

PROCEEDINGS OF THE

Twelfth Coastal Engineering Conference

September 13-18, 1970 • Washington, D C.

Volume I

Sponsored by the

Coastal Engineering Research Council
Technical Council on Ocean Engineering
Waterways, Harbors and Coastal Engineering Division
National Capital Section
of ASCE

American Shore and Beach Preservation Association
International Association for Hydraulic Research



Published by the American Society of Civil Engineers
345 East 47th Street, New York, N Y 10017

\$14 00

ACKNOWLEDGMENTS

This Conference was sponsored jointly by the Coastal Engineering Research Council of the American Society of Civil Engineers and the American Shore and Beach Preservation Association. Cooperating organizations were

Waterways, Harbors, and Coastal Engineering Division, ASCE
National Capital Section, ASCE
Technical Council on Ocean Engineering, ASCE
International Association for Hydraulic Research

FOREWORD

The Twelfth Conference on Coastal Engineering marks the twentieth year since the first conference was held at Long Beach, California, in October 1950. It appears appropriate at this time to present a brief history of the research councils which have sponsored these conferences over the years.

In March 1949 the late Professor Boris A. Bakhmeteff of Columbia University was invited to the University of California, Berkeley, to present a special lecture entitled, *The Engineer in the World of Today*. At that time Professor Boris A. Bakhmeteff was chairman of the Research Committees of both the American Society of Civil Engineers and The Engineering Foundation. He observed in his discussions with Dean Morrrough P. O'Brien during his stay in Berkeley that there were numerous research councils in the country to sponsor and coordinate research in various fields, but none existed for studying waves and related problems. Following this suggestion Dean O'Brien prepared a proposal for the formation of a Council on Wave Research and submitted it to The Engineering Foundation through the Hydraulics Division of the American Society of Civil Engineers. The A S C E Committee on Research approved the proposal and recommended to The Engineering Foundation that a grant be made to establish a Council on Wave Research. The Engineering Foundation Board at its semi-annual meeting in June 1950 approved of the Council with the grant becoming effective in October 1950. The Council was thus formed with Dean O'Brien as Chairman and J. W. Johnson as Secretary.

In 1963 The Engineering Foundation revised its policy on the support of Research Councils. With approval of The Engineering Foundation the Council on Wave Research proposed to the Board of Direction of the A S C E that the Council be incorporated in the A S C E and be renamed the Coastal Engineering Research Council. The A S C E approved of the establishment of the Council in May 1964 and designated the Waterways, Harbors, and Coastal Engineering Division to serve as liaison between the Council and the A S C E Research Committee. Dean M. P. O'Brien remains as Chairman of the Council with R. L. Wiegel as Vice-Chairman, and J. W. Johnson continuing as Secretary.

In October 1950 the University of California conducted an Institute on Coastal Engineering in Long Beach, California. This was conceived as a local meeting of engineers and scientists interested in shoreline problems. The aim was to aid engineers by summarizing the present state of the art and science related to the design and planning of coastal works rather than to present a series of original scientific contributions. The program consisted of thirty five invited papers, copies of which were distributed to those in attendance. This series of papers represented a rather thorough summary of coastal engineering as then practiced. The quality and scope of the papers and the need for a comprehensive and modern treatment of the subject convinced the sponsors of the conference that publication in a single volume was desirable rather than piecemeal in the scientific and technical journals. The newly-formed Council on Wave Research secured funds to underwrite the publication costs from the Engineering Foundation and the publication was entitled *The Proceedings of the First Conference on Coastal Engineering*.

Because of the success of the Long Beach Conference, invitations to cosponsor additional conferences were extended to the Council by various societies, universities, etc., with the result that subsequent conferences were held in Houston, Texas (1951), Cambridge, Massachusetts (1952), Chicago, Illinois (1953), Grenoble, France (1954), Gainesville, Florida (1957), The Hague, Netherlands (1960), Mexico City, Mexico (1962), Lisbon, Portugal (1964), Tokyo, Japan (1966), London, England (1968), and Washington, D C (1970). In addition, conferences on Ships and Waves (Hoboken, New Jersey, 1954), Coastal Engineering Instruments (Berkeley, California, 1955), and Civil Engineering in the Oceans I (San Francisco, California, 1967) also were sponsored by the research councils.

The proceedings of the various conferences were published by the Council on Wave Research with assistance from The Engineering Foundation until the formation of the Coastal Engineering Research Council in 1964, after which the proceedings have been published and distributed by the A S C E.

In view of the fact that the term coastal engineering appears to have been first used generally in connection with the Long Beach conference the following quotation from the preface of the proceedings of that conference is of interest.

“A word about the term “Coastal Engineering” is perhaps in order here. It is not a new or separate branch of engineering and there is no implication intended that a new breed of engineer, and a new society, is in the making

Coastal Engineering is primarily a branch of Civil Engineering which leans heavily on the sciences of oceanography, meteorology, fluid mechanics, electronics, structural mechanics, and others. However, it is also true that the design of coastal works does involve many criteria which are foreign to other phases of civil engineering and the novices in this field should proceed with caution. Along the coastlines of the world, numerous engineering works in various stages of disintegration testify to the futility and wastefulness of disregarding the tremendous destructive forces of the sea. Far worse than the destruction of insubstantial coastal works has been the damage to adjacent shorelines caused by structures planned in ignorance of, and occasionally in disregard of, the shoreline processes operative in the area.”

It is believed that the proceedings resulting from the conferences held over that past twenty years have done much to improve the art and science related to the design and planning of coastal works throughout the world.

J W Johnson, Secretary
Coastal Engineering Research Council

CONTENTS

ACKNOWLEDGMENTS iii

FOREWORD v

VOLUME I

WAVE THEORY, MEASUREMENTS AND ANALYSES

Chapter 1

CANADIAN WAVE CLIMATE STUDY – THE FORMATIVE YEAR
Laurence Draper 1

Chapter 2

OCEAN WAVE RESEARCH IN SOUTHERN AFRICA
J A Zwamborn, C. van Schaik, and A Harper 13

Chapter 3

SWELL AND STORM CHARACTERISTICS FROM COASTAL WAVE
RECORDS
Warren C Thompson 33

Chapter 4

MAXIMUM WAVE HEIGHT PROBABILITIES FOR A RANDOM
NUMBER OF RANDOM INTENSITY STORMS
L E Borgman 53

Chapter 5

SPECTRAL COMPUTATIONS ON PRESSURE WAVE GAUGE RECORDS
Manuel Mendes de Carvalho, Fernando Silveria Ramos,
and Carlos de Campos Moraes 65

Chapter 6

ANALYSIS OF WAVE RECORDS
D Lee Harris 85

Chapter 7

COMPARISON OF PRESSURE AND STAFF GAGE RECORDS
D Esteva and D Lee Harris 101

CONTENTS

Chapter 8		
DIRECTIONAL SPECTRA FROM WAVE-GAGE ARRAYS		
N N. Panicker and L E. Borgman		117
Chapter 9		
EQUILIBRIUM RANGE SPECTRA IN SHOALING WATER		
Takeshi Ijima, Takahiko Matsuo, and Kazutami Koga		137
Chapter 10		
WAVE INVESTIGATIONS IN SHALLOW WATER		
Winfried Siefert		151
Chapter 11		
EXPERIMENTAL STUDIES ON THE GENERATION OF WAVES IN SHALLOW WATER		
C T Kuo and Frederick L W Tang		179
Chapter 12		
WAVE FORECASTING FOR THE WEST COAST OF INDIA		
J Dattatri and P S. Renukaradhya		203
Chapter 13		
COMPILATION OF OCEAN AND LAKE WAVE STATISTICS		
John Simpson Hale		217
Chapter 14		
MACRO-TURBULENCE FROM WIND WAVES		
Chin Yuan Lee and Frank D Masch		223
Chapter 15		
SHEAR STRESS OF SEA BREEZE ON A SWASH ZONE		
Shih-Ang Hsu		243
Chapter 16		
ENERGY LOSSES UNDER WAVE ACTION		
P D Treloar and A Brebner		257
Chapter 17		
BOTTOM BOUNDARY-SHEAR STRESSES ON A MODEL BEACH		
P G Telek and M W Anderson		269

CONTENTS

Chapter 18		
VARIATION OF LONGSHORE CURRENT ACROSS THE SURF ZONE		
Edward B Thornton		291
Chapter 19		
HORIZONTAL WATER PARTICLE VELOCITY OF FINITE AMPLITUDE WAVES		
Yuichi Iwagaki and Tetsuo Sakai		309
Chapter 20		
A SYSTEM FOR MEASURING ORBITAL VELOCITIES IN WAVES		
M M Kolpak and P S Eagleson		327
Chapter 21		
SHOALING OF FINITE-AMPLITUDE WAVES ON PLANE BEACHES		
Robert K -C Chan and Robert L Street		345
Chapter 22		
PERIODIC WAVES SHOALING IN WATERS OVER STEEPLY SHOALING BOTTOMS		
Harihara Rama Ayyar		363
Chapter 23		
BREAKING WAVE SETUP AND DECAY ON GENTLE SLOPES		
Li San Hwang and David Divoky		377
Chapter 24		
AIR ENTRAINMENT AND ENERGY DISSIPATION IN BREAKERS		
Alfred Fuhrbóter		391
Chapter 25		
PROBABILITIES OF BREAKING WAVE CHARACTERISTICS		
J Ian Collins		399
Chapter 26		
CHARACTERISTICS OF WAVES BROKEN BY A LONGSHORE BAR		
E Clark McNair, Jr and Robert M Sorensen		415
Chapter 27		
VELOCITY FIELDS IN THE BREAKER ZONE		
M D Adeyemo		435

CONTENTS

Chapter 28		
DEVELOPMENT OF UNDULAR BORES IN ROUGH CHANNELS		
O Hawaleshka and S B Savage		461
Chapter 29		
COMPUTER MODELLING OF DIFFRACTION OF WIND WAVES		
Shou-Shan Fan and L E Borgman		473
Chapter 30		
INTERACTION BETWEEN WAVES AND CURRENTS		
Ivar G Jonnsson, Christian Skougaard, and John D Wang		489
Chapter 31		
EXPERIMENTS OF WAVE REFLEXION ON IMPERMEABLE SLOPES		
Carlos de Campos Moraes		509
Chapter 32		
LIMITING CONDITION FOR STANDING WAVE THEORIES BY PERTURBATION METHOD		
Yoshito Tsuchiya and Masataka Yamaguchi		523
Chapter 33		
HIGHER ORDER THEORY FOR SYMMETRICAL GRAVITY WAVES		
Peter L Monkmeyer		543
Chapter 34		
ANALYTICAL APPROACH ON WAVE OVERTOPPING ON LEVEES		
Hiroyoshi Shi-igai and Tsugio Kono		563
Chapter 35		
IMPULSE WAVES GENERATED BY LANDSLIDES		
J W Kamphuis and R J Bowering		575
Chapter 36		
WAVES GENERATED BY A PISTON - TYPE WAVEMAKER		
Ole Secher Madsen		589
Chapter 37		
PREDICTION CURVES FOR WAVES NEAR THE SOURCE OF AN IMPULSE		
Robert L Miller		609

CONTENTS

Chapter 38		
DIMENSIONAL ANALYSIS - SPURIOUS CORRELATION		
M S Yalin and J W Kamphuis		625
	VOLUME II	
	COASTAL SEDIMENT PROBLEMS	639
Chapter 39		
COASTAL PROCESSES FROM SPACE PHOTOGRAPHY		
Maynard M Nichols		641
Chapter 40		
REACH OF WAVES TO THE BED OF THE CONTINENTAL SHELF		
Richard Silvester and Geoffrey R Mognridge		651
Chapter 41		
ISOPACHOUS MAPPING OF THE LOWER PATUXENT ESTUARY		
SEDIMENTS BY CONTINUOUS SEISMIC PROFILING TECHNIQUES		
Newell T Stiles and Donald R Wiesnet		669
Chapter 42		
OBSERVATION OF SEDIMENT MOTION BY UNDERWATER-TELEVISION		
Gunter Luck		687
Chapter 43		
HISTORY OF THE DUTCH COAST IN THE LAST CENTURY		
W T Bakker and D Sj Joustra		709
Chapter 44		
STUDIES ON THE SHORE PROCESS AND WAVE FEATURES OF THE		
WESTERN COAST OF TAIWAN		
Kenneth S T Chang and Frederick L W Chang		729
Chapter 45		
STUDY OF MUDBANKS ALONG THE SOUTHWEST COAST OF INDIA		
N S Moni		739
Chapter 46		
TURBULENCE AND SEDIMENT CONCENTRATION DUE TO WAVES		
Kiyoshi Horikawa and Akira Watanabe		751

CONTENTS

Chapter 47		
EFFECTS OF NONUNIFORM WAVE ENERGY IN THE LITTORAL ZONE		
Victor Goldsmith and Joseph M. Colonell		767
Chapter 48		
LITTORAL TRANSPORT AND ENERGY RELATIONSHIP		
L. Bajorunas		787
Chapter 49		
SYNOPTIC OBSERVATIONS OF SAND MOVEMENT		
David B. Duane		799
Chapter 50		
UNDERWATER SURVEY SYSTEM FOR RADIONUCLIDE-TAGGED SEDIMENT TRACING		
E. H. Acree, H. R. Brashear, and F. N. Case		815
Chapter 51		
PROCESSING AND ANALYSIS OF RADIOISOTOPIC SAND TRACER (RIST) STUDY DATA		
H. R. Brashear, E. H. Acree, F. N. Case, P. A. Turner, and D. B. Duane		821
Chapter 52		
CLASS OF PROBABILITY MODELS FOR LITTORAL DRAFT		
William R. James		831
Chapter 53		
PROPERTIES OF LONGSHORE BARS IN THE GREAT LAKES		
James H. Saylor and Edward B. Hands		839
Chapter 54		
SAND TRANSPORT PHENOMENA ON COASTS WITH BARS		
M. Dyhr-Nielsen and Torben Sorensen		855
Chapter 55		
LABORATORY TESTS OF LONGSHORE TRANSPORT		
John C. Fairchild		867
Chapter 56		
INFLUENCE OF GRAIN SIZE ON LITTORAL DRIFT		
Jose Castanho		891

CONTENTS

Chapter 57		
COMPUTATION OF ALONGSHORE ENERGY AND LITTORAL TRANSPORT		
Theodor R Mogel and Robert L Street		899
Chapter 58		
CRATER SINK SAND TRANSFER SYSTEM		
Douglas L Inman and Roland W Harris		919
Chapter 59		
USE OF VOLCANOES FOR DETERMINATION OF DIRECTION OF LITTORAL DRIFT		
Per Bruun and Gish Viggooson		935
Chapter 60		
OFFSHORE BEACH NOURISHMENT SCHEME		
Robert A Dalrymple		955
Chapter 61		
BEACH NOURISHMENT AT VIRGINIA BEACH, VIRGINIA		
James W Bunch		967
Chapter 62		
UNDERWATER MOUND FOR THE PROTECTION OF DURBAN'S BEACHES		
J S Zwamborn, G A W Fromme, and J B Fitzpatrick		975
Chapter 63		
LABORATORY TESTS ON ARTIFICIAL SEAWEED		
W A Price, K W Tomlinson, and D H Willis		995
Chapter 64		
DYNAMICS OF A COAST WITH A GROUYNE SYSTEM		
W T Bakker, E H J Klein Breteler, and A Roos		1001
Chapter 65		
EXPERIMENTAL STUDY OF THE HYDRAULIC BEHAVIOUR OF INCLINED GROUYNE SYSTEM		
Júlio Patriarca Barcelo		1021

CONTENTS

Chapter 66		
LAND RECLAMATION AND GROIN-BUILDING IN TIDAL FLATS		
Hete Focken Erchinger		1041
Chapter 67		
EFFECT OF GROYNES ON ERODED BEACHES		
W A Price and K W Tomlinson		1053
Chapter 68		
CHARACTERISTICS OF SHINGLE BEACHES THE SOLUTION TO SOME PRACTICAL PROBLEMS		
A M Muir Wood		1059
Chapter 69		
COMPARISON OF FLUVIAL AND COASTAL SIMILITUDE		
Bernard Le Méhauté		1077
Chapter 70		
STUDY OF DURBAN HARBOR SILTING AND BEACH EROSION		
Jan Malan Jordaan, Jr		1097
CHAPTER 71		
ESTUARY INLET CHANNEL STABILIZATION STUDY USING A HYDRAULIC MODEL		
Theodore T Lee		1117
Chapter 72		
MODEL TESTS AND STUDIES FOR PORT RASHID, DUBAI		
Eric Loewy		1137
Chapter 73		
STUDY OF TOPOLOBAMPO'S BAY, MEXICO, ENTRANCE		
Héctor López Gutiérrez and Daniel Cervantes Castro		1151
Chapter 74		
TIDAL INLET PROBLEMS ALONG THE NEW ENGLAND COAST		
Oscar E Arpin		1171
Chapter 75		
OFFSET COASTAL INLETS		
Miles O Hayes, Victor Goldsmith, and Carl H Hobbs III		1187

CONTENTS

Chapter 76		
FIELD STUDY OF TIDAL INLET, BIMINI, BAHAMAS		
W Harrison, R J Byrne, J D Boone, and R W Moncure		1201
Chapter 77		
RECENT HISTORY OF EROSION AT CAROLINA BEACH, N C		
Limberios Vallianos		1223
Chapter 78		
RIO GRANDE BAR THE CASE HISTORY OF A LAGOON OUTLET INTO A TIDELESS SEA		
V F Motta		1243
Chapter 79		
SCOUR AROUND A CIRCULAR CYLINDER DUE TO WAVE MOTION		
Donald R Wells and Robert M Sorensen		1263
Chapter 80		
COMPARISON OF MODEL AND BEACH SCOUR PATTERNS		
John B Herbich		1281
Chapter 81		
VARIATION OF TOPOGRAPHY OF SEA BED CAUSED BY THE CONSTRUCTION OF BREAKWATERS		
Shoji Sato and Isao Irie		1301
Chapter 82		
EQUILIBRIUM PROFILES OF MODEL BEACHES		
Irvathur Vasudeva Nayak		1321
Chapter 83		
STOCHASTIC ANALYSIS OF BEACH PROFILE DATA		
Choule J Sonu and Myron H Young		1341
Chapter 84		
FIELD STUEDY OF SURATHKAL BEACH		
P Suryaprakasa Rao and P Kassim		1365
Chapter 85		
SEASONAL BOTTOM CHANGES, BOLINAS BAY, CALIFORNIA		
J W Johnson		1383

CONTENTS

Chapter 86		
SEDIMENT DISTRIBUTION AND ITS RELATIONS TO CIRCULATION PATTERNS IN BOLINAS BAY, CALIFORNIA		
P Wilde and T Yancey		1397

Chapter 87		
ON SUCCESSIVE SALTATION OF A SAND GRAIN BY WIND		
Yoshito Tsuchiya		1417

VOLUME III

COASTAL STRUCTURES AND RELATED PROBLEMS

Chapter 88		
RESEARCHES ON SEA-WALLS		
S Nagai		1431

Chapter 89		
PRESSURE OF WAVES AGAINST VERTICAL WALLS		
M E Plakida		1451

Chapter 90		
PLUNGING WAVE PRESSURES ON A SEMI-CYLINDRICAL TUBE		
Yuan Jen and Pang-Mou Lin		1469

Chapter 91		
LOADINGS ON LARGE PIERS IN WAVES AND CURRENTS		
Hsiang Wang		1491

Chapter 92		
EXPERIEMENTS WITH SAND-FILLED FLEXIBLE TUBES		
Per Roed Jakobsen and Arne Hasle Nielsen		1513

Chapter 93		
PRESSURE OF FLOATING ICE-FIELDS ON PILES		
Joachim Schwarz		1523

Chapter 94		
BREAKWATER AND QUAY WALL BY HORIZONTAL PLATES		
Takeshi Ijima, Shigeo Ozaki, Yasuhiko Eguchi, and Akira Kobayashi		1537

CONTENTS

Chapter 95		
INFLUENCE OF BREAKER TYPE OF RIPRAP STABILITY		
John P Ahrens		1557
Chapter 96		
DAMAGE FUNCTIONS FOR A RUBBLE-MOUND BREAKWATER UNDER THE EFFECT OF SWELLS		
Juan B Font		1567
Chapter 97		
HYDRAULIC RESISTANCE OF ARTIFICIAL CONCRETE BLOCKS		
Nobuo Shuto and Hiroshi Hashimoto		1587
Chapter 98		
USE OF ASPHALT IN BREAKWATER CONSTRUCTION		
K d'Angremond, J J Th Span, J Van der Weide, and A J Woestenenk		1601
Chapter 99		
HONOLULU REEF RUNWAY DIKE		
Robert Q Palmer and James R Walker		1629
Chapter 100		
FLOATING BREAKWATER FOR RESERVOIR MIRINAS		
Kenneth Chen and R L Wiegel		1647
Chapter 101		
FORCES ON A PONTOON IN THREE-DIMENSIONAL WAVES		
J Eie, A Traetteberg, and A Tjørnum		1667
Chapter 102		
RESONANCE OF MOORED OBJECTS IN WAVE TRAINS		
A J Hermans and G F M Remery		1685
Chapter 103		
HYDRODYNAMIC FORCES OF TWIN-HULL VESSELS		
Shen Wang		1701
Chapter 104		
BEHAVIOR OF A SLENDER BODY IN SHALLOW-WATER WAVES		
Hsiang Wang and Li-San Hwang		1723

CONTENTS

Chapter 105		
OIL BOOMS IN TIDAL CURRENTS		
Ralph H Cross and David P Hoult		1745
	PART 4	
COASTAL, ESTUARINE, AND ENVIRONMENTAL PROBLEMS		1759
Chapter 106		
ENVIRONMENTAL PLANNING OF A BAY AND COASTAL LAGOON SYSTEM		
Norman T Gilroy		1761
Chapter 107		
DETERIORATION AND RESTORATION OF COASTAL WETLANDS		
Sherwood M Gagliano, Hyuck J Kwon, and Johannes L van Beek		1767
Chapter 108		
RESEARCH FOR THE COASTAL AREA OF THE DELTA REGION OF THE NETHERLANDS		
J J Dronkers		1783
Chapter 109		
SEDIMENT POLLUTION IN COASTAL WATERS		
J van de Kreeke		1803
Chapter 110		
RECIRCULATION IN SHALLOW BAYS AND RIVERS		
R K Price, R A Dalrymple, and R G Dean		1813
Chapter 111		
NATURAL FLUSHING ABILITY IN TIDAL INLETS		
I B Mota Oliveira		1827
Chapter 112		
MATHEMATICAL MODEL OF MIXING IN NEW HAVEN HARBOR		
Michael D Disko, Robert A Norris, and Francis C Lutz		1847
Chapter 113		
FLUSHING PATTERN OF NON-REACTIVE EFFLUENTS		
Adel M Kamel		1867

CONTENTS

Chapter 114		
THE MEASUREMENT OF TIDAL WATER TRANSPORT IN CHANNELS		
R E Klein		1887
Chapter 115		
WATER CURRENT METER FOR MEAN FLOW MEASUREMENTS		
David Smith and W Harrison		1903
Chapter 116		
TRAPPING OF OUTFALL CONSTITUENTS BEHIND SILLS		
T Carstens and A Sjöberg		1917
Chapter 117		
SUSPENDED LOAD CALCULATIONS IN A TIDAL ESTUARY		
Brian A O'Connor		1931
Chapter 118		
PARTICLE VELOCITY MEASUREMENTS WITH A LASER DEVICE		
C A Greated and N B Webber		1951
Chapter 119		
DENSITY CURRENTS AND TURBULENT DIFFUSION IN LOCKS		
A Roy Halliwell and Martin O'Dell		1959
Chapter 120		
MEASUREMENT OF DENSITY CURRENTS IN AN IDEALIZED MODEL		
Timm Stuckrath		1979
Chapter 121		
COMPUTATION OF STORM SURGE		
Richard Silvester		1995
Chapter 122		
STATISTICAL PREDICTION OF HURRICANE STORM SURGE		
C Y Yang, A M Parisi, and W S Gaither		2011
Chapter 123		
ANALYSIS OF HURRICANE TIDES AT PADRE ISLAND, TEXAS		
Frank D Masch, Robert J Brandes, Floyd R Hill, and William A White		2031

CONTENTS

Chapter 124		
TURBULENCE IN HURRICANE-GENERATED COASTAL CURRENTS		
Stephen P Murray		2051
Chapter 125		
JAMAICA BAY HURRICANE BARRIER		
Frank L Panuzio		2069
Chapter 126		
MODEL STUDY OF THE TRANSFORMATION OF TSUNAMIS IN URADO BAY		
Shigehisa Nakamura, Yuichi Iwagaki, and Yoshito Tsuchiya		2089
Chapter 127		
TSUNAMIS SOME LABORATORY AND FIELD OBSERVATIONS		
Fredric Raichlen		2103
Chapter 128		
HEAD LOSS AT TSUNAMI-BREAKWATER OPENING		
Yoshiyuki Ito		2123
Chapter 129		
TIDAL WAVES IN SCHEMATIC ESTUARIES		
Hans Vollmers and Jürgen Sündermann		2133
Chapter 130		
DEFORMATION OF ROTATIONAL TIDAL CURRENTS IN SHALLOW COASTAL WATER		
Harald Göhren		2147
Chapter 131		
RESONANCE IN HARBORS OF ARBITRARY SHAPE		
Jiin-Jen Lee and Fredric Raichlen		2163
Chapter 132		
SPECTRAL RESPONSE OF HARBOR RESONATOR CONFIGURATIONS		
William James		2181
Chapter 133		
HARBOR STUDY FOR SAN NICOLAS BAY, PERU		
James M Keith and Emmett J Murphy		2195

CONTENTS

Chapter 134		
TIDAL MOTION IN BAYS		
O H Shemdin and R M Forney		2225
Chapter 135		
SURFACE OSCILLATIONS IN A TANK CAUSED BY A SUBMERGED JET		
Juan B Font, Omar Azpura, and Flora Aranguren		2243
Chapter 136		
EFFECT OF LONG PERIOD WAVES ON HYDROGRAPHIC SURVEYS		
Orville T Magoon and William O Sarlin		2251
Chapter 137		
SELECTION OF DISPOSAL AREAS FOR SPOIL FROM BALTIMORE HARBOR		
John F Hoffman		2267
Chapter 138		
WAVES GENERATED BY LARGE SHIPS AND SMALL BOATS		
M M Das and J W Johnson		2281



Hampton Harbor, New Hampshire

PART I. WAVE THEORY, MEASUREMENTS, AND ANALYSES

Webhannet River, Maine



CHAPTER 1

THE CANADIAN WAVE CLIMATE STUDY - THE FORMATIVE YEAR

Laurence Draper

National Institute of Oceanography, Great Britain

Director, Canadian Wave Climate Study, 1968-69
Department of Public Works

ABSTRACT

This paper describes the need for, and the factors involved in, the establishment of a Wave Climate Study, illustrated with particular reference to the Canadian Wave Climate Study

INTRODUCTION

The shortage of sea wave information is world-wide, and that which does exist has usually been obtained for specific purposes and is of value only in a very limited area. Of the existing information, a large part is incomplete in comparison with the desirable minimum of a year's continuously-sampled conditions, and much of that which has been collected systematically has been analyzed in ways which are difficult to interpret. Canadian waters were no better, and no worse, documented than most others, but the Canadian Department of Public Works, probably the major potential user of wave data, became concerned at the lack of information. The engineering design division had the foresight to see that techniques had advanced sufficiently to justify the setting up of an organization to devote itself solely to the collection of wave data to meet future needs. Because of the size of the country, the project envisaged was probably larger than any similar project which had previously been undertaken anywhere else in the world. Treasury approval was obtained for an exploratory phase, with a nominal budget of £183,000, and the author was privileged in being asked by the Chief Engineer of the Design Directorate, Mr G Millar, to direct the study in its formative year from October, 1968.

GENERAL JUSTIFICATION FOR A WAVE CLIMATE STUDY

The first part of any such study is largely an administrative exercise. Although the need to spend money is more than obvious to anyone who has ever had to dream up design wave characteristics, it has to be justified in some detail to the controller of the purse strings. Part of the justification

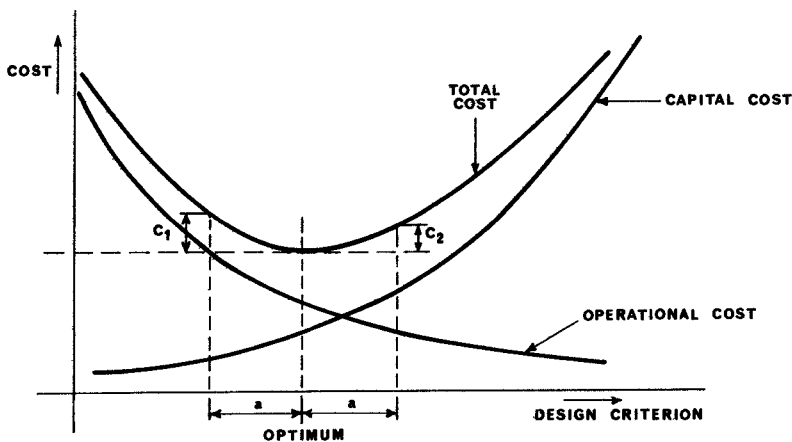


Figure 1 Schematic Relationship between Cost and Design Criteria

is not difficult to find, wherever structures have been built in exposed locations there must have been failures which have been expensive to remedy, and it is likely that it would be easy to find major repair bills totalling far in excess of the likely cost of any wave climate study. It is just conceivable that no major repair works have been necessary, in which case this is again a forceful argument in the minds of the Treasury Officials as it is most likely that the structures have been overdesigned, and that the initial capital outlay has been excessive. Figure 1, based on a diagram in a paper by J. Ploeg, suggests that there is a fairly sharp optimum cost of design for coastal structures, so that without a fairly good estimate of wave conditions, which are major parameters, it would be nearly impossible to come close to the optimum, and the cost would necessarily increase. As a consequence of this, it is reasonable to infer that the structure which is ultimately the cheapest will require occasional expenditure on maintenance and repair of storm damage. Wave conditions are only one, albeit major, of a number of parameters affecting the ultimate cost of a structure. The cost of failure is very much more than the actual rebuilding cost, for example, if a breakwater fails, in addition to the basic repair cost there will be the cost of overloading alternative ports and transport systems, and also the social costs, the latter may well have been completely neglected in many assessments and include the disruption of normal patterns of life and true unemployment costs (not just those of unemployment benefit), and possibly the costs of loss of life.

It cannot be pretended that good wave information alone will enable a designer to define the optimum precisely, but it should appreciably reduce deviations from the optima and make important savings in expenditure

STANDARDS FOR DESIGN

In the development of standards and criteria for the design of marine structures it is necessary to have reliable information, in some detail, on wave conditions which do, and are liable to, occur. The only way to ensure that criteria for waves are realistic is to study them, instrumentally and theoretically, in all geographical areas

Uses for wave information are legion. Apart from the obvious ones of design parameters for specific projects, and design standards in general, the results of a comprehensive wave climate study can be used for the assessment of utilization of all kinds of surface vehicles, ships, hydrofoils and hovercraft, drilling, pile-driving and pipe-laying vessels, and for many other civil, as well as military, purposes

PERSONNEL AND ORGANIZATION

The minimum personnel requirements of such a study, apart from a study Director, are for one or more Civil Engineers with marine experience, and preferably with a mathematical aptitude, a Hydrodynamicist with oceanographic experience to be responsible for data collection, for each field team a competent electronic engineer able to plan his own programme and work on his own, often in remote situations, and a technician able to work with him and on small boats. Diving experience in the field team would also be a useful attribute

The field team should preferably be supervised by the oceanographer, and the analysis of results would be undertaken jointly by him and the civil engineers, who would then be responsible for treatment of data and its interpretation for engineering purposes. Apart from technical prowess, enthusiasm for and appreciation of the value of the whole project are essential in every member of the whole study. The field team must have the ability to meet and win the confidence of all persons whose cooperation is required for the success of an installation

The engineers in the project must also be involved in the field work to help them appreciate the problems and difficulties involved, but their main task will be in the interpretation and application of data to real engineering problems. They will find themselves called upon to advise and pronounce on all manner of problems connected with waves. The study Director will probably have some difficulty in keeping a balance such that the group continues its research, and also helps those needing advice and often more substantial assistance, especially as they may well be the people on whom his field staff rely rather heavily for support in installing, running and maintaining equipment

The study must maintain close links with two groups who are generally regarded as distinct entities - at one end is the construction organization which may not be research oriented, and at the other end is the oceanographic research organization which might not be too interested in detailed practical applications of its work. The study should, if at all possible, house all its staff in close proximity to each other within one building, and also have its own laboratory and at least some workshop facilities. Only in this way can full discussion, essential in such a project, take place and all members of the staff be able to appreciate the problems and needs of the other parts of the project.

TASKS OF THE STUDY

Existing Data

One of the first tasks will be the tracking down and collection of all documents purporting to give wave information. The data in each one will have to be assessed, and listed according to its geographical location, so that when future needs arise it can be retrieved quickly. It is quite probable that very little data achieving the required standards will be found.

Known future needs

Many projects can be foreseen in general, if not in detail, several years in advance, so that a picture can be built up showing where requirements for wave information are likely to be concentrated. This information can often be obtained from area Public Works Authorities, Port and Harbour Authorities and major resource exploiters such as oil and mineral companies.

DEVELOPMENT OF A PLAN OF OPERATION

When all the existing data has been collected and opinions on future needs have been assembled (previous attempts at wave recording are indications that there may be more interest in those areas), it will be possible to propose areas in which general coverage stations should be placed. Usually these should be in open waters, placed so that each station samples wave conditions which are likely to be significantly different from those at any adjacent station. Possible specific locations can usually be determined from hydrographic charts of the area, in conjunction with land maps to give an indication of shore conditions, accessibility and density of habitation. The locations must be as exposed as possible and not suffer significantly from refractive effects, be shielded by reefs or sand bars, or be sheltered by long stretches of shallow water. If an underwater cable is to be used, a 'safe' landing zone must be available fairly conveniently, tidal currents should be as small as possible. Possible locations for housing the recording equipment, such as lighthouses or other officially-owned buildings on a coast, may be found from charts and land maps, the authorities concerned are often only too pleased to help by giving introductory letters for project personnel to present to lighthouse staff and others, asking them to give assistance during site surveys.

When specific locations have been decided it is then necessary to make site surveys. The actual visit to each site at which a cable may be brought ashore entails inspection on foot, preferably at low tide, to determine an actual route for the cable. The route must be as protected as possible to avoid sharp rocks and areas where boulders are liable to be moved by high waves. A major hazard for surface instruments is that they may be in collision with shipping, be stolen, or even used as targets for shooting practice, submerged instruments are less vulnerable, but can easily be trawled up, or the cable may be wrecked by a dragging anchor, in either case all local marine authorities and opinions must be sounded to determine the likelihood of misadventure. These will usually range from black despair to high optimism, the real answer usually lies between the two, and a crystal ball may well be needed before the final decision is taken.

Loss of information can, and will, occur through many different causes, in fact, wave recording is a highly hazardous operation, at least from the point of view of the resulting data. In planning the Canadian Study, it is intended to leave each recorder in operation for two years so that gaps in the first year's records can be patched with data from the second. In the relatively rare cases when the first year's records have insignificant gaps, the instrument can be withdrawn and moved elsewhere. In ice-free waters a year means twelve calendar months, but where the water is frozen over for part of the time, the "year" is taken to be the mean duration of time when substantial ice-cover is absent.

ASSESSMENT OF INSTRUMENTS

There is no universal wave recorder, but for most studies it may well be possible to standardize on one sub-surface pressure recorder, one surface buoy and one through-surface recorder. From the technical points of view of expertise in servicing and costs of spares, the virtues of having as few different types of instrument as possible are self evident. In the Canadian Study, it was initially intended to standardize on three types

- (1) N.I.O. Shipborne wave recorder. This can only be used for routine data collection where a vessel is stationary at one place for long periods - for example, on Light Vessels or Weather Ships, or where a vessel often revisits a station or small area for routine sampling purposes. In our case the two Canadian Ocean Weather Ships which operate on station P in the North Pacific were each already fitted with a Shipborne wave recorder. The only remaining Light Vessel in Canadian waters, the LURCHER, was scrapped as an economy measure less than a month before the equipment was due to be installed. One instrument was installed on the PORTE DAUPHINE, a Great Lakes Institute vessel, the one destined for LURCHER should be installed on a vessel belonging to the Canadian Centre for Inland Waters.

COASTAL ENGINEERING

- (2) Pressure recorder If at all possible the recorder should be capable of being monitored, so that a fault can be recognised at a very early stage. To achieve this it is necessary to use an underwater cable, but cables suffer badly from the vagaries of the sea, and may be damaged in a variety of ways which can reduce the insulation. For long-term installations it is essential that any damage which impairs the signal should be recognised at once. In a recorder which transmits back a voltage or a current, diminution of the insulation can result in an attenuated signal reaching the shore unit, and the presence of the trouble may not be recognised for a long time. Even when it is known that the record is in error, it may not be possible to determine with any certainty the time of onset of the trouble, and many perfectly good records may have to be scrapped. Possibly the most elegant alternative is the use of the frequency modulation system in which a pressure signal is converted in the transducer into a frequency signal, so that a frequency is transmitted up the cable. As long as the frequency can be discriminated from background noise, regardless of the state of the cable, a shore unit will record the correct pressure. Failure, when it comes, will be catastrophic, and will be immediately recognisable.

At the time when the Study was looking into the problem, only two types of F M wave recorders were commercially available. After testing one of each it was decided to standardize on the instrument designed and built by the National Research Council in Ottawa.

- (3) Surface buoy These instruments are intended for use where the water is deep and a pressure unit cannot be used, or where the distance to shore makes the cable cost prohibitive. They transmit by radio to a shore station, which may be twenty or thirty miles away. One of each of two different types were tested, and it was decided to standardize on the Waverider buoy built by Datawell of Holland.

Through-surface recorder In the first stages where only general area data was sought, there was no need for a through-surface recorder (they generally need to be fixed to an existing structure).

DATA HANDLING

In the Canadian Study it was intended initially to record by pen on paper charts, there were several reasons for this. The assessment of instruments was not due to be completed until the autumn of 1969, and until decisions had been made it was not possible to decide the type of digital equipment needed to match the outputs. In remote outstations the use of sophisticated equipment, especially if it is untried, can waste a great deal of time. Even if all the equipment had been well proven and was likely to give no trouble, the shortage of skilled technical staff would have reduced the number of installations which could be made in a given time. The philosophy at present is that if good chart records can be obtained they can be analyzed cheaply at headquarters by people other than technicians.

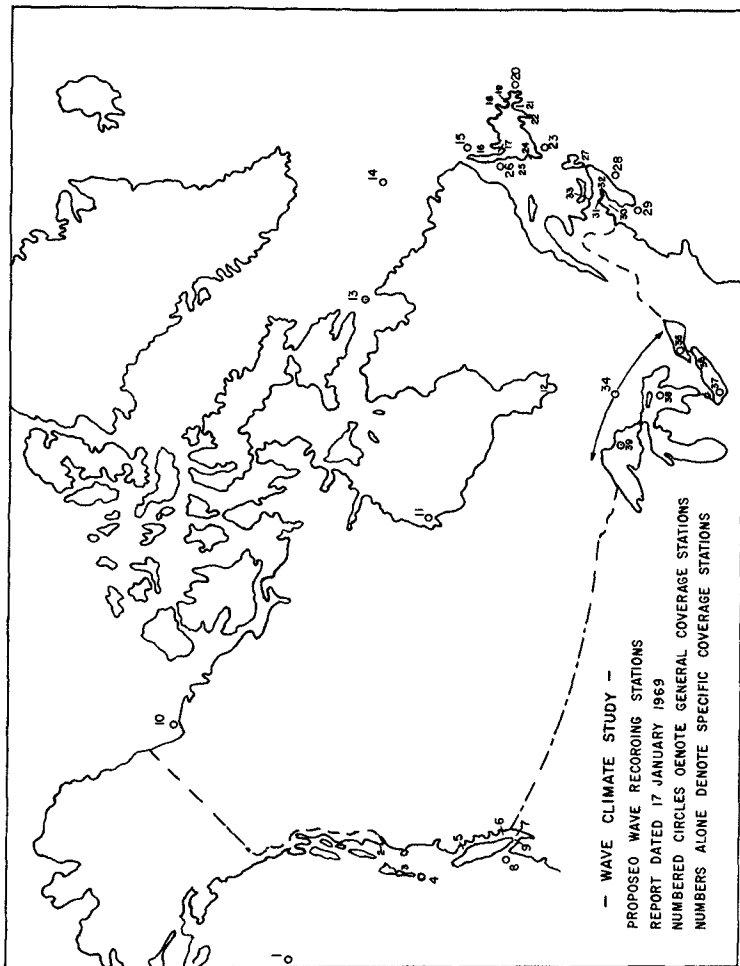


Figure 2 First proposal for Wave Recording Stations

One technique which needs to be investigated is the transmission of data over existing telephone lines back to headquarters. This would reduce the amount of data logging equipment needed, and have the great advantages that only one data logger would be required and could therefore be of high quality, and also that servicing staff would be easily available. It would have the disadvantage that spurious signals might be injected into the records by parts of the system out of our control and that recording might not always be possible at the required time due to congested lines.

The intention is to process the data, whether on charts or tape, following the recommendations given by the author² at the 1966 conference.

WIND DATA

A very important source of information from which wave data can be calculated is wind data. Measured or even observed wave data is sparse, but measured wind data is much more common and in many places is available for half a century or more. For calculations of extreme wave conditions the wind data may not be in the most useful form, the information needed is the most probable value of the highest mean wind, over durations up to 24 hours, likely to be exceeded once in some long period of time such as 20, 50 or even 100 years. If the basic measurements of mean hourly wind speed have been consistently made for at least ten years, an extrapolation can be made from them. The author is at present aware of only two countries where wind data is available in the required form, these being the United Kingdom³ and Canada⁴, where the data has recently been obtained by this Study. If this mean-hourly data is available, a further requirement for wave forecasting is information on the ratios of the mean wind speed over periods of from six to twenty four hours to the highest mean hourly speed in each storm. For Canada this was done for the 20 most severe storms at 21 typical stations, the mean speed over 24 hours was between 60% and 80% of the greatest mean hourly value, and the mean speed over six hours was between 80% and 90% of the greatest mean hourly value. For the U.K. some ratios have been calculated by Shellard (private communication) and the percentages were a little higher.

REFRACTION STUDIES

Any study group established to provide wave information will rapidly find itself being called upon to produce refraction diagrams. Several methods of doing this have been published, and one must be chosen and adapted to suit the computational facilities available, ideally the output should be drawn by a plotter. In the Canadian Study, the method devised by the U.S. Coastal Engineering Research Center was adapted⁵, with the output presented on a Benson Lehner plotter.

THE PROPOSALS AND ESTIMATED COSTS FOR THE CANADIAN STUDY

To achieve reasonable coverage of Canadian waters, 39 stations were designated (Fig 2), 9 being on the Pacific coast, 5 in northern waters, 19 on the Atlantic coast and 6 on the Great Lakes. Details of the specific proposals are not given here, as they are of local value only. The estimated total cost is just over one million dollars, spread over five years.

The staff requirements are for five persons in the first year building up to ten in the fourth year, the total number of man-years amounting to 40. At the end of the five years the study ought to achieve reasonable coverage of Canadian wave conditions, with data processed and presented in a standardized manner.

CONCLUSIONS

The needs for wave information are many, but the cost of a major comprehensive study is more than justified by the probable economies in construction and repair costs alone.

In the running of a Wave Climate Study, a lot will depend on the recruitment of staff with not only the appropriate abilities but with the sort of pioneer enthusiasm which is necessary in a small new project, in which there are few precedents and where improvisation is needed in isolated locations. Such a group must not only collect and analyse data, but it must be capable of acting as a consultant to interpret its findings and advise those who need the data and who will, in all probability, flock to it in increasing numbers. Indeed, maybe its major problem will be that of finding a way to limit the time spent in solving particular localized problems, as this can easily interfere with the task of making and interpreting field measurements - the first priorities of the study. At this stage it is hard to estimate what will happen after five years, but the author's feelings are that the group will be so involved in many projects that its continuation will be essential to the proper design of marine works in Canada, and that its usefulness in many other spheres as well will ensure its survival both as a data collecting and an engineering consultant agency.

ACKNOWLEDGEMENTS

The author wishes to thank all those people, too numerous to mention, without whose guidance, enthusiasm, friendship and hard work this project would never have become viable. He also wishes to express his appreciation to the Director of the National Institute of Oceanography, Dr G E R Deacon, C B E , F R S for his permission to undertake the task, and to his colleagues at Wormley who held the fort so admirably during his year's absence.

REFERENCES

- 1 PLOEG, J 1968 A General Discussion on the Selection of a Design Wave Second Marine Engineering Seminar Department of Public Works, Ottawa, Canada
- 2 DRAPER, L 1966 The analysis and presentation of wave data - a plea for uniformity Proc 10th Conf Coastal Engg 1, 1-11
- 3 SHELLARD, H C 1965 Extreme wind speeds over the United Kingdom for periods ending 1963 Climatological Memo No 50, Meteorological Office
- 4 DRAPER, I and 1960 Extreme mean wind speeds over Canada Marine Engineering Report No 14, Department of Public Works, Ottawa, Canada
- 5 WU, H J 1969 The application of a numerical method and computer program in a water-wave refraction study Marine Engineering Report No 12, Department of Public Works, Ottawa, Canada

CHAPTER 2

OCEAN WAVE RESEARCH IN SOUTHERN AFRICA

by

J A Zwamborn^x, C van Schaik^x, A Harper^x

ABSTRACT

Wave recording on a national basis in South Africa commenced in 1967, when an "Ocean Wave Research" project was initiated, aimed at obtaining reliable data on sea conditions around the shorelines of the Republic and South West Africa and to improve on wave prediction techniques

Various instruments are being used in this programme. Some of the problems encountered in practice with these instruments and the agreement between the results obtained using various wave recorders simultaneously at the same station are discussed. An indication of the volume of wave data so far obtained and the methods of analysing them are included.

INTRODUCTION

The realisation that accurate data on the wave conditions along the country's entire coastline and also over the continental shelf were indispensable for further coastal development and nearshore operations, has become evident in South Africa several years ago. Although wave records had been collected on an ad hoc basis in certain localities for many years, it was not until February, 1967 that the "Ocean Wave Research" project was initiated. This project was instigated by the South African National Committee for Oceanographic Research and is supported by various authorities and private bodies and aims at collecting wave data on a national and systematic basis. The work is being carried out by a research team from the Hydraulics Research Unit of the CSIR's National Mechanical Engineering Research Institute.

^x Head, Senior Technical Officer and Research Assistant respectively of the Hydraulics Research Unit of the CSIR's National Mechanical Engineering Research Institute, Stellenbosch, Republic of South Africa

OBJECTIVES AND PROGRAMME OF THE OCEAN WAVE RESEARCH PROJECT

The main objectives of the Ocean Wave Research project are to record and analyse wave conditions along the 4 000 km of coastline of South Africa and South West Africa, to correlate wave and wind data and to assist the South African Weather Bureau with wave forecasting

Wave recording stations are being operated or are being installed about 300 km apart, along the entire coastline. Moreover, records are supplemented by deep sea data obtained from five research vessels operating in the country's coastal waters (see Figure 1)

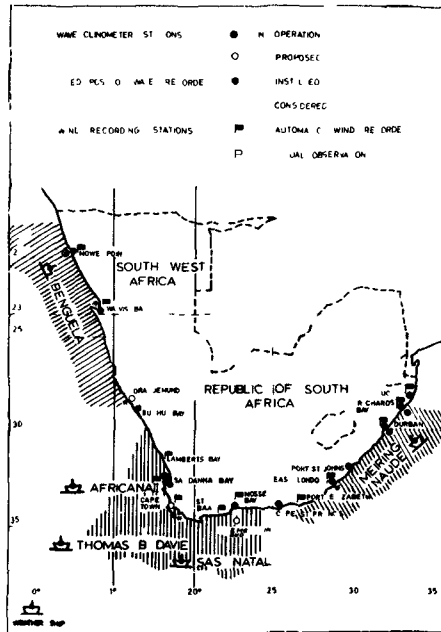


FIGURE 1 LOCATION OF WAVE RECORDING STATIONS

Most of the nearshore recording stations are in relatively shallow water of 10 to 30 m depth and the records obtained are only of local application. Using well-known refraction techniques, however, all the individual records are converted into deep sea values which not only apply to the recording area itself but they apply to much longer stretches of coastlines initially estimated to be as long as 300 km. Available data have confirmed the reliability of this estimate but

extensive correlation studies between the data from adjoining stations are being continued to establish the optimum spacing of recording stations

The full programme will run until 1975 at the earliest. It is possible that recordings at only a few key stations will continue on a permanent basis after this data

MEASURING INSTRUMENTS

When data from instruments are not available, visual wave records collected either from merchant ships or from lighthouses have to be used. The Ocean Wave Research project, however, aims at using only data obtained from wave recording instruments and relying as little as possible on visual observations. Instruments using optical, accelerometer, acoustic and pressure measuring systems are being used to obtain the wave recordings

Wave clinometer

The *wave clinometer* is an optical instrument developed in South Africa by the CSIR primarily for measuring wave direction. As can be seen in the photograph in Figure 2, it consists of a specially adapted telescope which is mounted on a stand and in such a way that its axis can be inclined at one of three fixed angles, namely 3° , 5° or $7\frac{1}{2}^{\circ}$ to the horizontal. The instrument is installed on shore at a fixed compass direction and the angle of inclination of the telescope fixed at one of these angles so that it can be focussed on the observation point at sea. To measure wave direction, a horizontal cross hair in the telescope is aligned with the wave crests by turning the telescope about its axis and the angle is recorded on a graduated disc mounted on the telescope.

Wave heights and wave periods are measured by observing the movements of an anchored floating buoy using the graduations provided in the telescope between which the image of the buoy moves. The wave heights obtained agree closely with the so-called significant wave height, H_s . By measuring the time for 20 waves to pass the buoy, the average wave period can be determined. This is found to represent both the significant wave period T_s and the zero crossing wave period

T_z closely. The buoys used are usually inflatable polyform spheres 0.5 m in diameter. Unfortunately, they are easily lost, due to such reasons as theft, running over by ships and interference by fish. Moreover, they do not usually last longer than about six months due to wear and tear. Since they are not costly, they are normally replaced at four monthly intervals.



FIGURE 2: WAVE OBSERVATION WITH WAVE CLINOMETER

Greater accuracy is achieved when the telescope is inclined in the 5° or $7\frac{1}{2}^\circ$ positions, thus the instrument should preferably be sited on a high vantage point. The water depth at the observation point should not be less than about 12 m, which means that the slope of the sea bottom should preferably be steep.

At present a total of eleven clinometers are installed around the coast, most of them in lighthouses (see Figure 1). The recordings are hand-punched on computer cards to facilitate subsequent analyses. Recordings can only be made during the hours of daylight and are normally made at 5.00, 10.00 and 15.00 hours G.M.T.

Shipborne recorder

The well-known *NIO shipborne wave recorder* is an accelerometer type instrument and consists of two identical units fitted under the waterline on each side of the ship's hull. Each unit contains an accelerometer and a static water pressure transducer, connected to a recorder unit normally installed in the ship's wheelhouse¹. The total vertical displacements of the ship are obtained by a double integration

(electronically) of the output of the accelerometers and averaging the two results. True wave height record is obtained after a correction is made for the ship's movements relative to the water surface by using the outputs of the pressure transducers. Wave directions are estimated by the crew using the ship's compass.

NIO recorders are installed on all five research vessels which operate in the areas shown hatched in Figure 1. Records of 15 min duration are made every six hours at 6 00, 12 00, 18 00 and 24 00 hours G M T daily. The records are in graphical form and adjustments have to be made to the wave periods to eliminate the influence of the ship's speed. In the past the graphic records were converted into digital form and punched on tape with a D-Mac pencil follower but arrangements have been made to install paper tape punch units in line with the graphical recorders to facilitate computer analyses of the data.

The NIO recorders give reliable results but should be calibrated at regular intervals and should be operated preferably by the ship's officers, or the scientist on board the research vessels.

Boersma recorder

The *Boersma wave height meter* is also an accelerometer type instrument. It is normally installed on a float and connected to an integrating and recording unit on board ship. In the early stages of the project the float, which is 1 m square, was launched from the weather ship (see Figure 1) but due to frequent cable breakage and instability of the float in heavy seas, it was later decided to install the accelerometer in the cabin of the 51 m long weather ship. Records are obtained daily for 15 min durations at 6 00, 12 00, 18 00 and 24 00 hours G M T. The records are in graphical form but a paper tape punch unit will be installed shortly.

Wave rider system

The *Dataveil wave rider system* is an accelerometer type instrument and consists of a telemetering buoy of spherical shape, anchored at sea and connected to a shore based receiving and punching unit. The buoy contains an accelerometer and transmitting unit, whereas the shore units contain the receiver, programmer, pen-recorder and punch-unit. Three buoys can be used with one receiver unit and they can be anchored

up to 50 km from the shore station

A Datawell wave rider system is installed at Mossel Bay (see Figure 1) where wave height records of 30 min duration are obtained automatically at 6 00, 12 00, 18 00 and 24 00 hours G M T daily. The records can be obtained either in graphical and/or punched form.

The shore unit of the wave rider system must be installed at a "civilised" place, since regular attendance is required for proper functioning. The Mossel Bay unit is installed at the radio station and has generally worked satisfactorily. The buoy is anchored some 35 km from the shore in 100 m deep water, which is close to the shipping lanes. The buoys have proved to be the weakest link in the system, since over a period of nine months, one buoy was lost and a second buoy was salvaged twice after it was presumed to have gone adrift. It is difficult to decide whether a reward should be offered for the retrieval of a lost buoy, since this may encourage the removal of the buoy on purpose.

Normal echo sounder

Normal echo sounders, which are acoustic type instruments installed on small boats, e.g. skiboats, are often used to obtain synoptic wave records to measure the effects of wave refraction and diffraction. Provided the boat is small and wave periods are relatively long, e.g. as in the case with swell, accurate wave records can be obtained with these instruments.

INES wave recorder

The *INverted Echo Sounder* or *INES wave recorder* is an acoustic type instrument developed by the Hydraulics Research Unit of the CSIR. It is a self-contained wave recorder which consists of a normal echo sounder housed in a waterproof canister placed in a supporting frame on the sea bottom. The transducer is fitted in the lid of the canister and the acoustic waves are reflected from the water surface, thus giving a continuous wave record (see Figure 3).

INES recorders are operating at three stations at present and another four stations will be operative shortly (see Figure 1). The instrument is left unattended on the sea bottom for up to five weeks, giving 15 min duration records at 6 00, 12 00, 18 00 and 24 00 hours.

G.M.T. daily. These records are in graphical form and are converted into digital form by a D-Mac pencil follower.



FIGURE 3: INES WAVE RECORDER

The INES recorders can be placed in any depth of water up to 36 m deep. Marker buoys indicate the position of the instrument, which are normally placed by divers to ensure that the tripod stand, which support the instrument, is in an upright position. They are serviced at monthly intervals normally by divers (see Figure 4) when the canister containing the instrument is released from the stand and brought to the surface. After servicing, it is taken down again. When operating in deep water, a spare serviced instrument is usually taken down by the diver on his first dive to replace the instrument which requires servicing. With this procedure, only one dive per instrument is required.

Good results have been obtained with these recorders but many problems have had to be overcome, e.g. leakage of the canister, breaking of the stylus and failure of the marker buoy mooring system.



FIGURE 4: PLACING OF INES WAVE RECORDER BY DIVERS

Ospos recorder

Ospos recorders are also being used. They are of the pressure type and are self-contained and can be left unattended for about four weeks. They are placed either on the sea bottom or suspended from an anchor on the sea bottom to "float" at a known distance, preferably 1 m below the lowest expected wave trough below the water surface. In deep water, therefore, there is considerable movement of the suspended instrument with wave action and this affects the results adversely. Moreover, since the depth of the transducer must be accurately known, the conversion from pressure changes to wave heights is dependent on the depth of submergence.

The instrument records pressure variations for durations of 15 min four times per day, usually at 6.00, 12.00, 18.00 and 24.00 hours G.M.T. The conversion from pressures to wave heights is very laborious and inaccurate and this recorder is used only if no other instruments are available.

CORRELATIONS BETWEEN VARIOUS INSTRUMENTS

Since the statistical analyses are based upon records obtained from different instruments, it is essential to check that their outputs are in good agreement².

Comparison of the wave directions read from a wave clinometer (inclined at 5°) with those obtained from aerial photographs specially made for this purpose showed a maximum deviation of 10° and an average deviation of 5°

A special correlation test was arranged at a point due west of Robben Island (Cape Town) in a water depth of 27.4 m on 2nd October, 1969 from 15 00 to 16 00 hours S A S T Simultaneous recordings were made using the following instruments

- (a) Boersma wave height meter (using the float)
- (b) INES wave recorder
- (c) Ospos wave recorder
- (d) NIO wave recorder on research vessel Africana II (NIO A)
- (e) NIO wave recorder on research vessel Benguela (NIO B)

A comparison of wave height and wave period distributions using a 30 min period of the records, are given in Figures 5 and 6

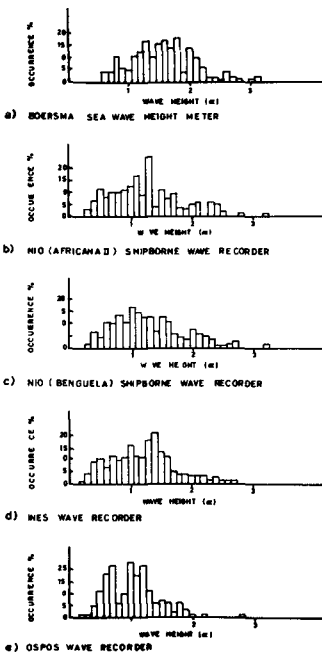


FIGURE 5 WAVE HEIGHT DISTRIBUTIONS

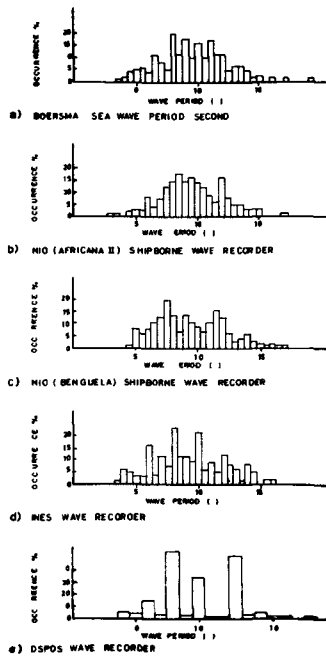


FIGURE 6 WAVE PERIOD DISTRIBUTIONS

The results show that the records of NIO recorders, installed on two different ships, are almost identical. The Boersma wave buoy seems to over-estimate the wave heights, especially for the lower wave group, whereas the Ospos generally gives wave heights which are too low. The INES records generally agree well with the NIO records, except for the maximum wave height. Wave periods agree well with each other except for the Ospos records.

In Figure 7 the smoothed energy density for a constant time interval of 1.8 seconds is plotted versus the frequency as obtained from the results of recordings with the INES wave recorder and NIO wave recorders on two different ships. It will be noted from this plot that the frequencies for maximum spectral density lie close to each other, although there are noticeable differences in the values for maximum spectral density, with the INES wave recorder giving the lowest values.

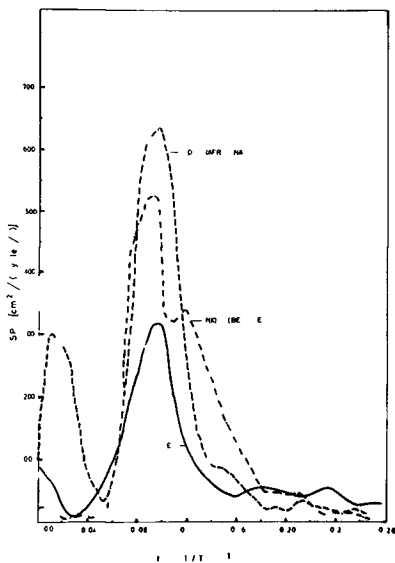


FIGURE 7 WAVE ENERGY SPECTRUM

AVAILABLE DATA

Data on ocean wave characteristics for the Ocean Wave Research project have been collected using the above-mentioned wave recording instruments since February, 1967 although wave data for certain areas have been collected since 1961. The number of recording stations has increased with the passage of time and the present situation is as shown in Figure 1.

The following instruments are in use:

- 11 Wave clinometers
- 5 NIO shipborne wave recorders
- 2 INES wave recorders
- 1 Wave rider system
- 1 Boersma wave height meter
- 1 Ospos wave recorder

The amount of data available from each instrument in its particular area or position is shown in Table 1 and Figure 8^{4,5,6,7}.

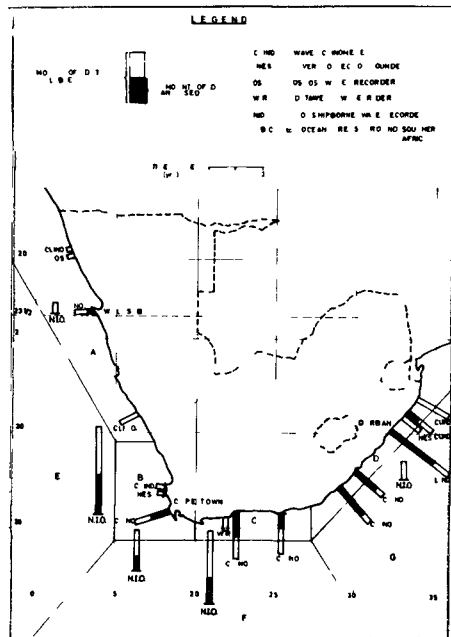


FIGURE 8 AVAILABLE WAVE DATA, MAY, 1970

WAVE ANALYSIS

The distance of approximately 300 km between wave recording stations, was assumed to be adequate to give a good overall coverage of the actual sea conditions along the coast of Southern Africa. Since, however, wave data are obtained from both shallow and deep water, they have to be converted to deep sea values to obtain a basis for comparison. This conversion is made using conventional refraction theories. The method used for the construction of the wave refraction diagrams by computer, is that described by Wilson of the U S Army Coastal Engineering Research Center^{8,9}. The correction of all wave directions to deep sea values is made by use of graphs on which deep sea wave direction versus nearshore direction at the recording point (found from the above refraction diagrams) are plotted.

The method used for the conversion of nearshore wave heights to deep sea values, is that developed by Dorrestein¹⁰ whereby the wave direction graphs referred to above are used to obtain the height correction factors. This method was found to be reliable and much quicker than the conventional method using pairs of orthogonals. In certain cases a correction for shoaling water also has to be made¹¹.

Wave clinometer records

Wave parameters obtained from the clinometer records are as follows

- (a) significant wave height (H_s)
- (b) significant wave period (T_s) or
zero crossing wave period (T_z)
- (c) wave direction

The clinometer records are converted to data applicable to deep sea by using the above-mentioned methods for the correction of the wave heights and directions. This entails the production by computer of refraction diagrams for each recording station using the most recent bathymetric chart. The wave clinometer records are obtained directly on hand-punched computer cards to facilitate the analysis procedure. The actual deep sea corrections, statistical analyses and tabulation of the data are now all done by computer.

Continuous wave records

The wave records obtained from the INES, wave rider, NIO and Ospos

instruments all lend themselves to the same type of analysis, although the records of the Ospos, which gives pressure fluctuations, first have to be converted to water level fluctuations. A computer programme is available to obtain the following wave characteristics from these records

- (a) cumulative wave height $(H)^x$ distribution
- (b) cumulative zero crossing wave period $(T_z)^x$ distribution
- (c) cumulative crest period (T_c) distribution
- (d) characteristic wave heights H_{50} , $H_{13.5}$, or H_s , H_1 and H_{max}
- (e) characteristic zero crossing wave periods $(T_z)_{50}$, $(T_z)_{13.5}$ or T_s and $(T_z)_1$
- (f) characteristic crest period $(T_c)_{50}$
- (g) the period of the maximum wave in the sample (T_{Hmax})

To reduce the cost of analysis by computer a simplified programme will be prepared to give the following information

- (a) wave heights H_{90} , H_{50} , $H_{13.5}$, H_{10} , H_1 and H_{max}
- (b) zero crossing wave periods $(T_z)_{50}$, $(T_z)_{13.5}$, $(T_z)_{10}$ and $(T_z)_1$
- (c) wave period of the maximum wave height viz T_{Hmax}
- (d) wave crest period $(T_c)_{50}$

The wave rider system already produces a punch tape output, but the records from the other instruments are in graphical form and must be converted to punch tape on the D-Mac pencil follower before computer analysis is possible

Statistical analysis and presentation of data

The deep sea wave characteristics are analysed to yield seasonal and yearly directional distributions. An example of the distribution of significant wave heights is shown in Figure 9. Standard forms of presentation are also used for cumulative distributions and exceedance curves. The standards used and methods of presentation are shown in Figure 10.

COMPARISON OF WAVE DATA

Cumulative distributions of wave direction, height and period for the various recording stations are plotted in Figures 11, 12 and 13

^x For definition of terms, see Appendix

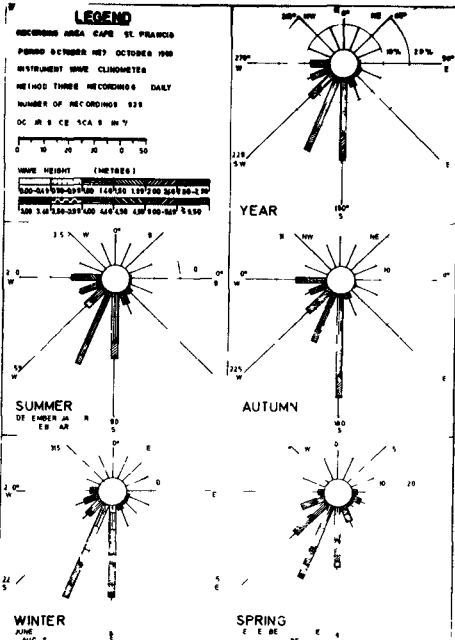
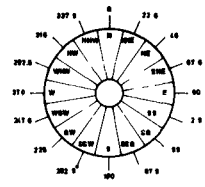


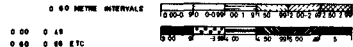
FIGURE 9 DEEP SEA WAVE HEIGHT ROSES FOR CAPE ST FRANCIS

DIRECTIONS

N	360	N
NNE	330	
NE	300	
ENE	270	
E	240	
ESE	225	
SE	180	
SSE	150	
S	90	
SSE	30	
SE	0	
ESE	330	
ENE	315	
N	270	
NNE	225	
NW	315	
NNW	330	
W	270	
WNW	285	
WSW	270	
W	225	
WSW	240	
WNW	225	
W	180	
WNW	165	
WSW	150	
W	90	
WNW	45	
WSW	0	



HEIGHTS



PERIODS



OCCURRENCE SCALE

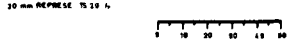


FIGURE 10 STANDARDS TO WHICH WAVE RECORDS ARE ANALYSED

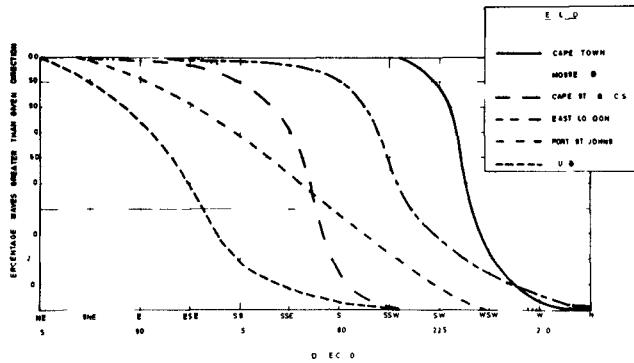


FIGURE 11 COMPARISONS OF WAVE DIRECTIONS CAPE TOWN TO DURBAN

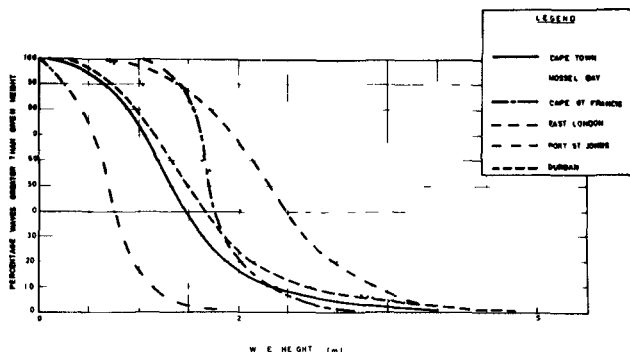


FIGURE 12 COMPARISONS OF WAVE HEIGHTS CAPE TOWN TO DURBAN

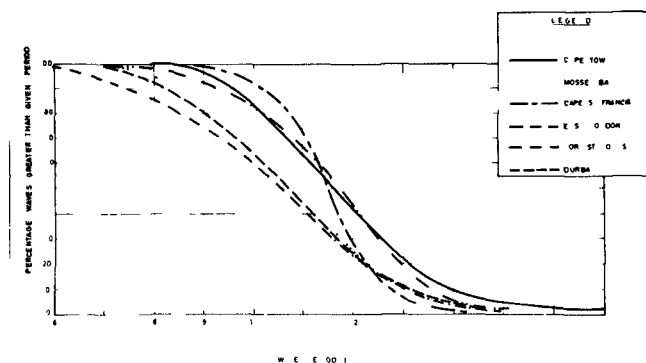


FIGURE 13 COMPARISONS OF WAVE PERIODS CAPE TOWN TO DURBAN

These figures show that there is an overall swing in the directions of wave approach from SW towards SE around the coast from Cape Town to Durban. There is no obvious trend in the variation of wave height along the coast, except that at East London and Port St Johns the waves are significantly higher and lower respectively than at the other stations. The wave period distributions indicate that there are two distinct areas, namely East London, Mossel Bay and Durban with an average median wave period of 10.7 s and Port St Johns, Cape St Francis and Cape Town with an average median wave period of 11.6 s.

From these data the distance between stations of 300 km so far

appears to be satisfactory More data will have to be obtained from some of the stations, however, before final conclusions on the suitability of this distance can be drawn

CONCLUSIONS

Since the commencement of the Ocean Wave Research project in 1967, data on wave conditions along the east and south coasts of Southern Africa have been systematically compiled The first data on wave conditions along the west coast will become available early in 1971 Already the project has provided the basic design data for various harbour and other coastal works, as well as for the present oil prospecting operations on the continental shelf

ACKNOWLEDGEMENTS

The energy spectra included in this paper were determined by J Forrer and L Langenegger Their assistance is acknowledged with thanks

REFERENCES

- 1 TUCKER, M J T A shipborne wave recorder Proc of the 1st Conference on Coastal Engineering Instruments Council of Wave Research The Engineering Foundation, 1956
- 2 HARPER, A Correlations between various ocean wave recording instruments Oceanography in South Africa Symposium, Durban, 1970
- 3 BLACKMAN, R B , TUKEY, J W The measurement of power spectra Dover Publications, Inc , New York
- 4 Ocean Wave Research Report No 1 Wave and wind conditions for the Natal and Western Cape coastal areas CSIR Report MEG 665, Pretoria, April, 1968
- 5 Ocean Wave Research Report No 2 Handleiding vir golfvoorspellings aan die Suid-Afrikaanse kus WNNR Verslag MEG 736, Pretoria, Januarie 1969
- 6 Ocean Wave Research Report No 3 Collection and analysis of ocean wave data South African practice CSIR Report MEG 741, Pretoria, January, 1969
- 7 Ocean Wave Research Report No 4 Wave and wind conditions for the Cape St Francis and Mossel Bay coastal areas CSIR Report MEG 804, Stellenbosch, 1969
- 8 WILSON, W S Development of a method for numerical calculation of wave refraction CERC, Tech Memo No 6, Washington, 1964

- 9 WILSON, W S A method for calculating and plotting surface wave rays CERC, Tech Memo No 17, Washington, 1966
- 10 DORRESTEIN, R Simplified method of determining refraction coefficients Jour Geophys Res Vol 65, 1960
- 11 GROEN, P Zeegolven Koninklijk Nederlands Meteorologisch Instituut No 111 'S Gravenhage, 1949

APPENDIX

GLOSSARY OF TERMS

- H - wave height the vertical distance between a wave crest and the preceding wave trough
- T_z - the average wave period obtained by dividing the duration of the entire wave record (in secs) by half the number of times the actual water profile crosses the mean water level
- T_c - the mean crest period obtained by dividing the duration of the entire record (in secs) by the number of crests in the record
- H_s - the average height of the highest one third of the waves occurring in a specified recording period
- T_s - the average period of the highest one third of the waves occurring in a specified recording period
- H_{max} - the greatest vertical height from crest to preceding trough in the record
- $T_{H_{max}}$ - the period of H_{max}
- H_{50} - 50 per cent of the waves occurring in a specific recording period are higher than H_{50}
- $H_{13.5}$ - 13.5 per cent of the waves are higher than $H_{13.5}$ ($H_{13.5} = H_s$ when distribution is Raleigh)

- H_1 - 1 per cent of the waves are higher than H_1
- T_{c50} - 50 per cent of the waves occurring in a specific recording period are longer than T_{c50}
- T_{z50} - 50 per cent of the waves occurring in a specific recording period are long than T_{z50}
- $T_{z13.5}$ - 13.5 per cent of the waves occurring in a specific recording period are longer than $T_{z13.5}$
- T_{z1} - 1 per cent of the waves occurring in a specific recording period are longer than T_{z1}

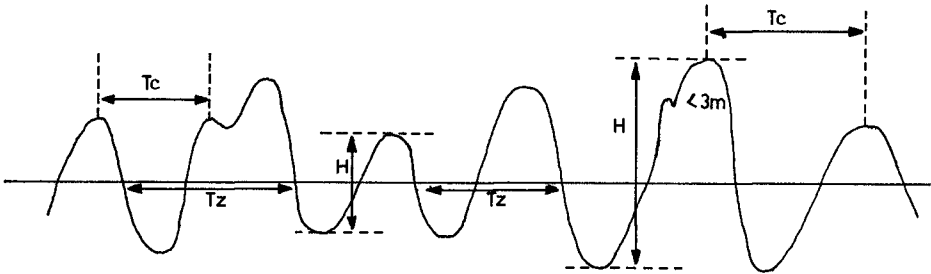


TABLE I AVAILABLE WAVE RECORDS MAY, 1970

PLACE/SHIP	POSITION	METHOD OF RECORDING	PERIOD	DEPRESSION OR DEPTH
St Lucia	Lighthouse	Visual Wave clinometer	Apr '61-Mar '62 Feb '68 -	5°
Richards Bay	North of bay mouth Opposite bay mouth	Wave clinometer INES	May '68 - Jan '69 -	3° 18 m
Durban	West Street Jetty Pilot boats S A S Bluff	Visual Visual Wave clinometer	Mar '61-Dec '61 Jan '68 - Apr '61-Nov '62	
Port St Johns	Radar station, Bluff 500 yds SW of Cooper Lighthouse	Wave clinometer Wave clinometer	July '65-Sept '69 Jan '70 -	7.5° 5°
East London	Cape Hermes Lighthouse Hood Point Lighthouse	Wave clinometer Wave clinometer	Feb '68 - June '67 -	7.5° 3°
Cape St Francis	Lighthouse	Wave clinometer	Oct '67 -	3°
Mosssel Bay	Cape St Blaize Lighthouse Deep sea (Area "C")	Wave clinometer Wave rider	June '67 - July '69 -	7.5° 100 m
Cape Town	Signal Hill	Wave clinometer	July '66-Dec '68	5°
Saldanha Bay	South Head Off South Head	Wave clinometer INES	Dec '69 - Jan '70 -	7.5° 30 m
Buchu Bay	Buchu Bay	Wave clinometer	Apr '69 -	5°
Walvis Bay	Pelican Point	Wave clinometer	May '69 -	3°
Mowe Point	Mowe Point Off Mowe Point	Wave clinometer Ospos	Apr '70 - Jan '70 -	5° 16 m
Africana II	Area "B"	NIO recorder	June '64 -	
Thomas B Davie	Area "B"	NIO recorder	Aug '67 -	
Meiring Naudé	Area "D"	NIO recorder	Apr '69 -	
S A S Natal	Areas "B" and "C"	NIO recorder	June '65-May '70	
Benguela	Area "A"	NIO recorder	Oct '69 -	

For areas
"A" to "D"
refer to
Figure 8

CHAPTER 3

SWELL AND STORM CHARACTERISTICS FROM COASTAL WAVE RECORDS

Warren C. Thompson, Professor of Oceanography
Naval Postgraduate School, Monterey, California

ABSTRACT

Manual analysis of strip-chart records from a conventional wave sensor at Monterey, California was found to yield a linear frequency shift associated with each arriving swell train, from which the origin time and travel distance of the swell could be computed. The use of surface weather maps allows identification of the source, and thereby yields an accurate determination of the deep-water arrival direction of the swell for use on the local coast. The wave records are analyzed for the frequency of the individual waves composing wave groups, f_g , consistency of the results obtained indicates that f_g is equivalent to the frequency of maximum energy density f_{max} , obtained by spectral analysis. Five swell sets studied were found to originate in North Pacific storms advancing toward Monterey. The seas in the fetch were fully arisen at the time of computed swell origin, and the surface to geostrophic wind ratio was 0.83. The dominant swell emerged from the fetch at a time when its group velocity equalled the velocity of the fetch toward Monterey.

INTRODUCTION

Barber and Ursell in 1948 published non-directional power spectra of ocean waves recorded on the coast of Cornwall, and showed that the spectral peak of swell arriving from a distant source shifts continuously toward higher frequencies, or short periods, with time. This shift is the result of dispersal of the broad band of frequency components generated in a sea that takes place during the propagation of the waves to a distant station, the energy in each component being transmitted at a velocity proportional to the frequency of the component, i.e., at group velocity. Barber and Ursell used the rate of increase in the frequency of the observed energy peaks to estimate the distance and time of swell origin, and identified swell sources at distances of 1200, 2800, and 6000 miles from the coastal wave station.

Subsequently, Munk, et al (1963) and Snodgrass, et al (1966) conducted notable experiments in wave measurement and analysis in the Pacific basin. In these studies, waves recorded daily and semi-daily at selected stations over several months were analyzed to determine their energy spectra, $E(f,t)$, as functions of frequency and time. The spectra were used to construct frequency-time (f-t) graphs on which were drawn contours of energy density. The resulting topography revealed pronounced linear ridges of high energy slanting across the graph which represent the arrival of swell trains generated by individual storms located in the South Pacific and South Indian Oceans at distances up to about 10,000 nautical miles (antipodal circumference).

of the earth) The distance from the storm to the station, and the origin time of the swell, were derived from the slope of the ridge line and from its intercept with the zero-frequency ordinate, respectively

As part of the study by Munk, Snodgrass, and colleagues, wave records from multiple-sensor arrays located on the continental shelf off San Clemente Island, California, and Honolulu, Hawaii, were analyzed for their direction spectra, $E(f, \theta, t)$, from which the directions to the swell sources, corrected for refraction, were determined. Comparison of the origin of swell trains computed from the wave data with the location of storms on weather charts gave good agreement.

The present paper introduces a non-spectral method of determining the frequency-time distribution of a swell train from coastal wave records. The f - t data thus obtained may be used to derive the source distance and origin time of the swell in the manner referred to above. This information, in turn, when used with synoptic weather charts permits identification of the storm, and provides a simple, accurate means of deriving the swell arrival direction in deep water off the recording station. The wave frequency is determined manually from wave groups appearing in strip-chart records. Evidence is offered to the effect that the frequency derived from wave groups, f_g , is equivalent to the frequency of maximum energy concentration, f_{max} , that is obtained from spectral analysis.

This study also probed into the conditions prevailing in the storm, and provided information concerning the stage in the storm history, and the state of development of the sea in the fetch, when the observed swell was produced. In addition, information was obtained on the relationship of the surface wind to the geostrophic wind prevailing in the fetch at the time of computed swell origin by an indirect means in which the surface wind was inferred from the frequency peak of the recorded swell train.

SYNOPTIC WAVE TRAINS

The wave records used in this study covered a period of 4-1/2 months in February-March 1967, November 1967, and March 1969, and were obtained using a conventional pressure sensor (Snodgrass Mark IX model) located in shallow water in southern Monterey Bay, California (Figure 1). The records were analyzed for wave height and period by procedures described in the next section.

Time plots of these parameters reveal an endless sequence of distinctive patterns representing the arrival of individual wave trains, each generated by a synoptic weather event occurring locally or somewhere in the Pacific Ocean. These synoptic wave trains sometimes arrive singly, and at other times two or more occur simultaneously. Nearly all swell trains recorded by the Monterey gauge have been found to originate in the North Pacific Ocean. Southern Hemisphere swell, which are observed occasionally on the adjacent open coast, experience extreme refractive divergence in reaching the Monterey gauge and are seldom detected.

Because of the sheltered location of the wave gauge, most of the 4-1/2 month period was marked by the arrival of swell trains, but seas generated in several local storms, and occasional low wind waves, were also recorded. In addition, there were several long quiet intervals of up to 12 days duration during which the wave height did not exceed 0.5 foot, and much of the time fell in the range from 0.1 to 0.3 foot.

Swell trains from distant storms are typified in a time plot by a narrow band of periods which decrease continuously with time. The swell height begins to increase about the time the first periods appear, reaches a peak, and eventually diminishes beyond detection. This characteristic height-period pattern is illustrated in Figure 3, in which may be seen three swell trains which arrived successively at Monterey during otherwise quiet sea conditions.

The initial period recorded among 13 swell trains studied ranged from 14.5 to 21.3 seconds, with the exception of the swell event of 22-28 March 1967 in which an initial period of 27.5 seconds was followed by a number of measurements above 20 seconds. In most swell trains, the period distribution terminates at a fairly well-defined cutoff in the range of 10 to 14 seconds, which reflects the submergence of the waning swell train below the rising energy level of the wind waves.

During those extended intervals when the wave height was half a foot or under, the periods were broad band and random much of the time, possibly reflecting the arrival of diffusely scattered wave energy. On several occasions, however, the period data clearly revealed the presence of a swell train when no trace of it was visible in the wave-height plot. The wave period is thus seen to be a sensitive indicator of swell even when the energy level is below that of the background.

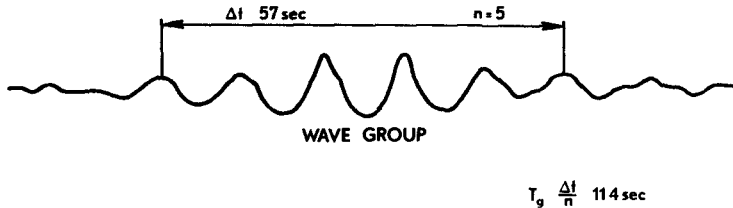
Waves from coastal storms, as seen in a time-series graph like that of Figure 3, are revealed by very short initial periods which increase with time and by a wide period scatter, characteristics which are representative of the broad spectrum in a sea. Periods decrease following passage of the wave peak and display a more limited scatter, which is consistent with the dispersive nature of young swell trailing in after the storm. Local seas, such as are caused by the commonly occurring sea breeze, produce a random scatter of periods ranging downward from about 6 seconds. No further attention will be directed to local wind waves or young swell in this paper.

ANALYSIS OF WAVE RECORDS

Wave Period

The wave data used in this study were recorded on Esterline-Angus strip-chart records, and were analyzed manually. The recorder was programmed to write a 5-minute fast trace (3 inches per minute) once every hour and a slow trace (3 inches per hour) the remainder of the time, from which, respectively, wave periods and wave heights were obtained.

As may readily be seen in a wave record, ocean waves characteristically display at intervals discrete wave groups composed of a variable number of more or less periodic waves. The average period of the individual waves contained in a wave group, T_g , is the period parameter used in this study. T_g may be determined from a wave record by measuring the time interval, Δt , for the passage of a selected number of waves, n , as illustrated in the diagram below. The measurement is made between those equivalent parts of the wave form that the analyst judges to give the best measure in each case, e.g., between selected crests, troughs, centers of wave mass, or centerline crossings.



At this point it is desirable to inquire into the physical significance of T_g since it forms the basis of this study. Within the conceptual framework of a sea surface composed of harmonic components of various period, extension of the rules for waveform interference stated by Manley (1945) to an ocean-wave spectrum leads to the conclusion that the apparent or mean period of the waves forming a group, or beat, T_g , is equal to the period of that component present having the greatest energy density. In the case of swell, the component of peak energy density can be considered to be the value T_{\max} , or its reciprocal f_{\max} , that would be obtained from spectral analysis of the wave records. As stated above, the frequency of the energy peak, f_{\max} , has been used with good success for calculating the origin time and travel distance of swell. The wave records analyzed in this study have not been subjected to spectral analysis for direct proof of the equivalence of T_g and T_{\max} , however, the writer believes that the consistency of the results obtained using T_g in examination of the wave-generating conditions at the swell source, which are described below, can have been achieved only if this condition were met.

With regard to practical considerations in the analysis of wave records, the wave-group method of determining the period has the important advantage over the conventional significant-period (T_s) procedure of quick application. It also yields a number of values of T_g in the 20-minute or so length of wave record needed to obtain T_s . In addition, two or three wave groups in

superposition are frequently observed in the wave records, and the wave-group method has the further important advantage of providing the periods of each A time-series graph of wave data shows the simultaneously occurring periods to be associated with independent wave trains from different sources, and thus provides additional insight into the synoptic nature of the wave trains present. For best results in the application of the wave-group method, the judgment of an analyst having a basic understanding of wave-interference phenomena is required. The task of discriminating individual wave groups and measuring T_g remains for the present beyond the capability of machine programming.

In order to assure the quality of the period measurements in this study, care was taken to avoid phase shifts and also the small secondary swell waves that occasionally appear in a wave group, and to account for occasional missing waves in a sequence. Not infrequently during quiet intervals the waveform assumed a variety of highly irregular shapes. In spite of their bumpy appearance these waves often occurred in a regular sequence, and the values of T_g obtained were found to be consistent with the periods derived from sets of well-defined waves.

For the interval covered by this study, the value of T_g derived from every swell group identified in the wave records was measured and graphed. Within the limits of Figure 3, for example, no data have been omitted, and all waves, whether sea or swell, are represented. The occurrence of obviously spurious period values was found to be quite low.

The period data reveal variable amounts of scatter when graphed as a time series, as may be seen in Figure 3. The scatter is attributed to the spectral bandwidth of the waves, and to subjectivity inherent in the selection and measurement of the wave groups. In regard to the latter, the precision of period measurements is estimated to be about 0.2 second for a group consisting of 5 waves, and 0.1 second or less for groups of 10 or more waves. An idea of the overall precision can be obtained from the observation that out of 582 wave groups (of 4 or more waves per group) composing a randomly selected month of data, 62% contained 4 to 6 waves, and 9% had more than 10 waves. The number of waves in a group was found to be independent of the period.

Wave Height

Wave heights, determined to 0.1 foot, were derived from one-hour and three-hour samples of the slow-trace portions of the strip-chart record using a shortcut method developed for the purpose. The method involves estimating visually the crest amplitude, $A_{67\%}$, such that one-third of the wave envelope exceeded this amplitude. The trough amplitude was estimated in the same way. The crest and trough amplitudes, which differ because of wave asymmetry in shallow water, were summed to give $H_{67\%}$, and then converted into the significant wave height, H_s , using the empirical relationship $H_s = 1.35 H_{67\%}$ obtained from the statistical height parameters given

by Pierson, Neumann, and James (1955) The method requires a strip-chart recording made at a speed such as to compress the waves time-wise but not beyond the point at which individual crests and troughs can be distinguished

This slow-trace method of height analysis is a simple operation which involves no counting of waves It has the important advantage of speed over other manual techniques, and can effect a major savings of time when a number of analyses are made The method can be applied much more quickly, for example, than the analysis method that is based on the identification and measurement of a single wave in a fast-trace record having a height that represents some percentage level in a statistical height distribution Another advantage of the slow-trace method is that the height variability associated with wave groups and energy bursts which frequently are present in the records is averaged out by treating a long record This results in a wave-height time series that displays relatively little scatter, as is illustrated in Figure 3 Intervals of unusually high or low wave groups having durations of 10 or 15 minutes are not uncommon, and bias the heights derived from the conventional 20-minute fast-trace Random comparisons showed the heights derived from the slow-trace method and the conventional zero-upcrossing method to agree within 20% in most instances

Wave-height information is not needed for the purpose of obtaining the swell origin distance and travel time from a wave record, although it is useful, when examined in conjunction with the wave period, for deducing the synoptic characteristics of arriving wave trains in a time-series graph The relative wave height is needed, however, for identification of the period of the peak waves in a swell train, T_p The latter is used for probing into the state of development of the sea that produced the swell and for estimating the surface wind at the time of swell origin, as discussed below

Shallow-Water Effects

It is possible, in theory, for the frequency of maximum energy density in swell to shift across the spectrum as the waves travel from deep water to the sensor because of shoaling transformations A shift of this sort would alter the source distance and origin time computed for the swell It is also possible for the largest waves to appear at the sensor either earlier or later than in deep water for the same reason Advance or retardation of the swell peak would, in turn, result in erroneous values deduced for the surface wind speed in the fetch, which is discussed later Accordingly, an analysis was made to determine the magnitude of the shift in the wave peak with both frequency and time, and these changes were found to be negligible

An idea of the magnitudes of the shallow-water coefficients at the sensor site, and their variation with frequency, may be gained from Figure 2 The coefficients, as given by linear wave theory, are defined as follows

$$\text{Shoaling coefficient} \quad K_s = (C_o/2V)^{1/2}$$

$$\text{Refraction coefficient} \quad K_r = (d_o/d)^{1/2}$$

$$\text{Hydrodynamic coefficient} \quad K_h = (\cosh kh)^{-1}$$

where C = phase (wave) velocity, V = group velocity, d = wave-orthogonal separation, k = wave number ($2\pi/L$), L = wave length, h = mean sensor depth (24 feet), and subscript o refers to deep water. Energy losses due to bottom friction were considered negligible because of the relatively narrow, deep shelf offshore. Accordingly, the energy density at the sensor, $E(f)$, relative to that in deep water, $E_o(f)$, for a given frequency component in an arriving wave train is given by

$$E(f) = (K_s K_r K_h)^2 E_o(f)$$

The curve of K_h applies only to Swell Train 1 of 21-23 February 1967 (Figure 3) which arrived from 311° . The variation of $(K_s K_r K_h)$ with frequency is seen to be small over the range of wave periods observed (20 to 12 seconds). Curves of $(K_s K_r K_h)$ for North Pacific swell arriving from other directions also display relatively small variation, but differ somewhat in magnitude.

SWELL ORIGIN AND DIRECTION

Determination of Swell Source

Using spectral analysis of wave records, Munk, et al., (1963) observed that a swell train arriving from a distant storm is revealed as a prominent ridge line in the spectral density topography on a frequency-time (f - t) graph, and noted that ridge lines are linear or very nearly so ($df/dt = \text{constant}$). A straight ridge line (f - t line), in the context of linear wave theory, implies a point source for the swell in space-time, and provides a simple means for determining the apparent source distance and origin time. Thus, if the energy associated with each frequency component, f , generated in the sea is propagated at group velocity, $V_f = g/4\pi f$, over distance D from the source to the wave gauge in travel time $\Delta t = t - t_o$, measured from the origin time t_o , then

$$V_f = g/4\pi f = D/(t - t_o)$$

The slope of the f - t line is then $df/dt = g/4\pi D$. Accordingly, the apparent distance to the swell source is given by

$$D = \frac{1}{4\pi} \frac{515}{df/dt} \text{ (naut mi)},$$

where f is in cycles/second and t is in hours. The apparent origin time is given by the intercept of the f - t line with zero frequency.

In the present study, the values of T_g derived from the Monterey wave records were converted to f_g , and f - t graphs were constructed. Examples of three swell trains (from Figure 3) are shown in Figure 4 in which the linear character of the f_g distribution with time may be seen. From the 4-1/2 months of analyzed wave data, 13 swell trains were selected for study. Straight-line fits to each set of f_g data yielded source distances ranging from 1515 to 4270 naut mi.

Wave records from a single gauge provide no directional information for use in locating the coordinates of a fetch that produced a given set of swell. In fact, directional information at the Monterey gauge site would have little value for this purpose because refraction caused by extreme sheltering results in a nearly unidirectional approach for all swell.

The storm responsible for a recorded swell train was identified, however, using the computed origin time and distance combined with six-hourly synoptic sea-level pressure analyses produced by the Fleet Numerical Weather Central, Monterey. In all swell cases analyzed, an arc of radius D drawn from Monterey on a weather chart of time t_0 was found to intersect a storm system. All of the swell sets studied were found to originate in eastward-moving cyclonic storms in the North Pacific Ocean. The absence of southerly waves among the swell sets selected is probably due to extreme energy reduction by refraction in passing around the Monterey Peninsula, since Southern Hemisphere swell is recorded on the adjacent open coast.

In view of the fact that a storm system produces swell for the duration of its passage across the ocean, it appears that the point source computed from the wave records represents that moment and location in the storm history at which the maximum energy density in the sea directed toward Monterey was generated.

Deep-Water Direction

The deep-water wave direction, ψ_0 , is a parameter required for nearly all coastal engineering applications involving waves in shallow-water. Direct measurement of this quantity is difficult and expensive as conventionally done because it requires synchronous operation of closely spaced multiple wave sensors and complex data-analysis procedures. In addition, the sensor array is placed on the bottom in shallow water, and shoaling and refraction transformations must be applied to the data in reverse in order to obtain the deep-water direction spectrum if that is desired. For these reasons directional wave recording remains for the present in the realm of research and is not performed on an operational basis.

With regard to swell, the procedure described in the previous section, by which the source is identified using coastal wave data from a single sensor in connection with weather charts, permits construction on the appropriate weather chart of a great-circle trajectory from the swell source to the coastal station, and thereby provides an accurate measure of ψ_0 at the station as well as for other locations on the adjacent coast. Noting that the energy in a sea is proportional to the fourth (or fifth) power of the wind speed, the swell trajectory can logically be considered to originate at that point in the fetch where the wind velocity directed toward the coastal station is a maximum. The deep-water swell directions derived in this manner for five selected storms producing swell recorded at Monterey are listed in Table 1, and can be seen in relation to the fetch trajectories of each storm in Figure 5. As implied above, the deep-water wave direction is also the fetch azimuth from Monterey.

The beamwidth, or angular intercept, of the fetch as viewed from a coastal station, is determined by both the fetch width and distance, and varies during

the life of a storm. For the purposes of this study the fetch width was defined as that swath of the wind field directed toward Monterey within which the winds can generate 70% or more of the wave energy generated by the peak winds in the fetch. By this definition, the fetch beamwidth at Monterey, which is also the directional bandwidth of the arriving swell, was 3° to 4° at the time of computed swell origin for the five storms studied (Table 1). These values appear to be typical for most swell trains arriving at coastal stations from distant sources. Accordingly, for practical engineering purposes, swell arriving on the Pacific Coast can be considered unidirectional, and to originate at the source computed.

In the directional recording of Southern Hemisphere swell at San Clemente Island, California, and Honolulu, Hawaii, Munk, et al (1963) and Snodgrass, et al (1966) found the computed swell source to lie pretty consistently to the left of the fetch location obtained from weather charts. The authors suggested that the deviations were the result of local refraction uncertainties and insufficient accuracy in the relative positioning of the sensors. Deflection of the swell direction by ocean-current systems also appears to be a possibility. For North Pacific swell arriving on the Pacific Coast, ocean-current deflection might be expected to amount to several degrees from the great-circle swell trajectory.

Long-Range Triangulation

The results of this study indicate that the source of a swell train can be identified with certainty in most instances using the wave date from a single sensor coupled with weather charts, but occasionally more than one storm is present simultaneously at the computed origin distance. This was the case with Storm 3 shown in Figure 5 (Braunstein, 1970).

It appears that positive identification can be obtained consistently and automatically by long-range triangulation using the swell travel distances derived from two sensors placed some miles apart along the coast. The feasibility of this was tested using wave sensors at Monterey and Bolinas, California, separated by 90 naut. mi., for the swell train of 18-20 March 1969. The two stations happened to be nearly in line with the swell direction in this case, and the computed origin times and distances yielded an almost identical common source.

It is probable that location of swell sources by long-range triangulation will not give direction resolution that is as good as can be obtained using weather charts, however, the precision of deep-water swell directions obtained by this means may prove to be fully adequate for practical engineering purposes.

GENERATING CONDITIONS IN THE STORM

Swell Origin in Relation to Storm History

With the objective of determining the relationship between the computed swell source and the history of development of the storm, five swell trains recorded at Monterey were selected and the storms that produced them were intensively studied by Braunstein (1970) and the author through the use of

FNWC six-hourly synoptic weather charts Data pertaining to the swell trains and storms are presented in Table 1

Using objective methods devised for the purpose, Braunstein measured from successive weather maps the dimensions of the effective generating area and its azimuth and distance from Monterey From this information, distance-time (d-t) graphs were prepared for the five storms throughout their development A d-t graph for the fetch area that produced the swell train of 21-23 February 1967, shown in Figure 3, is presented in Figure 6 The point of maximum wind in the fetch is shown by the dashed line, and the front and rear limits of the fetch are indicated by the solid lines The speed of advance of the fetch with respect to Monterey is given by the slope of the curves The wind area is observed to have travelled rapidly in its early stages but slowed perceptibly about 00Z on 17 February

The movement of the wind field may also be seen in Figure 5, which shows the fetch tracks for the five storms The dots mark six-hourly positions of the point of maximum winds directed toward Monterey, and the small circle indicates the computed swell origin time The fetch trajectories labelled 1, 2, and 3 are associated with the storms that produced the three successive swell trains of Figures 3 and 4 The fetch tracks should not be confused with the trajectories of the storm centers, which are not shown

The computed swell source derived from the Monterey wave records may be seen in Figure 6 to lie within the fetch observed from the weather maps Also plotted are the lowermost, uppermost, and peak period components identified in the swell The lines emanate from the swell source and arrive at the gauge ($D = 0$ naut mi) at the times indicated The group velocity of each component is given by the slope of its line It may thus be seen that the peak swell component observed was generated when its group velocity coincided with the speed at which the fetch approached Monterey

The histories of all five storms studied were found to be similar They were characterized during their early phase of development by a high fetch speed, followed by reduced speed as the storm matured The swell source was located within the fetch envelopes in four cases, and near the fetch margin in the other The swell was found to emerge when the fetch velocity and the group velocity of the peak swell component generated were approximately coincident It is significant that the peak geostrophic wind velocity in the five storms occurred from 20 hours earlier to 33 hours later than the computed swell origin time, and that it exceeded the geostrophic wind observed at the time of computed swell origin by as much as 33 knots, thus indicating that the time of swell origin is largely independent of the time of occurrence of the maximum wind speed in the type of synoptic situation dealt with, i e, swell from an approaching storm The requirement for generating the maximum energy in the sea appears to be equivalence of the fetch velocity with the group velocity of the lowest frequency components with significant energy that can be generated by the surface wind present at the moment

Fully Arisen Sea and the V_s/V_g Ratio

The condition in which the fetch travels at the velocity of the lower frequency components generated permits those components to remain under the

influence of the generating winds for a long effective duration over a long effective fetch, thus allowing maximum energy buildup. If it is assumed that North Pacific storms ordinarily permit the development of fully arisen seas directed toward Monterey, and if it is further assumed that the peak period generated is conserved during its propagation to Monterey, then the peak swell period observed, T_p , can be used to estimate the surface wind speed that generated the sea from suitable spectral models for the fully arisen sea. Entering the Pierson-Moskowitz (1964) spectrum with the values of T_p associated with the five selected storms yielded the surface winds listed in Table 1.

Of particular interest in the forecasting of ocean waves from weather charts is the surface to geostrophic wind ratio. Accordingly, the surface winds obtained in the manner described were used to calculate V_s/V_g for each storm. The geostrophic wind used was that measured at the time of computed swell origin from the 12-mb band in the strongest portion of the pressure gradient occurring along that storm radius lying normal to the surface wind direction toward Monterey. The values obtained are listed in Table 1 and are illustrated in Figure 7.

As may be seen in the figure, the surface to geostrophic wind ratio is in close agreement for all five storms. Its mean value, 0.83, is in general accord with values quoted for the North Pacific, the North Atlantic, and the Greenland and Norwegian Seas (reviewed by Aagaard, 1969). The magnitude of the values obtained, along with their internal agreement, provide strong evidence to the effect that the seas producing the swell in all five storms were fully arisen or nearly so.

In the case of a non-fully arisen sea, the peak swell period measured would yield a low value of V_s/V_g that would lie on the left side of the curve in the figure. The smaller value of V_s/V_g for Storm 4 (0.78) might indicate that the sea was not quite fully developed, or it might reflect greater air-mass stability typical of the fall of the year (November). The other four storms occurred in February and March when air-mass stability is normally less, and their average value is a little higher (0.85).

The consideration that perhaps most North Pacific storms may produce fully arisen seas is of potential importance with regard to forecasting swell on the west coast of North America.

APPLICATIONS AND FUTURE DEVELOPMENTS

This study has demonstrated the fact that the source and deep-water direction of swell can be obtained by simple methods involving the manual analysis of coastal wave records from a conventional wave gauge and the use of ocean weather charts. The procedures described are best suited for use in economic situations and geographic regions where the availability of funds or technical expertise is limited, or computer facilities are not available, and a source of labor can be tapped.

Perhaps the most difficult problem in present-day swell forecasting is making an accurate prediction of the time of arrival of the peak waves. Based upon results obtained in this study, the author anticipates the development of a new method of swell prediction in which forecast products will include the rate of change of swell frequency with time, and the arrival time and frequency of the peak waves.

On coasts subject to costly shoreline damage by heavy swell, such as occasionally occurs on the California coast due to Southerly Swell, there is increasing need for an integrated program of forecasting and monitoring wave conditions. The author foresees the development of a swell warning system consisting of a network of coastal wave sensors from which recorded wave data will be transmitted automatically to an analysis center for continuous machine processing. Storm systems will be identified and tracked by long-range triangulation. The deep-water swell characteristics along the coast will be obtained by forecasting and by swell analysis for use in estimating the wave conditions expected on local beaches.

ACKNOWLEDGMENTS

This work was supported by the Office of Naval Research Foundation Grant to the Naval Postgraduate School, and by the Fleet Numerical Weather Central, Monterey.

REFERENCES

- Aagaard, K , 1969 Relationship between Geostrophic and Surface Winds at Weather Ship M J Geoph Res , 74, 13, 3440-3442
- Barber, B F , and F Ursell, 1948 The Generation and Propagation of Ocean Waves and Swell Phil Trans Roy Soc , A, 240, 527-560
- Braunstein, W J , 1970 Origin of Swell Recorded at Monterey, California M S Thesis, Naval Postgrad Sch , Monterey
- Manley, R G , 1945 Waveform Analysis Wiley & Sons, N Y , 275 pp
- Munk, W H , G R Miller, F E Snodgrass, and N F Barber, 1963 Directional Recording of Swell from Distant Storms Phil Trans Roy Soc , A, 255, 505-584
- Pierson, W J , G Neumann, and R W James, 1955 Practical Methods for Forecasting Ocean Waves H O Pub 603, 284 pp
- Pierson, W J , and L Moskowitz, 1964 A Proposed Spectral Form for Fully Developed Wind Seas Based on the Similarity Theory of S A Kitaigorodskii J Geophys Res , 69, 24, 5181-5190

Table 1 SWELL AND ASSOCIATED STORM CHARACTERISTICS

A Swell Characteristics

Swell train	Time of peak (GMT)	Peak period (T) _p	Freq change (df/dt)	Computed source dist (D)	Computed origin time (t) _o
1	21/21 Feb 67	17 0 sec	12 2 c/ks day	2970 NM	00/17 Feb 67
2	07/24 Feb 67	15 6	16 5	2210	08/20 Feb 67
3	23/25 Feb 67	14 5	17 1	2120	00/22 Feb 67
4	04/20 Nov 67	13 7	10 6	2240	15/15 Nov 67
5	01/19 Mar 69	19 0	16 2	3450	01/14 Mar 69

B Storm Characteristics at Computed Swell Source

Assoc storm	Fetch* azimuth (ψ) _o	Fetch* width (λ)	Geostro* wind (V) _g	Surface wind (V) _s	Wind ratio (V/V) _g
1	310°	3 9°	51 5 kn	45 3 kn	0 88
2	315	4 1	50 9	41 6	0 82
3	287	4 0	45 8	38 6	0 84
4	314	3 8	48 5	36 5	0 75
5	315	3 0	60 5	50 5	0 84

*From Braunstein (1970)

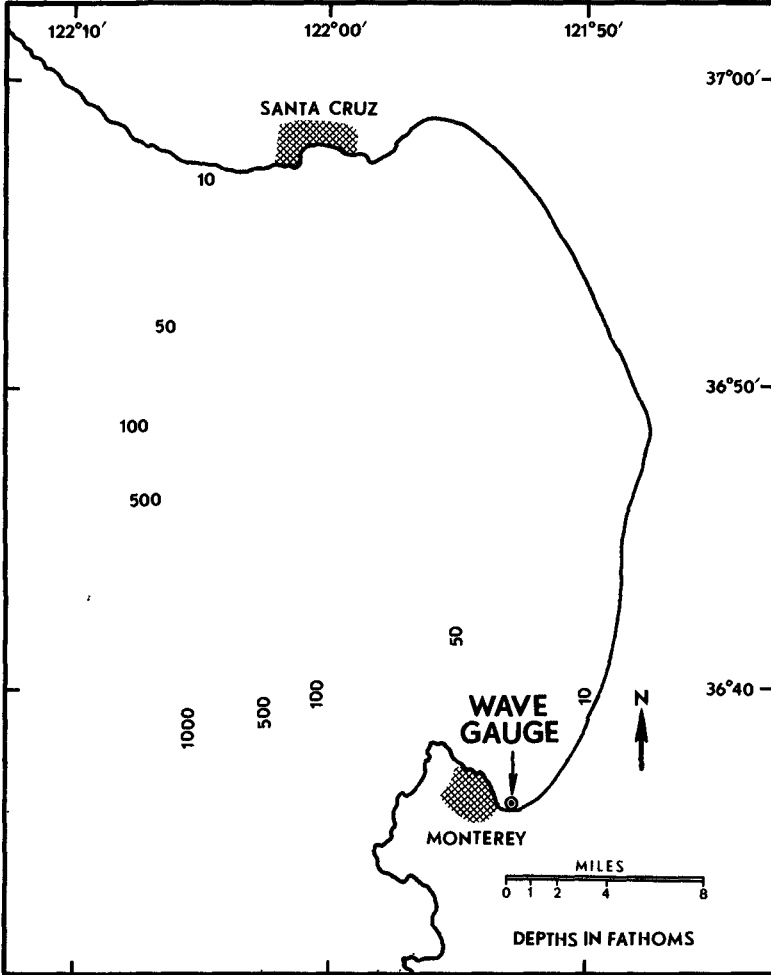


Figure 1 WAVE-GAUGE LOCATION IN MONTEREY BAY

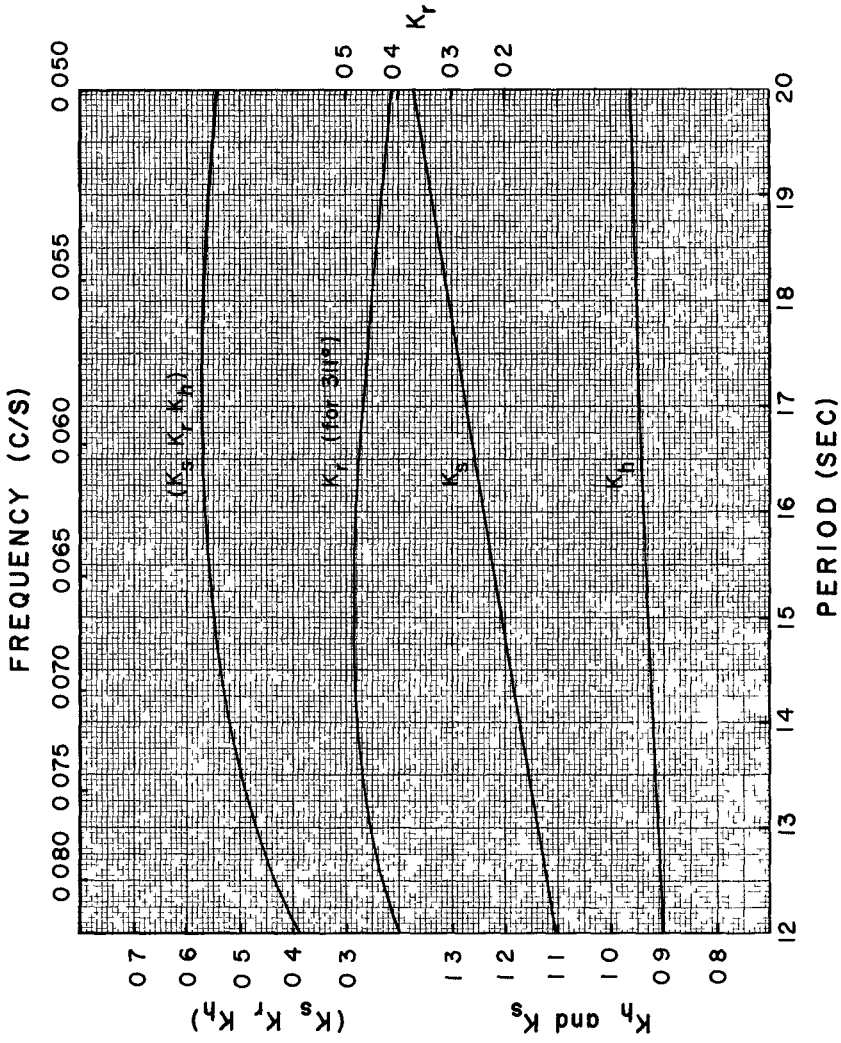


Figure 2 SHALLOW-WATER COEFFICIENTS FOR THE MONTEREY GAUGE

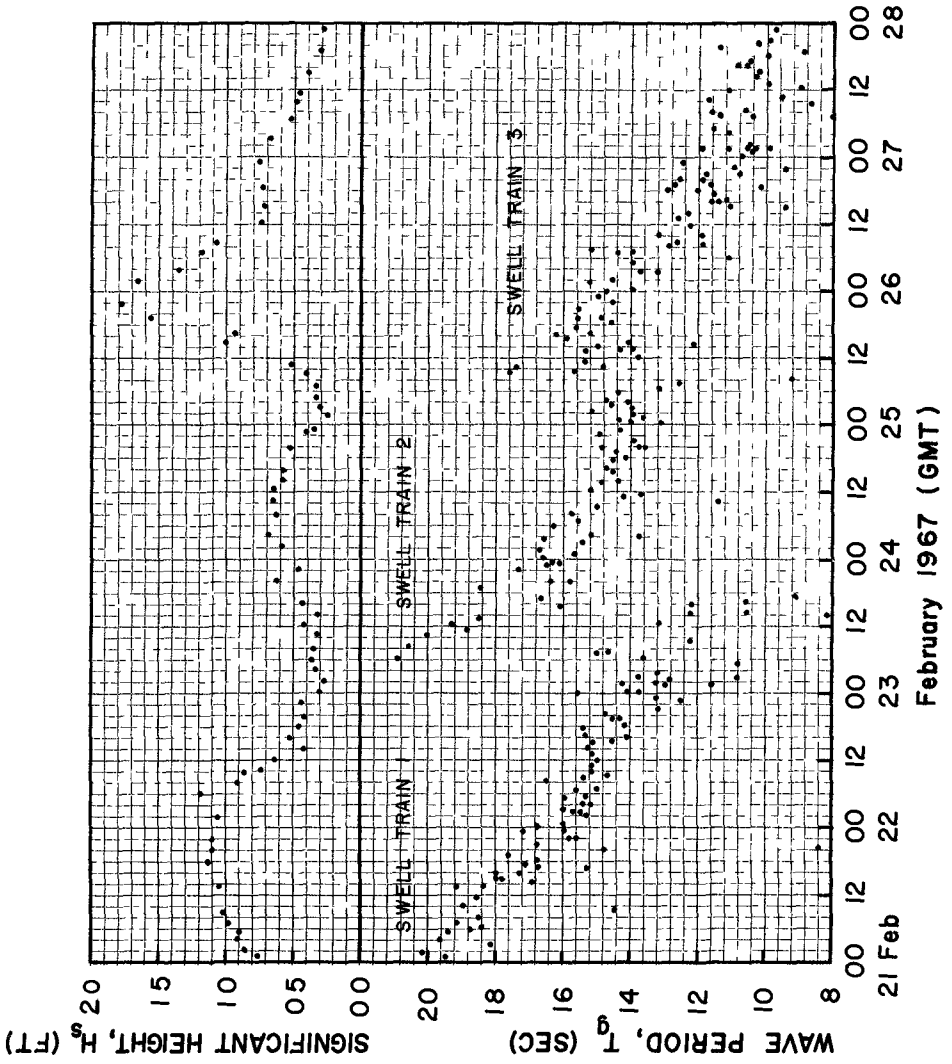


Figure 3 WAVE DATA FOR SWELL TRAINS 1-3

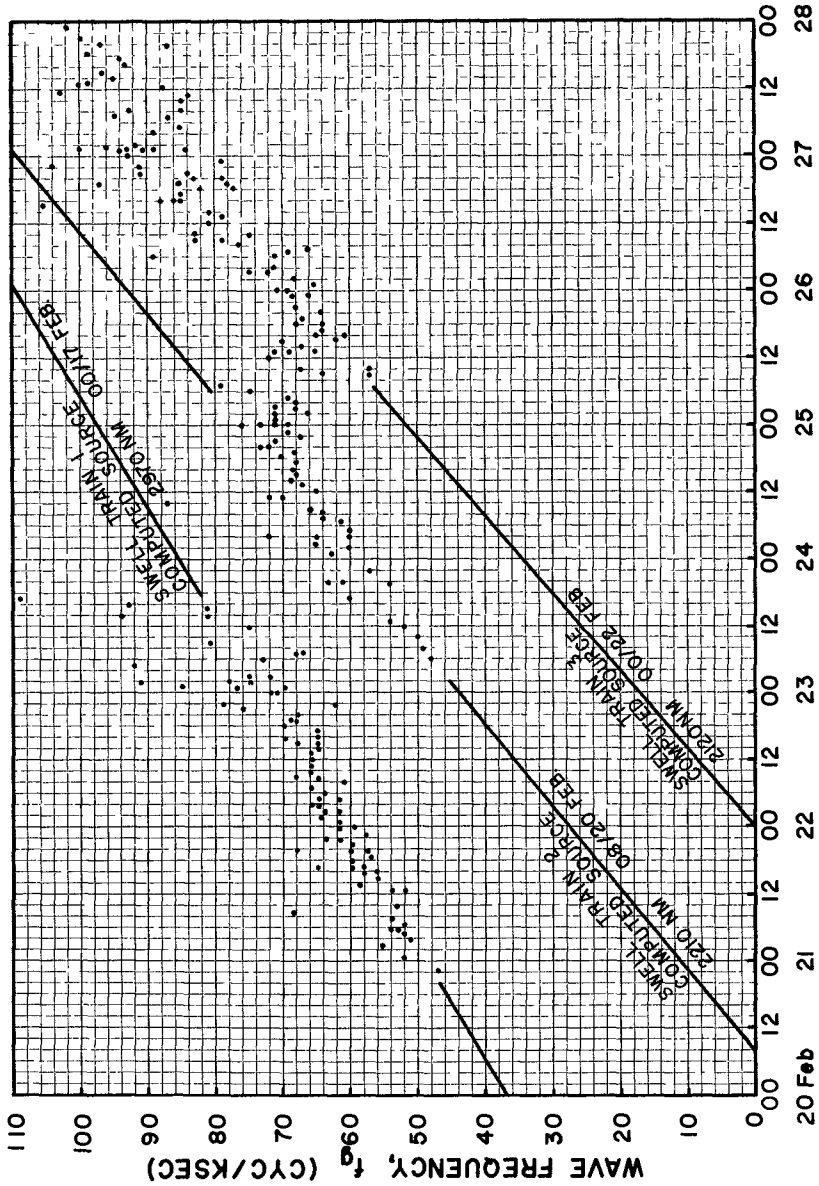


Figure 4 FREQUENCY-TIME DISTRIBUTION FOR SWELL TRAINS 1-3

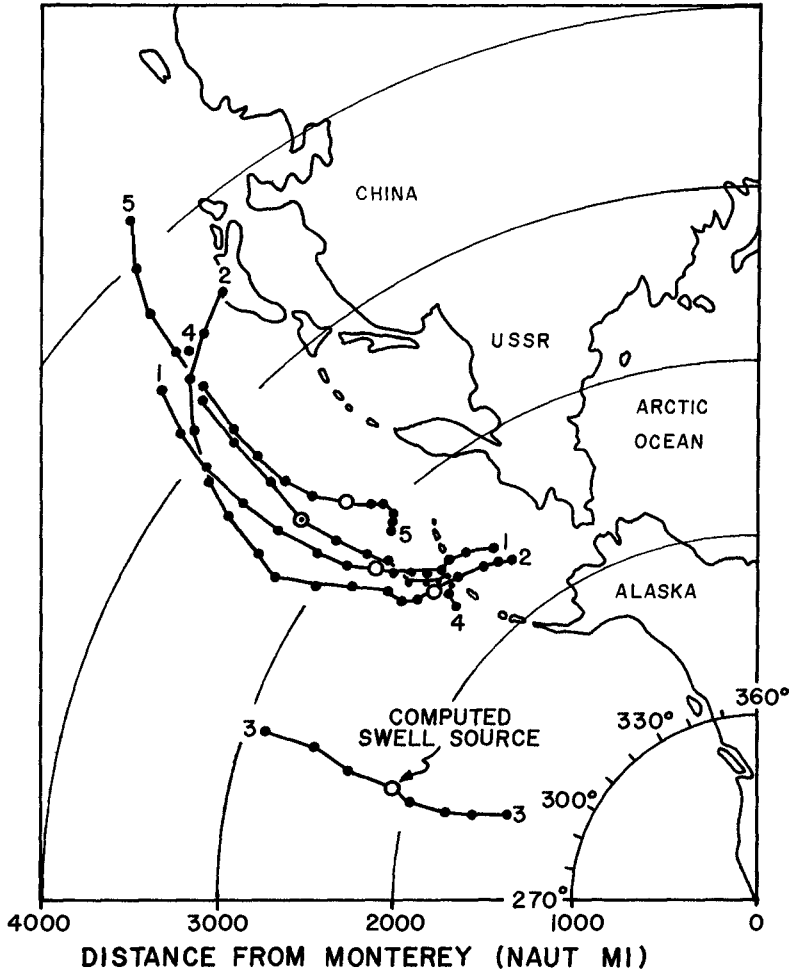
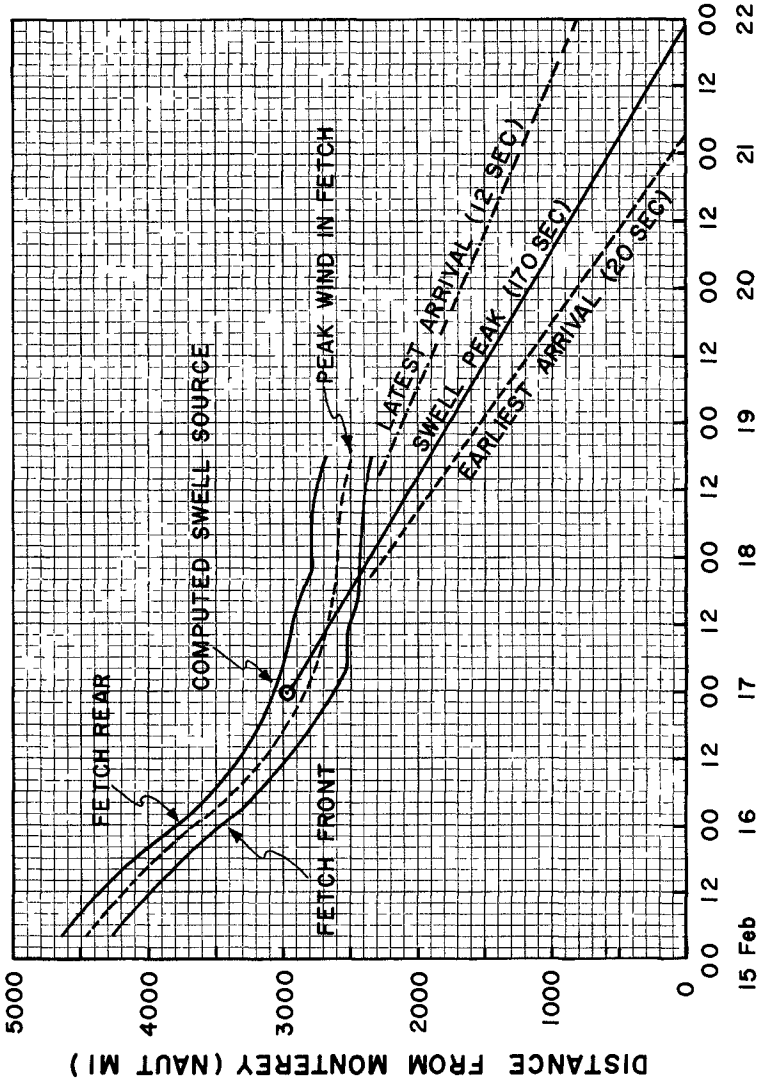


Figure 5 SIX-HOURLY FETCH LOCATIONS FOR STORMS 1-5
(after Braunstein, 1970)



February 1967 (GMT)
Figure 6: DISTANCE -TIME GRAPH FOR STORM I
 (after Braunstein, 1970)

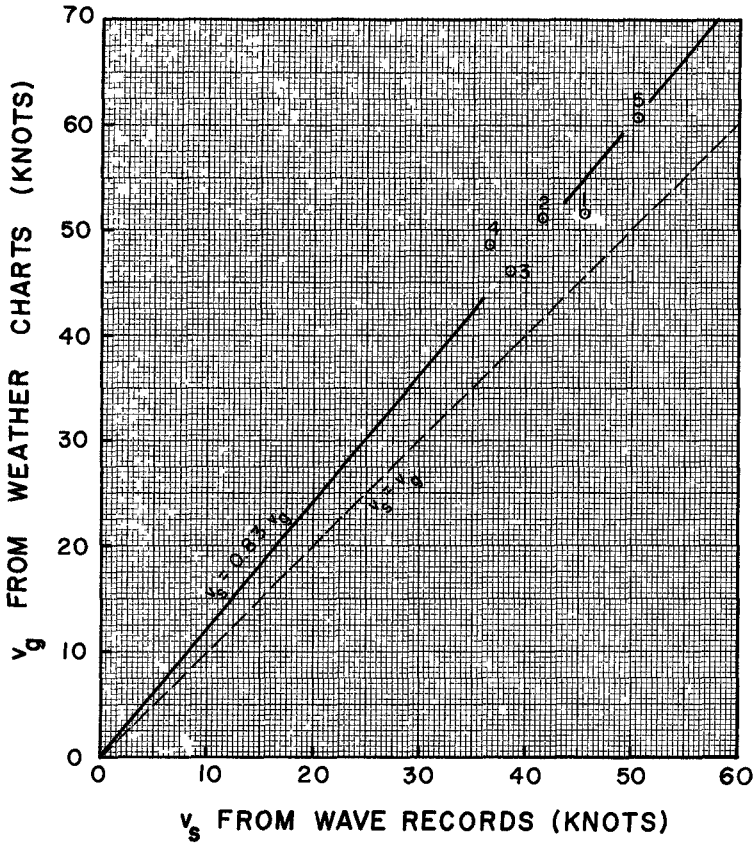


Figure 7 RELATIONSHIP BETWEEN SURFACE AND GEOSTROPHIC WINDS AT COMPUTED SWELL SOURCE FOR STORMS 1-5 (after Braunstein, 1970)

CHAPTER 4

MAXIMUM WAVE HEIGHT PROBABILITIES FOR A RANDOM NUMBER OF RANDOM INTENSITY STORMS

L E Borgman
Professor of Geology and Statistics
University of Wyoming

ABSTRACT

A very general model is presented for the probability distribution function for wave heights in storms with time-varying intensities. Some of the possible choices for functions in the model are listed and discussed. Techniques for determining the "equivalent rectangular storm" corresponding to a given historically recorded storm are developed. The final model formula expresses the probabilities for a random number of random length storms each with random intensities.

INTRODUCTION

The probability law for the largest of N independent, identically distributed random variables is covered quite well in statistical and scientific literature. Gumbel (1954) provides an excellent survey of the main elements of the theory. His book (Gumbel, 1958) gives a very complete bibliography and many additional details.

The application of these techniques to determine probabilities for the largest ocean wave heights in a sequence of N identically distributed and independent waves was developed by Longuet-Higgins (1952). What modifications are necessary to yield maximum wave probabilities for storms which vary in intensity with time? Furthermore, how would one obtain probabilities for the maximum wave in a random number of such time-varying storms? These questions will be considered in detail in the following.

PRELIMINARY ASSUMPTIONS

The basic assumptions needed in the development are

- (1) The probability distribution function

$$F_H(h) = P[H \leq h] \quad (1)$$

for wave heights is known as a function of time-varying intensity parameters. Here, and in later deviations, $P[]$ will denote the probability of the event indicated within the square brackets. The intensity parameters in $F_H(h)$ may be the root-

mean square wave height, a , if the Rayleigh distribution is used

$$F_H(h) = \begin{cases} 1 - e^{-h^2/a^2}, & \text{for } h \geq 0 \\ 0 & \text{for } h < 0 \end{cases}, \quad (2)$$

or the r m s wave height, a , and the breaking wave height if the clipped Rayleigh distribution is used

$$F_H(h) = \begin{cases} \frac{1 - e^{-h^2/a^2}}{1 - 2^{-H_b^2/a^2}}, & \text{if } 0 \leq h \leq H_b \\ 0 & \text{otherwise} \end{cases} \quad (3)$$

Another possibility is the Rice distribution outlined by Longuet-Higgins and Cartwright (1956) which depends on the r m s wave height and a parameter, ϵ , which is determined from the spectral density for the water level elevations

- (2) It will also be assumed that each wave height is statistically independent of the heights of its neighbors. This assumption is largely one of convenience. The theory is much harder without it. However, it has been shown theoretically that the limiting distribution for the maximum of random variables which are what is called "m-dependent" of each other is the same as the limiting distribution for independent random variables (Watson, 1954). The term, m-dependent, used here means that random variables in the sequence with more than m-1 other random variables between them are statistically independent of each other. It seems reasonable to assume that a wave height is at most interdependent with the first several wave heights occurring before and after it and essentially independent with waves further back into the past or forward into the future. Hence m-dependence seems reasonable for wave heights.

Since the limiting distribution is the same for independent as well as m-dependent random variables, one can tentatively presume the independence assumptions for wave heights will not lead to badly incorrect conclusions. It would appear that the independence assumption would lead to a conservative estimate of the maximum wave height probabilities, in any case. Longuet-Higgins and others have made this same assumption and it will be made here also.

- (3) It will also be presumed that there is a known, or estimated, function $T(t)$ such that for any small time interval dt , the number of waves in the interval is given by $dt/T(t)$.

A SINGLE TIME-VARYING STORM

Consider first N identically-distributed, independent wave heights, each with probability distribution function, $F_H(h, \underline{a})$. Here \underline{a} denotes the set of one or more intensity parameters which characterize the intensity of the sea conditions. For this situation, let $H_1, H_2, H_3, \dots, H_N$ be the N waves. The largest wave in the sequence will be less than or equal to h if, and only if, every one of the waves are less than or equal to h . Thus

$$P[\max H \leq h] = P[H_1 \leq h, H_2 \leq h, H_3 \leq h, \dots, H_N \leq h] \quad (4)$$

But since the wave heights are assumed independent of each other,

$$P[\max H \leq h] = P[H_1 \leq h] P[H_2 \leq h] P[H_3 \leq h] \dots P[H_N \leq h] \quad (5)$$

Finally since the N waves are taken to have the same probability distribution function

$$P[\max H \leq h] = \{F_H(h, \underline{a})\}^N$$

Suppose now that the time-varying storm can be subdivided into steps as shown in Table I below

TABLE I
FINITE STEP APPROXIMATION TO THE TIME-VARYING STORM

Time Interval	Number of Waves	Intensity	Interval Width	Period of Waves
t_0 to t_1	N_1	\underline{a}_1	Δt_1	T_1
t_1 to t_2	N_2	\underline{a}_2	Δt_2	T_2
t_2 to t_3	N_3	\underline{a}_3	Δt_3	T_3
t_{m-1} to t_m	N_m	\underline{a}_m	Δt_m	T_m

The probabilities for the maximum wave in the entire storm will be the product of the probabilities for each of the steps

$$\begin{aligned} P[\max H \leq h] &= \prod_{j=1}^m P[\max H \leq h \text{ in the } j^{\text{th}} \text{ step}] \\ &= \prod_{j=1}^m \{F_H(h, \underline{a}_j)\}^{N_j} \end{aligned}$$

It is being assumed that the waves within a step change intensity sufficiently slowly so that, to a fair approximation, they may be taken

as being identically distributed

It follows that the natural logarithm of $P[\max H \leq h]$ can be written

$$\log P[\max H \leq h] = \sum_{j=1}^m N_j \log F_H(h, \underline{a}_j) \tag{8}$$

If

$$N_j = \Delta t_j / T_j \tag{9}$$

is substituted into eq (8), one gets

$$\log P[\max H \leq h] = \sum_{j=1}^m (1/T_j) \log F_H(h, \underline{a}_j) \Delta t_j \tag{10}$$

Now let $m \rightarrow \infty$ and $\max \Delta t_j \rightarrow 0$ By the usual definition of an integral,

$$\log P[\max H \leq h] = \int_{t_0}^t [1/T(t)] \log F_H(h, \underline{a}(t)) dt \tag{11}$$

It is presumed that the integrand is continuous and uniformly bounded so that the stepwise expression in eq (10) becomes eq (11) in the limit

A SERIES APPROXIMATION

The distribution function $F_H(h, \underline{a}(t))$ will be expanded in a power series about some convenient value h_0 Several possibilities for h_0 are the breaking wave height, H_b , (if the maximum wave is probably going to be close to breaking), and the "expected" probable maximum, V , (which will be defined later) Thus, let

$$\log F_H(h, \underline{a}(t)) = b_0(t) + b_1(t)(h-h_0) + b_2(t)(h-h_0)^2 + \tag{12}$$

It is presumed that the distribution function is differentiable to the required order so that

$$b_0(t) = \log F_H(h_0, \underline{a}(t))$$

$$(1') b_1(t) = \frac{d}{dh} \log F_H(h, \underline{a}(t)), \quad h=h_0 \tag{13}$$

$$(2') b_2(t) = \frac{d^2}{dh^2} \log F_H(h, \underline{a}(t)), \quad h=h_0$$

etc

If eq (12) is substituted into eq (11), one gets

$$\log P[\max H \leq h] = B_0 + B_1(h-h_0) + B_2(h-h_0)^2 + \tag{14}$$

with

$$B_k = \int_{t_0}^t [b_k(t)/T(t)] dt, \quad k=0,1,2, \tag{15}$$

The evaluation of B_0, B_1, B_2 to whatever number of terms is desired gives a convenient representation of the probability of maximum height as

$$P[\max H \leq h] = \exp\{B_0 + B_1(H-h_0) + B_2(h-h_0)^2 + \dots\} \quad (16)$$

Presumably the first few terms would be sufficient for most situations since the higher order derivatives for most distribution functions become negligible as h grows large

THE COMBINATION OF SEVERAL STORMS

Another advantage of the representation in eq (14) is that it facilitates the determination of probabilities for the maximum for the combined wave heights in several storms. This is under the supposition that the same h_0 has been used for all the storms

Let $P_r[\max H \leq h]$ denote the probability that the maximum wave in the r^{th} storm is less than or equal to h . Suppose there are R storms to be considered. Then the probabilities for the maximum wave in the combined set of wave heights would be

$$\log P[\max H \leq h] = \sum_{r=1}^R \log P_r[\max H \leq h] \quad (17)$$

The function of h expressed by $P_r[\max H \leq h]$ can be evaluated from eq (11) for each storm. Alternatively, let B_{kr} be the B_k value from eq (15) for the r^{th} storm. Then if the same h_0 was used for each storm, one may write

$$\log P[\max H \leq h] = \sum_{r=1}^R B_{0r} + \sum_{r=1}^R B_{1r}(h-h_0) + \sum_{r=1}^R B_{2r}(h-h_0)^2 + \dots \quad (18)$$

That is, the B_{kr} can be added storm by storm. If B_k is redefined as $\sum_{r=1}^R B_{kr}$, then eq (16) gives the distribution function for the maximum height in the combined set of waves

The above development is appropriate for hindcasting the probabilities for maximum heights in storms whose fundamental time-varying intensities were measured or are known from other considerations. What about probabilities for future periods of time, say the next hundred years? One could take the historical record as given by Wilson (1957) and determine B_0, B_1, B_2 for each storm. Then the probability density jointly for (B_0, B_1, B_2) could be estimated from the data and used to make the extension to the future.

This procedure appears to have grave disadvantages in that $(B_0, B_1,$

B_2) are not "intuitive" quantities whose meanings are easy to interpret. One runs the risk of making mistakes because the unreasonableness of values arising apparently from the data are not recognized. A more trustworthy procedure would appear to be to shift over to intuitively interpretable values.

To fill this need, the concept of an "equivalent rectangular storm" will be introduced. A rectangular storm is defined to be one in which the intensity, wave period, and distribution function for the height of a single wave remain constant during the duration of the storm. The "equivalent rectangular storm" corresponding to a given historical storm will be that rectangular storm which leads to the same values of B_0 , B_1 , and B_2 as the historical storm. The constants for the "equivalent rectangular storm" will have intuitive meaning in characterizing the severity of the storm and in making predictions for the future.

PROBABILITIES FOR A RECTANGULAR STORM

A special development will be made for the maximum wave height in a rectangular storm as related to the intensity parameters \underline{a} and the number of waves, N . Let $w(h, \underline{a})$ be defined for N independent, identically distributed random wave heights, each with distribution function $F_H(h)$, as

$$w(h, \underline{a}) = N[1 - F_H(h, \underline{a})] \quad (19)$$

Then the distribution function for the maximum value may be written approximately (Cramer, 1946, p 286, eq 28.6.2, Borgman, 1961, pp 3296 - 3297, see eq (6)) for large values of N as

$$P[\max H \leq h] = \{F(h, \underline{a})\}^N = \left(1 - \frac{w(h, \underline{a})}{N}\right)^N \approx e^{-w(h, \underline{a})} \quad (20)$$

Hence

$$\log P[\max h \leq h] \approx N[1 - F_H(h, \underline{a})] \quad (21)$$

Gumbel (1954, p 13, eq 2.11) defines the "expected" largest value, V , of a variate to be the value V which satisfies the equation

$$w(V, \underline{a}) = N[1 - F_H(V, \underline{a})] = 1 \quad (22)$$

This has a physical interpretation in that $1 - F_H(V, \underline{a})$ is the probability, $P[H > V]$. Multiplying this probability by N gives the expected number of times wave heights will exceed V in the N occurrences. Hence V is that value such that on the average there will be exactly one exceedance in the N wave heights.

From eq (22)

$$N = [1 - F_H(V, \underline{a})]^{-1} \quad (23)$$

This can be inserted into eq (21) to give the approximation

$$\log P[\max H \leq h] \approx \frac{1 - F_H(h, \underline{a})}{1 - F_H(V, \underline{a})} \quad (24)$$

Now suppose that, paralleling eq (12), one expands $F_H(h)$ in a power series about h_0

$$F_H(h) = C_0 + C_1(h - h_0) + C_2(h - h_0)^2 + \quad (25)$$

Then keeping only the terms to second order

$$\begin{aligned} \log P[\max H \leq h] &\approx \frac{1 - C_0 - C_1(h - h_0) - C_2(h - h_0)^2}{1 - C_0 - C_1(V - h_0) - C_2(V - h_0)^2} \\ &= B_0' + B_1'(h - h_0) + B_2'(h - h_0)^2 \end{aligned} \quad (26)$$

with

$$\begin{aligned} B_0 &= (1 - C_0)/[1 - C_0 - C_1(V - h_0) - C_2(V - h_0)^2] \\ B_1' &= -C_1/[1 - C_0 - C_1(V - h_0) - C_2(V - h_0)^2] \\ B_2' &= -C_2/[1 - C_0 - C_1(V - h_0) - C_2(V - h_0)^2] \end{aligned} \quad (27)$$

The value of \underline{a} , N , and V for the equivalent rectangular storm will be determined by equating B_0' , B_1' , and B_2' to the B_0 , B_1 , and B_2 respectively given by eq (15) for the historical storm. Thus, to second order, the equivalent rectangular storm will be producing the same probabilities for maximum wave heights as did the historical storm

The equations to be solved are

$$\begin{aligned} D &= 1 - C_0 - C_1(V - h_0) - C_2(V - h_0)^2 \\ B_0 &= (1 - C_0)/D \\ B_1 &= -C_1/D \\ B_2 &= -C_2/D \end{aligned} \quad (28)$$

Here, h_0 is regarded as a previously selected (and thus known) value to expand about. Now the ratios

$$\begin{aligned} R_1 &= (B_1/B_0) = -C_1/(1 - C_0) \\ R_2 &= (B_2/B_0) = -C_2/(1 - C_0) \end{aligned} \quad (29)$$

can be computed from the values of B_0 , B_1 , and B_2 . If R_1 and R_2 are substituted into the expression for B_0 , one gets

$$B_0 R_2 (V - h_0)^2 + B_0 R_1 (V - h_0) + (B_0 - 1) = 0 \quad (30)$$

Hence V can be determined from eq (30) as a quadratic solution

Now $F_H(h, \underline{a})$ is typically a monotone decreasing function of storm intensity for fixed h . That is, a higher storm intensity normally means that there is a larger probability of exceeding the fixed h value or a smaller probability of being less than or equal to that h value. But eq (23) states that

$$F_H(V, \underline{a}) = 1 - \frac{1}{N} \quad (31)$$

Hence, the storm intensity can be determined from the value of N which is usually known, approximately at least, from other considerations. If the intensity of \underline{a} is a vector, reasonable interrelations between the components of \underline{a} must be imposed.

In summary the computational procedure for determining V and \underline{a} for the rectangular storm is as follows:

- (1) Calculate R_1 and R_2 from eq (29)
- (2) Determine V from eq (30)
- (3) Compute \underline{a} from eq (31) and the value of N

PROBABILITY GENERATING FUNCTIONS

In developing the probabilities for the maximum height in a random number of random length and random intensity storms, it will be natural to introduce various probability generating functions. A probability generating function for a random variable N is defined to be the infinite series

$$G_N(s) = \sum_{n=0}^{\infty} P[N=n] s^n \quad (32)$$

These functions have closed form for many probability laws (Borgman, 1961, p 3305, eq (21) - (27)). Two examples of particular usefulness are the probability generating functions for the Poisson and the negative binomial probability laws (Williamson and Bretherton, 1963, pp 9 - 10)

$$\text{Poisson} \quad P[N=n] = e^{-\lambda} \lambda^n / n! \quad (33)$$

$$G_N(s) = \exp[-\lambda(1-s)] \quad (34)$$

$$\text{Negative binomial} \quad P[N=n] = \binom{r+n-1}{n} p^r q^n \quad (35)$$

$$G_N(s) = p^r (1 - qs)^{-r}, \quad p + q = 1 \quad (36)$$

The mean and variance of the Poisson is λ . The corresponding mean and variance of the negative binomial are respectively

$$\text{mean} = rq/p \quad (37)$$

$$\text{variance} = rq/p^2 \quad (38)$$

$$\text{where } p + q = 1 \quad (39)$$

The negative binomial parameters, p , q , and r , can be estimated from the mean \bar{N} and variance $(N) = s^2$ by the method of moments as

$$\hat{p} = \bar{N}/s^2 \quad (40)$$

$$\hat{q} = 1 - \hat{p} \quad (41)$$

$$\hat{r} = \bar{N}\hat{p}/\hat{q} \quad (42)$$

PROBABILITIES FOR A RANDOM LENGTH STORM

Suppose a rectangular storm has a random length N and fixed intensity, \underline{a} . What is the probability law for the maximum wave height in the storm? Let $G_N(s)$ be the probability generating functions for N .

By eq (21), the approximate probability law for H given a particular value of $N = n$ is

$$P[\max H \leq h \mid N=n] \approx \{\exp[1 - F_H(h, \underline{a})]\}^n \quad (43)$$

Then for a random number of waves

$$\begin{aligned} P[\max H \leq h] &\approx \sum_{n=0}^{\infty} P[\max H \leq h \mid N=n] P[N=n] \\ &= \sum_{n=0}^{\infty} P[N=n] \{\exp[1 - F_H(h, \underline{a})]\}^n \end{aligned} \quad (44)$$

$$= G_N(\exp[1 - F_H(h, \underline{a})]) \quad (45)$$

A comparison of eq (44) with eq (32) will justify substituting the exponential for the argument s of the probability generating function

In practice one could use the guessed values of \bar{N} and s^2 together with the negative binomial probability law to determine the function $G_N(s)$. Alternatively another probability generating function could be used.

PROBABILITIES FOR RANDOM LENGTH AND RANDOM INTENSITY STORMS

If \underline{a} is also random, then eq (45) must be regarded as a probability given that intensity = \underline{a} . Let

$f_{\underline{1}}(\underline{a})$ = probability density for \underline{a}

Then

$$\begin{aligned} P[\max H \leq h] &= \int_{-\infty}^{\infty} P[\max H \leq h \mid \underline{1}=\underline{a}] f_{\underline{1}}(\underline{a}) d\underline{a} \\ &\approx \int_{-\infty}^{\infty} G_N(\exp[1-F_H(h,\underline{a})]) f_{\underline{1}}(\underline{a}) d\underline{a} \end{aligned} \quad (46)$$

PROBABILITIES FOR A RANDOM NUMBER OF RANDOM LENGTH
AND RANDOM INTENSITY STORMS

The final complication is to introduce a probability law for the number of storms, K , which may occur in the time interval for which predictions are made. Let $G_K(s)$ be the corresponding probability generating function. By the identical same argument leading to eq (45),

$$\begin{aligned} P[\max H \leq h] &= \sum_{k=0}^{\infty} P[\max H \leq h \mid K=k] P[K=k] \\ &= \sum_{k=0}^{\infty} \left\{ \int_{-\infty}^{\infty} G_N(\exp[1-F_H(h,\underline{a})]) f_{\underline{1}}(\underline{a}) d\underline{a} \right\}^k P[K=k] \end{aligned} \quad (47)$$

or

$$P[\max H \leq h] = G_K \left(\int_{-\infty}^{\infty} G_N(\exp[1-F_H(h,\underline{a})]) f_{\underline{1}}(\underline{a}) d\underline{a} \right) \quad (48)$$

The number of waves in a given storm may depend on \underline{a} . Hence the formula can be made a little more general by introducing the conditional probability generating function for N given \underline{a} . This final version of the formula would be

$$P[\max H \leq h] = G_K \left(\int_{-\infty}^{\infty} G_{N|\underline{a}}(\exp[1-F_H(h,\underline{a})]) f_{\underline{1}}(\underline{a}) d\underline{a} \right) \quad (49)$$

SOME FINAL COMMENTS

(1) The application of the above formula will obviously require a digital computer and detailed analysis of the historical data for the particular location of interest.

(2) The negative binomial appears to be the best choice for the two probability generating functions although, at least for Gulf of Mexico hurricanes, there is some basis for using the simpler Poisson probability generating function for $G_K(s)$.

(3) The possible choices for $F_H(h, a)$ were discussed at the beginning of the paper. Without more detailed information, the Rayleigh distribution appears to be as good a choice as any (Goodnight and Russell, 1963)

(4) The choice of $f_1(a)$ would have to depend strongly on the analysis of historical data or on meteorological considerations. Hence it is hard to make a guess as to a reasonable choice. However, a form of the gamma density would seem to be a good first guess.

(5) In this whole discussion, the randomness of wave period has been ignored. A more adequate model would certainly include this source of variation.

(6) An alternative approach to the maximum wave height might be made through the statistical theory of maxima and minima of a random function. Unfortunately, when such an approach is attempted, theoretical difficulties arise very quickly. Information on wave crest elevation probabilities can be obtained, however, by the random function type of analysis.

ACKNOWLEDGMENT

The research reported was supported in part by the Chevron Oil Field Research Company under a research gift to the University of California, Berkeley, and in part, by the Coastal Engineering Research Center, U S Army Corps of Engineers under Contract DACW-72-69-C-0001. The author gratefully acknowledges their financial assistance in the study.

REFERENCES

- Borgman, L. E. (1961) The frequency distribution of near extremes, Journal of Geophysical Research, 66, pp 3295-3307
- Cramer, Herald (1946) Mathematical Methods of Statistics, Princeton University Press, Princeton, New Jersey
- Goodnight, R. C. and Russell, T. L. (1963) Investigation of the statistics of wave heights, Jour Waterways and Harbors Div, ASCE, WW2, paper 3254, pp 29-54
- Gumbel, E. J. (1954) Statistical theory of extreme values and some practical applications, Applied Math Series 33, National Bureau of Standards, U S Govt Printing Office, Washington, D C
- Gumbel, E. J. (1958) Statistics of Extremes, Columbia Univ Press, N Y

Longuet-Higgins, M S (1952) On the statistical distribution of the heights of sea waves, Jour Marine Res , 11, pp 245-266

Longuet-Higgins, M S , and Cartwright, D E (1956) The statistical distribution of the maxima of a random function, Proc Royal Soc , A, 237, pp 212-232

Watson, G S (1954) Extreme values in samples from m-dependent stationary stochastic processes, Ann Math Statistics, 25, pp 798-800

CHAPTER 5

SPECTRAL COMPUTATIONS ON PRESSURE WAVE GAUGE RECORDS

by Manuel Mendes de CARVALHO*
Fernando Silveira RAMOS*
Carlos de Campos MORAES*

ABSTRACT

With a view to establish sea wave data processing procedures to be applied to records obtained at the Portuguese coast, a detailed study is made of different choices of certain parameters used in one-dimensional spectral analysis of a pressure wave gauge record. Statistics computed by the selected spectral procedure are then compared with results of a Tucker-Draper analysis of the same record. Finally a hindcast of sea conditions for the date and place of the record is made by different methods and comparisons with previous results are presented.

1 - INTRODUCTION

The study of the coastal sea wave regime in Portugal needs development both in programming an adequate deployment of sea wave gauges and in what concerns establishing the best data processing procedures. The authors form a research team charged at present with the study of the instrumentation and use of an irregular wave flume at LNEC. It is known that for a perfect simulation of irregular sea waves a detailed knowledge is necessary of the wave regimes to be reproduced. There are two phases to consider: the first is a qualitative one in which methods for sea wave data analysis and computation procedures are discussed and developed, the second is quantitative, results from the first being extensively applied, to try and acquire a more exact knowledge of the configuration of sea waves in the zone of interest.

The present paper relates to the above mentioned first phase. It represents the study path followed by the authors. Although most of the techniques presented are already known, it is thought that eventually some usefulness may be derived from reading it, particularly in pointing out some doubts and difficulties inherent in the methods used. The work being still restricted to the first phase, only one record was used. This record was made by a pressure wave gauge.

2 - CONDITIONS OF WAVE MEASURING, RECORDING AND ANALYSIS

In the approaches to Leixões Harbour (in the northwestern coast of Portugal) a pressure wave gauge is installed on the bottom at a mean depth of 22 m (Fig. 1). It is an autonomous St Chamond Granat pressure wave gauge, type LNH. Its working schedule is as follows: at both 0900 hrs and 2100 hrs a twenty-minute recording period starts, when the surface waves exceed 4 m it automatically produces a twenty-minute record every two hours. Normally a 250 milibar manometer is in use. The present study is based on a twenty-minute record made at 3 47 GMT on December 18th, 1968. For the record digitalization a Boscar LNF 630 projector by Benson, France, was used. This projector provides a twelvefold magnification of the 35 mm film from the wave gauge and can also handle 16 and 70 mm films. The computations were made in the LNEC's computing centre in a NCR-Elliott 4130 computer with 24 k 24-bit words and 3 magnetic tape handlers.

3 - SPECTRAL ANALYSIS

Estimates of the energy spectrum, $P(f)$, were obtained by the indirect method through the autocovariance function $c(\tau)$

$$P(f) = \int_{-\infty}^{+\infty} c(\tau) e^{-i2\pi f\tau} d\tau = TF [c(\tau)] \quad (1)$$

where TF means Fourier transform. A measure of the mean energy of the waves

* - Trainee Research Officers, Laboratorio Nacional de Engenharia Civil (LNEC), Lisbon, Portugal

during the record duration T_R is given by

$$c(0) = 2 \int_0^{+\infty} P(f) df \tag{2}$$

3.1 - Lag and spectral windows

If $Z(t)$ is the water surface elevation above an arbitrary level as a function of time, t , and at a certain place, then the autocovariance function is the mean value of $Z(t)Z(t+\tau)$ along time

$$c(\tau) = \lim_{T \rightarrow \infty} \frac{1}{T} \int_{-T/2}^{T/2} Z(t)Z(t+\tau) dt \tag{3}$$

$c(\tau)$ expresses covariance between $Z(t)$ and $Z(t+\tau)$, that is, between water surface elevations at any two instants separated by a time lag of τ secs. In case there are no periodicities in $Z(t)$, then $c(\tau)$ tends to zero as τ tends to infinity. If there is a periodicity in $Z(t)$, then an oscillation about zero, with the same period, appears in $c(\tau)$. In practice, the autocovariance function, $c(\tau)$, is computed as the mean value of $Z(t)Z(t+\tau)$ in the available recording interval, whose length or, rather, duration, is T_R . $c(\tau)$ never really damps out to zero, not only because T_R is finite but also owing to periodicities which always occur in records*. This leads to the necessity of truncating** the autocovariance function, that is, to consider instead of $c(\tau)$ the new function $c(\tau) D(\tau)$ where

$$D(\tau) = \begin{cases} 1 & , |\tau| \leq T_M \\ 0 & , |\tau| > T_M \end{cases}$$

$D(\tau)$ is the rectangular lag window and T_M is the maximum lag of the autocovariance function. Instead of $D(\tau)$ and to get more stability in the spectrum estimates, other functions or lag windows, $D_i(\tau)$ are used, which are also identically zero outside the interval $(-T_M, T_M)$ and take the value 1 for $\tau=0$. Using these lag windows, which is unavoidable in practice, leads to the fact that, for every frequency, one gets a weighted average of neighbouring values of the record spectrum. The weighting function is $Q_i(f) = TF [D_i(\tau)]$, the so-called spectral window corresponding to the lag window $D_i(\tau)$. In this study the Parzen, Tukey, Hamming, Bartlett and rectangular lag windows were considered. Their lag and spectral versions are presented in Fig. 3.

It is known that to each window there corresponds a statistical estimator for the spectrum. To choose one among these, various criteria have been proposed, most of them based in the minimization of the mean square error of the estimator or some function or functional of it. (See, for instance, Jenkins and Watts [4]). According to this kind of criteria the rectangular window distinguishes itself by being considerably worse than the others mentioned, which in turn are similar to one another in performance. In consequence the rectangular window should be avoided and the choice among the Parzen, Tukey, Hamming and Bartlett windows becomes of secondary importance, as compared, for example, with the choice of the maximum lag for $c(\tau)$, to be considered in 3.6. However, differences do exist and a choice had to be made.

The fact that the side lobes of the Parzen spectral window are much smaller and that its small variance originates narrower confidence intervals for the spectrum estimates led to its selection. For this window, the number of degrees of freedom of the spectrum estimates is $3.71 T_R/T_M$. The spectral window bandwidth is

* - As shown later, (see Fig. 2) the autocovariance function relative to the record considered is far from showing any tendency to become zero.

** - Of course, if $c(\tau)$ equalled zero only outside a very large interval a truncation would be in order.

$$b = \frac{1}{\int_{-\infty}^{+\infty} D^2(\tau) d\tau} = \frac{1}{\int_{-\infty}^{+\infty} Q^2(f) df} = \frac{1}{T_M} \quad (5)$$

and it is approximately the frequency interval between two practically independent spectrum estimates. It is seen that the smaller is b , the greater is the resolution of the estimates, i.e., the smaller is the influence exerted on an estimate by estimates in neighbouring frequencies. Applying the rectangular lag window is the same as simply truncating the autocovariance function. The spectrum obtained is termed the raw spectrum. The raw spectrum would be exactly equal to the true record spectrum if the autocovariance function were zero for $|\tau| > T_M$, which never happens in sea wave analysis. Using any other of the mentioned windows produces smoothed estimates, that is, more stable estimates. For a given window, if T_M is varied then stability and resolution increase or decrease in opposite senses. Fig. 4 shows the raw spectrum computed for $T_M = 80$ s and its Parzen smoothed version.

3.2 - Prewhitening and prefiltering

It is known that spectral windows delete accidental details of the spectrum, that is, they smooth it. In the process of smoothing, the spectrum estimate in a given frequency is influenced by the estimates in neighbouring frequencies. A sharp peak is "spread" over its neighbourhood in a way similar to the spectral window configuration.

5 This leads to the alteration of the true form of the spectrum. To avoid this difficulty as much as possible, Blackman and Tukey [7] suggested a prewhitening, that is a preliminary digital filtering of the record aiming to reduce the importance of its spectrum peaks. This is bringing the spectrum closer to that of a white noise.

The suggested digital filtering is in general

$$y_t = a x_t + b x_{t-1} \quad (6)$$

$\{x_t\}$ being the input time series and $\{y_t\}$ the output time series. The input and output spectra, $P_x(f)$ and $P_y(f)$ respectively, are then related by

$$P_y(f) = (a^2 + b^2 + 2ab \cos 2\pi f \Delta t) P_x(f) \quad (7)$$

In this way the spectral window will be applied to a spectrum without sharp peaks and the obtained spectrum $P_y(f)$ may then be corrected for prewhitening by (7).

Computations showed that, in the present case, estimates were practically the same with and without prewhitening. This led to giving up the use of prewhitening. As for other kinds of prefiltering, it was not deemed necessary to eliminate the spurious energy of very low frequencies. A first difference filter was nevertheless considered, as is suggested by Jenkins [4], results showing that it was not adequate, as its influence reaches regions of too high frequencies.

3.3 - Confidence intervals

Let $\bar{P}(f)$ be the smoothed spectrum estimate at frequency f , $P(f)$ the true value of the spectrum, χ^2_ν a random variable following the chi-square distribution with ν degrees of freedom and b the spectral window bandwidth. It can be proved that $2 T_R b \bar{P}(f)/P(f)$ is a random variable following the chi-square distribution with $2 T_R b$ degrees of freedom.

$$2 T_R b \frac{\bar{P}(f)}{P(f)} = \chi^2_{2 T_R b}$$

This permits confidence intervals to be constructed for the estimates. Those intervals will be

$$\left(\frac{\nu}{\chi^2_{\nu}(1-\alpha/2)} \bar{P}(f), \frac{\nu}{\chi^2_{\nu}(\alpha/2)} \bar{P}(f) \right) \quad (9)$$

where $1 - \alpha$ is the confidence level and $x_v(k)$ is a number such that

$$P(X_v^2 \leq x_v(k)) = k \tag{10}$$

In Fig 5, curves of variation with ν of $A(\nu) = \frac{\nu}{x_v(1-\alpha/2)}$ and $B(\nu) = \frac{\nu}{x_v(\alpha/2)}$ for $1 - \alpha = 80\%$ are presented

This was the confidence level used in the computations made. Most spectrum figures in this paper show a 80% confidence zone obtained in the manner described

3.4 - Sampling interval

From a continuous record a time series can be extracted using a certain sampling interval Δt (digitalization). If F_D is the frequency above which spectrum values are negligible one must have

$$F_D \leq \frac{1}{2\Delta t} \tag{11}$$

to avoid the so called aliasing. $F_N = \frac{1}{2\Delta t}$ is the Nyquist frequency. Aliasing is a consequence of the digitalization of the record. In fact, the result of digital computations is not the true spectrum $P(f)$ but the aliased spectrum

$$P_a(f) = \sum_{q=-\infty}^{+\infty} P(f - \frac{q}{\Delta t}) \tag{12}$$

If condition (11) is met, however, then (12) gives $P(f)$ values between 0 and F_D . Having fixed $T_M = 80$ s (and so, $b = 0.023$ cps), which is equivalent to having fixed resolution and stability of the estimates, computations were carried out with $\Delta t = 0.5, 1.0, 1.5, 2.0, 2.5$ and 3.0 s, corresponding to Nyquist frequencies of $1.0, 0.5, 0.33, 0.25, 0.20$ and 0.16 cps. As $F_D \approx 0.25$ cps in the present case, aliasing should be negligible for $\Delta t = 0.5, 1.0, 1.5$ and 2.0 s. In fact, it was seen that estimates were practically the same. For $\Delta t = 2.5$ and 3.0 s, that is, $F_D > F_N$, aliasing is already strongly apparent (Fig 6)

The conclusion is that inasmuch as there is no aliasing, the sampling interval may be as high as wished. In these computations $\Delta t = 2$ s could have been used

3.5 - Cutoff frequency

For reasons of economy, computation of spectrum values should not be carried much beyond F_D . Frequency F_C up to which calculations are made will be called cutoff frequency. One should then have $F_D < F_C < F_N$. The choice of F_C can have great influence in practical computation of the spectral moments

The spectral moment of order n is defined as

$$m_n = \int_{-\infty}^{+\infty} f^n P(f) df \tag{13}$$

For even values of n and since $P(f)$ is an even function, we may write

$$m_n = 2 \int_0^{+\infty} f^n P(f) df \tag{14}$$

In practice, estimates of m_n (even n) may be obtained from

$$m_n = 2\Delta f \sum_{r=1}^k (r\Delta f)^n P(r\Delta f) \tag{15}$$

with $k\Delta f = F_C$ and f being the frequency interval between two adjacent estimates of $P(f)$

Theoretically we have $m_0 = c(0)$ and so it is suggested that, in practice and with a view to calculating spectral moments, F_C be chosen such that

$$c(0) = 2 \Delta f \sum_{r=1}^k P(r\Delta f) \quad (16)$$

with $F_C = k\Delta f$

Fig 7 shows the variation with F_C of m_n values obtained from (15). It is seen that F_C should be chosen between 0.25 and 0.3 cps approximately

3.6 - Maximum lag for the autocovariance

The choice of T_M is very important, as on it are closely dependent the resolution and stability of estimates. A great T_M produces high resolution estimates owing to the narrow bandwidth of the spectral window, smoothing is however small and in consequence estimates present greater instability. If T_M is small then the inverse is true we get small resolution and great stability. A compromise is therefore necessarily between stability and resolution.

Three criteria for the choice of T_M were considered

a) The window closing technique

This technique is suggested by Jenkins [4] and consists in considering successively increasing T_M values, or, equivalently, decreasing b values (window closing), which will have the effect that initially obscured spectrum details will become more defined. There are no rules to decide when certain details, as, for instance, a peak which is beginning to show, are real or due to instability. Jenkins suggests that three spectra should be presented, computed for T_M values from the range where the initial form of the spectrum starts to change, that is, where after the initial convergence of shape a divergence begins to appear. Fig 8 shows that the general spectrum configuration is kept until T_M reaches about 70 s. Afterwards, a swelling begins to appear around frequency 0.12 cps and it becomes quite distinct when $T_M \approx 90$ s. A T_M value of about 80 s seems therefore indicated.

b) Using the rectangular lag window

If the autocovariance function $c(\tau)$ is zero for $|\tau| > \tau_0$, using the rectangular lag window with $T_M > \tau_0$ produces the true record spectrum. If one uses $T_M < \tau_0$, negative values may appear for the spectrum, which is an indication that T_M is not sufficiently high (Barber [6]). This could eventually serve as a criterion for the choice of T_M . Yet, in practice, with sea wave records, the autocovariance function never really comes to zero however great we may make T_M . This is due to periodicities which always turn up in natural records and the result is that negative values may always arise whatever the T_M . Fig 9 shows that, though T_M was increased tenfold, negative estimates show no tendency to disappear. On the other hand, when the autocovariance function looks like the one pictured in Fig 2, where there are regions of almost total damping, as in the neighbourhood of $\tau = 44$ s, a rectangular lag window truncation in that region should produce a spectrum equal to one from a record for which $c(\tau) = 0$ from that region on. This spectrum should not exhibit negative values, that is really the case when, in the present computations, $T_M = 44.5$ s was used, as is seen in Fig 9. The conclusion to draw is that using the rectangular lag window is not a satisfactory way to decide on T_M .

c) Variation of ϵ with T_M

One parameter to which the name spectrum width is generally given is

$$\epsilon = \sqrt{\frac{m_0 m_4 - m_2^2}{m_0 m_4}} \quad (17)$$

where m_n is defined by (13) ϵ values computed by (15) from spectra in which T_M

varied from 27 s to 222 s and where F_C was constantly equal to 0.3 cps are presented in table 1 and graphically in Fig 11. It is seen that for $T_M > 70$ s the ϵ value varies only very slightly. This may mean that a sufficiently high value for T_M has been reached.

Table 1

VARIATION OF T_M									
$\Delta t = 0.5$ s									
$F_C = 0.3$ cps									
T_M	22	44.5	50	60	70	80	89	100	222.5
ϵ	0.61	0.56	0.55	0.55	0.54	0.54	0.54	0.54	0.53
m_0	0.50	0.51	0.51	0.51	0.51	0.51	0.51	0.51	0.51
f_{peak}	0.085	0.080	0.080	0.080	0.080	0.080	0.080	0.08	2 peaks
$P(f_{peak})$	3.17	4.55	4.79	5.15	5.41	5.59	5.69	5.77	Low smoothing

These 3 criteria considered, it was decided to use 80 s as an adequate value for T_M , which is about 6 to 7 times the period corresponding to the peak frequency of the spectrum.

3.7 - Record partition

The record was partitioned in four 5-minute parts. Table 2 and Fig 10 show results of computations made. m_0 values increase clearly from the 1st to the 2nd part and from the 2nd to the 3rd part. The 3rd and 4th part values are about the same. Spectrum variations may have different reasons. They may result from the fact that we are now dealing with four different samples and variation may be merely statistical in nature. These variations should, perhaps, be considered large, which might mean that a five-minute period is too short for getting a representative record. Since m_0 is a measure of the mean energy of sea waves, another reason for the variations may be that the record should not be considered completely stationary. In future, when an extensive study is undertaken of records made at the same date as this one, the matter may be clarified further.

Table 2

	FIVE MIN	FIVE MIN	FIVE MIN	FIVE MIN
ϵ		0.54		
m_0		0.51		
f_{peak}		0.08		
$P(f_{peak})$		5.59		

ϵ	0.51	0.53	0.54	0.54
m_0	0.39	0.45	0.57	0.60
f_{peak}	0.09	0.08	0.08	0.08
$P(f_{peak})$	3.18	4.88	5.75	5.74

ϵ	0.53
m_0	0.42
f_{peak}	0.085
$P(f_{peak})$	3.96

ϵ	0.55
m_0	0.51
f_{peak}	0.08
$P(f_{peak})$	5.28

ϵ	0.54
m_0	0.59
f_{peak}	0.08
$P(f_{peak})$	5.72

ϵ	0.53
m_0	0.47
f_{peak}	0.08
$P(f_{peak})$	4.50

ϵ	0.55
m_0	0.54
f_{peak}	0.08
$P(f_{peak})$	5.44

3.8 - Variation of some statistics with T_M , Δt and F_C

Tables 1, 3 and 4 show the variation of ϵ , m_0 , f_{peak} and $P(f_{peak})$ with T_M , Δt and F_C respectively. Variation of ϵ with the same parameters is also shown in Fig 11.

As said in 3.5 variation of Δt will not influence spectrum estimates, as long as $F_D \leq F_N$. This is illustrated in table 3.

Convergence of ϵ values when T_M increases is apparent from table 1 and Fig 11, from $T_M = 70$ s onwards. f_{peak} is practically the same for all T_M but $P(f_{peak})$ increases with the closing of the spectral window since the influence of neighbouring low values steadily decreases. This increase, however, is small for $T_M > 80$ s. m_0 values vary only slightly with T_M and F_C as seen in tables 1 and 4. It is clear that F_C should

exert no influence on f_{peak} and $P(f_{peak})$. Choice of F_C is nevertheless very important for the calculation of ϵ as is seen in Table 4 and Fig 11, and should be made according to 3 5

Table 3

$c(0)=0.506$	Variation of Δt			
	0.5	1.0	1.5	2.0
ϵ	0.52	0.53	0.53	0.53
m_0	0.506	0.506	0.506	0.506
f_{peak}	0.080	0.080	0.080	0.080
$P(f_{peak})$	5.59	5.58	5.65	5.56

Table 4

$c(0)=0.506$	Variation of F_C				
	0.150	0.200	0.250	0.300	0.650
ϵ	0.45	0.50	0.52	0.52	0.79
m_0	0.495	0.505	0.506	0.506	0.507
f_{peak}	0.08				
$P(f_{peak})$	5.59				

3 9 - Conclusions

The considerations made from 3 1 to 3 8 led to the adoption of the following characteristics for the final computation of the bottom spectrum

- No prefiltering
- Window Parzen
- Maximum lag 80 s
- Cutoff frequency 0 3 cps
- Sampling interval 0 5 s (although this could have been wider the corresponding computations were already available)
- 80% confidence intervals

The number of degrees of freedom was 55 and the bandwidth 0 023 cps. The resulting values for ϵ , m_0 , f_{peak} and $P(f_{peak})$ are presented on table 1. Value computed for $c(0)$ was 0 5056

This final bottom spectrum is shown in Fig 12

Table 5

4 - WAVE STATISTICS AND WAVE HEIGHT DISTRIBUTION

4 1 - Computations of wave statistics by the Tucker-Draper method

The Tucker-Draper method [8], [9], was used to compute the statistics of Table 5. By this method, the fundamental values read from the record are T_Z (mean zero up crossing period), H_1 (sum of the highest crest with the lowest trough), H_2 (sum of the second highest crest with the second lowest trough). To obtain surface values H_1' from bottom values H the classical Hydrodynamics Formula was used

$$H_1' = H \operatorname{ch} \frac{2 \pi d}{L} \tag{18}$$

where d (depth) = 23 3 m

$$L \text{ (wave length)} = \sqrt{gd \left(1 - \frac{\pi d}{4 \cdot 68 T_Z^2}\right)} T_Z^* \tag{19}$$

g being the acceleration of gravity

Computations were based on the digitalized record using a sampling interval $\Delta t = 0.5$ s

4 2 - Wave height distribution compared with the Rayleigh distribution

Wave height in the present paper is the distance between the le

* - This formula is derived from $c = \sqrt{\frac{gL}{2\pi}} \operatorname{th} \frac{2\pi d}{L}$ by a series expansion of the th and substituting L by its approximate value $L = \sqrt{gd} T_Z$

T_Z	10 8
ϵ	0 58
H_1	4 5
H_2	3 5
H_1'	7 1
H_2'	5 5
$(H_s)_1$	2 8
$(H_s)_2$	2 4
$(H_s)_1'$	4 4
$(H_s)_2'$	3 8
$(m_0)_1$	0 48
$(m_0)_2$	0 35

vels of a crest and the preceding trough. For the record considered, Fig. 13 shows that the wave distribution is different from the Rayleigh distribution, which was to be expected since $\epsilon \approx 0.51$, a value greater than the limit (0.4) below which, according to Cartwright and Longuet-Higgins [10], wave heights follow reasonably well that distribution.

5 - COMPARISON BETWEEN WAVE STATISTICS OBTAINED FROM THE PRESSURE RECORD BY SPECTRAL ANALYSIS AND THE TUCKER-DRAPER METHOD

In Table 6 wave statistics obtained from the pressure record by spectral analysis and the Tucker-Draper method are compared.

Both for m_0 and H_s a pair of values is presented corresponding to calculations made from H_1 e H_2 .

6 - CORRECTION TO SURFACE OF PRESSURE RECORD STATISTICS

Though the aim of the work undertaken is mainly the processing of digital data extracted from wave records, which makes unimportant the nature (surface or bottom) of the record used, a comparison of results arising from a weather hindcast with those from spectral analysis and the Tucker-Draper method is possible only if a correction to surface is applied to the latter. Formula (18) was used with and without the instrument factor 1.25 which is recommended by the makers of the LNH type pressure wave gauge as adequate for the correction to surface of the significant wave height. The same formula, without the instrument factor, and the linearity hypothesis for spectrum decomposition as a sum of infinitesimal sinusoids leads to the following relation between surface and bottom spectra, $P_s(f)$ and $P_d(f)$ respectively

$$P_s(f) = P_d(f) \cdot ch^2 \frac{2\pi d}{L(f)} \quad (20)$$

where $L(f)$ is the wave length corresponding to frequency f .

It should be noted that (1) the instrument factor is very important and an investigation should be made to determine if the recommended value of 1.25 is adequate for sea wave regime at the Portuguese Coast, (2) formula (20) is based on an unverified hypothesis, namely, on linearity of the spectrum decomposition as a sum of infinitesimal sinusoids. In Fig. 14 results of the surface correction for the spectrum are shown. Some pertinent remarks are the following:

- The peak of the surface spectrum occurs at frequency 0.085 cps, which is very close to the one of the bottom spectrum.
- The existence of a second peak at 0.11 cps may or not have a physical significance (as, for instance, a local storm superimposed on the pre-existent one) as pointed out in 3.6 a).
- Up from $f = 0.13$ cps, $P(f)$ values increase without any physical significance. Owing to the great depth (23.3 m) of the recording wave gauge, $ch \frac{2\pi d}{L}$ values increase rapidly to absurd results from that frequency on.

7 - WAVE HINDCAST FOR DECEMBER 18th, 1968

7.1 - Analysis of the synoptic charts

Examining the synoptic charts for some days prior to December 18th, 1968, it is apparent that the pressure field has taken a little varying shape in the last three days (Fig. 15), the isobars following approximately a northwesterly direction, and that Leixões is included in the generating area over which this three-day storm actuated. As will be seen later the sea should be considered as fully arisen.

Table 6

	S P	T-D
ϵ	0.54	0.58
m_0	0.51	0.48 0.35
H_s	2.84	2.8 2.4

7 2 - Approximate determination of the fetch to be considered

In Fig 16, the maximum fetch relating to the meteorological situations of the storm days (16th, 17th and 18th) is delimited by a dashed line. After a mean wind speed during the storm is fixed, it can be seen that any of the indicated fetches is greater than the minimum fetch corresponding to a fully arisen sea.

7 3 - Wave refraction up to the wave gauge site

Recorded values at Leixões at a depth of 23.3 m cannot be transformed in off-shore values without some criticism.

An examination of Fig 17* reveals, waves following a course close to NW have a refraction coefficient given by H_e/H_o (where H_e is wave height at the harbour entrance and H_o the corresponding off-shore value) which is independent of period (the latter varying between 10 and 17 s) and has a nearly constant value of 0.7 approximately. This is the adopted value for a correction of statistics for off-shore conditions, according to a rough, yet seemingly adequate, procedure for the present case. Concerning the course followed by waves the following remarks should be noted. It was not possible to secure radar photographs made at Leixões and so there is no direct information on which course to consider. However, the shape of the isobars shows that that course should be close to NW. On the other hand, for a better accuracy of the H_e/H_o coefficient, a refraction plan including the wave gauge site should be available, indeed, elements provided in [2] concern only the harbour entrance. Therefore the adopted 0.7 value should not be accepted unreservedly.

7 4 - Hindcast

7 4 1 - Observations from North Atlantic Weather Ships

For a wave hindcast for the day the pressure record was made, knowledge of wind, sea and swell data provided by the North Atlantic Weather Ships is necessary. According to their position and keeping in view the NW direction of the storm, the most important ships are, by increasing order of distance to Leixões: K ship (730 km), J ship (1500 km) and C ship (2400 km).

K ship is the only one included in the zone common to the three fetches indicated in Fig 16 and, even so, she is outside the minimum fetch corresponding to a fully arisen 30-knot wind sea, as will be seen later. This is then the ship from which the most important information stems, as regards waves at Leixões (Fig 18).

We may roughly guess at the day and the period of time in which waves recorded at Leixões were passing by each one of the three ships (Table 7). Once more we are simplifying things by assuming that the propagation speed is $V_T = g T/4\pi$ and considering the period range to be 8 to 16 s.

Table 7

Ship	Distance to Leixões (km)	T (s)		Time to reach Leixões (hr)	Ship passed on	
		8	16		day	hr
K	730	8	6.2	33	16	19
		16	12.5	16	17	12
J	1500	8	6.2	67	15	9
		16	12.5	33	16	19
C	2400	8	6.2	108	13	16
		16	12.5	54	15	22

Table 8

Ship	Swell			Sea	
	Dir	H (m)	T (s)	H (m)	T (s)
K	W	6	12	9.5	10
	(const)	(const)	(const)	(8-10)	(const)
J	276	7.5	12	6.5	8.5
	(270-282)	(7-8)	(const)	(6-7)	(8-9)
C	-	-	-	5	8
	-	-	-	(4-6)	(7-9)

Table 8 is a résumé of sea and swell conditions recorded by each one of the three ships in such a way that waves could have arrived at Leixões during the twenty-minute recording period at 3 a.m. on December 18th, 1970.

* - Reproduced from Fig 5 in [2].

Another important problem in the application of the two most common forecasting methods (SMB and PNJ) concerns the choice of a mean wind speed likely to have occurred during the storm. Fig 16 shows that the mean values of wind speed recorded at K ship on the two days before Dec 18th are

Dec 16th U = 42 knots (a)
Dec 17th U = 32 knots (b)

Assuming that the sea is fully arisen (Leixões being included in the generating area) it will be interesting to know land-recorded values at the closest weather station to Leixões (Pedras Rubras)

Table 9

Day		17		18
Hour		6	18	6
Dir		W	NW	W
Speed (knots)	Pedras Rubras	22	14	18
	Leixões	29	20	26

Mean value at Leixões (sea) U=25 knots (c)

With U values indicated in (a), (b) and (c) a mean value should now be adopted. If a Neumann spectrum is chosen corresponding to U=30 knots according approximately with the pressure spectrum (Fig 14) and assuming a fully arisen sea, the following minimum values are obtained for duration and fetch $t_m^m = 23$ h, $F_m = 518$ km. Hence, in fixing U, only Leixões and K ship should be considered (K ship is even beyond F_m in case U=30 knots)

In short with mean U values of 25 knots (at Leixões) and 32 knots (during the previous 24 hours) and now reasoning backwards, the choice of U=30

knots seems to be adequate as the mean prevailing wind speed which brought about the fully arisen sea relative to the Dec 18th storm

7.4.2 - Forecasts of the S M N *

Based in lighthouse observations the S M N wave forecast for Dec 16th, 17th and 18th was "strong northwesterly waves" which corresponds to wave heights between 2.5 and 5.5 m

7.4.3 - The Sverdrup-Munk-Bretschneider Method (S M B)

For U=30 knots and assuming a 800 nautical mile fetch corresponding approximately to Dec 18th, we get $t=50$ h, $H_s=6.09$ m, $T_s=14$ s

There is small accuracy in the choice of fetch, but observing Fig 1-7 on page 19 in [3] one can see that wave characteristics vary only slightly between 800 and 1000 miles. The mean wind speed of 30 knots can be assumed constant during two days which corresponds approximately to $t=50$ h

Wave forecast for the wave gauge zone, taking into account a H_e/H_o value of 0.7 is then $H_s=4.3$ m

7.4.4 - Pierson-Neumann-James method (P N J)

As mentioned above a 30-knot Neumann spectrum was chosen according approximately with the pressure spectrum (Fig 14)

The corresponding hindcast statistics have the following off-shore values

$$\begin{aligned} H_s &= 6.6 \text{ m} & H_{av} &= 3 \text{ m} \\ H_{1/10} &= 8.3 & T_{av} &= 8.5 \text{ s} \\ & & f_{peak} &= 0.08 \text{ cps} \end{aligned}$$

Taking into account the correction for the wave gauge zone we get

$$\begin{aligned} H_{av} &= 2.1 \text{ m} & H_s &= 4.4 \text{ m} & H_{1/10} &= 5.7 \text{ m} \end{aligned}$$

* - Serviço Meteorológico Nacional (Portuguese Weather Service)

8 - COMPARISON OF COMPUTED AND HINDCAST SURFACE SIGNIFICANT WAVE HEIGHT VALUES

Tucker-Draper method

$$H_s \text{ (from } H_1) = 4.42 \text{ m}$$

$$H_s \text{ (from } H_2) = 3.78 \text{ m}$$

Taking the arithmetic mean and correcting to surface with $\frac{2\pi d}{L}$ only, we get $H_s = 4.1$ m. If the instrument factor 1.25 recommended by Chatouls is used, then $H_s = 5.1$ m.

P N J method $H_s = 4.4$ m

S M B method $H_s = 4.3$ m

S M N forecast for Dec. 18th Wave heights between 2.5 and 5.5 m

These values are close to one another and so it seems reasonable to conclude that at Leixões, on December 18th, 1968, the surface significant wave height was 4 to 5 m.

9 FINAL SUMMARY OF THE MORE NOTEWORTHY ASPECTS OF THIS PAPER

Partial detailed conclusions were drawn in preceding chapters of seemingly more salient aspects. A summary of important points is

- The sampling interval may be as high as 2 s if spectral analysis only is intended
 - If a smaller interval is used, which means a higher Nyquist frequency (F_N), then a convenient cutoff frequency (F_c) should be chosen, possibly according to coincidence of m_0 and $c(0)$
 - A good estimate of the spectrum width depends on a well balanced choice of some parameters, especially on the cutoff frequency
 - A good choice of maximum lag for the autocovariance function is of great importance to spectral analysis
 - Results from record partition seem to indicate that a more careful study must be made of the necessary record duration
 - Some aspects of wave data acquisition which are well-known yet should be kept in mind concern
 - correction to surface of bottom spectra (lack of linearity) and of bottom statistics (adequate instrument factor)
 - great influence of depth on wave attenuation
 - faulty characteristics of pressure records for spectral analysis of sea waves
 - For hindcast and related meteorological problems, the usual difficulties arise in fetch determination (to the resolution of this problem, directional spectra may provide a useful contribution). It is also important to make a realistic criticism to sea wave data secured from meteorological services, indeed, it is frequent to detect absurd correlations between wave heights and periods and sometimes fallacious distinctions are made between sea and swell.

As final conclusion we would like to stress the importance of a close collaboration between different techniques used in Maritime Hydraulics. This collaboration is essential for an intimate connexion in the development of both the physical (meteorology, oceanography, fluid mechanics) and the mathematical approaches.

ACKNOWLEDGEMENTS

The authors are grateful to the Instituto Hidrografico for the facilities granted concerning reading and digitizing wave records. They are also in debt to Dr Anílmio de Azevedo from the Serviço Meteorológico Nacional for the meteorological elements provided and their interpretation.

REFERENCES

- [1] - Bonnefille, Germain, Lepetit - Statistiques des houles naturelles mesurées par le houlographe autonome type LNH, Houille Blanche nº 8, 1967
- [2] - Reis de Carvalho, J J e D Vera-Cruz - Regime de ondulação no Porto de Leixões, Estudo realizado para a Sacor, LNEC, Julho de 1964
- [3] - Shore Protection, Planning and Design, Technical Memorandum nº 4, CERC (formerly Beach Erosion Board), 3rd Edition, June 1966
- [4] - Jenkins, G M and D G Watts - Spectral Analysis and its applications, Holden-Day, San Francisco, 1969
- [5] - Barber, N F - Experimental Correlograms and Fourier Transforms, Pergamon Press, 1961
- [6] - Barber, N F - A plea for the rectangular lag window, Ocean Wave Spectra, Prentice-Hall, Englewood Cliffs, 1963
- [7] - Blackman, R B and J W Tukey - The Measurement of Power Spectra from the Point of View of Communications Engineering, The Bell System Technical Journal, January and March, 1958
- [8] - Tucker, M J - Analysis of Records of Sea Waves, Proceedings of the Institution of Civil Engineers, October 1963
- [9] - Draper, L M - The Analysis and Presentation of Wave Data - A plea for Uniformity, Proceedings of the Xth Conference on Coastal Engineering, Tokyo, 1966
- [10] - Cartwright, D E and M S Longuet-Higgins - The Statistical Distribution of the Maxima of a Random Function, Proceedings of the Royal Society, A, 237, 1956

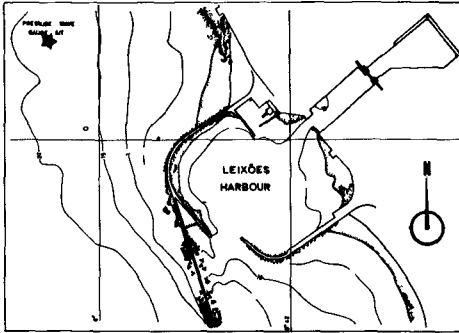


Fig 1 - Wave gauge site

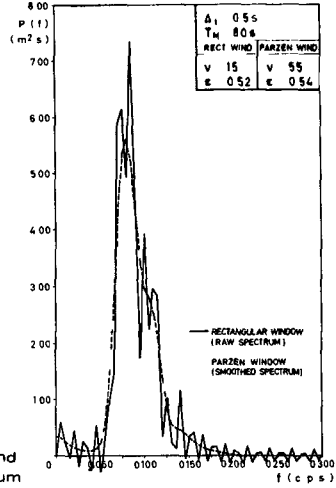


Fig 4 - Raw and smoothed spectrum

Fig 2 - Autocovariance function

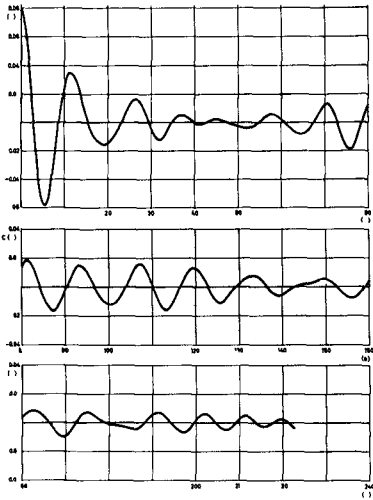
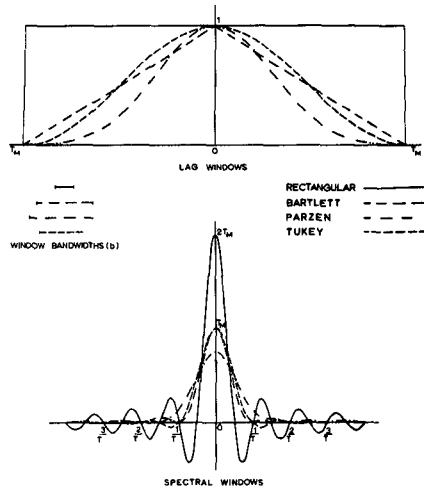


Fig 3 - Windows considered



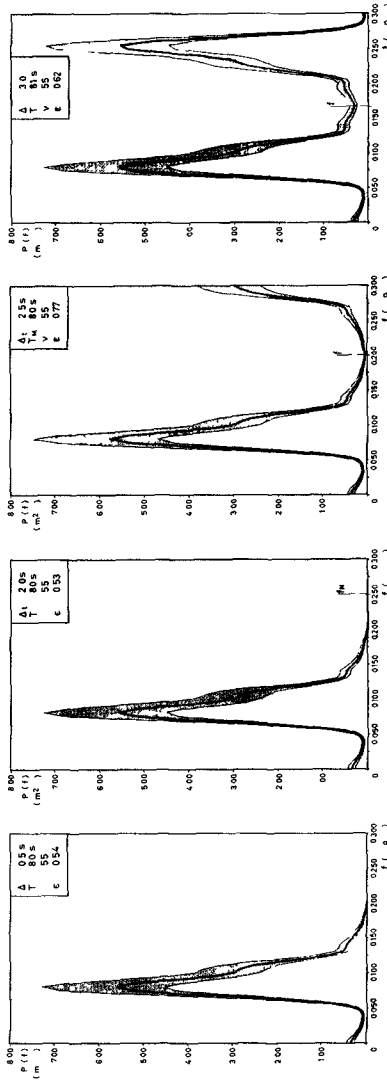


Fig 6 - Effect of Δt on aliasing

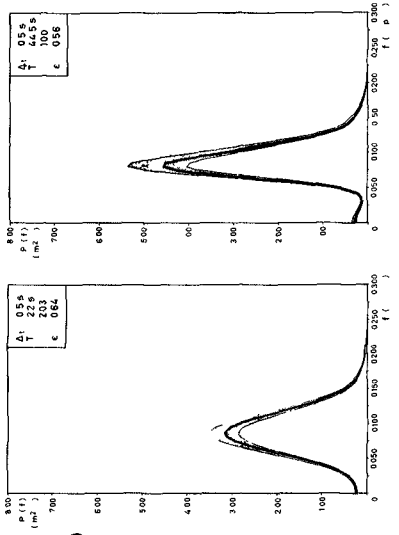


Fig 8 - The window closing technique (cont next page)

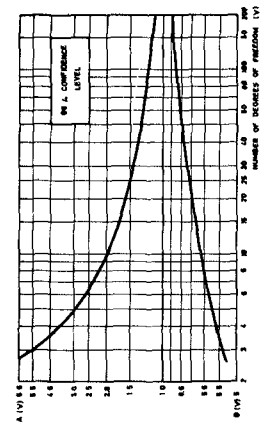
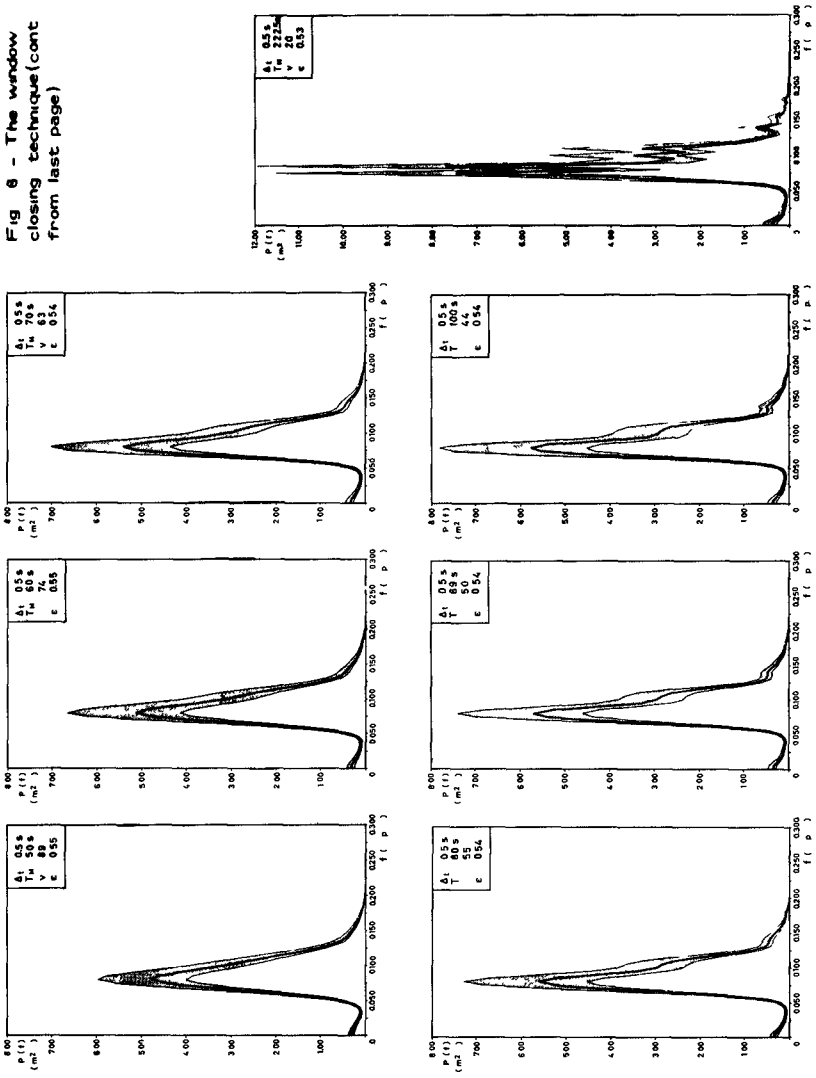


Fig 5 - Variation of the confidence interval with v

Fig 8 - The window closing technique (cont from last page)



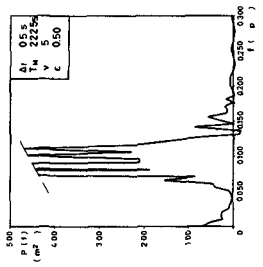
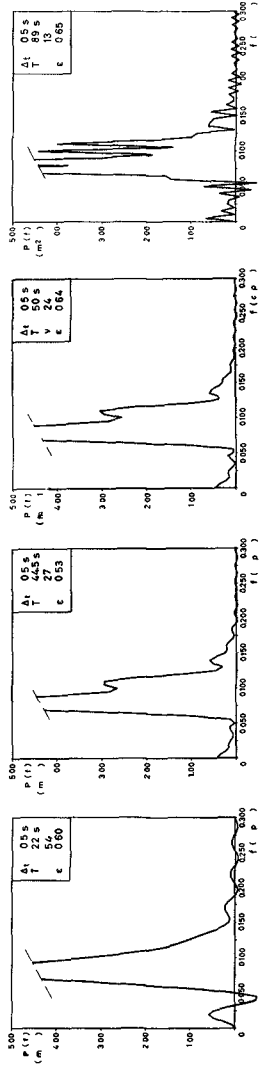


Fig 9 - The rectangular lag window and the choice of T_M

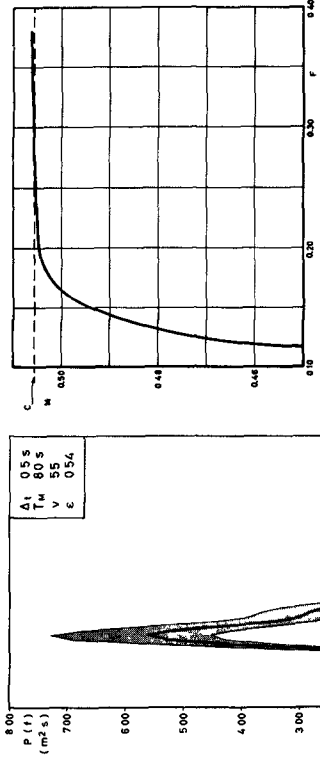


Fig 7 - Variation of m₀ with f_c

Fig 12 - Selected bottom spectrum

Fig 10 - Record partition

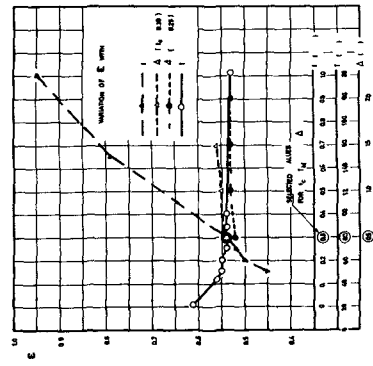
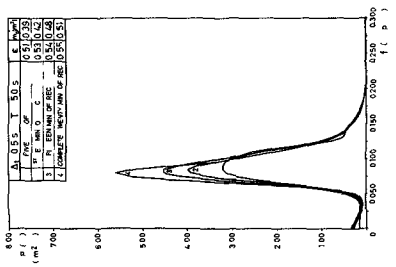
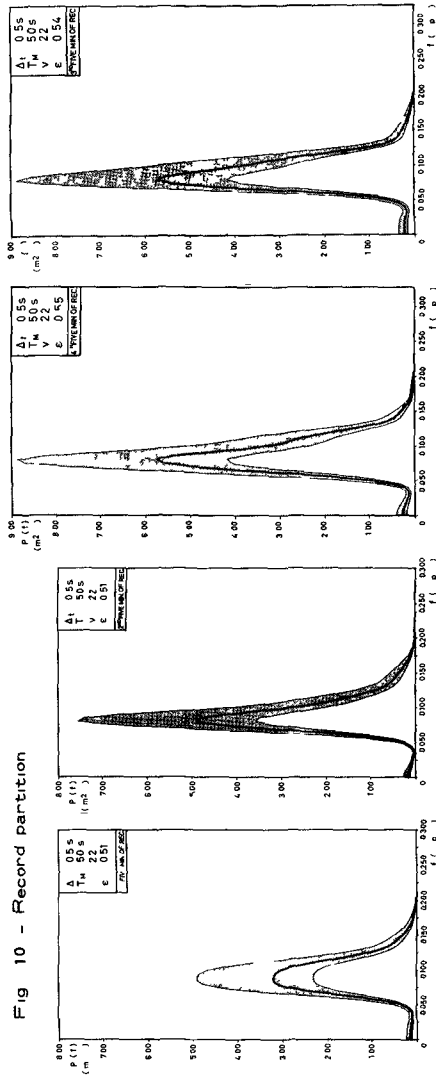


Fig 11 - Variation of E with Δ , T_m and C

Fig 14 - Surface version of bottom pressure spectrum compared with Neumann spectrum

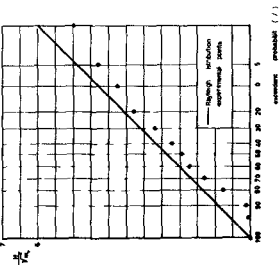
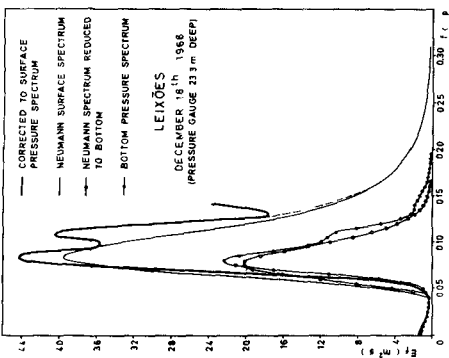


Fig 13 - Exceedance probabilities of bottom wave heights compared with Rayleigh distribution

Fig 15 - Synoptic charts

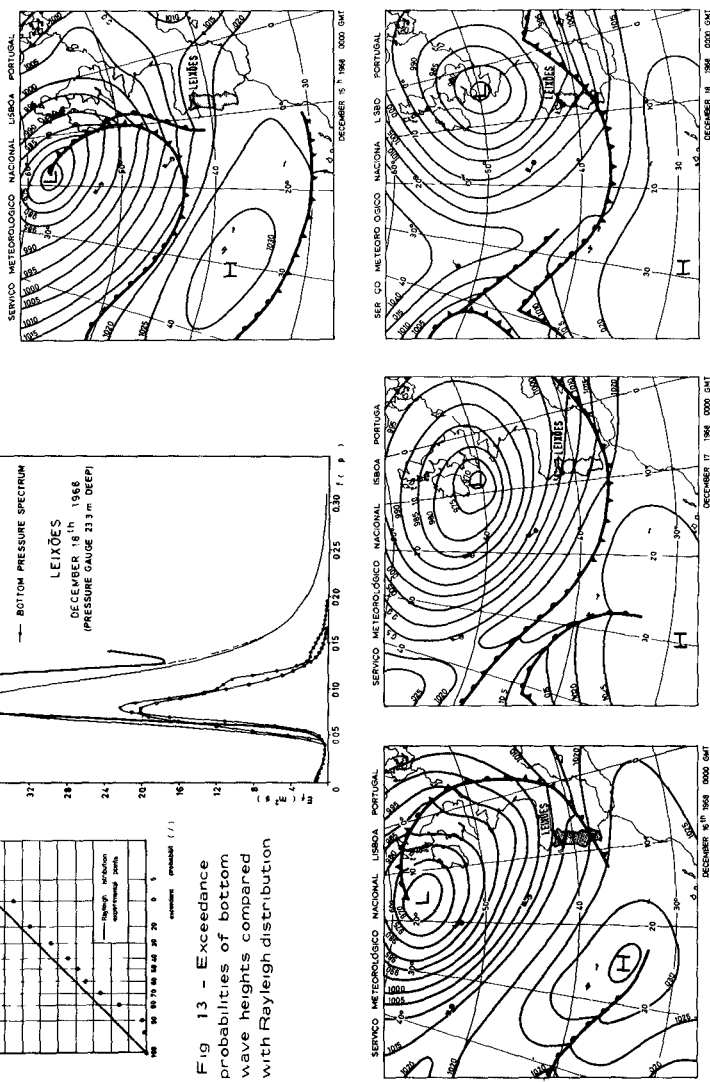


Fig 16 - Fetch delimitation

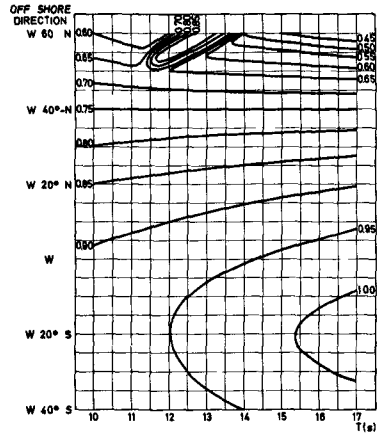
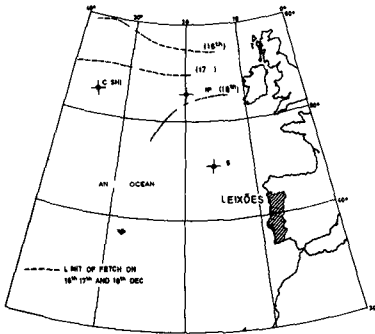


Fig 17 - Refraction coefficients at Leixões harbour entrance

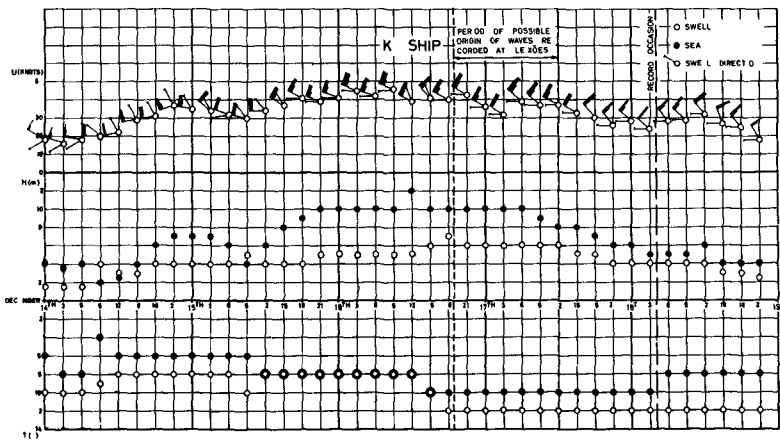


Fig 18 - Observations at North Atlantic K weather ship

CHAPTER 6

THE ANALYSIS OF WAVE RECORDS

by

D Lee Harris

Research Division, U S Army Coastal Engineering Research Center
Washington, D C

ABSTRACT

Data obtained from two surface profile wave gages and two pressure wave gages at the Steel Pier in Atlantic City, New Jersey, are used to check the consistency of the analysis variables obtained from a given set of records by several commonly used analysis procedures

All estimates of the characteristic height tested are found to be correlated better than 86 The estimates of characteristic period are not so satisfactory and in some cases are below 25 Consideration of several proposed definitions of the characteristic period indicates that they are based more on convenience in data processing than on application of the derived data Consideration of the use of wave data in engineering design shows that no one definition of the period can be satisfactory for all applications The best definition of the characteristic wave period for a given engineering problem can be specified only when the dynamic aspects of the problem have been identified

INTRODUCTION

The concept of a "significant wave height" and a "significant wave period" which can be used to characterize a wave field is appealingly simple It suggests a simple transition from the experimental results in a laboratory wave tank and the theoretical results obtained with monochromatic wave theory to the phenomena that occur in the real ocean

This concept was first introduced when sailors were asked to report the height and the period of " the larger, well formed waves, and omit entirely the low and poorly formed waves " as part of the synoptic weather reports from ships Comparison of early wave gage records, with visual observations, led to the opinion that the wave height "H " given by visual observers was the average height of the one-third highest individual waves, " $H_{1/3}$ " Figure 1, taken from Ross (1966) and based on an earlier figure by Cartwright (1962) provides some perspective on the reliability of this approximation Figure 1 is based on 905 pairs of visual and instrument observations from a weather ship equipped with a shipboard wave recorder For the data included in this figure $H_{1/3} = 1.1 H_v$ Comparisons of shipboard observations by two or more observers are given by Hogben and Lumb (1964, 1967) and likewise show considerable scatter

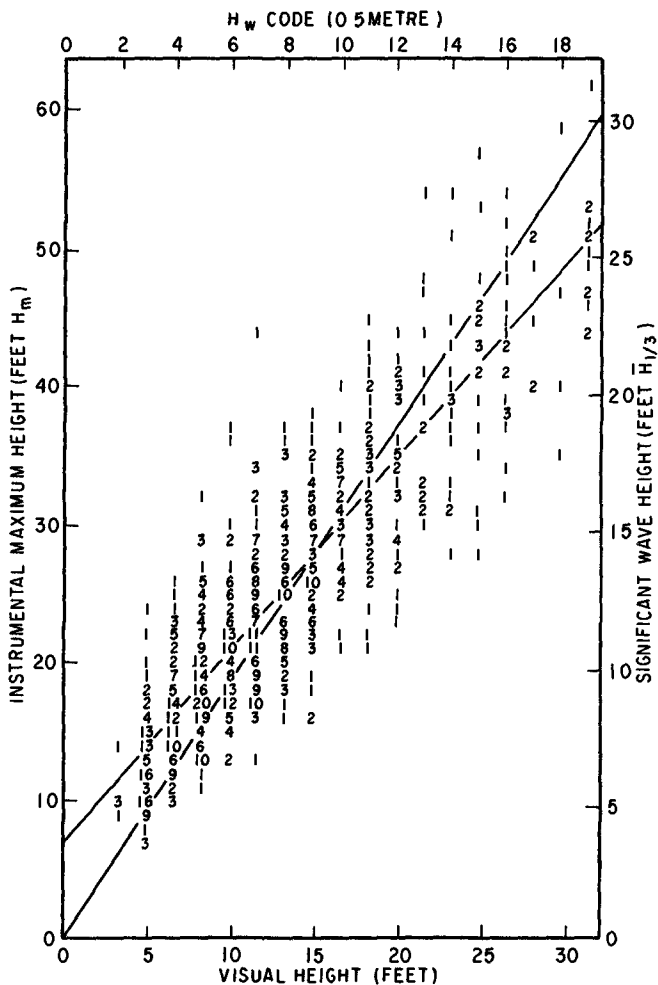


Figure 1 Comparison of instrument and visually observed heights (after Ross)
 For the data in the above figure $H_{1/3} = 1.1 H_v$

Many wave records have been analyzed by listing the heights and periods of individual waves for the determination of $H_{1/3}$ and the corresponding period $T_{1/3}$. This process is rather tedious and not truly objective, for there is no purely objective way of making a clear distinction of which perturbations on the record are waves that should be counted and which are ripples that should be omitted.

This problem is illustrated by Figure 2, where simultaneous records from four wave gages, located within a 12-foot circle on the Steel Pier in Atlantic City, are shown. Note that some of the waves appearing on the surface gage records do not appear on the pressure records, and that almost any procedure for determining which waves should be counted would accept some waves on one surface record that would be rejected on the other.

OTHER DEFINITIONS OF WAVE PERIOD

To obtain a more objective measure of the wave period, various writers (Draper, 1966, Tucker, 1961) have suggested using the average period of all zero up-crossings as the characteristic period. Both of these depend somewhat on the resolution of the wave recording system and Tucker's depends on a practical method for determining the zero line. Draper suggests that it can be estimated by eye. Thus two different estimates may lead to two different values. If interest is centered on the wind-generated waves, it would be more appropriate to consider crossing of a trend line. The difference would not be important with large waves and small tides, but it could be significant with large tide ranges and small waves. This latter combination can be important in sedimentation problems.

Since 1965, it has been customary at CERC to identify the most prominent period in a 7-minute wave record as the significant wave period.

To clarify the meaning of wave period estimates, it is useful to note that according to the linear theory for monochromatic progressive waves,

$$h(t) = \bar{h} + A \cos(kx - \sigma t - \phi) \quad (1)$$

$$w = \sigma A \frac{\sinh k(z+D)}{\sinh kD} \sin(kx - \sigma t - \phi) \quad (2)$$

$$u = \sigma A \frac{\cosh k(z+D)}{\sinh kD} \cos(kx - \sigma t - \phi) \quad (3)$$

$$p = \rho A C^2 k \frac{\cosh k(z+D)}{\sinh kD} \cos(kx - \sigma t - \phi) \quad (4)$$

$$k^2 C^2 = \sigma^2 = gk \tanh kD = (4\pi^2)/T^2 \quad (5)$$

where w , u are the vertical and horizontal components of velocity, p the

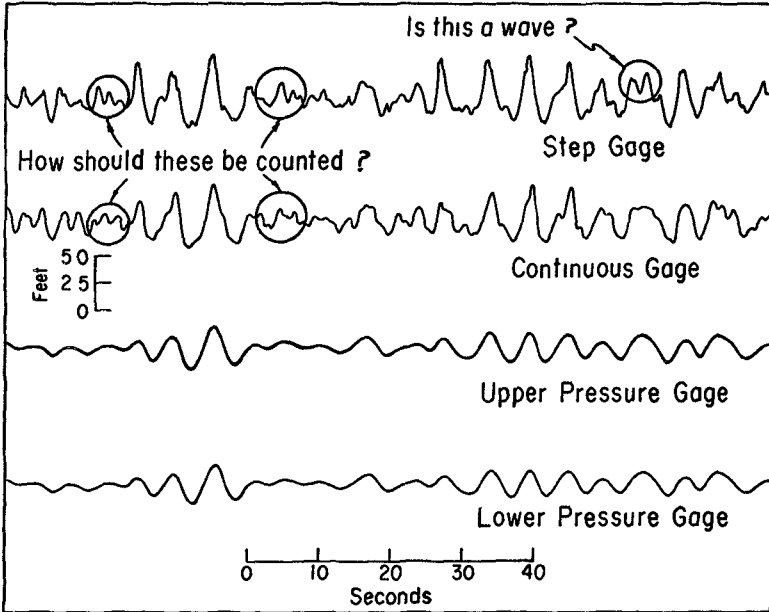


Figure 2 A sample of the simultaneous record from four wave gages at the Steel Pier in Atlantic City, N J , illustrating the difficulty in deciding which perturbations are to be considered as waves in determining $H_{1/3}$ Records (a) and (b) are for pressure gages, (c) and (d) are pressure gages with (d) about 6 feet below (e)

pressure, k the wave number, σ the frequency, ϕ the phase at $kx = \sigma t$, C the phase speed, T the period, ρ the density and g the acceleration of gravity. The origin of z is taken at the water surface and the upward direction is taken as positive. Since, for any given value of D , there is a one-to-one relationship between period, frequency, wave number, wave length and phase velocity, functions which logically depend on any one of these parameters may be expressed unambiguously as functions of the period.

In the more general case when several wave trains are present, it is more useful to consider

$$h(t) = \bar{h} + \sum_{m=1} A_m \cos(k_m x - \sigma_m t - \phi_m) \quad (6)$$

Similar expressions may be readily constructed for u , w , and p . In general k_m and x should be regarded as vectors with $k_m \cdot x$ as the scalar product of the vector wave number, k_m and the position vector x . This detail is not important here, however, for if the gage position is fixed, $k_m \cdot x$ is constant for each m , and may be absorbed into the phase angle ϕ_m . This procedure will be followed in the remainder of the paper. If the sequence of σ_m , important in a given application is known in advance, as in the case of astronomical tides, the most expedient analysis procedure for the calculation of the amplitudes A would be a least squares evaluation of the coefficient s , a_m , b_m , in the expression

$$h(t) = \bar{h} + \sum_{m=1} [a_m \cos \sigma_m t + b_m \sin \sigma_m t] \quad (7)$$

$$\begin{aligned} A_m^2 &= a_m^2 + b_m^2 \\ \phi_m &= \tan^{-1} b_m/a_m \end{aligned} \quad (8)$$

If the sequence of σ_m is not known in advance, and this is the usual case, the amount of arithmetic involved in the solution can be greatly reduced by choosing $\sigma_m = 2m\pi/T_a$, where T_a is the period of record selected for analysis.

It can be shown by Parseval's relation that the sum of all the A_m^2 is equal to the variance of $h(t)$. It can also be shown that the variance of $h(t)$ is proportional to the average potential energy of the wave (Kinsman, 1965, p. 145ff). According to Taylor (1937), this is the idea Rayleigh had in mind when he first introduced the concept of an energy spectrum.

If one value of A_m^2 , say A_s^2 is much larger than all of the others, it seems natural to select T the corresponding period, $T = 2\pi s/T_a$ as the significant period. If there are many A_m^2 's with nearly the same magnitude it may be desirable to regard the true energy as a continuous function of

the frequency and the computed A_m^2 as estimates of this function, integrated over a small frequency interval centered on σ_m . When this procedure is followed, it seems natural to define the significant period as the period corresponding to the peak energy density per unit frequency. If the wave energy is known, or estimated, as a continuous function of the frequency, a simple transformation of variables provides the energy as a function of the wave period. Thus, the significant wave period could be defined as the period of maximum energy density per unit period.

Short definitions of six proposed measures of the significant wave period are listed below.

- 1 The average period of the one-third highest waves, $T_{1/3}$
- 2 The period most prominent in the record, T_{CERC}
- 3 The average period of all waves, T_{all}
- 4 The average period of all waves that cross the mean water level, T_{ZUC}
- 5 The period of maximum energy density, T_{PM}
- 6 The period corresponding to frequency of maximum energy density, T_{FM}

The last of these seems most suitable for a study of wave dynamics, and is suggested as a standard. The first two definitions have been proposed for convenience in collecting data, and the third and fourth to make the determinations more objective and reproducible.

OTHER DEFINITIONS OF WAVE HEIGHT

Since the energy of a simple wave is proportional to the square of the wave height, it is natural to define a measure of the wave height in terms of the square root of the average energy. This estimate, called the root-mean-square wave height by Tucker (1961) is equivalent to the standard deviation of the wave record and is defined by

$$H_{RMS} = \left[\frac{1}{N} \sum_{n=1}^N [h(n\Delta t) - \bar{h}]^2 \right]^{1/2} \quad (9)$$

where $h(n\Delta t)$ is the water surface elevation at time $t=n\Delta t$, and \bar{h} is the mean water level for the analysis interval. Thus H_{RMS} , unlike $H_{1/3}$, has a clear physical definition and can be easily determined by either digital or analog computers. Both theoretical and empirical evidence suggest that the average value of the ratio $H_{1/3}/H_{RMS}$ is about 4. The actual value obtained from a given observation depends on the full wave spectrum.

Since 1965, it has been customary at CERC to estimate the significant wave height as the N'th highest wave in a 7-minute wave record where N is a function of the selected period and is approximately 1/6 of 420 seconds divided by the "significant period". This procedure can be performed very rapidly by making use of suitable transparent nomograms, but the determination of the "most prominent period in the record" is too subjective to be readily programmed for a computer.

Draper (1966), making use of some work by Tucker (1961), proposed a more objective system which can be readily programmed. The standard deviation of the wave record called H_{RMS} by Tucker is estimated from the highest and lowest water elevations in the record, and the significant wave height is estimated as the product of the sum of the highest and lowest departures of the surface elevations from its mean position and a factor, which depends on the period of zero up-crossings.

A COMPARISON OF THE PARAMETERS AS EVALUATED BY SEVERAL DEFINITIONS

Since 1966, CERC has been making a digital record from the step resistance wave gage at the Steel Pier in Atlantic City, New Jersey. A computer program has been developed for calculating each of the measures of wave height and period discussed above with the exception of T_{CERC} and H_{CERC} which must be obtained manually. This program has been used to analyze the records from November and December of 1966.

It has been found, for the records analyzed, that all of the measures for wave height are highly correlated. The correlation matrices for the principal measures are shown in Tables I and II. Consequently, it appears to make relatively little difference how a record is analyzed to obtain wave height, since very nearly the same answer is obtained for any method. The Fast Fourier Transform algorithm of Cooley and Tukey (1965), often called the "FFT" was used to analyze records 1024 seconds (17 minutes, 4 seconds) long for the computation of energy spectra. This permits a detailed definition of the spectrum with a frequency resolution slightly better than 10^{-3} Hertz.

Spectra with resolution per unit frequency similar to that obtained with the auto-correlation technique (Blackman and Tukey, 1958), were obtained by averaging across frequency bands of constant width. Spectra in terms of energy density per unit period were computed by averaging across frequency bands of variable width.

The correlation matrices for the various measures of the wave period are given in Tables III and IV, and a comparison of a few of the individual estimates in Table V. It can be seen that two estimating procedures which may agree to within 1 second in some cases, may differ by as much as 10 seconds in other cases. The correlation appears to be better for the higher waves. This is shown in Figure 3, in which the ratio of T_{FM} to T_{CERC} is shown as a function of H_{RMS} . H_{RMS} is a measure of wave height defined on page 6.

TABLE I
CORRELATION MATRIX FOR WAVE HEIGHT ESTIMATES
Atlantic City, N J , December 1966 (84 records)

	H_{RMS}	H_{CERC}	H_{Tucker}	$H_{1/3}$
H_{RMS}	1 000	958	987	970
H_{CERC}	958	1 000	908	917
H_{Tucker}	987	908	1 000	948
$H_{1/3}$	970	917	948	1 000

H_{RMS} is the Standard Deviation of the Record

H_{CERC} is the Value Obtained from the Analysis System Used at CERC Since 1965

H_{Tucker} is the Estimate of H_{RMS} Based on the Highest Crest and Lowest Trough as Recommended by Tucker (1961)

$H_{1/3}$ is the Average Value of the One-Third Highest Waves as Obtained by a Digital Computer

H_{CERC} is based on a seven-minute record Other estimates are based on records of 1024 seconds

The correlation between records of 420 seconds and 1024 seconds duration is approximately 0.98

TABLE II
 CORRELATION MATRIX FOR WAVE HEIGHT ESTIMATES
 Atlantic City, N J , November 1966 (129 records)

	H_{RMS}	H_{CERC}	H_{Tucker}	$H_{1/3}$
H_{RMS}	1 000	949	982	938
H_{CERC}	949	1 000	945	868
H_{Tucker}	982	945	1 000	918
$H_{1/3}$	938	868	918	1 000

See Table I for explanation

TABLE III
 CORRELATION MATRIX FOR WAVE PERIOD ESTIMATES
 Atlantic City, N J , December 1966 (84 records)

	T_{FM}	T_{CERC}	T_{PM}	T_{ZUC}	T_{a11}	$T_{1/3}$
T_{FM}	1 000	564	402	264	- 037	028
T_{CERC}	564	1 000	510	390	038	135
T_{PM}	402	510	1 000	583	236	365
T_{ZUC}	264	390	583	1 000	751	867
T_{a11}	- 037	038	236	751	1 000	951
$T_{1/3}$	028	135	365	867	951	1 000

T_{FM} is the period corresponding to the frequency of maximum energy density per unit frequency

T_{CERC} is the most prominent period as determined by the CERC method (see text)

T_{PM} is the period of maximum energy density per unit period

T_{ZUC} is the average period of zero up-crossings

T_{a11} is the average period between maxima in the record

$T_{1/3}$ is the average period of the one-third highest waves

T_{CERC} is based on a seven-minute record All other measures are based on a record of 1024 seconds

TABLE IV
 CORRELATION MATRIX FOR WAVE PERIOD ESTIMATES
 Atlantic City, N J, November 1966 (129 records)

	T _{FM}	T _{CERC}	T _{PM}	T _{ZUC}	T _{all}
T _{FM}	1 000	725	581	493	131
T _{CERC}	725	1 000	615	552	,236
T _{PM}	581	615	1 000	648	260
T _{ZUC}	493	552	648	1 000	710
T _{all}	131	236	260	710	1 000

See Table III for explanation

TABLE V
 ESTIMATES OF THE "CHARACTERISTIC WAVE PERIOD"
 ESTIMATES USING VARIOUS DEFINITIONS
 CERC STEP RESISTANCE WAVE GAGE, STEEL PIER, ATLANTIC CITY, N J
 DECEMBER 1966

Day	Hour	T _{FM}	T _{CERC}	T _{PM}	T _{ZUC}	T _{a11}	T _{1/3}
2	1600	9 1	7 0	8 0	4 2	2 3	3 3
2	2000	10 6	12 0	8 0	4 2	2 2	3 3
3	0000	10 6	11 0	10 0	4 5	2 5	3 6
3	0400	12 7	13 0	11 0	5 4	2 9	4 4
3	0800	12 7	12 0	11 0	4 7	1 9	2 4
3	1200	12 7	13 0	11 0	4 4	2 0	2 6
3	1600	12 7	11 0	11 0	4 5	2 2	3 3
3	2000	12 7	11 0	2 0	3 5	2 3	2 8
4	0000	10 6	5 0	2 0	3 4	2 3	3 0
4	0400	12 7	10 0	2 0	3 6	2 3	3 0
4	0800	5 8	6 0	5 0	4 6	2 7	3 8
4	1200	6 4	7 0	5 0	4 5	3 0	4 2
4	1600	9 1	10 0	8 0	5 0	2 7	4 3
4	2000	8 0	8 0	7 0	5 4	3 2	4 7
5	0000	9 1	8 0	8 0	5 3	3 3	4 8
5	0400	10 6	11 0	5 0	6 2	4 2	5 9
5	0800	12 7	9 0	12 0	6 2	3 1	4 7
5	1200	12 7	14 0	11 0	6 5	3 7	5 6
5	1600	12 7	12 0	11 0	5 8	3 1	5 1
5	2000	15 9	12 0	6 0	6 2	3 5	5 2

See Table III for explanation

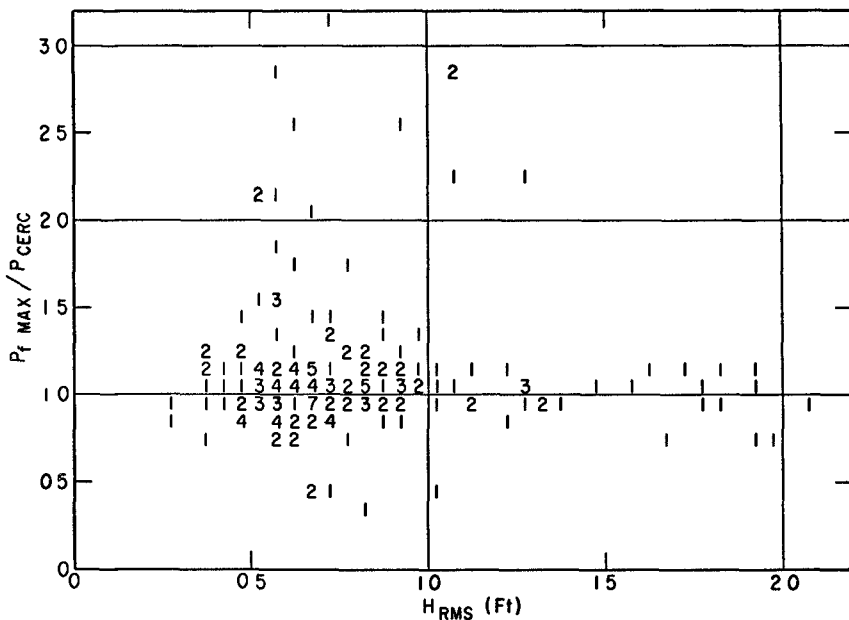


Figure 3 The ratio of $T_f \text{ max}$ to T_{CERC} as a function of H_{RMS}
 The numbers represent the number of cases in which the observation fell in 0.1 x 0.05 foot square

THE INTERPRETATION OF A CHARACTERISTIC WAVE PERIOD

For linear wave theory there is a one-to-one correspondence between period, frequency, wave length, wave number and phase velocity. Because of this, experimental results obtained with monochromatic waves are often tabulated or graphed as a function of period. A careful analysis, however, may show that one of the other variables is more fundamental to the problem. Thus in coastal engineering design, the wave period may be used to specify either the characteristic time scale or the characteristic length scale of some process due to waves. A little reflection on the physical processes involved will show that no one variable can provide the best estimate of the time and space scales for all processes due to a given sea state. This can be seen most clearly by considering a Fourier Transform of the wave record.

The energy spectrum for the wave height can be expressed in the form

$$E_h(\sigma_m) d\sigma = A_m^2 \quad (10)$$

The corresponding expressions for the spectra of the velocity components are obtained from (2) and (3) in the form

$$E_w(\sigma_m) d\sigma = A_m^2 \sigma_m^2 \left[\frac{\cosh k(z+D)}{\sinh kD} \right]^2 \quad (11)$$

$$E_u(\sigma_m) d\sigma = A_m^2 \sigma_m^2 \left[\frac{\cosh k(z+D)}{\sinh kD} \right]^2 \quad (12)$$

The term σ_m^2 produces an amplification of the height spectrum with increasing frequency. Thus if the height spectrum is flat or contains two or more nodes of nearly the same value, the peak of the velocity spectrum, on the surface, is likely to occur at a higher frequency than the peak of the height spectrum. The terms in square brackets decrease with depth and decrease more rapidly with increasing frequency. Thus the peak of the velocity spectrum will have a tendency to shift toward lower frequencies with increasing depth.

Equation (5) can be used to eliminate C^2 from (4) to obtain

$$p = \rho g A \frac{\cosh k(z+D)}{\cosh kD} \cos(\sigma t - \phi)$$

The horizontal displacement, X , may be obtained from (3) by integration with respect to time to obtain

$$X = A \frac{\cosh k(z+D)}{\cosh kD} \sin(\sigma t - \phi)$$

The corresponding spectra are

$$E_p(\sigma) d\sigma = \rho^2 g^2 A^2 \left[\frac{\cosh k(z+D)}{\cosh kD} \right]^2$$

$$E_\chi(\sigma) d\sigma = A^2 \left[\frac{\cosh k(z+D)}{\cosh kD} \right]^2$$

At the surface the peak of these spectra must agree with the peak of the height spectra, but the high-frequency components are attenuated with depth more than the low frequency components. Thus with relatively flat or bimodal spectra, there is a tendency for the peak of the spectrum to shift toward low frequencies.

Other transformations, which will produce other changes in the spectra, and in the period which seems to be most important will be appropriate to some engineering problems.

It seems that no one definition of the "significant period" for a wave field in which waves of several frequencies are present, can provide the best value for use in all engineering calculation.

SUMMARY AND CONCLUSIONS

The wave-height estimates obtained from any particular wave gage by any of the analysis procedures tested are consistent, in the sense that the ranking of estimates obtained by one procedure will be nearly the same as that obtained by any other analysis procedure tested. But a scale correction may be necessary to obtain the best fit between data analyzed by two different procedures.

The period data obtained by different analysis procedures are not consistent and the estimates of a characteristic wave period have little value unless the procedure used in obtaining the period estimate is known. Comparisons between wave periods may be more satisfactory when the data are stratified in some way which makes the data sample more homogenous. Restricting attention to waves more than 3 feet high is one such stratification which improves the consistency of the estimates. Other forms of stratification may also be useful.

It appears that the best procedure for engineering design will be to disregard the tabulated periods, and to consider every period that might reasonably occur, along with the given height estimate, to determine the critical conditions or the design wave.

The best choice for a design wave for a particular environment depends on the problem to be considered. No single value can be sufficient for all problems.

REFERENCES

- Blackman, R B and Tukey, J W , *The Measurement of Power Spectra*, American Telephone and Telegraph Co , 1958, reprinted by Dover Publications, New York
- Cartwright, D E , "A Comparison of Instrumental and Visually Estimated Wave Heights and Periods Recorded on Ocean Weather Ships", National Institute of Oceanography, October 1962
- Cooley, J W and Tukey, J W , "The Fast Fourier Transform", *IEEE Spectrum*, Vol 4, p 63-70, 1967
- Draper, L "The Analysis and Presentation of Wave Data - A Plea for Uniformity", *Proceedings of Tenth Conference on Coastal Engineering*, ASCE, New York (1967)
- Esteva, D and Harris, D L , "Analysis of Pressure Wave Records and Surface Wave Records", *Proceedings of Twelfth Conference*, ASCE, Washington (1970)
- Hogben, N and Lumb, F E with Appendix by Cartwright, D E *The Presentation of Wave Data from Voluntary Observing Ships*, National Physical Laboratory, Ship Division, London, 1964
- Hogben, N and Lumb, F E , *Ocean Wave Statistics*, National Physical Laboratory, Ministry of Technology, London, 1967
- Kinsman, B , *Wind Waves*, Prentice-Hall, Inc , Englewood Cliffs, N J (1965) p 676
- Ross, D B , "Recent Developments in Remote Sensing of Deep Ocean Waves", *The New Thrust Seaward*, Transactions of the Third Annual MTS Conference, the Marine Technological Society, Washington, D C (1967), p 371-393
- Taylor, G I , "The Spectrum of Turbulence", *Proceedings, Royal Society*, A164, p 476-490, 1938 Reprinted in Friedlander, S K and Topper, L *Turbulence, Classic Papers on Statistical Theory*, Interscience, New York, 1961
- Tucker, M J , "Simple Measurement of Wave Records", *Proceedings of the Conference on Wave Recording for Civil Engineers*, N I O (1961) Also in Dock & Harbor Authority, Vol 42, p 231

CHAPTER 7

COMPARISON OF PRESSURE AND STAFF WAVE GAGE RECORDS

by

D Esteva and D Lee Harris
Research Division, U S Army Coastal Engineering Research Center
Washington, D C

ABSTRACT

Simultaneous records from two pressure gages located at different depths, a step-resistance relay gage, and a continuous-wire staff gage have been collected at Atlantic City, N J

Spectra and cross-spectra are computed using the Fast Fourier Transform Algorithm (FFT) method proposed by Cooley and Tukey Individual harmonics of the pressure energy spectra are compensated for pressure attenuation according to classical theory Results indicate better agreement is obtained between the wave height and the spectra computed from the compensated pressure gages and those computed from the continuous-wire staff gage than between the two surface gages

Values of coherences are near .98 in the energy-containing part of the spectrum, and are always larger for the pressure-continuous wire staff cases than for the two surface gages which are displaced from each other only 12 feet in the horizontal

1 INTRODUCTION

Two basically different types of wave gages are widely used by coastal engineers One, called a surface-profile gage, produces a record which is considered to represent the actual elevation of the water surface at a point for each instant of time The other, called a pressure gage, produces a continuous record of the pressure at some fixed position beneath the surface The amplitude of the pressure pulses generated by waves is attenuated with depth, and short waves are attenuated more than long waves

To compensate for this attenuation, a theoretical correction is commonly applied to the record from a pressure gage Several recent comparisons of the records from surface-profile gages with compensated records from pressure gages have shown systematic differences (Hom-ma, Horikawa and Komori (1967)) In general, the differences have been attributed to inadequacy of the compensation formula

The Coastal Engineering Research Center (CERC) has established a facility at the Steel Pier in Atlantic City, New Jersey, for obtaining simultaneous records from several wave gages This installation is being used to compare surface-profile gages of various designs, and to obtain more information about the performance of pressure gages

A comparison of the records obtained from two pressure transducers, a step resistance relay gage described by Williams (1970), and a continuous wire gage is presented in this paper

2 THE INSTALLATION

The step-resistance wave gage has been installed for many years on one of the pilings supporting the Steel Pier at Atlantic City. The other three gages were installed on a 4-inch outside diameter, heavy-duty steam pipe jettied into the sand bottom and secured to the Pier deck about 12 feet to the northeast of the step resistance gage. The lower pressure transducer is immediately above the bottom of the continuous wire gage and the upper pressure transducer about 5.5 feet above the first. All gages are on the seaward end of the pier, about half a mile from the mean water line.

The mean depth at the gage site was determined as 15.5 feet MLW by lead line soundings a few days before and after the experiments. Extensive surveys a few months earlier and later showed that the gage site was near the center of a shallow depression. The depth within 200 feet of the instruments varied from 11.0 to 16.6 feet, with an average value near 14.0 feet MLW. A sketch of the installation is shown in Figure 1.

The signal from each sensor is obtained in the form of a DC voltage. All signals are transmitted to the CERC laboratory in Washington by telephone line.

The transmission was accomplished by using channels two through five of the IRIG multiplex channels as described in TELEMETRY STANDARDS, June 1962, Document 106-60, and in many other publications on telemetry. The transmission coefficient for the system is near unity for all frequencies less than 6 hertz. In the laboratory, the signals are separated and converted back to DC voltages. A digital voltmeter is used to measure the signal and the voltage is recorded on computer compatible magnetic tape at a rate of four samples per second from each gage.

3 THE ANALYSIS PROCEDURE

The Fast Fourier Transform Algorithm (FFT) suggested by Cooley and Tukey (1966) was used to analyze observations 1024 seconds (17 minutes and 4 seconds) long. This procedure gives 1024 harmonics with periods of 1 second or longer. The initial record, expressed as a departure from the mean, was multiplied by a cosine Bell Taper function as suggested by Bingham, Godfrey and Tukey (1967) prior to the analysis in order to decrease the leakage of energy between spectral lines. That is to say, the FFT was applied to the series

$$\tilde{Y}(n\Delta t) = \frac{1}{2}(Y(n\Delta t) - \bar{Y})(1 - \cos \frac{2\pi n\Delta t}{T}) \quad (1)$$

Linear monochromatic wave theory was used to obtain the compensation function needed to compute the amplitude of the surface disturbance from the observed pressure disturbance for each harmonic according to the equation

$$C(m) = \frac{\cosh(k(m)H)}{\cosh(k(m)G)} \quad (2)$$

where $C(m)$ is the compensation function for the m 'th harmonic, $k(m)$ is the wave number of the m 'th harmonic, G is the height of the pressure transducer above the bottom and H is the mean thickness of the water column above the bottom during the observation. The wave number is given by the implicit equation

$$(2\pi T)^2 = gk(m) \tanh k(m)H \quad (3)$$

where T is the length of the observation (1024 seconds in this study) and g is the acceleration of gravity. Thus the compensation factor appropriate to each specific frequency is applied to that harmonic.

The Fourier Transforms were used to compute energy spectra for each gage record, the compensated record from the pressure transducers, and the cross-spectra between the records from the continuous wire gage and each of the other gages.

The detailed spectra obtained in this way contain more than 1000 individual spectral lines. The results are easier to grasp if some of this detail is suppressed, so the individual spectral values have been grouped into bands of 17 lines each.

4 RESULTS

Eighty-three observations, taken 2 hours apart during December 19-26, 1969 were analyzed. A sample of the resulting spectra, as obtained directly from the records of the four gages and from the compensated pressure records is shown in Figure 2. The spectrum from the continuous-wire record has been superimposed on all others. The data in this Figure are normalized with respect to the frequency band with period between 3 and 19.69 seconds. The short-period cutoff was imposed because the spectrum of the pressure record at higher frequencies has little correlation with the surface spectrum. The long-period cutoff was imposed because the step-resistance gage shows an excessive amount of energy at longer periods for some of the observations. The spectra computed from the compensated pressure records agree very well with that from the continuous-wire record within this period band.

Figures 3 and 4 show a comparison of the wave heights as estimated from the continuous-wire gage and from the pressure gages compensated for hydrodynamic attenuation as described above. The root mean square wave height, which is equal to the standard deviation of the wave record, is used as a measure of the wave height because unlike the "significant wave height" it is clearly and objectively defined. Figure 5 shows the same comparison for

the records obtained from the step resistance relay gage. A tendency for the step resistance gage to record higher waves than the other gages is apparent. This tendency has also been noted by Hom-ma, Horikawa and Komori. These authors attributed this effect to wave runup on the gage or its support. It has been determined that wave runup has affected the records from the step resistance wave gage at Atlantic City. This step gage is no longer being used.

Different mounting arrangements have been used at some other locations. It seems likely that the installation at Atlantic City leads to larger runup than that experienced at some other installations. The possibility that the differences between the records of the step gage and the continuously variable gages is due to the digital nature of the record from the step gage was investigated by truncating the resolution of the continuous wire gage to correspond with that of the step gage. The results of the analysis of the truncated record did not differ significantly from those of the analysis of the original record.

It should be noted that the agreement between the compensated pressure records and the continuous-wire record is better than that between the two surface-profile records. The continuous-wire gage has been used as the standard in this comparison partly because of this better agreement and partly because wave runup is known to affect the accuracy of the step resistance gage.

The average factor needed to convert the wave heights as determined from the upper pressure transducer compensated by individual lines to those determined from the continuous-wire gage was found to be .98 with a correlation coefficient of .999. For the lower pressure transducer this factor becomes 1.04, with a correlation coefficient of .999. Even when the entire spectrum is compensated by the factor computed for the frequency of maximum energy density the factor is 1.08 with a correlation of .997. The agreement reported here is much better than most of those cited in the review paper by Grace (1970). The improved agreement is believed to result partly from the use of a more satisfactory surface gage system, partly because the FFT procedure permits a more precise determination of the frequencies of maximum interest than the procedures used by earlier investigations, and partly because the correction was applied to the individual harmonics in the spectrum.

5 ACCURACY OF THE COMPENSATION FACTOR AS A FUNCTION OF FREQUENCY

Hom-ma, et al, have studied the function $n(f)$ defined by the relation

$$E(f)_{\text{sfr}} = n(f)E(f)_{\text{cp}} \quad (4)$$

where f is the frequency, and the subscripts sfr and cp refer to the surface wave record and the compensated pressure record. The function $n(f)$ has been computed from our data for all bands containing as much as 5 percent of the total energy in a given spectrum. The function $n(f)$ based on all records from the upper pressure transducer is shown in Figure 6. The mean value of $n(f)$ is plotted as a circle and the standard deviation is shown by a vertical line. A similar plot based only on those observations in which H_{RMS} exceeded 1 foot is given in

Figure 7 The two values for which no standard deviations are shown consisted of single observations. Similar results, but with a little more scatter, were derived for the lower pressure transducer, as shown in Figures 8 and 9.

It is noted that both the deviation of the mean value of $n(f)$ from its theoretical value of unity and the scatter of the individual values is greater for low waves than high waves, and greater for the lower pressure transducer than for the upper one. From these results we are led to believe that the deviation results more from the presence of pressure impulses caused by factors other than surface gravity waves than from nonlinear effects due to the finite amplitude of the wave. This is especially likely at high frequencies where the large value of $c(m)$ would greatly amplify small impulses. In general, we feel that values of $c^2(m)$ greater than 25 should not be used at this installation.

6 CROSS SPECTRUM RESULTS

The cross spectra calculations for band widths of 0.017 Hertz showed a coherence of .95 between the continuous-wire gage and the pressure gages in most bands containing more than 5 percent of the total energy in the spectrum. The coherence between the two surface gages was slightly lower but still above .90.

Computations of the phase lags between the continuous-wire and the pressure gages showed that the phase of the wave advances slightly with increasing depth. This effect tends to increase with frequency. A phase shift of this kind has been predicted by Battjes (1968) and Mei and Chu (1970).

REFERENCES

- Bingham, C , Godfrey, M D and Tukey, J W , 1967, "Modern Techniques of Power Spectrum Estimation", IEE Trans Audio Electro-acoustics, Vol AU15, No 2, pp 56-66
- Battjes, J A , "Refraction of Water Waves", Journal of the Waterways and Harbors Div , Proceedings of the American Society of Civil Engineers, Vol 94, 1968, pp 437-450 , No WW4
- Cooley, J W and Tukey, J W "The Fast Fourier Transform", IEEE Spectrum, Vol 4, p 63-70, 1967
- Draper, L , "Attenuation of Sea Waves with Depth", La Houille Blanche, Vol 12, No 6, 1957, pp 926-931
- Gerhardt, J R , Jehn, K H and Katz, I , "A Comparison of Step-Pressure - and Continuous-Wire-Gauge Wave Recordings in the Golden Gate Channel", Transactions of the American Geophysical Union, Vol 36, No 2, 1955, pp 235-250
- Glukhovskii, B K , "Study of Wave Attenuation with Depth on the Basis of Correlation Analysis", Meteorologiya i Gidrologiya, No 11, 1961, pp 22-30, Electricite de France, Centre de Recherches et d'Essais de Chatou, Traduction 1343
- Grace, Robert A , "How to Measure Waves", Ocean Industry, Vol 5, No 2, 1970, pp 65-69
- Harris, D L , "The Analysis of Wave Records", Coastal Engineering, Proceedings of Twelfth Conference, 1970
- Hom-ma, M Horikawa, K , and Komori, S , "Response Characteristics of Underwater Wave Gage", Proceedings of the 10th Conference on Coastal Engineering, Tokyo 1966", pp 99-114
- Mei, C C and Chu, Vincent, "Slowly Varying Stokes Waves", Journal of Fluid Mechanics (1970)
- Williams, Leo C , Technical Memorandum No 30, Dec 1969, U S Army Corps of Engineers, Coastal Engineering Research Center, 1969

LEGEND TO FIGURES

- Fig 1 Sketch of installation (not to scale)
- Fig 2 Computed frequency energy spectra from continuous wave gage superimposed on computed spectra from a) compensated upper pressure gage, b) uncompensated upper pressure gage, c) compensated lower pressure gage, d) uncompensated lower pressure gage, e) step resistance relay gage
- Fig 3 Comparison of RMS heights, compensated upper pressure gage vs continuous wire gage
- Fig 4 Comparison of RMS heights, compensated lower pressure gage vs continuous wire gage
- Fig 5 Comparison of RMS heights, step resistance relay gage vs continuous wire gage
- Fig 6 The function, $n(f)$ for the upper pressure gage for all samples
- Fig 7 The function, $n(f)$ for the upper pressure gage for high wave samples
- Fig 8 The function, $n(f)$ for the lower pressure gage for all samples
- Fig 9 The function, $n(f)$ for the lower pressure gage for high wave samples

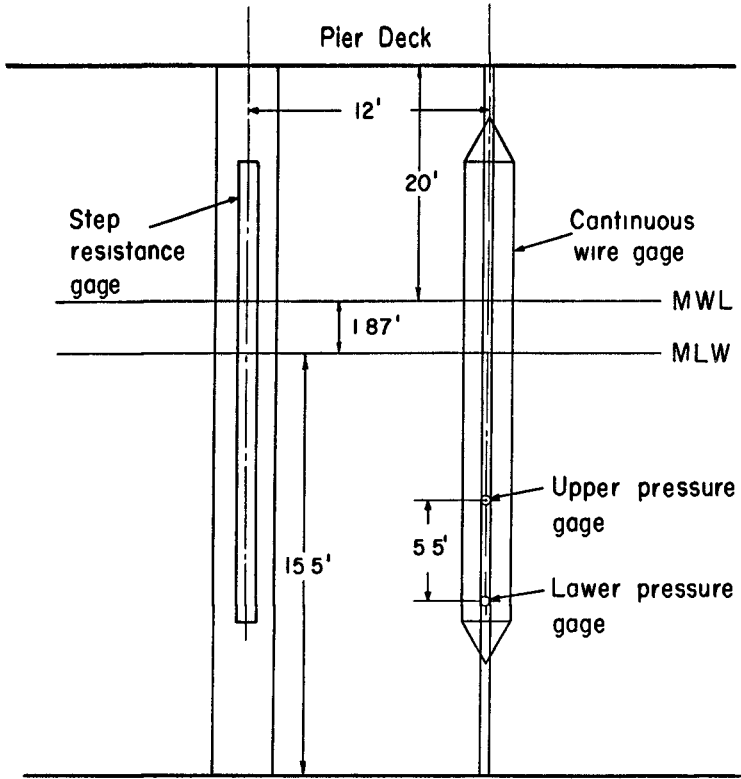


Fig 1 Sketch of Installation (not to scale)

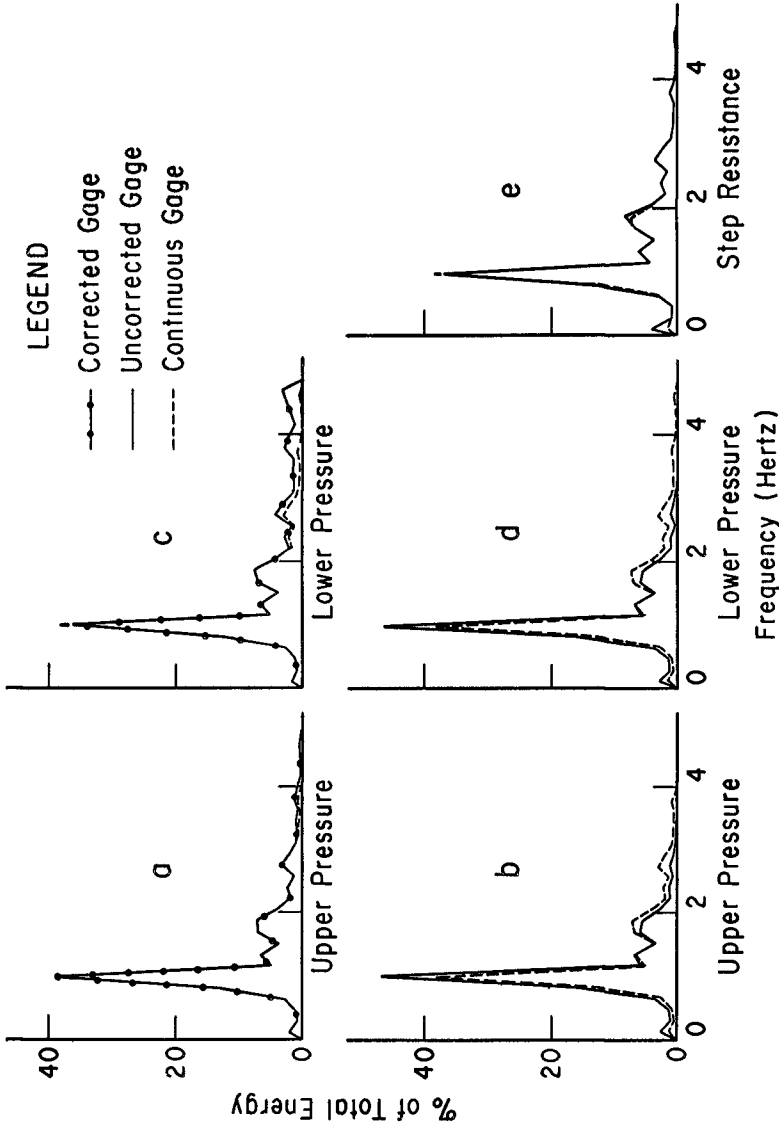


Fig 2 Computed Frequency Energy Spectra from continuous wave gage superimposed on computed spectra from a) compensated upper pressure gage, b) uncompensated upper pressure gage, c) compensated lower pressure gage, d) uncompensated lower pressure gage, e) step resistance relay gage

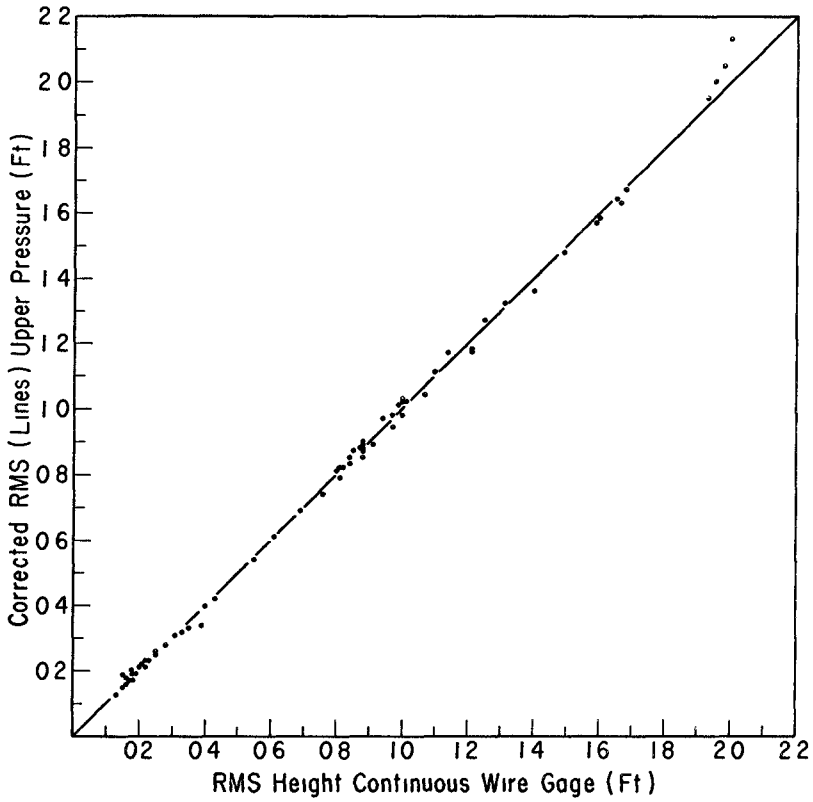


Fig 3 Comparison of RMS heights, compensated upper pressure gage vs continuous wire gage

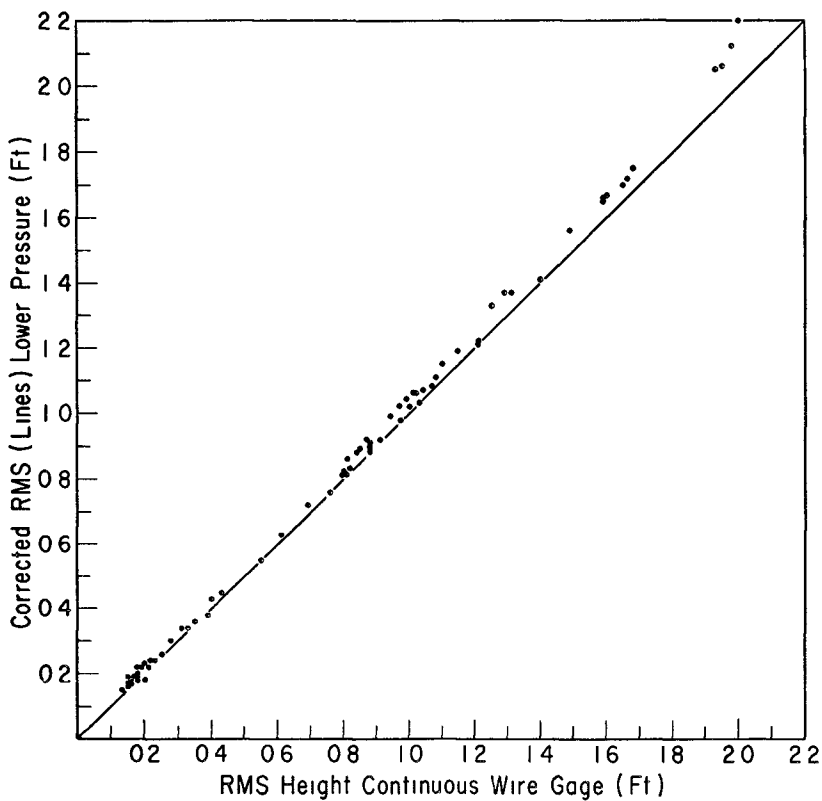


Fig 4 Comparison of RMS heights, compensated lower pressure gage vs continuous wire gage

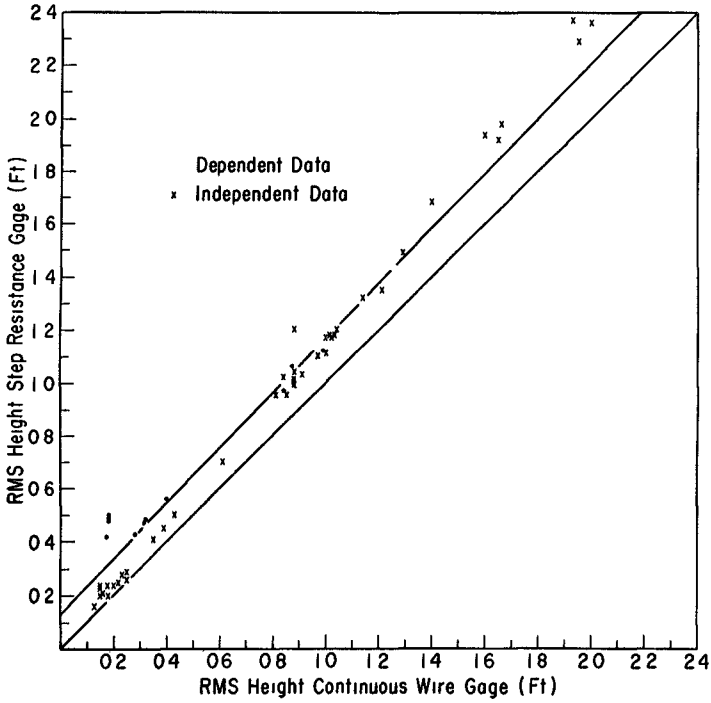


Fig 5 Comparison of RMS heights, step resistance relay gage vs continuous wire gage

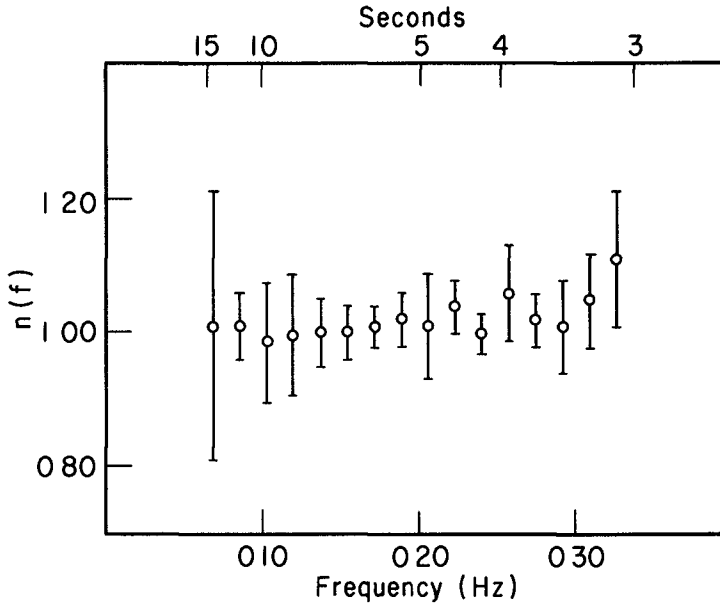


Fig 6 The function, $n(f)$ for the upper pressure gage for all samples

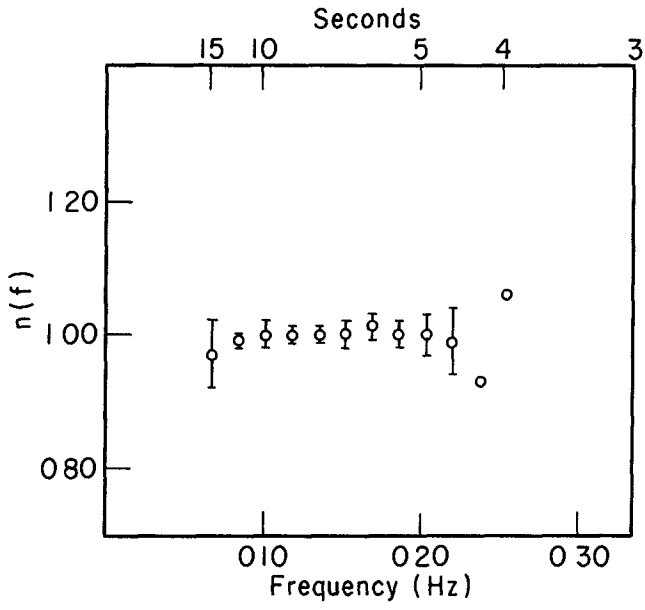


Fig 7 The function, $n(f)$ for the upper pressure gage for high wave samples

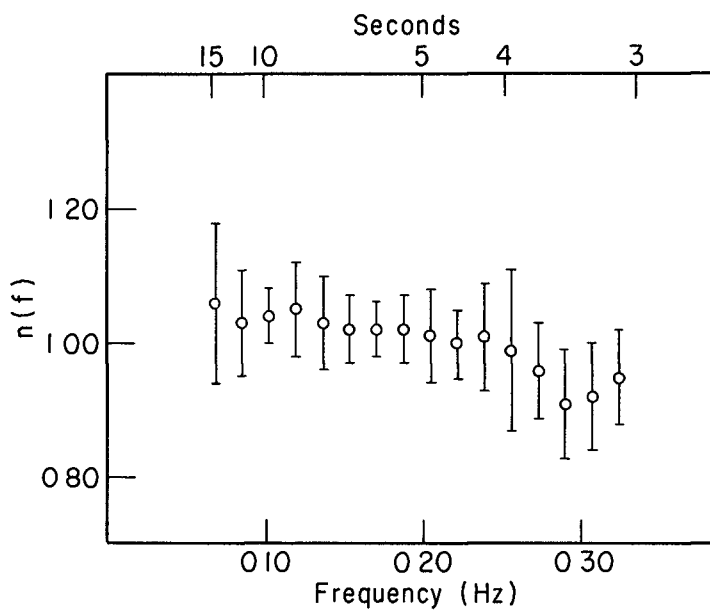


Fig 8 The function, $n(f)$ for the lower pressure gage for all samples

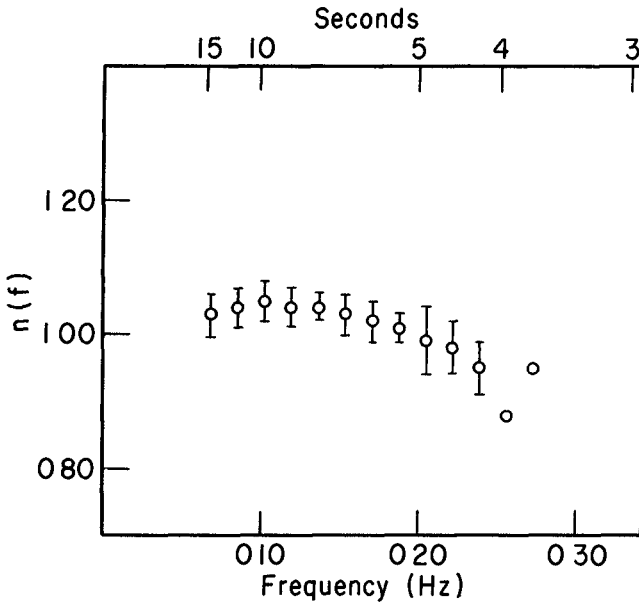


Fig 9 The function, $n(f)$ for the lower pressure gage for high wave samples

CHAPTER 8

DIRECTIONAL SPECTRA FROM WAVE-GAGE ARRAYS

by

N N Panicker

Graduate Student, Dept of Civil Engineering
University of California, Berkeley, Calif

and

L E Borgman

Professor of Geology and Statistics
University of Wyoming, Laramie, Wyoming

SYNOPSIS

The ocean surface may be considered to be composed of many waves traveling at different directions with different frequencies. A graphical plot showing the allocation of wave energy to the different component frequencies and directions is the directional spectrum. Directional spectrum has many applications in Coastal Engineering. Herein an analytical procedure is developed to obtain the directional spectrum from records of an array of wave gages. The two methods developed are the "locked phase method" and the "random phase method". The locked phase method can be used to obtain the distribution of both phase as well as energy of the waves with respect to frequency and direction and is a deterministic approach. The random phase analysis, on the other hand, is more suitable for wind waves in the ocean and yields just the distribution of energy alone as in most other procedures of spectrum analysis. The procedures programmed for computers are checked using simulated data and laboratory data. Wave records of the Pacific Ocean obtained off Point Mugu, California, on a 5-gage array were analyzed using the method developed and examples of the directional spectra obtained are presented.

INTRODUCTION

When confronted with a design or operation in the ocean environment, an engineer invariably needs to know how high the waves are and from which direction they are coming. Had ocean waves been single sinusoids, one could immediately obtain the height and direction of the waves. But waves in the ocean do not look like sinusoids. At best

the ocean surface may be thought of being the result of adding together very many sinusoids of various frequencies traveling in various directions. Therefore one has to specify the particular wave for which the height and direction are desired. As frequency, f , inverse of the period of the component wave, is the least easily changeable wave parameter, the component wave may be specified by its frequency. So, the problem is to obtain the wave amplitude a_1 and direction θ_1 for the various component frequencies, f . But to consider the ocean surface to be composed of a finite number of sinusoids is a poor approximation. A better approximation would be obtained if one lets the number of component simple harmonic waves to approach infinity and the frequency interval, Δf , between them to approach zero. The individual wave amplitudes, a_1 , in this case must approach zero in order for the overall wave heights to maintain a finite, mean square value. However, in this limiting process the quantity $a_1^2/2\Delta f$ remains finite and therefore it can be plotted as a continuous function of frequency. If the quantity $a_1^2/2\Delta f$ is plotted against frequency, the area under the curve within the frequency band of Δf is $a_1^2/2$, but this is proportional to the wave energy contributed by that frequency band because the energy of a simple harmonic wave of amplitude a_1 in a medium of unit weight γ is $\gamma a_1^2/2$ per unit width of crest, see, for example, Wiegel (44). In the same manner the number of component directions may be assumed to approach infinity to yield a continuous function of direction and the area under that curve for any angular width will be proportional to the energy of the waves traveling in those directions for a particular frequency. Alternately, the above two plots can be combined into a two-dimensional plot which will show the distribution of energy with respect to frequency and direction. This is the Directional Spectrum.

USES OF DIRECTIONAL SPECTRA

Directional spectrum shows the distribution of wave energy against frequencies and directions. Therefore, it specifies the wave climate more completely than any other way, ideally. When only some particular information like the predominant wave period and height alone are needed, that can be obtained from the directional spectrum. R M S wave height, for example, is the volume under the directional spectrum. Scott (37) and Neumann and Pierson (34) provide equations for the significant wave height from R M S wave height assuming different distributions for the frequency spectrum. As Wiegel (46) pointed out, there are still situations where the significant wave concept is useful to the design engineer, but it might be possible to obtain that information from the directional spectrum. Nevertheless, there are many engineering problems where directional spectra are the necessary input data for the correct design or prediction. For example, for the study of the diffraction of wind waves directional spectrum is necessary and, in fact, Wiegel and Mobarek (45) and Fan (19) successfully used it for the study of diffraction of laboratory wind waves. Refraction of ocean waves is another problem where the directional spectrum is needed and Karlsson (24) used it for practical cases. In the design of offshore towers and piles directional spectrum is useful for the analysis of vibration and three-dimensional analysis.

of structures with torsional loads Malhotra and Penzien (29) have succeeded in developing the procedure for analyzing tower structures using the spectrum and indicated the need for the directional spectrum For structures subjected to random forces, in general, a design by the method of simulation on a computer is highly suited and directional spectra are the suitable input data Borgman (11) showed how this can be done for offshore pile structures by linearizing wave forces Directional spectrum is necessary for the prediction of the response of ships and floating drilling vessels to sea conditions as the spectra of their motions can be obtained from the directional spectra of the sea It is, in fact, used by naval architects (see for example, Abkowitz, Vassilopoulos and Sellars (1)) Even for the design of an ocean outfall sewer, directional spectrum may be useful because, as Wiegel (43) pointed out, mixing and wave spectra are related Once a single wave model for longshore transport is established, directional spectrum may prove to be specifically cut out for the study of littoral transport because it provides at once the three crucial parameters of the problem, viz the wave energy, frequency and direction Another major use for directional spectrum is in wave forecasting and hindcasting In hindcasting the location of the origin of storms and the path of swell can be deduced from the variation of the non-stationary directional spectra, see Munk et al (32)

When directional spectra become available for desired locations, several other uses also may be found for them The problem at present is its non-availability for almost any place Here again, barring the huge expenses involved in the collection of necessary data, the main hurdle is the lack of a valid, dependable computational procedure to obtain directional spectra in a routine manner

REVIEW OF METHODS USED

The most direct way of obtaining the directional spectrum is to obtain the sea surface elevations over an area by stereophotographs and to analyze these data to get the directional spectra This was done in the Atlantic Ocean by W J Pierson and his group, see Cote et al (17), and in a much more modest scale by Ijima et al (23) From the story of the Stereo Wave Observation Project [Cote et al (17)] one realizes how arduous and expensive this method is Kinsman (25) therefore doubts whether it will ever become habit forming Another successful method applicable for deep ocean is to take records of the elevation and tilt of a free floating buoy as used by Longuet-Higgins, Cartwright and Smith (27) From the water surface elevation and the slopes in two coordinate directions they computed the first five coefficients (i.e. two harmonics) of the Fourier series expansion of the directional spectrum To remove the appearance of negative energy they used a smoothing function $w_2 = \frac{8}{3} \cos^4 \frac{\phi}{2}$ The net result of having a directional spectrum represented only up to two harmonics and then smoothing it is to get a very broad angular width for the spectrum If more accuracy is needed, records of the water surface curvatures are to be obtained Ewing (18) also obtained a sequence of ten records

of the directional spectra from the motions of a floating buoy located in the North Atlantic

The use of an array of wave recorders to measure wave parameters and the computation of directional spectrum from it was tried by several workers Barber (3) was probably the first to suggest it The wave-gage array could be one-dimensional (line array) or two-dimensional If one can make sure that no wave comes from one of the sides of a line array, a line array can be used to obtain directional spectrum Barber and Doyle (4), described a procedure to get the directions of swells by using just two gages Stevens (39) described the procedure to obtain directional spectrum from a line array and used it for an array in Buzzards Bay Macovsky and Mechlin (28) described a possible method of using a line array of inverted acoustic fathometers mounted on the deck of a submarine Two-dimensional arrays, in general, would be more appropriate for a general situation Barber (6) discussed a general theory of gage arrays and suggested ways to compare the directional resolving power of different arrays Mobarek (31) found that the discrete energy method was the most successful of the methods for the estimation of directional spectra for laboratory wind waves Fan (19) used a 4-gage array in the form of a star and compared the Fourier transform method and Least Square Method by simulation technique to obtain the directional spectra He found that the Fourier Transform Method gave better results for higher frequency components and the Least Square Fitting Method gave better results for lower frequency components Two-dimensional arrays have also been used in the ocean Munk, Miller, Snodgrass and Barber (32) used three bottom pressure gages forming an equilateral triangle with sides about 900 ft in 330 ft of water and obtained the direction of long period swell from the data Bennett, Pittman and Austin (7) and Bennett (8) described a 6-gage array in the form of a Pentagon with one gage at the center, which was used off Panama City, Florida in the Gulf of Mexico at depths of 63 ft and 104 ft Bennett (8) essentially used the procedure of Munk et al (32) by fitting a single wave of a particular frequency to the cross-spectrum equations This may, perhaps, be sufficient to obtain the direction of long period swell But as Tukey (42) pointed out, in analyzing or thinking about a computational process involving several layers of approximations, or the propagation of sampling fluctuations through several layers of transformations, step-by-step analysis is not likely to be enough and an analysis of the overall process is needed

A few other methods have also been reported Nagata (33) measured orbital motions with electromagnetic current meters and used it to obtain the directional spectra Ford, Timme and Trampus (20) used a triset sensor made up of three vertical surface-penetrating wave staffs located at the corners of a right triangle of side about 5 ft to obtain the three outputs, viz two components of wave slope and the average wave amplitude at the sensor From these they calculated the directional spectrum accurate up to 2 harmonics just in the same way as Longuet-Higgins et al (27) did Simpson (38) had a similar arrangement but the probes at the apices of the right triangle

measured orbital velocities instead, and the side of the triangle was about 3 ft. By this arrangement he could obtain the first 4 harmonics of the directional spectra. Suzuki (40) proposed another method of determining the directional spectra of sea waves using a wave gage and a wave direction meter which can record X and Y component of wave force acting on a bottom mounted sphere.

There may, perhaps, be many more ingenious ways of obtaining the directional spectra. But it seems to the authors that wave gage arrays might be the most convenient arrangement for collecting data in a routine way to determine the directional spectra. Hence a general theory for the determination of directional spectra from records of wave gage arrays and a computer program for it were developed. A brief description of the theory and the results obtained are described below. The equations for use when the wave gages measure surface elevations are presented here. The detailed development of the general case will be given in a separate report.

A THEORY FOR GAGE ARRAYS

The Modes of Analysis

Two modes of analysis are developed - the locked phase method and the random phase method. The locked phase mode of analysis is essentially a deterministic approach where the phases of the component waves are assumed to be fixed. Hence the analysis provides both the distribution of energy with frequency and direction as well as the distribution of phase angle with frequency and direction. In the random phase method the phases of component waves are considered to be random and independent of each other, hence they average out in the analysis. The locked phase mode of analysis is appropriate to situations where phase is locked to particular values, such as in a wave tank with flapper. The random phase mode of analysis, on the other hand, is applicable to situations where phase changes randomly with time as in narrow band surf or wind waves.

Locked Phase Mode of Analysis

The wave surface elevation, q , at a given instant of time t , is considered to be the result of superposition of a large number of simple harmonic waves each with its own frequency and direction. Let the amplitudes of the component waves be $a_0, a_1, a_2, \dots, a_m, \dots, a_M$ and frequencies $f_0, f_1, f_2, \dots, f_m, \dots, f_M$ and let them propagate in all directions between $-\pi$ and π . Let φ be the phase and θ the direction of wave. Let the coordinates of gage j in an array be x_j and y_j and let the wave number be $k = 2\pi/\text{wave length}$. Then the water surface elevation at gage j at time t can be written as

$$q_j(t) = \sum_{m=0}^M \int_{-\pi}^{\pi} a_m(\theta) \cos [kx_j \cos\theta + ky_j \sin\theta - 2\pi f_m t + \varphi_m(\theta)] \quad (1)$$

The subsequent development will make use of the Fast Fourier-Transform technique [see Cooley & Tukey (16), Cochran et al (15), Bergland (9) or Bingham, Godfrey and Tukey (10)] Let the length in time of the water surface elevation record be T and let the discrete time interval of recording be Δt Let T and Δt be such that $N = \frac{T}{\Delta t}$ be a power of 2 One gets the complex amplitude spectrum A_m by taking the FFT of the surface elevation record q_n

$$A_m = \Delta t \sum_{n=0}^{N-1} q_n e^{-12\pi mn/N} \quad (2)$$

Let the directional distribution be represented as a finite Fourier series in complex form as below

$$\begin{aligned} a_m(\theta) e^{i\varphi_m(\theta)} &= F(\theta) \\ &= \frac{a_0 + ia'_0}{2} + \sum_{n=1}^N [(a_n + ia'_n) \cos n\theta + (b_n + ib'_n) \sin n\theta] \quad (3) \end{aligned}$$

To determine the directional spectrum one therefore has to evaluate the coefficients $a_0, a'_0, a_1, a'_1, b_1, b'_1$ etc After going through some mathematical manipulations, one can come up with the following two equations for the real and imaginary parts of the FFT coefficients A_m of the surface elevation record for each gage

$$\begin{aligned} \Re(2A_m^{(j)}/\pi T) &= a_0 A_{0j}^* - (a'_1 A_{1j}^* + b'_1 B_{1j}^*) - (a_2 A_{2j}^* + b_2 B_{2j}^*) \\ &\quad + (a'_3 A_{3j}^* + b'_3 B_{3j}^*) + (a_4 A_{4j}^* + b_4 B_{4j}^*) - \quad (4) \end{aligned}$$

$$\begin{aligned} \Im(2A_m^{(j)}/\pi T) &= a'_0 A_{0j}^* + (a_1 A_{1j}^* + b_1 B_{1j}^*) - (a'_2 A_{2j}^* + b'_2 B_{2j}^*) \\ &\quad - (a_3 A_{3j}^* + b_3 B_{3j}^*) + (a'_4 A_{4j}^* + b'_4 B_{4j}^*) + \quad (5) \end{aligned}$$

In these equations,

$$A_{nj}^* = 2 \cos n\beta J_n(kD) \quad (6)$$

and

$$B_{nj}^* = 2 \sin n\beta J_n(kD) \quad (7)$$

where

β = angle of gage j from origin

$J_n(kD)$ = Bessel function of order n with argument
kD in which k = wave number and D = distance
of the gage from the origin

Once the coefficients a_n, a'_n, b_n and b'_n are evaluated from the above equations up to the number of harmonics feasible with the number of gages, one may obtain the energy and phase by the following relationships

$$a_m^2(\theta) = |F(\theta)|^2 \tag{8}$$

$$\varphi_m(\theta) = \arg [F(\theta)] \tag{9}$$

Random Phase Analysis

Let $p(f, \theta)$ be the directional spectral density function valid for $f > 0$ and $-\pi \leq \theta < \pi$. Then it can be shown, after Pierson and Marks (35), that the water surface elevation $q(x, y, t)$ at gage j at time t can be symbolically written as

$$q(x, y, t) = 2 \int_0^\infty \int_{-\pi}^\pi \sqrt{p(f, \theta)} df d\theta \cos (kx \cos \theta + ky \sin \theta - 2\pi ft + \varphi) \tag{10}$$

$q(x, y, t)$ here ends up with a Gaussian probability density for any fixed x, y and t , because of the normal convergence criterion [Brown (14), Loeve (26), Takano (41)]. The cross covariance between water surface elevations at two gages therefore turns out to be independent of phase. The directional spectrum may be represented as a finite Fourier series of the form

$$p(f, \theta) = \frac{a_0}{2} + \sum_{n=1}^N (a_n \cos n\theta + b_n \sin n\theta) \tag{11}$$

Here the Fourier series coefficients a_n and b_n are to be evaluated. In terms of the co- and quad- spectrum for each pair of gages the following two equations can be written down

$$\text{Co-spectrum}_{j\ell} = \pi [a_0 A_{0j\ell}^* - (a_2 A_{2j\ell}^* + b_2 B_{2j\ell}^*) + (a_4 A_{4j\ell}^* + b_4 B_{4j\ell}^*) - \tag{12}$$

$$\text{Quad-spectrum}_{j\ell} = \pi [(a_1 A_{1j\ell}^* + b_1 B_{1j\ell}^*) - (a_3 A_{3j\ell}^* + b_3 B_{3j\ell}^*) + (a_5 A_{5j\ell}^* + b_5 B_{5j\ell}^*)] \tag{13}$$

The co-spectrum and quad-spectrum can be calculated from the FFT coefficients on gage j and gage ℓ . The quantities A_n^* and B_n^* are as below

$$A_n^* = 2 \cos n\beta J_n(kD) \tag{14}$$

and

$$B_n^* = 2 \sin n\beta J_n(kD) \tag{15}$$

- where β = angle between gage j and gage ℓ
- D = distance between the gages,
- k = wave number = $2\pi/\text{wave length}$ and
- J_n = Bessel function of order n

The unknowns are the Fourier series coefficients a_0, a_1, b_1, a_2, b_2 etc. There are two equations for each pair of gages and two unknowns for every harmonic.

Least square analysis is used to make coefficient estimates. In both procedures, a unidirectional wave train will produce analytical results spread over an angular band width, because only a finite number of Fourier coefficients can be estimated.

COMPUTATION OF DIRECTIONAL SPECTRA

A very general computer program was developed to compute the directional spectrum, the details of which will be reported subsequently. The analytical procedure and the scheme of computation was verified for their validity and workability by computation of known directional spectra using the scheme. The directions obtained out of the computer checked very well with the known directions of the simulated wave as well as regular waves generated in the laboratory when the respective data were fed in. However, there was considerable angular spread in the results obtained for directions. These were due to leakage, finite length of data and the truncation of Fourier series representing directional spectra. It was also noticed that there was considerable negative energy showing up in the spectra. As the negative energy caused by the presence of one wave may foul up with the positive contribution from another wave in the system, the presence of negative energy may affect appreciably the directional resolution. Hence this had to be cured. For this a non-negative smoothing function $W_2(\varphi)$ was applied where

$$W_2(\varphi) = R_N \cos^{2N} \left(\frac{\varphi}{2} \right) \quad (16)$$

in which R_N is a coefficient to be obtained for each harmonic. Borgman (12) has described the procedure to apply this smoothing. The smoothing, however, broadens the angular spread of the directional spectrum and decreases the value of the spectral peak. The problem of de-smoothing the spectra seems to be very important and perhaps Medgyessey (30) may yield some clues.

The scheme of computation developed was used to compare the directional resolving power of some two-dimensional arrays by simulating a single wave train and comparing the response to it from different gage arrays. Figures 1 and 2 tabulate the relevant quantities for comparison. The difference between the two tables is that the quantities in Table 1 are obtained without W_2 smoothing, whereas the quantities in Table 2 are smoothed. A comparison shows that all the arrays considered give the direction correctly, but there is a difference in the angular spreads and the values of spectral peaks. For a single wave train the spectrum should have been theoretically a Dirac delta function, i.e. a spike. So, the narrower the angular spread and the higher the peak, the better the resolving power of the array. By this token, out of the five gage arrays tested, the CERC array seems to be the best. Figure 3 gives the plots of smoothed directional spectra obtained for different arrays for various input directions.

Input wave direction	3-GAGE CIRC			1-GAGE STAR			5-GAGE PENTAGON			6-GAGE HEXAGON			5-GAGE PLUS		
	Peak Spectral Density	Maximum Side-lobe	Minimum Side-lobe	Peak Spectral Density	Maximum Side-lobe	Minimum Side-lobe	Peak Spectral Density	Maximum Side-lobe	Minimum Side-lobe	Peak Spectral Density	Maximum Side-lobe	Minimum Side-lobe	Peak Spectral Density	Maximum Side-lobe	Minimum Side-lobe
-90	1 87111	0 25676	-0 11661	0 98037	0 11427	-0 22266	1 00077	0 15734	-0 23329	0 98637	0 14361	-0 22791	0 54866	0 10918	-0 14352
80	1 87641	0 -6657	-0 12757	0 98217	0 14733	-0 22034	0 98187	0 15297	-0 23493	0 98476	0 14447	-0 22289	0 54762	0 10757	-0 14163
-70	1 87116	0 25783	-0 11931	0 98653	0 14723	-0 22474	0 98569	0 13525	-0 21877	0 98363	0 14402	-0 22431	0 54479	0 10624	-0 13537
-60	1 86699	0 26044	-0 12718	0 98929	0 14320	-0 22070	0 98266	0 16019	-0 23962	0 98411	0 14437	-0 22384	0 54563	0 10953	-0 13522
0	1 86571	0 24650	-0 11769	0 98653	0 11723	0 22474	0 98398	0 16117	-0 23933	0 98363	0 14402	-0 22431	0 54850	0 11436	-0 13522
-10	1 85183	0 21709	-0 11777	0 98217	0 14733	-0 22773	0 97211	0 11121	-0 22459	0 98476	0 14447	-0 22289	0 54850	0 11436	-0 13532
-30	1 85945	0 24825	-0 11255	0 98057	0 14427	-0 22566	0 97645	0 14736	-0 23020	0 98637	0 14361	-0 22291	0 54563	0 10953	-0 13522
-20	1 83773	0 23238	-0 10213	0 98217	0 14733	-0 22773	0 99980	0 16013	-0 23718	0 98476	0 14447	-0 22289	0 54479	0 10624	-0 13557
-10	1 85535	0 24408	-0 10648	0 98653	0 14723	-0 22474	0 98749	0 15734	-0 23420	0 98363	0 14402	-0 22431	0 54762	0 10757	-0 14163
0	1 83199	0 22419	-0 10833	0 98929	0 14320	-0 22069	0 98631	0 13020	-0 21345	0 98411	0 14437	-0 22384	0 54968	0 10918	-0 14352
10	1 84111	0 -1108	-0 10618	0 98653	0 11723	-0 22171	0 98749	0 15734	-0 23420	0 98363	0 14402	-0 22431	0 54782	0 10757	-0 14163
-30	1 84771	0 -548	-0 10211	0 98217	0 11733	-0 22771	0 99980	0 16011	-0 23718	0 98176	0 14417	-0 22289	0 54179	0 10621	-0 13537
30	1 84111	0 -1923	-0 1111	0 98077	0 11127	-0 22866	0 97613	0 11736	-0 23020	0 98637	0 11361	-0 22289	0 51363	0 10953	-0 13522
50	1 84111	0 -170	-0 11777	0 98217	0 11715	-0 22771	0 97211	0 11121	-0 22159	0 98176	0 11117	-0 22289	0 51850	0 11136	-0 13532
70	1 84111	0 -16	-0 1176	0 98653	0 11743	-0 22171	0 98698	0 16117	-0 24933	0 98363	0 11102	-0 22431	0 51850	0 11136	-0 13532
90	1 84111	0 -101	-0 11718	0 98653	0 11540	-0 23070	0 99486	0 16019	-0 23962	0 98111	0 11137	-0 22384	0 51850	0 11136	-0 13522
110	1 84111	0 -376	-0 11111	0 98653	0 11723	-0 22171	0 98929	0 15423	-0 21877	0 98363	0 11102	-0 22111	0 51179	0 10621	-0 13537
130	1 84111	0 17	-0 1177	0 98176	0 11715	-0 22111	0 98187	0 15297	-0 21911	0 98176	0 11117	-0 22289	0 51762	0 10757	-0 14163
150	1 84111	0 -34	-0 11111	0 98077	0 11127	-0 22866	1 00077	0 11711	-0 23129	0 98637	0 11361	-0 22291	0 51966	0 10918	-0 13532

FIG 1 DIRECTIONAL RESOLVING POWER OF DIFFERENT WAVE GAGE ARRAYS
 DIRECTIONAL SPECTRA OBTAINED FOR AN INPUT WAVE OF AMPLITUDE
 0.1 AND PERIOD 2 SEC WITHOUT SMOOTHING

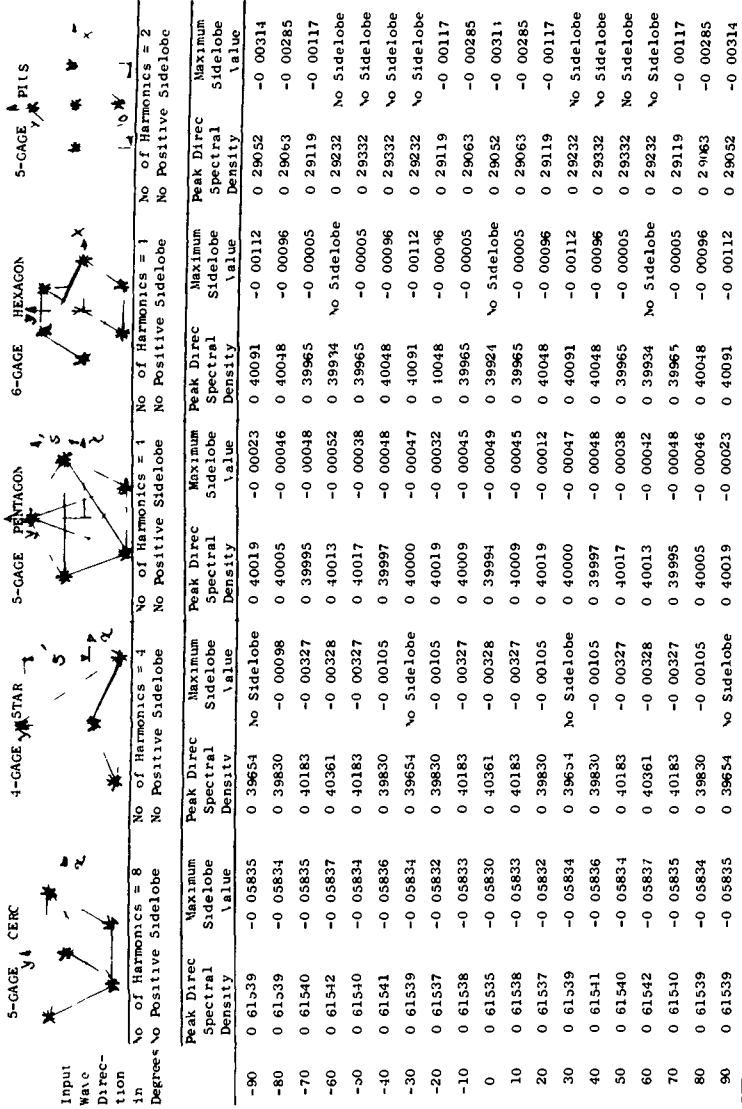


FIG 2 DIRECTIONAL RESOLVING POWER OF DIFFERENT GAGE ARRAYS
 DIRECTIONAL SPECTRA OBTAINED FOR AN INPUT WAVE TRAIN OF PERIOD
 2 SEC AND AMPLITUDE 0.1' WITH W₂ SMOOTHING

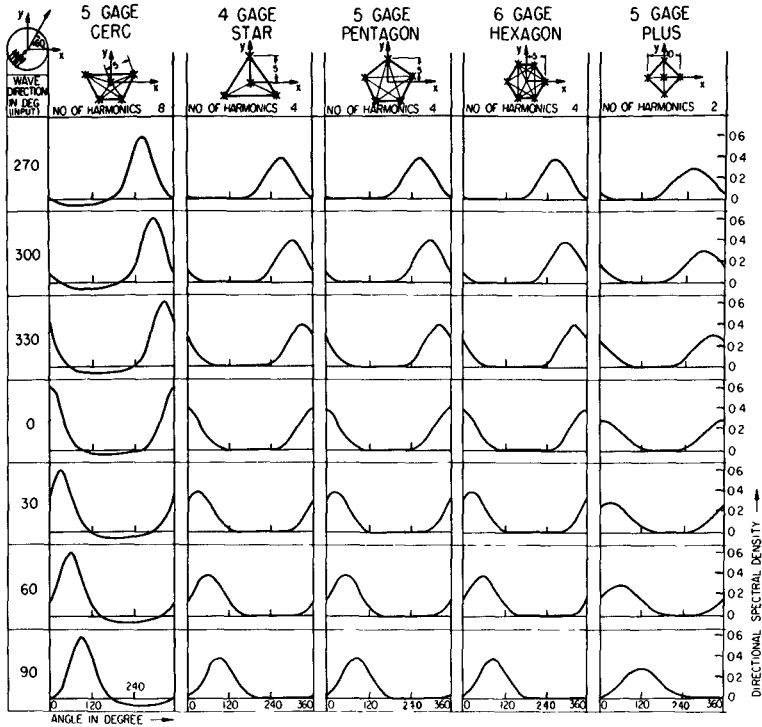


FIG 3 DIRECTIONAL RESOLVING POWER OF GAGE ARRAYS
 DIRECTIONAL SPECTRA OBTAINED ON DIFFERENT ARRAYS WITH W_2
 SMOOTHING FOR FREQUENCY 0.5 Hz FOR A SINGLE WAVE TRAIN OF
 PERIOD 2 SEC AND AMPLITUDE 0.1' COMING FROM DIFFERENT
 DIRECTIONS

Analysis of Data From the Pacific Ocean

Figure 4 gives the location map and Fig 5 the gage orientation for a 5-gage array put up by the Coastal Engineering Research Center in the Pacific Ocean off Point Mugu, California. This array was specifically designed for the determination of directional spectrum of ocean waves of periods between 7 sec and 25 sec, see Borgman and Panicker (13) for the design. The gages were subsurface pressure transducers placed 3 feet from the bottom at a water depth of 30 feet and 1600 feet away from the shore. The wave data were analyzed for directional spectrum using the method developed. Some examples of results obtained are given below.

The choice of a frequency band for averaging the spectra was made by studying Fig 6 which shows the effect of the use of different frequency bands for averaging. When the band width is large, the confidence interval of the spectral estimate is close, but the spectrum obtained is rather too smooth, see, for example, the spectrum obtained when averaging is made in blocks of 64 FFT coefficients, i.e., in band width of 64/1024 Hz. The spectrum is so smooth that it does not show the bimodality indicated by most other cases with block averaging in narrower frequency band width. But when the block averaging is done in too narrow a frequency width, as in block averaging of 4 Fourier coefficients, the spectrum shows much erratic nature. Tentatively, therefore, it was decided to average in blocks of 32 FFT coefficients and 16 FFT coefficients. Figure 7 shows a comparison of the spectra obtained at the different gages. They compare well but there is some discrepancy at peak frequencies. Figures 8 and 9 show typical directional spectra obtained for the locality using the random phase method of analysis described. The spectral densities shown are based on pressure in ft of water and not adjusted for surface elevations. The dominant directions would not be affected, anyway. Figure 8 shows a comparison of the directional spectra obtained at two different times. Notice the arrival of the prominent swell in the morning of March 28. Figure 9 shows a contour plot of directional spectrum obtained with a block averaging of 16 FFT coefficients, or a frequency band width of 16/1024 Hz. The typical bimodal spectrum of the Pacific coast can be seen with the ridges showing the strong sea and swell, both being shown to come generally from the West South West.

CONCLUSIONS

The following conclusions may be drawn from the above discussions:

- 1 Use of wave gage arrays seems to be well suited for the determination of directional spectra in a routine manner.
- 2 The analytical procedure and the scheme of computation developed seem to work well for the different situations tested, viz numerically simulated data, laboratory data and ocean data.

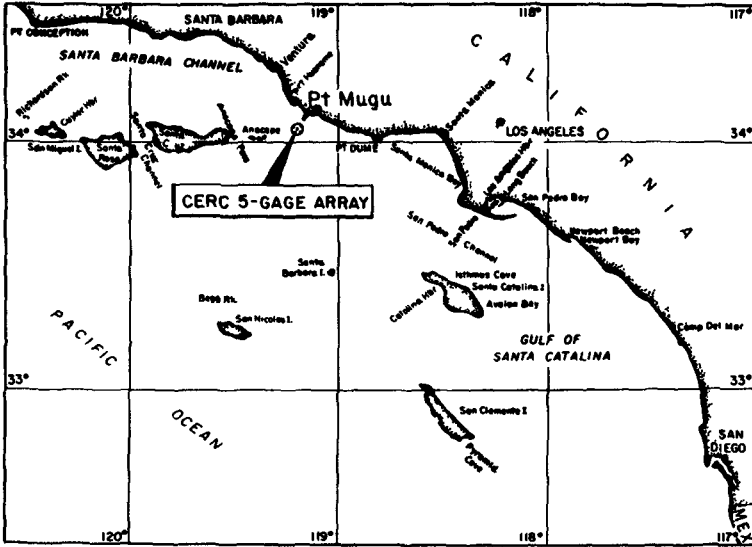


FIG 4 LOCATION MAP OF CERC 5-GAGE ARRAY OFF POINT MUGU, CALIFORNIA

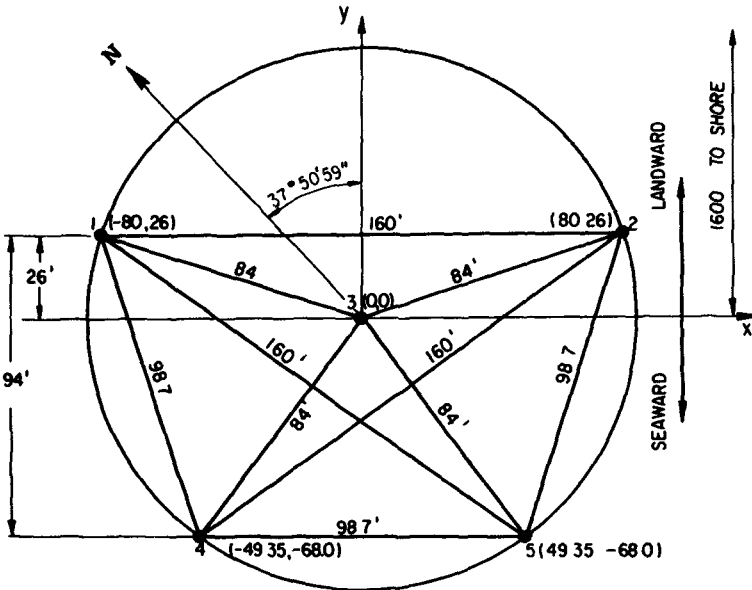


FIG 5 CERC ARRAY OF WAVE GAGES OFF POINT MUGU, CALIFORNIA

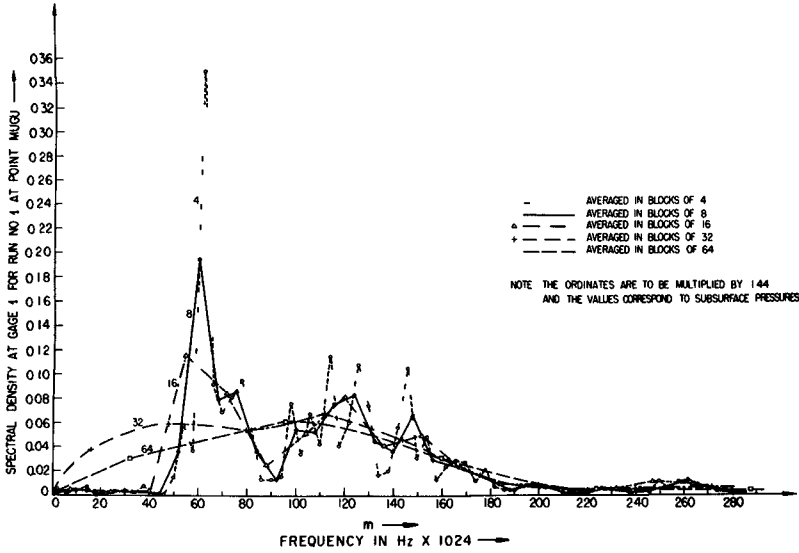


FIG 6 SPECTRA AT GAGE 1 OFF POINT MUGU FOR RUN NO 1, AVERAGE IN BLOCKS 4, 6, 16, 32 and 64

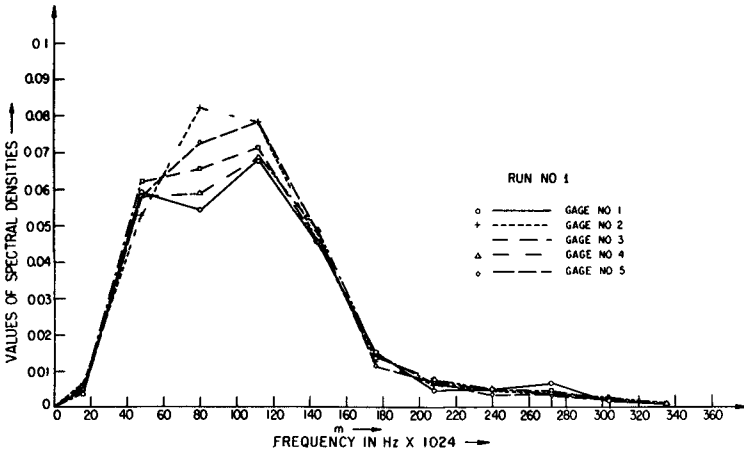
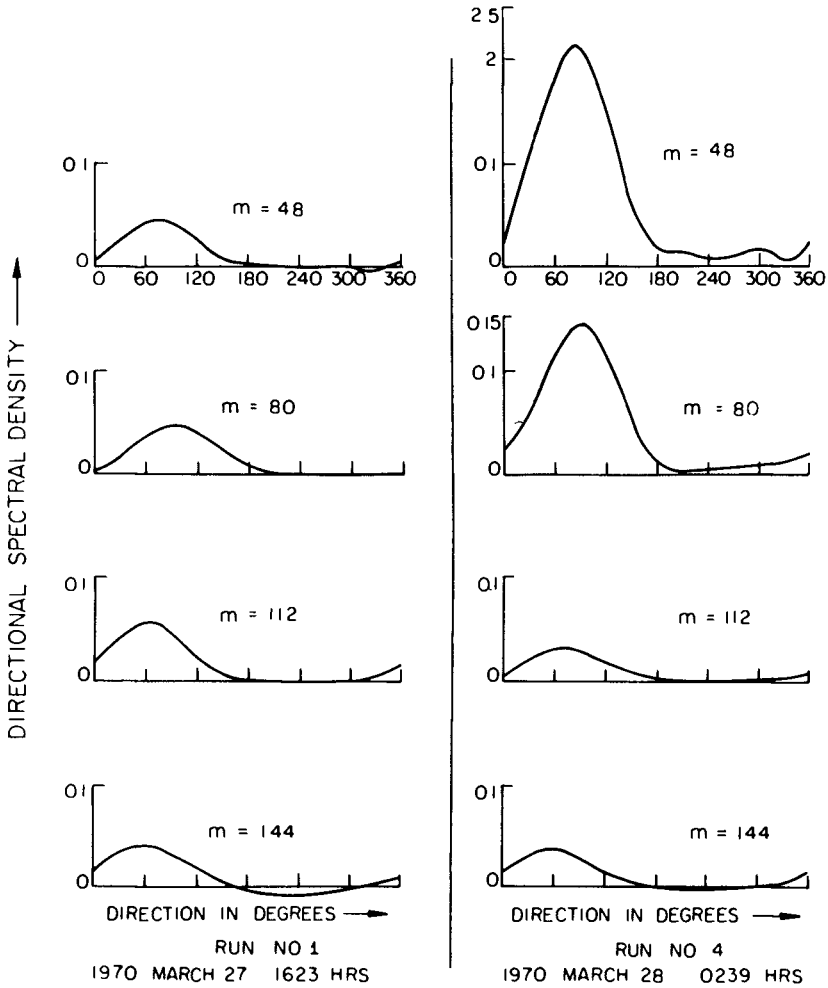


FIG 7 SUBSURFACE PRESSURE SPECTRA AT POINT MUGU AT GAGES 1, 2, 3, 4 AND 5 AVERAGED IN BLOCKS OF 32



NOTE FREQUENCY $f = \frac{m}{1024}$ LENGTH OF BLOCKS IN AVERAGING
 SPECTRA = 32 NO OF HARMONICS TO WHICH DIRECTIONAL
 SPECTRAL DENSITY FUNCTION IS REPRESENTED = 4

FIG 8 DIRECTIONAL SPECTRA OBTAINED FROM CERC 5-GAGE
 ARRAY OFF PT MUGU, CALIFORNIA

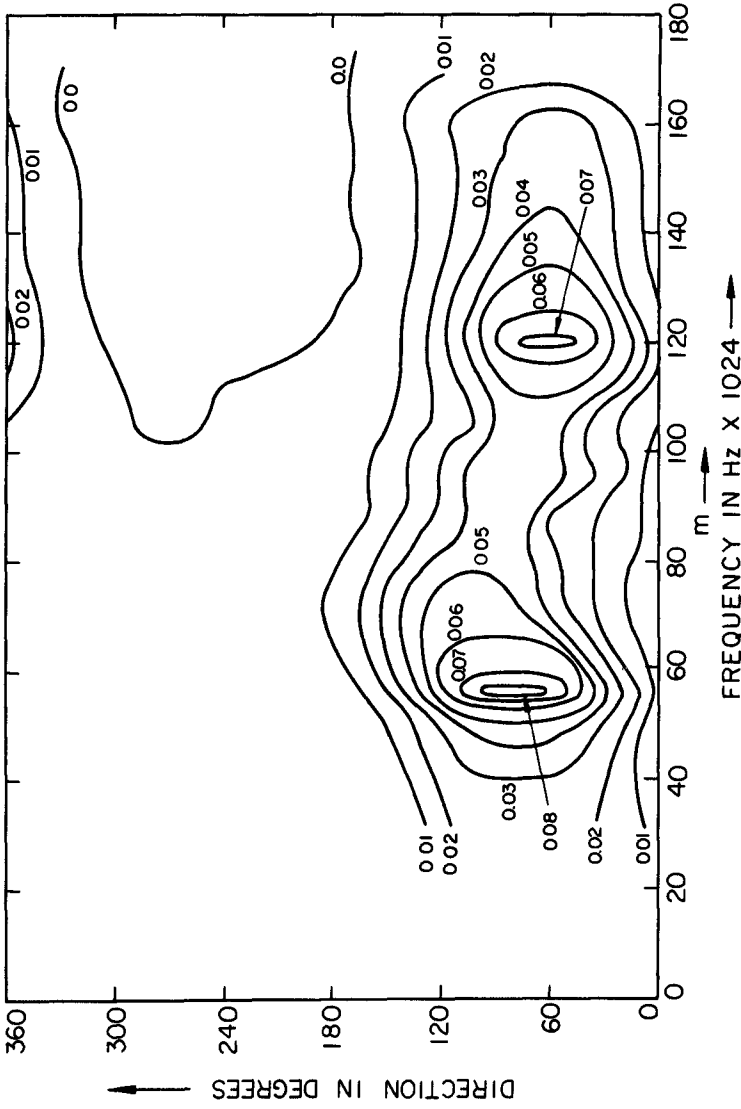


FIG 9 SPECTRA OBTAINED AT POINT MUGU, CALIFORNIA FROM CERC 5-GAGE ARRAY FROM RUN 1, MARCH 27, 1970 AT 1623 HOURS

- 3 Much more research work is needed in almost all aspects of the problem

ACKNOWLEDGMENT

The work presented herein was partially supported by Contract DACW 72-68-C-0016 with the Coastal Engineering Research Center, Corps of Engineers, U S Army. The authors express their appreciation to fellow research workers and to the staff of the Coastal Engineering Research Center who were extremely helpful in every aspect of the work. Professor R L Wiegel of the University of California, Berkeley, contributed greatly to the quality of the work by discussions, encouragement and other help which are highly appreciated. The assistance of Mr Dennis Dufalla of the Computer Science Division of the University of California, Berkeley, is also gratefully acknowledged.

REFERENCES

- 1 Abkowitz, M A , Vassilopoulos, L A and Sellers, F H , "Recent developments in seakeeping research and its application to design," Transactions, Society of Naval Architects and Marine Engineers, vol 74, pp 194-259, 1966
- 2 Abramowitz, M and Stegun, I A , Handbook of Mathematical Functions, Dover Publications, Inc , New York, 1965
- 3 Barber, N F , "Finding the direction of travel of sea waves," Nature, vol 174, pp 1048-1050, Dec 4, 1954
- 4 Barber, N F and Doyle, D , "A method of recording the direction of travel of ocean swell," Deep-Sea Research, vol 3, pp 206-213, 1956
- 5 Barber, N F , "Some relations to be expected between the directional spectra of swell observed at different times and places on the ocean," New Zealand Journal of Science, vol 1, no 2, pp 330-341, June, 1958
- 6 Barber, N F , "Directional resolving power of an array of wave detectors," Ocean Wave Spectra, Prentice-Hall Inc , Englewood Cliffs, N J , pp 137-150, 1961
- 7 Bennett, C M , Pittman, E P and Austin, G B , "Data processing system for multiple series analysis of ocean wave induced bottom pressure fluctuations," 1st U S Navy Symposium on Military Oceanography, pp 379-415, June 1964

- 8 Bennett, C M , "A directional analysis of sea waves from bottom pressure measurements," Transactions of the National Symposium on Ocean Sciences of the Atlantic Shelf, Marine Technology Society, 1965
- 9 Bergland, G D , "A guided tour of the FFT," IEEE Spectrum, pp 41-52, July 1969
- 10 Bingham, C , Godfrey, M D and Tukey, J W , "Modern techniques of power spectrum estimation," IEEE Transactions of Audio and electroacoustics, vol AU-15, No 2, pp 56-66, June 1967
- 11 Borgman, L E , "Ocean wave simulation for engineering design," Proceedings of the ASCE Conference on Civil Engineering in the Oceans, San Francisco, pp 31-74, Sept 1967
- 12 Borgman, L E , "Directional spectra models for design use," Technical Report HEL 1-12, Hydraulic Engineering Laboratory, University of California, Berkeley, June 1969
- 13 Borgman, L E and Panicker, N N , "Design Study for a Suggested Wave gage array off Point Mugu, California," Technical Report HEL 1-14, Hydraulic Engineering Laboratory, University of California, Berkeley, January 1970
- 14 Brown, L J , "Methods for the analysis of non-stationary time series with applications to oceanography," Technical Report, HEL 16-3, Hydraulic Engineering Laboratory, University of California, Berkeley, May, 1967
- 15 Cochran, W T , et al , "What is the FFT?" IEEE Transactions on Audio and Electroacoustics, vol AU-15, no 2, pp 45-55, June 1967
- 16 Cooley, J W and Tukey, J W , "An algorithm for the machine calculation of complex Fourier series," Mathematics of computation, vol 19, pp 297-301, April 1965
- 17 Cote, L J et al , "The directional spectrum of a wind generated sea as determined from data obtained by the Stereo Wave Observation Project," Meteorological Papers, New York University, vol 2, no 6, June 1960
- 18 Ewing, J A , "Some measurements of the directional wave spectrum," Journal of Marine Research, vol 27, no 2, 1969
- 19 Fan, S S , "Diffraction of wind waves," Technical Report HEL 1-10, Hydraulic Engineering Laboratory, University of California, Berkeley, October 1968
- 20 Ford, J R , Timme, R C and Trampus, A , "A new method for obtaining the directional spectrum of ocean surface gravity waves," presented at the Marine Technology Society 3rd Annual National Conference, Surface Wave Measurements Session, June 1967

- 21 Graybill, F , "An introduction to linear statistical models," McGraw-Hill Book Co , Inc , New York, 1961
- 22 Hasselman, K , Munk W and MacDonald, G , "Bispectra of ocean waves," Ch 8 of Time Series Analysis edited by M Rosenblatt, John Wiley & Sons, Inc , 1963
- 23 Ijima, T and Matsuo, T , "Study on waves in surf zone," Proceedings, 15th Conference on Coastal Engineering in Japan, 1968
- 24 Karlsson, T , "Refraction of continuous ocean wave spectra," Proceedings of the ASCE, Journal of the Waterways and Harbors Division, vol 95, no WW4, pp 437-448, Nov 1969
- 25 Kinsman, B , Wind Waves, Prentice-Hall, Inc , Englewood Cliffs, N J , 1965
- 26 Loeve, M , Probability Theory (3rd edition), D van Nostrand Co , Inc , New York, 1963
- 27 Longuet-Higgins, M S , Cartwright, D E and Smith, N D , "Observations of the directional spectrum of sea waves using the motions of a floating buoy," Ocean Wave Spectra, Prentice-Hall Inc , Englewood Cliffs, N J , pp 111-132, 1961
- 28 Macovsky, M L and Mechlin, G , "A proposed technique for obtaining directional wave spectra by an array of inverted fathometers," Ocean Wave Spectra, Prentice-Hall, Inc , Englewood Cliffs, N J , pp 235-242, 1961
- 29 Malhotra, A K and Penzien, J , "Stochastic analysis of off-shore tower structures," Report No EERC 69-6, Earthquake Engineering Research Center, University of California, Berkeley, May 1969
- 30 Medgyessy, P , Decomposition of superpositions of distribution functions, Publishing House of the Hungarian Academy of Sciences, Budapest, 1961
- 31 Mobarek, I E , "Directional spectra of laboratory wind waves," Proceedings of the ASCE, Waterways and Harbors Division, vol 91, no WW3, August 1966
- 32 Munk, W H , Miller, G R , Snodgrass, F E , and Barber, N F , "Directional recording of swells from distant storms," Royal Society of London, Philosophical Transactions, Series A, vol 255, pp 505-584, April 18, 1963
- 33 Nagata, Y , "The statistical properties of orbital wave motions and their application for the measurement of directional wave spectra," Journal of the Oceanographic Society of Japan, vol 19, no 4, 1964

- 34 Neumann, G and Pierson, W J , "Known and unknown properties of the frequency spectrum of wind generated sea," Ocean Wave Spectra, Prentice-Hall Inc , Englewood Cliffs, N J , pp 9-25, 1961
- 35 Pierson, W J and Marks, W , "The power spectrum analysis of ocean wave records," Transactions, American Geophysical Union, vol 33, 1952
- 36 Pierson, W J , "Wind generated gravity waves," Advances in Geophysics, vol 2, Academic Press Inc , New York, pp 93-178, 1955
- 37 Scott, J R , "A sea spectrum for model tests on long-term ship prediction," Journal of Ship Research, Society of Naval Architects and Marine Engineers, vol 9, no 3, Dec 1965
- 38 Simpson, J H , "Observations of the directional characteristics of sea waves," Geophysical Journal of the Royal Astronomical Society, vol 17, pp 93-120, January 1969
- 39 Stevens, R G , "On the measurement of the directional spectra of wind generated waves using a linear array of surface elevation detectors," Unpublished manuscript, Reference No 65-20, Technical Report of Woods Hole Oceanographic Institution, Woods Hole, Mass , April 1965
- 40 Suzuki, Y , "Determination of approximate directional spectra for coastal waves," Report of the Port and Harbor Research Institute, Japan, vol 8, no 4, pp 43-101, December 1969
- 41 Takano, K , "On some limit theorems of probability distributions," Annals of the Institute of Statistical Mathematics, Tokyo, vol 6, pp 37-113, 1954
- 42 Tukey, J W , "The sampling theory of power spectrum estimates," Symposium on Application of Autocorrelation Analysis to Physical Problems, Woods Hole, Mass , pp 47-67, June 1949
- 43 Wiegell, R L , "Some engineering aspects of wave spectra," Ocean Wave Spectra, Prentice-Hall, Inc , Englewoods Cliffs, N J , pp 309-321, 1961
- 44 Wiegell, R L , Oceanographical engineering, Prentice-Hall Inc , Englewood Cliffs, N J , 1964
- 45 Wiegell, R L and Mobarek, I E , "Diffraction of wind generated water waves," Proceedings, Tenth Conference on Coastal Engineering, vol I, p 185-197, 1966
- 46 Wiegell, R L , "Waves and their effects on pile-supported structures," Technical Report HEL 9-15, Hydraulic Engineering Laboratory, University of California, Berkeley, March 1969

CHAPTER 9

Equilibrium Range Spectra in Shoaling Water

by

Takeshi Iijima⁽¹⁾, Takahiko Matsuo⁽²⁾ and Kazutami Koga⁽³⁾

Abstract

In shoaling water on sloping beach, waves break by hydraulic instability due to the finiteness of water depth, so that frequency spectra of waves in surf zone must have any limiting form similar to the equilibrium spectrum given by Phillips(1958). In this paper, authors have derived an equilibrium form of spectra for surf waves from the limiting wave condition at constant water depth by Miche(1944) and from breaking wave experiments on sloped bottom by Iversen(1952). The results are compared with surf wave spectra obtained from field observations by means of stereo-type wave meter devised by the authors(1968).

By means of this spectrum and by deep water wave spectra for various wind conditions, significant wave heights and optimum periods of limiting waves in surf zone are calculated.

1 Introduction

By dimensional considerations, Phillips(1958) has shown that in the frequency spectrum of deep water wind waves the energy spectral density $\Phi(\sigma)$ of saturated high frequency component is proportional to σ^{-5} powers of frequency as shown by the following equation

$$\Phi(\sigma) = \beta g^2 \sigma^{-5} \quad (1)$$

where g is gravity acceleration and β is non-dimensional constant, for which Phillips has given numerically 0.0117 from observed data and Pierson(1964) has obtained 0.00810 from observed spectra on the North Atlantic Ocean.

L_0 is independent of wind conditions and is interpreted as representing a limiting spectrum for waves breaking in deep water in the state of hydraulic instability.

As for waves breaking in shoaling water, the limiting wave height is determined by instability depending on water depth h and the similar limiting spectrum should exist, which, of course, is independent on wind conditions but depends only on water depth and gravity acceleration in the range of gravity waves.

(1) Professor of Kyushu University, Fukuoka, Japan

(2) Lecturer, Oita Technical College, Oita, Japan

(3) Master Course Student, Kyushu University

Here, we assume straight shore line with constant slope and waves incident normally, so that one-dimensional waves without refraction effect

2 Derivation of equilibrium range spectrum

From observed wave record of a train of waves at a point of depth h in surf zone, apparent individual wave height \tilde{H} and wave period \tilde{T} of all the waves are measured in spite of breaking and non-breaking and then wave length \tilde{L} of the wave at water depth h are calculated by small amplitude wave relation. Then, we obtain a scatter diagram of \tilde{H}/\tilde{L} related to h/\tilde{L} as shown in Fig 1, which was obtained from wave record of 17 minutes long at depth of 5.7 meters on the Coast of Miyazaki (Pacific Coast of Kyushu)

The envelope curve through the upper limit of scattered points in the figure is interpreted to show the limiting wave condition for the depth h .

For a train of single sinusoidal waves, the limiting condition at constant depth for h/L larger than about $1/20$ is given by Miche (1944) as follows

$$H/L = \frac{1}{7} \tanh \frac{2\pi h}{L} \quad (2)$$

For deep water ($h/L \rightarrow \infty$), H/L is $1/7$ and for shallow water long waves ($h/L \rightarrow 0$), eq 2 gives $H/h \approx 0.9$, which is somewhat larger than 0.78 by solitary wave theory. For the bottom of constant slope, we have not yet theoretical relation but Iversen (1952) has shown experimental relations of H_b/H'_0 and h_b/H'_0 to H'_0/L_0 for bottom slopes $\alpha = 1/10, 1/20, 1/30$ and $1/50$, where H'_0, L_0 are deep water wave height and length and H_b, h_b are wave height and water depth of breakers. From these experimental relations, an empirical relation of H/L and h/L similar to eq 2 is obtained as follows

$$H/L = \frac{1}{7} \tanh \left[f(\alpha) \frac{2\pi h}{L} \right], \quad f(\alpha) = \cosh 3.5 \alpha^{3/5} \quad (3)$$

where α is bottom slope. Above relations are shown in Fig 1 for $\alpha = 0$ and $1/10$. Eq 3 may give somewhat larger values for $h/L < 1/20$ for single sinusoidal waves but for actual random waves the form of eq 3 may be assumed to represent approximate relations of limiting apparent wave height \tilde{H}_{max} and length \tilde{L} derived from apparent wave period \tilde{T} for all h/\tilde{L} . Accordingly, we assume next relation for limiting apparent waves

$$\frac{\tilde{H}_{max}}{\tilde{L}} = C_1 \tanh \left[f(\alpha) \frac{2\pi h}{\tilde{L}} \right] \quad (4)$$

Where C_{11} is assumed to be constant

As for actual waves with continuous spectrum, the limiting wave height \tilde{H}_{max} is interpreted as the result that all the phases of component waves whose periods are within narrow range of period band between $\tilde{T} - \Delta\tilde{T}/2$ and $\tilde{T} + \Delta\tilde{T}/2$ centered at period \tilde{T} happened to coincide and their spectral wave heights were summed up to attain the limiting height \tilde{H}_{max} . And for sufficiently narrow width of $\Delta\tilde{T}$, the component waves within the period band are considered to have nearly equal spectral wave height H_T proportional to the limiting wave height \tilde{H}_{max} , that is,

$$H_T \propto \tilde{H}_{max} \quad (5)$$

Therefore, from eq 4 we have

$$H_T = \text{const } \tilde{L} \tanh \left[f(\alpha) \frac{2\pi h}{\tilde{L}} \right] \quad (6)$$

Assuming that the number of component waves within the period band is N and they are mutually independent, the total energy density within the period band of $\tilde{T} - \Delta\tilde{T}/2$ and $\tilde{T} + \Delta\tilde{T}/2$ is

$$N \cdot \frac{\rho g}{8} \text{const } \tilde{L}^2 \tanh^2 \left[f(\alpha) \frac{2\pi h}{\tilde{L}} \right]$$

Accordingly, the total frequency spectral energy density $\Phi(\sigma)\Delta\sigma$ between $\sigma - \Delta\sigma/2$ and $\sigma + \Delta\sigma/2$ is given by the following equation.

$$\Phi(\sigma)\Delta\sigma = \text{const } N \tilde{L}^2 \tanh^2 \left[f(\alpha) \frac{2\pi h}{\tilde{L}} \right] \quad (7)$$

The number of component waves N in above equation is considered to become large when the period band $\Delta\tilde{T}$ becomes wide, but to become small when the period \tilde{T} becomes large for limited length of wave record. Accordingly, we may assume the following relation

$$\text{const } N = \text{const } \frac{\Delta\tilde{T}}{\tilde{T}} = \text{const } \frac{\Delta\sigma}{\sigma}, \quad (\sigma = 2\pi/\tilde{T}) \quad (8)$$

Now, eq 7 is written as follows

$$\begin{aligned} \Phi(\sigma)\Delta\sigma &= \text{const } \tilde{L}^2 \cdot \tanh^2 \left[f(\alpha) \frac{2\pi h}{\tilde{L}} \right] \\ &= \text{const } (2\pi)^2 \frac{h^{5/2}}{g^{1/2}} \frac{\tanh^2 \left[f(\alpha) \frac{2\pi h}{\tilde{L}} \right]}{\left(\frac{2\pi h}{\tilde{L}} \right)^2 \left(\frac{\sigma^2 h}{g} \right)^{1/2}} \Delta\sigma \\ &= \text{const } (2\pi)^2 \frac{h^{5/2}}{g^{1/2}} F \left(\alpha, \frac{\sigma^2 h}{g} \right) \Delta\sigma \quad (9) \end{aligned}$$

where

$$F(\alpha, \frac{\sigma^2 h}{g}) = \frac{\tanh^2 [f(\alpha) \frac{2\pi h}{L}]}{(\frac{2\pi h}{L})^2 (\frac{\sigma^2 h}{g})^{1/2}} \quad (10)$$

In above equations, $2\pi h/L$ is determined as a function of $\sigma^2 h/g$ by the following equation

$$\sigma^2 h/g = \frac{2\pi h}{L} \tanh \frac{2\pi h}{L} \quad (11)$$

In eq 10, when $\sigma^2 h/g$ becomes large, $2\pi h/L$ tends to $2\pi h/L_0$ and F tends to $(\sigma^2 h/g)^{-1/2}$, and when $\sigma^2 h/g$ becomes small, F tends to $f^2(\alpha) (\sigma^2 h/g)^{-1/2}$

Accordingly, from eq 9 it is seen that

$$\Phi(\sigma) = \text{const} (2\pi)^2 g^2 \sigma^{-5} \quad \text{for deep water waves} \quad (12)$$

$$\Phi(\sigma) = \text{const} \cdot (2\pi)^2 f^2(\alpha) h^2 \sigma^{-1} \quad \text{for shallow water waves} \quad (13)$$

Comparing eq 12 with eq 1,

$$\text{const} \cdot (2\pi)^2 = \beta$$

Thus, eq 9 is determined as follows

$$\Phi(\sigma) = \beta \frac{h^{5/2}}{g^{1/2}} F(\alpha, \frac{\sigma^2 h}{g}) \quad (14)$$

Above equation is considered to represent the equilibrium spectrum of surf waves

3 Comparisons with observations

The observation of surf waves is difficult because of various troubles in setting and maintaining wave meters. The authors(1968) have devised a stereo-type wave meter, with which field observations at Miyazaki Coast and Nata Coast of Kyushu were carried out. Fig 2 is an example of observed frequency spectra at Nata Coast. Fig.3 and 4 are non-dimensional plot of frequency spectra at Miyazaki- and Nata Coast, respectively, in which the curves are equilibrium spectra by eq 14 for $\alpha = 0$ and $1/10$ with $\beta = 0.00810$.

In Fig.3, measured spectral densities for large $\sigma^2 h/g$ attain to the equilibrium values but for small $\sigma^2 h/g$ measured densities are lower than the latter

This seems to be due to the fact that few waves are breaking by the effect of finite depth and only high frequency waves are saturated by local wind. In Fig.4 measured energy densities almost attain to the equilibrium values, which mean that almost waves are breaking by the effect of finite depth.

4 Estimation of limiting significant waves in surf zone

Assuming that eq 14 is the limiting spectral energy density at water depth h , the limiting spectrum for given wind conditions at the depth may be estimated by the following considerations.

In Fig 5, suppose that various spectra are drawn in linear scale and the curve MN is equilibrium spectrum at given water depth. When the spectrum of off-sea wind waves is given by the curve MWQ, the spectrum to be observed at the point of depth h should be given by the curve MCQ, which is the limiting spectrum for the given wind condition. When the spectrum of offsea swell is given by the curve ASQ, the spectrum at depth h should be the curve ABCQ, which is the limiting spectrum for given swell. Fig 6 shows an example of offsea wind wave spectrum for wind speed $U = 15$ m/s, fetch length $F = 400$ km, which is proposed by the authors as shown in Appendix, and equilibrium spectra at water depth $h = 8$ meters for bottom slope $\alpha = 0$ and $1/10$.

Fig 7(a)(b) are significant wave height and its optimum period of limiting waves calculated by above-derived limiting spectrum at various water depth for fetch length 100 km and 400 km with wind speed 15 m/s and 30 m/s.

5 Conclusions and remarks

Omitting the effect of wave refraction and directional distribution of wave spectrum, the equilibrium spectrum of surf waves at water depth h is represented by eq 14, by means of which and a proposed fetch- or duration spectrum of offsea wind waves the limiting spectrum at any depth is estimated as shown in Fig 6.

Up to date, for design purposes of surf zone structures the limiting wave height by such an equation 2 or 3 is frequently used as design wave height. But in some cases, it seems to be more reasonable to use such a limiting spectrum as above. The effect of directional distribution of wave spectrum should be considered in future.

Appendix

Derivation of Duration and Fetch Spectrum

We assume the general form of frequency spectrum as follows

$$\Phi(\sigma) = \alpha_* g^2 \sigma^{-5} \exp\left\{-\beta_* \left(\frac{g}{\sigma U_*}\right)^4\right\} \quad (A1)$$

where g is gravity acceleration, U_* is friction velocity of wind and α_* , β_* are non-dimensional constants

Above spectrum has the maximum energy density $\Phi(\sigma_0)$ at frequency σ_0 as follows

$$\Phi(\sigma_0) = \alpha_* g^2 e^{-\frac{5}{4}} \sigma_0^{-5} \quad (A2) \quad \frac{\sigma_0 U_*}{g} = \left(\frac{4}{5} \beta_*\right)^{1/4} \quad (A3)$$

from which we obtain

$$\beta_* = \frac{5}{4} \left(\frac{\sigma_0 U_*}{g}\right)^4 \quad (A4) \quad \alpha_* = \frac{e^{5/4}}{g^2} \Phi(\sigma_0) \sigma_0^5 \quad (A5)$$

The time development of the maximum energy density of wind generated-wave spectrum is given by Phillips(1966) as follows

$$\Phi(\sigma_0) = A \frac{U_*^4}{g^2} \frac{\sinh(\mu \sigma_0 t)}{\mu \sigma_0}, \quad A = 240 \left(\frac{\rho_a}{\rho_w}\right) \approx 3.46 \times 10^{-4} \quad (A6)$$

where ρ_a and ρ_w are densities of air and water and μ is coupling coefficient of air-sea interaction

Substituting eq A4, A5 and A6 into eq A1, we obtain as duration spectrum

$$\Phi(\sigma, t) = A e^{5/4} \frac{U_*^4}{g^2} \left(\frac{\sigma_0}{\sigma}\right)^5 \frac{\sinh(\mu \sigma_0 t)}{\mu \sigma_0} \exp\left\{-\frac{5}{4} \left(\frac{\sigma_0}{\sigma}\right)^4\right\} \quad (A7)$$

Meanwhile, Pierson(1964) has proposed the following spectrum for fully-developed wind waves

$$\Phi(\sigma) = \alpha g^2 \sigma^{-5} \exp\left\{-\beta \left(\frac{g}{\sigma U}\right)^4\right\} \quad (A8)$$

where $\alpha = 0.00810$, $\beta = 0.74$ and U is mean wind speed at 19.5 meters high above mean sea surface, which is related to U_* and U_{10} (wind speed at 10 meters above mean sea level) by the following empirical relationships

$$U = k U_* \quad k = 1.60 + \frac{1}{\sqrt{C_{10}}} \quad (A9)$$

$$\Pi_{10} = \frac{\Pi_*}{\sqrt{C_{10}}} \quad C_{10} = (0.80 + 0.114 \Pi_{10}) \times 10^{-3} \quad (A10)$$

For any given wind speed, the maximum energy density $\Phi(\sigma_0)$ of duration spectrum should lie always on the saturated spectrum curve of that wind speed given by eq A8, so that equating eq A6 to eq A8, we obtain next relation for σ_0 at any duration time t

$$\frac{A}{\alpha} \Pi_*^4 \left(\frac{\sigma_0}{g}\right)^4 \frac{\sinh \mu \sigma_0 t}{\mu} = \exp\left\{-\beta \left(\frac{g}{K \Pi_* \sigma_0}\right)^4\right\} \quad (A11)$$

Eq A7 together with eq A11 gives duration spectrum

Fetch length χ is related to duration time t by the following equation

$$\chi = \frac{1}{2} C_0 t \quad (A12)$$

where C_0 is the phase velocity of waves with frequency σ_0

Thus, fetch spectrum is obtained from duration spectrum as follows

$$\Phi(\sigma, \chi) = A e^{\frac{5}{4} \frac{\Pi_*^4}{g^2} \left(\frac{\sigma_0}{\sigma}\right)^5 \frac{\sinh(2\mu \sigma_0 \chi / C_0)}{\mu \sigma_0}} \exp\left\{-\frac{5}{4} \left(\frac{\sigma_0}{\sigma}\right)^4\right\} \quad (A13)$$

By the relation $\sigma_0 = g/C_0$, duration and fetch spectrum is written as follows

$$\Phi(\sigma, t) = A e^{\frac{5}{4} g^2 \sigma^{-5} \frac{\sinh(\mu \frac{g t}{U_*} / \frac{C_0}{U_*})}{\mu} \cdot \frac{1}{(C_0/U_*)^4} \exp\left\{-1.25 \frac{(g\sigma/U_*)^4}{(C_0/U_*)^4}\right\}} \quad (A14)$$

$$\Phi(\sigma, \chi) = A e^{\frac{5}{4} g^2 \sigma^{-5} \frac{\sinh(2\mu \frac{g \chi}{U_*} / \frac{C_0}{U_*})}{\mu} \cdot \frac{1}{(C_0/U_*)^4} \exp\left\{-1.25 \frac{(g\sigma/U_*)^4}{(C_0/U_*)^4}\right\}} \quad (A15)$$

In above equations, coupling coefficient μ is given by Phillips(1966) as a function of C/U_* . But when fetch spectrum is given by eq A15, the significant wave height $H_{1/3}$ is shown by following equation

$$\frac{g H_{1/3}}{\Pi_*} = 4.00 \sqrt{\frac{A}{5}} e^{5/8} \left(\frac{\sinh(2\mu \frac{g \chi}{U_*} / \frac{C_0}{U_*})}{\mu} \right)^{1/2} \quad (A16)$$

And also from observation data, significant wave height is empirically related to wind speed by the following equation by Wilson(1965)

$$\frac{g H_{1/3}}{\Pi_*} = \frac{K_3}{C_{10}} \left[1 - \frac{1}{\left\{ \sqrt{C_{10} K_4} \left(\frac{g \chi}{U_*} \right)^2 + 1 \right\}^2} \right], \quad K_3 = 0.30, K_4 = 0.004 \quad (A17)$$

Equating above two equations, coupling coefficient μ is obtained for C_0/U_* with parameter U_* as shown in Fig A1 Fig A2 is an example of fetch spectrum

References

- Phillips, O M (1958) " The Equilibrium Range in the Spectrum of Wind-Generated Waves " J Fluid Mechanics, Vol 4
- Miche, A (1944) " Mouvements ondulatoires de la mer en profondeur constante ou decroissante " Annales des ponts et chaussées, Vol 114
- Iversen, H W (1952) " Laboratory Study of Breakers " Gravity waves Nat Bur Standards Cir No 521
- Pierson, W J and L Moskowitz (1964) " A Proposed Spectral Form for Fully Developed Wind Seas based on the Similarity Theory of S A Kitaigorodskii " J Geoph Res Vol 69, No 24
- Ijima, F and T. Matsuo (1968) " Observation of Surf Waves by Stereo-Wave Meter " Coastal Engineering in Japan, Vol 11
- Phillips, O M (1966) " The Dynamics of the Upper Ocean " Cambridge University Press
- Wilson, B W (1965) " Numerical Prediction of Ocean Waves in the North Atlantic for December, 1959 " Deutsch Hydr Z Jg 18 Ht 13

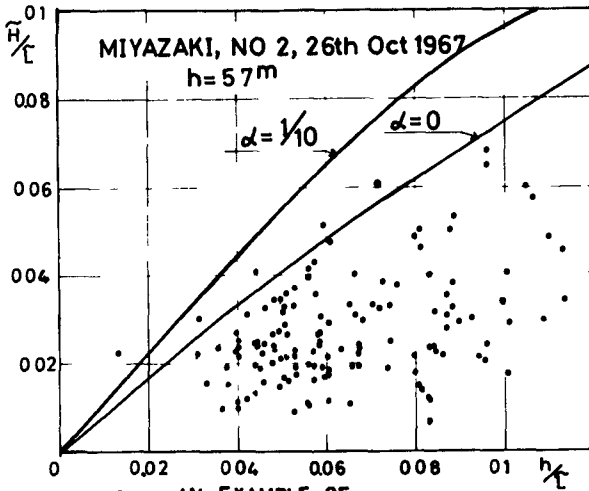


Fig -1 AN EXAMPLE OF SCATTER DIAGRAM

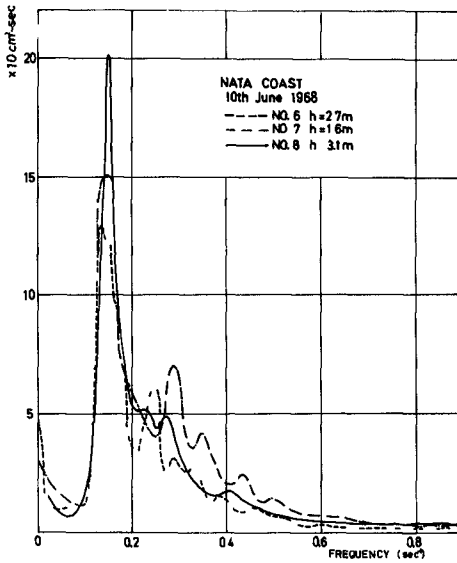


Fig 2 EXAMPLES OF FREQUENCY SPECTRA

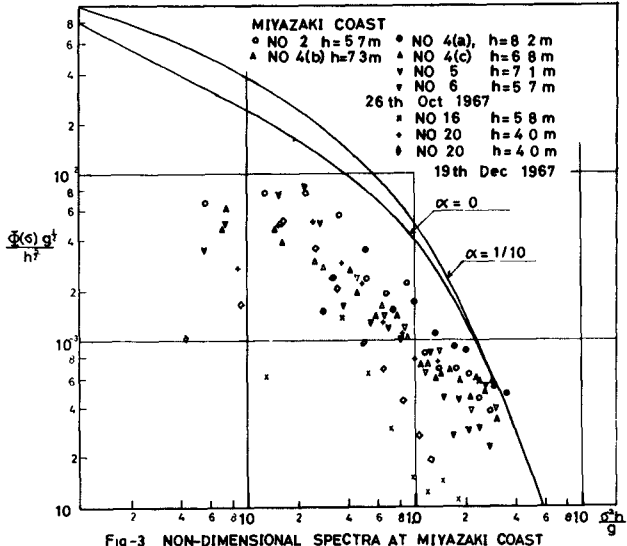


Fig-3 NON-DIMENSIONAL SPECTRA AT MIYAZAKI COAST

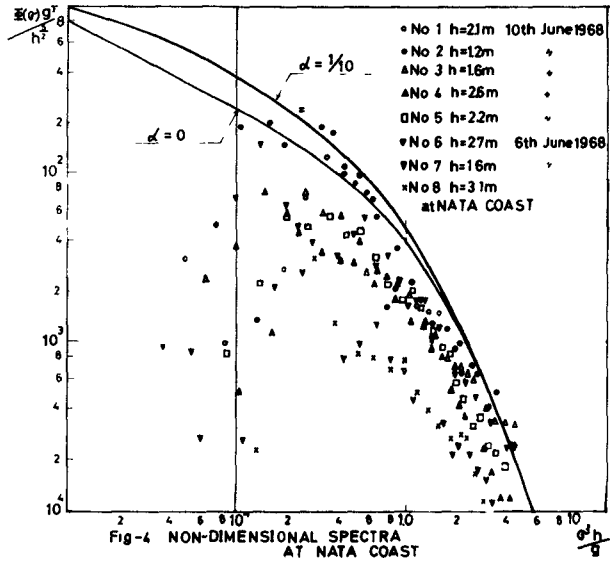


Fig-4 NON-DIMENSIONAL SPECTRA AT NATA COAST

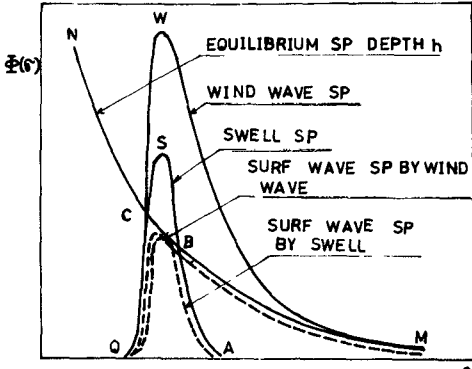


Fig -5, EXPLANATION SKETCH

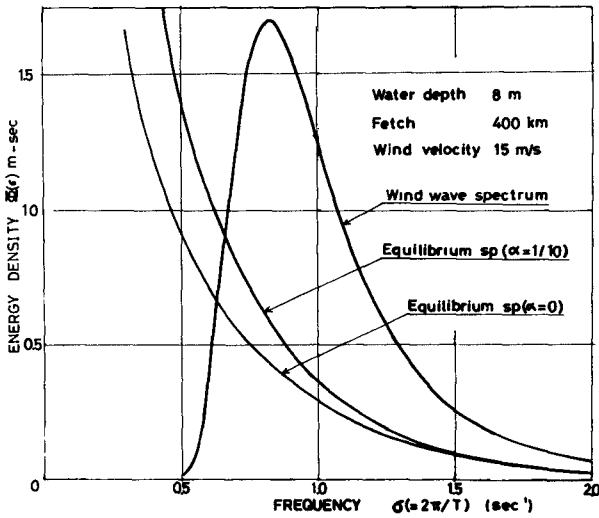


Fig -6 Limiting Spectra at Depth of 8 meters for an Offsea Wind Wave Spectrum

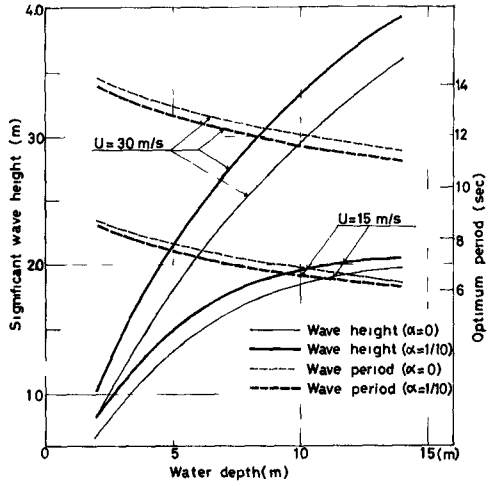


Fig-7(a) LIMITING SIGNIFICANT WAVES FOR FETCH LENGTH 100KM

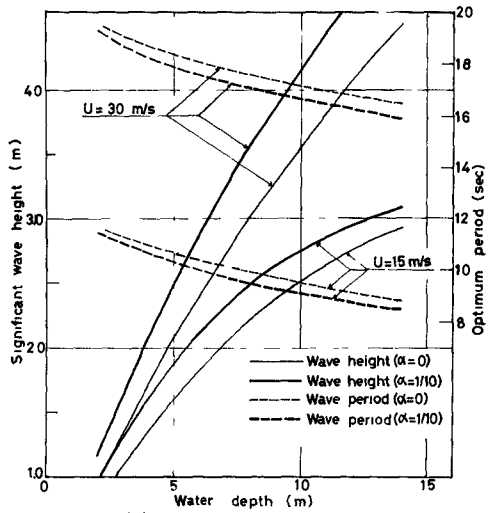


Fig-7(b) LIMITING SIGNIFICANT WAVES FOR FETCH LENGTH 400 KM

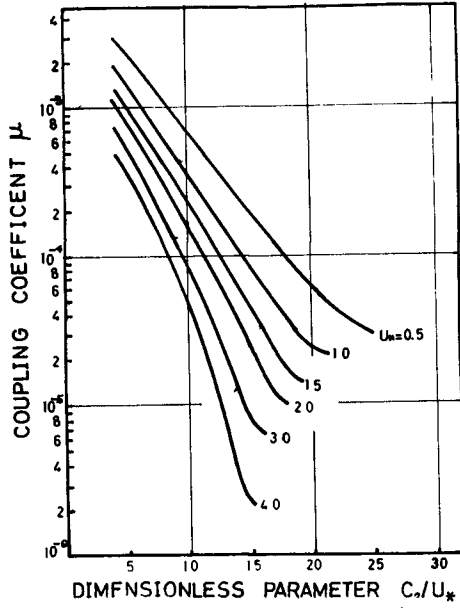


Fig -A1 RELATIONS ON μ AND C_s/U_* AND U_*

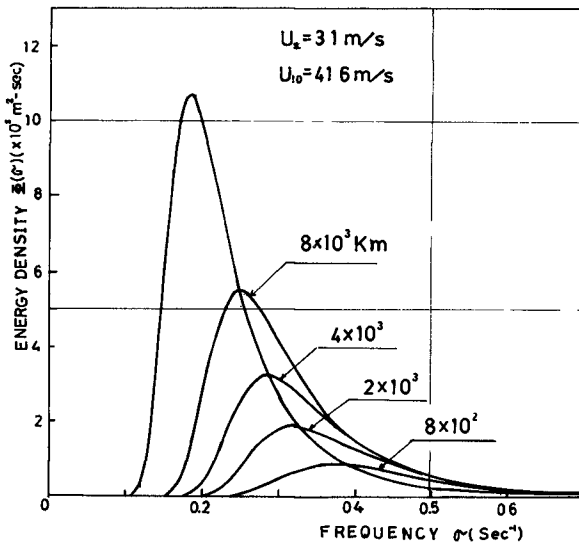


Fig -A2 FETCH SPECTRUM

CHAPTER 10

WAVE INVESTIGATIONS IN SHALLOW WATER

Dr -Ing. Winfried Siefert

Strom- und Hafenbau Hamburg
Forschungsgruppe Neuwerk, Cuxhaven, Germany

Abstract

=====

Examination of the significant heights of zero-crossing waves in the Elbe Estuary has yielded two noteworthy results: 1 In the deeper water of the estuary, the value of the quotient relating the significant and the mean wave heights is larger than on the bordering tidal flat. 2. The value of this function is dependent on the height of the waves; on the tidal flat this dependency is considerably more sensitive than in deeper water. With increasing wave height the value of significant wave height divided by mean height becomes smaller

The propagation direction of waves moving onto the tidal flat is contingent upon the position of intertidal channels. Such channels sharply reduce the possible propagation directions. The waves nearly always move up-channel regardless of the wind direction.

It is possible to derive special wave period and wave height distributions representing the conditions in very shallow water.

I. Introduction

As part of a general research program investigating the hydrologic, hydrodynamic and morphologic characteristics and changes in the Elbe Estuary, wave measurements are carried out (Laucht, 1968, and Fig 1). Few recordings - at least in Germany - have been made of waves in the nearshore zone, consequently, no data was available for the Elbe Estuary at the beginning of this program. Only a minimal amount of information on wave behavior in morphologically complex nearshore areas is found in the literature (Koele and de Bruyn, 1964; Wiegel, 1964, US Army, 1966). It was therefore necessary to tailor an investigation program to fit these special conditions.

Concurrent wave measurements have been made at 6 stations, and in 1970 an additional 7 stations on the tidal flat will be added. Of the present 6 stations, 3 are located on the edge of the Elbe channel in water depths from 5 to 10 m, and 3 are located on the tidal flat in depths of less than 2 m (Fig. 2). Expanded records of 2 to 5 minute duration are recorded at preset intervals, following the Wemelsfelder principal. The results presented here are based primarily on the "Hundebalje" station located between the dune island Scharhorn and the island of Neuwerk on the "high tidal flat" bordering an intertidal channel system. At mean high tide the water reaches a depth of 1.5 m at this point.

II. Interpretation of Wave Records

A Significant Wave Values

Expanded records from the various stations give only wave height and period and thereby only part of the signi-

ficant wave characteristics which must also include wavelength, wave propagation direction and velocity. The latter items can be obtained from radar and aerial photographs, however, these techniques don't yield the height and period (Siefert, 1969). An attempt is presently being made to combine aerial photo analysis with wave gauge records to bring together the height, frequency and directional spectrums.

Following currently accepted methods, the records were analyzed for the mean values \bar{H} and \bar{T} of the zero-crossing waves as well as $H_{1/3}$, $T_{H_{1/3}}$, and $H_{1/10}$. From these values, the ratios $C_{1/3}$, $C_{1/10}$, etc. were calculated.

It is commonly believed that wave parameters such as the mean or significant wave height are of somewhat limited use. However, even in an area with extreme depth variations, these values still serve to give the engineer a relatively good picture of the waves. Therefore, for preliminary work the calculation of spectrums can be omitted in favor of using the significant wave values. For construction planning, characteristics such as mean, significant and maximum wave heights and periods are more useful than spectrum analyses.

In the investigation area it is common to have several wave systems coming from different directions converging and overlapping one another. These systems can have quite different heights and periods depending on their origin and age. A typical Gaussian distribution, as found in the theoretical treatment of Cartwright and Longuet-Higgins, or a Rayleigh distribution for a very narrow wave spectrum, are seldom present (Koele and de Bruyn, 1964). When several systems overlap it becomes impossible to measure a mean wave-length or height of each system. The high degree of scattering in the wave

values precludes analytical treatment of data from this area until the mathematics of non-linear superposition is developed to a point where the spectrum can be calculated for shallow water (Wiegel, 1969).

In spite of these restrictions, the measured wave heights yield some interesting facts regarding the changes that take place in waves as they move into shallow water

B. Integration of the Dominant Wind Values

The values \bar{H} and \bar{T} from the wave records were classified according to wind velocity and direction. The wind parameters prevailing during the 6 to 12 hour period preceding the measurement were categorized into various wind sectors (Schrader, 1968). For wind directions from SW to N, the waves from the open sea are responsible for the waves in the channels and on the tidal flat. For these directions, the wind conditions prevailing outside the tidal flat area (Scharhornriff station, Fig. 2) must be considered. The division of the land wind directions (N to SW) is based solely upon the topography near the recording station. In Fig. 3, therefore, the wind sectors at the Scharhornriff station apply to the entire investigation area, whereas the sectors at the Hundebalje station apply only to records from this station.

Aerial photographic analysis of the wave-length changes as waves move into shallower water showed that classic wave theory could not be applied in this topographically complex region (Siefert, 1969). As a result, the attempt has been made to work with the changes in wave height as the waves progress into shallower water.

III Waves in Shallow Water

=====

A Comparison of Significant Wave Values in Deep and Shallow Water

In order to achieve a reliable shallow water - deep water comparison, over 500 records from the 6 recording stations were analyzed for both mean and significant wave values using the zero-crossing method. This amounted to a comparison of the tidal flat readings (from the Scharhorn-West, Scharhorn-Süd and Hundebalje stations) with the deeper water results (from the Scharhornriff, Scharhorn-Nord and Luchtergrund stations (see Fig. 2)).

Wave Parameter	Tidal Flat	8 m Water Depth
$C_{\tau} = \frac{T H_{1/3}}{T}$	1.11	1.30
$C_{1/3} = \frac{H_{1/3}^*)}{\bar{H}}$	1.49	1.52
$C_{1/10} = \frac{H_{1/10}}{\bar{H}}$	1.76	1.90
$\frac{H_{1/10}}{H_{1/3}}$	1.18	1.24

*) see Figure 4

All of the values show a tendency toward uniformity as the waves reach shallower water, i.e., $H_{1/10}$ and $H_{1/3}$ become somewhat smaller in relation to the mean wave height. This is caused by a form of "sorting" in which the highest waves, which control the values of $H_{1/10}$ and $H_{1/3}$ in deeper water, are removed from the spectrum in shallower water. Therefore it is understandable that the ratio $C_{1/10}$ should become smaller faster than the ratio

$C_{1/3}$ The change in the wave spectrum is also clearly seen in the decreasing values of C_r on the tidal flat

So one can not rely on having constant wave ratios in the coastal area. This applies to the wave heights as well as the periods. The value of $C_r = \frac{T H_{1/3}^3}{\bar{T}}$ for the deeper Elbe Estuary, as well as off the Dutch coast (Svasek, 1969), is 1.30, whereas on the tidal flat the value drops to 1.11. This lower figure corresponds well to the 1.10 calculated by Sibul (1955) for shallow water in a wind-wave channel (see Wiegel, 1964).

A further point should be mentioned which apparently is frequently overlooked in the evaluation of zero-crossing waves. As Fig. 4 shows, using a deep water station (Scharhornriff) and a tidal flat station (Hundebalje) as examples, the ratio $C_{1/3} = \frac{H_{1/3}}{\bar{H}}$ is dependent not only on location but also on the mean wave height H . Higher waves produce a more uniform wave spectrum; on the tidal flat the uniformity is achieved more quickly than in deeper water.

Variances in the directional spectrum of the waves as they reach the tidal flat are shown in Fig. 5 where the main wave systems seen in two series of aerial photographs are presented (see also Siefert, 1969). In the inner portion of the Elbe Estuary, nearly all wave directions can be developed depending upon the wind. However, this multiplicity of propagation directions is almost instantly reduced as the waves enter the tidal channels. The illustration shows propagation directions from WNW and E, a difference of 120° in the deep Elbe channel. This difference is reduced to 30° in the Hundebalje channel. This would seem to indicate that waves always move up-channel on the tidal flat regardless of wind direction.

B. Distributions of Wave Periods and Wave Heights

Everyone is aware of the large scattering in the relation of mean wave heights and periods, especially under the influence of complex topography and tidal conditions. Furtheron it is known that the heights and periods of individual waves seem to be nearly without any relation. The only facts that become clear are that the highest wave in a spectrum does not belong to the longest period and that the longest period belongs to a wave of about mean height. Therefore it is useful to split further investigations into analyzing separate period and height distributions.

Fig. 6 gives some characteristic period spectra in the form of cumulative distributions of the ratio of individual and mean periods in Gaussian paper. The comparison gives an interesting result: The distributions of Bretschneider and Putz are not the same, but similar, and both are derived for deep water waves. The spectra in the Elbe channel and the adjacent breaker zone (3 to 12 m) as well as those on the tidal flats (1 to 3 m) are different from those. The period spectrum of the waves obviously becomes wider with decreasing water depth. So it seems that the well-known theoretical Rayleigh-distribution is characteristic only for waves in very shallow water. The analytical variation of this distribution is possible by raising the factor "2" in the formula of the Rayleigh-distribution with increasing water depth.

Opposite developments can be noticed with the wave heights. To the usually used Rayleigh-distribution after Longuet-Higgins there belongs a value $C_{1/3} = 1.60$. Many authors found that this value is not always constant (see Wiegel, 1964). Investigations in the Elbe estuary show that the mean value is less than 1.60 and that the quotient becomes smaller with increasing wave height, but not at any point with the same rate (Fig. 4). The cumulative distributions of the wave heights in Fig. 7 give characteristic

curves for every $C_{1/3}$. As $C_{1/3}$ decreases with increasing mean wave height, the wave height spectrum then must become narrower. This apparent relationship between the width of the spectrum and $C_{1/3}$ can be expressed as a relation between the factor φ in the formula of the wave height distribution

$$P \left(\frac{H}{H} \right) = 1 - e^{-\frac{\pi}{4} \left(\frac{H}{H} \right)^\varphi}$$

and $C_{1/3}$:

$C_{1/3}$	1,35	1,40	1,45	1,50	1,55	1,60	1,65
φ	2,94	2,70	2,50	2,32	2,15	2,00	1,86

This relation is valid up to 99.8% and more. The following progress of the curves in Fig. 7 to a finite value indicates the influence of water depth, as there must be a maximum wave height even with the probability zero.

For a certain mean wave height in a certain place on the tidal flat, one can get the value of $C_{1/3}$ by Fig. 4, and further on Fig. 7 gives the complete wave height distribution in dependence on $C_{1/3}$.

Summarizing the investigations it can be stated that the period spectrum of waves progressing into shallow water becomes wider while at the same time the height spectrum becomes narrower. This fact has to be considered during further investigations, but we hope to find some general characteristics that may be applied to similar areas elsewhere.

C Wave Heights on the Tidal Flat

Tidal conditions result in the wave height on a tidal flat being controlled by the water level, i.e., the tidal phase. In addition to the tidal fluctuations, the water level is strongly influenced by wind thereby yielding complex relationships:

- a) Wave height as a function of wind and water level
- b) Water level as a function of wind

Some considerations may illustrate this double dependency of wave height on wind. When a constant water level is present (or in water deep enough to make such fluctuations insignificant) relationships can be established between wave height and wind. The Hundebalje station serves as a good example to show the influence of the wind on the water level. In the German Bight, and particularly near the coast, strong SW to N (sea) winds result in an accumulation of water and therefore increased mean tidal levels; NE to S (land) winds drive the water away from the coast and result in lower water levels. Because wave height is dependent on wind velocity and water level, higher waves can form on the tidal flat under sea wind conditions. In contrast, land winds produce an increase in wave height coupled with a lowering of the water level. The wave height can increase only as long as the first effect remains larger than the second; further increases in wind velocity will result in a decrease in wave height. It is therefore possible that hurricane force winds from some directions will produce no waves at all on the tidal flat if it falls dry.

This relatively simple hypothesis could be verified on the basis of one year's measurements at the Hundebalje station. The events during land wind conditions could be particularly well defined during a long east wind period.

Figure 8 shows the mean wave height \bar{H} in relation to the wind velocity from various sectors for three water levels (HW + 1 m, HW, HW - 0.5 m). As would be expected, the individual values are scattered. For clarity only the lines of highest \bar{H} are shown. It can be seen that during periods of land winds from sectors 1 to 3 (346° to 210°) the waves never reach an \bar{H} of over 37 cm on the tidal flat. For a ratio between significant and mean wave height of $\frac{H_{1/3}}{\bar{H}} = 1.46$ (Fig. 4) the significant wave height for this location during N to SW winds is

$$H_{1/3} = 54 \text{ cm.}$$

From Figure 8 it can be seen that the highest waves do not develop when the water level (at a wind velocity of 19 to 22 m/sec) reaches the HW level (1.9 m), but rather a level some 20 cm lower. Thus, with a water depth of 1.7 m, mean wave heights up to 37 cm can be expected.

The maximum possible wave height is also of particular interest. The maximum height will develop under westerly winds when both wave height and water depth are increasing. It is too early to set an absolute height limit based on only one year's measurements, particularly when these include relatively few storm-wind periods. During W to NNW wind (sector 6, Fig 3) with Beaufort force 10 (about 27 m/sec) waves with a mean height of 60 cm were recorded. The significant wave height was 85 cm. The recording is being continued.

The dependency of wave propagation direction on water depth is shown in the fact that the highest waves on the tidal flat develop during W to NNW wind (sector 6). During these times the Hundebalje recording station on the tidal flat lies directly in the wind shadow of the island of Scharhörn (Fig 3). The fetch of about 1.5 km over water depths from 0 to 1.9 m is not sufficient to generate mean wave heights of over 50 cm. The relation-

ship in Fig. 9 between wave height on the tidal flat (Hundebalje) and in about 8 m depth off the tidal flat (Lichtergrund) shows that the highest waves are recorded on the flat at the times when the highest waves off the flat are recorded (sector 6, $268^{\circ} - 354^{\circ}$).

It should again be stressed that the results obtained from the Hundebalje station apply only to its immediate area. The station was placed on a tidal channel in order to measure waves by their ingress on the tidal flat. On the higher parts of the flat away from channels, other conditions prevail which result in smaller waves. The wave spectrum on the tidal flat exhibits extreme local variations.

IV. List of Symbols

=====

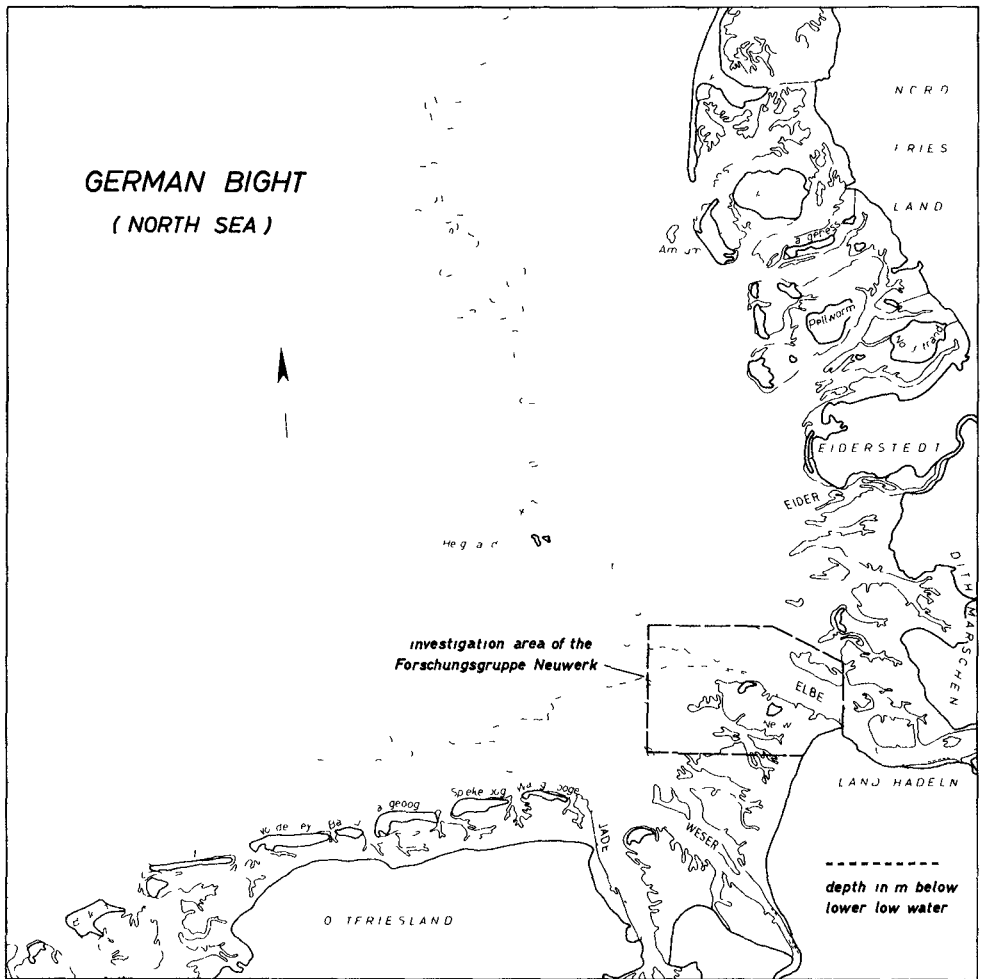
$C_{1/3}$	Ratio of Wave heights $\frac{H_{1/3}}{\bar{H}}$
$C_{1/10}$	Ratio of Wave heights $\frac{H_{1/10}}{\bar{H}}$
C_{τ}	Ratio of Wave periods $\frac{T_{H_{1/3}}}{\bar{T}}$
\bar{H}	Mean height of the zero-crossing waves
\bar{H}_{\max}	Maximum from number of mean wave heights
$H_{1/3}$	Significant wave height = average height of the highest one-third of the zero-crossing waves
$H_{1/10}$	Average height of the highest one-tenth of the zero-crossing waves
HW	Mean high tide
\bar{T}	Mean period of the zero-crossing waves
$T_{H_{1/3}}$	Mean period of the highest one-third of the zero-crossing waves (i.e. the significant waves)

V References

- =====
- Koele, L.A. and de Bruyn, P.A.: Statistical Distribution of Wave Heights in Correlation with Energy Spectrum and Water Depth. Proceedings, 9th Conference on Coastal Engineering, 1964
- Laucht, H.: Ursachen und Ziele der Hamburger Küstenforschung an der Elbmündung. Hamburger Küstenforschung, Heft 1, 1968
- Schrader, J.P.: Kennzeichnende Seegangsgroßen für drei Meßpunkte in der Elbmündung. Hamburger Küstenforschung, Heft 4, 1968
- Siefert, W.: Seegangsbestimmung mit Radar und nach Luftbildern. Hamburger Küstenforschung, Heft 7, 1969
- Svasek, J.N.: Statistical Evaluation of Wave Conditions in a Deltaic Area. Proceedings, Symposium Research on Wave Action, Delft, Holland, 1969
- U.S. Army Coastal Engineering Research Center: Shore Protection, Planning and Design. Technical Report No. 4, 1966
- Wiegel, R.L.: Oceanographical Engineering. Prentice-Hall Inc., Englewood Cliffs, N.J. 1964
- Wiegel, R.L.: Waves and their Effects on Pile-Supported Structures Proceedings, Symposium Research on Wave Action, Delft, Holland, 1969

Fig 1

German Bight
with Investigation Area of the Forschungsgruppe Neuwerk





Wave Investigation in the Elbe Estuary
 ● recording stations
 - - - edge of the area investigated by aerial photos

Fig 2

Classification of Wind Directions for Station Hundebalje

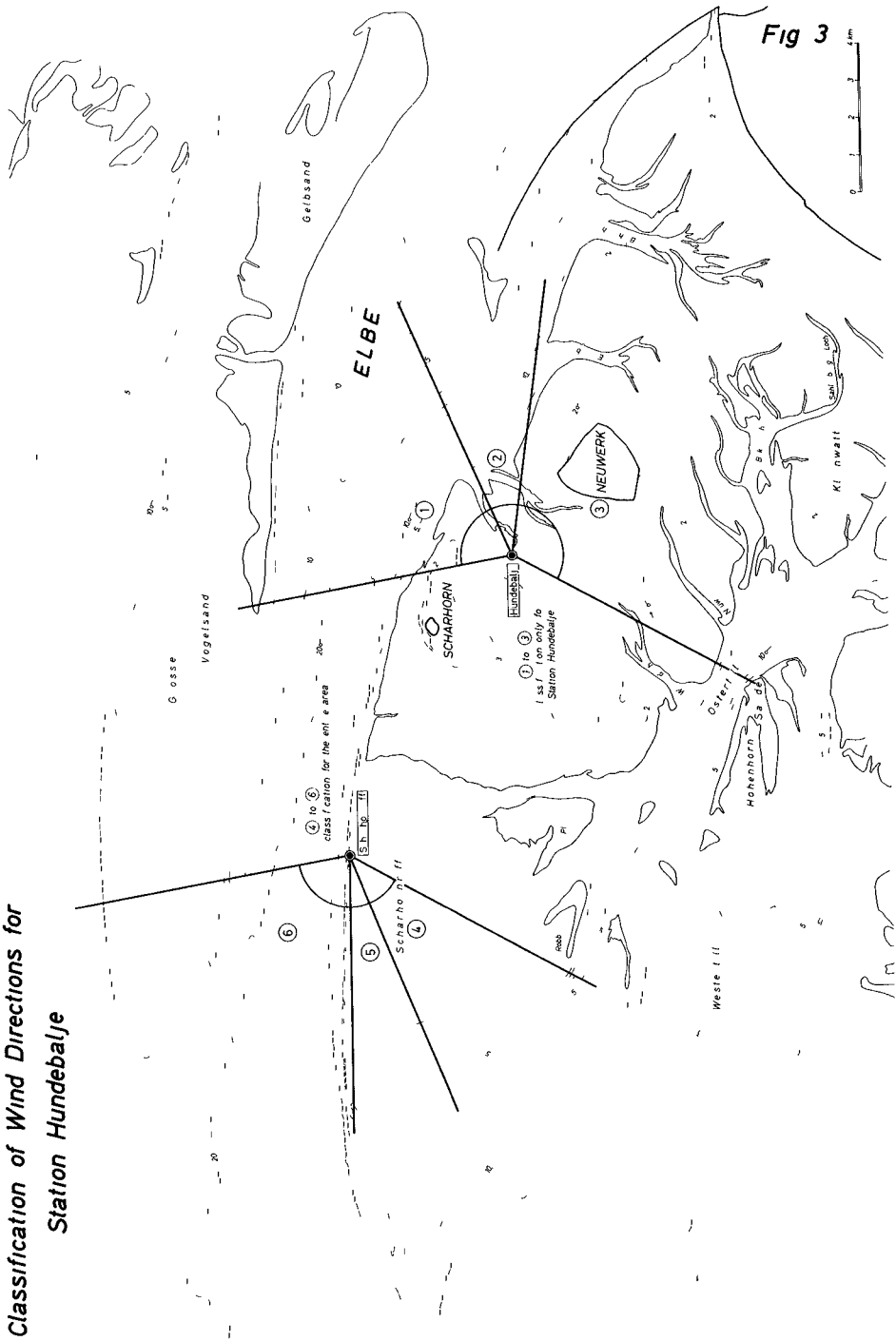


Fig 4

Quotient of Significant Wave Height $H_{1/3}$ and Mean Wave Height \bar{H} versus \bar{H}

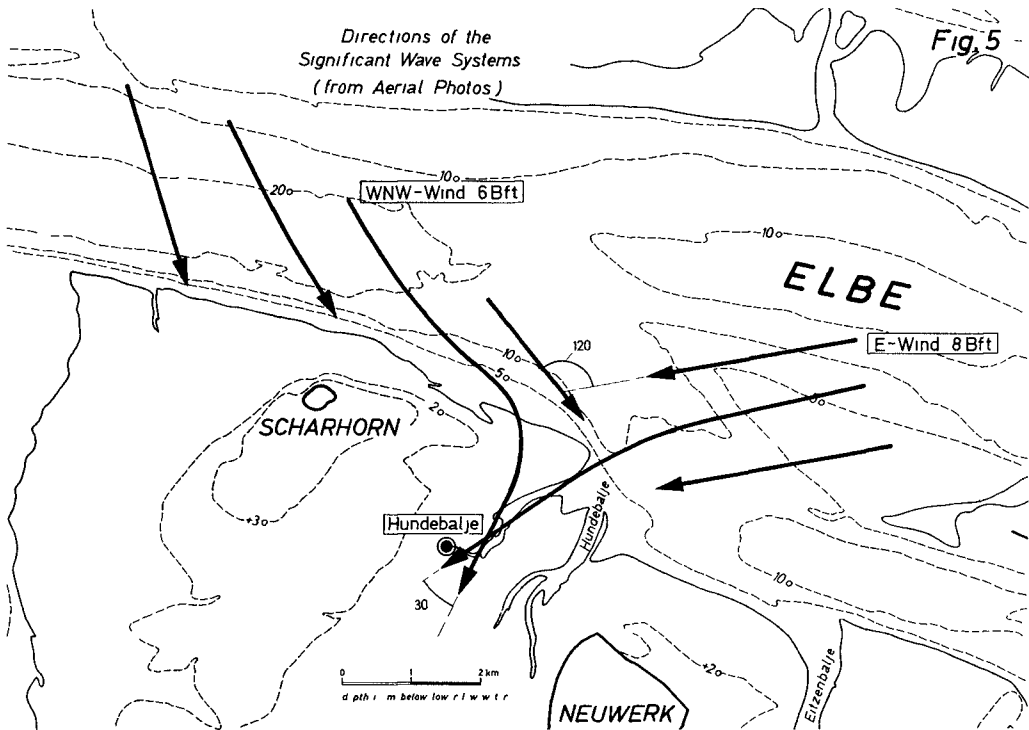
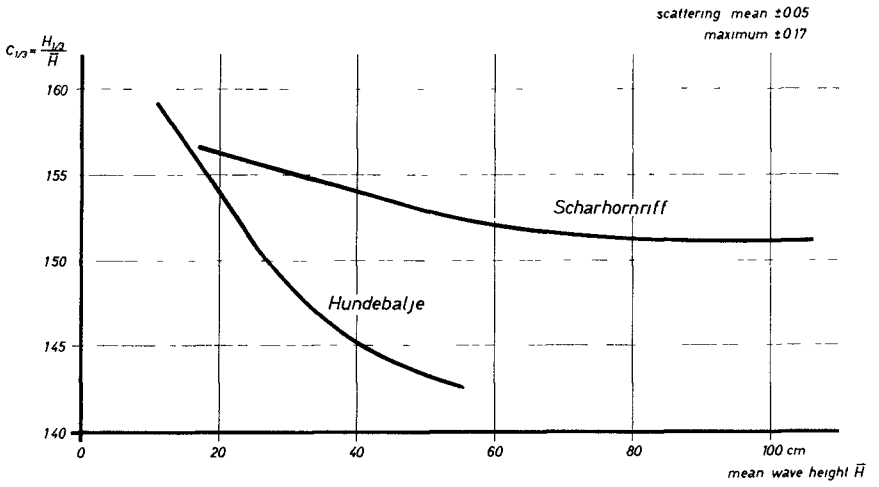


Fig 6

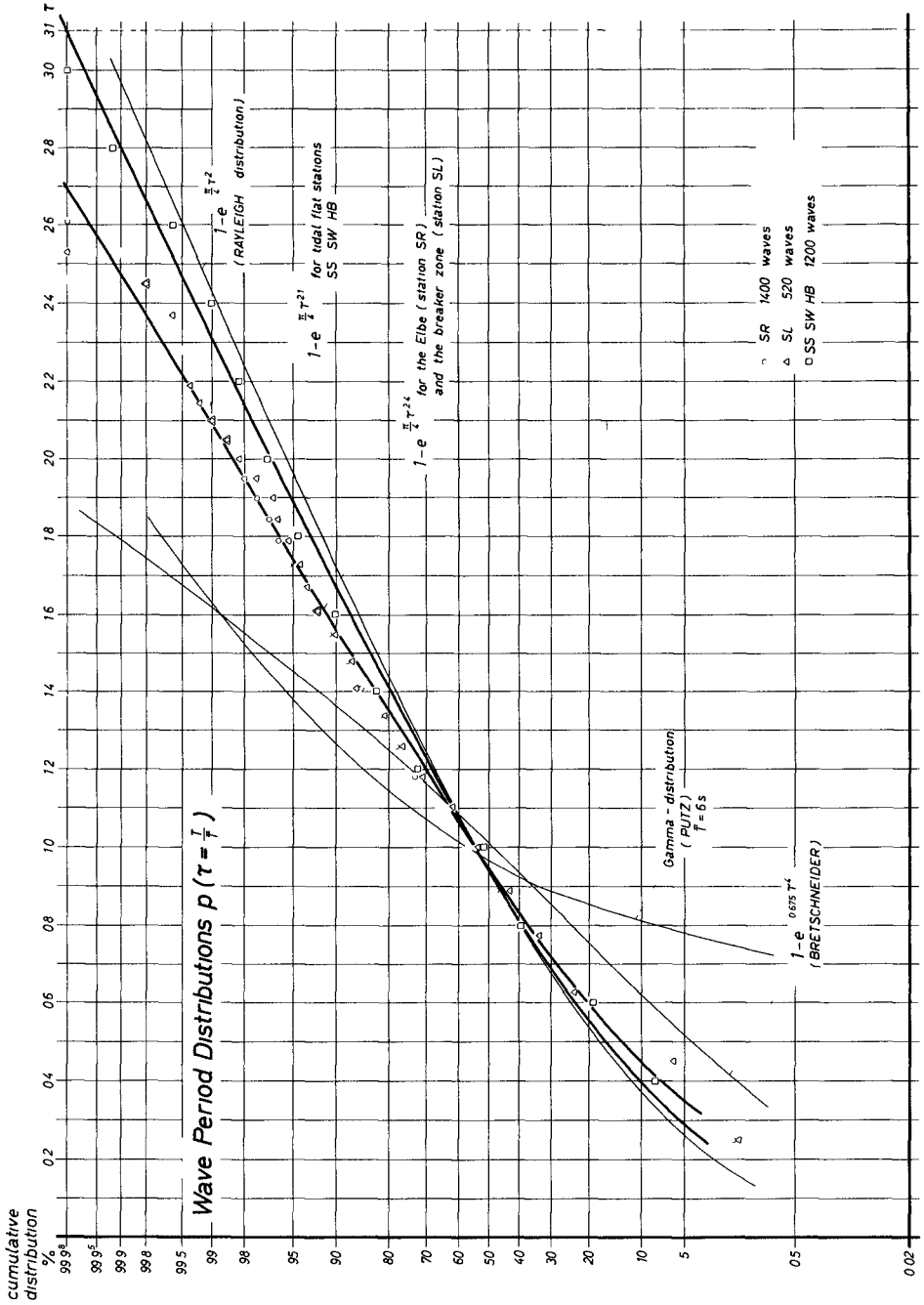


Fig 7

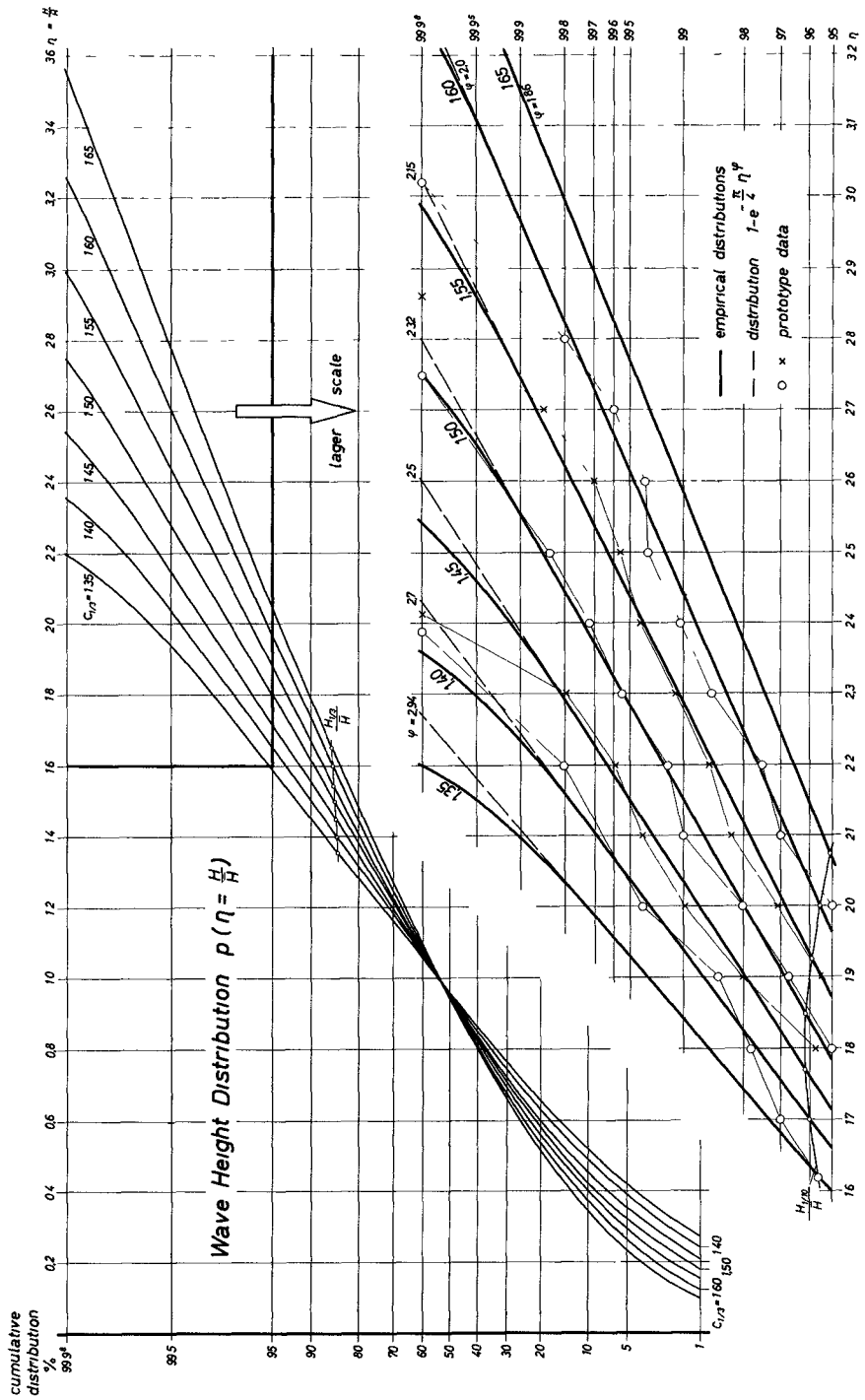
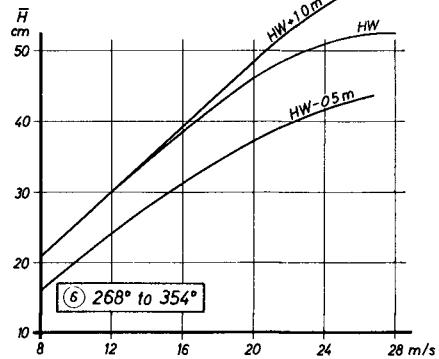
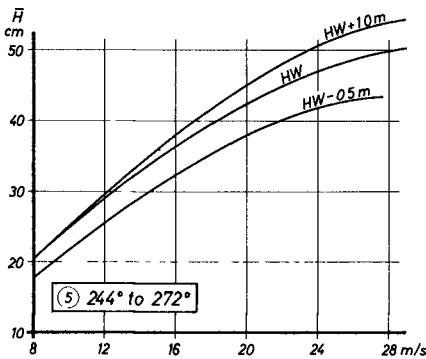
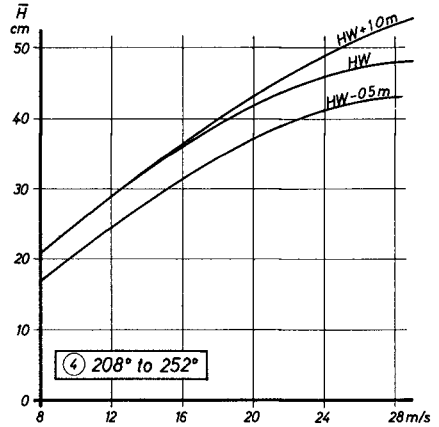
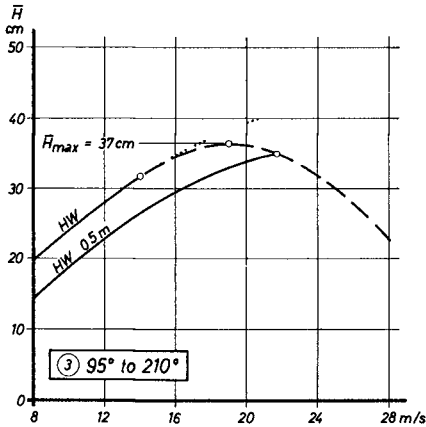
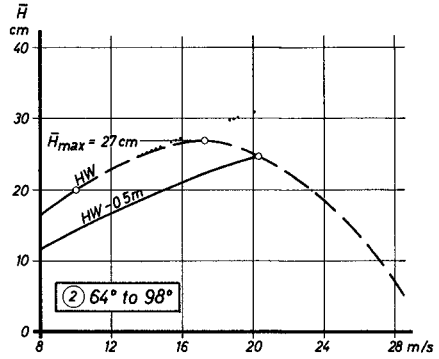
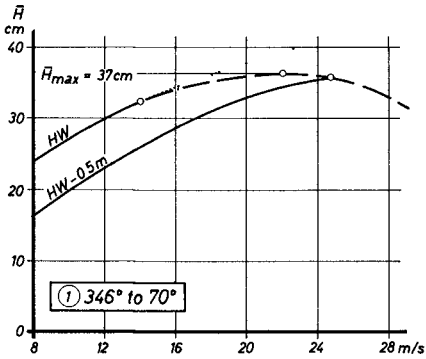
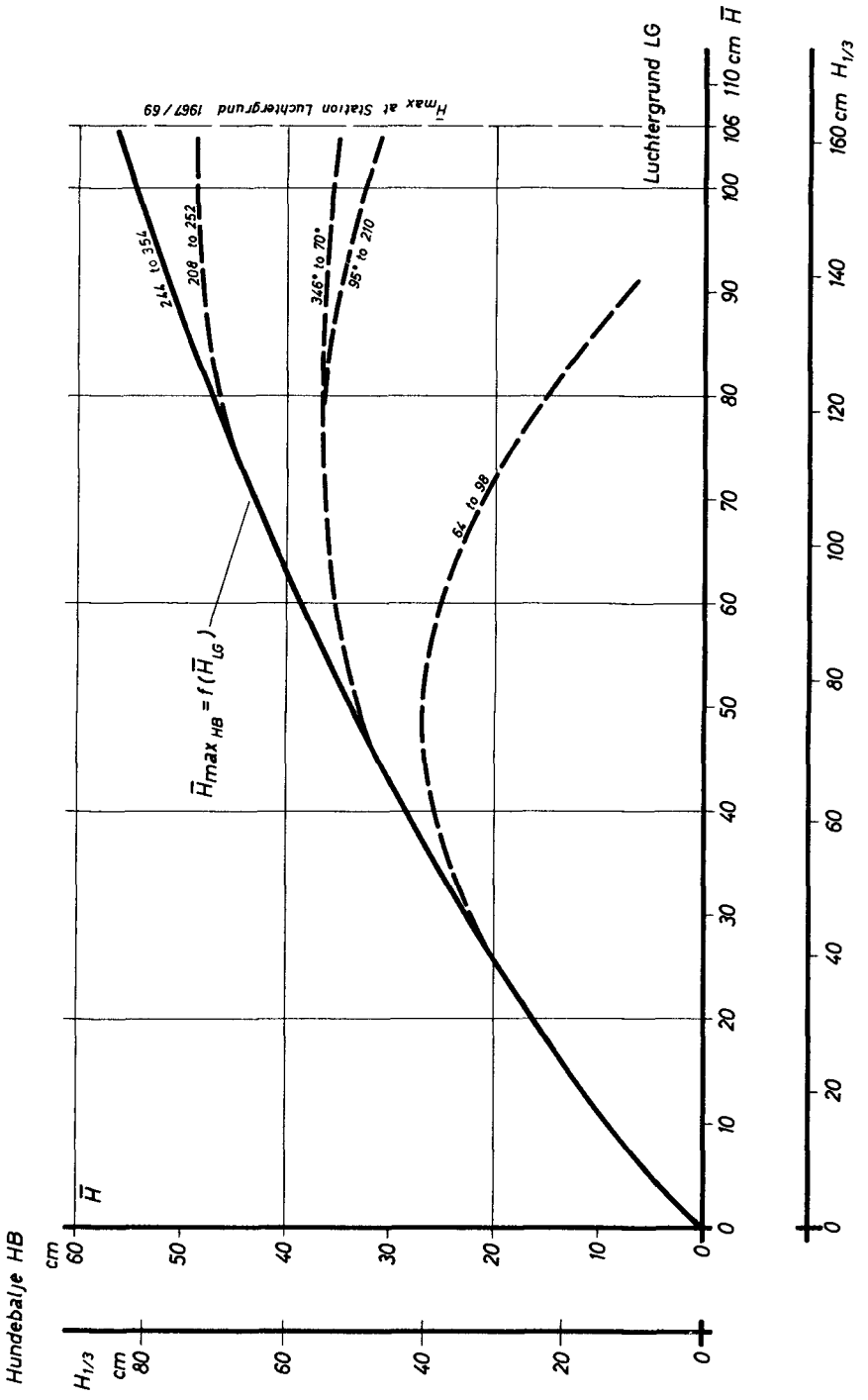


Fig 8

Station Hundebalje
Relation between Wave Heights and Wind
 (Depth of Water 19m at HW)



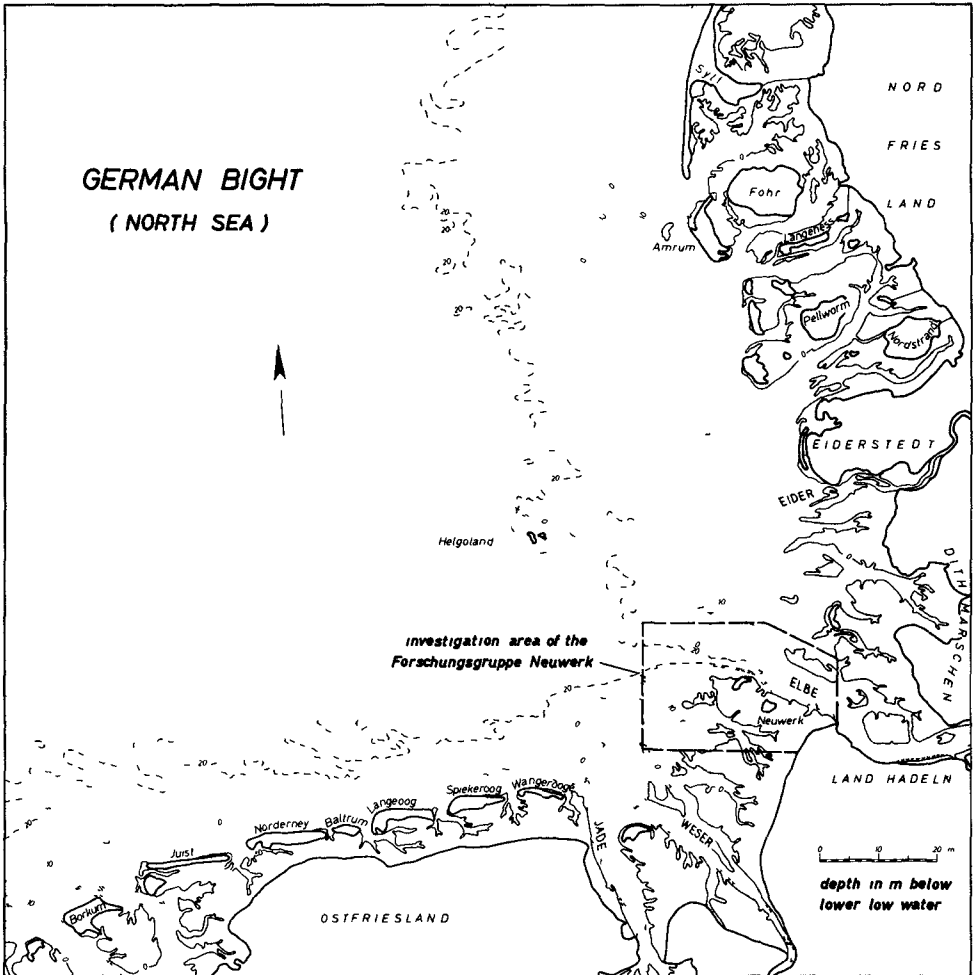
Relationship between Mean Wave Heights at Station Hundebalje for Different Wave Directions and Wave Heights in Deep Water (Station Luchtergrund)



Fig

Fig 1

**German Bight
with Investigation Area of the Forschungsgruppe Neuwerk**



**Classification of Wind Directions for
Station Hundebalje**

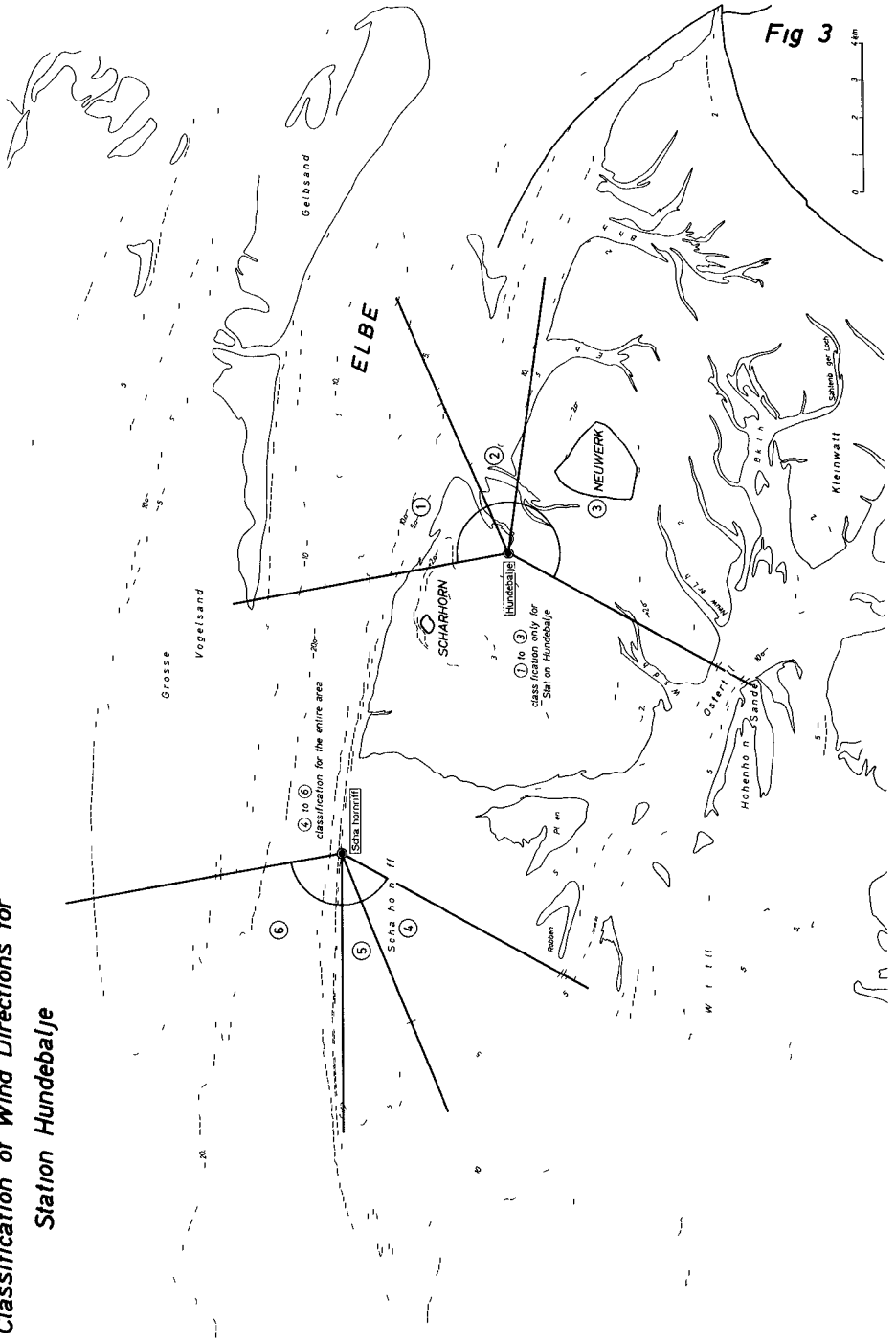


Fig 3

Fig 4

Quotient of Significant Wave Height $H_{1/3}$ and Mean Wave Height \bar{H} versus \bar{H}

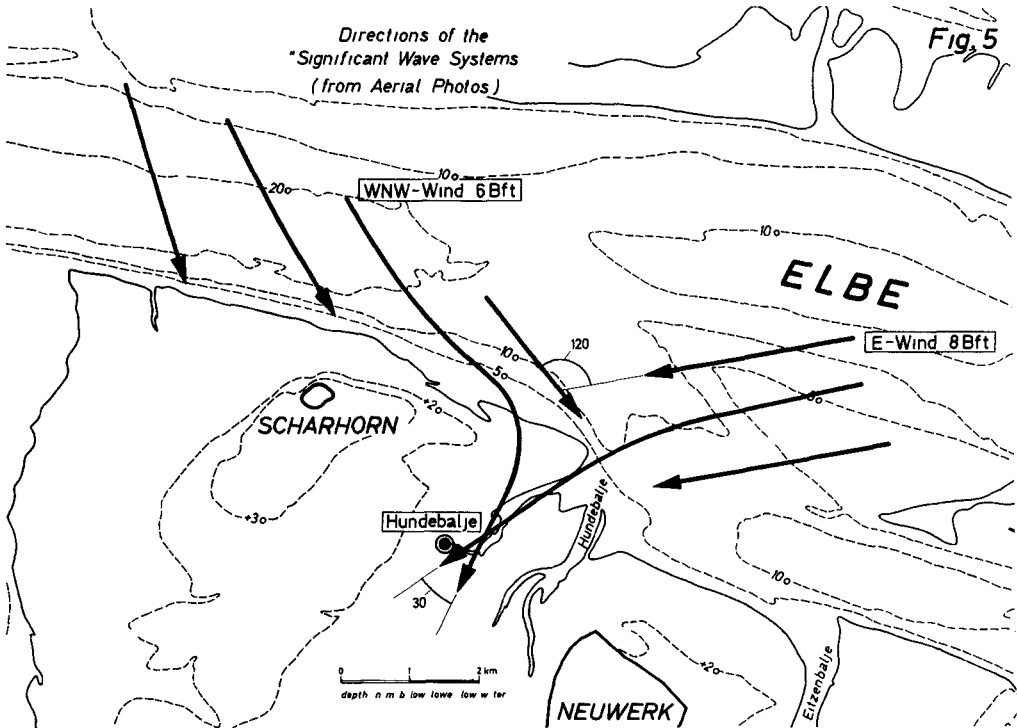
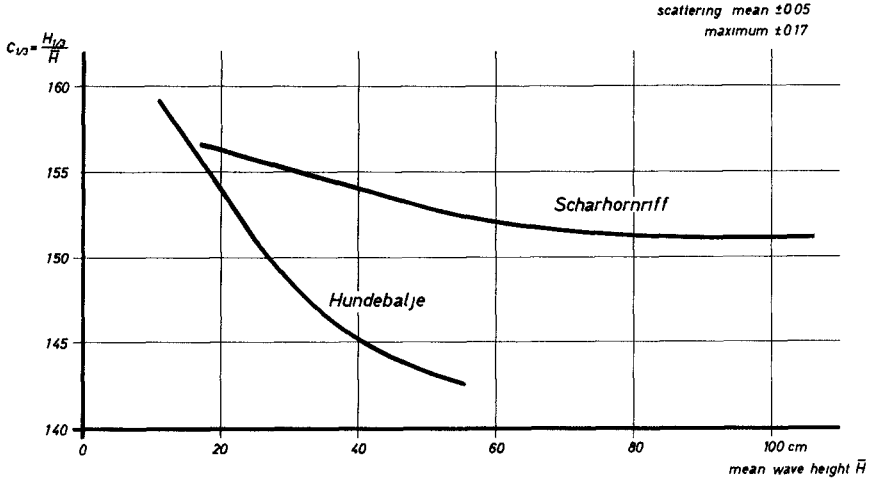


Fig 6

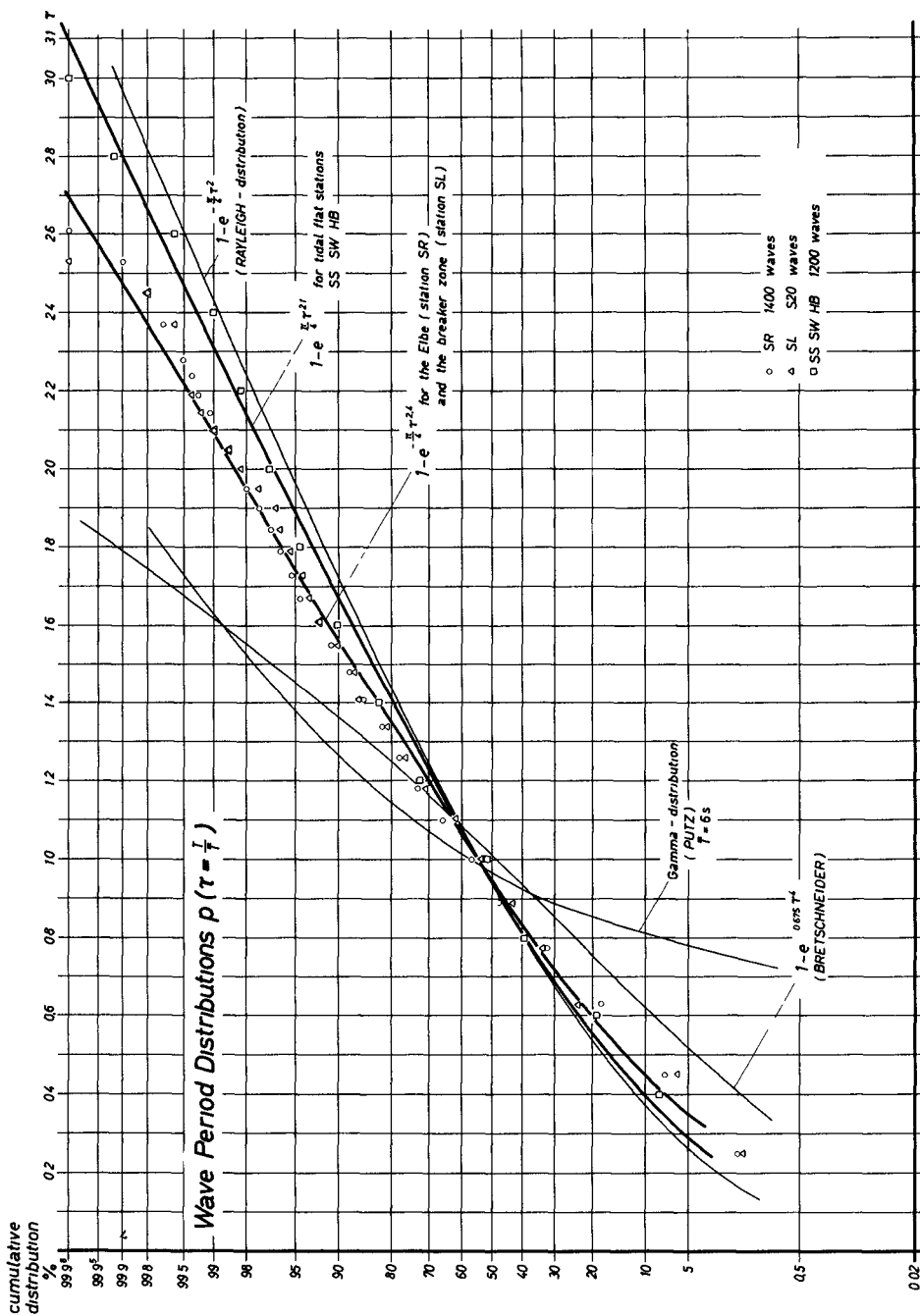


Fig 7

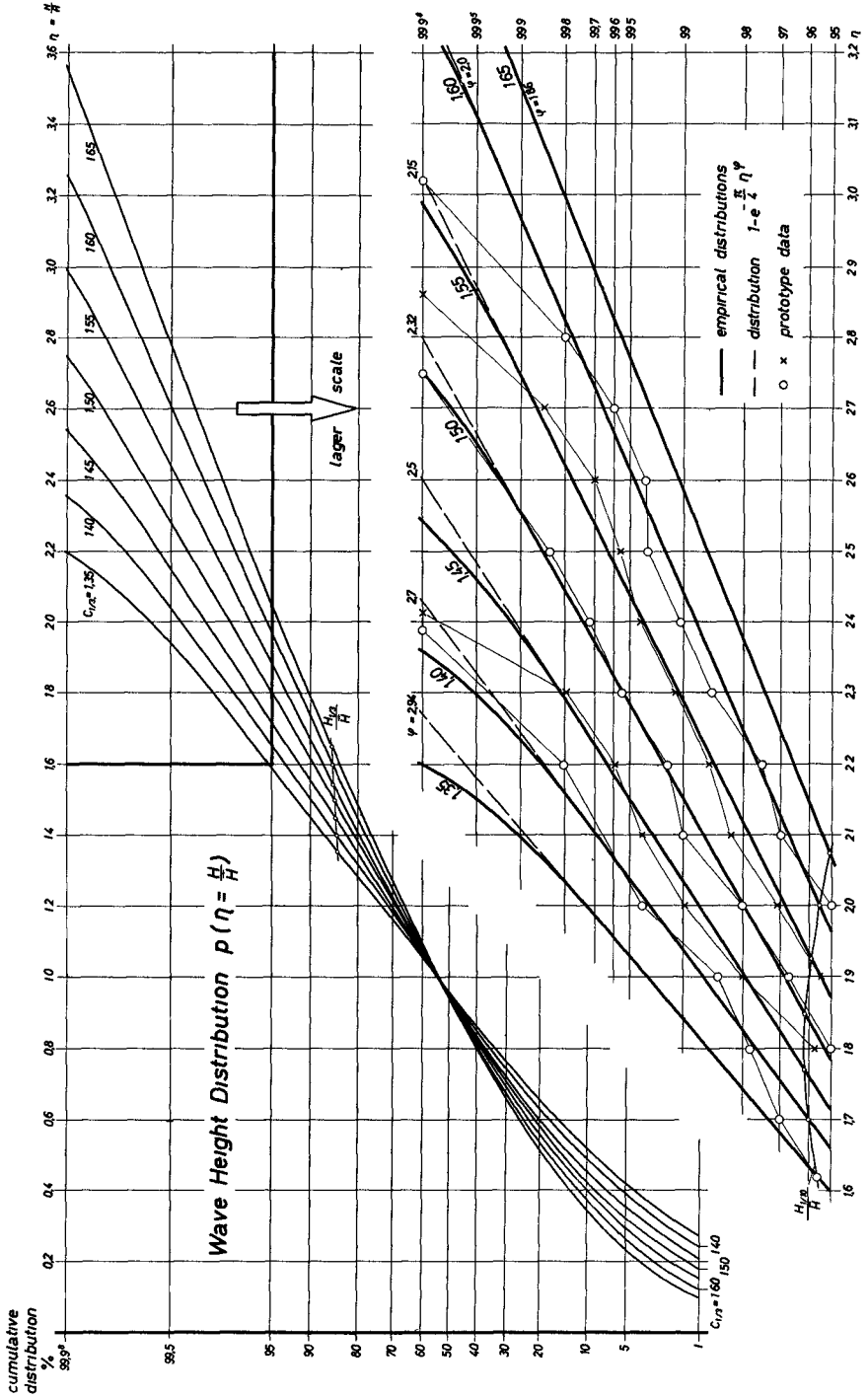
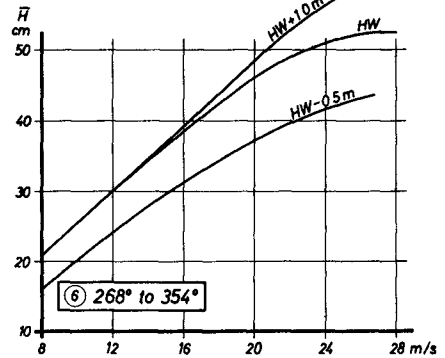
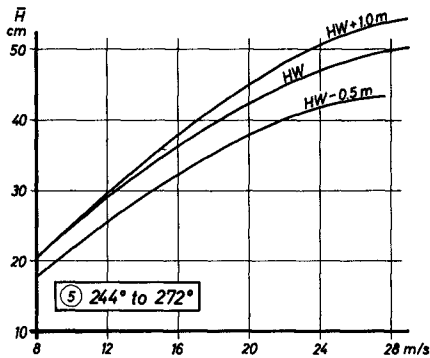
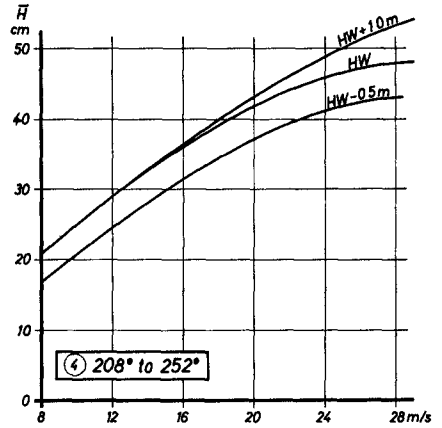
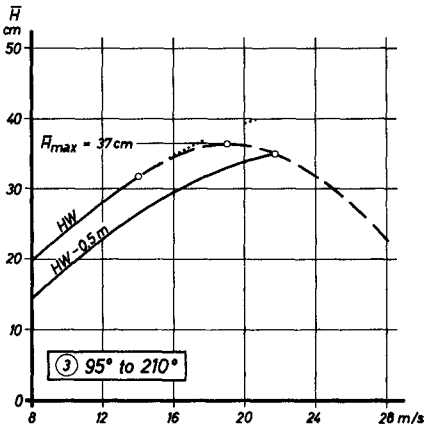
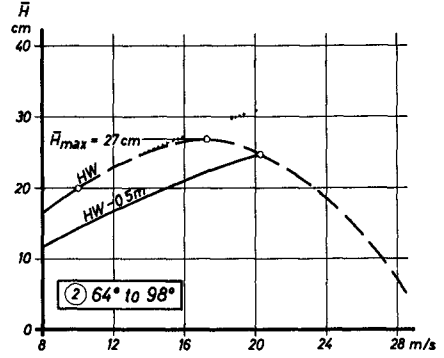
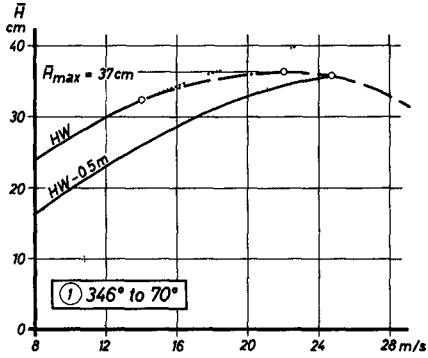


Fig 8

Station Hundebalje
Relation between Wave Heights and Wind
 (Depth of Water 19m at HW)



Relationship between Mean Wave Heights at Station Hundebalje for Different Wave Directions and Wave Heights in Deep Water (Station Luchtergrund)

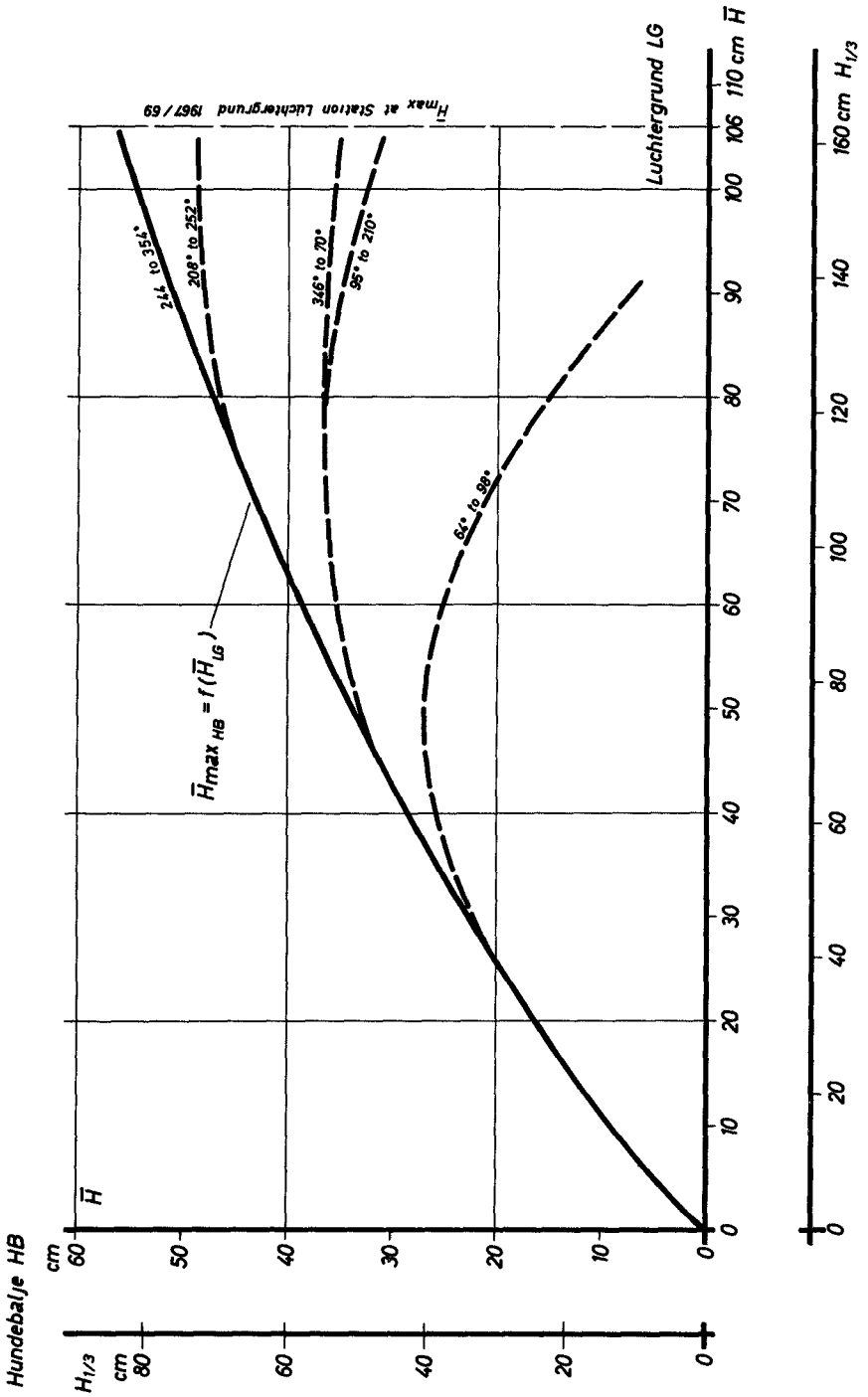


Fig 9

CHAPTER 11

EXPERIMENTAL STUDIES ON THE GENERATION OF WAVES IN SHALLOW WATER

C. T. Kuo

Associate Professor
Frederick L. W. Tang, Dr. Eng.
Professor and Chairman
Hydraulic Engineering Department
Cheng Kung University
Tainan, City, Taiwan
Republic of China

SYNOPSIS

The seas in front of China coast such as Yellow Sea, East China Sea and Taiwan Straits are all located on continental shelf. In consequence, waves approaching these coasts are generated in shallow water area in comparison with wave length. The authors has developed tangible calculation procedures for evaluating the wave features in such areas in stationary or moving fetches (1). However, the basical formulas of calculation are derived from experimental data of Bretschneider and Thijsse. In order to investigate the generating process of shallow water wind waves and obtain more detailed informations for correcting calculation criteria, a series of experiments have been performed at a wind tunnel of 75 meters in length. Various investigations on the relationships between waves and wind as well as water depth are to be submitted in this paper.

In addition, the situation of wind wave coexistence with regular wave is studied from experiments, because it resembles the superposition of refracted and local wind waves on the western coast of Taiwan.

SIGNIFICANT WAVE FEATURES

From the experiments, the wave heights and periods increase with wind velocities and fetch lengths, however, they reach fully arisen state more rapidly than deep water waves, only a few minutes in the experiments. After fully arisen, a portion of high waves begin to break and reduce their heights slightly, however, the waves recover their heights after advancing a short distance and then they break partially, such phenomena repeat again and again especially in the cases of the wind being strong. The wave periods remain increasing within the fetch length in these experiments, however, it can be expected that the wave periods and heights may become constant if the fetch length is long enough.

The experimental curves of $gH_{\frac{1}{3}}/U^2$ versus gF/U^2 with parameter gd/U^2 as shown in Fig. 1³ have the same tendency with the curves of Bretschneider (2), however, our data are larger than those of Johnson, Huft and Hamada, and even larger than the values predicted from the fetch graph of SMB in the region of gF/U^2 in Fig. 2 are located below breaking limit and Bretschneider's steady state of friction coefficients equal to 0.01. In Fig. 3 the experimental result of the relationship between $gT_{\frac{1}{3}}/U$ versus gF/U^2 is quite agreed with deep water waves.

Statistical characteristics of wave heights and periods have also been calculated. As shown in Fig. 4 and 5 the probability distribution corresponds sufficiently to Gaussian's rather than Rayleigh's. The ratios between various 1/nth wave heights are as follows.

$$\begin{aligned} H_{\frac{1}{3}}/H_{ave} &= 1.38 & (1.60) \\ H_{\frac{1}{6}}/H_{\frac{1}{3}} &= 1.16 & (1.27) \\ H_{max}/H_{\frac{1}{3}} &= 1.39 & (1.64) \end{aligned}$$

Any of the numbers is smaller than the theoretical value of Longuet-Higgins (in parenthesis). The ratios of 1/nth wave height to root-mean-square wave height H_{rms} are as follows.

$$\begin{aligned} H_{ave}/H_{rms} &= 0.94 \\ H_{\frac{1}{3}}/H_{rms} &= 1.30 \\ H_{\frac{1}{6}}/H_{rms} &= 1.55 \end{aligned}$$

They seem to be little concern with spectral width parameter.

On the whole, there is no substantial difference between the statistical properties of wind waves in shallow and deep water.

SPECTRAL ANALYSIS

The power spectra are calculated from experimental records by Blackman-Tukey's method. Sampling time interval Δt is 1/10-1/15 sec., total number of data is $N = 800$, maximum time lag m equals 40, and folding frequency $f_m = 5$ cps (or 0.375 cps). The degree of freedom calculated by Tukeys formula is 40, in consequence, confidence limit in 10% is 0.73-1.30.

At early stage, the spectra grow continuously as the fetch length becoming longer till saturation state is reached. While the fetch lengths extend, the lower frequency parts of the spectral curves increase their density, as Fig. 6,7,8.

The relationship between wave spectra and wind velocity has the same tendency of deep water waves. Namely in same fetch length and water depth, the spectra grow with wind velocity being increasing. As Fig. 9 & 11, if the depth is small, the spectral density is smaller than that of deep water waves, as shown in Fig. 12, 13, 14, for same wind velocity. The greater the wind velocity is the earlier the low frequency portion of spectrum developed, and the wider the frequency band becomes. In any case, the high frequency side of equilibrium range decays remarkably and can be represented by f^{-n} .

The connection between $T_{1/3}$ and optimum period T_{op} is to be $T_{1/3} = 1.23 T_{op}$ in our experiments, and $T_{1/3} = 1.23 T_{ave} = 1.23 T_{rms}$, accordingly $T_{rms} = T_{ave} = T_{op}$.

Phillips pointed out the shape of spectral curves in high frequency side should be:

However, Hamada proved that $\Phi(f) = \beta g^2 f^{-5}$, and n will be larger than 5 in deep water wave spectra. Our experiments also reveal $n = 7-10$ in shallow water waves.

The relationship between H and $E = 2 \int \Phi(f) df$ is the same as deep water waves, namely $H_{1/3} = 2.83 \sqrt{E}$. As shown in Fig. 15.

STUDIES ON THE COMPOSITION OF REGULAR AND WIND WAVES

According to the special topography of western coast of Taiwan, the beach is very flat and the waves approach from Taiwan Straits are breaking on offshore bars. The distance between bars and the main coast or sea dike is still as long as 5 km. Local wind waves are overlapping on the waves after broken. To investigate such a phenomenon in order to offer design criteria for sea dikes, we generated regular waves by flap type wave generator and blow wind simultaneously in the same wind wave channel. The regular wave spectra are shown in Fig. 16 and the spectra of wind wave while regular wave are not to be existing are shown in Fig. 17. Fig. 18 shows the result spectra of overlapping. Apparently there are two kinds of waves existing independently. However, if the regular wave steepness is large such a phenomenon disappears as Fig. 19. The comparison of the energy of resultant wave energy and energy calculated by linear summation is shown in Fig. 20. In case of broken waves superposed by wind waves as the case of western coast of Taiwan. Wave height in front of sea dike can be approximately calculated by $H^2 = H_w^2 + H_R^2$.

CONCLUSION

From experimental data described above following conclusions can be made.

1. The generation procedure of shallow water waves is closed resembling to deep water waves, however, the duration for fully arisen is much shorter.
2. In the range of our experiments wave period seems not to be significantly influenced by water depth. The wave height increases with fetch length increasing, however, they are smaller than deep water waves due to the influence of water depth.
3. If wave spectra of shallow wave area are available, the significant wave height can also be calculated by $H_{\frac{1}{3}} = 2.83 \sqrt{E}$, ($E = 2 \int \phi(f) df$).
4. In the problem concerning superposition of two series of waves, if the steepness is small, the resultant wave heights can be calculated by linear summation of their energies.

REFERENCE

1. Frederick L. W. Tang: Researches on Calculation of Waves on Long Shoaling Beaches. Jour. of Civil and Hydraulic Engineering, Taiwan Provincial Cheng Kung University. Feb. 1970.
2. Breschneider: Generation of Wind Waves Over a Shallow Bottom. B. E. B. Tech. Memo No. 51 Oct. 1954.

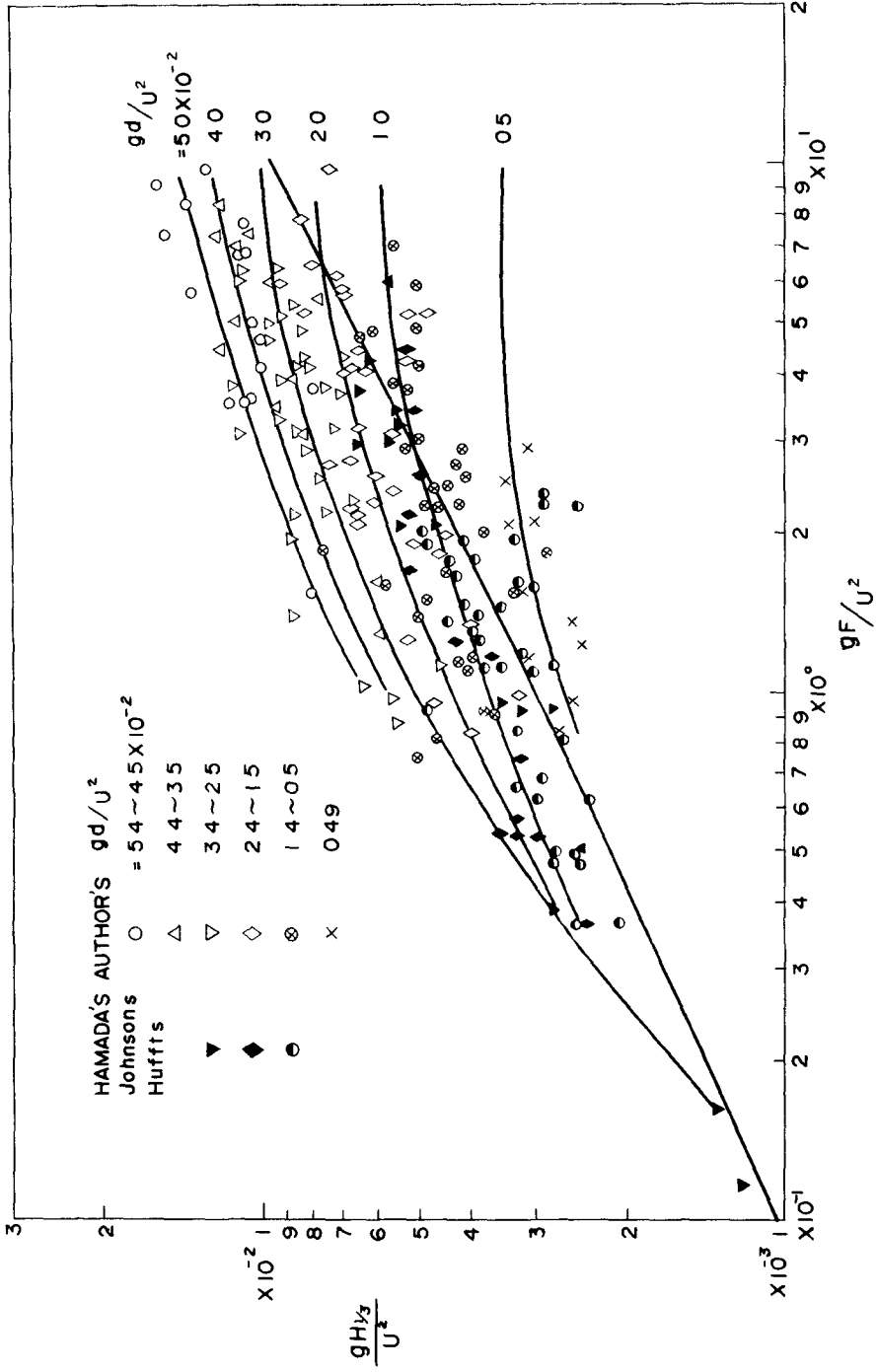


Fig 1

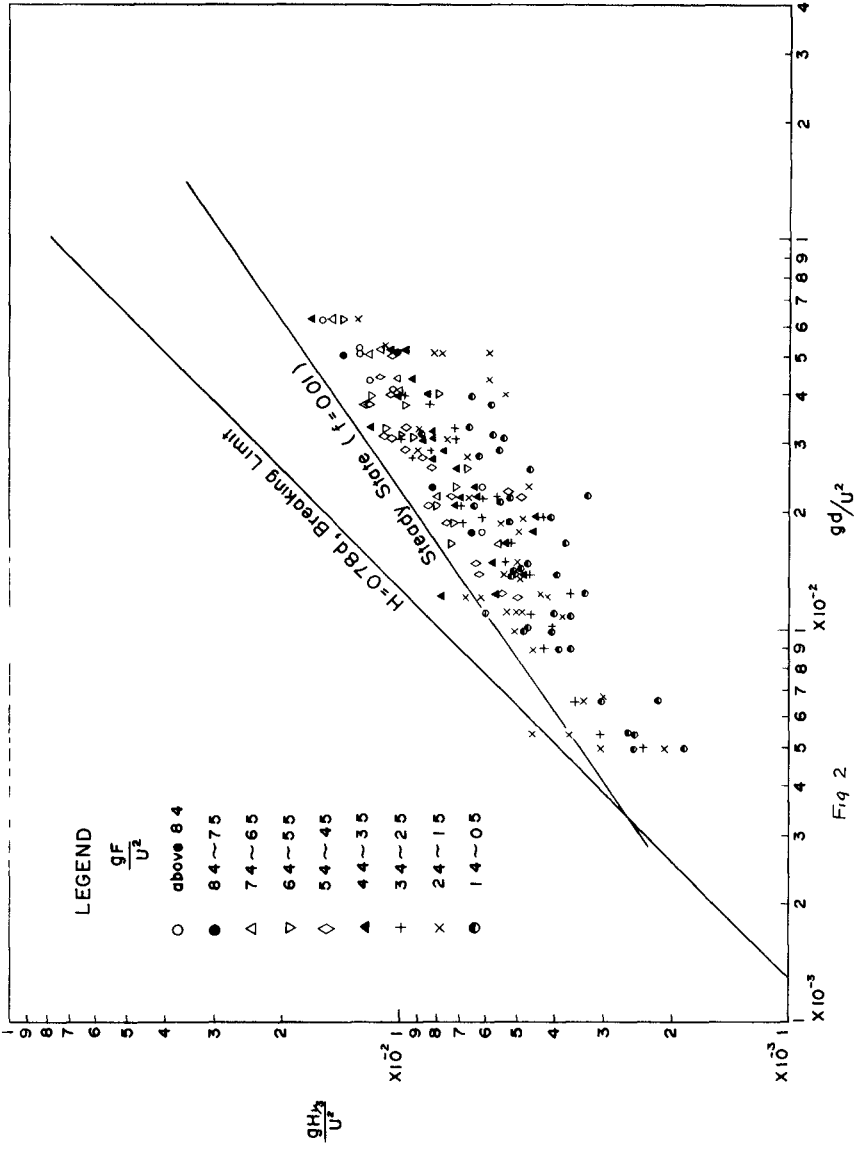


Fig 2

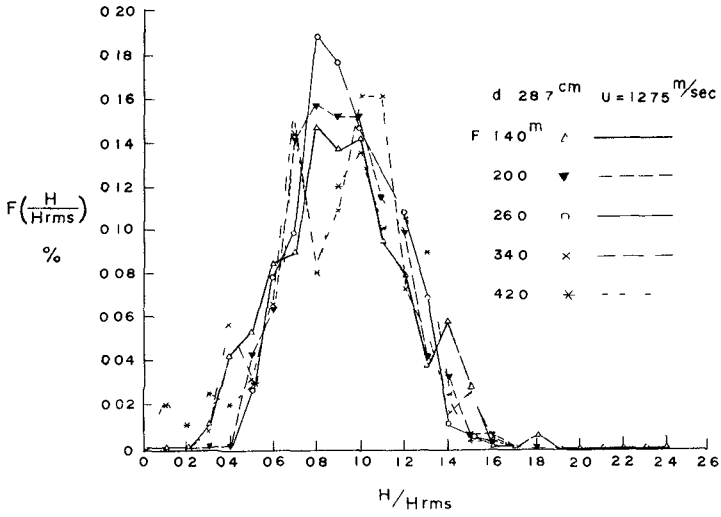
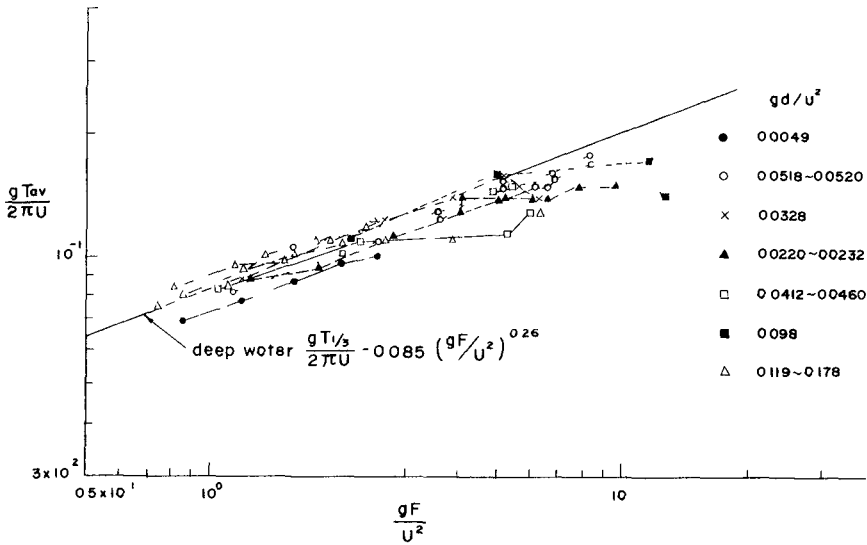


Fig 4



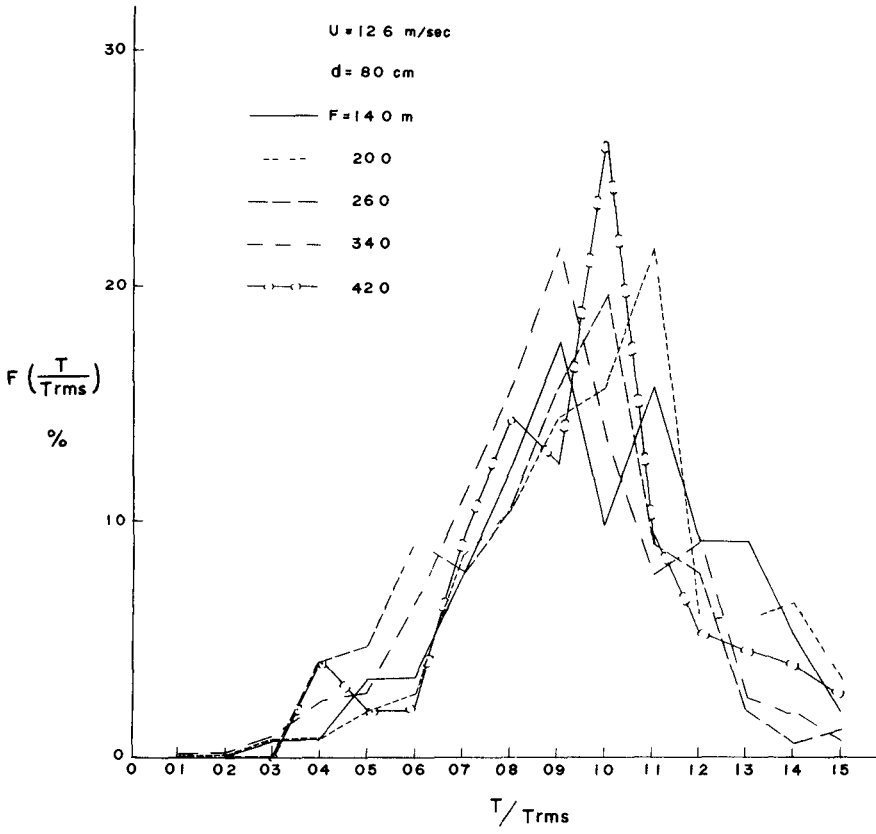


Fig 5

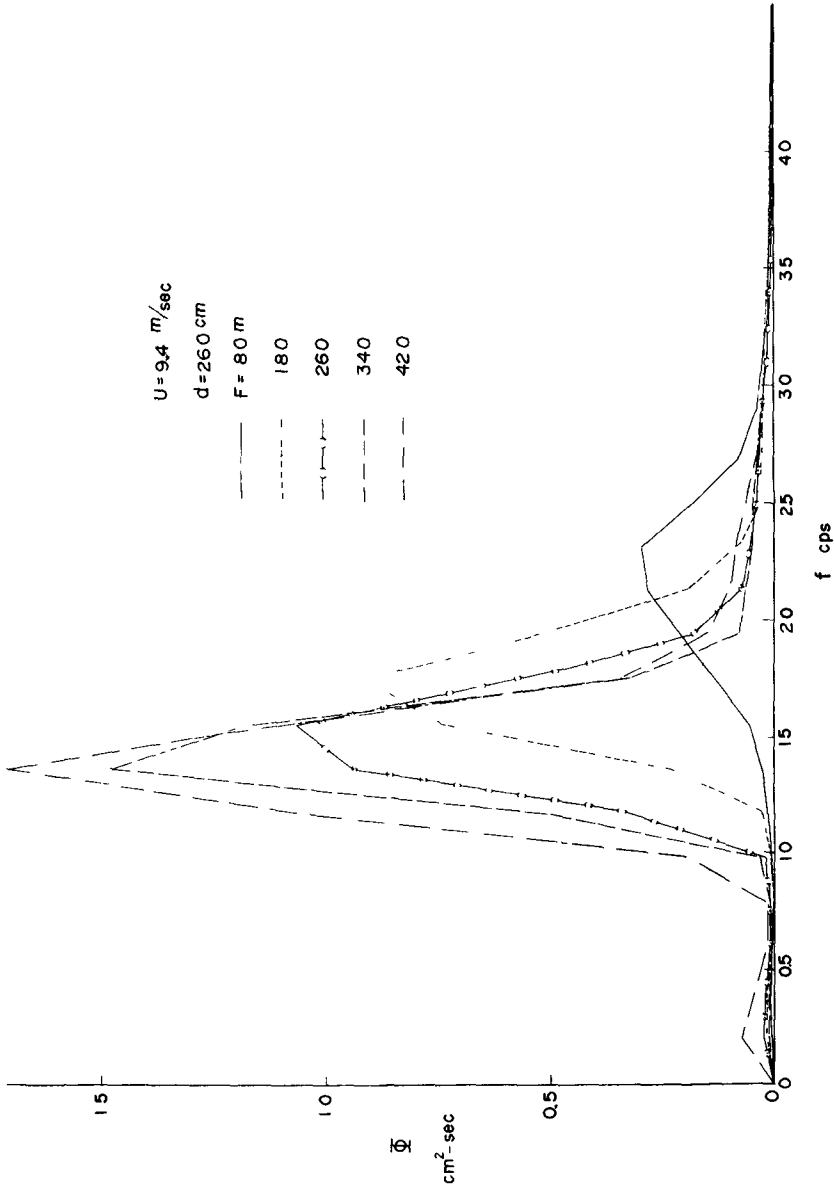


Fig 6

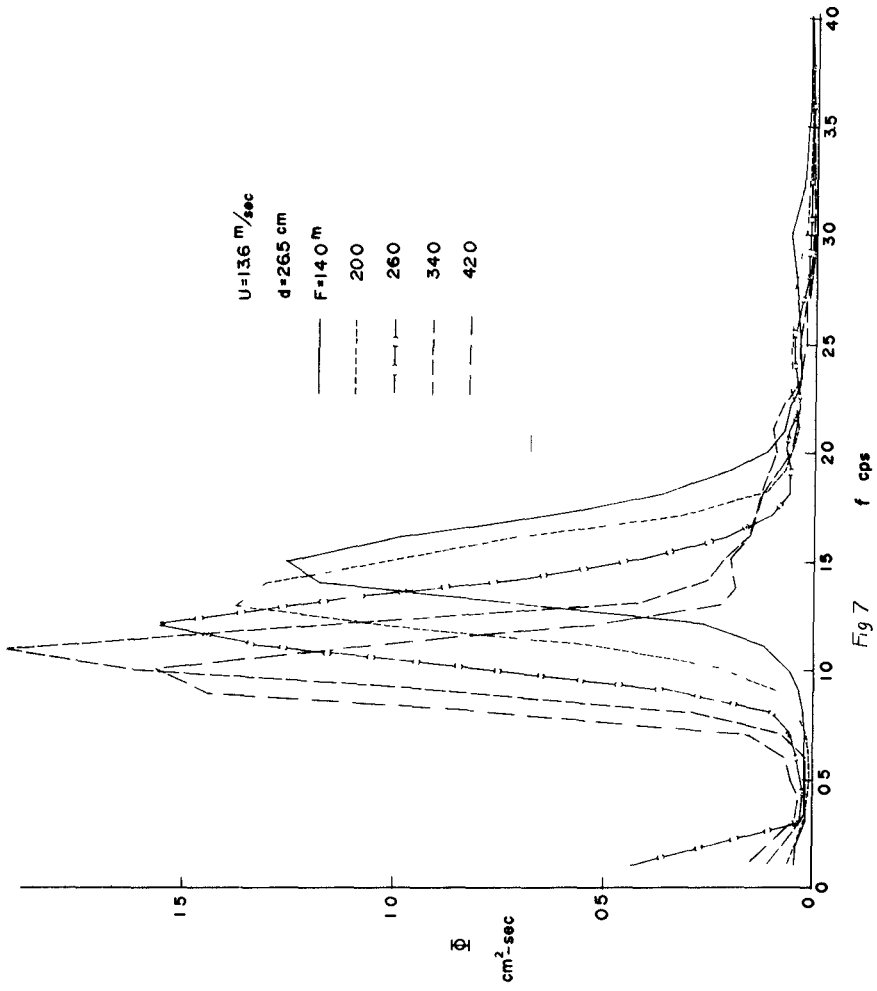


Fig. 7

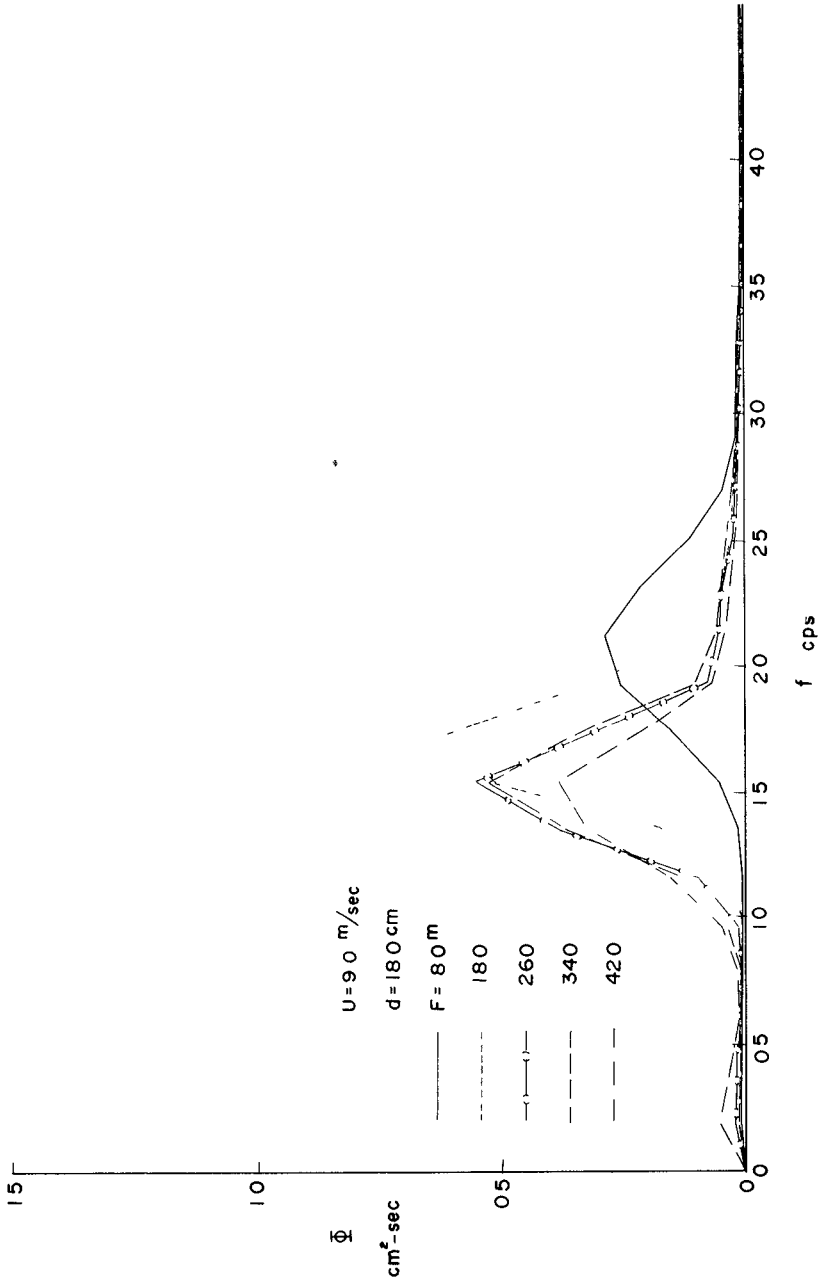


Fig 8

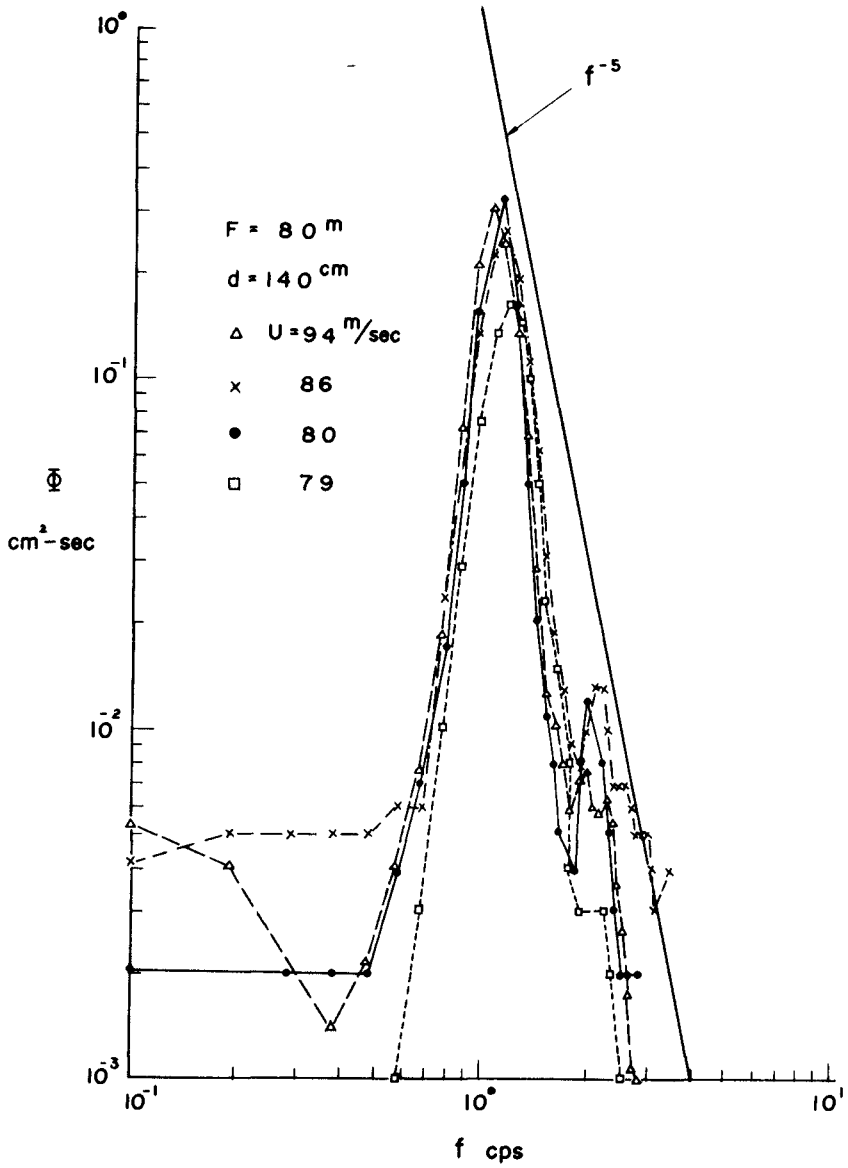


Fig 9

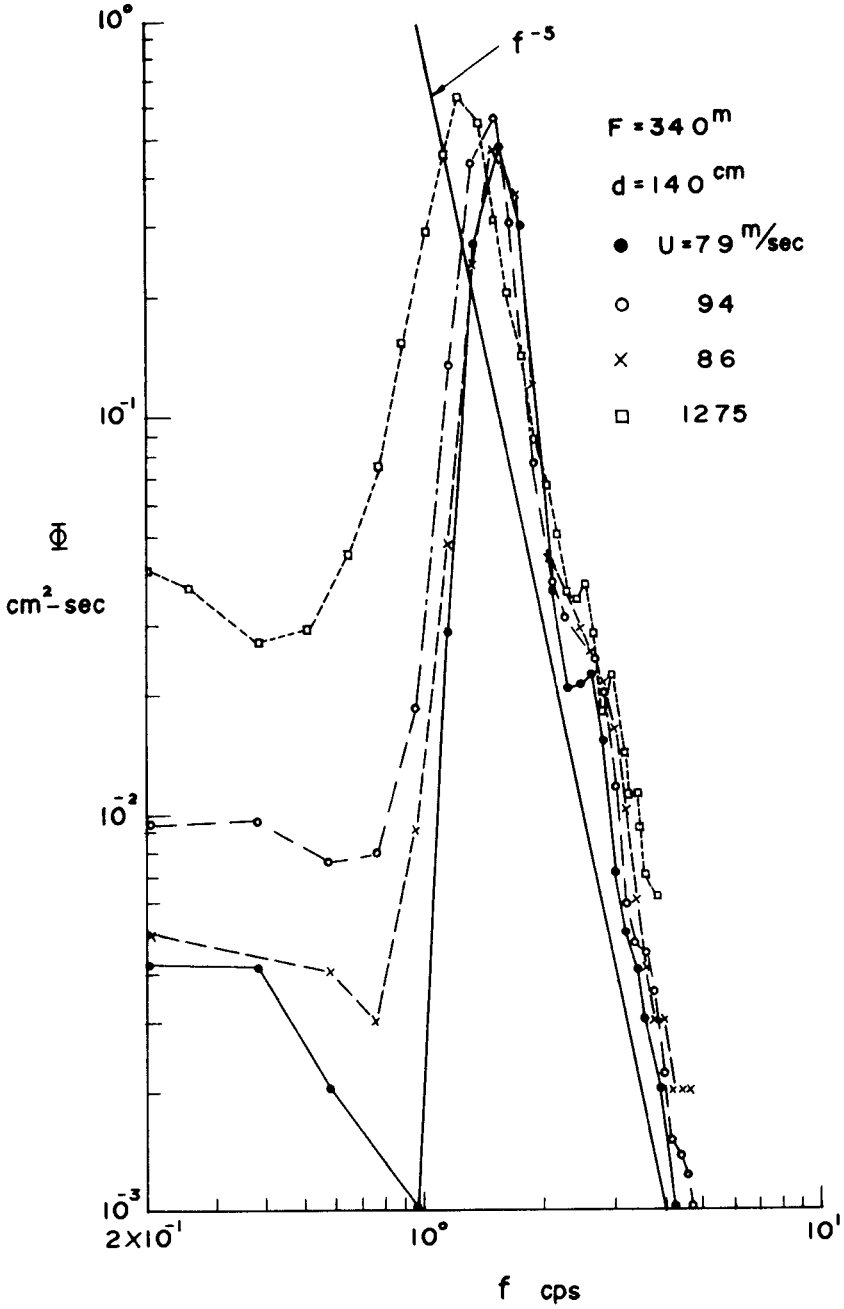


Fig 10

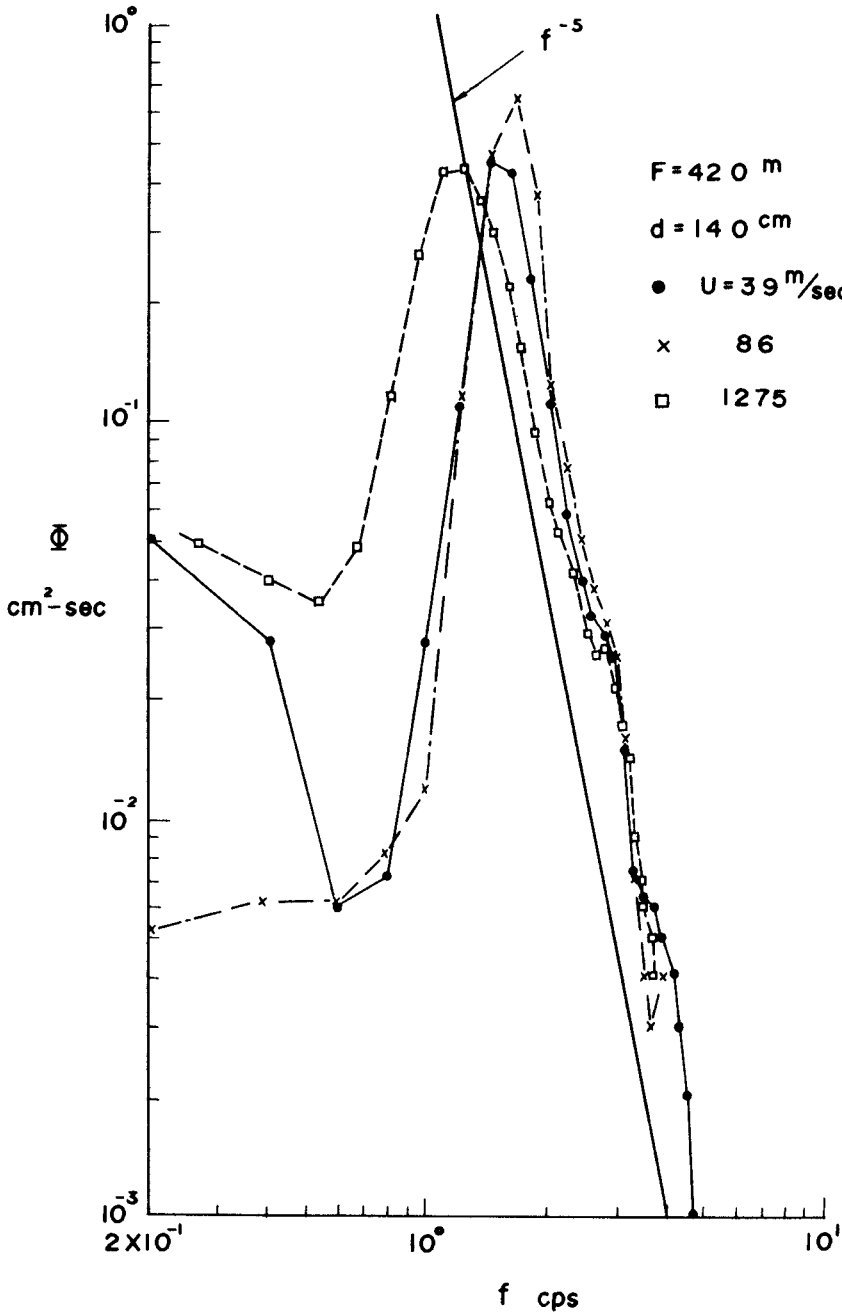


Fig 11

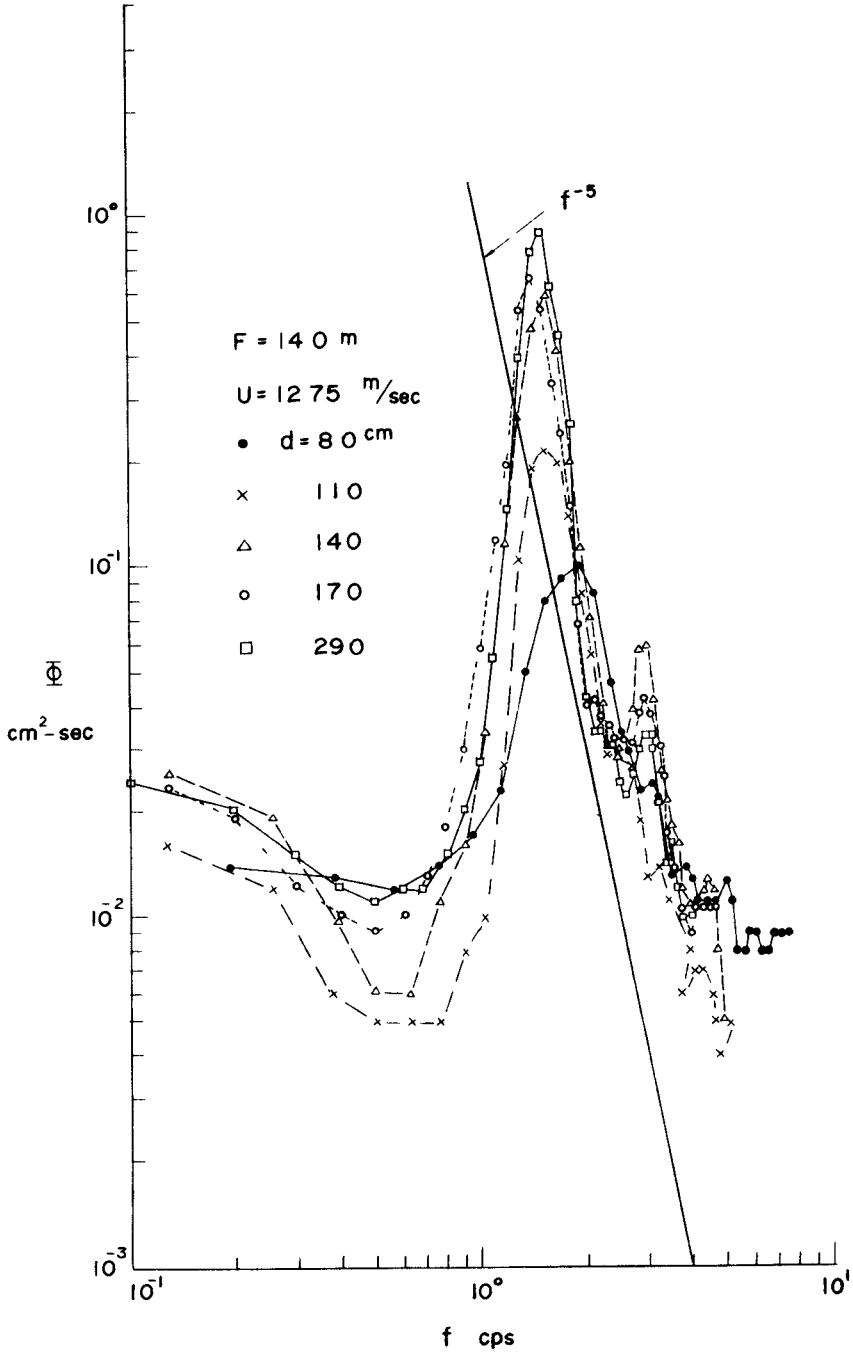


Fig 12

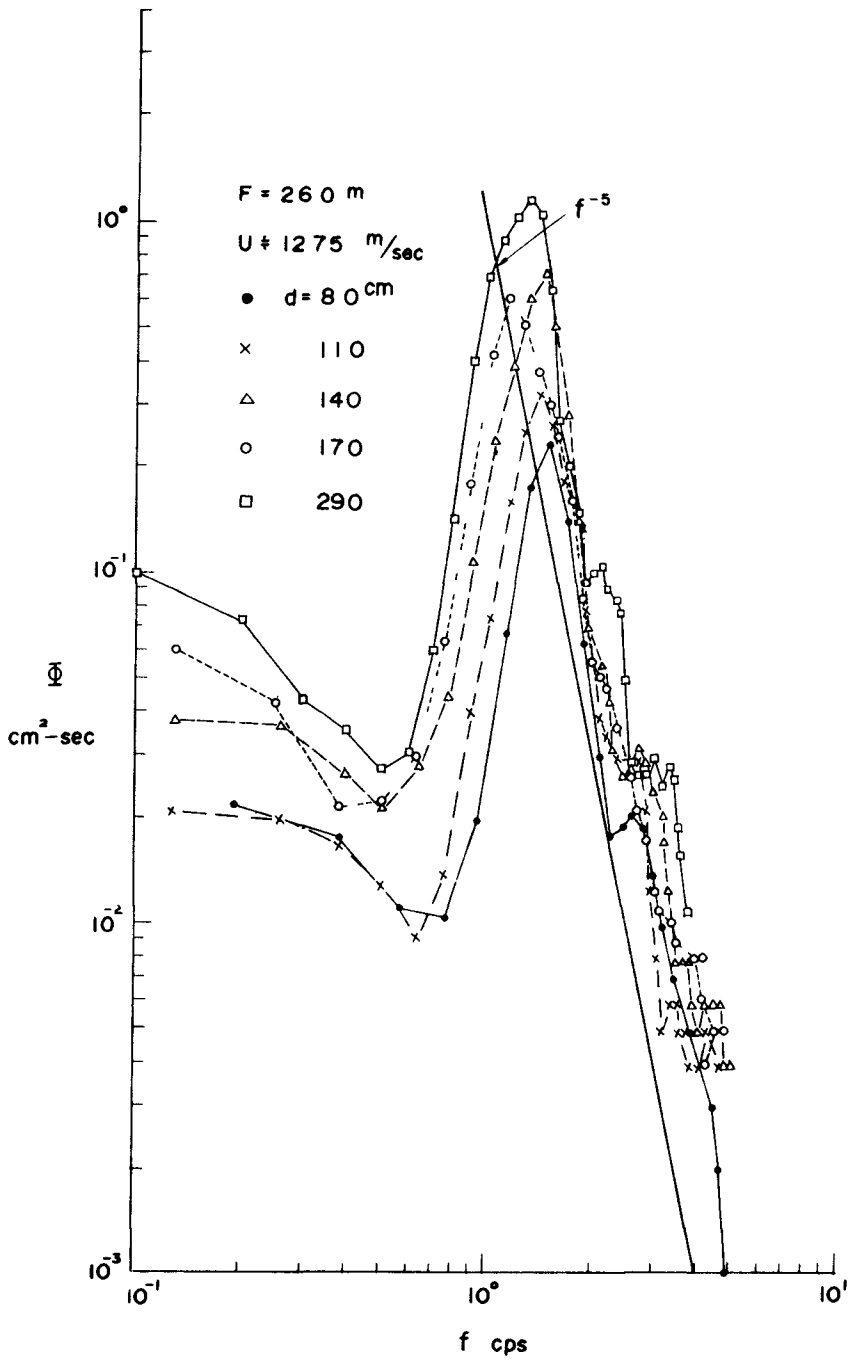


Fig 13

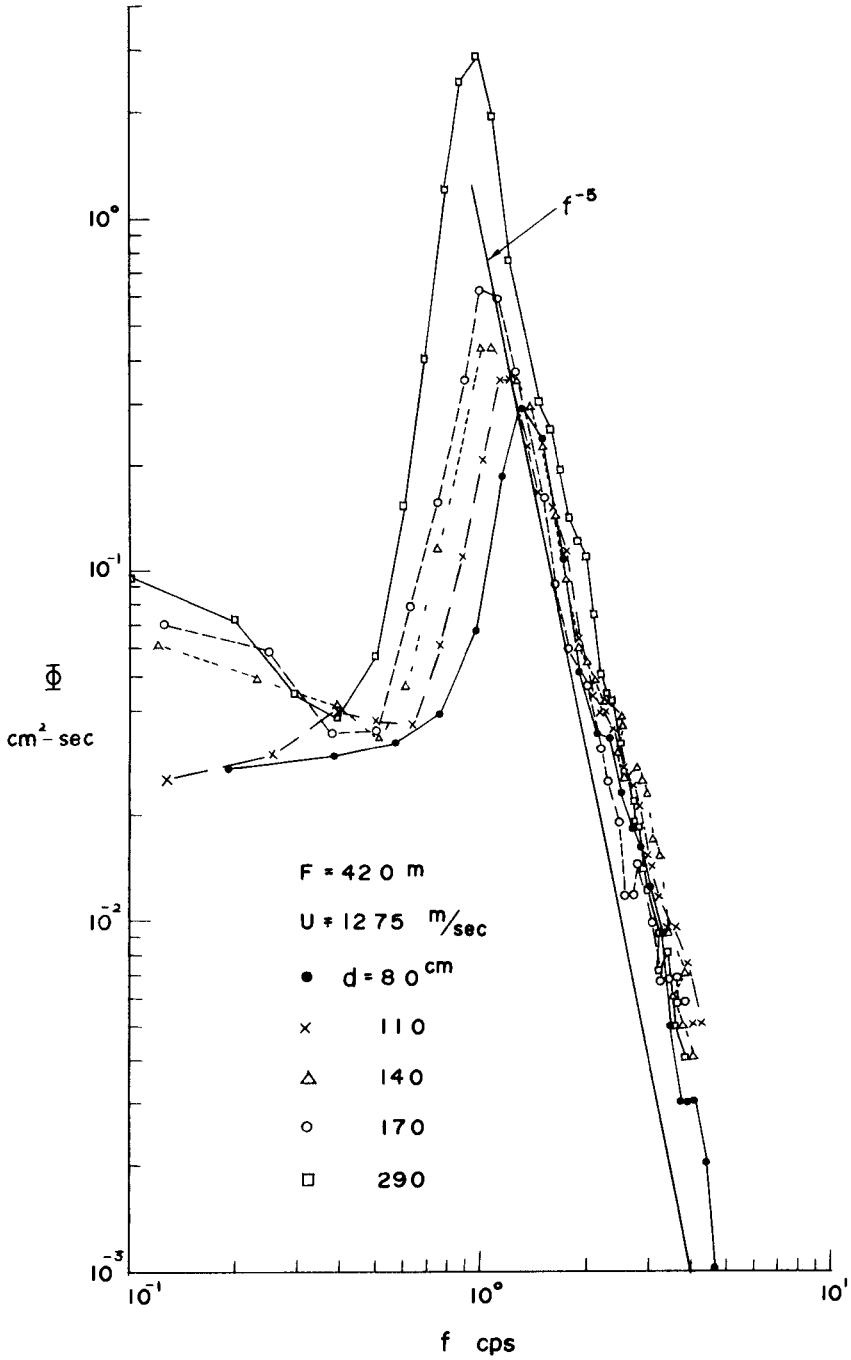


Fig 14

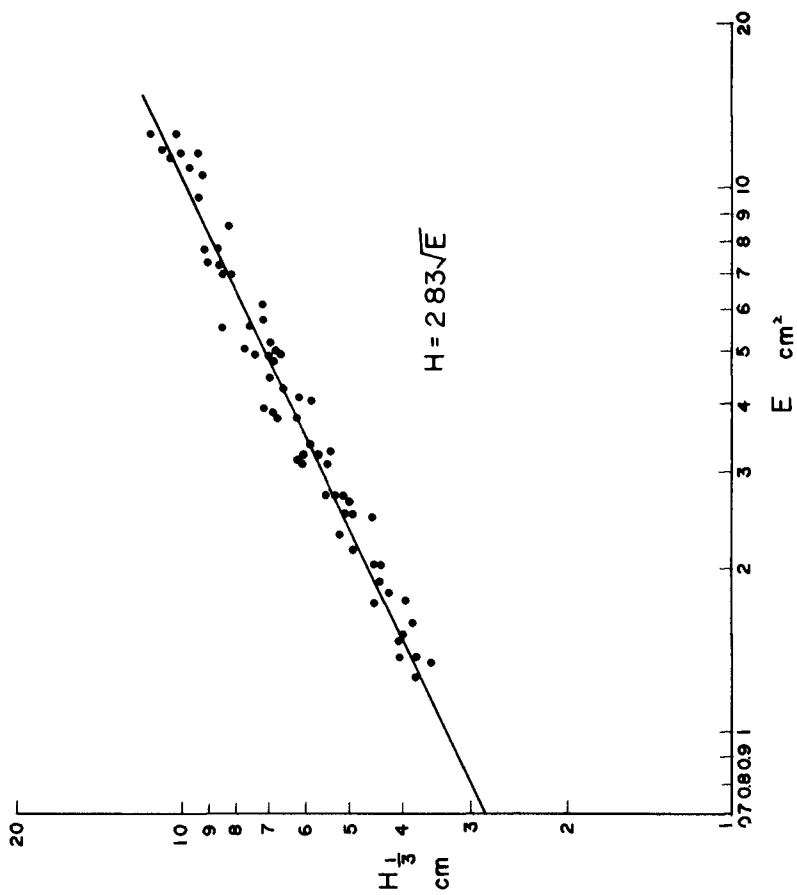


Fig 15

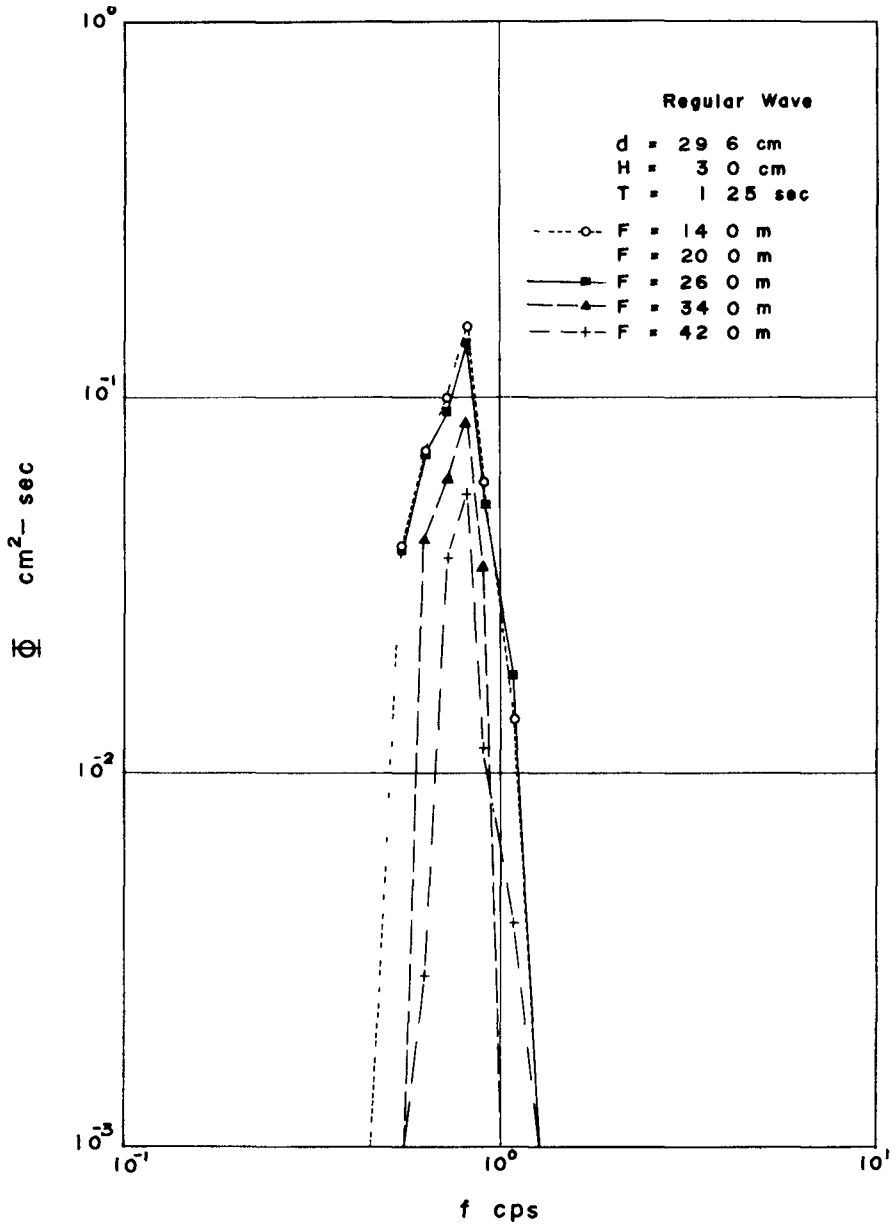
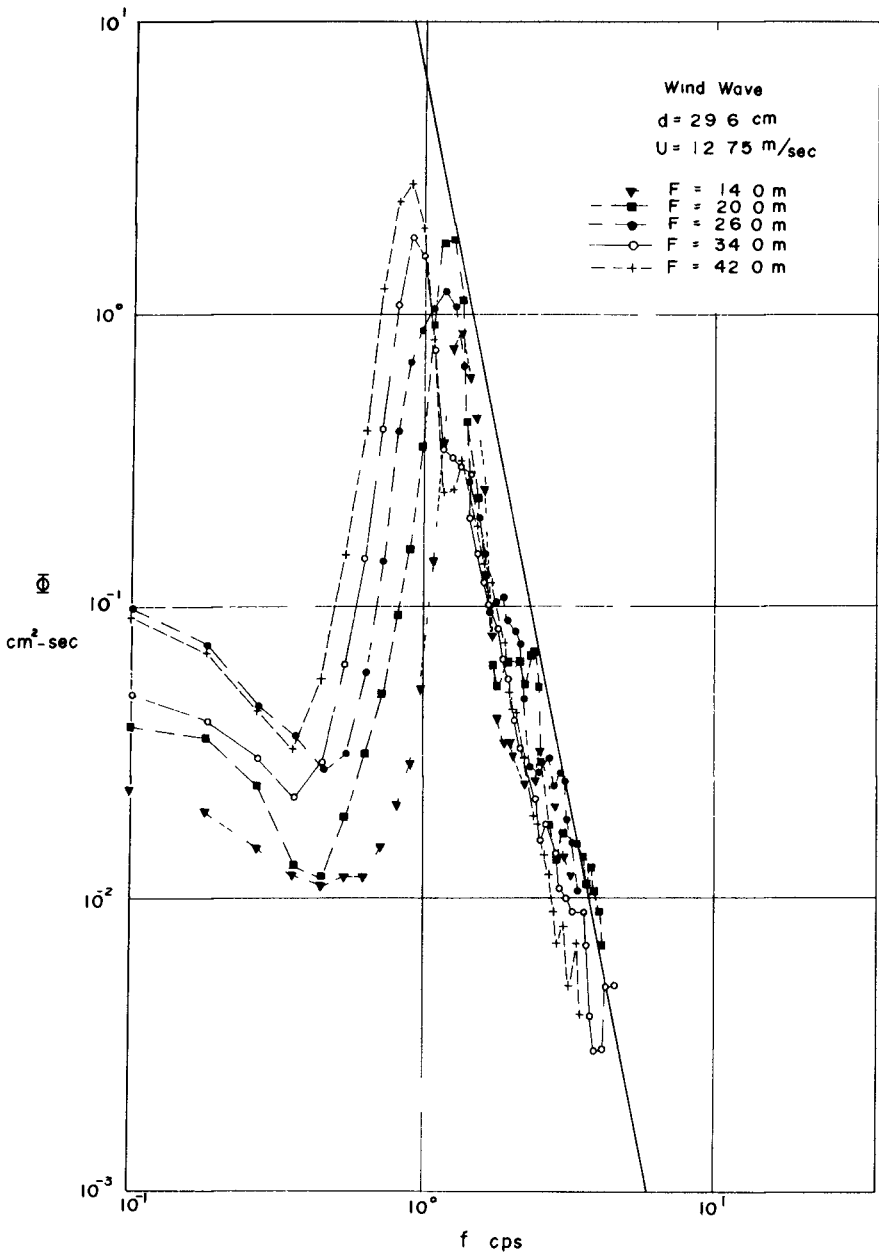


Fig 16



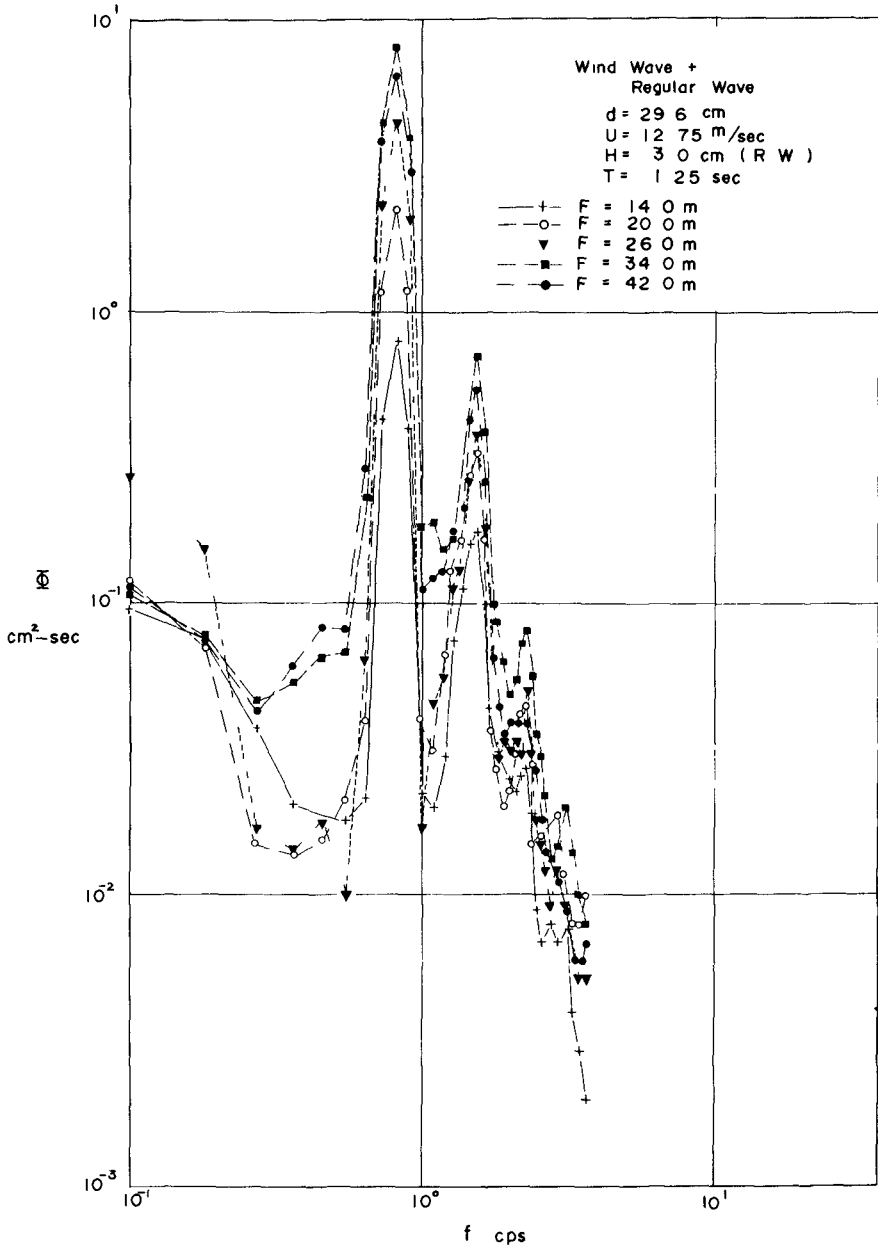


Fig 18

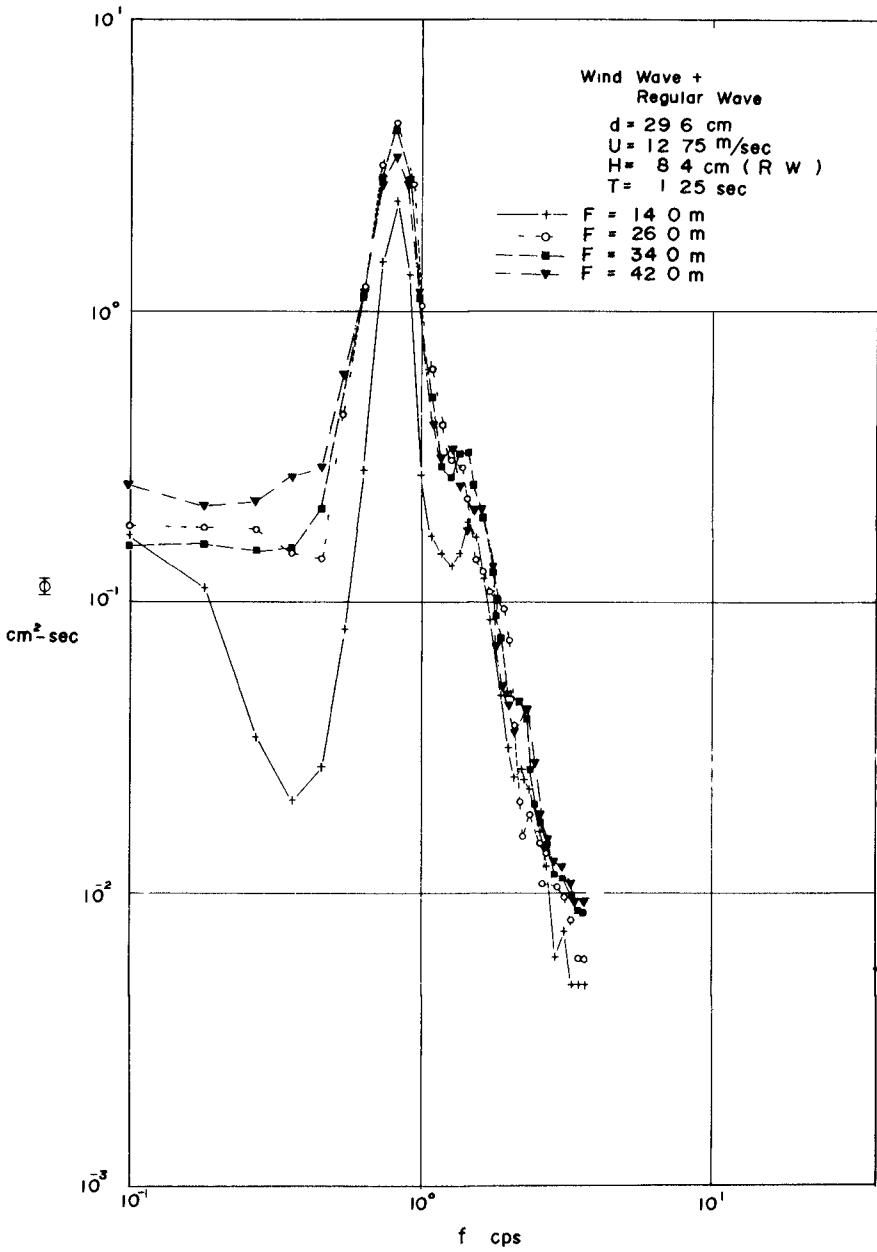


Fig 19

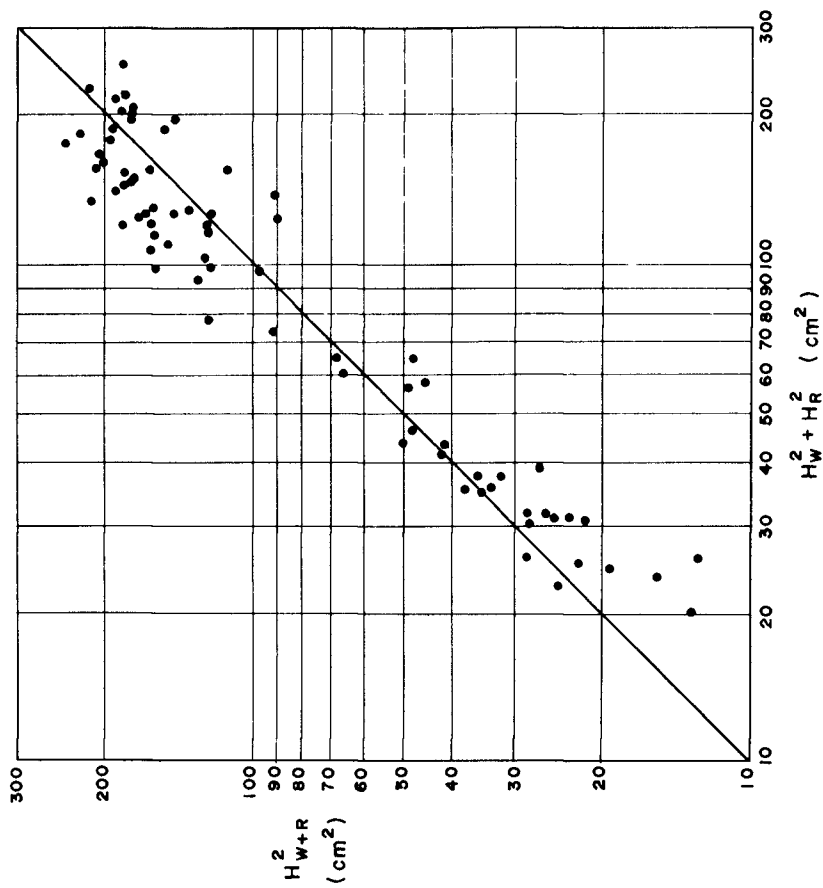


Fig 20

CHAPTER 12

WAVE FORECASTING FOR THE WEST COAST OF INDIA

J. DATTATRI *

AND

P S. RENUKARADHYA **

ABSTRACT

The applicability of the general Wave Forecasting procedures like the SMB and the PNJ methods, to the Indian coasts is studied. The study consisted in analysing the Synoptic charts to obtain the necessary wind characteristics. The computed wind characteristics were used in the above Forecasting methods to yield significant wave heights. These were compared with the wave characteristics as recorded by a sub-surface pressure type recorder after suitable modifications to account for the attenuation of wave pressure with depth.

The predicted wave heights compare well with the recorded wave heights and the SMB method predicts wave heights better for the case studied.

1. INTRODUCTION. Adequate foreknowledge of waves is essential for any coastal Engineering work. One of the ways of obtaining this necessary information about the wave characteristics is by installing wave recorders at suitable places along the coastline to obtain continuous records of waves. These records are statistically analysed to yield the required design wave height data. There are hardly any such recorders installed on the Indian coasts to the authors' knowledge. As such in the absence of any

* Department of Civil Engineering, Karnataka Regional Engineering College, Surathkal, India.

** Formerly Post-Graduate student, Marine Structures Section, Karnataka Regional Engineering College, Surathkal, India.

recorded wave data, in most cases the only alternative will be Wave Forecasting to get the required design wave height.

The two commonly used methods of Wave Forecasting are the Sverdrup-Munk-Bretschneider method (hereafter referred as the SMB method) and the Pierson-Neumann-James method (PNJ method). These methods are based almost entirely on field data and as such can be used with confidence in areas from where the field data is taken. These methods cannot be directly used for the Indian coasts without verifying their applicability.

The primary aim of the present paper is to study the general applicability of these Wave Forecasting methods to Indian Coasts. For this purpose the South-West Monsoon period of 1968 was considered for the analysis, since it is during this season the strong monsoon winds generate the heavier seas. This work was possible thanks to the Wave Recorder installed near the Mangalore Harbour Project area situated 10 KM to the south of the College.

2. ANALYSIS: The analysis consisted in Hindcasting the waves by the SMB and the PNJ methods for the Mangalore area on the West Coast of India from known meteorological conditions and comparing the Hindcast waves with the recorded waves.

The study consisted of three stages, (i) analysis of weather maps (synoptic charts) to get the required meteorological data, (ii) wave Hindcasting (iii) analysis of wave records and comparison of recorded waves with Hindcast waves.

2.1 Meteorological Data:- The Indian Daily weather maps published twice a day by the Indian Meteorological Department, Poona, were used to obtain the required meteorological data (wind speed, direction,

and duration, Fetch length and width and Decay distance). These weather maps are prepared with very scanty data, particularly over the Arabian Sea and the Bay of Bengal, which render any data based on them very approximate. The present analysis is subject to that limitation.

2.1(a) Wind characteristics:- The wind velocity over the generating area was determined by computing the Geostrophic Wind velocity(5)* from the isobar spacings and applying the corrections for isobar curvature and the air-sea temperature differences as given in T.R-4(6) to yield the surface wind speeds.

The wind direction was assumed to be parallel to isobars and the wind duration was fixed by a study of the changes in the successive synoptic charts.

Comparison with a few observed wind velocities from ships' reports showed that the computed wind velocities were not much differing from the observed velocities.

The use of the geostrophic wind equation over the generating area for the Mangalore Coast can be questioned. G.F. Taylor (5) recommends that the geostrophic wind equation should be used for latitudes above 20°. The generating areas for the Mangalore coast generally lies between 10° and 18° latitude N. (Latitude of Mangalore is 12° 52' N) The equation therefore is likely to give inaccurate results with tendencies for the computed wind velocities being on the higher side. In the absence of any other method for finding the wind velocity, the Geostrophic wind equation inspite of its limitations was used.

* Numerals in parenthesis refer to corresponding items in the list of references given at the end.

2.1(b) FETCH:- The generating areas were demarcated on the synoptic charts according to procedures laid down in T.R-4(6). For most cases in the monsoon periods the isobars are straight and practically run East-West and the generating areas can be marked with a fair degree of accuracy. The fetch length, width, decay distances and angles required for the PNJ method were directly scaled from the synoptic charts.

2.2 WAVE HINDCASTING: As mentioned earlier the SMB and the PNJ methods were used for wave hindcasting. The procedure for the SMB method was as that given in T.R-4(6) while that for the PNJ method was that given in Pierson et al (3).

The wave heights, periods and the time of arrival at the required hindcasting point were determined according to the standard procedures.

2.3 WAVE CHARACTERISTICS - RECORDED: The observed wave heights were obtained from the analysis of the wave records, recorded by the wave recorder.

The Wave Recorder is of the frequency modulated pressure type. The Recorder is kept at a depth of 6.2 metres from the M.W.L. and the water depth at the place is 7.5 metres.

The wave heights as recorded need to be modified to account for the attenuation of wave pressure with depth. From theoretical Wave Hydrodynamics (7) the surface wave height H is related to H' obtained from a pressure recorder by the following equation.

$$H = H' \frac{\text{Cosh } 2\pi d/L}{\text{Cosh } 2\pi d/L (1-3/d)} \quad \dots\dots\dots(1)$$

where z = distance below still water level to the recorder

d = depth of water where the recorder is installed

L = wave length in water of depth d

In the above attenuation factor the wave length L , must be known. A close look at any wave record will show the wave heights and periods continuously changing. If the attenuation factor is to be applied for each individual wave heights based on its period, with no computer facilities available, the work is very tedious and time consuming. As an approximation it was decided to use the average period of the waves in the sample under consideration for computing the above attenuation factor.

To investigate the probable error involved, some random samples of the wave records were selected, each of at least 15 minutes duration. The significant wave height were calculated using attenuation factors based on the individual periods of each wave in the 15 minute record as well as the average period. The results of this investigations is shown in Table 1.

This random survey as summarised in Table - 1, shows that the percentage error involved if the average period is used to be less than 6% This is insignificant particularly in view of the findings that an additional factor together with the above attenuation factor may be required to get the correct surface wave heights from a sub-surface recorder. As such the attenuation factor is based on the average period only.

The attenuation factor as given by Equation - 1 has been recognised to be inaccurate to correlate the underwater wave pressure with the surface wave heights. Based on simultaneous surface and sub-surface observations many investigators have proposed an additional

TABLE - 1

Sample No.	Significant wave heights			Percentage error based on individual period attenuation factor
	Without attenuation factor Inches	With attenuation factor based on average period inches	With attenuation factor based on individual factor inches	
1	24.40	29.00	30.00	-3.3
2	28.40	34.00	36.00	-5.5
3	27.00	32.20	33.70	-4.45
4	43.60	53.00	53.20	-0.38
5	47.20	57.50	58.00	-0.86
6	44.76	55.60	59.00	-5.75
7	68.90	85.50	87.00	-1.73
8	64.00	78.50	81.20	-3.20
9	58.60	69.20	69.80	-0.86
10	50.89	63.50	63.10	+0.63
11	21.26	26.70	25.40	+5.1
12	18.60	22.70	23.80	-4.60
13	38.50	52.30	53.30	-1.87
14	26.60	34.80	37.00	-5.80
15	26.90	35.60	37.50	-5.00

factor to be used. As summarised by Masashi Homma et al (2) this factor designated n is normally taken as a constant for the analysis. This modifies equation - 1 to equation - 1(a) as follows

$$H = n H' \frac{\cosh 2\pi d/L}{\cosh 2\pi d/L (1-z/d)} \quad \dots 1(a)$$

Seiwell (2) recommends a value of 1.35 for n , in Japan (2) a value of 1.3 to 1.5 is used, while laboratories National D'Hydraulique, France (2) recommends a value of 1.25, on the other hand Draper and Glukhovskiy (2) have presented formulas giving n as a function of relative water depth d/L . Cicslak and Kowalski (1) recommend a value of 1.25

In the absence of any definite criteria to fix this value of n , $n = 1.25$ is used in the analysis

3. REDUCTION OF DEEP WATER WAVES TO SHALLOW WATERS The waves as predicted by the Forecasting methods are deep water waves. Since the Wave Recorder is in shallow waters, the predicted deep water waves have to be reduced to shallow water waves to allow for refraction and shoaling. With the crests travelling parallel to coasts, the bottom contours also being practically parallel to the coast and the coast being a very flat one, the refraction and shoaling coefficient are very nearly unity so that the waves as predicted are directly compared with the recorded waves.
4. RESULTS OF THE ANALYSIS: Fig. 1 gives the significant wave heights as predicted by the SMB and the PNJ methods and the recorded significant wave heights over the active monsoon months of June and July. It is observed that the predicted wave heights are consistently smaller than the recorded heights for smaller wind velocities (upto 15 Knots). For wind velocities greater than 15 Knots there is a strong tendency for the predicted wave heights to be more than the recorded heights. Between the two methods, the SMB method appears to be closer to the recorded wave heights than the PNJ method.

Fig. 2 and Fig.3 show the comparison between the predicted wave heights and the recorded wave heights for the two methods. No doubt there is scatter since we are dealing with data which are subject to errors but the reasonable agreement cannot escape the attention.

The other results of the study reported elsewhere (4) can be summarised as;

(1) the generating areas for the waves that reach the Mangalore area on the West Coast of India, lie between 10° and 18° latitude North and 64° and 74° E longitudes

(2) the fetch lengths in the monsoon period lies between 200 to 600 NM

(3) the maximum calculated wind velocity is about 40 Knots while generally it is around 25 Knots

(4) the general direction of wave travel is between $S 35^{\circ}W$ and $N 65^{\circ}W$ since the range of wind direction is found to be between these limits. The predominant direction is from west.

5. CONCLUSIONS:- The planning, design and construction of any Coastal Engineering structure requires knowledge of wave characteristics. At present on the Indian Coast in most places the required design wave height is obtained from Wave Forecasting.

In this study undertaken at the Coastal Engineering Section of the Karnataka Regional Engineering College, Surathkal, India the primary aim was to investigate the applicability of the general Wave Forecasting methods like the PNJ and the SMB methods to Indian Coasts.

The present analysis indicates that the predicted wave heights compare well with the recorded wave heights and between the two

methods used, the SMB method predicts wave heights which are nearer to recorded wave heights.

- 6 ACKNOWLEDGEMENTS Much of the work reported herein was undertaken by the Junior author (PSR)(4) in partial fulfilment of the requirements for the degree of Master of Technology (Marine Structures) of the University of Mysore, Mysore.

Acknowledgement is gratefully made to Prof. Ev.Nielsen formerly UNESCO Professor in Coastal Engineering in the College, who initiated Coastal Engineering studies in the College and was in overall charge of the project. The authors thank the authorities of the Mangalore Harbour Project ~~XXXXXXXXXX~~ for kind permission to use the wave records. The paper is published with the permission of the College authorities.

References

1. Cicslak A and Kowalski T., "Wave pressure attenuation" XXII International Navigation Congress Section II, Subject 5, Paris 1969.
2. Masashi Himma, Kiyoshi Horikawa and Shuzo Komori, "Response Characteristics of underwater wave gauge", Coastal Engineering in Japan Vol9, 1966
3. Pierson W.J., Neumann G. and James R.W., "Practical methods for observing and Forecasting ocean waves", U.S. Navy Hydrographic office, Pub.No.603, 1955.
4. Renukaradhya P.S., "Wave Forecasting and Hindcasting for the West Coast of India", thesis submitted to the University of Mysore in partial fulfilment of the requirements for the Master of Technology in Marine Structures.
5. Taylor G.F., "Elementary Meteorology", Prentice Hall, Inc., Englewood cliffs, N.J. 1954.

6. U.S. Army Coastal Engineering Research Center, "Shore Protection, Planning and Design", Technical Report No.4, 1966.
7. Wiegel R.L., "Oceanographical Engineering", Prentice-Hall, Inc., Englewood cliffs, N.J., 1964.

--X-X--

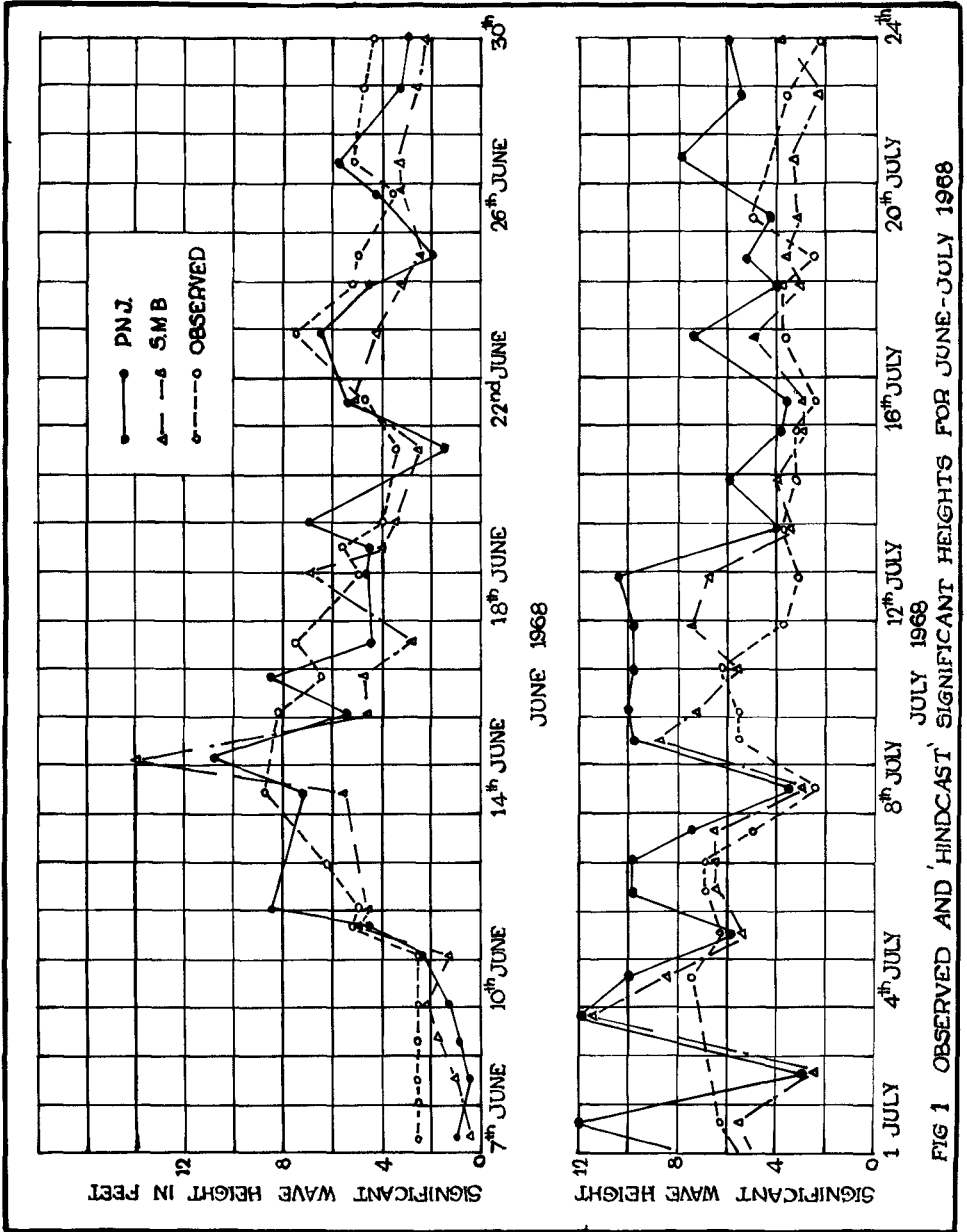


FIG 1 OBSERVED AND 'HINDCAST' SIGNIFICANT HEIGHTS FOR JUNE-JULY 1968

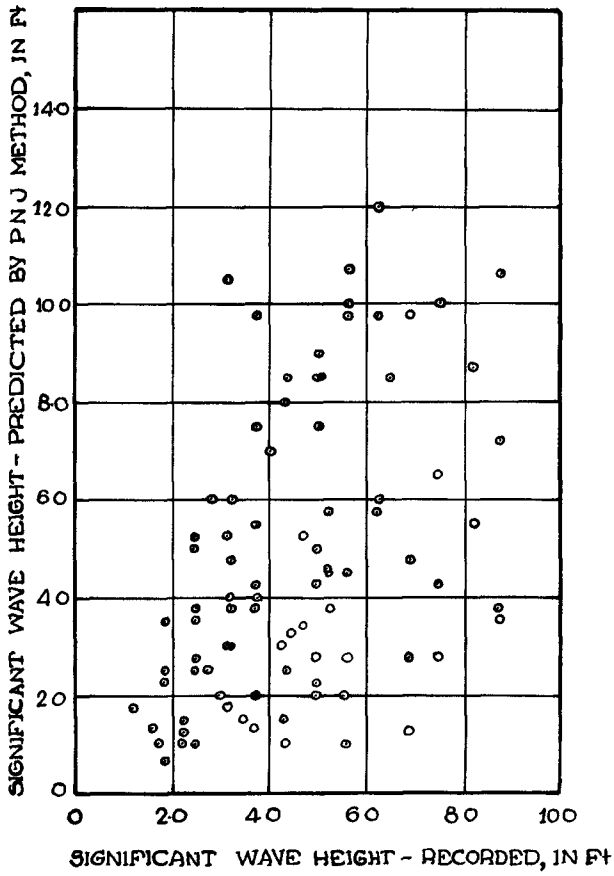


FIG 2 SIGNIFICANT WAVE HEIGHTS PREDICTED [PNJ METHOD] VERSUS RECORDED

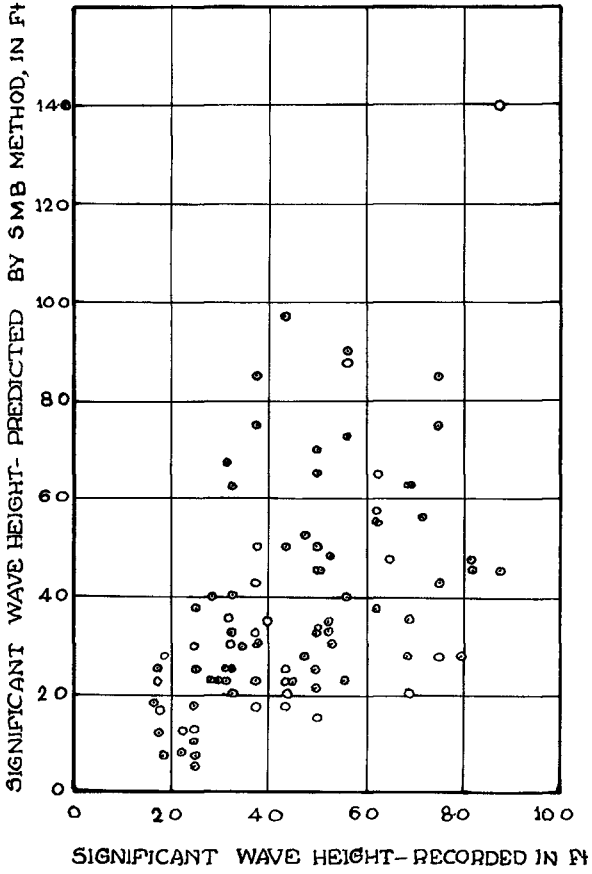


FIG 3 SIGNIFICANT WAVE HEIGHTS PREDICTED [S M B METHOD] VERSUS RECORDED

CHAPTER 13

COMPILATION OF OCEAN AND LAKE WAVE STATISTICS

John Simpson Hale
Head, Coastal Engineering Group
Los Angeles County
Los Angeles, California

RESUME AND COMMENTS

The wave program described in this paper is one intended to provide wave statistics by having our Los Angeles County life guards observe the wave heights, directions and periods.

Mark-sense cards and high speed data processing equipment and computers are used to handle the volumes of statistics.

While some scientists are planning very accurate, costly solutions to the problems of wave statistics, agencies are reluctant to venture into an expensive, elaborate wave surveillance program requiring a large quantity of personnel.

I feel that neither the accuracy of present day design or construction methods warrant "split hair" accuracy in wave surveillance.

The method described in this paper will provide a practical solution if the statistics are handled as follow

1. Wave statistics are gathered continuously over many years of time.
2. A standard is set to check the observed values.
3. Large rare damaging storm conditions will be developed by any reasonable means available until enough years of observation have passed to provide adequate statistics.

TEXT

With good wave statistics, we can provide a design that will prevent the insipient failure that occurs, occasionally, with various coastal structures such as coastal homes, hotels, jetties, groin systems with sand fills, breakwaters, bulkhead walls, etc.

This wave compilation program coupled with surveys showing shoreline movement is all that is needed to design coastal structures for today's coast line profiles as well as for predicted coast line profiles that might exist 20 years from now.

This paper will be confined to the problems of wave statistics.

Wave statistics, used in my work, must include wave heights, periods and directions and be compiled in a way that gives the results of daily observation, individual storm energies, resulting azimuths, resulting energies, root mean square wave heights and average periods.

Our wave observation program is planned to be a continuous program for years to come and will include observations in areas of special interest along miles of Los Angeles County Coast Line.

Hindcast wave statistics have been compiled on the deep water side of the island maze that surrounds our County, but the effects of island sheltering and wave refraction have to be calculated to make these wave statistics usable as design waves along the shores of the continent. This is a laborious method of compiling design wave values even with the use of present day computers. The method doesn't have the accuracy or the usefulness that the wave compilation system discussed in this abstract will illustrate.

After investigating deep water buoy type wave gauges, shallow water pressure gauges, and many other systems, we decided to tabulate wave statistics by visual observations from chosen points along our shoreline.

The chosen points were shoreline areas of future design, areas where man-power is available and areas involving unusual shoreline culture and contours. There were

points where much of the tabulated data could be converted, by applying wave refraction calculations, to deep water waves. The deep water waves could then be used to tabulate wave statistics in coast line areas, where wave observations were not recorded. This was to enable us to provide wave statistics for larger coast line areas.

A great volume of work is eliminated in data retrieval and tabulation by the use of mark sense cards and the I. B. M. 1620 and 360 systems. Our process will supply the wave statistics needed by the County of Los Angeles at little additional cost and may be the type of program that many coastal engineering groups can implement.

The procedure enables us to use County lifeguard personnel without interruption of their daily duties. The lifeguards will mark the wave observations on mark-sense cards which are easily edited and processed with our I. B. M. 1620 computer. Neither personnel time to edit, nor the cost of machine time is a large quantity. The direction of the waves is observed with a vane compass, the periods are timed with the second hand on a wrist watch or stop watch and the average wave heights will be obtained by comparing wave heights to swimmers, rocks, surfboard riders, etc. Observations are made twice a day with each observation being over a period of five minutes or more. The wave conditions are averaged during each observation and the resulting values marked on the specially prepared mark-sense cards.

This statistical sample is quite small but is often enlarged considerably by the fact that the lifeguards observe the waves for a number of minutes prior to the above five minute period.

While the most accurate immediate use of these statistics will be for beach improvement projects, observations over many years will provide enough statistics to allow us to make accurate calculations for rock construction and other types of coastal structures.

The mid range wave conditions, in our County, are those most important in shaping the beaches because of the large energy provided as the results of their frequency of occurrence.

Just one year's observation will result in average statistical waves close to the correct values for the entire family of wind formed waves.

Years of tabulating the above statistics would enable us to do the following

1. In the design of a barrier groin system, we can determine from the tabulated resultant wave direction

the plan view alignment of the shoreline and the realignment with changing storm waves.

2. By diffraction calculations, we can determine the wave heights inside a Harbor.
3. We can determine the height of groins from wave statistics. Uprush resulting from the compiled statistics can be added to the tidal averages to determine how high a groin has to be to provide for sand over topping.
5. Knowing the beach profile movement, we can use the wave statistics to determine the height of buildings on the shoreline, the type of foundations to be used, the height of the bulkhead walls and revetment structures.
6. From the wave statistics we can determine the size rock for revetments, breakwaters and jetties and the dynamic and static forces that coastal structures must resist. The designs of these and many other types of coastal structures are dependent on the Coastal Engineer's having these basic wave statistics.

After recording the name of the beach, the position on the beach and the date, the lifeguards record the average breaking wave heights, directions and periods. These tabulations are made twice everyday during the year.

The following list shows symbols and a resume of the basic formulas used by our I. B. M. computers to compile these wave statistics.

List of Symbols

H_b	=	Breaking height of wave observed by lifeguards
d	=	Breaking depth of wave observed by lifeguards
n	=	Value used in computation of shoaling co-efficient
π	=	$\pi = 3.1416$
L	=	Shallow water length of wave
L_0	=	Deep water length of wave
H_0	=	Height of deep water wave
T	=	Period of wave observed by lifeguards
C	=	Inshore velocity of wave
C_0	=	Deep water wave velocity
g	=	Gravity
E_n	=	Energy in millions of foot lbs/foot of beach
N	=	Number of observations
W	=	Weight of water

Computations

$$d = H_b \times 1.28 \text{ (Approximate)}$$

$$C = \sqrt{gd} \text{ (Approximate)}$$

$$L = C \times T$$

$$C_0 = 512 \times T$$

$$L_0 = 512 \times T^2$$

$$n = \frac{1}{2} \times \left[\frac{1 \times (4 \pi d/L)}{\sinh(4 \pi d/L)} \right]$$

$$H_b/H_0 = \frac{\sqrt{1/2 \times 1/n \times L_0/L}}{L}$$

$$H_0 = H_b/H_b/H_0$$

$$* E_n = W \times H^2 \times C/8 \times 10^6 = W \times H_0^2 \times C_0/16 \times 10^6$$

Root Mean Square Wave Height = $\sqrt{\sum H_b^2/N}$

Arithmetic Average For T = $\sum E_n \times 16 / (W \times \sum H_0^2 \times 512)$

* Greater accuracy was obtained by converting H_b to H₀ and calculating E_n by the use of the following

$$E_n = W \times H_0^2 \times C_0/16 \times 10^6$$

All energy values are in millions of foot pounds.

Most of these listed formulas are commonly used in the Coastal Engineering field, but the solutions used for resulting azimuths, energies and average periods are special innovations. Resulting energy is calculated by making vectors from each observation. The vectors are formed by wave direction and calculated energy. The machine mathematically joins the vector ends and calculates the resultant direction and energy. The formula for the average period calculation is shown in the preceding tabulations.

The program tabulates each daily observation and will calculate the resulting azimuths, energy, root mean square wave height, and average period for any time duration the computer operator desires.

Once the data has been edited and sorted for the I B M 1620, it takes only 7 minutes to tabulate an entire years observations for one point on the County Coast line.

This type of tabulation will very quickly give the design engineer wave statistics that he can convert to any type of design use. Accuracy is well within the limits needed. The data processing program for the I B M 1620 and 360 systems is available in the Office of the Los Angeles County Engineer, where it is filed as "Library Program No. TG016".

BIBLIOGRAPHY

1. SHORE PROTECTION, PLANNING AND DESIGN (Technical Report No. 4--third edition, 1966) published by The Department Of The Army, Corps Of Engineers, Coastal Engineering Research Center.
2. COMPILATION OF OCEAN AND LAKE WAVE STATISTICS by John S. Hale. I. B. M. 1620 Data Processing System, Library Program No. TG016 in the Department of County Engineer Office, Los Angeles County 1969.
3. HANDBOOK OF HYDRAULICS, fifth edition, by Horace W. King, 1963.
- *4. WAVE STATISTICS FOR SEVEN DEEP WATER STATIONS ALONG THE CALIFORNIA COAST prepared by the National Marine Consultants, 1960.
- *5. A STATISTICAL SURVEY OF OCEAN WAVE CHARACTERISTICS IN SOUTHERN CALIFORNIA WATERS prepared by the Marine Advisors, 1961
- *6. A STATISTICAL STUDY OF WAVE CONDITIONS AT FIVE OPEN SEA LOCALITIES ALONG THE CALIFORNIA COAST prepared by The University Of California, Scripps Institution of Oceanography, 1947.
7. BEACHES AND COASTS by Cuchalaine A. M. King, 1960
8. THE MOVEMENT OF BEACH SAND by James C. Ingle, 1966.

*Thanks to the Department of The Army, Los Angeles District, Corps of Engineers for Loan of This Material.

CHAPTER 14

MACRO-TURBULENCE FROM WIND WAVES

Chun-Yuan Lee¹ and Frank D. Masch²

ABSTRACT

Laboratory studies in a wind wave flume were carried out to investigate the macro-scale turbulence associated with wind waves and white cap conditions. Velocity fluctuations in water were measured with a hot film anemometer and parametric correlations between wind waves and turbulence characteristics were established. Measured data were recorded in analog form, digitized and stored on magnetic tape. Auto-covariance functions and power spectral density functions were then obtained for all sample records.

Results showed that the depth of the penetration of the macro-scale turbulence increased rapidly with wind speed but the rate of penetration diminished at the higher wind speeds. This rate of macro-turbulence penetration was found to vary inversely with wave height and wave steepness. Most turbulent fluctuations having frequencies equal to or higher than the frequency of the ambient surface waves were confined to the zone of macro-turbulence penetration although some disturbances such as vortex rings and other turbulence associated with white cap wave conditions occasionally penetrated to greater depths. It was found that the energy dissipation increased with wave height and that almost all wave energy dissipation was concentrated near the water surface.

INTRODUCTION

Turbulence has been analyzed and described variously in terms of instantaneous velocity fluctuations, correlation functions, power spectral density functions, eddy viscosity, mixing length, and turbulent shear stress. Yet, much of the experimental work on fluid turbulence has been on the relatively special cases of steady flow or plane Couette flow. Most of this experimentation has been largely conducted in wind tunnels, pipes and conduits. Very little experimentation has been on the "basics" of the phenomenon of macro-turbulence created by wind induced waves.

The objectives of this investigation are (1) To obtain some insight into the phenomenon of macro-turbulence in large natural bodies of water due to wind induced waves and (2) To establish empirical parametric correlations between the major interrelated elements of the macro-turbulence phenomenon. Underlying this investigation is the requirement to seek feasible practical solutions to the subsidiary objectives of pollution control based on the efficient use of the natural mixing and dispersion processes in natural bodies of water.

¹ Assistant Professor of Civil Engineering, Tri-State College, Angola, Indiana

² Special Consultant for Fischlin, Zurich, Switzerland and Austin (on leave from The University of Texas at Austin)

Energy from wind is imparted to water through shear stress at the interface, the "sheltering effect" on the lee side of individual waves, or the action of turbulent pressure fluctuations of the air stream. Some of the energy is absorbed in the form of a thin surface layer of flow called wind drift. Some energy is dissipated through viscosity in orbital motions of water particles. Additional dissipation occurs when surface drift interacts with orbital motions and wave breaking. As the wind grows stronger and the waves approach fully developed conditions, energy dissipation continues to increase until an equilibrium state is reached with respect to energy input from the wind. It appears that the increased energy dissipation results mostly from intensified interaction between the wind, wind drift, wave breaking, and orbital motion of water particles. Since these are mainly surface phenomena, it can be inferred that the macro-scale turbulence induced by wind waves is highly anisotropic. Thus, auto-correlation and power spectrum functions appear to be the most viable means of analysis. Furthermore, since the diffusive action of turbulence is believed to be determined mainly by the larger eddies, primary emphasis is placed on the lower frequency portion of the power spectrum.

Systematic measurements in a wind wave flume gave sample records of surface waves and velocity fluctuations for various combinations of water depths and wind speeds. Assuming random Gaussian processes, each sample record was regarded as representative of the entire ensemble. Comparisons of auto-correlation functions of surface waves and those of velocity fluctuations permitted evaluation of an arbitrarily defined depth of penetration of macro-turbulence. Relative intensity of turbulence at different depths from the surface can also be inferred from power spectrum functions. This information permits a more realistic assessment of the effects of wind and waves on the mixing and dispersion processes in natural bodies of water.

EXPERIMENTAL APPARATUS AND TEST PROCEDURES

Experimental Apparatus

All experiments were carried out in a 70 ft wind wave flume at The University of Texas at Austin. This flume is 11 ft wide, 2-1/2 ft deep, and is equipped with a 4500 cfm blower. The blower is attached so that air is drawn in at the upwind end of the closed flume through a vaned intake and then discharged through the blower to the atmosphere at the downwind end of the flume. The wind velocity was controlled by a vane installed at the throat section in the flume near the blower. This arrangement had the advantages that wind speed inside the flume could be effectively reduced without causing large pressure drops in the flume, and by leaving the entrance unobstructed, the streamlined guide vane produced relatively uniform inflow of the wind at all wind speeds. Wind velocities up to 40 fps were obtainable in the flume and were measured with a standard Prandtl-type pitot tube connected to a Uehling Type-B inclined draft gage. Wave absorbers were installed at the end of the flume to help dampen out oscillations and reduce reflections.

Continuous records of the heights and periods of the wind generated waves were measured with parallel wire wave gages inserted through the top cover of the flume. The outputs from the wave gages were recorded on a two channel oscillograph equipped with carrier preamplifiers.

To measure velocity fluctuations in fluids, many approaches have been tried. Macovsky [1] found that impurities in water prevented stable operation of hot-wire anemometers. Beginning in 1949 studies were undertaken at MIT to develop an instrument for turbulence measurements in water which would be free from the troubles encountered by hot-wires. This effort resulted in an impact tube-pressure cell combination, Ippen, et al [2] which measured the fluctuation in dynamic head at the tip of the impact tube by means of the change in electrical capacitance between a diaphragm and a fixed electrode. However any device based on this principle has relatively low natural frequency, picks up static pressure fluctuations as well as the dynamic head associated with the velocity fluctuations and is suited best for measurements of low intensity turbulence. Lumley [3] reported the use of a hot-thermistor probe for measuring turbulence. The main disadvantage of this device is the difficulty in attaining high frequency response.

The measurements involved in this study were made with the Heat Flux System Model 1010 constant temperature hot-film anemometer. This instrument consists basically of a power supply, wheatstone bridge, feedback amplifier, and readout meter. The bridge has two fixed resistance legs, a cylindrical sensor, and a three stage resistance decade. The frequency response reported by the manufacturer ranges from 0 cps to 1,000 cps.

The cylindrical hot-film sensor consists of a pyrex glass rod coated with a thin platinum film and sputtered with a thin layer of quartz. The platinum and quartz coatings are each approximately 10^{-5} inches in thickness. The quartz coating reduces bubble formation and electrical shunts across the sensor. This helps to eliminate the requirement for pure water and greatly reduces the effect of contamination of the surface. The sensor used in this study was 0.002 inches in diameter and 0.040 inches long.

In order to obtain a good calibration, an effort was made to assure the kinematical resemblance between the conditions of operation and calibration. Since a fixed sensor inserted into a water body under wave action experiences a periodic flow that changes direction continually each cycle a special calibration unit was built. This unit consisted of a half-horsepower electrical motor and a Vickers transmission and gear combination that supported an aluminum rod which held the sensor holder in a vertical position while undergoing an "irrotational rotation". This resulted in a periodic circular motion of the sensor relative to the still water. The amplitude of the circular motion could be adjusted by varying the position of the supporting points. Prior to a series of measurements analog wave records were obtained and samples of wave heights were chosen at random intervals and plotted against the corresponding wave periods. After about 30 waves had been obtained and plotted in this way a distance equal to the model wave amplitudes was taken as the distance from the axis of the wheel to the supporting points of the aluminum rod. This corresponded to the amplitude of the circular motion for the sensor. During calibration, the rotating speed of the wheel was first maintained constant long enough for the angular speed to be measured and for the output from the hot-film anemometer to be observed and recorded. As some effect of the supporting rod vibration was present during calibration, the average value of the output was assumed to represent the true sensor velocity. A second speed was then maintained and recorded as before. Repetition of this process before each series of velocity fluctuation measurements enabled the determination of the mean velocity experienced by the sensor under various wave actions.

The sensor stand was placed 60 feet from the entrance section of the flume. This location provided a long fetch yet remained some distance from the downwind end of the flume. During actual operations two external sources contributed to the vibration of the sensor, and gave signals irrelevant to the velocity fluctuations. The first was the vibration of the flume due to the blower and motor. The second was the vibration of the support rod for the sensor unit caused by the drag of the wind and waves in the flume. The following measures were taken to reduce the vibration of the sensor. First, the sensor stand was built of steel channels solidly welded together and was used to support the sensor independently of the flume. Secondly, the support rod was firmly attached to the sensor stand inserted through a hole in the top cover of the flume, and fastened with a very thin wire at the lower end near the sensor to dampen out vibrations. Finally the throat section connecting the flume and the blower was cut and re-sealed by masking tape to practically eliminate the transmission of vibration from the blower to the flume.

Water in the flume was kept clean by regular replacement. Before any measurements were taken with the hot-film sensor, new water was allowed to stand in the flume at least 24 hours to reduce the air content of the water and thus, the chance of bubble formation at the surface of the sensor which tended to create hot spots on the sensor surface and cause "erosion" of the quartz coating. If the quartz coating is deteriorating the cold resistance of the sensor drifts and no meaningful measurements are possible. Under such conditions the sensor soon fails completely.

Test Procedures

All experiments associated with the present study were designed in such a way that the characteristics and relative intensities of wind wave turbulence at various distances below the still water surface could be compared with one another under statistically constant wave conditions. In order to attain this objective, the water depth in the wave flume was first set at a predetermined level, a constant wind speed was maintained and the sensor was inserted into the water to measure the velocity fluctuations at a fixed point below the actual water surface, and a sample record was measured. The elevation of the sensor was then changed successively until sample records were obtained for a number of points uniformly spaced over the depth. Usually the spacing was taken to be 0.1 foot and the uppermost point was about 0.05 to 0.1 foot below the still water level, depending upon the wave conditions. This constituted one series of sample records from which information could be derived and the lower limit of penetration of the macro-scale turbulence associated with the wind waves estimated. The wind speed was then varied and the experiment repeated. Finally, the water depth was also varied to provide new wave conditions under different wind speeds.

Theoretically, sample record should be as long in real time as possible but there are several limitations to this requirement. To avoid the appearance of a squeezed or even blurred trace and to minimize human error in the digitizing process widely spaced records are desirable. These considerations favor a higher chart speed which means a shorter sample record in real time for a constant length of strip chart. Since the dimensions of the digitizing machine (the Pencil Follower) limited the effective chart length to about three feet (90 cm) a chart speed of 20 mm/sec was selected for all measurements. This chart speed and resulting chart length represented an actual operation time of 45 seconds and covered from 90 to 150 waves. When digitized, from 1800 to 3000 discrete points were obtained to describe the original sample record.

ANALYSIS OF RESULTS

Basic Data

Measurements of surface waves and velocity fluctuations were made at water depths of 0.7, 1.0 and 1.2 ft respectively. Three different wind speeds were applied successively at each water depth resulting in three series of measurements reflecting the variations of water particle velocity fluctuations at different depths. A total of 96 sample records were obtained. Wind velocity profiles at the center of the flume and contour lines of wind velocity in a cross-section were also obtained. Generally speaking, the wind velocity distributions in the wave flume were relatively uniform and the maximum cross-sectional velocity ranged from 13 to 40 fps with the corresponding Reynolds number varying from 2.44×10^4 to 7.51×10^4 .

Mathematical Considerations

It is desirable at this point to make a summary analysis of the variables and the relations involved in the application of the stochastic process model approach adopted for this study. There are many useful expositions and interpretations of the mathematical rationale underlying such methods in standard texts on stochastic methods, noise theory and random process analysis [4, 5, 6].

Suppose a stationary random process $y(t)$ has been given in the form of a time history record. The mean value μ is

$$\mu = \lim_{T \rightarrow \infty} \frac{1}{T} \int_0^T y(t) dt \quad (1)$$

where T is the length of the record. The mean square value ψ^2 is

$$\psi^2 = \lim_{T \rightarrow \infty} \frac{1}{T} \int_0^T y^2(t) dt \quad (2)$$

and the positive square root of this value is called the root mean square or rms value. The variance, σ^2 , is

$$\sigma^2 = \lim_{T \rightarrow \infty} \int_0^T [y(t) - \mu]^2 dt \quad (3)$$

The positive square root of the variance is called the standard deviation. By expanding Eq. (3), it can be shown that

$$\mu^2 = \sigma^2 + \psi^2 \quad (4)$$

The auto-covariance function $C(\tau)$ is defined as

$$C(\tau) = \lim_{T \rightarrow \infty} \frac{1}{T} \int_{-T/2}^{T/2} y(t) y(t + \tau) dt \quad (5)$$

when the mean value of μ of the process is assumed to be zero. When $\mu \neq 0$

$$C(\tau) = \lim_{T \rightarrow \infty} \frac{1}{T} \int_{-T/2}^{T/2} [y(t) - \mu] [y(t + \tau) - \mu] dt \quad (6)$$

In Eqs (5) and (6) τ represents a time lag. $C(\tau)$ is also frequently called the "autocorrelation function" although this term should be applied to the normalized ratio $C(\tau)/C(0)$.

The power spectral density function $P(f)$ may be defined as

$$P(f) = \int_{-\infty}^{\infty} C(\tau) e^{-i2\pi f\tau} d\tau \quad (7)$$

where f is the frequency of the fluctuation of the process at a certain point in the frequency domain and $i = \sqrt{-1}$. It can be seen that $P(f)$ and $C(\tau)$ are Fourier transforms of each other. From the stationary hypothesis the auto-covariance function is an even function of τ , and from Eqs (5) and (6), it can be seen that $C(\tau)$ is a real function. Thus,

$$\begin{aligned} C(\tau) &= \int_{-\infty}^{\infty} P(f) e^{i2\pi f\tau} df \\ &= \int_{-\infty}^{\infty} P(f) \cos 2\pi f\tau df + i \int_{-\infty}^{\infty} P(f) \sin 2\pi f\tau df \\ &= \int_{-\infty}^{\infty} P(f) \cos 2\pi f\tau df = \text{real function} \end{aligned} \quad (8)$$

By inverse transformation or a similar argument

$$P(f) = \int_{-\infty}^{\infty} C(\tau) \cos 2\pi f\tau d\tau \quad (9)$$

Since $C(\tau)$ is an even function $P(f)$ should also be even. The above relations for the real valued two-sided power spectral density function $P(f)$ may be simplified to

$$P(f) = 2 \int_0^{\infty} C(\tau) \cos 2\pi f\tau d\tau \quad (10)$$

The physically realizable one-sided power spectral density function $V(f)$ is defined by

$$V(f) = 2 P(f) = 4 \int_0^{\infty} C(\tau) \cos 2\pi f\tau d\tau \quad (11)$$

$0 \leq f < \infty$

For practical applications, the record lengths are limited and the y values involved in the actual calculations are uniformly distributed along the time axis. Discrete forms of the above equations for numerical calculations, are given as follows

$$\mu \approx \bar{y} = \frac{1}{N} \sum_{I=1}^N y(I) \tag{12}$$

where N is the total number of data points. The auto-covariance C_M is given by

$$C_M = \frac{1}{N - M + 1} \sum_{I=1}^{N - M + 1} y(I) y(I + M - 1) \tag{13}$$

where $l = 1, 2, 3$, N and M = 1, 2, 3. M_l In this study M_l is assumed to be N/10. The lag time $\tau = (M-1)\Delta t$ for a data sampling interval Δt .

The power spectral density function V(f) is calculated from

$$V_J = \text{one-sided power spectral density function} \\ = 2\Delta t \left\{ C_1 + 2 \sum_{K=2}^{M_l - 1} C_k \cos [(K - 1)(J - 1)\pi / (M_l - 1)] + C_{M_l} \cos [(J - 1)\pi] \right\} \tag{14}$$

where $J = 1, 2, 3$, M_l . This is an estimate of the power spectrum associated with the discrete covariance function defined by Eq. (13) rather than the continuous function of Eq. (16). For this discrete cosine transformation the spectral estimates at any frequency are affected by the energy in neighboring frequencies. It is apparent, therefore, that a smoothing operation is desirable. In this study, the Hanning procedure, [7], was performed on the above raw spectrum V_J , to obtain the so-called refined spectrum U

$$U_1 = 0.5V_1 + 0.5V_2 \\ U_{M_l} = 0.5V_{M_l - 1} + 0.5V_{M_l} \\ U_l = V_l + 0.5(V_{l - 1} + V_{l + 1}) \tag{15}$$

where $l = 2, 3, 4, \dots, (M_l - 1)$. Note that in order to facilitate computer programming, the notation is such that U_1 stands for $C(0)$, U_2 for $C(\Delta t)$, U_l for $C[(l - 1)\Delta t]$, etc. Eqs. (12), (13), (14) and (15) form the basis for the numerical evaluation of the auto-covariance and power spectral density function.

Digitizing and Computing Procedures

To digitize the sample records, each paper chart was placed on a 51" x 54" table with a magnetic field below the surface. The curve on the chart was traced with a special "pencil" which responded to the magnetic field and identified its position in terms of x- and y-values in arbitrary but predetermined units. These digitized values as well as calibration and identification data were stored on a magnetic tape through an incremental

tape recorder. By means of a high speed digital computer, the raw data were decoded and transformed into grid point data uniformly spaced on the time axis using a straight-line fit. Wave characteristics, auto-covariance and power spectral functions were calculated and then tabulated and plotted on microfilm.

Interpretation of Results

A random process may be classified as wide-banded if it consists of fluctuations of various frequencies, narrow banded if the range of frequencies is limited. The auto-covariance function of a wide-band random process diminishes rapidly as the lag time is increased, for a narrow-band random process the diminishing rate is slow [1]. Inspection of the auto-covariance plots for each test series (Fig. 1 is illustrative of a typical test series) revealed that the surface wave fluctuations appeared as narrow-band random processes and velocity fluctuations appeared as wide-band random processes near the water surface and narrow-banded at greater depths. Thus the spatial pattern of transition of the velocity records from one type of fluctuation to the other gives an estimate of the depth of penetration of wind-wave induced macro-turbulence.

For each power spectral plot of surface wave record (Fig. 2 is typical) there is only one major peak which always centers around the frequency corresponding to the mean wave period which, for this study, varied from about 0.38 to 0.63 seconds. For velocity fluctuations measured near the water surface, there is also a major peak centering around the frequency of the mean surface wave, but the smaller peaks at higher frequencies are relatively significant. However, for velocity fluctuations measured at a considerable distance below the surface, the trend is again toward the dominance of a major peak centering around the frequency of the mean surface wave.

The power spectral density function for random data describes the general frequency composition of the data in terms of the spectral density of its mean square value. Integration of the power spectral density function between two frequency values represents the amount contributed to the mean square value by the power spectrum within these limits. Comparison of all the power spectra for a given series of experiments (i.e., for a given combination of water depth and wind speed) permitted the determination of the common lower and upper frequency limits for the first major peak at the mean surface wave frequency. Integration of the power spectrum between these two limits was designated by A_1 . Beyond the upper limit of A_1 the power spectrum decreased in magnitude rather rapidly until a point was reached beyond which it began to flatten out. The change in the slope of the power spectrum was generally somewhere around 8 cps. A common frequency value of this turning point for each series of experiments was also determined from the power spectrum. Integration of the power spectrum between the upper limit of A_1 and this point was designated as A_2 . It was assumed that A_1 essentially represents the contribution from wave motion to the mean square value while A_2 represents the contributions from macro-scale turbulent motions. Although turbulent motions of larger scale comparable to wave motions supposedly were compounded into A_1 , the effect was assumed insignificant and the ratio of A_1 to A_2 was regarded as an indicator of the relative strengths between wave motion and wind wave induced turbulence. In other words, a small A_1/A_2 ratio implies a high turbulent intensity due to wind waves.

Results

Relying mainly on the spatial variation of auto-covariance the depth of penetration of macro-turbulence was estimated for each combination of wind speed and water depth. These data are plotted in Figs 3 through 6. Figure 3 shows that the depth of penetration increases rapidly with maximum wind speed in the flume when the wind speed is relatively low, but the rate of increase diminishes rapidly at higher wind speeds. The maximum wind speed was taken from wind velocity profiles at 0.3 to 0.4 feet above the still water level. In Fig 4, it is seen that when the wave height is small, the depth of penetration increases rapidly with wave height but as the wave height is increased, resistance to increase in depth of penetration becomes stronger. In Fig 5, the ratio, $H_1/10/T^2_{1/10}$, which is proportional to wave steepness using the one-tenth wave height and the corresponding wave period is plotted against depth of penetration. At small steepnesses the penetration increases rapidly, but for the steeper waves, there appears to be a lower limit to the penetration. Since the wave speed c is proportional to the wave period T , $U^2/T^2_{1/10}$ is related to the wave age c/U , where U is the wind speed. Using the same maximum wind speed as in Fig 3, Fig 6 indicates that the depth of penetration correlates quite well with wave age.

Values of A_1/A_2 also were plotted against water depths. Figure 7 is typical of these plots. It is clear that the relative turbulent intensity is much higher near the water surface than below. This tendency is much more evident with lower wind speed than with high wind speed. On the other hand the overall relative intensity of turbulence is much higher for high wind speed (CS 10V01 series) where the return flow is stronger than for low wind speed (e.g. CS 10V04).

For the surface waves, a small A_1/A_2 ratio means widening of the frequency band or a confused sea surface condition. It was interesting to note that the ratio A_1/A_2 correlated quite well with the wave steepness in a way which suggests that the white cap wave condition and consequently the turbulence level in a wind wave system grow in accordance with the characteristic wave steepness.

SUMMARY AND CONCLUSIONS

It is well known that larger eddies generate smaller eddies through inertial interaction thereby transferring energy to the smaller eddies which consume most of the kinetic energy of turbulence through viscous dissipation. However Von Karman and Lin [7] assumed that the eddy diffusivity might be regarded as a parameter determining the character of the turbulence in the lower-wave number range. In other words the diffusive action of turbulence is determined mainly by the larger eddies. Hence, it can be expected that once the behavior of the macro-turbulence is understood, the relative intensity and spatial distribution of the smaller energy-dissipating eddies could be inferred. This point is reinforced by the tendency for confinement of macro-turbulence to a surface layer a few wave heights in thickness and the existence of high relative turbulent intensity near the water surface. This confirms the finding of Stewart and Grant [8] who based on a study of energy-dissipating eddies concluded that almost all wave dissipation is concentrated near the water surface and decreases rapidly with depth from the surface. Thus rapid and effective mixing near the water surface can be expected in a body of water subject to wind waves.

While direct application of the results of this laboratory study to field situations has to be confirmed by further investigation, the results derived here disclose, qualitatively, the general tendencies under comparable field situations. The main conclusions from this study may be summarized as follows: (1) The depth of the macro-scale turbulence penetration due to the wind induced waves increases rapidly with maximum wind speed but the rate of increase diminishes at higher wind speeds. There is a limiting depth of macro-turbulence penetration which is not exceeded even if the wind velocity is further increased. (2) The rate of increase in the depth of penetration of macro-turbulence varies inversely with wave height, wave length and wave steepness. (3) Most turbulent fluctuations having frequencies higher than the mean frequency of ambient surface waves are confined to the zone of macro-turbulence penetration. This suggests that wind wave induced turbulence is a phenomenon confined essentially to the surface layer with thickness of a few wave heights. However, certain vortex rings or some disturbances associated with white cap wave conditions occasionally penetrate to greater depths, but the elements of the vortex spirals deteriorate into an admixture of random, small scale eddies.

ACKNOWLEDGMENT

This study was supported in part by the Federal Water Quality Administration under Grant 5 RO1 WP00705

REFERENCES

- [1] Macovsky, M S , "The Measurement of Turbulence in Water", Rep No 670, David Taylor Model Basin, Washington, D C , 1948
- [2] Ippen, A T , Tankin, R S , and Raichlen, F , "Turbulence Measurements in Free Surface Flow with an Impact Tube-Pressure Cell Combination", Tech Rep No 20, Hydro Lab, MIT, Cambridge, Mass 1955
- [3] Lumley, J L , "The Constant Temperature Hot-Thermistor Anemometer", Symposium on Measurement in Unsteady Flow ASME, Hydraulics Division Conf Worcester, Mass 1962
- [4] Bendat Julius S , and Piersoll, Allen, G , Measurement and Analysis of Random Data, John Wiley and Sons Inc 1966
- [5] Lee, Y W , Statistical Theory of Communication, John Wiley and Sons, Inc , 1963
- [6] Blackman R B , and Tukey, J W The Measurement of Power Spectra from the Point of View of Communications Engineering, Dover Publications, Inc , 1958
- [7] Karman Th von, and Lin, C C , Advances in Applied Mechanics, 2, 1, 1951
- [8] Stewart, R W , and Grant, H L , "Determination of the Rate of Dissipation of Turbulent Energy Near the Sea Surface in the Presence of Waves", Journal of Geophysical Research, Vol 67, No 8, July, 1962

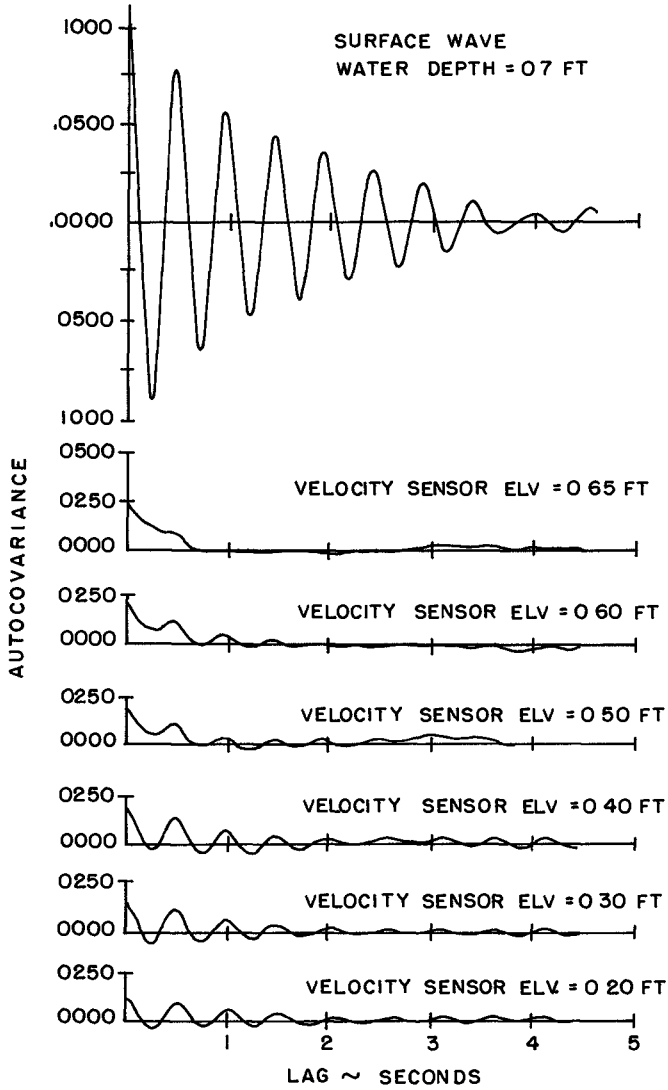


FIG 1 AUTOCOVARANCE VS LAG TIME

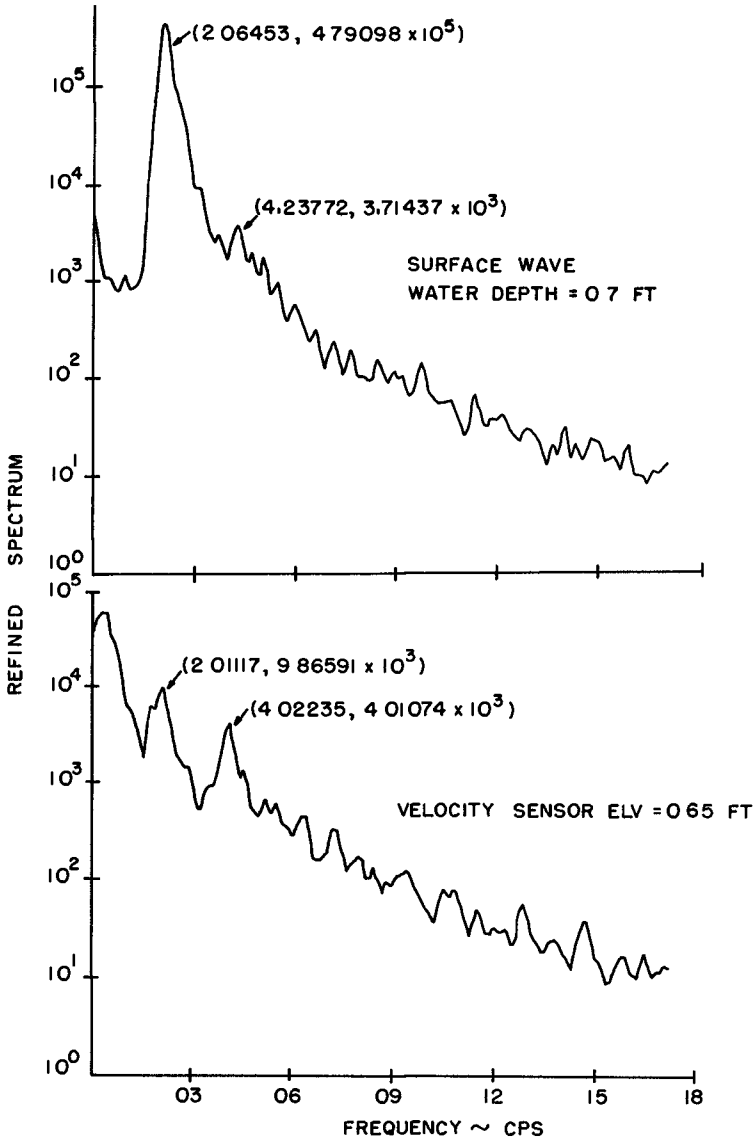


FIG 2A POWER SPECTRAL DENSITY VS FREQUENCY

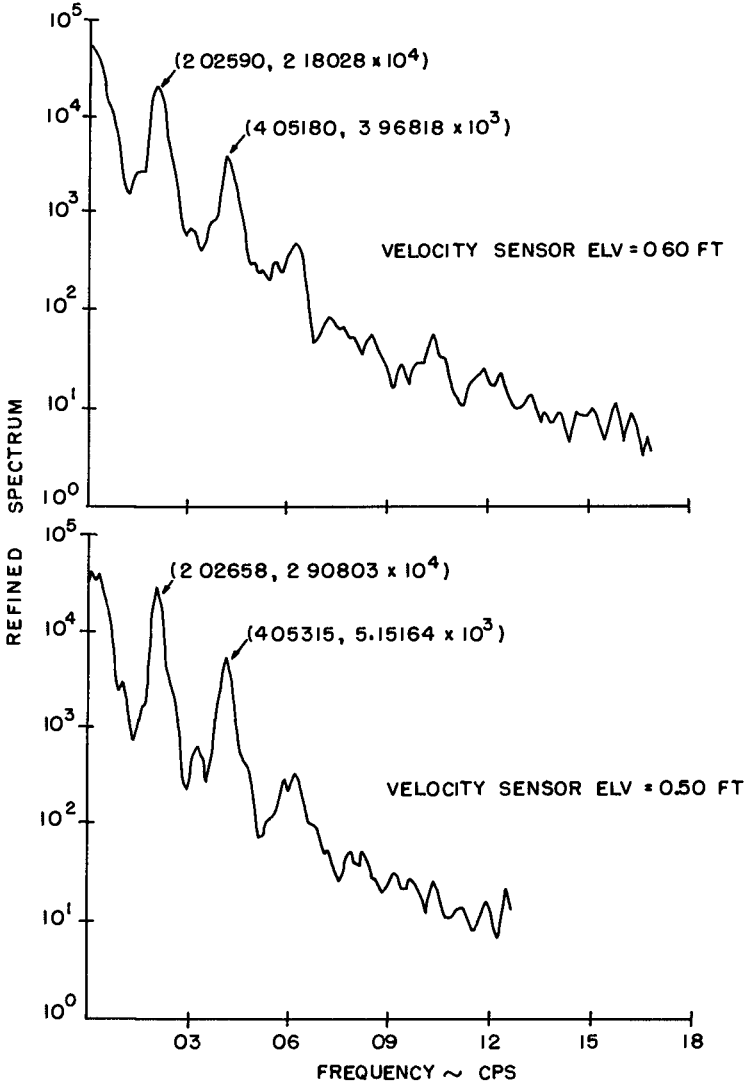


FIG 2B POWER SPECTRAL DENSITY VS FREQUENCY

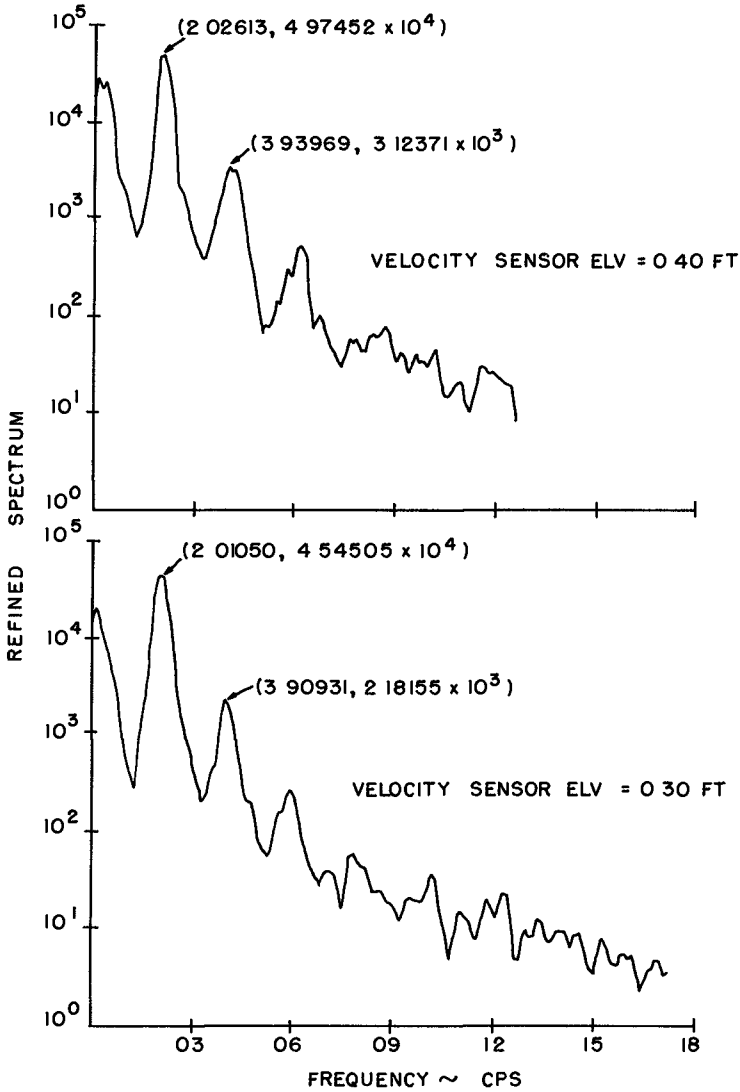


FIG 2C POWER SPECTRAL DENSITY VS FREQUENCY

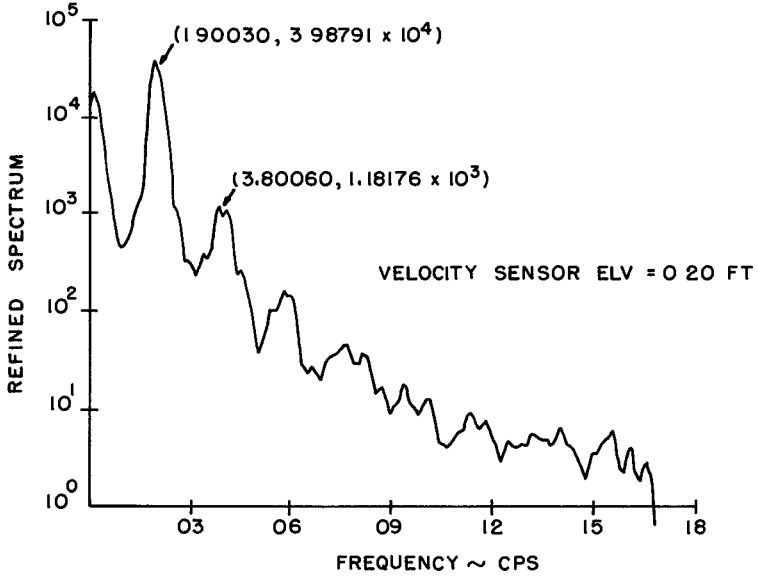


FIG 2D POWER SPECTRAL DENSITY VS FREQUENCY

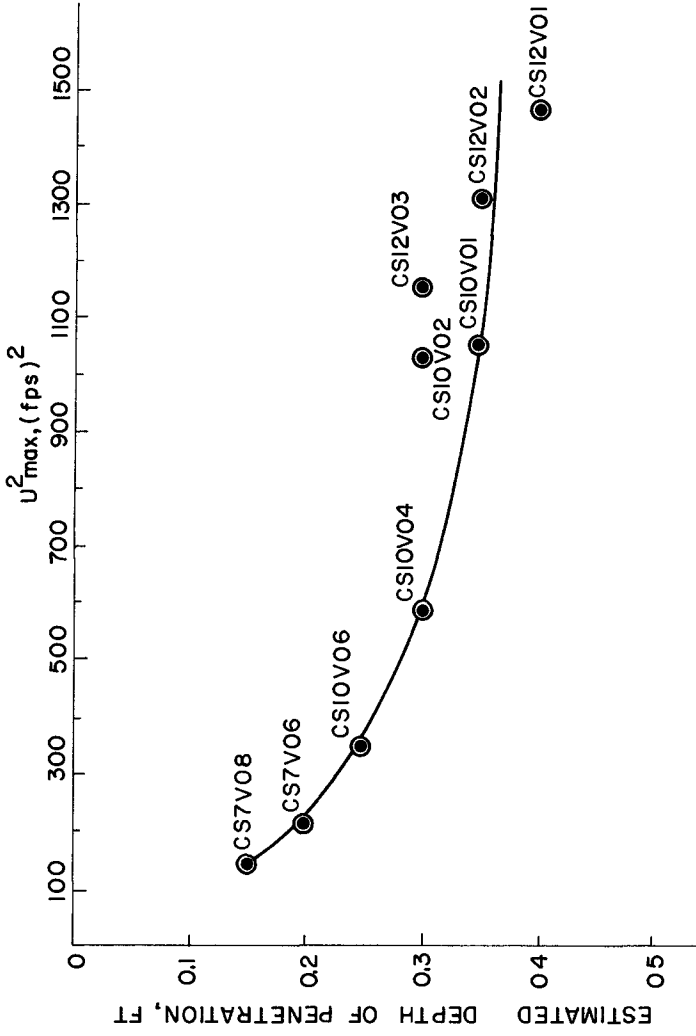


FIG 3 ESTIMATED DEPTH OF PENETRATION OF MACRO - TURBULENCE vs MAXIMUM WIND SPEED

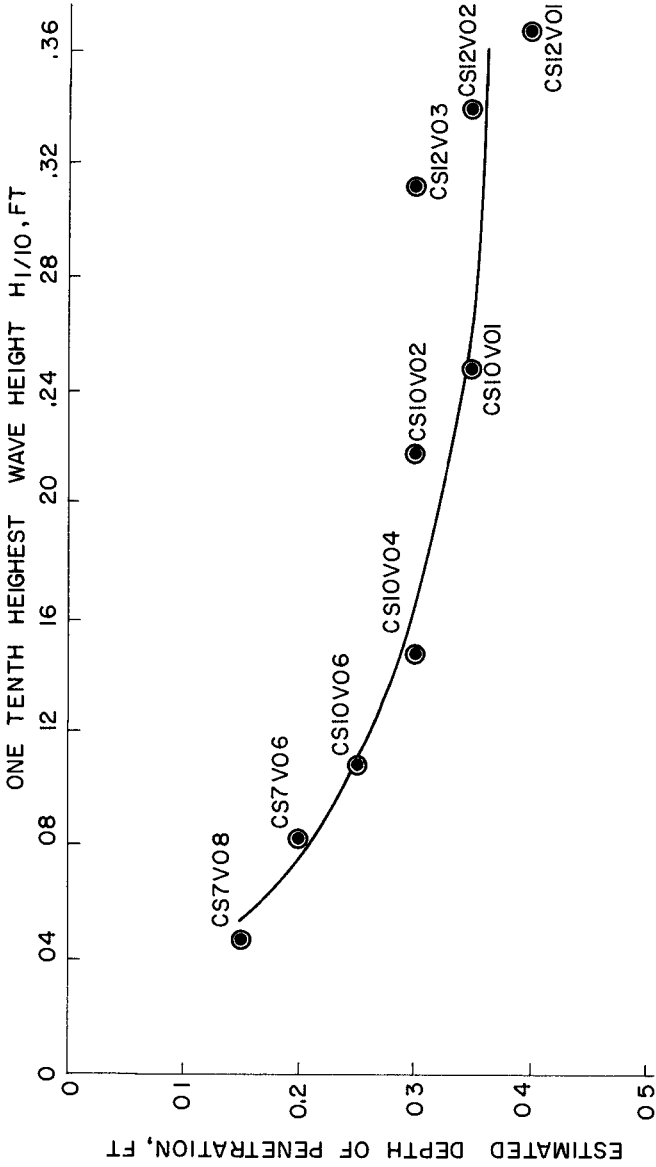


FIG 4 ESTIMATED DEPTH OF PENETRATION OF MACRO - TURBULENCE vs H_{1/10}

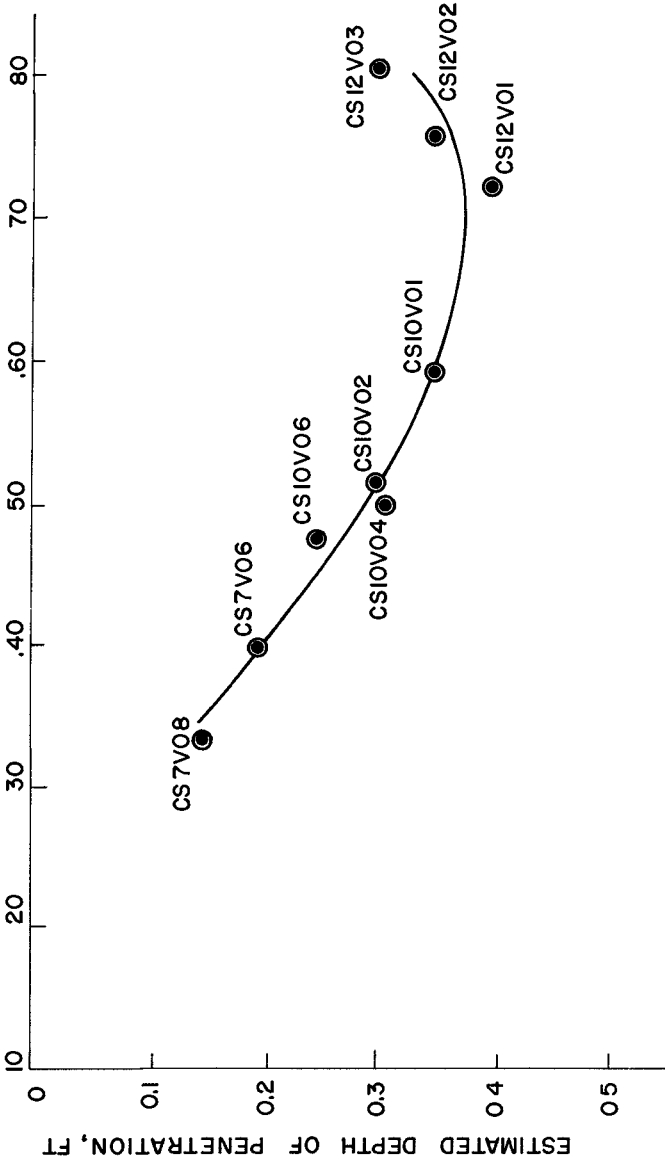


FIG 5 ESTIMATED DEPTH OF PENETRATION OF MACRO-TURBULENCE vs $H_{1/10}^2 / T_{1/10}^2$

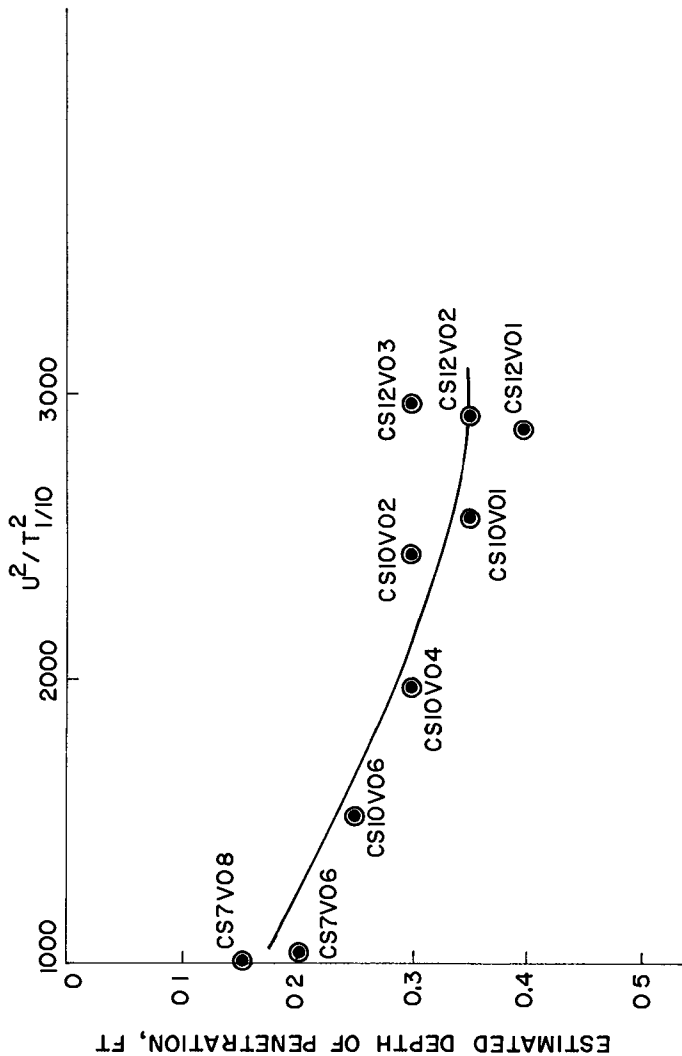


FIG 6 ESTIMATED DEPTH OF PENETRATION OF MACRO-TURBULENCE vs U^2/T^2

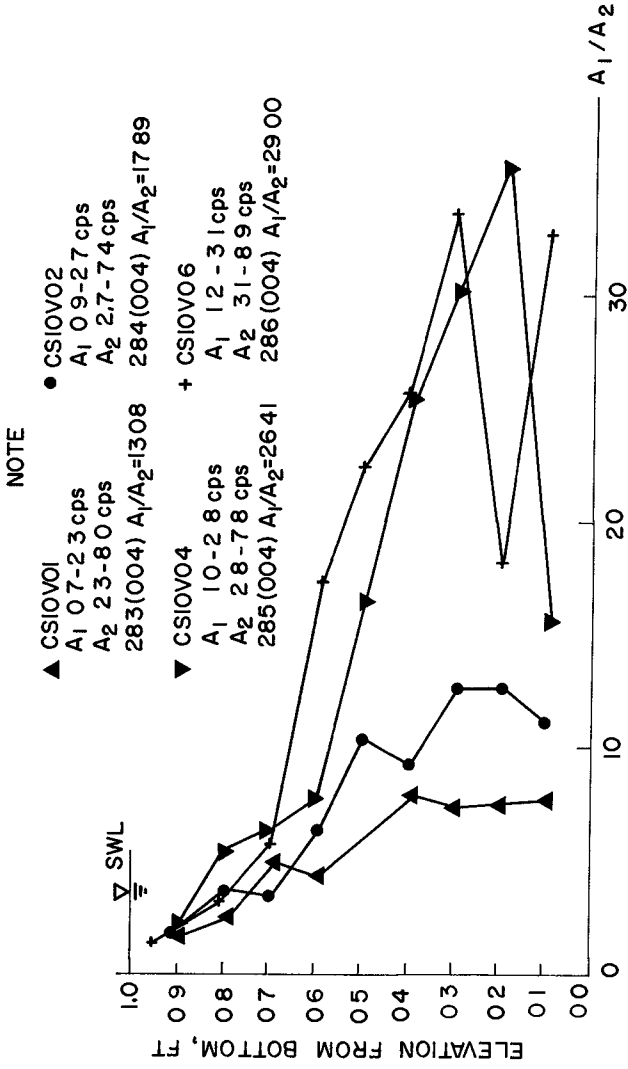


FIG 7 RATIO A₁/A₂, CSIOV01, V02, V04 & V06 SERIES

CHAPTER 15

THE SHEAR STRESS OF SEA BREEZE ON A SWASH ZONE

By Shih-Ang Hsu
Coastal Studies Institute
Louisiana State University
Baton Rouge, Louisiana 70803

ABSTRACT

Measurements of shear stress under the effect of a sea breeze were made by simultaneous wind and temperature profiles over a shore near Fort Walton Beach, Florida. It was found that the sea breeze in the surface boundary layer is in the atmospheric free-convection regime. The measured shear stress coefficient is in conformity with that obtained by other investigators by the sea surface tilt method under the unstable condition. For coastal applications, the result is found to be more reliable than those assumed coefficients obtained under neutral stability for this localized coastal wind system.

INTRODUCTION

In coastal areas, especially on tropical, subtropical, and marine desert coasts, and on the shores of relatively large lakes, we can observe in the course of a day the reversal of onshore and offshore winds, called sea breeze and land breeze, respectively. Perhaps the most lucid synopsis of the main features of these local wind systems has been presented by Defant (1951). Baralt and Brown (1965) have compiled an excellent annotated bibliography on this subject. It should be noted that whereas a hurricane or storm may cause extensive damage to coastal structures, the sea breeze is a persistent phenomenon and may, in the long run, be more important. For instance, loss of beach sand into the backshore area as a result of sea breeze is an urgent engineering problem, examples are found especially in coastal Peru, Libya, Florida, and the Cape Hatteras National Seashore.

The mesoscale structure as a function of space and time and particularly the hypothesis of land- and sea-breeze systems which are governed by the circulation theorem have been observed and verified on the Texas coast by Hsu (1970). Some of the microstructure of the frontal characteristics and the diurnal clockwise rotation of the system with time owing to the Coriolis effect have been observed and presented elsewhere (Hsu, 1969a), this paper will study the surface shearing stress aspect of the sea breeze.

The sea breeze is effective in generating waves and currents (Murray, personal communication), which in turn transport sediments in the littoral environment (Sonu, personal communication). Also, eolian sand transport (Sonu, personal communication) and air pollution (Neiburger, 1969) in the coastal zone are closely controlled by this localized wind system. Since in the nearshore areas that are frequently affected by diurnal local wind systems the lapse rate is rarely adiabatic and buoyancy forces must be considered, the wind shear stress coefficients obtained under the near-neutral condition (see, e.g., Wu, 1969) cannot be used under these local wind conditions, as previously pointed out by Hsu (1969b). It is hoped that this study will fulfill the need for coefficient values under the sea breeze situation.

THEORETICAL CONSIDERATION

The following derivation for the sea breeze regime in the surface boundary layer is due to McPherson (1968) and is an expanded version of that presented by Estoque (1961).

It is presumed that in the layer immediately above the surface the viscous forces acting on a fluid element are much larger than the inertial forces, thus the horizontal momentum equations and the thermodynamic equation for the layer become

$$\frac{\partial}{\partial Z} \left(K \frac{\partial u}{\partial Z} \right) = 0 \quad (1)$$

and

$$\frac{\partial}{\partial Z} \left(K \frac{\partial \theta}{\partial Z} \right) = 0 \quad (2)$$

where K is an eddy exchange coefficient, assumed to be the same for both heat and momentum transfer, u is the magnitude of the horizontal wind, and θ is the potential temperature. If K is known as a function of height Z , the equations can be integrated to obtain u and θ in the boundary layer.

Under conditions of free convection--that is, when the buoyant forces dominate the mechanical forces--the expression of K used is

$$K = \lambda Z^2 \left(\frac{g}{\bar{\theta}} \left| \frac{\partial \theta}{\partial Z} \right| \right)^{1/2}, \quad R_1 < -0.03, \quad (3)$$

as discussed by Priestley (1959). Here λ is an empirical constant, g is the acceleration of gravity, and $\bar{\theta}$ is a layer-mean potential temperature.

in the layer in which the Richardson number (R_1) is evaluated Eqs (1) and (2) may be written as

$$K \frac{\partial u}{\partial Z} = U_*^2 \quad (4)$$

and

$$K \frac{\partial \theta}{\partial Z} = \theta_* U_*, \quad (5)$$

where U_* , θ_* are termed the "friction velocity" and "friction temperature" respectively. From Eqs (4) and (5) we obtain

$$\frac{\partial u}{\partial Z} = \frac{U_*}{\theta_*} \frac{\partial \theta}{\partial Z} \quad (6)$$

and

$$\frac{\partial \theta}{\partial Z} = \frac{\theta_*}{U_*} \frac{\partial u}{\partial Z} \quad (7)$$

For the free-convection regime, we use Eqs (3) through (7) and obtain

$$\frac{\partial u}{\partial Z} = \left[\frac{U_*^5 \bar{\theta}}{\lambda^2 g |\theta_*|} \right]^{1/3} Z^{-4/3} \quad (8)$$

and

$$\frac{\partial \theta}{\partial Z} = \left[\frac{U_*^2 \theta_*^2 \bar{\theta}}{\lambda^2 g} \right]^{1/3} Z^{-4/3} \quad (9)$$

Eqs (8) and (9) can be integrated to give

$$u = -3 \left[\frac{U_*^5 \bar{\theta}}{\lambda^2 g |\theta_*|} \right]^{1/3} Z^{-1/3} + \text{Constant} \quad (10)$$

$$\theta = -3 \left[\frac{U_*^2 \theta_*^2 \bar{\theta}}{\lambda^2 g} \right]^{1/3} Z^{-1/3} + \text{Constant} \quad (11)$$

The expressions for turbulent shear stress (τ) and surface shear stress (τ_o) are

$$\tau = \rho U_*^2 \quad (12)$$

and

$$\tau_o = \rho C_z U_z^2 \quad (13)$$

where ρ is the density of air and C_z is a dimensionless "shear stress" or "drag" coefficient for the height Z

Combining Eqs (12) and (13) gives

$$C_z = \left(\frac{U_*}{U_z} \right)^2 \quad (14)$$

Thus, from simultaneous temperature- and wind-profile measurements in the atmospheric boundary layer and from Eqs (8) through (14), the values of C_z and τ_o are obtained

FIELD EXPERIMENT AND DATA ANALYSIS

Field Site and Experiment

The experiment site (see Figs 1 and 2) was located on the Gulf Coast near Fort Walton Beach, Florida. The site (86°43'W, 30°24'N) has an approximate east-west shoreline orientation. It has been used to study the local wind system (Hsu, 1969a). The experiment related to the present study was designed to measure the temperature and wind profiles in the surface boundary layer as shown in Eqs (8) through (11) and was performed during the month of May 1970.

Instrumentation

The main instrument used for this study was a Thornthwaite Wind Profile Register System (Model 106) with 6-unit, 3-cup fast response mounted 20, 40, 80, 160, 240, and 320 cm above the beach surface (Fig 1). The anemometers have a distance constant of better than 1 meter and are rugged enough to withstand limited exposure to a marine atmosphere (Seesholtz, 1968). Note that the system is portable so that during the experiment it is quickly and easily moved to a desired location.

Temperatures were measured at 170, 360, and 550 cm above a grass-



Fig. 1. Cup anemometer array located in the swash on the coast of the Gulf of Mexico near Fort Walton Beach, Florida. Hot-wire anemometer, also part of the instrumentation, is shown in the background.

free berm surface by three identical recording hygrometry systems (Taylor Instrument Company, Series 76J, having readings within ± 1 percent of any given chart range). The sensors were mounted on a 10-meter meteorological tower. An all-purpose wind-recording system (Science Associates, Inc., No. 162) at the 10-meter level above the surface made wind speed and direction measurements as the reference level. For detailed information about these instruments and their installation, relevant manuals should be consulted.

Data Reduction

Wind velocities measured by the Thornthwaite Wind Profile Register System were recorded by a Thornthwaite's Digital Printout Recorder (system model 706), which uses the well-known Polaroid reproduction process. A system of mirrors and mechanical level movements moves the image of a row of counters by small increments along the length of the film card. During the experiment an exposure of the register image is made on command from a timer after each movement of the image. A 15-minute time interval was used for the present study. The readings of the counters are then entered on the film card at the start of the period and again at the end. The difference is obtained and the corresponding wind speed in centimeters per second is determined from the appropriate conversion table supplied by the manufacturer.

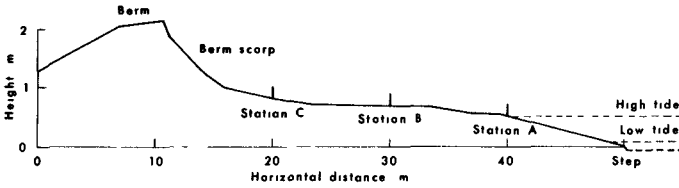


Fig 2 Beach profile on the coast of the Gulf of Mexico near Fort Walton Beach, Florida, during the experimental period, between May 20 and May 26, 1970

Method of Data Analysis

Our immediate concern is to examine the validity of Eq (10) under sea breeze conditions. First, by integrating Eq (10) between any two heights a and b , we have

$$U_b - U_a = 3 \left[\frac{U_*^5 \bar{\theta}}{\lambda^2 g |\theta_*|} \right]^{1/3} (a^{-1/3} - b^{-1/3}) \quad (15)$$

This may be written

$$y = a_0 + a_1 x \quad (15a)$$

where

$$y = U_b - U_a$$

$$a_0 = 0$$

$$a_1 = 3 \left[\frac{U_*^5 \bar{\theta}}{\lambda^2 g |\theta_*|} \right]^{1/3} \quad (15b)$$

$$x = a^{-1/3} - b^{-1/3}$$

We plot the observations for each run in the form y against x , plotting one point for each available pair of heights. Eq (15a) shows that, if the data do follow the free-convection form, the points lie on a straight line. This method is similar to that used by Webb (1970). Eqs (15a) and (15b) have also been obtained by the least-squares technique. Table 1 gives as an example the least-squares values of each correlation.

Table 1 Sea Breeze Wind Profiles on the Swash near Fort Walton Beach, Florida

May 22, 1970		Measured Wind Profiles (Speed vs Height)					Least-Squares Values#		
15-Minute Ending Time		Wind Speed at 20 cm	Wind Speed at 40 cm	Wind Speed at 80 cm	Wind Speed at 160 cm	Wind Speed at 240 cm	Wind Speed at 320 cm	Correlation Coefficient	Y Axis Intercept
Hr	Min	cm/sec	cm/sec	cm/sec	cm/sec	cm/sec	cm/sec	r	a ₀ , cm
800*		139	154	168	196	226	267	61	25 1
15*		152	169	185	213	248	276	69	21 8
30*		138	149	164	189	216	244	66	19 7
45*		130	144	158	181	200	227	73	15 6
900*		160	176	192	209	223	242	86	9 6
15**		190	211	227	247	254	262	98	2 6
30**		209	235	258	282	291	300	99	2 6
45**		240	272	303	341	361	377	96	9 1
1000		266	304	336	367	382	395	99	4 1
15		282	323	360	393	410	426	99	5 1
30		297	340	380	416	431	447	99	4 1
45		300	346	379	406	421	435	99	2 2
1100		337	389	424	455	466	480	99	- 0 0
15		354	407	443	472	484	499	99	0 1
30		369	428	465	493	507	523	99	- 0 2
45		374	431	468	501	518	535	99	2 4
1200		347	413	448	478	494	511	99	0 1
15		322	382	417	444	456	471	99	- 1 4
30		312	381	421	447	462	477	99	- 2 6
45		298	362	394	419	434	448	98	- 1 4
1300		326	395	431	460	472	488	98	- 2 6
15		270	324	353	374	385	398	98	- 1 6
30		250	301	326	345	352	361	98	- 3 8
45		233	279	300	316	324	332	97	- 2 8
1400		213	252	270	284	291	299	98	- 1 8
15		205	242	261	275	282	290	98	- 1 6
30		202	240	258	273	280	287	98	- 1 9
45		190	231	249	262	267	275	96	- 3 1

Table 1 continued

May 22, 1970		Measured Wind Profiles (Speed vs Height)						Least-Squares Values# (Eqs 15, 15a, and 15b)		
15-Minute Ending Time	Wind Speed at 20 cm cm/sec	Wind Speed at 40 cm cm/sec	Wind Speed at 80 cm cm/sec	Wind Speed at 160 cm cm/sec	Wind Speed at 240 cm cm/sec	Wind Speed at 320 cm cm/sec	Correlation Coefficient	Y Axis Intercept	r	a, cm
Hr Min CDT										
1500	201	238	256	271	278	286	98	-	1	3
15	198	240	260	277	285	294	98	-	1	5
30	216	263	290	307	317	326	98	-	2	3
45	230	280	310	330	342	352	99	-	1	7
1600	265	319	355	374	386	396	99	-	3	2
15	276	335	374	401	414	428	99	-	1	5
30	266	318	358	383	396	406	99	-	2	0
45	230	280	312	332	345	355	99	-	1	5
1700	246	300	332	351	363	373	98	-	2	8
15	230	277	313	332	343	352	99	-	2	5
30	237	291	323	342	351	360	98	-	4	2
45	213	259	291	307	316	322	98	-	4	2
1800	216	264	298	317	328	336	99	-	2	9
15	232	286	326	346	356	364	98	-	4	8
30	222	270	302	320	327	335	98	-	4	3
45	216	265	301	321	332	340	99	-	3	1
1900	227	277	314	335	345	353	99	-	3	7
15	237	289	328	349	361	369	99	-	3	5
30	224	277	314	335	345	352	99	-	4	6
45	217	265	301	321	332	339	99	-	3	3
2000	204	252	285	302	310	315	98	-	5	2
15	200	247	279	296	305	311	98	-	4	2
30	193	238	268	282	291	296	98	-	4	4
45	176	215	243	257	264	268	98	-	4	2
2100	166	205	231	245	251	256	98	-	4	0
15	174	214	242	255	262	267	98	-	4	2
30	167	204	230	244	249	254	98	-	4	0
45	159	192	216	228	233	237	98	-	3	7

Table 2 continued

May 22, 1970		Measured Wind Profiles (Speed vs Height)				Least-Squares Values#			
15-Minute Ending Time		Wind Speed at 20 cm	Wind Speed at 40 cm	Wind Speed at 80 cm	Wind Speed at 160 cm	Wind Speed at 240 cm	Wind Speed at 320 cm	Correlation Coefficient	Y Axis Intercept
Hr	Min	cm/sec	cm/sec	cm/sec	cm/sec	cm/sec	cm/sec	r	a ₀ , cm
		163	190	212	231	236	241	99	- 1 0
	15**	111	127	143	163	174	187	92	6 8
	30**	44	48	59	74	88	135	40	21 9

#Least-squares values are obtained from Eqs 15, 15a, and 15b for the atmospheric free-convection regime, which has pronounced nonlogarithmic wind profile

*For reference only Land breeze regime

**Sea breeze and land breeze fronts, for reference only

coefficient (r), as well as the y-axis intercept (a_0) It can be seen from this table that, in the whole sea breeze range from 1000 to 2200 CDT, $r > .96$ and $-5.2 \text{ cm} < a_0 < 5.2 \text{ cm}$, which is within the experimental error In other words, these observations verify that the sea breeze is in the atmospheric free-convection regime and that its wind profile in the surface boundary layer can be represented by Eq (10)

Similar analyses were made for temperature profiles under sea breeze conditions whenever wind profiles were measured Thus, the U_* and θ_* values are obtained from these observations, as mentioned previously Note that, on the basis of the findings by Priestly (1959), Dearnorff and Willis (1967), and Dyer (1967), the value of λ was chosen to equal unity and was used in the present analysis

SURFACE SHEAR STRESS OF THE SEA BREEZE

Since the main purpose of this paper is to provide the shear stress coefficient (C_z) under the sea breeze condition, and since usually $Z = 10$ meters is taken as reference level, Figure 3 shows the required results It can be noted immediately from this figure that the $C_{10} \times 10^3$ value for a given wind speed is greater than that under neutral and stable conditions (e g , Roll, 1965) This is not surprising inasmuch as the sea breeze itself is set up by the differential heating between land and water (Hsu, 1970) Thus the buoyancy forces must play the dominant role, as demonstrated in Table 1

The result is consistent with the findings by J and M Darbyshire (1955), who showed that atmospheric stability has a very marked effect on the tilt of the water surface in response to the wind In measuring the surface slope of a lake under different thermal conditions, they obtained stress coefficients that, for a given wind speed, were twice as great in unstable cases as in stable ones According to Roll (1965), the Darbyshires' result is also in conformity with the findings of several authors in different regions of the world (see references given by Roll, 1965)

Since the shear stress coefficient may also be affected by the fetch of the wind (e g , J and M Darbyshire, 1955, and Roll, 1965), the annotated bibliography compiled by Baralt and Brown (1965) for the sea breeze structure in various parts of the world and a summary of local winds by Defant (1951) may be consulted Furthermore, since the land and sea breeze systems, which are governed by the circulation theorem, have been verified by Hsu (1970), the fetch may be estimated from wind observations (see Eq 8 in Hsu, 1970), provided that the value of the coefficient of friction can be estimated on the basis of accurate geomorphological survey of the coastal area in question (see also the discussions by Haurwitz, 1947) An example of the mesoscale structure, including the fetch study of the sea breeze, is given by Hsu (1970)

As for coastal applications, Murray (personal communication) found that the computed shear stress value based on Figure 3 for a given wind speed fits his wind-induced current prediction and observation under the

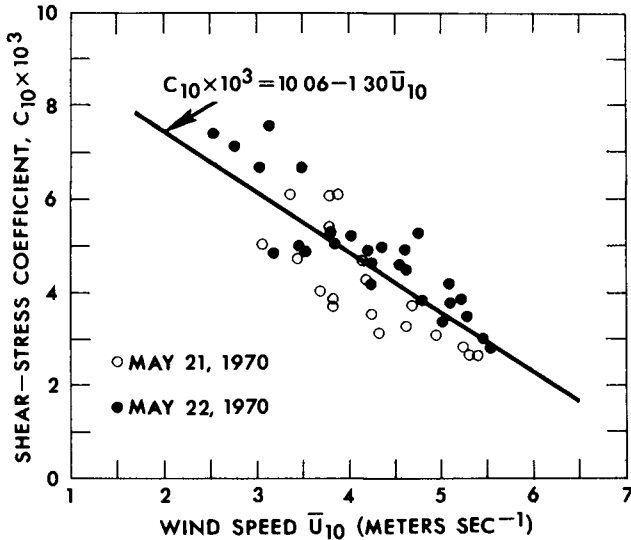


Fig 3 Measured shear stress coefficients under the sea breeze condition. Each point is calculated from a 15-minute time average from both air temperature and velocity profiles. Correlation coefficient of the least-squares fit for the straight line is 0.80.

sea breeze condition more reliably than that based on the neutral stability coefficient (e.g., Wu, 1969).

CONCLUDING REMARKS

While this study is intended to provide the shear stress coefficient under the sea breeze condition, caution should be exercised in applying the result, which may not be applicable to other coastal winds, such as the land breeze, coastal mountain and valley winds, and other synoptic and subsynoptic wind systems. It is suggested that before this result can be applied some knowledge of sea breeze meteorology may be needed. In this connection, papers by, among others, Defant (1951), Baralt and Brown (1965), and Hsu (1969a and b and 1970) may be consulted.

ACKNOWLEDGMENTS

This study was supported by the Geography Programs, Office of Naval Research, through the Coastal Studies Institute, Louisiana State University, under Contract N00014-69-A-0211-0003, NR 388 002. Appreciation is expressed to personnel of Eglin Air Force Base, particularly to Marshall Cartledge, for permission to occupy the site during the experiment. Thanks also go to Norwood Rector and Stanley Sandifer, who helped perform the experiment.

REFERENCES

- Saralt, G L , and R A Brown, 1965, The land and sea breezes an annotated bibliography Final Report on Mesometeorological Field Studies, Dept of Geophysical Sciences, Univ Chicago, 61 pp
- Darbyshire, J , and M Darbyshire, 1955, Determination of wind stress on the surface of Longh Neagh by measurement of tilt Quart J Roy Meteorol Soc , 81 333-339
- Deardorff, J W , and G E Willis, 1967, The free-convection temperature profile Quart J Roy Meteorol Soc , 93 166-175
- Defant, F , 1951, Local winds Compendium of Meteorology, Am Meteorol Soc , pp 655-672
- Dyer, A J , 1967, The turbulent transport of heat and water vapour in an unstable atmosphere Quart J Roy Meteorol Soc , 93 501-508
- Estoque, M A , 1961, A theoretical investigation of the sea breeze Quart J Roy Meteorol Soc , 87 136-146
- Haurwitz, B , 1947, Comments on the sea-breeze circulation J Meteorol , 4 1-8
- Hsu, S -A , 1969a, Land- and sea-breeze fronts near 50 cm on the Gulf coast Bull Am Meteorol Soc , 50 880-882
- _____, 1969b, Comments on paper by J Wu, 'Wind stress and surface roughness at air-sea interface ' J Geophys Res , 74 5562
- _____, 1970, Coastal air-circulation system observations and empirical model Monthly Weather Rev , 98 487-509
- McPherson, R D , 1968, A three-dimension numerical study of the Texas coast sea breeze Technical Report No 15, Atmospheric Science Group, College of Engineering, Univ Texas, Austin, 252 pp
- Neiburger, M , 1969, The role of meteorology in the study and control of air pollution Bull Am Meteorol Soc , 50 957-965
- Priestley, C H B , 1959, Turbulent transfer in the lower atmosphere Chicago (Univ Chicago Press), 130 pp
- Roll, H U , 1965, Physics of the marine atmosphere New York (Academic Press)

- Seesholtz, J R , 1968, A field investigation of air flow immediately above ocean surface waves Mass Inst Technol Dept Meteorology Technical Report, 138 pp
- Webb, E K , 1970, Profile relationships the log-linear range, and extension to strong stability Quart J Roy Meteorol Soc , 96 67-90
- Wu, J , 1969, Wind stress and surface roughness at air-sea interface J Geophys Res , 74 444-455

CHAPTER 16

ENERGY LOSSES UNDER WAVE ACTION

by

P D Treloar,
Research Associate,
Department of Civil Engineering,
Queen's University at Kingston

and

A Brebner,
Professor,
Department of Civil Engineering,
Queen's University at Kingston

ABSTRACT

Wave-height attenuation measurements were made in two identical flumes of different widths and the results used to separate bottom energy losses from sidewall energy losses. These energy losses, in the form of rates of energy dissipation, were then compared with their theoretical values as calculated by solving the linearized Prandtl boundary layer equations and evaluating the Rayleigh dissipation function. Using these results, an adjusted formula for the wave-height attenuation modulus was determined.

INTRODUCTION

Up to the present time no direct measurements of the sidewall and bottom rates of energy dissipation in laminar boundary layers, produced by progressive, oscillatory gravity waves in a wave flume, have been made. A comparison between these experimental values and their related theoretical values would be valuable as the results could be used to produce an adjusted formula for the wave-height attenuation modulus α , which is defined by the equation

$$\frac{H}{H_0} = e^{-\alpha x} \quad \text{--- --- --- --- --- --- --- --- --- --- --- 1}$$

where H₀ is the wave-height at position x = 0 and H is the subsequent wave-height at position x, in the direction of wave propagation Eagleson (1) and Iwagaki and Tsuchiya (2) measured the bottom shear forces produced by a wave by measuring the shear on a plate fitted flush with the flume bottom. Their results led to values of α_b, (where α_b is the attenuation modulus which results from the bottom boundary layer), which did not agree with the theoretical values of α_b, the formula for which is derived by the authors mentioned. In model harbour tests it is often necessary to have an accurate estimate of this attenuation modulus in order that the prototype wave-heights may be interpreted from the model measurements. This is because harbour models are constructed according to the Froude modelling law whereas the model wave amplitude attenuation is normally a viscous phenomenon

GENERAL APPROACH

In order to separate bottom and sidewall friction effects it is necessary to have two flumes which are identical except for their widths. Since the space rate of change of average wave power per unit plan area, ∂P̄/∂x, is equivalent to the sum of the average time rates of energy dissipation per unit plan area on the bottom and sidewalls, dE_b/dt and dE_w/dt respectively, the following simultaneous equations can be written

$$\begin{aligned}
 B_1 \frac{\partial \bar{P}_1}{\partial x} &= -(B_1 \frac{d\bar{E}_b}{dt} + 2h \frac{d\bar{E}_w}{dt}) \quad \text{--- --- --- 2} \\
 B_2 \frac{\partial \bar{P}_2}{\partial x} &= -(B_2 \frac{d\bar{E}_b}{dt} + 2h \frac{d\bar{E}_w}{dt})
 \end{aligned}$$

where B is flume width, h is still water depth and the subscripts 1 and 2 refer to the two separate flumes. If the quantities ∂P̄₁/∂x and ∂P̄₂/∂x are known, then the equations can be solved for dE_b/dt and dE_w/dt. These equations must be solved for the case when the wave parameters, wave period T, wave height H and still water depth h, are the same in both flumes because then the values of dE_w/dt and dE_b/dt are the same in the two flumes. Thus it becomes necessary to determine experimental values for ∂P̄/∂x in the two flumes. Now since P̄, from first order wave theory, can be written as

$$\bar{P} = \gamma H^2 C_g / 8 \quad \text{--- --- --- --- --- --- --- --- --- --- --- 3}$$

where γ is the specific weight of the fluid and C_g is the wave group velocity, it is possible to write ∂P̄/∂x as

$$\frac{\partial \bar{P}}{\partial x} = \gamma H / 4 \frac{dH}{dx} C_g \quad \text{--- --- --- --- --- --- --- --- --- --- --- 4}$$

for constant T and h . First order wave theory was used because the horizontal water particle velocities are described best, in this case, by this theory, (Le Mehauté et al (3)), and because the first order approximation to the solution of the wave equation satisfies the boundary conditions at the free surface as well as other theories, (Dean (4)). It now becomes obvious that it is necessary to determine wave height versus distance attenuation curves for waves with the same periods and depths in the two flumes. Equation 4 can then be evaluated and equations 2 solved.

EXPERIMENTAL TECHNIQUE

The Coastal Engineering Laboratory of Queen's University at Kingston has two similar flumes of width 2 ft and 3 ft and length 150 ft. They are constructed from concrete and the inside walls were cement plaster which has been sanded smooth and painted. However, in order to obtain sufficient difference between attenuation rates in the two flumes, an aluminum sheet wall was constructed in the 2 ft flume to make a temporary flume 6 inches wide. The flumes had identical motors and similar flap-type paddles.

The wave-heights in the 6 inch flume were measured using a carbon-strip probe and those in the 3 ft flume using a capacitance plate probe. Both of these instruments have similar accuracy, (± 0.002 ft) in comparison with a hook gauge. Risaltex "horse-hair" mats were used to make beaches which absorbed the energy of the incident waves. The reflection coefficient was always less than 5%.

The useful measuring length for each flume was about 25 ft out of a total length of some 150 ft. This distance was not long enough to produce a sufficient number of wave-height versus distance data points. For this reason the flume was "lengthened" using the following known method which is described by Battjes (5). The wave-heights were measured at two stations 25 ft apart, wave-height at $x = 0$ ft and wave-height at $x = 25$ ft. The wave paddle was then adjusted so that the wave-height measured at $x = 25$ ft was now produced at $x = 0$ ft in the flume. The wave-height produced at $x = 25$ ft is now the wave-height which would have been produced at $x = 50$ ft if the flume had been long enough. By repeating this procedure the flumes were "lengthened" considerably. In fact the paddle was adjusted so that the wave-height measured at $x = 0$ ft, for each "lengthening" increment, was within ± 0.3 mm of the required wave-height. The difference in wave-height decrements for waves of initial height differing by this small quantity would be very small. Each measurement was performed three times, the wave-height decrement being taken as the average of these values.

The wave-heights at stations were measured by moving the measuring device over a distance of one half wavelength on both sides of the station, thus measuring two maxima and two minima of the

incident-reflected wave interference profile. Then, assuming linear attenuation over a short distance, and assuming first order wave motion, the wave-height at a station can be shown to be equal to

$$H = 1/8(A+3B+3C+D)$$

where, in this case, A, B, C and D are the consecutive values of the maxima and minima taken from the recorder profile

DIMENSIONAL ANALYSIS OF ENERGY DISSIPATION

The rate of energy dissipation in the laminar bottom boundary layer can be written in the functional form

$$d\bar{E}_b/dt = f(a_s, \tau, \mu, \rho)$$

where μ is fluid viscosity, ρ is the fluid density and a_s is the length of the bottom fluid particle motion. Using dimensional analysis this equation becomes

$$d\bar{E}_b/dt = \rho a_s^3 / \tau^3 \cdot \phi(a_s^2 / \tau \nu) \quad \text{--- --- --- 5}$$

where ν is kinematic viscosity. It is well known that for laminar flow conditions a viscous force is proportional to the first power of a velocity, i.e.

$$\text{Force} \propto \text{velocity}$$

Now the rate at which work is done, or energy dissipated, is given by the relationship

$$\text{Rate of work} = \text{Force} \times \text{average velocity}$$

$$\text{i.e. Rate of work} \propto (\text{velocity})^2$$

or in this case

$$d\bar{E}_b/dt \propto u_o^2 \quad \text{--- --- --- --- 6}$$

is taken, where u_o is the horizontal velocity of fluid particles at the upper limit of the boundary layer. Thus equation 5 can be written in the form

$$d\bar{E}_b/dt = \rho (a_s / \tau)^3 \cdot \phi((a_s / \tau)^2 \cdot \tau / \nu)$$

which, upon putting $u_o = \text{constant} \times a_\delta/T$

$$d\bar{E}_b/dt = \rho u_o^3 \phi_1 (u_o^2 T/\nu) \quad \text{--- --- --- --- } 7$$

In order that equation 6 can be satisfied, ϕ must be of the form

$$\phi = \text{constant} (u_o^2 T/\nu)^{-1/2} \quad \text{--- --- --- } 8$$

By suitable arrangement and substitution of equation 8 in equation 7, the following is obtained

$$\begin{aligned} d\bar{E}_b/dt_{\text{experimental}} &= \text{const } d\bar{E}_b/dt_{\text{theoretical}} \\ &= D d\bar{E}_b/dt_{\text{theoretical}} \end{aligned}$$

and in a similar way the sidewall rate of energy dissipation functional relationship produces

$$\begin{aligned} d\bar{E}_w/dt_{\text{experimental}} &= \text{konst } d\bar{E}_w/dt_{\text{theoretical}} \\ &= F d\bar{E}_w/dt_{\text{theoretical}} \end{aligned}$$

The subscript "theoretical" indicates the theoretical equation for the rate of energy dissipation D and F are constants

From the above analysis it is obvious that, once the rates of attenuation curves for wave-height have been determined in the two flumes for waves with the same period and water depth, the constants D and F can be determined. One experiment only is required. However nine experiments were performed in order to reduce the effect of experimental error. The periods used were 0.91, 1.08 and 1.21 seconds. The water depths were 4.1, 5.6, 7.9 and 10.0 inches. The selection of these values ensured that the wavelength to depth ratios would be in the range $0.7 < L/h < 10$, the lower limit being for deep water waves and the upper limit being the commonly accepted limit for cnoidal waves. Maximum wave steepness was about 0.05. To ensure that the boundary layers remained laminar, the criterion for laminar oscillatory boundary layers under waves derived by Collins (6) was used, this being that

$$R_E = \frac{u_o \delta}{\nu} < 160$$

where δ is a boundary layer thickness parameter defined as

$$\delta = (\nu T / \pi)^{1/2}$$

In addition, the water surface was kept clean and the condition of an immobile surface never occurred. Energy dissipation as a result of surface films was not considered to be of importance.

RESULTS AND CONCLUSIONS

The experiments were performed as described and the results tabulated. The next step was to fit a suitable equation to the experimental results so that equation 4 could be evaluated. This was done by assuming exponential attenuation and linearizing equation 1

$$\ln H = \ln H_0 - \alpha x$$

Using the least squares technique and a weighting function of H^2 , the values of α and H_0 were determined. Table 1 shows the experimental values of α together with their related theoretical values. The data was found to fit this form very well. The fit was tested using the parameter

$$R^2 = 1 - \frac{\sum (H - H_i)^2}{\sum (H_i - \bar{H})^2}$$

where

$$\bar{H} = \frac{1}{n} \sum_{i=1}^n H_i$$

n is the number of data points obtained for a particular attenuation curve and H_{12} is the wave-height at position x_1 along a flume. The values of R^2 were better than 0.995 in all cases.

Grosch and Lukasik (7) determined an attenuation equation for finite amplitude waves. This equation was also tried and the results of regression analysis showed that their equation fitted the data almost as well as the exponential equation. However, the latter, because of its easier mathematical form, was used for evaluating equation 4.

With experimental values of α and H_0 determined, the values of rates of energy dissipation on the bottom and sidewalls can be separated. For constant values of T and h , the constants D and F will not vary with change in H as both the theoretical and experimental rates of energy dissipation are then functions of H^2 only. Tables 2 and 3 show theoretical and experimental rates of energy dissipation, calculated for an H value of 20 mm, for the bottom and sidewalls respectively, together with the values of D and F . The values of D and F are

$$D = 1.48 \pm 0.15$$

$$F = 0.94 \pm 0.09$$

at the 95% confidence limits. These values show that theory considerably underestimates the rate of energy dissipation on the flume bottom, whereas for the sidewalls, theory is very close to experiment. The fact that first order theory and experiments agree quite well for energy dissipation on the side walls, whereas this is not the case for bottom losses, cannot be satisfactorily explained. It is not thought that energy dissipation at the fluid surface as a result of surface films is the cause for the approx 50% difference since the experimental surface was certainly not immobile by any stretch of the imagination.

Using a method similar to that demonstrated by Eagleson (1), an equation for the adjusted attenuation modulus for bottom and sidewalls was determined

$$\alpha_{b+w} = \frac{k}{B} \left(\frac{TY}{\pi} \right)^{1/2} \left(\frac{1.48Bk + 0.94 \sinh 2kh}{2kh + \sinh 2kh} \right) \quad \text{--- -- 9}$$

where $k = 2\pi/L$ and L is wavelength. This adjusted modulus would, for the case of a wide, shallow flume, be considerably larger than the well-known theoretical value.

TABLE 1TABLE OF THEORETICAL AND EXPERIMENTAL
ATTENUATION MODULI

Depth	3 ft flume		6 inch flume	
	Theoretical	Experimental	Theoretical	Experimental
<u>T = 1 21 seconds</u>				
10 0 inches	0 00107	0 00108	0 0037	0 00306
<u>T = 1 08 seconds</u>				
4 1 inches	0 00315	0 00464	0 00675	0 00784
5 6 inches	0 00213	0 00246	0 00543	0 00570
7 9 inches	0 00143	0 00170	0 00451	0 00446
10 0 inches	0 00115	0 00116	0 00412	0 00356
<u>T = 0 91 seconds</u>				
4 1 inches	0 00337	0 00453	0 00758	0 00933
5 6 inches	0 00227	0 00300	0 00620	0 00714
7 9 inches	0 00156	0 00214	0 00543	0 00550
10 0 inches	0 00125	0 00159	0 00515	0 00521

TABLE 2
 TABLE OF THEORETICAL AND EXPERIMENTAL VALUES
 OF $\frac{d\bar{E}_b}{dt}$

Depth	$\frac{d\bar{E}_b}{dt}$ has units ft lb /ft ² /sec		F
	$\frac{d\bar{E}_b}{dt}$ exp x 10 ³	$\frac{d\bar{E}_b}{dt}$ theor x 10 ³	
<u>T = 1 21 seconds</u>			
10 0 inches	0 166	0 131	1 27
<u>T = 1 08 seconds</u>			
4 1 inches	0 742	0 450	1 65
5 6 inches	0 361	0 290	1 24
7 9 inches	0 249	0 178	1 40
10 0 inches	0 151	0 118	1 28
<u>T = 0 91 seconds</u>			
4 1 inches	0 615	0 437	1 41
5 6 inches	0 390	0 270	1 45
7 9 inches	0 275	0 148	1 86
10 0 inches	0 162	0 090	1 79

TABLE 3

TABLE OF THEORETICAL AND EXPERIMENTAL VALUES
OF $\frac{d\bar{E}_w}{dt}$

Depth	$\frac{d\bar{E}_w}{dt}$ has units $\text{ft lb} / \text{ft}^2 / \text{sec}$		D
	$\frac{d\bar{E}_w}{dt}$ exp $\times 10^3$	$\frac{d\bar{E}_w}{dt}$ theor $\times 10^3$	
<u>T = 1 21 seconds</u>			
10 0 inches	0 173	0 225	0 77
<u>T = 1 08 seconds</u>			
4 1 inches	0 521	0 583	0.89
5 6 inches	0 422	0 420	1 01
7 9 inches	0 273	0 303	0 90
10 0 inches	0 191	0 239	0 80
<u>T = 0 91 seconds</u>			
4 1 inches	0 726	0 636	1 14
5 6 inches	0 485	0 462	1 05
7 9 inches	0 287	0 329	0 99
10 0 inches	0 244	0 262	0 93

REFERENCES

- 1 Eagleson, P S (1962), "Laminar Damping of Oscillatory Waves", Proc A S C E , Vol 88, pp 155-181, Hy 3
- 2 Yuichi Iwagaki and Yoshito Tsuchiya, (1966), "Laminar Damping of Oscillatory Waves Due to Bottom Friction", Coastal Engineering Conference, Tokyo, 1966, pp 149-174
- 3 Le Mehauté, B , Divorky, D and Lin, A , (1968), "Shallow Water Waves A comparison of Theories and Experiments", Coastal Engineering Conference, London, 1968
- 4 Dean, R G (1965), "Stream Function Wave Theory, Validity and Application", Coastal Engineering Specialty Conference, Santa Barbara, 1965
- 5 Battjes, J S (1965), "Wave Attenuation In A Channel With Roughened Sides", Coastal Engineering Specialty Conference, Santa Barbara, 1965
- 6 Collins, J I (1963), "Inception of Turbulence At the Bed Under Periodic Gravity Waves", Jour Geophs Res , Vol 68, pp 6007-6014
- 7 Grosch, C E and Lukasik, S J (1963), "Discussion of Laminar Damping Of Oscillatory Waves", Proc A S C E , Vol 89, No Hy1, pp 232-239

CHAPTER 17

BOTTOM BOUNDARY SHEAR STRESSES ON A MODEL BEACH

by

P G Teleki

Department of Geology, Louisiana State University, Baton Rouge, and
U S Army Coastal Engineering Research Center, Washington, D C

and

M W Anderson, A M , ASCE

Department of Structures, Materials and Fluids
University of South Florida, Tampa

SYNOPSIS

The maximum amplitude of shear stress in the bottom boundary layer of water waves was evaluated with a Preston probe inclined on a 1:12.5 slope beach. Near bottom velocity profiles were obtained in laminar and developing turbulent flow conditions from which the experimental boundary layer thicknesses were evaluated. Agreement between experimental bottom velocities and those calculated from Airy theory deteriorate with decreasing depth on the beach resulting in lower shear stress values than predicted by linear theory. The measured boundary layer thickness on the slope exceeds the predicted for horizontal bottom, increasing shoreward to some critical depth outside the breaker zone from where it decreases shoreward. The influence of roughness on the shear stress distribution is considerable in the "offshore" region, but becomes negligible near the breaker zone. On a smooth bottom the coefficient of friction agrees with Kajiura's expression.

INTRODUCTION

In order to quantitatively evaluate nearshore sediment transport, it must be recognized that substantially more is required to be known about oscillatory boundary layers, the magnitude of energy dissipation due to bottom friction and fluid turbulence and about the effect of permeability in various sediments, in other words about the physical phenomena near the fluid-solid interface. Our present knowledge on the flow of fluid near the bottom boundary is negligible because analytical solutions of mass transport exist only for laminar flow and for horizontal impermeable boundary. Nature prescribes, in contrast, sloping beaches, loose boundaries and waves undergoing transformation and breaking. Furthermore, at this time we cannot yet solve the equations for turbulent boundary layer in unidirectional steady flow, let alone when waves are present. One of the early efforts of investigating the nature of the oscillating laminar

boundary layer was Eagleson's (1959) Solutions for the horizontal boundary were given by Longuet-Higgins (1958), Grosch (1962) and Iwagaki, et al (1967) Turbulent boundary layers were investigated by Jonsson (1963) and Horikawa and Watanabe (1968) The authors of the latter reference employed Kajiuura's (1968) theory for turbulent boundary layers with some success Direct measurement of boundary shear stress and evaluation of the friction coefficient have been made by Eagleson (1959) and Iwagaki et al (1965) The indirect method of velocity measurements has been applied by Jonsson (1963), Horikawa and Watanabe (1968) and Sleath (1968) Sleath's results are particularly interesting because he used a permeable bottom boundary One of his conclusions was that increase in the permeability of a sandy bottom brings about an increase in the near bottom mass transport velocity Experiments by Horikawa and Watanabe, employing the hydrogen bubble technique, hold out promise toward understanding not only the measurement of instantaneous velocities and boundary layer thickness but a very critical aspect of boundary layer research, namely phase differences between the velocities within and outside of the boundary layer and between the local velocities and the boundary shear stress

The use of the Preston probe for evaluating boundary shear stress from measurements of dynamic pressure is well known from literature for unidirectional turbulent flows Its theoretical development is due to Preston (1954) who used the probe on smooth boundaries Evidence for its applicability to rough boundaries was presented by Hwang and Laursen (1963) and Ghosh and Roy (1970) Nece and Smith (1970) used an enlarged version of the probe on loose boundary of a tidal estuary with partial success The Preston probe, as presented in this report, has not been applied to oscillating flows nor to a sloping bottom In presence of waves, pressure gradients will necessarily be present in the direction of flow Hsu (1955) and Patel (1965) have given proof of the probe's use in pressure gradients In addition, Hsu (1955) extended its use to laminar flow

The aim of this paper is to report on some aspects of the oscillating flow near the bottom, in particular about resistance on a sloping beach and its manifestation in velocity and shear stress distributions near a solid boundary The theoretical developments of Kajiuura (1968) for the oscillating boundary layer were followed Velocity and shear stress measurements were obtained for various wave conditions, a fixed slope, smooth and a rough boundary in a wavetank, using the indirect method of a Preston probe

THEORETICAL CONSIDERATIONS

For the case of unsteady flow of a viscous, incompressible fluid flow the Navier-Stokes equations of motion, two-dimensional case, is given as

$$\rho \left(\frac{\partial u}{\partial t} + u \frac{\partial u}{\partial x} + v \frac{\partial u}{\partial z} \right) = - \frac{\partial p}{\partial x} + \mu \frac{\partial^2 u}{\partial z^2} \quad (1.1)$$

where the x-axis is positive in the direction of wave propagation, z is the vertical coordinate measured positive upward, ρ is the fluid density, μ is the viscosity, p is pressure and u, v are the local velocity terms in the horizontal and vertical directions respectively, defined

$$u = - \frac{\partial \phi}{\partial x} \tag{1 2}$$

and
$$v = - \frac{\partial \phi}{\partial z} \tag{1 3}$$

so that the condition of continuity is met by

$$\frac{\partial^2 \phi}{\partial x^2} + \frac{\partial^2 \phi}{\partial z^2} = 0 \tag{1 4}$$

given ϕ as the velocity potential. Defining d as the local water depth positive upward from the free surface, U as the free stream velocity, and δ the boundary layer, the boundary conditions are

$$z = -d, u = 0, v = 0 \quad \text{at the bottom}$$

$$z = \delta, u = U(x,t) \quad \text{at the outer edge of the boundary layer}$$

$$z \rightarrow \infty, u = U(x,t) \quad \text{at the free surface}$$

Introducing harmonic velocity components

$$\begin{aligned} U(x,t) &= \bar{U}(x) + U'(x,t) \\ U'(x,t) &= U(x)e^{i\sigma t}, \sigma = 2\pi/T \end{aligned} \tag{1 5}$$

$$\bar{U}'(x,t) = 0 \tag{1 6}$$

$$\begin{aligned} u(x,y,t) &= \bar{u}(x,y) + u'(x,y,t) \\ v(x,y,t) &= \bar{v}(x,y) + v'(x,y,t) \\ p(x,t) &= \bar{p}(x) + p'(x,t) \end{aligned} \tag{1 7}$$

we integrate Eq 1 1 over one wave period and obtain

$$\rho \left(\frac{\partial \bar{u}}{\partial t} + \bar{u} \frac{\partial \bar{u}}{\partial x} + \overline{u' \frac{\partial u'}{\partial x}} + \bar{v} \frac{\partial \bar{u}}{\partial z} + \overline{v' \frac{\partial u'}{\partial z}} \right) + \frac{\partial \bar{p}}{\partial x} - \nu \frac{\partial^2 \bar{u}}{\partial z^2} = 0 \tag{1 8}$$

for the flow in the boundary layer. Using the same procedure, the averaged expression for the flow outside the boundary layer will be

$$\rho \left(\frac{\partial \bar{U}}{\partial t} + \bar{U} \frac{\partial \bar{U}}{\partial x} + \overline{U' \frac{\partial U'}{\partial x}} + \bar{v} \frac{\partial \bar{U}}{\partial z} + \overline{v' \frac{\partial U'}{\partial z}} \right) + \frac{\partial \bar{p}}{\partial x} - \nu \frac{\partial^2 \bar{U}}{\partial z^2} = 0 \tag{1 9}$$

Because its effect is negligible we can omit the viscous term in Eq 1 9 and extract the pressure term

$$-\frac{\partial \bar{p}}{\partial x} = \rho \left(\frac{\partial \bar{u}}{\partial t} + \bar{u} \frac{\partial \bar{u}}{\partial x} + \overline{u' \frac{\partial u'}{\partial x}} \right) \quad (1 10)$$

having also neglected the terms containing v , assuming that the vertical velocity is small. Substituting Eq 1 10 into Eq 1 8, gives

$$\frac{\partial \bar{u}}{\partial t} + \bar{u} \frac{\partial \bar{u}}{\partial x} + \overline{u' \frac{\partial u'}{\partial x}} - \left[\frac{\partial \bar{u}}{\partial t} + \bar{u} \frac{\partial \bar{u}}{\partial x} + \overline{u' \frac{\partial u'}{\partial x}} \right] = \mu \frac{\partial^2 \bar{u}}{\partial z^2} \quad (1 11)$$

which describes the total velocity distribution

Based on the parameter $\delta/L \ll 1$ (where L is the wavelength), we make the assumption that the contributions represented by the nonlinear convective terms (except turbulence) are numerically not significant. Therefore we rearrange Eq 1 11 to show the defect velocity relationship

$$\frac{\partial}{\partial t} (\bar{u} - \bar{U}) = \frac{\partial}{\partial z} \left(\frac{\tau}{\rho} \right) \quad (1 12)$$

where

$$\tau = \mu \frac{\partial u}{\partial z} \quad (1 13)$$

and

$$\tau = K_{\infty} \frac{\partial u}{\partial z} \quad (1 14)$$

are the laminar and turbulent horizontal shear stress relationships respectively, and the dynamic viscosity $\mu = \rho \nu$. Eq 1 12 is the expression for oscillatory mean motion in the boundary layer based on potential theory. According to Schlichting (1960), the validity of Eq 1 12 can be established if the laminar boundary layer thickness

$$\delta_L = (2\nu/\sigma)^{\frac{1}{2}} \quad (1 15)$$

The Laminar Case

Recalling that u is the horizontal velocity in the boundary layer and U just outside the layer, so that

$$u(x,y,t) = U(x,t) = a/d \quad C \sin(kx - \sigma t) \\ \lim_{z \rightarrow \delta} \quad (2 1)$$

where C is the wave celerity, " a " the wave amplitude and $k = 2\pi/L$ is the wave number. Grosch (1962) has shown that for $a/d \ll 1$ or a/d near $(kx - \sigma t) = 0$ the linearized theory in the laminar case provides an adequate description of the flow because the sum of all the terms $O(a/d)$ in the nonlinear solution for the bottom shear stress equal the linear solution and are hence negligible. The solution becomes analogous to the Blasius series for steady flows.

The steady state solution of the velocity in the boundary layer can be written as

$$u_o = U[\sin(kx-\sigma t) - e^{-z/\delta_L} \sin(kx-\sigma t - z/\delta_L)] \quad (2\ 2)$$

where the subscript "o" refers to boundary conditions, δ_L is defined in Eq 1 15 and

$$U = \frac{\pi H}{T} \sinh^{-1} kd \quad (2\ 3)$$

is the velocity immediately outside the boundary layer

Iwagaki, et al (1967) based on Grosch's solution obtained the approximate expression for the bottom shear stress

$$\tau_o / (\rho u_o^2) = R^{-1/2} \sin(kx - \sigma t - \pi/4) \quad (2\ 4)$$

where the local Reynolds number is

$$R = \frac{u_o^2 T}{2\pi\nu} \quad (2\ 5)$$

and the phase difference between U and τ_o is $\pi/4$

The maximum shear stress was given by Iwagaki, et al (1967) as

$$\frac{\tau_o \max}{\rho g H} = \frac{\sqrt{2\nu}}{g \sinh kd} \left(\frac{\pi}{T}\right)^{3/2} \quad (2\ 6)$$

$$\tau_o \max = \rho \hat{J} \left(\frac{2\nu\pi}{T}\right)^{1/2} \quad (2\ 7)$$

which shows that the amplitude \hat{J} , of the local boundary shear stress is a function of the local free stream velocity amplitude (therefore the water particle excursion distance) and a boundary layer thickness. The wave height $H = \frac{1}{2}a$ is applicable to sinusoidal wave profiles

In the laminar case we can describe the flow regime with the appropriate Reynolds number, which should contain the parameters for the boundary layer thickness, local velocity and viscosity. Hence, re-arranging Eq 2 5, we get

$$R^{-1/2} = \frac{1}{U} \left(\frac{2\nu\pi}{T}\right)^{1/2} = \frac{\nu}{U} \frac{\sqrt{2}}{\delta_L}$$

and

$$R^{1/2} = \frac{U\delta_L'}{\nu} = R_S \quad (2\ 8)$$

where $\delta_L' = (\nu/\sigma)^{1/2} = \delta_L/\sqrt{2}$ for smooth bottom. The Reynolds number in Eq 2 8 is identical with Kajiura's (1968) and that of Horikawa and Watanabe (1968)

For laminar flow we now nominally define the wave friction coefficient to be of the form

$$C_f \hat{U}U = n(\tau_o/\rho) \quad (2.9)$$

where n must be determined from experiments. For the case of smooth bottom laminar flow Kajiura (1968) approximates the amplitude of the friction coefficient by

$$\hat{C}_f = 1/R_S \quad \text{for } R < 200 \quad (2.10)$$

for the case of the smooth boundary. Introducing now z_o , as the characteristic roughness length, so that when

$$D = 30 z_o \quad (2.11)$$

we have the equivalent Nikuradse's roughness expressed, we follow Kajiura's notation and write the Reynolds number for the rough boundary as

$$R_R = \frac{\hat{U}D}{\nu} \quad (2.12)$$

and the friction coefficient can be expressed as

$$\hat{C}_f = 1.70 \left(\frac{\hat{U}}{\sigma z_o} \right)^{-2/3} \quad (2.13)$$

The Turbulent Case

From experiments of steady turbulent flow (e.g., see Clauser, 1954) we know that the turbulent boundary layer structure is threefold, consisting of the inner or laminar sublayer at the wall, the outer or defect layer near its outer edge, the two connected by the overlap layer. A similar breakdown for oscillatory layers was suggested by Jonsson (1966).

The general form of the turbulent velocity profile can be written as

$$\frac{u}{u^*} = A \log \left(\frac{zu^*}{\nu} \right) + C \quad (3.1)$$

which in the presence of roughness on the wall is modified to read

$$\frac{u}{u^*} = A \log \left(\frac{zu^*}{\nu} \right) + C - \frac{\Delta u}{u^*} \quad (3.2)$$

where $\Delta u/u^*$ represents the vertical shift of the logarithmic profile caused by the roughness elements, A and C are constants to be appraised experimentally and

$$(u^*)^2 = \tau/\rho \quad (3.3)$$

$$\text{Similarly } (u_o^*)^2 = (\tau_o/\rho) \quad z = 0 \quad (3.4)$$

is the shear velocity

and the shear stress is given by

$$\tau = K_z \partial u / \partial z \tag{3 5}$$

K_z is Kajiura's (1968) eddy viscosity (i.e., the Boussinesq effective viscosity) of the form

$$K_z = \begin{cases} \nu & \text{in the inner layer} \\ \kappa u_0^* z & \text{in the overlap layer} \\ K_d & \text{in the outer layer} \end{cases} \tag{3 6}$$

where $K_d = K \hat{U} \delta_L^1$, $K = 0.2$ is a universal constant, δ_L^1 is defined in Eq 1.15 and $\kappa = 0.4$ is Kármán's universal constant. Eq 3.6 is in relation to a smooth boundary. For the rough case the overlap expression of Eq 3.6 applies for $z_0 < z < \delta$, except when $(\delta_L^1/D) < 1$ in which case

$$K_z = 5.53 \kappa u_0^* z_0 \tag{3 7}$$

for the laminar sublayer. Kajiura's eddy viscosity assumption is based on analogy to steady state flow. It presents the possibility, however, of being an improved estimate because it takes the structure of the layer into consideration. But as Clauser (1956) pointed out for steady flow, "the turbulent eddies introduce shearing stresses for which no reliable method of calculation exists", and this phenomenon should only be more complex in time periodic flows.

Even small changes in bottom roughness will drastically alter the profile of the turbulent boundary layer, which makes the vertical distribution of K_z difficult to establish. Liu (1967, as quoted by Kline, 1969, vol. I, p. 529) showed that changing z_0 can result in a change of K_z by a factor of four in the defect layer. Indeed, Horikawa and Watanabe (1968) showed that K_z attenuates with respect to z on both smooth and rippled boundaries, therefore further research is needed before accepting the formulations given in Eq 3.6, 3.7, and 3.8.

The friction coefficient for the smooth bottom in turbulent flow is given by Kajiura as

$$\hat{C}_f = (R_S m y_L)^{-2} \text{ for } R_S > 200 \tag{3 9}$$

with
$$m = \frac{1}{2} \sqrt{\frac{\kappa}{N}}, \quad N = \text{Const} \approx 12 \quad \text{assumed} \tag{3 10}$$

$$y_L = \frac{2D_L}{\sqrt{\kappa N \delta_L}} \quad (3.11)$$

$$D_L = N\nu/\hat{u}^* \quad (3.12)$$

where y_L is the distance between the bottom and the lower limit of the overlap layer, we obtain the the aid of Eq 2.8 the approximate expression

$$\hat{C}_f = \left(\frac{\hat{u}_0^*}{\hat{U}}\right)^2 \quad (3.13)$$

For rough boundaries Kajiura gives

$$\hat{C}_f = \left(\frac{60 z_0 \sigma}{\kappa \hat{U} y_R}\right) \quad (3.14)$$

where y_R is the upper limit of the laminar sublayer

For $\hat{U}/\sigma z_0 < 1000$ Eq 3.14 can be approximated by Eq 2.13

The Preston Probe

Preston (1954) assumed that in turbulent flow on a smooth boundary a region must exist close to the wall in which the "law of the wall" of the form

$$\frac{U}{u^*} = f_1 \left(\frac{zu^*}{\nu}\right) \quad (4.1)$$

applies, so that the local shear stress at the boundary τ_0 , can be related to the velocity distribution by measuring the differential pressure Δp , with a modified Pitot tube in contact with the wall. The inter-relations are

$$\frac{\Delta p}{\tau_0} = f_2 \left(\frac{u^* d}{\nu}\right) \quad (4.2)$$

and

$$\frac{\tau_0}{\rho v^2} = f_3 \left(\frac{\Delta p d^2}{\nu^2 \rho}\right) \quad (4.3)$$

where f_2, f_3 denote functional dependence, and d is the outside diameter of the probe. The logarithmic expression obtained by Preston (1954)

$$\log_{10} \frac{\tau_0 d^2}{4\rho v^2} = 2.604 + 7/8 \log_{10} \frac{\Delta p d^2}{4\rho v^2} \quad (4.4)$$

was modified by Hsu (1955) for the laminar sublayer (hence for laminar

boundary layers) to read

$$y^* = \frac{1}{2} \log_{10} \left(\frac{8}{4+t^2} \right) + \frac{1}{2} x^* \quad (4.5)$$

and for the turbulent portion

$$y^* = \log_{10} k + \frac{7}{8} x^* \quad (4.6)$$

Where $y^* = \log_{10} (\tau_{od} / 4\rho v^2)$ and $x^* = \log_{10} (\Delta p d^2 / 4\rho v^2)$, t = the ratio of inner to outer diameter of the stagnation tube and should be in the vicinity of 0.6, $k = I(t)$ and $I(t)$ is given by Hsu in tabulated form

Preston also advanced the hypothesis that the relationships presented in Eqs. 4.2 and 4.3 are independent of the x -wise pressure gradient in the turbulent boundary layer. Patel (1965) indicated, however, that for severe favorable and adverse pressure gradients the Preston probe overestimates skin friction. The analytical solution given by Yalin and Russell (1966)

$$\tau_o = \rho(\alpha U^2 + \beta g S \delta) \quad (4.7)$$

given g as the gravitational acceleration and α, β as empirical constants, takes into consideration the instantaneous position of the free surface S , thus the pressure gradient. It is clear therefore, that to avoid the influence of vertical accelerations on the local static pressure, as well as the influence of wave set-down near the breaker zone, initial evaluation of flow parameters with the Preston probe must be restricted to $S=0$, i.e., to the wave crest and wave trough, or approximately $(kx - t) = 0$

EXPERIMENTAL APPARATUS AND PROCEDURE

Experiments were carried out in a fixed level, concrete floor, concrete and plexiglas-wall wavetank designed by the authors and constructed in 1968-69 at Louisiana State University. Dimensions of the channel were 65x3x3 feet and it is shown in Figure 1. A fixed angle beach was constructed at the downstream end of the tank with a slope of 1:12.5, covered with aluminum sheet to provide a smooth surface. For part of the tests sand of uniform size was attached to the beach face in thickness of one grain dimension ($z_o = 0.0123$ ft).

Resistance type wave gauges and the Preston probe were suspended from a forward-reverse gear, variable speed carriage and positioned with the aid of point gauges. A Sanborn Model 150 oscillograph served as the excitation source and recording unit for the wave and pressure recording. Waves with fixed periods of $T=1.0, 1.5, 2.0$ seconds were generated with a bottom-hinged paddle-type wavemaker. The surface configuration of these waves were quite asymmetric for low frequencies and high amplitudes, consequently they were damped using various combinations of baffles following recommendations of Keulegan (1968). An undamped short period wave train is shown in Figure 1.

Figure 1. Experimental set-up showing the wavetank, instrument carriage with Preston probe, and pressure transducer. Beach is nearest observer.



Since the Preston probe was to be used in wave boundary layers, the calibration procedure had to conform to the oscillatory motions experienced. For this purpose a variable stroke, variable frequency calibrating apparatus was built whose real time response was recorded by a linearsyn differential transformer. This enabled calculation of both the pressure-velocity relationship for the probe and the associated time lag. Differential pressures were sensed by a Pace 90B pressure transducer.

For the given wave periods the wavemaker stroke was changed to provide two wave amplitudes, noted as "large" and "small" in the graphs.

Water depth was fixed at 2.0 feet in the horizontal floor portion of the tank. Waves were measured in this part of the channel as well as adjacent to the Preston probe, aligned with the sloping bottom (Figure 2). The definition sketch for the probe is presented in Figure 3. Measurements of the differential pressure were made under the wave crests and troughs only by orienting the probe upslope and downslope, keeping other conditions the same. Adjustments for the phase difference between the surface, the free stream velocity and the velocity in the boundary layer were recorded. Measurements were carried out first on a smooth, then on a roughened bottom keeping other conditions the same. Water temperature was regularly recorded during the experiments.



Figure 2. Preston probe aligned with rough boundary. Static probe is in front.

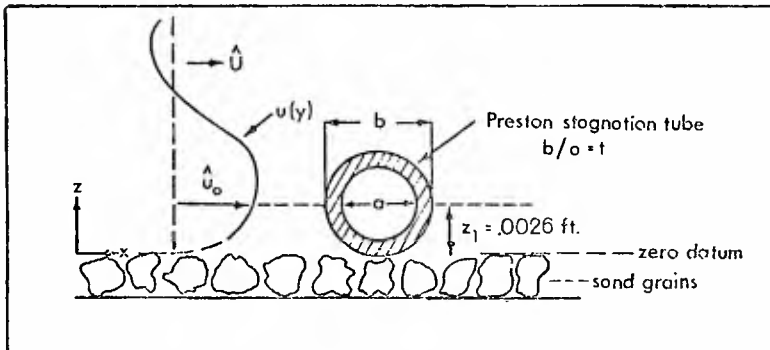


Figure 3. Preston probe resting on rough boundary, definition sketch

EXPERIMENTAL RESULTS

Rigorous evaluation of the velocity distributions on a slope, relative to waves undergoing transformation and without specific knowledge about boundary layer structure, growth and separation during a wave cycle will have to await further experimentation and a solution to the nonlinear phenomena experienced. Results presented on the velocity profiles on a sloping bottom are therefore exploratory only. In Figures 4, 5, 6, a set of profiles are illustrated from one of the experiments conducted on a smooth bottom with "small" amplitude waves.

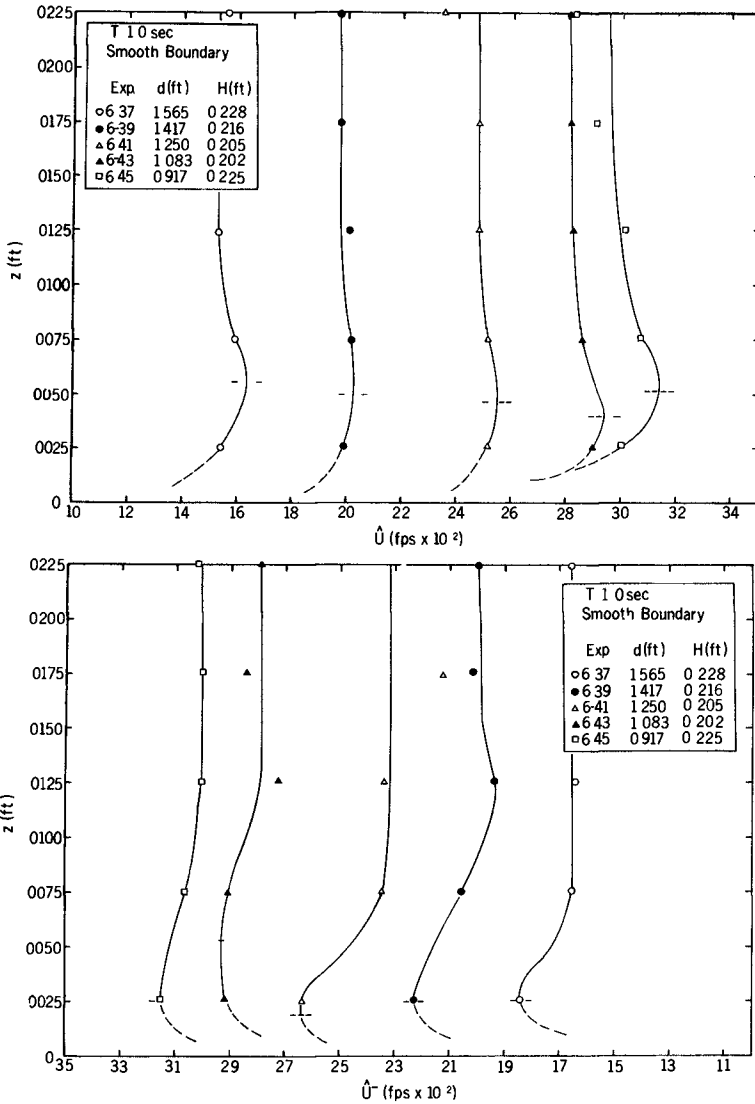


Figure 4 Experimental velocity profiles for T=1.0 second on smooth boundary. Upper graph shows measurements under wave crests, lower graph, wave troughs.

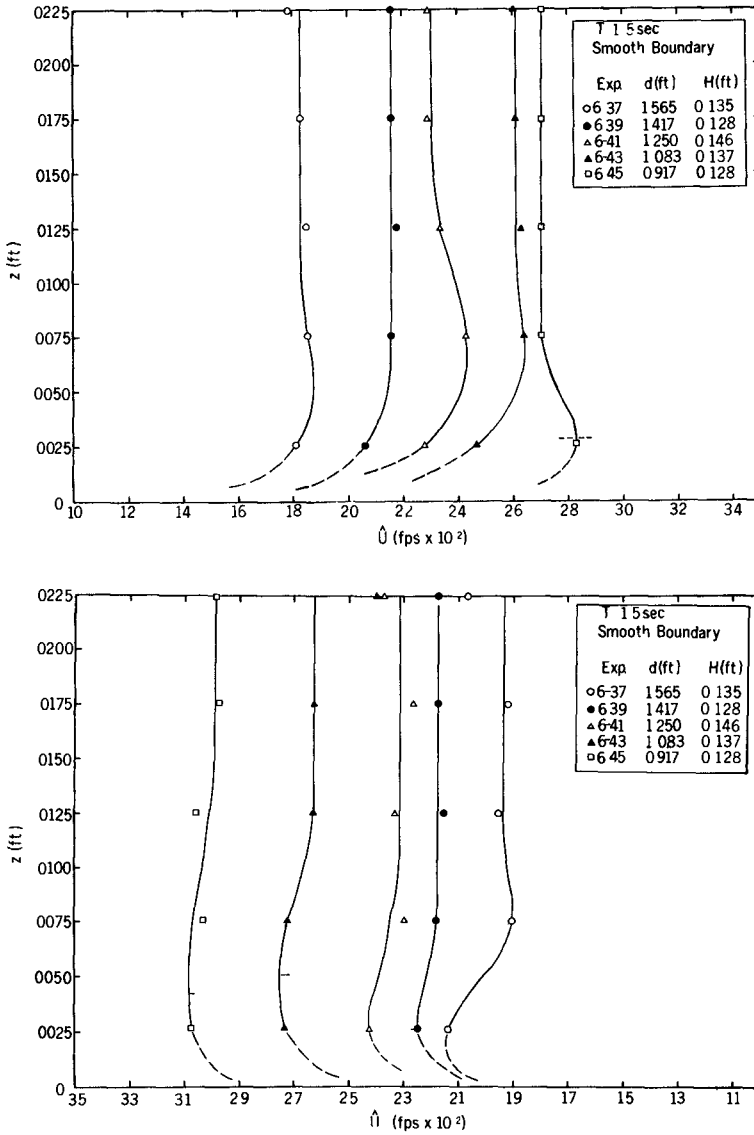


Figure 5 Experimental velocity profiles for T=1.5 seconds on smooth boundary Upper graph refers to wave crests, lower refers to wave troughs

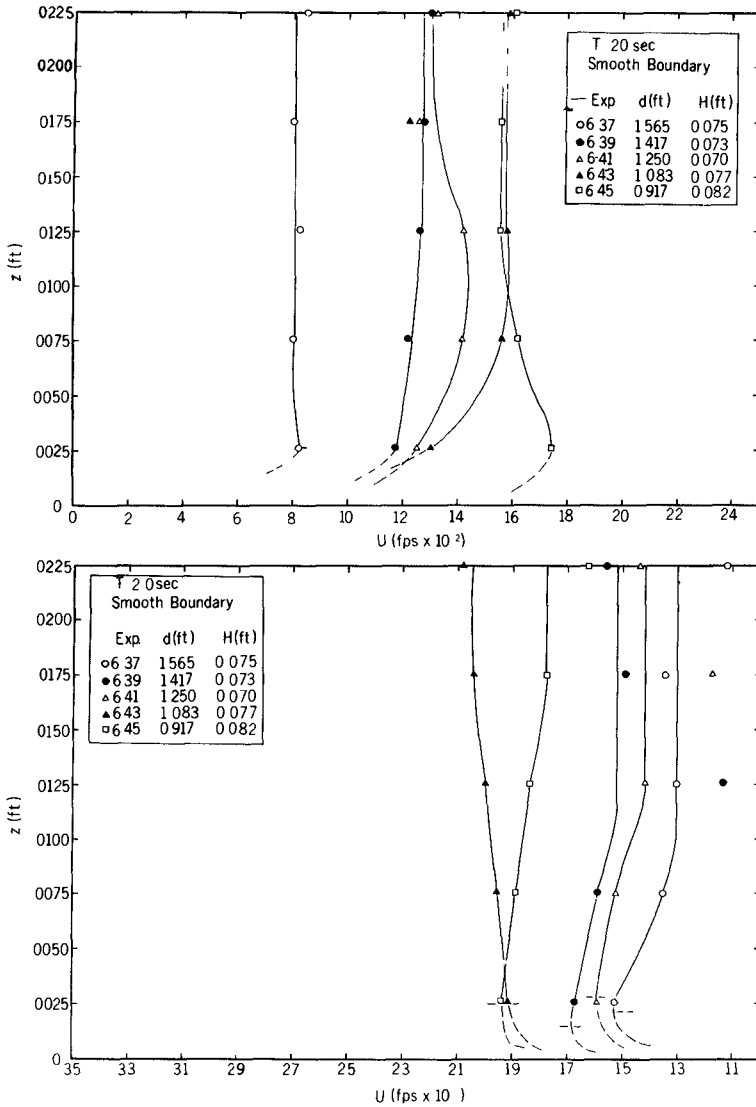


Figure 6 Experimental velocity profiles for T=2.0 seconds on smooth boundary. Upper graph measurements with respect to wave crests. Lower graph wave troughs.



Figure 7. Boundary layer obtained with injected dye on a rough boundary.

Visual confirmation of the presence of a boundary layer is shown in Figure 7, showing displacements of a dye streak upslope, indicative of incremental mass transport with successive wave cycles. The dashed lines of Figures 4 - 6 refer to the elevation of the maximum velocity in the boundary layer $\hat{u}_0 \text{ max}$ following the procedure of Eagleson, Dean and Peralta (1958). Experimental values of \hat{U} , were found to agree very well for "deep" water on the slope, but the agreement declined for decreasing water depth and the linear model was found to overestimate the measured values. It should be noted the maximum reflection (H_r/H_i) was less than 10% for any one test. Grosch's (1962) criterion for neglecting nonlinear terms in the N-S equation was $a/d < .01$; it was exceeded in all cases. The effect of the convective velocity terms should be additive under the crest and subtractive under the wave trough with respect to linear values (Eq. 2.3).

Experimental data on boundary layer thicknesses are presented in Table 1 for various combinations of wave amplitude, water depth and wave period. Values of $\hat{\delta}$ exceed the theoretical $\hat{\delta}_L$ (Eq.1.15), by factors of 3 to 8. Boundary layer thicknesses were found to be greater under wave crests than under wave troughs, this is no doubt influenced by vertical accelerations prior to attainment of \hat{U}_{max} under the crest. Growth of the layer is also affected by the contribution of upslope mass transport which allows a longer excursion distance for its development. This phenomenon occurs on both smooth and rough boundaries. The effect of roughness is to increase $\hat{\delta}$. The contribution is more under wave crests and this is to be expected because the rate of boundary layer growth accelerates with increasing roughness element size. Wave amplitude influence on $\hat{\delta}$ was difficult to discern, more tests are needed to evaluate this relationship. In some cases, boundary layers were observed to grow to some maximum value offshore of the breaker zone from which point $\hat{\delta}$ diminished shoreward, the reversal usually taking place at $d \approx 1.0$ foot.

Table 1 EXPERIMENTAL BOUNDARY LAYER THICKNESSES (in 10^{-3} feet)

		$\hat{\delta}$								δ_L
Wave Ampl		"Large"				"Small"				
Boundary		Smooth		Rough		Smooth		Rough		
Wave	-	Crest	Trough	Crest	Trough	Crest	Trough	Crest	Trough	
d/T^2										
1 56		11 9	6 9	15 3	13 1	12 5	7 6	12 3	7 0	1 79
1 42		16 7	7 3	7 5	10 2	12 5	9 4	12 5	7 1	
1 25		15 8	8 0	7 3	12 5	12 5	10 3	17 2	-	↓
1 083		22 6	6 2	13 5	7 1	16 3	10 6	17 5	10 4	↓
0 92		8 1	10 6	7 5	-	17 5	17 5	7 5	-	↓
0 695		14 5	7 5	11 3	7 6	11 5	6 2	12 0	14 5	2 18
0 629		12 6	8 2	14 6	11 2	15 0	8 4	10 7	-	↓
0 555		8 7	8 7	16 1	-	16 2	10 5	13 3	18 2	↓
0 481		12 6	9 0	16 4	5 7	12 0	13 8	10 5	16 5	↓
0 407		15 0	9 5	11 1	16 2	7 5	14 4	8 2	13 7	↓
0 391		14 5	12 5	16 8	12 1	6 0	10 1	11 6	5 9	2 54
0 354		-	14 1	12 4	10 2	14 0	11 2	8 5	10 6	↓
0 312		12 6	14 1	9 5	7 6	13 5	12 5	10 3	8 2	↓
0 271		7 0	8 9	15 4	10 7	12 0	17 5	12 2	17 4	↓
0 229		8 7	5 9	13 0	-	12 5	12 5	16 2	12 5	↓

The classification of boundary conditions in terms of the prevalent flow regime, i e to establish where laminar gives way to turbulent flow is a difficult task Kajiura specified the transition region as

$$25 < IR_S < 650 \text{ for smooth bottom}$$

$$\text{and } 100 < IR_R < 1000 \text{ for rough bottom}$$

Collins' (1963) critical Reynolds number of 113 (by transformation) is in the range for IR_S . Both ranges are wide and until a universal velocity distribution for oscillatory boundary layers is established, we do not know when to assume inception of turbulence or when full turbulence appears. Considerable data fell into the transition ranges specified above. The critical Reynolds numbers of $IR_S = 250$ for the smooth bottom and $IR_R = 500$ for the rough boundary are proposed.

Evaluation of boundary shear was based on Eqs 4 5 and 4 6, using the given critical Reynolds numbers. Maximum amplitudes of the shear stress were corrected for phase lag. The distribution of $\tau_{0 \text{ max}}$ upslope is shown in Figure 8 corresponding to wave crests and in Figure 9 for wave troughs.

Although the rate of increase varies depending on wave period and amplitude, the trends are linear. The dependence on wave amplitude is clearly discernible, higher shear stresses are associated with "large" amplitude waves. In "deep" water initial values of $\tau_{0 \text{ max}}$ are smaller under wave troughs than under wave crests. Convergence was noted, however, for both cases of boundary conditions on nearing the breaker zone, indicating also that the effect of roughness used becomes negligible for very shallow water.

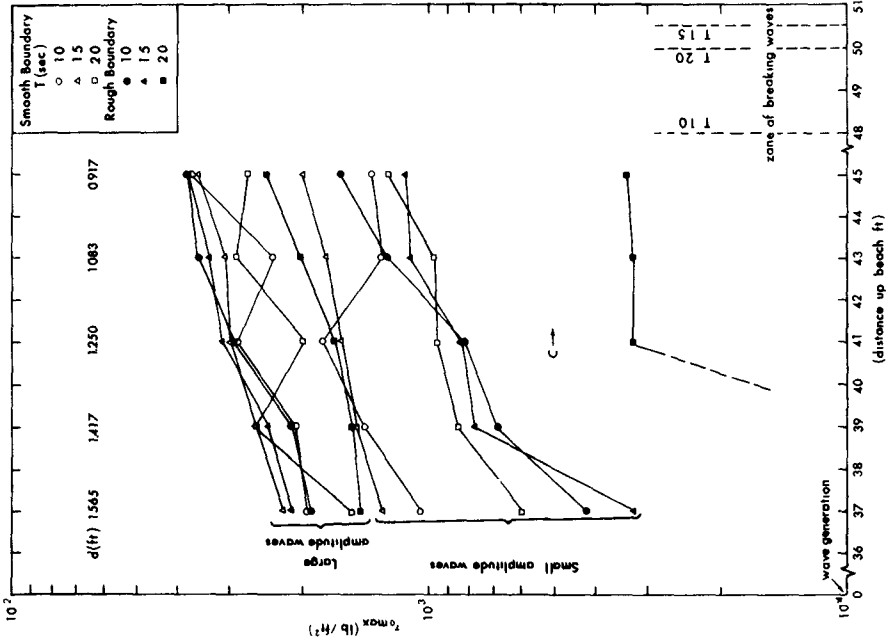


Figure 9 Shear stress distribution upslope corresponding to wave troughs

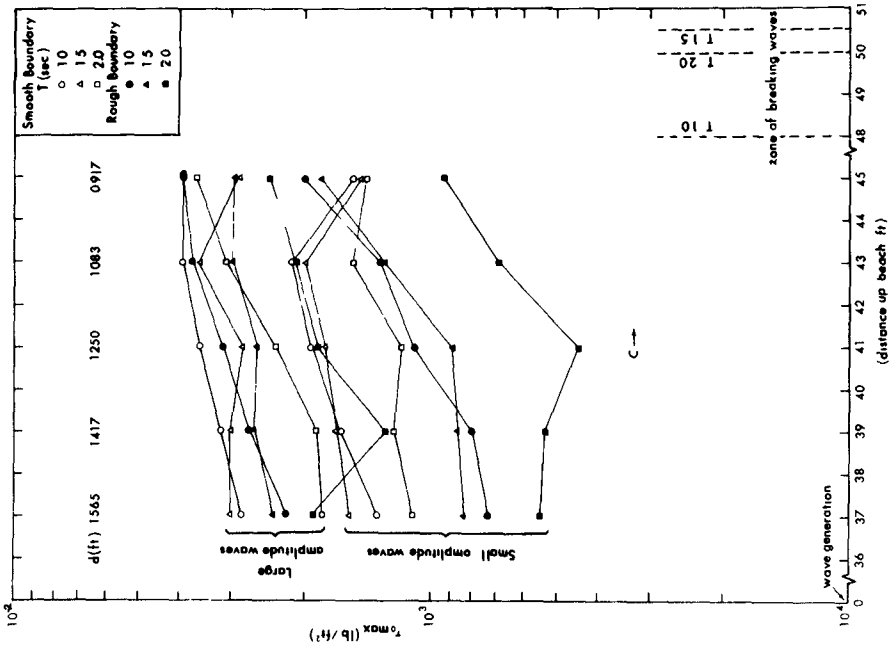


Figure 8 Shear stress distribution upslope corresponding to wave crests

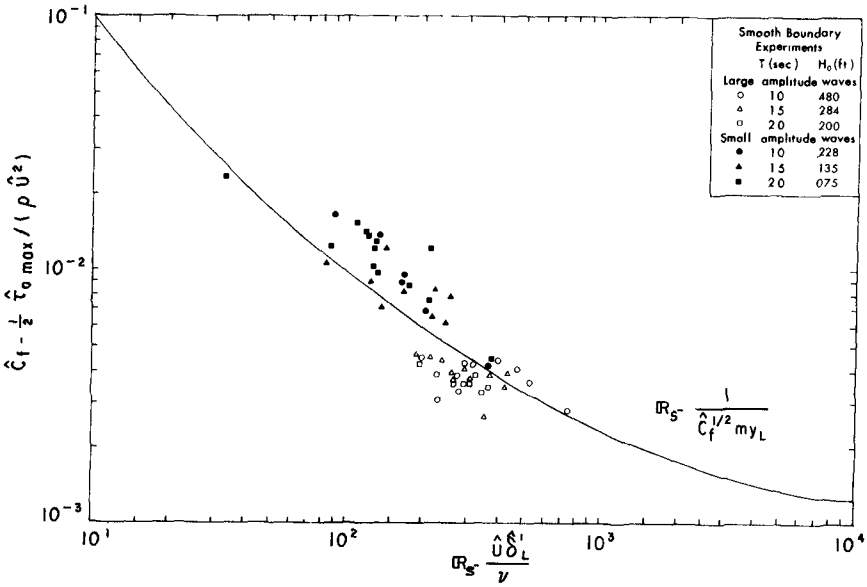


Figure 10 Relation between the coefficient of friction \hat{C}_f and the Reynolds number \mathbb{R}_S for smooth boundary

The relation between the shear stress and the corresponding velocity is dependent upon the coefficient of friction, whose value is a function of boundary conditions and the local flow regime. For the smooth bottom Figure 10 is presented where agreement between Kajiwara's curve and the computed \hat{C}_f is very good for $n = \frac{1}{2}$. This is in contrast with $n=2$ for the rather widely used \hat{C}_f (e.g., see Eagleson, 1959). It is shown that the friction coefficient increases for decreasing wave amplitude.

In presence of boundary roughness, Eq 2.13 is applicable when $\hat{U}/\sigma_o < 1000$, and this condition is validated for the test cases. In Figure 11 the linear trends show that the friction coefficient increases for increasing wave frequency, decreasing Reynolds numbers and decreasing wave amplitude.

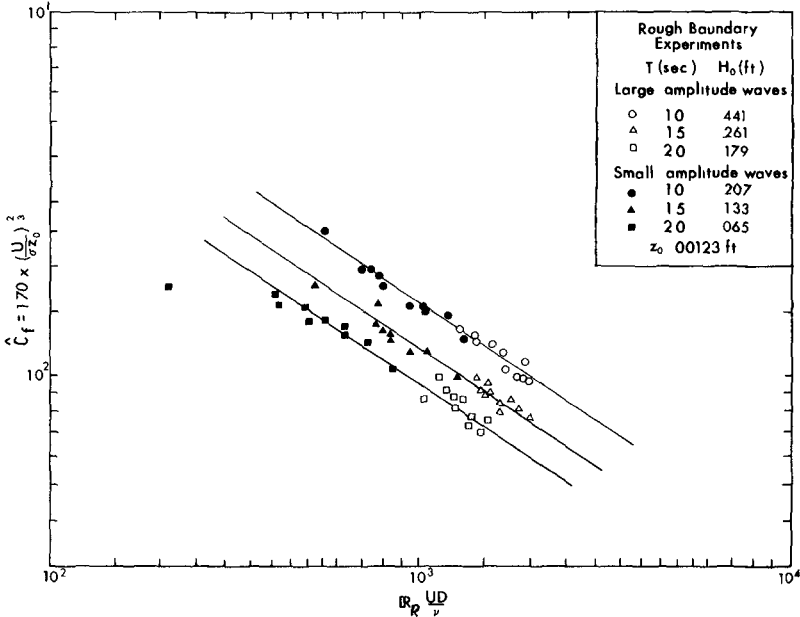


Figure 11 Relation between the coefficient of friction \hat{C}_f and the Reynolds number R_R for rough boundary

CONCLUSIONS

Laboratory investigations of boundary layer thickness, near bottom velocity profiles and bottom friction were carried out on a slope with the aid of a Preston probe in hopes of initiating greater understanding about littoral sediment transport. The use of Preston probe is limited under oscillating flow conditions although its simplicity of construction and applicability to both laminar and turbulent flows is appealing. Wave boundary layers are complex phenomena in time and space and their analysis on a sloping bottom presents considerable difficulties. The thickness of fully developed layers greatly exceeds the theoretical, and this is probably the result of non-negligible vertical accelerations and the presence of mass transport. The nonlinear effects could not be appraised for the velocity distribution and the agreement between the theoretical and experimental reference velocity only occurs for relatively deep water. The shear stress distribution appears to have a linear relation to decreasing water depth, with higher amplitudes as wave height is increased.

REFERENCES

- Clauser, F , 1954, Turbulent boundary layers in adverse pressure gradients, *J Aero Sci* , 21 91-108
- Clauser, F , 1956, The turbulent boundary layer, *Adv in Appl Mech* , 4 1-51, Academic Press, New York
- Collins, J I , 1963, Inception of turbulence at the bed under periodic gravity waves, *J Geophys Res* 68(21) 6007-6014
- Eagleson, P S , 1959, The damping of oscillatory waves by laminar boundary layers, *Mass Inst Tech , Hydrodyn Lab Tech Rpt* 32, 37 p
- Eagleson, P S , Dean, R G and Peralta, L A , 1958, The mechanics of the motion of discrete spherical bottom sediment particles due to shoaling waves, *U S Army Corps of Engrs, Beach Erosion Board Tech Memo* 104, 41 p
- Ghosh, S N and Roy, N , 1970, Boundary shear in open channel flow, *Proc ASCE, J Hydr Div* , 96 (HY4) 967-994
- Grosch, C E , 1962, Laminar boundary layer under a wave, *Phys of Fluids* 5 1163-1167
- Horikawa, K and Watanabe, A , 1968, Laboratory study on oscillatory boundary layer flow, *Coastal Engineering in Japan* 11 13-38
- Hsu, E Y , 1955, The measurement of local turbulent skin friction by means of surface Pitot tubes, *David Taylor Model Basin Rpt* 957
- Hwang, L S and Laursen, S M , 1963, Shear measurement technique for rough surfaces, *Proc ASCE, J Hydr Div* 89(HY2) 19-37
- Iwagaki, Y , Tsuchiya, Y and Chen, H , 1967, On the mechanism of laminar damping of oscillatory waves due to bottom friction, *Bull Dis Prev Research Institute, Kyoto University*, 16(3), 49-75
- Iwagaki, Y , Tsuchiya, Y and Sakai, M , 1965, Basic studies on the wave damping due to bottom friction, *Coastal Engrg in Japan*, 8 37-49
- Jonsson, I G , 1963, Measurements in the turbulent wave boundary layer, *Proc IAHR Conf* , London, 85-92
- Jonsson, I G , 1966, On the existence of universal velocity distributions in an oscillatory turbulent boundary layer, *Coastal Eng Lab Tech University, Denmark, Basic Res Prog Rpt* 12 2-9
- Kajiura, K , 1968, A model of the bottom boundary layer in water waves, *Bull Earthquake Res Inst* , Tokyo University 46 75-123
- Keulegan, G H , 1968, Wave damping effects of screens, *U S Army Corps of Engineers Waterways Exp Sta Rpt* 2-12, 62 p
- Kline, S J , Morkovin, M V , Sovran, G and Cockrell, D J , 1969, Computation of turbulent boundary layers - 1968, *Proc AFOSR-IFP-Stanford Conf* , vol I, p 529
- Longuet-Higgins, M S , 1958, The mechanics of the boundary layer near the bottom in a progressive wave, *Proc 6th Conf Coastal Engineering, Gainesville, Fla, Ch* 10 184-193
- Nece, R E and Smith, J D , 1970, Boundary shear stress in rivers and estuaries, *Proc ASCE, J Waterways & Harbors Div* 96(WW2) 335-358
- Patel, V C , 1965, Calibration of the Preston tube and limitations on its pressure gradients, *J Fluid Mech* 23(1) 185-208
- Preston, J H , 1954, The determination of turbulent skin friction by means of Pitot tubes, *J Royal Aero Soc* 58 109-121
- Schlichting, H , 1960, *Boundary layer theory*, McGraw-Hill, N Y 647 p
- Sleath, J F A , 1968, The effect of waves on the pressure in a bed of sand in a water channel and on the velocity distribution above it, *unpub Ph D Thesis, St John's College, Cambridge*, 141 p
- Yalin, M S and Russell, R C H , 1966, Shear stresses due to long waves, *J Hydr Res* , 4(2) 55-98

CHAPTER 18

VARIATION OF LONGSHORE CURRENT ACROSS THE SURF ZONE

Edward B Thornton
Assistant Professor of Oceanography
U S Naval Postgraduate School
Monterey, California

ABSTRACT

The wave-induced longshore current variation across the surf zone is described for a simplified model. The basic assumptions are that the conditions are steady, the bottom contours are straight and parallel but allow for an arbitrary bottom profile, the waves are adequately described by linear theory, and that spilling breakers exist across the surf zone. Conservation equations of mass, momentum, and energy, separated into the steady and unsteady components, are used to describe second order-wave-induced phenomena of shoaling waves approaching at an angle to the beach. An expression for the longshore current is developed, based on the alongshore component of excess momentum flux due to the presence of unsteady wave motion. Wave set-down and set-up have been included in the formulation. Emphasis in the analysis is placed on formulating usable predictive equations for engineering practice. Comparison with experimental results from the laboratory and field show that if the assumed conditions are approximately fulfilled, the predicted results compare quite favorably.

INTRODUCTION

A knowledge of the variation and extent across the surf zone of the longshore current is important in design considerations of structures placed in the littoral area. This kind of information is particularly important for groins or similar structures designed to impede sand movement since the longshore current is a primary mechanism for sand transport. On the other hand, it is often desirable to have natural bypassing about jetties constructed for navigational purposes at inlets and harbors. The distribution of effluent, introduced onto beaches and into the littoral zone, is also influenced by the currents in the surf zone. There is a very real need for a more complete understanding of the littoral zone so that further improvements and preservation of our beaches can be based on more rational and concrete approaches.

The study of the area in and about the surf zone presents a difficult problem due to its very complex nature. A proper treatment of the surf zone must consider a three-dimensional problem of unsteady fluid motion and is further complicated by moving interfaces at the upper and lower boundaries, that

is, at the water surface and sediment bottom. The hydrodynamics of the littoral zone can be characterized by two idealized systems of either a longshore current or rip current system which can occur for seemingly similar conditions. Thus, it is necessary to make definite and simplifying assumptions in order to make the problem tenable to a theoretical approach.

This analysis considers the steady-state distribution of quantities on a line normal to the shoreline. A schematic of the surf zone area is shown in Figure 1. The analysis is restricted to the case of an arbitrary bottom profile with straight and parallel contours in the y-direction (parallel to the beach). The x-direction is perpendicular to the beach.

CONSERVATION EQUATIONS

A convenient starting point for this analysis is a statement of the general conservation equations of mass, momentum, and energy fluxes applicable to unsteady flow. The analysis is not concerned with the internal flow structure of the fluid, hence, the derivation can be simplified by integrating the conservation equations over depth. Conservation equations which have already been developed by Phillips [1] are used and are presented below.

The conservation equations are applied to wave motion, but they are equally applicable to general turbulent motion. The unsteady velocity field of the wave motion can be expressed in the same manner as in the treatment of turbulent motion as the sum of its mean and fluctuating parts.

$$\vec{u} = (U_1(x,y,t) + u_1'(x,y,z,t), w(x,y,z,t)) \quad i = 1,2 \quad (1)$$

where (1,2) refer to the horizontal coordinates (x,y), respectively, and z is the vertical coordinate. The tensor notation is used only for horizontal components of water particle motion. The mean current is assumed uniform over depth for simplicity. The pressure term can be stated similarly. These expressions can be substituted into the mass, momentum, and energy equations, and the mean and fluctuating contribution identified.

The conservation equations are averaged over depth and time (one can consider averaging over a few wave periods). For the case of waves superposed on a mean current, all the wave motion is identified with the fluctuating quantity which, when integrated over the total depth, can contain a mean contribution due to the waves. The time averaging of the equations for a general development, being over a short interval compared to the total time, does not preclude long term unsteadiness in the mean motion.

A Conservation of Mass

The general conservation of total mass per unit area can be expressed

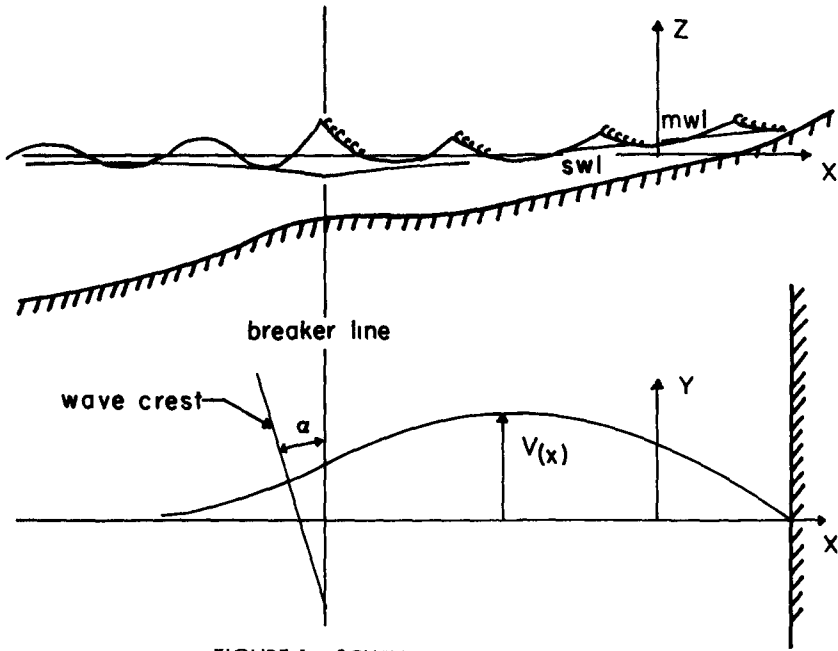


FIGURE 1 SCHEME OF THE SURF ZONE

$$\frac{\partial}{\partial t} \rho D + \frac{\partial}{\partial x_i} \tilde{M}_i = 0 \quad i = 1, 2 \quad (2)$$

D is the total averaged depth of water which can include a mean elevation $\bar{\eta}$, above (or below) the still water depth h, so that

$$D(x, y, t) = (\bar{\eta} + h) \quad (3)$$

The overbar shall be used to signify time averages. The total mass flux \tilde{M}_i can be partitioned into its mean and fluctuating components

$$\tilde{M}_i = \bar{M}_i + M_i \quad (4)$$

B Conservation of Momentum

The equation defining the conservation of horizontal momentum is derived by integrating the momentum equation over depth and averaging in time. The balance of total momentum per unit area can be expressed

$$\frac{\partial}{\partial t} \tilde{M}_i + \frac{\partial}{\partial x_j} (\tilde{U}_i \tilde{M}_j + S_{ij}) = T_i + R_i \quad (5)$$

Here \tilde{M}_i denotes the total horizontal momentum per unit area. Hence, the first term on the left represents the rate of change of the total mean momentum per unit area which includes both the current momentum and wave momentum

\tilde{U}_i is the total mean transport velocity. The second term on the left of Equation expresses the momentum flux of a steady stream together with an excess momentum flux term S_{ij} arising from the superposed unsteady motion, where

$$S_{ij} = \int_{-h}^{\bar{\eta}} (\rho u'_i u'_j + p \delta_{ij}) dz - \frac{1}{2} \rho g D^2 \delta_{ij} - \frac{M_i M_j}{\rho D} \quad (6)$$

and δ_{ij} is the Kronecker delta. The unsteady terms in the integral contain contribution from the mean motion, the last two terms represent the hydrostatic pressure and mean momentum flux contained in the integral term and is subtracted out so that the term represents only the excess momentum flux due to the unsteady motion. The last term is generally of higher order, but very near and inside the surf zone the term is of second order and consistent with this analysis, however, its maximum contribution is only four percent and this term will be neglected. The term T_i is given by

$$T_i = -\rho g (\bar{\eta} + h) \frac{\partial \bar{\eta}}{\partial x_i} \quad (7)$$

and represents the net horizontal force per unit area due to the slope of the free water surface

R_i is the time mean averaged shear stress which must be included in any realistic treatment of the surf zone where dissipative effects occur. The integrated form of the resistance term is given by

$$R_i = \int_{-h}^{\eta} \frac{\partial \tau_{j1}}{\partial x_j} dz + \overline{\tau_{\eta i}} - \overline{\tau_{hi}} \quad 1, j = 1, 2 \quad (8)$$

where τ_{j1} includes the combined lateral shear stresses of waves and currents and the last terms are the surface and bottom shear stress respectively

In the development of the conservation equations, no restrictions are placed on the wave slopes or amplitudes. Also, no restrictions are placed on the fluctuating motion so that the equations are equally applicable to wave or turbulent motion.

DESCRIPTION OF THE WAVE FIELD

A Waves outside the Surf Zone

It is known that, due to the fluctuating water particle motion of the waves, there is a momentum flux component. If the waves have a direction component parallel to shore, a longshore current can be generated due to changes in the longshore momentum flux component of the shoaling waves. In waves, the momentum flux is the sum of the pressure and the product of two velocities. It can be shown that the average momentum flux is nonlinear in wave height. In order to specify the excess momentum flux of the waves, it therefore becomes necessary to consider nonlinear, or higher order, effects of the wave motion.

The development presented here retains terms to the second order in amplitude (first order in energy and momentum) and neglect all higher order terms. The wave solution is substituted directly into the conservation equations providing a means for describing the wave-induced mean motions. In making this substitution and dropping all terms of orders higher than the second, only knowledge of the first order (linear) wave water particle velocities and surface elevation is necessary. This is because, in expanding and then averaging over the period, the terms involving higher order quantities in velocity and surface elevation go to zero. The pressure must be known to the second order in wave height, however, the average second order pressure component can be determined from the first order water particle velocities and surface elevation terms. Thus, only the linear wave solution is required.

B Waves inside the Surf Zone

Inside the surf zone, energy is dissipated due to the generation of turbulence in wave breaking, bottom friction,

percolation, and viscosity. The waves in the surf zone constitute a non-conservative system in which the use of potential flow theory is no longer valid. In fact, there is no analytical description available for the waves in the surf zone. Hence, one is required to make rather gross assumptions and then to test these assumptions experimentally. The linear wave theory will be retained as the input to the conservation equations, but with modification to the wave amplitude and speed. The wave height inside the surf zone is controlled by the depth and is of the same order of magnitude. Thus, even the second order theory in wave height is a rather poor assumption, but seems to agree surprisingly well with measurements of some phenomena.

Spilling breakers lend themselves to a physical treatment since the potential energy and momentum flux of the waves inside the surf zone can be expressed approximately in analytical form. If the beach slope is very gentle, the spilling breakers lose energy gradually, and the height of the breaking waves approximately follows the breaking index curve. The height of the wave, H , is then a function of the total depth, D , as given by

$$H = \kappa D \quad (9)$$

where the breaking index, $\kappa = 0.78$, as predicted by the solitary wave theory.

It is further assumed that the kinetic and potential energy are equally partitioned so that the total wave energy can be described in terms of the wave height which is a function of the depth.

$$E = \frac{1}{8} \rho g H^2 = \frac{1}{8} \rho g \kappa^2 D^2 \quad (10)$$

This is a non-conservative statement of the energy distribution within the surf zone.

The waves inside the surf zone are assumed to retain their simple harmonic character so that the wave profile and water particle velocity are described by

$$\eta = \frac{H}{2} \cos(k_1 x_1 - \sigma t) \quad (11)$$

$$\vec{u} = \frac{H}{2} \frac{g}{c} \frac{k_1}{k} \cos(k_1 x_1 - \sigma t) \quad (12)$$

where k is the wave number, σ the wave frequency and c the wave speed. The expression for the horizontal water particle velocity is based on the Airy wave theory and has been simplified for shallow water.

In very shallow water, the waves are non-dispersive with the wave speed being only a function of the depth. It has been found experimentally that a reasonable approximation to the wave speed in the surf zone is that predicted by the solitary wave theory

$$c = \sqrt{g(H + D)} = \sqrt{g(1 + \kappa) D} \quad (13)$$

Since the bottom contours are parallel, Snell's law can be used to account for the changes in wave direction due to refraction. The wave angles are referred to the breaker wave angle which is the commonly measured angle in the study of the surf zone. Hence,

$$\sin \alpha = \frac{c}{c_b} \sin \alpha_b \quad (14)$$

where the subscript "b" refers to the breaker line. Refraction due to shear flow is neglected and can be shown to be of minor importance.

The excess momentum flux tensor can be determined by substituting the wave expressions into Equation (6). In general terms of energy, group velocity, c_g , and wave speed, c , an expression applicable to both inside and outside the surf zone is given by

$$S_{ij} = \begin{vmatrix} E \frac{c_g}{c} \cos^2 \alpha + \frac{E}{2} \left(\frac{2c_g}{c} - 1 \right) & \frac{E}{2} \frac{c_g}{c} \sin 2\alpha \\ \frac{E}{2} \frac{c_g}{c} \sin 2\alpha & E \frac{c_g}{c} \sin^2 \alpha + \frac{E}{2} \left(2 \frac{c_g}{c} - 1 \right) \end{vmatrix} \quad (15)$$

The effects of turbulence and surface tension have not been included.

LONGSHORE CURRENT FORMULATION

The wave field has been completely specified. These results may now be substituted into the general conservation equations to describe wave-induced phenomena inside and outside the surf zone.

Recalling the analysis is restricted to the case of an arbitrary bottom profile with straight and parallel contours in the y -direction, the water depth is then a function of the x -direction only. Since the distribution of mean properties of the wave field is a function of the depth, this eliminates any y -dependence. An exception to this was found by Bowen [2]. Using the fact that incident waves can excite transversal waves, commonly called edge waves, he showed that if these waves are standing waves, or only slowly progressive, gradients in the mean water surface can be developed in the longshore direction which in turn can result in

circulation cells. Thus, a more exact formulation has to assume suitable spatial averaging in the longshore direction so as to preclude the effects of any transversal waves.

It is assumed that wave reflection is negligible. This assumption is justifiable outside the surf zone for gently sloping bottoms. The present analysis is most valid for spilling breakers which implies a gently sloping bottom. The wave reflection is least for this type of breaker condition and is assumed negligible inside the surf zone as well.

Shear stresses at the surface due to the wind are neglected.

The problem can be conveniently discussed by considering separately the areas outside and inside the surf zone. A determination of the distribution of mass transport and energy of the waves is first necessary in order to solve for the wave-induced currents.

A Mass Transport Velocity

Due to the absence of any y -dependence, the mass conservation Equation (2) reduces to

$$\frac{\partial \tilde{M}_x}{\partial x} = 0 \quad (16)$$

Integration gives

$$\tilde{M}_x = \text{constant} = 0 \quad (17)$$

which must be equal to zero since the beach forms a boundary in the x -direction. This then says

$$U_x = - \frac{M}{\rho D} \cos \alpha \quad (18)$$

which states that there is a mean reverse current balancing the mass transport onshore due to the wave motion. This must be true everywhere, both inside and outside the surf zone, to ensure that there is no accumulation of mass or growth of currents in the y -direction in order to maintain steady-state conditions in accordance with the original assumptions.

B Changes in the Mean Water Level

The changes in the mean water level must be determined inside the surf zone in order to specify the variation of wave energy since the waves are assumed proportional to the total depth of water. The changes in the mean water level can be determined from the x -momentum equation given by

$$\frac{\partial}{\partial x} S_{xx} = T_x = - \rho g D \frac{\partial \bar{\eta}}{\partial x} \quad (19)$$

where shear stresses are neglected and time dependence, y-gradients and net mass flux in the x-direction are all zero. This equation states that there is a change in the mean water level to balance the excess momentum flux of the waves. Longuet-Higgins and Steward [3] have solved Equation (19) for the case of wave approaching to an arbitrary plane bottom using linear wave theory. Outside the surf zone they found

$$\bar{\eta} = - \frac{H^2}{8} \frac{k}{\sinh 2kh} \quad (20)$$

where the negative sign indicates a set-down which is a function of the local conditions only.

Inside the surf zone the changes in mean water level are again determined from Equation (19). It is assumed that the excess momentum flux tensor inside the surf zone can be expressed in terms of the energy and wave speed in the same form as in shallow water. This assumption implies that even under the breaking waves, water particle motion retains much of its organized character as described by linear wave theory.

The excess momentum flux decreases inside the surf zone due to the decreasing wave height as energy is dissipated. This results in a wave set-up inside the surf zone given by

$$\bar{\eta} = K(h_b - h) + \bar{\eta}_b \quad (21)$$

where the set-down at the breaker line $\bar{\eta}_b$ can be determined from Equation (20) and

$$K = \frac{1}{1 + \frac{8}{3k^2}} \quad (22)$$

Bowen et al [4] conducted laboratory studies verifying the theory predicting the changes in mean sea level for waves normally incident to the shoreline. The effect of waves approaching at an angle is neglected in the above formula but was shown by Thornton [5] to result in a maximum change in the total depth of less than 2 per cent.

C Distribution of Currents Outside the Surf Zone

There is a component of excess momentum flux directed parallel to the shore due to the oblique wave approach. The question of whether a current can be generated is investigated by considering the general y-momentum equation. Applying the previous assumptions, Equation (5) can be written

$$\frac{\partial S_{xy}}{\partial x} = R_y \quad (23)$$

where the time dependent term is zero, the gradients in the y-direction are zero and the conservation of mass equation showed that $\dot{M}_x = 0$. If it is assumed that outside the surf zone that energy is conserved, that is, no dissipation of energy, then the stress term will be zero. Therefore, the change of momentum flux due to the waves and mean motion in the y-direction is zero--there is no driving force for generating a current outside the surf zone. The only wave-induced current far outside the surf zone is then due to the mass transport velocity which is weak.

With the mean water profile and energy distribution specified, the variation of the longshore current across the surf zone can be determined. The y-momentum equation inside the surf zone can be written the same as that outside the surf zone. Inside the surf zone energy is dissipated due to turbulence and bottom friction and the stress term is important. In order to solve for the longshore current inside the surf zone, an appropriate description of the resistance term composed of both bottom and internal shear stresses is required.

D Bottom Shear Stress

It is desired to determine the combined bottom shear stress due to waves and currents. It is assumed that the total instantaneous bed shear stress for combined waves and currents is related to the velocity by

$$\vec{\tau}_h = \rho \frac{f}{2} \vec{V} |\vec{V}| \quad (24)$$

where \vec{V} is the resultant instantaneous velocity vector of the combined wave and current motion, and f is the friction factor. Since the problem has been formulated as a combination of wave and current motion, it proves convenient to resolve the shear stresses into components in the direction of the wave and current components. Resolving the component shear stresses in the direction of the velocity vectors results in the shear stress and velocity vectors being conformal. Hence, the shear stress component for the wave motion can be written

$$\vec{\tau}_{hw} = \vec{\tau}_h \frac{\vec{u}_w}{\vec{V}} = \rho \frac{f}{2} |\vec{V}| \vec{u}_w \quad (25)$$

where \vec{u}_w is the instantaneous velocity of the wave motion measured just above the frictional boundary layer near the bottom and \vec{V} is the mean motion which was assumed uniform over the depth and in the longshore direction only.

Similarly, for the shear stress in the direction of the mean current

$$\vec{\tau}_{hy} = \vec{\tau}_h \frac{V}{\vec{V}} = \rho \frac{f}{2} |\vec{V}| V \quad (26)$$

If friction factors for the wave and current motion are now defined,

$$f_y = f \left| \frac{\vec{v}}{V} \right| \quad f_w = f \frac{|\vec{v}|}{|\vec{u}_w|} \quad (27)$$

This results in the shear stress components given in a form consistent with experimental results

$$\vec{\tau}_{hw} = \rho \frac{f_w}{2} \vec{u}_w |\vec{u}_w| \quad (28)$$

$$\tau_{hy} = \rho \frac{f_y}{2} V^2 \quad (29)$$

The shear stress for waves, as defined in Equation (28) is in the same form as given by Jonsson [6] for which information of the friction factor was found experimentally. He found, further, that the friction factor was practically constant over an oscillation period. The constancy of the friction factor for particular flow conditions is an important result which allows for a better analytical determination of the combined shear stress due to waves and currents. Using the available data from several sources, he found that the friction factor for wave motion alone for rough turbulent boundary layers (as usually found in nature) could tentatively be represented by

$$\frac{1}{4\sqrt{f_w}} + \log \frac{1}{4\sqrt{f_w}} = -0.08 + \log \frac{\xi_h}{r} \quad (30)$$

where r is a measure of roughness, and ξ_h is the maximum water particle excursion amplitude of the fluid motion at the bottom as predicted by linear wave theory

$$\xi_h = \frac{H}{2} \frac{1}{\sinh kh} \quad (30a)$$

Equation (30) is based on the roughness parameter r being a measure of the ripple height. The wave friction factor is seen to be a function of the wave characteristics. This is because, for granular beds consisting of a particular grain size, the ripples adjust their dimensions according to the wave motion, and it is the ripple geometry that determines the effective roughness. The difficulty in using the quadratic shear stress formula is in stipulating the friction factors. The wave friction factor is seen to be a function of the wave properties for a deformable bed, that is, the fluid motion, whereas, the friction factor for steady currents for rough turbulent boundary layers is only a function of the system geometry. It would seem reasonable to expect that for weak currents, as compared to the water particle motion of the waves, that the wave dynamics would dominate the hydrodynamical system. For this reason, it is desirable to use the combined bottom shear stress in terms of the wave

friction factor alone, even though it is less well defined than the friction factor for steady currents

For the problem at hand, the bottom shear stress directed parallel to shore can be written in terms of the wave friction factor by combining Equations (27) and (28) which results in the form

$$\tau_{hy} = \frac{\rho f_y}{2} V^2 = \rho \frac{f_w}{2} \left| \overline{u_{wh}} \right| V = \rho f_w \frac{H}{2\pi} \frac{g}{c} V \quad (31)$$

where shallow water waves are assumed

E Lateral Shear Stress

It is necessary to include the lateral shear stress in the formulation. If the lateral shear stress is not included, a velocity discontinuity at the breaker line is predicted due to the abrupt change in momentum flux here. The lateral shear stress effectively couples the adjacent elemental water columns together resulting in a diffusion of momentum in a direction perpendicular to shore. The lateral diffusion of momentum flux seaward across the breaker line results in the momentum flux inside the surf zone driving the currents outside, the lateral diffusion of momentum shoreward results in the maximum velocity displaced shoreward.

Considerable success has been achieved using Prandtl's mixing length hypothesis for specific problems. This concept will be utilized to relate the internal shear stresses to the mean flow. The expression for the internal shear stress can be given in terms of the mean turbulent Reynolds stress which is compared to a "Boussinesq" approach

$$\tau_{xy} = -\rho \overline{u'v'} = \rho \epsilon_v \frac{\partial V}{\partial x} \quad (32)$$

where ϵ_v is the kinematic eddy viscosity

The variation of the turbulent velocity component in the y-direction is given in accordance with Prandtl's hypothesis by

$$v' = \lambda' \frac{\partial V}{\partial x} \quad (33)$$

where λ' denotes a mixing length which can fluctuate with time. From Equation (32), the kinematic eddy viscosity can then be written

$$\epsilon_v = -\left| \overline{u'v'} \right| \quad (34)$$

For the case of superposed waves and currents, it is natural to consider the length over which momentum is transferred as equivalent to the water particle excursion due to the wave motion and the velocity fluctuation u' equal to that of the water particles in the waves

Because u' and l' are in quadrature, the absolute value of the product is necessary in order to obtain a non-zero value. The mixing length l' can be interpreted as a measure of the turbulent scale and u' as a measure of turbulent intensity. This interpretation is not unreasonable physically. Examination of actual energy spectra of turbulence occurring in the surf zone shows that most of the fluctuating energy is associated with the waves.

The kinematic eddy viscosity can be evaluated by recalling Equations (12) and (30a). It will be assumed for simplicity that shallow water wave conditions apply, so that

$$\epsilon_v = \frac{H^2}{8\pi^2} \frac{gT}{h} \cos^2 \alpha \quad (35)$$

Evaluating the internal shear stress term by substituting Equation (32) gives

$$\int_{-h}^{\eta} \frac{\partial \tau_{xy}}{\partial x} dz = \int_{-h}^{\eta} \rho \frac{\partial}{\partial x} (\epsilon_v \frac{\partial V}{\partial x}) dz = \rho D \frac{\partial}{\partial x} (\epsilon_v \frac{\partial V}{\partial x}) \quad (36)$$

where ϵ_v and V are independent of z .

The total resistance term, including internal and bottom shear stresses, is then given by

$$R_y = \rho D \frac{\partial}{\partial x} (\epsilon_v \frac{dV}{dx}) - \rho \frac{f_w}{2\pi} \frac{g}{c} H V \quad (37)$$

F Distribution of Currents Inside the Surf Zone

The variation of the longshore current inside the surf zone can be solved by equating the changes in excess wave momentum to the resistance forces. Substituting for S_{xy} from Equation (15) gives

$$\frac{\partial}{\partial x} [E \sin \alpha \cos \alpha] = R_y = \rho D \frac{\partial}{\partial x} (\epsilon_v \frac{dV}{dx}) - \rho \frac{f_w}{2\pi} \frac{g}{c} H V \quad (38)$$

The height, celerity, refracted angle of the waves, and, hence, changes in momentum flux inside the surf zone can be expressed in terms of the local depth of water. Substituting Equations (10), (14), and (35) into Equation (38) gives

$$AD^{3/2} (1 - 0.7 \frac{D}{D_b} \sin^2 \alpha_b) \frac{\partial D}{\partial x} = \rho D \frac{\partial}{\partial x} (\epsilon_v \frac{\partial V}{\partial x}) - \frac{\rho \kappa}{2\pi} f_w \sqrt{\frac{gD}{(1+\kappa)}} V \quad (39)$$

where

$$A = \frac{5}{16} \rho g \kappa^2 \frac{\sin \alpha_b}{\sqrt{D_b}} \quad (40)$$

This is a general equation expressing the changes in momentum flux across the surf zone in terms of the total local depth of water. Included in the formulation is the set-up of water and the effects of wave refraction inside the surf zone. This equation is subject to the restriction that the waves be described as spilling breakers, and, hence, the depth continuously decreases shoreward from the breaker line. Thus, the momentum flux decreases monotonically inside the surf zone since both the energy and wave angle decrease with decreasing depth.

This development is similar to that by Bowen [7] in an investigation limited to a plane beach in which he assumes linear bottom friction and constant kinematic eddy viscosity in order to obtain an analytical solution.

The inclusion of the bottom friction requires Equation (39) to be solved numerically. Also a general method of solution is sought for comparison to the arbitrary field conditions. Boundary conditions imposed on the problem inside the surf zone are for $D = 0$, $V = 0$ corresponding to conditions at the intersection of the water line and the beach, and for $D = D_b$, $V = V_b$ corresponding to conditions at the breaker line.

A similar solution can be sought outside the surf zone where it is now assumed that the driving force for the currents outside the surf zone is zero--the changes in the momentum flux directed parallel to shore are zero. The y-momentum Equation (38) reduces to

$$D \frac{\partial}{\partial x} \left(\epsilon_v \frac{\partial V}{\partial x} \right) - \frac{f_w}{2\pi} \frac{g}{c} H V = 0 \quad (41)$$

where now the force driving the currents is due to lateral momentum flux resulting from a coupling of the adjacent vertical faces of the differential water column across the breaker line. This is to say that currents outside the surf zone are being driven by the longshore currents inside the surf zone due to coupling across the breaker line.

The boundary conditions imposed on the formulation outside the surf zone are that the velocity approaches zero far away from the breaker line ($D \rightarrow -\infty$) and that the velocities and velocity gradients inside and outside the surf zone match at the breaker line.

COMPARISON OF THEORY AND EXPERIMENT

The laboratory results of Galvin and Eagleson [8] are used to test the predictive equations. The only parameter that is necessary to be chosen is the roughness in order to utilize the predictive equations. A value of $r = 0.0033$ feet (1mm) was chosen for the concrete beach which is a reasonable value. The kinematic eddy viscosity is completely specified by the kinematics of the flow field. The resulting

velocity distribution is shown in Figure 2. The distributions of the kinematic eddy viscosity and friction factor are also shown in Figure 2. The kinematic eddy viscosity is a maximum at the point of breaking, where the maximum momentum exchange would be expected to take place, and decreases to zero at the shoreline. The friction factor varies slowly except near the beach where f_w increases very rapidly and approaches infinity at the intersection of the beach and the still water line.

Other cases and a more complete text is given by Thornton [5]. In general, surprisingly good correlation is found considering that the only parameter chosen is the roughness in order to completely specify the longshore velocity distribution.

The same equations are applied to the field data taken by Ingle [9]. The velocity distribution is shown in Figure 3. The bottom profile is shown in the same figure. Information concerning the bathymetry outside the surf zone is lacking so a bottom slope of 0.01 is assumed. The kinematic eddy viscosity and friction factor distributions are also shown and are similar to those found for the laboratory beaches. The friction factors for the laboratory and field are of the same order of magnitude, owing to the fact that the friction factor is not only dependent on the roughness but also the wave characteristics. The kinematic eddy viscosity for field conditions is several orders of magnitude greater than the value found for laboratory conditions owing to the greater turbulent scales.

CONCLUSIONS

It was shown that the component of excess momentum flux due to the presence of the unsteady wave motion (sometimes called a "radiation stress") directed parallel to shore can generate longshore currents. Changes in the excess momentum flux, as the waves shoal, must be balanced by a resistance force in order to maintain the assumed steady-state conditions. The component of excess momentum flux perpendicular to the beach is responsible for wave set-down outside the surf zone and wave set-up inside the surf zone. These changes in the mean water level were included in the longshore current formulations.

Logical means of introducing the friction factor associated with the bottom shear stress term was presented--the friction factor being related to the wave and bottom roughness characteristics. A mixing length hypothesis and the kinematics of the wave motion were combined in order to define the internal shear stresses. Comparison of experimental results from the laboratory and field with the derived theory shows that the predicted results compare favorably if the assumed conditions are approximately fulfilled.

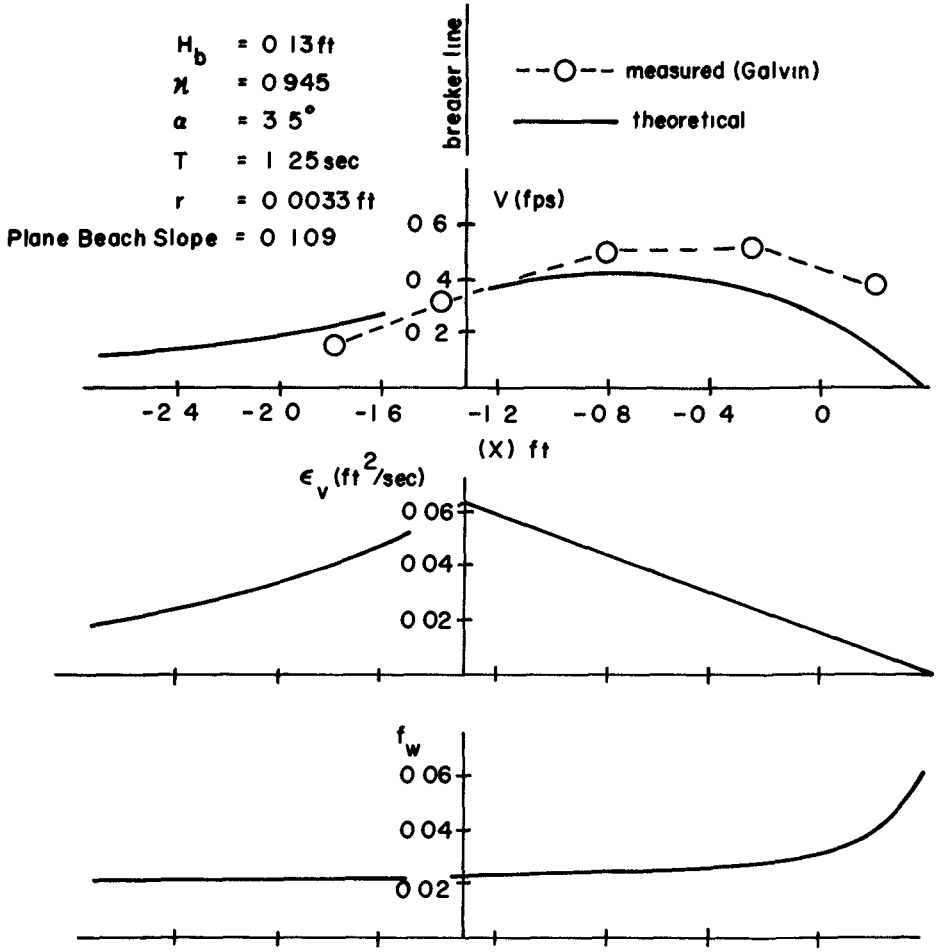


FIGURE 2 VELOCITY DISTRIBUTION ACROSS THE SURF ZONE FOR LABORATORY BEACH

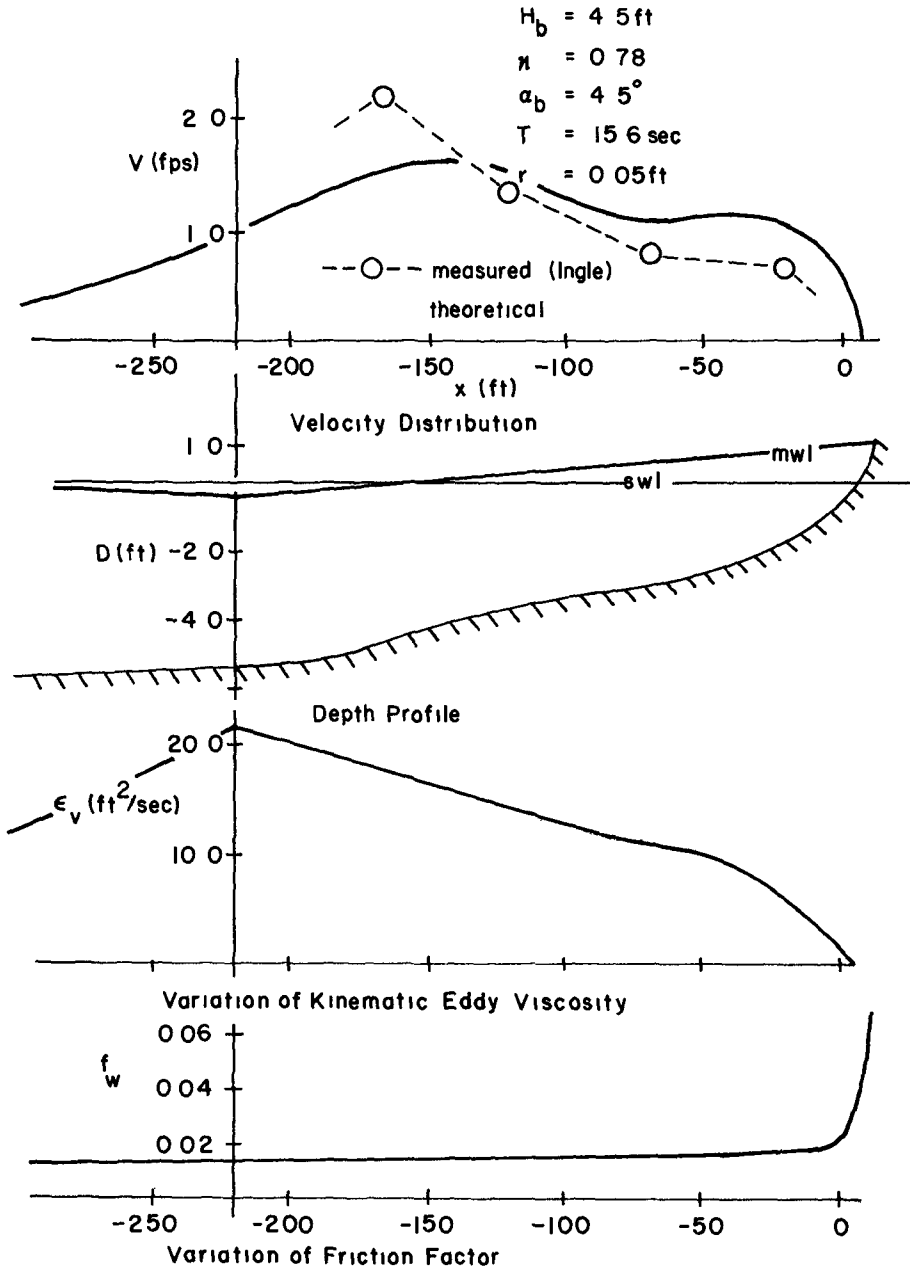


FIGURE 3 VELOCITY DISTRIBUTION ACROSS SURF ZONE, TRANCAS BEACH, CALIFORNIA

REFERENCES

- 1 Phillips, O M , The Dynamics of the Upper Ocean, University Press, Cambridge, 22-70, 1966
- 2 Bowen, A J , Rip Currents, Doctoral Thesis, Scripps Institution of Oceanography, 1967
- 3 Longuet-Higgins, M S and Stewart R W , A Note on Wave Set-up, J of Marine Res , 21 4-10, 1963
- 4 Bowen, A J , Inman, D L and Simmons, V P , Wave 'Set-down' and 'Set-up', J of Geophys Research, 73, 8 2559-2577, 1968
- 5 Thornton, E B , Longshore Current and Sediment Transport, Dept of Coastal and Oceanographic Engineering Tech Rpt No 5, University of Florida, 1969
- 6 Jonsson, I G , Wave Boundary Layers and Friction Factors, Proc Tenth Conf Coastal Eng , ASCE, 127-148, 1966
- 7 Bowen, A J , The Generation of Longshore Currents on a Plane Beach, J of Marine Research, 27, 2 206-215, 1969
- 8 Galvin, C J and Eagleson, P S , Experimental Study of Longshore Currents on a Plane Beach, Coastal Eng Res Center Tech Memo No 10, U S Army Corps of Engrs , Washington, D C , 1965
- 9 Ingle, J O , Jr , The Movement of Beach Sand, Elsevier Publishing Co , Amsterdam, 1966

CHAPTER 19

HORIZONTAL WATER PARTICLE VELOCITY OF FINITE AMPLITUDE WAVES

Yuichi Iwagaki
Professor
and
Tetsuo Sakai
Postgraduate

Department of Civil Engineering
Kyoto University
Kyoto, Japan

ABSTRACT

This paper firstly describes two methods to measure vertical distribution and time variation of horizontal water particle velocity induced by surface waves in a wave tank. These two methods consist of tracing hydrogen bubbles and using hot film anemometers, respectively.

Secondly, the experimental results by the two methods are presented with the theoretical curves derived from the small amplitude wave theory, Stokes wave theory of 3rd order, and the hyperbolic wave theory as an approximate expression of the cnoidal wave theory.

Finally, based on the comparison of the experimental data with the theoretical curves, the applicability of the finite amplitude wave theories, which has been studied for the wave profile, wave velocity, wave length and wave crest height, is discussed from view point of the water particle velocity.

INTRODUCTION

The water particle velocity induced by surface waves is one of the most important factors to solve the wave breaking mechanism, wave forces acting on submerged structures, mechanism of suspension and diffusion of materials by waves, and so on. However, there have been very little experimental data^{1,2,3,4}, because of difficulty of the measurement. Among the laboratory experiments of the water particle velocity, the data taken by Le Méhauté and others⁴ using tracers of neutrally buoyant particles show by the comparison with the predicted values from the various small amplitude and finite amplitude wave theories that no theory is uniformly valid. This conclusion makes us confused in applying finite amplitude wave theories to practical problems. It is necessary, therefore, to check the validity of the conclusion.

Recently, a new method to measure the water particle velocity was proposed, which is by using hydrogen bubbles as tracers, that is, tracing motions of hydrogen bubbles generated in water by electrolysis every very short period, to measure the water particle velocity induced by waves^{5,6}. This method is a very useful tool to measure vertical distributions of the water particle velocity at a particular phase of waves. On the other hand, in order to measure time variation of the water particle velocity, the hydrogen bubbles method is not so useful, but the use of a hot film anemometer is suitable, which was primarily developed for turbulence measurements in water⁷. These two methods were applied in this study to measure the water particle velocity induced by waves in a wave tank. As mentioned above, vertical distribution of the horizontal water particle velocity under the wave crest was measured by the method of tracing hydrogen bubbles, and time variation during one wave period at a definite height from the tank bottom was measured by a hot film anemometer.

This paper presents the experimental results of the horizontal water particle velocity obtained by these two methods, and comparison with theoretical values calculated from the small amplitude wave theory, Stokes wave theory of 3rd order⁸, and the hyperbolic wave theory⁹ as an approximate expression of the cnoidal wave theory of 2nd approximation¹⁰. Based on the comparison between the theories and the experiments, the applicability of the finite amplitude wave theories for the water particle velocity is discussed.

EXPERIMENTAL APPARATUS AND PROCEDURE

EXPERIMENTAL APPARATUS

The wave tank at Department of Civil Engineering, Kyoto University which has a wave generator of piston type was used in the experiments.

Method of tracing hydrogen bubbles The experimental apparatus to measure the water particle velocity by this method is shown in Fig 1. A platinum wire of 0.05mm in diameter was used as a negative pole to generate hydrogen bubbles in water. One end of the wire was attached to the tank bottom and stretched vertically, and the other end was connected with the pointgauge set a few centimeters high above the wave crest height. Four pieces of copper plates (15cm × 37cm), which were put on both side wall glasses of the wave tank around the negative pole, were used as positive terminals. One wave gauge was mounted side by side with the negative pole in the transverse direction of the wave tank, while the other wave gauge was mounted as far as about 2m from it. Two wave gauges were connected to the recorder. The equipment to load pulse voltages on the terminal can supply output voltages of 400V, with the pulse period of 4 ~ 700ms and the pulse width of 0.4 ~ 70ms. Photographs of hydrogen bubbles generated along the platinum wire and moving with flow were taken with a camera through the side wall glass.

Method of using hot film anemometer Two hot film anemometers of type 55D05 and their probes of type 55D85 made by DISA were used. The anemometer amplifies electrically heat convected from the probe which is one of bridge resistances. The probe, as shown in Fig 2, consists of a thin metal film as electrically heated resistance and its support. This anemometer is of

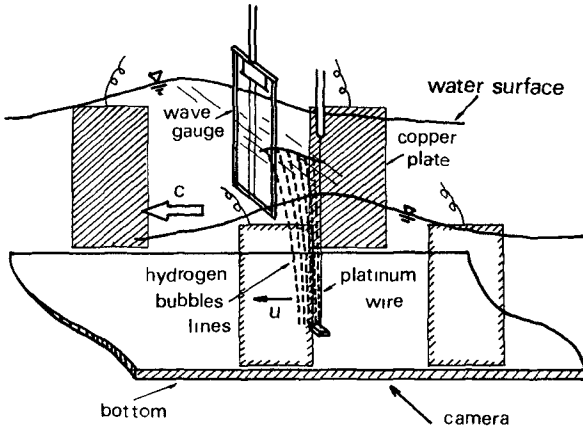


Fig 1 Schematic figure for measurement of water particle velocity by method of tracing hydrogen bubbles

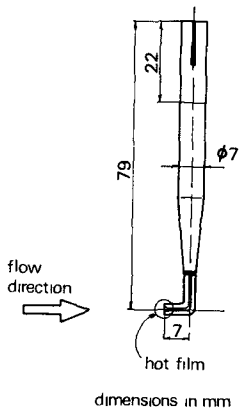


Fig 2 Probe of hot film anemometer

constant-temperature type designed for measuring energy required to keep always probe resistance (therefore probe temperature) constant (operating resistance)

When fluid flows as shown in Fig 2, the probe can detect its current velocity, but not its opposite current velocity. Therefore, if the probe is mounted confronting waves as shown in Fig 3(1), the record of the anemometer is reliable when the water level is higher than the still water level (full line), but not reliable when the water level is lower than the still water level and the flow direction becomes opposite. In addition, the probe can not detect opposite change of the flow direction. On the other hand, if the probe is mounted following waves as shown in Fig 3(2), the record is reliable even when water level is lower than the still water level (full line), but the other part of the record is not reliable.

In the experiments, two probes and one wave gauge were mounted side by side in the transverse direction. Especially, two probes of the hot film were set at the same height, confronting each other (see Fig 4). The other wave gauge was mounted as far as about 2m from the probes. All of two hot film anemometers and two wave gauges were connected to the recorder.

EXPERIMENTAL PROCEDURE

Method of tracing hydrogen bubbles Among the waves generated by the wave generator, one wave which became fully stable and was not influenced by the reflected waves from another end of the tank was selected. Just before the crest of this wave passed over the negative pole, pulse voltage of a proper period Δt began to be loaded. Lines of hydrogen bubbles generated along the platinum wire are transported by the flow in the direction of wave propagation under the wave crest. The photograph in this state was taken by a 35mm camera. At the same time, the records of waves at the wire position and as far as about 2m from the wire were taken. When pulse voltage is loaded on the terminal, the wave gauge can detect it and the disturbance appears in the record. Therefore, the time t_0 when the first pulse was loaded can be detected (if the time when the crest of a selected wave passes over the wire is put as $t=0$, $t_0 < 0$).

The m th and $(m+1)$ th hydrogen bubble lines were selected on the film, so that the arithmetic average $t_0 + \{m - (1/2)\} \Delta t$ of $t_0 + (m-1) \Delta t$ and $t_0 + m \Delta t$ becomes the smallest (see Photo 1). Reading the distance between these m th and $(m+1)$ th lines and dividing it by Δt , the horizontal water particle velocity u at the phase of $t/T = [t_0 + \{m - (1/2)\} \Delta t]/T$ was obtained approximately (T the wave period). This process was repeated at different heights above the tank bottom, and the vertical distribution of the horizontal water particle velocity was obtained.

Test conditions are shown in Table 1, where h is the water depth, H the wave height, and p the pulse width. The opening and shutter speed of the camera were always $1/4$ and $1/125$ sec.

Method of using hot film anemometer After the value of operating resistance of two hot film anemometers was set to be 1.00 ~ 1.15 time of cold resistance value, the calibration curves of two anemometers were determined by

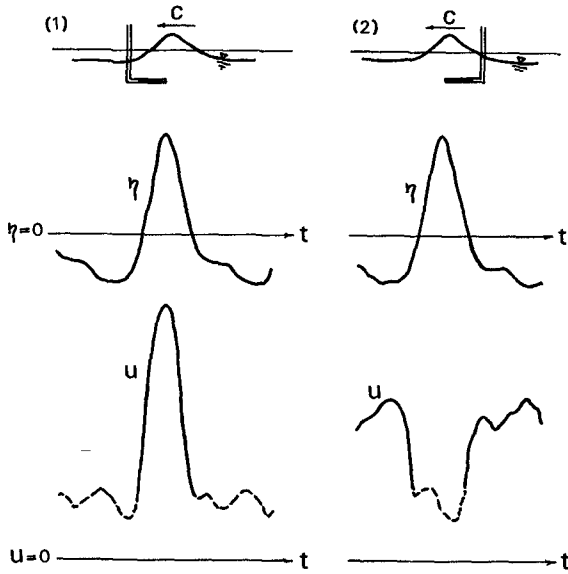


Fig 3 Relation between direction of probe and record of hot film anemometer

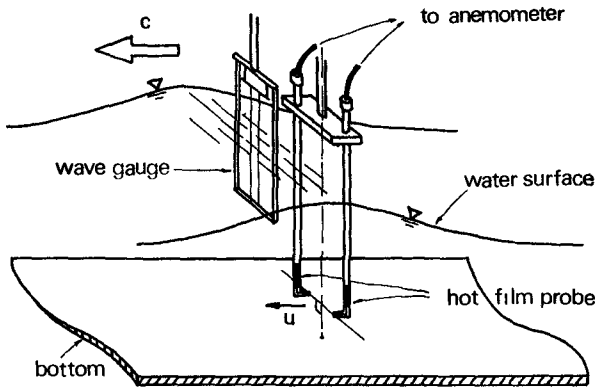


Fig 4 Schematic figure for measurement of water particle velocity by hot film anemometer



Photo 1 Hydrogen bubble tracer

Table 1 Conditions of experiments by method of tracing hydrogen bubbles

h (cm)	T (sec)	H (cm)	Δt (msec)	p (msec)	$T\sqrt{g/h}$	H/h
30.5	0.93	9.08	40	20	5.3	0.298
20.9	0.96	7.22	20	10	6.6	0.345
16.0	0.94	5.22	20	10	7.4	0.326
13.0	0.95	3.98	20	10	8.3	0.306
16.0	1.10	4.91	20	10	8.6	0.307
13.0	1.10	4.13	20	10	9.6	0.318
29.8	1.74	7.12	50	20	10.0	0.239
21.0	1.74	6.47	30	15	11.9	0.308
21.0	1.76	6.44	20	5	12.0	0.306
21.0	1.89	6.24	20	10	12.9	0.297
16.0	1.73	5.18	20	5	13.6	0.324
13.0	1.93	3.66	20	7	16.8	0.282

moving two probes with the carrier. The records of two confronting anemometers were read out using two calibration curves. The full lines in Fig 3(1) and (2) were selected, which are the part of the record of the anemometer confronting waves and that of the other anemometer following waves. These two curves were drawn up side down each other on the same figure, matching the phases of the waves, as shown in Fig 5. In general, as mentioned above, two records do not represent zero values but overlap where the real values of the velocity are zero. In order to obtain the time variation of the horizontal water particle velocity during one wave period, the records were modified assuming that the phase of $u=0$ was located where the absolute value of the upper record was equal to that of lower one, as shown in Fig 5.

In the experiments, the water depth h was constant, and the wave period T and the wave height H were variable. Test conditions are shown in Table 2, where z is the ordinate taken upwards from the still water level, and z_p is the depth of the probe, so that $z_p+h(z_p<0)$ means the height of the probe above the tank bottom. As shown in Table 2, the value of $(z_p+h)/h$ was always 0.05.

EXPERIMENTAL RESULTS

Fig 6(1)~(12) show the experimental results of the horizontal water particle velocity at the phase of the wave crest measured by the method of tracing hydrogen bubbles under the conditions of Table 1. u/\sqrt{gh} as dimensionless expression of u (g the gravity acceleration) is taken as an abscissa, and $(z+h)/h$ as dimensionless expression of the height from the bottom taken as an ordinate, with parameters of $T\sqrt{g/h}$, H/h and the wave phase t/T . In this figure, the experimental data are denoted by circles, and, for the same values of $T\sqrt{g/h}$, H/h and t/T , the vertical distributions based on the small amplitude wave theory, Stokes wave theory of 3rd order⁸ and the hyperbolic wave theory proposed by Iwagaki⁹ as an approximate expression of the cnoidal wave theory of 2nd approximation¹⁰ are shown for comparison with full, broken and chain lines, respectively.

The thick full lines in Fig 7(1)~(12) show the profiles of the waves measured simultaneously with the vertical distribution of the velocity. As in Fig 6, the wave profiles based on the three theories are also shown for comparison in the figure.

The thick full lines in Fig 8(1)~(10) show the continuous records of time variation of the horizontal water particle velocity during one wave period at $(z_p+h)/h=0.05$ measured by the hot film anemometers under the condition of Table 2 and the wave profiles recorded simultaneously. Other three thin lines show the theoretical curves as in Fig 7.

DISCUSSION

The error of the velocity measured by the method of tracing hydrogen bubbles, which results mainly from the error of reading films and the error of pulse period, will be approximately 3%. Also, the error of the velocity measured by the hot film anemometer occurs in the stage of determining the calibration curve, which will be approximately 3% too.

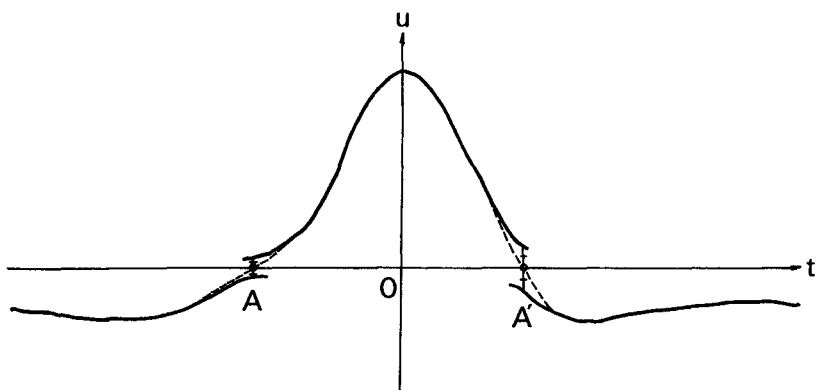


Fig 5 Schematic diagram for modification of record of water particle velocity by hot film anemometer

Table 2 Conditions of experiments by using hot film anemometer

h (cm)	T (sec)	H (cm)	z_p+h (cm)	$T\sqrt{g/h}$	H/h	$(z_p+h)/h$
16 0	1 03	6 72	0 80	8 1	0 420	0 05
16 0	1 30	6 86	0 80	10 2	0 429	0 05
16 0	1 58	6 04	0 80	12 4	0 378	0 05
16 0	1 83	7 21	0 80	14 3	0 448	0 05
16 0	2 08	7 05	0 80	16 3	0 441	0 05
16 0	2 39	4 89	0 80	18 7	0 306	0 05
16 0	2 63	5 06	0 80	20 6	0 316	0 05
16 0	2 84	4 13	0 80	22 2	0 258	0 05
16 0	3 07	4 11	0 80	24 0	0 257	0 05
16 0	3 40	3 66	0 80	26 6	0 229	0 05

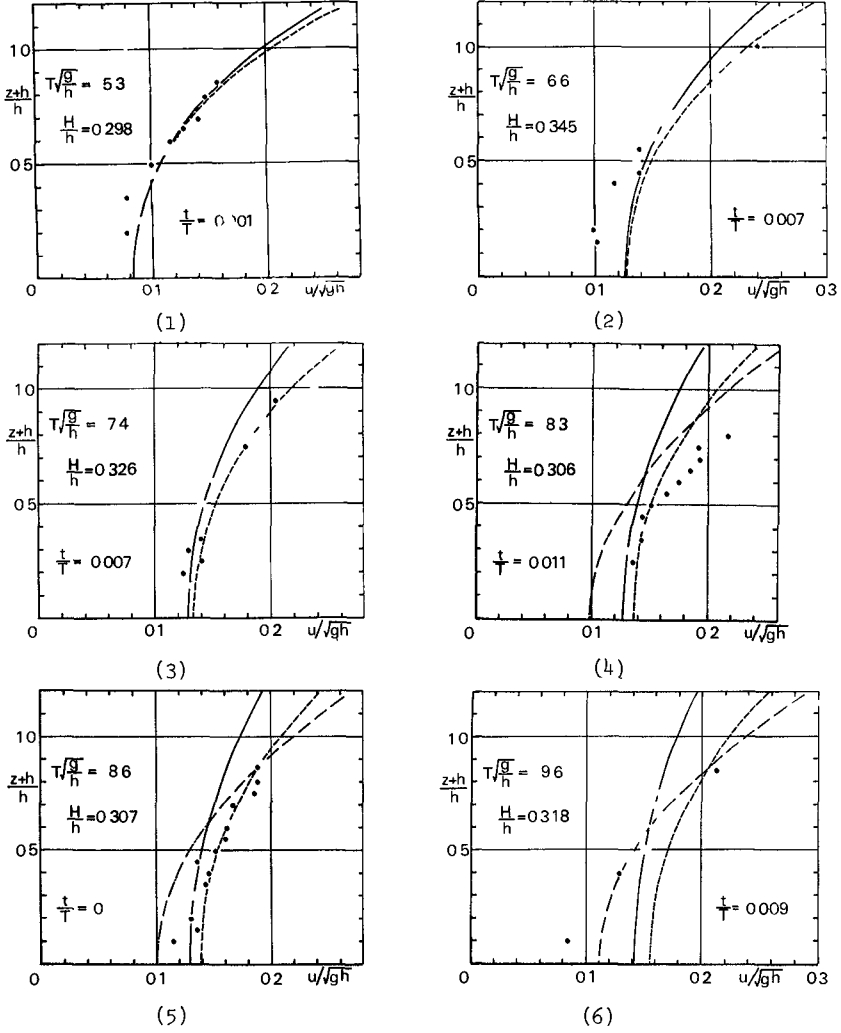
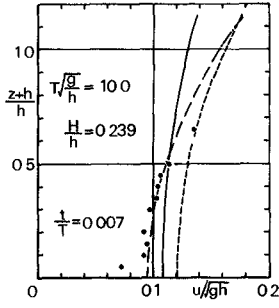
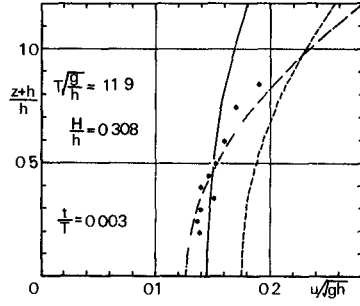


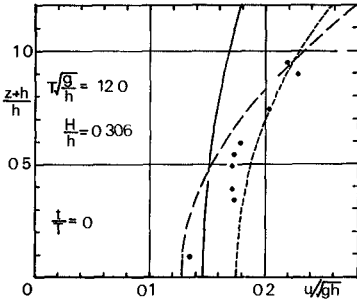
Fig 6(1)~(6) Vertical distribution of horizontal water particle velocity at phase of wave crest (full line small amplitude waves, broken line Stokes waves, chain line hyperbolic waves)



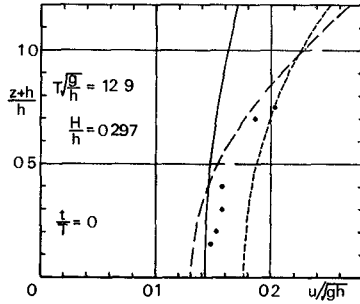
(7)



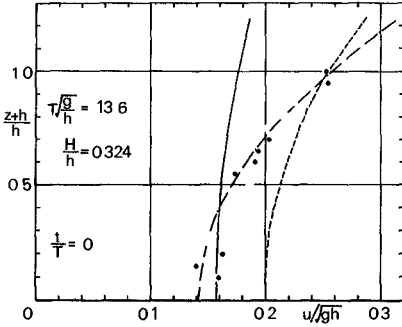
(8)



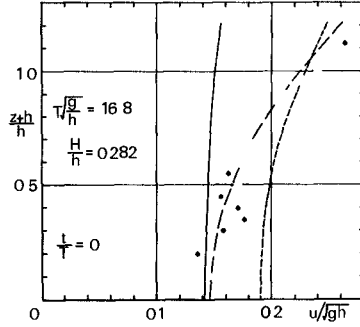
(9)



(10)



(11)



(12)

Fig 6(7)~(12) Vertical distribution of horizontal water particle velocity at phase of wave crest (full line small amplitude waves, broken line Stokes waves, chain line hyperbolic waves)

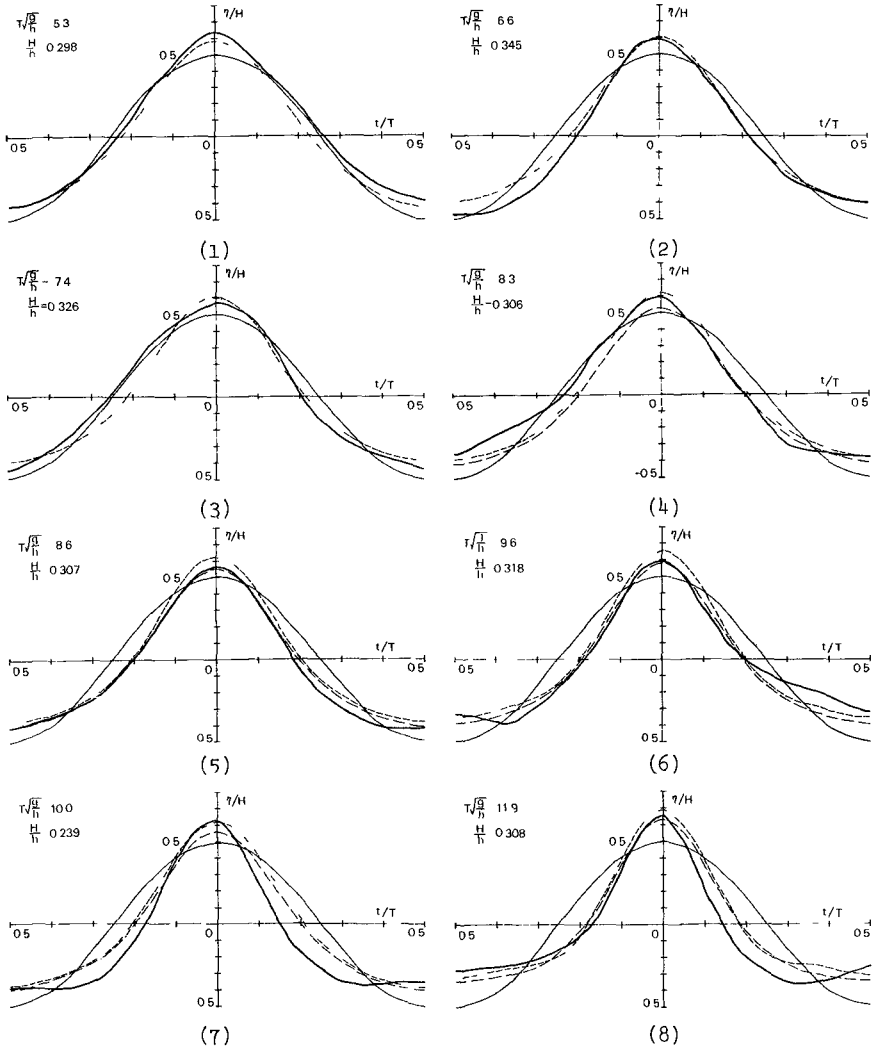


Fig 7(1)~(8) Time variation of water surface corresponding to Fig 6(thick full line experiment, thin full line small amplitude waves, thin broken line Stokes waves, thin chain line hyperbolic waves)

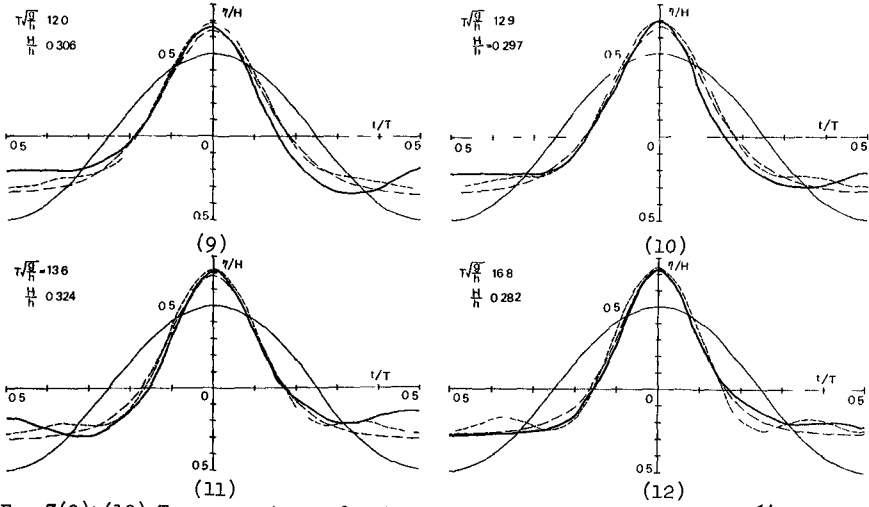


Fig 7(9)~(12) Time variation of water surface corresponding to Fig 6(thick full line experiment, thin full line small amplitude waves, thin broken line Stokes waves, thin chain line hyperbolic waves)

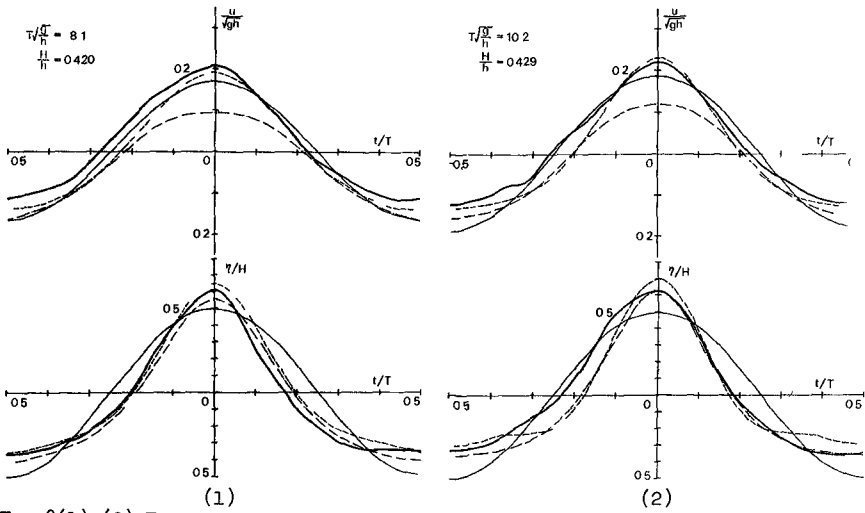


Fig 8(1),(2) Time variation of horizontal water particle velocity and corresponding water surface(thick full line experiment, thin full line small amplitude waves, thin broken line Stokes waves, thin chain line hyperbolic waves)

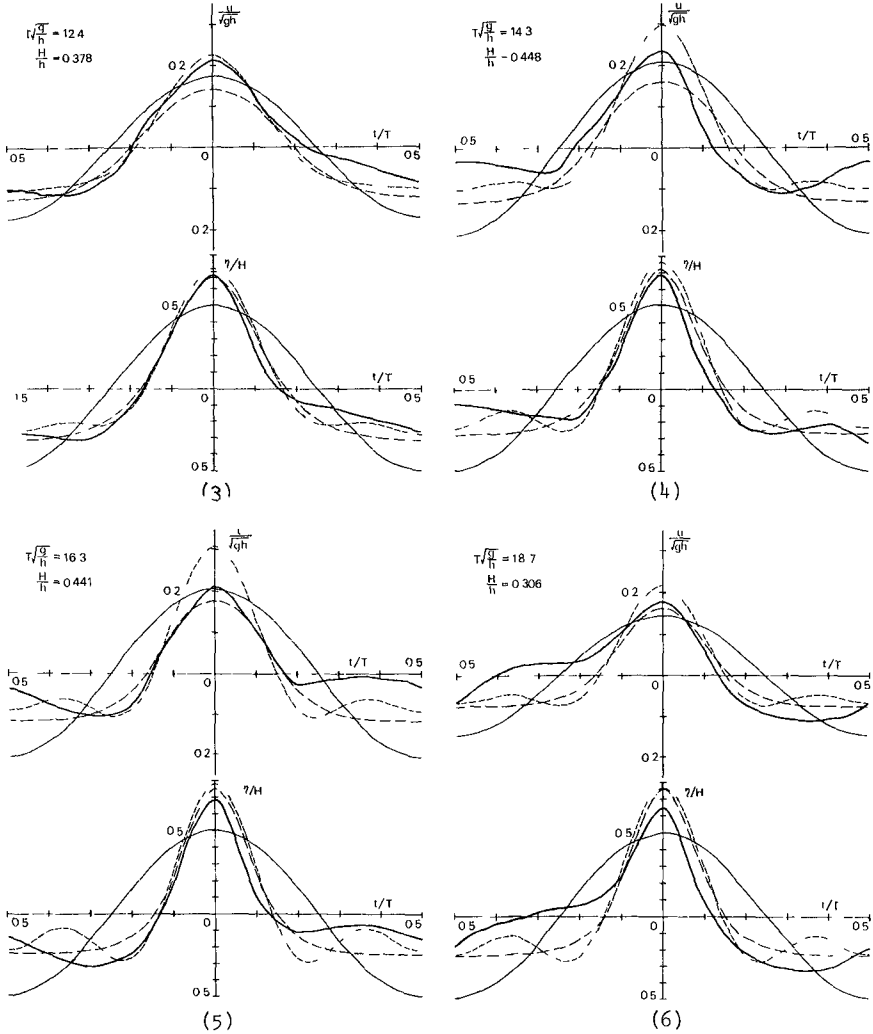


Fig 8(3)~(6) Time variation of horizontal water particle velocity and corresponding water surface(thick full line experiment, thin full line small amplitude waves, thin broken line Stokes waves, thin chain line hyperbolic waves)

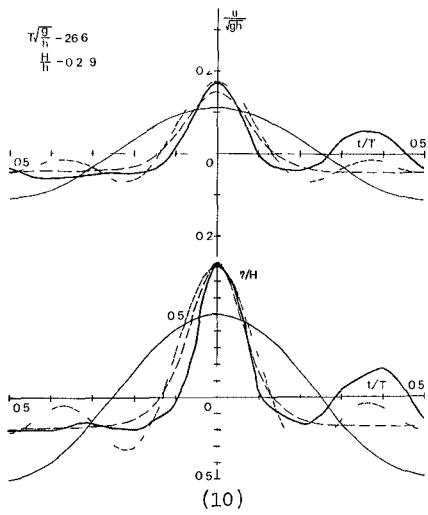
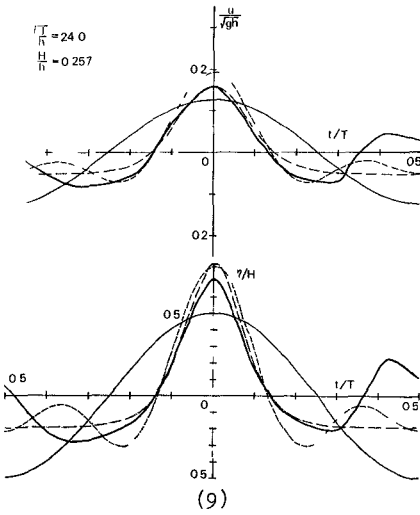
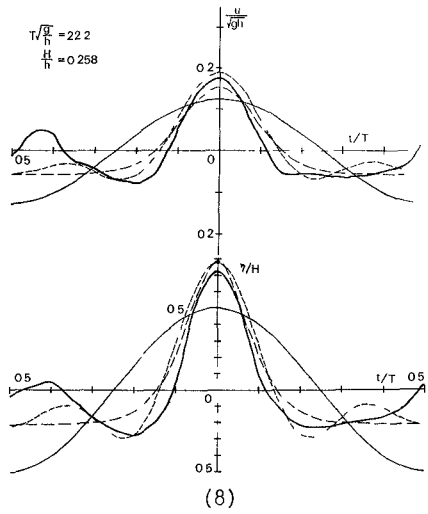
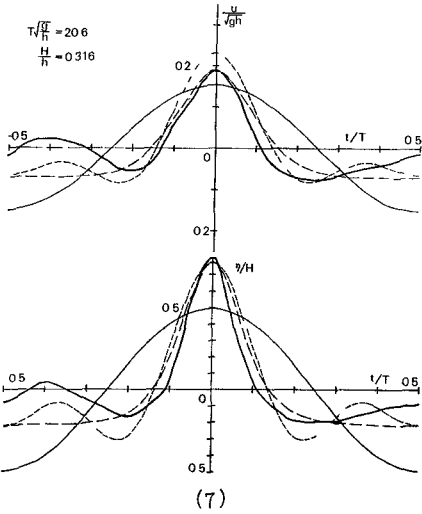


Fig 8(7)~(10) Time variation of horizontal water particle velocity and corresponding water surface(thick full line experiment thin full line small amplitude waves, thin broken line Stokes waves, thin chain line hyperbolic waves)

In Fig 6, the values of wave phase t/T are not always zero, but the absolute values exist between 0 and 0.01, which means that the data taken are regarded as at the phase of the wave crest. Generally speaking, among the theoretical curves of vertical distributions of the horizontal velocity, those of the small amplitude wave theory are steepest and the curves of the hyperbolic wave theory are most gentle. The value of the velocity based on the small amplitude wave theory is smaller all over the depth than that of Stokes wave theory, and the difference between them becomes largest at the water surface. On the other hand, the value based on the hyperbolic wave theory, in most cases, is smaller than that of the small amplitude wave theory near the bottom, but larger than that of Stokes wave theory near the water surface.

The experimental data were obtained generally at every height of 5% of the water depth from the bottom. However, in the region where $(z+h)/h < 0.1$, the velocity field induced by waves was disturbed by the obstacle of 5mm high to attach the platinum wire to the bottom, and in the region where $(z+h)/h > 1.0$ the velocity could not be measured because of insufficient generation of bubbles. In the case when $T\sqrt{g/h} = 5.3$, the experimental values have the same trend as two theoretical distributions based on the small amplitude wave and Stokes wave theories. In the cases when $T\sqrt{g/h} = 6.6$ and 7.4 , the experimental values agree fairly with those of Stokes waves. In the case when $T\sqrt{g/h} \geq 8.3$, the vertical distributions of the velocity based on the hyperbolic wave theory are also presented. In cases when $T\sqrt{g/h} > 8.6$, the experimental data are plotted between the theoretical curves of Stokes and hyperbolic waves. In general, when $T\sqrt{g/h} \geq 10$, the vertical distribution of the velocity under the wave crest can be explained well by the hyperbolic wave theory as an approximate expression of the cnoidal wave theory rather than Stokes wave theory.

Fig 7(1)~(12) show the comparisons between theories and experiments of the wave profile corresponding to each case of Fig 6 as mentioned above. It is evident that the experimental results of the wave profile are close to those of two finite amplitude wave theories rather than that of the small amplitude wave theory. However, it is very difficult to decide which finite amplitude wave theory is fit to the experiment on the wave profile from the figures. In other words, the difference between two finite amplitude wave theories is not clear in the case of the wave profile, but very clear for the vertical distribution of the velocity. It should be noticed that this fact is very significant when the wave force acting on submerged structures is estimated by the theory. Especially remarkable differences of the velocity between Stokes wave and hyperbolic wave theories appear near the bottom and above the still water level.

The probes of the hot film anemometer were mounted as high as 5% of the water depth above the bottom rather than near the water surface, because of avoiding risk of damage by exposing the probe in air. Tendencies of three theoretical curves of time variation of the velocity shown in Fig 8 are that the theoretical curves of Stokes and hyperbolic waves are sharper near the phase of the wave crest and flatter near the phase of the wave trough than that of the small amplitude wave theory, in the same manner as in the wave profile. However, in the cases when $T\sqrt{g/h} = 8.1$ and 10.2 , the velocity of hyperbolic waves at the trough is greater than that at the crest. This trend, which is of the cnoidal wave theory itself, occurs near the bottom only when

$T\sqrt{g/h} < 12.0$ and the value of H/h is large. Under the wave crest, the theoretical value of u/\sqrt{gh} of Stokes waves is largest and that of hyperbolic waves is smallest near the bottom when $T\sqrt{g/h} \leq 16.3$, and the value of hyperbolic waves shifts in the middle of small amplitude waves and Stokes waves when $T\sqrt{g/h} \geq 18.7$.

The experimental results of time variation of the horizontal velocity during one wave period show that, in general, the wave crest is sharper and the wave trough is flatter than those of small amplitude waves, in the same manner as the theoretical curves of finite amplitude waves. It is seen that the experimental curves near the crest are close to the theoretical values of Stokes waves when $T\sqrt{g/h} \leq 12.4$ and to those of hyperbolic waves when $T\sqrt{g/h} \geq 16.3$, although secondary waves appear at the wave trough. In the vertical distributions of the velocity shown in Fig 6, as mentioned above, the experimental values agree fairly with the hyperbolic wave theory when $T\sqrt{g/h} \geq 10$. However, in the experimental results of time variation of the velocity, the experimental values agree roughly with the theoretical curves of Stokes waves at least when $T\sqrt{g/h} \leq 12.4$. One of reasons of the discrepancy may be the difference of the values of H/h as shown in Table 1 and 2, that is, when $T\sqrt{g/h} \leq 16.3$ in Fig 8, values of H/h are greater than 0.4 in most cases, and considerably large compared with those in Fig 6.

In Fig 8, measured wave profiles are close to theoretical profiles of finite amplitude waves rather than those of small amplitude waves. However, differences between measured profiles and computed profiles based on two finite amplitude wave theories are not so clear as in the horizontal velocity.

In all cases of the experiments by the hot film anemometer, Reynolds numbers defined as

$$N_R = \frac{v \sqrt{\pi \sqrt{vT}}}{H} \sinh(2\pi h/L)$$

were calculated (v the kinematic viscosity). The maximum value among them is smaller than the critical Reynolds number $N_R = 160$ for transition from laminar to turbulent boundary layer by waves¹¹. Also, it was confirmed that the calculated thickness of the laminar boundary layer in this case, which is assumed to be the height from the bottom where the velocity becomes 99% of the velocity at the outside of the boundary layer, was 4.8 mm at maximum and smaller than the height of the probes from the bottom, 8 mm.

CONCLUSION

The authors described two methods to measure the horizontal water particle velocity induced by waves in the wave tank, the method of tracing hydrogen bubbles and the method of using a hot film anemometer. Experimental results of the vertical distribution of the velocity under the wave crest measured by the former method and time variation of the velocity during one wave period at a definite height from the bottom by the latter method were presented. Discussions were made compared with the theoretical values based on the small amplitude wave theory, Stokes wave theory of 3rd order and the hyperbolic wave theory as an approximate expression of the cnoidal wave theory of 2nd approximation.

After all, the following conclusions were obtained. The region, where the hyperbolic wave theory should be applied to the horizontal water particle velocity rather than Stokes wave theory, is $T\sqrt{g}/h \geq 10$, which was found for its vertical distribution under the wave crest, and $T\sqrt{g}/h \geq 14$ for its time variation during one wave period. It should be noted that, in computing the wave force acting on submerged structures, Stokes wave theory may give too small values of the horizontal water particle velocity at the water surface in the region $T\sqrt{g}/h \geq 10$.

ACKNOWLEDGEMENT

Part of this investigation was accomplished with the support of the Science Research Fund of the Ministry of Education, for which the authors express their appreciation. Thanks are due to Mr. T. Kawashima for his help during this investigation.

REFERENCES

- 1) Morison, J. R. and R. C. Crooke. The Mechanics of Deep Water, Shallow Water, and Breaking Waves, U. S. Army, Corps of Engineers, B. E. B., Tech. Memo No. 40, March, 1953, pp. 1-14.
- 2) Elliott, John G. Interim Report, Hydrodynamics Laboratory, Calif. Inst. of Tech., Contract Noy-12561, U. S. Navy, Bureau Yards and Docks, July, 1953.
- 3) Goda, Y. Wave Forces on a Vertical Circular Cylinder, Experiments and a Proposed Method of Wave Force Computation, Port and Harbour Technical Research Institute, Ministry of Transportation, Japan, Report No. 8, 1964.
- 4) Le Méhauté, B., D. Divoky and A. Lin. Shallow Water Waves. A Comparison of Theories and Experiments, Proc. 11th Conference on Coastal Engineering, 1968, pp. 86-107.
- 5) Schraub, F. A., S. J. Kline, J. Henry, P. W. Runstadler, Jr. and A. Littell. Use of Hydrogen Bubbles for Quantitative Determination of Time-Dependent Velocity Fields in Low-Speed Water Flows, Trans. ASME, Jour. of Basic Engineering, Vol. 87, 1965, pp. 429-444.
- 6) Horikawa, K. and A. Watanabe. Laboratory Study on Oscillatory Boundary Layer Flow, Proc. 11th Conference on Coastal Engineering, 1968, pp. 467-486.
- 7) Richardson, E. V. and R. S. McQuivey. Measurement of Turbulence in Water, Jour. of the Hydraulics Division, ASCE, Vol. 94, No. HY2, Proc. Paper 5855, March, 1968, pp. 411-430.
- 8) Skjelbreia, L. Gravity Waves, Stokes' Third Order Approximation, Table of Function, Council on Wave Research, The Engineering Foundation, 1959, pp. 1-337.
- 9) Iwagaki, Y. Hyperbolic Waves and Their Shoaling, Proc. 11th Conference on Coastal Engineering, 1968, pp. 124-144.
- 10) Laitone, E. V. The Second Approximation to Cnoidal and Solitary Waves, Jour. of Fluid Mechanics, Vol. 9, 1961, pp. 430-444.
- 11) Collins, J. I. Inception of Turbulence at the Bed under Periodic Gravity Waves, Jour. of Geophysical Research, Vol. 68, No. 21, 1963, pp. 6007-6014.

CHAPTER 20

A SYSTEM FOR MEASURING ORBITAL VELOCITIES IN WAVES

by M. M. Kolpak[†] and P. S. Eagleson *

Abstract

A single-ended, cylindrical hot-film sensor and a direction-vane transducer are studied as instruments for measuring flow fields in laboratory waves. Errors in the hot-film measurements are discussed in terms of sensor voltage and water temperature drifts, and directional sensitivity. The response of the direction-vane transducer is discussed in terms of the parameter b/r , which is the ratio of the vane chord length to the radius of curvature of the measured orbital flow.

The instruments are tested in a laboratory wave system, using stationary and traversing measuring techniques. The velocity measurements so obtained are compared to those obtained by a photographic technique, to determine instrument error. The flow speed comparisons indicate that the maximum hot-film error in flow speed measurements is between ± 5 and ± 10 inches/sec for the range 1 to 11 inches/sec tested. The flow direction comparisons indicate that the direction vane response is subject to errors larger than 5° for $b/r > 0.1$.

The study was carried out under the sponsorship of the Coastal Engineering Research Center at the Massachusetts Institute of Technology and is reported in full detail in the M.I.T. Hydrodynamics Laboratory Report No. 118.

Introduction

This is a study of the utility of a hot-film sensor and a direction-vane transducer in the laboratory measurement of velocity fields in water waves. It was motivated by a need for orbital data which is easier to obtain than by photographic techniques. The photographic techniques, in which neutrally buoyant particles are suspended in the wave flow and photographed, have the advantage that they produce relatively accurate data, but the disadvantage that the reduction of such data to flow speed and direction is so time consuming and tedious that the quantity of such data reduced to date is rather limited.

[†] Sr Research Engineer, Pan American Petroleum Corporation

* Head, Dept. of Civil Engineering, Massachusetts Institute of Technology

As an alternative to this method of measurement, a study was made of the use of the hot-film and direction-vane, which have electrical outputs that can be digitized and subsequently processed by computer to reduce the task of data reduction

For flow speed measurements the 6 mil diameter, single ended, cylindrical hot-film sensor shown in Fig (1) was studied. The sensor consists of an electrically heated metal film which conducts heat to the surrounding flow in proportion to the flow speed. When positioned so that its cylindrical axis is perpendicular to the plane of flow in a two dimensional wave flow field, the sensor can measure flow speed regardless of flow direction.

For measurements of flow direction, the direction-vane transducer shown in Fig (1) was studied. It consists of a neutrally buoyant vane 1.25" long, 0.3" wide and .004" thick, attached to a rotateable shaft. Fluid drag tends to align the vane with the direction of flow. By monitoring the angular orientation of the shaft with a sensing device in the transducer housing, it is possible to obtain measurements of flow direction in a two dimensional wave flow field.

The two instruments are mounted back to back on a strut and submerged to any location where simultaneous measurements of flow speed and direction are desired.

The Hot-Film Sensor

Experience with the hot-film sensor in this study showed that

1) The water in which measurements are made must be filtered to prevent output signal drift due to accumulation of dirt particles around the sensor.

2) The water must be deaerated to below about 16 ppm at 70°F dissolved gas content to prevent formation of gas bubbles on the sensor surface and the accompanying signal drift.

3) The overhear ratio, which is a measure of the degree to which the sensor is heated above the water temperature, must be less than about 1.15 to further prevent formation of gas bubbles on the sensor surface.

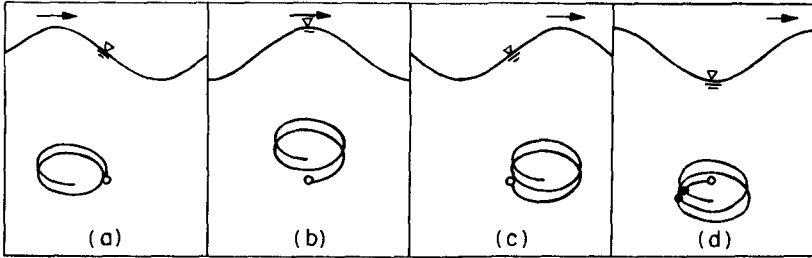
4) The presence of the sensor in the orbital flow field of wave motion can result in velocity and thermal disturbances in the flow which tend to remain in the vicinity of the sensor and interfere with measurement. These disturbances are illustrated schematically in Fig (2) where the wake emanating from the sensor is shown at four different times during the passage of a wave past a stationary sensor. Since the motion is orbital, the wake is orbital. And since the water in the wake is warmer than the surrounding water the wake tends to rise and have a spiral shape. Whenever a wave trough is passing the sensor, the sensor is crossed by previously formed loops of its own wake. Since the sensor is sensitive not only to flow speed but to water temperature, wake crossings therefore result in the aberrations of output signal schematized in Fig (2e) and (2f).



FIGURE (1) Hot-film Sensor and Direction-Vane Transducer mounted on Strut.

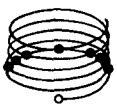
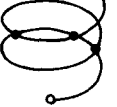


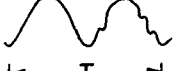

HEATED - WAKE EFFECTS

WAKE-TRACE CONFIGURATION UNDER PASSING WAVE



- STATIONARY SENSOR
- WAKE CROSSINGS

CONDITIONS FOR WAKE CROSSINGS

CONDITION	$K \ll 1$	$K < 1$	$K > 1$
WAKE TRACE			
	(e)	(f)	(g)
SENSOR VOLTAGE SIGNAL (FOR OVERHEAT > 110)			
	$\longleftarrow T \longrightarrow$	$\longleftarrow T \longrightarrow$	$\longleftarrow T \longrightarrow$

$$K = \frac{W_s}{(2A/T)}$$

W_s = VERTICAL VELOCITY OF BOUYANT WAKE

$2A$ = MINOR AXIS OF PARTICLE ORBITS

T = WAVE PERIOD

FIGURE (2)

Through experiments it was found that signal disturbances due to heat wake crossings are reduced to tolerably low levels when the overheat ratio is kept between 1.02 and 1.12. At the lower figure, however, the hot-film becomes relatively more sensitive to long term variations in water temperature than to velocity so that it is desirable to operate at around 1.10.

We may obtain estimates of the sensitivities of the hot-film by use of Kings Law type empirical heat transfer equations. For example, at 1.10 overheat ratio a 1% drift in the sensor's output voltage corresponds to a 5% velocity error. Also, a 1°F change in water at 1.10 overheat ratio results in a 3% velocity error unless corrections for temperature are made.

5) The hot-film sensors tested in this study have an undesirable sensitivity to flow direction, in spite of efforts by the manufacturer to avoid it. A typical calibration for directional sensitivity is illustrated in Fig. (3) which shows the result that the normalized sensor output voltage varies with flow direction when the direction of a constant speed flow is varied but kept perpendicular to the sensor axis at all times. The points are representative of a range of constant flow speeds and overheat ratios and tend to fall on the same curve which is very nearly sinusoidal. Even though the maximum variation is only about $\pm 3\%$ in voltage, this however translates to a $\pm 15\%$ velocity error unless corrected for. Such corrections were possible in the present study since the calibration points collapsed to a single sinusoidal curve, but even so, flow direction had to be known before the corrections could be made. Hopefully such sensitivity can be reduced as the art of sensor fabrication improves.

The Direction-Vane Transducer

Experience with the direction vane in shallow water waves has shown that 1) The vane can properly respond to changes in flow direction, but only near the free surface where the orbits are more nearly circular than near the bottom boundary of the flow where they are highly eccentric ellipses. Near the bottom the vane tends to lag the flow direction. The problem of predicting the vane's response error due to considerations of inertia and friction of the moving parts is complicated by the difficulty of obtaining a solution of the vane's dynamic equation of motion, which is highly non-linear. Furthermore, the forcing function in the equation, fluid drag on the vane, is not known for the general unsteady case, including the effects of virtual mass and separation. Although some approximations might be made about the drag force and numerical methods might be employed to solve the equations, no solutions were obtained in this study. Rather, it was decided to carry out some quantitative experiments first to establish criteria for the vane's response.

2) Apart from the dynamics, the fact that the vane is rigid whereas the flow is curvilinear means that the vane will generally lag the flow by an amount which is a function of b/r , where b is the chord length of the vane and r is the radius of curvature of the flow past the vane. This is illustrated in Fig. (4) where, schematically, we have, initially, several particles on either side of the vane identified by

DIRECTIONAL SENSITIVITY OF HOT-FILM SENSOR

$V' =$ DIRECTIONAL SENSITIVITY FACTOR $= V_{\theta} / V_A$

$V_{\theta} =$ SENSOR VOLTAGE FOR FLOW DIRECTION θ

$V_A =$ AVERAGE VOLTAGE OVER 360° RANGE

- EXPERIMENTAL POINTS FOR ALL COMBINATIONS OF
OVERHEAT = 110, 107, 105
VELOCITY = 3.5, 7.74, 12.12, 16.26 IN/SEC

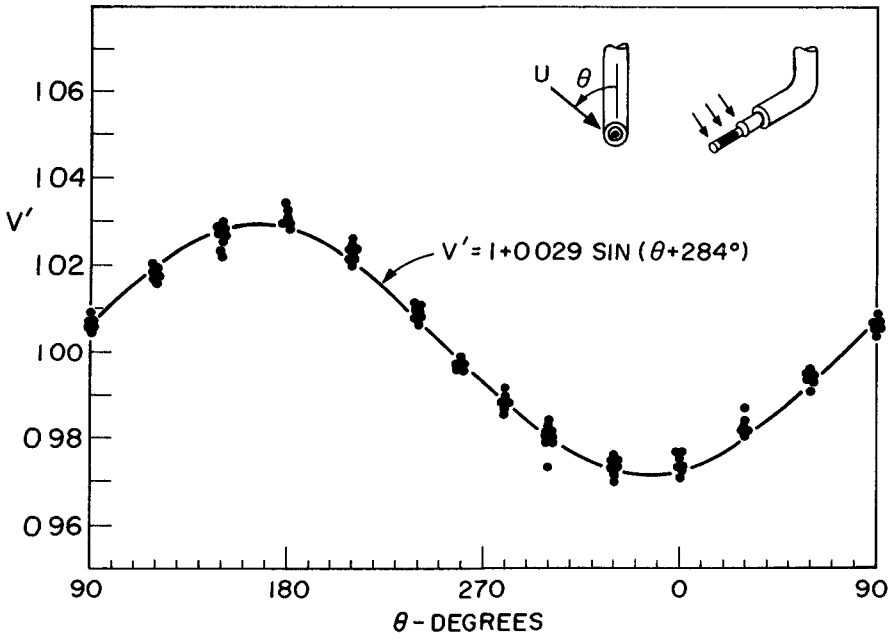


FIGURE (3)

KINEMATIC INCOMPATIBILITY

$$r < b$$

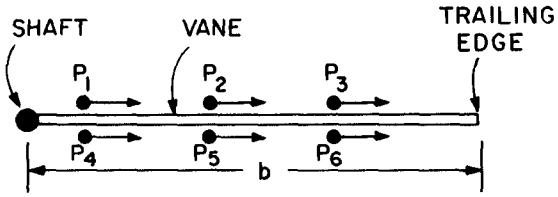


FIGURE (4a)

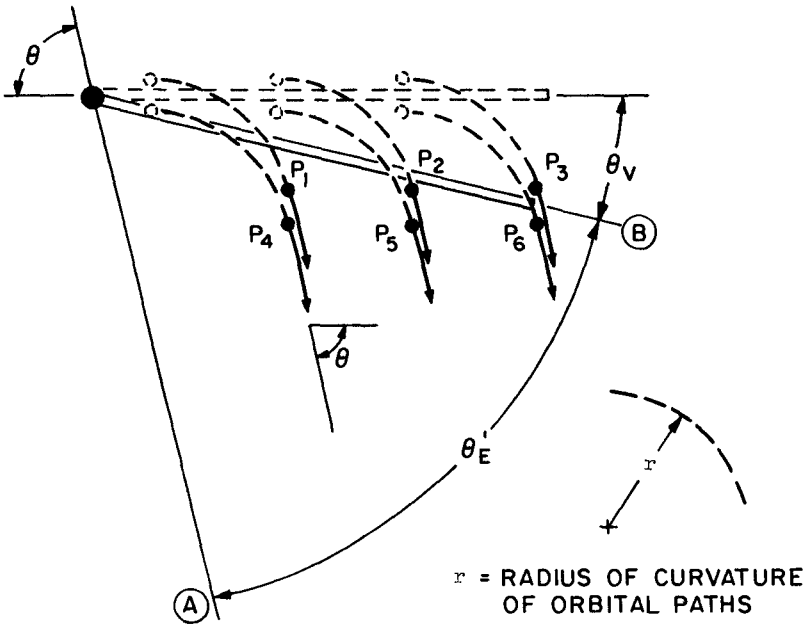


FIGURE (4b)

small circles, Fig (4a) For the sake of illustration, let the vane at this time be aligned with the direction of the flow It is seen that if the particles undergo portions of their undisturbed orbital motion, they move to the new locations shown in Fig (4b), but the rigid vane cannot possibly respond by pivoting about a fixed shaft and yet remain between the particles without deforming In fact, the vane will more likely point in the θ_v direction rather than in the actual direction θ of the flow This illustration is for the case of $b/r > 1$, but it can be extended for the case $b/r < 1$, and we realize that this purely kinematic consideration shows that the vane will in general lag the flow An approximate calculation of the resulting directional error, θ_E , yields

$$\theta_E = \sin^{-1}[b/2r] \quad (1)$$

which gives $\theta_E \leq 5^\circ$ for $b/r \leq 0.1$

To obtain experimental verification of this and some other quantitative aspects of the hot-film's response, measurements of the same flow field were made by the instruments and by a photographic technique and the results were compared to estimate instrument error

Measuring Techniques

The instruments were utilized in a number of ways

1) The "stationary" technique - here the instruments are submerged to a given depth and kept stationary for several wave periods' duration This is the simplest measuring technique, however, the response of the vane is rather limited by the small orbital radius of curvature near the wave tank bottom

2) The "transversing" techniques - these are represented in Fig (5) for the case of towing the instruments vertically upwards during measurement Referring to Fig (5a), as the instruments are towed upwards at uniform speed we obtain data along a straight line depth-time characteristic A-B If the flow is periodic, repeating itself exactly, every wave period, then portion C-B may be shifted by one wave period to D-E, so that the data can be viewed within the time domain of a single periodic wave Thus, by making several traverses, all at different beginning phase times, it is possible to fill the y-t plane with data Later, by subtracting the towing velocity vector from the relative flow vector measured, we obtain a mapping of the flow field along a vertical section through the flow The advantage of such a technique is that the radius of curvature and the flow speed of the relative flow past the vane are both larger than for the stationary technique and the vane response improves However, such improvements in response occur only during times when the vertical component of the flow is opposite to the direction of towing Thus to obtain data of superior relative accuracy a set of upward traverses is needed for $T/4 \leq t \leq 3\pi/4$ and a set of downward traverses for $0 \leq t \leq T/4$ and $3\pi/4 \leq t \leq T$, where T is the wave period and t is time

3) The "dual tow" technique - where it is possible to obtain measurements of flow direction using only the hot-film sensor and not the direction vane transducer The procedure is to first fill the

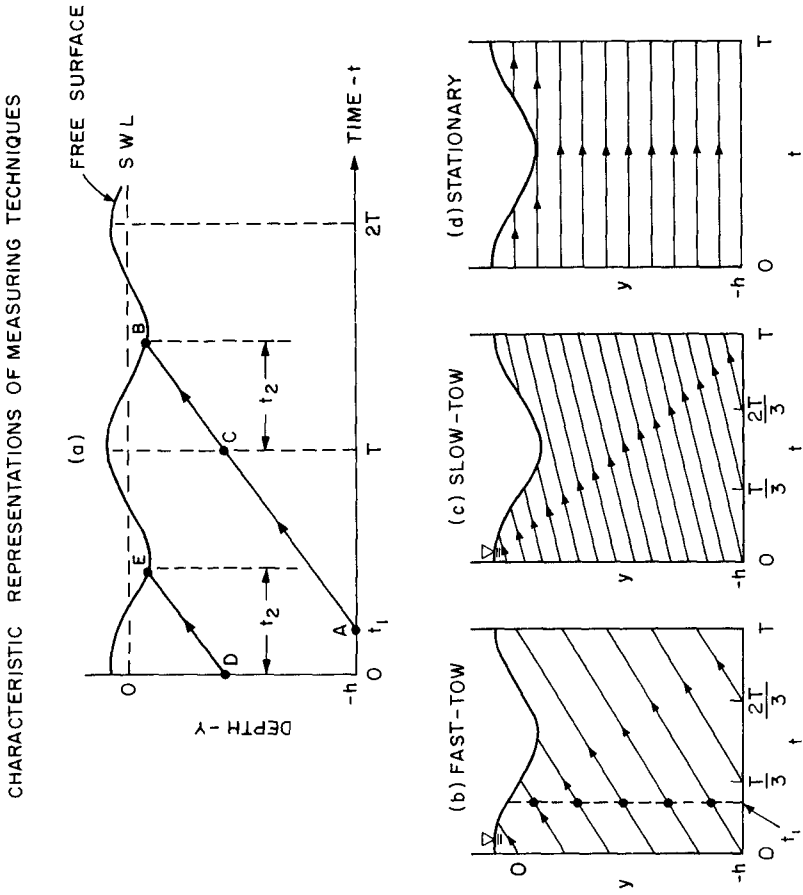


FIGURE (5)

depth-time plane with measured relative flow speed data, $R_1(y,t)$, having made traverses at towing speed S_1 . Then the measurements are repeated but at a different towing speed, S_2 , giving relative flow speed data, $R_2(y,t)$. The result is that at every point in the $y-t$ plane, we now have the four knowns, R_1 , S_1 , R_2 , S_2 , from which it is possible to solve for the two unknowns, U , the local flow speed, and θ , the local flow direction. With Fig (6) representing the vector diagram of the variables the Cosine Law for triangle ABC is,

$$R_1^2 = S_1^2 + U^2 - 2S_1U \cos(\pi - \theta) \quad (2)$$

and for triangle ABD,

$$R_2^2 = S_2^2 + U^2 - 2S_2U \cos(\pi - \theta) \quad (3)$$

Subtracting and rearranging, we obtain

$$U = \left[\frac{(S_2^2 - R_2^2)S_1 - (S_1^2 - R_1^2)S_2}{S_2 - S_1} \right]^{1/2} \quad (4)$$

from which U can be obtained since S_1 , S_2 , R_1 and R_2 are known. Equation (3) may then be used to solve for

Since Equation (4) yields only the principal values of U , additional information about whether the vertical component of U is up or down, is required to resolve the ambiguity. In practice, the position of the free surface may be used as an indicator.

Experimental Results

Typical experimental results for the stationary technique are shown in Fig (7), where the differences between hot-film measurements and photographic technique measurements are plotted against time for various depth locations, y/h , where y is the depth at measurement and h is the total depth. The hot-film error for this typical case is seen to be generally less than 1 in/sec for the range of flow speeds, 1 to 11 in/sec tested. These results are for plane progressive waves 4.3" high, 10.3 ft long and having a 1.474 sec period.

Similar comparisons of flow direction data for the stationary technique are shown in Fig (8). It is seen that near the free surface, $y/h = 0.138$, the direction-vane error is generally less than 10° for this case, whereas near the bottom, serious errors occur.

Fig (9) shows the decrease in direction errors achieved by utilizing the traversing technique.

Fig (10) shows the directional errors for the case of the dual-tow technique. Errors generally less than 10° were obtained even for locations well below the water surface.

VECTOR DIAGRAM FOR THE DUAL-TOW TECHNIQUE

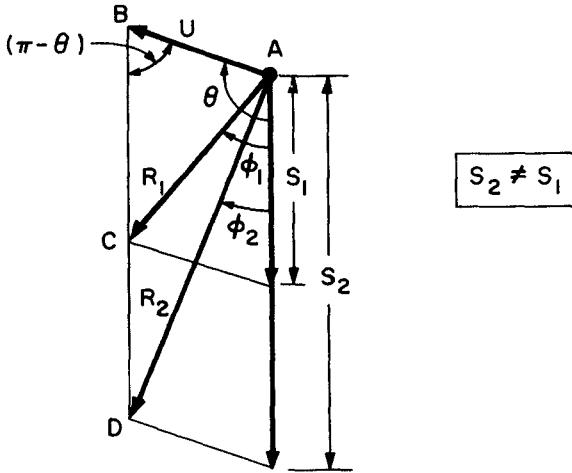


FIGURE (6)

VELOCITY ERROR
FOR
STATIONARY TECHNIQUE, STA - 15

$$U_E = U_{\text{HOT-FILM}} - U_{\text{PHOTOGRAPHIC}}$$

CURVE	①	②	③	④	⑤	⑥
$-y/h$	138	354	465	589	708	830

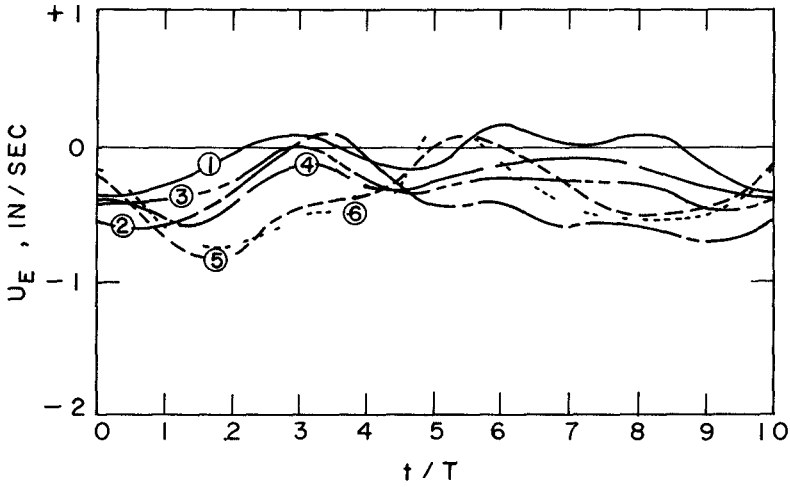


FIGURE (7)

DIRECTION - VANE ERROR
 FOR
 STATIONARY TECHNIQUE, STA +9

$$\theta_E = \theta_{\text{DIRECTION VANE}} - \theta_{\text{PHOTOGRAPHIC}}$$

CURVE	①	②	③	④	⑤
-y/h	217	395	545	704	882

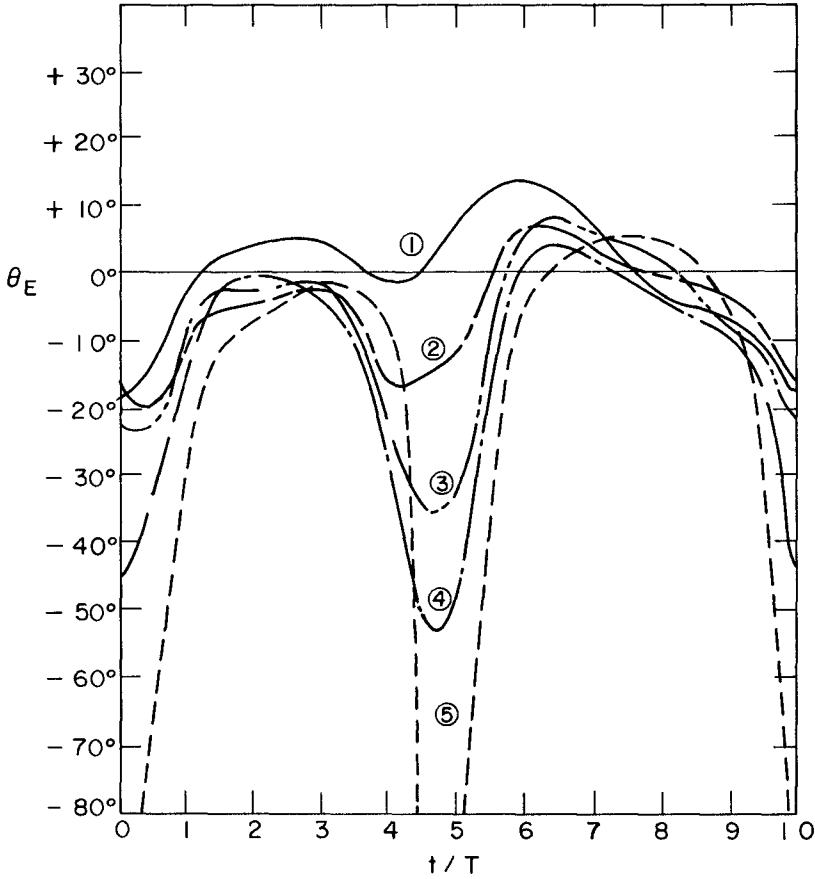


FIGURE (8)

DIRECTIONAL ERROR
FOR
FAST-TOWS UPWARDS, STA-15
TOWING SPEED = 10.2 IN/SEC

$$\theta_E = \theta_{\text{FAST-TOW}} - \theta_{\text{PHOTOGRAPHIC}}$$

CURVE	①	②	③	④	⑤
-y/h	138	354	465	589	708

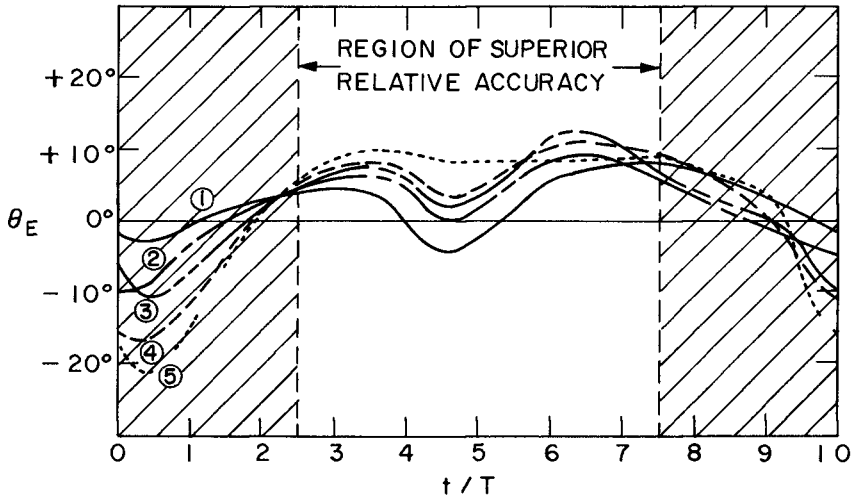


FIGURE (9)

DIRECTIONAL ERROR

FOR

DUAL-TOW, STA -15

TOWING SPEEDS = 0, 2.52 IN/SEC

$$\theta_E = \theta_{\text{DUAL-TOW}} - \theta_{\text{PHOTOGRAPHIC}}$$

CURVE	①	②	③	④	⑤
-y/h	138	354	465	589	708

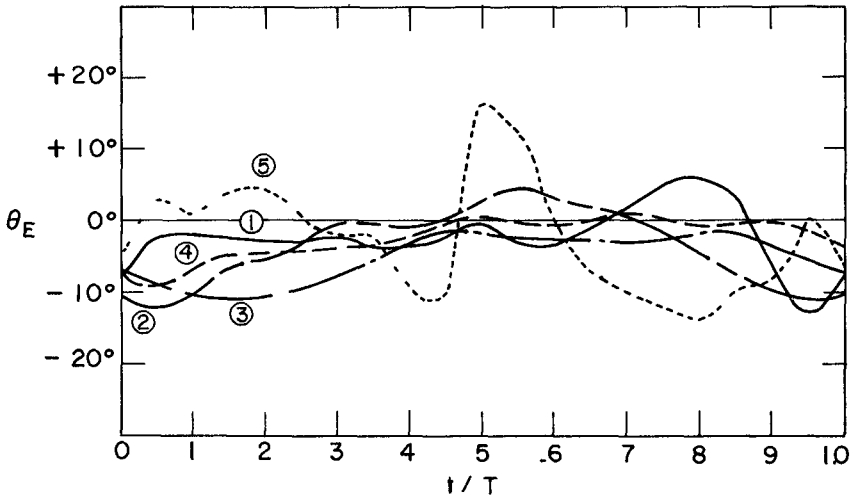


FIGURE (10)

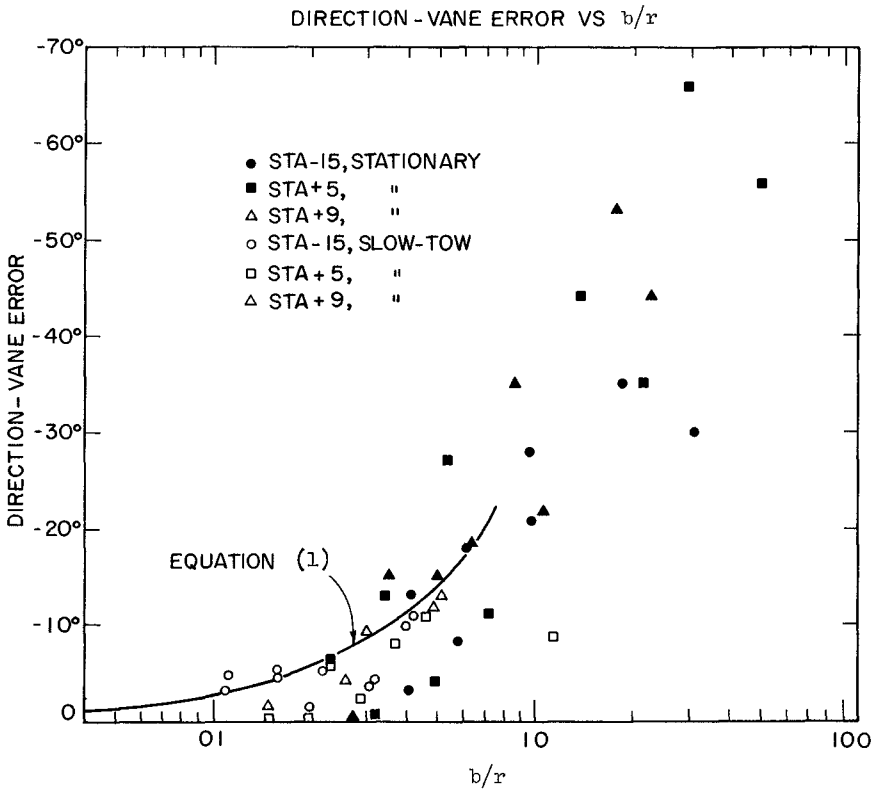


FIGURE (11)

Fig (11) shows experimental values for the vane plotted against the parameter b/r . The approximate relation for error given by Equation (1) appears to define the upper envelope of the points corresponding to small b/r fairly well. The data thus confirm that $\theta_E \leq 5^\circ$ for $b/r \leq 0.1$.

Conclusions

1) Since the problem of miniaturizing the physical dimensions of the vane sufficiently to make its chord length, b , an order of magnitude smaller than r , becomes prohibitive for the case of small laboratory waves, it appears that the direction-vane transducer is more suitable for larger scale wave flows, such as real ocean waves.

2) The directional sensitivity of the hot-film sensor appears to limit its accuracy at present to $\pm 15\%$ of the velocity measured unless corrections are made. Apart from this, the sensor can measure flow speed to within at least 10% of the velocity.

3) The dual-tow technique allows measurement of flow direction without the need for a separate direction measuring instrument. It is not scale dependent and thus makes possible measurements in small scale laboratory flow fields. However, the flow field must be periodic for the technique to be valid.

CHAPTER 21

SHOALING OF FINITE-AMPLITUDE WAVES ON PLANE BEACHES

Robert K -C Chan¹
Robert L Street,¹ M ASCE

ABSTRACT

This work focuses on the shoaling of large water waves with particular application to storm-generated waves and tsunamis. The specific objective is the exact simulation on a digital computer of finite-amplitude waves advancing on a beach of constant slope.

The study is based on the simulation technique called SUMMAC (the Stanford-University-Modified Marker-And-Cell Method). The flow field is represented by a rectangular mesh of cells and by a line of hypothetical particles which defines the free surface. Based on the Navier-Stokes equations, finite-difference equations were derived so that the entire flow configuration could be advanced through a finite increment of time. The pressure and velocity components are used directly as the dependent variables. Through extensive analyses and numerical experiments, this scheme was found to be computationally stable if the cell size and the time increment are properly selected.

As a specific example, the dynamics of a solitary wave passing from a zone of constant depth onto a sloping beach were simulated. Primary attention was focused on the details of the water particle motions and the changes in the amplitude and shape of the wave as it climbed the slope. The computed results are compared with the experiments with good agreement.

INTRODUCTION

The motion of water waves whose amplitudes are appreciable in relation to the water depth is nonlinear in nature (Stoker, 1957). Consequently the linearized theory (Lamb, 1945) does not provide adequate physical description of waves in the shallow-water zones. Most of the existing nonlinear analytical theories deal with a steady-state solution (See, e.g., Laitone, 1960, Dean, 1965, Monkmeyer and Kutzback, 1965). However, in shallow water the primary interest is in the transient aspect of the wave processes. It is quite difficult to treat time-dependent problems of this kind without recourse to computational methods.

At present several numerical methods are available for computing waves in shallow water and nonlinear terms are included to some extent (See, Street, et al., 1970, for a detailed summary). These methods retain in their governing equations the terms representing the kinetic energy of the vertical motion to varying degrees of accuracy. Only

¹Department of Civil Engineering, Stanford University, Stanford, California 94305

one space variable, namely x , is involved. Vertical variation of the fluid variables has been eliminated by integration or a series expansion approach and use of boundary conditions. These approximate theories generally produce good results for long waves of small but finite amplitude-to-depth ratio. However, more must be known about the internal distribution of pressure and velocity which must be incorporated in the governing equations of motion if one wishes to study waves of considerable amplitude.

Chan and Street (1970a) proposed a computing technique for analyzing two-dimensional finite-amplitude water waves under transient conditions. The method, called SUMMAC, is a modified version of the Marker-And-Cell method (MAC) which was originally developed by Welch, et al (1966). The essence of the modifications consists of a rigorous application of the pressure boundary condition at the free surface and of an extrapolation of velocity components from the fluid interior so that inaccuracy in shifting the free surface is kept at a minimum.

Thus, Chan and Street (1970a) outlined the basic features of SUMMAC and established its viability as an engineering research tool. The present work summarizes the earlier study, presents some essential new concepts and features, and finally, in giving a means of treating sloping beach problems, greatly broadens the realms of usage of MAC-type programs.

THE SUMMAC METHOD

The presently implemented SUMMAC is designed for simulating the unsteady motion of water waves in two space dimensions. The fluid is regarded as incompressible and the effect of viscosity is considered to be negligible.

To set up a computing network, the entire flow field is covered with a rectangular mesh of cells, each of dimensions δx and δy . The center of each cell is numbered by the indices i and j , with i counting the columns in the x -direction and j counting the rows in the y -direction of a fixed Cartesian coordinate system (Fig. 1). The field-variable values describing the flow are directly associated with these cells (Welch, et al, 1966). The fluid velocity components u and v and the pressure p are used as the dependent variables while the independent variables are x and y , the Cartesian space coordinates, and the time variable t .

In addition, there is a line of marker particles whose sole purpose is to indicate where the free surface is located. The marker-and-cell system provides an instantaneous representation of the flow field for any particular time during the evolution of the dynamics.

By neglecting viscosity, we can reduce the Navier-Stokes equations for an incompressible fluid to

$$\frac{\partial u}{\partial t} + u \frac{\partial u}{\partial x} + v \frac{\partial u}{\partial y} = - \frac{\partial p}{\partial x} + g_x, \quad (1)$$

$$\frac{\partial v}{\partial t} + u \frac{\partial v}{\partial x} + v \frac{\partial v}{\partial y} = - \frac{\partial p}{\partial y} + g_y \quad (2)$$

Here g_x and g_y are the components of gravity acceleration. All variables are dimensionless. The continuity equation is

$$\frac{\partial u}{\partial x} + \frac{\partial v}{\partial y} = 0 \quad (3)$$

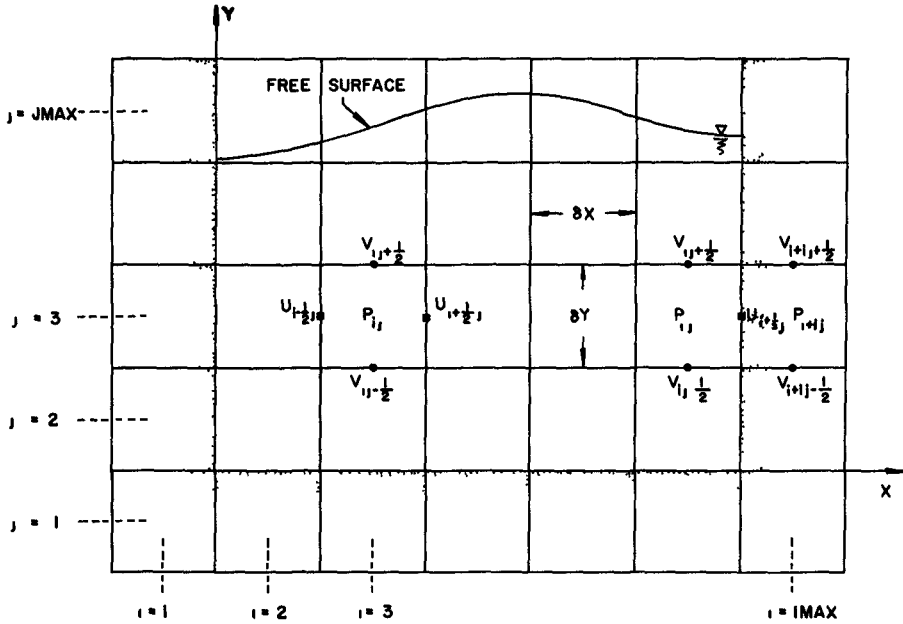


Fig 1 Cell Setup and Position of Variables

On the surface of a vertical impermeable wall, the boundary conditions are

$$u = 0, \quad \frac{\partial v}{\partial x} = 0 \quad \text{and} \quad \frac{\partial p}{\partial x} = g_x \quad (4)$$

Similar procedures can be followed to derive the boundary conditions for a horizontal solid boundary

$$v = 0, \quad \frac{\partial u}{\partial y} = 0 \quad \text{and} \quad \frac{\partial p}{\partial y} = g_y \quad (5)$$

For incompressible fluids with very low viscosity, such as water, it is sufficiently accurate to use the single condition on the free surface

$$p = p_a(x, t), \quad (6)$$

where p_a is the externally applied pressure at the free surface (Chan and Street, 1970a)

A finite-difference scheme can be derived from Eqs (1), (2) and (3) for cell (i, j) in Fig 1 as follows

$$u_{i+\frac{1}{2}, j}^{n+1} = u_{i+\frac{1}{2}, j}^* + \delta t \cdot g_x + \frac{\delta t}{\delta x} (p_{i, j} - p_{i+1, j}), \quad (7)$$

$$v_{i, j+\frac{1}{2}}^{n+1} = v_{i, j+\frac{1}{2}}^* + \delta t \cdot g_y + \frac{\delta t}{\delta y} (p_{i, j} - p_{i, j+1}), \quad (8)$$

$$D_{i, j}^{n+1} \equiv \frac{u_{i+\frac{1}{2}, j}^{n+1} - u_{i-\frac{1}{2}, j}^{n+1}}{\delta x} + \frac{v_{i, j+\frac{1}{2}}^{n+1} - v_{i, j-\frac{1}{2}}^{n+1}}{\delta y} = 0, \quad (9)$$

where $D_{i, j}^{n+1}$ is the velocity divergence, u^* and v^* are contributions to $u_{i, j}^{n+1}$ and $v_{i, j}^{n+1}$, respectively, by pure convection. Variables with the superscript $n+1$ are related to the $n+1$ th time step while those lacking a superscript are evaluated at the n th step. If the original MAC scheme is used, u^* and v^* are evaluated by

$$u_{i+\frac{1}{2}, j}^* = u_{i+\frac{1}{2}, j} + \delta t \left[\frac{u_{i, j}^2 - u_{i+1, j}^2}{\delta x} + \frac{(uv)_{i+\frac{1}{2}, j-\frac{1}{2}} - (uv)_{i+\frac{1}{2}, j+\frac{1}{2}}}{\delta y} \right], \quad (10)$$

$$v_{i, j+\frac{1}{2}}^* = v_{i, j+\frac{1}{2}} + \delta t \left[\frac{(uv)_{i-\frac{1}{2}, j+\frac{1}{2}} - (uv)_{i+\frac{1}{2}, j+\frac{1}{2}}}{\delta x} + \frac{v_{i, j}^2 - v_{i, j+1}^2}{\delta y} \right] \quad (11)$$

Substituting Eqs (7) and (8) into Eq (9) and requiring $D_{i, j}^{n+1} = 0$ lead to the pressure equation

$$p_{i, j} = \frac{1}{Z} \left(\frac{p_{i+1, j} + p_{i-1, j}}{\delta x^2} + \frac{p_{i, j+1} + p_{i, j-1}}{\delta y^2} + R_{i, j} \right), \quad (12)$$

where

$$z \equiv 2 \left(\frac{1}{\delta x^2} + \frac{1}{\delta y^2} \right) , \quad (13)$$

$$R_{1J} \equiv - \frac{1}{\delta t} \left[\frac{u_{1+\frac{1}{2},1}^* - u_{1-\frac{1}{2},1}^*}{\delta x} + \frac{v_{1,1+\frac{1}{2}}^* - v_{1,1-\frac{1}{2}}^*}{\delta y} \right] \quad (14)$$

Near the free surface "irregular stars" (Fig 2) must be used to derive a special equation for pressure so that, in the discrete sense, the free surface condition [Eq (6)] is applied at the exact location of the surface and not in a nearby cell center where p is normally defined. Let $\eta_1, \eta_2, \eta_3, \eta_4$ be the lengths of the four legs of the irregular star (Fig 2) and p_1, p_2, p_3, p_4 be the values of p at the ends of these legs. By expressing p_1, p_2, p_3, p_4 in terms of Taylor series expansions about the point $(1, j)$, Chan and Street (1970a) obtained

$$p_{1J} = \frac{\eta_1 \eta_2 \eta_3 \eta_4}{2(\eta_2 \eta_4 + \eta_1 \eta_3)} \left[\frac{\eta_3 p_1 + \eta_1 p_3}{\eta_1 \eta_3 \left(\frac{\eta_1 + \eta_3}{2} \right)} + \frac{\eta_4 p_2 + \eta_2 p_4}{\eta_2 \eta_4 \left(\frac{\eta_2 + \eta_4}{2} \right)} + R_{1J} \right] \quad (15)$$

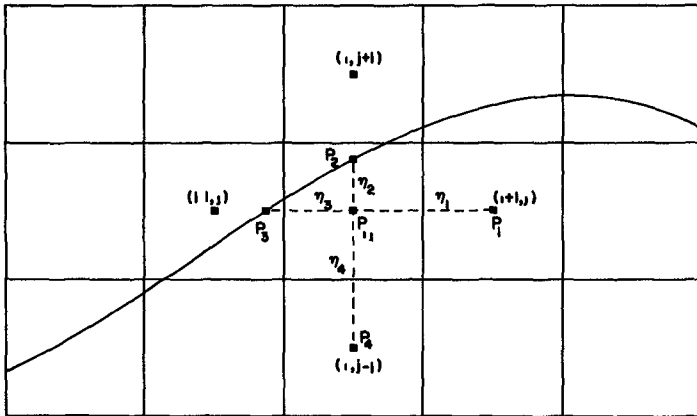


Fig 2 Irregular Star for P Calculations

A complete set of initial data -- the u and v fields and

the position of a line of particles depicting the free surface -- are needed to start the computation. The initial pressure p need be known only approximately. A hydrostatic distribution is adequate, because the p field is obtainable if u and v are given. Chan and Street (1970b) described a method of generating the flow fields of a solitary wave which may be used as the initial condition in simulating the shoaling process.

The evolution of the fluid dynamics is calculated in "cycles" or time steps. At the start of each cycle the source term R_{1j} for each cell is evaluated by Eq (14). The pressure p is computed only for those cells whose centers fall within the fluid region. Equation (12) is used if the centers of the four neighboring cells are all located on the fluid side of the free surface. If any of these neighboring centers lies beyond the free surface, then Eq (15) is used. The Successive Over-Relaxation method is employed to solve for p , with Eqs (12) and (15) being the iteration formulas. The iteration is terminated when the condition

$$|p_{1j}^{(m)} - p_{1j}^{(m-1)}| < \epsilon_p \quad (16)$$

is met for every cell, where (m) means the m th iteration and ϵ_p is a predetermined small positive number.

Now we can compute the new velocities using Eqs (7) and (8). Then, each free surface marker particle is advanced to its new position by

$$x_k^{n+1} = x_k^n + u_k^{n+1} \delta t, \quad (17)$$

$$y_k^{n+1} = y_k^n + v_k^{n+1} \delta t, \quad (18)$$

where x_k and y_k refer to the position of the k th particle and the particle velocities u_k and v_k are interpolated from the velocity fields at the n th time step. Thus, a cycle is completed and the next one can be immediately started.

BOUNDARY CONDITIONS ON A SLOPE

A set of boundary conditions can be rigorously obtained for a plane beach of constant slope which coincides with the diagonal of the cells (Fig 3). The main consideration in deriving an equation for p_{1j} which lies on the beach face is the conservation of mass. In Fig 3 we require that the net flow into the triangular region equal zero at the n th time step, viz ,

$$u_{1-\frac{1}{2}J}^{n+1} \delta y - v_{1J+\frac{1}{2}}^{n+1} \delta x = 0 \tag{19}$$

By substituting Eqs (7) and (8) into Eq (19) we have

$$P_{1J} = \frac{1}{Z_1} \left(\frac{P_{1-1J}}{\delta x^2} + \frac{P_{1J+1}}{\delta y^2} + R_{1J} \right) \tag{20}$$

where

$$Z_1 \equiv \frac{1}{\delta x^2} + \frac{1}{\delta y^2} , \tag{21}$$

$$R_{1J} \equiv \frac{1}{\delta t} \left(\frac{u_{1-\frac{1}{2}J}^*}{\delta x} - \frac{v_{1J+\frac{1}{2}}^*}{\delta y} \right) + \left(\frac{g_x}{\delta x} - \frac{g_y}{\delta y} \right) \tag{22}$$

In the iterative solution of the p field, Eq (20) is used at a beach cell

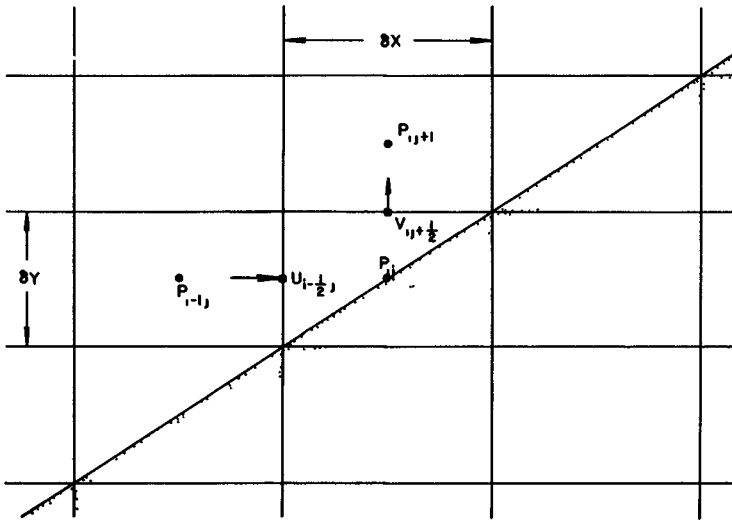


Fig 3 Definition Sketch for Computing p

Now, consider the diamond-shaped control volume for computing the convective contribution $u_{1+\frac{1}{2}j}^*$ (Fig 4) The total influx of the u-momentum is as follows

Through Face 1

$$M_1 = -\delta x v_{1+1j+\frac{1}{2}} \left(\frac{u_{1+\frac{1}{2}j} + u_{1+\frac{3}{2}j+1}}{2} \right) \quad (23)$$

Through Face 2

$$M_2 = \delta y \left(\frac{u_{1-\frac{1}{2}j} + u_{1+\frac{1}{2}j}}{2} \right)^2 - \delta x \left(\frac{v_{1j-\frac{1}{2}} + v_{1j+\frac{1}{2}}}{2} \right) \left(\frac{u_{1-\frac{1}{2}j} + u_{1+\frac{1}{2}j}}{2} \right) \quad (24)$$

Through Face 3

$$M_3 = \delta x v_{1j-\frac{1}{2}} \left(\frac{u_{1+\frac{1}{2}j} + u_{1-\frac{1}{2}j-1}}{2} \right) \quad (25)$$

Through Face 4

$$M_4 = \delta x \left(\frac{v_{1+1j-\frac{1}{2}} + v_{1+1j+\frac{1}{2}}}{2} \right) \left(\frac{u_{1+\frac{1}{2}j} + u_{1+\frac{3}{2}j}}{2} \right) - \delta y \left(\frac{u_{1+\frac{1}{2}j} + u_{1+\frac{3}{2}j}}{2} \right)^2 \quad (26)$$

The area of the control volume is $\delta x \delta y$ Therefore, by relating the net inflow of the u-momentum to its rate of increase, we obtain

$$\left(\frac{u_{1+\frac{1}{2}j}^* - u_{1+\frac{1}{2}j}}{\delta t} \right) (\delta x \delta y) = M_1 + M_2 + M_3 + M_4 \quad (27)$$

or, by rearranging,

$$u_{1+\frac{1}{2}j}^* = u_{1+\frac{1}{2}j} + \frac{\delta t}{\delta x \delta y} (M_1 + M_2 + M_3 + M_4) \quad (28)$$

The total $u_{1+\frac{1}{2}j}^{n+1}$ is then

$$u_{1+\frac{1}{2}j}^{n+1} = u_{1+\frac{1}{2}j}^* + \delta t g_x + \frac{\delta t}{\delta x} (p_{1j} - p_{1+1j}) \quad (29)$$

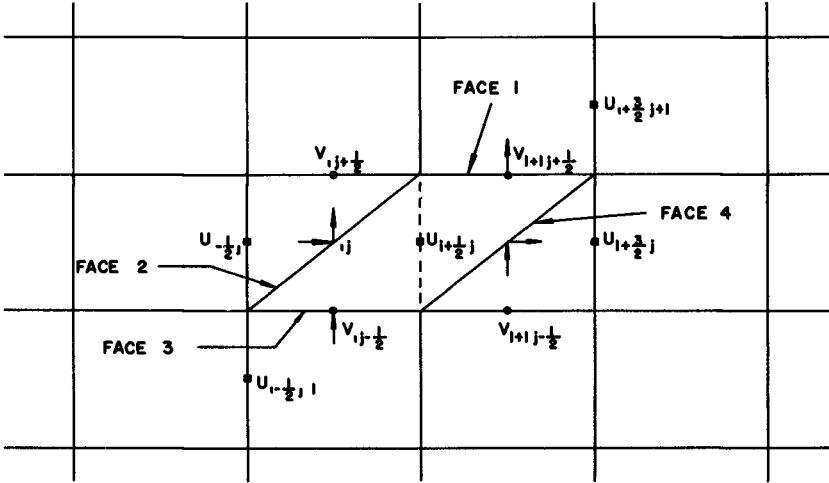


Fig 4 Definition Sketch for Computing u

If Face 4 is the beach face, then $M_4 = 0$ because there is no flow across it. Similarly, we use $M_3 = M_4 = 0$ if both Face 3 and Face 4 are solid boundaries.

To evaluate v^{n+1} near the beach face, a different type of diamond-shaped control volume is used (Fig 5). Again, the concept of balancing momentum within the control volume is employed to compute the convective contribution $v_{1j+\frac{1}{2}}^*$. The total influx of the v-momentum is as follows:

Through Face 1

$$M_1 = -\delta y u_{1+\frac{1}{2}j+1} \left(\frac{v_{1j+\frac{1}{2}} + v_{1+j+\frac{3}{2}}}{2} \right) \tag{30}$$

Through Face 2

$$M_2 = \delta y \left(\frac{u_{1-\frac{1}{2}j+1} + u_{1+\frac{1}{2}j+1}}{2} \right) \left(\frac{v_{1j+\frac{1}{2}} + v_{1j+\frac{3}{2}}}{2} \right) - \delta x \left(\frac{v_{1j+\frac{1}{2}} + v_{1j+\frac{3}{2}}}{2} \right)^2 \tag{31}$$

Through Face 3

$$M_3 = \delta y u_{1-\frac{1}{2}J} \left(\frac{v_{1J+\frac{1}{2}} + v_{1-1J-\frac{1}{2}}}{2} \right) \quad (32)$$

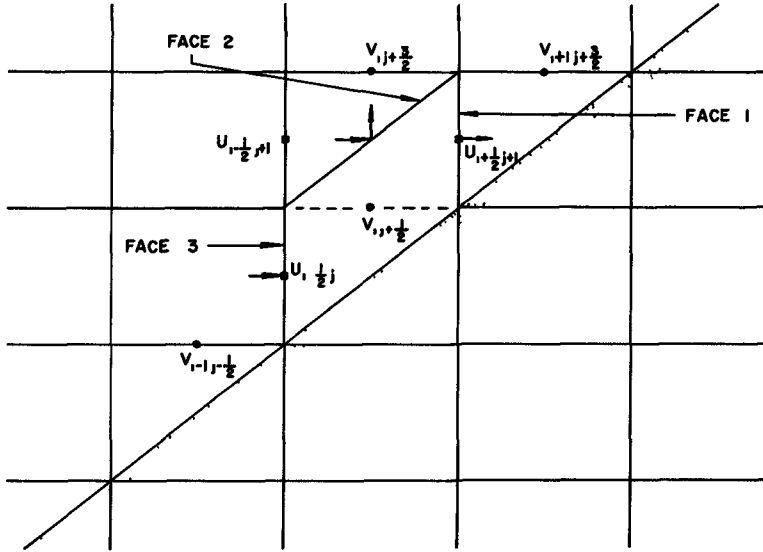


Fig 5 Definition Sketch for Computing v

Balancing the net inflow of the v -momentum with its rate of increase, we have

$$\left(\frac{v_{1J+\frac{1}{2}}^* - v_{1J+\frac{1}{2}}}{\delta t} \right) (\delta x \delta y) = M_1 + M_2 + M_3 \quad (33)$$

or

$$v_{1J+\frac{1}{2}}^* = v_{1J+\frac{1}{2}} + \frac{\delta t}{\delta x \delta y} (M_1 + M_2 + M_3) \quad (34)$$

The total $v_{1J+\frac{1}{2}}^{n+1}$ is then

$$v_{1J+\frac{1}{2}}^{n+1} = v_{1J+\frac{1}{2}}^* + \delta t g_y + \frac{\delta t}{\delta y} (p_{1J} - p_{1J+1}) \quad (35)$$

APPLICATION TO THE SHOALING OF WAVES

The initial position of the wave crest was chosen such that neither the left-hand wall nor the beach influenced the wave at $t = 0$. The beach slope used first was $S = 0.05$ (1 on 20). Each cell had the dimensions $\delta x = 0.50$ and $\delta y = 0.025$. The time increment was $\delta t = 0.05$. The initial wave height was $H_0 = 0.25$.

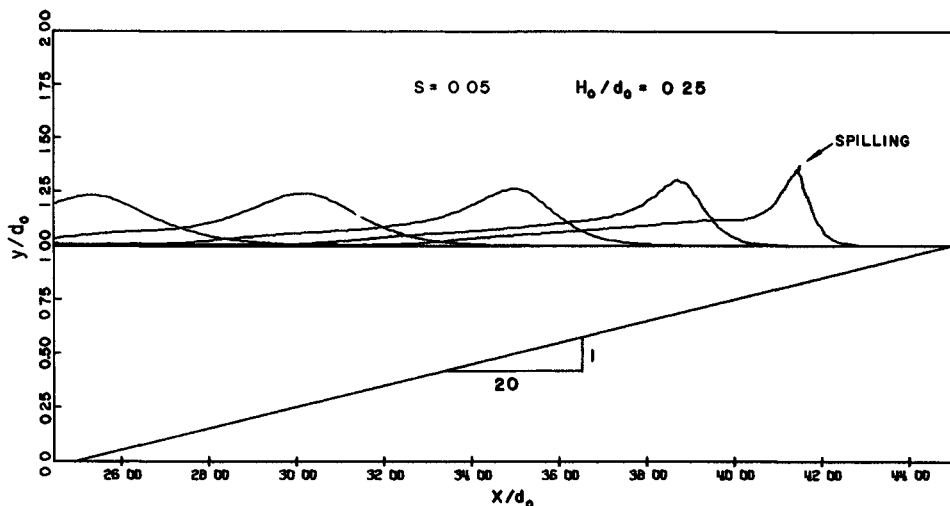


Fig 6 Shoaling on a 1/20 Slope (Surface Profiles)

When the wave advances into the beach section where the water depth decreases, its shape changes. The wave profiles at various stages of shoaling are shown in Fig 6. It is seen that the wave shape gradually loses symmetry on the beach. The wave has a steeper front than its hind part which looks like a long tail. At approximately $H/d = 2.0$, where H is the instantaneous wave height and d is the local still water depth under the wave crest, the wave crest peaks up with a very slight tendency to curl forward. This result is consistent with the observation of Ippen and Kulin (1955) that spilling rather than plunging occurs when a solitary wave of this magnitude breaks on the 1/20 slope. All these properties regarding the wave deformation also agree with the observations of Camfield and Street (1967).

The evolution of the fluid dynamics under the wave is best illustrated by the contour plots of the u and v fields. In Fig 7(a) the time history of the distribution of u is shown. On the two outermost contour lines, $u = 0.015$. Then the value of u is

increased by 0.030 per line toward the wave crest. Thus, $u = 0.375$ at the wave crest at $t = 0$. When the wave is well up the beach ($t = 23.00$), $u = 0.675$ at its crest. In Fig. 7(b) the motion of the v field is shown. To the left of the crest, the lowest contour line has $v = -0.015$, and v decreases by 0.030 per line toward the free surface. To the right of the crest, the lowest contour line has $v = +0.015$, and v increases by 0.030 per line toward the free surface. The line $v = 0$ lies between the lines $v = \pm 0.015$ and is not shown.

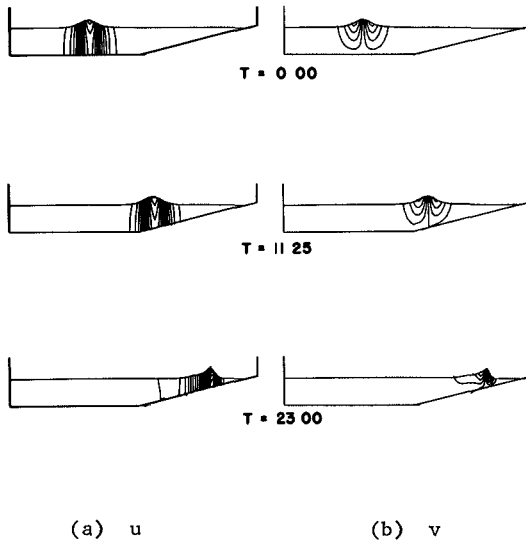


Fig. 7 Shoaling on a 1/20 Slope (Velocity Contours)

The contour lines in Fig. 7 were computed by using a plotting program developed by Schreiber (1968). The facility used was an IBM 2250 graphic display device in which the computed contour lines are shown on a TV screen. By directly photographing the surface of the screen, the contour plots were obtained. Several motion pictures have also been made with this apparatus. These graphical outputs prove to be valuable visual aids to an understanding of the physics in the waves.

In Fig. 8 the mass transport phenomenon in the mid-section of the beach is shown. A vertical line of fluid particles are moved forward from their initial position $x = 35.0$ by the passing wave. The mass transport here is of the translation-type as opposed to the oscillation-type in the periodic waves. Also, the wave induced motion on the beach is seen to be quite uniform throughout the water depth.

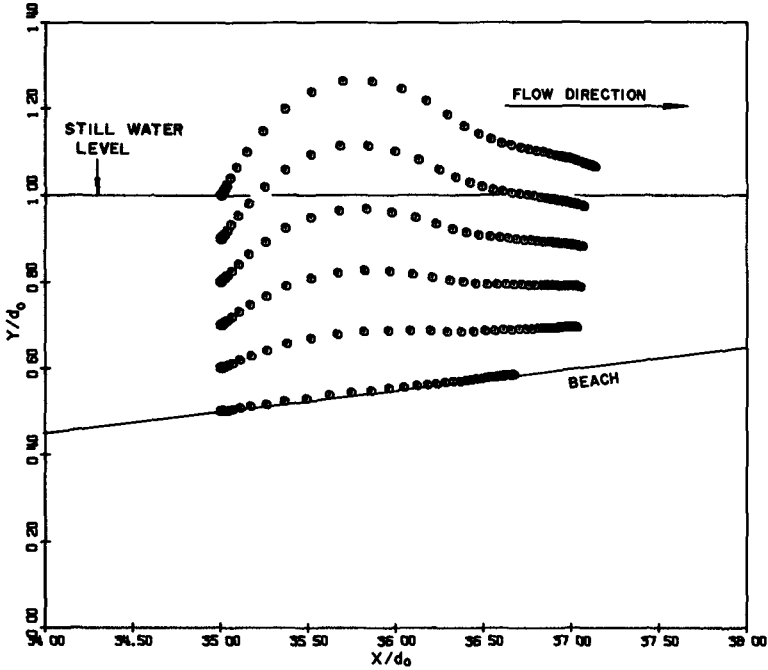


Fig 8 Shoaling on a 1/20 Slope (Particle Paths)

To study the growth of the wave height H as a function of the local water depth d , computations were conducted covering a range of the initial height-to-depth ratios (H_0/d_0). The results are compared with the experiments of Ippen and Kulin (1955) in Fig 9. Ippen and Kulin did not indicate the H_0/d_0 value associated with each data point, but H_0/d_0 is an important parameter in predicting the wave growth. The scattering of the measured data cannot be reconciled without knowledge of this parameter. However, the H_0/d_0 ratio clearly has a profound effect on the wave's initial reaction to the slope. Our results show that in the region $d/d_0 > 0.45$, a solitary wave with smaller H_0/d_0 has greater relative growth (H/H_0). The trend is reversed in the shallower region where $d/d_0 < 0.45$. For $H_0/d_0 = 0.10$ comparison was also made with the theories of Peregrine (1967), Madsen and Mei (1969) and the characteristics solution by Camfield and Street (1967) (Fig 10). With the exception of the characteristics solution, these theories seem to agree quite well.

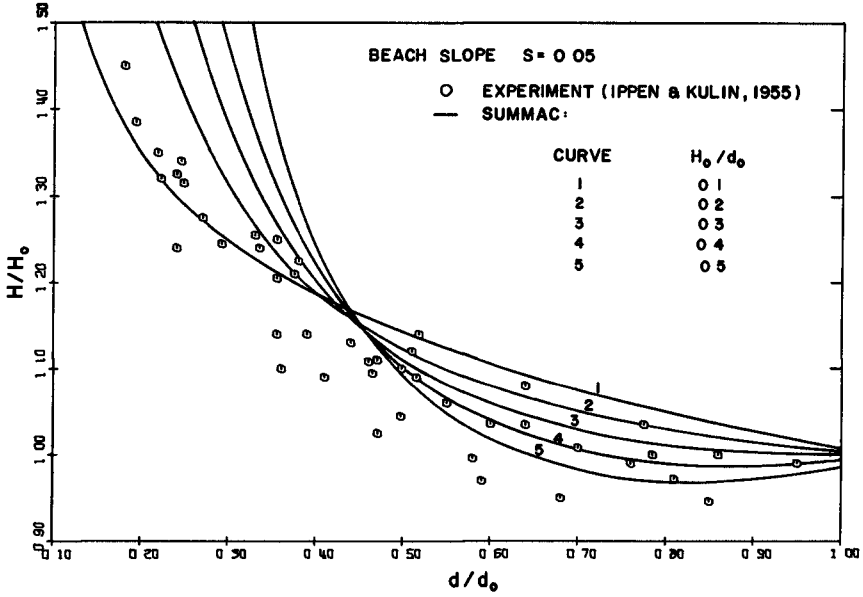


Fig 9 Growth of Wave Amplitude ($S = 0.05$)

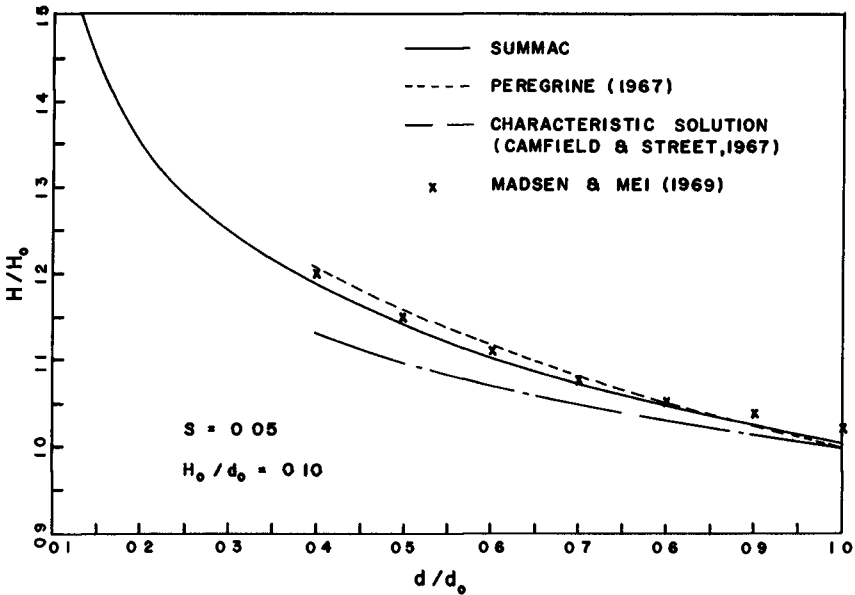


Fig 10 Comparison of Wave Amplitude Growth with Other Theories ($S = 0.05$)

Second, a wave with $H_0/d_0 = 0.10$ was shoaled on a beach with $S = 0.045$. In Fig. 11 the local height-to-depth ratio H/d is plotted against $x^*/d_b - 1/S$, where x^* is the distance measured from the intersection of the still water level and the beach and d_b (≈ 0.085) is the breaking depth. The solution agrees favorably with the measurement of Camfield and Street (1967).

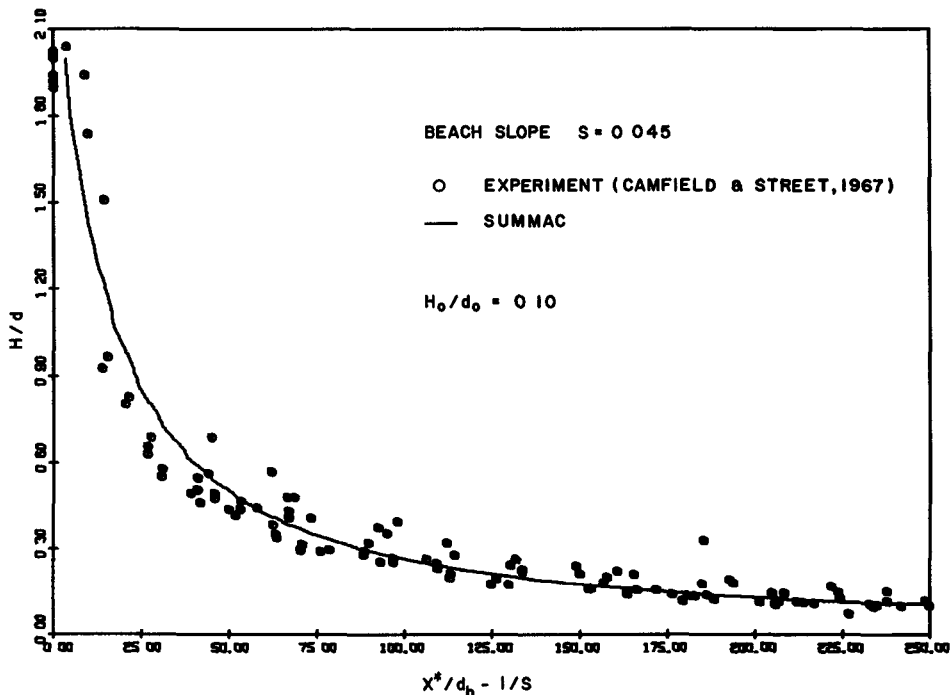


Fig. 11 Growth of Wave Amplitude ($S = 0.045$)

We also simulated wave run-up on a 45° slope which has direct application to the study of wave run-up on coastline structures such as rubble-mound breakwaters. The cell size was $\delta x = \delta y = 0.10$. The initial wave height was $H_0/d_0 = 0.48$ and a time increment $\delta t = 0.05$ was used in computation. The wave profiles at several stages of run-up are plotted in Fig. 12. Quantitative comparison of these profiles with experiments was not made because of the difficulty in obtaining a computed profile which corresponds to a measured profile in time. Nevertheless, the profiles closely resemble those observed by Street and Camfield (1966). We find the calculated envelope of the wave crests slightly higher than that of the experiment in the early stages of run-up, but the engineering interest is primarily in the prediction

of the maximum height of run-up R_o/d_o (Fig 12) The numerical model gave $R_o/d_o = 1.27$ which is equal to the measured value (Street and Camfield, 1966)

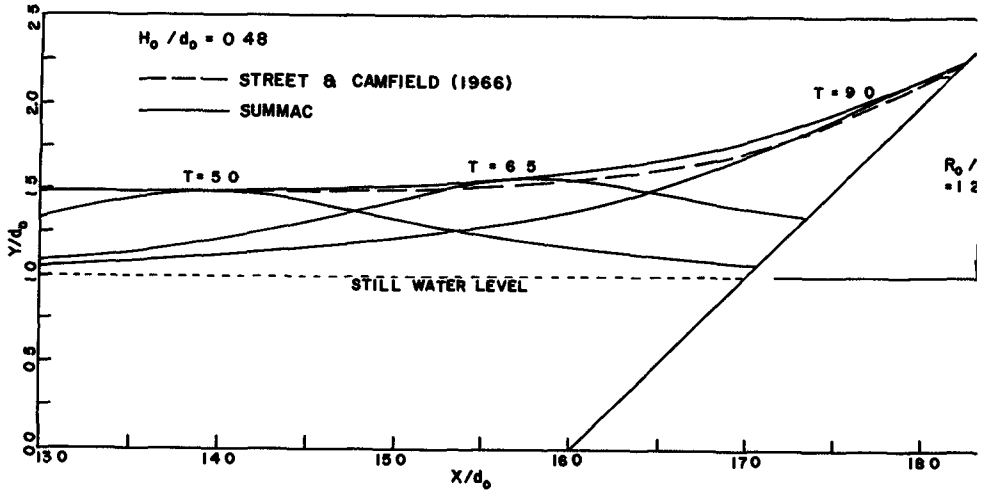


Fig 12 Run-up Profiles on a 45° Slope

CONCLUSIONS

The successful application of the SUMMAC technique to several physical problems indicates its usefulness as an engineering research tool for analyzing the dynamics of water waves in two space dimensions. It is capable of providing accurate quantitative results as well as qualitative descriptions [e.g., the prediction of wave run-up on a 45° slope]. In addition, rapid advance in the design of high-speed computing systems makes numerical modeling economically feasible.

While it is possible to employ the SUMMAC technique to attack a wide variety of water wave problems, some limitations inherent in the method must be noted. First, as a result of achieving a high degree of accuracy in applying the free surface pressure condition by using irregular stars, waves after breaking cannot be simulated. When breaking occurs, the computation must be terminated. Second, only non-turbulent flows are considered in our model. Although laminar viscous damping has little effect on large scale wave motions, energy dissipation due to the turbulence can be significant. However, recent studies by Gawain and Pritchett (1970) and by Pritchett (1970) show that it is feasible to implement a phenomenological simulation of turbulence in the MAC framework.

REFERENCES

- Camfield, F E and Street, R L , Dept of Civil Engrg Tech Rept No 81, Stanford University, Calif (1967)
- Chan, R K -C and Street, R L , Jour Computational Physics, 6, 1 (1970a)
- Chan, R K -C and Street, R L , Dept of Civil Engrg Tech Rept No 135, Stanford University, Calif (1970b)
- Dean, R G , Jour Geophysical Research, 70, 18 (1965)
- Gawain, T H and Pritchett, J W , Jour Computational Physics, 6, 1 (1970)
- Ippen, A T and Kulin, G , Dept of Civil and Sanitary Engrg Tech Rept No 15, Massachusetts Institute of Technology, Mass (1955)
- Laitone, E V , Jour Fluid Mechanics, 9 (1960)
- Lamb, Sir H , Hydrodynamics, Dover Publications (1945)
- Madsen, O S and Mei, C C , Jour Fluid Mechanics, 39, 4 (1969)
- Monkmeyer, P L and Kutzback, J E , Chapter 13, Coastal Engineering, Santa Barbara Specialty Conference, ASCE, New York (1965)
- Peregrine, D H , Jour Fluid Mechanics, 27, 4 (1967)
- Pritchett, J W , Information Research Asso., Inc , IRA-TR-1-70 (1970)
- Schreiber, D E , IBM Research Report, RJ499, IBM Research Laboratory, San Jose, Calif (1968)
- Stoker, J J , Water Waves, Interscience Publishers, Inc , New York (1957)
- Street, R L and Camfield, F E , Dept of Civil Engrg Tech Note No 85(1)-66, Stanford University, Calif (1966)
- Street, R L , Chan, R K -C , and Fromm, J E , 8th Symposium on Naval Hydrodynamics, CIT, Pasadena, Calif (1970)
- Welch, J E , Harlow, F H , Shannon, J P , and Daly, B J , Los Alamos Scientific Lab Rept LA-3425 (1966)

CHAPTER 22

PERIODIC WAVES SHOALING IN WATERS OVER STEPLY SLOPING BOTTOMS

by Dr. Harihara Rama AYYAR
Assistant Professor in Civil Engineering
Indian Institute of Technology, Madras, India.

Abstract

The bottom bed slope plays a vital role in the shoaling and breaking of periodic waves. This study aims at the understanding of the effect of steep slopes (range steeper than 1/10) on the breaking point and the breaker trajectory and the point of impact. This range of slope is often met with in the near-shore structures. Analytical investigations and model studies are outlined. The influence of slope on each of the significant breaker parameters is discussed.

1. INTRODUCTION

A train of periodic waves propagating on a sloping beach presents one of the most interesting and perhaps one of the most exciting phenomena in nature. Similar phenomena occur on the slopes of near-shore structures like sea-walls, breakers, dykes etc. A knowledge of the point of breaking and position of occurrence of maximum impact pressures due to breakers will be useful aids to the designer. It has been observed that beyond the point of breaking the particles move in a confused manner. Wave theories cannot be applied in this zone, at best till the breaking point only.

2. PERIODIC WAVES PROPAGATING IN SHOALING WATERS

It is known from IRY(1)'s theory of small amplitude waves, that the energy in a wave train is transported in the direction of wave propagation with the group velocity C_g . Considering a train of progressive waves advancing in water of variable depth, with change in depth being uniform and small RAYLEIGH(2) assumed that the mean rate of energy transport past all vertical sections is constant. Further it was assumed that since the change in depth is very gradual, the characteristics of the wave at any section are given by AIRY'S equations. This leads to the relation

$$\frac{H}{H_0} = \sqrt{\frac{2C \cosh^2 kh}{2k_1 + \sinh 2kh}} \quad (1)$$

$$\text{and } \frac{H/L}{H_0/L_0} = \sqrt{\frac{2\text{Cosh}^2 kh}{2kh + \sinh 2kh}} \cdot \text{Cotanh } kh \quad (2)$$

where H = Height of the incident wave (deep water)
 H_0 = Height of wave at any given location
 L_0 = Length of incident wave (deep water)
 L = Length of wave at any given location
 h = Local depth of water below SWL
 k = Wave number = $2\pi/L$

This solution, however, does not predict breaking, as it is based on the linear theory of AIRY.

STOKER(3) analysed the breaking problem based on the classical non-linear wave theory and the method of characteristics. The solution is however not explicit and calls for individual treatment. Only solutions for a few special angles of bottom slope were obtained. The solutions of STOKER do not predict the breaking point correctly (LE MEHAUTE(4)) and also predicts a bore even when the wave travels on a horizontal bottom. Moreover the results of STOKER always predict a spilling breaker observed only on mild slopes. On steep slopes plunging breakers are formed invariably.

3. SOLUTION BASED ON CLASSICAL NON-LINEAR SHALLOW WATER WAVE THEORY

The classical non-linear shallow water wave theory equations are

$$\frac{\partial}{\partial x} u (\eta + h) = - \frac{\partial \eta}{\partial t} \quad (3)$$

$$\frac{\partial u}{\partial t} + u \frac{\partial u}{\partial x} = -g \frac{\partial \eta}{\partial x} \quad (4)$$

where u = particle velocity in the horizontal direction (i.e. direction of wave advance)
 x = horizontal distance from the origin in the direction of wave advance.
 η = the vertical elevation of any particle on the free surface above SWL
 h = depth of water measured below SWL
 g = acceleration due to gravity
 t = the time reckoned from the moment the wave enters the sloping bottom.

The origin is taken at the intersection of SWL with the vertical at the foot of the slope (See Fig.1)

The equation can be expressed in terms of dimensionless quantities

$$x' = \frac{x}{l} \quad \text{where } l = nh$$

$$\eta' = \frac{\eta}{h}$$

$$u' = \frac{u}{u_0} \quad \text{where } u_0 = \sqrt{gh}$$

$$t' = \frac{t}{t_0} \quad \text{where } t_0 = n \sqrt{\frac{h}{g}}$$

The equations (3) and (4) will reduce to

$$\frac{\partial}{\partial x'} u' (1 - x' + \eta') = - \frac{\partial \eta'}{\partial t'} \tag{5}$$

$$\frac{\partial u'}{\partial t'} + u' \frac{\partial u'}{\partial x'} = - \frac{\partial \eta'}{\partial x'} \tag{6}$$

Along the characteristic directions

$$\frac{dx'}{dt'} = u' + C' \tag{7}$$

$$u' + 2C' + t' = \text{Constant}$$

$$\frac{dx'}{dt'} = u' - C' \tag{8}$$

$$u' - 2C' + t' = \text{Constant}$$

It is shown by GREENSPAN(5) and KISHI(6) that the initial positive characteristic is given by

$$x' = t' - \frac{1}{4} t'^2 \tag{9}$$

in the x-t plane. By changing over to a moving coordinate system, the slope of the wave front is obtained as

$$\frac{\partial \eta'}{\partial x'_m} = (1 - \frac{1}{2} t') \frac{\partial u'}{\partial x'_m} \tag{10}$$

By using the kinematic stability criterion that $u = C$ at the crest at the breaking point and using this relation in the integrated equation (10)

$$\eta' = (1 - \frac{1}{2} t') C' \tag{11}$$

But the property of the initial positive characteristic gives

$$C' = 1 - \frac{1}{2} t'$$

Hence
$$\eta' = (1 - \frac{1}{2} t')^2 \tag{12}$$

Suitable parameters are to be chosen to define the kinematics of the breaker. The following are chosen in this analysis.

h_B = Depth at breaking point below SWL
 y_B = Height of breaker crest above bed.

From the relations (9) and (12) and the geometry of the breaker, the following final relations will result.

$$\frac{h_B}{h} = \left(\frac{2m}{1+2m} \right)^{4/3} \quad (13)$$

$$\frac{y_B}{h} = 2 \left(\frac{2m}{1+2m} \right)^{4/3} \quad (14)$$

$$\text{and} \quad \frac{y_B}{h_B} = 2 \quad (15)$$

$$\text{where} \quad m = \eta \cdot \pi \cdot \frac{H}{L} \quad (16)$$

When friction and reflection effects are neglected, as was done in this analysis, one gets the relation (15) for the breaker geometry. This also confirms the thumb rule that breaking occurs at about the point where the wave height equals water depth. However the effects of reflection of wave energy are to be accounted for in the case of waves shoaling on steep slopes.

4. LABORATORY STUDIES IN FRANZIUS-INSTITUT AND CONCLUSIONS

As a result of a large number of model tests conducted by the author in the Franzius Institute in the Technical University of Hannover, West Germany the following conclusions were arrived at, by which the determination of the characteristics of breakers is made possible. Various bottom slopes (in the steep slope range) incident wave height and incident wave period were studied in a wave flume 4.5m X 0.5m X 0.9m with a paddle type wave generator, with provisions for changing the period as well as the height of the wave even during operation.

Instrumentation used consisted of a number of wave gauges of the parallel wire resistance type (gold-plated to prevent any chemical action) of different lengths to suit the local depth of water. The wave profiles were recorded by these wave gauges connected to a 3 channel electronic direct recording devices, which recorded the wave profile on a millimeter section paper run at the known speed. To ensure perfect linear relationship between the water level fluctuations and the records on paper special type of variable resistances were introduced in the circuit. This ensured linear relationship over a large range of wave height. The visual determination of the point of breaking was almost impossible. Therefore the wave statistics was collected along the flume and also above the sloping bottom.

A method was developed to determine the breaking point from the wave statistics thus collected, on the assumption that the trajectory of the breaker crest is a second degree curve. This follows from the fact that the particle velocity at the breaker crest at the breaking point is purely horizontal and equal to C , the phase velocity of the wave and in addition the particles are subjected to a gravitational acceleration g . That this is very much so is demonstrated by the shape of the plunging breakers in nature. A computer programme was written using the method of least squares and solving the resulting simultaneous equations by the diagonal matrix method (compact Gauss method). The computations were done in CDC-1604 digital computer. The breaking point was straightaway determined and then the breaker trajectory plotted. A back check was made to verify the degree of the curve (Fig.2). The agreement was quite good.

5. THE RETARDATION OF THE BREAKER

From dimensional analysis of the variables involved, it was found that the factors influencing the breaker characteristics are H/gT^2 and n (T is the period of the wave) which are the incident wave steepness and the bottom slope function respectively. The variation of Y_B/h_B with H/gT^2 was studied for all the slopes tested. The variation showed the same trend for all the slopes. A relation was established as follows

$$\frac{Y_B}{h_B} = \log \left\{ 40 \cdot n^{0.5} \cdot \left(\frac{H}{gT^2} \right)^{0.25} \right\} \quad (17)$$

(Fig.3) Note that the curves show the variation of Y_B/h_B with bed slope as well as the wave steepness (compare theory $Y_B/h_B = 2$)

The depth at the breaking point will help us to fix the location of breaking inception (Fig.4). For incident waves of given depth and period, the breaking depth remains almost constant for slopes flatter than 1/5. It was observed that for slopes flatter than 1/5, all the breaking action of the wave takes place shoreward of the breaking point. For slopes steeper than 1/5, the values of h_B increases sharply due to the seaward retardation of the breaker.

6. THE INFLUENCE OF A SLOPE ON BREAKER

Fig.(5) shows the influence of the bottom slope on the breaking of a wave.

The reflection coefficient is negligibly small for

a bed slope of 1/50, increases very slowly till a slope of 1/5 is reached and then increases sharply till the bed slope of 1/2 is reached and is then asymptotic till a factor of 1/0 is reached for vertical walls.

The breaking depth h_B is almost constant till a bed slope of 1/5 is reached, since the reflection is still very small of the order of 15%. The small decreasing tendency seen in the breaking depth is indeed negligible. For slopes steeper than 1/5 the breaking depth increases sharply showing that the breaker is retarded seawards. The breaker crest elevation y_B varies in a similar manner.

The variation of y_B/h_B is of interest. The theoretical value of 2 is never reached. The forces of reflection are almost negligible and frictional losses are small compared to the slopes 1/50 etc. For slopes flatter than 1/10 frictional losses increase. The effect of this is to reduce the potential energy growth and hence y_B/h_B decreases. For $n=10$ to $n=5$, the breaking action occurs shoreward, the waves still overcome the forces of reflection. A slight decrease is registered. For $n < 5$, h_B increases sharply due to retardation of the breaker. y_B also increases but at a slower rate. y_B/h_B decreases. The lowest value of 1.10 is reached for breaking clapotis.

7. THE POINT OF IMPACT

The point of impact of the breaker on the slope of the bottom boundary can be calculated once y_B and h_B are known. From the geometry of the slope (FUEHRBOETER)(7)

$$\Delta h = -h_B + y_B \left\{ 1 - \frac{1}{2n^2} (\sqrt{1 + 2n^2} - 1)^2 \right\} \quad (18)$$

The determination of the point of impact was checked on the model. With pressure cells connected to electronic direct recording devices (Honeywell ultraviolet light beam oscillograph), the impact pressure variation with respect to time is followed. Impact pressures were recorded at 6 points at 20cm intervals along the slope simultaneously. The maximum pressure corresponds to the direct impact of the breaker on the slope which helps to locate the point of impact. Comparison of the calculated values and measured values showed less than 8% error. The deviation of the curve $\Delta h/h_B$ for the slopes tested, from the curve computed from the linear theory applicable with reasonable accuracy for mild slopes is shown in Fig.(6).

8. ACKNOWLEDGEMENTS

The work reported here is a part of the doctoral work done by the author under the guidance of Prof.C.Rouvé and

Prof. W. Hensen in the Technical University of Hannover.
The author expresses his deep gratitude to them and to
Dr. Fuehrboeter for their help and guidance.

9. REFERENCES

1. AIRY, G.B. On Tides and Waves - Encyclopaedia
Metropolitana Vol 5, London, 1842.
 2. RAYLEIGH, LORD Hydrodynamical Notes
Philosophical Magazine, Vol 21, 1911.
 3. STOKER, J.J. The formation of Breakers and Bores -
Communications on Applied Mathematics,
Vol 1, 1948.
 4. LE MEHAUTE, B. A synthesis on Wave run-up -
Proceedings, American Society of Civil
Engineers, WW Dn., February 1968.
 5. GREENSPAN, H.P. On the breaking of water waves of finite
amplitude on a sloping beach - Journal
of Fluid Mechanics, Vol 4, Part I, 1958.
 6. FISHI, T. Transformation, Breaking and run-up
of a long wave of finite height -
Proceedings 8th Conference on Coastal
Engineering, 1962.
 7. FUEHRBOETER, A. Der Druckschlag durch Brecher auf
Deichbochungen - Mitteilungen des
Franzius-Instituts, Heft 28, Hannover,
1966.
-

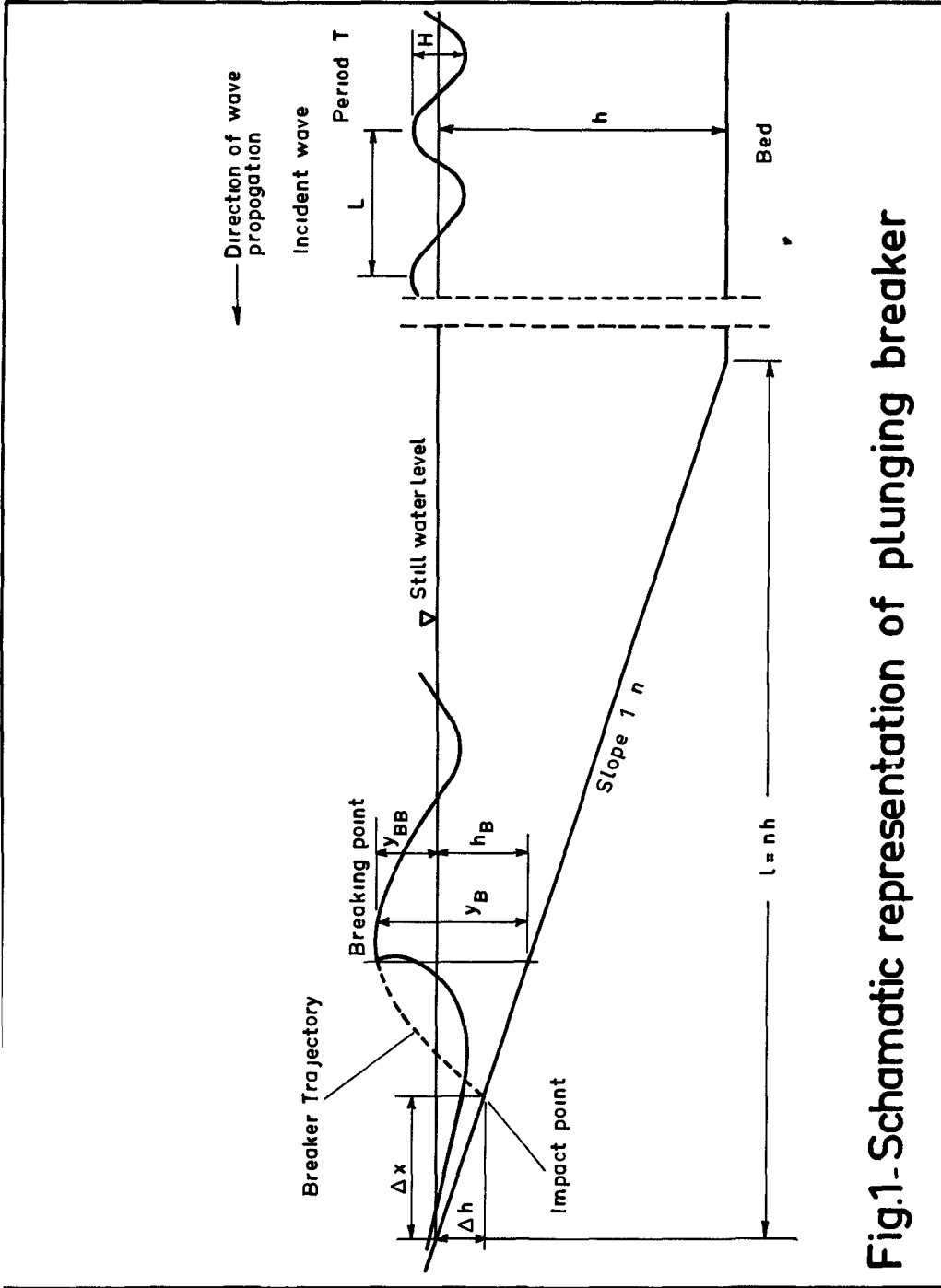


Fig.1-Schematic representation of plunging breaker

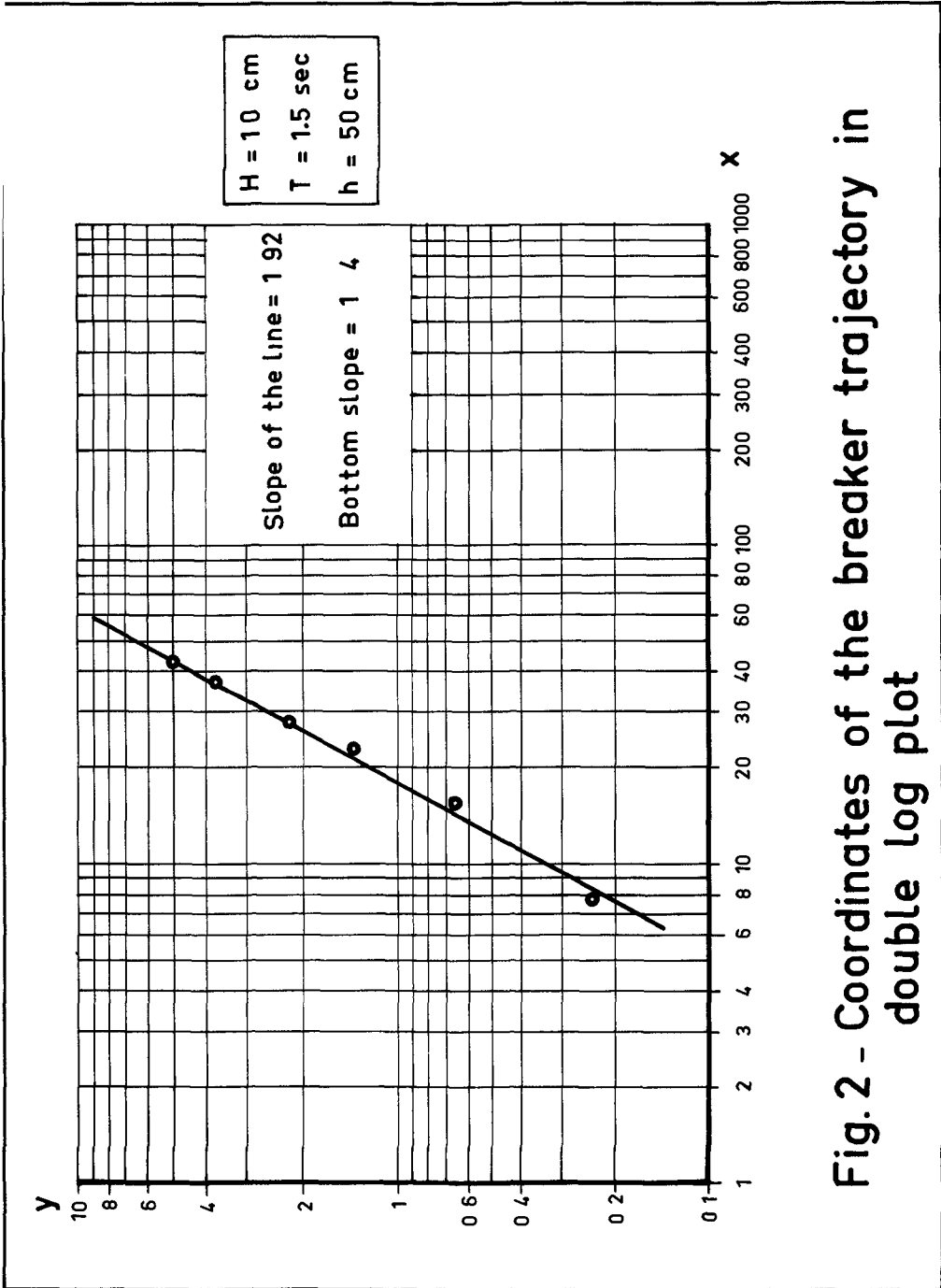


Fig. 2 - Coordinates of the breaker trajectory in double log plot

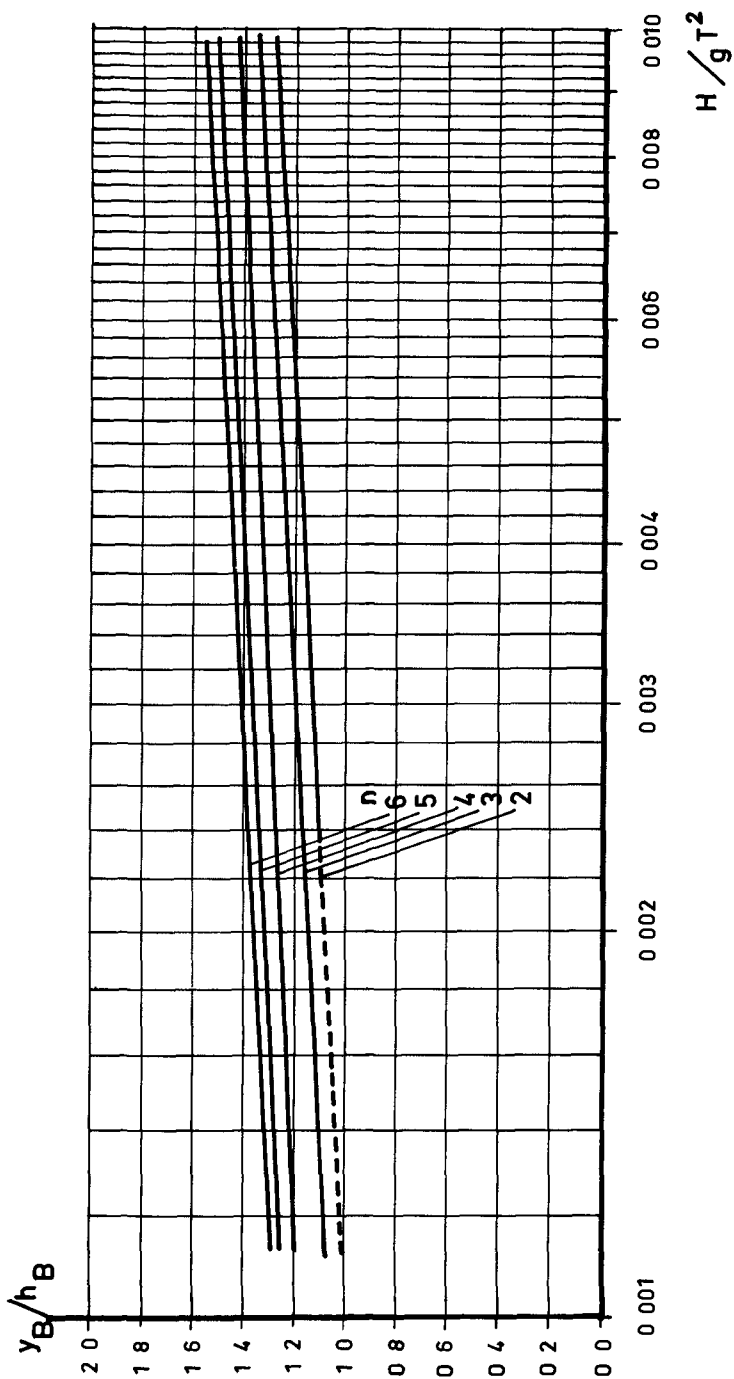


Fig.3 - Variation of y_B/h_B with H/gT^2 and the slope

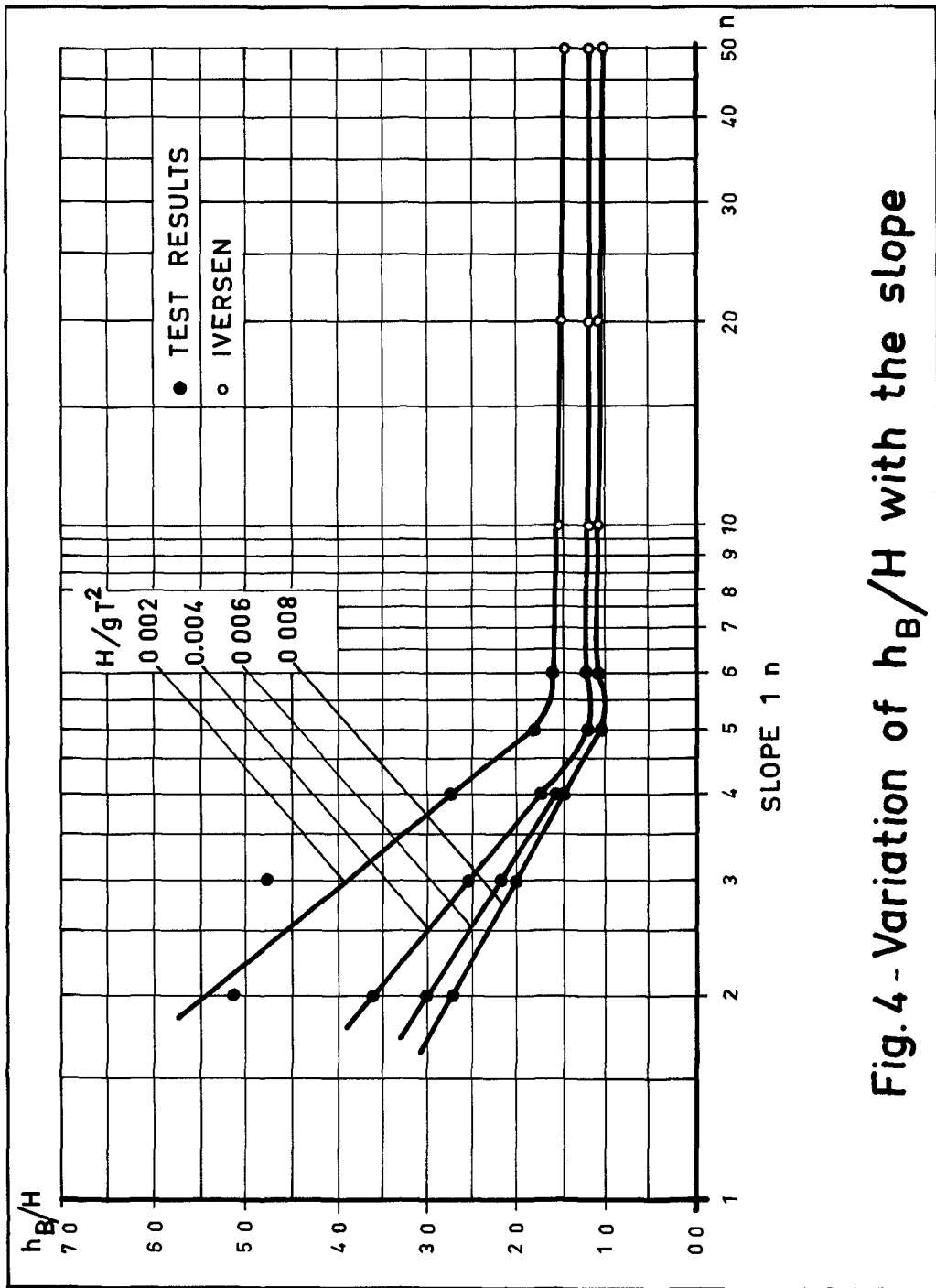


Fig. 4 - Variation of h_B/H with the slope

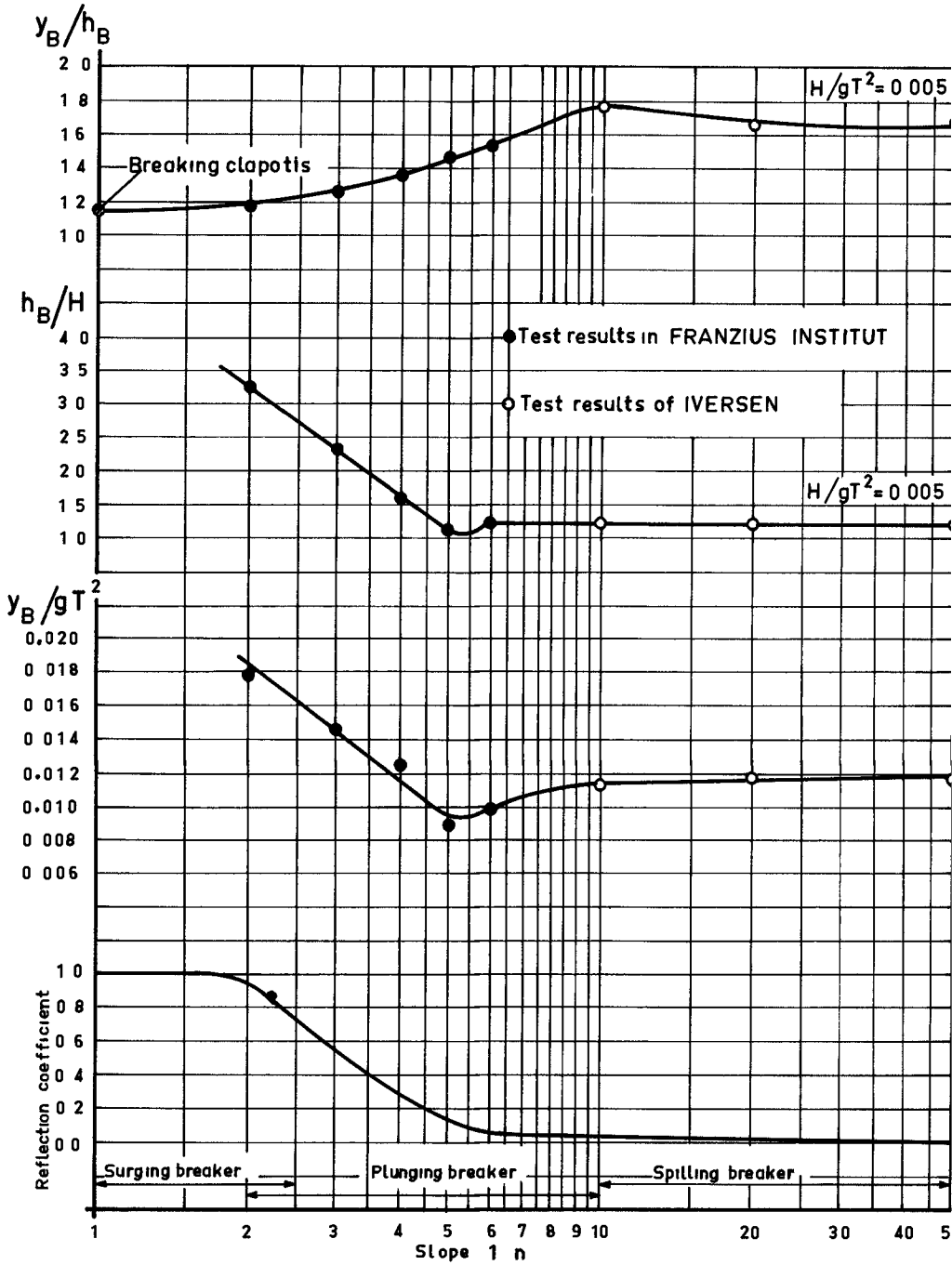


FIG. 5 - Influence of slope on breaking of waves

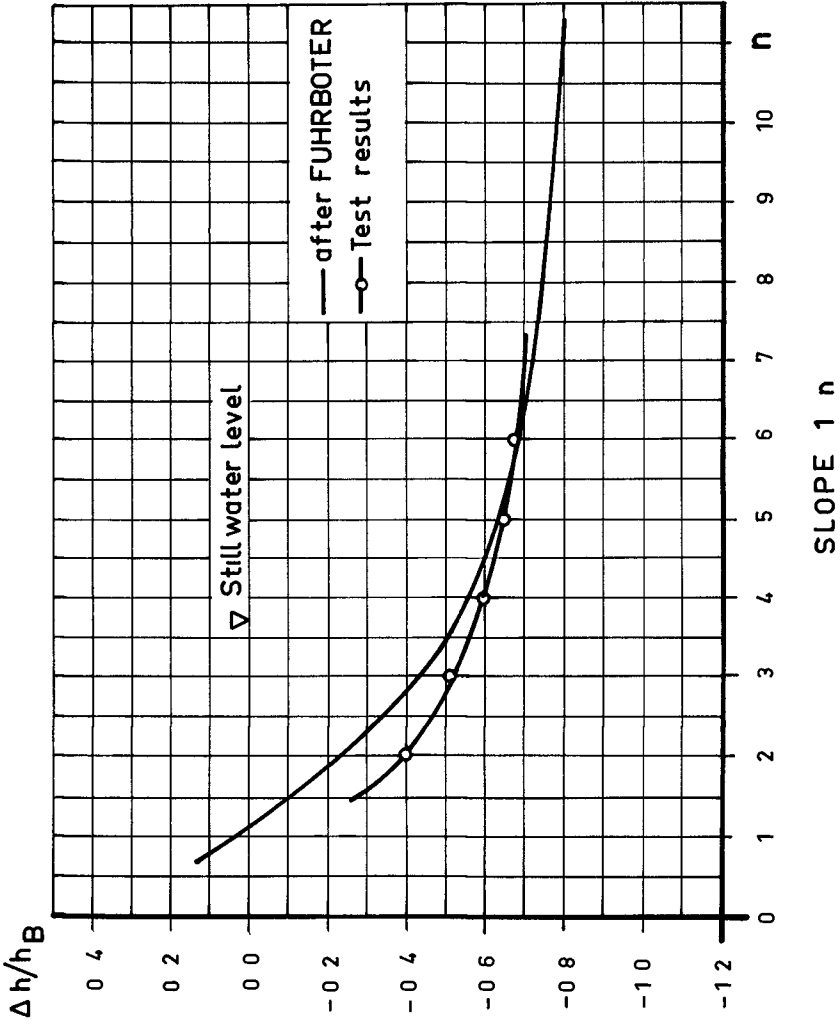


Fig. 6 - Variation of $\Delta h/h_B$ with slope

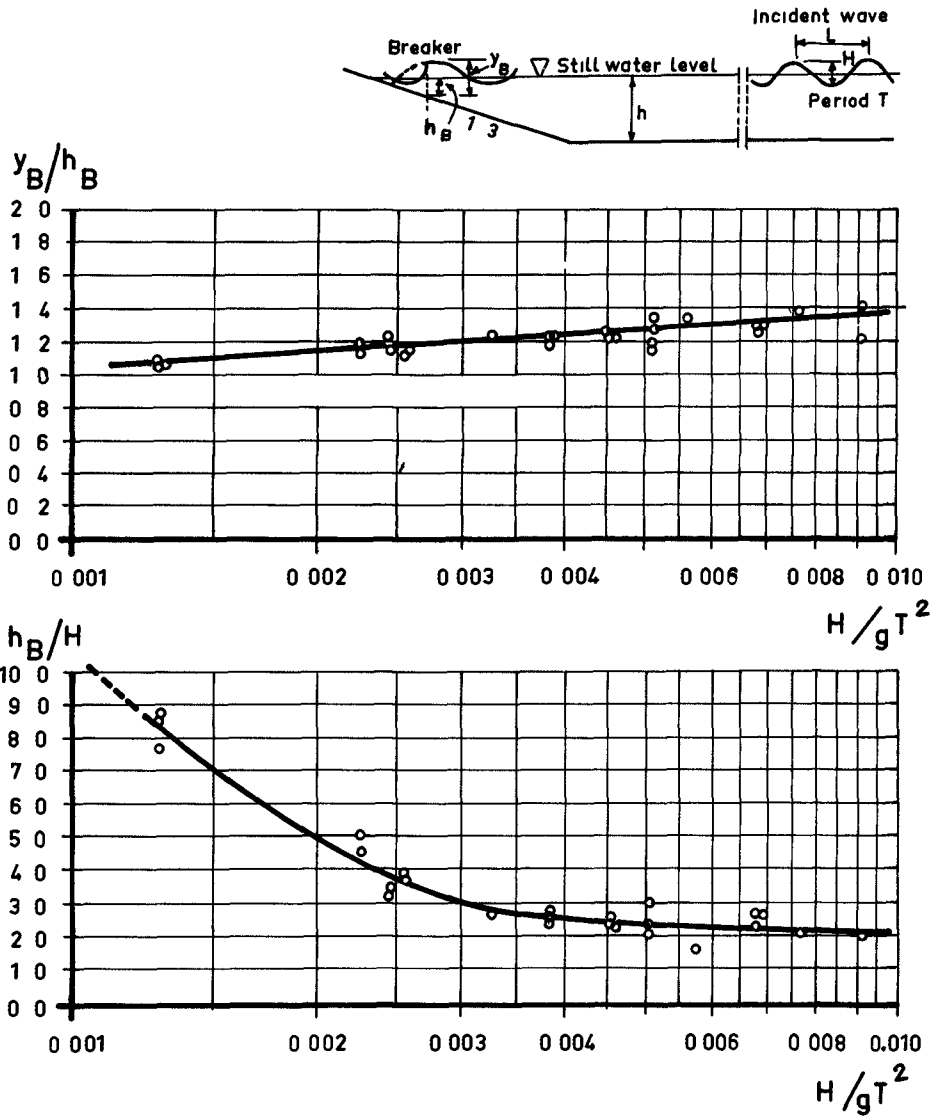


Fig.7 - Test results for the slope 1:3

CHAPTER 23

BREAKING WAVE SETUP AND DECAY ON GENTLE SLOPES

by

Li-San Hwang, Member
and
David Divoky, Visitor

ABSTRACT

Waves of large amplitude on a gentle slope may form spilling breakers which propagate shoreward and are slowly transformed. In addition, there occurs a modification of the mean water level termed wave setup. An analytical description based upon consideration of momentum flux has been developed which predicts this wave setup and the decay history of breaking wave height. The results have been compared with experiments and found quite satisfactory.

The effect of wave setup on breaking wave transformation is particularly important near the shoreline, where setup dominates the vanishing mean depth.

INTRODUCTION

The transformation of a breaking wave over a slope is a problem of obvious concern in the design and planning of coastal facilities. A number of investigators have considered this topic, including Freeman and LeMéhauté (1964), Horikawa and Kuo (1966), LeMéhauté (1962), Divoky, LeMéhauté, and Lin (1970), Nakamura, Shiraishi, and Sasaki (1966), and Street and Camfield (1966). The present contribution considers an essential aspect neglected in previous studies, the phenomenon of "wave set-up."

Set-up, while negligible seaward of the breaking point, becomes dominant with respect to still-water depth as the shore is approached. It is apparent, then, that any analysis of breaking wave height transformation should account for the set-up. Experimental investigations of set-up have been made by Saville (1961) and by Bowen, Inman, and Simmons (1968) with the result that the maximum elevation may be a significant fraction (~ 50%) of the breaking wave height. Additionally, measurements obtained during the Mono Lake explosion-wave tests indicated a set-up value equalling the maximum height of the superposed dispersive wave train (Van Dorn, et al, 1968). Hwang (1970) also investigated dispersive wave trains and found a fluctuating set-up of roughly half the peak wave height.

Wave set-up has been investigated extensively in a series of papers by Longuet-Higgins and Stewart (1960, 61, 62, 64) from an analytical approach. The difficulty in applying their results to the

Tetra Tech, Inc , Pasadena, California

surf zone, arises from the problem of finding an adequate description of the waves after breaking. Bowen, Inman, and Simmons (1968) assumed that the wave height remains a constant fraction of mean water depth after breaking and found, from a momentum balance, a linear set-up variation.

In this paper, a more detailed description of the wave transformation has been used so that height-decay and set-up are calculated simultaneously. The approach roughly follows Divoky, LeMéhauté, and Lin (1970) with the wave decay computed from an energy-dissipation model. The essential difference is that the set-up is included so that more realistic behavior is found near the shoreline, in particular, a significant surviving wave height is found at the still-water shoreline.

MODEL

Two governing equations are adopted in the present model. Firstly, a balance of forces across a fluid element (see, for example, Longuet-Higgins and Stewart, 1964), as shown in Figure 1, gives the momentum equation

$$\frac{dM}{dx} + \rho g(h+\xi) \frac{d\xi}{dx} = 0 \quad (1)$$

where M is the momentum flux, h is the still water depth, and ξ is the wave set-up. The energy dissipation rate is assumed to be a fixed fraction, B , of that of a bore of the same height. Then the standard formula (see, for example, Lamb, 1945) may be adopted--adjusted, of course, to conform to a moving jump, the result is

$$\frac{dE}{dx} = B \left(\frac{dE}{dx} \right)_{\text{BORE}} = B \frac{\rho g}{4} \frac{H^3 D}{y_t (y_t + H)} \quad (2)$$

In this expression the volume flux Q has been taken to be CD where C is the wave celerity and D is $(h+\xi)$, y_t is the depth below the trough (corresponding to the depth ahead of the jump) and (y_t+H) corresponds to the depth behind the jump. The assumption which has been made here is that B , which must account for all forms of energy dissipation, is constant within the breaking region.

To implement this simplified model, a suitable wave description must be chosen in order to calculate E and M . In this, we have followed the observation of LeMéhauté, Divoky, and Lin (1968), that the cnoidal wave theory of Keulegan and Patterson (1940) appears to give the best description of periodic waves in moderately shallow water and that this description may be adopted for gently spilling breakers with moderate success, of course, any non-breaking wave theory will be inadequate to describe violently plunging or surging conditions.

The following equations of cnoidal wave theory have been used

$$\eta = y_s - D = y_t - D + H \operatorname{cn}^2 \left[2K(k) \frac{x}{L} \right] \quad (3)$$

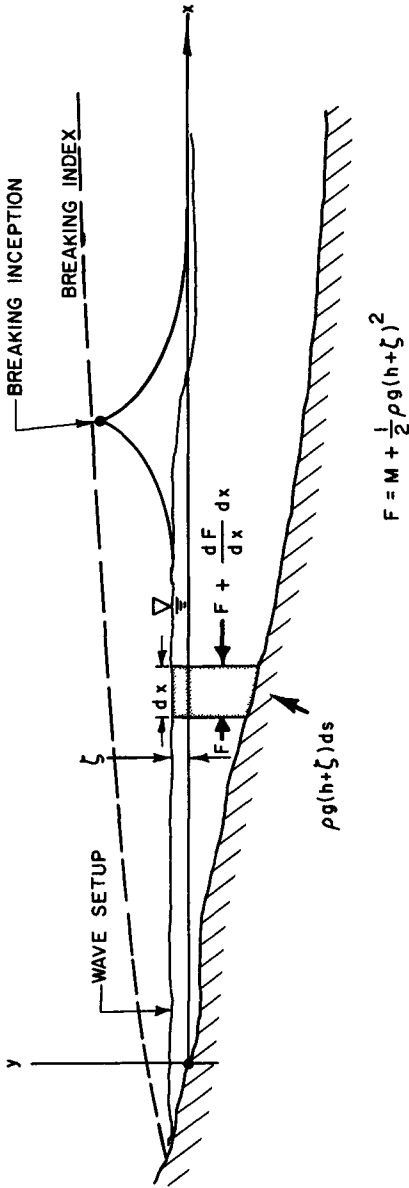


Figure 1 Coordinate System and the Balance of Forces on a Fluid Cross-section

$$L = \sqrt{\frac{16 D^3}{3H}} kK(k) \quad (4)$$

$$T\sqrt{\frac{g}{D}} = \sqrt{\frac{16 D}{3H}} \left\{ \frac{kK(k)}{1 + \frac{H}{k^2 D} \left[\frac{1}{2} - \frac{E(k)}{K(k)} \right]} \right\} \quad (5)$$

$$y_t = D - H + \frac{16 D^3}{3L^2 H} \left\{ K(k) [K(k) - E(k)] \right\} \quad (6)$$

For given values of H , D , and T , Equation (5) is used in an iteration procedure to find the elliptic parameter k^2 , which then allows calculation of all other quantities. In particular, we have evaluated the energy as

$$\begin{aligned} E &= 2(\text{POTENTIAL ENERGY}) = \rho g \int_0^L \eta^2 dx \\ &= \rho g L \left\{ -(y_t - D)^2 + \frac{H^2}{3k^2} \left[1 - k^2 + (2 - 4k^2) \left(\frac{y_t - D}{H} \right) \right] \right\} \quad (7) \end{aligned}$$

Calculation of the momentum flux from defining integrals poses a time-consuming and costly task even on a computer, since it involves repeated evaluation of the cnoidal wave properties. We have made the greatly simplifying approximation that

$$M \approx \frac{3}{2} \frac{E}{L} \quad (8)$$

a result essentially from Airy theory given by Longuet-Higgins and Stewart (1964). Following them, we consider this to be a not unreasonable assumption within the surf-zone, with the possible improvement that E and L are computed here from a more adequate wave theory.

The solution of Equations (1) and (2) begins with specification of a set of initial values for height, depth, set-up, and period. Equations (3) - (8) then give the wave properties at that point. For an advance by an increment dx toward shore, Equation (2) supplies the corresponding energy loss dE . An iteration procedure involving Equation (1) then gives new values of wave height and total mean depth consistent with the available energy.

A word concerning calculation of the elliptic parameter is in order. The cnoidal wave theory is of greatest interest when k^2 is extremely near unity. A direct expansion of E and K in terms of k^2 is then limited by problems of round-off in k^2 . This problem has been obviated by defining

$$P = -\log_{10} (1 - k^2)$$

E and K are written as power series in P rather than k^2 , and all calculations involved in Eqs (3) - (8) similarly suppress k^2 . P is an easily manageable number and is roughly the length of the string of nines in the decimal form of k^2 . In the present calculations P has varied from less than unity to above fifty.

RESULTS

A number of observations on wave transformation are summarized in Figure 2. The data of Horikawa and Kuo (1966) for a slope of 1/65 is shown in Figure 3 with the solid lines representing results of the present model with B taken arbitrarily as 0.8. The general trend appears quite good, and a somewhat better fit might have been obtained with other values of B. The comparison indicates that the data scatter is accounted for by the variation in deep water steepness, so that the transformation is not solely a function of bottom slope.

The dependence upon slope is indicated in Figure 4. Here, only slope is varied and the theoretical height transformation is shown. It is noted that the present model is probably better for gentle slopes than steep slopes, since all calculations of wave properties are based upon the assumption that the water depth is constant and equal to the local value.

Measurements of set-up are relatively few. A comparison of the present model with observations of Saville (1961) is shown in Figures 5 and 6.

The curves labelled "Calculated" represent the contributions to set-up in the breaking and non-breaking zones. The latter has been computed from (Longuet-Higgins and Stewart, 1964)

$$\xi = -\frac{1}{8} \frac{H^2 k}{\sinh 2kD}$$

where k is the wave number. The contribution due to breaking has been calculated by using observed values at the breaking point as initial values with ξ taken as zero (the portion due to breaking). The figures show that the general trends and magnitudes are correct and that the observed set-up "patches together" the portions contributed before and after the breaking point.

In all of the calculations shown so far B has been taken arbitrarily as 0.8, representing an energy dissipation rate 80% of that for a hydraulic jump of equal height. The dependence of results on this parameter is indicated in Figure 7, showing set-up for the conditions of Figure 6. It is seen that B = 0.6 would have shown better agreement with observation, but that the differences are relatively small.

DISCUSSION

The model presented here appears, from limited comparison with data, to be capable of adequate prediction of set-up and height decay in the breaking zone. Considerable improvement is possible, however.

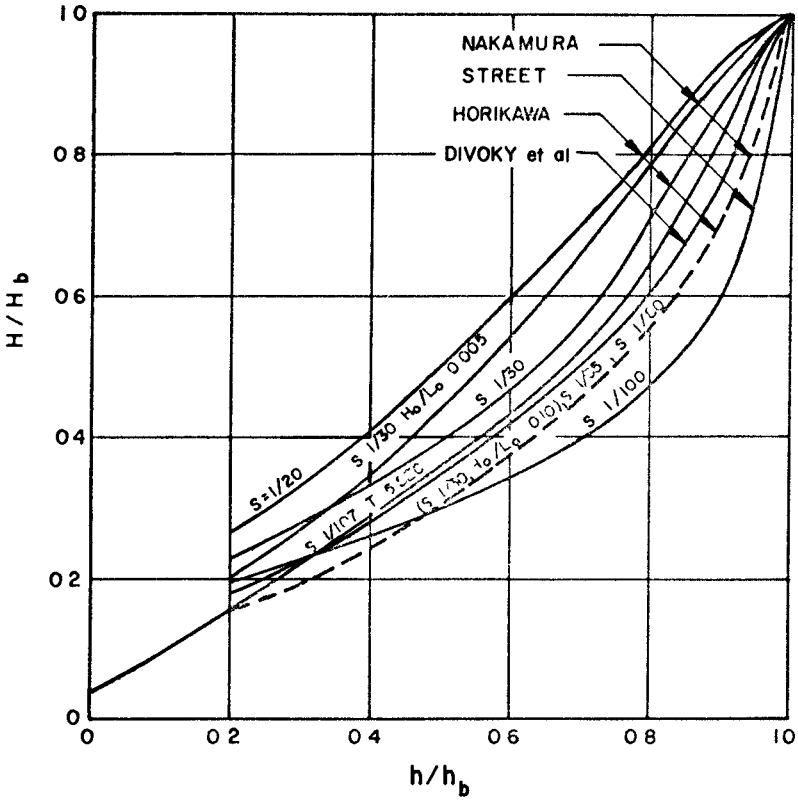


Figure 2 A Summary of Wave Transformation Data Shoreward of the Breaking Point

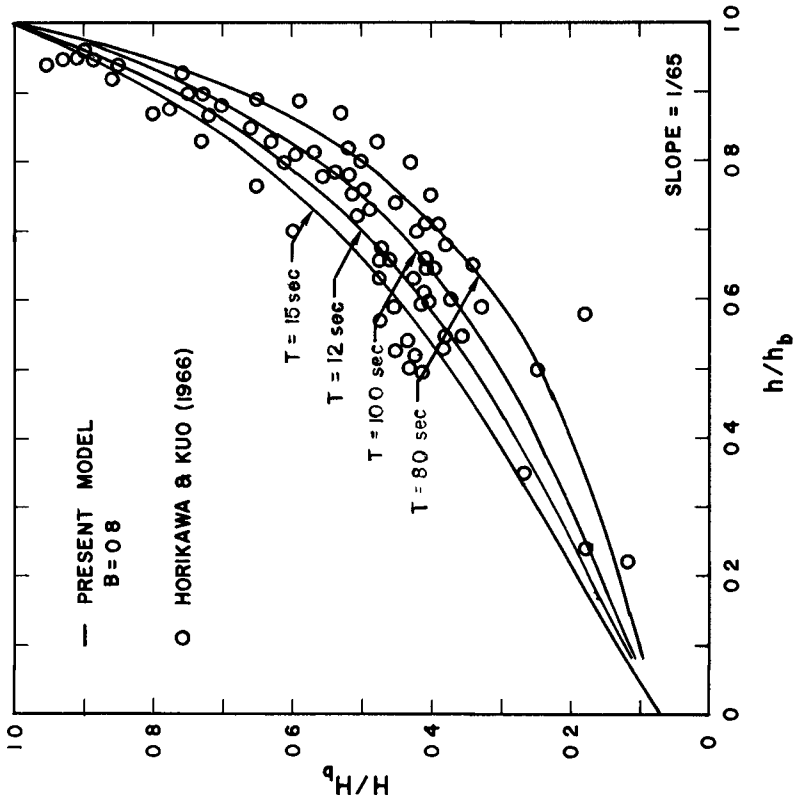


Figure 3 A Comparison of the Present Model with Data of Horikawa and Kuo (1966) for Wave Height Decay in the Breaking Zone

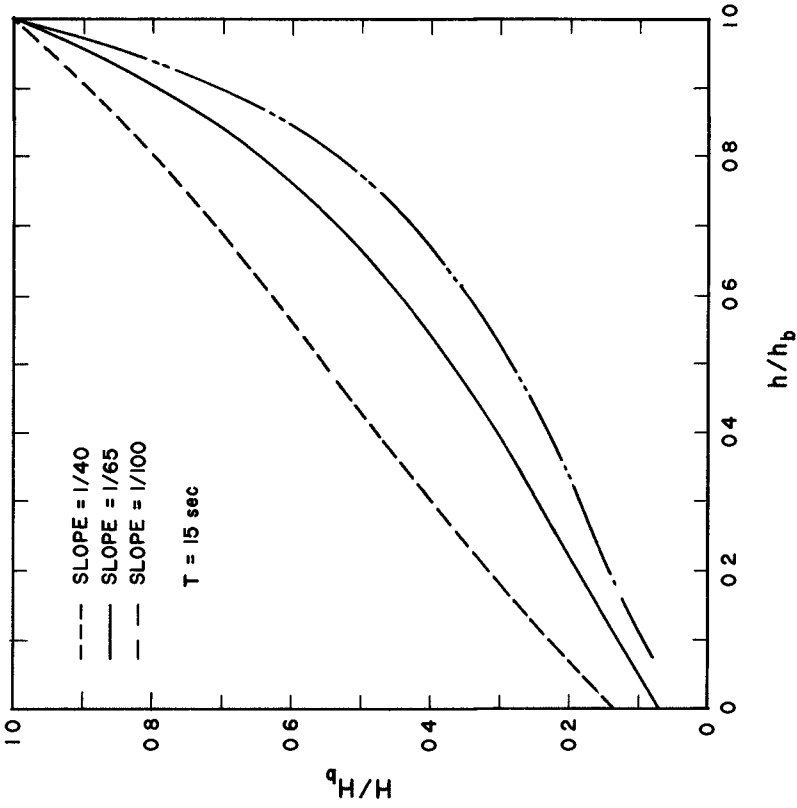


Figure 4 Results of the Present Model Showing Dependence of Height Decay in the Breaking Zone on Beach Slope

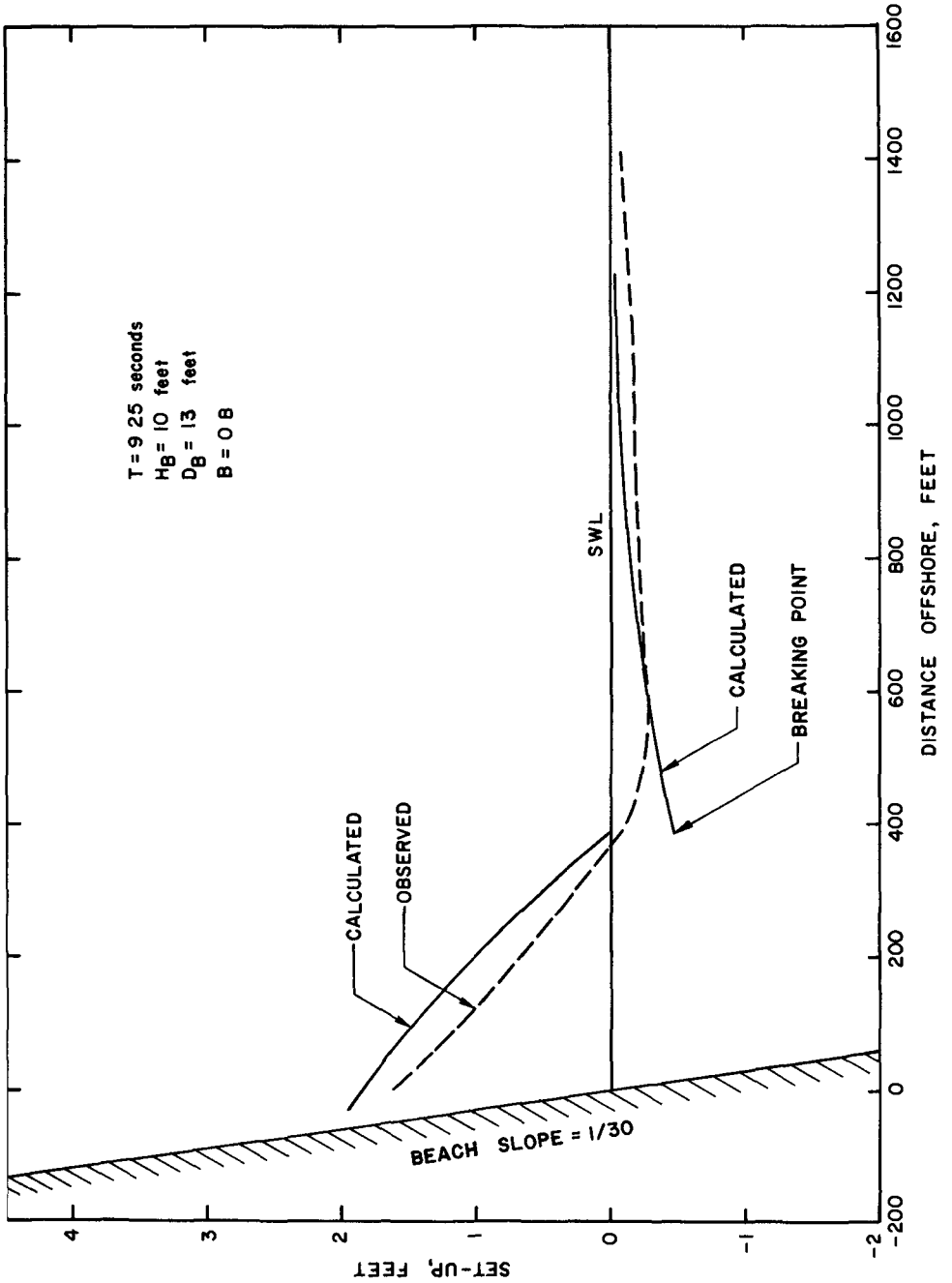
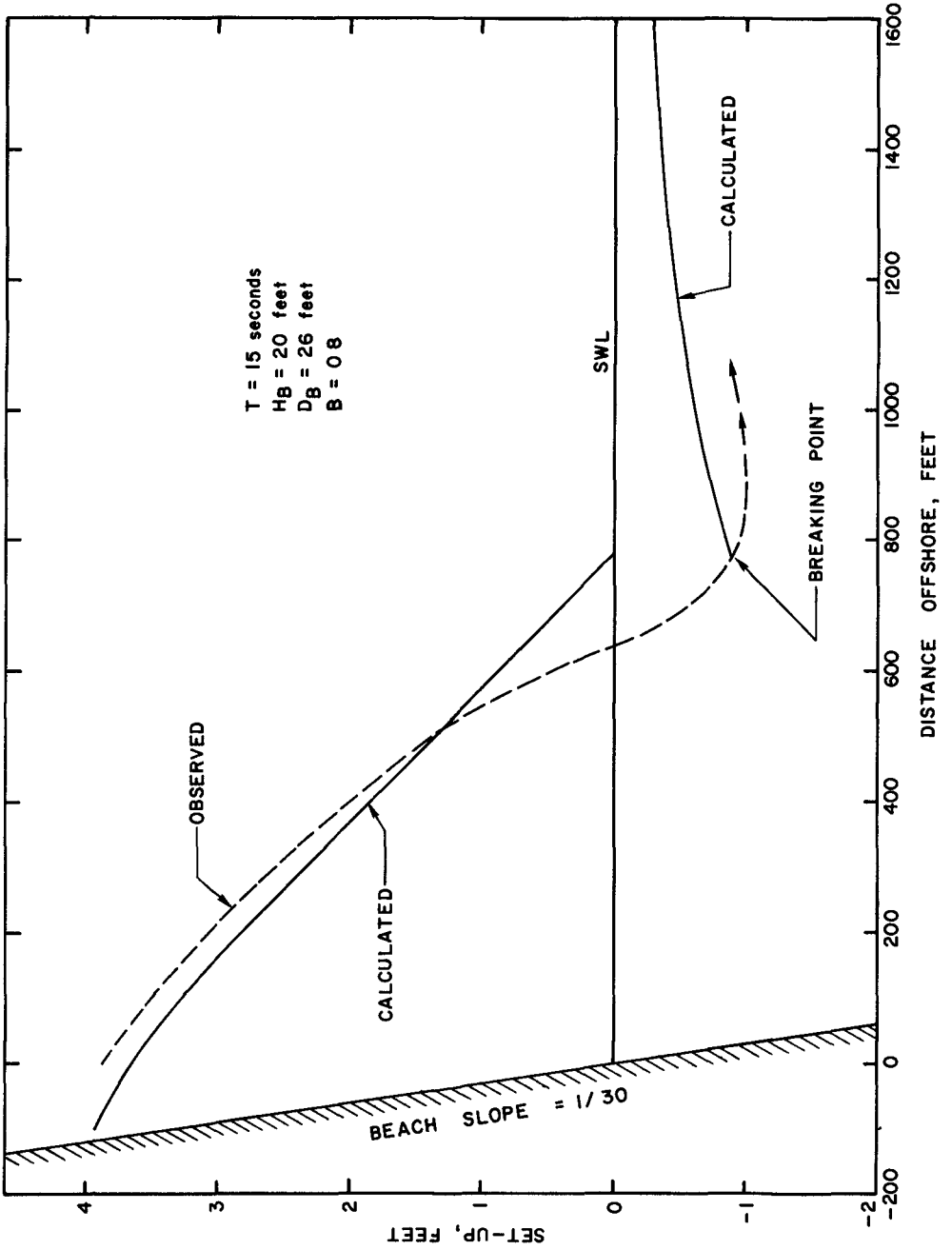


Figure 5 A Comparison of the Present Model of Breaking Wave Set-up with Data of Saville (1961)



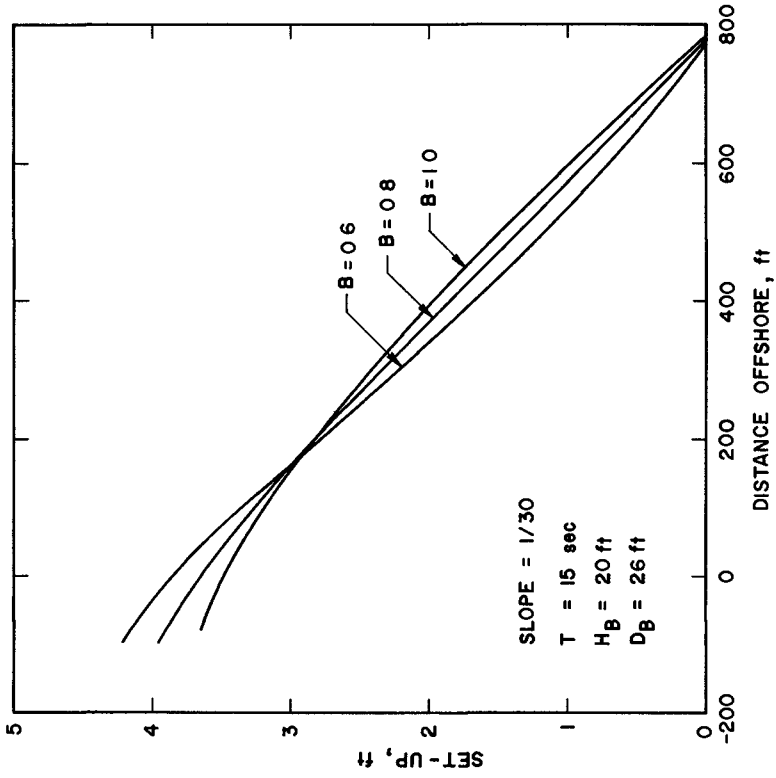


Figure 7 The Dependence of Breaking Wave Set-up (for the conditions of Figure 6) on the Breaking Parameter, B

In particular, the approximation to the momentum flux given in Equation (8) is especially primitive as noted, M can be computed directly from defining integrals, although this is difficult and inherently approximate for breaking waves if a non-breaking theory is adopted

The magnitude of the set-up at the shoreline is found, in accordance with the data of Saville (1961), to be quite large. It is pointed out that the Saville data, given in field magnitudes, was actually obtained in very small scale tests. Similarly, the data of Bowen, Inman, and Simmons (1968) was also taken at a small scale with periods on the order of one second and maximum set-up heights of a very few centimeters. For this reason, comparison with available data, including that of Saville, is somewhat problematic owing to the possibility of scale effects.

An interesting phenomenon observed by Bowen, Inman, and Simmons was a strong tendency for the set-up profile to become tangent to the beach slope, their analysis, which assumed a breaking wave height equal to a constant fraction of the total water depth, also showed this feature. The present model was unable to duplicate this, always showing a set-up profile convex-upward intersecting the beach, the data of Saville appears generally similar.

REFERENCES

- Bowen, A J, D L Inman, and V P Simmons (1968) "Wave 'Set-Down' and Set-Up," Journal of Geophysical Research, Vol 73, No 8
- Dvoky, D J, B J LeMéhauté, and A Lin (1970) "Breaking Waves on Gentle Slopes," Journal of Geophysical Research, Vol 75, No 9
- Freeman, J C and B J LeMéhauté (1964) "Wave Breakers on a Beach and Surge on a Dry Bed," ASCE, Journal of the Hydraulics Division, Vol 90, No HY2
- Horikawa, K and C T Kuo (1966) "A Study on Wave Transformation Inside the Surf Zone," Proceedings, Tenth Conf on Coastal Engineering, ASCE
- Hwang, Li-San (1970) "Wave Set-up of Nonperiodic Wave Train and Its Associated Shelf Oscillation," Journal of Geophysical Research, Vol 75, No 21
- Keulegan, G and G W Patterson (1940) "Mathematical Theory of Irrotational Water Waves," J Res NBS, Vol 24, No 1
- Longuet-Higgins, M S and R W Stewart (1960) "Changes in the Form of Short Gravity Waves on Long Waves and Tidal Streams," Journal of Fluid Mechanics, Vol 8
- Longuet-Higgins, M S and R W Stewart (1961) "The Changes in Amplitude of Short Gravity Waves on Steady Non-Uniform Currents," Journal of Fluid Mechanics, Vol 10
- Longuet-Higgins, M S and R W Stewart (1962) "Radiation Stress and Mass Transport in Gravity Waves, with Application to 'Surf Beats'," Journal of Fluid Mechanics, Vol 13, Part 4

- Longuet-Higgins, M S and R W Stewart (1964) "Radiation Stresses in Water Waves, A Physical Discussion with Applications," Deep-Sea Research, Vol 11
- Nakamura, M , H Shiraishi, and Y Sasaki (1966) "Wave Decaying Due to Breaking," Proc Tenth Conf on Coastal Engineering, ASCE
- Saville, T (1961) "Experimental Determination of Wave Set-up," Proc 2nd Tech Conf on Hurricanes, Miami, Fla
- Street, R L and F E Camfield (1966) "Observations and Experiments on Solitary Wave Deformation," Proc , Tenth Conf on Coastal Engineering, ASCE
- Van Dorn, W G , B LeMéhauté, and Li-San Hwang (1968) "Handbook of Explosion-Generated Water Waves Volume 1- State of the Art," Tetra Tech Rept TC-130, DASA - 1944

CHAPTER 24

AIR ENTRAINMENT AND ENERGY DISSIPATION IN BREAKERS

by Alfred FÜHRBOTER¹⁾

SUMMARY

Even in shallow water, only a part of wave energy is lost by turbulent viscosity and bottom friction, most of wave energy transfer takes place in the narrow zone of surf at the shore.

Till to the point of breaking, the theoretical conception of an one-phase flow may be applied to the problem. From beginning of breaking, however, the effect of aeration can not be neglected.

From a simple physical consideration, the sudden reduction of wave height and wave energy inside the surf zone can be explained by the entrainment of air bubbles into the water. Except compression and surface tension effects, most of wave energy is stored at first by the static energy of the air bubbles which are driven into the water.

Using idealized assumptions for calculation (uniform concentration of air bubbles a.s.o.), it can be shown that in a plunging breaker the wave energy is dissipated on a very short way (less than on wave length), for a spilling breaker however, this way is of the order of some wave lengths.

After formation of the air-water-mixture, the energy of the air bubbles is transformed by the microturbulence of the eddies in the turbulent wakes behind the uprising bubbles.

¹⁾Universitätsdozent Dr.-Ing., FRANZIUS-INSTITUT, Technical University of Hannover, Germany

So turbulence spectrum also is connected with the air content of the water, this shall be of importance for the sediment transport.

For model investigations of breaking waves heavy scale effects are to be expected from the air entrainment.

THEORETICAL CONSIDERATION

Inside the surf zone, wave height and energy are reduced suddenly by strong interactions, it shall be demonstrated here that the major part of wave energy is spent by surface interaction = air entrainment. For this demonstration, only simple assumptions and linear wave theory are used, the results would be essentially the same for higher order theories.

The total energy of a wave with the height H and the length L is on the width b

$$E = \frac{1}{8} \cdot \gamma \cdot b \cdot L \cdot H^2 \dots\dots\dots (1)$$

and a reduction of wave height dH gives the reduction of wave energy dE

$$dE = \frac{1}{4} \cdot \gamma \cdot b \cdot L \cdot H \cdot dH \dots\dots\dots (2)$$

The wave length L shall be stated to be constant during breaking.

This loss of (static and dynamic) energy must be transformed into other sorts of energy, so in turbulent motion and at last into heat by friction. But before the energy is going into turbulence, there is a transfer mechanism by air entrainment and foam production.

Fig. 1 shows a column of water with the height y and a volume of air Δy, when mixed together in such a matter, that there is a nearly uniform distribution of air bubbles in the water, the air concentration c, related to the vo-

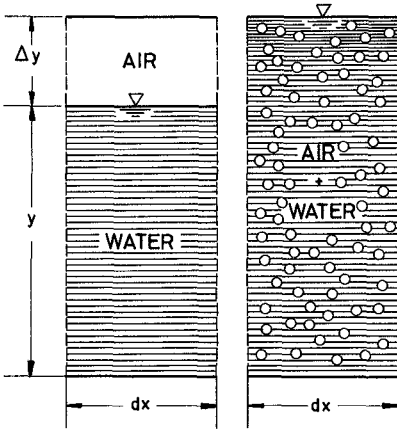


FIG. 1. - ENERGY CONSUMPTION BY AERATION

lumen with the height $y + \Delta y$, is

$$c = \frac{\Delta y}{y + \Delta y} \dots \dots \dots (3)$$

Neglecting the density of air, the static energy to bring a volume of air into the depth y below water surface is the same like to bring an equal volume of water into the height d above surface. For the length dx , the width b and an (uniform) air concentration c

therefore is (Fig. 1)

$$dE_{stat} = \gamma \cdot b \cdot dx \left(c \cdot \frac{y^2}{2} + \frac{\Delta y^2}{2} (1 - c) \right) \dots \dots \dots (4)$$

air in
water with

water
air above

level y

and with Δy from Eq. 3

$$dE_{stat} = \gamma \cdot b \cdot dx \cdot \frac{y^2}{2} \cdot \frac{c}{1-c} \dots \dots \dots (5)$$

This is only the static energy which is necessary to transfer the water column y and the air column Δy into a foam column $y + \Delta y$ (Fig. 1), additionally, energy losses by effects of (adiabatic) compression, surface tension and friction during the movement of the bubbles occur, these effects, however, are of small order compared with the static energy from Eq. 5.

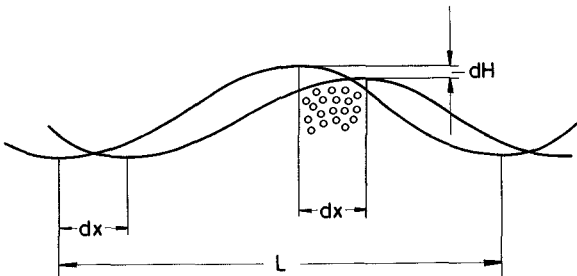


FIG. 2.

- WAVE HEIGHT REDUCTION

Now the reduction of wave height (Fig. 2) and the obligate loss of energy from Eq. 2 can be put together with Eq. 5 for the energy from aeration effect, with the assumption, that the energy amount dE on the way dx is spent completely for the aeration of a water column of the same length dx and the height y

$$\frac{dH}{dx} = -2 \cdot \frac{c}{1-c} \cdot \frac{y^2}{HL} \dots\dots\dots (6)$$

This is the differential equation for $H = H(x)$, the wave height inside the surf zone, for an evaluation, data are necessary for c and y , if there is no uniform distribution of the air bubbles, integrals have to be formed which represent the static energy of the air content.

But for a study only on the order of magnitude of aeration effect, for two special cases of breakers some rough assumptions can be made, so for the spilling breaker, that the depth of aeration is in a linear relation to the reduction of wave height $H(x)$

$$y \propto H(x) \text{ (spilling breaker)}$$

Then an integration of Eq. 6 gives with $H(x) = H_b$ for $x=0$ (point of breaking)

$$H(x) = H_b \cdot e^{-2 \cdot \frac{c}{1-c} \cdot \frac{x}{L}} \dots\dots\dots (7)$$

For a plunging breaker, in first approximation the depth of aeration y can be considered to be of same order of magnitude as the breaker height H_b and to be constant during the process of breaking.

$$y \propto H_b = \text{const (plunging breaker)}$$

Here integration of Eq. 6 gives with $H(x) = H_b$ for $x = 0$

$$H(x) = H_b \sqrt{1 - 4 \cdot \frac{c}{1-c} \cdot \frac{x}{L}} \dots\dots\dots (8)$$

On Fig. 3, the results of Eq. 7 and Eq. 8 are presented for air concentrations between 20 % and 40 % which may be probable for breaking waves. It is to be seen that for spilling breakers a way of some wave lengths is necessary for the reduction of initial wave height H_b , for the plunging breaker, however, a part of one wave length is enough for the total destruction of the wave, in agreement to observations in nature.

From wave theory as well as from the mechanism of the formation and the entrainment of the air bubbles, very many questions are open for the problem. Here only should be pointed out that even a simple model demonstrates clearly the importance of the aeration effect for the energy dissipation in surf zones, Eq. 7 and Eq. 8 together with Fig. 3 show that the aeration effect for itself is able to explain the high energy loss in breaking waves.

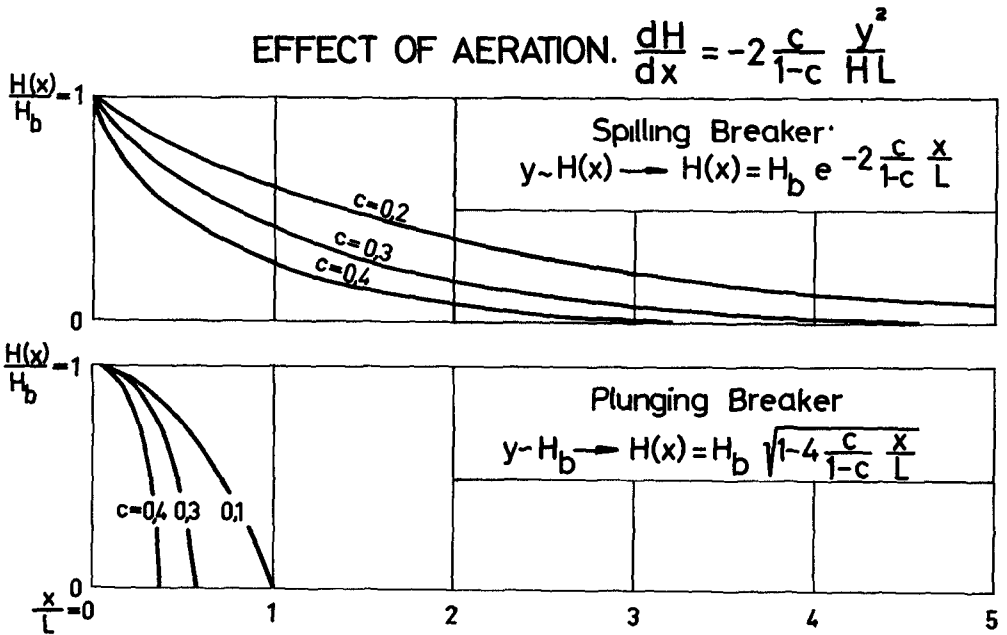


FIG. 3. - WAVE HEIGHT REDUCTION FOR SPILLING AND PLUNGING BREAKERS

DISCUSSION AND CONCLUSIONS

The static energy stored in the air bubbles afterwards is transformed in turbulent mixing and eddy production during the uprise of the bubbles to the surface. So the turbulence spectrum in the surf zone also is connected with aeration.

The amount of air entrainment, i.e. the concentration and distribution of air, is nearly unknown, especially for large breakers, but it seems to be sure that the air entrainment is not only a function of FROUDE's and REYNOLDS' but strongly also from WEBER's number. Surface tension and capillary effects will have influence on the process of breaking more for small than for large waves, for wave heights less than about one inch no aeration takes place. The interaction between a gas and a fluid is a well known but very complicated problem even for steady conditions in Processing and Chemical Engineering, for breaking waves the insteady process makes the difficulties increase, this is valid also for measurement of air concentration and distribution.

Indirectly, the investigations of SKLADNEV and KOPOV (ref. 4) give some ideas about the limits for scale models with breaking waves, they found for the special case of wave forces on a concrete slope that there are no scale effects for waves higher than 50 cm, waves from 3 cm till 120 cm were used for the test series, the wave height of 120 cm being thought as the prototype. For wave heights less than 50 cm, the forces scaled up after FROUDE's law became higher than measured with the prototype wave height of 120 cm, for waves 3 cm high more than two times. This effect is explained by the author explicitly by the decreasing air content. Similar considerations about the influence of the air content on impact forces (shock forces) also are given in ref. 1 and 2.

Even the beginning of breaking as "white capping" at the

wave crests is considered by HASSELMANN (ref. 3) to be a "strong interaction" compared with the "weak interaction" by bottom friction. Inside the surf zone, the water-air-interaction must be expected much stronger than the water-bottom-interactions.

Thinking the energy of an incoming wave at the point of breaking to be 100 %, it would be of highest interest to know how much percent of this energy is spent by water-air-interaction because only the difference can be effective for water-bottom-interactions, sediment transport, wave set-up and rip currents, wave run-up a.s.o.

Also of high importance is the question how far scale models are able to reproduce these processes, when the aeration effect is reduced by surface tension, the energy for the other effects mentioned above becomes higher than in prototype. So all problems of litoral processes are influenced by the aeration problem.

The production of air-water-mixtures by the different sizes and sorts of breakers therefore seems to be a first order problem for the physical process in surf zones. Measurements of air concentrations and bubble distributions are necessary together with wave height measurements in order to get a knowledge how much of the energy dissipation of a breaker is represented by the aeration effect given by Eq. 6.

REFERENCES

1. FÜHRBOTLER, A. Der Druckschlag durch Brecher auf Deichböschungen, Mitteilungen des Franzius-Instituts der Technischen Universität Hannover, Heft 28, 1966.
2. FÜHRBOTLER, A. Laboratory Investigation of Impact Forces, Paper No. 6, Symposium Research on Wave Action, Delft, March 24 - 28, 1969.

3. HASSELMANN, K. Weak Interaction Theory of
Ocean Waves, Basic Develop-
ments in Fluid Mechanics,
Vol. 2, Academic Press Inc.,
New York 1968.

4. SKLADNEV, M.F.
and POPOV, I.Ya.. Studies of Wave Loads on Con-
crete Slope Protections of
Earth Dams, Paper Nr. 7, Sym-
posium on Wave Action, Delft
March 24 - 28. 1969.

CHAPTER 25

PROBABILITIES OF BREAKING WAVE CHARACTERISTICS

J Ian Collins
Tetra Tech Inc
Pasadena California

ABSTRACT

Utilizing the hydrodynamic relationships for shoaling and refraction of waves approaching a shoreline over parallel bottom contours a procedure is developed to transform an arbitrary probability density of wave characteristics in deep water into the corresponding breaking characteristics in shallow water. A number of probability distributions for breaking wave characteristics are derived in terms of assumed deep water probability densities of wave heights, wave lengths and angles of approach. Some probability densities for wave heights at specific locations in the surf zone are computed for a Rayleigh distribution in deep water. The probability computations are used to derive the expectation of energy flux and its distribution.

INTRODUCTION

Many experimental investigations of breaking waves, longshore currents and littoral drift have been made. Sometimes the results have been expressed in terms of deep water wave characteristics and sometimes in terms of breaking wave characteristics making comparisons of various data a difficult task. In some instances the wave characteristics at some intermediate water depth are given. The laws of hydrodynamics can be used to relate deep and shallow water characteristics if bottom friction effects are neglected.

Earlier theoretical work of LeMéhauté (1961), LeMéhauté and Webb (1964) and LeMéhauté and Koh (1967) have proposed methods of computing shallow water wave characteristics in terms of deep water wave characteristics for periodic waves using first, third and fifth order Stokian wave theories.

It is well known that naturally occurring sea conditions can be characterized only in statistical terms. Such terms include the spectrum, the average wave height, significant wave height, mean wave period, etc. The sea state in deep water can be characterized by a probability distribution of wave heights, wave lengths and angles of approach to the shore.

The reason for the choice of characteristics in terms of probability distributions rather than the spectrum is purely for convenience in considering the behavior of waves in the surf zone as individual crests. Relationships between spectra and probability of wave height and wave period have been demonstrated by Longuet-Higgins (1952, 1957), Bretschneider (1959), Collins (1967) and others.

The usual method of treating a wave traveling in gradually varying water depths has been to use the wave theories for a horizontal bed and to account for the effects of bottom variation by considering energy conservation. Biesel (1951) and many others, and more recently Mei, Tlapa and Eagleson (1968) have proposed theoretical approaches to wave propagation over variable depth. The traditional method of treating waves over gradually varying bottom topography will be adopted. It will also be assumed that the linear wave theory (first order) can be applied up to the point of breaking. Non-linear effects (peak-up effect) which are important near breaking are, to some extent, empirically taken into account in the breaking criteria.

In this paper an attempt has been made to apply the hydrodynamic theories of shoaling, refraction and wave breaking to statistical models of the sea. Examples of computations are given for a plane beach. Generally the wave characteristics in deep water are assumed and the corresponding characteristics in shallow water including the surf zone are computed.

One-dimensional (wave height, wave length or wave direction) and two-dimensional (wave height and wave length) probability distributions are given. The general solution for a three-dimensional probability distribution is derived for two different wave breaking criteria.

The results of the computations of wave probabilities in shallow water are used to compute expected values of energy flux in the surf zone as a function of depth of water. A similar approach to determine longshore current distribution is proposed.

GENERAL DISCUSSION

Governing Equations of Wave Transformation

The dispersion relationship for waves is written

$$L_b/L_o = \tanh 2\pi d_b/L_b \quad (1)$$

where the subscript b refers to conditions at breaking, the subscript o refers to conditions in deep water (see figure 1). L is the wave length, d is the water depth.

Snell's law can be used

$$L_o/L_b = \sin \alpha_o / \sin \alpha_b \quad (2)$$

where d is the angle of the wave crest with the shoreline.

The choice of a suitable breaking criterion is required. Experimental investigations on this phenomenon in two-dimensional wave tanks have been made notably by Iversen (1952), Hamada (1963) and Suquet (1950). The following criterion fits the data very closely (after LeMehauté and Koh, 1967)

$$H_b/H_o = 0.76S^{1/7} (H_o/L_o)^{-1/4}$$

where S is the bottom slope and H is the wave height. For waves breaking at an angle, the bottom slope is actually $S \cos \alpha_b$ and H_o should be replaced by $H_o \cos^{1/2} \alpha_o$. The breaking criterion becomes

$$H_b/H_o = 0.76S^{1/7} \cos^{1/7} \alpha_b (H_o/L_o)^{-1/4} \cos^{3/8} \alpha_o \quad (3)$$

where S is the slope at breaking. An alternate breaking criterion was also used

$$H_b/d_b = 0.72 + 5.6S \quad (4)$$

if bottom friction effects are neglected then the wave height change up to breaking can be computed from the conservation of energy as $H_b = K_r K_s H_o$ which over a beach with parallel bottom contours will be used in the form

$$H_b/H_o = \left\{ \tanh k_b d_b \left[1 + 2k_b d_b / \sinh 2k_b d_b \right] \cos \alpha_b / \cos \alpha_o \right\}^{-1/2} \quad (5)$$

where

$$k_b = 2\pi/L_b$$

Equations 1, 2, 5 and 3 or 4 provide a system of equations such that a given deep water wave characterized by H_o, L_o, α_o yields a unique breaking wave

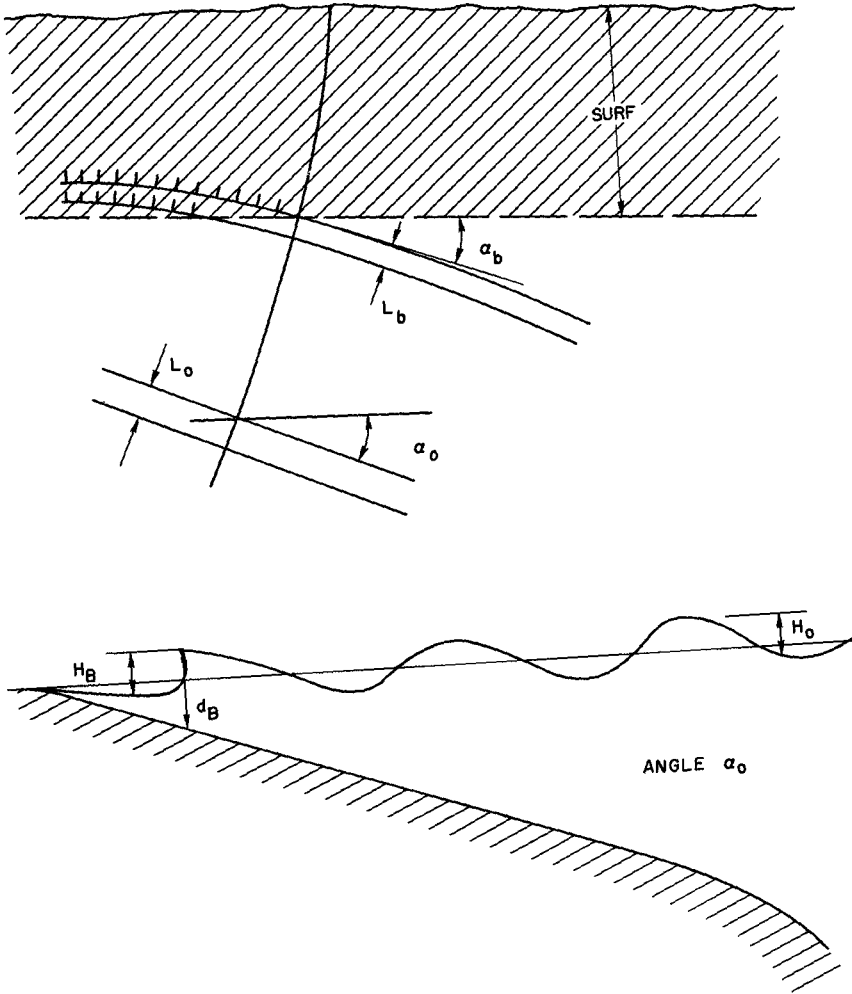


Figure 1 Illustration of Nomenclature Used In Wave Transformation

characterized by H_b, L_b, α_b . In fact the solution of these equations for the breaking characteristics requires a step-by-step or iterative procedure since the dependent variables cannot be separated.

Breaking Waves

The methods of the preceding section yield the information H_b, L_b, α_b, d_b for any specified deep water values H_o, L_o, α_o . Another problem of interest can be stated: given H_o, L_o, α_o - what is H, L, α at a specified location $d = d_c$? Three separate conditions must be recognized:

$$(a) d_c > d_b \quad (b) d_c < d_b \quad (c) d_c = d_b$$

When d_c is greater than d_b , Eqs. 1, 2, and 5 can be applied directly to compute H_c, L_c, α_c . The case $d_c = d_b$ can also be included. When d_c is less than d_b , the wave has broken farther offshore and some of its energy has been dissipated. The decay of wave height after breaking has been studied by Horikawa and Kuo (1966), Street and Camfield (1966), Nakamura, Shiraishi and Sasaki (1966) and Divoky, LeMéhauté and Lin (1969). The experimental results are summarized in Figure 2 (after Divoky et al. 1969).

For purposes of the present study, the wave height at $d = d_c$ after breaking was taken as

$$H_c = H_b \frac{d_c}{d_b} \tag{6}$$

1 e a linear wave height decay from the breaking point to the shore

The angle and wave length of the broken wave at $d = d_c$ were computed from the refraction laws for long waves

$$L_c = L_b \left(\frac{d_c}{d_b} \right)^{\frac{1}{2}} \tag{7}$$

$$\sin \alpha_c = \sin \alpha_b \left(\frac{d_c}{d_b} \right)^{\frac{1}{2}} \tag{8}$$

Probability Distributions

Assuming that the statistical properties of the deep water wave characteristics are known, the system of equations 2 through 5 will enable the determination of the statistical properties of shallow water waves up to breaking. The problem can be stated: given $p(H_o, L_o, \alpha_o)$ determine $p(H_b, L_b, \alpha_b, d_b)$ subject to the relationships of equations 1 through 5. At breaking, only three conditions need to be specified (The fourth can be found in terms of the other three). The general solution is,

$$p(H_b, L_b, \alpha_b) = p(H_o, L_o, \alpha_o) |J|^{-1} \tag{9}$$

where

$$|J| = \begin{vmatrix} \frac{\partial H_b}{\partial H_o} & \frac{\partial H_b}{\partial L_o} & \frac{\partial H_b}{\partial \alpha_o} \\ \frac{\partial L_b}{\partial H_o} & \frac{\partial L_b}{\partial L_o} & \frac{\partial L_b}{\partial \alpha_o} \\ \frac{\partial \alpha_b}{\partial H_o} & \frac{\partial \alpha_b}{\partial L_o} & \frac{\partial \alpha_b}{\partial \alpha_o} \end{vmatrix} \tag{10}$$

The partial derivatives have to be determined from equations 2 through 5. Generally it is seen that if equations 2 through 5 are differentiated by each variable H_o, L_o, α_o one at a time, a system of 12 simultaneous equations are derived which have to be solved for the partial derivatives before substitution into

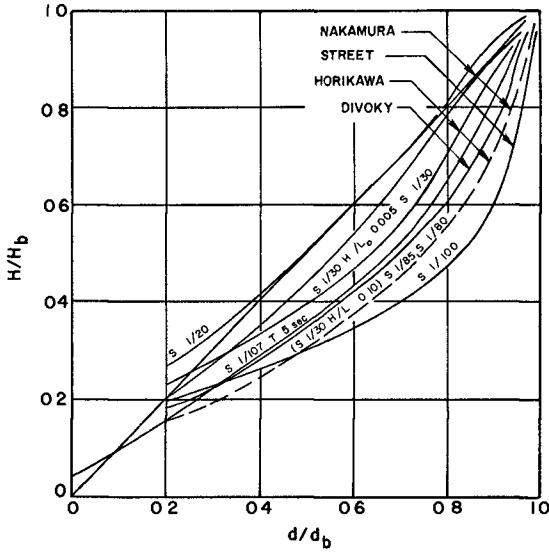


Figure 2 Summary of Experimental Data on Wave Height Decay After Breaking

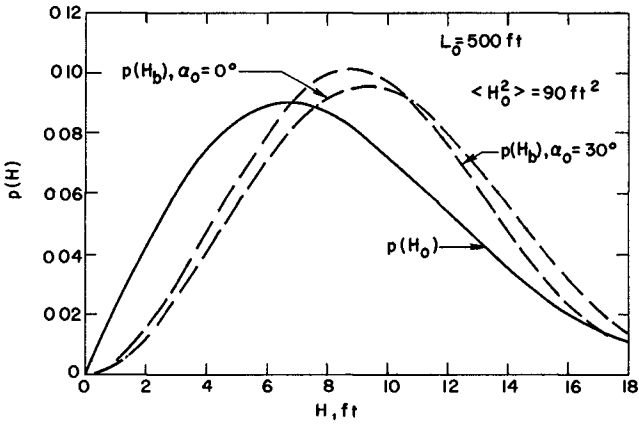


Figure 3 Probability Densities of Breaking Waves Height for Two Angles of Approach in Deep Water

equation 10 The entire procedure is straightforward (but tedious) unless J contains zeros Special consideration must be given to regions where J changes sign

SPECIFIC APPLICATIONS

One-Dimensional Probability Distribution

Assuming that the wave characteristics are specified in deep water such that

$$L_o = \text{constant} \quad \alpha_o = \text{constant}$$

H_o has the probability distribution

$$p(H_o) = 2H_o / \langle H_o^2 \rangle \exp \left[- H_o^2 / \langle H_o^2 \rangle \right] \quad (11)$$

$\langle \rangle$ denotes mean value

then

$$p(H_b) = p(H_o) \partial H_o / \partial H_b \quad (12)$$

$$p(L_b) = p(H_o) \partial H_o / \partial L_b \quad (13)$$

$$p(\alpha_b) = p(H_o) \partial H_o / \partial \alpha_b \quad (14)$$

The values of the differentials can be determined analytically or they can be calculated numerically by finite difference approximations

Examples of some sample cases computed for one-dimensional deep water probabilities are given as Figures 3 through 5 The probabilities shown are computed for breaking characteristics at whatever location they occur Figure 3 illustrates the effect on the probability of breaking wave heights for different angles of approach in deep water This probability is not too sensitive to the angle of approach

Figure 4 indicates the effect of various deep water wave lengths on the probability distribution of breaking wave heights for a deep water angle of approach of 30° As expected it is seen that increased deep water wave lengths lead to larger breaking wave heights The probability distributions are shifted toward higher values of wave height Figure 5 shows the effect of increased wave length in deep water on the angles of breaking waves for a Rayleigh-type deep water wave height distribution Once more as anticipated larger wave lengths tend to refract more and break more nearly parallel to the shore

Examples of computations for the probability densities of wave characteristics at a specific location are given as Figures 6 and 7 These two figures differ from figures 3 through 5 in that they present wave height probabilities at a fixed location Both broken and non-breaking waves are present All of the figures show a sharp rise in the probability density of wave heights at the breaking limit

Two-Dimensional Probability Distributions

The two-dimensional probability of breaking characteristics indicate the joint probability of breaking wave height and wave length Complete numerical computations have not been made since in this case the roots of the Jacobian must first be investigated One simplification which permitted numerical results to be obtained follows from the assumption that wave breaking occurs

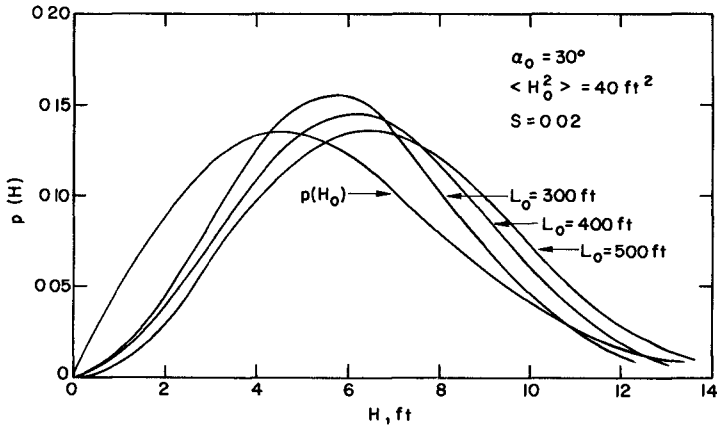


Figure 4 Probability Densities of Breaking Wave Heights for Various Deep Water Wave Lengths

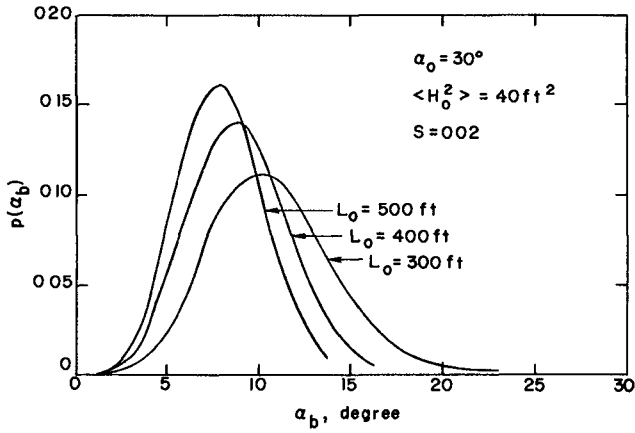


Figure 5 Probability Densities of Breaking Wave Angles for Various Deep Water Wave Lengths

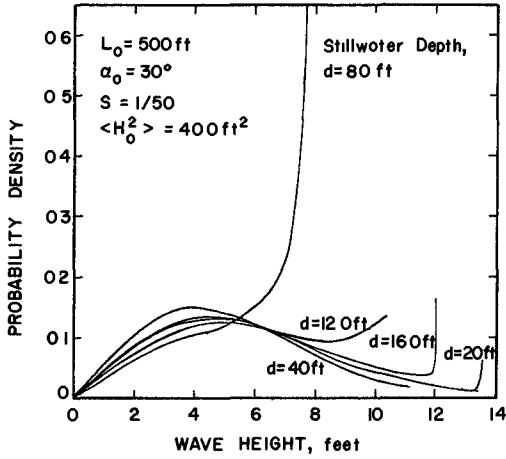


Figure 6 Probability Densities of Wave Heights at Specific Locations for $L_o = 500$ ft $\alpha_o = 30^\circ$ $S = 1/50$

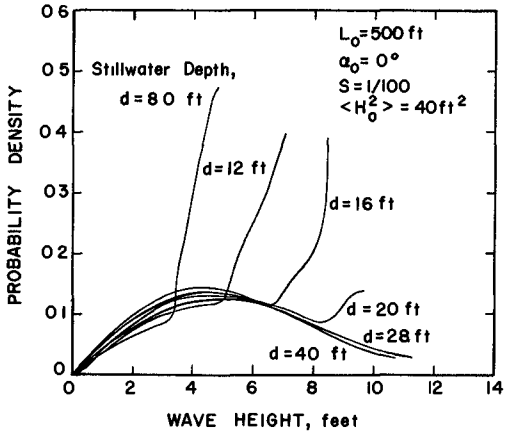


Figure 7 Probability Densities of Wave Heights at Specific Locations for $L_o = 500$ ft $\alpha_o = 0^\circ$ $S = 1/100$

in shallow water only, i.e. d/L at breaking is small. Then it follows that equation 5 becomes

$$H_b/H_o \approx \left[\cos \alpha_o / \cos \alpha_b \cdot 1/\sqrt{2k_d d_b} \right]^{\frac{1}{2}} \tag{15}$$

equation 1 becomes

$$L_b/L_o \approx k_b d_b \tag{16}$$

A comparison between equation 15 and equation 5 when $\alpha = 0$ is shown as Figure 8. It is seen that the differences are very small when d/L is less than 0.05.

Substitution of equations 16 and 2 into equation 15 yields the interesting result

$$H_b/H_o = 0.5 \left[\sin 2\alpha_o / \sin 2\alpha_b \right]^{\frac{1}{2}} \tag{17}$$

which has the limit $H_b/H_o = \left[L_o/L_b \right]^{\frac{1}{2}}$ when $\alpha_o = 0$ as might be expected.

The corresponding Jacobian is

$$J = \frac{\partial(H_o, L_o)}{\partial(H_b, L_b)} = \left\{ \frac{L_b}{L_o} - \frac{\cos \alpha_b}{\sin \alpha_o} \frac{\sin 2\alpha_o}{\cos 2\alpha_b} \right. \\ \left. \cdot \frac{1}{6A^2} \left(\frac{H_o}{L_o} \right)^{\frac{1}{2}} \right\} \frac{3A}{4} \left(\frac{H_o}{L_o} \right)^{-\frac{1}{4}} \cos^{3/8} \alpha_o \tag{18}$$

where $A = 0.76S^{1/7}$

Figure 9 shows an assumed deep water probability distribution $p(H_o, L_o)$ corresponding to a joint Rayleigh distribution with zero correlation between wave height and wave period (Bretschneider, 1959). The corresponding breaking wave characteristics $p(H_b, L_b) = p(H_o, L_o) |J|^{-1}$ are shown for

$\alpha_o = 0$ and $\alpha_o = 30^\circ$ as Figures 10 and 11 for the breaking condition of equation 3.

Figure 12 presents $p(H_b, L_b)$ for the depth limited breaking criterion.

It is seen from Figures 10 and 11 that the effect of the deep water angle of approach on breaking wave heights and lengths is relatively minor. A comparison of Figure 10 with 12 shows that the breaking wave steepness is very sensitive to the choice of breaking criteria.

Figure 13 compares the probability density of wave height determined from the one-dimensional computations and the marginal distribution for the two-dimensional distributions using two breaking criteria.

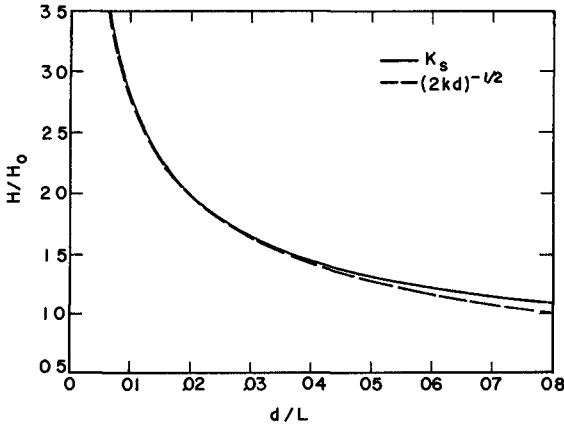


Figure 8 Comparison of Shoaling Coefficients Given by Equation 5 and Equation 17

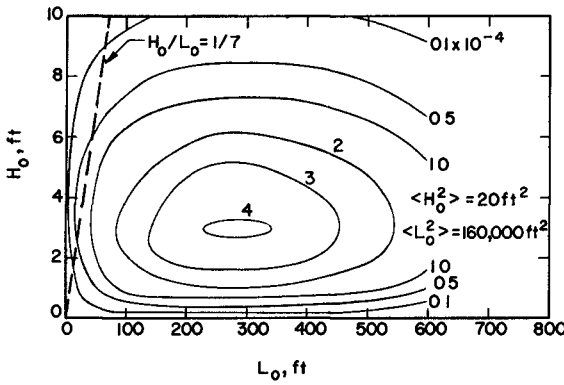


Figure 9 Two Dimension Probability Density of Deep Water Length and Wave Height for Joint Uncorrelated Raleigh Distribution

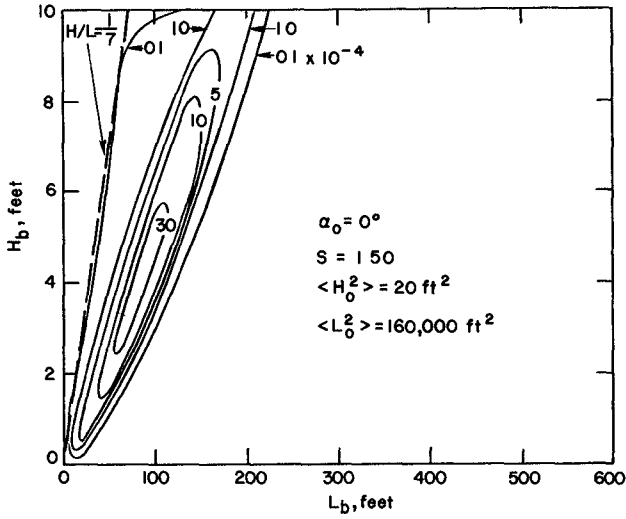


Figure 10 Two Dimensional Probability Density of Breaking Wave Characteristics for $\alpha_0 = 0$

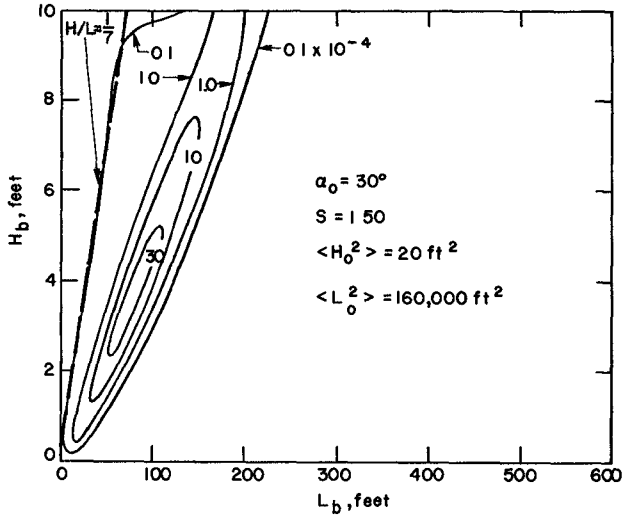


Figure 11 Two Dimensional Probability Density of Breaking Wave Characteristics for $\alpha_0 = 30^\circ$

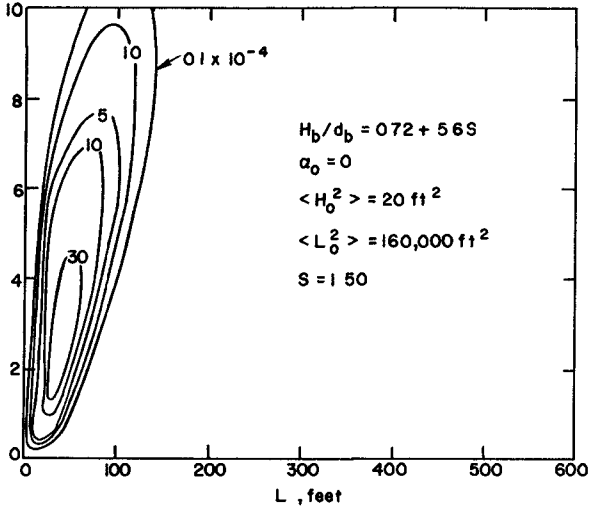


Figure 12 Two Dimensional Probability Density of Breaking Wave Characteristics for $\alpha_0 = 0$ and Depth Limited Breaking Criterion

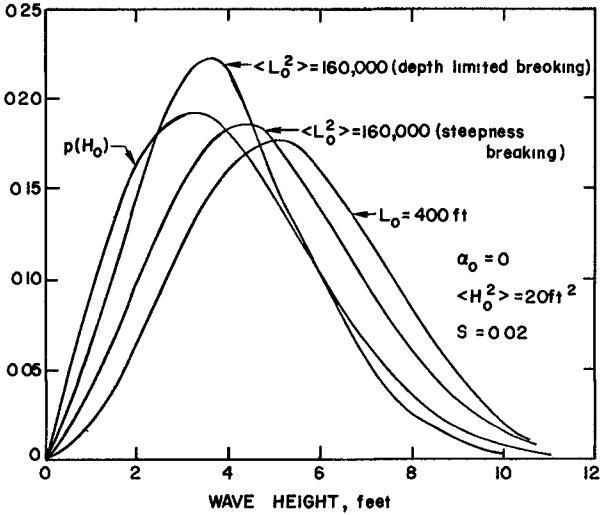


Figure 13 A Comparison of Marginal Distributions of Breaking Wave Heights from Two Dimensional Probability Densities with the Results for a One Dimensional Computation

LONGSHORE CURRENT AND ENERGY FLUX
FOR RANDOM WAVES IN THE SURF ZONE

The mean value of a function of H , L and α in a random sea can be derived from the equation for uniform periodic waves following a well known theorem of probability given a function of $f(x, y)$ in which the probability distributions of x and y are known, the mean value of the function $f(x, y)$ is given by

$$\langle f(x, y) \rangle = \iint f(x, y) p(x, y) dx dy$$

where $p(x, y)$ is the joint probability density of x and y . Hence a longshore current equation derived for uniform periodic waves, $V_L = V_L(H, L, \alpha)$ can be applied to random waves if the random values of H , L and α are weighted correctly.

The mean value of V_L in a random sea is given by

$$\langle V_L \rangle = \iiint V_L(H, L, \alpha) p(H, L, \alpha) dH dL d\alpha$$

which can be considered as the result of superimposing all of the wave heights, wave lengths and angles which are present and weighting the effect of each one by its probability of occurrence.

A set of sample calculations for longshore and onshore energy flux has been worked out. The mean longshore energy flux is given by

$$\begin{aligned} \frac{1}{\rho g} \langle F \rangle_L &= \iiint \frac{1}{8} \sqrt{\frac{g}{2\pi}} \frac{H^2 L n}{\sqrt{L_0}} \cos \alpha p(H, L, \alpha) dH dL d\alpha \\ &\quad \text{non-breaking} \\ &+ \iiint \frac{8}{3\sqrt{3}} \sqrt{\frac{g}{2\pi}} \left[\frac{(Hd)^3}{L_0} \right]^{\frac{1}{2}} \cos \alpha p(H, L, \alpha) dH dL d\alpha \\ &\quad \text{breaking} \end{aligned} \tag{19}$$

since

$$\Gamma = \sqrt{\frac{2\pi}{g}} \sqrt{L_0} \tag{20}$$

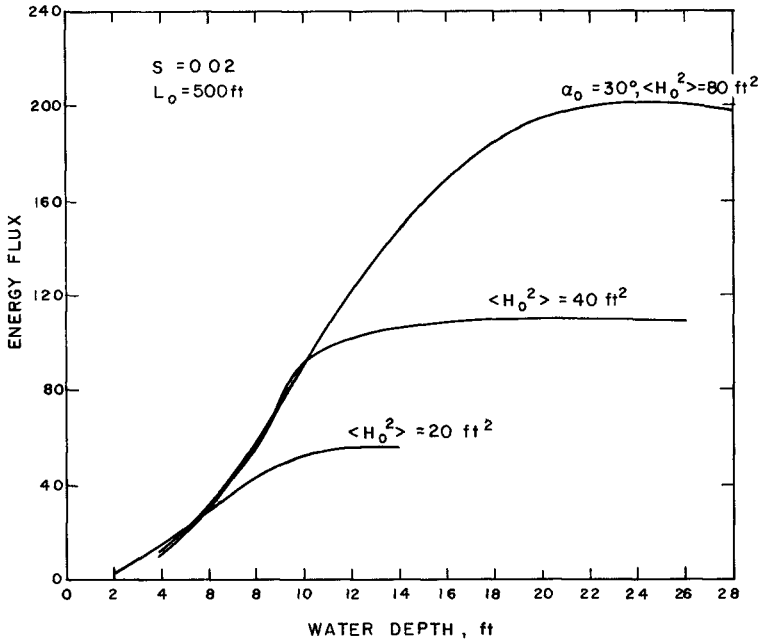
Also by definition $p(H, L, \alpha) dH dL d\alpha \equiv p(H_0, L_0, \alpha_0) dH_0 dL_0 d\alpha_0$ and the integrals can be approximated by summation

$$\begin{aligned} \frac{1}{\rho g} \langle F \rangle_L &= \frac{1}{8} \sqrt{\frac{g}{2\pi}} \sum \left\{ \frac{H^2 L}{\sqrt{L_0}} \cos \alpha p(H_0, L_0, \alpha_0) \Delta H_0 \Delta L_0 \Delta \alpha_0 \right\} \\ &\quad \text{non-breaking} \\ &+ \frac{8}{3} \sqrt{\frac{g}{2\pi}} \sum \left\{ \left[\frac{(Hd)^3}{L_0} \right]^{\frac{1}{2}} \cos \alpha p(H_0, L_0, \alpha_0) \Delta H_0 \Delta L_0 \Delta \alpha_0 \right\} \\ &\quad \text{breaking} \end{aligned} \tag{21}$$

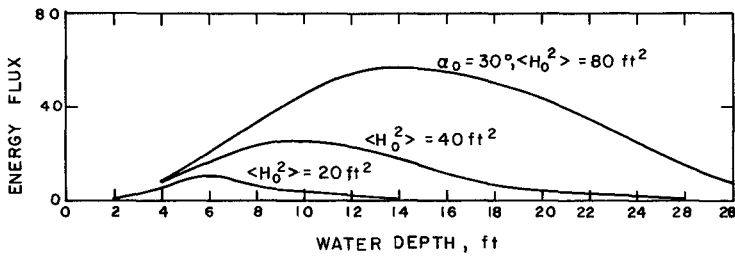
The mean onshore energy flux is defined with $\sin \alpha$ replacing $\cos \alpha$ in equation 21. An example of the computations using equation 21 is given as Figure 14. Figure 14 illustrates the variation of onshore energy flux in the surf zone. The variation of longshore energy flux is similar but absolute values of flux are smaller. In this figure the deep water wave length and angle of approach were taken as constant and the deep water waves were characterized by a probability distribution of wave heights.

REFERENCES

- Biesel F (1952) "Study of Wave Propagation in Water of Gradually Varying Depth" in Gravity Waves U S Department of Commerce N B S Circular 521
- Bretschneider C L (1959) "Wave Variability and Wave Spectra for Wind-Generated Gravity Waves" Technical Memorandum No 118 Beach Erosion Board August
- Collins, J I (1967) "Wave Statistics from Hurricane Dora", Journal Waterways and Harbors Division A S C E May
- Divoky D, LeMéhauté and Lin A (1969) "Breaking Waves on Gentle Slopes", A S C E Annual Meeting New Orleans Louisiana February
- Hamada T (1963) "Breakers and Beach Erosion" Port and Harbor Technical Research Institute Ministry of Transportation Japan
- Horikawa K and Kuo, C T (1966) "A Study on Wave Transformation Inside Surf Zone" Proc 10th Conference Coastal Engineering A S C E Vol 1
- Iverson H W (1952) "Laboratory Study of Breakers" in Gravity Waves U S Department of Commerce N B S Circular 521
- LeMéhauté B (1961) "Theoretical Study of Wave Breaking at an Angle with a Shoreline" Journal of Geophysical Research February
- LeMéhauté, B and Webb L (1964) "Periodic Gravity Waves Over a Gentle Slope at a Third Order of Approximation" Proc 9th Conference on Coastal Engineering, Lisbon
- Miche R (1944) "Mouvements Ondulatoires de la Mer en Profondeur Constante ou Decroissante" Ann des Pouts et Chau
- LeMéhauté B and Koh, R C Y (1967) "On the Breaking of Waves Arriving at an Angle to the Shore" Journal of Hydraulic Research, Vol 5 No 1
- Longuet-Higgins M S (1952) "On the Statistical Distribution of the Heights of Sea Waves", Journal of Marine Research, Vol 11 No 3
- Longuet-Higgins M S (1957) "The Statistical Analysis of a Random Moving Surface" Phil Trans Royal Soc of London A-966
- Méi, C C, Tlapa G A and Eagleson, P S (1968) "An Asymptotic Theory for Water Waves on Beaches of Mild Slope", Journal of Geophysical Research Vol 73 No 14 July
- Nakamura M, Shirouishi, H and Sasaki Y (1966) "Wave Decaying Due to Breaking" Proc 10th Conference Coastal Engineering A S C E Vol 1
- Street, R L and Camfield, F E (1966) "Observations and Experiments on Solitary Wave Deformation", Proc 10th Conf Coastal Engineering A S C E Vol 1
- Suquet F (1959) "Experimental Study on the Breaking of Waves", La Houille Blanche No 3 May-June



(a) Total Flux



(b) Breaking Flux

Figure 14 Onshore Energy Flux as a Function of Water Depth for Various Mean Square Wave Heights

ACKNOWLEDGMENT

This work was originally performed for the Office of Naval Research
Geography Branch under contract number N 00014-69-C-0107

CHAPTER 26

CHARACTERISTICS OF WAVES BROKEN BY A LONGSHORE BAR

By

E. Clark McNair, Jr.¹ and Robert M. Sorensen²

ABSTRACT

A two-dimensional model submerged offshore bar was installed in a Texas A&M Hydrodynamics Laboratory wave tank. Monochromatic waves with a range of heights and periods were generated at this bar for three different depths of water over the bar. For each wave, water surface time-histories were measured at points before and after the bar and spectral analyses of these measurements were performed.

The analysis of each wave record yielded an equivalent wave height which is proportional to the square root of the wave energy per unit surface area. The ratio of the reformed to incident equivalent wave height is shown to relate to the ratio of incident wave height to water depth over the bar. The predominant periods of the reformed waves are found to be the same as for the incident waves but the presence of energy at higher frequencies is also observed. The cause of these higher frequency waves is discussed.

INTRODUCTION

During parts of the year, generally the winter months, intense storms at sea generate waves that are quite steep. These waves, upon reaching the shore, will erode material from the beaches and deposit this material some distance from the shoreline. Continued deposition of material results in the formation of a longshore bar. A typical bar formation will have a rather gently sloping face toward the sea, a rounded crest, and a steep slope downward into a trough in the lee of the crest. These bar formations are generally of transient nature in shape and location.

After a wave breaks over the bar and reforms, questions arise concerning the characteristics and energy of the resulting wave form, particularly if expensive structures are to be placed where the wave can act on them or if the shore is composed of material which can be carried away by the waves. The object of the research described herein was to define some of the characteristics, particularly the heights and periods, of waves which have broken while passing a longshore bar and have reformed in the lee of the bar.

¹ Research Hydraulic Engineer, USAE Waterways Experiment Station, Vicksburg, Mississippi

² Assoc. Prof. of Civil Engineering, Texas A&M University, College Station, Texas

REVIEW OF THE LITERATURE

Investigations concerning breaking waves have been conducted by Iverson (7), Nakamura (9), and others (4, 5). However, the beach slopes used in those studies were such that the water depths never increased shoreward of the breaking point of the waves. The work of Iverson showed that if the beach slope and the deepwater wave steepness are known, several characteristics of the breaking wave, including the height of the wave and the water depth at the breaking point, can be predicted.

Investigations have also been performed with submerged rectangular breakwaters where waves approach the breakwater in fairly deep water, peak up and break over the relatively shallow structure, and then reform in the deeper water in the lee of the structure. Tests conducted by Dick (1) with such breakwaters indicated that as a wave passed over the structure and broke, it was reduced to a fundamental wave whose period was the same as the incident wave but whose height was lower than the incident wave. He also found lesser waves of higher frequency superimposed on the fundamental wave.

Nakamura, Shiraiishi, and Sasaki (10) also conducted experiments with submerged breakwaters. Their test results indicated alterations of wave length and period as the waves broke on the submerged dike. For instance, their data showed that for a depth in the lee of the breakwater equal to 10 percent of the deepwater wave length, the wave length in the lee of the breakwater was reduced to approximately 30 percent of the deepwater length and the wave period was reduced to approximately 60 percent of the deepwater period.

Diephuis (2) has reported on a hydraulic model study conducted at the Hydraulics Laboratory, Delft, Netherlands, to study the transmission of wave energy past submerged bars. Although much of his data were taken in the range of wave lengths and heights where surface tension and viscous effects play a large role in wave attenuation, his tests indicate that the wave heights in the lee of the bar where water depths are constant are some function of the deepwater wave steepness and that the heights of the reformed waves are more-or-less constant.

THE LABORATORY STUDY

A laboratory experiment was devised to study the characteristics of gravity water waves after the waves had encountered a two-dimensional long-shore bar and had broken while passing the bar. A model simulating a long-shore bar formation was designed and installed in a two-dimensional wave channel in the Hydromechanics Laboratory of Texas A&M University. Monochromatic, gravity water waves were generated toward this bar formation. Most waves broke as they passed over the bar and then reformed as they entered the deeper water in the lee of the bar. A limit on the waves studied was those waves that were on the verge of breaking but failed to do so. These waves did however distort and develop shorter period components. Re-

cordings of the water-surface time-histories were obtained before and after the bar. From the insight into the wave characteristics gained from these recordings, those characteristics which the wave possessed before reaching the bar were compared with the characteristics of the wave after it had reformed in the lee of the bar.

The laboratory model simulating the bar formation was fabricated by fashioning wood ribs to a predetermined shape and affixing a stiff aluminum covering to the ribs to form the bar surface. The shape of the model, as shown in Fig. 1, was chosen arbitrarily, but is believed to have a counterpart in nature. The height of the model crest above the channel floor was 0.75 ft and the total length of the model was 10 ft.

The model was attached to the floor of the channel by drilling and tapping threaded ways into the floor and passing bolts through the model into the ways. In this manner the model was securely fastened to the flume and showed little tendency to shift under the oscillating forces created by the passing waves.

The model was constructed with small tolerances between the aluminum covering and the walls of the channel. A caulking clay was forced into the spaces which did exist, to inhibit any leakage around or under the model.

In nature, a longshore bar formation is a steeper discontinuity in an already sloping beach. However, the sloping beach was not reproduced in this study. The channel floor, at constant elevation, served as the ocean floor so that the effects of bottom slope were not studied.

The wave channel in which this study was conducted is 2-ft wide by 3-ft deep by 120-ft long. The walls of the channel are glass so that tests may be observed visually. A pendulum-type wave generator was used to generate the monochromatic incident waves. The displacement of the wave generator was determined by the eccentricity of the rod connecting the generator to a motor-driven flywheel. The period of the generator was controlled by regulating the angular speed of the flywheel with the electric motor whose speed could be adjusted by the setting of a potentiometer. A wire-mesh wave filter was installed near the generator to attenuate the higher frequency noise waves superimposed on the incident wave. At the end of the flume, a permeable wave absorber minimized reflection of the reformed waves back into the testing area.

Water-surface time-histories were measured by a pair of capacitance-type wave probes. The circuitry of this system includes a capacitance bridge of which the probe forms one leg. Operation of the probe requires balancing the bridge by immersing the probe to its proper depth in the water and then balancing the bridge with an adjustable capacitor which forms another of the legs of the bridge. With the circuit so balanced, any displacement of the water surface from the mean water level will cause an imbalance of the circuit. The magnitude and sense of the imbalance is monitored and this signal is amplified. The amplified signal is then recorded by a dual channel strip-chart recorder to yield a record of water-surface position versus time at each probe location.

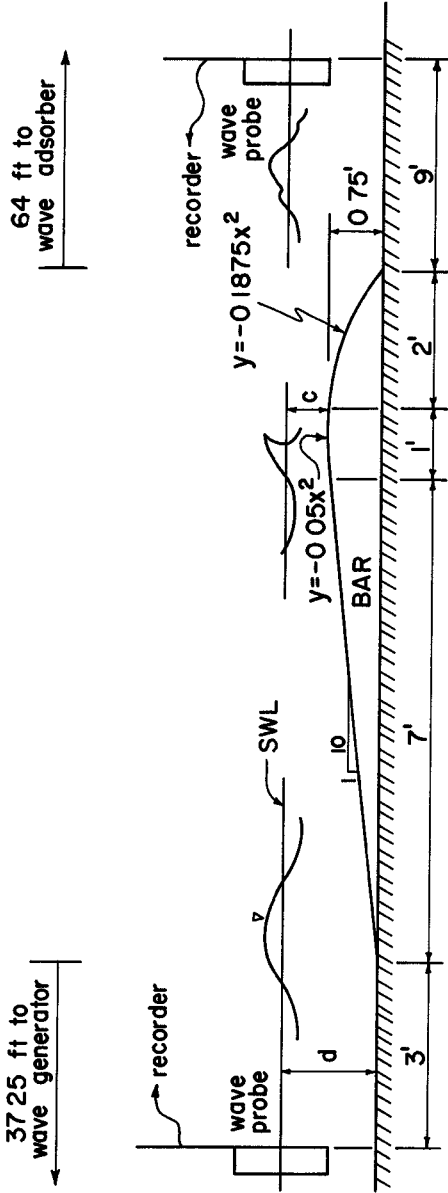


FIG 1 EXPERIMENTAL ARRANGEMENT

EXPERIMENTAL PROCEDURE

Several experimental runs with a range of wave characteristics were conducted for each of three water depths over the bar. These depths over the bar crest, C , were 1.5 in, 3.0 in, and 5.0 in giving total water depths, d , of 10.5 in, 12.0 in, and 14.0 in.

Two wave probes were installed in the channel at the locations shown in Fig 1 and calibrated before each set of test runs. The calibration was checked quite often during the study.

After each test run the wave channel was allowed to sit for several minutes to allow any ripples on the water surface or any oscillation of the water in the channel to dissipate.

With the water completely still, the wave probes and the recorder were switched on and the wave generator was started. Records of approximately one minute in length of the water-surface time-histories at the two probe locations were taken. The wave generator and recorder were then stopped, the water in the channel was allowed several minutes to still, and the test was repeated. After this repeat test, the amplitude and/or period of the wave generated were changed and the entire procedure was repeated for the new wave train.

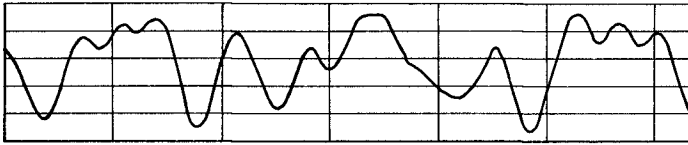
In addition, a wave probe was attached to a movable carriage atop the wave channel and attempts were made to measure any reflected waves from the bar formation by the envelope method (3). Although the procedure was repeated for waves of various steepnesses, in no instance were reflected waves detected.

EXPERIMENTAL RESULTS

The laboratory data were obtained in the form of recorder traces of the water-surface time-histories for the two wave probe locations shown in Fig 1. Samples of the recorder trace from each probe are shown in Fig 2.

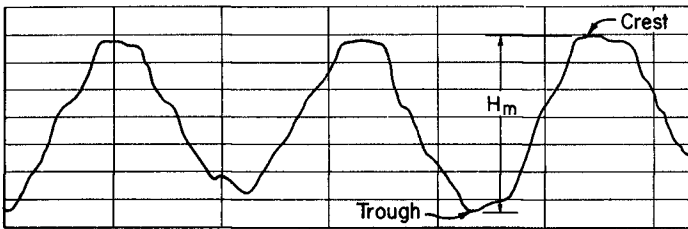
Wave heights were obtained from the wave records by measuring the vertical distance between the peaks and troughs of several successive waves and averaging these values. This procedure was easily followed for the relatively uniform incident waves, but the irregular wave forms which developed in the lee of the bar presented some difficulty. For those waves, the position of the crest and trough could not always be determined exactly, thus, there was some question concerning the heights obtained. Therefore, to provide a basis for comparison of test results as free as possible from subjectivity, a procedure was used in which an "equivalent" wave height was determined.

In order to evaluate the equivalent wave height, it was necessary to assume that the recorder trace of the water-surface time-history is periodic and may be expressed as a Fourier series.



A Trace of the re-formed wave

one
second



B Trace of the incident wave

FIG 2 A SAMPLE OF THE RECORDER TRACE

$$\eta(t) = \frac{a_0}{2} + \sum_{n=1}^{\infty} (a_n \cos n\sigma t + b_n \sin n\sigma t) \quad (1)$$

where $\eta(t)$ is the displacement of the water surface from mean water level at time t , a_0 is the mean displacement of the recorder trace from mean water level, a_n and b_n are Fourier coefficients, n is an integer coefficient, and σ is the angular frequency. The Parseval theorem for periodic functions (6) gives

$$\frac{\rho g}{T} \int_0^{\bar{T}} \eta(t)^2 dt = \frac{\rho g}{8} \sum_{j=1}^{\infty} H_j^2 \quad (2)$$

where ρ is the fluid density, g is the acceleration due to gravity, \bar{T} is the time length of the wave record, j is an integer, and H_j is the height of each constituent wave comprising a complex wave form. The right-hand side of Eq. 2 may be recognized as the total energy per unit surface area in the wave form obtained by adding the energy of each constituent of the wave. The incident equivalent height, H_{eq} , may now be introduced and defined by

$$\frac{1}{8} \rho g H_{eq}^2 = \frac{\rho g}{T} \int_0^{\bar{T}} \eta(t)^2 dt$$

or

$$H_{eq} = \left[2\sqrt{2} \left[\frac{1}{T} \int_0^{\bar{T}} \eta(t)^2 dt \right] \right]^{1/2} \quad (3)$$

The values of $\eta(t)$ were measured for all tests at time increments of 0.05 sec for record lengths, \bar{T} , ranging from 20 to 25 sec. These values were punched onto cards and the equivalent wave heights, as defined by Eq. 3, were evaluated numerically by a digital computer.

Although the equivalent wave heights need not have physical counterparts, they do provide an approximation of the measured wave heights. The plots in Fig. 3 and 4 for $C = 3.0$ in show this to be the case, particularly for the monochromatic incident waves. The measured heights, H_m and h_m , were obtained by averaging the heights of several successive waves from the recorder traces. H_m is the measured height of the incident wave and h_m is the measured height of the reformed wave. h_{eq} is the equivalent height of the reformed wave, defined in the same manner as H_{eq} . Table 1 lists pertinent data on the waves studied in these experiments.

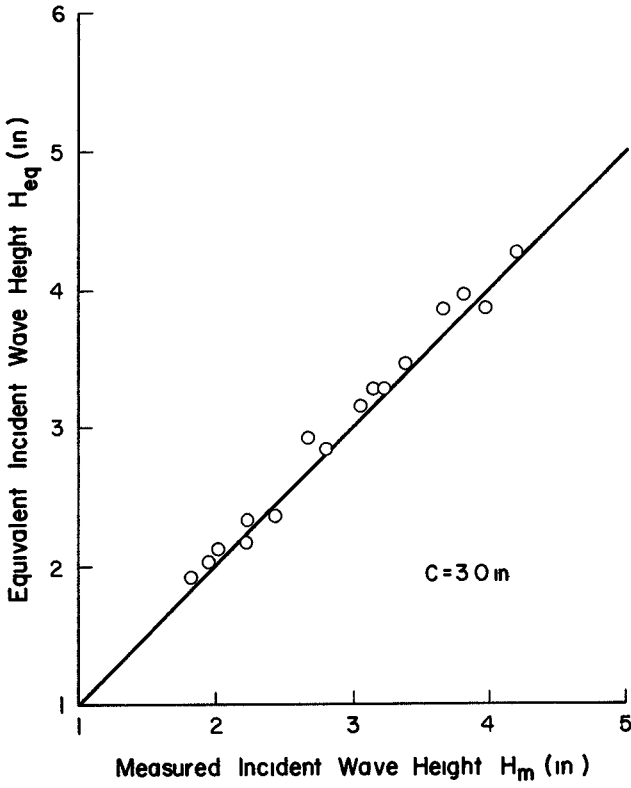


FIG 3-EQUIVALENT VERSUS MEASURED WAVE HEIGHT-INCIDENT WAVES

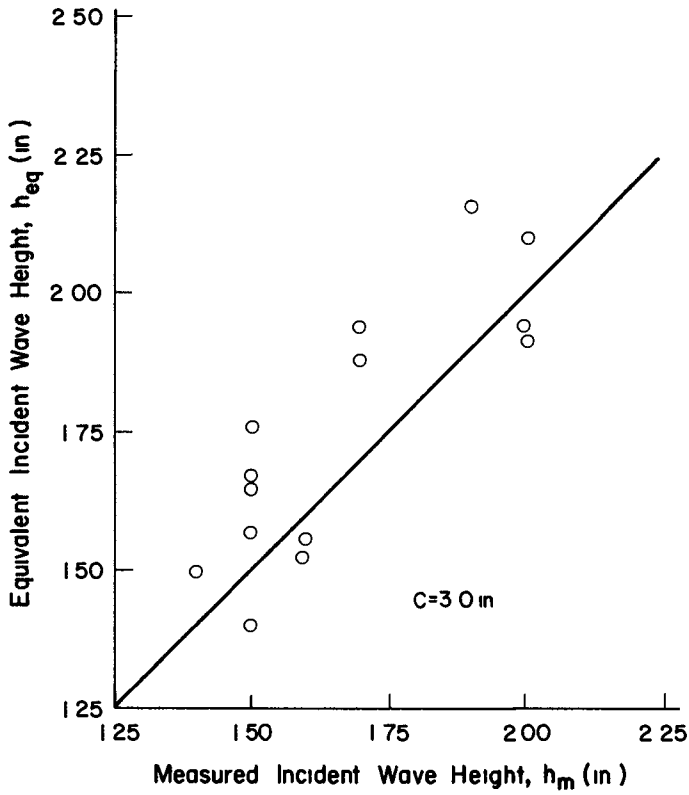


FIG 4—EQUIVALENT VERSUS MEASURED WAVE HEIGHT—REFORMED WAVES

TABLE I - WAVE DATA

Run Number	Depth Over Bar C (in)	Wave Period T (sec)	Heq (in)	heq (in)
1	1 5	1 22	1 75	0 76
2	1 5	1 00	1 90	0 64
3	1 5	0 85	1 84	0 61
4	1 5	0 73	1 62	0 51
5	1 5	0 84	1 56	0 52
6	1 5	1 22	1 54	0 53
7	1 5	1 21	1 14	0 47
8	1 5	0 92	1 33	0 52
9	1 5	1 20	2 29	0 81
10	1 5	1 69	2 04	0 63
11	1 5	1 71	2 17	0 71
12	1 5	1 21	2 52	0 78
13	1 5	1 23	0 99	0 51
14	3 0	2 24	3 04	1 93
15	3 0	2 17	3 79	2 14
16	3 0	2 19	2 03	1 49
17	3 0	1 94	1 90	1 58
18	3 0	1 93	2 68	1 90
19	3 0	1 81	3 67	2 08
20	3 0	1 57	2 36	1 40
21	3 0	1 54	3 96	1 87
22	3 0	1 58	3 14	1 57
23	3 0	1 32	4 19	1 92
24	3 0	1 33	3 38	1 76
25	3 0	1 35	2 14	1 49
26	3 0	1 10	2 02	1 40
27	3 0	1 14	2 41	1 54
28	3 0	1 10	3 20	1 67
29	3 0	0 90	2 79	1 64
30	5 0	1 26	3 45	2 65
31	5 0	1 54	3 20	2 71
32	5 0	1 98	5 21	2 78
33	5 0	2 53	4 54	2 96
34	5 0	1 92	4 34	2 42
35	5 0	1 47	5 64	2 74

Visual observations of the wave forms in the lee of the bar indicated that the water-surface history repeated itself in a time interval approximately equal to the period of the incident waves. However, a more rigorous determination of the period of the waves in the lee of the bar may be made by conducting a spectral analysis of the wave form. The assumption is made that the frequency at which the peak energy is located corresponds to the period of the wave. The spectral analysis will show the frequency band in which the peak energy is located in both the incident wave and the reformed wave. A comparison of the spectra of the incident wave and the spectra of the reformed wave will show if a shift in the location of the peak energy has occurred. If a shift has occurred, then the period of the wave will have changed during the breaking and reforming process.

The spectral analysis may be carried out using the data which were gathered earlier for the determination of the equivalent wave heights. A method for determining the wave spectra is presented by Kinsman (8) and is outlined here with some slight changes in constants.

With N values of $\eta(t_1)$ spaced at time intervals $\Delta\tau$ and with m as the lag, the sample autocorrelation function, r , may be computed

$$r(v\Delta\tau) = \frac{1}{N-v} \sum_{i=1}^{N-v} \eta(t_1) \eta(t_1 + v\Delta\tau) \tag{7}$$

where $v = 0, 1, 2, \dots, m$. The lag, m , is some fraction of the length of the record, usually less than $0.1N$.

The Fourier transform of the autocorrelation function is the energy spectrum, which is required. This transform may be effected by calculating the unsmoothed estimates of the spectrum as follows

$$L_{\tau=0} = \frac{1}{m} \left[\frac{1}{2}[r(0) + r(m\Delta\tau)] + \sum_{k=1}^{m-1} r(k\Delta\tau) \right] \tag{8}$$

$$L_{\tau=v} = \frac{2}{m} \left[\frac{1}{2}[r(0) + (-1)^v r(m\Delta\tau)] + \sum_{k=1}^{m-1} r(k\Delta\tau) \cos \frac{\pi kv}{m} \right] \tag{9}$$

$v = 1, 2, \dots, m-1$, and

$$L_{\tau=m} = \frac{1}{m} \left[\frac{1}{2}[r(0) + (-1)^m r(m\Delta\tau)] + \sum_{k=1}^{m-1} (-1)^k r(k\Delta\tau) \right] \tag{10}$$

where L is the unsmoothed spectral estimates at time $t = \tau$. The final smoothed estimates of the spectrum, Φ , are formed by the moving, weighted average

$$\Phi(v\Delta\tau) = \sum_{\tau=0}^m a_{v,\tau} L_{\tau} \quad (11)$$

where $v = 1, 2, \dots, m-1$, and

$$\left. \begin{aligned} a_{v,v-1} &= 0.25 \\ a_{v,v} &= 0.50 \\ a_{v,v+1} &= 0.25 \\ a_{v,1} &= 0 \end{aligned} \right\} \quad (12)$$

for $\tau \neq v-1, v$, or $v+1$. For the end points,

$$\left. \begin{aligned} \Phi(0) &= (L_0 + L_1)/2 \\ \Phi(m) &= (L_{m-1} + L_m)/2 \end{aligned} \right\} \quad (13)$$

Typical results of the spectral analysis are presented in Figs 5 through 10. These plots show that the peak energy of the incident wave and the peak energy of the reformed wave generally occur at the same frequency. Thus, the indication is that the basic period of a wave does not change as the wave passes over the bar, breaks, and reforms in the lee of the bar.

In all reformed wave records a second energy peak occurs at a higher frequency that is consistently twice the frequency of the incident wave. In a few cases, the peak value of this higher frequency energy is equal to or slightly exceeds the reformed energy of the incident wave frequency (see Fig 8 for example). In most cases, the peak energy at this higher frequency is only 20 to 40 percent of the main peak of the reformed energy spectra.

Also, in most of the reformed wave records analyzed, a very low level of energy with a frequency of approximately triple the incident wave frequency can be detected.

The ratio of reformed to incident equivalent wave height, heq/Heq , has been plotted against the deep water wave steepness, Heq/T^2 , (Fig 11) and against the relative depth over the bar crest, C/T^2 , (Fig 12). As can be seen, no correlation is apparent in either of these figures.

Fig 13 shows h_{eq}/H_{eq} plotted against the ratio of incident equivalent wave height to water depth over the bar crest, H_{eq}/C . The data for the 3 in and 5 in water depths plot together and produce a relatively well defined relationship between H_{eq}/C and h_{eq}/H_{eq} . Some of the scatter may be caused by the fact that some waves break over the bar crest while others break ahead of the crest.

The data for the 1.5 in depth fall below the other data, particularly for the low incident waves. This is possibly due to scale effects in the breaking of these low amplitude waves.

CONCLUSIONS

The objective of this investigation was to gain some understanding of the characteristics of monochromatic waves after they break over an offshore bar. Generally, most of the energy in the reformed waves is at the same period as in the incident wave but a large portion of the energy shifts to higher frequencies. The ratio of equivalent wave heights (square root of wave energy per unit surface area) before and after the bar depends primarily on the ratio of the incident wave height to water depth over the bar crest.

Further tests are planned for 5 in and greater (e.g. 7 in and 9 in) depths over the bar with waves that break and waves that do not break but are disturbed enough by the bar to cause the development of higher frequency components in the lee of the bar. These tests should better define the relationship between h_{eq}/H_{eq} and H_{eq}/C . They should also lead to a greater understanding of the reformed wave energy spectrum. Also, a closer look at the nature of the waves as they break as well as the point on the bar at which breaking occurs is needed.

ACKNOWLEDGEMENT

The support of the U S Army Corps of Engineers and the U S Army Engineer Waterways Experiment Station, Vicksburg, Mississippi during the senior authors period of graduate study and research on the problem of breaking waves is gratefully acknowledged.

REFERENCES

- 1 Dick, T M , "On Solid and Permeable Submerged Breakwaters", C E Research Report 59, Queen's University, Kingston, Ontario, Nov 1968, 144 p
- 2 Diephuis, J G H R , "Scale Effects Involving the Breaking of Waves", Proceedings, 6th Conference on Coastal Engineering, Gainesville, Palm Beach, and Miami, Fla , 1957, Chapter 11

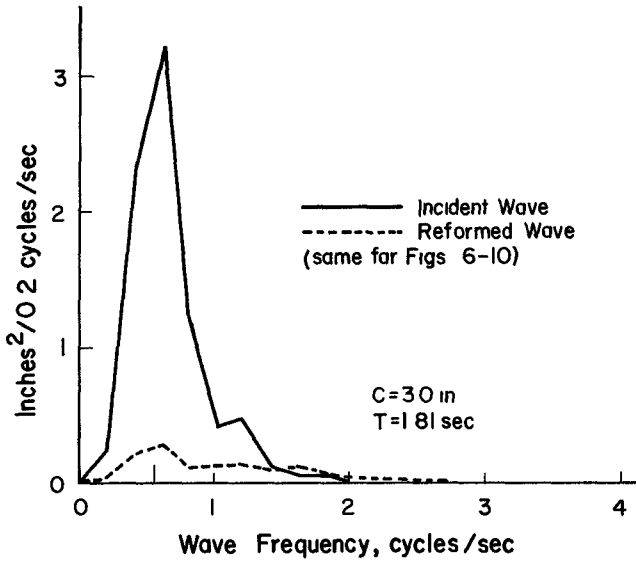


FIG 5 WAVE SPECTRA, RUN NO. 19

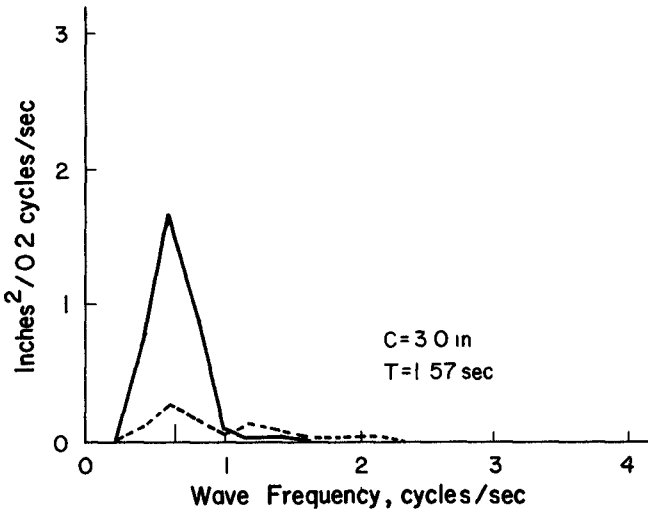


FIG 6 WAVE SPECTRA, RUN NO 20

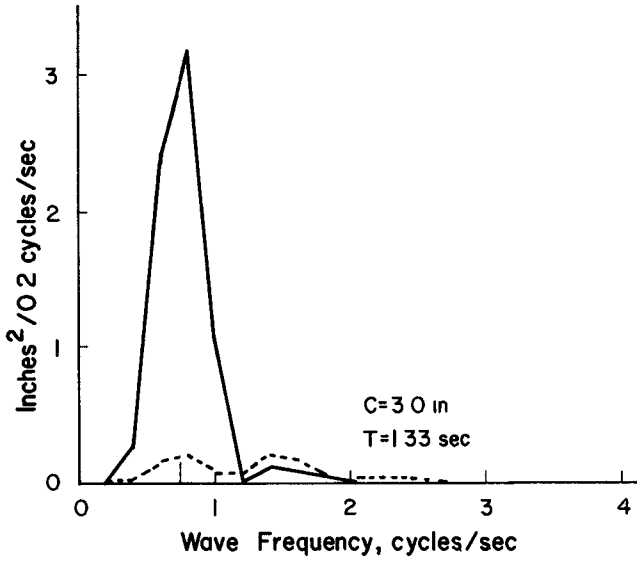


FIG 7 WAVE SPECTRA, RUN NO 24

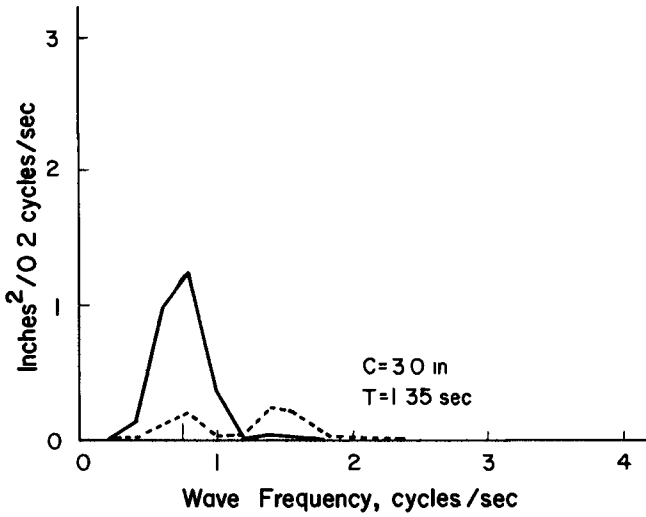


FIG 8 WAVE SPECTRA, RUN NO. 25

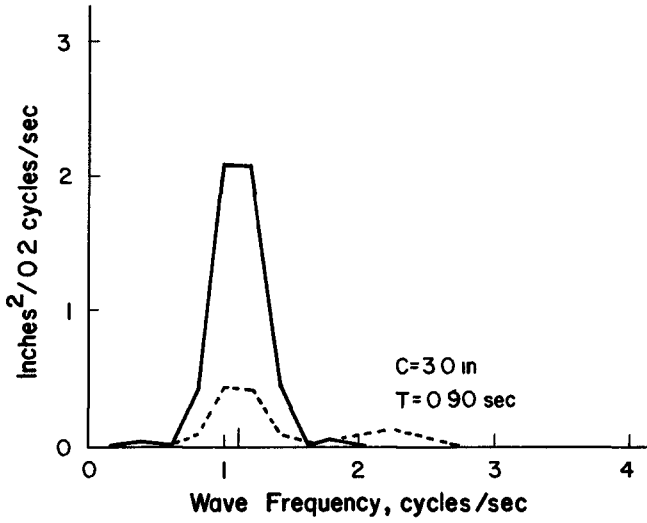


FIG 9 WAVE SPECTRA, RUN NO 29

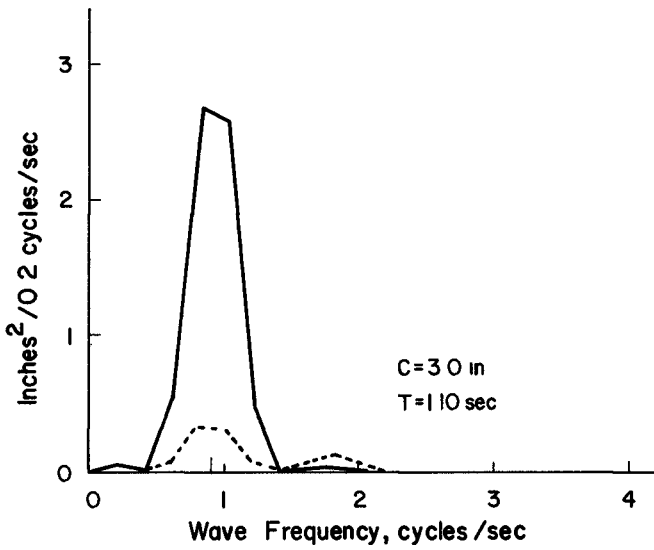


FIG 10 WAVE SPECTRA, RUN NO 28

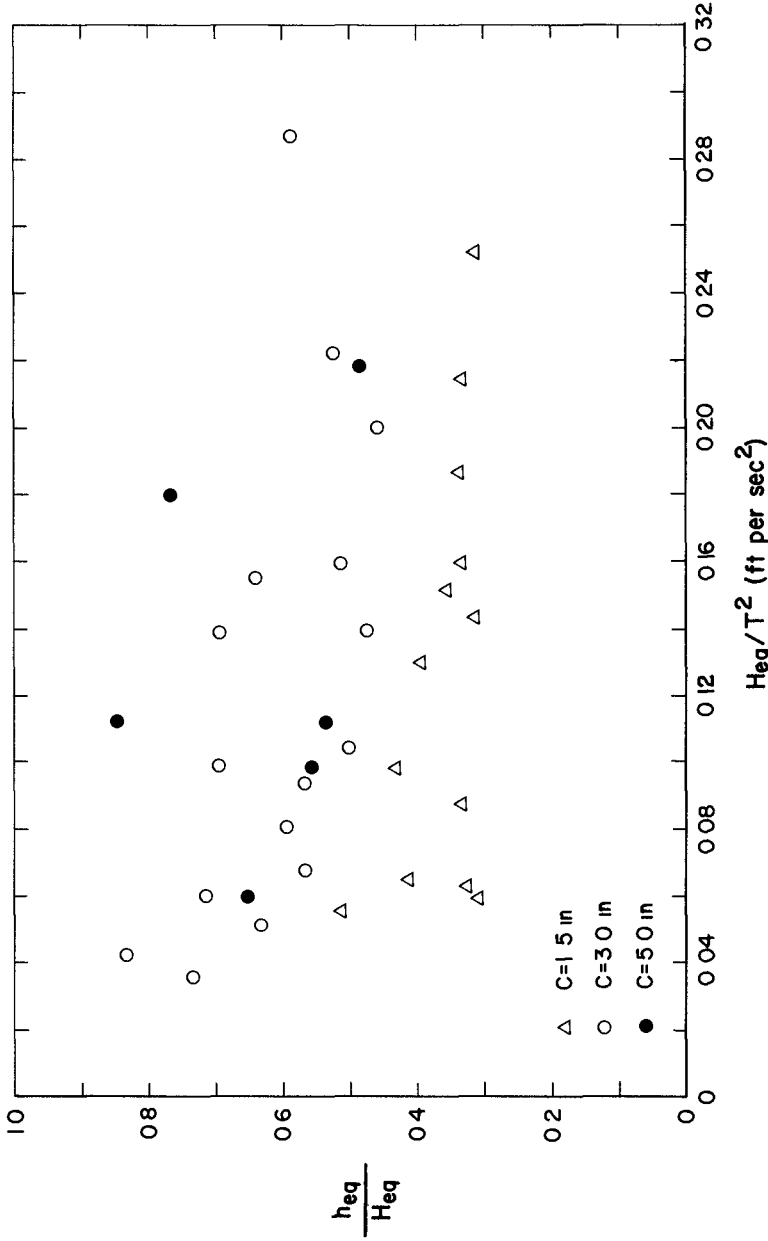


FIG II - h_{eq}/H_{eq} VERSUS H_{eq}/T^2 FOR ALL DEPTHS

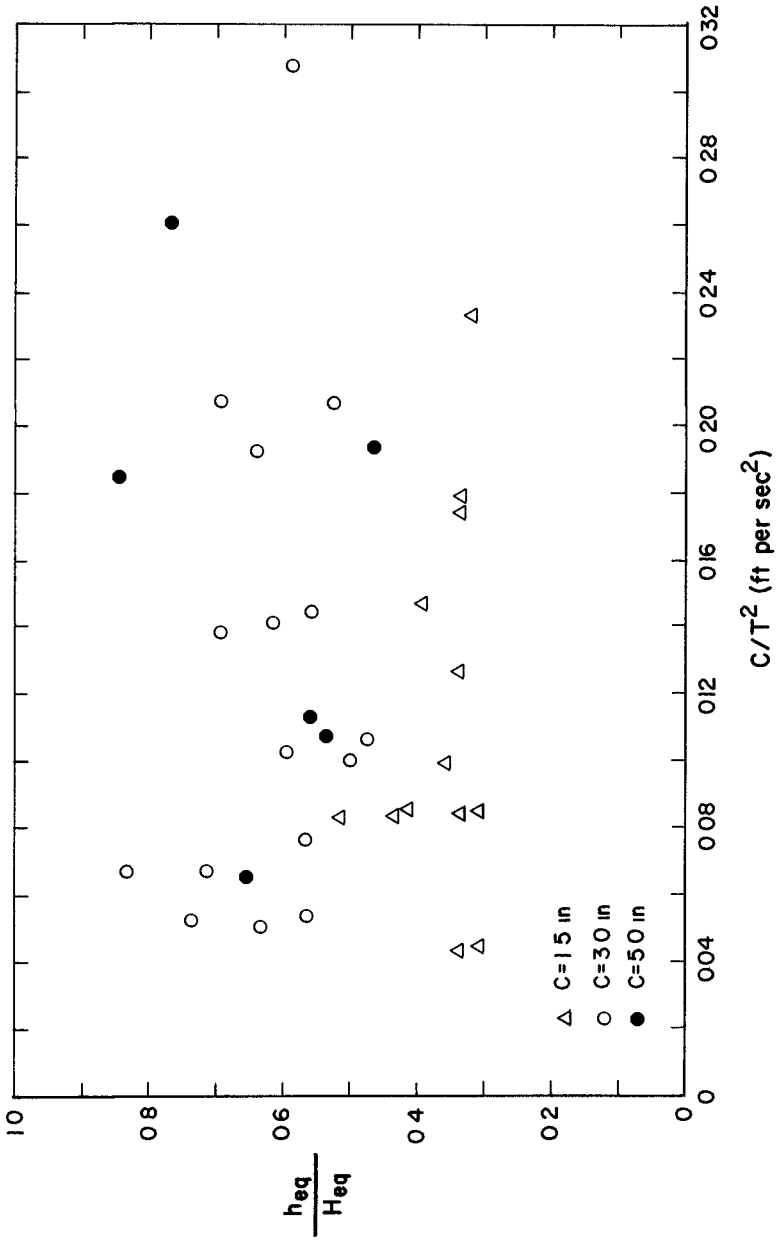


FIG 12- h_{eq}/H_{eq} VERSUS C/T^2 FOR ALL DEPTHS

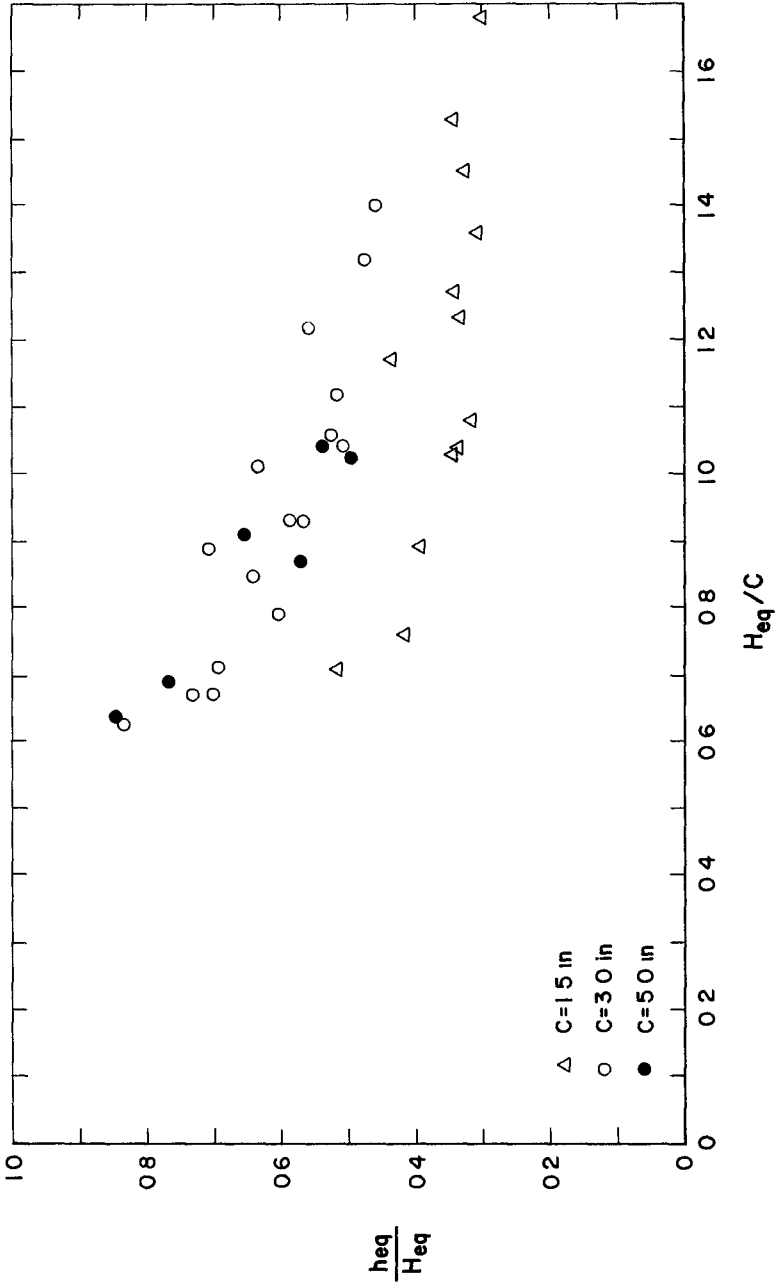


FIG 13- h_{eq}/H_{eq} VERSUS H_{eq}/C FOR ALL DEPTHS

- 3 Herbich, J B , "Experimental Studies of Wave Filters and Absorbers", Project Report No 44, University of Minnesota, St Anthony Falls Hydraulic Laboratory, St Paul, Minn , Jan , 1956
- 4 Hom-ma, M , and Horikawa, K , "Wave Forces Against Sea Wall", Proceedings, 9th Conference on Coastal Engineering, Lisbon, Portugal, 1954, Chapter 31
- 5 Horikawa, K , and Juo, C , "A Study on Wave Transformation Inside Surf Zone", Proceedings, 10th Conference on Coastal Engineering, Vol 1, Tokyo, Japan, 1966, Chapter 15
- 6 Ippen, A T , ed , Estuary and Coastline Hydrodynamics, McGraw-Hill Book Co , New York, 1966
- 7 Iverson, H W , "Laboratory Study of Breakers", National Bureau of Standards Circular 521, Gravity Waves Symposium, 1952
- 8 Kinsman, Blair, Wind Waves, Their Generation and Propagation on the Ocean Surface, Prentice-Hall, Inc , Englewood Cliffs, N J , 1965, Chapter 9
- 9 Nakamura, M , Shiraiishi, H , and Sasaki, Y , "Wave Decaying Due to Breaking", Proceedings, 10th Conference on Coastal Engineering, Vol 1, Tokyo, Japan, 1966, Chapter 16
- 10 _____, "Wave Damping Effect of Submerged Dike", Proceedings, 10th Conference on Coastal Engineering, Vol 1, Tokyo, Japan, 1966, Chapter 17

CHAPTER 27

VELOCITY FIELDS IN THE WAVE BREAKER ZONE

by

M. D. ADEYEMO, Ph.D. (Lond).

Faculty of Engineering, University of Lagos, Nigeria.

SYNOPSIS

The paper deals with the velocity fields in the neighbourhood of the breakers and the correlation between the wave asymmetry and the velocity asymmetry.

The velocity measurements were made on two beach slopes 1:9 and 1:18. Earlier work (3) showed that the two slopes produced different breaker types; the slope of 1:9 produced plunging breakers and the slope of 1:18 spilling breakers.

The velocities (velocity - time history) of the water particles were measured at a height of 5mm above the bed using the hydrogen bubble method combined with cine photography.

Two types of horizontal velocity asymmetry were defined and investigated, namely

- (1) horizontal velocity (Magnitude) asymmetry
- and (2) horizontal velocity (time) asymmetry.

It was found that there are both qualitative and quantitative correlation between the asymmetry of the wave, and the asymmetry of the resulting velocity field. As a result of the correlation two alternative expressions are given for the horizontal velocity (magnitude) asymmetry.

INTRODUCTION

In fairly deep water, the water particle horizontal velocities at the bottom are approximately equal for the shoreward and seaward motions, but as the waves moves into progressively shallow water of about $\frac{d}{L} < 0.15$, the asymmetry of the wave gives rise to the velocity differential of the water particles in the beachward and seaward directions, the onshore velocity of the water particles being greater in magnitude and of shorter duration than the offshore velocity. This behaviour thus leads to a definition of two types of horizontal velocity asymmetry, one based on magnitude and the other on time. They are defined as follows.

Horizontal velocity (magnitude) asymmetry =

$$\frac{\text{Maximum horizontal shoreward velocity}}{\text{Maximum horizontal seaward velocity}}$$

Horizontal velocity (time) asymmetry =

$$\frac{\text{Time for the shoreward motion}}{\text{Time for the seaward motion}}$$

The study on wave asymmetry where the effect of beach slope and shoaling on the magnitude of the wave asymmetry was examined had been reported by the author⁽³⁾. The present study is thus concentrated on the investigation of the velocity fields and the correlation of the velocity asymmetry and the wave asymmetry. The wave conditions used were the same as those used in the study on wave asymmetry⁽³⁾. The correlation of the wave asymmetry and the asymmetry of the orbital velocity field will be discussed later in the paper. A review of previous work on velocity studies of water particles under the action of waves is given below.

Review of Previous Work

Iversen⁽¹⁾ examined the kinematics of the water movement in breakers. He used particles of a mixture of xylene, carbon tetrachloride and zinc oxide for flow visualization. The movement of the particles was recorded on cine film, from which each particle velocity was obtained by noting the distance moved on the projected frames and the time interval of movement. The velocities obtained were plotted as vectors as shown in Fig. 1. Iversen, in addition, measured the backwash and crest velocities. He obtained the backwash velocities by averaging all particle velocities in the region of minimum depth in the backwash, and the crest velocities were obtained from the gradient of the crest position - time history. Iversen found that the backwash velocity was higher on a steep beach as compared to a flat beach. This was to be expected.

Hamada⁽⁵⁾ studied the particle velocity in wave motion in the region of the breakers. The velocity of flow was measured by means of a current meter which had several propellers driven by the action of water flow. A direct electric current in the circuit connected the current meter to an oscillograph, with one element of the oscillograph corresponding to one of the propellers. Hamada made orbital velocity measurements 3cm. from the bed. He noted the differential velocity in the shoreward and seaward directions. He found the ratio of backward velocity to forward velocity to vary between 1 : 1.16 to 1 : 1.29. However, his theoretical approach was to calculate the orbital velocity by the Airy theory and to add an estimated "residual" velocity (equivalent to the mass transport velocity). Since this was always positive, the resulting values gave a differential between the forward and backward velocities. His measurements are of interest, but his theoretical evaluation neglects the existence of orbital velocity asymmetry even in the absence of mass transport.

Inman and Nasu⁽⁶⁾ made a study of orbital velocity in shallow water at La Jolla California. The measurements were made near the bottom and just seaward of the breaker zone in water depths ranging from

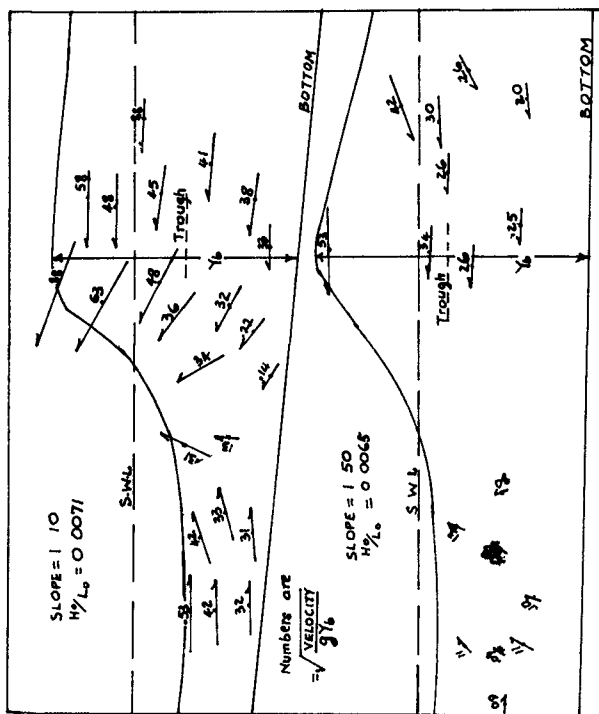


Fig. 1 Kinematics of a Breaking Wave (after Iversen (1) (1952))

about five to fifteen feet and wave heights of up to seven and a half feet. The orbital current meter consisted in the main of a cylindrical rod fixed rigidly at one end like a cantilever, and the system was arranged such that the orbital velocity could be interpreted from the bending of the rod caused by the force exerted by the moving water. A pressure type wave meter was used with the current meter, and both the wave meter and the current meter were mounted on a tripod. The current meter was mounted 0.82 ft. above the bottom. The bed had an average slope of about $\frac{1}{35}$ in the region where the orbital velocities were measured.

Inman and Nasu commented that the graph of the horizontal component of orbital velocity as a function of time resembled that of the wave pressure and they noted that the horizontal velocity seemed to be more dependent on the rate of change in level of the water surface during the passage of the wave than on the actual height of the wave. With reference to Fig. 2 after Inman and Nasu⁽⁶⁾ they noted that in the figure, the fourth wave was almost as high as those preceding it, but showed a more gradual rise in level from the preceding trough to the crest. The result was a very low crest velocity. In terms of the work reported in this paper, and in earlier papers by the author^(3,4) the statement of Inman and Nasu could be condensed into the statement that for waves of the same height, greater velocities are associated with greater wave slope asymmetry.

Inman and Nasu remarked that the maximum velocity under the wave crest was always onshore and that for almost all the waves analysed the mean onshore maximum velocity exceeded the offshore velocity. They compared the maximum orbital velocities with Solitary and Airy-Stokes waves. They gave the sum of the crest and trough velocities along the bottom aU for both Airy and Stokes waves as:

$$aU = |U_{\text{crest}}| + |U_{\text{trough}}| = \frac{2\pi H}{T} \frac{1}{\text{Sinh} \frac{2\pi d}{L}} \quad (1)$$

For the Solitary wave, they gave the maximum orbital velocity at the bottom aU as:

$$aU = \frac{1}{2} NC \quad (2)$$

where $C = \sqrt{g(H+d)}$ is the velocity of propagation of the wave crest. H is wave height and d water depth.

N is defined by the equations:

$$N = \frac{2}{3} \sin^2 \left[M \left(1 + \frac{2H}{3d} \right) \right] \quad (3)$$

and

$$\frac{H}{d} = \frac{N}{M} \tan^2 \frac{1}{2} \left[M \left(1 + \frac{H}{d} \right) \right] \quad (4)$$

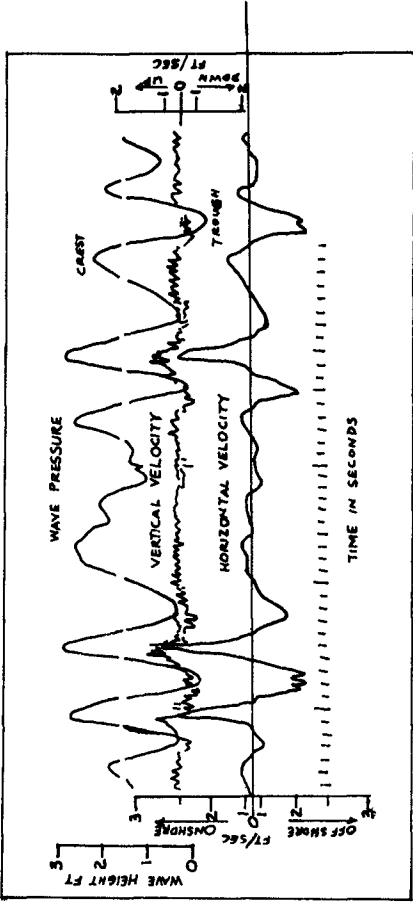


Figure 2 After Inman and Masu (6) (1956)

Inman and Nasu⁽⁶⁾ remarked that the measured velocities were on the average in better agreement with the Solitary wave than with the Airy - Stokes relations.

Ippen and Kulin⁽⁷⁾ studied the internal velocities of the Solitary wave at the break-point. They used droplets of a solution of xylene and n-butyl phthalate. The motion picture camera they employed was operated at 20 frames per second and they placed an auxiliary grid in the plane of the particles so that on the photographs the grid lines could be projected down into the wave itself. They conducted their studies on two types of breakers; the plunging breaker on a slope of 0.065 and the spilling breaker on a slope of 0.023. They commented that on the slope of 0.023 with a spilling breaker the maximum velocity was nearly equal to the crest celerity at the wave break point, and they noted that the maximum particle velocity seemed to occur just slightly shoreward of the highest point of the crest.

Some velocity studies were also carried out by Morison and Crooke⁽¹¹⁾ in a study of deep water, shallow water and breaking waves. They used a mixture of carbon tetrachloride, xylene and zinc oxide having approximately the same specific gravity as water. They found that the greatest horizontal particle velocity occurred when the wave was breaking, and they noted a velocity differential between the shoreward and seaward horizontal velocities. They concluded that the maximum horizontal particle velocity at the crest of the wave might attain the wave celerity as the wave broke, but that the phenomenon was confined to a very narrow region of water at the crest of the wave. This was not borne out by Miller and Zeigler's⁽⁸⁾ observations.

APPARATUS AND MEASURING TECHNIQUES

The technique used for the velocity measurements in the studies presented in this paper is a method usually called the "Hydrogen bubble method." Essentially it consists of a fine wire which forms the negative electrode of a D.C. circuit, while two metal plates, positioned at each side of the tank with a reasonable depth of the metal inside the water, serve as the second electrode. Hydrogen bubbles are formed on the negative electrode. The arrangement was such that the support for the wire and metal plates serving as the positive electrode were integral, (see plate 1). Two advantages of such an arrangement were that, as measurements were made at different positions along the beach, the apparatus could be moved intact. Secondly it was found that the quality of the bubbles was affected when the positive electrode was not close enough to the wire, as the circuit then became weak. The wire used in this work was 0.05mm diameter platinum wire, with brass plates as the positive electrodes.

Cine photography was employed and a suitable lighting arrangement was therefore devised. The camera used was a 16mm Reflex Bolex at 64 frames per second. With a wave period of 0.8 seconds, this gave approximately 50 pictures per wave cycle.

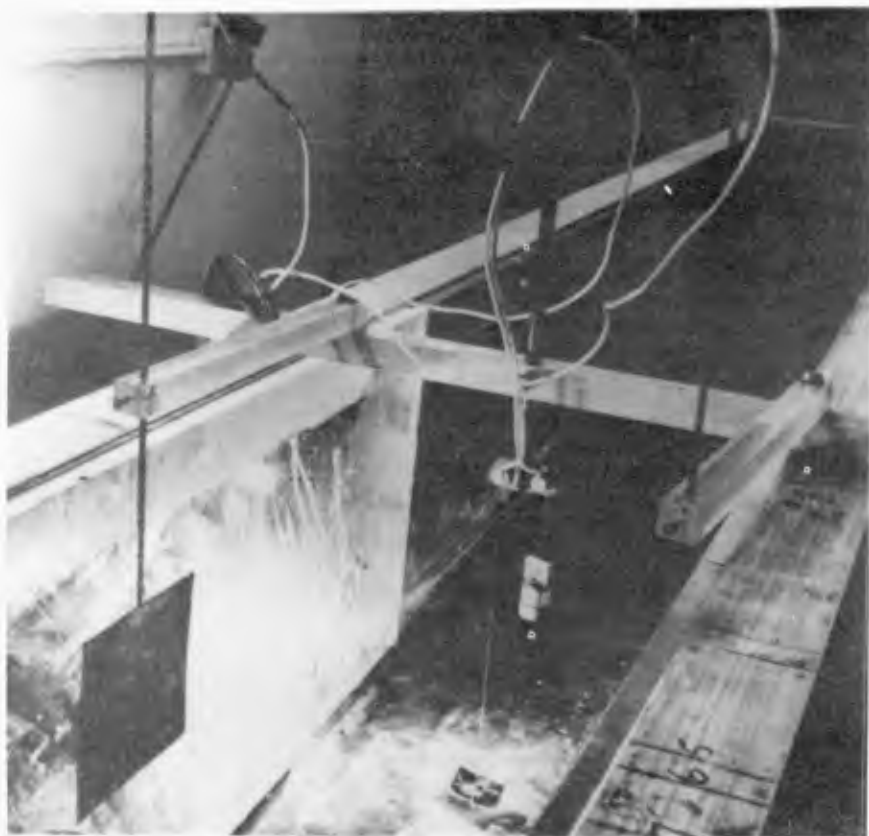


Plate I

For the lighting arrangement, an Aldis Tutor 1000 Watt slide projector was used. The light source was located on the opposite side of the channel to the camera, and orientated at an oblique angle to the channel. Slits were used to prevent stray lights from scattering in the water.

In operation, one end of the wire was fixed to the beach with a tape, while the other end was passed over a support and was tensioned by a suitable weight. The velocities close to the wire at the different positions were evaluated from the displacement of the bubbles generated at different but known times. The orbital velocity measurements were made at a height of 5mm above the bed, which was outside the wave induced boundary layer. These velocity measurements were made at several positions along the beach on two beach slopes 1:9 and 1:18 in the region $0/L < 0.15$ including the breakers. The two slopes were chosen on the basis of previous experiments(3, 4) which indicated that they are respectively representative of characteristically steep beaches with plunging breakers and flat beaches with spilling breakers.

The wave profiles and hence the different wave asymmetries for the different positions along the two beach slopes were also obtained using the capacitance-wire probe together with a visicorder.

EXPERIMENTAL RESULTS

Effect of Shoaling on Orbital Velocity Field

The velocity - time history for a full wave cycle at the different positions along the beach were obtained from the analysis of the cine films of hydrogen bubble blocks emitted from a wire positioned at these positions. The resulting curves are shown superimposed in figures 3 and 4. The two types of horizontal velocity asymmetry, one based on the magnitude of the shoreward-seaward velocities and referred to as the horizontal velocity (magnitude) asymmetry and the other based on the duration of the shoreward-seaward motion and referred to as the horizontal velocity (time) asymmetry were computed from the separate curves of the velocity - time variation for a wave cycle.

Figures 3 and 4 show how the orbital velocity-time curve changes in form as the wave progresses into shallower water. It can also be seen from the figures that the horizontal velocities increased in magnitude as the wave advanced into shallower water, and the greatest horizontal velocities occurred at the wave breaker position. It is interesting to note that the curves are closer together on the flatter beach slope of 1:18 than on the slope of 1:9 but that on each beach slope, the velocity seems to have a constant value at all positions along the beach 0.4 secs i.e. half the wave period after the passage of the wave crest, although the constant velocity varies in magnitude from one slope to another. It is evident from figures 3 and 4 that for each position on the beach, the maximum horizontal shoreward velocity did not occur directly under the wave crest but at a time 0.09T seconds after the passage of the crest (T is wave period).

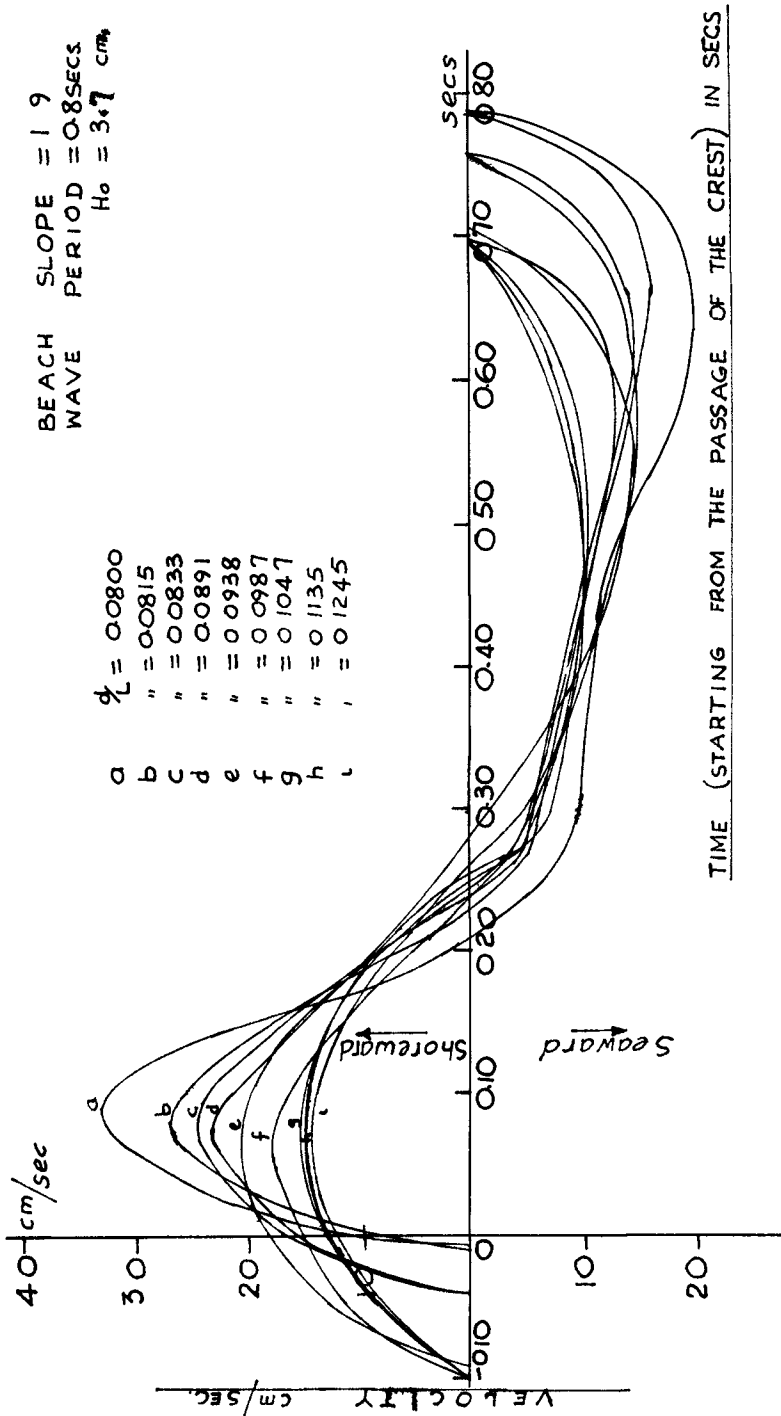


Fig 3 The Superposed graphs of Horizontal Orbital velocity For a Wave Cycle

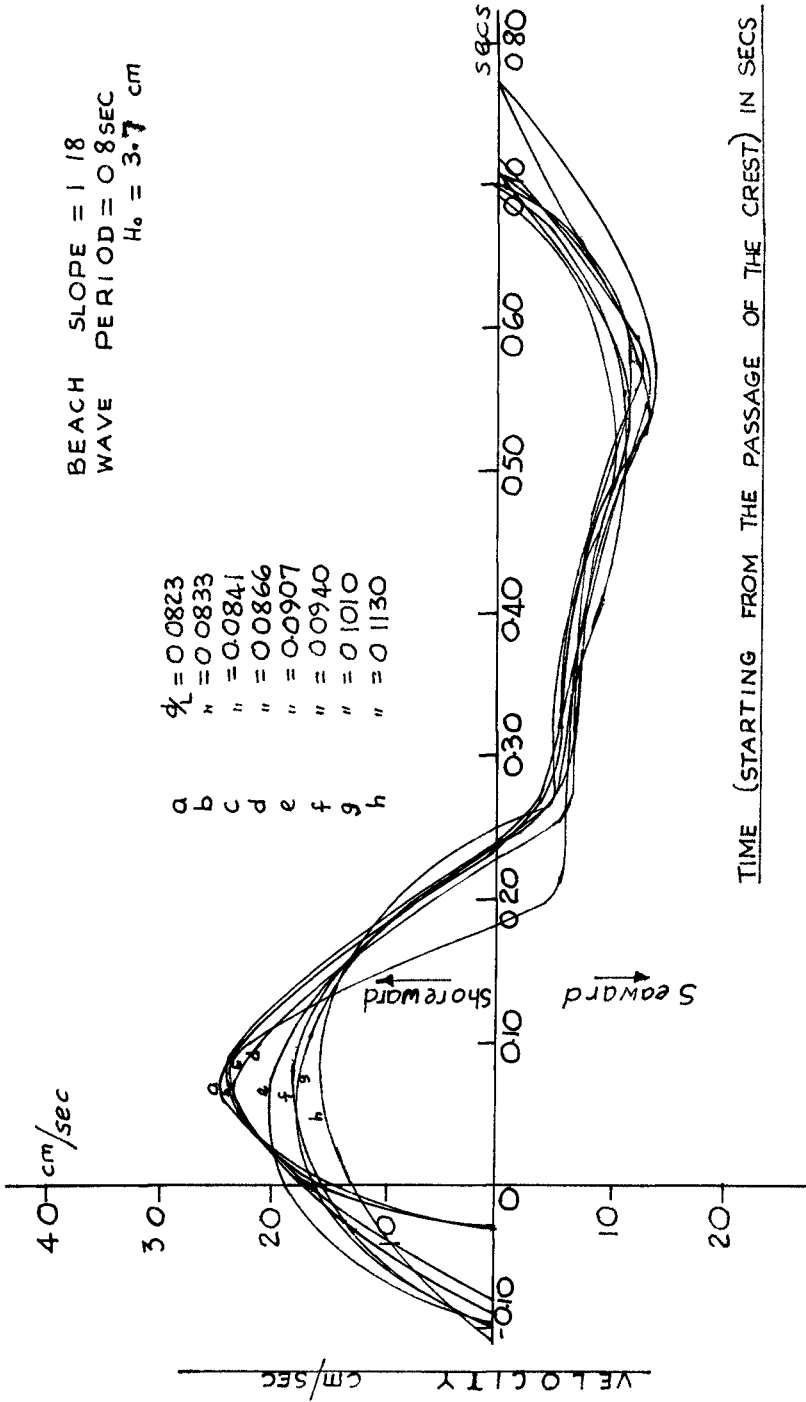


Fig 4 The Superposed Graphs of Horizontal Orbital Velocity For a Wave Cycle.

The graphs of horizontal velocity (magnitude) asymmetry against $\frac{d}{L}$ are shown in figure 5. It was found that for the two slopes of 1:9 and 1:18 the horizontal velocity (magnitude) asymmetry increased as the wave advanced into shoaling water and in each case was highest at the wave breaker position. At the $\frac{d}{L}$ value of 0.10 on the beach slope of 1:9 this asymmetry was found to be 1.57 while on the beach slope of 1:18 it was found to be 1.585. At the wave break-point on the beach slope of 1:9 the value of this asymmetry was found to be 1.63 while the corresponding value on the beach slope of 1:18 was 1.77.

In terms of absolute values of the horizontal velocities, the values on the steeper slope of 1:9 were found to be higher than those of on the flatter slope of 1:18, especially in the neighbourhood of the breakers, but the graph of the horizontal velocity (magnitude) asymmetry against $\frac{d}{L}$ (figure 5) indicated that the asymmetry values were higher on the flatter slope. In other words larger beach material could be set in motion on the steep slope, but a greater shoreward - - seaward differential would act on material on the flatter slope.

The graphs of horizontal velocity (time) asymmetry against $\frac{d}{L}$ are shown in figure 6. These show increasing asymmetry as the wave advances into shallower water. As noted in the introduction above, the horizontal velocity (time) asymmetry was defined as the ratio of the time for the shoreward motion to the time for the seaward motion, thus a small numerical value compared with unity denotes increasing asymmetry.

It was found that at the $\frac{d}{L}$ value of 0.10 the value of this asymmetry on the slope of 1:9 was 0.76 whilst on the beach slope of 1:18 the value was found to be 0.78. At the wave breaker position on the beach slope of 1:9 the asymmetry became 0.37 whilst the corresponding value on the slope of 1:18 was 0.49. Thus the shoreward motion takes a longer time on the flatter slope.

Fig. 7 illustrates the comparison between Stokes theoretical wave profile based on his third approximation, and a typical profile obtained in the present study. It can be seen that the Stokes Wave is less peaked than the experimental wave, and also, by virtue of its mathematical description, does not possess asymmetry about the vertical axis.

Figures 8 and 9 which compare the orbital velocities based on Stokes theory with those obtained experimentally, show that at a $\frac{d}{L}$ value of 0.0833, which is very close to the breakers, the theory clearly does not agree with the measurements (see figure 9). Farther seaward from the break-point, at a $\frac{d}{L}$ value of 0.1135 (figure 8), although the theoretical values were still much higher than the experimental values, for instance, by as much as 73% of the experimental value under the crest, and there was in addition a phase lag in the profile, nevertheless the comparison was better than in figure 9.

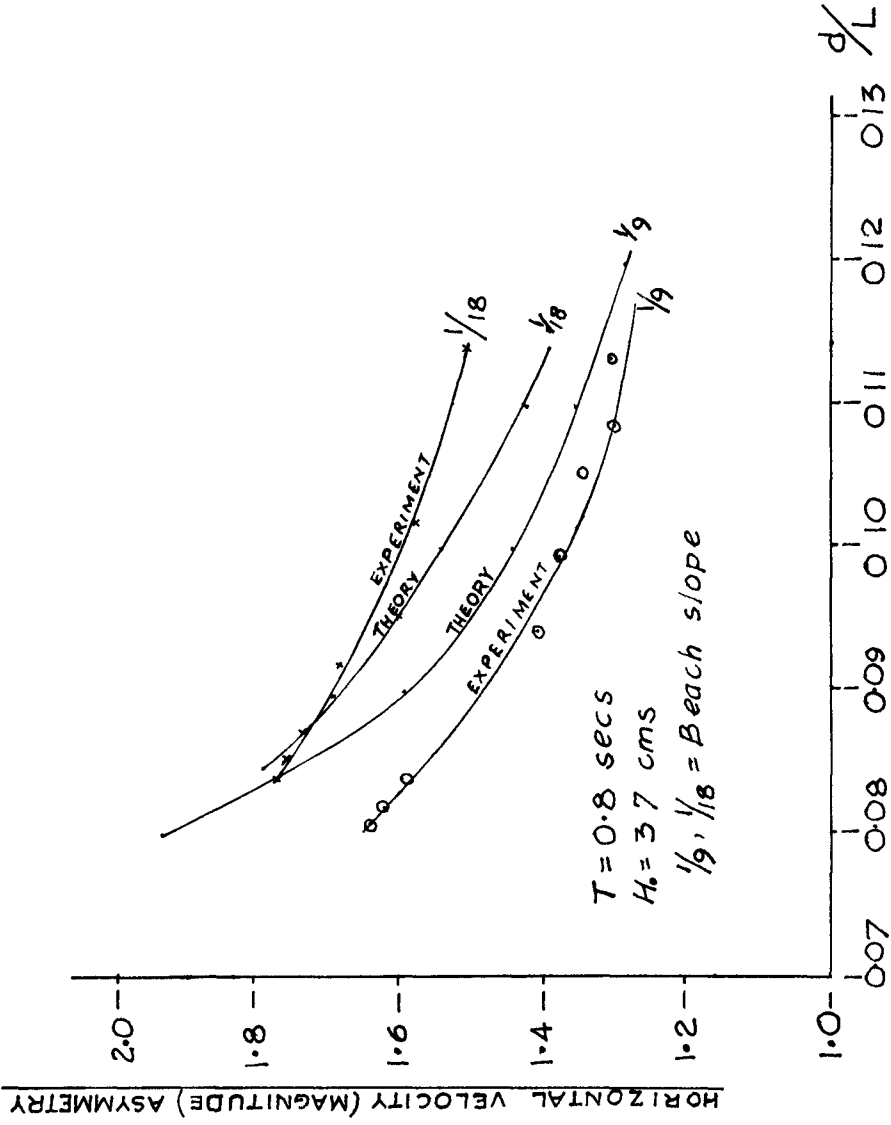


Fig 5 Graph of Horizontal Velocity (Magnitude) Asymmetry against d/L

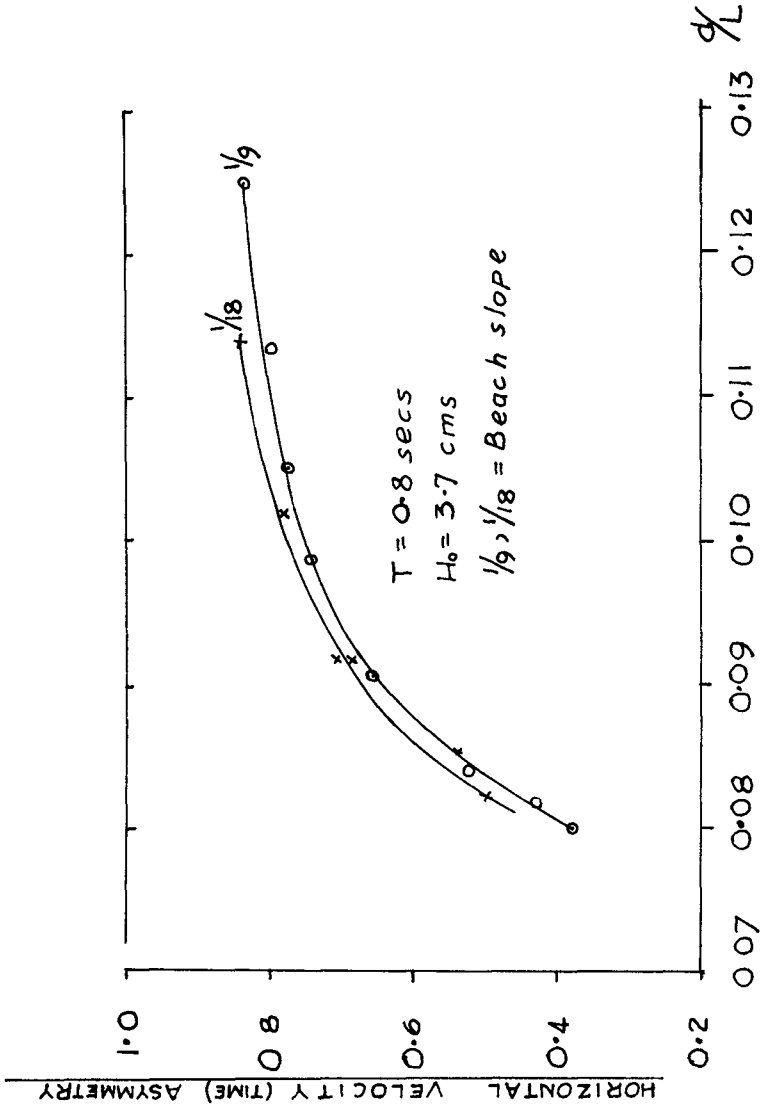
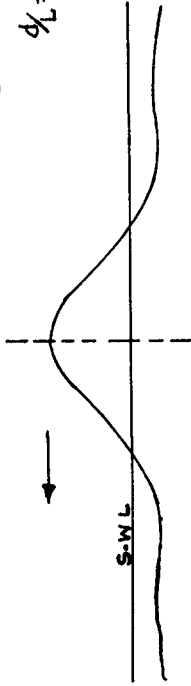


Fig 6 Graph of Horizontal Velocity (time) Asymmetry against d/L

STOKES FINITE AMP WAVE 3rd APPROX.
 $\frac{d}{L} = 0.07$ $H = 91 \text{ cm}$ $T = 0.8 \text{ secs}$

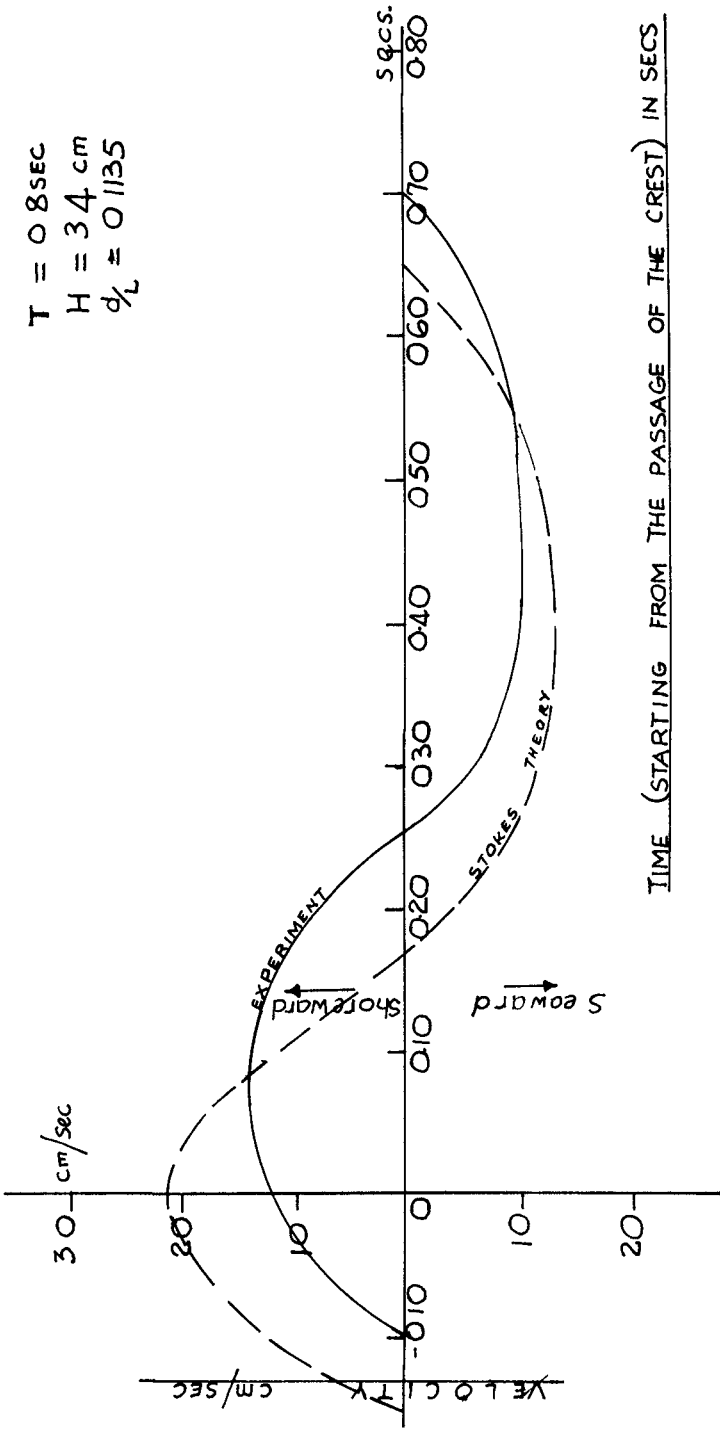


Theoretical Near-Breaking Wave. Stokes Finite Amplitude Wave,
 Third Approximation (after Miller & Zeigler (10))



Typical Experimental Profile Near the Break-point
 Figure 7

$T = 0.8 \text{ SEC}$
 $H = 34 \text{ cm}$
 $d/L = 0.1135$



TIME (STARTING FROM THE PASSAGE OF THE CREST) IN SECS

Fig. 3 Comparison of Stokes Theory with Experimental Results.

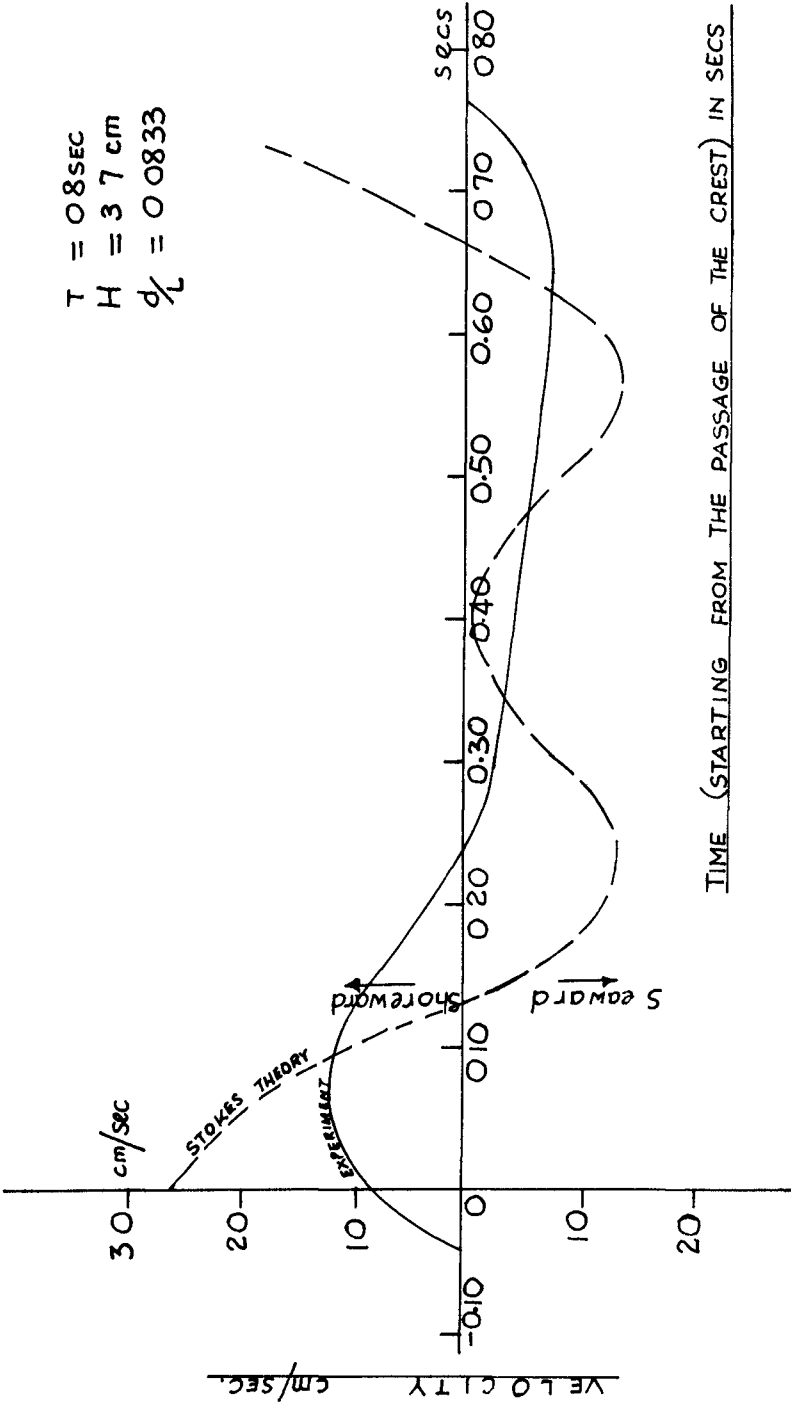


Fig 9 Comparison of Stokes Theory with Experimental Results.

The horizontal component of water particle velocity at a point (x, y) in water depth d is given to the second order of Stokes theory by the expression:

$$U = \frac{\pi H}{T} \frac{\cosh 2\pi \left(\frac{y+d}{L}\right)}{\sinh \frac{2\pi d}{L}} \cos 2\pi \left(\frac{x}{L} - \frac{t}{T}\right) + \frac{3}{4} \left(\frac{\pi H}{T}\right) \left(\frac{\pi H}{L}\right) \frac{\cosh 4\pi \left(\frac{y+d}{L}\right)}{\sinh^4 \frac{2\pi d}{L}} \cos 4\pi \left(\frac{x}{L} - \frac{t}{T}\right)$$

or in simplified form

$$U = A \cos 2\pi X + B \cos 4\pi X \quad \text{-----} \quad (5)$$

An inspection of equation (5) shows that the velocity components due to the first term on the right hand side are positive under the wave crest and negative under the trough, whilst the second term is positive under both crest and trough, and gives maximum negative components at $\frac{L}{4}$ and $\frac{3L}{4}$ from the crest. The net effect is to increase the value of the magnitude under the crest, and decrease it under the trough, thus producing asymmetry in the magnitudes of the orbital velocity. Fig. 10 compares the values of the horizontal velocity (magnitude) asymmetry given by the Stokes theory-equation (5) with the experimental results, and the theoretical values from equation (10). It can be seen that the divergence between the Stokes prediction and the experimental results was about 32% at a $\frac{d}{L}$ value of 0.11, with the divergence increasing shoreward but improving seaward.

For these reasons, one can conclude that Stokes theory is not directly applicable to the study of velocities in the near breaker zone.

Correlation Between Wave Asymmetry and Velocity Asymmetry

An important aspect of the work carried out by the author is the study of the correlation between the different types of wave asymmetry and the correlation between these and the resulting velocity asymmetry as the wave progressed into shallow water. The first aspect has been reported⁽⁵⁾.

Figure 11 shows the graphs of both the horizontal velocity (magnitude) asymmetry and the horizontal velocity (time) asymmetry plotted against the wave horizontal asymmetry H_A and H_A^1 for the beach slope of 1:18. The graphs show that a correlation exists between the velocity asymmetry and the wave asymmetry. The graph of horizontal velocity (magnitude) asymmetry against wave horizontal asymmetry H_A indicated that as the wave progressed into shallower water and the value of H_A decreased, indicating increased asymmetry,

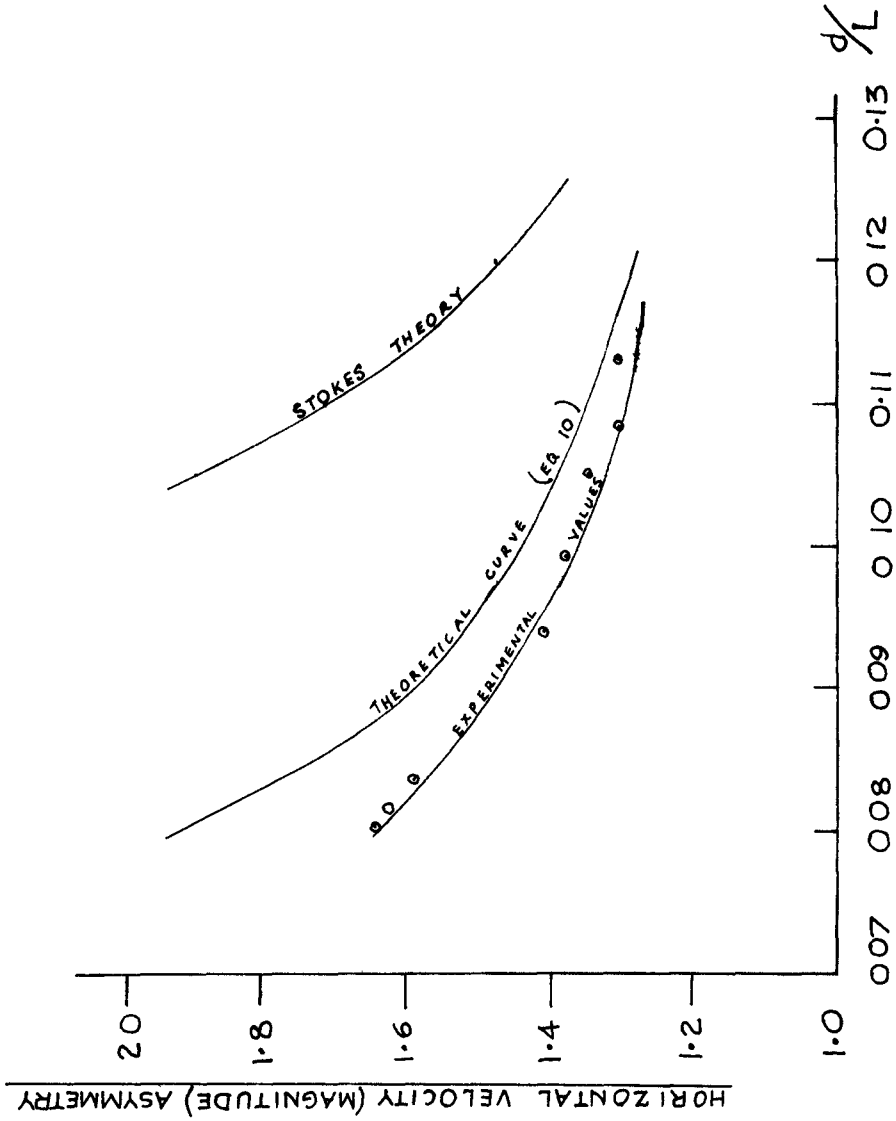


Fig 10 Comparison of Stokes theory with Experimental Results.

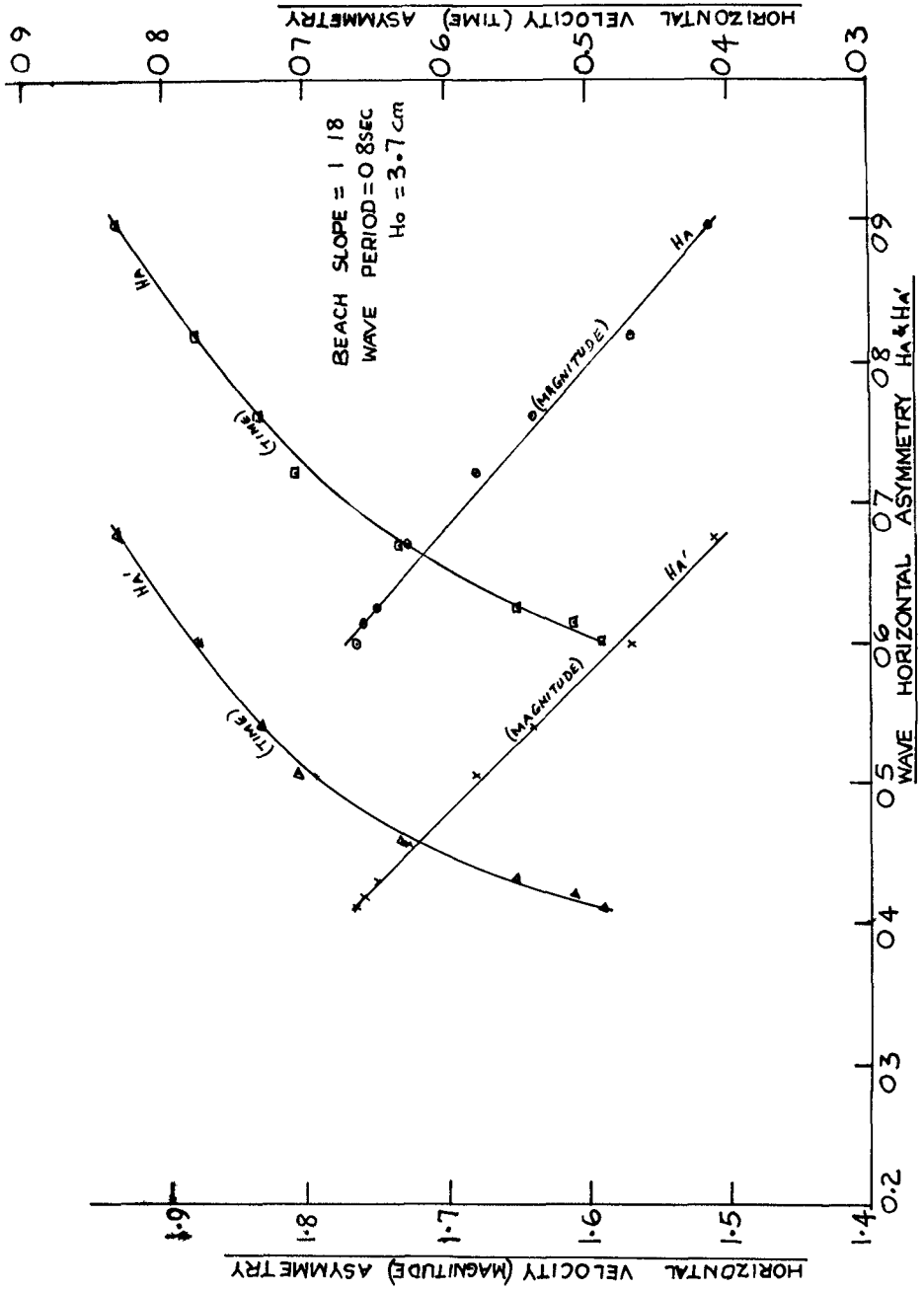


Figure 11 Graph of Velocity Asymmetry Against Wave Asymmetry.

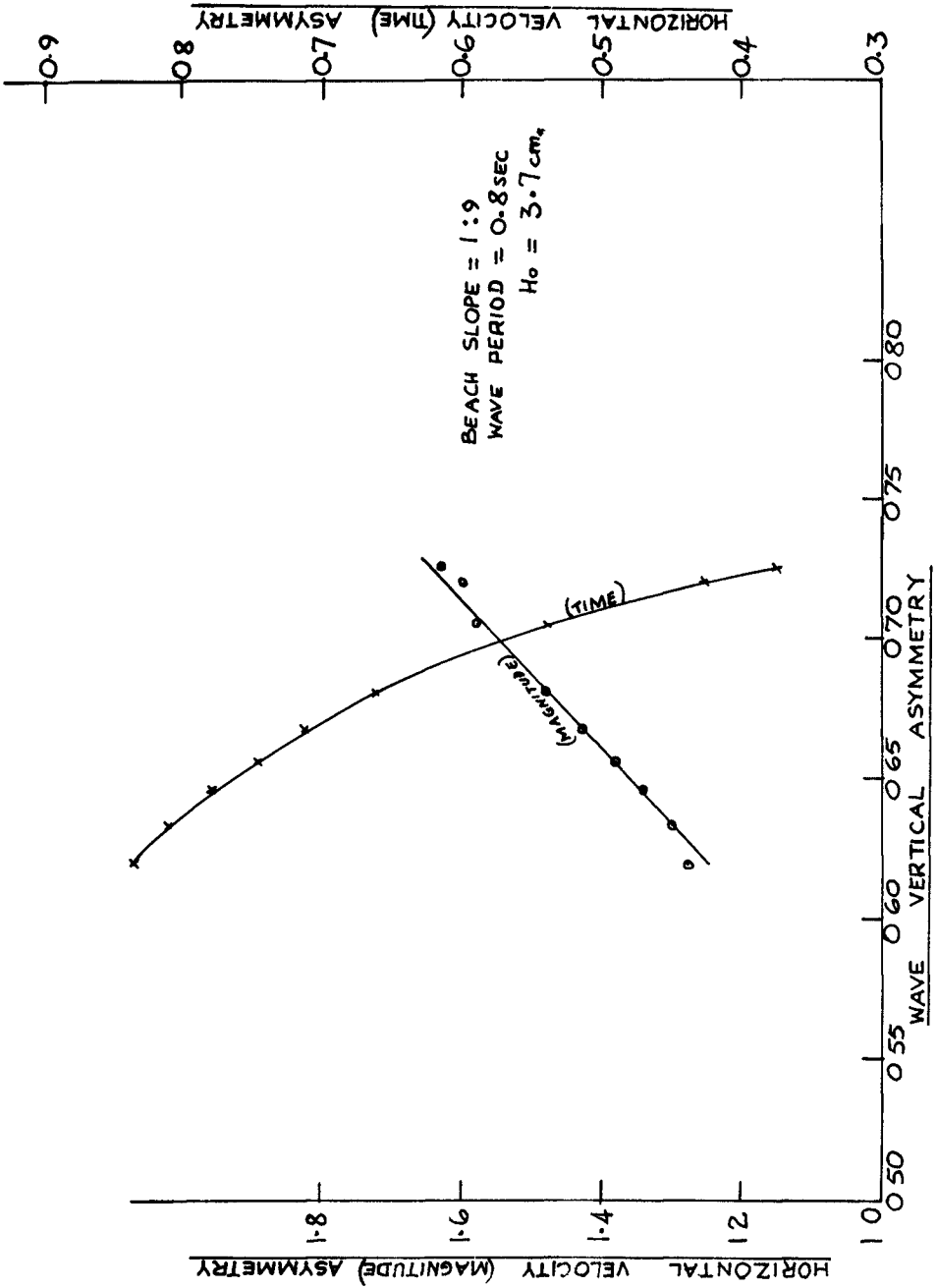


Fig 12 Graph of velocity Asymmetry Against Wave Asymmetry.

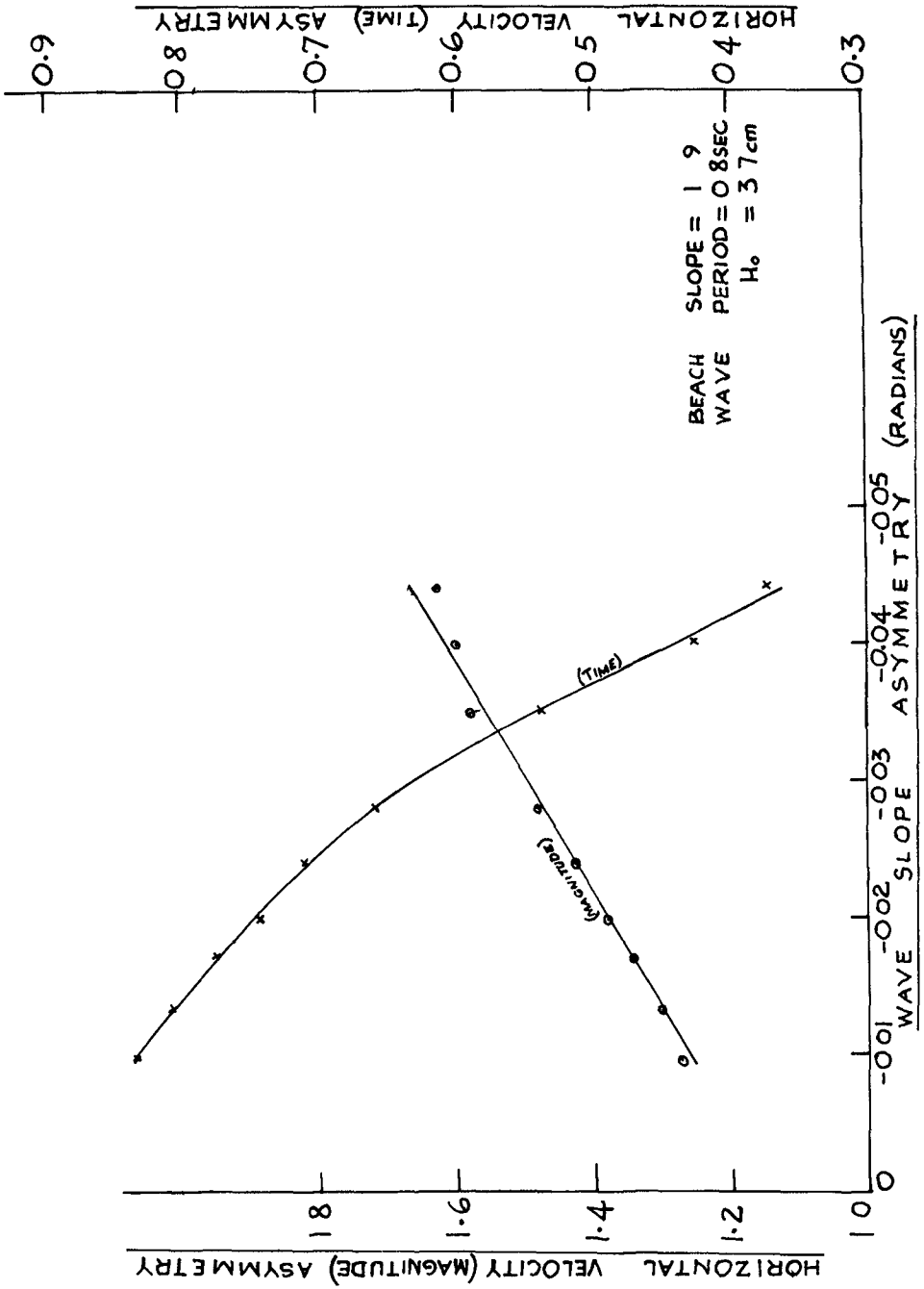


Fig 13 Graph of velocity Asymmetry Against Wave Asymmetry.

the horizontal velocity (magnitude) asymmetry also increased. For instance, when the value of the wave horizontal asymmetry H_A is 0.80 the value of the horizontal velocity (magnitude) asymmetry is 1.60, whereas when the value of H_A becomes 0.70 the value of the horizontal velocity (magnitude) asymmetry increased to 1.685 very near the wave break-point, the value of H_A becomes 0.60 the value of the horizontal velocity (magnitude) asymmetry is found to be 1.77. The graph of the horizontal velocity (magnitude) asymmetry against H_A followed a trend fairly similar to the graph of the horizontal velocity (magnitude) asymmetry against H_A . The graph of the horizontal velocity (time) asymmetry against H_A and H_A also show good correlations. The remaining graphs of the velocity asymmetry against the different types of wave asymmetry all show reasonably good correlation between the velocity asymmetry and the wave asymmetry. (see figures 12 and 13).

As a result of the studies the following relationships were obtained:

Let A_v = wave vertical asymmetry = $\frac{\text{Vertical distance from crest to S.W.L.}}{\text{Total wave height.}}$

S = wave slope asymmetry = $\frac{1}{2}(\text{Front face slope at S.W.L.} + \text{Back Face slope at S.W.L.})$ radians

$|S|$ = modulus of s

γ = beach slope.

V_{HMA} = Horizontal velocity (magnitude) asymmetry

H_A & H_{A1} = wave horizontal asymmetry

H_A = $\frac{\text{Horizontal distance from crest to front face at S.W.L.}}{\text{Horizontal distance from crest to back face at S.W.L.}}$

H_{A1} = $\frac{\text{Horizontal distance from crest to preceding wave trough}}{\text{Horizontal distance from crest to following wave trough}}$

The empirical relationships between V_{HMA} , S , γ , A_v and H_A are:

$$H_A = \frac{1.52}{e^\gamma} (1.18 - \sinh A_v) \quad \text{---} \quad (6)$$

$$V_{HMA} = 3.4 A_v - 0.78 \quad \text{---} \quad (7)$$

$$A_v = \frac{8.8}{e^\gamma} \tanh |S| + 0.5 \quad \text{---} \quad (8)$$

From the Cnoidal wave theory as developed by Korteweg and De Vries⁽⁸⁾, the wave vertical asymmetry A_v is given by

$$A_v = \frac{y_0 - d}{H} = \frac{16d^3}{3L^2H} \left\{ K(k) \left[K(k) - E(k) \right] \right\} \quad (9)$$

where y_0 = distance from the ocean bottom to the wave crest

d = still water depth

H = wave height (trough to crest)

L = wave length

$K(k)$ = complete elliptic integral of the first kind.

$E(k)$ = complete elliptic integral of the second kind.

k = modulus of the elliptic integral

From equations (9) and (7) we have

$$V_{HMA} = \left[\frac{18.1 d^3}{L^2 H} \left\{ K(k) \left[K(k) - E(k) \right] \right\} - 0.78 \right] \quad (10)$$

substituting for A_v from eq. (8) into eq. (7) gives

$$V_{HMA} = 3.4 \left\{ \frac{8.8}{e^{\gamma}} \tanh |S| + 0.271 \right\} \quad (11)$$

Also from the work of Biesel⁽²⁾, the wave slope asymmetry S is given by

$$s = m^2 \left(\frac{H_0}{2} \right)^2 \gamma \left\{ \frac{3 + \frac{md}{\tanh md} - 3 md \tanh md}{D^2 (\sinh md)^2 \tanh md} \right\} \quad (12)$$

$$\text{where } D = 1 + \frac{md}{\sinh md \cosh md}$$

$$\text{and } m = \frac{2\pi}{L}$$

substituting s from eq. (12) into eq. (11) gives

$$V_{HMA} = 3.4 \left\{ \frac{8.8}{e^{\gamma}} \tanh \left[m^2 \left(\frac{H_0}{2} \right)^2 \gamma \left\{ \frac{3 + \left(\frac{md}{\tanh md} \right) - 3 md \tanh md}{D^2 (\sinh md)^2 \tanh md} \right\} + 0.271 \right] \right\} \quad (13)$$

Thus equations (10) and (13) give expressions for V_{HMA} . However, of the two, equation (10) gives closer values to the experimental results in this work, and is the theoretical curve shown on figure 5. Values of $K(k)$ and $E(k)$ are tabulated in Masch and Wiegel⁽⁹⁾ (1961).

Comment

Figure 5 gives the impression that the theoretical predictions for horizontal velocity asymmetry are closer to the experimental values, for the steeper beach slope category. The correspondence is to within 5% in the region of $\frac{d}{L} = 0.10$ to 0.13 , and shows a difference of about 8% very close to the breakers where $\frac{d}{L}$ is approximately 0.08 . In fact, similar percentages apply in the case of the flatter beach slope, but the difference in the slope of the curves is more apparent and has the effect of offsetting the correlation.

Conclusions

The results show that the horizontal velocities increase in shoaling water, and for both slopes of 1:9 and 1:18 the greatest horizontal velocities occurred at the wave breaker position. The curves of the velocity-time history figures 3 and 4 show that the curves were closer together on the slope of 1:18 than on the slope of 1:9. It was however found that the velocity seems to have a constant value on each beach slope at all positions along the beach half the wave period after the passage of the wave crest; although the constant varies from slope to slope.

It was found that the maximum horizontal shoreward velocity did not occur directly under the wave crest but at a time $0.09T$ seconds after the passage of the crest. In terms of the values of the horizontal velocities, the values on the steeper slope of 1:9 were higher than those on the flatter slope of 1:18 especially in the neighbourhood of the breakers, but it was found that the values of the horizontal velocity (magnitude) asymmetry were higher on the flatter slope. Also the graph of the horizontal velocity (time) asymmetry against $\frac{d}{L}$ showed that the shoreward motion takes a longer time on the flatter slope.

The author is of the view that there must be a correlation between the wave asymmetry and the asymmetry of the velocity field resulting from the wave. The graphs of the different types of wave asymmetry defined by the author⁽³⁾ against the velocity asymmetry confirm that there are both qualitative and quantitative correlation between the wave asymmetry and the velocity asymmetry. As a result of the correlation two alternative expressions are given for the horizontal velocity (magnitude) asymmetry, one based on the Cnocidal wave theory and the other based on the work of Biesel⁽²⁾.

The paper also shows that Stokes theory is not directly applicable to the study of the velocity patterns in the near breaker zone.

In drawing conclusions from the study of the velocity fields associated with asymmetrical waves on varying beach slopes it is important to note that Miller and Zeigler⁽¹⁰⁾ observed three broad classes of wave asymmetry on a beach of only one slope. It is clear, as they suggest, that in nature in addition to the importance of beach slope, breaker shapes are affected by the interaction of different wave trains, and by the timing and magnitude of the backwash. It seems probable that the observations of Inman and Nasu⁽⁶⁾ that higher orbital velocities are associated with wave shape asymmetry must be considered in relation to the fact that their measurements were also made in nature, and that more than one wave train is likely to be present.

The author considers that investigations of the velocity fields very close to the bed should eventually provide a quantitative basis for evaluating the accretion and depletion of sediment under wave action. The magnitude and duration of the shoreward and seaward orbital velocities are important in sediment movement under wave actions. The magnitude of the maximum velocity is associated with initiating the motion and the asymmetry of the velocity fields determines the direction and extent of the net movement. The author thus considers that the quantitative correlation of the wave characteristics with the asymmetry of the orbital velocity fields would most probably lead to the correlation of wave characteristics with sediment movement.

Acknowledgements

The author wishes to express his gratitude to Prof. A. H. Chilver, the Chadwick Professor of Civil and Municipal Engineering, University College, London, where this work was carried out, and to Dr. P. H. Kemp who supervised the work.

The author also wishes to thank D. W. Vale, T. G. Gurman and Mick Gregory for their help in the experimental aspects of the work.

REFERENCES

- (1) Iversen, H. W. - Waves and breakers in shoaling water. Proc. Third Conf. Coastal Engineering 1952 pp. 1-12.
- (2) Biesel, F. - Study of Wave Propagation in water of gradually varying depth. Gravity waves circular No. 521 Nat. Bureau of Standards, Washington D.C. 1951.
- (3) Adeyemo, M. D. - Effect of beach slope and shoaling on Wave Asymmetry. Proc. Eleventh Conf. Coastal Engineering, London. 1968.

- (4) Adeyemo, M.D. - Wave transformation in shallow water. La Houille Blanche No. 6. 1969.
- (5) Hamada, T. - Breakers and beach erosions. Rept. Transportation Tech. Res. Inst. Tokyo. Report No. 1. Dec., 1951.
- (6) Inman, D. L. and Nasu, N. - Orbital velocity associated with wave action near the breaker zone. Beach Erosion Board. Washington D.C. Tech. memo No. 79, 1956.
- (7) Ippen, A. T. and Kulin, G. - The shoaling and breaking of the solitary wave. Proc. Fifth Conf. Coastal Engineering. Sept., 1954.
- (8) Korteweg, D. J., and De Vries, G. - On the change of form of long waves advancing in a rectangular canal, and on a new type of long stationary waves. Phil. Mag. 5th series 39, 1895 pp. 422 - 443.
- (9) Masch, F. D. and Wiegel, R. L. - Cnoidal waves - Tables of Functions Council on Wave research. The Engineering Foundation Richmond, California. 1961. 129 pp.
- (10) Miller, R. L. and Zeigler, J. M. - The internal velocity field in breaking waves. Proc. Ninth Conf. Coastal Eng. 1964.
- (11) Morison, J. R. and Crooke, R. C. - The mechanics of deep water, shallow water breaking waves. Beach Erosion Board. Tech. Memo. No. 40. 1953.

CHAPTER 28

THE DEVELOPMENT OF UNDULAR BORES WITH FRICTION

by

O Hawaleshka* and S B Savage**

ABSTRACT

A theoretical and experimental study of the initial development of undular bores in two-dimensional, rectangular channels with and without boundary friction was performed. Equations similar to those of Boussinesq, but including higher order and wall friction terms are presented and solved numerically by an implicit finite difference method. A Pohlhausen-type boundary layer momentum integral method is used to obtain the wall shear stress distribution under a developing long wave from the consideration of the boundary layer underneath it. The solution is performed in a quasi-iterative manner proceeding from the friction coefficient calculation for an initially assumed wave profile to the inclusion of this coefficient in the calculation of a new wave profile at an advanced time. Comparisons of theoretical and experimental results are given. For the initial development of the undular bore with which the present work is concerned, the measurements are found to be in reasonable agreement with the theoretical predictions. The effect of the wall shear stress manifests itself mainly in a slight reduction of the wave amplitudes.

INTRODUCTION

Bores are transitions between two essentially uniform liquid flows. A turbulent breaking zone is associated with "strong" bores, but if the depth change is relatively small, the bores are termed weak and may consist of a train of undular waves following the head wave. These waves are found to be closely approximated by the elliptic or cnoidal wave form of Korteweg and DeVries (1). This class of waves to which the solitary wave belongs as well is characterized by constancy of shape and a marked resistance to decay, in contrast to such waves as the non-linear shallow water waves of Airy that regardless of their initial smallness will eventually grow, steepen and break. Ursell (2) has

* Assistant Professor, Mechanical Engineering Department, University of Manitoba, Winnipeg, Manitoba, Canada

**Associate Professor, Department of Civil Engineering and Applied Mechanics, McGill University, Montreal, Quebec, Canada

distinguished various types of shallow water waves by the parameter $\alpha\lambda/h^3$ where values of $\alpha\lambda/h^3 \gg 1$, $\alpha\lambda/h^3 \sim O(1)$ and $\alpha\lambda/h^3 \ll 1$ correspond to the Airy theory, the nonlinear theory of cnoidal and solitary waves and the linearized theory respectively

Such bores may be created in many ways. For example the opening of lock gates will form positive surges in the canal and negative ones within the lock. A sudden stoppage of a turbine in a power station creates a positive surge in the supply channel and a negative one in the tail race channel. Similar bores are formed in tidal estuaries at rising tide.

It is of interest to be able to predict the development of such bores and related waves, taking account of frictional effects. Up till now, most investigations of undular bores were performed for conditions where these effects were neglected or were treated in an approximate manner by the use of, for example, some average value of a Chezy coefficient (cf. ex. Benjamin & Lighthill (3), Sandover & Taylor (4), Sandover & Zienkiewicz (5), Sturtevant (7), Peregrine (6), Murota (8)).

In this paper we treat the problem of an undular surge or an arbitrary long wave, considering the effect of boundary friction. This shear effect is obtained from the computation of the development of the boundary layer underneath the advancing wave.

EXPERIMENTAL SETUP AND PROCEDURE

An aluminum channel with glass side walls was used during the tests, (fig. 1). Its dimensions are 30 feet length, 12 inches wide and 18 inches deep, and was typically filled to a depth of four inches of water. A close-fitting piston with a maximum stroke of three feet and with a continuously variable velocity was installed at one end of the channel and was actuated hydraulically. It was found that with suitable combinations of piston stroke, speed and water depth a complete range of bores as well as a reasonable approximation to a solitary wave could be produced. Care was taken to provide seals around the wetted portion of the piston, effectively eliminating leaks.

The surface profiles resulting from the motion of this piston were measured at several stations along the channel by streamlined, immersed, variable-resistance probes and recorded together with the piston motion on a six channel recorder. Electronic filters were used to remove unwanted higher frequencies from the signals. The wave-measuring equipment was built by Kempf-Remmers. The accuracies obtained were essentially limited by the capillary effects of the water. The probes themselves were of fiberglass construction in the shape of a symmetrical streamlined profile with conducting strips on each side of the probe's leading edge. Production run calibrations were done statically before each run, since a test dynamic calibration showed no appreciable difference.

Some dye studies of the boundary layer under the advancing wave were performed to record visually the bottom boundary layer development.

Photographic records of surface profiles, in particular at the initial stages of the piston motion were taken by both still and cine cameras

The test procedure involved the measurements of the wave profiles for various non-dimensional piston speeds U_p from 0.1 to 0.5 and for still water depths ranging from two to five inches

THEORETICAL APPROACH

1 Equations of Motion

We make use of the equations derived by Su and Gardner (9) for non-linear dispersive shallow water waves. These are in non-dimensional form

$$\frac{\partial h}{\partial t} + \frac{\partial}{\partial x}(h\bar{u}) = 0 \tag{1}$$

$$\frac{\partial(h\bar{u})}{\partial t} + \frac{\partial}{\partial x} \left[h\bar{u}^2 + \frac{h^2}{2} - \frac{h^3}{3} (\bar{u}_{xx} + \bar{u}\bar{u}_{xx} - \bar{u}_x^2) \right] \tag{2}$$

where $h = \frac{h^*}{h_0}$, $t = t^* \sqrt{\frac{g}{h_0}}$, $x = \frac{x^*}{h_0}$, $y = \frac{y^*}{h_0}$

$$\bar{u} = \frac{1}{h} \int_0^h \frac{u^*}{\sqrt{gh_0}} dy$$

The starred variables are dimensional and h is the local water depth, t is time, x and y are the horizontal and vertical coordinates, u is the horizontal component of velocity, \bar{u} is the depth averaged velocity, g is the gravitational acceleration and h_0 is the undisturbed reference depth, see fig 2

Equations (1) and (2) are similar to the Boussinesq equation but include the higher order terms

$$\frac{\partial}{\partial x} \left[\frac{h^3}{3} (\bar{u}\bar{u}_{xx} - \bar{u}_x^2) \right]$$

in equation (2). We can approximately account for the effects of wall friction by the addition of the term

$$\text{Friction term} = - \frac{fh\bar{u}|\bar{u}|}{R} \tag{3}$$

to the left hand side of equation (2), where R is the dimensionless hydraulic radius at any station,

$$R = \frac{hb}{2h+b}$$

and b is the dimensionless channel width b/h_0

2 Calculation of the friction coefficient from a Momentum Integral consideration of the boundary layer developed by a long wave

We now carry out an approximate momentum integral analysis in order to calculate the friction coefficient f , to be used for the friction term (3) which is added to equation (2). The notation in this section is somewhat different from the previous one and unless otherwise noted unstarred variables refer to physical quantities.

Consider the development of a laminar two-dimensional boundary layer under a long wave advancing with speed u_F into still water of depth h_0 . In the boundary layer analysis the inviscid fluid velocity u_i is approximated as equal to the depth-averaged value obtained from the integration of the long wave equations. Fig. 3 shows the situation when brought to a quasi-steady state with respect to the wave front, and also defines the notation to be used. In this quasi-steady frame the boundary layer equations are

$$\frac{du}{dx} + \frac{dv}{dy} = 0 \quad (4)$$

$$u \frac{du}{dx} + v \frac{dv}{dy} + \frac{1}{\rho} \frac{dp}{dx} = \nu \frac{d^2u}{dy^2} \quad (5)$$

where the symbols have the usual meanings. Upon integration we obtain the common boundary layer momentum integral equation

$$\frac{d\Theta}{dx} + (2\Theta + \delta^*) \frac{1}{u_e} \frac{du_e}{dx} = + \frac{\tau_0}{\rho u_e^2} \quad (6)$$

where Θ and δ^* are the momentum and displacement thicknesses respectively and the wall shear stress is defined by

$$\frac{\tau_0}{\rho} = \nu \left. \frac{du}{dy} \right|_{y=0} \quad (7)$$

Equation (6) is solved by assuming a suitable form for the velocity profile in the boundary layer, a procedure first suggested by Pohlhausen. We take the fourth degree polynomial

$$\frac{u}{u_e} = f(\eta) = \frac{U_w}{U_e} - \left(\frac{U_w}{U_e} - 1 \right) (2\eta - 2\eta^3 + \eta^4); \quad \eta = \frac{y}{\delta} \quad (8)$$

which satisfies the conditions of $f(\eta) = \frac{U_w}{U_e}$ at $\eta = 0$, and 1 for $\eta = 1$. From this we can obtain $k_1 = k_1(x)$ and $k_2 = k_2(x)$ as defined by

$$\Theta = k_1 \delta \quad (9)$$

$$\delta^* = k_2 \delta \quad (10)$$

We have as well

$$\frac{dU_e}{dx} = - \frac{du_i}{dx} \quad ; \quad u_e = u_w - u_i \quad (11)$$

and
$$\frac{\tau_0}{\rho} = \frac{\nu}{S} \frac{du}{dz} \Big|_{z=0} = -\frac{\nu}{S} (2u_1) \tag{12}$$

Hence (6) becomes

$$\frac{1}{2} \frac{d\Theta^2}{dx^2} - \frac{1}{u_e} \frac{du_1}{dx} \left(2 + \frac{k_2}{k_1}\right) \Theta^2 = -2\nu k_1 \left(\frac{u_1}{u_e^2}\right) \tag{13}$$

After defining

$$\Xi = \Theta^2 \tag{14}$$

and the Reynolds Number

$$Re = \frac{h_0 \sqrt{gh_0}}{\nu} \tag{15}$$

we obtain

$$\frac{1}{h_0} \frac{d\Xi}{dx} - \frac{2}{u_e} \left(\frac{du_1}{dx}\right) \left(2 + \frac{k_2}{k_1}\right) \frac{\Xi}{h_0} = -\frac{4k_1}{Re} \left(\frac{u_1}{u_e^2}\right) \tag{16}$$

or, in non-dimensional form

$$\frac{d\tilde{\Xi}}{d\tilde{x}} - \frac{2}{\tilde{u}_e} \frac{d\tilde{u}_1}{d\tilde{x}} \left(2 + \frac{k_2}{k_1}\right) \tilde{\Xi} = -\frac{4k_1}{Re} \frac{\tilde{u}_1}{\tilde{u}_e^2} \tag{17}$$

where $\tilde{x} = x/h_0$, $\tilde{z} = z/h_0$, $\tilde{u}_1 = u_1/\sqrt{gh_0}$ and $\tilde{u}_e = u_e/\sqrt{gh_0}$

Experimental conditions define Re, and k_1 and k_2 are known from the assumed form of the boundary layer profile, equation (8). Equation (17) may be solved for $\tilde{\Xi}$ and hence for Θ and S . If we define the wall shear stress

$$\tau_0 = \frac{1}{2} \rho f u_1^2 \tag{18}$$

we may now calculate the coefficient of friction f from the equation

$$f = -\frac{4\nu}{S u_1} \tag{19}$$

The local value of f is now used in the long wave equations (1)-(3) for the computation of the development of the wave profile

3 Method of Solution

Assuming a suitable initial profile for the long wave we may integrate equation (17) - using a fourth order Runge-Kutta numerical integration and thence determine all the parameters of the boundary layer developing under this surge. In particular from equation (19) we obtain the friction coefficient distribution with x , corresponding to this initial profile. This friction coefficient is assumed to be constant

over the wetted perimeter across any cross-section of the flow. It is then fed into an implicit, finite central difference method of solution for equations (1)-(3), allowing the computation of a new wave profile at an incrementally advanced time. This new wave profile is then used in equation (17) to calculate a friction coefficient distribution corresponding to it. The solution proceeds in such a quasi-iterative fashion until the entire flow region of interest is covered.

A square mesh spacing of $\Delta x = \Delta t = 0.2$ was used in most computations. The general finite differences solution followed the method outlined by Wachspres (10). The governing equations (1)-(3) are expressed as simultaneous, central (3-point) finite difference equations at each grid point at the desired time step and solved by a forward elimination, backward substitution technique (line inversion).

Special procedures are required near the starting and ending boundaries since full central differences cannot be evaluated there. To reduce computation time, we specify initially a small portion of the x-axis ($t = 0$) and add new data points for the undisturbed liquid ahead of the advancing wave as it becomes necessary.

RESULTS

Figure 4 shows the comparison of our theoretical results with and without the effect of friction. We note that the main effect of the wall shear stress manifests itself mainly in the reduction of the wave peaks. The troughs seem relatively unaffected. This is in contrast to some experimental results given by Sandover and Zinkiewicz (5) who note that the troughs become shallower as the friction increases.

The value of the friction coefficient calculated in this manner is typically of the order of 3.0×10^{-3} far from the head wave. At the start of the wave the friction coefficient is very large but decreases rapidly with distance from the very beginning of the wave.

Figures 5 and 6 give comparisons of experiments with theory with the friction taken into account. The agreement is generally good in particular at the lower non-dimensional piston speed $u_0 = 0.1$. The first peak is well described but the theory indicates lower peaks for the trailing waves. The troughs are well predicted. The agreement becomes better with increasing time. For $u_0 = 0.2$ the agreement is less good, the theory seeming to exaggerate the actual swings of the peaks and troughs. The wavelength is well represented.

The above remarks are confirmed by figures 7 and 8, where we show the growth of the first peak and of the first wavelength from theory and experiment for cases with and without wall friction.

CONCLUSIONS

The method shown seems to reproduce the initial development of the undular bore reasonably well. It indicates the trends of behaviour regarding the influence of wall friction. For the experimental conditions described herein the effect is fairly small.

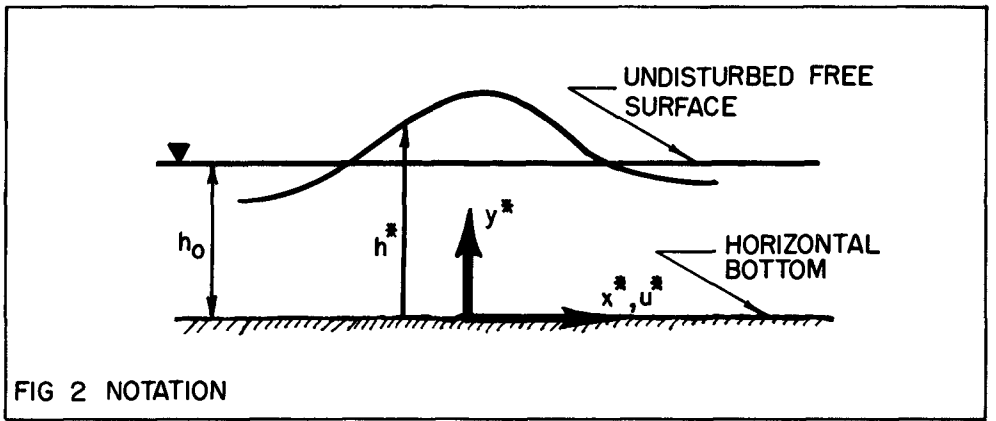
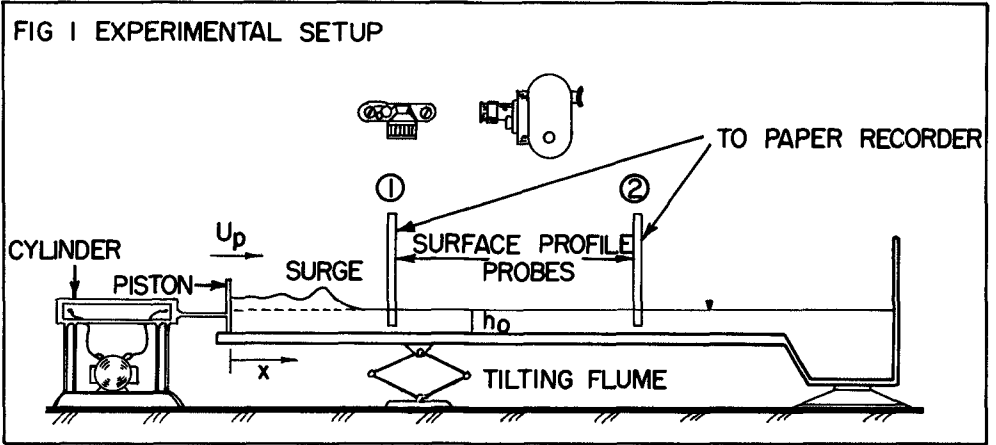
The analysis of the friction coefficient development is limited by the assumed form of the boundary layer velocity profile. It is possible that velocity reversals may appear as the wave develops and undulations become larger. These changes would invalidate the boundary layer approach described.

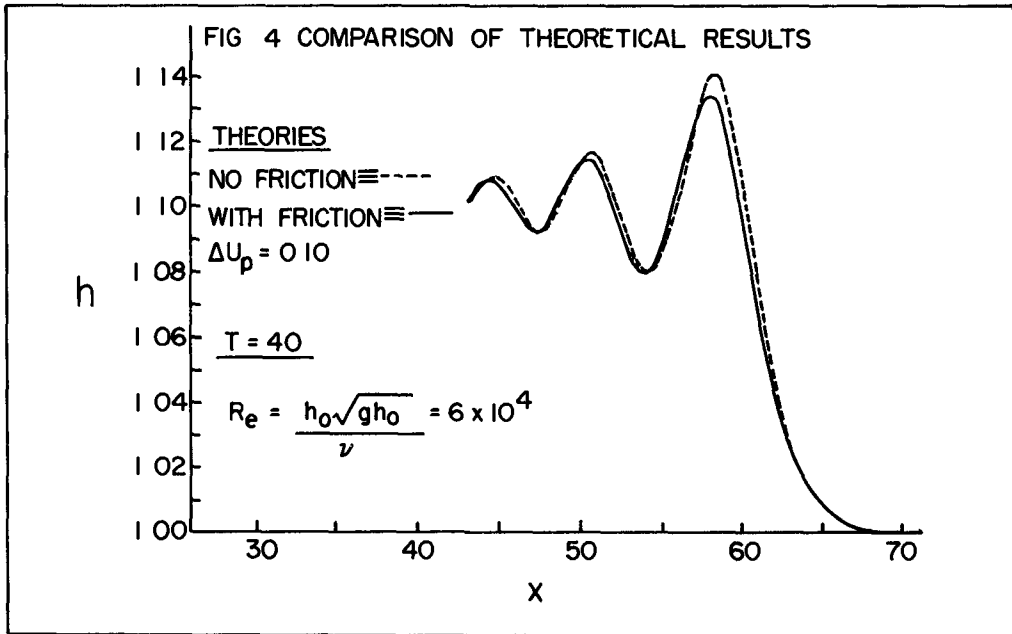
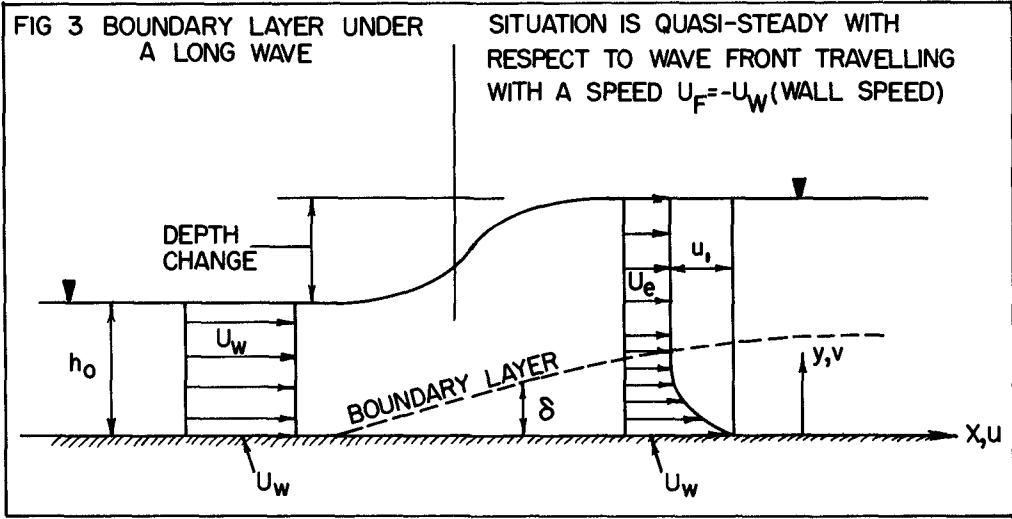
The above method (without friction) has been extended and applied successfully to various problems where the depth is variable, in particular to the development of a solitary wave crossing a bar or a trench, the solitary wave climbing a beach and to the development of an undular bore moving up a beach. These results will be given in a forthcoming paper.

BIBLIOGRAPHY

-
- 1 Korteweg, D J & deVries, G , 1895, Phil Mag (V), 39, 422-443
 - 2 Ursell, F , 1953, The Long-Wave Paradox in the Theory of Gravity Waves, Proc Camb Phil Soc 39, 685-694
 - 3 Benjamin, T B & Lighthill, M J , 1954, On Cnoidal Waves and Bores, Proc Roy Soc A, 224, 448-60
 - 4 Sandover, J A & Taylor, C , 1962, La Houille Blanche, 17, 443-455
 - 5 Sandover, J A & Zinkiewicz, O C , 1957, Experiments on surge waves, Water Power, 9, 418-424
 - 6 Peregrine, D H , 1966, Calculation of the Development of the Undular Bore, J Fl Mech (25), 2, 321-330
 - 7 Sturtevant, J , 1965, Implications of experiments on the weak undular bore, Phys of Fluids, vol 8, 6
 - 8 Muroka, A , 1966, Tenth Conf Coastal Engrg , 24, 382-395
 - 9 Su, C H & Gardner, C S , 1969, Derivation of the Korteweg-deVries Equation and Burger's Equation, J Math Phys ,10,3, 536-39
 - 10 Wachspress, E , 1960, Numerical Solution of Boundary Value Problems, Mathematical Methods for Digital Computers, Ralston, A & Wilf, H S ed , Wiley

=====





WAVE AMPLITUDES AT FIXED X

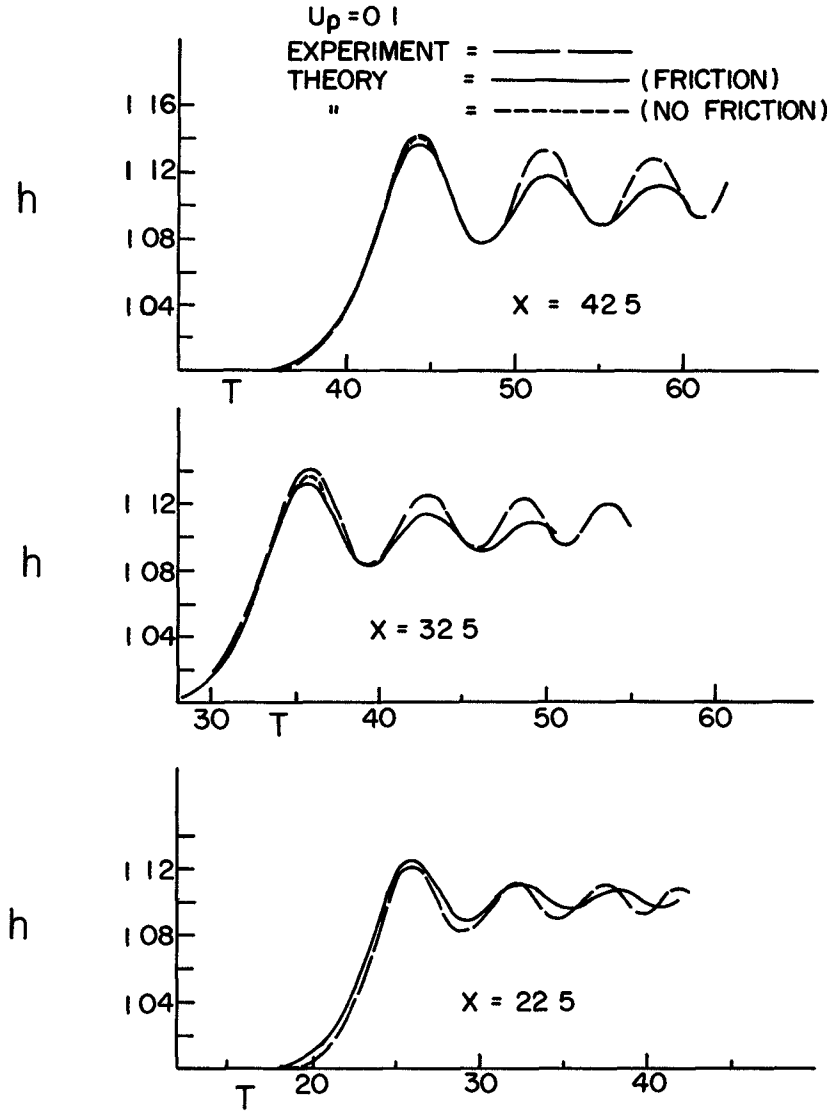


FIG 5 DEVELOPMENT OF AN UNDULAR BORE , $U_p = 0.1$

WAVE AMPLITUDES AT FIXED X

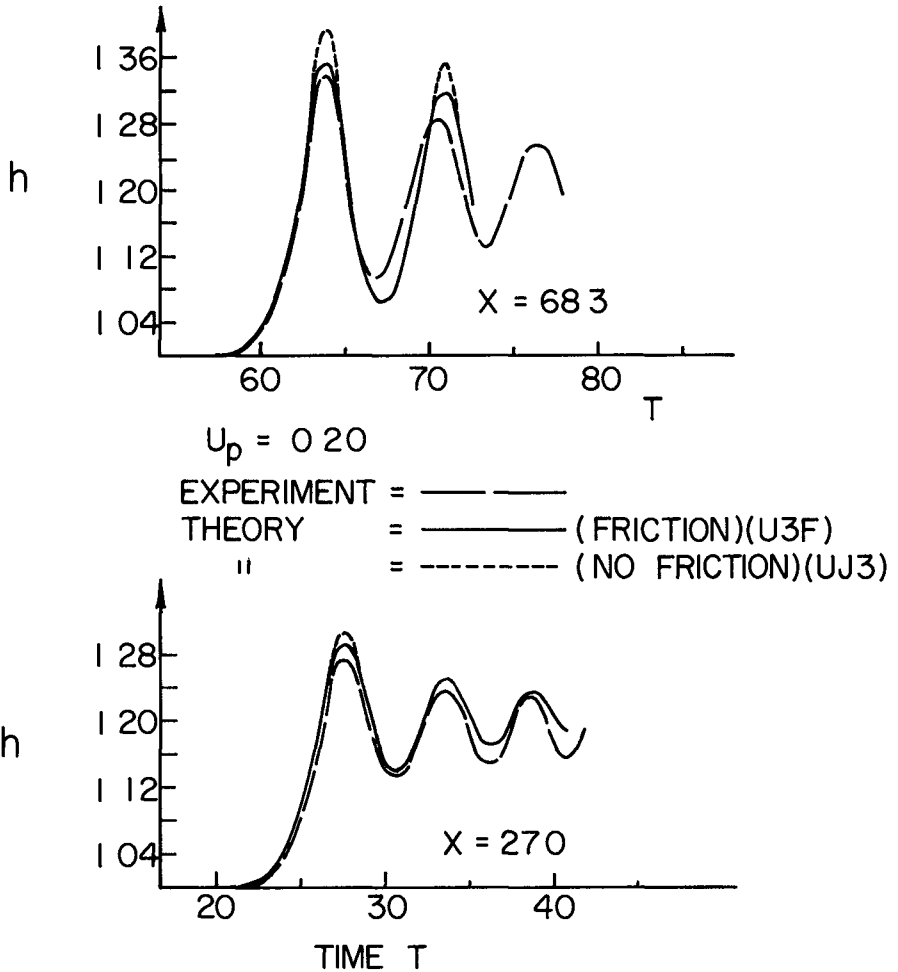
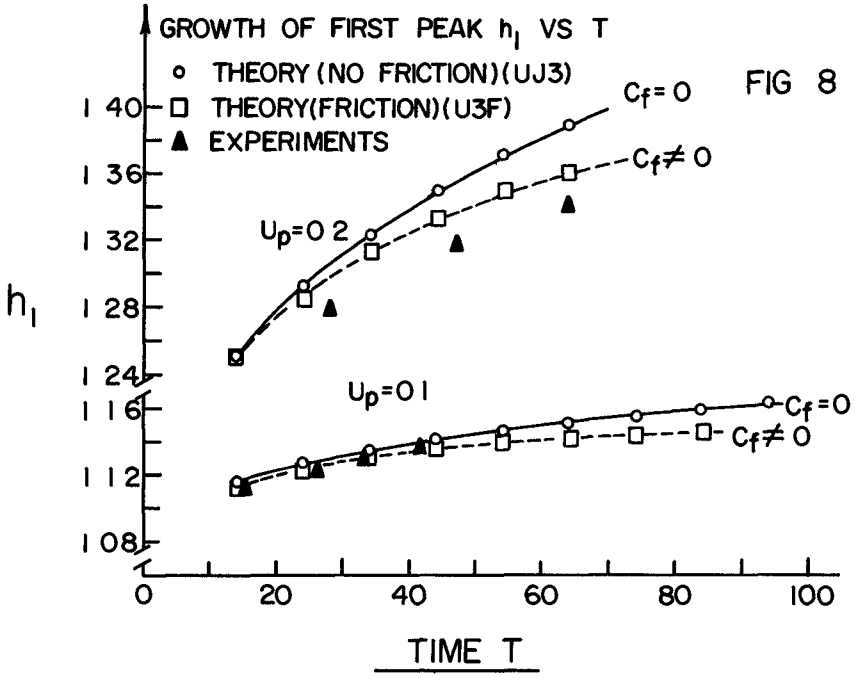
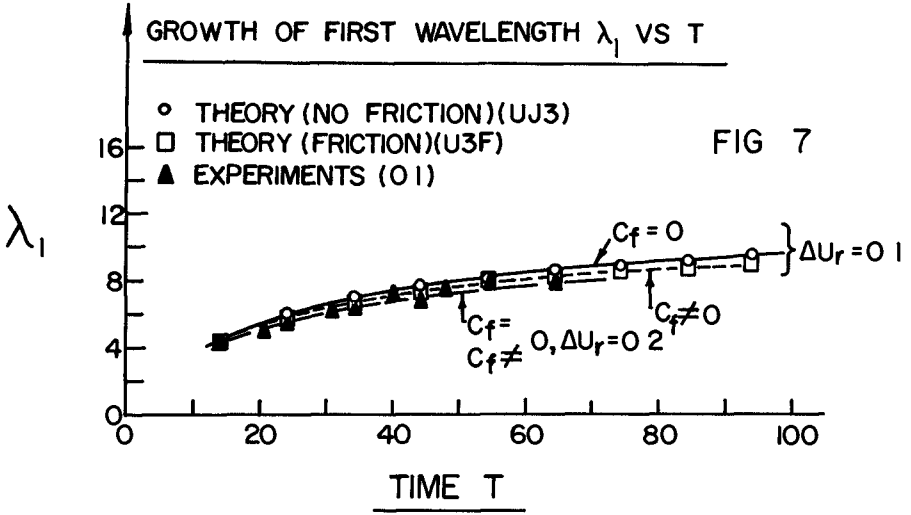


FIG 6 DEVELOPMENT OF AN UNDULAR BORE ; $U_p = 0.2$



CHAPTER 29

COMPUTER MODELLING OF DIFFRACTION OF WIND WAVES

by

Shou-shan Fan¹ and L E Borgman²

ABSTRACT

A digital computer model for diffraction of wind waves behind a breakwater is developed. The model combines the hydrodynamic theories and the concept of directional spectra. It is designed so that it may be used not only for the study of the wind wave diffraction problem behind breakwaters but also for the investigation of experimental (or field) data analysis procedures of other kinds. An extensive study of optimum data length, lag number and gage spacings in wave gage arrays is presented.

I INTRODUCTION

Unlike monochromatic waves, wind waves are quite complicated in nature. Their heights and lengths are irregular. The crest length along each wave crest is relatively short and their forms are not permanent. Each portion of the water surface has a different shape. The wave speed, frequency, and direction of advance vary from one wave to the next. Because of the difficulties of an analytical treatment of such a complicated situation, an approach through simulation techniques offers many advantages [4].

The three types of simulation commonly used are laboratory (physical), electronic analog, and digital computer. In the following, only the digital simulation procedures will be outlined.

II SIMULATION OF WIND WAVES

Wind waves can be simulated digitally in several ways, such as superposition and digital filter techniques [1]. In the following development, only the filtering procedure will be employed.

Let $y(t)$ be the wave surface elevations recorded by 4 gages in front of a breakwater. Each of the $y(t)$ can be expressed by the summation of the products of d and x (see eq (1)). Here, x is a sequence of normal random deviates. For computational convenience the random numbers have been selected so that they have a zero mean and variance of one.

¹Former graduate student, University of California, Berkeley
Oceanographer, Coastal Engineering Research Center, Washington, D C

²Former Associate Professor, University of California, Berkeley
Professor, University of Wyoming, Laramie, Wyoming

The "d" values are digital filter coefficients and can be represented in terms of the Fourier coefficients, A_n and B_n obtained from the Fourier approximation of the system functions $K^n(f)$ as shown by eqs (2)-(4)

The values of $K(f)$ are determined from the cross-spectral densities which are Fourier transform of the cross-covariance functions (eqs (5), (6))

If the probability distributions of the spectra are assumed to be circular normal (eq (10)), then the normalized cross-spectral density functions can be expressed as the functions of Bessel functions (eqs (7)-(9))

In short, if the spectral forms of waves are assumed (such as that given by Bretschneider [5] and Pierson and Moskowitz [6]) we can simulate the wind waves with digital computation

As already mentioned previously these simulated random waves have very complicated natures and the conventional diffraction theories cannot be applied. To deal with this kind of problem, we introduce the concept of directional spectrum

III CONCEPT OF DIRECTIONAL SPECTRUM

Random waves can be thought as composing of infinite number of monochromatic component waves, each of which has a different frequency and phase and propagate along a different direction. Since it is known that, to a linear approximation, the conventional diffraction theories are applicable to these monochromatic waves, our problem has then become the question of "how to determine the directional spectrum?"

At the present time, there are several ways available for estimating the directional spectrum. But, only one of those methods, [1,2] will be discussed. It considers the directional spectral density function as the product of $PS(f)$ and $D(\theta)$, where $PS(f)$ is spectral density which varies solely with frequency and $D(\theta)$ is a function of direction and possible frequency (see eq (13))

There are several ways to estimate $D(\theta)$. One of them is based on the assumption that $D(\theta)$ is circular normal. In that case, it can be approximated in terms of Bessel functions as shown in eq (14)

The spectral density function can be estimated by the conventional spectral analysis technique using either the covariance function approach or the techniques arising from the fast Fourier Transform algorithm

IV SIMULATION OF DIFFRACTION OF PLANE WAVES [3,4]

Mathematically, the propagation of a plane wave is described by the boundary value problem with a second order partial differential equation of elliptic type (eq (15)) and three boundary conditions (eqs 16,17,18). By applying the method of separation of variables, the boundary value can be solved

Due to the presence of a semi-infinite breakwater, located along the X-axis with one tip at the origin and the other at $x = +\infty$, an additional boundary condition of

$$\frac{\partial \phi}{\partial y} = 0$$

should be introduced. For the reason of generality and convenience, a polar coordinate system is adopted here. Accordingly, the amplitude for incident wave and diffracted wave can be determined.

Since the diffraction coefficient, k' is defined as the ratio of incident wave height over the diffracted wave height, it can be estimated by the modulus of $F(r, \theta)$ for the diffracted waves. Their mathematical equations and solutions are given in the Appendix III.

V THE APPLICATIONS OF SIMULATION TECHNIQUE

Simulation may be used to explain various features of data sampled from the field or to examine the consequences of selected theories. In addition, it can be used to determine

- (a) optimal data length (Fig 1). For this case, optional length = 2048.
- (b) optimal maximum number of lags (Fig 2). For this case, optional lag = 50.
- (c) effects of smoothing on the spectral density estimates (Fig 3). The results have indicated that
 - (1) for shorter data length, there is a great difference between the outputs of unsmoothed and smoothed cases but there seems to be no difference between Hanning or Hamming smoothing.

and that

- (11) for very long record, there is no difference no matter whether they have been smoothed or not.

REFERENCES

- Borgman, L E , "Ocean Wave Simulation For Engineering Design", Report HEL-9-13, University of California, Berkeley, October 1967
- Borgman, L E , "Directional Spectra Models For Design Use", Report HEL-1-12, University of California, Berkeley, 1969
- Fan, Shou-shan, Cumming, J , Wiegel, R L , "Computer Solution of Wave Diffraction by Semi-infinite Breakwater, Report HEL-1-7, University of California, Berkeley, July 1967
- Fan, Shou-shan, "Diffraction of Wind Waves", Report HEL-1-10, University of California, Berkeley, August 1968
- Bretschneider, C L , "Wave Variability and Wave Spectra For Wind Generated Gravity Waves", BEB, TM-118, August 1959
- Pierson, W J , Jr , & Moskowitz, L , " A Proposed Form For Fully Developed Wind Seas Based On The Similarity Theory of S A Kitaigoroskii, Jour Geophy Res , Vol 69(1964), No 24

APPENDIX I

Simulation of Complicated Wind Wave Profiles

Let $y_1(t)$, $y_2(t)$, ..., $y_m(t)$ be M - time series

$$y(t) = \sum_{n=-N}^N d_n x(t-n\Delta t) \quad (1)$$

where $n = 0, 1, 2, \dots$

Δt = time interval

x = random deviates

and the digital filter coefficients

$$d_0 = A_0 \quad (2)$$

$$d_n = A_n + B_n \quad \}$$

$$d_{-n} = A_n - B_n$$

where

$$A_n = \frac{1}{F} \int_0^F R[\hat{K}(f)] \cos\left(\frac{n\pi f}{F}\right) df$$

$$B_n = \frac{1}{F} \int_0^F I_m[\hat{K}(f)] \sin\left(\frac{n\pi f}{F}\right) df \quad (3)$$

$$F = \frac{1}{2\Delta t} = \text{Nyquist frequency}$$

and

$$\hat{K}(f) = A_0 + \sum_{n=1}^N \{A_n \cos\left(\frac{1n\pi f}{F}\right) - iB_n \sin\left(\frac{1n\pi f}{F}\right)\} \quad (4)$$

f = frequency, cps

$$i = \sqrt{-1}$$

The system function can be also written as

$$\begin{aligned}
 K_{11}(f_k) &= [s_{11}(f_k)] \\
 K_{m,1}(f_k) &= [s_{m,1}(f_k)]^{\frac{1}{2}} \\
 K_{m,n}(f_k) &= \{s_{m,(m-1)}(f_k) - \sum_{j=1}^n [K_{mj}(f_k)][K_{jn}(f_k)]\} / K_{nn}(f_k) \\
 K_{m,m}(f_k) &= [s_{mm}(f_k) - \sum_{j=1}^{m-1} |K_{mj}(f_k)|^2]^{\frac{1}{2}}
 \end{aligned} \tag{5}$$

where

$$s_{mj}(f) = CS_{mj}(f) + i QS_{mj}(f) \tag{6}$$

$CS_{mj}(f)$ = co-spectral density for gages m and j

$QS_{mj}(f)$ = quad-spectral density for gage m and j

Assuming the circular normal function (eq 10 below) for the angular distribution of energy at a given frequency, the normalized density between gages m and j can be expressed as

$$\frac{CS(f)}{PS(f)} = J_0(A_{mj}) + \frac{2}{I_0(a)} \sum_{n=2,4,6}^{\infty} (i)^n [I_n(a) J_n(A_{m_j})] \cos n\gamma_{mj} \tag{7}$$

and the normalized quad-(or quadrature-) spectral density between gages m and j is

$$\frac{QS(f)}{PS(f)} = \frac{2}{I_0(a)} \sum_{n=1,3,5}^{\infty} (i)^n [I_n(a) J_n(A_{m_j})] \cos(n\gamma_{mj}) \tag{8}$$

where

$$I_n(a) = I_{-n}(a) = (i)^{-n} J_n(ia) \tag{9}$$

= Modified Bessel Function of order n

a = a circular normal parameter = measure of dispersion of the circular normal

α = a circular normal parameter = modal direction of circular normal energy distribution

$$f(\xi, a) = \frac{e^{a \cos(\theta - \alpha)}}{2\pi I_0(a)} \quad (10)$$

θ = the angle between the positive x-axis and the direction of the wave propagation, measured counterclockwise

ξ = the wave angle departure from the mean = $\theta - \alpha$

$$A_{mJ} = 2\pi D_{mJ} / L$$

D_{mJ} = distance between wave gages m and j

L = wave length appropriate for the frequency, f

γ_{mJ} = the angle between direction of main energy and the line connected gage m and gage j

$$= \beta_{mJ} - \alpha$$

β_{mJ} = the angle between the x-axis and the line connected gage m and gage j

$$i = \sqrt{-1}$$

APPENDIX II

DIRECTIONAL SPECTRUM

1 Directional spectral density function, $p(f, \theta)$

(a) It has the property of

$$p(f, \theta) df d\theta = \Sigma [\text{Mean-Square Wave-Surface fluctuations}] \quad (11)$$

$$(df)(d\theta)$$

In other words,

$$p(f, \theta) df d\theta = \text{variance of sea surface fluctuations obtained by adding together only the waves with frequency and direction of travel in the } (df, d\theta) \text{ rectangle centred at } (f, \theta) \quad (12)$$

(b) It gives the allocation of the total variance among the various frequencies and directions

(c) It can also be considered as an allocation of wave energy (since the wave energy per unit sea surface is proportional to the variance)

2 Estimation of directional spectral density

$$p(f, \theta) = PS(f) D(\theta) \quad (13)$$

$$D_f(\theta) = \frac{e^{a \cos(\theta - \alpha)}}{2\pi I_0(a)} \quad (\text{Circular Normal Function})$$

$$= \frac{1}{2\pi} + \sum_{n=1}^{\infty} \frac{I_n(a)}{\pi I_0(a)} \cos\left(n\theta - \frac{n\pi}{2}\right) \quad (14)$$

(α and a may be functions of frequency in the general case)

APPENDIX III

Diffraction of Plane Wave

(A) BOUNDARY VALUE PROBLEM FOR PLANE WAVE PROPAGATION

1 Partial diff eq $\frac{\partial^2 \phi}{\partial x^2} + \frac{\partial^2 \phi}{\partial y^2} + \frac{\partial^2 \phi}{\partial z^2} = 0$ (15)

2 Boundary Conditions

(i) At an impervious and rigid bottom

$$\frac{\partial \phi}{\partial z} \Big|_{z=d} = 0$$
 (16)

which d = still-water depth

(ii) At the free surface

(a) Kinetic Surface Boundary Condition

$$\frac{\partial \phi}{\partial z} = \frac{d}{dt} [\eta(x,t)] = \frac{\partial \eta}{\partial t} + \frac{\partial \eta}{\partial x} u + \frac{\partial \eta}{\partial t} = \frac{\partial \eta}{\partial t} + u \frac{\partial \eta}{\partial t} \text{ at } z = \eta \text{ (non-linear)} \quad (17)$$

$$\frac{\partial \phi}{\partial z} = \frac{\partial \eta}{\partial t} \text{ at } z = 0 \text{ (linear)}$$

(b) Dynamic Surface Boundary Condition

$$-\frac{\partial \phi}{\partial t} + \frac{1}{2} (u^2 + v^2 + w^2) + g\eta = 0, \text{ at } z = 0 \text{ (non-linear)} \quad (18)$$

$$\eta = \frac{1}{g} \frac{\partial \phi}{\partial t} \text{ at } z = 0 \text{ (linear)}$$

3 Solutions

$$\phi = F(x,y) Z(z) T(t) \quad (19)$$

$$\phi = A e^{-1ket} \cosh [k(z+a)] F(x,y)$$

For a plane wave travelling in the y-direction

$$F(x,y) = e^{-ky} \tag{20}$$

Sommerfeld's radiation condition $F = 0 \left(\frac{1}{r} \right)$ (21)

$$r = \sqrt{x^2 + y^2}$$

Wave amplitude, $A = \frac{Akc}{g} \cosh(kd)$ (22)

wave period, $T = \frac{2\pi}{kc}$ (23)

wave velocity $c = \sqrt{\frac{g}{k} \tanh(kd)}$ (24)

wave length, $L = \frac{2\pi}{k}$ (25)

wave number, $k = \frac{2\pi}{L}$ (26)

$$= \frac{Akc}{g} \cosh(kd) \sin [k(ct-y)] \tag{27}$$

B THE PROBLEM WITH THE PRESENCE OF A BREAKWATER

(semi-infinite breakwater)

1 an additional boundary condition

$$\frac{\partial \phi}{\partial y} = 0 \text{ at } y = 0, x \geq 0 \tag{28}$$

This implies that

$$\frac{\partial F}{\partial y} = 0 \text{ at } y = 0, x \geq 0 \tag{29}$$

2 for incident waves

$$F_1(r, \theta) = e^{-ikr \cos(\theta - \theta_0)} \quad (30)$$

3 the free wave surface can be given as

$$= \frac{A_1 k c}{g} [\cosh(kd)] e^{ikct} F(r, \theta) \quad (31)$$

4 for diffracted waves

$$F_d(r, \theta) = f(\sigma) e^{-ikr [\cos(\theta - \theta_0)]} + f(\sigma') e^{-ikr [\cos(\theta - \theta_0)]} \quad (32)$$

$$\sigma = 2\sqrt{\frac{kr}{\pi}} \sin \frac{1}{2}(\theta - \theta_0)$$

$$\sigma' = -2\sqrt{\frac{kr}{\pi}} \sin \frac{1}{2}(\theta - \theta_0)$$

$$f(\sigma) = \frac{1}{\sqrt{2}} e^{i\pi/4} \int_{-\infty}^{\sigma} e^{(i\pi/2)t^2} dt$$

$$f(\sigma') = \frac{-1}{\sqrt{2}} e^{i\pi/4} \int_{-\infty}^{\sigma} e^{(i\pi/2)t^2} dt$$

$$F_d(r, \theta) = \rho(r, \theta) e^{i\xi(r, \theta)} \quad (33)$$

$$a_d = \frac{A k c \rho}{g} \cosh(kd) \quad (34)$$

5 Diffraction coefficient

$$k' = \frac{2a_d}{2a_1} = \rho$$

$$k' = |F_d(r, \theta)| \quad (35)$$

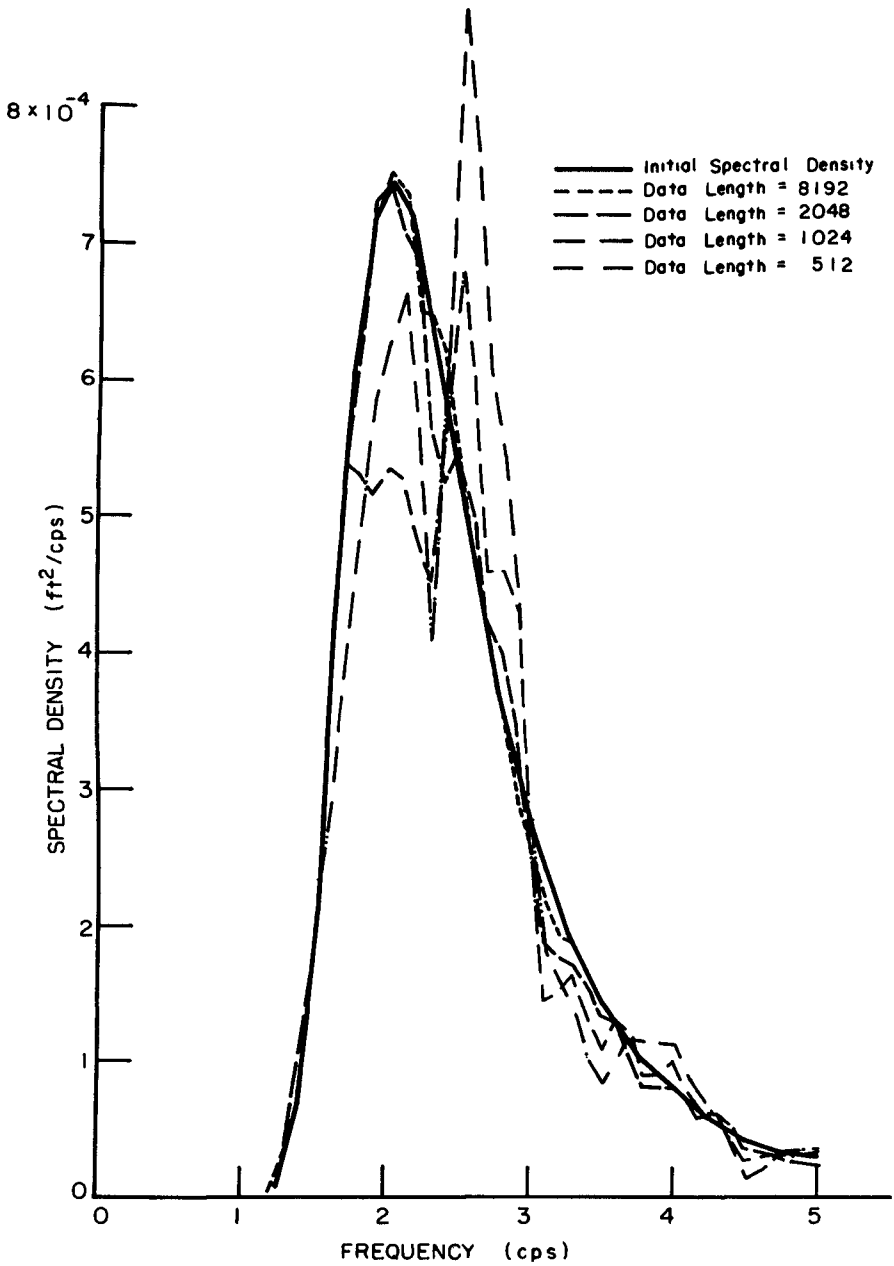


FIG 1 ESTIMATES OF SPECTRAL DENSITIES FOR VARIOUS LENGTH OF DATA

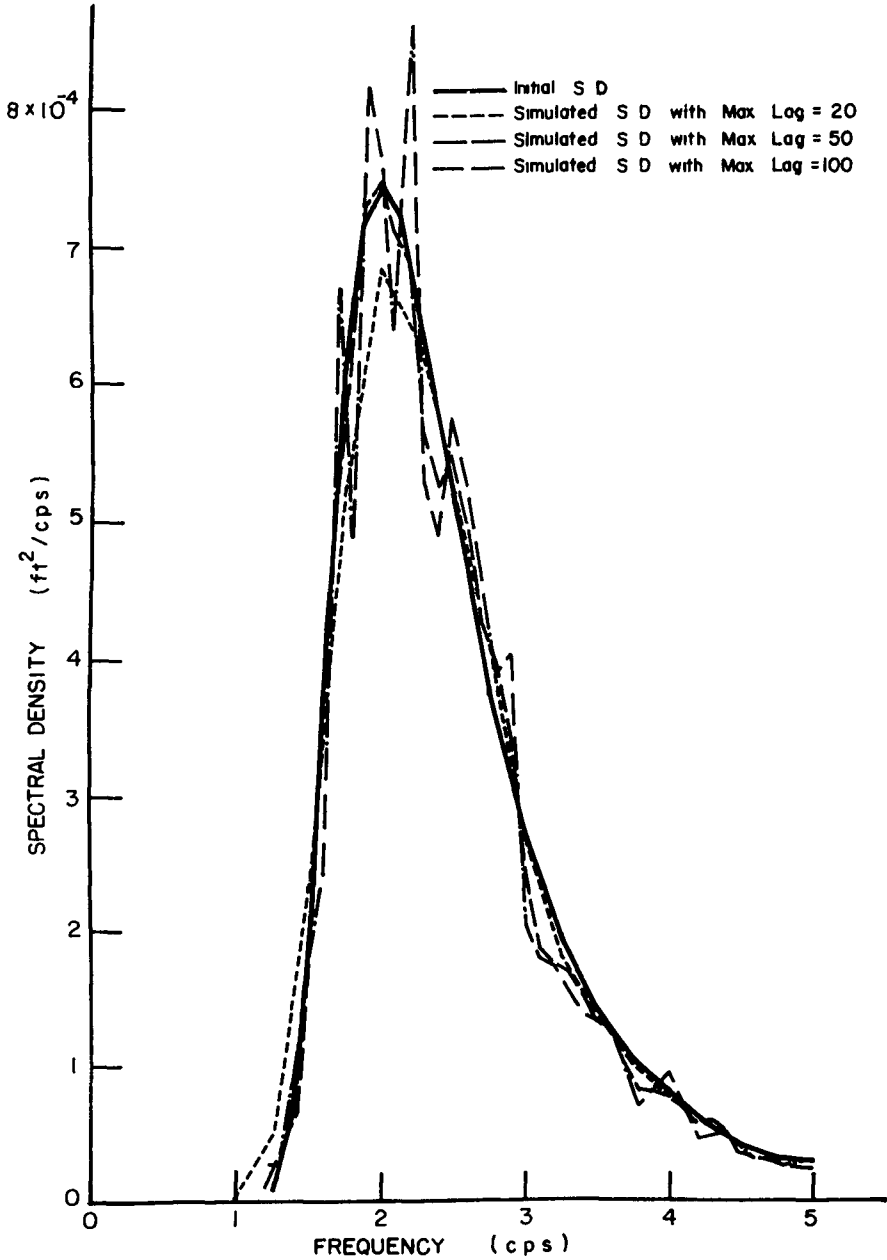


FIG 2 ESTIMATES OF SPECTRAL DENSITIES (2048 DATA LENGTH) FOR VARIOUS MAXIMUM LAGS ON THE COVARIANCE FUNCTIONS

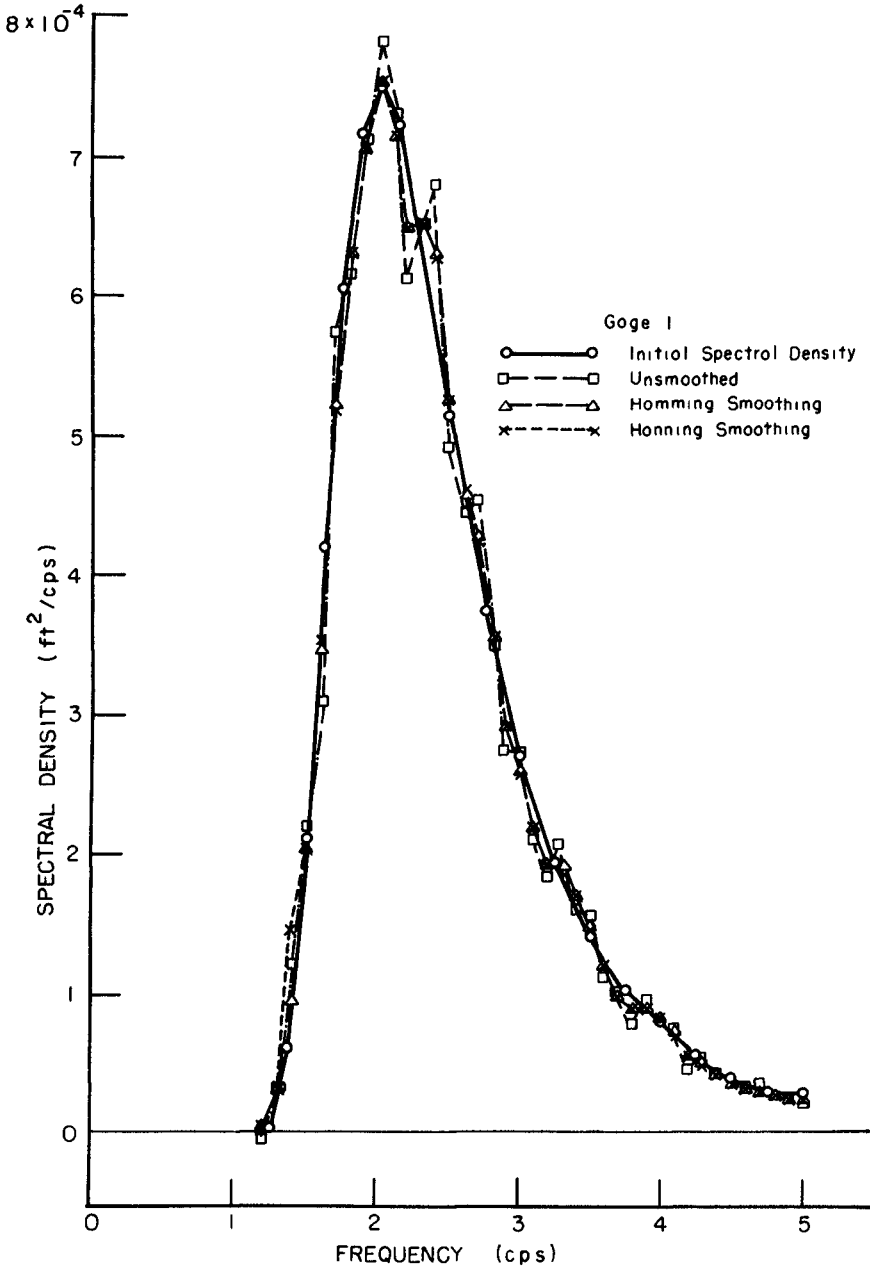


FIG 3 EFFECTS OF SMOOTHING ON THE SPECTRAL DENSITY ESTIMATES FOR DATA LENGTH 8192 AND MAXIMUM LAG 50

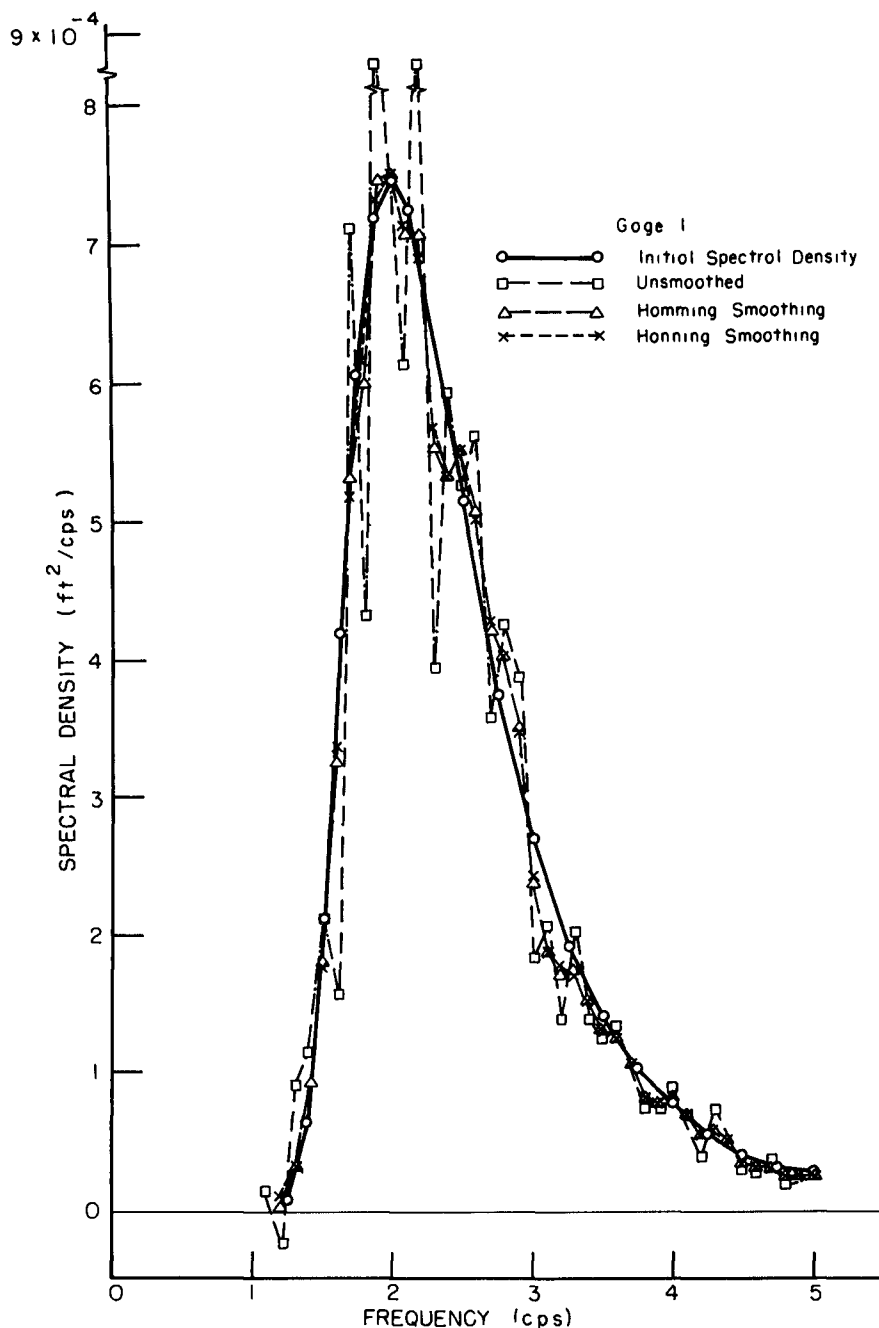


FIG 4 EFFECTS OF SMOOTHING ON THE SPECTRAL DENSITY ESTIMATES FOR DATA LENGTH 2048 AND MAXIMUM LAG 50

CHAPTER 30

INTERACTION BETWEEN WAVES AND CURRENTS

Ivar G Jonsson
Ph D , Coastal Engineering Laboratory

Christian Skougaard¹
M Sc , Coastal Engineering Laboratory

John D Wang
Graduate Student

Technical University of Denmark

ABSTRACT

This paper presents some theoretical results of a general study of the interaction between surface gravity waves and a steady current. Assuming irrotational flow and a second order Stokes wave motion, the main objects of the paper have been

- a To present a simple graphical method for the computation of the wave length in a current field
- b To introduce the concept of the mean energy level for a periodic wave motion with a steady current superimposed
- c To utilize this for the calculation of the "current-wave set-down" for a two-dimensional motion with a constant discharge over a gently sloping bottom
- d To present a complete set of conservation equations for the case considered under point c
- e To present graphs and tables for the variation in length and height of wave for the case considered under point c

No experimental results are presented

1 INTRODUCTION

Aspects of non-linear interaction between gravity waves and a current motion have received increasing attention during the last 10 years. The works by Longuet-Higgins and Stewart [5], [6], and Whitham [8] are already classics. The mechanism is intimately connected with the so-called radiation stress.

However, there are still basic features related to this problem that are not widely known. One of these is the important concept of the mean energy level for a periodic, irrotational flow (For a pure wave motion the mean energy level was introduced by Lundgren [7]). One of the objects of the present study is to show how this concept can yield the "current-wave set-down" in a simple way, and to demonstrate how it affects the conservation equations for a two-dimensional current-wave motion propa-

¹Present address Municipality of Roskilde, Denmark

gating over a gently sloping bed (see Fig 5-A) The conservation equations for wave crests and energy are solved to yield graphs and tables for the variation in wave length and wave height for this situation The wave length graphs and tables can be used, though, for any angle between wave front and current direction provided the current velocity is replaced by its component in the direction of the wave orthogonal A graphical method for the determination of the wave length in a homogeneous current field will also be introduced This method permits a simple discussion of various domains where different solutions are applicable

Energy losses are neglected in this paper The current velocity is assumed to be steady and constant over the water depth, and only surface waves are considered A second order Stokes expansion is used in the calculations

2 NOTATION

c	(m/s)	Wave celerity
c_g	(m/s)	Wave group celerity
D	(m)	"Geometrical water depth" ($= h + \Delta h$, see Fig 4-A)
E	(Nm/m ²)	Mean specific wave energy ($= 1/8 \gamma H^2$)
\bar{E}_F	(Nm/m/s)	Mean energy flux per unit width
F_w	(N/m)	Radiation stress
g	(m/s ²)	Acceleration due to gravity
H	(m)	Wave height
h	(m)	"Physical water depth" (see Fig 4-A)
Δh	(m)	"Current-wave set-down" (see Fig 4-A)
k	(m ⁻¹)	Wave number ($= 2 \pi/L$)
L	(m)	Wave length
MEL		Mean energy level (see Fig 4-A)
MWL		Mean water level (see Fig 4-A)
n	(dim less)	c_{gr}/c_r
p	(N/m ²)	Pressure
q	(m ³ /m/s)	Discharge per unit width ($= h U$)
q^*	(dim less)	Dimensionless discharge per unit width ($= q/(c_o L_o)$)
s_v	(dim less)	Slope of straight line in Fig 3-B
T	(s)	Wave period
t	(s)	Time
U	(m/s)	Current velocity (positive in direction of c)
u	(m/s)	Horizontal particle velocity
w	(m/s)	Vertical particle velocity
x	(m)	Horizontal co-ordinate

z	(m)	Vertical co-ordinate
β	(rad)	Angle between wave front and current (interval 0 to $\pi/2$)
γ	(N/m ³)	Specific weight of water
η	(m)	Water surface elevation
ρ	(kg/m ³)	Density of water
ϕ	(m ² /s)	Velocity potential ($u = -\partial\phi/\partial x$, etc)
ω	(s ⁻¹)	Angular frequency ($= 2\pi/T$)
$\bar{\quad}$		Mean value sign

Suffix a denotes "absolute"

Suffix b denotes "bottom"

Suffix o denotes "deep water with U equal to zero"

Suffix r denotes "relative" (to the current)

Suffix t denotes partial differentiation with respect to time t

3 WAVES IN A HOMOGENEOUS CURRENT FIELD

Consider a region of constant water depth h, where the absolute wave period T_a and the current velocity U are given

WAVE LENGTHS

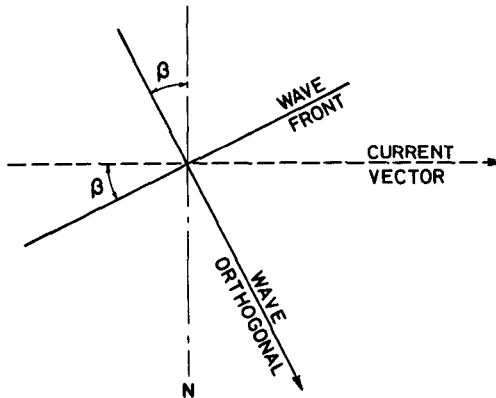


Fig 3-A Definition of the angle β

If β is the angle between wave front and direction of current (Fig 3-A), the following four equations are available to determine the unknowns the absolute and relative wave celerities c_a and c_r , the wave length L, and the relative period T_r

$$L = c_a T_a \quad (3.1)$$

$$L = c_r T_r \quad (3.2)$$

$$c_a = c_r + U \sin \beta \quad (3.3)$$

$$c_r = \sqrt{\frac{gL}{2\pi} \tanh kh} \quad (3.4)$$

where k is the wave number The current velocity U is considered positive to the same side of the normal N as is indicated by the positive direction of the wave orthogonal β lies, by definition, in the interval $0 \leq \beta \leq \pi/2$ (3 1) to (3 4) now yield for determination of L

$$\sqrt{\frac{h}{L} \tanh kh} = \sqrt{\frac{h}{L_0} \left[1 - \frac{U \sin \beta T_a}{h} \frac{h}{L} \right]} \tag{3 5}$$

where L_0 is defined as

$$L_0 \equiv \frac{g}{2\pi} T_a^2 \tag{3 6}$$

i e the deep water wave length with U equal to zero

(3 5) determines implicitly h/L as a function of h/L_0 and $U \sin \beta T_a/h$, and the equation can be solved by iteration (see chapter 6) It is not evident, however, whether a solution to (3 5) is unique - or whether it exists at all A graphical representation of (3 5) reveals this Writing (3 5) as

$$F(h/L) = G(h/L) \tag{3 7}$$

it appears that graphically h/L can be found as the value of the abscissa for the intersection of the F - and G -curves, see Fig 3-B The F -curve is unique, and values can be extracted from a "conventional" wave table

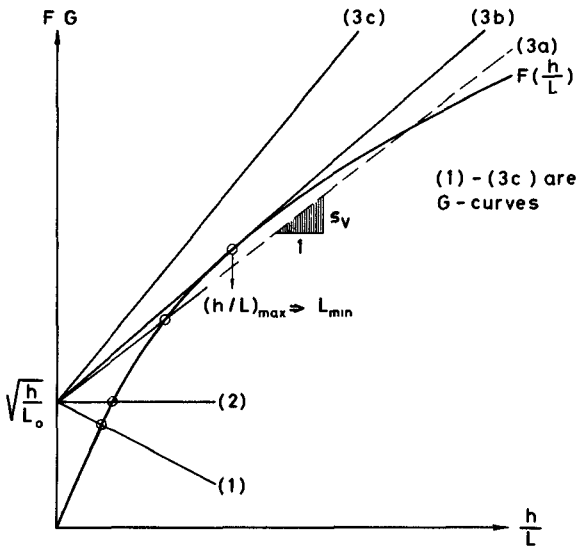


Fig 3-B Graphical determination of L (schematic)

The G-curves are straight lines through the point $(0, \sqrt{h/L_0})$, with a slope of 1 horizontal to s_v vertical, where

$$s_v = -\sqrt{\frac{h}{L_0}} \frac{U \sin \beta T_a}{h} = -\sqrt{2\pi} \frac{U \sin \beta}{\sqrt{g h}} = -\frac{U \sin \beta}{c_0 \sqrt{h/L_0}} \tag{3 8}$$

Here c_0 is defined as

$$c_0 \equiv \frac{g}{2\pi} T_a \tag{3 9}$$

i.e. the deep water wave celerity with U equal to zero

Fig 3-B now enables us to discuss the solution(s) to (3 5) in detail (h, T_a and β are assumed constant, so s_v becomes directly proportional to $-U$)^a For U positive we have case (1), and a unique solution exists for L This also applies to case (2), where U is zero For a negative current (case (3)), there are three possibilities In case (3a) there are theoretically two solutions for L If it is argued that the variation of L must, for physical reasons, be continuous for $U \rightarrow 0$, only one solution is possible This means that the larger value for L should be chosen, as shown in the figure In case (3b) the G-curve is a tangent to the F-curve, and U has attained its minimum value (always negative), as has the wave length, $L = L_{min}$ This case of "maximum counter-current" corresponds to

$$\sqrt{\frac{h}{L} \tanh kh} = \frac{1}{1-n} \sqrt{\frac{h}{L_0}} \tag{3 10}$$

with

$$n = \frac{c_{gr}}{c_r} = \frac{1}{2} \left[1 + \frac{2kh}{\sinh 2kh} \right] \tag{3 11}$$

c_{gr} being the relative wave group celerity From (3 5) and (3 10) we then find that the absolute wave group celerity is zero for $L = L_{min}$

$$c_{ga} = c_{gr} + U \sin \beta = 0 \tag{3 12}$$

(It will be shown in chapter 5 that in the case of a two-dimensional wave motion ($\sin \beta = 1$) progressing against a current over a gently sloping bed, the wave height reaches infinity at the water depth at which (3 12) is fulfilled) In case (3c) there is no solution for L It is readily seen from Fig 3-B that - other things being equal - a positive current "lengthens" the waves whereas a negative current "shortens" them

A full account of the graphical method, including its practical application, is found in [4] Solutions to (3 5) (with $\sin \beta = 1$) are presented in chapter 6

For deep-water waves (for instance $h/L > 0.5$) (3 5) can be solved explicitly

$$L = \frac{1}{4} L_0 \left[1 + \sqrt{1 + 4 \frac{U \sin \beta}{c_0}} \right]^2 \tag{3 13}$$

MOMENTUM AND PRESSURE FORCES ("STRESSES")

In this paper wave heights will be calculated only for two-dimensional flow Stresses and energy fluxes will therefore be calculated only

for the special case $\beta = \pi/2$ Taking mean values over period T_a , the following total force (normal "stress") over depth h and per unit width is found in a section at right angles to the current vector (and so in this case also to the direction of wave propagation)

$$\sigma = \frac{1}{2} \gamma h^2 + \rho h U^2 + F_w \quad (3.14)$$

In this expression, F_w is the radiation stress

$$F_w = \frac{1}{16} \gamma H^2 \left[1 + 2 \frac{2kh}{\sinh 2kh} \right] = \left(2 \frac{c}{c_r} - \frac{1}{2} \right) E \quad (3.15)$$

where E is the mean specific wave energy The first two terms in (3.14) are readily discernible

ENERGY FLUX

The mean energy flux over depth h and per unit width depends upon the zero level for potential energy, since a net current is present Taking the mean water level as level we find for $\beta = \pi/2$ in a section at right angles to the current vector

$$\bar{E}_{f,MWL} = \frac{1}{2} \rho h U^3 + (U + c_{gr}) E + U F_w \quad (3.16)$$

This expression has already been given by Longuet-Higgins and Stewart [5]

The paradox arises that although (3.16) may be interpreted physically, it is of no direct use for the calculation of the wave height variation on a non-uniform current (because of the variation in the mean water level) This will be elucidated in chapters 4 and 5

In these and the subsequent calculations the following restriction on a Stokes wave must be borne in mind For long waves the "Ursell parameter" (HL^2/h^3) must not exceed a certain number

4 THE MEAN ENERGY LEVEL

As a computation of the wave height variation requires a knowledge of the mean energy flux at any station corresponding to the same horizontal datum, it is imperative to determine the variation in the MWL over an "arbitrary" (here gently sloping) bottom In other words, the "set-down" of the MWL is wanted The discussion is confined to periodic, irrotational flows These two conditions are written in the frames in Fig 4-A (For simplicity we consider two-dimensional flow only)

In the figure we have a sloping, known bottom and a sloping, but unknown, MWL And we have a horizontal datum, $z = 0$ The mean water level is given by

$$\bar{\eta} = z_b + h \quad (4.1)$$

so the determination of the MWL calls in fact for a definition of the water depth h In the present case, which is a second order theory in wave height, but is also a "zero-order bottom-slope theory", it is natural to define the water depth from the mean bottom pressure

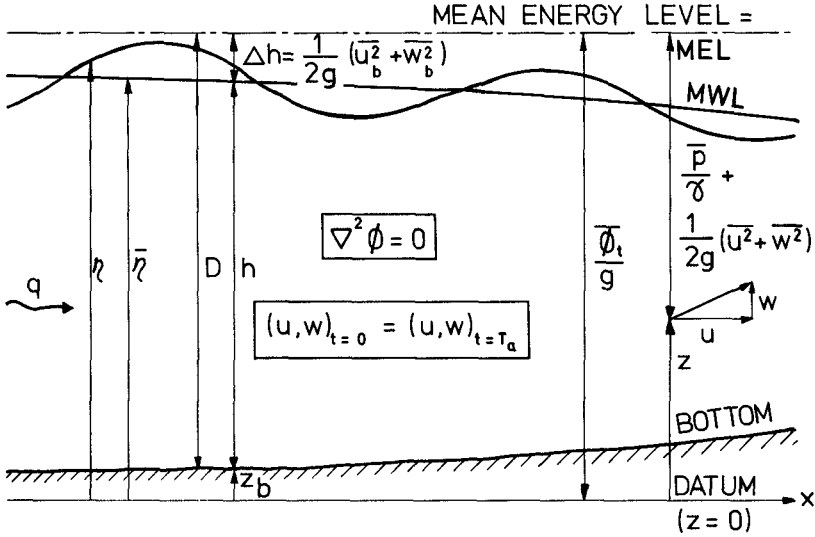


Fig 4-A Illustration of the "set-down" (schematical)

$$h = \frac{1}{\gamma} \bar{p}_b \tag{4 2}$$

We still have not utilized the fact, that the flow is irrotational and periodic. The Bernoulli equation - presented with mean values over period T_a - is therefore introduced

$$z + \frac{\bar{p}}{\gamma} + \frac{1}{2g} [\bar{u}^2 + \bar{w}^2] = \frac{1}{g} \bar{\phi}_t = \text{const} \tag{4 3}$$

(ϕ is defined, so that $u_1 = -\partial\phi/\partial x_1$) The fact that the right hand side is independent of x and \bar{z} is easily seen from

$$\frac{\partial}{\partial x_1} \left(\frac{\partial \phi}{\partial t} \right) = \frac{\partial}{\partial t} \left(\frac{\partial \phi}{\partial x_1} \right) = 0 \tag{4 4}$$

since the flow is periodic

This means that a constant horizontal level is now found which is inherently connected with the flow itself - and independent of the arbitrary datum. From the datum we can mark $\bar{\phi}_t/g$ vertically, and we will arrive at the same level for any x . This level will be called the mean energy level (MEL), since it contains the three terms that are analogous to conventional steady hydraulics. Combining (4 1), (4 2) and (4 3) (at the bottom) we find the MWL

$$\bar{h} + \frac{1}{2g} (\bar{u}_b^2 + \bar{w}_b^2) = \frac{1}{g} \bar{\phi}_t = \text{const} \tag{4 5}$$

Since the constant in (4 5) is the distance from the datum up to the MEL, the set-down of the MWL - as defined by (4 1) and (4 2) - is

$$\Delta h \equiv D - h = \frac{1}{2g} (\overline{u_b^2} + \overline{w_b^2}) \quad (4.6)$$

(D could be termed the "geometrical depth", in contrast to h, which is a "physical depth") Assuming the discharge q to be finite anywhere, it appears from (4.6) that the set-down Δh is in fact the depression of the MWL at an arbitrary depth below the MWL at infinite depth. And this depression equals the mean velocity head at the bottom.)

The actual analytical expression for the set-down in our two-dimensional combination of a steady current and a wave motion is found as follows. It is assumed that locally, we can use the velocity potential corresponding to a horizontal bottom. This is - correct to second order - with MWL as datum.

$$\begin{aligned} \phi = -Ux + \frac{Hc_r}{2} \frac{\cosh k(z+h)}{\sinh kh} \sin(\omega_a t - kx) \\ + \frac{3}{32} \frac{c_r}{k} (kH)^2 \frac{\cosh 2k(z+h)}{\sinh^4 kh} \sin 2(\omega_a t - kx) \\ + \frac{gH^2}{8hc_r} x + \left(\frac{1}{2} U^2 + \frac{gH^2}{16h} \frac{2kh}{\sinh 2kh} - \frac{gH^2}{8h} \frac{U}{c_r} \right) t \quad (4.7) \end{aligned}$$

(4.7) assumes $\bar{\eta} = 0$, so (4.5) - (4.7) yield directly

$$\Delta h = \frac{U^2}{2g} + \frac{H^2}{16h} \frac{2kh}{\sinh 2kh} - \frac{H^2}{8h} \frac{U}{c_r} \quad (4.8)$$

for two-dimensional flow. It will be observed in (4.8) that, in addition to the "current set-down" (first term) and the "wave set-down" (second term, see [7] and [1]), an interaction term appears. (This last term was unfortunately missing from two previous publications from our laboratory Progress Report No. 6 and a loose enclosure in Progress Report No. 7. This error was corrected in [3] p. 20, where some other Corrigenda were also presented.) Note that although (4.8) contains a negative term if U is positive, Δh can never become negative, according to (4.6).

It should be added that the set-down for a pure wave motion has been measured in a wave channel by Bowen et al. [1]. They found that the theory predicts the set-down outside the surf zone very well. (They also found the set-up inside the surf zone.)

5 TWO-DIMENSIONAL WAVE TRANSFORMATION

The two-dimensional current-wave system, which now will be considered in some detail, is shown schematically in Fig. 5-A. The five main unknown quantities that we want to calculate are: The wave length L, the current velocity U, the set-down Δh , the "physical water depth" h and the wave height H (c_a , c_r and T_a can hereafter be found from (3.1) - (3.4), with $\sin \beta = 1$). We assume that we know the absolute wave period T_a , the discharge q, the bottom topography $D = D(x)$, and the deep-water wave height H_0 (where the current is zero).

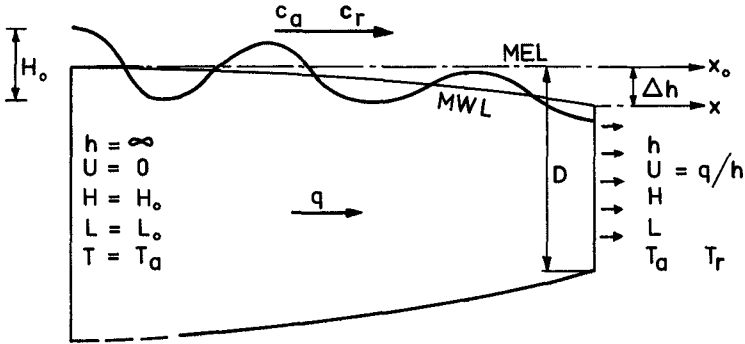


Fig 5-A Definition sketch for wave transformation

CONSERVATION EQUATIONS

To solve the problem, we must set up all the relevant conservation equations. Only the energy concept presents us with some difficulty in this connection. As pointed out in chapter 3, the expression for the mean energy flux with MWL as zero level cannot be used in a non-uniform flow since this level is constantly changing. However, the existence of the MEL, which was found in the preceding chapter to be independent of the horizontal coordinate(s), overcomes this difficulty.

In accordance with Fig 5-A we find the following expression for the mean energy flux with MEL as reference

$$\bar{E}_{f,MEL} = \bar{E}_{f,MWL} - (\gamma h \Delta h) U \tag{5 1}$$

$$= \left(1 + \frac{U}{c_r}\right) (U + c_{gr}) E \tag{5 2}$$

using (3 16) and (4 8) (An erroneous expression for \$\bar{E}_{f,MEL}\$ was presented in some earlier publications from this laboratory, see the comments to (4 8)). As, according to our assumptions, (5 2) must be constant, we can now write down the complete set of conservation equations

Wave crests $\omega_a = \omega_r + k U$	(5 3)
Mass $\frac{d}{dx} (h U) = 0$	(5 4)
Momentum $\frac{dF}{dx} + \frac{d}{dx} (\rho h U^2) - \gamma h \frac{d(\Delta h)}{dx} = 0$	(5 5)
Energy $\frac{d}{dx} \left[\left(1 + \frac{U}{c_r}\right) (U + c_{gr}) E \right] = 0$	(5 6)
Bottom topography $h + \Delta h = D$	(5 7)

(5 3) is the conventional way of expressing wave crest conservation. In order to get to a practical formula, the expression for the relative wave celerity (3 4) must be used. The mass and momentum equations have a direct physical interpretation and require no further comment ($-d(\Delta h)/dx$ is the slope of the MWL). The energy equation is less obvious. It should be noted, though, that (5 6) is a special case of Garrett's adiabatic invariant expression,[2]. It is directly seen from (5 6), that H reaches infinity at the water depth at which the absolute wave group celerity is zero. It is interesting to recognize this "dynamical" limit as the "kinematical" limit (found in chapter 3), yielding the minimum wave length. The last conservation equation may seem a trifle sophisticated, if not superfluous. This is in a way true for a pure wave motion. Our degree of approximation does not permit a discrimination between D and h for the determination of L , H and Δh for this case. However, when a current is present, the first term in (4 8) is by definition a zero-order term, and adjustment should be made for this, as described later.

PRACTICAL EQUATIONS

The conclusion of the foregoing discussion is that although the conservation equations are fundamental, they are not applicable for direct calculations. A new set of practical equations are therefore

$\sqrt{\frac{h}{L} \tanh kh} = \sqrt{\frac{h}{L_0} \left[1 - q^* \frac{h/L}{(h/L_0)^2} \right]}$	(5 8)
$h U = q$	(5 9)
$\Delta h = \frac{U^2}{2g} + \frac{H^2}{16 h} \frac{2kh}{\sinh 2kh} - \frac{H^2}{8 h} \frac{U}{c_r}$	(5 10)
$\frac{H}{H_0} = \left[2 \frac{c_r}{c_0} \left(\frac{c}{c_r} + \frac{q^*}{(c_r/c_0)(h/L_0)} \right) \left(1 + \frac{q^*}{(c_r/c_0)(h/L_0)} \right) \right]^{\frac{1}{2}}$	(5 11)
$h + \Delta h = D$	(5 12)

with

$$q^* \equiv \frac{q}{c_0 L_0} \quad (5 13) \quad \text{and} \quad \frac{c_r}{c_0} = \sqrt{\frac{h/L_0}{h/L} \tanh kh} \quad (5 14)$$

(5 8) is simply a rewriting of (3 5) with $\sin \beta = 1$ (Now assumed to be valid for a gradually varying water depth) (5 9) and (5 11) are (5 4) and (5 6) integrated. The momentum equation is replaced by the Δh -expression (4 8) (which in fact can be deduced directly from the conservation equations)

The equations are solved as follows for given values of D , q , T and H_0 (not all combinations are admissible). First h and U are found from (5 9) and (5 12), with $\Delta h = U^2/2g$ and subcritical flow assumed. L_0 , c_0 and q^* are calculated from (3 6), (3 9) and (5 13). Next, L is found from (5 8), either by iteration, or graphically, as explained in chapter 3 (with $s_v = -q^*/(h/L_0)^{3/2}$), or read from Fig 6-A, or interpolated in Table 6-a or 6-b. H is calculated from (5 11), (3 11) and (5 14), or read from Fig 6-B. A new value of Δh is then calculated from (5 10), (5 9) and (5 12) hereafter yield the final value of U , which should be used to correct the first term in (5 10), to give the final value of Δh (and h). In this way we should have taken account of all terms $O(H^2)$. (The calculations can of course be repeated in an iterative manner to give "full numerical reciprocity" between D and h . It should be borne in mind, though, that the increase in accuracy is formal). If h were given (measured), instead of D , the calculations and considerations are straightforward.

6 TABLES AND GRAPHS FOR L AND H

WAVE LENGTHS

(5 8) was solved numerically by a Newton-Raphson iteration method on a digital computer. The results are plotted in Fig 6-A ("constant discharge curves")

For q^* positive, the h/L_0 - limits have been so chosen that the Froude number is smaller than one, and h/L goes up to about 0.5. Outside the latter limit, deep-water expressions will normally suffice. Here (3 13) gives (with $\sin \beta = 1$)

$$\frac{L}{L_0} = \frac{1}{4} \left[1 + \sqrt{1 + 4 \frac{q^*}{h/L_0}} \right]^2 \quad (6 1)$$

(The former limit is of course unrealistic. Near such a high Froude number the curvature of the mean water surface becomes so large that the assumptions for our theory become invalid.) The straight line corresponding to h/L equal to 0.5 indicates that shallow-water conditions are not "typical" for the higher q^* -values. The shallow-water wave length is found from (5 8)

$$\frac{L}{L_0} = \sqrt{\frac{2\pi h}{L_0} + \frac{q^*}{h/L_0}} \quad (6 2)$$

Of particular interest is the existence of maxima and minima for a number of positive q^* -values. This is due to the fact that the steady increase in current velocity - as the depth decreases - tends to lengthen the waves, while the decrease in depth tends, in itself, to have the opposite effect. The possibility of horizontal tangents can also be seen directly from (3 11) and the following expression, which is valid for constant values of T_a and q

$$\frac{dL}{dh} = \frac{L}{2h} \frac{(2c_{gr} - c_r) - 2U}{c_{gr} + U} \quad (6 3)$$

For q^* negative, the upper limit for h/L_0 was chosen (arbitrarily) as 0.61. The lower limit was chosen so that the wave length L comes as close to L_{\min} as the selected values of h/L_0 allow (see Table 6-b). In the limit $L = L_{\min}$ (see (3 10) and the pertaining discussion), the numerical value of the Froude number will be smaller than one, see [4]. It is immediately obvious that for q^* smaller than -0.05 (appr.) deep-water conditions prevail, and (6 1) can be used. It will also be seen that in the case of a negative discharge we have the same trend as for no current. L decreases monotonously with decreasing depth.

In Table 6-a, numerical values of L/L_0 are presented for $|q^*| \leq 0.02$. (It should finally be mentioned that Fig 6-A and Tables 6-a and 6-b can also be applied in the three-dimensional case, Fig 3-A. Here we take as "current velocity" in (5 13) the component in the direction of the wave orthogonal.)

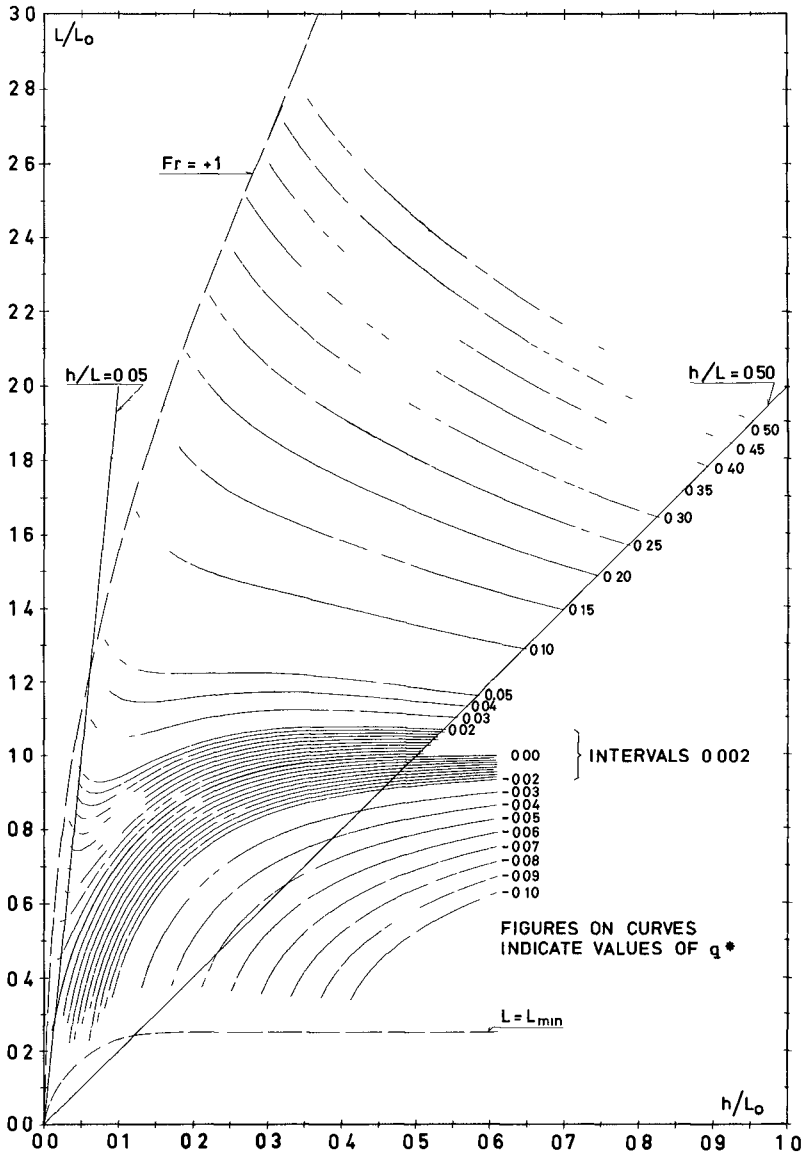


Fig 6-A "Constant discharge curves" for L/L_0

h/L_0	q^*	0	+0.002	+0.004	+0.006	+0.008	+0.010	+0.012	+0.014	+0.016	+0.018	+0.020
0.00	0.000											
0.01	0.248	0.450										
0.02	0.347	0.450	0.551	0.652								
0.03	0.420	0.491	0.560	0.628	0.696	0.763	0.830					
0.04	0.480	0.534	0.587	0.639	0.691	0.742	0.793	0.844	0.895	0.946		0.996
0.05	0.531	0.575	0.618	0.661	0.703	0.745	0.786	0.828	0.869	0.910		0.951
0.06	0.575	0.613	0.649	0.686	0.722	0.757	0.792	0.827	0.862	0.897		0.931
0.07	0.614	0.647	0.679	0.711	0.743	0.774	0.804	0.835	0.865	0.896		0.926
0.08	0.649	0.679	0.707	0.736	0.764	0.792	0.819	0.846	0.874	0.900		0.927
0.09	0.681	0.707	0.734	0.759	0.785	0.810	0.835	0.860	0.884	0.909		0.933
0.10	0.709	0.734	0.758	0.782	0.805	0.828	0.851	0.874	0.896	0.919		0.941
0.11	0.735	0.758	0.780	0.802	0.824	0.846	0.867	0.888	0.909	0.920		0.950
0.12	0.759	0.780	0.801	0.822	0.842	0.862	0.882	0.902	0.921	0.941		0.960
0.13	0.780	0.800	0.820	0.840	0.859	0.878	0.897	0.915	0.934	0.952		0.970
0.14	0.800	0.819	0.838	0.856	0.875	0.893	0.910	0.928	0.946	0.963		0.980
0.15	0.818	0.836	0.854	0.872	0.889	0.906	0.923	0.940	0.957	0.973		0.990
0.16	0.835	0.852	0.869	0.886	0.902	0.919	0.935	0.951	0.967	0.983		0.999
0.17	0.850	0.867	0.883	0.899	0.915	0.931	0.946	0.962	0.977	0.992		1.007
0.18	0.864	0.880	0.896	0.911	0.927	0.942	0.957	0.972	0.986	1.001		1.015
0.19	0.877	0.892	0.907	0.922	0.937	0.952	0.966	0.981	0.995	1.009		1.023
0.20	0.888	0.903	0.918	0.933	0.947	0.961	0.975	0.989	1.003	1.016		1.030
0.21	0.899	0.914	0.928	0.942	0.956	0.970	0.983	0.997	1.010	1.023		1.036
0.22	0.909	0.923	0.937	0.950	0.964	0.977	0.990	1.004	1.017	1.029		1.042
0.23	0.918	0.931	0.945	0.958	0.971	0.984	0.997	1.010	1.023	1.035		1.048
0.24	0.926	0.939	0.952	0.965	0.978	0.991	1.003	1.016	1.028	1.040		1.052
0.25	0.933	0.946	0.959	0.972	0.984	0.996	1.009	1.021	1.033	1.045		1.057
0.26	0.940	0.953	0.965	0.977	0.990	1.002	1.014	1.025	1.037	1.049		1.060
0.27	0.946	0.958	0.971	0.983	0.995	1.006	1.018	1.030	1.041	1.053		1.064
0.28	0.952	0.964	0.976	0.987	0.999	1.011	1.022	1.033	1.045	1.056		1.067
0.29	0.957	0.968	0.980	0.992	1.003	1.014	1.025	1.037	1.048	1.059		1.069
0.30	0.961	0.973	0.984	0.995	1.006	1.018	1.029	1.039	1.050	1.061		1.072
0.31	0.965	0.977	0.988	0.999	1.010	1.020	1.031	1.042	1.052	1.063		1.073
0.32	0.969	0.980	0.991	1.002	1.012	1.023	1.034	1.044	1.054	1.065		1.075
0.33	0.972	0.983	0.994	1.004	1.015	1.025	1.036	1.046	1.056	1.066		1.076
0.34	0.975	0.986	0.996	1.007	1.017	1.027	1.037	1.047	1.057	1.067		1.077
0.35	0.978	0.988	0.999	1.009	1.019	1.029	1.039	1.049	1.059	1.068		1.078
0.36	0.980	0.991	1.001	1.011	1.020	1.030	1.040	1.050	1.059	1.069		1.079
0.37	0.983	0.992	1.002	1.012	1.022	1.032	1.041	1.051	1.060	1.070		1.079
0.38	0.984	0.994	1.004	1.014	1.023	1.033	1.042	1.051	1.061	1.070		1.079
0.39	0.986	0.996	1.005	1.015	1.024	1.033	1.043	1.052	1.061	1.070		1.079
0.40	0.988	0.997	1.006	1.016	1.025	1.034	1.043	1.052	1.061	1.070		1.079
0.41	0.989	0.998	1.007	1.017	1.026	1.035	1.043	1.052	1.061	1.070		1.079
0.42	0.990	0.999	1.008	1.017	1.026	1.035	1.044	1.053	1.061	1.070		1.078
0.43	0.991	1.000	1.009	1.018	1.027	1.035	1.044	1.052	1.061	1.069		1.078
0.44	0.992	1.001	1.010	1.018	1.027	1.035	1.044	1.052	1.061	1.069		1.077
0.45	0.993	1.002	1.010	1.019	1.027	1.036	1.044	1.052	1.060	1.068		1.077
0.46	0.994	1.002	1.011	1.019	1.027	1.036	1.044	1.052	1.060	1.068		1.076
0.47	0.995	1.003	1.011	1.019	1.027	1.035	1.043	1.051	1.059	1.067		1.075
0.48	0.995	1.003	1.011	1.019	1.027	1.035	1.043	1.051	1.059	1.067		1.074
0.49	0.996	1.004	1.012	1.020	1.027	1.035	1.043	1.051	1.058	1.066		1.074
0.50	0.996	1.004	1.012	1.020	1.027	1.035	1.043	1.050	1.058	1.065		1.073
0.51	0.997	1.004	1.012	1.020	1.027	1.035	1.042	1.050	1.057	1.065		1.072
0.52	0.997				1.027	1.034	1.042	1.049	1.057	1.064		1.071
0.53	0.997				1.027	1.034	1.041	1.049	1.056	1.063		1.070
0.54	0.998								1.062	1.069		
0.55	0.998											
0.56	0.998											
0.57	0.998											
0.58	0.999											
0.59	0.999											
0.60	0.999											

NOTE BELOW DOTTED STEP-CURVE WE HAVE $h/L_0 > 0.5$

Table 6-a Values of L/L_0 (positive discharge)

INTERACTION

h/L_0	0	-0 002	-0 004	-0 006	-0 008	-0 010	-0 012	-0 014	-0 016	-0 018	-0 020
0 00	0 000										
0 01	0 248										
0 02	0 347	0 240									
0 03	0 420	0 348	0 270	0 169							
0 04	0 480	0 425	0 367	0 304	0 227						
0 05	0 531	0 486	0 439	0 390	0 336	0 272					
0 06	0 575	0 537	0 497	0 456	0 413	0 365	0 310	0 223			
0 07	0 614	0 581	0 546	0 511	0 474	0 434	0 391	0 341	0 275		
0 08	0 649	0 619	0 589	0 557	0 524	0 490	0 454	0 414	0 369	0 311	
0 09	0 681	0 654	0 626	0 597	0 568	0 537	0 505	0 471	0 434	0 392	0 341
0 10	0 709	0 684	0 659	0 633	0 606	0 578	0 549	0 519	0 487	0 452	0 412
0 11	0 735	0 712	0 689	0 664	0 640	0 614	0 588	0 560	0 531	0 500	0 467
0 12	0 759	0 737	0 715	0 693	0 670	0 646	0 622	0 596	0 570	0 542	0 512
0 13	0 780	0 760	0 739	0 718	0 697	0 674	0 652	0 628	0 604	0 578	0 551
0 14	0 800	0 781	0 761	0 741	0 721	0 700	0 679	0 656	0 634	0 610	0 585
0 15	0 818	0 800	0 781	0 762	0 743	0 723	0 703	0 682	0 660	0 638	0 615
0 16	0 835	0 817	0 800	0 781	0 763	0 744	0 725	0 705	0 685	0 664	0 642
0 17	0 850	0 833	0 816	0 799	0 781	0 763	0 745	0 726	0 706	0 687	0 666
0 18	0 864	0 848	0 831	0 815	0 798	0 780	0 763	0 745	0 726	0 707	0 688
0 19	0 877	0 861	0 845	0 829	0 813	0 796	0 779	0 762	0 744	0 726	0 708
0 20	0 888	0 873	0 858	0 843	0 827	0 811	0 794	0 778	0 761	0 743	0 726
0 21	0 899	0 884	0 870	0 855	0 839	0 824	0 808	0 792	0 776	0 759	0 742
0 22	0 909	0 895	0 880	0 866	0 851	0 836	0 821	0 805	0 789	0 773	0 757
0 23	0 918	0 904	0 890	0 876	0 862	0 847	0 832	0 817	0 802	0 786	0 770
0 24	0 926	0 912	0 899	0 885	0 871	0 857	0 843	0 828	0 813	0 798	0 783
0 25	0 933	0 920	0 907	0 894	0 880	0 866	0 852	0 838	0 824	0 809	0 794
0 26	0 940	0 927	0 914	0 901	0 888	0 875	0 861	0 847	0 833	0 819	0 805
0 27	0 946	0 934	0 921	0 908	0 896	0 882	0 869	0 856	0 842	0 829	0 815
0 28	0 952	0 939	0 927	0 915	0 902	0 890	0 877	0 864	0 850	0 837	0 823
0 29	0 957	0 945	0 933	0 921	0 908	0 896	0 883	0 871	0 858	0 845	0 832
0 30	0 961	0 950	0 938	0 926	0 914	0 902	0 890	0 877	0 865	0 852	0 839
0 31	0 965	0 954	0 942	0 931	0 919	0 907	0 895	0 883	0 871	0 859	0 846
0 32	0 969	0 958	0 947	0 935	0 924	0 912	0 901	0 889	0 877	0 865	0 853
0 33	0 972	0 961	0 950	0 939	0 928	0 917	0 905	0 894	0 882	0 871	0 859
0 34	0 975	0 965	0 954	0 943	0 932	0 921	0 910	0 899	0 887	0 876	0 864
0 35	0 978	0 968	0 957	0 946	0 936	0 925	0 914	0 903	0 892	0 881	0 869
0 36	0 980	0 970	0 960	0 949	0 939	0 928	0 918	0 907	0 896	0 885	0 874
0 37	0 983	0 973	0 962	0 952	0 942	0 932	0 921	0 911	0 900	0 889	0 879
0 38	0 984	0 975	0 965	0 955	0 945	0 935	0 924	0 914	0 904	0 893	0 883
0 39	0 986	0 977	0 967	0 957	0 947	0 937	0 927	0 917	0 907	0 897	0 887
0 40	0 988	0 978	0 969	0 959	0 950	0 940	0 930	0 920	0 910	0 900	0 890
0 41	0 989	0 980	0 971	0 961	0 952	0 942	0 933	0 923	0 913	0 903	0 894
0 42	0 990	0 981	0 972	0 963	0 954	0 944	0 935	0 925	0 916	0 906	0 897
0 43	0 991	0 983	0 974	0 965	0 955	0 946	0 937	0 928	0 919	0 909	0 900
0 44	0 992	0 984	0 975	0 966	0 957	0 948	0 939	0 930	0 921	0 912	0 902
0 45	0 993	0 985	0 976	0 967	0 959	0 950	0 941	0 932	0 923	0 914	0 905
0 46	0 994	0 986	0 977	0 969	0 960	0 951	0 943	0 934	0 925	0 916	0 908
0 47	0 995	0 986	0 978	0 970	0 961	0 953	0 944	0 936	0 927	0 919	0 910
0 48	0 995	0 987	0 979	0 971	0 963	0 954	0 946	0 938	0 929	0 921	0 912
0 49	0 996	0 988	0 980	0 973	0 964	0 956	0 947	0 939	0 931	0 923	0 914
0 50	0 996	0 989	0 981	0 973	0 965	0 957	0 949	0 941	0 933	0 924	0 916
0 51	0 997	0 989	0 981	0 974	0 966	0 958	0 950	0 942	0 934	0 926	0 918
0 52	0 997	0 990	0 982	0 974	0 967	0 959	0 951	0 943	0 936	0 928	0 920
0 53	0 997	0 990	0 983	0 975	0 968	0 960	0 952	0 945	0 937	0 929	0 922
0 54	0 998	0 990	0 983	0 976	0 968	0 961	0 953	0 946	0 938	0 931	0 923
0 55	0 998	0 991	0 984	0 976	0 969	0 962	0 954	0 947	0 940	0 932	0 925
0 56	0 998	0 991	0 984	0 977	0 970	0 963	0 955	0 948	0 941	0 934	0 926
0 57	0 998	0 992	0 985	0 978	0 970	0 963	0 956	0 949	0 942	0 935	0 928
0 58	0 999	0 992	0 985	0 978	0 971	0 964	0 957	0 950	0 943	0 936	0 929
0 59	0 999	0 992	0 985	0 979	0 972	0 965	0 958	0 951	0 944	0 937	0 930
0 60	0 999	0 992	0 986	0 979	0 972	0 966	0 959	0 952	0 945	0 938	0 932

NOTE BELOW DOTTED STEP-CURVE WE HAVE $h/L > 0.5$

Table 6-b Values of L/L_0 (negative discharge)

WAVE HEIGHTS

The wave heights - calculated from (5 8) and (5 11) - are plotted in Fig 6-B Note how the "shape" of the curves corresponding to a constant positive discharge differs from that corresponding to $q^* = 0$ The outmost left part of these curves correspond to Froude numbers close to one (see also Fig 6-A, with comments) For negative discharges we end with infinite wave heights in the limit $L = L_{\min}$

7 NUMERICAL EXAMPLES

In the examples results are only given with normal slide-rule accuracy

EX 7-a CALCULATION OF L , H , Δh , h AND U FROM T_a , q , D AND H_o

Two-dimensional flow is assumed, and the following quantities are given

$T_a = 8.0$ s, $q = 10.1$ m²/s, $D = 9.5$ m, $H_o = 1.6$ m (corresponding to a deep-water steepness $S_o = 1.6\%$)

In the first approximation, H is put equal to zero in (5 10), so we find from (5 9) and (5 12), by iteration

$\Delta h_1 = 0.0583$ m, $h_1 = 9.4417 \approx 9.44$ m, $U_1 = 1.07$ m/s

From (3 6), (3 9) and (5 13) $L_o = 1.5680^2 = 100$ m, $c_o = 1.5680 = 12.5$ m/s, $h/L_o = 0.0944$, $q^* = 0.00808$

By interpolation in Table 6-a we then find $L/L_o = 0.795 \Rightarrow L = 79.5$ m (without the current, the wave length would be 69.5 m, for the same values of D and T_a)

$h/L = 9.44/79.5 = 0.119$, so we find from (5 14) and (3 11)

$c_r/c_o = 0.709 \Rightarrow c_r = 8.86$ m/s (without the current the wave celerity

would be 8.69 m/s), and $c_{gr}/c_r = 0.853$

(5 11) then gives $H/H_o = 0.804 \Rightarrow H = 1.29$ m (without the current the wave height would be 1.50 m, for the same value of H_o)

The new value of Δh from (5 10) $\Delta h_2 = 0.0583$ m

+ 0.0078 m - 0.0027 m ≈ 0.0634 m $\Rightarrow h_2 \approx 9.44$ m = h_1 So within slide-rule accuracy we find $U = 1.07$ m/s, $\Delta h = 0.0634$ m (without the current the set-down would be 0.0094 m), $h = 9.4366$ m (≈ 9.44 m)

Finally from (3 1) and (3 2) $c_a = 79.5/8.0 = 9.93$ m/s and $T_r = 79.5/8.86 = 8.98$ s

EX 7-b CALCULATION OF WAVE HEIGHT FROM BOTTOM PRESSURE CELL

This example demonstrates how the wave height H can be determined for a two-dimensional flow, when the below mentioned parameters have been measured It also shows specifically the effect of a current

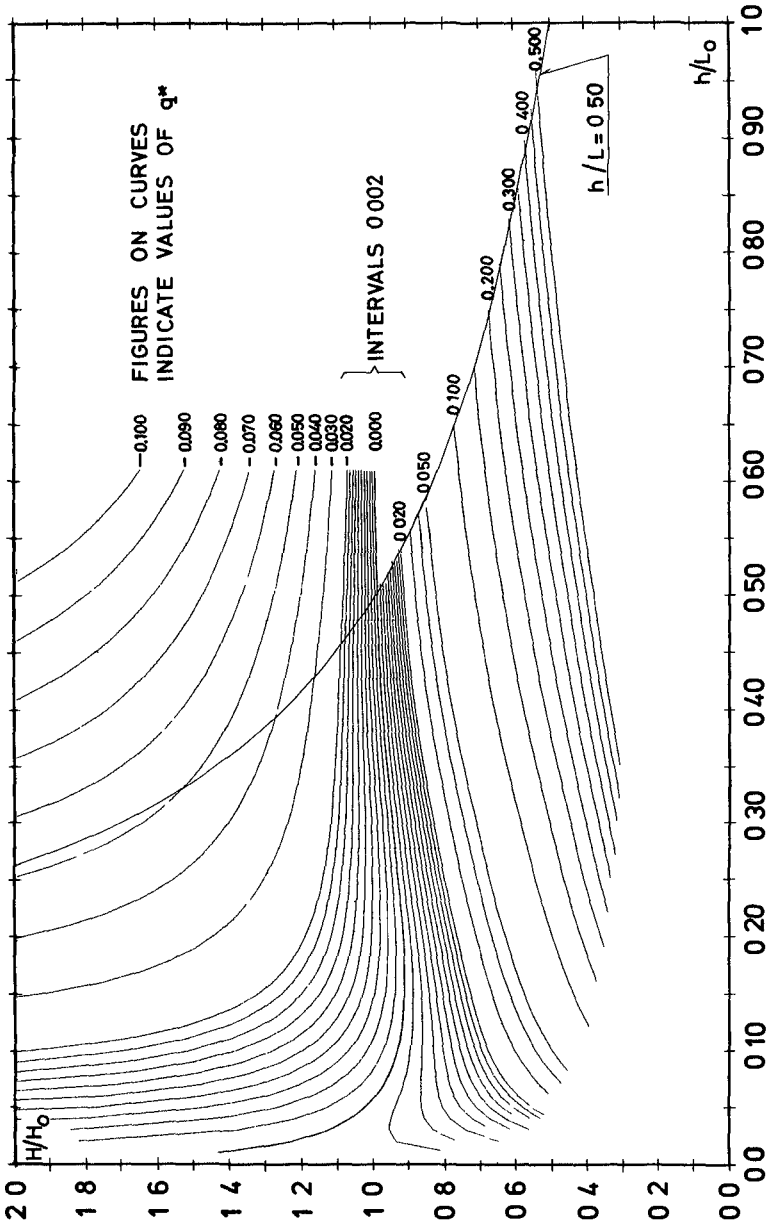


Fig 6-B "Constant discharge curves" for H/H_0

Measured parameters

$$h = 850 \text{ m}$$

$$U = -0.70 \text{ m/s} \quad (\text{is a counter-current})$$

$$T_a = 60 \text{ s}$$

and $\max \Delta p_b = 3400 \text{ N/m}^2$ ($1 \text{ N} = 1 \text{ kg m/s}^2$), where Δp_b is the difference between actual pressure and hydrostatic pressure corresponding to MWL ($\equiv \gamma h$) at the bottom, (here considered measured with a pressure cell at the bottom)

The calculations proceed thus

$$L_o = \frac{9.81}{2\pi} 60^2 = 562 \text{ m} \quad (3.6)$$

$$h/L_o = 850/562 = 0.151$$

$$c_o = \frac{9.81}{2\pi} 60 = 9.36 \text{ m/s} \quad (3.9)$$

$$q^* = 850(-0.70)/(9.36 \times 562) = -0.0113 \quad (5.13)$$

Using linear interpolation in Table 6-b we obtain

$$L/L_o = 0.712$$

hence $h/L \equiv (h/L_o)/(L/L_o) = 0.151/0.712 = 0.212$

Using the first order expression only, we have for the wave amplitude

$$H/2 = \max \Delta p_b \cosh kh/\gamma$$

$$\cosh kh = 2.03$$

and so the wave height becomes

$$H = 2 \times 3400 \times 2.03 / (1000 \times 9.81) = 1.41 \text{ m}$$

If the current were not noticed, then $L/L_o = 0.820$ from Table 6-a or 6-b and $h/L = 0.151/0.820 = 0.184$

$$\cosh kh = 1.75$$

$$H = 2 \times 3400 \times 1.75 / (1000 \times 9.81) = 1.21 \text{ m}$$

$$\frac{\Delta H}{H} = \frac{1.41 - 1.21}{1.41} \quad 100\% = 14\%$$

is in this case, neglectation of the current will give wave height 14% too small (A positive current will have the opposite effect)

It is not difficult to find realistic sets of values for h , U and T_a that lead to higher values of $\Delta H/H$ (as defined above). This aspect shows the importance of considering the effect of a possible current. The phenomenon may be one of the factors which can obscure the direct comparison in a coastal zone between wave heights as measured at the water surface and as calculated from pressure cell recordings at the bottom.

8 REFERENCES

- [1] Bowen, A J , Inman, D L , and Simmons, V P (1968) Wave "Set-Down" and Set-Up J Geophys Res 73, 2569-2577
- [2] Garrett, C J R (1967) Discussion The Adiabatic Invariant for Wave Propagation in a Nonuniform Moving Medium Proc Roy Soc , A, 299, 26-27
- [3] Jonsson, I G (ed), (1969) Index to Reports 1-19 (1961-1969) Basic Res -Prog Rep 20 Coastal Engrg Lab and Hydraulic Lab , Techn Univ Denmark
- [4] Jonsson, I G (1970) Graphical Determination of the Wave Length in a Homogeneous Current Field Basic Res -Prog Rep 21, 19-26 Coastal Engrg Lab and Hydraulic Lab , Techn Univ Denmark
- [5] Longuet-Higgins, M S , and Stewart, R W (1960) Changes in the Form of Short Gravity Waves on Long Waves and Tidal Currents J Fluid Mech 8, 565-583
- [6] Longuet-Higgins, M S , and Stewart, R W (1961) The Changes in Amplitude of Short Gravity Waves on Steady Non-Uniform Currents J Fluid Mech 10, 529-549
- [7] Lundgren, H (1963) Wave Thrust [\equiv Radiation Stress] and Wave Energy Level Int Assoc Hydr Res , Proc 10th Congress 1, 147-151, London
- [8] Whitham, G B (1962) Mass, Momentum and Energy Flux in Water Waves J Fluid Mech 12, 135-147

CHAPTER 31

EXPERIMENTS OF WAVE REFLEXION ON IMPERMEABLE SLOPES

by Carlos de Campos MORAES*

ABSTRACT

Results from experiments on the reflective power of smooth and rough impermeable slopes are presented. The importance of relative depth to the regular scatter diagram of the function $R=R(\delta_0)$ and the need for an adequate computational wave theory through which no significant alterations are introduced in the determination of reflective power is pointed out. Stokes 2nd order corrections are introduced. These help find a superior value for the reflexion coefficient and destroy the mentioned regularity of the scatter diagram. A regular scattering of experimental points, also of function $R=R(\delta_0)$, where, however, for constant steepness, reflexion decreases when relative depth increases, is found in rough slope tests. In this case, the more inclined is the slope, the greater is the influence of roughness.

1 - INTRODUCTION

Some of the approaches used for determining the reflexion coefficient of a given parameter are based on direct recording of incident and reflected wave trains (these are the "wave tail" and "subtraction" methods described in [1] by Goda and Abe), others on the recording of clapotis. Calculation procedures using maxima and minima of these clapotis range from the simplest - immediate application of the small amplitude assumption through the well-known formula

$$R = (\text{Max}-\text{min})/(\text{Max}+\text{min}) \quad (1)$$

to more elaborate cases in which approximations of different orders are used. Stokes II (as developed by Carry [2]), Stokes III (as proposed by Goda and Abe [1]), cnoidal theory, etc. More sophisticated methods exist as, for instance, Santon's and Marcou's method developed in Grenoble, which applies harmonic analysis to the clapotis profile as recorded at three points [3], [4], [5].

The present paper concerns results of tests where the reflective power of smooth and rough impermeable slopes was studied.

Use was made of the method of recording maxima and minima of clapotis. The aim was above all to study the validity range of the linear theory small amplitude assumption and acquire an idea of errors introduced by its application.

2 - RANGES OF PARAMETER VARIATION IN TESTS

Systematic tests were performed in a 20 m long and 0.80 m wide flume with a total depth of 0.55 m. This flume is equipped with a monochromatic translation actuator. Results of the tests are studied in the following.

Absolute water depth (d) was kept constant and equal to 0.35 m since the slope concerned a semi-indefinite plane. Local or offshore relative depth, d/L or d/L_0 , respectively varied then only owing to L_0 variation, that is, owing to T , which took values between 0.8 and 2.2 s.

In most cases concerning the presentation of results, periods 1.0, 1.6 and 2.2 s were selected corresponding the following relative depths

T (s)	d/L	d/L ₀
1.0	0.25	0.22
1.6	0.13	0.09
2.2	0.09	0.05

* - Traine Research Officer, Laboratório Nacional de Engenharia Civil (LNEC), Lisbon, Portugal

Going along the decreasing order of relative depths, the first of those three cases presents waves satisfying Miche's condition for non-appearance of secondary crests ($d/L > 0.15$). These waves are best suited for elementary computations, according to the linear theory small amplitude assumption. The second case (which occupies an intermediate position in the set of tests) includes waves corresponding to finite amplitude wave theories. To them the different Stokes approximations may be applied according to the rigour demanded. The case of the least relative depth comprises waves calculation of which enters the domain of cnoidal wave theory*.

As for steepness, its off-shore value (δ_0) varies approximately between 0.3 and 3%. These are the most common limits for sea waves. It was endeavoured to secure a great range of values corresponding to unbroken waves. Also, tests were carried further whenever breaking occurred for increasing steepness. However, beyond a certain point it was impossible to get acceptable clapotis from the point of view of regularity.

The plane slope inclination varied, for the set of tests, from the minimum 10% value to vertical inclination.

Roughness, which was introduced in the second part of the tests made, consisted of sand glued to the slope. Of course, the greater the intended roughness, the greater the used sand grain size. The sift hole diameter \underline{r} was used to characterize absolute roughness. This factor was made non-dimensional by means of the wave length. The resulting parameter r/L_0 , a measure of relative roughness, took values between 1.3×10^{-4} and 240×10^{-4} .

3 - TEST RESULTS

3.1 - Smooth slopes

In Fig. 1, a graphic diagram of $R = R(\delta_0)$, points corresponding to 10%, 15%, 20% and 30% slope tests are plotted.

Fig. 2 comprises four $R(\delta_0)$ plots corresponding to 40%, 50%, 100% and vertical slopes.

In the first set of tests (Fig. 1) points corresponding each one of the four inclinations cluster around similar curves. In each inclination only an experimental scattering of points occurs, with no period separation.

On the other hand, in the second set of tests a regular scattering of periods occurs. For constant δ_0 values a decrease of R is apparent when \underline{I} increases. The same phenomenon is noted for run-up experiments (Fig. 5).

3.2 - Rough slopes

In Fig. 4 four diagrams relating to rough slope tests are selected, absolute roughness being in each case a constant.

It is seen that in every case two type of point scattering are present, according to slope variation. For 20% and 30% a regular scattering of periods is observed, now, however, in the opposite sense. For constant δ_0 values, R and \underline{I} values increase or decrease together. For vertical inclination (and also for 100% inclinations, though no diagrams are presented) again a regular scattering of periods is observed as in the case of smooth slopes.

4 - INTERPRETATION OF RESULTS

4.1 - Introduction

With a view to simplifying the language used, the following designations are adopted

* - However, according to Ursell's parameter

$$U = \frac{H}{d} \left(\frac{L}{d} \right)^2 \quad (2)$$

cnoidal theory should be applied only for $U > 100$. Taking into account the highest wave of the tests (6.75 cm) and the local wave length ($L = 3.9$ m) corresponding to the off-shore wave length $L_0 = 7.55$ m ($T = 2.2$ s) we get $U = 24$.

ted for characterization of the three mentioned scattering types

- experimental scattering
- smooth type regular scattering
- rough type regular scattering

An attempt shall be made to interpret occurrence of regular scattering in the high of an explanation relative to computations in a case and of physical order in another. That is physical causes are perhaps related to energy dissipation phenomena which in turn are the reason for the decrease in the slope reflective power. Changes undergone by the wave in its orbital velocity field, when it is propagating in decreasing relative depths, with an increasing turbulence and finally reaching breaking point or energy dissipation due to slope roughness are cases in which the physical factor is indisputable. The decrease in reflective power may however be fictitious, that is, it may merely result from an inefficient computation method.

4 2 - Smooth slopes

4 2 1 - Influence of relative depth on reflexion computations

It is known that the best suited wave theory for computations of the relevant parameters is determined by relative depth. It should be noted, however, that the parameter t/L (where t is the horizontal distance measured from still water level to the slope base projection on the surface and L is the local wave length) may be of great importance.

d = 0.35 m					SLOPE								
					10%	15%	20%	30%	40%	50%	100%	200%	vert
					t (m)								
T(s)	L ₀ (m)	L(m)	d/L ₀	d/L	3.50	2.33	1.75	1.17	0.88	0.70	0.35	0.18	0.00
0.8	1.00	0.97	0.3506	0.3584	3.58	2.39	1.79	1.19	0.90	0.72	0.36	0.18	0.00
1.0	1.56	1.42	0.2244	0.2458	2.46	1.64	1.23	0.82	0.61	0.49	0.25	0.12	0.00
1.2	2.25	1.86	0.1558	0.1881	1.88	1.25	0.94	0.63	0.47	0.38	0.19	0.09	0.00
1.4	3.06	2.28	0.1145	0.1535	1.54	1.02	0.77	0.51	0.38	0.31	0.15	0.08	0.00
1.6	3.99	2.69	0.0876	0.1301	1.30	0.87	0.65	0.43	0.33	0.26	0.13	0.06	0.00
1.8	5.05	3.09	0.0692	0.1132	1.13	0.75	0.57	0.38	0.28	0.23	0.11	0.06	0.00
2.0	6.24	3.49	0.0561	0.1004	1.00	0.67	0.50	0.33	0.25	0.20	0.10	0.05	0.00
2.2	7.55	3.88	0.0464	0.0903	0.90	0.60	0.45	0.30	0.23	0.18	0.09	0.04	0.00

Schoemaker and Thijssse have pointed out [6] that that parameter is the main cause of energy dissipation and indicated that for an almost total reflexion we must have $t/L \leq 0.25$, and for a very small reflexion then $t/L \geq 0.5$.

In a small inclination slope (15%, for instance) two waves of different lengths, which propagate, before reaching it, in different relative depths, will in the end have traveled over zones with same relative depth (of course one lagging behind the other). This period does not exert a selective action. This is the type of tests corresponding to "experimental scattering" which was found for 10%, 15%, 20% and 30% slopes.

For strong inclinations (greater than 40%), the fact that t/L is small makes the two waves propagate in different relative depths when they bear on the slope. Thus, a proper wave theory for computations is essential. For the shorter wave a deeper water theory seems best suited while for the longer one a shallow water theory is indicated. This seems to be the evident explanation for the occurrence of the "smooth type regular scattering".

In fig 3 is shown the influence of inclination on R for constant values of T and

can be easily noted the different aspect of the phenomenon in inclinations up to 40% and from this value up to vertical in what concerns the shorter period (1 0s) and the longer ones (1 6s and 2 2s)

4 2 2 - Miche's theory

The steepness maximum value, δ_{max} , of a wave theoretically capable of total reflexion on a slope which is at an angle α with the horizontal has been defined by Miche [7] as

$$\delta_{max} = \sqrt{\frac{2\alpha}{\pi}} \frac{\sin^2 \alpha}{\pi} \tag{2}$$

the theoretical reflexion coefficient being

$$R' = \frac{\delta_{max}}{\delta_o} \tag{3}$$

for $\delta_{max} < \delta_o$ If $\delta_{max} \geq \delta_o$ then $R' = 1$

The actual reflexion coefficient is

$$R = \rho R' \tag{4}$$

where ρ is the so-called slope intrinsic reflexion coefficient

The diagram $R' = R'(\delta_o)$, Fig 6, shows that up to an 40% inclination and within the steepness range of the tests, R' values present a first constant 100% "landing" The smaller the inclination, the smaller is this landing For slopes of inclination greater than 40% and about (but not quite) 3% steepness, theoretical reflexion is always total for steepness values up to 3%

Greater δ_o values are more and more unlikely in nature For instance, for a 100% slope it is $\delta_{max} = 11.26\%$

This 40% inclination value (for results corresponding to the steepness range of the tests, as said before) separates in fact the two domains of experimental results: experimental scattering and regular scattering

4 2 3 - Stokes' 2nd order corrections

According to

$$1/\alpha = \frac{2\pi}{\text{th} \frac{2\pi d}{L}} \left(1 + \frac{3}{2 \text{sh}^2 \frac{2\pi d}{L}} \right) \tag{5}$$

α values were computed as a function of d/L

T(s)	d/L	α	T(s)	d/L	α
0 8	0 3584	0 1458	1 6	0 1301	0 0382
1 0	0 2458	0 1118	1 8	0 1132	0 0277
1 2	0 1881	0 0782	2 0	0 1004	0 0206
1 4	0 1535	0 0541	2 2	0 0903	0 0157

following Carry's procedure [2] These α values were used to compute

$$D = \frac{M}{2\alpha L} + \frac{m}{2\alpha L} \tag{6}$$

where M and m are maximum and minimum of the recorded clapotis

Fig 7 shows a diagram taken from [2] where the corrective value μ is determined which will allow the calculation of the new reflexion coefficient β (value corrected according to Stokes' 2nd order theory)

$$\beta = \mu R \quad (7)$$

where R is computed from (1)

In Fig 2, the corrected experimental points (black symbols) and the uncorrected points (white symbols) are presented linked by line segments which provide a measure of the amplitude of the introduced correction

In Fig 8, the percentage of introduced correction ($\frac{\beta - R}{R}$) is plotted as a function of δ_o , inclination and \underline{T}

The following points are noted

- Using a higher order wave theory will decrease the regular scattering of periods R being corrected for values close or equal to 100%. Proximity to this value seems to depend on the approximation order of the used wave theory

- Correction increases with period, \underline{l} e , decreases with relative depth (see Fig 8), which agrees with what was said above about the wave characteristics relating to depth

- Correction increases when either inclination or steepness increase

4 3 - Rough slopes

4 3 1 - Influence of relative roughness

In rough slopes, the regular scattering of periods is due, as said above, to two reasons

- "rough type regular scattering" for low inclinations (20% and 30% in the case of the tests performed) in which the greater the relative roughness (\underline{l} e the smaller is L_o relative to \underline{r}) the greater the energy dissipation. This explains that, for the same slope, longer period waves dissipate less energy

- "Smooth type regular scattering" for higher inclinations, in which, for the same absolute roughness, energy dissipation is smaller than in low inclination slopes. The effect of the separation of the experimental points due to insufficient approximation of the used wave theory overrules the physical effect of energy dissipation through roughness

Fig 9 shows experimental results obtained for equal values of relative roughness. They confirm the given explanation for small inclinations, the "rough type regular scattering" disappears. For vertical inclination the smooth type regular scattering remains

2nd order corrections for rough slopes are not presented in this paper

4 3 2 - Variation of the slope intrinsic reflexion coefficient

According to formula (4) and to Fig 10 diagrams, the intrinsic reflexion coefficient decreases with steepness until a minimum value is reached corresponding to $\delta_o = \delta_{max}$, afterwards it increases to values greater than δ_o

When a slope's actual reflexion coefficient is estimated from the theoretical reflexion coefficient R^1 one should not take a constant β value, taking the steepness into account

4 3 3 - Roughness influence on inclination from the point of view of energy dissipation

It is known that in a flume the maximum bottom orbital velocity for a wave which is propagating with height H and length L is given by

$$v_{max} = \frac{H \pi}{\sin \alpha} \sqrt{\frac{g}{L}}$$

and that this velocity value is concerned with energy dissipation by roughness

This v_{max} value increases very rapidly when inclination decreases, energy dissipation also increases as a consequence of roughness

Fig 11 shows, for a 30% slope, the decrease of reflective power due to the roughness increase. The same strong effect is not present for the case in which the inclination is greater than 100%

REFERENCES

- [1] - GODA, Yoshimi and ABE, Yoshiki - Apparent Coefficient of Partial Reflection of Finite Amplitude Waves Report of the Port and Harbour Research Institute vol 7 N° 3 September 1968
- [2] - CARRY - Clapotis partiel La Houille Blanche N° 4, Août - Septembre 1953 p 482-494
- [3] - SANTON, L , MARCOU, C - Enregistrement graphique du profil d'une houle produite en laboratoire Houille Blanche N° 3 de 1953 p 411-417
- [4] - SANTON, L - Enregistrement graphique du profil d'une houle de laboratoire , analyse harmonique Proc 5th Conf Coastal Engineering, Grenoble, France, September 1954 p 189-206
- [5] - CASTRO, C - Etude du coefficient de reflexion de la houle de laboratoire pour des talus plans, lisses et rugueux
- [6] - SCHOEMAKER, H J e THIJSSSE, TH - Investigations of the reflection of waves IAHR, 3th Meeting, Grenoble, September 1949
- [7] - MICHE - Le pouvoir reflechissant des ouvrages maritimes exposés à l'action de la houle Annales des ponts et chaussées, année 121, N° 3, 1951, p 285-319

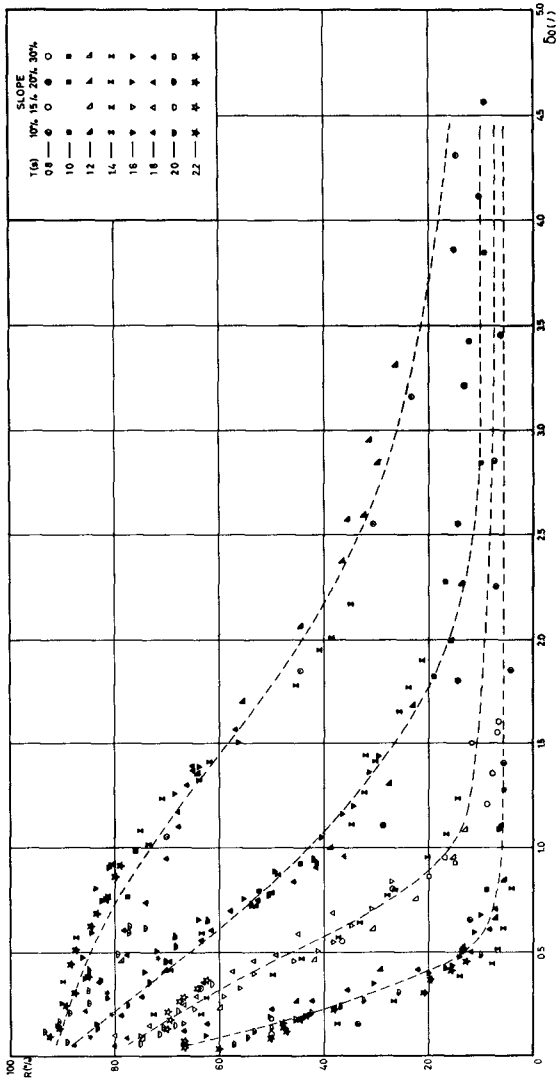


Fig 1 - Tests with smooth slopes of 10%, 15%, 20% and 30%

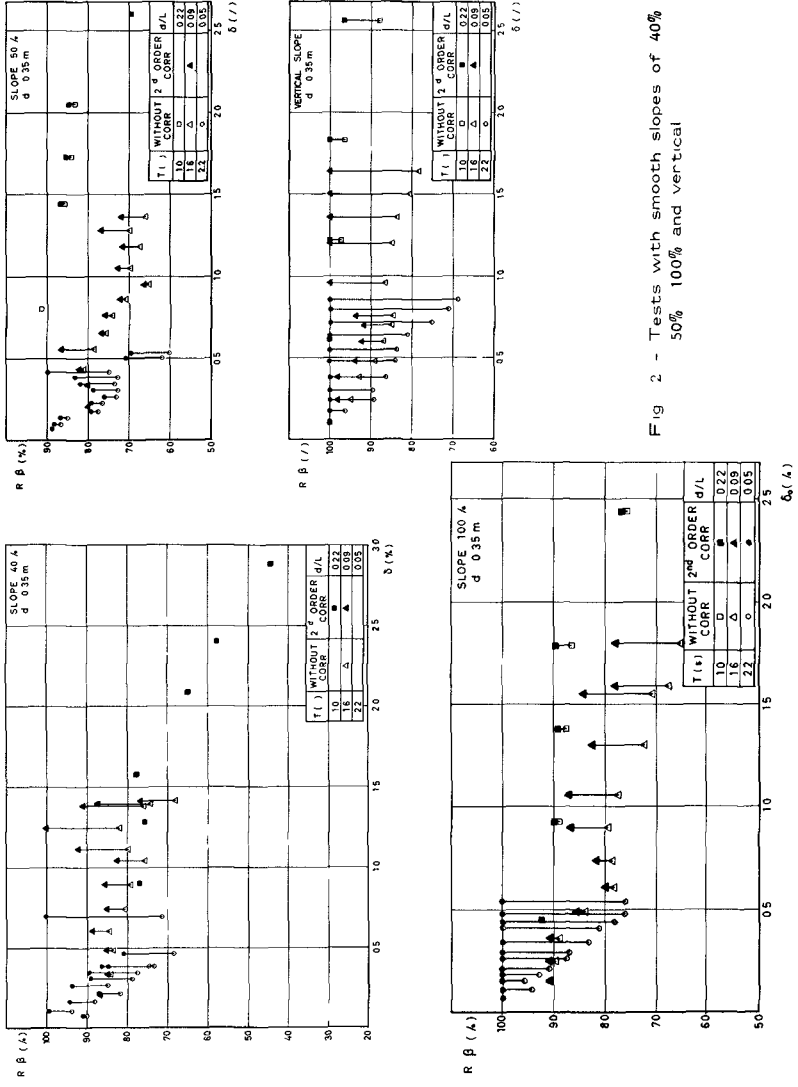


Fig 2 - Tests with smooth slopes of 40%
50% 100% and vertical

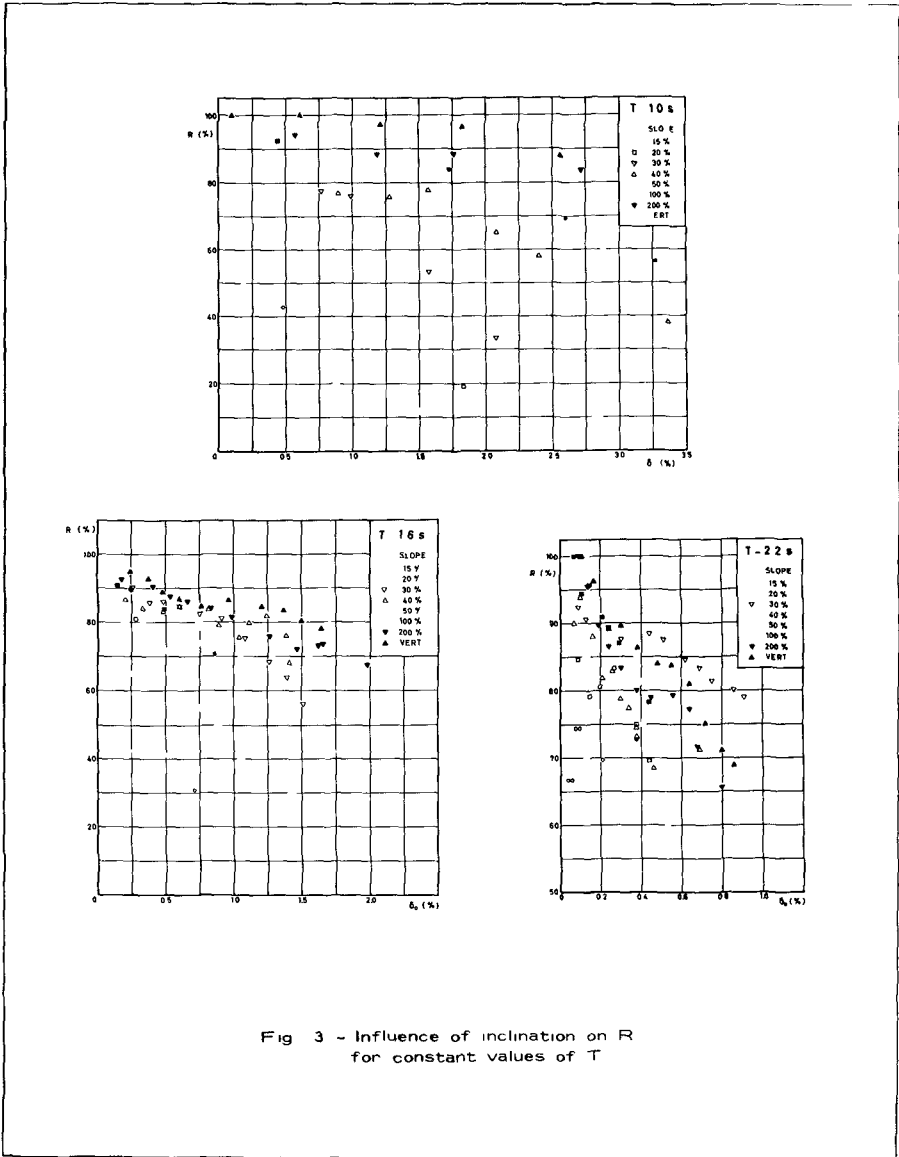


Fig 3 - Influence of inclination on R for constant values of T

Fig 4 - Tests with rough slopes

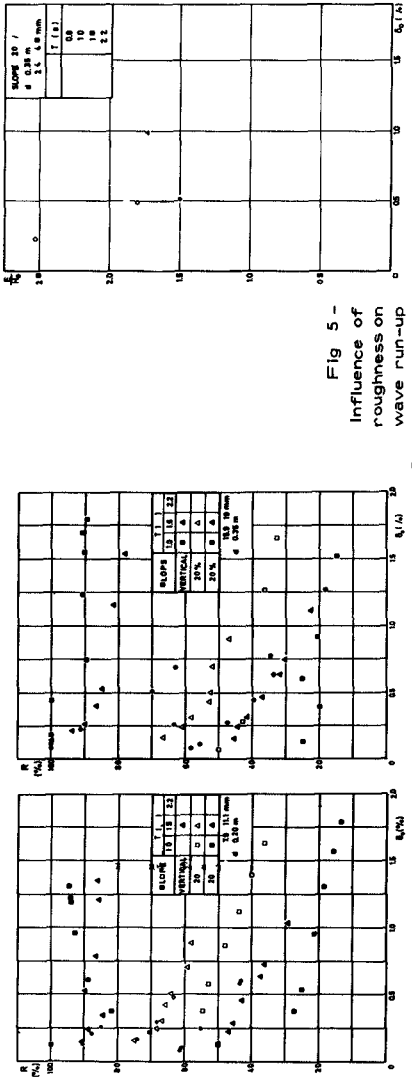
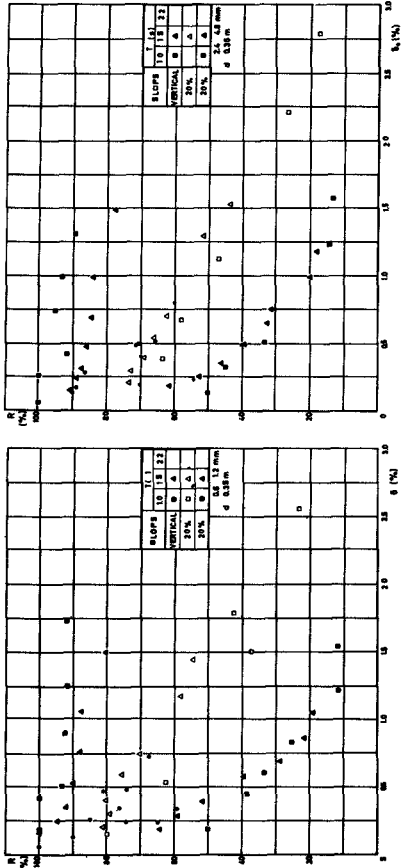


Fig 5 - Influence of roughness on wave run-up

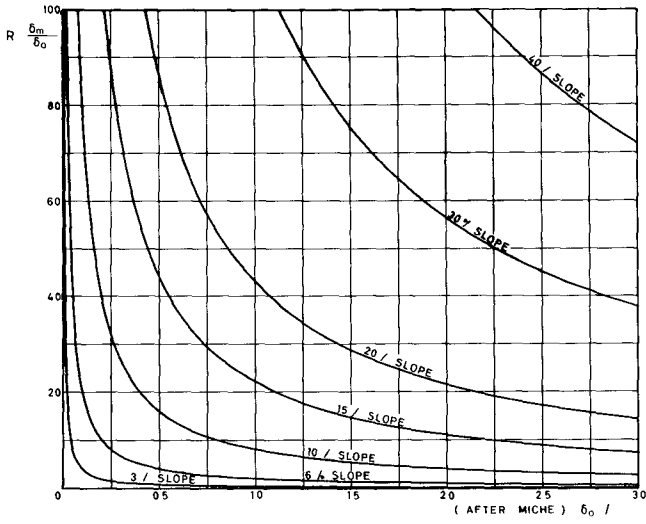


Fig 6 - Miche's theoretical reflexion coefficient

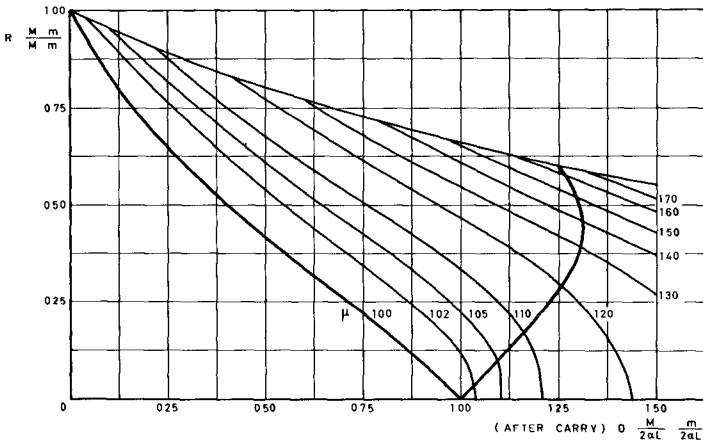


Fig 7 - Graph for the 2nd order corrections

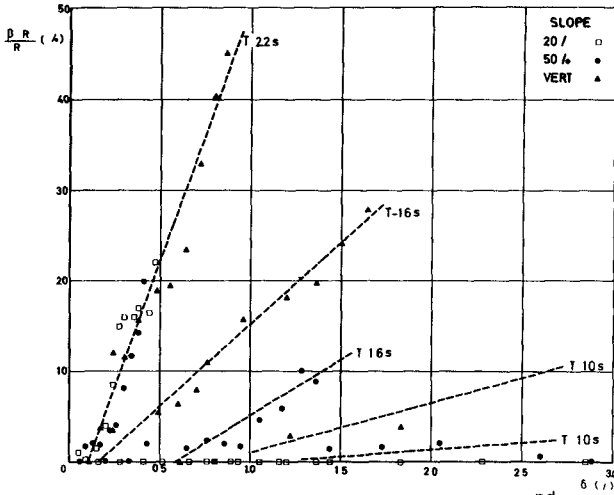


Fig 8 - 2nd order corrections for the reflexion coefficient according to the period and slope

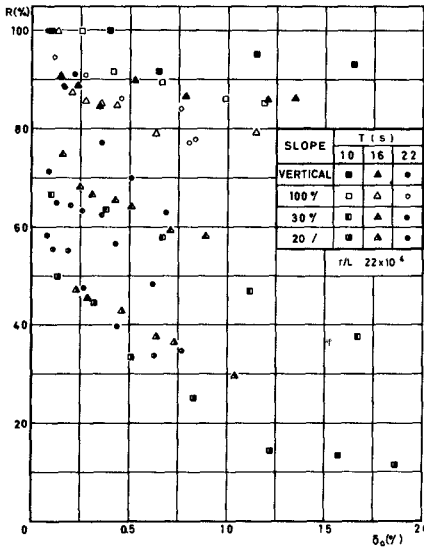


Fig 9 - Reflexion coefficient for the same relative roughness

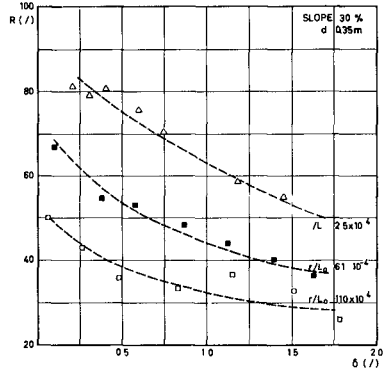
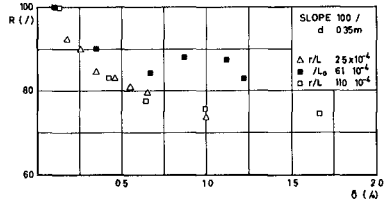
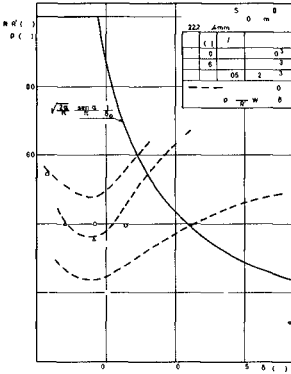
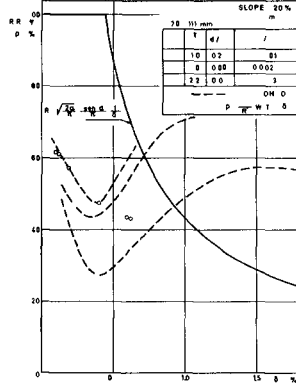
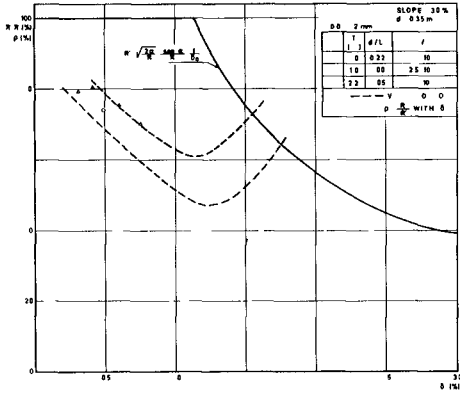


Fig 10 - Variation of ρ with off-shore steepness

Fig 11 - Influence of roughness on R for different slopes

CHAPTER 32

LIMITING CONDITION FOR STANDING WAVE THEORIES BY PERTURBATION METHOD

Yoshito Tsuchiya
Professor of Coastal Engineering

and

Masataka Yamaguchi
Research Assistant of Coastal Hydraulics
Disaster Prevention Research Institute
Kyoto University, Kyoto, Japan

ABSTRACT

The purpose of this paper is to make clear the validity and limiting condition for the application of the finite amplitude standing wave theories by the perturbation method. In a numerical example, the errors of each order solution of these theories for two non-linear free surface conditions are computed for various kinds of wave characteristics and compared with each other.

Some experiments on the wave pressure on a vertical wall by standing waves were carried out and a plot of the limiting condition for the application of these theories is proposed based on the comparison with theoretical curves.

In addition, as an example of the application of these theories, the change of characteristics of wave pressure of standing waves accompanying the overtopping wave on a vertical wall is discussed.

INTRODUCTION

Up to the present, the finite amplitude standing wave theories have been studied by many researchers such as Penny and Price, Kishi and etc. In 1960, Tadjbaksh and Keller derived the third order solution of finite amplitude standing waves in shallow water by means of the perturbation method with two additional conditions. Although the calculation for the higher approximation is very complicated, this method has often been used to solve such non-linear differential equations, because approximate solutions of arbitrary orders can be derived systematically. Recently the fourth order solution of the finite amplitude standing wave theories in shallow water was obtained by Goda in 1966.

The perturbation method is a formal one and no mathematical proof for the convergence of the solutions by this method is given. Solutions by this method are only approximate ones. Consequently, the validity and limiting condition for the application of these theories to physical phenomena are subject to question. To clarify these problems, we have carried out some investigations by the numerical consideration of the validity for two non-linear free surface boundary conditions using these theories and by the comparison between the theoretical curves based on these theories and experimental results for the wave pressure of standing waves.

Moreover, as an example of the application of these theories, the change of the characteristics of the wave pressure of standing waves accompanying the overtopping wave is discussed in comparison with the results of standing waves described already

NUMERICAL CONSIDERATION FOR THE BOUNDARY CONDITIONS AT FREE SURFACE

(1) Two Non-Linear Boundary Conditions at Free Surface

Since these solutions are only approximate ones as mentioned above, the two non-linear boundary conditions at the unknown free surface, namely the kinematic condition prescribing the particle motion at the free surface and the dynamic condition describing the pressure at the free surface to be constant on the basis of Bernoulli's theorem are not satisfied rigorously by these solutions and errors for these conditions always exist. So, we investigate to what extent the perturbation solution of each order satisfies these conditions by computing numerically the errors of each order solution for these non-dimensionalized conditions for various kinds of wave characteristics expressed by dimensionless parameters

The kinematic and dynamic conditions are given respectively as

$$v = \partial\eta/\partial t + u(\partial\eta/\partial x) \quad \text{at } y = \eta \quad (1)$$

$$\partial\phi/\partial t + (1/2)(u^2 + v^2) + g\eta = 0 \quad \text{at } y = \eta \quad (2)$$

Let ξ_1 and ξ_2 be the errors of kinematic and dynamic conditions for the solutions. These errors can be written in dimensionless form respectively as

$$\xi_1 = [\sqrt{k/g} \{v - \partial\eta/\partial t - u(\partial\eta/\partial x)\} / \sqrt{gh}]_{y=\eta} \quad (3)$$

$$\xi_2 = [\{k\eta + (k/g)(\partial\phi/\partial t) + (k/2g)(u^2 + v^2)\} / kh]_{y=\eta} \quad (4)$$

in which x is the horizontal coordinate at the still water level, y the vertical coordinate, directed upward positive, t the time, ϕ the velocity potential, u and v the horizontal and vertical particle velocities respectively, η the free surface elevation, h the depth of water, g the acceleration of gravity, $k=2\pi/L$ and L the wave length

If these conditions are rigorously satisfied by the solutions, ξ_1 and ξ_2 would be identically zero. However, as the solutions are approximate, the equality is not satisfied. Accordingly, by substituting these solutions into Eqs (3) and (4) and comparing the magnitude of these errors with each of them, we can investigate which solution has the best fitness for these conditions.

We introduce the following criteria to evaluate the boundary condition errors

$$(E_1)_R = (\xi_1)_{\max} - (\xi_1)_{\min} \quad (5)$$

$$(E_2)_R = (\xi_2)_{\max} - (\xi_2)_{\min} \quad (6)$$

and

$$(E_3)_R = \sqrt{\xi_1^2} = \sqrt{\left[\frac{M-1}{n=1} \sum_{n=1}^{M-1} \{(\xi_1)_{n-1}^2 + 4(\xi_1)_{n-1}^2 + (\xi_1)_{n+1}^2\} \right] / \{3(M-1)\}} \quad (7)$$

$$(E_4)_R = \sqrt{\xi_2^2} = \sqrt{\left[\frac{M-1}{n=1} \sum_{n=1}^{M-1} \{(\xi_2)_{n-1}^2 + 4(\xi_2)_{n-1}^2 + (\xi_2)_{n+1}^2\} \right] / \{3(M-1)\}} \quad (8)$$

which are according to Dean's criteria, where $(\xi_1)_{\max}$ and $(\xi_1)_{\min}$ show the largest and smallest values of ξ_1 and ξ_2 calculated at each point respectively, M is the number of calculation point and bar indicates the average, and the validity of the wave theories can be investigated with the aid of numerical calculations

(2) The Fitness for Boundary Conditions of the Theories

Fig 1 shows one of the time variations of E_1 and E_2 at a vertical wall calculated for given values of $T/\sqrt{g/h}$ and h/H where T is the wave period and H the amplitude of standing waves. Notations 1, 2, 3 and 4 in Fig 1 indicate the first, the second, the third and the fourth order solutions respectively. It is found from the figure that the fourth order solution has the best fitness for these conditions of the four theoretical curves.

The relation between $(E_1)_R$ and $(E_2)_R$ of each order solution at the wall and $T/\sqrt{g/h}$ in the case where the value of h/H is constant, where black points in these figures designate the breaking point of standing waves of each order solution calculated according to the criterion derived by Penny and Price are shown in Fig 2. It is found from Fig 2 that the higher approximate solutions certainly have better fitness for these boundary conditions within a limited range of wave characteristics. It is also found that the errors for these boundary conditions do not always decrease for the higher approximation, when the value of $T/\sqrt{g/h}$ becomes larger.

Graphs expressing the areas where the boundary condition errors decrease for the higher approximation are given in Fig 3 according to each criterion. Fig 3 shows that the perturbation solution of each order has a limited area of wave characteristics where the errors for the boundary conditions do not decrease by higher approximation, but there is a small difference between the areas for kinematic and dynamic conditions.

Fig 4 is the same as Fig 3 but is evaluated according to Dean's criterion, Eqs (7) and (8) for all phases of wave motion.

EXPERIMENT ON THE WAVE PRESSURE OF STANDING WAVES

(1) Experimental Equipment and Procedure

The wave tank used in this experiment is 63 m long, 0.5 m wide and 0.65 m deep and belongs to the Ujigawa Hydraulic Laboratory. It has a piston type wave generator at the end and a caisson equipped with five pressure gages at about 39.5 m from the end. In the experiment, the time variations in water level and wave pressure along the wall due to standing waves formed by wave reflection at the vertical wall were measured. Since waves of sufficiently large height which the value of h/H is smaller than 2.8 could not be generated in the case of the experiment with uniform depth, a slope composed of 1/60 (3 m long) and 1/400 (20 m long) was constructed on the bottom of wave tank as shown in Fig 5, so that the waves of very large height near wave breaking were generated. Experiments were carried out by changing the wave height, while the wave period and the water depth were determined by keeping the value of $T/\sqrt{g/h}$ constant. The wave characteristics used in the experiment are tabulated in Table 1.

(2) Experimental Results and Considerations

Fig 6 shows the comparison between the theoretical curves already discussed and the experimental results for the wave crest height above the still water level η_0/H . The notations are the same as those in Fig 1 except for the notation SHUTO which indicates the second approximation to stationary long

waves of finite amplitude derived by Shuto as the interaction problem of cnoidal waves. The theoretical curves agree comparatively well with the experimental results, but the theoretical curve of the second order approximate solution tends to deviate from the experimental results, as the value of h/H becomes smaller and the value of $T/\sqrt{g/h}$ larger.

Fig. 7 is an example of the comparison between the theoretical curves and the experimental results for the wave pressure distribution along the wall at phase of wave crest, in which the theoretical wave pressure above the still water level is assumed to be triangular which connects the maximum point of elevation of water level with a point of wave pressure at the still water level, where p is the wave pressure and ρ the density of fluid. The fourth order solution agrees well with the experimental values in the case of considerably large amplitude waves when the value of $T/\sqrt{g/h}$ is relatively small, but the other solutions give excessive values because of the insufficiency of approximation for calculation.

Fig. 8 shows the comparisons between the theoretical curves and the experimental results for wave pressure at a point on the wall at phase of wave crest, where the notation KISHI is the second order approximate solution derived by Kishi using the Penny and Price method. When the value of $T/\sqrt{g/h}$ is relatively small as seen in Fig. 8(a), the fourth order solution agrees well with the experimental values, but the lower order solutions deviate from the experimental results as the value of h/H becomes small. In the case where the value of $T/\sqrt{g/h}$ becomes larger as shown in Fig. 8(e) and (h), the fourth order solution also tends to deviate from the experimental results in the case of small h/H . The larger the value of $T/\sqrt{g/h}$ becomes, the larger the value of h/H , which the experimental values deviate from the theoretical curves corresponding to each order approximate solution except for the stationary long wave theory becomes. The theoretical curve for the stationary long wave theory agrees relatively well with the experimental results for large h/H as the value of $T/\sqrt{g/h}$ becomes larger, but in the case of small h/H , it deviates rapidly. This may be due to insufficiency of approximation order for the calculation.

Fig. 9 indicates the comparison between the theoretical curves and the experimental results for the time variations of water level and wave pressure on the wall. It is found that the experimental results approach the theoretical curves of the higher order approximate solutions in Fig. 9(a), that they do not agree with the experimental results in Fig. 9(b) due to the distortion of theoretical curves of the third and the fourth order solutions, and that the theoretical curve of stationary long wave agrees well with the experimental results only for the wave form.

Using the results obtained from the detailed comparison for the wave pressure of standing waves, a plot of the limiting conditions for the application of the theories is proposed in Fig. 10. This figure shows that the limiting condition of the second order solution is confined to the area in which the value of $T/\sqrt{g/h}$ is relatively small and the value of h/H large. Also this shows that the area of poor correspondence between the theoretical results and the experimental ones exists, although the third and the fourth order solutions have relatively wide areas of applicability and that the area of correspondence for the stationary long wave theory is restricted to the area of relatively large value of $T/\sqrt{g/h}$.

EXPERIMENT ON THE WAVE PRESSURE WITH WAVE OVERTOPPING

(1) Experimental Equipment and Procedure

The experimental equipment used is same as in th previous section Experiments were carried out alternatively for the case of the wave pressure accompanying the overtopping wave and standing waves The characteristics of waves and the crest height of wall are presented in Table 2

(2) Experimental Results and Considerations

The relation between the theoretical curves and the experimental results for wave crest height above the still water level is shown in Fig 11, where the white circles indicate the case of standing waves, the other circles indicate the case of the wave pressure accompanying the overtopping wave and H_c is the crest height of wall Experimental results for standing waves accompanying the overtopping wave agree relatively well with theoretical curves on the basis of the theories within a range of the experiment, although in the case of $T/\sqrt{h}=10$ they are a little less than the experimental values for the standing waves in spite of the scatter

Fig 12 shows the comparison between the theoretical curves of the fourth order solution calculated by taking into account the reduction of wave height due to the wave overtopping and the experimental results for the wave pressure distribution along the wall at phase of wave crest in the case of wave overtopping It is seen from Fig 12(a) that even if the wave height in comparison with the crest height of wall increases considerably, the change of the wave pressure due to the presence of wave overtopping may apparently disappear when the reduction of the wave height at the wall can be taken into account and that the theoretical curves agree well with the experimental results Fig 12(b) describes the effect of the crest height of the wall on the wave pressure distribution It is seen that the theoretical curve agrees well with the experimental results in spite of the difference in the crest height of wall

Fig 13 is the comparison between the theoretical curves of wave pressure at a point on the wall at phase of wave crest and the experimental results for the overtopping wave The theoretical curves agree fairly well with the experimental results in spite of the existence of wave overtopping within a range of the limiting area for the application of the theories corresponding to each order solution found out in the previous section if the reduction of wave height at the wall can be taken into account However, when the wave height increases considerably in comparison with the crest height of wall and becomes near the breaking wave height, the experimental results for the overtopping wave are a little less than those for standing waves This may be due to the change of the field of wave motion because of the increase of the rate of wave overtopping Accordingly, the value of H/H_c is an important parameter which dominates the change of wave pressure caused by wave overtopping as well as the phenomenon of wave overtopping itself

Fig 14 shows the time variations of the water level and wave pressure, where the theoretical curve is based on the fourth order solution The absolute values of experimental results for the overtopping wave decrease in comparison with those of standing waves with the same wave characteristics, while the values agree fairly well with theoretical ones in both the case, if the reduction of wave height

is taken into account But the second peak of double humped wave pressure record disappears and then an unsymmetric wave pressure record appears

The relation between the relative amplitude in the water level at the wall H/H_c and the one for the overtopping wave H/H_c is given in Fig 15 as evaluated by reducing of wave height due to the wave overtopping It is found that the rate of reduction of wave height is almost uniquely determined by the value of H/H_c , regardless of the wave period

CONCLUSIONS

The main results of this investigation are summarized as follows

1 As a result of detailed numerical and experimental considerations for the finite amplitude standing wave theories, the limiting conditions for the application of these theories are presented and it is verified that the approximate solutions for various orders of the theories are valid within a certain range of h/H and $T/\sqrt{g/h}$ corresponding to each order of approximation

2 If the rate of reduction of wave height at the wall caused by wave overtopping can be taken into account, these theories are applicable for estimating the wave pressure of standing waves on a wall in the case where wave overtopping exists within a range of the limiting area of applicability of the theories except for relatively large values of H/H_c

ACKNOWLEDGEMENT

Part of this investigation was accomplished with the support of the Science Research Fund of the Ministry of Education, for which the authors express their appreciation Thanks are due to Dr Iwagaki, Professor, Department of Civil Engineering Kyoto University, for his cordial encouragement during this investigation

REFERENCES

- Dean, R G (1967) Relative validities of water wave theories Proc of Conf on Civil Eng in the Oceans, pp 1-30
- Goda, Y and Kakizaki, S (1966) Studies on standing waves of finite amplitude and wave pressure Report of Port and Harbor Research Institute Ministry of Transport, Vol 5, No 10, pp 1-50 (in Japanese)
- Kishi, T (1957) Clapotis in shallow water Journal of Research of PWRI, Vol 2, Research Paper 5.
- Penny, W G and Price, A T (1952) Finite periodic stationary gravity waves in a perfect liquid Phil Trans A, Vol 224, pp 254-284
- Shuto, N (1968) Stationary long waves of finite amplitude Proc of the 15th Conf on Coastal Eng in Japan, pp 212-219 (in Japanese)
- Tadjabakh, I and Keller, J B (1960) Standing surface waves of finite amplitude J Fluid Mech, Vol 8, pp 442-451

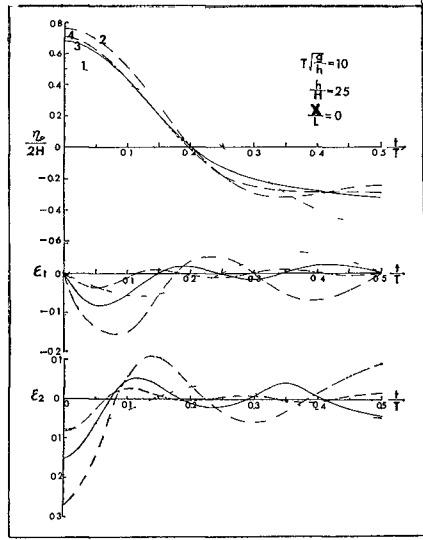
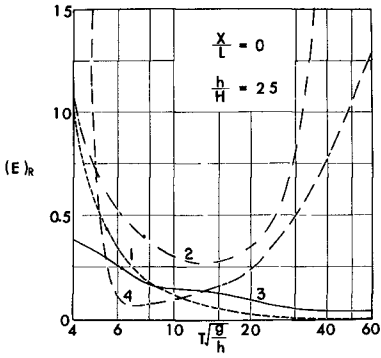
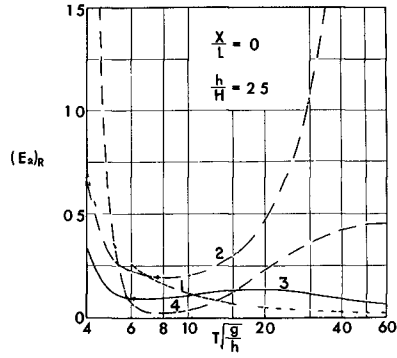


Fig 1 Time variations of E_1 and E_2 at vertical wall



(a)



(b)

Fig 2 Relation between $(E_1)_R$ and $(E_2)_R$ of each order solution at wall and $T/\sqrt{g/h}$

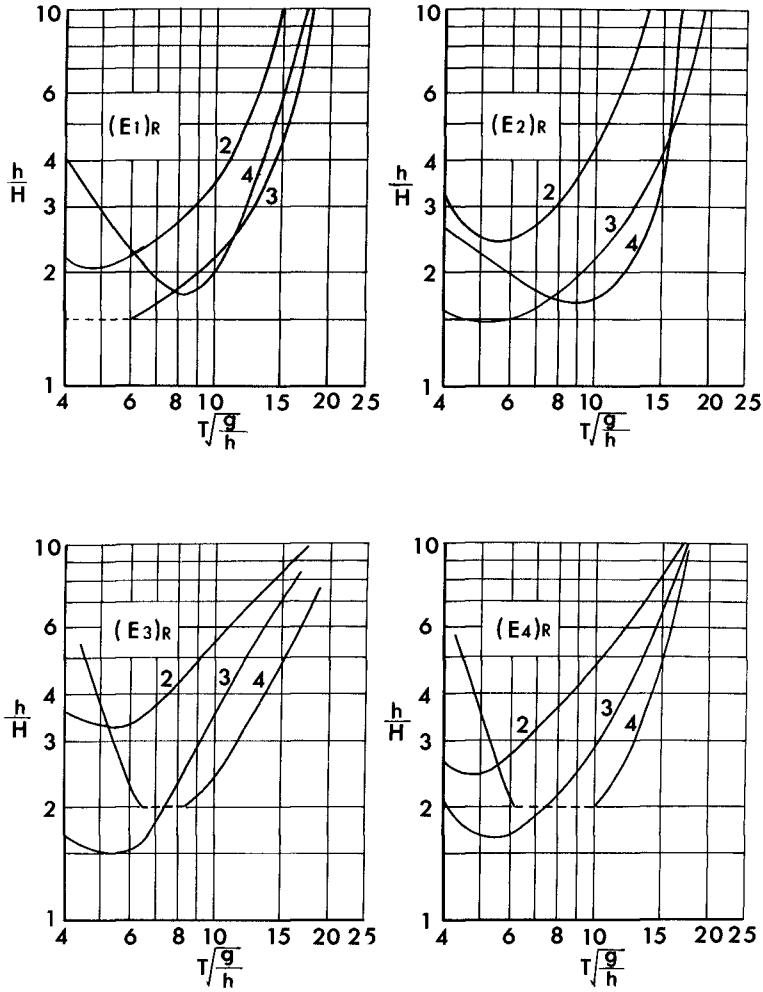


Fig 3 Decreasing areas, estimated approximately, of free surface boundary condition errors for validity of finite amplitude standing wave theories by higher approximation

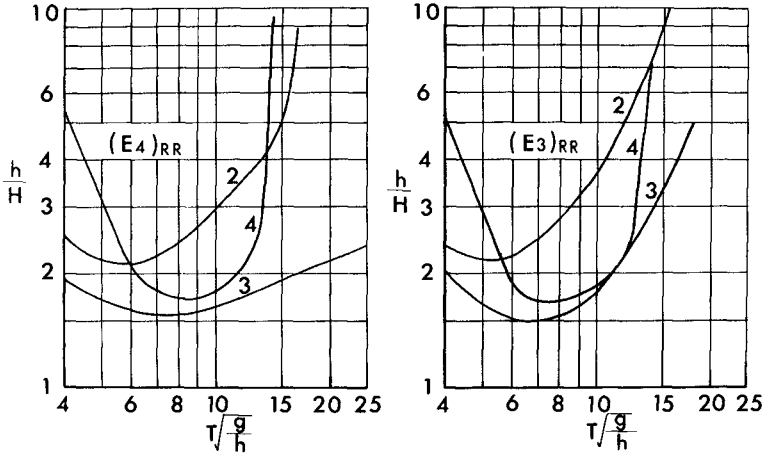


Fig 4 Decreasing areas, estimated approximately, of free surface boundary condition errors for validity of finite amplitude standing wave theories by higher approximation

Table 1 Wave characteristics used in the experiment on standing waves

$T\sqrt{g/h}$	h(cm)	T(sec)	H(cm)
6	25.0	0.958	10.70~2.05
	20.0	0.857	6.72~3.18
8	20.0	1.143	10.51~1.45
	25.0	1.278	7.11~2.97
	17.5	1.069	5.80~4.30
10	20.0	1.427	10.00~1.42
	25.0	1.597	8.36~3.05
	17.5	1.336	4.97~3.00
12	17.5	1.603	9.50~1.01
	20.0	1.714	5.93~2.98
	15.0	1.485	4.34~1.52
14	15.0	1.732	9.21~1.23
	20.0	2.000	6.08~1.84
16	15.0	1.979	9.20~1.01
	12.5	1.807	2.61~2.44
18	12.5	2.033	6.78~1.03
	10.0	1.818	2.31~0.73
20	10.0	2.020	5.04~1.15

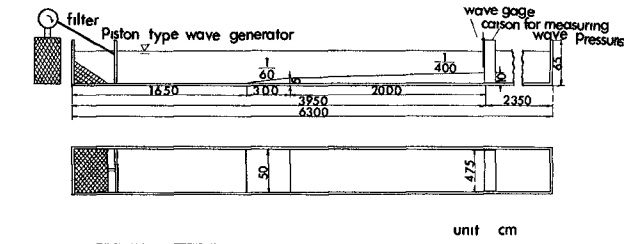
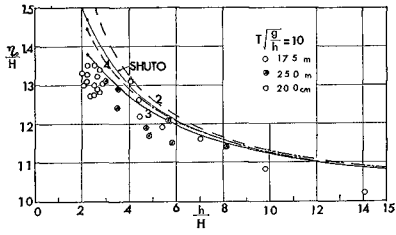
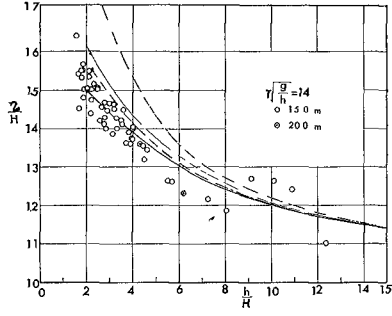


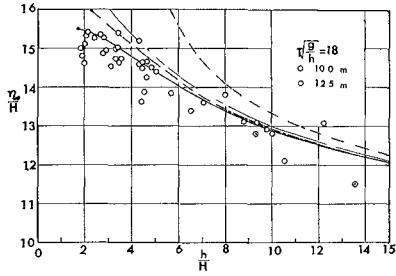
Fig 5 Schematic sketch of wave tank used



(a)



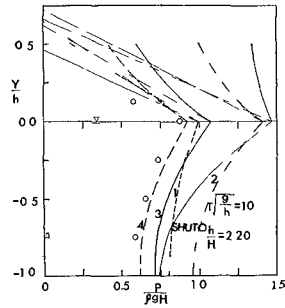
(b)



(c)

Fig 6 Comparison between theoretical curves and experimental results for wave crest height above still water level

Fig 7 Comparison between theoretical curves and experimental results for wave pressure distribution along wall at phase of wave crest



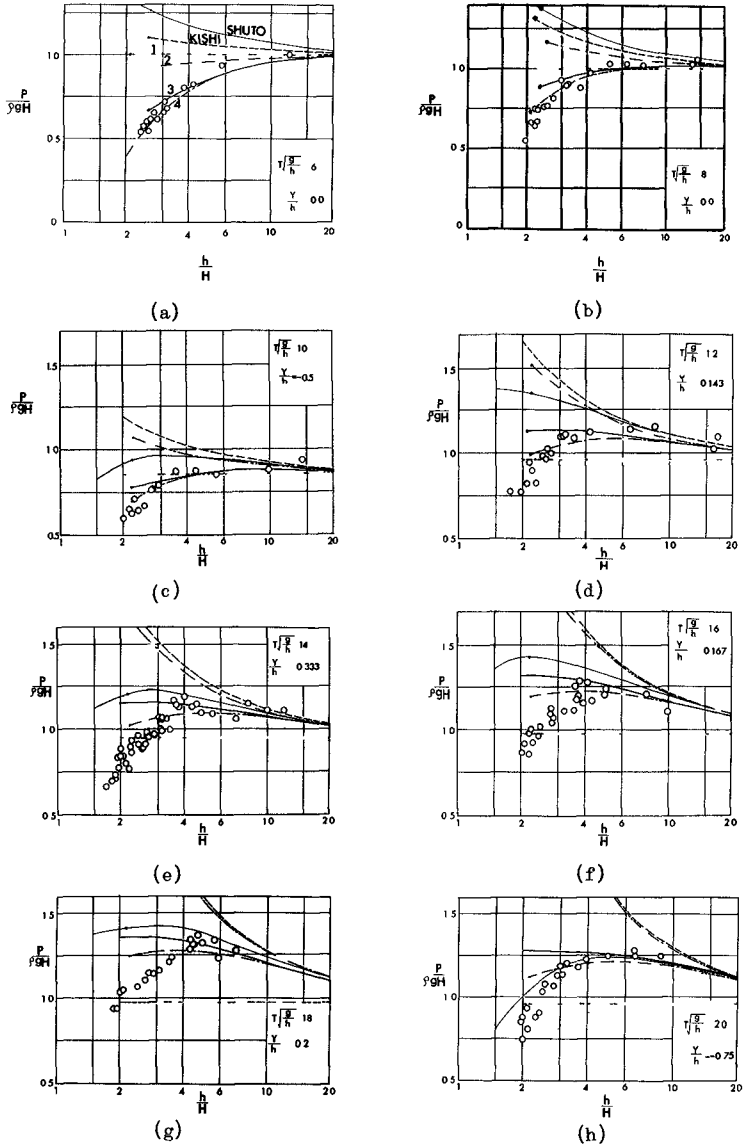
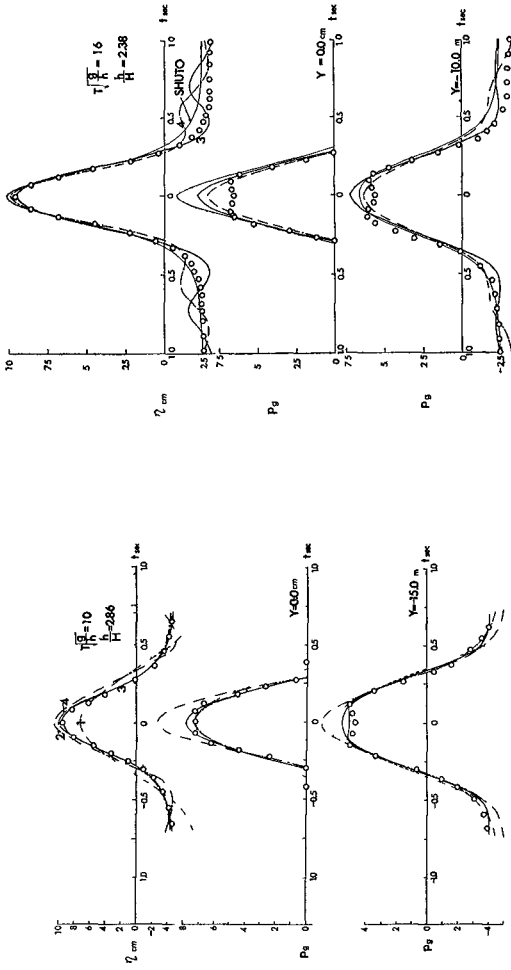


Fig 8 Comparison between theoretical curves and experimental results for wave pressure at a point on wall at phase of wave crest



(a)

(b)

Fig 9 Comparison between theoretical curves and experimental results for time variations of water level and wave pressure on wall

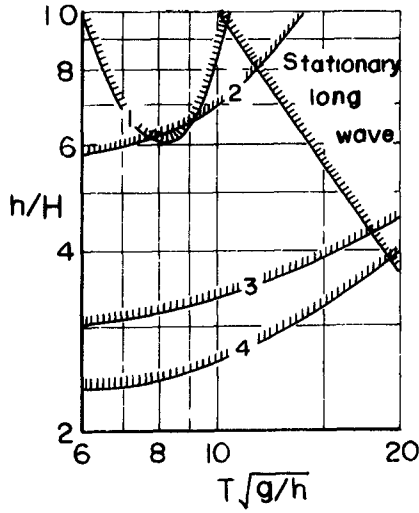


Fig 10 Limiting conditions for application of finite amplitude standing wave theories

Table 2 Wave characteristics used in the experiment on standing waves with wave overtopping.

$T\sqrt{g/h}$	T(sec)	h(cm)	Hc(cm)	H(cm)
8	1 143	20 0	5 0	10 50~4 91
10	1 429	20 0	5 0	12 38~4 40
	1 336	17 5	2 5	9 87~2 89
	1 336	17 5	5 0	9 70~4 60
	1 336	17 5	7 5	8 53~5 26
	1 237	15 0	5 0	8 58~4 50
12	1 604	17.5	5 0	9 22~3 70
14	1 732	15 0	5 0	9 58~4 01
16	1 979	15 0	5 0	9.12~3.39
18	2 033	12 5	5 0	8 28~3 04

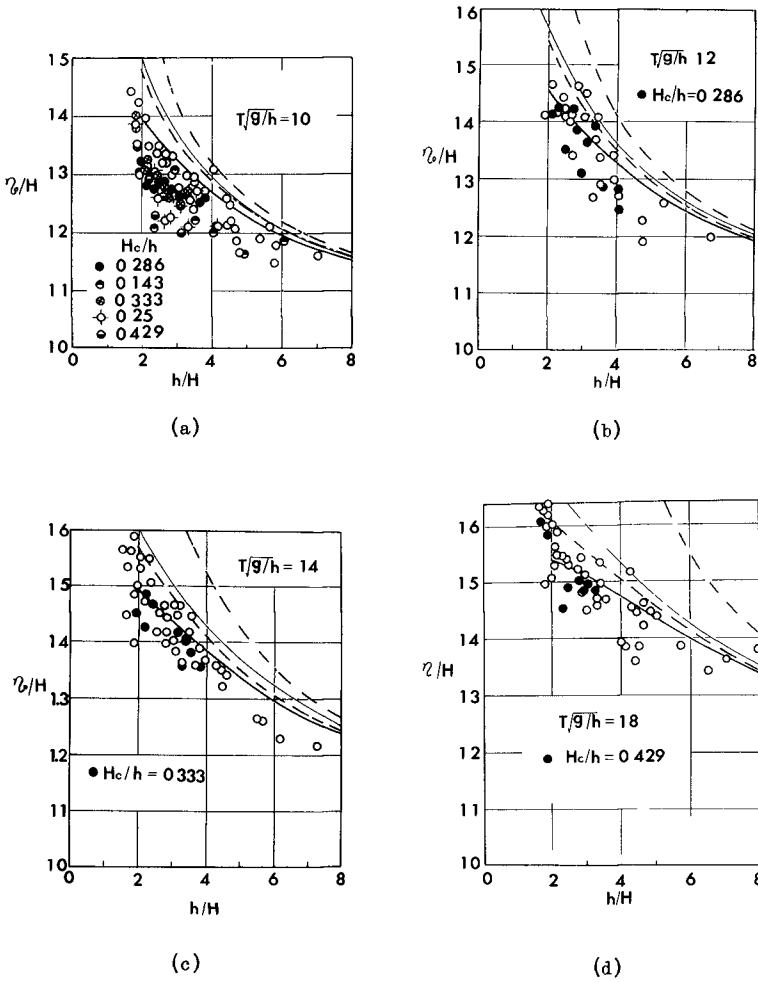
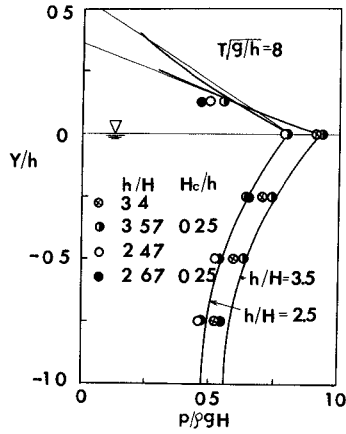
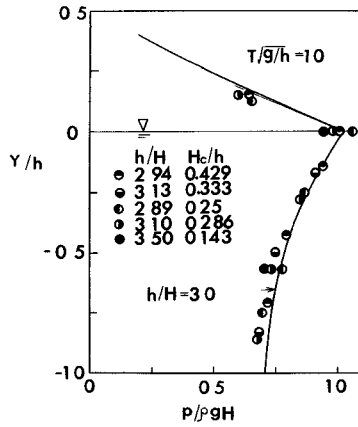


Fig 11 Comparison between theoretical curves and experimental results for wave crest height above still water level in the case where wave overtopping exists



(a)



(b)

Fig 12 Comparison between theoretical curves and experimental results for wave pressure distribution along wall at phase of wave crest in the case where wave overtopping exists

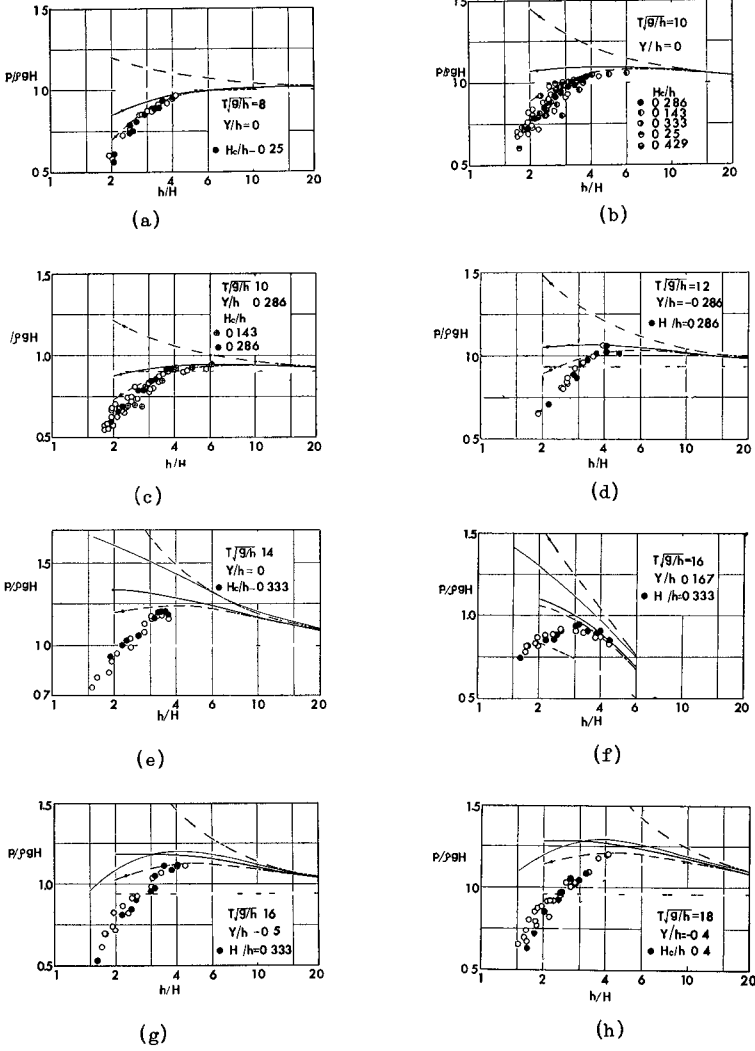
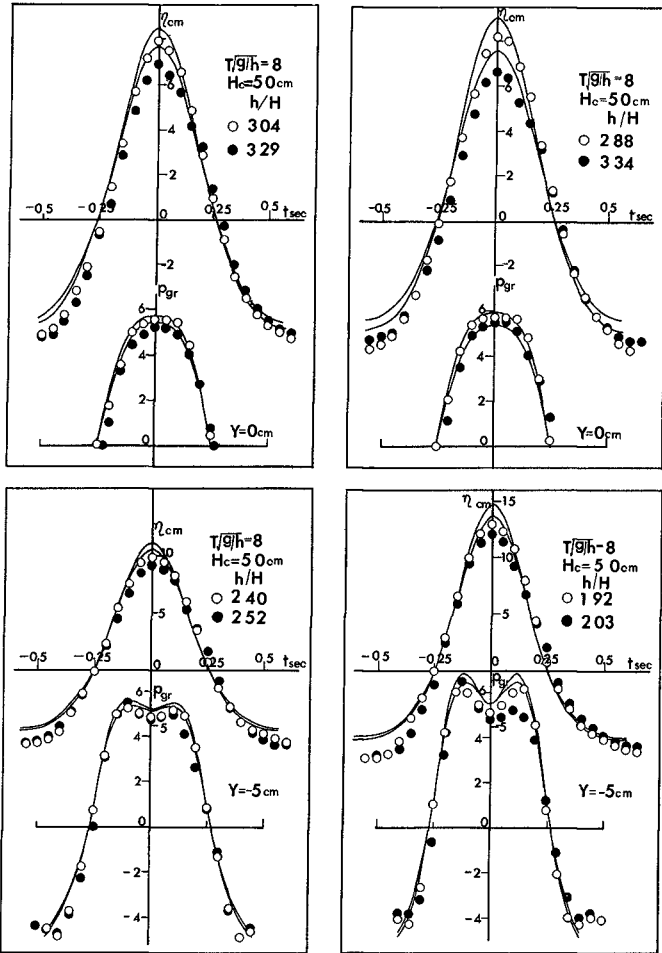
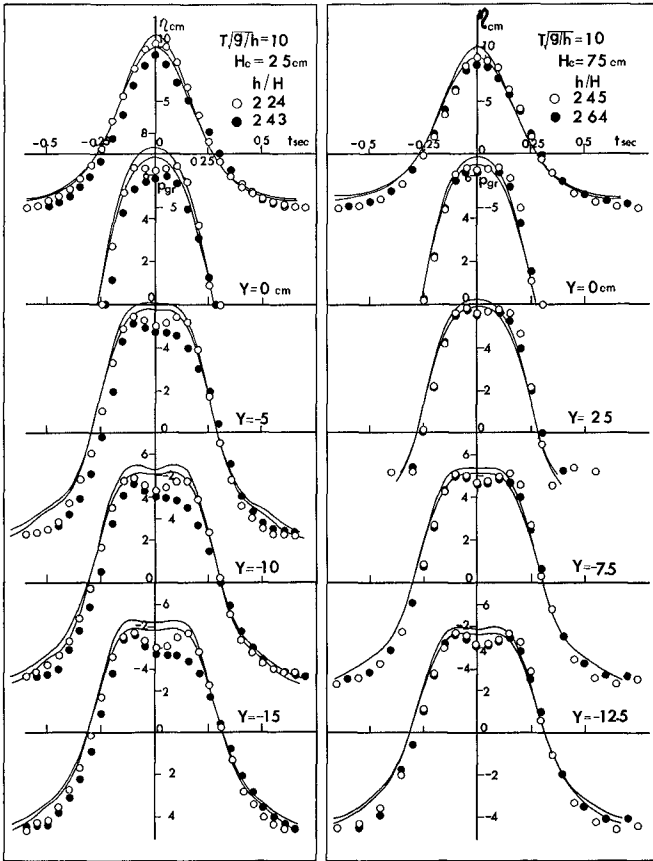


Fig 13 Comparison between theoretical curves of wave pressure at a point on wall at phase of wave crest and experimental results in the case where wave overtopping exists.



(a.)

Fig 14 Comparison between theoretical curves and experimental results for time variations of water level and wave pressure on wall in the case where wave overtopping exists



(b)

Fig 14 Comparison between theoretical curves and experimental results for time variations of water level and wave pressure on wall in the case where wave overtopping exists.

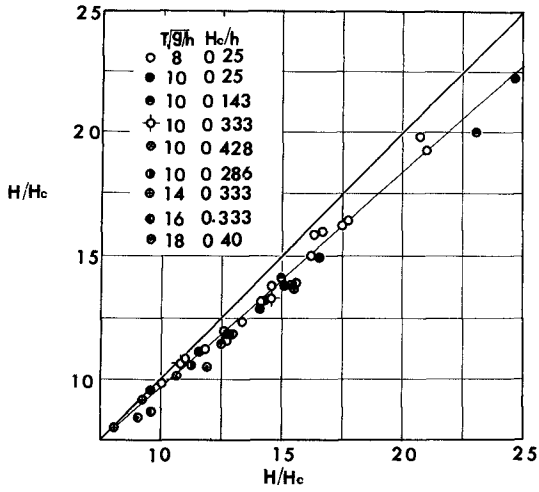


Fig 15 Relation between relative amplitude in water level at wall H/H_c and one for overtopping wave H/H_c

CHAPTER 33

A HIGHER ORDER THEORY FOR SYMMETRICAL GRAVITY WAVES

by Peter L. Monkmeyer
Professor of Civil Engineering
University of Wisconsin, Madison

ABSTRACT

A higher order theory is presented for symmetrical, non-linear gravity waves. As a consequence of the generality employed, the theory includes the full range of possible wave lengths, water depths and wave heights that may be encountered, and brings them into one unified formulation. Thus, the theory encompasses both linear and non-linear waves, including Airy waves, Stokes waves, cnoidal waves and the solitary wave.

Based on the work of Nekrasov, a complex potential in the form of an infinite series is developed to describe the flow field. The potential satisfies the bottom (horizontal) condition as well as the kinematic surface condition exactly. Furthermore, the dynamic surface condition is satisfied by numerical calculation of the series coefficients which appear in the complex potential. The calculation of these coefficients is accomplished by solving a set of non-linear algebraic equations, with the aid of a Newton-Raphson iteration procedure and matrix inversion.

Coefficients of the complex potential have been obtained for a fifth order analysis and preliminary results are presented in tabular form. A brief discussion of the characteristics of the waves, including wave speed, wave shape and the height of the highest possible wave follows.

INTRODUCTION

Water waves and their characteristics have received a great deal of attention by mathematicians, geophysicists and engineers over the past century and a half. In particular, numerous theories have been developed to describe the characteristics of symmetrical, periodic, progressive waves. Among the more classical papers are those by Stokes (1847, 1880), Rayleigh (1876), Boussinesq (1872), Korteweg and DeVries (1895), Levi-Civita (1925), and Struik (1926). Reviews of some of these works, as well as many more recent publications may be found in publications by Stoker (1957), Wiegel (1964), Kinsman (1965), Ippen (1966) and Neumann and Pierson (1966). No attempt will be made here to review the many recent contributions. However, of particular interest, especially for applications of the theory, are the works of Mash and Wiegel (1961), Skjelbreia and Hendrickson (1962), Laitone (1963) and Dean (1965).

The wealth of literature on the subject of periodic water waves reflects to some extent the lack of a unified approach. An effort to resolve this problem was made by Nekrasov (1951), followed

by Milne-Thomson (1969) and Thomas (1968) Nekrasov first formulated the wave problem in general terms, and concluded his analysis with a non-linear integral equation

The present study reexamines the work of Nekrasov and his successors and presents it in a manner which should be more useful in practice More specifically, a method is developed to compute coefficients which may be used to calculate the various characteristics of the waves

Since the theory presented herein is general, it covers the entire range of possible wave lengths, water depths and wave heights that may be encountered Thus it encompasses both linear and non-linear waves including Airy waves, Stokes waves, cnoidal waves and the solitary wave As a consequence it gives promise of simplifying the choice of the appropriate theory - a problem which currently faces the practitioner

SOLUTION OF THE WAVE PROBLEM

DEVELOPMENT OF THE THEORY

The wave theory which will be developed herein applies to progressive, symmetrical, gravity waves moving over the free surface of an inviscid, incompressible liquid, in an oscillatory manner Furthermore the waves are two-dimensional and, except for the special case of infinite depth, they move over a horizontal bottom No restriction is placed on liquid depth, D , wave length, L , or wave height, H Hence the theory is comprehensive and includes the full range of constant-profile waves, from Stokes waves to cnoidal waves and the solitary wave, as well as from small-amplitude waves to large-amplitude waves and the so-called "highest wave"

A train of oscillatory waves is moving from right to left over the surface of the liquid in question with wave speed, c By superimposing a uniform flow from left to right of the same speed as that of the waves, the wave profiles are brought to rest The net effect is to provide a steady flow from left to right, bounded by the fixed profile formed at the free surface and the impervious boundary at the bottom The steady flow-field will be seen to be considerably more amenable to study than would be the unsteady, progressive-wave field

In Fig 1 the steady wave is depicted and the more important constants are defined For convenience in the development the coordinates are described in complex terms and the physical plane is the z -plane, where z is the complex variable and x and y are the real and imaginary axes respectively The y -axis is chosen to pass through the crest of the wave, C , in order to assure symmetry The free surface is defined by $y_0 = y_0(x)$ and the still water level is located at $y = y_s$, a distance which remains to be determined It should be noted that the depth, d , usually defined as the distance from the still water level to the bottom will equal the sum of y_s and D

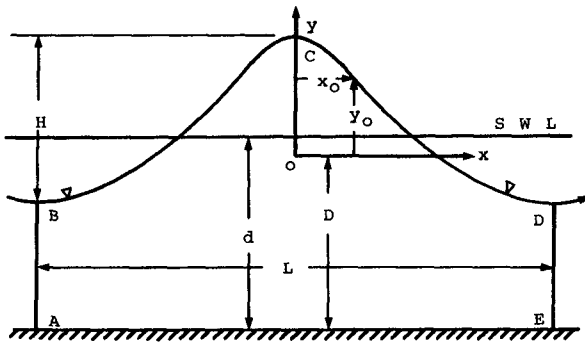


Fig 1 - The z -Plane

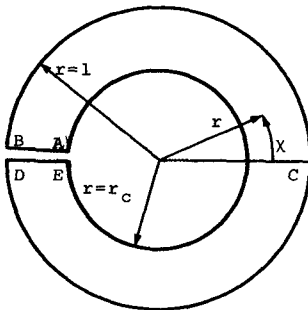


Fig 2 - The ζ -Plane

Since the flow is irrotational, an assumption which has been discussed by Stokes (1847), the complex potential is given by

$$w = \phi + i\psi \quad (1)$$

where ϕ is the potential function and ψ is the stream function. Furthermore, the complex potential is analytic and so the Cauchy-Riemann equations, which may be related to the velocity components, u and v , are given by

$$u = \frac{\partial \phi}{\partial x} = \frac{\partial \psi}{\partial y} \quad \text{and} \quad v = \frac{\partial \phi}{\partial y} = -\frac{\partial \psi}{\partial x} \quad (2)$$

Substitution of these expressions into the continuity and irrotational conditions results in Laplace's equation for each function,

$$\nabla^2 \phi = 0 \quad \nabla^2 \psi = 0 \quad (3)$$

respectively

At the free surface the kinematic boundary condition requires that the surface be a streamline. For convenience, this bounding streamline is defined as

$$\psi = 0 \quad \text{at } y = y_0 \quad (4)$$

The dynamic boundary condition at the free surface is expressed by the Bernoulli equation with pressure equal to zero,

$$q_0^2 + 2gy_0 = K_0 \quad \text{at } y = y_0 \quad (5)$$

where q_0 is the speed of a surface particle and K_0 is a constant (twice the so-called "Bernoulli constant")

The lower boundary condition is kinematic and requires that the horizontal bottom be a streamline. In order to reflect the volume rate of flow between the two bounding streamlines,

$$\psi = -cD \quad \text{at } y = -D \quad (6)$$

where " cD " equals the two-dimensional flow rate observed in the z -plane

Up to this point the relevant differential equations, together with the appropriate boundary conditions which describe the flow, have been presented. The two fundamental problems which immediately present themselves are that the location of the free surface is unknown and the dynamic boundary condition is non-linear. In order to deal with the first problem a conformal transformation will be employed. The purpose of this transformation is to redefine the problem in an auxiliary plane, the ζ -plane, where the location of the free surface is known.

The particular conformal transformation to be used, is an outgrowth of the work of Nekrasov (1951), as well as a subsequent

analysis by Milne-Thomson (1969) and Thomas (1968) More specifically, it is an extension and generalization of the special deep-water case considered by Monkmeyer and Kutzbach (1965) The transformation is given as follows

$$z = \frac{1L}{2\pi} \left[\ln(\zeta) + \frac{\pi}{2K} \sum_{j=1}^{\infty} \frac{a_j}{j} \exp\left\{i \operatorname{am}\left(\frac{-2jK}{\pi} \ln \zeta\right)\right\} \right] \quad (7)$$

where K is the complete elliptic integral of the first kind and the a_j 's are a set of real coefficients which are as yet unknown Moreover, ζ , which is the complex variable describing the coordinates of the ζ -plane is given in polar form by

$$\zeta = r \exp(i\chi) \quad (8)$$

where r is the radial coordinate and χ the angular coordinate of the ζ -plane as shown in Fig 2 Finally, $\operatorname{am}(\)$ is the amplitude of the elliptic integral of the first kind

One may verify, by application of the mapping function, Eq 7, that the region bounded by ABCDE in the z -plane is a mapping of the equivalent region inside the unit circle in the ζ -plane, subject only to the proper evaluation of the constant coefficients, a_j In fact it may be shown that the boundaries AB, DE and EA are mapped exactly from the z -plane to the ζ -plane, regardless of the values of the coefficients, a_j The boundaries AB and DE transform exactly as a consequence of the periodicity of the transformation The exact transformation of the lower boundary DE follows from the characteristics of the elliptic function, $\operatorname{am}(\)$ The choice of this particular conformal transformation was essentially dictated by the exact transformation of the bottom boundary As a by-product of the bottom transformation it is required that

$$\frac{K'}{K} = \frac{4D}{L} \quad (9)$$

where $K'(m) = K(1-m)$, and m is the parameter of the complete elliptic integral of the first kind This is a convenient formula since it permits a consideration of the entire range of waves for all wave lengths and depths In particular it facilitates inclusion of the two limiting cases, $L \rightarrow \infty$ and $D \rightarrow \infty$, since $K \rightarrow \infty$ in the first instance and $K' \rightarrow \infty$ in the second Eq 9 may therefore be used to convert Eq 7 and many of the following equations, if the limiting case of the solitary wave is of interest or if cnoidal waves are to be expressed in terms of depth rather than wave length

The transformation can also be applied to the boundary conditions, Eqs 4, 5 and 6, to generate the equivalent conditions in the ζ -plane,

$$\psi = 0 \quad \text{at } r = 1 \quad (10)$$

$$q_o^2 + 2gy_o = \kappa_o \quad \text{at } r = 1 \quad (11)$$

and

$$\psi = -cD \quad \text{at } r = r_c \quad (12)$$

where

$$r_c = \exp\left(-\frac{2\pi D}{L}\right) \quad (13)$$

The validity of these representations of the boundary conditions is verified in Fig 2. Moreover it should be noted that Eqs 10 and 12 are precisely the boundary conditions for a portion of a clockwise irrotational vortex in the ζ -plane, so that the complex potential for the flow in this plane may be written

$$w = \frac{1cL}{2\pi} \ln \zeta \quad (14)$$

By separating real and imaginary parts of this expression and rearranging terms,

$$\chi = -\frac{2\pi\phi}{cL} \quad (15)$$

and

$$r = \exp\left(\frac{2\pi\psi}{cL}\right) \quad (16)$$

It is therefore apparent that χ is a normalized form of the potential function and r is the exponential of the normalized stream function

To this point the physical problem in the z -plane has been transformed to one in the ζ -plane and two of the boundary conditions, Eqs 10 and 12, have been satisfied by the complex potential, Eq 14. It therefore remains to satisfy the dynamic surface condition, Eq 11, and this will be done by a proper choice of the coefficients in the conformal transformation. The remaining portion of this analysis is devoted to a method for calculating these coefficients so that the dynamic condition will be satisfied, approximately. The degree of approximation will depend on the truncation of the infinite series which makes up the conformal transformation. The greater the number of terms retained, the more nearly the dynamic condition will be satisfied.

Before proceeding to a calculation of the complex velocity, which will be needed in an examination of the Bernoulli condition on the free surface, it is necessary to substitute the complex potential in the ζ -plane, Eq 14, into the conformal transformation, Eq 7, in order to obtain the complex potential for the z -plane. The result may be regarded as the general wave equation,

$$z = \frac{w}{c} + \frac{1L}{4K} \sum_{j=1}^{\infty} \frac{a_j}{j} \exp\left[i \operatorname{am}\left(-\frac{4jK}{cL} w\right)\right] \quad (17)$$

For the limiting case of infinite depth, K approaches $\pi/2$ and $\operatorname{am}(\)$ approaches its argument. Therefore Eq 17 reduces to the deep-water equation,

$$z = \frac{w}{c} + \frac{1L}{2\pi} \sum_{j=1}^{\infty} \frac{a_j}{j} \exp\left[-i \frac{2j\pi}{cL} w\right] \quad (18)$$

On the other hand for the limiting case of infinite wave length, it should be noted that, after Eq 9 is introduced, K' approaches $\pi/2$ and $\text{am}(\)$ approaches $\text{gd}(\)$, the gudermannian. Therefore, Eq 17 reduces to the solitary wave equation,

$$z = \frac{w}{c} + \frac{12D}{\pi} \sum_{j=1}^{\infty} \frac{a_j}{j} \exp[1 \text{gd}(-\frac{j\pi}{2cD} w)] \quad (19)$$

Now along the free surface, $\psi = 0$, where we wish to apply the dynamic boundary condition, Eq 17 becomes

$$z_o = \frac{\phi}{c} + \frac{1L}{4K} \sum_{j=1}^{\infty} \frac{a_j}{j} \exp[1 \text{am}(-\frac{4jK}{cL} \phi)] \quad (20)$$

or in terms of the dimensionless potential function, χ ,

$$z_o = -\frac{L\chi}{2\pi} + \frac{1L}{4K} \sum_{j=1}^{\infty} \frac{a_j}{j} \exp[1 \text{am}(\frac{2jK}{\pi} \chi)] \quad (21)$$

Taking real and imaginary parts of Eq 21 one obtains

$$x_o = -\frac{L\chi}{2\pi} - \frac{L}{4K} \sum_{j=1}^{\infty} \frac{a_j}{j} \text{sn}(\frac{2jK}{\pi} \chi) \quad (22)$$

and

$$y_o = \frac{L}{4K} \sum_{j=1}^{\infty} \frac{a_j}{j} \text{cn}(\frac{2jK}{\pi} \chi) \quad (23)$$

where $\text{sn}(\)$ and $\text{cn}(\)$ are Jacobian elliptic functions. These two equations are parametrically related through χ to define the shape of the free surface. In order to make them somewhat more tractable, it is convenient to replace the elliptic functions by their expansions in sine and cosine series respectively (see Milne-Thomson (1950)). Eqs 22 and 23 therefore become

$$x_o = -\frac{L}{4K} \left(\frac{2K\chi}{\pi} + \sum_{j=1}^{\infty} \frac{b_j}{j} \sin j\chi \right) \quad (24)$$

and

$$y_o = \frac{L}{4K} \sum_{j=1}^{\infty} \frac{c_j}{j} \cos j\chi \quad (25)$$

where

$$b_j = \frac{2\pi}{m^{1/2} K} \sum_{k=1}^j \frac{\frac{1}{k} a_k q^{j/2k}}{(1-q^{j/k})} \quad (26)$$

and

$$c_j = \frac{2\pi}{m^{1/2} K} \sum_{k=1}^j \frac{\frac{1}{k} a_k q^{j/2k}}{(1+q^{j/k})} \quad (27)$$

where

$$k = j, \frac{j}{3}, \frac{j}{5}, \dots, 1$$

and only integer values of k are included in the summation, and where

$$q = \exp\left(-\pi \frac{K'}{K}\right) \quad (28)$$

For the limiting case of deep water waves

$$b_j = c_j = a_j \quad (29)$$

whereas for the limiting case of the solitary wave

$$b_j = \frac{4}{\pi} \sum_{k=1}^j a_k \quad (30)$$

and

$$Kc_j = \pi \sum_{k=1}^j \frac{1}{k} a_k \quad (31)$$

with k defined as for Eqs 26 and 27

In view of Eqs 24 and 25 it is now possible to reexpress the complex variable, z_o , that was given in Eq 21, as follows

$$z_o = \frac{1L}{2\pi} \left[\ln \zeta_o + \frac{\pi}{2K} \sum_{j=1}^{\infty} \left[\frac{c_j + b_j}{2} \zeta_o^j + \frac{c_j - b_j}{2} \zeta_o^{-j} \right] \right] \quad (32)$$

where, on the free surface, Eq 8 reduces to

$$\zeta_o = \exp(i\chi) \quad (33)$$

By differentiating Eq 32, the complex operator

$$\frac{dz_o}{d\zeta_o} = \frac{1L}{2\pi} \frac{f(\zeta_o)}{\zeta_o} \quad (34)$$

is obtained, where

$$f(\zeta_o) = \frac{\pi}{2K} \sum_{j=0}^{\infty} \left(\frac{c_j + b_j}{2} \zeta_o^j - \frac{c_j - b_j}{2} \zeta_o^{-j} \right) \quad (35)$$

$$= R_o \exp(i\theta_o), \text{ say} \quad (36)$$

and where

$$b_o = c_o = \frac{2K}{\pi} \quad (37)$$

Moreover, the modulus, R_o , of the function $f(\zeta_o)$ is given by

$$R_o^2 = \left[\frac{\pi}{2K} \sum_{j=0}^{\infty} b_j \cos j\chi \right]^2 + \left[\frac{\pi}{2K} \sum_{j=0}^{\infty} c_j \sin j\chi \right]^2 \quad (38)$$

and the argument, θ_o , of $f(\zeta_o)$ is given by

$$\theta_o = \cos^{-1} \left[\frac{\sum_{j=0}^{\infty} \frac{\pi}{2K} b_j \cos j\chi}{R_o} \right] \quad (39)$$

The above relations may now be employed, together with Eq 14, to derive an expression for the complex velocity, as follows

$$u_o - iv_o = \frac{dw}{dz_o} = \frac{dw}{d\zeta_o} \frac{d\zeta_o}{dz_o} = \frac{c}{f(\zeta_o)} = \frac{c}{R_o} \exp(-i\theta_o) \quad (40)$$

and therefore

$$u_o = \frac{c}{R_o} \cos \theta_o \quad \text{and} \quad v_o = \frac{c}{R_o} \sin \theta_o \quad (41)$$

and furthermore

$$q_o^2 = \frac{c^2}{R_o^2} \quad (42)$$

The dynamic free surface condition, Eq 11, may now be written

$$\frac{c^2}{R_o^2} + 2gy_o = K_o \quad (43)$$

an expression which was apparently first derived by Nekrasov (1951) who proceeded to derive a non-linear integral equation. In addition, with the aid of the following dimensionless terms

$$\begin{aligned} x'_o &\equiv \frac{4K}{L} x_o = \frac{K'}{D} x_o & y'_o &\equiv \frac{4K}{L} y_o = \frac{K'}{D} y_o \\ c' &\equiv \frac{c}{\sqrt{\frac{gL}{4K}}} = \frac{c}{\sqrt{\frac{gD}{K'}}} & \hat{K}_o &\equiv \frac{K_o}{\frac{gL}{4K}} = \frac{K_o}{\frac{gD}{K'}} \end{aligned} \quad (44)$$

Eq 43 becomes

$$c'^2 + 2y'_o R_o^2 = \hat{K}_o R_o^2 \quad (45)$$

where

$$y'_o = \sum_{j=1}^{\infty} \frac{c_j}{j} \cos j\chi \quad (46)$$

and, with the aid of trigonometric identities,

$$R_o^2 = \left(\frac{\pi}{2K}\right)^2 \left[D_o + 2 \sum_{j=1}^{\infty} D_j \cos j\chi \right] \quad (47)$$

where

$$D_o = b_o^2 + \sum_{k=1}^{\infty} \frac{b_k^2 + c_k^2}{2} \quad (48)$$

$$D_j = A_j + B_j + C_j \quad j = 1, 2, 3, 4 \quad (49)$$

$$A_j = \sum_{k=j}^{\infty} \frac{b_{k-j} b_k + c_{k-j} c_k}{2} \quad j = 1, 2, 3, 4 \quad (50)$$

$$B_j = \sum_{k=0}^{(j-1)/2} \frac{b_k b_{j-k} - c_k c_{j-k}}{2} \quad j = 1, 2, 3, 4 \quad (51)$$

and

$$C_j = \frac{1}{4} (b_{j/2}^2 - c_{j/2}^2) \quad \text{for } j = 2, 4, 6, 8 \quad (52)$$

$$= 0 \quad \text{for } j = 1, 3, 5, 7$$

By substituting Eqs 46 and 47 into Eq 45, the problem of the general symmetrical wave of finite amplitude is reduced to one of finding the solution to the equation,

$$c'^2 + 2 \left[\left(\sum_{j=1}^{\infty} \frac{c_j}{j} \cos j\chi \right) - \frac{k_0}{2} \right] \left[\left(\frac{\pi}{2K} \right)^2 (D_0 + 2 \sum_{j=1}^{\infty} (A_j + B_j + C_j) \cos j\chi) \right] = 0 \quad (53)$$

It is of interest to note that to this point no approximations have been made. Therefore Eq 53 is an exact representation of the problem.

In order to solve Eq 53 for a finite number of coefficients, it will be necessary to truncate the infinite trigonometric series which appear in the equation. Therefore Eqs 46, 47, 48 and 50 become

$$y'_0 \approx \sum_{j=1}^n \frac{c_j}{j} \cos j\chi \quad (54)$$

$$R_0^2 \approx \left(\frac{\pi}{2K} \right)^2 \left[D_0 + 2 \sum_{j=1}^n D_j \cos j\chi \right] \quad (55)$$

$$D_0 \approx b_0^2 + \sum_{k=1}^n \frac{b_k^2 + c_k^2}{2} \quad (56)$$

$$A_j \approx \sum_{k=j}^n \frac{b_{k-j} b_k + c_{k-j} c_k}{2} \quad j = 1, 2, 3, 4 \quad n \quad (57)$$

Furthermore, by combining and expanding these equations, one obtains

$$y'_0 R_0^2 \approx \left(\frac{\pi}{2K} \right)^2 \left[\sum_{k=1}^n \frac{c_k}{k} D_k + \sum_{j=1}^n \sum_{k=1}^n \frac{c_k}{k} (D_{k-j} + D_{k+j}) \cos j\chi \right] \quad (58)$$

where absolute value signs are omitted on the subscripts of D_{k-j} , and furthermore, $D_k = 0$ if $|k| > n$. Since harmonics higher than the n th have been omitted, Eq 58 is not exact.

The expressions for R^2 , Eq 55, and $y' R^2$, Eq 58, may now be substituted into Eq 45. By equating the coefficients of the harmonics, one obtains

$$c'^2 + 2 \left(\frac{\pi}{2K}\right)^2 \sum_{k=1}^n \frac{c_k}{k} D_k = \hat{K}_0 \left(\frac{\pi}{2K}\right)^2 D_0 \quad (0\text{th harmonic}) \quad (59)$$

$$\sum_{k=1}^n \frac{c_k}{k} (D_{k-j} + D_{k+j}) = \hat{K}_0 D_j \quad (j\text{th harmonic}, j=1,2,3 \dots n) \quad (60)$$

where absolute value signs are omitted on the subscripts of D_{k-j} , and furthermore D_k vanishes if $|k| > n$

Since the unknown terms in Eqs 59 and 60 are all functions of the height of the wave, it is appropriate to add an equation for wave height. The wave height is seen to be equal to the sum of the displacements of the crest and trough from the x-axis. Therefore, using Eqs 23 and 9,

$$H = (y_0)_{x=0} + (-y_0)_{x=\pi} = \frac{L}{2K} \sum_{j=1}^n \frac{a_j}{j} = \frac{2D}{K'} \sum_{j=1}^n \frac{a_j}{j} \quad (61)$$

$j = 1, 3, 5, 7$

and in dimensionless form,

$$H' = 2 \sum_{j=1}^n \frac{a_j}{j} \quad j = 1, 3, 5, 7 \quad (62)$$

Eqs 59, 60 and 62 are therefore seen to constitute a set of $(n+2)$ equations in $(n+2)$ unknowns $(c', \hat{K}_0, a_1, a_2, a_3 \dots a_n)$ for any desired value of the dimensionless wave height, H' .

COMPUTER SOLUTION

In setting up the equations for computer solution, the coefficient, \hat{K}_0 , is eliminated between the first of Eqs 60 ($j=1$) and each succeeding equation ($j=2, 3 \dots n$), thereby reducing Eqs 60 to $(n-1)$ equations in $(n-1)$ unknowns $(a_1, a_2, \dots, a_{n-1})$ for a fixed value of a_n . After the unknown coefficients are assumed, the simultaneous solution of these $(n-1)$ non-linear equations is accomplished with the aid of a Newton-Raphson iteration. By this technique the problem is reduced to one of obtaining the solution of a set of $(n-1)$ linear equations at each iteration. The matrix is then inverted using triangular decomposition and a solution of the set of equations is obtained for corrections on the assumed values of a_1, a_2, a_{n-2} and a_{n-1} . The entire procedure is repeated until the corrections are small enough to be neglected. After the coefficients have been computed, Eqs 61, 60 (first harmonic) and 59 are solved to yield H', \hat{K}_0 and c' respectively. The entire procedure is repeated iteratively until the coefficients \hat{K}_0 and c' are evaluated for uniform-interval values of H/L , which are appropriate for tabular presentation.

Computations were made on the University of Wisconsin UNIVAC 1108 computer. A fifth order solution was undertaken and some preliminary results are shown in Tables 1 and 2. In these tables the dimensionless wave height, H/L , is calculated correct to ± 0.00001 , while all other terms appearing in the tables were computed correct to at least the last place shown. It should be noted that this precision is significant for the lower values of wave height where the convergence of the a_j series is rapid and a fifth order solution is sufficient. As the wave height increases, however, the truncation of the trigonometric series which replace the elliptic functions as well as the omission of higher harmonics in the development of $(y' R_o^2)$, result in a less accurate satisfaction of Eq. 53. As a consequence the dynamic boundary condition, Eq. 5, is only satisfied approximately. By developing higher order solutions, greater than the fifth order solution considered here, the accuracy can be improved.

DISCUSSION

No specific attempt will be made at this point to compare the new theory with those which exist. The primary objective at the present is to develop the method of solution and to prepare sample tables of the coefficients.

Nevertheless it is already possible to indicate some agreement with the existing theories. In an earlier paper, Monkmeyer and Kutzbach (1965) compare the theory with that of Stokes (1880) to reveal that the basic equation for deep water, Eq. 18, is common to both theories. Stokes was, of course, limited in his ability to carry out computations to higher orders, and so restricted his attention to the well-known fifth-order theory. The success of this theory in deep water has been the prime stimulus for using a fifth order approach in the present work. Following Stokes, Wilton (1914) developed a twelfth order solution for deep water waves and Monkmeyer and Kutzbach (1965) developed a fifteenth order solution. These higher order computations resulted in little deviation from the fifth and third order theories, especially in the prediction of wave speed. Only in wave shape did the fifteenth order theory diverge from the lower order theories, as might be expected.

Wave speed may be computed with the aid of Eq. 59. However, since this equation demands considerable computation, a more convenient approach is to print out the wave speed together with the wave coefficients as shown in Tables 1 and 2. The wave speeds obtained in Table 1 show excellent agreement with those of Stokes' third and fifth order theories for deep water waves (see Monkmeyer and Kutzbach, 1965).

In order to describe the wave shape or profile of a wave, one may choose to use the parametric set of equations,

$$x_o = \frac{LX}{2\pi} - \frac{L}{4K} \sum_{j=1}^n \frac{a_j}{j} \operatorname{sn}\left(\frac{2jK}{\pi} \chi\right) \quad (22)$$

Table 1

FIFTH ORDER WAVE COEFFICIENTS

L/D = .00000

H/L	H/D	C'	\hat{K}_0	A(1) B(1) C(1)	A(2) B(2) C(2)	A(3) B(3) C(3)	A(4) B(4) C(4)	A(5) B(5) C(5)
.140	.000	1.1063	1.3825	.33811 .33811 .33811	.25489 .25489 .25489	.21308 .21308 .21308	.18215 .18215 .18215	.15343 .15343 .15343
.130	.000	1.0900	1.3304	.32414 .32414 .32414	.23004 .23004 .23004	.18174 .18174 .18174	.14753 .14753 .14753	.11848 .11848 .11848
.120	.000	1.0756	1.2816	.30833 .30833 .30833	.20519 .20519 .20519	.15253 .15253 .15253	.11702 .11702 .11702	.08910 .08910 .08910
.110	.000	1.0628	1.2366	.29086 .29086 .29086	.18038 .18038 .18038	.12534 .12534 .12534	.09024 .09024 .09024	.06467 .06467 .06467
.100	.000	1.0513	1.1954	.27177 .27177 .27177	.15575 .15575 .15575	.10026 .10026 .10026	.06712 .06712 .06712	.04487 .04487 .04487
.090	.000	1.0412	1.1582	.25101 .25101 .25101	.13154 .13154 .13154	.07756 .07756 .07756	.04772 .04772 .04772	.02943 .02943 .02943
.080	.000	1.0323	1.1250	.22855 .22855 .22855	.10806 .10806 .10806	.05755 .05755 .05755	.03207 .03207 .03207	.01799 .01799 .01799
.070	.000	1.0246	1.0958	.20440 .20440 .20440	.08573 .08573 .08573	.04051 .04051 .04051	.02009 .02009 .02009	.01006 .01006 .01006
.060	.000	1.0180	1.0705	.17861 .17861 .17861	.06500 .06500 .06500	.02665 .02665 .02665	.01149 .01149 .01149	.00502 .00502 .00502
.050	.000	1.0124	1.0491	.15131 .15131 .15131	.04638 .04638 .04638	.01601 .01601 .01601	.00582 .00582 .00582	.00215 .00215 .00215
.040	.000	1.0079	1.0315	.12270 .12270 .12270	.03035 .03035 .03035	.00846 .00846 .00846	.00248 .00248 .00248	.00074 .00074 .00074
.030	.000	1.0045	1.0177	.09299 .09299 .09299	.01737 .01737 .01737	.00365 .00365 .00365	.00081 .00081 .00081	.00018 .00018 .00018
.020	.000	1.0020	1.0079	.06246 .06246 .06246	.00782 .00782 .00782	.00110 .00110 .00110	.00016 .00016 .00016	.00002 .00002 .00002
.010	.000	1.0005	1.0020	.03137 .03137 .03137	.00197 .00197 .00197	.00014 .00014 .00014	.00001 .00001 .00001	.00000 .00000 .00000

VALUES OF THE COMPLETE ELLIPTIC INTEGRAL OF THE FIRST KIND

$k = 1.5707963$ $k' = \text{INF.}$ $M = .0000000$ $K'/K = \text{INF.}$

Table 2

FIFTH ORDER WAVE COEFFICIENTS

L/D = 2.00000

H/L	H/D	C'	λ K_0	A(1) B(1) C(1)	A(2) B(2) C(2)	A(3) B(3) C(3)	A(4) B(4) C(4)	A(5) B(5) C(5)
.140	.280	1.1090	1.3908	.34108 .34172 .34044	.25736 .25784 .25688	.21331 .21562 .21482	.18393 .18427 .18358	.15467 .15496 .15438
.130	.260	1.0926	1.3381	.32696 .32757 .32635	.23229 .23273 .23186	.18179 .18396 .18328	.14906 .14934 .14878	.11954 .11977 .11932
.120	.240	1.0781	1.2888	.31101 .31159 .31043	.20722 .20761 .20683	.15243 .15445 .15388	.11830 .11852 .11808	.08997 .09014 .08981
.110	.220	1.0652	1.2433	.29340 .29394 .29285	.18219 .18253 .18185	.12508 .12696 .12649	.09128 .09145 .09111	.06536 .06549 .06525
.100	.200	1.0537	1.2016	.27415 .27466 .27363	.15734 .15763 .15704	.09986 .10159 .10121	.06793 .06806 .06781	.04540 .04548 .04532
.090	.180	1.0434	1.1639	.25322 .25369 .25275	.13290 .13314 .13265	.07705 .07861 .07832	.04833 .04842 .04824	.02979 .02985 .02974
.080	.160	1.0344	1.1304	.23058 .23101 .23015	.10919 .10940 .10899	.05695 .05834 .05813	.03250 .03256 .03244	.01823 .01826 .01820
.070	.140	1.0266	1.1008	.20623 .20662 .20585	.08664 .08680 .08648	.03986 .04109 .04094	.02036 .02040 .02033	.01020 .01023 .01019
.060	.120	1.0200	1.0752	.18023 .18056 .17989	.06570 .06583 .06558	.02598 .02704 .02694	.01165 .01167 .01163	.00510 .00511 .00509
.050	.100	1.0144	1.0534	.15269 .15298 .15241	.04688 .04697 .04680	.01536 .01625 .01619	.00590 .00591 .00589	.00218 .00219 .00218
.040	.080	1.0099	1.0356	.12383 .12406 .12360	.03069 .03075 .03063	.00787 .00858 .00855	.00252 .00252 .00251	.00075 .00076 .00075
.030	.060	1.0064	1.0217	.09386 .09403 .09368	.01757 .01760 .01753	.00318 .00371 .00370	.00082 .00082 .00082	.00019 .00019 .00019
.020	.040	1.0039	1.0117	.06304 .06316 .06292	.00791 .00792 .00789	.00076 .00112 .00112	.00017 .00017 .00017	.00002 .00003 .00003

VALUES OF THE COMPLETE ELLIPTIC INTEGRAL OF THE FIRST KIND

K= 1.5825517 K'= 3.1651034 M= .0294372 K'/K= 2.0000000

$$y_o = \frac{L}{4K} \sum_{j=1}^n \frac{a_j}{j} \operatorname{cn}\left(\frac{2jK}{\pi}\chi\right) \tag{23}$$

or to avoid the elliptic functions, but at the expense of some accuracy,

$$x_o = -\frac{L\chi}{2\pi} - \frac{L}{4K} \sum_{j=1}^n \frac{b_j}{j} \sin j\chi \tag{24}$$

$$y_o = \frac{L}{4K} \sum_{j=1}^n \frac{c_j}{j} \cos j\chi \tag{25}$$

Numerical values relating x_o and y_o may be obtained by substituting arbitrary values of the normalized potential function, χ . This procedure is adequate for a graphical presentation of the wave shape. Stokes (1880) suggests that, with the aid of Lagrange's theorem (Whittaker and Watson, 1963), the two equations may be reduced to one.

It should be observed that the depth, D , differs from the depth to stillwater, d , by the elevation of the stillwater level, y_s (see Fig 1). The computation of y_s , and therefore, d , may be accomplished by noting that the net area bounded by the free surface and the stillwater level vanishes. Therefore

$$0 = \int_0^{L/2} (y_o - y_s) dx_o \tag{63}$$

By substituting the parametric profile expressions, Eqs 24 and 25, the equation may be solved for the dimensionless stillwater elevation

$$y'_s = \frac{\pi^2}{4K} \sum_{k=1}^n \frac{b_k c_k}{k} \tag{64}$$

Sample profiles for deep water waves are presented by Monkmeyer and Kutzbach

In order to study the characteristics of the highest possible wave it will be necessary to add one further restriction to those imposed by Eqs 59, 60 and 61. This restriction, which was first suggested by Stokes, affects the Bernoulli equation which describes the dynamic upper boundary condition. In effect Stokes suggests that for a fluid particle on the surface to reach the highest possible point above the surface, the wave crest, it must give up all of its kinetic energy. Hence at this point it has no velocity and the crest is a stagnation point. The dynamic boundary condition, Eq 45, therefore reduces to

$$2y_o' = \hat{k}_o \quad \text{at } r = 1, \chi = 0 \tag{65}$$

or substituting for y_o' with the aid of Eq 23

$$2 \sum_{k=1}^n \frac{a_k}{k} = \hat{k}_o \tag{66}$$

Since this equation adds no new unknowns to those already appearing in Eqs 59, 60 and 62 its inclusion results in a set of $(n + 3)$ equations with $(n + 3)$ unknowns, H' no longer being arbitrary but now considered as an unknown

For the deep water case using the fifteenth order theory Monkmeier and Kutzbach show that

$$(H/L)_{\max} = 0.1442$$

This compares well with Michell's (1893) result of

$$(H/L)_{\max} = 0.142$$

and Havelock's (1919) conclusion that

$$(H/L)_{\max} = 0.1418$$

No precise computations of the highest wave have been made for the finite waves considered herein. However, Eq 57 has been used to determine whether or not the wave data obtained in the preliminary computations includes waves that exceed the highest. This check showed for example that for $L/D = 6.0$, the maximum wave lies between $H/L = 1.3$ and 1.4 , which is in good agreement with the breaking index curve of Reid and Bretschneider (1953).

CONCLUSION

A higher order wave theory has been developed for the full range of waves from Stokes waves to cnoidal waves to the solitary wave and from small amplitude waves to finite amplitude waves and the "highest wave". By means of a conformal transformation the problem is reduced to obtaining a solution to a non-linear set of equations. Solutions of these equations using a high speed digital machine have been obtained to fifth order for L/D values of 0.0, 2.0, 4.0 and 6.0, and samples of this data are presented in tabular form.

A consideration of some preliminary results as well as earlier results of the deep water case, suggest that the theory is in good agreement with existing theories. Furthermore, it appears that this theory may provide a comprehensive practical means for wave analysis of the full-range of symmetrical waves from deep-water to shallow-water.

ACKNOWLEDGEMENTS

The derivation of the basic theory was completed while the writer was a guest researcher at the River and Harbor Laboratory of the Technical University of Norway, Trondheim, Norway. In particular the writer wishes to thank Director H. Berge and Dr. T. Carstens for providing him with the opportunity to complete the theoretical analysis.

Also, this research was supported in part by the National Science Foundation and the State of Wisconsin under the University of Wisconsin Sea Grant Program.

REFERENCES

- Airy, G B (1845) Tides and waves Encyclop Metropol, London
- Boussinesq, J (1872) Theorie des onde et de remous qui se propagent le long d'un canal rectangulaire horizontal, en communiquant au liquide contenu dans ce canal des vitesses sensiblement pareilles de la surface au fond, J Math Pures Appliquees, ser 2, vol 17, pp 55-108
- Dean, R G (1965) Stream function wave theory validity and application Proceedings - A S C E Coastal Engineering Conference, Santa Barbara, 1965, pp 269-300
- Havelock, T H (1919) Periodic irrotational waves of finite height Proc Roy Soc London, ser A, vol 95, pp 38-51
- Ippen, A T (1966) Estuary and coastline hydrodynamics McGraw-Hill Book Co, New York
- Kinsman, B (1965) Wind waves Prentice-Hall, Inc, Englewood Cliffs, N J
- Korteweg, D J and G DeVries (1895) On the change of form of long waves advancing in a rectangular canal and on a new type of long stationary waves Phil Mag, 5th ser, vol 39, pp 422-443
- Laitone, E V (1963) Higher approximation to nonlinear water waves and the limiting heights of cnoidal, solitary and Stokes' waves Technical Memorandum No 133, Beach Erosion Board, Corps of Engineers, U S Army (now Coastal Engineering Research Center)
- Levi-Civita, T (1925) Determination rigoureuse des ondes d'ampleur finie Math Annalen, vol 93, pp 264-314
- Mash, F D and R L Wiegel (1961) Cnoidal waves-Tables of functions Council on Wave Research, The Engineering Foundation, University of California, Richmond, California
- Michell, J H (1893) On the highest waves in water Phil Mag, ser 5, vol 36, pp 430-437
- Milne-Thomson, L M (1969) Theoretical hydrodynamics Fifth edition, Macmillan Co, New York, pp 428-435
- Milne-Thomson, L M (1950) Jacobian elliptic function tables Dover Publications, Inc, p 13
- Monkmeyer, P L and J E Kutzbach (1965) A higher order theory for deep water waves Proceedings - A S C E Coastal Engineering Conference, Santa Barbara
- Nekrasov, A I (1951) The exact theory of steady waves on the surface of a heavy fluid Izdat Akad Nauk, SSSR, Moscow, Mathematical Reviews 15 (1965), 654 (translated by Math Res Ctr U S Army, Univ of Wis)
- Neumann, G and W J Pierson, Jr (1966) Principles of Physical Oceanography Prentice-Hall, Inc, Englewood Cliffs, N J
- Rayleigh, Lord, (1876) On waves Phil Mag, ser 5, vol 1, pp 257-279, also Scientific Papers, vol 1, Cambridge University Press, 1899, pp 252-271
- Reid, R O and C L Bretschneider (1953) Surface waves and offshore structures, Texas A M Research Foundation, Technical Report, October
- Skjelbreia, L and J A Hendrickson (1962) Fifth order gravity wave theory with table of functions National Engineering Science Co, Pasadena, Calif
- Stoker, J J (1957) Water waves Interscience Publishers, Inc, New York

- Stokes, G G (1847) On the theory of oscillatory waves Trans Camb Phil Soc, vol 8, p 441, also Mathematical and Physical Papers, vol 1, Cambridge University Press, 1880, pp 197-229
- Stokes, G G (1880) Supplement to a paper on the theory of oscillatory waves Mathematical and Physical Papers, vol 1, Cambridge University Press, pp 314-326
- Struik, D J (1926) Determination rigoureuse des ondes irrotationnelles periodiques dans un canal a profondeur finie Mathematische Annalen, vol 95, pp 595-634
- Thomas, J W (1968) Irrotational gravity waves of finite height a numerical study Mathematika, vol 15, part 2, Dec, pp 139-148
- Whittaker, E T and Watson, G N (1963) A course of modern analysis 4th edition, Cambridge University Press, Cambridge
- Wiegel, R L (1964) Oceanographical engineering Prentice-Hall, Inc, Englewood Cliffs, N J
- Wilton, J R (1914) On deep water waves Phil Mag, ser 6, vol 27, pp 385-394

APPENDIX - NOTATION

- A] see Eq 50
- a] coefficient of the jth harmonic - see Eq 7
- am() amplitude of the elliptic integral of the first kind
- B] see Eq 51
- b] coefficient - see Eq 26
- C] see Eq 52
- c] wave speed
- c'] the dimensionless wave speed - see Eq 44
- c] coefficient - see Eq 27
- cn() Jacobian elliptic function
- D] depth measured from the origin
- D_j] see Eqs 48 and 49
- d] depth measured from stillwater
- f(ξ)] see Eq 35
- g] acceleration due to gravity
- gd()] gudermannian
- H] wave height
- H'] dimensionless wave height - see Eq 62
- i] $\sqrt{-1}$
- j] integer which identifies the jth harmonic - see Eq 8
- K] complete elliptic integral of the first kind (parameter - m)
- K'] complete elliptic integral of the first kind ($K'(m) = K(1-m)$)
- K₀] Bernoulli constant for free surface streamline
- K₀] see Eq 44
- k] integer which identifies the kth harmonic
- L] wave length
- l] integer which identifies the lth harmonic
- m] parameter of the complete elliptic integral of the first kind, K

n	integer which identifies the highest harmonic and the order of the analysis
q_0	magnitude of the particle velocity at the free surface
R_0	modulus of $f(\zeta_0)$ - see Eq 38, also = c/q_0
r	radial coordinate in the ζ -plane
r_c	radius of AE in the ζ -plane
$sn(\)$	Jacobian elliptic function
u	x-component of the particle velocity
u_0	x-component of the particle velocity at the free surface
v	y-component of the particle velocity
v_0	y-component of the particle velocity at the free surface
w	complex potential $\equiv \phi + iy$
x	horizontal coordinate in the z-plane
x'	dimensionless horizontal coordinate
x_0	horizontal free surface coordinate in the z-plane
x'_0	dimensionless horizontal free surface coordinate
y	vertical coordinate in the z-plane
y'	dimensionless vertical coordinate
y_0	vertical free surface coordinate in the z-plane
y'_0	dimensionless vertical free surface coordinate
y_s	still water elevation in the z-plane
y'_s	dimensionless still water elevation
z	$\equiv x + iy$ and refers to the physical plane
z_0	complex variable at the free surface
ζ	$\equiv r \exp(i\chi)$ and refers to the auxiliary plane
ζ_0	$= \exp(i\chi)$, or ζ at the free surface
θ_0	argument of $f(\zeta_0)$ - see Eq 39, also local slope angle of the free surface in the z-plane
π	$\equiv 3.1415927$
ϕ	potential function
χ	tangential coordinate in the ζ -plane, also a normalized form of the potential function
ψ	stream function

CHAPTER 34

ANALYTICAL APPROACH ON WAVE OVERTOPPING ON LEVEES

Hiroyoshi Shi-igai, Dr Eng ,M Eng ,M of JSCE.*

Tsugio Kono, B Eng ,M of JSCE**

1 Analytical Approach

An analytical approach to evaluate the amount of overtopping for given conditions is studied in this paper. Here, the wave overtopping is considered as a similar phenomenon to the flow over a weir changing the depth with respect to time.

The theoretical approaches used by many scholars have been mostly based on the dimensional analysis. In this paper, however, another kind of approach is tried, which is rather deterministic, in order to get a general view of wave overtopping mechanism.

The well-known formula which expresses the discharge over a sharp-edged weir is as follows:

$$q = \frac{2}{3} m \sqrt{2g} y^{\frac{3}{2}} \quad (1)$$

where q is the discharge per unit width, m is the discharge coefficient and y is the overflow depth. It is usually admitted that Eq (1) is valid only for steady flow. However, if we assume that y does not change very rapidly with respect to time, Eq (1) may be used for the analysis of wave overtopping. Writing that

$$y = z(t) - z_0 \quad (2)$$

* Associate Professor, Asian Institute of Technology, Bangkok, Thailand

** Research Associate, Department of Civil Engineering, Tokyo Institute of Technology, Tokyo, Japan

where $z(t)$ is the surface elevation of waves over the levee measured from SWL, and z_0 is the elevation of the top of the levee, we can obtain the quasi-steady equation for the overtopping discharge

$$q(t) = \frac{2}{3} m \sqrt{2g} (z(t) - z_0)^{\frac{3}{2}} \quad (3)$$

Further, we write $z(t)$ as

$$z(t) = z_m F(t) \quad (4)$$

where $F(t)$ is a non-dimensional function of time which expresses the wave profile at the levee z_m is approximately equal to the wave run-up height but not the same one, because normally wave run-up height R is measured without any overtopping. If there is overtopping, the reflection rate must change and R and z_m cannot be of the same value.

Using Eq (2), Eq.(3) and Eq (4), we obtain.

$$q = \frac{2}{3} m \sqrt{2g} (kH_0)^{\frac{3}{2}} \left\{ F(t) - \frac{z_0}{kH_0} \right\}^{\frac{3}{2}} \quad \text{for } F(t) \geq \frac{z_0}{z_m} \quad (5)$$

$$q = 0 \quad \text{for } F(t) < \frac{z_0}{z_m}$$

where k is defined as:

$$k = z_m / H_0 \quad (6)$$

If m and k are constant for a wave period, we integrate q with respect to time

$$Q = \int_{t_1}^{t_2} q dt$$

$$= \frac{2}{3} m \sqrt{2g} (kH_0)^{\frac{3}{2}} \int_{t_1}^{t_2} \left\{ F(t) - \frac{z_0}{kH_0} \right\}^{\frac{3}{2}} dt \quad (7)$$

where $F(t) > \frac{z_o}{kH_o}$ for $t_1 < t < t_2$ Q is the total discharge of overtopping for a period per unit width of the weir Eq (7) can be expressed as a non-dimensional form, which is

$$\frac{Q}{TH_o\sqrt{2gH_o}} = \frac{2}{3} \frac{mk^{\frac{3}{2}}}{T} \int_{t_1}^{t_2} \left\{ F(t) - \frac{z_o}{kH_o} \right\}^{\frac{3}{2}} dt \tag{8}$$

where T is the wave period The left hand side is a kind of Froude Number Fig 1 and Fig 2 show the schematic diagrams for the definitions Eq (8) may be simplified if the wave profile can be approximated by triangular waves

$$\frac{Q}{TH_o\sqrt{2gH_o}} = \frac{2}{15} mk^{\frac{3}{2}} \left(1 - \frac{z_o}{kH_o} \right)^{\frac{5}{2}} \tag{9}$$

For sinous waves we obtain Eq.(10)

$$\frac{Q}{TH_o\sqrt{2gH_o}} = \frac{4}{3} mk^{\frac{3}{2}} \frac{1}{T} \int_{t_1}^{\frac{T}{4}} \left\{ \sin \frac{2\pi}{T} t - \frac{z_o}{kH_o} \right\}^{\frac{3}{2}} dt \tag{10}$$

where $t_1 = \frac{T}{2\pi} \sin^{-1} \frac{z_o}{kH_o}$

Though Eq (9) looks very simple, it gives us fairly good results as is shown Fig 3, if we choose the value of k carefully, while the value of k is affected by so many factors Fig 4 shows the variation of k with respect to H_o/L and α , the slope of levees The value of k is much less than the value of R/H_o , which is for the case without overtopping, while both of them take the maximum value at $\tan \alpha \approx 0.35$

Eq (9) may be arranged to ^{the} conventional form obtained through dimensional analysis as follows

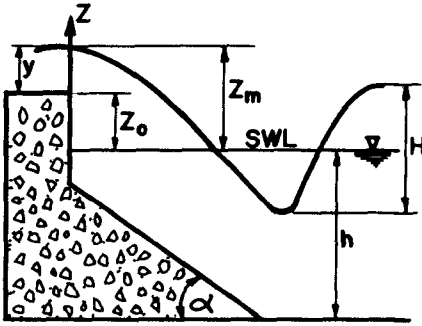


Fig 1 Definition sketch (1)

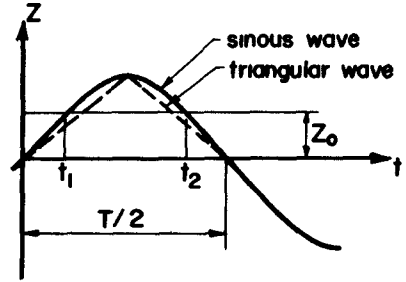


Fig 2 Definition sketch (2)

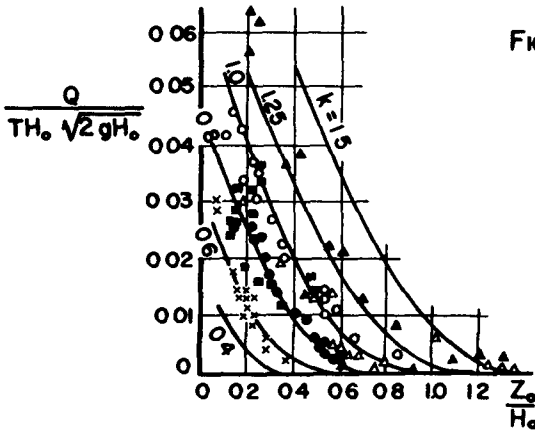


Fig 3 Eq (9) and experimental data

RUN	α, S	Note
x	1	90°
o	2	30°
•	3	30°, 90°
▲	4	1/10, 1/3 * ,wind
△	5	1/10, 1/6 * ,wind
■	6	1/6 **

* done by B E B
** done by W E S

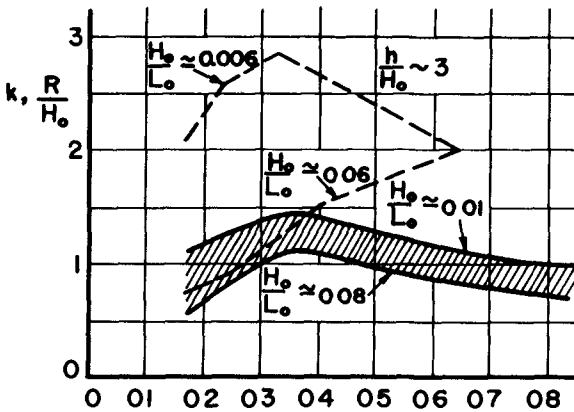


Fig 4 Variation of k with respect to α , the levee slope

k ———
R/H₀ - - - -

Note Value of R/H₀ is after Iwagaki⁸⁾

$$\frac{2\pi Q}{H_o L_o} = \frac{4\pi}{15} \sqrt{2gH_o} \frac{T_m}{L_o} \left(1 - \frac{z_o}{kH_o}\right)^{\frac{5}{2}} \quad (11)$$

Normally, Eq (10) gives us the better results but Eq (9) also gives us a satisfactory result. The effect of wind can also be expressed by the change of k , while the breakers' effect may not

2 Computer Experiment

For engineering purposes, what we need is the "prediction". Wave-overtopping phenomenon is a combination of statistical and deterministic factors, since wave period and wave height, for example, are statistical variables, while over-topping caused by a given wave can be a deterministic phenomenon. In this section the authors treat each over-topping as a completely deterministic process for the given wave conditions, which may include some statistical characteristics. The frequency response function being known, we can estimate the total amount of wave overtopping if all the informations of wave characteristics are available. However, we face the following problem: Can we estimate the total amount of wave over-topping by the statistical parameters only? Already this attempt has been done by Tsuruta and Goda by using authors' formula, Eq (9)⁷⁾. They estimated the expected amount of overtopping for irregular waves by using $H_{1/3}$. However, the authors would like to point out that the amount of over-topping depends upon the wave period as well as the wave height, and also that though Eq (9) is dimensionless, it is not very convenient to use it directly as the response function, since it includes H_o in both sides.

Another important point which is related with the prediction problem is that the response function is highly non-linear. Therefore the usual statistical values, $H_{1/3}$ for example, may not be a suitable

parameter at all. In order to study this point, some numerical experiments were carried out at AIT in Bangkok.

The following assumptions are made:

1. For simplicity Equation (9) is used instead of sinusoidal wave formula in the modified form.

2. Wave height H_0 and Wave period T follow Rayleigh distribution.

3. Cross correlation of H_0 and T is very small.

The modification of Eq (9) is as follows:

$$\frac{Q}{Z_0^2} = \begin{cases} C' \frac{(\zeta-1)^{5/2}}{\zeta} \tau & (\zeta > 1) \\ 0 & (\zeta \leq 0) \end{cases} \quad (12)$$

$$\text{where } C' = \frac{2}{15} \sqrt{2} \text{ m} \quad (13)$$

$$\tau = T \sqrt{\frac{g}{Z_0}} \quad (14)$$

and

$$\zeta = k \frac{H_0}{Z_0} \quad (15)$$

Eq (12) is convenient for prediction, since normally Z_0 is given and the variable of left hand side is only Q . H_0/\bar{H}_0 and T/\bar{T} may follow the following Rayleigh distributions:

$$p\left(\frac{H_0}{\bar{H}_0}\right) = \frac{\pi}{2} \frac{H_0}{\bar{H}_0} \exp\left[-\frac{\pi}{4} \left(\frac{H_0}{\bar{H}_0}\right)^2\right] \quad (16)$$

$$p\left(\frac{T}{\bar{T}}\right) = 2.7 \left(\frac{T}{\bar{T}}\right)^3 \exp\left[-0.675 \left(\frac{T}{\bar{T}}\right)^4\right] \quad (17)$$

where $p(\)$ means the probability density functions, and

\bar{T} and \bar{H}_0 mean the ensemble averages.

Eq (16) and Eq (17) are only examples, since in fully developed seas $p(\frac{H}{H_0})$ is Gaussian. Anyhow the numerical experiment is always possible if $p(\frac{H}{H_0})$ and $p(\frac{T}{\bar{T}})$ are given.

The procedure of numerical experiment is as follows:

1 Prepare the necessary values for the numerical experiments. They are Z_0 , \bar{T} , \bar{H}_0 and k . If the levee slope is given, k may be estimated from Fig 4. m can be 0.6.

2 Compute $T/\sqrt{Z_0 T}g$ and $k\bar{H}_0/Z_0$.

3 Generate H_0/\bar{H}_0 and T/\bar{T} which are statistically random but follow the given probability density. Normally, if they are random, the cross correlation is rather small. However, we should compute the cross correlation always.

4 Compute the values of τ and ζ , which are expressed by Eq (14) and Eq (15).

5 Compute Q/Z_0^2 by the use of Eq (12).

6 Repeat the above procedure for a certain number of times, say one hundred.

7 Compute the summation of Q/Z_0^2 . Also compute $H_{1/3}$ and $T_{1/3}$ statistically.

The above procedure is enough for design purposes, since we can estimate the total amount of overtopping. Through this information, we can determine, for instance, the capacity of the pump to drain the water.

exerted by overtopping

The numerical experiments were carried out for the case that \bar{H}_o , \bar{T} , $\bar{T}/\sqrt{Z_o/g}$ and $k\bar{H}_o/Z_o$ are all equal to unity. The computer used for the experiment is IBM 1130. The results are shown in Table 1. Each run contains one hundred of waves and $H_{o1/3}$, $T_{1/3}$, \bar{H}_o and \bar{T} are statistically obtained. For comparison, $H_{1/3}$ and $T_{1/3}$ are computed by Eq (18) and (19)

$$\text{'Computed' } H_{o1/3} = 1.60 \bar{H}_o \quad (18)$$

$$\text{'Computed' } T_{1/3} = \bar{T} \quad (19)$$

For each wave the value of Q/Z_o^2 is computed and its mean value is obtained through Eq (20)

$$\frac{\sum_{i=1}^{100} \left(\frac{Q}{Z_o^2}\right)_i}{100} = \bar{q}_m \quad (20)$$

Again for comparison, $\bar{q}_{\text{computed}}$ is obtained, which is defined by

$$C_o' \left(\frac{T}{\bar{T}}\right)_{1/3} \frac{\{(H_o/\bar{H}_o)_{1/3} - 1\}^{\frac{5}{2}}}{(H_o/\bar{H}_o)_{1/3}} = \bar{q}_c \quad (21)$$

From Table 1 the values of \bar{q}_c are always greater than those of \bar{q}_m , which means \bar{q}_c is in safety side for design purposes. Among seven runs of experiment, which contain 700 waves, there is a case that $\bar{q}_m = 0.945 \bar{q}_c$. This fact shows us that for a quick estimation, the use of $H_{o1/3}$ and $T_{1/3}$ may be a good approximation. However, the numerical experiments are more desirable for the actual design purposes.

3 Conclusions

As conclusions we may say the followings

1 Eq (9) gives us a fairly good prediction for the discharge of wave overtopping, though it contains two empirical factors

2 The above empirical factors, however, do not change vigorously at least for the existing experimental data

3 Theoretically speaking, the use of $H_{o1/3}$ and $T_{1/3}$ for the estimation of overtopping are doubtful

4 According to the limited number of computer experiments, the estimated values of over topping obtained by the use of $H_{o1/3}$ and $T_{1/3}$ are always greater than the statistically obtained values

5 However, this formula may be useful by the use of $H_{o1/3}$ and $T_{1/3}$ in order to get the first approximation of wave overtopping caused by a set of irregular waves

6 For the design purposes the computer experiment is highly recommended since already we obtained the response function which is expressed by Eq (9) or Eq (12)

Table 1 - Results of Numerical Experiment

Run	$H_{1/3}$		$T_{1/3}$		\bar{q}		(1)/(2) factor
	Measured	Computed	Measured	Computed	(1) Measured	(2) Computed	
1	1 35	1 45	1 10	1 12	3.83×10^{-3}	12.1×10^{-3}	0 317
2	1 44	1 35	1 10	1 05	4 43	6 36	0 695
3	1 49	1 49	1 10	1 10	7 35	14.1	0 521
4	1 43	1 39	1 05	1 00	6 85	7 20	0 945
5	1 33	1 31	1 04	1 00	4 79	8 14	0 590
6	1 39	1 39	1 04	1 00	5 46	7 13	0 765
7	1 43	1.42	1 00	1.08	5 69	9 80	0 581

Note: All are non-dimensional variables

"Measured" means statistically obtained values

"Computed" means the values obtained by mean values

(for example $H_{1/3} = 1.6 \bar{H}$)

Each run includes 100 of waves

Bibliography

- 1 Carrier, G F and Greenspan, H P Water waves of finite amplitude on a sloping beach, Jour of F M , Vol 4, 1958
- 2 Gei, C Report on the model test of sea-dike cross-section of Hsin-Chu Tidal Land, The Tainan Hyd. Lab Bulletin No 6, Taiwan, China
- 3 Kikkawa, H , Shi-iga1, H and Kono, T On the experimental study of over-topping over the vertical wall, The Report of Annual Conf of JSCE, 1966 (in Japanese)
- 4 Kikkawa, H , Shi-iga1, H and Kono, T Fundamental Study of wave over-topping on levees, Coastal Engineering in Japan, Vol 11, 1968
- 5 Saville, Jr , T : Wave run-up on shore structures, Proc ASCE, Vol 82, 1956
- 6 Sibul, O J and Tickner, E G Model study of over-topping of wind generated waves on levees with slopes of 1 3 and 6, Beach Erosion Board Tech Memo No 80, 1956
- 7 Tsuruta, S and Goda, Y.. Expected discharge of irregular wave over-topping, Proc of Coastal Engineering, Vol II, 1968, London
- 8 Iwagaki, Y , Shima, A and Inoue, M Effects of wave height and sea water level on wave overtopping and wave run up, Coastal Engineering in Japan, Vol 8, 1965

CHAPTER 35

IMPULSE WAVES GENERATED BY LANDSLIDES

J W Kamphuis
Associate Professor of Civil Engineering,
Queen's University at Kingston, Canada

R J Bowering
Engineer, Manitoba Water Resources,
Winnipeg, Canada

ABSTRACT

A study programme has been initiated to investigate the impulse waves generated by landslides originating entirely above the water surface. It may be seen that the characteristics of this wave depend mainly on the slide volume and the Froude number of the slide upon impact with the water. The resulting wave goes through a transition period. For the highest wave (usually the first), the wave height becomes stable relatively quickly and decays exponentially during the period of transition, the wave period continues to increase for a long time, the velocity of propagation may be approximated very closely by solitary wave theory.

INTRODUCTION

Impulse waves generated by landslides have long been a menace in certain localities and the study of this phenomenon has been carried out at an accelerated rate in the 1960's, perhaps as a result of disasters of major proportions such as at Valont (2). In coastal areas, these slides are also not uncommon and Miller (4) gives a number of examples.

An attempt is made in this paper to determine the relation between the generated impulse waves and the various parameters of the slide and the receiving body of water. Some studies of underwater slides and of slides under simplified conditions have been performed, Wiegel (9), Prins (5,6) and Wiegel et al (10), but little is known about slides originating above the water surface, sliding into the body of water at various angles.

Theoretical work has also been done for simplified generating conditions e.g. Unoki and Nakano (7), Kranzer and Keller (3) and Ursell (8). In this paper no attempt has been made to express the results on a theoretical basis.

The purpose of the present paper is to approach a highly complex, non-linear problem entirely experimentally, invoking as little simplification as possible. The test series is yet incomplete and the analysis is part of a continuing program.

EXPERIMENTAL TECHNIQUE

Experiments were carried out in a 45 m long flume, 1 m wide, with water depths, d , ranging from 23 to 46 cm¹. The landslides were modelled using a tray (Fig 1), loaded with a varying number of units of constant specific gravity and of zero porosity. The tray was placed at various distances above the water to roll down a roller ramp. In Fig 2 this ramp is shown with the tray in position at the top of the ramp. The angle of the ramp with the water surface, θ , was adjustable, as was the front slope of the tray, α . The tray was released using a quick release mechanism and the velocity of impact with the water, V , was measured using a combination of stroboscope illumination and prolonged photographic exposure of a series of lines on the top of the tray.

The resulting waves were measured continuously at three locations, 3.35, 9.45 and 17.1 m from the point of impact. These locations are called a, b, and c respectively.

The record from the first wave probe (a) was also squared and integrated by analogue methods. The wave energy was calculated, using a digital computer programme, by a combination of

$$E_o = \rho g C_a \int \eta^2 dt \quad (1)$$

and

$$E_s = \frac{8}{3\sqrt{3}} H^{3/2} d^{3/2} \quad (2)$$

where E_o is the energy contained in a deep water wave using oscillatory wave theory, E_s the energy by solitary wave theory, ρ the water density, g the acceleration of gravity, C_a the phase speed of the wave at location a, η the wave record, t the time and H the maximum wave height. The phase speed C_a , was measured using the elapsed travel time between probe a and an on-off probe, located at still water level, very close to probe a.

DIMENSIONAL ANALYSIS

For the experimental study, any property, A , of the wave may be stated as a function of the following parameters

$$A = f(l, w, h, V, \beta, \theta, \rho_s, \rho, \mu, g, d, x, t) \quad (3)$$

where l , w and h are the length, width and thickness of the slide, β is the angle between the front face of the slide and the horizontal ($\beta = \theta + \alpha$), ρ_s is the density of the slide, μ is the dynamic viscosity of the water, x is the distance from the point of impact and t is the elapsed time.

1 A summary of the notation may be found at the end of the paper



Fig. 2: Roller Ramp

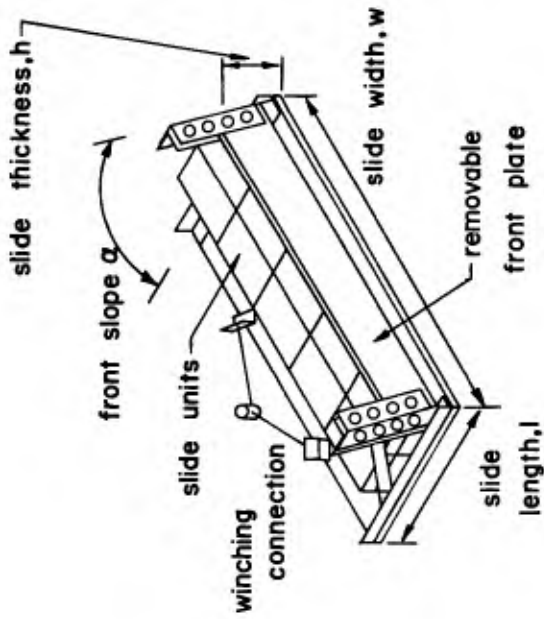


Fig. 1: Model Slide

Eq 3 may be written in dimensionless form as

$$\pi_A = \phi_A \left(\frac{1}{d}, \frac{w}{d}, \frac{h}{d}, \frac{V}{\sqrt{gd}}, \beta, \theta, p, \frac{\rho_s}{\rho}, \frac{\rho d \sqrt{gd}}{\mu}, \frac{x}{d}, t\sqrt{\frac{g}{d}} \right) \quad (4)$$

Because the tests were performed in a two dimensional flume, the term w/d becomes irrelevant. Early in the tests it became evident that the slide volume and the related kinetic energy of the slide upon impact with the water are very important terms and therefore $1/d$ has been replaced by the two-dimensional slide volume per unit width expressed in dimensionless form as

$$q = \frac{1}{d} \times \frac{h}{d} \quad (5)$$

The kinetic energy upon impact can be obtained by the following combination

$$k = \frac{1}{2} \left(\frac{\rho_s}{\rho} \right) \left(\frac{1}{d} \right) \left(\frac{h}{d} \right) \frac{V^2}{gd}$$

Because shear was negligible throughout, the Reynolds number can be neglected and Eq 4 becomes

$$\pi_A = \phi_A \left(q, \frac{h}{d}, \frac{V}{\sqrt{gd}}, \beta, \theta, p, \frac{\rho_s}{\rho}, \frac{x}{d}, t\sqrt{\frac{g}{d}} \right) \quad (6)$$

where π_A represents the dimensionless form of any dependent quantity A

Thus for maximum wave height at any probe

$$\frac{H}{d} = \phi_H \left(q, \frac{h}{d}, \frac{V}{\sqrt{gd}}, \beta, \theta, p, \frac{\rho_s}{\rho}, \frac{x}{d} \right) \quad (7)$$

and for the wave energy at the first probe

$$\frac{E}{\rho gd^3} = \phi_E \left(k, \frac{h}{d}, \frac{V}{\sqrt{gd}}, \beta, \theta, p, \frac{\rho_s}{\rho} \right) \quad (8)$$

Here q has been replaced by k , a more relevant parameter

For the speed of propagation of the waves

$$\frac{C}{\sqrt{gd}} = \phi_C \left(q, \frac{h}{d}, \frac{V}{\sqrt{gd}}, \beta, \theta, p, \frac{\rho_s}{\rho}, \frac{x}{d}, t\sqrt{\frac{g}{d}} \right) \quad (9)$$

and for the wave period

$$T\sqrt{\frac{g}{d}} = \phi_T \left(q, \frac{h}{d}, \frac{V}{\sqrt{gd}}, \beta, \theta, p, \frac{\rho_s}{\rho}, \frac{x}{d}, t\sqrt{\frac{g}{d}} \right) \quad (10)$$

Throughout the tests, except for one isolated test series, p and ρ_s/ρ were not varied ($p = 0, \rho_s/\rho = 2.7$). Further work needs to be done to test the effect of these parameters. The work also needs to be extended to higher values of slide volume, q or kinetic energy, k .

The test results therefore only apply to relatively small rock slides, originating above the water level.

TEST RESULTS

The wave records obtained were very much as expected. At probe a, the wave train consisted of one large wave followed by a short train of smaller, trailing, oscillatory waves. At probe b, the large leading wave had lengthened considerably and decreased in height. It had passed some of its energy to the following wave train. The train of oscillatory, following waves had also lengthened. At probe c, the wave height appeared to have reached a stable or almost stable value. The wave train was now very long, the large wave itself having attained a wave length of the order of 20 to 30 times the depth of water.

The first wave was always the highest in the train except for test series 52 where θ is 90° .

Maximum Wave Height The test results indicate the dimensionless parameters in Eq. 7 that exercise the greatest influence on the wave height are q , the volume per unit width of the slide and $F = V/\sqrt{gd}$, the Froude number of the slide upon impact with the body of water. The other parameters only introduce variations to the basic relationship. All test results have been plotted against q .

Typical test results are shown in Fig. 3 and it may be seen that H_c/d varies directly with $\log q$. This is not true for H_a/d , the wave height nearest the point of impact. From comparison of wave heights at a, b and c, it appears that H_c/d is stable, i.e. the wave height does not decrease significantly beyond probe c. The subsequent figures focus on this stable wave height and the other two measured wave heights are related to it by a wave height attenuation function discussed later in this section.

The effect of the slide thickness on the stable wave height is indicated in Fig. 4. For thick slides, defined as $h/d > \frac{1}{2}$, the relation between H_c/d and q is relatively constant. For thin slides, defined as $h/d < \frac{1}{2}$, a decrease in h/d results in smaller wave heights.

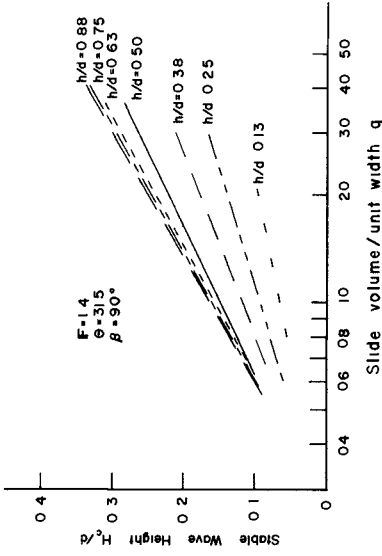


Fig 4 Effect of Slide Thickness on the Stable Wave Height

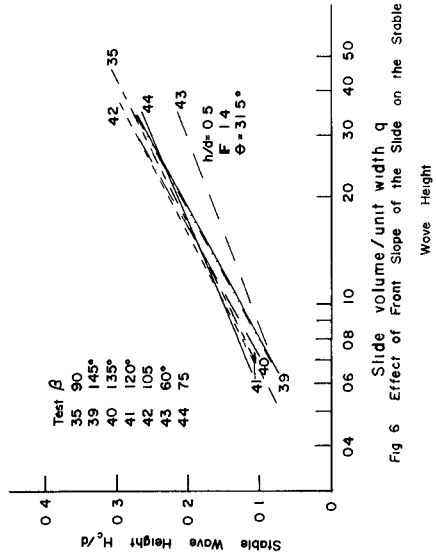


Fig 6 Effect of Front Slope of the Slide on the Stable Wave Height

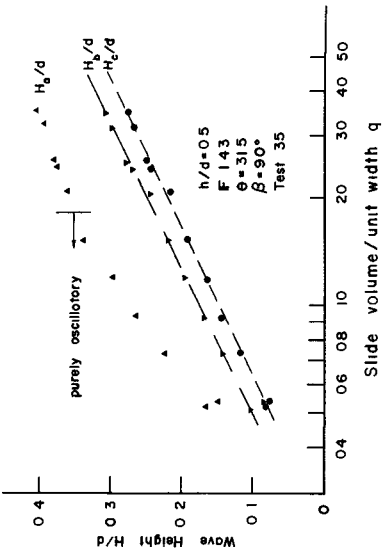


Fig 3 Wave Height as a Function of Slide Energy

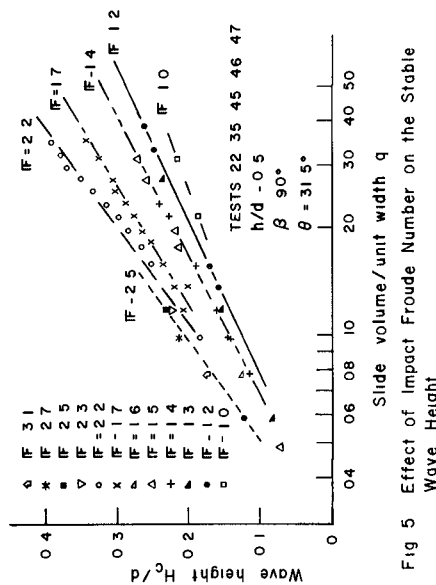
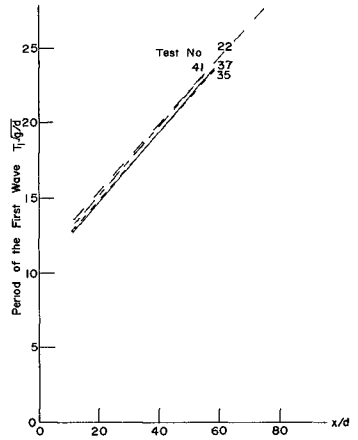
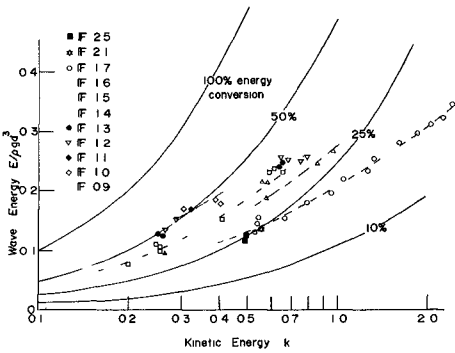
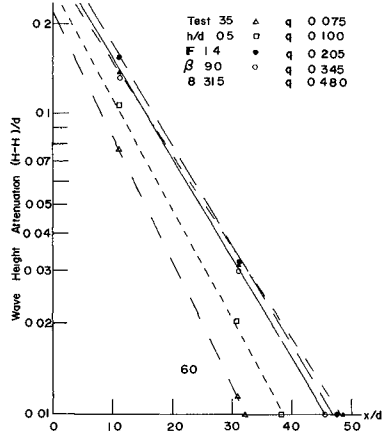
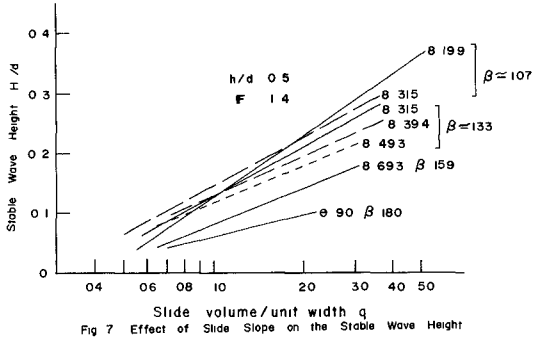


Fig 5 Effect of Impact Froude Number on the Stable Wave Height



For the range of Froude numbers tested (Fig 5) it may be seen that the stable wave height increases significantly with the Froude number of the slide upon impact

An increase in the front slope of the slide, β , appears to increase the slope of the relation between H_c/d and q . For large slides the resulting wave height increases with β , for small slides, it decreases with β . In addition, for $\beta < 90^\circ$ there is a general reduction in agitation. An example of the effect of β on H_c/d has been plotted in Fig 6

As θ increases, the generated wave is decreased slightly except for small slides - Fig 7. The results of test series 51 and 52 have also been plotted - not to indicate the effect of θ but to represent a possible overlap with the results of Prins (5,6) and Wiegel (9,10)

In Fig 3 it may be seen that $H_a > H_b > H_c$. This can be attributed mainly to dispersion, i.e. the passing of energy from the highest wave to the trailing train and the lengthening of the whole wave train. Experimentally it was found that the decrease in wave height is exponential and that the wave height for most tests decreased little beyond probe c. An example is shown in Fig 8. The slope of the lines is almost constant for all tests and the intercept varies as a function of q .

Wave Energy The test results involving wave energy may be plotted similar to Figs 3 to 7, but it is more convenient to plot them as a function of k , the dimensionless kinetic energy. As an example - Fig 9 - the effect of Froude number has been plotted and on the same graph the lines of constant % energy conversion have been shown.

Velocity of Propagation The velocity of propagation, between probes b and c, of the highest wave in the wave train was found to be within 1% of the following theoretical approximation for a solitary wave

$$\frac{c}{\sqrt{gd}} = 1 + \frac{\eta_{\max}}{2d} \quad (11)$$

This corresponds to Eq 9 because $\eta_{\max}/2d$ is simply another function of the right hand side of Eq 9

Wave period $T_1\sqrt{g/d}$, the dimensionless period of the first wave in the wave train has been plotted against distance along the flume in Fig 10. It may be seen that the wave period increases linearly with distance along the flume. It was found that all the other parameters of Eq 10 exercised a negligible influence on the relation between $T_1\sqrt{g/d}$ and x/d .

DISCUSSION

The wave forms obtained from the tests varied from a pure oscillatory wave train to a wave approaching solitary wave configuration, followed by an oscillatory wave train. Comparison with Prins (5, Fig 10) would indicate his experience to be similar. At no time during the tests were bores generated and therefore the results presented here can only be viewed as partial, also in this respect.

Under these conditions the test results indicate that a stable wave height is generally obtained within 80 depths from the point of impact.

Maximum Stable Wave Height A definite relation exists between the stable wave height and the volume of the slide. This relation can be expressed as

$$\frac{H_c}{d} = C_1 + C_2 \log q \quad (12)$$

where both C_1 and C_2 are functions of the remaining dimensionless parameters of Eq 7. But Fig 5 indicates that the wave height is also highly dependent on Froude number. Taking this into account, the relationship which approximates the test results most closely is

$$\frac{H_c}{d} = F^{0.7} (0.31 + 0.20 \log q) \quad (13)$$

This can be used as a good estimate of the stable wave height for $0.05 \leq q \leq 1.0$, as long as the slide is thick, i.e. $h/d \geq \frac{1}{2}$, the front angle of the slide is 90° or greater and the angle of the slide plane is about 30° . Eq 13 can also be used as a conservative estimate for slides where $\beta < 90^\circ$, or $\theta > 30^\circ$ and an estimate of the built-in factor of safety may be obtained from the figures presented in this paper. For the case $\theta < 30^\circ$, Eq 13 could be unsafe.

Eq 13 is purely empirical. Unoki and Nakano (7) conclude that theoretically $\eta \sim$ initial impulse. Since for each test series V was kept almost constant, this reasoning should lead to $\eta \sim$ slide volume for each test series. However, this appears not to be the case, indicating that the system is highly non-linear and that the theoretical approach of (7) overestimates the generated wave height. The theoretical approach of Kranzer and Keller (3) could perhaps be applied as an approximation, if the "initial" water surface, immediately after impact of the slide, were known. This is virtually impossible because of splash and because the slide takes a finite time to enter and travel through the body of water.

The changes in the relation of H/d on q for the parameters treated in Figs 4 to 7 can be explained from the physical phenomenon. It must be remembered that in all cases with the exception of Fig 5, the Froude number is constant, therefore slide volume is synonymous with kinetic energy on impact.

Referring to Fig 4, as the slide becomes thinner, it imparts less energy to the water, dissipating more of the remaining energy by bottom impact.

As the impact Froude number increases, Fig 5, the kinetic energy upon impact increases for the same slide volume. This results in greater wave heights as well as greater splash and bottom impact.

Fig 6 indicates that a decrease in β beyond 90° causes the front of the slide to become more streamlined. The slide then imparts less energy to the water.

As θ decreases, the distance of travel of the slide through the water becomes greater and therefore it is expected that a greater amount of the energy of the slide goes into wave generation. Also, the generation mechanism changes to more of a pushing action.

Wave Height Attenuation Fig 8 is an example of the pattern of wave height attenuation found generally. Because the attenuation is represented by straight lines of constant slope, the decrease in wave heights can be expressed as

$$\frac{H}{d} = \frac{H_c}{d} + C_3 e^{-C_4 \left(\frac{x}{d}\right)} \quad (14)$$

where C_3 is a function of the other parameters in Eq 7, C_4 appears to be constant at 0.08. For values of $0.1 < q < 1.0$, Eq 14 can be approximated by

$$\frac{H}{d} = \frac{H}{d}(\text{stable}) + 0.35 e^{-0.08 \left(\frac{x}{d}\right)} \quad (15)$$

Wave Energy For the range of values tested the wave energy is generally from $\frac{1}{4}$ to $\frac{1}{2}$ the kinetic energy of the slide upon impact. For test 52, the vertically falling slide only 10 to 20% of the kinetic energy was converted into wave energy. Thus the slide at an angle appears to be considerably more efficient than the vertical one. The kinetic energy of the slide at the time of impact is a rather difficult term to assess in the field. An easier estimate is the potential energy of a slide and this figure has been used by Johnson and Bermel (1) and Wiegand (9) for laboratory generation of impact waves and by Miller (4) in assessing slides in the field. The conversion from potential energy to kinetic energy upon impact is entirely different

in all three cases, however, and the complex mechanism in the field slides cannot be adequately simulated by simplified laboratory models. For that reason, kinetic energy upon impact was used which leaves the transfer function of field potential energy to kinetic energy only to be determined, circumventing an additional, similar function for each particular laboratory situation.

Velocity of Propagation With wave lengths of the order of 20 to 30 times the depth, the waves are by definition shallow water waves and their characteristics can be approximated by the solitary wave theory, once the waves become of constant form. Therefore the velocity of propagation should be approximated by the expression for the phase velocity of a solitary wave (Eq 11). The close comparison between actual values and theoretical values was indeed surprising.

Wave Period The various dimensionless parameters, other than the distance from the point of impact had very little influence on the wave period of the first wave and this wave period may be defined from plots similar to Fig. 10 as

$$T_1 \sqrt{\frac{g}{d}} = 11 + 0.225 \left(\frac{x}{d} \right) \quad (16)$$

This indicates that, although wave height and velocity of propagation of the first wave have reached a stable value at probe c, the wave period and wave length have not. Therefore the first wave continues to stretch out, tending to become a true, solitary wave, of infinitely long period, with no or only slight decrease in wave height. The periods of the trailing waves exhibit the same tendency although their increase in period is not linear with x/d through the range of x/d tested.

PRELIMINARY COMPARISON WITH FIELD RESULTS

Properly monitored field data are difficult to obtain because of the unexpected and disastrous nature of the slides. In an attempt to see how relevant the model tests are and as an indication of the applicability of formulae such as Eq. 13, the slides listed by Miller (4, p. 66) were used as field examples.

The model tests are two-dimensional and therefore can be expected to give a conservative indication for the three-dimensional field results.

Most of the slides listed by Miller are rock slides and all originated above the water surface. The volume and width of the slide front are only mentioned simultaneously in three cases thus reducing the list to only three examples. For one of these, the Shimabara Peninsula slide, the slide volume was greater than the range of q tested. For the other two, the Loen Lake slide of 1936 and the Tafjord slide of 1934, Eq. 13 gives a reasonably close estimate wave height.

A great deal more work needs to be done in this area.

CONCLUSIONS

The impulsively generated waves resulting from the sliding of a rock mass into a body of water have been investigated

A series of tests has been performed to determine the effect of various parameters describing the slide and the receiving body of water on the generated impulse waves. In this test series all slides were impervious and of rock density. The volumes of the slides were kept relatively small and so the test results are only applicable to small and medium sized slides of rock which originate above the water surface and slide into relatively large bodies of water.

For these conditions it was found that the wave height stabilized very quickly and can be described as a function of the slide volume and Froude number on impact (Eq 13). All other parameters appear as relatively small modifications to this function. The wave height attenuation between a location close to the site of impact and the point where the wave height has stabilized can be described by an exponential function (Eq 15).

The wave energy varies for these tests from $\frac{1}{4}$ to $\frac{1}{2}$ of the input kinetic slide energy. The velocity of propagation of the highest wave can be described adequately by solitary wave theory. Its wave period increases linearly with distance for the distance range tested. Some very preliminary work on field data indicates that Eq 13 can be used to predict or hindcast field wave heights.

ACKNOWLEDGEMENTS

The authors are grateful to Dr. A. Brebner for initiating this study and contributing during this program. Also they are indebted to the National Research Council of Canada for financial assistance.

REFERENCES

- 1 Johnson, J W , and Bermel, K J , "Impulse Waves in Shallow Water as Generated by Falling Weights", Transactions American Geophysical Union, Vol 30, No 2, April 1949, pp 223-230
- 2 Kiersch, George A , "Valont Reservoir Disaster", Civil Engineering, March 1964, pp 32-39
- 3 Kranzer, Herbert C , and Keller, Joseph B , "Water Waves Produced by Explosions", Journal Applied Physics, Vol 30, No 3, March 1959, pp 398-407
- 4 Miller, Don J , "Giant Waves in Lituya Bay, Alaska", U S Geological Survey Professional Paper 354-C, 1960
- 5 Prins, J E , "Water Waves Due to a Local Disturbance", Proceedings Sixth Conference Coastal Engineering, The Engineering Foundation Council on Wave Research, 1958, pp 147-162
- 6 Prins, J E , "Characteristics of Waves Generated by a Local Disturbance", Transactions American Geophysical Union, Vol 39, No 5, Oct 1958, pp 865-874
- 7 Unoki, S , and Nakano, M , "On the Cauchy-Poisson Waves Caused by the Eruption of a Submarine Volcano", Oceanographic, May 4, pp 119-141
- 8 Ursell, F , "On the Waves Generated by a Local Surface Disturbance - personal communication, mentioned in (10),
- 9 Wiegel, R L , "Laboratory Studies of Gravity Waves Generated by the Movement of a Submerged Body", Transactions American Geophysical Union, Vol 36, No 5, Oct 1955, pp 759-774
- 10 Wiegel, R L , Noda, E K , Kuba, E M , Gee, D M and Tornberg, G F , "Water Waves Generated by Landslides in Reservoirs", Journal of the Waterways and Harbours Division, ASCE, Vol 96, No WW2, May 1970, pp 307-331

NOTATION

- A = general dimensional expression for wave parameters,
 a = location of first wave measuring probe,
 b = location of second wave measuring probe,
 C = velocity of propagation of the wave,
 c = location of third wave measuring probe,
 d = depth of water,
 E = wave energy,
 E_o = wave energy in deep water from oscillatory wave theory,
 E_s = wave energy by solitary wave theory,
 F = Froude number,
 f = dimensional function,
 g = acceleration of gravity,
 H = maximum wave height,
 h = thickness of the slide,
 k = dimensionless kinetic energy of the slide,
 l = length of the slide,
 p = porosity of the slide,
 q = volume per unit width of the slide,
 T = wave period,
 t = time,
 V = velocity of impact of the slide,
 w = width of the slide,
 x = distance from the point of impact of the slide,
- α = angle between the bottom and the front face of the slide,
 β = angle between the front face of the slide and the horizontal, ($= \alpha + \theta$)
 η = wave record,
 θ = angle between the slip plane (roller ramp) and the water surface,
- μ = dynamic viscosity of the water,
 π = general dimensionless expression for wave parameters,
 ρ = density of water,
 ρ_s = density of the slide material,
 Φ = dimensionless function,
 ϕ = dimensionless function,

CHAPTER 36

WAVES GENERATED BY A PISTON-TYPE WAVEMAKER

by

Ole Secher Madsen

Research Division, U S Army Coastal Engineering Research Center
Washington, D C

ABSTRACT

When a wavemaker generates a finite number of waves, it has been found that one of the first and one of the last waves in such a burst is considerably larger than the average. A mathematical model, based on the linearized governing equations, is used for the particular problem of the waves generated by a sinusoidally moving piston-type wavemaker starting from rest. Theoretical results for the magnitude of the large wave relative to the average agree fairly well with experiments, however, the actual wave height is smaller in the experiments than predicted by theory. It is shown, by extending the classical wavemaker theory to second order, that finite amplitude effects do not offer an explanation. However, pistons rarely fit the tank dimensions exactly, and an approximate evaluation indicates that the discrepancy between predicted and observed wave heights can be attributed to the effects of leakage around the piston.

1 INTRODUCTION

One of the major problems encountered, when performing tests in a wave tank, is to account for the influence of reflected waves. Within the framework of linear theory we can deal with this problem (see Ursell, et al, 1960), when the magnitude of the reflected wave is small compared with that of the incident wave. However, in cases where the reflection from the far end of the tank is large, this is no longer possible. To overcome this problem, some coastal engineering tests are performed using the "burst method", in which the wavemaker generates waves only so long as no significant reflection from the far end of the tank has yet reached the wavemaker. After the wavemaker is stopped, time is allowed for the reflections to die out, before a new burst is generated. This procedure essentially eliminates the influence of even large reflections, but as is often the case, eliminating one problem creates another.

Figure 1 shows the surface profile recorded by a fixed gage 45 feet from a wavemaker, which generates a burst of 15 waves. A prominent feature is evident. One of the first and one of the last waves arriving at a particular station is considerably larger than the average. The effects of these large waves on test results have been of concern to engineers at the Coastal Engineering Research Center (CERC) where e.g., rip-rap stability is determined from tests employing the burst method.

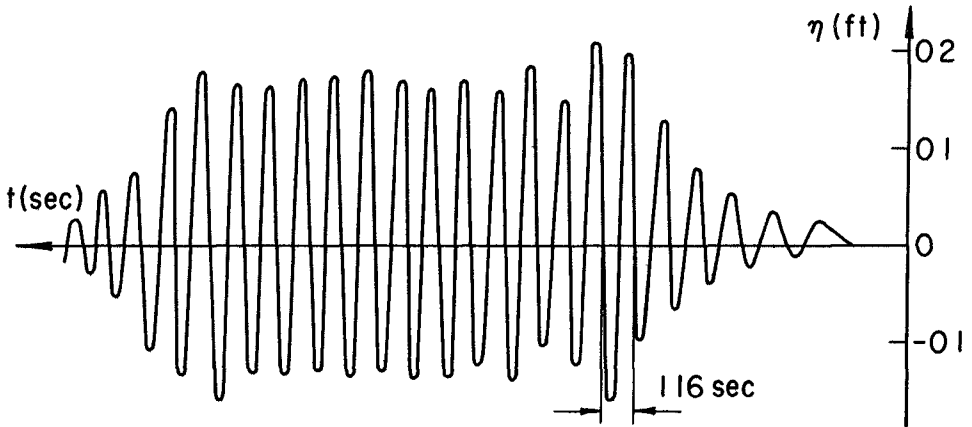


Figure 1 Surface profile recorded 45 feet from a sinusoidal piston-type wavemaker starting from rest and generating 15 waves ($T = 1.16$ sec, $h = 1.5$ ft, Stroke of wavemaker = 0.33 ft)

The study presented in the following was undertaken in an attempt to gain insight into the nature of these large waves and, if possible, to find a way to eliminate them

The large waves are clearly associated with the transient, i.e., the starting and stopping of the wavemaker, to which the classical wavemaker theory (Havelock, 1929, Biésel and Suquet, 1951, Ursell, et al., 1960) does not apply. However, Kennard (1949) has solved the linearized governing equations based on the assumption of potential flow starting from rest, and we adopt his solution as the theoretical model for the particular problem of a sinusoidally moving piston-type wavemaker starting from rest (Section 2.1)

The question is: How accurately will the linear theory predict the development of laboratory waves, which more often than not are quite nonlinear? From the theory of progressive waves we know that the second order nonlinear Stokes' wave sharpens the crest and flattens the trough when compared with the linear first order solution, but that the wave height remains unchanged. Thus focusing on wave height, rather than amplitude, the linear solution is likely to cover at least slightly nonlinear waves. This is supported by the experimental confirmation of the classical wavemaker theory by Ursell, et al. (1960). A much more serious limitation of the results from a linearized theory stems from the instability of sinusoidal waves, i.e., for relatively short waves ($\text{depth/length} = h/L > 0.216$) the Benjamin-Feir side-band instability (Benjamin, 1967), and for moderately long waves ($h/L < 0.09$), the occurrence of secondary crests (Galvin, 1968, Madsen et al., 1970)

With these limitations in mind, the theoretical results for wave heights are tested against experiments for three cases ($h/L = 0.24$, 0.197 , 0.132) in Section 2.2, and it is found that the predicted and observed magnitudes of the large waves relative to the average agree reasonably well. However, the theory overestimates the actual wave height. This was also found by Ursell et al. (1960) for waves of fairly large steepness and was attributed to possible nonlinear effects. In Section 3 the classical (linear) wavemaker theory is advanced to second order, and it is found that finite amplitude effects cannot be considered responsible for the difference between observed and predicted wave heights.

An approximate evaluation of the amount of leakage through the gaps between the piston and the tank walls and the influence of this leakage on the height of the generated wave is performed in Section 4. It is found that the discrepancy between observed and predicted wave heights may be attributed to leakage around the piston, which establishes confidence in the wave heights predicted by the linear theoretical model adopted.

Section 5 discusses the possibility of utilizing the large effect of leakage on the height of the generated waves to eliminate the large waves in a burst.

2 LINEAR SOLUTION FOR A WAVEMAKER STARTING FROM REST

2.1 Theory

Assuming irrotational motion the linearized equations governing the motion generated by a wavemaker (see Figure 2) are

$$\nabla^2 \phi = \phi_{xx} + \phi_{yy} = 0 \quad -h \leq y \leq 0 \quad (2.1)$$

$$\phi_y = 0 \quad y = -h \quad (2.2)$$

$$\eta_t - \phi_y = 0 \quad y = 0 \quad (2.3)$$

$$\phi_t + g\eta = 0 \quad y = 0 \quad (2.4)$$

and at the wavemaker, which is characterized by its position, $\xi(y,t)$

$$\phi_x = \xi_t(y,t) = u(y,t) \quad x = 0 \quad (2.5)$$

where subscripts indicate partial differentiation and g is the acceleration of gravity.

- Assuming the motion to start from rest,

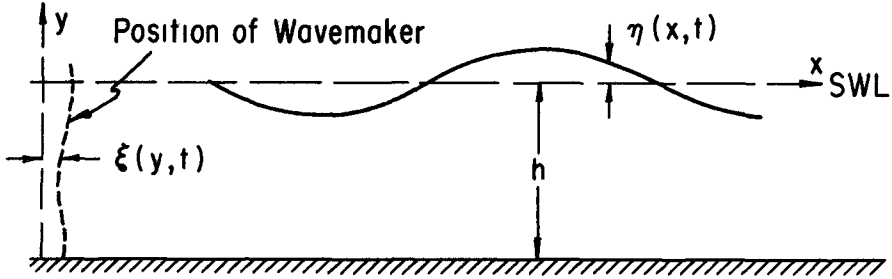


Figure 2 Definition of Symbols

$$\phi(x,y,0) = \phi_t(x,y,0) = \xi(y,0) = \xi_t(y,0) = 0 \tag{2.6}$$

the solution for the surface profile has been obtained by Kennard (1949)

$$\eta(x,t) = \frac{2}{\pi} \int_0^\infty dk \int_0^t d\tau \int_0^{-h} dy \frac{\cos \sigma(t-\tau) \cos kx u(y,\tau) \cosh k(y+h)}{\cosh kh} \tag{2.7}$$

where

$$\sigma^2 = gk \tanh kh \tag{2.8}$$

k being the wave number

For the particular case of a sinusoidal piston-type wavemaker, which runs for a length of time, t', we have

$$u(y,t) = \begin{cases} 0 & t \leq 0 \\ U \sin(\omega t + \delta) & 0 < t \leq t' \\ 0 & t > t' \end{cases} \tag{2.9}$$

and inserting this in (2.7), we can perform the integration with respect to y and τ to obtain

$$\eta(x,t,\delta) = \frac{2}{\pi} \frac{U}{\omega} \int_0^\infty dk \frac{\tanh kh}{k} \frac{\omega^2}{\omega^2 - \sigma^2} \cos kx \tag{2.10}$$

$$[(\cos \sigma t - \cos \omega t) \cos \delta + (\sin \omega t - \frac{\sigma}{\omega} \sin \sigma t) \sin \delta]$$

Realizing that

$$\frac{U}{\omega} = \xi_0$$

is the amplitude of the wavemaker motion and introducing the dimensionless variables (indicated by asterisks)

$$\begin{aligned} (x^*, y^*) &= h^{-1} (x, y) \\ t^* &= \sqrt{\frac{g}{h}} t \\ k^* &= kh \end{aligned} \tag{2 11}$$

the solution can be written

$$\frac{\pi}{2} \frac{\eta(x, t, \delta)}{\xi_0} = I_1 \cos \delta + I_2 \sin \delta \tag{2 12}$$

where

$$I_1 = \int_0^\infty dk^* \frac{\tanh k^*}{k^*} \frac{\omega^{*2}}{\omega^{*2} - k^{*2} \tanh k^*} (\cos \sqrt{k^* \tanh k^*} t^* - \cos \omega^* t^*) \cos k^* x^* \tag{2.13}$$

and

$$I_2 = \int_0^\infty dk^* \frac{\tanh k^*}{k^*} \frac{\omega^{*2}}{\omega^{*2} - k^{*2} \tanh k^*} (\sin \omega^* t^* - \frac{\sqrt{k^* \tanh k^*}}{\omega} \sin \sqrt{k^* \tanh k^*} t^*) \cos k^* x^* \tag{2 14}$$

This solution as it stands is valid only so long as $t < t'$. However, we may add the solution satisfying the boundary condition at $x = 0$

$$\phi_x^i = u^i(y, t) = \begin{cases} 0 & t \leq t' \\ -U \sin(\omega(t-t') + \delta') & t > t' \end{cases} \tag{2 15}$$

and due to the linearity of the governing equations the sum of these solutions will satisfy the boundary condition given by (2 9) provided

$$\delta' = \delta + \omega t' - 2 m \pi \tag{2 16}$$

where m is an integer

Thus in short we may write the solution as

$$\eta(x, t) = \begin{cases} \eta(x, t, \delta) & 0 < t \leq t' \\ \eta(x, t, \delta) - \eta(x, t-t', \delta') & t > t' \end{cases} \tag{2 17}$$

where the right-hand sides are calculated from (2 12)

The integrals I_1 and I_2 have removable singularities and are evaluated by numerical integration using the trapezoidal rule with a stepsize

equal to 0.05 the period of the integrand and the upper limit of integration equal to 16. The results were tested for accuracy by varying the stepsize and the upper limit of integration. As a further check the numerical solution was found to approach the classical solution to the wavemaker problem (Biésel and Suquet, 1951) as t became large.

Taking $x = \text{constant}$ in (2.12) we can compute the surface elevation at a particular station along the tank as a function of time, which corresponds to the surface profile recorded by a fixed gage. If we define the wave height as the difference in surface elevation between a trough and the preceding crest, we may describe the development taking place some distance from the wavemaker in terms of the sequence of wave heights as the waves arrive at this station. For a station 30 times the depth from the wavemaker, the computed variation in wave heights relative to the wave height in the final periodic state, H/H_p , is shown in Figure 3 for three depth-to-length ratios.

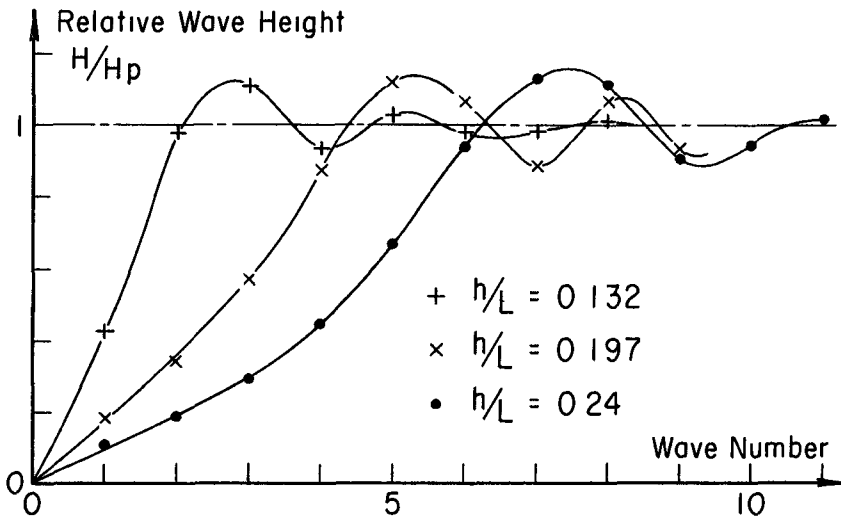


Figure 3 Computed variation in relative wave height of waves generated by a piston-type wavemaker starting from rest, as they reach a station 30 x depth from the generator

It shows that after the disturbance arrives, the wave height increases, overshoots but finally attains the constant value corresponding to the final periodic state. This type of behavior, which predicts a large first wave, is analogous to the response of a slightly damped mechanical system to an exciting force.

2.2 Comparison with Experiments

The large waves in a burst had previously been studied experimentally in CERC's 72-foot tank by John Ahrens, Hydraulic Engineer at CERC, and records of the surface profile obtained 16 and 45 feet from the wavemaker serve for a detailed comparison with the result computed from (2.12)

The wavemaker, piston type, is electronically controlled and was set to start from its mean position going backwards, i.e., corresponding to $\delta = -\pi/2$ in (2.9). The wavemaker was stopped manually, and if it was stopped off its mean position it would abruptly take this position. Since it is very difficult to avoid this final impulse, which will influence the last part of the burst, the comparison is only carried out for the first waves in a burst. The depth, h , was 1.5 feet and for each period the experiment was repeated three times, giving practically identical results for the part of the burst used for the comparison.

The experiments show second order effects (wave steepness = $H/L = 0.03 - 0.06$) in that crest amplitudes are larger than trough amplitudes, however, as was indicated previously and in view of the results obtained in Section 3, this effect is essentially eliminated by comparing wave heights rather than amplitudes. The comparison is presented in Table 1 as the variation in wave heights as the waves arrive at the particular stations, and it is obvious from the results that the actual wave heights differ considerably. However, if we compare the variation in wave heights relative to the wave height in the final periodic state, which for the experiments is taken as the average wave height in a burst excluding the large waves, the agreement between computed and experimental wave heights in this sense seems good. The larger discrepancy for the shortest wave, $h/L = 0.24$, may be attributed to the Benjamin-Feir side-band instability.

3 APPROXIMATE SECOND ORDER WAVEMAKER THEORY

The application of a linear theory as a predictor of the motion generated by a wavemaker starting from rest was found to be relatively successful. The large difference between the actual computed and experimental wave heights noted in Table 1 is naturally of minor importance once a particular wavemaker has been calibrated. However, if the observed discrepancy can be explained as other than the inadequacy of the linear solution, an understanding of the responsible mechanism will not only help us in designing more efficient wavemakers and maybe eliminate the need for calibrations, but it will give us confidence in the results obtained from the linearized governing equations, also for problems different from the one treated here. We therefore proceed to investigate if the large difference in wave heights can be attributed to finite amplitude effects as Ursell et al. (1960) suggested.

Based on a Lagrangian formulation Fontanet (1961) derived the complete second order solution to the wavemaker problem. His solution, however, is extremely difficult to evaluate, and for this reason we outline an approach using the more familiar Eulerian description. Due to the nonlinear instabilities mentioned previously (Benjamin-Feir instability for short waves, secondary waves for long waves), we need

Wave No	16 feet from Wavemaker				45 feet from Wavemaker				
	H feet		H/H _p		H feet		H/H _p		
	Exp	Comp	Exp	Comp	Exp	Comp	Exp	Comp	
1	0 305	0 370	0 85	0 9	0 155	0 183	0 43	0 44	h/L = 0 132
2	0 368	0 412	1 02	1 0	0 305	0 405	0 85	0 98	
3	<u>0 387</u>	<u>0 424</u>	<u>1 08</u>	<u>1 03</u>	<u>0 387</u>	<u>0 456</u>	<u>1 08</u>	<u>1 11</u>	
4	0 345	0 408	0 96	0 99	0 354	0 387	0 98	0 94	
5	0 357	0 418	0 99	1 02	0 360	0 424	1 00	1 03	
6	0 362	0 396	1 01	0 96	0 361	0 404	1 00	0 98	
1	0 142	0 181	0 42	0 44	0 061	0 068	0 19	0 16	h/L = 0 197
2	0 331	0 393	0 99	0 95	0 112	0 138	0 34	0 34	
3	<u>0 352</u>	<u>0 457</u>	<u>1 05</u>	<u>1 11</u>	0 194	0 236	0 59	0 57	
4	0 341	0 384	1 02	0 93	0 296	0 363	0 91	0 88	
5	0 334	0 408	1 00	0 99	<u>0 369</u>	<u>0 468</u>	<u>1 13</u>	<u>1 13</u>	
6	0 343	0 412	1 02	1 00	0 315	0 442	0 96	1 07	
7	0 330	0 391	0 98	0 95	0 318	0 366	0 97	0 89	
8	0 333	0 419	0 99	1 02	0 337	0 444	1 03	1 08	
9	0 339	0 416	1 01	1 01	0 327	0 384	1 00	0 93	
1	0 110	0 130	0 30	0 28	0 045	0 049	0 15	0 11	h/L = 0 24
2	0 254	0 287	0 71	0 62	0 068	0 085	0 20	0 18	
3	<u>0 420</u>	0 479	<u>1 17</u>	1 03	0 117	0 136	0 35	0 29	
4	0 366	<u>0 512</u>	1 02	<u>1 10</u>	0 170	0 209	0 51	0 45	
5	0 369	0 437	1 02	0 94	0 275	0 318	0 82	0 68	
6	0 368	0 459	1 02	0 99	<u>0 403</u>	0 441	<u>1 21</u>	0 95	
7	0 359	0 465	0 99	1 00	0 372	<u>0 524</u>	1 12	<u>1 13</u>	
8	0 364	0 472	1 01	1 02	0 300	0 519	0 90	1 12	
9	0 359	0 466	0 99	1 00	0 363	0 427	1 09	0 92	
10					0 310	0 446	0 93	0 96	
11					0 347	0 474	1 04	1 02	

Table 1 Comparison Between Computed and Experimental Wave Heights
 (Depth = 1 5 feet)
 (Underlined values correspond to the largest wave)

only consider intermediate waves, i e , $0.21 \leq h/L \leq 0.09$ For large t the solution to the first order (linear) equations given in Section 2 is the classical wave-maker theory (see e g , Biésel and Suquet, 1951) For a piston-type wavemaker,

$$u(y,t) = \xi_t = U \sin \omega t, \quad \xi = -\xi_0 \cos \omega t \tag{3 1}$$

and denoting the first order solution by a superscript, ⁽¹⁾, the classical solution reads

$$\phi^{(1)} = C_0 \cosh k_0 (y+h) \cos(k_0 x - \omega t) - \sin \omega t \sum_{n=1} C_n \cos k_n (y+h) e^{-k_n x} \tag{3 2}$$

$$\eta^{(1)} = \eta_0 \sin(k_0 x - \omega t) - \cos \omega t \sum_{n=1} \eta_n e^{-k_n x} \tag{3 3}$$

and

$$p^{(1)} = p^{(1)} + \rho g y = \text{pressure due to the wave} =$$

$$- \rho g \left[\eta_0 \frac{\cosh k_0 (y+h)}{\cosh k_0 h} \sin(k_0 x - \omega t) + \cos \omega t \sum_{n=1} \eta_n e^{-k_n x} \frac{\cos k_n (y+h)}{\cos k_n h} \right] \tag{3 4}$$

where

$$C_0 = \frac{2 U \sinh k_0 h}{k_0 h + \sinh k_0 h \cosh k_0 h} \frac{1}{k_0} \tag{3 5}$$

$$g k_0 \tanh k_0 h = \omega^2$$

$$C_n = \frac{2 U \sin k_n h}{k_n h + \sin k_n h \cos k_n h} \frac{1}{k_n} \quad (n \geq 1) \tag{3 6}$$

$$g k_n \tan k_n h = -\omega^2 \quad (n - \frac{1}{2})\pi < k_n h < n\pi$$

$$\eta_0 = \frac{\tanh k_0 h}{n_1} \xi_0 \quad n_1 = \frac{1}{2} \left[1 + \frac{2k_0 h}{\sinh 2k_0 h} \right] \tag{3 7}$$

$$\eta_n = \frac{2 \sin^2 k_n h}{k_n h + \sin k_n h \cos k_n h} \xi_0 \tag{3 8}$$

The first terms in (3 2), (3 3) and (3 4) represent a progressive wave, whereas the summations (inertia terms) express the correction necessary to account for the wavemaker motion not being exactly that

of the particles in a progressive wave with the given period and depth. For long progressive waves, we know that the horizontal particle velocity is practically independent of y , and this suggests that the necessary correction, i.e., the sum of the inertia terms, is small when a piston-type wavemaker generates long waves. Similarly, large corrections are needed when short waves are generated by a piston-type wavemaker. This was clearly demonstrated in calculations by Biésel and Suquet (1951). We also note, (3.2) combined with (3.6), that the exponential behavior of the inertia terms means that their importance becomes negligible within a small distance, of the order $3h$, from the wavemaker.

In advancing the theory to second order we proceed as outlined by Stoker (1957) by assuming a perturbation solution and expanding the boundary conditions at the free surface and at the wavemaker around $y = 0$ and $x = 0$, respectively. Denoting the second order solution by superscript (2) we have the governing equations,

$$\nabla^2 \phi^{(2)} = \phi_{xx}^{(2)} + \phi_{yy}^{(2)} = 0 \quad -h \leq y \leq 0 \quad (3.9)$$

$$\phi_y^{(2)} = 0 \quad y = -h \quad (3.10)$$

$$\begin{aligned} \phi_y^{(2)} + \frac{1}{g} \phi_{tt}^{(2)} = -\frac{1}{g} \{ (\phi_{ty}^{(1)} \eta^{(1)})_t + \phi_{xt}^{(1)} \phi_x^{(1)} + \phi_{yt}^{(1)} \phi_y^{(1)} \} \\ - \phi_{yy}^{(1)} \eta^{(1)} + \phi_x^{(1)} \eta_x^{(1)} \quad y = 0 \end{aligned} \quad (3.11)$$

where (3.11) is obtained by combining the dynamic and kinematic conditions to obtain a condition in $\phi^{(2)}$ only. The second order profile, $\eta^{(2)}$, is given by

$$\eta^{(2)} = -\frac{1}{g} \{ \phi_t^{(2)} + \phi_{ty}^{(1)} \eta^{(1)} + \frac{1}{2} [(\phi_x^{(1)})^2 + (\phi_y^{(1)})^2] \} \Big|_{y=0} \quad (3.12)$$

and the boundary condition at the wavemaker

$$\phi_x^{(2)} = -\phi_{xx}^{(1)} \xi \quad x = 0 \quad (3.13)$$

where we have used that $\xi = O(\eta)$ except for very long waves (see (3.7)).

The troublesome part of the determination of $\phi^{(2)}$ from (3.9), (3.10), (3.11) and (3.13) is the inhomogeneous equation (3.11). However, under the assumption of $t \rightarrow \infty$, $\phi^{(1)}$ and $\eta^{(1)}$ are as given by (3.2) and (3.3) and it can be shown that at $y = 0$ the maximum value of the inertia terms is of the order $1/4$ of the term associated with the progressive wave so

long as $h/L < 1/4$ It, therefore, seems to be a reasonable approximation to neglect the inertia terms when substituting $\phi^{(1)}$ and $\eta^{(1)}$ into (3 11) With this approximation the solution satisfying the equations (3 9) through (3 11) is the well known Stokes' second order solution for progressive waves (see e g , Ippen, 1966)

$$\phi_p^{(2)} = - \frac{3}{8} \omega \eta_0^2 \frac{\cosh 2k_o (y+h)}{\sinh^4 k_o h} \sin 2(k_o x - \omega t) \tag{3 14}$$

and

$$\eta_p^{(2)} = - \frac{1}{4} k_o \eta_0^2 \frac{\cosh k_o h (\cosh 2k_o h + 2)}{\sinh^3 k_o h} \cos 2(k_o x - \omega t) \tag{3 15}$$

However, we have not yet included the boundary condition $x = 0$, (3 13), which reads

$$\begin{aligned} \phi_x^{(2)} &= - \phi_{xx}^{(1)} \quad \xi(y, t) = \\ [C_o k_o^2 \cosh k_o (y+h) \cos \omega t + \sin \omega t \sum_{n=1} C_n k_n^2 \cos k_n (y+h)] \xi(y, t) \end{aligned} \tag{3 16}$$

We have previously justified the neglect of the inertia terms in the boundary condition at $y = 0$, however, this cannot be justified for all y 's at $x = 0$ unless the wave length is restricted further ($h/L < 0(0 1)$) Introducing (3 1) in (3 16) and using the relationship among η_0 and C_o we obtain

$$\phi_x^{(2)} = -\xi_o \left[\frac{g \eta_0}{\omega} k_o^2 \frac{\cosh k_o (y+h)}{\cosh k_o h} \cos^2 \omega t + \sin \omega t \cos \omega t \sum_{n=1} C_n k_n^2 \cos k_n (y+h) \right] \tag{3 17}$$

Clearly the solution (3 14) does not satisfy this boundary condition Using $\cos^2 \omega t = \frac{1}{2} (\cos 2\omega t + 1)$ and taking only the periodic part of (3 17) we see that we have a residual periodic boundary condition at $x = 0$

$$\begin{aligned} (\phi_R^{(2)})_x &= \phi_x^{(2)} - (\phi_p^{(2)})_x = - \frac{g \eta_o^2 k_o^2}{2\omega} \left\{ \frac{n_1 \cosh k_o (y+h)}{\sinh k_o h} - \right. \\ &\left. \frac{3}{2} \frac{\cosh 2k_o (y+h)}{\sinh^3 k_o h \cosh k_o h} \right\} \cos 2\omega t - \sin 2\omega t \frac{\xi_o}{2} \end{aligned}$$

$$\sum_{n=1} C_n k_n^2 \cos k_n (y+h) = U_R^{(2)}(y) \cos 2\omega t + \sin 2\omega t \sum_{n=1} (V_R^{(2)}(y))_n \tag{3 18}$$

Introducing

$$\phi_R^{(2)} = \phi^{(2)} - \phi_P^{(2)} \quad (3\ 19)$$

in the governing equations, which are linear in $\phi^{(2)}$ we see that $\phi_R^{(2)}$ is the solution to (3 18) and the homogeneous equations

$$\nabla^2 \phi_R^{(2)} = 0 \quad -h \leq y \leq 0 \quad (3\ 20)$$

$$(\phi_R^{(2)})_y = 0 \quad y = -h \quad (3\ 21)$$

and

$$(\phi_R^{(2)})_y + \frac{1}{g} (\phi_R^{(2)})_{tt} = 0 \quad y = 0 \quad (3\ 22)$$

i.e., the same governing equations as those for the first order solution, except for the more complicated boundary condition (3 18) at $x = 0$. The solution, however, can be found from the classical solution to the linear problem as a sum of ϕ_R 's, which we may combine and the progressive part can be written as

$$\phi_{R, \text{ Progressive}}^{(2)} = C_0^{(2)} \cosh k_0^{(2)}(y+h) \cos(k_0^{(2)}x - 2\omega t + \psi) \quad (3\ 23)$$

where $C_0^{(2)}$ and ψ are found by combining the ϕ_R 's and

$$4 \omega^2 = g k_0^{(2)} \tanh k_0^{(2)} h \quad (3\ 24)$$

We can therefore express the velocity potential far from the wavemaker to the second order

$$\phi = \phi_{\text{Progressive}}^{(1)} + \phi_P^{(2)} + \phi_{R, \text{ Progressive}}^{(2)} \quad (3\ 25)$$

or in physical terms the periodic waves generated by a wavemaker can be expressed as

- (1) A first harmonic linear wave of amplitude η_0
- (2) A second harmonic coupled with the first harmonic to give the second order Stokes' wave corresponding to the linear solution
- (3) A second harmonic free wave of small amplitude

This description agrees with that of Fontanet (1961), and when combined,

we see that the surface elevation at a fixed value of x can be expressed as

$$\eta = \eta_0 (\sin \omega t + \epsilon_1 \sin(2\omega t + \psi_1)) \quad (3.26)$$

where $\epsilon_1 \ll 1$. This type of surface elevation was shown by Ursell et al., (1960) to give a wave height, $H = 2\eta_0(1 + O(\epsilon_1^2))$. Thus for small ϵ_1 , the wave height of nonlinear waves, as recorded by a fixed gage, is practically the same as that predicted by a linear theory.

This analysis was carried out assuming the final periodic state to be reached, and suggests that when results for periodic waves obtained from a linear theory are compared with experiments, a comparison of wave heights should essentially eliminate the influence of finite amplitude. From this we conclude that the large difference between computed and experimental wave heights noted in Table 1 can hardly be attributed to nonlinear effects.

4 THE INFLUENCE OF LEAKAGE ON THE HEIGHT OF THE GENERATED WAVES

The results of Ursell et al. (1960) indicated that the discrepancy between measured and predicted wave heights increases from the order 3% to 10% with an increase in wave steepness from 0.03 to 0.045. This does not agree with the experiments at CERC, which show a larger discrepancy (of the order 15%) between theory and observation as well as the opposite trend, i.e., decreasing discrepancy with increasing wave steepness. In the experiments by Ursell et al. the leakage around the wavemaker was reduced by a rubber foam lining between the piston and the walls and bottom of the tank, whereas no such provision was taken in the CERC experiments. This suggests that leakage around the piston may have a large influence upon the height of the generated wave. A series of experiments performed at CERC (Tenney, 1969) serve as further evidence of the influence of leakage on the height of the generated waves. Two holes were drilled through a piston, the area of the holes was approximately 0.29% of the wetted area of the piston. It was found that the difference in wave height between the waves generated with these holes closed and open was of the order 2.8% - (1.6% - 4.0%).

4.1 Waves Generated by an Oscillating Flow Through a Slot

To evaluate the influence of leakage let us start by examining the waves generated by the oscillating flow through a slot which extends over the width of the generator.

For a slot of height Δ a distance Y below the free surface, we have

$$u(y,t) = \begin{cases} 0 & y > -Y + \Delta \\ v_0 \sin \omega t & -Y \leq y \leq -Y + \Delta \\ 0 & y < -Y \end{cases} \quad (4.1)$$

which, with the notation used in Section 3, gives the solution

$$C_0 = \frac{4}{2k_0 h + \sinh 2k_0 h} \frac{1}{k_0} v_0 [\sinh k_0 (-Y+\Delta+h) - \sinh k_0 (-Y+h)] \quad (4\ 2)$$

For small Δ we may write this as

$$C_0 = \frac{4 \sinh k_0 h}{2k_0 h + \sinh 2k_0 h} \frac{1}{k_0} \left\{ v_0 \frac{\Delta k_0 \cosh k_0 (-Y+h)}{\sinh k_0 h} \right\} \quad (4\ 3)$$

which written in this form by comparison with (3 5) clearly shows the generated progressive wave to be the same as that generated by a piston-type wave generator having a velocity given by

$$U = U' = v_0 \frac{k_0 \Delta \cosh k_0 (-Y+h)}{\sinh k_0 h} \quad -h \leq y \leq 0 \quad (4\ 4)$$

In particular we see that for a gap between the wavemaker and the bottom of the tank, $Y = h$,

$$U'_B = v_B \frac{k_0 \Delta_B}{\sinh k_0 h} = v_B \frac{\Delta_B}{h} \frac{k_0 h}{\sinh k_0 h} \quad (4\ 5)$$

with indices introduced for clarity

Clearly, the influence of leakage between the sidewalls and the piston is not as easy to handle rigorously. This leakage is probably one of the mechanisms responsible for the generation of transverse waves, however, if the width of the tank is small compared with the wave length of the generated waves, it seems physically reasonable that the waves generated by an oscillating flow, $v_s(y) \sin \omega t$, through a vertical slot of width Δ_s may be approximated as the waves generated by a piston-type wavemaker, having the prescribed motion

$$U'_s = v_s \frac{\Delta_s}{b} \quad (4\ 6)$$

where b is the width of the wave tank, and v_s is the average of $v_s(y)$ over the depth

Thus in principle, if v_B and v_s are known, we can find, at least with some accuracy, the generated waves, as those generated by an ideal piston-type wavemaker having the prescribed motion

$$u(y,t) = (U'_B + U'_s) \sin \omega t \quad (4\ 7)$$

However, is the potential theory really appropriate? When the water is

forced through the small gaps into the ambient fluid one might expect a considerable energy loss due to turbulence. In a study of the forced heave motion of a rectangular cylinder of large draught, i.e., small distance between bottom and cylinder ($\Delta_B \approx 0.06 h$), Svendsen (1968) found the radiated wave to be accurately predicted by potential theory. Thus, an inviscid theory seems indeed to give reliable results, however, contrary to Svendsen's study, the major problem in our case is determining the velocities.

4.2 Determination of the Leakage Velocity

In order to attack this problem we must first specify the conditions on both sides of the generator blade. If we assume that the region behind the wavemaker is occupied by an absorber beach, which corresponds to the CERC 72-foot tank, a reasonable assumption is that waves are generated in both directions and that these waves are the same, but 180° out of phase.

With this assumption the pressure due to the sinusoidal motion (3.1), of the piston on the front side is given by (3.4) and the pressure due to the wave on the back of the piston is of equal magnitude but opposite sign. If we restrict our analysis to moderately long wave ($h/L < 1/4$) the influence of the terms in (3.4) with exponential behavior in x , the inertia terms, is small compared with that of the term associated with the progressive wave. Thus, we may approximate the pressure difference between the two sides of the piston, Δp , by

$$\Delta p = p_{\text{front}}^+ - p_{\text{back}}^+ \approx 2\rho g \eta_0 \frac{\cosh k_0(y+h)}{\cosh k_0 h} \sin \omega t \quad (4.8)$$

where η_0 is given by (3.7)

This pressure difference will produce a flow through the gaps between the piston and the sides and the bottom of the tank. The velocity, v , of this flow may be estimated from Bernoulli's equation. Neglecting friction and the unsteadiness of the motion we have

$$v^2/2g = \Delta p/\rho g \quad (4.9)$$

In particular we get for the gap at the bottom, $y = -h$, by introducing (4.8) and defining v to be positive when directed towards the front of the piston, that

$$v(y = -h) = -\text{Sign} \{ \sin \omega t \} 2 \sqrt{\frac{g \eta_0}{\cosh k_0 h}} \sqrt{\sin \omega t} \quad (4.10)$$

To comply with the type of boundary condition assumed in (4.1), we can expand the time dependence of (4.10) in a Fourier Series. This has been done by Keulegan (1967), and retaining only the term associated

with $\sin \omega t$, we get

$$v(y = -h) \approx -2.22 \sqrt{\frac{g\eta_0}{\cosh k_0 h}} \sin \omega t \quad (4.11)$$

or with the notation used in Section 4.1 we have

$$v_B = -2.22 \sqrt{\frac{g\eta_0}{\cosh k_0 h}} \quad (4.12)$$

To find the leakage velocity through the gaps along the sides of the piston, we proceed in a similar manner, and taking the average leakage velocity over the depth, h , as the mean of the velocity at $y = 0$ and $y = h$ we get

$$v_s \approx -1.11 \sqrt{g\eta_0} \left(1 + \frac{1}{\sqrt{\cosh k_0 h}} \right) \quad (4.13)$$

4.3 Decrease in Wave Height Due to Leakage Around the Piston

By substituting (4.12) and (4.13) into (4.5) and (4.6) respectively, we get from (4.7) that the leakage around the piston produces waves, whose characteristics are approximately those of the waves generated by an ideal piston-type wavemaker having the prescribed motion

$$U' = -\sqrt{g\eta_0} \left(2.22 \sqrt{\frac{1}{\cosh k_0 h}} \frac{\Delta_B}{h} \frac{k_0 h}{\sinh k_0 h} + 1.11 \frac{\Delta_S}{b} \left(1 + \sqrt{\frac{1}{\cosh k_0 h}} \right) \right) \quad (4.14)$$

Comparing (4.14) with (3.1) we see that the leakage around the piston will decrease the amplitude of the generated waves by an amount $\Delta\eta_0$, which may be found from

$$\frac{\Delta\eta_0}{\eta_0} = - \left(2.22 \sqrt{\frac{1}{\cosh k_0 h}} \frac{\Delta_B}{h} \frac{k_0 h}{\sinh k_0 h} + 1.11 \frac{\Delta_S}{b} \left(1 + \sqrt{\frac{1}{\cosh k_0 h}} \right) \right) \frac{\sqrt{g\eta_0}}{U} \quad (4.15)$$

where η_0 is found from (3.7)

To test the validity of (4.15) some experiments were performed in the CERC 72-foot tank, which has a width, $b = 1.5$ feet. Measurements gave $\Delta_B = 0.28$ inches and $\Delta_S = 2 \times 0.1 = 0.2$ inches. With water depth $h = 1.5$ feet, the wave height, H_{exp} , as recorded 16 feet from the generator serve for the comparison presented in Table 2

h/L	ξ_0 (feet)	H_{exp} (feet)	$2\eta_0$ (feet)	Difference Observed %	Difference from (4 15) %
0 132	0 167	0 239	0 274	12 8	17 8
	0 251	0 367	0 411	10 7	14 6
0 197	0 115	0 228	0 272	16 2	15 8
	0 173	0 356	0 410	13 2	12 9
	0 230	0 477	0 545	12 5	11 2
0 240	0 125	0 300	0 352	14 8	12 7
	0 167	0 390	0 471	17 2	11 1
	0 196	0 466	0 553	15 3	10 2

Table 2 Comparison of observed reduction in wave height with that predicted from (4 15)

When considering the number of assumptions made in deriving (4 15), the agreement between predicted and observed reduction in wave height must be considered good. It is therefore concluded that the main part of the discrepancy between observed and predicted wave heights noted in Table 1 can be attributed to the influence of leakage around the piston. As a further check on the reasoning leading to (4 15), the reduction in wave height due to two holes in the piston, corresponding to the experiments by Tenney (1969) mentioned earlier, gave a predicted reduction of 2.1%, which compares favorably with Tenney's 1.6 - 4.0%.

The neglect of friction and unsteadiness made in order to arrive at (4 9) was tested by mounting a fitted 3/4 inch plywood board to the front of the piston blade. This increased the thickness of the blade from 1/4 inch to 1 inch, and since this had no significant effect on the height of the generated wave, this assumption seems justified.

It is interesting to note that the area of the gaps around the piston is of the order 2.7% of the wetted area, and that leakage through these gaps reduces the wave height by about 15%. This large effect of leakage through a small area, which is even more pronounced in the experiments by Tenney, may explain the results of Ursell et al. (1960), whose "seal" around the piston might not have been 100% effective for the large pressure difference between the two sides of the piston associated with the steepest waves. When one considers the large gap, which may exist at the

bottom in the case of a flap-type generator hinged at the bottom, the large effect of leakage through this gap may also explain why a group of Neyrpic engineers (1952) observed a discrepancy of 30% between theoretical and measured wave heights of waves generated by a flap-type wavemaker

5 CONCLUSION

In the preceding sections we have used a theoretical solution, based on the linearized governing equations, to predict the height of the waves generated by a piston-type wavemaker starting from rest. By comparison with experiments it was found that the theoretical model predicted the relative wave heights fairly accurately, and that the difference between predicted and observed wave heights could be attributed to the influence of leakage around the piston rather than to the inadequacy of the linear model. Thus the material presented essentially serves to establish confidence in the theoretical model adopted.

As stated in the Introduction, the problem initiating this study was the large first and last waves in a burst (Figure 1). Since the large last wave can be eliminated by the use of a drop-gate or a similar structure, the preceding sections have concentrated on the development taking place as the wavemaker is started. Computations show that the relative magnitude of the large first wave depends weakly on the position of the wavemaker, as it is started, and that this is smallest, when the wavemaker is started from its extreme positions. This dependence is, however, insignificant at stations far from the wavemaker, and consequently offers no solution to the problem of eliminating the large first wave.

From the analogy between Figure 3 and the response of a mechanical system to an exciting force, it is seen that the large first wave may be eliminated by starting the wavemaker slowly increasing the amplitude of its motion to the desired value. If this is possible and how it is most efficiently achieved can be determined by means of our theoretical model. Most wavemakers being of the type, which does not permit a change in stroke during operation, seems to render this solution impractical. However, this is where it might be possible to utilize the surprisingly large effect of leakage on the height of the generated waves. By controlling e.g. the area of the gap between the bottom and the piston, it would, in principle, be possible to change the height of the waves generated by a wavemaker having a constant stroke. If this effect can be used to eliminate the large first wave remains to be seen. However, this effect does seem to offer the possibility of generating amplitude modulated waves with a conventional wavemaker.

ACKNOWLEDGMENT

The work described herein is a portion of the research program of the U. S. Army Corps of Engineers and its Coastal Engineering Research Center. Permission to publish is appreciated. The author wishes to thank Mr. John Ahrens, Hydraulic Engineer at CERC, for making his experiments available for comparison with the computed results.

REFERENCES

- Benjamin, T B (1967), "Instability of Periodic Wave Trains in Nonlinear Dispersive Systems", Proceedings of the Royal Society, Series A, No 283
- Biéssel, F and Suquet, F (1951), "Les Appareils Générateurs de Houle en Laboratoire", La Houille Blanche, Vol 6, No 2, pp 147-165
- Fontanet, P (1961), "Theorie de la Génération de la Houle Cylindrique par un Batteur Plan", La Houille Blanche, No 1, pp 3-28
- Galvin, C J, Jr (1968), "Shapes of Unbroken Periodic Gravity Water Waves" (Abstract), Transactions of the American Geophysical Union, Vol 49, No 1, p 206
- Havelock, T H (1929), "Forced Surface-Waves on Water", Philosophical Magazine, Series F, Vol 8, pp 569-76
- Ippen, A T (Editor) (1966), "Estuarine and Coastline Hydrodynamics", McGraw Hill, New York
- Kennard, E H (1949), "Generation of Surface Waves by a Moving Partition" Quarterly of Applied Mathematics, Vol 7, No 3, pp 303-312
- Keulegan, G H (1961), "Tidal Flow in Entrances", Committee on Tidal Hydraulics, U S Army Corps of Engineers, Tech Bulletin No 19
- Madsen, O S, Mei, C C and Savage, R P (1970), "The Evolution of Time-Periodic Long Waves of Finite Amplitude", Journal of Fluid Mechanics, Vol 44, pp 195-208
- Neyrpic (1952), "Les Appareils Générateurs de Houle en Laboratoire, La Houille Blanche, Vol 7, No 6, pp 779-801
- Stoker, J J (1957), "Water Waves", Interscience, New York
- Svendsen, I A (1968), "On the Forces Induced on a Rectangular Cylinder by a Forced Heave Motion with Draught-Depth Ratio Close to Unity", Journal of Hydraulic Research No 4, pp 335-360
- Tenney, L W (1969), "Wave Height Variation Caused by Holes in the Wave Generator Blades", (Unpublished Report) Coastal Engineering Research Center
- Ursell, F, Dean, R G, and Yu, Y S (1960), "Forced Small-Amplitude Water Waves A Comparison of Theory and Experiment", Journal of Fluid Mechanics, Vol 7, Part 3, pp 33-52

CHAPTER 37

PREDICTION CURVES FOR WAVES NEAR THE SOURCE OF AN IMPULSE

Robert L. Miller
Department of the Geophysical Sciences
The University of Chicago

The Problem

The general problem of single-impulse induced waves has been under experimental investigation by the author for several years. The present paper is confined to a presentation of the wave modes which are to be expected for various permutations of displacement velocity and displacement length at the impulse source. Other portions of the study will be published elsewhere.

It is clear that a number of geometric arrangements in the laboratory may be made to generate impulse waves, for example, sudden upthrust or dropdown of a block on the tank bottom analogous to block faulting on the sea-floor in nature, or a hinged flap moving on the bottom analogous to the undulatory bottom motion which may occur during seismic disturbances on the sea floor. However, it is my opinion that the impulse generator which is most simple and most easily related to contemporary generalized theory, is a single piston thrust at one end of the wave tank which pushes the fluid down channel. (See Figure 1) As an additional simplification, the investigation is carried out for the flat bottom, fixed depth case, relegating the effect of varying depth to a later study.

The parameters of the impulse may thus be adequately described by the dimensionless variables l/d (where l is distance the piston is displaced, and the constant, d , is the undisturbed water depth) and a piston Froude number \bar{V}/\sqrt{gd} (where \bar{V} is the piston speed and \sqrt{gd} is the long wave velocity). The range of dimensionless piston displacements and piston velocities were chosen to cover reasonably well (where information is available), the movements of natural impulse generators. This includes coastal landslides entering a body of water, iceberg calving, seismic movements of various kinds, and explosions. None of the types of natural impulse generators referred to above are clearly modeled by a horizontal piston motion, although in many cases, the resultant of the natural motion may fit rather well, thus indicating the generality of this simple model.

Permutations of l/d and \bar{V}/\sqrt{gd} (or $F_{\bar{V}}$) through the selected range yields a series of points on the $l/d, F_{\bar{V}}$ plane. If a $l/d, F_{\bar{V}}$ plane is fixed at some arbitrary distance from the end of the piston motion, each point on the plane may be further described in terms of wave mode, some sort of wave speed, wave amplitude, etc. If a single wave is tracked down channel, it will be indicated by a fixed point on the $l/d, F_{\bar{V}}$ plane representing initial generating conditions. However, the nature of the wave mode, and the magnitude of wave speed and amplitude will change during the transformations which occur as the impulse wave progresses down channel. Thus, although the position of the point on the $l/d, F_{\bar{V}}$ plane does not change for a series of distances from the piston, the value or nature of the parameters for that point, will change. This yields a series of graphs consisting of $l/d, F_{\bar{V}}$ planes at various fixed

distances from the piston, which indicate the changes in wave mode, Froude number and maximum amplitude (Figures 5, 6 and 7)

Since the impulse waves are undergoing transformations and decay as they progress down channel, the question of a meaningful velocity must be considered. In this study, two velocities are measured. The first is a "phase velocity". A fixed point on the wave profile is tracked on multichannel oscillograph records. It is assumed that the transformations take place slowly relative to the short distance between two recording stations, and that the error in this approximation is not large. This method which yields an average velocity between points approximately 2.5 meters apart is in maximum error in the bore range near the piston where transformation is rapid and improves down channel. Thus, 2.5 meters is regarded as a characteristic "transformation distance" for these wave channel experiments. The Froude number representing this measurement of velocity is referred to as F_c , and the results are shown in Figure 6.

The second velocity in this study is the Boussinesq (1872) velocity of propagation of a volume element of the impulse wave. We have succeeded in devising an electronic system which will measure this velocity but due to space limitations, the method and results must be published elsewhere.

Sensing and Recording System

The surface time history of the impulse waves is obtained through capacitance probe sensors at a series of stations along the channel (Figure 2, D). The wave sensor is basically an amplitude modulated square wave generator. As the probe is immersed in the fluid, the capacitance increases, resulting in a modulated envelope directly proportional to the instantaneous degree of immersion. For details see L. F. McGoldrick, 1969.

The probe is constructed of #17 gage hypodermic tubing with a polyethylene sleeve (O.D. 1.94 mm) forming the dielectric (Figure 3a). Capacitive sensitivity is 20 pfd/cm giving a signal sensitivity of 0.5 V/cm.

The probe unit is driven by a 20 V D.C. power supply. The wave information in D.C. volts from the probe activates an operational amplifier (Fig. 2, C and Fig. 3) programmed as a subtracting amplifier, deleting the signal due to static water level (Fig. 2, A), and also serving as the resultant output sensitivity control (Fig. 2, E). This proved to be very useful when the experiments required an array of probes, and led to standardized calibration for all probes. The signal from the subtracting amplifier activates an oscillograph recorder for graphic analysis of wave properties (Figure 4).

The signal from the subtracting amplifier also goes to a second operational amplifier programmed to interact with a capacitor to perform a graphic integration of the wave amplitude (Fig 2,B and Fig 3) The output from this unit activates an oscillograph recorder for graphic analysis of the wave volume (Figure 4) A ramp control is used to offset potential that may have accumulated in the integrator unit before the arrival of the wave

This brief summary given in this section will be considerably amplified in a forthcoming technical report, White and Miller, Tech Rept No 10, 1970

Results

Figure 5 shows the changes in wave mode as a function of distance from the impulse source Four initial wave modes are recognized These are, in order of increasing initial energy with the lowest first, "sinusoid", "solitary", "undular bore" and fully developed bore (See Figure 4)

The following conclusions are drawn

- 1 The fully developed bore decays rapidly to the unbroken undular bore form (Figs 5, 6, 7)
- 2 The lead wave of the undular form takes on the "solitary" mode leaving behind the rest of the "undular" wave In several cases, the second and even the third undulations in turn take on the "solitary" mode (Figs 5e,f)
- 3 The "sinusoid" mode generated at short piston displacements transforms gradually as the trailing trough rises to the undisturbed water level, and finally enters the "solitary" mode (Figs 5a-f)

¹The term "solitary" is applied to the stable, symmetrical form which satisfies the following conditions

- 1) both leading and trailing portions asymptotically approach the static level
- 2) phase velocity agreed well with Laitone's 1961 wave speed equation taken to the first three terms $C = \sqrt{gd} \left(1 + \frac{1}{2} \frac{H}{d} - \frac{3}{20} \left(\frac{H}{d} \right)^2 + \right.$
- 3) amplitude as a function of volume, agrees well with the relationship given by Kuelegan and Patterson, 1940 $h_1 = \frac{3Q^2}{16H^3}$ where h_1 is max amp, Q is cross-sectional area, and H is static water depth

- 4 The Froude number² gradient indicates no striking irregularities, and indicates that all wave modes are in the breaking regime at approximately $F_{\bar{v}} = 1.26$ (Figure 6)
- 5 The experimentally established line dividing the breaking region from the unbroken region seems to be independent of wave mode. The breaking wave region occupies about half of the l/d , $F_{\bar{v}}$ plane very near the impulse source at $D/d = 10$ and decreases steadily toward the upper right corner at $D/d = 188$ (Figure 5)
- 6 There appears to be no alternative to the conclusion that given a predictable distance down channel from the impulse source, all impulse waves will assume the "most stable" mode in agreement with the prediction of Boussinesq, 1872, i.e. the "solitary" form has the minimum "moment of instability" and in agreement with the discussion in Keulegan and Patterson, 1940 p. 87
- 7 The decay sequence for a fully developed bore at the impulse source is: Bore \rightarrow undular bore \rightarrow lead undulation becomes solitary, + trailing undular bore consisting of remaining undulations \rightarrow lead undulation solitary + second undulation becomes solitary \rightarrow in several runs three successive solitary forms have emerged from the preceding undular form

Discussion

The graphs given in Figures 5, 6 and 7 form a relatively complete set of prediction curves for waves created by a horizontal impulse, surface to bottom. From these graphs, it is possible to predict the wave type, maximum wave amplitude, and maximum "phase speed" for any impulse wave within the estimated natural impulse generating range. These are open ended predictions, however. For example, the published l/d for "Shot Baker" at Bikini in the late 1940's is approximately 5.5 (Johnson and Bernel, 1949). The $F_{\bar{v}}$ value is undoubtedly very high but not available. In the landslide case, I have estimated l/d to be about 8.0 based on examination of landslide scars on coastal charts, if one takes avalanche figures for displacement velocity, the $F_{\bar{v}}$ values may easily exceed 40.0. Large scale seismic movements are particularly difficult to estimate, but for a submarine overthrust, l/d less than 1.0 and $F_{\bar{v}}$ less than 0.3 may be reasonable. In general, natural impulses yielding l/d values in excess of 9.0 coupled with $F_{\bar{v}}$ greater than 1.0

²Since this Froude number is based on an average phase velocity, it is insensitive to changes in velocity over the wave profile during transformations. I have found that the Boussinesq velocity on the other hand does bring out these changes quite clearly.

should not change the pattern of the prediction graphs. The wave mode will be either an undular bore or fully developed bore, with the same transition and decay sequence found in this study, differing only in magnitude. I feel extrapolation in this sense is justified. The very low λ/d high F_v corner of the graphs is a different matter. My present generating system will not produce impulses in this region. It would appear that some other sort of impulse generating mechanism should be devised for this region of the $\lambda/d, F_v$ plane.

Finally, it seems suggestive that the linear theoretical models for impulse waves of the type discussed in Lamb (1932, Art 238ff) are inadequate. For example, Cauchy-Poisson wave trains are not generated by this type of impulse mechanism in which the initial conditions include a velocity and surface elevation. This is in clear contrast to the experiments of Prins 1958 where the initial conditions include a surface elevation but no initial velocity. It is interesting to note that Prins found wave modes similar to those described in this paper but also for the low energy impulse, obtained an oscillatory wave region of the Cauchy-Poisson type. It is possible that a similar type of wave may exist in the low λ/d very high F_v region (Figure 5) which in my study was not investigated. Further development of the more realistic non-linear models, Perigrine 1968, is required to fit the "real" case
1969,

Acknowledgements are due to Robert V. White who is responsible for a major portion of the sensing and recording system, to L. F. McGoldrick for advice and comment on almost all phases of the study, and to J. M. Witting for several illuminating discussions. This study was supported by the Office of Naval Research Geography Branch, N0014-67-A-0285-0013

Bibliography

- Boussinesq, J Theorie des ondes etc Liouville's Jour Vol 17, 1872
- Johnson, J W and K J Bermel Impulsive waves in shallow water as generated by falling weights Trans A G U V 30, No 2, April, 1949, pp 223-230
- Kuelegan, G H and G W Patterson Mathematical theory of irrotational translation waves Jour of Res of Nat Bur Standards, Vol 24, R P 1272, 1940
- Laitone, E V Higher approximation to non-linear water waves and the limiting heights of Cnoidal, Solitary and Stokes waves Inst of Eng Res Tech Rept 89-6, Berkeley, Calif, 1961
- Lamb, H Hydrodynamics, 6th Edition, Dover Press (1st' Ed) 1932
- McGoldrick, L F A system for the generation and measurement of capillary-gravity waves Office of Naval Research, Tech Rept No 3, August 1969
- Miller, R L and R V White A single impulse system for generating solitary, undulating surge and gravity shock waves in the laboratory Tech Rept No 5, Fluid Dynamics Lab, Dept Geophys, Univ of Chicago, 1966
- Perigrine, D H Long waves in a channel of arbitrary cross-section Jour Fluid Mech 32, 353-365, 1968
- ibid, Solitary waves in trapezoidal channels Jour Fluid Mech 35, 1-6, 1969
- Prins, J E Characteristics of waves generated by a local disturbance Trans A G U Oct 1958 pp 865-874
- White, R V and R L Miller An electrical system for sensing and analysing wave properties including integration and differentiating capability Tech Rept No 10, Fluid Dynamics Lab, Dept Geophys Sci, Univ of Chicago (In press)

Figure Captions

FIGURE

- 1 Schematic of wave generating and wave sensing system For details of the wave tank facility see Miller & White, 1966
- 2 Flow sheet for wave recording and integrating systems
- 3 Detailed schematic of operational amplifiers, wave recording and integrating
- 3a Capacitance probe unit for sensing waves
- 4 The four possible wave modes due to a single horizontal impulse The cross-sectional area of fluid displaced by the piston is matched against the cumulative curve (integration over wave height) B in the figure This produces a cut-off point (A) on the wave trace where the cross-sectional area under the wave trace is equivalent to the cross sectional area of the fluid volume at the impulse source due to the several damped back and forth oscillations which occur after the magnetic brake has been applied
- 5 The wave mode field as a function of impulse displacement ℓ/d and speed of displacement in Froude number form $F_{\bar{V}}$ or (\bar{V}/\sqrt{gd}) for fixed distances from the impulse source ℓ is piston displacement d is undisturbed water depth D is distance from impulse source and $\bar{V} = \ell/t$ where t is elapsed time during piston displacement Note that in 5a at $D/d = 10$ closest to the source, there is no "solitary" wave region, whereas the "solitary" region is significant $D/d = 65$, and dominant at $D/d = 150$
- 6 Froude number gradient, $F_{\bar{V}}$, superimposed on the wave mode field at $D/d = 10, 65, 150$ Note that the breaking region retreats steadily toward the upper right corner with increase in distance from impulse source, and that the breaker line always lies between $F_{\bar{V}} = 1.25$ and 1.30
- 7 Maximum wave amplitude gradient superimposed on wave mode field for $D/d = 10, 65, 150$ Because of the relatively coarse contour interval, the abrupt drop in maximum amplitude from smooth to breaking appears only in Fig 7b, at $D/d = 65$

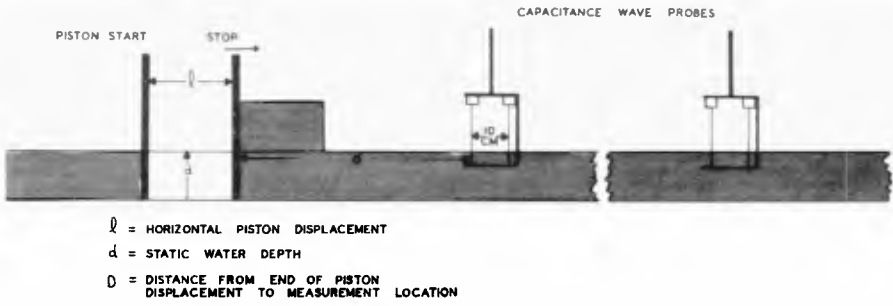


Fig. 1

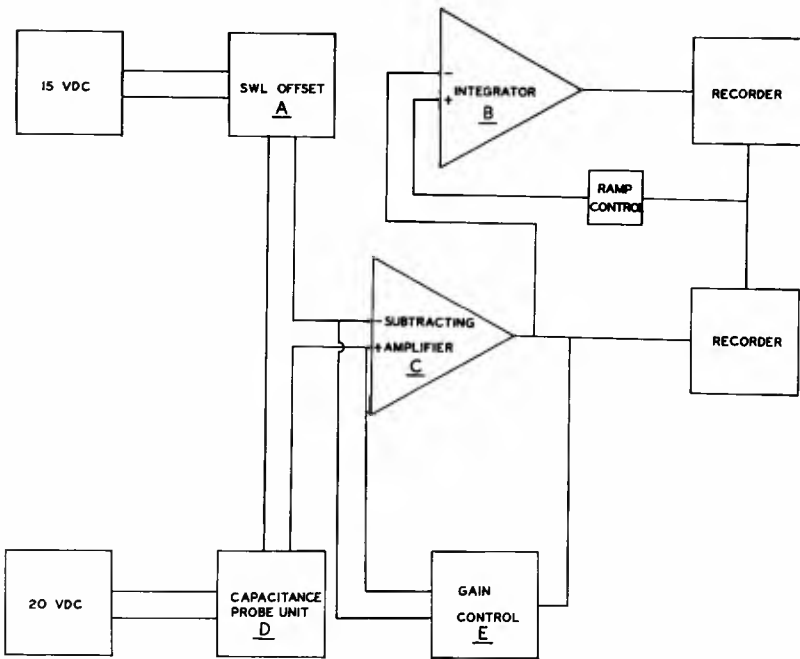


Fig. 2

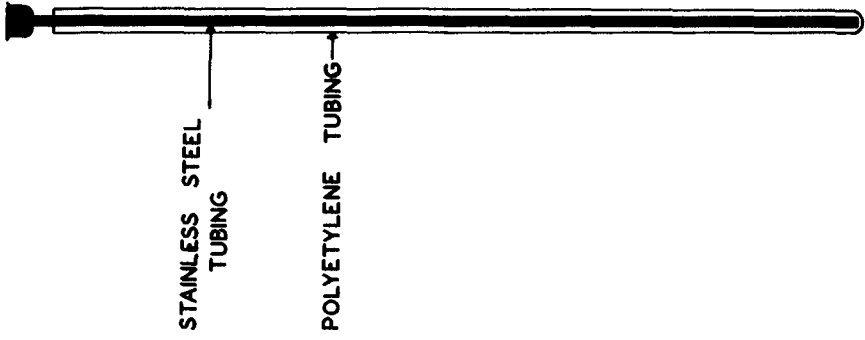


Fig 3a

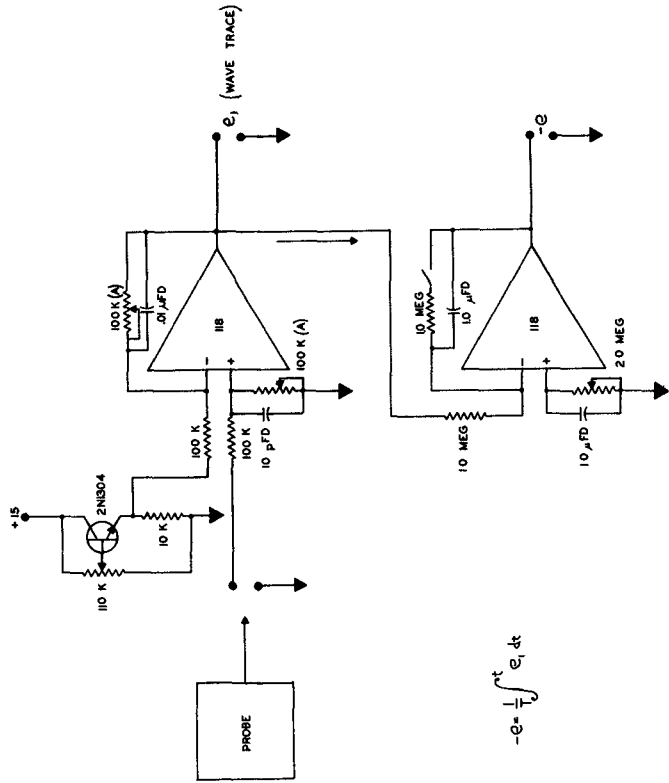
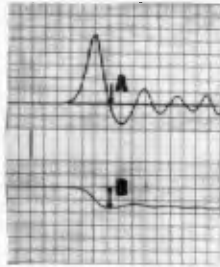
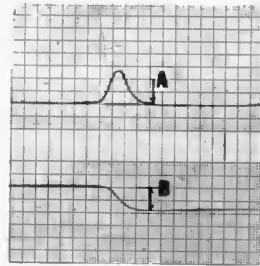


Fig 3

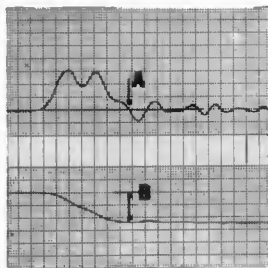
WAVE MODES



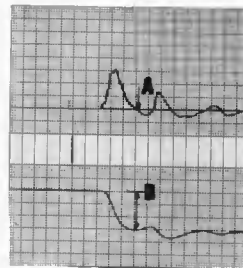
"SINUSOIDAL"



"SOLITARY"



UNDULAR BORE



FULLY DEVELOPED BORE

Fig. 4

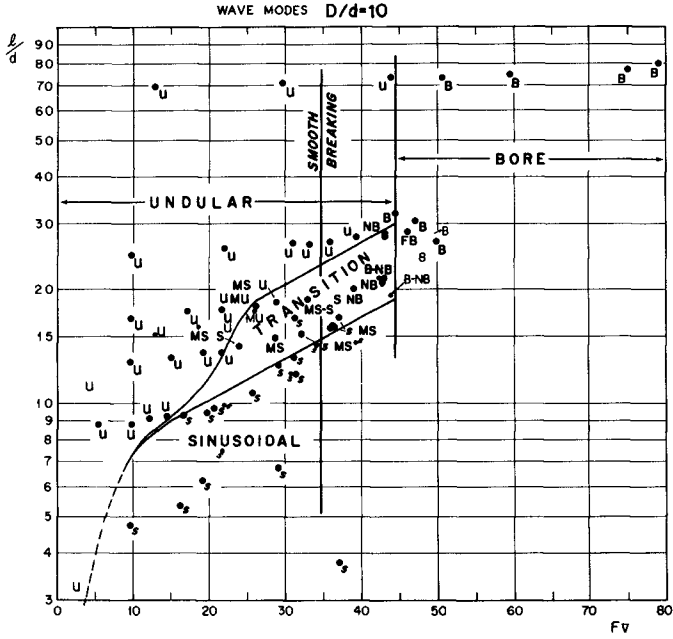


Fig 5a

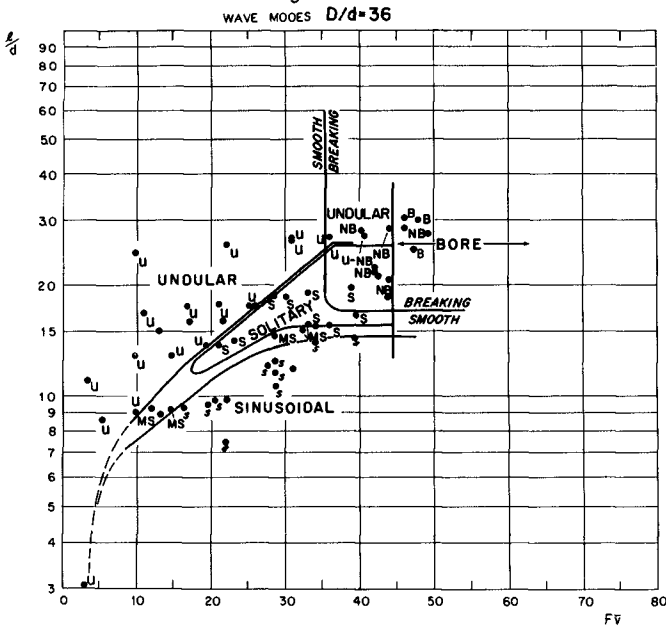


Fig 5b

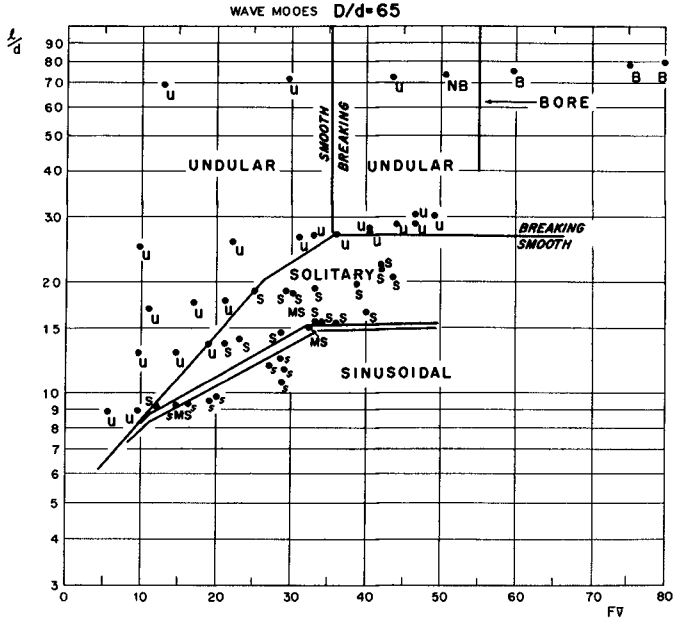


Fig 5c

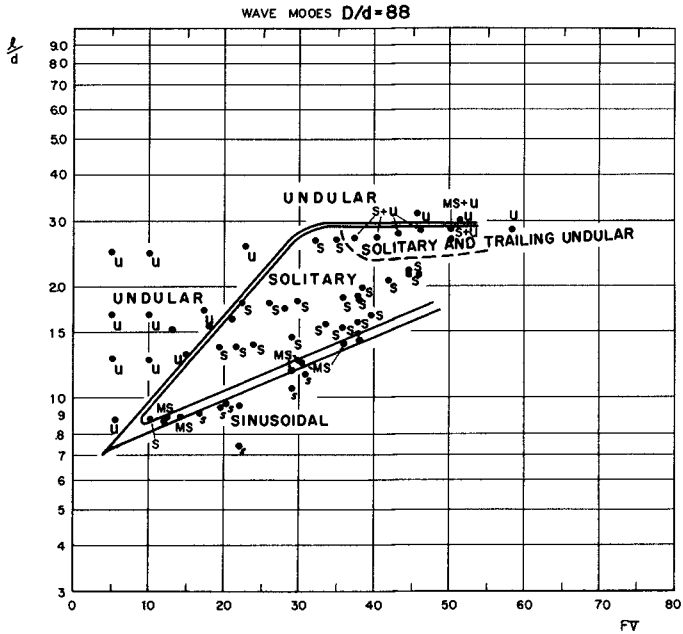


Fig 5d

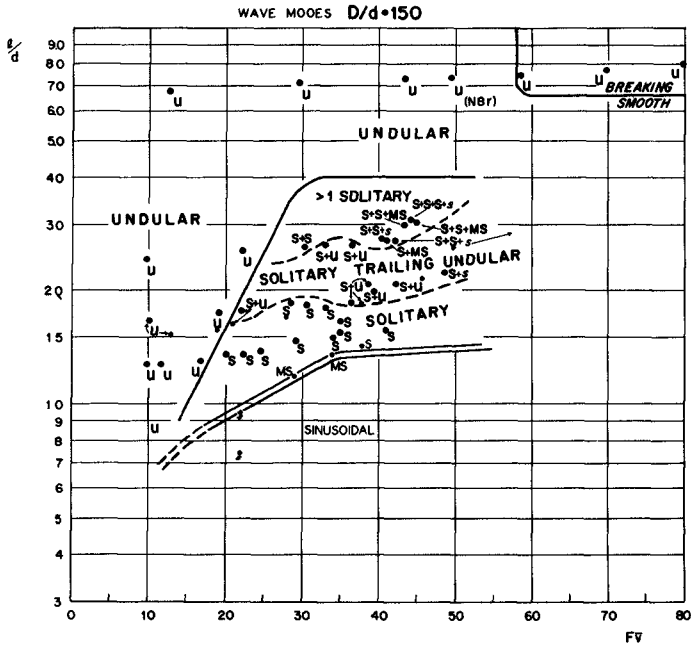


Fig 5e

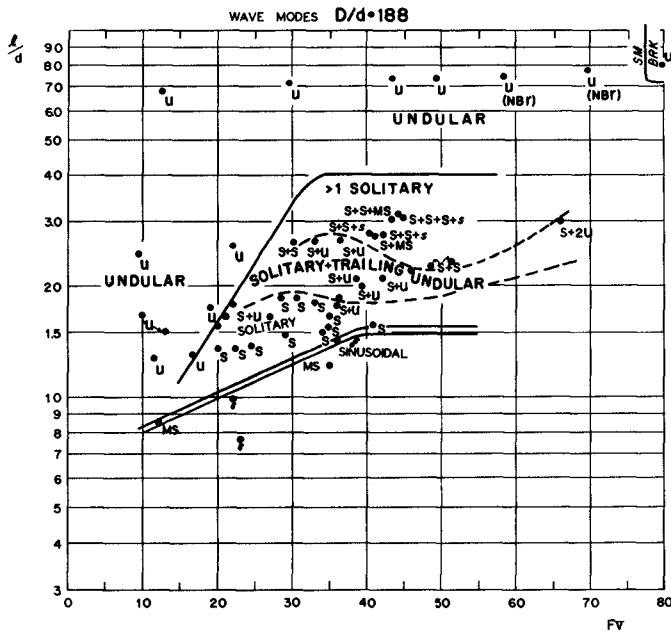


Fig 5f

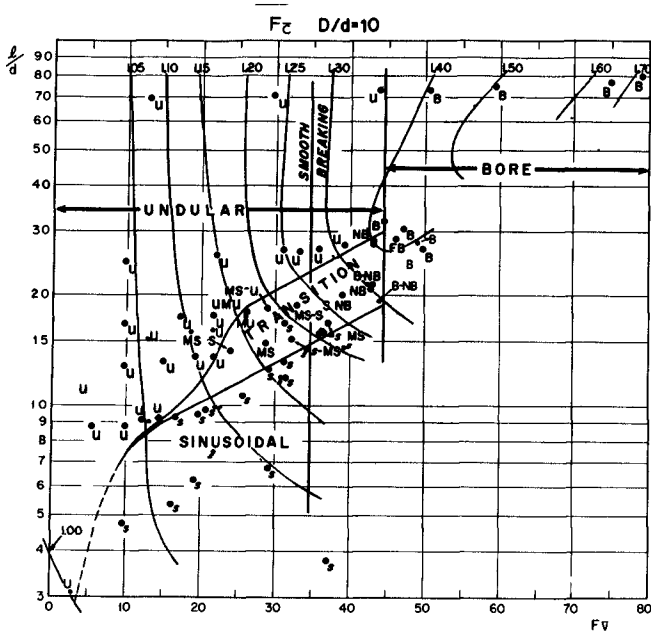


Fig 6a

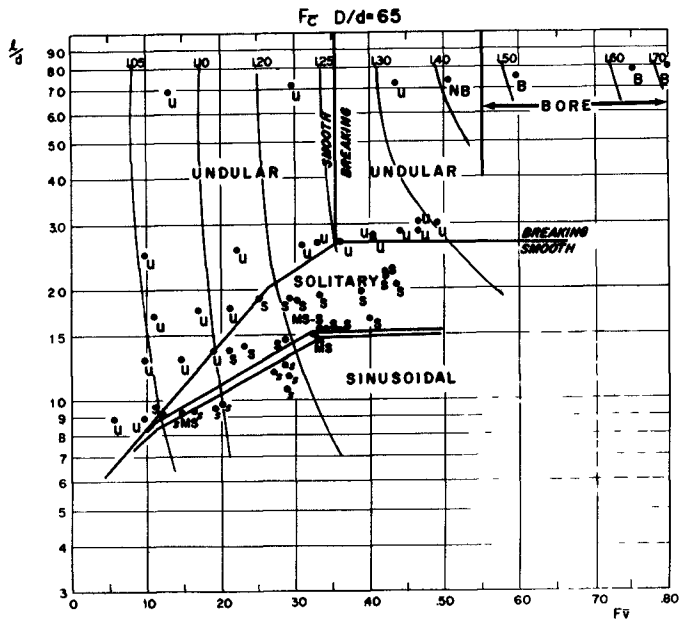


Fig 6b

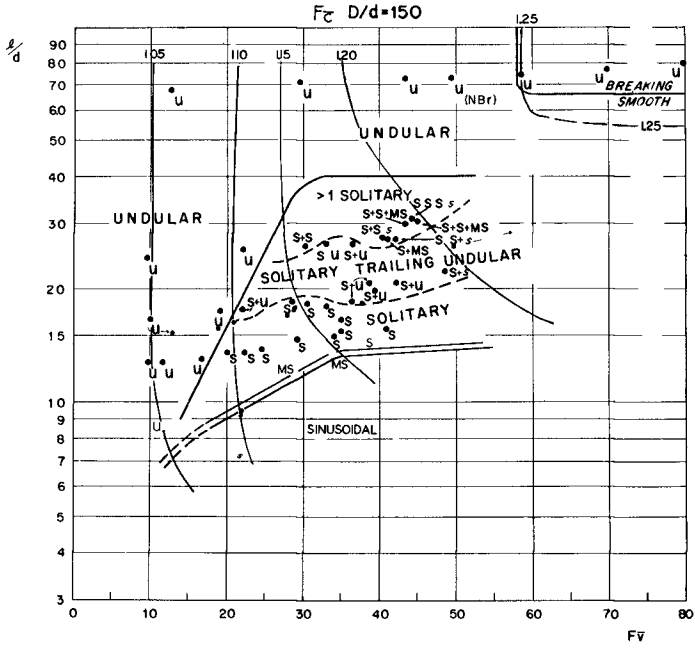


Fig 6c

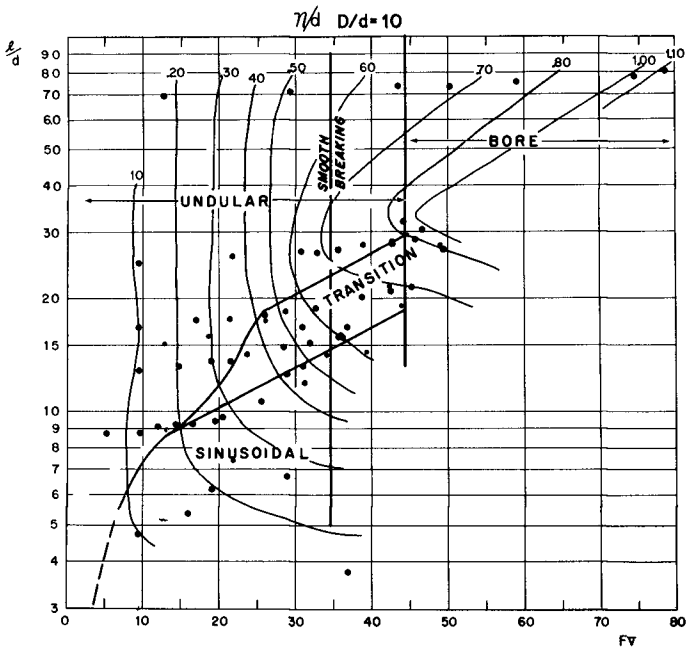


Fig 7a

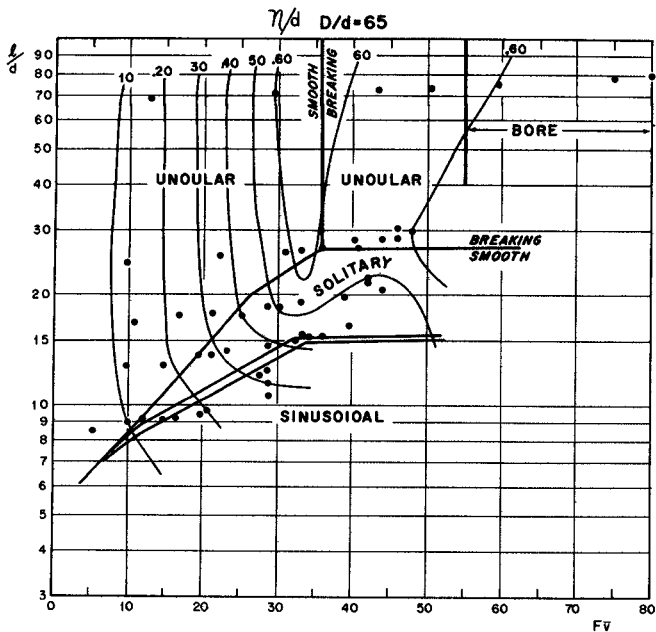


Fig 7b

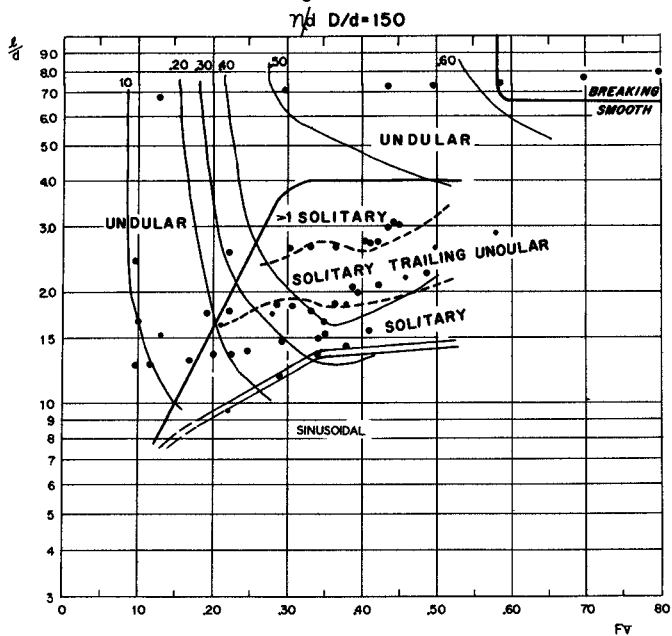


Fig 7c

CHAPTER 38

DIMENSIONAL ANALYSIS - SPURIOUS CORRELATION

by

M S Yalin
Professor, Department of Civil Engineering,

and

J W Kamphuis
Associate Professor, Department of Civil Engineering,
Queen's University at Kingston, Canada

ABSTRACT

Dimensional analysis and errors leading to spurious correlation are presented using a number of practical examples

INTRODUCTION

The theory of dimensions has been subject of considerable controversy and only in the last few decades has it been agreed that dimensional methods can serve as a powerful tool in experimental investigations of physical phenomena. Its effectiveness becomes especially noticeable when the number of factors involved is large and the theoretical knowledge is insufficient.

However, like any other mathematical tool, the theory of dimensions can supply correct and useful results only if it is properly applied. One example of improper application is the introduction of an exaggerated and sometimes simply of a nonexistent correlation between the experimental results. The purpose of the present paper is to analyse these kinds of spurious correlation.

OUTLINE OF GENERAL PRINCIPLES

For detailed information on the principles of the theory of dimensions the reader is referred to Refs (1), (2), (3), here only those points will be mentioned which have a direct bearing on the present analysis.

In general, a physical phenomenon corresponding to a specified geometry can be described by a number of independent quantities a_1, a_2, \dots, a_n referred to as the characteristic parameters. Accordingly any quantitative property b of the phenomenon under consideration must be given by a functional relation such as

$$b = f(a_1, a_2, \dots, a_n) \quad (1)$$

where the quantities a_1 and b are usually dimensional. Since all

physical relations must be dimensionally homogeneous, using the Π theorem of the theory of dimensions, one can express the above relation in a dimensionless form as

$$Y = \Phi (X_1, X_2, \dots, X_{n-k}) \quad (2)$$

Here, k is the number of fundamental units, while Y and X_j ($j = 1, 2, \dots, n-k$) are the following dimensionless power products

$$Y = b \prod_{i=1}^k a_i^{\beta_i} \quad (3)$$

$$X = a_j \prod_{i=1}^k a_i^{\alpha_i} \quad (4)$$

The dimensionless quantities Y and X_j can be interpreted as the dimensionless versions of b and a_j respectively. The k parameters a_i ($i = 1, \dots, k$) which are common in the expressions of X_j and Y are often called the basic quantities or the "repeaters".

Although either system may be used in experimental work, Eq. 2 has some definite advantages over Eq. 1 and these are described in standard works on the theory of dimensions, e.g. Refs (1, 2, 3). The most important advantages are -

- a) Eq. 2 is independent of the system of units used,
- b) the number of variables on the right hand side of the equation has been reduced by k ,
- c) the dimensionless variables (X_j) are criteria of similarity

VARIATION OF THE DIMENSIONLESS CHARACTERISTICS, SPURIOUS CORRELATION

In a correctly designed experimental investigation, the variation of Y is achieved by varying only one X_j at a time. In such cases, one deals with a set of functions of only one variable, as below

$$Y_j = \Phi (\text{Const}_1, \text{const}_2, \dots, X_j, \dots, \text{const}_n) = \phi_j(X_j) \quad (5)$$

Accordingly in the following, the consideration of Eq. 2 will be replaced by its special case, Eq. 5, while the subscript j will be omitted

Differentiating Eqs. 3 and 4, one arrives at the following relations which represent the most general versions of variation of Y and X_j

$$dY = b \prod_{i=1}^k a_i^{\beta_i} \left[\frac{db}{b} + \sum_{i=1}^k \beta_i \frac{da_i}{a_i} \right] \quad (6)$$

$$\frac{dY}{Y} = d(\ln Y) = d(\ln b) + \sum_{i=1}^k \beta_i d(\ln a_i) \quad (7)$$

$$dX = a_j \prod_{i=1}^k a_i^{\alpha_i} \left[\frac{da_j}{a_j} + \sum_{i=1}^k \alpha_i \frac{da_i}{a_i} \right] \quad (8)$$

$$\frac{dX}{X} = d(\ln X) = d(\ln a) + \sum_{i=1}^k \alpha_i d(\ln a_i) \tag{9}$$

Three typical methods of variation of Y and X_j are discussed below

Case I Variation of Y and X is achieved by varying b and a only and by keeping the basic quantities a₁ constant. Substituting da₁ = 0 into Eqs 6 and 8, one arrives at

$$\frac{dY}{dX} = C \frac{db}{da} = C' \frac{db}{dX} \tag{10}$$

where

$$C = \frac{\prod_{i=1}^k a_i^{\beta_i}}{\prod_{i=1}^k a_i^{\alpha_i}} \quad \text{and} \quad C' = \frac{\prod_{i=1}^k a_i^{\beta_i}}{\prod_{i=1}^k a_i^{\alpha_i}} \tag{11}$$

Hence, the variation of Y with X is proportional to the variation of b with a (and of b with X) and therefore the dimensionless relationship between Y and X is merely a scaled down version of the dimensional relationship between b and a (The scale of the ordinate is C times the scale of the abscissa)

For example, consider the decay of an impulsively generated wave with distance (4). The wave height H (which should be identified with b) may be plotted against the distance, s (to be identified with a) as in Fig 1a. On the other hand, one can plot the dimensionless quantities $Y = \frac{H}{h}$ and $X = \frac{s}{h}$ against each other - Fig 1b. Since the common parameter h, the water depth (which is to be identified with one of a₁) has not been varied, Figs 1a and 1b are merely scaled down versions of each other. For the present example C = 1 and thus the curves in Figs 1a and 1b are geometrically similar. From Eqs 7 and 9 it follows that

$$\frac{d(\ln Y)}{d(\ln X)} = \frac{d(\ln b)}{d(\ln a)} = \frac{d(\ln b)}{d(\ln X)} \tag{12}$$

is also valid, which implies that, in the case under consideration, the variation of Y and X in a logarithmic system is identical to that of b and a (or of b and X)

Case II Variation of Y and X is achieved by keeping the parameter a constant and by varying b and one or more of basic quantities a₁. Substituting da = 0 into Eqs 7 and 9 one obtains

$$\frac{d(\ln Y)}{d(\ln X)} = \frac{d(\ln b)}{d(\ln X)} + m \tag{13}$$

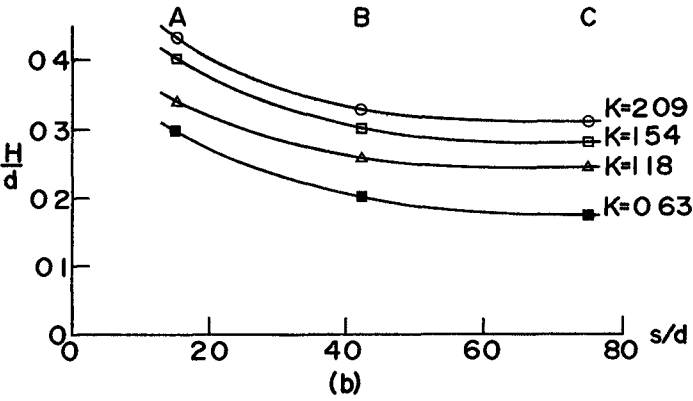
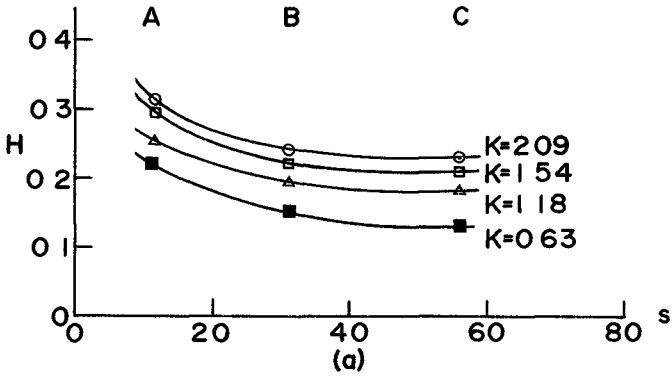


Fig 1 Dimensional and Dimensionless Plots

where

$$m = \frac{\sum_{i=1}^k \beta_i \frac{da_i}{a_i}}{\sum_{i=1}^k \alpha_i \frac{da_i}{a_i}} = \frac{\sum_{i=1}^k \beta_i d(\ln a_i)}{\sum_{i=1}^k \alpha_i d(\ln a_i)} \tag{14}$$

If only one of the basic quantities, e.g. a_1 is varied, then the expression for m reduces to

$$m = \frac{\beta_1}{\alpha_1} \tag{15}$$

The present case is very common in practice

Consider, for instance, the familiar plot of the drag force acting on a sphere in an infinite fluid flow (Fig 2) The dimensional relationship - analogous to Eq 1 - is

$$F = f(U, D, \rho, \mu) \tag{16}$$

where F is the drag force, U the velocity of the undisturbed flow, D , the sphere diameter, ρ the fluid density and μ the dynamic viscosity. The quantities F, μ, U, D and ρ must be identified with b, a, a_1, a_2 and a_3 of Eq 1 respectively

The dimensionless form - analogous to Eq 2 - is

$$Y = \frac{F}{U^2 D^2 \rho} = \phi(X) = \phi\left(\frac{UD\rho}{\mu}\right) \tag{17}$$

Note that Eq 16 contains four variables whereas Eq 17 contains only one, i.e. the problem has been simplified considerably by introducing the dimensionless form! Let us now assume that the variation in flow is achieved by varying only one basic quantity (common parameter) U . The variation of U alone will certainly induce the variation of the drag force F and the experimental procedure carried out in this manner will form an example for the present case. The experimental relation between Y and X shown in Fig 2 indicates that

$$\frac{d(\ln Y)}{d(\ln X)} = -1$$

is valid. On the other hand from the expression for Y and X (Eq 17) it follows that $m = -2$. Accordingly, Eq 13 gives

$$\frac{d(\ln b)}{d(\ln X)} = \frac{d(\ln Y)}{d(\ln X)} - m = 1$$

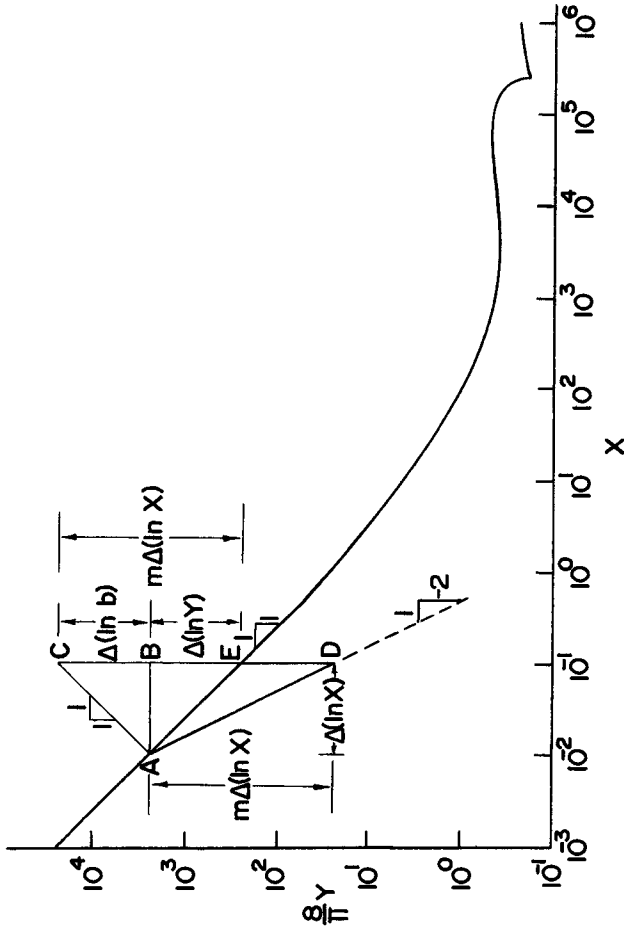


Fig 2 Drag Force on a Sphere

and in terms of finite differences

$$\Delta (\ln Y) = \Delta (\ln b) + m \Delta (\ln X)$$

In Fig 2 the increment $\Delta(\ln X)$ along the abscissa is shown by the horizontal distance \overline{AB} , the decrement $\Delta(\ln Y)$ along the ordinate being \overline{BE} . In Fig 2 the decrement \overline{BE} is shown as the algebraic sum of the increment $\Delta(\ln b) = \overline{CB}$ and the decrement $m\Delta (\ln X) = \overline{BD} = \overline{CE}$, i.e. as implied by the equation above. It follows, that the correlation between Y and X, achieved by varying a_1 (and consequently b) is as legitimate as that achieved by varying a (and b) as in the previous case. The difference is that in the case I the variation \overline{AE} is achieved directly, whereas in the present case it yields itself as the "resultant" of the "component variations" \overline{AC} and \overline{AD} .

Note, however, that the variation of Y with X can characterise the variation of b with a only, as has been shown in the case I. It cannot characterise the variation of b with any of the common parameters a_1 . Observe from Fig 2 that the value of Y decreases (along \overline{AE} with X, whereas the value of b increases (along \overline{AC}) with $a_1 = U$.

Case III Variation of Y is achieved without varying b. Substituting $d(\ln b) = 0$ into Eqs 7 and 9, one obtains

$$\frac{d(\ln Y)}{d(\ln X)} = \frac{m}{1 + \frac{k}{\sum_{i=1}^n \alpha_i} d(\ln a_i)} \tag{18}$$

and if a is kept constant,

$$\frac{d(\ln Y)}{d(\ln X)} = m \tag{19}$$

Eq 19 is simply Eq 13 without the first term which reflects the influence of the variation of b, the dimensional term responsible for the existence of Y. Hence a correlation between Y and X, obtained as described above is completely spurious. Indeed the correlation implied by the present case can only be due to the variation of the common quantities a_1 . If the parameters a_1 vary only, then the quantities Y and X also vary, and Y can be plotted against X in the form of a curve, even if b in actual fact does not depend on a at all. With reference to Fig 2, the curve of spurious correlation is the line \overline{AD} which implies the following case of Eq 19

$$\frac{d(\ln Y)}{d(\ln X)} = -2$$

and which is due to the variation of the common quality $a_1 = U$ alone. Hence, even if F had not been a function of μ at all, by applying the procedure described in the present case, one could still obtain a

correlation between Y and X, in the form of the line \overline{AD} , which would, of course, be completely spurious

Integrating Eq 19, one obtains

$$Y = CX^m \quad (20)$$

which is a straight line in the logarithmic system of co-ordinates and where C is given by

$$C = \frac{b}{a^m} \prod_{i=2}^k a_i^{(\beta - m\alpha_i)} \quad (21)$$

It follows that

- a) any correlation between Y and X obtained without varying b is spurious (unless a special subset of Eq 16 is chosen, where U, D, o and μ are not independent, thus violating the basic assumptions),
- b) in a log-log system of co-ordinates, this spurious correlation forms a straight line,
- c) the position and slope of the straight line of spurious correlation is, a priori, predictable, it is determined by Eqs 19 and 20

When analysing experimental plots, in case of doubt it is advisable to determine and plot the family of straight lines S_1 of spurious correlation (Fig 3) and to check the trend of the experimental points accordingly. If the dimensional analysis has been performed improperly and the original quantities are not truly independent, then the variation of a_1 brings about unexpected variation in a or b and spurious correlation will take place along a curve Γ (Fig 3). This is also a point to be kept in mind

A special case occurs when experimentally

$$Y = \phi(X) = CX^m \quad (22)$$

and the lines of spurious correlation and genuine correlation coincide

Consider, for example, the length $\Lambda = b$ of dunes forming on the bed of a two dimensional rough turbulent flow with a mobile bed. According to (5), this length may be expressed by the following functional relation

$$\Lambda = f(D, \rho, v_*, h) \quad (23)$$

where $D = a_1$ is the grain size, $\rho = a_2$ is the fluid density, $v_* = a_3$ is the shear velocity and $h = a_4$ is the flow depth

The relation above can be expressed in dimensionless form

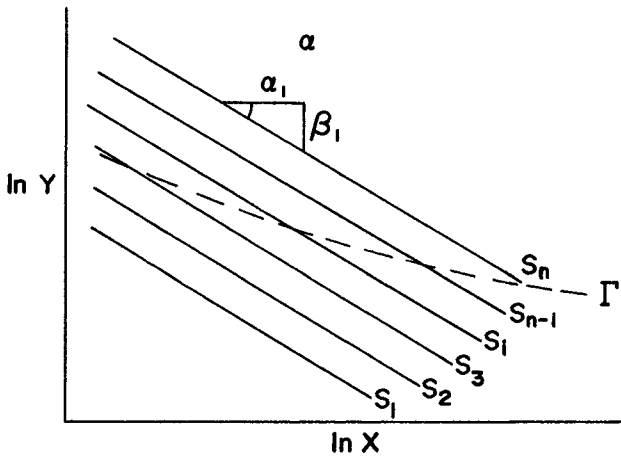


Fig 3 Lines of Spurious Correlation

as follows

$$Y = \frac{\Lambda}{D} = \phi(X) = \phi\left[\frac{h}{D}\right] \quad (24)$$

If the grain size $D = a_1$ is varied only, then Eqs 20 and 21 give

$$Y = CX \quad (25)$$

which implies that the lines of spurious correlation in a log-log system are straight lines with slope $m = 1$. On the other hand, the experimental results (obtained from experiments where $\Lambda = b$ is varied over a large range) indicate that the genuine correlation between Y and X is given by the linear relation

$$Y = 2\pi X \quad (26)$$

which also a straight line with the slope $m = 1$

The lines of spurious correlation and the real relationship can coincide as in example above only if the parameter a_1 is a "spurious parameter". This can be deduced from Eqs 3, 4 and 20 and indeed, the relation above which can be expressed as

$$\Lambda \approx 2\pi h \quad (27)$$

indicates (contrary to the theoretical expectation) that the dune length Λ actually does not depend on the grain size $a_1 = D$

EXAGGERATION OF THE ACTUAL CORRELATION

In practical applications, an existing correlation is often exaggerated by plotting common quantities along both co-ordinate axes (6). The explanation is given here in terms of a dimensionless system, however, the same argument is true for dimensional quantities

Consider the functional relation

$$Z = \psi(X) \quad (28)$$

where Z is the product

$$Z = Y X^N \quad (29)$$

and where Y implies

$$Y = \phi(X) \quad (30)$$

From Eq 28 one obtains

$$d(\ln Z) = d(\ln Y) + N d(\ln X)$$

and thus

$$\frac{d(\ln Z)}{d(\ln X)} = \frac{d(\ln Y)}{d(\ln X)} + N \tag{31}$$

This equation indicates how in a log-log system of co-ordinates the rate of change with X can be increased by plotting the product $Z = YX^N$ rather than simply Y versus X

For example if

$$\frac{d(\ln Y)}{d(\ln X)} = \tan \theta = 1$$

then the plot Y vs X is a 45° straight line, as shown in Fig 4 a. It is assumed that the experimental points forming this straight line are scattered in a "ribbon" of the thickness w_a

If the product $Z = YX^N$ is used as ordinate, and if for example the value of N is 2, then from Eq 30

$$\frac{d(\ln Z)}{d(\ln X)} = 1 + 2 = 3$$

is valid, which implies that the straight line becomes steeper by a factor 3, while the thickness of the scatter-ribbon decreases by a factor

$$\frac{w_b}{w_a} = \sqrt{\frac{1 + N^2 \tan^2 \theta}{1 + \tan^2 \theta}} = \sqrt{\frac{5}{2}} = 1.58$$

(Fig 4b) Thus the relative thickness of the scatter ribbon, i.e.

$$\frac{\text{thickness of scatter-ribbon}}{\text{length of the line}}$$

is reduced by factor

$$\frac{1 + N^2 \tan^2 \theta}{1 + \tan^2 \theta} = \frac{5}{2} = 2.5$$

One can say that the correlation can be improved 2.5 times by plotting $Z = YX^2$ rather than simply Y against X. Such an "improvement" is nothing else but an optical illusion and is not legitimate, for the dimensionless version of the quantity b under investigation, as supplied by the π - theorem, is Y, not YX^N . These kinds of illegitimate plots are recognisable by the presence of the parameter a (which should be present only in the expression of X) in the power product implying the ordinate.

SUMMARY

The experimenter is free to choose between a dimensional representation, Eq 1, or a dimensionless representation, Eq 2 of the

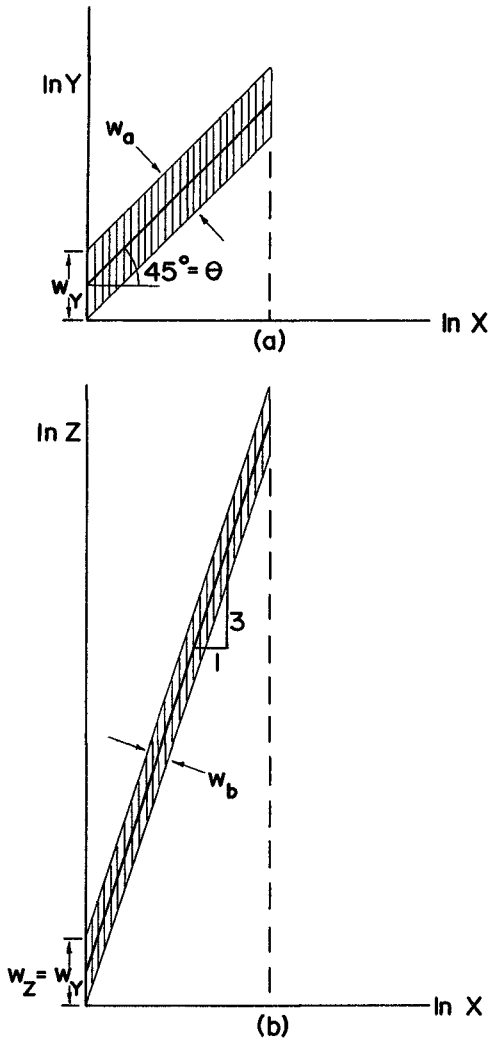


Fig 4 Exaggerated Correlation

phenomenon under investigation. The latter is found to have certain obvious advantages. Once a decision is made, all the subsequent analysis is expressed in terms of the system chosen. For instance if the dimensionless system is chosen, then the results should not be interpreted in terms of the individual dimensional parameters that form the dimensionless variables since the real variables of the experiment are the dimensionless variables.

The usual cause of spurious correlation is the appearance of common quantities along both co-ordinate axes. This is true for both a dimensional and a dimensionless system. This must not be confused with the appearance of common dimensional parameters along both co-ordinate axes when dimensionless variables are plotted against each other.

In addition, when considering dimensionless variables, care must be taken that the relationship between Y and X is not brought about only by variation of one or more of the repeating dimensional parameters common to both.

ACKNOWLEDGEMENTS

The authors wish to thank Dr A. Brebner who urged the writing of this paper.

APPENDIX 1 - REFERENCES

- 1 Sedov, L. I., Similarity and Dimensional Methods in Mechanics, Academic Press, New York, 1959.
- 2 Langhaar, H. L., Dimensional Analysis and Theory of Models, John Wiley and Sons, New York, London, 1962.
- 3 Birkhoff, G., Hydrodynamics, a Study in Logic, Fact and Similitude, Princeton, Harvard University Press, 1950, Dover, 1955.
- 4 Kamphuis, J. William and Bowering, Richard. "Impulse Waves", 12th Conference on Coastal Engineering, Washington, Sept. 1970.
- 5 Yalin, M. S., "Geometric Properties of Sand Waves" Journal of the Hydraulics Division, ASCE, Vol. 90, No. HY5, Sept. 1964, pp. 105-119.
- 6 Benson, Manuel A., "Spurious Correlation in Hydraulics and Hydrology", Journal of the Hydraulics Division, ASCE, Vol. 91, No. HY4, July 1965, pp. 35-42.

APPENDIX II - NOTATION

a_1	=	dimensional basic quantities (repeaters),
a_j	=	non repeating dimensional independent quantities,
b	=	dimensional dependent parameter,
C	=	constant,
D	=	diameter or grain size,
F	=	force,
f	=	dimensional function,
H	=	wave height,
h	=	depth of flow,
K	=	constant,
k	=	number of fundamental units,
m	=	constant (usually slope),
N	=	exponent,
s	=	distance,
U	=	approach velocity,
v_*	=	shear velocity,
w	=	scatter band width,
X_j	=	dimensionless independent variable,
Y	=	dimensionless dependent variable,
Z	=	dimensionless dependent variable,
α_1	=	exponent,
β_1	=	exponent,
Λ	=	dune length,
μ	=	dynamic viscosity,
Π	=	product,
ρ	=	density,
Σ	=	sum,
Φ	=	dimensionless function,
ϕ	=	dimensionless function of a single dimensionless variable



West Hampton, New York

PART 2. COASTAL SEDIMENT PROBLEMS

East Hampton, New York



CHAPTER 39

COASTAL PROCESSES FROM SPACE PHOTOGRAPHY

By Maynard M. Nichols
Virginia Institute of Marine Science
Gloucester Point, Virginia 23062, U.S.A.

ABSTRACT

Photographs taken from space provide a new source of data concerning coastal processes. By utilizing the high vantage point and broad view orbiting space cameras can record little known large-scale processes at short time intervals. Major outflow plumes, fresh-salt water "fronts", turbidity maxima and massive effluents are among the wide range of features displayed. It is shown from selected examples how coastal processes can be evaluated from space photography and how the information may be of use for solving certain problems as a supplement to field and other remote sensing data. By 1972 satellite photography will be available on a routine basis for many coasts of the world. Engineers are urged to consider the potential for improving their information which space photography has to offer.

Introduction

The "promise of space" has commanded a great deal of attention in recent years. In particular, considerable credit has been given to the potential usefulness of space photography. It has been asserted that space photography can record the location of fish-rich upwellings and mineral deposits, it can detect pollutants and diseased crops and inventory various natural resources, all on a global basis. Though photography has contributed a great deal to our knowledge in many fields, study of coastal processes important to the coastal engineer, has been limited. In recognition of this gap, this paper directs attention to space photography as a new source of information on aspects of coastal processes. What coastal features can be recorded by space photography? How can processes be evaluated? And of what earthly good are space photographs to problems of coastal engineering?

Already more than one thousand photographs of coasts have been obtained from Gemini and Apollo flights which point up the possibilities of studying certain processes from space. Recorded for the first time are major "fronts", massive effluents, and shelf-wide perturbations. Dramatic as they are, these are only a prelude to photographs anticipated on a routine basis from the up-coming ERTS (Earth Resources Technology Satellites) program in 1972.

But before we can utilize space photography we need to consider the nature of coastal features as photographic subjects and the character of space photography itself

Coastal Subjects

In contrast to terrain features, coastal features vary widely from land to water, and with depth, from surface to subsurface. Beaches, tidal flats, marshes, submerged bars, grass beds, bottom sediments, slicks, and plankton blooms are among the range of subjects. Varying in geometric size from a few meters to tens of kilometers and with time, hourly, daily and monthly, they present a full spectrum of rapidly changing contrasts. Best understood are those features of small geometric size and relative long time scale, least known are those of large-scale which occur at short time scales. Because of the very wide range and transient nature of different coastal subjects, practical problems of recording photographic information are great. Not only are reflecting qualities of the subject frequently masked by atmospheric phenomena but image contrast is often lost and illumination changed within the water. Our understanding of these recording vagaries is limited, and ground truth at the time of photography is seldom available. It is small wonder why photography has not been extensively utilized for study of coastal processes as it has in other fields. Despite the fickleness of coastal subjects and their illumination, the orbital space camera has certain characteristics of advantage for study of coastal processes.

Character of Photography.

From an altitude of over 200 km, the space camera can record more than 40,000 sq km of coast, e.g. Figure 1¹. Its broad view and synoptic record make it possible to examine in toto large scale features of the water, wave patterns, and shoals, as well as marshland, coastal terrain and cultural features, all in a single photograph. Even when only central parts of the photograph are examined, geometric fidelity is good and lighting uniform over a relatively large area, greater than 8,100 sq.km. Such a quality is difficult to obtain from conventional low altitude aerial photography. Because of the great distance above the optically turbulent atmosphere photographic "clarity" is good (Harvey and Myskowski, 1965), and color distortion small. Whereas image scale is reduced to about 1:1,000,000 and effective resolution limited to 40-100 meters, detail "lost" by low resolution is more-or-less "integrated" into color or tone anomalies depicting major features. Once in orbit the great strength of the satellite-borne camera is its ability to look at coastal phenomena at frequent intervals, once every 90 minutes to 17 days for a year or more.

¹ Reproductions in color are available from the Technology Application Center, University of New Mexico, Albuquerque, New Mexico, 87106, U S A. The illustrations used here do not fully portray the content of the original color photography.

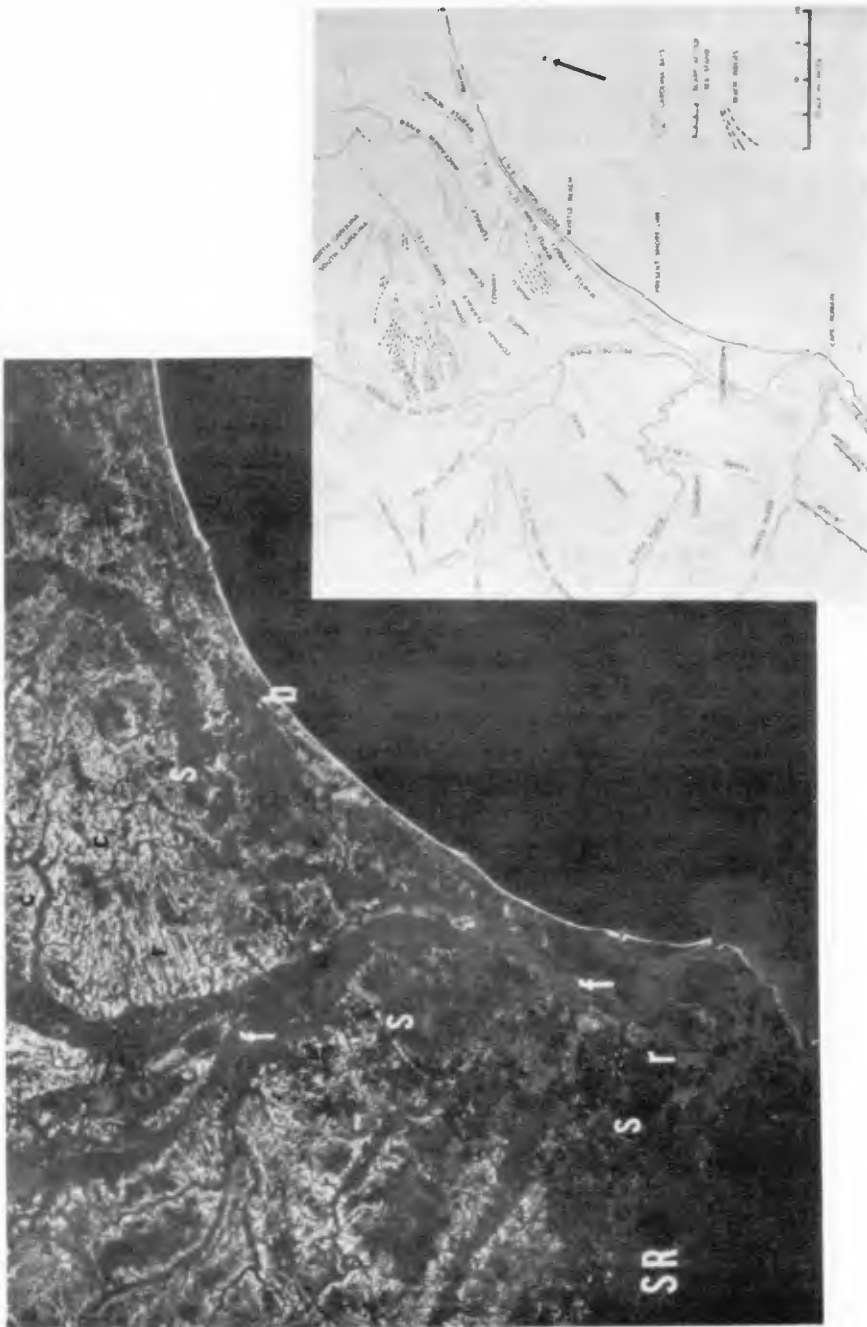


Figure 1. Apollo 9 photograph (AS9-26D-3793D) of the Atlantic coast of South Carolina, U. S. near Cape Romain. Beaches (b) extend for 100 kms along the coast while effluent plumes mark river mouths. Light tones inland are cultivated areas. Varied patterns of vegetation and cultivated areas define shoreline scarps (s) and former beach ridges (r). Marsh and tree covered floodplains border major rivers (f) and Carolina bays (c) are portrayed in a dark tone. A major water diversion is proposed, Santee River (SR). Annotated features, inset.

Waves

Because low resolution of the space camera "filters out" dimensional and directional detail, only long-period waves are recorded by photography. They are observed mainly in glitter patterns around oceanic islands and continental headlands. When traced to storm-generating sources with the aid of meteorological satellite photography, long period wave data is of value for forecasting waves propagated into coastal areas. Amenable to analysis are refraction patterns and landward changing wave dimensions that relate to decreasing water depth and the location of shoals, and in turn to wave-stirred sources of suspended materials or turbidity. Procedural details for photographic analyses of glitter patterns are given by Cox and Munk (1954) and for spectral distributions of long period waves, by Libby, et al (1969).

Coastal Morphology

Space photography is of value for portraying morphological features especially in regions where base maps are not available. In remote areas like mangrove swamps and ice bound coasts they may be the chief source of information on coastal configuration. Where relief changes are small and difficult to observe on the ground, many coastal features often show up more clearly on photographs. For example, linear features like ancient shoreline scarps (Figure 1) can be traced for more than 150 km despite their discontinuous nature with gaps of 20 km, and subtle relief, less than 6 m. The photographs reveal coastwide trends more clearly than a good map. Other patterns often revealed clearly on photography include beach ridges and dunes, drainage systems, broad patterns of salt marsh, evaporite deposits, and limits of tidal flooding on flats. Spatial relations of these features can be further evaluated on a regional basis in a context of major sediment sources and dispersal routes.

Shoreline Changes

In keeping with traditional use of aerial photography, space photographs can be used to measure changes in shoreline configuration and thus identify major sites of erosion or accretion. With proper control, scaling and rectification (Colvocoresses, 1970) different positions of the shoreline can be established by comparing common image points taken from time to time according to practices for aerial photography (Moffitt, 1969, and Langfelder, 1968). Old charts may be used to identify positions of former shorelines (Fig. 2) which are comparable to those in space photographs if sufficient control is available. However, relatively low ground resolution of present space photography limits application to shorelines having large changes (greater than about 300 m) over extended periods such as deltaic coasts and storm-washed beaches. Frequent coverage of shorelines by future satellites could record the opening or closing of tidal inlets in the aftermath of storms so that changes can be quickly assessed and corrective measures planned.

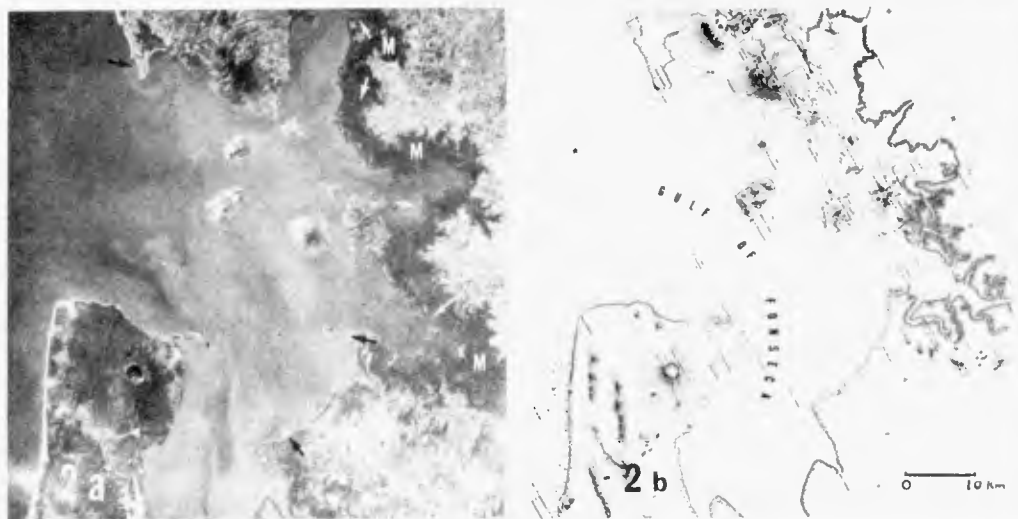


Figure 2A. Black and white reproduction of Apollo 9 color photograph (AS9-19-3019) over the Gulf of Fonseca, Pacific Coast of Honduras, March 9, 1969. Shore consists of mangroves (dark tone, M) as part of a landward extending zone 8 km wide. Locally barrier beaches (b) and spits (s) are visible. Light grey tone of the Gulf indicates turbid water supplied either by entering rivers or from wave-stirred tidal flats. Arrows directed landward indicate sites of major shoreline erosion, arrows seaward, sites of accretion.

Figure 2B. Corresponding hydrographic chart largely based on British Surveys of 1838. Depths in fathoms.

Coastal Drift:

Color and tone anomalies that record the distribution of discolored water provide a visible tracer of drift along the coast. By sensing light scattered by suspended materials in near surface water, these anomalies are fashioned into distinct patterns which reflect the direction of flow. Most obvious are seaward expanding plumes representing suspended sediment discharged off mouths of bays and rivers. Often they are prolonged downstream as "streaks" from wave-stirred bank tops or shoals. Less obvious in relation to their source are great rip-like patterns extending seaward from shore in eddy configurations (Fig. 3A) or as narrow tongues (Fig. 3B). Where opposing flows occur, "fish-hook" patterns or asymmetrical interfacial waves develop. Such indicators may be used together with other data to compile a coast-wide chart of drift for an area of interest. Similar indicators may be of use to evaluate the character and direction of flow around structures like an interference eddy seaward of the jetties at

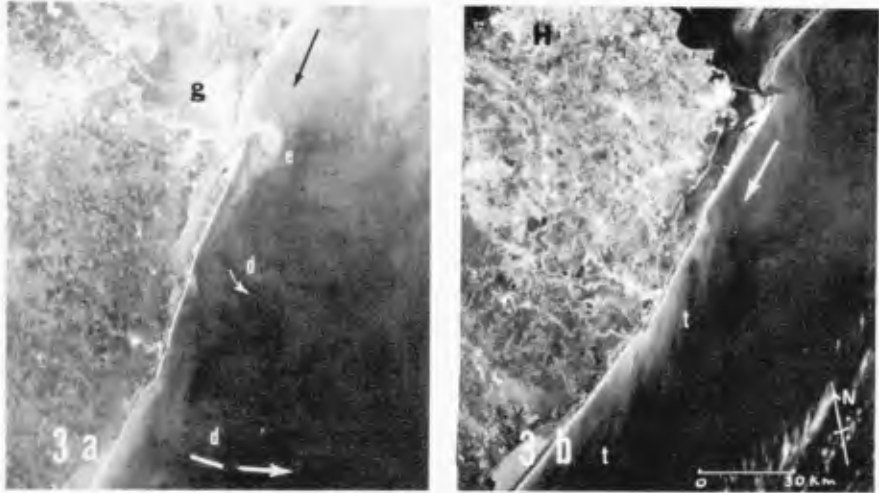


Figure 3A. Space photograph (S66-63064) taken from Gemini XII over the Texas Coast, U.S. Nov. 14, 1966. Eddy-like perturbations, (light grey tones) in the water mark offshore drift (d). In Galveston Bay (g) light tone portrays sediment discharged from a dredging operation. Debris laden outflow forms an interference eddy (e) in the coastal drift (arrow).

Figure 3B. Space photograph (AS9-26A-3728A) of the same portion of the Texas Coast, near Houston (H) March 8, 1969. Narrow tongues extending seaward (t) are in contrast to perturbations of figure 3A. Inferred coastal drift, arrow.

Galveston Bay (Fig. 3A). Within the Bay a light-colored streak marks turbid water emanating from a dredging operation. But, striking as the patterns are they are ephemeral and necessarily limited to suspended materials carried only in near surface water, often only a fraction of the total suspended load. Therefore, it seems essential to supplement the photographic record by extensive field measurements not only to gain a more complete "picture" of coast-wide drift but to "calibrate" the imagery as well.

Offshore Drift:

It was not until space photographs of the Gemini flights were available that the possibility of widespread dispersal of nearshore sediments was appreciated. First recognized by Stevenson (1967) in

coastal water off Texas, turbid perturbations were traced as far as 150 km from shore. Just as rip currents relieve rising water levels in the surf zone these large scale features are believed to carry water offshore in response to a coast-wide build-up of sea level. Later coverage of the same coast taken on Apollo 9 in 1969 portrays seaward extending tongues 22 km offshore. A day later along the same coast (AS9-22-3464 and AS9-22-3465 not printed) after the wind had shifted from onshore to offshore with passage of a front, the tongues were largely replaced by dark masses of relatively "clear" water common to offshore areas. Although the available examples are but a few snapshots of a whole "movie film" of rapidly changing drift patterns they do give an indication of widespread sediment dispersal to be expected.

In another example, figure 4, a large plume leads seaward from Cape Lookout, North Carolina. Seaward from the point, shoals are recorded as a light-toned shredded pattern representing large sand waves and these are interfingered with dark tongues representing tidal channels in deeper water. Beyond the charted limit of the shoals, an indistinct plume extends 60 km offshore. Its seaward edge is truncated by the Gulf Stream and trails northward as a narrow tongue. Concentrations of suspended material sampled in near-surface water close to the time of photography were relatively low, less than 2 mg/L and materials consisted of quartz sand (60%) mixed with plankton and detritus. Although the rate of drift is not recorded, the photograph shows where suspended sediment is going in relation to potential sources on the shoals or along the shore. If this drift persists over the long-term, perhaps it could be utilized as an avenue of transport to discharge pollutants across the shelf and into the ocean.

Utilization of photography for measurement of current speed has been successfully accomplished using stereo parallax techniques with aerial photography, Cameron (1952) and Waugh (1964). It seems feasible to use a similar approach with space photography if an economical means of "seeding" currents on a large scale can be developed.

Problems:

In practice the user of space photography is faced with a number of problems which must be recognized. The dynamic character of the subject creates a special problem for collecting ground truth. In some areas it would seem that sampling of selected sites at the moment of photography would suffice for large areas but the wide range of environments, each with characteristics of its own, and the variety of unpredictable local conditions make ground truth data collection an enormous task.

In addition to understanding the subject, use of the photography depends on an understanding of various colors, tones and density anomalies in the photograph. Excellent progress has been made (Ross, 1969) in developing techniques which enhance images and extract spectral data to determine water depth and turbid patterns. Yet, the three dimensional

character of hydrographic imagery is incompletely understood; often turbid features cannot be differentiated from bottom features. It seems sensitometric techniques have exceeded our ability to reduce imagery data to meaningful and quantitative information.

At the present stage of progress space photography is no alternative for field sampling. Instead it can assist in planning field work, extend coverage and direct it to profitable sites. The need for rapid, synoptic and timely data on a regional basis demands that new dimensions in data collection and processing be added to improve our knowledge of coastal processes.



Figure 4. Black and white reproduction of color Apollo 9 photograph (AS9-20-3127) over Cape Lookout (CL), N.C. March 12, 1969. Seaward expanding plume (broken arrow) leads from shoals (s) dissected by tidal channels (c) Gulf Stream "front" (f), inferred coastal drift (arrow) nearshore.

References

- Cameron, H L , 1952 The measurement of water current velocities by parallax methods Photogrammetric Engineering, Vol 18, p 99-104
- Colvocoresses, A P , 1970 ERTS-A satellite imagery Photogrammetric Engineering, June, p 555-560
- Cox, C. and W Monk, 1954 Statistics of the sea surface derived from sun glitter, effect of slicks Journal Marine Research, Vol 2, p 222-226
- Harvey, D I and E P Myskowski, 1965 Physics of high altitude photography In Photographic considerations for aerospace, Hall, H J and Howell, H K , Eds , Lexington, Mass , Itek Corp , p 1-22
- Langfelder, J , Stafford, D and M Amein, 1968 A reconnaissance of coastal erosion in North Carolina School of Engineering, Dept of Civil Engineering, North Carolina State University, Raleigh, N C , contract report ERD-238, 127 p
- Libby, L M , W F Libby, and S S Lawrence, 1969 Measurement of ocean waves in a satellite photography Rand Corp Miscell Docum AD696-492, p 1-9
- Moffitt, F H , 1969 History of shore growth from aerial photographs Shore and Beach, Vol 37, No 1, p 23-27
- Ross, D S , 1969 Color enhancement for ocean photography In Oceans from Space, Badgley, P C , Miloy, L and Childs, L , Eds , p 50-63
- Stevenson, R E , 1967 View of the earth from space Journal of Geological Education, Vol 16, no 3, p 83-90
- Waugh, J E , 1964 Photogrammetric measurements of tidal currents Journal of the Surveying and Mapping Division, Proc Am Soc Civil Engineers, paper no 3857, Su 1 , p 17-29

CHAPTER 40

Reach of Waves to the Bed of the Continental Shelf

RICHARD SILVESTER

Professor of Coastal Engineering
Asian Institute of Technology, Bangkok, Thailand
(seconded from Dept of Civil Eng , University of Western Australia)

and

GEOFFREY R MOGRIDGE

Research Assistant
Queen's University, Ontario, Canada
(formerly Dept of Civil Eng , University of Western Australia)

ABSTRACT

The physiography of Continental Shelves and their major composition of sediment indicate strongly their terrigenous origin and their smoothing by wave action. This premise is supported by the geologic time over which waves have existed and the mass-transport velocity in these relatively shallow depths, particularly the net movement within the wave boundary layer at the bed. A given wave train arriving obliquely to the shore can transport material along the coast, both beyond the breaker line and within the surf zone. It is shown that for equal over-all discharge in the two zones, the average sediment concentration offshore close to the bed need be reasonably small, indicating that transport near the beach could be a fraction of that from the breakers to the reach of the waves. This latter limit is shown to extend at least half way across the Shelf, with possibilities of greater reach when more realistic prototype conditions are introduced into experiments.

INTRODUCTION

The margins of landmasses are made up mainly of mildly sloped under-water zones which are termed Continental Shelves. The legally accepted limit for these, where the slope increases substantially, has been taken as 100 fathoms (183 metres), although the accumulation of data over decades has shown⁽¹⁾ that the edge of this feature is closer to 65 fathoms (120 metres).

Of the various classifications of Shelves the most important to the coastal engineer is the sediment accreted variety, which provides the widest marine margins available and also make up the largest percentage area of all Shelves. Hayes⁽²⁾ reports that 80% of the inner Shelf is covered by gravel, coral, shell, sand or mud, the last two constituting around 70%. Another important fact is that material is still being furnished to these zones by the rivers of the world⁽³⁾.

Whilst the sediment is supplied at specific locations along the coastlines, it is spread relatively evenly along them by wave action and possibly currents. Whilst geographers and geologists have stressed the role of tidal and other oceanic streams in this distribution process, it would seem that wave action could well be the predominant agent in this massive task. The following observations would appear to support this thesis.

(a) Where waves (particularly swell) arrive obliquely to a reasonably long length of coastline there is evidence of accretion at the down-coast area and a dearth of movable material in the upcoast region. The former occurs as an enlarged width of Continental Shelf and/or wide expanses of sedimentary plain. Such physiographic units⁽⁴⁾ are displayed on margins of enclosed seas as much as on boundaries of oceans where tidal currents are more pronounced.

(b) There are indications that the net littoral drift in places is in the opposite direction to the strongest tidal streams. For example on the Mozambique coast the predominant drift is northward whilst the strongest tides run southwards. This is understandable when it is realised that lengthy orbital water particle motions of tidal period will be circular and will suffer shearing stresses near the bed, and thus contain large scale vortices in both horizontal and vertical planes. The net transverse movement over a tidal cycle, particularly near the bed may thus be negligible or random in any direction.

(c) When a Continental Shelf consists of sediment over its complete width it has a mean slope of 0.002⁽¹⁾, being steeper near shore and milder at the edge. The uniformity of this profile over long lengths of coastline, and from one landmass to another, does not seem to correlate with the vast differences in tidal range or tidal currents associated therewith. As noted previously, totally enclosed seas, such as the Mediterranean, Baltic etc., should have Shelves only at river outlets if tidal action were the sole or major source of energy distribution.

(d) The edge of the Shelf, demarcating the limit of sweeping action by waves, has already been noted as around 65 fathoms (= 390 ft = 119 metres). This is around the reach or limit of influence of 13 second waves. It has been shown elsewhere⁽⁵⁾ that waves of this period are predominant in the ocean wave spectra generated in the storm zones of the oceans. Such waves traverse the oceans with very little loss of energy. Hence most oceanic margins of the world receive swell waves with periods from 11 to 15 seconds. The western margins of Continents⁽⁶⁾ in particular have swell incidence from the strong westerly gales in the 40° to 60° latitudes in both hemispheres. In enclosed seas where the spectra of waves are limited to the local storm centres, swell from major generating areas of the oceans being excluded, the Shelf edge is not so deep. In the Mediterranean it approximates 50 fathoms and in the Red Sea it is nearer to 30 fathoms, where sediment has accumulated.

(e) A ubiquitous feature of coastlines is the crenulate shaped bays formed by sedimentary sections between rocky headlands. The sculpturing of this shape has been shown to be the work of waves arriving

obliquely to the coast⁽⁷⁾ These bays are of vastly differing size, some encompassing many miles length of coast and some miles width of Shelf They indicate that waves can modify the sea bed to substantial depths and finally bring the bed and shoreline profiles into a compatible equilibrium with the direction of the most persistent swell waves in the adjacent ocean area The orientation of such bays has been used to determine the net sediment movement around the coastlines of the world⁽⁴⁾

(f) Finally, the oscillatory motion of the water particles at the bed produced by wave propagation involves a net advance each wave period which has a maximum value at the sea bed This is particularly so for small ratios of depth to wave length, and so is relevant to this discussion of predominant swell waves with periods from 11 to 15 seconds This net motion is termed mass transport and results from the viscous forces creating a boundary layer in the oscillatory motion of the water particles near the bed This boundary layer is in the order of 1 to 2 centimeters thick and yet the mass transport velocity is maximum within it Thus, if bed particles can be lifted temporarily from the floor during part of the wave cycle they can readily be carried forward in the net advance of the water itself As soon as the bed is so affected small ripples and then dunes form⁽⁸⁾, so creating a rough bed which changes the boundary conditions The ability of the waves to disturb bed particles is thus increased, so that sediment transport due to mass transport is enhanced The point of concern here is the comparison of this force with that of a tidal stream Whilst this latter may be strong at the surface, where it is most noticeable, it will be greatly reduced as the bed is approached, and be practically zero near the boundary layer previously mentioned Its transporting efficiency is further decreased by the vortices accompanying it, as noted earlier

From the above discussion it is seen that waves appear to have exerted a great influence on the sediment existing on Continental Shelves The motions of particles are slow and are in fact zero for large periods of a year, when wave heights or periods are too small for adequate reach to the bed However, when it is realised that waves, both storm type and swell, have been available on the oceans since their inception, there has been a surfeit of time for Shelves to be accumulated and even for vast expanses of landmasses to have been accreted

LONGSHORE COMPONENT OF MASS TRANSPORT

The mass transport velocity at the seabed has been derived theoretically for the case of waves of very small height, a smooth bed and laminar boundary layer⁽⁹⁾ An empirical relationship has also been found for the case of a rough bed and laminar or turbulent boundary layer⁽¹⁰⁾ It is thus possible to compute this net advance in the direction of wave propagation at any point across the Continental Shelf when the wave characteristics are known

Assuming a wave arrives at the edge of a uniformly sloped Shelf at some given deepwater angle, it is possible to compute the shoaling and refraction coefficients for it and find its angle to the shoreline during

propagation towards the shore. The variable wave height can be substituted into the bed mass-transport equation, assuming a roughness for the floor and the status of the boundary layer. This latter is determined from a knowledge of the limiting wave height for a given wave train when the transition from laminar to turbulent boundary layer occurs. The longshore component of the mass transport can be determined at each location to give its distribution across the Shelf.

For smooth or rough bed and laminar boundary layer, we have

$$\frac{U_L g T^3}{H_o^2 \sin \alpha_o} = \frac{k}{A} \quad \text{-----(1)}$$

where U_L = longshore component of mass-transport velocity at bed
 g = acceleration due to gravity
 T = wave period in seconds
 H_o = deep-water wave height
 α_o = deep-water angle of crest to bed contour
 k = dimensionless factor dependent on

$$D/\delta = D(\pi)^{1/2}/4 \cdot 6(\nu T)^{1/2}$$

where D = dimension of bed roughness (grain diameter or ripple height)
 δ = boundary layer thickness
 ν = kinematic viscosity of seawater

Experimental values of k derived by Brebner et al.⁽¹⁰⁾ give values as in Figure 1

$$A = (1 - \sin^2 \alpha_o \tanh^2 2\pi d/L)^{1/2} \left[\tanh 2\pi d/L \left(1 + \frac{4\pi d/L}{\sinh 4\pi d/L} \right) \right] \sinh^2 2\pi d/L / \cos \alpha_o$$

where d = water depth
 L = wave length

(The expression for A is graphed in Figure 2)

For the smooth and rough bed turbulent boundary layer condition, Brebner et al.⁽¹⁰⁾ found

$$\frac{U_L g T^{2.6}}{H_o^{1.2} \sin \alpha_o} = \frac{28.9}{A^{0.6}} \quad \text{for fps units} \quad \text{-----(2)}$$

(Unlike Eq (1) this relationship is not dimensionally homogeneous, indicating the need for further experimental confirmation)

The transition from laminar to turbulent boundary layer as found by the same workers⁽¹⁰⁾ can be expressed as

$$\frac{H_o^2}{T\nu} = 8150 A \quad \text{-----(3)}$$

It will be seen in the subsequent calculations that turbulent boundary layer conditions exist for nearly all the waves and depths chosen

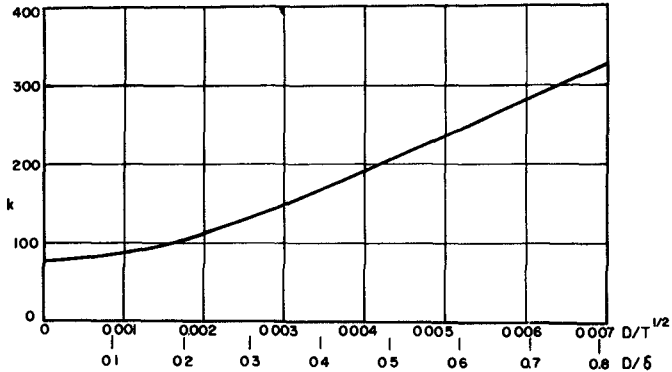


Fig 1 Values of k in equation (1) from roughness height in proportion to boundary layer thickness or $D/T^{1/2}$

AVERAGE WAVE SPECTRA

In order to determine some reasonable values of wave height and wave period to substitute in the above equations, the optimum storm conditions of the oceans must be assessed. As noted elsewhere⁽⁵⁾, the 35 knot wind is the strongest that can normally generate a fully arisen sea. Winds of higher velocity either have limited duration or fetch (or both), so restricting the waves to $H_{1/3} = 33$ ft and T_{max} to 12 seconds. The energy distribution curve⁽¹¹⁾ for this condition is depicted in Figure 3 where it is seen that the equivalent triangular distribution indicates upper and lower engineering limits of 19.4 and 4.2 seconds respectively. Proportional energy values for wave bands centered on 8, 10, 12, 14 and 16 seconds result in wave train heights ($H_{1/3}$) of 3.2, 4.9, 5.3, 4.2 and 2.0 feet respectively, based upon proportional areas under the curve.

If these wave trains emerged from a fetch a long distance away they would arrive at the Continental Shelf separately. The total energy available at any one time would depend upon the angular and radial dispersion from the fetch, but the resultant wave heights would be in proportion to those computed above for the discrete wave bands. For the purpose of this comparison it will be assumed that waves of all periods are arriving from the one direction, with the crests angled at 50° to the uniform and straight underwater contours.

In Figure 4 is depicted the Continental Shelf with uniform slope of 0.002:1. Conditions at each d/L_0 value represent the mean for a certain width of Shelf, from which it can be seen that $(\Delta d/L_0)(b/L_0) = 0.002$

so that
$$b = (\Delta d/L_0) \cdot 5.12 T^2 / 0.002$$

At intermediate depths the differential $\Delta d/L_0$ is the difference of values midway between adjacent points, whilst at the extremities of $d/L_0 = 0.01$ or 0.5 the outside half width is assumed the same as the inner half (e.g. $\Delta d/L_0 = 0.015 - 0.005 = 0.01$). The b values are listed in Table I. The product $b U_L$ represents a mass transport discharge across the Shelf width b per unit depth of liquid at the bed. When multiplied by a thickness to which U_L is considered to apply ($\frac{1}{2}$ " has been assumed), the discharge of water in this layer of liquid is obtained. The summation $\Sigma b U_L / 24$ gives the said discharge across the active width of the Shelf (Σb) for the wave train under consideration. Although calculations have been carried out to $d/L_0 = 0.5$, the limit of disturbance of the respective components (derived later) is indicated by the double lines in Table I.

EQUAL SEDIMENT TRANSPORT IN SURF ZONE AND OFFSHORE

For the wave conditions specified in Table I it is possible to compute the littoral drift in the surf zone by one of the many relationships available. The one employed here is that presented by Castanho⁽¹²⁾ which has been discussed elsewhere⁽¹³⁾. The volume of sediment passing a plane normal to the beach per unit of time (e.g. ft^3/sec) can be expressed as

$$Q = \omega H_0^2 L_0 E_r \sin \alpha_0 / 7 T \gamma_s \quad \text{-----(4)}$$

where Q = volume of sediment of specific weight γ_s passing a plane normal to the beach per second ($\gamma_s = 110 \text{ lb/ft}^3$)
 ω = specific weight of seawater ($= 64 \text{ lb/ft}^3$)
 H_0 = deep water wave height (ft)
 L_0 = deep water wave length (ft)
 E_r = $\frac{\text{energy dissipated}}{\text{longshore energy component}}$ (see Ref 13)
 α_b = angle of crest to beach at breaking (deg)
 α_0 = deep water approach angle (deg)
 T = wave period (secs)

Values have been computed in Table I for $\alpha_0 = 50^\circ$ and the respective wave heights and wave periods

Let it be assumed that an equal volume of material is passing the plane beyond the breaker line, out to the reach of each wave train. Also let it be assumed that sediment particles are moving at the same net speed as the water near the bed (i.e. in the $\frac{1}{2}$ " thick layer previously employed). Then the concentration of sediment by volume to accomplish this task can be calculated, as listed in Table I.

It is seen that for the wave characteristics chosen the concentration necessary for equal transport offshore and in the surf zone are feasible. Whilst the longshore velocity U_L is substantially reduced, the further from the beach and the longer the wave period, the widths of Shelf over which these operate are substantially enlarged.

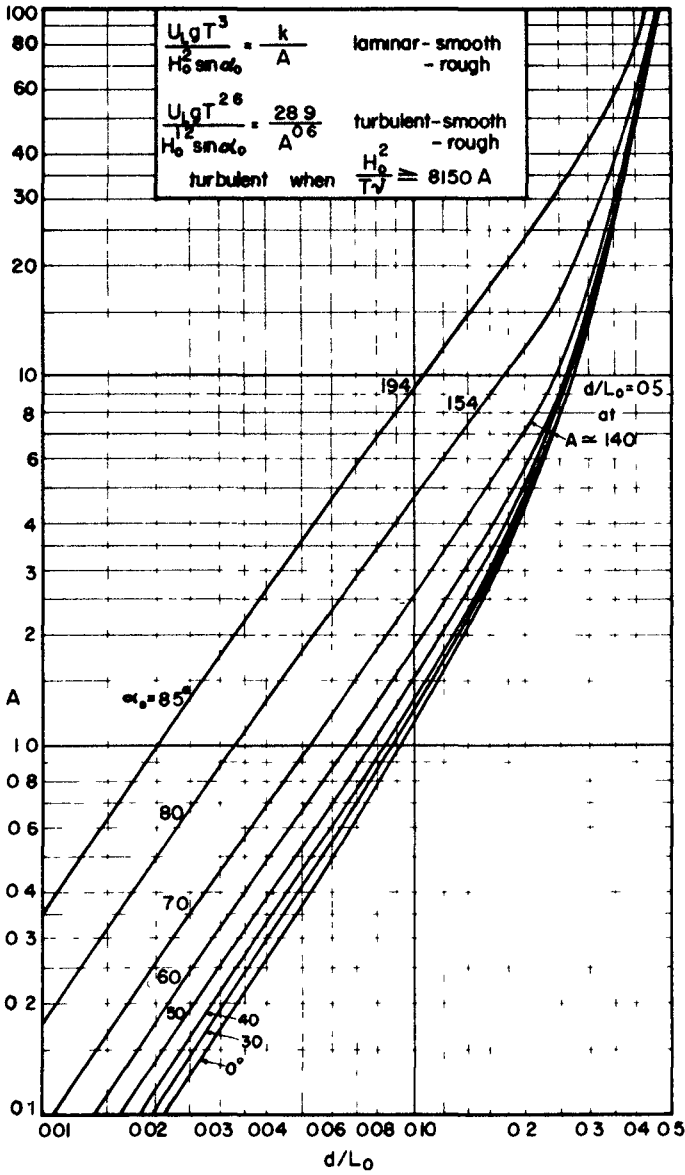


Fig 2 Factor A used in equations (1)(2) & (3)

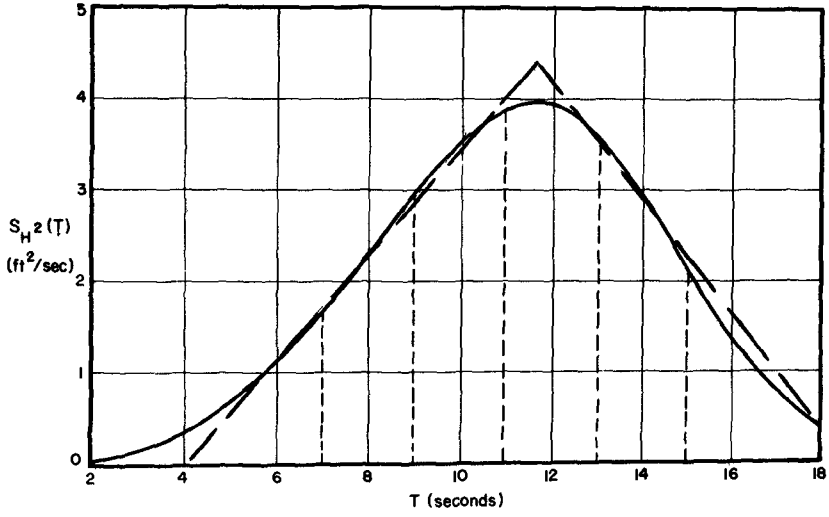


Fig 3 Energy distribution curve for a fully arisen sea generated by a 35 knot wind

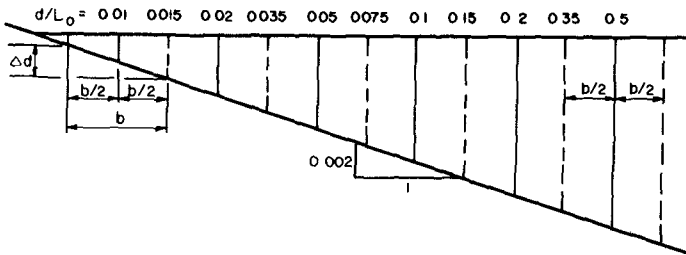


Fig 4 Assumed uniform Continental Shelf for purposes of calculations in Table I

Table I Longshore mass transport in various wave trains across portion of the Continental Shelf (See Figure 2)

$\alpha_o = 50^\circ$ $\sin \alpha_o = 0.766$		8	10	12	14	16	T secs	
			3 2	4 9	5 3	4 2	2 0	H feet
			2 10	1 75	2 59	6 56	43 0	$g T^3 / H_o^2 \sin \alpha_o 10^3$
			2 3	2 49	3 63	7 13	24 4	$g T^2 6 / H_o 1^2 \sin \alpha_o 10^3$
			14 35	26 9	26 3	14 1	2 78	$H_o^2 \pi / T v 160^2 \geq A$
d/L_o	0 01	-	-	-	-	-	$U_L \times 10^3$ (laminar) ⁽¹⁾	
$\Delta d/L_o$	0 01	78 1	72 1	49 5	25 2	7 4	$U_L \times 10^3$ (turbulent) ⁽¹⁾	
A	0 048	1 64	2 56	3 69	5 02	6 55	$b \times 10^{-3}$ (feet)	
$A^{0.6}$	0 161	128 0	183 0	183 0	127 0	48 5	$b \times U_L$	
	0 02	-	-	-	-	-		
	0 02	41 2	38 0	26 1	13 3	3 9		
	0 138	3 28	5 12	7 40	10 04	13 10		
	0 305	135 0	195 0	193 5	133 8	51 0		
	0 05	-	-	-	-	-		
	0 04	18 3	16 9	11 6	5 9	1 7		
	0 530	6 56	10 24	14 80	20 08	26 20		
	0 685	120 0	173 0	171 7	123 0	44 5		
	0 10	-	-	-	-	-		
	0 075	9 8	9 1	6 2	3 2	0 9		
	1 52	12 30	19 20	27 70	37 70	49 10		
	1 28	120 5	174 8	172 0	121 0	44 2		
	0 2	-	-	-	-	1 4	Note For laminar conditions it is assumed that $D/T^{1/2} = 0.007$ equivalent to ripples 1/4" to 1/3" high on bed	
	0 2	4 8	3 8	3 0	1 5	-		
	5 10	32 9	51 2	73 8	100 5	131 0		
	2 64	158 0	195 0	221 5	150 5	183 2		
	0 5	1 1	1 3	0 9	0 3	0 05		
	0 3	-	-	-	-	-		
	140	49 2	76 8	110 5	150 5	196 0		
	19 4	54 2	99 9	99 5	45 0	9 8		
(1) U_L (feet/sec)	0 075	0 20	0 3	0 325	0 31	limiting d/L_o		
(2) $MT = \Sigma b U_L / 24$ (ft ³ /sec)	1 00	0 50	0 75	0 87	0 80	prop of last b		
(3) G littoral drift (ft ³ sand/sec) (1 ft ³ = 110 lbs)	383	823	886	636	335	final $b \times U_L$		
(4) Concentration by volume	2 3	3 2	3 4	2 3	5 4	$\Sigma b U_L$ MT in 1/2" layer ⁽²⁾ $c^{(3)}$ $c^{(4)}$		

INCIPIENT MOTION OF BED PARTICLES

Before sediment particles can be carried forward and backward by the oscillatory motion of the water particles near the bed, they must be removed from the bed. This topic needs much more active research, but results are available from a number of workers on the incipient motion of sand particles under wave action. The differences and similarities of their results have been discussed elsewhere⁽⁸⁾, but it can be concluded that, as the replication of bed conditions has tended towards the prototype scale of action, the greater has been found the reach of the waves. The types of equipment employed in generating the necessary oscillatory water motion have been described elsewhere⁽¹⁴⁾. A more recent rig, used at the University of Western Australia⁽¹⁵⁾, essentially oscillates a block of water with amplitudes and periods applicable at the sea bed. Results from these tests are presented in Figures 5A & B.

The empirical formulae derived for incipient motion of sand particles on a flat bed can be put into similar dimensionless form as in equations (5) to (17).

The relationship by Abou Seida⁽²⁹⁾ cannot be written in such a form but a modification and iterative process carried out by Mogridge⁽²⁵⁾ permits it to be plotted as in Figure 5. The graph of Bonnefille and Pernecker⁽¹⁷⁾ consisted of two curves which have been modified into one for the presentation in the figure. The condition of the boundary layer has been indicated in the equations or been presumed (?).

$$\text{Bagnold}^{(16)} \text{ (laminar ?)} \quad \frac{U_{\max}}{(s-1)^{2/3} g^{2/3} D^{1/3} T^{1/3}} = 3.18 \quad \text{-----(5)}$$

$$\text{Bonnefille and Pernecker}^{(17)} \text{ (laminar)} \quad \frac{U_{\max} \nu^{1/6}}{(s-1)^{5/6} g^{5/6} D^{1/2} T^{1/2}} = 0.072 \quad \text{-----(6)}$$

$$\text{Bonnefille and Pernecker}^{(17)} \text{ (turbulent ?)} \quad \frac{U_{\max} \nu^{19/30}}{(s-1)^{16/15} g^{16/15} D^{6/5} T^{1/2}} = 0.01 \quad \text{-----(7)}$$

$$\text{Bonnefille and Pernecker}^{(17)} \text{ (modified)} \quad \frac{U_{\max} \nu^{5/18}}{(s-1)^{8/9} g^{8/9} D^{2/3} T^{1/2}} = 0.069 \quad \text{-----(8)}$$

$$\text{Carstens et al}^{(18)(19)(20)} \text{ (turbulent)} \quad \frac{U_{\max}}{(s-1)^{1/2} g^{1/2} D^{1/2}} = 3.5 \quad \text{-----(9)}$$

$$\text{Eagleson and Dean}^{(21)} \text{ (laminar)} \quad \frac{U_{\max} \nu^{1/2}}{(s-1) g D T^{1/2}} = 0.131 \quad \text{-----(10)}$$

$$\text{Goddet}^{(22)} \text{ (turbulent)} \quad \frac{U_{\max}}{(s-1)^{2/3} g^{2/3} \nu^{1/24} D^{1/4} T^{3/8}} = 3.0 \quad \text{-----(11)}$$

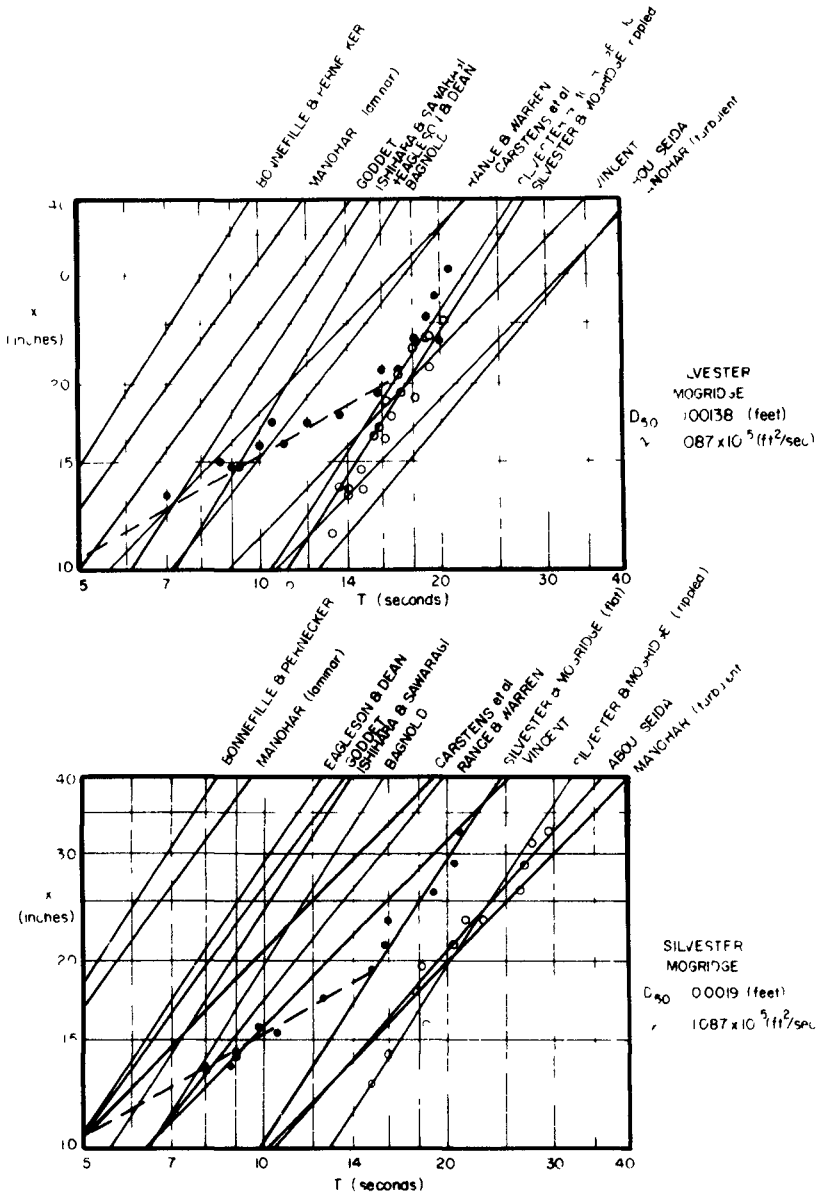


Fig 5 Wave periods (T) and amplitudes (x) at the sea floor to produce incipient motion on a flat bed with sand particles of mean dia A = 0.00138 ft (0.42 mm) and B = 0.0019 ft (0.58 mm)

Ishihara Sawaragi⁽²³⁾
(turbulent) $\frac{U_{max}}{g^{3/4}(s-1)^{3/4}D^{1/4}} = 0.093$ -----(12)

Manohar⁽²⁴⁾(laminar) $\frac{U_{max} \nu^{1/3}}{(s-1)^{2/3}g^{2/3}D^{2/3}} = 0.159$ -----(13)

Manohar⁽²⁴⁾(turbulent) $\frac{U_{max}}{(s-1)^{0.4}g^{0.4}D^{0.2}\nu^{0.2}} = 7.45$ -----(14)

Silvester and Mogridge⁽²⁵⁾
(flat bed) $\frac{U_{max} \nu^{1/18}}{(s-1)^{7/9}g^{7/9}D^{1/3}T^{1/2}} = 0.034$ -----(15)

Rance and Warren⁽²⁶⁾(sand) $\frac{U_{max}}{(s-1)^{3/5}g^{3/5}D^{2/5}T^{1/5}} = 0.69$ -----(16)

Vincent⁽²⁷⁾(turbulent) $\frac{U_{max}}{D^{1/2}} = 19.1$ -----(17)

The U_{max} can also be expressed in terms of amplitude of motion when the wave period is known or assumed, in which form these equations have been graphed in Figures 5A & B, for $D_{50} = 0.00138$ and 0.0019 ft respectively. Also assumed in the figures is $\nu = 1.087 \times 10^{-5}$ (ft²/sec), $s-1 = 1.6$ and $g = 32.2$ ft/sec². It is seen immediately that these relationships are not compatible, probably through being extrapolated beyond the zones of verification.

Also included in the figures are the results of the authors' tests, the black dots representing flat bed conditions and the open circles the rippled surface produced from prior oscillatory motion. For the flat bed two relationships were found, one in which x varied approximately as $T^{1/2}$ for smaller x and T values, and the second in which x varied as $T^{3/2}$. The transition from the one to the other occurred at $x = 20.5$ " and $T = 17$ seconds in Figure 5A, and $x = 19$ " and $T = 15$ seconds in Figure 5B. Sleath⁽²⁸⁾, in his velocity measurements in the boundary layer at the bed of a wave tank, found a parameter $U_{max} D_{50}/\nu$ which displayed the transition in the velocity profile from laminar to one still laminar but influenced by vortex formation around the grains of sand. Appropriate substitutions from the above tests give values for incipient particle motion of 82.5 and 116 for the 0.00138 and 0.0019 ft diameter sands respectively.

Sleath observed his critical condition to occur at a value approximating 50. He states "This may be compared with the value of $U_{max} D/\nu = 200$ obtained from the formula proposed by Manohar (1955)⁽²⁴⁾ for the transition from laminar to turbulent conditions with sand of median diameter = 0.0445 in. It is probable that the phenomenon observed by Manohar and his colleagues was vortex formation rather than turbulence."

Carstens et al⁽¹⁸⁾⁽¹⁹⁾⁽²⁰⁾ from their tests with oscillating water in a conduit obtained U_{max} values when certain changes in the bed were observed For the sand size $D = 0.00097$ ft and $v = 11.0 \times 10^{-6}$ ft²/sec the following values of $U_{max} D_{50}/v$ were obtained

boundary layer transition commences (sand bed)	56.3
boundary layer transition commences (smooth bed)	74.8
incipient bed motion, bed undisturbed	71.3
spontaneous appearance of ripples	94.0
fully turbulent boundary layer (smooth bed)	119

From these values it seems quite probable that Manohar's observations were commencement of turbulence. A significant observation of the above results is that incipient bed motion and even ripple formation occurred before full turbulence was experienced in the boundary layer. It is at such a stage that mass transport will exert its influence on the bed particles. As seen in Figures 5A & B the presence of ripples on the ocean floor will produce incipient motion at smaller amplitudes of the water particles for a given wave period, or at longer periods for a given amplitude. However, the curves for this more realistic condition do not match the one equation, so the conservative flat bed relation of equation (15) has been put in terms which are graphed in Figure 6.

With this diagram a wave of any specific period in a certain depth of water will have to have a minimum height in order to initiate particle movement on a flat bed. The respective heights and periods for a fully arisen sea of a 35 knot wind previously derived are indicated in Figure 6. It is seen that the 12 and 14 second waves can disturb sediment at over 200 feet depths. This is half way across the Continental Shelf.

It is believed that for similar wave conditions the ability of waves is greater than that indicated in Figure 6 due to the following prototype phenomena

- 1 Velocities of water particles near the ocean bed may be higher than those derived by first order theory
- 2 The interaction of wave trains of slightly differing period can generate greater instantaneous velocities than implied in the present analysis
- 3 Wave trains angled to each other produce vortices of large dimensions with associated turbulence which may disturb the bed more readily
- 4 In storms at sea, where fetches are changing location and orientation continually, waves may move in opposite directions so creating clapot¹ or partial clapot¹. These create high water particle velocities near the bed. They will also temporarily build up furrows of material which will be readily swept away when the standing wave has dispersed
- 5 Currents and internal waves associated with tidal action at the

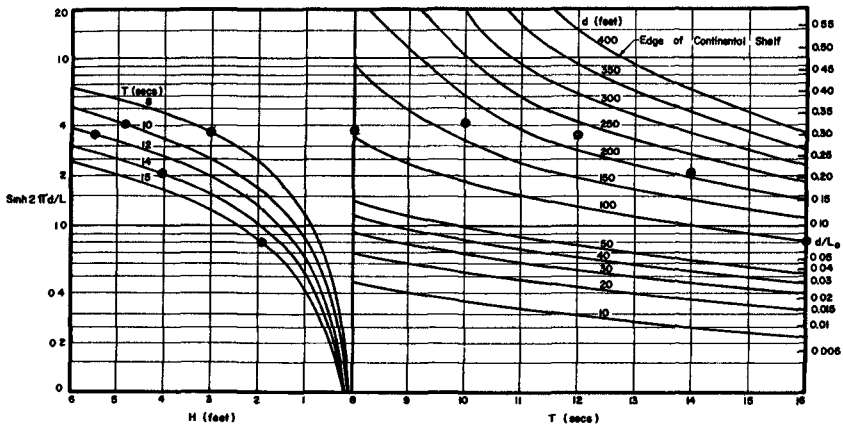


Fig 6 Wave conditions for incipient motion on a flat bed for sand
 $(D_{50} = 0.00065 \text{ ft} = 0.2 \text{ mm})$

edge of the Shelf could assist the waves in disturbing the bed at these larger depths

6 Shell debris on the sea floor can initiate movement of sand particles sooner than for rippled or smooth beds. Carsten's tests⁽¹⁹⁾ showed that, with small protruberances on the bed, motion is initiated at about half the water particle velocity of that for a smooth sand bed. This implies in Figure 6 that the same reach can be effected with half the wave heights previously considered. It can be shown by drawing curves in the left hand side of the figure with half the wave height for each period band, that for the original wave heights the reach is increased about 30%. For example, the 5.5 ft high 12 second wave which had a reach of 230 ft for rippled bed conditions can influence a bed at 300 ft depth which contains shell-like debris on it.

7 It is possible that fish life is concentrated heavily at the floor of the ocean. Any motions by them on or near the bed will disturb sediment which the mass transport of the waves will carry into and along the shore.

These prototype conditions could increase the concentration of suspended sediment above those recorded in model studies. They could also effect movement well above the boundary layer, on which the previous comparison was based.

CONCLUSIONS

1 Since the major proportions of Continental Shelves consist of sediment which has accreted to around the 400 feet depth, it would appear that wave action is the predominant spreading agent

2 The mass-transport due to wave action is at a maximum within the boundary layer at the bed where initial suspension of material occurs

3 Roughness of the sea floor due to the sediment particles or undulations formed thereon would appear to increase the mass-transport velocity and assist in the initial disturbance of the bed

4 For an oblique wave train, the mass-transport velocity at the bed, and its longshore component, can be computed at all depths across the Continental Shelf, to the limit where shoaling invalidates the theory employed

5 With certain simplifying assumptions, it can be shown that for equal sediment transport within the surf zone and beyond the breaker line for a given wave train, the volumetric concentration of sediment within the 1/2" bottom layer of water does not have to exceed 5%

6 Empirical relationships of wave and sediment characteristics for incipient motion on a flat bed vary considerably, with those utilizing prototype velocities and amplitudes in their experimental rigs showing a greater reach of wave action

7 Further tests are required to verify beyond all doubt that the average wave spectra to be expected over the Continental Shelves can sweep sediment on them to their recognised outer limit. These tests should include normal marine debris on the bed, so that initiation of sediment motion and the frictional effects on the boundary layer can be studied

8 More analytical and experimental work needs to be carried out on mass-transport, both for simple wave trains and the more complex water and sediment systems

REFERENCES

- (1) Shepard F P Submarine Geology (2nd Ed) Harper Row, 1963
- (2) Hayes M D "Relationship between coastal climate and bottom sediment type on the inner Continental Shelf" Marine Geol 5, 1967, 111-132
- (3) Stoddart D R "World erosion and sedimentation" Water, Earth and Man (Ed R J Chorley) Methuen (London), 1969
- (4) Silvester R "Sediment movement around the coastlines of the world" Proc Conf Inst Civil Engrs (London), 1962, 289-315
- (5) Silvester R and S Vongvisessomjai "Computation of storm waves and swell" Proc Inst Civil Engrs (In Press)
- (6) Davies J L "A morphogenic approach to world shorelines" Ann of Geomorph 8, 1964, 127-142
- (7) Silvester R. "Stabilization of sedimentary coastlines" Nature (London) 188, 1960, 467-469
- (8) Silvester R. "Sediment movement beyond the breaker zone" Trans Instn Engrs Aust CE12, 1970, 63-71
- (9) Longuet-Higgins M S "Mass transport in water waves" Phil Trans Roy Soc London, A245, 1953, 535-581
- (10) Brebner A , J A Askew and S W Law "The effect of roughness on the mass-transport of progressive gravity waves" Proc 10th Conf Coastal Eng , Vol 1, 1966, 175-184
- (11) Silvester R and S Vongvisessomjai "Energy distribution curves of developing and fully arisen seas" J Hyd Res (In Press)
- (12) Castanho J "Breaking waves and littoral drift" (in Portugese) Lab Nac de Eng Civil (Lisbon) Mem No 275, 1966
- (13) Silvester R "Beach profiles and littoral drift assessment" La Houille Blanche 24, 1969, 615-621
- (14) Silvester R "Modelling of sediment motion offshore" J Hyd Res 8, 1970, 227-259
- (15) Mogridge G R "Testing sediment movement due to wave action" Proc ASCE 96 (HY7), 1970, 1587-1604
- (16) Bagnold R A "Sand movement by waves, some small scale experiments with sand by very low density" Proc Inst Civil Engrs 27, 1947, 447-469
- (17) Bonnefille R and L Pernecker "Debut d'Entrainment des Sediments per la Houle" Proc 11th Congress IAHR Vol V, 1965, 207-208

- (18) Carstens M R , F.M. Neilson and H D Altınbilek "An analytical and experimental study of bed forms under water waves" Georgia Inst Tech Final Rep Proj A-798, 1967
- (19) Carstens M R and F M Neilson "Evolution of a duned bed under oscillatory flow" J Geoph Res 72, 1967, 3053-3059
- (20) Carstens M R ,F.M Neilson and H D Altınbilek "Bed forms generated in the laboratory under an oscillatory flow analytical and experimental study" Coastal Eng Res Centre, Tech Mem No 28, 1969
- (21) Eagleson P S and R G Dean "Wave induced motion of bottom sediment particles" Trans ASCE 126 (Pt I), 1961, 1162-1189
- (22) Goddet J "Etude du Début d'Entrainement des Materiaux Mobiles sous l'Action de la Houle" La Houille Blanche 15, 1960, 122-135
- (23) Ishihara T and T Sawaragi "Fundamental studies of sand drifts" Coastal Eng in Japan 5, 1962, 59-65
- (24) Manohar M "Mechanics of bottom sediment movement due to wave action" Beach Erosion Board, TM 75, 1955
- (25) Mogridge G R "Sediment transport due to wave action" Thesis University of Western Australia in partial fulfilment of Master of Engineering Degree
- (26) Rance P J and N.F Warren "The threshold of movement of coarse material in oscillatory flow" Proc 11th Conf Coastal Eng , Vol 1, 1968, 487-491
- (27) Vincent G E "Contribution to the study of sediment transport on a horizontal bed due to wave action", Proc 6th Conf Coastal Eng , 1958, 326-355
- (28) Sleath J F A "Velocity measurements close to the bed in a wave tank" J Fluid Mech 42, 1970, 111-123

CHAPTER 41

ISOPACHOUS MAPPING OF THE LOWER PATUXENT ESTUARY SEDIMENTS BY CONTINUOUS SEISMIC PROFILING TECHNIQUES

Newell T Stiles and Donald R Wiesnet
U S Naval Oceanographic Office
Washington, D C 20390

ABSTRACT

The thickness and extent of the sediment cover in the Patuxent Estuary has been determined using a high-frequency, high-spatial resolution, shallow penetration, continuous seismic profiling system. From these data, an isopachous map was prepared. The isopachous map provides the subbottom information required to determine optimum locations for placing test equipment on the river bottom.

Mud filled depressions, acoustically transparent to 12-kHz sound pulses, occur mainly to the north of Half Pone Point, and east of the present channel. Based on the identification of first subbottom reflectors, these depressions are as much as 16 feet thick. The dominance of the thicker deposits east of the channel and evidence of a submerged terrace indicates that either the channel has migrated to the west, or that the channel of the Patuxent River at this location was larger in the past and has subsequently filled in much of the material in the eastern edge. Maximum penetration at the scarp of the submerged terrace was 36 feet beneath the water-sediment interface. This study demonstrates the use of seismic profiling techniques for collecting and presenting data required for coastal engineering applications.

INTRODUCTION

The Maryland State Road Commission is considering plans to build a bridge across the Patuxent River near Solomons Island, Maryland (Figure 1). The proximity of the bridge to the existing naval test range located between Point Patience and Hooper Neck may require relocation of the test range. A knowledge of the strength characteristics of the river bottom are critical for effective use of the test range. Instrument packages may sink into soft muddy sediments and become impossible to locate or retrieve, other instruments could be damaged because of impact with hard sandy materials. In order to delineate these two sediment materials, a seismic investigation was conducted from Town Point northward to Broomes Island (Figure 2).

This paper deals with the use of the isopachous map to present continuous seismic reflection data of the sediment cover in the Lower Patuxent Estuary. An isopachous map shows the varying thickness of a designated stratigraphic unit by lines of equal thickness (isopachous lines). The stratigraphic unit used in this study is the acoustically transparent sediment cover, which is composed of fine-grained silt- and clay-size sediments.

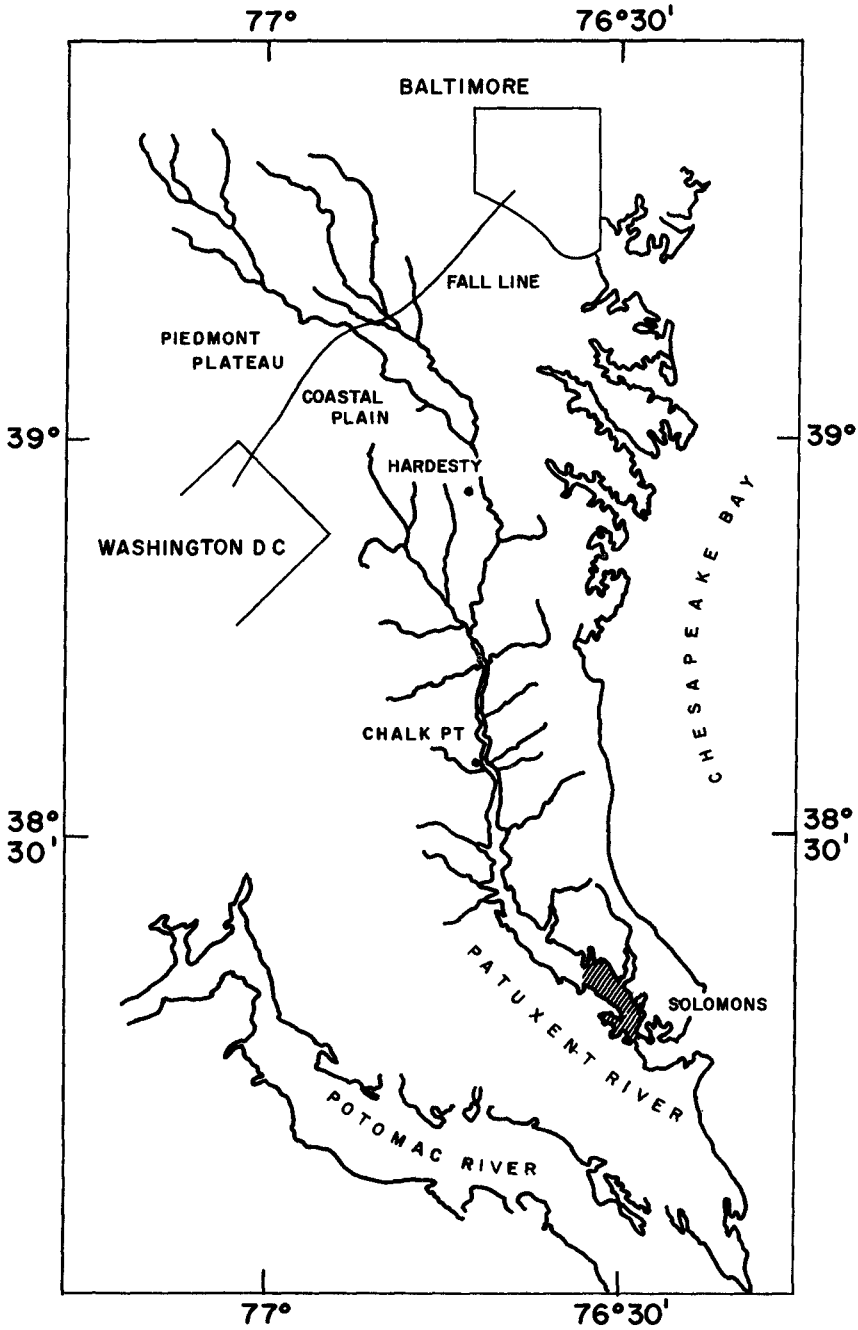


FIGURE 1 INDEX MAP SHOWING AREA OF STUDY

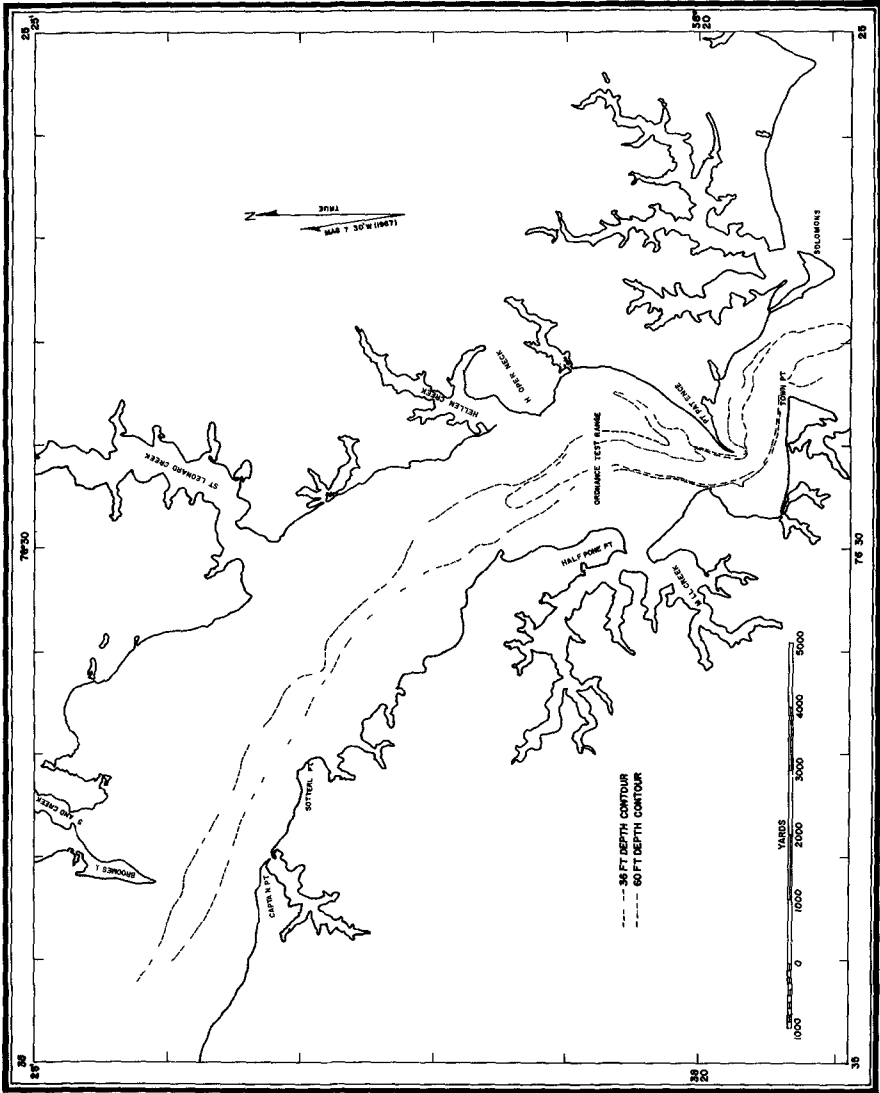


FIGURE 2 BATHYMETRIC CHART OF LOWER PATUXENT ESTUARY

The Patuxent River drainage basin lies entirely within the state of Maryland and occupies 930 square miles (Crooks, O'Bryan and others, 1967). The mouth of the Patuxent Estuary is located where the river enters Chesapeake Bay. The upper limit of the sea salt water ranges from 27 miles (Chalk Point) to 56 miles (Hardesty) above the mouth. The portion of the waterway between the upper limit of tidal influence and the limit of sea salt intrusion is designated the tidal river (Pritchard, 1967, and Owen, 1969). Between the upper limit of the sea salt intrusion and the mouth of the river is the estuary. The Patuxent has been termed moderately stratified by Pritchard (1967), and Owen states "The Patuxent Estuary has a normal two-layered flow associated with an intermittent three-layered flow." Chesapeake Bay itself is a moderately mixed estuary.

Owing to the abundance of readily accessible erodible material in the Coastal Plain the sediment yield of the drainage basin is fairly high, 235 tons per square mile at Hardesty near the estuary head (Johns Hopkins University, 1966). Figure 3 shows the change in the lower estuary channel from 1859 to 1944. Although the location of this cross section is not shown, depth and width values correspond with the segment of the estuary between Helen Creek and Broomes Island (Figure 2).

PROCEDURE

Continuous seismic profiles of the Patuxent River between Town Point and Broomes Island were recorded during the period 7 to 10 May 1968. Work was performed on a 45-foot utility boat provided by the U S Naval Ordnance Laboratory Test Facility. The transducer was rigidly mounted on the side of the boat three feet beneath the water surface. A total of 19 tracks were run over a distance of 30 nautical miles (Figure 4). Boat speeds of about three to four knots were maintained for all traverses. Positioning was determined from the two triangulation towers located at Point Patience.

The seismic profiler, nicknamed a "Mud Penetrator" (Yules and Edgerton, 1964), consists of three main components: (1) an acoustic transceiver and recorder (EG&G, Model 254 Seismic Recorder), (2) a transmitter/receiver transducer (EG&G, Model 228A Pinger Probe), and (3) a gasoline powered electric generator. The system operates at an acoustic frequency of 12-kHz which is sufficiently high so that only fine-grained sediments can be effectively penetrated.

The technique for continuous seismic profiling of subsurface acoustic horizons uses a repetitive sound source which propagates acoustic wave fronts through the water and subsurface materials. As these wave fronts encounter materials of contrasting acoustic impedance--normally manifestations of geologic stratification or boundaries--echoes are returned to the surface, sensed by the transducer, and then synthesized by the recorder to produce a real-time, continuous profile of the water column,

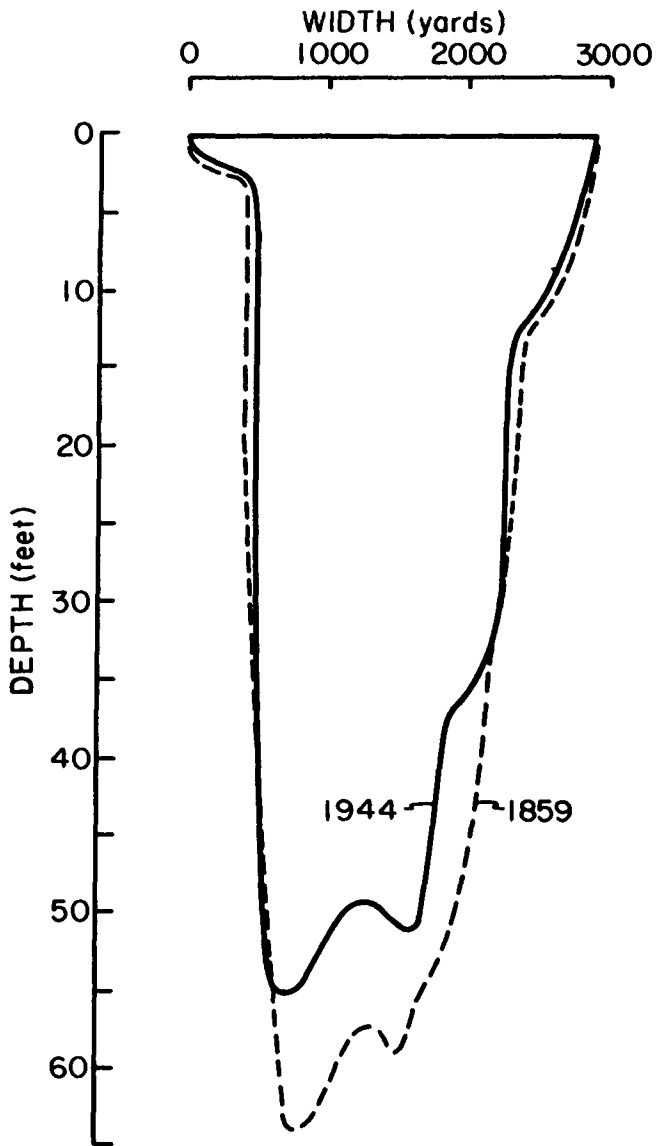


FIGURE 3. SEDIMENTATION IN THE PATUXENT ESTUARY.
(AFTER JOHNS HOPKINS UNIVERSITY, 1966)

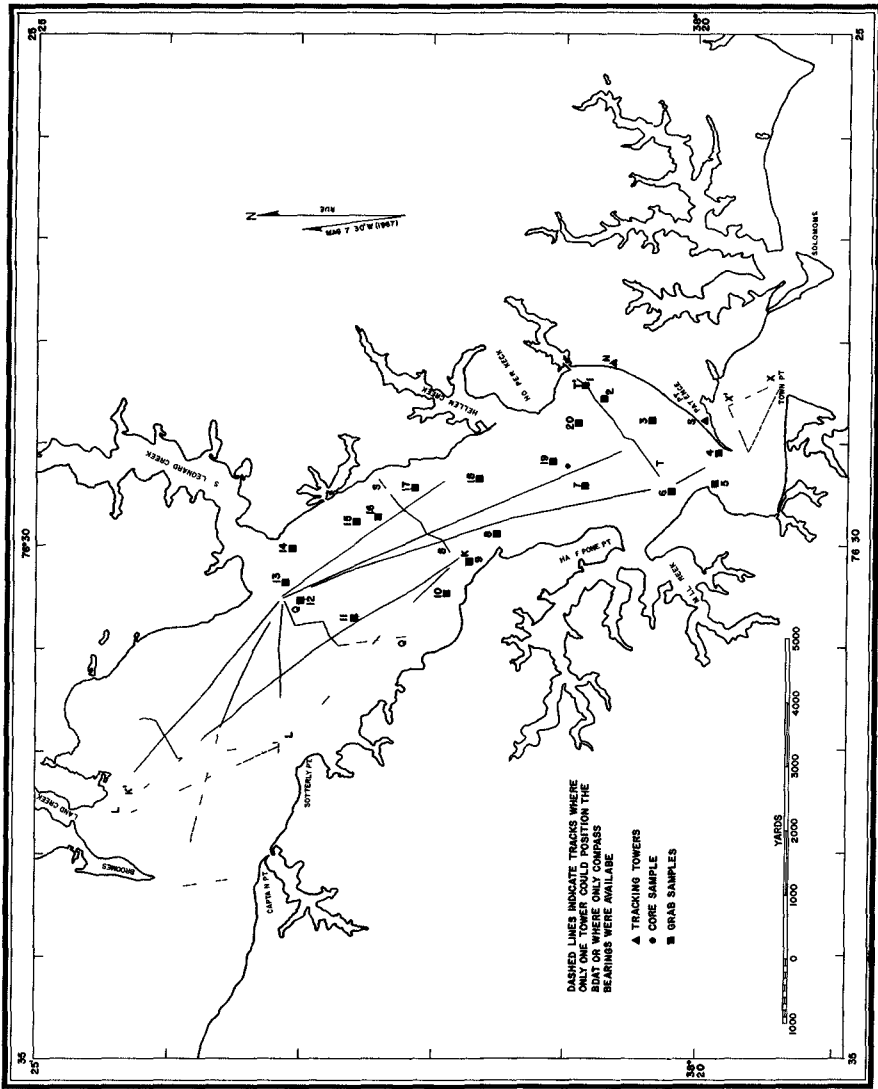


FIGURE 4 LOCATION OF BOAT TRACKS AND SEDIMENT SAMPLES

bottom, and subbottom The vertical scale is in time (milliseconds) and the horizontal scale is a function of recorder-paper speed and ship speed The time values shown on the seismic records are total travel times (two-way times) and must be halved for computing thickness Conversion of the time scale to thickness is accomplished by multiplying one-half the total travel time by a sound speed factor All depths in this report are based on a sound speed of 1500 meters per second in both the water and sediment. This value corresponds closely with measured values on two core samples obtained near the mouth of the Patuxent Estuary (Stiles and Wiesnet, 1970).

Analysis of the seismic profiles in this investigation is based on the following premise. Observed subsurface geologic features on the seismic record are acceptable as proof of existence of subbottom structure However, the converse of this statement is not necessarily true The absence of subbottom structure on the seismic record does not always mean that a subbottom reflector does not exist The absence may indicate masking by a cover of sand, gravel, or other coarse-grained material For a given frequency, mud is normally much less attenuating than sand or coarser grain sediments In most cases where a mud cover overlies a coarser grain sediment mass, the impedance contrast will be sufficient to record the thickness of the mud Exceptions may exist where the thickness of the surface cover is too great for the acoustic energy of the particular seismic system to penetrate and return to the sensor

Development of an isopachous map from seismic profile records requires identification of a particular reflecting horizon which corresponds to a designated stratigraphic unit, transferring the thickness values (e g, in this paper, the distance between the first subbottom layer and the water-sediment interface) on to a track chart, and contouring these values

DISCUSSION OF RESULTS

Results of this investigation are presented in the form of annotated seismic profiles and an isopachous map Interpretation of the seismic records was based in part on previous work with this system Earlier studies by Breslau and Edgerton (1968) in the Gulf of La Spezia, and by Stiles and others (1969) in four Vietnamese rivers have shown that the acoustic energy of this system is not capable of penetrating coarse-grained sediments, such as sands or gravels, whereas, fine-grained materials, such as silts and clays, are transparent to the 12-kHz sounds of the system After completion of the isopachous map, 20 sediment samples were collected Comparison between the sediment properties from these bottom samples which were collected simultaneously with seismic profiles corroborates the interpretation of seismic profiles in this investigation (Figure 5 and Table I)

The stratigraphic unit used in this study is the acoustically transparent sediment cover. This sediment cover is composed mainly of fine-grained silt- and clay-size sediments,

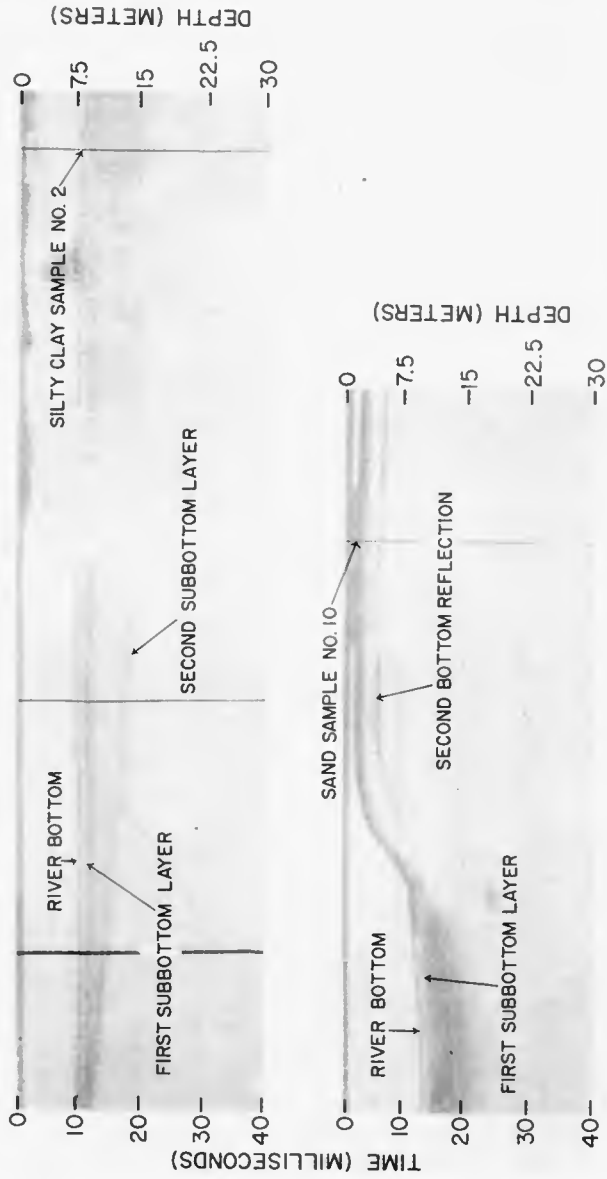


FIGURE 5. COMPARISON BETWEEN SEDIMENT TYPE AND ACOUSTIC PENETRATION.

TABLE I
SEDIMENT PROPERTIES AND ACOUSTIC PENETRATION

SAMPLE NO	COARSE FRACTION >0.0625 mm %	FINE FRACTION <0.0625 mm %	MEAN DIAMETER mm	WET UNIT WEIGHT g/cm ³	WATER CONTENT % dry wt	SEDIMENT TYPE	ACOUSTIC PENETRATION m
1	43	57	0.012	1.23	161	sand and clay	1
2	11	89	0.003	1.14	224	silty clay	2-7
3	12	88	0.004	1.25	172	silty clay	2
4	88	12	0.094	1.65	74	sand	0
5		-- NO	ANALYSIS	--		shells	0
6	98	2	0.242	1.72	34	sand	0
7	70	30	0.914	1.19	194	clay and shells	3
8	10	90	0.003	1.15	231	silty clay	1
9	21	79	0.006	1.13	245	silty clay	1
10	99	1	0.236	1.59	33	sand	0
11	21	79	0.005		233	silty clay	1
12		-- NO	ANALYSIS	--		shells	0
13	42	58	0.014	1.25	178	sand and clay	6
14	95	5	0.168	1.74	34	sand	0
15	90	10	0.119	1.61	45	sand	0
16	83	17	0.098	1.53	49	sand	0
17	51	49	0.109	1.16	216	clay and shells	4
18		-- NO	ANALYSIS	--		shells	0
19	95	5	0.179	1.78	45	sand	0
20	24	76	0.006	1.19	200	silty clay	2

collectively referred to as mud. The reflecting horizon used in all cases is the first subbottom layer. Where penetration does not occur, the surface materials consist of coarse-grain sediments. Both the opaque surface and subsurface reflectors are assumed to consist of similar sediments. Selected longitudinal and transverse profiles are shown in Figures 6 through 9. Location of these seismic profiles are shown in Figure 4. The isopachous map is shown in Figure 10.

Analysis of the seismic records shows numerous objects partially submerged on the river bottom. The largest object is shown protruding from the bottom near the southern end of Profile L - L' (Figure 6), which is believed to be either a part of the mooring buoy plotted on U S Coast and Geodetic Survey Chart No 553 or a sunken barge (James Green, Naval Ordnance Laboratory Test Facility, Solomons, Maryland, oral communication). Green indicated that in addition to the barge there are many metallic objects scattered on the river bottom. Some of these artifacts are probably the same objects observed on the seismic records (Figures 7 and 9). In addition to the objects lying on the river bottom, many reflections presumably caused by fish were recorded in the water column (Figure 9).

Subbottom layers are present in a majority of the seismic profiles north of Half Pone Point (Figure 10). Depressions filled with mud are as much as 16 feet thick. One of the clearest records of subbottom structure is shown on Profile K - K' northwest of the "Black Hill" structure (Figure 7). We assume that the subbottom reflecting layer is mainly composed of quartz sands or oyster shells (Table I). The same reflecting horizon forms a terrace further northwest along Profile K - K' (Figure 7). Similar terrace-shaped structures are present on the northeastern margin of Profiles Q - Q' and S - S' (Figure 8). A terrace consists of two parts, the inclined portion is called the scarp and the flat lying part is called the tread. In this paper, the term terrace is used even if only the scarp portion of the terrace is observed on the seismic record. Indications of terraces are seen on these bottom profiles and clearly show that they are composed of highly reflecting materials (i.e., sands or shells) with enough coherency to maintain slightly inclined slopes. The vertical exaggeration between the profile record and the true slope angle should be realized. The angle of the scarp shown in Profile Q - Q' is approximately 10 to 12 degrees. A submerged terrace is visible on the northeastern edge of Profile T - T' (Figure 9). The stairlike terrace is traced on the record as a second subbottom layer, and is clearly an abandoned feature not related to the present river channel. Maximum penetration at the deepest portion of the lower scarp is approximately 36 feet beneath the water-sediment interface. It is assumed that the first subbottom layer has a higher concentration of fine-grained sediments than those reflecting horizons previously discussed, and thus is partially transparent to the acoustic energy of the system.

The feature labeled on Profile K - K' as a "Black Hill" was viewed on several seismic records over this area. The areal extent and shape

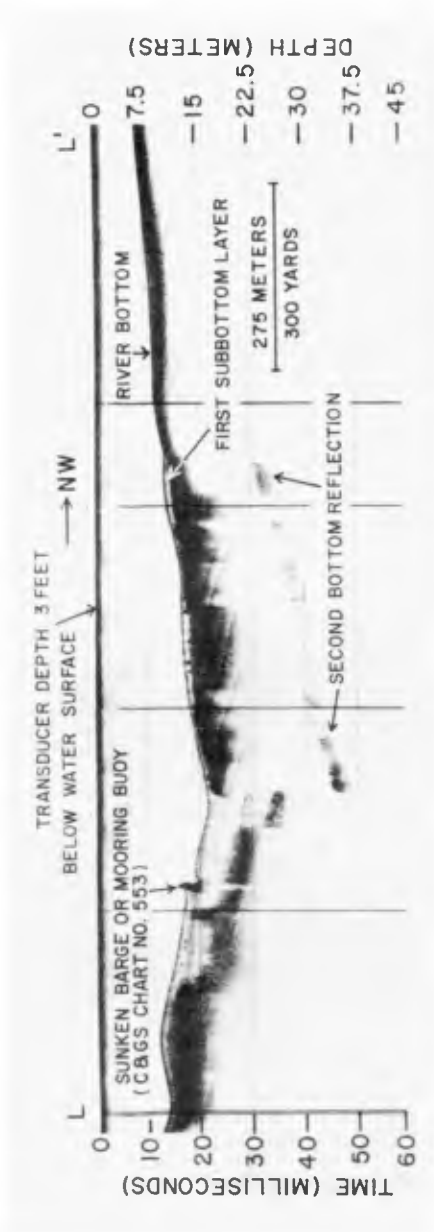


FIGURE 6. SEISMIC PROFILE OF LOWER PATUXENT ESTUARY (L - L').

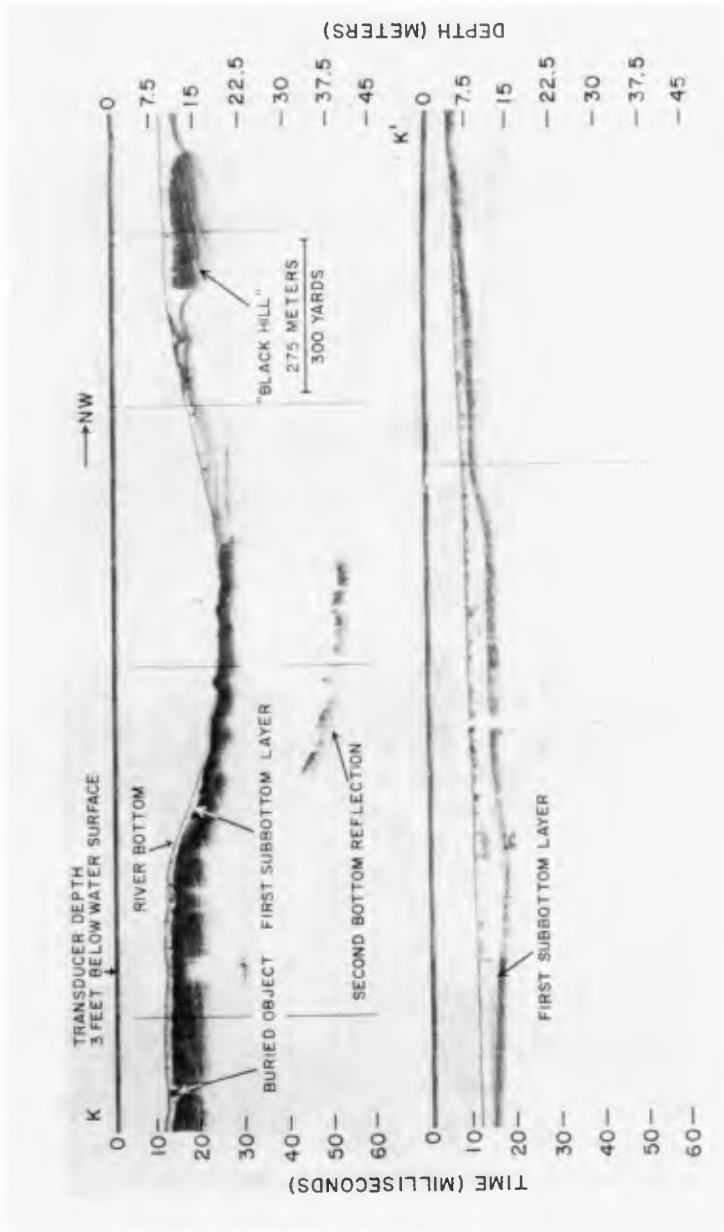


FIGURE 7. SEISMIC PROFILE OF LOWER PATUXENT ESTUARY (K - K').

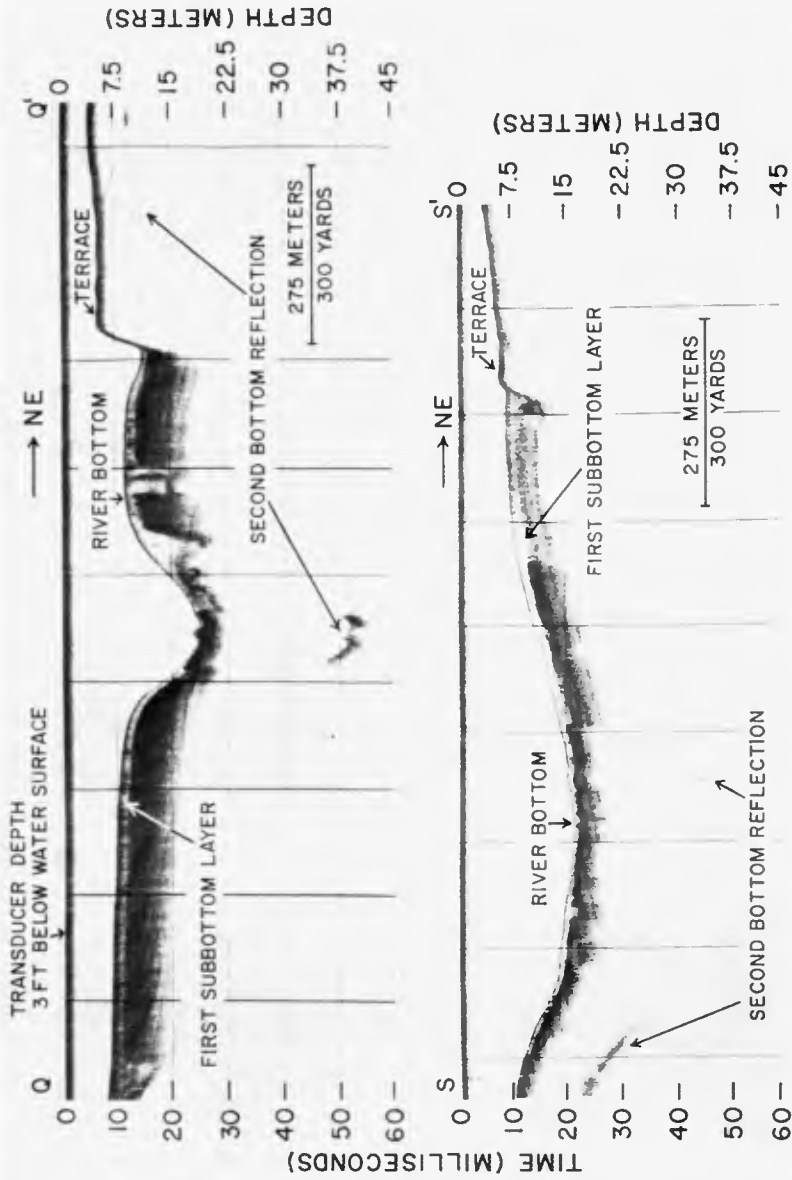


FIGURE 8. SEISMIC PROFILES OF LOWER PATUXENT ESTUARY (Q - Q' AND S - S').

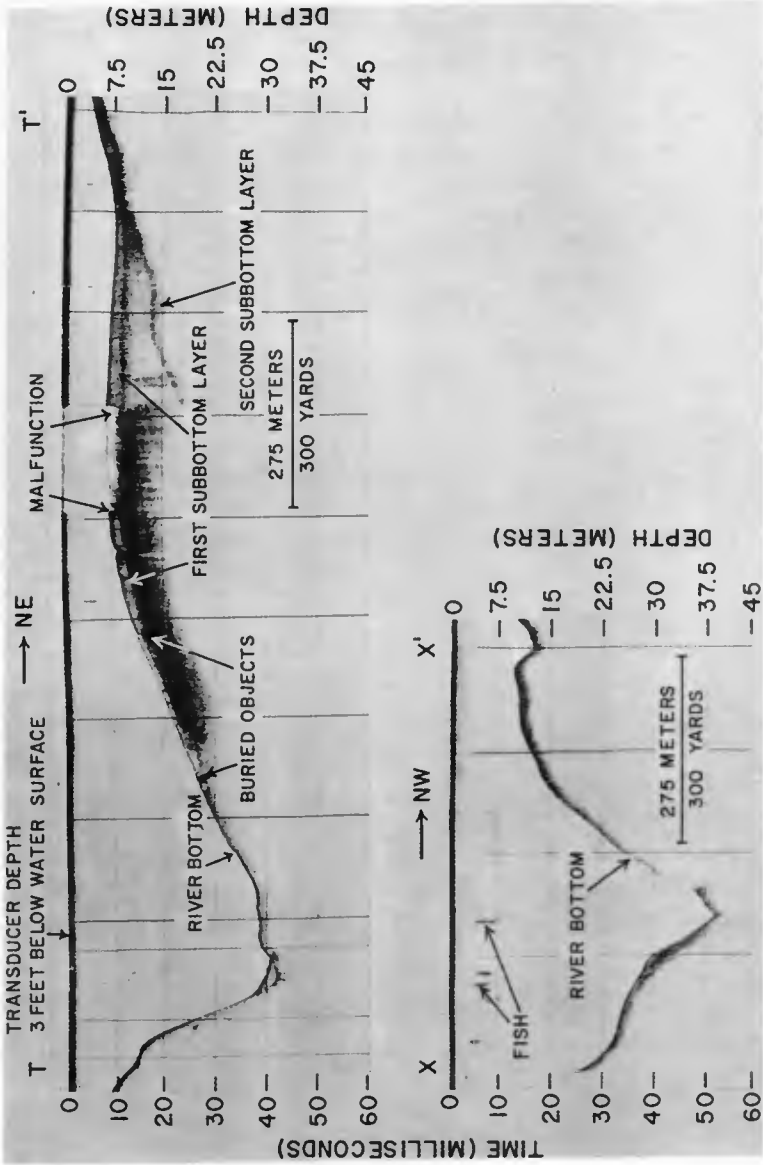


FIGURE 9. SEISMIC PROFILES OF LOWER PATUXENT ESTUARY (T - T' AND X - X').

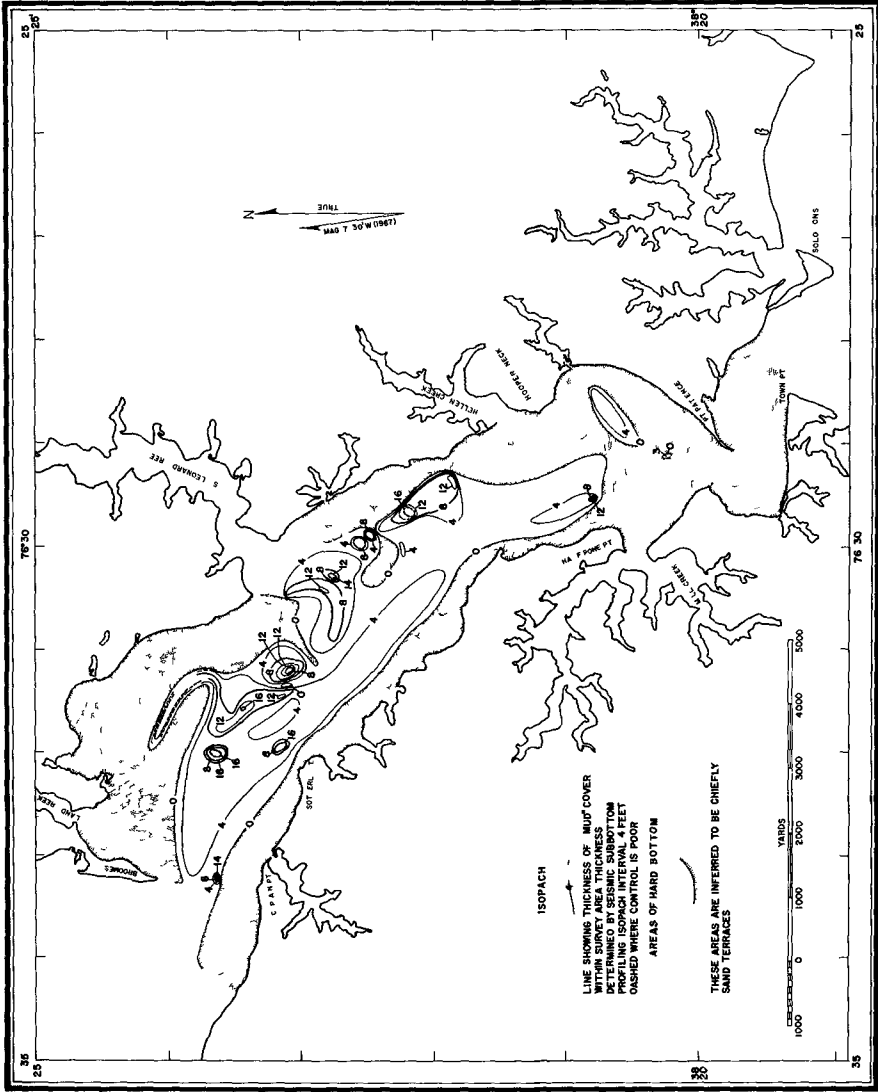


FIGURE 10 ISOPACHOUS MAP OF LOWER PATUXENT ESTUARY

of this structure is shown on the isopachous map (Figure 10). The structure is almost circular and lies directly northwest of the crescent-shaped mud hole at the mouth of St. Leonard Creek. The two almost circular 16-foot mud holes between Sotterly Point and Island Creek also closely resemble in profile and plan view this "Black Hill" structure. Although the cause or nature of these structures is not known, it is believed that they may be oyster beds that have been covered during a period of prolonged sedimentation.

CONCLUDING REMARKS

The work performed for this investigation demonstrates the stratigraphic variability of the surficial mud cover in the lower Patuxent River Estuary. The thickness and extent of the mud cover is based on the occurrence of acoustic discontinuities seen on the seismic record. These discontinuities occur only in areas where fine-grained materials, which are transparent to the 12-kHz sound, overlie coarse-grained sediments. Where penetration does not occur, the surface materials are coarse grained. Both the opaque surface and subsurface reflectors are assumed to consist of similar materials.

Depressions filled with mud occur mainly to the north of Half Pone Point (Figure 10). The thickest mud layers lie to the east of the present channel. These mud-filled depressions are as much as 16 feet thick. The dominance of the deeper holes to the east plus the occurrence of a submerged terrace indicates that either the channel of the Patuxent River at this location was much larger in the past and has subsequently filled in much of the material on the eastern edge, or that the channel has migrated to the west.

The presence of terraces on the edges of the channel was used as evidence for plotting the areas of hard bottom on the peripheral edges of the river (Figure 10). Although it was not possible to profile to the shoreline because the water was too shallow, it is safe to conclude that the materials which comprise the terraces extend also to the shoreline.

The majority of the sediments below Half Pone Point allowed little acoustic penetration (Figure 10). The presence of coarse-grained sediments is supported in part by divers from the Naval Ordnance Laboratory Test Facility. These divers have indicated that the elliptical mud hole north of Point Patience, as shown in Figure 10, extends northward and is a part of the large deposit of mud shown in the center of the river channel. These divers also have indicated that small mud holes lie slightly north of Town Point.

Recommendations for future study regarding the stratigraphic variability of the surficial mud cover are directed toward two potential problem areas. More work is needed in defining the sediment properties responsible for acoustic reflections in the study area. Secondly, little is known of

the riverine and estuarine dynamics causing the distribution of sediments Owen (1969) states that "a distinguishing feature of the Patuxent Estuary is its intermittent transition from a two-layer flow system to a three-layer flow system, a transition which occurs most often in the month of April " On the basis of this concept of a two-layer flow system, i e , a net bayward (or seaward) flow of less saline (lighter) water at the surface and a net landward flow of more saline (heavier) water near the bottom, Meade (1969) has presented evidence that bottom sediments in Atlantic Coastal Plain estuaries are transported landward Some questions that remain to be answered are In the various flow layers is there some process going on differentiating sediment types? Of the materials brought down by the river, how much and what type of material is trapped in the estuary? What is the spatial distribution and temporal variation of this flow system which may control the distribution of sediments?

This study demonstrates the use of seismic profiling techniques for collecting and presenting data required for coastal engineering applications Other possible coastal engineering applications for this type of work are (1) determining the thickness of a particular stratum for estimating dredging or excavation costs as well as for obtaining construction materials, (2) foundation studies, (3) harbor mapping, (4) slope stability studies, (5) spoil location, and (6) location of tunnels and pipelines

ACKNOWLEDGEMENTS

We would like to express our special thanks to Dr Lloyd Breslau, former Head of the Coastal Oceanography Branch, U S Naval Oceanographic Office, now with the U S Coast Guard, whose guidance and valued advice during the field phase of this investigation are deeply appreciated His helpful comments and review of the manuscript are gratefully acknowledged

Appreciation is expressed to Dr Jerry Schubel of the Chesapeake Bay Institute, The Johns Hopkins University, Mr Leo Fisher of the U S Naval Oceanographic Office, and Mr Ralph Hightower and Mr Arne Yensen of the U S Naval Ordnance Laboratory for their suggestions and review of this manuscript

REFERENCES

- Breslau, L R , and Edgerton, H E , 1968, The Sub-Bottom Structure of the Gulf of La Spezia SACLANT ASW RESEARCH CENTRE, Technical Report No 129, 81p
- Crooks, J W , O'Bryan, D , and others, 1967, Water Resources of the Patuxent River Basin, Maryland U S Geological Survey Hydrologic Investigations Atlas HA-244, 5 sheets
- Johns Hopkins University, 1966, Report on the Patuxent River Basin, Maryland--Prepared by the members of the Water Management Seminar The Johns Hopkins University, Baltimore, Maryland, 228p
- Meade, R H , 1969, Landward Transport of Bottom Sediments in Estuaries of the Atlantic Coastal Plain Jour Sedimentary Petrology, Vol 39, No 1, p 222-234
- Owen, W , 1969, A Study of the Physical Hydrography of the Patuxent River and its Estuary Chesapeake Bay Inst , The Johns Hopkins University Technical Report 53, 78p
- Pritchard, D W , 1967, What is an Estuary Physical Viewpoint in Estuaries, G H Lauff (editor), AAAS Publication No 83, p 3-5
- Stiles, N T , Breslau, L R , and Beeston, M D , 1969, The Riverbed Roughness and Sub-Bottom Structure of the Main Shipping Channel to Sai Gon, RVN (Nga Bay, Long Tau, Nha Be, and Sai Gon Rivers) Proc , 12th Conf on the Naval Minefield, Naval Ordnance Laboratory Technical Report 69-69, Vol 1, p 327-368
- Stiles, N T , and Wiesnet, D R , 1970, Isopachous Mapping of the Lower Patuxent Estuary Sediments by Continuous Seismic Profiling Techniques U S Naval Oceanographic Office Informal Report No 70-37, 26p
- U S Coast and Geodetic Survey, 1969, C & GS Chart No 553, Chesapeake Bay, Patuxent River and Vicinity, Maryland U S Dept of Commerce, Washington, D C , Scale 1 40,000, 8th Edition, April 14, 1969
- Yules, J A , and Edgerton, H E , 1964, Bottom Sonar Search Techniques Undersea Technology, November, p 29-32

CHAPTER 42

OBSERVATION OF SEDIMENT MOTION BY UNDERWATER-TELEVISION

Dipl Ing. Gunter Luck

Researchstation for Island- and
Coastprotection, Norderney, Germany

ABSTRACT

For observation and interpretation of sedimentological movements an Underwater Television set-up is employed, which is described in the following paper. The so long achieved results and experiences are exemplified.

THE TV SET-UP

Since springtime 1968 an Underwater-Television set-up is employed for special sedimentological researches in the Juist-Norderney oceanic region (East Frisian Islands), which is bestowed by the German Research Association (Fig 1). The TV set-up - in transportable execution - is constructed for use in free waters to a depth of 100 m. The main equipments are as follows (Fig 2a/b).

- 1 TV camera in a cylindrical case of stainless steel, resistant to pressure, with outfit for necessary correct contact when fixing the at times used sight- and lighting-

supplements The TV camera is fitted out with a multi-pole contact-plug for connection with the camera-cable and the wireless control-transmission for focus.

Diameter 76 mm; length 447,5 mm; test pressure 48 atu, weight 6,7 kg in the air and 4,5 kg in the water

1 Supplementary lens for free sight for general free water observations (opening angle 103° in the air and 72° in the water).

2 Underwater widespread lights

1 Underwater photo camera with an underwater flashlight

1 Camera cable, length 100m, diameter 25 mm

1 Control unit with electronic regulator

1 Distribution unit

1 Reproduction unit (screen diagonal. 36 cm)

1 Video tape recorder

Further there are providently kept ready accessories and spare pieces such as tubes, incandescent-lamps, packings, service-box and so on In anticipation it was to be expected, that due to the small range of sight the set-up only can be used from an anchoring ship Therefore the TV camera and the photo camera were mounted in a fourlegged frame (Fig 3), which can be placed on the sea floor by aid of a crane The reproduction-unit, control-mechanisms, video tape recorder and so on were firmly installed on a ship (Fig 4)

PRIMARY INVESTIGATIONS AND EXPERIENCES

In the first half-year of researches (summer 1968) above all the apparativ feasibilities of the TV set-up were tested,

specially taking into consideration the particular conditions in the extreme turbid waters of the tidal flat. In detail there was to find out

- 1 The most effective use of the set-up (observations from anchoring or sailing ship). Further the best distances from object to sea bottom had to be found, simultaneously using the most favourable focal depth.
- 2 Ascertainment of the most effective search light arrangement to receive the most contrasting pictures as well as the best efficiency of light evolution.
3. Dependency of the TV work on meteorological conditions.
4. Dependency of the observations on the different turbidness of the water.

These investigations had the following results

- 1 In the turbid waters of the tidal flat the use of the TV set-up is only reasonable at continuous fine weather and during slack water (Fig.5). As soon as the current exceeds the critical velocity of erosion or sedimentation, the rate of suspension increases so quickly, that it is no longer possible to gain an interpretable picture (Fig.6).
- 2 After atmospheric disturbances and great water motion also during slack water the rate of turbidity in the tidal flat is for a longer time so intense (up to three and four days), that observations of the sea bottom are not possible

Whereas after continuous fine weather it might be possible to observe the sea bottom during the first and perhaps even the second turbulent tide. At wind forces of more than 6 Bft and at high current velocity connected with high waves an observation of sedimentary movements is absolutely impossible.

3. Even on the most favourable conditions the distance between the objective and the sea bottom must not exceed 35 cm (TV picture 40 x 40 cm).
4. The conditions improve obviously, when the set-up is employed in deeper waters abroad the tidal flats. The visibility is much better and the times of observation can be extended (Fig.7). Nevertheless the range of turbidity is so extensive, that the distance objective - sea bottom only may amount to 55 cm (TV picture 60 x 60 cm).
5. These only small distances between objective and sea bottom, available due to the local boundary conditions, don't allow observations from the sailing or drifting ship. As for each observation the anchor has to be set, it is only possible to work stationary and the researches take much time. For this reason the TV method in the sediment research is severely limited.

SOME OBSERVATION RESULTS

In the research years 1969 and 1970 it was possible to perform aimed sedimentological observations. Besides general observations of regional movements in the research area it was tried to gain

knowledge of the sedimental process on the tidal flats and specially to find an optical definition of the critical velocity of erosion and sedimentation. Without entering into the details of the researches the main results can be resumed as follows

- 1 Only in exceptional cases the suspended matters and the sediments, transported on the bottom, are separated more or less exactly. Considering the hitherto existing observations a thus strict separation actually can ensue only within the compass of high current velocity and therefore strong sediment motion on the bottom (Fig 8a/b). In regions with lower velocities, which nevertheless still are capable of transporting, a differentiation of the motion on the bottom and the transport of suspended matter is not possible. Therefore the moved materials have to be considered as one unity.
2. As already mentioned the range of visibility very much depends on the meteorological conditions of the foretides. When the foretides were influenced by storm, the rate of turbidity is intensified still for a longer time. Whereas as undisturbed progress of the foretides the rate of suspended matter for the present is still normal, even after commencing atmospheric disturbance and higher current velocity. Therefore at the same current velocity and otherwise similar conditions the concentration of the suspended matter differs very much.
- 3 Of still more importance to the suspended matter are the

seasonable varying biological conditions. Thus the rate of suspended matter is much higher on midsummer after full development of vegetation, than for example in winter or springtime. After the long lasting quiet and warm summer 1969 in the whole oceanic region of Norderney the rate of suspended matter was much higher than in springtime 1970, which was preceded by an extreme long winter.

- 4 The physical process of suspension is essentially determined by the suspended matter's appearing not in equal dispersion but in flakes (Fig 9). These flakes are in nearly permanent hovering motion and only settle occasionally for short times during slack water. At insignificant turbulence, when the preceding tides had been quiet and the current velocity is lower than some 15 cm/s, the flakes fall to the bottom in a sudden process. As soon as the current velocity has risen to some 20 cm/s, the flakes are absorbed by the current.

At the microscopical and chemical analysis of these flakes one could discern particles of different sizes and origin, which adhere to a scarcely visible organic slime, showing a strong positive albumen- and occasionally a cellulose-reaction (Fig 10 a/b). Here it is probably the question of reduction products of marine organisms. This supposition is confirmed by the rich bacterial trimming. These slimes, being scarcely perceptible in the microscope, become well visible in the flash light beam and can be observed clearly in the television picture as flakes. In volume the slimes preponderate, whereas the quartz crystals and other mineral particles as well as diatom shells, chitin scraps, filaments

etc prevail in weight.

Measuring and ascertaining the rates of suspended matters there was not paid enough attention to these flake structures untill now. In the floating water these flakes and pure mineral particles are to be found close together. During the sedimentation- and erosion-process this different physical deportment of flaky and pure mineral sediments causes different sedimentation- and erosion-phenomena, which however are temporary without transition.

- 5 Seldom the transportation process near the bottom has a continuous run, but the sediment moves in intermittent veils. This discontinuity also was to be observed at the progress of small ribs. The motion of the sediment increases, when also shells are transported or animals move on the ground (Fig 11 a/b). Thus a small rib disappeared (length some 20 cm, height some 5 cm), which first seemed to be rather stable, while a crayfish was crossing it. The whole sand supply at once turned to suspension.

The discontinuity of the transport near the bottom is still additionally intensified, when the sediments come into the waves' sphere of action. In this case the sediments move on paths, which relate to the direction of the current and waves. When the waves work in the same direction as the current, the motion is rolling. Do the directions mould an angle, this rolling progress passes over to a more saw-tooth-shaped path.

6. A series of researches was performed, especially tended to the optical ascertainment of the critical velocity of erosion and sedimentation. In spite of a great expenditure however, so long it was not possible to undertake a single-valued fixing of these critical velocities. The process of sediment reception by the current proceeds most floating, locally however very much differing, without a possibility of observing the beginning of this phenomenon. The process of sedimentation is still more opaque, because only very seldom the whole sediment is deposited during slack water. With diminishing velocity the process of erosion also doesn't turn slidingly to the process of sedimentation, as before the beginning of sedimentation there exists a higher range of velocity, which doesn't erode the material near the bottom any longer, but still transports more or less suspended matters.

CONCLUSION

The observations of sedimentological processes of motion with the underwater television set-up showed the limits of its efficiency. The extraordinary value of the so long achieved investigations is to be found especially in the fact, that the processes of motion were made visible and partly interpretable.

The sediment transport's predominant dependency on the meteorological conditions of the foretides and specially the development of the suspended matter as consequence to the biological phenomena was unobjectionably discerned and proved

It was not possible to ascertain a connexion between the at times locally measured current-velocity, rate of suspended matters, grain distribution of the sediment near the bottom and so on. A separate treatment of the bottom-near transport of sediments and the suspended matters is only possible in those exceptional cases, in which high velocities put the whole bottom material in rolling, jumbling and at last pushing motion. As a rule - in the tidal flats and oceanic regions with low current velocity - the water contents flaky and pure sediments in proportionate distribution, whereat however at low turbulence the density of the suspended matter can increase with depth.

The in past times theoretical formed conceptions to ascertain sedimentological processes of motion, which predominantly depended on the current velocity and the critical velocity of erosion, are - appreciating the observation results, gained with the under water television - only little satisfying.

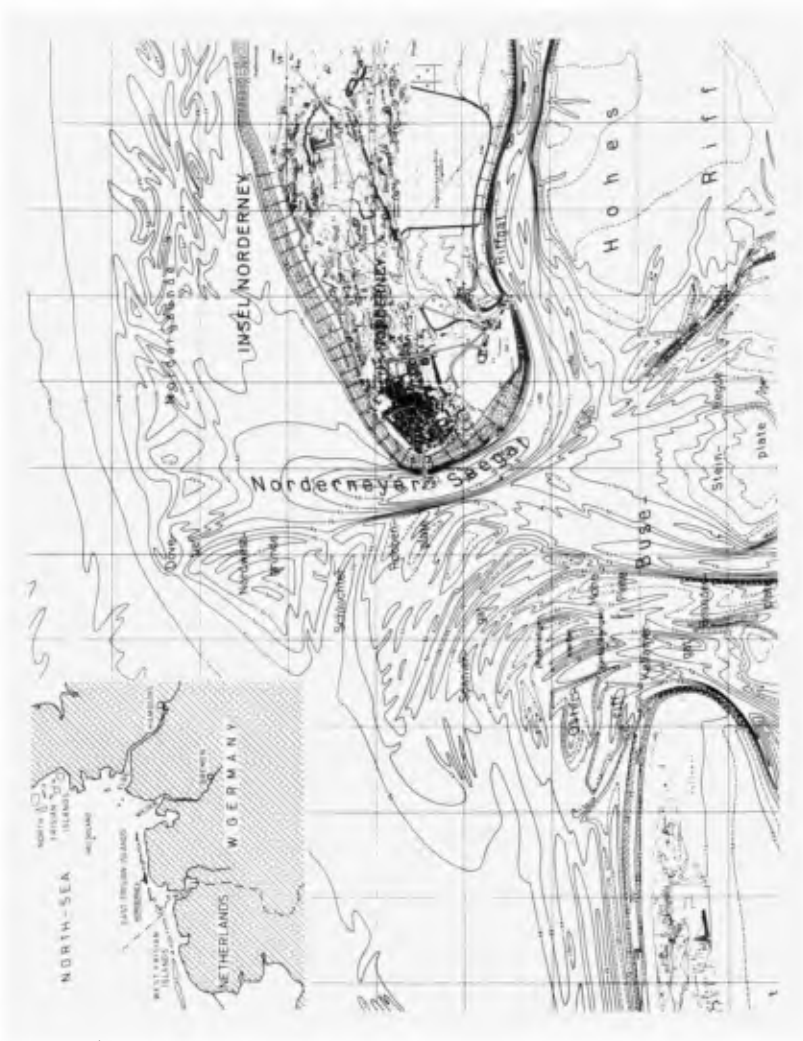


Fig.1 Research region around Juist-Norderney Islands



Fig. 2a TV camera (center), photo camera (left), flashlight (right) and searchlights (behind)



Fig.2b Lower deck television set-up with monitor (top), distribution unit (bottom right), control unit with moisture warning inset, operating inset for photo equipment, operations inset for intercommunication system (bottom center) and video tape recorder (left)



Fig.3 Four-legged support frame on deck



Fig.4 Workshop "Burchana" of the Norderney Researchstation, where the TV set-up is installed.

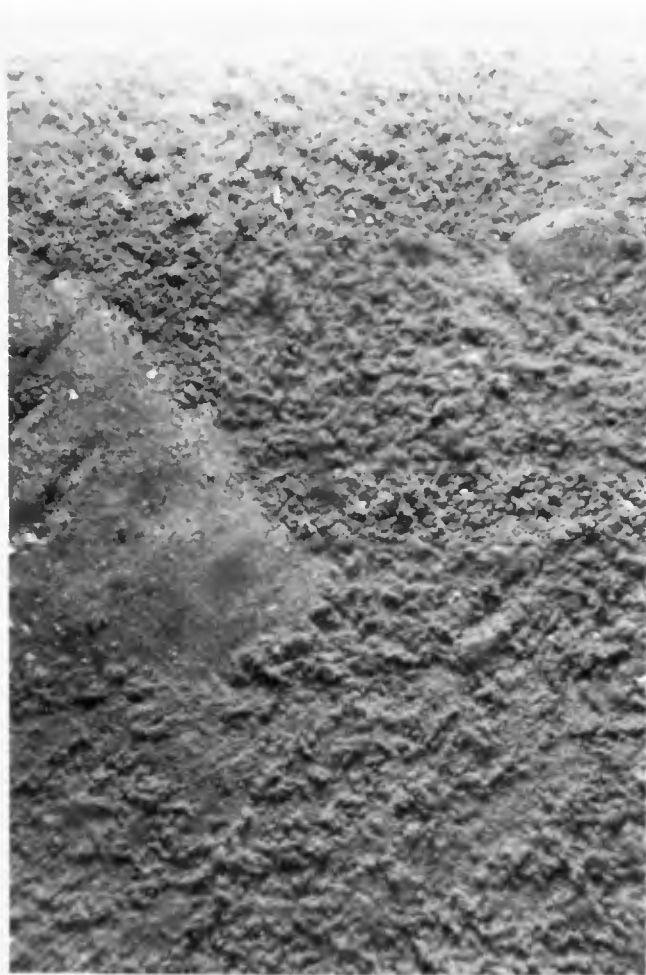


Fig.5 Bottom in a narrow channel of the tidal flat during slack water. The ground is covered with flaky sediments. A small area of sand in the left-hand section of the photograph is still uncovered.



Fig.6 At great water motion in the tidal flat it is impossible to gain an interpretable picture.



Fig.7 Sea bottom in the north of Norderney island (water depth some 26 m). The visibility is much better than in the tidal flat.

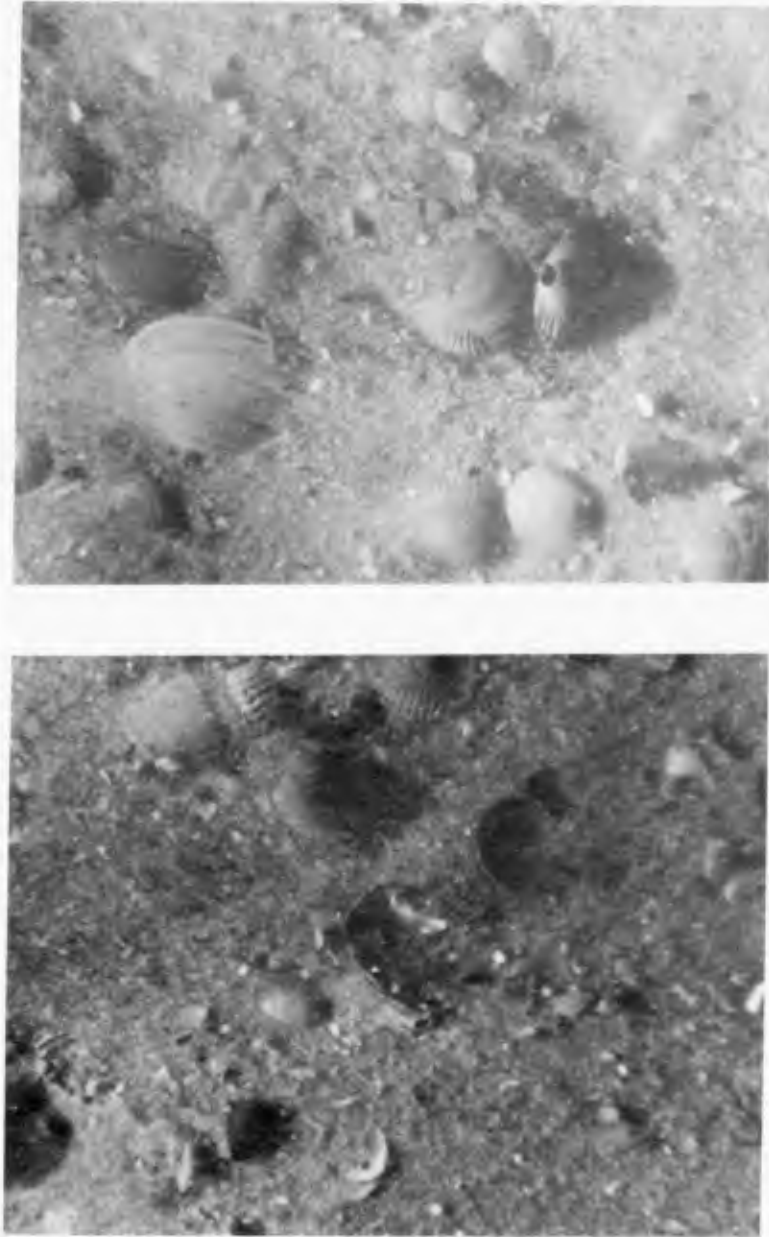


Fig.8a/b Two photographs of the same spot in a narrow channel with high current velocity (some 80 cm/s). Sand and shells jump, roll and slide along. The temporal distance between figure a and b is four seconds.



Fig.9 Flaky material covers the bottom for a short time during slack water.



Fig.10b The same flake in still higher enlargement (about 10 times larger) with mineral and organic ingredients.

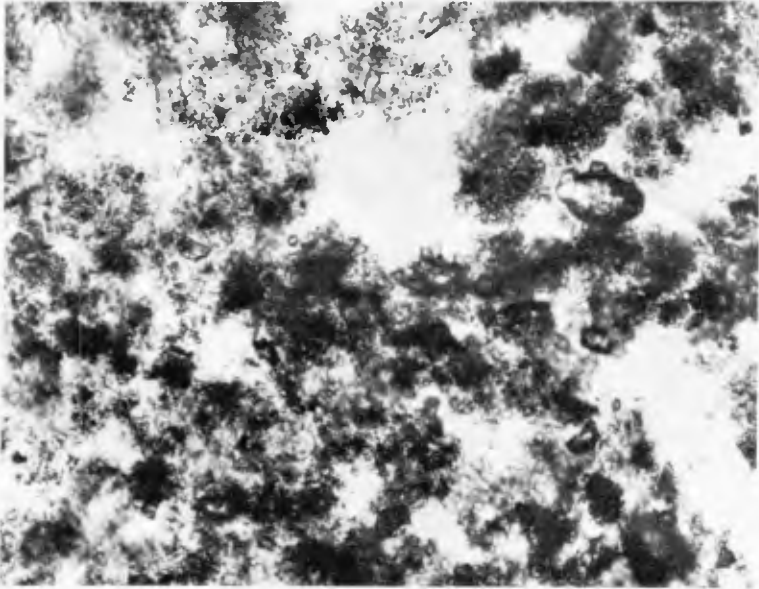


Fig.10a Flake in microscopical enlargement. In front mineral particles (sand, diatom-shells etc.) in black and dirty grey, in the light grey background organic slimes.



Fig.11a Ripplemark abroad the tidal flat
in 18 m water depth, current velocity
some 20 cm/s.



Fig.11b The same ripplemark one minute later.

CHAPTER 43

THE HISTORY OF THE DUTCH COAST IN THE LAST CENTURY

by W.T. Bakker¹⁾ and D.Sj. Joustra²⁾

ABSTRACT

The purpose of this paper is

1. Publishing some available coastal measurements and computations of more than local importance
2. Investigation on the influence of groynes in practice.
3. Investigation on the motion of the gullies in the outer deltas.

The following conclusions are drawn

1. The gross littoral drift along the dutch coast is in the order of 1.5 to 2 mln m^3 /year, (computed with the CERC-formula) the resulting net drift is mostly within the order of accuracy of the computation.
2. The erosion of the areas with groynes was much less than the erosion of the adjacent areas, partially this effect is due to lee-side scour but mainly to decreased erosion in the protected area.
3. The gullies in the outer deltas of the Wadden mainly turned clockwise, which is probably the direction of the resultant transport there.

INTRODUCTION

The dutch coast consists of three parts (fig. 1)

1. The Rhine-Schelde Delta
2. The uninterrupted coast of Holland
3. The Wadden area

It is a sandy coast ($D_m \approx 200\mu$), the tidal difference varies between 4 m near the Belgium border, down to 1.5 m near Hook of Holland, to 1.3 m near den Helder and then up again to 1.8 m near the German Island Borkum. The gully systems in the Rhine-Schelde delta and that of the inlets between the Wadden Islands in the North have quite a different shape, since the tidal basins are quite different. In the South the basins are rectangular with an open short side towards the sea and in the North they are rectangular with the long side parallel with the coast-line, this side is bordered by the Wadden Islands with narrow inlets in between. Therefore the Wadden coast can be compared with lagoon coasts, as they occur in many parts of the world. The Wadden Sea is a tidal flat, which is submerged during every high tide. Most information will be given about the Holland coast and the Wadden area, as DRONKERS [1] stresses the research in the Delta-area.

1) Senior Engineer Coastal Eng. Res. Dept., Directorate for Hydr. Res., Rijkswaterstaat

2) Lieutenant of Spec. Services 3rd Class Royal Dutch Navy Reserve

The main purpose of this paper is to supply data, which enables international comparison. This paper gives largely a summary of many reports of regional study-branches of Rijkswaterstaat, made over a period of about 50 years. From the former papers, covering the same subject, special attention is asked for WENTHOLT (1912)[2] who investigated especially the effect of groynes, van VEEN (1936) [3], who treated the origin of the Dutch coast and the shape of the gullies, van BENDEGOM [12], [22], [4], who investigated the hydraulic laws for the motion of the gullies, van STRAATEN [5], who considered the directional effects of winds, waves and currents and concluded that the sand drift must be strong (west to east) along the northern barrier islands and small between Katwijk and Texel, EDELMAN and EGGINK [6] who drew morphological conclusions from the curvature of the coast. PER BRUUN and GERRITSEN [7] treated the cross section of gullies and the stability of coastal inlets. BIJKER and SVAŠEK [8] give a treatise about IJmuiden harbour. The following paper gives more recent data than WENTHOLT, the conclusions of van VEEN, van STRAATEN, EDELMAN and EGGINK are reviewed in the light of modern theories about sand transport of CERC, BIJKER and SVAŠEK, making use of tidal computations.

BEACH MEASUREMENTS

Figure 2 and 3 show the erosion and accretion of the low-tide line, the high-tide line and the dune foot in periods of 10 year. First the 10-year average of each of these lines was determined, for instance 1856 - 1865, the distance between two successive 10-year averages is plotted in fig. 2 and 3. It is indicated where groynes, seawalls or harbour moles are present and when they are constructed.

The area of the Holland coast (fig. 2) is highly influenced very much by the building of the harbour moles of Hook of Holland and IJmuiden in 1870. The low-tide line shows the influence of climatologic changes [5], overall much erosion between 1860 and 1880 and accretion between 1880 to 1900. These periodical changes are attenuated very much in the line of the dune foot and here one finds the general trend as indicated by EDELMAN and EGGINK [6] a general accretion of $\frac{1}{2}$ m/year, with erosion near Hook of Holland and den Helder (fig. 4). The Hondsbossche Seawall lies at the moment much further seaward than the adjacent dunes because of the erosion of the dunes.

The influence of the harbour moles (length 1400 m) of IJmuiden built in 1870 is shown in detail in fig. 5. Fig. 2 shows, that the low-tide line and high-tide line obtain stability about 1900, but that the dune foot changes up to 1930. Fig. 5 gives an upper view on the 5-years average of the low-tide and high-tide line (seaward scale exaggerated with respect to the longshore scale). The total gain was 9.10^6 m³ in the North and 6.10^5 m³ in the South [8].

In 1965 the harbour moles were enlarged to 3000 m. Fig. 5 shows on the right hand side the change of the mean of the low-tide and high-tide line since 1965. Now the accretion on the South side is more than on the North side. Although a changing of the wave climate may have been of influence [5], [8], also the fact must be important, that at the moment an extensive area with only small

currents prevents the entrainment of material from the surf zone around the head of the mole.

The changes of the Wadden Islands are shown in fig. 3. The changes at the ends are large compared to the changes in the middle of the islands, partly due to the changes in the gully-systems in the inlets, the silting up of a gully causes that a shoal grows together with the end of the island. After that, a sandwave along the coast is generated [9]. Obvious is the relatively large erosion on both ends of Texel. We shall return to this subject.

GROYNES

The Dutch groynes have a length of about 200 m, the distances between the successive groynes can be found from fig. 6 to 8 (about 200 m). In the considered area they are broad-crested stone structures, lying at about mean sea-level. In order to investigate the behaviour of groynes in practice three areas were considered, on which groynes were constructed during the period of the measurements South-Holland km 97 to 105 (fig. 6), North-Holland km 8 to 20 (fig. 7, derived from [11]) and Vlieland km 41 to 52 (fig. 8). Constructed is the 5-year average of the low-water line, (for instance 1858 to 1862 for 1860), the scale perpendicular to the reference-line is 10 times exaggerated in fig. 8 and 20 times in fig. 6 and 7 with respect to the longshore direction. In each figure two successive lines are plotted together, the black fields show the erosion in 10 years, the grey fields the accretion. The groynes built from 1853 - 1862 are plotted through the line of 1860, and so on. The hatched area gives the protected coastal area. Fig. 8 seems a striking proof of the benefit of groynes. The erosion near km 47 to 51 in 1860/70 can hardly be ascribed to the groynes 5 km away. The reduction of the erosion after the building of the groynes is quite clear. Of course, this does not mean that groynes are the most economic way of coastal protection.

The same kind of effect can be seen in fig. 6, 1860/70, although less convincingly. The influence of the lee-side scour plays here also a big role. A rough estimation of this lee-side scour (giving also a measure for the net littoral drift in this zone) about $100.000 \text{ m}^3/\text{year}$ (erosion of about 2 m/year over 3 km). Less clear still is fig. 7. The Northern part of this area is subject to the movement of the Schulpengat, the Southern branch of the inlet of Texel. The lee-side scour on the Northern side can be observed clearly (km 20, 21, 1860 to 1880 etc.), and also the inverse the accretion near km 13, 14 between 1900 and 1910 on the luff-side.

Analysis of the effect of the groynes is very difficult. Comparison with unprotected parts of the beach has no sense, since groynes are constructed only on eroding beaches. A before- and after-comparison will be obscured by climatological changes (cf fig. 3, low-waterline)

We chose the areas of fig. 6, 7 and 8 for comparison (all eroding beaches, gradually more and more protected with groynes) and computed for each area for each 10-year period the mean erosion/year of the protected part and of the unprotected part (fig. 9a, b, c). Thus the erosion on the same area could be compared, when this

area was protected (later on) or not (in the beginning) In order to eliminate local influences all three areas were put together and again the mean erosion per year of the protected and of the unprotected area were computed (fig. 9d). An impression of the climatological changes gives fig. 9e, in which the mean regression and progression per 10-year period of the low-tide line of the uninterrupted coast of Holland is shown. Only the relative changes are of importance. In fig. 9f finally the erosion of the protected part of fig. 9d is plotted against the erosion of the unprotected part, from which a considerable reduction of the erosion can be concluded. Although nearly all the considered unprotected areas were subject to lee-side scour, fig. 8 shows that the reduction is not mainly caused by that, but that the building of groynes reduced the erosion.

SAND TRANSPORT BY WAVES AND TIDES

Van STRAATEN [5] and EDELMAN and EGGINK [6] both give qualitative considerations about the sand transport by waves. Since their publications so many data have been collected, about the relation between the longshore component of the wave energy and the sand transport, that it is worthwhile to apply such formulae to the dutch coast, in order to obtain more quantitative conclusions. However, these conclusions can be not better than the available data the visual wave observations on the dutch light-vessels. These measurements from 1949 to 1957 have been statistically treated by DORRESTEIN [10], giving for each wave condition, (characterized by height, period and direction of the waves) the probability of occurrence. From [10], the longshore component of the wave energy flux P_1 has been computed, defined by

$$P_1 = \frac{1}{8} \rho g H_{br}^2 C_{br} \sin \varphi_{br} \cos \varphi_{br}$$

in which ρg = specific weight water, H = wave height, C = wave celerity, φ = angle of wave incidence and the index br refers to the breaker zone.

The exact way of computation is treated in [14].

The accuracy is very low, because it is impossible to get an accurate significant H , C and φ in the breaker zone from visual wave data from a distance of 10 km. It was necessary to make a lot of assumptions [14]. The results are given in the table above fig. 12, and fig. 10 shows a probability distribution.

It is easy to compute from this the mean energy flux and the mean littoral drift Q using the CERC-formula, which can be transferred [14] in

$$Q^* = 2300 P_1 \quad (Q^* \text{ in } m^3/\text{year}, P_1 \text{ in } W/m')$$

However, the used data and formulae are not accurate enough to justify this computation, also because the probability distributions are about symmetrical. Only along the Vlieland coast the resultant drift is significant (about $\frac{1}{2}$ mln m^3/year).

The gross littoral drift (sum of transport in both directions) is found to be of the order of 1.5 to 2 mln m^3/year (thus about 1 mln m^3 in each direction).

Assuming for instance no influence of tides, the distribution of the littoral drift over the surf zone has been computed by an adapted method proposed by SVAŠEK [8], the way of computation is pointed out in another paper of this conference [13]. The result for Scheveningen is shown in fig. 11.

Considering which one is most important, the influence of waves or tides, in [15] and [16] the driving forces of waves and currents are investigated.

In order to get an impression of the influence of the tide, a tidal computation has been carried out with the numerical tidal model of which fig. 12 gives the scheme [19]. We assumed a gully system parallel and perpendicular to the coast. On the ends the vertical tide was given, in the knots the vertical tide was computed and in the gullies the horizontal tide. The computerprogram was developed by BOOY according to the explicit leap-frog method, non-linear terms were considered, but Coriolis was neglected. In each gully at every time was computed $\sum Bvh \cdot \Delta t$, in which B is the width of the gully, v the current velocity, h the water depth at that moment and Δt the time step. From this, the resultant currents, indicated in the upper figure of fig. 12 were found, about 3 cm/sec in the shallow regions and 6 cm/sec in the deeper regions. A computation, taking the tidal currents into account, based on a simplified BIJKER-method (cf [8]) is in preparation.

THE OUTER DELTAS

The boundary conditions for the motion of the coast are given by the inlets. Therefore it is important to consider the motion of the gullies. Fig. 13 and 14 give the motion of the gullies in the inlets of Texel and Vlie respectively. The arrows give the motion of the gullies since the last recording. What is known about these deltas?

The cross-section of the gullies reasonably fit in with the theory PER BRUUN and GERRITSEN [7]. As a variation HARING [20] found, that the quotient of the tidal volume (ebb + flood) and the total profile area of the gully was about 55 cm/sec, except for the inlet of Texel and the inlet of the Vlie, where it was 75 cm/sec (cf DRONKERS [1]). This higher velocity might be some influence of littoral drift. Van VEEN [21] states, that the largest gullies are mainly orientated in the direction of the greatest water gradient, averaged per tide. If the tidal amplitude is everywhere the same (which is often not the case), this direction is perpendicular to the cotidal lines (fig. 17) the gradient between A and B is much larger than between A and C.

Two reasons can be given for erosion of the coast near these inlets. As has been pointed out by van BENDEGOM [22], the submerging of the Wadden during flood tide takes place with larger velocities than the retreating of the water over the shoals during ebb-tide. Thus, the water looses here a part of its sediment, which makes, that the Wadden shoals reach an equilibrium at about the mean water level. Now the relative sea-level rising in the Netherlands during the last 20 centuries was about 6 cm/century, which would result in a "sand hunger" of the Wadden shoals of about 1 mln m³/year (distributed over all inlets).

However, this will mostly be confined to finer sediments (D_m about 100-150 μ).

The second reason is that the water during the flood tide gets an acceleration, entering the inlet, but that during the ebb-tide it gets a retardation and this will give a jet-stream with vortices on its side. Therefore in the gullies near the beaches, there is surplus of flood discharge and in the center gully a surplus of ebb discharge. The flood erodes the beaches and the ebb gives an outer delta, which can reach up to mean sealevel (Noorderhaaks in inlet of Texel. This delta gives a shelter against these waves, which would transport material away from the delta. As the waves come alternately from both directions, this process reinforces the erosion of the beaches near the inlets. Thus the erosion of Texel could be rather well explained [23]. After some time an equilibrium should be reached.

Two reasons can be given too for the motion of the gullies a meandering effect and a longshore sand drift. It will be clear, that the resulting sand drift perpendicular to the gully can not be derived from the velocity of the gully because of the meandering effect. The big sand transport in the gullies can be attributed to the high current velocities and this meandering.

The motion of the gullies and the effects of their orientation has been investigated (fig. 16). The line in the middle of each of the bars gives the orientation of the gully in course of time. The width of the bar gives the development of representative cross section. As far as they were known, the time-integrated slope of the water-surface as a function of the orientation have been mentioned (fig. 16¹⁾). It gives no evidence about the van Veen-theory.

In fig. 18, derived from fig. 16, the turning of the gullies in the dutch Wadden delta is shown. Mainly they turn clockwise, although very slowly and there is a slight indication (correlation coeff..24), that the large gullies turn slower than the small ones.

ACKNOWLEDGEMENT

The authors gratefully acknowledge the aid of the Study Services Hoorn, IJmuiden and Delfzijl of Rijkswaterstaat in providing the data, published here.

REFERENCES

- [1]. dr. J.J. Dronkers, Research for the coastal area of the Delta region of the Netherlands, C.E.C., Washington 1970.
- [2]. ir. L.R. Wentholt, Stranden en strandverdediging, Delft Doctor's Thesis 1912.
- [3]. ir. J. van Veen, Onderzoekingen in de hoofden Delft, Doctor's Thesis 1936.
- [4]. dr.ir. J. v. Veen, Eb- en vloodschaarsystemen in de Nederlandse getijwateren. Tijdschr. Kon. Ned. Aandr. Gen. 67 pp. 45-65.

¹⁾ These have been derived from van Veen 21 and Ferguson 24

- 5] dr. L.M.J.U. van Straaten, Directional effects of winds, waves and currents.
 Geologie en Mijnbouw 23, 1961.
- 6] ir. T. Edelman and drs. D.N. Eggink, Some characteristics of the dutch coast C.E.C. 1962.
- 7] Per Bruun and ir. F. Gerritsen, Stability of coastal inlets.
- 8] prof.dr.ir. E.W. Bijker and ir. J.N. Svasek, Two methods for determination of morphological changes, induced by coastal structures.
 Int. Nav. Congr. 1969.
- 9] ir. W.T. Bakker , A mathematical theory about sandwaves.
 Shore and Beach, Oct. 1968.
- 10] dr. R. Dorrestein , Wind and wave data of Netherlands light-vessels. Med. en Verh. K.N.M.I. no. 90.
- 11] L. Knop , Onderzoek Noordzeekust Petten-Huisduinen.
 Study Service Hoorn Rijkswaterstaat nr. 584.
- 12] ir. L. van Bendegom, Beschouwingen over riviermorfologie.
 De Ingenieur 59, 24 jan. 1947.
- 13] ir. W.T. Bakker, ir. E.H.J. Klein Breteler and A. Roos,
 The dynamics of a coast with a groyne system
- 14] ir. W.T. Bakker , Computation littoral drift with Svasek-method. Rijkswaterstaat, Dept. for Coastal Res. Rep. W.W.K. 69-7.
- 15] ir. W.T. Bakker and H.J. Opdam, Influence of waves and tides on the littoral drift in the surf zone.
 Rijkswaterstaat, Dept. for Coastal Res. Rep. W.W.K. 70-8.
- 16] H.J. Opdam , A wave tide model for the dutch coast.
 M. Sc. thesis, Delft 1970.
- 17] A.J. Bowen , The generation of longshore currents on a plane beach.
 Journal of Marine Research 27 no. 2, May 1969.
- 18] E.H.J. Klein Breteler, Zandtransport bij Katwijk.
 M Sc. thesis, Delft 1970.
- 19] ir. E.H.J. Klein Breteler, A tidal model for the coast of Hook of Holland - IJmuiden.
 Rijkswaterstaat, Dept. for Coastal Res. Rep. W.W.K. 70-10.
- 20] J. Haring , Oppervlakte van het dwarsprofiel van de Nederlandse zeegaten als functie van het getij-volume.
 Rijkswaterstaat, Delta Works, Rep. K 251
- 21] ir. J. van Veen , Zeegat van het Vlie (1934).
 Rijkswaterstaat, Dir. Benedenrivieren
- 22] ir. L. van Bendegom, Grondslagen der kustverdediging,
 Rijkswaterstaat.
- 23] ir. Th.J.C. Wijnant, Littoral drift near Texel.
 Rijkswaterstaat, Dept. for Coastal Res.

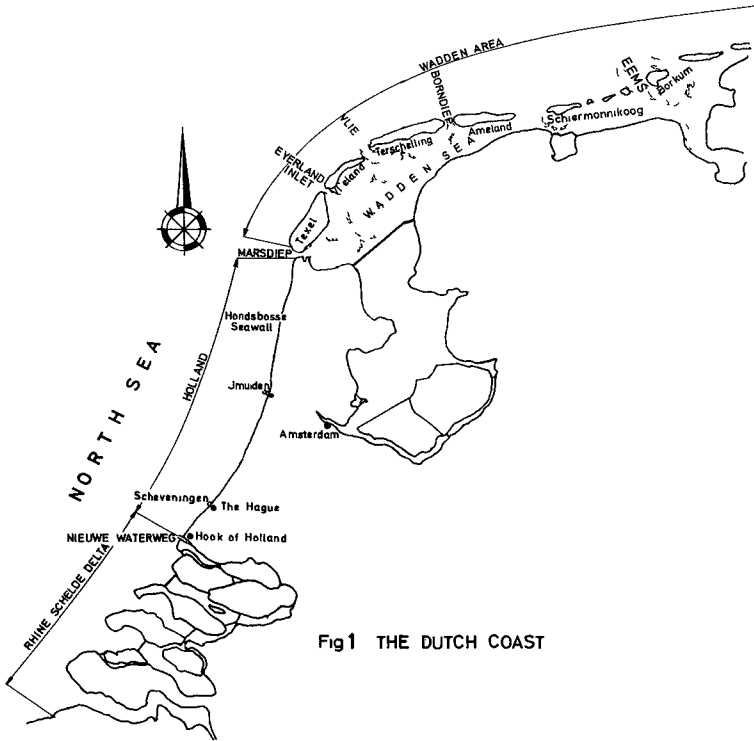


Fig 1 THE DUTCH COAST

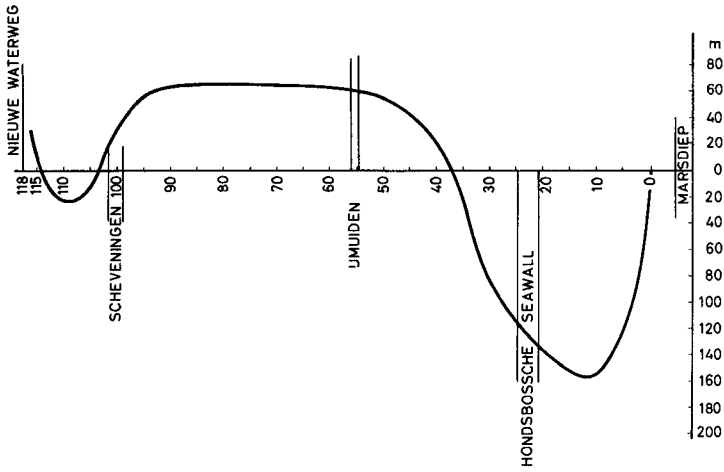


Fig 4 MEAN DUNE-FOOT MOVEMENTS FROM 1860 TILL 1960 BETWEEN NIEUWE WATERWEG AND MARSDIEP

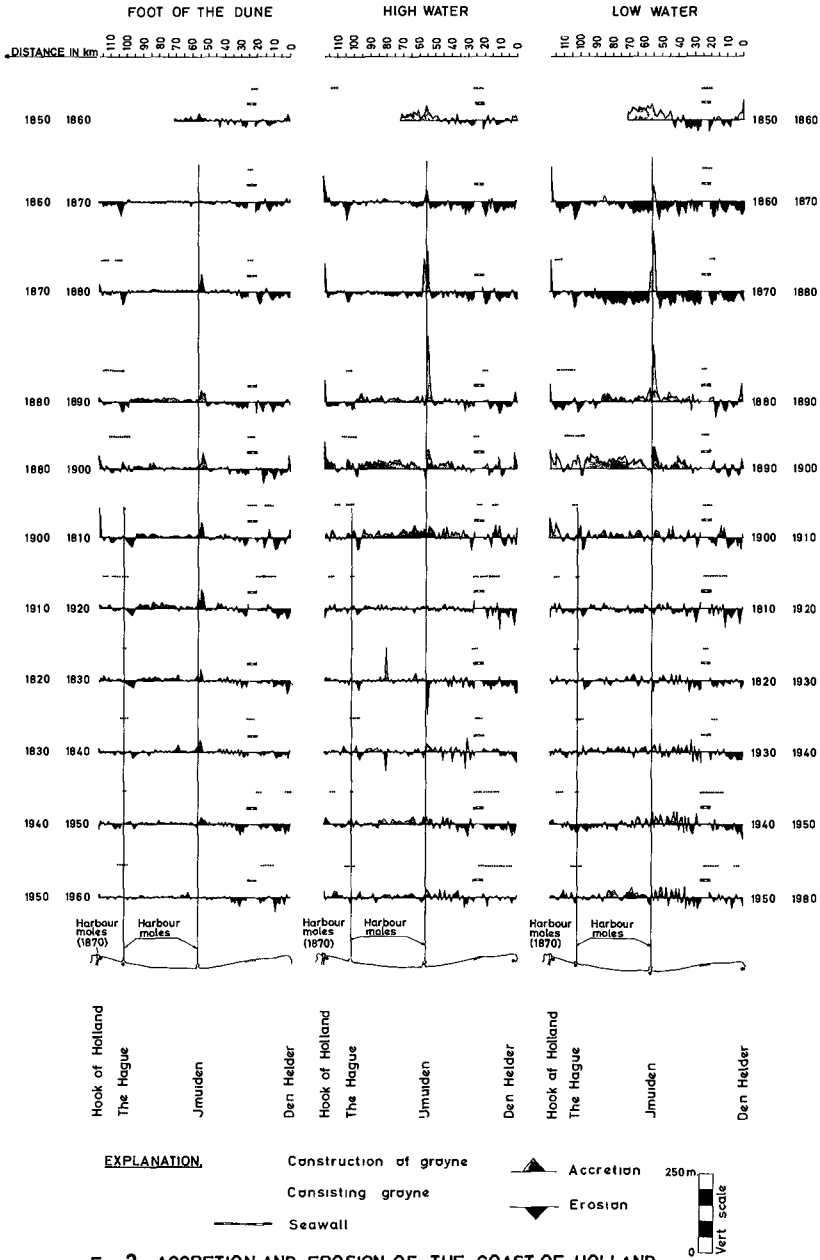


Fig 2 ACCRETION AND EROSION OF THE COAST OF HOLLAND

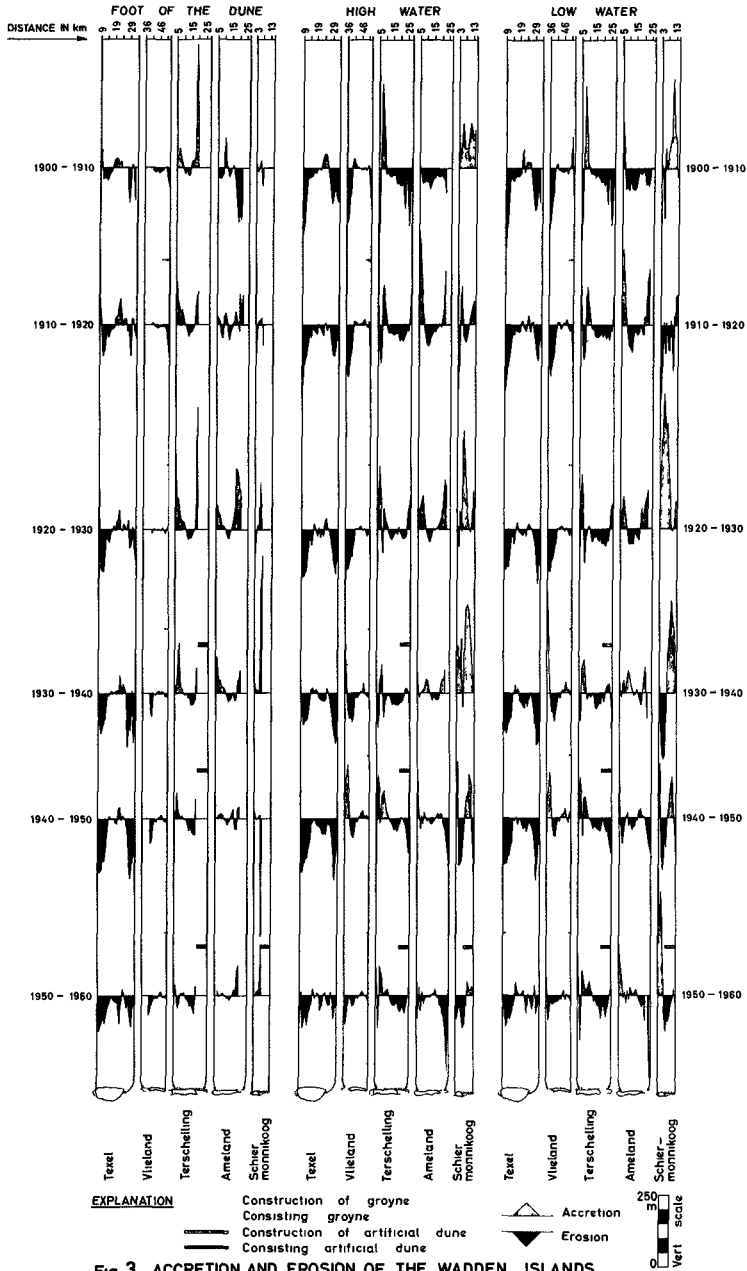


Fig 3 ACCRETION AND EROSION OF THE WADDEN ISLANDS

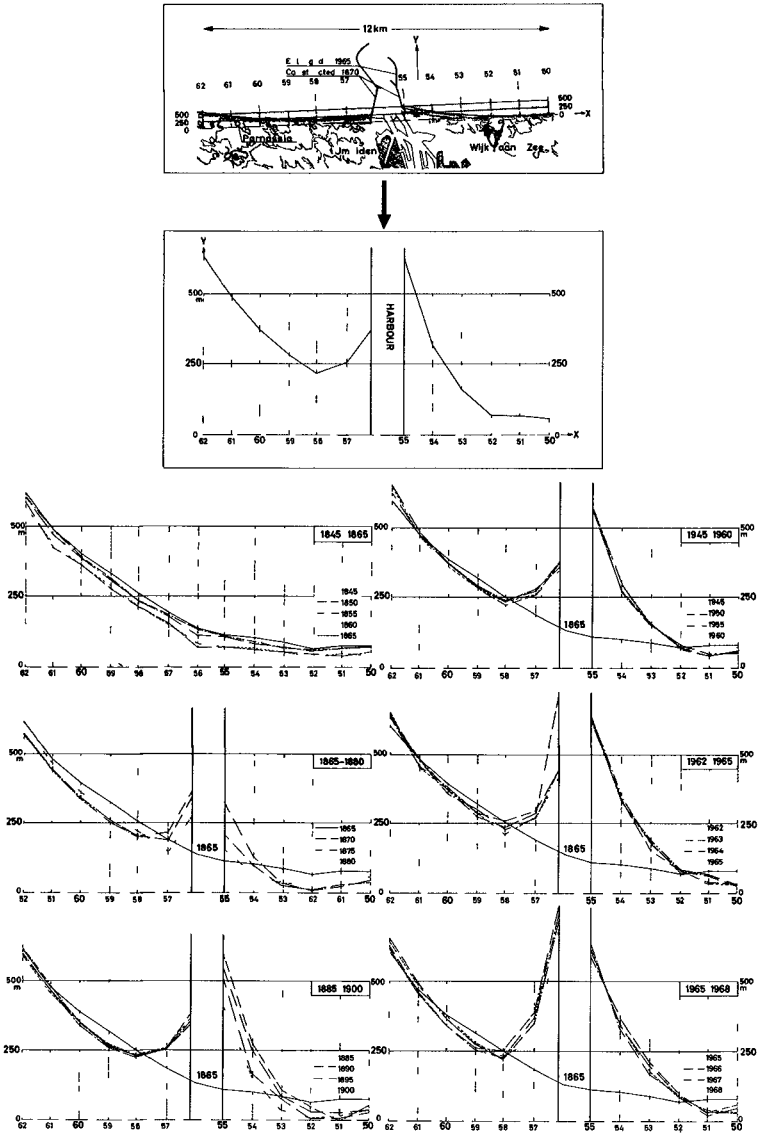


Fig 5 DEVELOPMENT OF THE WATERLINE NEAR UMUIDEN

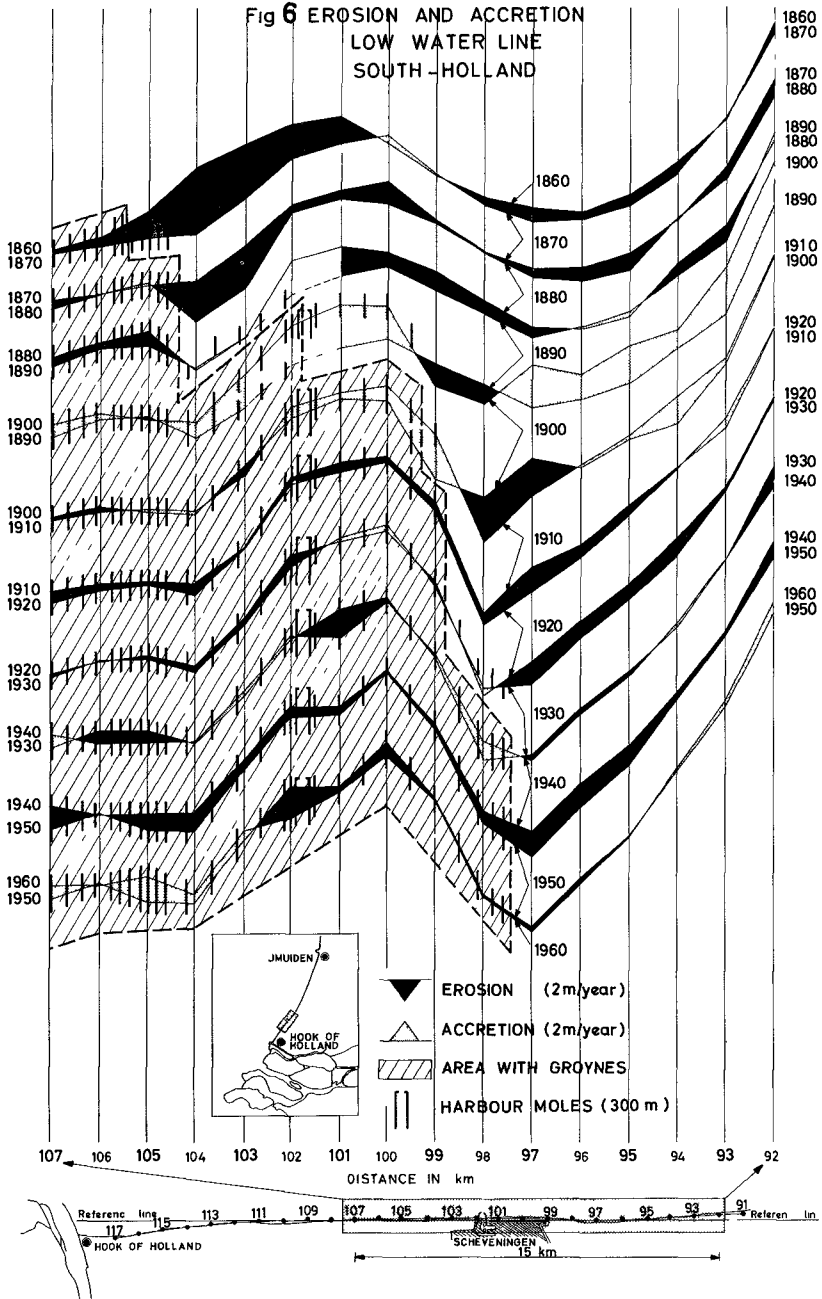


Fig 7 EROSION AND ACCRETION

LOW WATER LINE
NORTH-HOLLAND

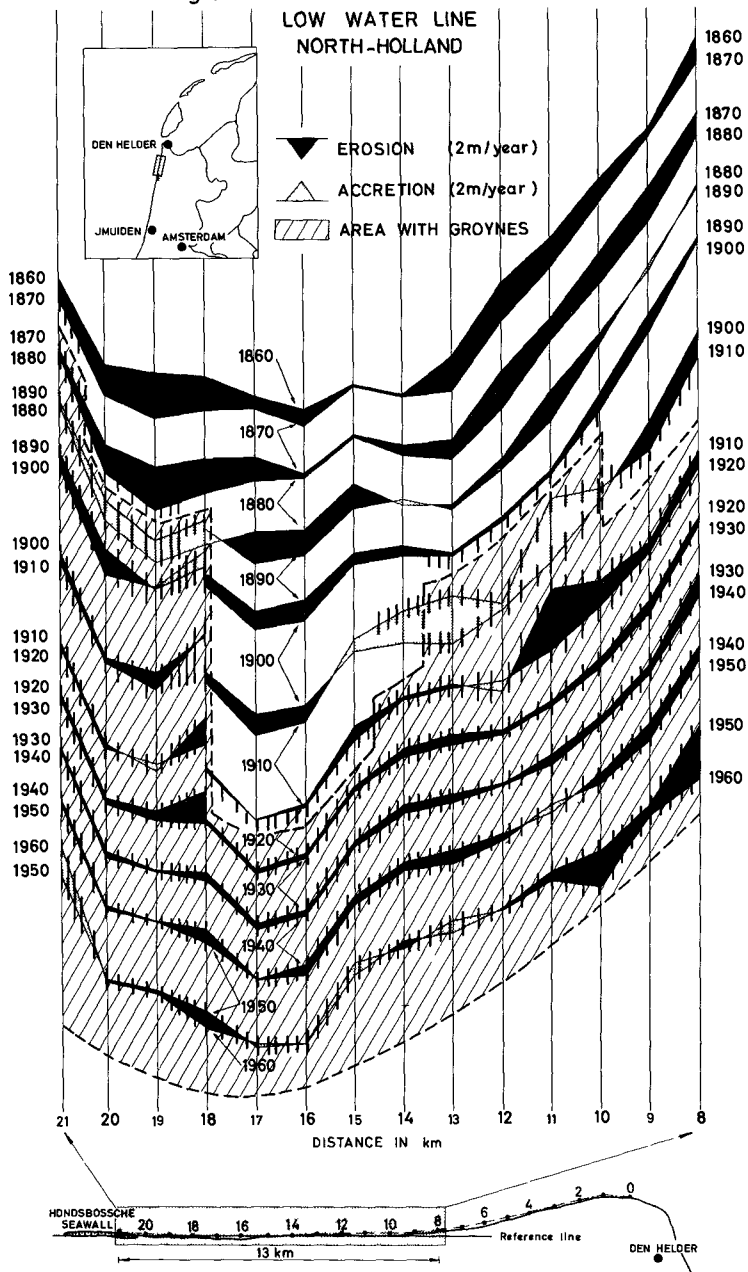
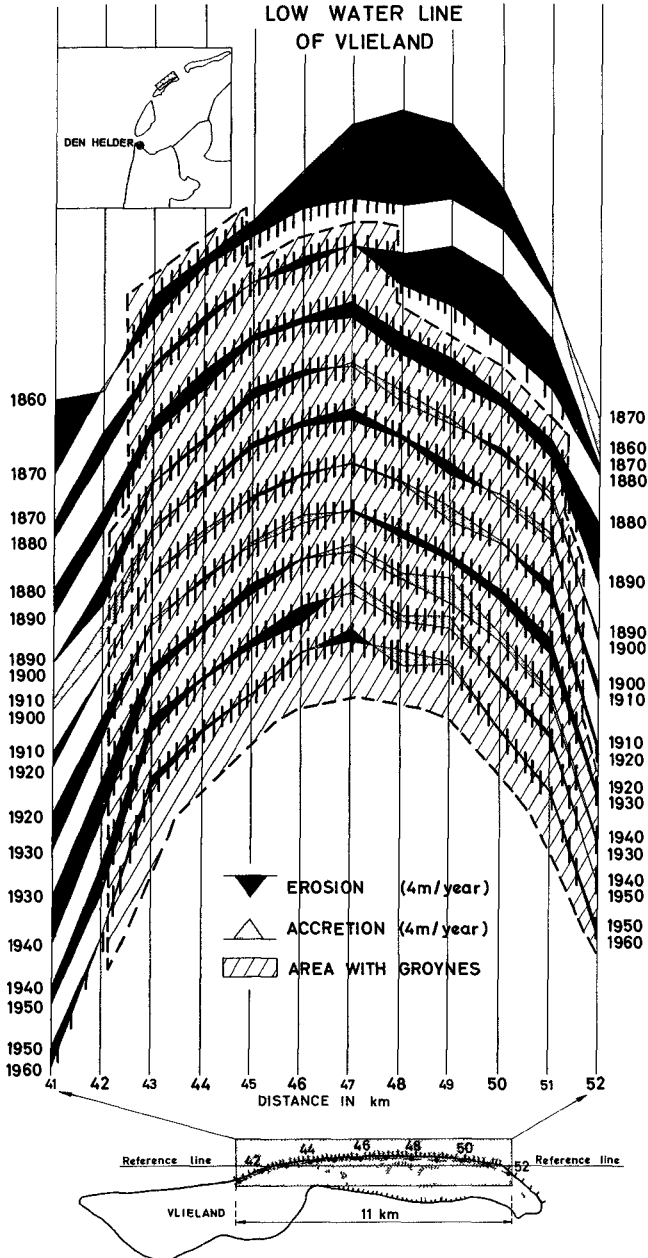


Fig 8 EROSION AND ACCRETION
LOW WATER LINE
OF VLIELAND



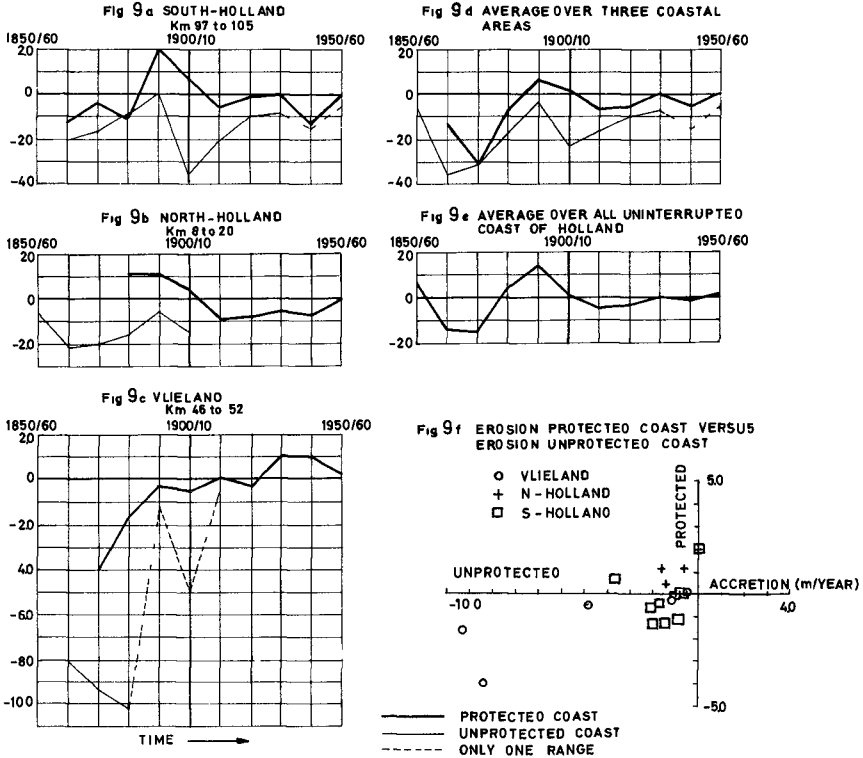
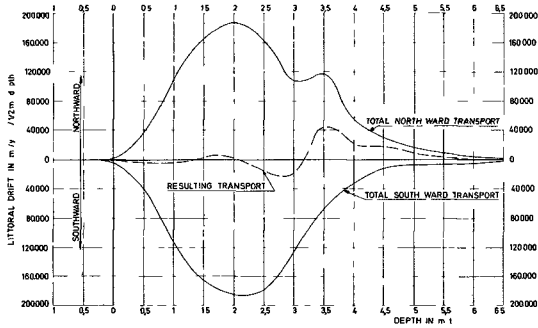


Fig 9 COMPARISON OF EROSION IN m/YEAR OF PROTECTED AND UNPROTECTED AREAS



Site	Orientation of the coast with respect to the North	<p>Fig 10 THE PROBABILITY DISTRIBUTION OF THE LONGSHORE COMPONENT OF THE WAVE ENERGY FLUX NEAR SCHEVENINGEN</p>
Vlieland	060° - 240°	
Texel	030° - 210°	
IJmuiden Scheveningen	015° - 215° 045° - 225°	

Probability in ‰ of P_1 (from North to south)

Min. 1)	-33	-31	-25	-23	-19	-17	-15	-13	-11	-9	-7	-5	-3	-1	-
Max. 1)	-31	-29	-23	-21	-17	-15	-13	-11	-9	-7	-5	-3	-1	0	0
Vlieland	-	-	-	-	-	-	.03	.27	.25	1.2	.82	8.9	32	166	210
Texel	-	-	-	.13	-	.13	.25	.50	.76	2.4	4.3	19	56	203	287
IJmuiden	-	.52	.17	.24	.42	.70	-	1.1	3.1	8.7	3.4	26	120	159	323
Scheveningen	.13	-	-	-	.27	-	.92	1.6	.35	5.6	2.0	26	119	200	355

Probability in ‰ of P_1 (from South to North)

Min. 1)	0	0	1	3	5	7	9	11	13	15	17	21	23	29	0
Max. 1)	0	1	3	5	7	9	11	13	15	17	19	23	25	31	-
Vlieland	529	155	53	29	11	5.4	1.4	1.0	1.1	.84	.81	.34	.42	.12	261
Texel	401	196	70	31	6.1	4.2	2.1	.61	.84	.47	.24	.23	-	-	312
IJmuiden	299	272	86	15	4.0	.88	1.3	.15	-	-	-	-	-	-	379
Scheveningen	316	188	92	28	10	6.0	.56	2.9	-	.56	.22	.44	-	-	329

1) Lower limit (min.) and Upper limit (max.) of P_1 expressed in KW/m^2

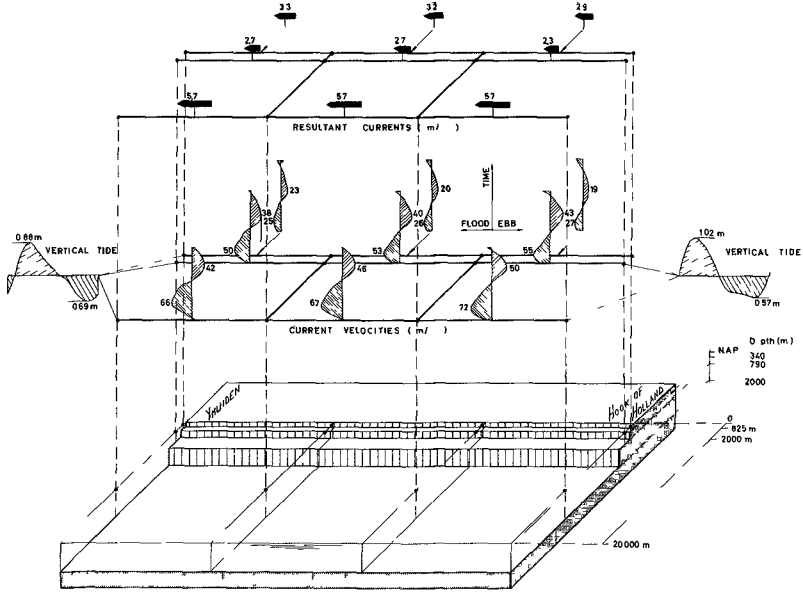
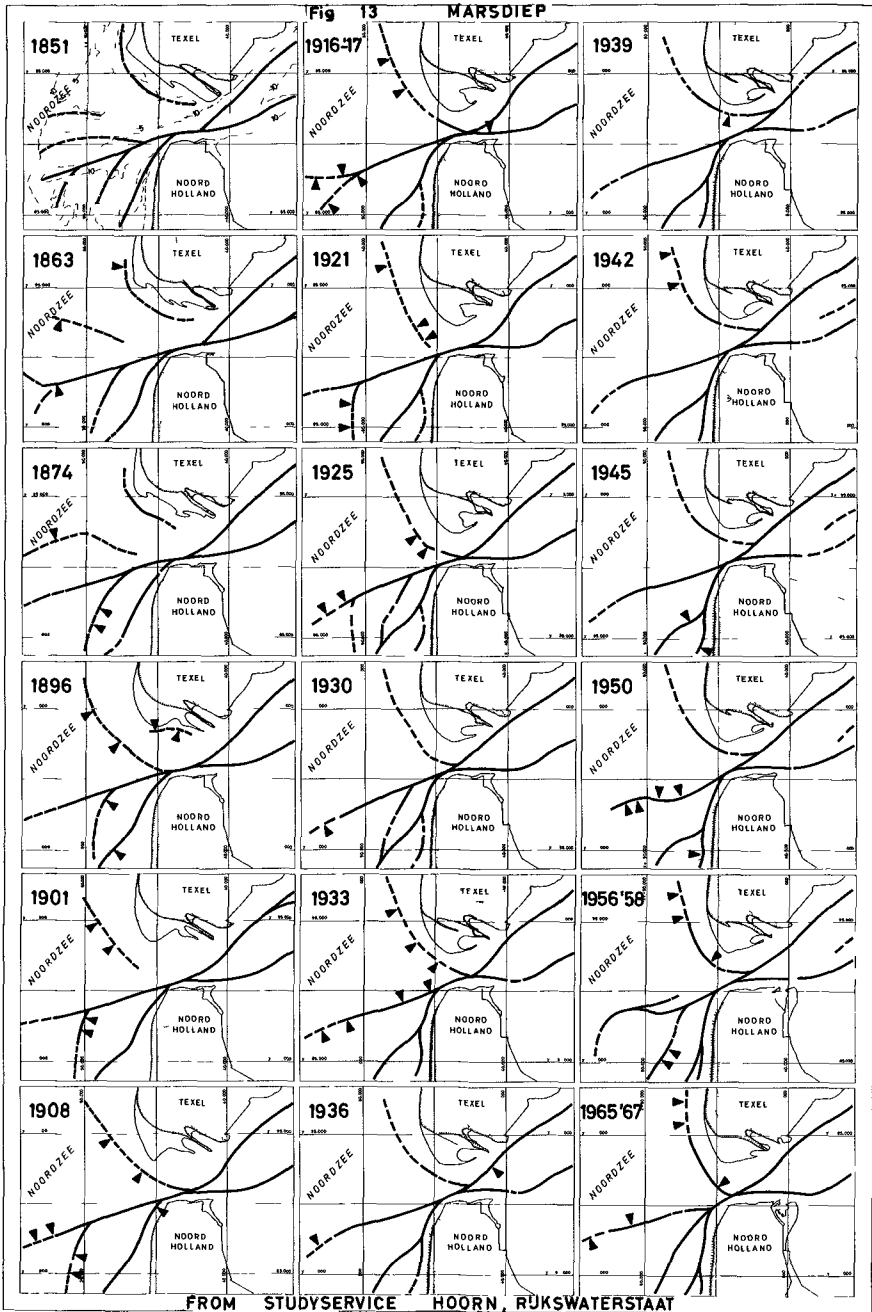
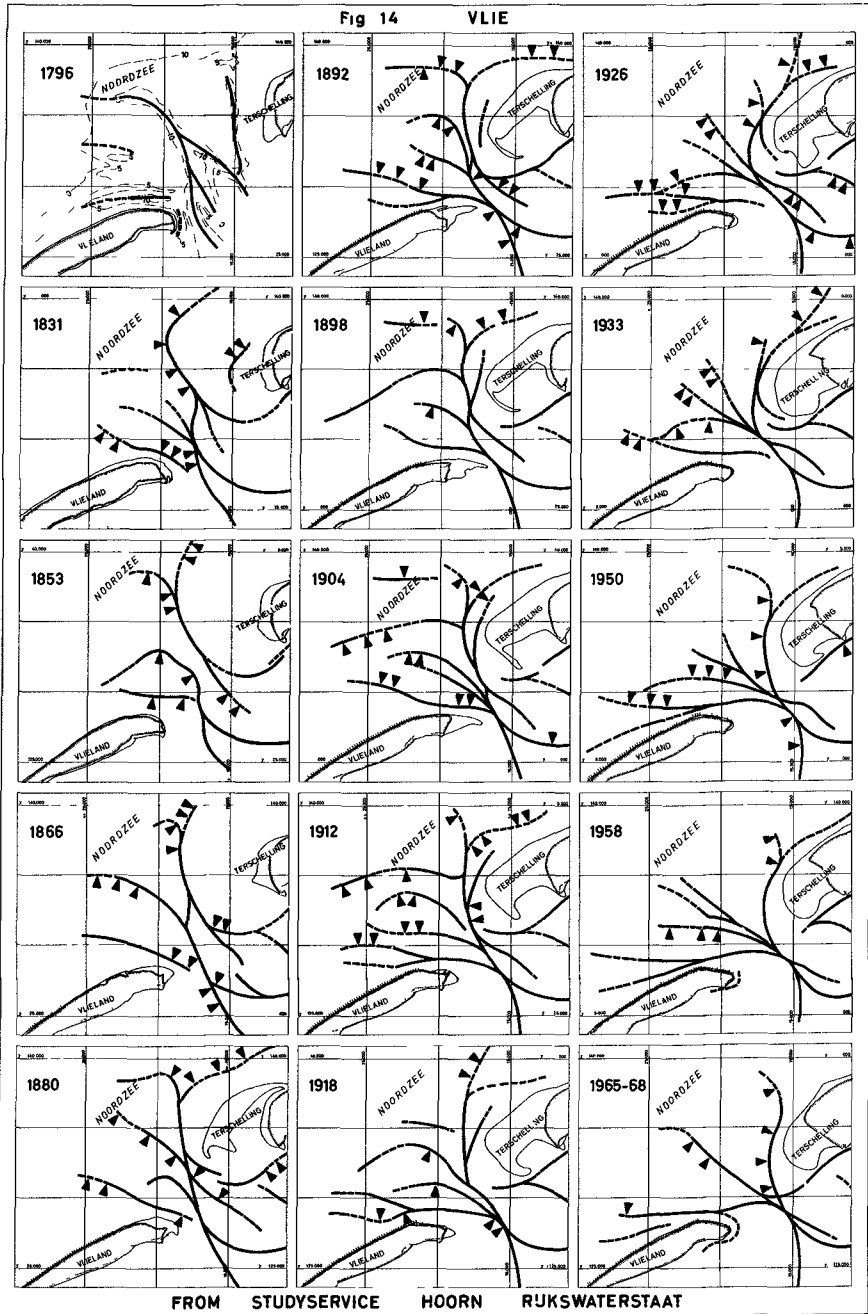


Fig 12 TIDAL MODEL





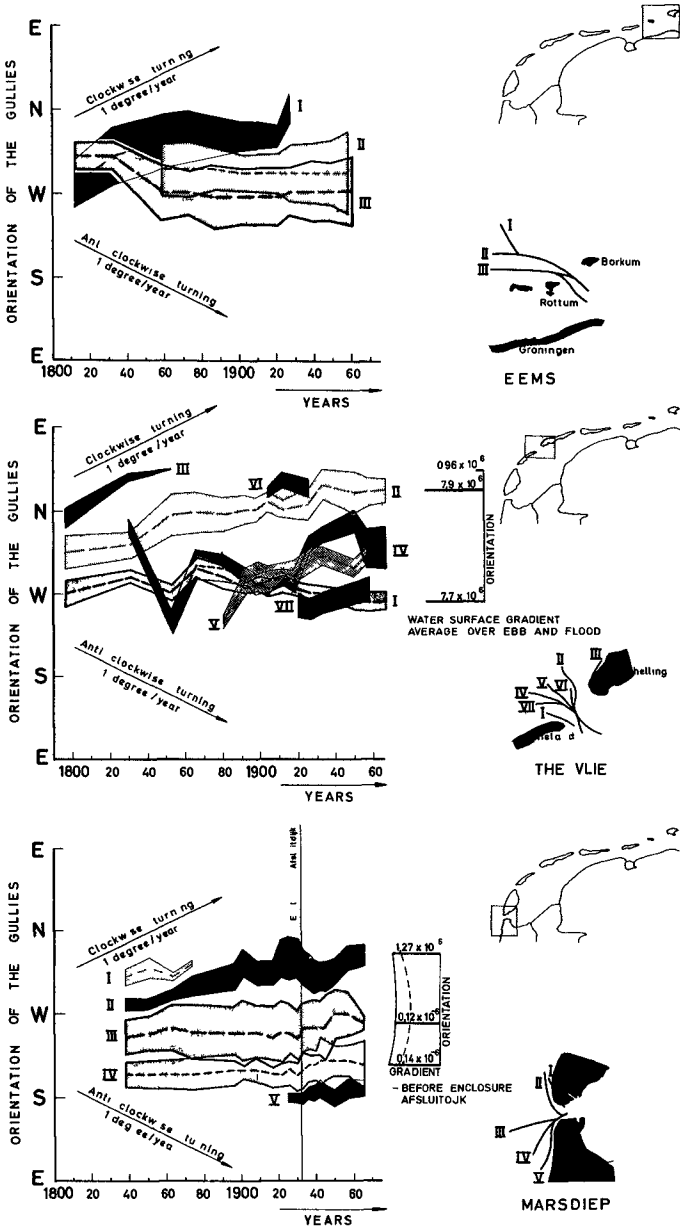


Fig 16 THE DIRECTION AND THE WET SURFACE OF THE GULLIES

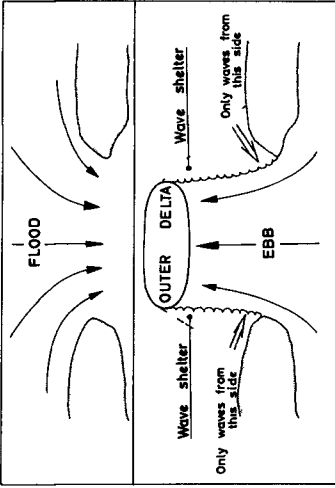


Fig 19 Erosion of the coast by tides and waves near on inlet

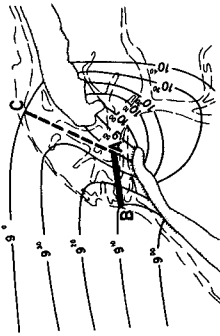


Fig 17 Orientation of gullies according to VAN VEEN theory

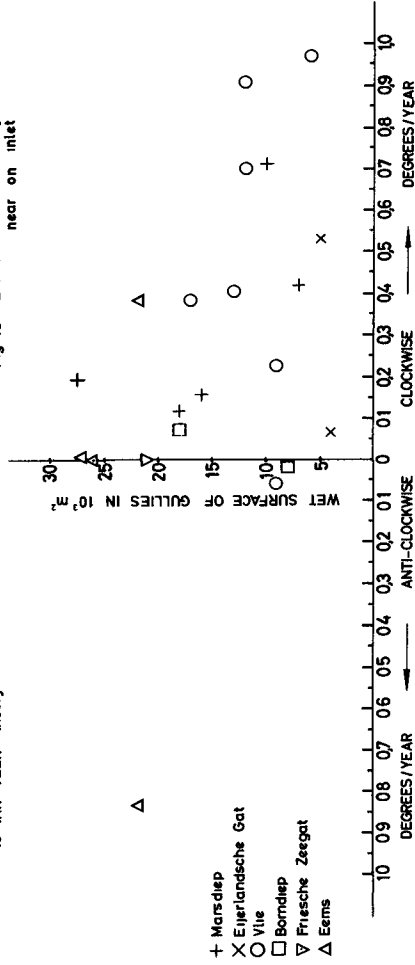


Fig 18 The correlation between the wet surface and the moving of the gullies

CHAPTER 44

STUDIES ON THE SHORE PROCESS AND WAVE FEATURES OF THE WESTERN COAST OF TAIWAN

Kenneth S T Chang, Chief Engineer
Taiwan Land Resources Development Commission, R O C

Frederick L W Tang, Professor
Hydraulic Engineering Department, Cheng Kung University, R O C

SYNOPSIS

The western coast of Taiwan has been accumulated to vast area of tidal flats by the sediment transported from numerous torrential streams. According to the aerial photographs, 53,800 hectares of tidal land are worth being reclaimed. However, this coast suffers from waves generated by winter monsoons as well as waves and swells caused by typhoons in the summer. Studies on the historical processes and future development of the shoreline are of great significance.

The ancient topographical data in An-Ping and Tseng-Pa areas as well as recent coastal line variations of Tseng-Pa and Yulin are reported in this paper, also the general features of waves along this coast are described. The future of the coast is predicted as a conclusion.

HISTORICAL DATA ON COASTAL CHANGE

Taiwan is the eastern province of the Republic of China that is surrounded by the sea (Fig 1) and has a total coastline of 1,566 kilometers. The type of the west coast is one of deposition, and there is a large area of tidal flats formed before long ago. At the present there are 53,800 hectares tidal land to be developed.

According to historical data and results analyzed, this coast extended offshore since 1624 until 1961 as shown in Fig 2 and Table 1. Here An-Ping coast means the coast area nearby the city An-Ping, and Tseng-Pa coast means the coast area between rivers Tseng-wen and Pa-Chang.

WAVE CHARACTERISTICS ON THE COAST

From September to March of last year, anticyclones of large intensity (some 1040 millibars) occur continuously in the vicinity of Bering Lake and move due southeast. Finally, they weaken and vanish in the Pacific Ocean.

While the anticyclone is moving, wind from NE or NNE direction blows over the East China Sea and Taiwan Strait with velocities of 10-20 m/sec. Due to the long duration of the wind, relatively large waves are generated. According to measured data in the middle and south section of the coast, waves 2-3 meters high and 6-8 seconds in period exist on this coast most of the winter. The steepness of these waves are large and the bed materials of the coast are as fine as 0.2 mm. Apparently the sand of the coast is eroded by the waves and is moved in a southerly direction.

In the summer months, winds from SW-S blow in the afternoon and the velocity rarely exceeds 10 m/sec. Waves generated by such wind are small, however, during these months typhoons frequently occur and cause considerable damage. The waves caused by typhoons sometimes are 7 meters in height and 12 seconds in period. These waves and swells also cause shoreline changes on the coast. The coast is severely eroded and the sand drift moves offshore. The coast does recover the sand when the winter monsoons begin.

RECENT SHORELINE PROCESSES OF TSENG-PA AND YULIN

There are a series of offshore dunes along the Tainan coast. After the Tseng-Wen polder was reclaimed, most of the dunes became more stable than before. Only near the inlets between the dunes were changed seriously during the winter monsoons, thereby causing damage to the north dike of the polder Tseng-Wen. Sometimes, owing to the fluctuation of climate and sea level during typhoons, the dunes are broken and new inlets are formed. The tendency of shoreline processes in this area is one of erosion (Fig. 3).

By means of hydrographic surveys and aerial photographs, we also provided valuable evidence of coastal and offshore changes in the Yulin area (Fig. 4). Profiles in this area are shown in Fig. 5. The shoreline process in this area is one of erosion.

CONCLUSIONS

1. The western coast of Taiwan was the result of deposition by north to south drift during ancient times. The sources of supply of sand drift was from high mountains and torrential streams.
2. According to the wave characteristics and bed material, this coast now suffers by erosion.
3. In ancient times the sand supply exceeded that which was eroded. The rivers have been regulated since the beginning of this century and also soil conservation works have been constructed. Thus the coast has begun to erode because of the sand supply which has been considerably decreased.

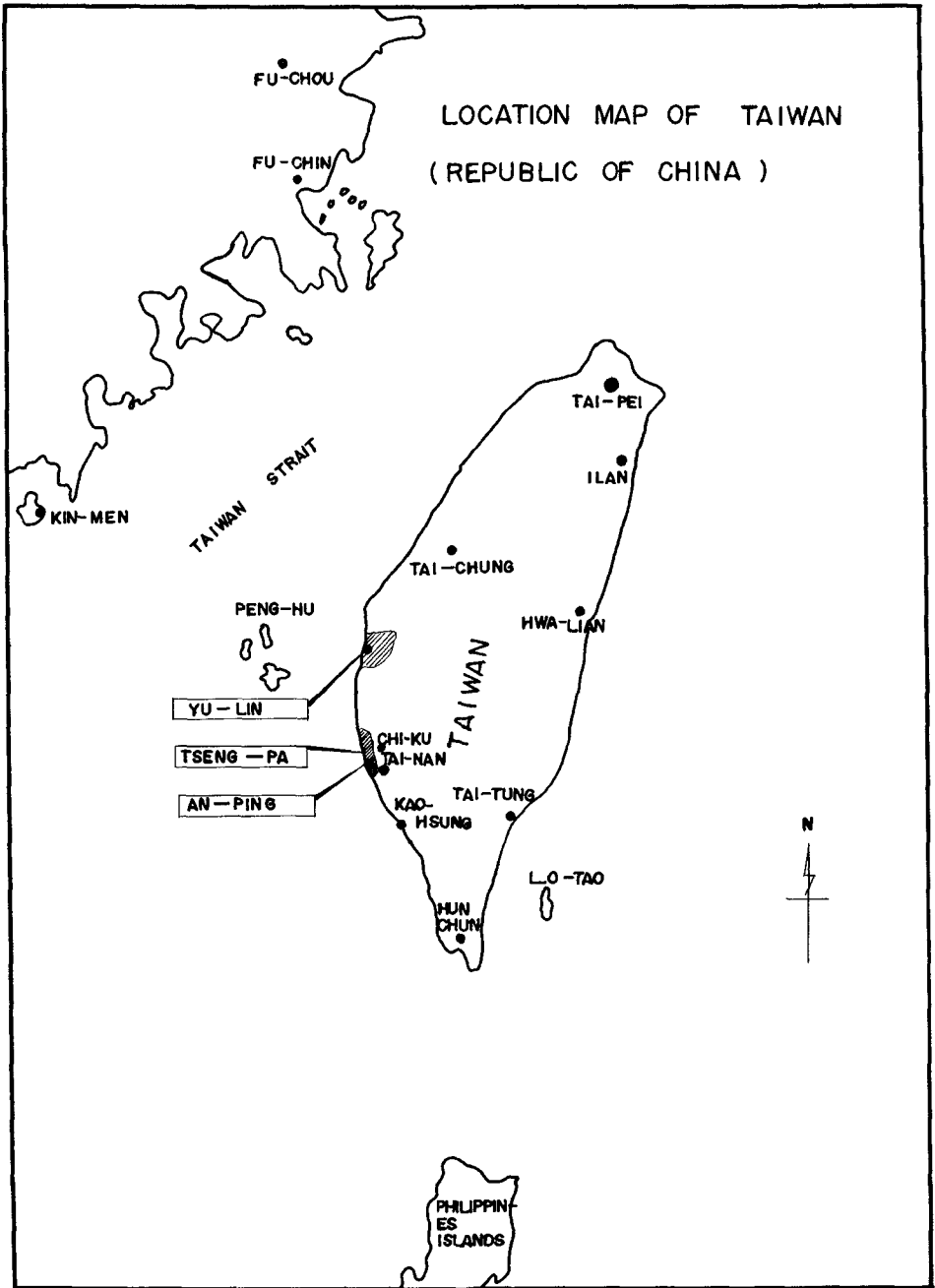
- 4 Although the erosion is not serious today, methods of shore protection must be undertaken. The reclamation of tidal land is of great significance from the economical point of view.
- 5 The shore process of this coast is very complicated and interesting, and detailed studies should be conducted.

SHORELINE PROCESSES OF AN-PING COAST

TABLE 1

THE PERIOD OF COASTAL ACCRETION	PERIOD	THE MAIN FORMATION AND TYPES OF THE COAST	THE UTILIZATION OF COAST AND TIDAL LAND	DATA RESOURCES	
ANCIENT (TAI-KIANG) PERIOD		CRUSTAL MOVEMENT UPLIFTING MOTION GEOLOGICAL CONDITION SANDY COAST FORMATION DEPOSIT ALLUVIUM TYPE BAY SURROUNDED BY OFFSHORE BARS ACCRETION RATE 33.4 M/YEAR UPLIFTING MOTION IN CRUSTAL MOVEMENT		TAIWAN HISTORY	
	FIRST STAGE	FROM 1624 TO 1662 (38) YEAR	MANY OFFSHORE BARS FORMED NATURAL HARBOUR BAY AGE IN EARLY YOUNG STAGE	VESSELS ANCHORAGED IN THE BAY A SMALL AMOUNT OF SALT PANS WAS RECLAIMED	TAIWAN HSIN HISTORY
	MIDDLE STAGE	FROM 1662 TO 1722 (60 YEARS)	SEDIMENTATION IN THE BAY BARS INCREASED AGE IN EARLY YOUNG STAGE	DITTO	TAIWAN HSIN HISTORY
	LAST STAGE	FROM 1722 TO 1822 (100 YEARS)	OFFSHORE BARS ENLARGED AND CONNECTED WITH LAND FORMED LAGOONS THE FORM OF BAY VANISHED AGE IN YOUNG STAGE	SALT PANS INCREASED AND RECLAIMED FISH PONDS	KAHSIUNG HARBOUR HISTORY
RECENT COASTAL PERIOD	FROM 1822 TO 1894 (72 YEARS)	CRUSTAL MOVEMENT UPLIFTING MOTION GEOLOGICAL CONDITION SANDY COAST FORMATION DEPOSIT ALLUVIUM TYPE LAGOONS SILTED UP LAND OFFSHORE BARS BECAME NEW COAST, PRODUCED NEW RIVERS AND NEW OFFSHORE BARS FORMED AGE IN YOUNG STAGE ACCRETION RATE 27.9 M/YEAR	VESSELS ANCHORAGED IN THE BAY SALT PANS AND FISH PONDS INCREASED AND ALSO SETTLERS INCREASED	KAHSIUNG HARBOUR HISTORY	
NOWADAYS PERIOD (EARLY STAGE)	FROM 1894 TO 1945 (51 YEARS)	1 AN-PING COAST BECAME STABLE LAND 2 TSENG-PA COAST (OLD SHAW-LOONG COAST) NEW OFF-SHORE BARS AND LAGOON FORMED AGAIN AGE IN YOUNG STAGE OTHER ITEMS SAME AS BEFORE	MODERN HARBOUR WAS CONSTRUCTED MUCH MORE SALT PANS AND FISH PONDS WERE RECLAIMED	HISTORY OF TAIWAN ECONOMICS AND OLD MAPS	
NOWADAYS PERIOD (NEW STAGE)	FROM 1945 TO (21 YEARS)	TYPE 1 AN-PING COAST ALREADY FIXED OFFSHORE BAR AND TIDAL LAND NO LONGER EXISTING AGE IN MATURE STAGE 2 TSENG-PA COAST - OFFSHORE BARS CONTINUOUSLY ACCRETED AND LAGOON WAS FORMED	TIDAL LAND WAS DEVELOPED WITH MODERN TECHNICS	HISTORY OF TAIWAN ECONOMICS AND OLD MAPS	
TOTAL	342 YEARS	ACCRETION RATE LAN-PING 28.2 M/YEAR 2 TSENG-PA 16.3 M/YEAR			

FIG 1



SHORELINE PROCESSES OF AN-PING COAST

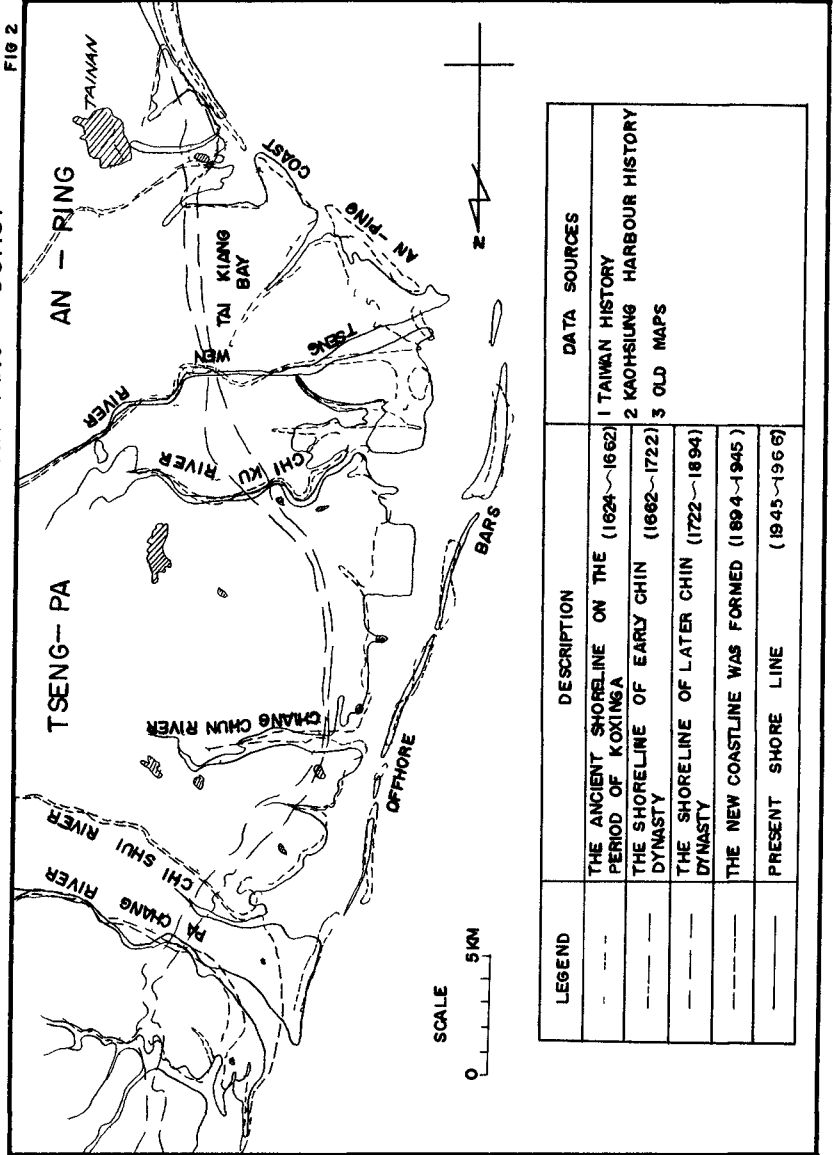


FIG 2

LEGEND	DESCRIPTION	DATA SOURCES
---	THE ANCIENT SHORELINE ON THE PERIOD OF KOXINGA (1624~1662)	1 TAINAN HISTORY
---	THE SHORELINE OF EARLY CHIN DYNASTY (1662~1722)	2 KAOHSIUNG HARBOUR HISTORY
---	THE SHORELINE OF LATER CHIN DYNASTY (1722~1894)	3 OLD MAPS
---	THE NEW COASTLINE WAS FORMED (1894~1945)	
---	PRESENT SHORE LINE (1945~1966)	

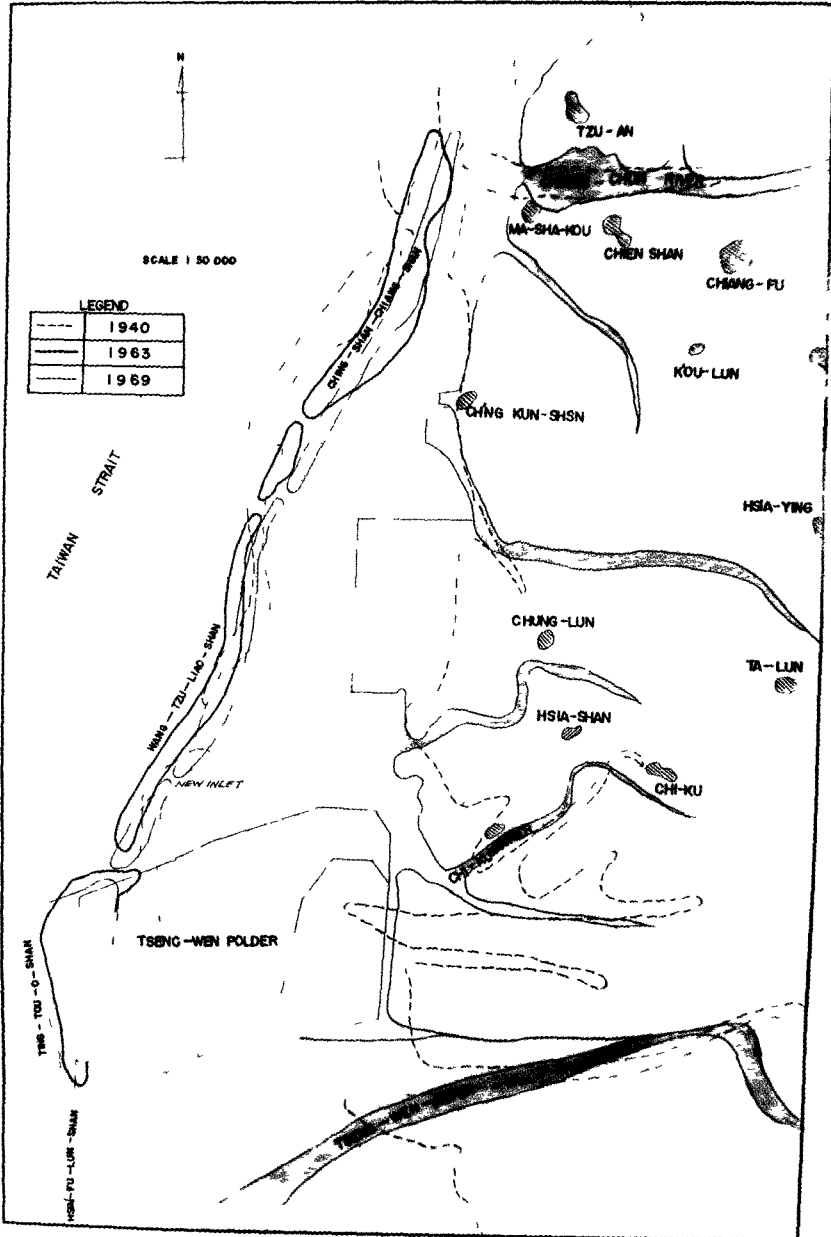


Fig 3 Map Showing the Variation of Shoreline on Tseng-Wen River to Chiang-Chun River

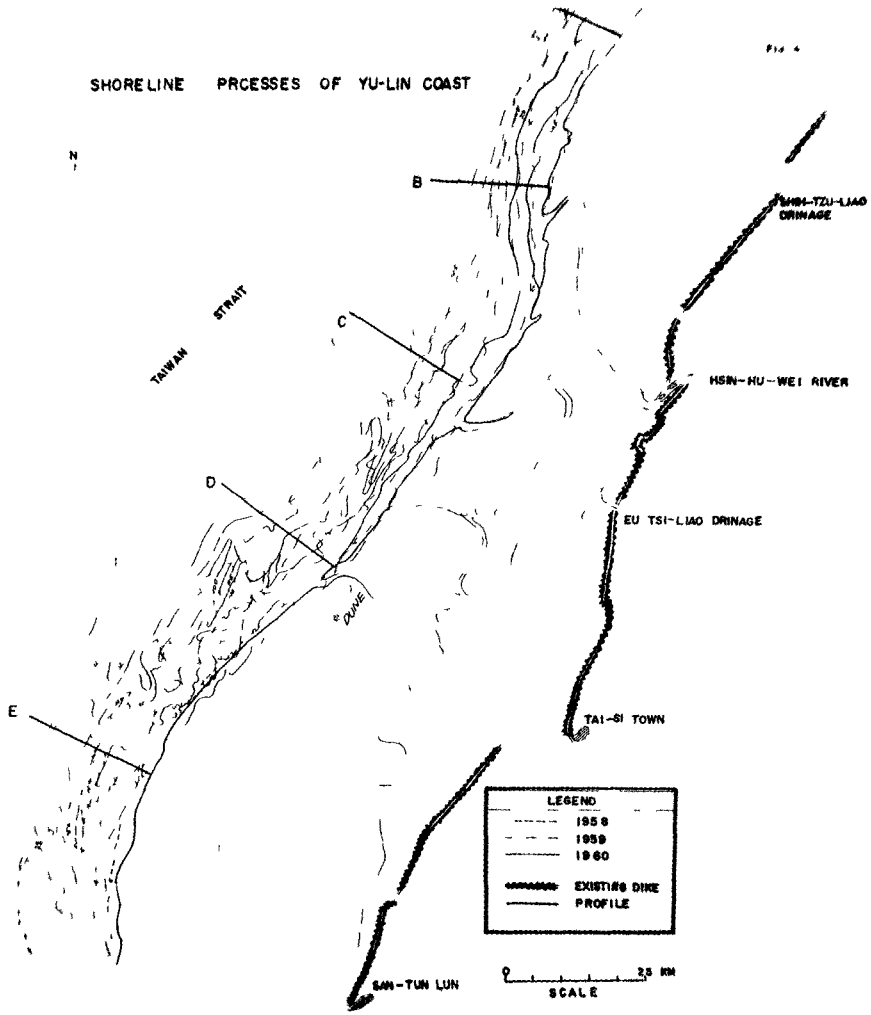
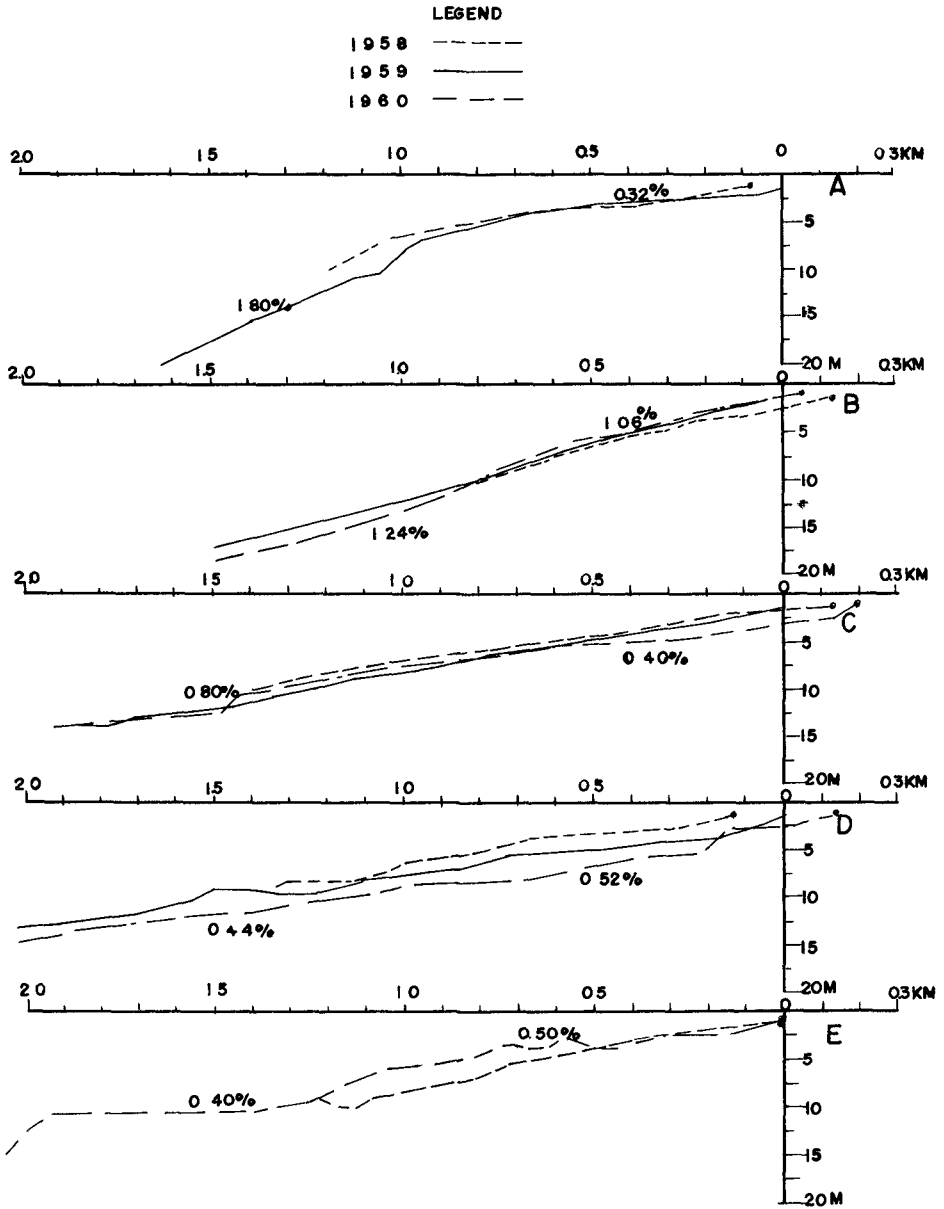


Fig 4 Shoreline Processes of Yu-Lin Coast

PROFILES OF YU-LIN COAST

FIG 5



CHAPTER 45

STUDY OF MUDBANKS ALONG THE SOUTHWEST COAST OF INDIA

by N.S.MONI **

ABSTRACT

The formation and behaviour of 'Mud Banks' is a phenomenon peculiar to the Southwest Coast of India. They are unique in their formation as well as functions. The paper deals with the history of mudbanks, their locations, causes of their formation, the nature of material and their sources. The behaviour of the mudbanks and their influence on the stability of the coast is also reported. The mudbanks act as storehouses of littoral material. It is also the initiator of erosion on its downdrift areas. It is noted that the material stored in the mudbanks must be advantageously utilised in stabilising the shores adjacent to it and for reclamation. Of extreme importance is the recognition that mudbanks are closely associated with the stability of the Southwest Coast of India and is a factor to be reckoned in any programme of coastal development or protection in this area.

INTRODUCTION

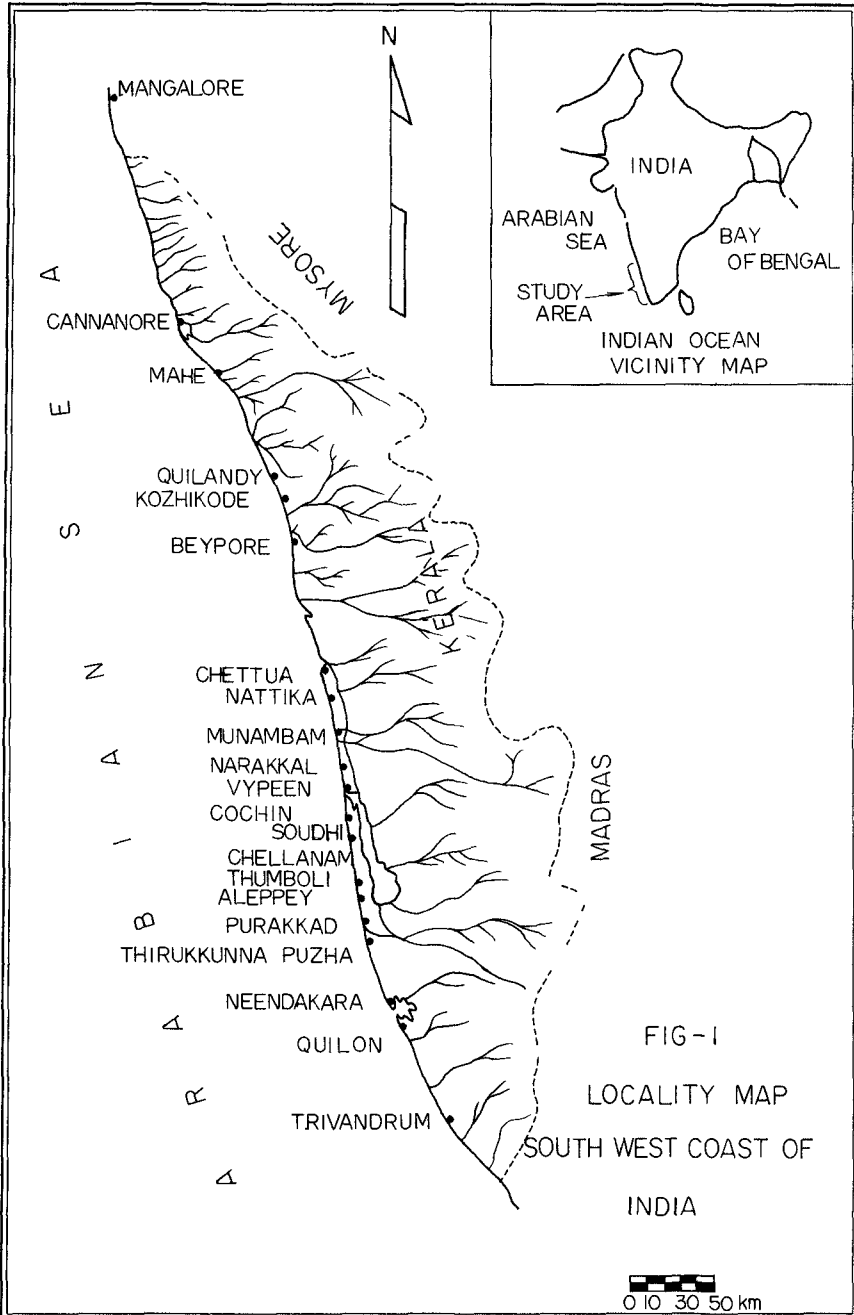
In the Southwest Coast of India, certain inshore areas have a special property of dampening wave action and producing regions of calm water even during the rough monsoon season due to the dissipation of wave energy in the large quantity of colloidal suspension in the region. These regions are generally known as the 'Mud Banks'. They are unique in their formation as well as functions. The mudbanks form part of the sediment activity along the coast. They directly influence the equilibrium conditions of shore in its vicinity. The mudbank regions are considered to be a 'boon' by the local populace as these areas which are calm during the monsoons abound in Prawns, Sardines, Mackerals and Soles.

LOCATION

There are four well known mudbanks along the Southwest Coast of India- one near Cochin, one near Alleppey and two near Kozhikode.

**

Deputy Director, Coastal Engineering Division,
Kerala Engineering Research Institute, Peechi, Kerala, INDIA
(now on deputation, as) Colombo Plan Participant (O.T.C.A)
Port and Harbour Research Institute, Nagase, Yokosuka, JAPAN



Historical records relating to the mudbanks at Cochin and at Alleppey are available from 1840. Of these four, three mudbanks are either at or near the outlets of rivers and lagoons while the fourth one at Alleppey is not any where near an outlet. There are other mudbanks which are known to have existed during the past twenty years. They are located at:

Mahe (South of Mahe river outlet)
 Beypore (South of Beypore river outlet)
 Nattika (South of Chettua outlet)
 Munambam (Soth of Periyar river outlet)
 Soudha (South of Cochin outlet)
 Thumboli (North Of Alleppey)
 Thrikkunnappuzha (South of Thottapalli Artificial Cut)

The study area of 560 km and the location of the mudbanks are given in Figure 1

HISTORY OF MUDBANKS

The earliest known record of the existence of mudbanks dates as far back as 1678, in Pinkerton's 'Collections of voyages and travels' given in the Administration Report of 1860 of Travancore (India). Dr. King, of the Geological Survey Of India in his report 'Considerations on the Smooth water anchorages or mudbanks of Narakkal (Cochin) and Alleppey on the Travancore Coast' (1881) has given an account of the migration and formation of the two mudbanks. According to his report, the range of migration of the Alleppey mudbank is twentyfour km between Alleppey and Purakkad and that of the Cochin mudbank is twenty km between Narakkal and Cochin. An organised attempt to study the mudbanks was made by Sir R.C. Bristow, and these are detailed in his books 'History of Malabar Mudbanks', 1938 Vol. I and Vol. II. This throws light on the origin, formation and other features of the mudbanks. The historical data of the Cochin and Alleppey mudbanks are given in Figures 2A and 2B.

Cochin Mudbank

The record of history of this mudbank is available from 1841. No perceptible change was reported between 1841 and 1861. From 1861 to 1881 it has moved southwards for 15 km. In 1890 the mudbank was located north. Till 1924 the movement was gradual towards south. In 1937, it crossed the Cochin approach channel and caused considerable silting. It moved further south. Between 1950 and 1968 the mudbank was located both in the north and south of the Cochin outlet.

Alleppey Mudbank

This mudbank was first reported in 1678. Again it was located in the same region in 1725. In 1827 it was reported 24 km south. In 1860 and in 1890 it was located near the Alleppey Pier (northern limit). In 1896 it was 10 km south and in 1902, 25 km south. In 1924 to 1928 it was located at the Alleppey Pier. Then onwards it was moving to the south. In 1937 it was 8 km to the south of the Pier. From 1950 to 1968 it was located between 8 to 16 km south of the Alleppey Pier.

FIG- 2A
HISTORY OF MUDBANKS

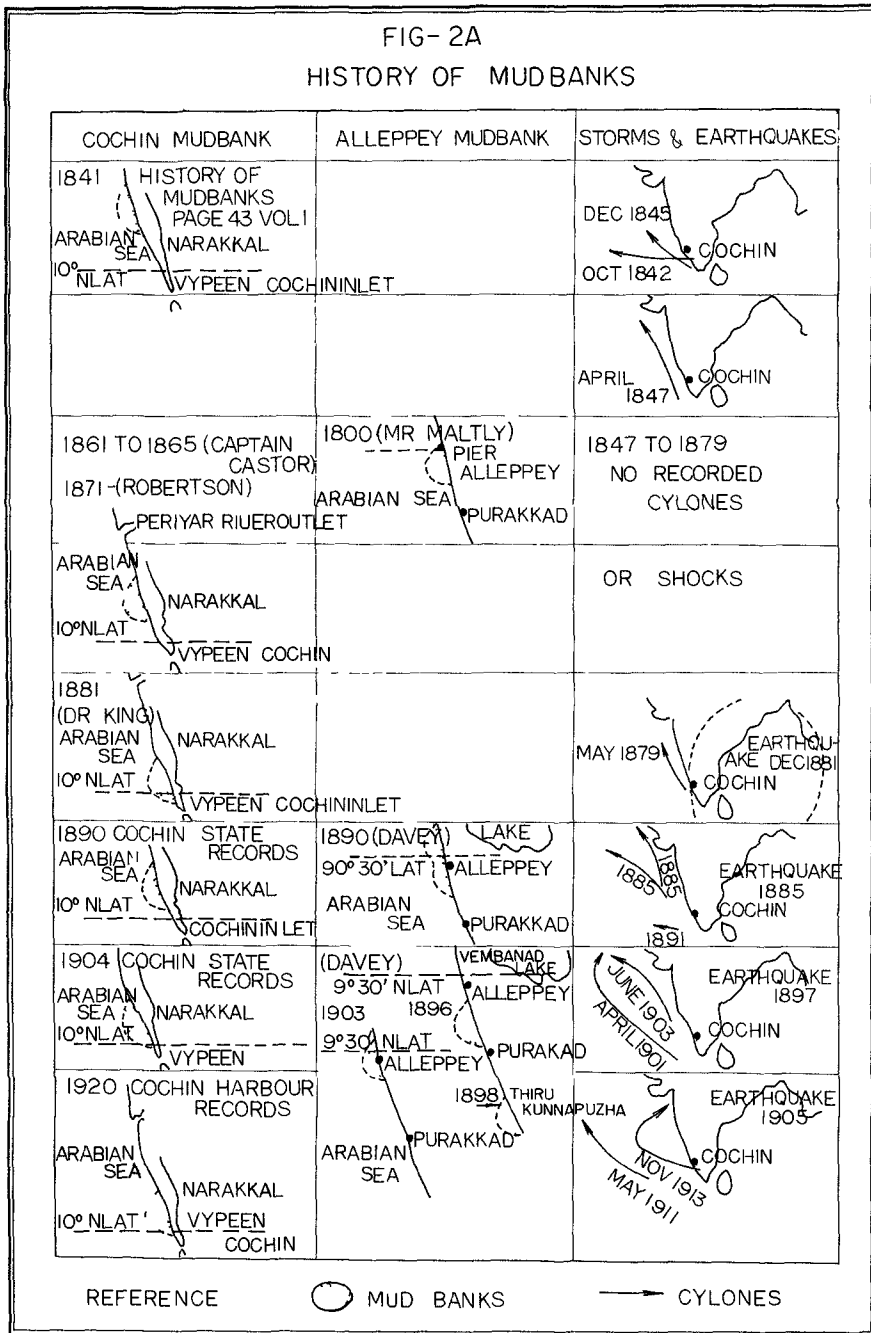
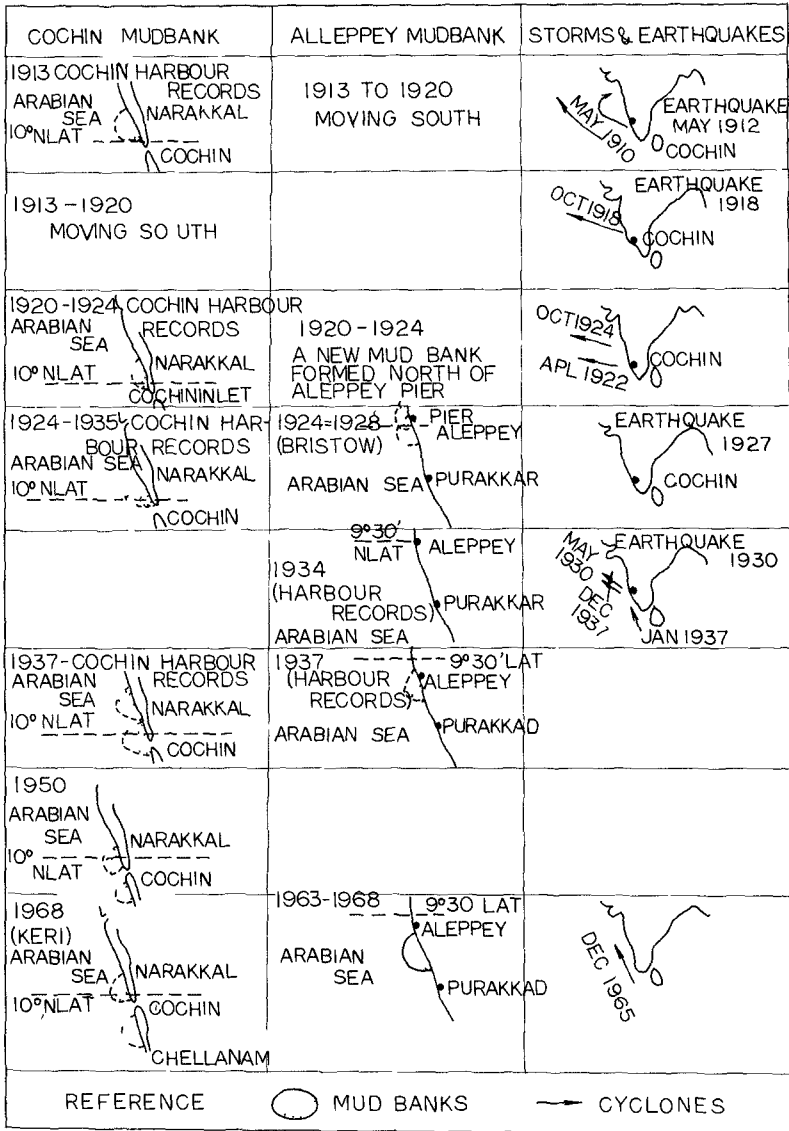


FIG - 2B
HISTORY OF MUDBANKS



PHYSICAL FACTORS AND LITTORAL MOVEMENTS

The physical factors, shore effects and littoral drift have bearing on the mudbanks and are detailed below.

Winds, Waves and Tides

The data was developed from the daily weather charts of the Indian Meteorological Department. The predominant direction of the prevailing winds along the shore is from west and northwest during May to September (monsoon season). From the wave rose diagrams it is observed that during the monsoon season, the predominant direction of waves is from west and those from northwest are contributory factors during July, August and September. The largest computed waves were between 5m and 6m in height. The mean wave height can be taken as 1.8m with a period of 8 to 10 seconds. The tides are semidiurnal and vary with a mean range of 0.8m at the south end to 1.8m at the northern limit. Storm tides occur all along the coast during the monsoon.

Offshore and Foreshore Zones

The continental shelf of this coast has a gradual slope upto 10 fathoms after which there is a steep fall. The distance of the 100 fathom line from the shore varies from 82km at the north to 45km at the south. In general the foreshore has a slope of 1 on 5 to 1 on 10 above LW with flatter underwater slopes. The foreshore slope in the mudbank regions are flatter compared to those on the adjacent sides. A typical example is given in Figure 3.

Field observations at selected reaches in the coast indicate that there are seasonal changes in the beaches. Erosion is experienced from April to September, after which the beach begins to accrete. The berm crest in certain cases fluctuates within wide limits - even upto 70m in a season.

Littoral Drift

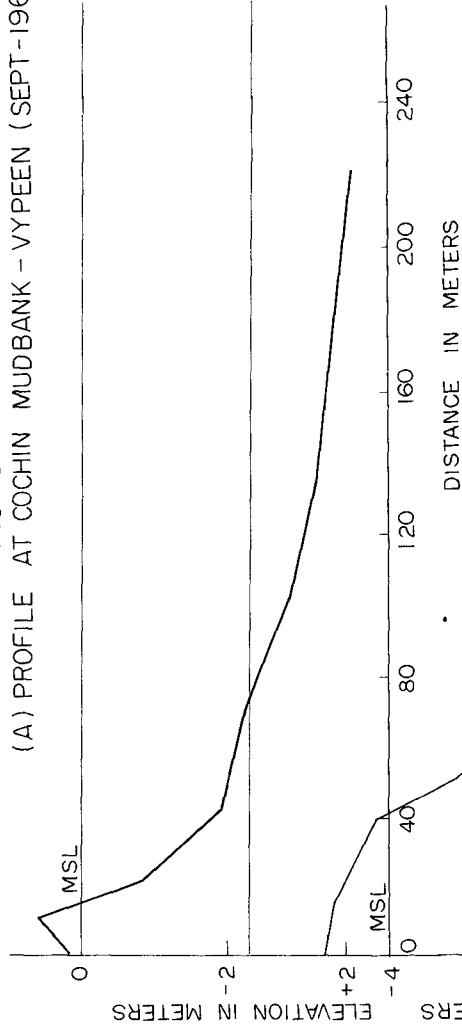
Littoral drift varies with the seasons of the year but is predominantly from north to south. This predominance is evident from the analysis of wave data, evidence from headlands and bays, migration of spits and inlets and observations of groins and jetties.

NATURE, FORMATION AND ORIGIN OF MUDBANKS

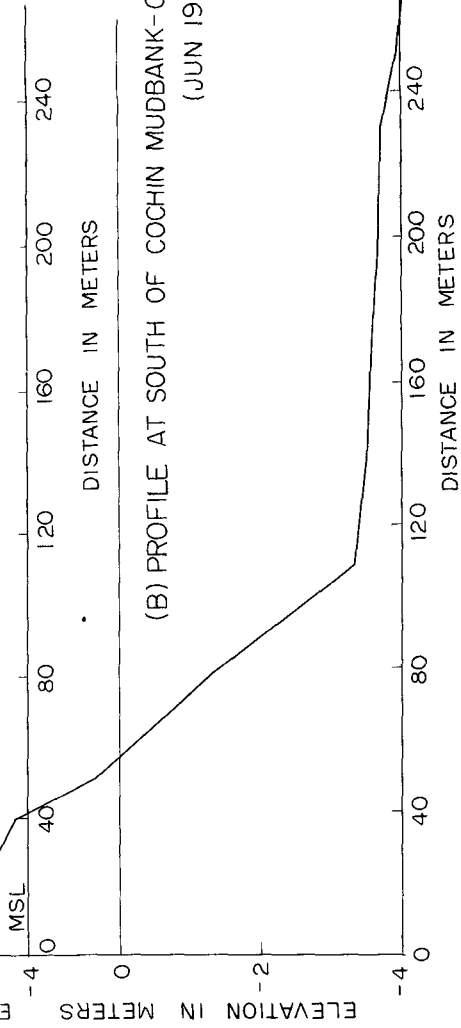
Geologically the Southwest Coast of India is of recent age, its formation dating back to the early Tertiary period. Borings at Cochin show that there are deposits of alluvial material for 100m to 125m overlying rock. It is noticeable that the portion of the coast from Kozhikode to Trivandrum where the mudbanks are confined is coincident with the presence of alluvial belt backed by laterite deposits at no long distance from the coast. The general distribution of sediments in the continental shelf of this coast indicate that

FIG - 3

(A) PROFILE AT COCHIN MUDBANK - VYPEEN (SEPT-1966)



(B) PROFILE AT SOUTH OF COCHIN MUDBANK - CHELLANAM (JUN 1965)



the inner shelf (upto 20 fathoms) consists of greenish black, poorly sorted clayeys and clayey silts and the outer shelf (20 fathoms) to 100 fathoms) consists of well sorted fine and medium sand with abundant shell fragments.

Analysis of samples from the seabed in the mudbank region reveal the following. They are greenish black and deep slaty in colour and cohesive and plastic to touch. Granulometric analysis indicate that it consists predominantly of silt and clay fractions, with less than 5% of fine sand. (Figure 4) The heavy mineral fraction average 2%. The samples taken at the top of the bed reveal that the top layer of the bottom mud is in a state of liquidity.

Samples from the sea bottom upto 10m adjacent to the mudbanks and also from the inland backwaters were analysed and compared with the mudbank samples. The samples from the mudbanks and from the adjacent sea bed showed close resemblance and similar characteristics. The granulometric analysis of samples taken from inland backwaters and mudbanks also showed similar characteristics.

The mudbanks are situated near and not too distant from the river outlets except in the case of Alleppey mudbank which is separated from the Vembanad backwater by a narrow strip of alluvial belt.

The analysis suggests that the origin of the material in the mudbanks is from the deposits of laterite and alluvial formation of the interior brought by the rivers.

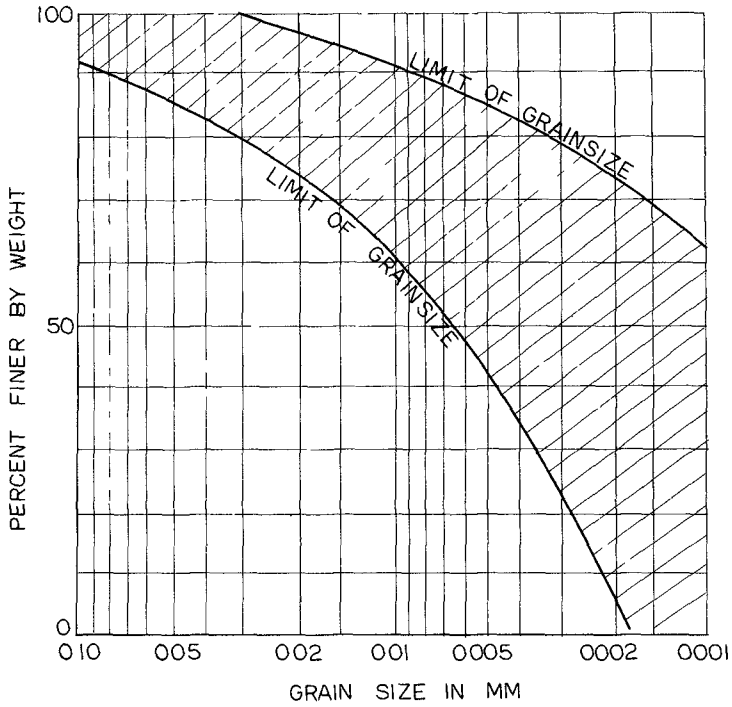
The mudbanks are formed by a single or a combination of the undermentioned causes:

- i) By the gradual deposition of clay and silt brought by the rivers during the monsoon season
- ii) By the throwing up of the already existing mud in the seabed by the waves
- iii) Their exists a waterbearing strata along the coast. The appearance of the mudbanks is coincident when the waterlevel in the backwaters adjacent to the coast is high. When the water level rises in the backwaters during the monsoon, it is likely that silt and clay may be thrown up through the waterbearing strata connecting the backwater and sea.

It is interesting to note that the effect of the mudbanks are felt about a week after the beginning of the monsoon. The rivers and backwater systems discharge large quantities flood discharge and sediments into the sea through the numerous perennial and seasonal outlets and by seepage through barrier beaches separating the backwaters from the sea. Further the sea bed is agitated by the action of the waves and the material is thrown in suspension. The monsoon swells provide a continuous source of energy to maintain the colloidal suspension which alternately dampen the waves progressively and finally the sea becomes completely calm within the area.

BEHAVIOUR OF MUDBANKS

Observation of the Cochin and Alleppey mudbanks indicate that they change in shape and size with the seasons. The length along the coast varies from 6km to 10km and the width upto 8km. By tracking the



ENVELOPE OF GRAINSIZE CURVES
OF COCHIN MUD BANK
SAMPLES

FIG 4

mudbanks it is noted that they migrate with the seasons, but the predominant direction of movement is towards south (during June-July) These confirm the findings of the earlier observations taken in 1937-1938. It is also noted that the migration of the mudbanks conform to a cyclic pattern similar to those of the uncontrolled inlets in this coast.

MUDBANKS AND SHORE STABILITY

The effect of the mudbanks on the equilibrium conditions of the coast adjacent to it was studied with particular reference to the Cochin and Alleppey mudbanks. The shore sectors located south of the two mudbanks are subjected to progressive shore recession. An examination of historical evidence and field observations indicates that the mudbanks provide the key to the shore stability in these two sectors.

- Mudbanks affect the coastal processes in the following ways
- 1) Traps the littoral material from the updrift side and thereby prevents its downcoast movement
 - ii) Causes refraction of waves on its sides
 - iii) Causes accretion within the mudbank area

Trapping of littoral material

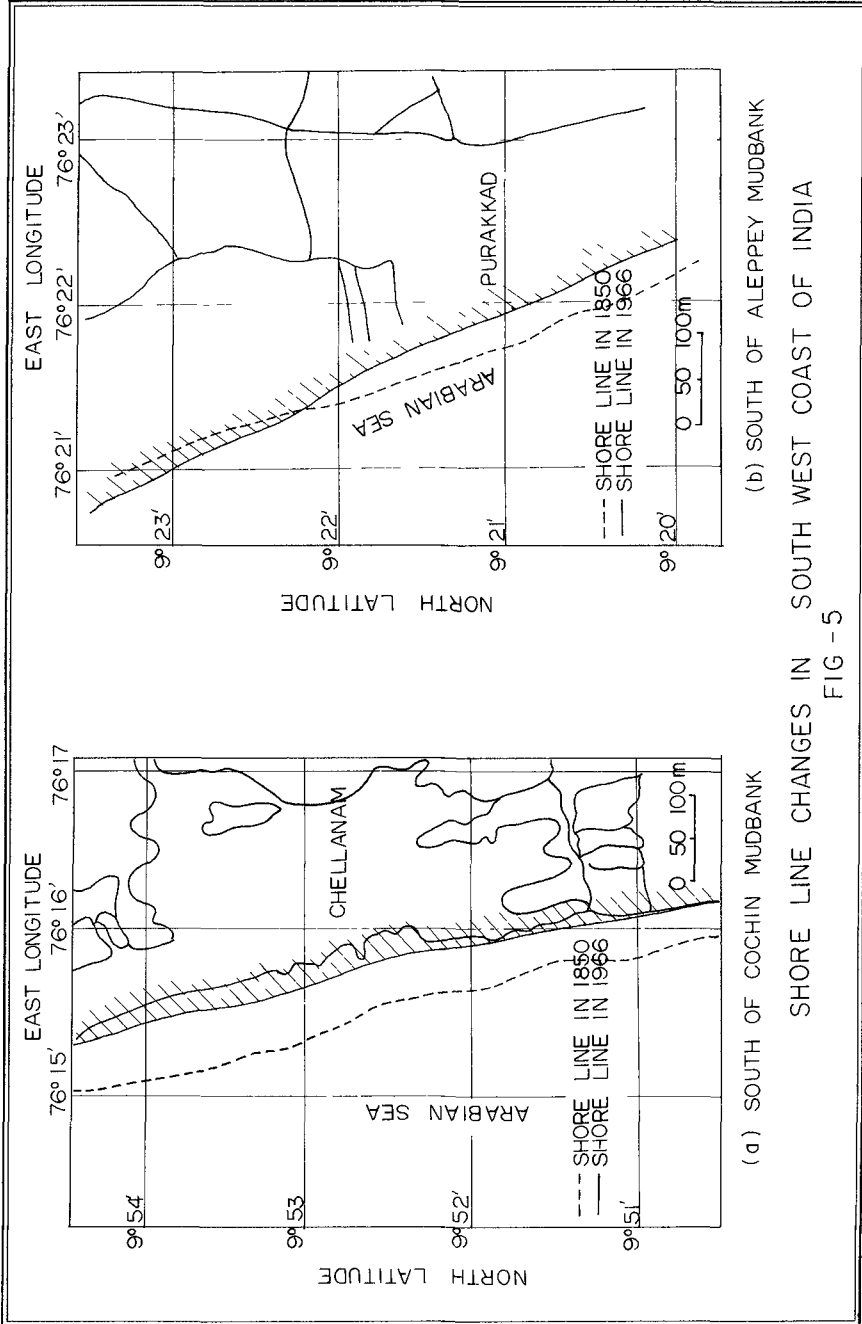
As the littoral material transported by the alongshore movement reaches the mudbank, its further movement is arrested as a result of the damping of the waves. Hence the in the immediate downdrift is starved of littoral supply and the coast is eroded to make up for the deficiency. Comparison surveys prepared from authentic maps indicate that there is consistent retrogression of shoreline, especially in the zones south of the Alleppey and Cochin mudbanks. The shorelines had receded 360m during the past 120 years south of the Alleppey mudbank and 600m during the same period south of the Cochin mudbank (Refer Figure 5).

Refraction of waves on the sides of the mudbank

The mudbank act as a long, wide breakwater. As the waves approach the mudbank, they tend to refract. The refracted waves turn towards the mudbank on its leeside causing a reversal in the general direction of the drift from a nodal zone in the downcoast and causes movement of material towards the mudbank from its leeside. Observations confirm this phenomenon. This aggravates the eroding tendency on the downcoast side.

Accretion within the mudbank

Within the mudbank, littoral material accumulates, thereby accreting the shore within it. Absence of waves preclude littoral movement through the mudbank and hence materials once trapped within it is prevented from moving out. The mudbank acts as a storehouse of littoral material. There is progressive growth of headland. The shoreline has advanced by 1250m during the past 50 years in the Cochin zone and by 500m during the past 15 years in the Alleppey zone.



EVALUATION

Mudbanks have the special property of dampening wave action and producing areas of calm water even during the roughest monsoon season. They decisively influence the shore processes and are effectively disturbing the equilibrium conditions of the coast adjacent to them. They are acting as storehouses of littoral material. The material stored in the mudbanks must be advantageously utilised in stabilising the eroding shores on its downdrift side and for reclamation by a coordinated programme. Of extreme importance is the recognition that mudbanks are closely associated with the stability of the southwest coast of India and is a factor to be studied further and reckoned in any programme of coastal development or protection in this area.

REFERENCES

1. Bristow, R.C., 'The History of Malabar MudBank', Vol. I, Cochin Port Trust., 1938.
2. Bristow, R.C., 'The History of Malabar Mudbank', Vol. II, Cochin Port Trust., 1938.
3. Joglekar, D.V., Gole, C.V., Mulekar, S.N., 'Studies on siltation of Cochin Port', Proceedings of XIX International Navigation Congress., 1957.
4. Kerala Engineering Research Institute, 'Annual Report', 1964.
5. Damodaran, R., Hridayanadhan, C., 'Studies of the MudBanks of the Kerala Coast', Symposium on Coastal and Nearshore Oceanography, C.S.I.R., 1966.
6. Moni, N.S., Nambiar, K.K.M., 'Study of seasonal variations in the Beaches of the Kerala State', Irrigation and Power Journal, Vol. 24 No. 2, 1966.
7. Richard T. Russel, 'Rivers, Plains, and Sea Coasts!', University of California Press, Berkeley., 1967.
8. Moni, N.S., George, M.M., Nambiar, K.K.N., 'Study of Beach Profiles in & near the Surf Zone of the Kerala Coast taken using Sled', Thirtieth Annual Research Session of C.B.I.P., 1968.
9. Kerala Engineering Research Institute, 'Studies on Coastal Erosion', (Internal Report), 1969.

CHAPTER 46

TURBULENCE AND SEDIMENT CONCENTRATION DUE TO WAVES

Kiyoshi Horikawa
Professor
and
Akira Watanabe
Postgraduate

Department of Civil Engineering
University of Tokyo
Tokyo, Japan

ABSTRACT

A new electrolytic turbulence transducer has been developed in order to measure the turbulent velocity fluctuation superposed on the oscillatory flow velocity. The aim of the present paper is firstly to describe the outline of this transducer and secondly to introduce some of the experimental results. The main items of the results are, 1) the vertical distribution of turbulence intensity averaged over one wave cycle, where the turbulence is induced by ripples which appear on the movable bed of wave flume, and 2) the correlation between the turbulence intensity and the characteristics of sediment particles at the same level such as their fall velocity and sediment concentration.

INTRODUCTION

The authors have had a strong interest in the fundamental mechanism of suspended sediment due to wave action. In the previous papers the authors have described their results related to the following subjects:

- 1) The vertical distribution of suspended sediment concentration due to waves (Hom-ma and Horikawa, 1962, Hom-ma, Horikawa and Kajima, 1965),
- 2) The general relationships to determine the size of sand ripples which appear on the movable bed owing to progressive waves (Hom-ma and Horikawa, 1962),
- 3) The critical water depth for the onset of bed material movement due to waves (Horikawa and Watanabe, 1967), and
- 4) The measurement of velocity distribution in the vicinity of bottom boundary in the oscillatory flow field, from which the characteristics of shear stress and of eddy viscosity been evaluated (Horikawa and Watanabe, 1968)

All of these studies are successive approaches to clarify the basic mechanism of suspension phenomena in a wave field

The following equation is commonly used as the fundamental equation for determining the vertical distribution of suspended sediment concentration averaged over one wave cycle \bar{m}

$$\frac{d}{dz} (K_z \frac{d\bar{m}}{dz}) + w_o \frac{d\bar{m}}{dz} = 0 \quad (1)$$

Where w_o is the fall velocity of suspended sediment particle, K_z is the vertical eddy diffusivity, and z is the vertical axis taken upward from the bottom. In order to solve the above equation the value of K_z should be evaluated beforehand, hence in the previous papers the authors treated the above problem based on the assumption that K_z could be replaced by the eddy viscosity ϵ_m . This kind of treatment should be valuable from the engineering point of view, but may not be powerful to clarify the basic questionnaires on the suspension phenomena, such as how to determine the concentration at a certain elevation near bottom which is used as a measure to define the vertical distribution of suspended sediment concentration.

In the region where the sediment movement is active, the flow in the vicinity of sea bottom is, generally speaking, in the turbulent flow condition, and the vortices are generated behind sand ripples which are formed along the sea bottom. These vortices induce the turbulence with higher frequencies in the oscillatory flow field. These processes stated above must keep the motivative activities on suspension phenomena, hence it seems to be of essential importance to clarify the turbulence characteristics in an oscillatory flow field in order to understand the real state of questioned phenomena.

ELECTROLYTIC TURBULENCE TRANSDUCER (ELET)

In order to measure the mean velocity in an oscillatory flow field, Jonsson(1963) applied a miniature current meter, while Iwagaki(1969) applied a hot-film anemometer. On the other hand the authors(1968) used the hydrogen bubble technique to measure the velocity in a thin boundary layer.

With regard to the turbulence in an oscillatory flow no data is available to be used. The main reasons why the measurement of turbulent velocity fluctuation in the vicinity of bottom boundary under the oscillatory flow is difficult are as follows.

- 1) The direction and magnitude of the main flow in the oscillatory flow field vary in time differing from the states of steady flow field.
- 2) The time variation of flow circumstance has been occurred in a rather short period such as one to several sec.

3) In the case of rippled rough bottom, a vortex with relatively big size (the diameter of vortex being one to several cm in laboratory) has been formed behind each ripple. Under these complicated situations it is awfully difficult to apply such a standardized measuring technique for obtaining each component of turbulent velocity fluctuation as a measurement of hot-film anemometer, the reliability of which has been verified in steady water flow. Binder (1967) reported the applicability of the electrokinetic turbulence meter, the principle of which is to measure the electric potential fluctuations induced by the translation of electric double layers. The disadvantage of this transducer is represented by the fact that the output is zero under the laminar flow condition. That is to say, the output is affected by the flow characteristics even though the current velocity is the same.

From these points of view the authors have been devoting their efforts to develop a new electrolytic turbulence transducer, herein after the authors will call it shortly as ELETT, and have a confidence in getting reliable data by using ELETT.

Figure 1 shows the schematic diagram of the instrumentation system. When the D.C. voltage is charged between a cathode of platinum wire and an anode of carbon rod, both of which are immersed in water, some part of water neighbouring those is electrolyzed to ions or gases. The flow produces a variation in electric resistance between the electrodes. Therefore the out-of-balance electric current in the Wheatstone's bridge is affected by the flow velocity at the cathode. The actual length of sensing element is about 1 mm.

In Figure 2 is shown the calibration curve between the velocity V and the output of sensor I. Figure 3 shows the direction-sensitivity $M(\varphi)$ of the ELETT sensor, where φ is the angle between the flow and a certain direction normal to the sensor.

When a probe which consists of a pair of sensors as shown in Figure 1 is used, the ratio between the output from one sensor and that from the other depends on the flow direction.

Table 1 is to summarize the processes how to determine the velocity component in a certain direction. The output I is a function of the velocity V and the direction angle φ , and is likely to be separated into two independent functions $S(V)$ and $M(\varphi)$ as shown in Equation (1). The calibration curves for $S(V)$ and $M(\varphi)$ are given as shown in the previous Figures 2 and 3. By using Figure b in Table 1, a newly defined function of $K(\varphi)$ can be calculated as shown in Figure c. The absolute value of V , the velocity component U , the direction angle φ , and the outputs I_1 and I_2 are defined as given in the stated diagram. Hence the outputs I_1 and I_2 are written as Equations (11) and (111) respectively, and the output ratio I_1/I_2 is expressed by the stated relation in Table 1. From Figure c the absolute value of direction angle $|\varphi|$ is deter-

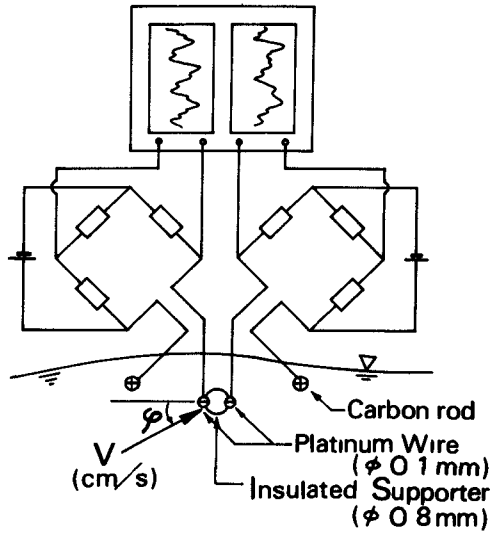


Fig. 1 Instrumentation system for velocity measurement.

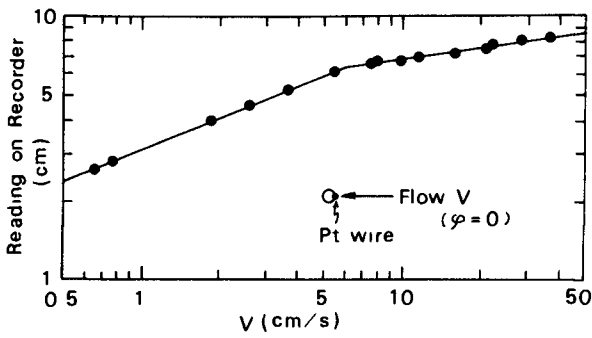


Fig. 2. Calibration curve for ELETT

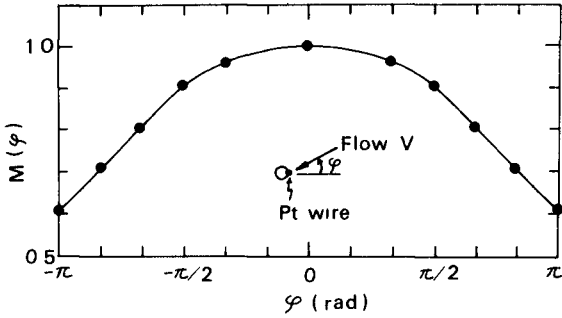


Fig 3 Direction-sensitivity of ELETT

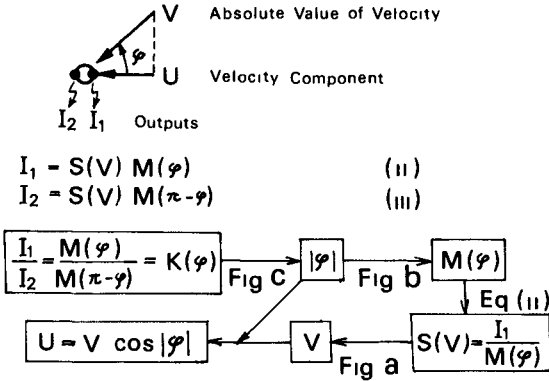
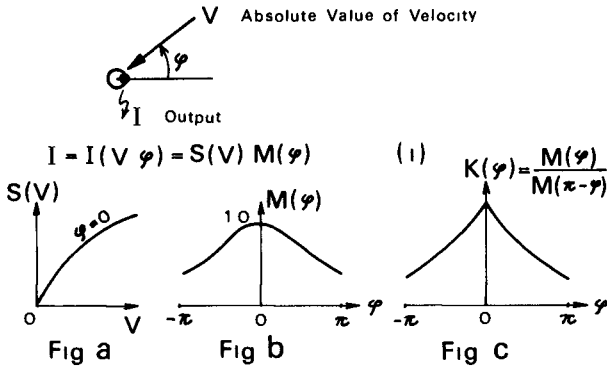


Table 1 Process diagram of velocity component reduction

mined By using Figure b we can get $M(\varphi)$, from which the value of $S(V)$ can be read by the help of Equation(11) Next the absolute value of V can be obtained by using Figure a, and hence the value of U is also calculated

TURBULENCE CHARACTERISTICS MEASURED BY ELETT

The laboratory measurements by ELETT was conducted in a wave flume under the following conditions the water depth was 30 cm, the wave height and period of fundamental mode were 7.93 cm and 1.35 sec respectively, and the water temperature was 8 °C The medium diameter and the sorting coefficient of standard sand placed on the flume bed with the thickness of 15 cm were 0.20 mm, and 1.15 respectively The rise and pitch of ripples which appeared on the flume bottom were 0.95 cm and 5.7 cm respectively

Figure 4 indicates one example of the time history of the horizontal velocity component which was measured by ELETT The thick line in this figure is for the measured horizontal velocity component U . Here it is necessary to separate the turbulence fluctuation from the combined original record In the present case of laboratory experiment, it was found that the amplitude of the second harmonic of surface wave profile was as small as 3 % of the fundamental mode, through the harmonic analysis of the wave record Hence the authors defined temporarily the turbulence velocity fluctuations u as the remainder after subtracting the fundamental mode of the velocity U_1 from the corresponding original data of horizontal velocity U In Figure 4 the fundamental mode velocity was expressed by a thin line, while the turbulence velocity fluctuation defined above was expressed by a broken line The same procedure was applied to the vertical velocity component.

Figure 5 shows the amplitude ratio between the calculated value of the vertical velocity component on the basis of Airy's theory W_{cal} and the fundamental mode value of the measured vertical velocity component W_{meas} . This diagram indicates that there exists a vertical motion in a considerably large scale even within a region near the bottom boundary For example $W_{meas} \approx 2$ cm/sec at $z \approx 0.5$ cm According to the oscillatory turbulent boundary layer theory presented by Kajiura(1964, 1968), where the vertical component of velocity was neglected, the thickness of the turbulent boundary layer in the present case was estimated as about 3.5 cm Even if the above thickness is larger than the rise of ripple, the vertical velocity component seems not to be neglected owing to the fact that the stated value is comparable to the horizontal one in the vicinity of ripples The authors believe that the Kajiura's theory on the oscillatory boundary layer flow should be modified with the consideration of the above stated fact

Here the turbulence intensity is defined as the root mean square of the turbulence fluctuation In Figure 6

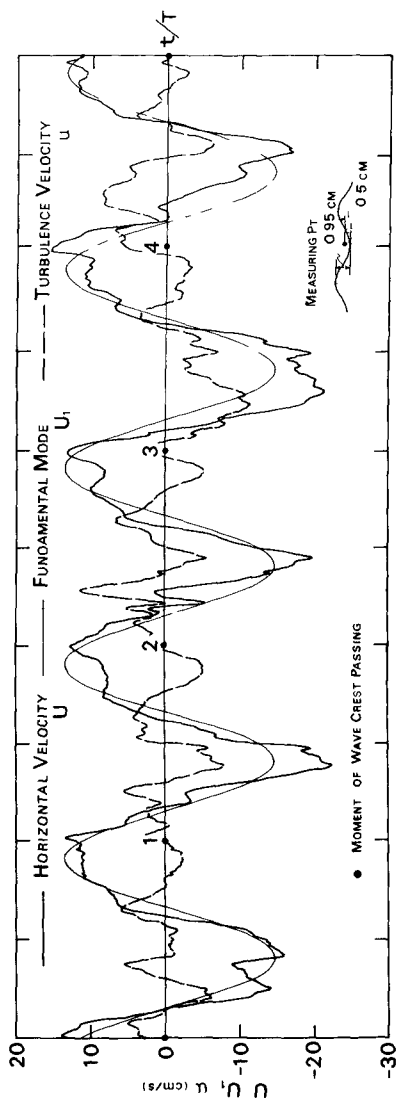


Fig 4 Time history of horizontal velocity component

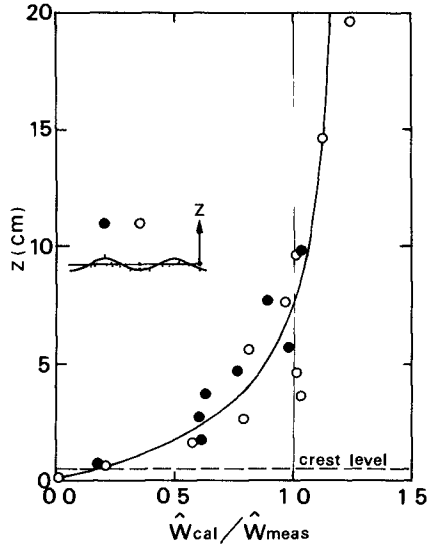


Fig 5 Amplitude ratio of W_{cal} to W_{meas}

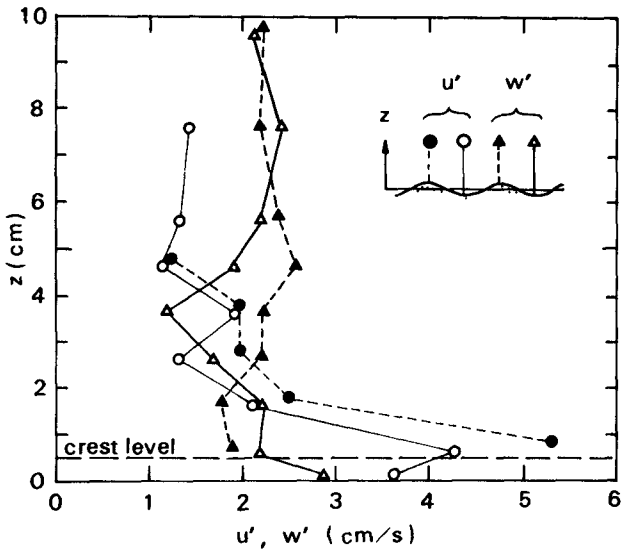


Fig 6 Vertical distributions of turbulence intensities, u' and w' .

are shown the vertical distributions of horizontal and vertical components of turbulence intensity. This diagram indicates that the vertical intensity $w' = \sqrt{w'^2}$ is nearly constant independently of the measuring position, while that the horizontal intensity $u' = \sqrt{u'^2}$ is very high near the bottom boundary. The value of $(u'^2 + w'^2)$, which is related to the total energy of turbulence, is decreasing monotonously with the height above the bottom. These are quite interesting and important facts to investigate the source mechanism of suspended materials from bottom.

Figure 7 is for the normalized spectral energy density $F(n)$ of the horizontal component of turbulence fluctuation u given in Figure 4, where n is a frequency. The range of the major energy content is situated at low frequencies less than 4 cps, and the so-called -7 power law seems to be applicable at higher frequencies larger than about 10 cps. From the latter fact the micro scale of turbulence in time is said to be 0.1 sec. This value seems to be pretty large compared with the result in an air flow, but is in fair agreement with the value obtained by Raichlen (1967), who measured the turbulence intensity of steady flow in an open channel by using a hot-film anemometer. The spectrum computation was made under the condition of 1) the degrees of freedom being about 30 and 2) the lag window being the Hanning procedure.

The different expression of turbulence energy spectrum $n^2 F(n)$, which is related to the rate of turbulence energy dissipation, is shown in Figure 8, from which two peaks are observed at 2~3 cps and 7 cps. Taking consideration of the oscillatory flow pattern in the vicinity of sand ripple and of the wave period of 1.35 sec, the authors believe that the former peak corresponds to the vortex or circulation formed behind a ripple, while that the latter peak corresponds to the turbulence itself induced by the vortex stated above. This kind of approach must be quite valuable to find out 1) the essential reason why such a typical distribution curve as an L shape is appeared in the vertical distribution of suspended sediment concentration, and 2) the critical elevation beyond which a certain sand particle can not exist as a suspended sediment.

RELATIONSHIP BETWEEN SUSPENDED SEDIMENT CONCENTRATION AND TURBULENCE CHARACTERISTICS

The photo-transistor type concentration meter was developed at the Coastal Engineering Laboratory, University of Tokyo (Hom-ma and Horikawa (1963)) and has been improved step by step during the last several years. The circuit diagram of the present instrumentation system is shown in Figure 9. By using this instrument the time history of suspended sediment concentration was recorded under the same condition as the velocity measurement. The above measurements were conducted along the vertical lines above both a crest and a trough

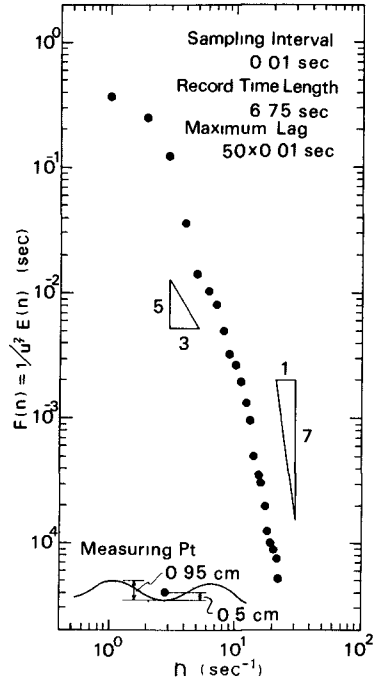


Fig 7 Spectral density distribution of horizontal turbulence component (1), $F(n)$

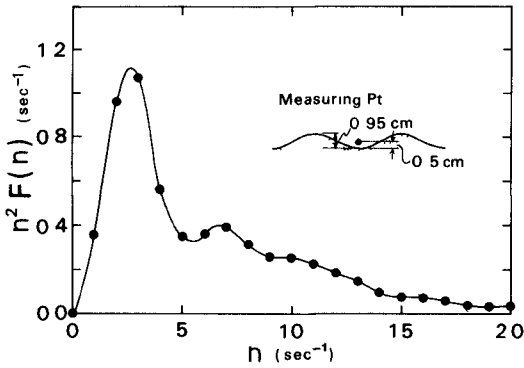


Fig 8 Spectral density distribution of horizontal turbulence component (2), $n^2 F(n)$

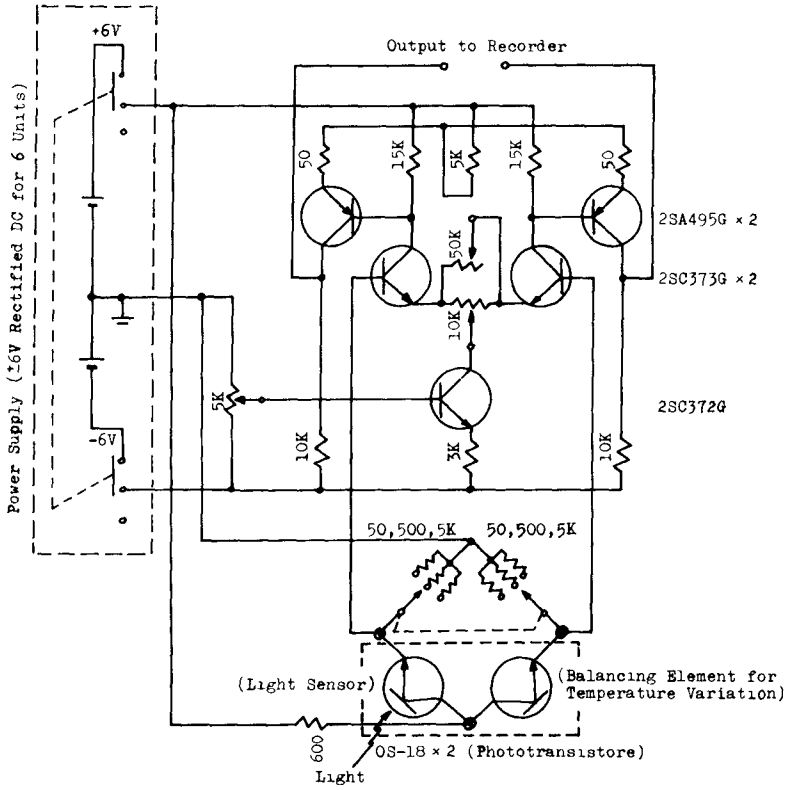


Fig 9 Circuit diagram of photoelectric concentration meter unit

of a certain sand ripple

From the recorded data were determined the time mean concentration \bar{m} and the root mean square value of the fluctuation in sediment concentration $\sqrt{m'^2}$, where m' is its fluctuation determined as the difference between the instantaneous value of sediment concentration m and the time mean concentration \bar{m} . In Figure 10 are shown the vertical distributions of \bar{m} , $\sqrt{m'^2}$ and $\sqrt{m'^2}/\bar{m}$. The last is the value of root mean square of m' normalized by the local mean concentration. From this diagram the following tendencies are observed

- 1) The vertical distribution of mean sediment concentration \bar{m} has an L shape which has commonly been observed in field and in the previous experiments.
- 2) The vertical distribution of these values above the ripple crest are slightly different from, but are basically the same as those above the ripple trough.
- 3) The root mean square $\sqrt{m'^2}$ has its greatest value near the bed and decreases as the elevation increases.
- 4) The distribution of the normalized value $\sqrt{m'^2}/\bar{m}$ is roughly similar to that of the intensity of vertical turbulence component which is shown in Figure 6.

Figure 11 is to show the comparison between the intensity of vertical turbulence component w' and the fall velocity w_0 of sediment particles sampled at corresponding elevations by using a syphon tube. It should be mentioned that the magnitudes of w' and w_0 are comparable.

As stated in INTRODUCTION of this paper Equation(1) is used as the fundamental equation to determine the vertical distribution of mean sediment concentration \bar{m} . By using the analyzed data of sediment concentration and of sediment fall velocity, the value of diffusion coefficient K_z at each elevation can be evaluated on the basis of Equation(1)

On the other hand the following relationship can be taken as an analogue of the eddy viscosity ϵ_m

$$\epsilon_m = -\frac{\overline{uw}}{\partial \bar{U} / \partial z} \sim \frac{\mathcal{L}(\partial \bar{U} / \partial z) \overline{w}}{\partial \bar{U} / \partial z} \sim \mathcal{L} \overline{w} \sim \mathcal{J}_E w'^2 \quad (2)$$

where u and w are the turbulence fluctuation in horizontal and vertical directions respectively, \bar{U} is the mean value of horizontal velocity component, z is taken positive upward, w' is the intensity of vertical turbulence fluctuation, \mathcal{L} is the mixing length, and \mathcal{J}_E is the Eulerian integral time scale related to w . The value of \mathcal{J}_E is calculated by the following equations

$$\left. \begin{aligned} \mathcal{J}_E &= \int_0^{\infty} R_E(\tau) d\tau \\ R_E(\tau) &= \frac{\overline{w(t)w(t+\tau)}}{w'^2} \end{aligned} \right\} \quad (3)$$

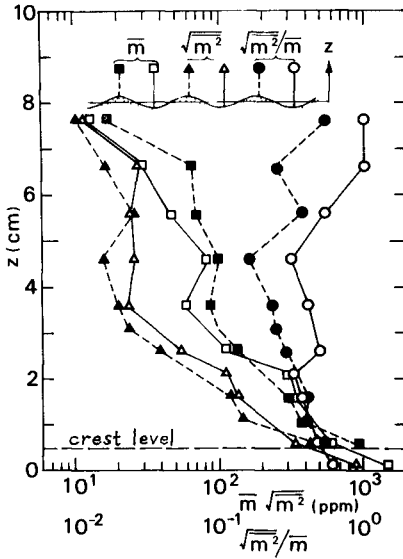


Fig 10 Vertical distributions of mean concentration \bar{m} , concentration fluctuation $\sqrt{\bar{m}^2}$ and $\sqrt{\bar{m}^2}/\bar{m}$

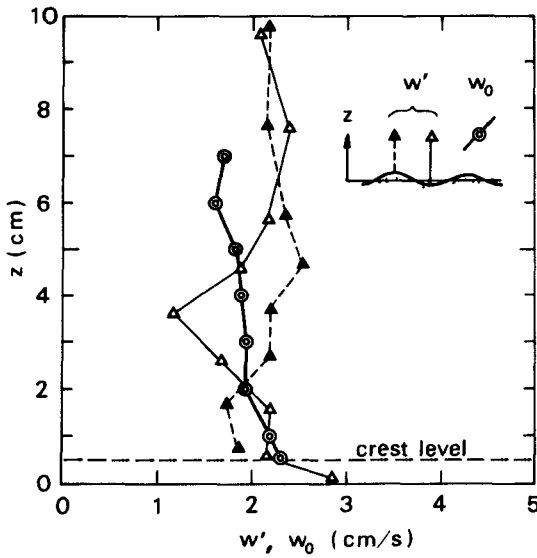


Fig 11 Comparison between vertical turbulence intensity w' and fall velocity w_0

where R_E is a coefficient of Eulerian time correlation

In order to compare the vertical distribution pattern of K_Z with that of $\mathcal{J}_E w'^2$, the values of both factors calculated through the stated methods were plotted in Figure 12. It is quite interesting that the distribution pattern of K_Z is rather similar to that of $\mathcal{J}_E w'^2$. There are still numerous uncertainties remained unsolved, hence it is certainly needed to accomplish further studies related to the following subjects, such as 1) to reevaluate the order of the term $d(\overline{m'w})/dz$ which was neglected in Equation (1), and 2) to find out the precise expression for ϵ_m . The authors have the strong intention to improve the newly developed instrumentation system of ELETT in order to get more accurate data, and also to accumulate much more data with the aim of finding the generalized relationship between the diffusion coefficient K_Z and the eddy viscosity ϵ_m .

CONCLUSIONS

In order to clarify the mechanism of suspension phenomena due to progressive waves, it is of essentially importance to observe and to understand the turbulence fluctuation characteristics under the oscillatory flow condition. On the basis of the above concept the authors developed a new anemometer named as ELETT (electrolytic turbulence transducer) and obtained a certain amount of measuring data. This is at any rate the preliminary approach to attack the turbulence characteristics induced by oscillatory flows, hence there are many problems to be solved in future. For example to establish the linearization of instrument output, to make clear the frequency characteristics of this instrument, and to find out more rational way of separating the turbulence fluctuation from the actual velocity record are the problems with which the authors have confronted at present.

The authors believe that the relationship among the turbulence intensity, the bottom roughness and the wave characteristics might be clarified in future owing to the further accumulation of laboratory data. The vertical distribution of turbulence intensity may be attacked theoretically on the basis of the turbulence energy equation. The authors have an intention to proceed the present treatment to the following directions in order to understand more clearly the relationship between the suspended sediment concentration and the turbulence characteristics. These are

- 1) to reevaluate the effect of convective term on a suspended sediment concentration, and to reconsider the expression of eddy viscosity; these are to find out the rational expression for the diffusion coefficient and for the vertical distribution of suspended sediment concentration
- 2) to make clear the characteristic concentration at a certain elevation, which is used as a measure to determine the vertical distribution of suspended sediment concentration, the characteristic concentration stated above is

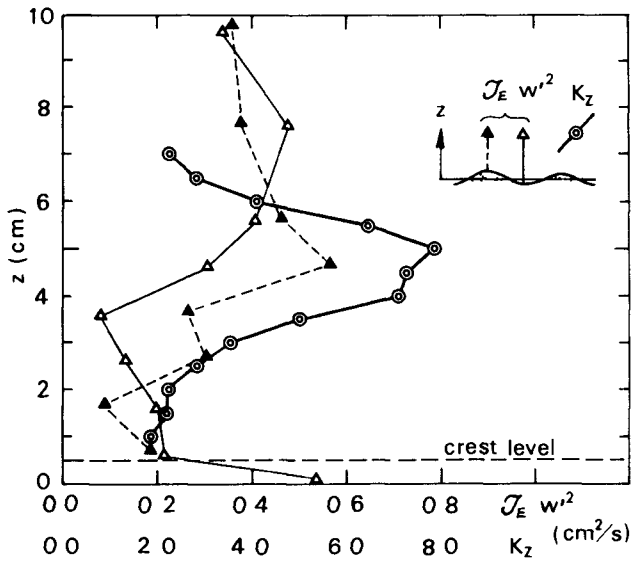


Fig 12 Comparison between analogue of eddy viscosity $\mathcal{T}_E w'^2$ and eddy diffusivity K_z

expected to have a close relationship with the Reynolds stress in the vicinity of bottom. The transducer reported here seems to be applicable to measure the Reynolds stress, therefore the pick-up and data processing system which are suitable for the present purpose should be developed in future.

ACKNOWLEDGEMENT

The work reported herein is a part of investigations carried out at the Coastal Engineering Laboratory, University of Tokyo, under the support of the Scientific Research Fund of the Ministry of Education in Japan.

REFERENCES

- Binder, G (1967) Potential fluctuations generated by turbulence on a small wire, Proc. 12th Congress, I A H R
- Hom-ma, M. and K. Horikawa (1962) Suspended sediment due to wave action, Proc 8th Conf on Coastal Engng
- Hom-ma, M and K Horikawa (1963) A laboratory study on suspended sediment due to wave action, Proc. 10th Congress, I A H R
- Hom-ma, M, K Horikawa and R Kajima (1965) A study on suspended sediment due to wave action, Coastal Engng. in Japan, Vol. 8
- Horikawa, K and A Watanabe (1967) A study on sand movement due to wave action, Coastal Engng. in Japan, Vol 10
- Horikawa, K. and A Watanabe (1968) Laboratory study on oscillatory boundary layer flow, Proc. 11th Conf on Coastal Engng
- Iwagaki, Y. and T Sakai (1969) Experiments on water particle velocity of finite amplitude waves, Proc 16th Conf. on Coastal Engng in Japan (in Japanese)
- Jonsson, I G (1963) Measurement in the turbulent wave boundary layer, Proc 10th Congress, I A H R
- Kajiura, K (1964) On the bottom friction in an oscillatory currents, Bull. Earthq Res Inst., Univ of Tokyo, Vol 42.
- Kajiura, K. (1968) A model of the bottom boundary layer in water waves, Bull. Earthq Res. Inst., Univ of Tokyo, Vol 46.
- Raichlen, F. (1967) Some turbulence measurements in water, Jour. Engng Mech Div, Proc. ASCE, Vol. 93, No EM 2.

CHAPTER 47

EFFECTS OF NONUNIFORM WAVE ENERGY IN THE LITTORAL ZONE

Victor Goldsmith¹
and
Joseph M. Colonell²

Abstract

Bi-weekly monitoring of four closely-spaced permanent beach profile stations located on the northeast end of Monomoy Island (Cape Cod) has revealed major variations in the amount of erosion and accretion occurring along this portion of the Massachusetts shoreline. During the 27-month monitoring period a close relationship was observed between changes in the beach and offshore portions of the profiles. Three distinct types of bars were noted:

- (1) Subtidal bars which are parallel to the shoreline and located one to two thousand feet off those portions of the shoreline undergoing relatively small amounts of beach erosion,
- (2) Subtidal bars which are perpendicular to the shoreline and attached to areas of the shore undergoing large amounts of erosion, and
- (3) Large intertidal bars which are oriented obliquely to the shoreline and associated with the formation of the ebb-tidal delta and the resulting wave refraction patterns.

The large variations in erosion and accretion occurring along the beach at any one time are related to the nonuniform distribution of energy within the waves arriving at this section of the coastline. This nonuniformity of wave energy is attributed to refraction of the waves around the irregular bathymetry offshore from Monomoy, and it appears to produce shoreline protuberances of sand which are flanked updrift and downdrift by erosional zones.

Wave refraction calculations indicate zones of alternately converging and diverging orthogonals in the wave fronts impinging upon Monomoy Island, with a correlation observed between the zones of converging orthogonals, i.e. wave energy concentrations, and the areas of the beach presently undergoing the greatest amounts of erosion.

¹Institute of Coastal Research, Department of Geology, University of Massachusetts, Amherst, Mass., 01002

²Associate Professor, Department of Civil Engineering, University of Massachusetts, Amherst, Mass., 01002

INTRODUCTION

Rhythmic beach topography and its relationship to adjacent intertidal and subtidal bathymetry has been discussed by several authors (Bruun, 1954, Robinson, 1960, Homma and Sonu, 1963, Sonu et al, 1966, Bakker, 1968, Sonu, 1968, Dolan and Ferm, 1968, Van Beek, 1969, Niederoda and Tanner, 1970) Attempts to relate nonuniform shoreline changes to wave refraction over irregular offshore bathymetry has been limited to large-scale effects (Munk and Taylor, 1947, Shepard and Inman, 1950, Jordaan, 1964, Roberts, 1964) In this study the nonuniform wave energy distribution produced by wave refraction over uneven offshore bathymetry is related to the large variations in erosion and accretion occurring at closely-spaced intervals on Monomoy Island

Monomoy Island is located on the "elbow" of Cape Cod, Massachusetts Monomoy was formed in Holocene time as a sand spit in response to the longshore currents resulting from the dominant northeast and east-northeast waves impinging upon the outer beach of Cape Cod

Since June 1968, twelve beach profiles on Monomoy Island and four profiles on Nauset Beach to the north have been monitored at bi-weekly intervals throughout the year Approximately twice per year, fathometer profiles have been run to extend these profiles seaward from the high tide line to a distance of one and one-half miles from shore Fathometer profiles parallel to the shore were also obtained The variations in erosion and accretion occurring at these closely-spaced profiles are quite significant This discussion is limited to the four northernmost profiles on Monomoy so that variations between these profiles, and their relationship to changes in the offshore region, may be examined in detail (Fig 1)

BEACH PROFILES

The northernmost profile, M-1, underwent 35 feet of erosion on the terrestrial portion of the profile in the first year of observations (June 1968 to June 1969) but was accretional during the second year (Fig 2) In the offshore area of the M-1 profile a series of intertidal swash bars had migrated to the northwest (i.e., onshore and into the page) during the period of these observations (Fig 2) This movement is a

result of the refraction of northeast waves around the large ebb-tidal delta so that these waves actually approach from the southeast at the M-1 profile location. One of the swash bars has become attached to the beach 300 feet north of the M-1 profile, causing a large accumulation of sand south of the bar at the M-1 profile (Fig. 3).

The changes observed at the other three profiles suggest a slightly different interpretation but, nevertheless, illustrate the close relationship between changes in the terrestrial and offshore portions of the profiles. The second profile, M-6, underwent 30 feet of erosion the first year (Fig. 4). However, the rate of erosion increased substantially during the second year such that by March 1970 the beach had retreated 135 feet at the M-6 location. Since March 1970 this profile has undergone

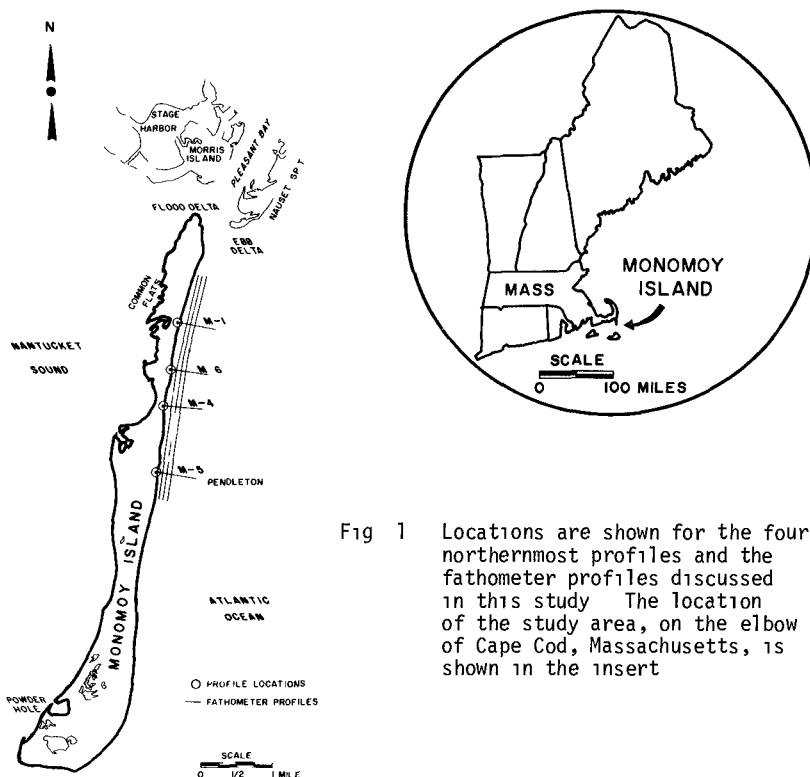


Fig. 1 Locations are shown for the four northernmost profiles and the fathometer profiles discussed in this study. The location of the study area, on the elbow of Cape Cod, Massachusetts, is shown in the insert.

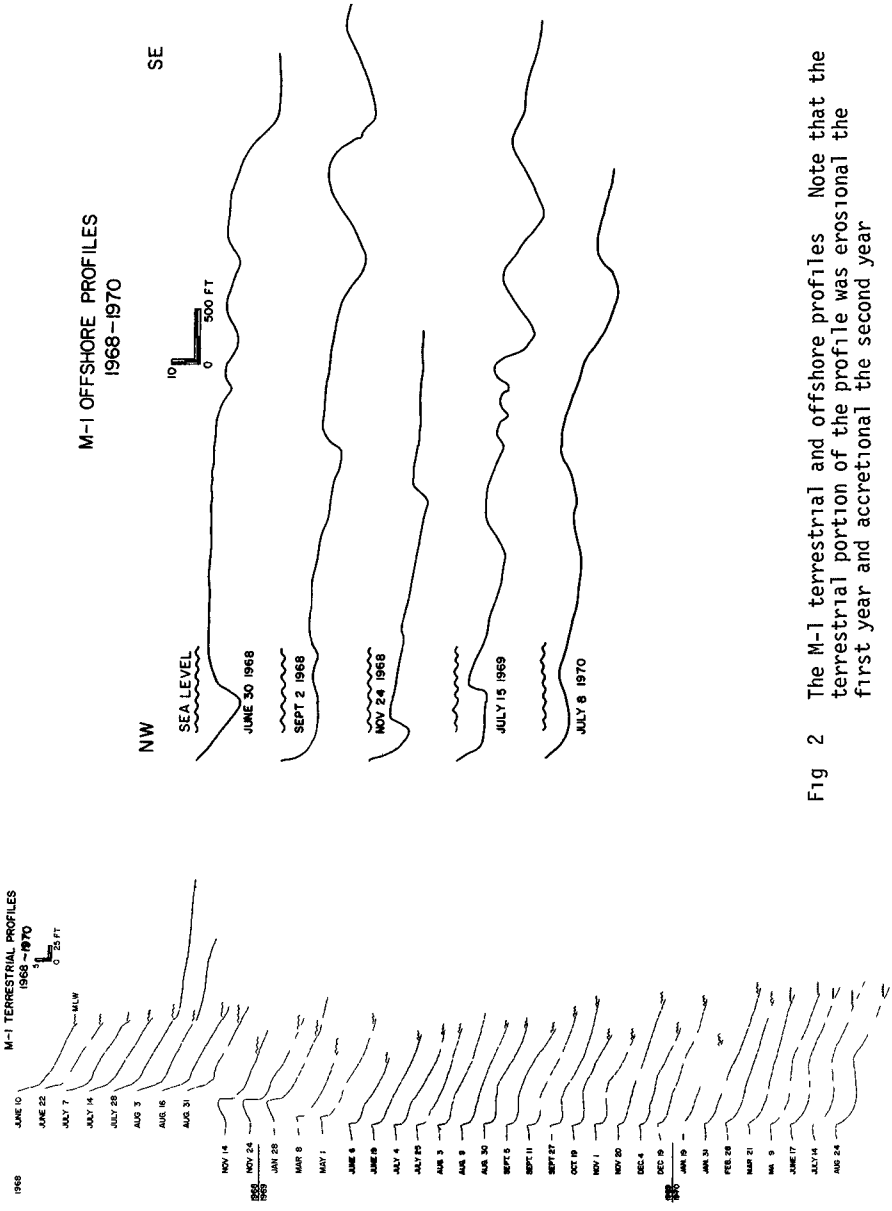


Fig 2 The M-1 terrestrial and offshore profiles. Note that the terrestrial portion of the profile was erosional the first year and accretional the second year



September 1969



September 1968



July 1970

Fig. 3. Migration of a large intertidal swash bar to the northwest resulting from wave refraction around the ebb-tidal delta. In September 1968 the bar was opposite the profile, 600 feet from shore, and separated by a 12-foot deep channel. Note the waves approaching from the southeast. After the bar became attached to the shore in September 1969 the M-1 profile, south of the bar, became accretional as observed in July 1970.

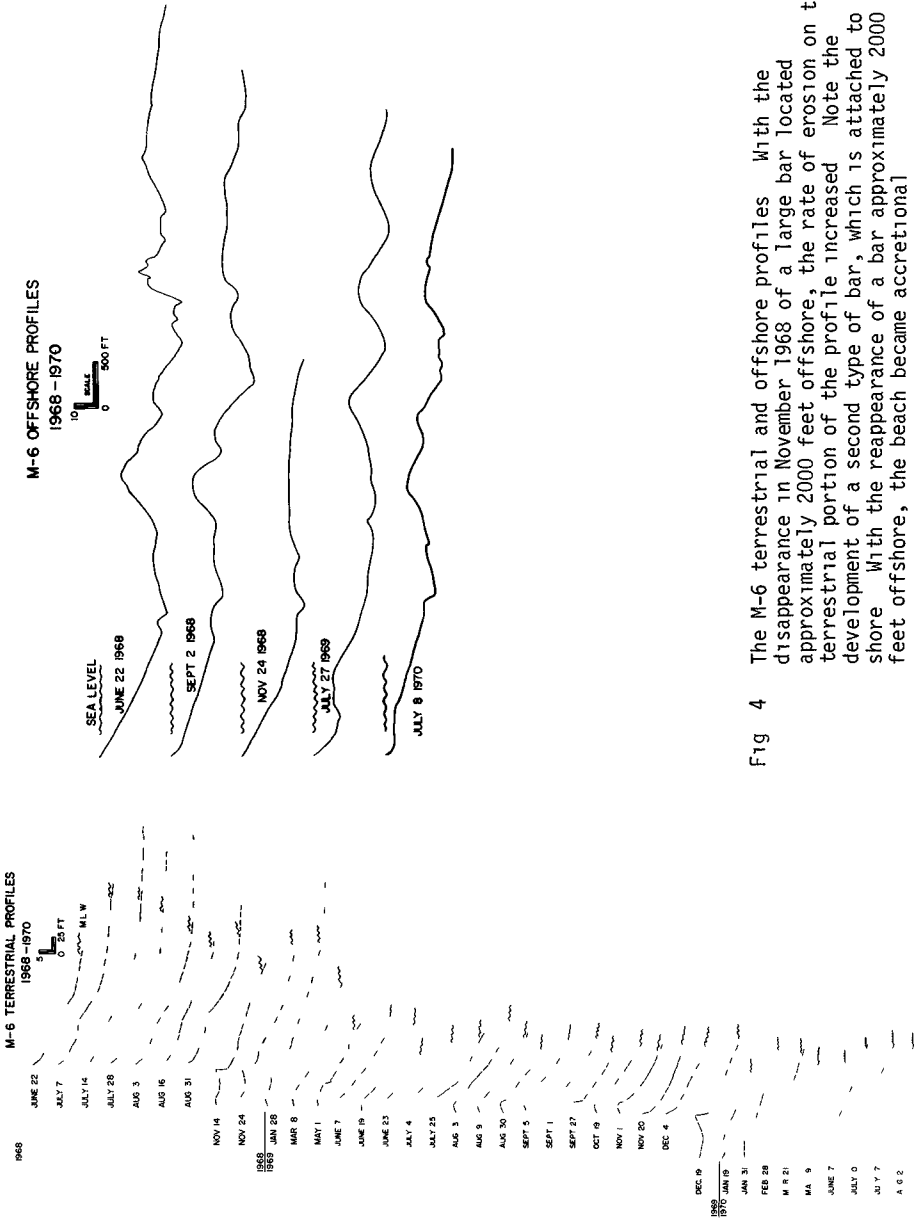


Fig 4 The M-6 terrestrial and offshore profiles. With the disappearance in November 1968 of a large bar located approximately 2000 feet offshore, the rate of erosion on the terrestrial portion of the profile increased. Note the development of a second type of bar, which is attached to the shore. With the reappearance of a bar approximately 2000 feet offshore, the beach became accretional.

approximately 50 feet of accretion. In June 1968 a large bar with an elevation of twelve feet above the adjacent sea bed, was located approximately 2000 feet from shore and oriented parallel to the shore. By November 1968 this bar had disappeared from the profile and the terrestrial portion of the profile had become highly erosional. With the development of a new bar on the profile, as seen in the July 1970 fathometer profile, the rate of erosion decreased sharply and the profile became accretional. Associated with the severe erosion was the development of a shoreline protuberance of sand downdrift from the M-6 profile (Fig. 5).

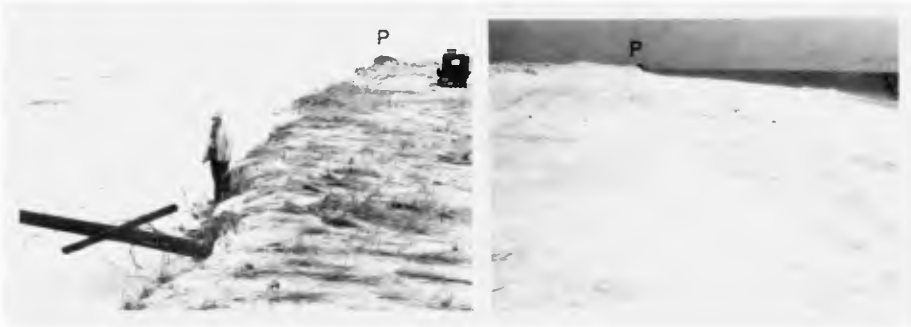


Fig. 5. Two views of the M-6 beach protuberance on December 19, 1969. The updrift erosional zone is shown on the left (looking south), and the accretional zone, downdrift from the view on the left, is shown on the right (looking north). Point P is the same in each photograph.

The offshore extension of the protuberance, in the form of an attached subtidal bar oriented approximately perpendicular to the shoreline, is recorded in the July 1969 fathometer profile (Fig. 4).

The M-4 profile is located at the narrowest part of the island (600 feet wide at high tide), yet it underwent the least amount of change in both the terrestrial and offshore portions of the profile (Fig. 6).

The M-5 profile is located adjacent to a beach protuberance much like the one near the M-6 profile. Therefore, the M-5 profile is similar in behavior to the M-6 profile in that an offshore bar parallel to the shore, is present when the terrestrial portion is accretional and absent when the terrestrial portion is most erosional (Fig. 7). During the erosional

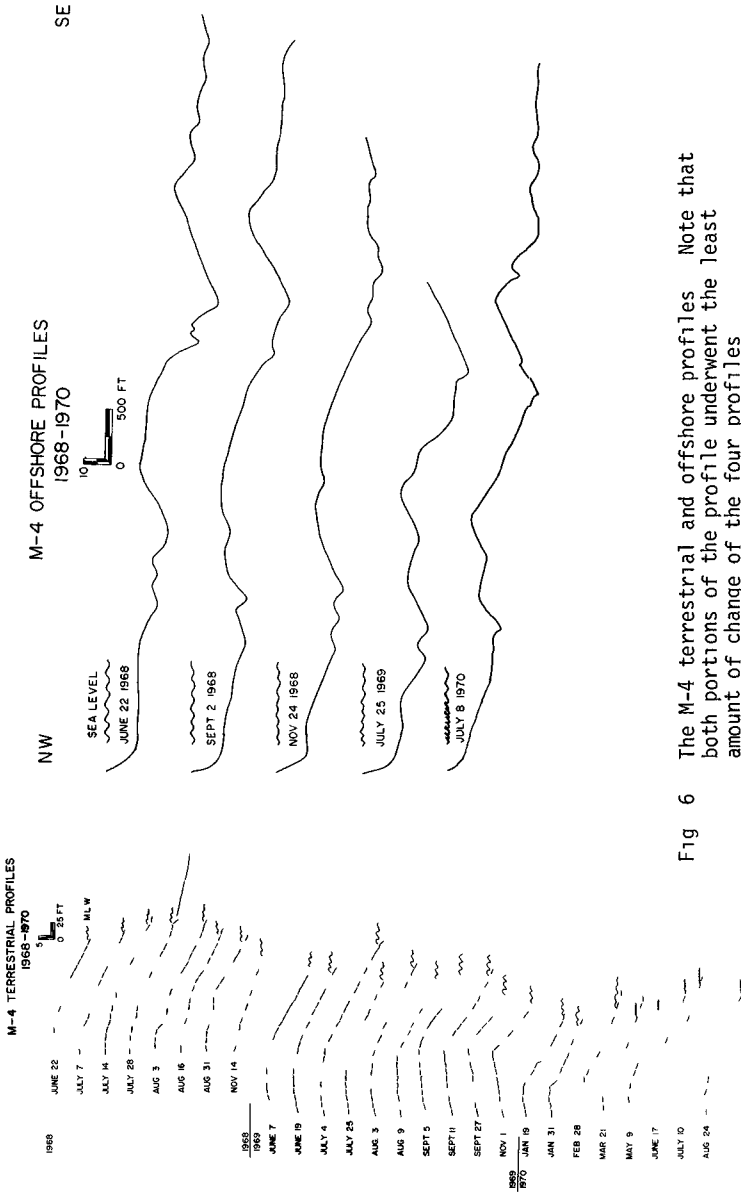


Fig 6 The M-4 terrestrial and offshore profiles Note that both portions of the profile underwent the least amount of change of the four profiles

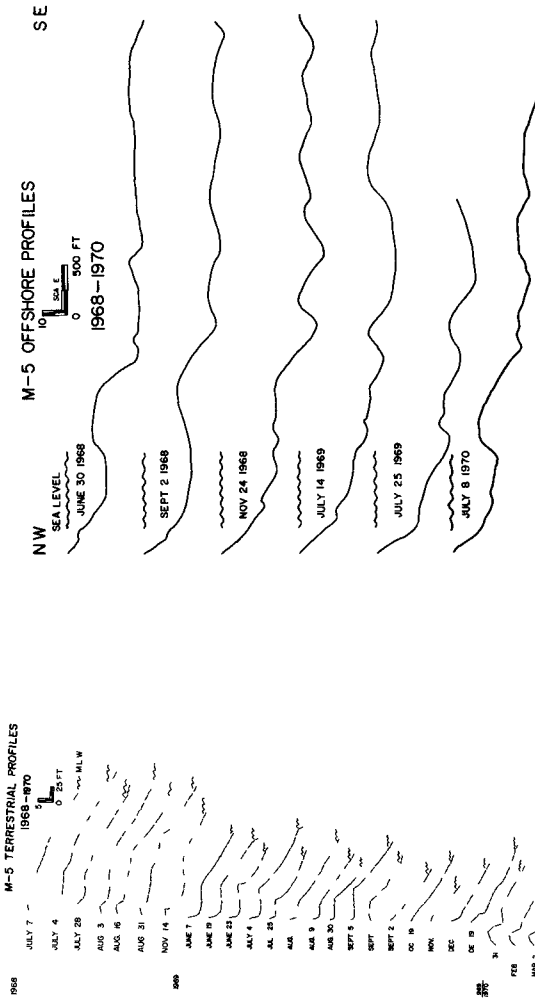


Fig 7 The M-5 terrestrial and offshore profiles. Note that with the disappearance of a large bar approximately 1200 feet from shore in July 1969, the beach became more erosional. With the development of a new bar in the previous location in July 1970 the rate of erosion decreased sharply.

periods the second type of subtidal bar, which is perpendicular to the shoreline, began to form and is recorded on the July 25, 1969, fathometer profile. The close relationship between erosional zones and the presence of subtidal bars perpendicular to the shoreline and attached to the shore is illustrated in Figure 8.

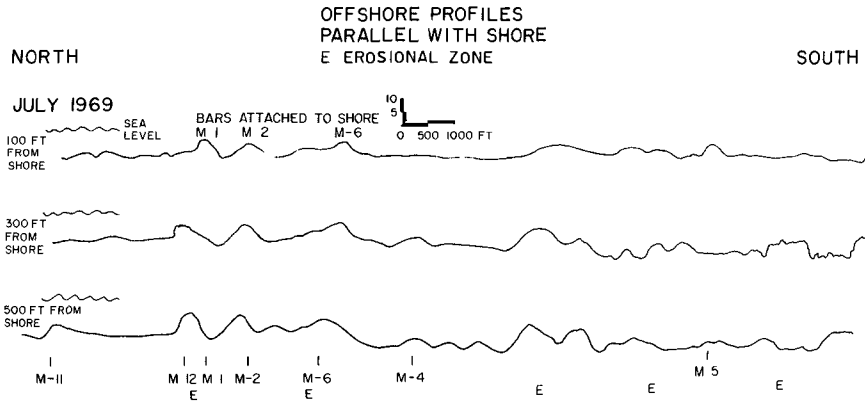


Fig. 8 Fathometer profiles run parallel with, and 100, 300, and 500 feet from shore. The areas of the Monomoy shoreline undergoing the severest amounts of erosion are indicated with the letter E. Note the correlation between the maximum erosion and the presence of nearshore subtidal bars which are perpendicular to the shoreline.

A summary of the erosion or accretion occurring at these four closely-spaced profiles during the 27 months of observations is given in Figure 9 and Table 1. It is readily apparent that there is a large variation in the rate of beach retreat along this shoreline. This suggests the hypothesis that there is a considerable spatial variation in the wave energy arriving at Monomoy Island and that the formation of the beach protuberances can be associated with this nonuniformity of wave energy in the littoral zone.

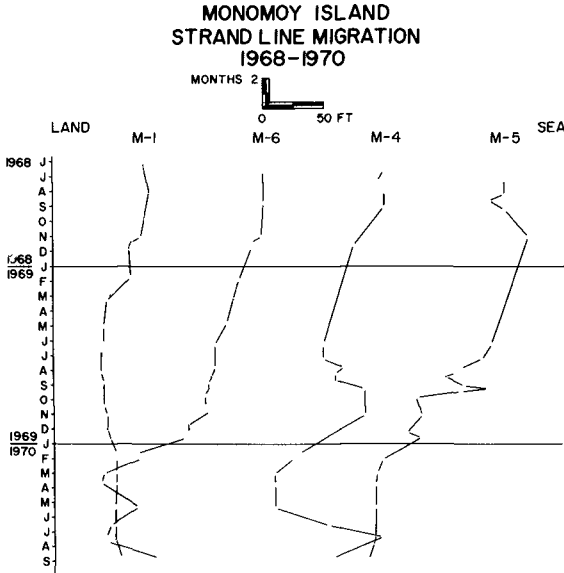


Fig 9 Rates of erosion and accretion at four permanent beach profiling stations located approximately one mile apart on Monomoy Island. Leftward movement of the line under the profile number indicates erosion, while movement to the right indicates accretion.

	<u>M-1</u>	<u>M-6</u>	<u>M-4</u>	<u>M-5</u>
June 1968 - June 1969	35	30	35	0 Feet
June 1969 - March 1970	-10	105	40	75
March 1970 - August 1970	<u>-7</u>	<u>-50</u>	<u>-48</u>	<u>6</u>
TOTALS	18	85	27	81

Table 1 Summary of beach retreat at four profiles on Monomoy Island. Negative amounts signify beach advance (accretion).

WAVE REFRACTION

A mechanism by which zones of wave energy concentration can be produced is illustrated schematically in Figure 10. Waves passing

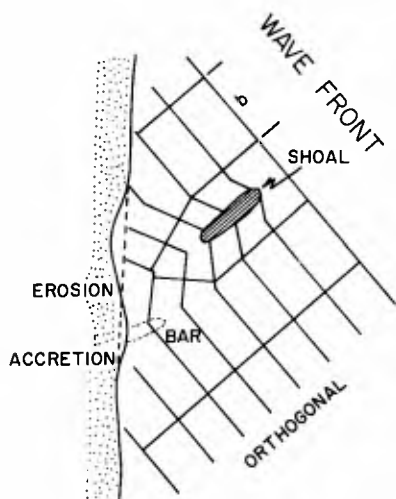


Fig. 10. A schematic diagram (left) illustrates the effects of wave refraction over irregular offshore bathymetry. This process results in differential erosion of the shoreline and causes segments of the shoreline to orient themselves perpendicularly to the dominant wave approach direction. Three beach protuberances are shown in the northward view of Monomoy Island (right).

over the highly irregular bathymetry offshore of Monomoy are refracted such that alternate zones of converging and diverging orthogonals are produced, indicating portions of the wavefront with increased or decreased wave energy concentration. When that portion of the wave front which contains the higher wave energy concentration impinges upon the shoreline, an increased rate of erosion can be expected to occur along that portion of the shoreline.

To test this hypothesis, a series of wave refraction computations were made with the aid of a digital computer (CDC 3600), using the Stanford University Wave Refraction Program originally developed by Dobson (1967) and adapted by the authors for use at the University of Massachusetts Research Computing Center. The computational techniques employed by this program have been summarized by Mogel et al (1970).

The bathymetric grid used in these computations is shown in Figure 11. The wave periods and approach directions chosen for the computations were based on the authors' personal observations of the dominant waves approaching Monomoy, and on deep water observations of the waves in the Marsden Square adjacent to Monomoy as compiled by the National Oceanographic Data Center. The wave refraction diagrams resulting from the computations are illustrated in Figures 12 through 15 on the following pages.

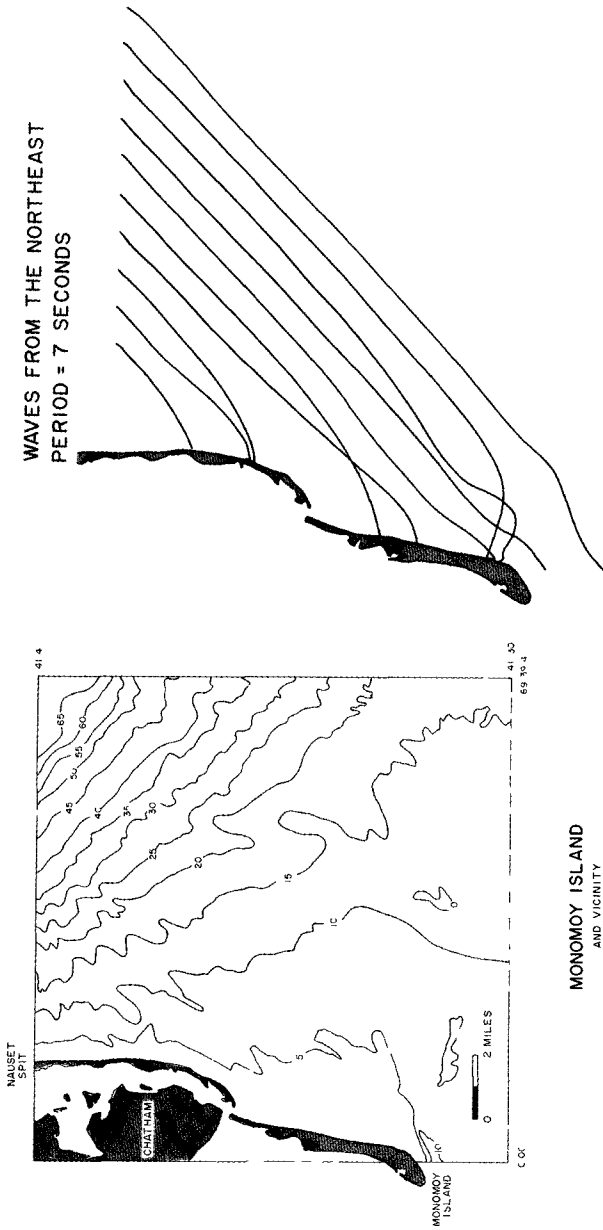


Fig 11 Bathymetric data used in the wave refraction computations covered the area shown as a square grid with a 0.2 nautical mile spacing. The original C & G S Chart (No. 0708N-51) upon which this grid is based has a one-fathom contour interval.

WAVES FROM THE NORTHEAST
PERIOD = 7 SECONDS

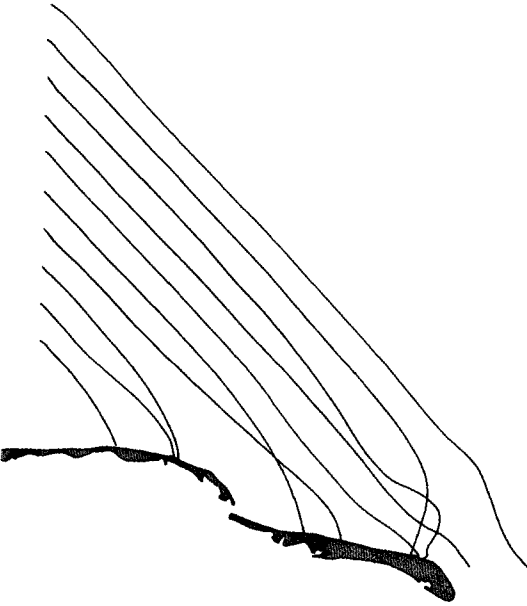


Fig 12 Refraction diagram showing rays (orthogonals) for waves from the northeast with 7-second period. Initial separation of rays is one nautical mile.

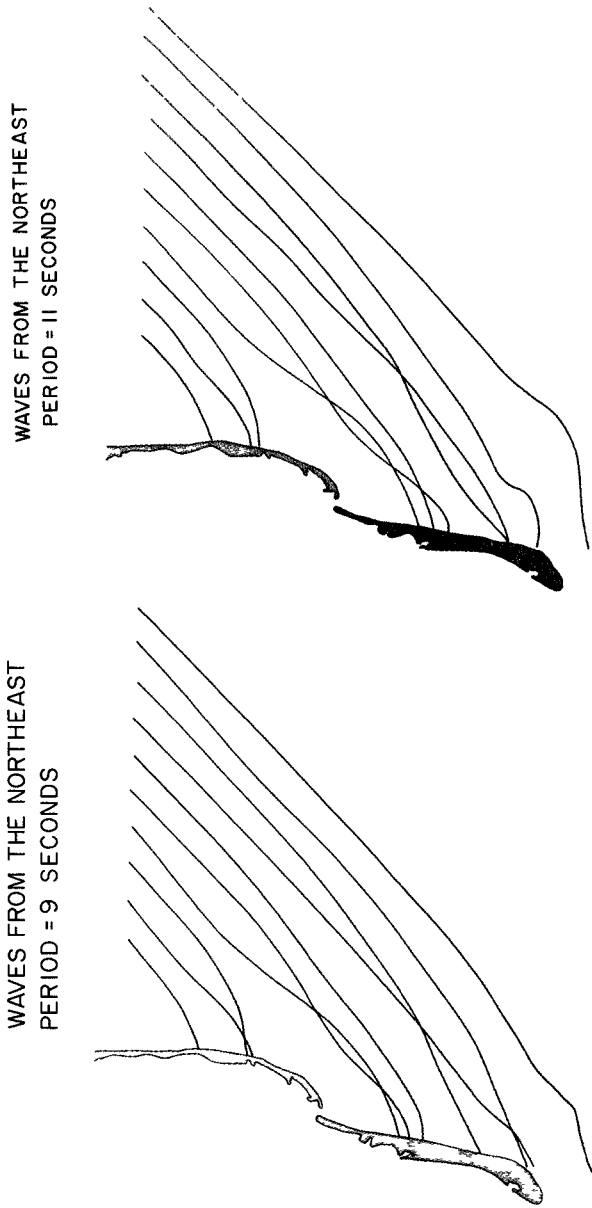
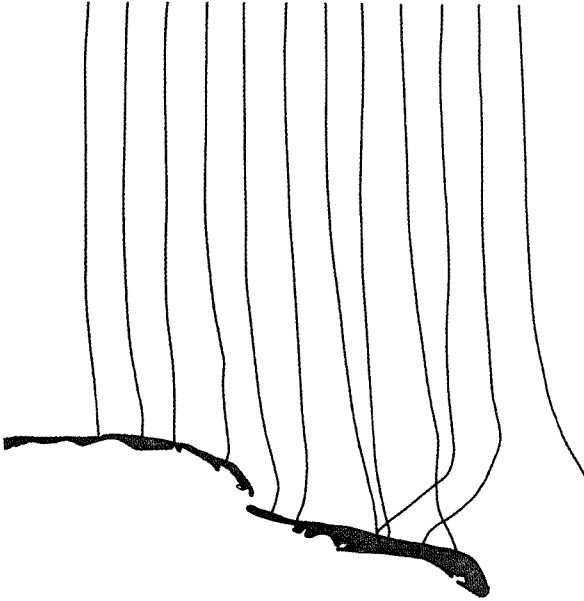


Fig 13 Refraction diagrams showing rays for waves from the northeast with 9-second (left) and 11-second periods (right) Initial separation of rays is one nautical mile

WAVES FROM THE EAST
PERIOD = 9 SECONDS



WAVES FROM THE EAST
PERIOD = 7 SECONDS

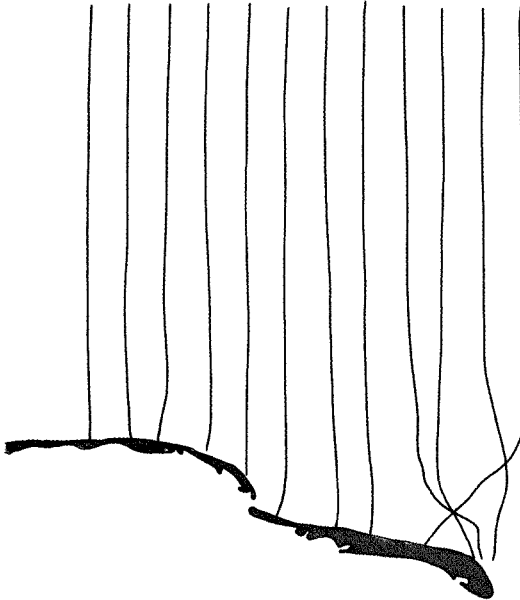


Fig 14 Refraction diagrams showing rays for waves from the east with 7-second (left) and 9-second periods (right) Initial separation of rays is one nautical mile

WAVES FROM THE EAST
PERIOD = 11 SECONDS

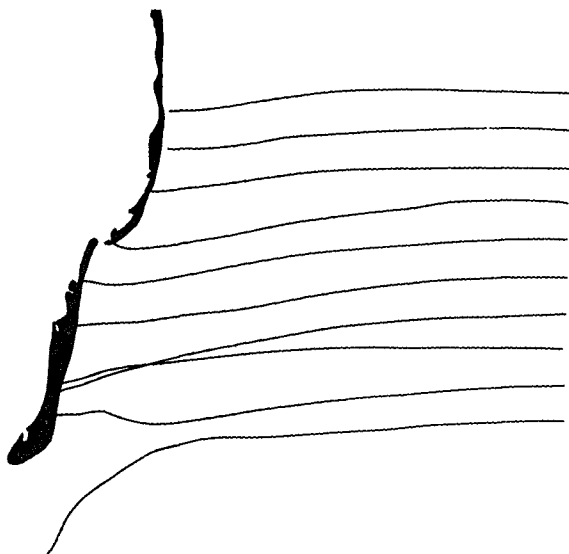


Fig 15 Refraction diagram showing rays for waves from the east with 11-second period. Initial separation of rays is one nautical mile.

CONCLUSIONS

Wave refraction computations indicate that wave energy is distributed rather unevenly along closely-spaced intervals of the Monomoy Island shoreline. Field data suggest a strong correlation between concentrations of wave energy and those portions of the shoreline which are undergoing increased rates of erosion producing shoreline protuberances of sand which are flanked updrift and downdrift by erosional zones. This implies that areas of increased erosion can be predicted by wave refraction computations and that coastline changes resulting from variations in the offshore bathymetry may be similarly predicted.

ACKNOWLEDGMENTS

This work was supported by the Coastal Engineering Research Center, U S Army Corps of Engineers, Contract DACW 72-67-C-0004. Dr Miles O Hayes, supervisor of the project, provided much constructive discussion and criticism. Thanks and appreciation are expressed to members of the UMass Coastal Research Group for their assistance. Special acknowledgment goes to Yvonne Goldsmith, Frank Raffaldi, Wayne Dowdall, John Gifford, Eugene Rhodes, Stewart Farrell, and Richard Callahan, who assisted in the field. The University of Massachusetts Research Computing Center provided support through a grant to cover computer expenses. The U S Fish and Wildlife Service granted permission to conduct the studies and provided storage facilities on the Monomoy Island National Wildlife Refuge.

REFERENCES

- Bakker, W T , 1968, A mathematical theory about sand waves and its application on the Dutch Wadden Isle of Vlieland Shore and Beach, October, p 5-14
- Beek, J van, 1969, Systematic changes of rhythmic beach topography (Abs) Geol Soc of Amer Ann Meeting, p 229
- Bruun, Per, 1954, Migrating sand waves or sand humps, with special reference to investigations carried out on the Danish North Sea Coast Proc Fifth Conf on Coastal Engineering, p 269-295
- Oobson, R S , 1967, Some applications of a digital computer to hydraulic engineering problems Technical Report No 80, Department of Civil Engineering, Stanford University, Stanford, California
- Dolan, R and Fern, J C , 1968, Crescentic landforms along the Atlantic coast of the U S Science v 159, p 637-639
- Homma, M and Sonu, C , 1963, Rhythmic pattern of longshore bars related to sediment characteristics Proc Eighth Conf on Coastal Engineering, p 248-278
- Jordaan, J M , 1964, Effects of hydrographic changes due to nearshore dredger dumping on wave refraction and littoral sand balance Proc Ninth Conf on Coastal Engineering, p 310-322
- Mogel, T R , Street, R L , and Perry, B , 1970, Computation of along-shore energy and littoral transport Proc Twelfth Conf on Coastal Engineering
- Munk, W and Taylor, M A , 1947, Refraction of ocean waves, a process linking underwater topography to beach erosion J of Geol , v 54, p 1-26
- Niederoda, A W and Tanner, W F , 1970, Preliminary study of transverse bars Marine Geology, v 9, p 41-62
- Roberts, J A , 1964, The reshaping of South Beach, Crescent City, Calif , after the tsunami of 27-28 March 1964 Paper presented before the Beach Erosion Control Conf , Calif State Dept of Water Resources, Santa Monica, Calif , 18 p
- Robinson, A H W , 1960, The hydrography of Start Bay and its relationship to beach changes at Hallsands Geogr J , v 127, p 63-77
- Shepard, F P and Inman, D L , 1950, Nearshore circulation related to bottom topography and wave refraction Trans Am Geoph Un , v 31, p 196-212
- Sonu, C J , McCloy, J M and McArthur, D S , 1966, Longshore currents and nearshore topographies Proc Tenth Conf on Coastal Engineering, p 525-549
- Sonu, C J , 1968, Collective movement of sediment in the littoral environment Proc Eleventh Conf on Coastal Engineering, p 373-400

CHAPTER 48

LITTORAL TRANSPORT AND ENERGY RELATIONSHIPS

L. Bajorunas
National Oceanic and Atmospheric Administration
Detroit, Michigan 48226

The littoral transport rates in the Great Lakes were obtained two distinctly different ways, long-term averages from drift accumulations and hourly averages were measured in the St. Clair River which receives sand from Lake Huron beaches. Statistical analysis of both the recorded energy elements and measured sediment transport rates indicates that a combination of energy elements and environmental factors consisting of wave power and duration, current speed, and length of shoreline produces the best correlation with the transport rate. Dimensional analysis expands the process-response model by including sediment-size and specific-weight parameters.

INTRODUCTION

The St. Clair River, which emerges from Lake Huron, carries little sediment during calm lake conditions, however, during storms, it transports significant amounts of sediment from Lake Huron beaches adjoining the river. Extensive measurements were made during the spring and fall of 1965 to determine the amount and characteristics of the sediment transported both in suspension and as bedload by the St. Clair River. Simultaneous recordings were made of the energy elements in Lake Huron that could contribute to the pickup of sediment from the beaches and transportation downdrift into the St. Clair River.

SEDIMENT TRANSPORT

Measurement methods

The St. Clair River heads at the southern end of Lake Huron (Fig. 1) where it passes through a restricted and narrow reach, "The St. Clair Rapids", with water velocities up to 2 m/s and associated extreme turbulence. Exposure to lake waves and very heavy vessel traffic prohibited the use of this reach and, therefore, a river cross-section further downstream was selected for measurement of sediment transport. Insignificant deposition has been observed in the reach of the river between the lake and the metering section, which is at the shoal just downstream of the first river bend and some boat slips.

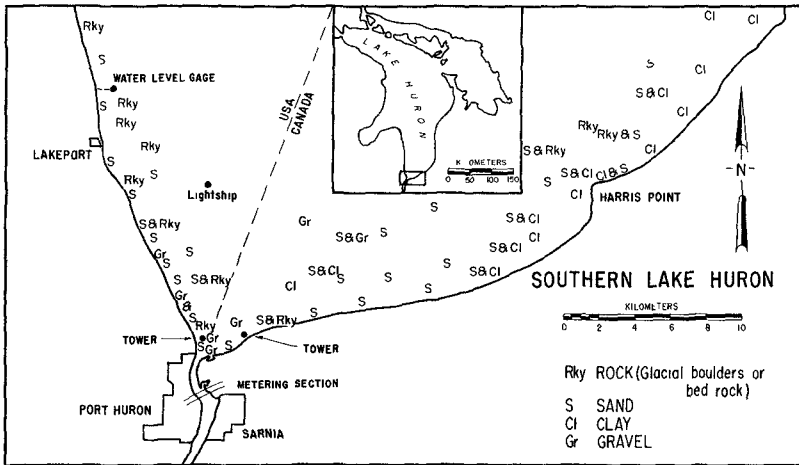


Fig 1 Southern Lake Huron

The river cross-section was divided into eight panels for the purpose of sediment measurement. Water samples were taken and current velocities recorded at 0.1 depth intervals at the mid-vertical of each panel. A second water sampler, simultaneously took samples at a constant 0.4 depth. Each vertical was sampled twenty times, and the complete river crossing produced at least 160 samples. U.S. P-61 suspended sediment samplers and Price current meters were used in the data collection program. The sand moving within five centimeters of the river bottom was trapped in an Arnhem bedload sampler. The time required for sampling one panel, including the time for positioning of the survey boat, was about one hour. It would have been possible to complete a river crossing in a day but weather and heavy vessel traffic caused unexpected delays and on only one occasion was a river crossing completed in a single day.

Transport rates

The measured concentration of suspended sediment by weight ranged from 0.3 to 90 ppm, with an average of about 10 ppm. The sediment transport in suspension was determined using the standard method of the current velocity times the cross-sectional area times the suspended sediment concentration. An average density of 1700 kg/m^3 was used to change the suspended sediment transport rate by weight into rate by volume. Repeated sampling at the 0.4 depth shows that the concentration is subject to considerable variation with time. In addition to the seemingly random variation some regular pulsation in sediment concentration was observed, which in no way can be related with the flow in the St. Clair River.

The bedload was determined by extrapolating the measured rate in the sampler to represent the transport over the panel width. Sediment movement along the river bed amounted to a fraction of one percent of the suspended sediment and was not considered further. The measured rates of suspended and bedload sediment are given in Table 1. Table 1 also lists the sum of the measured values and the estimated total transport in the river. In two cases the measurements were insufficient for a reasonable estimate. Comparison of the measured portion of the transport with the estimated total gives some indication of the magnitude of errors.

TABLE 1 SUSPENDED AND BEDLOAD SEDIMENT IN ST CLAIR RIVER

Date	River panels								Sum of meas	Estim total trans
	1	2	3	4	5	6	7	8		
SUSPENDED SEDIMENT m^3/hr										
14 May	9 2	18 5	14 6	6 2	10 8	8 5*	6 2*	3 0*	59 3	77
17 "	4 1	6 6	5 3	7 3	--	--	--	--	23 3	34
19 "	6 6	12 5	9 2	15 2	9 3	5 9	5 3	2 0	66 0	66
20 "	6 4	8 7	10 9	--	--	--	--	--	26 0	48
21 "	2 7	7 5	13 3	12 9	--	--	--	--	36 4	54
3 Jun	8 9	13 9	10 2	9 2	--	--	--	--	42 2	62
4 "	--	--	--	--	6 8	7 7	5 3	1 9	21 7	68
14 "	22 6	35 6	--	--	--	--	--	--	58 2	160
15 "	15 4*	26 4*	24 2	11 0	12 1	9 9	7 7	3 3	68 2	110
16 "	10 4	16 2	16 4	10 7	--	--	--	--	53 7	79
3 Nov	3 2	--	--	--	--	--	--	--	3 2	--
4 "	22 9	41 5	28 4	37 7	--	--	--	--	130 5	190
6 "	--	--	--	--	10 9	4 1	6 6	3 4	25 0	78
9 "	30 6	46 8	27 0	19 8	19 8	18 0	12 6*	5 4*	162 0	180
10 "	--	--	--	--	--	--	3 6	1 7	5 3	--
18 "	40 5	64 0	46 4	48 6	37 5	--	--	--	237 0	300
19 "	--	--	--	--	--	9 5	8 9	4 4	22 8	110
BEDLOAD SEDIMENT, $10^{-3}m^3/hr$										
19 May	9	10	9	15	9	9	9	6	76	
8 Nov	2	5	7	16	5	14	4	3	56	

*estimated

Sediment Characteristics

A detailed description of the sediments in St Clair River was published by Duane (1967) and, therefore, only a summary is given here. The suspended sediment is mostly of the fine sand size, ranging from 0.11 mm to 0.17 mm, with a few particles reaching 1.0 mm size. Material is dominantly quartz although other minerals and organic matter are present. The bedload sediment size ranges from 0.25 mm to 2.6 mm.

Samples from Lake Huron beaches show the same composition and grain-size characteristics as the suspended load and bedload of the St Clair River. Areal extent of sand along lower Lake Huron is depicted in Fig. 1. Mandelbaum (1966) reported that sediment in the St Clair River delta at the entrance to Lake St Clair contains some finer grain sizes than those measured in the river.

ENERGY ELEMENTS

Elements measured

In addition to the primary variables, wind speed and direction, wave height and period, and current speed and direction, some elements probably only remotely related to the study were recorded, such as barometric pressure, and air and water temperature. Lake level and river discharge data were available from continuous data collection programs on the lakes. Instrumentation was placed at five locations (see Fig. 1) on the Coast Guard Light Ship, on two specially erected towers, and on two submerged tripods. Towers, as described by Duane and Saylor (1966) were placed near the east and west shores in 5.7 m and 6.6 m depths, respectively. Submerged tripods were located between the shore and the towers in 1.5 m depth and supported current meters only. Data pertinent to the sediment sampling periods are listed in Table 2.

TABLE 2 MEASURED ENERGY ELEMENTS

Date	Lake Level m	Wind		East Shore			West Shore		
		Speed m/s	Dir hr	Wave Height cm	Wave Per s	Curr Speed cm/s	Wave Height cm	Wave Per s	Curr Speed cm/s
14 May	175 68	3 3	NE 4	--	--	--	6	3 0	16
17 "	175 77	4 2	W 10	18	3 3	10*	11	3 4	17
19 "	175 76	4 0	N 8	25	3 0	11	17	3 2	20
20 "	175 77	4 3	N 13	--	--	9	12	3 1	18
21 "	175 71	4 2	SE 4	--	--	9	6	3 4	17
3 Jun	175 80	5 5	N 9	40	3 1	9	36	3 2	12
4 "	175 77	3 9	N 6	12	3 0	9	--	--	14
14 "	175 84	7 6	N 34	61	4 2	15*	37	3 6	20*
15 "	175 82	8 8	N 5	77	3 6	18	37	3 5	24
16 "	175 83	7 5	N 3	60	3 2	15*	29	3 2	15
4 Nov	176 02	5 6	N 11	64	7 5	27	53	4 1	15*
6 "	175 86	3 8	S 25	8	3 7	3	--	--	21
9 "	175 92	4 3	NW 22	41	5 2	40	46	4 5	10
18 "	175 92	5 3	W 42	31	6 2	110	--	--	--
19 "	175 89	1 8	W 15	29	5 4	10	--	--	--

Recorded current direction on the listed days was towards the St Clair River despite the variable winds.

*estimated

Overwater wind was recorded at the two towers and at the Light Ship. The wind over this rather small area was quite uniform. The data listed were obtained from the tower near the west shore. Wind persistence was defined as the period of time prior to sediment sampling having essentially the same wind speed and direction as that recorded during the sediment sampling period. All higher wind speeds, lower speeds of less than one hour duration, and deviations of less than 45° in direction were included in the determination of persistence.

Waves were also recorded at the two towers and near the Light Ship. The wave gage near the Light Ship was difficult to maintain due mainly to excessive cable length. The data recorded at this location were insufficient for analysis. Wave recordings taken at the two tower locations were more successful, but even in these locations some records were missing, as was the case on 18 November when the highest sediment movement was measured. Heights listed in Table 2 are of significant waves, which are defined as four times the standard deviation of the wave gage record. The linear average values read from wave spectra curves produced by the Coastal Engineering Research Center were multiplied by a factor of 2.7 to obtain significant waves. The 2.7 factor was derived from data by Cole (1967). The wave periods are those at which maximum energy was produced. Analyses of several 20 minute wave records taken at different times during the sediment sampling period were averaged to obtain the listed values. No attempt was made to estimate the missing waves from wind records. Cole concluded on the basis of carefully recorded wind and wave data that existing wind and wave relationships were producing marginal results.

Currents were recorded at four locations. One current sensor was attached to each tower and the other two sensors were placed on the two tripods. The propeller type current sensors were placed in a tube about 10 cm above the bottom. These so-called ducted current meters were responsive to currents along the axis of the tube, which was oriented parallel to the shoreline. The direction indicator was freely suspended and assumed the direction of dominant current. Current speed and direction were both recorded, however, Table 2 lists only current speeds recorded on the tripods. The currents at the times listed were always toward to the head of the river. The meters frequently jammed during operation due to sand particles or weeds lodging between tube and propeller. Some missing current data were estimated with reasonable accuracy either from the records immediately preceding or following the missing records or from the currents recorded on the towers. The estimated values are so indicated.

Lake Huron levels and outflows are recorded by the U. S. Lake Survey. Levels are recorded by five water-level gages, with those recorded at the Lakeport gage listed. In addition to the long-term gradual change of lake levels caused by the changing water volume there are frequently quite large local water level changes caused by wind and barometric pressure. In contrast with the oceans, lunar tides in the Great Lakes are quite small, not exceeding 15 cm. During the sediment sampling periods, however, only insignificant short-term changes in lake level were recorded. The flow in the St. Clair River has a small day-to-

day variation and was gradually increasing from 4700 m³/s in May, to 4900 m³/s in June, and to 5200 m³/s in November

ANALYSIS OF TRANSPORT FACTORS

Littoral transport is affected by numerous factors basically related to the sediment supply and characteristics, and energy in its various forms. A brief discussion of the more obvious factors and their numerical evaluation follows.

Sediment Characteristics

Recent investigations utilizing both models and the natural environment point to the important effect the sediment size distribution has on the movement rate in littoral environments. However, no agreement exists on magnitude of that effect. A comprehensive study of sediment movement in the ocean environment was made by Ingle (1966). He found that sediment transport doubles with the change in sediment size from 0.14 mm to 0.20 mm, and increases by 20% for the change from 0.20 mm to 0.28 mm. Model studies by Larras (1966) indicate that the maximum transport takes place when the median diameter of the sediment is 0.9 mm. Material finer or coarser than this moves at significantly lower rates. For example, fine sand of the size on Lake Huron beaches moves at one third the rate of the 0.9 mm size sediment. Contrary findings are reported by Iwagaki and Sawaragi [Homma, (1966)]. Their equation indicates that sediment movement decreases with increase of the square root of sediment diameter. In present study the dimensional analysis, discussed later, indicates that transport increases with the square root of sediment size. This is in general agreement with findings by others for the fine to medium sand.

Sediment must be freely available along the shoreline for equilibrium to exist between energy and the volume of sediment in movement. In the study area, sand on the east shore extends northeastward for about 20 km and ends before Harris Point. The areal extent of sand on the west shore cannot be clearly assessed, although it is estimated to be in the order of 20 km. Sediment movement in this location is somewhat retarded by scattered rocks of glacial origin.

Effective Shoreline and Wave Duration

Two limiting factors in sediment transport must be considered: the length of unobstructed shoreline and the duration of wave action. The wave duration is the limiting factor for very long shorelines, however, long shorelines without either natural or man-made barriers to sediment movement rarely exist. More frequently the length of unobstructed shorelines sets the limit to sediment transport. This phenomenon in nature, however, is rather complex due to the continuous variation of both the energy elements during a storm and the sediment characteristics along a shoreline. Statistical methods must therefore be applied when considering observations in nature. The effect of shoreline length was investigated by Bajorunas (1961) based on long-term drift accumulation on the updrift side of harbors or natural barriers. Present

investigations consider a variable duration of wave action over a given length of shoreline Persistence of wind speed and direction is used here as an index of the duration of waves

Effective Shoreline in the 1961 study varied from 2 to 67 km with the wave duration undetermined Since sediment data was obtained from accumulations extending over long periods, sometimes exceeding 90 years, it seems that any reasonable wave duration could be applicable and that the transport is, therefore, limited by the effective shoreline rather than by wave duration It is difficult to isolate the effect of the shoreline in the empirical littoral transport and energy equation derived in 1961 It was therefore necessary to replace that equation

$$Q = 19 E_0 \sin \alpha_0 (1 - e^{-0.023S \cot \alpha_0}) \tag{1}$$

by the theoretically less desirable

$$Q = 4.5 E_0 \sin 2\alpha_0 (1 - e^{-0.04S}) \tag{2}$$

where Q is the annual littoral transport, cubic yards in equation (1) and m³ in (2)

E₀ is the annual deepwater wave energy, millions of foot-pounds in equation (1) and 10⁶ joules in (2)

S is the effective length of shoreline, miles in (1) and km in (2)

α₀ is the angle between the shoreline and the wave crest

Fig 2 contains the 1961 data which depicts transport per energy unit versus the effective shoreline

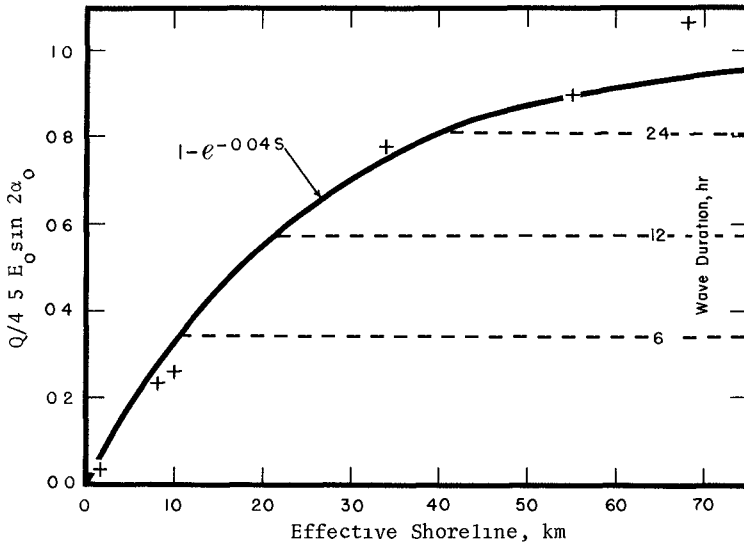


Fig 2 Effect of shoreline on littoral transport

Wave Duration in the present study was based on recorded wind persistence and varied from 3 to 34 hours while the effective shoreline was about 20 km. Data in Fig 3 indicate that the wave duration is a significant factor in sediment transport if less than about twelve hours. The effective shoreline becomes the determining factor for longer periods and on these occasions the transport per energy unit remains more or less constant. The effect of wave duration was expressed mathematically as $(1 - e^{-0.07D})$ based on meager field data and on the assumption that it must have an exponential form similar to that derived for effective shoreline.

The dependence of drift rates upon both the wave duration and effective shoreline requires selection and use of that factor which restricts the transport more.

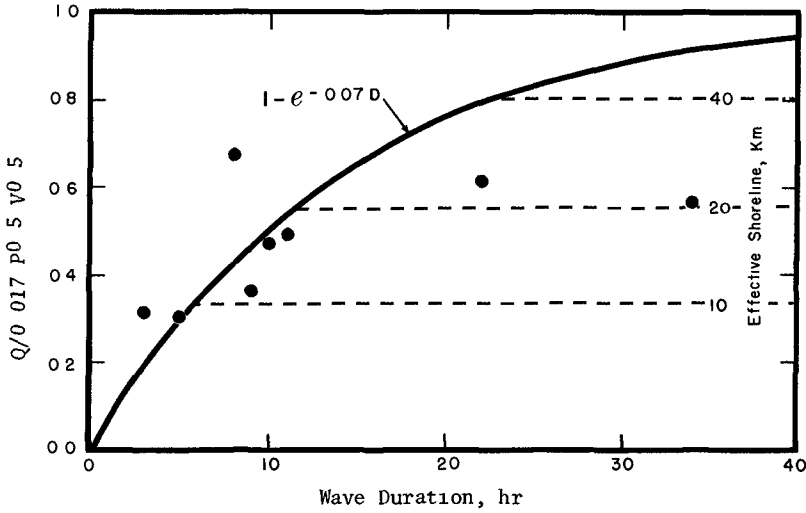


Fig 3 Effect of wave duration on littoral transport

Energy Elements

Wave power, as used here, was derived from wave energy and wave frequency. The wave energy per unit width of wave crest is expressed as

$$E = 0.125 \gamma H^2 L \tag{4}$$

where γ is specific weight of water
 H is wave height
 L is wave length

Considering the rather small waves in this particular case, the correction for wave shape was deleted and the wave length was expressed by $gT^2/2\pi$, where T indicates wave period. The energy transmitted to the

shore by wave train in a time period t is equal to $E_t = nEt^{-1}t$, where n is the ratio of wave group velocity to the phase velocity and is, in this case, approximately 0.5. The wave energy exerted over a time period t is thus

$$E_t = (32\pi)^{-1} \gamma g H^2 T t \quad (5)$$

The above equation is correct for any unit system. The equation can further be simplified to $E_t = 960 H^2 T t$, if the international system (SI) is used where the wave energy is expressed in joules. To conform with the sediment transport, $t = 3600$ s was used here. Wave frequency, if considered as an independent factor, greatly improves the correlation between sediment transport and energy elements. The combination of wave energy and wave frequency results in wave power ($P = Ef$), where the wave height is the only significant element. This would indicate that the wave height and not the wave length or wave period has an effect on the transport rate.

Currents It becomes obvious from the analysis of the data collected, that wave energy alone or in combination with the angle of wave approach is not sufficient to define the movement of material. In this particular location, moreover, with its prevailing winds from the west and currents from the east, the results would be erroneous. When the waves and currents come from differing directions the sediment saltation is necessarily complex, however, net movement in the study area was always in the direction of the currents. One can speculate then that waves lift the material and the currents transport it in the direction of flow. Previous observations of shoaling in a harbor also indicate that sediment moves in the direction of currents [Bajorunas and Duane, (1967)]

Investigations of lake currents by Saylor (1966) indicate that currents generated by winds reach equilibrium with the wind at about 0.033 of the wind speed. This occurs in a rather short period of one to three hours. Currents persist for days after wind cessation, and therefore have quite stable patterns in geographic locations where certain winds prevail, such as the Great Lakes with their predominantly westerly winds. Currents in the open lake flow 10-15 degrees to the right of the wind direction with current speed and direction practically independent of surface wave activity. Currents in nearshore locations are modified by shoreline configuration and, depending on that configuration, might flow against the wind. Occurrences of this type were recorded frequently in the study area. The data establishes a strong relationship between the volume of sediment being transported and the current speed. There is no apparent upper limit for this relationship.

RELATIONSHIPS

Logarithmic plotting (not shown) of the rate of sediment transport, adjusted for effective shoreline and wave duration, against a factor consisting of a combination of wave power and current speed indicates that transport is directly related to the square root of this factor and the relationship can be expressed as follows if $f(S,D)$ denotes the

limiting effects either of the shoreline or the wave duration

$$Q = 0.39 x (P v)^{0.5} f(S, D) \quad (6)$$

where x represents the unknown dimensions of the numerical factor. Analysis indicates that sediment characteristics, expressed by sediment size d and by specific weight of sediment in water $g(\rho-1)$, will satisfy the dimensional requirements. Average values of the sediment in the study area, $d = 0.14$ mm, and $\rho = 2.4$ g cm⁻³, allow us to determine the numerical value of x . Thus, the equation (6) becomes

$$Q = 3.9 [P v d (\rho-1)^{-1} g^{-1}]^{0.5} f(S, D) \quad (7)$$

where Q is littoral transport, m³/hr

3.9 is constant, dimensionless factor

P is wave power, J/s, computed as hourly wave energy times wave frequency

v is nearshore current speed, m/s

d is average sediment size, mm, fine to medium sand sizes only

ρ is sediment density, g cm⁻³

g is acceleration due to gravity, ms⁻²

$f(S, D)$ is the lower value of either $(1 - e^{-0.04S})$ or $(1 - e^{-0.07D})$

where S is effective shoreline, km, and D is duration of waves, hr

Fig. 4 provides a comparison of the measured transport with that computed by equations (2) and (7)

SUMMARY

The littoral transport rates in the Great Lakes were obtained two distinctly different ways. The long-term averages were derived from drift accumulations over periods sometimes exceeding 90 years on the updrift side of harbors or natural barriers. The hourly averages were directly measured in the St. Clair River into which sediment moves from Lake Huron beaches. At the same time sediment characteristics were determined and recordings of the energy elements analyzed to relate them with the measured sediment transport rates.

Analysis of data indicates that

1. Wave power and nearshore currents are the main elements in sediment movement. On occasions when the current is flowing counter to the waves, sediment moves with the current. One can speculate that waves are lifting material and the current is transporting it in the direction of flow. Transport rate is directly related to the square root of wave power and current speed.

2. Length of sediment-contributing shoreline, exposed to waves and currents, is a significant factor in determining the transport rate. Analysis of data on shorelines varying from 2 to 67 km in length indicates that transport grows exponentially with the shoreline length towards a steady-state value.

3. History of acting elements, as expressed by wave duration,

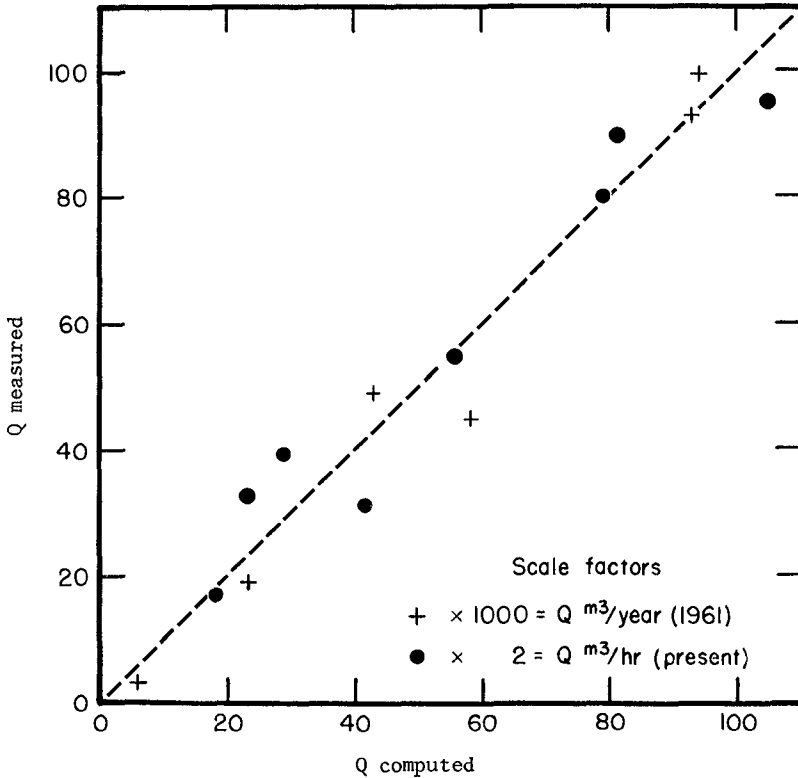


Fig 4 Comparison of measured littoral transport with computed

helps to explain the transport growth and is a limiting factor in cases of short wave duration on a long shoreline. Wave duration, which varied from 3 to 34 hours, has a similar effect to that of shoreline length, the effect increases exponentially with the increase in duration towards a steady-state value.

4 Transport increases with the square root of sediment size. This conclusion was reached indirectly by dimensional analysis and generally agrees with observations in oceans and models for the fine and medium sand size.

5 Equations utilizing wave energy, angle of wave approach, and shoreline length could provide reasonable estimate of sediment movement on an open shoreline along which the wind, waves, and current progress in the same direction. They would fail, however, in the complex wave and current environment, in such environment the nearshore current speed and direction is an essential factor.

ACKNOWLEDGEMENTS

The field collection of data, laboratory procedures, and analysis were carried out in connection with the general research program of the Great Lakes Research Center, U S Lake Survey, Army Corps of Engineers. Permission granted by the Chief of Engineers to publish this information is appreciated. Fieldwork was directed by Dr D B Duane, presently with the U S Army Coastal Engineering Research Center. Essential assistance was provided by Mr W P Ward in analysis of the sediment data and Mr P C Liu in wave energy calculations.

REFERENCES

- Bajorunas, L (1961) Littoral transport in the Great Lakes, Proc 7th Coastal Eng Conf, Council on Wave Res, Univ Calif, Berkeley, 326-341
- Bajorunas, L and Duane, D B (1967) Offshore bars and harbor shoaling, J Geophys, Res, 72, 6195-6205
- Cole, A L (1967) An evaluation of wind analysis and wave hindcasting methods as applied to the Great Lakes, Proc Tenth Conf Great Lakes Res, Intern Asso for Great Lakes Res, Ann Arbor, Mich, 186-196
- Duane, D (1967) Characteristics of the sediment load in the St Clair River, Proc Tenth Conf Great Lakes Res, Intern Asso for Great Lakes Res, Ann Arbor, Mich, 115-132
- Duane, D B, and Saylor, J H (1966) Portable Great Lakes research towers, Proc Ninth Conf Great Lakes Res, Intern Asso for Great Lakes Res, Ann Arbor, Mich, 295-300
- Homma, M (1966) Coastal sediment studies in Japan, Univ of Tokyo, 11 p
- Ingle, J C (1966) The movement of Beach Sand, Univ of S Calif, 221 p
- Larras, J (1966) Cubes de sable charries par la houle parallelement a la cote, Annales des Ponts et Chaussees, Paris, 71-76
- Mandelbaum, H (1966) Sedimentation in the St Clair River delta, Proc Ninth Conf Great Lakes Res, Univ of Michigan, Ann Arbor, 192-202
- Saylor, J H (1966) Modification of nearshore currents by coastal structures, Misc paper, Lake Survey District, Corps of Engineers, Detroit, Michigan, 14 p

CHAPTER 49

SYNOPTIC OBSERVATIONS OF SAND MOVEMENT

David B Duane
Chief, Geology Branch
U S Army Corps of Engineers
Coastal Engineering Research Center
Washington, D C

ABSTRACT

The U S Army Corps of Engineers' Coastal Engineering Research Center, in cooperation with the Atomic Energy Commission, initiated a multi-agency program to create a viable radioisotopic sand tracing (RIST) program. Other agency participants in this program have been the Los Angeles District, Corps of Engineers, U S Air Force (First Strategic Aerospace Division), U S Navy (Pacific Missile Range), U S Army Mobility Equipment Command, National Aeronautics and Space Administration, and the State of California (Dept of Navigation and Ocean Development). CERC, together with the AEC's Oak Ridge National Laboratory has developed tagging procedures, hardware development, field surveys and data handling techniques that permit collection and analysis of over 12,000 bits of information per hour over a survey track of approximately 18,000 feet. Data obtained with the RIST system can be considered as nearly synoptic observations of sediment transport in a single environmental zone or in adjacent beach, surf and offshore zones.

Using sand tagged with isotopes of gold, experiments have been carried out at several sites on the California coast: Surf, Point Conception area, Point Mugu, and Oceanside. Data from the studies carried out in beach areas unmodified by littoral barriers indicate that under a given set of wave conditions the alongshore velocity of sediment transport differs from zone to zone such that transport seaward of peaking-breaking waves < transport on the beach face < transport in the plunge and surf zone. Because of these differences, tracing surveys confined solely to the foreshore or offshore zones produce data only partially indicative of transport in the zone of immediate concern to coastal engineers.

INTRODUCTION

Recognizing the engineering need to better understand coastal processes, the U S Army Corps of Engineers' Coastal Engineering Research Center, in cooperation with the Atomic Energy Commission, initiated a multi-agency program to create a viable radioisotopic sand tracing (RIST) program. To date cooperating agencies have included the Los Angeles District, Corps of Engineers, U S Mobility Equipment Command, the U S Air Force 1st Strategic Aerospace Division and Western Test Range, U S Navy Pacific Missile Range, the National Aeronautics and Space Administration, and the State of California Department of Navigation and Ocean Development. In addition to the development of the techniques and technology necessary to trace nuclide labelled particles in the marine environment objectives can be summarized as understanding the mechanics

of sediment movement, both entrainment and transport, patterns of movement, and the volume of sediment movement. Relative to the application of these goals to engineering needs, field experiments have been carried on straight coastal segments unaltered by engineering works as well as coastal segments effected by engineering works such as groins and harbor jetties.

Tagging procedures, hardware development, field surveys and data handling techniques have been developed in cooperation with AEC's Oak Ridge National Laboratory that permit collection and analysis of over 12,000 bits of information per hour over survey track of approximately 18,000 feet. Details of model studies, tagging procedures, detection instrumentation, and data handling are discussed elsewhere in these proceedings (James, Acree et al, and Brasheer et al). However for clarity and perspective some statements about these items are necessary to this discussion. Search for isotopes and tagging procedures suitable for sand tracing have emphasized two criteria, health physics and the engineering behavior of tagged sand (Duane and Judge, 1969, Acree et al 1969). To date, isotopes of gold (198/199) have been used most extensively. The gamma energy (0.4 Mev) is suitable as is the three day half life.

Sand indigenous to a study area is collected approximately 4 weeks before the scheduled field experiment and shipped to Oak Ridge National Laboratories where it is tagged and returned via common carrier to the field site. Tagging is a surface tag but is done in such a manner as to simulate a mass tag (Stevens, et al 1969). Tests were conducted at CERC to determine if the gold tagging process modified the characteristics of the untagged sand. No detectable differences in specific gravity occurred and there was no observable change in the shapes of grains. Overall hydraulic equivalence of the tagged sand to the naturally occurring sand was demonstrated by granulometric analyses conducted on the CERC Rapid Sediment Analyzer (a device used to determine the grain size distributional characteristics of sediment, especially grains in the size range from 62 to 2,000 microns, as they settle through a 1-meter column of water). Distance to be covered and areas involved in most field operations require a mobile detector system with continuous transmission of data to an on-board data recording system. The detector vehicle developed is a ball like device which is towed behind an amphibious vehicle (Fig 1). Signal from the detectors is transmitted by cable to the recording system on-board the amphibious vehicle. By means of a programmed interrogator other data pertinent to surveying is coordinated with the radiation data and read into the real time data display and on to punched paper tape.

Surveying is accomplished at a speed of approximately three knots (5 ft per second). Data obtained with the RIST system can be considered as nearly synoptic observations of sediment transport in a single zone or on adjacent beach inshore and offshore zones.

FIELD EXPERIMENTS

Field experiments involving tracing of sand simultaneously in one or more of the three environmental zones have been carried out at several California

sites Surf, Pt Conception, Pt Mugu, and Oceanside. In each program at least one shore perpendicular line source was emplaced and followed for several days as the dispersal pattern continued to grow. In some programs a point source was also utilized to more specifically identify the movement of sand from a particular location. During most recent experiments conducted at Pt Mugu, as well as on the small beach in the harbor at Oceanside, patterns of sediment movement were observed that were similar to those observed during the initial experiments at Surf (Duane, 1970). These indicate that the observed patterns are real and operative on any beach, and indicative of natural processes.

At Pt Mugu the first line source (comprised of 30 packets each containing approximately 15 cc of sand in water soluble material and placed 30 feet apart) was emplaced from approximately -3 ft MLLW to -30 ft MLLW. Two wave sets were active: a shorter period higher wave from the west was dominant. The first RIST survey was made 5 hours after injection (Fig 2). Evident is a rapid dispersion in the swash zone, movement upcoast is greater in the breaker and surf zone than on the beach face. At least one survey per day was made for the next 3 days as the dispersal pattern developed. Swell during the 3 days was from the southwest $H = 3$ to 5 ft, $T = 12$ seconds, superposed was a wind chop directed from the northwest with an 8 second period. Currents seaward of the breaker zone were north as were those measured in swash zone, although some reversals there were noted. Typical of currents measured offshore are depicted in Figure 3. Seventy-two hours after injection a zone apparently void of tagged material separated the offshore zone from the inshore zone and the beach face. This zone void of labelled sand coincides with the approximate seaward limit of the zone of peaking and breaking waves.

On 28 September oceanographic conditions changed and a second line injection was made, approximately 1,000 feet downcoast. This line extended from approximately -1-foot MLLW to approximately -18 ft MLLW. Patterns of sediment movement observed from this injection are unidirectional. Swell during the next several days was from the northwest $H = 3$ ft $T = 12$ sec. Currents offshore and in the swash zone were downcoast (Fig 4). Zonal differential transport rate exists but is not of the same relative magnitude as that observed previously, movement of sand towards the beach face is also evident (Fig 5). The gap in radioactivity along the injection line and observed at the first Pt Mugu drop coincident with the low tide breaker zone developed rapidly and seemed to grow in width. To gather additional data on the movement of sand in and from the breaker zone during oceanographic conditions then extant, a point source was emplaced there. The dispersal pattern of tagged sand was monitored three times in 27 hours. Obvious movement is alongshore and to the beach and alongshore (Fig 6). Greatest alongshore rate is in the breaker zone and not the beach face. No tagged sand was observed to move seaward through the surf and breaker zone.

The oceanographic mileaux adjacent to an engineering structure such as a breakwater is somewhat different than the mileaux adjacent an unmodified coastal segment. This is amply demonstrated by the water depth in which sand was observed moving at Oceanside -28 ft MLLW (Fig 7). This depth is nearly twice that observed offshore at Pt Mugu, and under closely similar wave conditions. At Oceanside during the time of observations, no sediment was noted moving through the structure. Clearly observed, however, was southward

jetty and shore-parallel movement of nuclide labelled sand up to and slightly into the harbor entrance under a southerly directed current and wave regime (Fig 8) Several days later under northerly directed wave and current regime two point sources of labelled sand, were emplaced one in the harbor entrance at -18 ft MLLW and one offshore at -30 ft MLLW Evident is a bifurcating transport system The sand placed in the harbor entrance moved into and down the dredged channels, the seaward point source moved northward parallel to the bottom contour and did not enter the harbor (Fig 9)

SUMMARY

During periods when only one wave train impinges on the coastline unidirectional transport is evident In these instances, marked truncation of labelled sand occurs updrift (within 10 ft) of the injection site Further these data indicate that under given wave conditions the alongshore velocity of sediment transport differs from the offshore zone through the inshore zone to the beach face such that transport seaward of peaking - breaking waves < transport on the beach face < transport in the inshore (plunge and surf) zone A conceptual model for this process is illustrated in Figure 10 Dimensions of these zones would change with tide and wave regime

Present technology and techniques make the RIST system a useful engineering and research tool However, while the identification of the zonal differential transport rate as well as the pattern of sediment movement is of some use to the practicing engineer, full practical value into design considerations will not be reached until the zonal volume rate of transport is obtained Types and dimensions of sedimentary structures observed offshore, in the surf zone, and on the beach are indicative of differing depths of active sand transport Isotope data and plugs of fluorescent and radioactive sand also indicate differing depths of sand movement in different environmental zones These differences, coupled with the differing lateral transport rates introduce complexities to realistic determination of volume sediment movement in the nearshore zone Simple diffusion models are unsuited and any studies confined to one environmental zone cannot relate the true picture of sediment transport in the nearshore zones important to the coastal engineer Work within the RIST program is continuing toward a solution to the problem of volume rate of sand transport with indications of some success although it is premature to report that progress herein

REFERENCES

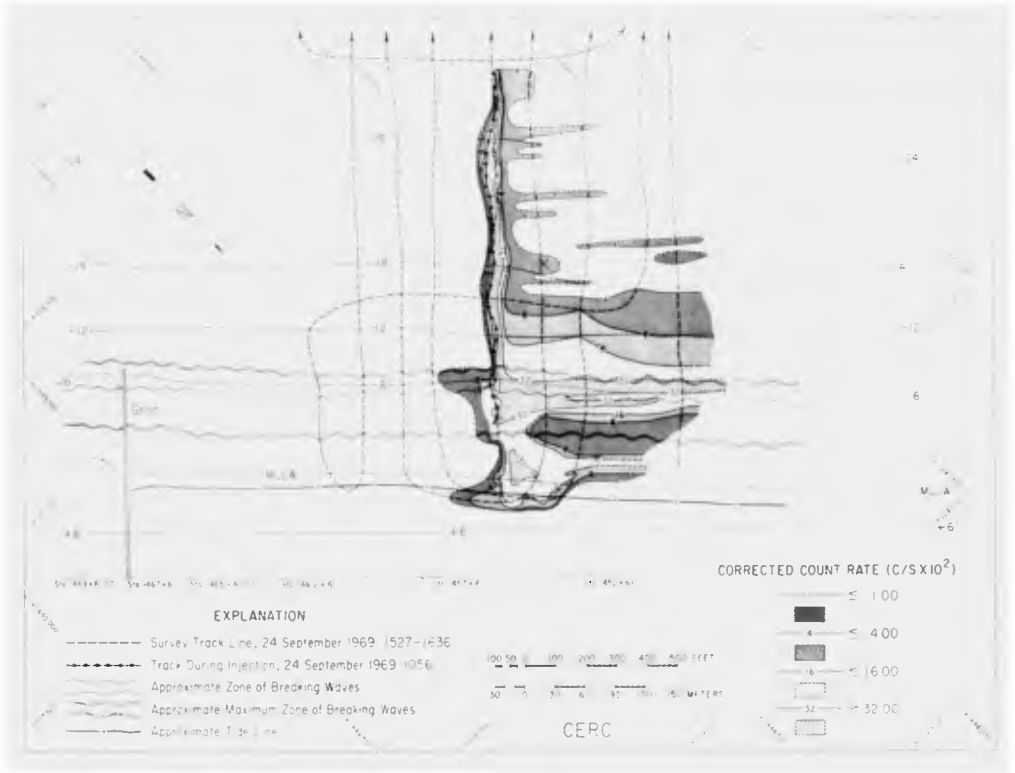
- Acree, E H , Case, F N , Cutshall, N H , and Brashear, H R , (1969), "Radioisotopic Sand Tracer Study (RIST) Status Report for May 1966-April 1968", ORNL-4341, Contract No W-7405-eng-26
- Acree, E H , Brashear, H R , & Case, F N (1970), "A System for Tracing Radio-nuclide-Tagged Sand", (this volume)

- Brashear, H R , Acree, E H , Case, F N , Turner, P A , and Duane, D B
(1970), "Analysis of Radioisotopic Sand Tracer Study Data" (this volume)
- Duane, D B , (1970), "Tracing Sand Movement in the Littoral Zone Progress
in the Radioisotopic Sand Tracer (RIST) Study, July 1968-February 1969",
U S Army Coastal Engineering Research Center, Miscellaneous Paper 4-70
- Duane, D B , and Judge, C W , 1969, "Radioisotopic Sand Tracer Study, Point
Conception, California, Preliminary Report on Accomplishments July 1966-
June 1968", U S Army Coastal Engineering Research Center, Miscellaneous
Paper 2-69
- James, W R (1970), "A Class of Probability Models for Littoral Drift,"
(this volume)

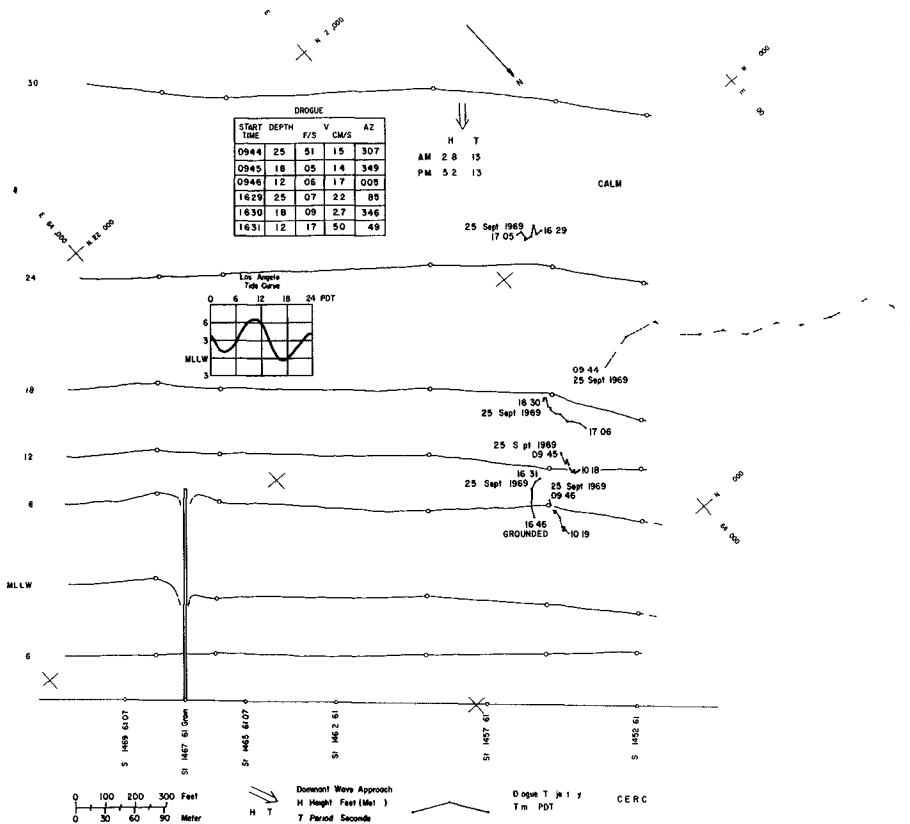


Amphibious LARC XV towing radiation detector vehicle entering surf. The ball-like device is connected to the LARC and the onboard data acquisition system by means of electromechanical cable.

FIGURE 1

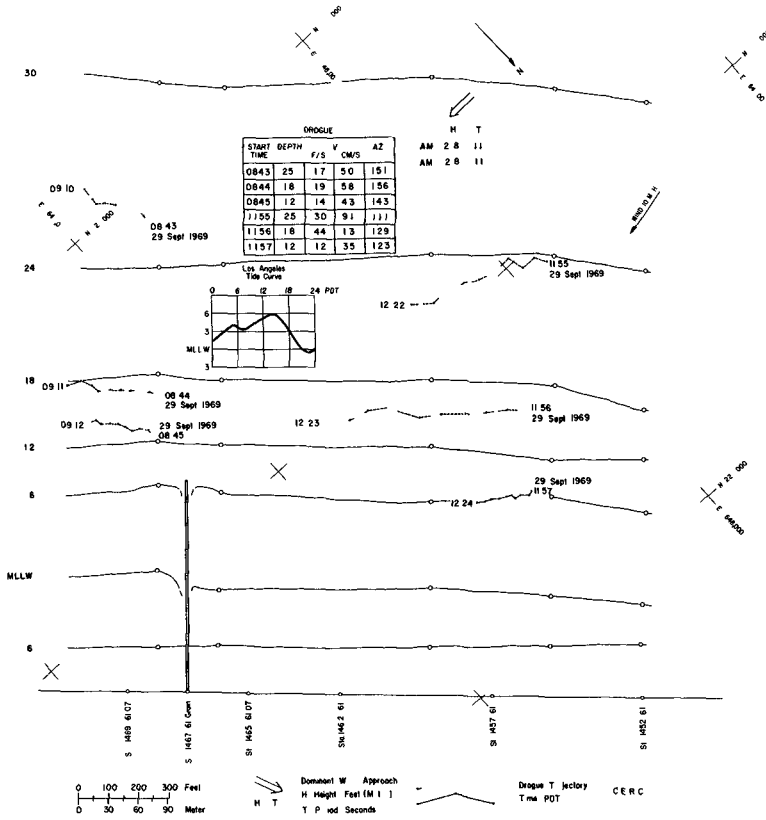


Dispersal pattern of gold-tagged sand observed approximately 5 hours after injection. Note that in this and all site figures, the groin had no panels emplaced and structurally was a pier.



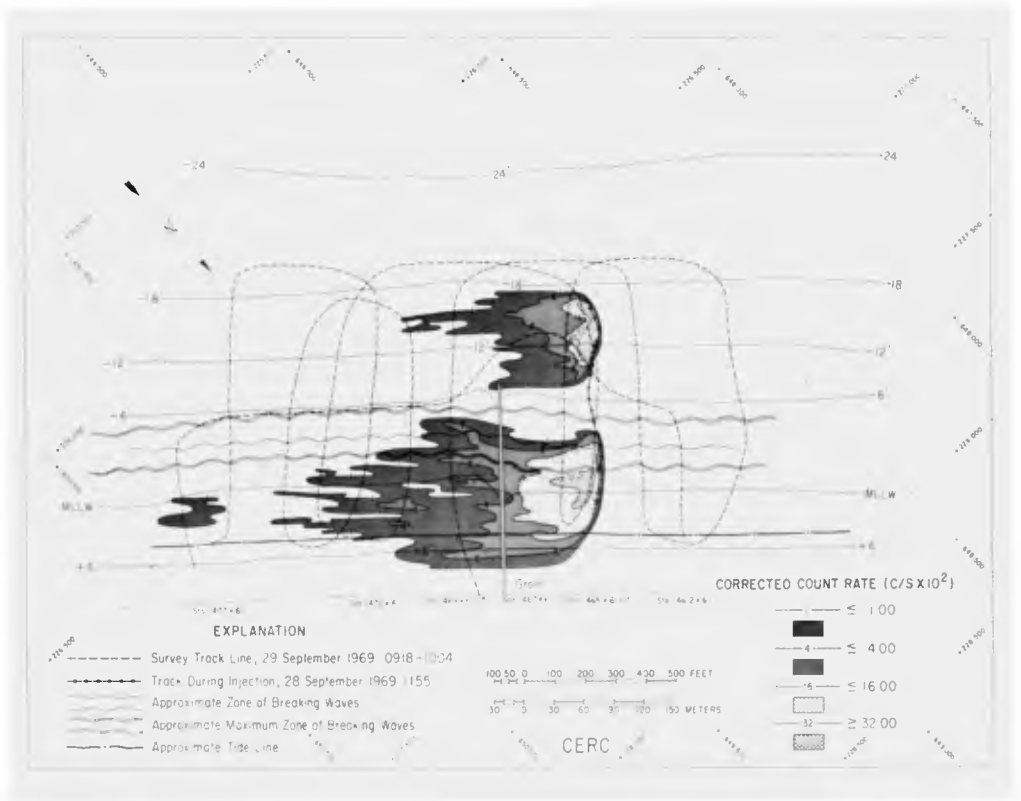
Current drogue patterns, velocities, and tide curve representative of conditions during tests 24-27 September, 1970

FIGURE 3



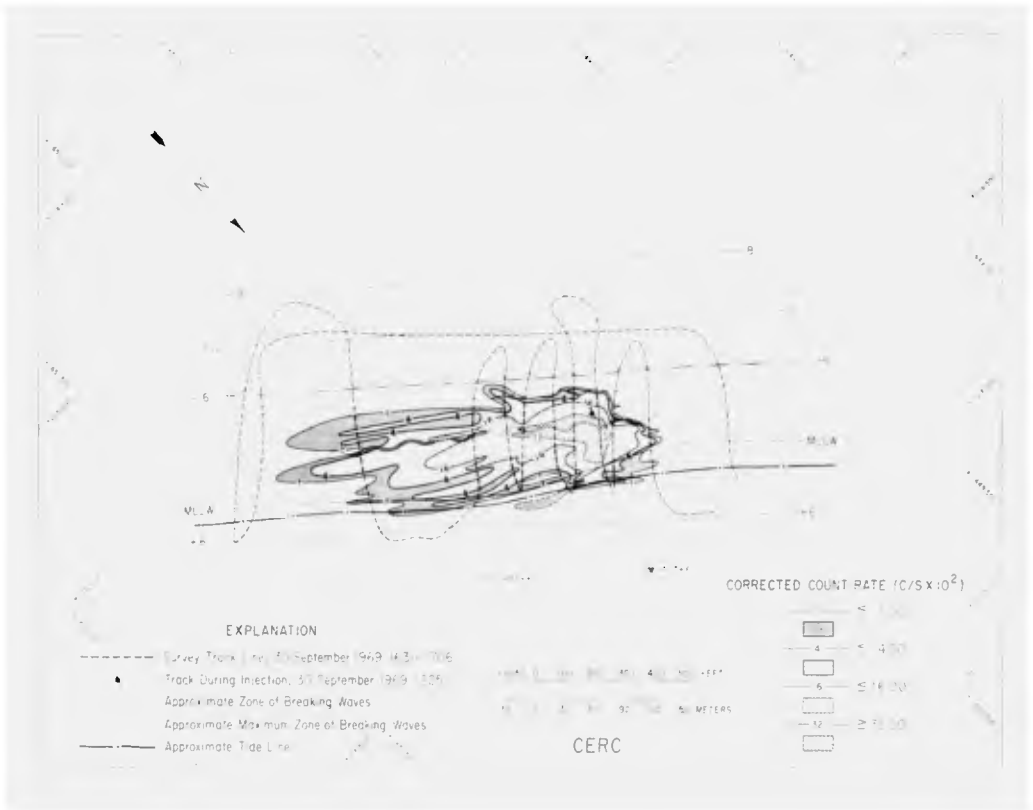
Current drogue patterns, velocities, and tide curve representative of conditions during tests 28 September-1 October, 1970

FIGURE 4



Dispersal pattern of gold-tagged sand observed approximately 23 hours after injection. Note patterns of sand moving through the pier-like structure.

FIGURE 5



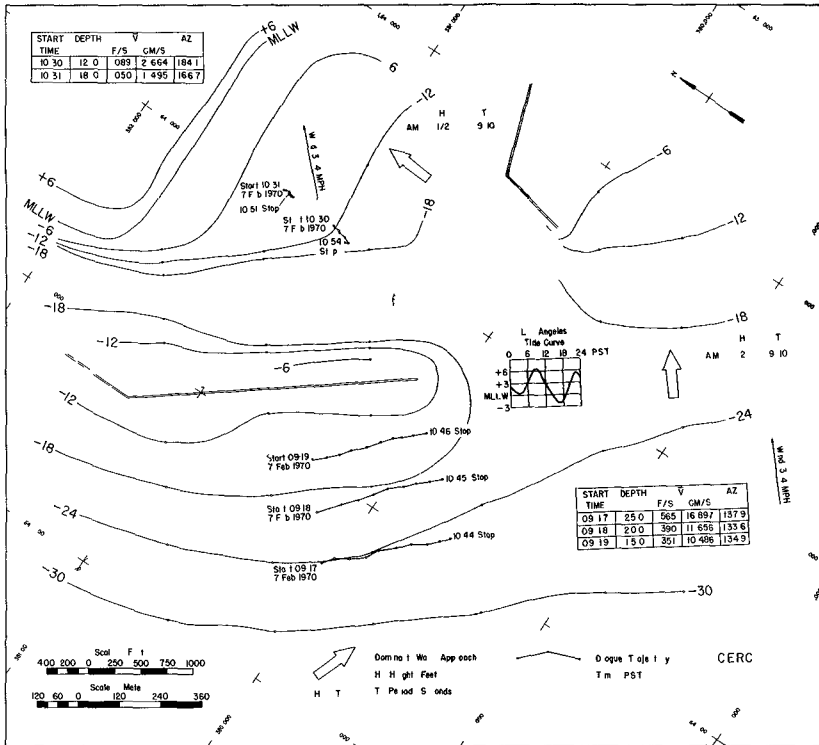
Dispersal pattern of gold tagged sand observed approximately 4 hours after emplacement as a point source in the surf zone.

FIGURE 6



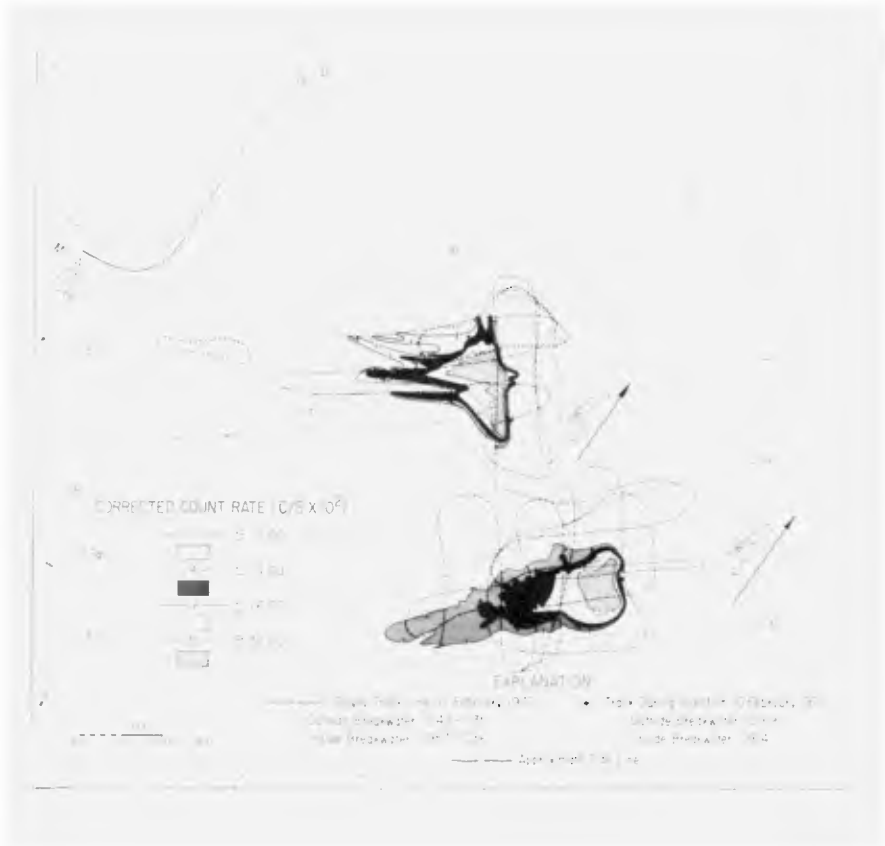
Dispersal patterns of gold-tagged sand placed outside and inside harbor approximately 48 hours after emplacement.

FIGURE 7



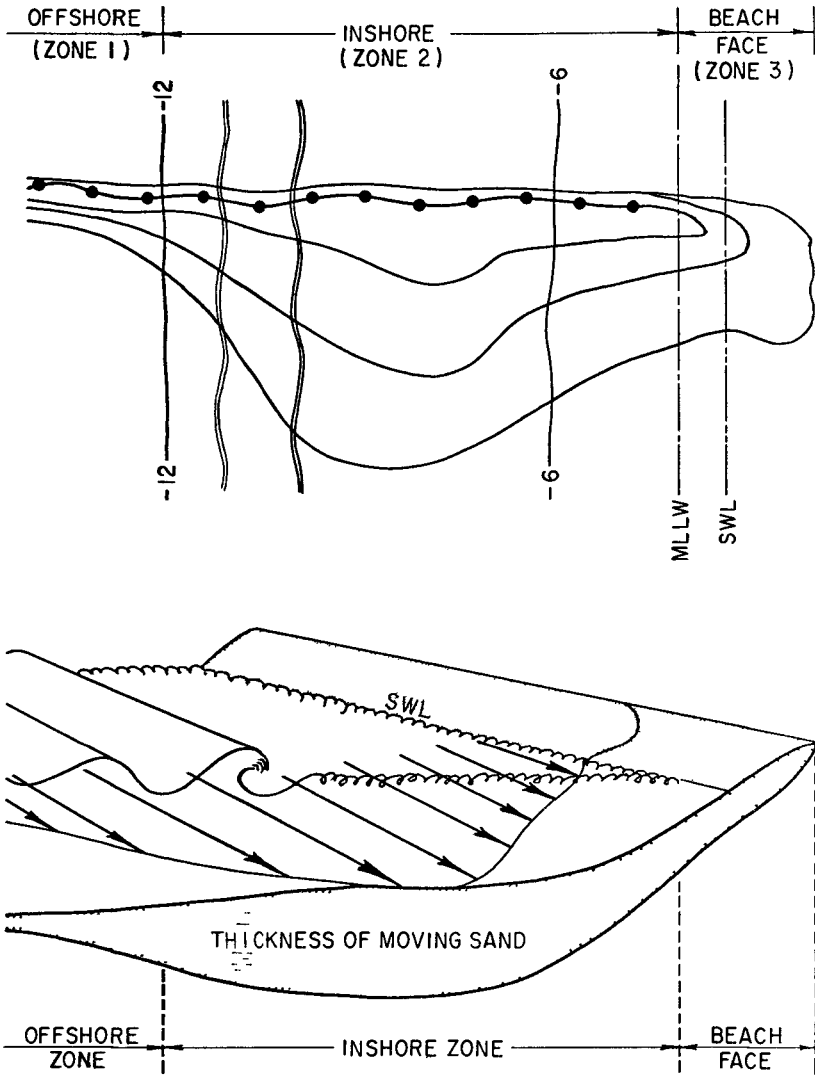
Current drogue patterns, velocities, and tide curve representative of conditions during tests 4-8 February 1970

FIGURE 8



Dispersal patterns of two point source injections of gold-tagged sand observed approximately 24 hours after injection and just after sea and swell had returned to eastward-directed approach.

FIGURE 9



Conceptual model for sediment transport in the littoral zone, numbers refer to depth of bottom below mean lower low water (MLLW) (A) Schematic map of sand dispersal system showing regions of high, medium, and low level radiation (B) Schematic isometric projection showing relative thickness of sand layer involved in transport, length of arrows proportional to rate of transport

FIGURE 10

CHAPTER 50

AN UNDERWATER SURVEY SYSTEM FOR RADIONUCLIDE-TAGGED SEDIMENT TRACING¹

E H Acree, H R Brashear, and F N Case

Oak Ridge National Laboratory
Oak Ridge, Tennessee

ABSTRACT

Survey equipment for use in tracing sediment tagged with radionuclides has been designed and field tested. The system is unique in its ability to operate on the dry beach, in the surf, and in deep water, making it possible to synoptically examine the beach face, surf zone, and off-shore marine environment. The ball-shaped radiation detector vehicle is towed behind an amphibious vessel. Data are collected on punched tape at a rate of one set of data (position, radiation counts, time) every two seconds. Gold-198 and xenon-133 have been used for tagging sand indigenous to the survey area under study. Operational characteristics and detection sensitivity are discussed.

This underwater survey system was developed for use in the RIST program which is under the direction of the U S Army Corps of Engineers, Coastal Engineering Research Center. The survey system was designed and built at Oak Ridge National Laboratory and was sponsored by the U S Atomic Energy Commission, Division of Isotopes Development.

The design criteria for the instrument were

- 1 It must be capable of operating as a gamma spectrometer
- 2 It must automatically correlate radiation counts, position, and time
- 3 It must be capable of operating on the beach face, in the surf zone, and off shore

¹Research sponsored by the Division of Isotopes Development, U S Atomic Energy Commission, under contract with the Union Carbide Corporation

The components of the basic detector unit are shown in Fig. 1. The detectors are 2 in. by 2 in. sodium activated cesium iodide crystals



Fig. 1. Underwater Detector Components

enclosed in aluminum cans which have 0.030-in.-thick walls. Since the detectors are exposed to water pressure, a 1/2-in.-thick Plexiglas light pipe is used as a pressure barrier between the crystals and the photomultiplier tubes. Four detector assemblies and the preamplifier are mounted in a water-tight chamber suspended from the axle

of an open mesh ball-like cylinder (Fig. 2). As the "ball" rotates on the stationary axle, the detectors remain oriented toward the surface over which the ball rolls.



Fig. 2. Radiation - Detector Vehicle

When designing the underwater survey vehicle, we were concerned with its ability to travel over moderately rocky areas that are common to the West Coast. The ball design, chosen over a sled-type, functions well over rocks that are up to 1 to 2 ft in diameter and over rock outcrops. It is fabricated from rectangular steel bars to form an open lattice with a minimum of shielding of the detectors. The entire device is covered with expanded metal to exclude stones and other debris. The detector chamber is weighted with lead to maintain the detectors in a vertical position.

The ball was tested for underwater tracking characteristics at the U S Naval Ship Research and Development Center in Washington to determine hydrodynamic performance. The physical characteristics of the vehicle are listed in Table 1.

Table 1 Physical Characteristics of Detector Vehicle

Overall width, in	50
Overall diameter, in	30
Housing width, in	42
Height, in	30
Distance from center shaft to tow point, in	32
Weight in air, lb	505
Weight in fresh water, lb	410

The minimum length of cable required to maintain the detector vehicle in a surveying position on the ocean bottom is shown in Fig. 3.

We are using approximately 100 ft of cable and travel at a speed of approximately 3 knots. The vehicle is very stable under these conditions, and during an average survey the detector vehicle will cover approximately 1% of the total survey area.

A schematic of the overall survey system is shown in Fig. 4.

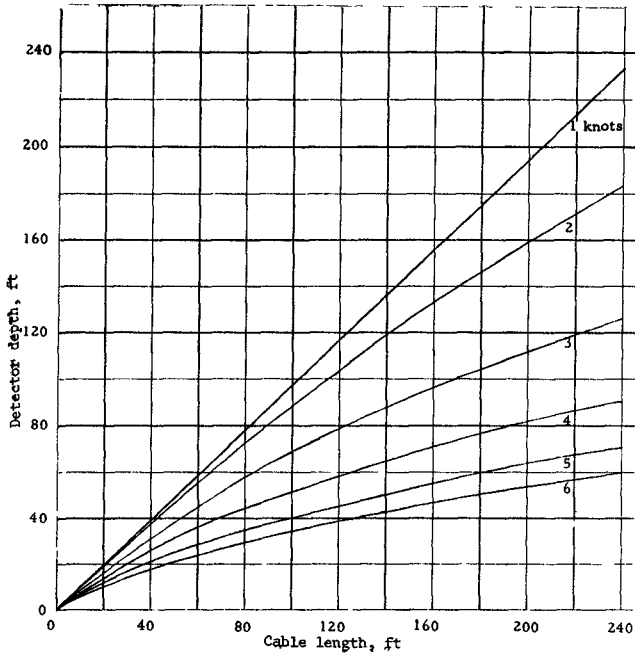


Fig 3 Minimum Required Cable Length as a Function of Detector Depth for Various Speeds

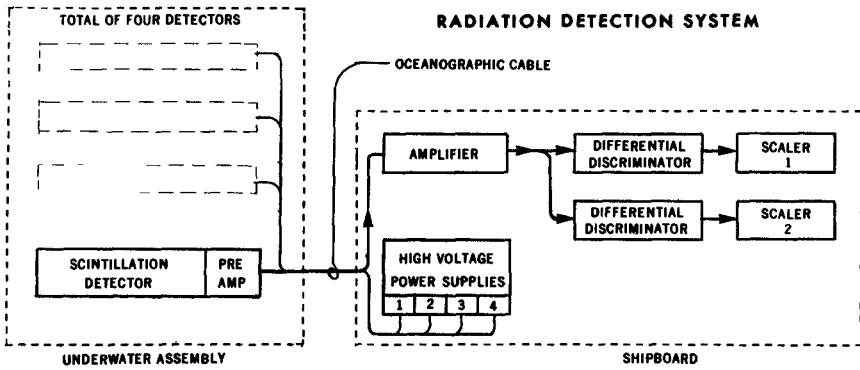


Fig 4 RIST Survey System Schematic

Signals from the individual detectors are mixed in the preamplifier whose output is matched to a 50-ohm coaxial cable which carries both the positive 24 V dc power to the preamplifier and the output voltage pulses. The coaxial cable is part of a wire bundle that has an additional eleven conductors which provide high voltage to the photomultiplier tubes. High voltage to each tube is supplied by individual power supplies which permit gain adjustment of the tubes so that the responses from all four detectors will be equal. The cable assembly also serves as the tow cable and has a tensile strength of 30,000 lb. The preamplifier output is amplified with a linear amplifier and feeds two differential discriminators for choosing which segment of the gamma spectrum is to be recorded. The output signals from the discriminators are used to drive two buffered scalers. The print-out control unit samples each scaler and records the data on an 8-level punched paper tape. The printout control unit also samples a scaler which generates a line number, a scaler which generates time, and the boat position data. The boat position is determined by use of a microwave system which provides two distances from two fixed positions on shore. A complete set of data can be collected once a second or in multiples thereof by switch selection on the console. The data readout presents a log of line number, time, radiation channel No 1, radiation channel No 2, distance 1, distance 2, and water depth.

The punched tape is used to provide data input to a computer for interpretation and the preparation of contour maps. The detection sensitivity of the detector system submerged in water for gold-198-199 is 2.3×10^3 counts/sec when the activity concentration is $1 \mu\text{Ci}/\text{ft}^2$.

The tow vessel that is currently being used for surveying is an amphibious vessel (LARC-15) which is approximately 60 ft long. This craft can easily operate in 6- to 8-ft breakers.

In our early field tests with this equipment, xenon-133 tagged into sand indigenous to the test area was used as the tracing material. While sand injection and health physics problems are greatly simplified with xenon-133, the quantity of activity that can be introduced into a survey area is limited to approximately 40 liters of sand tagged with approximately 800 mCi of xenon-133. This small quantity of activity tends to

limit the scope of surveys We are currently using a gold-198-199 mixture The amount of activity that we can use is only limited by the equipment used to transport and dispense it Our recent experiments were conducted with 10 Ci of activity tagged onto approximately 1/2 liter of sand The use of the survey equipment is not limited to xenon-133 and gold-198-199, because it functions as a gamma spectrometer and can be used to monitor any gamma radiation above 30 keV Other possible applications for this equipment are conducting natural background surveys in inland lakes and streams and prospecting for heavy mineral deposits

CHAPTER 51

PROCESSING AND ANALYSIS OF RADIOISOTOPIC SAND TRACER (RIST) STUDY DATA*

H R Brashear

Instrumentation and Controls Division
Oak Ridge National Laboratory

E H Acree
F N Case

Isotopes Division
Oak Ridge National Laboratory

P A Turner
D B Duane

Coastal Engineering Research Center
Washington, D C

ABSTRACT

Data collected during the Radioisotopic Sand Tracer (RIST) field tests are processed through digital computers. Data treatment requires computing and plotting the detector position and correcting the corresponding radiation count rates for radioactive decay. The field data are recorded on punched paper tape which is then edited and transferred to magnetic tape for input to data reduction programs. The navigation data, which are in the form of distances to shore-based microwave responder beacons, are tested for spurious values by comparison with the theoretical maximum travel distances of the survey vehicle between successive fixes. The navigation ranges are then converted to rectangular geographical coordinates.

Present emphasis is in the development of computer programs to construct a count rate surface from data collected along track lines. This technique facilitates machine contouring and enables numerical integration of the count rate surface. The ultimate goal is to obtain an estimate of mean direction and volume of littoral transport and a radiation material balance to be used to check the results. Several programs required to accomplish these tasks are operating at the Coastal Engineering Research Center (CERC) and the Oak Ridge National Laboratory (ORNL).

*Research sponsored by the Division of Isotopes Development, U S Atomic Energy Commission, under contract with the Union Carbide Corporation

Data processing for the Radioisotopic Sand Tracer (RIST) Study is computer oriented to handle the large volume of collected data which are digital in form and represent parameters that must be correlated to obtain sand transport rates. Figure 1 enumerates the objectives of the computer programs.

Fig 1 Objectives of Computer Programs

-
- 1 Assembling the data in graphical form
 - 2 Interpolation to establish the count rate surface within the survey area
 - 3 Computation of the surface rate and direction of the sand movement
 - 4 Correlation of other data with survey data to calculate volume rate of sand transport
 - 5 Correlation of the volume rate of sand transport with ocean conditions for fundamental studies in sand transport
-

To accomplish the first objective of assembling the data in graphical form, two programs are operational one at the Coastal Engineering Research Center and the other at the Oak Ridge National Laboratory. The data collection system¹ shown in Fig 2 illustrates the automatic correlation of three parameters necessary in assembling the data in graphical form.

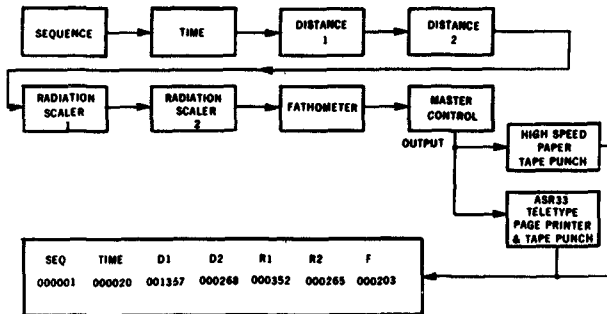


Fig 2 Data Collection System

¹An Underwater Survey System for Radionuclide-Tagged Sediment Tracing
E H Acree, F N Case, and H R Brashear

The data are collected on punched paper tape in a serial fashion to form a line of data. Each line of data consists of numbers which represent time, tow vehicle position, radiation count rate, and water depth. Time and radiation units have buffers so the data can be recorded while new data are being taken. These buffers permit data to be taken at 2-sec intervals with no instrument dead time due to readout. Tow vehicle position is represented by D1 and D2, the distances between the tow vehicle and two fixed shore stations. The distances are measured at the same time that the time and radiation values are transferred to the buffers for readout. Water depth measurements are near the first part of each data cycle, but are not as precisely timed.

One survey may have up to 2000 lines of data, which is approximately the capacity of one roll of paper tape. A normal survey consists of 1700 lines of data. An average of four surveys are made each day, producing 47,600 six-digit numbers, an average field test yields a total of 380,800 six-digit numbers.

Data stored on punched paper tape are copied onto magnetic tape for computer input. The tow vehicle positions are calculated from D1 and D2, using either the law of cosines or the intersection of two circles, depending upon which coordinate system is desired. The law of cosines is used to place the tow vehicle on a geographical grid, and the intersection of two circles is used for placement on an arbitrary x-y coordinate grid. The validity of each location is checked by comparison with the previous location. If the separation distance between the two locations is greater than the theoretical distance possible, the location is changed. This change is based on the average velocity and direction of the tow vehicle.

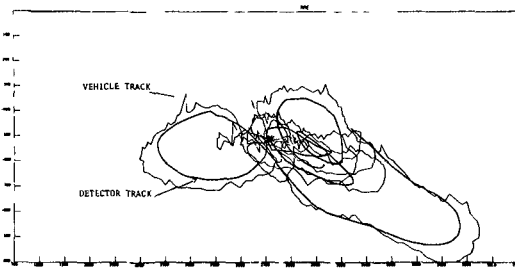


Fig 3 Plot of Tow Vehicle and Detector Path

Figure 3 is a computer-directed machine plot of a tow vehicle path and detector vehicle path with no corrections for the tow vehicle locations. The irregularities are due to errors from the range-finding equipment in measuring the distances.

from the tow vehicle to each shore station. The location of the detector vehicle, which is towed approximately 100 ft behind the tow vessel, must be calculated by performing a series of approximations. These approximations are quite accurate due to the frequency of obtaining tow vehicle position. The initial detector vehicle position is determined on an arbitrary basis. The second position is determined by computing the equation of the line which connects the first detector vehicle position with the second tow vehicle position. The actual length of the tow cable, minus any correction due to water depth, is used as the distance from the tow vehicle (along the computed line) to the second detector vehicle position. Subsequent detector vehicle positions are determined in a similar manner. As each detector vehicle position is calculated, the corresponding time and radiation count rates are assigned to that position. In Fig. 3, the paths of both vehicles are drawn by straight lines connecting successive calculated positions.

Radiation data are scanned to obtain an average radiation background count rate (due to natural radioactive material). All radiation count rates are adjusted by subtracting the average background, and the adjusted count rates which are equal to or greater than the background are corrected for radioactive decay by the following formula:

$$R_{CD} = \frac{R}{E^{-\lambda t}}$$

- where R_{CD} = radiation counts corrected for decay (counts/sec)
 R = radiation counts $\geq 2x$ average background (counts/sec)
 E = base of natural logarithm
 λ = decay constant of isotope used in test
 t = time from tagged sand insertion (unit)

Figure 4 is a machine plot of numbers which represent ranges of corrected count rates calculated from data obtained at Point Mugu, California, in September, 1969.

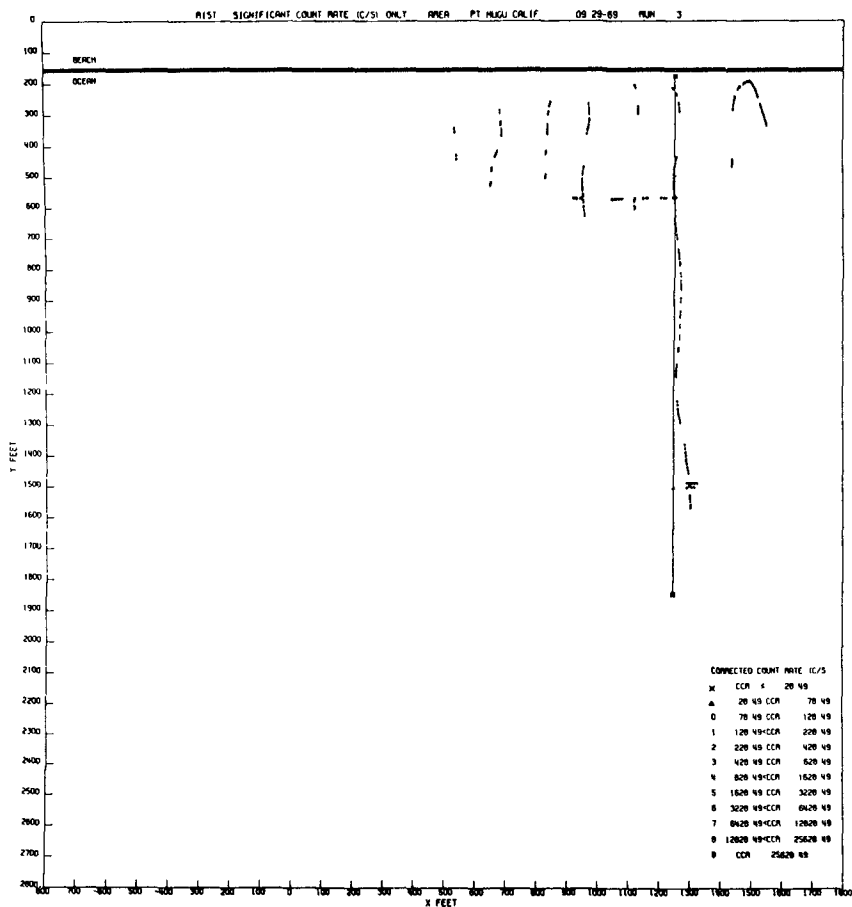


Fig 4 Calculated Radiation Count Rate Ranges Over Detector Track

Figure 5 is an enlargement of Fig 4 in the area of significant radiation count rates. All background count rates have been omitted to make the trend of sand movement more apparent. The computer programs allow more than one survey to be plotted on a single map to enhance the distribution pattern as it develops.

R N

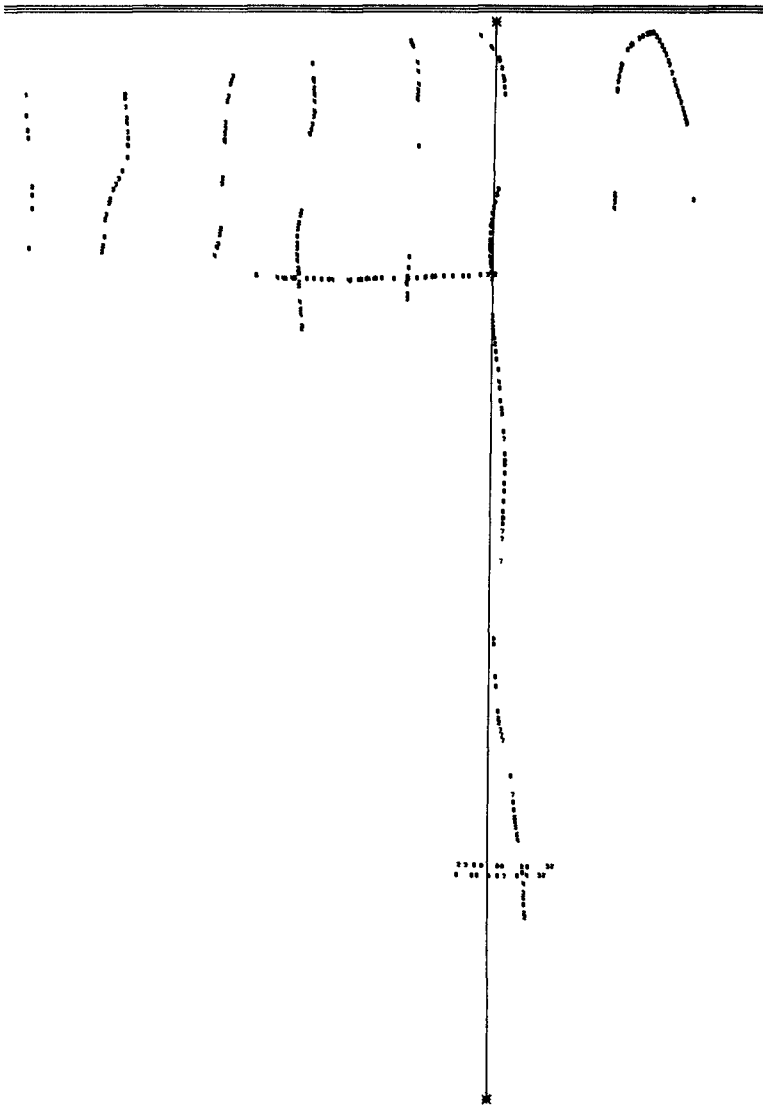


Fig 5 Section of Fig 4, Area of Significant Count Rates

The second objective, interpolation of data, is required because it is physically impossible to sample every square foot of the study area. Several programs are either operational or near operational to complete the count rate surface and machine draw radiation intensity contours. One of the programs is a linear interpolation technique. This program divides the x-y coordinate system into a grid adjacent to the x and y axes having square areas of 25 ft on a side. In general the x-axis lies parallel with the beach. In the studies to date the predominate directions of sand movement have been parallel or perpendicular to the beach. The interpolation is done in either or both directions depending on the preliminary indication of sand movement direction.

The second step in this program is to assign all square areas which have radiation count rates within an area a single count rate, which is the average of all radiation count rates within that area. Figure 6 is the result of the second step of the program. The results here are much like the data display of radiation count rates along the detector vehicle track of the first program, but somewhat simpler due to a grouping of numbers.

The third step computes radiation count rates for those areas with no count rates assigned. Interpolation is made only between areas which have real data. The interpolation is linear, and the average radiation count rate of two areas is assigned to the area halfway between the two areas. The formula used is

$$R_{1+K,J} = R_{1,u} - \frac{(R_{1,J} - R_{1+L,J})}{L} (L - K)$$

where R = radiation value of the area

i = x location of area of larger R data

j = y location of area

K = x location of area for R interpolation

L = x location of area of smaller R data

If interpolation is desired in both the x and y direction, the interpolation is done independently in each direction and the average of the two is used as the final value.

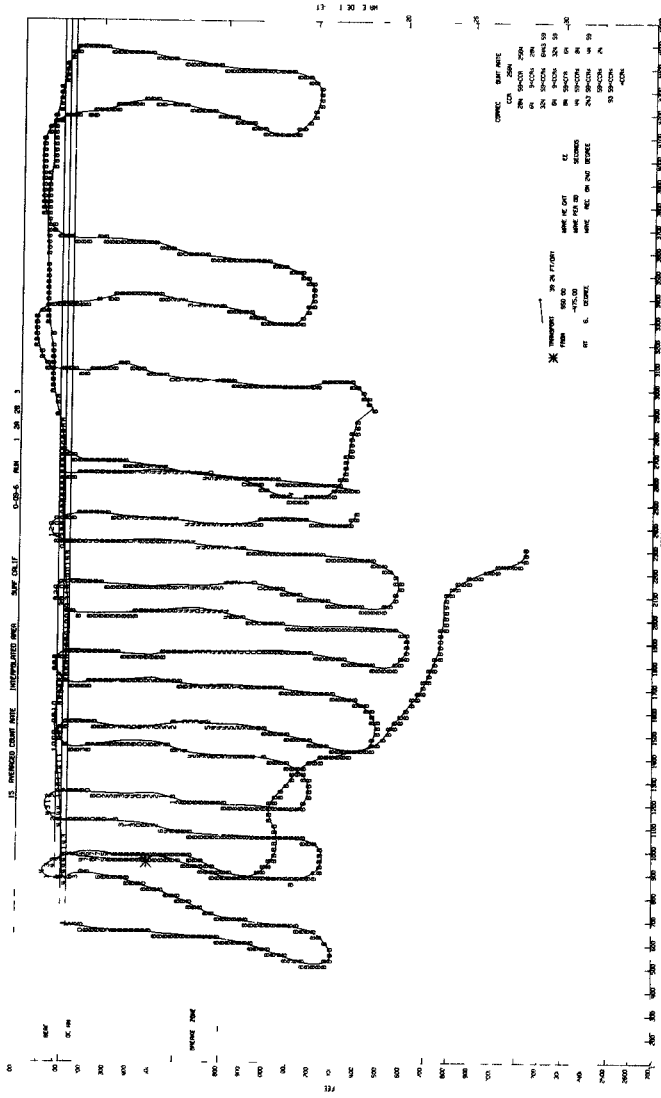


Fig 6 Count Rate Assigned to Significant Count Rate Areas

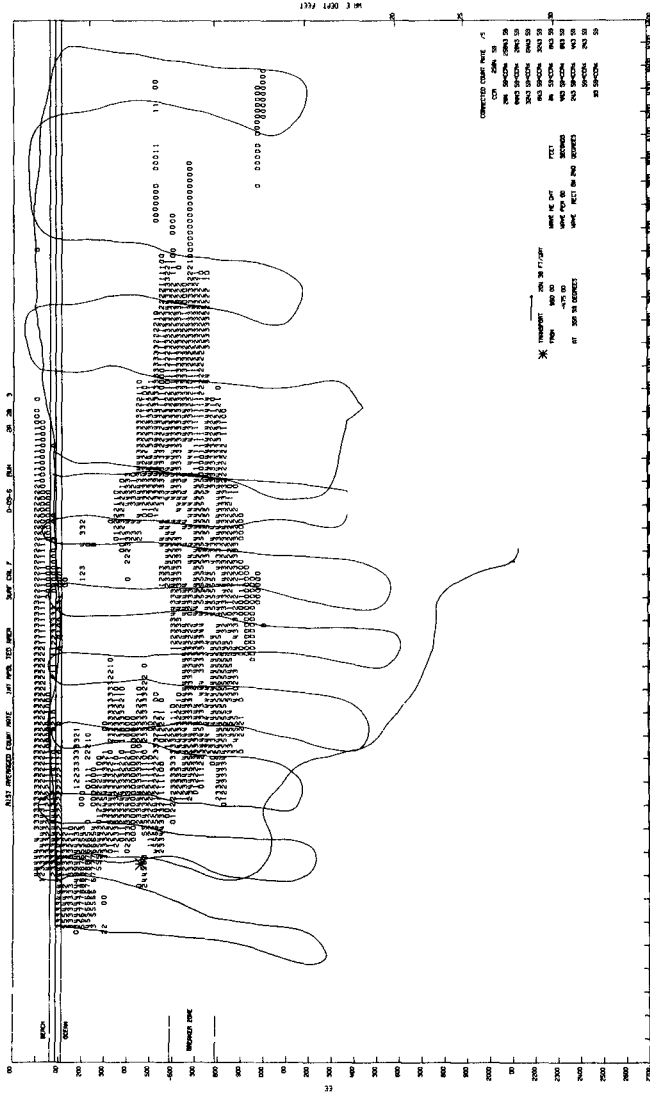


Fig 7 Contour Map Derived by Linear Interpolation of Radiation Data

Figure 7 is the completed map using the linear interpolation method. All background radiation count rates have been omitted for clarity.

Beyond the initial plotting of trackline data, present emphasis at CERC is slightly different from that at ORNL. The procedure being tested at CERC for RIST survey data is to use a weighted least-squares fit of a plane through the centroid of each grid cell containing a data point. The area surrounding each grid mesh point is divided into octants, and each octant is searched for the nearest data point to the grid centroid. Once the search is completed, the nearest point in each octant is used to construct a weighted least-square fit of a plane through the centroid. Each data point is assigned a weight which is an inverse function of the distance from the data point to the grid centroid.

This procedure has been tested by generating a random surface with a double Fourier series and evaluating it at 100 randomly distributed points in a plane. When interpolated over a uniform grid, these points produced a surface that appeared similar to the original surface, but with reduced variance. The numerical approximation routine has not been tested yet with a hypothetical trackline superimposed on the random surface. It has already been observed that, in certain instances with real data, the routine produces grid point values that are artifacts of the numerical approximation procedure. Although the result is not as aesthetically appealing as a handdrawn contour map of the data, it does provide a quick first approximation of the survey area. Testing and evaluation of the two approaches is being made at CERC and ORNL, but at present is incomplete.

Correlation of data for fundamental studies and volume-rate of sand transport are in the early stages of development.

CHAPTER 52

A Class of Probability Models for Littoral Drift

William R James
Special Assistant
Coastal Engineering Research Center
Washington, D C

Introduction

The major goal in the development of sediment tracer technology is to produce an accurate method for the field measurement of short term volume littoral rate. Many of the technical difficulties involved in tagging, injecting, and sensing the movement of radioisotope sand tracers in the littoral zone have been overcome by the RIST project. However, quantitative determination of volume drift rate requires more than knowledge of tracer position in time and space. A mathematical model is required to relate the flux of tracer material to the sediment flux.

A linear (or average) rate of tracer transport along the coastline can be measured to a fair degree of accuracy with tracers. These measurements, when determined from tracers injected along a line source which span the transport zone, can be used to provide an estimate of an areal transport rate. However, it is not obvious how to measure the third dimension, depth of transport. This, of course, is needed to provide the desired estimate of volume transport rate.

This problem arises, even if the relation of tracer concentration to burial depth is everywhere known without error. Sediment transport does not occur as a sheet of constant thickness moving at a constant rate. If this were so tracer concentration would rapidly attain a uniform concentration over a fixed depth and no tracers would appear below that depth. In fact no observations of the relation between tracer concentration and burial depth support this model as even a first approximation.

Studies such as those of Courtois and Monaco (1969) and Hubble and Sayre (1964) suggest that the concentration of tracers is related to burial depth in a complex fashion. The concentration on the surface is finite, but not maximal. The concentration increases with depth to some point where a maximum is reached and diminishes in a "long tailed" fashion.

If sediment transport occurred as a sheet of uniform thickness, and tracers were thus uniformly distributed over the range of that thickness, one measure of depth of movement would be the mean of the maximum observed tracer depth. A more stable estimate, if this condition was assumed only to approximate reality, would be to double the observed mean depth of burial.

Yet the observed distribution curves so strongly deny the original hypothesis that neither of these methods can be relied upon. What is needed is a model for sediment particle burial which admits the observations as realizations and directs the form of estimation. This paper attempts to present a class of such models which lead to a particularly simple form for the calculation of littoral volume drift rate.

The Conceptual Model

Assume a two dimensional sediment transport system which includes only depth of burial and transport direction. The motion of sand particles is initiated by the passing of a surge. As wave crests pass over a point particles are alternately lifted from the sea floor, transported, and re-deposited. Inasmuch as wave height and period are random variables, the depth to which material is eroded from the sea floor varies with each wave.

When the wave train impinges obliquely upon the shoreline a net long-shore current is superimposed upon the oscillatory motion so that particles suspended by the passing surge are subjected to a net motion along the shoreline. Contrary to the situation in uniform flow, it is the individual energy pulses which control the erosive mechanism and the wave climatology as a whole which controls the transporting mechanism. Short period high waves do not effect littoral drift if they are directed onshore. The long-shore current is the transporting mechanism, but is not the erosive mechanism except in extreme cases.

The Probability Model

For the purposes of this development the elevation of a point on the sea floor can then be considered to change instantaneously through a series of erosional and depositional increments. Define the thickness of the erosional increment accompanying the passage of the i th surge as ϵ_i , and the thickness of the following depositional increment as δ_i . Both ϵ_i and δ_i are assumed to be random variables with equal expectations (μ). Particles which are eroded are assumed to mix in transport so that the depth below the sediment-water interface at which they are redeposited is independent of the depth from which they were eroded.

At time zero tracer particles are injected on the surface. Initially all tracer particles will be eroded, transported and redeposited. As successive erosional and depositional episodes occur, some of the tracer particles will become buried below normal erosional depths, thus occupying sites of relative stability. Ultimately an equilibrium state will be reached where the concentration of tracer particles with depth of burial will no longer change. This state will be that where the probability of erosion of particles buried at a given depth times the proportion of tracer particles buried at that depth precisely equals the probability that a freshly eroded particle will be deposited at that depth times the total probability that a tracer particle is eroded, for all depths.

Certain characteristics of the equilibrium distribution can be derived without knowledge of the specific probability density functions describing erosional and depositional increment thicknesses

Define

$f_{1+1}(z)dz$ = the probability that after the 1th surge passes, a tracer particle is buried between depths z and $z+dz$

$f_{new}(z)dz$ = the probability that a particle which is eroded by the 1th surge, is redeposited between depths z and $z+dz$

$P_{move}(z)$ = the probability that a particle buried at depth z is eroded by the 1th surge

$P_{stay}(z)$ = the probability that a particle buried at depth z is not eroded by the 1th surge

$f_{\epsilon}(\epsilon)d\epsilon$ = the probability that the thickness of an erosional increment is between ϵ and $\epsilon+d\epsilon$

$F_{\epsilon}(\epsilon) = \int_0^{\epsilon} f_{\epsilon}(x)dx$ = the probability that the thickness of an erosional increment does not exceed ϵ

Then $P_{stay}(z) = 1 - F_{\epsilon}(z)$, and $P_{move}(z) = F_{\epsilon}(z)$

Define Pm_1 = the total probability of a tracer particle being eroded by the 1th surge, independent of burial depth

$$Pm_1 = \int_0^{\infty} [1 - F_{\epsilon}(z)]f_1(z)dz$$

Then

$$f_{1+1}(z) = F_{\epsilon}(z)f_1(z) + Pm_1 f_{new}(z)$$

An equilibrium probability distribution of tracer burial depth will be obtained when

$$f_{1+1}(z) = f_1(z)$$

Define this distribution as $f_{eq}(z)$

Then

$$f_{eq}(z) = F_{\epsilon}(z)f_{eq}(z) + Pm_{eq} f_{new}(z)$$

or,

$$f_{eq}(z) = \frac{P_{m_{eq}} f_{new}(z)}{[1 - F_e(z)]}$$

It now remains to relate the fresh deposition burial law ($f_{new}(z)$) to the probability density for depositional increment thicknesses

Define

$f_{\delta}(\delta)d\delta$ = the probability that a random sample from the probability distribution of depositional increments has thickness between δ and $\delta+d\delta$

$g_{\delta}(\delta)d\delta$ = the probability that the depositional increment within which a freshly deposited particle falls has thickness between δ and $\delta+d\delta$

Then in order to maintain a volume balance

$$g_{\delta}(\delta)d\delta \propto \delta f_{\delta}(\delta)d\delta$$

$$\text{As, } \int_0^{\infty} g_{\delta}(\delta)d\delta = 1$$

$$\text{and, } \int_0^{\infty} \delta f_{\delta}(\delta) d\delta = \mu$$

$$\text{then, } g_{\delta}(\delta)d\delta = \frac{\delta f_{\delta}(\delta)d\delta}{\mu}$$

From the mixing in transport assumption, a particle which falls within a depositional increment of size δ is equally likely to fall at any depth between the surface and the base of the increment

Thus

$$f_{new}(z|\delta) = \begin{cases} \frac{1}{\delta} & 0 < z < \delta \\ 0 & z > \delta \end{cases}$$

Then the joint probability density of depth of burial and size of depositional increment is given by

$$\begin{aligned} f_{new}(z, \delta) &= f_{new}(z|\delta) g_{\delta}(\delta) \\ &= \frac{(1/\delta) \delta f_{\delta}(\delta)}{\mu} \end{aligned}$$

or,

$$f_{\text{new}}(z, \delta) = \frac{f_{\delta}(\delta)}{\mu} \quad 0 < z < \delta < \infty$$

$$= 0 \quad z > \delta$$

Then the probability distribution describing burial depths of freshly deposited particles is given by

$$f_{\text{new}}(z) = \int_z^{\infty} f_{\text{new}}(z, \delta) d\delta$$

$$= \int_z^{\infty} (1/\mu) f_{\delta}(\delta) d\delta$$

or,

$$f_{\text{new}}(z) = \frac{1 - F_{\delta}(z)}{\mu}$$

where $F_{\delta}(z)$ = the probability that a random sample from the probability distribution of depositional increments has thickness less than z

The resulting equilibrium distribution of burial depths is thus

$$f_{\text{eq}}(z) = \frac{Pm_{\text{eq}}}{\mu} \frac{[1 - F_{\delta}(z)]}{[1 - F_{\epsilon}(z)]}$$

A significant special case being

$$f_{\text{eq}}(0) = (Pm_{\text{eq}}/\mu)$$

For this class of probability models, the total surface concentration of tracer material is independent of the specific probability laws governing erosional and depositional increment thicknesses

Volume Littoral Drift Rate

Even more important is the implied relation between the rate of tracer transport and the volume rate of littoral drift

At equilibrium

1 The expected proportion of tracer particles moving with each passing surge is $P_{m_{eq}}$

2 The average distance of movement is defined as $E(\Delta X)$
Thus the average longshore tracer velocity is

$$v_x = P_{m_{eq}} E(\Delta X) / \Delta t$$

$$Q \approx \mu E(\Delta x) / \Delta t$$

$$\mu = P_{m_{eq}} / f_{eq}(0)$$

$$E(\Delta x) / \Delta t = v_x / P_{m_{eq}}$$

Thus
$$Q = \frac{P_{m_{eq}}}{f_{eq}(0)} \frac{v_x}{P_{m_{eq}}}$$

Or
$$Q \approx v_x / f_{eq}(0)$$

Volume drift rate is simply the tracer centroid velocity divided by the total surface concentration of tracer material, both of which are measurable quantities

These results can be applied to the three dimensional case if one assumes that diffusion of material in the shore-normal direction is negligibly small. In this case, for a line injection the littoral drift rate is given by

$$Q = \int \frac{v_x(y)}{f_{eq}(0/y)} dy$$

where the integral is taken across the entire zone of transport

Concluding Remarks

Before the above equations can be relied upon, it is necessary to test some of the underlying assumptions both in the laboratory and in the field. Experiments are presently being designed at CERC and elsewhere for this purpose.

References

- Courtois G and Monaco, A (1969), "Radioactive Methods for the Quantitative Determination of Coastal Drift Rate", Marine Geology, v 1, pp 183-206
- Hubbell, D W and Sayre, W W (1964), "Sand Transport Studies with Radioactive Tracers," ASCE, vol 90, HY 3, pp 39-68

CHAPTER 53

PROPERTIES OF LONGSHORE BARS IN THE GREAT LAKES

by

James H Saylor

Edward B Hands

National Oceanic and Atmospheric Administration

Detroit, Michigan 48226

Longshore bars are permanent features of nearshore bathymetry along the windward coasts of the Great Lakes. The stability and permanency of these features have been noted by numerous investigators, but movements of the bars and troughs in relation to varying lake levels and incident wave energies are not fully understood. Studies of nearshore bathymetry and sediment properties were conducted during 1967 and 1969 along a forty-five kilometer reach of the eastern coast of Lake Michigan.

Results show that the offshore bars migrate significantly due to changes in lake level, a rise of one-half meter in the surface of Lake Michigan between 1967 and 1969 was accompanied by a shoreward movement of bar crests and troughs over a distance averaging 30 meters. Elevations of the crests and troughs are also built upward toward new equilibrium levels during rising water levels, but elevating of the crests lags the increase in stage. Extensive shore erosion occurs because of the reduced effectiveness of longshore bars in dissipating incident wave energy. The average crest depth was found to increase linearly in the offshore direction. Average distances between crests increase exponentially. These relationships are preserved during the bar growth and shifting that accompanies long term changes in lake level.

Bar troughs are characteristically crescent shaped, with no abrupt changes in slope. Bathograms from several ranges show atypical trough configurations consisting of flat bottoms with discontinuities in slope on ascent to adjacent crests. This unusual trough shape is indicative of an immobile stratum exposed along the bottom of the trough.

INTRODUCTION

Longshore bars are permanent features of nearshore bathymetry along the windward coasts of the Great Lakes where an abundant supply of sand-size sediment is present. The bars and intervening troughs are oriented essentially parallel to the shoreline. Along the eastern coast of Lake Michigan the longshore bars are continuous in coastal reaches exceeding many tens of kilometers, and the structure of these remarkable features has been described by numerous investigators. The continuous bars are usually three or four in number in Lake Michigan, although as many as five or six have been observed. As a rule, the

spacing between bars increases in the offshore direction, so that the distance between the first and second bars is less than the distance between the second and third bars as one proceeds toward deep water. The trough associated with each bar occurs inshore of the crest, and the height of the crest above the trough also increases going offshore, with the exception that the bar farthest offshore is often of small height and configured as a long, gently-sloping swell of the lake bottom lying just lakeward of the more typical longshore bar structures.

The longshore bars of Lake Michigan were first described by Desor (1851), and more comprehensively investigated by Evans (1940, 1942). The observations of bar structure made by Evans have been widely reported (e.g., Shepard (1950) and Zenkovitch (1967)), and constitute the framework of present knowledge. There have been relatively few studies concerning movements of the bar structures due to varying incident waves and currents, or due to long-duration variations in water surface elevation. Evans (1940) concluded that minor readjustments in the positions of bars and troughs may occur with changes in intensity or direction of incident waves, but that the bars do not migrate in response to significant increases in water surface elevation. He believed that an increase in water level would strand the deeper bars as relicts, and that a new set of crests and troughs would be built inside them. The only shoreward migration of bars would be associated with a lowering of lake level, which would decrease the water depth over the innermost bar and cause currents or waves of translation across it. With these conditions, Evans felt that the innermost bar would move shoreward as a subaqueous dune. Davis and McGeary (1965) studied the stability of nearshore topography in southeastern Lake Michigan during the summer months of 1963. Their results agreed with Evans' findings that the offshore bars do not move appreciably. Bajorunas and Duane (1967) studied nearshore topography in a similar environment in southeastern Lake Superior and contrary to previous findings, they showed that considerable movement of bars can occur during just a few months. In southeastern Lake Michigan, Hawley and Judge (1968) indicated that the bars and troughs do migrate from year to year, but they did not identify a regular and consistent pattern of movement.

This paper describes the results of an investigation of bar stability conducted during 1967 and 1969 on the eastern coast of Lake Michigan. The reach of coast studied extends about 45 km, centered about Little Sable Point (Figure 1). Twenty-nine range lines were established perpendicular to the shoreline at nearly equally-spaced intervals throughout the study area. Topography was monitored along each range line from the back beach to an offshore water depth of about 9 m, which is a depth in excess of that in which the bar structures occur. Sediment samples were collected along each range and grain-size distributions determined in the laboratory. Wave height and period and wind speed and direction were recorded continuously from an offshore platform. The platform was erected at a site where the water depth was 6 m, and it was located about 500 m north of the Pentwater jetties, near the northerly end of the study area, and 400 m from the strandline. Water surface elevation and current speed and direction were also monitored from the platform during the investigations.

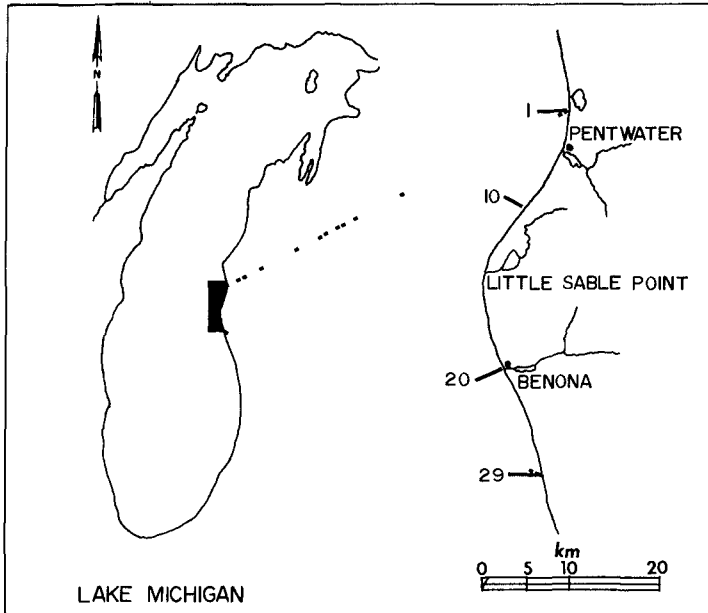


Fig 1 Location of study area and selected ranges

CHARACTERISTICS OF OFFSHORE BARS

From casual observation of the eastern Lake Michigan coast by either personal visits or inspection of aerial photographs, the continuity and regular spacing of the offshore bars and troughs are striking features. However, if the nearshore topography is studied in more detail over a lengthy reach of the coast, the regularities of bar structure become more obscure. The spacing and number of bars vary from range to range, as does the depth of water over the crests and the distance of the bars from shore. The most pronounced variations occur in shallow water near shore. The shallow-water bar, or bars, may not conform to the trend of the shore, as do deeper bars, but will sometimes merge at an angle with the beach face. In other reaches, the coastal ridge may appear as an alignment of discontinuous shoals, a crescentic bar (horns and cusps directed toward shore), or simply a perturbation on the outer edge of a bench lying below the swash zone. Such coastal bar forms are also more variable in time than the deeper longshore bars. They are continually subject to changes in size and position, and may disappear and reform in the course of a few days. Just south of the Pentwater jetties the entire sequence of longshore bars is virtually absent. The jetties, which extend about 150 m into the lake, disrupt littoral drift and as a consequence the fully-developed sequence of bars is not observed again until one proceeds abouts 1 km south. From this location southward to the vicinity of Little Sable Point, a quartet of well-developed bars persists with

little variation in geometry. At Little Sable Point, the inflection point between a northeasterly and southwesterly trending coast, the regularity of bar-trough configuration is again broken. The smooth, regular bar pattern is replaced by an irregular profile which more closely resembles that found on ocean coasts exposed to a wide variety of wave trains. A regular sequence of bars is reestablished south of the point and persists throughout the southerly 20 km of the study area. The crests are deeper and more widely spaced in this reach, however.

In spite of the variations in bar structure from range to range, the entire reach of Lake Michigan coast studied is typified by the presence of three, and in several subreaches four, essentially-continuous longshore bars. The spacing and depth of these bars, while not constant, do fit remarkably simple patterns. These bars conform with the classical descriptions, in that the elevation of crest above trough (height) increases going offshore, as does the spacing between crests. The depth of water over successive crests increases linearly in the offshore direction, as illustrated in Figure 2, which shows the average values observed during 1969 for ranges 1 through 15, and ranges 18 through 29. The continuous bar nearest shore is labeled in the figure as crest 2 because of the frequent presence of one or more low amplitude bar-like structures between it and the strandline. In all reaches studied, the crest elevations of the three continuous bars exhibit a nearly linear distribution, although the slope of the line connecting crest elevations does vary along the coast as illustrated in the figure, and the bars are deeper south of Little Sable Point than they are to the north.

Between the continuous bar nearest shore and the strandline, one or more bar-like structures are occasionally observed. If more than one are present, the depth of water over the crests is nearly the same and averages about 0.5 m. These shallow-water features show much variability from range to range and they are not continuous along the coast for lengthy distances. The 1967 investigations were conducted in the northern third of the coastal reach and during the summer months of June through August. During this period the shallow-water crests were always present, but they were not as prevalent on the same ranges during the 1969 studies made during the spring and fall months. The summer months on Lake Michigan are characterized by moderate winds and waves, with storms occurring infrequently, while during spring and fall the coast is subjected to frequent intervals of high wave stress. Thus, the shallow-water features are prominent in summer when the deeper and permanent bars are inactive and lie below the depth of the normal wave forces. They represent the reworking of the nearshore sediment due to moderate waves which pass unaltered across the deeper bars. Intense storm waves effect the entire bottom structure and disrupt the shallow-water structures built under moderate wave conditions.

Much variability in bar structure also occurs offshore from the three continuous crests. In the northern parts of the study area, a fourth continuous bar is present and the depth of water over its crest is linearly related to the depth of water over the three shallower continuous crests. In this region, the fourth continuous bar conforms with the characteristics of the inner three, as the amplitude and bar

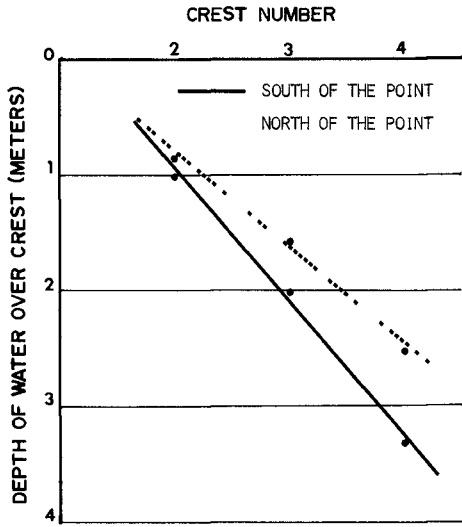


Fig 2 Average depth of water over successive bar crests

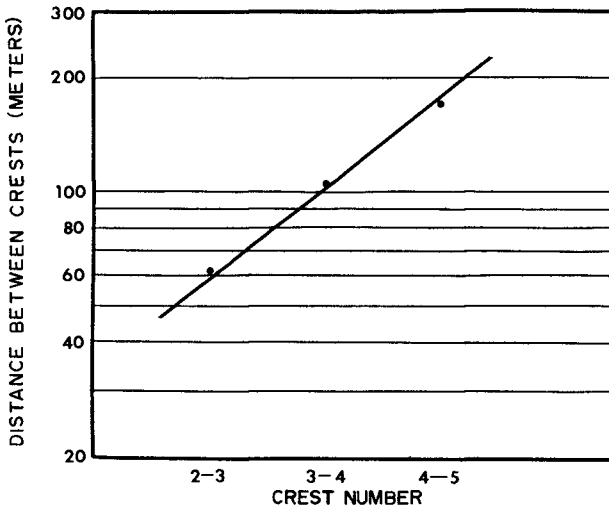


Fig 3 Average distance between bar crests based on measurements at 29 sites over approximately 45 km

spacing increase in a regular fashion going offshore. Outside of the quartet of continuous crests, a long-crested, low-amplitude swell of the lake bottom is sporadically present on various ranges. The northern half of the reach south of Little Sable Point is also characterized by four continuous crests, while near the southerly end of the coastal reach only the three continuous crests are present. Again, the low-amplitude swell occurs lakeward of the continuous features on only several of the range lines.

The depth of water over the crests of shallow-water bars and of the deep lake bottom swells does not fit the linear distribution observed for the continuous crests. At both ends, the observed water depths are greater than those which would be obtained from interpolation of the linear trend for the persistent triplet. If the linear distribution of crest elevations is truly representative of an equilibrium longshore bar structure, as is certainly suggested by the consistent observations, the deep swells of the lake bottom must be representative of bar formation at a depth where there is insufficient energy expended by breaking waves for full bar development. This is perhaps to be expected, since the deep crests would cause wave breaking only for the most intense and infrequent Lake Michigan storms. The sporadic occurrence of the deep swells, and the development of four continuous bars in two subreaches, would be the result of the variations in wave intensity along the coast due to wave refraction and differences in exposure.

The spacing between crests in the offshore direction does not increase in a linear fashion, but rather increases exponentially. The spacing between bars shows more variability than the depth of water over the crests, although there are clearly defined distributions. Figure 3 shows the bar spacings observed during the spring of 1969 in the entire coastal reach. The numbering scheme for the crests shown on the figure is the same as used previously, i.e., crests 2-4 refer to the three bars continuous along the coast. The spacing between crests varies considerably as the offshore gradient varies from range to range. At Little Sable Point, for example, the slope is greater than it is at the northern end of the study area, so that the bars are compressed together even though an exponential increase in spacing is still observed in the offshore direction.

The ratio of water depth over the trough (D_t) to depth over the crest (D_c) falls between 1.1 and 2.1. Keulegan (1948) reported that this parameter remained fixed even as other measures of the bar changed due to varying wave conditions. The average value of 1.5 from our data agrees closely with value 1.5 (below 11w) given by Shepard (1950) as most typical of Pacific beaches, and with the average of 1.69 determined by Keulegan in wave tank experiments. It should be noted, however, that choice of reference level (mlw, 11w, etc.) and method of calculating the average can significantly alter the results. Further, no relationship between the type of bottom material and D_t/D_c could be found even though the bottom material was found to exert a major influence on bar profile configuration, as will be discussed later.

In examining bar measurements made on the Pomeranian coast by Otto

and Hartnack (in Keulegan, 1948) and on Lake Michigan by Evans (1940), Keulegan felt that there was field evidence that D_t/D_c increases with increasing distance of the bar from shore. No significant difference was found in this ratio for the three persistent bars (2, 3, and 4) in this study. A lower value of 1.3 for the outer bar contributes to the evidence that the outer bar, which is out of the reach of frequent wave disturbance, has not yet been able to build to an equilibrium state.

The physical significance of the linear increase in depth of water over successive crests and of the exponential increase in bar spacing is not readily apparent. The water depth at which incident wind waves break is a constant fraction of the depth, i.e., the waves break when the wave height is on the order of 0.8 of the water depth. Thus, a linear increase in water depth over the crests going offshore would imply a linear decrease in the height of waves breaking on successive crests in the onshore direction. Since wave energy is proportional to the square of the wave height, the energy dissipated on each bar would not decrease in a linear manner, and the energy dissipated on each crest may play an important role in determining bar spacing. However, it is probable that the large wave heights are associated with the longer wave lengths incident on the coast so that the process of breaking across successive bars can filter out wave lengths as well as wave heights. The wave length may also be a factor in determining bar spacing.

BAR STABILITY

After reaching record low levels in 1964, the water surface elevation of Lake Michigan increased steadily through 1969 (Figure 4). According to Evans' (1940) hypothesis, the rise in lake level should have stranded the deeper bars as relicts, with a new set of longshore bars built inside them. But the observations do not indicate that this has occurred. On the contrary, the bars have built upward toward the water surface and moved inshore. Figure 5 shows bottom elevations measured along two ranges in the northern third of the study area which typify the observations in this coastal reach. The profiles were measured during the summer of 1967 and the spring and fall of 1969.

An onshore movement of bars and troughs is unmistakable, and for the profiles shown in Figure 5 averages about 30 m. The direction of movement in relation to long-duration changes in lake level is exactly opposite to the movements hypothesized by Evans (1940), who indicated that onshore movement of the shallower continuous bars would be associated with falling lake levels. During the summer months the deeper bars exhibit much stability, in agreement with summer observations made by Davis and McGeary (1965). Comparison of aerial photographs may also give a misleading interpretation of bar stability unless the cyclical changes with respect to water surface elevation are taken into account.

The average depths of water observed over successive crests during the summer of 1967 and spring of 1969 are compared in Figure 6 for those ranges studied both years. If the bars were static, fossil fea-

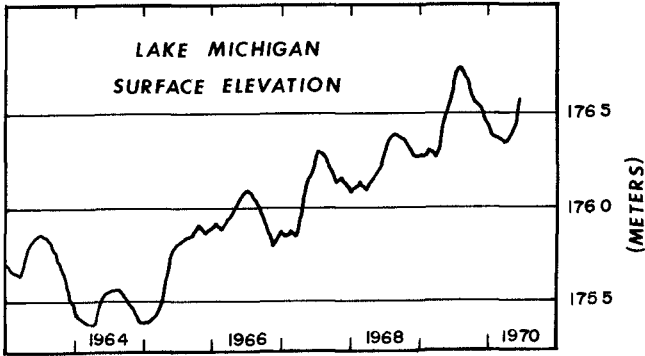


Fig 4 Hydrograph of monthly mean levels of Lake Michigan since the record low of 1964 (IGLD, 1955)

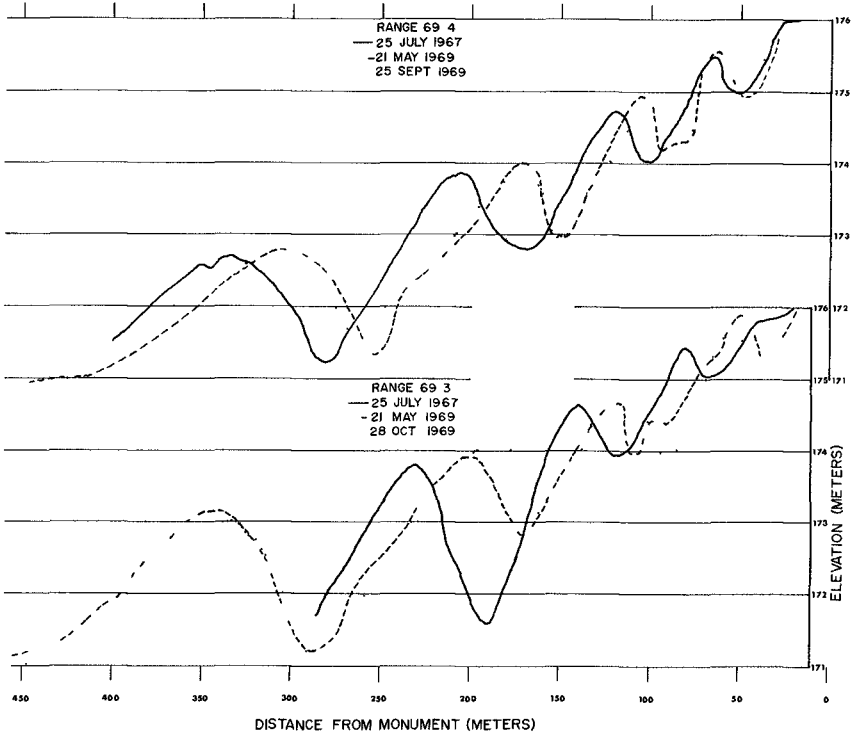


Fig 5 Movement of bars and troughs

tures, they would simply have been drowned during the subsequent rise in lake level, i.e., the 1969 depths would merely plot 0.31 m above the 1967 depths. But this is not what occurs. The bars have responded to the rising lake level by building upward in a manner to preserve fixed depths below the water surface. Discrepancy between the 67 and 69 depths increases toward deep water (where the response is slower), but even on the deeper bars the difference in depth is less than the change in lake level.

The most rapid movements of bottom material are associated with the spring and fall intervals of frequent high wave intensities. The fall season is most important because wind across the lakes is accelerated due to unstable air stratification above the warm lake surface, whereas stable stratification occurs in spring and summer over the cold lake surface. Thus, lake elevation during the fall months is perhaps the determining factor in the establishment of equilibrium nearshore topography, and in this sense the profiles measured during the summer of 1967 and the spring of 1969 are probably representative, at least for the deep water ends of the profiles, of conditions established during fall of the previous year. For a considerable part of the ice-free season, an increase in water surface elevation allows higher amplitude waves to propagate to the shoreline than would be possible if the profiles were fully adjusted to an equilibrium state. These non-equilibrium stages are associated with extensive beach erosion and structural damage. Conversely, during low lake levels the longshore bars are more effective in dissipating the incident wave energy, and the shallow-water areas are unusually stable. Noting the annual cycle of water surface elevation in Lake Michigan as shown in Figure 4, it is to be expected that the beach is most vulnerable to erosion during the early summer months of peak water level.

TEXTURE OF BOTTOM SEDIMENTS

A fine grain, very well sorted quartz sand is the typical bottom sediment from the water's edge out to a depth of 9 m and from range 1 to range 29, 45 km south. While diving with the aid of SCUBA, a few pools of colloidal clay (about a meter in diameter and a few centimeters in thickness) were noted, resting gently over scattered depressions in the bottom. None of the more than 270 bottom samples had so much as 1% by weight in the silt-clay size range, i.e., $<4\phi$, where $\phi = -\log_2$ diameter in mm. Toward the other end of the size range granules and pebbles, though uncommon, did occur at the strandline along some reaches of the coast and they appeared in a few samples from specific troughs.

Sieving the sediment on $1/4\phi$ intervals disclosed a small but clear trend toward finer material on the crests away from shore. Superimposed on this classical pattern is a tendency for trough samples to be coarser, more poorly sorted, and more negatively skewed than samples from the adjacent bar (Figure 7). Changes in these three textural parameters can most simply be viewed as expressing the absence, on crests, of some material from the coarse end of the normal size distribution.

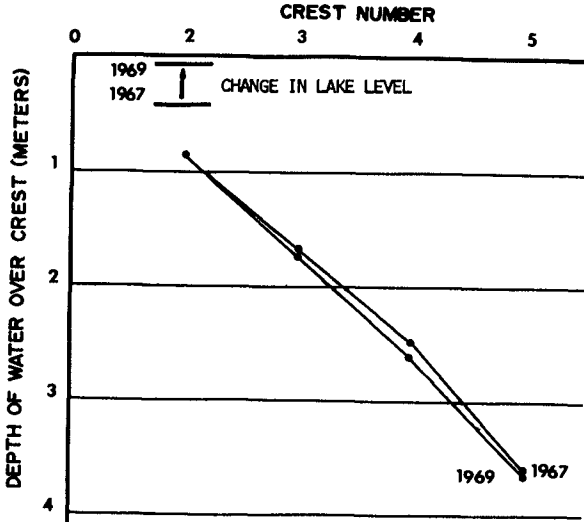


Fig 6 Average crest depths measured at ten sites in 1967 compared with the results of 1969 measurements from the same area

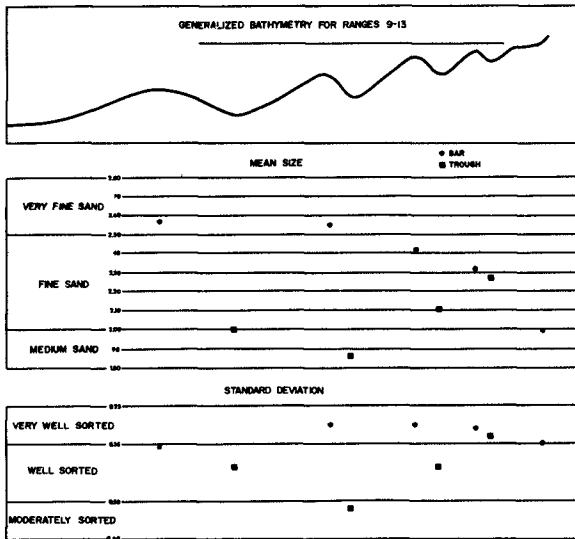


Fig 7 Average textural parameters of crest and trough samples from ranges 9-13 Trough samples are coarser and more poorly sorted than samples from adjacent troughs

These observations are in accord with the principal theories on bar genesis, in as much as the various theories all envision some winnowing action at trough sites with concomitant deposition on a bar site located immediately lakeward

Figure 7, illustrating textural variations in an offshore direction, is based on the average values from the various bars on ranges 9-13 during 1969. In addition to the accumulation of slightly coarser sand at the troughs, which appears to be a general rule, we found a few troughs floored with a relict, immobile material. Therefore, to examine size variations of just the mobile fraction in the longshore direction, the crest samples were averaged for the three persistent bars which occur on each range, and the results are shown in figure 8. A regional trend emerged, the finest material in littoral transit and stable within the surf zone accumulates in the area just north of Little Sable Point (in the vicinity of range 10). This reach of the coast occupies an intermediate position between shore bluffs that mark the intersection of the modern shoreline with glacial moraines. A high bluff (>50m) to the north is subject to periodic slumping as indicated by the presence of recently uprooted trees in the shallow water at the toe of the bluff and by the testimony of residents. This source of new material to the littoral system lies about 5 km beyond the northern limit of the area sampled, but as shown by the pattern of accretion and recession around the Pentwater jetties the net longshore drift is from the north in this region and the bluff appears to be a source of sediment to the nearshore zone as far south as Little Sable Point. Cobbles lie at the toe of the bluff and the finer constituents eroded from the moraine debris are redistributed by littoral drift. Clays and silts in suspension evidently move considerable distances alongshore, but are ultimately diffused into deeper water prior to burial. The sand load becomes gradually finer in its direction of flow away from the bluff toward Little Sable Point, Figure 8. The transport of some of the coarse sand reaching Pentwater may be arrested by the jetties there. South of Little Sable Point the moraine again meets the shoreline, and in the past has contributed fresh material to the shore environment. However, because of the configuration of the coast (Figure 1) the northwesterly storms are less important here than southwesterlies which cause littoral drift in this region toward the north. The finer sediments in the vicinity of range 10 are protected somewhat from northerly drift by the Point. Northwestery storms likewise fail to induce strong littoral flow at this point since the waves approach normal to shore. Therefore, it is not unreasonable that moving away from glacial bluffs to the north and south toward this zone of converging littoral currents, increasingly finer and more mobile sediments are encountered. It should be pointed out that the spatial variations in texture, (alongshore, offshore, and bar versus trough) are small ($\sim 3/4\phi$) and would not have been disclosed by the still common practice of sieving at $1/2\phi$ intervals.

BAR GEOMETRY AND COMPOSITION

A relationship between sand size and slope of the beach has been demonstrated by Bascom (1951). Moreover, wave tank experiments at the Coastal Engineering Research Center (Saville and Watts, 1969) have

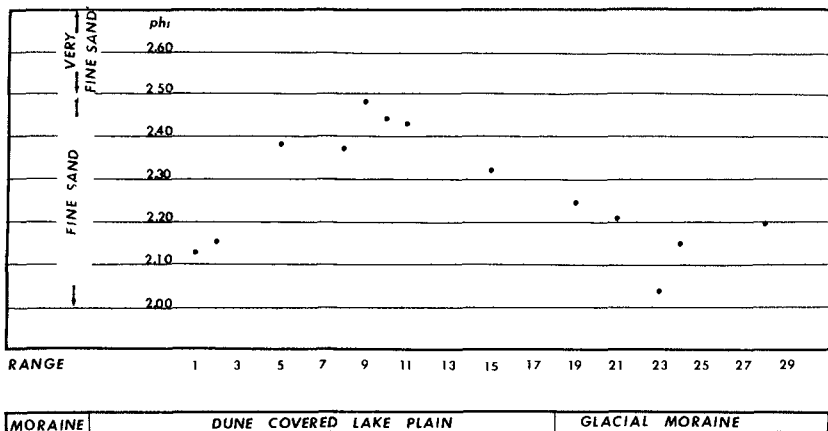


Fig 8 Longshore variation in mean diameter of mobile sediment

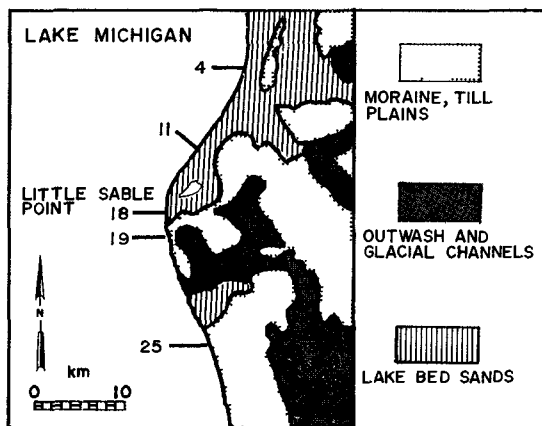


Fig 9 Location of ranges with boulder-paved troughs and their relationship with glacial formations onshore (From Michigan Geological Survey, 1955)

shown a tendency for bars to build slightly farther offshore as the grain size of the sediment is decreased. The textural variations discussed in the preceding section are, however, too small to relate to changes in bar morphology. The response of profile configuration to radical changes in bottom composition, several orders of magnitude greater than the variations revealed by sieve analysis, will be discussed here.

Longshore bars occur on tidal as well as tideless bodies, inland lakes as well as open oceans. The resulting forms are quite variable, reflecting local sediment response to a particular energy environment. In spite of this variability, longshore troughs in sandy material are characteristically U-shaped. It was therefore surprising to find on the fathograms several profiles exhibiting flat and even convex upward trough floors. In each instance investigation using SCUBA revealed the presence of a rock pavement at these sites of anomalously shaped troughs.

The rocks were from cobble to boulder size (0.1 to several meters in diameter) and ran the gamut of lithologies through sedimentary, igneous, and metamorphic types. This indicates the necessity of glacial transport to explain their occurrence on the shore of Lake Michigan. Three of the five ranges with flat bottom troughs are indeed directly offshore from truncated glacial moraines. The occurrence of boulders on these three southern ranges is thus readily explainable as an effect of post glacial coastal erosion. Boulders also floor troughs on ranges 4 and 11, and these are separated by kilometers from the nearest boulder clay deposit. Evidently the glacial moraines formerly extended considerably farther westward (Figure 9).

The correlation between atypically shaped troughs and the presence of boulder pavements seems well established by this study. The use of grab samplers (VanVeen, 1936; Shipek, 1965), so routinely employed in surveys of shallow-water sediments, fail to reveal the rock pavements due to the large size of individual rocks (0.1-2m) and the elongate, patchy distribution of the deposit. Likewise, Hough's method (1952) for identifying bottom composition by interpreting the density and thickness of fathogram traces also failed to reveal these substantial changes in bottom type. Rock pavements do however reveal their presence by effecting profile configuration. They interrupt normal profile development, causing abrupt changes in slope and flat to convex upward troughs (Figure 10). This previously unrecognized relationship permits the use of fathograms to infer the presence of clay, gravel, boulder, or bedrock substratum and the thickness of mobile sediment.

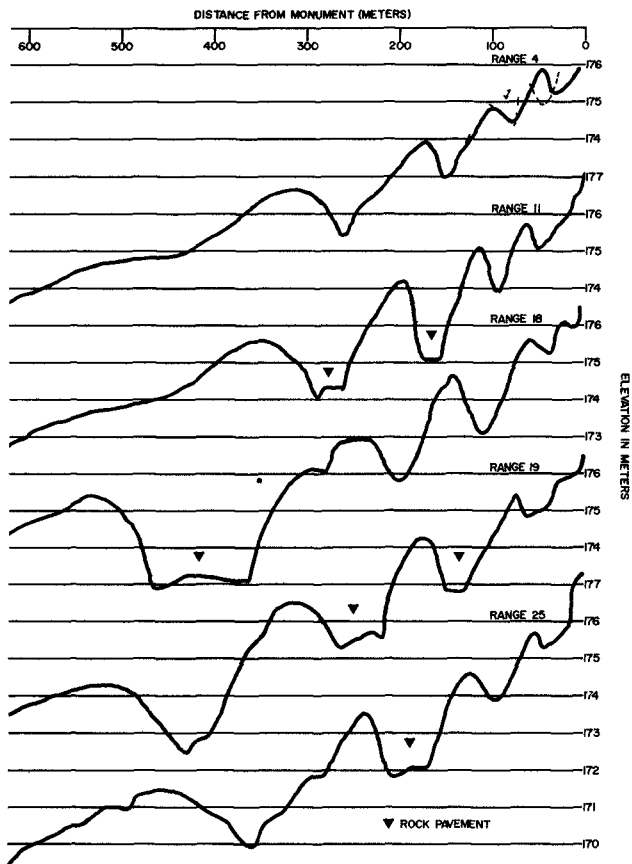


Fig 10 Atypical, flat-bottom troughs arise where immobile strata interrupt normal profile development

REFERENCES

- Bajorunas, L and D B Duane
1967 Shifting offshore bars and harbor shoaling Jour Geophysical Res ,
V 72, No 24, 6195-6205
- Bascom, W N
1951 Relationships between sand size and beach face slope Transactions
American Geophysical Union, V 32, No 6, 866-874
- Davis, R A and D F R McGeary
1965 Stability in nearshore bottom topography and sediment distribution,
southeastern Lake Michigan Proc 8th Conf on Great Lakes Res , Pub
No 13, Great Lakes Res Div , Univ Mich , Ann Arbor, Mich , 222-231

- Desor, E
1851 On the superficial deposits of the district In Foster, J W and J D Whitney, Report on the Geology of the Lake Superior Land District, Part 2, Wash , D C , 258p
- Evans, O F
1940 The low and ball of the eastern shore of Lake Michigan Jour Geology, V 48, No 5, 476-511

1942 The origin of spits, bars, and related structures Jour Geology, V 50, No 7, 846-865
- Folk, R L and W C Ward
1957 Brazos river bar a study in the significance of grain size parameters Jour of Sed Petrology, V 27, No 1, 3-26
- Hawley, E F and C W Judge
1969 Characteristics of Lake Michigan bottom profiles and sediment from Lakeside, Michigan to Gary, Indiana Proc 12th Conf on Great Lakes Res , International Association for Great Lakes Research, 198-209
- Hough, J L
1952 Fathogram indications of bottom materials in Lake Michigan Jour of Sed Petrology, V 22, No 3, 162-172
- Keulegan, G H
1948 An experimental study of submarine sand bars Beach Erosion Board, Tech Rept 3
- Martin, H M
1955 Map of the surface formations of the southern peninsula of Michigan Mich Geol Survey Pub 49
- Saville, T Jr and G W Watts
1969 Coastal regime, recent U S experience Proc 22nd International Navigation Congress, Reprint 3-70, Coastal Engineering Research Center, Washington, D C
- Shepard, F P
1950 Longshore bars and longshore troughs U S Beach Erosion Board, Tech Mem 15, 32p
- Shipek, C J
1965 A new deep sea oceanographic system in Ocean Science and Ocean Engineering Trans of the Joint Conf and Exhibit, Marine Tech Soc and Am Soc Limnology and Oceanography, 14-17, V 2, 999-1008
- Van Veen, Johann
1936 Onderzoekingen in de Hoffden Landsdrukkerij, The Hague, 252p
- Zenkovitch, V P
1967 Processes of Coastal Development Interscience Publishers, New York, N Y 738p

CHAPTER 54

SOME SAND TRANSPORT PHENOMENA ON COASTS WITH BARS

M. Dyhr-Nielsen, Research Engineer
and
Torben Sørensen, Director
Danish Institute of Applied Hydraulics
Copenhagen, Denmark

1. INTRODUCTION

Longshore wave currents and their influence on the sand transport phenomena in the shore zone have attracted the attention of numerous researchers. Also the existence of transverse, secondary currents, superposing the longshore component, has been known for years, but less attention has been given to analysis of their effect on the sediment movement.

This paper presents some examples of the influence, these relatively weak transverse currents may have on the processes in the shore zone. They have a parallel in the effect of secondary currents in alluvial streams, which, although weak, give rise to such an impressive phenomenon as meandering.

All conclusions below are based on simple, qualitative considerations of the physics of the system. A strict mathematical, quantitative approach to the problem does not seem possible with the present knowledge of the fluid dynamics in the shore zone, and much further research into these complex phenomena remains, of course, necessary.

2. NET CURRENTS IN THE SHORE ZONE

Longshore currents

It is well known that the breaking of waves in shallow water exerts a force on the water body between the breaker zone and the shore. This is due to the existence of the wave thrust [Lundgren 1963], found by integrating the flux of momentum and the wave pressure over the water depth in a wave period. The wave thrust has the same direction as the wave orthogonals.

It is also known that the longshore component of the wave thrust generates longshore currents in the trough between breakers and shore. An equation of equilibrium of the forces in the longshore direction may in principle be established to yield an expression for the longshore velocity. This approach is physically sound, but lack of sufficient knowledge of the bed shear stress generated in the complex movement in and behind the breaker zone renders this approach impracticable at this moment. Furthermore the stochastic aspects of the problem are undoubtedly very important and cannot at present be grasped in mathematical form.

Circulation currents

The component of the wave thrust parallel to the shore generates the longshore currents.

Similarly, the component perpendicular to the shore generates circulating currents in the cross section. These currents were first observed by Bagnold [Bagnold 1940] and have since been verified by many others. In the following a simple qualitative explanation of the generation of these currents is given, and their occurrence is related to specific properties of the wave motion.

Bottom currents under shoaling, nearly-breaking waves

The deformation of the waves approaching the breaker zone will increase the wave thrust I in the shoreward direction, so that the thrust I_2 in section 2 is greater than I_1 in section 1, see Fig. 1. Therefore the resulting thrust I_R on a control volume from section 1 to section 2 has an offshore direction. This force is compensated by a decrease in mean water level in an onshore direction, creating a static water pressure reaction P_R against I_R .

The strong deformation of the orbital velocity profile of a wave immediately before breaking causes I_R to act at a higher level over the bottom than P_R . Hence an equilibrium in the moments can only be obtained if there is a resulting force along the bottom, i.e. a resulting shear stress T . T must act on the water body in a seaward direction, and in a shoreward direction on the bottom. The waves will contribute to this, as the resulting shear stress due to wave motion will have an onshore component, but near the breaker zone this appears not to be sufficient, and a shoreward bottom current will superpose the wave motion.

The existence of shoreward currents under nearly-breaking waves can clearly be observed in a laboratory flume.

Bottom currents under surfing waves

After breaking the wave proceeds for some wave lengths as a surfing wave. The heavy energy losses will reduce the wave height, and the wave thrust will decrease in the onshore direction, see Fig. 2. The resulting wave thrust I_R acting on the control volume will now have a shoreward direction. A rise in mean water level will give a static pressure reaction P_R , but due to the high particle velocities at the water surface, I_R will attack at a higher level than P_R .

Equilibrium in the moments again requires the existence of a resulting bottom shear stress T , but now acting shoreward on the water volume and seaward on the bottom. Hence under surfing waves the wave movement must be superposed by a resulting bottom current in a seaward direction.

This current can also be observed in a laboratory flume.

Circulating currents

Under the breaker line, the onshore and offshore bottom currents under the waves will meet. Observations in a flume have shown, that there is only a very small transport of water through the breaker zone near the bottom. Circulating cells are formed as shown in Fig. 3 whereby the return flows for the bottom currents are established. Fig. 3 shows a two-breaker zone where the surfing waves are regenerated and a secondary breaker zone is formed. Two circulating cells are formed between the breaker lines, preventing transport in the bottom zone from the inner to the outer cell.

If the surfing waves reach the shore like in Fig. 4, only one cell is formed, and transport from the shore to the outer breaker line will occur. This has a very important effect on the coastal sediment transport as will be shown later.

3. EFFECTS ON SEDIMENT TRANSPORT

Formation of longshore bars

It has been shown above that waves breaking on a sloping plane will generate secondary currents directed towards the breaker line. This will have an accumulating effect on the grains on the bottom, moving them towards the breaker line where they build up a bar.

The shape will stabilize when the slope gets so steep that the bottom current cannot transport the sand up over

it, or when there is equilibrium between the amount of sand carried up by the bottom current and the sand returned in suspension at higher levels. At present it is not possible to tell which of these two conditions is the governing factor.

The position of the bar is closely connected to the position of the breaker line. Therefore, on tidal shores where this position is changing rapidly with the tidal cycle, distinct bars can only be expected to occur under severe wave conditions. Hence the existence of bars is more likely to occur in the winter as a result of more frequent storms.

The lower waves in the summer will not break over the bar, so the accumulating effect is replaced by an onshore bottom current that will erode the bar configuration and change the winter-profile to a summer-profile.

Formation of transverse bars

In certain cases the situation with a two-breaker zone may change to a one-breaker zone, where the surfing waves from the outer breaker line are not regenerated but extends to the shore as shown in Fig. 4 and 5. It might for instance happen when the depth over the outer bar is increased by erosion or dredging.

In this case a shoreward bottom current extends from the shore to the outer breaker line, see Fig. 4. This current will carry at least a part of the material transported on the inner bar out to the outer bar. Studies of bottom topographies in the nature have shown, that in connection with this a transverse bar is formed.

The deficit in the near shore transport downstream of the transverse bar affects the stability of the beach profile. Erosion of the beach occurs in the downstream region in order to reduce the deficit and satisfy the transport capacity of waves and currents downstream of the transverse bar.

The stable beach

It has been shown in laboratory tests that the wave steepness, defined as the ratio between wave height and wave length, has a high influence on the stability of a beach. Waves steeper than a certain value were shown to erode the beach profile while waves below this steepness would build up the beach.

The existence of secondary currents seems to offer a simple explanation of this. Consider a plane beach with slope 1:n, see Fig. 6. A wave of height H will break at a depth approximately equal to H . Hence the distance from the shore to the breaker line will be approximately $n H$.

It is obvious that if this distance is large, surfing waves are formed and seaward bottom currents are generated. But if the breaker line is very close to the shore this is not the case and the breaker will instead form a swash wave on the beach. Surfing waves are able to remove sand from the shore, whereas swash can move sand up on the beach for the following reasons: Swash has the highest velocity and hence the highest transport capacity, when the water is moving shoreward, and seepage losses reduce the seaward transport capacity further when the water is running back.

Assuming that the change between surf and swash happens when the breaker line is distance $k L$ from the shore, where L is the wave length. Now a simple similarity consideration gives the limiting wave steepness H/L for the stable beach as $H/L = k/n$.

It can be seen that the critical steepness depends on the slope of the beach. This may have some implications for model tests with movable bed and a distorted scale. The effect of distortion on the slope of a beach might change an eroding wave in the nature to an accumulating wave in the model.

Meandering in the shore zone

An interesting observation of some shore line configurations may be mentioned in this connection.

On a 10 km long reach south of Hvide Sande on the west coast of Denmark it is possible to detect a periodic fluctuation on the shore line and of the outer bar. The wave length of this fluctuation is about 3000 m, and the amplitude of the order 100 - 200 m. Hence with 3000 m interval the width of the beach is relatively large, and in between it is relatively narrow. This pattern has been remarkably stable in the 9 years for which this shore has been studied in detail, although it has been superposed by local erosions and accretions in connection with the formation and passage of transverse bars.

If the area between the bar and the shore is considered as a "river" carrying the longshore current, the ratio between the width of this river (about 300 m) and the length of its "meander" (about 3000 m) is the same as found for meanders in alluvial rivers. From this it seems possible that the longshore current in certain aspects is similar to an alluvial river. The observations of formation of dunes in the trough between bar and shore [Zenko- vich 1967] further support this assumption.

A similar "meander" pattern in a smaller scale has been observed on other Danish coasts.

4. THE "HVIDE SANDE" STUDY

Investigations in the prototype

Hvide Sande is a small harbour town on the west coast of Denmark. It is located on a narrow sand spit in a tidal outlet which is now controlled by sluices. The undisturbed coast profile at Hvide Sande has two parallel bars and the resulting sand transport along the shore has a southward direction.

To stabilize the outlet two 100 m long groyne were constructed in 1931, but these had no significant influence on the outer bar. In the fifties the depth over the outer bar was considered too shallow for safe navigation and in order to improve the conditions a 400 m long groyne was constructed about 100 m north of the outlet, see Fig. 7.

This groyne crossed the outer bar and forced it to move seaward. Furthermore a strong erosion took place on the outer bar at least up to 3 km south of the new groyne in the following 3-4 years as the supply from north was temporarily cut.

Hence in October 1966 the original bar was significantly reduced over long reaches south of the groyne. In the same period a severe erosion of the beach occurred at a point about 3 km south of Hvide Sande. (Similar attacks were reported 6 and 10 km to the south, in places where the "meandering" had narrowed the beach.) In connection with this soundings in April 1967 showed that transverse bars had been formed in the winter of 1967 connecting the near-shore bar with the remnants of the outer bar, see Fig. 8. Just south of these bars the severe erosions were observed. The transverse bars migrated towards south with a velocity of about 600 m/year, changing the points of attack on the beach so that the erosion in a point decreased or was substituted by a temporary accretion after the passage of the bar.

South of the transverse bars the outer bar was built up again, which indicates that the outer bar was supplied with sand from the shore zone as mentioned above. The erosion of the outer bar in connection with the groyne construction changed the breaker regime from a two-breaker zone to a one-breaker zone causing the formation of the transverse bar.

It should be mentioned that transverse bars have been observed at many other locations, for example at the upstream side of a groyne where the beach transport has to leave the shore to get around the groyne. They are also found on coasts without manmade interference, but again in connection with local erosion of the beach.

Model tests

With the purpose of studying the effect of the groyne constructions on the wave current patterns during storms three fixed bed models were built. The horizontal scale was 1:300, the vertical scale 1:100. The models illustrated the situation in 1927 before any groynes were built, in 1961 with the two small groynes just before construction of the big groyne, and in 1967 3 years after the big groyne was completed.

As the bottom currents were of major interest they were traced by plastic balls having a diameter of 1 cm and a settling velocity of 7 cm/sec. These balls were shown to be light enough to follow the wave current but heavy enough to stay at the bottom.

The movement of the balls showed clearly the existence of resulting transverse bottom currents as mentioned in section 2, as they always had a velocity component towards the breaker zone. But an even more convincing demonstration came from the injection of small (1 mm ϕ) polystyrol grains which were transported seaward under surfing waves and shoreward under nearly-breaking waves. The accumulating effect of the circulation currents concentrated the grains under the breaker lines where they were transported downstream in very narrow bands parallel to the shore.

That something similar happens in the nature has been demonstrated by Ingle in his studies of the movement of dyed grains on beaches in California [Ingle 1966].

The only exception from the pattern above was found in the region where the beach erosion had been reported. Here the relatively low outer bar caused a change from a two-breaker zone to a one-breaker zone, and the grains were transported from the bar near the shore out to the outer bar. In the two other models where the outer bar was undisturbed this did not occur.

Hence it was concluded that the heavy beach erosions were a secondary effect of the groyne construction. The erosion of the outer bar and the change in the breaker zone regime, caused by temporary cutting of the sand transport from north, gave rise to the formation of transverse bars, and these in turn were responsible for the erosion of the beach.

REFERENCES

- Bagnold, R. A. (1940). Beach formation by waves; some model experiments in a wave tank. J. Inst. Civ. Engrs., London, 15, 27-52.

Ingle, J. C. (1966). The movement of beach sand. Elsevier, Amsterdam.

Lundgren, H. (1963). Wave thrust and wave energy level. Internat. Assoc. Hydr. Res., 10th Congr., London, I.20, 147-151.

Zenkovich, V. (1967). Processes of coastal development. Interscience Publishers, New York.

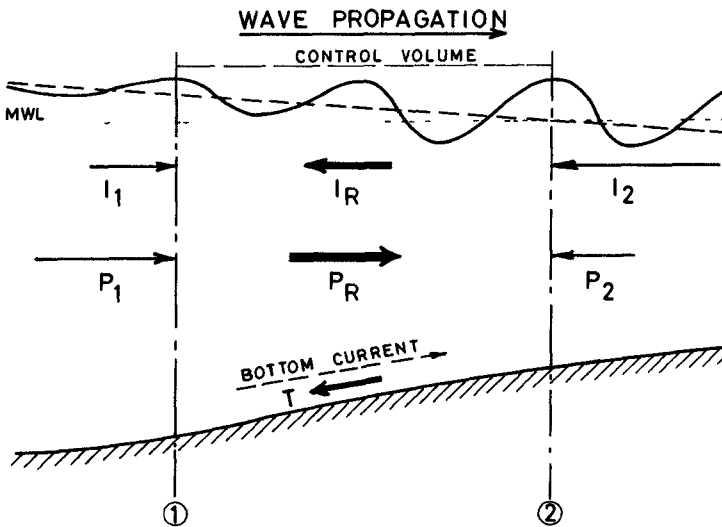


FIG 1 WAVES NEAR BREAKER ZONE

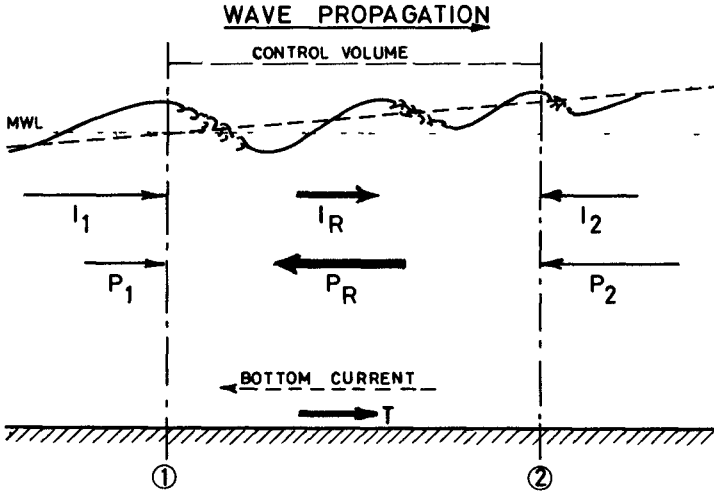


FIG 2 SURFING WAVES

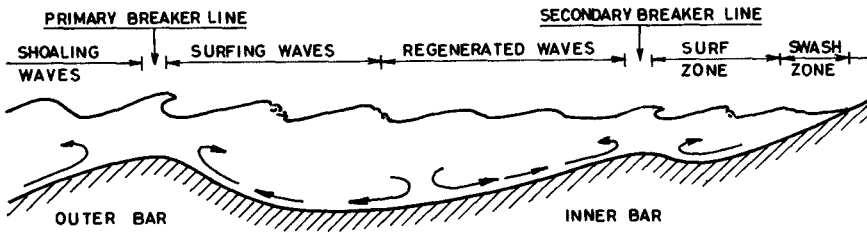


FIG 3 BOTTOM CURRENTS IN A TWO-BREAKER ZONE

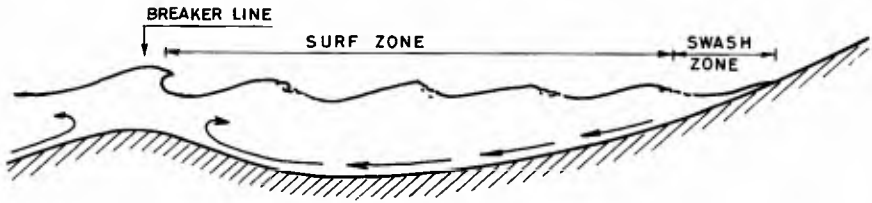


FIG. 4 BOTTOM CURRENTS IN A ONE-BREAKER ZONE

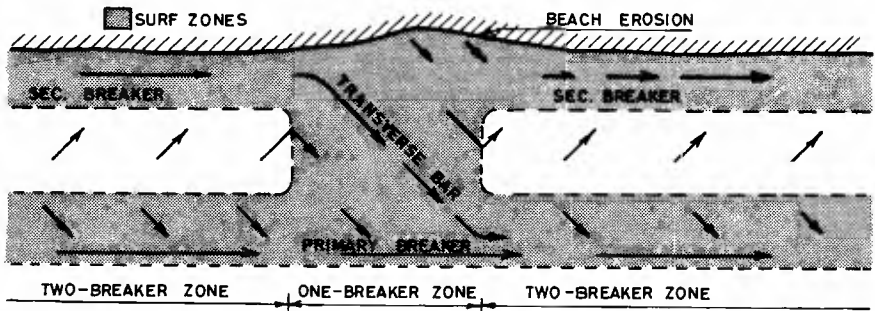


FIG. 5 TRANSVERSE BAR

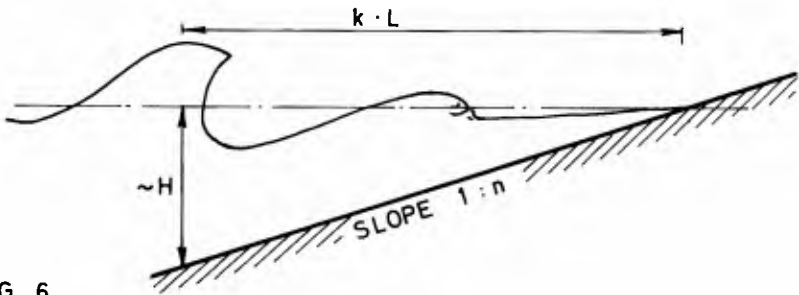


FIG. 6

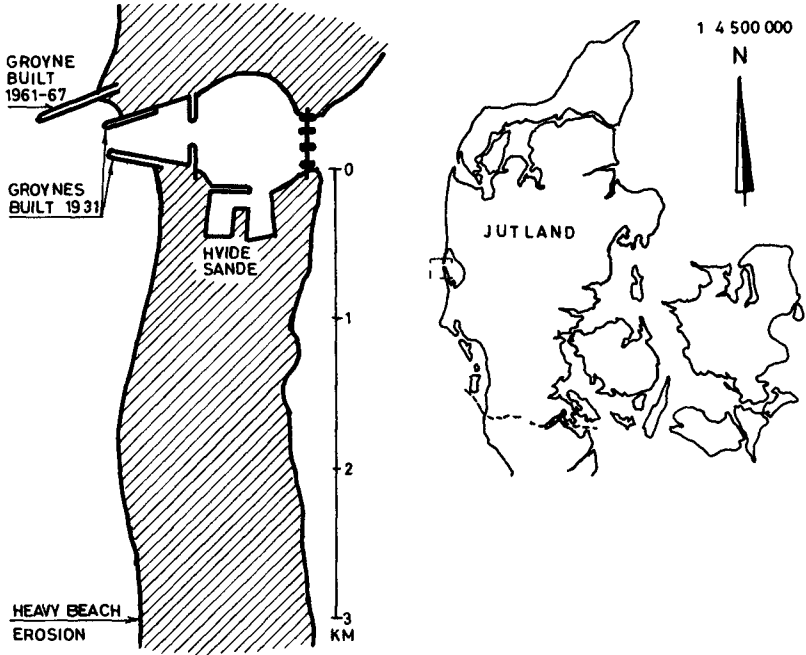


FIG 7 STUDY AREA

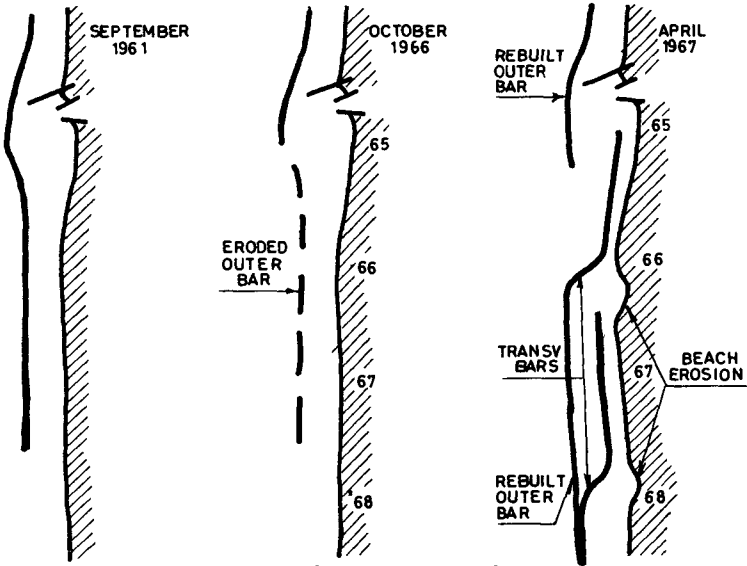


FIG 8 FORMATION OF TRANSVERSE BARS

CHAPTER 55

LABORATORY TESTS OF LONGSHORE TRANSPORT

by

John C Fairchild, M , ASCE
Research Hydraulic Engineer
U S Army Coastal Engineering Research Center
Washington, D C

ABSTRACT

Tests were made in CERC's Shore Processes Test Basin with waves approaching the toe of a test beach at a 30-degree angle. Beach material was quartz sand with median diameter of 0.22 millimeter which, in most tests, was molded to a 1 on 10 slope before starting a test. Long crested waves generated in a constant depth of 2.33 feet traveled over the beach, shoaled and were refracted before breaking near the shoreline. The breaking action caused the sand to be transported along the shore in the direction of the longshore component of the wave energy flux. Transport rates of 2 to 170 cubic yards per day were measured, with the lower rate within the range of laboratory rates reported by Savage⁽¹⁾ and the higher rate comparable to field rates reported by Watts⁽²⁾ for South Lake Worth Inlet, Florida. Analysis includes correlation of the measured rates to the longshore wave energy flux, and in some tests, to the longshore current. Transport rates, defined by visual fit curve of the data, are about 3 times the rates indicated by the CERC TR-4 design curve for a longshore energy range of 0.016 to 0.760 millions of foot pounds per foot of shore per day.

I INTRODUCTION

General

Water waves impinging obliquely on a sandy shore scour and suspend shore materials causing them to move along the shore in the direction of the longshore component of the wave energy flux. The amount of material moving depends primarily on the wave breaker angle and the energy of the waves impinging on the shore. However, the amount of material moving at a given energy flux is influenced by the wave steepness, breaker type, sand size, and the beach slope, and experience indicates that these factors may act to increase or decrease the longshore transport, where there is little or no change in the wave energy flux.

The amount and direction of longshore transport is important in the planning and design of shore improvements. Reliable field data on longshore transport is required in the design and economic evaluation of jetties, navigation inlets, beach erosion projects, and hurricane protection projects. Data, usually of questionable accuracy, is available for a few coastal areas, but present coverage is inadequate and field data is expensive and difficult to get. Therefore, CERC has for some time had underway a program to obtain laboratory data which would define basic relationships and which might be used with field data to more quickly and less expensively provide the relationship between longshore wave energy flux and longshore sand transport.

Laboratory Tests

This report presents results from laboratory tests of longshore transport (3,4,5,6) made in CERC's Shore Processes Test Basin (SPTB). Tests were made with waves approaching the beach at a 30 degree angle in a constant depth of 23.3 feet. Figure 1 is a plan view typical of the test set-ups used, showing the wave generators and the test beach, with the sand trap at the downdrift end and the feeder beach at the updrift end.

Beach material was a uniformly sized sand with a median diameter of 0.22 millimeter. In most tests the beach was molded to a 1 on 10 slope before starting wave action. Several tests, including some groin tests in 1957 (1) and 1958, were started on a "150 hour profile slope", which was an equilibrium slope determined from 150 hours of wave action. Other tests in 1959 and earlier were started on a 1 on 20 slope.

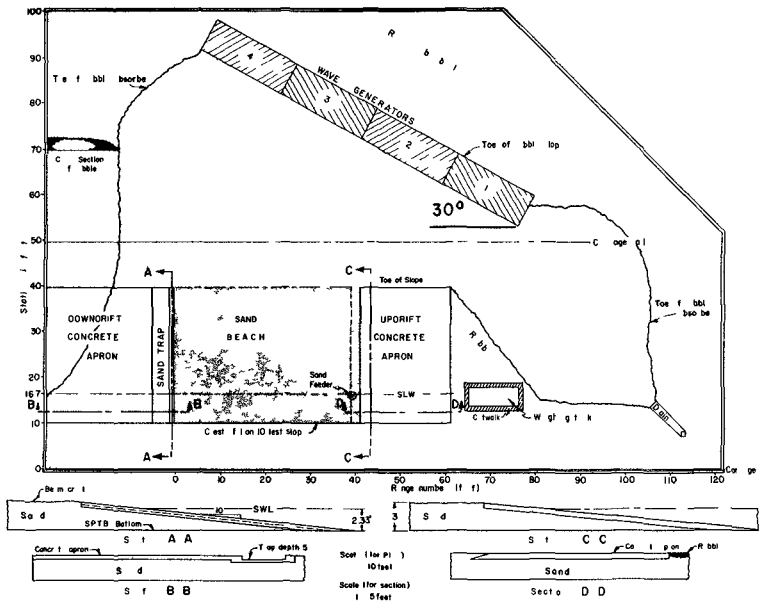


FIGURE 1 LONGSHORE TRANSPORT TEST LAYOUT IN THE NORTH SECTOR OF SPTB (1966)

Tests were carried out by generating long crested waves which traveled from the wave generator to the toe of the beach slope in a constant water depth. As waves continued over the beach they shoaled and were refracted before breaking. When the waves broke, part of their energy was dissipated in turbulence, scouring and suspending sand, part was transformed into a longshore current and part was reflected from the beach. The wave action scoured the beach sand, forcing it into suspension, to be carried along the shore by the longshore current. Also, the swash and backwash of the waves

caused the sand to move onshore and offshore, with a resultant slantwise movement along the shore

In summary, the wave action caused the sand to move along the shore in the breaker zone, in the swash zone and in the deeper offshore zone. The sand moved onshore and offshore, and with continued wave action, the bottom profile progressed toward an "equilibrium profile" characterized by a reduced transport rate and a reduced onshore-offshore exchange of material.

Purpose

The purpose of the tests was to measure the longshore transport rate for a range of wave characteristics, and to establish a correlation between the measured rates and the corresponding longshore components of wave energy flux. Longshore transport rates were measured in tests, wherein sand moving along the shore was deposited in a sand trap from which it was pumped and weighed under water. Longshore components of wave energy flux were computed from measured wave heights and calculated wave breaker directions.

From an engineering viewpoint, the purpose encompassed the obtention of laboratory data to define basic relationship for use with field data, to more quickly and economically improve and develop previous correlations between wave energy flux and longshore transport rate.

OBSERVATION AND MEASUREMENT

General

The sand (0.22mm quartz), water depth (2.33 ft at toe of beach), and angle of wave generator with initial shoreline (30°) were constant in the tests.

TABLE 1
TEST VARIABLES

Experimental Variables	Range of Variables Tested
1 Wave period	1.25 to 3.75 seconds
2 Wave generator stroke	2.0 to 15.0 inches
3 Depth at beach toe	2.30 to 2.33 feet (bottom uneven)
4 Initial slope	1 on 10 to 1 on 20
5 Beach material	0.22mm median diameter quartz sand
6 Angle of waves to toe of slope	30°, constant for all tests
7 Test time	25 to 100 hours
8 Layout of basin	training walls or flume to open basin

TABLE 2

WAVE CONDITIONS AND TEST SET-UP CHANGES
 *(total hours in test)

Test No	Wave Conditions				t*	Set-up Changes
	T, sec	Ecc, inches	H, ft			
1-58	1 50	1 00	176	60		Starting slope 1 on 20, T was sequenced in 15 minute intervals at T=1 50, 1 30, 1 50, 1 76, etc , no sand fed on feeder beach after 35 hours
2-58	1 50	1 00	176	70		Starting slope 1 on 20, T was varied as in test 1-58, feeder beach maintained throughout entire test
2a-59	3 00	2 35	192	80		Starting slope 1 on 10, T was sequenced in 15 minute intervals at T=2 50, 3 00, 3 75, 3 00, etc, upbeach training wall curved for wave refraction, beach length 90 feet
3a-59	3 00	2 35	192	50		Beach length reduced to 30 feet along SWL, other conditions same as Test 2a-59
4a-59	2 18	1 75	210	50		Starting slope 1 on 10, updrift trng wall re-curved by wave refraction for new T, sequenced in 15 minute intervals at T=1 94, 2 18, 2 50, 2 18, etc
1-59	1 50	1 00	176	25		Starting slope based on a 150 hour "equilibrium profile", segment of downbeach training wall from carriage rail to toe of slope, removed, T was varied same as in test 1-58
2-59 Phase 1	1 50	1 00	176	32		Same starting slope as 1-59, above, T was varied same as in test 1-59, downdrift training wall completely removed
2-59 Phase 11	3 00	2 35	192	80		Starting slope was the beach slope at end of Phase 1, T was sequenced as in test 2a-59
3-59	3 00	2 35	192	75		Starting slope 1 on 20, updrift training wall curved along wave refraction orthogonal, T was sequenced as in test 2a-59
4-59	3 00	2 35	192	50		Starting slope 1 on 20, wave period constant
5-59	3 75	2 35	140	50		Starting slope 1 on 20, wave period constant
6-59	2 50	2 35	246	50		Starting slope 1 on 20, wave period constant
1-60	2 18	1 75	210	50		Starting slope in this and all subsequent tests, 1 on 10, downdrift training wall reinstalled, and curved for wave refraction, T was sequenced as in test 4a-59
2-60	2 18	3 50	420	26		Wave Height increased as shown, T was sequenced in test 4a-59

TABLE 2, cont'd
 *(total hours in test)

Test No	Wave Conditions			t*	Set-up Changes
	T sec	Ecc, inches	H, ft		
3-60	3 00	2 35	192	28	A repeat of test 3a-59 conditions to check transport of suspended sand past the sand trap
4-60	2 18	5 00	614	25	Test at maximum wave height for generators, T was sequenced as in test 4a-59
5-60	3 00	4 70	422	26	Increased wave height as shown, T was sequenced as in test 2a-59
6-60	2 18	2 50	300	50	To test intermediate wave height value
7-60	1 36	1 50	320	50	To test maximum height at minimum period, T was sequenced in 15 minute intervals at T=1 25, 1 36, 1 50, 1 36, etc
1-61	3 00	2 35	192	50	Wave period changed every 5 instead of every 15 minutes, T was sequenced as in test 2a-59
2-61	3 00	2 35	192	50	Wave period changed at 1 minute intervals, T was sequenced as in test 2a-59
3-61	3 00	2 35	192	50	To compare results with test 4-59 (started on a 1 on 20 slope) Constant wave period
5-61	3 00	2 35	192	50	Wave period varied continuously from T=3 75 to T=2 50 through the mean, 3 00 seconds and return
6-61	2 50	2 35	246	50	Constant wave period, for comparison with results of test 6-59 (1 on 20 slope)
7-61	3 75	2 35	140	50	Constant wave period, for comparison with results of test 5-59 (1 on 20 slope)
1-61	3 75	2 35	140	50	Constant wave period, test of sand feeder, elevation 2 ft above SWL
2-62	3 75	2 35	140	25	Same as 1-62, elevation 0 1 ft above SWL
3-62	3 75	2 35	140	25	Same as 1-62, elevation at SWL
4-62	3 75	2 35	140	25	Constant wave period, to investigate effect of extraneous wave
6-62	1 50	0 94	172	48	Constant wave period, feasibility test of sand tracers
8-62	1 50	0 94	172	30	Same as 6-62, longer half life tracer, T was constant up to t=8 hours and wave varied as in test 1-58 after 8 hours
1-64	3 75	2 35	140	50	Constant wave period, offshore area divided into 8 flumes
1-65	3 75	2 35	140	40	Special constant wave period test, open test basin, rubble around test area

TABLE 2, cont'd
 *(total hours in test)

Test No	Wave Conditions			t*	Set-up Changes
	T sec	Ecc, inches	H, ft		
2-66	2 18	2 35	290	25	Same set-up as test 1-65, reduced wave period was constant
3-66	1 25	2 00	480	50	Constant minimum period for a stable wave and 2 inch eccentric
5-62	3 00	7 50	750	40	A special test attempting to measure the maximum transport rate possible in the SPTB

Five other variables under the experimenter's control were wave period, wave height, initial beach slope, test duration and basin geometry. Although not as simple a variable as others noted above, basin geometry changes from test to test included, the general configuration of the test layout, test beach length, arrangement of training and splitter walls, and sand feeding techniques. These changes were made after continuing observation and analysis, in the hope that they would improve the quality of the data in the tests.

Table 1 outlines the experimental variables and the range of these variables tested. This table gives an overview of the test variables within the positive control of the project engineer. Table 2 is a more detailed listing of the wave conditions and test set-up changes by test number, with the last column giving a running commentary of test-to-test changes in set-up. The variables listed in Table 2 include wave height, wave period and test duration, and each of these plus five other areas of observation and measurement are discussed separately in the following paragraphs.

Wave Height

Wave recordings using strip chart recorders were made regularly in the tests using parallel wire wave sensors placed along the toe of the beach slope. Spot recordings were also made at other locations in the test basin. Wave heights were determined from an analysis of the wave recordings, as the average height of ten successive waves.

As the tests continued, wave heights were found to vary significantly, from point to point, and with time as at a fixed point. Special wave measurements tests were made in 1963 and 1964 attempting to identify the cause or causes of the wave height variability. The measurement results were not conclusive. Another series of tests in the SPTB are presently investigating wave reflection as a cause of wave height variability in inclosed basins such as the SPTB. With continued testing and consideration of wave energy analysis in the tests, the large wave height variability (up to and exceeding a factor of 2) made it difficult to confidently specify a causative wave height in relation to a measured transport rate. Specifying a causative height - say from reflection-free waves in the SPTB was difficult because of the short distance for wave travel and the long length of the waves. For the longer wave periods only two waves could be measured before wave reflection from the beach began to affect the measurements.

Because of the length limitation in the SPTB, the measurements of wave height used in this report were made in CERC's 72-foot tank under experimental conditions equivalent to a 1/2 scale Froude model of the depth, eccentrics and periods tested in the SPTB. When the SPTB wave conditions were reduced to 1/2 scale, the 72-foot tank was long enough to generate sufficient reflection-free waves from which a sound evaluation of the wave heights was possible.

Considerable care was taken in measuring the wave heights in order to have heights as free from reflection effects as practicable. Only those waves which reached the wave gage before reflected waves returned from the absorber beach were used. For example, a wave period of 3.75 seconds and water depth of 2.33 feet in the SPTB reduces to a wave period of 2.65 seconds and 1.17 feet, respectively, at 1/2 scale. At this period and depth the wave length in the 72-foot tank was 15.6 feet which would allow for measurement of 7 to 8 reflection-free waves in a 60-foot spacing between a wave sensor and an absorber beach. These measurements in the 72-foot tank provided wave heights for 8 wave generator eccentrics, over a range of wave periods. The range of wave periods was 1.25 to 3.75 seconds with minimum wave heights of the order of 0.1 foot and maximum wave heights up to .75 feet. Figure 2 is a graph of the wave height measurements made in the 1/2 scale Froude model, plotted as prototype SPTB values.

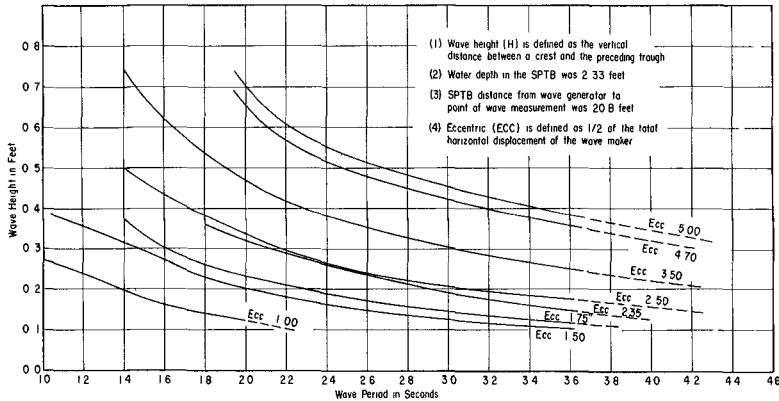


FIGURE 2 WAVE CHARACTERISTICS IN THE SPTB REDUCED FROM 1/2 SIZE FROUDE MODEL MEASUREMENTS IN THE 72-FOOT WAVE TANK

Wave Period

Wave period, T, could be arbitrarily selected within a range of 1 to 4 seconds on the SPTB wave generators. Dial settings, corresponding to specific wave periods in seconds, were made on a varidrive motor, which was electronically coupled by remote cable to a 7 1/2 horsepower A C drive motor for each wave generator. Since there was "drift or noise" in the electronic control system, dial settings of the wave periods were calibrated at frequent intervals. Also, wave period, once selected, was closely monitored to keep it constant. Monitoring was done by visually timing rotations of the wave generator eccentric arm by stop watch. Monitored values

were checked against the variable dial settings and when needed, corrections were made promptly. Wave period checks were made generally at 15 minute intervals for both variable and constant period tests. The variable period tests were varied in sequence above and below the mean wave period and height at a fixed time interval. In most of the tests this time interval was 15 minutes but in test 1-61 it was 5 minutes and in test 5-61, period and height variation was continuous. The last column in Table 2 gives some detail on wave period sequencing.

Longshore Transport

Longshore transport is the movement of material along the shore in the littoral zone by waves and currents⁽⁷⁾. In the laboratory tests under discussion, longshore transport rate is defined operationally as the rate of accumulation of beach material in a sand trap on the downdrift end of the test beach. The material accumulated from the sand trap, using eductors and hose line, into a weighing bin where it was weighed while submerged. Submerged weights were converted to their equivalent dry weights (or weights in air) by multiplying them by the factor, $\rho_s / (\rho_s - \rho_w)$, where ρ_s and ρ_w are the specific gravities of quartz and water, respectively. Using this factor to convert submerged weights to dry weights assumes that the sand is 100% quartz. These dry weights of sand, along with the time between weighings, were used to compute the longshore transport rates. Generally, transport rates were computed for the first hour or a lesser time, and in 5-hour intervals to the end of the test. In a few cases, rates were computed for periods of 15 minutes.

Sand Feeding

The feeder beach area was a small area at the updrift end of the test beach where sand was fed into the wave swash in order to maintain the test beach. The sand feeder at the updrift end of the sand beach, shown in Figure 1, is in the feeder beach area. In earlier tests, a variety of methods were used to feed sand into the feeder beach, and to maintain a hydrography in the feeder beach area similar to that which develops downdrift of it. The initial method was to stockpile sand on the beach, and to shovel sand from the stockpile directly into the wave swash. Later methods included dumping from an overhead boom-supported bin, wheelbarrow dumping and the discharge of a water-sand slurry into the wave swash. Also, wheelbarrow lots were dumped at the shoreline and then shoveled directly into the wave swash, similar to shoveling from a stockpile. Except for the discharge of sand slurry by hose line, which scoured the beach, sand feeding methods were adequate to keep the tests going. What appeared to be needed was a method of continuous sand feeding, with a minimal influence on the natural action-reaction between wave and beach.

In 1962 a method for sand feeding⁽⁸⁾ was introduced which enabled an automatic and continuous feeding of wet sand into the wave swash. The method made use of a vertical cylindrical sand feeder which deposited wet sand continuously and automatically into the wave swash. The sand feeder, shown in Figure 3 with functional parts indicated, is basically a vertical cylinder filled with sand and water. It had been modified by welding a cone section at the bottom to retard the flow of wet sand through it. Another modification was a supply line at the top for keeping the sand feeder supplied with sand.

In the absence of waves, the sand in the sand feeder mouth rested directly on the sand beach tending to stabilize the column of sand in it but with some noticeable oozing of sand about the mouth. In the presence of wave action,

and so long as the sand was maintained at a constant level, the sand feeder was observed to feed at a fairly consistent rate. The two main factors



FIGURE 3 AUTOMATIC SAND FEEDER

affecting the rate of sand fed through the feeder and onto the beach were the weight of sand and water in the feeder and the scouring action at the mouth of the feeder due to the wave swash and backwash. The weight of the sand and water in the feeder acted to force sand out at the mouth and onto the beach, while the wave swash and backwash scoured the beach under the feeder mouth making it easier for sand to be forced out and onto the beach. The amounts of sand fed into the sand feeder or onto the feeder beach were obtained by weighing the sand while submerged- the same method used to obtain the weight of sand deposited in the sand trap.

Beach Soundings

Soundings of the test beach were made regularly. The first sounding was made on a smooth molded beach before any waves acted on it. This initial sounding was made after submerging the beach for one or two days, to allow time for settling of the material before the start of wave action. Subsequent soundings were made after one hour and five hours of wave action and thence at 5-hour intervals to the end of a test. Soundings were made from a level railing using a telescoping sounding rod with a hinged aluminum foot. Readings were made with respect to a still water level datum to one thousandth of a foot; and recorded areally on a survey sheet, analogous to the method of recording elevations in plane table surveys. Figure 4 is a contour chart of the beach obtained by contouring along points of equal depth as recorded in sounding surveys in test 4-60 after 25 hours of wave action.

Test Duration

In the earlier tests, there were no hard and fast rules for determining the length of a longshore transport test. However, there were general principles, and the philosophy of these was, that during longshore transport measurement there be a meaningful similarity between the test beach profiles and typical profiles found on natural beaches. Based on this philosophy, tests were run until the beach profiles had reached a condition defined as "equilibrium profile". "Equilibrium profile" is defined as the near constant or minimum change stage of a beach profile under the sustained action of

constant condition waves (9) When tests neared an equilibrium profile stage, longshore transport rate decreased, becoming fairly constant in some tests

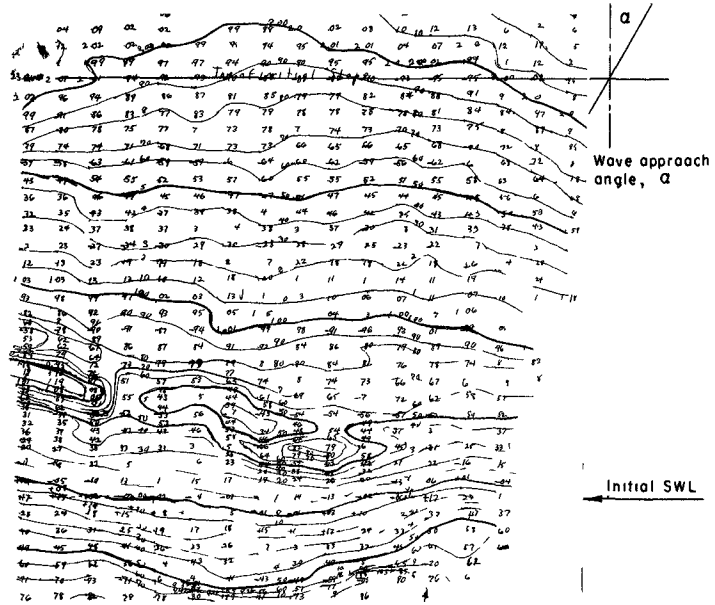


FIGURE 4 BEACH CONTOURS AFTER 25 HOURS IN TEST 4-60

Wave action time required for a test beach to reach an equilibrium profile stage generally ranged from 15 to 30 hours depending on the wave period, wave height and the starting beach slope. Tests started on a 1 on 10 slope generally reached equilibrium in less time than tests started on a 1 on 20 slope. While an equilibrium profile stage was observed to occur as early as 15 hours, and as late as 30 hours, typical tests were run for 50 hours and while a large number of the tests were run 50 hours, a few tests exceeded 100 hours and several repeat tests were run only 25 hours. Fifty hours was usually enough time for a smooth beach to reach an equilibrium profile stage, with 20 hours or more remaining for observation and measurement under a fairly "steady state" condition, of continuing but reduced, profile adjustment and longshore transport rate.

Longshore Current

Estimates of the longshore current velocity were made from timings of fluorescein dye travel in the surf zone. Generally, two estimates were made, one for the updrift and one for the downdrift part of the test beach. The dye was squirted into the wave uprush by a plastic "squeeze" bottle. Actual clockings observed the travel time of the leading or downdrift edge of a dye trace, and not the travel time of the dye-patch center. Since the leading edge of the dye trace was timed, the rates estimated are probably maximum rates for the wave conditions tested.

Water Temperature

Water temperature was taken hourly and in some tests more frequently. Dial type thermometers were used, mounted on a rod, where the dial was visually accessible and the sensing element remained submerged. Water temperature data, although taken regularly, did not seem to be of any direct usefulness in the analyses of the tests. However, considerable data on wave induced suspended sediment (10) and also on suspended sediment in rivers (11) have shown that water temperature does effect the quantity of sediment in suspension, and since these tests were made in an outdoor facility, subject to a significant range of water temperature change, it was felt that the temperature measurements, though not of immediate usefulness in the analysis, were justified in terms of their anticipated value in some future analysis. The water temperature data observed in the tests is available at CERC.

TABLE 3
WAVE PARAMETERS

Ref* No	T, Sec	H ft	H _b ft	d _b ft	E _b **	d _b ^o	K _R	E _a ***
3-66	1 25	0 48	363	459	4 17	16	95	1 08
7-60	1 36	0 32	310	399	3 17	14	94	0 66
(6)	1 50	0 18	227	294	1 65	12	93	0 29
(3)	2 18	0 21	325	410	5 86	10	94	0 86
6-60	2 18	0 30	410	522	10 45	10	94	1 58
2-60	2 18	0 42	507	660	17 94	12	94	3 22
4-60	2 18	0 62	642	854	32 48	13	94	6 29
(2)	2 50	0 25	386	495	10 46	9	94	1 43
(11)	3 00	0 19	355	452	10 24	7	93	1 07
5-60	3 00	0 42	596	760	37 00	9	94	5 05
(8)	3 75	0 14	309	388	8 99	5	93	0 68

* Indicates a specific test, or the number of tests as (6) in row 3

** E_b is in ft lbs/ft crest/wave

*** E_a is in ft lbs/ft of shore/wave

ANALYSIS OF TESTS

A single longshore transport test included the specification of a wave and test set-up condition, test operation, measurements, observations and analysis. The first part of Table 2 lists the test number, eccentricity, height, period, and duration. The second part of Table 2 contains comments on special aspects of the test set-up.

Table 3 lists measured and computed parameters associated with the waves, and Table 4 lists the longshore wave energy flux and the measured transport rates. The wave height, H, as listed in both Tables 2 and 3, is the wave

height appropriate to the offshore part of the test area, where the water depth was 2 33 feet. This height can be read from Figure 2 by taking a wave period and a wave generator eccentric from those listed in Table 2 for a given test number.

Thus far this report has considered the tests in general. The following paragraphs present a test by test description of four representative tests.

Representative Tests

Tests selected for discussion are representative of the entire series of 36 tests. The representative tests are tests numbered 4-60, 4-62, 1-64, and 3-66. The longshore transport in each representative test was measured over 25 or more hours at a specified wave height and period in the general setup illustrated in Figure 1. Wave conditions span the full range of the wave conditions tested, test layouts are typical of the different aetups tested, the range of transport rates approximate the total range of all rates tested, and, testing problems are felt to be typical. Tests selected for discussion are also special in that each test usually represents a specific type of set-up. For example, some of the types of set-up in representative tests were a maximum wave height condition in test 4-60, dividing the offshore basin area into wave flumes in tests 4-62 and 1-64, and eliminating training and splitter walls entirely in test 3-66.

Test 4-60

Test 4-60, made in the North Section of the SPTB, had the highest height and largest transport rate of the five tests run at a 2.18 second period. The period, T , was changed at 15-minute intervals through a sequence of wave periods as indicated in Table 2 for test 4a-59. Initial wave action began on a molded, 1 on 10 beach slope at a wave period of 1.94 seconds. See Tables 2 and 3 and Figure 2 for details of wave conditions.

The emphasis in test 4-60 was in measuring the transport rate at a mean period of 2.18 seconds for the maximum wave height obtainable at this period. This test resulted in an average longshore transport rate of 9,880 pounds of sand per hour, 45% higher than the immediately preceding test, and nearly 4 times higher than the previous maximums. As a result of the higher rate, the test apparatus and personnel were hard-pressed just to keep the test going and to make the observations and measurements. One of these tasks was simply feeding enough sand, properly, to keep the test beach from eroding seriously. Another task was keeping the wave generators operating as smoothly and as continuously as possible, since at a higher rate, smoothness of operation was difficult to maintain and wave machine stops due to breakdown or run-away were frequent.

Longshore transport sand feeding and longshore current results for test 4-60 are summarized in Figure 5. Note the correlations in Figure 5 between longshore transport and downdrift longshore current, and between sand feeding rate and updrift longshore current. Compilations of the data from all the tests, including that used to plot Figure 5, are available at CERC.

Test 4-62 and 1-64

Changes in Tests 4-62 and 1-64 included the installation of splitter walls in the offshore portion of the test layout to study wave height variability.

The splitter wall in Test 4-62 was installed parallel to, and 10 feet updrift of the downdrift training wall. The splitter wall was conceived because repeated visual observations of wave profiles and the results of wave height

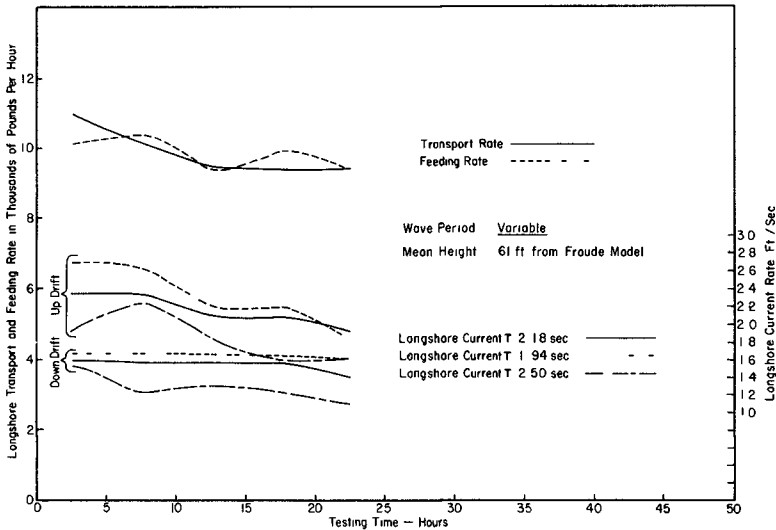


FIGURE 5 TEST NO 4-60, RELATIONSHIP OF LONGSHORE TRANSPORT, SAND FEEDING AND LONGSHORE CURRENT TO TESTING TIME

measurements suggested that a significant variation in wave height with distance across the basin was caused by resonance between training walls. The visual observations were views of the water surface profile along a wave crest as outlined against the wave generator blade at the instant of generating the wave crest. Figure 6 is a schematic drawing of the modes of profiles observed. Mode 1 was observed only for the longer period waves - say 3.75 seconds or longer. Modes 2 and 3 were also observed, with mode 3 generally associated with shorter wave periods.

The function of the splitter wall was to change the mode of the cross basin wave. It was further hypothesized that placing the splitter wall 10 feet ($L/4$) updrift of the training wall, placed it at an antinode of a cross basin wave. A splitter wall placed at the antinode would impede the cross basin flow and thus force the wave mode to change with a possible lessening of wave height variability across the basin. The two curves in Figure 7 for a 3.75 second period show that the total range of the wave height variability was reduced, and that the initial bimodal distribution of wave height was changed.

The test set-up for Test 1-64 was a further application of splitter walls in which 7 splitter walls divided the offshore test area into 8 flumes, each 5 feet wide. The reasoning, as in Test No. 4-62, was that the splitter walls should change the mode of a cross-basin wave hypothesized to be a cause of

wave height variability across the basin. Wave height measurements showed that the 7 splitter walls in Test 1-64 did change the distribution of wave heights, as a single wall did in Test 4-62, but had little effect in reducing the wave height variation. In summary, measurement results in Test 1-64, Test 4-62 and a similar four-flume test suggest that the wave height variability is independent of the spacing between training or splitter walls.

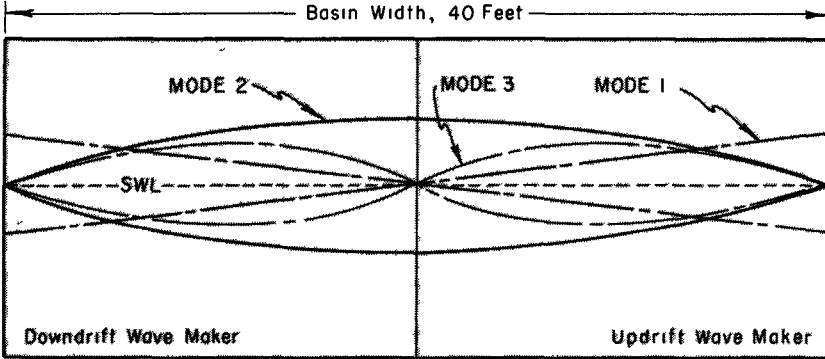


FIGURE 6 SCHEMATIC DRAWING, ILLUSTRATING VISUALLY OBSERVED WAVE MODES IN THE SPTB

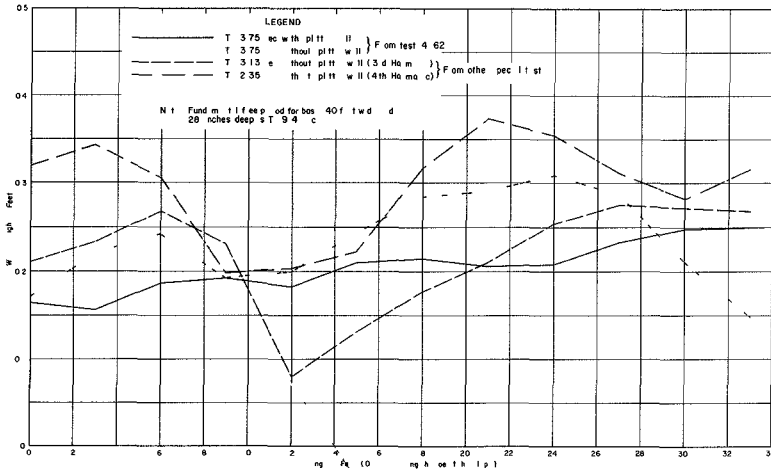


FIGURE 7 COMPARISON OF WAVE HEIGHT BEFORE AND AFTER INSTALLING THE SPLITTER WALL IN TEST NO 4-62

Longshore transport, sand feeding and longshore current results for Tests 4-62 and 1-64 are summarized in Figure 8. Note the correlations in Figure 8 between downdrift longshore current and longshore transport rate. Also note similar correlations between the sand feeding rate and the updrift longshore current.

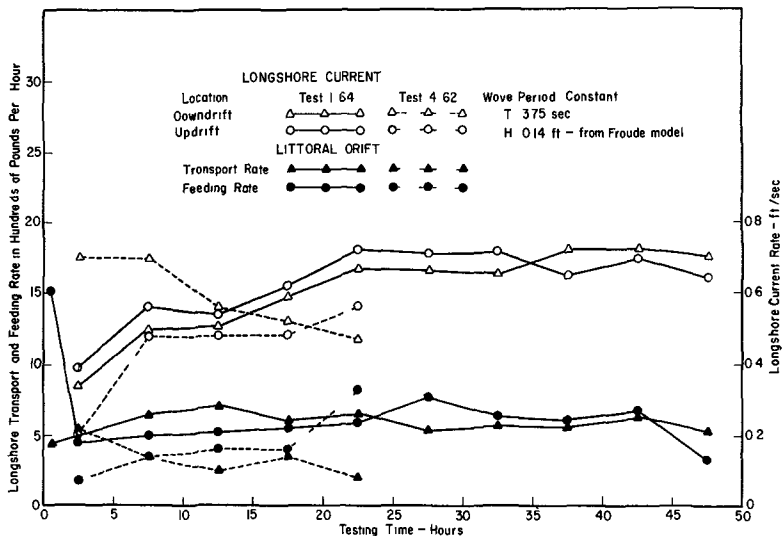


FIGURE 8 TEST NO 4-62 AND 1-64, RELATIONSHIP OF LONGSHORE TRANSPORT, SAND FEEDING AND LONGSHORE CURRENT TO TESTING TIME

Test 3-66

Test 3-66, completed in October 1966, was the last test completed. With two important differences, the test set-up was similar to the set-up for Test 1-64 described in the previous section. The first difference was the deletion of all training and splitter walls and the use of a longer beach necessitating the generation of a longer crested wave (80 feet in contrast to 40 feet in Test 1-64 and other prior tests). The second difference was the installation of a concrete slope, 20 feet wide, immediately updrift of the feeder beach as shown in Figure 1. The first difference, an open basin set-up, was designed to reduce variability in wave height, by eliminating some reflective surfaces (the training walls) and the second, an updrift concrete slope, was designed to provide a more natural longshore current. It was reasoned that wave reflection could be a significant contributor to the wave height variability problem and that the small distance between the training wall and the feeder beach area in previous tests may have hindered the development of a natural longshore current.

Test 3-66 was a constant wave period test with a high wave steepness. It had a high wave energy relative to the wave energies in many other tests. Wave breaker type in the test was spilling to plunging and yet the transport rate seems relatively low for its relative wave energy level among the tests.

TABLE 4

LONGSHORE WAVE ENERGY FLUX AND LONGSHORE TRANSPORT RATES
 (E_a is in millions of ft lbs/ft of shore/day)*

Test No	E_a *	Q in yds ³ /day at test times			Average
		0-5 hrs	20-30 hrs	40-50 hrs	
1-58	017	2 36	2 65	2 77	2 49
2-58	017	1 94	2 09	2 19	2 42
2a-59	031	15 62	13 20	13 28	14 23
3a-59	031	10 56	13 54	13 88	13 77
4a-59	034	19 72	18 38	16 53	18 17
1-59	017	1 83	1 93	-	1 97
2-59					
Ph 1	017	2 73	2 45	-	2 46
Ph 2	031	1 23	3 59	1 77	4 57
3-59	031	6 83	13 30	12 30	11 44
4-59	031	7 19	9 52	11 64	9 73
5-59	016	5 65	6 15	4 58	5 78
6-59	049	8 32	7 62	6 69	7 19
1-60	034	17 30	19 92	21 71	19 48
2-60	128	61 06	56 20	-	61 03
3-60	031	14 24	17 20	-	16 05
4-60	250	92 98	80 03	-	83 64
5-60	145	96 42	132 80	-	121 32
6-60	063	40 06	39 83	38 04	40 62
7-60	042	13 70	8 11	7 20	8 91
1-61	031	20 16	18 63	15 76	17 88
2-61	031	23 04	19 56	20 00	20 41
3-61	031	12 88	8 03	8 18	9 20
5-61	031	19 64	19 70	18 01	19 18
6-61	049	30 16	27 94	31 29	29 59
7-61	016	6 22	2 26	3 64	3 37
1-62	016	3 01	5 99	4 92	5 63
2-62	016	2 31	5 12	-	5 13
3-61	016	3 14	4 77	-	4 77
4-62	016	4 53	2 88	-	2 88
6-62	015	9 21	7 23	6 80	7 44
8-62	015	5 98	6 08	-	6 11
1-64	016	3 50	5 43	4 97	5 05
1-65	016	15 70	5 49	-	8 90
2-66	063	26 18	34 95	-	33 12
3-66	095	19 76	9 65	7 77	10 55
5-62	763	special test, Q=171 32 yd ³ /day			

The longshore current rate is quite high and seemed by direct observation to be out of step with the transport rate in the test. The wave breaking turbulence appeared to remain very much near the water surface and seemed too weak to really stir up the bottom boundary layer.

Longshore transport, sand feeding and longshore current rates for Test 3-66 are summarized in Figure 9. These tests results also show a correlation between longshore transport and downdrift longshore current rate and between sand feeding rate and the updrift longshore current rate.

Discussion of Longshore Transport Data

As described earlier, rates of longshore transport, sand feeding and longshore current have been compiled for each of the tests. Reduced and compiled rates and associated littoral drift data are available at CERC. Some

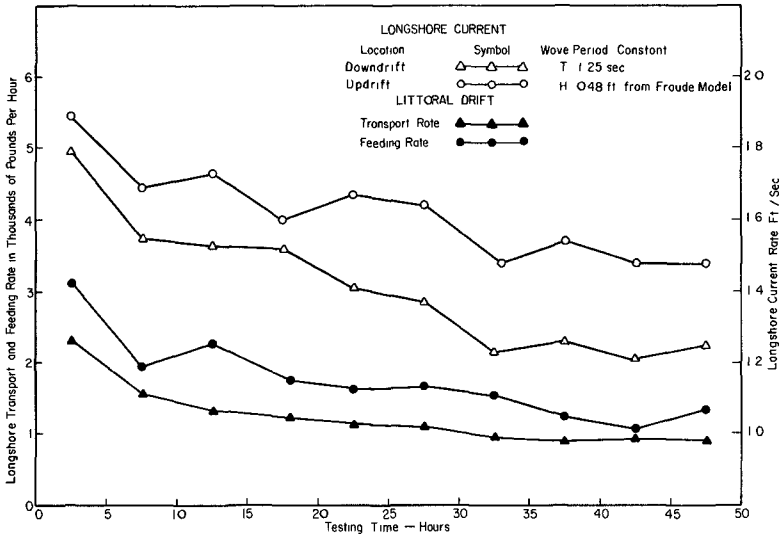


FIGURE 9 TEST NO 3-66, RELATIONSHIP OF LONGSHORE TRANSPORT, LONGSHORE CURRENT AND SAND FEEDING TO TESTING TIME

of this data has been summarized and is shown in Table 4. The data in Table 4 gives the test number, longshore wave energy, E_a , and the longshore transport rate, Q , at test times of 0-5, 20-30 and 40-50 hours. The rates listed are volumetric rates based on a conversion factor of 105 pounds per cubic foot (satisfactorily checked by volumetric measurements of the sand) to obtain rates for the dry weight, or weight in air of the sand, as described in the section on "Longshore Transport".

The transport rates vary considerably, as the values in Table 4 show. The greatest variation appears to be in the long period - low energy tests run at a constant wave period. Eight of these tests are listed in Table 4, each with a longshore energy flux, E_a , of 0.16 millions of foot pounds per foot of beach per day. Figures 10 and 11, respectively, give a graphical comparison of transport rate and longshore current rate variation with test time for ten selected tests. The ten tests include the four representative tests described in the previous section. The data on Figures 10 and 11 indicate, that tests with higher transport rates generally have higher longshore current rates and vice versa. Several tests corroborate this similarity, but there are two notable exceptions. One is Test 3-66 having a very high steepness and another is Test 1-64 with a very low steepness. Another similarity is the increases and decreases of longshore transport and longshore current rates which appear to be fairly well correlated. In most tests, the variations in longshore current are

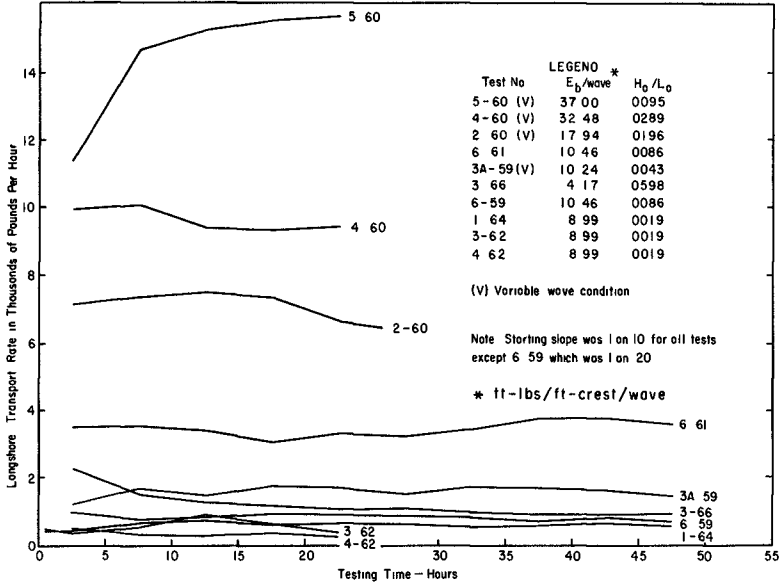


FIGURE 10 COMPARISON OF LONGSHORE TRANSPORT RATES IN REPRESENTATIVE TESTS

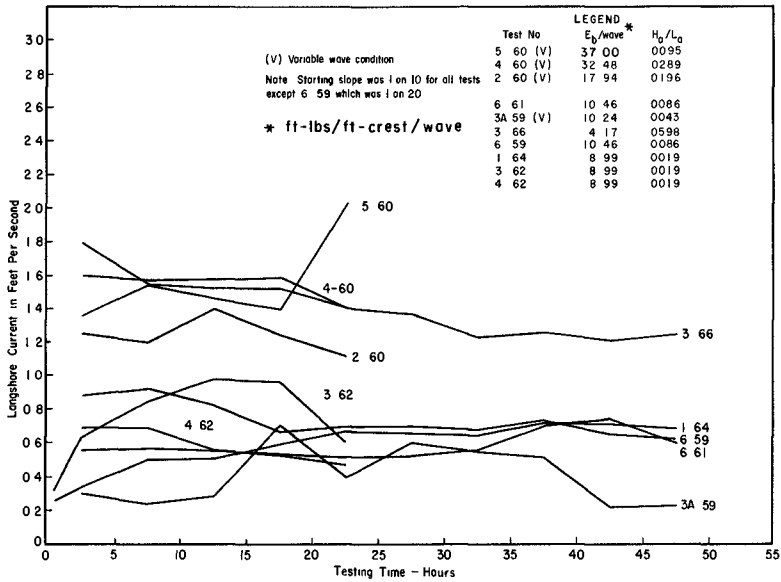


FIGURE 11 COMPARISON OF LONGSHORE CURRENT RATES IN REPRESENTATIVE TESTS

noticeably greater than the variations in longshore transport. Actually, the transport rates appear steady when compared with the quite variable longshore current rates.

Energy Flux - Longshore Transport Correlation

The total wave energy per unit crest width in one wave length of an oscillatory wave⁽⁷⁾ is given by $E_t = \frac{1}{8} \rho g H^2 L [1 - M \frac{H^2}{L^2}]$ where $\rho = w/g$ is the mass density of water (fresh water = 1.94 slugs/ft³) and M is an energy coefficient defined as $\frac{\pi^2}{2 \tanh^2(2\pi d/L)}$. When considering a single wave at the breaking depth the above formula may be re-written as

$$E_b/\text{wave} = 1/8 \rho g H_b^2 L_b \left[1 - M_b \frac{H_b^2}{L_b^2} \right], \text{ where the subscript, b, refers to wave break-}$$

ing conditions. This formula was used in these tests to compute the wave breaker energy per wave. Calculations were carried out on a desk calculator using the Modified Solitary Wave Theory - wave breaker indices curves and Weigels Tables in CERC TR-4. Wave breaker height, H_b , breaker depth, d_b , and wave breaker energy, E_b , are tabulated in Figure 3 for discrete combinations of wave height and period.

Wave breaker angle, α_b , and wave refraction coefficient, K_R , were obtained empirically using the analytic expression, $K_R = \sqrt{\frac{\cos \alpha_0}{\cos \alpha}}$, of Snell's law in a nomograph of d/L_0 , α_0 , and K_R ⁽¹²⁾. In using the nomograph, it was assumed that α_0 was 30° which was the wave approach angle in a constant depth of 2.33 feet in the test set-up. The breaker depth, d_b , was used in the expression d_b/L_0 , to enter the nomograph and the angle, read from the graph was considered as α_b , even though it was not based on the theoretical deep water for the respective wave periods. When the wave breaker energy, E_b , per wave was multiplied by $\cos \alpha_b \sin \alpha_b$ and K_R^2 the product was the longshore component of the wave energy flux, E_a , in foot pounds per foot of shore per wave. These last three parameters, α_b , K_R , and E_a are tabulated in Table 3. E_a is also tabulated in Table 4, in millions of foot pounds per foot of beach per day.

The final results are given in Figure 12 as a scatter plot of longshore wave energy flux versus longshore transport rate at test times of 20-30 hours. The visual best fit curve drawn through the points is based only on the 1 on 10 starting-slope tests. Figure 12 also includes the suggested design curve of the wave energy-longshore transport relationship excerpted from CERC's TR-4. Results plotted in Figure 12 include a total of 36 points which includes eight points for the relatively low energy - low transport, constant period tests. Most of the points falling on or near the CERC TR-4 curve have a 1 on 20 starting slope. The maximum point on the curve is from a special test of four hours duration. In this test, sand moving past the downdrift end of the beach dropped over a vertical ledge and formed a mound of sand, which was measured volumetrically by a method of successive surveys.

Most of the data point scatter in the longshore transport rates is not felt to be just simple data scatter per se, but is more likely meaningful scatter.

For example, the legend in Figure 12, which categorizes the results into only four discrete classes, cannot adequately account for significant influences on the longshore transport rate caused by wave height variability, wave breaker type, model effects at the sand trap and at the feeder beach, or wave diffraction. All of these causes, admittedly influence longshore transport rates in model basins, and the influence of one, wave diffraction, was tested and demonstrated in the SPTB at CERC (13)

Summary

A total of 36 tests were completed for the following experimental conditions, wave periods of 1.25 to 3.75 seconds, and wave heights of 0.14 to 0.75 feet in a constant water depth of 2.33 feet between a wave generator and the beach. Waves were generated at a 30° angle to the beach with portable wave generators, which when used singly, generated a wave crest 20 feet long, or when used - say in groups of five - generated a continuous wave crest 100 feet long. Waves, so generated, traveled in the constant depth to a molded sand slope, where they impinged along a variable length shoreline from 30 to 95 feet, depending on the length of wave crest generated and the test set-up conditions. In addition to variable period, height, length of wave crest generated and shoreline length, specific tests were either variable about some mean period and height or they were constant, with starting slopes of 1 on 10, 1 on 20, or a 1 on 30 equilibrium slope.

As waves shoaled and broke along the 0.22 mm median-diameter sand beach, they caused the sand to move downdrift where it was deposited in a sand trap. Amounts of sand deposited in a given time were reduced and compiled as longshore transport rates. Longshore wave energy flux, computed from measured wave heights and calculated wave breaker angles is plotted against measured longshore transport rates in Figure 12. The results in the plot are compared with the suggested

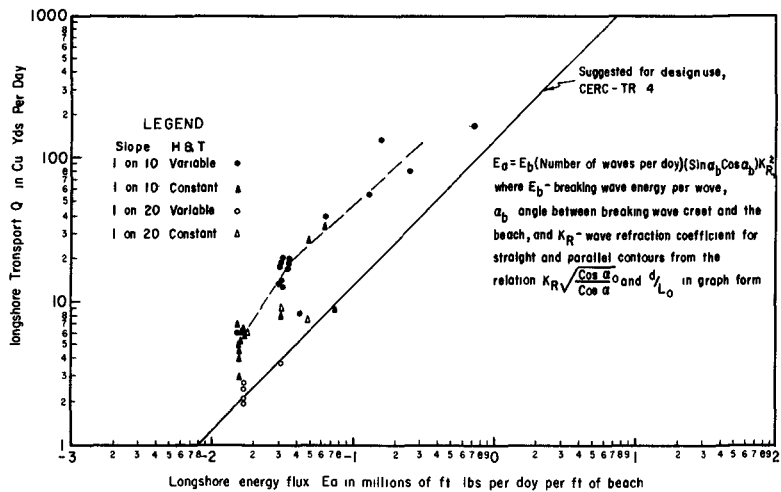


FIGURE 12 RELATIONSHIP BETWEEN THE LONGSHORE COMPONENT OF WAVE ENERGY AND THE LONGSHORE TRANSPORT RATE

design curve of the longshore wave energy flux - longshore transport relation from CERC TR-4. Transport rates along the best fit curve of the laboratory data range from a low of about 6 yd^3 per day to a high of 170 yd^3 per day, and exceed the CERC TR-4 design curve rates by an average factor of 3.

Conclusions

It is concluded that the laboratory rates, noted above as exceeding the CERC design rates by a factor of 3, are at least as large as indicated in Figure 12, and except for some test difficulties noted above, would be larger than indicated. Moreover, transport rates would be expected to be higher if, (1) tests were run continuously, not intermittently, and (2) at a changing water level, simulating a tide, instead of a constant water level.

A localized and deep wave scour immediately updrift of the sand trap, restricted the transport to that in suspension in some tests, and thus reduced the transport rate. In several tests, bars, cuts and cusps developed along the shoreline, and it is felt that these features reduced the transport rate. In addition, accumulation of pebbles armored the beach locally against the waves in some tests, which was judged to have reduced the transport rate.

It is also concluded that the actual wave height, defined as the effective wave height impinging along the test beach, was significantly higher than the scaled-up Froude model height used to compute the wave energy. Figure 13 is presented in support of this conclusion, as a typical result from the wave height variability measurements. It shows that the average sustained height of the SPTB waves exceeded the Froude model height by 46 percent in a wall compartmented basin and by 71 percent in an open basin. It is important to note here, that if these percentages were applied in Figure 12, the plotted points

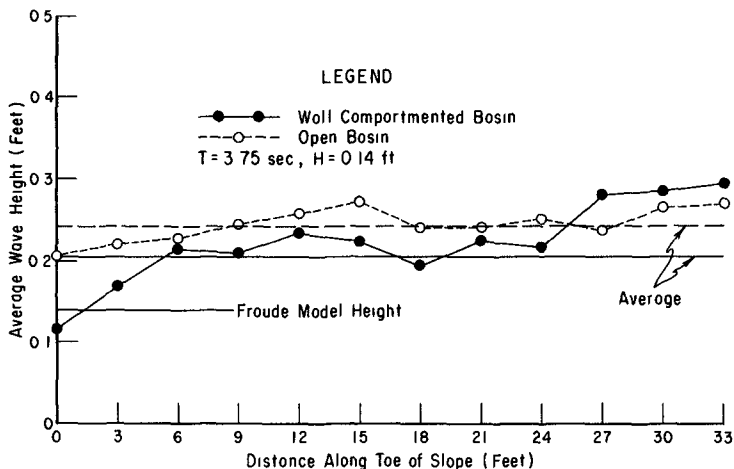


FIGURE 13 COMPARISON OF WAVE HEIGHT VARIABILITY AT A CONSTANT WAVE CONDITION IN A WALL COMPARTMENTED BASIN AND AN OPEN BASIN

would move to the right by a factor of about 2 to 3 and then fall much nearer, or even cluster about the CERC TR-4 curve. While such good agreement would indeed be gratifying, it must be recognized that some part of the increase in height (energy) illustrated in Figure 13 was caused by reflected waves, either from the beach, the wave generator or both.

Recommendations

It is recommended that in future tests, consideration be given to running some tests continuously to completion, with a tide range superposed on the mean water levels. It is further recommended that wave height variability, wave breaker type, model effects at trap and feeder beach and wave diffraction effects be monitored and documented in future tests and so become part of the test results.

It is also recommended that in future tests, consideration be given to short period tests of the order of 10 minutes to be made - say in the middle of a test beach length - somewhat removed from the influences of trap, feeder beach and wave diffraction. Such tests might be made by interfacing sheet plastic along a profile line vertically, and laterally along the bottom for collecting sand drifting past the interface. At the same time measurements could be made of the wave height at the toe of the beach profile and at the peak height before wave breaking. Wave measurements and analysis should account for the percent of a wave height which is due to wave reflection.

ACKNOWLEDGMENT

Acknowledgment is extended to Thorndike Saville, Jr., Chief, Research Division, who provided general guidance during this work, R. P. Savage, Assistant Chief, Research Division, who provided guidance and who, with C. J. Galvin, Jr., Chief, Coastal Processes Branch, reviewed the final draft of this report, and R. P. Stafford, who reduced, compiled and helped to analyze the data.

The work described herein is a portion of the research program of the U. S. Army Corps of Engineers and its Coastal Engineering Research Center. Permission to publish this information is appreciated.

REFERENCES

1. Savage, R. P., "Laboratory Study of the Effects of Groins on the Rate of Littoral Transport Equipment Development and Initial Tests," Beach Erosion Board Technical Memorandum No. 114, 1959.
2. Watts, G. M., "A Study of Sand Movement at South Lake Worth Inlet, Florida" Beach Erosion Board Technical Memorandum No. 42, 1953.
3. Savage, R. P., "Laboratory Determination of Littoral Transport Rates", Journal of Waterways and Harbors Division, ASCE, v. 88, No. WW2, May 1962.
4. Krumbain, W. C., "Shore Currents and Sand Movement on a Model Beach", Beach Erosion Board Tech. Memo No. 7, 1944.
5. Shay, E. A., and Johnson, J. W., "Model Studies on the Movement of Sand Transported by Wave Action Along a Straight Beach", Issue 7, Series 14, Inst. of Engrg. Res., Univ. of Calif., 1951 (unpublished).

- 6 Sauvage, D , and Vincent, G , "Transport Littoral Formation de Fleches et de Tombolos", Proc of the Fifth Conference on Coastal Engineering, Grenoble, France, 1954
- 7 "Shore Protection, Planning and Design", Coastal Engineering Research Center Technical Report No 4, Third Edition, 1966
- 8 Savage, R P , "A Sand Feeder for Use in Laboratory Littoral Transport Studies", Bulletin of the Beach Erosion Board, Vol 15, 1961
- 9 Rector, R L , "Laboratory Study of Equilibrium Profile of Beaches", Beach Erosion Board Technical Memorandum No 41, 1954
- 10 Fairchild, J C , "Suspended Sediment Sampling in Laboratory Wave Action", Beach Erosion Board Technical Memorandum No 115, 1959
- 11 Straub, L D , "Effect of Water Temperature on Suspended Sediment Load in an Alluvial Stream", Proceedings of the Sixth General Meeting of IAHR, The Hague, 1955
- 12 U S Navy Hydrographic Office, "Breakers and Surf", Publication Number 234 and Supplement, 1950
- 13 Fairchild, J C , "Wave Diffraction in a Laboratory Movable-Bed Set-up", Coastal Engineering Research Center, Bulletin and Summary of Research Progress, Fiscal Years 1967-69, Vol III, 1970

CHAPTER 56

INFLUENCE OF GRAIN SIZE ON LITTORAL DRIFT

José Castanho*

Influence of grain size in sediment transport depends on flow conditions. For bed load transport a maximum probably exists for load discharge as a function of grain size. The important parameter seems to be the ratio τ_0/τ between the threshold shear stress and the flow shear stress.

1 It has been pointed out** that authors interested in littoral drift sometimes reach very different conclusions as to the influence of grain size.

In fact, prototype observations made in California beaches by Inman have shown that littoral drift was practically independent of grain size.

On the other hand, L. Bajournas concluded from dimensional analysis considerations that littoral drift should increase with the square root of grain size. According to this author this result agrees with observations made in prototypes and in models for medium and fine sands.

Finally, laboratory tests conducted by Larras and Bonnefille at Chatou Laboratory (France) revealed clearly the existence of a maxi-

* - Research Engineer, Laboratório Nacional de Engenharia Civil, Lisboa, Portugal

** - See for instance the General Report S II C 4 of the International Congress on Navigation, Paris - 1969, by J. Larras.

mum for littoral drift as a function of grain size

In the present paper an attempt is made to show in a more qualitative than quantitative manner that the divergence of results obtained by different researchers is explained by the fact that the influence of grain size should be variable according to circumstances, namely how far one is from the beginning of the sediment movement

2 - It is commonly accepted that littoral drift is a function of wave and sediment characteristics

$$Q_1 = f(\text{wave, sediment})$$

As wave characteristics one should consider H (wave height), T (wave period) and α (wave obliquity) As for sediment, the important parameters are the submerged specific weight (γ'_s) and grain size (D)

Some other factors with possible influence on Q_1 , such as beach slope and bed roughness, wind up being functions either of wave or sediment characteristics or both and so we may ultimately write

$$Q_1 = f(H, T, \alpha, \gamma'_s, D)$$

3 - Now let us consider, according to some authors, the following schematic model for littoral drift sediments are moved by the longshore current in a direction parallel to the shore line, waves, with their turbulence, merely "prepare" material to be moved

That being so, to a given wave (H, T, α) on a given beach will correspond a certain longshore current and consequently a certain shear stress τ , so that we may write

$$Q_1 = f(\tau, \gamma'_s, D) \quad (1)$$

In the above formula D means the direct influence of grain size, the indirect influence corresponding to beach slope and bed roughness being implicit in τ

4 - Equation (1) is formally identic to the equations accepted for unidirectional flow, namely Meyer-Peter's and Einstein's formulas if we consider that bed-load transport is predominant relative to the transport in suspension

The direct influence of grain size in load discharge can be easily understood if in equation (1) we put $\tau = \text{const}$, $\gamma'_s = \text{const}$ and compute Q_1 as a function of D

Meyer-Peter's formula is based on the concept of threshold shear stress and can be written

$$q'_s = 8 \left(\frac{g}{\gamma} \right)^{1/2} (\tau - \tau_0)^{3/2} \quad (*) \quad (2)$$

In this formula, q'_s is the load discharge weighed underwater and γ is the water specific weight. The threshold shear stress τ_0 may be computed by

$$\tau_0 = 0.05 \gamma'_s D$$

Calculations carried out on equation (2) for natural sand ($\gamma'_s = 1.6$) and for two distinct values of τ ($\tau = 0.1 \text{ kg/m}^2$ and $\tau = 1 \text{ kg/}$

* - Rigorously one should write τ' instead of τ , with $\tau' = \mu \tau$, where μ is a coefficient which takes into account the relationship between bed form roughness and the roughness due to grain size. For the sake of simplicity we will put $\mu = 1$

$/m^2$) led to the results presented in Fig 1, where the weighed out of water load discharge (q_s) is plotted against the grain size (D)

It can be concluded that after Meyer-Peter's formula load discharge is zero for sufficiently great sizes and grows as size gets smaller. For sufficiently small sizes, bed-load discharge tends to remain a constant*.

Einstein's formula for bed-load transport is based on the probability of motion of bottom particles and the load discharge q_s is given

by means of two parameters ψ and ϕ

$$\psi = \frac{\rho_s - \rho}{\rho} \frac{D}{Rl} \quad \phi = \frac{s}{\rho_s g} \left(\frac{\rho}{\rho_s - \rho} \frac{1}{gD^3} \right)^{1/2}$$

ψ = flow parameter

ϕ = transport parameter

ρ_s = specific mass of sediment

ρ = specific mass of water

R = hydraulic radius**

l = unit head loss

The relationship between ψ and ϕ is plotted in Fig 3

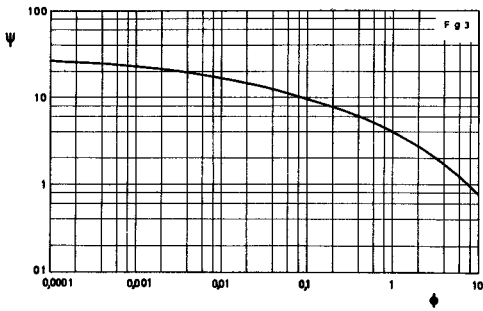
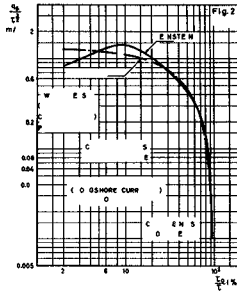
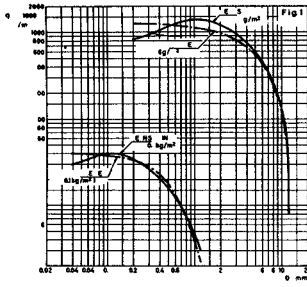
Introducing in ψ the concept of shear stress

$\tau = \gamma Rl$ and taking $\gamma_s = 2600 \text{ kg/m}^3$ (natural sand) the funda

mental parameters can be written, in metric units

* - This will be true as long as the transport is made predominantly through bed load discharge

** - Again, one should also write $R' = \mu R$. For simplicity we will take $\mu = 1$



$$\psi = 1600 \frac{D}{\tau}$$

$$\phi = 10^{-4} \frac{q_s}{d^{3/2}} \quad (3)$$

Calculations on equations (3) for $\tau = 0.1 \text{ kg/m}^2$ and $\tau = 1 \text{ kg/m}^2$ led to the results plotted in Fig 1. It can be seen that in this case a maximum of load discharge exists for a size D varying with τ .

These results are in qualitative agreement with Larras and Bonefille results.

Also we may say that they agree with Bajournas results. Indeed, if the load discharge increases with the square root of the sediment size for a certain range of diameters, and if, for sufficiently great diameters, the load discharge is zero, then there must exist a maximum of load discharge as a function of grain size.

5 - A more suggestive interpretation of the above results may be achieved by plotting $Q_1/\tau^{3/2}$ as a function of $\frac{\tau_0}{\tau}$ (Fig 2). In this plot the value of τ_0 was computed from $\tau_0 = 0.05 \gamma'_s D$ which would be true for unidirectional flow.

It is the author's impression that the curves in Fig 2 may also be assumed valid in case of longshore current movement if for τ_0 a smaller value than the above is taken*, that is, if τ_0 is divided by a parameter $W > 1$ which would represent the "help" granted by the wave itself to the longshore current in the "preparation" of the material

* - The same results would be obtained if a greater value of τ were taken.

to be moved

According to this reasoning, the relative value of littoral drift will depend on the zone of Fig 2 plot where one is working. The influence of diameter will be represented through the parameter τ_o and the effect of the additional turbulence due to waves will be represented by the parameter W .

Situations indicated in Fig 2 for waves and currents should be frequent for the usual materials in prototypes and in models.

The above reasoning may explain certain observed facts. Let us consider the case of a movable bed model subject to wave and current* action in which both waves and current are reproduced in the Froude scale.

For a given τ we may find ourselves in the extreme right of the plot in case of currents, while for waves (lesser τ_o) we may be working in the middle zone. Hence, load discharge by wave action is comparatively greater than the one due to current action. This fact, observed in different laboratories, is one of the great difficulties in the calibration of estuary models, where waves and currents have equal importance. These difficulties have been avoided both by enhancing the effect of currents and by reducing the effect of waves.

* - River or tidal current

6 - CONCLUSIONS

a) Influence of grain size on sediment transport depends on the flow conditions. If the transport is mainly in suspension, then load discharge should decrease when the diameter increases. When the transport is mainly through bed load discharge, then discharge will at the beginning increase with increasing diameter reaching a maximum and decreasing afterwards.

b) The value of the grain size for which the maximum transport is attained depends on the flow shear stress.

c) The influence of grain size is expressed through the parameter τ_0/τ . It is very different for conditions near the beginning of the sediment movement (great τ_0/τ) and for conditions of fully developed movement (small τ_0/τ).

d) In the case of currents (tidal or river currents) τ_0 may be computed from $\tau_0 = 0.05 \gamma_s D$. In the case of transport due to wave action (longshore current) τ_0 should be divided by a coefficient W which depends on the wave characteristics. (It should be noted that dividing τ_0 by W is the same as multiplying τ by W).

CHAPTER 57

COMPUTATION OF ALONGSHORE ENERGY AND LITTORAL TRANSPORT

Theodor R. Mogel¹

Robert L. Street,¹ M. ASCE

Byrne Perry¹

ABSTRACT

This work encompasses a study of the littoral regime of a section of the coastline of the city and county of San Francisco, California. The study included a complete refraction analysis of all applicable deep water wave directions and periods, the determination of breaker locations, and a computation of alongshore energy and potential littoral transport for seven stations located just offshore along the thirty foot depth contour. The waves are refracted from deep water locations to the shoreline using the Stanford Wave Refraction computer program. Wave breaking is assumed to take place whenever the computed wave height exceeds 0.78 times the local water depth. The effect of limiting the refraction coefficient is explored since the refraction theory, in analogy with its parent theory of geometric optics, fails along caustic curves and predicts unreasonably large values for the refraction coefficient.

1 INTRODUCTION

The proper design of coastal structures, improvements or controls depends crucially upon an accurate estimate of the amounts of sand supplied to or lost from the shore region. The most significant portion of the sand supply is the littoral drift--the material of the beach and nearshore bottom moved by the action of waves and currents. The rate and direction of littoral transport or the movement of littoral drift is dependent on many factors, among which are the alongshore components of water-wave energy, currents, availability of littoral drift, its size characteristics, shapes and mineral compositions, tide range, and beach slope. Unfortunately, neither the precise mechanism of transport nor the interaction of the various factors is clearly understood (1-5). The present work is based on the concepts that the principal supply of energy for the movement of littoral drift comes from water waves impinging upon the shore and that an empirical relationship (1,4) between transport and alongshore energy is the most appropriate means for estimating the potential littoral transport.

¹Department of Civil Engineering, Stanford University, Stanford, California 94305

1 1 The Purpose and Scope of the Study

This paper reports on a study (6) of the littoral regime of a section of the coastline of the City and County of San Francisco, California, from the Golden Gate Bridge to Mussel Rock, south of the southerly boundary of the City and County of San Francisco. The original study includes a complete refraction analysis of all applicable deep-water wave directions and periods, determination of the locations of wave breaking, application of 12 monthly tables and an annual table of digitized deep-water wave characteristics (7), calculation of alongshore energy and potential littoral transport, and tabulation of shallow-water wave direction and refraction coefficients for the San Francisco coastline. Here we review the original results and explore the effect of limiting the maximum value that the refraction coefficient can attain (8,11)

1 2 The Plan of the Study

The basic inputs to the study were the hindcast deep-water wave statistics (7) compiled for a deep-water station (number 3, Ref 7) almost due West from San Francisco. By use of a computer program that carried out a refraction analysis of waves of all applicable periods, heights and directions represented in the wave statistics tables, the deep-water values were carried to seven points distributed in shallow water along the San Francisco shoreline (fig 1). Then a second computer program computed the alongshore energy components of the waves and, utilizing an empirical relation between these energy components and littoral transport (1,4), computed the monthly and annual potential transport at the seven points on the shoreline. All computations were carried out and plots and printed tables were generated by an IBM 360, Model 67 digital computer with an associated CALCOMP 750 plotter. All programs were written in FORTRAN IV.

The Refraction Program solves the refraction equation and the wave intensity equation along each individual wave ray for arbitrary bottom shapes. The theoretical bases for the computer program were given in detail by Dobson (9) and are discussed briefly below (cf., Ref 10). The bottom hydrographic data in digitized form and contoured grid maps for two study areas were supplied by the San Francisco Engineer District of the U S Army Corps of Engineers. The INNER GRID or study area covered the immediate vicinity of the San Francisco shoreline from Pirates Cove, north of the Golden Gate, to south of Mussel Rock at the southern boundary of the County with a 215 unit by 150 unit grid (333 33 feet per grid unit). The OUTER GRID or study area covered the coast from shore to approximately the 300 fathom contour and approximately from the mouth of the Russian River in Sonoma County to the City of Santa Cruz in Santa Cruz County with a 303 unit by 199 unit grid (1666.67 feet per grid unit) of much greater size. The INNER GRID provided the detailed bottom contours needed for an accurate prediction of wave behavior in shallow water near the coast, while the OUTER GRID provided the link to the deep-water wave conditions. Figures 1a and 1b show CALCOMP (computer) contour plots of the hydrography described by the grids of depths. Waves ranging in period from 4 to 20 seconds and in height from 1 to 25 feet and

coming from directions between North and South-Southeast were considered

The Drift Program utilizes a linear relation between alongshore energy components and potential littoral transport. The alongshore energy components are calculated from output supplied by the Refraction Program and the deep-water wave statistics.

2 METHOD OF COMPUTATION

2.1 Refraction

2.1.1 Theory and Background

The theoretical basis of the present refraction computations is well known (10-12) and will only be touched on here. In effect the same theory is commonly employed in hand computations and only the implementation for the computer led to differences in detail. The original version of the theory comes from the physical science of geometrical optics, the key result of which is Snell's law. A detailed discussion of the method was given by Dobson (9).

The main feature that has been added for the computer work is a technique for fairing a smooth surface through the known bottom depth data. A quadratic surface is constructed to give the best fit in the sense of least squares to the local point and its surrounding neighbors. Thus, the bottom is always represented as a smoothly-varying surface. Starting from a known point on a grid and in a given initial direction, the computer program constructs a single wave ray (or orthogonal) step-by-step across the grid. Because the fitted bottom surface is smooth, and hence differentiable, the equation of wave intensity (equivalently wave height) may be solved at each step in the ray construction process, and the relationship between initial and present wave height carried forward continuously along a single ray. This is an essential feature of the analysis without which the breaking height location computations, described below, would not have been feasible. The refraction technique has proved very satisfactory in many test cases, as shown by comparison with exact theory and hand computations (9). Battjes (13) has recently shown that, according to both linear and nonlinear theory, the energy flux in wave propagation in three dimensions is always directed along the wave rays (orthogonals) [our wave intensity equation is based on this fact] regardless of the wave amplitude gradients and that refraction of water waves over bottoms of small slope can indeed be considered as a case of wave propagation through an inhomogeneous (depth varies), two-dimensional medium. This is in agreement with the method used in the present work and current practice.

The refraction theory, in analogy with its parent theory of geometric optics, fails along caustic curves and predicts unreasonably large values for the refraction coefficient K_r near the caustic curve. Pierson (8,11) gave justification for the approximate limit $K_r^2 \leq 2.0$ and we have run test cases for $K_r^2 \leq 2.0$, $K_r^2 \leq 4.0$, and $K_r^2 < \infty$.

2.1.2 Technique

The refraction program constructed rays on either the OUTER GRID (303 x 199 grid units) or the INNER GRID (215 x 150 grid units). The depth data at the intersection points of the grids was provided by the San Francisco Engineer District and was digitized from their bottom hydrography charts. A match line for transfer of computations from one grid to the other was established.

The calculation of littoral transport requires the shallow-water wave height and direction at the point of breaking of every possible wave in the three-dimensional matrix of deep-water statistics (parameterized by deep-water height, direction and period). Accordingly, on an inward run from deep to shallow water, the refraction program punched a data card whenever breaking occurred on the INNER GRID, only those breaking points near the beach were retained. For the range of wave heights and periods considered in this study, breaking was assumed to occur whenever the height of a particular wave exceeded 0.78 times the local water depth. While more sophisticated criteria are available (12), it appears that none is significantly more accurate on the average for prototype waves in our period range. Furthermore, in view of the basis of the refraction analysis on linear theory, a more refined breaking criteria does not appear warranted.

The objective of the refraction analysis was to bring one ray from deep water to each of the seven target points near the shore for each applicable deep-water direction and period. Because local wave height is a linear function of deep-water height, all the results for the heights between 2 and 24 feet were obtained from a single ray computation. In view of the complex hydrography of the San Francisco shore region, it was decided to work outward from each target station with fans of rays, the rays in each fan having a different period. New fans were generated until a set of results were obtained in deep water that would permit us to run a complete set of applicable waves in from deep water (corresponding to the wave statistics). It was not possible to generate the necessary data on an outgoing run because the refraction coefficient calculation is not valid for rays started in shallow water (the starting condition of parallel rays is not correct there). Therefore, it remains necessary to retrace outgoing rays from deep water inward. In some cases it was possible to begin with incoming rays of specific period and direction and to hit a target station by using trial-and-error and the information known about adjacent stations.

A study of the hindcast data (7) shows that the wave statistics are given for 22.5-degree direction segments, two-second period intervals and two-foot height intervals. We used the mid-direction, mid-period and mid-heights in our refraction calculations. In light of the difficulty of hitting a given direction with an outward running ray or a given station with an inward ray we established tolerance criteria of ± 5 degrees on direction when running outward and an x-distance tolerance of ± 4 grid units when running in. Tests of the results showed that no large changes in wave characteristics occurred within these tolerances. In any case the majority of the runs are well within the tolerance limits which seem reasonable in view of the expected accuracy of the hindcast deep-water statistics.

2 1 3 Notes on Computer Programming

The results of the present study were obtained on an IBM 360/67 digital computer and an off-line CALCOMP 750 plotter. The program is an extension of the Stanford Refraction Program originally developed for the IBM 7090. Dobson (9) has given a very thorough documentation including flow charts for the main program and subroutines in the original program, except for the CALCOMP subroutine calls which are highly installation dependent.

The primary changes made in the original Stanford Program have been related either to differences between the IBM 7090 and IBM 360/67 computers or improvements in the graphical displays and printed or punched outputs of the program.

For the present study the program has been specifically modified to do the following:

- a Read the Depth data and associated fixed grid and ray constants and identifiers from Disc storage in the machine.
- b Plot wave rays on a map (Fig 1). The map includes labeled X and Y axes, a north direction arrow, suitable contours (stored on Disc also), and identification block giving relevant parameters and identification. The contours on the INNER GRID are the shoreline and 30-foot contours, while only the shoreline is shown on the OUTER GRID. If the ray is to continue to another grid, the map also shows the match line outline of the next grid.
- c Create a punched card data deck to continue wave rays on another grid. The X- and Y-coordinates in the data deck have been converted to the new coordinate system. The data deck is complete with all necessary title and end-of-set cards so that it may be loaded for the next run without further processing.
- d Create a punched-card data deck giving coordinates and wave parameters at the 30-foot contour for each wave ray.
- e Create a punched-card data deck with one card for each deep-water wave height on each ray when the wave breaks ($H/D > 0.78$) for heights of 2 to 24 feet in increments of 2 feet. These cards contain, in addition to the wave height, direction, period and spacial location, the shoaling coefficient, the deep-water height, the water depth and the local angle between the wave ray and the gradient of the bottom topography.
- f Limit the refraction coefficient to a specific value.

Figures 1a and 1b show sample plotter output from the refraction program. A ray was started a short distance to each side of each of the actual rays used to better illustrate the shifting of the wave front. Tables 1a and 1b are the printouts generated for one of the rays shown in the figures.

2 2 Littoral Transport

2 2 1 Analysis and Hindcast Data

National Marine Consultants compiled deep-water wave statistics based upon meteorological records and charts for the years 1956, 1957 and 1958 for seven deep-water stations along the California coast (7). The wave hindcast data for deep-water sea (generated by local wind) and swell were given as height-period-direction average frequency distributions in percent monthly and annually. A digitized data deck for Station 3 (Latitude 37 6 degrees N, Longitude 123 5 degrees W) was provided the authors by the San Francisco Engineer District. This station is due west of San Francisco. As none of the other stations were close to this area, Station 3 was the only data source, cf., Fairchild (3) who interpolated between several stations for an east-coast study.

The treatment of deep-water wave statistics and littoral transport calculations was based on the methods of Saville (14) and Fairchild (3). In particular, sea and swell energies were added linearly, and the significant wave heights, corrected in accordance with Fairchild (3) and Saville (14), were used to estimate the wave energy at the shore. The refraction analysis used the dominant wave period, as outlined by Saville (14), associated with the significant wave heights given in the statistical data.

Littoral transport was computed from the alongshore energy components derived from the combination of wave statistics and refraction program output for the seven shallow-water stations shown in Fig 1b. An empirical littoral transport equation was obtained from Fig 2-22 of CERC Technical Report No. 4 (1). According to this figure, the potential littoral transport past a point on shore and caused by a given period wave of given deep-water height and direction is

$$Q = 128E_a \cdot 10^{-6} \text{ cu yds/month}$$

where

$$E_a = 0.58E_a F_{ijk}$$

$$E_a = 5400 \frac{\gamma H_b^2 L_o}{TK_s^2} \sin \alpha_c \cos \alpha_c = 1.77 \cdot 10^6 \frac{H_b^2 T}{K_s} \sin \alpha_c \cos \alpha_c$$

in ft-lbs/ft of beach/day,

α_c = angle between wave ray and the gradient of the bottom hydrography in degrees,

γ = specific weight of sea-water = 64 lbs/ft³,

H_b = shallow-water wave height at breaking in feet,

T = wave period in seconds,

K_S = the shoaling coefficient at breaking,

L_o = the deep-water wave length in feet = $5.12T^2$

F_{ijk} = WAVES (I,J,K,L) = fraction of a month that waves of given height, period, direction and month occur in deep water = (percent per month) (days per month)/100

The actual (as opposed to potential) littoral transport may be less than Q if bottom bed material is not available at the point in question. The factor 0.58 is required (14) to reduce the given deep-water spectral energy for significant waves to the proper average energy that causes littoral transport. Note that in this analysis the littoral transport caused by waves of varying heights will occur where the wave breaks, thus, for each station location our transport results reflect the alongshore transport on the average through the broad-band breaking or surf zone (see Fig 4) created by a set of deep-water waves whose common point is that they all pass through (or near) a given station location (1 through 7) on the 30-foot contour along the San Francisco shoreline.

The machine calculations were checked by hand for those cases in which only one deep-water wave height for a given period and direction had a nonzero occurrence in a month or for the year.

2.2.2 Programming and Output

The operation of the program that calculates the alongshore energy and potential littoral transport is particularly simple and proceeds as follows:

- a The program reads the digitized sea data (Table 3, Ref 7) and constructs WAVES (I,J,K,L) for the sea data for each month.
- b The program reads the swell data and adds it to the appropriate WAVES (I,J,K,L).
- c The program reads a refraction-program-punched input card for a particular deep-water height, direction, period and station (always starting with the 24-foot height and working downward) and constructs E_a' for that card. Cards are read and energies calculated until all the heights for a given ray are surveyed, and their energies are added together to find the total energy for that period and direction. Only the last complete height survey (24 feet to 2 feet) is used to calculate the transport, i.e., only the breaking zone contiguous to the beach is considered to cause transport. No allowance has been made for energy losses in prior breaking zones away from the beach (see Sec 4.2).
- d The program repeats c for the remaining periods and directions.

- e The littoral transports Q corresponding to the E_a^{\sim} for each period and direction are computed
- f Tables of E_a^{\sim} and Q are constructed for each station

3 RESULTS AND DISCUSSION

3.1 Transport and Energy Tables

The tables of littoral transport and alongshore energy components computed by the Drift Program for the three limits on K_r are given in Tables 2 and 3 for each of the seven stations of the study. Results are given for each month in the year and the annual total transport as a station. A positive sign indicates energy components and transport motion up-coast or generally North.

As noted above (Secs. 2.1.3 and 2.2.1) the alongshore energy component computation is based upon the local angle α_c at breaking between the wave ray and the gradient of the bottom hydrography (the perpendicular to the local bottom contour). We considered the use of the mean gradient direction of the beach as a whole near any given station in lieu of the local gradient. Tests with this concept had predictable results, namely, the transport and energy components vary widely for small changes in mean beach gradient direction. Because of the complex hydrography near the shore (Fig. 1b) and the wide zone of breaking (Fig. 2) the direction of a ray at the breaking point for a given wave is not correlated to any observable mean beach gradient direction. Accordingly, no computations utilized an α_c based on mean beach gradients, rather, the ray direction was correlated with the bottom contour at the actual breaking point.

As can be seen from the alongshore energy and littoral transport tables (Tables 2, 3, & 4), limiting the maximum value of K_r tends to make the calculated energy and transport more uniform. The majority of the alongshore energy at each station is the result of a few rays. When some of these rays pass through or near a caustic and their K_r is not restricted, their dominance is exaggerated and they break further from shore. By limiting the maximum value that K_r can attain, the dominance of these waves is reduced and they break closer to the beach zone. Station 1, for example, has a ray from the west which contributes most of the energy and transport. When this ray crosses the 30 ft contour $K_r = 3.67$. When K_r is restricted to a more reasonable value, the dominance of the ray diminishes and the net transport is brought into line with the transport of station 3 as expected because the bottom hydrography near these two stations is similar.

3.2 Unusual Features

Several features of the bottom hydrography are worth noting. The Farallon Islands are the visible portion of a shoaling region which lies mainly between 60 fathoms and the surface. Long waves, in particular, are affected by this region. The peaked nature of the region causes bending of the longer waves which is quite unpredictable and led to much of the tedium of locating the starting positions of these longer waves.

The Fourfathom Bar blocks or diverts much of the wave energy of the longer period waves from the Golden Gate area. The small energy and transport figures for stations 6 and 7 are a direct result of this blocking effect. The Southern and Central portions of the San Francisco Bar also severely bend the rays. However this effect is quite predictable.

3.3 Comparison with other studies

Kamel (15) made a study of sand transport along the California Coast in the Russian River-Point San Pedro reach using, mainly, radioactive tracer and heavy mineral concentrations. His study predicts a general transport in the southerly direction. In the region between the Golden Gate and Merced Lake (our stations 4 and 2) no predominant direction of transport was predicted and the radioactive tracer samples predicted a Southern transport near our stations 1 and 3. However a close examination of the heavy mineral concentration data for the same region shows a Northern transport for the same region.

Adding to the uncertainty Johnson (16) states in his study of the Half Moon Bay-Russian River region that little if any material is transported in this littoral zone. Our results indicate, with the exception of station 2, a northerly direction of sand transport. Johnson (16) also concludes that there is no major source of littoral materials along the Half Moon Bay-Russian River region indicating that perhaps the experimental results revealed not what is taking place now but what has taken place over geologic time.

4 Conclusions

4.1 Conclusions based on the present results

In this study we brought together three essential ingredients to synthesize the potential littoral transport and alongshore energy. The combination of deep-water hindcast wave statistics, linear refraction of wave components and an empirical relation between energy and transport produced energy and transport patterns which clearly show that

- 1) The average annual transport and energy direction is north.
- 2) The Farallon Islands and their associated shoaling region both block wave energy from the shore and bend and focus wave rays to zones not otherwise reachable.
- 3) Limiting the maximum value of K_r produces energy and transport predictions which are more uniform and realistic.

However it must be emphasized that the littoral transport results are obtained from an empirical energy-transport relation developed for other coastal areas and based on very scattered data (4,5). Accordingly, within the accuracy of the hindcast data and the linear refraction analysis, we consider the alongshore energy distribution to be accurate, but the potential (computed) littoral transport can only be considered as a qualitative indicator of the actual transport.

4.2 Recommendations for Modification of the Present Technique

Three problem areas arise in connection with the present study. First, a large effort in terms of man-hours and computer time is expended in selecting the desired wave rays for each deep-water wave direction and period that run to each station. Second, and more significant, no account is made of energy losses that occur through wave breaking on bars and other shoaling regions far from the beach area. Third, the relationship between energy and sand movement rests on little in the way of sound principles and analysis. Thornton (5) has recently made a start in remedying this situation, but his success is limited.

Battjes (13) proposes a refraction technique in which the wave characteristics are determined as continuous field variables over an entire grid. This method requires the solution of a pair of non-linear partial differential equations, but would give the necessary data at all points along a shoreline. However his method would require large amounts of storage ($\sim 10^6$ words for our Outer Grid) and long run times (probably more than 10 minutes per wave direction and period). Our present program has none of these problems.

The greatest need, however, is to find a way to account for energy loss when a wave breaks offshore before coming into the breaker zone. Battjes (13) technique assumes no energy losses from the wave system so would suffer from some of the present inaccuracies.

ACKNOWLEDGEMENT

The basic refraction and littoral drift studies were carried out under Contract No. DACW07-68-C-0054 for the U. S. Army Engineer District, San Francisco, Corps of Engineers.

REFERENCES

- 1 Shore Protection, Planning and Design, Tech Rep No 4 (3rd ed), U S Army Coastal Engineering Research Center, Dept of the Army, Corps of Engineers, Washington, D C , June 1966
- 2 J W Johnson and P S Eagleson, "Coastal Processes," Estuary and Coastline Hydrodynamics, McGraw-Hill Book Co , Inc , New York, Chapter 9, 1966
- 3 J C Fairchild, "Correlation of Littoral Transport with Wave Climate along Shores of New York and New Jersey," Tech Memo No 18, U S Army Coastal Engineering Research Center, Dept of the Army, Corps of Engineers, Washington, D C , November 1966
- 4 T Saville, Jr , G M Watts, " Coastal Regime, Recent U S Experience," XXII International Navigation Congress, Paris, 1969
- 5 E B Thornton, "Longshore Currents and Sediment Transport," Tech Rep No 5, Department of Coastal and Oceanographic Engineering, University of Florida, Gainesville, Florida, December, 1969
- 6 Street, R L , T Mogel and B Perry, "Computation of the Littoral Regime of the Shore of San Francisco County, California, by Automatic Data Processing Methods," Final Report, Contract No DACW07-68-0054, U S Army Engineer District, San Francisco, Corps of Engineers, 1 January 1969
- 7 "Wave Statistics for Seven Deep Water Stations Along the California Coast," National Marine Consultants, Santa Barbara, California, December 1960
- 8 W J Pierson, "The Interpretation of Crossed Orthogonals in Wave Refraction Phenomena," Tech Memo No 21, Beach Erosion Board, Corps of Engineers, January 1951
- 9 R S Dobson, "Some Applications of a Digital Computer to Hydraulic Engineering Problems," Tech Rep No 80, Dept of Civil Engineering, Stanford University, Stanford, California, June 1967, DDC AD No 659309
- 10 G H Keulegan, J Harrison, "Tsunami Refraction Diagrams by Digital Computer," J Waterways and Harbor Division, Proc ASCE, V96, No WW2, Paper 7261, May 1970
- 11 W J Pierson, G Neumann and R W James, Practical Methods for Observing and Forecasting Ocean Waves by Means of Wave Spectra and Statistics, U S Navy Hydrographic Office, Publication No 603, 1955

- 12 R L Wiegel, Oceanographical Engineering, Prentice-Hall, Inc , Englewood Cliffs, New Jersey, 1964
- 13 J A Battjes, "Refraction of Water Waves," J Waterways and Harbor Division, Proc ASCE, V 94, No WW4, Paper 6206, November 1968
- 14 T Saville, Jr , "North Atlantic Coast Wave Statistics Hindcast by Bretschneider-Revised Sverdrup-Munk Method," Beach Erosion Board Tech Memo No 55, Dept of the Army, Corps of Engineers, Washington, D C , November 1954
- 15 A M Kamei, "Littoral Studies Near San Francisco Using Tracer Techniques," Tech Memo No 131, Beach Erosion Board, November 1962
- 16 J W Johnson, "Nearshore Sediment Movement--Central California Coast," Coastal Engineering, ASCE Santa Barbara Specialty Conference, Chapter 23, October 1965

TABLE 1A OUTER GRID COMPUTER PRINTOUT SAMPLE

SAN FRANCISCO		COAST		OUTER GRID		DATE		9/11/70	
SET NO	1	PERIOD =	13 00 SECS	RAY NO	36	TIME STEP =	18 7823 SECS	KR KS	KS
PCINT	X (GU)	Y (GU)	ANGLE (DEG)	DEPTH (FT)	MAX DIF (PERCENT)	LENGTH (FT)	SPEED (FPS)	KR KS	KS
								DIMENSIONLESS	B2
1	136 88	188 20	-110 50	1805 99	0 00	865 35	66 57	1 00	1 0000
30	129 26	167 83	-110 50	1805 99	0 00	865 35	66 57	1 00	1 0000
60	121 38	146 75	-110 46	494 91	1 67	864 05	66 47	1 00	0 9954
90	114 62	125 84	-103 59	233 24	0 57	818 46	62 96	0 77	0 9388
120	111 64	105 33	-93 31	172 90	1 45	768 62	59 12	0 53	0 5772
150	111 66	86 28	-88 91	119 77	0 94	689 85	53 07	1 33	1 4559
180	113 12	70 10	-77 81	64 04	0 35	544 15	41 86	0 47	0 4849
* 183	113 41	68 73	-77 77	58 05	2 73	522 16	40 17	0 47	0 4774
210	115 21	59 26	-79 49	30 65	2 65	320 50	30 23	0 54	0 4957
240	118 24	50 73	-72 80	19 82	6 14	393 38	24 64	1 05	0 8825
270	117 86	44 39	-116 34	4 86	50 96	161 58	12 43	0 64	0 3895
300	116 83	41 46	-108 34	0 65	229 16	39 51	4 58	0 64	0 4925
315	116 28	41 08	-136 92	-0 00	8421 00	35 34	0 37	2 81	0 3689
RAY STOPPED, REACHED SHORE X = 116 58, Y = 41 08									

TABLE 1B INNER GRID COMPUTER PRINTOUT SAMPLE

SAN FRANCISCO		COAST		INNER GRID		DATE		9/11/70	
SET NO	1	PERIOD =	13 00 SECS	RAY NO	36	TIME STEP =	3 7357 SECS	KR KS	KS
PCINT	X (GU)	Y (GU)	ANGLE (DGS)	DEPTH (FT)	MAX DIF (PERCENT)	LENGTH (FT)	SPEED (FPS)	KR KS	KS
								DIMENSIONLESS	B2
1	47 02	142 80	-95 67	90 76	1 76	865 35	66 57	1 00	1 1377
20	46 59	132 45	-87 13	92 76	1 76	630 15	48 47	1 06	0 9274
40	47 10	121 72	-85 28	85 91	1 90	612 12	47 09	1 08	0 9333
60	47 59	111 25	-94 16	81 03	0 42	598 37	46 03	1 09	1 1524
80	49 12	101 06	-92 78	74 25	0 38	578 03	44 46	1 12	1 1875
100	50 65	91 54	-79 35	60 76	0 40	532 33	40 95	1 17	1 2022
120	52 44	82 73	-77 43	53 05	0 51	502 43	38 65	1 19	1 2007
140	54 47	74 98	-75 19	44 75	0 54	466 45	35 88	1 19	1 1656
160	56 47	67 01	-75 76	37 09	0 43	428 85	32 99	1 17	1 1103
* 162	56 65	66 29	-76 12	35 83	0 53	422 18	32 48	1 17	1 1046
** 167	57 05	64 56	-78 21	32 67	0 89	404 75	31 13	1 18	1 0960
** 167	57 12	64 23	-78 85	29 43	0 61	385 73	29 67	1 20	1 0900
* 170	57 23	63 60	-80 45	27 56	0 65	374 17	28 78	1 21	1 0867
* 171	57 28	63 31	-81 32	27 45	0 33	346 97	26 69	1 24	1 0793
* 172	57 32	63 26	-81 33	27 36	0 37	331 99	25 53	1 26	1 0749
* 173	57 36	63 24	-82 13	27 25	0 11	319 29	24 79	1 28	1 0703
* 174	57 41	62 76	-82 40	27 13	0 73	307 37	23 94	1 30	1 0656
* 175	57 46	61 81	-83 61	26 96	0 53	293 80	23 24	1 32	1 0611
* 177	57 45	61 81	-83 71	26 82	0 66	283 35	22 80	1 34	1 0566
* 180	57 48	61 23	-87 17	18 03	12 68	206 95	18 18	1 44	1 0470
* 181	57 49	61 05	-87 65	7 46	13 65	199 57	15 35	1 51	1 0361
* 190	57 50	59 61	-92 02	4 10	10 64	148 62	11 43	1 53	1 0330
196	57 47	59 07	-94 50	-0 25	-652 68	87 09	6 70	2 23	0 9985
TOPPED, REACHED SHORE X = 57 47, Y = 59 07									

TABLE 2 ALONGSHORE ENERGY FOR $K_r < \infty$ (10^6 ft-lbs/ft of beach)

STATION	1	3	2	5	4	6	7
JAN	3489	1452	4180	22092	5031	666	225
FEB	4625	3114	8302	21418	8030	244	1084
MAR	2167	1180	2705	10584	2583	-9	4
APR	769	824	-39	5195	2642	2617	177
MAY	104	347	-261	1253	1271	-143	169
JUN	-429	-80	-247	-1717	75	-3	1
JUL	-361	-56	-90	-1163	34	-5	2
AUG	-411	-45	-182	-1043	35	23	2
SEP	-92	110	152	-27	349	-20	7
OCT	305	226	297	1206	1049	384	70
NOV	982	89	88	2669	839	1081	-5
DEC	1866	603	1009	5857	1430	1171	-14
TOTAL	13014	7764	15914	66324	23368	6006	1722

POTENTIAL LITTORAL TRANSPORT FOR $K_r < \infty$ (10^3 cubic yards)

STATION	1	3	2	5	4	6	7
JAN	447	186	535	2828	644	86	29
FEB	592	399	1063	2741	1027	31	139
MAR	277	151	346	1355	331	-1	1
APR	98	105	-5	665	338	335	23
MAY	13	44	-33	160	163	-18	22
JUN	-55	-10	-32	-220	10	0	0
JUL	-46	-7	-12	-149	4	1	0
AUG	-53	-6	-23	-134	4	3	0
SEP	-12	14	20	-4	45	-3	1
OCT	39	29	38	154	134	49	9
NOV	126	11	11	342	107	138	-1
DEC	239	77	129	750	183	150	-2
TOTAL	1665	993	2037	8488	2990	770	221

TABLE 3 ALONGSHORE ENERGY FOR $K_r \leq 2$ (10^6 ft-lbs/ft of beach)

STATION	1	3	2	5	4	6	7
JAN	3029	1440	-184	6701	3708	21	225
FEB	3719	3006	199	7888	6822	319	1084
MAR	1410	1097	-616	1963	1564	35	4
APR	392	789	156	1420	2001	579	177
MAY	-196	342	-185	-806	462	12	169
JUN	-556	-80	-198	-1722	75	37	1
JUL	-435	-56	-67	-1162	34	9	2
AUG	-469	-45	-182	-1044	35	37	2
SEP	-251	107	-192	-496	166	30	7
OCT	13	211	-594	-49	458	-18	70
NOV	179	89	-644	-304	330	-49	-5
OEC	943	562	-1673	925	881	-28	-14
TOTAL	7778	7462	-4179	13314	16536	984	1722

POTENTIAL LITTORAL TRANSPORT FOR $K_r \leq 2$ (10^3 cubic yards)

STATION	1	3	2	5	4	6	7
JAN	388	184	-24	858	475	3	29
FEB	476	385	26	1010	873	41	139
MAR	180	140	-79	251	200	4	1
APR	50	101	20	182	256	74	23
MAY	-25	44	-24	-103	59	2	22
JUN	-71	-10	-25	-221	10	5	0
JUL	-56	-7	-9	-149	4	1	0
AUG	-60	-6	-23	-134	4	5	0
SEP	-32	14	-25	-63	21	4	1
OCT	2	27	-76	-6	59	-2	9
NOV	23	11	-82	-39	42	-6	-1
OEC	121	72	-214	118	113	-4	-2
TOTAL	996	955	-535	1704	2116	127	221

TABLE 4 ALONGSHORE ENERGY FOR $K_r \leq 1.41$ (10^6 ft-lbs/ft of beach)

STATION	1	3	2	5	4	6	7
JAN	3200	1357	6	3233	2921	168	128
FEB	3130	2537	1477	5295	4478	346	625
MAR	902	792	-496	882	1229	83	-9
APR	260	583	-243	-13	1426	60	101
MAY	-342	295	-171	-961	294	61	92
JUN	-593	-80	-190	-1712	75	53	1
JUL	-456	-56	-63	-1160	34	15	2
AUG	-486	-45	-182	-1041	35	45	2
SEP	-327	67	-159	-499	133	60	4
OCT	-237	163	-446	-334	353	64	34
NOV	-179	89	-578	-468	273	62	-8
DEC	642	434	-1902	228	739	133	-19
TOTAL	5514	6136	-2947	3450	11990	1150	953

POTENTIAL LITTORAL TRANSPORT FOR $K_r \leq 1.41$ (10^3 cubic yards)

STATION	1	3	2	5	4	6	7
JAN	410	174	1	414	374	22	16
FEB	401	325	189	678	573	44	80
MAR	115	101	-64	113	157	11	-1
APR	33	75	-31	-2	183	8	13
MAY	-44	38	-22	-123	38	8	12
JUN	-76	-10	-24	-219	10	7	0
JUL	-58	-7	-8	-149	4	2	0
AUG	-62	-6	-23	-133	4	6	0
SEP	-42	9	-20	-64	17	8	1
OCT	-30	21	-57	-43	45	8	4
NOV	-23	11	-74	-60	35	8	-1
DEC	82	56	-243	29	95	17	-2
TOTAL	706	787	-376	441	1535	149	122

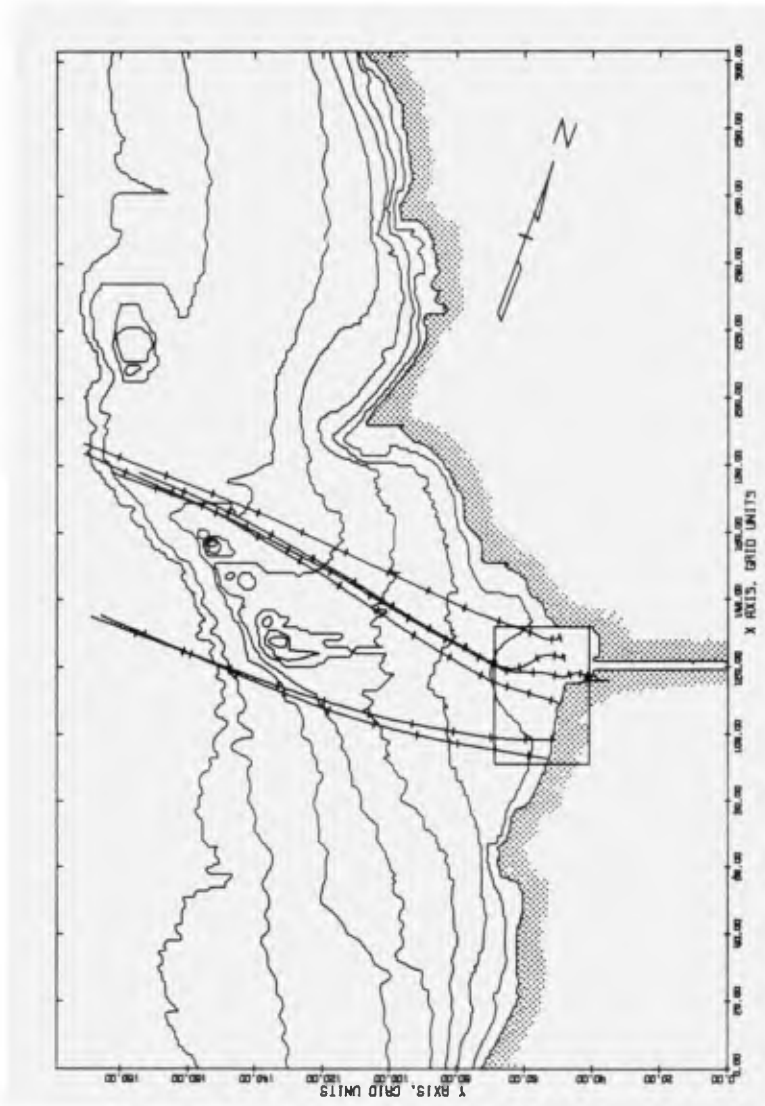


FIGURE 1A
OUTER GRID CONTOUR MAP and
13 SEC. WAVE RAYS TO STATIONS 1,2,3,4,5,7

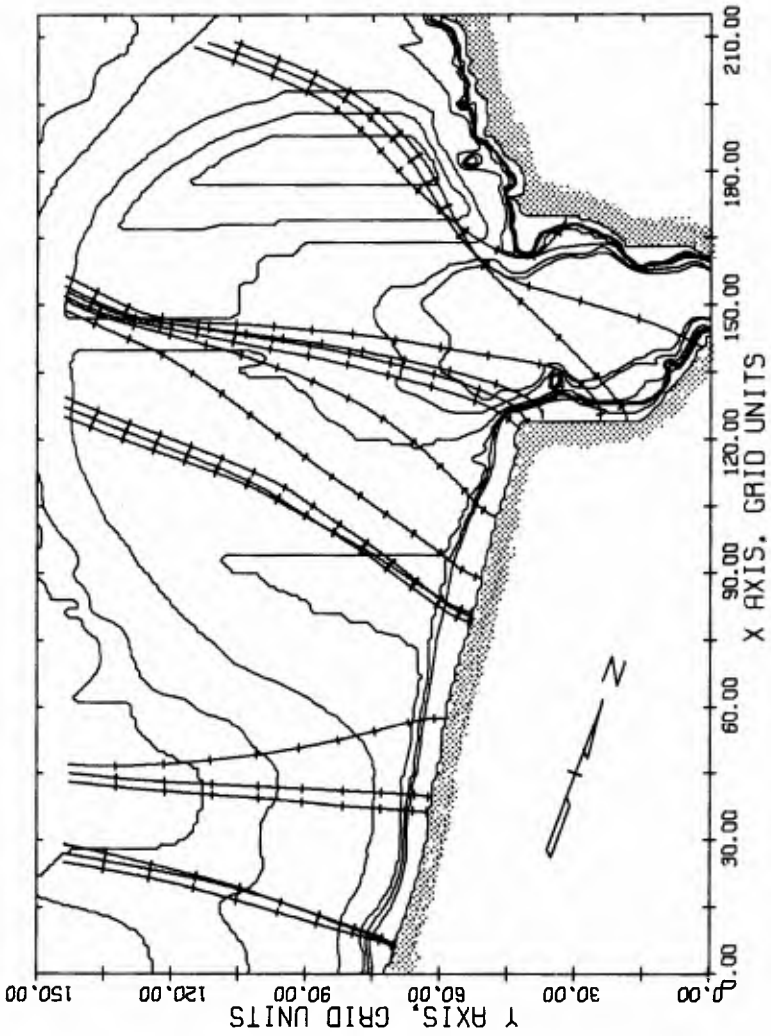


FIGURE 1B

INNER GRID CONTOUR MAP and
13 SEC. WAVE RAYS TO STATIONS 1,2,3,4,5,7

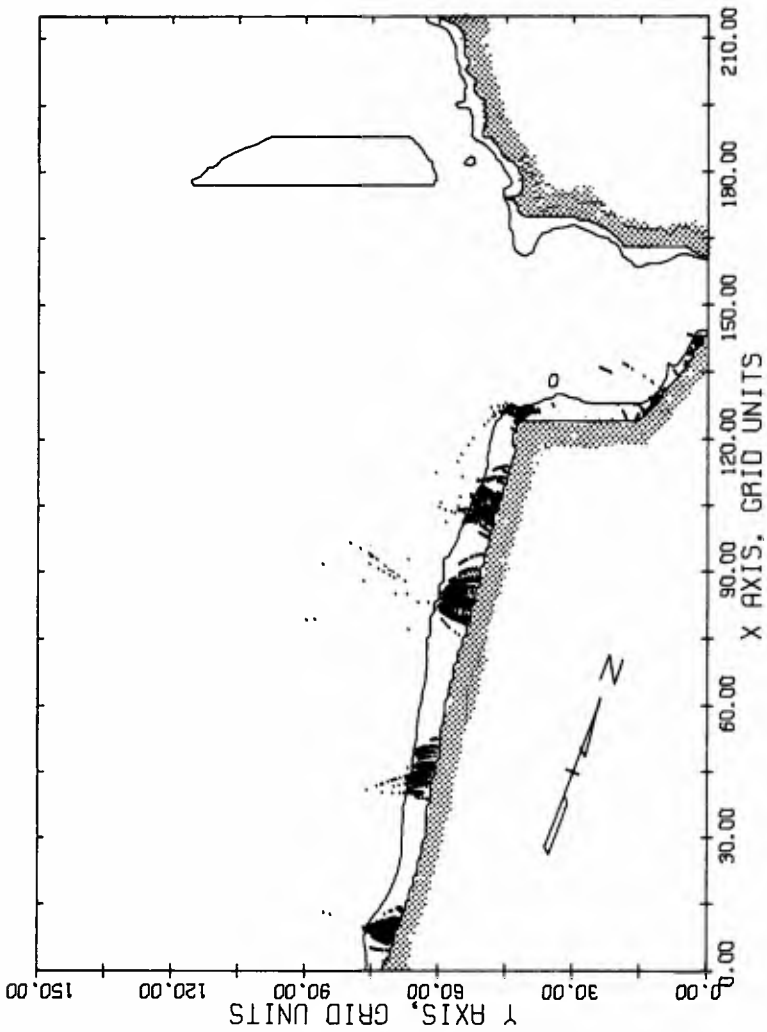


FIGURE 2

SCATTERGRAPH
Showing Breaking Locations for the Case $K_r < \infty$

CHAPTER 58

CRATER-SINK SAND TRANSFER SYSTEM

by

Douglas L Inman
Scripps Institution of Oceanography, University of California
La Jolla, California 92037

and

Roland W Harris
Dredging Engineer, currently with Leedshill-Deleuw
Dacca, East Pakistan

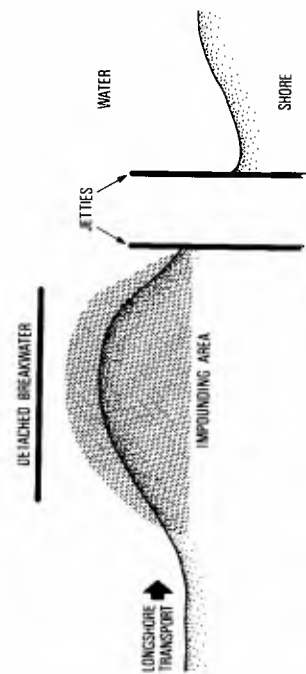
ABSTRACT

A sand transfer system that requires no surface impounding area and that can be installed and operated at low cost is proposed. The system consists of a hydraulic jet assembly operating from the bottom of a sand crater. A jet pump and suction mouth are located at the lowest point of a crater-like depression dredged into the sea floor. The crater acts as a gravity-fed sink for sand and other cohesionless material, thus serving the dual purpose of a mechanism for collecting sand and a sub-surface impounding area for the accumulation of sand.

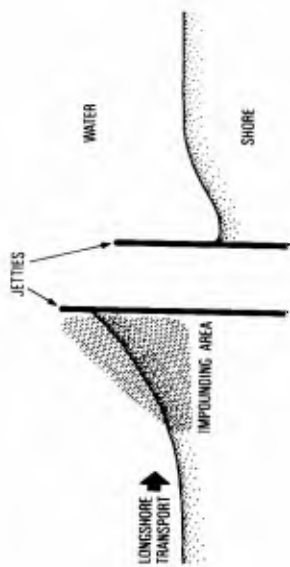
INTRODUCTION

The large volumes of sand transported by waves and currents in the nearshore zone has always presented a serious problem to the coastal engineer (Johnson, 1957). The problem is particularly serious with engineering structures associated with the entrances to harbors and coastal lagoons. Coastal structures that interrupt the longshore transport of sand produce local areas of accretion on the up-coast side of the structures and corresponding areas of erosion on the down-coast side. In time, both the accretion and the erosion become problems, whose common solutions require that the accreted material be bypassed to the area of erosion. Over the years various procedures have been developed to handle the bypassing of sand around coastal structures, (Eaton, 1951, Watts, 1966, Tornberg, 1968).

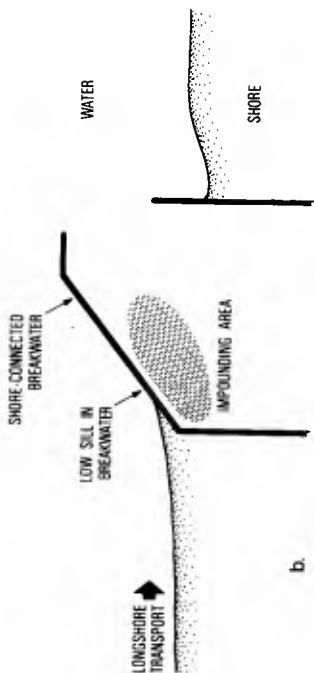
All of these bypassing procedures require the construction of "impounding" or storage areas where the sand accumulates until its volume is sufficient to warrant bypassing by suction dredge or other means. Impounding requires that the longshore transport of sand be intercepted before it reaches the entrance channel. This is usually accomplished by building a suitable structure, which commonly takes one of the forms illustrated in Figure 1. All of these procedures involve expensive construction and maintenance. Further, to attain maximum efficiency the impounding areas must be large, thus occupying valuable coastal area.



② DETACHED BREAKWATER



① JETTIED ENTRANCE



③ SHORE-CONNECTED BREAKWATER

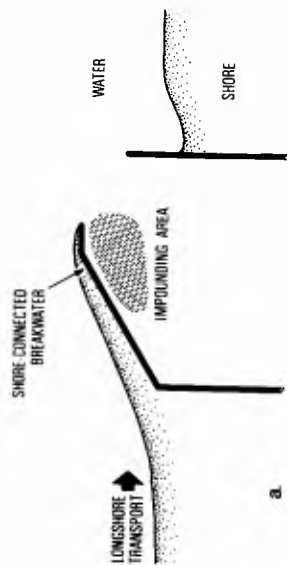


Figure 1. Schematic diagrams of the types of impounding areas associated with entrances to harbors and coastal lagoons (after Watts, 1966). Prototype examples include: (1) South Lake Worth Inlet, Florida (Watts, 1963); (2) Channel Islands Harbor, and Port Hueneme, California (Herron and Harris, 1966); (3a) Santa Barbara, California (Wiegel, 1959); and, (3b) Masonboro Inlet, North Carolina (Magnuson and Rayner, 1966).

Considerations of the overall budget of sand in the nearshore areas of the world show that the problem has a more basic aspect than just that of sand bypassing. Beach sand has become an important natural resource that is diminishing in quantity at an alarming rate. This has come about because man has progressively decreased the supply of sand to the beaches by damming rivers and has interrupted its longshore movement with coastal structures. On the other hand, the loss of sand from the nearshore zone, either down submarine canyons or by other means, remains at a high rate (Inman and Frautschy, 1966). Various procedures, such as dredging sand from the continental shelf (Taney, 1965) and pumping sand from coastal impoundment areas (Herron and Harris, 1962) have been suggested for supplying sand to undernourished beaches.

The increasing need for sand bypass systems and for beach nourishment systems makes it apparent that the development of different, more efficient sand transfer systems is an urgent necessity if we are to retain our coastal zone resources. Accordingly, a sand transfer system that requires no surface impounding area and that can be installed and operated at low cost is proposed.

CRATER-SINK SAND TRANSFER SYSTEM

The crater-sink sand transfer system consists of a hydraulic jet assembly operating from the bottom of a sand crater. The hydraulic jet assembly consists of a suction mouth, a jet pump, a drive-water pipe, and, a delivery pipe that transports the sand-water mixture away from the crater site (Figure 2). Since the suction mouth is located at the lowest point of a crater-like depression in the sea floor, the crater acts as a gravity-fed sink for sand and other cohesionless material. Sand transported to the perimeter of the crater will cascade down the sides of the crater to the suction mouth where it becomes available for transfer. Thus, the crater-sink serves the dual purpose of a mechanism for collecting sand and a sub-surface impounding area for the accumulation of sand. When located in the entrances to harbors and inlets, it provides the greatest depth of water in the entrance channel where it is needed. Once installed the system is stationary and the only moving parts are in the drive-water pump. When required, the jet pump assemblage and delivery pipe can be floated to the surface for maintenance, as discussed in the section on installation.

HYDRAULIC JET ASSEMBLY

Recent developments in jet pump technology now make it practical to use hydraulically driven jet pumps to move sand through pipelines. The excessive wear rates caused by the highly abrasive sand-water mixtures have been markedly reduced in recently designed pumps. The new designs have resulted from experiments (1) on the optimum shape and angle for the nozzle entry into the throat of the Venturi section of the pump (Figure 3), and, (2) with various types of resistant linings for the

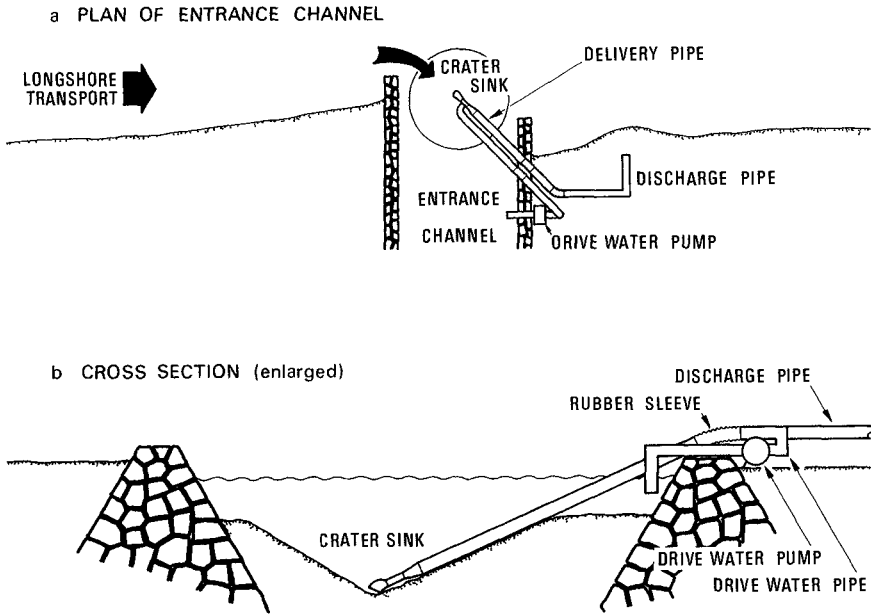


Figure 2 Schematic diagram of crater-sink sand transfer system when used to bypass sand across the entrance to a harbor or lagoon

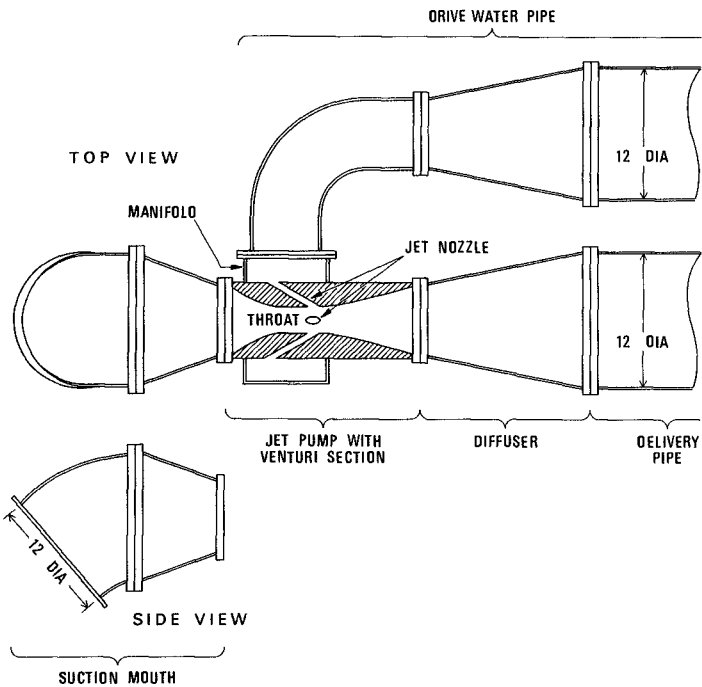


Figure 3 Schematic diagram of the hydraulic jet assembly

Venturi throat of the pump (D M Frazier, 1967, W G Fraser, unpublished manuscript, J V Barker, 1969)

Improved jet pumps of this type have been in use for several years as suction booster pumps behind the cutter head on suction dredges. Experience by various users ^{*/} indicates that the wear life of a jet pump, before requiring new plastic linings, is now measured in millions of cubic yards rather than hundreds of thousands of cubic yards. The basic rate of pumping for a jet pump driving a 12-inch ID delivery pipe would be in excess of one million cubic yards of sand per year. This includes approximately 25% down-time for maintenance.

The hydraulic jet assembly driving the crater-sink sand transfer system consists of a suction mouth, jet pump, diffuser, and delivery pipe. The jet pump consists of a cylindrical cast steel Venturi section which is fitted with a series of peripheral nozzles (Figure 3). The nozzles are inclined towards the centerline of the Venturi throat, and are driven by water supplied to the cylindrical manifold surrounding the Venturi section. Drive water is supplied to the manifold through a separate pipe which is fed by a water pump.

The delivery pipe is coupled to the jet pump by a diffuser which increases the diameter of the Venturi section to that of the delivery pipe. The delivery pipe brings the sand to the landing pipe, where it may be discharged at the shoreline through a short discharge pipe. If the sand is to be discharged at a more distant point, then a booster pump driving an extended discharge line must also be installed, as shown in Figure 7.

INSTALLATION AND CHARACTERISTICS OF THE CRATER-SINK

The initial installation can be made in several ways. If the thickness of cohesionless sand is sufficient to provide a crater of the desired size, the crater can be excavated by the hydraulic jet assembly. The assembly could be floated and towed to the site, where it could then be flooded with water and used to excavate itself into place. The crater will then be developed as the delivery pipe is extended from a handling barge or ship (Figure 4a).

If the thickness of cohesionless sand above a consolidated soil horizon is thin, then it will be necessary to excavate a crater of the desired size, using conventional methods such as a suction dredge with a rotary cutter head. Once the crater is formed then the jet pump and discharge pipe can be floated over the site, flooded with water and the rig set into position (Figure 4b).

^{*/} For example, jet pumps have been used by General Construction Co., Portland, Oregon (personal communication), Pacific Dredging Co., Long Beach, Calif (personal communication), Western-Pacific Dredging Co., Portland, Oregon, Utah Dredging Corp., San Francisco, Calif, and, the U S Corps of Engineers, Portland District (Fraser, unpublished manuscript). Also, a jet pump system for offshore sources of sand has been recommended by Govatos and Zandi (1969).

In the absence of currents, the crater walls would normally stand at the static angle of repose of the sand which is about 30 degrees. Thus, the minimum size of the crater would be that occurring for static conditions, where the diameter would be approximately four times its depth, and the volume of the crater would equal about 4/2 times the cube of its depth. Therefore, a 50 foot deep crater would have a minimum circular perimeter with a diameter of about 200 feet, and a volume of 20,000 yd³, while a 100 foot deep crater would have a minimum diameter of 400 feet and a volume of 155,000 yd³.

The dynamic effects of currents flowing across the sand crater would result in crater slopes that are less than the static angle of repose, and thus increase the periphery and the volume of the crater. Also, the effective collecting periphery of the crater-sink would be extended by the sand transported to the rim of the crater by currents. The effect of currents and wave action on crater shape is not clearly understood and should receive further study.

The successful functioning of the crater-sink concept requires that the crater be sited so as to intercept the longshore transport of sand. Entrance channels tend to migrate along the coast in the direction of the longshore transport as well as in an on-offshore direction with changing wave and current conditions (Inman, 1950, p 15). Thus, the construction of a short up-coast jetty to stabilize the location of the "transport path" of the littoral drift is important in siting the crater-sink (Figure 2). The principal function of a down-coast structure would be the protection of the site for the drive-water pump and the landing and discharge pipes.

Excavation of the Crater Sink with the Jet Unit

The equipment for this operation is shown schematically in Figure 4a and includes a suitable barge with ground tackle and lifting gear and a drive-water pump. The jet pump end of the assembly of delivery and drive-water pipes is suspended from a barge in such a way as to provide both vertical control and horizontal control of the suction mouth. The delivery pipe is fitted with pontoons which support the delivery pipe for transporting the sand away from the crater site.

After the crater is excavated the pipeline and jet assembly are moved to the beach where the pontoons are removed, the pipelines are lengthened to suit the installation and stability tanks are attached. The shore ends of the drive-water pipe and delivery pipe are blanked off at the landing pipe and air is pumped into both pipes. Since there is less buoyancy at the jet pump end of the pipes, the suction mouth will always float lower than the rest of the pipe, thus effectively preventing a large loss of air through the suction mouth. When the assembly has been floated into the correct position air is vented at the landing pipe position and the jet pump end of the assembly begins to descend, the descent rate being controlled by the residual air in the pipes. After

sinking into position, the discharge pipe is connected to the shore end of the landing pipe, and the drive-water pipe is connected to the drive-water line from the drive-water pump. Raising of the hydraulic jet assembly is carried out in the reverse procedure as described above.

EXTENSION OF CRATER-SINK BY FLUIDIZATION

It would appear that the perimeter of the crater-sink could be effectively extended in any desired direction by fluidizing the sand bed. A sand body tends to behave as a fluid when the fluid pressure in the pore spaces at any level are equal to or greater than the immersed weight of sand above this level. This technique is widely used in industry for the transport and mixing of granular-fluid media (Flood and Lee, 1968) and could be used to extend the effective perimeter of a crater-sink system without requiring an increase in the depth or width of the crater. It would appear that this could be accomplished by installing a length of pipe, fitted with jet holes, that extended from the crater-sink to some distant shoal. If the pipe were laid along the bottom with jet holes in the "down-position", then pumping water at a high rate through the pipe would activate the jets and cause the pipe to bury into the sand bed. Once in place, a reduced pumping rate could be employed that would fluidize the sand above the pipe, without causing it to jet further into the bed. As long as the bottom of the crater is deeper than the shoal the fluidized layers of sand, under the influence of gravity, will flow towards the crater-sink (Figure 5).

The extension of a crater-sink by long fluidization units appears to be particularly applicable to long, narrow entrance channels, which commonly result in the formation of shoals outside of the entrance (Figure 6). This application is essentially the reverse of that suggested by Hagyard, et al (1969), which would have employed a one mile long fluidization unit located off Westport Harbor, New Zealand, to transport sand from the entrance channel into deeper water. However, the experiments performed by Hagyard, et al (1968) on fluidizing velocities, depth of burial of pipe, and the shape of the fluidized zone above the pipe, should also apply to the crater-sink concept. In fact, since the installation proposed here would involve relatively short fluidization units operating over relatively steep slopes and feeding continuous sand sinks, its application should be less critical than that suggested by Hagyard, et al. However, the technology for fluidizing natural sand beds has not been perfected, and it is quite apparent that both applications require further study before committing them to prototype conditions (Wilson and Mudie, in preparation).

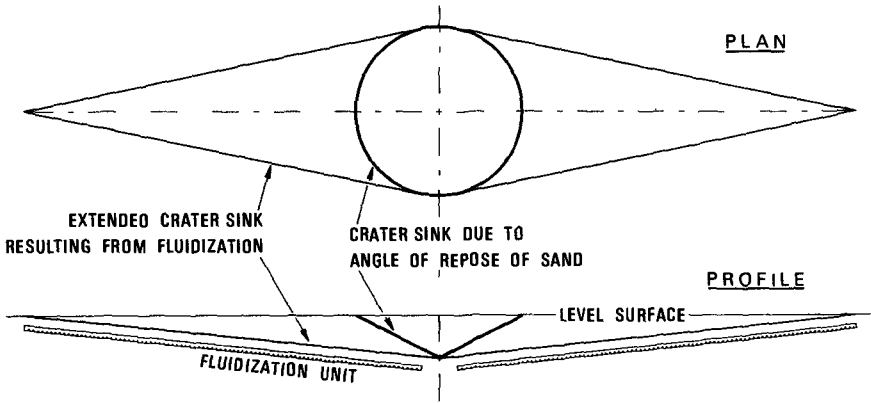


Figure 5 Extension of the periphery of the crater-sink using two fluidization units (Refer to Figure 6)

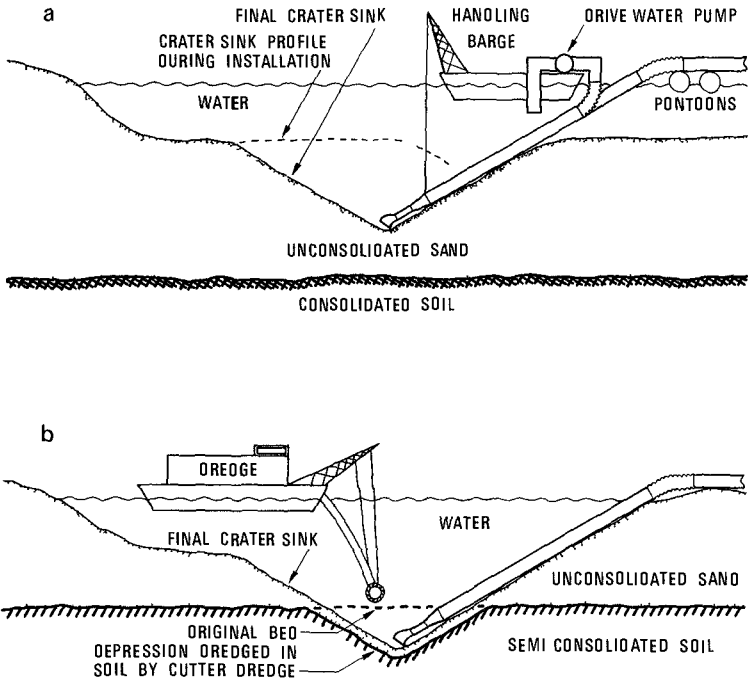


Figure 4 Schematic diagram showing the various methods of constructing the crater-sink (1) direct installation from a barge or boat using the hydraulic jet assembly as a dredge and (b) excavation of a crater into semi-consolidated soil using conventional suction dredge with a rotary cutter head

CHARACTERISTICS OF A TYPICAL INSTALLATION AT A SANDY INLET

As stated previously, additional research is warranted before the crater-sink concept and its extension by fluidization is employed in the field. However, it is instructive to consider the characteristics of such an installation as based on present understanding.

Consider the crater-sink sand transfer system that would be required to maintain an entrance channel 20 feet deep and 500 feet wide through an inlet where the net longshore transport is known to be 400,000 cubic yards per year. Assume that there are occasional reversals in the direction of transport, amounting to about 100,000 cubic yards, so that the system must be capable of pumping in excess of 500,000 cubic yards per year. Further, assume that there is a tendency for a bar to form offshore from the inlet, so that the perimeter of the crater-sink must be extended for 1000 feet offshore from the end of the up-coast jetty. This situation is analogous to that shown schematically in Figure 6 and listed in Table 1, and is a fairly common one along the sandy coastlines of the world.

For an inlet of this type a hydraulic jet assembly pumping from the bottom of a 50 foot deep crater would probably provide sufficient perimeter for the basic crater. The minimum width of the crater would be about 200 feet as determined by the static angle of repose of the sand, while the dynamic width in the presence of waves and currents would probably be about 300 feet as shown in Figure 6. A vertical lift of 70 feet and a horizontal delivery distance of about 400 feet is within the capacity of existing jet pumps. If the basic crater can be extended seaward by installation of a 1000 foot long fluidization unit it would then be possible to extend and maintain the channel through the central portion of the offshore bar as shown in Figure 6.

The use of turn pipes and rubber sleeves permits accommodation of a variety of bottom profiles, while providing lateral stiffness and maintaining alignment. Life of the equipment can be extended by exchanging sand delivery and drive-water pipes when the former wear thin.

The operating schedule for the jet pump would depend upon demand. For example, the pump could be turned on every 24 hours and would then operate until the sand fill in the crater had been removed. During times of low wave activity it would operate perhaps one or two hours per day, while during times of pronounced longshore transport it could operate 24 hours per day.

Table 1 Characteristics of crater-sink sand transfer system (extended by fluidization) when used to bypass sand around an inlet and entrance channel. Sand is to be discharged directly on the beach face near the landing pipe as shown schematically in Figure 6

ENTRANCE CHANNEL AND INLET

water depth	20 ft
channel width	500 ft
distance to offshore bar	700 ft
longshore transport rate of sand, net	400,000 yds ³ /yr
longshore transport rate reversed direction	100,000 yds ³ /yr
total required sand pumping capacity	500,000 yds ³ /yr

CRATER-SINK

crater depth	50 ft
water depth at center of crater	70 ft
crater width - minimum (still water)	200 ft
crater width - maximum with waves and currents	300 ft
crater length - minimum	1,200 ft
crater length - maximum	1,300 ft

HYDRAULIC JET ASSEMBLY

jet pump*/	Venturi throat diameter	10 in
	nozzles - number	4
	nozzles - diameter	1 in
	rated flow capacity	approx 5,500 gpm (12 ft ³ /sec)
		total flow

Table 1 (Continued)

drive-water pump**/	flow capacity	2,200 gpm (5 ft ³ /sec) 250 horsepower
delivery pipe	length (jet pump to landing pipe	300 ft
	diameter I D	12 in
elevation of discharge point above mean water level		10 ft

*/ For example, jet pump model 12 in, manufactured by Pacific Coast Engineering Co , Alameda, California

**/ For example 2200 gpm at 150 psi, 250 horsepower, electric driven water pump, manufactured by Byron-Jackson Pump Co , Los Angeles, California

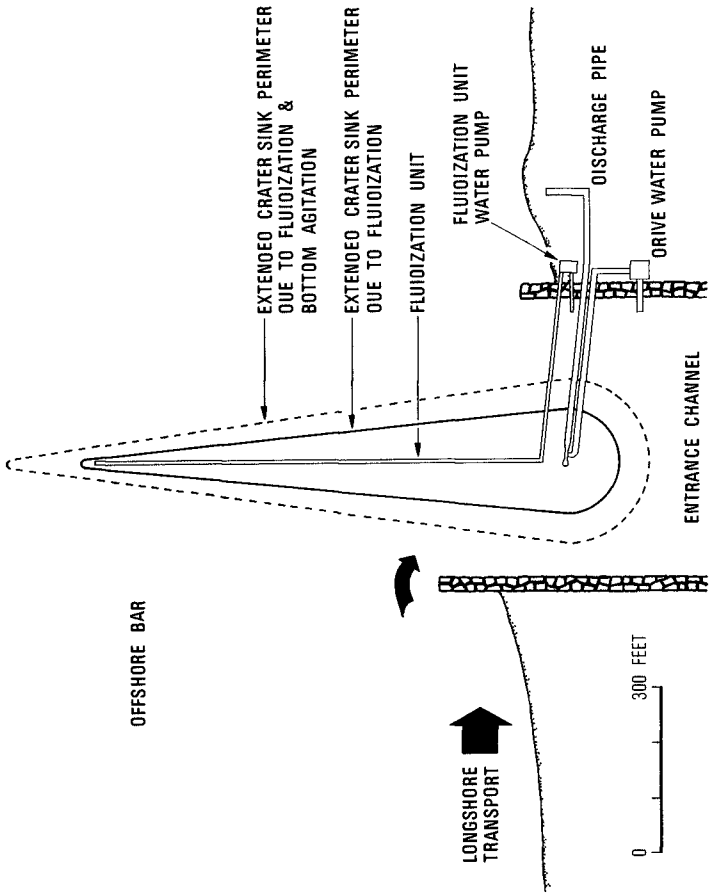


Figure 6 Schematic diagram of a fluidized crater-sink employed for sand bypassing at an inlet with offshore bar

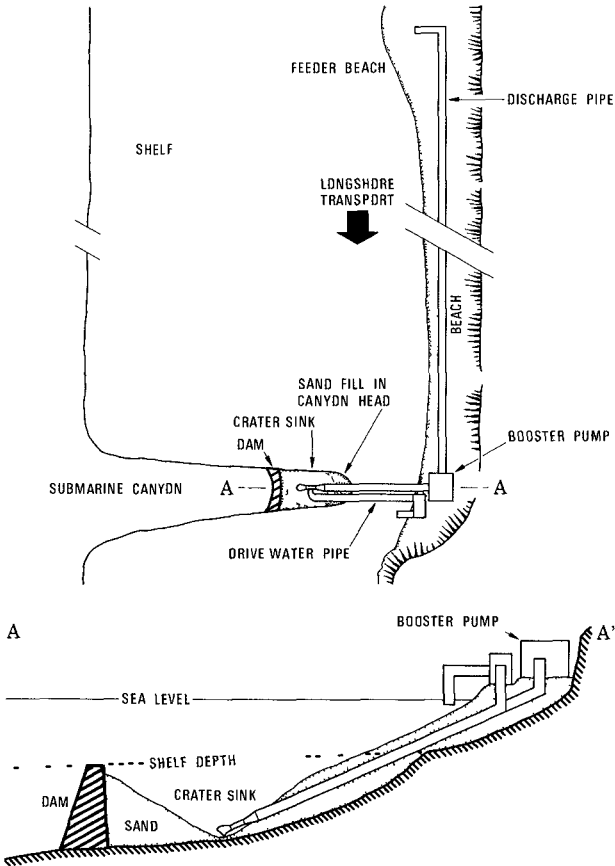


Figure 7 Schematic diagram of the crater-sink sand transfer system used to recycle sand in a littoral cell with longshore transport. Sand trapped by a sub-surface dam across the head of a submarine canyon is pumped up-coast to a feeder beach where it again becomes available for longshore transport.

CONCLUSIONS

The advantages of the crater-sink sand transfer system over conventional dredging appear to include (a) simple, inexpensive equipment requiring a minimal amount of labor, (b) lower operating costs, (c) no obstruction to navigation, (d) elimination of the up-coast sand impounding area, and, (e) the ability to operate throughout the year, thus providing a continuous bypass operation which maintains the natural drift rates along the coast and eliminates the down-coast zone of erosion

Once perfected, it would appear that a crater-sink sand transfer system would have a variety of coastal and inland applications. In addition to its use at sandy inlets (Figures 2 and 6), it would appear to have potential for pumping sediment from dams that have intercepted the supply of sand formerly brought to the coast by streams and rivers. Also, the sand transfer system could be used to recycle sand to feeder beaches on a coast with littoral drift. Sand trapped on the down-coast end of a beach could be pumped to feeder beaches along the up-coast portions of the beach where it again becomes available for longshore transport as illustrated schematically in Figure 7.

ACKNOWLEDGMENTS

The authors are indebted to George M. Watts, U. S. Army Corps of Engineers, Coastal Engineering Research Center, and John D. Mudie, Scripps Institution of Oceanography, for valuable suggestions and critical reading of the manuscript. This paper represents, in part, application of concepts developed by the University of California, San Diego, under contract with the Advanced Research Projects Agency.

REFERENCES

- Angas, W. M., 1960, "Shark River inlet sand bypassing project", Jour. Waterways and Harbors Div., Amer. Soc. Civil Engin., vol 86, WW 3 paper 2599, p 29-47
- Barker, J. V., 1969, "The PACECO jet stream system", World Dredging and Marine Construction, June p 28-30
- Eaton, R. W., 1950, "Littoral processes on sandy coasts", Proc. First Conf. on Coastal Engin., Council on Wave Research, the Engineering Foundation, p 40-54
- Flood, H. W. and B. S. Lee, 1968, "Fluidization", Scientific American, vol 219, no 1, p 94-104
- Fraser, W. G., "Development of a dredge jet pump", Pacific Coast Engineering Company, 5 pp (unpublished)

- Frazier, D M , 1967, "New dredging techniques using an annular jet", Proc of WODCON, World Dredging Conf , p 115-131
- Govatos, G and I Zandi, 1969, "Beach nourishment from offshore sources", Shore and Beach, vol 37, no 2, p 40-49
- Hagyard, T , I A Gilmour, W D Mottram, 1969, "A proposal to remove sand bars by fluidization", New Zealand Jour Sci , vol 12, p 851-64
- Herron, W J Jr , and R L Harris, 1966, "Littoral bypassing and beach restoration in the vicinity of Port Hueneme, Calif", Proc Tenth Conf Coastal Engin p 651-675
- Inman, D L , 1950, "Beach study in the vicinity of Mugu Lagoon, Calif", Beach Erosion Board, Corps of Engin , Technical Memo 14, 47 pp
- Inman, D L and J D Frautschy, 1966, "Littoral processes and the development of shorelines", Coastal Engineering, Santa Barbara Specialty Conference, Amer Soc Civil Engin p 511-36
- Johnson, J W , 1956, "Dynamics of nearshore sediment movement", Amer Assoc Petrol Geologists Bull , vol 40, p 2211-2232
- Johnson, J W , 1957, "The littoral drift problem at shoreline harbors", Jour Waterways and Harbors Div , Amer Soc Civil Engin , vol 83, WW1, paper 1211, 37 pp
- Magnusom, N C and A C Rayner, 1966, "Stabilization of Masonboro Inlet", Shore and Beach, vol 34, no 2, p 36-41
- Taney, N E , 1965, "A vanishing resource found anew", Shore and Beach, vol 33, no 1, p 22-26
- Tornberg, G F , 1968, "Sand bypassing systems", Shore and Beach, vol 36, no 2, p 27-33
- Watts, G M , 1966, "Trends in sand transfer systems", Coastal Engin Santa Barbara Specialty Conf , Amer Soc Civil Engin , p 799-804
- Watts, G M , 1953, "Study of sand movement at South Lake Worth Inlet, Florida", Beach Erosion Board, Corps of Engineers, Technical Memo, 42, 24 pp
- Weigel, R L , 1959, "Sand bypassing at Santa Barbara, Calif", Jour Waterways and Harbors Div , Amer Soc Civil Engin , WW 2 paper 2066, 30 pp
- Wilson, C R and J D Mudie (in preparation), "Comments on the removal of sand bars by fluidization", New Zealand Jour of Science

CHAPTER 59

USE OF VOLCANOES FOR DETERMINATION OF DIRECTION OF LITTORAL DRIFT

By

Per Bruun and Gísli Viggooson

The Technical University of Norway

Abstract - The title of this paper may sound like a joke. Correctly the title ought to be "Determination of Direction of Littoral Drift on the South Coast of Iceland by Geomorphological Approach". In order to check the results of such study based on the movements of river entrances and their geometry the use of an accelerometer buoy to be placed in offshore open waters for collection of wave data combined with the results of meteorological data was discussed. Then the volcano Surtsey suddenly emerged from 400 ft depth (Nov 1964) and its huge outpours of volcanic material built up an "offshore pole station", where the shoreline development provided some information which supported conclusions from the shoreline study on the mainland. Computation of wave energy input provided further information.

GEOMORPHOLOGICAL APPROACH

OBSERVATIONS OF RIVER OUTLETS

The littoral drift on the Icelandic south coast was investigated by means of topographic surveys and aerial photos including

Survey by the Danish Geodetic Institute, 1906
 Survey by the Danish Navy, ab 1926
 Aerial photography, 1945 (Icelandic Survey Dept)
 Aerial photography, 1960
 Aerial photography, 1960 U S Navy
 Aerial photography, July 1963 (Icelandic Dept of Light-
 houses and Ports)
 Aerial photography, Aug 1963 (Icelandic Dept of Light-
 houses and Ports)

Most of these surveys were undertaken during the summer period, when the littoral drift because of winds from South East tends to be westward This may have considerable influence on the geographical direction of the outlets of minor rivers on the South Coast while the major streams will not change the general orientation of the outlet which points in the direction of the predominant littoral drift

The results of studies of this material are depicted on Fig 1, indicating that the littoral drift at Holsá is eastward, that the drift at the shore between Affall until west of Holsos is neutral, that the drift from west of Jokulsá and up to Dyrholaey probably is eastward although some minor outlets demonstrate westward direction which, as mentioned above, most likely is a seasonal phenomenon Furthermore that the littoral drift just east of Dyrholaey is westward

Professor Trausta Einarsson in his article on "Suðurstrond Islands og mundunarsaga hennar" published in Tímarit, Verkfræðingafélag Islands (Proceedings of the Icelandic Engineering Association), No 1-2, 1966 in section IV "Raðir foksandshóla og forsöguleg staða strandarinnar" explains the development of shore and shoreline configuration west of Dyrholaey from the outlet of Thorsá and up to Reynisfjall towards the East He takes a closer look at the shores at Dyrholaey Based on the development of ancient and recent shorelines it is quite clear that the shore between Klifandi (Figs 1 and 3) and Skogá (Figs 1 and 2) has been a "neutral area", which means that the net drift has been relatively small or the drift has taken place in opposite directions

according to season and in almost equal quantities on a year round basis. The sediments which washed down to shore by the rivers apparently drifted in part towards the Dyrholaey (Dyrhola-island) building up a tombolo (barrier connecting island and main land) and partly westwards towards Vestmannaeyjar (islands south of Iceland - see Fig 1) which caused the development of another major tombolo inside the wave shadow of these islands (Fig 2). With enough "patience" and material available the Vestmanna Islands would finally become connected to the mainland provided current concentrations between island and mainland would not make this development impossible.

This confirms the results of the observations of direction of outlets mentioned above. The orientation of the shoreline west of Dyrholaey is almost constant 27 degrees north of west.

OBSERVATIONS OF SHORELINE DEVELOPMENT OF VOLCANOE SURTSEY

It is in this respect interesting to note the development of shorelines at the volcano Surtsey as studied by Thorarinnsson (Surtsey Research Progress Reports Nos II and III 1966 and 1967) and by Norrman (Surtsey Research Progress Report No IV, 1968).

Surtsey is a submarine volcano, which erupted on Nov 14th, 1963 (Fig 4) at about 100 meters depth. In 6 days an island 600 m long and almost as wide with top elevation of 60 meters came into existence.

Gradually the configuration of the island changed to hoof shape, which immediately after Nov 26th (Fig 5) normally was open towards the southwest. Sometimes a barrier blocked the opening, however, but it only lasted until it was broken down by the surf, or until it was blown away by explosions from the volcano. After the middle of December the island became nearly circular, later more squared because two sides developed to be almost parallel as explained below.

Figs 6 and 7 show the development of shorelines at Surtsey during the period from 1964 to 1967 when coarse lava and pebbles normally were available in a narrow beach around the island for long migration by wave action. During extreme storms the solid lava could become exposed, however, in certain sections of the shore. As it may be seen from the figures, the general trend of shoreline development was towards a rectangular shape with rounded corners against SW. The island has two almost parallel sides running SW-NE and an accumulation area on the NE side which developed a lagoon between two beach ridges growing out from SW, typical for an "angular foreland". The orientation of the two parallel sides is given in the figures. It may be seen that the average orientation of the two parallel sides in 1964 was 27 degrees E of N, which is identical with the orientation of the shoreline west of Dyrholaey

WAVE ENERGY APPROACH

An attempt was made to study this situation in a more rational way by evaluating the wave energy input on the south coast of Iceland in order to find the direction of shoreline with "neutral drift". No wave energy data were available however. The procedures were based on the Los Angeles formula

$$Q = \frac{1}{2} k_1 w e \sin 2\alpha_b \quad (1)$$

where Q = the total amount of sand moved in littoral drift past a given point per year by waves of given period and direction

w = total work accomplished by all waves of a given period and direction in deep water during an average year

e = wave energy coefficient at the breaker line for waves of a given period and direction. It is the ratio between the distance between orthogonals in deep water and at the shore line

α = angle between wave crests at the breaker line and the shore line, or the angle between orthogonals and the normal to the shore line (i.e. $\alpha = \alpha_b$)

k_1 = factor depending on dimensional units and empirical relations. It varies with beach slope, grain size, and other variables

The wave energy coefficient may be written $e = \cos \alpha_o / \cos \alpha_b$ and $\sin 2\alpha_b = 2 \sin \alpha_b \cos \alpha_b$

$$\text{hence } e \sin 2\alpha_b = 2 \cos \alpha_o \sin \alpha_b \quad (2)$$

The relationship between $\sin \alpha_o$ and $\sin \alpha_b$ for different steepness ratios of the waves is given in Fig 8

Neglecting energy dissipation and reflection the total work may be written

$$w = \frac{\gamma H_{1/3}^2 C_{1/3}}{16} \quad \text{ft-lbs/sec/ft of crest} \quad (3)$$

Eqs (1), (2) and (3) combined gives

$$Q = \frac{1}{2} 6,3 \cdot 10^8 \quad k \quad H_{1/3}^2 \quad T_{1/3} \quad e \sin 2\alpha_b \quad \text{ft-lbs/year/ft of crest} \quad (4 a)$$

$$Q = 6,3 \cdot 10^8 \quad k \cdot H_{1/3}^2 \quad T_{1/3} \quad \cos \alpha_o \sin \alpha_b \quad \text{ft-lbs/year/ft of crest} \quad (4 b)$$

where $H_{1/3}$ and $T_{1/3}$ are the significant wave height and period

Wind conditions in Iceland are characterized by cyclones moving from SW giving rise to variable wind fields. The average duration of a cyclone moving from SW towards Iceland is 1 to 3 days. The predominate direction of wind wave

propagation is towards NE. Usually the cyclones pass south of Iceland but they may also pass north of Iceland Fig 9 shows the characteristic situation during the winter and summer seasons Fig 10 demonstrates the characteristic wind direction for the three paths of the cyclones As it may be noted from Fig 10 the cyclones give rise to strong winds from the east when they pass south of Iceland In this situation waves propagate from three directions, SW, S and E Field experiments show that high waves from SW occur although the wind has blown from E for some time

Because of the fact that no wave data were available and the Los Angeles formula refers to an average year, it was necessary for a preliminary evaluation to use the average wind conditions Available wind data are meteorological observations covering a period of 10 years Wind data from three meteorological stations, located in the area between Vestmannaeyjar and Dyrholaey, were statistically evaluated Fig 11 shows frequency diagram The average wind speed ranged from 12 to 22.5 knots Hindcasting was based on the SMB method The problem here, as usual, is to determine the fetch A 22.5 knots wind generates a fully developed sea at a fetch of about 135 NM (nautical miles) and a duration of about 14 hours. The wave energy is a function of H^2 and T , and the SMB diagrams indicate that wind speeds of 12 to 20 knots have no practical influence on the significant wave height, when the fetch increases from 100 NM to 250 NM However, there is an increase of one second in the significant wave period For waves generated by the cyclones moving from SW, it is therefore realistic to select a fetch of 250 NM for W and SW For the other directions a fetch of 135 NM was selected This agrees with results of Danish investigations on wave action for the harbour of Vestmannaeyjar The results of hindcasting as well as the calculation of the deep water energy is shown in Table 1

Each direction represents a sector of 45 degrees The actual shore boundary conditions including true shore orientation west of Dyrholaey are shown in Fig 12. In Fig. 13 the shoreline was turned 5 degrees clockwise in order to observe the possible influence of this on the drift direction computed

on the basis of input of longshore wave energy

As shown in Fig 12 the W and SE sectors are bounded respectively 39 and 36 degrees, and only half of the E sector is represented west of Dyrholaey. Wind direction from the E tends to concentrate in the area around Dyrholaey, partly due to the Bernoulli effect from the nearby Myrdalsjökull (glacier) east of Dyrholaey. West of Dyrholaey the wind blows along the shore and increases the longshore wave energy. Moreover the wave energy west of Dyrholaey also increases due to a combination of diffraction and refraction at Dyrholaey. In this preliminary evaluation, it is difficult to calculate the wave energy from east representing the average year. It is possible however, to estimate roughly the wave energy coefficient "e" in Equation (1)

The maximum input of wave energy is determined approximately by the geometric shadow line which gives $e = 0.5^2$. The minimum input of wave energy is determined approximately by the 27 degrees diffraction ray which gives a diffraction coefficient of about 0.10 approximately 1 km west of Dyrholaey or $e = 0.1^2$. Due to the refraction, one may expect a wave energy coefficient between $e = 0.5^2$ and $e = 0.3^2$.

Diffacted waves are only of importance in the area immediately west of Dyrholaey. They break under an angle of approximately 25 degrees with the shoreline. Further westwards refraction of waves towards the shore takes place, developing low swells which are superimposed by wind waves corresponding to actual fetches west of Dyrholaey.

The numerical calculations carried out in Tables 1-5 with $e = 0.4^2$ and ave $H/L = 0.025$ (Table 1) refer to the area immediately west of Dyrholaey. It may be noted that the H/L -ratio plays an important role, and that turning the shoreline 5 degrees clockwise from the actual direction (Fig 13) changes the resultant energy balance from eastward predominance to westward predominance thereby causing westward drift. This still refers to the area just west of Dyrholaey. Further westward the importance of E winds tends to decrease because

of the shadow by the Dyrholaey headland This in turn would create more tendency to eastward drift Assuming that this is correct, the shoreline should develop slightly convex (turn clockwise) up towards the Dyrholaey apart from a small area influenced by leese side erosion just west of the Dyrholaey point As it may be seen from Figures 2 and 3 this is actually the way shoreline configuration developed It is therefore evidenced that the orientation of shoreline of about 27 degrees N of W is close to the direction which causes neutral drift The correct average direction may be a few degrees more as is in fact also indicated by the early development of shorelines at Surtsey

CONCLUSION

Although none of the methods used are exact in the true sense of the word, the similarity of the results are noteworthy The development of shorelines of volcanoes popping up from the bottom of the sea, like Surtsey, may be used to determine the direction of littoral drift on nearby shores As a good luck other methods are available, however

List of figures

- Fig 1 Iceland Littoral drift investigation on the
Icelandic south coast
- Fig 2 South coast of Iceland From Dyrholaey to Thorsa
- Fig 3 South coast of Iceland The area around Dyrholaey
- Fig 4 Surtsey two days after its eruption, Nov. 16, 1963
- Fig 5 Surtsey has emerged from the bottom of the sea on
Nov 26, 1963
- Fig 6 Surtsey, Oct 23, 1964
- Fig 7 Outlines of Surtsey during 1965 to 1967
- Fig 8 Relationships between $\sin \alpha_o$ and $\sin \alpha_b$ for
different steepness ratios of the waves
- Fig 9 Characteristic cyclones and dominating wind
directions
- Fig 10 Characteristic wind direction for the three paths
of the cyclones
- Fig 11 Wind frequency diagrams, the south coast of Iceland
- Fig 12 The shore boundary conditions west of Dyrholaey
- Fig 13 The shore boundary conditions west of Dyrholaey
when the shore line is turned 5 degrees clockwise

List of tables

- Table 1 Hindcasting
- Table 2 $e \sin 2\alpha_b$ corresponds to Fig 12 for various
steepness ratios
- Table 3 $e \sin 2\alpha_b$ corresponds to Fig 13 for various
steepness ratios
- Table 4 Littoral drift west of Dyrholaey (Solution of
Eq (4 a) and (4 b))
- Table 5 Littoral drift west of Dyrholaey when the shoreline
is turned 5 degrees clockwise (Solution of Eq
(4 a) and (4 b))

Table 1 Hindcasting

Direction	Wind	Fetch	$H_{1/3}$	$T_{1/3}$	$H_{1/3}/L_{1/3}$	Duration	$W_{Eq} (3)$
	Knots	NM	ft	sec		hours	ft-lbs/ft/year
E	22 5	135	8 5	7 9	0 027	14	$3600 \cdot 10^8$
SE	12 5	135	3 6	5 8	0 021	20	$474 \cdot 10^8$
S	12 0	135	3.3	5 7	0 020	21	$390 \cdot 10^8$
SW	14 5	250	5 0	7 3	0 018	30	$1150 \cdot 10^8$
W	12 0	250	3 5	6 5	0 019	35	$500 \cdot 10^8$

Table 2 $e \sin 2 \alpha_b$ corresponds to Fig 12 for various steepness ratios

Fig 12		Fig 8		$e \sin 2 \alpha_b = 2 \cos \alpha \sin \alpha_b$	
Direction	α_o	H/L		H/L	
		0 02	0 03	0 02	0 03
S-43° E	70°	0 31	0 37	0 212	0 253
S	27°	0 19	0 23	0 321	0 41
SW	18°	0 13	0 16	0 24	0 304
W-3° S	60°	0 32	0 373	0 32	0 37

Table 3 $e \sin 2 \alpha_b$ corresponds to Fig 13 for various steepness ratios

Fig 13		Fig 8		$e \sin 2 \alpha_b = 2 \cos \alpha \sin \alpha_b$	
Direction	α_b	H/L		H/L	
		0 02	0 03	0 02	0 03
S-40° E	72°	0 31	0 366	0 192	0 229
S	32°	0 215	0 262	0 365	0 434
SW	13°	0 092	0 118	0 179	0 23
W-3° S	55°	0 312	0 364	0 358	0 418

Table 4 - Littoral drift west of Dyrholaey Fig 12
(Solution of Eq (4 a) and (4 b))

Direction	α_0	Reduction of wave energy from dom direct	Q in cubic yards per year	
			H/L	
			0 02	0 03
E	~	$0.5(0.4)^2$	- 110 k 10^8	- 110 k 10^8
S-43° E	70°	$2.20/45=0.89$	- 43 k 10^8	- 51 k 10^8
S	27°	1 0	- 63 k 10^8	- 80 k 10^8
SW	18°	1 0	+ 142 k 10^8	+ 175 k 10^8
W-3° S	60°	$2.195/45=0.87$	+ 69 k 10^8	+ 80 k 10^8
			- 5 k 10^8	+ 14 k 10^8
			ave Q = + 5 k 10^8	

+ means eastward drift
- means westward drift

Table 5 - Littoral drift west of Dyrholaey when the shoreline
is turned 5 degrees clockwise Fig 13
(Solution of Eq (4 a) and (4 b))

Direction	α_0	Reduction of wave energy from dom direct	Q in cubic yards per year	
			H/L	
			0 02	0 03
E	~	$0.5(0.4)^2$	- 110 k 10^8	- 110 k 10^8
S-40° E	72°	$2.18/45=0.8$	- 36 k 10^8	- 43 k 10^8
S	32°	1 0	- 72 k 10^8	- 85 k 10^8
SW	13°	1 0	+ 103 k 10^8	+ 132 k 10^8
W-3° S	55°	$2.195/45=0.87$	+ 78 k 10^8	+ 91 k 10^8
			- 37 k 10^8	- 15 k 10^8
			ave Q = - 26 k 10^8	

+ means eastward drift
- means westward drift

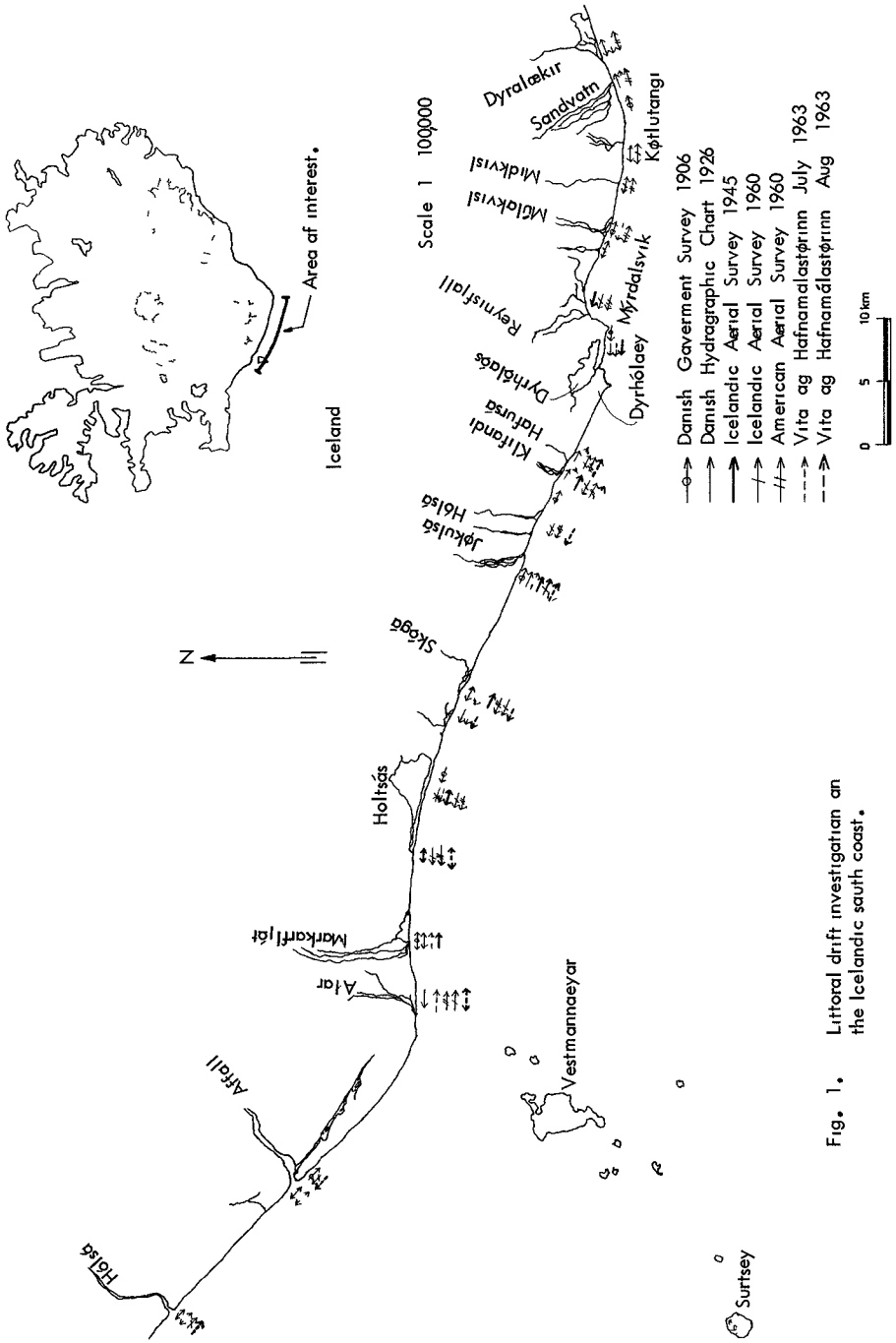


Fig. 1. Littoral drift investigation on the Icelandic south coast.

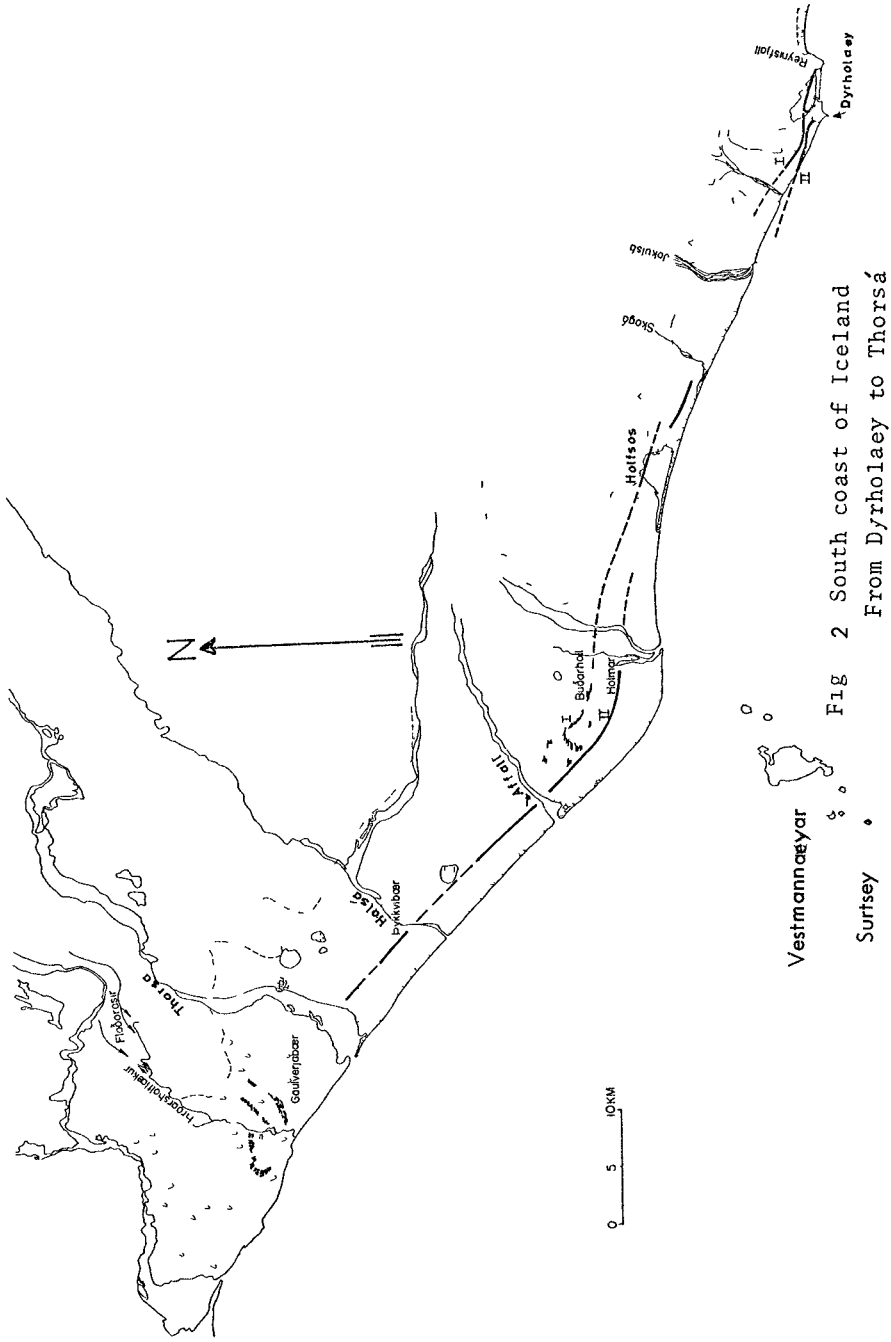


Fig 2 South coast of Iceland
From Dyrhólaey to Thorsá

Vestmannaeyjar
Surtsey

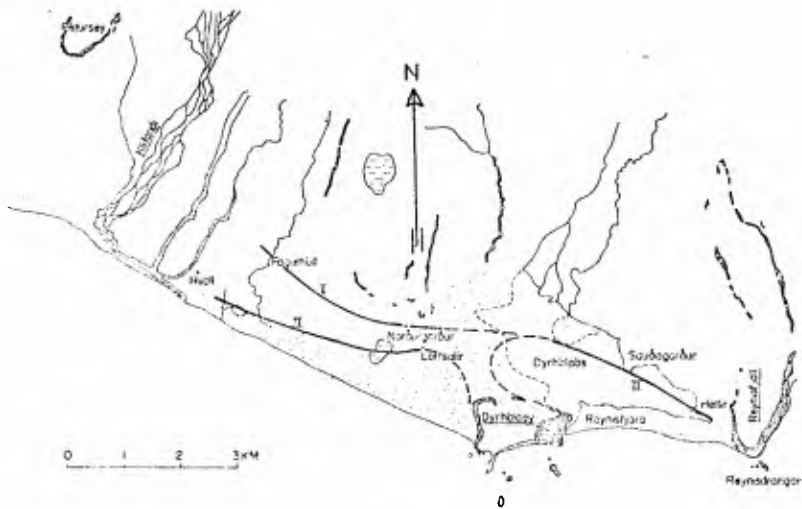


Fig. 3 South coast of Iceland
The area around Dyrhólaey



Fig. 4. Surtsey two days after its eruption, Nov. 16, 1963



Fig. 5. Surtsey has emerged from the bottom of the sea on Nov. 26, 1963



Fig. 6. Surtsey, October 23, 1964

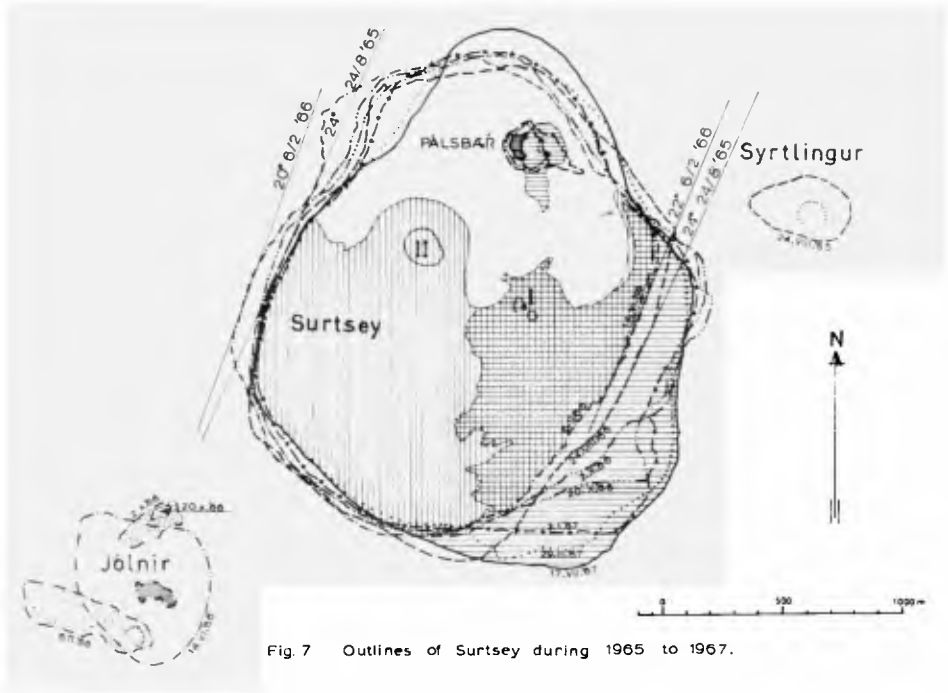


Fig. 7 Outlines of Surtsey during 1965 to 1967.

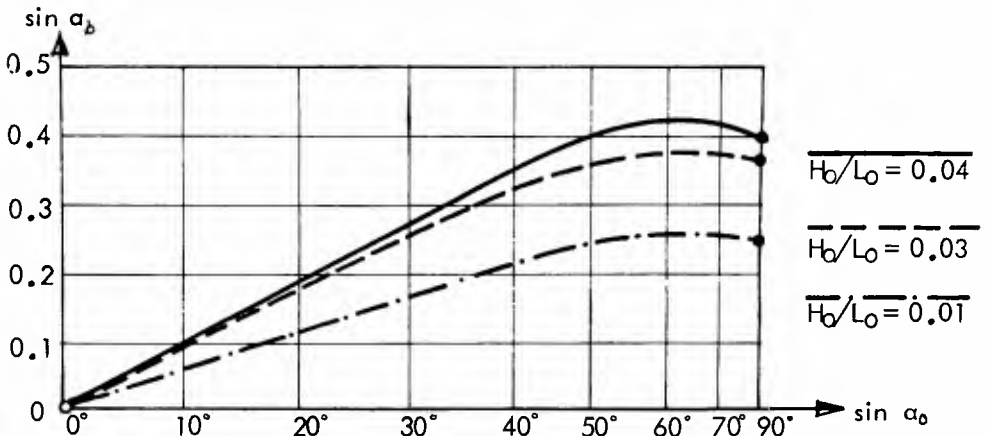


Fig. 8. Relationships between $\sin \alpha_0$ and $\sin \alpha_b$ for different steepness ratios of the waves.

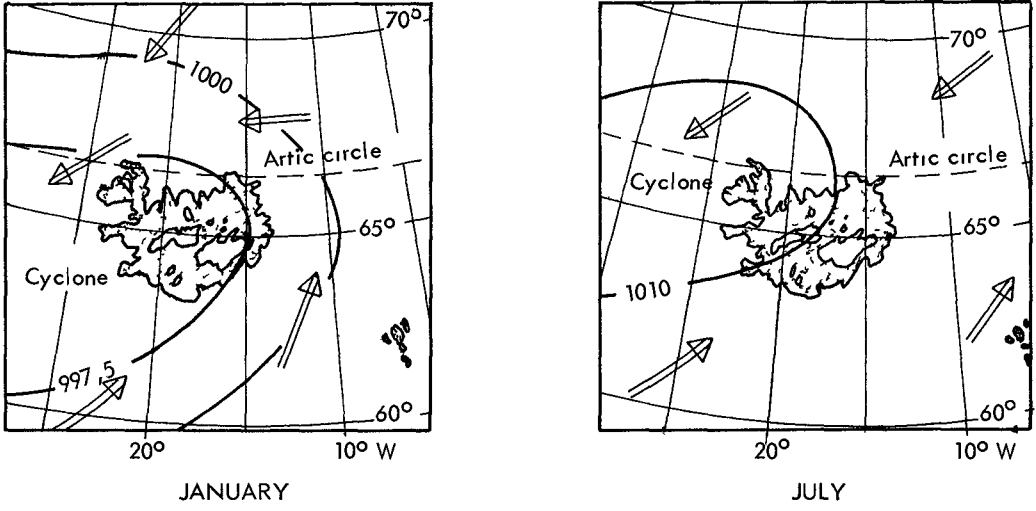


FIG 9 Characteristic cyclones and dominant wind directions

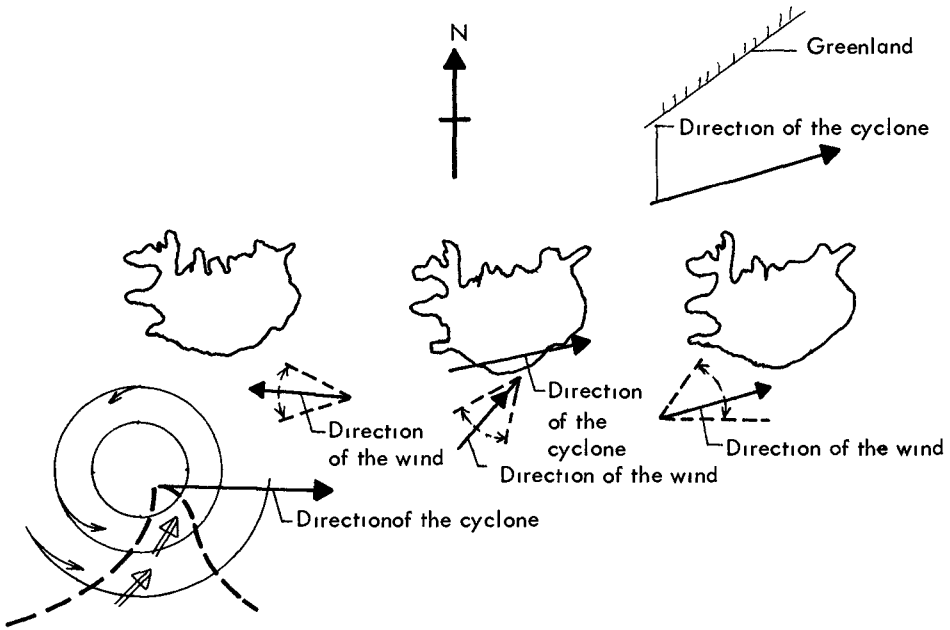


FIG 10 Characteristic wind direction for the tree paths of the cyclones

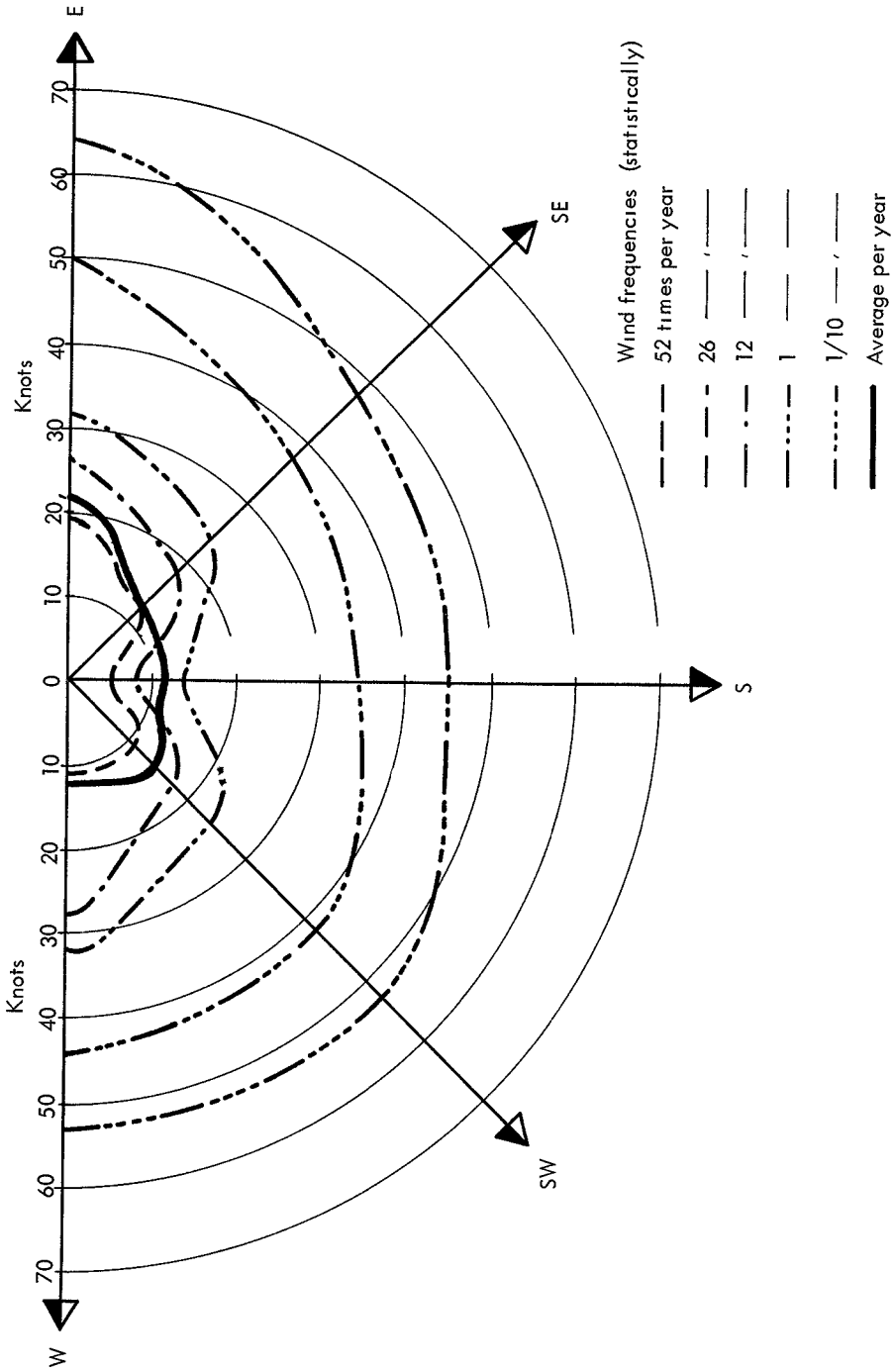


FIG 11 Wind frequency diagram, the South coast of Iceland

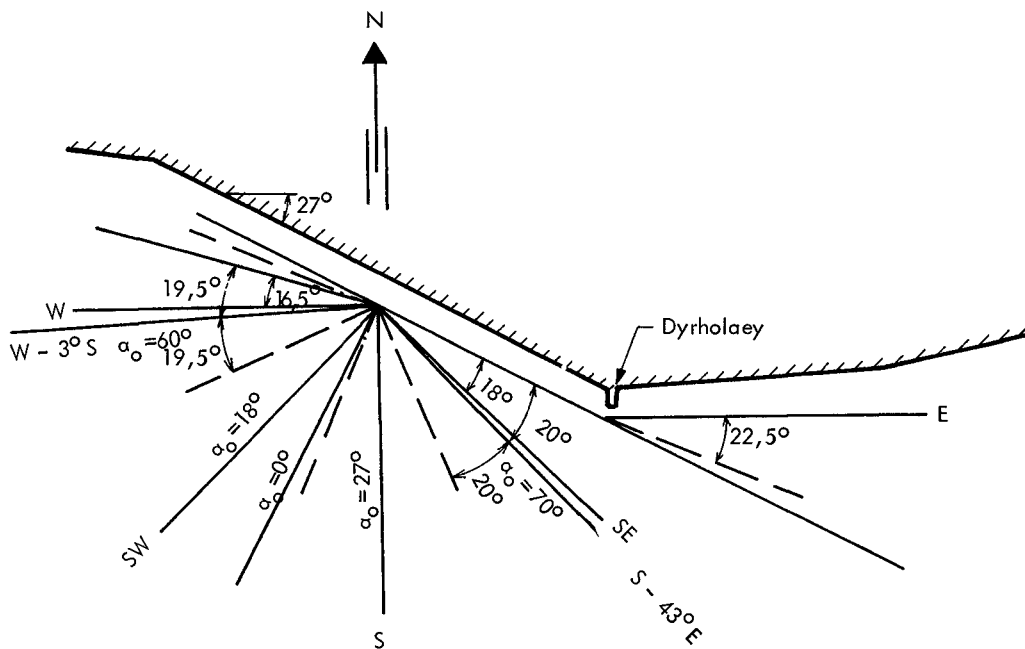


FIG 12 The boundary conditions west of DYRHOLAELY

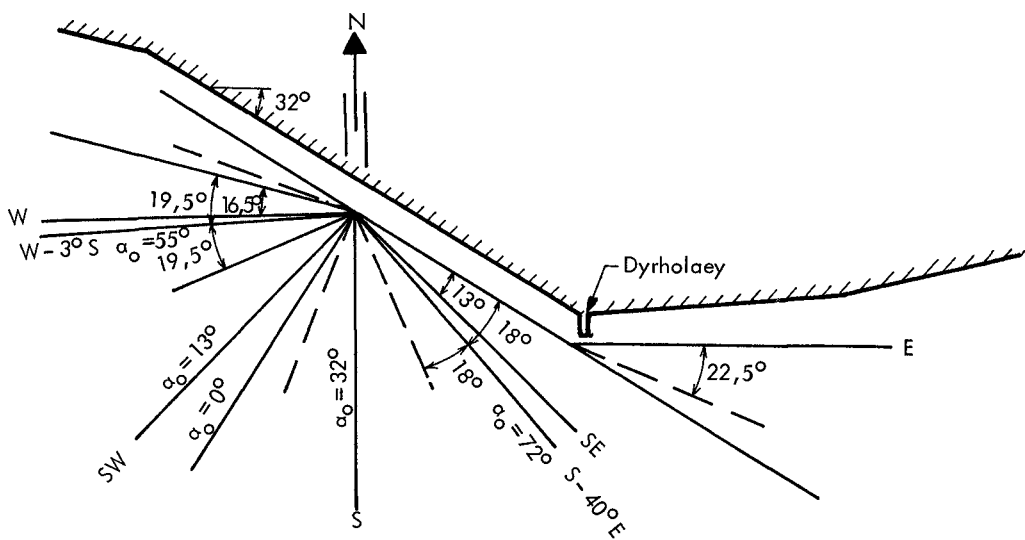


FIG 13 The boundary conditions west of DYRHOLAELY when the shoreline is turned 5 degrees clockwise

CHAPTER 60

AN OFFSHORE BEACH NOURISHMENT SCHEME

by Robert A Dalrymple

Department of Coastal and Oceanographic Engineering
University of Florida
Gainesville, Florida

Abstract

The University of Florida has conducted a series of tests to evaluate the effectiveness of beach nourishment from offshore sources by a specially designed drag scraper. The field work, over a nine-month study period, included hydrographic surveys, fluorescent sand tracing, and a sand sampling program for two scraper sites at Jupiter Island, Florida.

The conclusions provide information as to the effect of the borrow pits and the dredged sand on the beach characteristics, the mechanisms of the filling of the pits, and the efficiency of the drag scraper.

Introduction

As beach erosion becomes more of a critical problem, extensive sources of sand are necessary for the artificial replenishing or rebuilding of beaches. At Jupiter Island, on the east coast of Florida, where erosion has been quite severe due mainly to a large inlet to the north, onshore sources of nourishment sand were being depleted in a beach rehabilitation program begun in 1957, and it became necessary to find another readily available source.

In 1963, Dickerson, Inc. of Stuart, Florida began nourishing the beaches with a specially designed Sauerman drag scraper (See Gee, 1963). The scraper consists of a three-drum hoist powered by a 260 horsepower engine, which pulls a bottomless, three cubic yard capacity bucket over a wedge-shaped offshore borrow area, demarcated by two anchored buoys. The buoys are 850 feet offshore and about 500 feet apart, floating between them is a mooring float which guides the scraper bucket over the borrow area. The scraper is able to make over 300 round-trips of the bucket per day, placing the recovered sand at the base of the winding machine. See photographs 1 to 4.

During 1967 and 1968, the Department of Coastal and Oceanographic Engineering (DCOE) conducted a field study of the two borrow areas (denoted Areas I and II) at which the drag scraper operated. The purpose of the study was (1) to determine if the scraper was a viable method of beach nourishment, (2) to determine if spoil placed on the beach returned directly to the borrow area, and (3) to estimate the efficiency of the scraping operation.

During the first part of the summer of 1967, from May until the end of June, the scraper was at Area I, then it was moved two miles south to Area II.

where it operated until August 4, when it shut down for the season. The scraper was contracted to recover 30,000 cubic yards of sand at each site, the total being the estimated annual erosion at the developed section of Jupiter Island (Coastal Engineering Staff, 1957). The unit cost of the sand was 50¢ per cubic yard.

Environmental Data

At both locations, the shoreline is straight and the beach is narrow. The offshore profile is shallow. The dune lines have been protected by sloping energy absorbing seawalls, and adjustable groins had been placed on the beach in 1963.

Waves in the summer at Jupiter Island approach from the southeast and are generally small, as large ocean swell are blocked by the Bahama Islands from reaching shore. During the winter, however, the wave climate becomes very severe and predominantly comes from the northeast. In 1967, the seasonal shift between the summer and winter wave climate occurred on September 4, with the onset of a period of northeast storms.

The littoral drift follows the wave direction. It is mild and from the south in the summer, and more intense and from the north in the winter. The net quantity of littoral drift passing Jupiter Island inside the 18' contour has been estimated by the Corps of Engineers as 230,000 cubic yards per year. Its direction is north to south.

Offshore Effects

At both areas, when the scraper began operation, pits were dug about 175 feet offshore in about 9 feet of water. These lengthened in the offshore direction into oval depressions 500-600 feet long and 300 feet wide, as scraping continued, until maximum recorded depths of 14 and 17 feet were reached at each area.

During the scraping operation, the summer littoral current moved large quantities of suspended sand, kicked up by the fast-moving scraper bucket, northward, resulting in the formation of a bar on the north side of the borrow pit. This "shoulder" bar became quite large at both sites as scraping continued, covering an area about two-thirds the area of the borrow pit, and a height of 3 feet above the bottom. See figure 1.

At Area I, after the scraper was stopped and moved to Area II, the offshore borrow pit began to change shape slowly under the action of waves and currents. The elevation contours of the pit became more rounded, and the bottom of it shoaled about one foot during the first two months. The shoulder bar, during this time, was moved shoreward, by wave action concentrated on it by refraction at the hole, and filled the trough that had previously separated it from the beach.

Soon after the scraper was shut down for the season at Area II, the wave climate changed. Northeast storms during early September brought about the seasonal littoral drift reversal and the larger winter waves. This more

severe wave climate caused rapid shoaling of the borrow pits. Calculated shoaling rates for the bottom of the borrow pits from August 31 to September 22 were 22 foot per day at Area II and 1 foot per day at Area I, which was a much shallower pit by this time. These fill rates are much higher than rates calculated for borrow pits examined by Watts (1963).

The high fill rate at Area II produced a migration of the borrow pit. As seen in Figure 3, the pit had moved southward. A simple experiment in a movable bed hydraulic model showed that a hole in a sand bed, under the action of a unidirectional current, was filled from the upstream side, while sand was eroded from the downstream side--the net result being filling of the hole, coupled with translation downstream.

The shoulder bar, at Area II, was moved both shoreward and into the borrow pit, by the northeast waves, the shoulder bar here was a more important factor in the filling of the borrow pit than at Area I, due to the intensity of the littoral current. See figure 2.

At Area II, 1000 pounds of fluorescent tracer were placed in the spoil pile on the beach in front of the scraper, 20 days after scraping was discontinued. The purpose of the test was to estimate the return of dredging spoil to the borrow pit. Sand samples taken in the borrow pit subsequently showed some tracer being incorporated offshore into the filling borrow pit. However, this recovered tracer was very fine grained, and did not represent a direct return of all the spoil to the borrow pit, but rather the natural action of beach sorting. The fill material, including the tracer, had a median diameter of 13 mm and was well sorted, whereas the natural beach sand and the tracer had a median diameter of 29 mm. Watts (1963), too, has observed fine grained material in filling borrow pits. The sources of the fill material in the pits are longshore current and wave transported material, the shoulder bar, particularly at Area II, and the transversally transported fine-grained dredge material, moved offshore by natural beach sorting processes.

By the following summer, both pits had filled entirely and the bottom topography was similar to that of the previous summer.

Beach Effects

During scraper operation, the dry beaches at both areas grew, as the spoil pile was dispersed by wave action and due to the natural onshore movement of sand during the summer. The Mean Sea Level (MSL) contour moved seaward an average at each station of 5 feet at Area I and 34 feet at Area II. However, by the next summer, June 28, beach surveys showed significant erosion had occurred during the winter, after the scraper was shut down, with an average net loss after the whole year of 20 feet and 42 feet at the beaches.

Stability

No major beach stability problems were observed, however, they may be created if the drag scraper operates too near shore. If the borrow pit is dredged very deep, slumping of the foreshore can occur, with the dredged sand returning directly to the borrow pit. Also, as pointed out by Rector (1966),

sand moved offshore by steep waves during storms, will fill the borrow pit and be lost to the beach, as this material will not be returned to the beach by natural action when the wave climate becomes less severe. For Jupiter Island, where winter and summer bars exist, it was recommended that the scraper recover sand from an area offshore of the normal location of the winter bars, thus ensuring there would be no sand lost from the beach by natural processes.

An additional stability problem may arise if the offshore sand is much finer than the natural beach sand. This would also be the case if the scraper returned to the same place for additional spoil. The fine sand would probably be quickly removed from the beach by wave action.

As mentioned previously, the incidental deposition of the shoulder bar by the drag scraper provides a stabilizing effect. When the longshore current changed to southward, the deposited sand was moved on to the beach and into the pit, thus removing some of the aforementioned hazard of normal beach sand being lost to the pit during storms.

Efficiency

The present scraper design was observed in the field by DCOE personnel to be unable to carry its full capacity due to its design. Volume estimates of the beach spoil pile and the offshore borrow pit and shoreline monitoring showed that the scraper did not move the quantity of sand necessary to match or exceed the annual erosion.

Conclusions

The drag scraper technique is a viable method of beach nourishment, provided it recovers sand in a quantity to balance or exceed the annual amount of erosion.

Only the fine grained dredge material returns to the borrow pit under normal operation. Primary sources of pit fill material are the littoral drift and the shoulder bar, built by suspended sand.

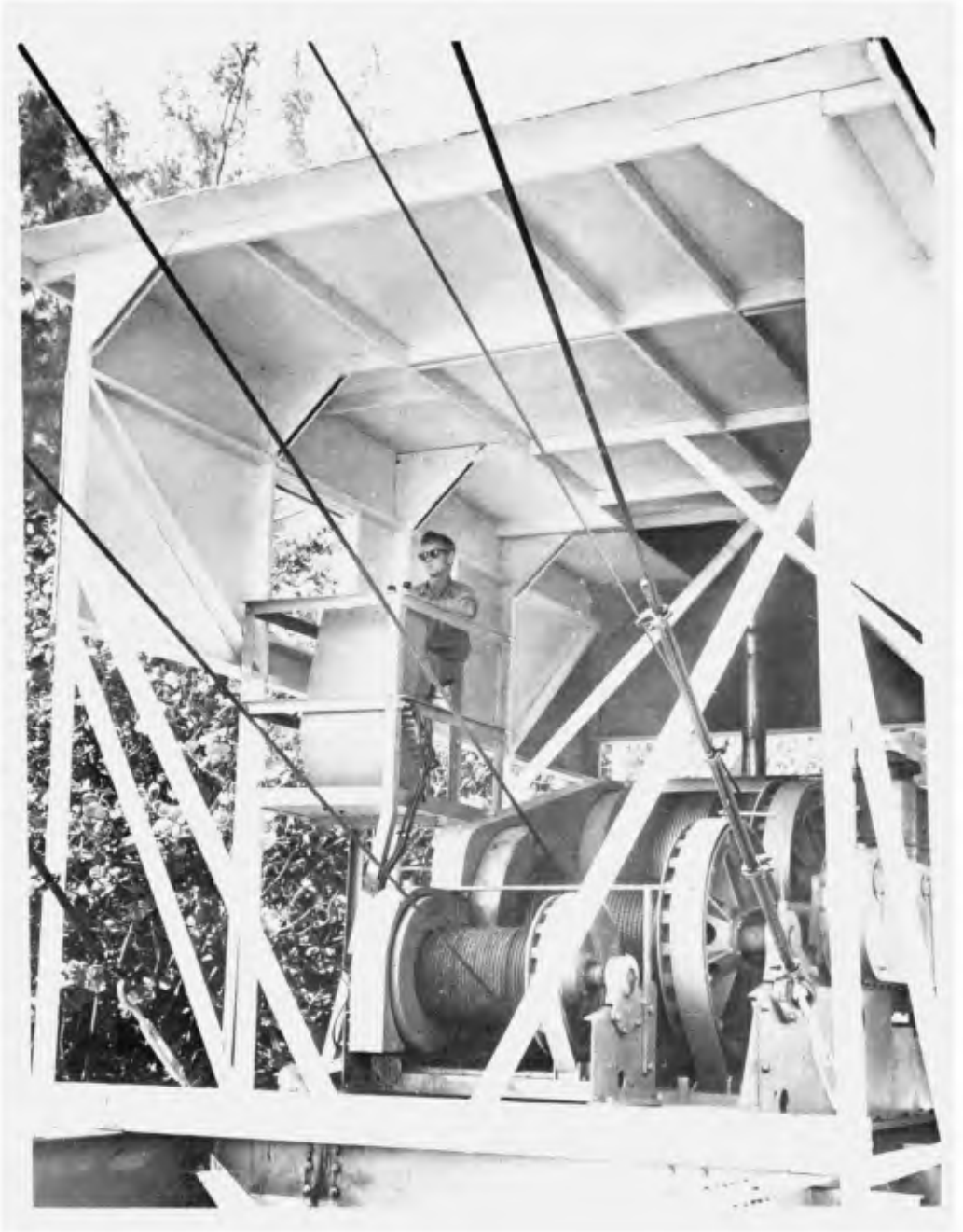
Beach stability is ensured if the scraper dredges sand compatible with the natural beach sand and from an area at a sufficient distance from the shore.

Acknowledgements

Mr James A Purpura, Associate Professor at the Department of Coastal and Oceanographic Engineering, initiated this project and directed the field program. The study was funded cooperatively by the Jacksonville District, U S Army Corps of Engineers and the Florida Bureau of Natural Resources. The photographs are courtesy of Dickerson, Incorporated.

References

- 1 Coastal Engineering Staff, Coastal Engineering Investigation at Jupiter Island, Technical Progress Report No 5, Florida Engineering and Industrial Experiment Station, March, 1957
- 2 Gee, Herbert C , Beach Nourishment from Offshore Sourcea, ASCE Journal of Waterways and Harbors, Vol 91, No WW3, August, 1965 Discussion by R L Rector, No WW2, Vol 92, May, 1966
- 3 Watts, George M , Behavior of Offshore Borrow Zones in Beach Fill Operations, Int Assoc for Hydraulic Research Congress, London, 1963



Photograph 1. Winch System for the Sauerman Drag Scraper



Photograph 2. Drag Scraper Bucket and Spoil Pile



Photograph 3. Drag Scraper in Action. Note the large amount of suspended sand in borrow area.



Photograph 4. Aerial View of Drag Scraper

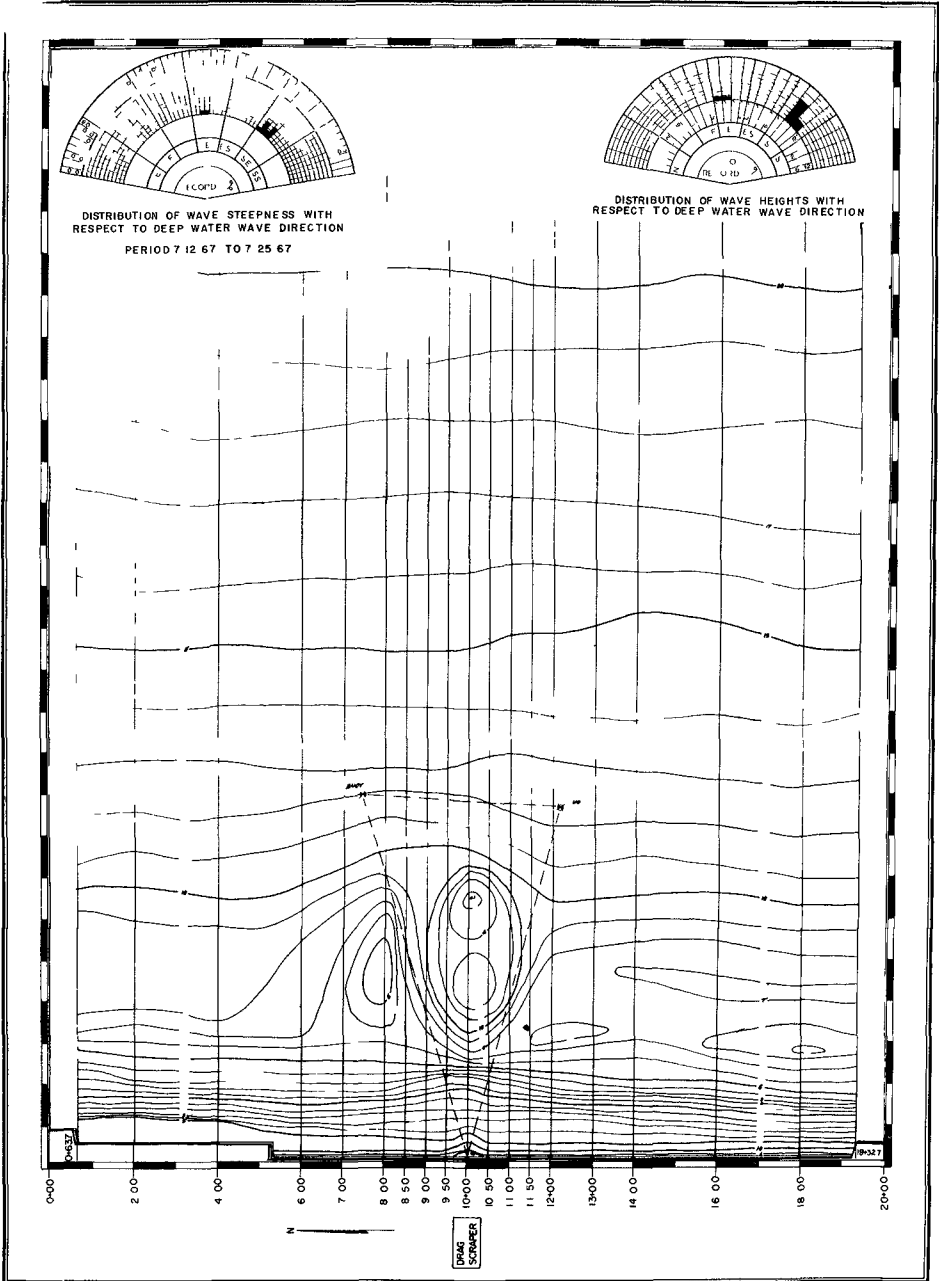


Figure 1 Hydrographic Survey, Area II No 3,7-25-67

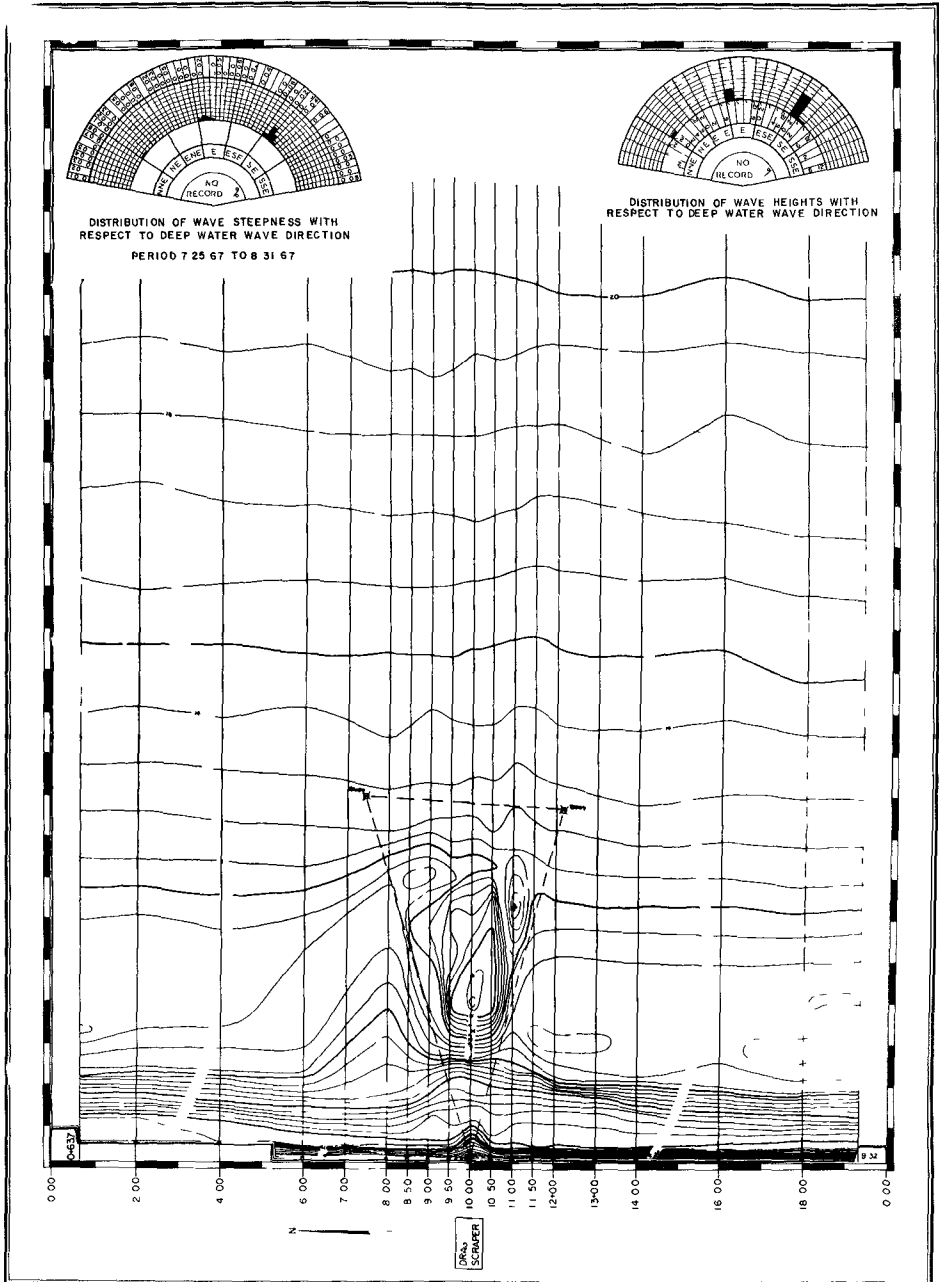


Figure 2 Hydrographic Survey, Area II No 4, 8-31-67

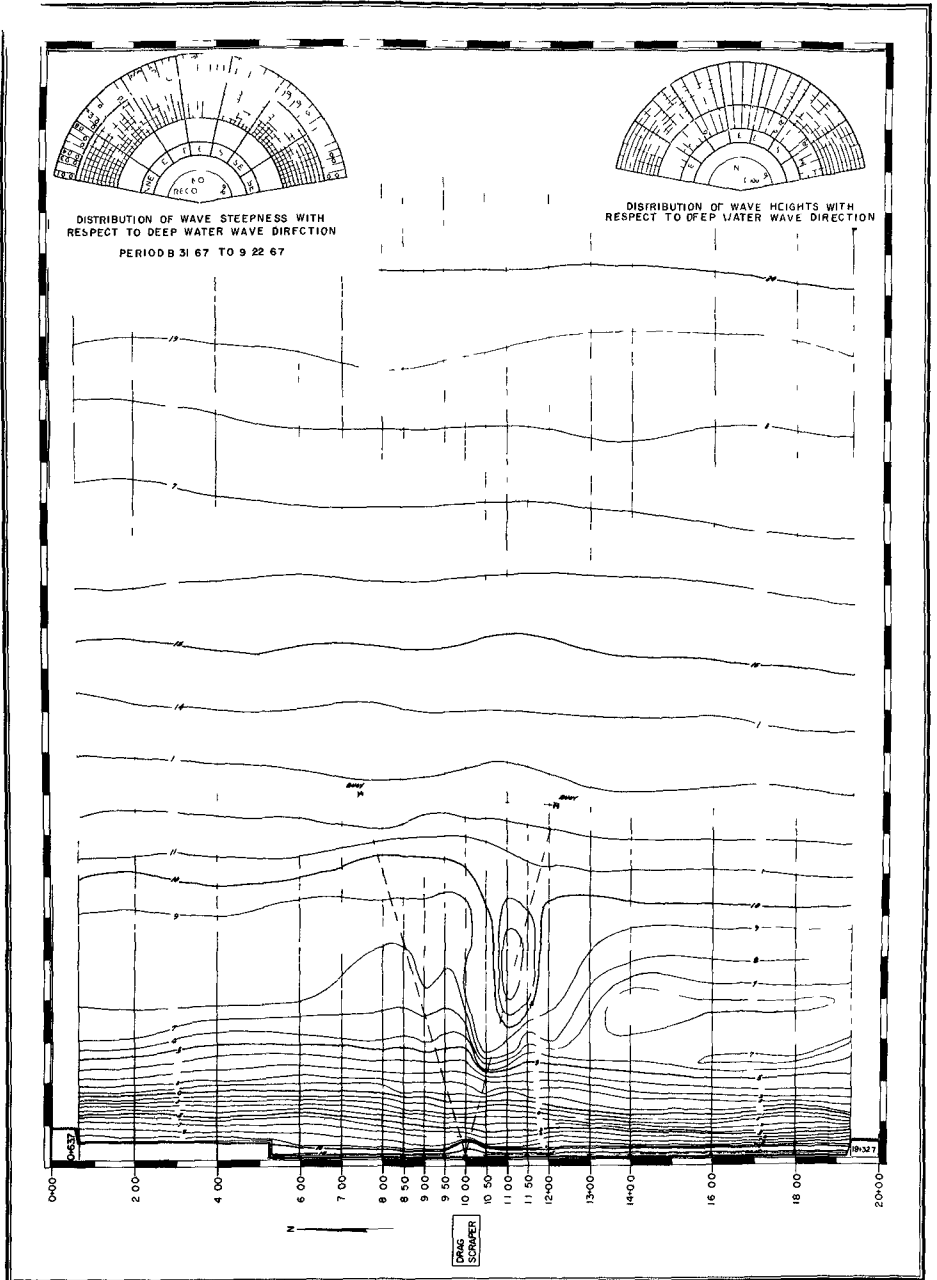


Figure 3 Hydrographic Survey, Area II No 5,9-22-67

CHAPTER 61

Beach Nourishment at Virginia Beach, Virginia

James W Bunch
Army Corps of Engineers
Norfolk, Virginia

ABSTRACT

Aspects of the Federal beach erosion control project at Virginia Beach, Virginia are described with particular emphasis directed to the sources, characteristics, costs, methods of placement and quantities of material periodically placed on the beach following project inception. The beach response to nourishment is analyzed on the basis of yearly survey records compiled from data gathered by the sea-sled direct leveling technique. The quantity of annual nourishment material required to maintain present beach dimensions is determined to be approximately 141,000 cubic yards.

INTRODUCTION

In the present appraisal, information gathered by a comparison of bathymetric surveys is used as a basis for evaluating the beach response and annual sand nourishment requirement at Virginia Beach, Virginia. Survey data gathered by the sea-sled direct leveling technique and collected annually over seventeen identical ranges for a three-year period (1966-1969) were employed in the appraisal.

DESCRIPTION OF STUDY AREA

Virginia Beach, as shown in figure 1, is located on the east coast of Virginia, about 19 miles east of Norfolk, Virginia and 3.5 miles south of Cape Henry which is the south point of the entrance to Chesapeake Bay. The shoreline in the area bears South 12°36' East.

The existing Federal beach erosion control project here extends from Rudee Inlet to 49th Street and includes the 3.3 miles of coastline treated in this paper (figure 2). A concrete bulkhead and promenade, within the limits of the project, was constructed by local interests in 1927. It extends from 7th to 35th Street and is supported on two rows of piling generally parallel to the shore. A wooden bulkhead, constructed by local interests, extends from 35th to 49th Street.

Tides at Virginia Beach are semidiurnal. The mean range of tide is 3.4 feet and the spring range is 4.1 feet.

Waves reaching the area are predominately from the southeastern quadrant during the summer and from the northeastern quadrant during the winter. The greatest yearly percentage of waves arrive from the

east-northeast and range between 1 and 6 feet. Calms prevail approximately 19 percent of the time. Available evidence suggests that the predominant direction of the littoral drift in the area is from south to north. An analysis of winds and waves reaching Virginia Beach indicates that the predominant energy applied to the shore is from the northeast quadrant. However, observations and surveys of the jetties at Rudee Inlet and an experimental groin at Seventh Street clearly suggest a net northerly drift. This anomaly with respect to the direction of the littoral movement has been attributed to the possible assistance of a tidal eddy extending for some distance south of the Chesapeake Bay entrance.

DESCRIPTION OF EXISTING FEDERAL BEACH EROSION CONTROL PROJECT

The existing Federal beach erosion control project at Virginia Beach includes (a) artificial placement of suitable sand fill on the ocean shore to provide and maintain a beach berm having a width of approximately 100 feet at elevation 5.4 m s l with a 1 on 15 foreshore slope extending to the natural bottom and (b) a deferred system of groins to be constructed if experience indicates that it is more economical than periodic sand nourishment. The project is now being maintained with dredging equipment owned by the Virginia Beach Erosion Commission, a state agency.

Nearly \$200,000 is being expended annually to maintain the project of which 50 percent is borne by the Federal Government.

BORROW AREA

Material for beach nourishment during the study period was dredged from the Owl Creek Estuary (Fig. 2). The remaining available material in this area is estimated to be sufficient to supply the annual nourishment requirements through 1970. For a source of future nourishment material, the Virginia Beach Erosion Commission has acquired state-owned lands on the south side of Owl Creek containing approximately 500,000 cubic yards of fine sand. This will provide sufficient material to nourish the beach for approximately four years, or to early 1975 at the heretofore proposed annual rate of 130,000 cubic yards.

The median diameter of nourishment material during the period 1964 - 1969 was 26 mm as compared to 31 mm for natural material found on the beach.

EQUIPMENT USED

Figure 3 shows the normal layout of dredging plant equipment when operating in the Owl Creek borrow area. It includes a 10-inch hydraulic cutterhead dredge, a 10-inch floating booster station at

the foot of Mediterranean Avenue, and a fixed booster station at Seventh Street. The pipeline is 15,000 feet long when discharging at its farthest point, usually between 21st Street and 22nd Street. A 12-inch dredge has just been purchased for the purpose of keeping Rudee Inlet open and will also be available to pump sand on Virginia Beach.

COST

For dredging work only, Table I indicates the cost per cubic yard of placing material on Virginia Beach during the period of investigation.

Table I
Cost of Beach Nourishment

FY 1966	\$1 41
FY 1967	1 51
FY 1968	2 91
FY 1969	0

QUANTITIES OF MATERIAL DREDGED

Table 2 indicates the quantities of new source material pumped by the dredge annually during the study period.

Table II
Quantities of New Material Pumped on Beach

FY 1966	117,000 cubic yards
FY 1967	119,000 cubic yards
FY 1968	6,000 cubic yards
FY 1969	0

COMPARISON OF SURVEYS

Comparison of the 1966, 1967, 1968 and 1969 surveys, which were made using an identical method over the nearshore and offshore profiles, yields what is thought to be an accurate indication of beach response in the project area and is summarized in Table III.

The nearshore profile over which surveys were made extends from the bulkhead line for a distance of 400 feet oceanward. Including berm material which was in excess of design dimensions, the deficiency in the design berm of 150,000 cubic yards that existed in June 1966 was reduced to 110,000 cubic yards in 1967. The deficiency in the design berm for July 1968 was 209,000 cubic yards or an increased deficiency of 99,000 cubic yards over July 1967. Similarly, a deficiency in the design berm for June 1969 of 330,000 cubic yards represents an increase of 121,000 cubic yards over July 1968.

The offshore profile, as defined for survey purposes, extends from the bulkhead line to the 25-foot depth contour. Including excess berm material, there was an indicated loss of approximately 392,000 cubic

yards of material from the offshore area between 1966 and 1967. This is equivalent to 0 30-foot over the entire project. Between 1967 and 1968 there was an indicated gain of 7,600 cubic yards which is a negligible gain over the entire project. In 1969, the offshore profiles indicated a loss of 221,000 cubic yards of material from the previous year. This is equivalent to 0 20-foot over the entire project.

Overall, during the three-year period, 1966-1969, the net loss of material over the nearshore profile has been 179,000 cubic yards while the net loss over both profiles was 605,000 cubic yards. During the same period, a total of approximately 242,000 cubic yards of suitable material has been placed on the beach. On the basis of the foregoing figures, there has been an apparent loss of 847,000 cubic yards or an average annual loss of approximately 282,000 cubic yards of material in the problem area. Total nearshore losses of 179,000 cubic yards indicate an average annual loss of approximately 141,000 cubic yards in the project area. Consequently, a quantity of suitable nourishment material, totaling at least 141,000 cubic yards should be placed in the project area to maintain present beach dimensions.

Table III

<u>Fiscal Year</u>	<u>Suitable Material Pumped On Beach (Cubic Yards)</u>	<u>Deficiency from Design Berm (Nearshore) (Cubic Yards)</u>	<u>Net Change in Nearshore from Previous Year (Cubic Yards)</u>	<u>Net Change in Nearshore & Offshore from Previous Year (Cubic Yards)</u>	<u>Net Change in Offshore Area (Cubic Yard)</u>
1966	117,000	150,000			
1967	119,000	110,000	+ 41,000	- 392,000	- 433,000
1968	6,000	209,000	- 99,000	+ 8,000	+ 107,000
1969	0	330,000	- 121,000	- 221,000	- 100,000

As indicated in Table III, although a state of erosion or accretion may occur on the beach during any given year, an opposite condition may result in the offshore reaches. As more survey data becomes available, the relationship between nearshore and offshore profile changes can possibly be determined.

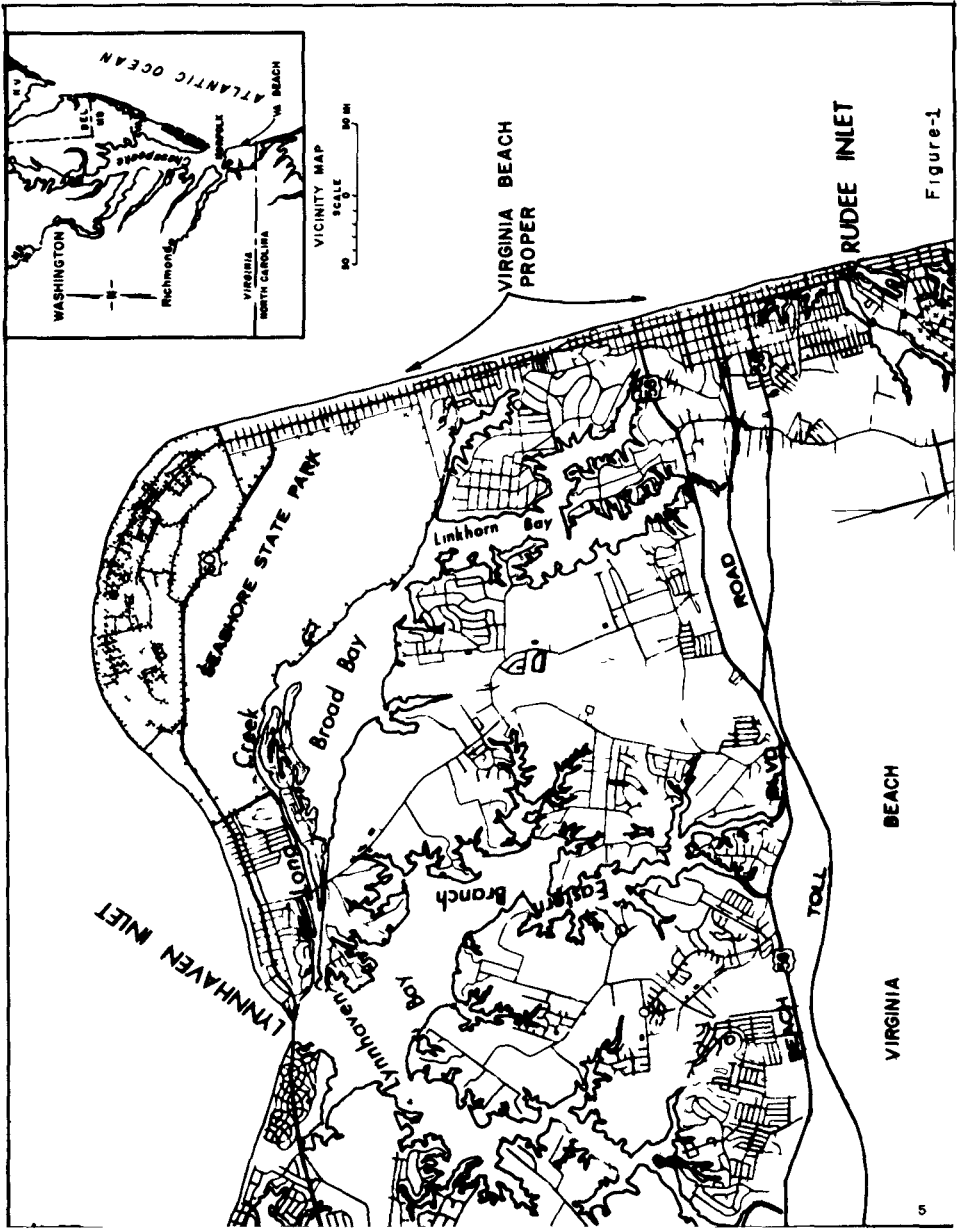


Figure-1

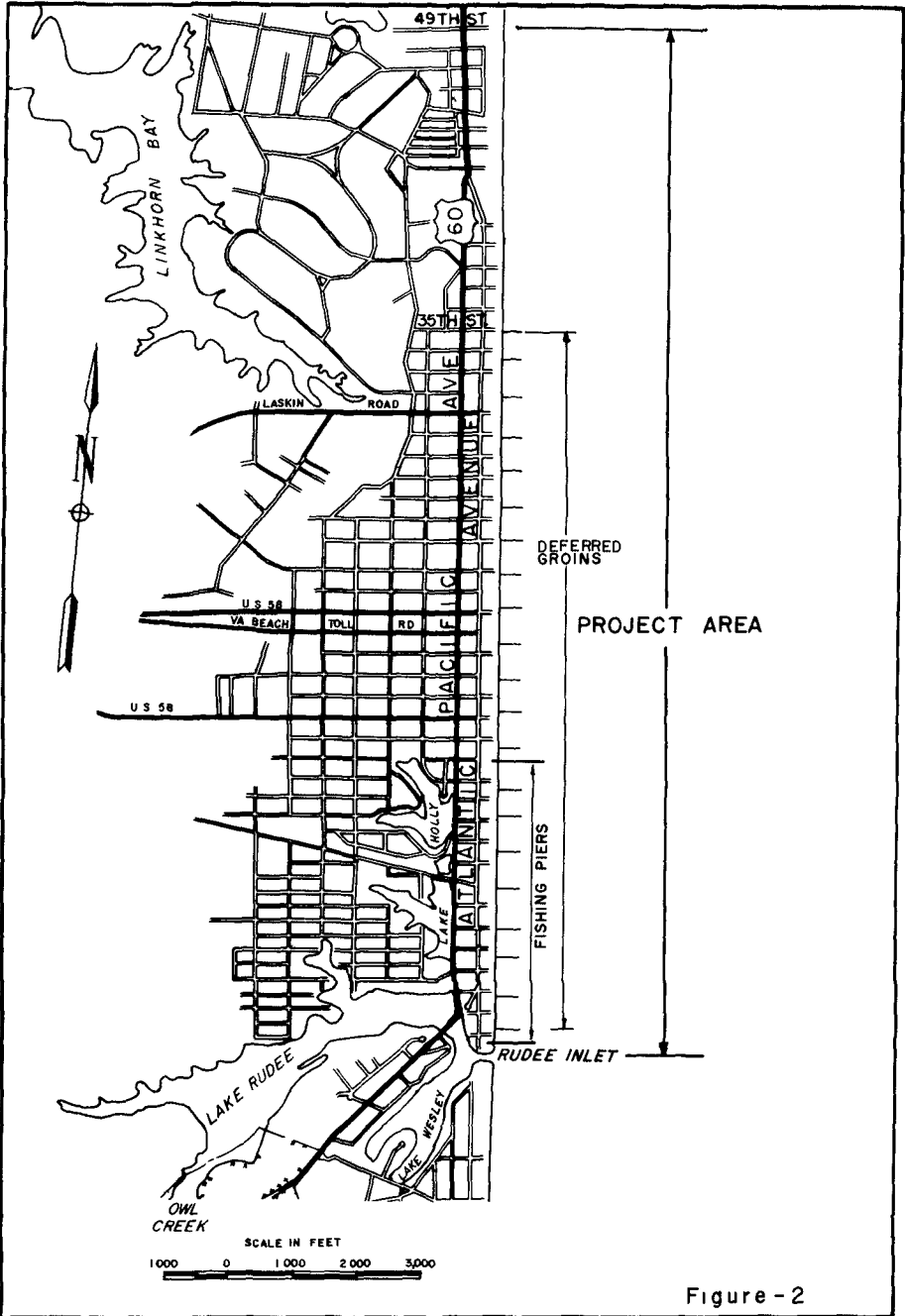


Figure - 2

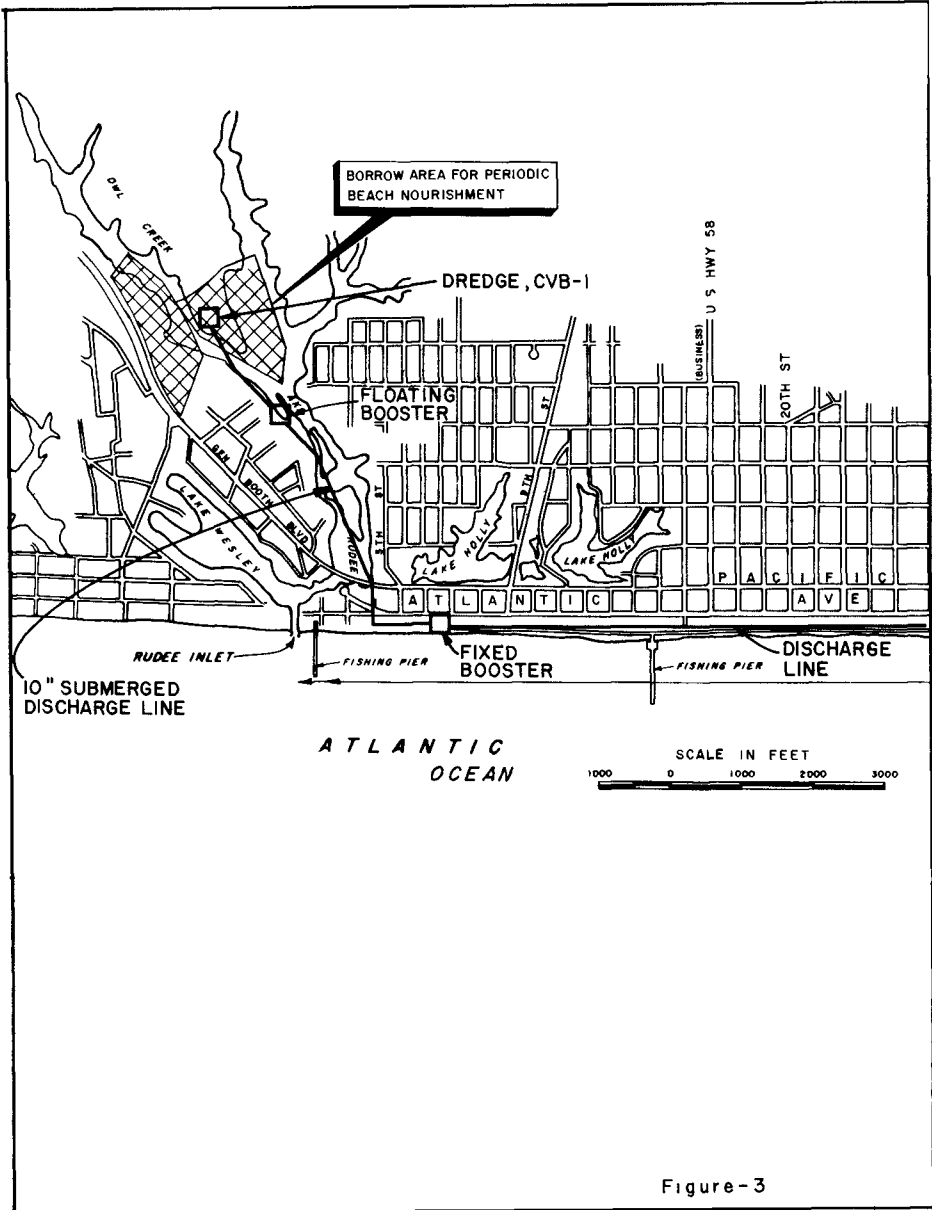


Figure-3

CHAPTER 62

UNDERWATER MOUND FOR THE PROTECTION OF DURBAN'S BEACHES

by

J A Zwamborn^x, G A W Fromme^x, J B FitzPatrick^x

ABSTRACT

The construction of an underwater mound of sand for the protection and improvement of Durban's beaches has been recommended on the basis of intensive investigations. These investigations included prototype measurements of beach changes as related to recorded sea conditions, basic scaling tests in which these beach changes were reproduced to scale in movable bed models and tests of the proposed underwater mound in models, using different scales in order to eliminate possible scale effects.

The test results showed that, provided the shear-settling velocity similarity criterion is satisfied, beach changes can be reproduced in a movable bed model to a reasonable degree of accuracy. Optimum dimensions for the cross section of the mound were determined on the basis of the criterion for erosive and non-erosive wave conditions which was derived from the prototype beach profile changes and confirmed by model tests. The resulting dimensions are a mound of sand about 4.5 km long, about 1200 m offshore, reaching to 7.3 m below LWOST, with side slopes of 1 in 25 and a crest width of 61 m.

Of the total quantity required (8 000 000 m³) some 2 500 000 m³ of sand, available from harbour dredging works in Durban Bay, had been dumped by May, 1970. Model predictions on mound stability and beach improvements were confirmed to a high degree of accuracy by the full scale events.

^x Head, Chief Research Officer and Research Assistant respectively, Hydraulics Research Unit of the National Mechanical Engineering Research Institute, South African Council for Scientific and Industrial Research, Stellenbosch, Republic of South Africa

INTRODUCTION

As part of an investigation into the siltation of the entrance to Durban harbour, South Africa's biggest port and the erosion of the adjoining ocean beaches, various possibilities for the protection and improvement of these beaches, which make Durban South Africa's premier holiday resort, were studied between 1962 and 1964¹. The causes of the deterioration of Durban's beach and conventional methods to improve the situation, e.g. groynes, are described by Jordaan in a separate conference paper². Subsequent to Jordaan's work, the senior author developed a possible solution, which emerged from the necessity of finding a suitable dumping site for material dredged from the harbour entrance and from the harbour extension works in Durban Bay³. This scheme consisted of dumping the spoil along a line parallel to the beach line some 1 200 m offshore, in an attempt to form a continuous underwater sand ridge eventually of some 4.5 km long (see Figure 1)

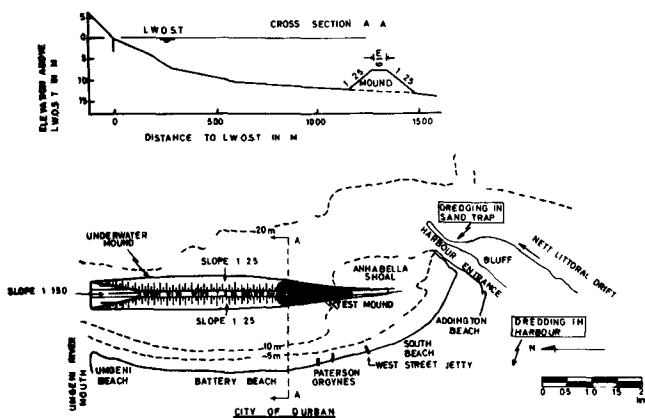


FIGURE 1 SCHEMATIC LAYOUT OF THE DURBAN UNDERWATER MOUND

If such an underwater mound could be built up to a sufficient height and provided it would remain fairly stable, it would act as a selective wave filter, e.g. low waves would pass unhindered, whereas large erosive waves would break on the mound and thus lose much of their energy. As a result, beach building conditions were expected to improve in the lee of the mound and due to the reduction of the

incident wave heights, longshore sand bar and trough dimensions were expected to be reduced, resulting in safer bathing conditions

THE UNDERWATER MOUND

Although underwater *breakwaters* have been built before for the protection of certain beach areas, particularly in Japan, the underwater mound scheme, when conceived in 1963, is believed to have been the first application of an artificially placed sand bar to protect the leeward beaches. Large amounts of sand are available from harbour dredging works at Durban but since trailing-suction dredgers are used, it is impractical to discharge the sand directly onto the beaches. Nearshore dumping, in an attempt to feed the beaches, was tried at Long Beach, New Jersey and Santa Barbara, California^{4,5}, both attempts were, however, unsuccessful because the sand remained where it was dumped instead of moving onto the beach.

This evidence strengthened the idea that dredging spoil could be used to build an offshore underwater sand ridge or mound which would be sufficiently stable to form an effective beach protection scheme. In this way a solution would be obtained for both the beach problem and the problem of finding a satisfactory dumping site. Preliminary tests and calculations based on breaker depth functions³ showed that the mound should reach a height of at least 7.3 m below LWOST^x to be effective. Since this is also the minimum depth in which most of the available hopper dredgers could safely operate, this height was accepted for the further investigations. In the field it was established that side slope with underwater dumping would not be steeper than about 1 in 25 and this slope was therefore used in the model tests.

The final scheme which eventually evolved is shown in Figure 1. The proposed underwater mound runs parallel to the Durban beaches in a water depth varying from 7 to 16 m. Its crest level is 7.3 m below LWOST, the crest width 61 m, the length about 4.5 km and the total quantity of sand required is about 8 000 000 m³. A gradual slope of 1 in 150 is included at the northern end of the mound to minimise side effects.

^x Low Water Ordinary Spring Tide

Before the above scheme could, however, be recommended to the Durban Corporation, it was necessary to establish whether the underwater mound would remain sufficiently stable and what its effect would be on the beaches. Because of the uniqueness of the problem, it was decided, firstly, to carry out extensive research into *basic scaling problems* for movable bed models, whereafter optimum dimensions of the mound and the stability of the mound and its effect on the beaches were determined in movable bed models. It was also decided to supplement the model tests with the construction of a 1 200 m long test section off the Durban beach, to establish mound stability and possible sand migration from the mound under prototype conditions

BASIC SCALING TESTS

Detailed measurements of beach changes, wave conditions and sand sizes were made for a beach section along West Street Jetty, Durban, during 1965⁶. Using these data, tests were carried out in a 0.23 m wide wave flume, applying the following scale ratio's

horizontal scale ratio	$L_r = 200$
vertical scale ratio	$h_r = 72$
geometric distortion	$S_r = h_r/L_r = 1/2.78$
hydraulic time ratio (tides)	$t_r = 23.6$ (based on Froude's law)
wave period scale	$T_r = h_r^{1/2} = 8.47$

The average value of the mean grain sizes, d_m , along West Street Jetty was found to be 350 micron. Three separate series of tests were carried out using sand ($d_m = 250$ micron) and anthracite ($d_m = 190$ and 270 micron) with a specific gravity of 1.35. Wave conditions, as measured in nature including tides, were reproduced to scale in these tests. All the wave conditions were tested until equilibrium profiles had been reached.

The results of these tests⁷ showed that with the 270 micron anthracite, the average prototype beach slope of 5 per cent was correctly reproduced. Moreover, the general beach shapes as well as the quantitative changes compared remarkably well. On the other hand, the results from the tests with 250 micron sand and 190 micron anthracite, did not compare with nature at all, average beach slopes found in the

model being 8 and 3 per cent respectively

It has been shown^{8,9} that in the case of river models with a movable bed, good similarity between model and prototype is achieved when, apart from the Froude and friction criteria, the shear-settling velocity criterion is also satisfied, viz $(V_x/W)_r = (hs)_r^{1/2} / W_r = 1$, in which V_x is the shear velocity, W is the settling velocity of the mean grain size and subscript r denotes prototype to model ratio. To reproduce the 350 micron prototype sand in accordance with the shear-settling velocity criterion either sand with $d_m = 120$ micron, or anthracite with $d_m = 260$ micron should have been used in the tests. The 270 micron model anthracite thus almost satisfied the above criterion and since this material resulted in nearly correct reproduction of prototype events, it is concluded that, for the model scales used for the tests, the *shear-settling velocity criterion must be satisfied to correctly reproduce coastal changes*⁹

CRITERION FOR EROSIVE AND NON-EROSIVE CONDITIONS

It has been shown^{7,10} that beach deformations relative to an equilibrium beach slope, 1, are a function of the deep water wave steepness, H_o/λ_o and the parameter $(gHo)^{1/2}/W$ (g is acceleration due to gravity, H_o wave height and λ_o wave length). The beach profiles measured along West Street Jetty, as related to particular wave conditions, were divided into erosive, non-erosive and equilibrium profiles and from the results the criterion shown in Figure 2 was obtained (put $S_r = 1$), which defines the conditions for accretion, erosion or a neutral profile in case of the Durban beach with its 5 per cent equilibrium beach slope

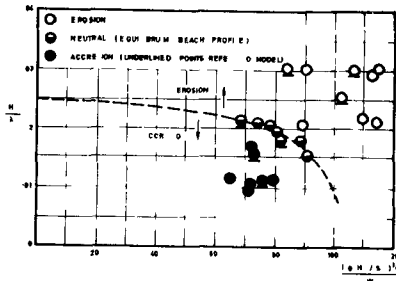


FIGURE 2 CRITERION FOR EROSIVE AND NON-EROSIVE CONDITIONS

So far only prototype conditions have been considered. Assuming now that model tests are made of beach deformations and that the criterion $(hs)_r^{\frac{1}{2}} = W_r$ is satisfied, the beach deformation will become a function of⁷

$$\text{deformation} = f \left(Ho/\lambda_o, \frac{(gHo/S_r)^{\frac{1}{2}}}{W} \right)$$

This expression is applicable to both model and prototype ($S_r = 1$ for prototype). In Figure 2 are also shown the test results with the 270 micron anthracite which closely agree with the prototype data. This yields further proof of the importance of the shear-settling velocity criterion.

Although it is realised that these findings are based on a limited amount of data, it may nevertheless be concluded that a reasonably accurate criterion has been established to differentiate between erosive and non-erosive wave conditions. This criterion has proved invaluable for the interpretation of the results of additional scaling tests and for the determination of the optimum dimensions of the mound (see following sections). Moreover, since for points on the dividing line neither erosion nor build up occurs, it is suggested that this line be used to define the conditions which yield the *equilibrium beach profile* which is of particular value for model tests.

The criterion shown in Figure 2 only applies to the Durban conditions, viz a slightly protected beach with 350 micron sand and 5 per cent beach slope. However, using the relationship between beach slope and average grain size given by Wiegel¹¹, the Durban results can be extended to cover a range of beach slopes and grain sizes. In Figure 3 a generalised criterion is given for *slightly protected* beaches, which clearly shows the influence of beach slope, β . Using Wiegel's data, similar criteria can be derived for protected and unprotected beaches. Extensive tests are at present being undertaken at the University of Stellenbosch to check on the validity of the generalised criterion.

ADDITIONAL TESTS ON SCALE EFFECTS

In the above it was shown that the shear-settling velocity ratio must be satisfied in the case of a model, with $L_r = 200$ and $h_r = 72$, to ensure proper reproduction of prototype events. It remained to establish

whether this criterion also applied to other scale ratios to be used for the model tests on the underwater mound Tests on scale effects, as listed in Table I, were therefore carried out using a typical section of the Durban beaches with 350 micron sand as a basis for the tests

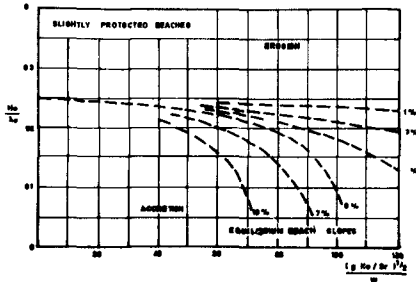


FIGURE 3 GENERALISED CRITERION FOR EROSIIVE AND NON-EROSIVE CONDITIONS

TABLE I TESTS ON SCALE EFFECTS

Test Series	L_r	h_r	$\frac{1}{S_r}$	Sediment	Mean grain size, d_m (micron)		Width of flume (m)
					Req for $(\frac{v_s}{w})_r = 1$	Available	
1	200	200	1	Anthracite	135	150	0 23
2	200	100	2	"	205	190	0 23
3	72	72	1	"	180	190	1 22
4	72	18	4	Mine sand	200	225	1 22

For all the above tests model sediment was used which nearly satisfied the shear-settling velocity ratio and test conditions included both erosive and build up type waves Resulting model beach profiles were compared with those predicted on the basis of Figure 2 and it was found that definite scale effects were present for the smallest model (1 in 200 undistorted) but for all scales equal to or larger than $L_r = 200$ and $h_r = 100$ the model results closely agreed with the predictions⁷

Thus it may be concluded that models in the range of scales listed in Table I (excluding the smallest scale) and for which the shear-settling velocity ratio is satisfied, may be relied upon to reproduce prototype conditions to a reasonable degree of accuracy

OPTIMUM DIMENSIONS OF THE MOUND

Initially (1964) the dimensions of the mound were rather arbitrarily chosen, i.e. a crest width of 92 m, side slopes of 1 in 9 and reaching to 7.3 m below LWOST. From early echo sounders made in 1966 over a test section of the mound, it was found that the dumped sand reached an equilibrium underwater slope of 1 in 25. This slope was therefore accepted for all subsequent model tests.

Although the underwater mound is a long way from the beach, since its function is to cause the larger waves to break over it, its behaviour could well be similar to that of a bar in the main breaker zone. Keulegan has found that for a nearshore bar to be stable for different wave steepnesses, the depth of crest immersion must be about half the water depth^{12,13}. As can be seen from Figure 1 the main body of the mound will be in about 15 m water depth and thus the crest should reach to about 7.5 m below LWOST. Based on this and considering the required depth for safe manoeuvring of the hopper dredgers, the original crest level of 7.3 m below LWOST was maintained for the further tests on the mound. To determine an effective crest width for the mound, both fixed bed and movable bed model tests were carried out in the 0.23 m and 1.22 m wide wave channels.

The *fixed bed* model tests were performed for a beach and mound cross section just north of the Patterson Groynes (Section A-A, Figure 1). The water depth near the mound in this area is 13 m, side slopes of 1 in 25 and a crest level of 7.3 m below LWOST were used. The tests were carried out in the 0.23 m wide flume at an undistorted scale of 1 in 100, using crest widths of 0, 30, 61 and 92 m respectively. Tides were not reproduced, the tests were performed at MSL^x.

The results of the tests are shown in Figure 4 where the incident wave heights are plotted against the wave heights in the lee of the mound. It should be noted that with no breaking of waves over the mound, the reduction in wave height due to the mound is about 30 per cent but as soon as the waves start to break the reduction increases rapidly. From Figure 4 it is clear that the mound is significantly

^x Mean Sea Level, i.e. 0.9 m above LWOST for Durban

effective only when the crest width is at least 61 m. In this case wave heights behind the mound are limited, due to breaking, to 2.5 m irrespective of the incident wave height. A further rather insignificant reduction to 2.25 m is effected by an increase in crest width to 92 m. On the basis of these tests it was therefore concluded that the crest width of the mound should be at least 61 m.

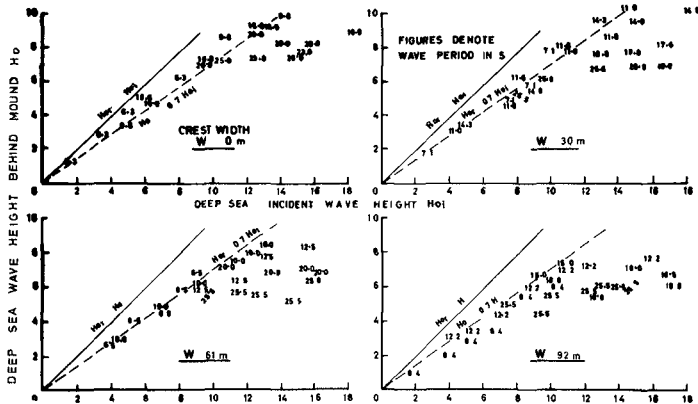


FIGURE 4 RELATIONSHIPS BETWEEN MODEL WAVE HEIGHTS SEAWARDS AND BEHIND THE MOUND

In Figure 5 are shown density patterns of waves recorded in Durban with a wave clinometer over the period 22/7/65 to 27/10/66, superimposed on the criterion for erosive and non-erosive waves (see Figure 2). The full lines in Figure 5 represent incident wave conditions as recorded in Durban, whereas the dotted lines enclose the reduced wave conditions behind a 61 m wide underwater mound. It is clear from a comparison of these density patterns that the balance between erosion and build up will be disturbed by the mound and accretion can be expected to take place until a new equilibrium beach profile is established. For the incident waves 30 per cent of the waves lie in the erosion zone and 70 per cent in the build up zone (of course the smaller waves in the build up zone are too small to cause any sand movement so that the large difference in the percentages is misleading). When a similar percentage division between erosive and non-erosive waves is assumed, the expected new equilibrium beach slope in the lee of the mound would be steeper if the generalised criterion given in Figure 3 would still apply to the

conditions behind the mound Although the latter is probably not the case, there is a strong indication that the equilibrium beach slope behind the mound will be somewhat steeper than the beach profile without the mound

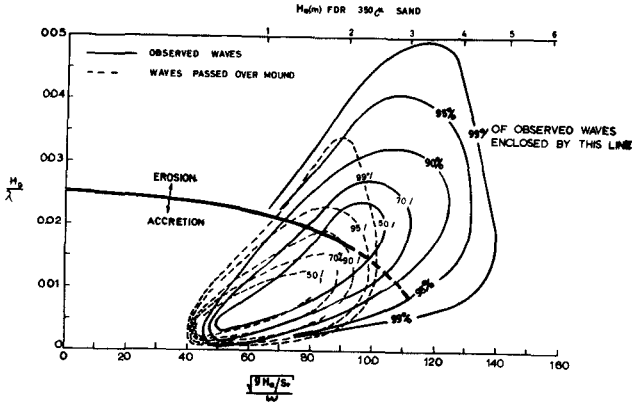


FIGURE 5 DENSITY PATTERN OF OBSERVED WAVES AND WAVES AFTER PASSING OVER MOUND

The percentages erosive waves behind mounds with different crest widths were calculated in the same way as for the 61 m wide mound The results, shown in Table II, emphasise the validity of the conclusion reached earlier that the crest width should be 61 m

TABLE II PERCENTAGES EROSIIVE WAVES

Without mound	With mound with crest width (m)			
	0	30	61	92
30	10	5½	3	2½

This conclusion was further confirmed by *movable bed* model studies which showed a significant improvement on the beaches only for a crest width of 61 m and over⁷ The dimensions of the underwater mound as shown in Figure 1 viz mound crest level at 7.3 m below LWOST, side slopes 1 in 25, crest width 61 m and total volume about 8 000 000 m³ were therefore accepted

WIND-WAVE FLUME TESTS

In order to study the long term stability of the proposed mound and its effect on the beaches tests were performed in the CSIR's 120 m long, 3 m wide wind-wave flume^{14,15} For these tests a beach section at Battery Beach was used (see Figure 1) with a 1 in 25 beach slope above and 1 in 40 below low water The beach sand had an average diameter of 350 micron whereas the sand in the mound was assumed on average 250 micron The choice of the model sediment was based on the shear-settling velocity criterion The scale factors used are given in Table III

TABLE III SCALES FOR WIND-WAVE FLUME TESTS

Scale ratio	Mound	Beach
vertical scale h_r	50	50
horizontal scale L_r	50	150
wave period scale $T_r = h_r^{1/2}$	7.06	7.06
hydraulic time scale (tides) $t_r = L_r/h_r^{1/2}$	7.06	21.25
sedimentological time scale $(T_s)_r \approx 10t_r$	70	212
model sediment (anthracite) mean grain size (micron)	190	360

As can be seen from Table III different scales were used to model the mound and the beach although they were tested at the same time This was essential because no distortion could be allowed for the mound, since the wave attenuation for a distorted mound, i e with a too small crest width relative to the wave length, would be too small (see Figure 4) Since the whole object of the underwater mound is beach improvement, the time scales pertaining to the beaches were adopted for the entire system

Wave conditions as recorded in Durban from June, 1965 to June, 1967 (2 years) were schematised and scaled down in accordance with the above scale ratio's Recorded wave height spectra were found to agree closely with the Rayleigh distribution of wave heights which could very nearly be reproduced in the flume by a combination of machine and wind generated waves (see Figure 6)

A continuous test, representing the two years prototype conditions, was carried out whereby two models, one with and the other without the mound were tested simultaneously side by side in the flume. Profiles were measured after each wave condition and a typical result is shown in Figure 7, which shows the beach and mound sections after an extremely severe storm condition. Even with these large waves the mound remained virtually stable, whereas a considerable improvement, due to the mound, is noted on the beach (2.5 m vertical or 90 m horizontal).

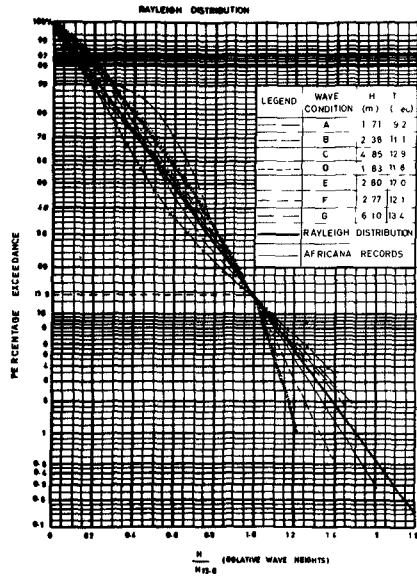


FIGURE 6 WAVE HEIGHT SPECTRA

The maximum change of the crest level of the mound was found to be 1 m and the maximum horizontal movement about 40 m for the entire period of the test. As was expected, a slightly steeper beach slope established under most conditions as a result of the presence of the mound.

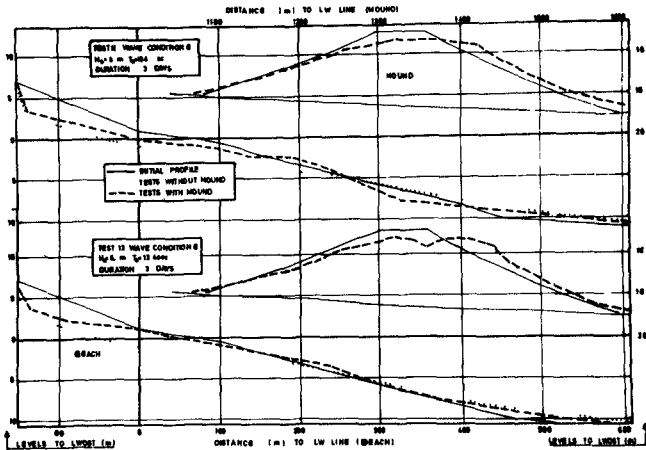


FIGURE 7 LONG TERM MOUND STABILITY AND BEACH CHANGES

On the basis of this extensive test programme, it was concluded that the underwater mound (as shown in Figure 1) would remain virtually stable, with maximum crest level fluctuations of about 1 m and that the beaches in the lee of the mound would significantly improve

CONSTRUCTION OF TEST SECTION

In order to investigate dumping techniques, stability of the dumped sand, side slopes and possible sand migration from the dumping area towards the nearby harbour entrance or the roadstead, it was decided to supplement the model tests with the construction of a test section of the underwater mound (see Figure 1) Sand dumping started in June, 1966 at the most southern end of the mound and the test mound was virtually completed in November, 1966 when some 700 000 m³ of sand, coming from dredging works in Durban Bay, had been dumped (see Figures 8 and 9) By this time the test mound had reached a height of 8 to 8.5 m below LWOST over a length of about 1 200 m with side slopes of 1 in 25

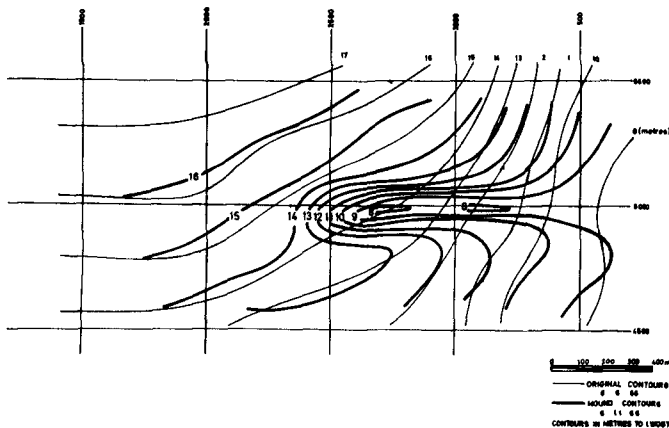


FIGURE 8 BUILD UP OF TEST MOUND AFTER FIVE MONTHS

The test mound provided answers to most of the above questions No difficulties were encountered with dumping with a 1 000 m³ capacity hopper dredger in 8 m water depth, in fact the contractor found it advantageous to dump in this area because of the shorter haulage Weekly echo sounding surveys were made of the area to check on the dumpings and sand quantities calculated from these surveys are compared in

Figure 9 with the dumping records. This comparison shows close agreement and it was thus concluded that there was no loss of sand and that the dumped sand remained in place.

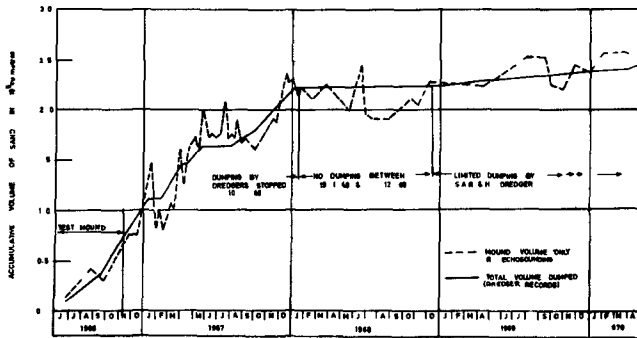


FIGURE 9 ACCUMULATIVE QUANTITIES OF SAND IN THE MOUND FROM JUNE 1966 TO APRIL 1970

This was further confirmed by detailed sediment movement studies. Sieve analyses of the sand in the mound area were carried out before dumping commenced. The mean grain sizes of the sand on the sea-bottom were found to vary between 212 and 340 micron. Samples from the sand in the hopper collected daily by the dredger crew showed fluctuations in mean grain size from 130 to 495 micron. Subsequent sampling operations of the sea-bottom at strictly controlled positions provided some evidence of the stability of the dumped sand but this evidence was not conclusive because of these large variations. A better check was obtained from the separation of heavy and light minerals by using heavy liquid (bromoform, $s.g. = 2.88$). The heavy mineral content of the samples was found to be throughout much higher in the original sea bed than in the dumped sand from the dredging site. The high content of heavy minerals in the sand on the sea-bottom is due to an abundance of ilmenite, magnetite and garnets, while the dumped sand is rich in light feldspars, calcites and clay minerals (phyllosilicates). Six weeks after dumping started, when $130,000 \text{ m}^3$ had been dumped, a considerable reduction in the heavy mineral content of the sand collected from the dump area could be discerned, while samples collected from the surrounding areas showed no change at all.

Finally, tests were performed using fluorescent tracers dumped at the site of the test mound. Earlier model results were confirmed by these tests in that sand movements, if any, were found to be inshore. Recorded sand grain velocities varied between 5 to 30 mm/s for significant wave heights from 1 to 2 m.

Based on these results it was concluded that the underwater mound could be expected to remain stable and that no sand from the mound would move towards either the harbour entrance or the roadstead seaward of the mound.

FURTHER CONSTRUCTION OF THE MOUND

Some 1 500 000 m³ of sand were dumped between November, 1966 and January, 1967 (see Figure 9). The main 1 000 m³ hopper capacity dredger ceased operating in August, 1967 and was replaced by three hopper barges with a capacity of 120 m³ each. No dumping took place during 1968, which provided an ideal opportunity to study the stability of the completed part of the mound. From the end of 1968 onwards limited amounts of sand were dumped by the South African Railway dredgers, carrying out maintenance dredging of the harbour entrance. To date (May, 1970) a total of some 2 500 000 m³ has been dumped.

In Figure 9 are shown the cumulative quantities dumped as recorded by the dredger masters, in comparison with quantities calculated from echo sounding surveys. These surveys were made weekly or fortnightly during intensive dumping periods to control the dumping and at monthly intervals after January, 1968. It is clear from Figure 9 that no sand is permanently lost from the mound, although fluctuations in quantities do occur as a result of adverse wave conditions. For instance, a 20 per cent reduction occurred after a storm in August, 1966 (significant wave height $H_s = 2.4$ m, wave period $T_s = 14$ s, direction ESE) and a 23 per cent loss occurred, mainly from the incomplete sections of the mound, after a storm in June, 1968 ($H_s = 3.5$ m, direction S). However, in both cases these losses were regained by natural forces and it thus appears that the mound, once it has been built up to the required level of 7.3 m below LWOST, is reinstated naturally even after considerable temporary losses of sand.

THE STABILITY OF THE MOUND

In the above it has been shown that the sand quantities in the completed section of the mound do not change materially as a result of the actions of the sea. Figure 10 gives an example of contours of the mound for December, 1969 and comparisons with similar surveys before and after this date showed that no significant displacement of the mound takes place¹⁶

This is further borne out by a study of some of the cross sections of the mound shown in Figure 11 (for positions of cross sections refer to Figure 12). These cross sections are based on echo sounding surveys made during 1969 when no dumping took place, except at the northern extremity of the mound (sections 1000 to 1500, see Figure 12). The profiles show random variations with a maximum fluctuation in crest levels of 1 m and maximum lateral movements of the crest of the mound of about 75 m.

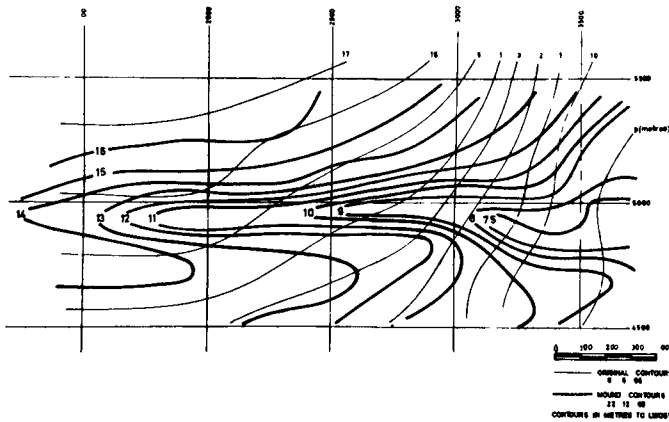


FIGURE 10 DEPTH CONTOURS OF THE UNDERWATER MOUND AS ON 22.12.69

Although it can be seen from Figure 11 that, except for section 3300, the mound did not yet have the required cross section, the agreement between these recorded movements with those obtained in the model tests, viz 1 m crest level variation and about 60 m lateral movement, are extremely good.

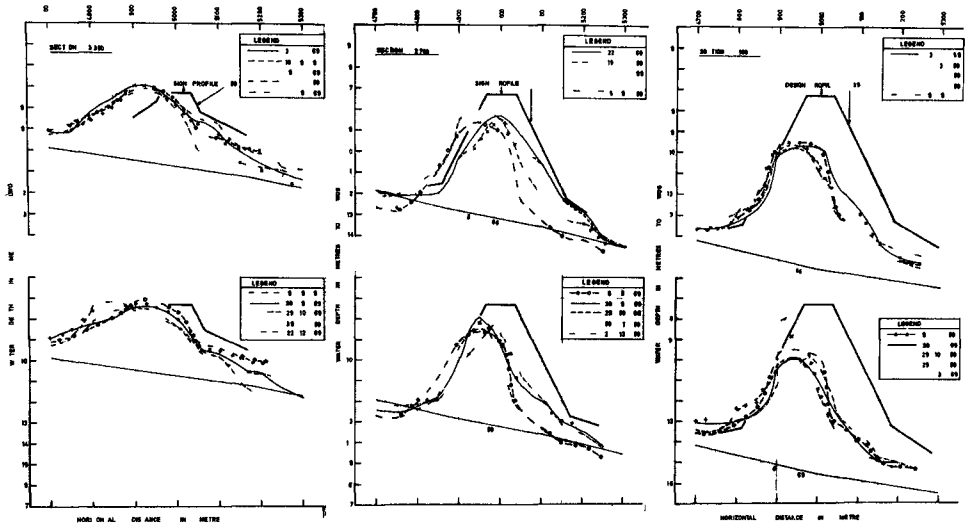


FIGURE 11 BEHAVIOUR OF UNDERWATER MOUND CROSS SECTIONS DURING 1969

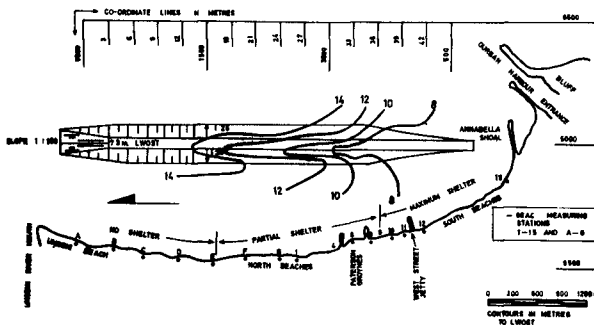


FIGURE 12 SCHEMATIC PLAN OF THE DURBAN UNDERWATER MOUND AS ON 22 12 69

EFFECT ON THE BEACHES

As can be seen from Figures 11 and 12, the underwater mound is still far from complete. Only $2\,500\,000\text{ m}^3$ had been dumped by May, 1970 against the required $8\,000\,000\text{ m}^3$ and the crest level is only reasonably close to the required 7.3 m below LWOSt over a length of some $1\,500\text{ m}$, which is about one third of the required length of the mound. The most logi-

cal method in assessing the beaches therefore, is to compare the beaches in terms of the amount of protection they receive from the partly completed mound. A sub-division is made between beaches receiving full protection (south beaches), partial protection (Patterson Groynes area) and zero protection (northern beaches to Umgeni mouth) (see Figure 12)

Figure 13 shows the overall effect on the beaches since the construction of the mound started. The 100 per cent is based on the average of the measured sand volumes on the beaches above mean sea level for the period November, 1965 to May, 1966 and all subsequent monthly measurements were compared with these values.

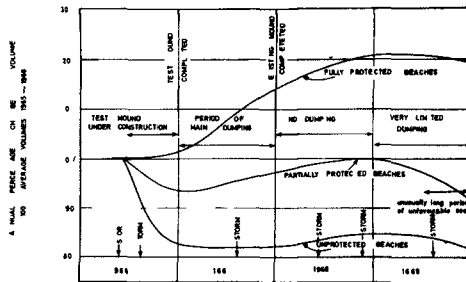


FIGURE 13 EFFECT ON BEACHES FOR VARIOUS DEGREES OF PROTECTION

Although even at the south end the mound has not yet reached its full design crest width, it is clear from Figure 13 that the fully protected beaches greatly benefited from the mound (about 20 per cent increase in sand quantities) whereas partially protected beaches show less improvement and those unprotected appear to loose sand.

The partially protected beaches were close to equilibrium at the end of 1968 but they show a decline in beach volumes during 1969. This was caused by a severe storm with 4.5 m high SE'ly waves which occurred on the 22nd August, 1969. This was the most severe storm since the devastating storm in May, 1966 which caused severe erosion of the northern beaches (see Figure 13) and the first major test of the completed section of the mound. The mound stood up to the test extremely well, hardly any loss of sand was recorded and crest levels remained within 0.5 m the same as before the storm.

The effect of the storm on the beaches was serious, as can be expected from a storm of such magnitude. The northern unprotected

beaches showed a loss, compared with the condition just before the storm, of 21 per cent against 33 per cent for the May, 1966 storm, the partially protected central beaches lost 16 per cent, which is the same as in 1966, whereas the protected beaches lost only 8 per cent against 20 per cent in May, 1966

It is thus clear that the completed section of the underwater mound has considerably improved the beaches in its lee, as was predicted on the basis of the model tests

CONCLUSIONS

The following conclusions may be drawn from the Durban underwater mound studies

- (a) An underwater mound of sand of the correct dimensions offers an effective beach protection scheme
- (b) Such a mound of fine to medium sand may be expected to remain virtually stable under most wave conditions and if losses occur during severe storms, natural processes will re-build the depleted mound to its original size
- (c) Reliable results, i e accurate predictions of prototype events, were obtained from movable bed models which were designed in accordance with the *shear-settling velocity* criterion

The entire mound will have to be built to provide protection to all the beaches between the harbour entrance and the Umgeni mouth It is expected that the mound will be completed in about 2 to 3 years, using sand from future harbour extension works in Durban Bay

ACKNOWLEDGEMENTS

The continual and very stimulating support of this work by the Durban Corporation and in particular of the then Direction of Special Works, Mr A Kinmont, is gratefully acknowledged

REFERENCES

- 1 JORDAAN, J M Durban harbour siltation and beach erosion investigations CSIR Contract Report CMEG 558, Pretoria, South Africa, September, 1963

- 2 JORDAAN, J M Study of Durban harbour silting and beach erosion
Proc XIIth Conference on Coastal Engineering, Washington, September, 1970
- 3 ZWAMBORN, J A Underwater mound for the protection and improvement of Durban's ocean beaches Preliminary investigations
CSIR Contract Report CMEG 596, Pretoria, South Africa, July, 1964
- 4 HALL, J V Test of nourishment of the shore by offshore deposition of sand Techn Memo No. 17, B E B , June, 1950
- 5 HALL, J V Artificially nourished and constructed beaches
Techn Memo No 29, B E B , December, 1952
- 6 ZWAMBORN, J A , VAN WYK, W Durban beach protection Interim Report No 5 CSIR Report MEG 528, Pretoria, South Africa, July, 1964
- 7 ZWAMBORN, J A , VAN WYK, W Some positive results in reproducing coastal processes in models CSIR Symposium Paper S 37, Stellenbosch, South Africa, June, 1969
- 8 ZWAMBORN, J A Reproducibility in hydraulic models of prototype river morphology La Houille Blanche, No 3, 1966
- 9 ZWAMBORN, J A Hydraulic models CSIR Report MEG 795, Stellenbosch, South Africa, July, 1969
- 10 IWAGAKI, Y , NODA, H Laboratory study of scale effects in two-dimensional beach processes Proc VIIIth Conference on Coastal Engineering, Mexico City, 1962
- 11 WIEGEL, R L Oceanographical engineering Prentice-Hall, Inc /Eaglewood Cliffs, N Y
- 12 KEULEGAN, G H Depths of offshore bars Techn Memo No 8, Beach Erosion Board, Washington, July, 1945
- 13 B E B Longshore bars and longshore troughs Techn Memo No 15, Beach Erosion Board, Washington, January, 1950
- 14 VAN WYK, W Durban beach protection Long term mound stability and beach improvement CSIR Report MEG 852, Stellenbosch, September, 1969
- 15 ZWAMBORN, J A CSIR's new wind-wave flume is amongst world's longest S A Engineer, Vol 58, No 595, December, 1967
- 16 FITZPATRICK, J B Stability of underwater mound for the protection of Durban's beaches Symposium Paper No G4, Oceanography, 1970, CSIR, Durban, South Africa

CHAPTER 63

LABORATORY TESTS ON ARTIFICIAL SEAWEED

W A PRICE - Senior Principal Scientific Officer
K W TOMLINSON - Senior Scientific Officer
D H. WILLIS - Scientific Officer

Hydraulics Research Station, Wallingford, Great Britain

ABSTRACT

Tests are described in which the effect of artificial seaweed on bed sediment movements due to waves was studied in a model. Water velocities near the bed and coal particle velocities on the bed, within the seaweed array, were measured over a range of wave conditions and densities of packing of the seaweed. The water velocity measurements were erratic, probably due to additional turbulence caused by the seaweed. Coal particle movements on the bed were slowed down in the presence of seaweed.

Introduction

A paper was presented to the 11th Conference on Coastal Engineering entitled, "The Effect of Artificial Seaweed in Promoting the Build-up of Beaches," see Ref 1. This paper described tests conducted in a laboratory wave channel using a beach of crushed coal, in addition to full-scale tests on the beach at Bournemouth, England. Anchorage problems stopped the full-scale tests before meaningful results could be obtained although some accretion had occurred inshore of the seaweed array. In the model, the presence of artificial seaweed offshore caused a build-up of the beach levels. An explanation of this build-up was suggested from the theory of wave propagation in a two-layered liquid of differing viscosities.

Since that time further laboratory investigations have been carried out to attempt to find an optimum arrangement of seaweed, and to test the applicability of the viscosity theory over a range of wave heights, periods and densities of seaweed packing.

Test Procedure and Results

The artificial seaweed was a white polypropylene ribbon 3 mm wide having a specific gravity of 0.93. Twenty strands of this, 0.30 m long, formed a clump which was stapled to the plywood floor of a wave channel. Clump spacing was varied to make three seaweed arrays, each 4.60 m long and 0.61 m wide.

Clumps at 150 mm \times 150 mm = 120 clumps

Clumps at 75 mm \times 75 mm = 420 clumps

Clumps at 50 mm \times 50 mm = 990 clumps

The wave channel was 28.5 m long and 0.61 m wide, with a mean water depth at the seaweed of 0.43 m. At the offshore end a paddle generated single-frequency waves. The tests were carried out with a fixed bed and landward of the seaweed installation was a pebble spending beach, 10 m long parabolic in shape.

Fourteen wave conditions, with periods from 1.5 sec to 2.5 sec and heights from 50 mm to 150 mm were generated for the channel bed without seaweed and for each seaweed installation. Observations were made of the wave orbital velocities near the bed and of the movement of coal particles along the bed.

1 Wave orbital velocities near the bed A miniature propeller current meter was placed 10 mm above the bed and connected to an instantaneous ratemeter to give a continuous record of orbital velocities during one wave period. This record was integrated to obtain the net wave induced drift, and divided by the wave period to give the mean drift velocity at the point of measurement. It was assumed that an increase in the landward drift velocity offshore might be expected to produce an increased landward sediment transport, and hence a build-up of levels inshore and on the beach.

The results are shown in Fig. 1a, b and c. It is apparent that there is little correlation between the density of seaweed packing and drift velocity. Some tests were repeated, and the net drift velocities were found to vary by as much as $\pm 300\%$. Differences of 200% were found with only a 75 mm change in the horizontal position of the propeller. The instruments were checked frequently to ensure that they were operating correctly.

The conclusion was reached, therefore, that the seaweed created additional turbulence, making velocity readings at a single point unrepresentative of water movements over the entire array. In order to study conditions over the array as a whole, the movement of coal particles along the bed was also measured.

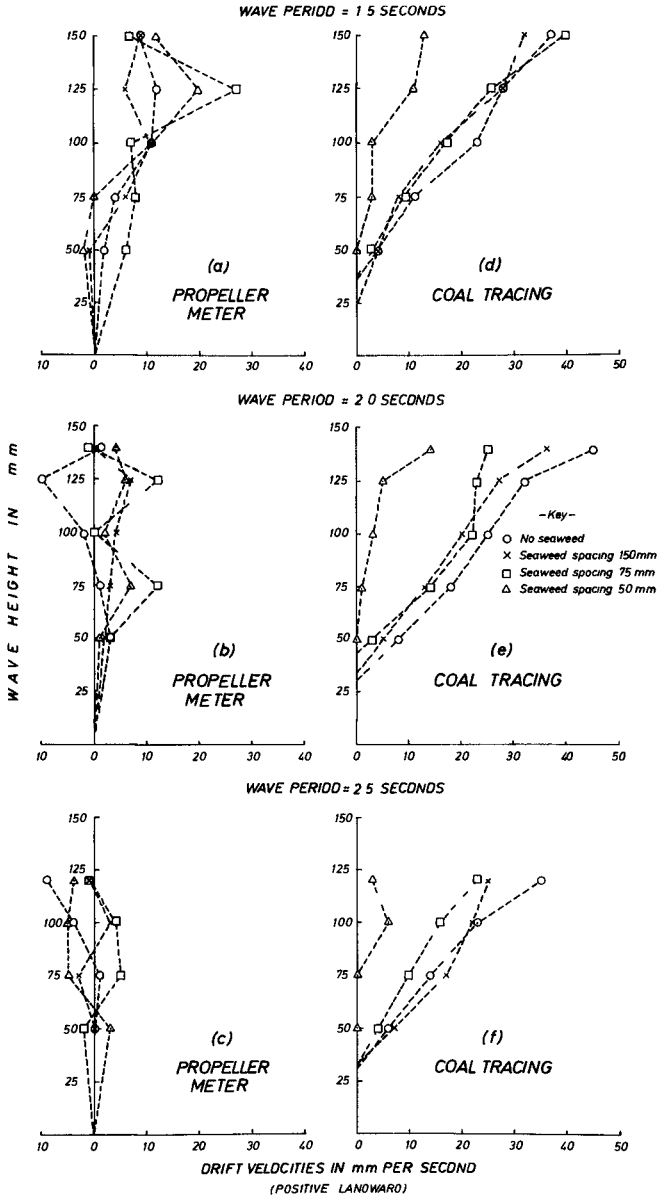


FIG 1

2 Movement of coal particles along the bed Coal particles were injected on the bed, and the number of waves required to move a particle over a known distance was counted. The net drift velocities found in this way are plotted on Fig 1d, e and f

These figures show a trend towards lower net drift velocities with denser seaweed packing, and with the exception of one seaweed installation, the results were repeatable. For the exception, seaweed at a clump spacing of 50 mm, turbulence was markedly greater with larger waves even the boundary layer behaved turbulently, and the coal dispersed in all onshore directions rather than parallel to the channel axis, with lower waves, the coal collected at scattered points in the array where bed shear was insufficient to move it

Discussion

In interpreting the results of the propeller meter tests, the method of analyzing the data must be considered. Wave induced drifts towards and away from the beach were calculated by integrating the velocity records and these were subtracted to obtain the net drift. The net drift so obtained was of the same order as the probable error in the velocity measurements. In addition, there were obvious differences in the shape of the velocity record for repeated tests. The lack of correlation between drift velocity and seaweed packing was probably due to the combined effects of computational error and turbulence.

The coal particle experiments, however, gave some interesting results. Of the fourteen wave conditions tested, all but three showed drift velocities with seaweed less than or equal to those without seaweed. Furthermore, in seven cases there was a definite trend towards lower drift velocities with denser seaweed packing, and only for a clump spacing of 150 mm with 1.5 sec waves was there a large incongruity. These results are not consistent with those predicted from the theory of wave propagation in a two-layered liquid of differing viscosities.

The results of the present series of tests suggest that the presence of artificial seaweed inhibits the transport of sand from the offshore seabed towards the beach. This appears to contradict the findings of the earlier tests in which a build-up of the beach was measured shoreward of the seaweed installation. However, the earlier build-up may not have been due to increased shoreward bed-load transport, but caused by a reduction in wave steepness due to attenuation of the wave height by the seaweed. In addition, the two series of tests were not truly comparable. First, the response of the instruments dictated wave periods for the most recent series greater than the 1.33 sec of the first series, and second, the use of a coal beach in the

original tests introduced the factors of beach slope, grain size distribution and suspended sediment load, none of which were present in the tests reported here

The results of the coal tracing indicate that artificial seaweed may have an application in uni-directional flow as a sediment trap, reducing the velocity gradient and bed shear and causing accretion within the array

Reference

- 1 PRICE, W.A , TOMLINSON, K W , and HUNT, J N The effect of artificial seaweed in promoting the build-up of beaches Proceedings 11th Conference on Coastal Engineering, London, 1969, Vol 1 pp 570-578

This report is published by permission of the Director of Hydraulics Research, Wallingford, England

CHAPTER 64

THE DYNAMICS OF A COAST WITH A GROUYNE SYSTEM

by W.T. Bakker, E.H J. Klein Breteler, and A. Roos

Coastal Research Department, Rijkswaterstaat
The Hague, Netherlands

ABSTRACT

This paper is a continuation of the paper with the same name, presented on the XIth Conference on Coastal Engineering by the first author [1], in which a mathematical theory was given about the behaviour of a coast after the construction of a groyne system. Now this paper extends the former paper theoretically and practically.

1. Theoretically a computer program has been made in which the influence of diffraction behind the groyne has been taken into account.
2. Practically the coastal constants used in the theoretical model of the coast will be expressed in terms of wave height and wave direction, based on the theory of SVASEK [2].

Results are given of computations with a coastal model in which the coast is schematized to one line (one-line theory) and a model in which the coast is schematized to a beach line and on inshore-line (two-line theory).

The influence of changing wave conditions is investigated.

INTRODUCTION

The construction of a groyne has the following effects (fig. 1)

1. Prevention of the littoral sanddrift in the area between the coastline and the head of the groyne.
2. Prevention of the longshore current in the same area.
3. Formation of a sheltered area at the lee-side of the groyne, caused by the diffraction.
4. Changing the wave height by reflection

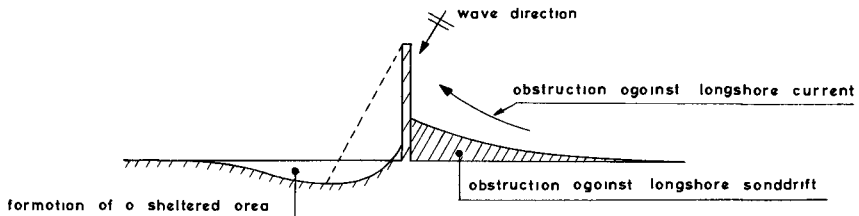


Fig 1 The effects of the construction of a groyne

The former paper dealt only about the first aspect, now we shall pay attention to the first and the third aspect. The second and fourth one will be investigated in the future.

ONE-LINE THEORY

The theory given here is an extension of the theory of PELNARD-CONSIDERE [3] .

PELNARD-CONSIDERE assumes, that the profile of the coast always remains the equilibrium profile, so that he only needs to consider one coastline, being one of the contourlines. He assumes no currents, constant wave direction, small angle of wave incidence and a linear relation between angle of wave incidence and the littoral drift.

The derivation of his theory is summarized in [1] .

For the littoral drift he finds

$$Q = Q_0 - q \frac{\partial Y}{\partial x} \dots (1)$$

in which Q = littoral drift.

Q_0 = littoral drift at the point, where

$$\frac{\partial Y}{\partial x} = 0.$$

$q = \frac{\partial Q}{\partial \varphi}$ = the derivate of the littoral drift Q to the angle of wave incidence φ .

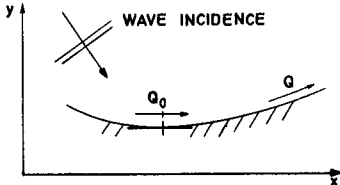


Fig 2 Littoral drift along the coast

He finds, that the accretion is proportional to the curvature of the coast

$$\frac{\partial Y}{\partial t} = \frac{q}{D} \frac{\partial^2 Y}{\partial x^2} \dots (2)$$

From this equation the coastline y as a function of x and t can be found for many boundary conditions. Pelnard-Considère gives analytical solutions of his equations. The interrupted line in fig. 5 shows the accretion and erosion near a groyne according to his theory. He assumes that wave height and wave direction are constants along the coast. At the lee-side of the groyne however, the wave height is less and the waves have an other direction, as a result of the diffraction.

We introduce diffraction in the theory of Pelnard-Considère

. The equations become more complicated, that's why we have to give numerical solutions. The derivation of the one-line theory including diffraction is given in appendix A'1.

For the littoral drift the same formula of Pelnard-Considère remains of value

$$Q = Q_0^* - q^* \cdot \frac{\partial Y}{\partial x} \dots (3)$$

but now Q^* and q^* are functions of x .

The effect of the diffraction can be splitted in a stationary effect and an instationary effect. This can be made clear in the following way (fig. 4).

If everywhere wave height and wave direction are the same, a straight coastline is stable, the transport is everywhere the same. If the wave height and the wave direction change in x-direction, the transport will change also and therefore the coastal shape has to adapt itself in order to make the transport everywhere the same again and give a stable coastline. In appendix A1 a mathematical formulation of this problem is given. The transport has been taken proportional to the square of the wave height and to the angle of wave incidence. A possible stable coastline y_0 as a function of x is found (appendix A1), ruled by the differential equation

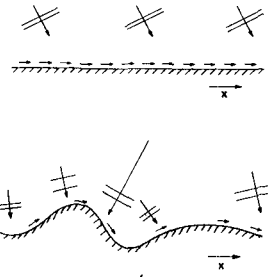


Fig 4

$$\frac{dy_0}{dx} = \varphi_x - \frac{\varphi_\infty}{h^2} \dots \dots \dots (4)$$

in which φ_x is the angle of the waves with the x -axis, φ_∞ the angle of wave incidence far from the groyne and h is the ratio between the wave height at an arbitrary point $(x,0)$ to the wave height at $x = \infty$, h is a function of x .

A short analysis of (4) learns, that if the wave height should be everywhere the same ($h=1$) this would give

$\frac{dy_0}{dx} = \varphi_x - \varphi_\infty$, thus the changing of the coastal direction is equal to the changing of the wave direction.

However, the problem of diffraction near a harbour mole is more intricate.

As the groyne stops all the transport, and as at $x = \infty$ the transport remains Q_0 , a stable coastline can never be achieved.

We split the coastline y into two parts, y_0 being a stationary effect of the diffraction¹⁾ and y' , being an unstationary effect

$$y(x,t) = y_0(x) + y'(x,t) \dots \dots \dots (5)$$

As shown in appendix A1, the equation for the unstationary part y' becomes about (2), but with an additional term, because q^* is a function of x

$$\frac{\partial y'}{\partial t} = \frac{q^*}{D_{tot}} \frac{\partial^2 y'}{\partial x^2} + \frac{1}{D_{tot}} \frac{dq^*}{dx} \cdot \frac{\partial y'}{\partial x} \dots \dots \dots (6)$$

in which $q^* = Ah^2 \dots \dots \dots (7)$

1) y_0 is the stable coastline, which would develop, if an artificial nourishment Q_0 would be administered on the lee-side of the groyne.

A is a proportionality constant, being investigated in the chapter "coastal constants".

The amount of h and Φ_x in (4) and (7) in the diffraction case is found from the simplified theory of PUTNAM and ARTHUR [4].

The unstationary part y' can be found by numerical integration of equation (6).

Superposition of y_0 and y' , according to (4) gives the coastline $y(x,t)$.

For the calculation of the coastlines a computerprogram has been made. Fig. 5 shows the calculated development of a coast with one groyne. Comparison of the interrupted and the solid line gives an impression of the influence of diffraction.

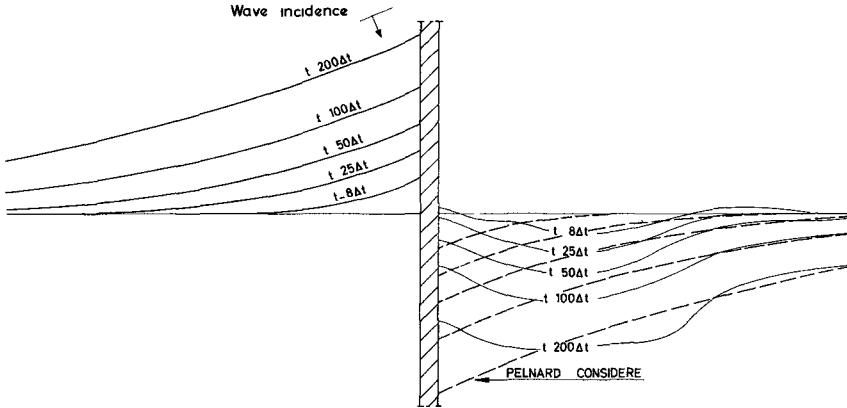


Fig 5 Accretion and erosion near a groyne numerical solution with diffraction (one line theory)
The dotted lines at the right hand gives erosion according to Pelnard - Considere

With the computerprogram we calculated the behaviour of the coastline between two groynes with the influence of diffraction. The result is shown in fig. 6.

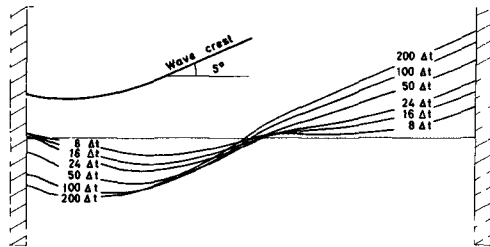


Fig 6 Behavior of the coastline between two groynes (one-line theory)

TWO-LINE THEORY

Now we schematize the coastal profile to two lines, the beach (y_1) and the inshore (y_2'). This gives the possibility to take the off- and onshore transport into account.

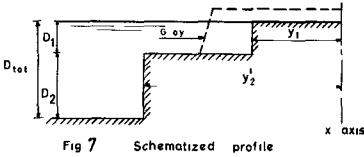


Fig 7 Schematized profile

In top view one sees two lines at a distance y_1 and y_2' from the x-axis. The "equilibrium distance" is the distance $y_2' - y'$ between beach and inshore, when the profile is an equilibrium profile.

The following dynamic equations are assumed.

If the distance $y_2' - y'$ is equal to the equilibrium distance W , no interaction is assumed. If the distance $y_2' - y_1$ is less than W , the profile is too steep and an offshore transport will be the result. An onshore transport will occur in the opposite case.

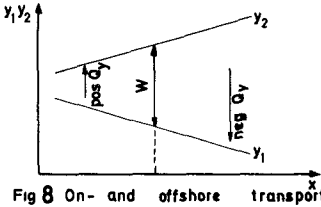


Fig 8 On- and offshore transport

We linearize this relation and take for the offshore transport Q_y per unit length

$$Q_y = q_y \{y_1 - (y_2' - W)\} \dots (9)$$

in which q_y is a proportional constant with the dimension $[1/t]$. It is a function of x . For a simpler notation, we denote

$$y_2 = y_2' - W \dots (10)$$

Then (9) becomes

$$Q_y = q_y (y_1 - y_2) \dots (11)$$

With respect to the littoral drift, the assumption of PELNARD-CONSIDERE is applied, both for beach and inshore, the transport is linearized

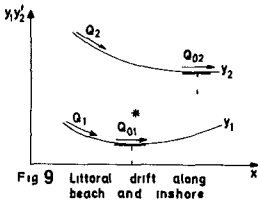


Fig 9 Littoral drift along beach and inshore

$$Q_1 = Q_{01}^* - q_1^* \frac{\partial y_1}{\partial x} \dots (12a)$$

$$Q_2 = Q_{02} - q_2 \frac{\partial y_2}{\partial x} \dots (12b)$$

in which Q_{01} and Q_{02} are respectively the transports where $\frac{\partial y_1}{\partial x} = 0$.

Q_{01}^* is a function of x , Q_{02} is a constant. q_1^* and q_2 are proportionality factors, q_1^* is a function of x and q_2 is a constant.

In appendix A2 the derivation of the two-line theory is given. The beach line y_1 is splitted into two parts, analogue to (4).

$$y_1(x, t) = y_0(x) + y_1'(x, t) \dots (13)$$

in which $y_0(x)$ is the same function as given in (8).
 For the accretion along the beach and the inshore we find

$$\frac{\partial y_1'}{\partial t} = \frac{q_1^*}{D_1} \frac{\partial^2 y_1'}{\partial x^2} + \frac{1}{D_1} \frac{\partial q_1^*}{\partial x} \cdot \frac{\partial y_1'}{\partial x} - \frac{q}{D_1} (y_1' + y_0 - y_2) \dots (14)$$

$$\frac{\partial y_2}{\partial t} = \frac{q_2}{D_2} \frac{\partial^2 y_2}{\partial x^2} + \frac{q}{D_2} (y_1' + y_0 - y_2) \dots \dots \dots (15)$$

These are two simultaneous partial differential equations. For the calculation of the beach line y_1 and the inshore line y_2 we made a computer program in which the equations are solved numerically (appendix A2). In fig. 10 the development of a coast with one groyne is shown.

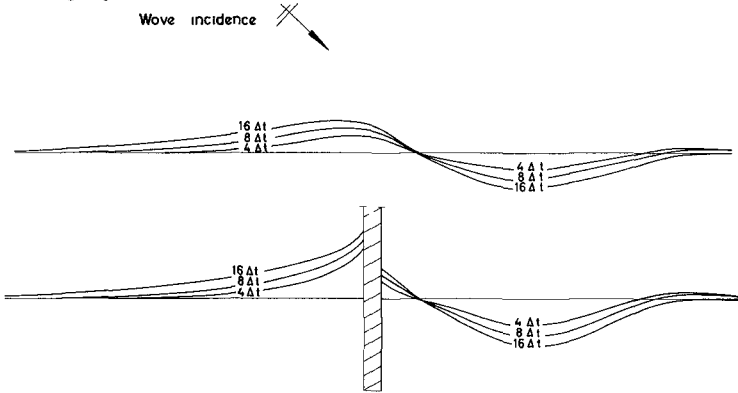


Fig 10 Accretion and erosion near a groyne numerical solution with diffraction (two-line theory)

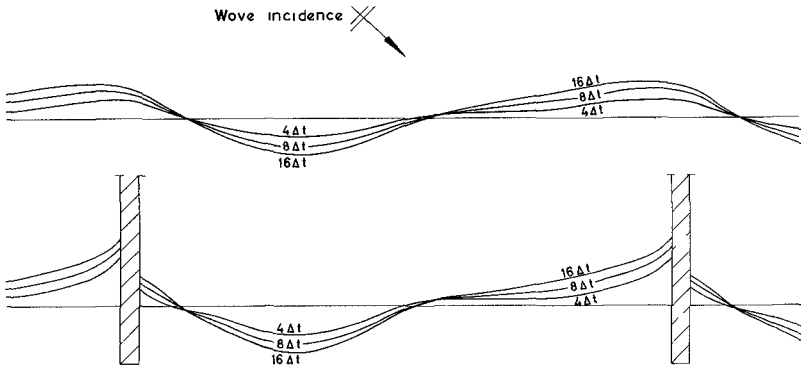


Fig 11 Behaviour of beach and inshore between two groynes (two-line theory)

From a coast with an infinite row of groynes, we calculated the development of the coastal shape between two groynes. This is shown in fig. 11.

COASTAL CONSTANTS

In this chapter some expressions will be derived for the coastal constants, respectively using the one-line and the two-line theory. For the one-line theory the CERC-formula will be used, for the two-line theory the SVASEK-variation of this [2]. It is assumed, that the transport is confined to the breaker-zone.

$$D_{tot} = D_{br} \dots \dots \dots (16)$$

Considering the longshore theory of BOWEN 6 it may be expected that the transport takes place over a distance 1 to 1,5 times the breaker zone, and that most of the transport is confined to the breaker zone. Probably it is better to assume for D_{tot} the depth occurring at a distance $1\frac{1}{2}$ times the width of the breaker zone. In this case the factor q becomes less, for a concave profile about 100% to 80% of the computed value.

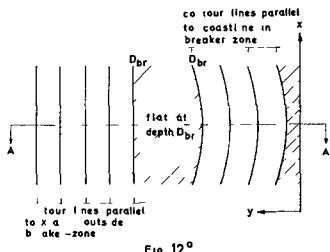


Fig 12^a

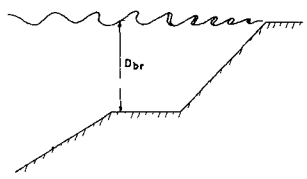


Fig 12^b profile A-A

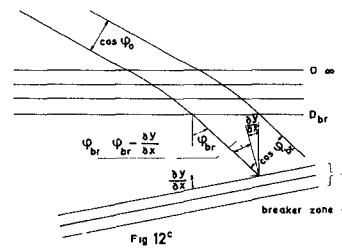


Fig 12^c

One-line theory

We assume the topography and notation according to fig. 12. The CERC-formula relates the longshore transport Q to the longshore

component of the wave energy flux

$$Q = 1.4 \times 10^{-2} H_o^2 C_o K^2 \sin \varphi_{br} \cos \varphi_{br} \dots (17)$$

in which H_o = wave height in deep water
 C_o = phase velocity in deep water
 K = refraction coefficient
 φ_{br} = angle of wave incidence in the breaker zone

From fig. 12 can be derived

$$\varphi_{br} = \varphi_{br}' - \frac{\partial Y}{\partial x} \quad (\frac{\partial Y}{\partial x} \text{ small}) \dots (18)$$

$$Q_o = 1.4 \times 10^2 H_o^2 C_o K^2 \sin \varphi_{br}' \cos \varphi_{br}' \dots (19)$$

$$q = \frac{dQ}{d(\frac{\partial Y}{\partial x})} = 1.4 \times 10^{-2} H_o^2 C_o K^2 \cos 2 \varphi_{br}' \dots (20)$$

One can write

$$H_{br} = A_2 D_{br} \dots (21) \text{ and } C_{br} \sqrt{g D_{br}} \dots (22)$$

in which A_2 and A_3 can be taken from any wave theory or measurements (for instance, solitary wave theory [?])

$$A_2 = 0.78 \text{ and } A_3 = 2 \times 0.78).$$

Conservation of wave energy between wave rays gives

$$H_o^2 C_o K^2 = H_{br}^2 C_{br} = A_2^2 A_3 g^{\frac{1}{2}} D_{br}^{5/2}$$

This makes

$$Q_o = A_1 A_2^2 A_3 g^{\frac{1}{2}} D_{br}^{5/2} \sin \varphi_{br}' \cos \varphi_{br}' \dots (23)$$

$$q = A_1 A_2^2 A_3 g^{\frac{1}{2}} D_{br}^{5/2} \cos 2 \varphi_{br}' \dots (24)$$

in which $A_1 = 1.4 \times 10^2$

Often $\cos \varphi_{br}$ can be taken equal to 1.

Now it is easy to give numerical values to the proportionality constants, used elsewhere in this paper, for instance, in (?)

$$A = 1.4 \times 10^{-2} H_o^2 C_o K^2$$

and in appendix A1, (A10)

$$\Delta t = \frac{D_{tot}}{Ah_{max}^2} \frac{(\Delta x)^2}{2}$$

$$\Delta t = \frac{D_{br}}{A_1 A_2^2 A_3 g^{\frac{1}{2}} D_{br}^{5/2} h_{max}^2} \frac{(\Delta x)^2}{2}$$

$$\Delta t = \frac{1}{2A_1 A_2^2 A_3 h_{max}^2} \frac{(\Delta x)^2}{D_{br} \sqrt{g} D_{br}}$$

Two-line theory

In the two-line theory, the coastal constants mentioned in fig. 13 are of importance. The exact definitions are given in (9) and (12). The constant q_y , which defines, how the offshore transport changes, when the profile changes, will be treated in a separate paper in the future. Some investigation about this constant has already been done 8 .

The coefficients Q_{01} , q_1 , Q_{02} and q_2 will be computed with the SVASEK-theory 2 which only treats the longshore transport. SVASEK neglects the longshore transport outside the breaker-zone. We assume, that the profile outside the breaker-zone has reached already its equilibrium profile, and that the on- and offshore transport can be neglected there. The assumed profile topography can be like given in fig. 14 (see next page), more natural than shown in fig. 7. SVASEK assumes, that the littoral drift between two depth contours is proportional to the longshore component of the loss energy between these contourlines (2 , formula 5 - 7)

$$\Delta Q = A_1' \cdot \Delta \left(\frac{H^2 C}{K^2} \right) K_m^2 \sin \varphi_m \cos \varphi_2 \dots (25)$$

in which $Q =$ littoral drift between two depth contours $D - \frac{1}{2} \Delta D$

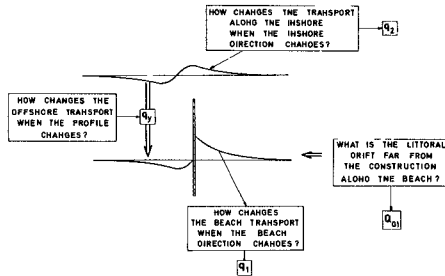


Fig 13

and $D + \frac{1}{2} \Delta D$, $\Delta \left(\frac{H^2 C}{K} \right) = \text{difference}$

between $\frac{H^2 C}{K}$ on both dept contours

$K_m, \varphi_m = \text{value of refrac-}$

tion coefficient K and angle of wave incidence φ in the midst between the depth contours. It appears (appendix A3), that ΔQ can be written

$$\Delta Q = 3A_1 A_2^2 A_3 g^{\frac{1}{2}} D_1^{\frac{1}{2}} \Delta D \sin \varphi_m \cos \varphi_m \dots (26)$$

and after some simplifications, treated in appendix A3, the following constants are found for small angle of wave incidence

$$Q_{o1} = A_1 A_2^2 A_3 g^{\frac{1}{2}} D_1^3 D_{br}^{-\frac{1}{2}} \sin \varphi_{br}'$$

$$q_1 = A_1 A_2^2 A_3 g^{\frac{1}{2}} D_1^{2\frac{1}{2}}$$

$$Q_{o2} = A_1 A_2^2 A_3 g^{\frac{1}{2}} (D_{br}^3 - D_1^3) D_{br}^{-\frac{1}{2}} \sin \varphi_{br}'$$

$$q_2 = A_1 A_2^2 A_3 g^{\frac{1}{2}} (D_{br}^3 - D_1^3) D_{br}^{-\frac{1}{2}}$$

The factor $A_1 A_2^2 A_3 g^{\frac{1}{2}}$ varies between 2.37×10^{-2} and $3.85 \times 10^{-2} \sqrt{\text{m/sec}}$, dependent of the kind of waves (harmonic or random).

VARIABLE WAVE CONDITIONS

There has to be distinguished the influence of variable wave conditions on the coastal constants and the influence of the boundary conditions.

Influence variable wave conditions on coastal constants

The derivation used for the PELNARD-CONSIDÈRE-formula (2) keeps its validity when the littoral drift Q , the stationary transport Q_o and the constant q are averages over a year instead of instantaneous values. However, it will not be directly clear, which value has to be taken for D_{tot} . In order to estimate D_{tot} it is useful to compute first the distribution of the littoral drift perpendicular to the coast. An example of such a distribution gives fig. 15. The yearly littoral drift between two

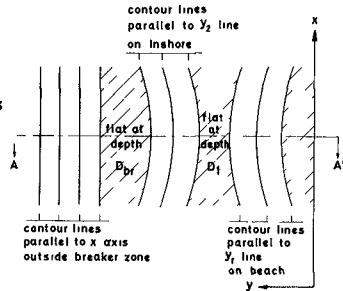


Fig 14a Upper view

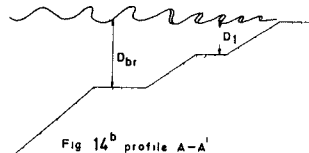
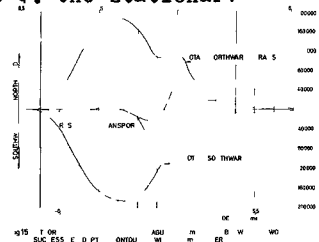


Fig 14b profile A-A'

..... (27)

..... (28)



depth contours $D - \frac{1}{2} \Delta D$ and $D + \frac{1}{2} \Delta D$ is computed with the aid of (26), which becomes in case of variable wave conditions ($\cos \varphi_b$ has been taken and Snell's law has been applied)

$$\Delta Q = 3A_1 A_2^2 A_3 g D^2 \Delta D \sum_{\substack{\text{all wave classes} \\ \text{for which } D < D_{br}}} \frac{\sin \varphi_0}{C_0} fr(H, T, \varphi) \dots (29)$$

in which $fr(H, T, \varphi)$ denotes the frequency of occurrence of a wave class for which H , T and φ lie between certain values (for instance $\frac{1}{2} m < H < 1 m$, $5 \text{ sec} < T < 6 \text{ sec}$, $30^\circ < \varphi < 60^\circ$). More details about the computation are given in [9]

From the distribution of the transport Q_{01} and Q_{02} are found (fig. 16)

$$Q_{01} = \sum_{0 < D < D_1} \overline{\Delta Q} \dots (30)$$

$$Q_{02} = \sum_{D > D_1} \overline{\Delta Q}$$

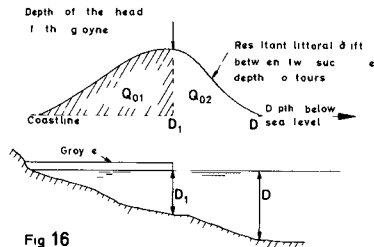


Fig 16

After that, q_1 and q_2 can be found by repeating the computation according to (29), but with a "wrong" coastal direction, which has been turned over an angle $\Delta \varphi$, say 15° . This gives the interrupted line in fig. 17, instead of the solid line, which represents the transport distribution for the original coastal direction.

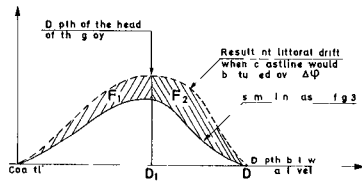


Fig 17

Now q_1 equals $F_1 / \Delta \varphi$ (F_1 is the left-handed hatched area in fig. 17) and $q_2 = F_2 / \Delta \varphi$.

From the transport distribution, also a reasonable guess about D_{tot} can be made.

Influence variable wave conditions on the boundary

This paper is concentrated on two effects of a groyne prevention of the littoral sand drift and formation of a sheltered area. We shall investigate these two effects in case of changing wave conditions.

When the wave direction changes periodically for instance according to

$$\varphi = \hat{\varphi} \sin \omega \varphi t \dots (31)$$

this generates a sandwave near a groyne (fig. 15, [10])

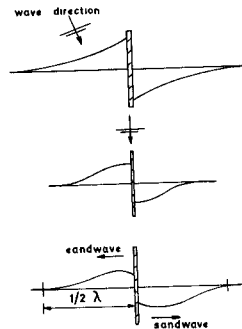


Fig 18 Generation of sandwaves by variable wave direction

$$y = \frac{\hat{\phi} \lambda_{\phi}}{2\pi\sqrt{2}} e^{-k_{\phi} x} \cos(\omega_{\phi} t - k_{\phi} x) \dots (32)$$

in which

$$\lambda_{\phi} = \frac{2\pi}{k_{\phi}} = 2\sqrt{\pi \frac{g}{D_{tot}}} T_{\phi} \dots (33)$$

T_{ϕ} being the period of the fluctuations of ϕ and λ_{ϕ} being the length of the sandwave.

Using (24) and taking $A_1 = 1.4 \times 10^{-2}$, $A_2 = 0.4$, $A_3 = \sqrt{1.4}$, this gives

$$\lambda_{\phi} = .183 D_{br}^{3/4} (g T^2)^{1/4} \dots (34)$$

Taking as an example $T_{\phi} = 1$ week, this makes $\lambda_{\phi} = 324$ m. Now the decay of this sandwave is very strong within $\frac{1}{2}\lambda_{\phi}$ it is attenuated to 4%. Thus, outside this area, no influence of the stopping of the littoral drift by the groyne will be observed. In case of the two-line theory D_{br} in (34) probably can be replaced by D_1 , $\hat{\phi}$ has to be replaced by ϕ_{01} , according to (A36) The second influence of the groyne is the wave-shelter. We shall assume first, that the sheltered area is large with respect to $\frac{1}{2}\lambda_{\phi}$. As in (12a), Q_0 and q_1 become functions of x , called Q_{01}^* and q_1^* . Consider fig. 19. The influence of diffraction will be neglected with respect to the influence of changing wave conditions.

The computation of Q_{01} and q_1 in area A can be performed according to (29), (30) and fig. 14. But applying (44) to area B, all wave classes with $\phi_0 \geq 75^\circ$ must be excluded in the summation, in area C all wave classes with $\phi_0 \geq 45^\circ$, and so on.

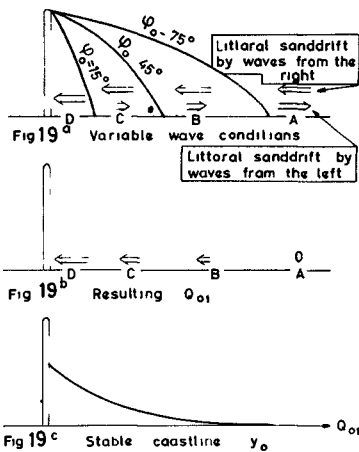
When, for instance, the resulting transport in area A would be zero for a coastline parallel to the x-axis (fig. 19a), the transport

$$Q_{01}^* \left(\frac{\partial y_1}{\partial x} = 0 \right) \text{ (started because it}$$

changes in x-direction) will be larger and larger (in negative direction) in the areas B, C and D_1 , and also q_1^* will change

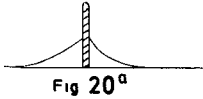
Now we have returned to the normal computer program, treated in (5) to (7) and in appendix 3, only with other values for y_0 and y' than the diffraction cases.

The stable coastline y_0 can be found from continuity for y_0 the transport is everywhere the same



$$\begin{aligned}
 [Q_{01}]_{x=\infty} &= Q_1 \rightarrow [Q_{01}]_{x=\infty} = \\
 &= Q_{01}^* - q_1^* \frac{dy_0}{dx} \rightarrow \frac{dy_0}{dx} = \frac{Q_{01}^* - [Q_{01}]_{x=\infty}}{q_1^*} \quad . \quad . \quad (35)
 \end{aligned}$$

From (35) the stable coastline y_0 can be found, which gives the initial value of the unstationary part y_1'

Fig 20^aFig 20^b

In case of changing wave conditions, and no resultant drift, the final coastal shape near one single groyne will become just the stable shape y_0 , because then everywhere the resultant drift is zero. This will give accretion on both sides of the groyne, which will be withdrawn from a very long stretch of coast (fig. 20a). In case of a row of groyne, the sand for the accretion near the groyne is withdrawn from the area in the midst between the groyne, and only near the boundary of the groyne system some real accretion can be expected (fig. 20b). However, after some time this sand will move to the areas between the groyne, and so this shelter effect may give some accretion (in case of no resultant drift), starting from the boundaries of the groyne system

In case $\frac{1}{2}\lambda\phi$ is not small with respect to the sheltered area, the best way of computation is a kind of "hindcasting", using the one-line or two-line computer program described before, and changing the wave conditions during the program. This has been done at the Coastal Research Department of Rijkswaterstaat.

N B The vertical scale of fig 5 and 6 is 5 times and of fig. 10 and 11 is 10 times exaggerated.

APPENDIX

A1. One-line theory Assumptions and formulae (diffraction)

Assumptions littoral drift proportional to the angle of wave incidence and to the square of the wave height (fig. A1)

$$Q = Ah^2 \left(\varphi_x - \frac{\partial Y}{\partial x} \right) \dots \dots \dots (A1)$$

in which A is a proportionality constant and h is the ratio between the wave height at $x = x$ and the wave height at $x = \infty$ Eq (A1) is a special case of (3)

Continuity $\frac{\partial Y}{\partial t} = - \frac{q}{D_{tot}} \frac{\partial Q}{\partial x} \dots \dots \dots (A2)$

Using (3) $\frac{\partial Y}{\partial t} = \frac{1}{D_{tot}} \left(q^* \frac{\partial^2 Y}{\partial x^2} + \frac{\partial q^*}{\partial x} \cdot \frac{\partial Y}{\partial x} \right) - \frac{1}{D_{tot}} \frac{dQ_o}{dx} \dots \dots (A3)$

The stable coastline y_o from (5) is a solution of (A2), or (A3) Continuity gives Q is constant for y_o . The amount of Q can be derived from the condition at infinity

$h = 1$, $\varphi_x = \varphi_\infty$, $\frac{\partial Y}{\partial x} = 0$, from (A1) follows (4)

$$A \varphi_\infty = Ah^2 \left(\varphi_x - \frac{dy_o}{dx} \right)$$

Eq (6) can be derived from (A3) by substituting y_o in (A3) and subtracting this equation from (A3).

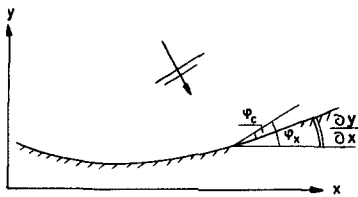


Fig A1

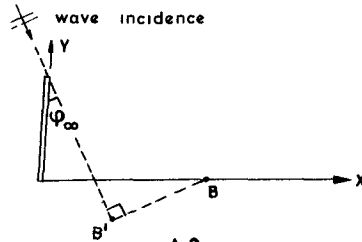


Fig A2

For the determination of the values of φ_x and h the simplified diffraction theory of PUTNAM and ARTHUR [4] is used.

It can be shown[11] that φ_x is about equal to

$$\varphi_x = \varphi_\infty - \frac{\lambda}{2\pi} \frac{d\epsilon}{dx} \dots \dots \dots (A4)$$

in which λ - wave length diffracted wave and ϵ = phase difference of the waves between B and B' (fig. A2). B = point on x-axis, for which y_o is computed.

Substitution of this result in (4) and integration gives the relation between y_0 and the basic data of diffraction h and Θ

$$y_0 = -\frac{\lambda}{2\pi}\Theta + \varphi_\infty \int \frac{h^2 - 1}{h} dx \dots (A6)$$

The first term of the right hand side of (A6) is the influence of the turning of the waves, the second term gives the influence of changing the wave height by diffraction.

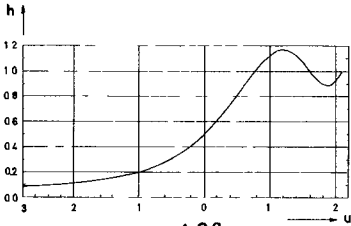


Fig A3^a

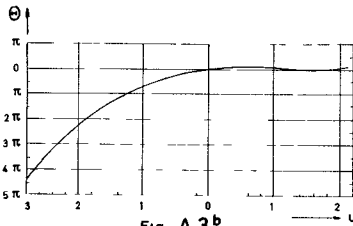


Fig A3^b

Fig A3 WAVE DIFFRACTION ACCORDING TO PUTNAM AND ARTHUR [6]

Θ and h as a function of $u = \frac{2\sqrt{AB-AB'}}{\lambda}$ according to PUTNAM AND ARTHUR [4] are shown in fig. A5.

Unstationary part y'

(6) has been taken as a difference equation, taking

$$q_{max} = Ah_{max}^2 \dots (A7)$$

$$\Delta t = D_{tot} \cdot (\Delta x)^2 / 2q_{max} \dots (A10)$$

Substituting (A7) and (A10) in (6), from three adjacent points of a curve at time t one point of the curve at point $t + \Delta t$ can be found (explicit method)

$$y' [x, t + \Delta t] = \left(\tilde{q} [x + \Delta x] / 8 + \tilde{q} [x] / 2 - \tilde{q} [x - \Delta x] / 8 \right) \cdot y' [x + \Delta x, t] + \left(-\tilde{q} [x] + 1 \right) \cdot y' [x, t] + \left(-\tilde{q} [x + \Delta x] / 8 + \tilde{q} [x] / 2 + \tilde{q} [x - \Delta x] / 8 \right) \cdot y' [x - \Delta x, t] \dots (A11)$$

in which $\tilde{q} = q^* / q_{max}$ has been introduced to avoid instability.

Boundary conditions at $x = 0$ no transport and therefore

$$\frac{\partial y}{\partial x} = \frac{dy}{dx} + \frac{\partial y'}{\partial x} = \left[\frac{\partial \varphi}{\partial x} \right]_{x=0} \dots (A12)$$

Substitution of (4) in (A12) gives

$$\frac{\partial y'}{\partial x} = \psi_x - (\psi_x - \frac{\psi_{\infty}}{h^2}) = \frac{\psi_{\infty}}{h^2} \dots \dots \dots (A13)$$

We can write this equation into differences and express $y'[-x]$ in $y'[\Delta x]$ This gives for the boundary point at the lee-side

$$y'[0, t + \Delta t] = - (-\bar{q}[\Delta x]/8 + \bar{q}[0]/2 + q[-\Delta x]/8) \cdot 2\Delta x \cdot \frac{\psi}{h^2}_{x=0} + (-q[0] + 1) \cdot y'[0, t] + \bar{q}[0] \cdot y'[\Delta x, t] \dots \dots \dots (A14)$$

The expression for the luffside can be found by changing everywhere in (A14) Δx by $-\Delta x$.

A2 Two-line theory

(14) and (15) can be derived by substitution of the dynamic equations (12_a, b) in the continuity equations

$$\left. \begin{aligned} \frac{\partial Q_1}{\partial x} + Q_y + D_1 \frac{\partial y_1}{\partial t} &= 0 \\ \frac{\partial Q_2}{\partial x} - Q_y + D_2 \frac{\partial y_2}{\partial t} &= 0 \end{aligned} \right\} \dots \dots \dots (A17)$$

We state $\Delta t = cD(\Delta x)^2/q_{1max}$ and call $q_y \cdot (\Delta x)^2/q_{1max} = q'_y$

in which c is a coefficient to get a stable numerical process. Then the following difference equations are derived

$$y'_1 [x, t + \Delta t] = c \cdot D \left\{ (\bar{q}_1 [x + \Delta x]/4 + \bar{q}_1 [x] - \bar{q}_1 [x - \Delta x]/4) \cdot y'_1 [x + \Delta x, t] + (D/CD_1 - 2q_1 [x] - q'_y) \cdot y'_1 [x, t] + (-\bar{q}_1 [x + \Delta x]/4 + q_1 [x] + q_1 [x - \Delta x]/4) \cdot y'_1 [x - \Delta x, t] - q'_y (y_0 [x] - y_2 [x, t]) \right\} \dots \dots \dots (A21)$$

$$\begin{aligned}
 & y_2 [x, t + \Delta t] - \\
 c. & \frac{\Gamma}{D_2} \left\{ (J_2 [y + \Delta x, t] + J_2 [y - \Delta x, t]) \cdot q_2 / q_{1\max} + \right. \\
 & \quad \left. + (D_2 / cD - 2q_2 / q_{1\max} - q'_y) y_2 [x, t] + \right. \\
 & \quad \left. q'_y (y'_1 [x, t] + y_0 [x]) \right\} \dots \dots \dots (A22)
 \end{aligned}$$

The boundary conditions for y' , can be found by substituting $x = 0$ and (lee-side)

$$y'_1 [-\Delta x] = y'_1 [\Delta x] \quad \Delta x \cdot \frac{\Phi_\infty}{[h^2]_{y=0}} \dots \dots \dots (A23)$$

A3. Coastal constants according to the adapted SVASEK-theory
 SVASEK assumes, that the littoral drift between two depth contours is proportional to the longshore component of the loss of energy between these contour lines ((25))

We assume that in the breaker zone $\cos y = \cos \varphi$ for ' and we neglect the influence of the refraction factor K inside the breaker zone

$$Q = A'_1 \cdot \Delta (H^2 C) \sin \varphi \cos \varphi \dots \dots \dots (A25)$$

We assume, that the relations between H and D and between C and D according to (21) and (22) on the boundary of the breaker zone remain their validity inside the breakerzone (spilling breaker)

$$H = A_2 D \dots \dots (A26)$$

$$C = A_3 g D \dots \dots (A27)$$

Thus the difference in $H^2 C$ between two adjacent depth contours equals

$$\Delta (H^2 C) = \frac{d}{dD} (A_2^2 A_3 g^{\frac{1}{2}} D^{2\frac{1}{2}}) \Delta D = \frac{5}{2} A_2^2 A_3 g^{\frac{1}{2}} D^{1\frac{1}{2}} \Delta D \dots \dots (A28)$$

Now first the stationary transport Q_0 will be computed, according to SVASEK's theory. In this case all contour lines are parallel and Snell's law is valid

$$\frac{\sin \Phi}{\sin \Phi_{br}} = \frac{C}{C_{br}} = \sqrt{\frac{D}{D_{br}}} \dots \dots \dots (A29)$$

Substitution of (28) and (29) in (25) gives ΔQ , expressed in D

$$\Delta Q = \frac{5}{2} A_1 A_2^2 A_3 g D^2 D_{br}^{-\frac{1}{2}} \Delta D \sin \Phi_{br} \cos \Phi_{br} \dots \dots (A30)$$

We find the total transport by integration over the depth. Again we assume $\cos \Psi = \cos \Phi$.

$$Q_0 = \int_0^{D_{br}} \Delta Q dD = \frac{5}{6} A_1 A_2^2 A_3 g^{\frac{1}{2}} D_{br}^{2\frac{1}{2}} \sin \Phi_{br} \cos \Phi_{br} \dots (A31)$$

Comparison of (A31) and (23) leads to the conclusion, that for parallel depth contours the relation should exist

$$A_1' = \frac{6}{5} A_1 \dots \dots \dots (A32)$$

The reason is, that SVASEK multiplies the component of the wave energy with $\sin \Phi$ instead of $\sin \Phi_{br}$ and in the breakerzone $\sin \Phi$ is less than $\sin \Phi_{br}$. Thus the transport between two depth contours will be, in general, using (A25) (A29) and (A32)

$$\Delta Q = 3 A_1 A_2^2 A_3 g^{\frac{1}{2}} D^{\frac{1}{2}} D \sin \Phi_m \cos \Phi_m \dots \dots (A33)$$

In 12 has been considered in detail how the littoral drift changes when the beach and inshore direction change in case of the topography at fig. A5 (cf fig. 14).

Using SVASEK's assumptions and a proper use of Snell's law, for the littoral drift along the inshore is found

$$Q_2 = A_1 A_2^2 A_3 g^{\frac{1}{2}} (D_{br}^3 - D_1^3) D_{br}^{-\frac{1}{2}} \sin \Phi_{br} \cos \Phi_{br} \dots \dots (A34)$$

and for the transport along the beach

$$Q_1 = A_1 A_2^2 A_3 g^{\frac{1}{2}} D_1^{2\frac{1}{2}} \sin \Phi_{10} \cos \Phi_{10} - \frac{\partial y_1}{\partial x} \cos 2\Phi_{10} + \frac{\partial y_2}{\partial x} (1 - \frac{1}{2} \sin 2\Phi_{10} \cos \Phi_{br}) \frac{\cos^2 2\Phi_{10}}{\cos^2 \Phi_{10}} (A35)$$

in which Φ_{10} is the angle of incidence of the wave on the beach (fig. A5), which occurs, when the inshore is parallel with the x-axis

$$\Phi_{10} = \arcsin \left(\sqrt{\frac{D_1}{D_{br}}} \sin \Phi_{br}' \right) \dots \dots \dots (A36)$$

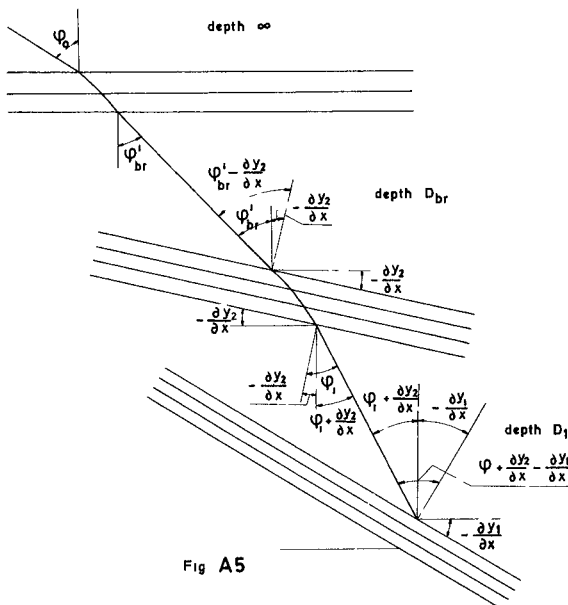


Fig A5

in which Φ_{br}^1 is the breaker angle, if the inshore would be parallel to the x-axis.

For small angle of wave incidence, (A35) can be written

$$Q_1 = A_1 A_2^2 A_3 g^{\frac{1}{2}} D^{2\frac{1}{2}} \left[\sin \Phi_{10} - \frac{\partial y_1}{\partial x} + \frac{\partial y_2}{\partial x} \left(1 - \sqrt{\frac{D_1}{D_{br}}} \right) \right] \quad (A37)$$

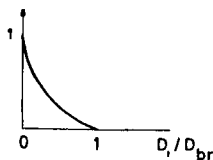


Fig A6

Influence direction inshore
Influence direction beach
versus D_1/D_{br}

($1 - \sqrt{D_1/D_{br}}$) times the influence of the direction of the beach. This function is shown in fig. A6.

The formulae for q_1 and q_2 can be derived by differentiation of (A34) and (A35) to $\frac{\partial y_1}{\partial x}$ and $\frac{\partial y_2}{\partial x}$ respectively. For Φ_{br} equals

$$\Phi_{br} = \Phi_{br}^1 - \frac{\partial y_2}{\partial x}$$

Thus the derivative to $\frac{\partial y_2}{\partial x}$ is minus $d\Phi_{br}$

The influence of the inshore on the beach has been neglected.

REFERENCES

1. W.T. Bakker The dynamics of a coast with a groyne system
C.E.C. XI, London 1968, ch. 31.
2. E.W. Bijker and J.N. Svasek Two methods for determination of morphological changes by coastal structures.
XXIInd. Int. Nav. Congress, Sect. II, subj. 4, pp 181-202.
3. R. Pelnard-Considère Essai de théorie de l'évolution des formes de révages enplages de sable et de galets. IVme Jaunnées de l'Hydraulique Paris 13-15 Juin 1954.
4. J.R. Putnam and R S. Arthur Diffraction of Water Waves by Bredewaters
Trans. A.G.U. Vol. 29, 4, Aug. 1948.
5. E.W. Bijker Littoral drift as function of waves and current. Publ. 58 Delft Hydr. Lab.
6. A.J. Bowen The generation of long shore currents on a plane beach J. Mar. Res. Vol. 27, May '69
7. J. Mac. Cowan On the highest wave of permanent type.
Phil. Mag. (V) Vol. 38 pp. 351-357.
8. W.T. Bakker The influence of dune height on dune erosion.
Rijkswaterstaat, Dept. for Coastal Res.
9. W.T. Bakker Computation of littoral drift with the Svasek-method. Rijkswaterstaat, Dept. for Coastal Res. Rep. W.W.K. 69-7.
10. W.T. Bakker The Coastal Dynamics of Sandwaves and the Influence of Brakewaters and Groynes.
Rijkswaterstaat, Dept. for Coastal Res.
11. W.T. Bakker The influence of diffraction near a harbour mole on the coastal shape
Rijkswaterstaat, Dept. for Coastal Res. Rep. W.W K 70-2.
12. W.T. Bakker The relation between wave climate and coastal constants Rijkswaterstaat, Dept. for Coastal Res. (yet unpublished).

CHAPTER 65

EXPERIMENTAL STUDY OF THE HYDRAULIC BEHAVIOUR OF INCLINED GROUYNE SYSTEMS

Júlio Patriarca Barceló

Research Officer Department of Hydraulics
Laboratório Nacional de Engenharia Civil Lisboa Portugal

SYNOPSIS

This paper presents the results of an experimental study on the behaviour of inclined groynes and a short discussion on the optimization of groyne systems. It supplements a paper presented at the XI Coastal Engineering Conference (London, 1968). In the present paper both studies are applied to the design of a groyne system located to the south of the Tagus estuary (near Lisbon), where a serious erosion has been under way.

1 - INTRODUCTION

Groynes are one of the most applied coast protection structures because, owing to their transverse position, they detain long shore drift, which is the main cause of serious coastal erosion phenomena (see fig 1). Groynes have practically no influence on transport normal to the coast but this, in addition to being usually small, tends to balance in the annual wave cycle. Groynes can be used to stop longshore drift, which may cause undesirable depositions in certain zones (case of beaches in dynamic equilibrium), or to protect beaches where the supply of material is exceeded by the losses. In any case, a single groyne or a group of groynes can be used, the latter - called a groyne system - being particularly important owing to applications in long sand shores.

The hydraulic optimization of groyne systems (structural questions, although influenced by the hydraulic behaviour, belong to the stability of maritime structures) is extremely important because groynes must obey economic requirements and simultaneously must provide beach stretches satisfactory for recreational purposes,



Fig. 1 - Erosion in Caparica beach, January 1970



Fig. 2 - Groyne system tested in the 1st stage of the study

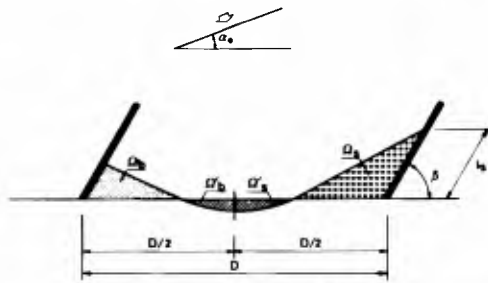


Fig. 3 - Schematic drawing of the testing setup



Fig. 4 - View of a test ($\beta = 50^\circ$; $\alpha_0 = 20^\circ$)

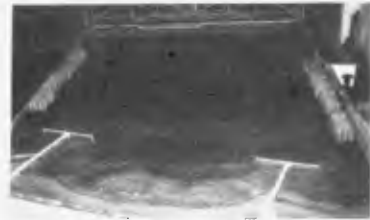


Fig. 5 - Test of T-groynes ($\alpha_0 = 20^\circ$)

which, together with coast protection, is their main object. This leads to the use of long very spaced groynes, which in addition to affording a satisfactory protection against wave erosion and providing wide beach stretches satisfactory for recreational purposes, improves the landscape of these. A groyne system is functional when it meets these requirements.

A paper was presented at the XI Coastal Engineering Conference (London, 1968) describing an experimental study of the hydraulic behaviour of systems of groynes normal to the bathymetric curves [1] (see fig 2). This study is now complemented by the present study on inclined groynes, which also contains some consideration on the optimization of groyne systems based on the results of both studies, and an instance of application to a serious case of erosion in the Portuguese coast (Caparica and Cova do Vapor beaches).

2 - EXPERIMENTAL TECHNIQUE

The tests were carried out in a tank (with a net area of about 8 m x 18 m), fitted with a translation wave machine. The plain sine waves generated had periods from 1.0 to 1.3 s, heights between 3.00 cm and 5.50 cm and obliquities of 20° , 10° and 5° (α_0 - obliquity of the breaking wave - see fig 3). The mobile material used was pumice stone with a unit weight of 1.46 gf/cm^3 and a median diameter of about 1.5 mm. The tests began with a beach with a transverse slope of $i = 8\%$. The still water level remained constant, i.e. tides were not reproduced. Fixed, high, and impermeable groynes were tested and the beach stretches between them can be considered as independent physiographic units.

The testing setup was as extensive as possible so that the evolution of beach stretches between groynes could be studied in detail (see figs 4 and 5). The interference of the tank borders with the transport of sediments was taken into consideration but it was only in one test of very inclined groynes that it was neces

sary to reproduce the area near the downdrift groyne with a fixed bed and to remove mobile material beyond this groyne. The curve of fig 6, plotted from the quantities removed, represents drift at

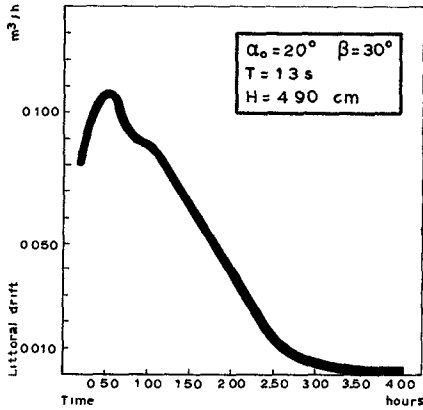


Fig 6

the end of the groyne versus the duration of the test. It should be noted that the conclusions drawn are not invalidated by the absence of updrift feed, which corresponds to the most adverse conditions in the extreme updrift groyne.

The inclinations considered were those affording the best protection to groyne roots, inclinations symmetrical of these were not tested as they obviously are of no practical interest. The study was completed with tests of T-groynes for comparison with the former results.

The measurement and bottom surveying methods used were those described in [1]. Fresh water was used and the flow can be considered as turbulent. Systematic tests to no particular scale were also carried out as the testing setup represents no specific case.

3 - EXPERIMENTAL RESULTS

On the whole inclined groynes (see fig 3) operate roughly as normal groynes ($\beta = 90^\circ$), i.e. beaches initially with a uniform transverse slope of 8% reach final equilibrium conditions essentially depending on the characteristics of the wave for each value of β . The characteristic parameters of the operation of groynes are those indicated in [1], but the following are particularly relevant in the present study: accretion areas Ω_s and Ω_b , total accretion area $\Omega = \Omega_s + \Omega_b$, evolution l_s of the beach near the downdrift groyne, spacing D between groynes, length c of the groynes, and value

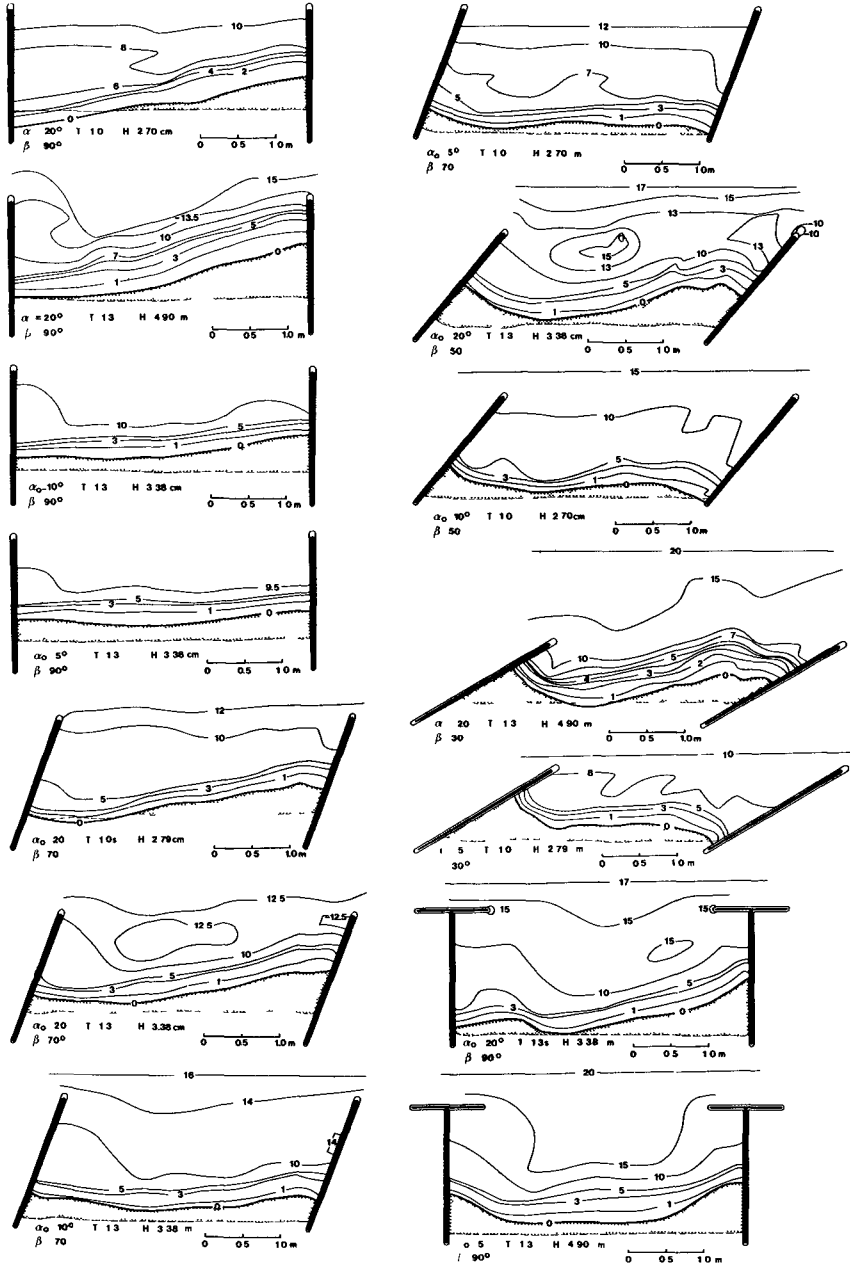


Fig 7 - Typical plans of final equilibrium conditions of the tested cases

$H_0^2 C_0$ proportional to the transmitted wave power (H_0 and C_0 are the wave height and the wave speed in infinite depth, respectively)

Detail characteristics of the evolution of beach stretches will be taken into consideration and the efficiency of inclined groynes will be defined in function of these characteristics

The detail characteristics of the evolution of beach stretches are presented in fig 7, which shows the final equilibrium condition for the different typical cases studied, the dotted line represents initial conditions in the beach for a zero water level, the indicated value of the wave height, H , concerns the depth where the wave generator is placed. Groynes with $\beta = 90^\circ$ may cause erosions near the updrift groynes for the maximum obliquities tested, whereas accretions extend throughout the width of the beach stretch for lower obliquities, in which transverse movements predominate. For $\beta = 70^\circ$ the overall behaviour of the groyne system is not changed, but erosion hazards near the updrift groyne decrease, and for obliquities of $\alpha_0 = 20^\circ$ there is even deposition throughout the beach stretch, owing to the shelter afforded by the updrift groyne, for smaller obliquities, the beach retreats near the downdrift groyne and the area Ω_s decreases. For $\beta = 50^\circ$ the increase in the accretion area Ω_b and in the protection afforded by the root of the updrift groyne grow more marked. For smaller obliquities regression increases near the downdrift groyne and the areas Ω_s decrease. For $\beta = 30^\circ$ the beach stretch can hardly be considered as a physiographic unit for large obliquities, for smaller obliquities considerable erosions occur in the root of the downdrift groyne and the areas Ω_s are appreciably reduced. T-groynes operate roughly as normal groynes but the protection afforded to the groyne roots is present in all cases and the symmetry of areas Ω_b and Ω_s is more marked.

The two most relevant parameters for the definition of the efficiency of groynes (accretion areas and evolution of the beach near the downdrift groyne) are defined in fig 8, which represents

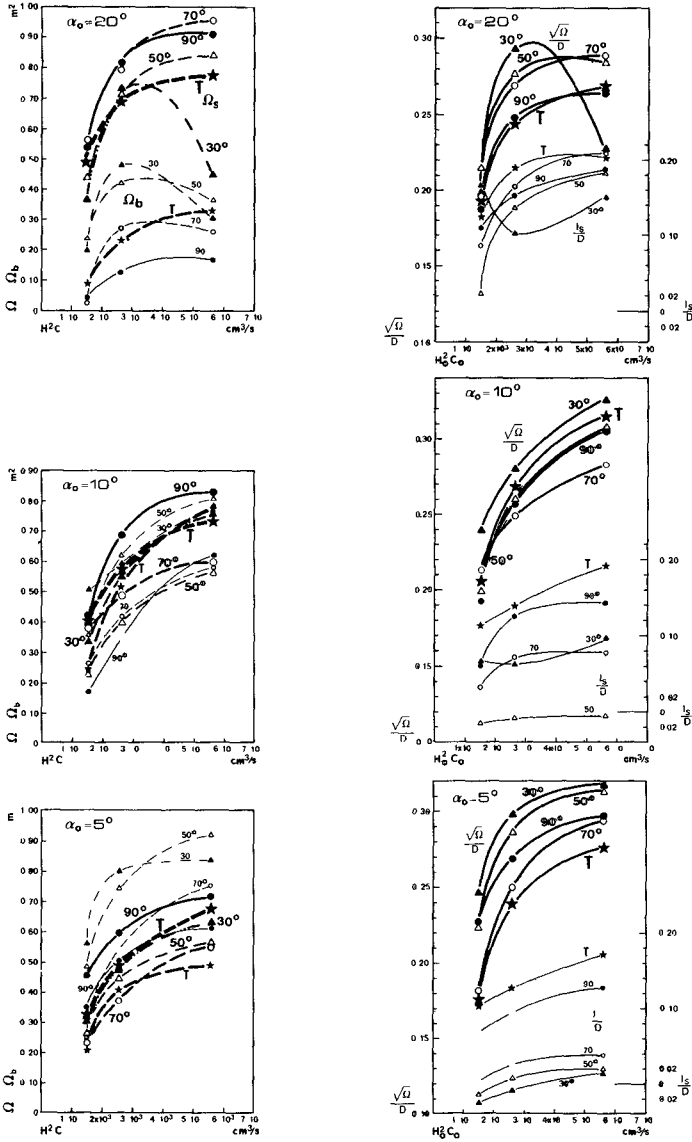


Fig 8 - Curves of the parameter defining the efficiency of groynes in function of the transmitted wave power

the curves of Ω_s and Ω_b (thick and thin lines respectively) with dimensions which give an idea of the values observed in the model tests, and the curves of $\sqrt{\Omega}/D$ together with those of l_s/D (dimensionless values suitable for practical applications) The figure also presents the curves of these parameters in function of the value $H_o^2 C_o$ proportional to the transmitted wave power for each obliquity α_o of the breaking wave It is from these dimensionless values that the efficiency of the groyne types tested will be defined For $\alpha_o = 20^\circ$ the maximum efficiency corresponds to $\beta = 70^\circ$, if the increase not only of $\sqrt{\Omega}/D$ but also of l_s/D is taken into account For $\alpha_o = 10^\circ$ the groynes with $\beta = 90^\circ$ are the most efficient taking into account the fact that l_s/D is larger for $\beta = 90^\circ$ although the values of $\sqrt{\Omega}/D$ are higher for $\beta = 30^\circ$ For $\alpha_o = 5^\circ$, groynes with $\beta < 90^\circ$ yield values of l_s/D which are very low or correspond to erosions, so that the maximum efficiency is obtained for $\beta = 90^\circ$ T-groynes are not more efficient than normal groynes ($\beta = 90^\circ$), their only advantage being the absence of erosions in the groyne roots

The efficiency of the different groyne types was defined for the maximum transmitted wave power

These results agree with Prof Nagai's {2}, as regards both the inclinations of the groynes and the values of the ratio c/D

4 - PRACTICAL APPLICATION

Portuguese beaches are extremely valuable assets for our economy due to their variety and remarkable natural conditions, so that they must be improved, and protected against the serious phenomena of erosion which endanger them

One of the most serious erosion phenomena in the Portuguese coast occurred in the beaches of Cova do Vapor and Caparica, a long sand expansion south of the Tagus estuary near Lisbon From the situation presented in fig 9, which prevailed in 1929, erosion begun due to the collapse of the natural protection afforded by the sand formation north of the beaches, which ends at the

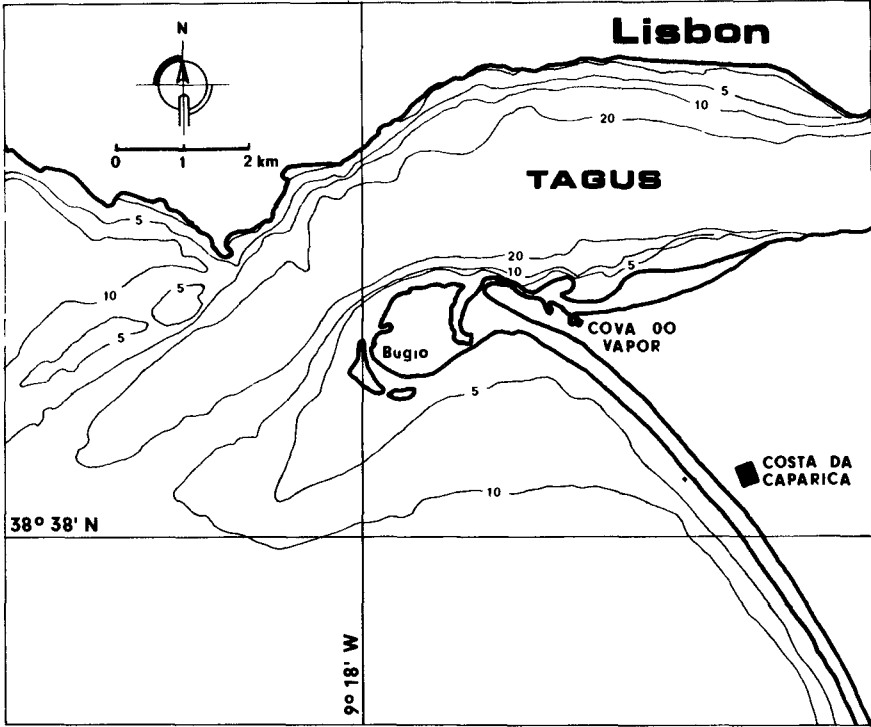


Fig 9 - Caparica and Cova do Vapor beaches (1929)

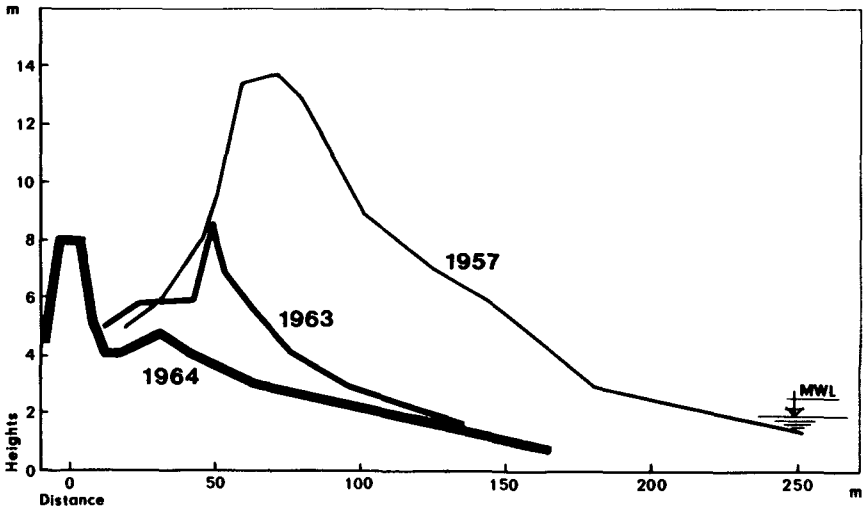


Fig 10 - Evolution of transverse profiles in Caparica (transverse profile in the dike root)

zone of the Bugio lighthouse. The very oblique approach of the waves caused northward sand movements from the central zone of Caparica beach, where the obliquity of the wave action was very reduced or even normal to the coast so that the beach south of Caparica was very stable.

When the natural protection to the north collapsed an intense longshore drift began that formed a spit in the root of the existing formation, this spit was fed in part by the sands carried northward, the remainder being deposited in the channel of the Tagus estuary, the great depth of which avoided serious disturbances. This phenomenon began to affect Caparica practically in 1960 in the form of the erosion mechanism illustrated in fig 10. The first emergency measures, taken in 1959, consisted in the construction of a groyne (see fig 11, E3) and were followed by a frontal protection structure and groynes E_1 (1962) and E_2 (1963) at Cova do Vapor. When the waves cut the sand dunes between Cova do Vapor and Caparica a dike with a light structure was built (1959) to protect the urban areas in the neighbourhood, located below the mean level of the sea, against the runup of spring tide waves.

The situation grew worse after 1964 when serious destructions occurred in the central zone of Caparica, so that the dike was strengthened and a frontal protection core was built at its root, together with a short groyne, which, of course, proved entirely useless. Obviously the influence zone of the groyne built at Cova do Vapor was too small to protect the southern beach and the other protection works in the same site merely helped to form a resisting core that prevented the entire destruction of the zone and of the small village in it. Other emergency measures were taken after 1964, so that the situation evolved to the state presented in fig 12 (a comparison of which with fig 11 shows the evolution in 1963-1969) after the groyne E_2 was extended and the beach between Cova do Vapor and Caparica was entirely eroded except for a small zone protected by the first groyne built, the northern spit moved under the influence of the waves up to the NATO jetty

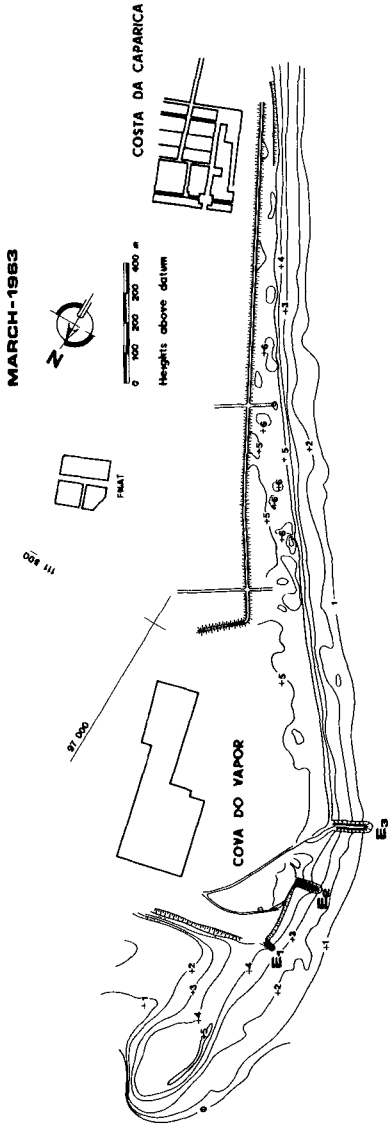


Fig 11 - Plans of Cova do Vapor and Caparica beaches (March 1963)

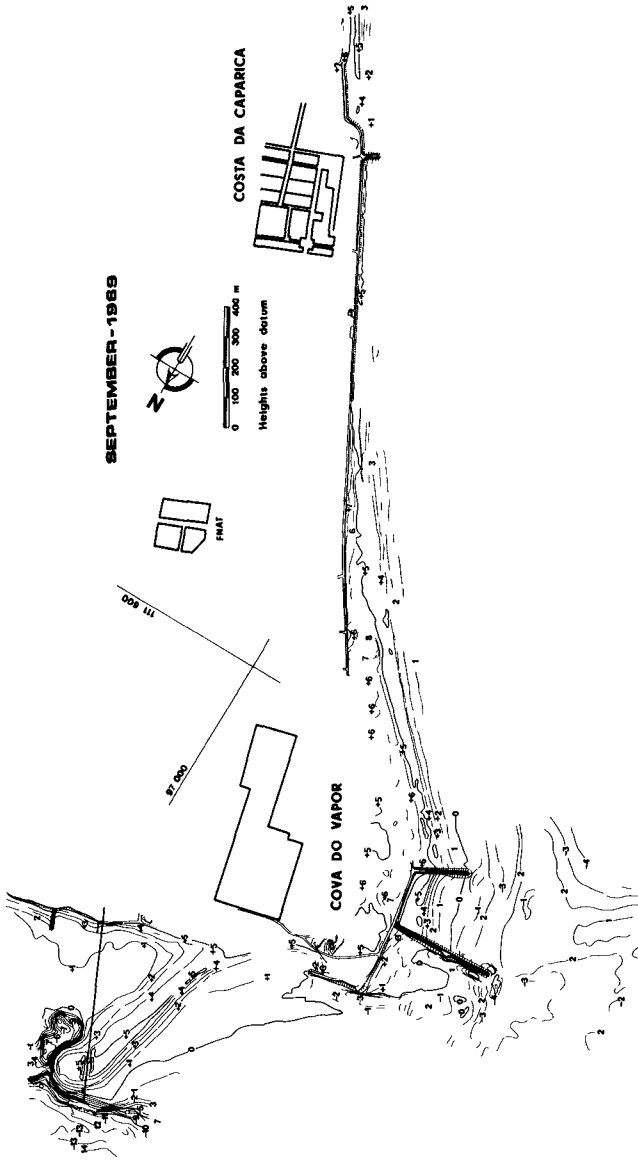


Fig 12 - Plans of Cova do Vapor and Caparica beaches (September, 1969)

also shown in fig 12 According to the studies carried out {3} the littoral drift in this zone is estimated in $1\ 000\ 000\ m^3/year$ At the same time, owing to changes in the sea-bottom relief and their influence on the wave action, a rapid erosion started in the central zone of Caparica particularly serious in the beaches to the south (see fig 1) Another emergency structure for frontal protection was built and subsequently strengthened in the central zone of Caparica

The main physiographic characteristics of the beaches of Covado Vapor and Caparica have been very rapidly presented Many comprehensive studies of this case were carried out by official and private bodies charged with and interested in the development and exploration of marine zones Owing to insufficient means, deficient policies of beach protection and development, and uncoordinated activities of the different official and private bodies involved emergency structures — some of which entirely unsuited — were resorted to, but did not prevent the loss of one of the best Portuguese beaches

Figures 13 and 14 give an idea of conditions in Caparica beach before the erosion begun and now (July 1970) The groyne E_2 (fig 11 and 12) is now being extended, and the construction of a groyne system and the strengthening and extension of the frontal protection structure {4} are in preparation The groyne system is made up of units which, although very long, have a reduced effective length and a small spacing and are located at very high elevations With such a system, the restoration of the beach is out of question, as the existing groynes to the north cannot operate efficiently for lack of supply from the south due to the disappearance of the beach On the other hand the southern stretch of the beach will tend to be eroded away up to the extended frontal protection structure, which will have to be exaggeratedly strengthened These measures, planned a long time ago for hydrographic conditions no longer prevailing, are unsuited to the present needs and will never



Fig. 13 - Caparica beach before erosion begun



Fig. 14 - Caparica beach in July 1970 (low water level)



Fig. 15 - Scheveningen beach (The Hague, Netherlands)

provide a beach with real recreational and touristic interest. As an instance of a system of functional groynes, the one built at Scheveningen beach (The Hague, Holland) is presented, the construction was very expensive owing to the extraordinary structural perfection of the groynes, but the results were excellent (see fig 15)

The restoration and protection of these beaches requires an artificial feeding and a system of functional groynes, i.e. long very spaced groynes. The artificial feeding would restore e.g. 1963 conditions, as shown in fig 16. The northern spit is represented in the figure, because studies on the touristic development of Cova do Vapor carried out in 1966 for the TECHINT project [3], recommended the construction of a long groyne in the northern end and the creation of an extensive beach mainly at the cost of sand dredged from the spit, in which a pleasure boat port (represented by the dotted line in the figure 16) would also be built. The solution recommended here for the present conditions would require the straightening and protection of the bank, upstream of the root of groyne E_0 , the artificial restoration of the beach being necessary to the south of E_2 alone. This location of groyne E_0 is preferable to the one shown in fig 12, which would leave two groynes very near one another disturbing the operation of groyne E_0 .

By means of the plan presented in fig 16 it would be possible not only to recover the beaches and protect the coast to the south of Caparica but also to avoid the extension and strengthening of the frontal protection structure. Obviously a more detailed study of this plan (which is no more than a typical solution), could yield a better and more economical solution. A single very long groyne to restore the natural connexion with Bugio together with a large volume of sand to restore the beach (a natural restoration being impossible owing to lack of supply and the irreversibility of erosion) would leave a long stretch of beach without protection making possible local erosions, so that the solution presented is preferable.

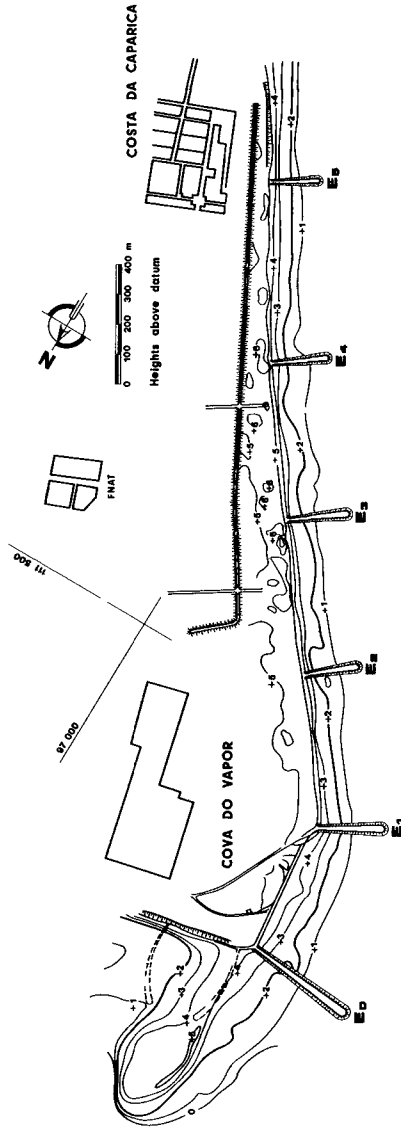


Fig 16 - Groyne field drawn on the March 1963 survey (Cova do Vapor and Caparica beaches)

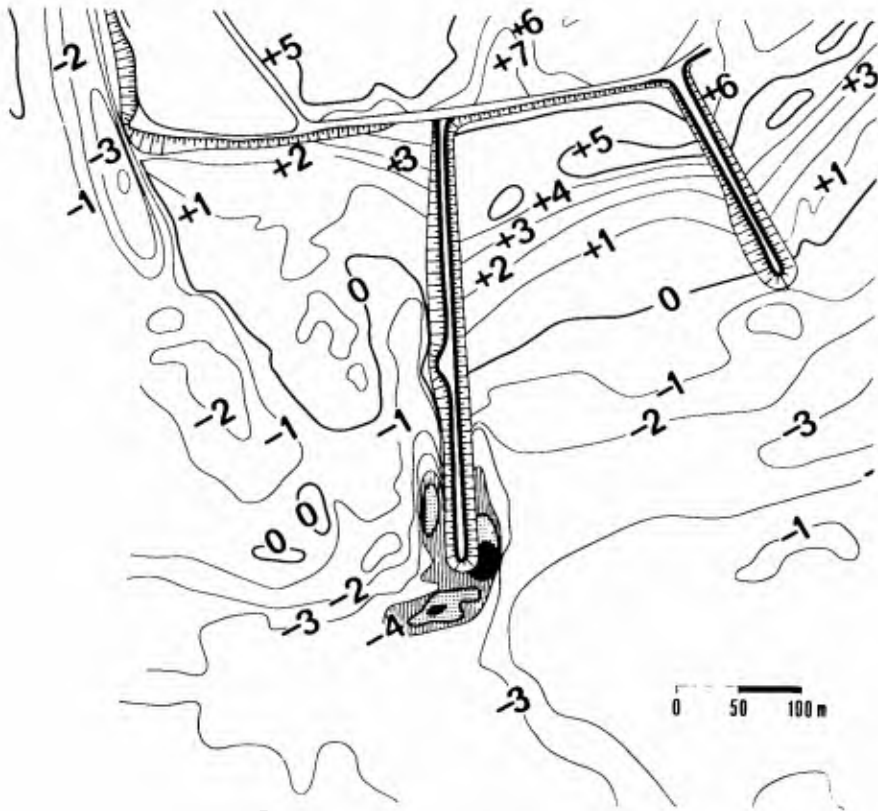


Fig. 17 - Plan of the groyne in Cova do Vapor (September 1969)



Fig. 18 - Detail of the construction of groyne in Cova do Vapor



Fig. 19 - Erosion at the ends of the groyne obtained in the models

The typical solution presented for the groyne system takes into account the two studies carried out. As wave conditions are variable, groynes with $\beta = 90^\circ$ were chosen. The obliquities α_o considered are 10° in the zone from Cova do Vapor to the middle of the dike, and 5° from this point to the central zone of Caparica. The reference line for calculating the length of the groynes will be the bathymetric curve +2.00 m. For $\alpha_o = 10^\circ$, $c/D = 3.5$ and for $c = 150$ m, $D = 520$ m (groynes E_1 to E_4), for $\alpha_o = 5^\circ$, $c/D = 4.0$, which for $c = 150$ m yields $D = 600$ m (E_5). Groyne E_5 may be shorter ($c = 100$ m, above +2.00 m) because the zone updrift of this groyne would be stable and obliquities are very small, an inversion to the south being even possible with small obliquities.

It should also be noted that an efficient system does not depend on the location of the groynes alone. Their structure and certain constructional details are also essential. As an instance, the case of groyne E_2 (fig 11 and 12) is presented. Excavations shown in the fig 17, occurred at its end, in concentric zones at depths -4, -5, -6, the darker zones corresponding to the last depth. These peculiarities seriously interfered with the construction of the groynes and caused an exaggerated use of rockfill. An adequate base of the groynes protecting the adjacent sea floor against erosion is essential but, as shown in fig 18, these groynes lack such a special base. As can be seen in fig 19 erosions at the end of the groynes occur even in the model tests, those shown having been observed in tests carried out in the first stage of these studies.

5 - CONCLUSIONS

- The angle of the groynes with the shore line is a function of the obliquity α_o of the waves. For high obliquities ($\alpha_o = 20^\circ$) the maximum efficiency corresponds to inclined groynes with $\beta = 70^\circ$. For intermediate ($\alpha_o = 10^\circ$) and low ($\alpha_o = 5^\circ$) obliquities, normal ($\beta = 90^\circ$) groynes are preferable to inclined groynes.

In variable wave conditions efficiency will be defined in function

tion of the range of obliquities of the waves present. In this case normal groynes ($\beta = 90^\circ$) are recommended.

It should not be forgotten that inclined groynes are longer (increased c) for the same spacing D . For $\alpha_0 = 20^\circ$, groynes with $\beta = 70^\circ$ are 30% longer than normal groynes ($\beta = 90^\circ$), whereas the increase in the area Ω of the inclined groyne is 20% only. The fact that groynes with $\beta = 70^\circ$ protect the root of the updrift groyne against erosion should be taken into account.

— T-groynes are not more efficient than normal groynes, except for $\alpha_0 = 10^\circ$, and even then the difference is small (see fig 8). Their only advantage lies in preventing erosion near the roots of the groynes. Nevertheless they are not recommended because, in addition to their construction being more expensive, they disturb the utilization of the beaches for sea baths.

— The hydraulic optimization of groyne systems must take into account not only the ratio c/D , the values of which were defined in {1}, but also the inclination of the groynes according to the criteria presented above. A judicious application of these results must obviously be based on a knowledge as complete as possible of physiographic conditions in the involved zone, and other questions must also be taken into account such as the stability and the crest elevation of the groynes (the latter basically depends on the transverse profile of the beach and its evolution).

Another basic point to be borne in mind when designing systems of functional groynes and which may help to reduce the volume of the structure is that its object is not, as a rule, entirely to stop the littoral drift occurring in zones of the beach variable under the action of tides, but to preserve a certain area of the beach. On the other hand littoral drift is more marked for high tide levels, precisely the conditions in which groynes operate most efficiently. This leads to adopting groynes, which although long, do not extend to very low levels.

— The cooperation of the different official and private bodies interested in the exploration of marine zones seems extremely important. Protecting structures should be thoroughly studied and designed, and constructed without delay, emergency or experimental structures are strongly disapproved, all the more so as the present knowledge in this field makes them entirely unnecessary.

— In the case of Cova do Vapor and Caparica, the essential solution for the restoration and improvement of the beaches is their artificial feeding and a functional compartmentation of the beaches by means of a system of groynes.

LITERATURE

- {1} - BARCELÓ, J P - Experimental Study of the Hydraulic Behaviour of Groyne Systems *Memória nº 350 do Laboratório Nacional de Engenharia Civil Lisboa 1969*
- {2} - NAGAI, S , KUBO, H - Motion of sand particles between groins *Journal of the Waterways and Harbors Division. ASCE, vol 84, No WW5 December 1958 Part 1*
- {3} - TECHINT - *Estudo do aproveitamento turístico da área da Cova do Vapor Lisboa Outubro 1966*
- {4} - DIRECÇÃO DOS SERVIÇOS MARÍTIMOS (MOP-DGSH)- *Projecto de defesa e valorização turística das praias a sul da embocadura do Tejo Lisboa Junho 1966*

CHAPTER 66

LAND RECLAMATION AND GROIN-BUILDING IN THE TIDAL FLATS

by

Heie Focken Erchinger *)

COASTAL PROTECTION BY RECLAIMING LAND

Along the North Sea coast of Germany there are two large areas where land reclamation work in the tidal flats is being carried out. One is on the coast of Schleswig-Holstein and the other in Ostfriesland, on the coast and along the estuary of the river Ems near the border with the Netherlands. Conditions and working methods for land reclamation in tidal flats as well as the development of new groin constructions on the Ostfriesian coast are described below.

Before the middle of this century, land reclamation was done mainly for reclaiming new fertile soil for agricultural purposes on the tidal flats. Nowadays, the aim of reclaiming land is for coastal protection, for the reclaimed foreland has many favourable effects on the dikes:

*) Oberbaurat, Chief of the Coastal Protection Department
in Lower Saxony, 298 Norden/Ostfriesland, West Germany

1. The run-up of waves on the dike is reduced as the waves break on the foreland with spilling breakers (FÜHRBÖTER 1966) and are thus prevented from reaching the slope of the dike with all their vehemence. During the storm surge on Febr. 16th, 1962 for instance, this was observed distinctly as to be seen in figure 1.
2. Wave-wash on the slope of the dike becomes considerably smaller.
3. The land before the dike, in the case of a dike failure in a storm surge, also prevents a failure of the base from taking place so that even at mean high water level the sea cannot enter the land.
4. An expensive rubble slope for the protection of the dike is not necessary.
5. For the upkeep of the grass and clay covered dike, it is important to find sods and clay near the dike on the reclaimed land.

For coastal protection a 200 m wide strip of land in front of the dikes is needed. This was found in research works carried out by Prof. Hensen, Technical University, Hannover.

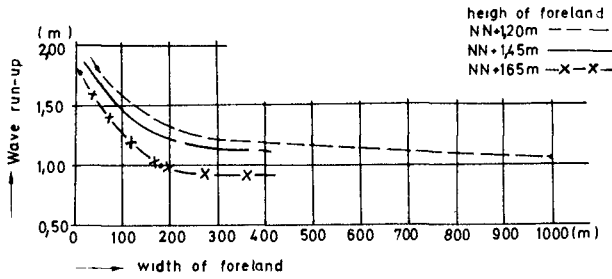
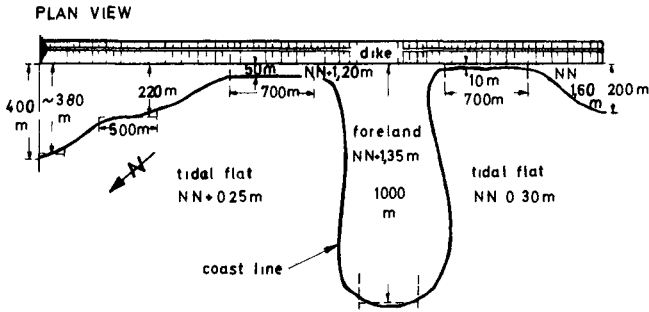
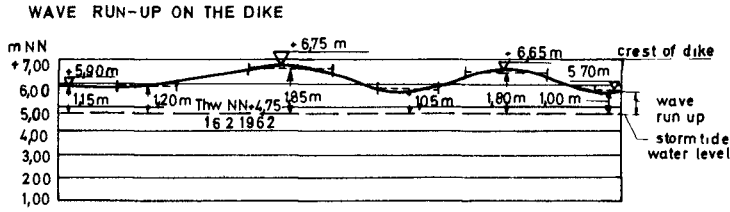


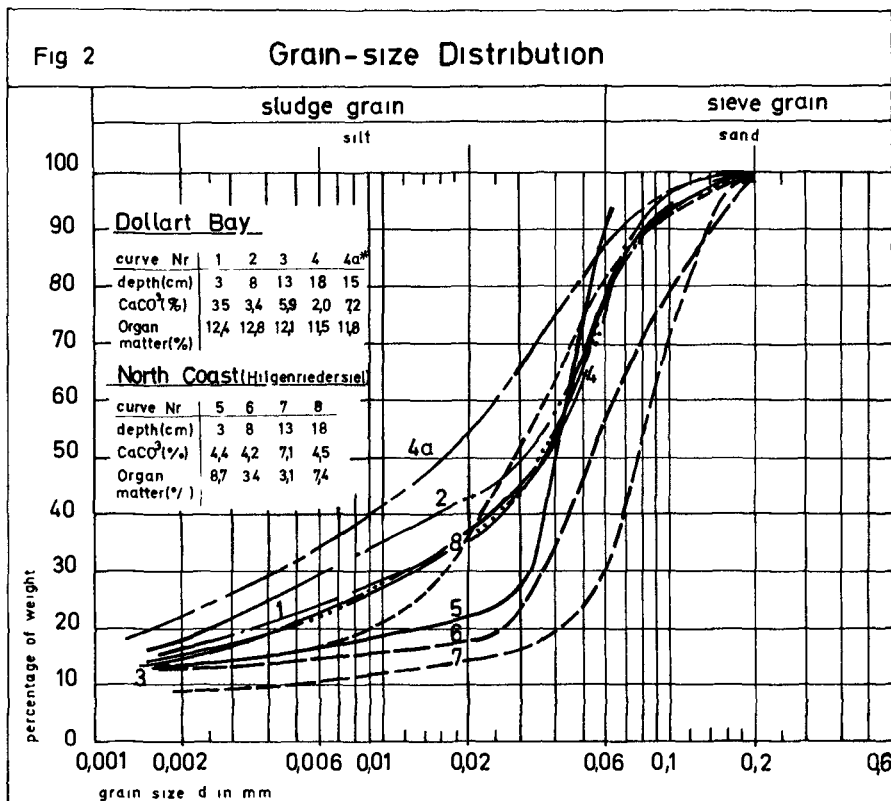
Fig 1 Relation between wave run up and width and height of the foreland (KRAMER, LIESE LUDERS 1962)

CONDITIONS AND WORKING METHODS FOR LAND RECLAMATION

For reclaiming new land, rectangular sedimentation fields, measuring about 100 by 200 m, are constructed of groins. Hence, the fields are saved from strong currents and wave movements so that the sedimentation of sand and silt can be allowed to take place unhindered. Through the inlet in the groin on the sea-side, called "cross groin", the water can enter and leave the field quickly. During the calm period, the settling and a part of the suspended solids precipitate on the soil.

It is of interest to know something about the origin of the solids which could be classified as Sand, Clay Minerals, Organic Matter and Calcium Carbonate. The composition of the sediment varies considerably along the Ostfriesian coast. Near the brackish water region of the river Ems and the Dollart Bay the clay mineral and organic material contents are relatively high. Along the North coast the sediment contains more sandy material (Figure 2).

The rate of sedimentation and the composition of the sediment depends also on the work of the molluscs, which prepare the fine organic material and clay minerals by building small lumps of silt (KAMPS, 1962). The gills, which are used by these creatures for breathing, also



*Sample 4a from the sedimentation field, all the other samples from grass covered foreland

serve the purpose for the collection of food, which they sieve out from water. In this process, sand and mud components, which are of no value to the creature are collected and covered with slime, out of which the coarse material, which in this case would be sand and some or-

ganic matters is ejected at the inlet, while the fine material, including the mud, is discharged together with the other remnants of digestion in the form of tiny lumps, strongly joined together. For reclaiming land it is very important that these lumps effect a higher rate of sedimentation which is rich in clay and organic matter. The important molluscs on the Ostfriesian tidal flats are Mussels (*Mytilus edulis* L.), Cockles (*Cardium edule* L.) and Gapershells (*Mya arenaria* L.).

Our knowledge in this difficult matter is not complete. For instance Mr. Raudkivi of New Zealand is of the opinion, that in brackish water the rate of sedimentation is dependent upon the change in the electric charge of the single solids as they come in from fresh water (RAUDKIVI, 1967).

It is relevant to mention some aspects of plant-growth and ditch-building in the sedimentation fields. When the terrain in the fields has reached a height, at which plant-growth can be expected, that is about 30 to 40 cm below mean high water level, ditches are dug at regular intervals by special excavators.

Figure 3 shows the hydraulic excavator, mounted on a pontoon, which is cable-operated and slides on the ground. On the higher fields with vegetation a ditch-milling-cutter is used for making ditches. The earliest natural

plants to take root in the sedimentation fields are Glasswort (*Salicornia herbacea* L.) and Cordgrass (*Spartina Townsendii*). A rank plant-growth effects a greater calmness on the field, facilitating better sedimentation and hence a more clayey soil.

When the terrain has reached mean high water level, the first plant of the grass-family to take root is the Sea Poa (*Puccinellia maritima* Parl.).



Fig. 3

THE CONSTRUCTION OF THE GROINS

Although methods of land reclamation are not different on shallow and deeper tidal flats, the construction of the groins depends on the level of the flats. Formally, the reclamation of land for agricultural purposes was done mainly on shallow tidal flats. The groins were built of brushwood and earth. They were constructed of two rows of wooden piles with compact brushwood in between and wooden planks at the leeside to prevent permeation. The piles are held together on top with wire (figure 4).

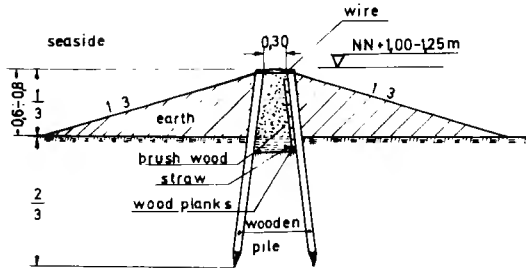


Fig 4 Brushwood groin

Occasionally the cross-groin at the sea-side is strengthened with fascine mattresses (figure 5).



Fig. 5

In deeper tidal flats it was necessary to construct the groins

more solid by using new materials. So far five types of groins have been developed for this purpose:

1. A precast concrete unit with a height of 50 to 90 cm. Each unit has a length of 1 m, the weight is 900, 1200 and 1800 kg (figure 6).

They are set on top of a wooden sheeting on either side. The joints between the single units are made close

with a special joint ribbon of foamed Polyäthylen held in a groove at one side of the unit.

2. A flexible tube of plastic web with a diameter of about 1 m is filled with sand

by hydraulic dredging and takes the form of a sausage (figure 7). The plastic web is woven of small strips of a polyäthylen membrane. Normally, the sandy soil can be taken from the ground of the tidal flat at a small distance to the building site. It is an inexpensive method to construct groins.

Besides, the following construction works are made use of, when the abovementioned types are not high and heavy enough.

3. A groin with a core of earth, with plastic mem-



Fig. 6



Fig. 7

brane (Polyathylen) around this and concrete blocks interlocking horizontally and vertically on top. A wooden sheeting and wooden planks fastened to the wood piles encloses the groin on both sides. A woven mat of reed above the plastic membrane, protects these from getting damaged (figure 8) (ERCHINGER, 1967).

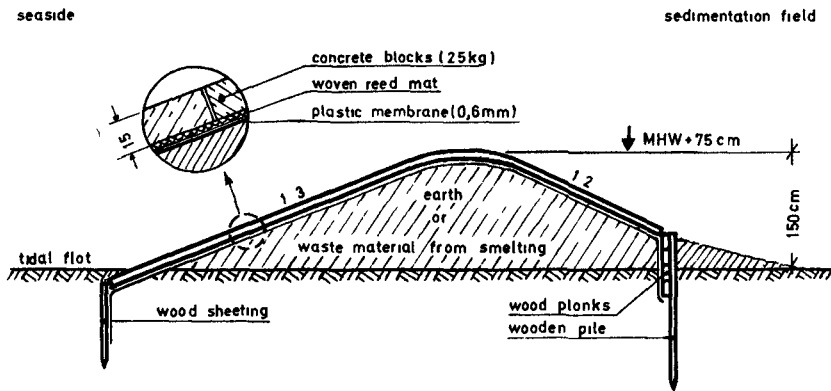


Fig 8 Section through a groin

4. This type is nearly the same as the third, but the surface is covered with quarry stones instead of concrete blocks and with steeper slopes. As the layer of the stones is about 40 cm thick, this construction needs much more material than the type with concrete blocks, which is to be transported to the building site. Transport on the flats is difficult and expensive.
5. This construction is chosen when the area in front of the dikes is to be filled up by hydraulic dredging and an embankment is to be built at the sea-side. Instead

of the plastic membrane, we take a plastic web which is woven very close, so that even the finest particles of sand and silt cannot get through (figure 9). However, it is necessary for the outlet of the water and for preventing water pressure under the surface.

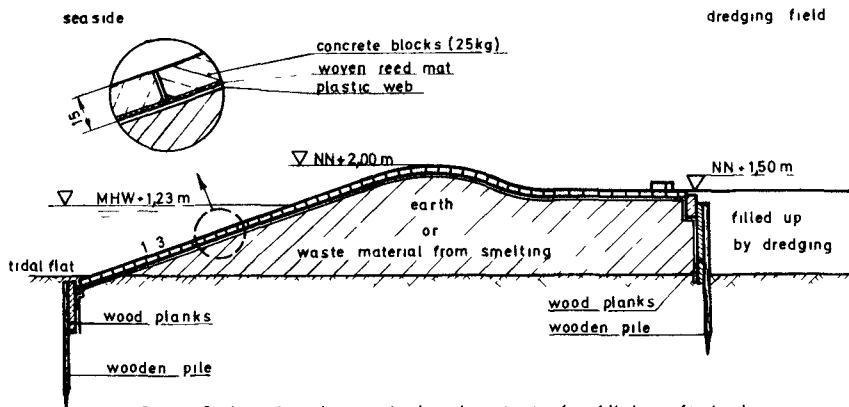


Fig 9 Section through an embankment in front of a filled up foreland

In some cases of groin construction of the last three types, waste material from smelting has been taken for the core of the groin. This material has been found to be very usefull. Its hydraulic substance, which formed a 50 cm thick and hard layer on the tidal flats was so stable, that even loaded heavy motor vehicles could use this as a road to transport the material to the building site. This ist a great advantage, considering that it is derived from waste material.

In 1965, the smelting industry, the Hoesch Concern, made a test with 100 000 t of waste material, containing residues and scrap heaps as well as mud and dust from the smelting process. A forefield in front of a dike was created with this material. This was done in the expectation to make the waste products useful for dike protection and also as a means to get rid of this substance from the vicinity of the foundries, with insufficient storage capacity for this (HAUKE, 1968).

Several scientists have inquired into the chemical and biological consequences of this waste material at the surrounding tidal flat area. No unfavourable effect has been found (KÜSTENAUSSCHUSS, 1969).

REFERENCES:

- ERCHINGER, H. F.. Küstenschutz durch Vorlandgewinnung. Wasser und Boden 19, H. 10, 1967
- FUHRBOTER, A. Der Druckschlag durch Brecher auf Deichböschungen. Mitteilung des Franzius-Institutes für Grund- und Wasserbau der Technischen Universität Hannover, Heft 28, 1966
- HAUKE, M. Deichsicherung mit Verhüttungsrückständen. Helgolander wissenschaftliche Meeresuntersuchungen 17, 1968
- KAMPS, L. F. Mud Distribution and Land Reclamation in the Eastern Wadden Shallows. Rijkswaterstaat Communications Nr. 4, The Hague, 1962
- KRAMER, J., LIESE, R. Die Sturmflut vom 16./17. Februar 1962 im Niedersächsischen Küstengebiet. Die Küste 10, 1962, H. 1
- LUDERS, K. Deichsicherung durch Verhüttungsrückstände. Die Küste 18, 1969, Hsg.. Küstenausschuß Nord- und Ostsee, Kiel-Wik, Feldstraße 251/253
- KÜSTENAUSSCHUSS NDRD-UND DSTSEE
- RAUDKIVI, A. J. Loose Boundary Hydraulics. Pergamon Press, Oxford a. o., 1967

CHAPTER 67

THE EFFECT OF GROYNES ON ERODED BEACHES

W A PRICE - Senior Principal Scientific Officer

K W TOMLINSON - Senior Scientific Officer

Hydraulics Research Station, Wallingford, Great Britain

ABSTRACT

Laboratory tests are described, in which the effect of impermeable groynes on an eroded beach was studied. A beach was allowed to reach equilibrium for a particular wave climate and supply of littoral material. The foreshore was then manually eroded, and the beach allowed to return to equilibrium with and without groynes. It was found that the presence of groynes increased the rate of accretion but did not significantly build up the inshore beach beyond the stable levels. Bed levels seaward of the groynes were increased.

Introduction

As part of the continuing research into the effects of groynes on beaches being carried out at the Hydraulics Research Station, the authors presented a paper to the 11th Conference on Coastal Engineering, see Ref 1, describing laboratory tests to study the effect of permeable and impermeable groynes on a beach that was stable for a particular wave climate and a given supply of littoral material. These tests showed that on the part of the beach between high water and low water levels the groynes induced little or no build-up. However, accretion was found seaward of the impermeable groynes. It was concluded that this offshore build-up was necessary in order that, at equilibrium, the littoral transport that formerly travelled along the foreshore could pass seaward of the groynes. The permeable groynes tested had little effect on either inshore or offshore levels.

Since then, the more practical case of groynes installed on an eroded beach has been studied. The tests were conducted in the same wave basin as the previous series, see Fig 1. This facility allows the generation of waves at an angle to the beach using the serpent-type wave generator shown plus tides and littoral currents, although the littoral current

generator was not used during these tests

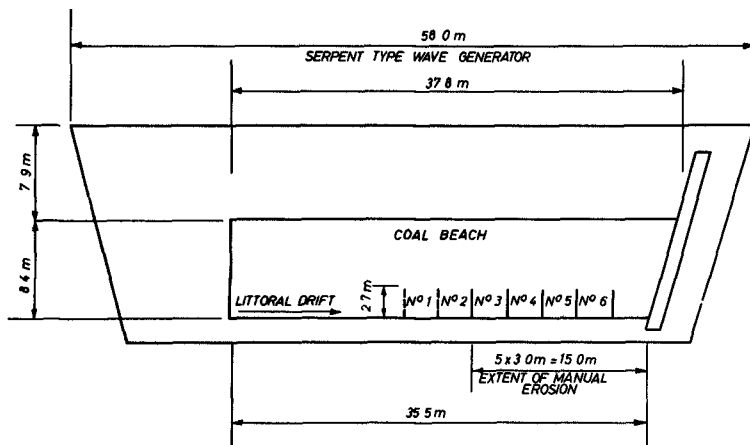


FIG 1 DETAILS OF WAVE BASIN

Test Procedure

In the absence of groynes, waves and tides were generated to bring the beach to equilibrium. The waves were 65 mm high at mean water level, with a period of 1.15 seconds and an angle of approach of 5 degrees in deep water. The tidal period was 75 minutes, with a range of 0.12 m. Beach material was crushed coal of specific gravity 1.35 and median grain size 0.8 mm. The experiments were continued until a comparison of successive beach surveys showed that little change was taking place and the quantity of littoral material trapped at the downdrift end of the beach was the same as that fed in at the updrift end, this normally required at least 25 tides.

An eroded beach, 15 m long, was then created at the down-drift end by removing material between high and low water to an average depth of 25 mm. Five impermeable groynes were placed on the eroded beach. The groynes, shown as solid lines in Fig 1, were 2.7 m long and about 35 mm high, spaced at 3.0 m, $1\frac{1}{2}$ times the horizontal distance from high water to low water.

Again the same waves and tides were generated and the littoral transport measured. Beach material was fed to the updrift beach at the average rate measured on the equilibrium

beach Beach surveys were made at 1, 3, 5, 10, 15 and 20 tides, at which time the beach had returned to its equilibrium profile

The experiment was then repeated with no groynes on the eroded beach

Calculation of Results

The parameter selected for the comparison of beaches was the volume of coal within groyne compartments. The six compartments for which volumes were calculated are defined in Figs 1 and 2, all compartments were 3.0 m long, 2.7 m wide and a maximum of 0.28 m deep

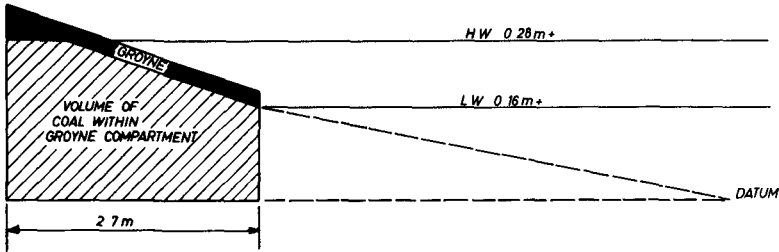


FIG 2 BEACH ZONE REFERRED TO IN CALCULATIONS

Although not bounded on both sides by groynes, compartments 1 and 2 were included to show the effect of groynes on the updrift beach

Three cross-sections were measured in each compartment 0.15 m from the groynes or boundaries, and on the compartment centre-line. Volumes were then calculated using the trapezoidal rule. These volumes were plotted in Fig 3

- (i) Stable beach without groynes
- (ii) Eroded beach without groynes after 1, 3, 5, 10, 15 and 20 tides
- (iii) Eroded beach with groynes after 1, 3, 5, 10, 15 and 20 tides

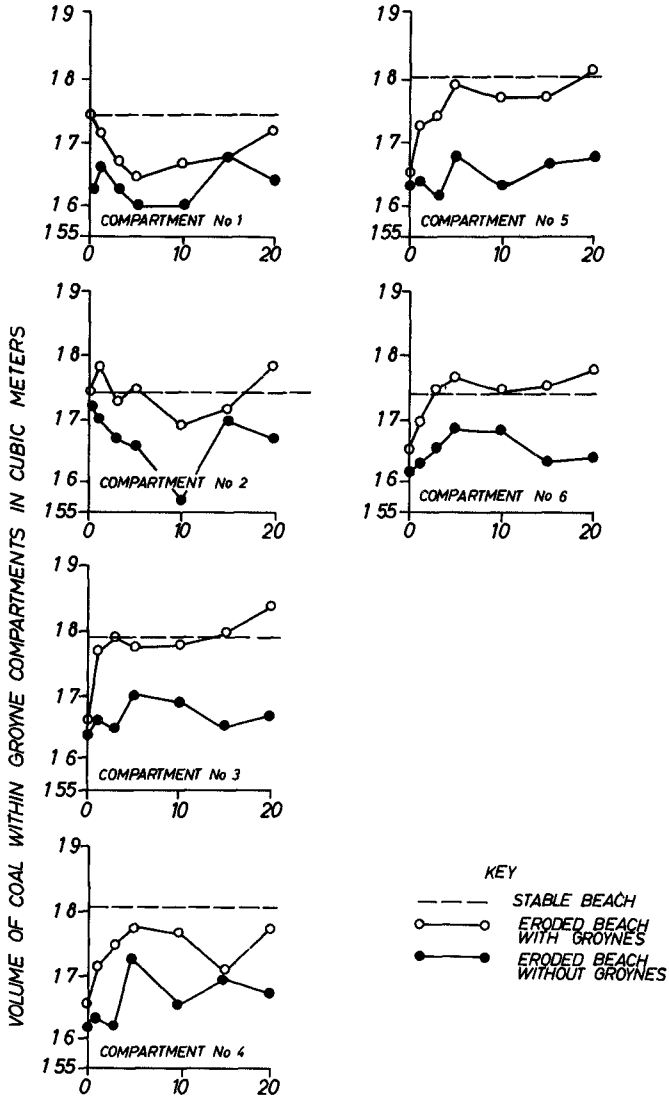


FIG 3 BEACH CHANGES WITH TIME

Interpretation of Results

The changes with time in the volumes of material in each compartment with and without groynes can be seen in Fig 3. In addition, the volumes for the stable beach, before manual erosion, are indicated.

Clearly, the rate of accretion in the groyne compartments, Nos 3, 4, 5 and 6, was greater in the presence of groynes. This increased rate of inshore accretion was accompanied by a build-up in bed levels offshore of the groynes, not shown in Fig 3, necessary in order that at equilibrium the littoral transport that formerly travelled along the foreshore might travel seaward of the groynes. With groynes, the beach had returned to its equilibrium profile in approximately 20 tides, without groynes, the experiment was terminated at 20 tides since it was clear that the beach was returning to the equilibrium profile, although slowly.

No significant build-up of the groyned beach was found above the stable levels, with the exception of the accretion already mentioned seaward of the groynes.

Conclusions

The following conclusions might be drawn from the results of the present series of tests:

- 1 Groynes will increase the rate of accretion on an eroded beach if there is a sufficient supply of littoral material.
- 2 The presence of groynes will not result in a build-up of the inshore beach above the stable open beach levels for the given wave climate and supply of littoral material.
- 3 Bed levels seaward of groynes will be increased in order that a uniform littoral drift may be maintained along the coast.

Acknowledgement

The authors wish to thank Mr H Hashimoto who carried out the experimental work at the Hydraulics Research Station while on a grant from the Japanese Government.

This report is published by permission of the Director of Hydraulics Research, Wallingford, Great Britain

References

- 1 PRICE, W A and TOMLINSON, K W "The effect of groynes on stable beaches" Proc 11th Conf on Coastal Engineering, 1968, Vol 1

CHAPTER 68

CHARACTERISTICS OF SHINGLE BEACHES THE SOLUTION TO SOME PRACTICAL PROBLEMS

A. M. Muir Wood
Partner, Sir William Halcrow & Partners

ABSTRACT

Shingle beaches differ from sand beaches mainly in the mode of transport of the material and in the permeability of the beach. The typical beach forms are in consequence different and the typical problems of beach stabilisation require different types of solution.

The mechanism of littoral drift of shingle is controlled predominantly by the action of the breaking wave, on a groined beach a simple theory is advanced to relate drift to groyne length and spacing.

Longitudinal sorting of shingle sizes is a specially notable sign of a stable beach. Well marked size-sorting transversely to the coastline is a more general characteristic.

Examples of schemes of management are provided for a beach with high littoral drift and a beach which has to be controlled as artificial cells.

The accretion shingle beach may in suitable circumstances develop a steep in-shore profile - examples are given of such.

FORCES CONTROLLING THE BEACH PROFILE

The extensive literature on the engineering properties of a natural beach is principally concerned with fine to medium sand foreshores. In consequence, a number of generalisations have been made concerning the properties of a beach that do not apply, however, to a shingle or even to a coarse sand beach. The object of this paper is to discuss some of the properties specific to a shingle beach and briefly to describe solutions relevant to the typical problems that arise with them. By definition, a shingle beach is one in which the median particle size D_{50} is larger than 10mm. The mean size is most often in the range 10-40mm.

South-east Britain is well provided with natural shingle beaches and Fig. 1 illustrates a number of the lengths of coastlines concerned. The main reason for the predominance here of shingle is that the principal constituent, flint pebbles, was originally formed in the massive chalk which has since been widely eroded over this area. Secondary fluvial and marine deposits have provided copious sources of flint (silica) which have been washed inshore as the sea level rose following the most recent glaciations. Once the flint pebbles become well rounded they tend to be reduced gradually in size by attrition rather than to be reduced to sand by fragmentation.

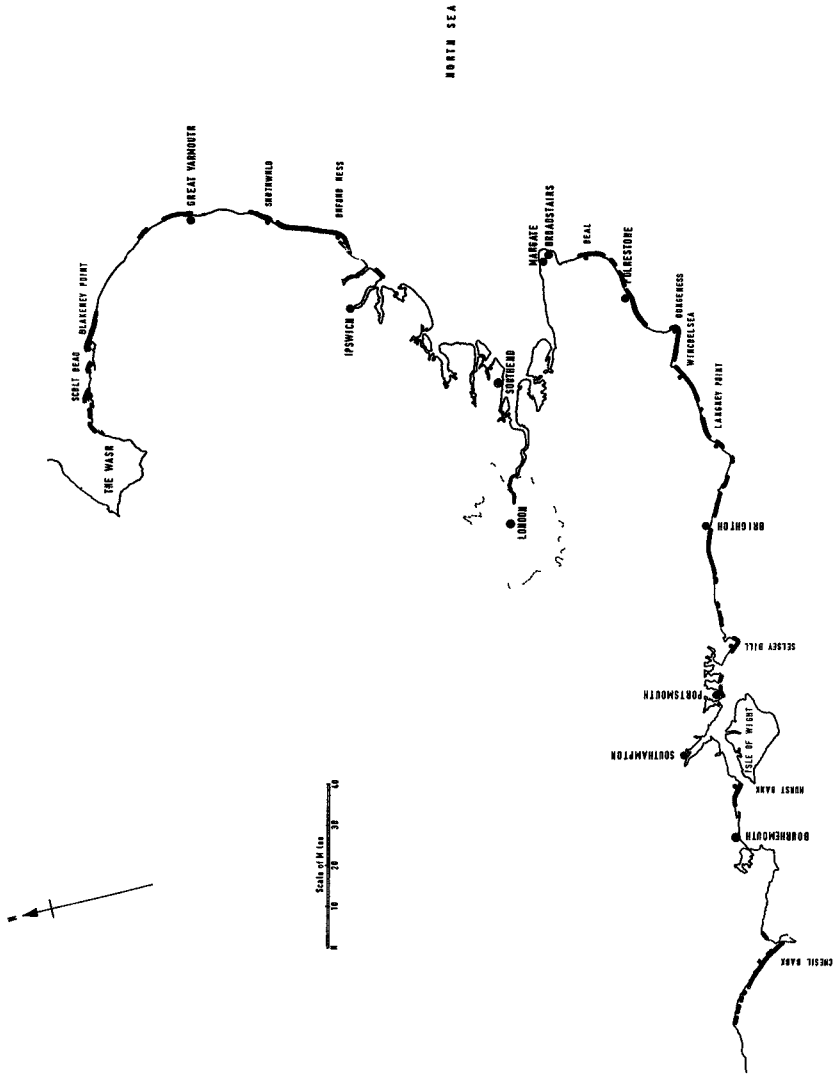


Fig 1- PRINCIPAL SHINGLE BEACHES OF THE SOUTH AND EAST COAST OF BRITAIN

The main differences between the coastal behaviour of shingle and sand are related to the mode of transport and to the permeability of the beach. Whereas sand is moved by the sea predominantly in saltation and, near and inshore of the breaker line, in suspension, shingle is shifted by sliding and rolling along the bottom. The significance of this difference is that, whereas sand will tend to be moved in the direction of the vector representing residual wave velocity plus tidal velocity, shingle is only moved during that part of the wave velocity cycle in which a certain threshold value is exceeded. Generally this threshold value will be little below maximum velocities at the situation and in consequence the direction of high velocity will greatly predominate. In addition, the amount of work required to move shingle on the seabed in substantial quantities is such that this movement will generally be confined to areas of high rate of dissipation of wave energy, i.e. landward of the breaker line. Shingle immediately to seaward of this line, except where the offshore bed is steep, will tend to move shoreward, if disturbed at all, on account of the asymmetrical shape of the wave leading to higher shoreward orbital velocities.

The shingle beach, with a typical slope of 1:10 or steeper, is appreciably steeper than the equilibrium sand beach and this is largely due to the extent of percolation of the swash of the breaking wave into the shingle beach, leading to a diminution of the downwash. To treat this phenomenon in a very simple instance, we may consider the lower bound of the velocity of steady percolation of water into a beach at gradient S to be k/\sqrt{S} which is about 60m/s for a typical value of permeability, k , of 10^{25} cm/e for a beach at 1:10 slope.

To attempt theoretically to calculate the shape of a beach profile, even for a regular train of waves, would be extremely complicated since, apart from the non-uniformity of the material of the beach, we have to be able to calculate the fluctuating degree of saturation of the beach, and the effects of drag and lift on the surface particles on the beach. A point of interest is that the percolation of water into the beach will entail the flow lines of the swash flow and, to a lesser degree, the downwash flow, converging towards the beach and the bed velocities at any instant will therefore tend to be greater than they would be over an impermeable bed of comparable roughness, where the flow lines would be parallel to the bed. The bed profile will be expected generally to be convex upwards since the ratio of return to upward flow will tend to diminish higher up the beach.

Referring to Fig. 2, the force P_1 necessary to dislodge a submerged pebble up a beach of gradient β and limiting angle of repose ϕ is given by

$$P_1 = mg \left(\frac{\rho_s}{\rho_w} - 1 \right) \sin (\phi + \beta) \quad (1)$$

where ρ_s and ρ_w are respectively specific weight of pebble and water.

Similarly the force P_2 necessary to dislodge a pebble down the beach is given by

$$P_2 = mg \left(\frac{\rho_s}{\rho_w} - 1 \right) \sin (\phi - \beta) \quad (2)$$

The energy flux of the swash and backwash may be represented respectively as

$$E_1 = \frac{1}{2} \rho_w v_1 \bar{u}_1^2 \quad (3)$$

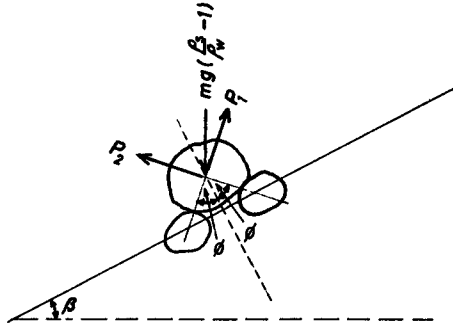


Fig 2 FORCES ACTING ON AN EXPOSED SHINGLE PEBBLE

and

$$E_2 = \frac{1}{2} C_D V_2 \bar{u}_2^2 \quad (4)$$

V_1 and V_2 represent volumes of water with mean specific energy $\frac{1}{2} \bar{u}^2$.

P_1 may be considered as related to u , steady water velocity parallel to and up the beach, by

$$P_1 = \frac{1}{2} C_L m u^2 / \rho_s \quad (5)$$

where C_L is a coefficient with lift and drag components. P_2 is similarly related to velocity down the beach.

The number of uphill and downhill dislodgements may then be considered by eqns. (3), (4) and (5) to be proportional to E_1 and E_2 respectively. For a stable profile there must be a balance of dislodgements and, if $E_2 = cE_1$, from eqns. (1) and (2), considering the threshold values of P_1 and P_2 ,

$$c = \sin(\phi - \beta) / \sin(\phi + \beta) \quad (6)$$

$$\text{i.e. } c = (\tan \phi - \tan \beta) / (\tan \phi + \tan \beta) \quad (7)$$

a result similar to that obtained by Bagnold¹ by consideration of the work done by the swash and downwash in moving pebbles up and down the beach.

A study of natural shingle beach profiles after drawdown by storms indicates generally a profile which may be represented between beach crest and beach step level approximately as a parabola. Thus, Kemp's records² of three sections of the Chesil Beach (A, B and W) fit closely to the same parabola above the level of the step.

This beach grading given by Kemp² indicates D_{10} sizes as 6mm, 4mm and 20mm at A, B and W respectively. The coefficients of permeability are to be expected therefore to be approximately in the ratios 1.2, 1.0 and 2.2 respectively, provided the same beach grading extends to appreciable depth. One factor to explain the common profile may be the greater work done in transporting mobile beach material up and down the beach where the particle size is finer and thus compensating for lower volumetric loss $(V_1 - V_2)$ by higher specific energy loss, $(\frac{1}{2}u_1^2 - \frac{1}{2}u_2^2)$

A shingle beach usually exists in the presence of sand in the inshores (and often also offshores) zones. A certain amount of sand is therefore generally in suspension, following breaking of the wave, and this sand tends to percolate into the beach. As a result, apart from the mobile shingles near the surface, the interstices of the beach will be more or less charged with sand, effective permeability, even of a relatively thick depth of predominant shingle, will be correspondingly reduced. The thickness of mobile shingle mainly controls the critical height and period of wave that will provoke draw-down of the beach by its incapacity to absorb an adequate fraction of the water in the swash.

There are certain typical profiles to be recognised on a shingle beach. The accreting beach has a profile concave upwards becoming convex upwards as the storm crest is reached. On the eroding beach, the concave upward curve runs into a sharp scarp at the head, with the slope immediately below the scarp standing at the critical angle of repose of the beach material. During the course of recovering, one or more secondary crests form at the limit of the swash of the breaking waves but below the upper crest, the upper crest represents the height reached by the breaking sub-critical wave at a time of high mean sea level, ('critical' waves refers to the waves that just begin to draw the beach down).

LITTORAL DRIFT OF SHINGLE

Generally rip currents play no appreciable role in longshore movement of shingle inshores of the breaker zone. This movement is caused predominantly by the direction of up-rush of the breaking waves and, though the downwash usually returns fairly directly down the beach, this contributes to a certain extent when the breaking waves approach very obliquely.

For a natural foreshore, most of the longshore movement of shingle probably occurs in the upper part of the beach. In particular, as the foreshore slope is known to vary considerably with the state of the tide during periods of storm, increased littoral drift is to be expected in an area of high tidal range, other factors remaining unchanged.

When a sea wall is present, extreme flattening of the beach occurs when storm waves come into contact with the wall, and yet higher rates of littoral drift may therefore be associated with the consequent change of profile with each tide.

With the variations of weather, tide and mobility of a shingle beach profile it is unlikely that any direct general relationship will be found between longshore energy flux and littoral drift even for the same beach, and no reliable quantitative solution of general applicability is foreseeable, without separation of the many parameters.

The concept of Pelnard-Consideré³, expressing littoral drift for given wave energy flux as directly proportional to the angle between the crest of the breaking wave and the beach line, may be expected to be applicable as a first approximation where $\sin 2\alpha \sim 2\alpha$, α being the angle of approach of the wave to the foreshore, but the interesting development of this theory by Bakker⁴ cannot be applied directly to the typical shingle beach. Bakker supposes an equilibrium between variable littoral drift and the consequential onshore and offshore movement between the foreshore and the inshore area. His principle is based upon a concept of a unique stable beach profile but, as illustrated by Fig. 3, the shingle profile in the upper beach will adopt an angle so different from that of the sand in the lower beach that it is possible to have variations in size of the shingle wedge without resulting onshore and offshore motion. In consequence, where it is required to provide groynes to maintain a shingle beach, the criterion will mainly depend upon the extent to which the toe of the shingle beach extends seaward of the groyne at a time of appreciable littoral drift. It appears to be the general experience, although there are exceptions to this rule, that the sand in the inshore and offshore zones becomes adapted to the general line of the shingle beach. Thus, if the shingle can be maintained in adequate quantities to provide natural protection, the lower beach will adjust itself accordingly.

Referring to Fig. 3, if the predominant angle of approach of the wave crest to the natural coastline is α_0 and the system of groynes is required to reduce littoral drift from Q_0 to Q_g , then the groyne must provide a beach crest line making an angle of α_g with the original coastline, where the suffices 0 and g relate to the original and the groyned conditions and α_g to the change in the angle of approach of the waves to the beach crest due to the groyne. At the present time we do not know how to relate the reduction of littoral drift ($Q_0 - Q_g$) to the extent of projection of the toe of the beach, at times of storm, beyond the seaward end of the groyne. The following makes a first attempt to such a relationship.

For a system of groynes built sufficiently high to prevent overtopping, the degree of reduction of longshore motion of shingle past each groyne will depend only on the position of the toe of the mobile beach, (probably situated at or inshore of the breaker point) relative to the end of the groyns.

If we assume that littoral drift

$$Q = K\alpha \quad (8)$$

for constant wave characteristics, where α is the angle of approach of the wave to the beach and K is a constant for the particular situation, then, where groynes cause the angle of approach of the waves to be reduced from α_0 to α_g (see Fig. 3)

$$Q_0 = K\alpha_0 \quad (9)$$

$$Q_g = K\alpha_g \quad (10)$$

But, at a groyne, where the distance in plan of the mobile beach from crest to toe is L and the projection of the toe beyond a groyne is a, (Fig. 3), for steady flow conditions of littoral drift we may postulate

$$Q_g = K'a/L \quad \text{where } K' = Kf(\alpha) \quad (11)$$

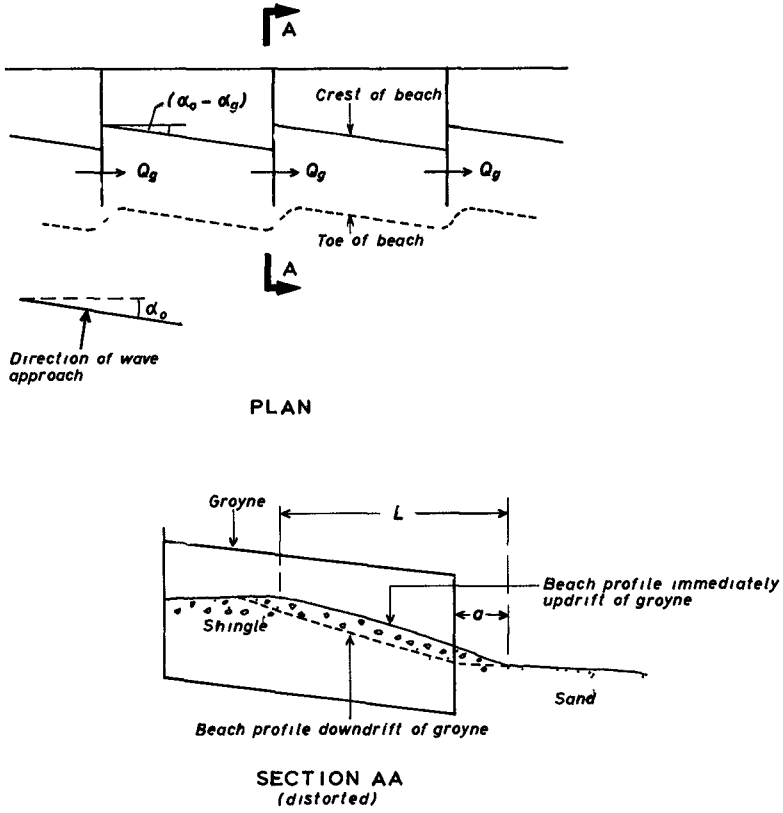


Fig 3 A SHINGLE BEACH IN EQUILIBRIUM ON A GROYNED FORESHORE

At a groyne, the line of the toe of the beach will tend to maximise drift past the groyne, i.e. locally $\alpha \rightarrow \pi/4$ if we suppose that for large values of α , $Q = \frac{K}{2} \sin 2\alpha$. Then

$$K' = K \sin \pi/4 \cos \pi/4 = K/2 \quad (12)$$

and hence, from eqns. (10), (11) and (12),

$$Q_g (=K'\alpha_g) = Ka/2L. \quad \text{Hence } \alpha_g = a/2L$$

whence for given value of a and L , Q_g may be estimated as a fraction of Q_0 , from eqns. (9) and (10).

LONGITUDINAL SORTING OF SHINGLE

Many references may be found to the sorting of shingle by sea waves to produce longitudinal size grading along a beach. Shingle of the largest size tends to move towards the zone of the highest degree of exposure to the waves. A classic example of this phenomenon is found at Chesil Beach (see Fig. 1) where the most significant features are as set out in Table 1.

TABLE 1

Significant Features of Chesil Beach

Distance from West Bay (km)	Average offshore slope (0-5 fathoms)	Average longitudinal diameter of pebbles (cm)	
		Foreshore (Ref 12)	Seabed (Ref 12)
0	1:75	0.86	
6.1	1:50	1.16	4.5
7.2	1:50	1.16	3.0
11.3	1:20	1.56	2.0
12.6	1:20	1.64	3.5
15.1	1:20		3.0
17.1	1:20		4.8
21.4	1:20	3.36	3.2
23.8	1:20	3.64	5.0
25.6	1:12	4.28	6.0
28.0	1:25	5.89	

Jolliffe⁶ describes a number of experiments on beaches at Deal and Winchelsea (see Fig. 1) to record the relative rate of littoral drift by means of tracer pebbles of different sizes matched to the range of pebble sizes present on the beaches. He found a significant correlation between the size of pebble and the rate of littoral drift, the size of greatest mobility being related to the wave height.

On a beach comprising an assemblage of shingle sizes, we may consider that a pebble will begin to move when drag and lift cause the pebble to rotate about a line between points of contact with other pebbles. Fig. 2 indicates how, on a beach of pebbles of different sizes, this force will bear the least ratio to the pebble mass for the pebble of the largest diameter. Moreover, once set in motion by a wave, translational and rotational inertia will tend to cause a large pebble to travel considerably further than a small one. The pebble of small size will tend to become rebedded into the beach with drag from downward percolation opposed to wave lift.

For a given beach and given wave climate there must be a size of pebble so large that it is only infrequently dislodged. Pebbles below such a size may be expected to undergo some degree of longitudinal sorting if there is a longshore component of wave energy flux. For a beach which is in long term stability, but which is subjected to different directions of littoral drift by different sizes of waves, the sorting should be a significant feature, and generally it appears so to be. This effect may arise from the different degree of exposure to prevailing winds and swell or from different degrees of refraction of different types of waves.

The size grading along Chesil Beach might be explained principally by increasing exposure to the Atlantic as one proceeds along the beach towards its south-east extremity. This increase is due not only to differences in sheltering afforded by Start Point, the west headland of the bay, but also to the increasing depth of water offshore in the same sense.

Reverse drift of shingle along Chesil Beach, i.e. towards the north-west, will occur under the action of waves generated within the English Channel, but these will only be of a height to affect the smaller sizes of shingle. Further studies are warranted here to observe differences in long-shore mobility of shingle of different sizes and gradings subjected to a varying wave climate.

It is to be noted that for a beach not in long-term equilibrium little sign of longitudinal sorting is likely to be observed unless it is subjected to long-term cycles of reversal of drift. Nor is this effect likely to be observed on a groyned foreshore except in individual groyne bays, for the reason of the interference with natural drift caused by the presence of the groynes.

BEACH REPLENISHMENT: A SYSTEM OPERATED AT DUNGENESS

Possibly the finest long-term continuous records of shingle movement available anywhere up to the present day are those relating to Dungeness (see Fig. 1). Here the existence of a pattern of shingle ridges, looking like a magnified fingerprint, permits a reconstruction of events over nearly 2,000 years!

In recent years the Ness has been building out towards the east-south-east at a rate of 3-4m per year, at the expense of erosion along the south coast of the feature. As indicated in Fig. 4 the changeover from erosion to accretion occurs at a point about 700m west of the Ness proper. It will be noted that this change must be accounted for by the angle of approach becoming super-critical i.e. greater than that for maximum littoral drift, since the degree of sheltering is reduced from west to east and the extent of refraction of the dominant south-westerly waves is reduced in the same direction.

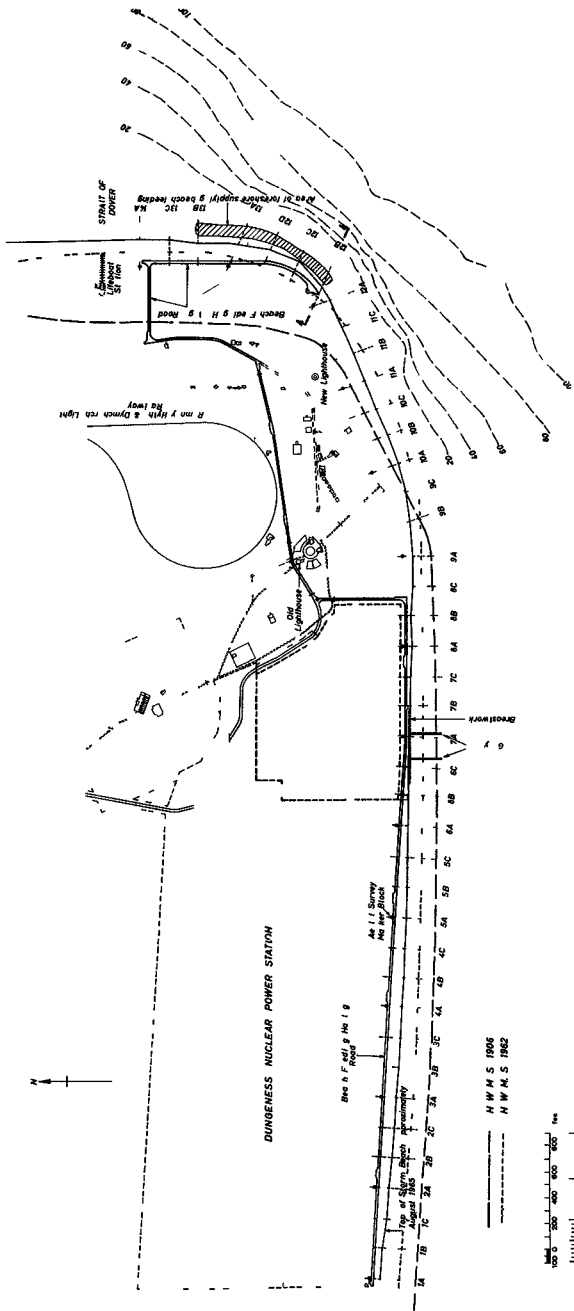


FIG 4 PLAN OF THE SOUTH - EASTERN TIP OF DUNGENESS

Since 1965 a scheme of beach recharge has been operated to stabilise the shoreline between Sections 1A and 8B (Fig. 4) where it forms a frontage to the existing and projected Nuclear Power Stations. Shingle for this purpose, won from the foreshore and upper beach in the vicinity of the Ness, has been transported each year in lorries to the Power Station frontage and tipped on the beach at recharge points. These tips build out to form shingle breakwaters on the foreshores and it is to be expected that, as they persist virtually throughout the winter, they will reduce the erosion updrift from the points of recharge.⁶ Making due allowance for the local and short term variations, this effect appears to be supported by the figures set out in Table 2.

The plan of the beach has been subdivided by section lines about 30m apart and fixed points have been selected at intervals along these lines seaward from the crest of the beach which is at about 6m above O.D. (approximate mean sea level). Vertical co-ordinates of the shingle level at such points are provided each year from an aerial survey taken at the time of Low Water Spring Tides (about 3m below O.D.) in August. The volumes of shingle in each sub-division of the beach are then provided by a computer program and on these data the beach recharge plan for the following winter is formulated.

It is to be noted, in Table 2, that during 1965/66, the year of inception of the scheme, a considerably higher degree of beach feeding was undertaken than during subsequent years. Table 2 also indicates the annual variation in the longshore movement of shingles and in the quantity arriving at the Ness. The Power Station foreshore is now virtually stable from year to year and it seems reasonable to assume that any variations in the beach profile below low water of spring tides could be ignored, the volume changes provided by the computer data then being actual volume changes on the beach. However, as the Ness is still advancing into deep water, allowance has now been made for the volume of shingle accretion on the steep face to the Ness below low water. The volumes of shingles arriving at the Ness, shown in Table 2, also include an allowance for accretion north of the northernmost section of the surveyed area.

In view of the detailed records available of the shingle movement over four consecutive years it was decided to study the possible relation between wave energy in the area of the Ness and the rates of erosion and accretion along the foreshore. However, there are no wave records available directly applicable to Dungeness. The nearest records are on the Varne and Dyck lightships, but in the enclosed waters of the eastern English Channel differential sheltering is an important factor. Consequently, since there is no significant long period swell in this part of the Channel, wind records may be used to derive at least a first order estimate of longshore wave energy flux and wind records were available from the Dungeness lighthouse. These records were analysed into durations (T) of wind speeds from points of the compass from east through south to west for winds of Beaufort Force 8 and higher.

A wave energy spectrum was then obtained, using the simplified graphical relationship prepared by Darbyshire and Draper⁶ to provide maximum wave heights and thence the corresponding significant wave heights (Hs). The total annual energy flux factors ($KH_s^3 T_{C_{5m}} 2\sigma$) were calculated and these are indicated in the final column in Table 2, the positive figures indicating energy from winds west of the south sector. The comparison of these flux factors, which are proportional to the total longshore energy flux, with the figures in Table 2 either for net littoral drift or for material arriving at the Ness, shows no general relationship, although the highest flux factor is associated with the highest movement of material. However, the trend of recharge does generally follow the factors and with a few more years experience it might be possible to use these calculated factors to predict the quantity of recharge necessary, though some form of survey would be necessary to determine the optimal points of recharge.

TABLE 2

Shingle Recharge and Littoral Drift at Dungeness (in cubic metres)

Section of Shore		Year				
		1965-66	1966-67	1967-68	1968-69	1969-70
1A-4A	R	-	-	20600	12600	
	L	-1800	-2300	-16100	-1300	
4A-5C	R	8000	19000	-	11500	
	L	-800	-1600	-4100	-4900	
5C-7A	R	43000	-	7400	9500	
	L	-10100	1000	-700	-3400	
7A-8B	R	23000	5400	4400	6400	
	L	-900	-1000	-3000	-2200	
1A-8B	R	74000	24400	32400	40000	
	L	-13600	-3900	-23900	-11800	
Estimated quantity of shingle arriving at the Ness		80000	30000	90000	55000	
Energy flux factor		6.7	6.5	10.1	2.2	

R = Shingle Recharge

L = (Littoral drift into section) -(Littoral drift out of section)

It will be noticed in Table 2 that a large volume of recharge at a section of the shore is generally associated with a high rate of loss. This is no doubt due to the form of tipping, which is always onto the end of the tip, and where no recharge is made at the adjacent downdrift section a build up of beach only occurs against the following point of recharge. It is noticeable that in 1968-69 when a fairly even distribution of recharge was made the loss of material was also fairly evenly distributed along the beach.

Prior to 1965, the average annual loss of material along the length between Sections 1A - 8B amounted to about 25,000 cubic metres per year.

CONTROL OF A BEACH AT SEAFORD WITHOUT EXTERNAL REPLENISHMENT

The coast protection problem at Seaford (see Fig. 1) is fundamentally one of retaining a shingle beach without the benefit of natural recharge. Seaford was originally established behind a natural shingle bank and there are many hundreds of years of history of the variations in the position of the mouth of the River Ouse through this shingle bank. Since the 18th Century the river has been trained to flow through Newhaven Harbour to the west of Seaford. From 1847 the east harbour breakwater arm has prevented easterly drift of shingle and has also affected the wave pattern that arrives around the perimeter of the bay. For the prevailing south-westerly winds this has the effect of causing a reversal of drift, i.e. towards the west, along the westernmost protected length of foreshore.

For many years sea walls and conventional groynes have been constructed at Seaford during which period the sea continued to encroach, causing considerable damage and the collapse of sea walls. The natural drift along this foreshore towards the east has not been measured but is probably of the order of 10^2 cu.m of shingle per year. The economics of a beach recharge scheme have been examined but this is highly uneconomic in the absence of long term supplies of natural shingle nearby. The only alternative scheme that could continue to place reliance on natural shingle as the principal medium of protection is one that would contain the shingle along the protected length. The object was then to determine the minimum length of groyne to ensure effective containment of the shingle. An empirical approach is to suppose that a shingle beach, being relatively thin over a solid chalk bottom, may at times of storm be dragged out to sea so that its toe corresponds approximately to the breaker point of the largest waves. Model studies carried out by the Hydraulics Research Station² generally pointed to a similar limit of shingle movement, although allowance has to be made for the fact that, while the several relevant hydrodynamic dimensionless factors were satisfied (Yalin, 1963)⁴, the material shape and grading were very different from the natural shingle.

The form of construction of long groynes decided upon had to be much more robust than conventional groynes taken out approximately to low water. The groynes, erected initially and experimentally as a timber gantry faced with steel sheet piling, were subsequently converted into mass concrete groynes built in cellular sheet-piled coffer dams. They are taken out to a point at which the bed level is approximately 6m below mean sea level (O D) and at the eastern end the principal groyne was constructed to provide, in addition, a sewer outfall.

In view of the inclination of the beach crest to the shoreline for zero drift, it is necessary to sub-divide the length into intermediate cells to avoid the need for a large amount of continuous redistribution of shingle from the east end towards the west. A small amount of redistribution can be tolerated and it is not necessary for the intermediate long groynes to be taken out far enough to achieve full cutoff. The tidal range here is approximately 5.5m on Neap Tides and 6.0m on Spring Tides. As a result, the redistribution necessary to maintain an adequate beach in the area of maximum scour (i.e. near the point of reversal of drift) amounts to about 5,000 cu.m. per year for storm waves of about 3m height and 6/7 seconds period.

Periodical aerial surveys establish that the overall shingle quantities along the foreshore remain approximately constant and also indicate the volume appropriate for periodical distribution.

An insidious cause for failure of sea walls on shingle beaches can be attributed to undermining by the sea near the time of High Water, which action can then become obscured to view on account of partial recovery of the beach at Low Water. At Seaford it was observed that, while the upper layers of shingle are maintained relatively clean as a result of the mobility of the shingle in stormy weather, the lower shingle tends to become charged with finer shingle, sand and chalk particles, carried by the water percolation through the beach. It is, consequently, possible to determine after heavy storms the depth to which the beach has been disturbed. The chalk particles act as a cementitious binder so that the side of an excavation made after a heavy storm stands vertical, immediately below the base of the mobile beach. The depth to which the beach has been disturbed at vulnerable points is recorded and compared against previous records, against the known levels of the wall facing and of the surface

chalk in which, generally, at Seaford, the wall is founded. Although local availability of heavy plant for maintenance for these works facilitates this simple method of control, in the absence of such plant, some simple penetrometer device, or a heavy ring around a pile, might be used for the same purpose. At Seaford trials of alternative geophysical methods of locating the boundary were unsuccessful.

REGIME OF A NATURALLY ACCRETING BEACH

The natural regime of a shingle beach is usually confused by tides, by the presence of a well marked division between the medium to coarse shingle of the upper beach and fine to medium sand of the lower beach, also by highly variable winds and currents. The natural form of a beach may best be studied where such factors do not intervene and the characteristics of a beach in Thessalonika help to illuminate this aspect.

The beach in question is situated in a bay on the southwest coast of the Sithonia Peninsula facing the Gulf of Kassandra. The beach is contained by rock headlands and is largely composed of particles of natural quartzite graded from fine gravel to coarse sand. The schistose rocks drop away into deep water and there is little fine material in suspension in the sea. The beach material has been carried to the bay by a river which flows into it. The beach in consequence represents the stable profile of a slowly accreting beach fed from this source. Fig. 5 indicates how the grading and sorting factors vary around the margin of the bay. It is seen that the material becomes very well sorted for size as it travels away from the river mouth, with the size adjusted to the degree of exposure to the waves.

Fig. 6 shows a typical profile of the shore taken to a depth of about 30m below sea level. Contrary to the normally accepted shingle beach profile, seaward of the step, situated approximately on the breaker point for the maximum height of significant wave of about 1.7m, the shore drops steadily away into deep water, at a slope of 30° - 32° around the bay, except locally near the river mouth. The absence of an appreciable fraction below coarse sand size, coupled with a low coastal current, permits the bed material to stand at an angle a little below its natural angle of repose of about 36° . Further to seaward from this steep slope there is a variable flatter slope at a gradient of about 1 in 10 in which the material is predominantly fine sand. In Fig. 5, samples A-J are from the foreshore, samples S1, S3, S5 and S7 are from the steep inshore bed and samples S2, S4, S6 and S8 are from near the foot of the steep inshore slope.

It is interesting to compare the profile of the Sithonia beach with that at Dungeness Point (see Fig. 6) where a shingle beach is accreting in very different conditions, but nevertheless exhibits the same steep inshore feature.

In general therefore one can say that a naturally accreting shingle beach will tend to develop a profile of a foreshore that is concave upwards, steepening towards the crest to the angle of repose, an onshore section flattening to a step at the breaker point, then changing seawards to a convex upward profile, finally arriving at a steep section seaward of the low water mark which assumes a slope a little flatter than the angle of repose. The lower features of this general profile, however, are frequently obscured by accumulation of sand against the shingle beach. Fine to medium sand would only accumulate at a steep angle in deep still water, on account of its susceptibility of movement by relatively small

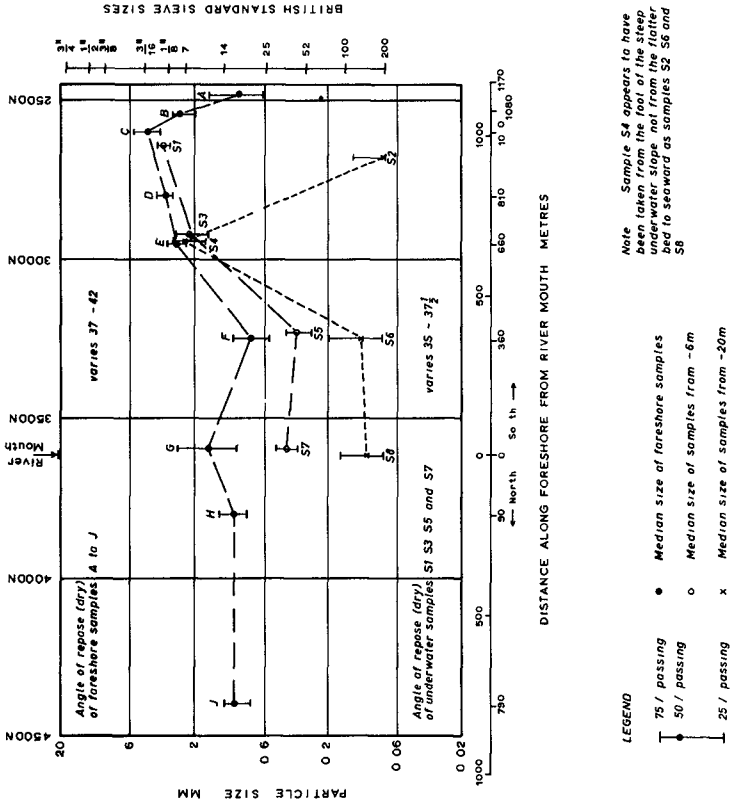


FIG 5 PARTICLE SIZE GRADING ALONG SITHONIA BEACH

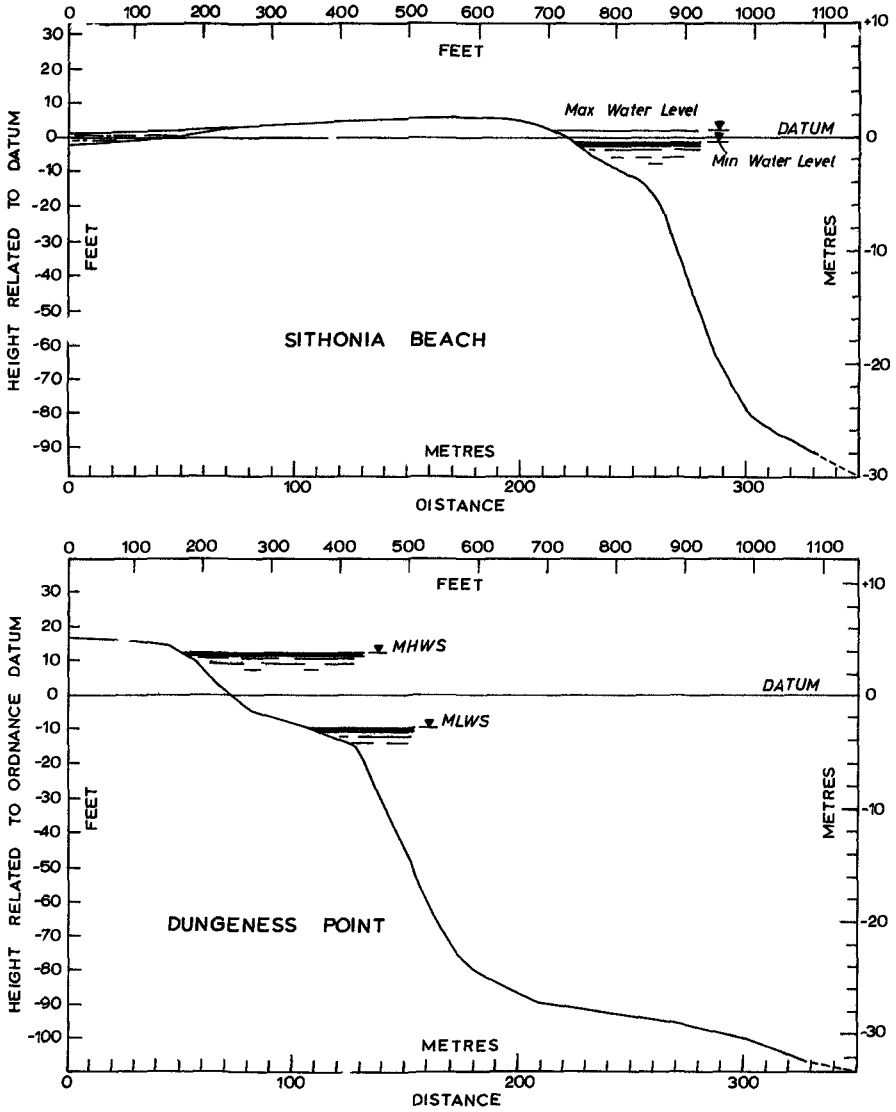


Fig 6 - PROFILE OF ACCRETING BEACHES AT SITHONIA AND DUNGENESS.

oscillatory currents, the susceptibility being attributable not only to the grain size of the material but also to its proneness to rippling. An eroding shingle shore, on the other hand, will not develop the steep offshore feature, even in the absence of sand.

REFERENCES

1. Bagnold, R.A Mechanics of marine sedimentation, The Sea, 3, Interscience Publishers Inc., (1963) pp 507-528
2. Kemp, P H A field study of wave action on natural beaches, I A H.R. Xth Congress, 1, Paper 1.18 (1963) pp 131-138
3. Pelnard-Considers R. Essai de theorie de l'evolution des formes de rivage en plage de sable et de galets IV same Journée de L'Hydraulique Question IV (Paris) 1956.
4. Bakker, W T The dynamics of a coast with a groyne system. XIth Conf. on Coastal Engineering, London (1968) Vol II pp 492-517
5. Carr, A.P. Size grading along a pebble beach Chesil Beach, England Jnl. of Sedimentary Petrology, Vol 39, No 1 (Mar 69) pp 297-311
6. Jolliffe, I P Experiments designed to compare the relative rates of movement of different sizes of beach pebble. Proc. Geol. Assoc. Vol 75 (1964) pp 67-86.
7. Lewis, W.V. The formation of Dungeness Foreland. Geogr. Jnl. Vol 60 (1932) pp 309-324.
8. Derbyshire, M. & Draper, L. Forecasting wind-generated sea waves, Engineering (5th April 1963) pp 482-484.
9. Hydraulics Research Station Seaford Sea Wall: protection by artificial fill. Report EX 209 (May 1963).
10. Yalin, M.S A model shingle beach with permeability and drag forces reproduced. XIth Congress Int. Assoc. Hyd. Res., London (1963).
11. Nsate, D J M Underwater pebble grading of Chesil Beach. Proc. Geol. Assoc. Vol 78 (1967) Pt. 3 pp 419-426.

Note Tables 2 reproduced by permission of South Eastern Region of the Central Electricity Generating Board

CHAPTER 69

A COMPARISON OF FLUVIAL AND COASTAL SIMILITUDE

By Bernard Le Mehaute, D Sc
Vice-President, Tetra Tech, Inc
Pasadena, California

ABSTRACT

A comparison of the conditions of similitude for movable bed scale models of rivers and estuaries on one hand, and beaches and shorelines on the other hand, is presented. It is demonstrated that despite the fact that the knowledge in sediment transport by wave action is less advanced than in the case of steady current, the conditions of similitude for beaches are less stringent than for rivers. In particular, the effect of relative roughness is comparatively unimportant in the case of beaches, while the necessity of similitude of head loss imposes an imperative condition in the case of scale models of rivers. An introduction to a natural law of distortion for beaches is presented in analogy with the Lacey condition for rivers.

INTRODUCTION

Belief in movable bed scale model technology is somewhat mystical--God's existence can be proven by logic, while as many reasons can be proposed for proving the opposite. This belief is not a matter of logic--it is a matter of faith. Similarly, agnostic specialists in sediment transport can easily find many reasons why similitude of movable bed scale models is not possible. On the other hand, hydraulic engineers believe in movable bed scale model technology as a tool for solving practical problems and guiding their intuition. Sometimes this belief or disbelief is completely irrational. One finds the scientist who does not want to admit that this tool could be of practical value and one also finds the engineer whose faith in his scale model fringes on the rim of superstition, while he should know its limit of validity. The analogy can be further prolonged by considering that different scale model practices and technology prevailing in different hydraulic laboratories correspond to slightly different religions. But the road to salvation is not unique--despite some disagreement between laboratories on what should be done, none of these methods is "completely wrong". One can only discuss what could be the most universal approach--the better approach actually being the one which is the best mastered by individual experimenters.

A detailed investigation of what can and cannot be done in movable bed scale models dealing with coastal structures has been presented in a previous report (Fan and Le Mehauté, 1969). This presentation will be limited to some reflections which may not necessarily be original, but which are felt pertinent to this convention, which assembles agnostics as well as believers in movable bed scale models. One would like to clearly establish that the chance for success of a movable bed scale model dealing with shoreline processes is much higher than a movable bed model of fluvial hydraulics. Subsequently, the first kind of model will require less knowledge in the law of sediment transport and less astuteness on the part of the experimenter than the second kind.

The reasons which make a coastal model more reliable than a river model are

- a) A less imperative choice of the condition of similitude. This is discussed at length in the following. In general, coastal models do not

require any condition on bottom roughness, while the necessity of reproducing head loss in similitude in fluvial models imposes an additional condition upon the size of the model material to be used

- b) A wider choice of criteria of similitude in the case of a coastal model. One can always satisfactorily reproduce an observed shoreline evolution by adjusting wave height, period, direction, duration, or intensity of tidal current. (However, similitude of sand deposit taking place in a diffraction area may be subjected to scale effects.)

In fluvial hydraulics, the choice of criteria is limited to typical flood histograms and required fineness of topography. (Secondary meandering effect may not need to be reproduced in similitude.)

- c) The third reason for making coastal models more successful is related to the problem of hydraulic instability. A river flowing in its own alluvium is fundamentally unstable in the sense that if there is erosion, more water will flow, and, consequently, more erosion will follow. The study of a meandering river on a scale model is only possible if the banks are fixed. A meandering process can be reproduced on a scale model only if it obeys a well defined cycle, such as the Seine estuary.

In coastal processes if one excepts cusps and rip currents on long, straight beaches, the flow pattern is generally well determined by an imposed bottom topography. Short coastal engineering scale models always deal with well defined topography and man-made works, such as harbor entrances. Consequently, there is a general tendency towards a stable state: a dune tends to be flattened out and a channel tends to be filled.

- d) Finally, the last reason for the success of coastal engineering models is due to the fact that beaches are generally made of relatively uniform non-cohesive material, while rivers may present a much wider size distribution of material and have cohesive characteristics. The law of similitude for cohesive material cannot be established until more is known about the sediment transport of cohesive material.

PRELIMINARY REMARKS

Prior to entering this subject, it is pertinent to briefly recall some of the fundamental principles governing movable bed scale model technology.

- 1) Quoting L. F. Vernon-Harcourt, who continued the work of Reynolds:

"If I succeed in demonstrating with the model that the originally existing conditions can be reproduced typically, and if, moreover, by placing regulating works in the model, the same changes can be reproduced that were brought about by the training works actually built, then I am sure that I can take the third and most important step, namely, of investigating, with every promise of success, the probable effect of the projects that have been proposed."

This principle has been the basic guideline ever since.

- 2) A movable bed scale model must fulfill the following conditions:
- a) It must be exact *i.e.*, it must reproduce with exactness the natural phenomenon under study.

- b) It must be consistent i e it must always give the same results under the same conditions
 - c) It must be sensitive--or more exactly, its sensitivity has to be imposed by the fineness of the topography which needs to be reproduced for the phenomenon under investigation Secondary meandering flow, small benches, and at the limit ripples, will, of course, not need to be reproduced in the scale model
 - d) It must be economical, of reasonable size, and completed within a reasonable time interval
- 3) In a movable bed scale model, the basic similitude requirement is the reproduction of bottom evolution observed in the field even if it is not achieved through exact similitude of water motion (the way in which water motion is simulated must be logical so that it can be extended to future conditions) Reproducibility of test results under the same conditions is a general requirement for all experimental studies This requirement of the model also implies stability under random disturbances An unstable phenomenon cannot be studied adequately in a movable bed model

"For example, it would be illusive to study the stability of a river flowing in its own alluvium on a scale model because a simple bush or a local soil a little more cohesive can definitely guide a meander in a way different from the model result Such studies embody by their very nature a risk of complete failure "
(Le Méhauté, 1962)

- 4) It is important to distinguish between conditions of similitude and criteria of similitude The conditions of similitude are an ensemble of formulas deduced from the physical laws governing the phenomena under investigation e g , the similitude condition governing sediment transport is obtained by an analysis of the mechanics of sediment transport They have an absolute definition which cannot be changed unless an improvement in the knowledge of the physical law is obtained They are not chosen by the experimenter but are imposed on him Unfortunately, it is known that in the field of sediment transport, many phenomena still remain to be analyzed or clarified Thus, the conditions of similitude are not as well defined as they should be A choice of what is important will have to be based again on the knowledge of these laws obtained by "inspectional analysis"

In performing a model study, an experimenter must specify certain criteria such as model wave conditions and fineness of model bottom features The criteria of similitude is a free choice of the experimenter to a very large extent For example, sea states vary from day to day and from hour to hour The experimenter will choose, for the sake of simplicity as well as practical necessity, a characteristic wave condition and will only be able to reproduce simplified storm and swell conditions on the scale model He will choose the wave direction and the wave amplitude and the duration guided by his knowledge of natural conditions In particular, the wave generator will generate waves at an angle which corresponds to the dominant direction of storm wave energy Even though he is guided by his knowledge of wave statistics, his final choice will be determined by a trial and error method which permits him to reproduce the same bottom evolution as observed in the prototype This faithful reproduction of bottom evolution determines

the choice of the wave characteristics, rather than the strict conditions of similitude of wave motion

Other criteria of similitude will be to what extent he wants to reproduce the fineness of the bottom topography, a typical tide cycle, the currents and their variations with time, and so on. In summary, the criteria of similitude are specified by the experimenter as reasonable approximations for simplification of model operation

- 5) Movable bed scale models are distorted, i.e., the vertical scale is different from the horizontal scale. Distortion is not an engineering trick for reducing the size of the model and the bottom friction, but is the extrapolation of a natural observed phenomenon. The method to obtain a satisfactory scale model is first to obey the law of nature, even though this law may not be fully understood. For example, a small river flowing in its own alluvium can be considered a distorted model of a large river. This means that the ratio depth to width of the small river is comparatively greater than the relative depth of the larger one. The ratios of depths μ and widths λ are approximately related by the law of Lacey ($\lambda^2 = \mu^3$), in accordance with the "regime theory". Similarly, a beach in a protected area has a relatively steep slope, while a beach in an exposed area tends to have a more gentle slope (Wiegel, 1964). The vertical scale being defined by the ratio of incident wave heights, a protected beach can be considered as a distorted scale model of an exposed beach. In both the case of the river and the beach, the choice of distortion becomes a stringent condition to be respected quantitatively, however, the natural law determined by statistical observation of natural phenomena needs to be modified in the case of a river model due to the fact that scale models generally do not use the same material as the prototypes in order to satisfy other conditions of similitude. On the other hand, natural distortion based on the use of sand is compatible with other conditions of similitude in the cases of beaches as will be seen in the following. However, the use of sand would rather be discarded as leading to too large a distortion and, subsequently, to large scale effects.
- 6) To the old teaching tradition which consists of presenting a parallel between Froude and Reynolds similitude, I would prefer to make a parallel between what we can call "short model" and "long model". In a short scale model, viscous friction is unimportant as compared to gravity and inertia, therefore, it is governed by Froude similitude. Also, energy dissipation may result from a fully turbulent condition, as in the case of a hydraulic jump or a wave breaking on a beach. Boundary layer effects in both cases are unimportant. The dissipative forces are also proportional to the square of velocity like the inertial forces. (A small hydraulic jump is a scale model of a large hydraulic jump under proper depths-discharge relationships.) This is the generalized Froude similitude.

On the other hand, in a long model, friction has a definite influence on the flow pattern; therefore, in addition, a similitude of head loss is required. This head loss is a function of the Reynolds number, but is not determined by the so-called Reynolds similitude requiring an equality of Reynolds numbers. Therefore, similitude for long models requires, in addition to the Froude similitude, another condition which makes long models more difficult, if not impossible, to handle. The model of a smooth concrete-lined gallery cannot provide a "Froudian" discharge under similar pressure head, since the friction coefficient can only be larger at a smaller Reynolds number (Moody diagram). On the other hand, the head loss in the scale model of a rough (rocky) gallery can be adjusted for the same friction factor insuring the Froude similitude to be satisfied.

The magnitude of long shore currents and location of rip currents may, to some extent, depend upon friction characteristics of the beaches, in which case the study of this phenomena would have to be considered as belonging to the categories of long models, and therefore, may not be studied on scale models. Nevertheless, most scale model studies have to deal with short coastal structures (like entrance of harbor), and therefore, the water motion is not too dependent upon the friction coefficients. The main dissipative mechanism is due to wave breaking. If viscous damping is too significant, as in the case where the wave has to travel a long distance in very shallow water, it just means that the model is not properly designed. However, very rarely do we have to be concerned with adjustments of roughness for similitude of energy dissipation, and coastal models can be considered as short models. On the other hand, as has been pointed out previously, a similitude of head loss is imperative for models of rivers and estuaries--these are long models. Despite this adjustment, vertical velocity distribution being a function of the Reynolds number could never be in similitude.

- 7) This relative advantage of a short model is somewhat balanced by the lack of knowledge of sediment transport by wave action. The law of sediment transport in rivers is relatively well understood. Therefore, the condition of similitude may be established with more certainty than in the case of beaches. Boundary layer characteristics do not vary too much from one place to another. While on the other hand, in the case of beaches, the boundary layer characteristics vary from offshore to the upsurge of the wave. A choice has to be made concerning which part of the beach we want to have the best similitude requirements. In general, it will be in the breaking zone, where the shearing force at the bottom is quadratic. However, it is to be realized that because of this variation of boundary layer characteristics from place to place perpendicular to the beach, a total similitude is impossible.
- 8) In designing a movable bed model, there are four basic unknowns namely, horizontal scale λ , vertical scale μ , sediment size δ , and sediment specific weight γ_s , which require at the most four basic equations. However, the horizontal scale is generally determined by economic considerations and available space. The three remaining unknowns are relatively well determined in the case of a river, by a well accepted unique set of conditions of similitude as summarized in a following section.

In the case of beaches, there is a great controversy concerning which condition of similitude should be imperative. This controversy is due on one hand to a lack of knowledge of the law of littoral processes but is also due to the fact that the road to a successful coastal model is not unique. As a matter of fact, a thorough analysis of the subject matter may only lead to two conditions which give us a free choice for one of the unknowns. These conditions are 1) an equality of ratio of shearing force to relative gravity, the shearing force being quadratic as in the case of a turbulent boundary layer, and 2) a second condition is imposed by the law of distortion of beaches (equilibrium profile of beaches) under different wave actions, which embodies globally many misunderstood phenomena. In addition to these two, one can choose somewhat arbitrarily another condition, such as a dynamic condition $^{n_u}/^{n_w} = \lambda/\mu$, where u is a horizontal current, w is the free fall velocity of the particles. One would rather choose an equality of boundary layer Reynolds number R_* . The theoretical formulation based on these assumptions is presented in the following section, based on the assumption that the scale for the friction factor is the same as in the case of a fully turbulent flow, as in the surf zone.

This relative freedom is partly due to the lack of understanding of the law of sediment transport under wave action. But it is also an indication of one of the reasons why coastal models are generally more successful than fluvial models.

- 9) It is pertinent to point out that since the only requirement of a movable bed model is a reproduction of bottom evolution, it is not necessary that this be achieved through exact similitude of water motion. Since the model is distorted, a similitude wave refraction and wave breaking only is being searched as a most satisfying condition, susceptible to producing satisfactory reproduction of long shore current and sediment transport distribution. This is achieved by keeping the ratio of wave lengths and wave heights like vertical scale μ . Based upon this condition, the following wave characteristics are preserved in the model: a) wave steepness, b) refraction pattern and angle or refraction with bottom contours, c) breaking angle of wave crests with shorelines if the distortion is not too large, and d) breaking depth.

Also, the scale for long shore current and mass transport velocities is approximately $\mu^{1/2}$. Therefore, the ratio of scales of wave particle velocity to current velocity is approximately unity.

A BRIEF REVIEW OF THE HYDRAULIC PROPERTIES OF SEDIMENTS UNDER WAVE ACTION AND CURRENT

- 1) It is first recalled that in the case of water waves, the laminar shear velocity u_* (see Appendix for notation) $u_* = \sqrt{\tau_o/\rho} = U_\delta^{1/2} (\nu\pi/T)^{1/4}$ (1)

U_δ is the amplitude wave bottom velocity $U_\delta = \pi T/\sinh kd$

For $R_\delta > 160$, the boundary layer flow is turbulent, then the turbulent bottom shear $\tau_o = \rho f U_\delta^2/8$ where f is the Darcy-Weisbach friction (2)

factor, and $u_* = \sqrt{\frac{f}{8}} U_\delta$ (3)

- 2) The hydraulic properties of a sediment particle are often represented by its fall velocity w in the water, defined by the equation

$$1.33 \frac{gD}{w^2} \gamma' = f \left(\frac{wD}{\nu} \right) \quad \text{or} \quad \frac{w}{\sqrt{\gamma'gD}} = f \left(\sqrt{\gamma'gD} D/\nu \right) \quad (4)$$

In Stokes range, $wD/\nu \ll 1$

$$\frac{w}{\sqrt{\gamma'gD}} = \frac{1}{18} \left(\sqrt{\gamma'gD} D/\nu \right) \quad (5)$$

- 3) In coastal processes, the sediment motion is caused by wave and tidal current actions. In studying such interactions, an important criterion is the critical condition initiation of sediment motion. Shields' criterion of the initiation of sediment motion is in the case of a steady current

$$\frac{\tau_C}{\rho g \gamma' D} = f_1(R_{*C}) \quad \text{where} \quad \tau_C \text{ is the critical shear stress} \quad (6)$$

$R_{*C} = u_{*C} D/\nu$ is the critical boundary layer Reynolds number based upon grain diameter D

$u_{*c} = \sqrt{\tau_C/\rho}$ is the critical shear velocity. If a boundary layer densi-
metric Froude number F_{*c} is defined as $F_{*c} = \frac{u_{*c}}{\sqrt{g\gamma'D}}$ (7)

then Equation (6) can be expressed as $F_{*c} = f(R_{*c})$ (8)

where F_{*c} is the critical boundary layer Froude number. For a given size of sediment, a critical velocity u_c can easily be derived by noting the relation $u = C_c u_y / \sqrt{g}$ where C_c is the Chezy coefficient (9)

Such criterion has also been investigated extensively in the case of sedi-
ments under wave action. It is remarkable that the criterion is identical with that of the steady current case, although the range of R_{*c} is consider-
ably smaller. For initiation of sediment motion due to wave action, the boundary layer Reynolds number R_{*c} based on grain diameter is given by

$$R_{*c} = 2.1 D \left(\frac{H^2}{\nu^3 T^3 \sinh^2 kd} \right)^{\frac{1}{4}} \text{ in a laminar boundary layer} \quad (10)$$

At present (1970) there is no experimental information on initiation of sediment motion due to combined wave and current actions known to the authors. Based upon dimensional consideration of similar nature as Equation (8), the criterion can be expressed as

$$F_{*c} = f \left(R_{*c}, \frac{u_{*w}}{u_{*c}}, \phi \right) \quad (11)$$

where F_{*c} and R_{*c} are critical boundary layer Froude and Reynolds numbers, based upon either wave or current shear velocities i e , u_{*w} or u_{*c} respectively. The parameter u_{*w}/u_{*c} shear velocity ratio represents the relative importance of wave and current effects. An additional factor is the angle of wave incidence to the current direction ϕ .

- 4) The volume transport rate of bed load q_s can be expressed in general as a function of boundary layer Reynolds number, R_* , boundary layer Froude number F_* and sediment size distribution

$$\frac{q_s}{u_* D} = f_1 (R_*, F_*, \sigma_D) \quad \text{or} \quad (12)$$

$$\frac{q_s}{u_* (u_*^2/g)} = f_2 (R_*, F_*, \sigma_D) \quad (13)$$

where q_s is the volume sediment transport rate per unit width. The effect of distribution of the sediment size is considered by including the geometric standard deviation σ_D .

Sediment transport by waves is mainly due to mass transport and longshore currents. On a beach, the onshore and offshore transport of sediments are reflected by the beach profiles. The alongshore transport of sediment (i e , littoral drift) is induced by longshore currents.

For bed load transport due to combined wave and current action, the volume rate is expected to be affected by two additional parameters,

namely, 1) the ratio of characteristic velocities between current and wave u_c/u_w , and 2) the incident angle of wave to the current direction ϕ , i.e.,

$$\frac{q_s}{u_x (u_w^2 / g)} = f(R_x, F_x, u_c/u_w, \phi, \sigma_D) \quad (14)$$

- 5) Beaches are formed by wave and coastal sediment interactions. Beaches are said to be in equilibrium when they reach stable profiles under relatively constant wave action. This means that the offshore and onshore transport of sediments are in balance. In general, the form of equilibrium profile of a beach depends upon the wave characteristics, such as wave height and wave length or wave steepness, sediment specific weight and sizes.

There is no well established law on beach equilibrium which can be applied both to offshore and surf zones, or to both natural sand and scale model light material. A study is now being conducted at Tetra Tech for this purpose.

- 6) The most commonly accepted relation for littoral drift is approximately

$$\frac{\gamma_f E}{2g(\gamma_s - \gamma_f)D} = K Q_s \left(\frac{\gamma_s - \gamma_f}{\gamma_f} \right)^{1/2} \left(\frac{1}{gD^3} \right)^{1/2} \quad (15)$$

where E is the longshore energy and K a constant coefficient (Manohar, 1962)

SIMILITUDE RELATIONS FOR MOVABLE BED RIVER MODELS

The similitude relations for movable bed river models are derived based upon similitudes on (Boucher and Le Mehauté, 1957) 1) basic flow characteristics and flow patterns, 2) head loss, 3) sediment transport characteristics and 4) kinematic condition on sediment motion.

As in a coastal model, there are four basic scale ratios to be determined namely, λ , the horizontal scale, μ , the vertical scale (or distortion), Ω , D , artificial sediment size, & γ' apparent specific weight. However, in many river model studies, an extra distortion is allowed for the river slope. Here, only the case with one distortion is discussed.

For similitude on basic flow characteristics and flow patterns, the model flow conditions are deduced based upon the Froudian law. The scale ratio of flow velocity n_u is $n_u = \mu^{1/2}$ and the time scale n_t is $n_t = \lambda \mu^{-1/2}$ (16)

For similitude of head loss, there are two conditions: 1) the energy gradient, and 2) the bed configuration. Based upon Chezy's formula

$$u = C_c \sqrt{d S_e} \quad \text{where } C_c \text{ is the Chezy coefficient} = \sqrt{8/f} \quad (17)$$

d is the water depth, R_h , the hydraulic radius for wide rivers, S_e is the energy gradient.

Since the energy gradient for a distorted model must be exaggerated by a factor of Ω , the scale ratio for the Chezy coefficient n_{C_c} is $n_{C_c} = \Omega^{-1/2}$ (18) and $n_f = \Omega$.

This condition is valid for movable bed models as well as for fixed bed models (For the latter, the head loss is set up experimentally without taking into account the relative roughness) For movable bed models, since the flow is kept fully turbulent, C_c can be expressed as $C_c = K (d/D)^{1/6}$ (19)

where K is a proportionality constant, and D is the sediment size

A necessary condition for this Equation for C_c to be applicable is that there should be no ripples or dune formation in the model This condition is

$$R_* = \frac{u_* D}{\nu} = 11.6 \frac{D}{\delta} > 500 \text{ (in the model), where } R_* \text{ is a boundary layer} \quad (20)$$

Reynolds number, $u_* = \sqrt{g d S_e}$ is the shear velocity The condition $R_* > 500$ implies $R > 500$ where $R = \frac{u R_h}{\nu}$ (i.e., the flow is fully turbulent in the

$$\text{model) Then the scale ratio for the sediment size } n_D \text{ is given by } n_D = \mu \Omega^3 \quad (22)$$

For the similitudes of sediment transport characteristics, there are three basic aspects namely, 1) initiation of sediment motion, 2) regimes of bed configuration and 3) bed load sediment transport characteristics So far, modeling of the suspension transport has not been carried out

The condition of initiation of sediment motion due to current action, as discussed in a previous section, is $F_C = f(R_{*C})$, where F_C is the critical boundary layer Froude number, and R_{*C} is the critical boundary layer Reynolds number (23)

Based upon the general formula for bed load transport rate per unit width, q_s can also be expressed in general functional relationship as

$$\frac{q_s}{u_* \left(\frac{u_*^2}{g} \right)} = f_2 (R_*, F_C, \sigma_D) \quad (24)$$

Based upon the above reasoning the similitudes of sediment transports including condition of initiation of sediment motion, require $n_{F_*} = 1$ (25)

$$n_{R_*} = 1 \quad (26) \quad \text{and} \quad n_{\sigma_D} = 1 \quad (27)$$

These Equations are entirely similar to those derived for coastal models They imply $n_{u_*}^2 n_{\nu}^{-1} n_D^{-1} = 1$ and $n_{u_*} = n_{U_\delta} (n_f)^{\frac{1}{2}} = \mu^{\frac{1}{2}} \left(\frac{\mu}{\lambda} \right)^{\frac{1}{2}}$ (28)

$$\text{or} \quad n_{\nu} n_D = \mu \Omega \quad (29)$$

In general, R_* in the field is large For large R_* , the sediment transport characteristics are approximately independent of R_* On the other hand, it is desirable to prevent occurrence of ripples in the model Thus, Equation $n_{R_*} = 1$ is relaxed in practice except specifying $R_* > 500$ in the model At large R_* , the sediment transport characteristics are believed to be dependent primarily on F_C On the model bed, it is undesirable to have extensive ripple formations because the model ripples often contribute too much flow resistance in comparison with the prototype condition and their effect is difficult to control

A kinematic condition of sediment motion is specified here as an additional basic similitude relation, a sediment in suspension travels distances in the

vertical and the horizontal directions proportional to its fall velocity w and its horizontal velocity u , (i.e. $x/y = u/w$, where x and y are horizontal and vertical distances of travel. This Equation gives an additional condition on the basic unknowns

$$\Omega = n_w/n_u = n_w \mu^{-\frac{1}{2}} \quad (31)$$

Considering the value of the fall velocity w , the scale ratio n_w is then given by $n_w = (n_v, n_D/n_{fw})^{\frac{1}{2}}$, where n_{fw} is the scale ratio of the function $f_w(wD/v)$. This condition cannot be expressed explicitly, because of the inclusion of n_{fw} . However, it is interesting to note that if one uses the same sediment in the model as in the prototype, $n_w = 1$, the above Equation reduces to $\lambda^2 = \mu^3$, which matches the Lacey relation based on river statistics, but $n_{F_x} = 1$ and $n_{R_v} = 1$ are then not verified

In summary, the similitude relationships of movable bed river scale models are determined from three conditions: 1) similarity of head loss $n_f = \mu/\lambda$, 2) similarity of sediment transport characteristics $n_{F_s} = 1$ and 3) kinematic condition of sediment motion $n_u = \lambda$ leading to a well defined distortion. In addition, there $\frac{n_u}{n_w} = \frac{\lambda}{\mu}$ should be no ripple formation in the model $R_* > 500$

The bed load transport formula, Equation (24) is used to obtain the time scale of bed evolution n_{tb}

$$n_{tb} = \lambda \mu / n_{qs} = \lambda^{5/2} \mu^{-2} \quad (34)$$

The kinematic conditions imply Lacey's law at $n_w = 1$. The Lacey's law is also compatible with the regime theory of rivers based upon statistical analyses of meandering rivers: width $\propto Q^{\frac{1}{2}}$, depth $\propto Q^{1/3}$. In scale relations, it gives identical relations as the one obtained by previous considerations, i.e.,

$$\lambda^2 = \mu^3 \quad (35)$$

which is often used as a guide in choosing λ and μ values. However, since this is derived by assuming identical model and prototype sediments, another relationship should be used in actual choice of scale ratios. This relationship can easily be verified quantitatively from the previous set of Equations where the particle fall velocity for the light scale model material is taken into account exactly.

SIMILITUDE OF SEDIMENT MOTION FOR COASTAL MODELS

Similitude of sediment motion means homogeneous scaling of sediment transport characteristics in the model, i.e., consistent quantitative relationships between the model and prototype transport quantities. For a distorted Froudan model, similitude of wave refraction insures

approximately identical u_c/u_w and ϕ values as in the prototype For constant $q_s/u_c \left(\frac{u_{*c}^2}{g} \right)$, it requires

$$n_{F_*} = 1 \quad (36) \qquad n_{R_*} = 1 \quad (37) \quad \text{and} \quad n_{\sigma_D} = 1 \quad (38)$$

(The condition $n_{\sigma_D} = 1$ is disregarded by most investigators) These

Equations give $n_{u_*}^2 = n_{\gamma'} n_D$ and $n_{u_*} n_D = 1$

The scale for n_{u_*} is actually difficult to define, since the boundary layer characteristics vary from offshore (viscous case or ripples) to the breaking zone, where it is fully turbulent, without ripples

In the first case (viscous) $n_{u_*} = \mu^{1/8}$

In the breaking zone $n_{u_*} = n_f^{1/2} \mu^{1/2}$

Considering the state of the art, it is difficult to assess the value of n_f If one assumes that f in the surf zone is a function of the relative roughness, as in the case of a river, then $n_f = \mu/\lambda$ Then $n_{u_*} \approx \mu \lambda^{-1/2}$

$$n_D = \lambda^{1/2} \mu^{-1} \quad (39) \qquad n_{\gamma'} = n_D^{-3} = \mu^3 \lambda^{-3/2} \quad (40)$$

The use of natural sand, $n_{\gamma'} = 1$, would require that $n_D = 1$ This implies that

model sand should be identical to the prototype sand In this case, Equation (40) gives $\lambda^{1/2} = \mu$, which could be considered as the natural distortion law

equivalent to Lacey condition $\lambda^2 = \mu^3$ for rivers Since the scale for the slope is equal to distortion $n_s = \frac{\mu}{\lambda}$, $n_s = \frac{1}{\lambda^{1/2}}$ (A natural beach subjected to 10 foot, 12 second waves of slope $\frac{1}{50}$ will have a $\frac{1}{100}$ scale model slope

of 1/5 when subjected to a 1 foot, 4 second wave) However, a lighter material than sand will actually insure less distortion and a more gentle scale model slope, therefore, less scale effects It is interesting to note that Equation $\lambda^{1/2} = \mu$ is compatible with $n_{F_*} = 1$ and also $n_{R_*} = 1$ Consequently, sand can be theoretically used on scale models of beaches

Although similitude of R_* and F_* are obtained based upon the bed load transport formula, the similitude relationships have the following additional implications 1) similitude of initiation of sediment motion, and 2) similitude of regimes of sediment motion

Thus, such similitude relationships imply a similar and homogeneous transport characteristic over the model as in the prototype However, there are several restrictions before the above equations for n_D and $n_{\gamma'}$ can be used These limitations are

- 1) Both the prototype and the model boundary layers are turbulent (this is certainly true in the surf zone)
- 2) The model friction factor is scaled according to distortion of $n_f = \frac{\mu}{\lambda}$
- 3) Size distributions of the sediments should be identical between model and prototype

- 4) Moreover, the analysis here does not apply in the case of a pebble beach. In such case, the condition of $n_{R_*} = 1$ is replaced by a limiting value of R_* , say, of 500

Theoretically, relationships between scales, distortion, artificial sediments, etc., are obtained based upon similitude of sediment transport characteristics and equilibrium beach profiles. Because of the uncertainties involved, certain preliminary wave tank experiments are necessary. The purpose of such wave tank experiments is to confirm the choice of distortion and artificial sediments. The similitude of sediment transport characteristics by selecting $n_{R_*} = 1$ and $n_{F_*} = 1$ gives not only the correct scaling of bed load transport, n_{R_*} but also the critical condition of sediment motion.

The condition $n_{R_*} = 1$ may then be too stringent and be replaced by a condition such as $R_* > R_{*,c}$, where $R_{*,c}$ is a minimum critical value for the scale model (say 160 implying a turbulent boundary layer).

An important scale ratio is the time scale of bottom evolution n_{tb} . The value of n_{tb} is usually determined in the process of reproduction of bottom evolution. Analytically, n_{tb} can be obtained from any sediment transport formula (15). For a coastal movable bed model, the littoral transport formula, is proposed here to be used for determining the value of n_{tb} .

$$n_{tb} = \frac{\lambda^2 \mu}{n_{Qs}^2} = \lambda^2 \mu^{-3/2} n_D^{-1} n_{Y'}^{1/2} \quad \text{where } n_{Qs} \text{ is the scale ratio of} \quad (41)$$

the littoral transport rate. This Equation is applicable only in the case of coastal problems where the littoral transport is the dominant sediment transport mechanism. For river models, a different formula has already been proposed. This formula is useful in predicting time scale of bed evolution in the model. At present, there are, to our knowledge, two sets of data available for comparison.

- 1) Cobourg Harbor Study (Le Méhauté and Collins, 1961)

Model conditions $\lambda = 1/200$, $\mu = 1/60$ Artificial sediment Gilsonite,
 $n_{Y'} = 0.0182$, $n_D = 7$.

Timescale by model reproduction of bottom evolution $n_{tb} = 25 \text{ min} \quad 1 \text{ yr}$

Timescale from proposed Equation $n_{tb} = 117 \text{ minutes} \quad 1 \text{ year}$

In this study, the model wave height was exaggerated, approximately, by a factor of two. A correction of the wave height scaling based upon the littoral drift equation gives $n_{tb} = 29 \text{ minutes} \quad 1 \text{ year}$, which is close to the predicted value.

- 2) Absecon Inlet Study (U S Waterways Experiment Station, 1943)

Model conditions $\lambda = 1/500$, $\mu = 1/100$ Artificial sediment Sand,
 $n_{Y'} = 1$, $n_D = 0.63$

Timescale by model reproduction of bottom evolution $n_{tb} = 13 \text{ hrs} \quad 1 \text{ yr}$

Timescale from proposed Equation $n_{tb} = 56 \text{ hours} \quad 1 \text{ year}$

Again there is a correction on the exaggeration of the model wave heights (a factor of about two) $n_{tb} = 14 \text{ hours} \quad 1 \text{ year}$

An additional correction is to be made due to the fact that 22 percent of time was not reproduced in the model when there was no littoral transport in the field $n_{tb} = 11$ hours 1 year

Thus, these predicted time scales compared favorably with observed values. The accuracy is estimated to be within 30 percent.

CONCLUSION

The success of a movable bed scale model depends upon the proper choice of distortion and material. Distortion is a natural observed phenomena, which needs to be strictly adhered to for similitude. Its choice can theoretically be justified in the case of a river, based on well defined conditions of similitude. These conditions lead to a Lacey type relationship close to $\lambda^2 = \mu^3$. The law $\lambda^2 = \mu^3$ prevails in the case where the same material (sand) is used in both the prototype and the model. This is the law of "natural distortion" which is not compatible with other conditions of similitude ($n_F = 1$, $n_T = \Omega$).

The choice of scales and material is less well defined in the case of beaches. However, for a given material and vertical scale, there is also a well defined rate of distortion based on the equilibrium profile of beaches. This approach compensates to a large extent for the lack of understanding of the law of sediment transport by wave action. If one assumes that the regime in the boundary layer is turbulent, the friction coefficient can be related to relative roughness (as in the case of a steady flow) and the same material, a law of "natural distortion" is also obtained such as $\lambda^{1/2} = \mu$. The first law is approximately verified by compilation of river statistics, while the second law ($\lambda^{1/2} = \mu$) is obtained from theoretical considerations. This law still needs to be proven, improved, or disproven from observation. For the time being, one can only insure that it gives a qualitatively observed trend (Wiegel, 1964). Lighter scale model material will insure a smaller rate of distortion. Therefore, the use of sand in movable scale models may provide too large a scale effect, even though it is now compatible with $n_{F*} = 1$ and $n_{R_c} = 1$. It is hoped that present studies on equilibrium profiles of beaches will solve some of the uncertainties that have been brought out in this paper. In the meantime, preliminary 2D tests are still necessary for determining distortion prior to designing any large 3D model.

It is also hoped that the present paper will help to demonstrate that movable bed scale model technology is not "magic witchcraft" after all.

ACKNOWLEDGMENTS

This study was sponsored by the Coastal Engineering Research Center, Washington, D C, under Contract DAC W 72-68-C-0020. The writer is indebted to Drs. I. Collins, E. Noda, and L. N. Fan for many fruitful discussions.

SUMMARY

Conditions of Similitude

Coastal	Fluvial
1) Similitude of wave refraction Time scale $n_t = \mu^{\frac{1}{2}}$ Velocity, current $n_u \approx \mu^{\frac{1}{2}}$ Similitude of wave breaking $n_{H_b} = \mu$	1) Normal Froude similitude for distorted model Time scale $n_t = \lambda / \mu^{\frac{1}{2}}$ Velocity $n_u = \mu^{\frac{1}{2}}$
2) $n_{F_*} = 1$ $n_{u_*}^2 = n_{V'} n_D$ (imperative)	2) $n_{F_*} = 1$ $n_{u_*}^2 = n_{V'} n_D$ (imperative)
3) $n_{R_*} = 1$ (not imperative, but recommended)	3) $R_* > 500$ no ripple (imperative)
4) Short model independent of relative roughness $n_{u_*} \approx \mu \lambda^{-\frac{1}{2}}$ if (?) $n_f = \mu / \lambda$ (surf zone)	4) Long model similitude of head loss, function of relative roughness $C_c = K \left(\frac{d}{D} \right)^{1/6}$ $n_{C_c} = \left(\frac{\lambda}{\mu} \right)^{\frac{1}{2}}$, $n_f = \mu / \lambda$ (imperative) $n_{u_*} = \mu \lambda^{-\frac{1}{2}}$ (turbulent boundary layer)
5) Suspension $\frac{n_u}{n_w} = \frac{\lambda}{\mu}$ (not imperative ?)	5) Suspension $\frac{n_u}{n_w} = \frac{\lambda}{\mu}$
6) Distortion imposed by equilibrium profiles of beaches (Still undetermined for light model material)	6) 2, 4, & 5 combined lead to a distortion with different material (imperative)
Natural distortion (same material), and where $n_f = \frac{\mu}{\lambda}$ $\lambda^{\frac{1}{2}} = \mu$ Compatible with $n_{F_*} = 1$, $n_{R_*} = 1$ but too large distortion (scale effects)	Natural distortion (same material) $\lambda^2 = \mu^3$ Compatible with "regime theory," but not with $n_{F_*} = 1$

Phenomena and Important Quantities	Similitude Relations	
	Fluvial	Coastal
A) <u>Geometry</u> Horizontal length Vertical length Distortion Ω Slope (river, beaches) S	λ μ μ/λ μ/λ	λ μ μ/λ μ/λ
B) <u>Water Motion Characteristics</u> Water depth d, wave breaking depth d_b Wave height H, breaking wave hgt H_b Wave length L Wave period T Refraction angle & wave breaking angle Wave diffraction, reflection Time scale t Particle velocity Mass transport longshore velocity Friction coefficient f Chezy coefficient C_c Viscous sublayer Shear velocity u_* Energy slope Head loss	μ $\lambda/\mu^{\frac{1}{2}}$ $\mu^{\frac{1}{2}}$ $\Omega^{-\frac{1}{2}}$ $(\mu\Omega)^{-\frac{1}{2}}$ $(\mu\Omega)^{-\frac{1}{2}}$ Ω μ	μ μ μ μ 1 Not in similitude $\mu^{\frac{1}{2}}$ $\mu^{\frac{1}{2}}$ $\mu^{\frac{1}{2}}$ Ω (for surf zone) $(\mu\Omega)^{\frac{1}{2}}$ (for surf zone) $R_\delta > 160$ $\mu^{1/8} R_\delta < 160$ (viscous)
C) <u>Sediment Characteristics</u> Sediment size D Apparent specific weight γ' Size distribution σ_D	$\lambda^{\frac{1}{2}} \mu^{-1}$ $\mu^3 \lambda^{-3/2}$ 1	$\lambda^{\frac{1}{2}} \mu^{-1}$ (for surf zone) $\mu^3 \lambda^{-3/2}$ 1
D) <u>Initiation of Motion</u> Critical boundary layer Reynolds number R_{*C} Critical boundary layer Froude number F_{*C}	$R_{*C} > 500$ 1	1 1
E) <u>Sediment Transport Characteristics</u> Boundary layer Reynolds number R_{*C} Boundary layer Froude number F_{*C} Volume of deposition or erosion Time of bed evolution	> 500 1 $\lambda^2 \mu$ $\lambda^{5/2} \mu^{-2}$	1 or $n_{u_*} n_D = 1$ 1 or $n_u^2 = n \gamma' n_D$ $\lambda^2 \mu$ $\lambda^2 \mu^{-3/2} n_D^{-1} n_{\gamma'}^{\frac{1}{2}}$

Comparison of Various Approaches for
Determination of Basic Scale Ratios of
A Coastal Movable Bed Model

Authors	Basic Relations	Method of Derivation
Goddet & Jaffry (1960)	$n_D = \mu^{17/20} \Omega^{8/5}$ $n_{\gamma'} = \mu^{3/20} \Omega^{-3/5}$	Sediment motion due to combined action of waves and currents
Valembois (1960)	$\Omega = n_{\gamma'}^{-1}$ $n_{\gamma'} n_D^3 = 1$ $\mu = n_{\gamma'}^3 n_D (n_H/\mu)^{-4}$	Kinematics of motion of suspended sediments Similitude of D Modified relation of initiation of sediment motion $D = KR_s^{8/9}$
Yalin (1963)	$n_D = \mu^{3/4} \lambda^{1/2}$ $n_{\gamma'} n_D^3 = 1$	Dimensional analysis
Bijker (1967)	$n_{\gamma'} n_D \Omega^{-1} = \mu n_{\mu r}$ $\Omega \leftarrow$ equilibrium beach profiles	Similitude of F_s
Present Method(1970)	$n_{\gamma'} n_D^3 = 1$ $n_{\gamma'} = \mu^3 \lambda^{-3/2} \quad \text{or}$ $n_D = \lambda^{1/2} \mu^{-1}$ $\Omega \leftarrow$ equilibrium beach profiles	Similitude of sediment transport characteristics, τ_e , F and R_s

LIST OF SYMBOLS

C_c	Chezy coefficient $(L^{1/2} T^{-1})^3$
d	depth of water
d_b	depth of water at breaking
D	mean sediment size
D_*	dimensionless sediment size = $\left(\frac{(\gamma_s - \gamma_f) g}{\nu^2 \gamma_f}\right)^{1/3} D = (R_* / F_*^2)^{2/3}$
E	wave energy flux per unit length of the crest (MLT^{-2})
f	Darcy-Weisbach friction factor
F_*	boundary layer densimetric Froude number = $u_* / \sqrt{\gamma' g D}$
F_*^C	critical boundary layer Froude number on initiation of sediment motion
g	acceleration of gravity
H	wave height
k	wave number = $2\pi/L$
L	wave length
n_{quantity}	scale ratio with subscripts denoting corresponding quantities = (value of model)/(value of prototype) e.g., n_L is the scale ratio of the wave lengths
q_s	volumetric sediment transport rate per unit width $(L^2 T^{-1})$
Q_s	volumetric sediment transport rate $(L^3 T^{-1})$
r	radial coordinate
R_h	hydraulic radius
R_δ	boundary layer Reynolds number = $U_\delta \delta / \nu$
R_{*c}	boundary layer Reynolds number based upon sediment size = $u_* D / \nu$
R_*^C	critical boundary layer Reynolds number on initiation of sediment motion
S	slope
S_e	energy gradient
t	time
t_b	time of bed evolution
T	wave period
u	horizontal velocity
u_C	critical velocity for sediment motion

u_c	shear velocity = $\sqrt{\tau / \rho}$
u_x	current shear velocity
u_x^c	wave shear velocity
U^w	horizontal velocity
U_δ	velocity immediately above the boundary layer
v	vertical velocity
w	sediment fall velocity
x	horizontal coordinate
y	vertical coordinate
δ	boundary layer thickness
δ_L	laminar boundary layer thickness parameter
δ_T	turbulent boundary layer thickness
γ_f	specific weight of the fluid
γ_s	specific weight of the sediment
γ'	apparent specific weight of the sediment = $(\gamma_s - \gamma_f) / \gamma_f$
λ	horizontal scale
μ	vertical scale, dynamic viscosity of the fluid (ML^2T^{-1})
ν	kinematic viscosity of the fluid
Ω	distortion = μ / λ
ξ	angle of wave incidence w r t the current direction
π	3.1416
ρ	mass density of the fluid
σ_D	geometric standard deviation of the sediment size distributions
τ	shear stress
τ_C	critical shear stress on the initiation of sediment motion

PARTIAL LIST OF REFERENCES

- Bascom, W N (1951), "The Relationship Between Sand Size and Beach-Face Slope", Trans AGU, 32, No 6, December, pp 866-874
- Bijker, E W (1967), "Some Considerations About Scales for Coastal Models with Movable Bed", Delft Hyd Lab , Pub No 50, Nov , 142 pages
- Bonnefille, R, and Perneckner, L (1965), "Note de Synthese Sur Les Mouvements Des Fonds Marins Sous L'Action des Courants et de La Houle", National Hydraulics Lab , Chatou Res and Exp't Center, France 66 pages
- Boucher, R , and Le Méhauté, B (1957), "L'etude Experimentale des Problemes de l'Hydraulique Fluviale", L'ingenieur, Montreal, pp 49-58
- Collins, J I (1963), "Inception of Turbulence at the Bed Under Periodic Gravity Waves", J of Geophy , Res , Vol 68, No 21, Nov , pp 6007-6014
- Divoky, D , Le Mehaute, B , and Lin, A (1969), "Breaking Waves on Gentle Slopes", AGU
- Eagleson, P S , Glenne, B , and Dracup, J A (1963), "Equilibrium Characteristics of Sand Beaches", J of Hyd Div , Proc ASCE, Jan , pp 35-57
- Fan, L N , and Le Mehauté, B (1969), "Coastal Movable Bed Scale Model Technology", Tetra Tech, Inc No TC-131
- Goddet, J (1960), "The Initial Stages of the Transport of Materials Under Wave Action" La Houille Blanche, No 2, March-April, pp 122-135
- Goddet, J , and Jaffry, P (1960), "Similitude Laws for Sediment Transport Under the Simultaneous Action of Waves and Currents", La Houille Blanche, No 2 March-April, pp 136-147
- Larras, J (1957), "Effet D'echelle Dans Les Etudes D'erosion du Sable Par La Houle Et Par Le Clapotis", Proc of 7th Cong If IAHR, Lisbon, Paper No A-5 13 pages
- Le Méhauté, B , and Brebner, A (1961), "An Introduction to Coastal Morphology and Littoral Processes", CE Dept , Res Rept 14, Queen's University, Jan , 46 pages
- Le Mehauté, B , and Collins, J I (1961), "A Model Investigation of Cobourg Harbor", CE Dept , Res Rept 17, Queen's University, July
- Le Mehaute, B (1962), "Theory, Experiments, A Philosophy of Hydraulics", J of Hyd Div , Vol 88, HY 1, Proc of ASCE, Jan pp 45-66

- Le Mehaute, B and Koh, R C Y (1967), "On the Breaking of Waves Arriving at an Angle to the Shore", *J of Hydraulic Research*, 5, No 1, pp 67-88
- Manohar, M (1962), Discussion of "Laboratory Determination of Littoral Transport Rate", by R P Savage, *J of Waterways and Harbors Div*, Proc ASCE, 88, No 4, Nov pp 144-147
- Savage, R P (1962), "Laboratory Determination of Littoral Transport Rates", *Journal of Waterways and Harbors Div*, Proc, ASCE, May, pp 69-92
- Saville, T Jr (1950), "Model Study of Sand Transport Along an Infinitely Long, Straight Beach", *Trans AGU*, 31, No 4, Aug pp 555-565
- Saville, T Jr (1957), "Scale Effects in Two-Dimensional Beach Studies", Paper No A-3, Proc of 7th Congress of IAHR, Lisbon
- Simmons, H B (1950), "Contribution of Hydraulic Models to Coastal Sedimentation Studies", Proc of 1st Conf on Coastal Engrg, Long Beach, 19 pages
- Simmons, H B (1966), "Tidal and Salinity Model Practice", Ch 18 of *Estuary and Coastline Hydrodynamics*, Ed by A T Ippen, pp 711-731
- Sitarz, J A (1963), "Contribution a l'Etude de L'evolution des Plages a Partir de la Connaissance des Profils D'equilibre", *Travaux du Center de Recherches et d'Etudes Oceanographiques*, Vol 5, Sept
- Valembois, J (1960), "Etude Sur Modele Du Transport Littoral Conditions De Similitude", Ch 18, Proc 7th Conf on Coastal Engrg, The Hague, pp 307-317 (English Translation, U S Army Corps of Engineers, Waterways Experiment Station, Translation No 65-7, July 1965)
- Vanoni, V A Brooks, N H and Kennedy, J F (1961), "Lecture Notes on Sediment Transportation and Channel Stability", W M Keck Lab of Hydraulics and Water Resources, Tech Report KH-R-1, Calif Institute of Technology, Pasadena, California, Jan
- Wiegel, R L (1964), "Oceanographical Engineering", Prentice-Hall, Inc, Englewood Cliffs, N J, 527 pages (p 359)
- Yalin, S (1963), "Method for Selecting Scales for Models with Movable Bed Involving Wave Motion and Tidal Currents", Proc of 10th Congr of IAHR, Vol 1, paper I 30, London

CHAPTER 70

STUDY OF DURBAN HARBOR SILTING AND BEACH EROSION¹⁾

Jan Malan Jordaan, Jr., M. ASCE²⁾

Abstract

A 1 : 300 vertical, 1 : 100 horizontal scale model of seven miles of coastline, including the major area of the port limits and the inner harbor, was constructed to study combined wave, tide and wind action on transport of sand along the coast.

The effects of three predominant conditions of swell and wind-waves on the state of the ocean front beaches were studied by observing relative changes in shoreline contours. Fluorescent-dyed sand tracers were also used in the model. The accumulation and dredging of sand near the harbor entrance was reproduced in the model and various dredging and storage proposals were carried out to scale on the model.

The model study enabled the cause of beach erosion to be attributed to the existence of an offshore shoal produced by the localized dumping of sand dredged from the harbor approaches. This shoal caused selective wave action along the coastline, which was reproduced to scale in the model. It was found that wind and tidal action had a major effect on the redistribution of sand on the beaches as modeled but a minor effect on the permanence of the harbor entrance channel. Apart from the interaction of dredged sand at times being fed to the beaches, the problem of beach erosion could be studied independently of that of harbor silting on the same model. Sand was fed to maintain a state of equilibrium on the southern approach beach to the harbor to simulate the littoral supply.

The northern beach downdrift of the harbor entrance, where the erosion problem existed, was found to be essentially starved of littoral supply, due to maintenance of the harbor entrance by dredging and offshore dumping.

The requirements of the model study also gave rise to a program of field data collection on the governing environmental factors, which in itself aided considerably to the diagnosis of the causes of the state of unbalance in the shoreline. The model study led to several proposed remedial schemes, certain of which have been adopted since completion of the model study. The model study was conducted by the South African Council for Scientific and Industrial Research, for the South African Railways and the City Council of Durban.

- 1) This work was conducted by the author while a Senior Research Officer of the Nat. Mech. Engrg. Res. Inst., South African Council for Scientific and Industrial Research, under contract with the South African Railways and the City Council of Durban.
- 2) Assistant Chief Engineer (Design), Department of Water Affairs, Pretoria, South Africa.

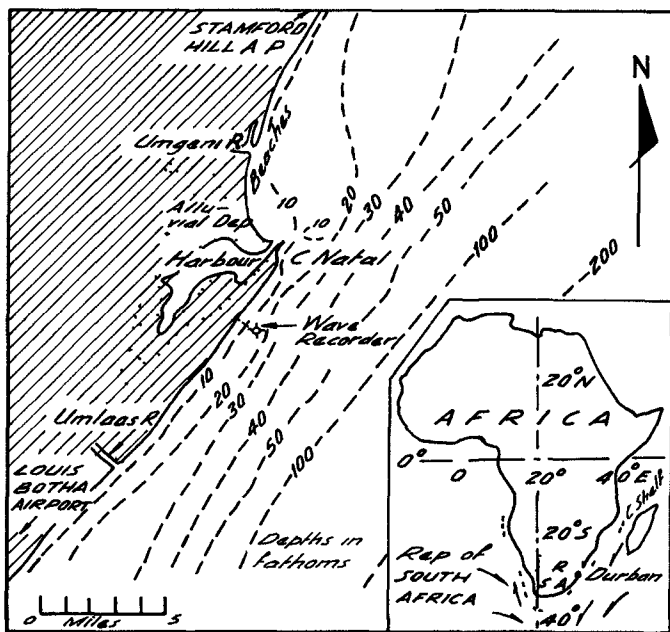


Figure 1 Plan of Vicinity and Location.

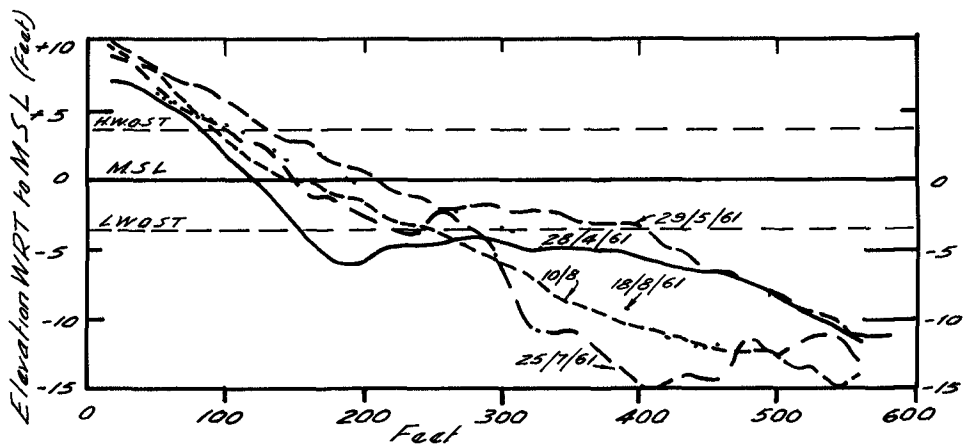


Figure 6. Variability of beach profiles at West Street Jetty, South Beach.

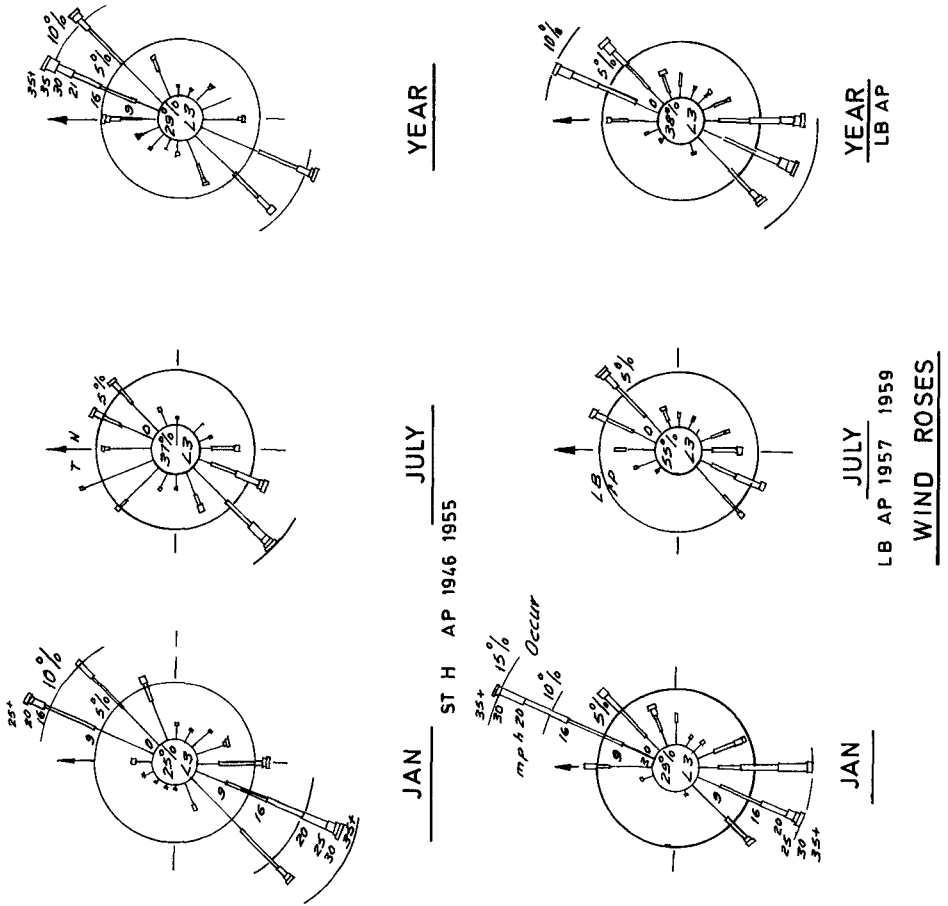


Figure 2. Wind roses for Stamford Hill and Louis Botha Airports, Durban.

1. Historical resume and statement of the problem

Durban is situated on South Africa's east coast around a natural bay which was first settled in 1824. It has since grown to become the country's largest port and most popular seaside resort (Fig. 1).

The Durban port is located at a geological irregularity of the otherwise straight coastline. The harbor entrance channel is formed between the 300 ft high projecting spur "The Bluff" and the 20 ft high estuarine formation "The Point". The nearshore area and the beaches are referred to as the Bluff side and the Bight respectively.

Before 1851 the estuarine channel remained open naturally, mainly as a result of tidal action and the protection afforded by the Bluff from SW to SE storms. The depth over the bar was, however, only about 6 feet at that time. In 1851 the harbour entrance-channel works were commenced. Breakwaters were built and extended at intervals on both the north and the south sides of the entrance, until the present state was reached in 1952 (Moffatt, 5).

At present the entrance channel is dredged to a width of 650 feet and is kept 42 feet deep in the channel proper and 48 feet deep at the bar. Maintenance dredging, which consists mainly of keeping the sand trap just south of the entrance approximately 54 feet deep, has steadily increased and now amounts to approximately 800,000 cubic yards a year (Fig. 5). One of the main aims of the investigation was to find means of reducing this amount.

The material which was dredged was mainly dumped offshore, in the earlier years up to 1938 in an area about $1\frac{1}{2}$ miles east of the entrance and thereafter at various distances south-east of the entrance. During more recent years, however, some of the material has been supplied for pumping to the beaches (Fig. 7a).

The second main task of the investigation was concerned with stabilizing Durban's ocean beaches (Fig. 6). The beaches are located between the Point and the Umgeni River mouth on Durban Bay which forms part of a concave portion of coast stretching north from Cape Natal (Fig. 1). In the past, due to this particular location, a rather stable condition must have existed (4). Due to the harbor entrance improvements the equilibrium of the sand movements was disturbed (3). During the earlier stages of breakwater building (1851-1903) large deposits, a result of greater protection against SW to SE swells, caused the beaches to progress generally seawards a distance of about 800 feet.

From 1938 until 1949 some 5 million cubic yards of sand was pumped to Vetch's Bight (Fig. 9) by S.A. Railway dredgers moored at the North Pier through a 42" dia. pipe (4).

From 1950 to 1953 sand was pumped from a suction plant just south of the South Breakwater directly to Vetch's Bight through a 16" dia. submarine pipeline across the entrance channel. Because insufficient sand collected near the suction plant in the Cave Rock Bight, after 1953 the original system with the Railway dredgers delivering sand to Vetch's Bight was resumed. It was presumed that initially 600,000 cubic yards of sand per annum would be pumped and,

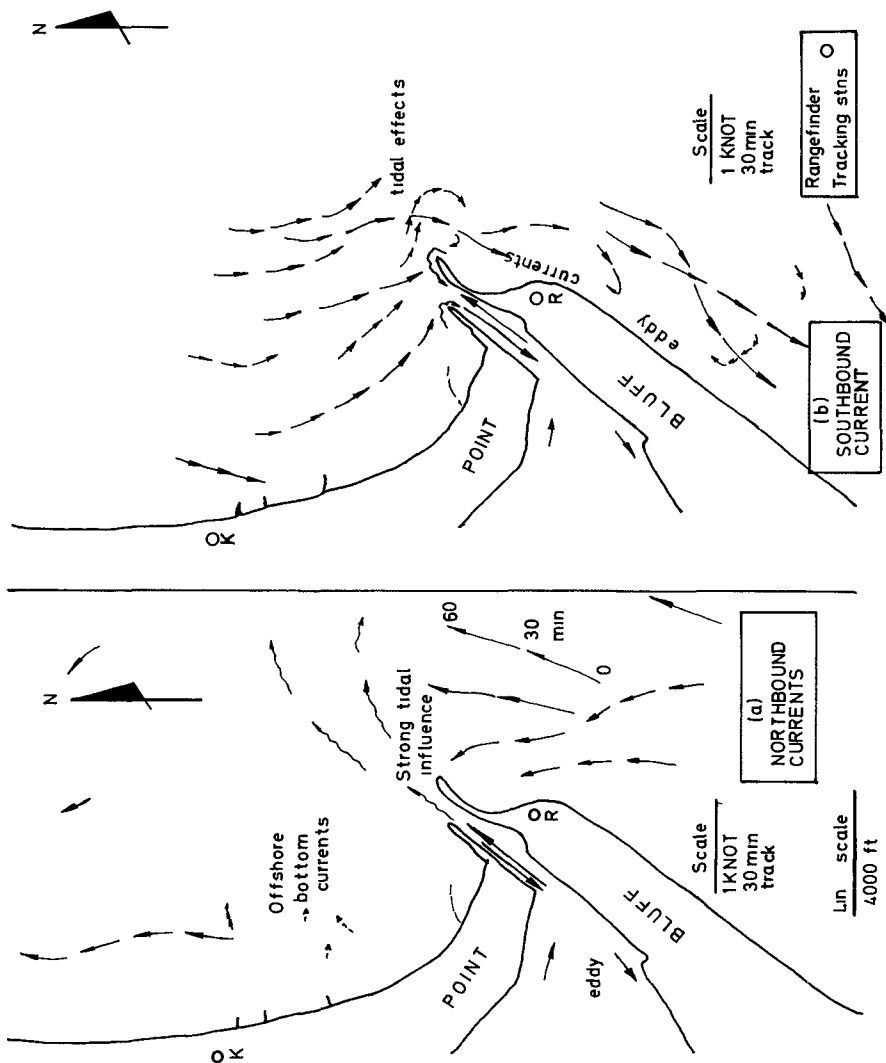


Figure 3. Typical Current Tracks with 10-ft Drogues on Floats, (Durban 1961-62).

FIGURE 3ab TYPICAL CURRENT TRACKS WITH 10 FT DROGUES ON FLOATS (DURBAN 1961 - 62)

after a period of building up, 300,000 cubic yards of sand would be available for maintenance. Moreover, two groins or breakwaters (Paterson Groynes) were built between 1954 to 1956 in order to stabilize the sand supplied to the Central Beach.

In 1960, at the start of this investigation, the supply of only one-third of the annual quantity of sand required for maintenance purposes could be realized, so that the Central Beach in particular was badly starved of sand. In addition, scour holes developed near the tips of the Paterson groins, causing a steep beach slope and dangerous swimming conditions near the groins.

2. Data Collection

In order to successfully perform a hydraulic model study such as the Durban investigation, a complete set of field data, covering both oceanographic, topographic and geomorphological aspects must be obtained. Oceanographic data were collected over a period of 26 months from October 1960 until November 1962.

Wind. The result of the analyses of wind records taken over ten consecutive years at Stamford Hill Airport and over three years at Louis Botha Airport are shown in Figure 2. The predominance of strong winds from north-easterly and south-westerly directions is striking. This fact was made use of in the layout of the model.

Waves. Long period waves (swell) and storm waves cause rapid migration of sand directly and also indirectly by wave-induced currents. Sand movements can be correlated with incoming wave energy. Proper wave records are therefore essential for the analysis of sand movement. Waves can be fully described by their direction of approach, height and period. Because wave patterns are often very complex the above values have to be expressed statistically.

Wave characteristics have been recorded over various periods at the beach front (West Street Jetty), at the harbor entrance and by inverted echo-sounder recorder 1 mile off the Bluff (?). Wave direction, refraction and diffraction were successfully recorded by means of aerial photography for three typical weather conditions. It is clear from Figure 9 that wave direction in the Bight area is very much affected by wave refraction, while in the Vetch's Pier area, diffraction plays an important role.

The six months echo-sounder records have been supplemented and combined with Pilot Boat logs and clinometer readings to give the wave energy roses shown in Figure 4. These wave roses are fully representative for an average year (6). A very severe storm occurred from 24th to 30th August, 1962 when the recorder was inoperative. Stereo-photo pairs of the waves during the peak of the storm were obtained from an aircraft and these, together with visual estimates of wave heights, led to the conclusion that waves up to 20 feet high and of 11 to 12 seconds period occurred near the harbor entrance. The persistence of swell from any one direction has been determined as normally three to four days. A persistency of seven days was never exceeded.

Currents. Even fairly weak currents can cause substantial sand

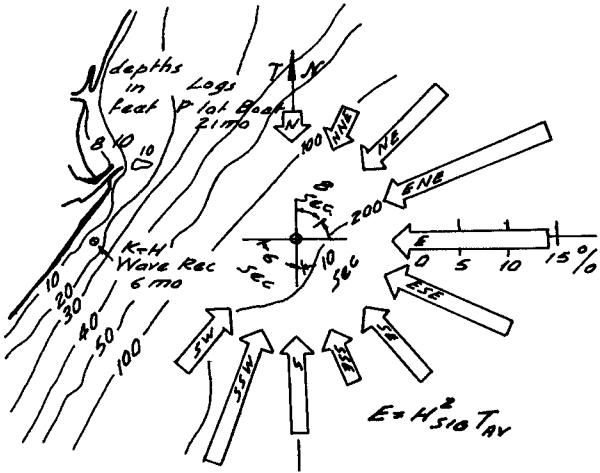
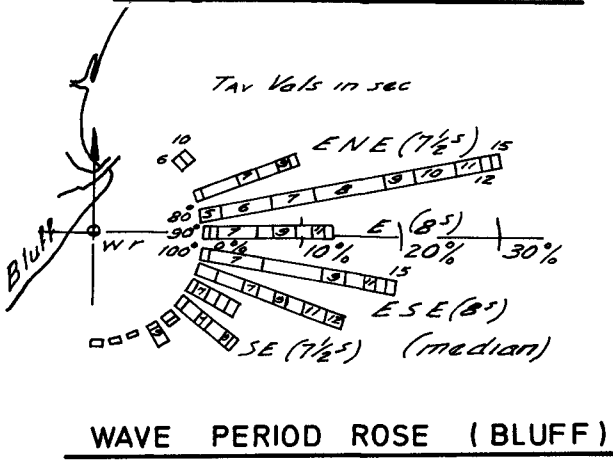
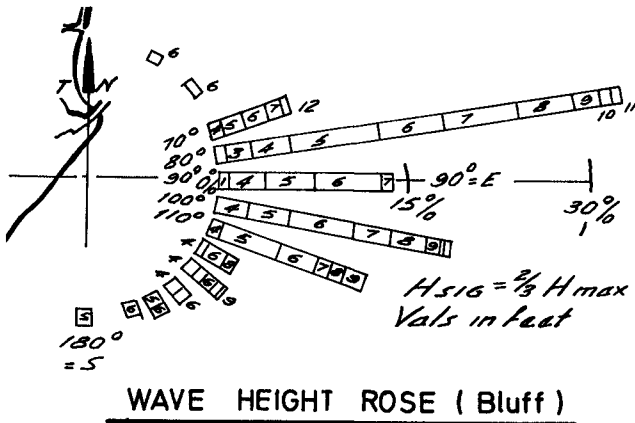


Figure 4. Wave Energy Distribution, offshore locations, Durban.

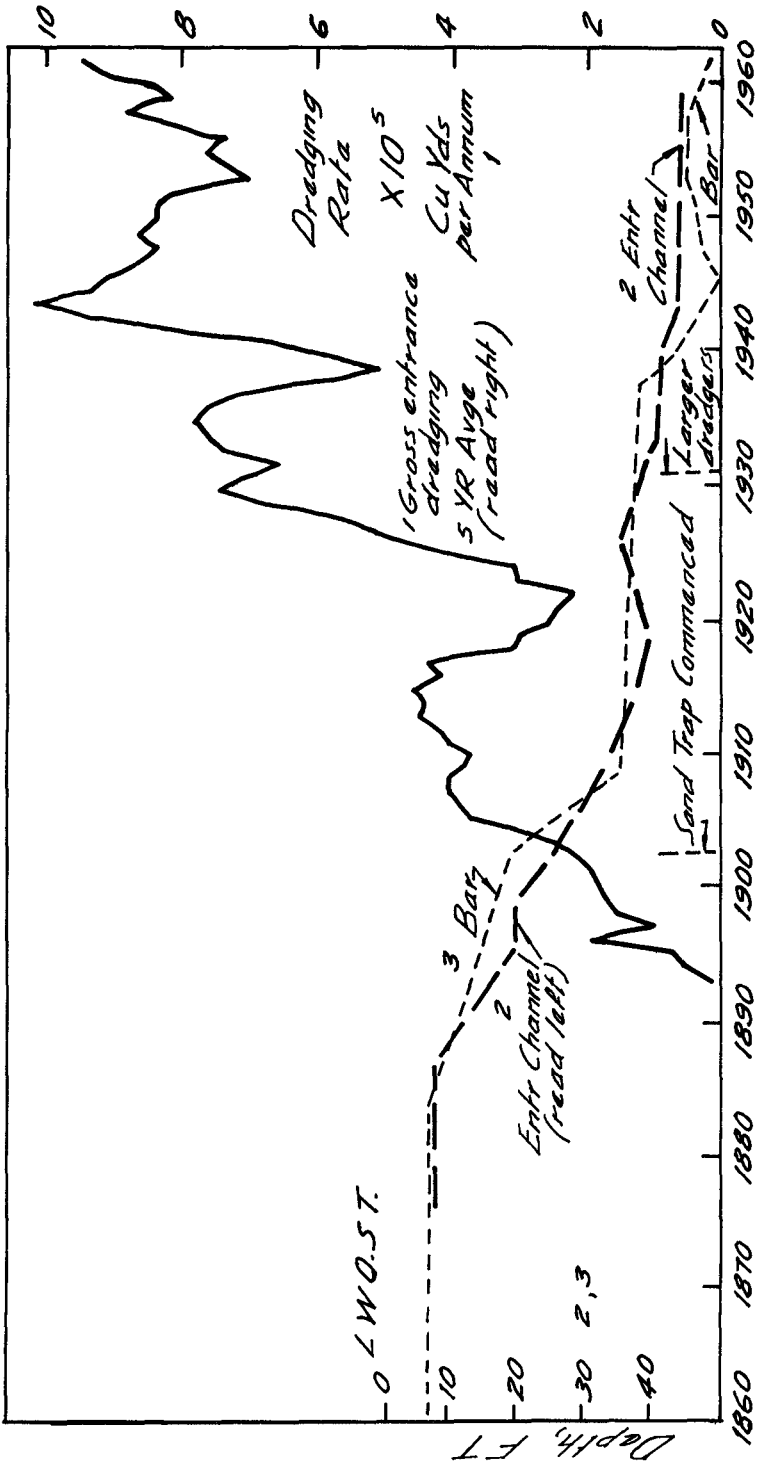


Figure 5. Dredging Rates per annum; entrance channel depths at various times.

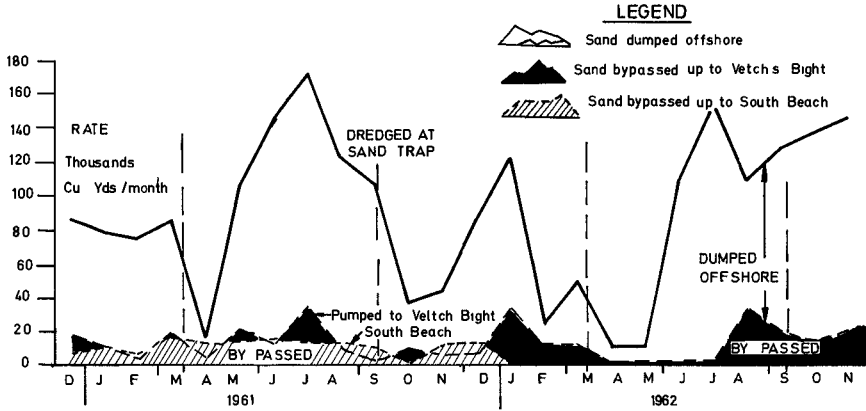


Figure 7a Distribution of Sand dredged, Sand dumped offshore and Sand pumped to Beaches (bypassed)

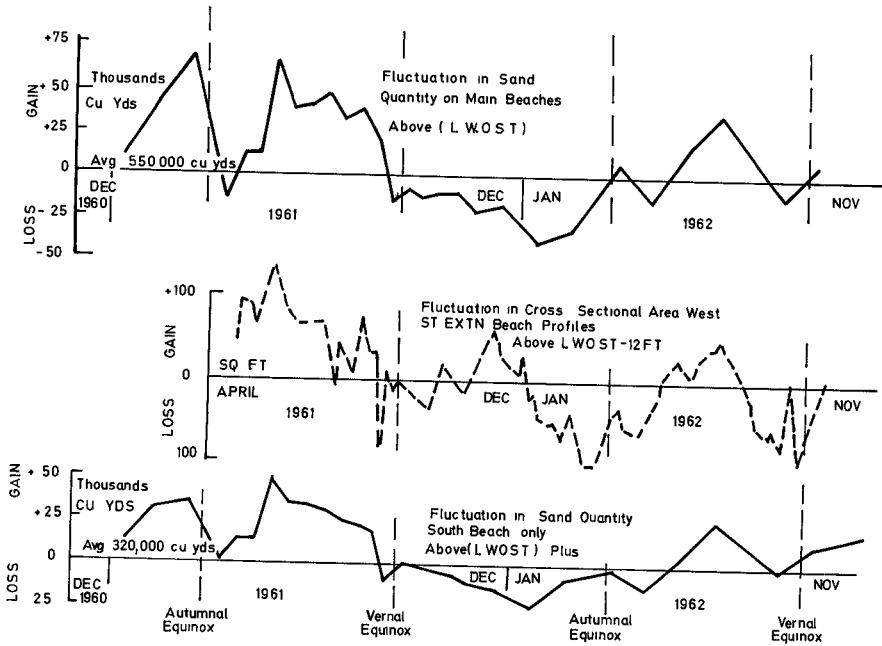


FIGURE 7 b Corresponding changes to beach sand quantities, mainly as affected by seasonal influence moving sand on- and offshore

movements when occurring concurrently with waves of swell which stirs up the bottom material into suspension. On the other hand, current velocities have to be about 1.25 knots to be able to transport material not already in suspension. The south bound Mozambique current, which is in general not found within the 100 fathom line, creates a counter current from south to north along the coastline at Durban. The extent and strength of this counter current has been found to be extremely variable.

For correct reproduction of prototype conditions in the model a better understanding of the current system near Durban was therefore called for. Measurements, spread over a period of nearly two years, included aerial photographic tracing of surface floats with drogues attached, propeller current meter measurements from a boat, tracking of floats with two rangefinders and measurements of bottom currents with jelly bottles.

3. Morphology

The quantities of sand in beaches above low water mark taken from regular fortnightly surveys made by the Durban Corporation are given in Figure 7b. The total and the South Beach quantities have also been plotted. A significant loss of sand is seen to have occurred at the equinoctial spring tides. A set of typical extremes in beach profiles taken along West Street Jetty over a period of eighteen months reflect the effects of various extreme conditions on underwater beach formation (Fig. 6). The maximum variation of beach level near mean sea level was found to be nine feet, corresponding to a beach width change of approximately 150 feet.

Dredging at Durban harbor started in 1884 in the entrance channel and in 1893 on the bar. From 1903 onwards dredging was concentrated more in the sand trap area. The data for floating five-year averages of annual dredging outside the harbor basin are plotted in Figure 5. Available records of channel and bar depths have been plotted as well. The correlation between dredged quantities, channel and bar depths can readily be seen from the figure. For the past several decades the South African Railways (S.A.R.) have made available to the Durban Corporation (D.C.) a certain quantity of sand per annum for beach renourishment. This sand is pumped by the S.A.R. and discharged just north of Vetch's Pier where it is retrieved by the D.C. pumping plant and discharged just north of West Street Jetty via booster stations. Records made available by the S.A.R. and D.C. for the two years 1961 and 1962 are presented in Figure 7a. The various monthly quantities dredged and pumped via the various pipe lines are shown.

Sand samples were taken at various places along the beaches and from the sea bottom in the area represented in the model (1). They showed significant differences in size distribution, hue and texture. The results yielded a basis for classifying the sand by size as well as by color and permitted interpretation to be made of the pattern of sand movement. This made the use of special tracer experiments unnecessary. The sand south of the Umgeni River down to the harbor entrance is rather fine, well-sorted

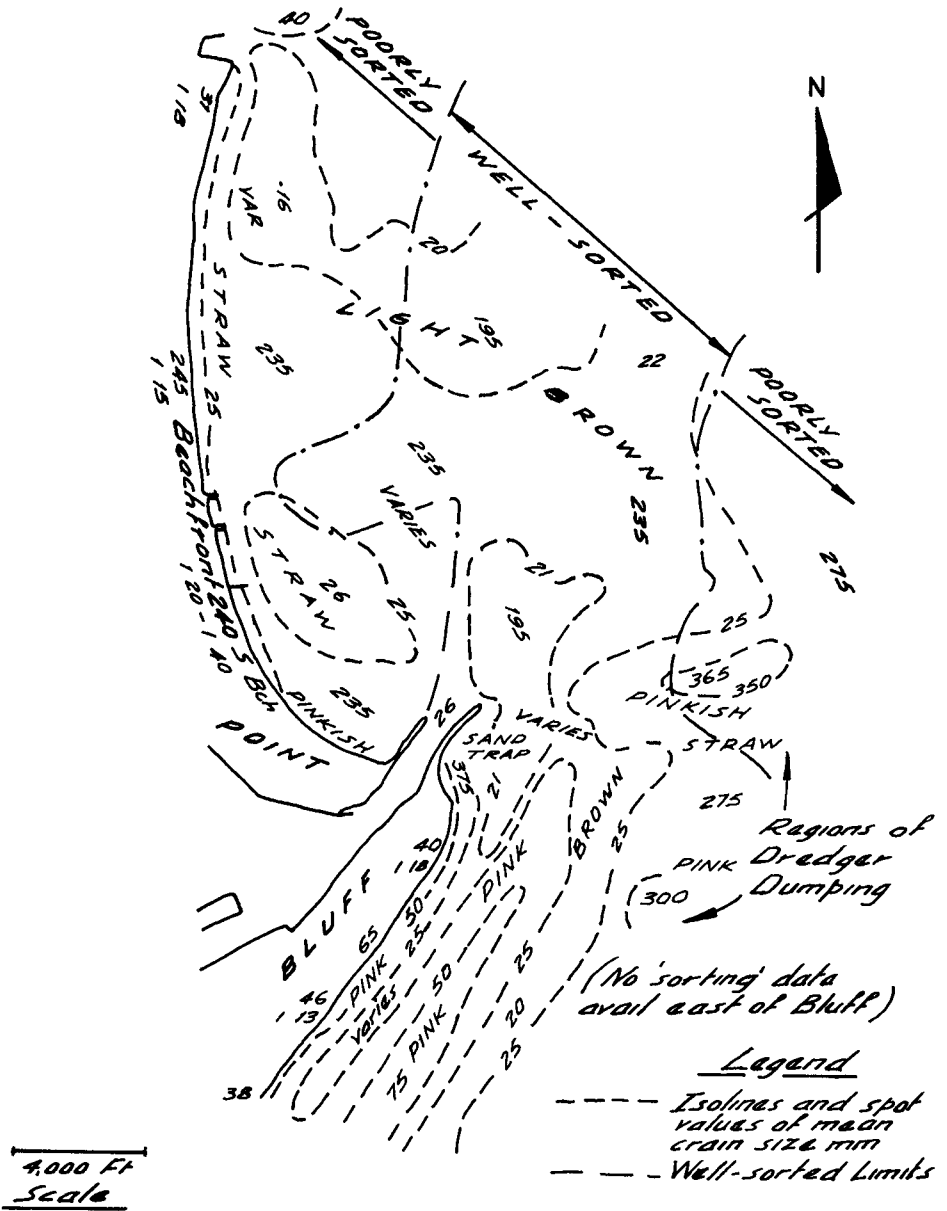


Figure 8. Sand size and color distribution, Durban 1961 - 1962.

DURBAN 1961 - 62

(closely sized) and rounded in shape. South of the harbor entrance on the Bluff beaches, the sand is very coarse, irregular in shape and it occurs in a wide band of sizes (Fig. 8). The most important observation is that the Bluff sands are distinctively colored - pink or red - compared to the Bight sands which are straw-colored. The presence of the pink color points to the fact that "The Dump" consists of Bluff sand dredged from the sand trap and dumped offshore. A remarkable finding was the close correlation between sand size and color. As a result of this correlation, Bluff sands could be identified elsewhere in the sampling area, both by color and by size.

4. The Model

Although theoretical considerations combined with an extensive measuring campaign in nature, can often yield an evaluation of the existing hydrological and morphological conditions, changes to the existing status can only be evaluated economically in a hydraulic model. More often than not, a distorted model, with vertical heights accentuated, is used as the most expedient solution. The Durban sand movement problem therefore called for a movable bed model. In order to reproduce the natural forces in the model as correctly as possible, besides the usual waves, current and tides, wind was also reproduced. This was quite unusual in a three-dimensional model. The model was built in Durban for reasons of convenience and suitable control. A Belman Hangar, belonging to the S.A.R. was made available for this purpose.

Model Scales. A 6.5 mile stretch of coastline, by 4 mile offshore distance had to be reproduced in the available space of the hangar-120 by 96 feet. Furthermore, a model wave height of about 1 inch minimum is required in order to avoid unscalable influences such as surface tension and viscosity effects. The following scale ratios were consequently selected:

Horizontal scale (except wave length): $L_r = 300$

Vertical scale (including wave length): $h_r = 100$

Further scale ratios follow from the Froude similitude law:-

Velocity scale (currents): $V_r = \sqrt{h_r} = 10$

Hydraulic time ratio (tides): $t_r = L_r/V_r = 30$

Celerity scale (shallow water): $C_r = \sqrt{h_r} = 10$

Wave period scale (for $\lambda_r = h_r$) $T_r = \lambda_r/C_r = 10$

Satisfactory results were obtained with fine beach sand as movable bed material, with specific gravity of 2.65 and a median diameter of 250 microns.

Construction. The construction of the model was a joint undertaking of the CSIR, the D.C. and the S.A.R. and took 9 months from October, 1960 to June, 1961. The main model structure consists of level concrete floor approximately 3 inches thick

and a surrounding concrete wall 2'3" high, forming a watertight basin. The model topography was moulded in concrete using asbestos templates, according to the 1960 offshore survey (Fig. 9).

Wind generation. To be able to reproduce wind effects from the predominant directions - NNE and SSW - a bank of 20 inch diameter axial flow fans was installed along the NE and SW boundaries of the model (Fig. 9). Each fan produced some 5000 cubic feet per minute free air which was blown horizontally over the model. The opening of the converging duct which covered the fans was 15 inches high. With the aid of guide vanes the air jet could be deflected at will. The maximum air velocity ranged from about 35 ft/s at the jet outlet to 6 ft/s at the beach front. More realistic, irregular and steep, wave shapes were obtained when using wind as well, than by the use of the wave generator alone.

Wave generation. Waves were created to scale in the model by three banks of unique pneumatic wave makers, oriented perpendicular to the three main directions of wave approach, viz. NE, ESE and SE (Fig. 9). The wave generators were made up of two-foot air-dome elements, surge chambers and diverging underwater nozzles. Air let into the domes periodically depresses the water surface, thus creating a wave at the nozzle outlet. The surge chambers were connected via four-arm rotary valves alternately to the suction and the compression ducts of a common blower. All four-arm valves, fitted on to a common rotating shaft. By turning each valve housing through a pre-determined angle, the phase between the individual 2-ft sections of the wave-maker could be set. In this way waves could be produced in any required direction, from 0.4 to 1.2 sec. in period and up to 2" high. The two separate drives for the shaft allowed the creation of a typical "sea" and swell combination coming from two different directions.

Currents. For the reproduction of currents axial-flow propeller pumps of 1½" and 6" diameter were used to circulate the water.

Tide Generation. The tides in the model were created by admitting water to and withdrawing water from the model according to a pre-set program controlled by a tidal synthesizer which produced a saw-tooth-shaped tidal curve.

Operation. As a result of the analyses of wave records it was found that three basic sea conditions, viz. NE, ESE and SSE and combinations thereof could be used to represent natural conditions. Quantitative measurements of loss and gain were obtained by measuring the change in the depth of sand over the fixed concrete bed, as well as by photographing contour strings from a traversing gantry tower spanning the model. Quantitative measurements of dredging rates were made by continuously weighing accretions "dredged" with a centrifugal pump and suction hose, the discharge of which was admitted under water into a constant volume skimming weighing tank.

Sedimentological time scale. Tests showed that the equivalent of the ¾ million cubic yards sand dredged annually can be moved from one area into another with SSE conditions in about

four hours when the bed material consists of 250 micron sand. In nature SSE stormy conditions only occur during about three per cent of the time, i.e. 260 hours per year. An approximate value of the sedimentological time scale, for SSE conditions is thus about 65.

Verification. Because a satisfactory correlation was found between model and prototype phenomena (wave, current and sand transport patterns), predictions made from the model regarding changes which might result from the coastal engineering structures envisaged in this investigation, may be regarded with confidence.

5. Results of Model Tests.

Littoral Drift. When not affected by dredging, the north bound littoral drift will encroach into the harbor entrance and eventually form a bar across, thus creating much the same conditions as existed in 1851, but shifted 3000 ft out to sea. Dredging is therefore necessary to prevent the siltation of the harbor entrance. It is the reduction of the necessary maintenance dredging which was aimed at with the testing in the model of the various remedial schemes.

From the diagnostic studies it was clear that with the present sand trap dredging technique, the gross northerly drift is removed (3). The main aim of the investigation was therefore to provide conditions which would ensure that only the net northerly drift will have to be dredged.

Standard Test Cycle. The conditions producing littoral drift to the north are SSE swell by itself or in combination with ESE swell, south-to-north current and S'ly wind. Under these storm conditions a yearly accrual in the sand trap of some 800,000 cubic yards, could be simulated in the model in about four hours.

Conditions under which a reduction of deposits in the Cave Rock Light can be expected are NE swell with NE wind. These two storm conditions were applied in the model in such a way that the energy distribution corresponded as near as possible to that found in nature.

<u>Phase</u>	<u>Swell direction</u>	<u>Period in sec.</u>	<u>Approximate duration, days</u> (storm)	<u>Wind direction</u>
I	SSE	10	1	SW
	NE	8	1	NE
	ESE	8	1	-
II	SSE	10	2.5	SW
	NE	8	4.5	NE
	ESE	8	2.5	-
III	SSE	10)	combined	
	ESE	7)	4.5	SW
IV	NE	8	2.5	NE
	SSE	10	2.5	SW
	NE	8)	combined	
	ESE	8)	4.5	NE

The foregoing test sequence consisting of four phases was used for most of the remedial scheme tests, the times given being as for nature, the cycle representing approximately one year's storm conditions in nature, (6).

Harbor Silting Prevention

A 1000-foot long mole off Cave Rock gave very promising results when tested in the model. To the north of the mole, an oscillation basin is formed between the mole and the South Breakwater which is well protected for SSE conditions.

Some 2.5 million cubic yards can be stored in the Cave Rock Bight before bypassing of the breakwater starts under prolonged SSE swell. Moreover, some 1.5 million cubic yards can accumulate south of the mole, bringing the total possible accumulation before there is any encroachment into the channel to some 4 million cubic yards, or 5 to 7 years storage capacity for the entire northerly littoral drift.

Due to NE'ly conditions, some sand will be moved out of the basin to the south again. Moreover, a large portion of the sand accumulated to the south of the mole is moved south, thus creating new storage capacity for SSE conditions, (Fig. 11), (6).

Beach Improvement structures tested

A system of Y-groynes with intermediate straight groynes, and the addition of spurs to the Paterson Groynes, yielded positive results in maintaining a beach everywhere except at the southern portion of the Lower Marine Parade, where a beach could only be maintained by intermittent sand renourishment or with offshore protection (Fig. 10).

Offshore breakwaters were investigated with the object of protecting existing and artificially created beaches and of building up new beaches in the lee of the structures. Solid reflecting and semi-solid partly-absorbing structures were tested in the model in a number of positions. A good build-up of the sheltered beaches was generally obtained and the initial fill was satisfactorily protected.

The optimum solution was found to be two 1000 foot long parallel breakwaters, approximately 2000 feet offshore. Two floating rafts, 900 by 300 feet in the same positions, tested as alternative measures, resulted in as good a protection of the beaches as the offshore breakwaters would give.

6. Summary of the main conclusions

a. Although conditions at Durban vary almost daily, neither seasonal nor yearly variations were found to be very significant. The field data collected over a period of two years could be considered representative.

b. Data collected over much longer recording periods than two years have to be processed when analysing geomorphological data. Nearshore surveys and dredging records extending many decades, proved an invaluable source of information. Color and size analysis and sand samples from the sea bottom yielded a method for classifying the sand which simplified the diagnosis of sand movement.

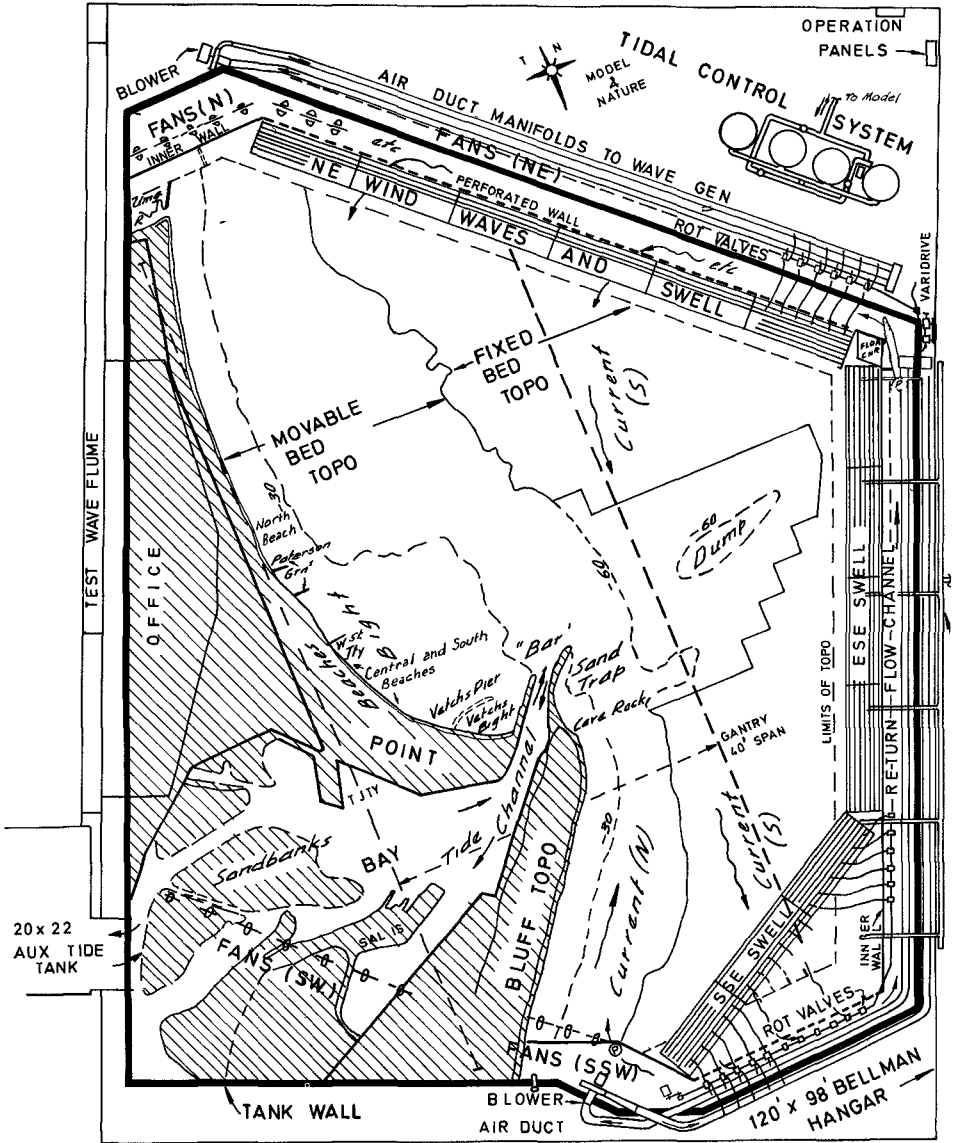


Figure 9 Plan of Durban Coastal Model

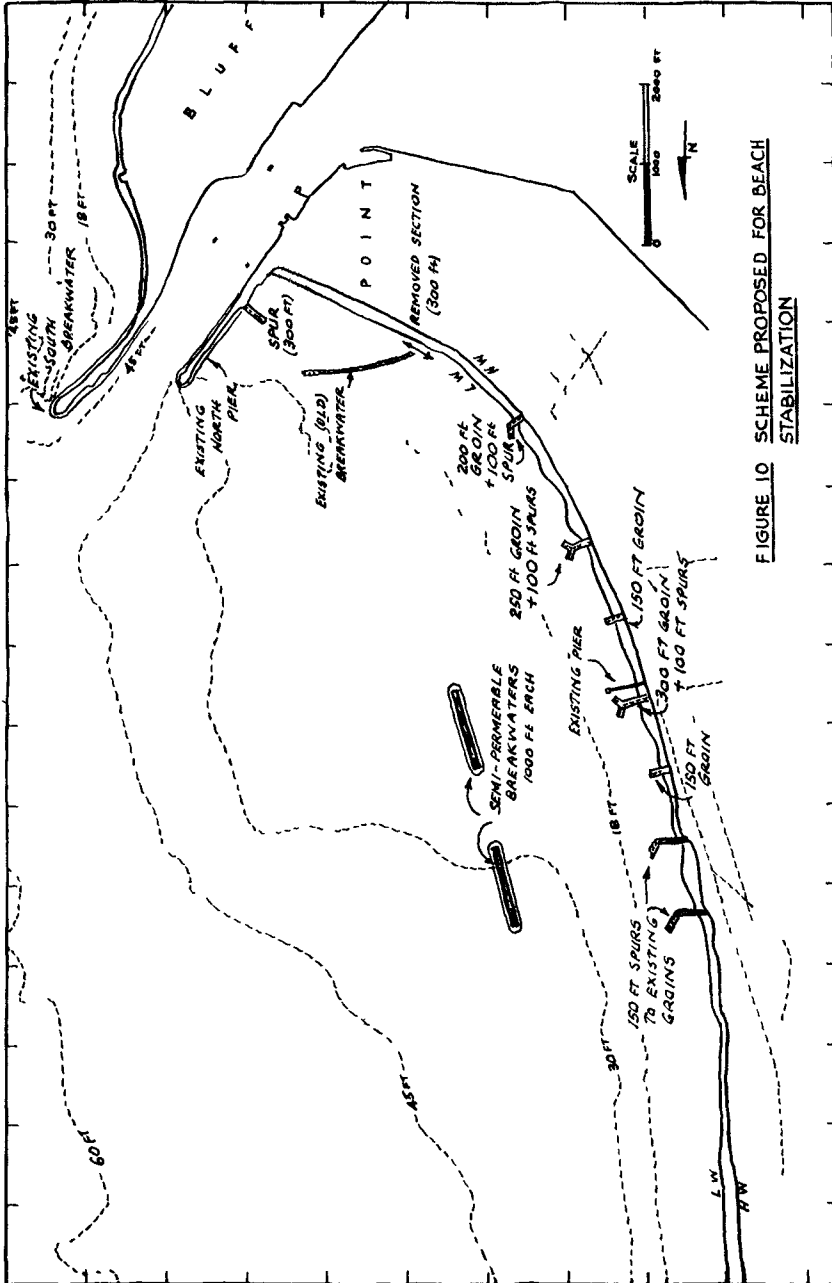


FIGURE 10 SCHEME PROPOSED FOR BEACH STABILIZATION

Figure 10. Scheme proposed for beach stabilization.

c. Progressive extension of the breakwaters and deepening of the harbor entrance, together with the associated maintenance dredging, resulted in a gradually increasing interception of the northerly littoral drift. The coastal areas north and south of the entrance channel can at present be regarded as two independent systems with reference to littoral processes. Observations indicate that the major movement of sand occurs close to the South Pier tip. Only relatively fine material can be carried in suspension across the harbor channel. The present state of the beaches is therefore not materially affected by the method of dredging south of the harbor entrance.

d. Nearshore bottom changes, mainly brought about by dumping of spoil, affect wave refraction in such a way that a concentration of wave energy in the Paterson Groynes area results for certain sea conditions(3). Partly due to this and partly due to the greater sheltering effect caused by the South Breakline has adapted itself into a new long-term equilibrium position, concave in plan compared with the 1851 conditions. Seasonal and short-term or storm effects can cause a redistribution of beach material in the beach and surf zones resulting in possible beach variations of up to 150 feet in width.

e. If dredging is interrupted altogether, the northerly sand drift eventually finds its way into the harbor entrance by creeping in, as a narrow band, around the South Pier tip. Dredging is therefore essential. A reduction in maintenance dredging rate can, however, be achieved when conditions are created such that only the net northerly littoral drift has to be covered with

It has been found in the model that this can be realised with various schemes, of which the one with a 1000 feet long mole off Cave Rock proved most advantageous. This scheme provides for an initial sand storage of some 4 million cubic yards, and anticipated reduction in maintenance dredging rate of some 25 per cent and a reserve storage volume of some 1.5 million cubic yards, (6).

f. As the present eight beaches have been found to be not subject to progressive erosion, improvement schemes were directed towards the formation of beaches in those areas where there are none at present and the protection and stabilisation of newly formed and existing beaches.

A scheme including two 1000-foot long offshore breakwaters or floating rafts, as well as a system of Y-groynes and additional groynes has proved to be successful in maintaining a beach everywhere, after the initial fill (1 million cubic yards) had been brought in to form a beach in the Central and South Beach areas.

With a groynes-only scheme (Fig. 10) it has been established in the model that, after an initial fill of approximately 250,000 cubic yards and with a maintenance sand pumping rate of about 10,000 cubic yards per year, a mean beach width above HW of some 55 feet in the Central Beach area and 250 feet in the North and South Beach areas could be maintained. Moreover, the groynes and spurs could successfully reduce seasonal variations to a negligible amount, (6).

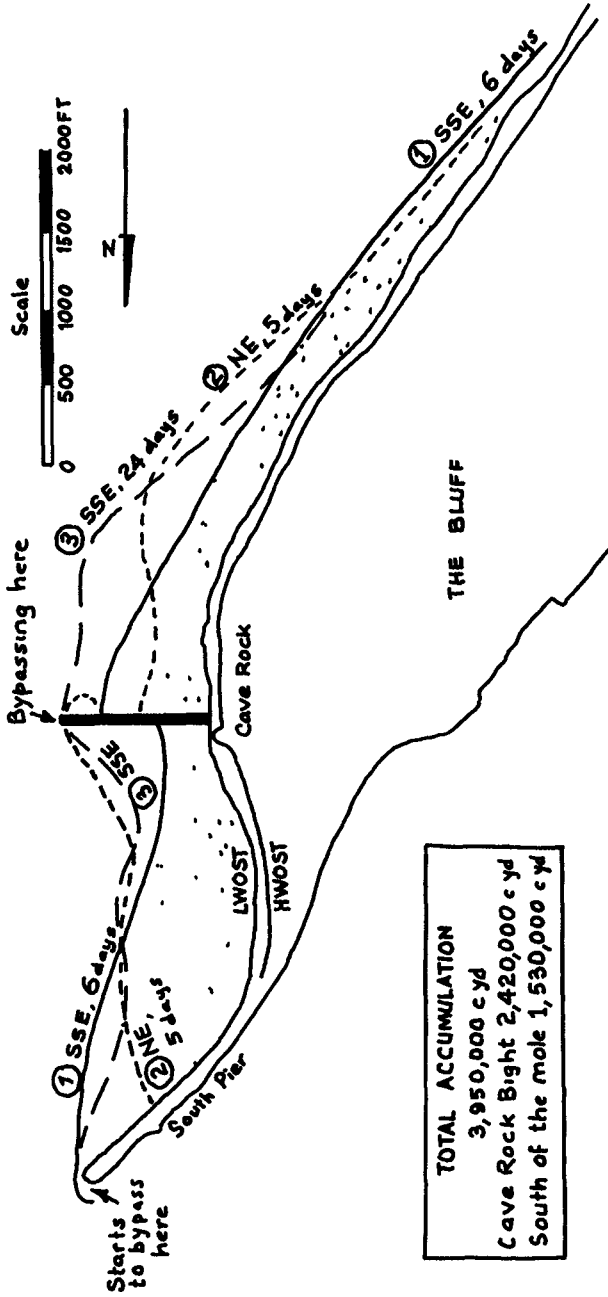


Figure 11. Fluctuation of accumulations, Mole (prop.) off Cave Rock.

An alternative scheme by which a continuous underwater sand mound be formed some 4000 feet offshore in the Durban Bight seemed to warrant further investigation, and was eventually adopted (7).

REFERENCES

1. Belderson, R.H. Thesis for the degree M.Sc., Geology Department, University of Natal, Durban, 1962.
2. Jordaan, J.M., Jr. Experience with recording of storm waves, swell and tide using an inverted echo-sounder off Durban (South Africa), International Hydrographic Review, Monaco, Vol XL, No. 2, July 1963, pp. 125-140.
3. Jordaan, J.M., Jr. Effects of hydrographic changes due to near-shore dredger dumping, on wave refraction and littoral sand balance. Proc. Ninth Conf. on Coastal Engineering, Lisbon, Portugal. June 1964, Pub. A.S.C.E., New York, 1964, pp. 310-322.
4. Kinmont, A. The nearshore movement of sediment at Durban. CSIR Symposium, No. 52, Pretoria, March 1961, pp.46-58.
5. Moffatt, H.R. The development of the Harbours of South Africa, Proceedings at the Western Cape Regional Convention, 1961, The S. Afr. Inst. of Civil Engineers, pp. 44-52, esp. 49, 50.
6. CSIR Report CMeg 558 Durban Harbour Siltation and Beach Erosion Investigation, Sept. 1963, Pretoria.
7. Zwamborn, J.A., G.A.W. Fromme and J.B. FitzPatrick. Underwater Mound for the protection of Durban Beaches. XII Conference on Coastal Engineering, Washington, 1970.

ACKNOWLEDGMENTS

The author appreciates the encouragement and assistance from Mr. R.E. Jones, then System Harbour Engineer, Mr. A. Kinmont, then City Engineer, Durban, Dr. H.G. Denkhous, Director CSIR National Mechanical Engineering Research Institute and other members of the Technical Committee and their organizations.

Mr. J.A. Zwamborn, Mr. W.G. van Lienden, Mr. J.B. FitzPatrick collaborated over long periods of time on this investigation and their unsparing efforts are greatly appreciated.

The author is indebted to all who contributed their time and efforts to the work herein reported.

Permission to present this paper was granted by the South African Railways Administration, the City Council of Durban, and the Council for Scientific and Industrial Research.

CHAPTER 71

ESTUARY INLET CHANNEL STABILIZATION STUDY USING A HYDRAULIC MODEL

Theodore T Lee
Associate Researcher

Look Laboratory of Oceanographic Engineering
University of Hawaii
Honolulu, Hawaii
U S A

ABSTRACT

A hydraulic model study was conducted to determine the most feasible means of reducing shoaling into a coastal inlet channel that had been used by loaded Landing Ship Tank (LST) class vessels serving the port of Tan My near Hue, Republic of Vietnam. The ultimate objective was to increase the time during which the channel will be open to navigation by improvements in physical configuration.

An extensive field data acquisition and analysis program was executed to provide basic information for model prototype correlation. This incidentally resulted in the re-evaluation of several empirical formulae being used for prediction of littoral transport and of tidal currents. The comprehensive field measurements of shoaling in the channel area also permitted the determination of the scale effects on the quantitative results of sediment deposition in the channel and on the time scale of bottom evolution.

The experiments were conducted systematically in three phases. The three-dimensional studies for Phase I and II were conducted using a rigid bed, sand or walnut shell covered (1/250 horizontal and 1/50 vertical scale) hydraulic model of a 15 sq mi ocean-estuary land area. Periodic long-crested waves (tides, tide/river induced currents) were simulated in the model. Phase I covered qualitative evaluation of nine improvement plans, from which a "BEST PLAN," an upshore jetty to protect the existing channel, was selected. Phase II covered qualitative and quantitative evaluation of four variants of the "BEST PLAN," from which the most effective and economical variant was determined. To insure reliability of quantitative results, comprehensive experiments were conducted using three different sediments ($D_{50} = 0.41$ mm and 0.90 mm, $\gamma = 1.35$ for two types of ground walnut shells and $D_{50} = 0.22$ mm, $\gamma = 2.65$ for sands), and three model scaling criteria (Froude Scaling, "Ideal Velocity" Scaling, and Modified Froude/Ideal Velocity Scaling). Phase III covered two-dimensional model tests, in a 180 foot flume, of the stability characteristics of the proposed rubble mound type jetty on a movable bed.

The major conclusions of this study include (1) the jetty, as postulated in the "BEST PLAN," would reduce annual maintenance dredging requirements by 74 to 84 percent, (2) a systematic three phase model study such as used in this investigation is most feasible (from a time-consumption viewpoint, use of light weight materials such as ground walnut shells may be more economical than use of natural sands as model material), and (3) use of theory alone in predicting a time scale for bottom evolution should be approached with caution especially where field data are not readily available.

INTRODUCTION

This paper describes the techniques used for a particular coastal inlet stabilization study using a hydraulic model in order to obtain an optimum solution to the excessive shoaling of the existing ship channel. The channel in question is located at Tan My, on the South China Sea Coast near Hue Republic of Vietnam. The shoaling results from significant storm waves during the winter and summer monsoon seasons dominated by wind waves from the Northeast during the period from November to January. Sediment contribution from the inland rivers (Huong, Bo and O Lau) is mainly deposited in the large estuary area with only negligible wash load diverted into the offshore channel area. To maintain a 20 ft deep and 300 ft wide ship channel considerable efforts were expended to keep the channel open by dredging (1.8 million cubic yards per year). Unfortunately, the duration of the relatively safe dredging periods are prohibitively short and infrequent. It was therefore considered necessary to construct permanent barrier structures in order to protect the Tan My Channel from shoaling so that the channel can be operationally useful for most time with minimum dredging maintenance.

The study (Lee, 1970) was sponsored by the Officer in Charge of Construction Republic of Vietnam Naval Facilities Engineering Command Department of the United States Navy.

DESCRIPTION OF STUDY AREA

The subject study covered a small area (3 miles by 5 miles) of the coastal line and offshore topography, the inlet, and a portion of the estuary. The boundaries of the project area to be modeled were selected on the basis of such criteria as (a) the model should extend to sufficient depth (10 fathoms) to obtain correct refraction patterns of waves approaching the shoreline from prevailing directions, including NE, N, and NNW, around the area of interest, (b) sufficient shore length should be provided to permit cutting a new channel through the spit and to allow a natural development of longshore current by water waves and (c) the boundary condition in regard to the flow should not change as various improvement plans for the inlet are studied in the model.

OCEAN ENVIRONMENTAL DATA ACQUISITION

An extensive field data acquisition and analysis program was executed in order to provide basic information for model prototype correlation.

Waves and Swell Wave climates simulated in the model were determined from observations by Lyon Associates (1968-1969), NAVFORV Weather, Saigon, RVN from wave budget analyses by Marine Advisors (Inman and Harris, 1966), and wave hindcasting by Glenn Associates (1966). The wave rose developed from most recent field observations is shown in Fig 1(a).

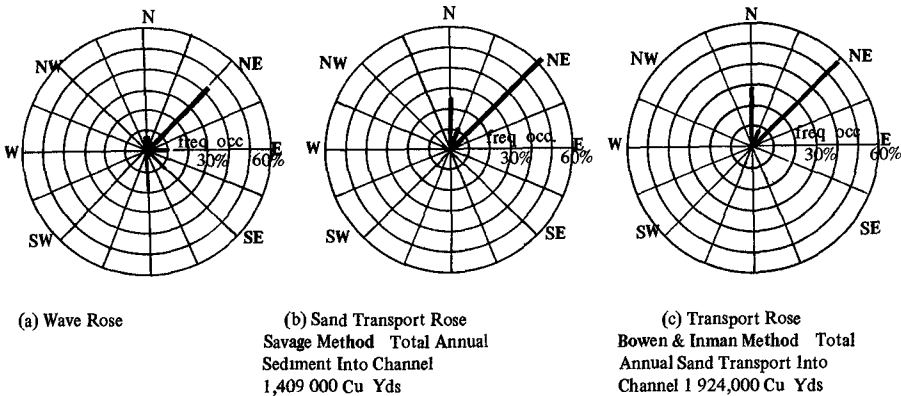


Fig 1 Wave and Sediment Transport Distribution

The following "Typical Waves" were used in the model tests for the selection of the "BEST PLAN"

	Wave height (feet)	Wave period (seconds)
Severe Storm Wave Condition	10	8
Normal Storm Wave Condition	5	5

Wave directions selected for model tests included NE, N, NNW. An analysis of the waves incident on the channel has shown that shoaling in the channel results as follows: 60% from NE, 25% from N, and 15% from NNW and other directions [Fig 1(b) and (c)]. Furthermore, the wave and swell data, wind information, and weather maps related to the period of Typhoon Bess (27 September 1968) were analyzed. It was found that the average wave climate incidentally corresponded to the Normal Storm Wave condition defined above: i.e. 5 ft high, 5 second period (from NE).

Tides and Tidal Currents The diurnal tide at Tan My was an average of 2.0 feet with a tidal period of 25 hours and 35 minutes. The semi-diurnal tide was 1.6 feet high and 12 hours and 47 minutes. Tide induced current in the Tan My entrance channel without river discharge was predicted, using the theoretical method of Keulegan (1967). The maximum velocities predicted compared reasonably well with those measured by Lyon Associates and by the U.S. Naval Oceanographic Office. The field measurements were made of tides and tidal currents at four locations as shown in Fig. 2.

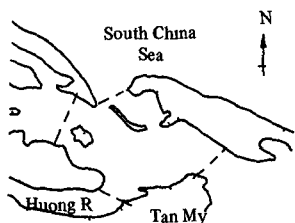


Fig. 2 Tide and Current Measurements at Four Stations

The Lyon's measurements involved detailed measurements of tidal current velocities covering the whole cross section at 0.2 and 0.8 of the water depth, from which the mean velocity through each section can be determined. Unfortunately, tides were not recorded continuously and the measurements at the sections were not made simultaneously. Ten series of measurements were made at each station during the 5 month period from September 1968 to January 1969. The measurements by the Naval Oceanographic Office were made simultaneously at each of the four stations but only currents at one or two points were recorded instead of numerous points at each station as done by Lyon. The measurements covered a four month period from December 1968 to March 1969. The field measurements helped verify somewhat the tide and tidal current predictions but it is not feasible to simulate such tides because the measurements include the effects of waves, river discharge, and longshore currents. Therefore, the tide simulated in the model was based on tide prediction and the tidal currents through the channel according to proper adjustments of tidal prism in the model estuary.

The maximum tide prism measured at Tan My was 47×10^6 m³/diurnal tide cycle as determined from the maximum mean tidal discharge of 1500 m³/sec measured by Lyon. This compared well with the 49×10^6 m³/diurnal tide cycle as estimated by Inman and Harris (1966).

The tide and tidal currents simulated in the model are considered adequate because the low tide range does not significantly affect the sand transport into the channel.

Hydraulic Regime Offshore Tan My Inlet For calibration of the model and study of the flow conditions in the inlet area, it was necessary to obtain current patterns. These patterns were obtained by the Naval Oceanographic Office using infra red techniques.

Huong (perfume) River Flow Based on frequency of occurrence of the Huong River flow, 500 m³/sec and 1,800 m³/sec were selected to simulate the normal and severe flood conditions. This seems to be high, but it would compensate for the omission of the contributions from the Bo and O Lau Rivers and reduce the scale effects of the use of sands as bed materials. (Flow measurements at Huong River during a 4 month period showed the maximum discharge was 1,250 m³/sec and averaged 300 m³/sec.)

Longshore Currents Offshore ocean currents upcoast of the Tan My Inlet were measured with float techniques but the measurements are not utilized because they were made too far offshore to be within the model limits. Subsequently, longshore currents of 2.0 ft/sec and 4.0 ft/sec were predicted by theory and simulated in the model for normal storm wave (5 ft high, 5 second period) and for severe storm wave (10 ft high, 8 second period) conditions respectively.

Sediment Properties. Beach samples were taken upcoast of the Tan My Inlet. The typical size distribution of sediment—the median diameter (D_{50})—was 0.41 mm. The sediment is 100 percent quartz, containing no carbonate, with a density of 2.65. The size distributions of both prototype and model sediments are shown in Fig. 3.

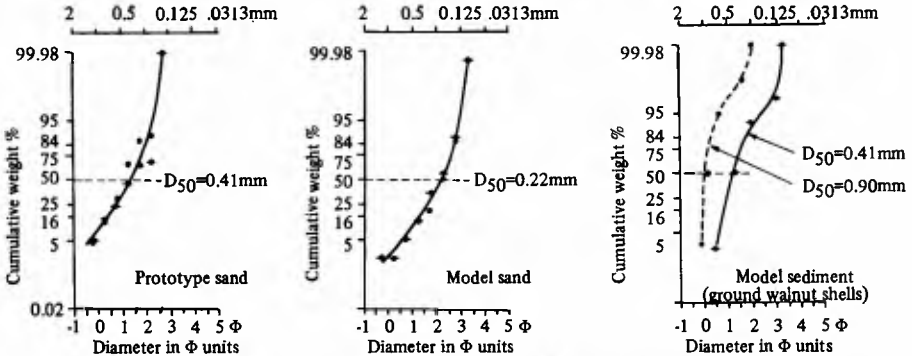


Fig. 3 Size Distribution of both Prototype and Model Sediments

Coastal Morphology. The shoreline evolution around Tan My Inlet from April through December 1968 was studied from the analyses of monthly uncontrolled aerial photographs. These photographs showed the unstable nature of the Tan My Inlet. A comparison of the coastal morphology at Tan My during August, September, and December 1968 is shown in Fig. 4. The stability parameter for Tan My is compared with other similar inlets in Table 1.

Shoaling and Dredging Information. An extensive study was made of the shoaling and dredging aspects at the Tan My existing entrance channel. Included are: annual sediment budget, sediment transport during a special storm (Typhoon Bess), bottom topography changes, and dredging studies. It was found that the total sediment transport into the existing channel amounted to 2.1 million cubic yards ($1.6 \times 10^6 \text{ m}^3/\text{year}$) as compared with 1.4 to 1.9 cubic yards per year (1.1 to $1.5 \times 10^6 \text{ m}^3/\text{year}$) predicted by theories of Savage (1959) and Bowen-Inman (1966) respectively [see Fig. 1(b) and (c)]. Based on the estimated inlet stability parameter (Bruun, 1969) the annual sediment transport would be 1.4 million cubic meters or 1.8 million cubic yards. This estimate was the basis for economic evaluation of the improvement plans.

Summary of Ocean Environment Data for Model Tests. The ocean environmental data selected for the model tests are summarized in Table 2.



Fig. 4 Coastal Morphology at Tan My Inlet

Table 1 INLET STABILITY

Inlet	Tide Prism (Ω) (m^3 /tide cycle)	Sand Transport (M) (m^3 /year)	$\frac{\Omega}{M}$	Stability*
Tan My	47×10^6			
Model		1.50×10^6	31	
Savage		1.08×10^6	43	
Bowen & Inman		1.46×10^6	32	
Dredge Record		1.61×10^6	29	
Average		1.40×10^6	34	Very Poor
Masonboro, N C (Bruun, 1966)			30	Very Poor
Ponce de Leon, Fla (Bruun, 1966)			40	Poor
Figueira da Foz, Portugal (Bruun & Gerritsen, 1960)			40	Poor
Oregon, N C (Bruun & Gerritsen, 1960)			80	Poor to Fair
* Very Poor	very much shoaling			
Poor	much shoaling			
Poor to Fair	significant shoaling			
Fair	some shoaling			
Good	neghible shoaling, $\frac{\Omega}{M} = 100$			

Table 2 SUMMARY OF OCEAN ENVIRONMENT DATA FOR MODEL TESTS

Environment	Normal Storm Condition	Severe Storm Condition
Wave and swell		
Wave height (ft)	5	10
Wave period (sec)	5	8
Wave direction	NE, N, NNW	NE, N, NNW
Tide		
Diurnal		
Tide range (ft)	2	2
Tide period or cycle	25 hr , 35 min	25 hr , 35 min
Semi Diurnal		
Tide range (ft)	1.6	1.6
Tide period or cycle	12 hr 47 min	12 hr , 47 min
Tide Prism	$47 \times 10^6 m^3$ /diurnal tide cycle	
Huong River Discharge (m^3 /sec)	500	500 and 1,800
Longshore Current (ft /sec)	1.8 2.0	3.6 4.0
Sediment Property		
Medium diameter (d_{50})	0.41 mm	0.41 mm
Density	2.65	2.65
Annual Sand Deposition into Channel (used in study)	1.8×10^6 (cu yds /year)	

THE TAN MY ESTUARY MODEL

Design of Model The model (Fig 5) has the following linear model scale ratios

- (a) Horizontal Scale $1/250 = n_1 = \lambda$
- (b) Vertical Scale $1/50 = n_d = \mu$
- (c) Model Distortion $1/5 = n_d/n_1 = \mu/\lambda = \Omega$

The vertical scale and model distortion were selected with due consideration of the scale effects, the artificial sediments to be used in the model, and prototype beach slope. In general most models of movable bed have a distortion ratio from 1.3 up to 1.8. The natural beach slope at Tan My is relatively gentle (1:60) and the equilibrium beach slope is changed with wave characteristics, thereby affecting the decision of choosing a single model distortion to satisfy all equilibrium beach slope conditions, therefore a 1.5 model distortion was selected. The selection of the vertical scale does not materially affect model results because the model has a semi movable bed rather than a movable bed. The foreshore and offshore beach slopes were maintained constant during the tests because the natural beach slope is relatively flat.

Similitude Relationship The model and prototype scale relationship for the Tan My Estuary Model for the Phase I and early Phase II tests is summarized by Lee (1970)

The following references were helpful: Fan and LeMehaute (1969), Byker (1967), Bruun, et al (1966)

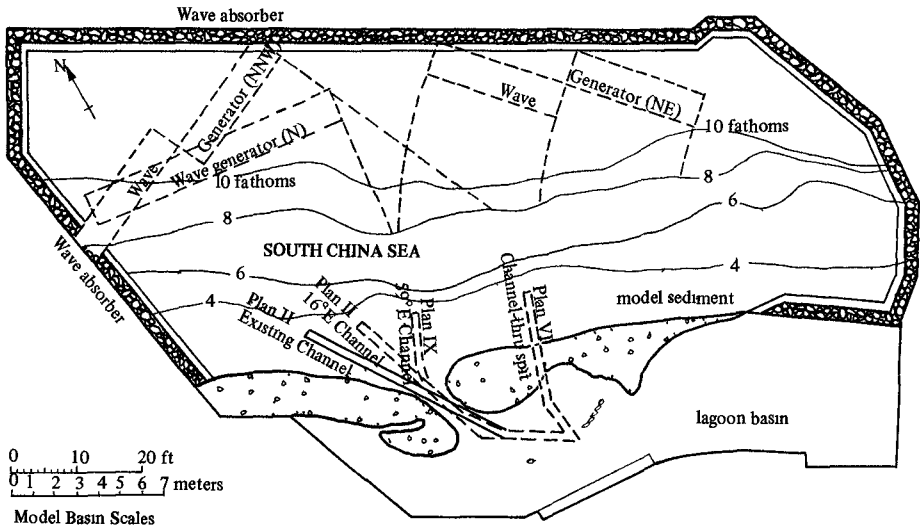


Fig 5 General Layout of Tan My Estuary Model

EXPERIMENTAL EQUIPMENT AND PROCEDURE

Ocean Environment Simulation, Measuring and Recording Apparatus

Wave Generators The wave generator for the three dimensional model tests was of the plunger type, capable of simulating long crested, periodic water waves. The wave generator for the 180 foot long wave flume was also of the plunger type, with a unique control unit. The generator is driven by a high torque, low speed hydrostatic pump motor. The hydrostatic drive is infinitely variable in speed in either direction off detent center from 1 to 60 rpm. The variable displacement hydraulic pump is driven at a constant speed by means of a 20 hp, 1750 rpm motor.

Tide Generator Tides of diurnal and semi-diurnal types were simulated by alternately pumping and draining water to and from the model basin. The outer ocean basin and inner lagoon basin were controlled separately. The tide generator was designed to reproduce tidal discharge through the inlet rather than tidal elevation differentials between the ocean and bay lagoon. The tide generator had a unique electro pneumatic flow control system which was simple and economical. It was calibrated by a cam arrangement to reproduce inlet flow by changing electrical voltage which in turn controlled the valve opening of the pipe lines.

River Flow Generator Huong River discharge was simulated by spilling water over a V weir into the estuary near the river mouth through a pumping system.

Other Measuring and Recording Systems Time-exposure photographs were used extensively to provide information on the speed and direction of currents in the inlet area and to illustrate graphically the eddy locations and current patterns. This helped evaluate the hydraulic regime of each particular improvement plan tested in the model. Current through the channel entrance was measured by timing the travel of a surface float over a known distance. Waves were measured by means of optical (Palmer, 1970) and electrode resistance type wave gauges. Tidal current and tide level variations were measured respectively and intermittently by float and point gauge techniques over the entire tide cycle to verify the outputs which had been calibrated. River flow was measured by a V shaped weir. Motion pictures were taken to document the pertinent tests of the entire study.

Experimental Procedure The following experimental procedure was followed:

1. Calibrate the three dimensional model after a series of preliminary tests to determine the most significant parameters which would affect the flow characteristics and the quantity and distribution of sediment transport and deposition in the channel. Relative effects of waves, tides, river discharge type of model sediment, artificial roughness were thoroughly investigated.
2. Conduct Phase I tests covering qualitative evaluation of nine channel improvement plans (Fig 6) from which a "BEST PLAN" (an upshore jetty to protect the existing Tan My channel) was selected.
3. Conduct Phase II tests covering the qualitative and quantitative evaluation of four variants (Fig 7) of the "BEST PLAN" from which the most effective and economical variant was determined.
4. Conduct Phase III tests in a large wave flume at a much larger scale to determine the stability characteristics of the rubble mound type jetty of the "BEST PLAN" against normal and severe storm wave actions.

MODEL STUDY AND RESULTS

Proof of Model The model base line is the quantity and distribution of sand deposited in the existing channel during a 35 day period, 9 August to 13 September 1968, which covered the period of Typhoon Bess, 31 August to 7 September. Field data on channel configuration at the beginning and end of the period were also available, as well as the quantity and location of dredging during the period. Excitation during the period was not measured. However, hindcasting procedures indicated that it likely was the Normal Storm Condition as shown in Table 1. Coincidentally, this condition also represents the average wave condition during the NE wave monsoon season. Therefore, model prototype correlation was also made of shoaling caused by normal, or long term wave action.

Because the orientation of the channel is unclear and the river flow through it during Typhoon Bess is unclear and shoaling is sensitive to these factors proper proof of the model on a quantitative basis was not possible. Therefore, only qualitative model prototype correlation was achieved during the Phase I tests. Subsequently, comprehensive tests with seven scaling criteria were conducted to relate their relationship quantitatively under Phase II tests which will be discussed later.

Furthermore, the favorable reproducibility of the bottom topography at the inlet [Fig 6(a)] and of the hydraulic regime (current pattern) in the model leads to the belief that the model prototype correlation is considered adequate with the data available for the purpose. Preliminary viewing of the imagery indicated that the eddy near the mouth of the Tan My Channel in the model appears also in the imagery [Fig 8]. The patterns appear to be consistent with a

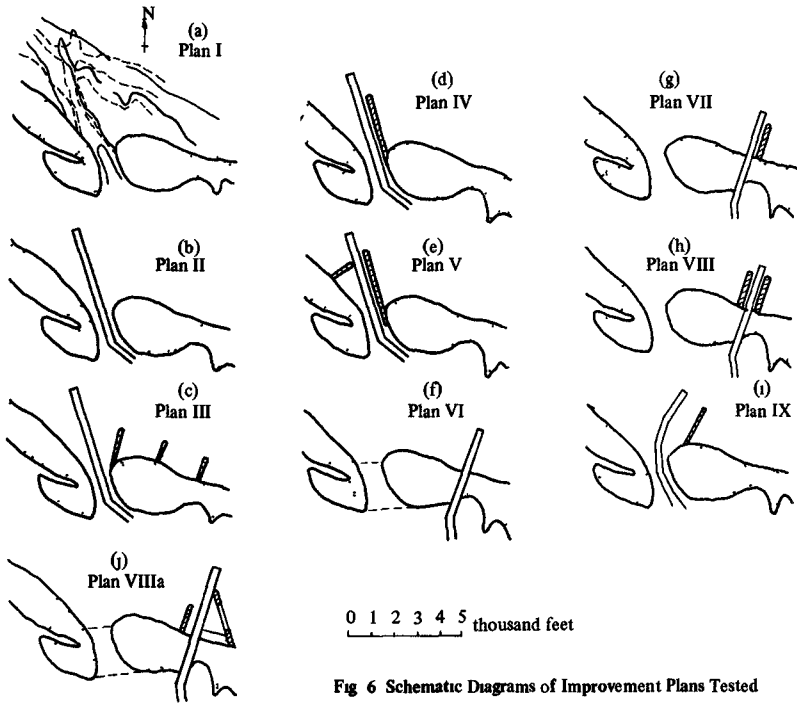


Fig 6 Schematic Diagrams of Improvement Plans Tested

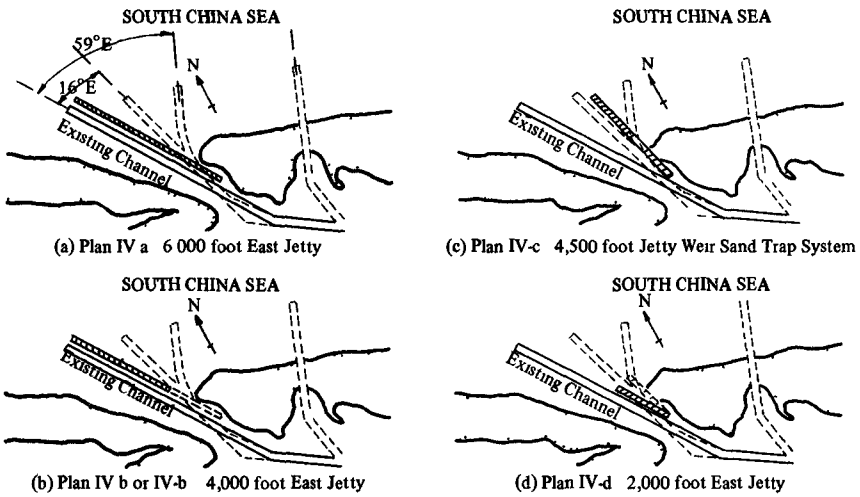


Fig 7 Schematic Diagrams of Four Variants of "BEST PLAN" Tested

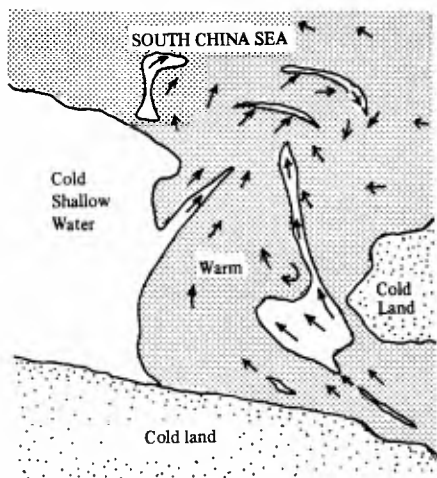
postulated, relatively small, clock-wise eddy just off the inlet (Wiemat, 1969). This favorable prototype-model relationship helped increase confidence in the model results. The distribution of peak shoaling area is consistent with actual prototype conditions observed over long periods of time under normal conditions. Also, the favorable comparability of the littoral transport (Table 3) by model, prototype, and prediction, and favorable comparability of measured and predicted tidal current (Table 4) have encouraged the preceeding of the model tests for subsequent test and evaluation of a variety of channel improvement plans.

Table 3. COMPARABILITY – LITTORAL TRANSPORT

Method/ Source	Littoral Transport (cu. yds./day)			
	(1) Normal wave NE, 5 ft., 5 sec.	(2) Storm wave NE 10 ft., 8 sec.	Ratio (2) / (1)	
Model measurement	Measured	10,500	79,900	7.57
Prototype	Calculated from dredging records	9,700	—	—
Prediction	Caldwell (1956)	10,500	53,750	5.13
"	Savage (1959)	18,500	50,000	5.90
"	Bowen & Inman (1966)	8,800	69,000	7.85
"	Bijker (1968)	6,450	48,900	7.59

Table 4. COMPARABILITY OF MEASURED & PREDICTED TIDE CURRENT

	max. mean current vel.	max. surface current vel.
Measured in model	0.093 ft./sec.	0.210 ft./sec.
Predicted by Keulegan (1967) method	0.078	0.175
Error	16%	17%



(a) Prototype Circulation Pattern
Infrared Imagery June 24, 1969



(b) Model Circulation Pattern

Fig. 8 Comparison of current circulation patterns, prototype vs. model

Phase I Qualitative Evaluation of Improvement Plans Phase I covered qualitative evaluation of nine (9) improvement plans [Fig 6] from which a 'BEST PLAN,' an upshore jetty to protect the existing channel, was designated. These sedimentation reduction plans involved four channel configurations. These were the existing channel, two channels rotated about 16° and 59° East, relative to the existing channel, and a new channel relocated through the spit about one mile upshore of the existing entrance. All these channel configurations (except the 59°E channel) were protected by groins and/or jetties upshore. In some cases downshore jetties were tested as well (Plans tested are shown schematically in Fig 6)

The quantity and distribution of sand transport into the channel for various test plans, as measured in the model are compared in Fig 9. It is shown that Plan IV, V, or VIII provides better protection from shoaling of the navigation channel, i.e. the existing channel or a new channel cut through the spit. Their relative merits will be described below.

The four unprotected channels [Fig 5]—two associated with Plan II, existing and 16°E, and IX and VI—behave similarly as a function of their orientation relative to the direction of the incident wave when the other excitations are constant, i.e. river, longshore, and tidal currents.

Their behavior is highlighted by a dominant constant river outflow which (both aided and opposed by the wave as well as by tidal and longshore currents) tends to generate eddies up and downcoast of the entrance, this action, in turn, builds a bar on the upcoast side and scours a hole on the downcoast side.

At the channel entrance, the wave generated current (mass transport plus oscillatory) tends at significant times to transport sediment into and up the channel. Thus, the quantity of sediment (Q) deposited in the channel should be a function of the ratio of component (Py) of the wave generated power (P) parallel to the centerline of the channel proportional to P. This appears not only to be the normal case, but also roughly a linear case for Test Condition I with NE waves with $H_o/L_o = 0.40$ incident on the four channels as indicated by a plot of P_y/P versus Q/ft of channel [Fig 10] where H_o and L_o refer to deep water wave height and length respectively, even though Johnson (1965) and others indicate transport should be dominantly offshore when $H_o/L_o = 0.025$.

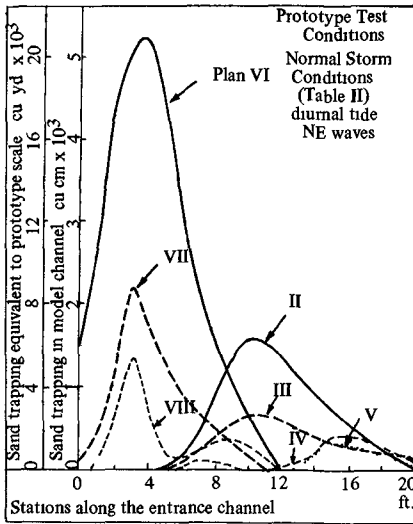


Fig 9 Comparison of Relative Merits of Various Plans for the Existing Entrance and New Entrance through the Spit

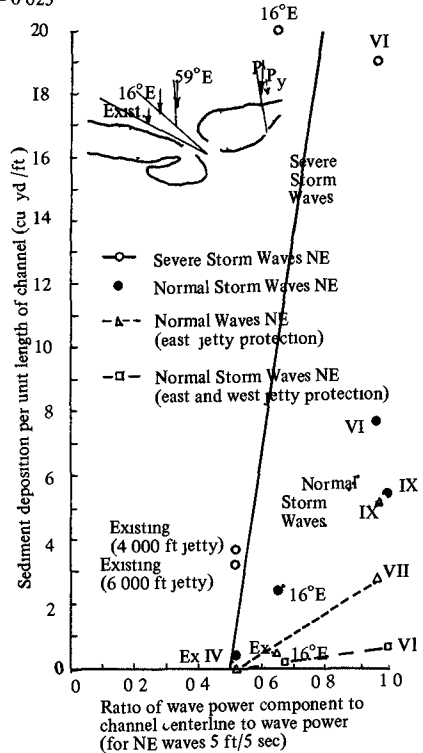


Fig 10 Correlation of Sediment Deposition in Four Channels Tested

A review of these data indicates that the existing, 16°, IX and VI channels are sediment retarders in that order of effectiveness this is attributable to the fact that the channel centerlines are 64, 49, 5, and 17 degrees, respectively, to the NE direction of the incident wave in deep water That is, the channel (existing) closest to perpendicular to the incident wave crests is the most effective sediment retarder

The four channels (two associated with Plan II—existing and 16°E—and IX and VI), when protected by a full length upshore jetty (Plans IV and VII), and partial length groin well upshore (Plan IX), behave predictably This predictability is, as in their unprotected condition somewhat a function of channel “heading” relative to the direction of incident waves The protected versions in all cases are more effectively self cleaning channels

An upshore jetty is considered entirely adequate as a channel protector The addition of a downshore jetty adds a quite small increase in effectiveness at the expense of inducing undesirable eddies at the entrance and is not recommended

It was found that the unprotected anti shoaling effectiveness of the four channels (existing, 16°E, 59°E and through the spit) varies inversely as the heading into the incident waves The existing channel with full upshore jetty is most effective (and the channel through spit the least effective) as designated “BEST PLAN

An upshore jetty weir sand trap system, such as at Masonboro Sound N Carolina, is no more effective as a total sedimentation retarder than a conventional system However, it reduces sedimentation into the channel (balance in trap), and hence merits further study only if preservation of downshore configuration is important

The reproducibility of the magnitude and distribution of sand deposited in the channel from run to run is close when the beach is stabilized, i e after two tide cycles for normal waves and four to six cycles of severe storm waves There is a variation of 1 to 12 percent, which is quite acceptable

Sand transport measured in the prototype and model compare well with those predicted theoretically by Savage (1959) and Caldwell (1956) for normal to moderate waves, and Inman (1966) for storm waves The comparison is poor for those predicted by Bijker (1968) i e 40 percent lower than those measured in the model and predicted by other methods (see Table 3)

Phase II Qualitative and Quantitative Evaluation of the BEST PLAN Phase II covered qualitative and quantitative evaluation of the most effective and economical variant of the “BEST PLAN” This phase of the study involved determination of the optimum length and orientation of the jetty among four variants [Fig 7] To insure reliability of the quantitative results, a series of comprehensive experiments were conducted with sand ($D_{50} = 0.22$ mm, $\gamma = 2.65$) and two sizes of light weight, ground walnut shell material ($D_{50} = 0.41$ and 0.90 mm $\gamma = 1.35$) as model sediment Three different model-similitude criteria were used in these tests, i e , Froude Law Scaling ‘Ideal Velocity’ Scaling, as proposed by Bijker (1967) of Delft University, and “Modified Froude Law/Ideal Velocity” scaling, as proposed by the Look Laboratory The time scale of bottom evolution was determined experimentally for each case and compared with theory

Three versions of the ‘BEST PLAN’ included jetties immediately upshore (east) of the existing channel, with lengths of 6,000, 4,000 and 2,000 feet, located along the channel bank a fourth version included a 4,500 foot jetty upshore of the channel bank to form a jetty weir sand trap system [Fig 7]

Three model similitude criteria were employed

Froude Criteria $n_v = n_u = n_d^{1/2}, n_H = n_d, n_T = n_d^{1/2}$

where n = scale ratio = value of model/value of prototype

v and u designate respectively current (tidal or river) velocity, and orbital velocity (wave)

d , H , and T designate vertical depth, wave height, and wave period

Ideal Velocity Criteria

$$n_v = \frac{n_\Delta n_D}{n_\mu}^{1/2} \quad n_{C_c}, n_u = n_v / n_{C_c} \quad n_H = n_u n_T \quad n_T = n_d^{1/2} \quad (\text{Bijker, 1967 pp 128-129})$$

where Δ , D , μ and C designate respectively relative apparent density of sediment, mean grain diameter, ripple coefficient, and resistance coefficient

Modified Froude/'Ideal Velocity' Criteria

$$n_v = \frac{n_{\Delta} n_D^{1/2}}{n_{\mu}} \quad n_{C_c}, n_u = n_d^{1/2}, n_H = n_d, n_T = n_d^{1/2}$$

Use Froude Criteria for wave characteristics, and 'Ideal Velocity' Criteria for current velocity (tidal and river flow)

The primary objectives were to

- (a) determine the appropriate time scales of sediment deposition, frequently referred to as time scales of bottom evolution,
- (b) determine the jetty effectiveness in each case,
- (c) determine annual maintenance dredging requirements after the jetty is built,
- (d) determine the effect of by passing when the jetty is built

Froude Law Scaling tends to distort sediment transportation similarity particularly in areas where oscillatory wave action is absent. However, this wave action tends to reduce the critical shear stress and/or velocity necessary for initial movement of material in the zone of littoral drift over that without wave action. For this reason, Froude Law Scaling may still be reasonable for use in wave induced sediment transportation.

Ideal Velocity Scaling relationship is established by Byker (1967) with due consideration of shear stress similitude for both tidal/river currents and wave orbital velocities toward reducing similarity distortion likely when Froude velocity scaling is used. This criterion requires that both the tidal/river and wave orbital velocities be exaggerated, hence the height of the waves and of the jetty which obstructs them must be exaggerated.

Modified Froude Law/Ideal Velocity scaling as established by the Look Laboratory is designed to reduce the wave height and model exaggerations necessary when 'Ideal Velocity' scaling is used. The tidal/river current velocities required in 'Ideal Velocity' scaling and the waves required in 'Froude Law' scaling are used in the 'Modified Froude Law/Ideal Velocity' scaling. The similitude relationship of these criteria is shown in Table 5.

Froude Law scaling criteria were applied to the tests in which sand was used as sediment. Lack of time and inadequate wave-generator capacities precluded application of two other scaling criteria to tests with sand. However, all three criteria were applied in tests using ground walnut shells as sediment material (in two grain sizes, $D_{50} = 0.41$ mm and 0.90 mm, respectively). However, when larger walnut shell material was used, the desirable similitude relationship for 'Ideal Velocity' criteria and 'Modified Froude Law/Ideal Velocity' criteria were adjusted as shown in Table 5. It was impractical to perform required exaggerations in wave height and tidal/river velocities because of limitations in the wave generator.

Test Procedure Excitation was by normal and severe storm waves from the NE, on the existing channel with or without upshore east jetty protection.

Because the rate of sediment transportation and deposition of ground walnut shell material is much faster than that of sand, the test was correspondingly shorter, i.e. periods of much less than a complete tide cycle, but including portions of both ebb and flood tides. After a view of the tidal/river current pattern obtained previously with sand for Plan II, it was concluded that there are ebb currents in the channel during approximately two thirds of a tide cycle, and flood currents during the remaining one-third period. The sediment deposited in the channel during a portion of tide cycle and during operation of ebb and flood currents (for 15 and 10 minutes respectively) was measured. These test results were used to extrapolate the anticipated deposition over a complete tide cycle (on a basis of proportional contributions, two third ebb current and one third flood environment).

The time scale for each case is dependent on the amount of sediment passing over the channel. Every effort was exerted to avoid a condition in which the model channel would be filled to capacity; therefore, there was unnecessary by pass of bed load material. Tests of short duration have resulted in negligible by passing over the channel during normal and severe storm wave conditions. The time scale under no bypassing condition was used to predict sediment deposition in the channel. Furthermore, deposition by waves from N and NNW was estimated using depositions experienced in earlier tests with sands. This is considered feasible because the 'BEST PLAN' does not provide significant protection against N and NNW waves, duration is significantly short.

Table 5 MODEL SCALING CRITERIA AND MODEL SEDIMENT AS APPLIED TO RESPECTIVE CRITERIA

Parameter	Froude Scaling (1)			'Ideal Velocity Scaling (2)			Modified Froude/ Ideal Velocity Scaling (3)		
	Sands	Small Walnut Shells	Large Walnut Shells**	Sands*	Small Walnut Shells	Large Walnut Shells**	Sands*	Small Walnut Shells	Large Walnut Shells**
scale ratio	(D ₅₀ = 0.22 mm)	(D ₅₀ = 0.43 mm)	(D ₅₀ = 0.90 mm)	(D ₅₀ = 0.22 mm)	(D ₅₀ = 0.43 mm)	(D ₅₀ = 0.90 mm)	(D ₅₀ = 0.22 mm)	(D ₅₀ = 0.43 mm)	(D ₅₀ = 0.90 mm)
n	1/250	1/250	1/250	(1/250)	1/250	1/250	(1/250)	1/250	1/250
n _d	1/50	1/50	1/50	(1/50)	1/50	1/50	(1/50)	1/50	1/50
n _H	1/50	1/50	1/50	(1/11)	1/28	(1/12)	(1/50)	1/50	1/50
n _T	1/7.07	1/7.07	1/7.07	(1/7.07)	1/7.07	1/7.07	(1/7.07)	1/7.07	1/7.07
n _v	1/7.07	1/7.07	1/7.07	(1/1.8)	1/4.5	(1/2.0)	(1/1.8)	1/4.5	(1/2.0)
n _u	1/7.07	1/7.07	1/7.07	(1/1.6)	1/3.9	(1/1.99)	(1/7.07)	1/7.07	1/7.07
n _h	1/50	1/50	1/50	(1/11)	1/28	(1/12)	(1/50)	1/50	1/50

Note * Tests were not conducted for 'Ideal Velocity scaling and Modified Froude/Ideal Velocity scaling with sands
 ** The parameters as shown in the parenthesis represent the theoretical values required for the large walnut shells but were modified due to simulation equipment limitations. The modified criteria will enable the study of size effects on quantitative results of sediment deposition

Summary of Phase II Test Results Figure 11 was prepared to facilitate comparison between the distribution of sediment deposition along the existing channel in the model with no jetty protection and related measurements in the actual channel before and after Typhoon Bess. All deposition quantities are normalized to represent average one day deposition during Typhoon Bess, considering both volume and respective time scales as indicated. It was found that

- (a) Distribution predictions made by use of the Froude Law Criteria, based on results with large walnut shell material, tend to be fair for the Typhoon Bess period
- (b) Distribution predictions tend to be fair, under the normal wave condition over a long period of time (for example, one year), either by use of Froude Law Criteria based on results with sands, by use of the "Modified Froude Law/Ideal Velocity" scale criteria or the "Ideal Velocity" scale criteria (as modified) based on results with large walnut shell material, or by use of "Ideal Velocity" scale criteria based on results with small walnut shell material
- (c) Quantitative prediction by use of the Froude Law scaling criteria based on results with sands, tends to be fair when one considers only comparison of the model time scale of bottom evolution with theoretical value. However, it is expected that quantitative prediction should be reasonably good if the appropriate time scale of bottom evolution or deposition factor is applied for each test (based on respective scaling criteria with either sands or walnut shell material)

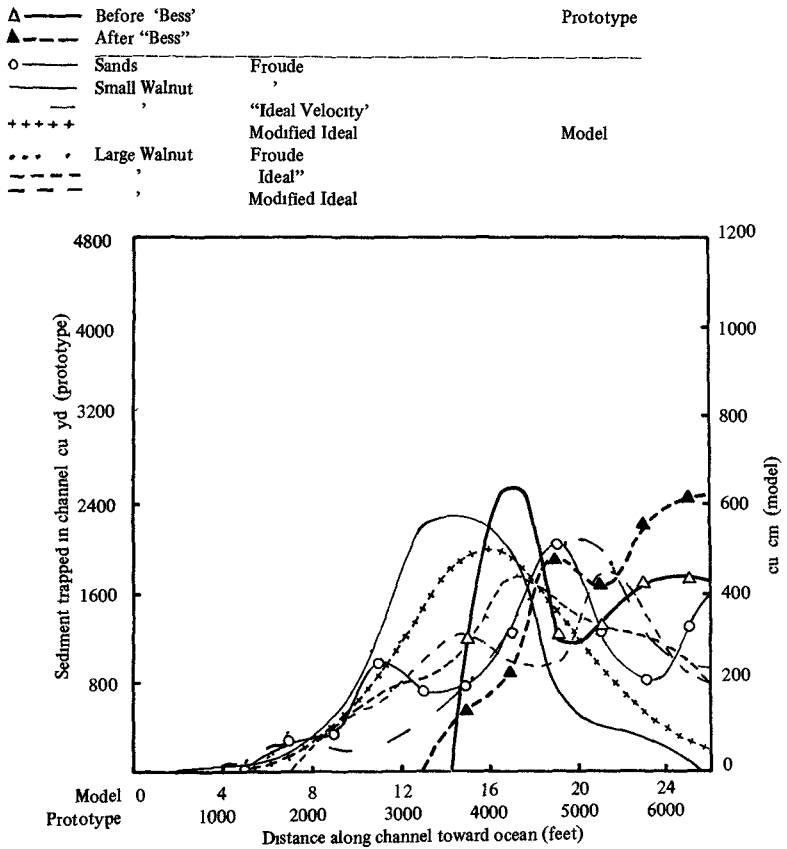


Fig 11 Model-Prototype Correlation

Time Scale Determination Time scales (the ratio of model time to prototype time for equal prototype sediment transport) were evolved for normal storm wave excitations using the three model scaling criteria and appropriate deposition in the model Measurement of the actual shoaling which occurred during Typhoon Bess is the basis for time scale determination for normal storm wave condition

As shown in Table 6, the time scales of bottom evolution vary significantly because the scale, at minimum is a function of scale factors of grain diameter, apparent density and wave height distortion However, they did not compare well with the theoretical values predicted using methods of either Manohar (1962), or Waterways Experiment Station (Fan and LeMehaute, 1969) The significant differences between theory and model results obtained with walnut-shell material raise the question of whether or not the theory is valid for the model scaling criteria used Further, the theory did not take the tide/river current scale effects into consideration in the formulation Further research is needed to determine the feasibility of using the theoretical time scale of bottom evolution in a movable bed study when no prototype quantitative data are available

Table 6 COMPARISON OF TIME SCALE OF BOTTOM EVOLUTION BETWEEN MODEL AND THEORETICAL VALUES

Time Scale of Bottom Evolution n_{tb}	Sand		Ground Walnut Shells				
	Froude	Froude	Small Grains		Froude	Large Grains	
			Ideal	Modified Froude/Ideal		Ideal (Modified)	Modified Froude/Ideal
Model	1/7.5	1/4820	1/6070	1/5400	1/3160	1/3585	1/2450
Theory *							
Manohar (1962)	1/97	1/410	1/1330	1/410	1/850	1/2750	1/2750
WES (Fan & LeMehaute 1969)	1/115	1/600	1/1940	1/600	1/1030	1/3340	1/3340

Effectiveness of the Jetty in Reduction of Maintenance Dredging Requirements It is predicted from the test results that the jetty will significantly reduce sedimentation in the existing channel (Table 7) The predicted reductions vary due to NE waves, from 82 to 99 percent when compared to sediment deposited in the unprotected channel with an average improvement of 91 percent The 87 percent reduction predicted by use of the Froude Law scale criteria (based on results with sands) is relatively conservative

Predictions of annual reduction by the jetty of sedimentation into the channel by waves from NE, N and NNW directions are also included in Table 7 (For greatest rigor, these require considerable prototype data, e.g. for calibration of the time scale of bottom evolution) Reductions in sedimentation are predicted on the order of 74 to 84 percent to the unprotected channel with an average value of 79 percent Deviations of about 5 percent may be expected between predictions based on the three scaling criteria It is concluded that the predictions (by use of the Froude Law scale criteria, based on results of tests in the model with sands) of quantities of sand deposits are adequate for engineering purposes

Table 7 PREDICTED "BEST PLAN PERFORMANCE (Based on Model Tests)

	Sand		Ground Walnut Shells				
	Froude	Froude	Small Grains		Froude	Large Grains	
			Ideal	Modified Froude/Ideal		Ideal (Modified)	Modified Froude/Ideal
Silting Reduction (NE Waves)	87%	86%	82%	93%	99%	94%	99%
Silting Reduction (all waves)	77%	76%	74%	81%	84%	81%	83%

* Manohar (1962) $n_{tb} = \lambda^2 \mu^{3/2} n_D^{-1} n_\gamma^{-1/2}$

WES (Fan & LeMehaute, 1969) $n_{tb} = \lambda^2 (n_H/\mu)^2 \mu^{3/2} n_D^{-3/4} n_\gamma^{-3/4}$

Effect of Bar By Passing Mechanics after Jetty Construction A prolonged test of the existing channel protected by a 6,000 foot long upshore East jetty (Plan IVa, Fig 7) was conducted using ground walnut shell material (small) as sediment. The purpose was mainly to study the vitally important process by which sediment bypasses around the jetty causing shoals to develop seaward of the protected channel area. These tests determine the usefulness of the improved channel system, including the equilibrium condition of updrift bar formation. By passing from the updrift to the downdrift, and bar development outside the channel entrance were also considered. The initial shoreline for the coast area updrift (East) of the jetty is considered to be the one formed by, and in equilibrium with excitation by severe NE storm waves.

The base for the study of by pass and off-entrance shoaling in which the excitation was Test Condition I was as follows: NE waves 5 ft/5 sec, and 500 m³/sec river flow, 1.8 ft/sec tidal current in one diurnal tide cycle (44 minutes in model), increments up to three tide cycles. As a result, a new equilibrium shoreline was formed as shown in Fig 12(a). Bottom profiles were taken through the beach area (Section A-A), around the channel entrance (Section B-B), and along the existing channel (Section C-C), as shown in Figure 12 (c), (d), and (e), respectively. These permit evaluation of the shoaling and by passing process as a function of time. It is interesting to note that the new equilibrium shoreline forms parallel to the incident NE wave and establishes after two tide cycles. This is equivalent to approximately 280 days in the prototype, using a time scale for bottom development of 1/4820 based on Froude Law scale criteria for no by passing.

Heavy shoaling developed upshore, and near the center of the 6,000 foot long jetty [Fig 12(c)]. A significant bar did not develop outside the channel entrance of the protected channel even after one additional tide cycle beyond the time necessary for the beach to attain equilibrium [Fig 12(d)]. This is perhaps controlled by the scouring effect of the high currents present offshore of the end of the jetty, and by the onshore component of the wave action which tended to curtail littoral drift, and caused deposition of sediments in other areas as noted in Fig 12(a). However, a bar of about 160,000 cubic yards did develop inside the channel entrance, with a peak at approximately 750 feet upstream from the end of the jetty. This bar represents about a year (420 days) of accumulation in the protected existing channel, with no dredging. It seems unlikely that the large bar would develop should the channel be maintained reasonably by periodic dredging.

Action of the waves, other than the normal NE storm waves, studied in these special tests (i.e. waves from N and NNW and severe NE storm waves) should tend to reduce, by erosion, the sediment trapped upshore of the jetty. This would act as a storage area for sediment driven into the area by NE waves, during the normal NE monsoon season. Thus, updrift of sediment into the channel should be inhibited.

As a result of these tests, it is concluded that

- 1 The effectiveness of the improved channel system (Plan IVa—6,000 foot long jetty upshore of the existing channel) can be maintained by dredging at a minimum level (21 percent of the original estimate without jetty protection)
- 2 Seasonal changes of wave action will help to maintain the effectiveness of the jetty. In particular, they will scour the upshore beach and make it a more effective trap during monsoon season. Thus, excessive dredging will not be required after the monsoon season. Delay in ship operation will be reduced to a minimum.

Findings and Conclusions of Phase II Study A 6,000 foot long jetty along the upshore bank of the existing channel is most effective and economical, with reasonable initial cost and minimum maintenance dredging requirements.

It was found that a jetty as postulated in the "BEST PLAN" would reduce the annual maintenance dredging required in the Tan My Inlet navigation channel (caused by NE wave induced shoaling) by 82 to 99 percent. This had been predicted with different model scaling criteria and types of sediment materials. A 10 percent error (5 percent on annual basis), attributable to scale effects, may be expected. No attempt was made to determine the relative merit of conflicting model scaling criteria. By consideration of the appropriate time scale of bottom evolution, one can obtain nearly the same quantitative results of annual dredging requirements. The "Ideal Velocity Scaling" with small walnut-shell material tends to predict most conservatively.

As far as the distribution of sediment deposition along the channel is concerned, none of the scaling criteria gave comparable distribution to that found in the prototype using Typhoon Bess conditions. However, model results (with sands using Froude Law scaling, with small walnut-shell material using 'Ideal Velocity' scaling, and with large walnut-shell material using "Modified Froude/Ideal Velocity" scaling or "Ideal Velocity," as modified) tend to give fair to good comparison of sediment distribution over long periods of time under normal conditions.

From the viewpoints of time consumption for a model study, the use of light weight sediment materials (such as the ground walnut shells used in this study) may be more economical than sands.

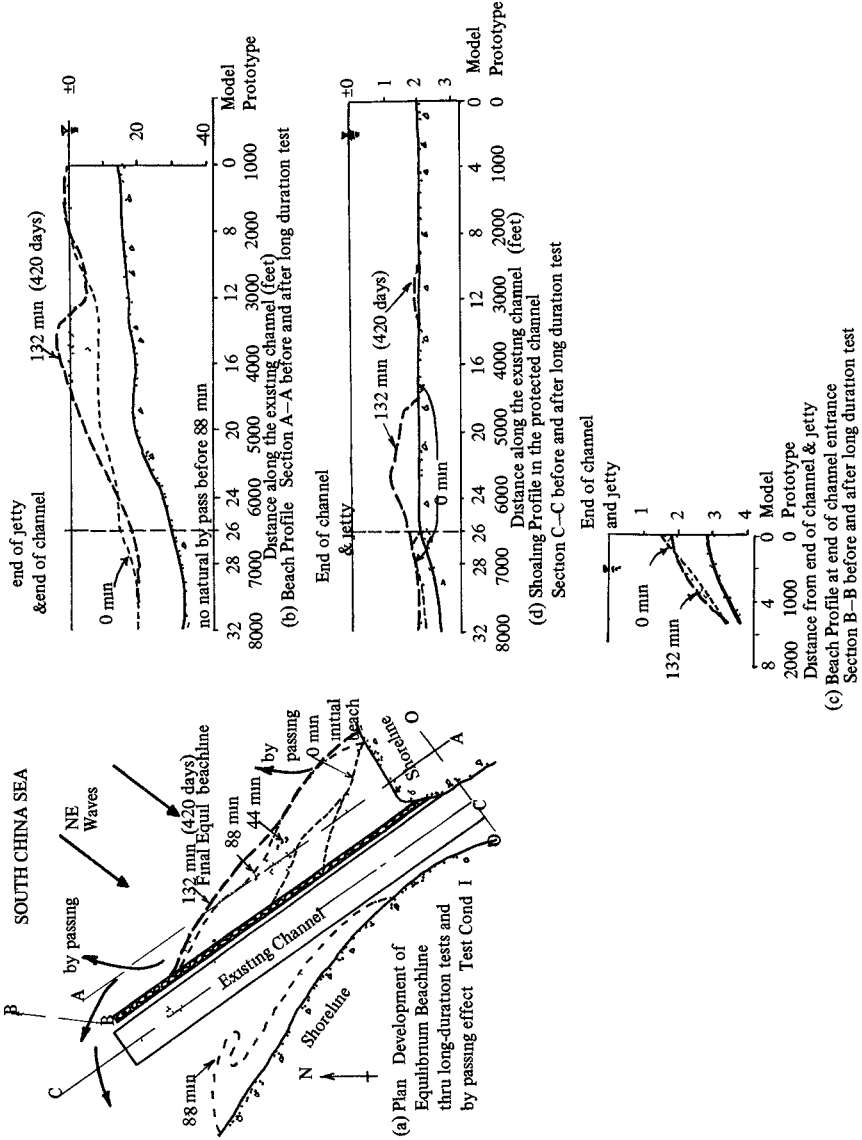


Fig 12. Prolonged Tests on By passing Characteristics of BEST PLAN IVa

Further research work on the model technology of a movable bed model is needed to clarify the uncertainties encountered in this study. Furthermore, an important point on the necessity of by pass operation should be discussed. Periodic by pass of the littoral drift that accumulated upshore of the jetty may be desirable only if the protection of the downdrift beaches from erosion is of vital importance and only when the value of the beaches is sufficient to justify the cost of such a by-pass operation. On the other hand, where preservation of the downdrift beach is not of major importance, as in the case of Tan My Inlet, the suggested "BEST PLAN" should be adequate to reduce substantially the maintenance dredging required in the navigation channel by trapping a significant portion of the predominant littoral drift on the updrift side of the jetty and by encouraging natural by passing of some of the untrapped portion.

Phase III Stability Characteristics of Rubble Mound Type Jetty of the BEST PLAN Phase III covered the two dimensional model studies which were conducted at a much larger scale in a 180 foot long wave flume. The objective here was to determine the stability characteristics of the rubble mound type jetty of the 'BEST PLAN' against storm wave action. From these tests, the jetty design was optimized. Tests and evaluations were made on the

basic designs of Fredric R Harris Inc for Jetty Sections IV and V. From these test results, the design was improved for use in this case (Fig 13).

Scale dimensions for tests were 1/20, 1/23.4 and 1/24.5. The tests were conducted with a 1/60 beach slope covered with sands (or walnut shells) as an erosible bed. Stone weight scaling followed the similitude by Hudson (1959) i.e.

$$\frac{(W_r)_m}{(W_r)_p} = \frac{(\gamma_r)_m}{(\gamma_r)_p} \left(\frac{L_m}{L_p} \right)^3 \left(\frac{(S_r)_p - 1}{(S_r)_m - 1} \right)^3$$

W_r = weight of stone

γ_r = specific weight of stone

$$S_r = \frac{\gamma_r}{\gamma_w}$$

γ_w = specific weight of water

The jetty was trapezoidal in cross section with 90 foot base, 15 foot wide crown, 24 feet high, with side slopes of 1 on 1.25. It rested in water 21 feet deep. Design configuration was rubble type rock in double layer at 6.4 or 10.3 tons each on the outside (armor), double layer at 0.3 tons each (as secondary cover), and quarry run of 2 inch size as both core and 4 foot thick base. It was intended to be overtopped by the design waves which, face on, were 14 feet high, with an 8

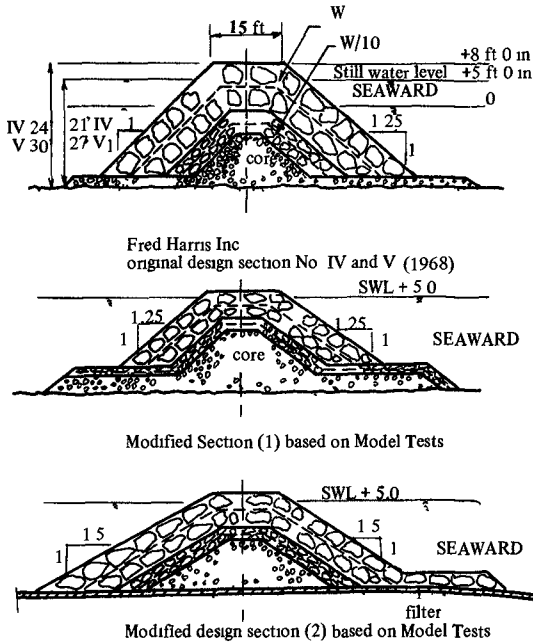


Fig 13

second period. However, toward conservatism, the jetty was tested in waves up to 20 feet high with a 10 second period.

Major findings were as follows:

1. A slope of 1:1.25 is acceptable for the 14 foot high design waves.
2. An armor stone size of 6.4 tons (for Jetty Section IV) and of 10.3 tons (for Jetty Section V) is adequate for the 14 foot high design waves under either low or high tide and storm surge conditions.

- 3 To prevent scouring under the jetty a layer of core materials should be extended beyond the armor stone toe with two layers of secondary stones placed over this layer of core material for protection An alternate for protection against sand scour is a plastic filter (such as Poly Filter X) extended in front of the jetty and under the sand with secondary stones above the sand as protection
- 4 A filter layer, preferably of plastic, is necessary in the prototype between the core material and the sand beach This could not be demonstrated in the model due to the effect of the scale, i.e., larger voids in the prototype than those in the model
- 5 Further testing of scouring depth at the jetty toe is necessary because of the discrepancies found between test results with sand and those with walnut shell material as erosible bed materials
- 6 The stability of the rubble mound jetty should be studied in a movable bed model particularly if the jetty is founded in a depth shallower than the critical depth for sand movement Otherwise the designer should specify that the jetty bottom should either extend below scour depth to be determined, or it should rest on a plastic filter
- 7 The filter system for a jetty should be designed with extreme care, particularly if the transitory currents induced by tidal and river flow along the longitudinal axis of the jetty are significant

CONCLUSIONS

The major conclusions of this study were

- 1 A 6,000 foot long rubble mound type jetty along the east bank of the existing channel [Fig 7] should be considered the 'BEST PLAN'—the most effective and economical solution of the exterior channel improvement at Tan My Inlet The rubble mound type jetty should be constructed of 6 4 to 10 3 ton armor stones with two layers of secondary stones and core materials laid underneath it A filter system must be carefully designed to avoid any failures due to erosion of the jetty foundation and toe
- 2 A semi movable bed model study of the inlet stability improvements, following the three phase experimental procedure reported herein, may be considered a feasible method by which to obtain both qualitative and quantitative results this is particularly so when sufficient prototype data are available to relate the time scale of bottom evolution
- 3 A jetty as postulated in the 'BEST PLAN' would reduce the annual maintenance dredging required in the Tan My Inlet navigation channel (caused by NE N, and NNW wave induced shoaling) by 74 to 84 percent This was predicted with different model scaling criteria and types of sediment materials By consideration of the appropriate time scale of bottom evolution, one obtained nearly the same quantitative results of annual dredging requirements 'Ideal Velocity' scaling with small walnut shell material tended to predict most conservatively

As far as the distribution of sediment deposition along the channel was concerned none of the scaling criteria gave distribution comparable to that found in the prototype using Typhoon Bess conditions However model results (with sands using Froude Law scaling with small walnut shell material using "Ideal Velocity" scaling and with large walnut shell material using 'Modified Froude/Ideal Velocity' scaling or 'Ideal Velocity,' as modified) tended to give fair to good comparison of sediment distribution over long periods of time under normal conditions

From the viewpoint of time consumption for a model study, the use of light weight sediment materials (such as ground walnut shells) may be more economical than use of sands Further research work on the model technology of a movable bed model is needed to clarify the uncertainties encountered in this study

- 4 Use of theory alone in predicting the time scale of bottom evolution should be done with caution, especially in cases where field data are not readily available for model prototype correlation This conclusion was quite obvious, at least for this study Further verification is needed
- 5 The quality of the model study is still greatly dependent on the quality and quantity of environmental data collected When adequate data are available to permit the determination of the time scale of bottom evolution the discrepancy between the results obtained with different scaling criteria and model sediment was not too large as one would expect normally Of course there are still many research problems involved in a movable bed model

ACKNOWLEDGEMENTS

The Officer in Charge of Construction, Republic of Vietnam, Naval Facilities Engineering Command sponsored the model study, the assistance provided by LCDR W H Kay, ROICC, and his staff is appreciated Mr J C Kray of NAVFAC furnished valuable comments Their permission to publish this paper is appreciated

The invaluable support given by the colleagues of this author is acknowledged, particularly that of Dr C L Bretschneider, Project Manager Mr J T O'Brien Director of Look Laboratory, Mr R Q Palmer Co Principal Investigator Messrs A R Fallon and David Lally and other study team members

The Research Corporation of the University of Hawaii monitored the contract of this study

REFERENCES

- Bijker, E W (1967), "Some Considerations about Scales for Coastal Models with Movable Bed," Pub 50, Delft Hydraulics Laboratory, Nov 1967
- Bijker, E K (1968), Littoral Drift as a Function of Waves and Current ' Proceedings of the 11th Conference on Coastal Engineering (London, Sept 1968), American Society of Civil Engineers, 1969
- Bowen, A J and D L Inman (1966) Budget of Littoral Sands in the Vicinity of Point Arguello Calif Tech Memo 19 U S Army Coastal Engineering Research Center, Dec 1966
- Bruun, Per J A Batties, T Y Chiu and J A Purpura (1966), "Coastal Engineering Model Studies of Three Florida Coastal Inlets" Bull 122 Florida Eng and Ind Experiment Station, University of Florida, Gainesville June 1966
- Caldwell, J M (1956), ' Wave Action and Sand Movement Near Anaheim Bay, Calif ' BEB TM 68, Feb 1956
- Fan, L N and B LeMehaute (1969) "Coastal Movable Bed Scale Model Technology," Final Report, U S Army Coastal Eng Research Center, (DACW 72 68-C-0020) by Tetra Tech, Inc , January 1969
- Glenn, A H and associates (1966) Meteorological-Oceanographic Evaluation for Planning, Design, Operation of Marine Facilities Along the Coast of South Vietnam General Report," 19 April 1966
- Hudson, R T (1959), "Laboratory Investigation of Rubble Mound Breakwaters," Journal Waterways and Harbors Division, Proceedings, ASCE, vol 85, no WW3, Sept 1959
- Inman, D L and R W Harris (1966) *Oceanographic and Engineering Report on Investigation of Sedimentation Siltng, and Dredging Requirements Various Locations, Republic of Vietnam, Contract NBY 79844 Daniel, Mann Johnson, and Mendenhall, Saigon Vietnam, June 30, 1966
- Keulegan, G H (1967), "Tidal Flow in Entrance Water Level Fluctuations of Basins in Communications with Seas," Tech Bull no 14, Committee on Tidal Hydraulics, Corps of Engineers, U S Army, Vicksburg, Miss July 1967
- Lee, T T (1970), "Model Investigation to Improve the Stability of Tan My Channel Hue, Republic of Vietnam," Technical Report 10, Look Laboratory University of Hawaii, Feb 1970 (Contract N 63185 69-C-0089)
- Lyon Associates, Inc (1968 1969) "Tan My Channel Study Field Measurements" OICC/RVN Contract P11 0088 Bi weekly Report No 1 through 10 dated Sept 1968 Jan 1969
- Manohar, M (1962), 'Discussion of Laboratory Determination of Littoral Transport Rate ' by R P Savage,' Jour Waterways and Harbors Div Proc ASCE 88, WW4 Nov 1962
- NAVFORV Weather Unit, Saigon, RVN (1968), Wave observations at Tan My during 1 Oct 1967 to 30 Sept 1968
- Palmer, R Q (1970) 'Optical Wave Recorder for Hydraulic Models,' LOOK LAB/HAWAII, vol 1, no 1, Jan, 1970
- Savage, R P (1959) "Laboratory Study of the Effect of Groins on the Rate of Littoral Transport Equip Development and Initial Test,' BEB TM 114, June 1959 (also TR-4, U S Army Coastal Eng Research Center)
- Wiemat, D R (1969) Letter to Mr R Steward concerning preliminary results of the Infra red imagery Survey of Tan My area 14 July, 1969

CHAPTER 72

MODEL TESTS AND STUDIES FOR PORT RASHID, DUBAI

ERIC LOEWY

Partner
Sir William Halcrow & Partners
Consulting Engineers, London

ABSTRACT

This paper is a factual account of studies carried out for the design of a new deep water harbour. As so often happens construction work had to be begun before many of the conclusions of the study were available so that alterations to the initial designs had to be made while work progressed. The studies comprised tidal and wave recordings and analysis, model studies to determine residual wave conditions at the quays, studies to determine the extent of littoral drift, the effect of the proposed works upon this and possible measures to counter downdrift erosion. In addition studies were made of the stability of the adjacent creek channel which had previously been the harbour and a mathematical model study was carried out of the effects on the creek regime of various proposed entrance works including the construction of an entirely new creek entrance channel through the new deep water harbour.

INTRODUCTION

The State of Dubai is situated on the southerly coast of the Strait of Hormuz which forms the seaward entrance of The Gulf (sometimes called the Persian or Arabian Gulf - see fig 1). The Capital Town of Dubai consists essentially of the twin towns of Dubai proper and Daira (fig 2) which lie astride the mouth of a tidal creek which has up to now formed its harbour. This harbour was used by country craft (dhow), lighters and other small vessels, with only very minor works on jetties and wharves up to approximately 1958. The combination of littoral drift towards the north east and the creek tidal flow resulted in a gradual migration of the creek entrance in the direction of the drift and, in the years after the last war, to a reduction in the depth of water available at the entrance. Starting in 1959 entrance training works were constructed and the channel dredged out to 8 feet below chart datum. These works caused an interruption of the littoral drift with consequent erosion of the downdrift site (figs 3 and 4).

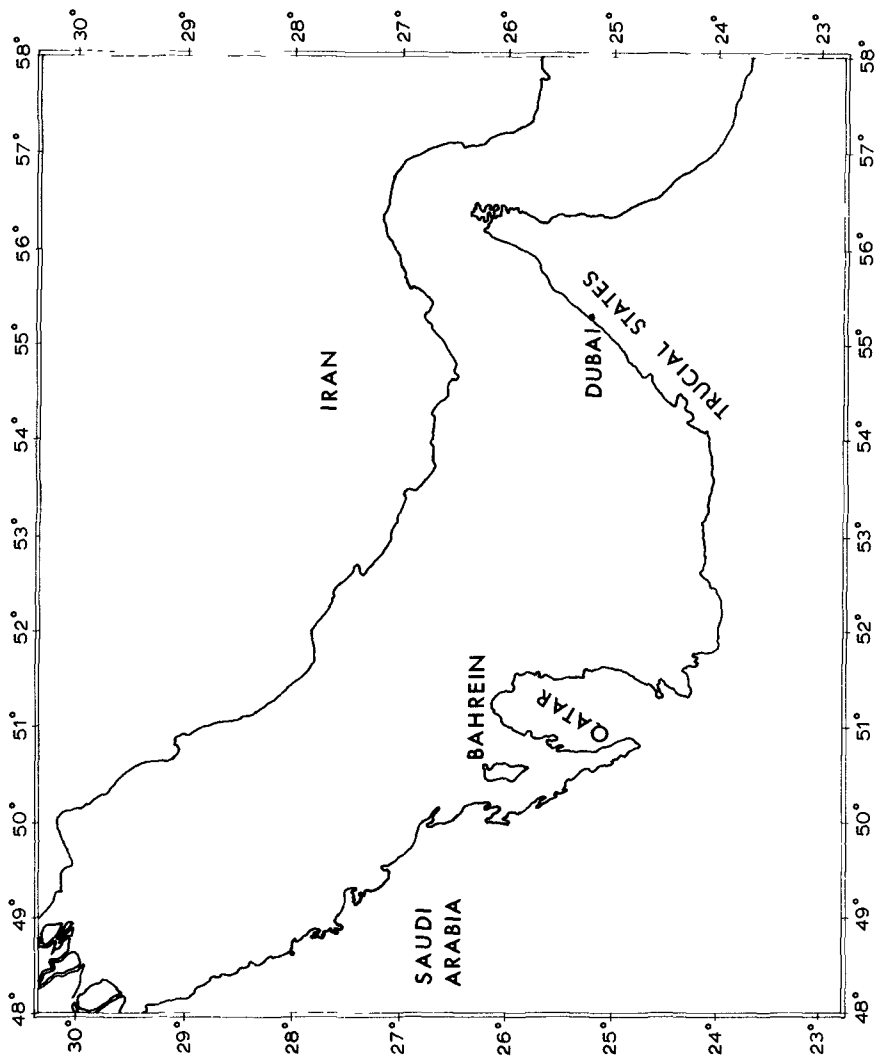
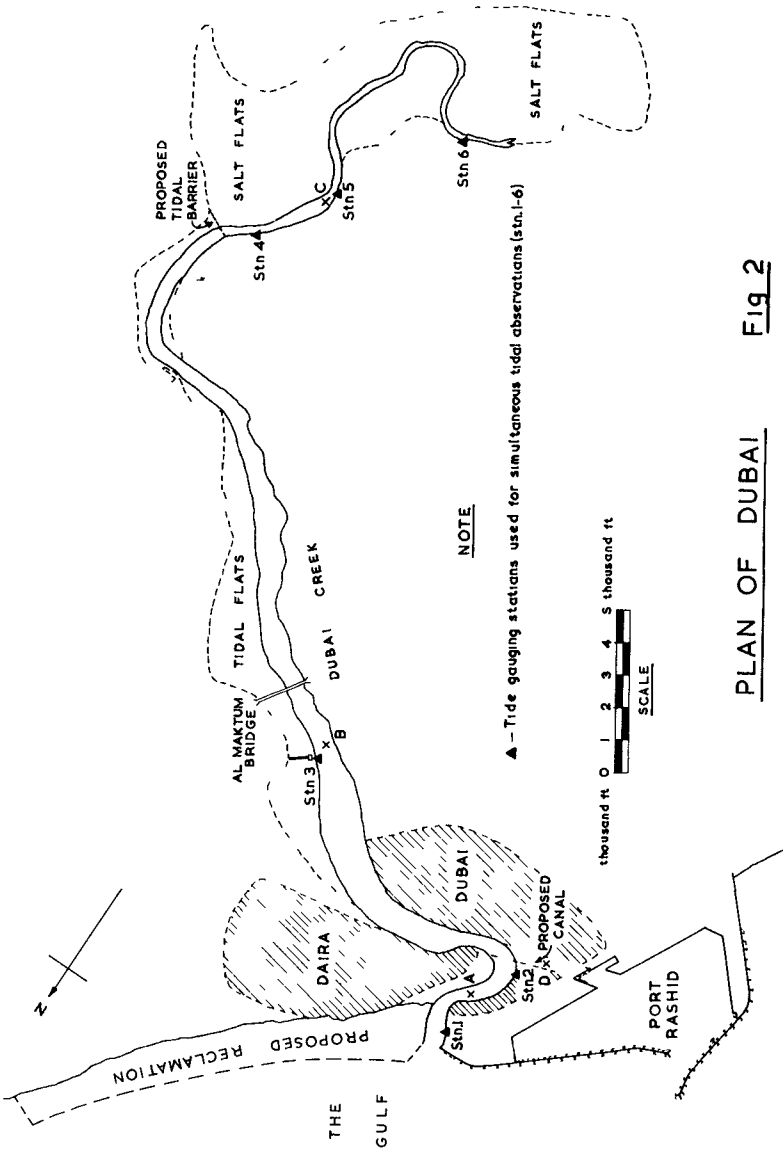


Fig 1 Plan of the Gulf



PLAN OF DUBAI Fig. 2



Fig. 3 DUBAI CREEK



Fig. 4 CREEK ENTRANCE

In 1966, as a result of oil being found in Dubai waters, His Highness the Ruler was enabled to embark upon the construction of a new deep water harbour, to be known as Port Rashid, immediately south-east of the creek entrance (fig 2) The new harbour, which will enclose a water area of approximately 350 acres and will provide 15 deep water berths each approximately 600 ft, long, is still in course of construction It will have a bed level at its entrance approximately 36 ft below chart datum and will be dredged to 30 5 feet below chart datum throughout Since the harbour works will form a solid barrier to the littoral drift for approximately one mile out to sea from the previous shore line it is clear that these are likely to have an even greater effect on the coastal regime than the creek entrance works

There are proposals to close or partly close the existing creek entrance and form a new canal link from the creek to the new harbour There is also a proposal to reclaim a coastal strip of land north east (downdrift) of the new harbour and protect this with a heavy sea wall which would have the effect of preventing further erosion there and transferring the erosion to less valuable land further along the coast

Model Tests and Studies were initiated to consider various aspects of the works The majority of these were carried out at the Hydraulics Research Station at Wallingford, England

INVESTIGATIONS

A tide recorder was set up on the side of a small jetty built out across the beach into the sea An analysis of the first year's tidal records was carried out by the Institute of Coastal Oceanography and Tides at Birkenhead, England The analysis demonstrated the extent of the "set up" which can occur at the south-east end of the Gulf On 25th January 1969 this was 12-18 inches continuously for a period of 12 hours Shorter period seiches up to 17 inches have also been recorded The tides are subject to a large diurnal inequality Their normal range is between MHHW + 5 5 ft (chart datum), MLHW + 4 4 ft, MELW + 2 6 ft and MLLW + 1 3 ft

An O S P O S wave recorder was installed This type of self-contained recorder was chosen in place of an instrument which would record on shore to avoid the danger of the connecting cable being broken by small vessels anchoring offshore For most of the recording period the O S P O S instrument was anchored approximately $\frac{3}{4}$ mile offshore in 36 ft of water (below chart datum) with the recorder tethered 8 to 10 ft below chart datum so as to be approximately 3 ft below what was anticipated to be lowest wave trough level The relationships and equations used in the analysis of the wave records were reduced to forms suitable for the Olivetti Programma 101 Desk Top Computer The analysis was carried out in accordance with Draper's procedure (ref 1) using the empirical corrections for attenuation worked out by Draper and Maxted (ref 2)

Since no commercially-available, proven, wave direction recorder of reasonable cost appeared to be available wave directions were estimated visually, normally twice daily. Twice daily observations were the most which could be expected from the already overbusy Resident Engineer's Staff but as the height recordings occurred 8 times per day (every 3 hours) it is obvious that considerable interpolation of wave directions had to be estimated with corresponding risks of error. There is no doubt that the development of a reliable, commercially-available, reasonably-inexpensive wave direction recorder would be very greatly welcomed.

WAVE ANALYSIS

To date six month's wave records have been analysed. The data has been adequate and sufficiently representative for wave height frequency prediction graphs to be drawn for "all directions" waves and for waves from 300°, the dominant direction, and from 330°, but not other directions. The "all directions" prediction (fig 5) drawn on probability graph paper, extended upwards to obtain a Once in 100 Years wave value, indicates a maximum deep water wave height of 34.5 ft in 100 years, 31.5 ft in 50 years, and 26.0 ft in 10 years. Using Darbyshire and Draper's relationships (ref 3) between wind speed and duration for the maximum possible fetch of approximately 500 nautical miles these maximum wave heights would require wind speeds of respectively 44, 45 and 36 knots for a period in each case of approximately 33 hours, or equivalent combinations of speed and duration.

In the restricted area of The Gulf the majority of wave patterns are composed of short-period waves. The recording of such waves led to difficulties which were not sufficiently appreciated at the beginning of the analysis. The first was locational, in that the record tended to be increasingly flattened the deeper the pressure-actuated instrument was tethered below the water surface. This was overcome in large measure but still required an attenuation factor adjustment before feeding the data into the computer. The second was instrumental, in that a considerable number of the 12 minute duration records were of waves about 1 foot in height, shown on the trace as 1 mm. The difficulty of classifying these in wave height steps was such that the analysis proved unreliable in the smaller ranges and in fact only derived maximum waves over 7 feet in height were plotted, the linear results being extended to cover predictions for lesser waves and extrapolated for waves beyond the scope of the instrument readings.

Estimation of the likely frequency of stated wave heights has so far been assessed only by reference to the British Ministry of Technology's statistical survey of wave characteristics estimated visually from Voluntary Observing Ships on their normal shipping passages (ref 4). It is interesting to note, however, the confirmation provided by maximum heights up to 25 feet being estimated at points a little further west in The Gulf during a storm in 1964.

The relationship between maximum wave height and maximum significant wave height was found during this analysis of six-months' recordings to be approximately 2 to 1, for the range of wave periods of between 4 and 9 seconds which was of principal interest and occurrence.

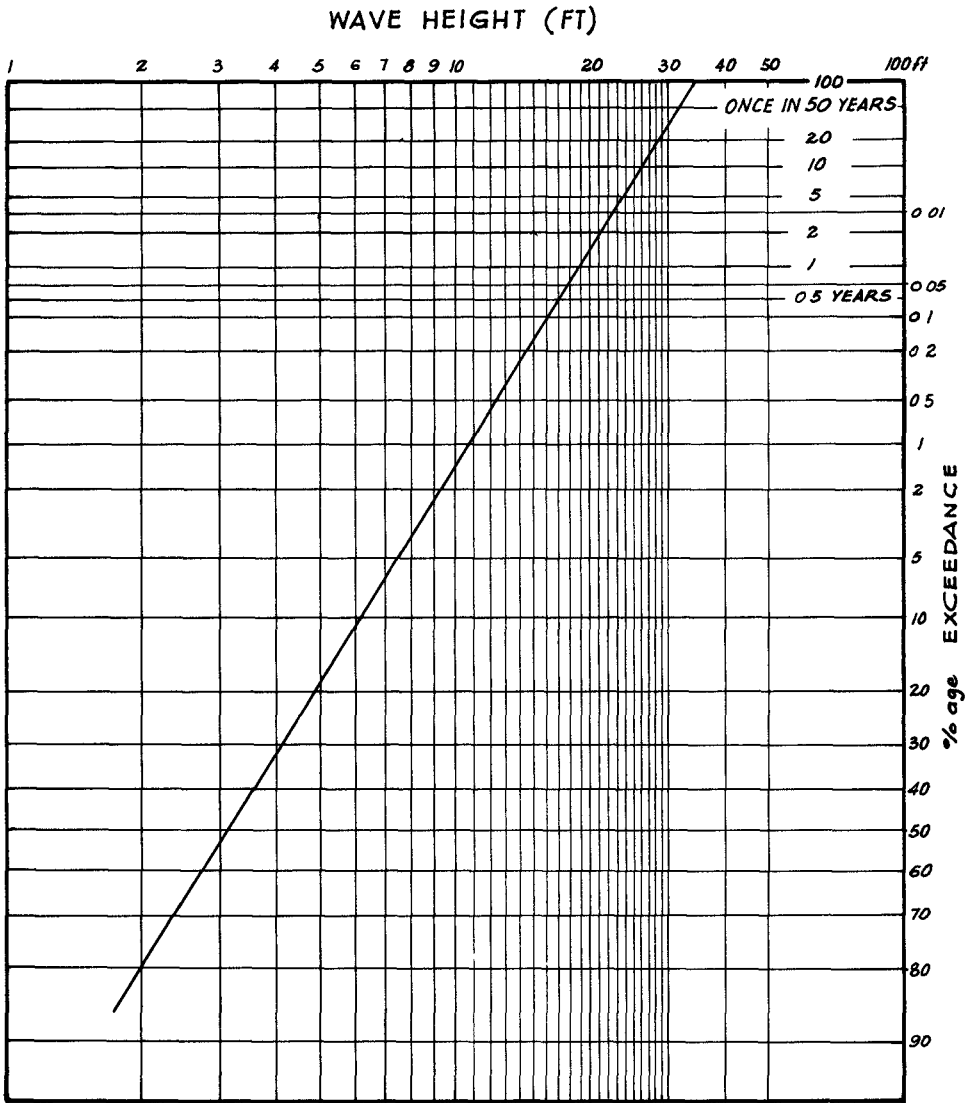


FIG 5 WAVE HEIGHT PREDICTION (all directions)

HYDRAULIC MODEL TESTS

A rigid bed hydraulic model of Port Rashid was constructed to a scale of 1:150. Waves of different equivalent heights, periods and directions were generated and directed on to the harbour and their residual heights along the quays were measured for a number of harbour layouts. A final harbour layout was chosen by this means. These model tests had to be carried out before any results could be obtained from the wave recorder. The waves used for the tests were therefore estimated from wave recordings taken further west in the Gulf and an assessment, using synoptic charts, of the corresponding waves off Dubai.

Idealised ship movement tests, using the same equivalent waves, were also carried out using models representing 10,000 dwt and 4,000 dwt vessels at the quays. The results of these model tests were satisfactory, except in the case of two berths when waves were from the north direction. This is in fact the direction in which the harbour entrance points so that there is virtually no obstruction to these waves. Although no prediction for waves from the north has been possible from wave recordings at Dubai for reasons mentioned previously it has become clear that considerable wave activity from that general direction is rare. This conclusion has since been confirmed by an analysis of the wave records from Voluntary Observing Ships steaming in the vicinity of Dubai. These records were kindly supplied by the British Meteorological Office.

In connection with the wave model a study was carried out of the extent to which waves could be generated within the enclosed harbour area over the greatest fetch of approximately 1.3 miles by strong winds blowing from approximately south west or north east. Although it was appreciated that these conditions would only occur infrequently, experience with the model showed that the resulting waves would not significantly hamper the working of ships alongside the quays.

No evidence was obtained that the natural period of oscillation of the harbour basin would give rise to seiches having periods or length of range which could affect moored vessels in Port Rashid, providing of course that such mooring lines and fenders were in appropriate combination of stiffness and softness which previous model and full-scale tests had shown to be suitable.

LITTORAL DRIFT

The coastal regime at and in the vicinity of Dubai was studied particularly in order to assess the effects of the construction of Port Rashid. As has been mentioned, training works were carried out between 1959 and 1962 at the entrance to Dubai Creek. These involved the construction of steel sheet-piled training walls to stabilise and maintain the creek channel into the sea out to approximately the seabed contour 8.0 ft below chart datum, this being a sufficient depth of channel for the country craft and lighter traffic at that time (fig 3).

Since the net littoral drift is south west to north east along the coast the effect of these training walls had been to cause accretion on the south west side and erosion on the north east side. By 1968 the down-drift erosion, which affected the densely-populated town of Daira, had begun to cause serious concern, though by about that time some natural sand by-passing of the creek had just begun to occur. There were therefore naturally fears of the effect of the very much bigger barrier of Port Rashid. Comparison of regular measurements of beach and bed levels on a number of lines perpendicular to the coast updrift of the training walls early led to the conclusion that the natural net rate of littoral drift was approximately 70,000 cu yds per year. In 1969 a further calculation was made based upon the relationship -

$$Q = 210 E^{0.8}$$

where Q = intensity of littoral drift in cu yds per day
and E = longshore wave energy in millions of foot-pounds per foot of beach per day

The net littoral drift per year calculated from this amounted to 79,000 cu yds. Again, because wave data from the wave recorder was not available when this calculation was made, the same assumptions as have been mentioned before were made regarding the waves. However since the two calculations showed such close agreement it was considered justified to assume a net littoral drift of the order of 80,000 cu yds per year from south west to north east and no further calculations have been undertaken using the results of the analysis of the first 6 months of actual wave records.

Based upon such an assessment of annual volume, it will be at least 20 years before any significant by-passing of sand across the entrance of Port Rashid is likely to occur. The form which this natural by-passing may take is uncertain and may well be unacceptable. During this time corresponding erosion of the downdrift coast of Daira will occur unless remedial measures are taken. Since this township is densely populated to the coastline this is obviously not a result which can be accepted and the Ruler is at present considering the adoption of one of several alternative solutions proposed to him. Artificial nourishment is one course, another, more favoured, is to concentrate the erosion length further downdrift, where the coastal strip is devoid of use or habitation, by carrying out protection and reclamation works from the creek entrance to beyond the downdrift end of Daira.

DUBAI CREEK

The influence of the creek flow upon the situation has not so far been mentioned because it does not appear that there is any significant outflow or inflow of bed material associated with it. As far as is known the creek has remained remarkably stable of recent years in these respects though there has undoubtedly been a gradual migration of the entrance towards the north east.

Normal sand by-passing did not apparently produce the formation of sand bars which cause navigational difficulties. But when the channel began to follow a course leading over a coral reef an unacceptable reduction in natural entrance depth resulted. The works carried out between 1959 and 1962 successfully relocated the entrance by a system of sheet piled training walls with dredging to restore and deepen slightly the channel linking the creek port with the sea.

With the firm proposal taken to construct the deep water port on the coast off Dubai, there followed naturally the suggestion of a connection by water between the already-flourishing Creek port, with its winding and restricted entrance, and the new harbour enabling cargo liners to discharge and export freight in security from wind and sea conditions. It was evident that the sediment loads and tidal velocities through the creek port had a large effect on the success of such a scheme to direct the flow into and out of the tidal basin upstream of the port and to close, wholly or partially, what would become the former entrance. Examination of this proposal could only be through model analysis, unfortunately time and cost limited the study to a mainly qualitative rather than a quantitative one, but nevertheless the results were instructive.

INVESTIGATION AND MATHEMATICAL MODEL

The creek is not fed by any surface streams, even intermittent ones, but there is a small amount of sub-surface seepage of water into the upper reaches and this seepage is very highly saline. In addition there are very extensive tidal flats at the head of the creek which are covered at high water and dry out at low water. These large areas of generally very shallow water are of course areas where high evaporation leads to increasing salinity. For these two reasons, therefore, the water at the head of the creek is considerably more saline than the sea and the water lower down the creek. This reverses the more usual situation in which fresh water flows into the head of a tidal inlet and the salinity decreases as the distance from the sea increases. A natural corollary of the situation at Dubai is that the highest salinities occur at low water. The result of this salinity pattern is that there is a net drift of water near the bed of the creek towards the sea, but the velocities involved are so low that this is not of significance as regards the transport of bed material.

No measurements are available to show up any areas of accretion or erosion either permanent or temporary in the creek or to indicate quantitatively any natural changes in the entrance channel. However it seems clear that there is a negligible transport of solids to the creek through sub-surface flows. The most likely sources are from wind-blown material and erosion of the bed or banks. Erosion does not appear to provide any overall change in the quantity of solid material entering or leaving the creek though there are local movements within it. Wind-blown sand undoubtedly does provide an input source, but such calculations as have been possible in this respect suggest that the quantity is small and that it is confined to the upper reaches. Due to a large diurnal inequality in the tides at Dubai the maximum ebb flows in the creek are greater than the maximum flood flows so that bed material from the creek tends to be flushed out into the sea rather than the reverse, and consequently the entrance channel remains open.

A large number of cross-sections of the creek were surveyed and tidal observations carried out simultaneously at six stations (fig 2) over a high spring tide cycle on 13/14 May 1968, with an extensive series of current velocity measurements taken during this cycle. The mathematical model of tidal flows in the creek, with the view to assessing the effects of various proposed schemes, was proved against this set of tide levels and flows. Because of the large diurnal inequality, which results in velocities and discharges on the fall of the major tide being much greater than the velocities and flows during any other period, subsequent analyses were directed towards determining the maximum velocities and volumes of water (tidal prism) leaving the creek on the ebb of the major tide under the conditions of 13th/14th May 1968.

Once the model had been satisfactorily proved the effects of proposed engineering works could be studied. These proposed works are indicated on Figure 2 and they comprised -

- (a) Construction of a canal link between Port Rashid and the creek and the closure or partial closure of the by-passed seaward end of the latter.
- (b) Construction of a tidal barrier near tide gauging station 4 to close off the salt flat area at the head of the creek. The object of the barrier would be primarily to reduce the tidal flow by eliminating the large storage volume contained in the tidal flats at the head of the creek. As a secondary object it would serve as a barrage to increase water level permanently above the barrier in a reach to which vessels would have access through a lock. Such a barrier might indeed be valuable but would probably be better sited further towards the sea so that the locked area would be able to serve the towns and the ships.

RESULTS AND CONCLUSIONS

The mathematical model quickly demonstrated that the tidal regime in the creek is at present dominated by two factors. These are the throttling effect of the narrow channel through the Town and the presence of the large inter-tidal flats storage volume at the head of the creek. As a result schemes to vary the entrance to the creek cannot alone greatly affect the regime except locally. The only practical scheme examined which caused an appreciable change in the whole regime was that to construct a tidal barrier blocking off the major portion of the inter-tidal flats storage volume.

The model was able to calculate water level, velocity and flow at any time at a number of selected points in the creek and proposed canal for the conditions resulting from the various schemes under the open-sea ebb tidal

conditions of the 13/14 May 1968 Volumes of tidal prisms could also be calculated for the various tide levels

Some actual mathematically-calculated figures may be of interest here At present the creek channel tidal maximum velocities vary greatly along its length Peak maximum velocity is 5.2 ft/sec at Section A (fig 2), reducing to 1.33 ft/sec at Section B and increasing again to 2.5 ft/sec at Section C Incipient sediment movement was calculated to correspond to a water surface velocity of 1.4 ft/sec for a 0.1 mm sand (taken as representative of the finer fractions of bed material) This means that at present some sediment movement towards the sea probably takes place in the upper reaches but not in the middle reaches In the lower reaches between the towns quite extensive movement would take place were it not for the fact that the bed here mainly consists of coral with limestone boulders and the quantity of sand is small It would appear therefore that there is probably some accumulation of bed material in the middle reaches though there are no indications that this is of serious proportions The bed sand lost in the upper reaches appears to be approximately made good by the wind-blown sand previously mentioned

When the proposed canal was introduced into the model, with varying proportions of the existing creek entrance channel remaining as well, it was found that the effect of such new entrance proposals on the tidal prism was limited to a maximum increase of 6.6 per cent because of the throttling effect of the reach through the town A large change in the entrance channel conveyance produced only a small change in the tidal prism As a result it was possible to work out a simple method of calculating the performance of any combination of entrance channels (so long as their combined conveyance exceeded the value of the existing entrance channel) This no longer required the use of the mathematical model

Provisionally it was considered that a canal link having a 340 ft wide rectangular section and a bed level 12 ft below chart datum, with the existing creek entrance completely closed off, would result in a peak maximum velocity of 4.4 ft/sec (at Section D, fig 2) This would be acceptable provided that the bed material was found to be suitable or was suitably protected Peak maximum velocities somewhat higher than 1.4 ft/sec would also be present within part of Port Rashid under the conditions of this arrangement

The effect of the tidal barrier was to decrease the tidal prism (major ebb tide 13th/14th May 1968) by causing a reduction in the canal peak maximum velocity from the 4.4 ft/sec quoted above to approximately 3.4 ft/second Policy on both these matters remains to be decided, as there are many other factors of a non-hydraulic kind to be taken into account

The Author appreciates the assistance given in preparing this paper by the Hydraulics Research Station Staff, particularly Messrs W A Price and K W Tomlinson, and of his colleague, Mr H E B Frederickson

REFERENCES

- 1 L Draper The analysis and presentation of wave data - A plea for uniformity Proc 10th Conf Coastal Engineering, 1966
- 2 L Draper and A V Moxted Graphs of attenuation of waves with depth Internal Report A17, National Institute of Oceanography 1962
- 3 M Darbyshire and L Draper Forecasting Wind-generated Sea Waves Engineering 5th April 1963
- 4 Ministry of Technology, United Kingdom Ocean wave statistics Her Majesty's Stationery Office, 1966

CHAPTER 73

STUDY OF TOPOLOBAMPO'S BAY, MEXICO, ENTRANCE

by

Héctor López Gutiérrez ¹
Daniel Cervantes Castro

SUMMARY

Brief examination of the geomorphological background of the Topolobampo's bay inlet is made

A theoretical study of the inlet and spits, based on field data such as wind, waves, tides, currents, bathymetric charts from 1875 to 1965, was developed in order to determine the most convenient position of an experimental channel dredged on 1963.

Radioactive tracer studies, photographic and periodical surveys of the inlet and the channel gave the information for the design of the definitive channel, which at present is behaving in accordance with the predicted way in the theoretical study

INTRODUCTION

The economical needs of the northwest of Mexico have led to the conclusion that a port is required at Topolobampo Bay.

1 Consulting Engineers

The main problem to establish the port has been the existence of a bar at the entrance of the bay. The study of such problem started in 1952 and several solutions have been given, most of them, considering the use of jetties, but these being so long, the solution have always been an economic obstacle for the port.

With that thought in mind, this study has been carried out, with the purpose of finding a solution based on a dredged channel across the bar, which has to be kept by small works or maintenance dredging.

I GEOMORPHOLOGICAL BACKGROUND

Topolobampo Bay is located at the northwest of Mexico (fig. 1), it has an approximate area of 48.85 km² and also has several shallow zones and secondary inlets. It is communicated with the Gulf of California through an inlet with a width of 4.5 km which is limited at its ends by two sandy spits called "Punta Copas" and "Punta Santa María". There are two perfectly defined channels, the main one that covers the whole bay with NE-SW direction up to "Punta Copas" where it changes to an E-W direction, up to Santa María where the second channel, called Lechuguillas, joins it. This latter channel is communicated with San Esteban Bay located in the northern zone. From there the inlet channel is formed with a S-SW direction.

Topolobampo Bay is communicated with Ohuira Bay by a narrow and deep pass (30 m). The latter bay with an extension of 148.00 km² is a very important factor in the bar's dynamics due to the great tidal prism generated by it.

The present shape is due to an evolution of the "Rio Fuerte" delta, whose first mouth combined with volcanic action, remolded a great part of Topolobampo and Ohuira bays (1).

Latest processes determined an emigration of the mouth towards the North, and its old delta continued as the main source for the littoral barriers that limit San Esteban, Topolobampo and San Ignacio bays. At the present time the "Rio Fuerte" continues as the main source of beach material.

Due to the wave characteristics acting in the zone as well as the induced currents produced by flood and ebb of the tide, a sandy bar has

been formed at the bay's entrance, with a length of 12 Km , a width of 2 Km and a depth of 2 3 m in a shape of a horse shoe, that joins "Punta Santa María" and "Punta Copas"

2 WINDS, WAVES, TIDES AND CURRENTS

2 1 Winds.

The prevailing and strongest winds come from the WNW, their main influence is the formation of seas which act from October to May, and from June to September there are others that produce swells from the SE The effect of both of them on the wind transport is of a secondary importance (2)

2 2 Waves.

Table 1

Type	Direction	$H_{1/3}$ (m)	T (sec)	Acting Time hr/year
Sea	WNW	1.25	5	3720
Swell	S30W	0.9	12	480
Swell	SSE	0.9	12	840

2.3 Tides

They are of the mixed type with a mean range of 0.823 m., and a spring tidal range of 1.80 m They were recorded simultaneously at four points in order to relate them with the observed currents (fig. 1)

2 4 Currents

The tidal currents are significant at the main channel (3) being the mean maximum velocity of 1.2 m/sec

From the field measurements it was obtained the following discharges distribution in everyone of the section indicated in fig. 2 and table 2 (4).

Table 2

1 Phase	2 Amplitude m	3 Section I	4 Section II	5 Section I+II	6 100 ⁵ /o-
Flood	1.25	66%	33.8%	99.8%	0.2%
Ebb	1.31	44%	31.6%	75.6%	24.4%
Flood	1.128	62%	28.7%	90.8%	9.3%
Ebb	1.037	51%	38.2%	89.2%	10.8%

Discharge in Section III = 100%

Column 3 shows that at Lechuguilla Inlet $Q_{\text{Flood}} = Q_{\text{Ebb}}$

Column 4 shows that the shallow zones have a considerable regulation effect.

Column 6 gives us an idea of the regulation capacity of the shallow zones.

3. LITTORAL DRIFT

The studies of grain sizes carried out in the bay as well as in the bar showed the presence of fine sand with a mean diameter ranging from 0.25 mm to 0.125 mm with a very good distribution

On the bar there are two defined types of sediment transport

3.1. Shoreward transport.

Produced by the swells that with their incidence almost normal to the shoreline and the bar itself as well as their length and period induce a transport towards the bar

3.2 Littoral transport

Due mainly to waves with a short period which effect is located at both

littoral barriers.

The analysis of these data lead to the computation (4), (5), that the littoral drift along the bar, in the zone in which it was going to be dredged, the channel was of the order of 360,000 m³/year. Larras, Pychkine and Manohar criteria were used (fig 3 and 4)

3.3 Suspended transport

Suspended transport measurements were made at the different velocity control sections, and it was found that the amount of suspended transport varies from 0 mg/lt up to 15.5 mg/lt, depending on the current velocity and the sections of study, being the maximum recorded values taken at the channel zone, finding out that at 6 m. depth and a velocity of 0.60 m/sec, the transport was 10 mg/lt, on the other hand, at 1 m depth in the same zone, it was recorded 5 mg/lt, which leads to the conclusion that its effect is of secondary importance.

4 BAR EVOLUTION FROM 1875 TO 1962

The analysis (4) was made considering the variations of the centroidal axis of the bar in order to study its movements in a plan view as well as in elevation (Fig 5)

It was observed that

- a Between 5° and 45° the bar tended to grow seaward, due probably to the channel effect of Punta Copas which dissipates the wave action from the SW. The maximum variation was 1300 metres for 1967
- b Between 45° and 75° exists a transition zone, because the bar showed movements towards WNW as well as to the bay, the reason for this behaviour could be the gradual disappearance of high ebb currents, that could oppose to the SW waves.
- c Between 75° and 120° the bar tendency was to grow towards the bay, due to the wave action in that zone in which there does not exist any definite active of tidal currents. Nevertheless, due to the sand transport diffusion and the channels that limit the zone, the movements are, as an average, 4 times smaller than the ones occurring between 5° and 45°

- d. From 127° up to 180° the bar tendency is growing towards the sea in a similar way to the first zone considered above, being the maximum movements between 150° and 165° , which are of the order of 1455 m. for 1962. This is due to the fact that some small bars appeared as a result of the littoral drift from the WNW and the very efficient hydraulic groin formed by the main outlet channel.

Depth variations.

Generally speaking, the vertical movements of the bar are not excessive, being up wards as well as downwards, these variations being noticeable at radiations 5° , 15° , 75° , 90° and 105° whose maximum relative values are 1.5 m., 1.55 m., 0.70 m., 1.35 m. and 1.30 m. respectively.

The rest of the zones tend to keep the same depth that in 1875, having small movements upwards as well as downwards. The most stable zones are the 45° , 60° , 127° , 180° , 150° and 180° .

The mean depth in the bar varies from 3 m. to 4 m., the 3.90 m. being the most stable depth which is located between 105° and 120° , the smallest depths are between 15° and 75° with a value of 3 m.

3. EXPERIMENTAL CHANNEL

In 1962, from theoretical results showed in the above paragraphs, the existing zone between 75° and 120° was chosen as the proper place for the dredging of the experimental channel as this had demonstrated the maximum stability.

The alignment of the channel was made following the tendency of the natural channel.

The design dimensions were

Bottom width	75 m
Slopes	5 1
Mean depth	7 m

The experimental channel had as a main function the precise evaluation of the littoral drift and hence its maintenance cost. In addition the channel would permit the access of small ships to the port.

From the date of its construction, periodical soundings were made, and during a four months period, in 1964, the channel dredging was suspended in order to be able to know if its natural tendency would be its accretion, maintenance or erosion. Simultaneously, a radioactive tracer study, was carried out (Fig 6)

The results of the experimental channel can be divided into two groups

- Channel behaviour
- Effects on the bar.

5.1 Channel behaviour

The amount of littoral drift that reached the channel, recorded in its initial phase, when its efficiency and discharge were still low, was of the order of 320,000 m³/year (360,000 m³/year computed) (fig 7). At that time, the mean currents velocities in the channel was 0.4 m/sec. From 1965 in which dredging was practically suspended, a tendency to increase the section has been observed. In table 3, the results of control soundings are shown, pointing out that in 1966, the channel velocities, for similar tide conditions were of 0.8 m/sec

Table 3

Date	Minimum depth	Maximum depth	Channel mean width at 6 m depth
July 1966	6.15	8.40	50
Aug 1966	6.90	8.65	60
Oct 1966	6.55	8.65	70
Nov. 1966	7.05	8.80	90
Dec 1966	7.10	8.70	75
Feb. 1967	6.95	9.00	100
Mar. 1967	6.80	8.75	115
Apr. 1967	7.35	9.15	150
Jun 1967	7.20	9.20	120
Sept. 1968	8.50	9.35	150

5.2 Effects on the bar

Immediately after dredging the experimental channel, a big shallow zone started its formation on the NW side of the bar, which was modified by the changes in wave action, but that in general, showed the tendency to increase in size in such a way that at present its distance from Punta Santa María is of only 150 m. Initially that distance was 1200 m (fig. 8).

6 RADIOACTIVE TRACERS INVESTIGATION

During a period of four months in 1964 a radioactive tracers investigation was programmed using a synthetic glass sample with Ta_2O_5 to obtain $T_a 182$ with a 250 milicurie of activity. The tendencies showed by the tracers checked notably with the results of the soundings in the same period of time (fig. 7). The accretion tendency observed at that time disappeared when the hydraulic efficiency of the channel was improved.

7 RESULTS ANALYSIS AND CHANNEL DESIGN

The analysis of the experimental channel behaviour shows a definite tendency to the increase of tidal currents velocities and hence an increase of the shear stress which represents a channel erosion. This effect is favoured by the shallow zones formed, so it can be assumed that the channel tends to an equilibrium state, due to the increase of its hydraulic efficiency when the tidal prism diffusion decreases due to the shallow zone and its concentration into the channel. This tendency can be natural or be increased in an artificial way by means of dredging in the channel so that it can acquire a stable section.

It is convenient to point out that in the analysed period there was a season (January to March 1967) in which the channel showed a tendency to accretion. This tendency corresponded to the forecast made by the computations and radioactive tracer studies, nevertheless, spring tides in April eliminated the accretion (7) continuing in such a way the self dredging of the channel. From that date up to now all the dredging work has been abandoned.

Providing that for navigation requirements the channel must have a minimum width of 150 m, 11 m depth and construction slopes 5:1 (fig. 6),

at present a dredging volume of 1,300,000 m³ is still required

Considering that the mean diameter of the sandy material that constitutes the bar in the channel zone is 0.125 mm, it is required a $\tau = 0.36 \text{ Kg/m}^2$ and a velocity of 25 cm/sec (8) in order that the bottom particles start their movements and taking into account that at present, mean maximum velocities have been measured with a value of 0.8 m/sec it is expectable that for spring tides the mean maximum velocity reaches similar values to that existing in the present main channel with a value of 1 m/sec (9)

Therefore, using the mean velocity of 0.8 m/sec, the following results in relation to the self dredging capacity of the channel are obtained

$$\tau = \frac{640}{2020} = 0.315 \text{ Kg/m}^2$$

In accordance with Kalinke's Formula

$$q_s = \frac{10 D \tau^{5/2}}{\rho^{1/2} D^2 \gamma^2 (S_s - 1)^2} = \frac{10 \times 0.56}{11.0 \times 125 \times 10^{-3} (1000)^2 (1.6)^2} =$$

$$= \frac{0.56}{3.5 \times 10^3} = 1.6 \times 10^{-4} \text{ m}^3/\text{seg/m.}$$

$$Q_s = 1.6 \times 10^{-4} \times 195 = 314 \times 10^{-4} \text{ m}^3/\text{sec}$$

$$M_s = 495,000 \text{ m}^3/\text{year}$$

$$\frac{M_s}{M_e} = \frac{495,000}{300,000} = 1.66 > 1$$

So the section will tend to increase (9) diminishing the shear stress, until the equilibrium between the channel capacity for washing out the accretion and the material transported from the bar is reached.

With the increased values of the velocities observed in the channel zone, it is very feasible that it could reach the value of 1 m/sec, and hence, the required shear stress required for the equilibrium is attained with a much bigger area than the one necessary for navigation purposes.

In other words, the channel in the way it has been designed, will not have any maintenance problems as depth concerns.

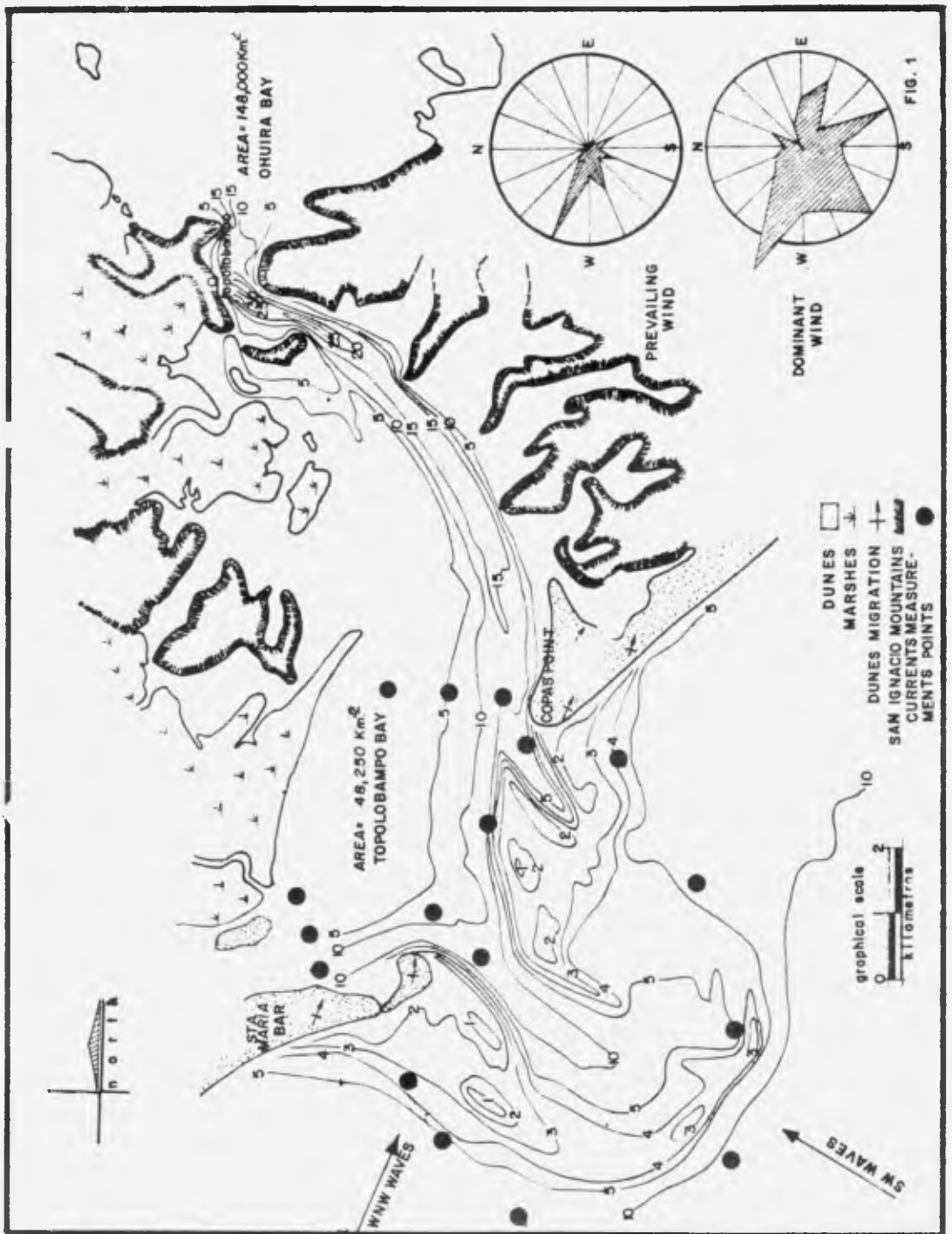
CONCLUSION

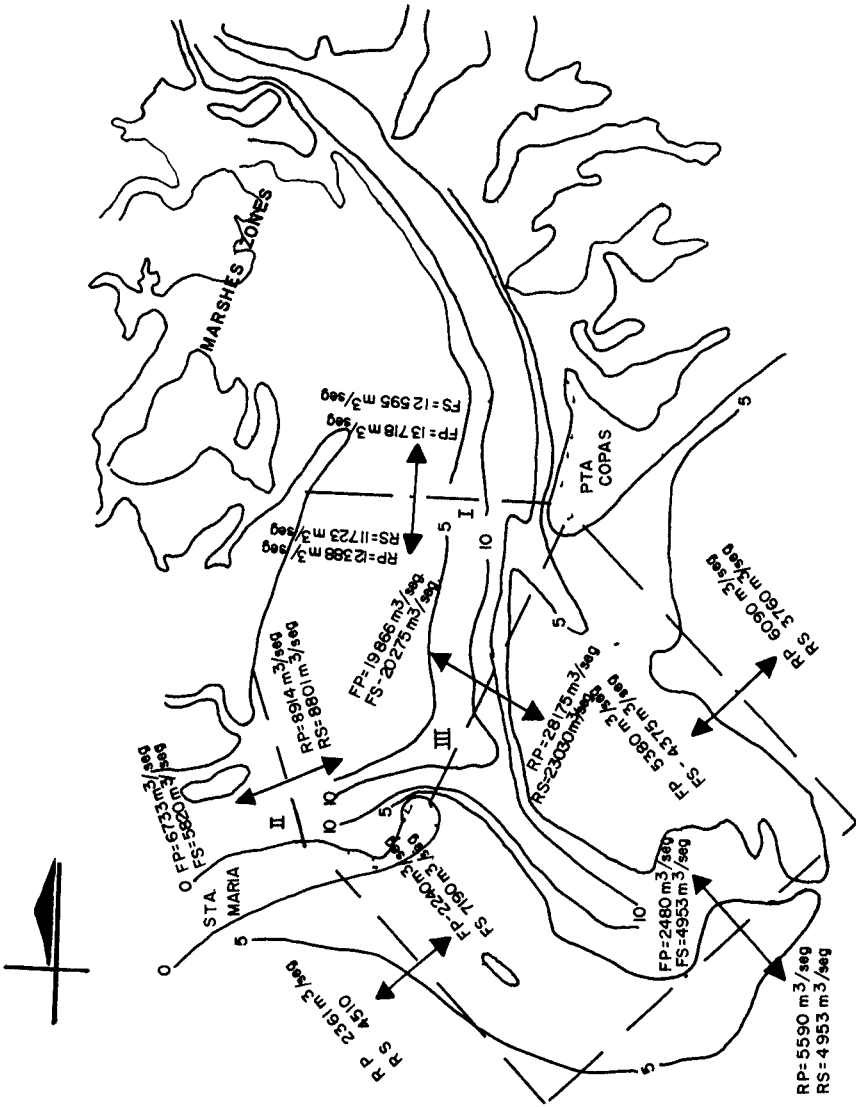
From the above study the following conclusions are obtained

- i The applied theoretical and experimental methods have been checked with nature results.
- ii The access channel has a definite tendency to be stable
- iii This stable status will be completely attained when, by navigation requirements, the channel gets at least 150 m. of bottom width and 11 m. depth
- iv The maintenance dredgings during certain seasons in the year will be small and very well located.

B I B L I O G R A P H Y

- 1 Ayala-Castañares A & F Pnleger - Informe final del Estudio de Geología Marina del Area de la Bahía de Topolobampo, Sinaloa Instituto de Geología México 1966
- 2 Cervantes C D - Nolas sobre Transporte Eólico Análisis de Diferentes Criterios utilizados para tratar de cuantificar el acarreo por viento Departamento de Estudios y Laboratorios, Secretaría de Marina Boletín Técnico No 1, Tomo II México, marzo 1966
- 3 López G H & J Aguilar - Análisis Hidráulico del Comportamiento de la Onda de Marea a través de la Bahía de Topolobampo y sus Efectos en la Barra Proc of the 8th Conference on Coastal Engineering
- 4 López G H - Estudio Integral del Acceso a la Bahía de Topolobampo, Sin Depto de Estudios y Laboratorios, Boletín Técnico No 2 y 3, Tomo II México, junio-septiembre 1966
- 5 De Alba L P - Estudio General del Acceso al Puerto de Topolobampo, Sin Aplicación de Trazadores Radioactivos Tesis Profesional México 1965
- 6 López G H - Aplicación de Radioisótopos a Problemas de Ingeniería de Costas Estudios en Topolobampo, Sin - Depto de Estudios y Laboratorios, Boletín Técnico No 1, Tomo I Mexico, 1965
- 7 Cervantes C D - Acceso al Puerto de Topolobampo, Sin - Primera Reunión para el Desarrollo del Puerto de Topolobampo (No publicado) 1969
- 8 Larras J - Embouchures, Estuaires, Lagunes et Deltas - Collection du Centre de Recherches et D'Essais de Cnatou Eyrolles, Paris 1964
- 9 Bruun P - Tidal Inlets and Littoral Drift Vol 2 - Ed Universitets Forlaget, Oslo, 1966





GENERAL TATTEN OF TIDAL CURRENTS

Fig No 2

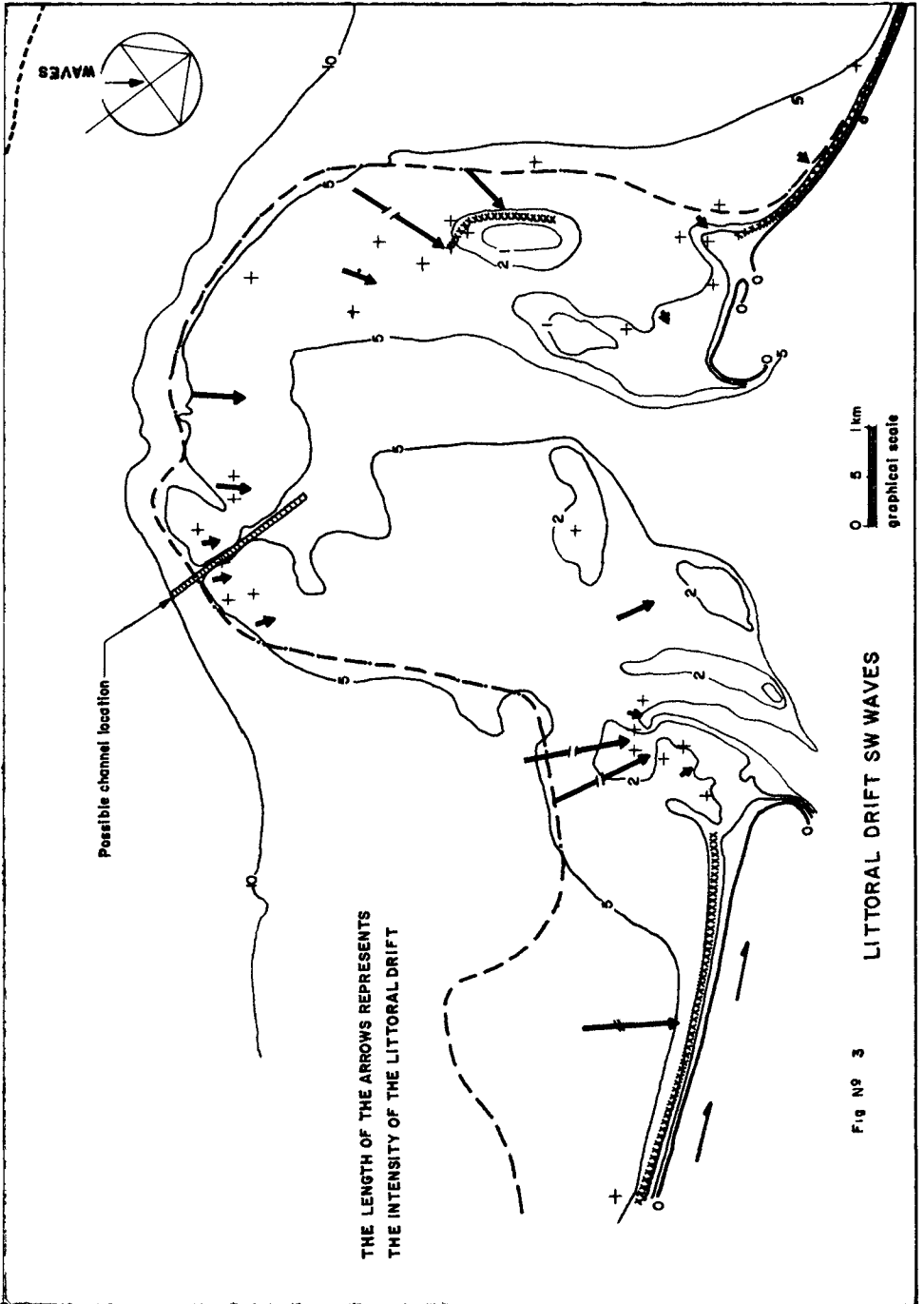
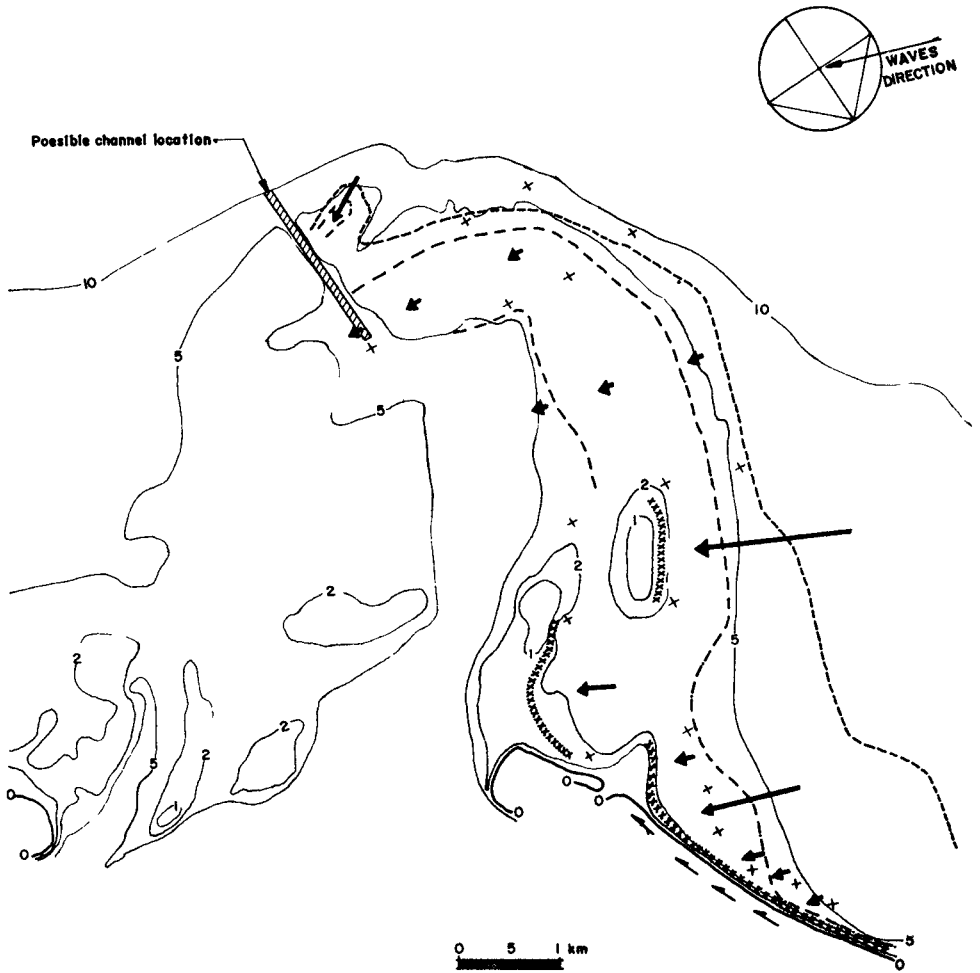
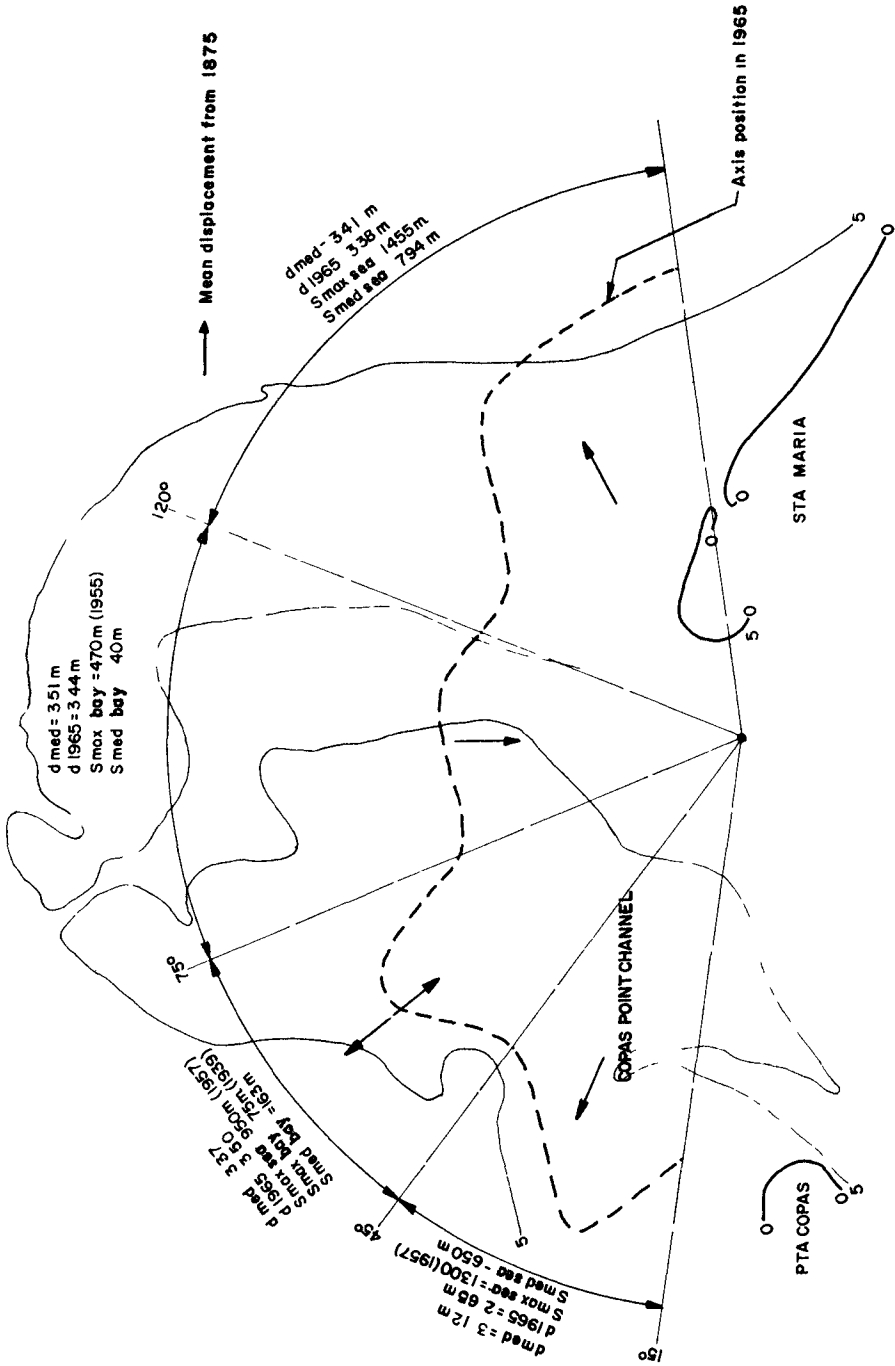


FIG N° 3 LITTORAL DRIFT SW WAVES



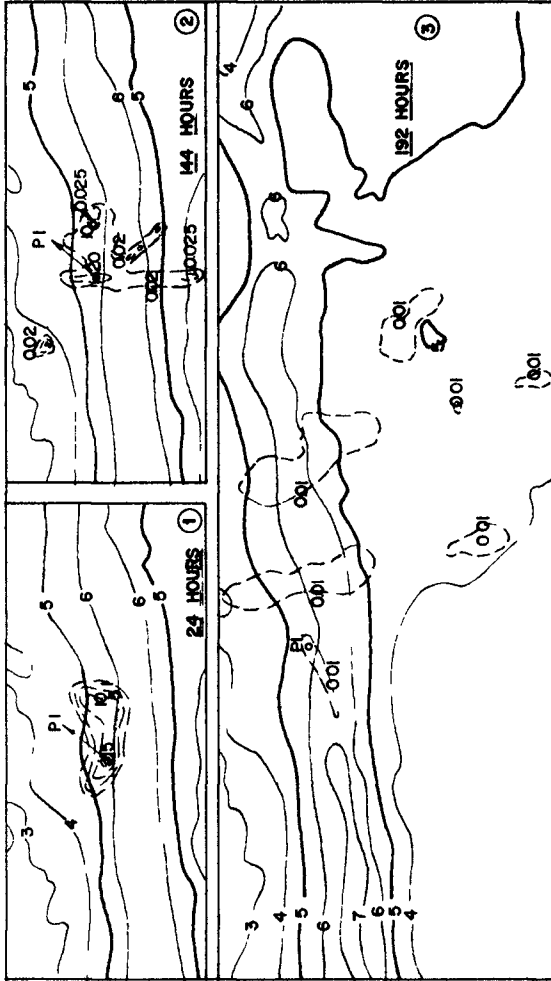
LITTORAL DRIFT WNW WAVES

Fig No 4



CENTROIDAL BAR AXIS VARIATIONS

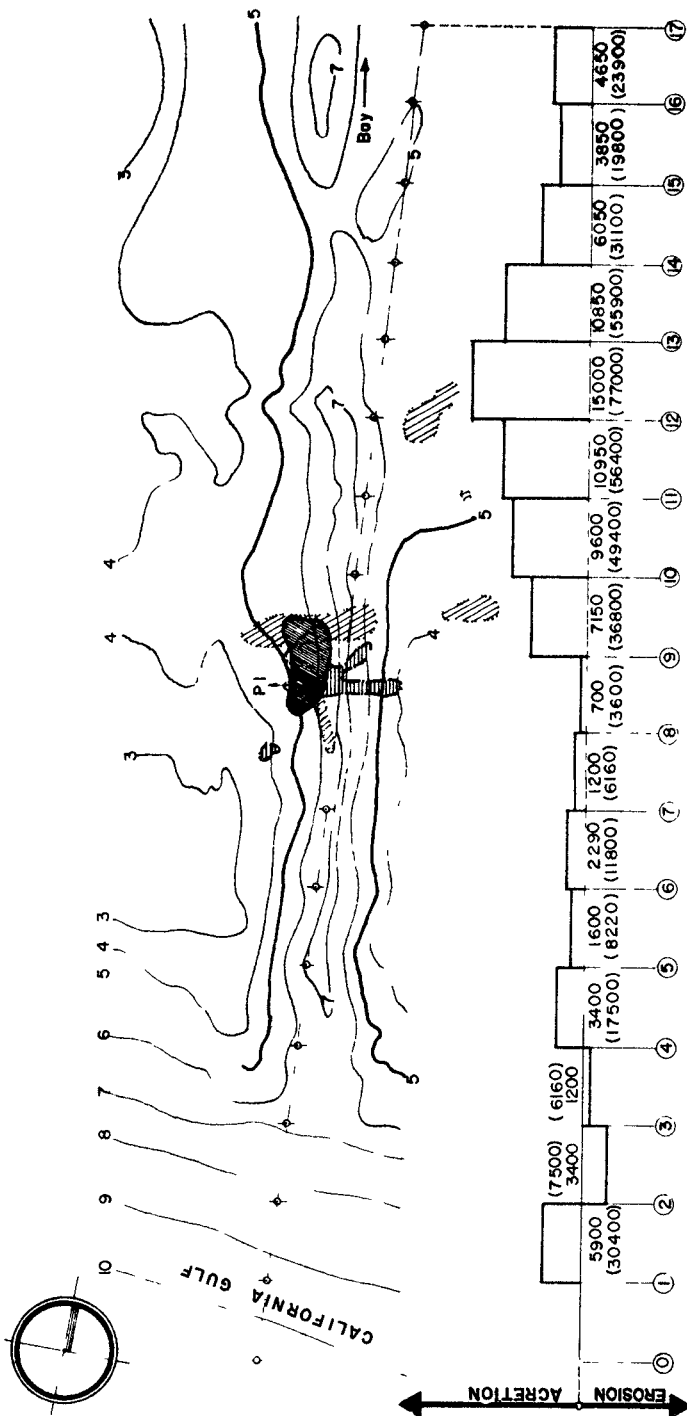
Fig No 5



**RADIOACTIVE TRACERS STUDY
IN THE EXPERIMENTAL CHANNEL**

ACTIVITIES IN MILICURIES
PI = IMMERSION POINT

FIG 6



EXPERIMENTAL CHANNEL BEHAVIOUR

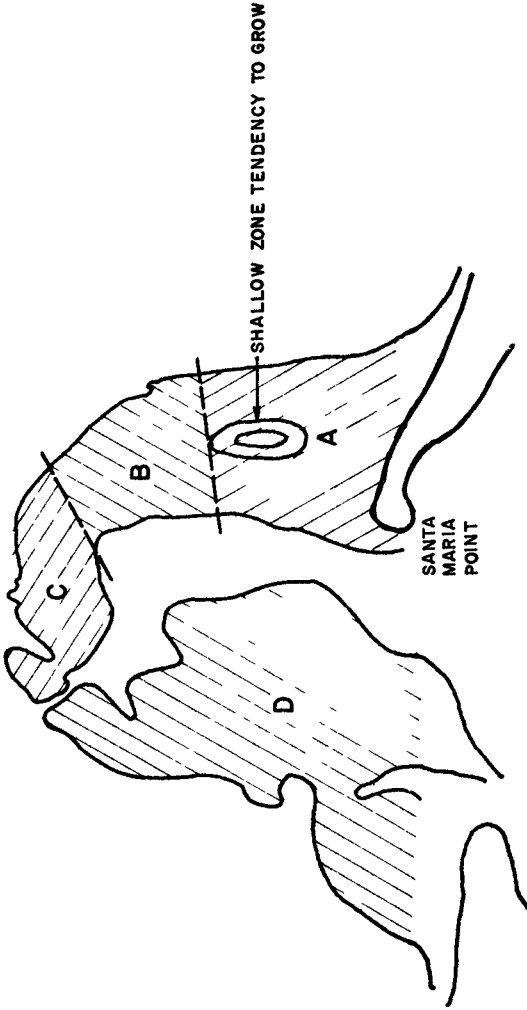


FIG. 8

CHAPTER 74

TIDAL INLET PROBLEMS ALONG THE NEW ENGLAND COAST

Oscar E Arpin

United States Army Corps of Engineers,
New England Division
Waltham, Massachusetts

ABSTRACT

The New England Division of the United States Army Corps of Engineers has created and improved many harbors along the New England coast for the benefit of commercial fishing and recreational boating fleets. A harbor, to be effective, must provide a protected area for boats and it must have a safe access, that is, a protected and stabilized tidal inlet. A coastal inlet has been defined as a waterway connecting a bay, lagoon or similar body of water with a larger body of water. The major engineering problems encountered in the development of harbors have involved stabilization of these inlets. The problems have been caused by excessive littoral drift resulting from erosion of the shorefront adjacent to the inlets by wave attack. Planning, designing, constructing, and modifying these inlets under very dynamic conditions is complex and difficult. Each inlet is unique. This paper discusses very briefly some of the problems encountered.

INTRODUCTION

Two principal factors are involved in producing littoral drift. One factor involves storm waves and tides. New England is often subjected to severe storms, including hurricanes (See Figure No. 1). New England has been battered by a severe hurricane on the average of once every five years during the last 60 years. The second factor involves geologic structure. Storm wave attack on unconsolidated materials results in severe shoreline recession and an excessive rate of littoral drift. The section of the New England coast where tidal inlet problems have been encountered is that extending southerly from Portland, Maine to and including Cape Cod and the offshore islands of Martha's Vineyard and Nantucket.

Littoral drift does not pose a problem along the coast of Maine extending between Portland and the Canadian border, as this shorefront is composed largely of massive ledge outcrops which are very resistant to erosion forces, in spite of severe storm wave attack and normal tide ranges up to 20 feet. The shore of Connecticut is composed largely of hard rock. Further, it is afforded some protection from severe storm

CORPS OF ENGINEERS

U.S. ARMY

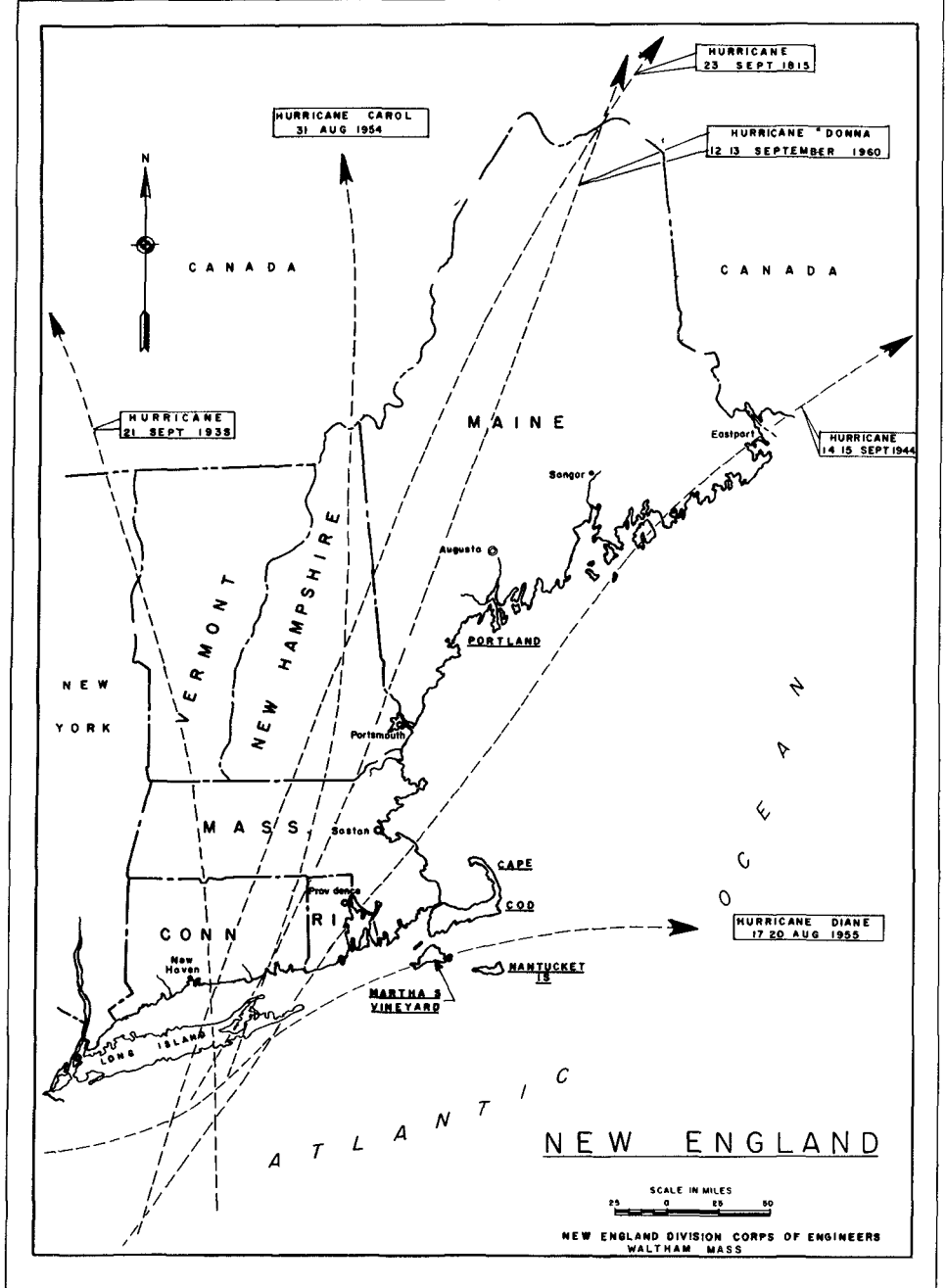


Figure 1

waves by Long Island to the south and it experiences tide ranges of relatively few feet. Thus, its coast remains irregular in configuration, whereas the shore of Rhode Island just to the east, also composed of unconsolidated glacial debris like that of Connecticut, is now almost straight with long sand barrier beaches. The primary differences are that the Rhode Island shore consists of boulders mixed with clay, uncemented and thus easily eroded, and the shore is directly exposed to severe storm waves from southerly quadrants. This coast, much of which is still privately owned, is relatively undeveloped. The littoral drift encountered in Narragansett Bay, Rhode Island and in Buzzards Bay, Massachusetts is not of major significance. The chief difficulty requiring attention within these bays is tidal flooding due to hurricanes.

Continuous battering of the unconsolidated materials of Cape Cod and the offshore islands of Martha's Vineyard and Nantucket by large waves generated over vast expanses of water, result in rapid and extensive erosion. For example, much of the south shore of Martha's Vineyard is estimated to be receding at a rate of 8 feet each year, involving sand losses of 400,000 cubic yards. Some portions of the south side of Nantucket Island and of the southeasterly side of the outer arm of Cape Cod are estimated to be receding at rates up to 15 feet each year.

Newburyport Harbor, Massachusetts

Man has studied storms and their generated waves and the geologic structure of the coasts for many years. He uses all the advanced and sophisticated knowledge available concerning coastal development. He conducts wave refraction, diffraction and reflection studies and makes mathematical and hydraulic model studies. He does all this and more, only to find that nature interjects a new unforeseen factor. An example of this occurred in February 1969 at Newburyport Harbor, Massachusetts, located 55 miles north of Boston, Massachusetts (See Figure No. 2). First, a little background. The Federal navigation project for this harbor was constructed in the early 1900's to stabilize the badly migrating inlet at the mouth of the Merrimack River which rises in central New Hampshire and has a drainage basin of about 5,000 square miles. The south jetty is nearly 2,500 feet long. The north jetty is over 4,100 feet long. Both jetties were built to an elevation of 12 feet above mean low water. In February, 1969 three northeast storms struck within a relatively short time of each other. The first prevailed during 9 and 10 February, the second from 19 through 21 February, and the third lasted for about 4 days, 24 through 27 February.

Storm waves from the northeast overtopped and diffracted around the end of the deteriorated north jetty. Waves from the east entered the inlet directly. These waves ran generally along the smooth face of the south jetty, then being rehabilitated, and attacked the shore fronting the United States Coast Guard Station located at the inshore end of the south jetty. The mean high water line receded 150 feet as a result of these

U. S. ARMY

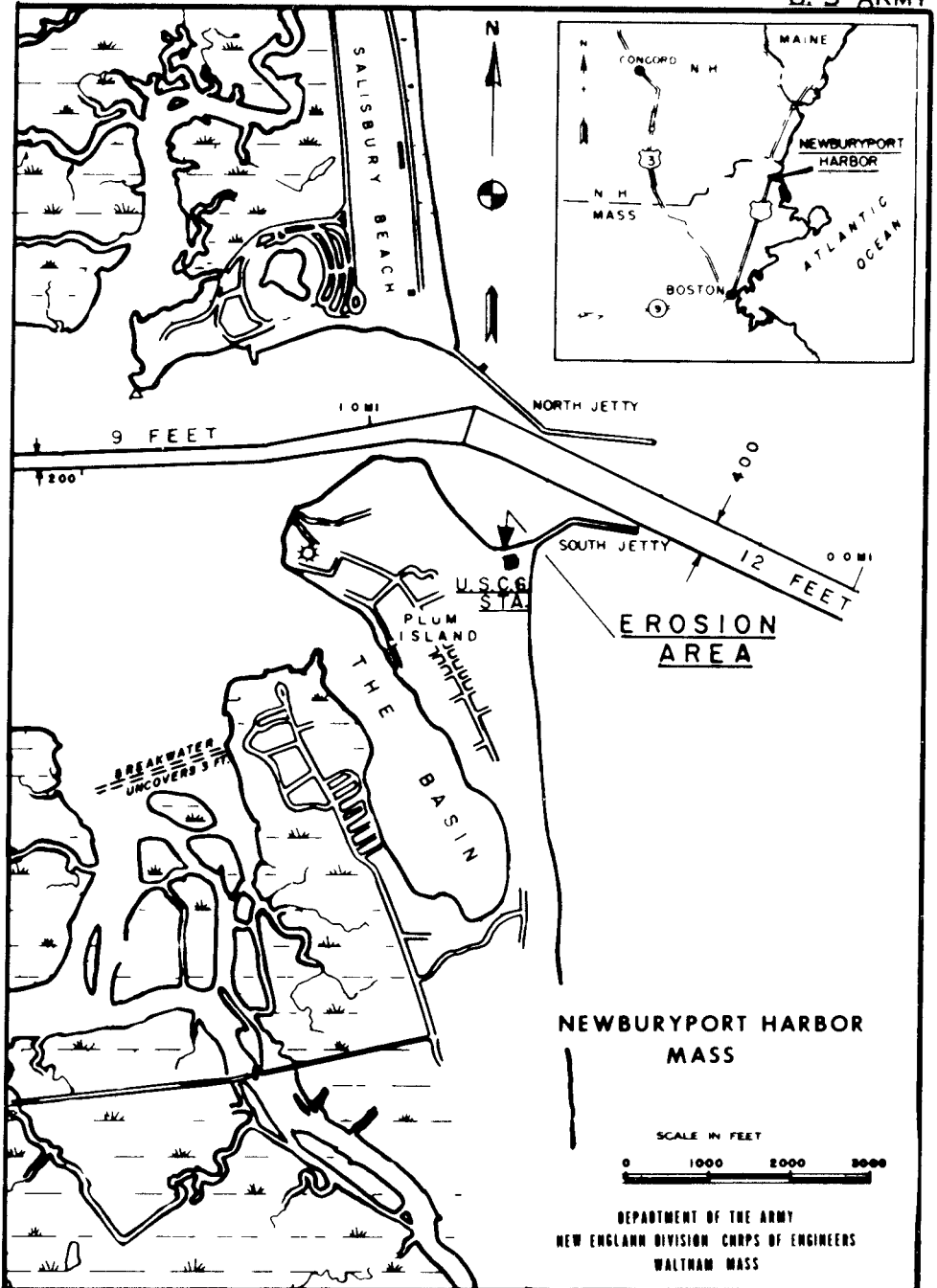


Figure 2

storms. The erosion, once triggered, continued at a more gradual rate toward the station. A special study was quickly made to determine what corrective measures were necessary to save the station, which was built in 1930 to provide emergency assistance to ships and small boats in distress offshore. A stone mound with sandfill, and revetment was recently completed to stabilize that shorefront. Erosion had reached one corner of the station at the time of initiation of the emergency work.

Green Harbor, Massachusetts

Another inlet problem recently developed at Green Harbor, Massachusetts, located 35 miles south of Boston (See Figure No. 3). The Commonwealth of Massachusetts and the Town of Marshfield have provided and maintained navigation improvements at this harbor for over 70 years. The jetties were constructed by the Commonwealth in 1898 and 1899. In 1969, the United States government, in financial cooperation with the State, County and Town governments, completed a modification of the existing project. The modification provided for sealing and extending the west jetty 200 feet to prevent littoral drift from passing through and around the end of the jetty and into the channel. It is interesting to note that the south to north drift at the inlet constitutes a local reversal of the overall predominant net north to south drift along these shores. Project modification also included raising the top of the east jetty from 12 to 14 feet above mean low water and dredging a harbor channel and anchorage.

Shortly after completion of these improvements, erosion began along the shore at the inshore end of the east jetty. Field observations and wave studies indicate that the erosion is probably the result of reflection of easterly waves off the smooth face of the west jetty extension with little reduction in wave height. A stone revetment and sandfill are being prescribed for stopping the erosion.

Andrews River, Massachusetts

In 1968, a new harbor was created in an area of negligible value marshlands within Andrews River in Harwich, Massachusetts, a small tidal creek on the south side of Cape Cod (See Figure No. 4). The project provides for a Federal entrance channel protected by stone jetties and a maneuvering area to serve a marina complex provided jointly by the Commonwealth and the town. The harbor was developed to accommodate the fast growing recreational boating fleet in the area. Nearby harbors had long been saturated. After much study and consultation between the New England Division and the Office of the Chief of Engineers in Washington, D. C., it was decided to defer construction of the west jetty until experience and observation showed the need for it. It was generally considered that the long jetty protecting and stabilizing the Wychmere Harbor inlet immediately to the west would also provide

CORPS OF ENGINEERS

U S ARMY

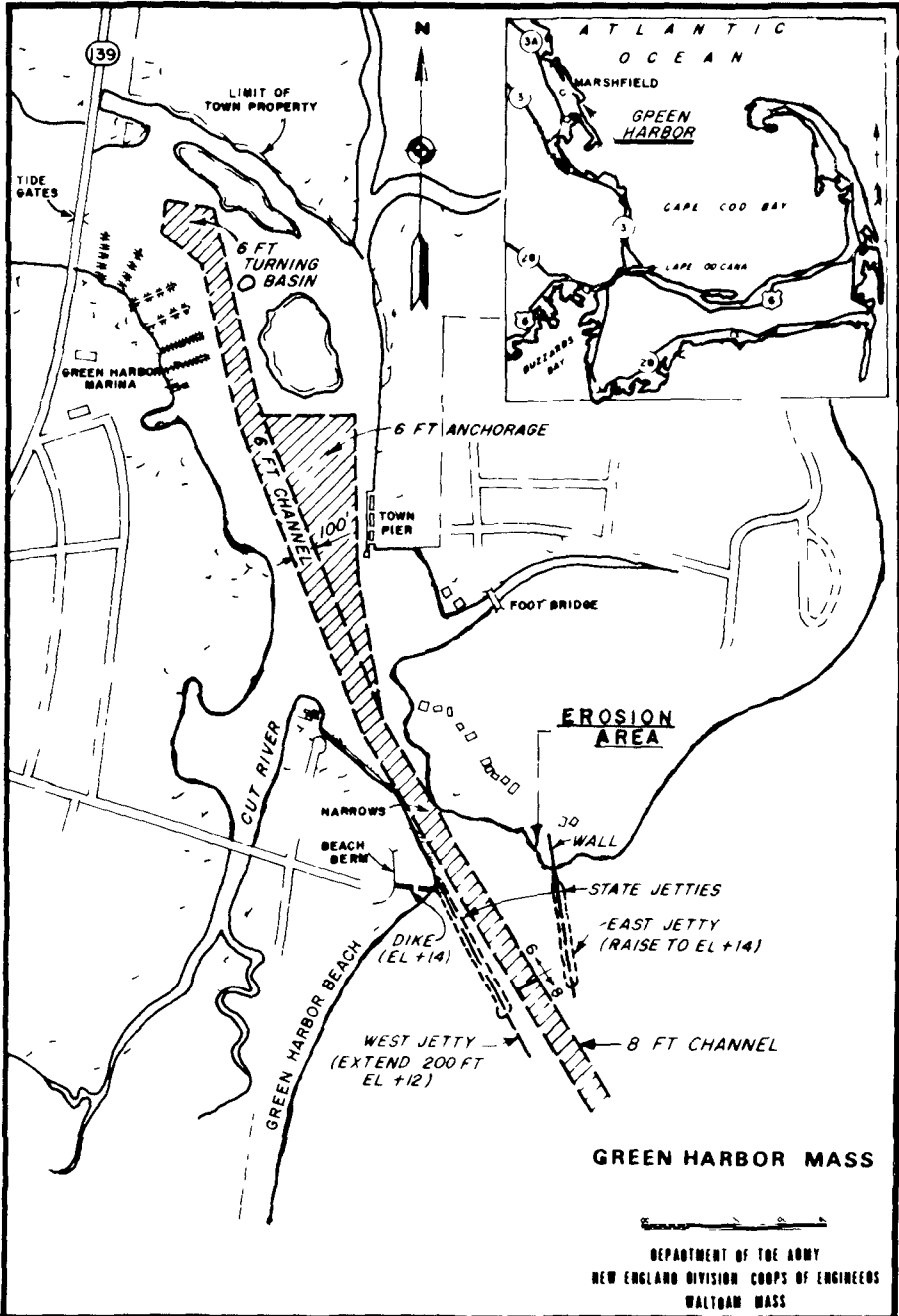


Figure 3

CORPS OF ENGINEERS

U S ARMY

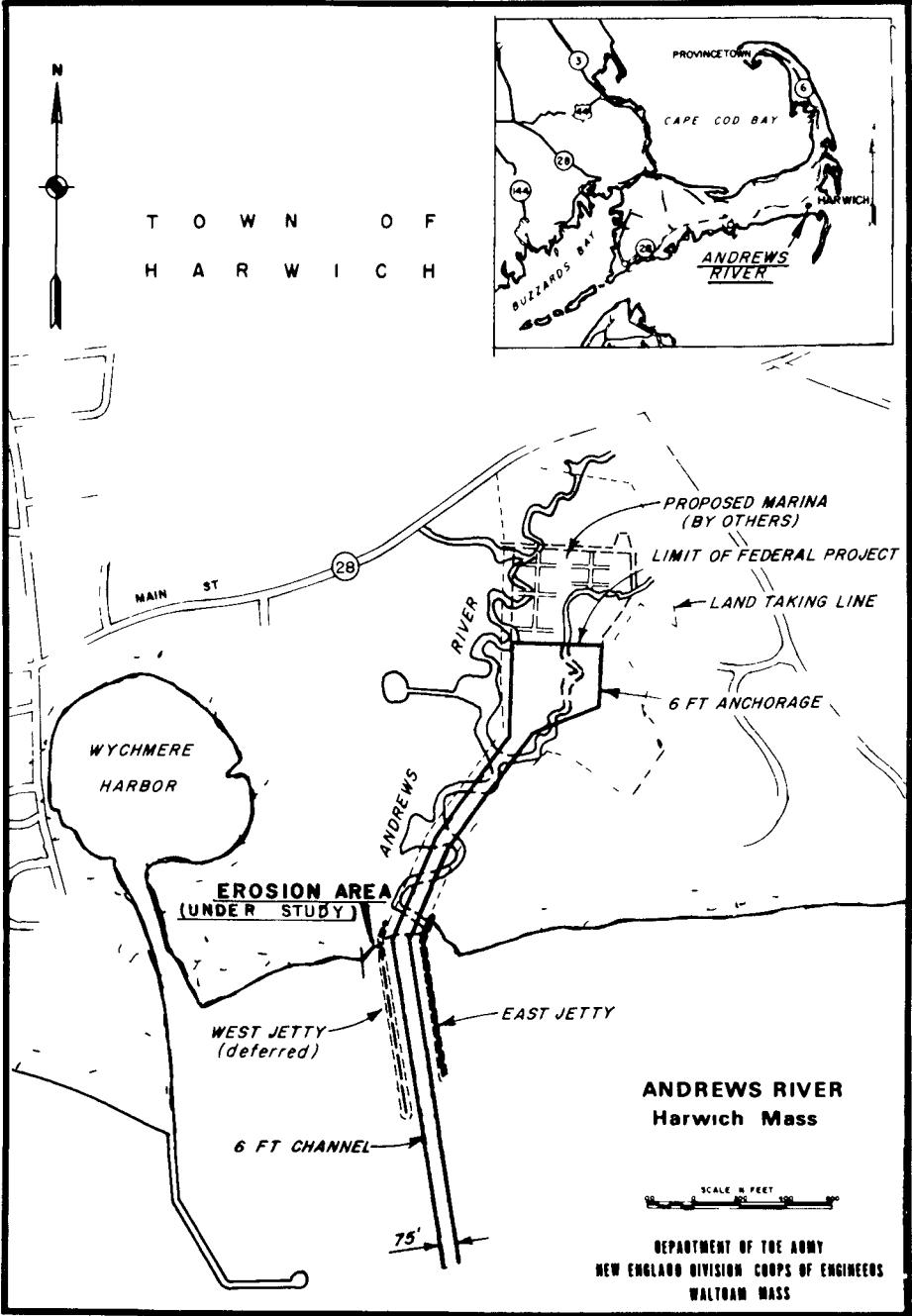


Figure 4

protection to and prevent the west to east littoral drift from fouling up the Andrews River inlet. Since completion of the project, erosion of the shore just west of the new inlet and shoaling of the entrance channel have occurred. Field observations and wave studies made to date indicate that south and southeasterly storm waves may be diffracting around the end of the Wychmere Harbor jetty and then moving easterly. More detailed studies are being made to determine if the west jetty should now be recommended for construction, or if some other corrective measure is required.

Scarboro River, Maine

In 1960, a problem was encountered during construction of a jetty at Scarboro River, a small shallow stream rising in the marshlands of the town of Scarboro, Maine about 17 miles southeast of Portland, Maine (See Figure No 5). The jetty was being built to impound excessive west to east littoral drift, which was rapidly shoaling the Federal entrance channel constructed several years earlier. When the jetty had been constructed 350 feet from the shoreline, severe scour occurred at the seaward end. The area of scour extended 100 feet beyond the end of the jetty, beyond which accretion occurred. The sea bottom in the area of scour went from 2 feet below mean low water to nearly 19 feet below mean low water. Consultation with known experts in the field of tidal hydraulics revealed that tidal currents were flowing nearly perpendicular to the jetty during both the ebb and flood tides resulting from a shift in tidal flow not anticipated. Also, the bottom materials were found to consist of very fine sand. A greater thickness of bedding, 3 to 4 feet instead of 18 inches, consisting of 10-150 pound stone placed at least 50 feet in advance of the core and armor stone, was found to be the answer to the problem.

Wells Harbor, Maine

As a result of the establishment of the Wells Harbor Committee in 1953 to determine what measures were necessary to develop a harbor at Wells, Maine (See Figure No 6), the Federal government constructed two converging stone jetties at the mouth of the Webhannet River to stabilize the migrating inlet. The project included dredging a channel and anchorage in the marshlands. During construction of the south jetty to its angle point, that is, where it then extends parallel to the channel, accretion of the northerly tip of Wells Beach took place. However, as construction of the jetty progressed to its full length of 940 feet parallel to the channel, erosion of the tip of Wells Beach occurred rapidly. Over 400 feet were lost in eight months. Concurrently, the north jetty, 640 feet long, was already nearly completely impounded, with littoral materials about to enter the inlet. These occurrences meant that the proposed anchorage would be directly exposed to easterly storm waves and to severe shoaling.

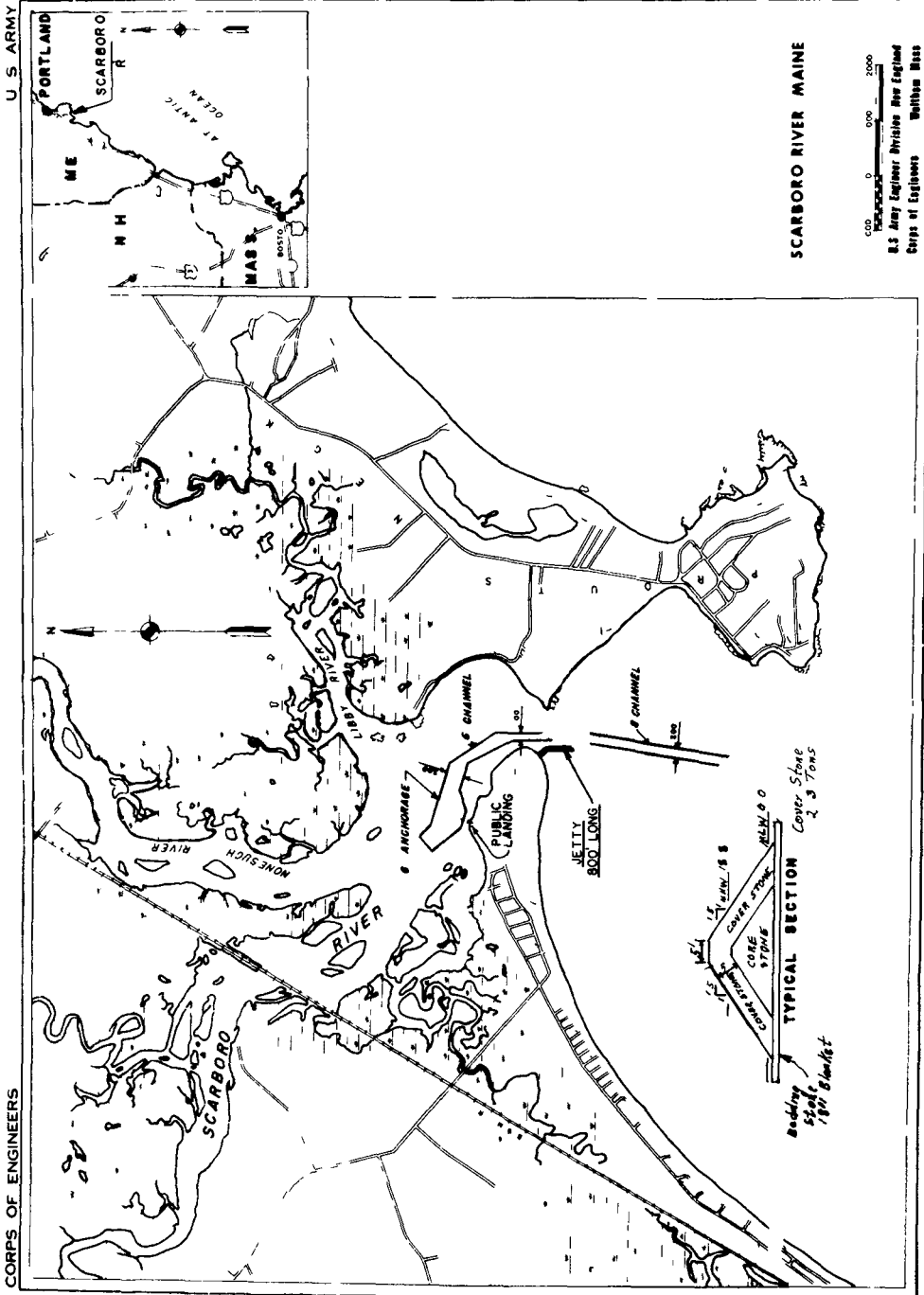


Figure 5

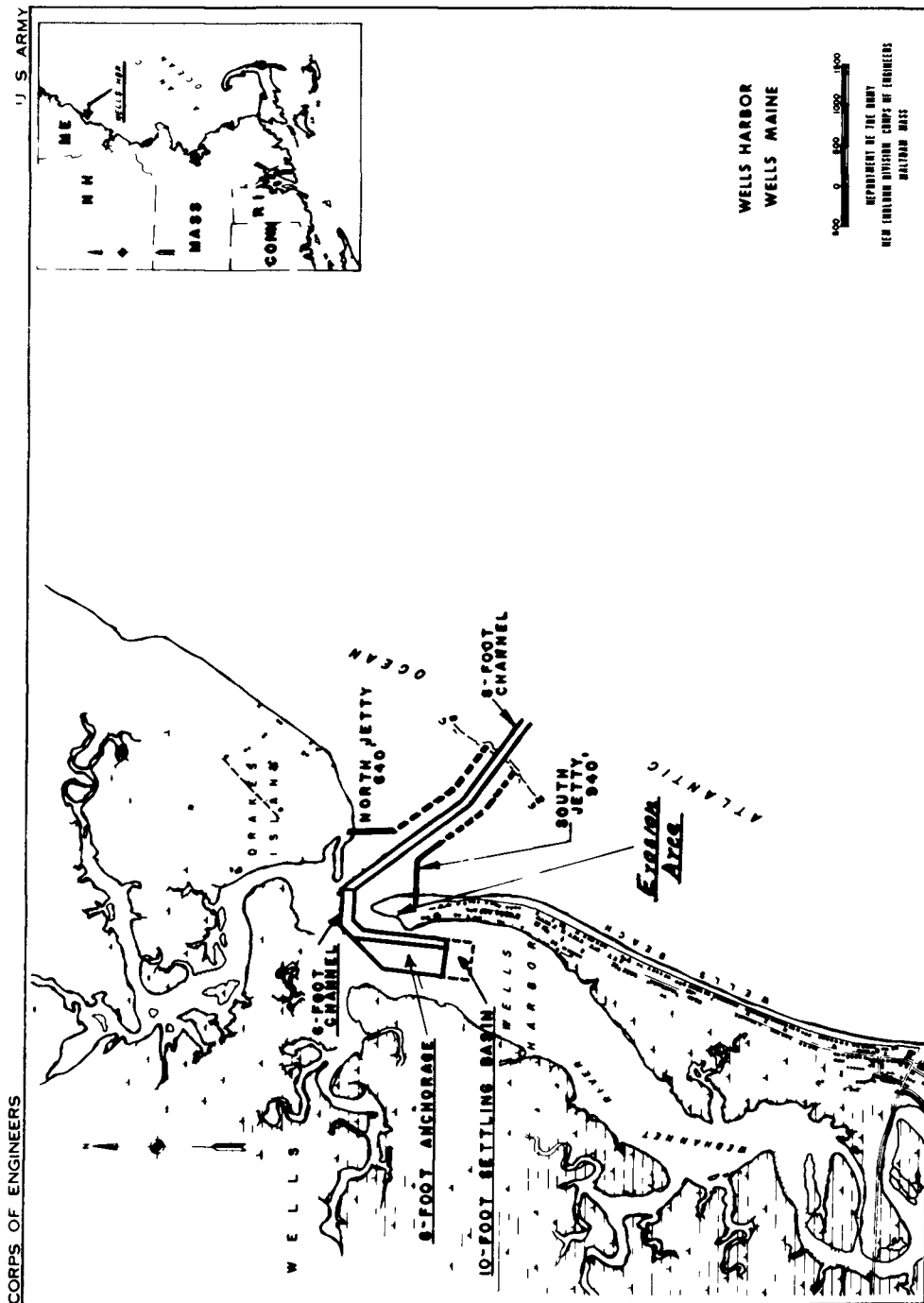


Figure 6

After discussions with the Committee on Tidal Hydraulics and representatives of the Waterways Experiment Station at Vicksburg, Mississippi, it was decided to construct a 100-foot long wave absorber along the inner end of the south jetty, place stone revetment along 680 feet of the tip of Wells Beach, and extend the north jetty. The channel and anchorage were then dredged. However, because of a continued high rate of shoaling, both from littoral drift and from sediments carried down the Webbannet River, both jetties were later extended to about the 8-foot depth contour and a 10-foot deep settling basin dredged at the upstream end of the anchorage to intercept river sediment. In spite of numerous problems encountered in the creation of Wells Harbor, it now is overcoming the growing pains and is beginning to function as planned. It is a safe harbor for the commercial fishing boats which transferred from nearby inadequate coves and for a new fleet of recreational boats which could not be accommodated at the saturated harbors to the north and south of Wells Harbor.

Chatham Harbor, Massachusetts

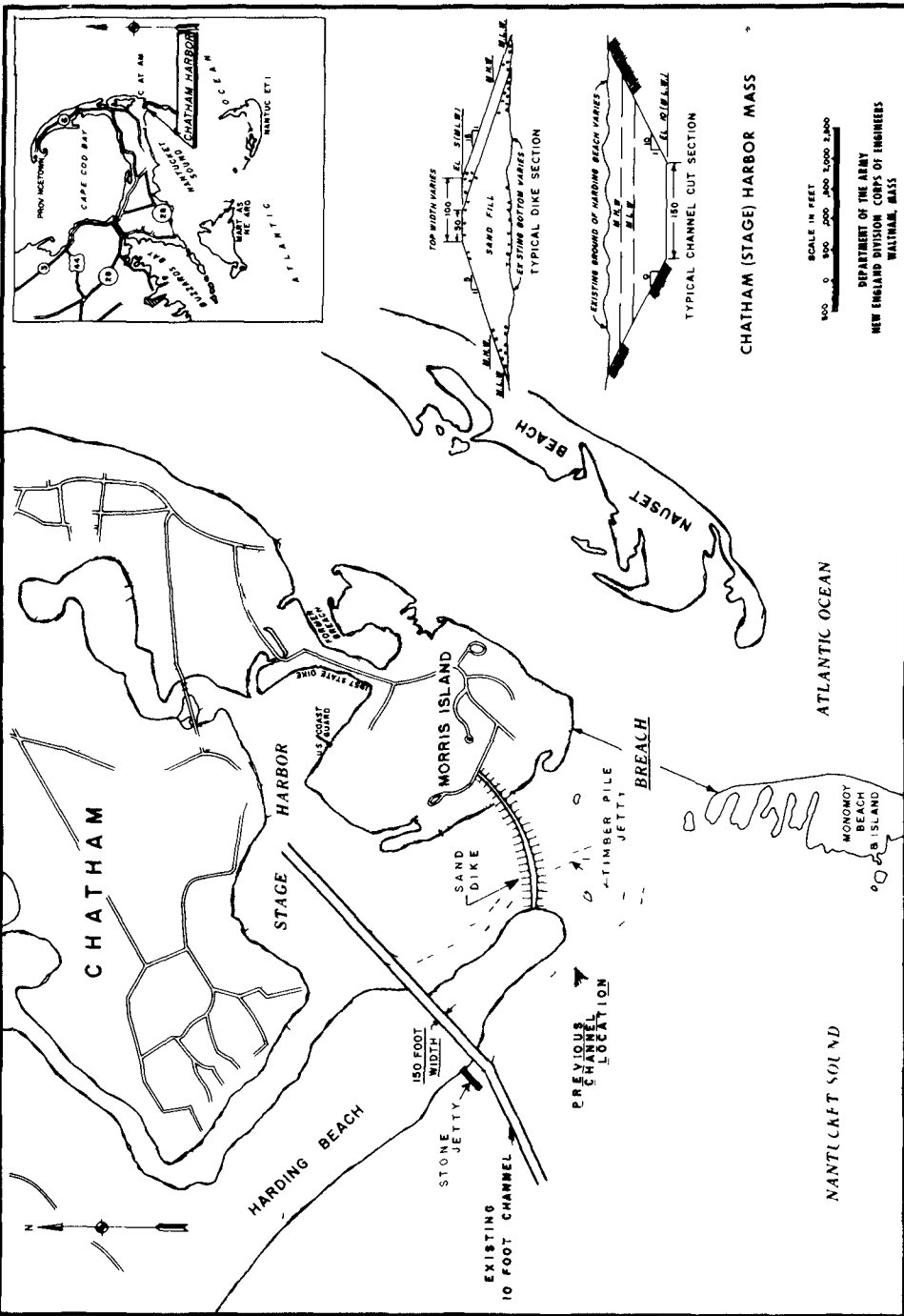
Chatham Harbor, Massachusetts is located on the southeasterly corner of Cape Cod in an area of very rapid and continuously changing shoreline conditions (See Figure No 7). The directions, rates, and amounts of littoral drift are extremely complex and variable. Planning and designing a modification of the existing Federal navigation project at Chatham Harbor proved to be difficult under these unique conditions. In 1956, Monomoy Beach, a long narrow barrier beach, was connected to Morris Island. At that time, it was breached by storm waves. The breach widened, deepened and became a continuous waterway. By 1961, sediment moved by the tidal currents through the breach, extended over a wide area and filled the existing Federal channel around the tip of Harding Beach. The shoaling continued to advance westward along the south side of Harding Beach toward the Chatham Roads approach channel. Concurrently, tidal flows in the vicinity of Harding Beach caused its tip to erode rapidly and the deep scour hole at the breach to extend toward Harding Beach and Chatham Harbor. Detailed studies found that the most feasible solution was to construct a sand dike between Morris Island and Harding Beach with a timber pile structure seaward of the dike to protect it against severe tidal currents, and relocate the channel through Harding Beach stabilized by a stone jetty. The improvement has proved to be successful.

Edgartown Harbor, Massachusetts

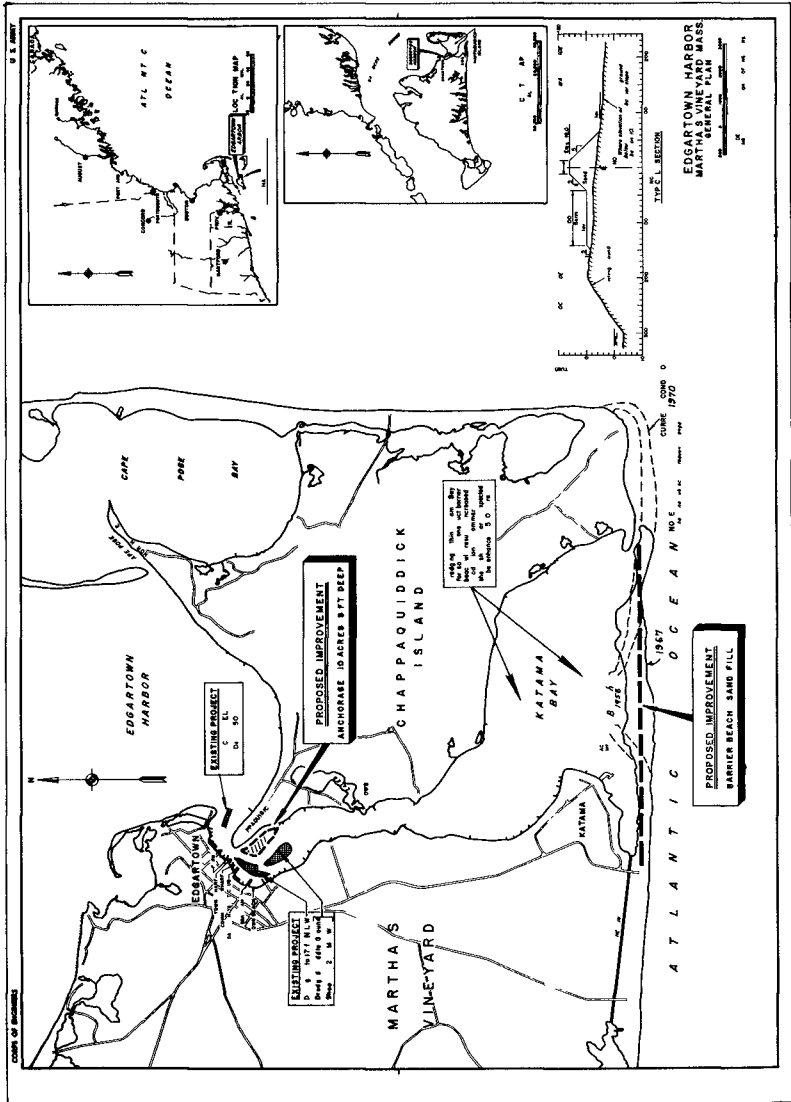
Edgartown Harbor, Massachusetts is located on the easterly end of Martha's Vineyard (See Figure No 8). The natural sand barrier beach extending for 3 miles along the south side of Katama Bay has had a history of breaches caused by storm waves recorded back to 1776. These breaches occur at the west to mid-portion of the barrier beach as the offshore hydraulic grade line lengthens and flattens in this area, the tidal currents diminish, and the beach narrows in width. The breaches result in excessive tidal currents at Edgartown Harbor and in shifting sands

U S ARMY

CORPS OF ENGINEERS



E C A 7



E 0118 0

within Katama Bay, which destroys the valuable shellfish crops in the bay. The breaches migrate to the east until they reach Chappaquidick Island at which time the westerly portion of the barrier beach is once again susceptible of a new breach. At present, the barrier beach connects Martha's Vineyard to Chappaquidick Island. A survey report now being forwarded to Congress for consideration for authorization, recommends that the barrier beach be raised and widened to prevent future breaches. The Fish and Wildlife Service of the United States Department of Interior, in cooperation with State and town fish and wildlife agencies, expects the improvement to result in a complete re-establishment of the shellfish industry within Katama Bay involving benefits of nearly two million dollars each year. In addition, the recreational boating fleet will be benefited.

CONCLUSIONS

As a result of the inlet problems discussed above, the following observations are offered. First, inlet jetties should be studied closely to avoid their construction with smooth faces resulting from placed stone, if it appears that this condition could contribute to excessive wave run-up, run-along, or reflection. All available advanced knowledge concerning inlet development should be utilized and exhaustive wave studies made for each inlet. Field observations of inlet sites should be made more often and more intensively. Every effort should be made by the coastal engineer to respond to the greatest desire and need of local interests while cooperating and coordinating fully with all affected interests to provide the optimum plan of improvement within the dictates of available funds and environmental controls.

It should be recognized that inlet problems can occur at any stage of development. It should also be recognized that changes in shorelines adjacent to inlet developments are a rather frequent occurrence. Congress responded to this recognition by including Section 110 into the River and Harbor Act of 1968, which authorizes the Corps of Engineers to provide corrective measures at shorefront areas shown to be adversely affected by Federal inlet improvements.

In summary, the coastal engineer should plan for all predictable factors, but he should be prepared to modify his plans at any time to correct for the unpredictable.

ACKNOWLEDGEMENTS

The information presented herein represents largely a summary of the very extensive and detailed studies made by coastal engineering experts of the New England Division office of the U S Army Corps of Engineers for each of the project areas discussed.

REFERENCES

- Task Committee on Small Craft Harbors (1964), Small Craft Harbors Development, Committee on Ports and Harbors, Journal of the Waterways and Harbors Division - Vol 90, No WW3
- U S Army Corps of Engineers, New England Division, Reports on the seven navigation projects discussed in this paper
- Watts, George M (1962), Mechanical Bypassing of Littoral Drift at Inlets, Journal of the Waterways and Harbors Division Proceedings of the American Society of Civil Engineers, Vol 88, No WW1
- Coastal Engineering Research Center (1968), Shore Protection Planning and Design, Technical Report No 4, 3rd Edition
- Sharp, Henry Staats, A M (1929), State Geological and Natural History - Bulletin No 46, Instructor in Geology, Columbia University, State of Connecticut
- Rhode Island Development Council (1955), Hurricane Tidal Protection in Narragansett Bay, R I
- Chute, Newton E , (1939), Geology of the Coastline Between Point Gammon and Monomoy Point, Cape Cod, Massachusetts
- U S Army Corps of Engineers, New England Division (1965) Massachusetts Coastal and Tidal Areas - House Document No 293, 89th Congress, 1st Session
- U S Army Corps of Engineers, New England Division (1962), Shore of the State of New Hampshire, Beach Erosion Control Study - House Document No 416, 87th Congress, 2nd Session

CHAPTER 75

OFFSET COASTAL INLETS

Miles O Hayes¹

Victor Goldsmith¹

Carl H Hobbs III¹

Abstract

Offset coastal inlets are common on the coasts of New England and the northern Gulf of Alaska. In both areas, the dominant waves approach the shore at an oblique angle, resulting in a strong net littoral drift. The most common type of offset on these coasts is a downdrift offset (i.e., the downdrift side of the inlet protrudes further seaward than the updrift side). Wave refraction around the ebb-tidal deltas at the inlets is an important process in the formation of the downdrift offsets, inasmuch as it creates a local reversal in drift direction just downdrift of the inlet, and allows sediment to accumulate there. Associated with the offset appears to be a segregation of tidal current flow in the inlets, with the ebb flow being more channelized than the flood.

The type of inlet offset at any one location can vary through time. Studies of the changes at the Hampton Harbor, New Hampshire, inlet from 1776 to the present show two reversals from updrift to downdrift offsets during that interval.

INTRODUCTION

An examination of coastal charts from almost any area in the world will reveal that coastal inlets are rarely symmetrical with respect to the placement of beaches on either side of the inlet. They are usually offset, either updrift or downdrift. As yet, no satisfactory theory or model has been proposed to explain these offsets.² Inlets with barrier spits that overlap adjacent downdrift barrier beaches, such as those of Long Island, N Y, seem in accordance with what might be predicted. However, many of the

¹ Institute of Coastal Research, Department of Geology, University of Massachusetts, Amherst, Massachusetts 01002

² This problem is under study by Cyril J Galvin, Jr of the Coastal Engineering Research Center, who considers the ratio of net drift to gross drift significant.

inlets of the New England and Alaskan coasts are offset in just the opposite direction, that is, the barrier beach downdrift from the inlet protrudes further seaward than the one on the updrift side. In fact, our studies indicate that this is by far the most common type of offset inlet on both the Alaskan and the New England coasts.

NEW ENGLAND INLETS

Over the period of the last five years, most of the sandy inlets on the New England coast have been studied by members of the Institute of Coastal Research, Department of Geology of the University of Massachusetts. With respect to coastal sedimentation, northeasterly storms, which generate waves that approach most of the shoreline obliquely from the northeast, have a dominant influence on the New England coast. These waves set up a net littoral drift to the south in most areas. At almost every inlet in New England, the barrier beach downdrift of the inlet (i.e., on the south side) protrudes further seaward than the one on the updrift side.

One of the most important processes in the accumulation of sand on the downdrift side of these inlets is wave refraction around ebb-tidal deltas. In the case of the Merrimack River Inlet, Massachusetts, the refraction of the dominant northeast waves causes waves to approach from the southeast, resulting in a northerly littoral drift at the south side of the inlet (Figs 1, 2, and 3). This reversal in drift direction on the downdrift side of the inlet serves to promote accumulation of sand to such an extent that the beach builds seaward at that point. A wave refraction diagram constructed for the inlet of the Merrimack River illustrates this principle (Fig 1).

ALASKAN INLETS

The depositional portion of the coastline of southeastern Alaska is similar in many respects to the New England coast. Important to the theme of this paper is the fact that most of the coastal inlets on this part of the Alaskan coast have downdrift

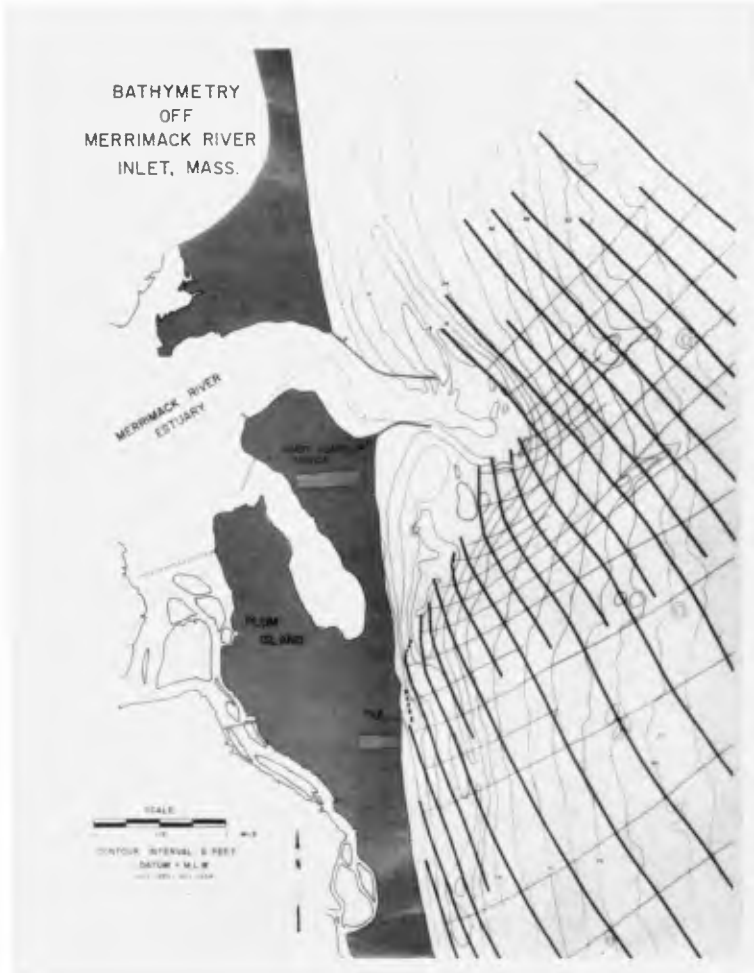


Fig. 1 Wave refraction diagram at the mouth of the Merrimack inlet, Massachusetts. Note that the refraction of the dominant northeast waves around the ebb-tidal delta has resulted in waves approaching from the southeast and thus in accretion at the south (i.e., downdrift) side of the inlet. Compare diagram with photographs in Figures 2 and 3. Wave fronts are approaching from the northeast with a period of 9 seconds.



Fig. 2 View looking south along the Plum Island beach, Massachusetts, just south of the Merrimack inlet. Coast Guard station in foreground is located on the wave refraction diagram of Figure 1. Note accumulation of sand on the south side of the groins and the oblique approach of the wave crests from the southeast. The groin field is located inside the ebb-tidal delta and is in an area of local reversal of longshore drift which results from wave refraction around the ebb-tidal delta (Fig. 1). In the far background of the photograph, drift resumes its normal southerly trend. Photograph taken June 1968.

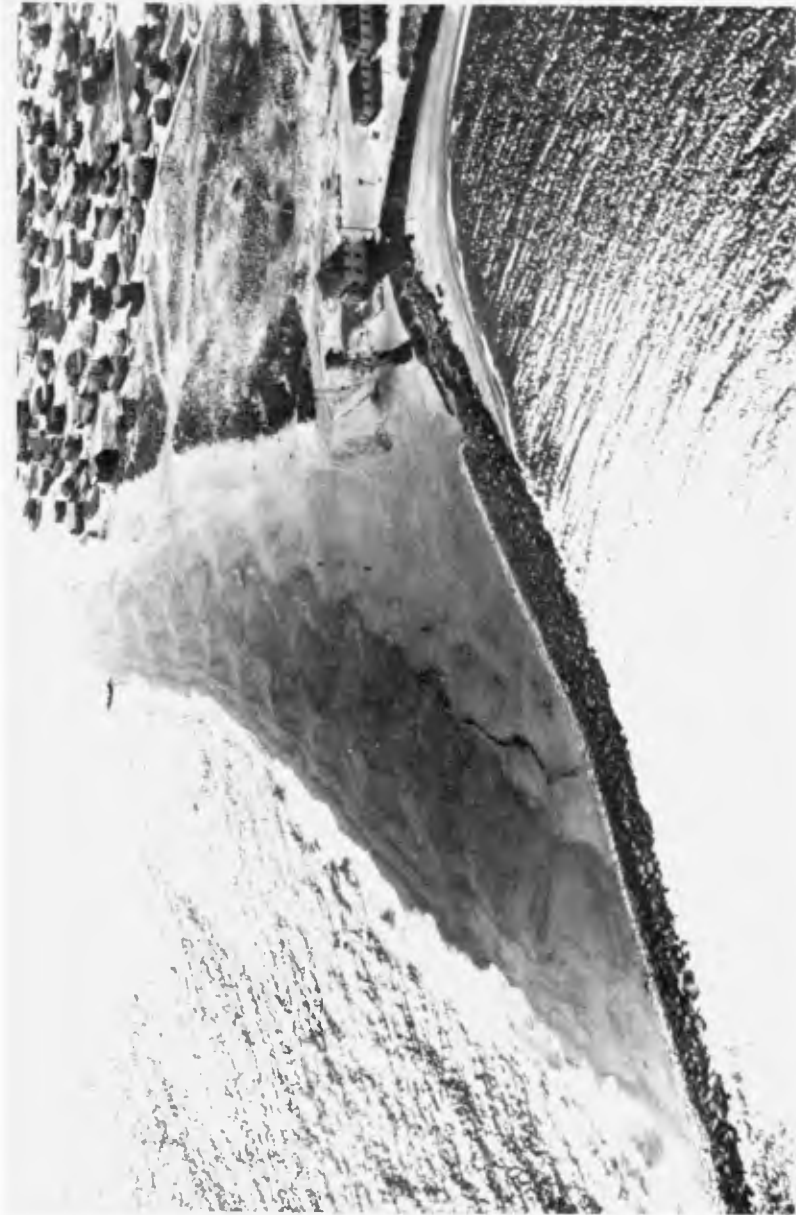


Fig. 3 South jetty of the Merrimack River inlet, Massachusetts, on 16 October 1969. Note the large accumulation and outbuilding of sand behind the Jetty, which was restored in the summer and fall of 1968. View looks south. This is further evidence for local reversal in drift direction on the downdrift side of the inlet. Compare with Figures 1 and 2.

offsets Net littoral drift is from east to west, as determined by geomorphologic evidence Figure 4 shows the lineation of coastal sand dunes in response to strong southeast winds These southeast winds are the result of low pressure centers that pass up the Aleutian Island chain and strike the Alaskan coast in the apex of the Gulf of Alaska

The coastal inlets off the Copper River Delta show pronounced downdrift offsets The barrier beaches on the west sides of the inlets have developed large seaward protrusions (Figs 5 and 6) Wave refraction appears to play an important role in the formation of downdrift offsets in this area (Fig 6)

DOWNDRIFT-OFFSET MODEL

From the study of approximately 15 offset coastal inlets, we have derived a simple model that we feel is representative of inlets with downdrift offset The model is given in Figure 7 Waves approaching the shore at an oblique angle produce a strong net littoral drift The supratidal portion of the beach on the downdrift side of the inlet usually protrudes seaward with the beach face of that portion of the barrier beach facing the oncoming waves The barrier beach on the updrift side is usually composed of multiple recurved spits, indicating strong transportation of sediment into the inlet Commonly, the intertidal portion of the inlet is also offset, in that large accumulations of sand on the ebb-tidal delta (usually swash bars) protrude further seaward on the downdrift side than on the updrift side The Barnstable inlet in Massachusetts is an excellent example of this type of offset

Another common feature of these coastal inlets is the segregation of ebb and flood flow Each inlet usually has a main channel that is oriented perpendicular to the shoreline and carries a large portion of the ebb flow The flood flow, on the other hand, tends to be distributed as a sheet with several individual flood channels developed in some cases Usually, the flood channels hug both beaches, flanking the main ebb channel A similar segregation



Fig. 4 Linear coastal dunes near the Bering Glacier, Alaska. Lineation is the result of strong southeast winds generated during southeasterly storms. View is towards the southeast. Sand spit and beach protruberances in background indicate strong littoral drift from east to west.



Fig. 5 Offset coastal inlet, Copper River Delta, Alaska. View is toward the east. Note the large seaward protrusion on the downdrift (west) side of the inlet with the linear beachface (arrow) perpendicular to the southeast, the dominant wave approach direction.



Fig. 6 Offset coastal inlet, Egg Island, Copper River Delta, Alaska. View is toward the east. Note the large protrusion on the downdrift (west) side of the inlet. Wave refraction (illustrated here) is thought to be an important process in slowing down and reversing littoral drift on the downdrift side of the inlet, with the downdrift protrusion building seaward as a series of ridge-and-runnel systems.

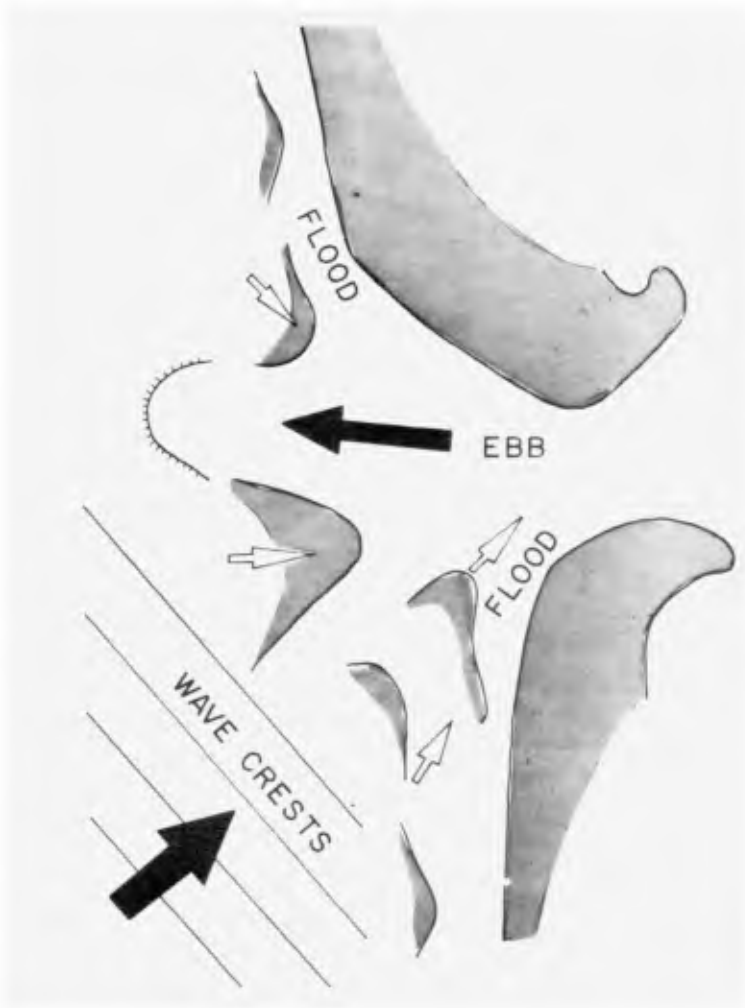


Fig. 7 A simple model for coastal inlets with down-drift offsets on the New England and Alaskan coasts. The down-drift side of the inlet, which is offset seaward, usually has a straight beach face perpendicular to the dominant wave approach direction. The ebb flow is channelized, whereas the flood current tends to develop as sheet flow across the intertidal swash bars and through minor flood channels.

of flow has been observed in model studies by Henry Simmons and his associates at Vicksburg (personal communication, September 1970)

We feel that the reason for this segregation of flow is the occurrence of time-velocity asymmetry of the tidal currents. Maximum flood velocities are usually late in the flood-tidal cycle, between mid-tide and high-tide. Similarly, the maximum ebb flow is between mid-tide and low-tide, usually quite close to low-tide. Thus, the ebb flow tends to be much more channelized than the flood, which flows in as a sheet. The exact relationship of this segregation of flow to inlet offset is unknown.

A spectacular example of a flood channel located on the down-drift side of an inlet, flanking the main channel, is shown in Figure 8. This figure, a photograph looking downdrift, shows large sand waves in this shallow flood channel which indicate transport toward the inlet. An inspection of the bedforms in the channel (on the ground) shows a complete predominance of flood flow in this channel.

HISTORIC CHANGES IN INLET OFFSET

Our studies of historical changes on the New England coast indicate that inlet offsets can change through time. A study of the inlet at Hampton Harbor, New Hampshire, shows that the offset of the inlet has passed through two cycles since 1776 (Fig. 9). In 1776, the northern beach overlapped the southern beach. By 1885 this pattern had reversed with the southern beach protruding further seaward than the northern beach. This cycle repeated again, with the inlet attaining its present configuration, with a southern protrusion, in 1931. The Merrimack River entrance, the next inlet to the south, shows a similar pattern of migration. This long term variation in inlet offset needs to be investigated in much greater detail.



Fig. 8 A flood channel on the downdrift side of an offset inlet, Strawberry Reef, Copper River Delta, Alaska (arrows indicate direction of flood current flow). The view is downdrift (southwest) looking out of the inlet. Flood-oriented sand waves in the middle distance indicate transport of sediment into the inlet. The flank of the main ebb channel is at the lower left-hand corner of the photograph. Photograph taken at low tide in July 1970.

HAMPTON INLET, N. H.
SHORELINE CHANGES

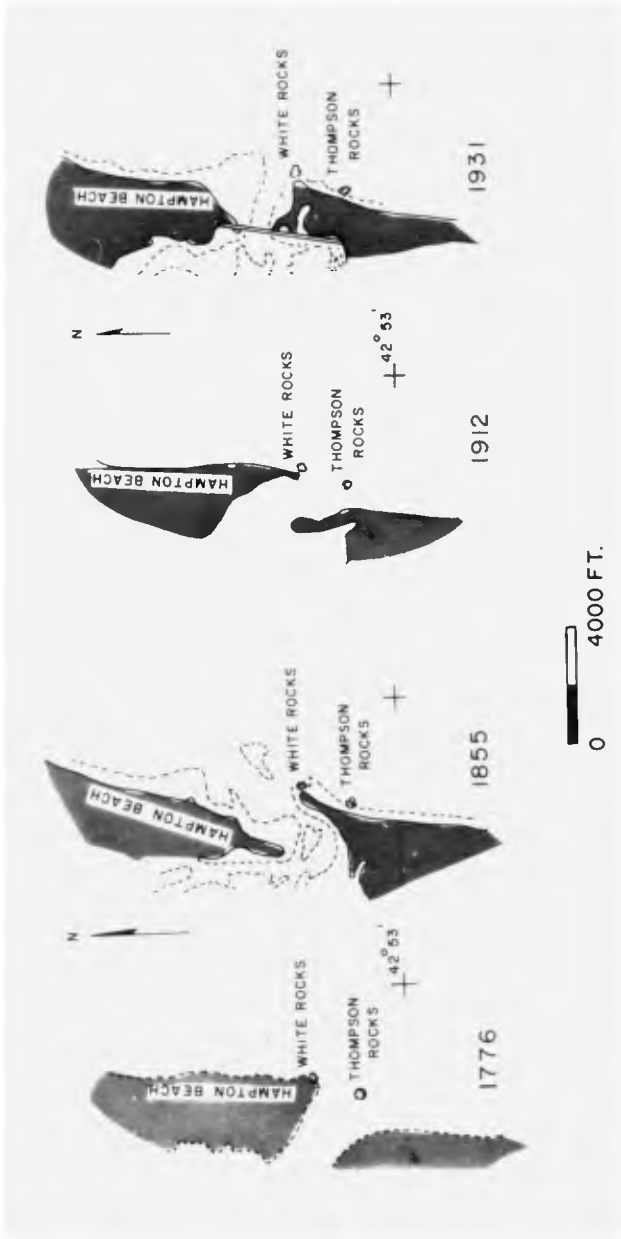


Fig. 9 Inlet changes at Hampton Harbor, New Hampshire, 1776-1931. Note that in 1776 and 1912, the updrift side of the inlet was further offset in a seaward direction, whereas in 1855 and 1931, the downdrift side of the inlet was further offset in a seaward direction.

SUMMARY

Coastal inlets of the shoreline of New England and the northern Gulf of Alaska show some striking similarities. Both of these areas are characterized by dominant waves that approach the shoreline obliquely, producing a large net littoral drift. Offset coastal inlets are common in both areas, the prevalent type being inlets with downdrift offset. We have presented a simple downdrift-offset model that we feel is typical of most of the inlets studied.

Associated with the downdrift offsets is a segregation of tidal current flow in the inlets, with the ebb flow being more channelized than the flood. How the flow segregation relates to inlet migration is one of the most important questions raised by our study.

In this paper we have dwelt on what we consider to be the most common type of offset in the area of study. The type of offset can and does vary from inlet to inlet, and, as indicated by our historic studies, can vary even at the same inlet through time.

ACKNOWLEDGMENTS

The observations reported in this paper were incidental to research being conducted in New England under contract DACW 72-67-0004 with the Coastal Engineering Research Center, U S Army Corps of Engineers, and in Alaska under contract N00014-67-A-0230-0001 with the Office of Naval Research (Geography Branch).

CHAPTER 76

FIELD STUDY OF A TIDAL INLET, BIMINI, BAHAMAS¹

W HARRISON, R J BYRNE, J D BOON, III, and R W MONCURE
Division of Physical, Chemical, and Geological Oceanography
Virginia Institute of Marine Science, Gloucester Point, Virginia 23062

ABSTRACT

The inlet bathymetry was mapped by standard photogrammetric techniques after photographing the bottom directly through the water column. The channel bottom is bare beachrock or is floored with bioclastic sands and gravels (S G = 2 84).

A nine-day time series of observations of current speed and direction, and water temperature and salinity was obtained at two depths at each of eight stations using tripod-mounted, telemetering sensor packages. Twelve-to-18-minute pulsations in the flow were often observed. Spectral analysis of near-surface current speeds shows significant peaks at 2 4, 3 2, 4 3, 6 7, and 12 3 hrs.

Evolution of sand ripples and dunes was monitored over a 200-ft distance during one tidal cycle. The pattern of growth illustrates the differences in bedform geometry which may be expected to influence friction coefficients. Evidence is presented for a bottom jet that is induced by flow over the crests of sand waves.

Tracer sand, sorted into two size groups and color-coded for identification, was released on a flood current. Sampling of color-coded tracer sand was conducted by divers using strips of grease-coated plastic tape. Spatial distribution of tracers in relation to the bedforms, and the importance to grain erosion of a natural mucoid coating, are noted.

INTRODUCTION

This study was designed to examine the hydrography and the fluid-sediment interactions in an inlet floored with carbonate sand. The approach adopted involved 1) describing the basic inlet geometry and the semi-permanent bedforms, 2) documenting the general flow field, 3) documenting the response of relatively small-scale bedforms to ebb and flood currents, and 4) conducting specific sand-tracer experiments.

Morphologically speaking, the inlet studied is a specialized tidal channel that connects waters of the Florida Straits with a shallow lagoon about eight square miles in area (Fig. 1). The lagoon is not enclosed, but opens to the Great Bahama Bank across a broad area of flats.

¹Contribution No. 359 of the Virginia Institute of Marine Science

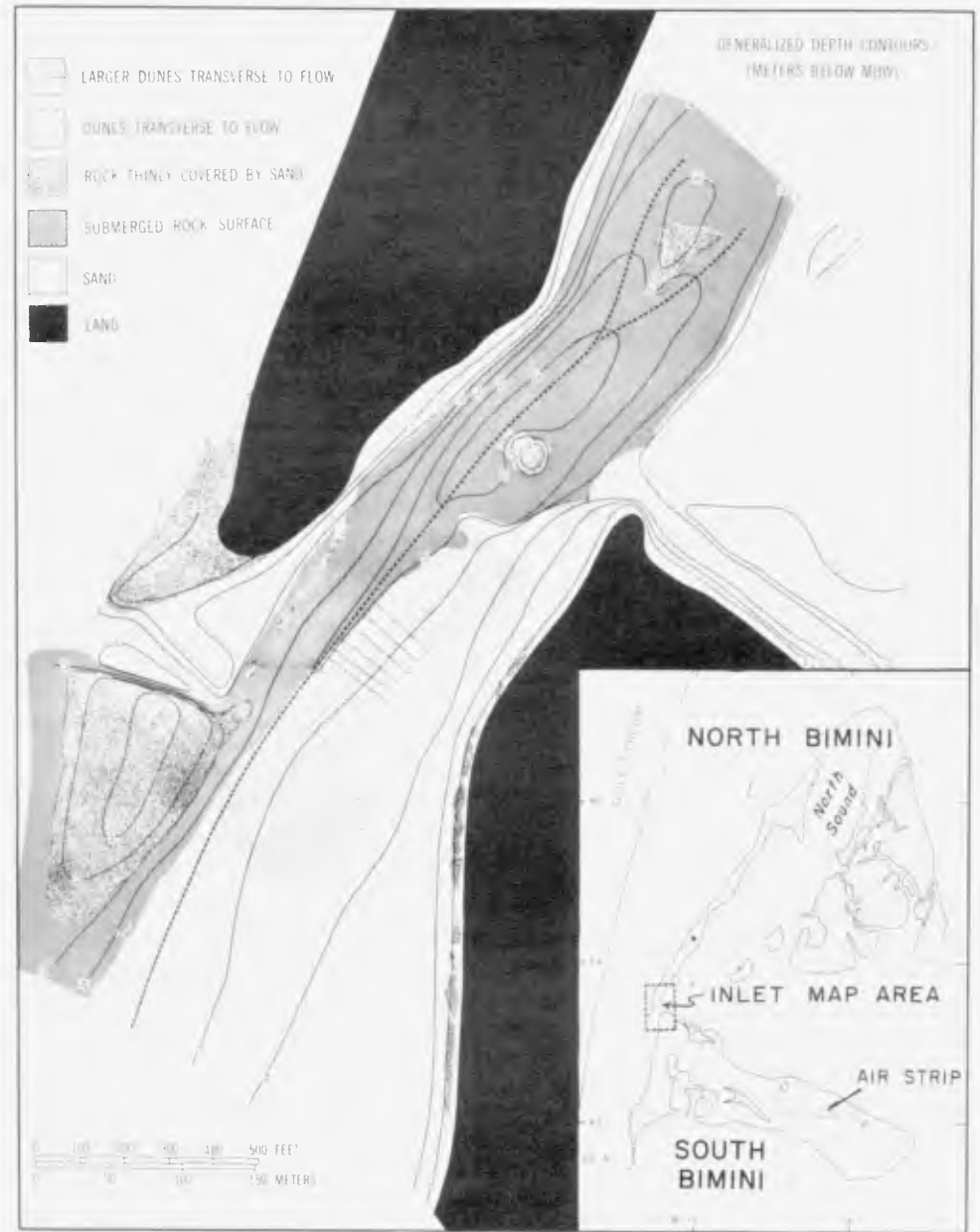


Figure 1.- Location, generalized bathymetry, and geology of Bimini Inlet channel.

Turekian (1957) felt that the lagoon was "host to three distinct water masses 1) an indigenous mass that moves in and out of the North Sound with the tides, 2) a mass entering from the Florida Straits through Entrance Point, and 3) a mass entering from the Bank" to the east

The tide range at Bimini varies between about 2.5 to 3.0 ft and sea level tends to rise or fall together at both Bimini and Miami (Wunsch, et al., 1969). Tides are of the semidiurnal type with a slight diurnal inequality. Propagation of the tide wave through the open lagoon is such that the ebb flow (to the southwest) through the inlet is about 30 percent longer than the flood.

Current speeds in the northern, constricted part of the inlet channel (Fig. 1) are high enough to sweep sediment from the beachrock floor. Some of the larger dunes in the central portion are composed of fragmented shell gravel. This gives way to sand with median grain diameters of 0.6 to 0.8 mm in the southern portion of the channel. Most of the grain surfaces in sand samples of shell hash taken from the central and southern portions of the inlet exhibit a glazed appearance when viewed under the binocular microscope. Sand-grain surfaces become more chalky, however, as one moves lagoonward (Bathurst, 1967). The specific gravity of sand grains from eight samples in the area of "dunes transverse to flow" (Fig. 1) was 2.84.

During the period of study, November 5-13, 1967, water temperature in the inlet channel varied between 20° and 27°C, salinity between 34 and 38 ‰, and density between 1.0201 and 1.0267 g/cm³. In May, 1955, Turekian (1957) found that salinity in the inlet varied between 36.0 and 37.0 ‰ and temperature ranged between 26.3 and 28.6°C over one tidal cycle.

DETERMINATION OF INLET GEOMETRY

Existing nautical charts of the Bimini Islands (British Admiralty Surveys of the 1840's) inadequately define the inlet geometry. Considering the general clarity of water at the inlet, it was decided to attempt bottom contouring by standard photogrammetric techniques.

To provide horizontal control for aerotriangulation, a base line 2319 ft in length was established by electrotape. Each end of the base line was pre-marked with a 4-x-4-ft, red plywood panel, the north end of the base being on North Bimini and the south end on South Bimini.

Five vertical control points on land were also established and pre-marked in the same manner. The levels were run with a Zeiss Opton level and were based on a tidal bench mark on North Bimini.

The photography as planned placed some photo centers over water with land areas on only one side. To facilitate the clearing of models during both aerotriangulation and compilation, seven floating targets (4-x-4-ft plywood) were anchored offshore to provide photographic images.

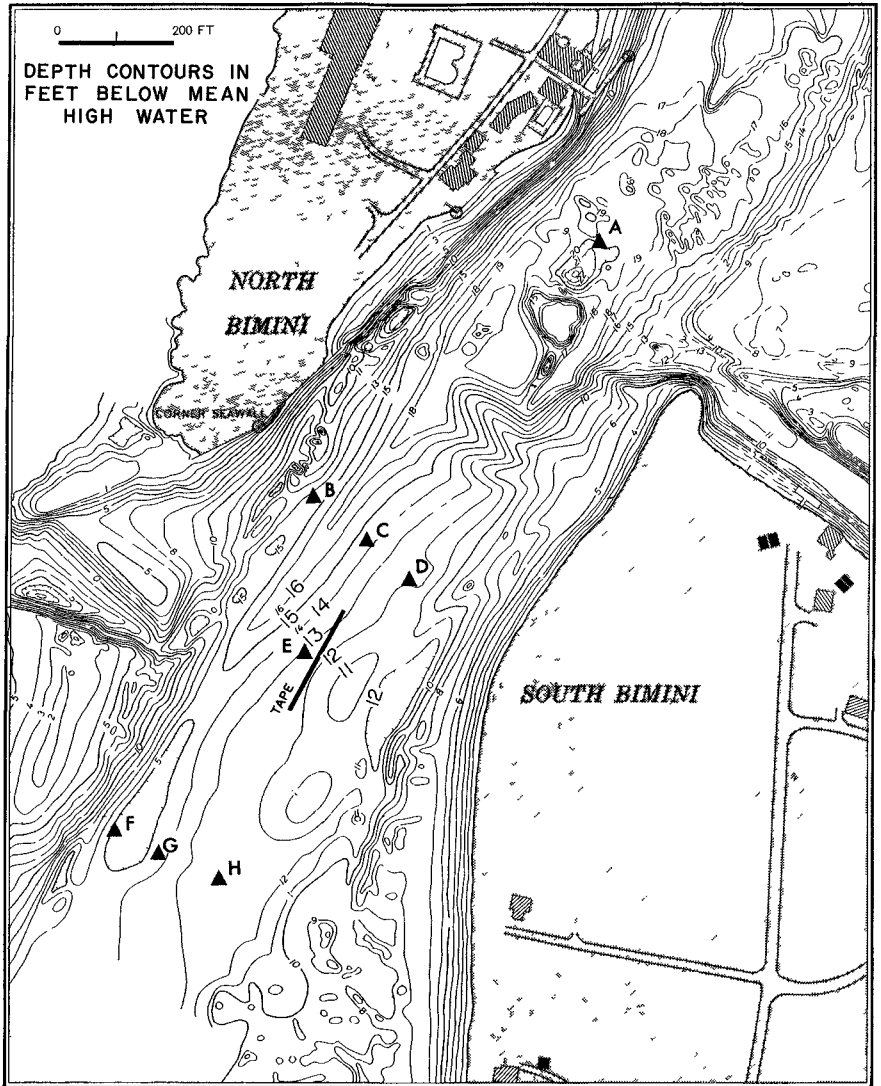


Figure 2 - Detailed bathymetry of inlet, locations of bottom-mounted sensor packages, and position of reference tape

A Wild RC-8 camera with a focal length of 152.29 mm, mounted in an Aerocommander aircraft, was used to obtain the photography on September 8, 1967. Film was Anscochrome D-200 with an ASA rating of 165. The flying height was 2000 ft above mean sea level, resulting in a photograph scale of approximately 1/4,000.

Aerotriangulation was by stereoplanographic methods using drilled glass plates. The contouring of the bottom (Fig 2) was accomplished on a Wild B-8 Plotter at 1/2,400 scale with a contour interval of one ft. The average correction for the refraction index of water for the models contoured was 1/4.

Hydrographic check lines run 45 days later indicated that the depth contours (Fig 2) were within ± 0.25 to 0.5 -ft for the shallow-water areas of the inlet. The "larger dunes transverse to flow" (Fig 1) were adequately brought out in the bathymetric contours and the hydrographic check lines showed them to be essentially stationary over the 45 days that had elapsed since they were photographed.

DOCUMENTATION OF FLUID PROPERTIES, WATER LEVEL, AND FLOW

Two tripod-mounted, "Geodyne" sensor packages were installed at each of the eight stations (A-H) shown on Figure 2. Each sensor package contained a platinum thermometer for measuring temperature, a toroidal cell for conductivity, a Savonius rotor for current speed, and a vane for current direction. A given pair of instrument packages were mounted in the tripod so that the Savonius rotor of one was one ft above the bottom while that of its companion was eight ft above the bottom. The mounting configuration was such that the flow pattern around a given rotor or vane was unaffected by the tripod legs or by the adjacent sensor package.

Each tripod was placed on a level part of the bottom and the sensor packages were hardlined to one of four shore-based stations. Each shore station contained a magnetic tape recorder and a radio transmitter. A given sensor was interrogated every six minutes, each interrogation involving five separate readings of current direction and speed and one each of temperature, conductivity, and reference.

Data from the four shore-based transmitters were sent by an RF link to a master station at the Lerner Marine Laboratory on North Bimini. At the master station, all data from the 16 sensor packages were recorded sequentially on computer-compatible magnetic tape. The entire system of sensors was continuously operated from 5 November through 13 November, 1967.

A bubbler-type tide gage was installed on North Bimini, the orifice was attached to the tripod at Station B.

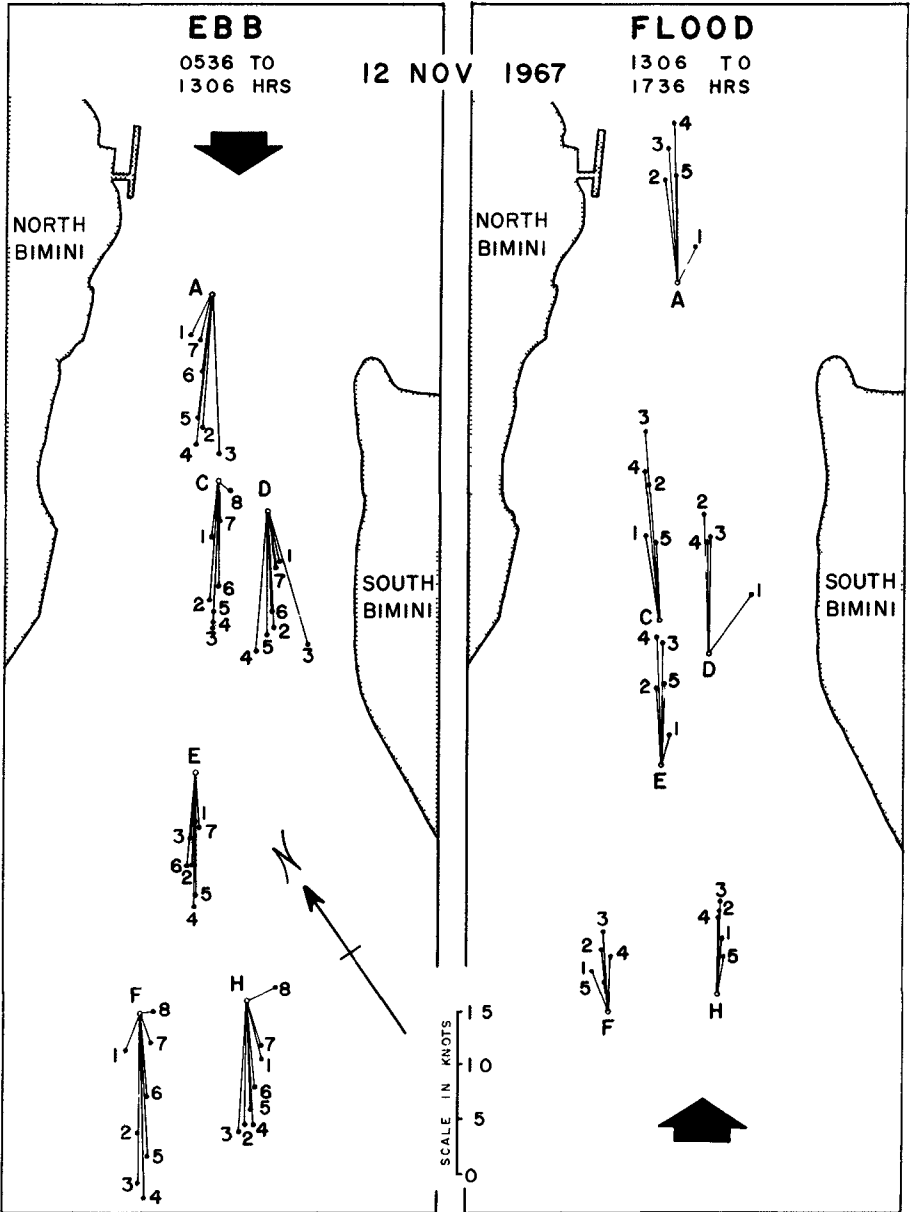


Figure 3 - Tidal-current vectors for a neap-tidal cycle (in hours after high-slack or low-slack water)

Data on maximum flow eight ft above the bottom are presented in Table 1. The absolute peak speed measured does not appear in Table 1 because it occurred prior to having all eight stations operational. This peak speed was 4.1 knots and was measured eight ft above the bottom at Station A. The time of measurement was during a maximum ebb flow that coincided with spring tides and a strong wind from the northeast that had been blowing for several hours.

TABLE 1 - NEAR-SURFACE VELOCITIES AT SELECTED STATIONS (5 Nov 67, through 13 Nov 67) (F = flood current, toward NE into lagoon, E = ebb current)

SENSOR STATION (fig 2)	MAXIMUM VELOCITY (kts, flood or ebb) (direction, true)	TIME (date) (hours, EST)	AVERAGE MAXIMUM VELOCITY (kts)		AVERAGE DEPTH BELOW SURFACE TO ROTOR (ft) (All rotors eight ft above bottom)
			flood	ebb	
A	2.3 F 31°	5 XI 67 2142 hrs	1.7	1.7	10.5
C	2.8 E 190°	11 XI 67 0824 hrs	1.7	1.9	4.0
D	2.1 F 04°	6 XI 67 0936 hrs	1.3	1.5	2.7
E	2.2 E 213°	11 XI 67 0618 hrs	1.3	1.7	3.3
F	3.3 E 195°	11 XI 67 0824 hrs	1.0	2.0	5.7
H	2.6 E 234°	6 XI 67 0142 hrs	1.6	1.4	4.0

An idea of tidal-current speeds and directions during a neap-tide flood and ebb cycle may be obtained from the vectors of Figure 3. It is interesting to note that the directional spread is less than 21° (Station D, ebb) at all stations during relatively strong flows.

An example of pulsations in the flow, for the upper rotor at Station E, is shown in Figure 4. Pulsations of this type were observed at all sensors and generally were of 12 or 18-minute frequency. Spectral analysis with a boxcar window failed to reveal any obvious power at these relatively high frequencies. Significant power was found at the tidal frequencies (6.7 and 12.3 hours) and at the sub-tidal frequency of 4.3 hours. Power peaks of possible significance were also noted at all stations at frequencies of 2.4 and 3.2 hours.

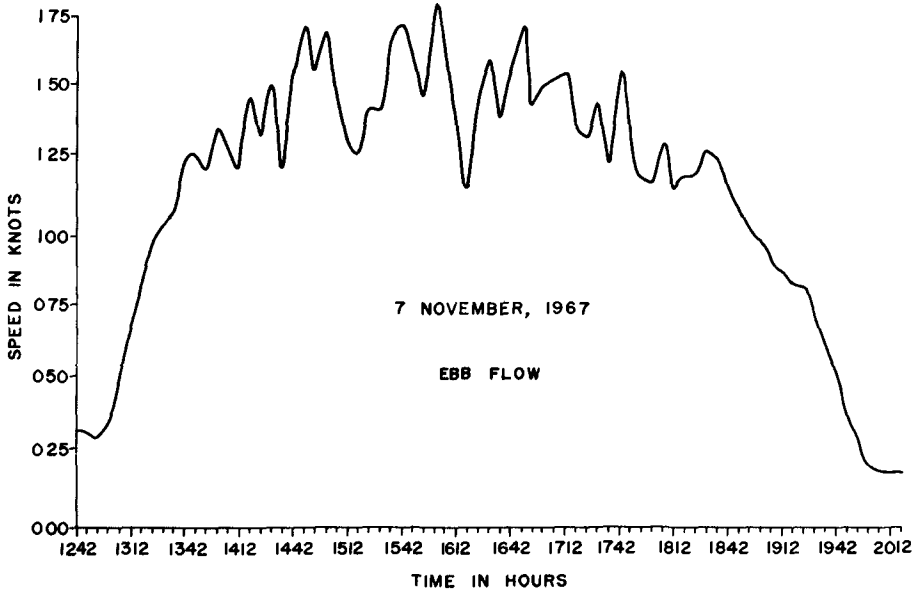


Figure 4 - Flow pulsations at upper rotor (eight feet off bottom) at Station E (Fig 2), during ebb flow

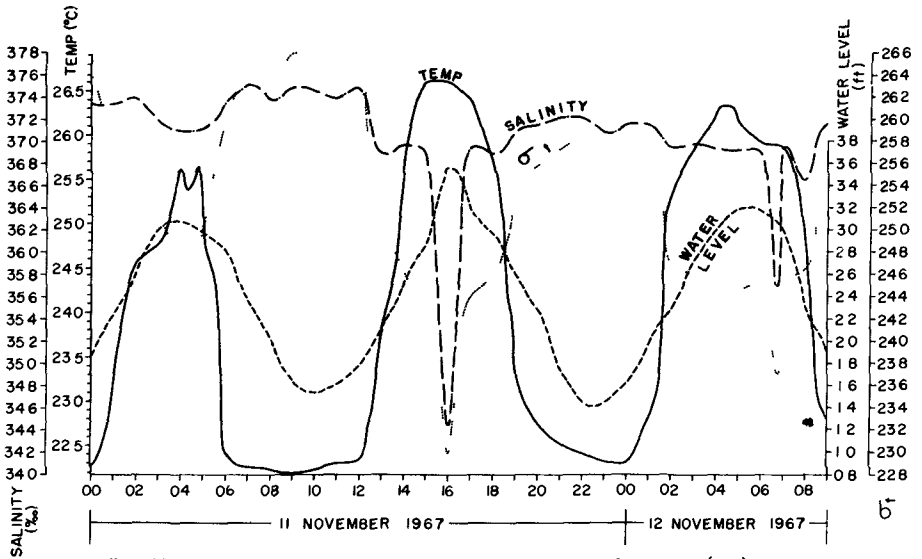


Figure 5 - Variation in salinity, temperature, and density (σ_t) at Station C (Fig 2), and water level at Station B, for 33 consecutive hours

A portion of the curves for variations in temperature, salinity, and sigma-tee at Station C and water level at Station B are plotted in Figure 5. The inverse relationship between sigma-tee and water level is due to the fact that in November, cooler, more-saline, high-density water flows out of the lagoon on ebb tide. This water is completely replaced at high tide by warmer, lower-salinity, less-dense Gulf Stream water. No density stratification was observed in this shallow channel of well-mixed waters.

BEDFORM MORPHOLOGY

Measurement Procedures

The goal of the bedform monitoring program was to measure changes in geometry and position of the various forms through the reversing flow of one tidal cycle. A fairly complete run was made on 13 November 1967. It started near the beginning of ebb flow and continued through one-half of the flood.

Photographic techniques were the prime tools in making the bedform measurements. Early in the survey a 200-ft, rigid tape measure (graduated in 1-ft intervals) was installed about one ft above the irregular bottom (Fig 2). About 15 ft to the west of the tape, and parallel to it, a wire guide-line was installed five ft above the bottom. The guide-line served to maintain the diver-photographer at a uniform distance from the tape and allowed him to control his progress in the rather swift flow. A second diver positioned himself behind the 200-ft tape. The second diver pushed a fork-like device into the sediment so that the elevation of the bed relative to the tape measure could be photographed. The fork device was composed of a series of 1/4-in rods welded at a 0.5-ft spacing to a rigid cross-member. Each rod was graduated in 0.1-ft intervals. The rigid cross-member had a bubble level cemented to it so that the upper member was horizontal, which in turn insured that the rods were vertical. Two forks were used, each was six ft long and three ft high.

A typical run was executed as follows. Two divers would descend at the upstream end of the tape. One diver would take the two forks to the tape and insert them, end to end, into the bed. The photographer-diver then took a still picture from the guide-line position. The other diver would then remove the upstream fork and place it in the downstream position for another photo, and so on. A single-photograph sequence of the bedforms generally took thirty minutes. Immediately before or after the still-camera sequence a run was made with a 16-mm movie camera. From the developed still-camera sequence, the configuration of sand bed relative to horizontal was reconstructed.

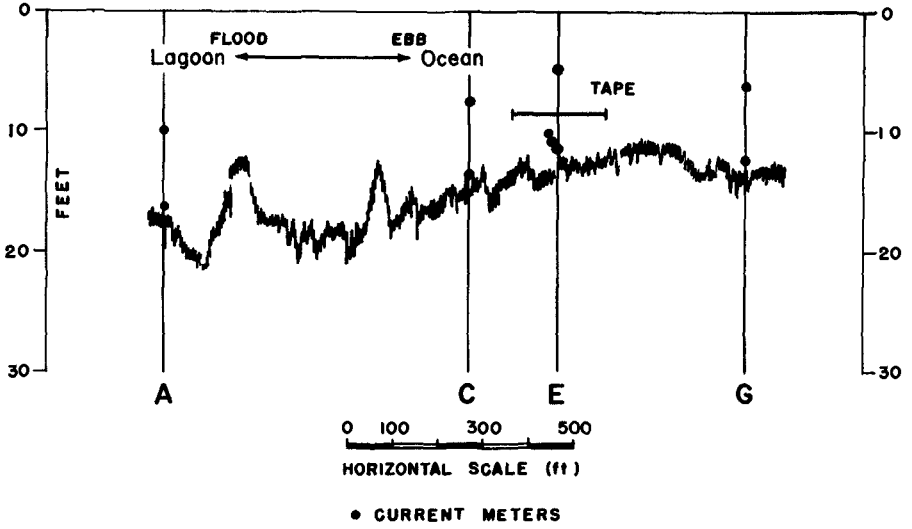


Figure 6 - Fathometer profile from sensor Stations A to C to E to G and vertical position of current meters

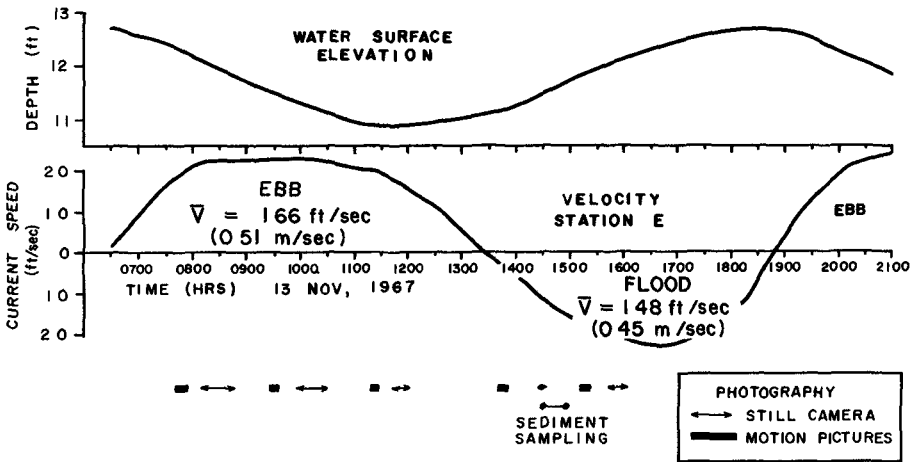


Figure 7 - Flow history and sampling times at Station E, 13 Nov, 1967

Field Setting

At any given time during the study three bedform length scales could be observed sand waves dunes, and ripples Inspection of Figure 1 shows that the sand waves exist only on the eastern side of the channel The dunes were long crested, the crest length being 10 to 15 times the wave length A fathometer run from stations A to C to E to G (Fig 2) is shown in Figure 6 There is a large rock outcrop at the northern end of the throat of the inlet, about 150 ft south of Station A A series of five sand waves had an average wave length of approximately 90 feet The fathometer profile shown was obtained during the slack water following a flood flow The fact that the ebb flow asymmetry still remains suggests that these bedforms are not strongly influenced by the flood flow Superimposed on these larger features were dunes and ripples that were modified by the reversing flow The position of the 200-ft tape is shown also, its northern end rests on the crest of the last sand wave Thus, the bedforms monitored included those in the lee of the sand wave crest, as well as those exposed to ebb flows of a converging nature Convergence was due to decreasing water depth in the direction of the southern end of the tape

The water surface time history and the velocity history at Station E on 13 November are shown in Figure 7 Also shown are the times when photographic sequences of the bedforms were obtained The velocity history illustrates the strong asymmetry in duration of the ebb relative to flood flow, which was found to be characteristic for this inlet The velocity history is at a mean relative depth (z/\bar{d}) of 0.66 (where z is the height of the rotor above the bottom and \bar{d} is the mean water depth) The mean velocities (integrating over the flow duration) for the ebb and flood are, respectively, 1.66 ft/sec and 1.48 ft/sec In summary, we have a condition in which the ebb flow is generally stronger and of appreciably longer duration Net sediment transport may then be expected to be seaward

Evolution of Bedforms

The sequence of events in bedform change is shown schematically in Figure 8 where, for descriptive purposes, the cycle is started at the end of flood (Fig 8a) With the reversal of flow (Fig 8b), the bed sediment is transported up the steep gravity face of the dune to form what dimensionally might be considered the new dune crest A train of ripples also occurs on the dune flank These ripples are all of smaller amplitude than the one derived from the old edge of the dune crest The dominant ripple length is approximately 1 to 1.5 ft

With continued ebb flow the primary crest overtakes some of the other ripples in its lee There is a consequent increase in amplitude and the growing ripple slowly becomes a dune (Fig 8c) As the new dune crest advances (in the ebb flow direction, Fig 8d), the ripples in its lee become increasingly less active due to sheltering action Other ripples are then observed translating up the upcurrent flank of the dune These are of small amplitude and approximately 2 to 2.5-ft in length (Fig 8e, f)

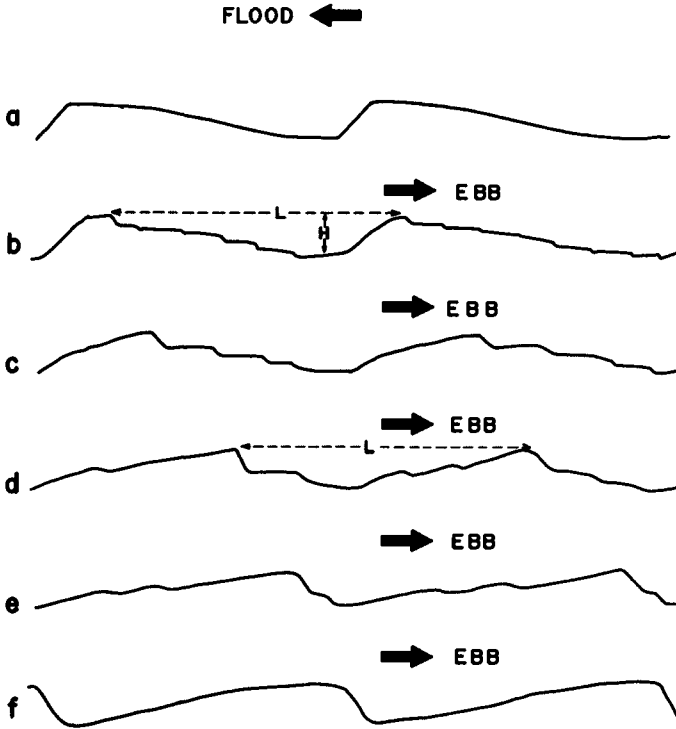


Figure 8 - Schematic bedform evolution

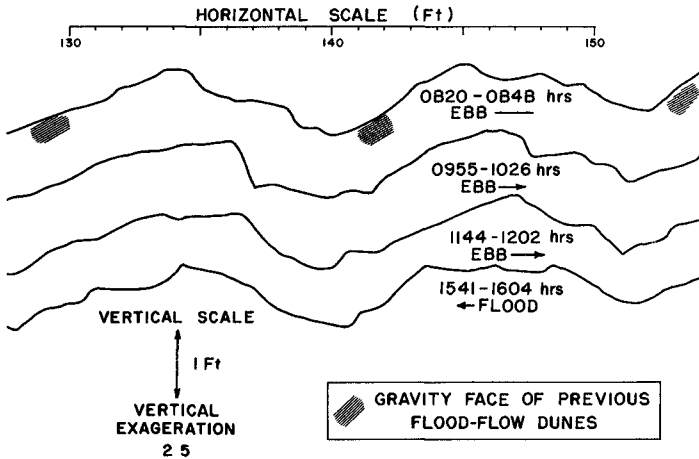


Figure 9 - Example of observed bedform changes during a tidal cycle

As the velocity of the ebb flow diminishes the dune crest slows its advance until bed transport stops, at which point the bedforms become dormant until the new flood flow is intense enough for grain transport. Some of the measured bedform changes are shown in Figure 9. The flow conditions for the various sampling times may be noted in Figure 7.

Throughout the study period visual observations indicated most of the sediment transport occurred via dune advance with no perceptible suspended load. Given the aforementioned asymmetry in strength and duration of the flow (Fig 7) it might be expected that the ebb flow dune advance would be greater than the flood flow dune retreat. This was observed to be the case over a three day period 10 November to 13 November. Successive measurements of ebb-flow, dune-crest positions indicated a mean net advance out of the inlet on the order of 1 foot per tidal cycle. This value is a very rough estimate as large variability was noted both in time and space.

The evolving nature of the dunes presents some problems in determining length characteristics, however, as a flow cycle starts a reversal, a distinctive crest is generated on each dune. This crest is the highest point above the downstream trough and it probably exerts a dominant influence on the gross wake characteristics for the dune. The dune wave length (L) is defined as the distance between a given dominant crest and the next downstream crest. Dune height (H) is defined as the vertical distance between the dominant crest elevation and the downstream trough.

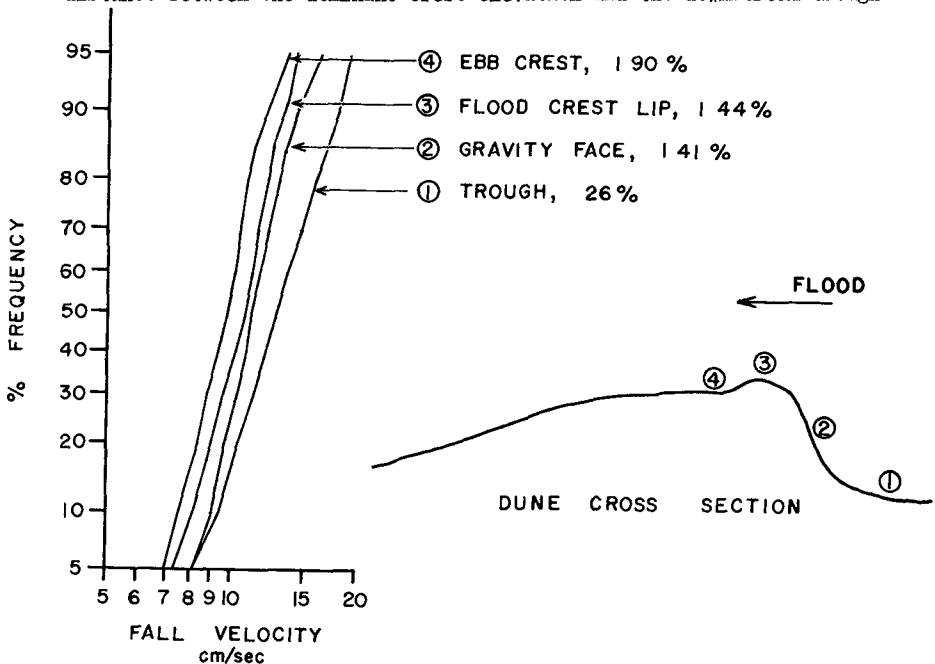


Figure 10 - Sediment fall velocity distributions. Values represent % weight of material larger than 2 mm

Inspection of the bedform profiles over the 200-ft distance indicated that the wave lengths and heights were significantly different for the northern half (115 ft) of the tape as opposed to the southern half. This is perhaps to be expected, as the first half encompasses those dunes which are formed in the lee of the large sand wave (see Fig. 6). The results, cast as averages, are shown in Table 2. Two facts deserve specific comment. First of all, it should be noted that during the ebb flow the dunes in the lee of the large sand wave have longer wave lengths and smaller heights than those beyond the direct influence of the sand wave. There is only scanty evidence for the flood flow, but that available (1541-1604 hrs), suggests a uniformity in dune height. The second point of interest is the relative stability of wave length and height (and, therefore, steepness) during the various phases of the reversing flow.

TABLE 2 - SIZE PARAMETERS OF DUNES

Parameter	Position on Tape (Ft.)	Time			
		0820- 0848 hrs	0955- 1022 hrs.	1144- 1202 hrs	1541- 1604 hrs.
\bar{L} (ft)	0-110	14.3	14.0	14.3	15.6
Range of L		9.5-18.5	9.5-20.0	10.0-20.0	10.0-18.0
	110-200	10.7	10.9	11.3	10.5
		9.5-12.5	9.0-12.0	10.0-13.0	9.0-13.0
\bar{H} (ft)	0-110	0.56	0.63	0.53	0.82
Range of H		0.27-1.10	0.25-1.4	0.25-1.20	0.25-1.0
	110-200	0.75	0.81	0.81	0.80
		0.50-1.00	0.60-1.00	0.5-1.00	0.50-1.0
\bar{L}/\bar{H}	0-110	30	33	32	25
		8-41	9-68	11-50	12-64
	110-200	16	14	14	15
		12-26	11-20	10-23	11-25

Dune Field Sediments

Sediment samples were obtained on 13 November during flood flow, about one hour after flow reversal. Samples were taken of the upper half-inch of the bed material on the dune flanks, crests, and troughs. The trough samples are biased, as large fragments of the conch *Strombus gigas* were not collected. Laboratory treatment consisted of a wet separation of the material greater than 2-mm, followed by a settling analysis of the finer fraction.

All of the grain-size distributions from the settling analyses closely approximated a log-normal distribution with very little variation in the geometric standard deviation, $\sigma_g = W_{84.1} - W_{50}$, which had an average value of about 1.2. The average median fall velocity of the trough material was about 12.6 cm/sec and at least 25 percent of the material (by weight) is larger than 2 mm. The sediments composing the dune flank and crest had a somewhat smaller median settling speed (10-11 cm/sec) and were generally less than 7 percent greater than 2 mm in mean size.

An example of these results is shown in Figure 10. The sequence shown was obtained during the flood flow when the flood crest was becoming established. Diver observations suggest that the small flood-flow crest is composed of material swept up the ebb-flow gravity face.

Flow Profile--Station E

In an attempt to obtain an estimate of the velocity profile over the dunes an auxiliary current-meter tripod containing two additional Savonius rotors was placed near Station E. Sampling of the rotors was synchronized with the two tripod-mounted Savonius-rotors and a sample of 46-seconds' duration was taken every six minutes. The relative positions of the four rotors are shown in Figure 6, the lowest rotor was about 1.5-ft above the sand interface, the remaining rotors were 2.1, 3.2, and 8.3 ft above the bottom.

During the ebb flow the rotor outputs indicated a larger speed near the bottom than that registered at the uppermost rotor (Fig. 6). This pattern persisted throughout the ebb flow until one-half hour before flow reversal at which time a normal profile was present. During the flood flow the enhancement of flow speed near the bottom was not present, instead, the flow was essentially uniform with depth.

It seems likely that the flow maximum near the bottom is a jet due to the sand wave field. The nature and development of jet flow over sand waves is being studied by J. Dungan Smith (Univ. of Washington). Smith (personal communication) has formulated a model predicting the jet and has documented jet occurrences in tidal flows. His early results indicate that the jet amplitude is a maximum when the sand wave height is about 20% of the water depth and that the jet is fully developed at the fifth wave in the field. The bedform conditions of the Bimini Inlet case described here are similar to those found by Smith. During flood flow the approach toward uniformity of velocity with depth is consistent with the fact the depth is then divergent downstream.

Discussion of Bedform Changes

Although past studies have delineated the significant variables that control bedform characteristics in unidirectional flow, there is no satisfactory formulation to predict the length and amplitude of bedforms found in the field. It may be anticipated that the problem is even more

complex in the case of reversing tidal flow. There are two main differences between the two cases. In the case of tidal flows the time variations in stage (and discharge) for a given flow direction occur in a few hours and bedforms may not come into equilibrium with the maximum flow speeds. Carey and Keller (1957), in a study of Mississippi River bedforms noted a bedform size dependence on discharge and postulate a lag between bedform change and change in stage. Secondly, with the change in flow direction the flow may encounter (as in this study) an established bedform morphology of reverse symmetry. The role of such initial conditions needs detailed attention.

Aside from flow-acceleration effects, it may be anticipated that friction factors during a flow cycle will be somewhat different for reversing flows as opposed to a unidirectional flow of equivalent maximum velocity, because the character and position of the separation zone in the lee of the crest changes in time. Model studies by Bayazit (1969) for ripples generated by reversing flows indicated friction factors less than those found for corresponding unidirectional flows. The difference between the two cases was attributed to a possible lack of bedform equilibrium with the reversing flow. In order to avoid the effects of acceleration, Bayazit used the maximum velocity in formulating a friction factor.

In the absence of detailed studies it has frequently been assumed that bedform development in an inlet may not differ significantly from a corresponding steady flow (Bruun, 1966). If such was the case one might expect to find a progression from ripples to dunes as the velocity increases and the reverse order as the velocity decreases. The present study indicates this view is probably oversimplified. For this case, the basic bedform sizes are stable through time with the major changes being simply a reversal of dune geometry. It is of interest to compare the dune lengths and heights observed here with those observed in unidirectional flow. Analysis of field data by Allen (1968) showed that the characteristic lengths of dunes were strongly correlated with flow depth although it was recognized that dune size is not a unique function of depth. Allen's relationships are, for lengths in meters

$$1) H_D = 0.086d^{1.19} \text{ and}$$

$$2) L_D = 1.16d^{1.55}$$

where H_D is dune height, d is flow depth and L_D is dune wave length. Because there was relative stability in the average dune length and height during the observation period (Table 2), the mean depths over the two tape segments were used to calculate the expected values from equations 1 and 2. For the lagoon side of the tape the computed wave length is 35.6 ft whereas the observed mean value is approximately 14.5 ft. The computed dune height is 1.6 ft and the observed mean is about 0.6 ft. For the oceanside segment of the tape the computed wave length is 28.2 ft and the observed is about 11.0 ft, for dune heights we find 1.32 ft versus an observed value of about 0.80 ft. The expected values from equations 1 and 2 are thus significantly larger than the observed mean values.

Generally it can be said that the resulting scour is strongly influenced by the pile and the wave characteristics. In most of the runs, very little to no bed movement could be observed away from the pile. The pile served as a catalyst to start the scour activity and once started around the pile it spread over a large area and extended in some cases great distances from the pile. Figs. 9 and 10 show some typical scour patterns obtained from the experiments.

CONCLUSIONS AND REMARKS

- 1 The critical velocity necessary to cause incipient motion in oscillatory flow appears to be lower than that for steady state flow.
- 2 The ratio of the maximum velocity on the pile boundary and the initial free stream velocity, is less than the value of 2.0 for potential flow theory.
- 3 Incipient motion on the pile boundary appears to be independent of $\frac{H}{h}$ and directly dependent on the parameters $\frac{h}{gT^2}$ and $\frac{d}{h}$.
- 4 $\frac{Su}{H}$ appears to be directly related to the sediment number N_s and the pile Reynolds Number N_{RP} .
- 5 A maximum of only 6000 waves are required to reach an ultimate scour depth and in most cases 3000 waves are sufficient.
- 6 The relative ultimate significant scour depth increases very rapidly at first, reaching three-fourths of its ultimate depth in the first 1000 waves, and increases more slowly after that until it reaches its ultimate depth.
- 7 Eddy forces, although initially influencing the scour patterns, do not appear to be of significance in the final scour pattern.
- 8 The scour pattern resulting is primarily influenced by the pile and the wave characteristics.
- 9 In all the scour experiments, the pile acted as a catalyst causing scour of the bed particles to be initiated whereas if the pile was not present little to no scour would have resulted.

To try and predict scour depths for a prototype case or relate these inconclusive results to a prototype would be presumptuous. To predict happenings or occurrences of a phenomenon in a prototype requires that there be similitude, both geometric and dynamic, between the model and prototype. This requires that similitude exists between the orbital velocities and orbital lengths (i.e. wave characteristics are similar), grain size and grain size distribution in the bed, roughness of the beds, and translation of the orbit due to drift. Without these similitudes erroneous conclusions could be reached in attempting to predict prototype conditions. The difficulties in acquiring similitude between prototype and model were pointed out by Posy and Sybert¹⁸ in their studies of scour around piles on offshore platforms. It required several years of study and experimentation before actual prototype conditions were duplicated in the model.

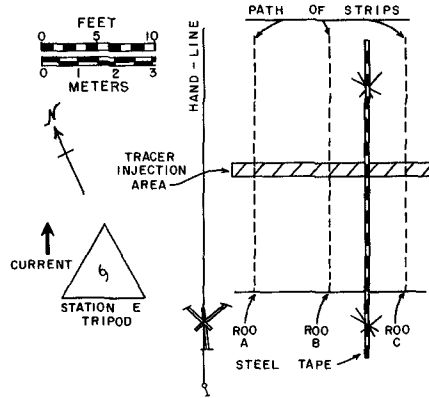


Figure 11 - Map View of Tracer Experiment Layout

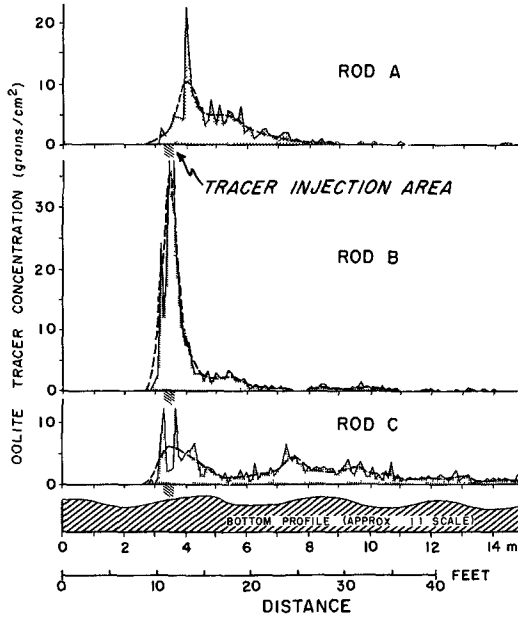


Figure 12 - Plot of Oolite Tracer Concentration versus Distance for Rods A, B, and C after the First Sampling Run

Plastic bags containing the tracers were placed within the injection area (Fig 11) by a diver who cut them open with a knife at the designated time of release. Recovery of released tracers was accomplished using 0.15 x 1.8 m strips of K & E drafting film (Herculene) coated with Dow-Corning 103 compound. These strips were unrolled on the bottom in a northerly direction parallel to a graduated steel tape. Three strips, fixed at one end by steel rods were unrolled simultaneously by divers according to the configuration shown on Figure 11. Four sampling runs were made at 30-minute intervals beginning at 1307 hours.

The recovered sampling strips were examined in the laboratory under ultraviolet light. Tracers were counted within a 10 cm² grid placed over the strips at 0.1 m increments for the full length of the tape. Tracer concentrations, expressed as the number of grains per cm², were then plotted against distance from the holding rods in meters. Figure 12 is a plot of the initial sampling run for rods A, B, and C. The dashed curves, intended for smoothing of the data, were obtained by dividing distance into 0.5 m class intervals and averaging grain concentrations therein.

In examining the data, it was immediately apparent that the quartz grains (0.59-0.84 mm) were present in smaller amounts than the oolite (0.30-0.59 mm) and that their distribution was more limited. A few quartz grains traveled as far as 15 m downstream in the first 30 minutes after the first release. Most of the quartz tracers, however, assumed an almost normal distribution about a point less than 1.0 m downstream from the release zone. The quartz tracers also appeared to be distributed uniformly in a lateral sense as evidenced by simultaneous comparisons between adjacent strips.

Oolite tracers were recovered in greater numbers and their distribution appears to have been more widespread than that of the quartz material. Following their release, significant concentrations of oolite (~1 grain/cm²) were found at maximum distances from the release zone after 30 minutes, also the greater mass of these tracers, while remaining some 1-2 m downstream from the release zone, showed markedly skewed distributions toward the downstream side (Fig 12, Rods A and B) with pronounced bi- or trimodality in many cases (Fig 12, Rod C). Moreover, the oolite tracers often showed great lateral variability, as seen through the simultaneous comparisons of adjacent strips, and temporal variability, as seen in time-sequential comparisons along each of the strip paths.

A bedform profile, obtained from photographs at the end of the flood current, is included in Figure 12 to show the relation of tracer concentration to bedforms.

In order to quantify the observed lateral and temporal variability in oolite tracer distribution, a two-way analysis of variance (Rods versus Runs) was conducted using the oolite data of the four runs for rods A, B, and C. The variable used in the analysis was tape distance in meters with

TABLE 3 - TWO-WAY ANALYSIS OF VARIANCE OF TRACER RECOVERY DATA (Variable is Tape Distance in Meters Tracer Colite)

ROD	SAMPLE	RUN 1	RUN 2	RUN 3	RUN 4
A	Mean	4 92	3 63	4 08	4 59
	Var	1 31	0 17	0 21	0 66
	Size	188	180	48	47
B	Mean	3 83	3 90	4 59	4 43
	Var	0 52	0 18	1 12	0 55
	Size	302	81	461	155
C	Mean	6 06	3 58	4 29	4 00
	Var	4 64	0 23	0 21	0 48
	Size	200	55	21	97

VARIATION SOURCE	SUMS of SQUARES	DEGREES of FREEDOM	MEAN SQUARE	F VALUE	CONFIDENCE LEVEL (PERCENTAGE)
TOTAL	2977 63	1834			
INTERACTION	459 05	6	76 51	67 41	> 99
ERROR	2074 00	1828	1 13		
ROD	178 52	2	89 26		
RUN	265 29	3	88 43		

the number of grains recovered at a particular distance serving as a frequency index for that distance. Each sample of tape distances was therefore an indicator of the distribution of the tracer population for which a mean and a variance could be estimated.

The object of the analysis was to determine whether or not tape distances could be pooled for all three rods and a separation of tape distance means effected between runs. After the analysis was run, significant interaction indicated that pooling could not be done and therefore separation of the means was not possible. Table 3 gives the results of this analysis.

A similar analysis was attempted for the quartz tracers. However, by using a one-way analysis of variance initially, it was learned that none of the means for runs could be separated due to their close similarity in value and the significant variance within each run. This result only confirmed the visual impression that the quartz tracers evidenced very little bulk movement.

DISCUSSION

The results obtained suggest that the oolite tracer exhibited a greater tendency toward transport than did the quartz tracer. Probably the oolite tracer was "undersized" for the existing flow regime in the inlet while the quartz tracer was close to the prevailing grain sizes on dune crests. Compared with the greater ebb current speed obtained at Station E (Av 1.7 knots, max 2.2 knots) it is not surprising that the flood current seemed to transport only a few quartz grains and that the distributions of these were less skewed. Caution must be used in this interpretation, however, because the effect of burial of tracer grains is unknown due to the sampling method employed. It has been instructive to the authors that an inlet such as the one at Bimini represents an extremely complex environment and even detailed measurements are inadequate for a clear picture of the way in which sand is transported. For example, lateral variability of apparent grain motion was much more evident than anticipated, bottom transport is truly a three-dimensional problem.

Although the results of the experiment are not conclusive, it seems evident that dunes play a major role in the distribution of tracer sands, and the modes of the concentration curves indicate points of grain accumulation which move slowly downcurrent with time. In some cases, grains apparently travel very quickly over a succession of dunes, but a majority of samples indicate that most of them are fixed by the dune topography and therefore travel at much slower rates. This slow transport is in keeping with the fact that the dunes themselves migrate very little during any given tidal cycle.

The Bimini Inlet sediments appear to possess an organic coating (Bathurst, 1966) which did not allow most of them to adhere to the greased sampling strips. All tracer grains were thoroughly dried and rewetted with detergent before release, they adhered very well to the strips. Although mucoid coatings or gelatinous mats are not common to the active sands typical of the Bimini Inlet (Bathurst, 1966, p. 90), there was clearly a difference in the surfaces of the in-situ and tracer grains. This then leaves the question of whether or not the in-situ grains experience a binding effect that is not otherwise apparent.

ACKNOWLEDGMENTS

All of the field work for this study was supported by the Atlantic Oceanographic and Meteorological Laboratories, of the Environmental Science Services Administration (ESSA), Miami, Florida. Logistical support was obtained from the Lerner Marine Laboratory (American Museum of Natural History) on North Bimini. Aerial photography and contour mapping was accomplished by the Photogrammetry Division, Coast and Geodetic Survey, ESSA.

This study could not have been accomplished without the concerted efforts of many individuals. We wish to express our great appreciation to Messrs F. Beugnet, S. Cofer, J. Falkenhoff, B. G. Grant, C. Kiersh, M. P. Lynch, E. W. Rayfield, G. Reynolds, and D. G. Tyler for their efforts in the field. R. W. Mathewson and his staff at the Lerner Laboratory were also most helpful in the field effort.

REFERENCES

- Allen, J. R. L. 1968. The nature and origin of bedform hierarchies. Sedimentology, 10: 161-182.
- Bathurst, R. G. C. 1967. Oolite films on low energy carbonate sand grains, Bimini lagoon, Bahamas. Marine Geology, 5: 89-109.
- Bayazit, M. 1969. Resistance to reversing flows over movable beds. Proc. ASCE, Jour. Hydraulics Div., 95(July 11:09-11:27).
- Bruun, P. 1966. Tidal Inlets and Littoral Drift, v. 2, Skjerpnes Offsettrykkeri, Trondheim, Norway, p. 1-193.
- Carey, W. C. and H. D. Keller. 1957. Systematic changes in the beds of alluvial rivers. Proc. ASCE, Jour. Hydraulic Div., 85(August 1-24).
- Turekian, K. K. 1957. Salinity variations in sea water in the vicinity of Bimini, Bahamas, B. W. I., Amer. Museum Novitates, No. 1822, 12 pp.
- Wunsch, C., D. V. Hansen, and B. D. Zetler. 1969. Fluctuations of the Florida current inferred from sea level records. Deep Sea Research (Suppl.) 16: 447-470.
- Yasso, W. E. 1962. Fluorescent coatings on coarse sediments, an integrated system. Office Naval Research, Geog. Branch, Tech. Rep. 1, 48 pp.

CHAPTER 77

RECENT HISTORY OF EROSION AT CAROLINA BEACH, N C

Limberios Vallianos, Chief, Coastal Engineering Studies Section,
Department of the Army, Wilmington District, and Member ASCE

ABSTRACT

The reaction of shores adjacent to salient features which interrupt along-shore processes has long been recognized as an important consideration in connection with the investigation of engineering works to be undertaken on shores characterized by a littoral drift regimen. Particular emphasis has been placed on the evaluation of shore changes related to major control structures at navigation entrances, however, manmade interruptions of small scope, which initially appear innocuous, can produce costly damage to the adjacent shores located on the downdrift side of the interruption.

The town of Carolina Beach, a seaside resort on the Atlantic Ocean in southeastern North Carolina, is a classic example of an area experiencing inordinate and costly erosion associated with an initially small manmade interruption on the updrift shore. In 1952, local boating interests excavated a channel through the updrift barrier beach to connect the Atlantic Ocean and a lagoonal area traversed by the Atlantic Intracoastal Waterway. The channel, located 8,000 feet north of the Carolina Beach town limits, soon developed into a small, permanent coastal inlet having a width of approximately 550 feet and a depth of 15 feet. In the ensuing 17-year period, 1952-1969, this inlet entrapped over 4 million cubic yards of littoral material, resulting in a concomitant downdrift erosion which progressed southward to the town of Carolina Beach. A protective beach fill placed along the town's ocean front in 1965 has suffered considerable erosion damage.

This paper develops and quantifies the cause and effect relationships of the problem generally in terms of the alongshore processes and, in so doing, also furnishes basic information in regard to the performance of the large-scale artificial beach fill placed along the ocean front of Carolina Beach in 1965.

INTRODUCTION

In October 1962, Congress authorized the construction of a beach fill, for the purpose of hurricane protection and beach erosion control, to extend from the northern town limits of Carolina Beach, N C, to the southern town limits of Kure Beach, N C, a distance of about 26,000 lineal feet. In April 1965, a portion of the project was completed by the placement of approximately 2,632,000 cubic yards of fill material along the 14,000 lineal feet of shore fronting the town of Carolina Beach (see FIGURE I). The geometric configuration of the fill consisted of a dune having a crest width of 25 feet, at an elevation of 15 feet above mean low water, fronted by a 50-foot-wide storm berm at an elevation of 12 feet above mean low water (see FIGURE II). Along the northernmost 3,700 lineal feet of constructed project, the storm berm was widened to 70 feet to provide an advanced beach-nourishment stockpile. Construction of the authorized project south of the town limits of Carolina Beach was deferred due to the inability of local interests to finance a portion of the non-Federal share of the project costs. Herein, reference to the authorized project applies only to the constructed section, specifically, that portion of the project fronting the town of Carolina Beach,
N C

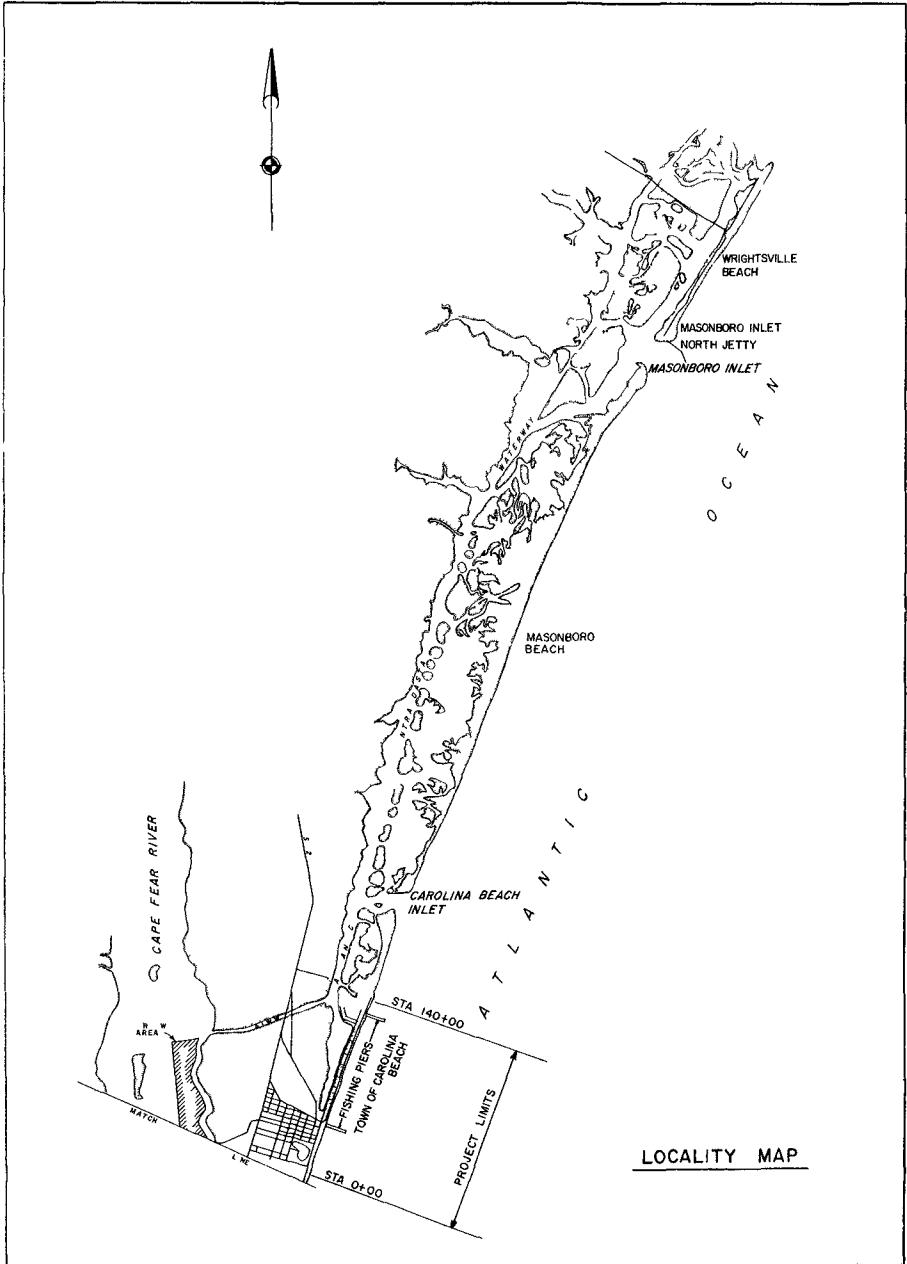


FIGURE I

U. S. ARMY

CORPS OF ENGINEERS

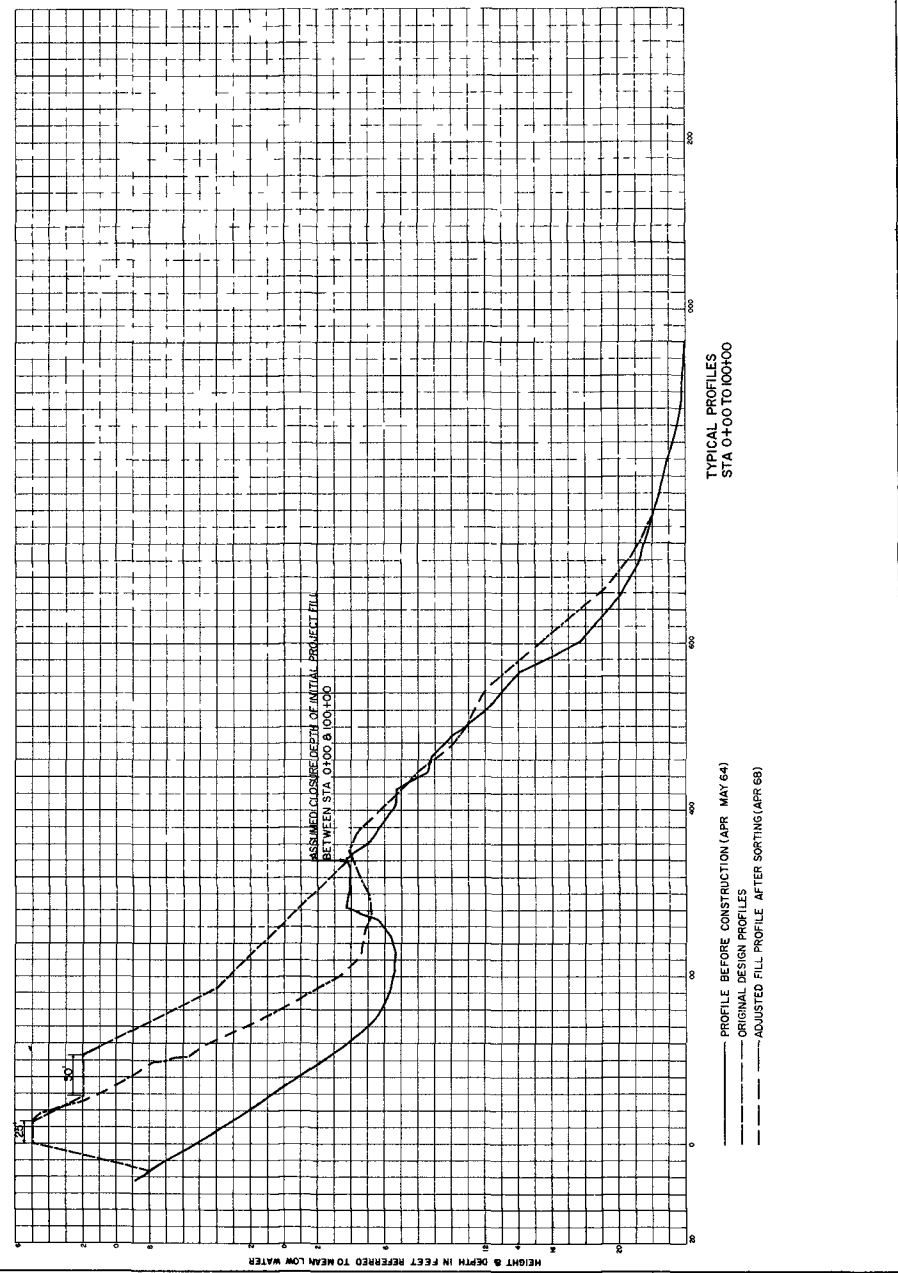


FIGURE II

Immediately following the construction of the Carolina Beach project, rapid erosion was manifest along the entire length of the fill structure. Though initial adjustments were expected, the actual changes, particularly those evidenced along the onshore section of the project, were much greater than anticipated during the planning and design phases of the project. In the first 2 years of project operation, erosion was a persistent phenomenon along the entire length of fill, however, the rate of erosion along the southern 10,000 feet of project was considerably smaller than that experienced along the northern 4,000 feet.

During the initial 2-year period, approximately 712,000 cubic yards of fill were lost from the entire profile, to seaward depths beyond the 22-foot mean-low-water contour, within the southern section of the project. This volumetric loss represents about 43 percent of the total in-place fill initially placed along that section of the project, therefore, in terms of fill, the degree of project protection was reduced by 43 percent. The attendant onshore changes resulted in an 82-foot recession of the high-water line in the initial 2-year period and the destruction of the horizontal storm berm of the design profile. By the end of the second year of operation, the southern 10,000 lineal feet of project stabilized and have remained in more or less the same condition to the present.

In the first 2 years of project operation, erosion along the northernmost 4,000 lineal feet of project was even more extensive than that which had occurred in the 10,000-foot southern section. Within the initial 2-year period, approximately 550,000 cubic yards of fill were lost from the active profile along this section of the project, which amounted to a 56-percent reduction in the total in-place fill. By March 1967, 2 years after initial construction, the high-water line along this section of project receded 140 feet, resulting in the total destruction of 1,500 lineal feet of dune and storm berm and the severe deterioration of an additional 1,200 feet of onshore fill section. This erosion was progressing rapidly in a southward direction and threatening the more stable southern section of the project. Therefore, in March 1967, emergency measures were implemented to alleviate the problem. These emergency measures involved restoration of the north end of the project by the placement of approximately 360,000 cubic yards of beach fill and the construction of a 405-foot-long groin near the north terminal of the project. The groin was considered necessary, as there appeared to be a reversal in the predominant direction of littoral transport at the north end of the project. In the year following the implementation of the emergency measures, approximately 203,000 cubic yards of emergency fill were lost to erosion and the major portion of the shoreline returned to about the same position it had prior to the emergency work. The shoreline immediately south of the groin, for a distance of about 400 feet, has remained relatively stable, and the rate of loss of emergency fill along this small segment of shore was about 42 percent less than that experienced along the remaining emergency section.

ENVIRONMENTAL FACTORS

Beach-profile characteristics Within the area of interest, the qualities of the normal beach profile are characterized by conditions existing along the southern 10,000 lineal feet of project. Along this area, sufficient time has now elapsed for the borrow material, placed in 1965, to be sorted and to establish itself on the profile in more or less a condition of dynamic equilibrium, as discussed below in connection with shore processes. Bottom-material characteristics are defined by the grain-size analysis of surficial sediment samples taken from two representative range lines along the active profile, contained

between the backshore and the 30-foot-depth contour (see TABLE 1) It will be noted that the resulting composite phi mean diameter is 1.69 (0.31 mm) and that the phi standard deviation is 0.91

TABLE 1

Characteristics of material on profile at Carolina Beach (May 1967)

Station	Sample	Phi mean (Mφ)	Phi standard deviation (Sφ)	Phi variance (Sφ ²)	
10+00	Top of berm	1.30	0.51	0.260	
	Mean high water	0.85	0.58	0.336	
	Mean sea level	1.46	0.40	0.160	
	Mean low water	0.76	0.47	0.221	
	-6	2.39	0.48	0.230	
	-12	2.16	0.59	0.348	
	-18	1.87	0.59	0.348	
	-24	No sample	-	-	-
	-30	1.57	0.61	0.372	
70+00	Top of berm	1.03	0.76	0.578	
	Mean high water	1.00	0.54	0.292	
	Mean sea level	1.25	0.39	0.152	
	Mean low water	0.38	0.54	0.292	
	-6	2.49	0.86	0.740	
	-12	2.66	0.45	0.203	
	-18	2.91	0.47	0.221	
	-24	3.13	0.52	0.270	
	-30	1.51	1.13	1.277	

$M\phi = 1.69$

$S^2 = 0.37$

$S\phi_{comp} = 0.91$ (see TABLE 4 for definition of $S\phi_{comp}$)

The associated average profile configuration, in terms of slope, is as follows

Depth range below mean low water	4 feet to 12 feet	12 feet to 18 feet	18 feet to 24 feet	24 feet to 30 feet
	1.22	1.29	1.50	1.167
Average slope				

The natural berm elevation is located at an elevation of about 8 feet above mean low water. The foreshore slope, extending from the berm crest to a depth of about -2 feet mean low water, averages 1 on 8. Between the -2 and -4-foot contours, the profile is characterized by an alongshore trough and submerged bar. Typical profiles are shown on FIGURE II.

Winds On an annual basis, winds blow onshore 38.8 percent of the time and offshore 50.0 percent of the time, with 11.2 percent representing calm conditions. With reference to onshore winds, 50.7 percent occur from the northeast and east. Normal wind speeds range up to 20 knots.

Waves During the fall and winter months, waves approach the area more frequently from the northeast and east, producing north to south littoral currents. During the spring (March, April, and May), a transition period is observed during which waves attack the shore with almost equal frequency from

all directions, resulting in frequent reversals in the direction of littoral transport. During the summer, waves are more likely to come from the south-east and south and produce northward drift. On an annual basis, the predominant direction of wave attack, in terms of energy level, is from the northeast and east, producing a net drift to the south. The most frequent waves affecting the area have heights ranging from 1 to 5 feet and periods of from 5 to 10 seconds.

Littoral currents Littoral current observations have indicated that during northeast and east wave attack, littoral currents north of station 140+00 are less than those south thereof. During southeasterly and southerly attack, currents north of station 140+00 were observed to be stronger than those south of that location.

Tides The normal tidal range in the vicinity of Carolina Beach is about 4.0 feet. The average spring range is 4.7 feet. Storms, particularly hurricanes, can cause considerable variation in these normal tides. For example Hurricane Hazel (15 October 1954) generated a tide of 12.7 feet above mean-low-water datum, which is the highest recorded tide in the study area.

SHORE PROCESSES - CAUSE AND EFFECT RELATIONSHIPS

General Prior to 1952, the shoreline between Masonboro Inlet, located 11 miles north-northeast of Carolina Beach, and New Inlet, located 9 miles south-southeast of Carolina Beach, constituted a continuous physiographic unit. This shoreline reach was characteristic of the general coastline of North Carolina, being comprised of plain, unobstructed sandy beach areas subject to reversals in the direction of littoral transport, but with a predominant southward movement of littoral material. The long-term average annual recession of the waterline was estimated to be of the order of magnitude of 1 foot.

In September 1952, local interests excavated a tidal inlet at a point approximately 7,500 feet north of the town limits of Carolina Beach, thus providing for the immediate area a direct connection between the Atlantic Intra-coastal Waterway (AIWW) and the Atlantic Ocean (see FIGURE I). This inlet, later to be known as Carolina Beach Inlet, rapidly developed as a permanent coastal feature having a low-waterline width of 550 feet and an associated cross-sectional area of 6,500 square feet. The ebb and flood flows are 300×10^6 and 450×10^6 cubic feet, respectively. Immediately following the development of this inlet, severe erosion was evidenced at the south shoulder of the inlet and has, over the 17-year period of the inlet's existence, progressed southward to the extent of seriously affecting the performance of the beach-restoration and hurricane-protection project constructed in 1965 along the 14,000 lineal feet of shoreline fronting the town of Carolina Beach. Though the effect of the inlet on the downdrift shore have been recognized for some time, in a broad qualitative sense, the full assessment of the shore processes involved and the quantification of the phenomena required the detailed synthesis of data accumulated in the 17-year period, 1952-1969 (the bulk of which were obtained between 1965 and 1969), in connection with a survey monitoring program involving the shores of Carolina Beach northward to and including the inlet complex. It has been through the collection of these data, as well as other recent information related to nearby shores, that a rational appraisal of the general problem can be made.

The total length of shoreline germane to this discussion extends 21,100 lineal feet between Carolina Beach Inlet and station 0+00 at the southern

terminal of the Carolina Beach project This reach of shoreline can be divided into three units, each of which has responded to shore processes in a distinctly different manner, though the causative factors are interrelated These units are designated herein as (a) Segment I - the 10 000 lineal feet of shore northward from station 0+00 at the south end of the Carolina Beach project to project station 100+00, (b) Segment II - the 4,000 lineal feet of shore extending northward from project station 100+00 to station 140+00 at the north end of the Carolina Beach project, and (c) Segment III - the 7,100 lineal feet of undeveloped shoreline between the Carolina Beach town limits and Carolina Beach Inlet

Segment I Survey records for the 19-year period, 1938 to 1957, reported in the original Carolina Beach project report show that the average annual recession rate was approximately 1 foot per year with a short-term maximum rate of 2 8 feet being observed in the period 1952-1957, during which the area had been exposed to four major hurricanes The volumetric loss of material for the entire active beach profile was estimated to be approximately 4 cubic yards per lineal foot of beach annually

Following the placement of artificial fill along Segment I, in connection with the construction of the Carolina Beach project, the effects of shore processes in this area were radically different during the first 2 years of project operation than those determined from historical records During these first and second years of project operation, April 1965-April 1966 and April 1966-April 1967, the shoreline receded at an average annual rate of 67 feet and 15 feet, respectively, with corresponding volumetric losses of fill material amounting to 370,000 cubic yards and 342,000 cubic yards In the third year of operation, April 1967-April 1968, a marked change occurred in the response of the artificial fill to shore processes, as the rate of shoreline recession decelerated to 5 feet per year and the volumetric change of material amounted to a slight accretion of about 17,000 cubic yards Shoreline movements and volumetric changes following project construction are given in FIGURE III and TABLE 2, respectively Surveys in 1969 indicate that the project is in essentially the same condition as observed in 1968 Full verification of the present project condition will depend on the results of surveys conducted in the summer of 1969 and winter period of 1970 However, on the basis of existing information, it can be assumed that the section of the Carolina Beach project within Segment I of the study area required 2 years of exposure to reach a state of dynamic equilibrium with the prevailing environment

The rapid recessions of the waterline in Segment I during the first 2 years of project operation were a result of profile adjustment along the active profile which terminates at depths between -22 and -30 feet mean low water, as well as net losses in material volume resulting from natural sorting action displacing fine material, which was incompatible with energy levels on the active profile, to depths seaward of the active profile Reference is made to FIGURE II, which shows the typical beach profile in Segment I prior to construction of the Carolina Beach project and the original design project profile It will be noted that the foreshore and offshore design profile slope of 1 on 20 terminates at a depth of 4 feet below mean low water and deviates from the natural profile by the exclusion of the offshore bar and trough situated at a depth of 4 to 6 feet below mean low water The adjusted project profile of April 1968 also given on FIGURE II, shows the actual profile closing at a depth of about 22 feet below mean low water, as well as the characteristic bar and trough Thus, displacement of the initial fill with the concomitant reduction of the onshore design section, was an inevitable eventuality of normal sorting action and the reestablishment of the normal profile configuration Note that the actual profiles shown on FIGURE II are for the month of April, during which average annual profile conditions obtain in the vicinity of Carolina Beach

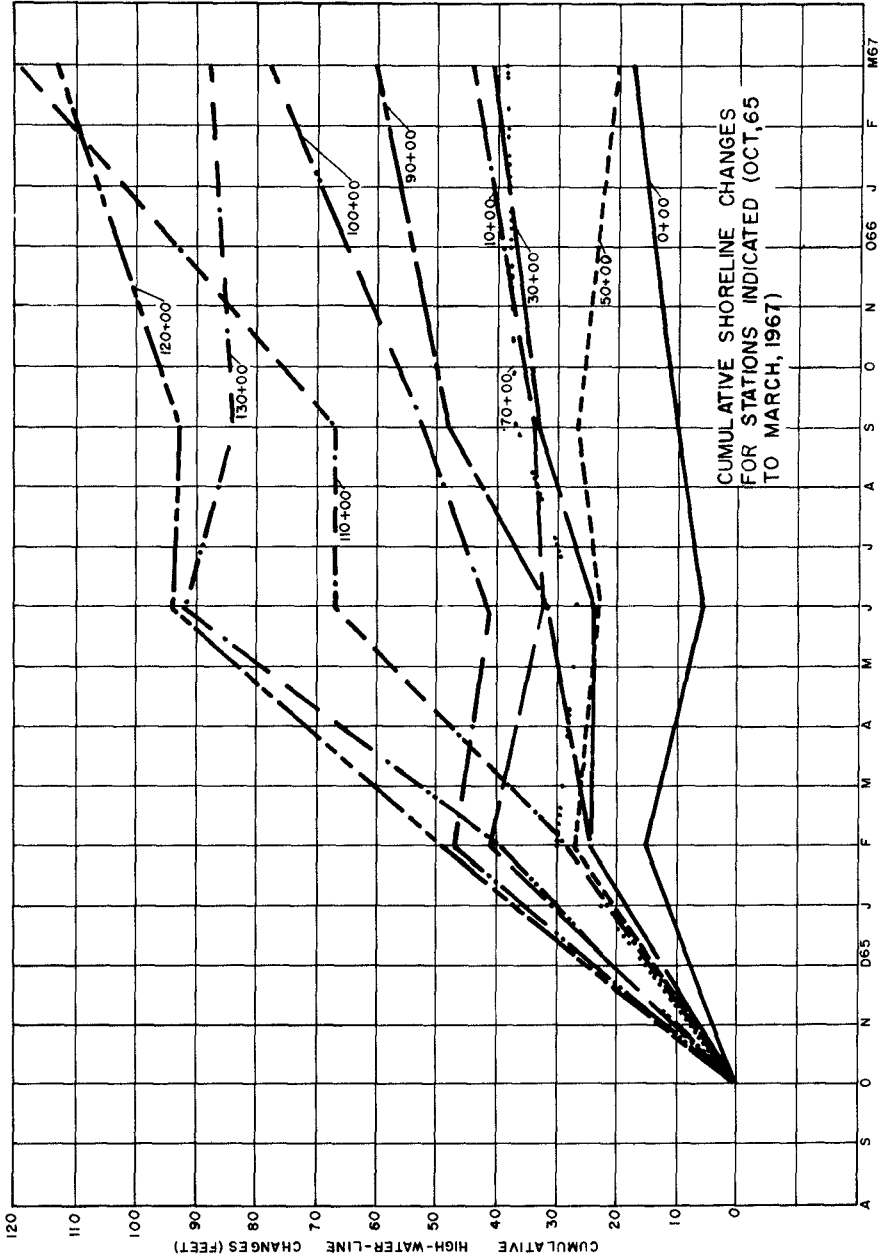


FIGURE III.

TABLE 2

Total volumetric change since construction of the project
(SEGMENT I - station 0+00 to station 100+00)

Period	Volumetric change during period (cubic yards)	Cumulative volumetric change by end of period (cubic yards)
As built to June 1966	-435,300	-435,300
June 1966 to September 1966	-143,800	-579,100
September 1966 to December 1966	-7,100	-586,200
December 1966 to May 1967	-172,000	-758,200
May 1967 to June 1967	+257,800	-500,400
June 1967 to October 1967	-29,000	-529,400
October 1967 to February 1968	-326,400	-855,800
February 1968 to April 1968	+156,700	-699,100
April 1968 to August 1968	+75,400	-623,700

NOTE + = accretion, - = erosion

Two computations were made in an attempt to determine the degree to which sorting of the original borrow material affected the rate of erosion of the project fill. The first computation consisted of a mathematical comparison of the size characteristics of the original borrow material to the size characteristics of the material composing the beach profile. The results of this computation indicated that for every cubic yard of borrow material remaining on the profile, 2.1 cubic yards of this material had to be sorted. The ratio of the total material sorted to the amount remaining on the profile after sorting action has occurred, as defined by W. C. Krumbein and W. R. James¹, is referred to as the "critical ratio" ($R_{\phi crit}$), where

$$R_{\phi crit} = \left[\frac{S_{\phi b}}{S_{\phi n}} \right] \left[e^{-\frac{(M_{\phi n} - M_{\phi b})^2}{2(S_{\phi n}^2 - S_{\phi b}^2)}} \right]$$

in which

$S_{\phi b}$ = standard deviation of borrow material, in phi units (1.28 in this case, see TABLE 3)

$S_{\phi n}$ = standard deviation of native material, in phi units (0.91 in this case, see TABLE 1)

$M_{\phi b}$ = phi mean of borrow material (0.88 in this case, see TABLE 3)

$M_{\phi n}$ = phi mean of native material (1.69 in this case, see TABLE 1)

¹See U. S. Army Coastal Engineering Research Center Technical Memorandum No. 16, "A Lognormal Size Distribution Model for Estimating Stability of Beach Fill Material."

TABLE 3

Characteristics of original fill material
placed between stations 0+00 and 100+00 - Segment I

Range	Sample elevation (m l w)	Phi mean (M ϕ)	Phi standard deviation (S ϕ)	Phi variance (S ϕ^2)
10+00	11	0 52	1 27	1 61
	9	0 02	1 82	3 31
	7	0 62	1 43	2 04
	5	0 70	1 38	1 90
	3	1 30	1 25	1 56
20+00	11	0 70	1 20	1 44
	9	0 45	1 27	1 61
	7	0 70	1 20	1 44
	5	1 27	0 84	0 71
	3	1 50	0 80	0 64
30+00	11	0 99	1 14	1 30
	9	0 77	1 07	1 14
	7	0 33	1 54	2 37
	5	0 84	1 24	1 54
	3	1 70	1 10	1 21
40+00	11	1 67	0 72	0 52
	9	1 31	0 78	0 61
	5	0 68	1 18	1 39
	3	1 00	1 19	1 42
50+00	11	0 53	1 33	1 77
	9	0 56	1 22	1 49
	7	1 33	1 13	1 28
	5	0 78	1 20	1 44
	3	1 74	0 75	0 56
60+00	11	1 21	1 01	1 02
	9	0 66	1 86	3 46
	7	0 28	1 64	2 69
	5	0 39	1 41	1 99
	3	1 01	1 41	1 99
70+00	11	1 20	1 40	1 96
	9	0 85	1 37	1 88
	7	0 37	1 13	1 28
	3	1 10	1 10	1 21
80+00	9	0 68	1 51	2 28
	7	0 77	1 31	1 72
	5	1 20	0 85	0 72
	3	1 05	0 97	0 94
90+00	11	0 73	1 44	2 07
	9	0 70	1 50	2 25
	7	0 94	1 00	1 00
	5	1 04	1 06	1 12
Average		M ϕ = 0 88		S ² = 1 56

The composite phi variance (S ϕ^2 comp) and standard deviation (S ϕ comp) are computed by

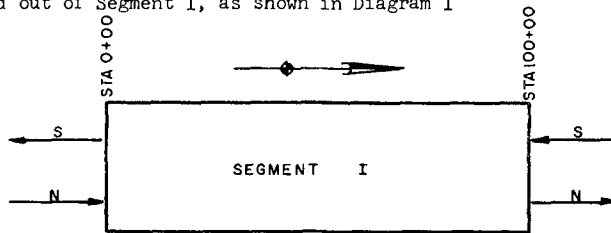
$$S\phi^2\text{comp} = S^2 + \frac{(B-A)^2}{12} = 1 56 + \frac{(0 92)^2}{12} = 1 63$$

$$S_{\phi comp} = 1.28$$

Where A is the average of the minimum phi-mean values obtained along the various ranges The value B is the average of the maximum phi-mean values

The second computation consisted of a determination of the ratio of borrow material placed within Segment I, which was subjected to sorting action, to the amount of that material which remained on the profile at the end of approximately 2 years of project operation. The ratio thus determined was 2.3, which compares extremely favorably with the computed "critical ratio". Since the two independent checks of this ratio resulted in essentially the same value, the implication is that most of the material lost from the project in Segment I was the result of sorting action displacing fine-grain material to depths seaward of the active profile. It is remarked that the entire artificial fill was not exposed to hydraulic action during the 4 years of project operation and this fact was accounted for in the sorting computations. Had the artificial fill been exposed to a storm of hurricane intensity with the attendant severe churning of the beach profile cover, larger quantities of fill would have been exposed to sorting action and the net losses of material would have, doubtless, been greater. It is worthy of mention that the analytical procedure used in arriving at the value of the "critical ratio" was not developed during the design phase of the Carolina Beach project. Had this procedure been available, the material losses experienced by the project in Segment I could have been predicted with a remarkably high degree of accuracy.

Insofar as the present conditions are concerned, the relative stability of the project in Segment I is apparently due to the balance of alongshore transport into and out of Segment I, as shown in Diagram 1.



WHERE S = TOTAL SOUTHBOUND LITTORAL DRIFT
N = TOTAL NORTHBOUND LITTORAL DRIFT

PRESENT ALONGSHORE PROCESSES IN SEGMENT I
DIAGRAM 1

Segment II and Segment III Prior to the opening of Carolina Beach Inlet in 1952, the shorelines of Segments II and III were continuous with, and on the same alignment as, Segment I. Therefore, the behavior of the entire shore area was more or less uniform. However, immediately following the opening of the inlet, dramatic changes began occurring in Segment III and, with time, progressed southward into Segment II. In the period 1952-1963, prior to the construction of the Carolina Beach project, the high-water line receded 1,135 feet at the shoulder of Carolina Beach Inlet, the north end of Segment III, and 37 feet at station 100+00, the south end of Segment II. The difference in the extent of recession near the inlet and at station 100+00 resulted in a change of alignment of the combined shoreline of Segments II and III with respect to Segment I. This change of alignment, which was later to have a prominent role

in the behaviour of the artificial fill in Segment II, was a natural development resulting from a deficit of littoral drift from the north, caused by material entrapment in the inlet shoal system. By way of a brief qualitative analysis of this phenomenon, the following explanation is given. The alongshore movement of littoral material results from the existence of an alongshore current generated by the obliquity of the wave crests attacking the shore, in other words, it can be assumed that, if the breaking-wave crests are parallel to the shore, little or no alongshore current exists and, consequently, there is no alongshore movement of beach material. When there is a substantial reduction in the quantity of littoral material to a segment of shore, that shore will erode to the extent of reaching some new state of equilibrium with the eroding forces. This was accomplished in Segment III, and to a smaller degree in Segment II, by the shore retrograding to an alignment approaching parallelism with the general approach of wave crests from the northeast sector of attack. As any given section of shore attains near parallelism with the attacking wave crests, it ceases to supply large quantities of material to the adjacent down-drift section, resulting in a downdrift progression of the erosion, as shown in Diagram 2.

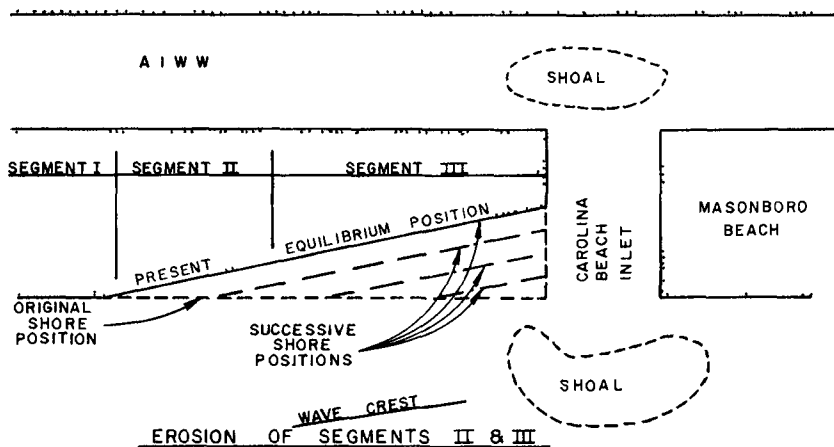


DIAGRAM 2

Of course, wave attack along the area of interest is neither uniform nor unidirectional and, moreover, there is some natural bypassing of material across Carolina Beach Inlet. However, the generalization outlined above is not only rational, in a theoretical sense, but validated by the time - space relationships of the erosion in Segments II and III, presented in TABLE 4. PHOTOGRAPH 1 clearly shows the change of shore alignment.

Immediately following the placement of artificial fill along Segment II in March 1965, severe erosion began and continued at an intense rate to March 1967. The cumulative shore recession in the 2-year period, March 1965-March 1967, amounted to 140 feet, with an attendant loss of 550,000 cubic yards of material, or an average annual loss in the 2-year period of 275,000 cubic yards. As a result of this severe erosion, emergency measures were implemented for Segment II in March 1967 by the construction of a groin at station 136+75 and the addition of 321,000 cubic yards of fill, of which 284,000 cubic yards were placed south of the groin and approximately 37,000 cubic yards were placed north of the groin. The emergency work was completed in May 1967. By May 1968,



PHOTOGRAPH 1 - VIEW NORTHWARD OVER CAROLINA BEACH PROJECT IN 1965. NOTE CHANGE OF SHORE ALIGNMENT CENTER BACKGROUND OF PHOTOGRAPH.



PHOTOGRAPH 2 - VIEW OF CAROLINA BEACH INLET IN 1969. NOTE OFFSET BETWEEN INLET SHOULDERS, AND WAVE REFRACTION PATTERN.

1 year after the placement of emergency fill, the net loss of this material amounted to 203,000 cubic yards, of which 175,600 were lost between stations 100+00 and 132+50. It is noted that, notwithstanding the groin, losses of emergency beach material in Segment II were extremely high, particularly in view of the fact that conditions observed in Segment I showed that the general area was experiencing some natural accretion in 1968. The rates of shoreline movements in Segment II, shown in comparison with shore-movement rates in Segment I, are presented on FIGURE III. Volumetric changes in Segment II are given in TABLE 5.

TABLE 4

Rate of shoreline movement at specified stations within Segment II and Segment III (1952-1963) (rate in feet per year)

Segment and station	Time period			
	1952-55	1955-57	1957-63	1952-63
<u>SEGMENT II</u>				
100+00	+3 0	-7 0	-5 3	-3 3
110+00	-3 7	-3 5	-7 8	-5 8
120+00	-9 7	-5 5	-9 0	-8 5
130+00	-12 0	-6 0	-13 0	-10 5
140+00	-14 0	-19 0	-43 0	-26 7
<u>SEGMENT III</u>				
150+00	-13 6	-25 0	-57 0	-39 4
160+00	-10 3	-60 0	-68 7	-51 0
170+00	-10 0	-107 0	-76 5	-63 9
180+00	-8 3	-139 0	-91 2	-77 2
190+00	-6 7	-156 0	-80 3	-74 0
200+00	-53 3	-100 0	-129 1	-103 2

NOTE + = accretion, - = erosion

TABLE 5

Total volumetric change since construction of the project (SEGMENT II - station 100+00 to station 140+00)

Period	Volumetric change during period (cubic yards)	Cumulative volumetric change by end of period (cubic yards)
As built to June 1966	-412,200	-412,200
June 1966 to September 1966	-64,300	-476,500
September 1966 to December 1966	-58,300	-534,800
December 1966 to March 1967	-15,200	-550,000
March 1967 to May 1967	¹ +284,000	(Fill)
May 1967 to June 1967	-54,400	-604,400
June 1967 to October 1967	-60,100	-664,500
October 1967 to February 1968	-158,000	-822,500
February 1968 to April 1968	+67,100	-755,400
April 1968 to August 1968	-9,300	-746,100

¹Not included in cumulative total

NOTE + = accretion, - = erosion

The quality of fill material placed in Segment II with the initial construction of the Carolina Beach project and later as part of the emergency measures was compared with the quality of borrow material used in Segment I, and it was found that all of the material was essentially of the same quality. Therefore, it can be assumed that the "critical ratio" for all the material placed in Segment II was of the order of magnitude of 2. Considering that the total loss of material in Segment II during the 3-year period, May 1965-May 1968, amounted to 753,000 cubic yards, the average annual loss of material from this area can be taken as 251,000 cubic yards. Of the total annual loss, a portion is allocated to sorting-action displacement to depths seaward of the active profile and the remaining portion is allocated to a deficit in the alongshore transport into Segment II. This deficit in alongshore transport, which in fact is the deficit in material transport imposed by Carolina Beach Inlet, is easily computed by applying the "critical ratio" to the total average annual loss of material experienced in Segment II, that is

$$\begin{aligned} \text{Alongshore deficit} \\ \text{in material transport} &= \frac{251,000}{2} = 125,500 \text{ cubic yards} \\ \text{(littoral drift)} & \end{aligned}$$

(say 130,000 cubic yards)

The shore processes in terms of annual alongshore movements in Segment II are represented schematically in Diagram 3. It is evident from Diagram 3 that the total annual alongshore transport phenomenon cannot be described without the development of two other conditions through which the values of B and N can be computed. Such conditions can be developed, as demonstrated below, by making certain assumptions, one of which is that all observed annual values of littoral transport represent average annual values over a relatively long period, specifically, the 17-year period, 1952-1969, in which Carolina Beach Inlet has been in existence.



- S = TOTAL SOUTHBOUND DRIFT OUT OF SEGMENT II**
- N = TOTAL NORTHBOUND DRIFT INTO AND OUT OF SEGMENT II**
- B = MATERIAL BYPASSING INLET AND TRANSPORTED ALONG SEGMENT III TO SEGMENT II**

ALONGSHORE MOVEMENTS IN SEGMENT II
DIAGRAM 3

In order to obtain a relatively accurate value of B, it is necessary to have a measured value of S, the total southbound drift. Such a value is available for the period June 1966-June 1967 for the shore of Wrightsville Beach, located 9 miles north of Carolina Beach (see FIGURE 1). It is remarked that Wrightsville and Carolina Beaches are exposed to the same wave climate and are composed of essentially the same material. In June 1966, a 3,600-foot-long weir-type jetty was constructed on the south end of Wrightsville Beach, at Masonboro Inlet. During the period June 1966-June 1967, approximately 150,000 cubic yards of littoral material were transported by natural forces across the weir section of the jetty and deposited in the lee-side deposition basin. In addition, an estimated 70,000 cubic yards of material accumulated on the updrift side of the jetty in the form of an accretion fillet. Therefore, the total southbound drift, S, was approximately 220,000 cubic yards, presuming that the accretion fillet, being small during the first year of jetty operation and in the shadow zone of the jetty, was not exposed to attack by waves from the southeast sector. Referring to Diagram 3, $B = 220,000$ cubic yards minus 130,000 cubic yards, or $B = 90,000$ cubic yards.

At this point, only the value of the northbound drift, N, remains to be computed. For the determination of this value, conditions at Carolina Beach Inlet are used to develop a continuity relationship for the total alongshore movement of material. Here, the assumption is made that, contrary to the natural southward bypassing of 90,000 cubic yards of material at Carolina Beach Inlet, there has been no significant northward bypassing at the inlet. The rationale on which this assumption is based is as follows. First, bypassing of material at an inlet is highly dependent on storm activity, as wave crests, encroaching on the sea shoal during normal sea conditions, are refracted to such an extent that they split and approach the inlet throat from both the updrift and downdrift directions, making bypassing difficult. This phenomenon is easily observed in the field or from aerial photographs and, in fact, is the reason for the multiple, confused chop existing on shoals. Moreover, the refraction phenomenon can, as at Carolina Beach Inlet, create permanent, but shifting, nodal zones on the shores near and adjacent to the inlet. However, during storm activity with attendant storm tides, high-energy levels, and short-period waves which are not too susceptible to refraction, natural bypassing can be accomplished. Therefore, since most storm activity to which Carolina Beach Inlet is subjected comes from the northeast sector of exposure, it can be assumed that the largest proportion of natural bypassing is in a southward direction. The second reason that bypassing in a northward direction is assumed small relative to southward bypassing is that the ocean shoreline on the north shoulder of the inlet is offset seaward from the shoreline on the south side by a distance of approximately 1,500 feet (see PHOTOGRAPH 2). This offset doubtless restrains the northward movement of material across the inlet. The phenomenon discussed above, insofar as normal sea conditions are concerned, is schematized in Diagram 4. Note that there would be no change in the general refraction pattern for normal conditions if the deepwater wave crest approached from the northeast quadrant under normal sea conditions. The actual refraction phenomenon is readily discernible in PHOTOGRAPH 2.

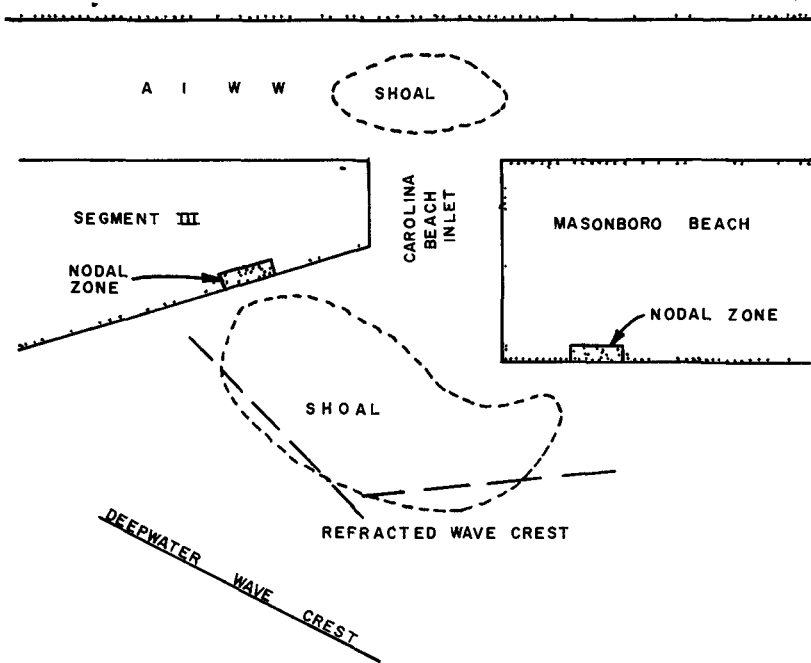


DIAGRAM 4

With acceptance of the assumption that northward bypassing at the inlet is insignificant, the value of the total northbound drift, N , can be computed by determining the total volume of material accumulated in the inlet complex during its 17 years (1952-1969) of existence. The total accumulation was determined from hydrographic surveys, dredging records in the AIWW, at the inlet throat, and from aerial photographs. This accumulation amounted to 4,160,000 cubic yards, of which 3,250,000 cubic yards were stored on the sea shoal, 680,000 cubic yards were deposited and removed from the AIWW, at the throat of the inlet, and 230,000 cubic yards were flushed into the marshes of Masonboro Beach at a point approximately 2,000 feet north of Carolina Beach Inlet as a result of a breakthrough which occurred during Hurricane Hazel in 1954. This breakthrough remained open as a small inlet for approximately 4 years, and was closed by natural forces. With a total storage of 4,160,000 cubic yards in a 17-year period, the average annual accumulation rate is 245,000 cubic yards. The value of N is determined from the continuity relationship

$$N + S - B = \text{Accumulation in the inlet}$$

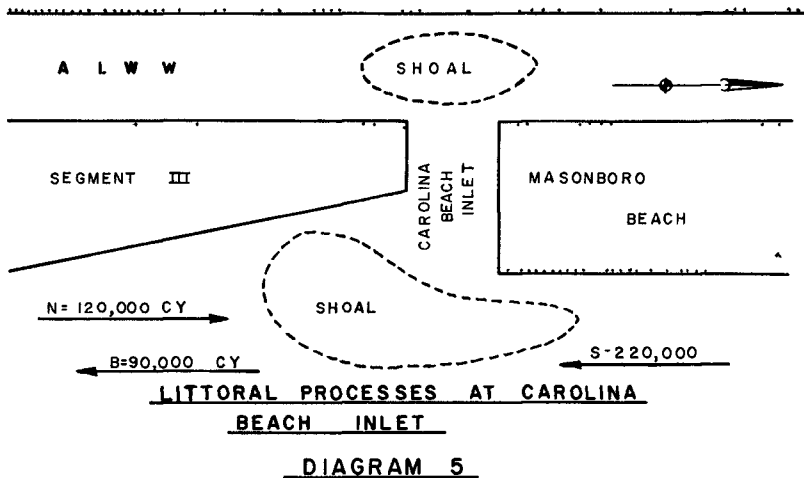
or

$$N + 220,000 - 90,000 = 245,000$$

$$N = 115,000 \text{ cubic yards}$$

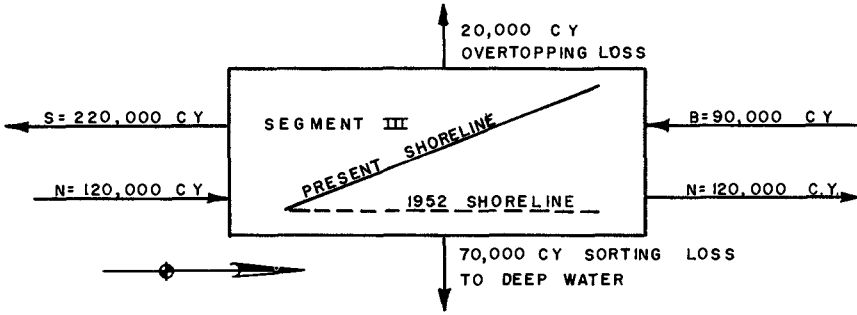
(say $N = 120,000$ cubic yards)

A schematic flow diagram of the computed average annual littoral process at the inlet is given in Diagram 5



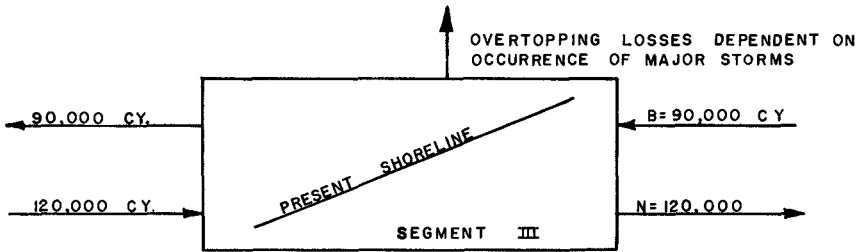
To formulate a complete shore-processes scenario for the Carolina Beach area, conditions along Segment III of the study area were also investigated. Surveys indicate that the total quantity of material eroded from Segment III during the 17-year period, 1952-1969, amounted to approximately 3,670,000 cubic yards, which results in an average annual loss of about 220,000 cubic yards, however, it was shown previously that the average annual deficit of material imposed by the inlet amounted to only 130,000 cubic yards. Thus, the remaining 90,000 cubic yards must be accounted for. These losses can, with reasonable assurance, be attributed to material lost from the beach profile through wave and/or tidal overtopping of Segment III and the quantity of material displaced seaward of the active beach profile as a result of sorting action. In connection with wave and tidal overtopping, Segment III is a low barrier ridge with a general maximum elevation between 4 and 5 feet above mean sea level. Therefore, wave and/or tidal overtopping is a frequent occurrence in this area during any given year, however, major overtopping losses are associated with hurricane events. From aerial photographs and existing topography, it was determined that the landward side of Segment III accreted westward into the adjacent marsh at a rate of approximately 20,000 cubic yards per year. Thus, there remains a value of 70,000 cubic yards lost through sorting action. In view of the severe erosion of the landmass in Segment III, it can be assumed that sorting losses were substantial. The assumed sorting action loss of 70,000 cubic yards results in a "critical ratio" of $\sqrt[2]{\frac{220,000}{220,000 - 70,000}} = 1.47$, which is not at all an unreasonable value. It is also noted that the quantity of material attributed to sorting losses beyond the active profile represents approximately 32 percent of the total loss. This corresponds closely to the "rule-of-thumb" value of 30 percent used, in the vicinity of Segment III, in determining the quantities of fine silt, peat, and clay lost in the placement of dredged fill. It is remarked that exposed peat laminae are found along much of the Segment III shoreline. The shore-processes scheme for Segment III is illustrated schematically in Diagram 6. It should be noted that the shore processes described above for Segment III relate to average conditions prevailing over the 17-year period that this section of shore was adjusting to a new

equilibrium condition as a result of changes produced in the littoral regime by Carolina Beach Inlet. As mentioned above, Segment III has generally attained a state of equilibrium through erosion and a reorientation of the shoreline. At present, the major effects of the littoral material deficit imposed by the inlet have been transferred to Segment II.



AVERAGE ANNUAL PROCESSES 1952 TO 1969

DIAGRAM 6(a)



PRESENT CONDITIONS

DIAGRAM 6(b)

Verification of computed values A condition used to verify the computed values, specifically N and S, is taken at Masonboro Inlet, which is exposed to the same gross littoral drift as Carolina Beach Inlet. In the 4-year interval, 1965-1969, two hydrographic surveys show that approximately 900,000 cubic yards of material have been deposited on the outer and inner shoals of Masonboro Inlet. In addition, approximately 170,000 cubic yards were removed from the inlet by hopper dredges in the period 1965-1969. Therefore, the total accumulation within the inlet during a 4-year period amounted to approximately 1,070,000 cubic yards, resulting from the intrusion of southbound and northbound drift. On an average annual basis, the deposition rate is about 270,000 cubic yards. Furthermore, the growth of the accretion fillet along Wrightsville Beach, updrift of the Masonboro Inlet Jetty, has an accretion rate of about 60,000 cubic yards per year for the 2-year period 1966 to 1968. Construction of the jetty began August 1965 and was completed June 1966. If it is assumed that the average of the 2-year fillet growth rate is representative of an average annual growth rate for the 4-year period of 1965-1969, the gross drift toward the inlet would be 270,000 cubic yards + 60,000 cubic yards = 330,000 cubic yards, which compares extremely well with the value $N + S = 340,000$ cubic yards. Note that natural inlet bypassing was not considered, as the inlet shoals are well shadowed by the jetty, also, the 1965-1969 period was free of major storm activity.

Conclusion The analysis presented above results in a rational understanding of shore processes in the study area from 1952 to the present. It is remarked that the quantitative values determined in the analysis represent only the average annual conditions for the data period of record used, and, moreover, insofar as shore processes are extremely nonuniform, wide variations from average annual values can occur in any given short-term period.

In closing, it is remarked that detailed plans for solving the erosion problem described herein have been formulated and are presently under review.

CHAPTER 78

RIO GRANDE BAR - THE CASE HISTORY OF A LAGOON OUTLET INTO A TIDELESS SEA

V. F. Motta

Head of the Coastal Division.
Hydraulics Research Institute
of the Federal University of
Rio Grande do Sul (Porto Ale-
gre, Brazil).

A b s t r a c t

Rio Grande harbour is situated inside the outlet of Lagoa dos Patos (9 910 km²) and Lagoa Mirim (3 770 km²). Most of the rivers in the State of Rio Grande do Sul, that are not tributaries of river Uruguay, flow into the two lagoons and the latter discharge through Canal do Norte into a tideless sea. Flood flows can exceed 20 000 cumecs. The outlet is on a sandy coast with littoral drift in both shoreline directions.

The time history of the outlet can be divided into three periods. Before breakwater construction, the bar was extremely unstable in lay-out, position and controlling depth. The latter ranged from 2.5 to 7 m. From 1911 to 1916 two 4 km long rubble mound breakwaters were built. They deepened the entrance channel to 8 - 10 m but a new bar came about further offshore entailing objectionable navigation conditions in the approach channel. No previous dredging was carried out as the breakwater construction proceeded out to sea, and as result a total of 14 million cubic metres was scoured out between the two breakwaters and discharged offshore to build up the new bar. Some improvement by dredging was not achieved until 1962.

The improvement of the approach channel lay-out as well as deepening the entrance to 14 m below datum are under consideration. Field and model investigations have been designed for this purpose.

I) The Coastal Environment and Hydraulic Conditions, Rio Grande harbour is situated inside the outlet of Patos Lagoon (9 910 km²) and Mirim Lagoon (3 770 km²). The key map of Fig.1 shows the area discussed in this paper. It lies near the southern border of Brazil, Rio Grande being the main port in the State of Rio Grande do Sul.

72-93

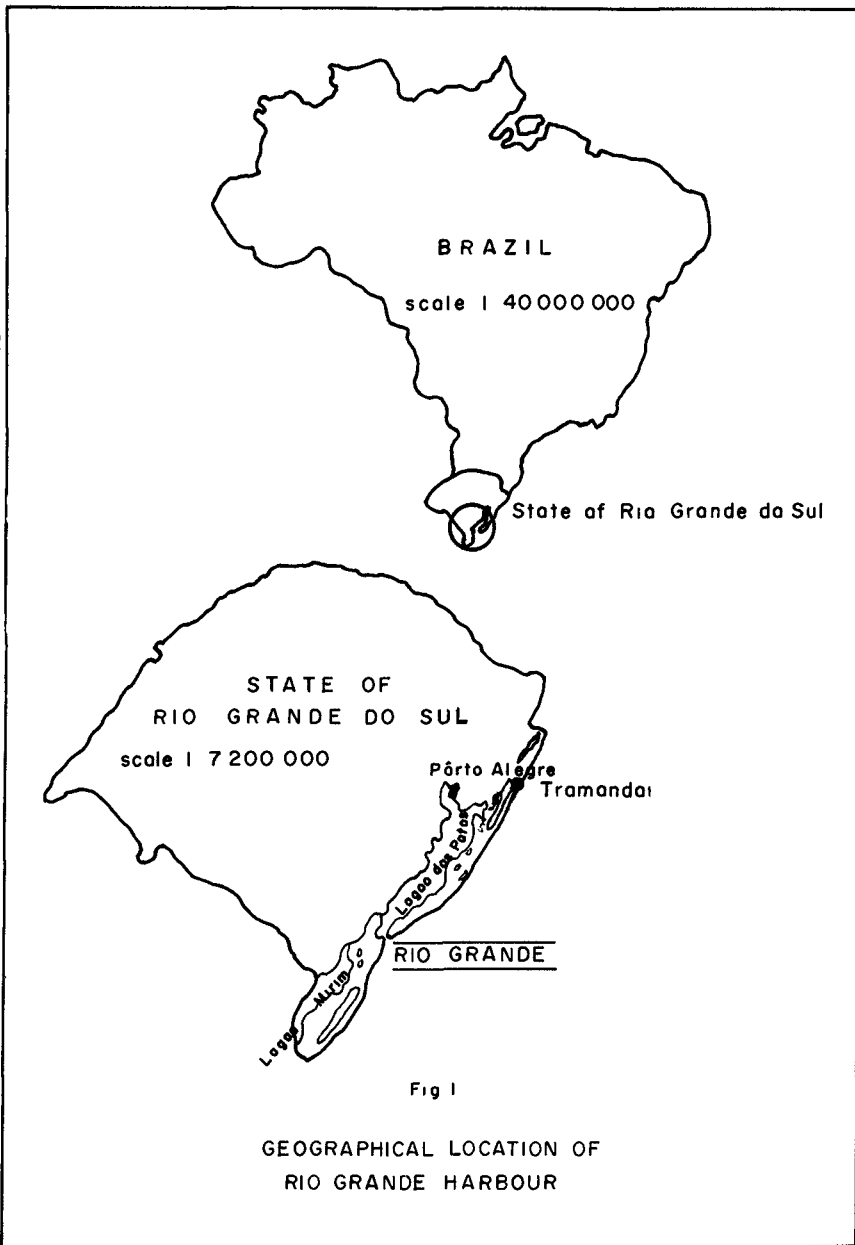


Fig 1

GEOGRAPHICAL LOCATION OF
RIO GRANDE HARBOUR

The coast of this State is a long barrier beach dividing several lagoons from the sea. Patos and Mirim lagoons are the two most important bodies of water. They are connected by a 70 km long channel, Canal São Gonçalo, and they discharge into the sea through a common outlet (Canal do Norte) on whose western bank the port of Rio Grande has been built. Most of the rivers in the State of Rio Grande do Sul, that are not tributaries of River Uruguay, flow into these two lagoons. As a result, the upland flow in Canal do Norte drains a basin with an area of 162 000 km², and peak flows can exceed 20 000 cumecs. Canal do Norte is quite stable in position, width, depth and length. Its width varies from 1.5 km at the mouth to about 3 km at the northern end, a major portion of its shipping channel being over 15 m deep.

The lagoon outlet lies on a sandy coast with littoral drift in both shoreward directions. The coast is fairly straight, flat, and uniform in profile, the offshore slope from the -1 to the -15 m contour being about 1%. The beach material is fine sand, a representative mean diameter being about 0.20 mm. The shoreline runs on a SW to NE alignment but the axis of Canal do Norte nearly coincides with a meridian, which accounts for its name the Portuguese for Northerly Channel.

According to [1] the main characteristics of the deep-water wave climate are the same from Punta del Este (in Uruguay) to Tramandai, some 320 km north of Rio Grande, where wave characteristics were recorded at a 20 m depth for more than a year, in 1962-63, in connection with the design of an offshore oil terminal. The main characteristic of this wave climate is that swell comes mostly from SE whereas the dominant and prevailing winds blow from NE. As a result, there is a marked correlation between wave periods and directions as shown in Fig. 2. The waves with the greatest energy (Fig. 3) and least steepness - therefore with the greatest transport capacity - come from SE which causes the northward littoral drift to be dominant over the southward drift. The latter is induced by the waves, mostly locally generated sea, from the NE quadrant.

The only indication available as to the intensities of this two-way littoral drift is that the average dominant littoral drift would be 1.5 times as great as the secondary drift. The average total annual volume of the dominant littoral drift would amount to some 100 000 m³ per year. These figures were arrived at from the results of a mobile-bed model investigation into the control of Tramandai inlet which was carried out in 1964 at the Hydraulics Research Institute of the Federal University of Rio Grande do Sul [2]. A time scale for bed movement was worked out by comparing model and prototype durations of the northward inlet migration when Tramandai inlet was uncontrolled, and the transport capacity of the waves reproduced in the model was measured by trapping sand at the down-drift end of the model. The total volume of littoral drift in a model year was then scaled up. The amount of 100 000 m³/year for the dominant drift seems rather lower than values reported for similar conditions in other parts of the world and may be due to the model improperly simulating suspended transport in the surf zone. On the other hand, it should be noted that the angle of attack of the dominant waves is usually small about 10° at a 20 m depth. Whatever the accuracy

72-43

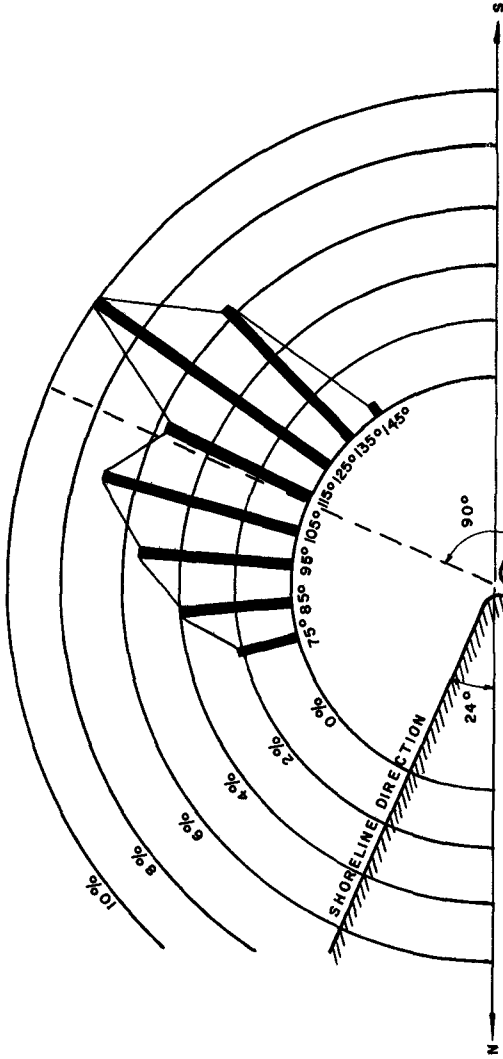


Fig 2
CORRELATION BETWEEN ANGLES
OF ATTACK (AT THE 20m DEPTH) AND
SIGNIFICANT PERIODS EQUAL TO OR
GREATER THAN 10% OFF TRAMANDA

72-43

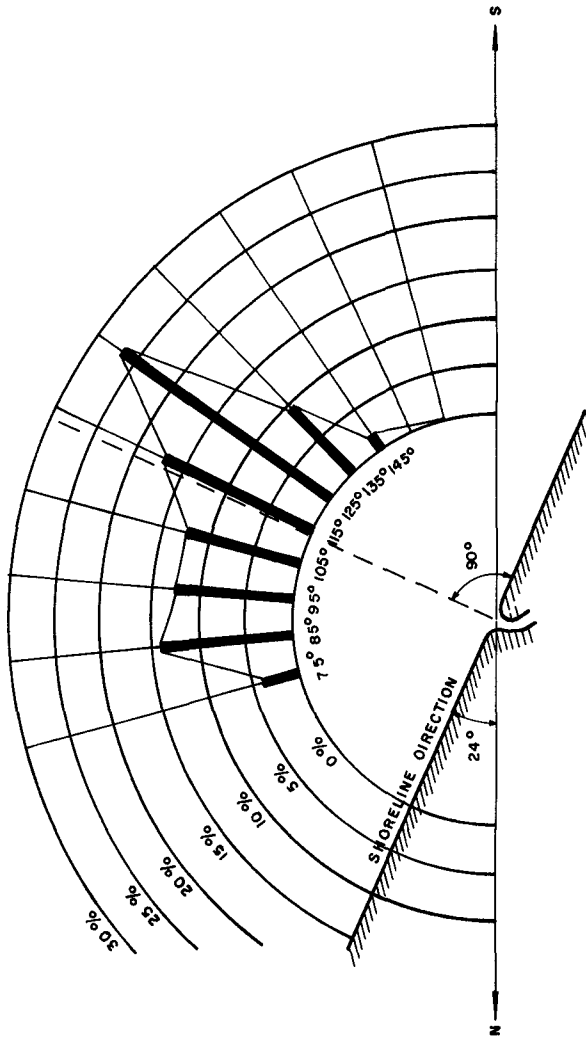


Fig. 3

CORRELATION BETWEEN ANGLES OF ATTACK (AT THE 20m DEPTH) AND WAVE ENERGY ($\Sigma H^2 T_e$) OFF TRAMANDAI

of the above estimate for littoral drift on the coast of Rio Grande do Sul may be, what is actually known is that the most frequent significant wave height is 1.5 m at the 20 m depth, and the most frequent significant wave period is 9 s. Wave heights of 4 m at the 20 m depth occur at least once in a year.

The most striking feature of Rio Grande harbour entrance is that fresh-water flow largely dominates over tidal flow in determining its hydraulic and morphological characteristics. This is the reason why the present paper refers to Canal do Norte as a "lagoon outlet" instead of adapting the usual expression "coastal inlet". While six sizable rivers flow into Patos Lagoon and five into Mirim Lagoon the sea off the harbour entrance is practically tideless. The area of Patos Lagoon alone is about three times as large as that of the IJsselmeer, the dammed Zuiderzee, in the Netherlands. On the other hand, the mean monthly tidal range is usually below half a metre. The overall result is that waterlevels as well as velocities, directions and durations of flow through Canal do Norte are mainly determined by a complex interaction between wind effects at sea and in the lagoon system, and fresh-water flow in the latter. Instead of periodical reversals of ebb and flood in Canal do Norte, the flow may be out to sea for several days on end in the rainy season if no strong winds blow from the south whereas strong winds from the south can bring about flow from the sea into the lagoons for several days in the dry season.

Increase in upland flow or northerly to northeasterly winds tend to cause ebb flow in Canal do Norte. Decrease in upland flow or winds from the south (SE to W) tend to cause flood flow. The greatest ebb discharges obviously take place when upland floods occur together with winds from N to NE. The greatest flood discharges are brought about by wind action from the south in the dry season.

The values of the upland discharges as well as the pattern of seasonal changes of rainfall and wind characteristics are such as to make ebb flows in Canal do Norte largely dominant over floods both in discharge values and durations throughout the year. Rainfall reaches a maximum in late winter, August and September, the southern Hemisphere winter and spring being the seasons with greater rainfall. Summer, December to March, is the dry season. Although northeasterly winds prevail over the year, they are more frequent from September to March. Winds from the southern quadrant are more frequent during the winter, from June to September. As a result, the greater upland discharges in winter counteract the flood-producing effect of the southerly winds. In the summer the effects of the northeasterly winds offset the decrease in upland flow to some extent.

One of the French engineers who built the breakwaters at the entrance in 1908-1916, M. B. Malaval [3], made an analysis of discharge values and durations of ebb and flood in Canal do Norte for six years (1908, 1911, 1912, 1913, 1914, 1915). The water surface profile was determined by two water level recorders 8 250 m apart, one near the port and the other near the entrance. Discharges were calculated with the aid of the Chezy formula, the assumptions on the value of the Chezy coefficient being controlled by some velocity measurements. The average results of Malaval's analysis for the six

years under consideration were as follows:

- 1) 2 604 hours of flood per year, or 108 days in a year, with a mean discharge of 6 767 m³/s, a mean velocity of 0.8 m/s, and an annual volume of 63 x 10⁹ m³,
- 2) 4 925 hours of ebb per year, or 205 days in a year, with a mean discharge of 8 650 m³/s, a mean velocity of 1.0 m/s, and an annual volume of 149 x 10⁹ m³,
- 3) 1 239 hours of slack water, or 52 days in a year, for which no flow was assumed.

Malaval's analysis did not take salinity effects into account.

Malaval also drew a list of ebb and flood periods with durations from 18 to 24 consecutive hours. He found an ebb period lasting for 19 consecutive days in July 1915 and a flood period lasting for 9 days in December 1915. On the average in a year he found for the ebb

2	periods	lasting	for	10	to	19	consecutive	days
5	"	"	"	5	"	10	"	"
18	"	"	"	2	"	4	"	"
21	"	"	"	1	whole	day		

and for the flood

1	period	lasting	for	5	to	9	consecutive	days
6	periods	lasting	for	2	to	4	consecutive	days
21	"	"	"	1	whole	day		

Analysis of flood and ebb durations in Canal do Norte more refined than Malaval's were not carried out to this day.

The two lagoons act both as large storage basins for the upland flow and sediment traps for the bed load brought down by the rivers. As a result, the sand in and around the harbour entrance is brought in by wave action on the continental shelf. The bed material is sand at the entrance and in the outer stretch of Canal do Norte. The inner stretch and the harbour basin have a muddy bed. Coastal currents are wind induced and can only cause sand transport in conjunction with waves.

II) The Uncontrolled Outlet and the Effects of Breakwater Construction.

The main object of this paper is the time history of the bar that came into being off the entrance to the lagoon outlet as a result of the interaction between the transport capacity of the waves and the flushing action of the upland flow. This time history can be divided into three periods

- 1) The situation of uncontrolled outlet, before breakwater construction in 1908-1916,
- 2) the changes which breakwater construction brought about,
- 3) the present situation that prevails since the bar, the shoreline and the outer stretch of Canal do Norte adapted themselves to the new conditions.

The time history of the bar is fairly well known as from

1883, annual surveys being available from that year to 1956 [4]. Surveys have been less frequent since 1956. Prior to 1883 the information available is poor.

Before breakwater construction the bar was extremely unstable in controlling depth, distance to the shoreline and pattern of the channels. Between 1883 - when the first comprehensive, reliable survey was carried out - and 1914 - when the influence of the breakwaters then under construction was brought to bear for the first time - the controlling depth varied in an erratic manner from a minimum of 2.5 m (1883) to a maximum of 7 m (1894). However, the most frequent values ranged from 4 to 5 m.

Figs. 4, 5 and 6 show the time history of the bar as taken from [4]. In Fig. 4 the annual values of the controlling depth are plotted from 1883 to 1956. Fig. 5 correlates the controlling depth to distances to a reference alignment joining two triangulation vertices on the shore. Fig. 6 is a plot of the variation in time of the least depths over the bar outside the shipping channel.

The distances from the reference alignment to the contour standing for the controlling depth ranged from a minimum of 2.8 km (in 1885, 1898 and 1899) to a maximum of 5.0 km (in 1892). The average distance of the controlling depth to the reference alignment was therefore 3.9 km (actual positions in 1886 and 1894). Very different values of controlling depth could be associated to a given value of distance to the reference alignment. For instance, the 4.0 km distance was associated to a controlling depth of 2.5 m (1883), 5.0 m (1902) and 6.0 m (1893). The 3.9 km distance was associated with values of 4.0 m (1886) and 7.0 m (1894). The minimum 2.8 km distance was associated with 3.0 m (1885) and 6.0 m (1898 and 1899). The maximum 5.0 km distance, which occurred only once (1892), was associated with 5.0 m.

Lack of reliable data for rainfall or upland discharges at the time under consideration in all the river basins involved precludes any attempt at correlating bar characteristics with upland flow values.

The lay-out of the main channel across the bar used to swing from SW to S and SE, although a SW alignment was most frequent. The instability of natural-channel pattern can also be seen in the different breakwater lay-outs proposed by different engineers at different times. Each proposed design was based on the most recent available survey.

While the bar underwent the changes discussed above the outlet itself, Canal do Norte, remained remarkably stable in position, width and depth. It is interesting to point out that the other lagoon outlet (Tramandai) and the mouths of small rivers (Chui, Mamputuba and Ararangua) on the same stretch of the Brazilian coast migrate northwards, in the direction of the dominant littoral drift. It appears that the stability of Canal do Norte was due to its much greater upland flow which flushed to considerable distances out to sea the sand brought in by the waves from the sides and in frontal action. At the other lagoon outlet and river mouths mentioned above the bar builds up much nearer the shoreline, and the interaction between littoral drift and the transport capacity of the upland flow in this tideless sea cause inlet migration.

72-43

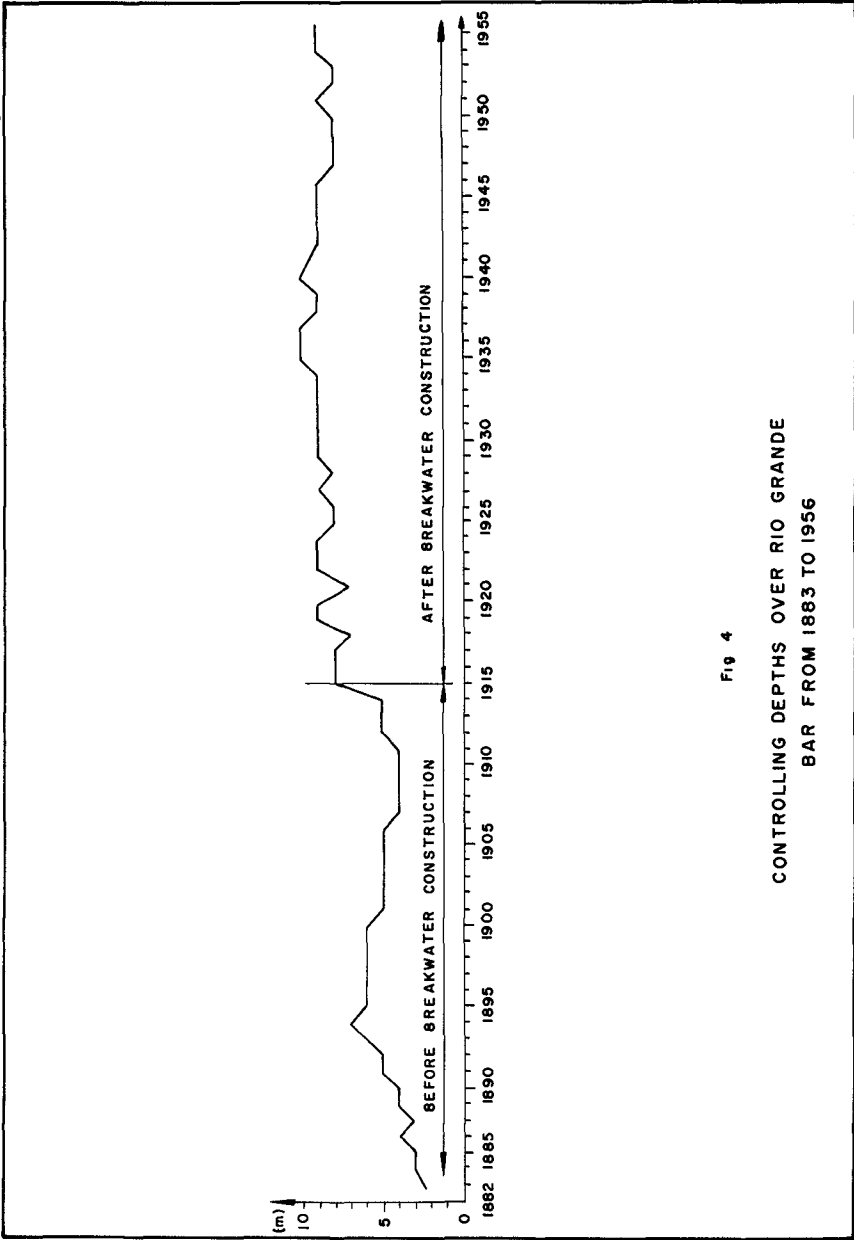


Fig. 4
CONTROLLING DEPTHS OVER RIO GRANDE
BAR FROM 1883 TO 1956

72-43

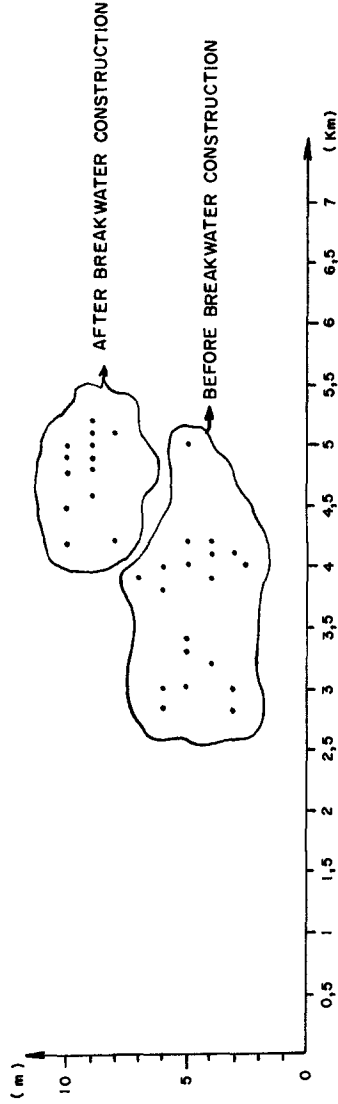


FIG 5
CORRELATION BETWEEN
CONTROLLING DEPTHS AND
DISTANCES TO SHORELINE

72-43

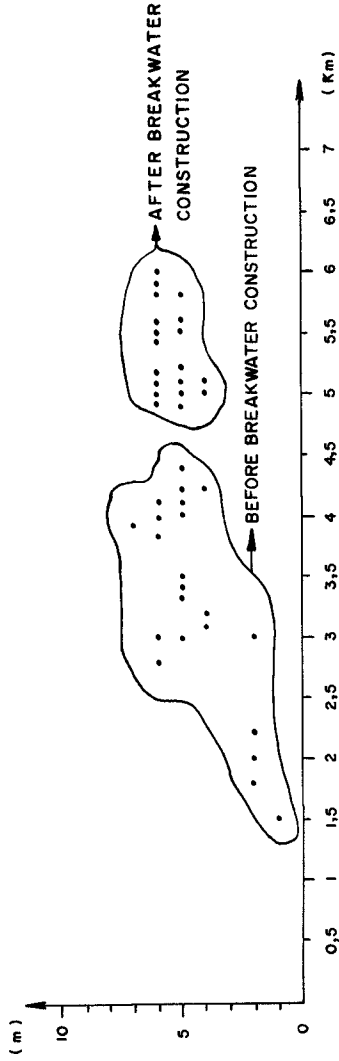


FIG 6

LEAST DEPTHS OVER THE BAR
OUTSIDE THE SHIPPING CHANNEL

On the other hand, the great instability of Rio Grande bar seems to be largely accounted for by the fact that upland flow, and not tidal flow, is the natural agent whose flushing action tends to preserve depths over the bar. Upland flow discharges are much less repeatable from year to year than would be tidal flow discharges in a place with a regular tide.

As far as it can be ascertained from the available surveys the shorelines on both sides of the lagoon outlet were fairly stable as long as it remained uncontrolled.

The earliest proposal for breakwater construction at Rio Grande was put forward by a British engineer, Sir John Hawkshaw, who was commissioned by the Brazilian Imperial Government in 1872 to report on methods to provide for a safe shipping channel across the bar. However, in his report [5] Hawkshaw pointed out that the size and cost of the required breakwaters would be such as to make the construction of a sheltered harbour at Torres, near the northern boundary of the State of Rio Grande do Sul, more advisable.

In 1883 the Brazilian Imperial Government entrusted a Brazilian engineer, H. Bicalho, with the task of carrying out the field surveys and design work to improve Rio Grande entrance. Bicalho [6] proposed the construction of two 4 km long breakwaters and requested the Government to seek the advice of a European or American engineer with a great experience in harbour entrance training to pass judgement on his proposal. The Government choice fell on the Dutch engineer, P. Caland, who had been in charge of the works for Rotterdam harbour entrance. Caland [7] approved of Bicalho's proposal with some minor changes in lay-out.

Hawkshaw, Bicalho and Caland were the first men to grasp the behaviour of Rio Grande bar and lay down rules for its improvement although the lack of the sea and swell concept in their time misled them as to the direction of the dominant littoral drift on the coast of Rio Grande do Sul because of the prevailing and dominant winds from NE.

Caland was prophetic in his recommendation that, when the breakwaters would be built, previous dredging should be carried out as the construction work proceeded out to sea in order to forestall scour caused by the increased transport capacity of the upland flow between the breakwaters, of which the formation of a new bar further offshore would be the inevitable result.

Breakwater construction was not started until 1908 when a French company was awarded a concession to build the breakwaters and dock facilities. Work in the breakwaters themselves was carried out from 1911 to late 1915, and major effects on the bar came about in 1914 which was a year with great rainfall and long, strong ebb flows in Canal do Norte. The Rio Grande breakwaters were the biggest hydraulic-engineering structures built in Brazil until some fifteen years ago, and at the time they ranked among the largest coastal works in the world. From 1922 to 1928, already under Brazilian administration, the outer 288 m of the eastern breakwater, which had been left in 1916 as a submerged dyke, were brought to the same top level (+ 3.00 m) as the remainder of the structure.

M. B. Malaval, one of the French engineers in charge of the construction work, left a detailed account [3] of its progress and

effects on the bed configuration. Malaval's paper followed up of deepening process from 1913 to 1919 in great detail.

Fig. 4, 5 and 6 bring out the effects of the breakwaters on the bar. Fig. 5 shows that the deepening of the former bar was quite sudden from 1914 to 1915 the plot jumps from 5 to 8 m. Ever since that occasion

- 1) the least controlling depth has always been above 7 m and this minimum only occurred in two years (1918 and 1921) in the time interval from 1915 to 1956, the most frequent value being 9 m (which occurred in 23 years), a value of 8 m occurring in 11 years, and the maximum between 9 and 10 m occurring in 4 years (1935, 1936, 1937 and 1940),
- 2) the range of the controlling-depth variation has decreased from 2.5 - 7.0 m before breakwater construction to 8-10 m as from 1922.

Fig. 5 proves that, in addition to increasing the controlling depth, breakwater construction increased its distance to the shoreline.

However, it can be seen from Fig. 6 that, although the breakwaters did increase the depths at the harbour entrance, the scheme was not entirely successful. The former bar was destroyed but a new bar built up further offshore. This fact entailed objectionable conditions for navigation at the entrance because the ships had to follow tight S - curve between the breakwater tip and the new bar. The radius of curvature did not exceed 500 m.

The obvious reason for this unhappy outcome was the fact that Caland's recommendation for previous dredging as breakwater construction proceeded out to sea went unheeded. No previous dredging was carried out, and as much as 14 million cubic metres of sand was scoured out between the breakwaters from January 1913 to January 1919 of which 10 million in 1914 alone. Such a huge volume was discharged offshore, and since it far exceeded the transport capacity of waves and currents offshore, a new bar came into being. The bed levels were irreversibly raised off the breakwater tips, and the interaction between the transport capacity of waves and upland flow has gone on ever since over the submarine mound thus created. Previous dredging has proved successful in forestalling the formation of a new bar at other harbour entrances [8].

The first approach channel to deepen was the one leading to the seaward end of the eastern breakwater. This channel was the main route to negotiate the entrance until 1962. The eastern channel was the first to deepen because construction of the eastern breakwater went ahead of that of the western breakwater. Another unfortunate feature of the construction work was the fact that advance of both breakwaters was not kept at the same distance to the shoreline. This seems to have been mainly due to difficulties in access to the western breakwater as a result of the 1914 upland floods which caused damage in a railway bridge. The western channel did not deepen completely until 1917 but in 1919 it was nearly 10 m deep. Adaptation of the bar and channels to the new conditions went on until 1922

when the new configuration became stable in its main features. Fig.7 reproduces the 1922 survey and shows the shipping lanes to negotiate the entrance.

Breakwater construction at Rio Grande harbour entrance had two other noteworthy effects. A deep scour hole developed around the eastern breakwater tip which eventually reached depths above 20 m. At the same time a shoal came about in the middle of the entrance which considerably reduced the available width between the breakwaters for shipping. The shoal developed in step with the scour hole, and it is believed to be formed by material from the latter. Velocity measurements carried out with floats in the late twenties sketched out the flow pattern and showed that, whereas ebb flows use the full width between the breakwaters, flood flows separate from the seaward end of the western breakwater and hug the eastern one. This flow concentration along the seaward end of the eastern breakwater is believed to be the main cause of the scour hole. However, both the scour hole and the middle shoal eventually reached equilibrium. To this day the shipping lane in the shelter of the breakwaters runs between the middle shoal and the western breakwater.

The other outstanding effect was beach accretion on both sides of the breakwaters although accretion on the western side was much greater than on the eastern side. Accretion on the western side was very fast shortly after breakwater construction. It amounted to a 200 m shoreline advance over a great length and went as far as Cassino beach some 6 km west of the western breakwater. Later on, the accretion slowed down and the shoreline on both sides seems to have reached a new equilibrium. Fig. 8 shows the shoreline position on both sides of the breakwaters in 1911, 1919, 1922, 1950 and 1956. Lack of adequate data on beach profile and boundaries in plan and elevation precludes a cubature of this accretion.

The outer portion of Canal do Norte was also considerably deepened by breakwater construction.

III) The Situation after Breakwater Construction.

The main outlines of the bed configuration that came about as a result of breakwater construction are fairly stable since the early twenties. The main features are the outer bar, the two 8 to 10 m deep approach channels between the bar and the breakwater tips compelling the ships to follow tight curves around the latter, the scour hole around the eastern breakwater seaward end, the middle shoal and the deep, wide Canal do Norte.

As already seen the controlling depth in the two outer approach channels fluctuates between 8 and 10 m. The depth over the top of the outer bar fluctuates between 5 and 6 m. However, in terms of volume the outer bar is far from stable, annual fluctuations of over 1 million cubic metres in a year having been detected. There is evidence to the effect that the volume of the bar is very sensitive to yearly changes of the natural forces at play. On the other hand, no correlation can be found between the volume of the bar and the controlling depth in either of the two approach channels.

The annual changes in volume of the bar have ranged from

72-43

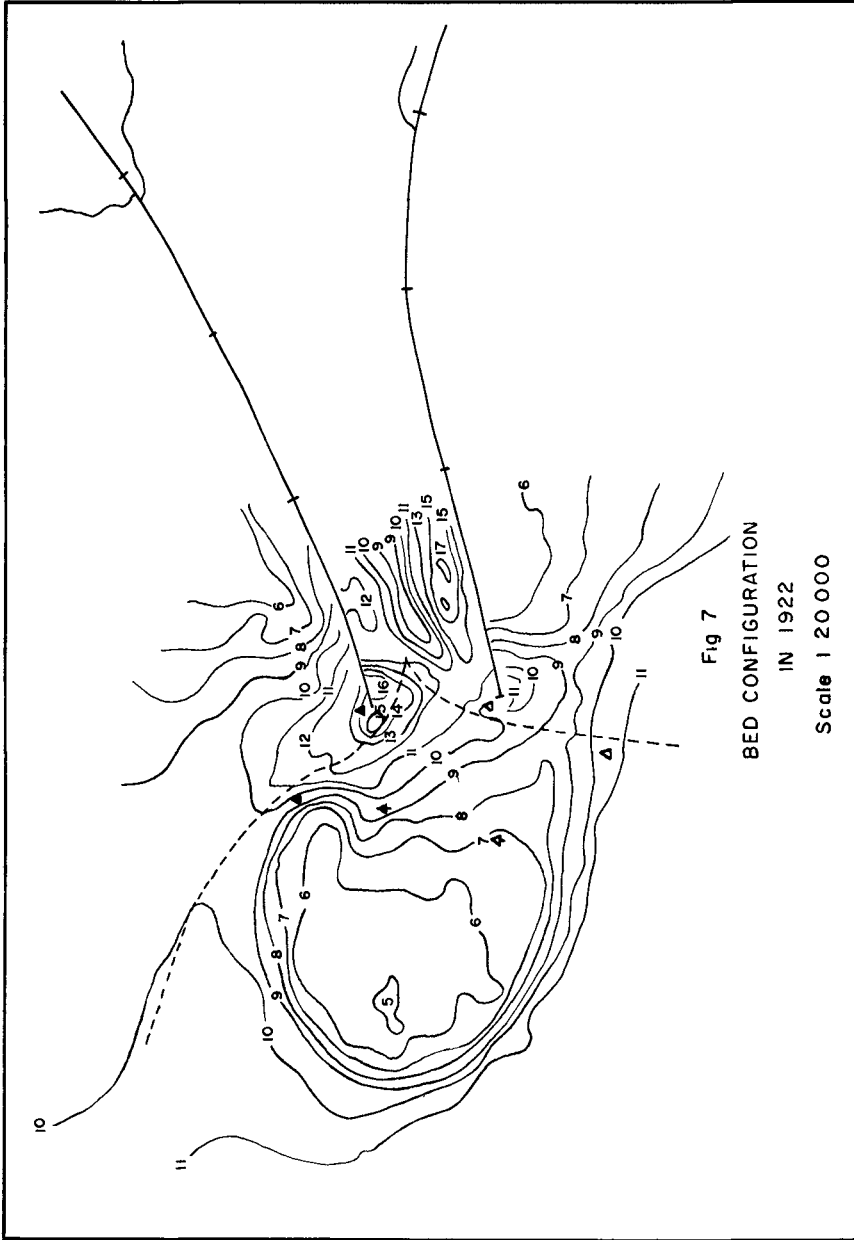
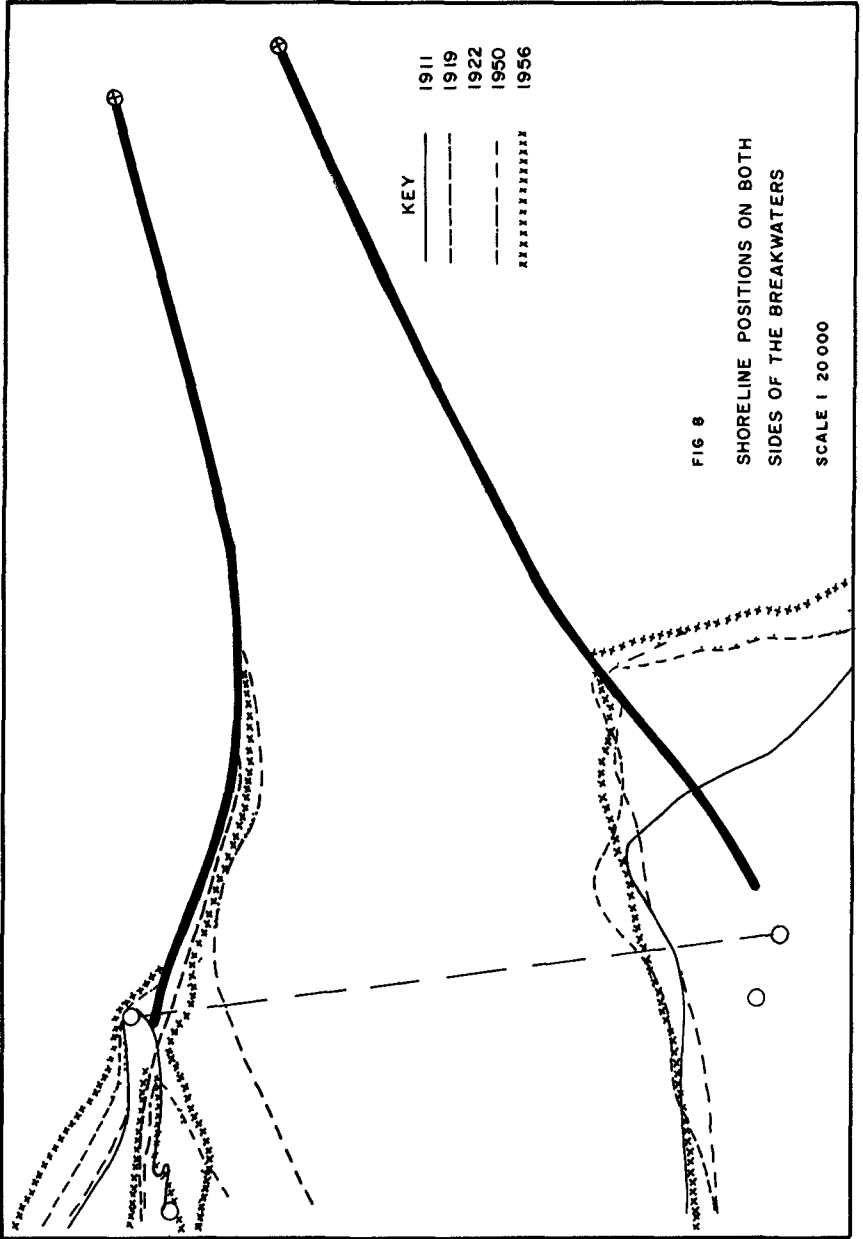


Fig 7
BED CONFIGURATION
IN 1922
Scale 1 20 000

72-43



2,000 m³ (1952-53) and 1 264 000 m³ (1929-1930) for accretion, and from 58 000 m³ (1931-32) to 1 238 000 m³ (1926-27) for erosion.

An important event that took place after breakwater construction was the great upland flow in April-May 1941, the greatest on record. The table below lists estimated mean monthly discharges in Canal do Norte for several months in 1941 |9|.

Month	Mean discharges (m ³ /s)
January	3 100
February	7 800
March	1 600
April	21 600
May	22 700
June	6 000
July	6 800

Surveys of Canal do Norte and the outer bar were made before and after the peak flows. Therefore, the effects of the high upland flow in April and May on the bed configuration could be readily assessed. The outer bar was displaced offshore, the - 6 m contour having moved nearly 500 m out to sea, the middle shoal was topped off, and the scour hole around the seaward end of the eastern breakwater filled up to some extent, the 18 m depth being reduced to 12 m. However, the effects of this powerful flushing action vanished in a few months.

Endless discussions were held in Brazil during the twenties and the thirties about remedial measures to improve shipping conditions at Rio Grande entrance but no action was taken. Several proposals were put forward with a view to extending the breakwaters or changing their top levels. Many modern coastal engineering concepts were not available at the time, and knowledge of the wave characteristic at the site was poor. As a result, in the light of modern ideas several of those proposals now seem ill-founded. One particular proposal |10| was bound to have disastrous effects, had it been implemented, because it was still implicitly based on the wrong assumption that, if the prevailing and dominant winds blow from NE, the dominant sand transport must be towards SW. It consisted of keeping the western breakwater as it is and extending the eastern breakwater in a curved shape.

No improvement was achieved until 1961-62 when a 12 m deep eastern approach channel was dredged in the outer bar in order to eliminate the S - shaped curves in the entrance route and provide for a greater radius of curvature which was increased to 1 400 m. No maintenance dredging was done but the total deposit in the dredged channel from January 1963 to October 1967 did not exceed 120 000 m³. In the most recent available survey (1965) the 12 m dredged depth had been reduced to 10.5 m. The maximum draught presently allowed by the harbour authority is 8.8 m (29 ft). Maintenance dredging in this channel is under way at the time of writing.

The Federal and State harbour authorities now contemplate improving Rio Grande harbour entrance and deepening it to 14 m. The Coastal Division of the Hydraulics Research Institute of the Federal University of Rio Grande do Sul (IPH da UFRGS) has acted as consulting engineer to the State dock and harbour authority by giving advice as to the problems to be solved and by making recommendations. In the light of the progress in dredging technology extension of the two 4 km long breakwaters is not deemed an economical solution. A new approach channel must be set up and maintained by dredging. The radius of curvature of the eastern approach channel is to be increased to 2,500 m, and the width at the bottom to 250 m. IPH da UFRGS has proposed to carry out a fixed-bed model investigation using radio-controlled model ships to determine the most suitable lay-out of the approach channel to be dredged outside the breakwaters. However, the State dock and harbour authority has preferred not to increase the 2,500 m value so as to keep the amount of capital dredging to a minimum.

In addition to dealing with the outer-bar problems the improvement of Rio Grande harbour entrance has to cope with the middle shoal between the breakwaters. A 14 m deep shipping channel with a 250 m width at the bottom cannot be accommodated between the middle shoal and the western breakwater. A mobile-bed model investigation is to be carried out into the means to eliminate the middle shoal or reduce the amount of maintenance dredging in a channel that cuts into it.

Dredged spoils in Canal do Norte are to be pumped ashore or dumped in dyked-in disposal areas. A radioactive tracer experiment is to be carried out to check on the suitability of the dumping grounds of the material presently dredged in the harbour basin.

Deepening the approach channel to Rio Grande is inseparable from building new dock facilities on the west bank of Canal do Norte. Depths along the quays of the present port to not exceed 10 m and cannot be increased because of structural reasons.

IV) Bibliographical References.

- 1) USNHO. "Sea and Swell Charts for the South Atlantic Ocean". Washington, 1st edition, 1948.
- 2) V. F. Motta. "The Model Investigation into the Control of Tramandai Inlet" (in Portuguese), Proceedings of the 2nd Brazilian Conference on Maritime Transport and Naval Engineering, Rio de Janeiro, 1967.
- 3) M. B. Malaval. "Travaux du Port et de la Barre de Rio Grande, Brésil". Ed. Eyrolles, Paris, 1922.
- 4) DNPVN. "Rio Grande Bar Surveys, 1883-1956" (in Portuguese). Compiled by C. M. Vassão, Porto Alegre, 1959.
- 5) Sir John Hawkshaw. "Report on Rio Grande do Sul Harbour". In "Rio Grande do Sul Bar and Harbour Works", Vol. III (in Portuguese), a compilation of several reports, Porto Alegre, 1924.
- 6) H. Bicalho. "Report of Rio Grande Bar Improvement Commission, 1883" (in Portuguese). Idem.
- 7) P. Caland. "Amélioration de la Barre du Rio Grande do Sul.

- Rapport Présenté au Gouvernement Brésilien". Rio de Janeiro, 1886
- 8) G. H. Farleigh, D. C. Coode, A. F. Dickson, J. Green. British Report to the 20th International Navigation Congress. Baltimore, 1961.
 - 9) F. Duprat da Silva. "Effects of the 1941 Flood" (in Portuguese). Rio Grande, 1941.
 - 10) H. C. Ripley. "Some Notes on the Rio Grande do Sul Bar Improvement". New York, 1925.
 - 11) V. F. Motta. "Report on Improving and Deepening Rio Grande Harbour Entrance" (in Portuguese). Submitted by IPH da UFRGS to Departamento Estadual de Portos, Rios e Canais, Porto Alegre, 1969.

CHAPTER 79

SCOUR AROUND A CIRCULAR CYLINDER DUE TO WAVE MOTION

Donald R. WELLS, LCDR, Civil Engineer Corps, U.S. Navy, Instructor of Ocean Engineering, Naval School, Civil Engineer Corps Officers, Port Hueneme, California

and

Robert M. SORLENSEN, Associate Professor of Civil Engineering, Texas A&M University, College Station, Texas

ABSTRACT

A vertical circular cylinder to simulate a pile was installed in the Texas A&M Hydrodynamics Lab two dimensional wave tank along with a built up section containing a horizontal bed of fine sand. This was subjected to monochromatic waves of differing characteristics and conditions for incipient motion were observed for each of three sands. Also, the magnitude and pattern of ultimate scour and the time interval required to reach this state were measured for six different conditions of wave steepness and relative depth.

These results were related to influential parameters, including wave, pile and sediment characteristics, and developed by dimensional analysis with consideration of the literature pertaining to past work on the movement of sediment by oscillatory flow. Conclusions regarding the critical flow velocity for incipient motion, the effect of the above parameters on incipient motion and ultimate scour depth, the time required for maximum scour, the significance of eddies generated by the pile, and the catalytic action of the pile in causing the initiation of scour are presented.

The above conclusions are also generally discussed in light of the difficulties involved in extending the results to prototype conditions.

INTRODUCTION

The scour of bed particles adjacent to an obstacle begins when the velocities and accelerations of the water particles cause hydrodynamic forces sufficient to overcome gravity and cause the bed particles to move. When the bed particles begin to tip from their angle of repose is defined as incipient motion and is the point where any study of scour must begin.

Incipient motion and scour have been studied extensively with regard to steady open channel flow but it has only been in the last two decades that research has been carried out in oscillatory motion. It is extremely difficult to formulate mathematical equations that represent accurately the phenomena of incipient motion, scour, and ultimate scour depth. Because of this difficulty no formulation of mathematical equations was attempted. However, the interrelationships and interdependency of the parameters were experimentally studied using terms derived by dimensional analysis.

The studies were conducted in a two dimensional wave tank using three uniformly graded commercial sands and monochromatic waves of various steepness and relative depth to produce the incipient motion and scour results

BACKGROUND

Incipient Motion It becomes obvious when reading the literature that there is no universally accepted definition for incipient motion. Because of this it is sometimes difficult to compare the results obtained by various authors. For the purposes of this study the definition put forth by Eagleson and Dean,¹ is best suited. They defined incipient motion as "an instantaneous condition reached when the resultant of all the active forces on the particle intersects the line connecting the bed particle contact points." The term "active" means all the forces due to water particle motion and gravity.

The first major work on incipient motion caused by oscillatory flow was done in 1954 by Li.² Using an oscillating bed in a still fluid, he found that the transition point from a laminar to a turbulent boundary layer occurred at a Reynolds number of 800 for a hydrodynamically smooth boundary. Several years later Vincent³ carried out similar experiments using a wave flume and found the Reynolds number for the transition point to be much less than that reported by Li. Both concluded that the transition point was a function of roughness and would vary depending on the characteristics of the bed material.

Eagleson and Dean¹ continuing work initiated by Ippen and Eagleson⁴ made a rigorous mathematical analysis of incipient motion and sediment transport and presented equations for both. Several other authors have presented equations for incipient motion notably Ko⁵, Vincent³, and Chepil.⁶ All of the equations presented are accurate within certain limits but none of them will predict the exact occurrence of incipient motion. This is primarily due to the inability to evaluate the coefficients of drag and lift and the influences of the angle of repose and bed particle geometry. Raudkivi⁷ presents a very good discussion of these problems.

Coleman⁸ recently has developed relationships between the drag coefficient, C_D , the lift factor, K , which is similar to the lift coefficient, C_L , and the Reynolds number. His equations, although for steady state conditions, do give a representation for the lift on a bed particle. Reference 9 presents an excellent discussion on incipient motion including an analysis and comparisons of the results of several authors. It also presents equations for incipient motion from various authors.

Scour Very little experiment work has been done on scour due to oscillatory wave motion. However, there exists a wealth of knowledge on scour in open channel flow. Since the forces that cause scour are somewhat similar for oscillatory flow as for open channel (steady state) flow, the knowledge gained from experiments in open channel flow can be applied with reservations to oscillatory motion. The majority of the work done on scour in oscillatory motion has been concerned primarily with scour of beaches and littoral sediment transport.

Murphy,¹⁰ Van Weele¹¹ and Ko⁵ studied scour in front of seawalls of various angles, and their results are summarized by Herbich et al.¹² They found that the ultimate depth of scour is a function of wave characteristics as well as the number of waves passing a given point where scour occurs and scour approaches its maximum value asymptotically after initially increasing very rapidly.

Roper, Schneider and Shen¹³ have shown that for steady state conditions in open channel flow the depth of scour is a function of the pier Reynolds number, defined as

$$N_{RP} = \frac{UD}{\nu} \quad (1)$$

where

U = horizontal free stream velocity,
 D = pile diameter, and
 ν = kinematic viscosity

They have further shown that the scour is influenced by the type of vortex system caused by the pier. For a circular pier a horseshoe vortex system is most generally formed. For nonsteady state conditions (oscillatory motion) this horseshoe vortex system may not have time to build up to such an intensity that it is shed and therefore the vortex system formed by oscillatory wave motion may not influence the scour. The influence of the bed particle size on scour is not generally known, however, studies conducted by Roper, Schneider and Shen¹³ show that when the bed particle size is greater than 0.52 millimeter, the particle size influences scour depth and when the particle size is less than 0.52 millimeter scour depth is independent of particle size.

Carstens¹⁴ has made extensive studies of the scour associated with different types of obstacles. From his study he has shown that the rate of scour caused by an object in the flow path is a function of the sediment number N_s , sediment grain geometry, and the ratio of the scour depth to the obstacle size. The sediment number is defined as

$$N_s = \frac{U}{\sqrt{(S_s - 1)gd}} \quad (2)$$

where

U = free stream velocity,
 S_s = specific gravity of sediment,
 g = acceleration of gravity, and
 d = mean sediment particle diameter

His studies were primarily conducted in steady flow. He presents equations for the ultimate scour depth associated with a vertical cylinder and for the relative scour depth as a function of the sediment number. However, all his equations are based on the supposition that the scour hole formed will have the appearance and form of an inverted frustum of a right circular cone having a base diameter equal to the pile diameter and a side slope equal to the angle of repose.

THEORETICAL CONSIDERATIONS

In this investigation the water particle motions, velocities and accelerations, and the forces they in turn produce were calculated using Stokes third order wave theory. This theory was chosen to be used after studying papers by Dean¹⁵ and Le Mehaute, Divoky and Lin¹⁶ and comparing the wave characteristics with the results published by these authors.

The forces causing bed particle motion are hydrodynamic and consist of the forces of drag, lift and inertia. However, since the force due to inertia is a function of d^3 whereas the force due to drag

is a function of d^2 and thus inertia forces will never predominate due to the small particle size, the force of inertia will be neglected. The total hydrodynamic force will therefore be the combination of the lift force and the drag force. The hydrodynamic forces are opposed by the force of gravity and influenced by bed particle geometry.

Drag The drag force is the combination of the form drag due to pressure differential and the viscous drag due to skin friction. The point through which the drag force acts is not necessarily the center of gravity of the bed particle but depends on the relative magnitude of the lift and drag force components which are functions of bed particle geometry, location and local Reynolds number. The steady force due to drag as developed in any elementary fluid mechanics text can be shown to be

$$F_D = \frac{C_D}{2} \rho A U^2 \quad (3)$$

where

- ρ = fluid density,
- A = projected area of object normal to flow direction, and
- C_D = drag coefficient

The coefficient of drag is a function of Reynolds number and bed particle geometry and is also influenced to some unknown extent by adjacent particles causing anomalies in the flow patterns.

Lift The relationship for the force due to lift is similar to that for form drag and is given by

$$F_L = \frac{C_L}{2} \rho A U^2 \quad (4)$$

where

- C_L = coefficient of lift and
- A' = projected area perpendicular to flow direction

The lift force is the resultant due to the pressure differential above and below the particle. The pressure differential is caused when the fluid velocity is increased as it passes over the top of the particle thereby decreasing the pressure. Since the pressure below the particle remains fairly static there is a pressure differential or lift force. A significant number of the studies conducted on forces related to particle movement have neglected the lift force, however, the proof that it does exist and is significant has been reported^{8 & 9}

The coefficient of lift has not been studied as extensively as the coefficient of drag primarily due to the difficulty in evaluating it. Coleman's⁸ work appears to give the best indications of its value.

Gravity The hydrodynamic forces are opposed by the weight of the particle, friction and the intergranular reactions. The friction and intergranular reaction are difficult to evaluate but the gravity force can be represented by the equation

$$F_g = \frac{\pi d^3}{6} (\gamma_s - \gamma_f) \quad (5)$$

where

$$\begin{aligned}\gamma_s &= \text{specific weight of the sand, and} \\ \gamma_f &= \text{specific weight of the fluid}\end{aligned}$$

Mechanics of Motion It is very difficult to study the motion of sand grains primarily due to their varying sizes, angularity, and distribution in a bed. Therefore, the problem must be simplified. This can be done by considering the sand grains to be spheres of uniform size. Referring to Fig. 1, it can be seen that the total hydrodynamic force F_T , is the combination of the lift and drag force.

For motion to occur the sum of the moments about point R must be zero or in other words, F_T times its moment arm, d , must equal F_g times its moment arm, $d \sin \phi$. When this condition exists incipient motion can occur. As pointed out by Coleman⁸, the lift force can be negative if the Reynolds number is below 100. It is therefore possible for the particle to be pushed into the bed rather than be lifted out or rolled along it.

The velocity, U , used in evaluating the results of these experiments will be the maximum water particle velocity that occurs at the bed and is the velocity associated with the wave crest for shallow water waves.

Flow around the pile and its relationship to scour Any obstacle inserted into the region of flow will cause the flow to be diverted around the obstacle. The flow velocity will increase as the flow deflects around the obstacle with a consequential reduction of pressure. Depending on surface roughness on the boundary, local Reynolds number, boundary shape and boundary layer characteristics, the flow can separate from the boundary causing a wake to occur behind the pile.

From potential flow theory, it can be shown that for flow around a cylinder the velocity of the flow at points on the cylinder ninety degrees from the initial direction of flow will be twice the initial velocity of flow. Because of the periodic direction changes of the flow and boundary layer development it is doubtful that the velocity of flow at the ninety degree points will become twice the initial velocity. In oscillatory flow the separation condition might not occur unless the distance the water particle moves is several pile diameters long. From observations it is felt that if the distance the water particle moves is approximately five or more pile diameters then separation should occur and eddies should form and be shed periodically from the pile.

In studies conducted by Roper, Schneider, and Shen¹³, it was shown that the vortex system formed by flow around an obstacle was related to the shape and size of the obstacle. They concluded that the eddy structure formed is the basic mechanism of scour and that the depth of scour was a function of the pier or pile Reynolds number, N_{RP} .

Because of the difficulties in evaluation lift and drag coefficients and intergranular reactions, a mathematical analysis of scour is beyond achievement.

Dimensional Analysis The significant variables influencing incipient motion are still water depth, h ; wave height, H ; wave period, T ; viscosity, μ ; acceleration of gravity, g ; densities of fluid and bed particles, ρ and ρ_s respectively; mean bed particle diameter, d ; and angle of repose ϕ . Using the Buckingham pi theorem the functional equation for incipient motion can be derived as

$$f\left(\frac{d}{h}, \phi, \frac{H}{h}, \frac{h}{gT^2}, \frac{h^2}{\mu T}, (\rho_s, \rho)\right) = 0 \quad (6)$$

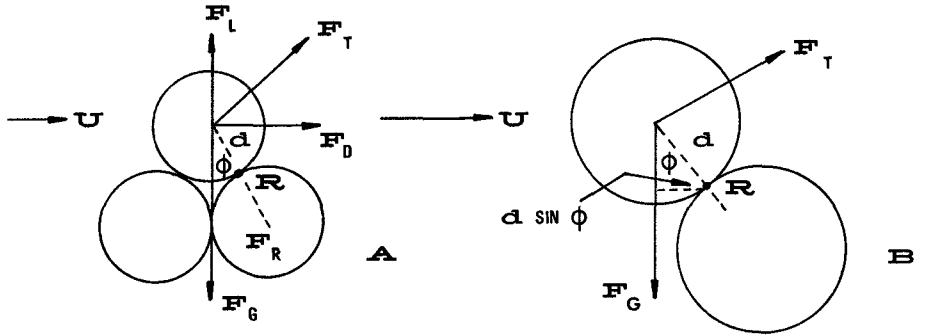


Fig 1 MECHANICS OF MOTION

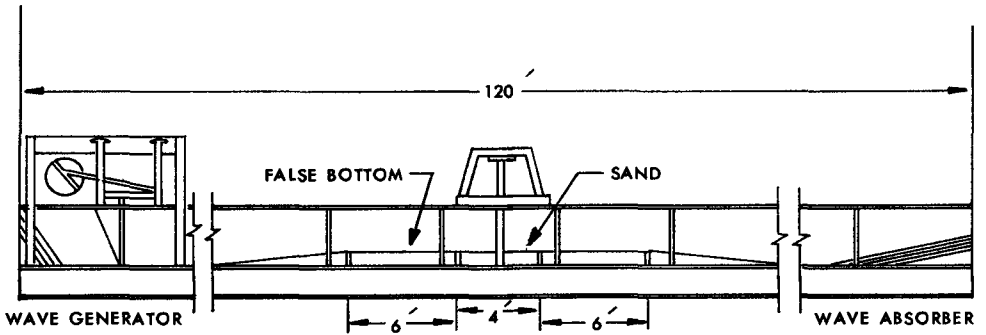


Fig 2 TEST APPARATUS IN THE WIND-WAVE CHANNEL

Since these experiments will use sand as a bed material the density of sand ρ_s will not change, also the density and viscosity of water will remain constant. Therefore the parameter $\frac{h^2}{\mu T} (\rho_s - \rho)$ will vary as $\frac{h^2}{T}$ varies. Since h and T are included in the $\frac{h}{gT^2}$ parameter the $\frac{h^2}{\mu T} (\rho_s - \rho)$ parameter can be dropped. Also it is doubtful that the angle of repose will be a significant parameter in these experiments, therefore, it will be discarded. That leaves the function relationship

$$\frac{d}{h} = F \left(\frac{h}{gT^2}, \frac{H}{h} \right) \quad (7)$$

which is to say that for incipient motion the relative particle size is a function of relative depth and relative wave height.

The variables considered to be significant for scour contain those considered for incipient motion and the additional variables of pile diameter, D , U , ultimate significant scour depth S_u and elapsed time t .

The orbital particle velocity, U , although not independent of those listed above was included so that the parameter N_s could be defined in its normally accepted form.

Again using the Buckingham pi theorem, the functional equation defining scour around a circular pile in oscillatory motion is

$$\frac{\bar{S}_u}{H} = f \left(\frac{H}{gT^2}, \frac{h}{gT^2}, N_{RP}, N_s, \frac{\bar{S}_u}{d}, \frac{H}{h}, \frac{t}{T}, \phi \right) \quad (8)$$

EXPERIMENTAL APPARATUS AND EQUIPMENT

The experiments on incipient motion and scour were conducted in a 120 foot long, 3 foot deep and 2 foot wide two dimensional wave channel (Fig. 2). A false bottom 6 inches deep and 16 feet long was constructed in the channel. At each end of the false bottom was a gradual slope to bring the wave up to the new depth at the top of the false bottom. The false bottom was split into three sections, two 6 foot sections at each end with 4 feet of the test sand in the center between the 6 foot sections. The 1½ inch diameter steel pile was placed in the center of the 4 foot sand test section and anchored to an aluminum frame above the wave tank to keep the pile vertical and stable.

Scour depth measurements were made using a depth probe that was attached to a device that could be rotated around the pile 360 degrees and extended up to 8 inches from the outer edge of the pile. The rotating ring was marked in degrees and the extended arm was marked in inches so that any scour measurement could be identified in polar coordinates.

The wave generator was an oscillating pendulum type whose stroke and consequently wave height can be varied by adjusting the eccentricity of the paddle arm on the flywheel. The period was varied through a variable rheostat that controls the speed of the flywheel. Wave heights and periods were measured by a capacitance wave gage connected to a Hewlett Packard Dual Channel Carrier amplifier recorder (Model No. 321). A mechanical counter was attached to the wave generator so that the number of waves generated could be determined.

EXPERIMENTAL PROCEDURES

Incipient Motion Prior to the start of each incipient motion run, the sand bed was leveled. The wave generator, set for a particular wave height and period, was started and the sand along the boundary of the pile was observed. The wave period was adjusted until several sand grains were observed to tip out of their position of rest and the wave characteristics were then recorded for that run. The wave period was then further adjusted to attempt to observe incipient motion on the bed far enough away from the pile so that the pile had no influence on the sand grains. These experiments were run for all three sands at depths of 15 inches and 8 inches and for approximately 15 runs per sand. Several paddle positions were used in making the runs in order to observe incipient motion for intermediate and shallow water waves. The bottom water particle velocity for each run was calculated using Stokes third order wave theory. The incipient motion data can be found tabulated in Appendix I of reference 17.

Scour For the experiments on scour, three experimental waves were selected of varying characteristics for each experimental wave at each depth are shown in Table 1. Runs were made for each sand at each depth for each wave for a total of 18 runs. At the start of each run the sand bed was leveled and measurements were made to ascertain the level of the bed.

The wave generator adjusted for a particular experimental wave, was then started and the wave period and height were recorded. Measurements of scour depth were made after each 200, 400, 800, 1200, 2000, 3000, etc. waves until there appeared to be no increase in scour depth after two successive measurements. This procedure was adjusted occasionally when it was felt that the run should be continued to observe scour pattern changes although there was no increase in scour depth. The scour depth measurements were made on a random basis, measuring the deepest scour holes and trying to use the same holes for each measurement as a control basis. This could not always be done because when ripples formed on the bed a scour hole would occasionally be filled in. The relative significant scour depth and the relative ultimate significant scour depth were calculated by averaging the scour depths for the deepest one third scour measurements and the latter being divided by the wave height. For each sequence point in a particular run, a collection of at least six data points was attempted but occasionally this could not be done due to the lack of scour holes. For each data point, the angle, distance from the pile and scour depth were recorded. At the completion of each run a number of data points were taken so as to be able to construct a contour map of the scour pattern. The data for the scour runs are tabulated in Appendix I of reference 17.

Three sands were selected for use in the experiments. The sands were all standard Ottawa sands that are produced with a controlled size distribution. Each sand was subjected to a standard ASTM sieve analysis to determine mean particle diameters. The data are shown in Table 2.

TABLE 1 EXPERIMENTAL WAVE CHARACTERISTICS

Test Wave	Depth, h in feet	Average wave height, H, in feet	Average wave period, T, in seconds	Average wave length, L, in feet	Relative depth $\frac{h}{L}$	Wave steepness $\frac{H}{L}$
(1)	(2)	(3)	(4)	(5)	(6)	(7)
1	1 25	0 16	3 8	24 74	0 0506	0 00647
	0 666	0 19	3 8	20 01	0 0333	0 00950
2	1 25	0 187	3 08	19 42	0 0644	0 00963
	0 666	0 13	3 08	15 14	0 0440	0 00858
3	1 25	0 275	1 875	10 85	0 1152	0 02530
	0 666	0 22	1 875	9 23	0 0721	0 02380

TABLE 2 EXPERIMENTAL SAND CHARACTERISTICS

Test Sand	Manufacture trade name	Mean grain diameter, d in millimeters	Average weight per grain in grams	Density in grams per cubic centimeter
(1)	(2)	(3)	(4)	(5)
1	Sawing sand	0 62	$2 314 \times 10^{-4}$	2 67
2	Crystal sand	0 325	$1 310 \times 10^{-4}$	2 66
3	Bond sand	0 30	$6 854 \times 10^{-5}$	2 665

PRESENTATION AND DISCUSSION OF RESULTS

Incipient Motion The occurrence of incipient motion was observed at the pile and on the bed and the maximum undisturbed bottom velocity for each case was calculated from the measured wave height and period. These were compared with the theoretical potential flow of two. The average velocity ratio for 11 experimental runs was 1.69. Further experimentation should be done for various pile sizes and roughnesses before any conclusions can be made as to what the velocity ratio will be and how it is influenced by roughness and pile size.

It was assumed that incipient motion was a function of the relative depth, the relative wave height, and the dimensionless particle size. These parameters were plotted on a log-log plot and are shown in Fig. 3 for incipient motion occurring at the pile boundary. Referring to Fig. 3, it can be seen that incipient motion appears to be influenced only slightly by the parameter $\frac{H}{h}$ and appears to be directly related by the parameters $\frac{h}{gT^2}$ and $\frac{d}{h}$. However, in the case of incipient motion on the bed, it appears to be independent of $\frac{H}{h}$ and $\frac{h}{gT^2}$. More data collection will be necessary before any conclusion can be drawn regarding incipient motion on a pile boundary except to say that the initiation of motion appears to be a function of the relative depth and dimensionless particle size. This, of course, is only true for sands since these experiments did not investigate non-cohesive materials of other specific gravities.

Reference 9 presents a collection of data regarding the incipient velocities for various materials for steady state conditions. A plot of these data along with the velocities calculated for incipient motion on the bed for the three experimental sands is shown in Fig. 4. As can be seen from the graph, the incipient velocities for the three sands fall on the lower boundary and below the region of data presented by reference 9. The reason for the lower values is not known except to say that for oscillatory motion, incipient motion appears to occur at a lower velocity. However, as pointed out by Vanoni⁹ in his discussion of the incipient velocity data, the curve for Shields (1936) data gave substantially higher incipient velocities than did that of Mavis and Laushey (1949) and the data of Hjulstrom (1935) did not compare to either of the other two curves. Because of the inconsistencies in the data for incipient velocities, Vanoni therefore recommends that critical shear stress be used as the parameter for comparing incipient motion rather than incipient velocity.

SCOUR

The dimensionless parameters developed for scour were calculated and their interdependency was studied by plotting the parameters. The parameter $\frac{\bar{S}_u}{H}$ was plotted against the wave steepness $\frac{H}{gT^2}$ for various values of relative steepness $\frac{H}{h}$; however, no conclusive relationship could be drawn from a study of the plot. It is, however, felt that as the wave steepness increases from a point of incipient motion the relative ultimate significant scour depth increases until a point is reached where for further increases in wave steepness a rapid decrease in scour depth occurs. The rapid decrease in scour depth is associated with the phenomena of ripple formation. It is conjectured that after the ripple formation becomes stable or well defined there will be no further significant increase or decrease in scour depth for further increases in wave steepness.

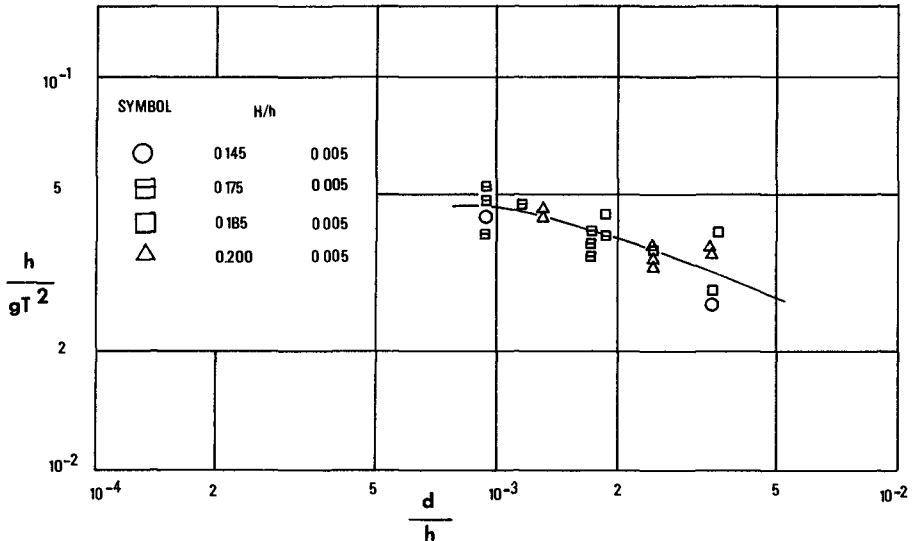


Fig 3 INCIPIENT MOTION OCCURRING ON THE PILE BOUNDARY FOR VARIOUS VALUES OF RELATIVE WAVE HEIGHT

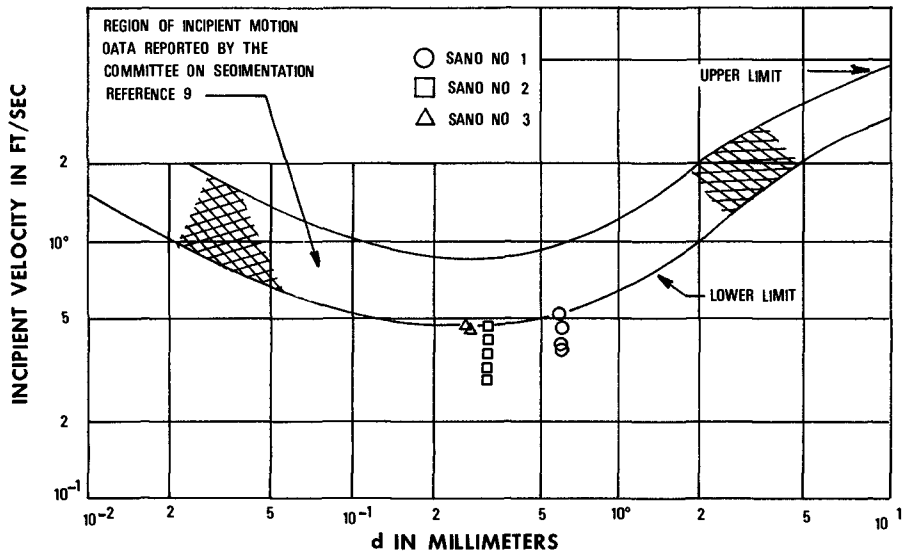


Fig 4 INCIPIENT VELOCITY AS A FUNCTION OF GRAIN SIZE

The parameters $\frac{\bar{S}_u}{d}$ and $\frac{h}{gT^2}$ were graphically studied to determine their relationship to each other. It was found that the relative ultimate significant scour depth is a function of relative depth and bed particle size. As the relative depth decreases for each bed particle size the relative scour depth increases slowly at first until a relative depth of approximately 1.5×10^{-3} is reached where the relative scour depth increases rapidly for decreases in bed particle size. Although relative ultimate significant scour depth is a function of relative depth and possibly a function of wave steepness, it appears to be primarily influenced by the sediment number N_s and the pile Reynold's Number N_{RP} .

Figs 5 and 6 show the functional relationship between the relative ultimate significant scour depth and the sediment number, N_s , and pile Reynold's number, N_{RP} , respectively. The incipient values of N_s and N_{RP} for each of the sands were calculated and included on Figs 5 and 6 to show that the curves actually have a rapid initial increase in $\frac{\bar{S}_u}{H}$. The functional relationship appears to be similar in both cases in that relative scour depth increases very rapidly from the point where incipient motion occurs to a maximum relative scour depth. Any further increase in N_s or N_{RP} results in a rapid decrease in ultimate scour depth reaching a point where the relative ultimate significant scour depth becomes independent of N_s and N_{RP} but not of bed particle size. It is unknown why the number 2 sand, which has a smaller mean diameter than the number 1 sand, has the maximum ultimate scour depth and also levels off at a higher relative scour depth than the number 1 sand. One possible answer could be, as was pointed out by Roper, Schneider, and Shea¹³, that when the bed particle size is less than 0.52 millimeter, the scour depth is independent of the bed particle size.

Figs 7 and 8 show the relationship between the relative significant scour depth and the parameter t/T which is the number of waves. These are typical curves and the remainder of the plots for all the runs can be found in Reference 17. The parameter $\frac{\bar{S}_u}{H}$ for each of the three sands is plotted versus the number of waves for a particular experimental wave so as to compare the relative significant scour for the three sands. The majority of the curves have a characteristic initial rapid increase in the relatively significant scour depth. Most of the curves reach their approximate ultimate condition after 2000 waves. Also the majority of curves reach characteristic plateaus where the scour activity is dormant for a period of time and then it starts to increase again. For the runs where ripple activity was dominant (Fig 8), the curves seem to reach a peak value rapidly followed by a decrease in relative scour depth for further increases in number of waves and then finally level off at the ultimate scour depth.

Intuitively one would think that Sand number 1 would have the largest relative significant scour followed by Sands number 2 and 3. However, this is not always the case and the reasons for it are unexplainable except for the reason pointed out by Roper, Schneider and Shen. For all the runs, the ultimate scour conditions are reached after 6000 waves.

SCOUR PATTERN OBSERVATIONS

The resulting scour patterns for each run were studied to determine the similarities or differences that might be attributed to wave characteristics or sand sizes. In almost all cases, scour initially started around the pile periphery and when eddies were formed, two relatively deep scour holes formed at the rear of the pile approximately 1 to 2 inches from the pile and 30 to 40 degrees from a normal to the wave direction. The two eddy influenced scour holes normally converged toward each other forming a ripple front. The rapidity of the formation of the ripples is dependent on the water depth, the wave characteristics and the mean particle diameter.

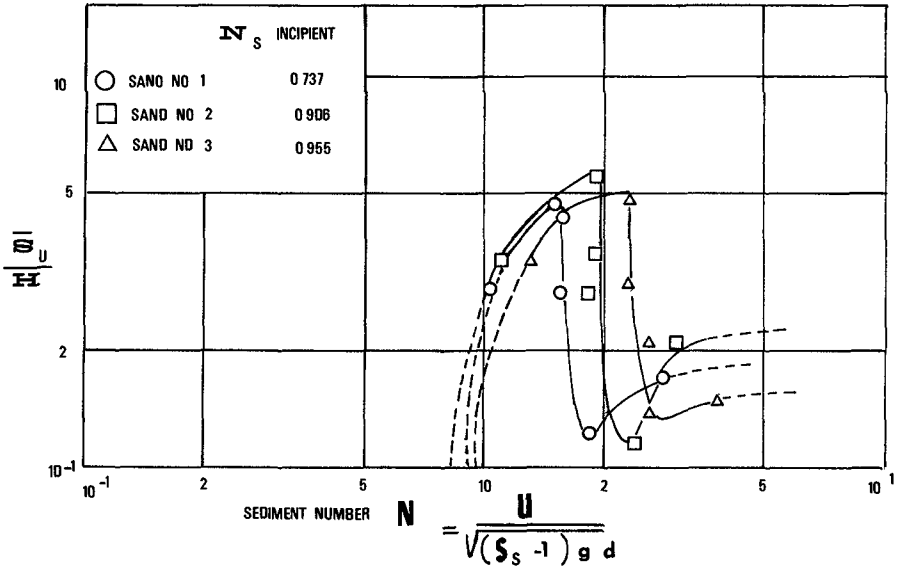


Fig 5 RELATIVE ULTIMATE SIGNIFICANT SCOUR DEPTH AS A FUNCTION OF THE SEDIMENT NUMBER

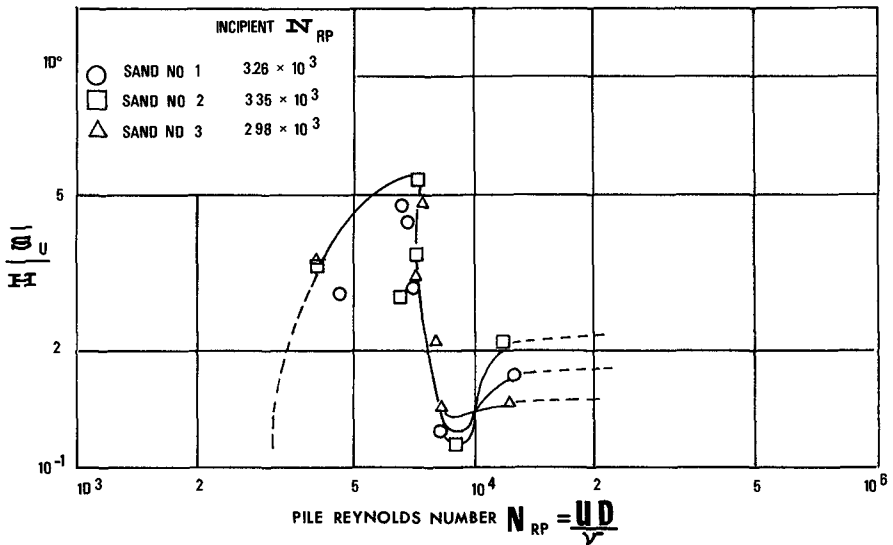


Fig 6 RELATIVE ULTIMATE SIGNIFICANT SCOUR DEPTH AS A FUNCTION OF THE PILE REYNOLDS NUMBER

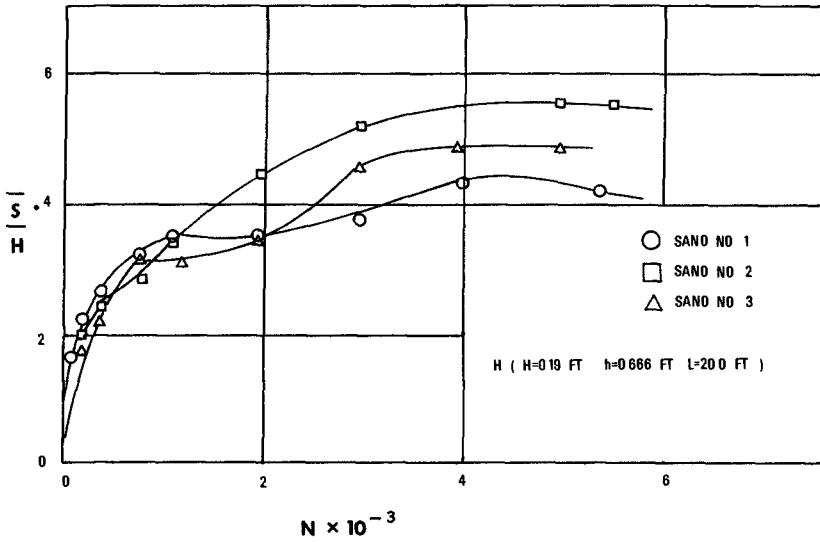


Fig 7 RELATIVE DEPTH OF SCOUR AS A FUNCTION OF NUMBER OF WAVES

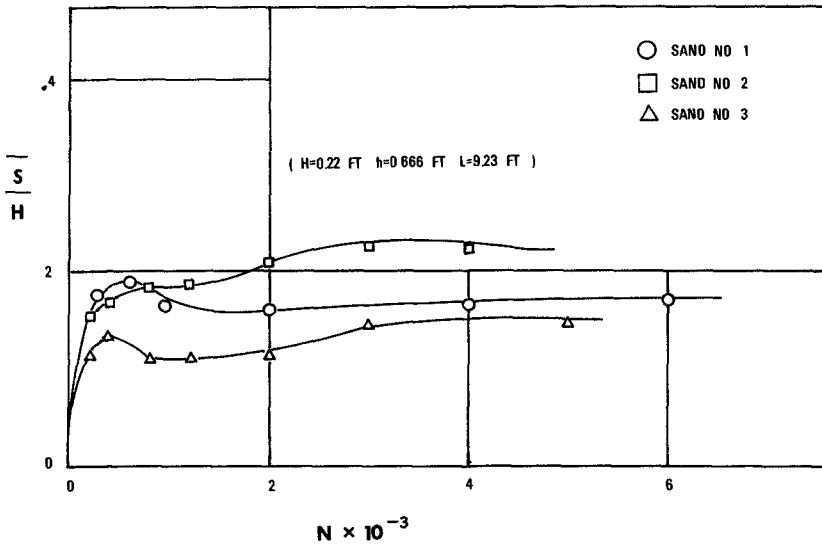


Fig 8 RELATIVE DEPTH OF SCOUR AS A FUNCTION OF NUMBER OF WAVES

Generally it can be said that the resulting scour is strongly influenced by the pile and the wave characteristics. In most of the runs, very little to no bed movement could be observed away from the pile. The pile served as a catalyst to start the scour activity and once started around the pile it spread over a large area and extended in some cases great distances from the pile. Figs 9 and 10 show some typical scour patterns obtained from the experiments.

CONCLUSIONS AND REMARKS

- 1 The critical velocity necessary to cause incipient motion in oscillatory flow appears to be lower than that for steady state flow.
- 2 The ratio of the maximum velocity on the pile boundary and the initial free stream velocity, is less than the value of 2.0 for potential flow theory.
- 3 Incipient motion on the pile boundary appears to be independent of $\frac{H}{h}$ and directly dependent on the parameters $\frac{h}{gT^2}$ and $\frac{d}{h}$.
- 4 $\frac{Su}{H}$ appears to be directly related to the sediment number N_s and the pile Reynold's Number N_{Rp} .
- 5 A maximum of only 6000 waves are required to reach an ultimate scour depth and in most cases 3000 waves are sufficient.
- 6 The relative ultimate significant scour depth increases very rapidly at first, reaching three fourths of its ultimate depth in the first 1000 waves, and increases more slowly after that until it reaches its ultimate depth.
- 7 Eddy forces, although initially influencing the scour patterns, do not appear to be of significance in the final scour pattern.
- 8 The scour pattern resulting is primarily influenced by the pile and the wave characteristics.
- 9 In all the scour experiments, the pile acted as a catalyst causing scour of the bed particles to be initiated whereas if the pile was not present little to no scour would have resulted.

To try and predict scour depths for a prototype case or relate these inconclusive results to a prototype would be presumptuous. To predict happenings or occurrences of a phenomenon in a prototype requires that there be similitude, both geometric and dynamic, between the model and prototype. This requires that similitude exists between the orbital velocities and orbital lengths (i.e., wave characteristics are similar), grain size and grain size distribution in the bed, roughness of the beds, and translation of the orbit due to drift. Without these similitudes, erroneous conclusions could be reached in attempting to predict prototype conditions. The difficulties in acquiring similitude between prototype and model were pointed out by Posey and Sybert¹⁸ in their studies of scour around piles on offshore platforms. It required several years of study and experimentation before actual prototype conditions were duplicated in the model.



Fig. 9. SCOUR PATTERN WAVE NO. 1 - 8 inch depth, Sand No. 2



Fig. 10. SCOUR PATTERN WAVE NO. 1 - 8 inch depth, Sand No. 3

However from the experiments conducted on scour it is felt that certain conjectures on prototype conditions can be made. The maximum scour measured in the experiments was approximately one pile diameter. It, therefore, is conjectured that the maximum scour observable in a prototype would be approximately equal to one pile diameter, which for a typical offshore pile of 4 to 6 feet would be approximately 5 feet. Kreig¹⁹ has reported observed scour depths on offshore platforms in the Gulf of Mexico of 8 to 10 feet and Posey and Sybert¹⁸ measured maximum scour depths of 13 feet with average scour depths of 8 to 10 feet for offshore platforms in line sands off Padre Island, Texas. The average pile diameter associated with the scour measurements made by Posey and Sybert¹⁸ was approximately 3 feet and there was a fairly significant littoral current present. It is important to note from the above discussion that exact similitude is very important. Without every condition duplicated between model and prototype (i.e., the littoral current) erroneous results will be had. The scour patterns for the Padre Island platforms had a dish or saucer appearance, that was much larger in shape than the platform. Scour patterns such as these would not normally be expected.

The conclusion that the scour is very rapid at first and decreases thereafter has been verified by Posey and Sybert¹⁸ who observed that the scour rate is high during the first year or two, and decreases thereafter.

REFERENCES

1. Eagleson, P. S., Dean, R. G., "Wave Induced Motion of Bottom Sediment Particles," *Transactions ASCE*, Vol. 126, 1961, Part 1, pp. 1162-1189.
2. Huon, Li, "Stability of Oscillatory Laminar Flow Along a Wall," *Technical Memorandum No. 47* Beach Erosion Board, 1954.
3. Vincent, G. E., "Contribution to the Study of Sediment Transport on a Horizontal Bed Due to Wave Action," *Proceedings Sixth Conference on Coastal Engineering, ASCE*, Dec. 1957, pp. 326-335.
4. Ippen, A. T., Eagleson, P. S., "A Study of Sediment Sorting by Waves Shoaling on a Plane Beach," *MIT Hydrodynamics Laboratory Report No. 18*, 1955.
5. Ko, S. C., "Scour of Flat Sand Beaches in Front of Seawalls," *Prinz Engineering Laboratory Report No. 2935*, Lehigh University, March 1967.
6. Chepil, W. S., "Equilibrium of Soil Grains at the Threshold of Movement by Wind," *Proceedings of Soil Science Society of America*, Vol. 23, pp. 422-428.
7. Raudkivi, A. J., *Loose Boundary Hydraulics*, Pergamon Press Ltd., London, 1967.
8. Coleman, N. I., "A Theoretical and Experimental Study of Drag and Lift Forces Acting on a Sphere Resting on a Hypothetical Stream Bed," *Proceedings Twelfth Congress, International Association for Hydraulic Research*, Vol. 3, Section C18, 19, 1967.
9. Vanoni, V. et al., "Sediment Transportation Mechanics: Initiation of Motion, Progress Report of the Task Committee on Preparation of Sedimentation Manual, Committee on Sedimentation," *Journal of the Hydraulics Division ASCE*, Vol. 92, No. HY2, Proc. Paper 4738, March 1966.

- 10 Murphy, H D , "Scour of Flat Sand Beaches Due to Wave Action," *Fritz Engineering Laboratory Report No 293 3*, Lehigh University, June 1964
- 11 Van Weele, B , "Beach Scour Due to Wave Action on Seawalls," *Fritz Engineering Laboratory Report No 293 3* Lehigh University, April 1965
- 12 Herbich, J B , Murphy, H D , Van Weele, B , "Scour of Flat Sand Beaches Due to Wave Action in Front of Seawalls" *Proceedings Coastal Engineering Santa Barbara Specialty Conference, Chapter 28, Oct 1965, pp 703 726*
- 13 Roper, A T , Schneider, U R , Shen, H W , "Analytical Approach to Local Scour," *Proceedings Twelfth Congress, International Association for Hydraulic Research, Vol 3, Section C18, 19, 1967*
- 14 Carstens, M R , "Similarity Laws for Localized Scour," *Journal of the Hydraulics Division ASCE, Vol 92, No HY3, Proc Paper 4818, May 1966*
- 15 Dean, R G , "Relative Validities of Water Wave Theories," *Proceedings, Conference on Civil Engineering in the Oceans, ASCE, San Francisco, 1967*
- 16 Le Me'haute', B , Divoky, D , Lin A , 'Shallow Water Waves A Comparison of Theories and Experiments," *Proceedings Eleventh Conference on Coastal Engineering, London, 1968*
- 17 Wells, D R , "Scour Around a Circular Pile Due to Oscillatory Wave Motion," a M S thesis, Texas A&M University, January 1970, unpublished
- 18 Posey, C J , Sybert, J H , "Erosion Protection of Production Structures," *Proceedings Ninth Congress, International Association for Hydraulic Research 1961, pp 1157 1162*
- 19 Kreig, J L , "Criteria for Planning an Offshore Pipeline," *Journal of the Pipeline Division ASCE, Vol 91, No PL 1, July 1965, pp 15 37*

CHAPTER 80

COMPARISON OF MODEL AND BEACH SCOUR PATTERNS

by

John B Herbich, Ph D , P E
Professor and Head
Coastal and Ocean Engineering Division
Texas A&M University
College Station, Texas 77843

ABSTRACT

Artificial or natural barriers may be divided into two classes, those from which waves are reflected and those on which waves break. In general, any intermediate type that gives a combination of reflection and breaking may set up severe erosive action of the beach in front of barriers. When the reflected waves are superimposed on the incident waves a stationary spatial envelope of the combined incident and reflected waves is produced. Previous laboratory studies indicated that the crests of the sand bed appear fairly closely under the nodes of the envelope and troughs of the scoured sand bed under the loops of the envelope. The predominant scouring pattern had a spacing between crests equal to one-half the wave length.

Other studies by Keulegan and Shepard established characteristic parameters for bar and trough depth for laboratory conditions and for several field locations. Their studies were compared with beach profiles taken along the Texas Gulf Coast.

Relationships between (a) scour depth and sand crest wave length, (b) between trough depth and sand bar depth and between wave characteristics and beach scour were established for selected locations along the Texas Coast.

INTRODUCTION

Natural or artificial barriers may be divided in two classes, those from which waves are reflected and those on which waves break. In general, any intermediate type that gives a combination of reflection and breaking may cause excessive erosive action seaward from the barrier.

One laboratory study was confined to non-breaking waves at the seawall and the main objective was to investigate the nature of scour of a flat, horizontal sand beach in front of a seawall due to wave action. Some of the results were presented at the Eleventh Conference on Coastal Engineering (1)*. Since then field data were acquired and analyzed for several locations along the Gulf of Mexico Texas coast. Another study by Sato et al, also in laboratory, principally dealt with waves breaking at the seawall. The principal objective of that investigation was to determine the basic characteristics and to determine possible measures to prevent erosion around coastal structures (2). The study was followed up by field investigations which indicated that beach scour depends not only on wave characteristics just in front of structures and wave reflection from the structures but also on the currents set up by waves around the structures.

Studies by Otto (3), Hartnack (4), Keulegan (5) and Shepard (6) dealt with laboratory or field studies on characteristics of offshore sand bars formed by waves.

In recent years a beach profile and jetty condition survey along the Texas Gulf Coast was undertaken (7) and preliminary analysis indicates that scour patterns and other characteristics resemble those obtained in laboratories and at other field locations.

Unfortunately data for waves which produced these patterns are very scarce, if at all available, so that any comparisons between laboratory and field conditions can only be very approximate.

LITERATURE REVIEW

Underwater sand bars are found in all parts of the world along the coastlines of lakes, seas and oceans. There may be only one distinct bar consisting of a crest, or ridge on the seaward side and a trough on the landward side, or there may be a series of bars with related crests and troughs.

The bar formations have been studied by geologists and geographers for over a century and considerable field data of the form, number of bars and dimensions are available. However, only a few laboratory

* Numbers in parenthesis refer to references at the end of paper

studies were made and only limited explanations of the hydromechanics process have been put forward

Field observations of form and dimensions of natural, underwater beach profiles were made along the Baltic Coast, Lake Michigan, California and the Texas Coast

Otto and Hartnack (3, 4) reported on measurements along the Pomeranian Baltic Coast, while Evans (8) reported field measurements of the bars along Lake Michigan. There were essentially three distinct bars measured on the Eastern shore of Lake Michigan

Keulegan (5) indicated that the form of experimental bars varies considerably from that of the natural bars. In general the natural bars are flatter and longer than the bars formed in a laboratory wave channel. This may be due in large part to the fact that one cannot scale down the size of sand used, as most of the laboratory investigations employed natural sands of approximately the same size as the prototype sands. It should also be noted that the laboratory beach profiles are usually subject to monochromatic waves while the prototype waves are usually irregular and contain a spectrum of wave heights and wave lengths. However, Keulegan also noted that the ratio of depth of crest (h_c) to the depth of the bar (h_T) was similar in the model and prototype

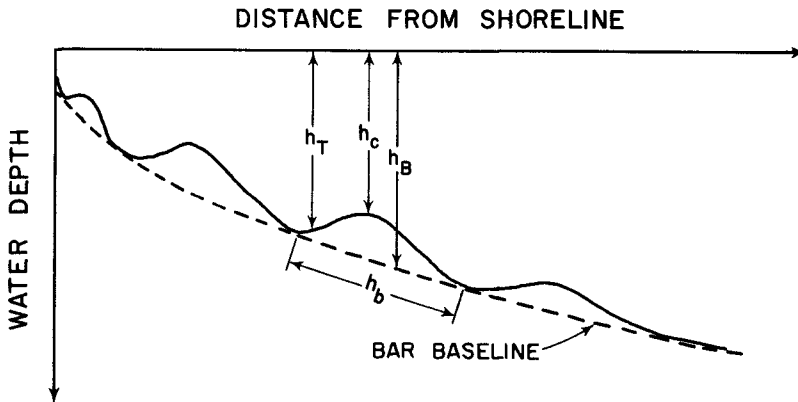


FIG 1 DEFINITION SKETCH

Shepard (6) examined thousands of beach profiles taken along the ocean piers in California and indicated that the troughs which lie between the shoreline and the submerged beach bars are formed by the plunging breakers and by the longshore currents which feed the rip currents. He also found that there is a relationship between the depth of the bars and troughs and the wave height

SAND SCOUR ON SLOPING SURFACES

Previous Investigations

Both Keulegan (5) and Shepard (6) conducted investigations concerning the characteristics of beach scour patterns in response to breaking waves. Keulegan conducted a series of laboratory experiments and found that the scour trough forms at the breaker plunge point, with a corresponding accumulation of sand, or the sand bar, forming just seaward of this location. It was found that after initiation of uniform wave patterns over the sloping bottom, a trough-bar complex developed rapidly, migrating onshore until an equilibrium position was reached. Thereafter only small changes in the scour pattern occurred. Similar results were reported by Herbich and Ko (1), indicating that the scour depth limit is approached asymptotically.

Shepard (6) summarized the results of three hundred and fifty three beach profiles taken at Scripps Pier at La Jolla, California.

Both Keulegan and Shepard stress the importance of wave characteristics as influencing the scour pattern. Keulegan's results show that the ratio of H/h_B

where H - wave height, and

h_B - distance from still water level to the bar base
(see Fig 1)

increases with wave steepness (H/L) up to a steepness of 0.04. For greater values of steepness the ratio of H/h_B is independent of wave steepness and remains constant at about 0.83. This relationship was found to be independent of beach slopes for slopes between 1:15 to 1:70.

Keulegan and Shepard also examined the ratio of h_T/h_C where

h_T = trough depth from still water level, and

h_C = sand crest depth from still water level
(see Fig 1)

Keulegan noted that the h_T/h_C ratio was practically independent of wave steepness and beach slope and computed an average value of 1.69 for his laboratory experiments.

Shepard also determined a relatively uniform relationship of h_T/h_C with an average value of 1.16 at Scripps Pier (using mean sea level as datum).

Current Investigations

A survey report prepared by U. S. Army Corps of Engineers (7) presents beach profiles taken at selected locations along the Texas Gulf Coast during the past several years. Analysis of these profiles was made to determine the characteristics of natural scour pattern along the coast, and to compare with previous laboratory and field studies. The data were analyzed for the following locations:

- (1) East Beach, Galveston, Texas (Fig 2)
- (2) Groin Area, Galveston, Texas
- (3) West Beach, Galveston, Texas
- (4) Panther Point, Matagorda - Port Aransas, Texas
- (5) Yarborough Pass, Padre Island, Texas

Since space limitation prevents reproduction of all tabulated data, only average values and selected sample data are given

Table I gives the average values of distances between sand crests (sand wave lengths) and average depth of scour for East Beach at Galveston Tables II through V gives similar information for Groin Area - Galveston, West Beach - Galveston, Panther Point - Matagorda - Port Aransas and Yarborough Pass, Padre Island

Fig 3 presents sample beach profile for East Beach at Galveston The crests of bars were joined to indicate the crest pattern along the beach section Fig 4 is for Panther Point and Fig 5 is for Yarborough Pass location

Relationship Between Scour Depth and Sand Crest Wave Length

Scour depth readings as well as scour wave length measurements were taken for all locations and a sample location is given in Fig 6 Although the scatter is considerable (as may be expected) the relationship may be approximated by a straight line having a slope of 0.004

Relationship Between Trough Depth and Sand Bar Depth

Values of trough depth to sand bar depth (h_T/h_C) were determined at each location along the Texas Coast for various times of the year

The ratio of trough depth to sand bar depth was plotted for three locations along the Texas Coast as a function of time (Figure 7) It will be noted that there is some annual variation in this ratio which, of course, may be caused by major storms, or hurricanes, but the variation is within fairly narrow limits of h_T/h_C For example for Matagorda Bay the variation is between 1.15 and 1.42, with an average value of about 1.25

Figure 8 shows the relationship for other locations in addition to locations shown in Figure 7 The data indicate that this ratio tends toward an equilibrium value characteristic of each location, but at times a significant deviation from this value may occur

Depth of trough is plotted in Figure 9, against the depth of bar for several field locations along the Texas Coast Field data from Washington and Oregon coast and data from California are also plotted as well as Keulegan's laboratory data Remarkably consistent results are obtained for all locations with field data ranging between h_T/h_C values of 1.16 and 1.60 The laboratory data gives a value of 1.69

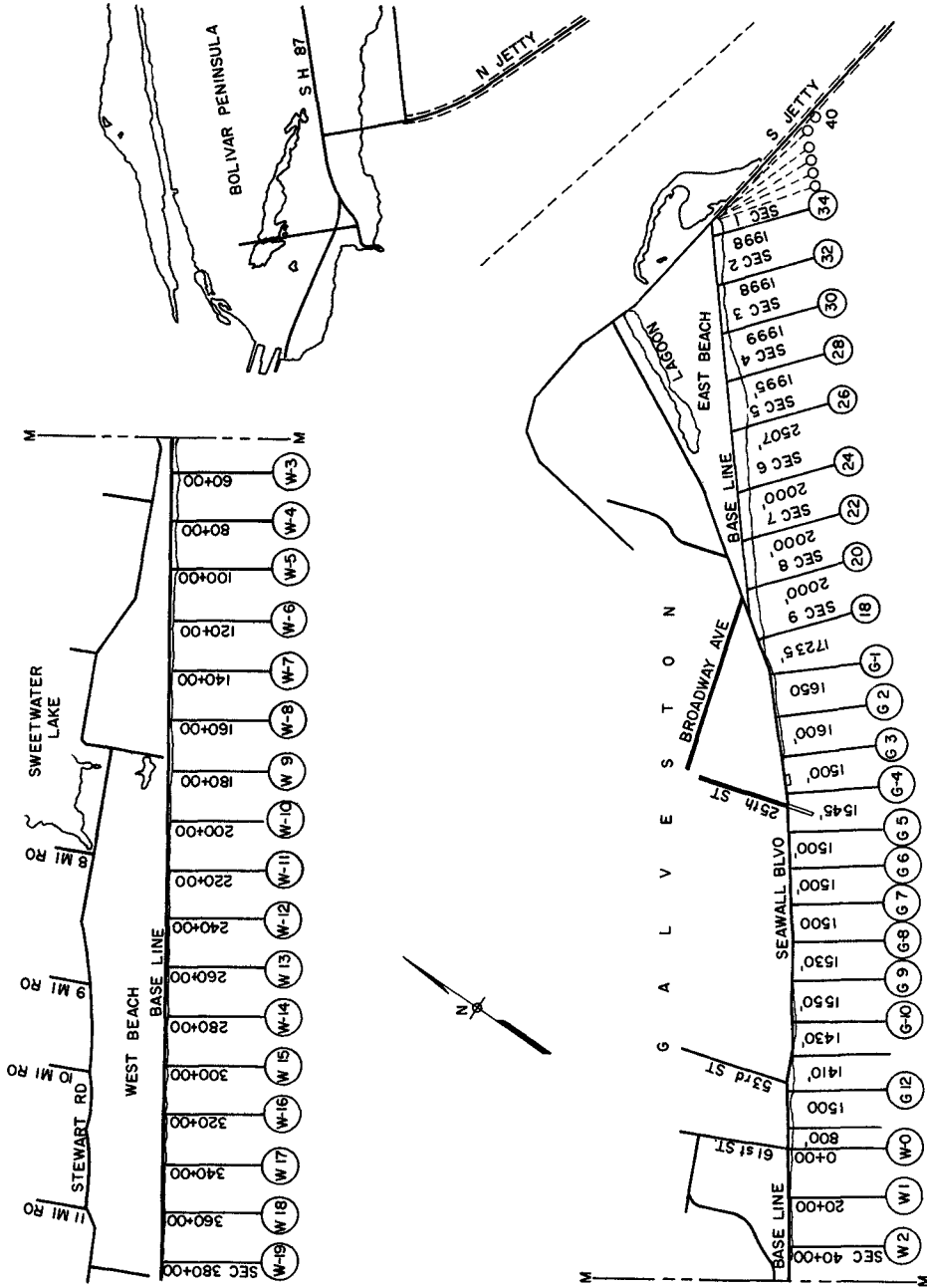


FIG 2 COMPARATIVE STUDY PLAN SHEET GALVESTON (FROM REF 7)

SCOUR PATTERNS

1287

EAST BEACH
GALVESTON, TEXAS

Section	Period	Average Distance Between Sand Crests (ft)	Average Depth of Scour (ft)
1	1934-68	301	76
2	1934-68	257	68
3	1934-68	354	99
4	1934-68	327	93
5	1934-68	298	97
6	1934-68	354	87
7	1934-68	277	1 23
8	1934-68	310	1 04
9	1934-68	272	73
10	1949-68	240	1 07
11	1949-69	314	70
12	1949-69	345	77
13	1949-69	252	89
Average		300	89

TABLE I

GROIN AREA
GALVESTON, TEXAS

Section	Period	Average Distance Between Sand Crests (ft)	Average Depth of Scour (ft)
14	1949-69	280	70
15	1949-69	202	48
16	1949-69	180	45
17	1949-69	286	88
18	1949-69	232	87
19	1949-69	247	67
20	1949-69	227	48
21	1949-68	305	1 38
22	1949-69	192	45
23	1949-69	206	44
24	1949-69	230	1 18
25	1949-69	207	26
26	1949-69	212	35
27	1949-69	187	49
28	1949-69	178	36
29	1949-69	165	48
30	1949-69	202	91
31	1949-69	242	35
32	1949-69	189	43
33	1949-69	186	37
34	1949-69	178	46
35	1949-69	178	68
36	1949-69	227	48
37	1949-69	181	58
38	1949-69	276	61
39	1949-69	221	47
40	1949-69	194	64
41	1949-69	220	77
42	1949-69	262	61
43	1949-69	279	62
44	1949-69	209	50
45	1949-69	195	37
46	1949-69	341	60
47	1949-69	230	61
Average		222	59

TABLE II

WEST BEACH
GALVESTON, TEXAS

Section	Period	Average Distance Between Sand Crests (ft)	Average Depth of Scour (ft)
0 + 00	1949-69	231	70
20 + 00	1949-68	200	80
40 + 00	1949-68	210	1 0
60 + 00	1949-68	215	95
80 + 00	1949-68	181	1 03
100 + 00	1949-68	304	75
120 + 00	1949-68	273	1 17
140 + 00	1949-68	178	1 3
160 + 00	1949-68	198	1 0
180 + 00	1949-68	363	78
200 + 00	1949-68	231	73
220 + 00	1949-68	244	83
240 + 00	1961-68	187	83
260 + 00	1961-68	218	1 07
280 + 00	1961-68	373	77
300 + 00	1961-68	311	87
320 + 00	1961-68	423	1 03
340 + 00	1961-68	184	70
360 + 00	1961-68	221	73
380 + 00	1961-68	184	67
400 + 00	1961-68	226	90
420 + 00	1961-68	202	60
440 + 00	1961-68	310	73
460 + 00	1961-68	333	67
470 + 00	1961-68	279	60
Average		251	84

TABLE III

COASTAL ENGINEERING

PANTHER POINT

MATAGORDA - PORT ARANSAS, TEXAS

Section	Date	Distance Between Sand Crests* (In Feet)	Avg	Depth of Scour, Ft	Avg
0 + 00	5/23/1967	85, 40, 50, 100, 70, 140, 100, 65	81		
0 + 00	11/5/1967	45, 100, 150, 150, 110, 85	107		
0 + 00	7/26/1968	104, 160	132	0 2, 0 5	0 35
0 + 00	10/10/1968	47, 57	52	0 4, 0	0 2
0 + 00	1/9/1969	150	150	0 3	0 3
0 + 00	3/10/1969	80	80	0 25	0 25
0 + 00	7/15/1969	165	165	0 8	0 8
0 + 00	1/21/1970	100	100	0 3	0 3
10 + 00	5/23/1967	45, 85, 70, 115, 95, 100, 70, 70	81		
10 + 00	11/5/1967	60, 90, 140, 160, 90, 100	107		
10 + 00	7/26/1968	152, 95	123	0 4, 0 6	0 5
10 + 00	3/10/1969	110, 40	75	0, 0	0
10 + 00	7/15/1969	95, 105, 90	97	0 4, 0 2, 0 15	0 25
20 + 00	5/23/1967	165, 70, 90, 100, 75, 95, 65, 125	98		
20 + 00	11/5/1967	70, 105, 180, 125, 45, 140	111		
20 + 00	7/25/1968	165	165	0 9	0 9
20 + 00	7/9/1969	283	283	0 8	0 8
20 + 00	3/10/1969	95	95	0 2	0 2
20 + 00	7/15/1969	190, 97	143	0 3, 0 8	0 55
20 + 00	1/21/1970	300	300	0 5	0 5
30 + 00	5/23/1967	100, 70, 60, 165, 75, 85, 80, 125	95		
30 + 00	11/5/1967	50, 115, 195, 125, 40, 180	118		
30 + 00	7/26/1968	235	235	0 6	0 6
30 + 00	1/9/1969	210	210	0 7	0 7
30 + 00	3/10/1969	95, 45, 75	72	0 4, 0 2, 0 1	0 22
30 + 00	7/15/1969	115, 207	161	0 4, 0 5	0 45
30 + 00	1/21/1970	153, 45	100	0 5, 0 4	0 45
All Sections	5/23/1967	Average	89		
All Sections	11/5/1967	Average	111		
All Sections	7/26/1968		152		0 33
All Sections	10/10/1968		52		0 20
All Sections	1/9/1969		214		0 6
All Sections	3/10/1969		77		16
All Sections	7/15/1969		133		44
All Sections	1/21/1970		150		43
0 + 00		Average	121	Average	46
10 + 00			97		25
20 + 00			171		59
30 + 00			142		48

* Some of the data relate to sand bars formed during the hurricanes which are now above water surface

TABLE IV

SCOUR PATTERNS

1291

YARBOROUGH PASS

PADRE ISLAND, TEXAS

Section	Date	Distance Between Sand Crests* (In Feet)	Avg	Depth of Scour, Ft	Avg
0 + 00	5/19/1967	160	160		
0 + 00	11/9/1967	160	160		
0 + 00	6/19/1968	160, 190	175		
0 + 00	1/7/1969	140	140	1	2
0 + 00	3/5/1969	110, 100	105	0 2, 1	0 6
0 + 00	7/11/1969	225	225	1 9	1 9
0 + 00	1/20/1970	125, 132	128	1 1, 1 5	1 3
10 + 00	5/19/1967	165	165		
10 + 00	11/9/1967	135	135		
10 + 00	6/19/1968	120, 210	165		
10 + 00	1/7/1969	115	115	2 5	2 5
10 + 00	7/11/1969	118	188	2 75	2 75
10 + 00	1/20/1970	110, 150	130	1 1, 1 5	1 3
20 + 00	5/19/1967	145	145		
20 + 00	11/9/1967	135	135		
20 + 00	6/19/1968	85, 250	168		
20 + 00	1/7/1969	125	125	1 8	1 8
20 + 00	3/5/1969	110	110	2 65	2 65
20 + 00	7/11/1969	215	215	2 0	2 0
20 + 00	1/20/1970	105, 110	107	1 0, 1 0	1 0
30 + 00	5/19/1967	175	175		
30 + 00	11/9/1967	110	110		
30 + 00	6/19/1968	145, 240	193		
30 + 00	7/11/1969	160	160	2 0	2 0
30 + 00	1/20/1970	210	210	2 4	2 4
All Sections	5/19/1967	Average	161		
All Sections	11/9/1967	Average	135		
All Sections	6/19/1968	Average	175		
All Sections	1/7/1969		127		2 25
All Sections	3/5/1969		108		0 88
All Sections	7/11/1969		197		2 16
All Sections	1/20/1970		135		1 37
0 + 00		Average	156	Average	1 5
10 + 00			150		2 2
20 + 00			159		2 1
30 + 00			170		2 2

* Some of the data relate to sand bars formed during the hurricanes which are now above water surface

TABLE V

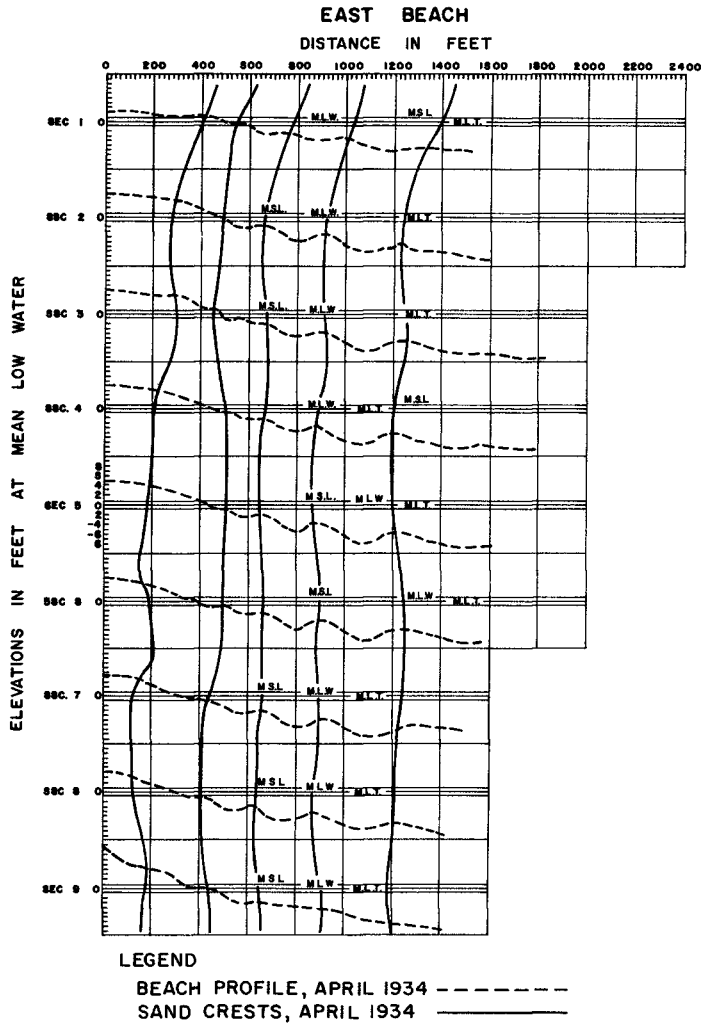
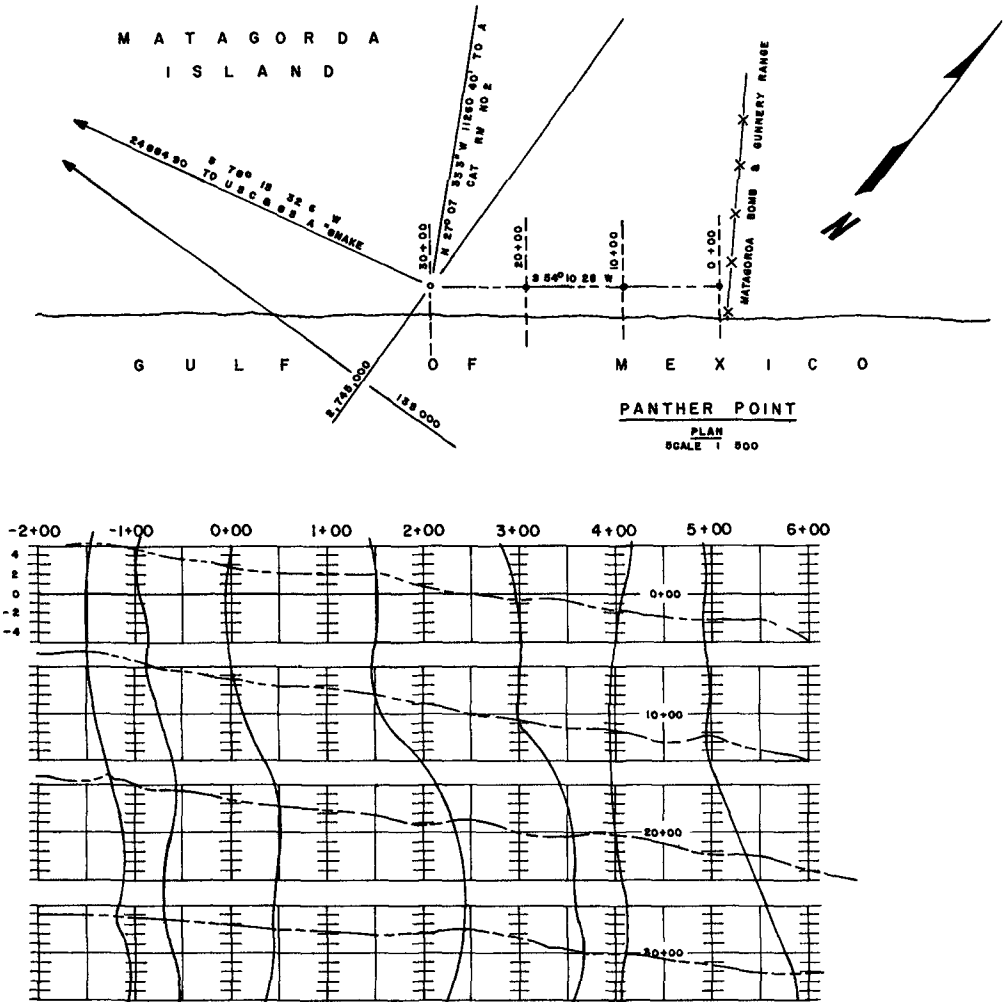
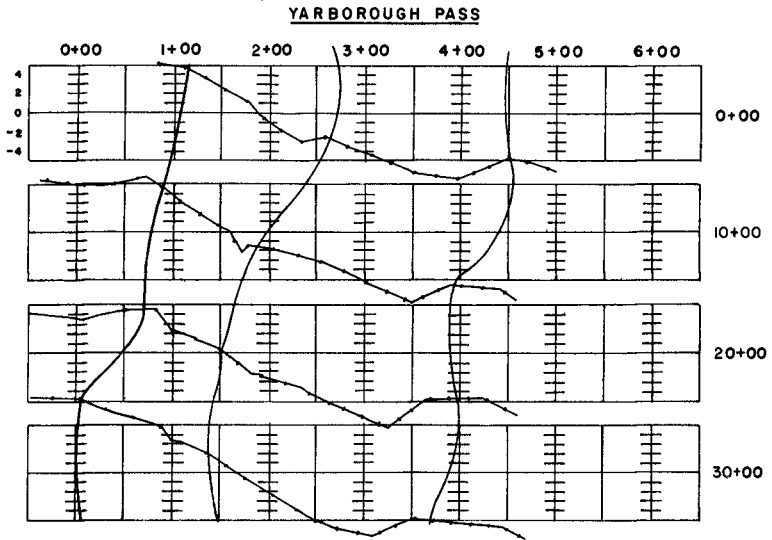
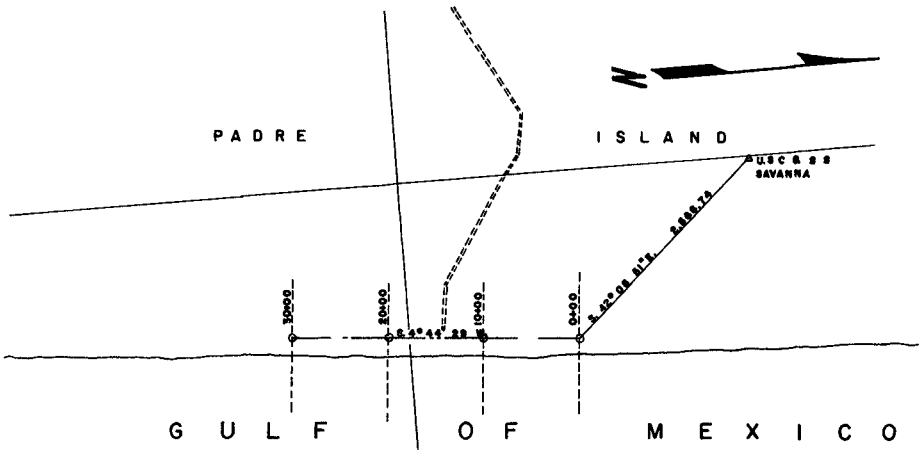


FIG 3 BEACH PROFILE AND SAND CRESTS AT EAST BEACH, GALVESTON (FROM REF 7)



LEGEND
 BEACH PROFILE, 5 NOV 1967 -----
 SAND CREST, 5 NOV 1967 _____

FIG 4 BEACH PROFILE AND SAND CRESTS
 AT PANTHER POINT (FROM REF 7)



LEGEND
BEACH PROFILE, 19 JUNE 1968 ————
SAND CREST, 19 JUNE 1968 ————

FIG 5 BEACH PROFILE AND SAND CRESTS AT YARBOROUGH PASS (FROM REF 7)

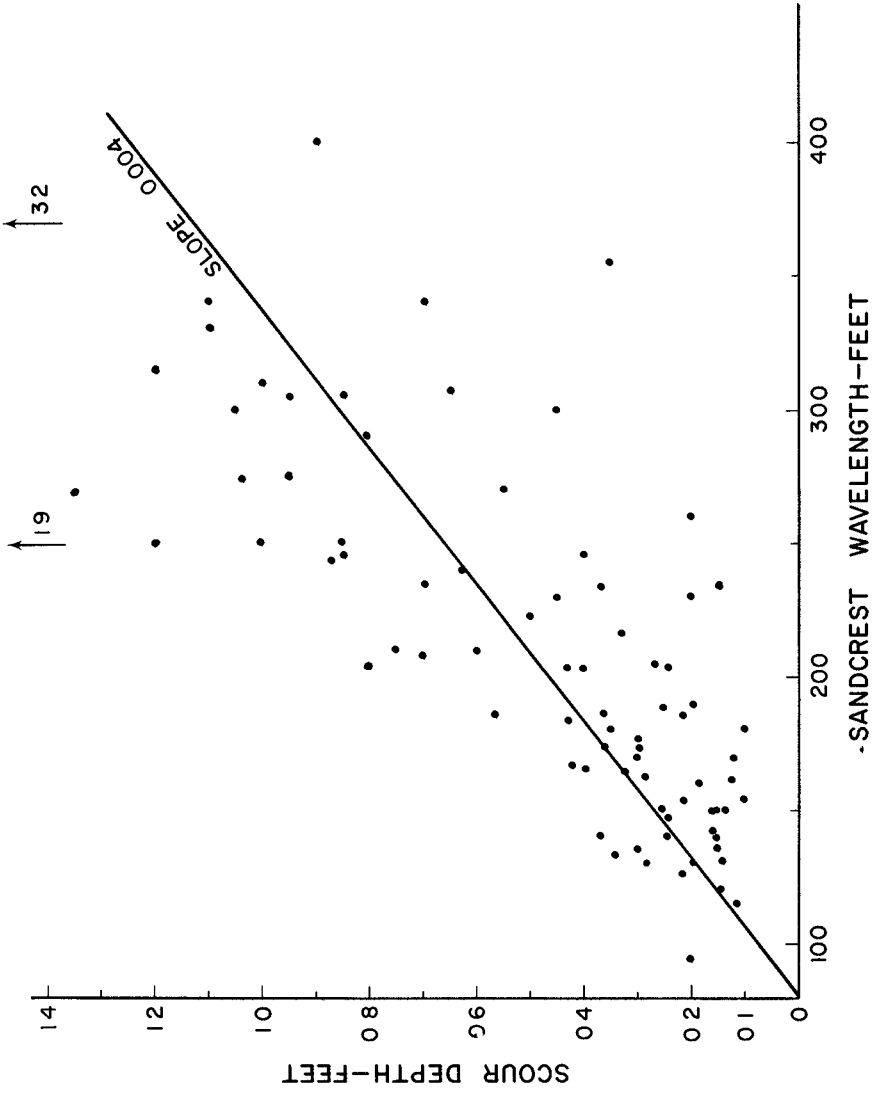


FIG 6 RELATIONSHIP BETWEEN DEPTH OF SCOUR AND SCOUR WAVE LENGTH FOR EAST BEACH AT GALVESTON, TEXAS

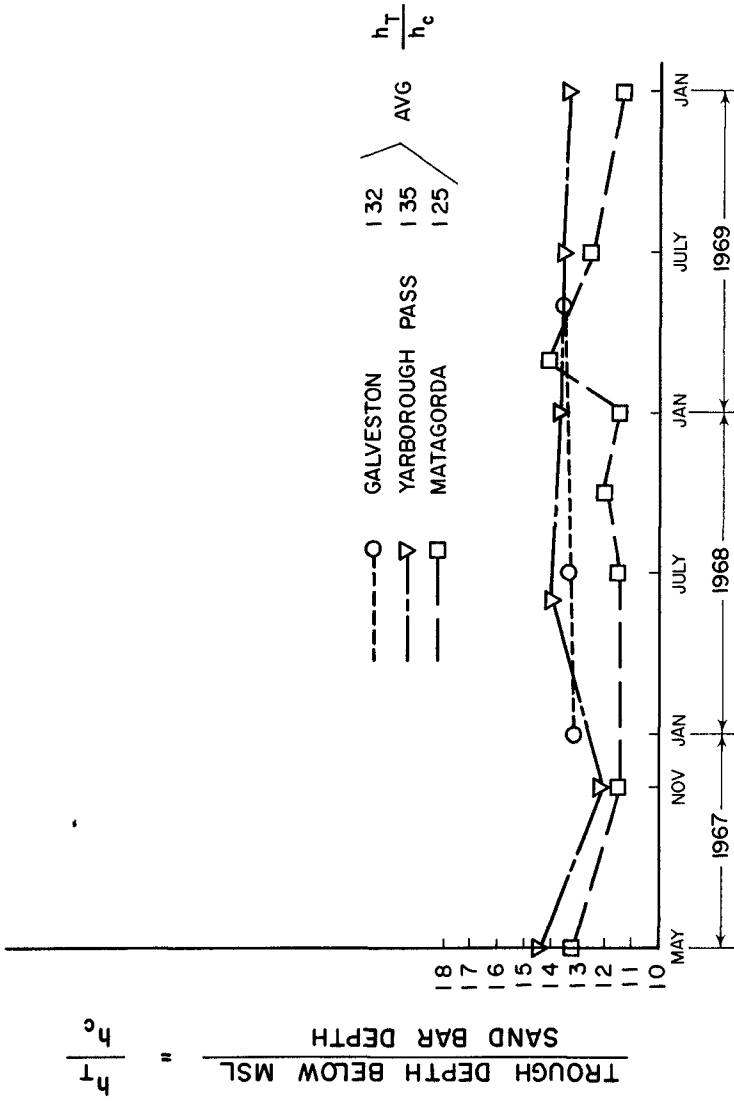


FIG 7 TROUGH DEPTH-SAND BAR DEPTH RATIO AS A FUNCTION OF TIME

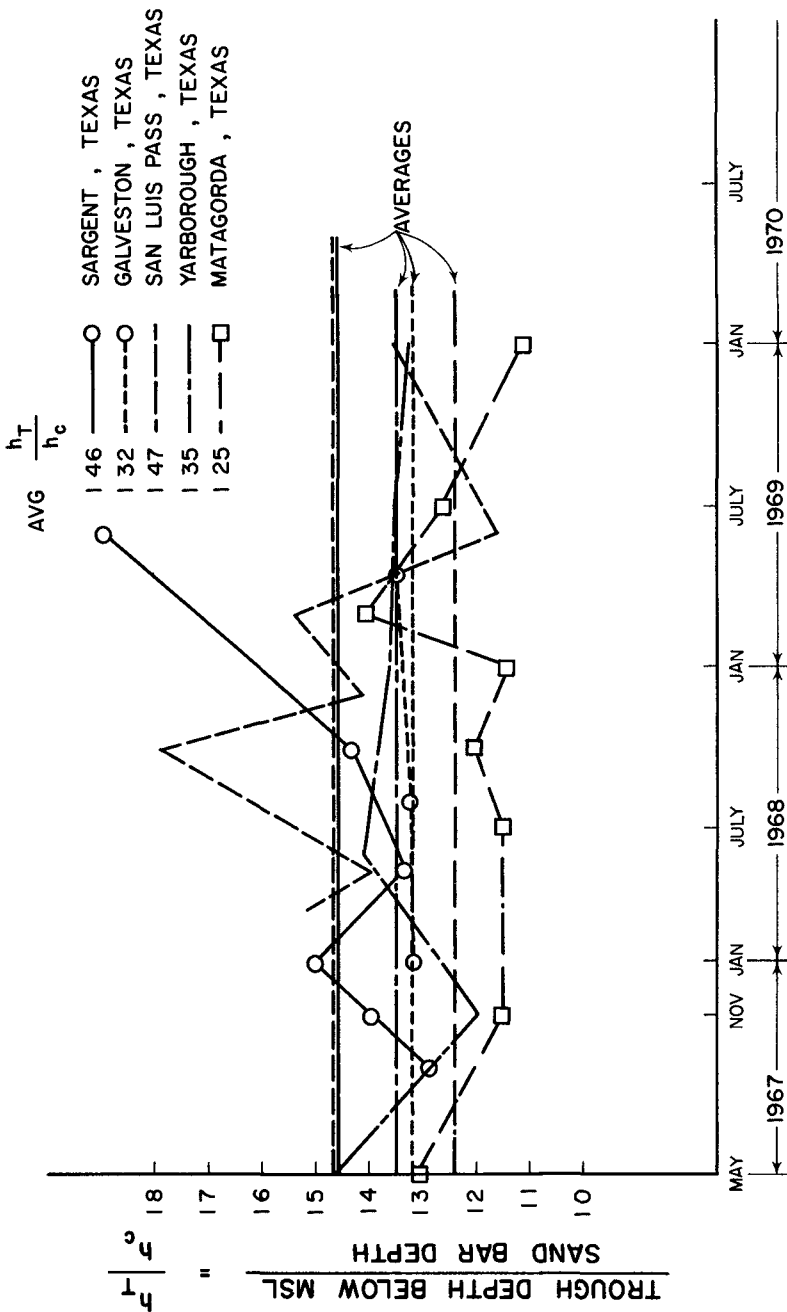


FIG 8 TROUGH DEPTH - SANDBAR DEPTH RATIO AS A FUNCTION OF TIME FOR SEVERAL TEXAS LOCATIONS

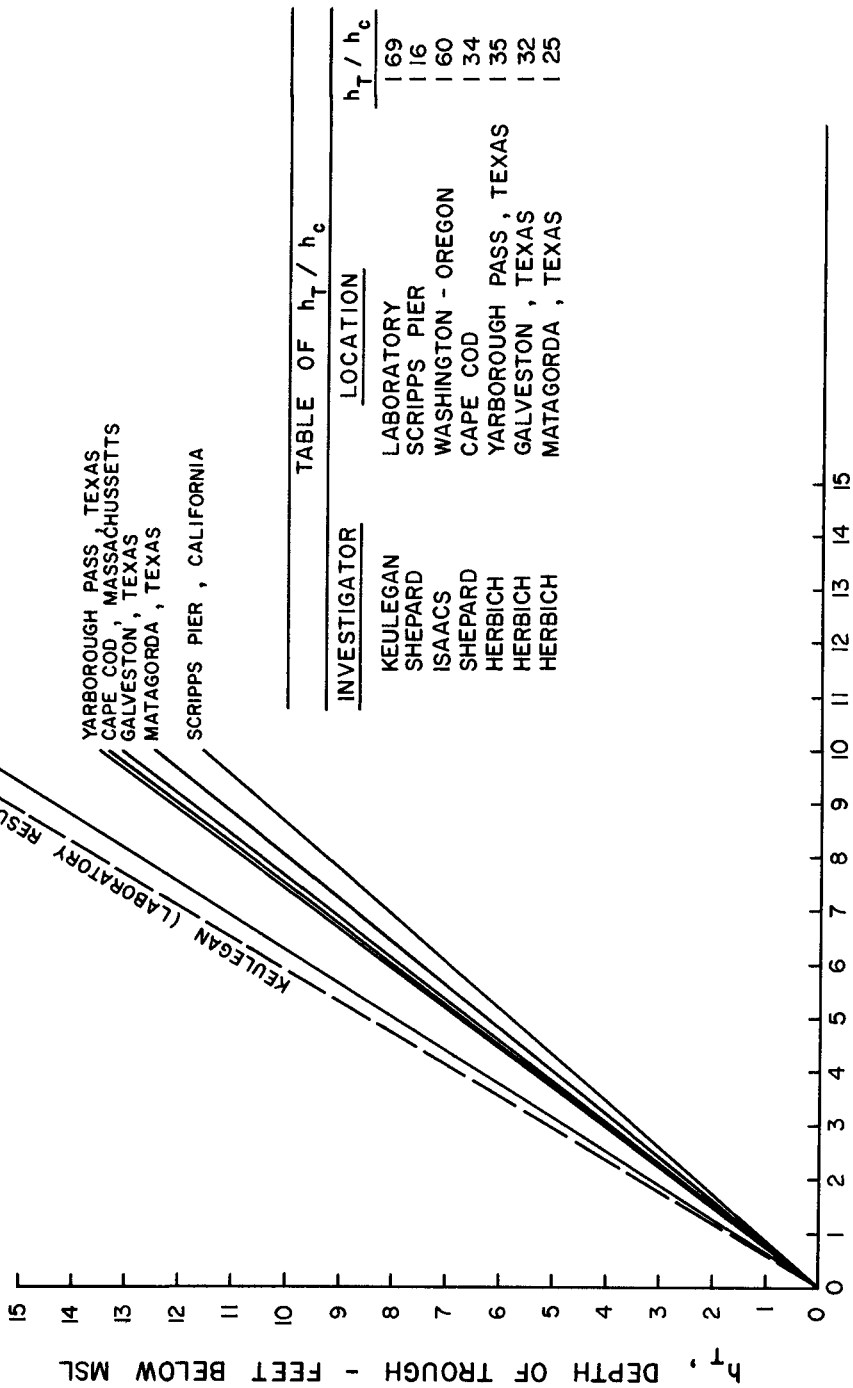


TABLE OF h_T / h_c

INVESTIGATOR	LOCATION	h_T / h_c
KEULEGAN	LABORATORY	1.69
SHEPARD	SCRIPPS PIER	1.16
ISAACS	WASHINGTON - OREGON	1.60
SHEPARD	CAPE COD	1.34
HERBICH	YARBOROUGH PASS, TEXAS	1.35
HERBICH	GALVESTON, TEXAS	1.32
HERBICH	MATAGORDA, TEXAS	1.25

h_c , DEPTH OF BAR - FEET BELOW MSL
 FIG 9 RELATIONSHIP BETWEEN DEPTH OF TROUGH
 AND DEPTH OF BAR

Relationship Between Waves and Beach Scour

Analyses of Texas beach profiles indicate that in most cases more than one bar-trough complex formation was created by wave action. Laboratory experiments by Herlich and Ko (1) and by Sato et al (2) have revealed that the distance between succeeding bar crests is a function of wave length, and was generally equal to one half the wave length generated, for several sand sizes employed.

In general wave data for locations where beach profiles are measured are very scarce, or difficult to obtain. For the purpose of this analysis wave data taken during hurricane Beulah (October 1967) at Galveston were obtained from the Coastal Engineering Research Center (9). The wave data were analyzed, using spectral methods, and equivalent wave height and period at maximum spectral density were obtained.

Beach profiles taken in January, 1968 were also analyzed. The results of the analyses are as follows:

Location	Average Length Between Crests (ft)	Average Deep** Water Wave Length (ft)	Average* Wave Length at 18' Depth	Average Scour Depth (ft)	Equivalent** Wave Height (ft)
East Beach	330	261	159	0.86	5.36
Groin Area	312	261	159	0.76	5.36

* Wave gauge was located at 18 ft depth

**Analyzed using power spectrum method

Comparison of the beach profiles at Galveston indicates that the average spacing between crests was greater than the deep water wave length and about twice as long as the average wave length at 18 ft depth, which does not agree with laboratory studies. The relationship between average scour depth and the average wave height is approximately equal to 0.160 for the East Beach area and equal to 0.142 for the Groin area.

CONCLUSIONS

Definite relationships exist between

- (1) trough depth and sand crest depth
- (2) average length between sand crests and the average wave length
- (3) average scour depth and average wave height
- (4) additional studies, particularly in the field, should be conducted

ACKNOWLEDGEMENT

Cooperation of Galveston District of U S Army Engineers in providing beach profile data along the Texas Coast is appreciated Assistance of Miss Rosella Duke, a civil engineering student and Messrs Ch Chestnutt, C McClenan and C Mason, graduate students in coastal and ocean engineering in data reduction is acknowledged

REFERENCES

- 1 Herbich, J B and S C Ko, "Scour of Sand Beaches in Front of Seawalls", Proceedings of the Eleventh Conference on Coastal Engineering, London, England, Chapter 40, pp 622-643, September 1968
- 2 Sato, S , M Tanaka and I Irie, "Study on Scouring at the Feet of Coastal Structures", Proceedings of the Eleventh Conference on Coastal Engineering, London, England, Chapter 37, pp 579-598, September 1968
- 3 Otto, T , "Der Darss und Zingst", Jahresber Geogr Ges Greisswald, Vol 12, 1911-12
- 4 Hartnack, W , "Uber Sandriffe", Jahresber Geogr Ges Greisswald, Vol 40-42, 1924
- 5 Keulegan, G H , "An Experimental Study of Submarine Sand Bars", Technical Report No 3, Beach Erosion Board, Corps of Engineers, U S Army, 40 pp , 1948
- 6 Shepard, F P , "Longshore-Bars and Longshore-Troughs", Technical Memorandum No 15, Beach Erosion Board, Corps of Engineers, U S Army, 31 pp , January 1950
- 7 "Texas Coast Inlet Studies", Galveston District, Corps of Engineers, U S Army, 1968, 1969
- 8 Evans, O F , "The Low and Ball of the Eastern Shore of Lake Michigan", Journal of Geology, Vol 48, p 476, 1940
- 9 Personal communication from Dr Harris, Coastal Engineering Research Center, U S Army Corps of Engineers, August 1970

CHAPTER 81

VARIATION OF TOPOGRAPHY OF SEA-BED CAUSED BY THE CONSTRUCTION OF BREAKWATERS

Shoji Sato and Isao Irie
Hydraulics Division, Port and Harbour Research Institute
Ministry of Transport
1-1, 3 Chome, Nagase, Yokosuka, Japan

INTRODUCTION

In Japan, many breakwaters or jetties have been constructed in the sandy beach from the past decade for new ports to cope with the development of industry. It is needless to say that the construction and prolongation of breakwaters or jetties cause the change of bottom-topography in their vicinity, but many points remain indistinct on this change of bottom-topography.

In this paper, some general properties on the change of the topography of sea-bed caused by the construction of breakwaters are discussed on the basis of the hydraulic sounding maps of several ports and the results of model tests. The terminology used in this paper is given in Figure 1.

VARIATION OF SEA-BED TOPOGRAPHY AT KASHIMA PORT

Port Kashima is located on the coast of Kashimanada facing the Pacific Ocean, as shown in Figure 2. Waves of the coast of Port Kashima approach from the direction almost perpendicular to the shore line, though the southerly waves exceed a little than the northerly waves. The maximum significant wave observed in the period from 1961 to 1968 is 5 m in height and 10.3 sec in period. The mean diameter of bottom material is about 0.15 mm in the offshore and 0.6-0.2 mm in the inshore. The alongshore littoral transport per year is estimated to be the order of 600,000 cubic meters both in the southerly and northerly directions on the basis of the hydraulic sounding data and the calculation of wave energy, though the littoral transport from the south exceeds a little that from the north in the sum of several years.

Figure 3 and 4 shows the position of equi-depth lines for each summer from 1963 to 1968.

In July 1963, the down-side breakwater and the jetty of the working basin were constructed as far as the alongshore bar. The shore line advanced up-side of the jetty and severe scouring was seen in the vicinity of the tip of the jetty.

In July 1964, the working basin was completed and the up-side breakwater was constructed for nearly 200 m. These parts of the breakwater was constructed with rouble stones. The equi-depth lines of 0 to 3 m advanced near the jetty of the working basin on the up-side,

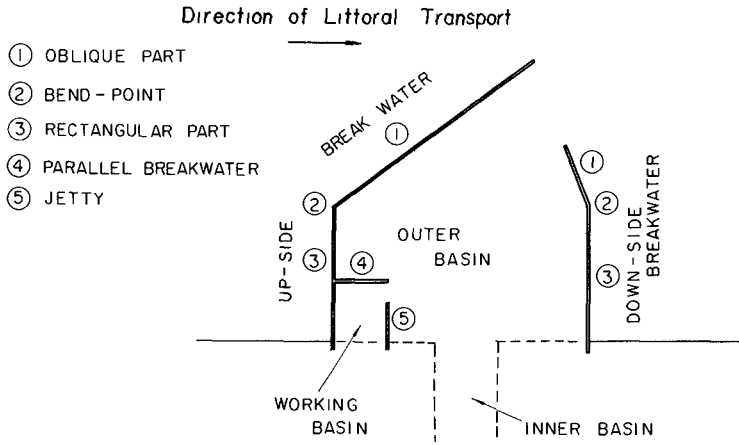


Figure 1 Terminology of each part.

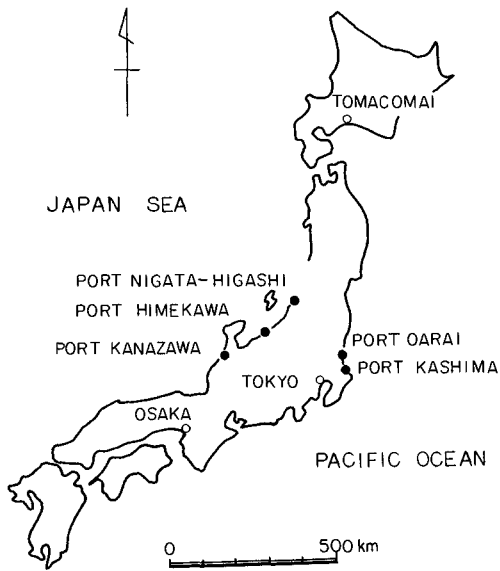


Figure 2 Position of ports

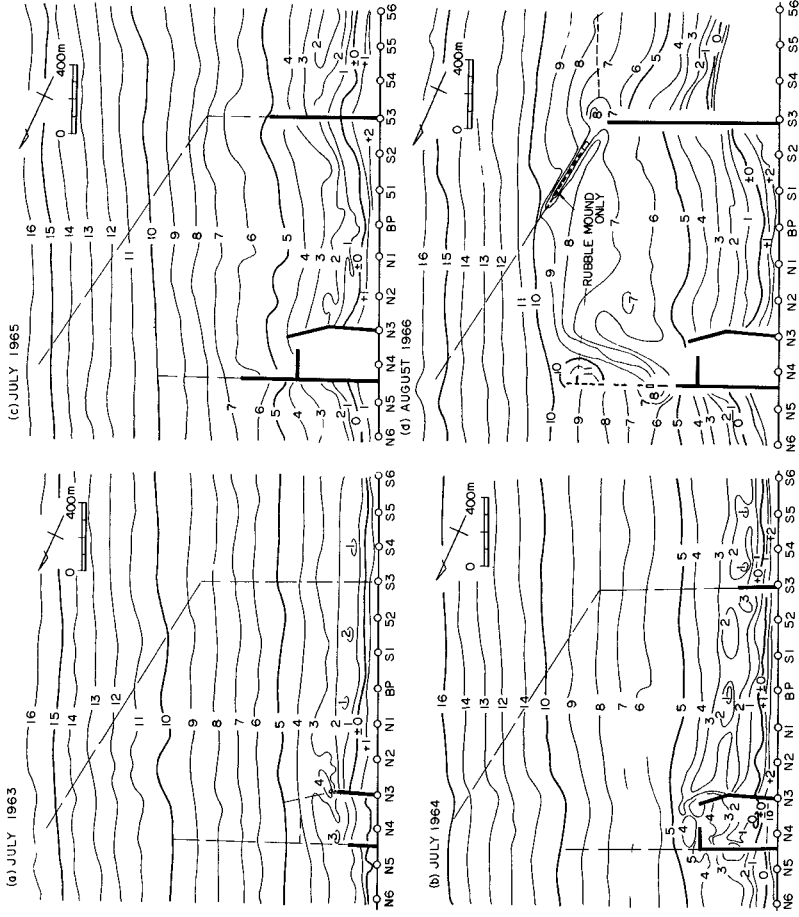


Figure 3 Variation of bed-topography at Port Kasrma, (a).

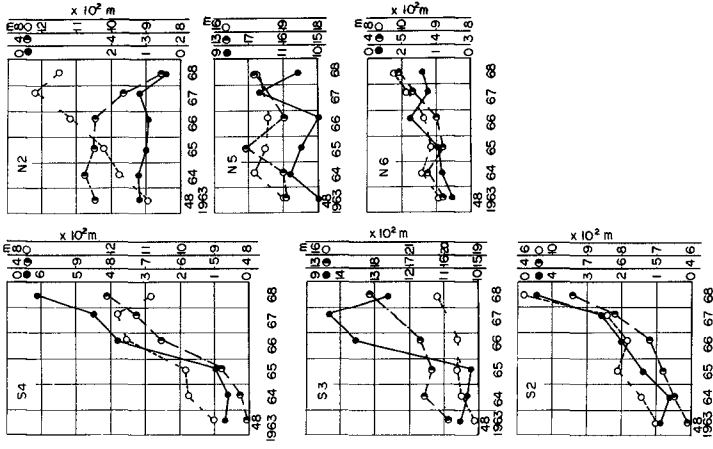


Figure 5 Time change of distances of depth-lines from the datum line at Port Kashima

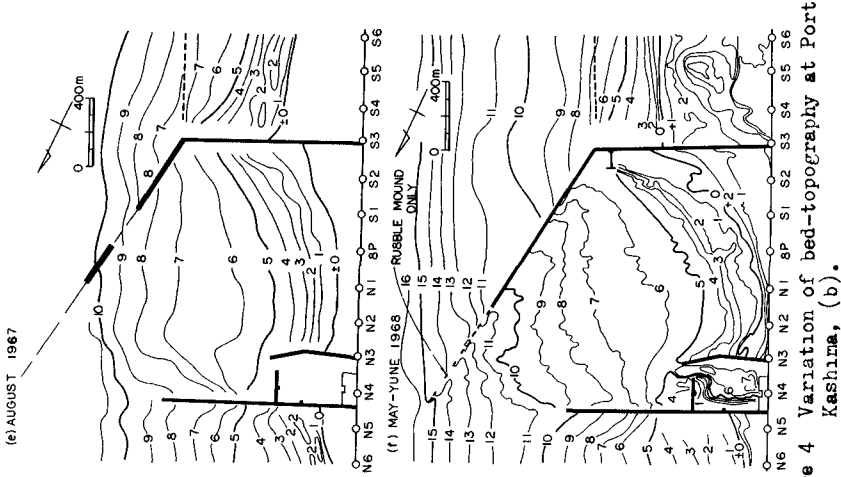


Figure 4 Variation of bed-topography at Port Kashima, (a), (b).

and alongshore bars advanced up-side of both jetty and breakwater and became indistinct down-side of them

In July 1965, the equi-depth lines shallower than 5 m in the outer basin move landward, especially at the center, near to the datum point BP. The longshore bar remained distinct on the out-side of the up-side breakwater, but is indistinct in the outer basin and on the down-side of the down-side breakwater. The advancement of shoreline out-side of the down-side breakwater is due to the discharge of materials dredged in the working basin.

In August 1966, the portion between the tip in July 1965 and the bend point of the up-side breakwater was constructed with concrete blocks. Thick dotted lines indicate the portion where only the rubble mound base of caissons is constructed. Scour along this rubble mound was more severe on the inside than on the out-side of it. Especially, the inside portion along that of the down-side breakwater is scoured remarkably and remarkable shoaling is seen within this scoured portion. The central portion of the outer-basin was shoaled and the equi-depth lines shallower than 5 m moved further landward than in 1965. The remarkable shoaling out-side of the up-side breakwater is due to the discharge of the materials dredged from the inner basin. The dredging of inner basin started in June 1965 by dredgers which entered in the part of the inner basin dredging from the working basin through the broken line shown in Figure 6. Therefore, the shoreline between the jetty and downside breakwater (between datum points S3 and N3) was not disturbed by the dredging.

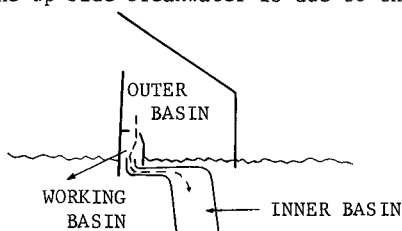


FIG 6

In August 1967 and May - June 1968, the equi-depth lines of 6 meters and less became still more landward-convex in shape and that of 7 m and more became seaward-convex in shape with the prolongation of the breakwaters. Moreover, the most receded point of shoreline was shifting towards the working basin. The equi-depth lines deeper than 7 meters outside of the up-side breakwater bulged offshoreward, on the offshore of the oblique part of the breakwater. The remarkable shoaling outside of the rectangular part of the up-side breakwater was mainly due to the discharged materials mentioned above, but some part of them passed through the breakwater into the basin and deposited in the vicinity of datum points S1 to S3.

Figure 5 shows time change of the distances of 0 m, 4 m, 8 m and other depth-lines from the datum line S6 to N6 at the points S4, S3, S2, N2, N5 and N6. The time change graph serves to make more clear the characteristics of the bottom changes described above. For example, at S2, the line of 0 m receded in July 1964 when the up-side breakwater was about 200 m in length and then advanced steadily and remarkably until 1968, the depth-lines of 4 and 6 m

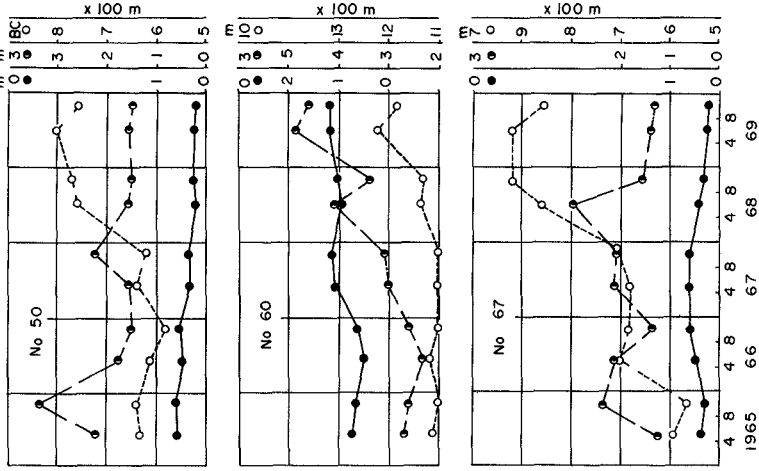


Figure 8 Time change of distances of depth-lines from the datum line at Port Kanazawa

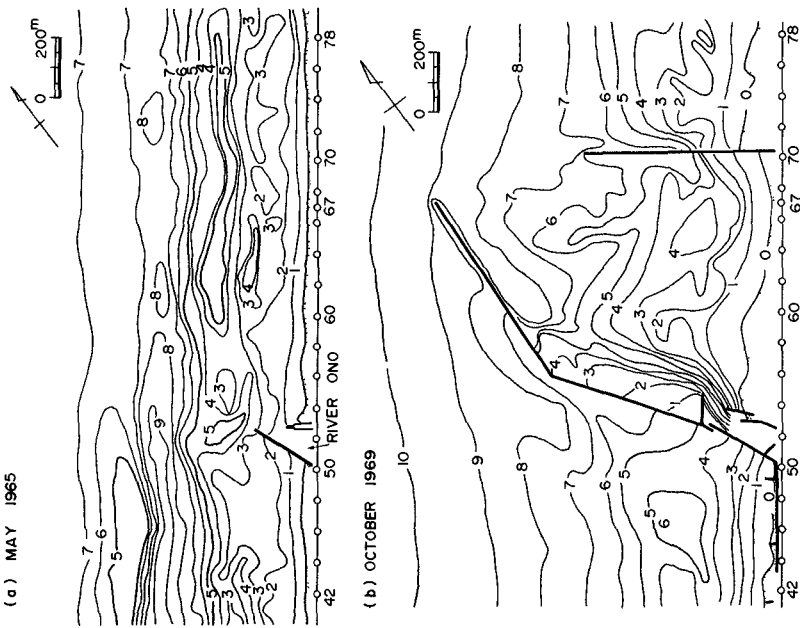


Figure 7. Variation of bed-topography at Port Kanazawa

continuing to advance through this period except for 6 m line in August 1966. These advances are remarkable in 1967 and 1968 when the oblique part of the up-side breakwater was being extended. Also, at N2, the depth lines of 0 and 4 m advanced in 1964 and then continued to recede, especially remarkably in 1967 and 1968. On the other hand, the line of 8 m at the same datum point advanced steadily except in 1968.

VARIATION OF SEA-BED TOPOGRAPHY AT KANAZAWA PORT

Port Kanazawa is located on the coast of Japan Sea as shown in Figure 2. The wave approach is in a direction almost perpendicular to the shoreline, though the southerly waves exceed the northerly waves a little similar to Port Kashima. Waves of 3 to 5 m in significant wave height and 7 - 10 sec in period very often attack during winter. But the sea is very calm in summer. The mean diameter of bottom materials is 0.15 - 0.3 mm in offshore zone. The littoral transport from the south is slightly more than that from the north.

Figure 7 shows the position of equi-depth lines in May 1965 and October 1969, and Figure 8 shows the time change of the distances of some equi-depth lines at the datum points Nos. 50, 60 and 67 from the datum line. The construction of the up-side breakwater began with prolonging the jetty which had existed at the mouth of River Ono, as shown in the sounding map of May 1965 of Figure 7.

From these figures, the pattern of change of bottom topography is found to be similar to that of Port Kashima except the severe recession of the shoreline outside of the up-side breakwater. This recession appeared in 1967 and 1968, as can be seen from the time change of 0 m at No. 50 in Figure 8, and hence a sea wall was constructed along the shore-line between the datum points 50 and 44 in the summer of 1968. The recession seems to be caused by the extension of the up-side breakwater in the direction oblique to the shoreline.

The line of BC of No. 50 in Figure 8 shows the time change of the longshore bar which existed about 630 m seaward of the datum line in May 1965. This longshore bar advanced with the prolongation of the breakwater though it became indistinct since 1968. The down-side breakwater began to be constructed in the spring of 1968, which caused the recession of shoreline near and inside of that breakwater as seen from the time change of 0 m line on the datum point No. 67 in Figure 8. The bottom material dredged in the channel extending from the mouth of River Ono were discharged on the outside of the down-side breakwater, which advanced the equi-depth lines there as seen in Figure 7.

VARIATION OF SEA-BED TOPOGRAPHY AT NIIGATA-HIGASHI

Port Niigata-higashi is located on the coast of Japan Sea, as shown in Figure 2. The predominant wave direction is NNW, almost perpendicular to the shoreline, but the westerly waves are slightly predominant than the easterly waves, and hence the direction of the net alongshore transport is from west to east along the shore. The other wave condition and the mean diameter of bottom materials are

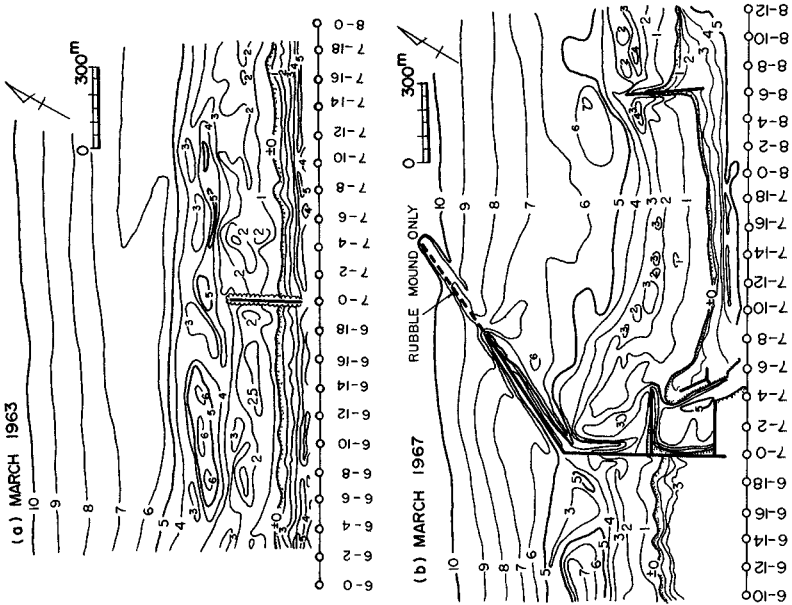


Figure 9 Variation of bed-topography at Port Niigata-higashi

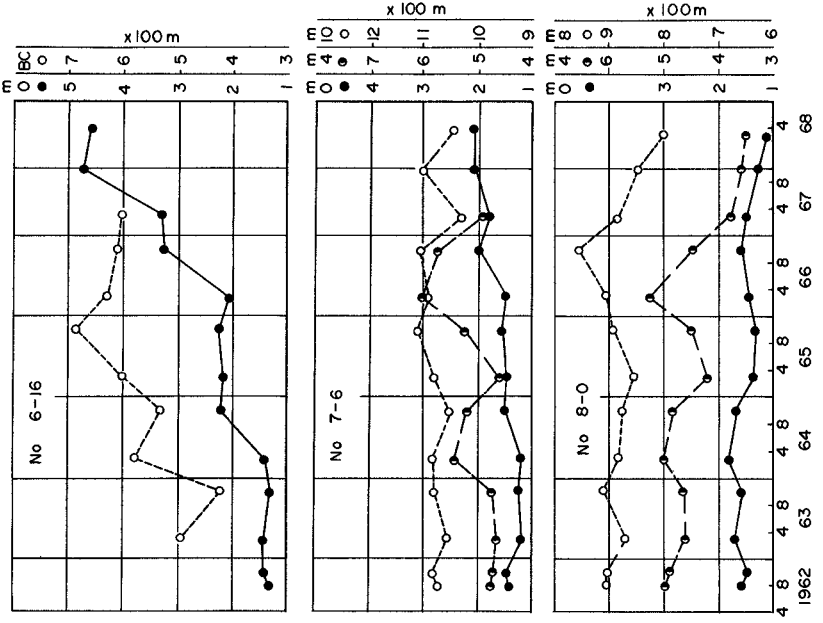


Figure 10. Time change of distances of depth-lines from the datum line at Port Niigata-higashi

nearly the same as those at Port Kanazawa. The construction works of breakwaters is stopped in winter due to severe waves similar to Port Kanazawa. Figure 9 shows the sounding maps of March 1963 and March 1967 and Figure 10 the time change of the distance from the datum line of a few equi-depth lines at the datum point Nos. 8-0, 6-16 and 7-6.

The above figures show the same tendency as Port Kashima on the bottom-change due to the construction of breakwater, though the deeper equi-depth lines did not become seaward-convex in shape in the map of March 1967. This is due to the down-side breakwater being still short. The down-side breakwater began to be constructed in 1966.

The inner basin was dredged by dredgers which entered from the working basin similarly to Port Kashima, and the dredged material was discharged on the outside of the up and down-side breakwaters. It caused the abrupt advancement of shoreline out-side of the breakwaters since 1964, as seen in the time change of 0 m line on No. 6-16 in Figure 10. As seen also in Figure 10, the alongshore bar advanced until October 1965, receded till March 1967, and then disappeared due to the above-mentioned discharged materials. 0, 4 and 8 m lines on No. 8-0 receded abruptly from 1966 when the down-side breakwater began to be constructed.

TOPOGRAPHY OF PORT OARAI AND HIMEKAWA

Port Oarai is located near to Port Kashima, and Port Himekawa between Port Kanazawa and Niigata-higashi as shown in Figure 2.

Figure 11 shows the sounding maps of Port Oarai in 1967. In this case, the bulge of equi-depth lines is not seen offshore of the oblique part of the up-side breakwater, but the shoaling is remarkable inside of the tip of breakwater. This seems to be due to the extension of the oblique part of the up-side breakwater at a small angle to the shoreline.

Figure 12 is for Port Himekawa in 1969. In this case, the rectangular part of the up-side breakwater is very short, and so the shoreline has advanced remarkably on the down-side to form a tombolo and has receded on the up-side of the breakwater.

MODEL TEST ON CHANGE OF SEA-BED TOPOGRAPHY CAUSED BY A JETTY

Some model tests were conducted on the change of sea-bed topography caused by a jetty in a basin, 30 m wide, 50 m long and 0.8 m deep. At first, a model beach of 18 m long in the direction of shoreline and of 1:15 bed slope was made with fine sand of about 0.2 mm in mean diameter. The model beach was attacked by waves which were 8 cm in height, 1.2 sec in period and 15 degree against the shoreline in wave direction. Moreover, sand was fed in the shoreline of up-side end so that the shore line there did not change during the wave action.

Change of bed-topography caused by a long jetty

Figure 13(a) shows the bed topography after two hours of wave

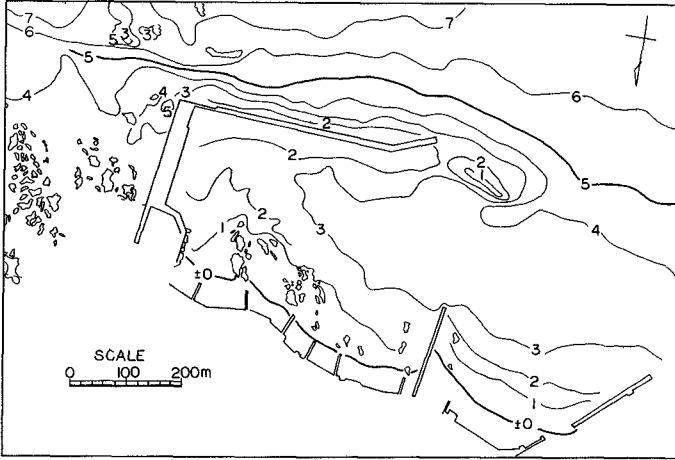


Figure 11 Port Oarai in 1967

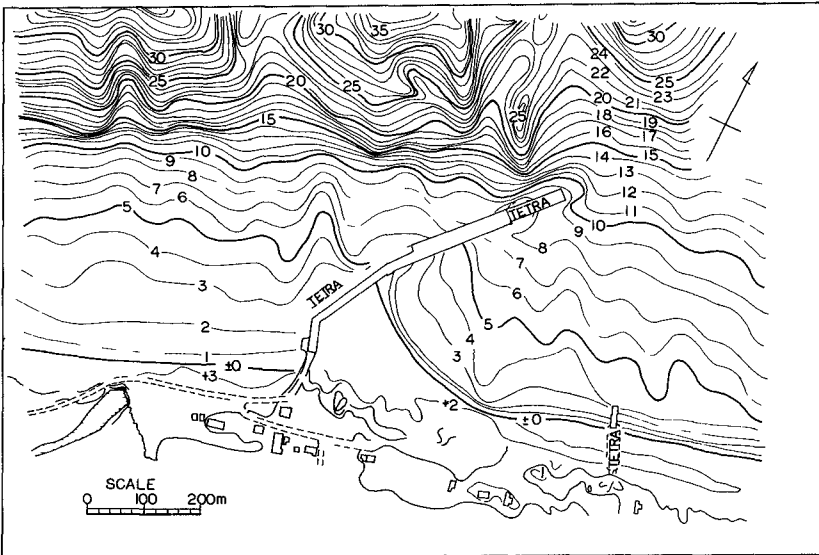


Figure 12 Port Hinekawa in 1969

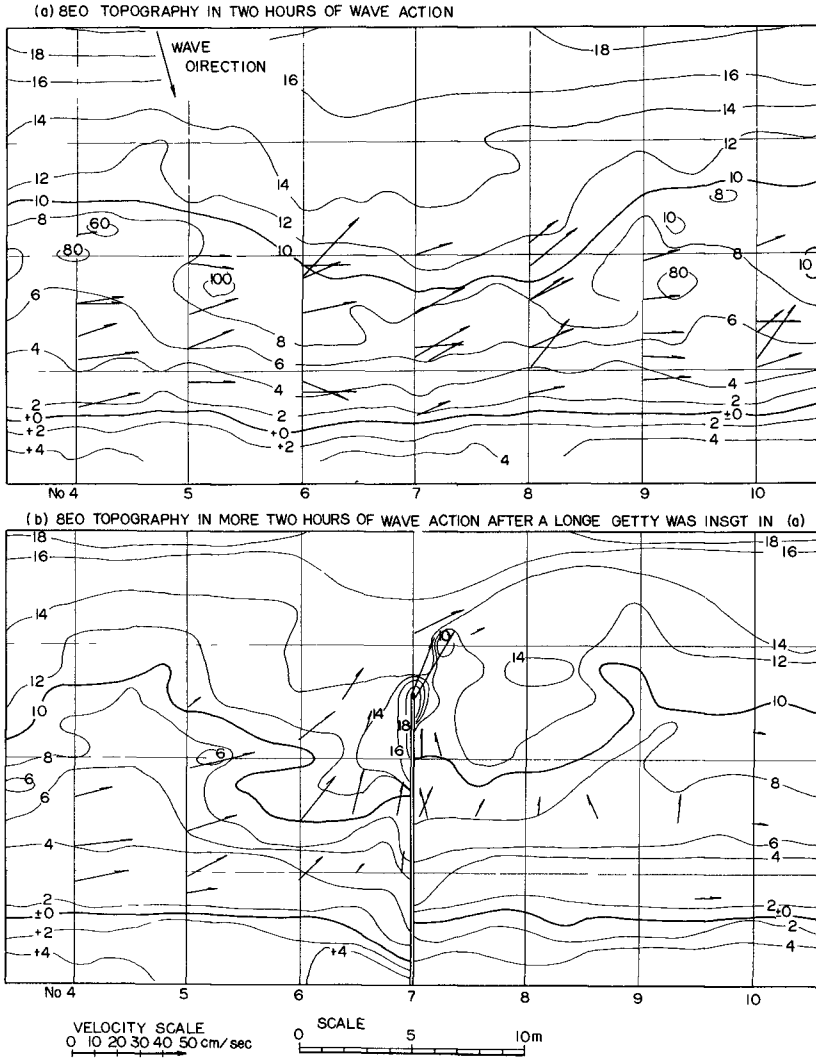


Figure 13 Changes of equi-depth lines and bottom currents by a long jetty (model test)

action on the above-mentioned initial model beach and Figure 13(b) shows the bed after an additional two hours of wave action, after a jetty was inset in the bed of (a). The arrow marks show bottom currents measured using a plastic ball of 1.5 cm in diameter filled with water, which moves along the bottom. The jetty was made with a plastic plate having smooth surfaces.

The longshore bar is seen between the equi-depth lines of 6 to 10 cm in (a), and it advances offshoreward in front of the datum point No 3 to 6 and 8 to 11. The bottom currents are flowing nearly parallel with the shoreline mostly, except that they go obliquely offshoreward on the up-side of the advancing part of the longshore bar.

In (b) with a jetty, there are seen severe scouring at the tip of jetty, scour along the jetty and erosion of the shoreline on the up-side of the jetty. The alongshore currents on the up-side of the jetty change their direction towards the tip of the jetty as they approach the jetty. Moreover, seaward currents exist along the up-side of the jetty from the foreshore. These alongshore currents and seaward currents join to become a strong current in the vicinity of the tip of the jetty, which cause the above-mentioned severe scouring there, together with the breaking wave along the jetty. The wave height is higher along the jetty than in the area away from the jetty, because the wave comes obliquely to the jetty, which results in the increase of disturbance of bottom materials and the rise of the water level at the foreshore near to the jetty. The rise of the water level causes the above-mentioned seaward bottom currents. The other hand, on the down-side of jetty, the area near to the jetty is by some degree sheltered by the jetty from waves, which results in the advancement of shoreline and the disappearance of alongshore bars.

Relation between length of a jetty and erosion of up-side foreshore

Figure 14 shows the change of bed topography for jetties of 2.0, 1.5 and 1.25 m long from the datum line with the same surface as the above-mentioned jetty of figure 13 and also for a jetty of 2.5 m long with the surface of rouble stones. In the figure, equi-depth lines are drawn by dotted lines for after two hours of wave action on the initial model beach of 1:15 in bed slope and by full lines for after an additional two hours of wave action after a jetty was inset.

The up-side foreshore near the jetty was eroded in (a) of 2 m long jetty as well as in Figure 13, changing little in (b) of 1.5 m long jetty and being accreted in (c) of 1.25 m long jetty. In (d) of 2.5 m long and rough surface jetty, the up-side foreshore was accreted. The rough surface, as well as the decrease of length, of the jetty serves in the decrease of wave height and the decrease of the offshoreward current velocity along the jetty, which results in the decrease of erosion and scour along the up-side of the jetty.

MODEL TEST ON CHANGE OF SEA-BED TOPOGRAPHY CAUSED BY TWO BREAKWATERS

Prior to the prolongation of the oblique part of the up-side breakwater at Port Kashima, model tests were conducted for different stages

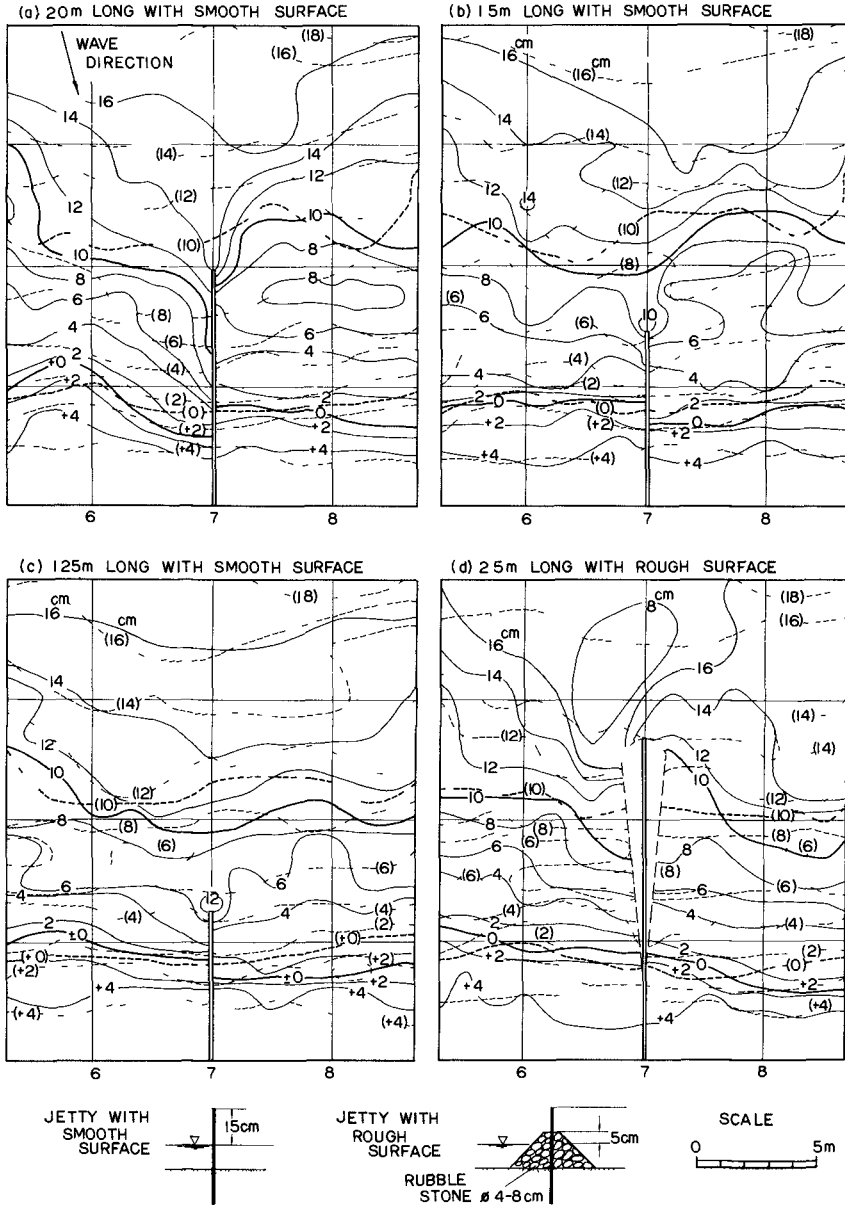


Figure 14 Relation between length of a jetty and erosion of up-side foreshore (model test)

of the construction of breakwaters in the same basin as the above-mentioned test. Figure 15 shows a part of the model tests. The up and down-side breakwaters were prolonged from the state in upper figure (a) to the state in the lower figure (b) and then waves were acted for four hours. The result by the wave action is shown in the lower figure. In this case, model waves in the offshore were 14 cm in height, 1.4 sec in period and 1 NE in direction. Model bed materials were sand of 0.22 mm in mean diameter and model scale was 1:200 in horizontal and 1:40 in vertical. Also, the model of breakwater was made by concrete blocks which was impermeable against water. Figure 16 shows the conditions of bottom currents and wave-heights for the bed condition in Figure 15(b).

Comparison of change of bottom topography between model and prototype

The length of breakwaters is not so much different between Figure 15(a) and Figure 3(d) though the latter has a little more extended breakwater than the former, and so also between Figure 15(b) and Figure 4(f). Therefore, the change of bottom topography from the above (a) to (b) of the model is compared with that from the above (d) to (f) of the prototype.

The offshoreward bulge of equi-depth lines near the oblique part of the up-side breakwater on the out-side, the advancement of all equi-depth lines near the up-side breakwater on the in-side, the shift of the most receded point of the shoreline towards the jetty of working basin and the shoaling of the center part in the outer basin are seen both in the model and the prototype. It is seen also in the model the tendency for equi-depth lines to become of landward-convex shape in the shallower area and of offshoreward-convex shape in the deeper area in the outer basin. The tendency of change of bed-topography coincides between the model and the prototype, though there is some difference on the intensity or rate of the change.

Distribution of waves and bottom currents

It is seen from (a) of Figure 16 that the wave height in the outer basin is larger in the portion extending from the mouth to the datum points N1 to N2 and smaller in the portion near the up-side breakwater. It is also seen from (b) of Figure 16 that there is currents circulating in the anti-clockwise direction in the outer basin. The velocity of the circulating current is smaller in the center of the outer basin and in the portion near the up-side breakwater. This indicates that the pre-described most eroded point of the shoreline have the higher wave and more rapid bottom current, and the pre-described shoaling portion in the center of the basin has the slower current. Also, the accumulation seen in the area near the up-side breakwater seems to be caused by the condition of current velocity and wave height which are smaller in the area near the up-side breakwater than in the area near the down-side breakwater.

CONCLUSION

The general characteristics of bottom topography change caused by the construction of breakwaters on a sandy beach are concluded from the foregoing chapters as follows. Figure 17 is the illustration of the

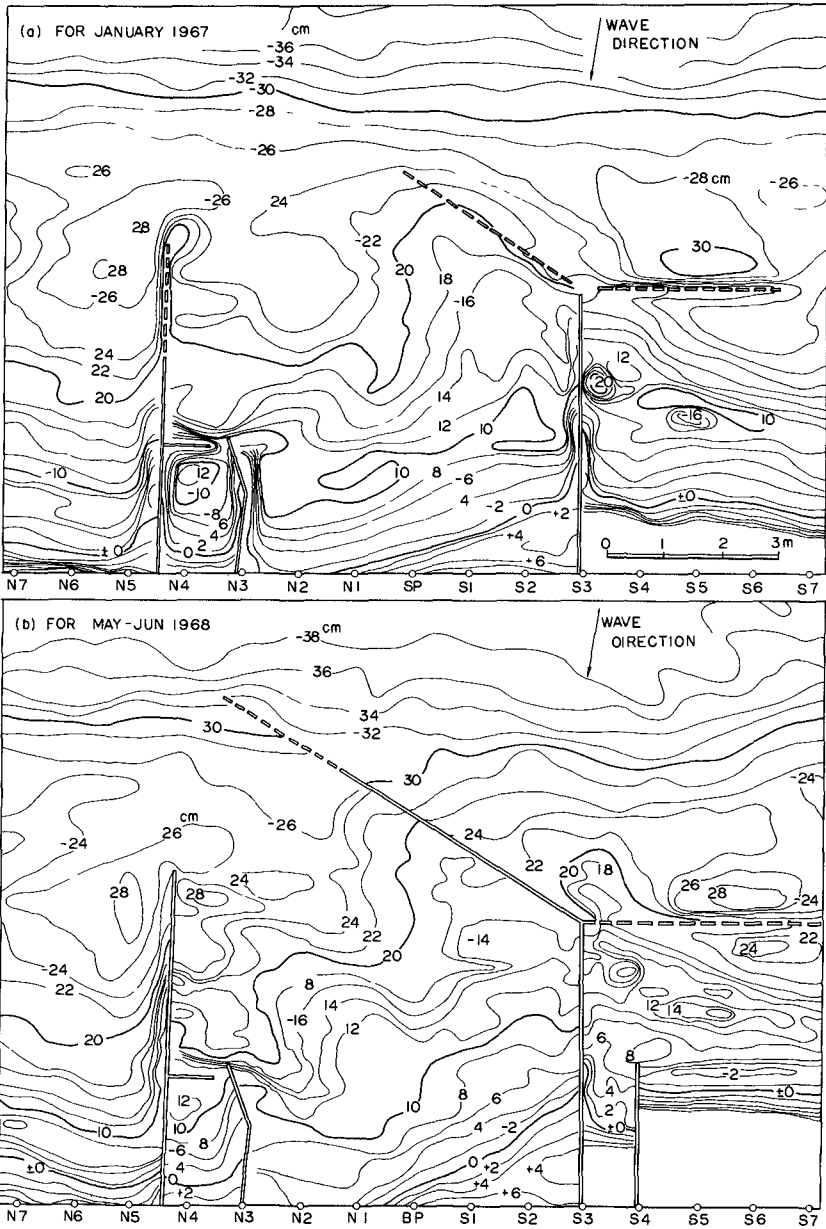


Figure 15 Change of bottom topography caused by the prolongation of breakwaters (model test of Port Kashima)

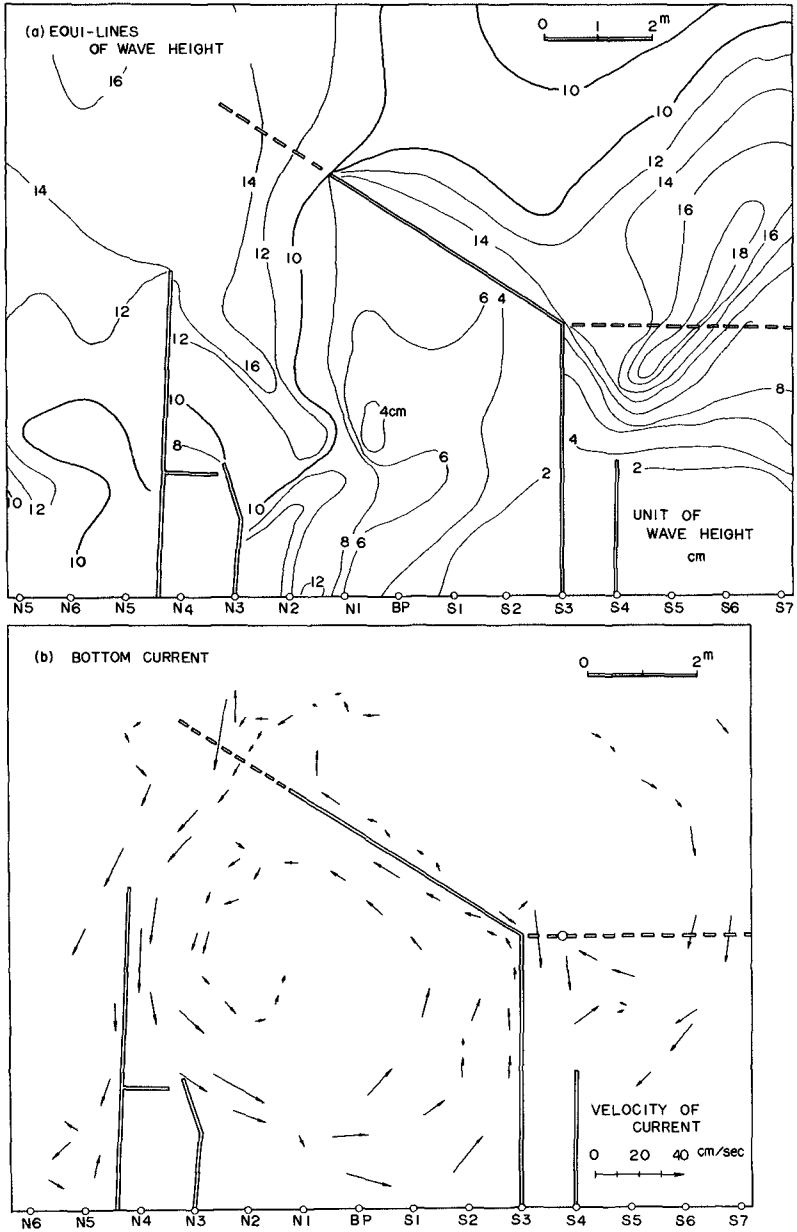


Figure 16 Distribution of waves and bottom currents for figure 15(b) (model test).

same

Out-side of the up-side breakwater

(1) The shore-line near to the breakwater advances offshoreward first and then stops or recedes according to the prolongation of the breakwater. In this case, the more oblique the direction of a breakwater is, the more severe the recession of shoreline is. Such recession of shoreline is less in the breakwater with rough side-surface than that with smooth surface as shown in the model test.

(2) The alongshore bar near to the breakwater advances offshoreward becoming distinct in shape with the prolongation of the rectangular part of the breakwater and stops or recedes becoming indistinct with the construction of the oblique part of the breakwater.

(3) The equi-depth lines near to the oblique part of the breakwater bulge offshoreward, as most of littoral drift carried along the shore moved seaward along the rectangular part to deposit offshore of the bend-point without moving directly along the oblique part of the breakwater. However, in the case where the rectangular part is short and the bending angle of the oblique part is large, such bulge of equi-depth lines does not occur but the shoaling tends to be remarkable inside the tip of the breakwater, **as in Port Oarai.**

Inside of breakwater (outer basin)

(1) According to the construction of an up-side breakwater, the shoreline advances in the part near to the breakwater and recedes in its down-side, namely, having a shape of landward-convex. The most receded point in this case moves towards the down-side with the increase of length of the breakwater. Such advancement of a shore line near to an up-side breakwater becomes larger when the direction of breakwater is oblique to the shoreline and is closely related to the diffraction of waves by the breakwater.

(2) The alongshore bar in the outer basin becomes indistinct or disappears with the prolongation of breakwaters.

(3) The scouring at the toe of the rouble mound is more severe inside of it than outside of it during the period before caissons are set on it. This seems to be due to the swirl formed inside the rouble mound by waves passing over it.

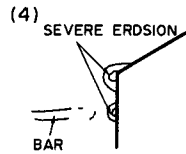
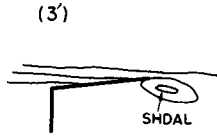
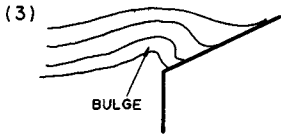
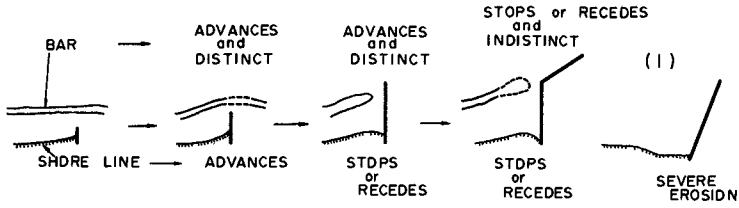
(4) When both up and down-side breakwaters are prolonged, equi-depth lines move landwards in the shallower zone and offshorewards in the deeper zone, namely, having a shape of landward-convex in the former and a shape of offshoreward-convex in the latter.

(5) Waves entering from the mouth progress near the down-side breakwater so that they erode the foreshore near to the down-side breakwater and produce circulating currents flowing from the down-side breakwater to the up-side breakwater and then to the center of the outer basin.

(6) In the shallower area, the bottom is eroded or scoured where

OUTSIDE OF THE UP-SIDE BREAKWATER

(1) and (2)



INSIDE OF BREAKWATERS (OUTER BASIN)

(1) and (2)

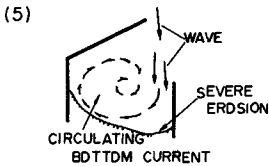
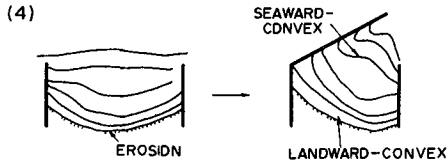
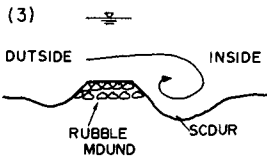
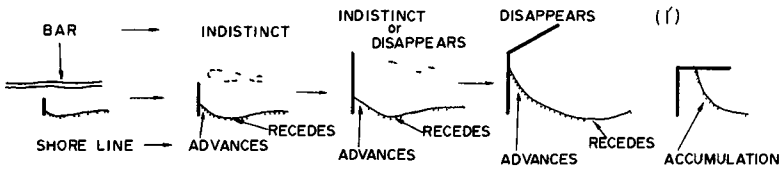


Figure 17 Typical pattern of outer topography caused by the construction of breakwaters

waves and bottom currents are more severe than its surroundings and is shoaled where they become weak and slow down. On the other hand, in the deeper area, the shoaling of bottom happens where bottom currents slow down rather than waves.

Outside of the down-side breakwater

The change of a shoreline to landward-convex in shape, the disappearance of alongshore bars, and the scour of bottom along the breakwater are seen often in the area near to the breakwater.

CHAPTER 82

EQUILIBRIUM PROFILES OF MODEL BEACHS

By Irvathur Vasudeva Nayak¹ A.M. ASCE.

ABSTRACT

The investigation reported herein covers two aspects of equilibrium beach profiles, namely, (a) the criterion governing their type and (b) their reflection characteristics. The problems are first analysed from dimensional considerations and then studied experimentally in laboratory wave flumes using different sizes of quartz, ground walnut shell and ground plastic as movable bed material. Empirical relations between pertinent parameters governing the beach process are given.

Introduction

The wave and hydrologic climate at a beach location is everchanging and the coastal engineers have always been interested in the deformation of the natural beach caused by wave action over a short or long interval of time. The resulting changes in beach characteristics, such as the type of profile, beach width, berm level, location and size of offshore bars, height of run-up, the rate and mode of sediment transport, areas of deposition and scour and the amount of energy absorbed or reflected from the beach, are often rapid. Coastal management requires a knowledge of the fundamental principles involved in the behaviour of the

¹ Professor and Head of Department of Applied Mechanics, & Hydraulics, K.R. Engineering College, Surathkal, INDIA
Formerly Graduate student, University of California, Berkeley, California.

beach material and research attempts have, long since, been directed to obtain analytical and empirical relations between the different pertinent variables involved in the extremely complicated beach process.

The study reported herein covers two aspects of equilibrium beach profiles, namely, criterion governing their type and reflection characteristics. The experiments relating to the criterion for the type of profile have been performed as series A and those of the latter as series B in two separate experimental units in the laboratory.

Part A. Criterion for type of profile.

Almost all the investigations that have been conducted to date have indicated that deep-water wave steepness is an important parameter related to the beach process and a critical value of this parameter characterises various elements of the phenomenon like the type of profile, mode and rate of transport and the type of breakers etc. In this part of the study an attempt is made to relate the variation in the critical value of deep-water wave steepness concerning the type of beach profile, "storm" or "summer", to the characteristic size and specific gravity of the beach material.

The type of equilibrium profile, storm or summer, that results from the action of waves in a two dimensional flume can be assumed to be governed by the following variables.

- (i) deep-water wave height, H_0
- (ii) wave period, T
- (iii) specific gravity of sediment in water, S
- (iv) median diameter of sediment, D

(v) depth of water in the channel, d

(vi) acceleration due to gravity, g

(vii) initial slope of beach, 1_0

(viii) standard deviation of grain size, σ

$$\begin{aligned} \text{i.e. type of profile} &= f_1 (H_0, T, S, D, \sigma, 1_0, g, d) \\ &= f_2 (H_0, L_0, S, D, 1_0, g, d) \end{aligned}$$

The role of viscosity of the fluid is of minor importance if we assume that the Reynolds number is sufficiently high and the entire phenomenon takes place well within the turbulent range. If the zone of sand movement is limited on the beach slope, the effect of depth of water can be neglected. The gravitational acceleration is constant. The standard deviation of grain size is of minor importance and from earlier studies one can find that the initial beach slope plays no major role in the phenomena. Thus considering the equilibrium condition which is independent of duration,

$$\begin{aligned} \text{Type of profile} &= f_3 (H_0/L_0, H_0/D, S) \\ \text{or} &= f_4 (H_0/L_0, H_0/SD, S) \end{aligned}$$

The problem can be also viewed as

$$\begin{aligned} \text{Type of profile} &= f (H_0, L_0, S, D) \\ &= f (H_0, L_0, V_f) \end{aligned}$$

considering that the fall velocity in water, V_f , characterises the sediment,

$$\text{i.e., type of profile} = f (H_0/L_0, \frac{\sqrt{gH_0}}{V_f})$$

The fall velocity can be taken to be proportional to the quantity $(\frac{S g d}{C_D})^{\frac{1}{2}}$

$$\begin{aligned} \therefore \text{Type of profile} &= f (H_0/L_0, \frac{\sqrt{g H_0}}{S^{\frac{1}{2}} g^{\frac{1}{2}} D^{\frac{1}{2}} C_D^{\frac{1}{2}}}) \\ &= f_5 (H_0/L_0, H_0/SD), \text{ disregarding} \\ &\text{the effect of } C_D. \end{aligned}$$

The parameter H_0/SD can also be taken as the ratio of a typical unit force exerted by the wave to unit resistance offered by the beach sediment, because the former is proportional to

$$\rho_f \times (\text{a characteristic velocity of flow pattern})^2 \times D^2$$

and the latter to the submerged weight of the grain of beach material, i.e., $g (\rho_s - \rho_f) D^3$. If the characteristic velocity is taken as $\sqrt{gH_0}$, the ratio becomes

$$\frac{\rho_f \cdot u_c^2 \cdot D^2}{g (\rho_s - \rho_f) D^3} = \frac{\rho_f u_c^2 / g}{(\rho_s - \rho_f) D} = \frac{H_0}{SD}$$

The ratio H_0/SD is also comparable to the ratio $1/\psi$ where ψ is the intensity of flow given by the expression

$$\psi = \frac{\rho_s - \rho_f}{\rho_f} \cdot \frac{Dg}{U^2},$$

an important quantity used in sediment flow problems.

Thus the ratio of wave height to the product of specific gravity in water and the median diameter of the sediment can be taken to be a very important parameter in the beach process.

The importance of the size of the beach material has been pointed out by Rector (1954) and the ratio of wave height to median diameter by Iwagaki (1962) (Fig.1). The present experiments were carried out in a wave flume shown in Fig.2. The wave height was noted with the help of a point gauge placed just offshore from the toe of the beach and was taken as twice the distance recorded between the crest of the wave and the still water level. This is correct in deep water. The beach profile was recorded by measuring the horizontal and vertical coordinates on a rectangular grid fixed to the side of the flume. The first four materials whose size distribution is given in Fig.4, were used as beach material in

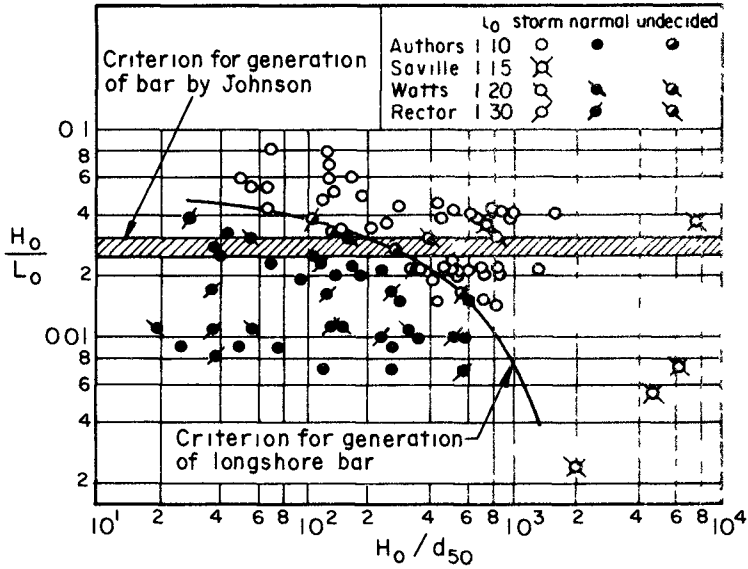


FIG 1 CRITERION OF BAR GENERATION (IWAGAKI)

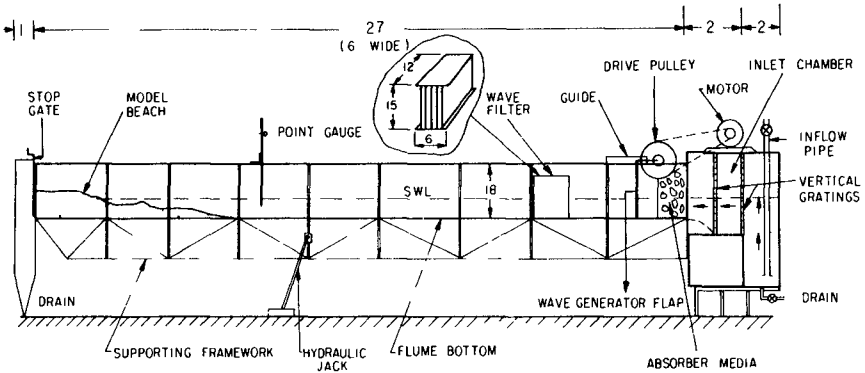


FIG 2 WAVE FLUME USED IN SERIES A

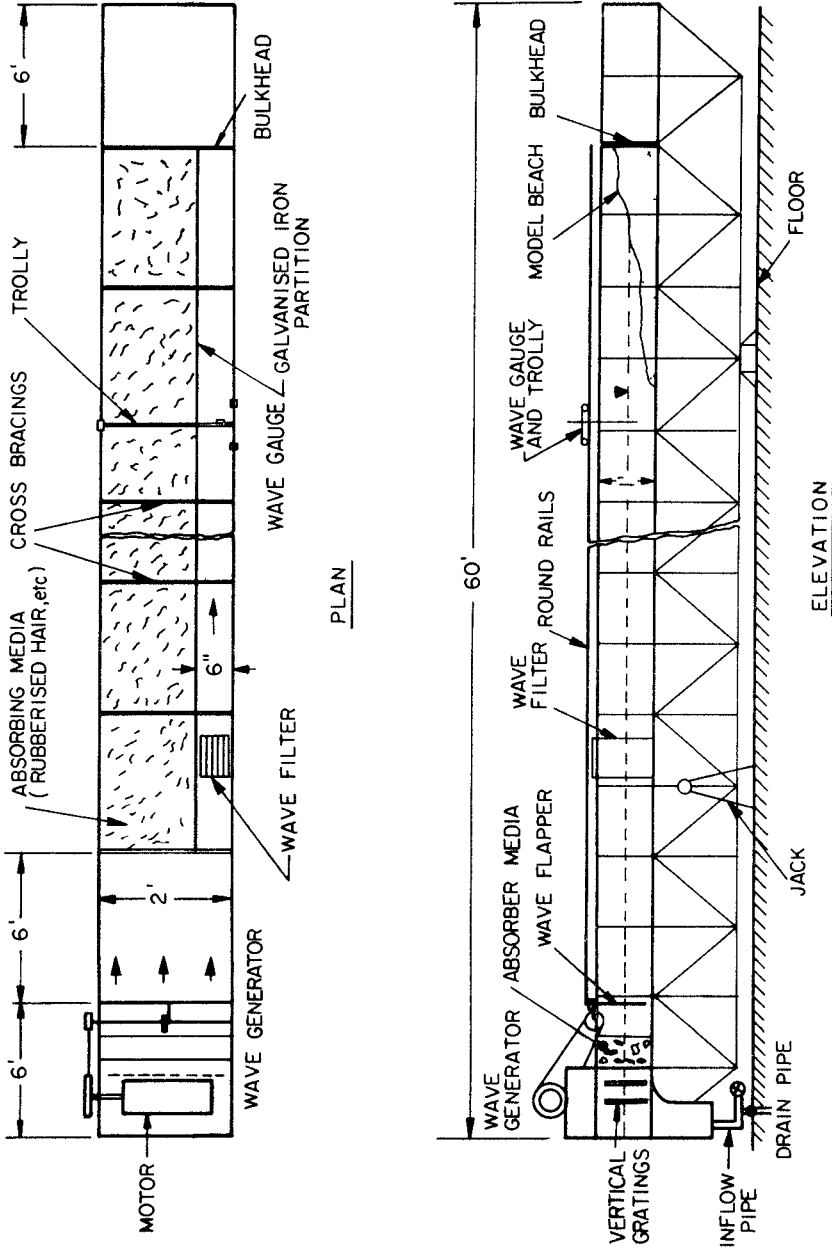


FIG 3 WAVE FLUME USED IN SERIES B

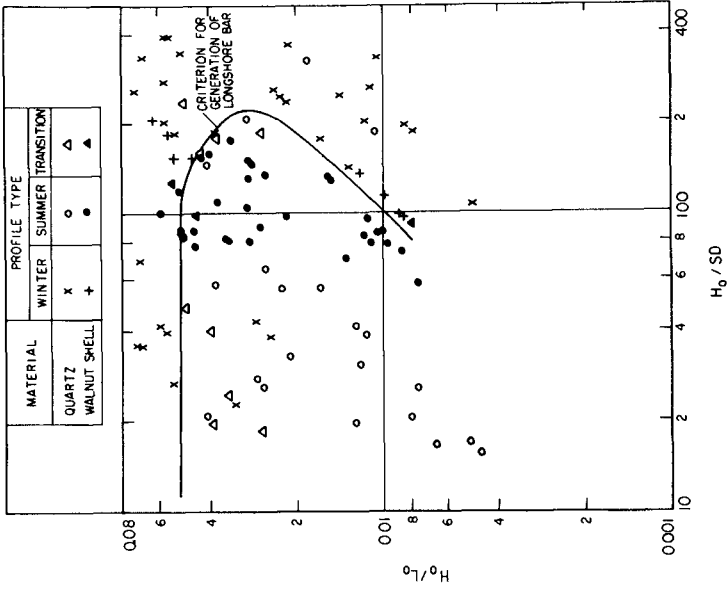


FIG 5 CRITERION FOR GENERATION OF LONGSHORE BAR

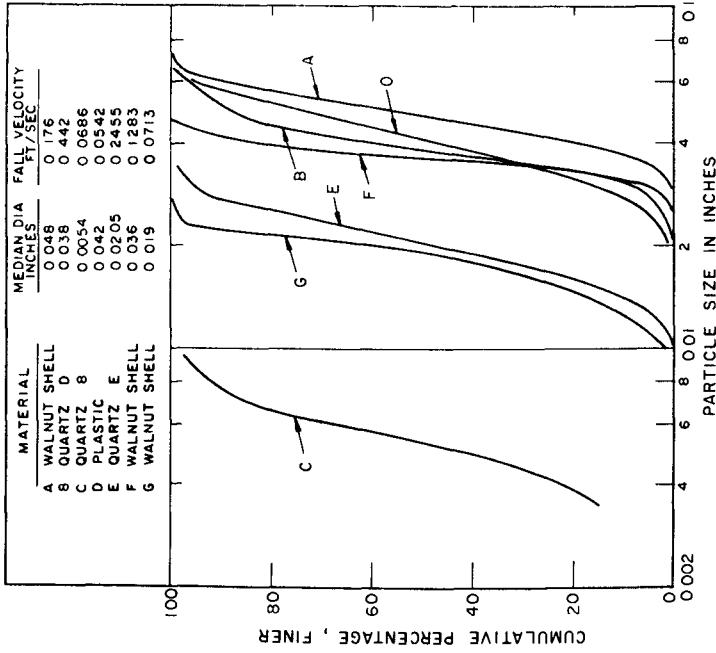


FIG 4 SIZE DISTRIBUTION OF MATERIALS

series A. In the case of each material, the depths of water used were 0.30, 0.35, 0.40, 0.45 and 0.50 ft. For each depth the following wave periods were used 1.86, 1.60, 1.26, 1.01, 0.845 and 0.72 secs. At the beginning of each group of experiments just enough material was placed in the flume such that the beach crest was generally located 1 to 2 ft. from the end of the flume. No particular initial slope was used. The beach was allowed to shape itself under wave action until equilibrium conditions were reached.

The criterion for the type of profile, summer or winter, based on this study has been shown in Fig.5 in terms of two parameters, namely, deep-water wave steepness, H_o/L_o , and the ratio of deep-water wave height to the product of specific gravity of the beach material in water and its median diameter, H_o/SD . In this plot the results of experiments with the two sizes of quartz sands and the walnut shell have been used.

The behaviour of the ground plastic was quite different. In none of the runs with this material were ripples observed or were the waves found to break. The material appeared "soupy" and proved a very efficient absorber of energy. Under wave action most of the material went into thick suspension and oscillated to the entire depth of the movable bed. For this reason the results of the ground plastic were not included in the plot of Fig.5. It is also to be noted that no correction has been applied to the observed wave heights to take into account the reflected wave component.

The curve separating the region of summer profiles from that of winter profiles in Fig.5 is a rising straight line in the range of wave steepnesses from 0.008 to 0.02. For the higher values of wave steepness,

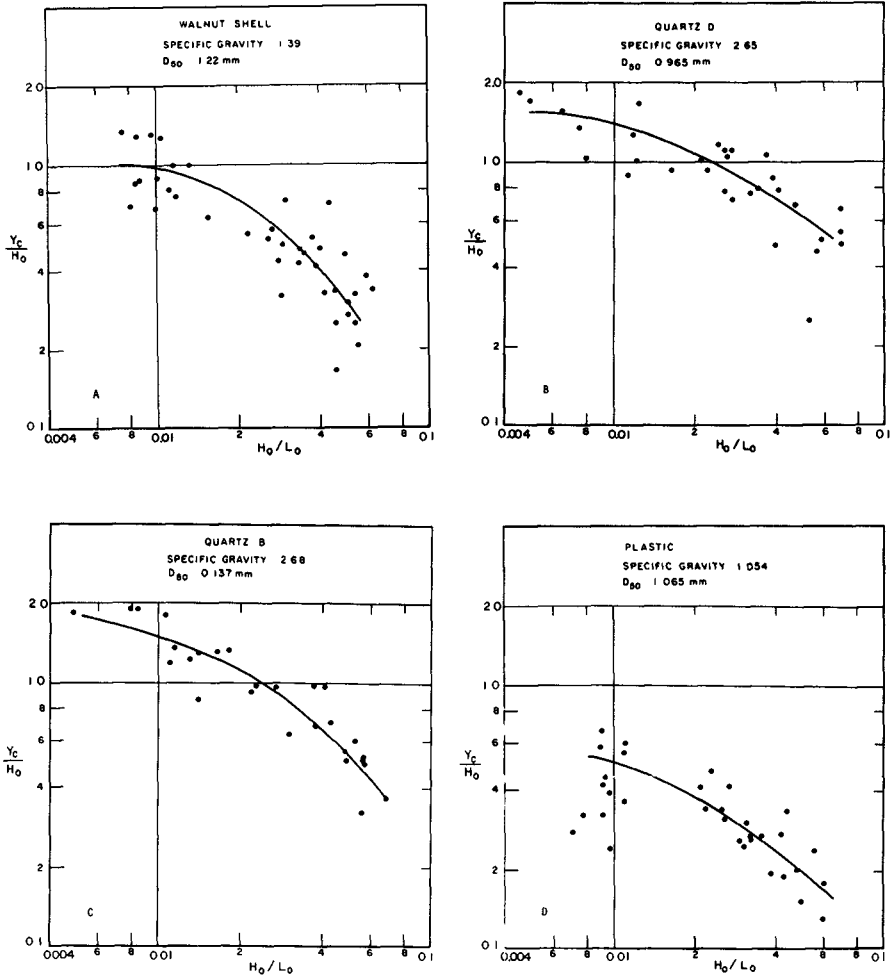


FIG 6 PLOT OF $\frac{Y_c}{H_0}$ VS H_0/L_0 FOR VARIOUS MATERIALS

the curve is a curved line from $H_0/L_0 \approx .05$ to $.03$, the value of the parameter h_0/SD increasing from 20 to about 220, where it turns round to join the straight line from the lower range. The curved line separating the two regions is, at the beginning, nearly horizontal for the range $H_0/SD \approx 20$ to 100. For the range of $H_0/SD = 80$ to 200 it was possible to get a storm profile for high values of wave steepness as well as low values with an intermediate range in which the profiles were of summer type without any bar. When compared with Fig. 1, the critical wave steepnesses obtained in this study are slightly higher probably due to the reflected energy not being taken into account. The results indicate that with certain combination of size and specific gravity it is possible to get "winter" profiles at low wave steepnesses as well as high ones with an intermediate range for which the profiles will be of "summer" type. This fact can be taken advantage of in achieving similarity in the type of profile in model studies.

Fig. 6 shows the dimensionless wave run-up observed for different materials plotted against the deep-water wave steepness. In each case the wave run-up decreases with increase in wave steepness because the steeper waves break farther offshore in greater depths. Plastic material gave the least uprush and the quartz sands the maximum while for walnut shell the value was intermediate to the other two. Irrespective of the size difference the value of the uprush was almost same for the quartz sands.

Part B Reflection characteristics

In this second part of the article the reflection characteristics of two-dimensional equilibrium profiles are considered. It is assumed that the action of a

given wave condition on a certain sediment results in a unique equilibrium profile when the waves are allowed to shape the beach for a sufficiently long time. The variables involved in the reflection phenomenon in that case will be

- (i) percentage of energy reflected from the profile, E_r
- (ii) wave height, H_0
- (iii) wave period, T
- (iv) median size of grains, D
- (v) mass density of sediment, ρ_s
- (vi) mass density of fluid, ρ_f
- (vii) depth of water, d

One can, then, write

$$E_r = f(H_0, T, D, \rho_s, \rho_f, d)$$

the assumptions regarding viscosity of the fluid and standard deviation of the grain size being same as in Part A. If the fall velocity, V_f , of the sediment is taken to characterise the sediment size and its density and the density of the fluid, then one can write

$$E_r = f_1(H_0, T, V_f, d)$$

Now

$$E_r \propto K_r^2$$

$$\therefore K_r = f_2(H_0, T, V_f, d)$$

or

$$f_3\left(K_r, \frac{H_0}{V_f T}, \frac{d}{V_f T}\right) = 0$$

in which V_f and T are taken as repeating variables.

This can also be written as

$$f_4\left(K_r, \frac{H_0}{V_f T}, d/h_0\right) = 0 \text{ if } V_f \text{ and } H_0 \text{ are taken}$$

as the repeating variables. The third parameter in these relations is important if the reflection coefficient, K_r , is measured in shallow water. Otherwise, the relation $F(K_r, H_0/V_f T) = 0$ should apply and it is this relation

which is empirically determined.

The experiments related to the second part of the study were conducted in a wave flume (Fig.3) 2' wide, 60' long and 1' deep. With the help of a longitudinal partition, only a narrow 6" wide section of the flume was used in the experiments. This ensured that the results were very little influenced by the secondary reflection taking place from the wave generator. Five different materials, i.e., all excepting the first and the third one in the list given in Fig.4, were used in this series of runs. The following depths of water and wave periods were utilised

d ft.	T secs.	d/L ₀
0.50	1.20	0.0678
0.45	1.20	0.0610
0.45	1.00	0.0878
0.40	1.00	0.0543
0.40	1.20	0.0781
0.30	1.00	0.0586

For each depth three different wave heights were applied by changing the stroke of the wave generator. The duration of each run was on an average two hours so that the beach attained substantial equilibrium before observations were made. The coefficient of reflection, K_r , was then found by recording the envelope of the wave system in front of the beach by a movable parallel - wire resistance type wave gauge and noting the wave heights at the node and anti-node of the wave system and using these values in the Keulegan formula. If H_n and H_1 are the wave heights registered at the node and anti node respectively, then according to the linear wave theory

$$K_r = \frac{h_1 - H_n}{h_1 + H_n}$$

The resulting error in using this expression for shallow water waves in the calculation of the reflection coefficient is considered negligible.

The empirical relationship between the reflection coefficient, K_r , and the parameter, $H_{o1}/V_f T$, as developed from dimensional considerations above is shown in Fig.9. This plot using ordinary scales along the two axes was found to be the best form of representing this relation. The reflection coefficient reduces sharply from a high value of approximately 0.55 to about 0.10 as $H_{o1}/V_f T$ increases from 0.1 to 0.5 and thereafter K_r shows little variation even when $H_{o1}/V_f T$ is increased up to 2.0. The results of the two quartz sands fell in the range of $H_{o1}/V_f T = 0.10$ to 0.37 and those of walnut shell and plastic in the range - 0.2 to 2.0.

Figs.7 and 8 show the same relation for the bed material of grain size 1 mm and 0.5 mm respectively, the results for these diagrams being taken from those of Fig.9. These figures have been drawn to observe the effect of size and specific gravity on the reflection coefficient. Within the same type of sediment, the smaller size showed a higher trend of values of K_r . This is due to the reduced permeability and roughness magnitude. However opposing this tendency is the fact that a larger quantity of the smaller size should be in movement and suspension for the same wave condition and this should lead to a reduction in the value of K_r indicating increased absorption of energy. The resulting trend noticed in the experiments shows, however, that the effect on reflection of the latter factor is not so significant at least in the range involved. A change in

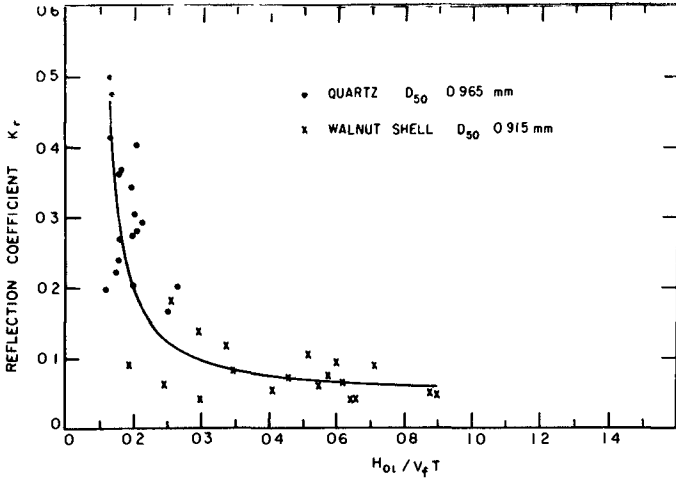


FIG 7 PLOT OF K_r VS $H_{01}/V_f T$ ($D \approx 1$ mm)

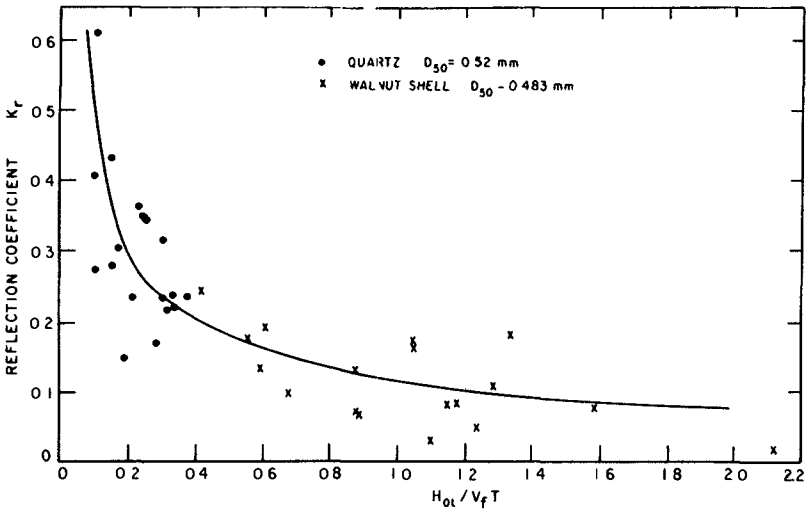


FIG 8 PLOT OF K_r VS $H_{01}/V_f T$ ($D \approx 0.5$ mm)

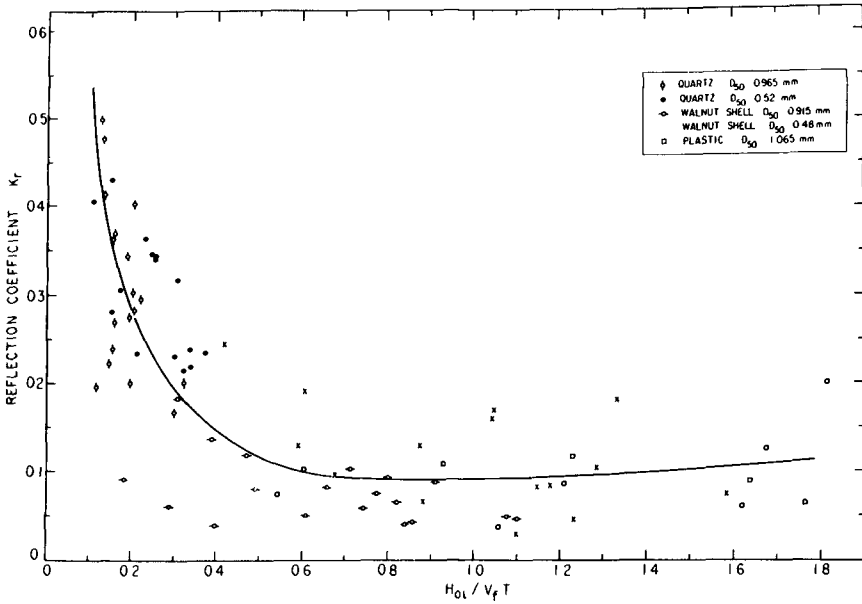


FIG 9 REFLECTION COEFFICIENT K_r VS $H_{01}/V_f T$

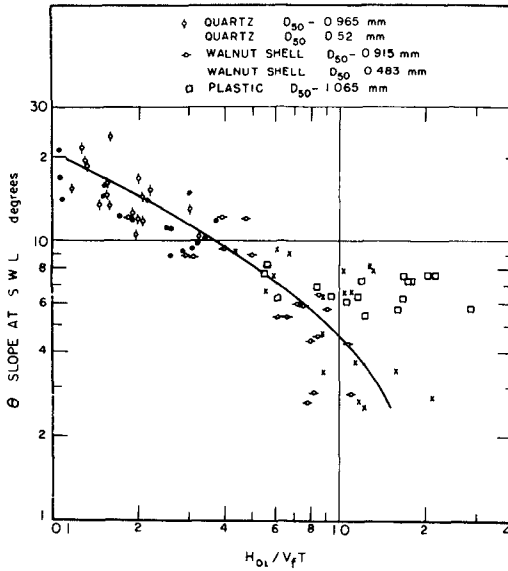


FIG 10 PLOT OF θ VS $H_{01}/V_f T$

specific gravity, however, markedly effects the value of K_r . If one assumes that the median diameter characterises the roughness magnitude as well as permeability, the effect of absorption of energy by the particles in motion at the bottom and those in suspension can be estimated by looking at the variation of l_r with $H_{o1}/V_f T$ for nearly the same size but different type of material. This can be done with the help of Figs. 7 and 8.

Figure 10 shows the variation of the slope of the profile at the still water level, θ , with the dimensionless parameter $H_{o1}/V_f T$ and Fig. 11, the variation of K_r with θ . The use of a less dense artificial sand leads to a lowering of the slope, θ . If the slope at still water level is taken to represent the slope of the profile, the effect of greater quantity of material being in motion and suspension at higher values of $H_{o1}/V_f T$ is enhanced by that due to the reduction in slope. The slope decreases regularly from about 22° to 2.5° as $H_{o1}/V_f T$ is increased from 0.1 to about 2.0. For the plastic material, however, the slope remains nearly the same with an average value of about 6.5° . The behaviour of this material was characteristically different from the rest as in series 1.

Fig. 12 is a logarithmic plot of slope at still water level versus incident wave steepness for all the materials. In all cases except the plastic the slope is found to increase as the steepness is decreased.

Fig. 13 is a comparison plot of the results of this study using a movable bed with Miche's theoretical values as well as those of Greslou and Mahe, empirically obtained, for smooth impermeable slopes at constant values of deep-water wave steepness. The range of values for wave steepness in all cases is .005 to .03. Although

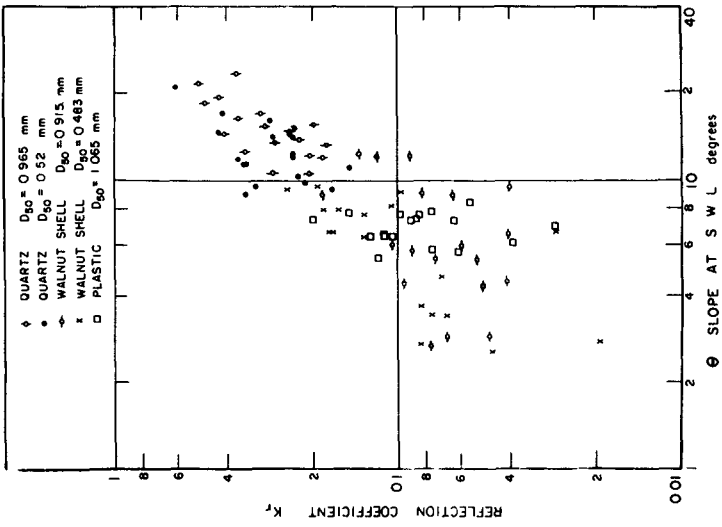


FIG 11 PLOT OF K_r VS θ

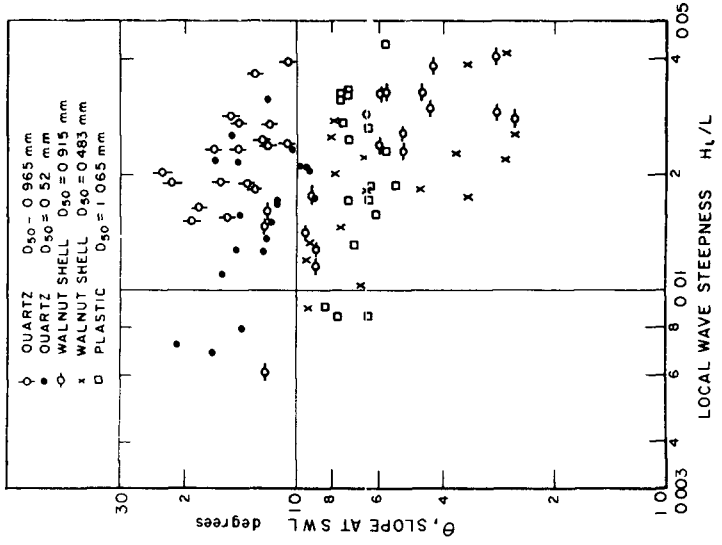


FIG 12 PLOT OF θ VS H_1/L

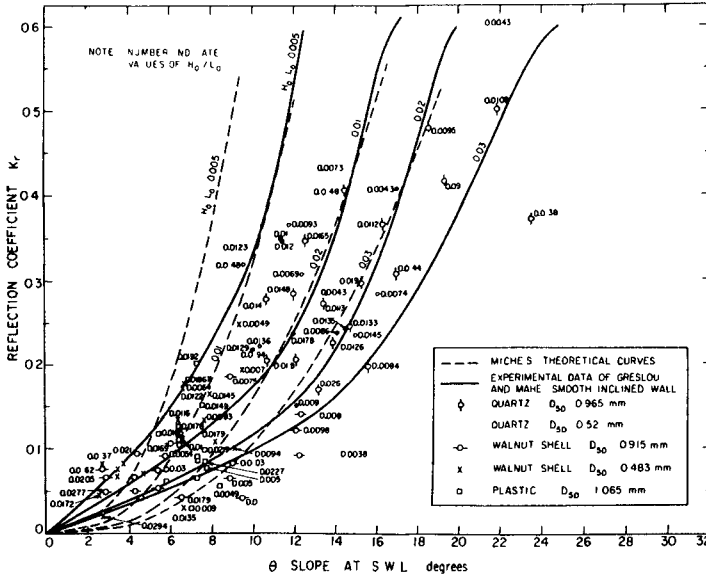


FIG 13 COMPARISON PLOT OF K_r VS θ

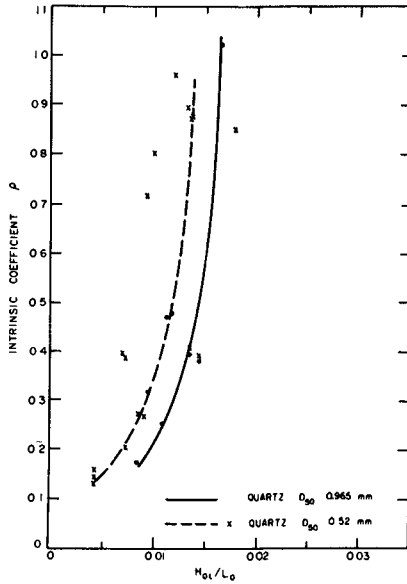


FIG 14 PLOT OF INTRINSIC COEFFICIENT, ρ VS H_{01}/L_0

the total spread of the results agreed very closely with Miche's and Greslou's curves, no clear pattern of distribution of wave steepness as a third parameter could be noticed in the case of the movable bed which includes the effects of roughness, permeability and suspension.

Fig. 14 gives the values of Miche's intrinsic coefficient, ρ , plotted as a function of the deep-water wave steepness for the two sizes of quartz sands. The average value of ρ was found to be 0.54 and 0.49 for the larger and smaller size of sand respectively. The values of the intrinsic coefficient for walnut shell and plastic were found to be higher than 1.00 on an average as the slope, θ , produced by these materials were much lower than 10° and Miche's theory was not applicable. The variation of ρ with H_{01}/L_0 follows the same pattern as that found in the studies at Minnesota for artificial wave absorbers.

Conclusions

1. The criterion for generation of a longshore bar can be described in terms of deep-water wave steepness and the term H_0/SD . Certain combination of size and specific gravity may produce storm-type profiles at high wave steepnesses as well as low ones with an intermediate range where the profiles are of summer type.
2. The parameter $H_{01}/V_f T$ is very significant in determining the reflection coefficient of model beaches formed of noncohesive, movable bed material of fairly uniform given size and density.
3. The reflection coefficient rapidly decreases as the parameter $H_{01}/V_f T$ increases and appears to attain a constant value of about 0.07 over the range of the present experiments. It does not appear to have any

distinct relationship with deep-water wave steepness.

4. The slope at still-water level is related to the term $H_{01}/V_f T$ in a well defined fashion. The slope is affected to a greater extent by specific gravity than grain size of sediment. It is also influenced by the incident wave steepness.

5. The value of Miche's intrinsic coefficient for beaches composed of natural quartz is found to be 0.5

ACKNOWLEDGEMENTS

The work reported herein was carried out towards the requirements of the Ph.D. degree at the University of California, Berkeley and the author would like to express his grateful thanks to Prof. J.W. Johnson for the advice and guidance received during the course of this study.

References

1. Nayak, I.V., "Equilibrium Profiles of Model Beaches", Hydraulic Engineering Laboratory Report No.HEL-2-25, University of California, Berkeley, May, 1970.

CHAPTER 83

STOCHASTIC ANALYSIS OF BEACH PROFILE DATA

By Choule J Sonu and Myron H Young
Coastal Studies Institute
Louisiana State University
Baton Rouge, Louisiana

ABSTRACT

Stochastic prediction of beach changes by means of a linear least-squares transfer function requires a knowledge of power spectra. Since most field data are too short to ensure stable analysis, an attempt was made to generate data artificially by a Monte Carlo simulation. A beach profile transition model which considers the beach profile as a dynamic system allows beach width, sediment storage, and surface configuration to be determined in successive profiles and simulates beach cycles associated with random waves which are in sufficient agreement with the actual observation. The simulated data are amenable to standard stochastic analysis to yield power spectra, cross spectra, coherence functions, and phase lags. Comparison of the results with those derived from actual data shows reasonable agreement. It appears that the process of beach sediment storage involves a combination of classes of Markov Gaussian random processes, whereas that of beach width resembles a white noise. Coupling between these two parameters occurs in the lower frequency range with periodicities longer than about 8 days. Moreover, the beach width shows phase advance before sediment storage. Although the beach profile transition model requires further refinement, especially in regard to quantitative response to waves of various magnitudes and characteristics, the basic concept of the model is sound and will probably explain beach changes in various types of world coasts.

INTRODUCTION

The process of beach change is stochastic in nature. It is also a Markovian process in the sense that the resulting beach profile is partly a function of the preceding profile. Stochastic analysis is a well-established method in many areas of geophysics (see, e.g., Blackman and Tukey, 1958) but has seldom been applied to the study of beach changes. An attractive feature of this approach is the possible design of an optimum transfer kernel function which will allow linear prediction of beach changes as extrapolated time series (Wiener, 1956, Lee, 1960).

A difficulty in the application of stochastic analysis to the process of beach change is the need for data with sufficient length. To illustrate the length of time required to gather a meaningful data set, consider semidiurnal sampling intervals and let the normalized standard error in a power spectrum be ϵ . This is calculated by (see,

e g , Bendat and Piersol, 1966)

$$\epsilon = \sqrt{m/N} \quad (1)$$

in which m is the maximum correlation lag value and N is the total sample size. The relationship between the sampling interval, Δt , the maximum correlation lag, m , and the equivalent resolution band width, B_e , is

$$\Delta t = 1/(B_e \quad m) \quad (2)$$

Assuming a modest 20 percent for ϵ and 2×10^{-3} cycles per hour (CPH) for B_e , the required total sample length is

$$\begin{aligned} \Delta t \times N &= 12 \times 10^3 \text{ hours} \\ &= 500 \text{ days} \\ &= 1 \text{ year } 4 \text{ months} \end{aligned} \quad (3)$$

A continuous field operation requiring such a long period of time is impractical, if not impossible.

To the writers' knowledge, the longest available beach profile data set is one representing 180 days of successive measurements by the Coastal Studies Institute, Louisiana State University, on an Outer Banks beach, North Carolina (Dolan et al , 1969). However, it is evident that the data are still far short of the desired length.

The purpose of this paper is to explore the possibility of generating beach profile data of desired length by means of stochastic simulation. In the first step, a beach profile transition model is established which describes the sequence of profile changes under accretive or erosional wave excitation. The beach profile is defined as a system which essentially incorporates three parameters: beach width, sediment storage (or profile cross section), and surface configuration. The pathways of transition of the surface configuration are dictated by the accretive and erosional wave actions, which are simulated by random numbers. The actual values for the remaining two variables to assume are determined by the Monte Carlo method. Time series of beach profiles thus generated are subjected to stochastic analysis. The resulting power spectrum, cross spectrum, coherence function, and phase lag between the beach width and the sediment storage are then compared with the results obtained with actual data.

DATA ACQUISITION

The field site was located at Nags Head, the Outer Banks, North Carolina (Fig. 1). The coastline was relatively smooth, trended in the north-south direction, and faced the Atlantic Ocean on the east. Rhythmic

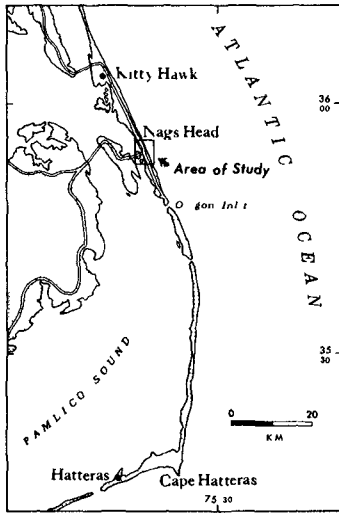


Fig 1 Location of Nags Head, site of field investigation

beach features such as lunate bars and cusped shorelines occurring on this coast have already been discussed (Sonu and Russell, 1966, Sonu *et al* , 1966)

Five traverses perpendicular to the shoreline were set up 30 feet apart. Stakes were set at 10-foot intervals on each traverse over the entire length of approximately 200 feet between the dune and the shoreline. The crests of the stakes were initially surveyed in reference to a permanent datum, so that the successive profile surveys read in rapid sequence the exposed lengths of the stakes. The accuracy of measurement of beach elevation was on the order of 0.01 foot.

The field investigation was conducted between October 1963 and May 1964. The profiles were measured at successive semi-diurnal low tides at intervals of approximately 12 hours 25 minutes. A step-resistance wave gage of the Coastal Engineering Research Center, placed 400 feet from the shore alongside a fishing pier, provided data.

Figure 2 shows the cumulative distribution of these wave data, which were processed from 2-minute strip chart records at 4-hour intervals for about 6 months. Waves higher than about 4.5 feet, representing a 25 percent probability of occurrence, broke over the outer bar, while those higher than about 2.5 feet, representing a 65 percent probability of occurrence, broke only over the inner bar. The median wave height was slightly above 3 feet, and the standard deviation was 1.8 feet. Wave periods occurred in a wide range, between 4 and 20 seconds.

Figure 3 shows the mean profile and histograms of semidiurnal elevation changes. Though there was an indication of net erosion on the upper beach level and of net accretion on the lower beach level, net equilibrium of sediment load was maintained over the entire profile. The higher intensity of elevation changes closer to the shoreline is indicated by the increase in the standard deviation with proximity to the shoreline. Elevation changes were particularly active in an 80-foot width immediately next to the shoreline where the beach was washed by most of the ordinary waves. Only storm waves coinciding with the flood tides sent swashes beyond this limit.

DERIVATION OF PROFILE TRANSITION MODEL

In many of the past studies on beach change, it was customary to represent the beach profile by single parameters. Thus, such parameters as beach width (or shoreline position relative to a fixed base line), beach face slope, and elevations at selected stations were singled out

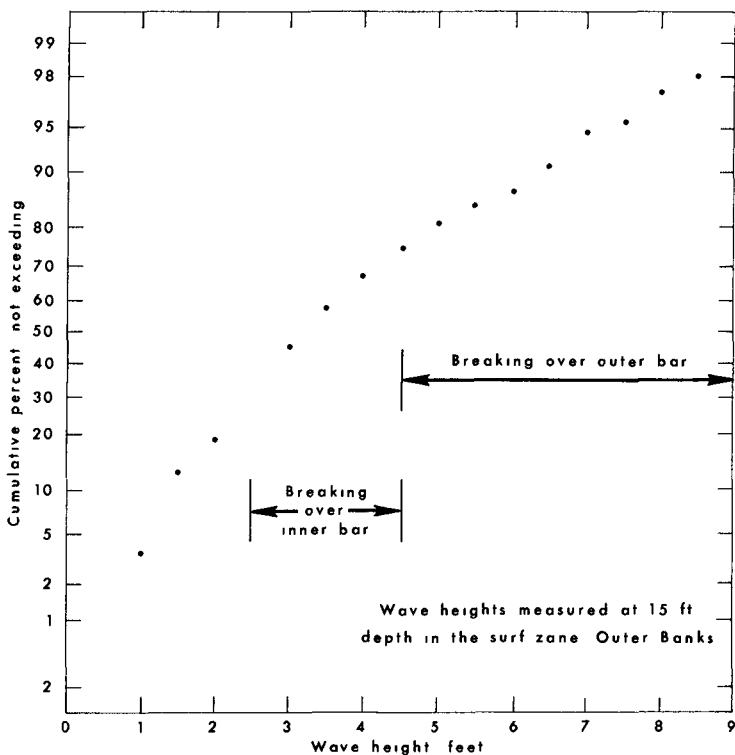


Fig 2 Cumulative distribution of wave heights from 6-month records between December 1963 and May 1964 at Jennette's Pier, Nags Head, North Carolina

and dealt with independently. However, such an approach fails to treat the beach profile as a dynamic system.

Sonu and van Beek (in press) introduced the idea that the beach profile may be represented as a system in which varying amounts of sediment would assume varying distribution patterns within the varying subaerial spaces. To describe this system, obviously, three parameters were needed: the beach width (X), which represented the subaerial space in a two-dimensional profile, the profile cross section (Q), which represented the amount of sediment accommodated in the subaerial beach space, and the surface configuration (Ω), which represented the manner by which the sediment was distributed. For brevity, Q may be referred to as "sediment storage."

The predominant occurrence of six major profile configurations (Ω) was noted, as follows (see Fig 4)

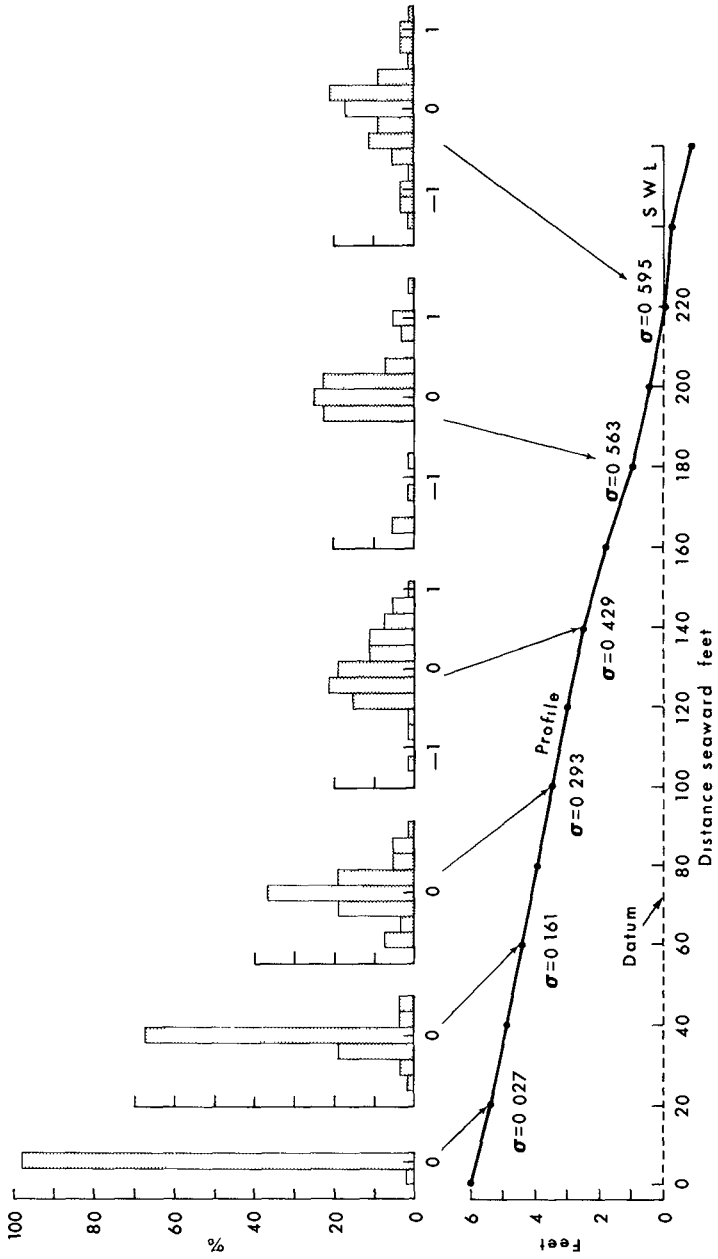


Fig 3 Histograms and standard deviations of semidiurnal elevation changes in the profile, shown relative to mean profile

- A smooth concave profile,
- A' concave profile having a berm at the lower beach elevation,
- B smooth linear profile,
- B' linear profile having a berm at the intermediate beach elevation,
- C smooth convex profile,
- C' convex profile having a berm at the upper beach elevation

The relationship among the three beach profile parameters is illustrated schematically in Figure 4. According to this diagram, accretion of the profile (e.g., increase in sediment storage Q) is accomplished through either growth in beach width (X) or transformation of surface configuration from concave to linear or from linear to convex profiles, in either case involving a profile with a berm. The pathways of profile transition are indicated by arrows. Since the profile C' represents the maximum state of accretion, no further climb of a berm, hence no further accretion, would occur once this profile was realized.

On the other hand, erosion of the profile (e.g., decrease in sediment storage Q) is accomplished through either decrease in beach width (X) or transformation of surface configurations from C to B or from B to A, the process involving only the smooth profiles. Note that profile A represents the maximum state of erosion, therefore, no further erosion would occur once this profile was formed.

Another interesting characteristic of the profile transition model herein described is that it explains the occurrence of beach cycles by random wave excitation, e.g., without considering cyclic energy input such as tides. Because of the unidirectional accretive transitions through A', B', C', and also because of the unidirectional erosional transitions through

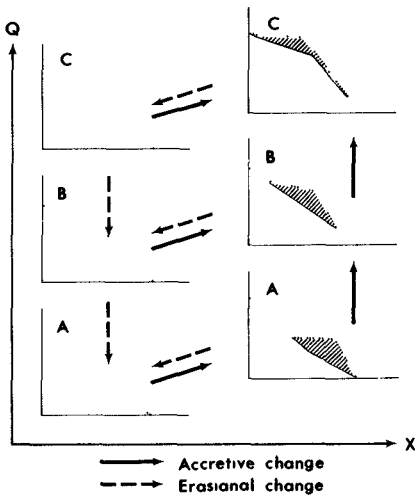


Fig 4 Beach profile transition model

C, B, and A, the beach changes in the long run are bound to produce a net loop of pathways connecting A, A', B', C', C, B, and back to A. A simulated analysis to test this cyclic characteristic was performed. Uniformly distributed random numbers were used to simulate random wave excitation, and the number of transition steps needed to complete a cycle at each trial was counted. Random numbers between 0 and 0.5 were considered to represent accretive excitation, those between 0.5 and 1 were considered to represent erosional excitation. A total of 3,000,000 trials were carried out on an IBM 360 Model 65 computer, and the result is presented as a histogram in Figure 5. The mode, which represented the most frequent number of steps required to complete a cycle was located at 18. The actual observed cycle had 20 steps, showing close agreement with the experiment.

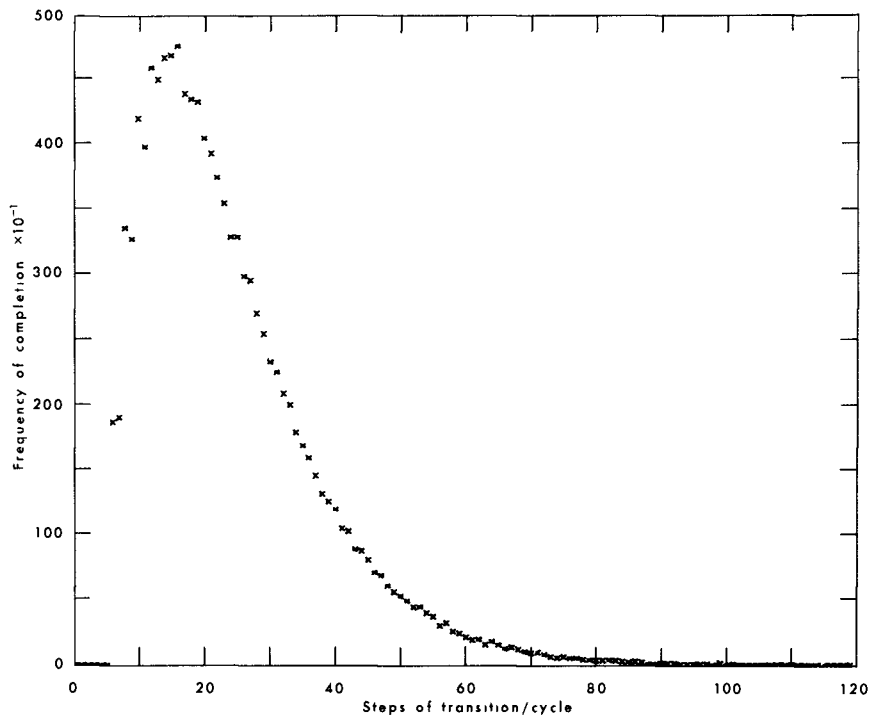


Fig 5 Histogram of the number of transition steps to complete a beach cycle upon 3,000,000 trials

DATA GENERATION

Each of the surface configurations, A, A', B, B', C, and C', was represented by a linear regression relationship between Q and X, as follows (see Fig 6)

For profiles A and A'

$$Q = 0.45 X$$

$$A \quad 32 < X < 46, \quad 29 < Q < 41 \tag{4}$$

$$A' \quad 46 < X < 55, \quad 41 < Q < 49$$

For profiles B and B'

$$Q = 1.00 X$$

$$B \quad 32 < X < 43, \quad 32 < Q < 43 \tag{5}$$

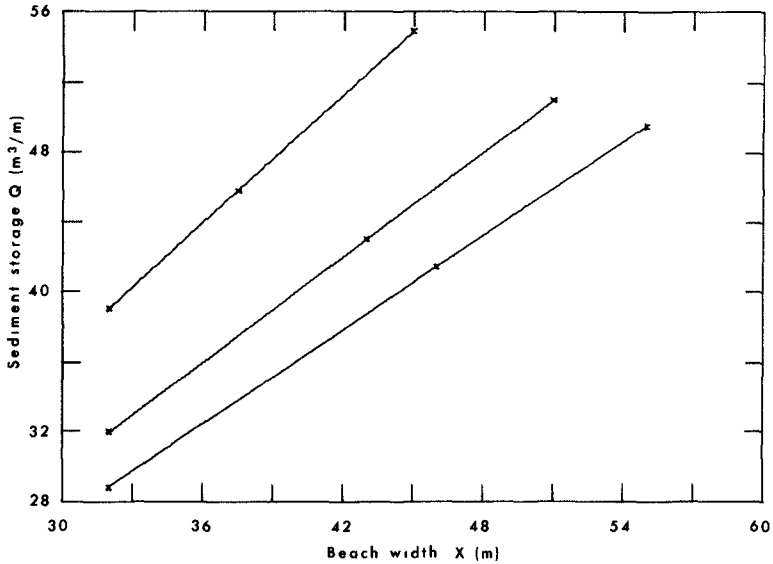


Fig 6 Representation of the beach profile transition model through linear regression relationships

$$B' \quad 43 < X < 51, \quad 43 < Q < 51$$

For profiles C and C'

$$Q = 1.22 X$$

$$C \quad 32 < X < 37, \quad 39 < Q < 46$$

$$C' \quad 37 < X < 45, \quad 46 < Q < 55$$

The derivation of these relationships has been given elsewhere (Sonu and van Beek, in press)

The first step of data generation by the Monte Carlo technique is to draw a random number to induce a profile transition. A number less than 0.5 meant accretive transition, and those larger than 0.5, erosional transition. In the next step, another random number was drawn to determine quantitative measures of the resulting profile, e.g., beach width X and sediment storage Q .

The quantitative profile was determined by using a random number as the proportional length in the corresponding regressive curve. A point thus located in the curve yielded a beach width (X) and sediment storage (Q) pair in accordance with Figure 6. The random number generator was provided by the "RANDU" subroutine of the IBM scientific sub-

routine package A uniform distribution-type generator was used in view of the nature of the problem These steps were repeated to generate a succession of data in regard to X and Q The total sample size was 6,000, it was limited by the computer storage capacity when spectral analysis was performed at the same time Figures 7 and 8 show part of the generated data

It was necessary to filter out low-frequency oscillations in order to eliminate the underlying trend This was done by smoothing with weighted running means

$$\tilde{X}(k) = \sum_{i=-n}^n X(k+i) W_{k+i} \quad (7)$$

in which $i = -n, -n + 1, \dots, n-1, n$

$$\{X(j)\}, j = k + 1 = 1, 2, \dots, N \quad (8)$$

are the original data, and

$$\{\tilde{X}(k)\}, k = n + 1, n + 2, \dots, N-n \quad (9)$$

are the smoothed data The weighting function W_j serves as a low-pass filter Therefore, the desired time series after removal of low frequencies is obtained as

$$X'(k) = X(k) - \tilde{X}(k) \quad (10)$$

$$k = n + 1, n + 2, \dots, N-n$$

Note that the sample size has now reduced to $N - 2n$

Figure 9 shows the response characteristics of the weighting functions An equal-weight smoothing function is a constant for all j 's, e g ,

$$W_j = 1/(2n + 1) \quad (11)$$

$$j = n + 1, n + 2, \dots, N-n$$

However, the range of summing, n , may vary, e g , $n = 10$ and 30 As shown in Figure 9, the equal-weight filter with a larger range of summation $n = 30$ gives a cutoff at lower frequencies, thus saving a greater portion of the higher frequencies for analysis than the filter using $n = 10$ This advantage is gained only at the expense of a larger amount of data, lost because the data length is reduced to $N - 2n$ ($N - 60$) Note also the prominent peaks, which exceed unity, followed by rippling effects, which

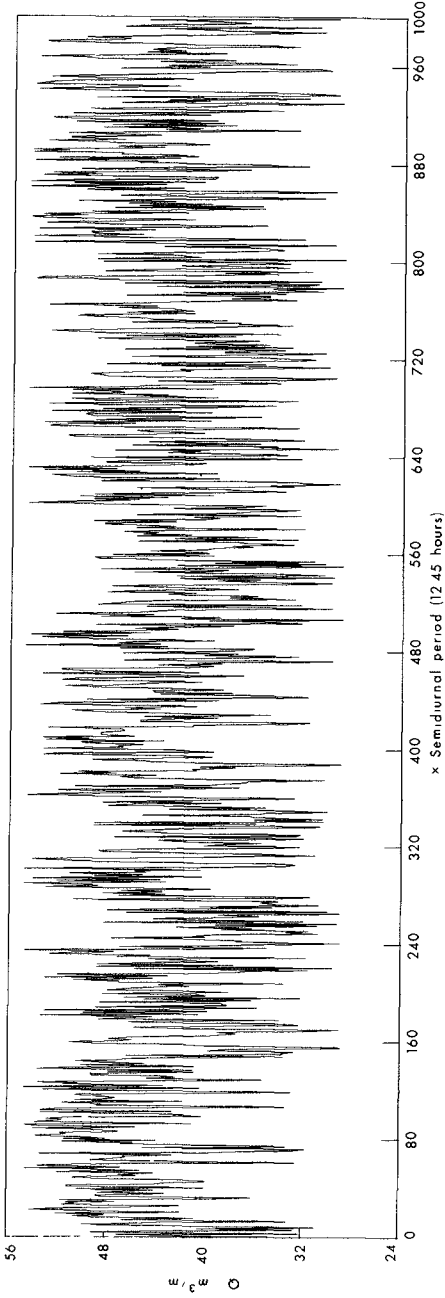


Fig 7 Artificially generated data, the beach sediment storage Q

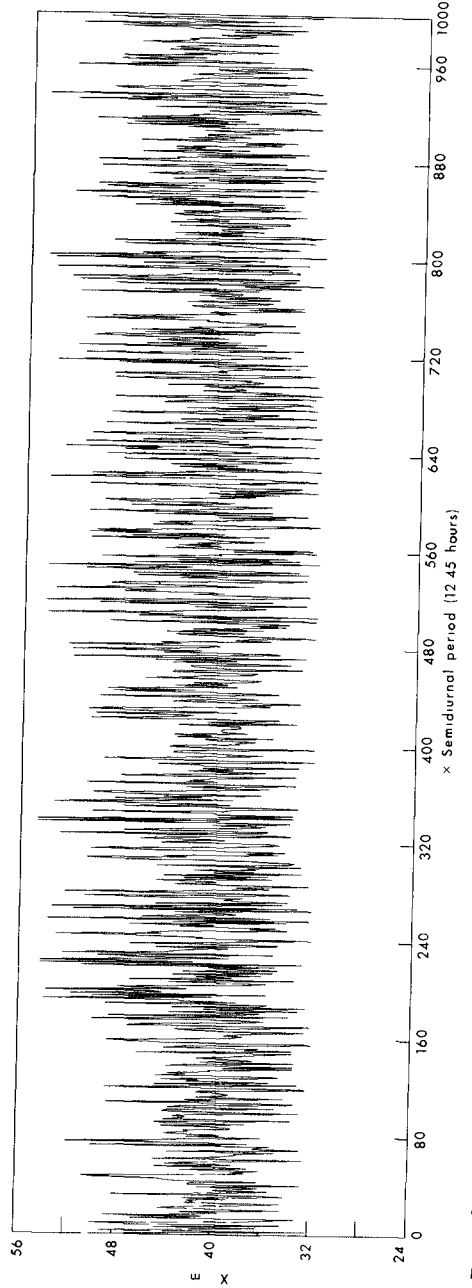


Fig 8 Artificially generated data

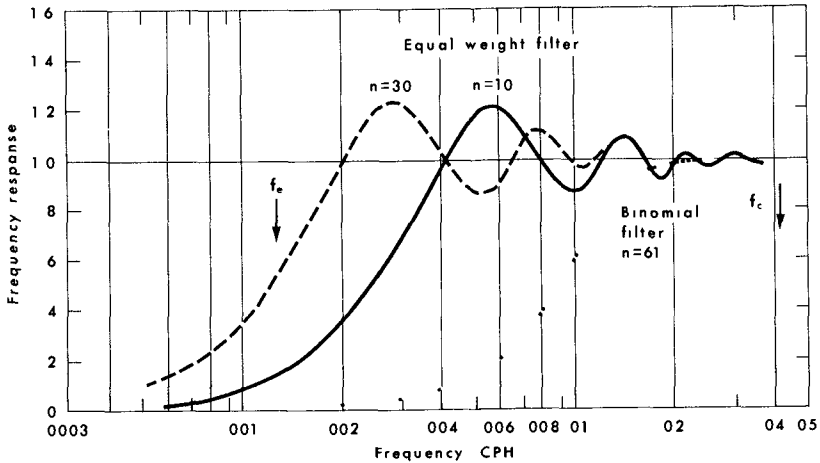


Fig 9 Frequency response characteristics of various high-pass (smoothing) filters

may produce corresponding false peaks in the power spectrum. It is also known that the equal-weight function produces polarity reversal in the filtered data (Holloway, 1958). These problems may be overcome by using a binomial weighting function. But, as seen in Figure 9, a cutoff at a sufficiently low frequency cannot be expected without a large n , hence a considerable reduction in the data size. After repeated trial-and-error calculations it was decided to use an equal-weight filter with $n = 10$ and a binomial filter with $n = 61$. Figures 10 and 11 show the real data and the filtered data, respectively, using the binomial filter for sediment storage.

DATA ANALYSIS

Table 1 shows the frequency resolution f_e and the Nyquist frequency f_c for the real and the simulated data.

Table 1 Frequency Resolution F_e and Nyquist Frequency f_c for the Real and Simulated Data

	f_e	f_c
Real data	0 0156	0 0402
Simulated data	0 0003	0 0402

The power spectrum, cross spectrum, coherence function, and phase

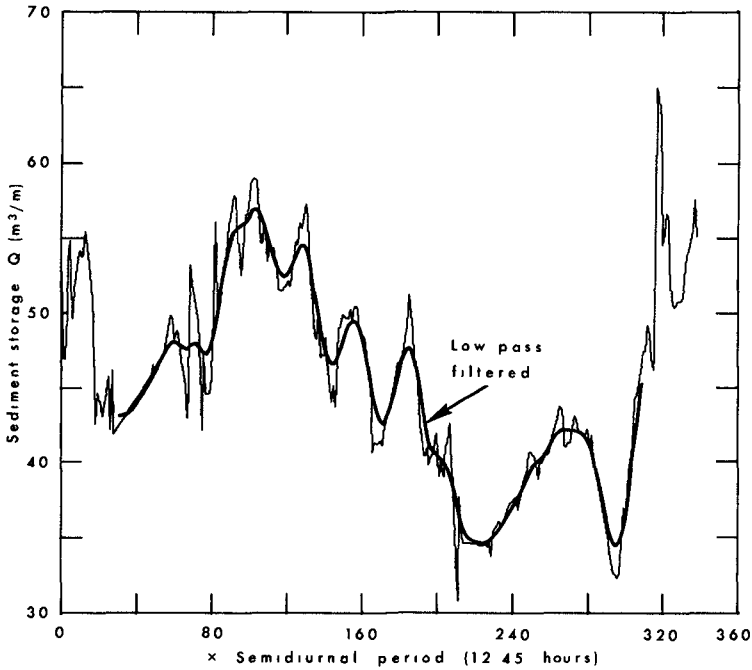


Fig 10 Original real data, the beach sediment storage Q, shown with the binomial low-pass filtered data in thick line

lag calculations in the present study are essentially the same as described by Blackman and Tukey (1958) and Bendat and Piersol (1966) However, the Fast Fourier Transform (FFT) program by Cooley and Tukey (1965) is used to improve the accuracy of calculation as well as to reduce computational time (see also Rothman, 1968)

The autocovariance function at the k-th lag is given as

$$R(k) = \frac{1}{N-k} \sum_{i=1}^{N-k} X(i) X(i+k) / R(0) \tag{12}$$

The one-side power spectrum can be calculated as a Fourier transform of the autocovariance function,

$$G\left(\frac{kf}{m}\right) = 2 \Delta t \left[R(0) + 2 \sum_{k=1}^{m-1} R(k) \cos\left(\frac{\pi k f}{m}\right) - (-1)^k R(m) \right] \tag{13}$$

The FFT subroutine computes the values within the brackets For

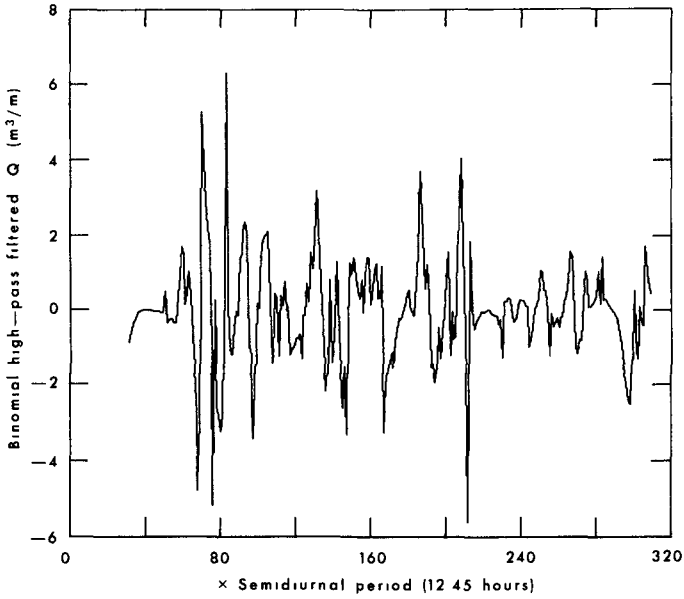


Fig 11 Real data upon subtraction of the binomial low-pass filtered data from the original data (n = 61)

stochastic representation, the final estimates are smoothed by Hanning's equation (see Blackman and Tukey, 1958)

The coherence function and phase lag of beach width and sediment storage are calculated by first obtaining the cross covariance functions between the time series data of X and Q

$$R_{XQ}(k \Delta t) = \frac{1}{N - k} \sum_{n=1}^{N-k} X_n Q_{n+k} \tag{14}$$

$$R_{QX}(k \Delta t) = \frac{1}{N - k} \sum_{n=1}^{N-k} Q_n X_{n+k} \tag{15}$$

The cross spectral function $G_{XQ}(f)$ is then obtained from the cospectrum and quadrature spectrum, which are the Fourier transform of the modified functions of the above cross covariance functions R_{XQ} and R_{QX} . These relations are given in equations (18) through (22)

$$G_{XQ}(f) = C_{XQ}(f) - jD_{XQ}(f) \tag{16}$$

in which $C_{XQ}(f)$ is the cospectrum, $D_{XQ}(f)$ is the quadrature spectrum, and $j = \sqrt{-1}$. They are related to the cross covariance functions as

$$C_{XQ}\left(\frac{k f}{m}\right) = 2 \Delta t \left[A_0 + 2 \sum_{i=1}^{m-1} A_i \cos\left(\frac{\pi i k}{m}\right) + (-1)^k A_m \right] \quad (17)$$

$$D_{XQ}\left(\frac{k f}{m}\right) = 4 \Delta t \sum_{i=1}^{m-1} B_i \sin\left(\frac{\pi i k}{m}\right) \quad (18)$$

where A_1 and B_1 are the modified cross covariance functions

$$A_1 = 1/2 (R_{XQ}(1 \Delta t) + R_{QX}(1 \Delta t)) \quad (19)$$

$$B_1 = 1/2 (R_{XQ}(1 \Delta t) - R_{QX}(1 \Delta t)) \quad (20)$$

Finally, the coherence function γ_k^2 and the phase angle ϕ_k can be obtained

$$\gamma_k^2 = \frac{C_{XQ}^2\left(\frac{k f}{m}\right) + D_{XQ}^2\left(\frac{k f}{m}\right)}{G_X\left(\frac{k f}{m}\right) G_Q\left(\frac{k f}{m}\right)} \quad (21)$$

$$\phi_k = \tan^{-1} \left(\frac{D_{XQ}\left(\frac{k f}{m}\right)}{C_{XQ}\left(\frac{k f}{m}\right)} \right) \quad (22)$$

The Monte Carlo method requires repeated trials of data generation and analysis so that the end product may be evaluated through the central limit theorem. In the present study, the results of the initial several trials were so similar to each other that no further calculation was pursued.

INTERPRETATION

Figure 12 shows the power spectrum for Q. The real-data spectrum using an equal-weight filter and one using a binomial filter show peaks in the spectral density at 0.003 and 0.008 CPH, respectively. A gross peak is also located near 0.010 CPH in the simulated power spectrum using a binomial filter. However, all these peaks are spurious since

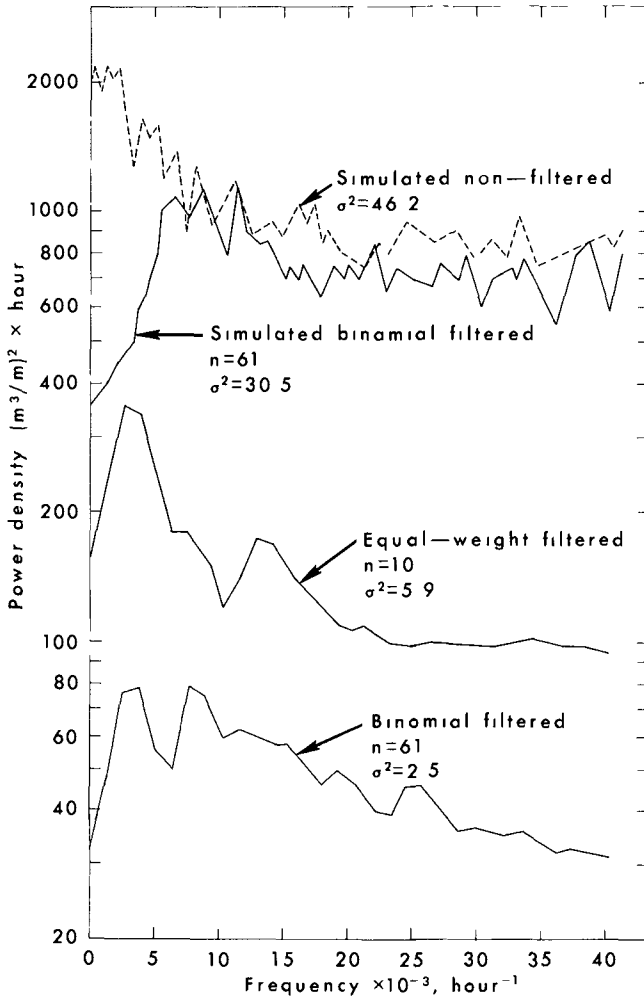


Fig 12 Power spectrum of Q (sediment storage)
 Data smoothed with equal-weight filter (n = 10),
 with binomial filter (n = 61), simulated data using
 binomial filter, and simulated data with no smoothing

they represent the effect of low-frequency cutoff by the high-pass filter used (see Fig 9) The true spectrum for the actual sediment storage Q is very likely to be a smooth curve which has no prominent peak but attenuates monotonically toward high frequencies (see Fig 17, case 1) This type power spectrum was indeed obtained from the simulated data in

which no high-pass filter was applied (The ripples are probably the result of intrinsic noise in the simulation process)

The minimum number of transition steps necessary to complete a beach cycle is six, representing a frequency of 0.013 CPH. The majority of beach cycles take more steps than six, which corresponds to frequencies shorter than 0.013 CPH. The most probable number of steps is 18, which gives a frequency of 0.0067 CPH. In Figure 12 beach cycles shorter than 0.013 CPH indeed constitute the major part of the simulated power density. Note particularly that a peak appears at 0.005 CPH, which is equivalent to a 16-step simulated beach cycle and hence approximates the observed 20-step beach cycle of the real data reasonably well. This peak is especially noteworthy because of its occurrence in the frequency range where the response has been considerably reduced by the high-pass filter.

There are smaller beach cycles in the analysis. For example, the four-step cycles through A, A', B', B, and A or through B, B', C', C, and B represent a frequency of 0.0201 CPH. The two-step cycles through A, A', and A, through B, B', and B, or through C, C', and C represent a frequency of 0.040 CPH. However, they fail to comprise a significant level of power spectral density.

The discrepancy between the actual and the simulated power spectra of Q is due mainly to the fact that in the simulation the profile transition was only allowed to take either erosional or accretive pathways, disregarding the third possibility, in which the profiles would remain unchanged. As a result, the variability was exaggerated in the simulation, leading to a larger value of power density (σ^2). This discrepancy may be adjusted as the interaction between the profile and wave characteristics is better established.

Power spectra for the real-data beach width X are shown in Figure 13. Both an equal-weight filter and a binomial filter are used in the analysis. The density concentration is found in the frequencies below 0.015 CPH, which corresponds to a period of 60 hours or a five-step transition period. Although the binomial filter allows only 40 percent or less response for this frequency range, the filtered spectra reveal peaks at 0.012 CPH as well as at 0.005 CPH. The 0.012 CPH frequency period corresponds to a period of about 83 hours or a 6.7-step transition period.

The simulated power spectrum for X , on the other hand, is quite inconsistent. Repeated calculations using different random numbers showed that individual peaks in this power spectrum were fortuitous. Therefore, they may average out only if a long record can be simulated in the analysis. The general trend of the simulated power spectrum for X strongly suggests a similarity to a white noise spectrum, which characterizes a consistent power density level for all frequencies. It is not immediately clear why the beach width should behave so differently from the sediment storage.

Figure 14 shows coherence functions between the beach width X and the sediment storage Q . The real-data coherence functions are obtained by using both equal-weight filter and binomial filter. Both curves show a high level of coherence. About 50 percent coherence is found for

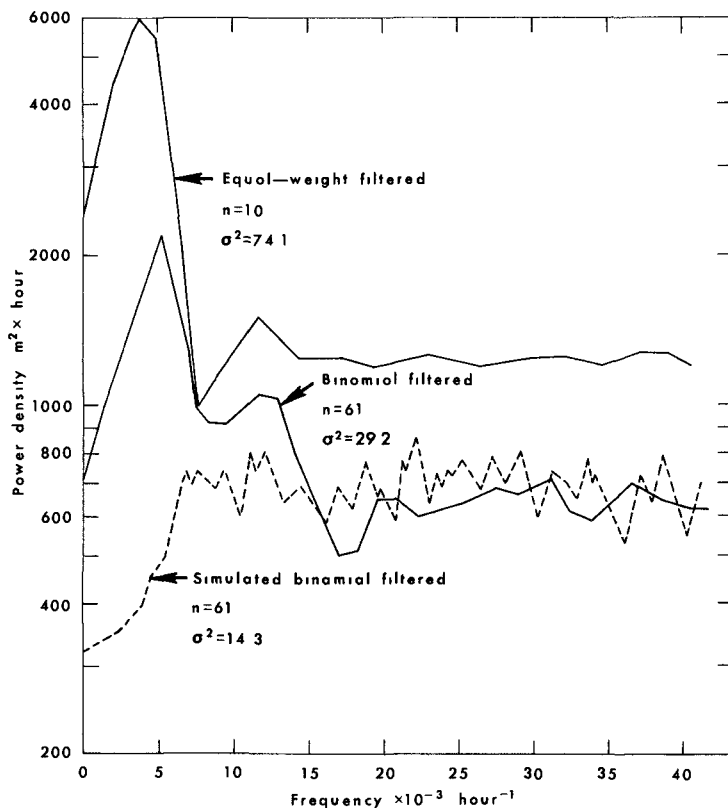


Fig 13 Power spectrum of X (beach width) Data smoothed with equal-weight filter (n = 10), data smoothed with binomial filter (n = 61), and simulated data

frequencies below about 0.005 CPH, which is a region where the beach width power spectrum displays a peak density. The coherence drops sharply to less than 20 percent at higher frequencies, which means that the coupling between the beach width and the sediment storage is basically a low-frequency phenomenon with periodicities of 8 days or longer.

A discrepancy with the above results is noted in the simulated coherence function. Here, the coherence is low at low frequencies and high at high frequencies. A probable explanation for this may be revealed from the following considerations. The beach process is basically a response to a weather regime which will change gradually with periodicities of several days. Consequently, following "persistence" in natural processes, the beach width change will essentially be a gradual process in which the effect of the preceding profiles

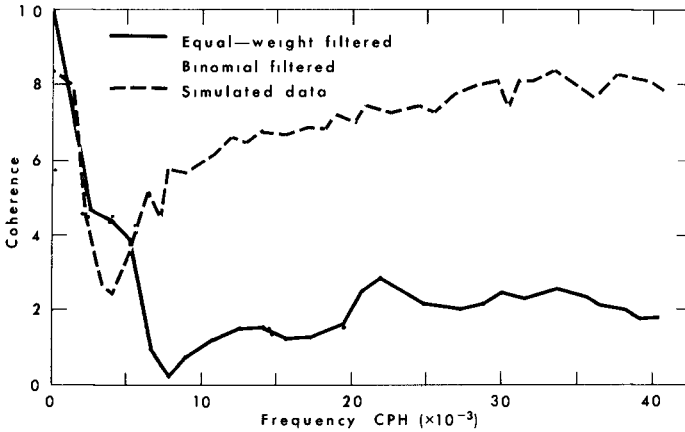


Fig 14 Coherence function for X and Q Data smoothed with equal-weight filter ($n = 10$), smoothed with binomial filter ($n = 61$), and simulated data

will persist for some time. In the data simulation, the effect of persistence was taken into consideration in the transition of surface configurations but not in the successive values of beach width and sediment storage. These parameters were determined by random numbers not influenced by their preceding values. Consequently, the coupling effect with periodicities on the order of the weather influence may not be expected. The high coherence at high frequencies in the simulated coherence function is not important because the power density in the corresponding frequency range is extremely low.

Figure 15 shows phase lags in the correlation between the beach width and the sediment storage. In the real data, the sediment storage lags behind the beach width in the low-frequency region, where a coherence coupling between the two parameters exists. At somewhat higher frequencies, however, this relationship is reversed, and eventually the phase difference disappears at frequencies higher than about 0.020 CPH, which corresponds to 2 days or less in period. In the simulated data, the phase lag of the sediment storage also lags behind the beach width. However, it appears at a much lower frequency than that of the real data. It is then followed by a reversed relationship and eventually reduces to a zero phase difference at frequencies higher than 0.020 CPH.

DISCUSSION

Dynamic beach transitions are Gaussian processes in nature. Therefore, these random processes deserve special attention for two reasons:

1. They approximate reasonably well a number of experimental data involving noise and random phenomena.

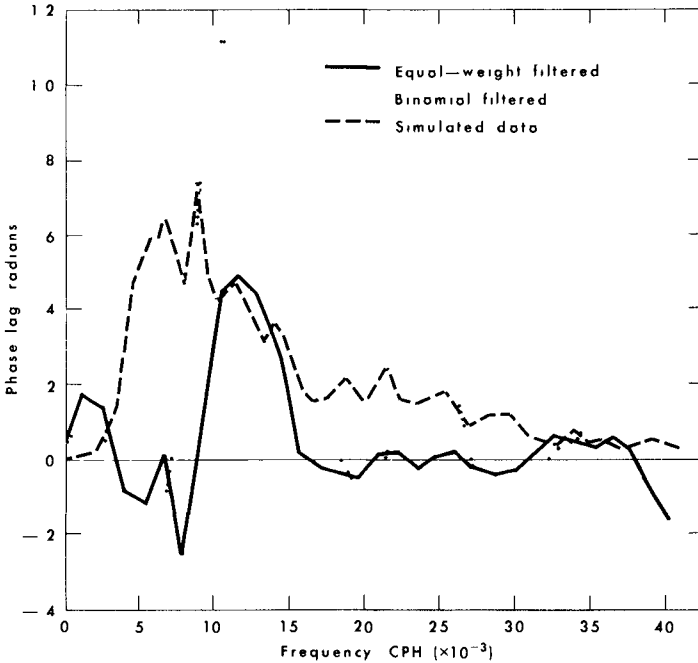


Fig 15 Phase lag for X and Q Data smoothed with equal-weight filter (n = 10), smoothed with binomial filter (n = 61), and simulated data

- 2 They arise from "multidimensional central limit theorem and, therefore, [are] of theoretical significance as an idealization of the superposition of small effects" (Bendat, 1958)

In the present case, a Markovian feature must also be considered, since according to the profile transition model the successive profiles are products not only of either accretive or erosional wave excitation but also of the preceding profile. Thus, a Markov Gaussian random process may possibly explain beach profile changes. According to Doob (1953), the stationary Markov Gaussian random process requires an exponential autocovariance function and hence necessarily a power spectrum of the form

$$G(f) = \frac{2k}{\pi} \frac{f^2 + (k^2 + c^2)}{f^4 + 2(k^2 - c^2) f^2 + (k^2 + c^2)^2} \tag{23}$$

in which parameters k and c are obtained by a curve fitting the autocovariance function in the low lag region, e g ,

$$R(\tau) = e^{-k|\tau|} \cos c \tau \quad (24)$$

Figure 16 shows the approximation of the real data autocovariance function fitted by equation (24), in which $c = 0.048$ CPH and $k = 0.024$ CPH. According to Bendat (1958), two types of power spectrum may result, depending on the relative size of $3c^2$ and k^2 (see Fig. 17). With the above values for c and k , it is obvious that $3c^2 > k^2$ for the sediment storage, hence the power spectrum of Q must have a peak density, contrary to the actual case. Moreover, for the theoretical power spectrum the power density is inversely proportional to f^2 , e.g.,

$$G(f) \propto f^{-2} \quad (25)$$

whereas in the present case

$$G(f) \propto f^{-1/3} \quad (26)$$

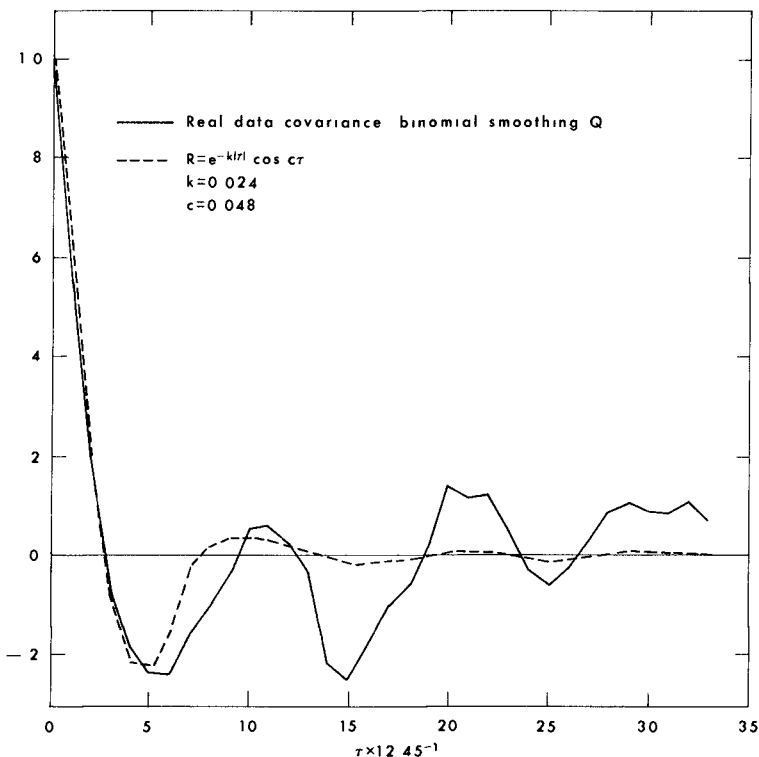


Fig. 16 Autocovariance function of the real data Q compared with the theoretical covariance function for Markov Gaussian random process

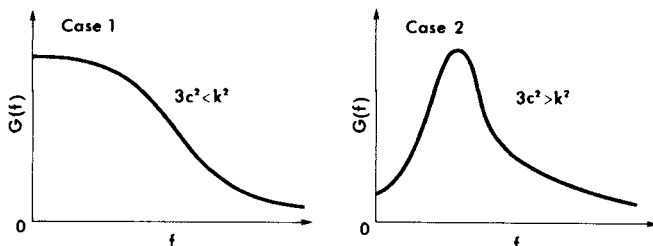


Fig 17 Two cases of power spectrum for Markov Gaussian random process (after Bendat, 1958)

The reason for this discrepancy is not immediately clear, but it seems possible that the actual example represents the superposition of two or more case 1 and/or case 2 situations

The time series simulation by means of a Monte Carlo technique, as demonstrated in this paper, appears to be reasonably successful. Areas of needed improvement are the interactions between waves and beach profiles. "Accretive" and "erosional" wave excitations, which are simulated by random numbers in the present study, need further clarification. According to Sonu and van Beek (in press), erosion of the beach profile is associated with a period of growth of waves, while accretion is associated with a period of wave decay. This relationship is more pronounced than the generally acknowledged effect of wave steepness. In fact, it is noted that waves of the same steepness could cause either erosion or accretion, depending on whether they occurred during growth or decay of a wave field. The basic mechanism controlling this relationship is not known. Also unknown is the extent of beach change as a function of wave energy. In the simulation study, it is assumed that each wave excitation would cause only one step of profile transition. More precisely, the number of steps per semidiurnal period (the speed of beach change) should vary by types of profiles as well as by waves.

The beach profile transition model, while requiring further refinement, appears to be basically sound. It is likely that various regional coasts may be represented by different regression areas in the Q-X plane. As indicated schematically in Figure 18, a type I coast may be found in an embayed coastline with a flat slope receiving little lateral supply of sediment, a small change in sediment balance may seriously affect the shoreline positions. A type III coast may be, on the other hand, a steep beach sufficiently close to the source of sediment supply so that it requires a large amount of sediment movement to cause appreciable dislocation of the shoreline. A type II coast is a typical ocean-exposed sandy coast, while type II' is exposed to limited fetch, such as on a lake or an inland sea. With accumulation of data, it is hoped that a generalized picture of beach profile transition model for various regions may be constructed in the entire Q-X plane.

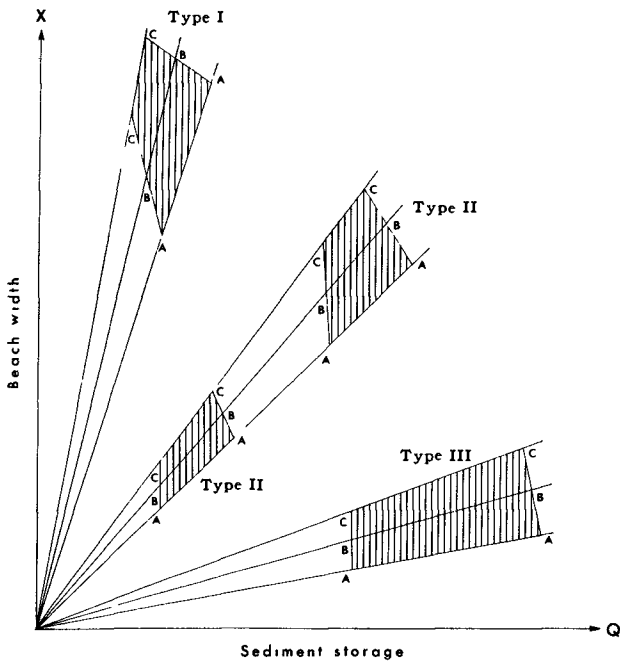


Fig 18 Suggestion for a generalized beach profile transition model for different types of coasts

ACKNOWLEDGMENTS

This study was supported financially by the Office of Naval Research, Geography Programs, under contract N00014-69-A-0211-0003, NR 388 002, with the Coastal Studies Institute, Louisiana State University Miss Sharon Dunn did the drafting

REFERENCES

- Bendat, J S , 1958, Principles and applications of random noise theory
New York (John Wiley and Sons, Inc)
- _____, and A C Piersol, 1966, Measurement and analysis of random data
New York (John Wiley and Sons, Inc)
- Blackman, R B , and J W Tukey, 1958, The measurement of power spectra -
from the point of view of communications engineering New York
(Dover Publications, Inc)
- Cooley, J W , and J W Tukey, 1965, An algorithm for the machine calcula-
tion of complex Fourier series Mathematics of Computers, 19 297-
301
- Dolan, R , J C Ferm, and D S McArthur, 1969, Measurements of beach
process variables, Outer Banks, North Carolina La State Univ ,
Coastal Studies Institute Tech Report No 64
- Doob, J L , 1953, Stochastic processes New York (John Wiley and Sons,
Inc)
- Holloway, J L , Jr , 1958, Smoothing and filtering of time series and
space fields Advances in Geophysics, vol 4, New York (Academic
Press, Inc)
- Lee, Y W , 1960, Statistical theory of communication New York (John
Wiley and Sons, Inc)
- Rothman, J E , 1968, The Fast Fourier Transform and its implementation
Decuscope, Digital Equipment Computer Users Society, vol 7, no 3
- Sonu, C J , 1969, Collective movement of sediment in littoral environ-
ment Proceedings, XIth Coastal Engineering Conference, Council
on Wave Research, London
- _____, J M McCloy, and D S McArthur, 1966, Longshore currents and
nearshore topographies Proceedings, Xth Coastal Engineering
Conference, Council on Wave Research, Tokyo
- _____, and R J Russell, 1966, Topographic changes in the surf zone
profile Proceedings, Xth Coastal Engineering Conference, Council
on Wave Research, Tokyo
- _____, and J L van Beek, in press, Systematic beach changes on the
Outer Banks, North Carolina J Ceol
- Wiener, N , 1956, The theory of prediction In (E F Beckenbach, ed)
Modern mathematics for the engineer New York (McCraw-Hill Book
Company, Inc)

CHAPTER 84

FIELD STUDY OF SURATHKAL BEACH

P. Suryaprakasa Rao* & P. Kassim **

ABSTRACT

Beach profile observations and sediment sampling were carried out for six months at frequent intervals to study the seasonal changes of the beach. The study is helpful in bringing out the qualitative and quantitative changes of the beach under varying wave and tide conditions. Useful information is obtained and presented regarding i) the maximum rate of erosion ii) the total quantity of material eroded iii) the critical wave steepness values which changed from depositing to eroding nature and iv) the sediment characteristics of the beach.

INTRODUCTION

This paper presents the results of a six month (February to August 1969) field study of the seasonal profile changes and sediment characteristics of a natural sand beach at Surathkal.

* Assistant Professor of Civil Engineering, Karnataka Regional Engineering College, Surathkal (India)

** Lecturer, I.K.M. College of Engineering, Quilon (India)
Formerly post graduate student at Karnataka Regional Engineering College, Surathkal (India)

Surathkal beach is on a straight reach of the West Coast of India facing the Arabian sea at a distance of 20 Km north of Mangalore. The beach material is well sorted sand having median diameters in the range of 0.2 to 0.4 mm. The climatic conditions on the coast repeat annually with remarkable regularity and uniformity. The beach is exposed to relatively uniform swells of low steepness arriving with crests parallel or nearly parallel to shore during fair weather season when the beach is built up. During the monsoon period, the wave height and the wave steepness are increased and the beach is eroded. The average tidal range is about 1 metre.

Beach erosion problems exist along some stretches of West Coast of India and the information obtained from this study could be useful in planning shore protection measures.

FIELD MEASUREMENTS AND OBSERVATIONS

1) Beach profiles:-

A stretch of beach of 200 metres length was selected for study and observation. Three cross sections, 100 metres apart, were marked by constructing two pillars for each section. The pillars were constructed on the storm berm where the waves do not normally reach. The line joining the three pillars nearer the water line was taken as the base line.

Levelling was done using a precise level along the three cross sections on the portion of the beach exposed at

low tide between the base line and the water line. The beach elevations given in the various figures are with respect to an arbitrary datum. Profile measurements were done at intervals of 3 to 9 days, the interval depending on the magnitude of the changes that occurred. A total of 33 measurements were made during six months. Surface sediment samples at various points along the profiles were collected during some of the observations.

11) Wave and Tide data:

Wave data was obtained from the wave records of the offshore subsurface pressure type wave recorder installed by the Mangalore Harbour Project authorities at Panambur about 10 Km. south of Surathkal beach. The waves were recorded for 15 minutes at 3 hour intervals during fair weather season and at closer intervals during monsoon period.

The maximum recorded wave heights and the corresponding periods for each day were available from the records. The maximum surface wave heights for each day were computed by using the corresponding pressure response factors.

For the periods of considerable changes in the beach profiles, the continuous wave records for the days were studied and representative strips, each of 15 minute duration, were analysed to find out the mean wave heights and the average periods. The surface mean wave height was computed and the corresponding deepwater mean wave height

had the same value as this because the shoaling and refraction coefficients were both nearly equal to unity for the prevailing conditions. The deepwater mean wave steepness was computed using the deepwater mean wave height and the deepwater wave length corresponding to the average period. Visual observations were also made to study the type and location of the breakers and width of surf zone.

The tide data was obtained from the tide recorder installed by the Mangalore Port authorities at Mangalore. The tidal range can be taken to be the same at Mangalore and Surathkal.

RESULTS OF STUDY

i) Seasonal beach profile changes:-

The period of study covered two distinct portions of the year. One was the premonsoon fair weather season upto middle of May when the beach was still being built up by processes of deposition which commenced at the end of the previous year's monsoon. The second one was the monsoon period from middle of May to August when the beach was eroded. After August the beach would again slowly start building up. The climatic conditions on the Coast repeat annually with remarkable regularity and hence the corresponding beach processes are also more or less repetitive in nature. Thus the study included the period when the beach process changed from depositional to eroding nature and the period when the total erosion

occured.

Typical beach profile changes at one of the three cross sections are shown in figure 1. upto about the middle of May, the beach was subjected to long period waves of low steepness and was being built up. The maximum wave height was less than one metre and the mean wave steepness was less than 0.002. The height and width of the summer berm increased to a maximum and the berm had a slope towards the land.

Fig.2 shows the beach profile changes during the period of erosion from middle of May to August. It is not as if there was continuous erosion during the period. There were periods of deposition in between but the net effect was one of erosion. The complete summer berm was progressively eroded.

During the latter half of May there was a graual increase in the maximum wave height from less than one metre to about 1.75 metres. The mean wave steepness also increased from about 0.002 to 0.003 and above as shown in fig.4. This is the period when the beach erosion has set in as can be seen from the beach profiles on 20th and 28th May in fig.2. Therefore the critical deepwater mean wave steepness value which changed the wave action on the beach from depositing to eroding nature lies between 0.002 and 0.003.

The maximum rate of erosion occured during the period 28th May to 5th June. The beach profiles at one

of the sections are shown in fig.3. Similar profile changes occurred at all the three cross sections. During this period the maximum wave height increased to about 2 metres; the mean wave steepness increased to 0.004; and this happened to be the spring tide period with an increased tidal range. It was computed from the three cross sections that, on an average, 15.8 metres width of berm was removed and 18.65 cu. metres of material per metre length of beach was eroded during this period. This gives a maximum rate of erosion of 1.18 cu.metres of material per sq.metre change in beach surface area in one week (i.e. 0.143 cu yds/ft²/week)

Fig.5 shows two profiles at one of the cross sections. One profile corresponds to the stage of maximum deposition and the other one to that of maximum erosion. From similar profile changes at the three sections, the total quantity of material eroded during the season was an average of 74 cu. metres per metre length of the beach and the average width of beach eroded was 31 metres. One sq.metre of change in beach surface area equals 2.39 cu. metres of beach material eroded (i.e. 1 sq.ft. of change in beach area equals 0.3 cu.yds.of material eroded). This, it may be observed, is a much smaller value compared to other exposed beaches in the world.

From such profile changes as shown in fig.5 it was also found that the active zone of the beach, the material of which partook in the beach processes, was confined to

a depth of about 3 metres.

Figs.6 and 6(a) show the profile changes at two of the cross sections. The beach profiles appeared to oscillate in response to a tidal cycle of about a month's duration. The profiles did not repeat exactly as the wave characteristics had not remained the same throughout the period.

Cusps were found to form on the beach during periods of deposition as well as erosion. They always formed during the neap tide periods and disappeared during the subsequent spring tides. The spacing of the cusps along the beach was regular and varied from 27 to 45 metres. The spacing of the cusps and the level difference between the valley and the ridge of the cusp formation increased with increase in wave height.

ii) Sediment Characteristics:

The median diameter of the beach sand was between 0.2 and 0.4 mm. The dune sand was finer than that on the berm. The sands on the dunes, berms and the foreshore were all well sorted with the sorting coefficient lying between 1.1 and 1.4. The grain size distributions were nearly symmetric with the skewness values lying between 0.9 and 1.1. There was no regular variation of median diameter with depth at a point on the beach and also along the beach at various points.

Relationship between grain size (median diameter in mm) and the foreshore slope on which it was resting is shown in fig.7. The curve is inserted in a similar plot given in

reference number 1 for comparison with other coasts. Sand of a given size within the range of 0.2 to 0.4 mm stands on a steeper slope on this beach.

Acknowledgements

The work reported here was done by the junior author, while at the College, for his thesis submitted in partial fulfilment of the requirements of the M.Tech. degree. Grateful acknowledgment is made to the Mangalore Harbour Project authorities for the wave data, to the Mangalore Port for the tide data and to Prof. Evald Nielsen, Unesco visiting Professor of Coastal Engineering at the College for his encouragement and overall guidance. Permission of the College authorities to publish this paper is appreciated.

REFERENCES

1. U.S. Army, CERC (1966). Technical Report No.4, Shore Protection, Planning and design.
2. Kassim P. (1969). A field study of seasonal profile changes and sediment characteristics of Surathkal beach. M.Tech. Thesis, K.R.Engg. College, Surathkal.
3. Shepard, F.P.(1963). Submarine Geology(2nd Edition): Harper & Row, Publ., New York.
4. King C.A.M. (1966) Beaches and Coasts (2nd reprint) Edwin Arnold Publ. Ltd., London.
5. John M. Darling (1964). Seasonal changes in beaches of the north Atlantic Coast of the United States. Prof., 9th Conference, Coastal Engineering.

6. Bascom, Willard J., (1954) Characteristics of natural beaches, Proc. 4th Conf. Coastal Engg., Berkeley, Calif.

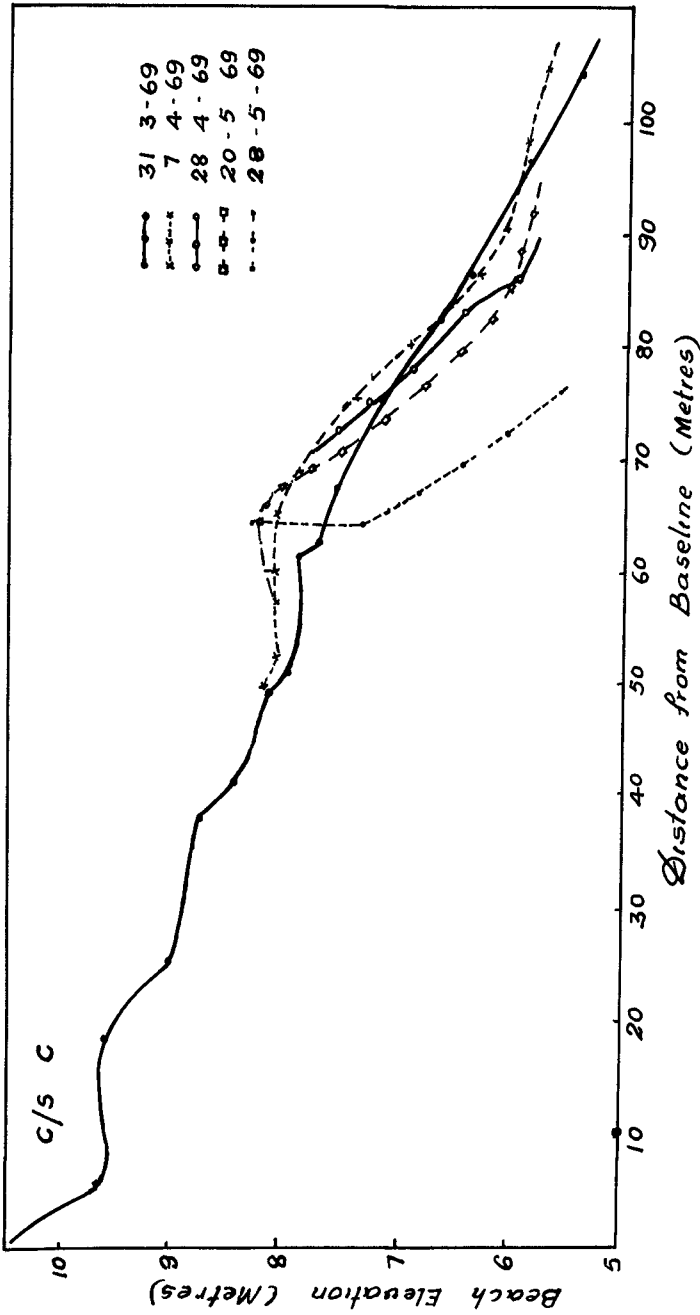


Fig 1. STAGES OF DEPOSITION

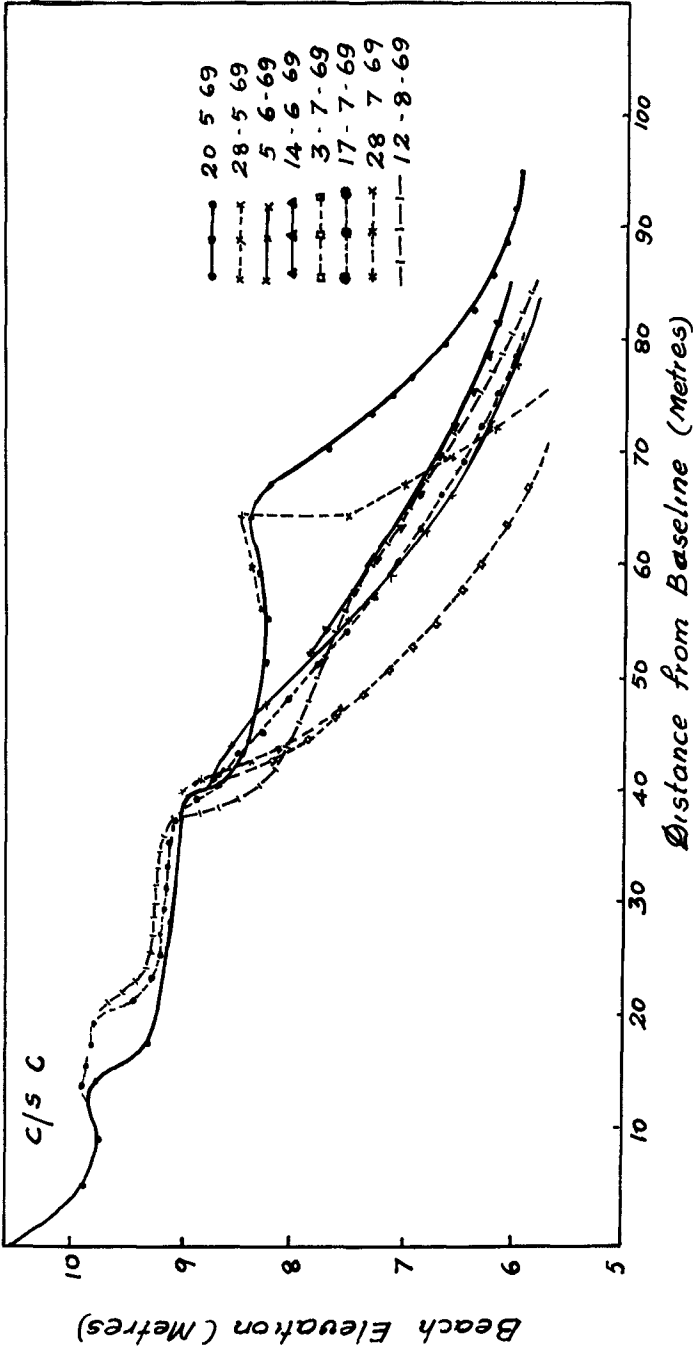


Fig 2 STAGES OF EROSION

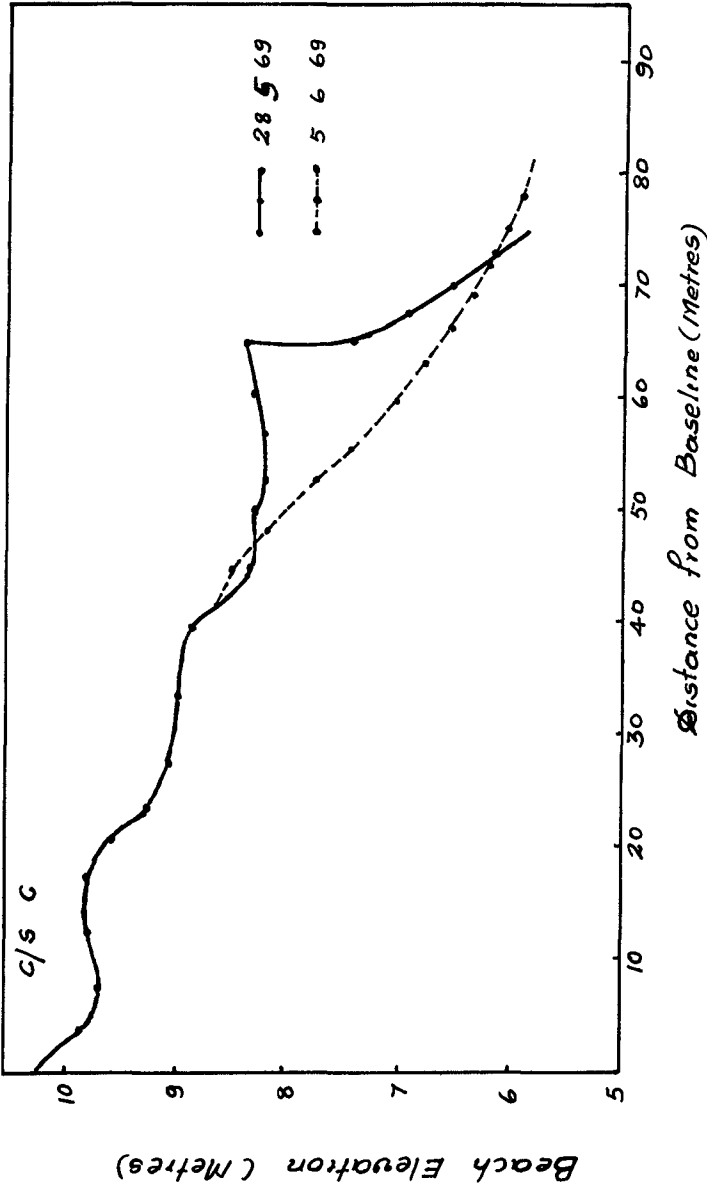


Fig 3 MAXIMUM RATE OF EROSION

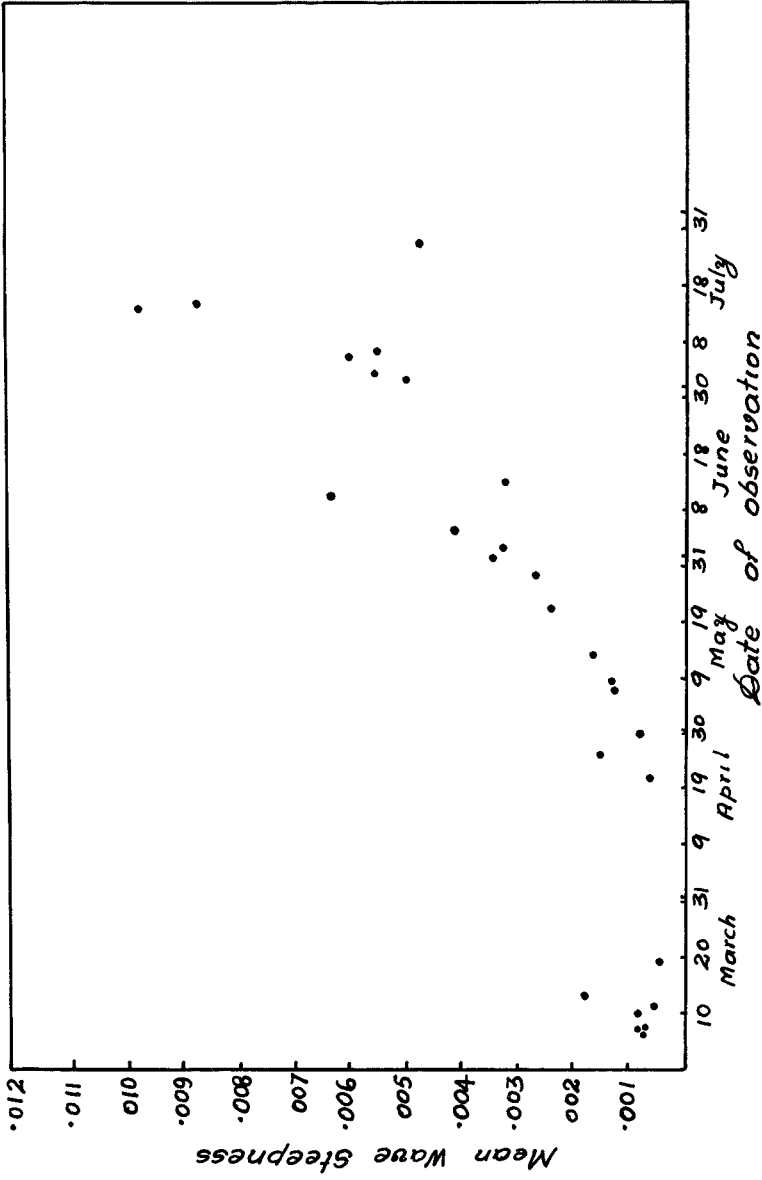


Fig 4 VARIATION OF MEAN WAVE STEEPNESS

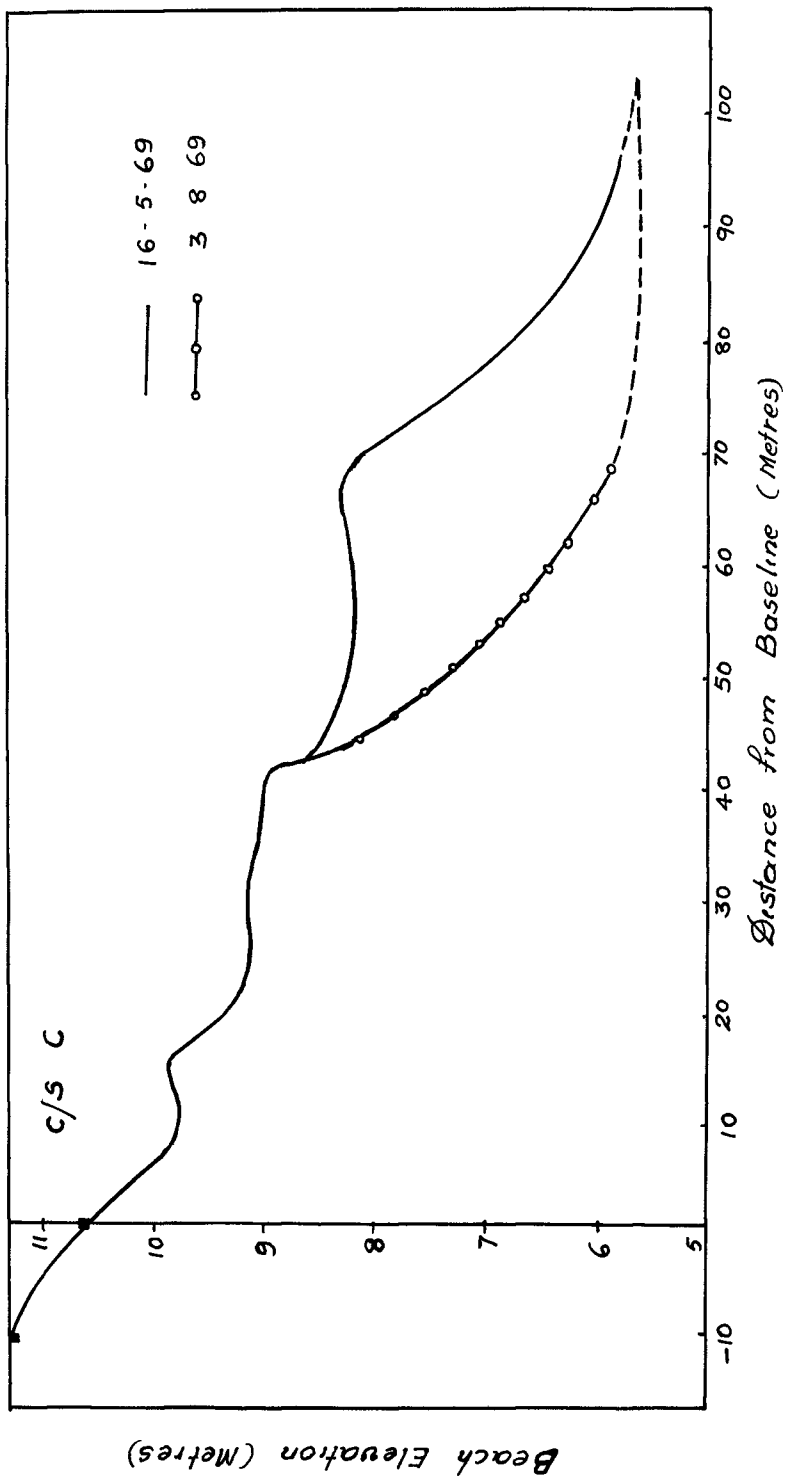
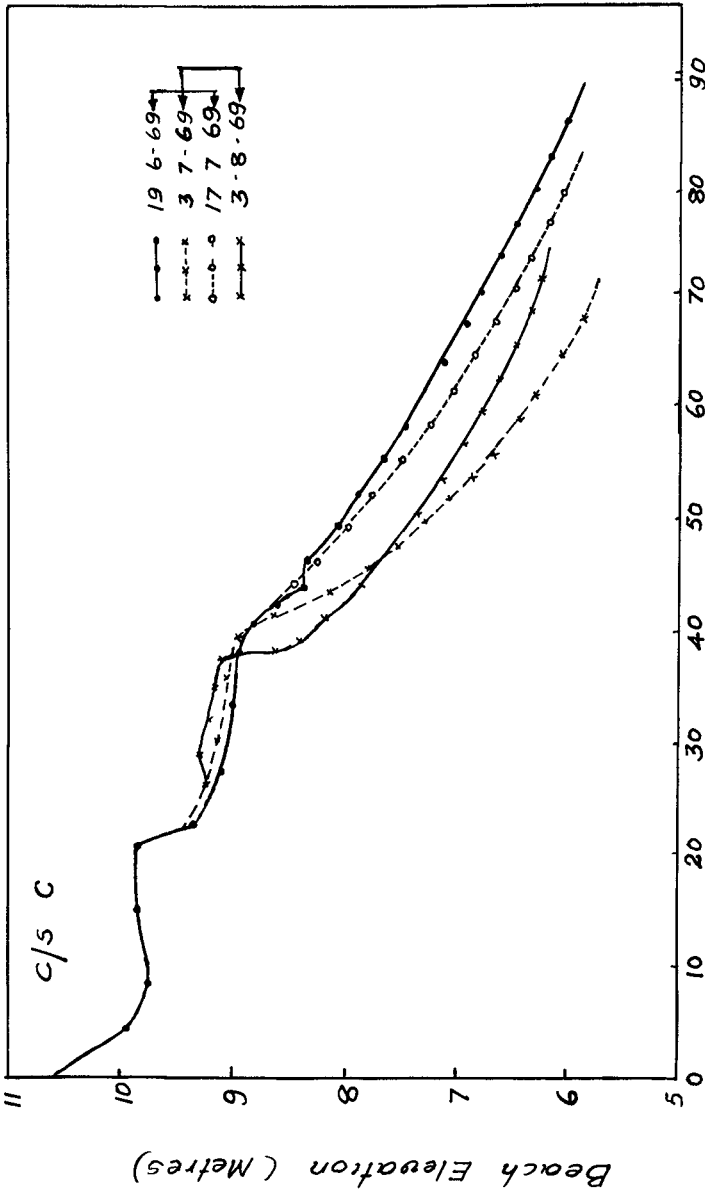


Fig 5 MAXIMUM EROSION



Distance from Baseline (Metres)
 Fig 6 RESPONSE TO TIDAL VARIATION

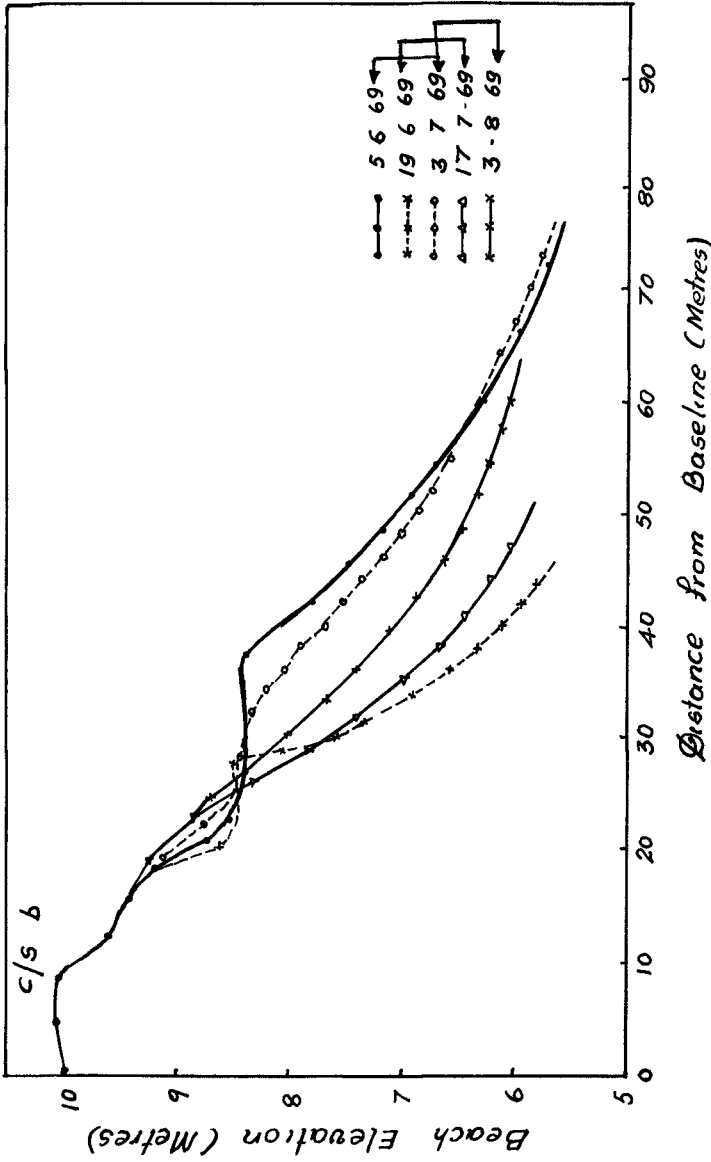


Fig 6(a) RESPONSE TO TIDAL VARIATION

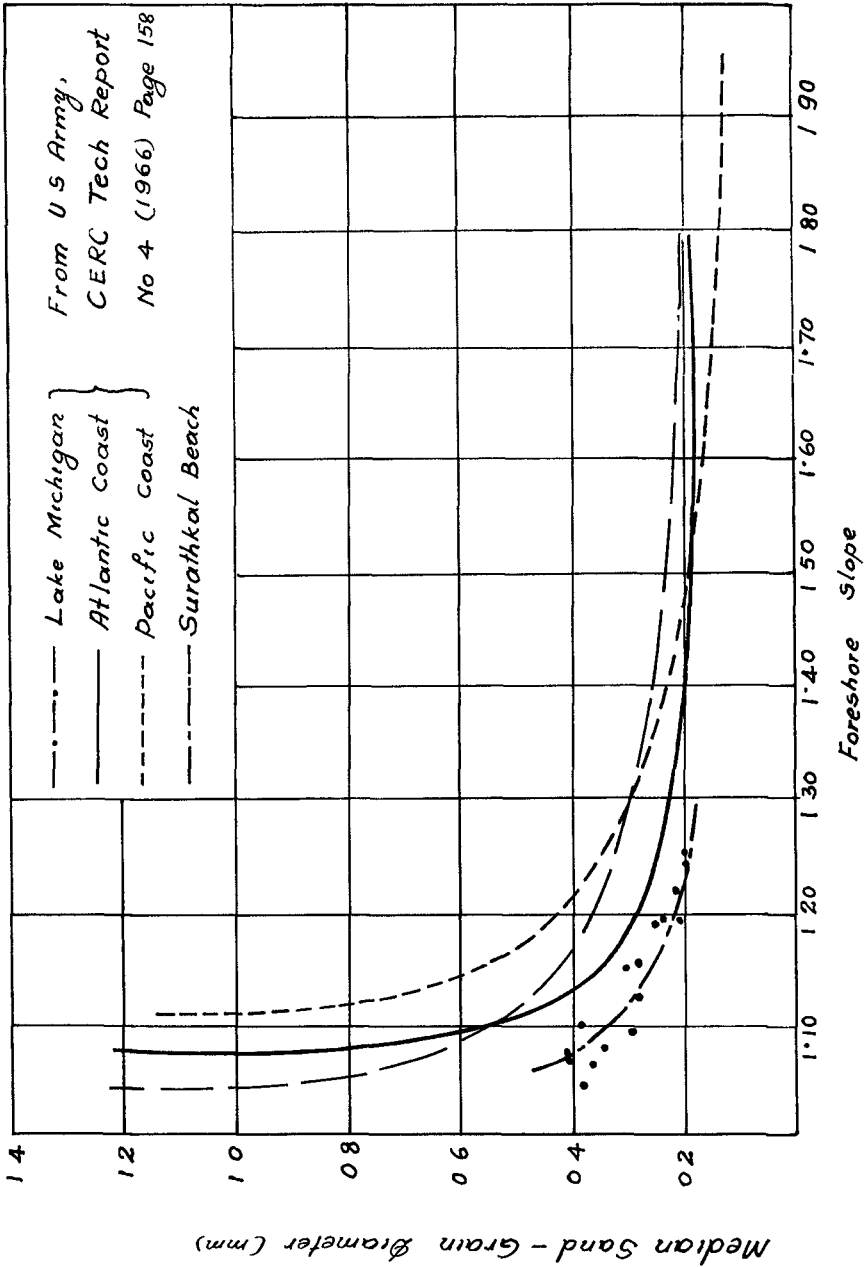


Fig 7 RELATIONSHIP BETWEEN GRAIN SIZE AND FORESHORE SLOPE

CHAPTER 85

SEASONAL BOTTOM CHANGES BOLINAS BAY, CALIFORNIA

J W Johnson
University of California
Berkeley, California

ABSTRACT

Five bottom surveys over a period of a year were made in the north portion of Bolinas Bay, California. Comparisons between successive surveys permitted an evaluation of the areas and depths of scour and fill with the seasons and were correlated with littoral current measurements. Data for a 22-year period also were available on the position of the mean high-tide line over a limited length of beach. These data showed a cyclic variation of the position of the high-tide line with the season with the most variation from year to year occurring during the spring months.

INTRODUCTION

In connection with a comprehensive study of the environment of a tidal lagoon, the inlet, and the adjacent ocean area at Bolinas, California (1)* numerous beach and bottom surveys were made at various times in the northern part of Bolinas Bay. The portion of Bolinas Bay in which repeat surveys of the bottom were made is shown in Figure 1. These surveys covering a year were made in May, August, and December in 1968, and in April and May in 1969. Five beach ranges were established along Stinson Beach by the Corps of Engineers in 1961 and profiles were determined in March and August of that year (Fig 1). They were resurveyed in March and April of 1969 by the California State Lands Commission. The State also established the location of the mean high tide line and several beach profiles along a 600 ft length of the beach on numerous occasions since 1948 (Fig 1). Twenty-seven surveys which were made during the years 1948-1970, inclusive, provide important information on seasonal profile changes on this semi-exposed beach. Wave data, observed simultaneously with the bottom and beach surveys, were obtained from a bottom pressure-type wave gage as well as visual observations of wave height and period, littoral currents, and beach characteristics at Bolinas and Stinson Beach.

WAVE CONDITIONS

The most important factors in the movement of sand in the nearshore area are wave action and tidal currents. Information on these factors

*See References

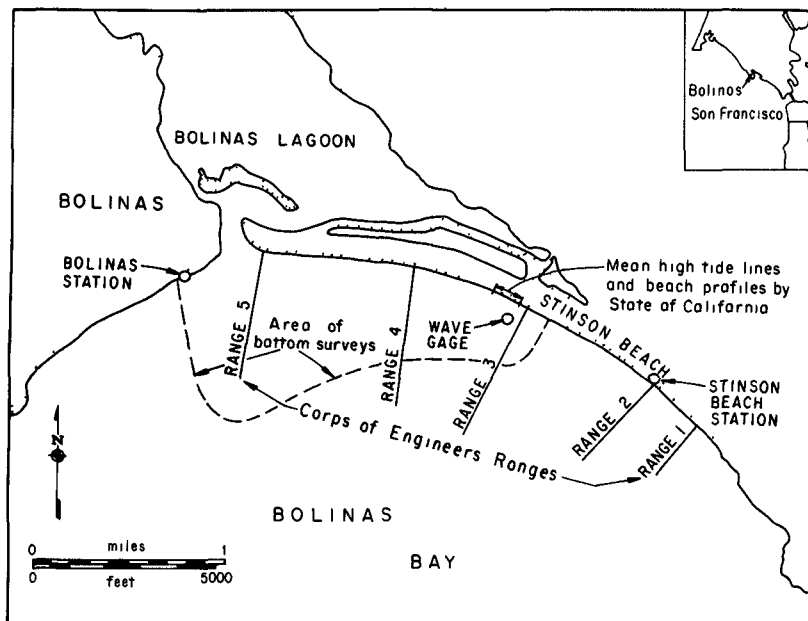


Figure 1 Location map, Bolinas Bay

in Bolinas Bay is provided by data obtained from a wave gage operated by the Bolinas Harbor District and visual surf observations made at the Stinson Beach State Park and at Bolinas for the Coastal Engineering Research Center (2). Figure 1 shows the locations of these stations. The visual observations are of course not as accurate as the wave gage data on height and period, but there is considerable additional information such as wave direction, wave type, wind data, direction and strength of littoral current, beach-face characteristics, tide conditions, etc. These data are of importance in the discussion below on the character and extent of sediment movement in the nearshore area of Bolinas Bay. For ready accessibility, the available data from the Coastal Engineering Research Center on wave period and the direction and strength of the littoral current have been plotted in Figures 2 and 3 for the Stinson Beach and Bolinas stations, respectively. It is evident from these two figures that there are extended periods of time when the littoral current prevailed in one direction. For example, during the period of February to June, inclusive, in 1969 the littoral current at Stinson Beach was generally in a southeast direction with a reversal in direction occurring only on about 15 days.

BOTTOM SURVEYS

To obtain a measure of the seasonal bottom changes in the offshore area each survey made between May 17, 1968 and May 16, 1969, inclusive,

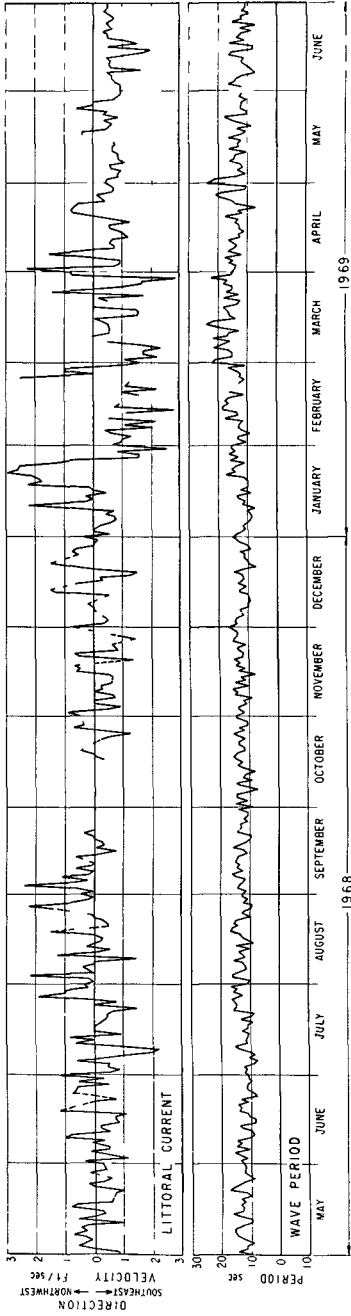


Figure 2 Wave period and littoral currents, Stinson Beach State Park, California, 1968-69

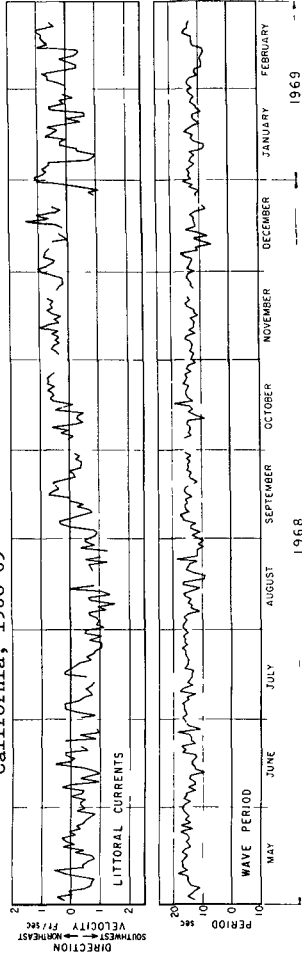


Figure 3 Wave period and littoral currents, Bolinas, California, 1968-69

was compared with the next following survey and the depth of scour or fill was noted on an overlay. These overlays were then contoured to give areas and depth of scour and fill occurring between the two dates. These comparison maps are shown in Figures 4-7, inclusive. Thus, Figure 4 is the result of comparing a survey made toward the end of the winter season (May 17, 1968) and a survey well into the summer season (August 21, 1968). The differences in depths between surveys are all minus, that is, depths in August were all deeper than in May. As will be shown below in connection with beach changes this indicates that sand is moved generally from the offshore area to create a fill on the beach face during the summer. This onshore movement is also illustrated by the fact that the 30 ft depth contour is closer inshore in August than in May.

Figure 5 shows a comparison between the summer survey of August 21, 1968 and the survey of December 19, 1968 which is at the beginning of the winter season. An area of scour occurred near the entrance of Bolinas Lagoon, but a general fill occurred over the remainder of the area surveyed, with the largest fill occurring near the surf zone-- probably such material was removed from the beach face and deposited immediately offshore by early winter storms. As a result of this general fill the position of the 30 ft depth contour in December was further offshore than in August.

Figure 6 shows a comparison between the winter survey of December 19, 1968 with a survey taken on April 15, 1969 which was toward the end of the winter season. This map shows a general scour of one to two feet in April compared with December. A deep area of scour occurred immediately offshore of the lagoon entrance. Areas of fill occurred on the west and northeast sides of the area mapped. As a result of the general scour the position of the 30 ft contour in April is slightly further inshore than in December.

Figure 7 shows a comparison between two surveys taken a month apart (April 15 and May 16, 1969) in the transition period from winter to summer conditions. A slight filling occurs in the offshore area, a considerable fill at the lagoon entrance, and a scour area on the westerly part of the area surveyed. Because of the limited coverage by the April survey, it is not possible to determine the source of the sand which filled much of the area represented by this map, however, it is possible that this sand has been shifted laterally from the west to the east as a result of the change in wave direction from the southwesterly direction in winter (April) to the more northwesterly direction at the beginning of summer (May).

That sand may be shifted laterally within Bolinas Bay is evident in Figure 8 which shows a comparison of the positions of several depth contours as they existed on May 17, 1968 and on May 16, 1969. Examination of this figure shows that the area opposite the entrance to Bolinas Lagoon has been filled generally by May 1969 compared with the May 1968, that is, over most of the area the May 1969 contours are seaward of the positions of the contours in 1968. On the other hand, at the easterly end of the map shown in Figure 8, a region of scour has occurred, that is, the 1969 contours are generally shoreward of the 1968 positions.

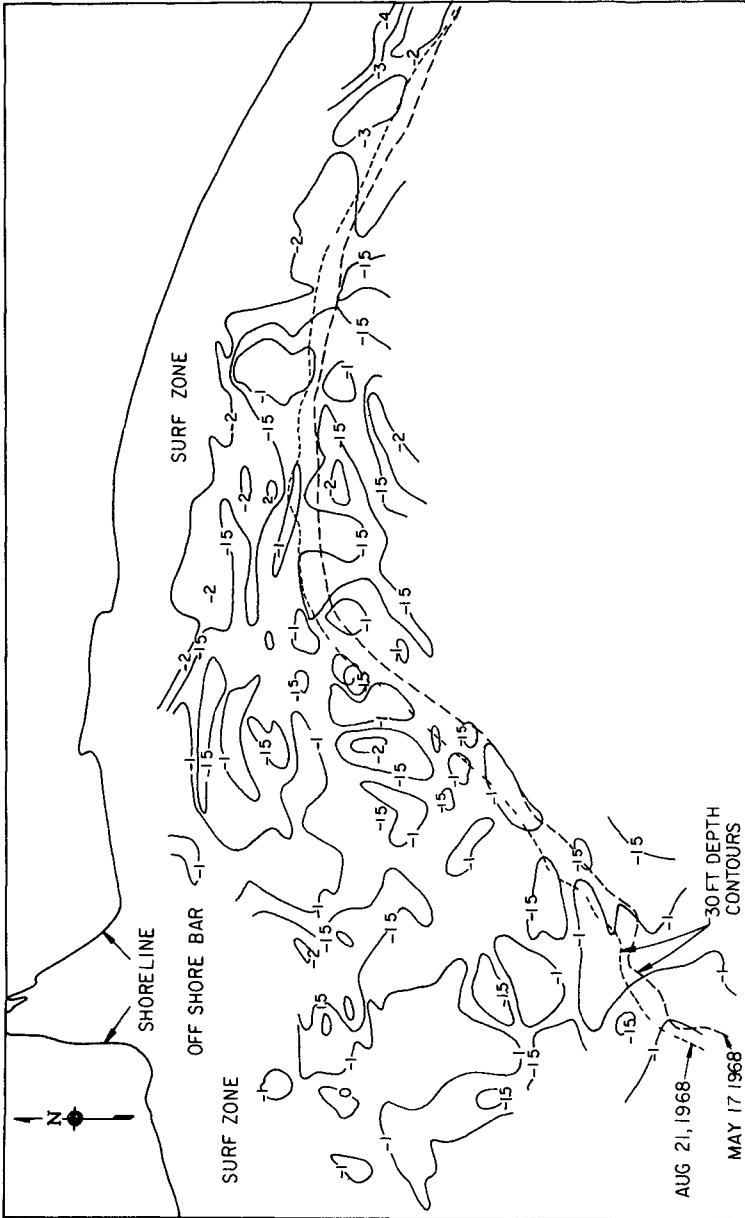


Figure 4 Areas of scour and fill between May 17, 1968 and August 21, 1968

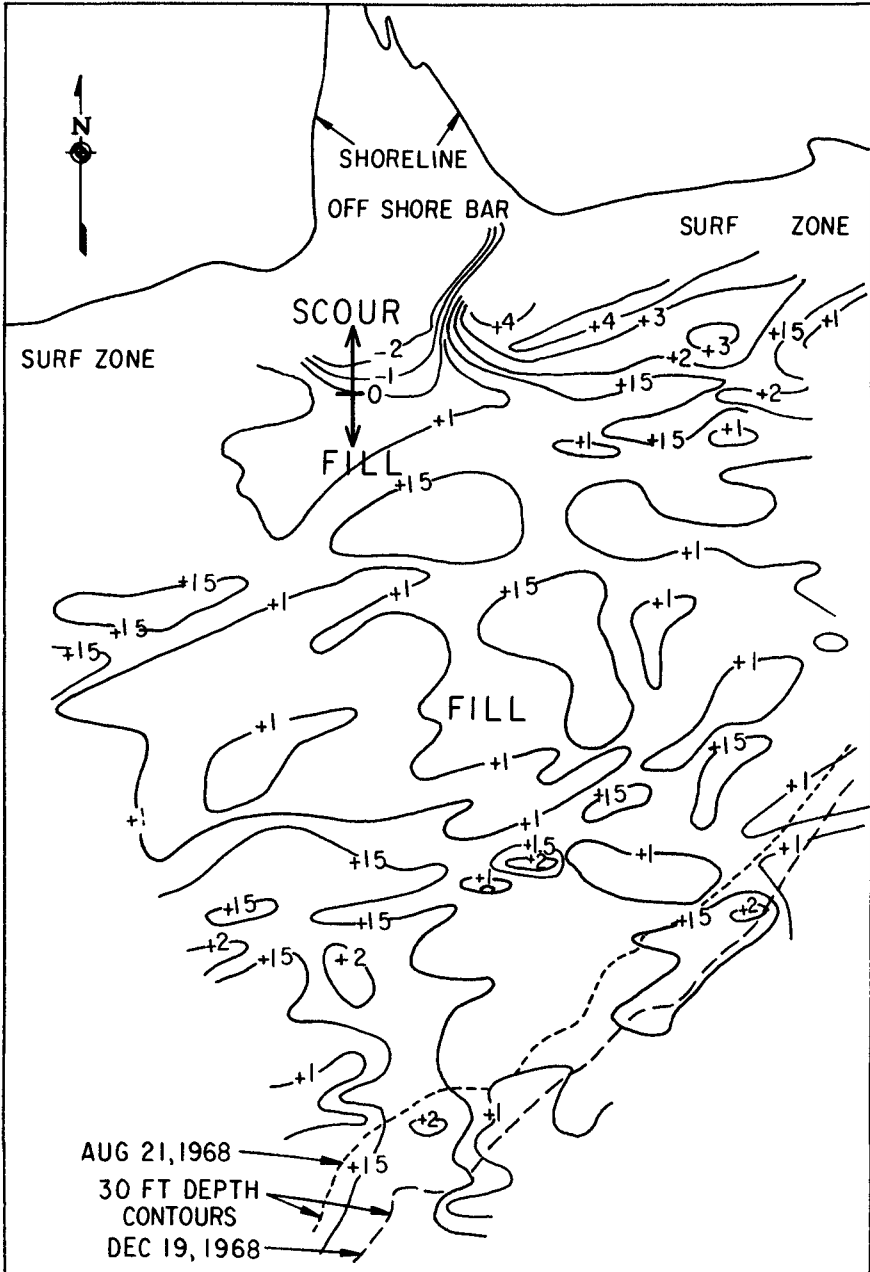


Figure 5 Areas of scour and fill between August 21, 1968 and December 19, 1968

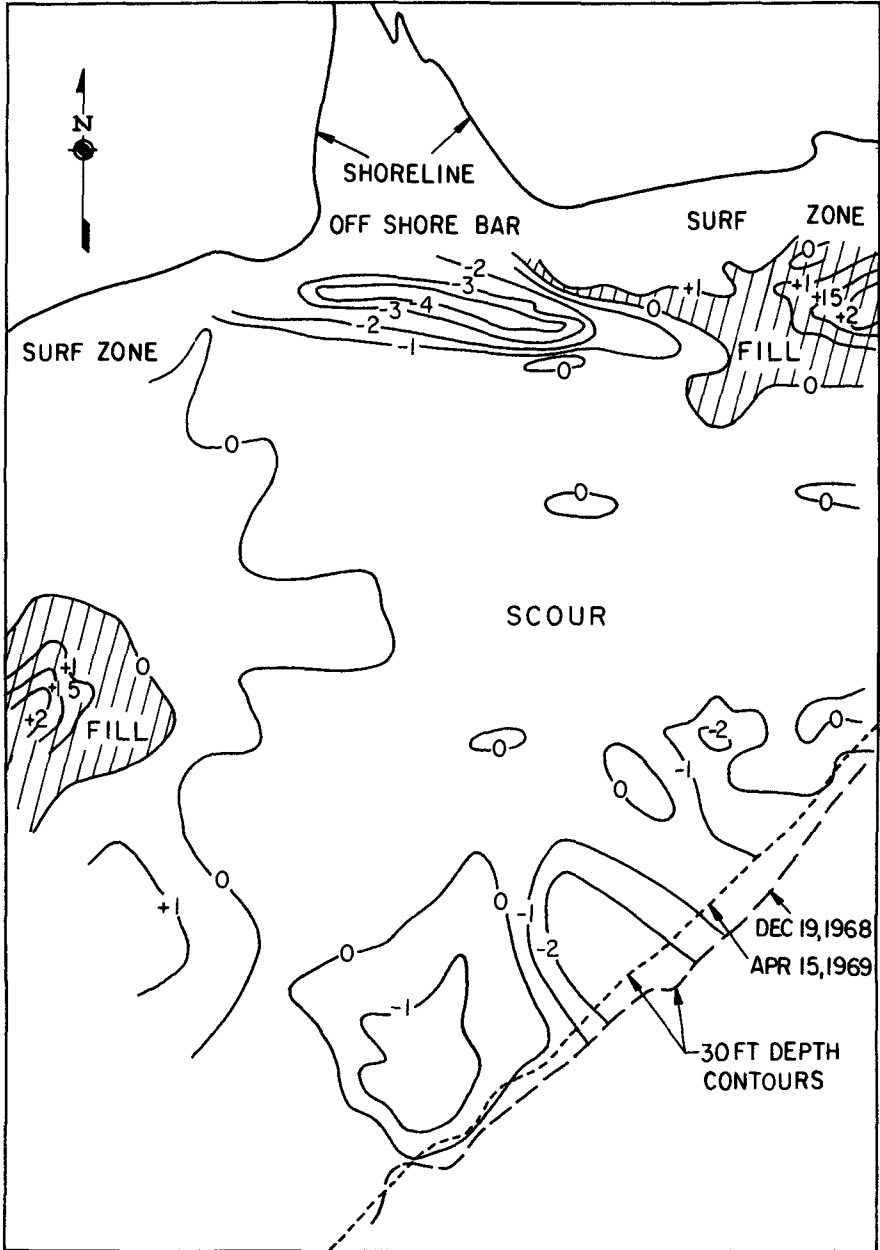


Figure 6 Areas of scour and fill between December 19, 1968 and April 15, 1969

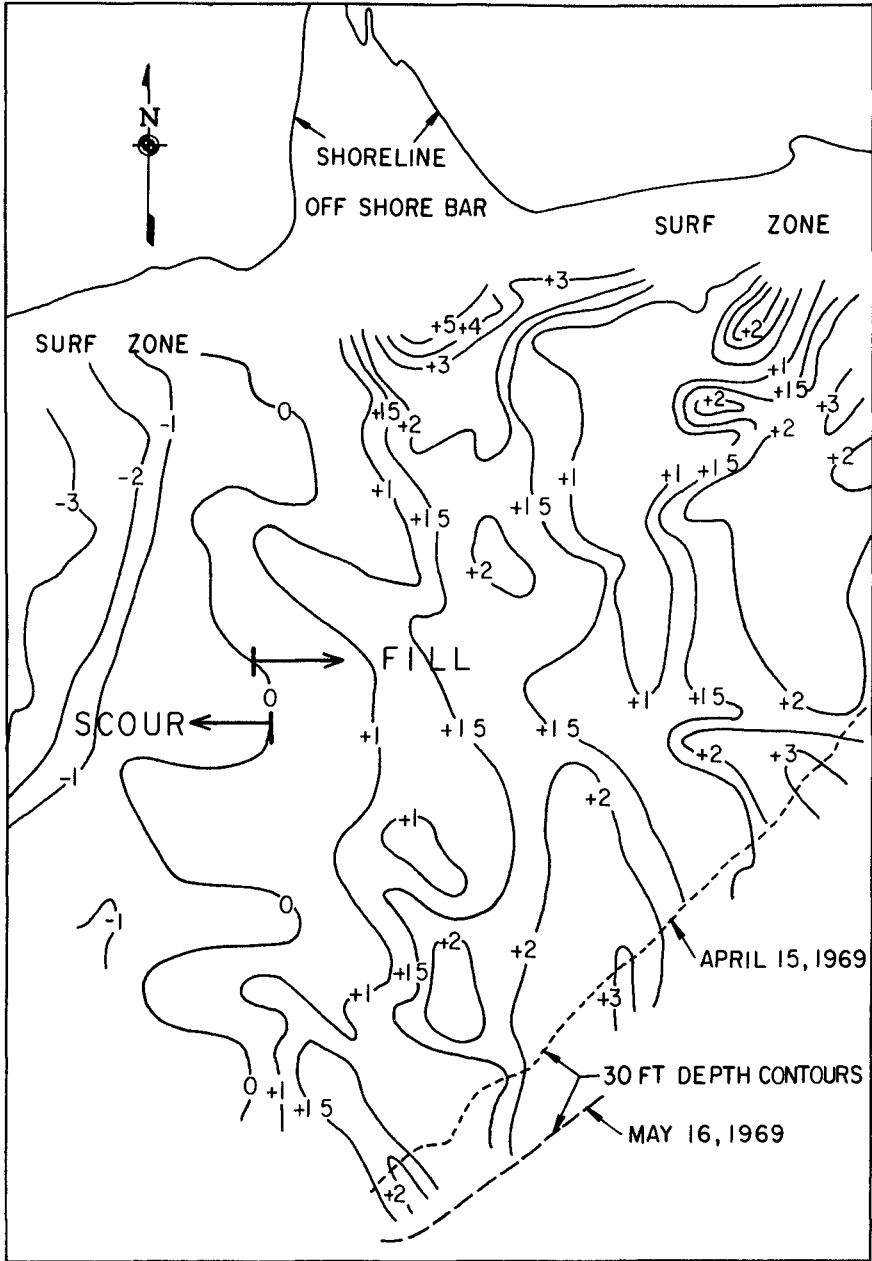


Figure 7 Areas of scour and fill between April 15, 1969 and May 16, 1969

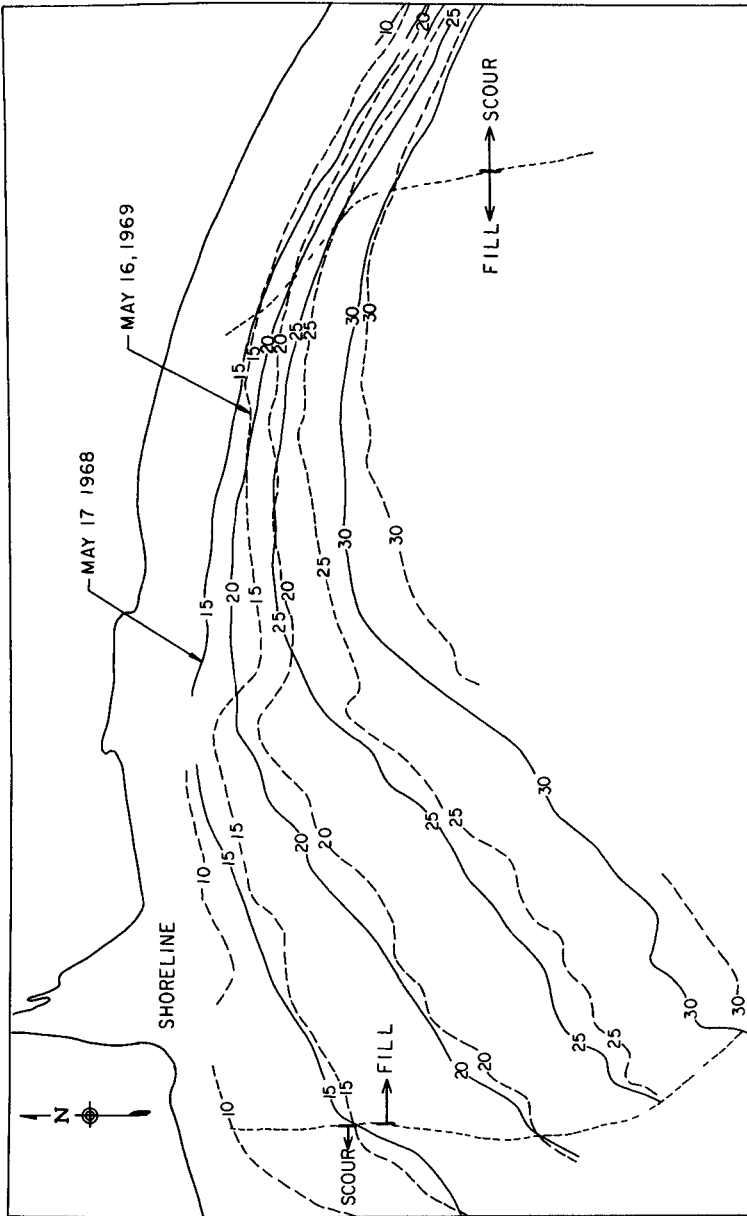


Figure 8 Comparison of bottom contour maps of May 17, 1968 and May 16, 1969

This indicates that, between the 1968 and 1969 surveys, sand appears to have been shifted northward from Stinson Beach into the north end of Bolinas Bay. Wave conditions and tidal currents in the coming year could possibly be of a character that the material would be shifted back in an east and southerly direction. It should be recognized in the comparison maps discussed above (Figs 4-8) that the actual depths of scour and fill are subject to some sounding error, but the areas of scour and fill show no randomness and are consistent with seasonal changes as generally observed elsewhere.

Other data which provide information on the general movement of sediment in the entire Bolinas Bay are presented in the following chapter by Wilde and Yancey in which heavy minerals are utilized as tracers. The reader is referred to that paper for details on procedures and conclusions. Other supplementary data on sediment movement in Bolinas Bay resulted from sand tracing studies along the beach face as obtained by the U S Geological Survey in connection with investigations of sedimentation and hydrology in Bolinas Lagoon (3). This study involved the placement of fluorescent-dyed sand on the beach at both the town of Bolinas (Brighton Avenue) and the Stinson Beach State Park and then periodically detecting the direction of movement away from the source by use of an ultraviolet lamp. Placement of sand at both localities was made on July 23-24, 1968 and then periodically sampled until late October 1968 when the dyed material either was completely scattered and buried or the dye strength had been greatly reduced.

The results of these limited and qualitative tests showed that at Bolinas the movement of sand was always eastward toward the entrance of Bolinas Lagoon, but no material ever crossed the lagoon entrance to the Stinson spit. Although the surf observations summarized by the Coastal Engineering Research Center showed a general westerly littoral current in this same locality during the period of the sand tracing studies (Fig 2), it is possible that the tidal currents into Bolinas Lagoon rather than wave generated littoral currents were instrumental in generally moving sand eastward along the beach at Bolinas.

In the case of the Stinson Beach State Park studies it was found that the dyed sands were moved in both the southeasterly and northwesterly directions, with some material being detected about one and one-half miles northwesterly up the beach two months after initial placement of the dyed sand. This might be expected upon examination of Figure 2 which shows that a northwesterly littoral current prevailed over most of the period, (August and September), following the start of the tracer tests.

BEACH CHANGES

It has long been established that beaches exposed to wave action undergo changes to their profiles throughout the year because of the seasonal changes in wave characteristics (4,5, and 6). One of the most important factors in determining the character of a beach profile is the ratio of wave height to wave length--a factor commonly referred to as the "wave steepness". During extended periods of low wave steepness,

low berms usually are built on the foreshore with very steep profiles on the beach face, and bars and underwater berms immediately offshore tend to disappear or become discontinuous. During periods of high wave steepness (storm or winter conditions) the beach face becomes less steep and the offshore underwater bars become more pronounced.

In the case of the beaches along Bolinas Bay the seasonal changes in their characteristics are less well defined than in the offshore area. This lack of beach data is primarily due to the difficulties and hazards of making accurate bottom surveys in the surf zone--especially during winter storms. It is to be noted that the hydrographic surveys used in preparing Figures 4-7, inclusive, were not made closer to shore than about the 8 ft depth contour. The data on seasonal beach changes are therefore confined to the beach profiles made by (a) the University of California (6) and (b) the Corps of Engineers in 1961 (7) and repeat surveys of these ranges by the California State Lands Commission in 1969. The location of the Corps' ranges is shown in Figure 1. Surveys by the State Lands Commission to determine the position of the mean high-tide lines over a limited length of the Stinson spit for the period 1948 to 1970 are of importance in evaluating beach changes in Bolinas Bay.

To provide an accurate measure of the seasonal fluctuations of the width of the beach at Stinson spit the data on the position of the mean high-tide line, as determined by the State Lands Commission and other sources on twenty-seven occasions from 1948 to 1970, are of considerable value. To obtain information on the position of the mean high-tide line the distance from a base line to the high-tide line was measured and plotted as shown in Figure 9 for the appropriate day of the month. There is an obvious cyclic pattern with the seasons as to the position of the high-tide line, but no precise relationship obviously exists because of the variation of intensity of wave attack that undoubtedly occurred from year to year. An upper and lower envelope has been drawn on Figure 9 to enclose the plotted points. Inspection of this plot shows that the position of the mean high-tide lines is more variable from year to year during the spring months than during late summer and fall. The distance between envelopes during the spring may amount to as much as 50 ft, and the beach at the mean high-tide line is approximately 150 ft wider in summer than in winter. The surveys of the five Corps of Engineers ranges showed an average difference in width of about 100 feet between winter and summer conditions at the mean high-tide level (7).

Of importance in connection with Figure 9 is the magnitude of the mean monthly wave height for the California coast as shown in Figure 10. This figure, plotted from data compiled by Galvin et al (1969), shows that the time of occurrence of the lowest mean monthly wave height occurs at about the same time (August) as does the time when the beach on Stinson spit (Fig 9) is the widest, that is, the beach is widest when the wave steepness is the lowest.

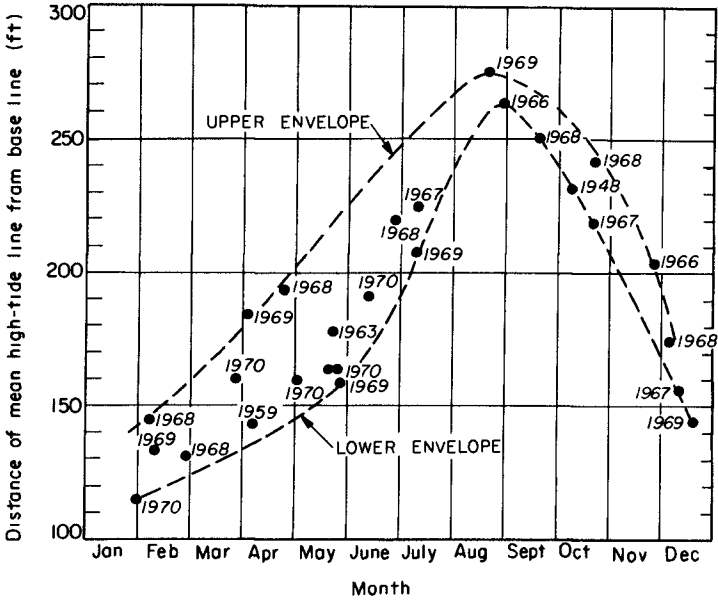


Figure 9 Seasonal variation of the position of the mean high-tide line, Stinson Beach spit 1948-1970 (Data compiled by California State Lands Commission)

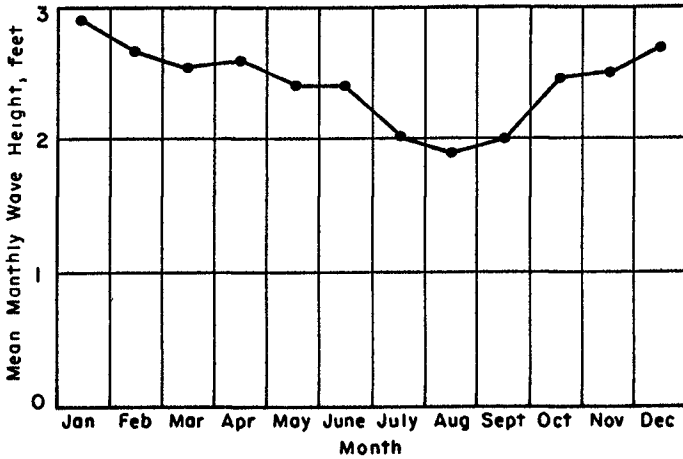


Figure 10 Mean monthly wave heights for the California coast From data for 31 station years compiled by C J Galvin, Jr , et al (1969)

SUMMARY

1 Five bottom surveys made in 1968-69 of the northern part of Bolinas Bay show an offshore-onshore movement in the depths between 8 ft and 35 ft below MSL as a result of varying wave conditions with the seasons. A survey in May 1969, when compared with a survey one year earlier in May 1968, shows an accretion in the northern part of Bolinas Bay and a scouring of the shoreline southward along the Stinson spit.

2 Repeat surveys at five ranges located along the Stinson spit show a seasonal change with the seasons, that is, the beach averages about 100 ft greater in width during the summer compared with the winter. Repeat surveys of the location of the mean high-tide line at one location on Stinson spit over a period of several years (1948-1970) shows a cyclic position of the high-tide line with the season with the most variation from year to year occurring during the spring months.

ACKNOWLEDGMENTS

This study was conducted for the Bolinas Harbor District in which Mr Norman T Gilroy was project coordinator and consultant planner. Data on the position of the mean high-tide line as provided by the California State Lands Commission is gratefully acknowledged.

REFERENCES

- 1 Gilroy, Norman T (1970) Bolinas Lagoon Its system of environmental dynamics and recommendations for its future preservation and utilization, Mill Valley, Calif
- 2 Corps of Engineers (1970) Littoral environment observation program in California, Preliminary report, February-December 1968, Misc Paper No 2-70, Coastal Engineering Research Center, Wash , D C
- 3 Ritter, John (1969) Preliminary studies of sedimentation and hydrology in Bolinas Lagoon, Marin County, California, May 1967-June 1968, U S G S Open-File Report, April 4, 1969
- 4 Johnson, J W (1949) Scale effects in hydraulic models involving wave motion, Transactions, Amer Geophysical Union, Vol 30, No 4, pp 517-525
- 5 Shepard, Francis P (1950) Beach cycles in Southern California, Beach Erosion Board Tech Memo No 20, Wash , D C
- 6 Trask, Parker D (1959) Beaches near San Francisco, California, 1956-57, Beach Erosion Board Tech Memo No 110, Wash , D C
- 7 Corps of Engineers (1965) Cooperative beach erosion study of coast of Northern California, Point Delgado to Point Ano Nuevo, San Francisco District, June 1965

- 8 Galvin, C J , Jr , D G Dumm, Jr , B R Sims, and L W Tenny
(1969) Nearshore visual wave observations for United States'
coastlines, U S Army Coastal Engineering Research Center
(unpublished)

CHAPTER 86

SEDIMENT DISTRIBUTION AND ITS RELATIONS TO CIRCULATION PATTERNS IN BOLINAS BAY, CALIFORNIA

P Wilde¹ and T Yancey²

ABSTRACT

Grain size and heavy mineral analyses of 6 cliff, 12 beach, and 44 marine sediment and rock samples from Bolinas Bay and its surrounding drainage area were done as part of a long term study of sediment transport on the continental shelf off Central California

Sediments in the bay are predominately very fine sands. Some samples, particularly adjacent to Duxbury Reef on the west, have a coarse sand to pebble component. The primary mode of the marine samples is in the range 0.88 to 1.25 mm, whereas, the primary mode for beach material is from 0.175 to 0.25 mm. The range of median diameters of the marine samples is from 0.07 to 0.14 mm. The median diameters show a trend of decreasing grain size seaward parallel to the depth contours except opposite the entrance to Bolinas Lagoon where a tongue of relatively coarser material cuts across the depth contours. The range of other statistical parameters are (1) sorting coefficient 1.10 to 1.41, (2) skewness 0.83 to 1.18, and (3) kurtosis 0.15 to 0.32.

Our sediment studies indicate

(1) The heavy mineral assemblage is predominantly green hornblende with secondary amounts of hypersthene and augite. Glauco-phane and jadeite occur in locally high concentrations near shore.

(2) The pattern of distribution of the heavy minerals shows (a) a tongue of high concentrations of minerals with a granitic source extending northwest from the San Francisco Bar, (b) flanked on the north and northeast by increasing landward concentrations of Franciscan metamorphic minerals.

(3) The major source of heavy minerals is the San Francisco Bar. Secondary contributions come from Bolinas Lagoon and the adjacent cliffs.

(4) The circulation in the Bay is primarily counterclockwise, produced by a combination of wave refraction around Duxbury Reef and the tidal Coast Eddy Current. The tidal influence, however, of Bolinas Lagoon is restricted to about one mile from the lagoon mouth. Circulation

¹ P. Wilde, Department of Civil Engineering, University of California, Berkeley, California

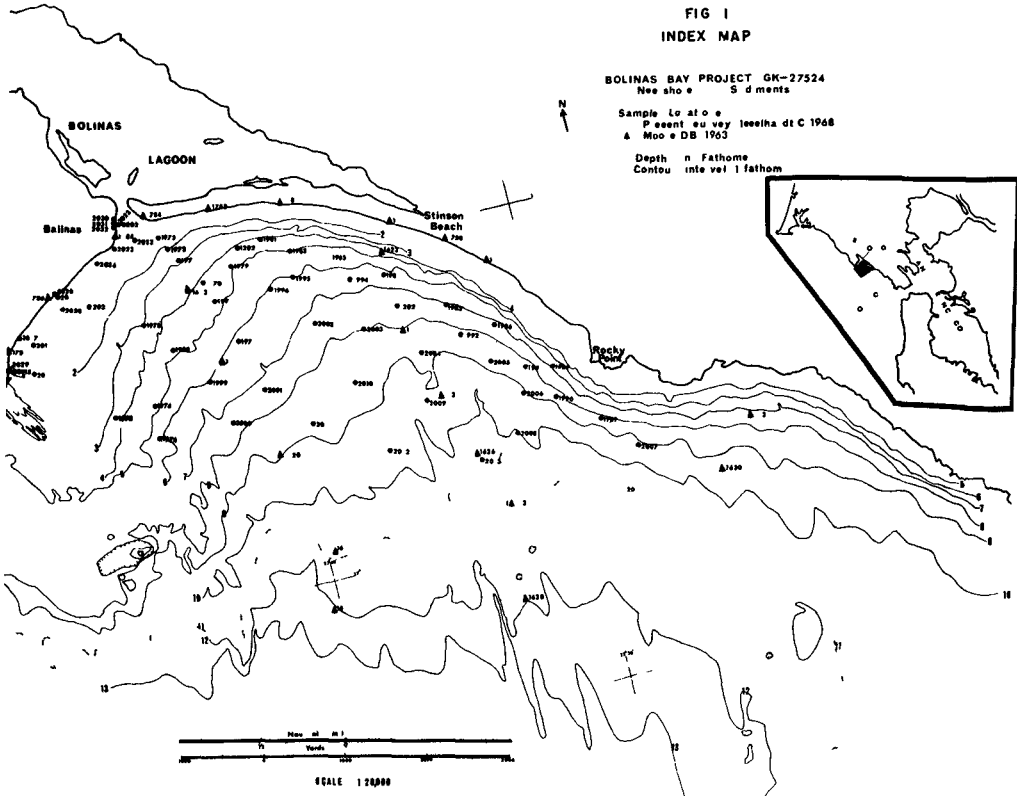
² T. Yancey, Department of Paleontology, University of California, Berkeley, California

patterns in the Bay greatly influence the sediment distribution

(5) The annual sediment flux in Bolinas Bay is about 300,000 cubic yards. The bottom sediments in the Bay are apparently in quasiequilibrium.

This report summarizes a comprehensive study of Bolinas Bay sediments given in Isselhardt and others, 1968, 1969, and Wilde and others, 1969. Bolinas Bay is a parabolic shaped embayment of the Pacific Ocean at the southern tip of the Point Reyes Peninsula, ten miles north of the entrance to San Francisco Bay (Fig 1). Bolinas Bay is bounded (1) on the north by the Bolinas Cliffs, (2) on the northeast by Sea Drift Spit, the barrier bar at the entrance to Bolinas Lagoon, (3) on the east by the Marin County Coast Ranges, (4) on the south by the Pacific Ocean, and (5) on the west by the shoals of Duxbury Reef. The long axis of the bay points towards Bolinas Lagoon and is oriented about N 40°W along the submarine trace of the San Andreas Fault.

FIG 1
INDEX MAP



The land area in the drainage adjacent to Bolinas Bay can be divided, east to west, respectively, into three topographic regions, (1) Bolinas Ridge which extends northeastward from Mount Tamalpais to Tomales Bay, (2) the San Andreas rift zone of rolling hills, sag ponds, and Bolinas Lagoon, and (3) the Bolinas Plateau with Duxbury Reef, a wave cut bench at the base of the western edge of the plateau (U S G S 7½ minute quadrangle Bolinas sheet) The main feature of the Bolinas region is the conspicuous rift valley of the San Andreas Fault, which is prominently expressed by Bolinas Lagoon In Bolinas Bay it can be traced, less conspicuously, in the submarine contours This rift separates structural blocks of greatly different geological composition, as well as acting as a focus for drainage within the region

Depth contours in Bolinas Bay generally are sub-parallel to the shore line (Fig 1) Bay bottom gradients are steepest on the eastern side near Rocky Point where the 10 fathom line lies one-half mile offshore The contours diverge to the west where adjacent to Duxbury Reef the 10 fathom line is one and three-quarters miles offshore

Two submarine channels heading southeast downslope can be traced seaward of 7 fathoms These channels are aligned with the northwest-southeast trend of the San Andreas Fault The channels empty into a depression lying between Bolinas Bay and the north rim of the San Francisco Bar (Potato Patch Shoal)

Changes in bathymetry with tidal fluctuations apparently are limited to a small region with an offshore bar just seaward of the entrance to Bolinas Lagoon (Ritter, 1969) Seasonal depth changes are being studied now by comparison of various precision depth surveys of the bay Preliminary results (Johnson, 1969) indicate that seasonal depth changes also are limited to shallow nearshore regions near the entrance to the lagoon

Tides

The Bolinas area has a mixed tide like San Francisco Bay, with a maximum range of 8 feet from higher high water to lower low water (Ritter, 1969, p 13)

Currents

Open Ocean Currents The major offshore current off the central California coast is the southwesterly flowing California Current which is the eastern return gyre of the clockwise circulation pattern of the North Pacific (Reid and others, 1958, U S Hydro, 1947) During the winter months a coastal northward flowing current called the Davidson Current (Reid and Schwartzlose, 1962) interposes itself between the coast and the California Current The Davidson Current flows during the periods of maximum water runoff and erosion (Hendricks, 1964) on the adjacent land areas Thus, the Davidson current probably carries a significant load of suspended sediment in a northward direction along the coast

Tidal Currents The most apparent water movements in Bolinas Bay are tidal, complicated by the configuration of the coastline and the inputs of the tidal prisms of both Bolinas Lagoon and San Francisco Bay. Strong non-surfing currents have been encountered by scuba divers near station 1627 (R. Zelwer, 1968, personal communication) in about 70 feet of water, which indicates tidal rather than wave produced currents. The Coast Eddy Current (U. S. Coast Pilot, no. 7, 1968, p. 152), a feature of the San Francisco Bay tide, flows north and counterclockwise north of the San Francisco Bar into Bolinas Bay.

Longshore Currents Longshore currents develop in response to the prevailing west-northwest swell (Fig. 2). Refraction of the waves about Duxbury Reef would produce a northerly drift north of the Golden Gate. Northwestern longshore currents within Bolinas Bay is suggested by the orientation of Sea Drift Spit across the mouth of Bolinas Lagoon. Drift measurements by dye drops (rhodamine B) and floating rubber balls by the U. S. Geological Survey (Ritter, 1969, p. 30), and by milk bottle caps (Brown and Caldwell Consulting Eng., 1961) indicate counterclockwise drift in the eastern portion of Bolinas Bay.

Geology

The Bolinas Bay drainage area is at the southern edge of the Northern Coast Ranges and is divided by the San Andreas rift zone into two distinct geological provinces (Fig. 3). The eastern section noted topographically as Bolinas Ridge consists entirely of Franciscan Formation rocks except for recent alluvium in stream valleys. In the Bolinas Bay drainage area the Franciscan consists of undifferentiated sandstones, chert, serpentine, and diabases. Feldspathic sandstone is the most abundant rock type (Gluskoter, 1962).

The area to the west of the San Andreas fault is in the Salinian Quartz Diorite province, although no granitic type rocks crop out in the Bolinas Bay drainage, such rocks are found nearby at Point Reyes, Tomales Point, and Bodega, and presumably are the basement rocks in the Bolinas area. Two Cenozoic formations, the Monterey and the Merced, form the surface exposures, except for patches of recent alluvium, over the entire Bolinas Peninsula. The Merced Formation, found as a thin band parallel to the fault, consists of fine grained, friable sandstones and siltstones with small amounts of fossiliferous sandstone and pebble conglomerates. The Monterey Formation is the most extensive unit found on the Bolinas Peninsula and forms the rapidly eroding cliffs extending from Duxbury Reef almost to the Bolinas Lagoon entrance. The Monterey rocks are predominantly tan to gray mudstones, silty mudstones, and siltstones with occasional lenses of sandstones.

The San Andreas rift zone is a jumbled mass of rock composed of slivers from formations on both sides of the zone. The fault is active and displacements of one foot vertically and 8-14 feet horizontally were recorded in the Bolinas area from the 1906 earthquake (Lawson, 1908, p. 70, 84). In fact, the epicenter of the 1906 earthquake was located near Bolinas Bay on the Pt. Reyes Peninsula.

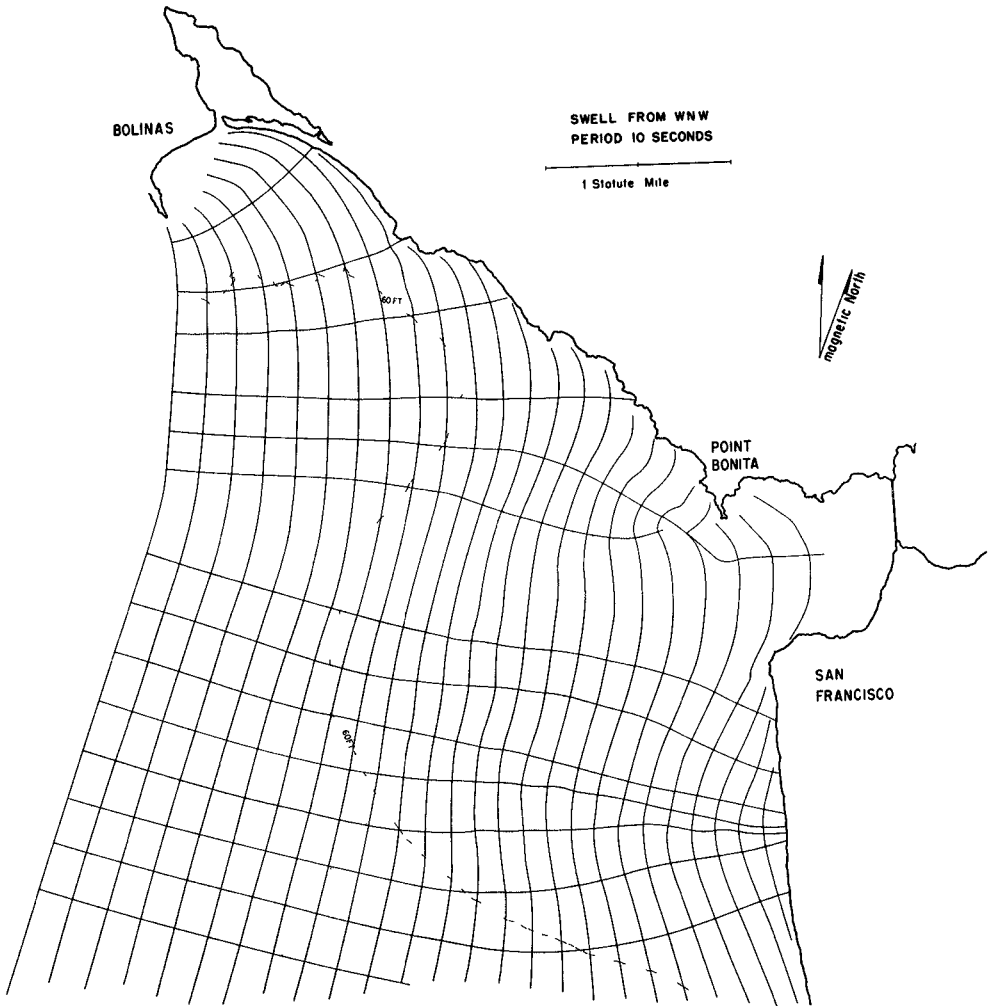


FIG 2 WAVE REFRACTION DIAGRAM (WNW, 10 SEC) FOR MARIN-SAN FRANCISCO AREA

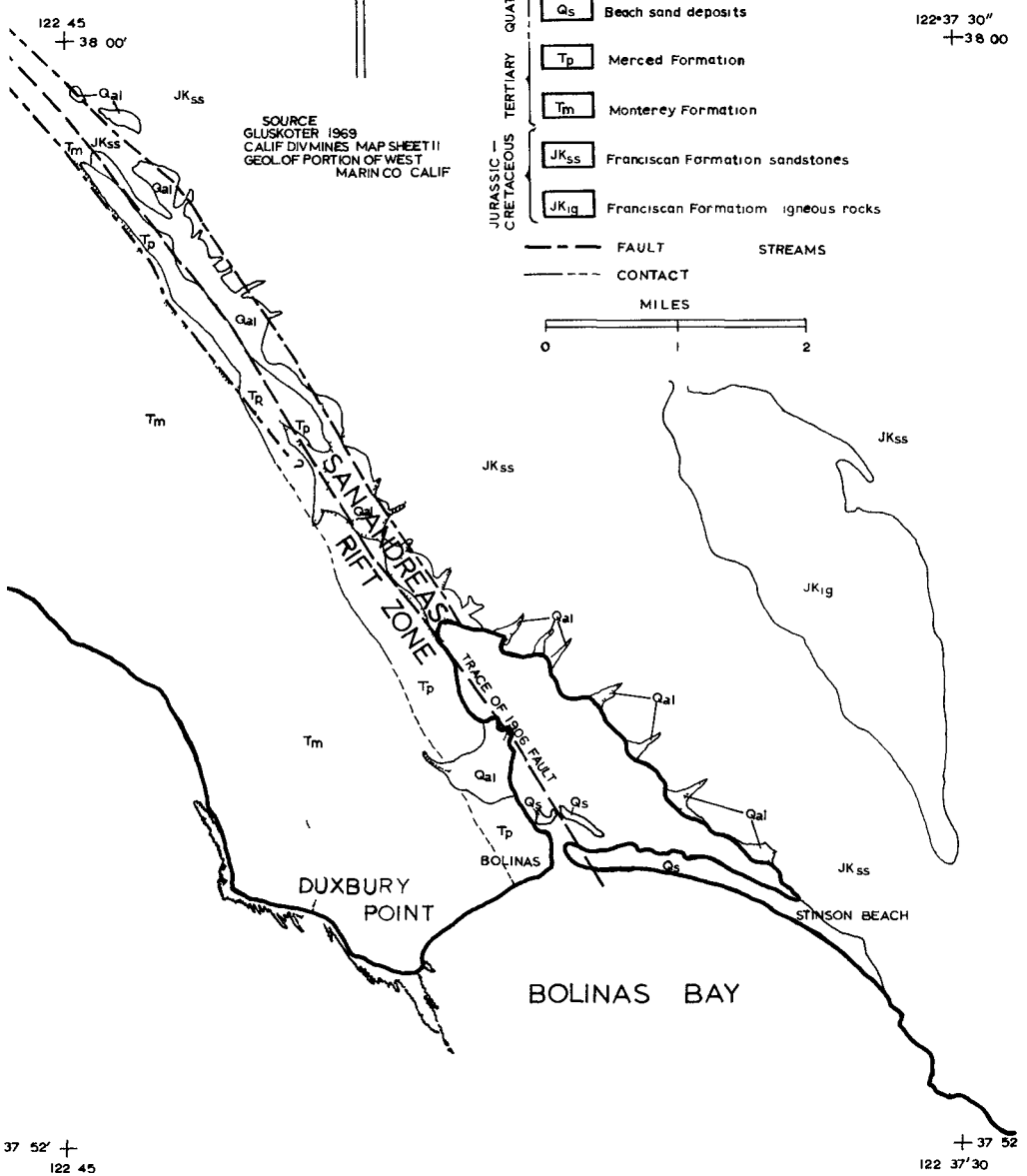
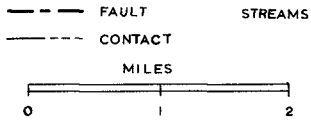
GEOLOGY OF THE BOLINAS BAY REGION

EXPLANATION

FIG 3



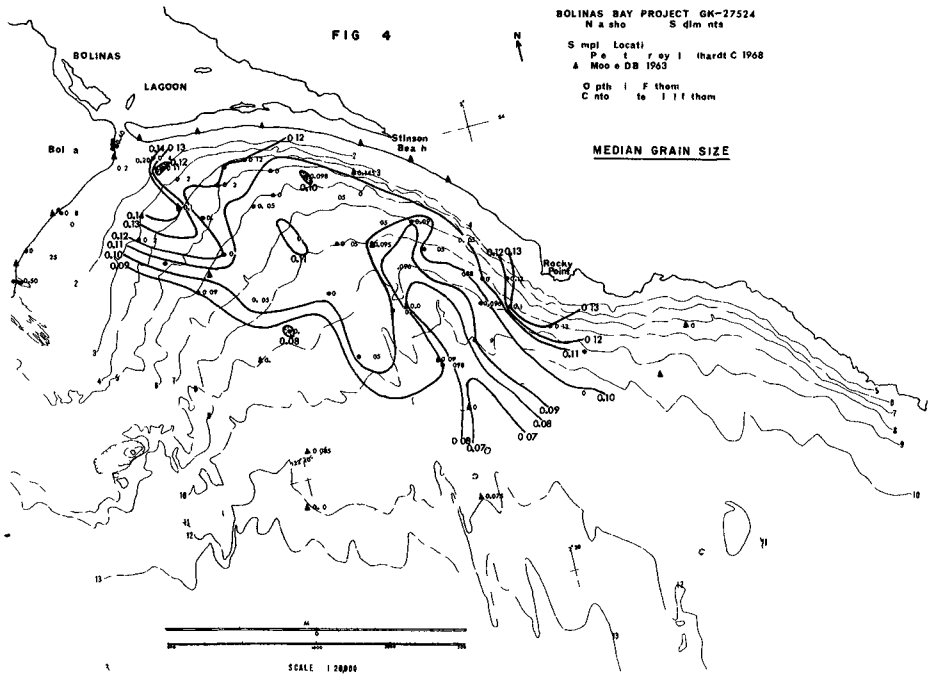
- | | | |
|------------------------|------|------------------------------------|
| QUATERNARY | Qal | Recent alluvium |
| | Qs | Beach sand deposits |
| TERTIARY | Tp | Merced Formation |
| | Tm | Monterey Formation |
| JURASSIC
CRETACEOUS | JKss | Franciscan Formation sandstones |
| | JKig | Franciscan Formation igneous rocks |



For more detailed information on the geology of the Bolinas area, see Weaver (1949), Gluskoter (1962, 1969), Galloway (1966), and Bailey (1964)

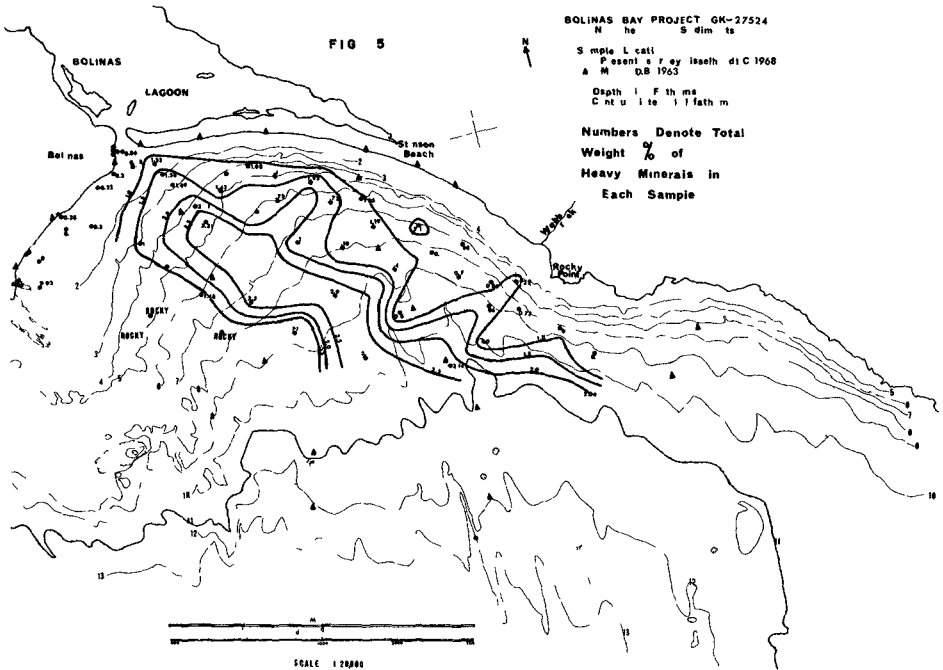
Grain Size Properties

The statistical parameters, median grain size, and sorting coefficient are derived from data presented in Isselhardt and others, 1968. The average of median grain size for the bay sediments is about 0.10 mm or fine sand, with extremes at 0.40 mm medium sand to 0.07 mm very fine sand. The median grain size generally decreases seaward paralleling the depth contours. Figure 4 shows variations of this trend as two lobes of coarser sediment extending (1) seaward from Rocky Point and (2) from the mouth of Bolinas Lagoon, and a band of finer grained sediment on the western margin of the bay next to Duxbury Reef. Topographic and bathymetric irregularities produce the Rocky Point and Duxbury Reef anomalies. Wave agitation around Rocky Point prevents fine material from depositing. While on the protected lee side of Duxbury Reef, finer particles may settle out. The lobe of coarser material near the mouth of Bolinas Lagoon presumably is a product of tidal action. Coarser sediment is carried seaward by the strong tidal currents measured by Ritter (1969) exiting the lagoon. Winnowing by tidal reversals prevents settling of finer material here.



Values of the sorting coefficient indicate all the samples are well sorted, with the expected gradient of poorer sorting seaward. The gradient is greatly masked by sample to sample variation, but deep samples have values of 1.20 or greater while shallow samples have values usually less than 1.20. The best sorting in the bay is associated as expected with the entrance to Bolinas Lagoon and with Rocky Point. The sorting roughly shows the same pattern as the median grain size, but much less clearly. In Bolinas Bay the sorting of the sediments is primarily a function of the grain size of the sediments, in both deep and shallow water.

Contours of weight percent heavy minerals (Fig 5) also gives strong indication of bottom currents flowing between the lagoon entrance and deeper water. The major trend is a linear concentration of heavy minerals aligned from the entrance to Bolinas Lagoon to the center of the bay. It extends between and connects the two tongues of coarse sediment noted on the median grain size chart, and apparently is caused by tidal currents.



Mineralogy

The heavy mineral assemblages reveal two discrete suites (1) in a mid-bay tongue typified by green hornblende and hypersthene, and (2) along the shore characterized by glaucophane and jadeite. Figure 6 shows the relative proportion of the two mineral suites in each sample plotted as a function of distance from shore. These data plotted on a map (Fig. 7) describe three zones: (1) off shore, for sediments of the hornblende + hypersthene suite, (2) near shore, for samples with a glaucophane + jadeite assemblage, and (3) at intermediate distance from shore where the two suites are mixed.

Provenance

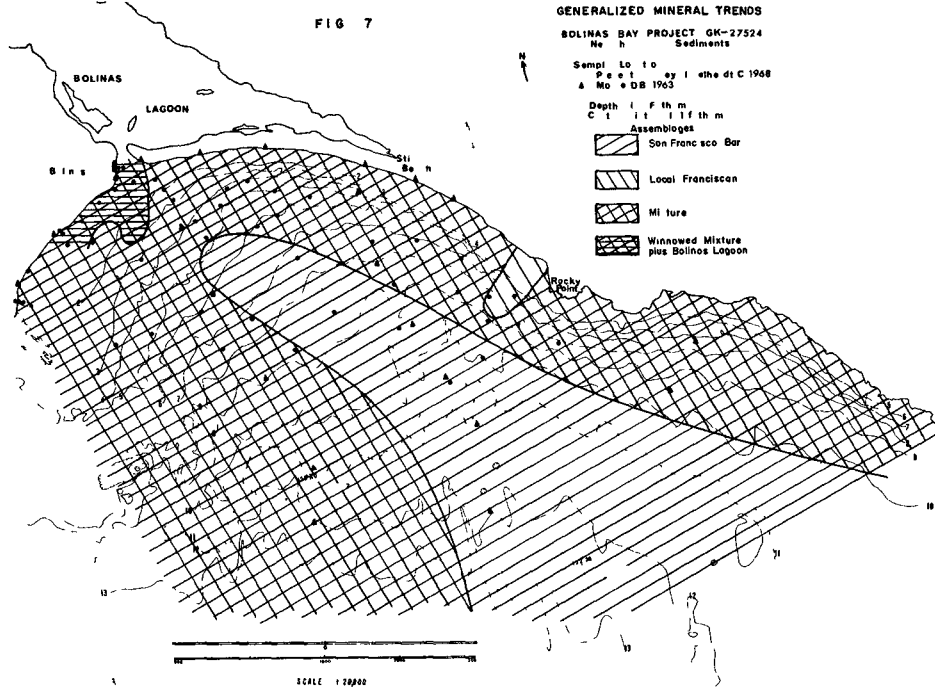
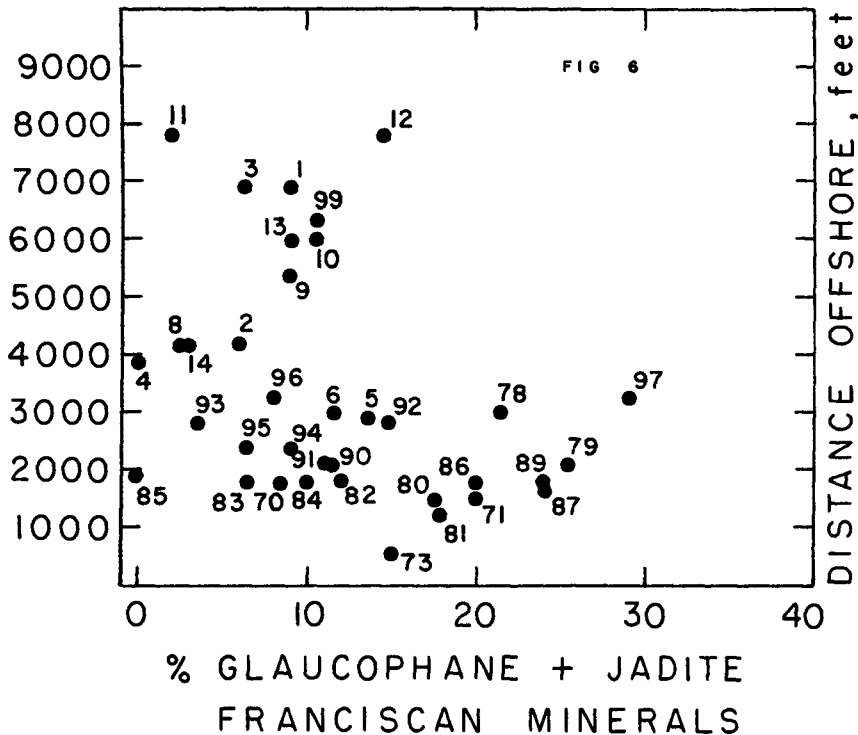
Potential sources for the sediments of Bolinas Bay are

- (1) Webb Creek drainage, which empties directly into Bolinas Bay,
- (2) drainage area of Bolinas Lagoon, with sediment transported from the lagoon into Bolinas Bay by tidal action,
- (3) sea cliff erosion of cliffs between Duxbury Reef and the town of Bolinas,
- (4) San Francisco Bar, with sediments transported into Bolinas Bay by northward flowing bottom currents,
- (5) rocks north and south of Bolinas Bay - sediments brought into the bay by longshore drift.

Webb Creek, draining Franciscan terrain, is the only stream that empties directly into Bolinas Bay. Sediments in Bolinas Bay adjacent to the mouth of Webb Creek contain high concentrations of glaucophane and jadeite, a typical Franciscan mineralogy, indicating a flow of Webb Creek sediments into the bay.

The mineralogy of bottom sediments in the lagoon (Helley, in Ritter, 1969) indicates that Pine Gulch Creek, the largest creek, principally contributes Monterey shale sediments to the lagoon, which is mixed with the contribution from the smaller streams with exclusively Franciscan drainage. As a result, Bolinas Lagoon sediments are dominantly of Monterey shale fragments, while containing a heavy mineralogy characteristic of Franciscan Formation sediments.

The Bolinas Cliffs are actively eroding and supply large amounts of sediment to Bolinas Bay annually. Helley (in Ritter, 1969) cites an annual rate of cliff erosion of 2-3 feet per year (determined by A. J. Galloway). The sea cliffs fronting on Bolinas Bay are 7000 feet long and are at least 120 feet high, and would give an annual yield of sediment of 72,000 cubic yards. The cliffs are composed mostly of Monterey shale, with lesser exposures of Merced Formation near the town of Bolinas.



The San Francisco Bar, to the south of Bolinas Bay, contains a very large reservoir of unconsolidated sediment, part of which is brought into Bolinas Bay by tidal currents. Sediments of the San Francisco Bar are characterized by higher concentrations of augite and hypersthene than are found in marine sediments to the northwest or south (Moore, 1965). The source of the hypersthene is the volcanic rocks and volcanic sediment of the Central Valley drainage area (Hall, 1965). Part of the sediments in Bolinas Bay are characterized by similar high concentrations of augite and hypersthene and thus are probably derived directly from the San Francisco Bar, carried by the northward flowing Coast Eddy Current (U S Coast Pilot, No 7, 1968, p 152).

The San Francisco Bar is formed of sediment brought to the Pacific through the Golden Gate from the Central Valley drainage area. U S Geological Survey estimates (in Homan and Schultz, 1963, p 4) of the sediment entering San Francisco Bay are from 7.2 to 9.6 million cubic yards per year. Table 1 shows the rates of sedimentation of San Francisco Bay and Bar for the past 101 years (Homan and Schultz, 1963). With the present rate of sedimentation, 2.9 to 5.3 million cubic yards of sediment per year passes through the bay and off the Bar. A portion of this volume must move north into Bolinas Bay by northward flowing currents.

The sea cliffs south of Bolinas Bay, between Rocky Point and Point Bonita, are a possible source for sediments in Bolinas Bay. However, sediment entering Bolinas Bay from this source would be carried northward by longshore drift, which would be blocked or directed seaward by the irregular shoreline, and its character would be masked by mixing with the San Francisco Bar sediments. Duxbury Reef acts as a barrier to sediment movement into the bay from sources north of Bolinas Bay. The reef forms a continuous barrier on the sea floor extending about two miles out into the ocean and acts as a baffle which traps sediment, or as a barrier to deflect it to the south. The reef completely blocks sediment movement into the shallow part of Bolinas Bay from the coastline to the northwest, and probably keeps it out of the bay entirely. Figure 7 shows these mineralogic trends.

Sediment Regime

Sediment Sources The data from mineralogical studies presented in this report permit us to distinguish two major and one minor source(s) of sediment for Bolinas Bay. A fourth source, of nondiagnostic mineral composition, is known from studies of sea cliff erosion. The first source is Bolinas Lagoon, which supplies sediment of a distinctive heavy mineral composition characterized by glaucophane and jadeite. Bolinas Bay sediments near the entrance to Bolinas Lagoon are of this composition, and there is a limited eastward dispersal of sediment from this source.

The other major source is the unconsolidated sediments of San Francisco Bar, south of Bolinas Bay, characterized by hornblende and hypersthene. Sediments derived from this source cover a large area in the southeast and central portions of the bay, in areas of the bay closest

to the bar. Sediment from the bar enters Bolinas Bay from the southeast, and is mixed with sediment from other sources. This sediment is moved into the bay by bottom currents in the deeper parts of the bay, in depths probably of 50-80 feet, where topographic gradients are low. This sediment does not enter the bay by longshore drift, and does not enter depths that lie within the regime of the surf zone (approx. 0-30 feet).

A third, and minor, source of sediment is Webb Creek near Rocky Point. Sediment with a Franciscan glaucophane-jadeite mineral composition enters Bolinas Bay at this place, and is spread a short distance to the north, west, and south of the point. The limited and equal distribution of sediment from Webb Creek shows that sediment bypassing around Rocky Point, from either the north or the south, is relatively unimportant. As a result, longshore drift on a long term basis is unimportant in sediment movement in the vicinity of Rocky Point. This supplies further evidence that sediment transported into Bolinas Bay from the San Francisco Bar enters through the deeper portions of the bay, outside the surf zone.

A fourth source of sediment, although indistinguishable by heavy mineral content, is present in the northwest corner of the bay. The sea cliffs between the town of Bolinas and Duxbury Reef are rapidly eroding at the present and deliver sediment directly into the bay. The relative importance of this source cannot be determined on the basis of heavy mineral data, but estimates of 72,000 cubic yards of erosion per year indicate that this is a major source of sediment.

Sediment Transport The sedimentary budget of Bolinas Bay is a function of (1) the volume, size distribution, and entry point of material introduced into the bay, and (2) the volume, size distribution, and exit areas for material leaving the bay. Within the bay these sediment fluxes are governed by (3) bottom currents which distribute the sediment, and (4) the bottom configuration which modifies the hydraulic regime causing transportation or deposition of sediment in a given area. The above four factors also, at least in part, are time dependent, some seasonal like the volume of stream discharge, or semi-diurnal like tidal fluctuations of the bottom currents. However, Johnson (1969) has shown that the changes in bottom configuration are limited to shallow areas near the mouth of the lagoon. Therefore, the mineralogic distributions shown in this report probably are valid for the generalized annual picture for the entire bay.

Sediment Budget As noted in the section on provenance, the major source of the sedimentary cover is San Francisco Bar. Secondary to this is the sediment from Bolinas Lagoon, and of least importance is Webb Creek. For the Bolinas Cliffs the rate of retreat of the cliffs is known, and volumes of sediment can be roughly determined.

As cited earlier in this report, the Bolinas Cliffs are presently eroding at a rate of 2-3 feet per year. Computing the area of cliff face subject to erosion, the resultant sediment yield to the ocean is determined to be approximately 72,000 cubic yards per year.

Ritter (1969) made measurements of the amount of sediment transported through the mouth of Bolinas Lagoon for one complete tidal day, a period of 25 hours, on October 24-25, 1967. Most of the sediment was moved during the major ebbtide, and the resultant of all portions of the tidal cycle was a net removal of about 330 tons of sediment from the lagoon for a 25 hour period. Projecting this over a full year, and using a density of 79 pounds per cubic foot, which Ritter (1969) determined to be the average density of sediments in Bolinas Lagoon, the resultant is a sediment yield of about 32,500 cubic yards per year. This figure is used as a minimum value of yearly sediment yield. The measurements were made at the end of the California dry summer season, when sediment yield is low. High sediment yields are associated with periods of high water runoff during the winter, which our calculations do not allow for, although it may be counterbalanced to a small degree by dry summer months with a lower sediment yield. A safe estimate would be an average of about 50,000 cubic yards per year.

No data on the amount of water flow, or suspended sediment content is available for Webb Creek, so an estimate of the sediment yield is made on the basis of the areal distribution of sediments derived from this source in the sediment cover of Bolinas Bay. A rough estimate of between 1,000-10,000 cubic yards per year can be made on this basis. Sediment yield of Webb Creek is augmented by sea cliff erosion of Rocky Point, which may provide as much, or more, sediment as Webb Creek proper. In any event, this source is not a major source of sediment to Bolinas Bay.

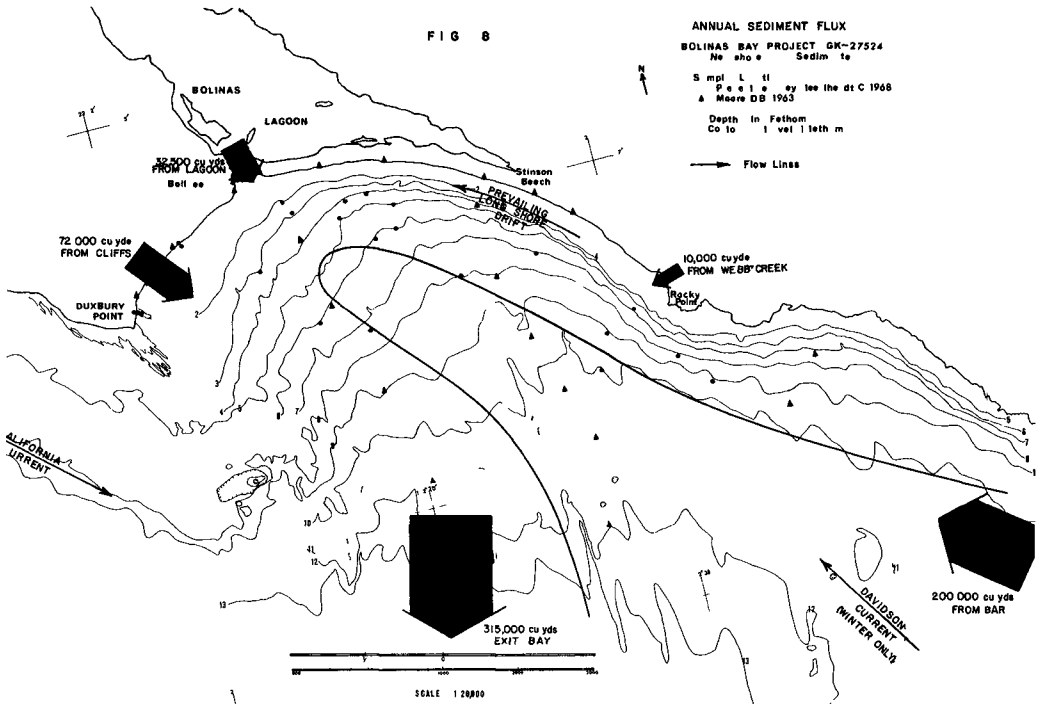
An estimate of the volume of sediment entering Bolinas Bay from San Francisco Bar can be made from the computed volume of sediment passing over San Francisco Bar. Sediment is transported over the bar at a rate of 2.9-5.3 million cubic yards per year. Assuming a fairly even radial dispersal off the bar, about 20% of this total will move towards Bolinas Bay, or about 800,000 cubic yards per year. Assuming that 25% of this amount will actually reach Bolinas Bay, with the remainder moving into deeper water, the resultant total is 200,000 cubic yards of sediment per year. Comparing the relative areal distribution of sediment in Bolinas Bay from each source, with a standard of about 50,000 cubic yards of sediment per year from Bolinas Lagoon, 200,000 cubic yards per year is a reasonable estimate of sediment yield to Bolinas Bay from San Francisco Bar.

Estimates of sedimentary inputs into Bolinas Bay are summarized in Table 1.

Figure 8 shows postulated sediment flux and non-tidal currents for the end of the winter season in Bolinas Bay. As seen in Fig. 7, the orientation of the heavy mineral provinces is not adequately explained by the non-tidal currents in Bolinas Bay. This is particularly true for the lobe of high hornblende-hypersthene emanating from the Potato Patch Shoals of the San Francisco Bar. The influence of the tides in governing the sediment distribution in Bolinas Bay is postulated as a two step process.

Table 1 Estimated Annual Sediment
Influx into Bolinas Bay

<u>Source</u>	<u>Volume</u>	<u>Authority</u>
Bolinas Cliffs	72,000 cu yards	rate from Galloway
Bolinas Lagoon	32,500 cu yards	Ritter
Webb Creek	1-10,000 cu yards	this report
San Francisco Bay	200,000 cu yards	estimation Holman & Schutz
TOTAL	314,500	
	315,000 cubic yards/year	



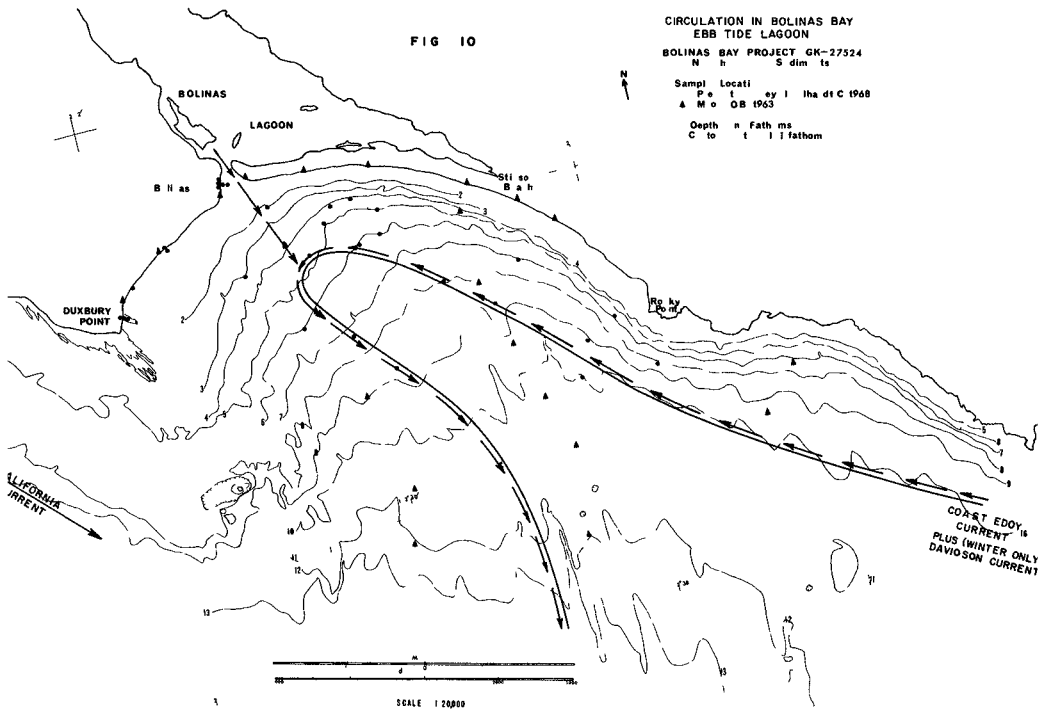
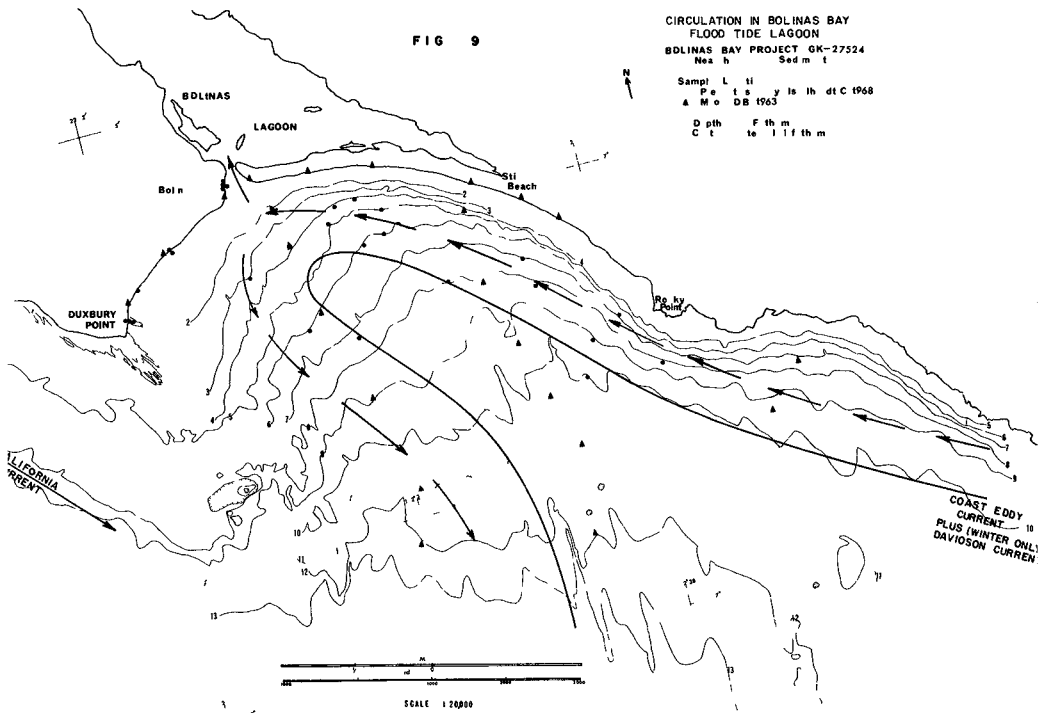
I During flood tide in the lagoon (Fig 9), the flow of water and entrained sediment to the northwest is at a maximum as (a) the Coast Eddy Current, (b) the Davidson Current, (c) longshore drift by wave refraction around Duxbury Reef, all act in consort with the incoming tide in the lagoon. Apparently the axis of transport is directed approximately along the 50 foot (8-9 fathom) line as shown by the orientation of the hornblende-hypersthene lobe.

II During ebb tide in the lagoon (Fig 10), the outflow from the lagoon combines with or produces the southwest return gyre of the Coast Eddy Current, which is reinforced to the southwest off the tip of Duxbury Reef by the California Current. The leading edge of the counterclockwise gyre, (a) entrains material from local sources which mixes with lagoonal material from the ebb tide on the southwest side, but (b) maintains on the inner side of the gyre the compositional integrity of the sediment brought from the San Francisco Bar. The gyre thus produces a northwest oriented lobe of San Francisco Bar material surrounded on three sides by sediments from local source areas.

The above models are based on an input from various sources of 315,000 cubic yards annually to Bolinas Bay (Table 1). Johnson (1969) has shown that the bottom configuration in deeper water does not change throughout the year. Thus, there is no net aggradation-degradation in Bolinas Bay. This implies quasi-equilibrium with a balancing outflow of approximately 315,000 cubic yards annually. With sediment added along the counterclockwise gyre (a) from the southeast from the San Francisco Bar, (b) from the northeast from Webb Creek, and (c) from the northwest from the lagoon and cliff erosion, the logical exit is to the southwest to deeper water on the shelf. This is indicated on the bathymetry map by (1) the steep seaward gradients in the channel adjacent to Duxbury Reef, and (2) two small channels emptying into the embayment which separates the bay from Potato Patch Shoals.

Acknowledgments

This work was sponsored by the Coastal Engineering Research Center, U S Army Corps of Engineers, by contract 72-67-C-0015, through the University of California.



References

- Bailey, E H , Irwin, W P , and Jones, D L , 1964, Franciscan and related rocks, and their significance in the geology of western California Calif Div Mines and Geology Bull 183, 177 p
- Brown and Caldwell, 1967, Interim report on the Bolinas watershed
Brown and Caldwell Consulting Engineers
- Cherry, J A , 1964, Sand movement along a portion of the northern California coast Univ of Calif , Inst of Eng Res Tech Report Series HEL-4-3, 150 p
- Cherry, J A , 1966, Sand movement along equilibrium beaches north of San Francisco Jour of Sed Petrology, v 36, no 2, p 341-357
- Galloway, A J , 1966, Geology of Northern California Calif Div Mines, Bull 190, p 429-440
- Gluskoter, H J , 1962, Geology of a portion of western Marin County, Calif unpub Ph D thesis, Univ of Calif , Berkeley, 184 p
- Gluskoter, H J , 1969, Geology of a portion of western Marin County, Calif Calif Div Mines and Geology, Map Sheet 11
- Hall, N T , 1965, Petrology of the type Merced Group, San Francisco Peninsula, California Univ of Calif , Berkeley, unpublished M A thesis, Geology, 127 p
- Hendricks, H L , ed , Compilation of records of surface waters of the United States, October 1950 to September 1960, part 11, Pacific slope basins in California U S Geol Survey Water-Supply Paper 1735, 715 p
- Homan, W J , and Schultz, E A , 1963, Model tests of shoaling and of dredge spoil disposal in San Francisco Bay Jackson, Miss , Federal Interagency Sedimentation Conf , 30 p
- Isselhardt, C , Osuch, L , and Wilde, P , 1968, Recent sediments of Bolinas Bay, Calif , Part A Introduction and grain size analysis, Univ of Calif , Hydraulic Engineering Lab , Tech Rept HEL-2-19, 55 p
- Isselhardt, C , Osuch, L , Yancey, T , and Wilde, P , 1969, Recent sediments of Bolinas Bay, Calif , Part B Mineralogical data Univ of Calif , Hydraulic Engineering Lab , Tech Rept HEL-2-22, 155 p
- Johnson, J W , 1969, Stabilization of the Bolinas Lagoon Inlet Report to Bolinas Harbor District, 40 p

- Minard, C R , 1964, The erosional and depositional history of the coast of northern California Univ of Calif , Inst of Engineering Research, Tech Rept HEL-2-10, 63 p
- Moore, D B , 1965, Recent coastal sediments Double Point to Point San Pedro, Calif Univ of Calif , Hydraulic Engineering Lab , Tech Rept HEL-2-14, 86 p
- Reid, J L , Roden, G I , and Wyllie, J G , 1958, Studies of the California current system Calif Co-op Ocean Fish Invest Progress Reports 1 July 1956 - 1 January 1958, p 27-56
- Reid, J L , and Schwartzlose, R A , 1962, Direct measurement of the Davidson Current off central California Jour Geophysical Research, v 67, p 2491-2497
- Ritter, J R , 1969, Preliminary studies of sedimentation and hydrology in Bolinas Lagoon, Marin County, Calif , May 1967-June 1968 U S Geol Survey Open File Report, Menlo Park, 68 p
- U S Coast and Geodetic Survey, 1947, Tide Chart, San Francisco Bay
- U S Coast and Geodetic Survey, 1968, United States Coast Pilot 7, Pacific Coast, Calif , Oregon, Washington, and Hawaii, Fifth edition, 380 p
- U S Hydrographic Office, 1947, Atlas of surface currents, north-eastern Pacific Ocean
- Weaver, C E , 1949, Geology of the Coast Ranges immediately north of the San Francisco Bay region, Calif Geol Soc of America Memoir 35, 242 p
- Wilde, P , Isselhardt, C , Osuch, L , and Yancey, T , 1969, Recent Sediments of Bolinas Bay, Part C, Interpretation and Summary of Results Univ of Calif , Hydraulic Engineering Research Lab , Tech Rept HEL-2-23, 86 p
- Yancey, T E , 1968, Recent sediments of Monterey Bay, Calif Univ of Calif , Hydraulic Engineering Lab , Tech Rept HEL-2-18, 145 p

CHAPTER 87

SUCCESSIVE SALTATION OF A SAND GRAIN BY WIND

Yoshito Tsuchiya
Professor of Coastal Engineering
Disaster Prevention Research Institute
Kyoto University, Kyoto, Japan

ABSTRACT

In order to establish the mechanics of sand transport in an air or water stream, the mechanics of saltation of sand grains should first be considered. In sand storms, most of the saltating sand grains on a granular bed have successively continued the saltation motion. In this paper, such a saltation motion is defined as successive saltation. A theoretical approach to the saltation of a single sand grain on a fixed granular bed is proposed on the basis of the equations of motion for the saltation and the dynamic characteristics of collision between a saltating sand grain and bed sand grains. Some experiments of the successive saltation of a single sand grain on a fixed granular bed were carried out to compare with the theoretical relationships. It was verified from the comparison that the theoretical relationships of the height and distance of saltation of a sand grain are in fairly good agreement in substance with the results of experiment.

INTRODUCTION

One of the crucial problems in the mechanics of sediment transport by wind is to establish the mechanics of the motion of sand grains near the bed. In 1941, Bagnold published a famous book entitled "The physics of blown sand and desert dunes", and investigated the motion of sand by wind defined as saltation and surface creep. Although many investigations have been conducted since then, the mechanics of the motion of sand grains have not yet been established completely. In 1951, Kawamura proposed an excellent theory of sand movement by wind based on the equation of motion of a sand grain by applying the drag force acting on the sand grain to the equation of motion but neglecting the virtual mass force since the force is usually very small compared with the drag force. Recently, Owen studied the mechanism of saltation of sand grains by wind to discover the velocity profile in a saltation layer and the rate of sediment transport.

On the other hand, in the case of water streams, in 1964 Yalin first established a theory of saltation of a sand grain by taking into consideration the uplift force acting on a sand grain, as measured by Einstein and Sammi and by Chepil and proposed a formula for the rate of sediment transport. And after that Kishi and Fukuoka recently carried out a basic experiment on the first saltation of a single spherical particle from the beginning of movement in a turbulent stream and modified Yalin's theory of saltation by taking into consideration the virtual mass force. The authors also conducted the same experiments as those done by Kishi and Fukuoka to make clear the mechanism of successive

saltation of a single sand grain from the beginning of motion and other basic experiments on the motion of sand grains in bed load. In addition the authors proposed a theoretical approach to the motion of sand grains, namely the sliding or rolling motion and the saltation motion, based on a different concept of the motion of a sand grain from the theories of Yalin and of Kishi and Fukuoka. In the theory there are two types of motion of a sand grain which has begun to move from the rest condition. The first one is defined as the rolling motion including the sliding one and the second the so-called saltation motion which the grain skips for a distance. With regard to the transition from the rolling motion to saltation it was pointed out from the photographs and the direct observations of motion that the grain always begins saltation after rolling for a certain distance. And it was concluded from the theory that the rolling distance is a function of the flow intensity and the ratio of the density of grain to that of fluid and that the distance decreases rapidly with the increase of flow intensity and of the density ratio. With regard to the hydrodynamic forces acting on a sand grain of which the size is large, both the drag and virtual mass forces were applied to the establishment of the equation of motion of a sand grain, because the so-called uplift force is considered to be very small compared with the drag force as measured by Chepil and calculated by Iwagaki.

In this paper, a modification of the theory is made based on the fact that the rolling and sliding motion do not exist in the case where sand grains are transported by wind and an application of the theory to the saltation of sand grains by wind is presented in comparison with some results of experiments on the successive saltation of a sand grain on a fixed granular bed.

THEORY OF THE SALTATION OF A SAND GRAIN

(1) Equation of Motion

Since the Reynolds number becomes very high in the motion of a sand grain in general, the quadratic law for drag forces is applicable to the equation of motion. It is assumed that the size of the grain is so large that the effect of turbulence on the motion is not taken into consideration. Although the hodograph space can be used in establishing the equation of motion, the equations are assumed to be established in the vertical and horizontal directions respectively, because the saltation height is assumed not to be very high compared with the saltation distance. Neglecting the Basset term which is one of the virtual mass forces, the equation of motion of a sand grain can be written as

$$\left. \begin{aligned} dW/dt &= \mp (3/4)C_D W^2/(\sigma/\rho+1/2)d - (\sigma/\rho-1)g/(\sigma/\rho+1/2) \\ dU/dt &= (3/4)C_D (u-U)^2/(\sigma/\rho+1/2)d \end{aligned} \right\} \quad (1)$$

in the vertical and horizontal directions respectively, in which W is the vertical velocity component of the sand grain, U the horizontal component, C_D the drag coefficient, d the diameter of the grain, g the acceleration of gravity, t the time and σ and ρ the densities of the grain and fluid respectively. And u in Eq. (1) denotes the velocity in a saltation layer which is a function of the ordinate.

Let the following dimensionless quantities be introduced into Eq. (1)

$$\left. \begin{aligned} U &= U/u^*, \quad \bar{W} = W/u^* \quad K^2 = (4/3)\{(\sigma/\rho - 1)gd/u^* C_D\} \\ \tau &= \{C_D/(\sigma/\rho + 1/2)\}(u^*t/d) \end{aligned} \right\} \quad (2)$$

in which u^* is the shear velocity and the solution under the initial condition that $\bar{W} = \bar{W}_0^*$ and $\bar{U} = \bar{U}_0$ at $\tau = 0$ becomes

$$\left. \begin{aligned} \bar{W} &= K\{(\bar{W}_0/K) - \tan K\tau\} / \{1 + (\bar{W}_0/K)\tan K\tau\} \\ \bar{U} &= u - (u - \bar{U}_0) / \{1 + (u - \bar{U}_0)\tau\} \end{aligned} \right\} \quad (3)$$

in the upward motion of the sand grain. And the solution for \bar{W} in the downward motion under the initial condition that $\bar{W} = 0$ at $\tau' = 0$ becomes

$$\bar{W} = -K \tan(K\tau') \quad (4)$$

in which τ' is the same expression as τ . Therefore, the velocity components \bar{W}_1 and \bar{U}_1 just before arriving at the bed can approximately

$$\bar{W}_1 \approx \bar{W}_0, \quad \bar{U}_1 = u - (u - \bar{U}_0) / \{1 + 2(u - \bar{U}_0)\bar{W}_0/K^2\} \quad (5)$$

In the case where the velocity in a saltation layer u is assumed to be constant because the saltation height is very small, further integration of Eq. (3) under the initial condition that $\xi (= x/d) = \eta (= z/d) = 0$ at $\tau = 0$ yields

$$\left. \begin{aligned} \bar{H} &= (2/3)\{(\sigma/\rho + 1/2)/C_D\} \log\{1 + (\bar{W}_0/K)\} - (2/3)\{(\sigma/\rho + 1/2)/C_D\}(\bar{W}_0/K) \\ \bar{L} &= (4/3)\{(\sigma/\rho + 1/2)/C_D\}\{2u\bar{W}_0/K - \log\{2(u - \bar{U}_0)\bar{W}_0/K^2 + 1\}\} \end{aligned} \right\} \quad (6)$$

in which \bar{H} is the saltation height, \bar{L} the distance, $\bar{h} = \bar{H}/d$ and $\bar{l} = \bar{L}/d$

(2) Collision and Rebound of a Saltating Sand Grain on Bed Grains

Fig. 1 shows a schematic diagram for the collision and rebound of a sand grain in which V_1 and V_2 denote the velocity vectors of saltating sand grain and the other notations are shown in the figure. Making some assumptions, the conservation law of momentum in the vertical and horizontal directions yields

$$\left. \begin{aligned} -eV_1 \cos(\gamma - \alpha) &= V_2 \cos(\pi - \beta - \gamma) \\ V_1 \sin(\gamma - \alpha) &= V_2 \sin(\pi - \beta - \gamma) \end{aligned} \right\} \quad (7)$$

in which e is the coefficient of rebound of a saltating sand grain. Introducing the quantities

$$\left. \begin{aligned} V_1 \cos \alpha &= U_1, \quad V_1 \sin \alpha = W_1, \quad V_2 \cos \beta = U_2 \\ V_2 \sin \beta &= W_2, \quad U_1 = -W_1 \cot \alpha = a_1 W_1 (\delta_1 < 0) \\ U_2 &= W_2 \cot \beta, \quad \delta = W_2 (\delta > 0) \\ \bar{W}_1 &= W_1/u^*, \quad \bar{U}_1 = U_1/u^*, \quad \bar{W}_2 = W_2/u^* \\ \bar{U}_2 &= U_2/u^*, \quad \bar{U}_1 = \delta_1 \bar{W}_1, \quad \bar{U}_2 = \delta_2 \bar{W}_2 \end{aligned} \right\} \quad (8)$$

the relationships between the velocity components just before and after the

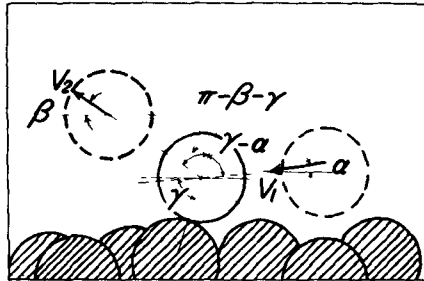


Fig. 1 Schematic diagram for collision of sand grain

collision can be expressed approximately as

$$\left. \begin{aligned} \bar{U}_0 &= e\bar{U}_1 \\ \bar{W}_0 &= e\{b_1\bar{U}_1 + b_2\bar{W}_1\} / \{b_3 + b_1(\bar{W}_1/\bar{U}_1)\} \end{aligned} \right\} \quad (9)$$

in which $b_1 = (1+e)\tan\gamma$, $b_2 = (1-e)\tan^2\gamma$ and $b_3 = (\tan^2\gamma - e)$

(3) First Saltation

In this paper the first jumping motion of a sand grain from the rest condition is defined as first saltation. In the sand movement by wind the rolling or sliding motion scarcely ever occurs. The friction force in the equation of motion can be neglected because the sand grain always begins to saltate just after the collision on a neighboring sand grain. Therefore the equation of motion of a sand grain for the motion from the rest condition to the saltation can be written as

$$dU'/dt = (3/4)\{C_D/(\sigma/\rho + 1/2)d\}(u - U')^2 \quad (10)$$

in which U' is the horizontal velocity of the grain and u' the velocity near the grain which may be affected by the velocity of fluctuation and assumed to be $\bar{u} = u'/u_*$. The integration of Eq (10) with the initial condition that $U' = 0$ at $t = 0$ yields

$$U'/u_*^2 = (3/4)u_*^2\tau / \{1 + (3/4)u_*\tau\} \quad (11)$$

From Eq (11) the relationship for the change of velocity with the distance under the assumption that C is very small can be expressed approximately as

$$U'/u_*^2 = u_*\sqrt{2(x/d)N} / \{1 + \sqrt{2(x/d)N}\} \quad (12)$$

in which $N = (3/4)\{C_D/(\sigma/\rho + 1/2)\}$

As described already, making the assumption that the sand grain begins to saltate just after the collision on a neighboring sand grain from the rest condition, the value of x/d in Eq

(12) is assumed to be that $x/d \approx 1$. Since the initial velocity of the grain for the first saltation can be estimated, putting the velocity into an approximate expression of Eq (6) for $(\bar{W}_0/K)^2 \ll 1$, the saltation height can be expressed approximately as

$$\begin{aligned} \bar{H} &= (1/2)\beta^2 A_*^2 \{(\sigma/\rho + 1/2)\} \\ &\{2N / (1 + \sqrt{2N})^2\} \{u_*^2 / (\sigma/\rho - 1)gd\} \end{aligned} \quad (13)$$

in which $\beta = \bar{W}_0/U_0$ and $A_* = \bar{u}$. By the same means the calculation for the saltation distance can also be made

(4) Successive Saltation

Although the successive

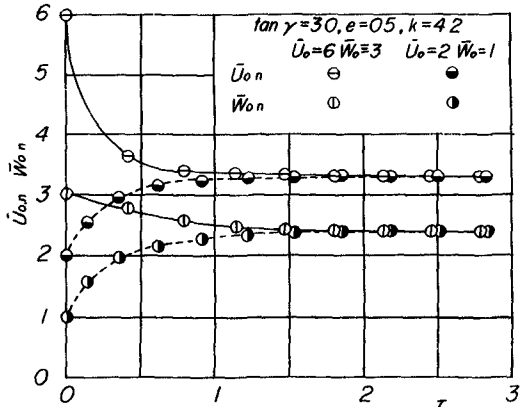


Fig 2 Changes of initial velocity of sand grain in successive saltation

saltation can be calculated by Eqs (5), (6) and (9) as seen in Fig 2, the velocity components of the saltating sand grain become constant after several saltations. Such a saltation is defined as the stationary saltation of which the velocity components in the vertical and horizontal directions are expressed by \bar{W}_s and \bar{U}_s respectively

Assuming that the sand grain has alternately taken saltation and rebound keeps the stationary velocity at the k-th step in saltation, the relationship can be obtained as

$$U_{k0} = P u \quad \bar{W}_{k0} = Q u \quad U_{k10} = U_{k0} = P u \quad \bar{W}_{k10} = \bar{W}_{k0} = Q u \tag{14}$$

Transformation of Eq (14) using Eqs (5), (6) and (9) yields approximately

$$\left. \begin{aligned} \bar{W}_s &= \lambda [(1+e) - \sqrt{(1-e)^2 + 2(1-e)/(\lambda(u/K))}] u/2 \\ \bar{U}_s &= [(1+e) - \sqrt{(1-e)^2 + 2(1-e)/[\rho(u/K)^2]}] u/2 \end{aligned} \right\} \tag{15}$$

According to Eq (15), it is seen that the values of \bar{W}_s and \bar{U}_s are real, since $e = 1$ in general, and then the roots in the equation also are real. As seen from Eq (15), the condition that $\bar{W}_s = \bar{U}_s = 0$ can be written as

$$u_*^2 / (\sigma/\rho - 1) g d = (2/3) (1/C_D) (1-e) e \lambda u_*^2 \tag{16}$$

which is generally different from the so-called critical flow intensity

It is concluded from the above description that the sand grain moving downstream, repeating saltation and rebound alternately, reaches a certain stationary velocity after several steps of successive saltation in the case where the flow intensity is larger than the critical one expressed by Eq (16) and that the initial velocity components in the vertical and horizontal directions in stationary saltation are expressed by Eq (15)

Although the height and distance of saltation of a sand grain are formulated by Eq (6) in connection with the initial velocities, without loss of generality, for simplicity, the following relationships can be used under the assumptions that $(\bar{W}_0/K)^2 \ll 1$ and $2(\bar{U}_0/K)^2 \ll 1$

$$\left. \begin{aligned} \bar{H} &= (2/3) \{ (\sigma/\rho + 1/2) / C_D \} (\bar{W}_0/K)^2 \\ \bar{L} &= (8/3) \{ (\sigma/\rho + 1/2) / C_D \} (\bar{U}_0 \bar{W}_0 / K^2) \end{aligned} \right\} \tag{17}$$

Putting Eq (15) into Eq (16), the relationship of the height and distance of saltation with the flow intensity and the condition of the granular bed can be written approximately as

$$\left. \begin{aligned} \bar{H}_m &= (1/6) \{ (\sigma/\rho + 1/2) / C_D \} \lambda [(1+e) - \sqrt{(1-e)^2 + 2(1-e)/(\lambda(u/K))}]^2 (u/K) \\ \bar{L}_m &= (2/3) \{ (\sigma/\rho + 1/2) / C_D \} \lambda [(1+e) - \sqrt{(1-e)^2 + 2(1-e)/[\lambda(u/K)^2]}]^2 (u/K)^2 \end{aligned} \right\} \tag{18}$$

in which \bar{H}_m denotes the mean values of saltation height and \bar{L}_m the mean values of saltation distance. From Eq (18), the value of λ can be expressed as

$$\lambda = 4 (\bar{H}_m / \bar{L}_m) \tag{19}$$

which is an empirical constant to be determined by the experimental results for the mean values of height and distance of saltation

(5) Distributions of Height and Distance of Saltation

Although the distribution characteristics of the saltation height and distance of a sand grain generally depend upon the characteristics of the velocity fluctuation of a sand grain just before and after its collision with bed grains, the dispersion characteristics of the angle of collision and the effect of turbulence on the motion of the grain, it is assumed that the distribution of height and distance of saltation is affected only by the characteristics of the velocity fluctuation

From this point of view, assuming that the density functions of the horizontal velocity of a sand grain both in first and stationary saltations $f_1(\bar{u})$ and $f_1(\bar{U})$ can be expressed respectively by the Gaussian distribution in the form

$$f_1(u) = (1/\sqrt{2\pi}\sigma_u) \exp\{-(u-u_m)^2/2\sigma_u^2\} \quad (20)$$

for first saltation and

$$f_2(\bar{U}) = (1/\sqrt{2\pi})(1/\sigma_U) \exp\{-(\bar{U}-U_s)^2/2\sigma_U^2\} \quad (21)$$

for stationary saltation, in which σ_u and σ_U are the standard deviations of the dimensionless horizontal velocities \bar{u} and \bar{U} respectively and are assumed to be

$$\sigma_u = \epsilon u_m \quad \sigma_U = \epsilon U \quad \epsilon = \text{const} \quad (22)$$

and \bar{u}_m is the mean value of \bar{u} , assuming that the relation between the horizontal and vertical velocities can be expressed generally by $\bar{w} = \lambda \bar{u}$, the density function of the saltation height can finally be written after some transformations as

$$f(\bar{H}) = (1/2\sqrt{2\pi})(1/\epsilon\sqrt{\bar{H}\bar{H}_m}) \exp\{-(\sqrt{\bar{H}} - \sqrt{\bar{H}_m})^2/2\epsilon^2\bar{H}_m\} \quad (23)$$

for both first and stationary saltation. Similarly the density function of the saltation distance can finally be expressed as

$$f(\bar{L}) = (1/2\sqrt{2\pi})(1/\epsilon\sqrt{\bar{L}\bar{L}_m}) \exp\{-(\sqrt{\bar{L}} - \sqrt{\bar{L}_m})^2/2\epsilon^2\bar{L}_m\} \quad (24)$$

EXPERIMENTS OF SUCCESSIVE SALTATION OF A SAND GRAIN

(1) Experimental Apparatus and Procedure

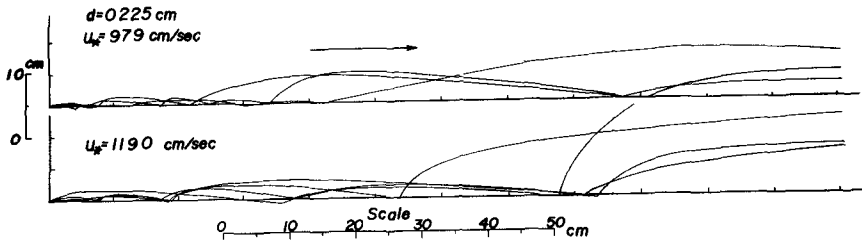
A wind tunnel, 21.6 m long, 0.75 m wide and 1.0 m deep was used in order to make clear the characteristics of successive saltation of a sand grain on a fixed granular bed. Properties of grains used in the experiments are shown in Table 1, in which ρ_0 is the density of water. Paths of saltation of a grain from the rest condition were photographed with a 16 mm high speed camera under various conditions of wind and the film was analyzed with a film motion analyzer. Wind velocity profiles in the wind tunnel were measured with a hot wire anemometer and the shear velocity was estimated by the wind velocity profiles measured based on the logarithmic law of velocity profile.

Table 1 Properties of grains used in the experiment

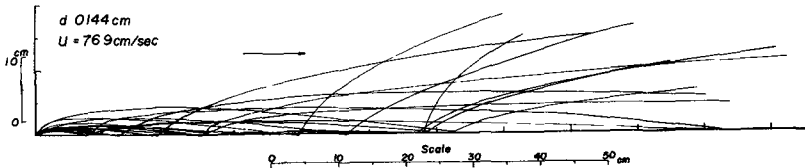
Kind of grains	Diameter d cm	Specific gravity σ/β_0
sand	0.225	2.624
	0.184	2.523
	0.144	2.474
seed	0.184	1.155
	0.144	1.155

(2) Results of Experiments

Fig 3 shows some examples of the successive saltation of sand grains and seeds respectively obtained in the experiment. From the results of the experiment the saltation angle β shown in Fig 1 were measured. Fig 4 describes the relationship between the angles in each step of saltation and the flow intensity in which β_1 , β_2 and β_3 are the saltation angles in the first, second and third saltations respectively. It can be found that the angle of the first saltation is mostly independent of the flow intensity and is approximately 40 degrees.



(a) In the case where sand grains were used



(b) In the case where seeds were used

Fig 3 Some examples of paths of saltating grains in successive saltation

Fig 5 shows a comparison between the experimental values of the height of first saltation and the theoretical relationship for the first saltation obtained by Eq (13) in which A_r is assumed to be 10.5 including the effect of turbulence.

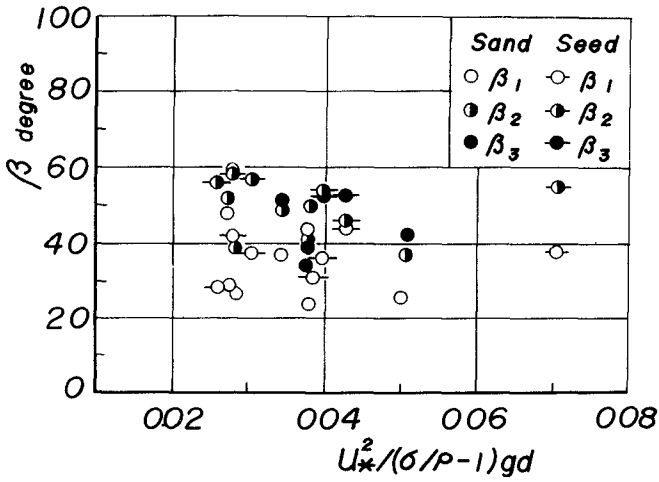


Fig 4 Variations of saltation angles with flow intensity

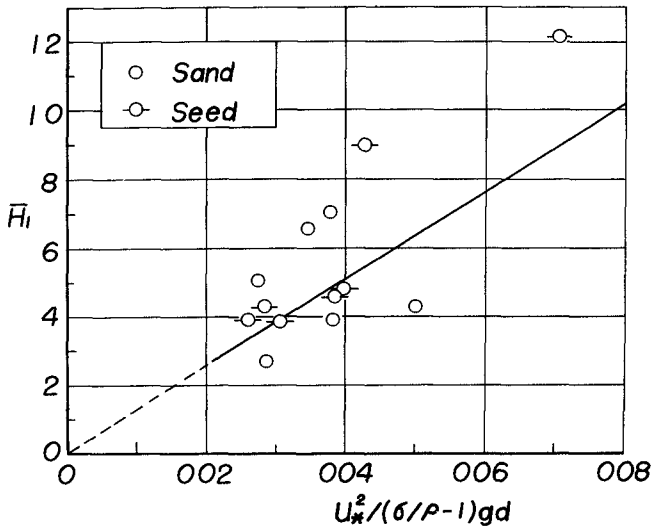


Fig 5 Comparison between theoretical relationship for the first saltation and experimental values

and β is determined by the best fit to the values of experiment which is estimated to be nearly 0.8. It is concluded from the comparison that the theoretical relationship for the first saltation is in good agreement with the experimental values though there is a large scatter.

Fig. 6 describes the variation of the value of λ which is the ratio of the saltation height to the distance with the increase of flow intensity. It is seen that the value of λ is nearly constant and is estimated to be 0.23. The value is different from that in a water stream because of the difference of col-

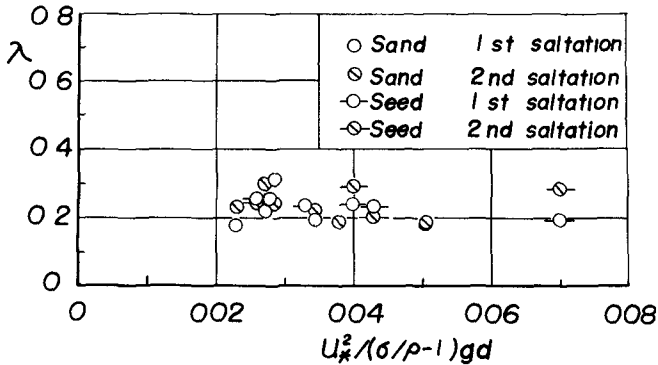


Fig. 6 Variation of value of λ with flow intensity

lision characteristics

Figs 7 and 8 show the comparisons between the theoretical curves of the saltation height and distance in stationary saltation and the experimental values for the first, second and third saltations. Experiments of more successive saltation than the third saltation could not be conducted due to the limitation of the experimental apparatus. Therefore a complete comparison between the theory for the stationary successive saltation and the experiment cannot be made. It is seen from the comparisons however that the experimental values in successive saltation tend to approach the theoretical curves for stationary saltation in which the value of A_1 is assumed to be the value corresponding to $H = 100$ because the saltation height is not small and the effect of velocity profile on the saltation should be taken into consideration. It is concluded that this theoretical approach to the saltation of a single sand grain by wind is in fairly good agreement with the results of experiments.

CONCLUSION

Although the phenomena of saltation of a sand grain by wind are very complicated, there generally exists some kinds of saltation such as first saltation, successive saltation and stationary saltation as defined in this paper.

A theory of successive saltation is established, based on the equations of motion of a sand grain and the dynamic relationship of the collision of a saltat-

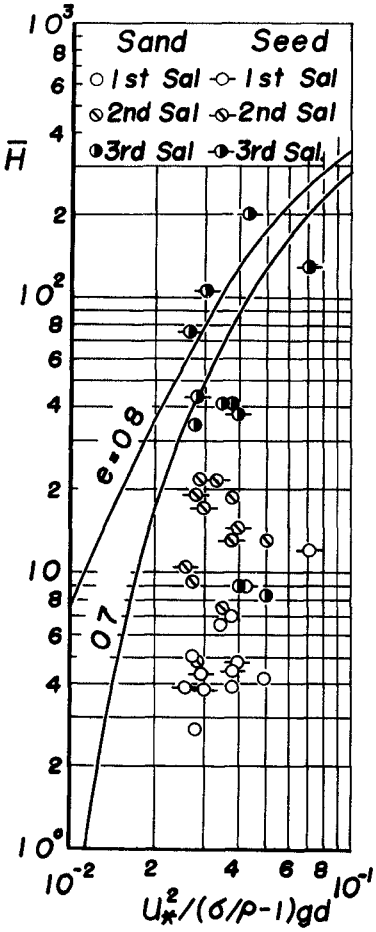


Fig 7 Comparison between theoretical curves of saltation height in stationary saltation and experimental values for first, second and third saltations

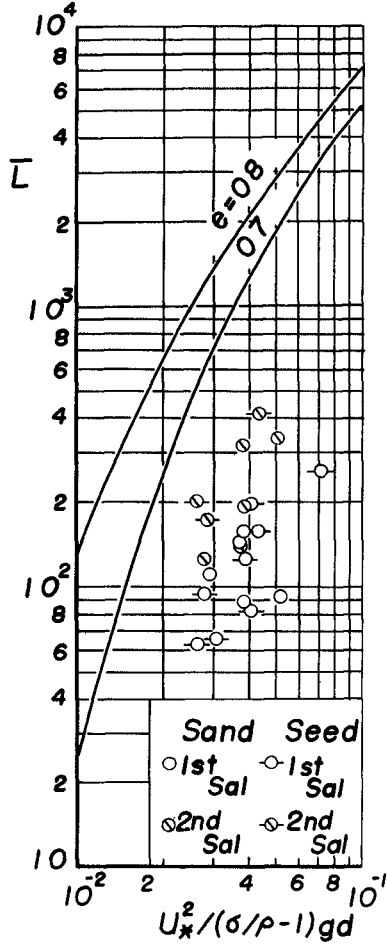


Fig 8 Comparison between theoretical curves of saltation distance in stationary saltation and experimental values for first, second and third saltations

ing sand grain with bed grains. It is concluded that the theoretical relationships for the saltation are in fairly good agreement with the results of the experiment although further comparisons should be made.

Further investigations on the saltation of sand grains will be conducted studying the saltation characteristics of sand grains in a water stream and comparing the results with the data of field observations in sand storms.

ACKNOWLEDGEMENT

The author wishes to acknowledge his sincere thanks to Mr T Shibano, Technical Officer, for his kind help in preparing this paper and to Mr Y Kawata, Graduate Student, for his kind help in conducting this investigation.

REFERENCES

- Bagnold, R A (1941) The physics of blown sand and desert dunes Methuen & Co Ltd, London
- Chepil, W S (1961) The use of spheres to measure lift and drag on wind-eroded soil grains Soil Sci Soc American Proc, Vol 25, pp 343-345
- Einstein, H A and Sammi, E L (1949) Hydrodynamic forces on a rough wall Reviews of Modern Phys, Vol 21, No 3, pp 520-524
- Iwagaki, Y (1956) Hydrodynamical study on the critical tractive force Trans JSCE, No 41, pp 1-21 (in Japanese)
- Kawamura, R (1951) Study of sand movement by wind Report of Tech Res Inst, Univ of Tokyo, Vol 5, pp 95-112 (in Japanese)
- Kishi, T and Fukuoka, S (1966) The mechanism of saltation of sand grains and the rate of sediment transport Proc 10th Conf on Hydraulics, JSCE, pp 59-64 (in Japanese)
- Owen, P R (1964) Saltation of uniform grains in air Jour Fluid Mech, Vol 20, Part 2, pp 225-242
- Tsuchiya, Y and Sumino, M (1967) Experiments on the mechanism of movement of a spherical sand particle on a granular bed in turbulent streams, Annuals, Disas Prev Res Inst, Kyoto Univ, No 10, pp 97-107 (in Japanese)
- Tsuchiya, Y, Watado, K and Aoyama, T (1969) On the mechanism of saltation of a sand particle in a turbulent stream (1), Annuals, Disas Prev Res Inst Kyoto Univ, No 12B, pp 475-490 (in Japanese)
- Tsuchiya, Y and Aoyama, T (1970) On the mechanism of saltation of a sand particle in a turbulent stream (2) -- On a theory of the successive saltation, Annuals, Disas Prev Res Inst, Kyoto Univ No 13B, pp 199-216 (in Japanese)
- Yalin, M S (1963) An expression for bed load transportation, Proc ASCE, Vol 89, HY3, pp 221-250



Baco Raton Inlet, Florida

PART 3. COASTAL STRUCTURES AND RELATED PROBLEMS

St. Johns River, Florida



CHAPTER 88

RESEARCHES ON SEA-WALLS

S Nagai
Professor of Hydraulics,
Dean of Faculty of Engineering,
Osaka City University, Osaka, Japan

ABSTRACT

In the recent decade, very wide areas of sea where the depths of water are from several meters to ten meters or more during storms have been reclaimed for industrial firms and port facilities in many places in Japan. As the incident wave energy in such cases is very large at the sea-walls, the protection of the reclaimed lands from wave overtopping by the conventional sea-walls of vertical type or composite-slope-and-berm type is generally impossible from an economical point of view. In Japan a special type of sea-wall, which is of such a type that a rubble-mound covered with specially shaped precast concrete armor blocks is built in front of the sea-wall to absorb most of the incident wave energy, has been constructed to protect the reclaimed lands from wave overtopping. Most of the sea-walls have been proved satisfactory after passing of typhoons over or near the sea-walls. The design of the sea-walls is presented here in by showing the comparisons between the experiments and prototypes during typhoons.

INTRODUCTION

Until about fifteen years ago most of sea-walls had been built on the shore line or in shallow water for the protection of low lands or coastal areas from the attack of high tides and storm waves. In such cases incoming wave energy is generally not large and the sea-walls can be designed only with the estimations of the change of the incoming wave characteristics before the waves reach the sea-walls and of the wave run-up on the sea-walls. In a recent decade, however, very wide areas of sea where the depths of water are several meters to ten meters or more during typhoons or storms have been forced to reclaim at many place in Japan, because of rapid expanding industries and increasing population. In the latter cases the incident wave energy at the sea-walls is much larger than that in the former cases, and the protection of the reclaimed land from wave overtopping during typhoons is so difficult that a conventional sea-wall of vertical type would need very high crowns with heights of two to several times the design wave height above the design sea level or a sea-wall of composite-slope and berm type would require a very large cross-section. Therefore the sea-walls of these two types are seldom possible to be designed from an economical point of view.

In Japan a special type of sea-wall has been constructed since around 1961 to protect reclaimed lands and coastal areas from wave overtopping. It is of such a type that a rubble-mound covered with specially shaped precast concrete armor blocks is built in front of the sea-wall in order to absorb most of the incoming wave energy.

The comprehensive experiments of the sea-walls of this type have been performed since 1960 in wind channels with a wind blower in Osaka City University, and numerous sea-walls have been designed and constructed in seas since 1961 by the use of the experimental results. Most of the

sea-walls have proved after attacks of storm waves during typhoons that the results obtained in the experiments were in a good agreement with prototype

PARAMETERS RELATED WITH WAVE OVERTOPPING
AND CLASSIFICATION OF OVERTOPPING

In the investigation to determine the quantity of wave overtopping from the sea-walls of special type mentioned above the following variables should be considered

- q = quantity of overtopping over the unit length of the sea-wall for a period,
 H = height of the incoming wave,
 L = length of the incoming wave,
 h_1 = depth of water at the toe of the rubble-mound,
 H_c = height of the crown of the sea-wall above the design sea level,
 H_r = height of the crown of the rubble-mound above the design sea level,
 α = slope of the sea bottom
 $\tan \alpha$ = slope of the rubble-mound,
 B = width of the crown of the rubble-mound,
 and
 V = wind velocity

These symbols are shown in Fig 1

If q_0 defines the volume of water transported shoreward by a shallow water wave for a period, it is given by the small amplitude wave theory

$$\begin{aligned} q_0 &= \int_0^{T/2} \int_{-h_1}^0 u \, dz \, dt \\ &= \int_0^{T/2} \int_{-h_1}^0 \frac{H}{2} \frac{2\pi}{T} \frac{\cosh \frac{2\pi}{L} (h_1 + z)}{\sinh \frac{2\pi}{L} h_1} \sin \left(\frac{2\pi}{L} x - \frac{2\pi}{T} t \right) dz \, dt \\ &= \frac{HL}{2\pi} \end{aligned}$$

If q/q_0 is used as a dimensionless parameter of wave overtopping, it is a function of the following dimensionless parameters

$$q/q_0 = f \left(h_1/H, h_1/L, H_c/H, H_r/H, B/H, \alpha, V/\sqrt{gH}, \tan \alpha \right) \dots \dots \dots (1)$$

when the permeability and roughness of the rubble-mound are kept constant

The dissipation of the energy of a wave striking the sea-wall with a rubble-mound covered with specially shaped precast concrete armors depends, to a considerable extent, on the characteristics of the armor blocks, that is, the permeability, the distribution of the voids of the armor layers and the roughness of the armors, as well as the slope of the rubble-mound, $\tan \alpha$, and the crown width, B . In practical designs the value of $\tan \alpha$ has mostly been taken 1.15 or 1.2 from an economical point of view and the stability of the armor blocks used on the slope. The crown width, B , of the rubble-mound also has usually been taken the width of two to three rows of the armor blocks from the same reasons as mentioned above

Therefore $\tan\alpha$ was kept 1.15 in our experiments, and most of B were taken four to six meters in prototype-scale. The velocity of wind has a great effect on the quantity of overtopping of a sea-wall when it exceeds about ten meters per second, but it was kept constant $V = 20$ to 25 meters per second in the experiments. According to the results of the experiments, in which B/H ranged from 1.0 to 4.0, and V/\sqrt{gH} were proved to have a negligibly small effect on overtopping. Finally the relative overtopping was shown as a function of the following five major dimensionless parameters

$$q/q_0 = f (h_1/H, H/L, H_c/H, H_r/H, 1), \dots \dots \dots (2)$$

when the shape and hydraulic characteristics of the rubble-mound is kept constant

When the depth of water at the toe of the rubble-mound, h_1 , is so small that the incoming wave breaks offshore the rubble-mound, it is rather easy to construct a sea-wall which can completely prevent the overtopping even during windy storms. However, when h_1 is equal to or larger than the depth of breaking of the incoming wave, it is generally seldom possible from an economical point of view to design a sea-wall of no-overtopping. As h_1 increases compared with H , the difficulty increases much more, and it cannot be helped to permit some quantity of overtopping from the sea-wall. The quantity of overtopping to be allowed depends upon the economical value of the land to be protected, the purpose of use of the area, the stability of the sea-wall and the scale of the drainage channel. According to the results of the experiments, the state and quantity of the overtopping can be classified into the four cases shown in Table 1 by the value of q/q_0 .

TABLE 1 CLASSIFICATION OF BEHAVIORS OF OVERTOPPING

Classification	Behavior of overtopping	q/q_0	Propriety
I	Only spray overtops (very well absorption of wave)	0 to 10^{-4}	Adequate for a sea-wall
II	Lumps of water overtop (higher limit applicable to a sea-wall)	10^{-4} to 5×10^{-3}	
III	A substantial part of wave over- tops (imperfect absorption of wave)	5×10^{-3} to 10^{-2}	Inad- equately for a sea-wall
IV	Large volume of wave overflows (poor absorption of wave)	10^{-2} to 10^{-1}	

EXPERIMENTAL EQUIPMENT AND PROCEDURES

The experiments were performed by dividing into two groups, one was concerned with sea-walls constructed in comparatively shallow waters with depths less than several meters, and the other concerned with sea-walls built in deeper waters with depths from about 8 meters to 14 meters. The former group of the experiments were conducted in 1963 and 1964, and the latter in 1966 and 1967. The wave channel used for both groups of the experiments is 50 m long, 1 m wide, and 1.65 m high, and has a wind blower by which winds of velocities up to 6.0 m per sec can be blown over the water waves generated by a wave-generator of flutter-type. The scale of the experiments used in both the groups is 1/20 horizontally and vertically. The characteristics of the waves tested and other conditions used in the experiments are summarized in Table 2. The 10 m-length of the bottom in front of the sea-wall has a slope of 1, and the remaining part of the bottom is flat.

TABLE 2 CONDITIONS USED IN EXPERIMENTS

Group of exper- iment	Water depth		Wave characteristics				Slope of bottom	Wind velocity	
	model	proto- type	model		proto- type			model	proto- type
	(h ₁)m cm	(h ₁)p m	Hm cm	Tm sec	Hp m	Tp sec	1	Vm cm/sec	Vp m/sec
Shal- lower waters	2 to 33	0.4 to 6.6	3 to 22	1.4 to 3.0	0.6 to 4.4	6.3 to 13.4	1/10 and 1/40	4.5	20
Deeper waters	40 to 70	8.0 to 14.0	10 to 25	1.12 to 2.8	2.0 to 5.0	5.0 to 13.0	1/100	4.5	20

The rubble-mound was made of quarry stones with diameters of about 2 cm to 3.5 cm (40 cm to 70 cm in prototype), and covered with two layers of precast concrete armor blocks such as hollow square, hollow tetrahedron, and N-shape blocks with dead weights of 250 grams and 750 grams (2 tons and 6 tons in prototype). The slope of the rubble-mound was kept 1.15.

as shown in Fig 1 The characteristics of the armor blocks used in the experiments are summerized in Table 3

TABLE 3 CHARACTERISTICS OF ARMOR BLOCKS USED IN EXPERIMENTS

Armor block	Weight in ton	Placing	NO of blocks per 100 m ²	Void ratio	K _d for no damage condition	
					Reg placing	Pell-mell
Hollow square	2	2 layers	80	49	20	13
Hollow tetrahedron	6	2 layers	42	66	11	7 6
Hollow N ₁	6	2 layers	45	53	20	-
Hollow N ₃	6	2 layers	49	61	20	-

The crown width of the rubble-mound, B, was taken the width required for placing 2 5 or 3 rows of the armor blocks used, from the experiences in seas of the stability and absorption of wave energy of the armor blocks

EXPERIMENTAL RESULTS

Effect of Water Depth at the Toe of the Rubble-Mound of the Sea-Wall

The volume of wave overtopping is greatly affected by the point of breaking of the incident wave, which can be divided into the following three cases

1 When the incident wave breaks offshore from the toe of the rubble-mound This case may be termed "Offshore Breaking", in which the overtopping is the minimum of the three cases

2 When the incident wave breaks at or near the toe of the rubble-mound This case may be termed "Breaking at Toe" The relative overtopping and relative run-up are the maximum of the three cases as seen in Fig 3

3 When the incident wave breaks on the slope of the rubble-mound This case is termed "Breaking on Slope" This case occurs when the rubble-mound is located in larger depth of water than the depth of breaking of the incident wave

The effect of h_1/L on q/q_0 is shown in Fig 3 in the cases when the relative crown heights of the sea-wall and rubble-mound, H_C/H and H_R/H , as well as the steepness of the incident wave, H/L , are kept constant. Fig 3 shows that q/q_0 is the maximum when the toe of the rubble-mound is located at a little larger depth of water than or near the point of breaking, i.e. $h_b = 1.28 H_b$ which is the breaking depth of solitary wave. The reason is attributed to the fact that the point of breaking of the incident wave somewhat moves toward offshore due to the existence of the rubble-mound.

However, when $h_1/H \geq 1.7$, in which the incident wave always breaks on the slope of the rubble-mound, the parameters of h_1/H and h_1/L have little effect of overtopping and run-up. The experimental results obtained at the Waterways Experiment Station (1) and Coastal Engineering Research Center (2) also showed roughly the fact that when the ratio of h_1/H is between 2.18 and 3.12 or as long as the waves break on the slope of a structure, h_1/H had little effect on wave run-up.

Effect of the Steepness of the Incident Wave

Fig 4 shows the effect of H/L of the incident wave on q/q_0 when H_C/H , H_R/H , and h_1/H are kept constant. Though the relative overtopping seems the maximum near H/L of about 0.025, sea-walls in general are designed by the characteristics of design waves decided from storm conditions at the site.

Effect of the Bottom Slope

According to comparisons of the results of the experiments, Figs 5 and 6, in which the bottom slope of the wave channel was changed 1/10 and 1/40, it was noted that the cases of $\beta = 1/10$ generally caused larger overtopping than those of $\beta = 1/40$, but the effect of the bottom slope on the overtopping was smaller than that of the other parameters.

Effects of the Relative Crown Heights of the Sea-Wall and Rubble-Mound

The effect of the relative crown height of the sea-wall, H_C/H , is shown in Figs 7 and 8 for the various values of the relative crown heights of the rubble-mound, H_R/H . It may be seen in Figs 7 and 8 that the value of H_C/H must be taken larger than 1.0 at least in order to be q/q_0 less than 5×10^{-3} which will be the higher limit applicable to the sea-walls. Figs 9 and 10 show the effect of H_R/H on q/q_0 for the scope of $1.0 \leq H_C/H < 1.3$, and also the effect of the bottom slope on q/q_0 . It may be understood in Figs 9 and 10 that in order to be q/q_0 less than 5×10^{-3} , H_R/H must be taken larger than 0.7 for the scope of the "Breaking at Toe" and $\beta = 1/40$, and $H_R/H > 1.1$ for the same scope of $\beta = 1/10$.

Relationships among q/q_0 , H_C/H and H_R/H for the Case of "Breaking on Slope"

As has been mentioned, when the value of h_1/H exceeds 1.7 the effect of h_1/H or h_1/L on q/q_0 is negligibly smaller than the other parameters, and in the scope of the "Breaking on Slope" the following relationship was found

$$\frac{H_c}{H} + \frac{H_r}{H} = C \dots\dots\dots (3)$$

in which C is a constant for a value of q/q_0 and a kind of armor block used on the slope of the rubble-mound. Figs 11 and 12 show the relationships in the scope of $h/L = 0.090$ to 0.450 for the various values of q/q_0 and the two kinds of armor block such as N_1 - and N_2 - blocks. Tables 4 and 5 show the values of C.

TABLE 4 VALUES OF C FOR N_1 -BLOCK

q/q_0	10^{-4}	10^{-3}	5×10^{-3}	10^{-2}
C	2.5	2.0	1.75	1.6

TABLE 5 VALUES OF C FOR N_3 -BLOCK

q/q_0	10^{-4}	10^{-3}	5×10^{-3}	10^{-2}
C	2.3	1.8	1.55	1.4

Effect of the Permeability of the Rubble-Mound

It has been well realized that the permeability and the shape of voids of rubble-mounds play a great role of the absorption of waves running up the slope of the rubble-mound. In order to prove the effect of the permeability and the shape of voids of the rubble-mound on the overtopping of sea-wall, the three kinds of N-shape armor block, shown in Fig 13, which have a same shape but different void ratios of 53 per cent for N_1 , 55 per cent for N_2 , and 61 per cent for N_3 , were used as the armor block of the rubble-mound, and tetrahedron blocks which have a different shape of voids and a void ratio of 66 per cent were also used. The experimental results are shown in Fig 14. Fig 14 shows that for a same shape of voids of armor layers the capacity to absorb waves increases as the void ratio increases, but for different shapes of voids of armor layers the capacity to absorb wave energy is not always proportional to the void ratio.

EFFECT OF RECURVATURE OF A SEA-WALL AND SIMILARITY ON OVERTOPPING

Taking the origin of the rectangular co-ordinates at the top of the recurvature of a sea-wall, as shown in Fig 15, the x-axis as positive toward the offshore direction, and the z-axis vertically upward, the equation of motion of a water mass, m, exerted by wind force are given by

$$m \frac{d^2x}{dt^2} = - P \dots \dots \dots (4)$$

$$m \frac{d^2z}{dt^2} = - mg + P_u \dots \dots \dots (5)$$

in which P denotes the horizontal component of the wind pressure acting from the offshore side, P_u is the vertical component of the wind pressure, and g defines the acceleration of gravity P is given by

$$P = \zeta \cdot w_a \cdot A \cdot \frac{V^2}{2g} \dots \dots \dots (6)$$

in which V denotes the wind velocity, A is the area of the water mass exerted by P, w_a = ρ_a · g = unit weight of air, and ζ defines the coefficient of drag which is a function of Reynolds number and the shape of the water mass

(1) A water mass of sphere

Letting the water mass be a sphere with a diameter of d, and let us calculate Reynolds number for d = 0.01 to 0.10 m, a wind velocity of 20 meters per second and at temperature of 20 degrees in Centigrade

$$Re = \frac{Vd}{\nu} = 1.33 \times 10^{-4} \text{ to } 1.33 \times 10^{-5}$$

The drag coefficient is nearly constant for the Reynolds number, i.e., ζ = 0.4 to 0.5

Taking ζ = 0.5, and m = (4/3)ρπr³ in which ρ is the density of water, and r is the radius of the water sphere,

$$\frac{d^2x}{dt^2} = - \frac{3}{16} \cdot \frac{\rho_a}{\rho} \cdot \frac{V^2}{r} \dots \dots \dots (7)$$

Let the velocity of the water mass be v₀ at t = 0 and x = 0, and the angle between the direction and the x-axis be θ₀,

$$\frac{dx}{dt} = - \frac{3}{16} \cdot \frac{\rho_a}{\rho} \cdot \frac{V^2}{r} t + v_0 \cos \theta_0 \dots \dots \dots (8)$$

and

$$x = - \frac{3}{32} \cdot \frac{\rho_a}{\rho} \cdot \frac{V^2}{r} t^2 + v_0 t \cos \theta_0 \dots \dots \dots (9)$$

The time, t_0 , which a water mass spends until it comes back again on the z-axis after leaving the top, O, of the sea-wall, is obtained from Eq 9

$$t_0 = \frac{v_0 \cos \theta_0}{\frac{3}{32} \cdot \frac{\rho_a}{\rho} \cdot \frac{v^2}{r}} \dots\dots\dots (10)$$

If V_u represents the upward component of wind velocity at the top of the sea-wall, P_u is given by

$$P_u = \zeta \cdot \rho_a \cdot g \cdot A \cdot \frac{V_u^2}{2g} = \frac{1}{4} \rho_a \cdot \pi r^2 \cdot V_u^2 \dots\dots\dots (11)$$

Assuming $V_u = \frac{1}{3} V$,

$$P_u = \frac{1}{36} \rho_a \cdot \pi r^2 \cdot v^2 \dots\dots\dots (12)$$

Substituting Eq 12 into Eq 5,

$$\frac{d^2 z}{dt^2} = -g + \frac{1}{48} \frac{\rho_a}{\rho} \frac{v^2}{r} \dots\dots\dots (13)$$

as

$$\frac{dz}{dt} = v_0 \sin \theta_0, \text{ for } t = 0$$

Integrating

$$z = v_0 t \sin \theta_0 + \frac{1}{2} \left(-g + \frac{1}{48} \cdot \frac{\rho_a}{\rho} \cdot \frac{v^2}{r} \right) t^2 \dots\dots\dots (14)$$

If the third term of the right hand side of Eq 14 is neglected, since it is approximately 20 per cent of the second term,

$$z = v_0 t \sin \theta_0 - \frac{1}{2} g t^2 \dots\dots\dots (15)$$

If t_z represents the time which a water mass spends until it falls again onto the x-axis by the gravity force after leaving the top of the sea-wall,

$$t_z = \frac{2 v_0 \sin \theta_0}{g} \dots\dots\dots (16)$$

Denoting by t the time which the water mass spends until it falls down into the land over the sea-wall after leaving the top of the sea-wall,

$$t_z \geq t > t_0 \dots\dots\dots (17)$$

The values of t_o , t_z , and $(1/2)t_o v_o \cos \theta_o$, which represents the horizontal flying distance of the water mass in the time of t_o are tabulated in Table 6 for $V = 10, 15$ and 20 m/sec, $V_o = 4$ meters per second, $r = 0.5, 1.0$ and 5.0 cm, and $\theta_o = 50^\circ$ and 60° .

TABLE 6 VALUES OF t_o , t_z , and $\frac{1}{2} t_o v_o \cos \theta_o$ ($\rho_a/\rho = 1/827$)

V (m/sec)	θ_o	r = 0.5 cm			r = 1 cm			r = 5 cm		
		t_o (sec)	t_z (sec)	$\frac{1}{2} t_o v_o$ $\times \cos \theta_o$ (m)	t_o (sec)	t_z (sec)	$\frac{1}{2} t_o v_o$ $\times \cos \theta_o$ (m)	t_o (sec)	t_o (sec)	$\frac{1}{2} t_o v_o$ $\times \cos \theta_o$ (m)
10	50°	1.14	0.63	1.47	2.27	0.63	2.93	11.4	0.63	14.7
	60°	0.88	0.71	0.88	1.76	0.71	1.76	8.80	0.71	8.80
15	50°	0.50	0.63	0.65	1.01	0.63	1.30	5.04	0.63	6.48
	60°	0.39	0.71	0.39	0.78	0.71	0.78	3.92	0.71	3.92
20	50°	0.28	0.63	0.36	0.57	0.63	0.72	2.85	0.63	3.68
	60°	0.22	0.71	0.22	0.44	0.71	0.44	2.20	0.71	2.20

Since t_o is larger than t_z in the scope surrounded by a thick line, the water mass does not jump into the land over the sea-wall. This means that if the water mass is assumed a sphere with a diameter of d , the water mass with $d \leq 1$ cm will jump into the land over the sea-wall when $V \geq 15$ m/sec, the water mass with $d \leq 2$ cm will jump into the land when $V \geq 20$ m/sec.

(2) A wall of water

Let us consider that the water spray over the top of the sea-wall is a wall of water with a thickness of b . Since the drag coefficient of the water wall is taken $\xi = 2$ for Reynolds numbers $Re = 5 \times 10^3$ to 10^6 , the horizontal component of the wind pressure per unit area is

$$P = \rho_a \cdot V^2 \dots\dots\dots (18)$$

Since $m = \rho \cdot b$, Eq 4 may be written

$$\frac{d^2 x}{dt^2} = - \frac{\rho_a}{\rho} \cdot \frac{V^2}{b} \dots\dots\dots (19)$$

Using the boundary conditions $dx/dt = v_0 \cos \theta_0$ and $x = 0$ for $t = 0$,

$$x = - \frac{1}{2} \cdot \frac{\rho_a}{\rho} \cdot \frac{v^2}{b} t^2 + v_0 t \cos \theta_0 \dots\dots\dots (20)$$

$t = t_0$ for $x = 0$ is given by

$$t_0 = \frac{v_0 \cos \theta_0}{\frac{1}{2} \cdot \frac{\rho_a}{\rho} \cdot \frac{v^2}{b}} \dots\dots\dots (21)$$

If P_u is neglected, t_z is given by Eq 16. As previously mentioned, only when the condition $t_z \geq t > t_0$ is satisfied, the water wall can fall into the land over the sea-wall. Table 7 is shown the values of t_0 , t_z , and $(1/2) t_0 v_0 \cos \theta_0$.

TABLE 7 VALUES OF t_0 , t_z , and $\frac{1}{2} t_0 v_0 \cos \theta_0$

V (m/sec)	θ_0	b = 1 cm			b = 5 cm			b = 10 cm		
		t_0	t_z	$\frac{1}{2} t_0 v_0$	t_0	t_z	$\frac{1}{2} t_0 v_0$	t_0	t_z	$\frac{1}{2} t_0 v_0$
		(sec)	(sec)	$\times \cos \theta_0$ (m)	(sec)	(sec)	$\times \cos \theta_0$ (m)	(sec)	(sec)	$\times \cos \theta_0$ (m)
10	50°	0 43	0 63	0 55	2 13	0 63	2 88	4 25	0 63	5 46
	60°	0 33	0 71	0 33	1 65	0 71	1 65	3 31	0 71	3 31
15	50°	0 19	0 63	0 24	0 95	0 63	1 22	1 89	0 63	2 43
	60°	0 15	0 71	0 15	0 74	0 71	0 74	1 47	0 71	1 47
20	50°	0 11	0 63	0 14	0 53	0 63	0 68	1 06	0 63	1 36
	60°	0 08	0 71	0 08	0 41	0 71	0 41	0 83	0 71	0 83

In Table 7 the scope enclosed by a thick line shows the cases of $t_0 > t_z$. According to Table 7, it may be known that a wall of overtopping with a thickness of one cm is blown down within one second into the land over the sea-wall by winds with velocities equal to or larger than 10 m/sec, and a wall of overtopping with a thickness of 5 cm by winds with velocities equal to or larger than 20 m/sec.

Similarity on Overtopping

(1) A water mass of sphere

Let us consider of a water mass of sphere with a diameter d overtopping a sea-wall. Assuming d_p , the diameter in prototype, is 3 cm to 10 cm, d_m , the diameter in model, the scale of which is 1/20 to prototype, is 1.5 to 5 mm.

Reynolds number pRe for a wind velocity in prototype of $V_p = 20$ m/sec is

$$pRe = \frac{V_p \cdot d_p}{\nu} = 4.0 \times 10^4 \text{ to } 1.33 \times 10^5$$

In the model

$$mRe = \frac{V_m \cdot d_m}{\nu} = 4.5 \times 10^2 \text{ to } 1.47 \times 10^3$$

Drag coefficients for the spheres are

$$\zeta_p = \sim 0.45 \text{ to } 0.5 \text{ in prototype,}$$

and

$$\zeta_m = \sim 0.60 \text{ to } 0.45 \text{ in model,}$$

thus, it may be assumed approximately $\zeta_p = \zeta_m$

This means that if a mass of water overtopping a sea-wall is a sphere with a diameter $d \geq 3$ cm, the motion of the water mass exerted by a wind of $V_p = 20$ m/sec may be stated to be approximately followed by Froude law of similarity, i.e. the results of the model experiment may be stated to be approximately similar to the results of the nature.

However, if the diameter of the water mass, d_p , is smaller than about 3 cm, $\zeta_p = \sim 0.4$ to 0.5 for $pRe = \sim 10^4$, as against $\zeta_m = \sim 0.6$ to 0.9 for $mRe = \sim 10^2$. Therefore we cannot expect a good similitude between model and prototype. But from a practical point of view on the water quantity of wave overtopping, the volume of such spray of water would be considered to be negligible small.

(2) A wall of water

Let us consider the overtopping as a wall of water. This may be the case when large overtopping is seen in prototype and model, as seen in Figs. 17, 18 and 19, therefore, this case would be the most important in wave overtopping over sea-walls.

If the overtopping of wave is assumed as a wall of water, the drag coefficient of the wall, ζ , is constantly two for all Reynolds numbers larger than 10^2 . It, therefore, may be stated that the results of experiments conducted by Froude law are similar to the results in the nature. Field observations of overtopping at sea-walls during typhoons have proved that this assumption is correct.

It may be concluded from the theoretical considerations described above that the recurvature of a sea-wall would have little effect on wave overtopping when wind velocity exceeds about 15 m/sec.

APPLICATION TO DESIGN OF SEA-WALLS AND VERIFICATION BY TYPHOONS

The results studied in our laboratory have been applied to the design of sea-walls in Japan since 1960 and those sea-walls have been tested by severe typhoons. All of the sea-walls which have undergone the natural tests have proved that the designs were satisfactory and there were generally a fairly good agreement between the experiments and prototypes. Some examples are presented herein.

(1) Sea-wall in the Port of Wakayama

This sea-wall was constructed in 1958 at a water depth of 7 m to 8 m below the Datum Line offshore a long sandy beach exposed to an open sea in the North Harbor of the Port of Wakayama, Wakayama Prefecture, which is one of the biggest industrial harbors for steel firms in Japan. This was the first big sea-wall that harbor engineers in Japan constructed to protect a reclaimed industrial land located offshore from wave overtopping. Fig 16 shows a cross-section of the sea-wall.

After completion it was severely hit three times consecutively in September of 1959, 1960 and 1961. Figs 17 and 18 show huge overtoppings of waves which were taken when the typhoon was located still far offshore from the harbor.

After calculations and experiments, it was recommended that the sea-wall should have a rubble-mound covered with precast concrete armors in front of the wall and a large drainage channel with a width of 20 m at the land-side of the sea-wall, as shown in Fig 19.

(2) Another Sea-Wall in the Port of Wakayama

The sea-wall, the cross-section of which is shown in Fig 20, was constructed in 1965 and 1966 to protect the industrial area of 1.8 million m^2 reclaimed at the northern part of the Wakayama North Harbor.

(a) When the height and period of the design wave are taken $H_p = 5.0$ m and $T_p = 9.0$ sec

Since $h_1/H = 8.74/5 = 1.75 > 1.7$, this case is "Breaking on Slope". For $H_c/H = 4.76/5 = 0.95 = \sim 1.0$ and $H_r/H = 3.76/5 = 0.75$, we obtain $q/q_0 = 5 \times 10^{-3}$ from Fig 11.

(b) When $H_p = 5.5$ m and $T_p = 13.0$ sec

Since $H/L = 0.041$ and $h_1/L = 0.065$, this case is on the critical condition between "Breaking at Toe" and "Breaking on Slope".

Using $H_c/H = 0.87$ and $H_r/H = 3.76/5.5 = 0.68$, we obtain $q/q_0 = 5 \times 10^{-3}$ for "Breaking at Toe", and from Fig 11 $q/q_0 = 8 \times 10^{-3}$ for "Breaking on Slope", which necessitate a large drainage channel as shown in Fig 20.

Decision of the Width and Depth of the Drainage Channel

The design conditions of the drainage channel

Δz = height from the bottom of the drainage channel to the x-axis

= (D L + 6.70 m) - (D L + 4.00 m) = 2.70 m

θ_0 = angle of the parapet wall to the x-axis = 70° ,

V = wind velocity = 20 m/sec,

The wave run-ups, R_u , for the design waves with heights of 5.0 m and 5.5 m and periods of 9 sec and 13 sec, respectively, were approximately 1.2 H according to the experiments carried out by using the model of the sea-wall shown in Fig 21.

Let us consider about the design wave with a height of 5 m and a period of 9 sec, and take the design sea level D L + 2 24 m. The velocity of a water mass of sphere with a diameter of d at the origin of the co-ordinates, O, is obtained by $v_0 = \sqrt{2 \times 9.8 (6.0 - 4.46)} = 5.5 \text{ m/sec}$

t_z which denotes the time that the water mass spends until it falls down on the bottom of the drainage channel over the sea-wall after leaving the origin O is given by

$$t_z = \frac{v_0 \sin \theta_0 + \sqrt{v_0^2 \sin^2 \theta_0 + 2g \Delta z}}{g} \dots\dots\dots(22)$$

By substitution of Eq 22 into Eq 9, the horizontal distance l_x which the water mass reaches at the time t_z from the origin O onto the channel bottom is obtained by

$$l_x = \frac{3}{32} \cdot \frac{\rho_a}{\rho} \cdot \frac{V^2}{r} t_z - v_0 t \cos \theta_0 \dots\dots\dots(23)$$

From Eqs 22 and 23 $t_z = 1.44 \text{ sec}$ and $l_x = 16.0 \text{ m}$ for $d = 0.01 \text{ m}$, $l_x = 6.7 \text{ m}$ for $d = 0.02 \text{ m}$

Considering a wall of water with a thickness of b, the horizontal distance l_x is obtained by substitution of Eq 22 into Eq 20, $l_x = 47.4 \text{ m}$ for $b = 0.01 \text{ m}$, $l_x = 22.4 \text{ m}$ for $b = 0.02 \text{ m}$, $l_x = 14.0 \text{ m}$ for $b = 0.03 \text{ m}$, and $l_x = 9.8 \text{ m}$ for $b = 0.04 \text{ m}$

The loci of those walls of water are shown in Fig 21. According to Fig 21, if the side wall with a height of 2 m from the bottom of the channel is constructed at a distance of $l_x = 17.5 \text{ m}$ from the origin O, the walls of water with thicknesses of more than $b = 2 \text{ cm}$ and the spheres of water with diameters more than one cm could be taken into the drainage channel.

The length of the sea-wall over which the design wave overtops simultaneously was decided about 350 m by the experiments, and the factor of safety for the maximum relative overtopping was taken two, therefore the maximum discharge of water for the drainage channel, Q_{max} , was

$$q = 8 \times 10^{-3} q_0 = 8 \times 10^{-3} \times 5 \times 88/2\pi = 0.56 \text{ m}^3/9\text{sec/m}$$

$$Q_{max} = 2q \times 350 = 393 \text{ m}^3/9\text{sec}$$

$$= 43.7 \text{ m}^3/\text{sec} = \sim 45 \text{ m}^3/\text{sec}$$

If the slope of the channel bottom is taken 1/1000, the width 20 m, and the depth 2 m, the channel can discharge Q_{max} safely.

After completion of the drainage channel, the sea-wall has undergone severe typhoons several times, and it has been reported due to the visual observations during the typhoons that the behaviors of the overtopping were quite similar to those of the experiments and almost all overtoppings were assembled into the channels and flowed down safely into the harbor basin.

(3) Sea-Wall of the Kansai Electric Power Co Ltd

The sea-wall was constructed in an open sea with a water depth of D L - 2.50 m to 3.00 m to protect a reclaimed land of about 38 acres which was used for an electric power plant of the Kansai Electric Power Co Ltd. The sea-wall was requested to be designed no-overtopping even

during the heaviest typhoon ever experienced there. After the calculations shown here and model experiments carried out on a scale of 1/20 in the wave channel shown in Fig. 2, the sea-wall shown in Figs. 22 and 23 was designed.

Estimation of the Overtopping during the Heaviest Typhoon

The significant wave height and period of the design wave were taken $H_{1/3} = 2.50$ m, and $T_{1/3} = 6.3$ sec. The highest high tide averaged for two hours including the highest tide ever recorded in the harbor was estimated D L + 3.80 m. Since $h_1/H = 5.80/2.5 = 2.3 > 1.7$, the case is "Breaking on Slope". Using $H_c/H = 3.95/2.50 = 1.58$ and $H_r/H = 1.75/2.5 = 0.70$, we obtain from Figs. 11 and 12, $q/q_0 = 5 \times 10^{-4}$ and 2×10^{-4} , respectively.

Since the tetrahedron blocks of two tons were used as the armor block of the rubble-mound, q/q_0 is estimated approximately 3×10^{-4} from Fig. 14. According to the experiments in which two high tides of D L + 3.80 m and D L + 3.30 m were used and the wind velocity used was always 20 m/sec, a few overtopping was seen for a tide of D L + 3.80 m and only a few spray was observed for a tide of D L + 3.30 m.

Shortly after the completion of the sea-wall, it was hit by one of the most severe typhoons ever observed in the harbor, the Second Muroto typhoon, which passed near over the location of the sea-wall on September 16, 1961. The highest tide during the typhoon was D L + 4.00 m and the average highest high tide for two hours was estimated approximately D L + 3.60 m. The maximum wave height was assumed 2.50 m or 3.0 m, and strong winds of from 20 m/sec to 35 m/sec blew from offshore for about 3 hr.

Pictures taken with the 8-mm movie camera near the top of the sea-wall during the typhoon showed that comparatively small volume of wave overtopping occurred sometimes over the top of the rubble-mound covered with the two layers of the hollow tetrahedron armors. However, there was no overtopping over the top of the sea-wall, as seen in Fig. 23. It was proved that there was a good agreement between the experiment and prototype.

APPENDIX - REFERENCES

- 1 "Wave Run-up and Overtopping, Levee Sections, Lake Okeechobee, Florida", Corps of Engrs., Waterways Experiment Sta., Tech. Report NO. 2-449, January, 1959.
- 2 Saville, Thorndike, "Wave Run-up on Shore Structures", Proc. ASCE, Vol. 82, NO. WW2, April, 1956.

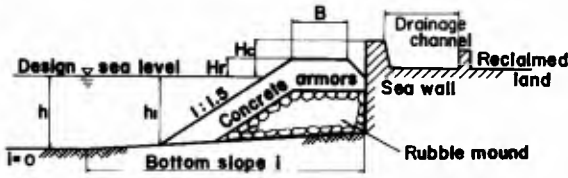


FIG. 1. - CROSS-SECTIONS TYPICAL TYPES OF SEA-WALL IN JAPAN
UPPER SECTION USED IN DEEPER WATERS
LOWER SECTION USED IN SHALLOW BEACH

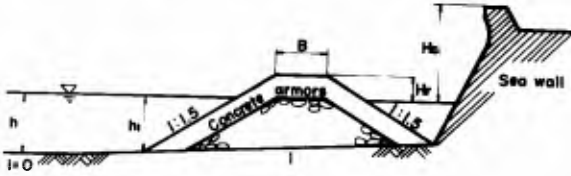


FIG. 2. - WAVE CHANNEL WITH A WIND BLOWER

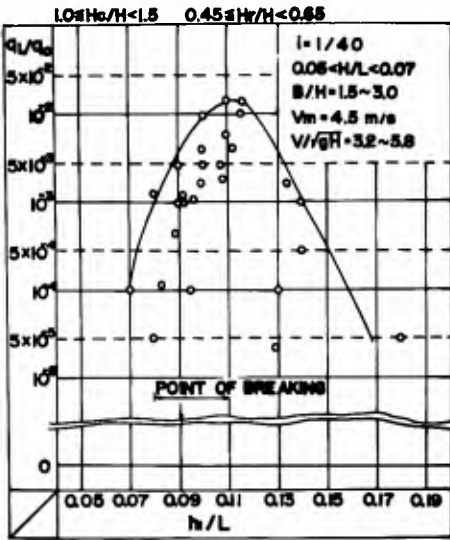


FIG. 3. - RELATIONSHIP BETWEEN RELATIVE OVERTOPPING AND H_1/L

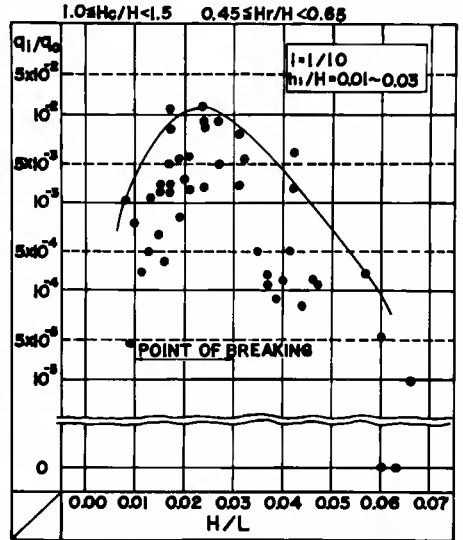


FIG. 4. - RELATIONSHIP BETWEEN q/q_0 AND H/L

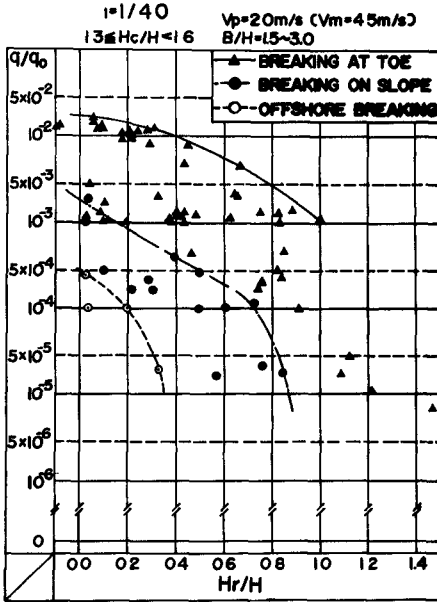


FIG 5 - RELATIONSHIP BETWEEN q/q_0 AND H_r/H , $i = 1/40$

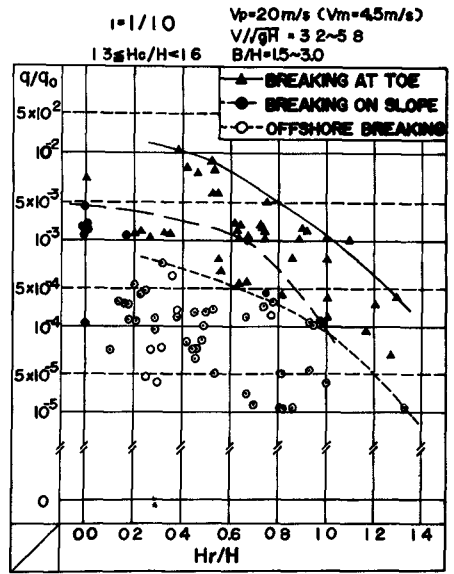


FIG 6 - RELATIONSHIP BETWEEN q/q_0 AND H_r/H , $i = 1/10$

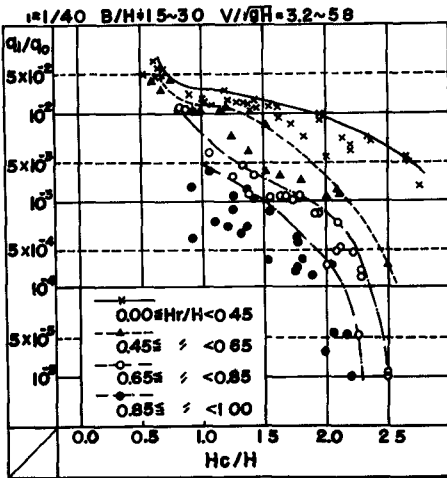


FIG 7 - RELATIONSHIP AMONG q/q_0 , H_c/H AND H_r/H

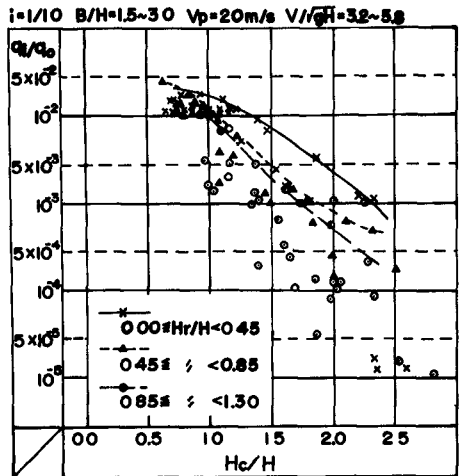


FIG 8 - RELATIONSHIP AMONG q/q_0 , H_c/H AND H_r/H

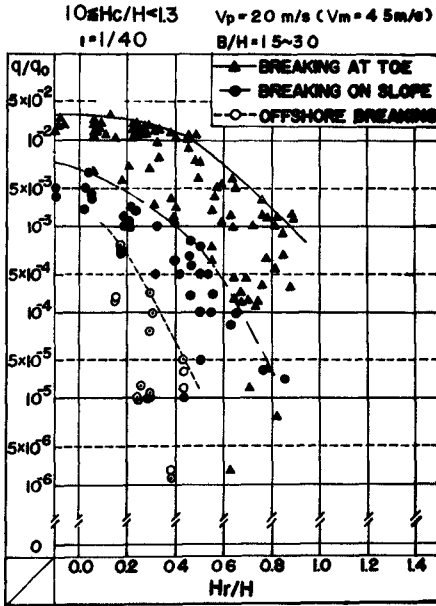


FIG 9 - RELATIONSHIP BETWEEN q/q_0 AND H_r/H , $1 = 1/40$

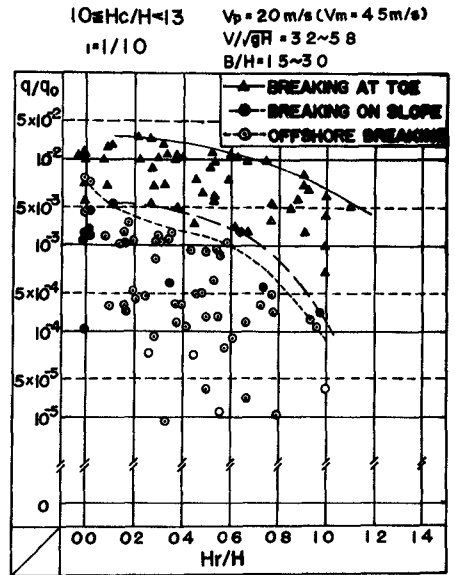


FIG 10 - RELATIONSHIP BETWEEN q/q_0 AND H_r/H , $1 = 1/10$

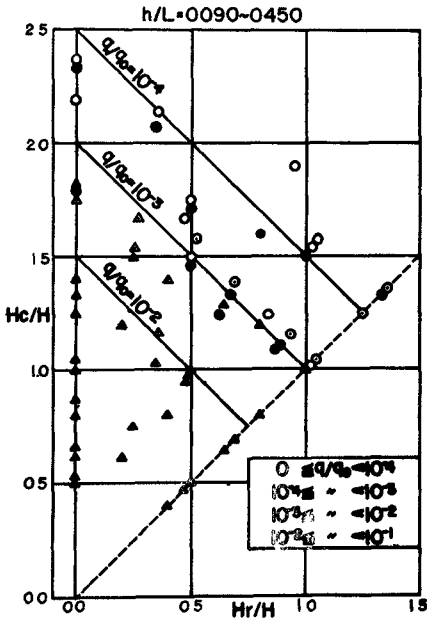


FIG 11 - RELATIONSHIP AMONG q/q_0 , H_c/H , AND H_r/H FOR N_1 -BLOCK

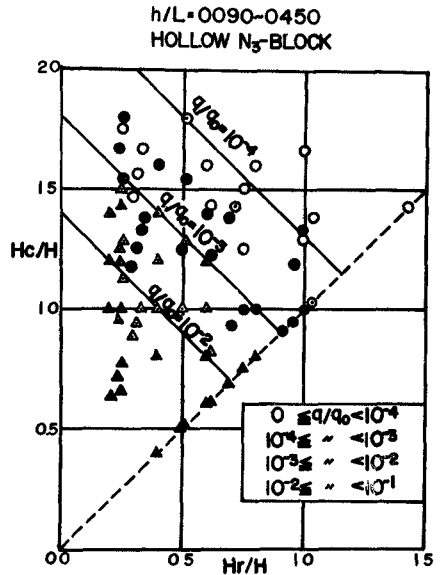


FIG 12 - RELATIONSHIP AMONG q/q_0 , H_c/H , AND H_r/H FOR N_3 -BLOCK

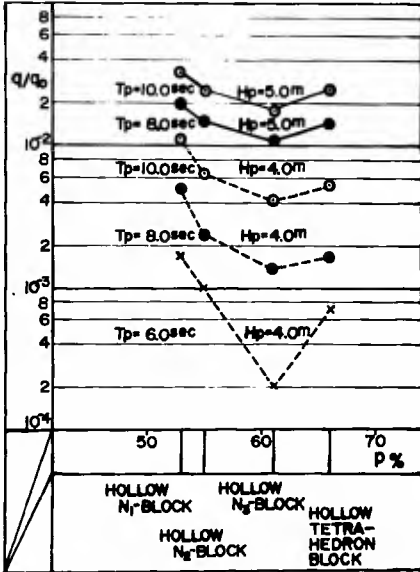


FIG. 14. - RELATIONSHIPS BETWEEN q/q_0 AND THE VOID RATIO AND SHAPE OF VOID OF ARMOR LAYERS



FIG. 13. - HOLLOW N-BLOCK

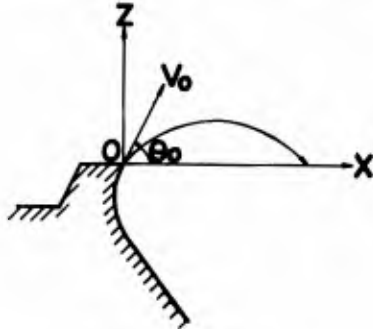


FIG. 15

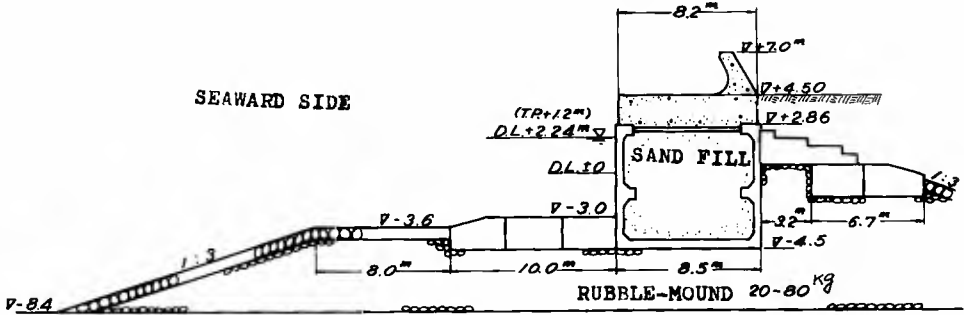


FIG. 16. - CROSS-SECTION OF THE SEA-WALL IN WAKAYAMA HARBOR BEFORE 1961

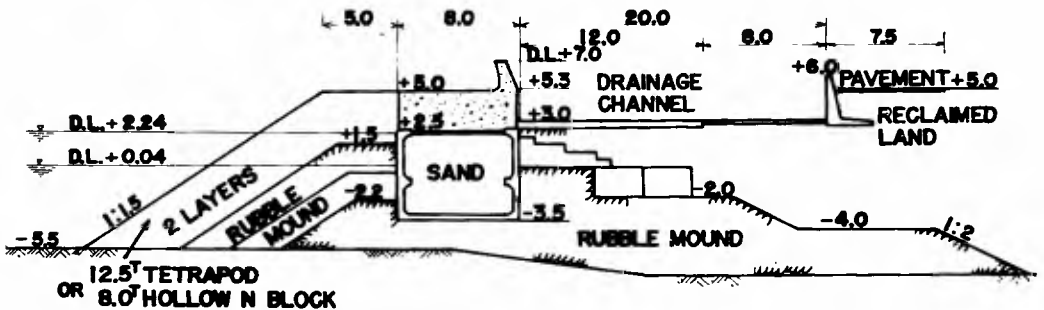


FIG. 19. - CROSS-SECTION OF THE SEA-WALL IMPROVED AFTER THE EXPERIMENTS



FIG. 17. - LARGE WAVE OVERTOPPINGS AT SEA-WALLS OF WAKAYAMA HARBOR



FIG. 18.



FIG. 20. - CROSS-SECTION OF THE SEA-WALL IN WAKAYAMA HARBOR

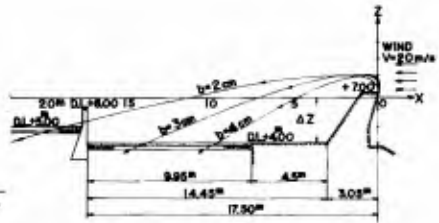


FIG. 21. - LOCI OF THE WALLS OF WATER OVERTOPPING THE SEA-WALL IN FIG. 20



FIG. 22. - CROSS-SECTION OF THE SEA-WALL OF THE KANSAI ELECTRIC POWER CO. LTD



FIG. 23. - SEA-WALL OF THE KANSAI E. P. CO. LTD. DURING A TYPHOON, 1961

CHAPTER 89

PRESSURE OF WAVES AGAINST VERTICAL WALLS

by M.E.Plakida^{*)} M.Sc.

Docent, Chief of Wave Laboratory of Moscow

Branch of Water Transport Institute

Moscow, U.S.S.R.

SUMMARY

This paper is concerned with the study of the breaking wave pressure exerted upon the breakwater of the vertical type. The method of calculation of the wave pressure, named the quasistatistical method, is based with the theory of the impact of the water jet on the vertical plane and some new results of the experimental data.

The formulas for the calculation of the pressure distribution of the breaking wave and the surf wave on the vertical wall are given.

INTRODUCTION

The following symbols are used in this paper.

- h - wave height;
- λ - wave length;
- τ - wave period,
- c - wave celerity;

*) U.S.S.R. Moscow. K-1, Sadovokudrinskaya Street 14-16, Ap.11.

- v --orbital velocity,
 p - pressure intensity,
 H - depth of water measured from SWL,
 H_{cr} - critical depth of water corresponding to the point of breaking wave,
 H_w - depth of water at the wall,
 γ - unit weight of water,
 g - 9.81 m/sec² - gravitation acceleration.

Up to the present time evaluation of the breaking wave force upon a breakwater of the vertical type presents a complex problem. For many decads this problem has requested very much attention from the harbour engineer, who has to deal with design and construction of breakwaters of the vertical type at a shallow sea.

There are several solutions of this problem, one of them makes use of the conception of the theory of the impact of a water jet upon a vertical plane. However, in spite of the fact that these investigations have been carried out during a long time the possibility of the conception of the impact of a water jet upon a vertical plane in full measure is not used.

This expression is given

$$p = k \gamma \frac{u^2}{2g} \quad (1)$$

where

- u - velocity of the water jet at the crest of a breaking wave,
 k - experimental coefficient equal to 1.7 (by Gaillard).

In their time D. Gaillard, D. Molitor and V. Trenuhin developed this direction suggesting to take into account $u = c + v$.

In 1940 N.Djounkovskiy [1] corrected this to $u=0.75c+v$. In 1958 M.Plakida [2] suggested the new corrections to the distribution of the surf wave pressure exerted upon the vertical wall, based upon the experimental investigation. As a consequence the resultant value of the wave pressure on the vertical wall could be decreased up to 20 per cent in comparison with the value given by N.Djounkovskiy [3].

It is necessary to note that summing up c and v makes no physical sense, this is explained by the absence of sufficient information about the kinematics of the breaking wave structure.

In this paper we have given as far as it was possible the development of the calculation method of the pressure distribution from the breaking wave and the surf wave on the vertical wall. Remaining at the conception of the impact of the water jet for the calculation of the wave pressure at the still water surface, we have used the standing wave theory of the first approximation and some experimental data for the calculation of the wave pressure at the foot of the vertical wall.

This expression is given

$$P_b = \frac{\rho h}{ch \frac{2\pi H_w}{\lambda}} \quad (2)$$

where

P_b - wave pressure (above hydrostatic) at the foot of the vertical wall.

We note that it was about twenty years ago, when the method of calculation of the breaking wave pressure, based on the use of the impact impulse of the breaking wave, was suggested. It is the second direction in the solution of this problem. However, the experimental data is insufficient for the full solution at the present time.

KINEMATICS AND DYNAMICS OF BREAKING WAVES

The breaking wave or the surf wave is developed when the deep water wave comes up to a shallow water and reaches the critical depth. The value of the critical depth varies in a very wide range $(1.0 + 2.5)h$. The critical depth within the limits $(1.5 + 1.8)h$ are accepted for the steepness of the deep water waves within $1:9 + 1:25$.

When the water depth in front of the vertical wall is $H > \frac{\lambda}{3}$ or at least $H \gg 3h$ and the depth on the berme at the foot of the wall is $H_w < H_{cr}$ then the deep water wave is broken on the berme at the wall surface; in this case the vertical wall is subjected to by the breaking wave action.

When in front of the vertical wall the sea bed is horizontal or gently sloping at least within $\frac{\lambda}{2}$ before the wall and the water depth is $H_1 < H_{cr}$ then the deep water wave is broken before the wall, in this case the vertical wall is subjected to the action of the surf wave.

It is seen that from the condition of development of the breaking wave and the surf wave the former exerts a greater wave pressure on the vertical wall than the latter for the same height and length of the deep water wave.

The experimental data show that the velocity of the water particles at the crest of the breaking and surf waves may be nearly equal to the wave celerity and even exceed it.

The value of this velocity is given as

$$u = \sqrt{gH} \quad (3)$$

The formation of the front steep slope of the wave, which is near to breaking, is the result of dragging of the foot of the wave, while the crest of the wave passes ahead because of different wave velocities of the particles in the crest and in the trough. The velocities of the water par-

ticles in the crest of the wave are greater and the velocities of the water particles in the trough of the wave are less than the average velocity of the wave at the still water surface. The kinematics of this phenomenon in detail is described by V. Shuleykin [4] based on the classical hydrodynamics formula

$$c = \sqrt{\frac{g\lambda}{2\pi} \operatorname{th} \frac{2\pi H}{\lambda}}, \quad (4)$$

taking in (4) $H = H_1 + 0,5h$ for the wave crest, and $H = H_1 - 0,5h$ for the wave trough (where H_1 - water depth from the sea-bed to the still water surface).

From the energetical point of view in the wave near to breaking the concentration of the potential energy occurs, as the deep water wave approaching shallow water decreases in length. In addition the wave energy is carried into shallow water with the full wave velocity as can be seen from the formula (5), when at $H \ll \lambda$ the second item \longrightarrow to 1.

$$u_0 = \frac{c}{2} \left(1 + \frac{2aH}{\operatorname{sh}2aH} \right) \quad (5)$$

where

u_0 - velocity of the transportation of the wave energy;

$$a = \frac{2\pi}{\lambda}.$$

Phenomenon of the breaking of the wave proceeds very rapidly and during very short time. It is accompanied by the transition of the potential energy of the dragged wave into the kinetic energy of the transitional movement of the water stream. When this stream reaches the vertical wall the phenomenon of the impact of the water jet directed to the wall and the wave reflection from the wall are observed.

The maximum wave pressure on the wall appears earlier than the maximum elevation of the water level at the wall. When the uplift of the water level is maximum the wave pressure decreases. The wave pressure does not exceed the value $(0.6 - 1.0) \gamma h$ at the still water surface.

EQUIPMENT AND EXPERIMENTS

The laboratory study of the action of the breaking and the surf waves on the vertical wall has been carried out in a flume of rectangular cross-section 23 m in length, 0,50 m wide. The water depth was 75 cm in the flume and the water depth at the foot of the wall was 15 cm. The vertical wall model was placed on the top of the prism, which was 60 cm above the flume bottom. The prism slope was 1:2.

The positions of the vertical plane of the wall were 25 cm and 82 cm from the prism edge (Fig.1). In the first case the wall is exposed to the action of the breaking wave and in the second case - to the action of the surf wave.

The waves were reproduced by the wave generator of the type of the flat paddle.

The wave pressures were measured by tensometric gauges. The wave heights were measured by electrical gauges. A sample of the oscillograph record is given on Fig.2.

Phases of breaking, wave deformation details and the moment of small ball indicators (prepared with bitumen and paraffin, their specific weight is equal to that of water) were recorded on 35 mm film at 24 frames per sec. A sample of film record is shown on Fig.3. It is seen that the indicator I between frames 15-17 has moved to the wall with maximum velocity before the impact.

Wave conditions of our experiments are given in table 1.

Table 1

Wave Conditions

Designation of wave conditions	H = 75 cm					H ₁ = 15 cm			
	h cm	λ cm	τ sec	$\frac{H}{\lambda}$	$\frac{h}{\lambda}$	h, cm	λ ₁ cm	$\frac{H_1}{h_1}$	$\frac{h_1}{\lambda_1}$
A-6-220-20	8.8	175	1.06	0.43	0.050	8.8	115	0.13	0.077
A-7-220-20	11.5	177	1.07	0.42	0.067	9.8	115	0.13	0.085
A-8-180-20	15.7	210	1.17	0.36	0.077	9.8	130	0.12	0.076
A-8-220-20	17.7	177	1.07	0.42	0.10	9.8	115	0.13	0.085

WAVE PRESSURE

After giving a short description of the kinematics and dynamics of the breaking wave and our experiments, we can begin to evolve the formulas for the calculation of the breaking wave pressure and the surf wave pressure exerted upon the vertical wall.

Our position is based on the formulas (1) - (3) and our experimental data. The following calculation method and formulas for the determination of the value of the pressure on the vertical wall from the breaking and surf waves is suggested.

Pressure of breaking waves. It is a matter of some difficulty to assume the value of the water depth H in formula (3). As a solution this complex question after some considerations we suppose possible to take a safe value of

$$H = H_{cr} = 1.8h \quad (6)$$

Substituting (6) and (3) in Eq. (1) we arrive at the expression for the maximum pressure of the breaking wave, which occurs at or in the vicinity of still water surface

$$p_0 = 1.5 \gamma h \quad (7)$$

where

p_0 — the maximum pressure of the breaking wave at the still water surface.

At the foot of the vertical wall rather calm wave conditions are observed (see the pressure fluctuation on the record of D_{10} on Fig.2).

There are traced (see Fig.4) two curves showing the fluctuation of the relative wave pressure at the foot of the wall. One of them is the experimental curve indicating the pressure of the breaking wave and the second is the theoretical curve showing the pressure of the standing wave. It is seen by the comparison of these two curves that the maximum pressure of the breaking wave at the foot of the wall appears earlier than the maximum pressure of the standing wave, calculated by the wave theory of the first approximation. As a result of this comparison of the two curves, we propose to base the calculation of breaking wave pressure at the foot of the vertical wall upon the formula (2).

The relationship between $\frac{p_c}{\gamma h}$ and $\frac{H_w}{h}$ is given on Fig.5 by the experimental data. This relationship is not linear as it may be expected. The greatest values of the relative wave pressure are found within $\frac{H_w}{h} = (1.2 - 1.5)$. The curve accepted by the construction rules acting in the USSR (SN -92-60) is also shown.

The maximum values of the breaking wave pressure measured and calculated are given in Table 2. These data were used for the experimental curve on Fig.5.

Table 2

Values of wave pressure at the bottom of a vertical wall (gr/cm²)

h cm	$\frac{H_w}{h}$	Calculated	Measured	$\frac{P_{15}^m}{P_{15}^c}$	$\frac{P_{15}^m}{\gamma h}$
		P_{15}^c	P_{15}^m	P_{15}^c	
8.8	1.70	7.6	5.7	0.76	0.86
11.5	1.30	9.9	10.9	1.10	0.94
15.7	0.96	14.0	12.8	0.92	0.82
17.7	0.85	14.6	13.0	0.93	0.74
mean				0.93	0.84

where:

P_{15}^m — significant wave pressure that for statistical purposes is defined as the average pressure of the highest one-third of all measured breaking wave pressures at the foot of the vertical wall;

P_{15}^c — wave pressure calculated by formula (2);

H_w — 15 cm, — water depth at the wall.

The elevation of water surface above the still water level at the vertical wall is observed within (0.5 — 0.8)h when the wave pressure is maximum. Taking into consideration some fluctuation of this value we propose to take

$$z = h \tag{8}$$

The breaking wave pressure exerted upon the foundation of the vertical wall is given as

$$W = 1/2 M_b P_b b \quad (9)$$

where.

$M_b = 0.9$ - experimental coefficient;

b - width of the wall.

Pressure of surf waves. The breaking wave and the surf wave possess the same physics of the breaking phenomenon. This allows us to use, in the case of the surf wave, the same formulas, that were mentioned above in the case of the breaking wave with following replacements:

1. h - the height of the deep water wave (which is equal to the breaking wave) is replaced by the height of the surf wave h_1 , calculated by the formula

$$h_1 = 0,65H \quad (10)$$

where

$H = H_w$ - in the case when the sea-bed is horizontal in front of the wall, and

$H = H_c = H_w + 0,5 \lambda_1 i$ - in the case, when the sea-bed is gently sloped;

where i - sea-bed slope.

2. λ - the length of the deep water wave is replaced by the length of the surf wave λ_1 , calculated by the formula

$$\lambda_1 = \lambda \operatorname{th} \frac{2\sqrt{H}}{\lambda_1} \quad (11)$$

The maximum pressure of the surf wave exerted upon a vertical wall occurs at $1/3 h_1$ above still water level according to our experimental data.

The elevation of water surface above the still water level in the case of the surf wave may be also taken as in the case of the breaking wave by the formula (8).

The surf wave pressure exerted upon the foundation of the vertical wall is given as

$$W = 1/2 M_s p_b b \quad (12)$$

where:

$$M_s = 0.7 - \text{experimental coefficient.}$$

The distribution of the pressure of the breaking and surf waves is shown on Fig.6.

CONCLUSION

1. The action of the breaking and surf waves upon the vertical wall was studied in the wave laboratory from the point of view of the kinematics and the dynamics. It was found possible to advance somewhat a quasistatistical method of the calculation of the wave pressure at the depth conditions

$$h \leq H_w \leq H_{or} = 1.8h$$

This suggestion is based on the conception of the impact of a water jet upon a vertical plane.

2. Our experimental data lies within of the following values:

- the wave steepness $\frac{h}{\lambda}$ from 0.05 to 0.10; and
- the relative water depth at the wall $\frac{H_w}{h}$ from 0.85 to 1.71.

3. The list of the formulas is given in the table 3.

Table 3

Formulas

Denomination	Breaking wave	Surf wave
1. Wave height and wave length	h, λ	h_1, λ_1
2. Maximum wave pressure p_0	$1.5 \gamma h$	$1.5 \gamma h_1$
3. Maximum wave pressure is found	At the S.W.L.	At $\frac{1}{3}h_1$ the S.W.L. above
4. Maximum wave pressure at the foot of the wall p_b ..	$\frac{\gamma h}{ch \frac{2\pi H_w}{\lambda}}$	$\frac{\gamma h_1}{ch \frac{2\pi H_w}{\lambda_1}}$
5. Elevation of the water surface above the still water level z	h	h_1
6. Wave pressure exerted upon the foundation of the wall W	$0.9 \frac{p_b b}{2}$	$0.7 \frac{p_b b}{2}$

REFERENCES

1. М.Э.Плакида. Давление от прибойных и разбитых волн на оградительные сооружения типа вертикальной стенки. Гидротехническое строительство № 8, 1965.
M.E.Plakida. Breaking wave and surf wave pressures against the vertical breakwaters. Hydrotechnical Construction No.8, 1965.
2. М.Э.Плакида. Исследование прибойной волны и ее воздействии на оградительное сооружение вертикального типа. Труды ЦНИИЭВТ'а. Вопросы гидротехники. Вып. XV, Москва, 1958.
M.E.Plakida. Investigation of surf waves and its action on the vertical breakwaters. Proc. CNIIEWT.Vol.XV, Moscow, 1958.
3. П.К.Вожич и Н.Н.Джунковский. Морское волнение и его действии на сооружения и берега. Машстройиздат.Москва, 1948.
P.K.Vojitch and N.N.Djeunkovskiy. Sea waves and its action on the constructions and the sheres.Machizdat. Moscow, 1948.
4. В.В.Шулейкин. Теория морских волн. Изв. А.Н. СССР, 1956.
V.V.Shuleykin. Sea wave theory. Izv. A.S. of U.S.S.R., 1956.

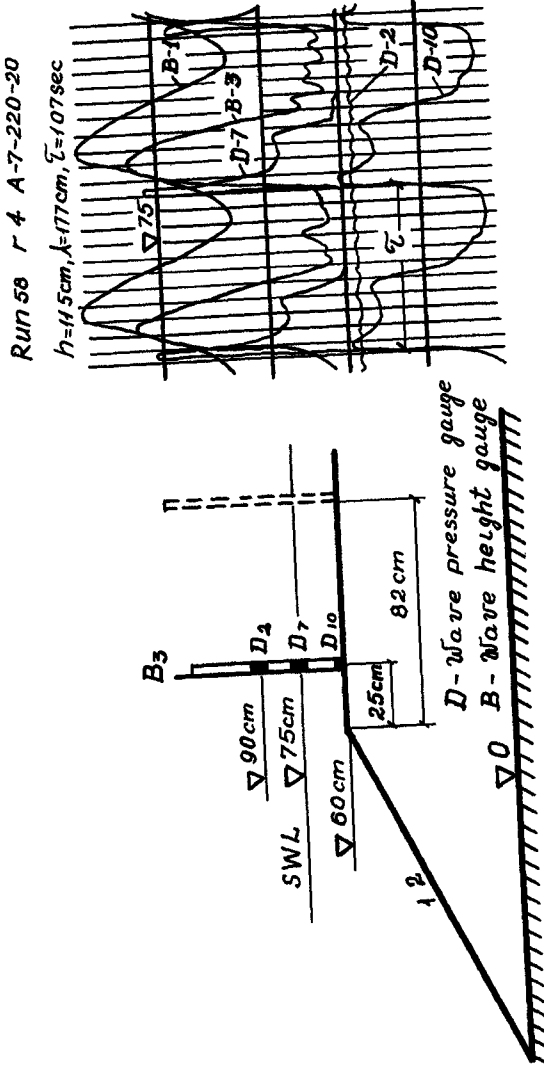


Fig. 2 Pattern of the oscillograph record

Fig. 1 Model scheme

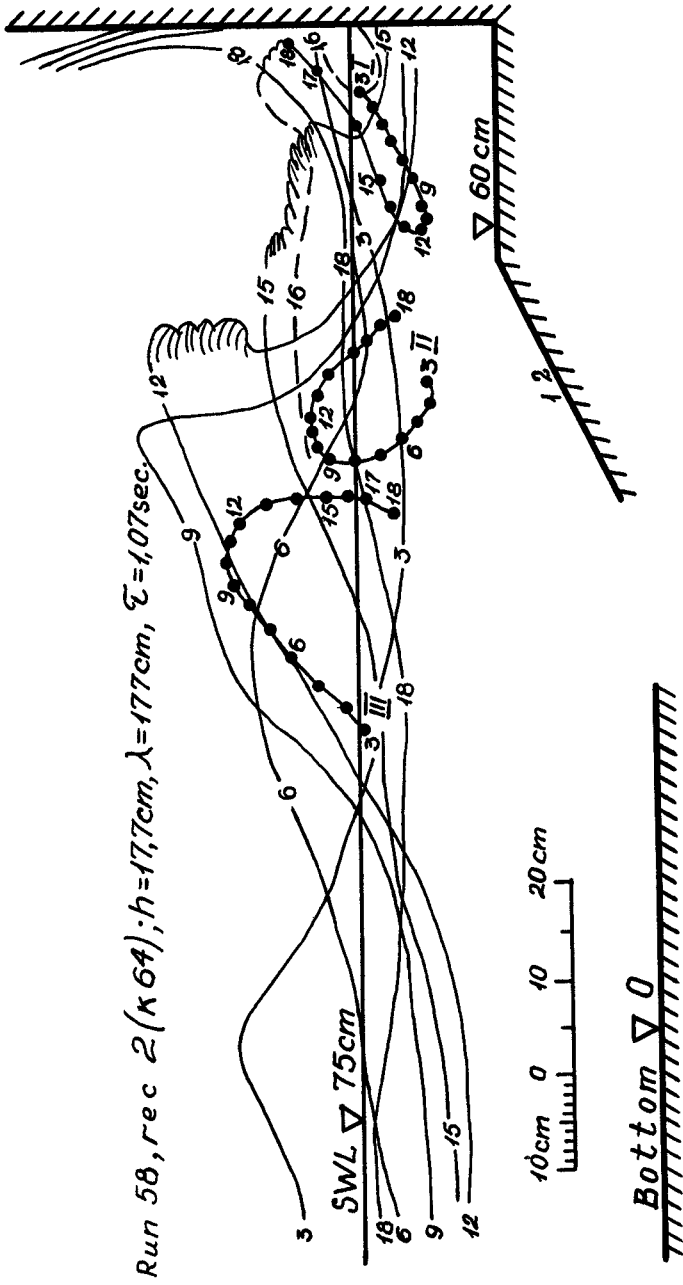


Fig 3 The breaking wave surface and the trajectories of the movement of water particles (Film 24 ca/sec)

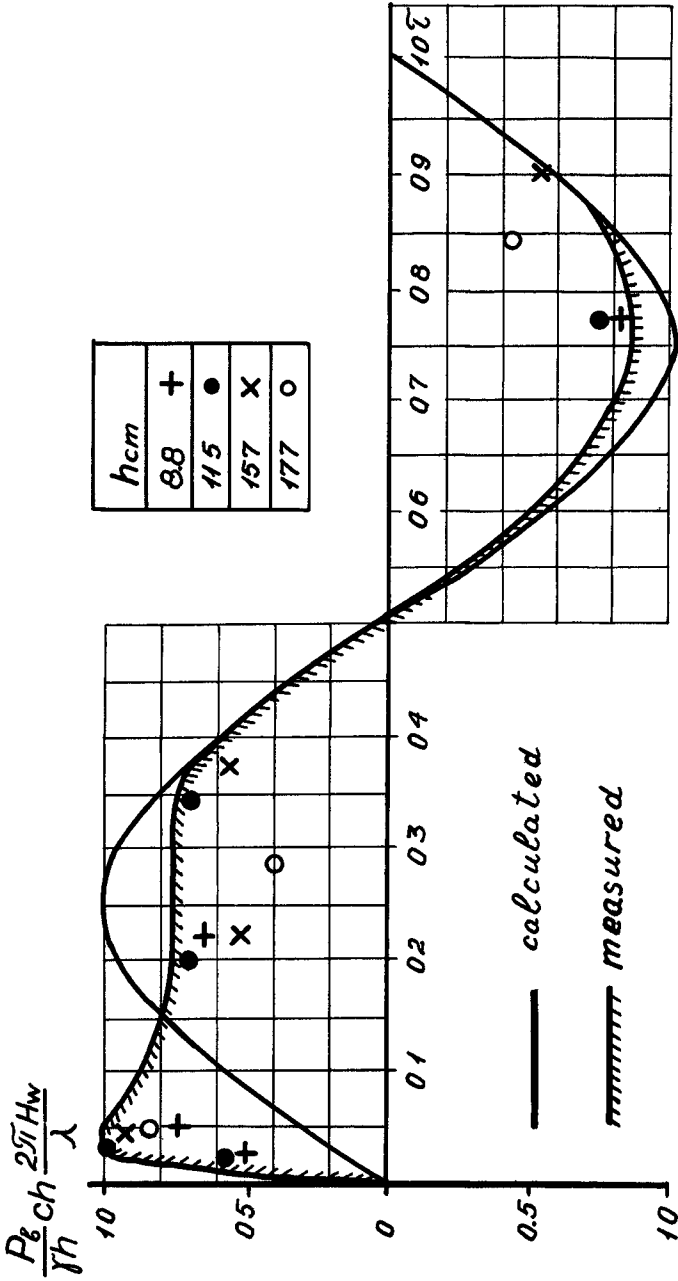


Fig. 4. Variation of the relative pressure at the bottom of the vertical wall

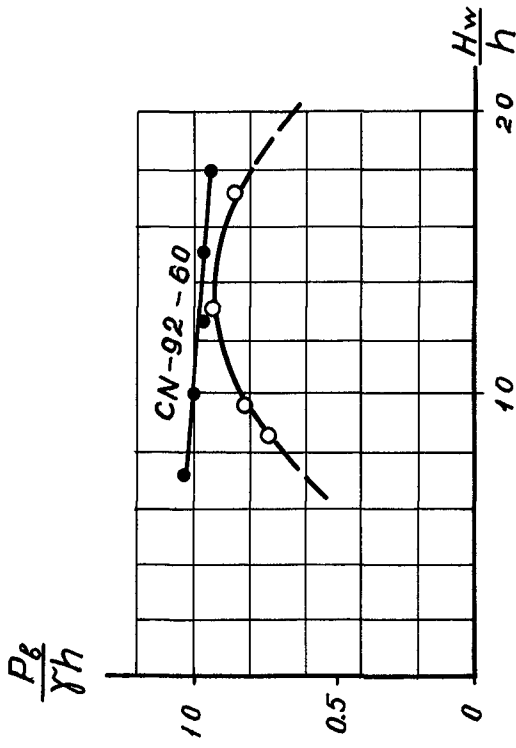
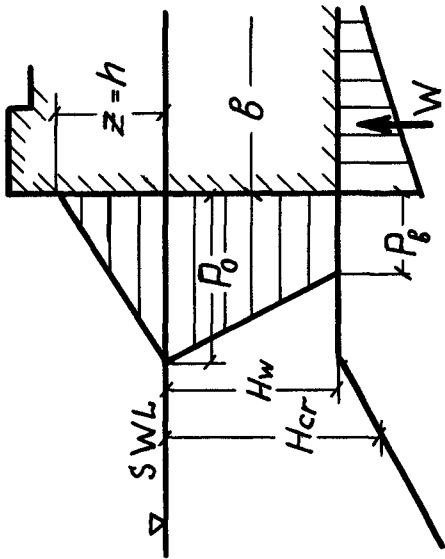


Fig 5 Relation between $\frac{P_b}{\gamma h}$ and $\frac{H_w}{h}$

a) Breaking wave

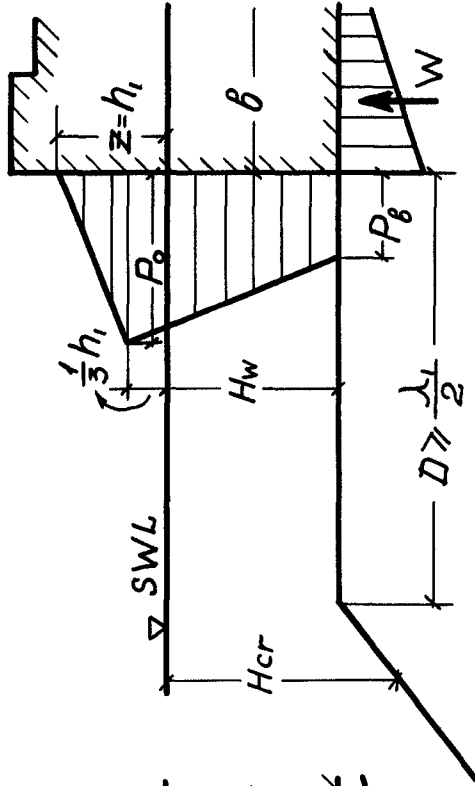
h, λ, τ



$$P_0 = 1.5\gamma h; P_\delta = \frac{\gamma h}{ch} \frac{2\pi H_w}{\lambda}$$

b) Surf wave

$h, = 0,65H_1; \lambda_1 = \lambda th \frac{2\pi H_w}{\lambda}; \tau$



$$P_0 = 1.5\gamma h_1; P_\delta = \frac{\gamma h_1}{ch} \frac{2\pi H_w}{\lambda_1}$$

Fig 6. Vertical distributions of the pressure of the breaking wave and the surf wave against the vertical wall

CHAPTER 90

PLUNGING WAVE PRESSURES ON A SEMI-CYLINDRICAL TUBE

by

Yuan Jen, Assistant Professor
Pang-Mou Lin, Graduate Student

Department of Coastal and Oceanographic Engineering
University of Florida-Gainesville, Florida
USA

ABSTRACT

Laboratory tests were made on a 6-inch diameter semi-cylindrical tube simulating a prototype concrete structure designed to be placed parallel to the coastline in the surf zone to intercept offshore transport of beach materials and thus preserving the beach. The model beach was of fixed bed type with a slope of 1 to 15. The crest elevation of the tube was set at the still water level for most of the test runs and the sloping beach intersected a flat channel bottom at a depth of 20.75"

The test parameters used may be summarized as follows

$$H/L = 0.005 \text{ to } 0.052$$

$$d/L_o = 0.027 \text{ to } 0.111$$

$$H/D = 0.26 \text{ to } 1.18$$

where H is the wave height measured at the toe of the beach, d is the water depth in the flat portion of the channel, D is the tube diameter, L is the wave length in the flat channel and L_o is the equivalent deep water wave length

The above test conditions resulted in plunging breakers on the beach except for a few test cases

Pressure measurements were made around the tube circumference, at an interval of 30 degrees azimuth angle, by using a high frequency response pressure transducer. It was found that the pressure distribution could be treated in two parts

- Part I During the wave uprush, an impact pressure of short duration was recorded at the front of the tube, followed by smoother pressure variations in time
- Part II During the wave downrush, the volume of water transported across the tube flowed back under gravity. The pressure distribution on the beach side of the tube was relatively steady during the flow reversing process

Solitary wave theory was used to compute the breaking wave height and wave celerity. The validity of analytical treatments were evaluated by comparison of measured and observed data. The impact pressures at the front of the tube occurred in somewhat random nature. The average impact pressure in dimensionless form $P_1/\gamma H$ was found dependent upon wave steepness. The maximum impact pressure decreases as the plunging wave steepness increases. Waves with $H/L < 0.01$ exert little impact. The impulse-momentum theory was applied to investigate the behavior of impact pressures. The pressure distribution on the tube surface during the wave downrush was treated as quasi-steady case in which the Bernoulli principle for steady state condition applies.

INTRODUCTION

The phenomenon of wave and structure interaction has long been a subject of vital interest to coastal engineers. Considerable information related to the forces acting on coastal structures due to the action of non-breaking waves can be found in the engineering literature, and dependable methods of predicting wave forces are available. However, despite the fact that a large number of published works also deal with breaking waves, few conclusions can be drawn in order to establish confidence in the design of coastal structures to be located in the surf zone. Analytical means of evaluating wave-structure interactions in the surf zone are difficult to derive because

- 1 Presently available wave theories are inadequate in describing the wave characteristics in the surf zone
- 2 Forces or pressures exerted by traveling breakers differ in magnitude from wave to wave, therefore the analysis of such forces must rely upon statistical means

The Coastal Engineering Laboratory, University of Florida, conducted a two phase study on a semi-cylindrical concrete tube structure, designed to be placed parallel to the beach at or near the mean water line to intercept the offshore transport of beach materials. The study includes

- Phase I - Movable Bed Model Study - To evaluate the stability of the structure under wave action
- Phase II - Fixed Bed Model Study - To measure the pressure distribution around the tube surface and to determine the wave loading

Only the results of Phase II will be presented in this paper, since the results of Phase I are mainly qualitative in nature. The effectiveness of the structure in trapping beach materials is beyond the scope of this paper.

MODEL SET-UP AND INSTRUMENTATION

The model study on wave pressures was performed in a 100 ft x 10 ft x 2.5 ft wave channel. A semi-cylindrical tube, 6 inches in diameter, was mounted on a fixed slope of 1 to 15 at a distance of 85 feet from the wave generator (see Figure 1). The water depths were 17.5 inches at low water and 20.75 inches at

high water The high water represents a case when the tube is barely submerged and most test runs were conducted at this water level Variable wave heights and periods were recorded by a parallel wire resistance-type wave gage located 22 feet in front of the test structure at the point where the channel bottom starts to flatten out A high sensitivity pressure transducer was mounted on a circular test section which was free to rotate about its center so that the pressure sensor could be moved to any desired location along the tube circumference When performing the tests, the transducer was rotated at every 30° interval and the same test condition was repeated for every transducer position The records showed that the wave inputs could be accurately reproduced and the pressure response at each location could be synchronized by using the wave records as references The calibration of the transducer was performed statically This method of calibration was considered to be sufficiently accurate since the transducer has a natural frequency of 10,000 Hz which is much higher than the input frequencies, and the natural period of the transducer was much shorter than the duration of shock pressure impulse

CHARACTERISTICS OF MODEL WAVES

Referring to the model set-up as shown in Figure 1, the model wave characteristics are adequately described at the gage location as

$$H/L = 0.005 \text{ to } 0.052$$

$$d/L_0 = 0.027 \text{ to } 0.111$$

$$H/D = 0.26 \text{ to } 1.18$$

where H is the wave height at the gage location, d is the water depth in the flat channel, D is the tube diameter, L is the wave length in the flat channel, and L_0 is the equivalent deep water wave length The measured wave heights range from 0.131 to 0.589 feet and the wave periods range from 1.73 to 3.50 seconds Wiegel (Ref 1) suggested that the waves in shoaling water just prior to breaking might be treated as a solitary wave as an approximation Wilson, Webb and Hendrickson (Ref 2) recommended the range of Ursell's parameter HL^2/d^3 within which the solitary wave theory is applicable The calculated Ursell's parameters for this study are between 15 and 36, well within their recommended range of 10 to 40 Therefore, in this study, the solitary wave theory will be used to describe the model waves measured at the wave gage During the tests, most waves broke on the 1:15 beach and the locations where white caps were first found as the wave advanced toward the tube were observed and recorded, so that the breaking depth d_b , measured from the still water level to the beach bottom, can be computed Figure 2 shows the relationships between H/T^2 and d_b/T^2 as compared to the usually referred breaking index curve A surprising result of the wave breaking data was that $H \approx H_b$, where H_b is the wave height at breaking (not measured) Galvin (Ref 3) found that

$$\frac{d_b}{H_b} = 1.40 - 6.85m \quad (1)$$

where m is the beach slope

Using Eq (1), we obtain, for the present slope of 1/15

$$\frac{H_b}{d_b} \approx 1.04$$

while Figure 2 suggests that $H/d_b = 1.1$, confirming the previous statement of $H \approx H_b$. The wave forms fit the description of "plunging breakers" by observation Iversen (Ref 4) found that the plunging breakers occurred when $H_o/T^2 = 0.05$ to 0.30 for 1:10 beach slope and $H_o/T^2 = 0.02$ to 0.20 for 1:20 beach slope Galvin (Ref 3) defined the occurrence of plunging breakers as

$$H_o/L_o m^2 = 0.9 \text{ to } 4.8$$

For this study, $H_o/T^2 = 0.01$ to 0.22 and $H_o/L_o m^2 = 0.44$ to 8.8. Reasonable agreement to suggestions by previous investigators was found in defining plunging breakers

TEST RESULTS AND ANALYSIS

Description of Pressure Time History

The variation of pressure in time as the plunging breakers passed through the tube structure can best be described by referring to Figure 3 in which the pressure time histories around the tube circumference are shown for a typical test condition. " θ " values shown in the figure are defined in Figure 7. During the wave uprush, as the wave front contacts the front face of the tube ($\theta = 0$ to 90°), pressures of high intensity and short duration were registered at the point of impact, this pressure will be referred to as "impact pressure", P_i , throughout this paper. Immediately after the impact, the pressures acting upon the front of the tube undergo a smooth continuous variation, normally decreasing in intensity, as the uprushing waves gradually lose their momentum due to the counteracting gravitational force. The secondary peak pressure registered immediately after the impact will be designated as P_s .

As a result of wave uprush, a certain volume of water is transported across the crest of the tube. The maximum run-up is attained when all the available kinetic energy is converted into potential energy. Under the influence of gravity this volume of water flows back across the tube and the wave downrush begins. The behavior of reversing flow resembles the case of flow across a spillway, except that the available head decreases with time. The pressure time histories recorded on the beach side of the tube ($\theta = 90^\circ$ to 180°) were quite steady during the flow reversing process. The reverse flow is suddenly interrupted by the impact accompanying the next oncoming wave, and the wave uprush is again repeated. In Fig 4, the pressure variation with respect to time is shown for two test cases. The times $t = 0$ and $t = T$ represent times of two consecutive impacts during which a high pressure intensities were found at the front of the tube for a short duration. Therefore, at $t = 0$ and $t = T$, the net resultant force on the tube is

definitely acting shoreward. At $t = 3T/4$, the tube is under the action of reversed flow, the front portion ($\theta < 90^\circ$) of the tube is subjected to pressures less than the hydrostatic pressure at still water level, while the back of the tube ($\theta > 90^\circ$) is subjected to some dynamic pressure in addition to the initial hydrostatic pressure. The net resultant force during the wave downrush is thus acting seaward. Repetitive wave actions will cause the tube to loosen on a beach. Additional instantaneous pressure distributions during impact are shown in Fig. 5.

The Impact Pressure P_i

Test results showed that the impact pressure intensity varied with every wave, even though the wave form at the toe of the sloping beach appeared to be rather uniform and periodic. Therefore, an appropriate evaluation of the pressure intensity should be based upon a statistical analysis. However, the number of waves available to analysis was limited because, after a certain length of time, the wave form became distorted by the reflection from the wave generator. Because of this restriction, only eight pressure peaks were averaged, and the dimensionless parameter $P_i/\gamma H$ is correlated with the wave steepness H/L in Fig. 6. " P_i " was the pressure difference between the pressure peak measured during the impact and the pressure just prior to the moment of impact. The maximum impact occurred as $T = 3.5$ seconds and $H = 0.282$ feet when the waves broke right in front of the tube. The wave steepness for this test case is 0.01. Fig. 6 clearly indicates that steeper waves exert a relatively lower impact as expressed in dimensionless form, because they break at a distance from the tube. For the few cases when $H/L < 0.01$, no appreciable breaking of the waves was observed, therefore the impact is relatively low.

In the following, an impact-momentum model is postulated to gain further insight to the behavior of impact pressures.

Refer to Fig. 7. As breaking waves impinge upon a portion of the tube surface, the normal force exerted on an element of the circumference Δl is equal to the rate of change of momentum in the radial direction. Thus we may write

$$-d(M_e U_r)/dt = P_i \Delta l \quad (3)$$

where " M_e " is the effective mass of the portion of water causing the momentum reaction on the element Δl and " U_r " is the radial velocity of the mass M_e . The "-" sign is inserted here to represent a case of decreasing momentum. The effective mass M_e is considered independent of time during the impact when the velocity of the mass is retarded, and may be expressed as

$$M_e = \rho b^* \Delta l \cos \alpha \quad (4)$$

providing that Δl is small. It is apparently unrealistic to treat the whole horizontal element of width " b " as solid, therefore the effective width is defined as " b^* " where b^* is much less than b . Substituting Eq. (4) into (3), we obtain

$$P_i = -\rho b^* \cos \alpha \frac{dU_r}{dt} \quad (5)$$

If the time variations of "P_i" and that of "U_r" are linear, as that assumed by Weggel (Ref 5), then Eq 5 can be integrated as

$$\int_0^{t_i} P dt = - \int_{U_0 \cos \alpha}^0 \rho b^* \cos \alpha dU_r \quad (6)$$

where t_i is the duration of impact and U₀ is the horizontal water particle velocity just before impact (see Figure 7) After integration, we obtain

$$P_i = \rho U_0 \left(\frac{2b^* \cos^2 \alpha}{t_i} \right) \quad (7)$$

$$\text{or } P_i = \rho U_0 U^*$$

where U* is a characteristic velocity which has an upper limit equal to the sonic speed in water

Eq (7) is reduced to dimensionless form through the following procedures

- (1) The celerity at breaking is computed from solitary wave theory as

$$C_b = \sqrt{g(H_b + h_b)} \quad (8)$$

where h_b is the breaking depth measured to the trough of the waves and is related to the still water depth d_b as

$$h_b = d_b - C_h H \quad (9)$$

where C_h = 0.2 to 0.4 from previous experimental studies

- (2) Recalling the previous discussion that

$$H \approx H_b \text{ and } \frac{d_b}{H} = \frac{1}{1.1} = 0.91,$$

we may write

$$P_i / \gamma H = (U_0 U^* / C_b^2) (1 - C_h + d_b / H) \quad (10)$$

or

$$P_1/\gamma H = (1.51 \text{ to } 1.71) U_o U^*/C_b^2 \quad (11)$$

Referring again to Figure 6 which shows $P_1/\gamma H = 1.9$ when the waves break right in front of the tube ($C_b \approx U_o$), Equation (11) implies

$$U^*/C_b = 1.11 \text{ to } 1.26$$

which shows U^* and C_b are in the same order of magnitude, much less than the sonic speed in water^b. The impact pressures shown in Figure 6 are much less than those observed by previous investigators who have dealt with wave pressure acting on vertical walls (Ref 6 to 10). The curvature of the tube, which is not as conducive to "shock" as plane surfaces, is mainly responsible for the reduction of impact pressure.

The Secondary Pressure P_s

After the initial impact, a sudden drop of pressure occurs and this pressure is termed "secondary" as was referred to previously. The concept of fixed hypothetical mass no longer applies here since there exists a continuous flux of mass toward the tube. The kinematics of flow around the tube surface are beyond a theoretical prediction, therefore an accurate estimate of P_s is difficult to obtain. Figure 8 shows the distribution of $P_s/\gamma H$ with respect to θ for different values of H/D . For simplicity, if one assumes that the horizontal velocity of water mass in front of the tube remains constant, then the mass flux in the radial direction is $\rho U_o \Delta l \cos \alpha$ and the rate of change of momentum in the same direction becomes $\rho U_o^2 \Delta l \cos^2 \alpha$, so the application of momentum principle gives

$$P_s = \rho U_o^2 \cos^2 \alpha$$

A similar analysis to that made on the impact pressure gives

$$P_s/\gamma H = (U_o/C_b)^2 \cos^2 \alpha (1 - C_h + d_b/H) \quad (13)$$

or

$$P_s/\gamma H = (1.51 \sim 1.71) (U_o/C_b)^2 \cos^2 \alpha \quad (14)$$

The upper limit of $P_s/\gamma H$ must occur when $U_o = C_b$, thus

$$(P_s/\gamma H)_{\max} = (1.51 \sim 1.71) \cos^2 \alpha \quad (15)$$

Eq (15) is plotted in Figure 8, the curve is shown to fit the envelope of all data $P_s/\gamma H$ decreases as H/D increases. The trend is reasonable since U_o/C_b values are smaller for large H/D values, and Eq (14) shows that " $P_s/\gamma H$ " is proportional to $(U_o/C_b)^2$

Pressures due to Reversed Flow

During the wave downrush, the flow reverses its direction under the influence of gravitational force. The flow patterns resemble those found across a spillway. The pressure distribution at the beginning and the end of the reversing flow are shown for six test conditions in Fig 9. At the beginning of wave downrush, the pressure distribution is believed to be hydrostatic since the motion of water particles was negligible at that instant, while at the end of wave downrush, the flow over the tube approaches a steady state so that the pressure distribution on the beach side of the tube ($\theta > 90^\circ$) remains unchanged for a short period of time. The overflow along the ocean side of the tube ($\theta < 90^\circ$) is curvilinear with relatively high speed. Negative gage pressures were often recorded for $\theta = 30^\circ$ and $\theta = 60^\circ$. The total resultant force during the wave downrush is therefore acting seaward, in contrast to the case of wave uprush.

SUMMARY AND CONCLUSIONS

It is found in this study that the uprush of plunging breakers exert little impact on a semi-cylindrical tube as compared to the "shock" pressure caused by waves breaking on a vertical wall. The " $P_i/\gamma H$ " value as defined in the paper is at maximum when waves break right in front of the tube ($H/L = 0.01$). Waves steeper than $H/L (> 0.01)$ break at a distance away from the tube and the resulting $P_i/\gamma H$ decrease as wave steepness increases. No noticeable impact was observed for waves with $H/L < 0.01$. An impulse momentum model gives

$$P_i = \rho U_o U^*$$

where

$$U^* = \frac{2b \cos^2 \alpha}{t_i}$$

and

$$P_i/\gamma H = (1.51 \text{ to } 1.71) U_o U^*/C_b^2$$

The characteristic velocity U^* is in the same order of magnitude as the wave celerity at breaking, C_b . Therefore, the impact pressure is much lower than the pressure of the water hammer type. Detailed characteristics of U^* could be studied by fast speed photography along with fast speed pressure recording systems. The "secondary pressure" as defined in the paper has a maximum value

$$(P_s/\gamma H)_{\max} = (1.51 \text{ to } 1.71) \cos^2 \alpha$$

when $U_o = C_b$

The above equation represents the envelope of the data $P_s/\gamma H$ becomes smaller as H/D increases. The validity of the equation

$$P_s/\gamma H = (1.51 \text{ to } 1.71)(U_o/C_b)^2 \cos^2 \alpha$$

could be evaluated by measuring U_o . During the wave downrush, wave pressures on the beach side of the tube seldomly exceed the net hydrostatic pressure caused by the wave run-up. The high speed curvilinear overflow on the ocean side of the tube results in some negative gage pressures so that the resultant force during the wave downrush is acting seaward, in contrast to the case of wave uprush during which the impact force is acting shoreward. The oscillatory behavior of the net resultant force creates a stability problem on the structure. When designing this type of structure, cut-off walls extending downward into the soil must be provided to resist sliding and overturning of the structure, and also, reducing the uplift pressure on the tube foundation.

ACKNOWLEDGEMENTS

This work was supported in part by the Gray Tech Industries, Incorporated, Mohnton, Pennsylvania. Dr. R. G. Dean kindly reviewed the paper and offered constructive suggestions.

REFERENCES

- 1 Wiegel, R L , Oceanographical Engineering, Prentice-Hall, Inc 1964
- 2 Wilson, B W , Webb, L M and Hendrickson, J A , The Nature of Tsunamis, Their Generation and Dissipation in Water of Finite Depth National Engineering Science Company, Technical Report, August, 1962
- 3 Galvin, C J , Jr , Breaker Travel and Choice of Design Wave Height, Journal of Waterways and Harbors Div , Proc ASCE, May, 1969
- 4 Iversen, H W , Waves and Breakers in Shoaling Water, Proc Third Conf on Coastal Engineering, 1952, pp 1-12
- 5 Weggel, J R and Maxwell, H C , Numerical Model for Wave Pressure Distributions, Journal of Waterways and Harbors Div , Proc ASCE, August, 1970
- 6 Weggel, J R and Maxwell, H C , Experimental Study of Breaking Wave Pressures, Offshore Technology Conference, Paper No OTC 1244, April, 1970
- 7 Kamel, A M , Shock Pressure on Coastal Structures, Journal of Waterways, Harbors and Coastal Engineering Div , Proc ASCE, August, 1970
- 8 Rundgren, L , Water Wave Forces - A Theoretical and Laboratory Study, Bull No 54, Institution of Hydraulics, Royal Institute of Technology, Stockholm, Sweden, 1958
- 9 Ross, C W , Laboratory Study of Shock Pressures of Breaking Waves, Beach Erosion Board Tech Memo No 59, U S Army Corps of Engineers, February, 1955
- 10 Nagai, S "Shock Pressure Exerted on Breaking Waves on Breakwaters" Journal of Waterways and Harbors Div , ASCE, Vol 86, No WW2, Proc Paper 2504, June, 1960

NOTATION

The following symbols are used in this paper

b	=	the width of a horizontal wave element
b^*	=	effective width of a horizontal wave element during impact
C_b	=	wave celerity at breaking
C_h	=	a coefficient
D	=	diameter of the semi-cylindrical tube
d	=	water depth measured to mean water level
d_b	=	water depth at breaking
H	=	wave height
H_o	=	deep water wave height
H_b	=	breaking wave height
h_b	=	breaking depth measured to the wave trough
L	=	wave length
L_o	=	deep water wave length
Δl	=	length of an element on the tube surface
M_e	=	effective mass of a horizontal wave element
m	=	beach slope
P_1	=	impact pressure
P_s	=	secondary pressure
T	=	wave period
t	=	time
t_1	=	duration of impact
U_o	=	approaching water particle velocity
U^*	=	a characteristic velocity defined by Eq (7)

- U_r = radial velocity component
 ρ = mass density of water
 θ, α = as defined in Fig 7
 γ = specific density of water

LIST OF FIGURES

- Figure 1 Model set-up for the pressure test
- Figure 2 The relationship between H/T^2 and d_b/T^2
- Figure 3 Samples of pressure recordings
- Figure 4 Typical pressure variations with respect to time
- Figure 5 Instantaneous pressure distributions when the pressure intensity at $\theta = 0$ is maximum
- Figure 6 Relationship between dimensionless impact pressure and the wave steepness
- Figure 7 Wave parameters during impact
- Figure 8 Distribution of dimensionless secondary pressure around tube surface
- Figure 9 Pressure variation during wave downrush

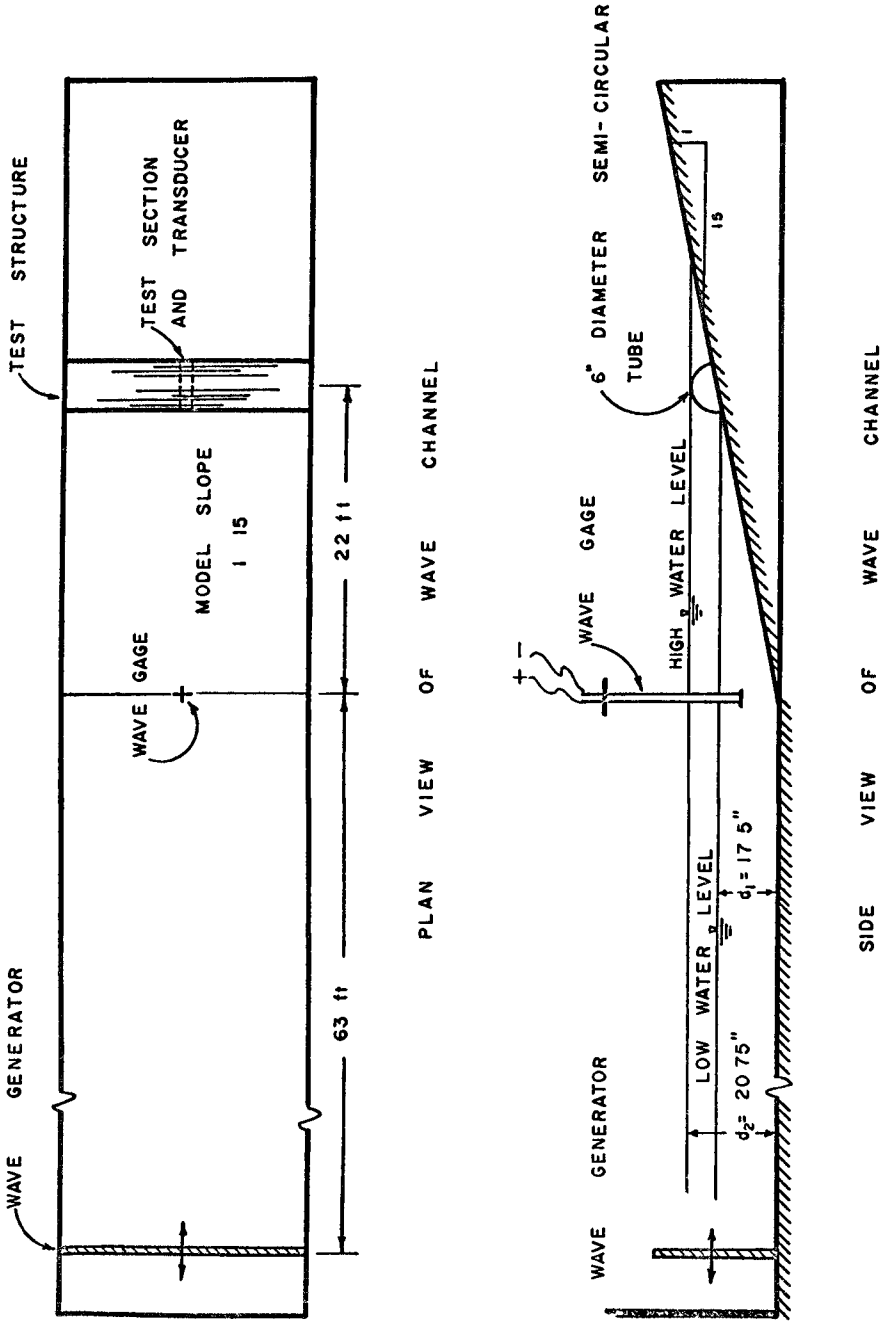


FIGURE 1 MODEL SET-UP FOR THE PRESSURE TEST

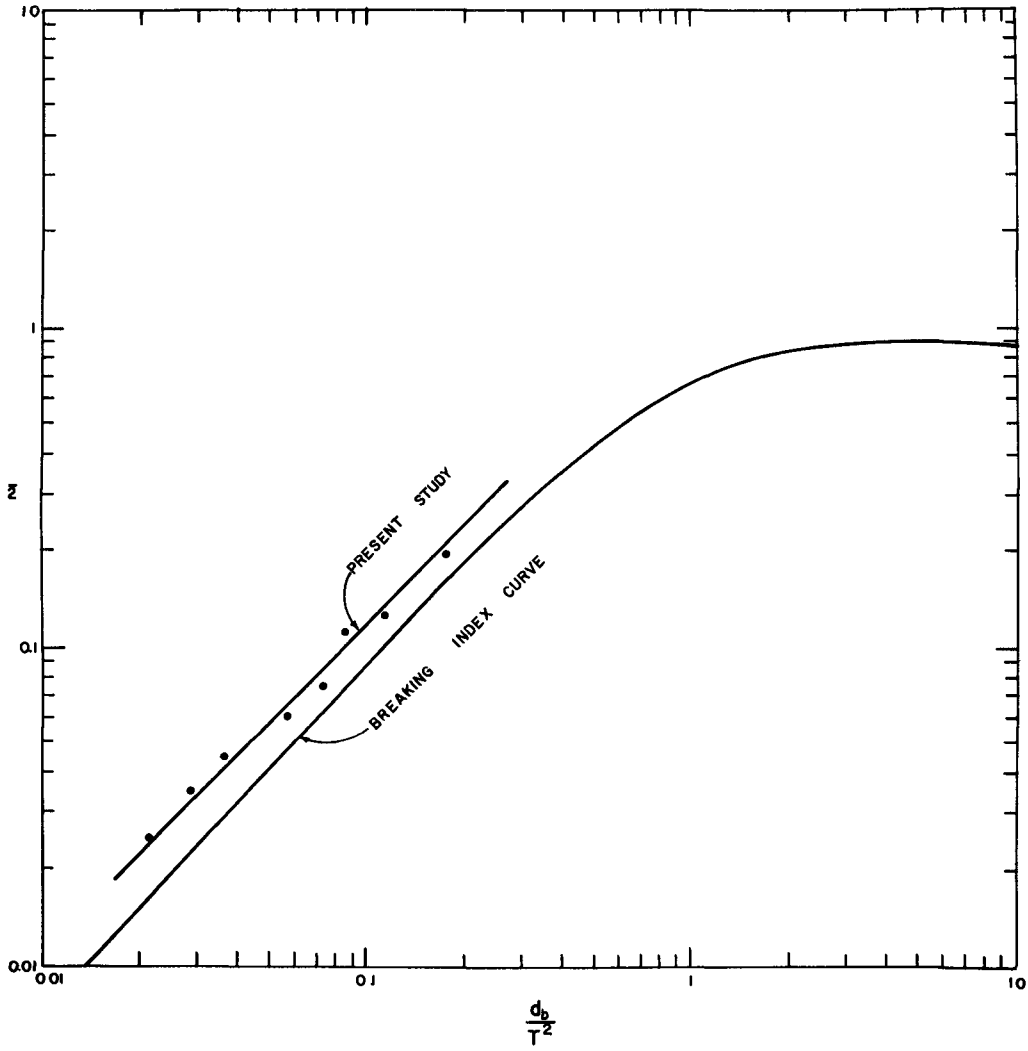


FIGURE 2 RELATIONSHIP BETWEEN H/T^2 & d_b/T^2

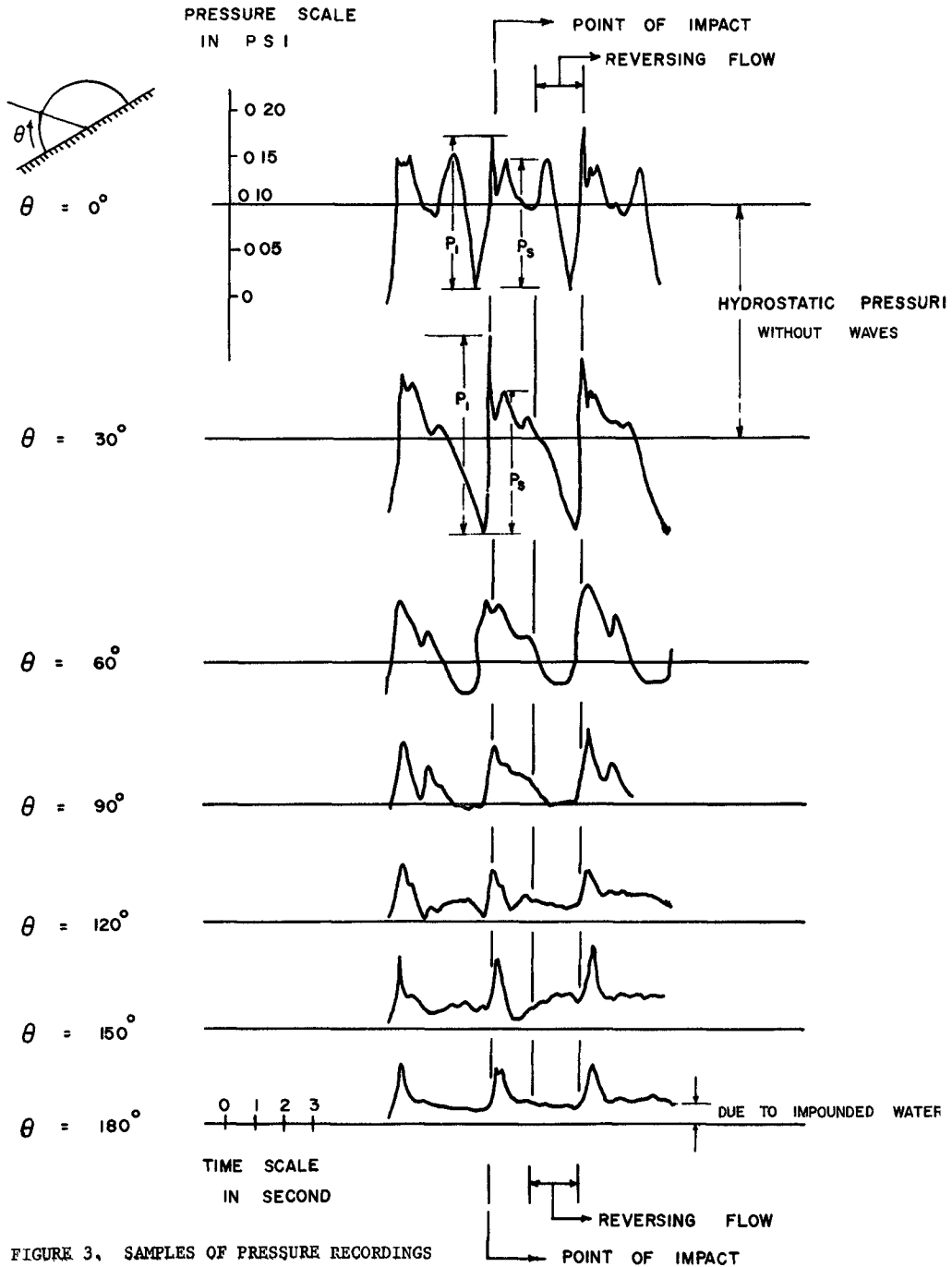


FIGURE 3. SAMPLES OF PRESSURE RECORDINGS

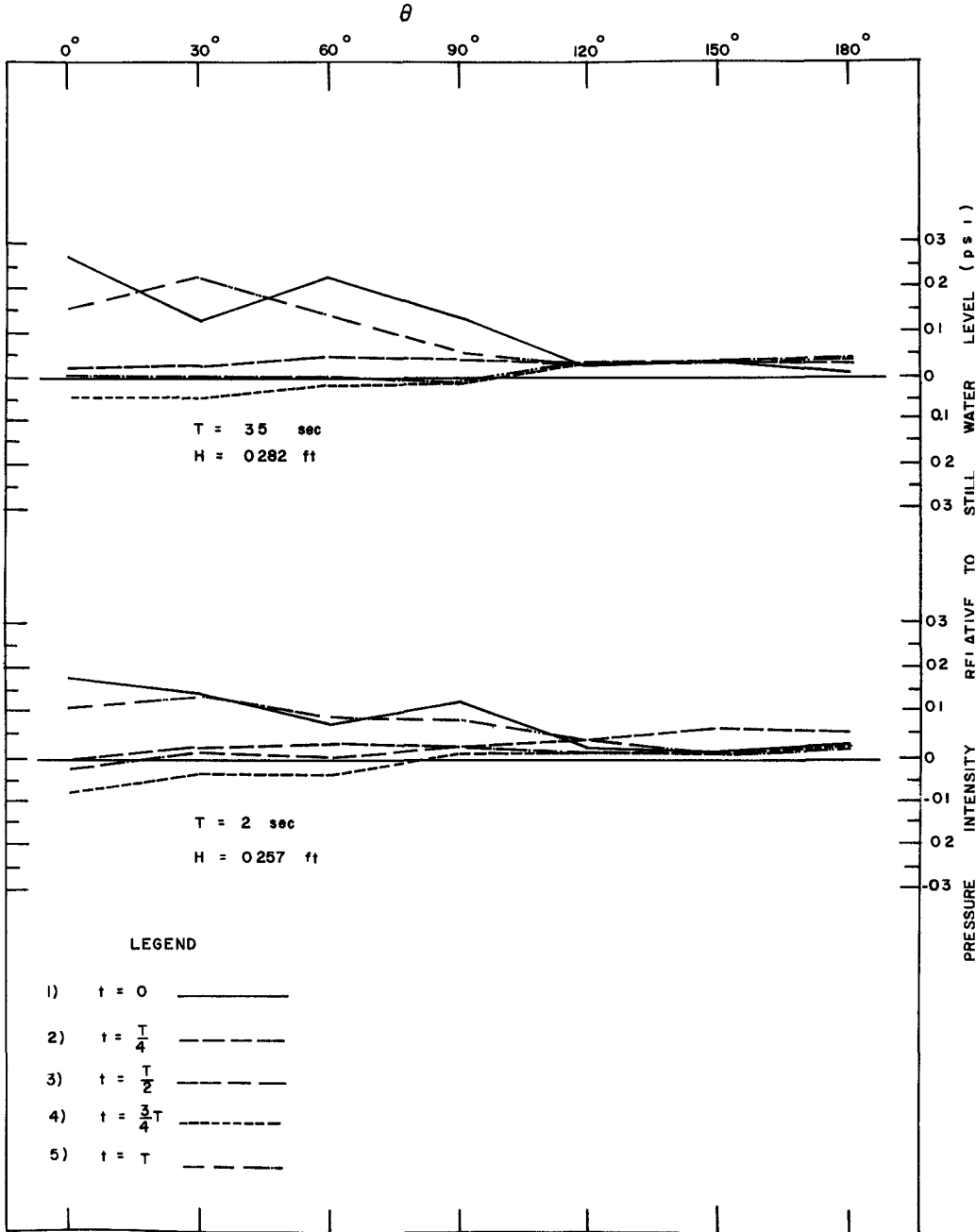


FIGURE 4 TYPICAL PRESSURE VARIATIONS WITH RESPECT TO TIME

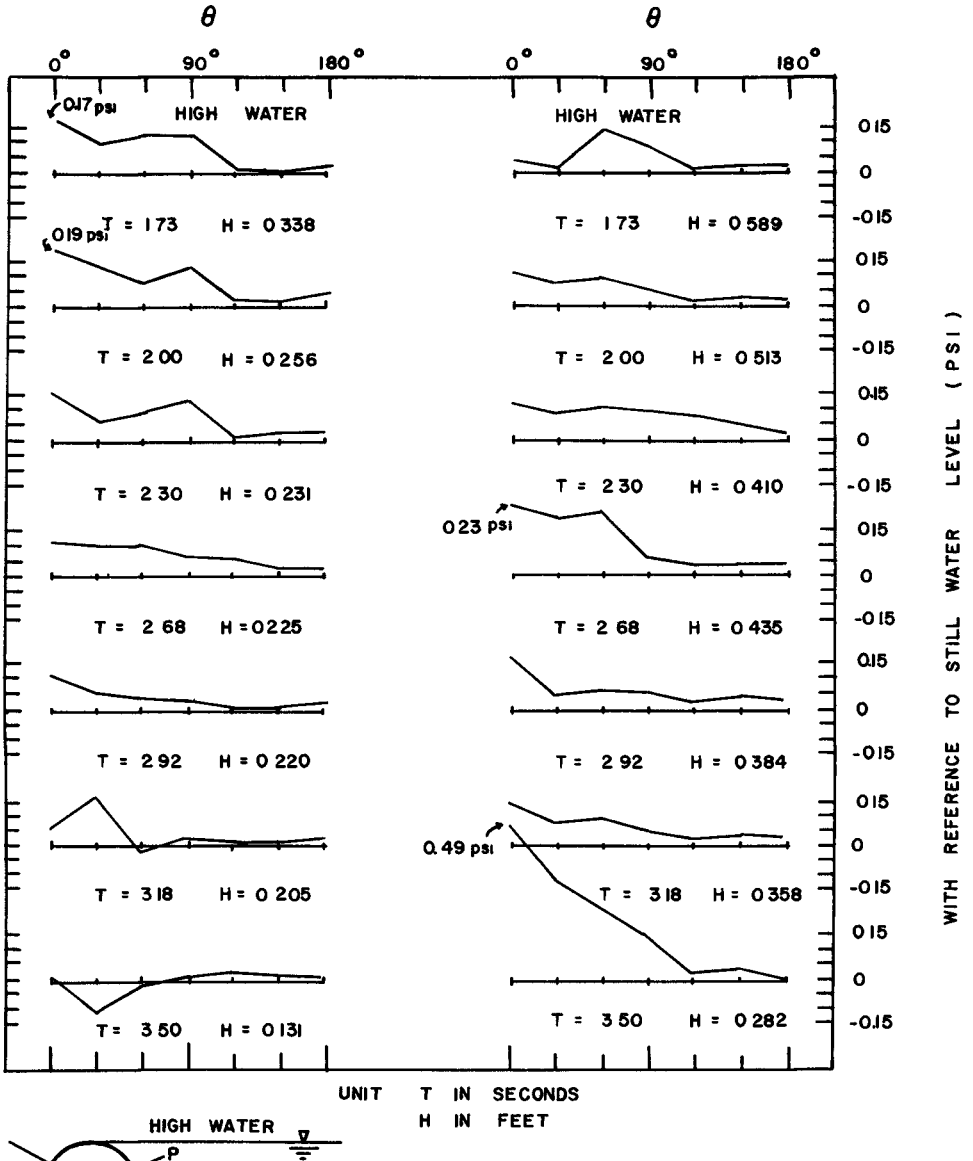


FIGURE 5 INSTANTANEOUS PRESSURE DISTRIBUTION AROUND THE SEMI-CIRCULAR TUBE WHEN THE PRESSURE INTENSITY AT $\theta = 0^\circ$ IS MAXIMUM

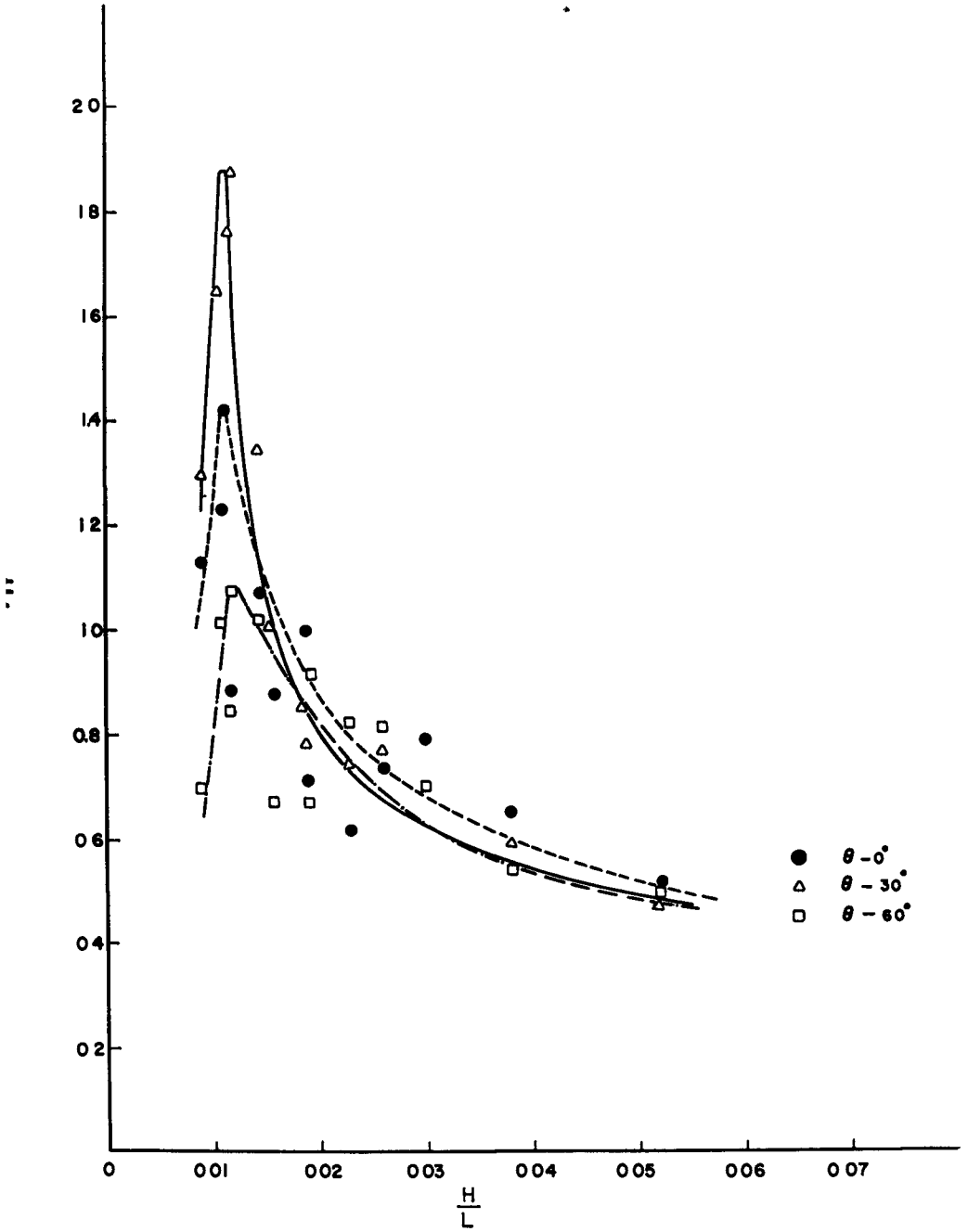


FIGURE 6 RELATIONSHIP BETWEEN DIMENSIONLESS IMPACT PRESSURE AND THE WAVE STEEPNESS

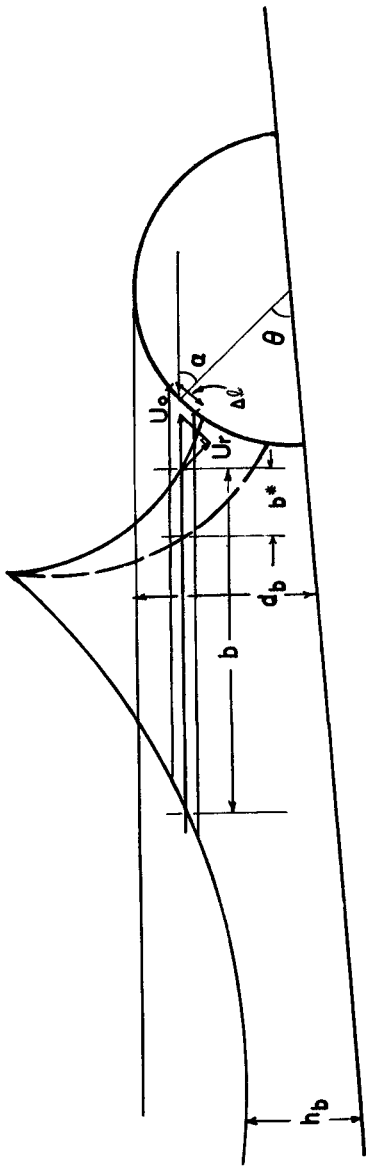


FIGURE 7 WAVE PARAMETERS DURING IMPACT

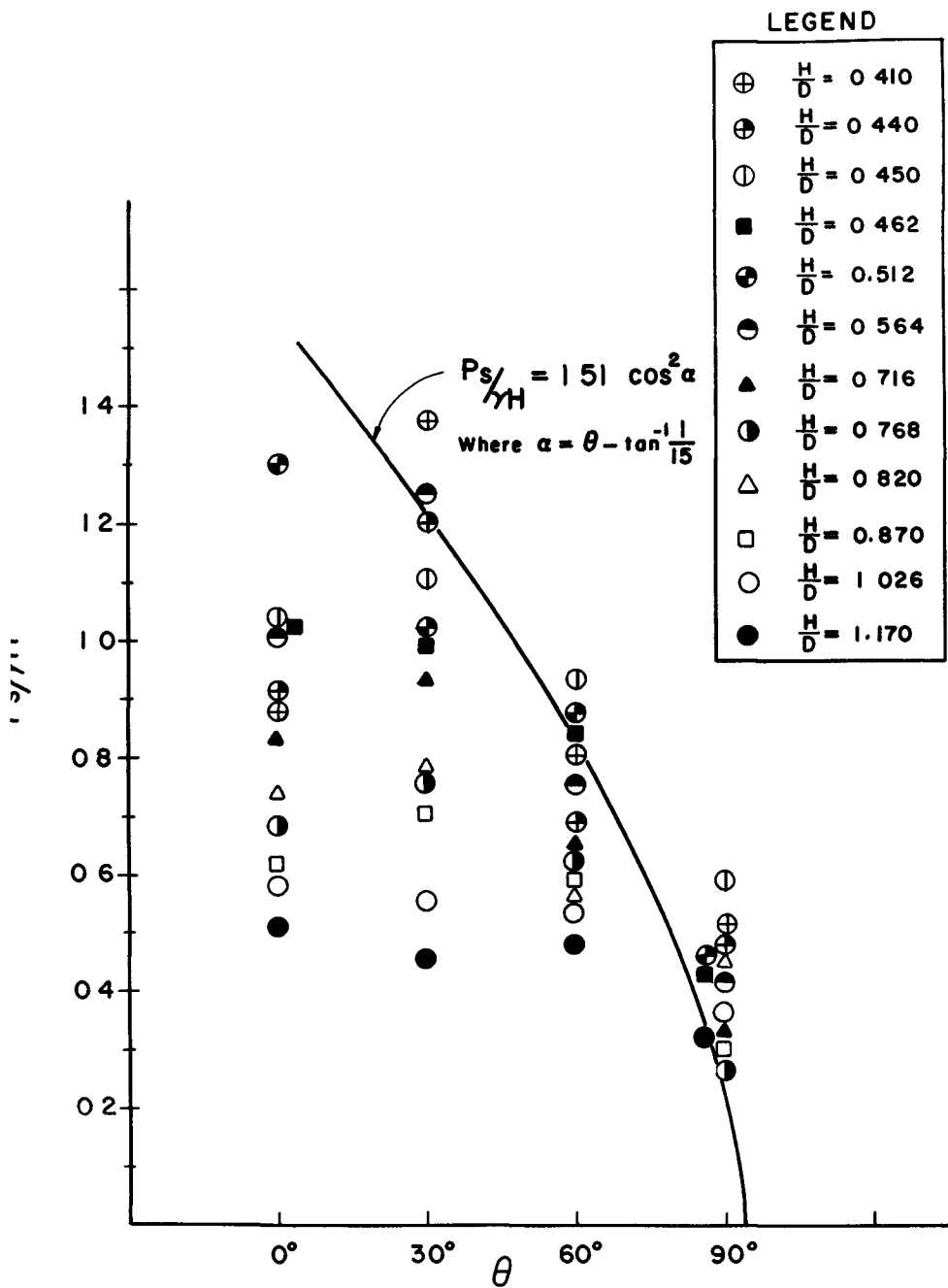


FIGURE 8 DISTRIBUTION OF DIMENSIONLESS SECONDARY PRESSURE AROUND TUBE SURFACE

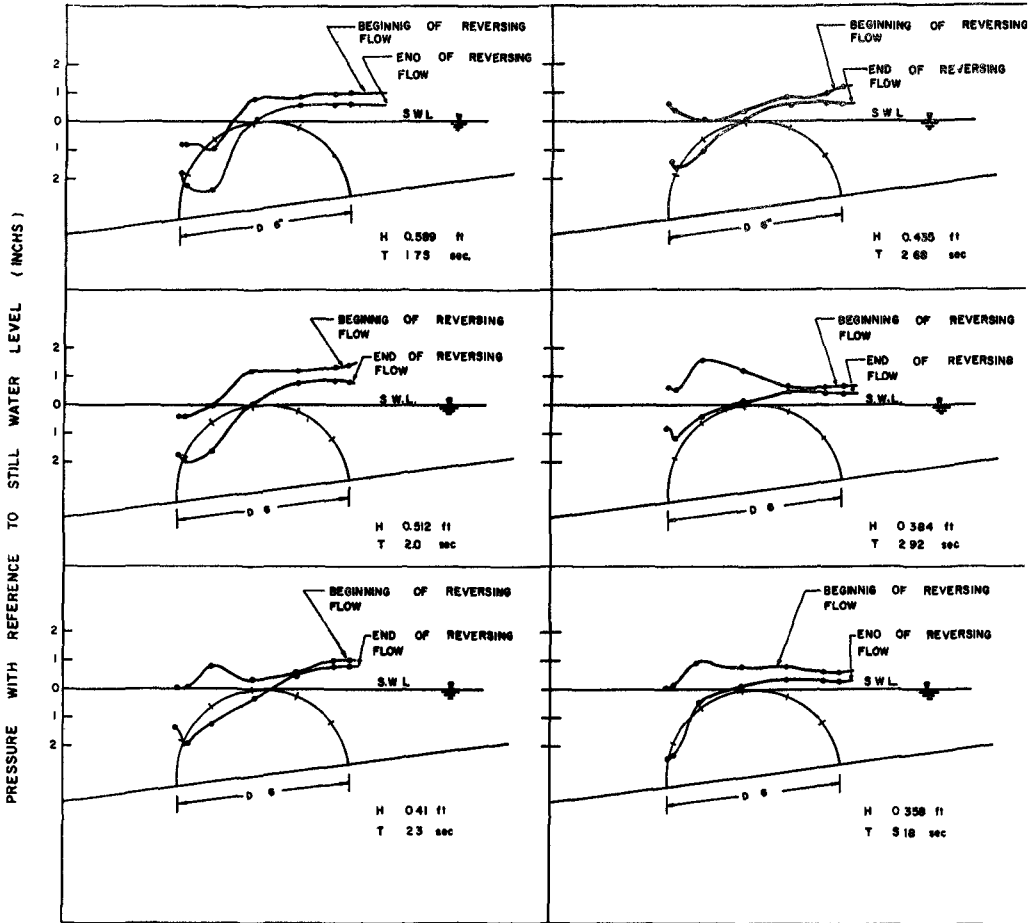


FIGURE 9 PRESSURE VARIATION DURING THE WAVE DOWNRUSH

CHAPTER 91

LOADINGS ON LARGE PIERS IN WAVES AND CURRENTS

by

Hsiang Wang

University of Delaware, Newark, Delaware

Abstract

Through scale-model tests, the forces, moments, and the pressure distributions, including impact pressures, were determined for large diameter piers extending through large-amplitude wave system in which current strengths vary. Tests were performed at 1/100 scale, simulating piers of the bridge for the Northumberland Strait Crossing, Canada. These piers are partially cylindrical with a base diameter of 100 feet. Close to the surface, where the wave action is greatest, they are conical. Waves up to 25 feet and current up to 4 knots have been reproduced in the laboratory, according to Froude similitude. The tests results fully support the known concept that, when the pier diameter is large in comparison with the wave length, inertial force becomes dominant. Generally, the presence of current, either with or against the wave train, results in a decreasing wave force. Semiempirical relations were developed for force predictions that require the experimental determination of a singular coefficient.

Introduction

The problems of predicting wave forces on a cylindrical-shaped structure are often categorized according to the magnitude of the linear dimensions of the object and of the wave field. Past advancement had been concerned mainly with the category of small-diameter cylinder under the action of small-amplitude waves (Morrison et al., 1949, Goda, 1964, Bretschneider, 1955, 1957). Some attention has been given to the analytical treatment of the problem of a large-diameter pile (in comparison to the wave length) with small-amplitude wave (McCamy and Fuchs, 1954, Bonnefille and Germaine, 1963). These theories still remain to be verified by experiment. When it comes to the problem of determining forces on a large-diameter cylinder protruding through a large-amplitude wave system, one quickly finds the lack of adequate information and reliable guidance. The difficulty lay in general the lack of an adequate mathematical model on the one hand and the scarcity of experimental data on the other. Therefore, the design of such a marine structure often presents a unique task of its own.

The present study dealt with the prediction of wave forces on the piers of the bridge for the Northumberland Strait Crossing. These piers are partially cylindrical with base diameter equal to 100 feet, close to the surface, where the wave action is greatest they are conical. According to the information provided by the Northumberland Consultants,

Ltd , the design storm is based on a 1 percent risk of occurrence once in 100 years resulting in wind of 95 mph on the northwest and southeast side of the crossing, respectively. Significant wave of 14 foot height and 7.0 to 7.7 seconds is to be expected. The extreme wave can be as high as 25 feet. The design problem becomes unconventional. Actually, this problem is further complicated because tidal current ranging from 0 to 4 knots is expected in the Strait. This alters the wave kinematics and hence wave-induced forces. Therefore, to obtain an engineering solution of this problem, one has little choice but to rely on the outcome of a scaled model test.

This experimental investigation is intended to provide sufficient information to meet the immediate need of the specific design problem in hand and at the same time to serve as foundation and verification for the development of a possible theory. It is realized that few model setups portray perfect dynamic similarity with their prototypes, and that, for all practical purposes, only the pertinent part of the phenomenon need be closely approximated. As a result of dimensional analysis, it is not the viscous action, but wave inertia that is to be evaluated in the present instance. Therefore, in addition to the absolute magnitude of the force and moment exerted on the structure, it is the above postulation with which the present investigation is concerned.

Dimensional Analysis and Scaling Laws

The problem in hand is that of determining from experiments on a model of reduced scale the dynamic forces imposed by shallow water waves of relatively high amplitude upon a system of piers of partly cylindrical, partly conical shape. An important aspect is that of determining the scaling laws to be applied.

When an obstacle, such as a pier, is placed in the channel, it experiences a hydrodynamic force. This force can be considered as consisting of two components respectively related to wave velocity and acceleration. The velocity related force in the horizontal direction is given by

$$F(V,u) = \frac{1}{2} \pi \rho \int_{-d}^{\eta} C_d [D(z)] [V(z) + u(z)]^2 dz \quad (1)$$

where V is the current velocity, u is the horizontal component of the wave orbital velocity, ρ is the density of the water, d is the water depth, η is the wave ordinate, D is the diameter of the pier, z is vertical ordinate and C_d is a drag coefficient. The drag coefficient is a function of, among other parameters, Reynold's number which is defined as

$$R = \frac{V D}{\nu}$$

where ν is the kinematic viscosity. The acceleration related force is given by

$$F(u) = \frac{\pi \rho}{4} \int_{-d}^{\eta} C_a [D(z)]^2 [\dot{u}(z)] dz \quad (2)$$

where C_1 is an inertia coefficient which depends mainly on the Ursell number

$$U_n(z) = \frac{4\pi^2 D(z)}{gT^2} = \frac{D(z)}{L}$$

The Ursell number is actually an inversed Froude number preferred in wave mechanics

The foregoing argument leads to the point that dynamic similarity requires that both Froude and Reynold's numbers be preserved. Since simultaneous Froude and Reynolds scaling of reduced model is impossible, a choice must be made. To this end it is brought out that the ratio of the acceleration force to the velocity force at any level of the pier is

$$\frac{\pi C_1 D(z)}{C_d H(z)}$$

and since the inertia and drag coefficients are of approximately equal value, the ratio reduces to $\pi D(z)/H(z)$. This ratio is always greater than unity even for the waves of extreme height and in the cylindrical portion of the pier much greater than unity, so that the acceleration force dominates the velocity force and the resultant hydrodynamic force is close to the acceleration components. The consequence of this is that the scaling should follow the Froude law.

The integration of Eq (2), which represents the acceleration component of the hydrodynamic force, cannot be carried out unless explicit expressions of C_1 and u can be obtained. The other alternative is to establish the functional relationship through dimensional analysis between this force component and other pertinent fluid, flow, and geometrical variables. By the latter method the following relation is obtained

$$\frac{F/(D^2 d)}{\rho H/T^2} = E_n \left(\frac{D}{L}, \frac{VT}{D}, \frac{H}{d}, \frac{V}{(gd)^{1/2}} \right) \quad (3)$$

Where E_n is a modified Euler number which represents a force coefficient, and T is the wave period, H is the wave height, and g is the gravitational acceleration.

Evidently the number of parameters involved makes a thorough investigation burdensome, further simplification is desirable. McCamy and Fuchs (1955) obtained analytically the amplitude of the wave force per unit height acting on a cylinder at depth z below the surface as

$$F(z) = \frac{\rho H L}{\pi} \frac{\cosh [2\pi(z+d)/L]}{\cosh 2\pi d/L} f_A \quad (4)$$

where

$$f_A = \frac{1}{[J_1'(\pi D/L)]^2 + [Y_1'(\pi D/L)]^2} \quad 1/2$$

and J_1 and Y_1 are Bessel functions of the first and the second kinds, respectively, and the prime denotes first derivative. Accordingly the total force is

$$F = \int_{-d}^d F(z) dz = \frac{\rho H}{\pi} \frac{L^3}{T^2} f_A \quad (5)$$

When $\pi D/L$ is small,

$$f_A \sim \left(\frac{\pi}{2}\right)^2 (\pi D/L)^2$$

and $F \sim \frac{\pi^2}{4} \frac{\rho H}{T^2} L D^2 \quad (6)$

On the other hand, when $\pi D/L$ is large,

$$f_A \sim \left(\frac{1}{2}\right)^{1/2} \pi \left(\frac{D}{L}\right)^{1/2}$$

and

$$F \sim \sqrt{1/2} \frac{\rho H}{T^2} L^{5/2} D^{1/2} \quad (7)$$

Physically, the last two equations imply that when D/L is small, the pier diameter is the controlling factor, whereas, when D/L is large, the effect of wave length becomes predominant. The present pier-diameter-to-wave-length ration ($\pi D/L$ ranges from 1 to 1.5) is believed to fall into the latter category. The force coefficient is redefined as

$$\frac{F/(L^{5/2} D^{1/2})}{\rho H/T^2} = C_m = C_m \left(\frac{VT}{D}, \frac{H}{d}, \frac{V}{(gd)^{1/2}}\right) \quad (8)$$

For the case of shallow water, this equation simplified further to

$$\frac{F}{g^{5/4} \rho H T^{1/2} D^{1/2} d^{5/4}} = C_{ms} = C_m \left(\frac{VT}{D}, \frac{H}{d}, \frac{V}{(gd)^{1/2}}\right) \quad (9)$$

The parameter VT/D is a Strouhal number written in the form preferred by Keulegan and Carpenter (1958), in the case of combined wave and current the more appropriate expression is $[V + U_m]T/D$, where U_m is the maximum horizontal particle velocity in the wave. This parameter characterizes the wake and eddy formations and is thus more directly related to viscous forces. It has been shown that, in the present case, the viscosity plays a minor role. Therefore, it is expected that the effect of the parameter

on the force coefficient is insignificant. In fact, the value of $[V + U_m]T/D$ varies from 1 to 3 for the range of variables in the present experiment. Keulegan and Carpenter were able to show that for the parameter as small as such no eddy shedding occurs. Consequently, the force coefficient remains practically constant. Finally, the force relation is simplified to

$$\frac{F}{g^{5/4} \rho_{HT}^{1/2} D^{1/2} d^{5/4}} = C_{ms} \left(\frac{H}{d}, \frac{V}{(gd)^{1/2}} \right) \quad (10)$$

Experimental Apparatus and Procedure

Facility

The experimental study was carried out in the wave tank shown in Fig 1. Stable waves of steep profile and of period ranging from 0.74 to 4 seconds for water depths as shallow as 6 inches can be generated at the test section. Current corresponding to controlled rates ranging from 500 to 4000 gpm can be developed either in or against the direction of wave propagation. A current deflector is fitted in way of the ports in the converging section to reduce the up-swelling action of the flow entering from the ports. A spending beach of 1:20 slope is installed at the end opposite from the wave generating section, to reduce wave reflection and to smooth the velocity distribution when the current is made to flow opposite the wave direction.

Pier Model

The pier model (Fig 2) is made of aluminum at a scale of 1/100 that of the prototype. It consists of four detachable sections so that, as water depth is varied, the position of the calm waterline remains relatively unchanged and approximately 1.5 to 2 inches above the top of the cylindrical portion of the pier. The pier model is fitted with three adaptors for diaphragm-type pressure transducers, two in the conical section and one in the uppermost section of the cylindrical body. Each cylindrical section of the model is also tapped for cavity-type pressure transducers. Generally, pressure transducers are sensitive to temperature fluctuations. When the pressure fluctuations to be measured are small, as in the present tests, temperature fluctuations can have a pronounced effect on the results. To minimize the possible error so introduced, the temperature of the transducers is matched to that of the water in the tank by continuously running a thin film of tank water over the transducers.

Two force gages are mounted to a 2-inch by 1/4-inch flat bar which is fixed on the side wall of the wave tank and protrudes into the pier through the opening at its top. These gages are for the measurement of the magnitude and point of application of the horizontal hydrodynamic force exerted on the pier. The lower gage is fixed to its flat-bar support and allowed to float in a force-transmitting adaptor which is fixed

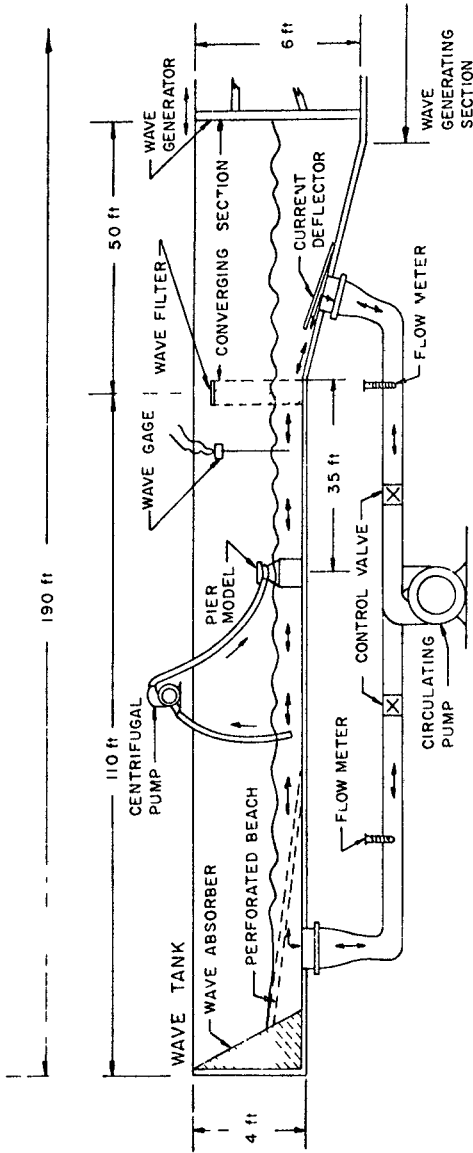


Figure 1
General Arrangement of Experimental Setup

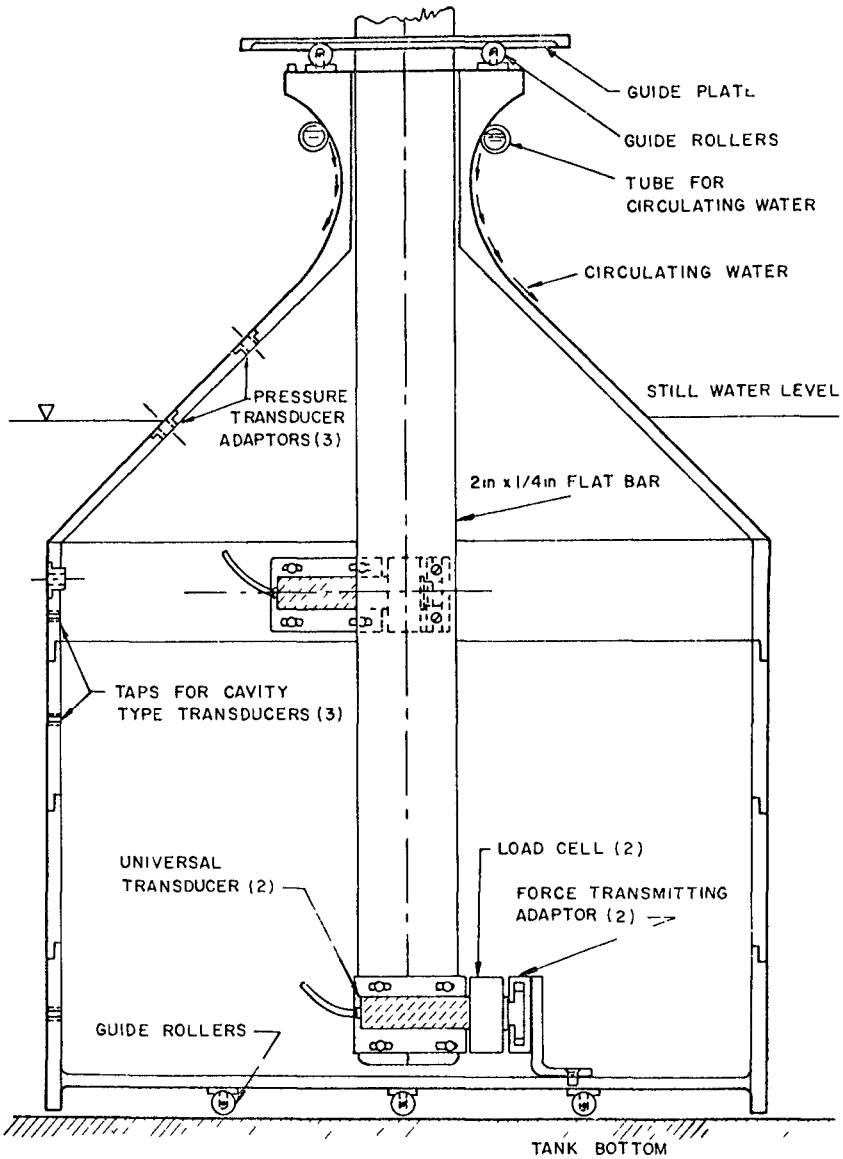


Figure 2
Pier Model

to the pier and designed to transmit only tension or compression in the horizontal direction. The upper gage is mounted in a reverse fashion, it is fixed to the pier and allowed to float in an adaptor fixed to the flat bar (Fig. 2)

Instrument

The flush diaphragm pressure transducers and the cavity pressure transducers are both of the resistive type and manufactured by Statham Instruments, Inc. The former, with a pressure range of 0 to 5 psig and a natural frequency of 3.5 KC, are used to measure the wave pressure on the pier in the region where waterline fluctuates and impact is likely to happen, whereas the latter, with a pressure range of 0.5 psi differential pressure, are used in the region that is always fully submerged.

The force gage consists of a Statham Universal Transducing Cell of Model UC3 and a load cell adaptor with a load range of 50 pounds. The Universal Transducing Cell is itself a basic sensing element made from strain gages and is capable of measuring a variety of physical parameters by using different adaptors. The load cell adaptor is, of course, as its name implies, an accessory for transmitting forces.

The water surface elevations were measured by resistance type gage consisting of a pair of surface-piercing parallel wires, across which an excitation voltage was impressed. The corresponding voltage variations caused by fluctuations of the wetted line on the gage were recorded in wave-forms on a paper by a Sanborn Recorder.

The current-velocity distributions across the test section were measured by conventional 0.25-inch Pitot tubes in conjunction with precision manometer which can be read to 0.001 inch.

Procedure

The magnitude and point of application of the horizontal force were determined for the various combinations of wave and current characteristics of Table 1. In these tests, the model of the pier was first made quasi-neutrally buoyant by ballasting. The model was then suppressed into the water by a horizontal bar mounted fixed to the side wall of the tank, but clear of the tank bottom. Guide rollers between the model and the bar confined the pier model to move in the horizontal direction. The force gages were mechanically biased to one-half of their full range so that they would respond in both tension and compression to a 25-pound maximum value. These gages were calibrated by applying through a set of pulleys known horizontal forces at the midpoint between gages.

The hydrodynamic pressure distribution was also determined for the combination of wave and current characteristics of Table 1 and for water depths of 6 inches and 12 inches corresponding to 50 and 100 foot full scale. In these tests, the model of the pier was mounted so as to be

TABLE 1
Test Schedule for Force and Pressure Measurement

Water Depth	Model (in)	6	9	12
	Prototype (ft)	50	75	100
Current Speed	Model (fps)	0, ± 0.2 , ± 0.4 , ± 0.6	0, ± 0.2 , ± 0.4 , ± 0.6	0, ± 0.2 , ± 0.4 , ± 0.6 , ± 0.8
	Prototype (Knots)	0, ± 1.2 , ± 2.4 , ± 3.6	0, ± 1.2 , ± 2.4 , ± 3.6	0, ± 1.2 , ± 2.4 , ± 3.6 , ± 4.8
Wave Height	Model (in)	1.4 3.0	1.4 3.0	1.4 3.0
	Prototype (ft)	12 25	12 25	12 25
Wave Period	Model (sec)	0.75, 0.85, 1.0	0.75, 0.85, 1.0	0.75, 0.85, 1.0
	Prototype (Sec)	7.5, 8.5, 10	7.5, 8.5, 10	7.5, 8.5, 10

fixed to the tank. The pressure was measured at five points along a meridian. Measurements were made for 30-degree increments in polar angle with respect to current and wave direction.

The impact pressure was sensed by transducers of the flush diaphragm type since in the region of impact the transducer is alternately wet and dry. Because of the short duration of the impact, the signal transmitted by the transducer, after being amplified, was displayed on an oscilloscope and photographically recorded.

Test Results and Discussion

Wave Force

A typical time record of the wave force exerted on the pier along with the history of the wave measured alongside the pier is shown in Fig. 3. From these records it is possible to determine the phase of the wave, with reference to the centerline of the pier, at which the wave force is a maximum. This maximum occurs when the wave node coincides with such centerline, for which condition the velocity-dependent force is a minimum. Thus, the maximum wave force is almost solely of acceleration-induced loading. This result supports the argument made under Dimensional Analysis and Scaling Laws.

It has been shown that the force coefficient defined in Eq. (2) is a function of the H/d and $V/(gd)^{1/2}$. The effect of wave steepness (H/d) on the force coefficient is found to be insignificant, at least in the tested range of H/d (0.08 - 0.4).

In the case of shallow water, in the present experiment, the parameter $V/(gd)^{1/2}$, which is determining the influence of current on wave kinematics, although just how this parameter is related to wave dynamics is, as yet, somewhat unexplained. The experimental results of C_{ms} plotted versus $V/(gd)^{1/2}$, are shown in Figs. 4, 5, and 6 for water depths of 6, 9, and 12 inches respectively. The heavy solid lines in these figures are based on averaged values. The force coefficient fluctuates in the region of positive $V/(gd)^{1/2}$. A reverse current of increasing strength, however, always results in smaller force. The values of $V/(gd)^{1/2}$ which corresponds to maximum C_{ms} fall in the region of 0 to 0.25.

The foregoing arguments lead to the point that the wave force acting on the (full scale) pier can be calculated from

$$F = C_{ms} \rho g^{5/4} H_T^{1/2} D^{1/2} d^{5/4}$$

where C_{ms} has to be determined by model test at the corresponding Froude number. The wave height H is the local wave height with the absence of the pier and the current.

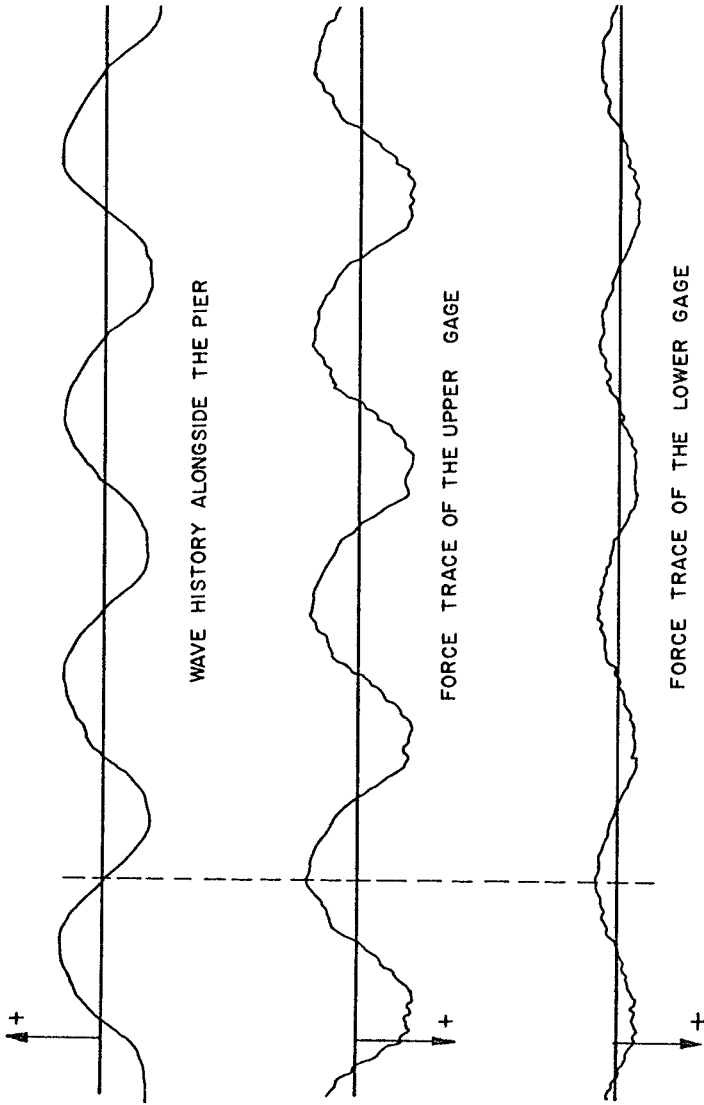


Figure 3
Example of Time Record of Force Measurement

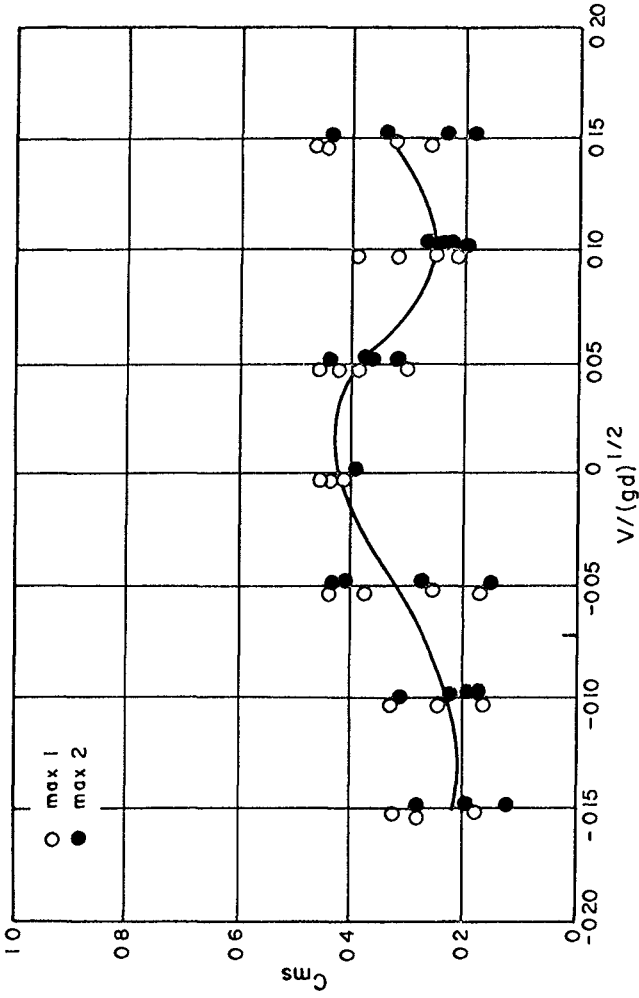


Figure 4
Force Coefficient versus Current Strength ($d = 6$ inches)

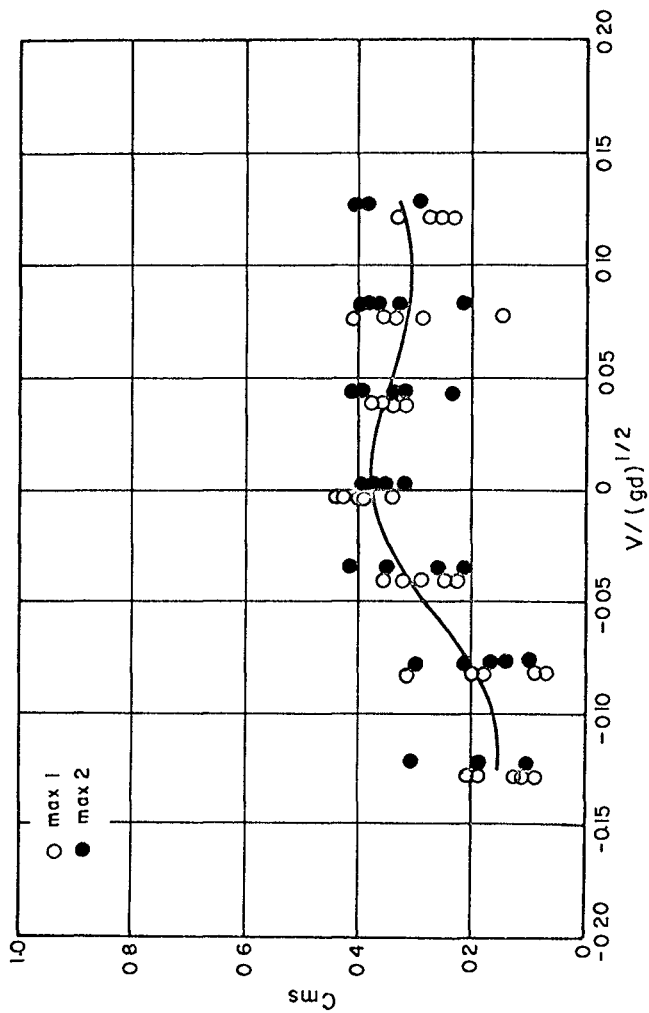


Figure 5

Force Coefficient versus Current Strength (d = 9 inches)

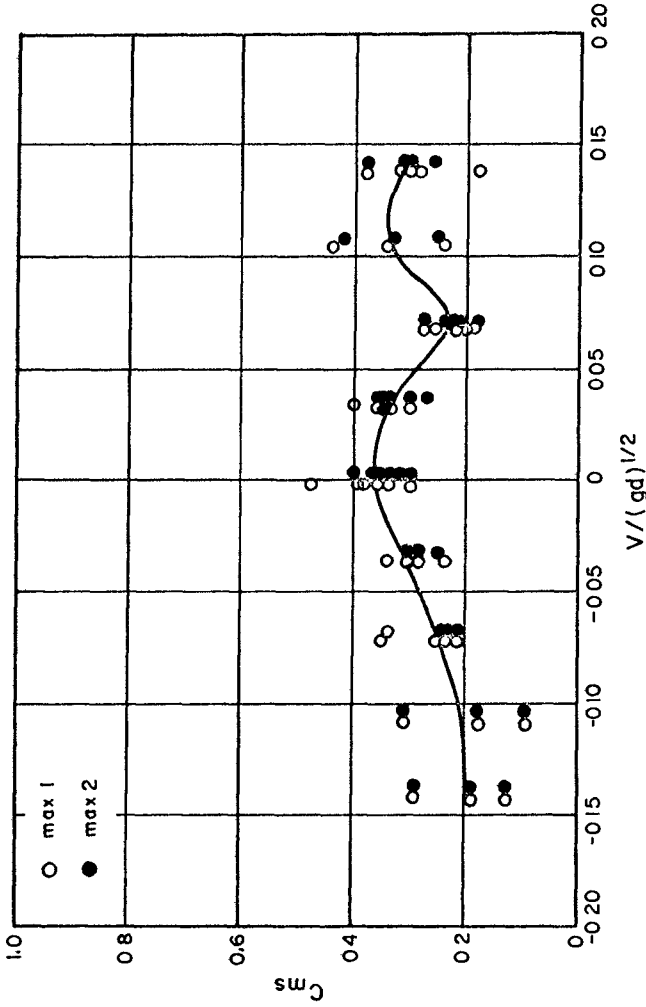


Figure 6
Force Coefficient versus Current Strength ($d = 12$ inches)

The wave force so obtained were generally larger than those computed by using the linear diffraction theory developed by McCamy and Fuchs (of the order of 20 - 30 per cent) It is also noted here that the experimental study dealt with a case of two-dimensional simulation in that the pier model was placed and tested in the middle of a straight channel which is approximately 40 feet away from either end of the current inlets This arrangement discounted the effects of channel constriction near which wave and current encounters and the flow is either accelerated or decelerated depending on the flow directions Experimental results reveal that the wave height at the test section with the absence of the pier model is always diminished by the effect of the current As a consequence, the greatest hydrodynamic loading exerted on the pier is obtained when the current is null, since the wave force is directly proportional to the wave height

However, one must be cautious to extend this conclusion to cases where three-dimensional effects mentioned above might be pronounced In fact, additional experiments were conducted in the tank and demonstrated that for long waves in shallow water the wave height was augmented by an oppose current

The point of application of the maximum horizontal force does not vary appreciably with change in test condition The mean values of the point of application measured from the mud line and their standard deviations are listed below

Water depth(d) (Inch)	Mean ($\frac{z}{d}$)		Standard deviation	
	Max 1	Max 2	Max 1	Max 2
12	0 535	0 525	0 049	0 055
9	0 585	0 555	0 053	0 073
6	0 575	0 550	0 085	0 098

The Max 1 and Max 2 are defined as in Fig 8

Wave Pressure

Pressure distribution about the pier was measured for water depths of 6 and 12 inches The pressure characteristics for both cases are quite similar Experimental results for the case of 12-inch depth only are presented here for the purpose of discussion Figure 7 illustrates the instantaneous pressure about the pier at a certain vertical position Figure 8 summarizes the results of maximum pressures as a function of angular and vertical position

The gross characteristics of the pressure about the pier model does not differ significantly from the case of a straight circular cylindrical caisson in the absence of current (Laird, 1955) - i e , neither the shape of the distribution curve nor the magnitude of the peak value ap-

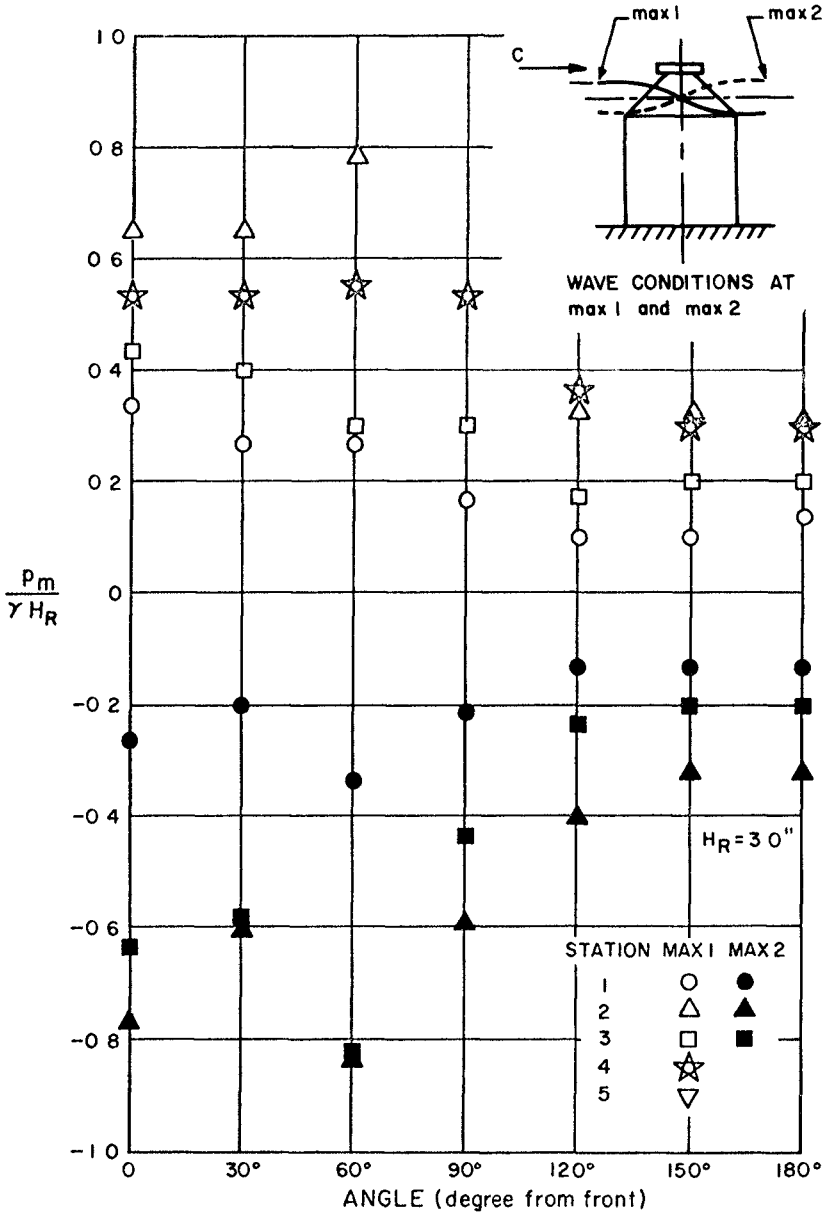


Figure 7

Pressure About the Pier at a Vertical Section

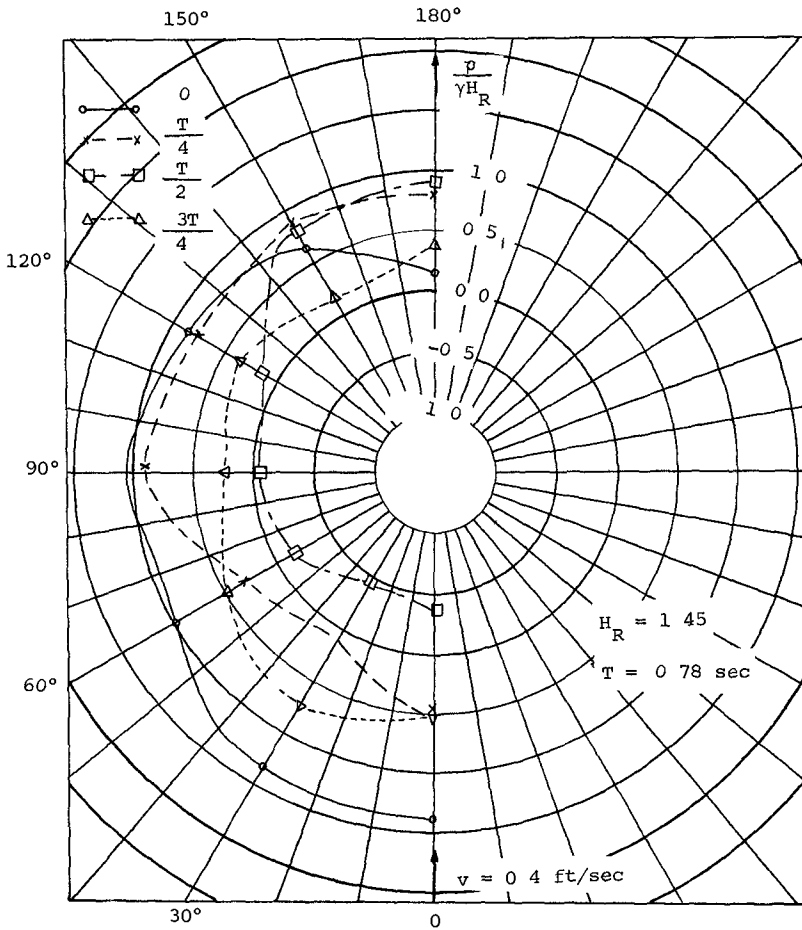


Figure 8

Maximum Pressures as a Function of Angular and Vertical Position
 ($v = -0.2 \text{ ft/sec}$)

peared abnormal with respect to the case of straight caisson. The effects of the conical upper section of the pier model are two fold (1) The wave pressure on this section itself is reduced considerably in comparison with that on a circular cylinder of comparable base diameter (2) The pressure on the cylindrical portion, immediately below the tapered section is also reduced, possibly due to the greatly reduced reflection by the conical section.

Note that the maximum pressure amplitude occurs either at or close to the forward stagnation point (facing waving and current) and is slightly smaller, or at most equal to, than that corresponding to a change in level equal to the wave height. This means that the wave is almost completely reflected by the cylindrical portion of pier.

The current affects the pressure distribution on the pier in the same manner as it affects the horizontal force, the magnitude of the maximum pressure fluctuates for increasing strength of forward current but decreases for increasing strength of opposed current. To a certain extent the presence of the current tends to deflect the wave front when waves approach the pier. This effect causes the location of the maximum pressure to shift away from the stagnation point.

The wave force exerted on the pier in the horizontal direction can also be obtained by integrating the pressure around the pier according to the following equation:

$$F = \int_0^{\eta(\theta)} dz \int_0^{2\pi} \frac{D(z)}{2} p(\theta, z) \cos\theta \cos\beta d\theta$$

or

$$F = \gamma D H_R \int_0^{\eta(\theta)} dz \int_0^{\pi} \frac{D(z)}{D} \frac{p(\theta, z)}{\gamma H_R} \cos\theta \cos\beta d\theta$$

where θ is the azimuth angle and β is the angle of normal of the surface measured from mud line. As an example, the maximum horizontal force for a specific case of $H_R = 1.45$ inch and $V = 0$ ft/sec was computed graphically and compared with the R result of direct measurement. Upon graphical integration values of

$$\int_0^{\pi} \frac{D(z)}{D} \frac{p(\theta, z)}{\gamma H_R} \cos\theta \cos\beta d\theta$$

are obtained. These values when plotted versus the height of pier (Fig. 9) can be used to construct the horizontal load distribution diagram on the

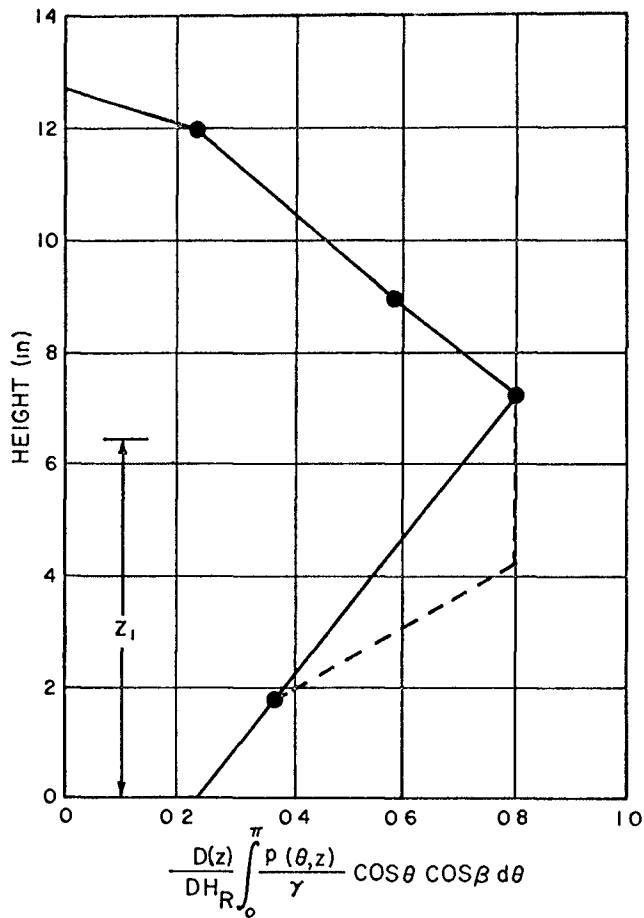


Figure 9

Load Diagram on Pier

pier The magnitude and the point of application of the total force calculated according to the force diagram which connects the data points by straight lines are respectively, 4 85 pounds and 6 4 inches The corresponding values in the direct measurement are 5 4 pounds and 6 3 inches The force magnitude obtained from pressure integration is 15 per cent smaller than directly measured This error results from the over simplified load diagram A more realistic, yet still simply constructed, load diagram is proposed and shown by the dotted line According to this modified load diagram, the magnitude and the points of application of the resultant force become 5 4 pounds and 6 1 inches

The load diagram also reveals two facts (1) A predominate portion of the total load applies on the middle section of pier Thus the point of application becomes insensitive to the variation of load magnitude This fact was observed and noted in the direct-force measurement (2) The horizontal load on the conical section contributes merely 10 per cent to the total load This leads to the explanation that the point of application of the horizontal force in the present geometrical configuration is considerably lower than that of a straight cylindrical caisson

Impact Pressure

With regard to the impact pressure measurement, Fig 10 shows a typical pressure traces displayed on the oscilloscope In the region of the upper tapered section, no impact was ever observed In the upper portion of the cylindrical section, impact of moderate magnitude (generally smaller than the maximum dynamic pressure) was observed occasionally when the backwash from the tapered section met the oncoming wave It was concluded that, for the present test conditions, the waves are neither steep enough or fast enough to induce significant impact loadings

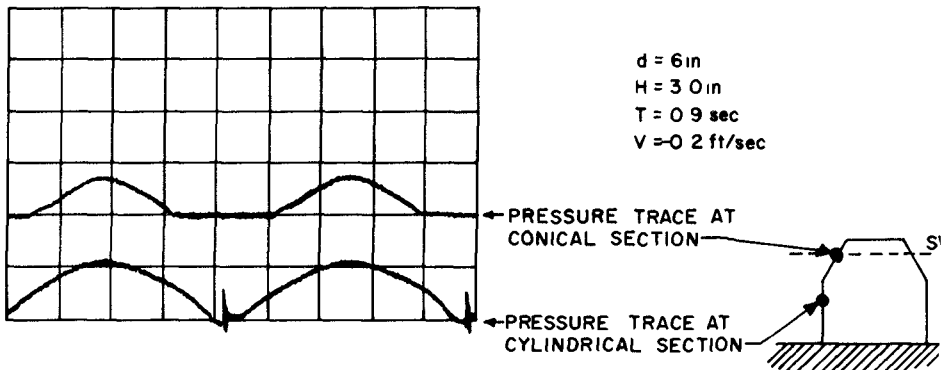


Figure 10

Examples of Time Record of Impact Pressure Measurement

Conclusions

Through scaled-model tests, the forces, moments, and the pressure distributions on the piers of the bridge for the Northumberland Strait Crossing have been determined. Geometrical simulations were partially fulfilled by placing the pier model in a wave channel that has a width of 4 feet. The test results fully support the known concept that when the pier diameter is large in comparison with the wave length, wave inertial force becomes predominant. Generally, the presence of current in either direction results in a decreasing in wave force unless the pier is located at the channel entrance where a relatively long wave encounters a strong current in a shallow water.

As far as the wave force is concerned, the conical pier section serves three functions: the total horizontal force is considerably reduced, the point of application of the horizontal force is lowered and becomes insensitive to the wave height, and the danger of wave impact is removed.

Measurements conducted in the wave tank provided the single experimental coefficient required to complete the result of dimensional analysis for this case. This coefficient is reasonably well behaved for a range of current strength and wave parameters. Consequently, all results reported herein are considered applicable for design purposes to bridge piers and to structures of similar geometry.

Acknowledgement

The program was sponsored by the Northumberland, Ltd of Canada. The permission of publication by the Department of Public Works of Canada is gratefully acknowledged. The author is also indebted to Dr Manley St Denis for his contribution and Drs Thomas Monti, and Ean Ma Caig, and Messrs Carlo Pentassuglia and James Cowley for their fruitful discussion.

References

- Bonnefille, R and Germain, P , "Wave Action on Isolated Vertical Cylinders of Large Dimensions," I A H R Congress, London, 1963
- Bretschneider, C L (1955), "An Evaluation of Inertia Coefficients in Wave Forces Experiments," Texas A & M Research Foundation Tech Report No 55-2
- Bretschneider, C L (1957), "Evaluation of Drag and Inertia Coefficients for Maximum Range of Total Wave Forces," Texas A & M Research Foundation Report No 55-5
- Goda, Y (1964), "Wave Forces on a Vertical Circular Cylinder," Port and Harbour Technical Research Institute, Japan, Report No 8
- Keulegan, Garkis H , and Carpenter, Lloyd H (1958), "Forces on Cylinders and Plates in an Oscillating Fluid," Journal of Research, National Bureau of Standards, 60, 5, May 1958
- Laird, A D K (1955), "A Model Study of Wave Action on a Cylindrical Island," Transactions American Geophysical Union, 36, 2 April 1955
- Longuet-Higgins, M S and Stewart, R W (1961), "The Changes in Amplitude of Short Gravity Waves on Steady Non-uniform Current," Journal of Fluid Mechanics, 10, part 4, June 1961
- MacCamy, R C , and Fuch, R A (1954), "Wave Force on Piles, a Diffraction Theory," U S Army Corps of Engineers, Beach Erosion Board, Technical Memorandum No 69, December 1954
- Morison, J R , Johnson, J W and O'Brine, M P (1953), "Experimental Studies on Forces on Piles," Proceedings of Fourth Conference on Coastal Engineering

CHAPTER 92

SOME EXPERIMENTS WITH SAND-FILLED FLEXIBLE TUBES

by

Per Roed Jakobsen, M sc , Danish Board of Maritime Works

and

Arne Hasle Nielsen, M Sc , Danish Institute of Applied Hydraulics

ABSTRACT

Experiments with the use of long sand-filled flexible plastic tubes ("Sand sausages") have been carried out for coastal protection purposes at several exposed locations along the Danish coasts since 1967. In general the results have been encouraging.

Several methods have been used to fill the tubes with sand. A simple inexpensive hydraulic method for easy filling of almost impermeable tubes on site has been developed by model and prototype experiments with promising results.

As a result of the experiments it seems likely that sand-filled tubes may be used with advantage as temporary structures, i.e. for full-scale pilot investigations and to solve acute problems, or they may be incorporated in more permanent structures.

1 INTRODUCTION

Flexible sand bags have been used in hydraulic engineering practice for many years, but due to the poor quality of available materials the use was mainly restricted until recent times to projects of non-permanent nature such as emergency flood control and protection of dikes.

However, with the development of fabrics of durable, strong synthetic fibres of nylon, polypropylene, etc., new possibilities have arisen for more permanent use of large sand bags in more exposed locations than could previously be considered.

The paper describes some preliminary experiments with long flexible sand tubes in coastal protection works that have been carried out in Denmark since 1967 by model and prototype experiments.

2 FILLING METHODS

One of the major problems in the economical use of long flexible sand tubes is filling the skin.

Several ingenious devices and filling methods have been developed for the filling of skins of permeable fabrics. The sand is usually transported into the tube by hydraulic pumping and the water escapes through the permeable fabric, leaving the sand grains in the tube.

In most cases the discharge tube is drawn backwards inside the tube with a speed corresponding to the rate of filling leaving the filled tube behind (Fig 1).

A much simpler and more economical hydraulic filling method which allows filling of sand tubes to almost any length above or below the water surface from the "front" end of the tube has been developed simply by using impermeable instead of permeable fabrics.

When the mixture of sand and water flows into the impermeable flexible tube, the sand settles out near the inlet until the cross-section has decreased so much that a small "river" is formed in the tube on top of the accreted material

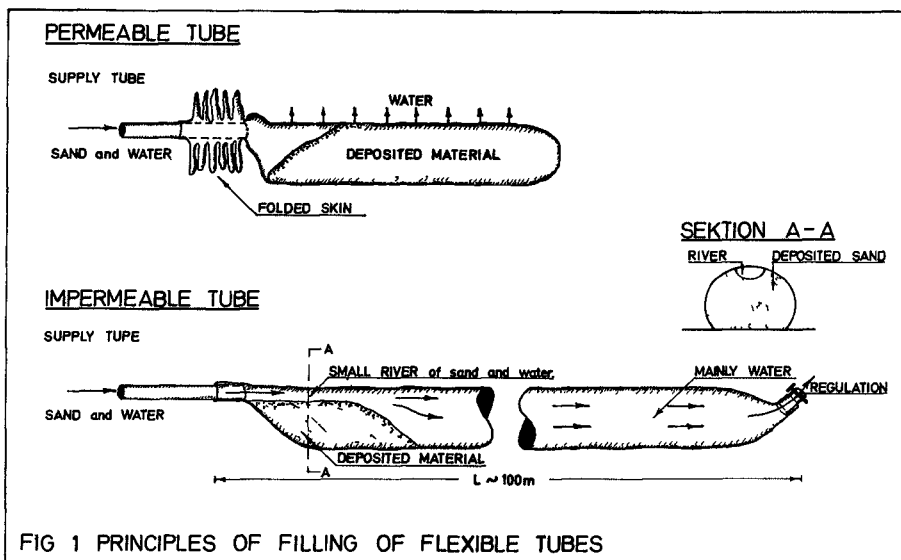


FIG 1 PRINCIPLES OF FILLING OF FLEXIBLE TUBES

The mixture of water and sand is now transported forward in the tube and the sand grains settle out in front of the already accreted material, while the water leaves the tube through an opening at the far end. By decreasing the outlet opening, the skin may be expanded by water pressure whereby an almost circular, filled cross-section can be obtained.

In laboratory tests the sand/water mixture was injected by sand-pumping, while in experiments in the field a different method was primarily employed: water was fed under high pressure through a type of diffuser into which the filling material was added directly.

The impression has been procured from the experiments that in principle almost infinitely long, large cross-section tubes can be filled by hydraulic pumping provided the skin is impermeable at the time of filling.

3 EXPERIMENTS IN NATURE

While the filling method was developed by model experiments the resistance of fabrics to atmospheric conditions, ultraviolet sun rays, ice, human activity, etc., was investigated by full scale experiment in nature where various types of constructions were also tested under different conditions.

Experiments were conducted in about 10 different locations, including sites on the exposed coasts of Jutland and on the more sheltered island coasts of Funen and Zealand.

The type of structures employed in natural locations so far has in most cases been groins, in some cases however revements and embankments have been built.

Cross-sections of the various structures have been (1) a single

tube, (2) one tube resting on two tubes, forming a triangular cross-section, and (3) two tubes placed at the sides of an interjacent sheet covering a sand-prism. Future plans call for experiments with multicellular cross-sections.

Tubes of a diameter of up to 100 cm have been filled to lengths of up to 100 meters, and at water depths of up to 3 meters.

Various methods have been tried to make the tubes in the structures behave as units. In some cases tubes have been lashed together by plastic ropes, in other cases tubes have been wrapped in filter sheets. Later experiments have involved weaving together the lower tubes in prism structures.



Fig. 2. Structures composed of sand tubes with diameter 0.7 m (1 tube on top of 2)

In almost all the structures installed on sandy beaches there has been a problem of bottom protection. (The authors are aware that in autumn 1970 sand-tube structures with a new form of bottom protection of filter sheeting have been erected on the coast of South Carolina, U.S.A.).

On shingle beaches there have been no problems of bottom protection.

In all the experiments tubes have been entirely unprotected; in less exposed locations such structures may have a working life of several years. For permanent use of tubes above the water surface, tubes should be protected by a covering layer of rocks or similar material.

The first sand-tube experiments conducted in Denmark took place in spring 1967. The only point worthy of mention in this connection is that one of the filled tubes, laid at a depth of water of approx. 100 cm and



Fig. 3. Tubes wrapped into a filter sheet.

thus protected against sunlight, is still intact, covered with barnacles, cockles and other sea-life.

Some of the experiments are illustrated and described below.

Fig 4 shows the small fishing town of Lønstrup on the west coast of Jutland. Tidal range is about 0.3 m but wind set-up may be about 1.5 m combined with heavy wave action.

The littoral South-North drift is estimated at approx. $500,000 \text{ m}^3$ p.a. On account of the poor condition of the existing high wooden groin, which was no longer able to ensure the necessary build-up of the beach, three sand tubes were laid out in 1967 along the foot of the groin. As anticipated, this caused a considerable build-up of the foreshore.

The tubes sank somewhat during the winter of 1967-68 although they had been given bottom protection in the form of filter sheeting - but they stopped sinking when they came to rest on an old stone layer, the remains of the foot protection of the wooden groin. Consequently another three tubes were added in 1968.

In autumn 1969 the structure was severely damaged during a military landing exercise.

The structure was repaired in 1970 as shown in the illustration, with a prism groin comprising three hydraulic filled tubes, diameter 0.7 m, lashed together with plastic ropes, the lower tubes woven together.

In spring 1969 an experiment began on the barrier beach south of the harbour at Hvide Sande on the west coast of Jutland (See Fig. 5). The experiment served three main purposes:

1. A further development of sand tube constructions.



Fig. 4. Sand tube groin (Lønstrup at the Danish North Sea Coast).

2. To obtain better knowledge of the applicability of sand tubes in coastal protection works.
3. Measures against a downdrift recession caused by a mole built to protect the Hvide Sande inlet.

The barrier is only about 1 km wide but has a natural protection of dunes.

The coast is exposed towards the west, prevailing winds from W-NW, and the N-S littoral drift is estimated at $400,000 \text{ m}^3$ p.a. Tidal range less than 0.8 m, wind set up may be up to + 3.0 m.

The constructions described in the following were with few exceptions made of three tubes laid out to form a prism. The tubes were permeable made of double layers of black polypropylene monofilament.

Group 1: Four beach groins. (Fig. 5).
35 m long, starting on the dune at a level of + 6-7 m, ending on the beach at level + 2 m.

Group 2: Two artificial beach ridges.
One half-moon shaped with a shingle drain under the middle section. Total length 70 m.
Laid out with top level - 0.2 m at the front and the ends at top level appr. + 1.0 m.
The construction never really worked because the permeable tubes over the drain were washed out by a gale during the construction period.



Fig. 5. Beach groins (Hvide Sande. The danish North Sea Coast).

The other ridge boomerang shaped.

Total length 70 m. Laid out on the beach at level + 1 m. After a short while the structure sank and is now buried in the sand.

Group 3: Two groins going from the dune foot to the still water line, spaced 120 m apart and at an angle of 20° north to the coast normal.

Group 4: As group three, now showing 20° south.

Finally two constructions in the form of dozed sand prisms normal and parallel to the coast covered with a filter sheet stitched on both sides to individual tubes; unfortunately the stitching was not strong enough and the structures failed after a short while.

Experimences:

The material has shown good resistance to the forces acting upon it. The tube structures must be held together by some means: It is essential to pay careful attention to the problem of bottom protection. Some attempts were tried with filter sheet but were not properly executed. Thus the "groins" and "ridges" followed the seasonal beach fluctuations down - but of course never up again.

A extensive measurement program following the experiments will be finished and finally evaluated in the summer of 1971 so far it can be stated that in the period summer 1969 to spring 1970 stabilisation of the beach has been noted.



Fig. 6. Enebærødde (Funen).

On the Enebærødde spit on the north coast of Funen a contractor has been conducting some experiments, that began in autumn 1969.

There was a minor erosion problem in the test field.

The tubes used were made of polypropylene lined with plastic D = 0.70 m.

There have been some interesting features in these experiments especially concerning some groins made of single tubes going to a water depth of approx. - 1.0 m. (Fig. 6).

1. The sand-tube groins in this relatively calm area had a significant traditional groin effect.
2. The groins did not show any damages in the breaker zone.
3. During the severe winter 1969-70 the tubes remained intact, although subjects to rather hard ice attacks.
4. The spit consists mainly of rather coarse material (shingle) but this has not apparently caused extra wear on the tubes,
5. but keeps them from sinking.

Lately - spring 1970 - sand tubes have been used for dune foot protection on an artificial spit along the Lime Inlet on the west coast of Denmark.



Fig. 7. Sydhalen (Thyborøn).

The tubes were laid out on the west beach of the spit and thus face the east part of the southern Thyborøn barrier; the construction is not therefore in a very exposed position. (Fig. 7).

The structure is a 2 x 100 m prism arrangement with three 70 cm diameter tubes made of polypropylene tubes lined with impermeable plastic foil.

On the southern section the tubes are lashed together with ropes while on the northern section the two lower tubes are woven together. Later sand will be dozed up between the eroded dune and the structure.

The tubes were filled very successfully by the hydraulic principle and had a very high filling degree, a level of about 90 % of the theoretical diameter being obtained.

In June 1970 the first 1 m diameter tube was laid out north of the harbour at the Skaw.

The effective height obtained was approx. 90 cm, the far end of the tube was positioned at a water depth of approx. 3.0 m.

It was build in an old landing stage, and accreted in a short while sand to a height varying from 0.20 m at depth 1.50 m to 1 m at the shore end.

Other projects have been carried out, and new are under preparation.

4 MATERIALS

Several types of polypropylene fabrics have been used for the skin of the tubes

White polypropylene very soon appeared to have an unsatisfactory resistance to the influence of ultraviolet sun rays, and the fibres of a black polypropylene monofilament had an unfortunate tendency to slide so the sand grains could be washed out

A woven black fabric, multiplex polypropylene splitfibre, seems to have solved most of these problems and has furthermore proved very resistant to icy conditions and to the effect of human activity, at bathing beaches for more than 1 year. When the hydraulic filling method is used the skin is lined with an inner tube of plastic foil to obtain impermeability.

Tubes with diameters of up to 1.0 m have been filled to lengths of up to 1.00 m and at water depths of up to - 3 m. The filling material has been natural beach sand with mean grain diameters of about 0.25-0.50 mm. A recent small test with hydraulic filling of a tube with a mixture of 1 part cement to 3 parts of sand has worked out well.

CONCLUSIONS

On the basis of preliminary experiments conducted hitherto the following conclusions may be drawn:

- (1) Impermeable sand tubes can be filled above and under the water to almost any length by hydraulic pumping.
- (2) The selected type of fabric has demonstrated relatively good resistance to the forces acting in coastal environment.
- (3) The experiments have shown that sand tubes may be used with advantage to solve minor coast problems, as temporary structures and for prototype pilot tests because the sand tubes can be easily removed.
- (4) If sand tubes are protected from sunlight and from human activity their use may be of a permanent nature.
- (5) Many problems are still unsolved and the use of tubes is still in the development stage. Work is in progress towards development of larger and more economical sizes of tubes.

CHAPTER 93

THE PRESSURE OF FLOATING ICE-FIELDS ON PILES

by Joachim SCHWARZ¹⁾

ES NOPSIS

In order to determine the maximum ice forces against structures, the compressive strength was investigated by laboratory tests on cubes of several ice species. The results contain the influence of temperature, velocity of deformation and direction of pressure on the cubic strength.

In order to employ these laboratory results for the calculation of structures, a relationship between the strength in laboratory tests and in nature was derived by measuring the pressure of floating ice-fields on a pile of a bridge, which crosses the tidal estuary of the EIDER River.

The investigation leads to an equation, which allows the calculation of ice pressure against piles.

INTRODUCTION

In cold regions the pressure of ice is decisive for the calculation of hydraulic structures. This pressure, however, is still unknown or just in development. It is therefore not surprising that in severe winters hydraulic structures will be destroyed by ice run.

In rivers the danger of ice pressure decreases with time, because the ice run in spring will be controlled by ice-breaker-

¹⁾Dr.-Ing., Scientific Assistant of the FRANZIUS-INSTITUT, Technical University of Hannover, Germany

A similar report was given by the author at the 1. Ice-Symposium of IAHR in Reykjavik, September 1970

ships and because the ice formation will be reduced by the heated water of power-stations.

In coastal regions there is no way of keeping the ice forces from structures and just in these locations the question of ice pressure becomes more and more important, for example by the offshore-construction of deep-water harbors, transloading-points for oil, light-houses and bridges.

Intensive ice research was started after World-War II., especially in USA, Canada and Russia with the investigation of fundamental properties of ice (6).

The problem of ice forces on structures has picked up during the last 10 years: KORZHAVIN (3, 1962) developed an equation to calculate the pressure of river ice in spring. This formula is based upon assumptions, which are only derived through laboratory tests. PEYTON (4, 1966) measured the ice pressure on the piles of a drilling-platform in Cook Inlet, Alaska. His qualitative results are in agreement with the investigations of the author. Some experimental work, carried out by oil companies (CROASDALE, 2, 1970) has not yet been published.

A general view about the present situation of research of ice pressure on structures was given by ASSUR (1, 1970) at the 1. Ice Symposium of IAHR, 8 - 10 September 1970 in Reykjavik.

GENERAL CONSIDERATION

The authors investigation (5, 1970) of the pressure of floating ice-fields on piles has been based on the assumption that the maximum pressure of ice is limited by its compressive strength. This strength was first of all ascertained in compression tests on cubes in order to determine systematically the different influences, such as temperature, velocity of deformation and direction of pressure. The received cubic strength can't be immediately employed for designing structures, because in nature the rupture of ice occurs in another way than in our laboratory tests. In nature the contact between ice and structure

is, for example, smaller than in the experiments between ice cube and pressure plate. Moreover the shape, the width of the structure and the thickness of ice has an influence upon the strength.

Because the fundamental strength properties nevertheless should be utilized for calculating ice forces, it was necessary to derive a relationship between the strength in laboratory tests and in nature. This was done by measuring the ice-forces on a pile of a bridge.

LABORATORY TESTS

Strength properties were investigated by compression tests on ice-cubes from river, lake and harbor (fresh-water-ice) and from the North-Sea, Baltic-Sea and brackish-water (salt-water-ice).

The edge lengths of the cubes were 10 cm. The tests were performed at ice temperatures of 0° , -10° and -20° C in two different directions (perpendicular and parallel to the growth-direction). The velocity of deformation was varied from $S = 3 \cdot 10^{-3} \frac{1}{\text{sec}}$ to $S = 3 \cdot 10^0 \frac{1}{\text{sec}}$. Plywood panels were placed between the cube area and the pressure plate, in order to average out the unevenness on the cube surface, so that the test results scattered only up to $\pm 5\%$.

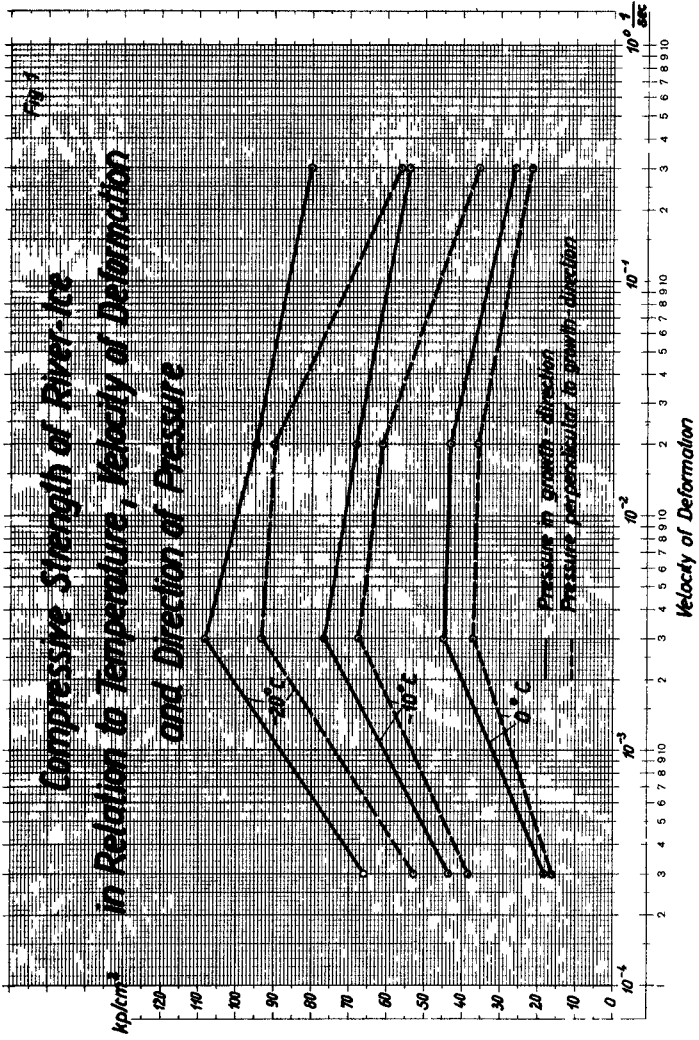
RESULTS

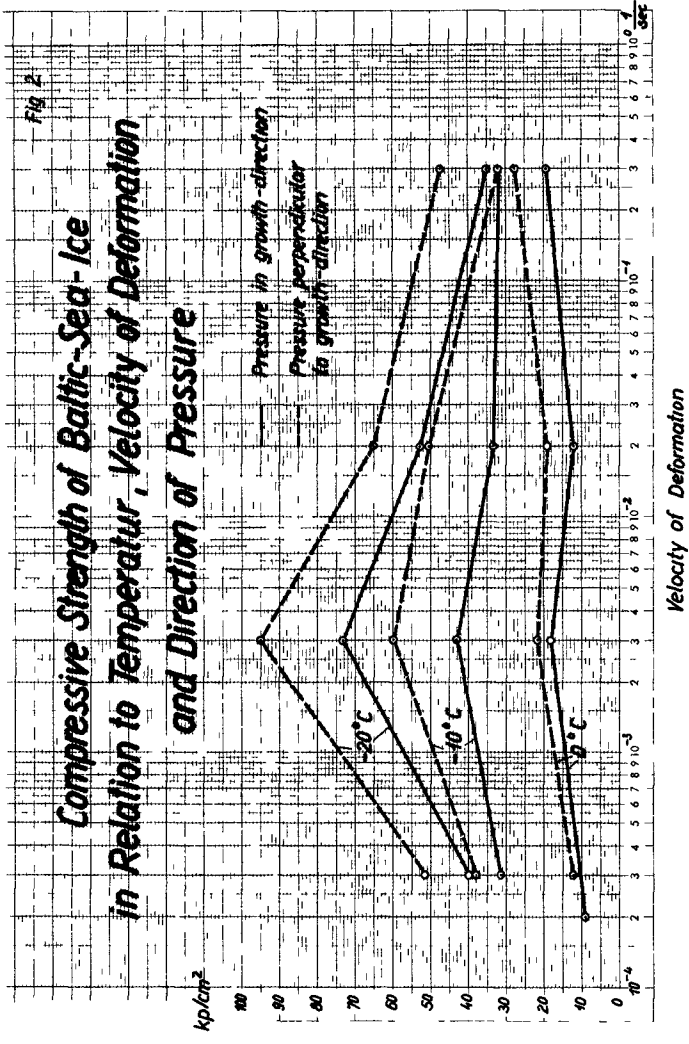
1. By lowering the temperature, the strength of ice increases at a rate of about.

$$\alpha = 4,5 \text{ kp/cm}^2\text{C with fresh-water-ice and}$$

$$\alpha = 2,5 \text{ kp/cm}^2\text{C with salt-water-ice.}$$

This strengthening is nearly linear down to -20° C. The lesser strength of salt-water-ice is attributed to the liquid brine cells within the ice.





2. At a deformation velocity of $S = 0,003 \frac{1}{\text{sec}}$ there is a maximum in strength (Fig. 1, 2). This result is explainable from the deflection-time-curve, shown in Fig. 3. The maximum appears at all ice species at the same strain rate and is more evident, the colder the ice is. The deformation velocity of $S = 0,003 \frac{1}{\text{sec}}$ corresponds to an ice sheet velocity of only a few cm/sec. That means, if the ice temperature is low, the maximum ice pressure in nature is to be expected just before the ice sheet stops.
3. If the pressure acts parallel to the growth direction, the strength of fresh-water-ice is 20 % higher (Fig. 1) than if the pressure direction is perpendicular to the growth direction. With salt-water-ice these relations are just the reverse.
4. Between air-content within the ice and strength exists a nearly linear relation.

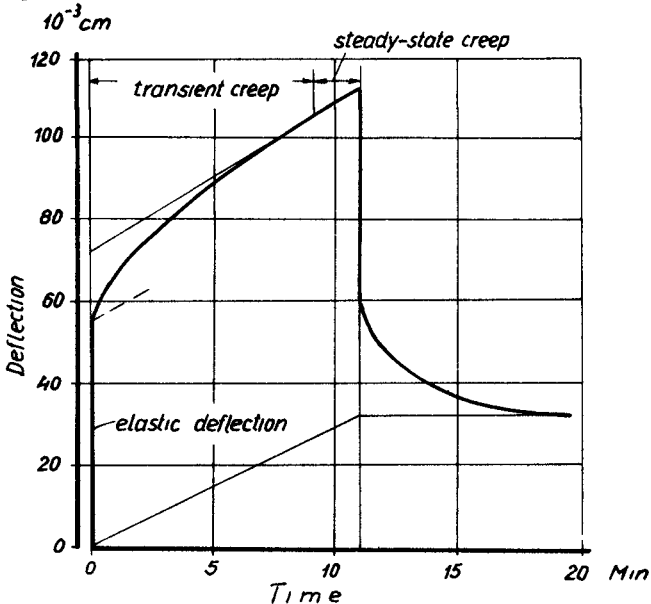


FIG. 3 DEFLECTION OF ICE VS TIME (TABATA, 7)

MEASUREMENT IN NATURE

The compressive strength of sea ice, as occurs in nature, was measured in winter 1967/68 and 1968/69 at a pile of a bridge, which crosses the tidal estuary of the Eider during the construction of a tidal barrier.

Along the entire German coast of the North Sea and also just outside the estuary of the Eider lie large flat areas (wadden ground), where ice fields can grow very quickly. These ice fields float up only at higher tides and then drift with the tidal current against the bridge, where the ice fields are cut up by the piles. In the hereby occurring state of stress the ice strength has maximum values.

The testing instrument consists of a shield with 50 pressure cells (Fig. 4), 5 in each altitude level halfway encompassing the pile (\emptyset 60 cm). The area of the pressure cells was



15 cm x 15 cm. In some of these pressure cells were situated smaller ones with areas of 25 cm² and 50 cm² in order to determine the relationship between strength and area of pressure. The shield was fixed on the sea-side of the pile (Fig. 5).

Insulating the electronic part of the pressure cell against salt water presented a particular problem. It was solved with BOSTIC-NEOSEAL and SILICON-CAOUTCHOUC.

FIG. 4 SHIELD WITH
50 PRESSURE CELLS



RESULT

In a paper of probability (Fig. 6) the strength of sea-ice in nature, related to several areas of pressure ($\sigma_{F'} \Rightarrow 25 \text{ cm}^2$, $\sigma_{F'} \Rightarrow 200 \text{ cm}^2$, $\sigma_{\phi} \Rightarrow 840 \text{ cm}^2 \Rightarrow$ the whole width of the pile at an ice thickness of 14 cm) was compared with the cubic strength from laboratory tests with the same ice.

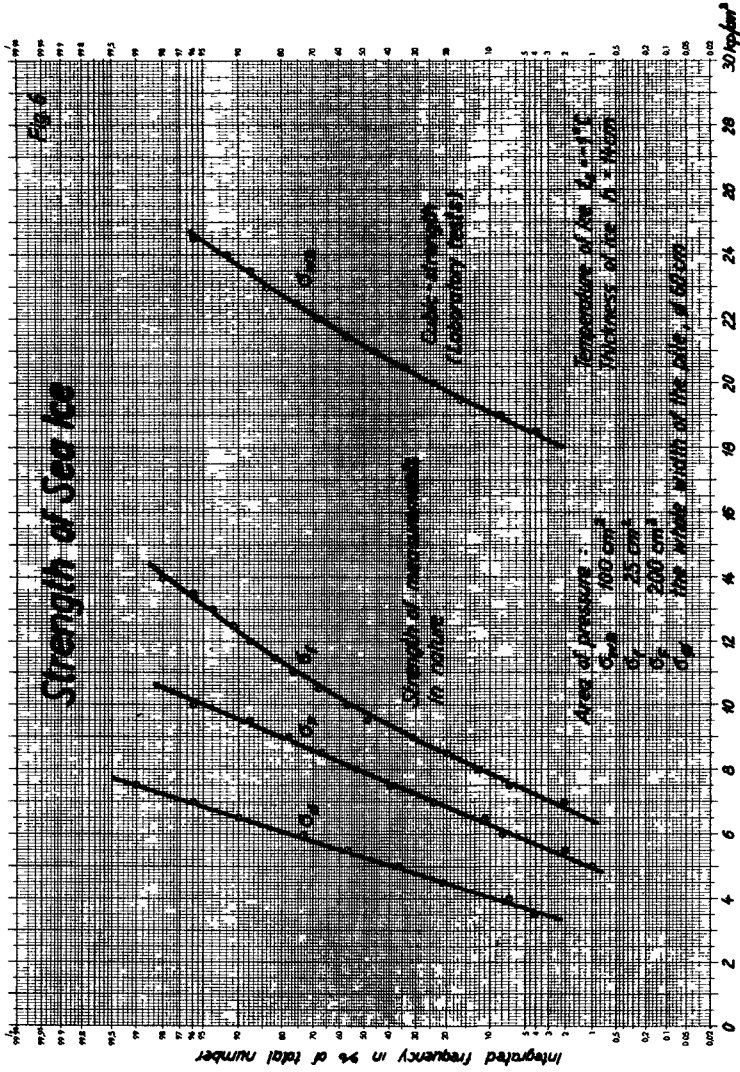
FIG. 5 POINT FOR MEASURING ICE PRESSURE ON A PILE OF A BRIDGE

1. If the pressure is related to an area of $F' = 200 \text{ cm}^2$ the compressive strength in nature ($\sigma_{F'}$) is only half of the cubic strength (σ_{WB})

$$\frac{\sigma_{F',99}}{\sigma_{WB,50}} = \kappa_{F'} = 0.5$$

This reduction of the cubic strength is attributed to the incomplete contact between ice and structure. Therefore κ is called contact coefficient, although this value includes the different state of stress in the cube pressure experiment and in nature.

2. If the area of pressure is only $f = 25 \text{ cm}^2$, the coefficient of contact increases to $\kappa_f = 0.56$.



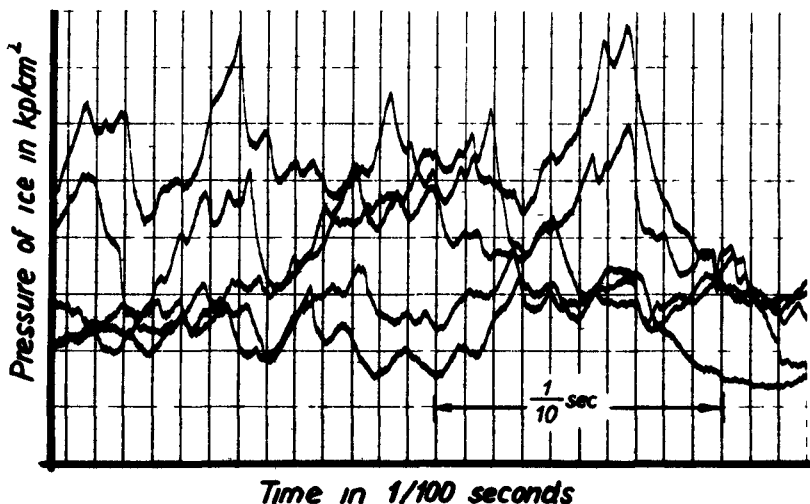


FIG. 7 ICE PRESSURE ON 5 SIDE BY SIDE PRESSURE CELLS

3. Because the peaks of pressure (Fig. 7) occur simultaneously only on 1 or 2 of the 5 side by side load cells - the others being largely unpressured - a second reduction factor from the proportion

$$\frac{\sigma_{\phi}}{\sigma_F} = 0,66 \text{ was ascertained.}$$

σ_{ϕ} is the mean pressure over the whole width of the pile \times thickness of ice, projected in the direction of floating. 0.66 takes into account first of all the shape of the structure, but also the increase of the area of pressure from 200 cm² to 840 cm².

4. From measurements of different thicknesses of ice follows, that the strength of ice increases, if the ratio thickness of ice to width of pile becomes greater (Fig. 8). This is caused by the increase of the

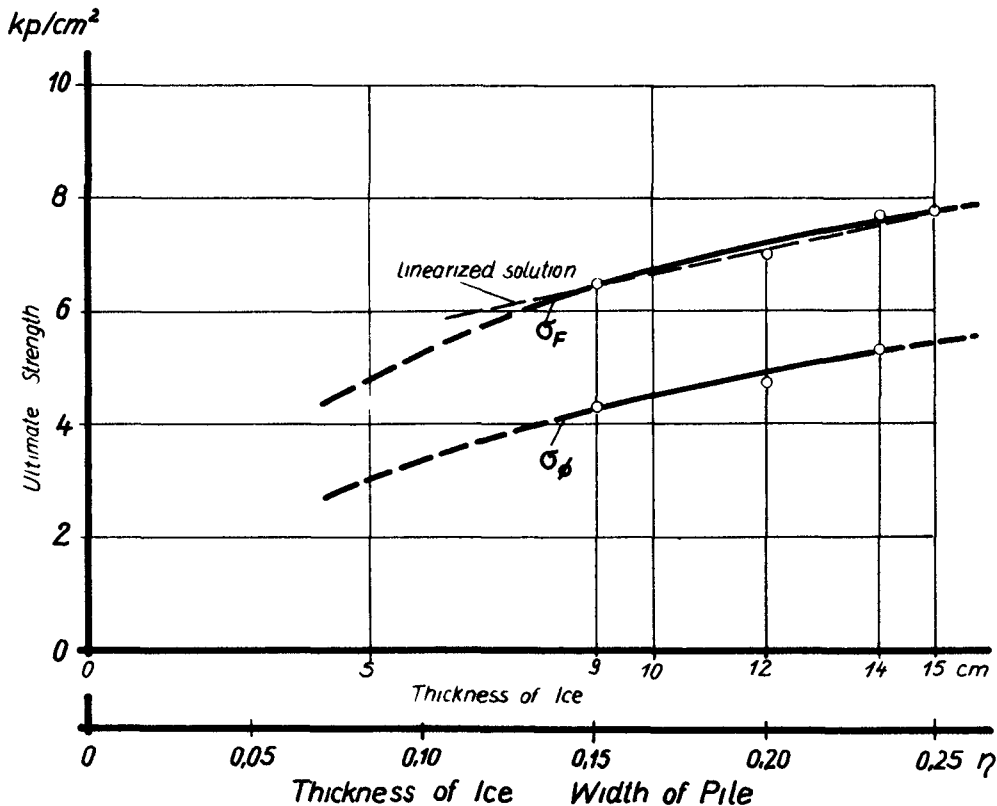


FIG. 8 RELATION BETWEEN ULTIMATE STRENGTH AND THE RATIO THICKNESS OF ICE TO WIDTH OF PILE

three-dimensional stress. If the ice sheet grows thicker, the number of planes of shear increases linearly, but also the extension of the planes of shear is lengthened, so that the strength increases exponentially.

5. The pressure of brittle ice with low cubic strength was nearly the same as the pressure of new ice, because of the closer contact between brittle ice and structure. It can be assumed, that the coefficient of contact decreases with lowering temperatures.

From the results of the laboratory tests and the measurements in nature the following equation is derived in order to determine the maximum pressure of floating ice-fields on piles

$$P = [0,5 \cdot 0,66(\sigma_{WB}(0^\circ \text{ C}) + 0,35 \cdot \alpha(t_L - t_w)) + 12,5(\eta - 0,15)] h \cdot b$$

0,5 = Coefficient of contact

0,66 = Coefficient of form (pile \emptyset 60 cm)

$\sigma_{WB}(0^\circ \text{ C})$ = Cubic strength of ice at 0° C and a deformation velocity of $S = 0,003 \frac{1}{\text{sec}}$

$0,35 \cdot \alpha(t_L - t_w)$ = Influence of temperature

α = Temperature factor

t_L = Air-temperature during the last 24 hours

t_w = Water-temperature

0,35 = Factor to get the mean temperature of the ice-sheet (after KORZHAVIN, 3)

$12,5(\eta - 0,15)$ = Influence of thickness in proportion to the width of pile

h = Thickness of ice

b = Width of pile

η = Thickness of ice width of structure

This equation should be extended to higher values of η .

REFERENCES

1. ASSUR, A. Forces Exerted by Ice on Marine Structures. Proceeding of 1. Ice Symposium of IAHR in Reykjavik, 8 - 10 September 1970, will be published in sommer 1971.
2. CROASDALE, K.R. The Nutcracker Ice Strength Tester and its Operation in the Beaufort Sea. Preprints of papers of the 1. Ice Symposium of IAHR in Reykjavik, 8 - 10 September 1970, Reykjavik Juli 1970.
3. KORZHAVIN, K.N. The Action of Ice on Engineering Structures. Publication of the Siberian Department of the Academy of Science of USSR, Novosibirsk, 1962 (in Russian).
4. PEYTON, H.R. Sea Ice Forces. Ice Pressure against Structures. Proceedings of Conference at Laval University Quebec, 1966, Ottawa 1968.
5. SCHWARZ, J. Treibeisdruck auf Pfähle. Mitteilungen des Franzius-Instituts für Grund- und Wasserbau der Technischen Universität Hannover, Hannover 1970.
6. WEEKS, W.,
ASSUR, A. The Mechanical Properties of Sea Ice. Ice pressures against Structures. Proceedings of Conference at Laval University Quebec, November 1966, Ottawa 1968.

7. TABATA, T. Studies of Visco-Elastic Properties of Sea Ice. Arctic Sea Ice. U.S. National Academy of Science.
National Research Council.
Publication 598. Washington 1968.

CHAPTER 94

Breakwater and quay Wall by Horizontal Plates

by

Takeehi Ijima ¹⁾, Shigeo Ozaki ²⁾, Yasuhiko Eguchi ³⁾ and Akire Kobayashi ⁴⁾

Abstract

Wave action to breakwater and quay wall by fixed horizontal plates as shown in Fig 4 and 5 are studied theoretically and experimentally. Transmission and reflection coefficients for breakwater are calculated as shown in Fig 6(a)(b), which suggest that only fixing the water surface by rigid plate is effective to reduce the transmitted waves for appropriate wave conditions. Pressure distributions to plates are calculated as shown in Fig 7 and total pressures are in Fig 8. Pressure distributions to horizontal plate and vertical wall of quay wall are shown in Fig 9 and 10, which show that the plate makes the pressure distribution to vertical wall more uniform than the one without plate and also submerged plates of breakwater and quay wall make the pressure distributions smooth.

Wave action in case when the region under plates is filled by permeable material are also calculated. The results suggest that the void of the material has the effect to elongate the plate and the fluid resistance acts as wave energy absorber.

1 Introduction

Piling up the fringed-column blocks as shown in Fig 1 into three or four layers, permeable breakwater and quay wall with vertical sides are constructed as shown in Fig 2 and 3. Photo 1 and 2 are actually constructed ones of Fig. 2 and 3, respectively, in Japan, as wave absorbing structures. Hydrodynamically, they are regarded as composed of horizontal slabs supported by vertical piles. Accordingly, wave actions to these structures are studied by investigating the effect of horizontal plates and then of the permeable material filled uniformly under the plates instead of piles.

2 Theory of breakwater by horizontal plate (without permeable material)

Suppose that a rigid horizontal plate of length $2l$ is fixed on water surface with constant water depth h and the water is divided at $x=0$ into three regions I, II and III as shown in Fig 4. Assuming small amplitude waves in perfect liquid and velocity potential in each region to be ϕ_1, ϕ_2 and ϕ_3 , we have the following Laplace's equations

$$\frac{\partial^2 \phi_i}{\partial x^2} + \frac{\partial^2 \phi_i}{\partial z^2} = 0 \quad (i = 1, 2, 3) \quad (1)$$

(1) Professor, Faculty of Engineering, Kyushu University, Fukuoka, Japan

(2) Director, the Fourth Harbour Construction Office, Ministry of Transportation

(3)(4) Research Assistant, Kyushu University

Bottom and surface conditions in region I and III are as follows

$$\frac{\partial \phi_v}{\partial z} = 0 \quad \text{at } z = -h, \quad \frac{\partial^2 \phi_v}{\partial t^2} + g \frac{\partial \phi_v}{\partial z} = 0 \quad \text{at } z = 0 \quad (v = 1, 3) \quad (2)$$

In region II, we have

$$\frac{\partial \phi_2}{\partial z} = 0 \quad \text{at } z = 0 \quad \text{and } z = -h \quad (3)$$

Fluid pressure in each region and surface profiles in regions I and III are as follows

$$\frac{p_v}{f} = -\frac{\partial \phi_v}{\partial t} - g z \quad (v = 1, 2, 3), \quad \zeta_v = -\frac{1}{g} \left(\frac{\partial \phi_v}{\partial t} \right)_{z=0} \quad (v = 1, 3) \quad (4)$$

where g is gravity acceleration and f is fluid density

Supposing the incident wave of frequency σ ($\sigma = 2\pi/T$, T is wave period) and reflected wave in region I and transmitted wave in region III, the velocity potential which satisfies Laplace's equation and bottom and surface boundary conditions in each region is given as follows

$$\phi_1(x, z, t) = e^{i\sigma t} \left[(Ae^{ikx} + Be^{-ikx}) \frac{\cosh k(z+h)}{\cosh kh} + \sum_{n=1}^{\infty} C_n e^{-k_n x} \frac{\cosh k_n(z+h)}{\cosh k_n h} \right], \quad (n = 1, 2, 3) \quad (5)$$

$$\phi_2(x, z, t) = e^{i\sigma t} \sum_{r=0}^{\infty} (D_r \cosh \frac{r\pi x}{h} + E_r \sinh \frac{r\pi x}{h}) \cos \frac{r\pi z}{h}, \quad (r = 0, 1, 2) \quad (6)$$

$$\phi_3(x, z, t) = e^{i\sigma t} \left[F e^{ikx} \frac{\cosh k(z+h)}{\cosh kh} + \sum_{n=1}^{\infty} G_n e^{k_n x} \frac{\cosh k_n(z+h)}{\cosh k_n h} \right] \quad (n = 1, 2, 3) \quad (7)$$

where k and k_n are eigenvalues determined by the following relations

$$\frac{\sigma^2 h}{g} = kh \tanh kh = -k_n h \tan k_n h, \quad (n = 1, 2, 3) \quad (8)$$

A , B and F are complex constants which represent the incident, reflected and transmitted waves, respectively, and C_n and G_n are standing waves which vanish at $|x| \rightarrow \infty$
 D_r and E_r are complex constants to be determined from the following boundary conditions

At the boundaries $x = \pm l$, continuities of horizontal fluid velocities and fluctuating wave pressures due to continuities of mass and energy flux through the boundaries require the following conditions

$$\frac{\partial \phi_1}{\partial x} = \frac{\partial \phi_2}{\partial x}, \quad \phi_1 = \phi_2 \quad \text{at } x = l \quad (9)$$

$$\frac{\partial \phi_2}{\partial x} = \frac{\partial \phi_3}{\partial x}, \quad \phi_2 = \phi_3 \quad \text{at } x = -l \quad (10)$$

Substituting eq 5, 6, 7 into eq 9, 10 and adding and subtracting, we obtain next

relations

$$\{Ae^{-ikl} - (B-F)e^{-ikl}\} \frac{\cosh k(z+h)}{\cosh kh} + i \sum_{n=1}^{\infty} (C_n - G_n) e^{-knk} \frac{kn \cosh kn(z+h)}{k \cosh knh} = -2i \sum_{r=0}^{\infty} \frac{r\pi}{kh} E_r \cosh \frac{r\pi l}{h} \cos \frac{r\pi z}{h} \quad (11)$$

$$\{Ae^{ikl} + (B+F)e^{-ikl}\} \frac{\cosh k(z+h)}{\cosh kh} + \sum_{n=1}^{\infty} (C_n - G_n) e^{-knk} \frac{\cosh kn(z+h)}{\cosh knh} = 2 \sum_{r=0}^{\infty} E_r \sinh \frac{r\pi l}{h} \cos \frac{r\pi z}{h} \quad (12)$$

$$\{Ae^{-ikl} - (B+F)e^{-ikl}\} \frac{\cosh k(z+h)}{\cosh kh} + i \sum_{n=1}^{\infty} (C_n + G_n) e^{-knk} \frac{kn \cosh kn(z+h)}{k \cosh knh} = -2i \sum_{r=0}^{\infty} \frac{r\pi}{kh} D_r \sinh \frac{r\pi l}{h} \cos \frac{r\pi z}{h} \quad (13)$$

$$\{Ae^{ikl} + (B+F)e^{-ikl}\} \frac{\cosh k(z+h)}{\cosh kh} + \sum_{n=1}^{\infty} (C_n + G_n) e^{-knk} \frac{\cosh kn(z+h)}{\cosh knh} = 2 \sum_{r=0}^{\infty} D_r \cosh \frac{r\pi l}{h} \cos \frac{r\pi z}{h} \quad (14)$$

Multiplying each terms of above equations by $\cos(r\pi z/h)$, integrating from $z = -h$ to $z = 0$ and using the following relations

$$\int_{-h}^0 \cos \frac{r\pi z}{h} \cos \frac{s\pi z}{h} dz = 0 \quad (r+s); = \frac{h}{2} \quad (r=s \neq 0), = h \quad (r=s=0)$$

$$\int_{-h}^0 \cosh k(z+h) \cos \frac{r\pi z}{h} dz = \frac{1}{k} \frac{\sinh kh}{1 + (r\pi/kh)^2}, \int_{-h}^0 \cosh kn(z+h) \cos \frac{r\pi z}{h} dz = \frac{1}{kn} \frac{\sinh knh}{1 - (r\pi/knh)^2}$$

we have following equations

$$\{Ae^{-ikl} - (B-F)e^{-ikl}\} \frac{\tanh kh}{1 + (r\pi/kh)^2} + i \sum_{n=1}^{\infty} (C_n - G_n) e^{-knk} \frac{\tanh knh}{1 - (r\pi/knh)^2} = -i r \pi E_r \cosh \frac{r\pi l}{h} \quad (15)$$

$$\{Ae^{ikl} + (B+F)e^{-ikl}\} \frac{\tanh kh}{1 + (r\pi/kh)^2} + \sum_{n=1}^{\infty} (C_n - G_n) e^{-knk} \frac{k \tanh knh}{kn [1 - (r\pi/knh)^2]} = kh E_r \sinh \frac{r\pi l}{h} \quad (16)$$

$$\{Ae^{-ikl} - (B+F)e^{-ikl}\} \frac{\tanh kh}{1 + (r\pi/kh)^2} + i \sum_{n=1}^{\infty} (C_n + G_n) e^{-knk} \frac{\tanh knh}{1 - (r\pi/knh)^2} = -i r \pi D_r \sinh \frac{r\pi l}{h} \quad (17)$$

$$\{Ae^{ikl} + (B+F)e^{-ikl}\} \frac{\tanh kh}{1 + (r\pi/kh)^2} + \sum_{n=1}^{\infty} (C_n + G_n) e^{-knk} \frac{k \tanh knh}{kn [1 - (r\pi/knh)^2]} = kh D_r \cosh \frac{r\pi l}{h} \quad (18)$$

Eliminating D_r and E_r in above equations and putting

$$Ae^{ikl} = a, \quad Be^{-ikl} = b, \quad Fe^{-ikl} = f, \quad C_n e^{-knk} = c_n$$

$$G_n e^{-knk} = g_n, \quad \pi l/h = H, \quad kh/\pi = \lambda_0, \quad knh/\pi = \lambda_n$$

$$F_{r,n} = \frac{\lambda_0^2 + r^2}{\lambda_n^2 - r^2} \frac{\lambda_n + r \tanh rH}{\sqrt{\lambda_n^2 + (r \tanh rH)^2}}, \quad \Phi_{r,n} = \frac{\lambda_0^2 + r^2}{\lambda_n^2 - r^2} \frac{\lambda_n + r \coth rH}{\sqrt{\lambda_n^2 + (r \coth rH)^2}}$$

$$\theta_r = \tan^{-1} \left(\frac{f}{\lambda_0} \tanh rH \right), \quad \varphi_r = \tan^{-1} \left(\frac{f}{\lambda_0} \coth rH \right) \quad (19)$$

the following two systems of linear simultaneous equations are provided

$$\frac{b+f}{a} e^{-i\theta r} + i \sum_{n=1}^{\infty} F_{r,n} \frac{c_n + g_n}{a} = e^{i\theta r} \quad (r = 0, 1, 2) \tag{20}$$

$$\frac{b-f}{a} e^{-i\psi r} + i \sum_{n=1}^{\infty} \Phi_{r,n} \frac{c_n - g_n}{a} = e^{i\psi r} \quad (r = 0, 1, 2) \tag{21}$$

where

$$F_{0,n} = \frac{\lambda_0}{\lambda_n}, \quad \Phi_{0,n} = \lim_{r \rightarrow 0} \frac{\lambda_0^2 + r^2}{\lambda_n^2 - r^2} \frac{\lambda_n + r \coth r H}{\sqrt{\lambda_n^2 + (r \coth r H)^2}} = \frac{\lambda_0^2}{\lambda_n^2} \frac{1 + \lambda_n H}{\sqrt{1 + (\lambda_n H)^2}} \tag{22}$$

$$\theta_0 = 0, \quad \psi_0 = \lim_{r \rightarrow 0} \tan^{-1}(r H \coth r H / \lambda_0 H) = \tan^{-1}(1/\lambda_0 H)$$

Eq 20 and 21 are regarded as equations for determining the unknowns $(b+f)/a$, $(c_n + g_n)/a$ and $(b-f)/a$ and $(c_n - g_n)/a$, respectively, so that we obtain b/a , f/a , c_n/a and g_n/a from eq 20 and 21. Thus, from eq 16 and 18, D_r and E_r are determined as follows

$$\begin{aligned} D_0 &= d_0/2 = \frac{a}{2\pi^2} \frac{\sigma^2 h}{g} \left[\left(1 + \frac{b+f}{a}\right) \frac{1}{\lambda_0^2} - \sum_{n=1}^{\infty} \frac{c_n + g_n}{a} \frac{1}{\lambda_n^2} \right] \\ D_r \cosh r H &= d_r = \frac{a}{\pi^2} \frac{\sigma^2 h}{g} \left[\left(1 + \frac{b+f}{a}\right) \frac{1}{\lambda_0^2 + r^2} - \sum_{n=1}^{\infty} \frac{c_n + g_n}{a} \frac{1}{\lambda_n^2 - r^2} \right] \\ E_r \sinh r H &= e_r = \frac{a}{\pi^2} \frac{\sigma^2 h}{g} \left[\left(1 + \frac{b-f}{a}\right) \frac{1}{\lambda_0^2 + r^2} - \sum_{n=1}^{\infty} \frac{c_n - g_n}{a} \frac{1}{\lambda_n^2 - r^2} \right] \end{aligned} \tag{23}$$

Letting the incident wave be $S_0 = \cos(kx + at)$, we have

$$a = i \alpha g e^{i k l} / \sigma \tag{24}$$

Thus, from eq 5,6 and 7, the velocity potentials are determined as follows

$$\Phi_1(x, z, t) = a e^{i \omega t} \left[\left\{ e^{i k(x-l)} + \frac{f}{a} e^{-i k(x-l)} \right\} \frac{\cosh k(z+h)}{\cosh kh} + \sum_{n=1}^{\infty} \frac{c_n}{a} e^{-k_n(x-l)} \frac{\cosh k_n(z+h)}{\cosh k_n h} \right] \tag{25}$$

$$\Phi_2(x, z, t) = a e^{i \omega t} \left[\frac{d_0}{2a} + \sum_{r=1}^{\infty} \left(\frac{d_r \cosh r H x / l}{\cosh r H} + \frac{e_r \sinh r H x / l}{\sinh r H} \right) \cos \frac{r H z}{h} \right] \tag{26}$$

$$\Phi_3(x, z, t) = a e^{i \omega t} \left[\frac{f}{a} e^{i k(x+l)} \frac{\cosh k(z+h)}{\cosh kh} + \sum_{n=1}^{\infty} \frac{g_n}{a} e^{-k_n(x+l)} \frac{\cosh k_n(z+h)}{\cosh k_n h} \right] \tag{27}$$

Surface profiles in regions I and III are given as follows

$$S_1(x, t) = \alpha e^{i(kl + at)} \left[e^{i k(x-l)} + \frac{f}{a} e^{-i k(x-l)} + \sum_{n=1}^{\infty} \frac{c_n}{a} e^{-k_n(x-l)} \right] \tag{28}$$

$$\zeta_3(x,t) = \alpha e^{i(kl+at)} \left[\frac{f}{a} e^{ik(x+l)} + \sum_{n=1}^{\infty} \frac{g_n}{a} e^{kn(x+l)} \right] \tag{29}$$

Reflection and transmission coefficients are as follows

$$K_r = |b/a|, \quad K_t = |f/a| \tag{30}$$

Pressure distribution $p_2(z=0)$ and the total pressure P_u to the horizontal plate are as follows

$$p_2(z=0)/\rho g d = e^{i(kl+at)} \left[\frac{d_0}{2a} + \sum_{r=1}^{\infty} \left(\frac{d_r}{a} \frac{\cosh rHx/l}{\cosh rH} + \frac{e_r}{a} \frac{\sinh rHx/l}{\sinh rH} \right) \right] \tag{31}$$

$$|P_u/2\rho g d l| = \left| \int_{-l}^l \frac{p_2(z=0)}{2\rho g d l} dx \right| = \left| \frac{d_0}{2a} + \sum_{r=1}^{\infty} \frac{d_r}{a} \frac{\tanh rH}{rH} \right| \tag{32}$$

3 Theory of quay wall with horizontal plate (without permeable material)

Suppose the vertical wall with horizontal plate of length l as shown in Fig 5. Boundary conditions for fluid motion in region I are just the same as the previous section and velocity potential ϕ_1 is given by eq 5. In region II, the condition $\partial\phi_2/\partial x = 0$ at $x=0$ is to be added, so that the velocity potential ϕ_2 becomes, putting $E_r = 0$, as follows

$$\phi_2(x,z,t) = e^{i\theta t} \sum_{r=0}^{\infty} D_r \cosh \frac{r\pi x}{h} \cos \frac{r\pi z}{h}, \quad (r=0, 1, 2, \dots) \tag{33}$$

Boundary conditions at $x=l$ is the same as eq 9

Following to the same process as previous section and using the same symbols as eq 19, simultaneous equations for b/a and c_n/a are provided in the same form as eq 20 as follows

$$\frac{b}{a} e^{-i\theta r} + i \sum_{n=1}^{\infty} F_{rn} \frac{c_n}{a} = e^{i\theta r} \quad (r=0, 1, 2, \dots) \tag{34}$$

Thus, the numerical results of eq 20 for breakwater are used as it is and D_0 and D_r are given as follows

$$D_0 = d_0/2 = \frac{a}{\pi^2} \frac{\sigma^2 h}{g} \left[\left(1 + \frac{f}{a}\right) \frac{1}{\lambda^3} - \sum_{n=1}^{\infty} \frac{c_n}{a} \frac{1}{\lambda_n^3} \right] \tag{35}$$

$$D_r \cosh rH = d_r = 2 \frac{a}{\pi^2} \frac{\sigma^2 h}{g} \left[\left(1 + \frac{f}{a}\right) \frac{1}{\lambda_0^3 + \gamma^2} - \sum_{n=1}^{\infty} \frac{c_n}{a} \frac{1}{\lambda_n^3 - \gamma^2} \right]$$

For the incident wave $\zeta_0 = \alpha \cos(kx + at)$, the velocity potential ϕ_1 is the same as eq 25 and ϕ_2 is as follows

$$\Phi_2(x, z, t) = a e^{i\omega t} \left[\frac{d_0}{2a} + \sum_{r=1}^{\infty} \frac{dr}{a} \frac{\cosh rHx/l}{\cosh rH} \cos \frac{r\pi z}{h} \right] \quad (36)$$

Reflection coefficient $K_r = |b/a|$ is identically equal to unity

Pressure distribution $p_2(z=0)$ and $p_2(z=-h)$, and the total pressure P_u and P_H to horizontal plate and vertical wall are given as follows

$$p_2(z=0)/\rho g d = e^{i(kl + \omega t)} \left[\frac{d_0}{2a} + \sum_{r=1}^{\infty} \frac{dr}{a} \frac{\cosh rHx/l}{\cosh rH} \right] \quad (37)$$

$$|P_u/\rho g d l| = \left| \int_0^l \frac{p_2(z=0)}{\rho g d l} dx \right| = \left| \frac{d_0}{2a} + \sum_{r=1}^{\infty} \frac{dr}{a} \frac{\tanh rH}{rH} \right| \quad (38)$$

$$p_2(z=-h)/\rho g d = e^{i(kl + \omega t)} \left[\frac{d_0}{2a} + \sum_{r=1}^{\infty} \frac{dr}{a} \frac{\cosh r\pi z/h}{\cosh rH} \right] \quad (39)$$

$$|P_H/\rho g d h| = \left| \int_{-h}^0 \frac{p_2(z=-h)}{\rho g d h} dz \right| = |d_0/a| \quad (40)$$

4 Breakwater and quay wall with double plates (without permeable material)

In cases of breakwater and quay wall with double plates at $z = 0$ and $z = -h/2$ as shown by dotted lines in Fig 4 and 5, velocity potential in region II must satisfy one more condition $\partial \Phi_2 / \partial z = 0$ at $z = -h/2$. This is done by taking even numbers for integers r in eq 6 and 33 (that is $r = 0, 2, 4, 6, \dots$)

5 Calculations

For various values of $\sigma^2 h/g = 2\pi h/L_0$ (L_0 is deep water wave length for period T), λ_0 and λ_n defined by eq 19 are calculated by eq 8 as shown in Table 1. And then, eq 20 and 21 are solved by means of electronic computer. For example, b/a , f/a , c_n/a etc for the case of $\sigma^2 h/g = 1.0$ and $l/h = 1.0$ are as shown in Table 2.

6 Calculated results for horizontal plate breakwater

Transmission and reflection coefficients K_t and K_r by eq 30 are shown in Fig 6(a) (b) for single and double plates. For the case of single plate with $l/h = 2.0$, $K_t = 0.53, 0.38$ and 0.28 for $\sigma^2 h/g = 0.5, 1.0$ and 1.5 , respectively, and so only 28%, 14% and 8% of incident wave energy are transmitted through the plate. Comparing Fig 6(a) with Fig 6(b), it is seen that if the total length of plates are equal in both cases (that is, $(l/h)_1 = 2.0$ corresponds to $(l/h)_2 = 1.0$), $(K_r)_1$ is always larger than $(K_r)_2$ and $(K_t)_1$ is smaller than $(K_t)_2$ for all $\sigma^2 h/g$, where suffix 1 and 2 show the cases of single plate and double plates, respectively. These properties are interpreted as

the result that when the water surface is fixed by horizontal plate, the fluid under the plate is constrained in motion, increases its inertial resistance to motion and behaves like as semi-rigid breakwater for short waves

Pressure distribution to plate by eq 31 are shown in Fig 7(a)(b), which show that the distribution for double plates is remarkably uniform compared with that of single plate. The total pressure by eq 32 is shown in Fig 8, from which it is seen that the averaged pressure per unit length of plate and per unit amplitude of incident wave for double plates is almost independent of l/h and approaches to the value for $l/h=0.5$ of single plate. These properties of pressure to the plate suggest that the submerged plate has the effect of making the pressure distribution uniform.

7 Calculated results for horizontal plate quay wall (without permeable material)

The pressure distribution to horizontal plate by eq 37 is shown in Fig 9 for single plate quay wall. As was shown for breakwater, the distribution for double plates is remarkably uniform compared with that of single plate. Pressure distribution to the vertical wall is in Fig 10. Compared with the one without plate (that is, $l/h=0$), the distribution is smooth even for single plate wall and the tendency is much clearer for double plates wall. Averaged total pressure to horizontal plate and vertical wall by eq 38 and 40 are in Fig 11 and 12, respectively. Comparing both figures, it is seen that for single plate wall the averaged pressure to horizontal direction becomes equal to that of vertical direction for larger l/h , and it is clearer for double plates wall. This means that the water in region II is constrained in motion by horizontal plate and vertical wall and the wave pressures are equalized to all directions.

8 Theory of horizontal plate breakwater and quay wall with permeable material

When permeable material is filled under horizontal plate, it causes resistance to the motion of fluid flowing through the void. For simplicity, we assume that the resistance is proportional to fluid velocity and the coefficient of resistance per unit fluid mass is μ and the void ratio is V . If u , w and p are actual velocities and pressure of fluid, equations of motion and continuity are as follows:

$$\frac{\partial u}{\partial t} = -\frac{1}{\rho} \frac{\partial p}{\partial x} - \mu u, \quad \frac{\partial w}{\partial t} = -\frac{1}{\rho} \frac{\partial p}{\partial z} - \mu w, \quad \frac{\partial u}{\partial x} + \frac{\partial w}{\partial z} = 0 \tag{41}$$

Letting the average velocities and pressure per unit volume of this region be \bar{u} , \bar{w} and \bar{p} , respectively, we have next relations:

$$\bar{u} = \nabla u, \quad \bar{w} = \nabla w, \quad \bar{p} = \nabla p \tag{42}$$

Then, eq 41 are rewritten as follows

$$\frac{\partial \bar{u}}{\partial t} = -\frac{1}{\rho} \frac{\partial \bar{p}}{\partial x} - \mu \bar{u} \quad \frac{\partial \bar{w}}{\partial t} = -\frac{1}{\rho} \frac{\partial \bar{p}}{\partial z} - gV - \mu \bar{w} \quad \frac{\partial \bar{u}}{\partial x} + \frac{\partial \bar{w}}{\partial z} = 0 \quad (43)$$

This average motion has velocity potential $\bar{\Phi}$ which satisfies Laplace's equation

Putting
$$\bar{u} = \frac{\partial \bar{\Phi}}{\partial x}, \quad \bar{w} = \frac{\partial \bar{\Phi}}{\partial z} \quad (44)$$

fluid pressure \bar{p} is given by the following equation

$$\frac{\bar{p}}{\rho} = -\frac{\partial \bar{\Phi}}{\partial t} - \mu \bar{\Phi} - gVz \quad (45)$$

The boundary condition for potential $\bar{\Phi}$ in region II of Fig.4 are $\frac{\partial \bar{\Phi}}{\partial z} = 0$ at $z = 0$ and $z = -h$, and from the continuity of mass flux at $x = \pm l$,

$$\frac{\partial \bar{\Phi}_1}{\partial x} = \frac{\partial \bar{\Phi}}{\partial x} \quad \text{at } x = l, \quad \frac{\partial \bar{\Phi}_3}{\partial x} = \frac{\partial \bar{\Phi}}{\partial x} \quad \text{at } x = -l \quad (46)$$

and also from the continuity of energy flux $p_1 = \bar{p}/V$ at $x = l$, $p_3 = \bar{p}/V$ at $x = -l$, so that

$$\frac{\partial \bar{\Phi}_1}{\partial t} = \frac{1}{V} \left(\frac{\partial \bar{\Phi}}{\partial t} + \mu \bar{\Phi} \right) \quad \text{at } x = l \quad (47)$$

$$\frac{\partial \bar{\Phi}_3}{\partial t} = \frac{1}{V} \left(\frac{\partial \bar{\Phi}}{\partial t} + \mu \bar{\Phi} \right) \quad \text{at } x = -l \quad (48)$$

Since the velocity potential in each region is given by eq 5,6 and 7 for breakwater, we obtain next relations corresponding to eq.20 and 21, using above conditions and the same symbols as eq 19

$$\frac{b+f}{a} + i \sum_{n=1}^{\infty} \frac{\lambda_n^2 + r^2}{\lambda_n^2 - r^2} \frac{\lambda_n + P_r e^{i\nu}}{\lambda_n + P_r e^{i(\nu-\pi/2)}} \frac{c_n + g_n}{a} = \frac{\lambda_0 + P_r e^{i(\nu+\pi/2)}}{\lambda_0 + P_r e^{i(\nu-\pi/2)}} \quad (r=0 \text{ or } 2) \quad (49)$$

$$\frac{b-f}{a} + i \sum_{n=1}^{\infty} \frac{\lambda_n^2 + r^2}{\lambda_n^2 - r^2} \frac{\lambda_n + Q_r e^{i\nu}}{\lambda_n + Q_r e^{i(\nu-\pi/2)}} \frac{c_n - g_n}{a} = \frac{\lambda_0 + P_r e^{i(\nu+\pi/2)}}{\lambda_0 + Q_r e^{i(\nu-\pi/2)}} \quad (r=0 \text{ or } 2) \quad (50)$$

where

$$P_r = \frac{rV \tanh rH}{\beta} \quad Q_r = \frac{rV \coth rH}{\beta} \quad P_0 = 0 \quad (51)$$

$$Q_0 = \lim_{r \rightarrow 0} rH \coth rH / \beta H = V/\beta H, \quad \beta = \sqrt{1 + (\mu/\omega)^2}, \quad \nu = \tan^{-1}(\mu/\omega)$$

Solving eq 49 and 50, we obtain b/a , f/a , c_n/a and g_n/a for breakwater, and then D_r and E_r are given as follows

$$D_0 = \frac{d_0}{2} = \frac{V}{2\beta} e^{i\nu} \frac{\omega^2 h}{g} \frac{a}{\pi^2} \left[\left(1 + \frac{b+f}{a} \right) \frac{1}{\lambda_0^2} - \sum_{n=1}^{\infty} \frac{1}{\lambda_n^2} \frac{c_n + g_n}{a} \right]$$

$$\begin{aligned}
 D_r \cosh rH &= d_r = \frac{V}{\beta} e^{\nu \sigma^2 h} \frac{a}{g} \frac{1}{\pi^2} \left[\left(1 + \frac{b+f}{a}\right) \frac{1}{\lambda b + r^2} - \sum_{n=1}^{\infty} \frac{1}{\lambda_n^2 + r^2} \frac{C_n + g_n}{a} \right] \\
 E_r \sinh rH &= e_r = \frac{V}{\beta} e^{\nu \sigma^2 h} \frac{a}{g} \frac{1}{\pi^2} \left[\left(1 + \frac{b-f}{a}\right) \frac{1}{\lambda b + r^2} - \sum_{n=1}^{\infty} \frac{1}{\lambda_n^2 + r^2} \frac{C_n - g_n}{a} \right] \quad (52)
 \end{aligned}$$

Surface wave profiles, reflection and transmission coefficients etc are given in the same form of eq 28, 29 and 30 etc, using b/a , f/a , c_n/a and g_n/a by eq 49 and 50. The fluid pressure in the region II is given by eq 45 for the incident wave

$S_0 = \alpha \cos(kx + \sigma t)$ as follows

$$\frac{p}{\rho g d} = \frac{\beta}{V} e^{\nu(kl + \sigma t - \nu)} \left[\frac{d_0}{2a} + \sum_{r=1}^{\infty} \left(\frac{d_r \cosh rH/l}{a \cosh rH} + \frac{E_r \sinh rH/l}{a \sinh rH} \right) \cos \frac{r\pi z}{h} \right] \quad (53)$$

Pressure distribution and the total pressure to horizontal plate are given as follows

$$p(z=0)/\rho g d = \frac{\beta}{V} e^{\nu(kl + \sigma t - \nu)} \left[\frac{d_0}{2a} + \sum_{r=1}^{\infty} \left(\frac{d_r \cosh rH/l}{a \cosh rH} + \frac{E_r \sinh rH/l}{a \sinh rH} \right) \right] \quad (54)$$

$$|P_w/2\rho g d h| = \frac{\beta}{V} \left| \left(\frac{d_0}{2a} + \sum_{r=1}^{\infty} \frac{d_r \tanh rH}{rH} \right) \right| \quad (55)$$

Above-mentioned results are for single plate breakwater. For quay wall, similar results are obtained by the same process as in section 5.

9 Calculated results for horizontal plate breakwater with permeable material

As an example, b/a , f/a , c_n/a , g_n/a and d_r/a , e_r/a by eq 49 and 50 for $\sigma^2 h/g = 1.0$, $l/h = 1.0$, $V = 0.5$ and $M/\sigma = 1.0$ are shown in Table 3.

Transmission and reflection coefficients for $l/h = 1.0$, $V = 0.5$ are shown in Fig 13 for parameter M/σ . When $M/\sigma = 0$, K_r and K_t are equal to those for $l/h = 2.0$ in Fig 6(a) for the case without permeable material. When $M/\sigma \neq 0$, K_r becomes smaller than that for $M/\sigma = 0$ and then it increases with the increase of M/σ . On the contrary, K_t decreases steadily with increase of M/σ . This means that the void has the effect to elongate the length l of the plate to l/V and the fluid resistance has the effect to resist to the incident wave and to cause energy dissipation in breakwater.

The pressure distribution to plate by eq 54 is shown in Fig 14. Compared with Fig 7(a), it is seen that the distribution is steeper than the case without permeable material and the tendency is remarkable for large $\sigma^2 h/g$. This coincides with the fact that the void has the effect to elongate the plate length.

It may be said that the submerged plate has the effect to make the pressure

distribution uniform but the submerged permeable material has the effect to make the distribution steep. The averaged total pressure by eq 55 is nearly equal to the case without permeable material.

10 Calculated results for horizontal plate quay wall with permeable material

For the same conditions as previous section, reflection coefficient K_r for quay wall is calculated as shown in Fig 15. K_r decreases steadily with the increase of $\sigma^2 h/g$, but not so with M/σ . For large values of $\sigma^2 h/g$, K_r is minimum for M/σ between 1.0 and 2.0. That is, reflection coefficient is the least for a particular value of M/σ depending on $\sigma^2 h/g$ and becomes larger for other values of M/σ . As seen from Fig 15, K_r is larger than 0.94 for $\sigma^2 h/g < 1.5$ and also by calculations for various values of l/h , it is found that K_r is almost constant for $l/h > 1.0$, that is, K_r is independent on the length of plate for $l/h > 1.0$. The fact that the reflection coefficient of quay wall does not decrease even for large values of M/σ and l/h is interpreted to be due to the small fluid velocity and the energy dissipation inside the permeable material under the horizontal plate.

11 Comparisons with the experiment

Using the wave channel of length 22 meters, width 1.0 meters and depth 0.6 meters with flap type wave generator, experimental measurement was carried out for single plate breakwater of $h = 40\text{cm}$ and $l = 40\text{cm}$ ($l/h = 1.0$) without permeable material, for incident wave amplitude α nearly constant of 3cm. Transmission and reflection coefficients are shown in Fig 16, in which each plotted datum is the mean value of 10 times measurements. Measured transmission coefficients agree well with theoretical values but reflection coefficients are lower than theory. The measured pressure distribution to plate is shown in Fig 17, which shows that the measured distributions are remarkably steeper than those of theoretical ones. These discrepancies might be due to wave overtopping and eddies generated at the front edge of plate. Measured average total pressure to the plate are shown in Fig 18, which shows good agreement with theory. For the case with permeable material, experiments are now under taken.

12 Conclusions and remarks

Theory of single plate breakwater for long waves are introduced by J. J. Stoker (1957) and the mathematical study of dock problems are presented by K. O. Friedrichs and H. Levy (1948) and others. In this paper we have tried the extension of Stoker's result to the case of general wave conditions by different method from these authors.

Main results of our study are summarized as follows

(i) For the case of breakwater without permeable material, a horizontal plate fixed rigidly at water surface behaves like as a semi-rigid breakwater for short surface waves and more incident wave energy is reflected for shorter waves and longer plate. The longer the plate is, the more steeply distributes the pressure along the plate. In case of double plates, the pressure distribution becomes remarkably smooth.

(ii) For the case of quay wall, the pressure distribution to vertical wall is remarkably uniform by the effect of horizontal plate, compared to the case without plate. The pressure distribution to plate is similar to that of breakwater, and the longer the plate is, the more equally becomes the averaged pressures to vertical wall and to horizontal plate. In other words, the horizontal plate at water surface of quay wall plays the role of pressure equalizer to horizontal and vertical directions. In case of double plates, pressure distributions to both directions becomes more smooth than the case of single plate.

(iii) When the region under the horizontal plate is filled by permeable material, the void has the effect to elongate the plate, so that for breakwater the transmission coefficient decreases and the reflection coefficient increases and for both of breakwater and quay wall the distribution of pressure along the plate becomes steeper than the case without permeable material. The effect of fluid resistance is partly to reflect the incident wave and partly to absorb wave energy, so that for breakwater the reflection coefficient increases and the transmission coefficient decreases and quay wall the decrease of reflection coefficient is not so remarkable. The pressure distribution along the plate and the vertical wall is not changed remarkably by the effect of fluid resistance.

References

- Stoker, J. J. (1957) "Water Waves" pp 430-436, Interscience Publishers
Friedrichs, G. O. and Levy (1948) "The Dock Problem" Communications on Pure and Applied Mathematics, Vol 1, pp 135-148

Table 1 λ_0 and λ_n for $\sigma^2 h/g$

λ $\sigma^2 h/g$	0 1	0 5	1 0	1 5	2 0
λ_0	0 10237	0 24564	0 38187	0 51624	0 65742
λ_1	0 98977	0 94700	0 89075	0 83459	0 78263
λ_2	1 99492	1 97440	1 94845	1 92251	1 89699
λ_3	2 99662	2 98303	2 96597	2 94889	2 93194
λ_4	3 99747	3 98730	3 97456	3 96182	3 94913
λ_5	4 99794	4 98985	4 97968	4 96951	4 95953
λ_6	5 99831	5 99155	5 98308	5 97462	5 96622

Table 2 (a) $\sigma^2 h/g = 1 0$, $l/h = 1 0$ (single plate)

$b/a = 0 5621 + 0 5434 i$ $f/a = 0 4334 - 0 4482 i$

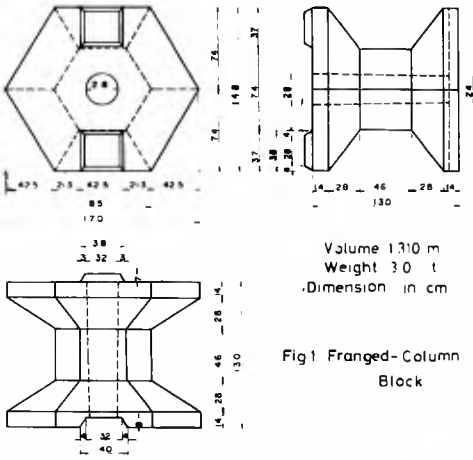
n	c_n/a		g_n/a	
1	- 0 1340	- 0 03753 i	- 0 05896	+ 0 02837 i
2	- 0 03114	- 0 01006 i	- 0 01050	+ 0 008075 i
3	- 0 01392	- 0 004658 i	- 0 004308	+ 0 003788 i
4	- 0 007891	- 0 002683 i	- 0 002340	+ 0 002195 i
5	- 0 005077	- 0 001742 i	- 0 001467	+ 0 001430 i
6	- 0 003532	- 0 001220 i	- 0 001003	+ 0 001003 i
7	- 0 002582	- 0 0008751 i	- 0 0007238	+ 0 0007374 i
r	d_r/a		e_r/a	
0	0 7063	+ 0 03396 i		
1	0 08366	+ 0 003990 i	0 06392	+ 0 05616 i
2	0 02246	+ 0 001071 i	0 01522	+ 0 01337 i
3	0 01004	+ 0 0004788 i	0 006499	+ 0 005710 i
4	0 005633	+ 0 0002687 i	0 003563	+ 0 003131 i
5	0 003594	+ 0 0001714 i	0 002242	+ 0 001969 i
6	0 002488	+ 0 0001187 i	0 001537	+ 0 001350 i
7	0 001823	+ 0 00008699 i	0 001118	+ 0 0009827 i

Table 2 (b) • $\sigma^2 h/g = 1.0$, $\beta/h = 1.0$ (double plate)
 $b/a = 0.001452 + 0.8682 i$ $f/a = 0.4963 - 0.0008301 i$

n	c_n/a		g_n/a	
1	- 1.592	- 1.422 i	- 0.7140	+ 0.08723 i
2	0.08463	+ 0.07888 i	0.03229	- 0.01117 i
3	0.6287	+ 0.5925 i	0.2284	- 0.09617 i
4	- 0.01199	- 0.01136 i	- 0.004250	+ 0.001953 i
5	- 0.1053	- 0.1001 i	- 0.03680	+ 0.01778 i
6	0.0006480	+ 0.0006171 i	0.0002243	- 0.0001119 i
7	0.002819	+ 0.002688 i	0.0009689	- 0.0004946 i
r	d_r/a		e_r/a	
0	0.6614	+ 0.3830 i		
2	0.004674	+ 0.002707 i	0.002614	+ 0.004496 i
4	0.0005754	+ 0.0003332 i	0.0003059	+ 0.0005262 i
6	0.0001629	+ 0.00009434 i	0.00008513	+ 0.0001464 i
8	0.00006688	+ 0.00003873 i	0.00003464	+ 0.00005959 i
10	0.00003387	+ 0.00001962 i	0.00001745	+ 0.00003002 i
12	0.00001962	+ 0.00001136 i	0.00001007	+ 0.00001732 i
14	0.00001247	+ 0.000007219 i	0.000006383	+ 0.00001098 i

Table 3
 $\sigma^2 h/g = 1.0$, $\beta/h = 1.0$, $V = 0.5$, $\mu/\sigma = 1.0$
 $b/a = 0.7769 + 0.1685 i$ $f/a = 0.1930 - 0.1239 i$

n	c_n/a		g_n/a	
1	- 0.06763	- 0.05141 i	- 0.02255	- 0.009455 i
2	- 0.01620	- 0.01236 i	- 0.003733	- 0.0008074 i
3	- 0.007329	- 0.005580 i	- 0.001490	- 0.0001913 i
4	- 0.004184	- 0.003178 i	- 0.0007981	- 0.00006291 i
5	- 0.002750	- 0.002051 i	- 0.0004964	- 0.00002332 i
6	- 0.001888	- 0.001430 i	- 0.0003377	- 0.000008349 i
7	- 0.001384	- 0.001046 i	- 0.0002429	- 0.000002015 i
r	d_r/a		e_r/a	
0	0.16771	- 0.17753 i		
1	0.03904	- 0.02638 i	0.028177	- 0.03108 i
2	0.01071	- 0.007101 i	0.007753	- 0.007868 i
3	0.004838	- 0.003176 i	0.003508	- 0.003445 i
4	0.002734	- 0.001784 i	0.001984	- 0.001915 i
5	0.001753	- 0.001138 i	0.001273	- 0.001215 i
6	0.001218	- 0.0007888 i	0.0008849	- 0.0008382 i
7	0.0008950	- 0.0005782 i	0.0006505	- 0.0006126 i



Volume 1.310 m³
 Weight 30 t
 Dimension in cm

Fig 1 Fringed-Column Block



Photo. 1

Dimension in Meters

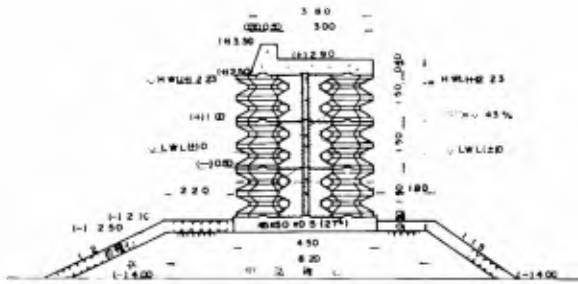


Fig.2 Breakwater by Fringed-Column Blocks
 (Port of Hakata)

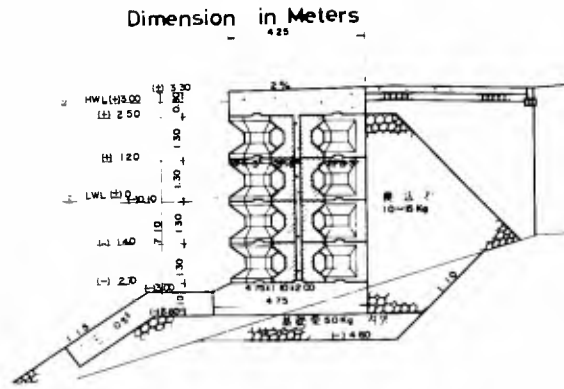


Fig.3 Quay Wall by Franged-Column Block (Tabira Harbour)

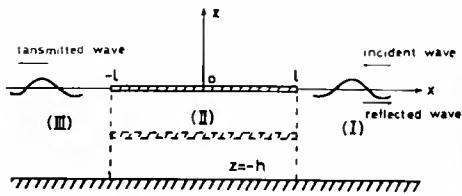


Fig- 4 Breakwater by Horizontal Plate



Photo. 2

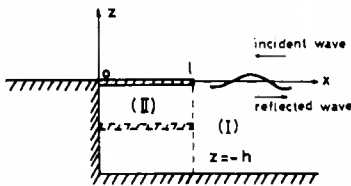
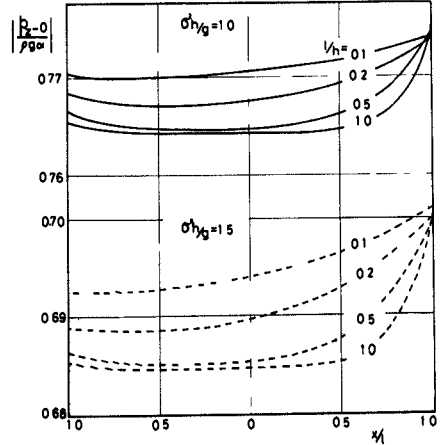
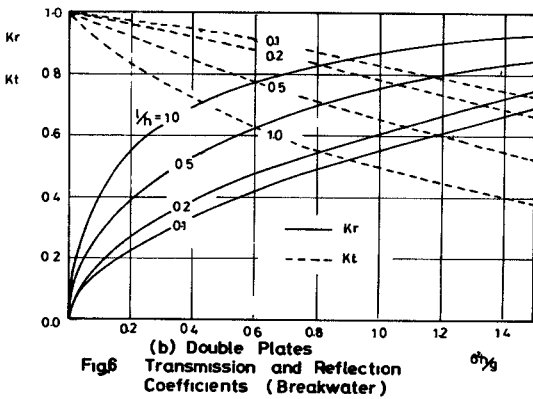
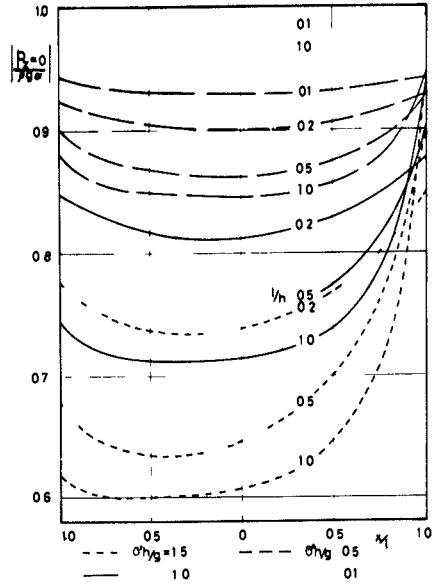
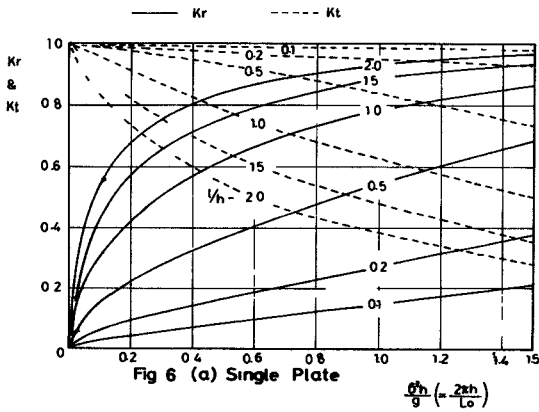
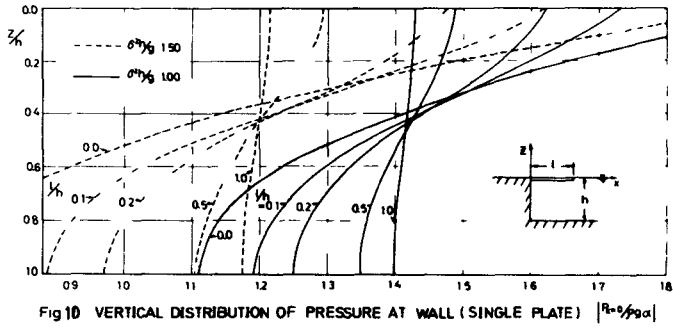
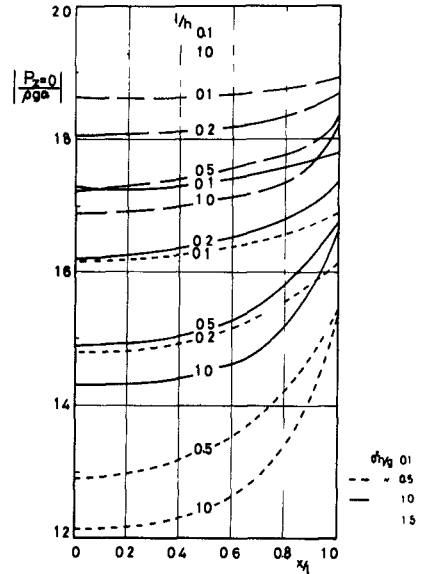
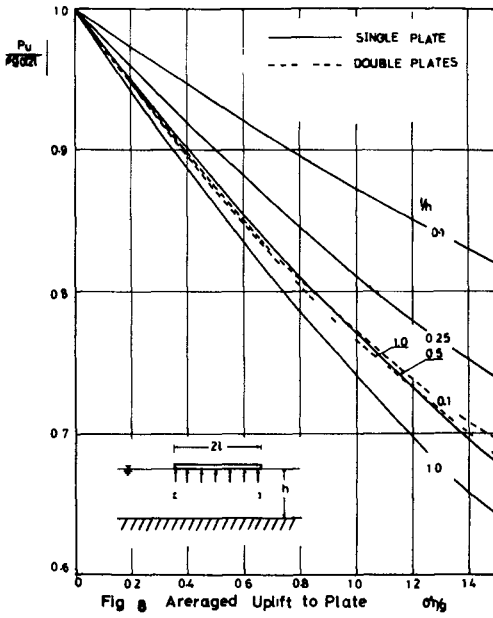


Fig- 5 Quay Wall with Horizontal Plate





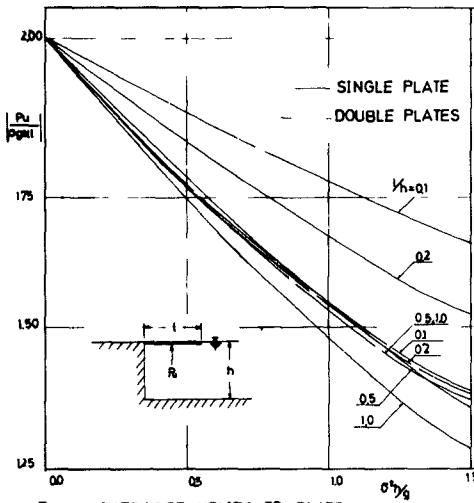


Fig 11 AVERAGED UPLIFT TO PLATE

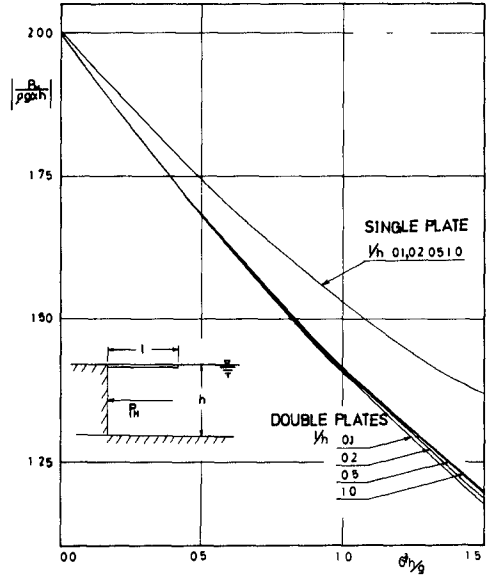


Fig 12 AVERAGED HORIZONTAL PRESSURE AT WALL

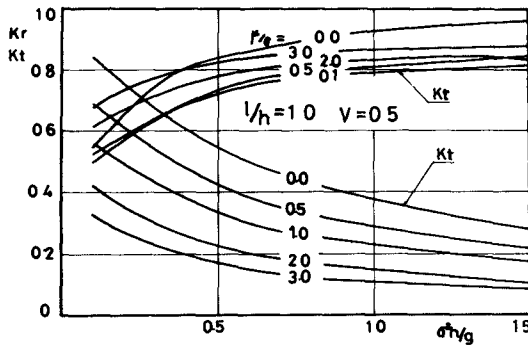
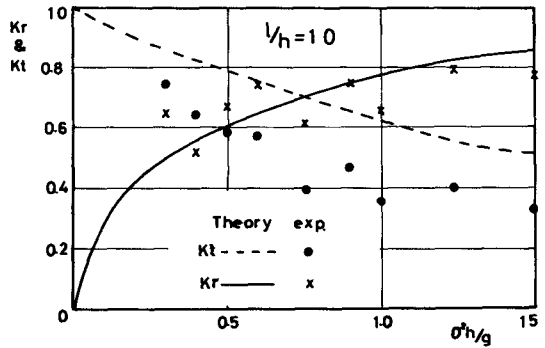
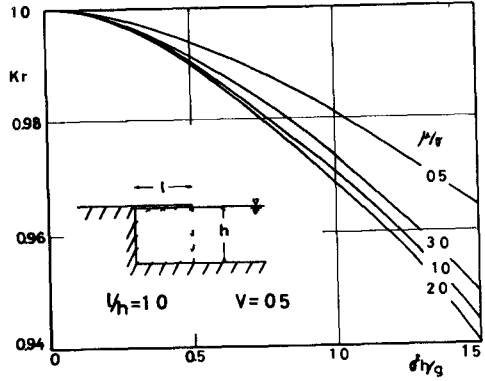
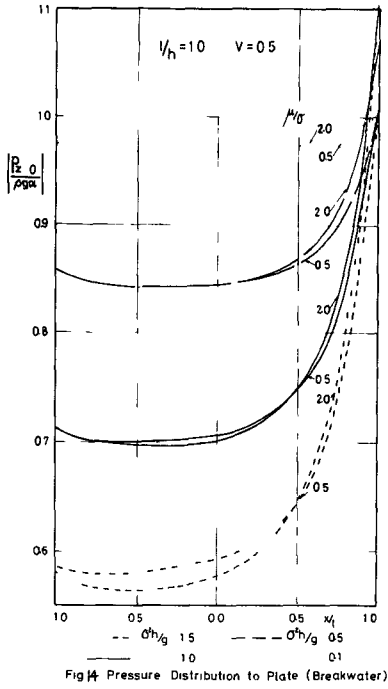


Fig 13 K_r and K_t of Breakwater



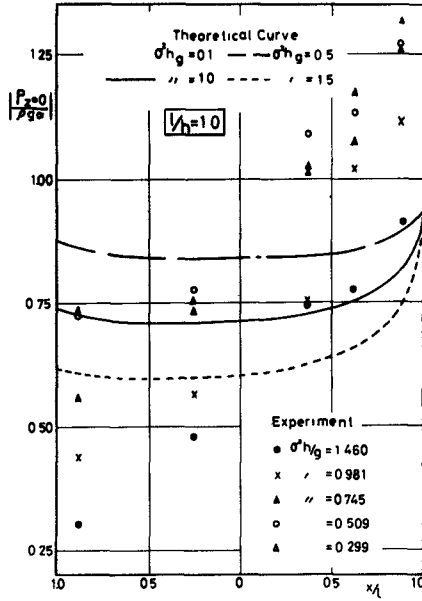


Fig.17 Pressure Distribution to Plate Theory and Experiment (Single Plate Breakwater)

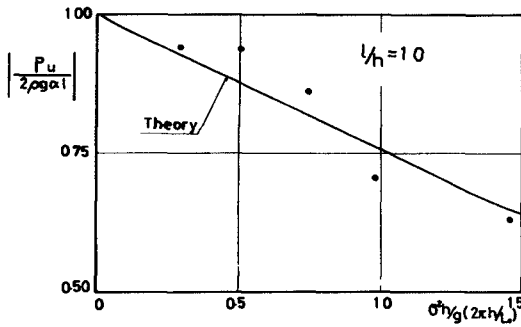


Fig.18 Total Pressure to Plate Theory and Experiment (Single Plate Breakwater)

CHAPTER 95

THE INFLUENCE OF BREAKER TYPE ON RIPRAP STABILITY

by

John P Ahrens, A M , ASCE
Oceanographer
U S Army Coastal Engineering Research Center
Washington, D C

ABSTRACT

Test data related to the stability of dumped quarry stone riprap under wave action is presented. The tests were conducted in the large 635-foot wave tank at the Coastal Engineering Research Center at near prototype scale. The data indicate that the stability of the riprap is strongly influenced by the type of breaker. The lowest riprap stability is associated with a breaker type intermediate between plunging and surging, sometimes referred to as a collapsing breaker.

INTRODUCTION

From February 1969 to June 1970, tests were conducted in the large 635-foot wave tank at the Coastal Engineering Research Center (CERC) to determine the relation of stability of dumped quarry stone riprap to wave action. During this period sixteen riprap protected earth embankments were subjected to progressively higher waves until the riprap failed. The embankments were all constructed to have an initial slope of 1 on 2.5, with a median armor stone weight of 28 pounds for ten tests and 79 or 80 pounds for six tests. The purpose of this study was to collect data related to riprap stability at nearly prototype scale so that current design criteria can be improved. The scope of the study includes riprap stability for waves in reservoirs and coastal waters. The sixteen tests described here represent all of the tests planned for a slope of 1 on 2.5, future tests will be conducted with slopes flatter than 1 on 2.5.

TEST CONDITIONS

All of the sixteen tests described here were conducted in the 635-foot wave tank at CERC. The width of this tank is 15 feet, the depth is 20 feet, the water depth used for all tests was 15 feet and the distance from the toe of the slope to the mean blade position was about 440 feet. Sideboards were placed along the top of the tank wall near the crest of the embankment to allow the crest of the embankment to be built to a height of 24 feet above the bottom of the tank.

The core of the embankment was composed of compacted earth, graded to a smooth 1 on 2.5 slope. Between the core and the armor there was a layer of filter stone about half a foot thick. The riprap was dumped

on the filter bed from a skip, no water was in the wave tank during the dumping. The riprap stone was quarry stone granite from near Occoquan, Virginia, with a specific gravity of 2.71. The median weight of the riprap stone was 28 pounds for tests SPL-1 through 10 and 79 or 80 pounds for tests SPL-11 through 16. The gradation of the riprap was measured by the ratio of the diameter of the 85% stone divided by the diameter of the 15% stone, $D(85)/D(15)$, this ratio was about 1.7 for all tests. The range in weights of the riprap stone was from about 4 times the median weight down to about 1/8 of the median weight. The general shape of the stones could be described as blocky, almost none of the stones had a ratio of their longest axis divided by their shortest axis greater than 4. The porosity of the riprap was 37.4% for the 28 pound stone and 38.7% for the 79-80 pound stone.

In order to include waves with characteristics similar to those observed on both reservoirs and in coastal waters, five wave periods were chosen for testing riprap stability. Each of the tests in this study were run at one of the following wave periods: 2.8, 4.2, 5.7, 8.5, and 11.3 seconds.

TEST PROCEDURES

Waves were run in short bursts during the stability tests so that the generator would be shut off just before the wave energy reflected from the slope could reach the generator blade. Between wave bursts there were brief interludes to allow reflected wave energy to dampen out. Prior to the stability tests there was a calibration phase of this study to determine the proper wave height to assign to a particular combination of generator stroke and wave period. During calibration waves were run in bursts with a wave absorber beach in the tank and the heights were recorded at several locations in the tank. The wave heights used in this study were all obtained during calibration and, therefore, include almost no influence of reflection.

A test was started by surveying the newly constructed slope on a square, 2.0 by 2.0-foot grid in the horizontal plane. The initial survey was then used as a reference with which to compare subsequent surveys. The slope was surveyed with a heavy, rigid sounding rod with a ball and socket foot, the foot was circular with a diameter of 0.5 feet. The height of the first waves run on the newly constructed slope was chosen to be about 30% lower than the height which was expected to dislodge armor stones. Waves were run, in bursts, on the embankment until it appeared that no further stones would be moved by waves of this height, in no case would less than 500 waves be run at a particular wave height and often over 1500 waves would be run before the slope was considered stable. After the riprap was demonstrated to be stable at a particular height the slope would be resurveyed and the wave generator would be adjusted to generate waves approximately 10% higher. The test procedure can then be summarized as, running enough waves at a given height until it appears that the slope is stable, then survey the slope and increase the wave height about 10% and repeat the cycle. The cycle was repeated until enough armor stones were removed to constitute

failure Failure, for these tests, was defined as having occurred when enough riprap stones were displaced so that the filter layer was exposed to wave action and core material was actually being removed through the filter layer

DISCUSSION

The purpose of these tests was to determine the relationship of the stability of dumped quarry stone riprap to wave action on slopes of 1 on 2.5. The primary measure of stability for these tests was the zero damage wave height. The zero damage wave height was estimated on the basis of the written notes made by observers of their impression of the damage occurring to the riprap during the tests, and from damage calculations obtained from the frequent surveys of the slope. By comparing a survey associated with some wave height with the initial survey, the volume of armor displaced and the maximum penetration of damage into the riprap layer were calculated and used to help estimate the zero damage wave height. Table I gives the estimated zero damage wave height for the various tests and also some other observed data. Appendix II explains the meaning of all symbols used in this paper.

Table I gives an average value of the runup ratio, R/H , for each test. The runup ratio is the average of a number of observations made for waves lower than the zero damage wave height, while the slope was still in good condition. Within the limited range of wave heights considered the runup ratio was approximately constant for each test. The initial slope, shown in Table I, was calculated by fitting a least squares straight line through the initial survey points. The initial slope was used as an estimate of how well the construction conformed to the planned 1 on 2.5 slope. Table I also shows the average riprap layer thickness, \bar{r} , for each test.

As the test series proceeded, the scatter in the zero damage wave height was greater than expected and appeared to be at least partly dependent on the wave period. This was not completely unforeseen, however, since a previous study on riprap stability conducted at CERC seemed to show some influence of wave period. The effect of the wave period was confused since these earlier tests were run in three different wave tanks at model scale ratios of from 1 to 30 to prototype. In addition, the previous riprap tests did not generally test a wide range of depth to wave length ratios, d/L , as they were oriented towards some specific riprap problems on reservoirs.

In Table II the stability number N_s , is defined and tabulated for each test by wave period and median armor weight. The stability number shown in Table II is useful for intercomparing riprap tests, having the same slope but different median weights (Hudson (2)). Table II shows that the lowest stability is associated with the four tests with a wave period of 4.2 seconds and the two tests at a period of 5.7 seconds with the larger median weight. There is relatively high stability for both the short period waves, $T=2.8$ seconds and for the long waves, $T=8.5$ and 11.3 seconds. Table II suggests that the breaker type may influence the riprap stability since it is related to the incident wave height and period.

TABLE I
OBSERVED TEST DATA

Test Designation	T (sec)	W ₅₀ (lbs)	H _{D=0} (feet)	H(FAIL) (feet)	\bar{r} (feet)	R/H	Initial Slope, 1/m
SPL-1	2 8	28	2 50	3 81	1 82	0 98	2 50
2	5 7	28	2 11	2 41	1 38	1 44	2 62
3	4 2	28	1 76	2 68	1 54	1 21	2 48
4	8 5	28	2 48	3 20	1 46	1 61	2 57
5	11 3	28	2 58	3 26	1 57	1 81	2 46
6	8 5	28	2 20	2 34	0 95	1 62	2 58
7	5 7	28	2 11	2 41	1 21	1 51	2 55
8	4 2	28	1 76	2 03	1 03	1 22	2 50
9	2 8	28	2 50	3 00	1 10	1 01	2 43
10	4 2	28	1 76	2 03	1 06	1 22	2 51
11	5 7	80	2 51	2 97	1 40	1 36	2 46
12	8 5	79	3 28	3 84	1 58	1 61	2 51
13	2 8	79	3 28	-	1 41	1 01	2 55
14	4 2	79	2 58	3 16	1 45	1 23	2 49
15	11 3	79	3 40	3 97	1 35	1 69	2 47
16	5 7	79	2 51	3 13	1 38	1 32	2 48

TABLE I

STABILITY NUMBERS BASED ON ZERO DAMAGE WAVE HEIGHTS

Median Weight	Wave Periods (seconds)				
	2 8	4 2	5 7	8 5	11 3
{ 28	2 66	1 87	2 25	2 64	2 75
{ 28	2 66	1 87	2 25	2 34	----
{ 28	----	1 87	----	----	----
{ 79	2 47	1 94	1 89	2 47	2 56
{ 80	----	----	1 88	----	----

$$\text{STABILITY NUMBER, } N_s = \frac{\gamma_s^{1/3} H_{D=0}}{W_{50}^{1/3} (S-1)}$$

Table II also suggests that for the tests with the lowest stability the median armor weight is proportional to the cube of the zero damage wave height given by Hudson's (2) formula

The breaker types for the six tests with low stability noted above (tests SPL-3, 8, 10, 11, 14 and 16) were all intermediate between surging and plunging. Galvin (1) calls this transitional type of breaker a collapsing breaker. Apparently collapsing breakers have characteristics which yield low riprap stability. Table III places each test into a breaker category based on the wave conditions observed for the test before and just after the zero damage wave height. Table III shows that the average stability number for the tests with collapsing waves is considerably lower than tests in the plunging or surging breaker category. Galvin's definitions of breaker types have been used throughout this study.

In order to more clearly show the effect of breaker type on riprap stability Figure 1 shows the riprap stability coefficient, K_{RR} , plotted versus the offshore breaker parameter H_0/L_{0m}^2 . The riprap stability coefficient is equal to the product of the cube of the stability number and the tangent of the slope angle, it is similar to the stability coefficient, K_{Δ} , which is frequently used in evaluating the stability of armor units in rubble-mound breakwaters. The offshore breaker parameter is useful for predicting the breaker type on a known slope for waves with known deep water steepness. The offshore breaker parameter for Figure 1 was computed by converting the zero damage wave height for each test to their equivalent deep water height. Figure 1 clearly shows the low stability associated with collapsing breakers. For these tests the transition between surging and collapsing breakers occurred between values of 0.08 and 0.10 of the offshore breaker parameter and the transition between collapsing and plunging occurred between values of 0.20 and 0.25 of the offshore breaker parameter.

CONCLUSION

Intuitively it seems reasonable that the manner in which the waves break on a slope will influence the stability of the armor protecting the slope. When a plunging breaker hits the armor stones with great impact, the impact has only a small component which is tangential to the slope, so that it takes a surprisingly large wave to dislodge armor stones. The uprush following the plunge is a turbulent, spongy mass of water with a great quantity of entrained air and has little impact against the stones. The return flow of the uprush appears to lack the volume, elevation and time to develop the strength to overturn the armor stones. In the case of a surging breaker the runup travels rather gently up the slope and the impact against the armor stones is slight. When riprap stones are removed by surging waves, it is by the return flow of the runup through, out of, and over the armor layer. The flow out of the armor layer tends to lift the stones and the return flow over the surface tends to overturn them. The breaker type transitional between plunging and surging, referred to as a collapsing breaker, has an uprush which seems to have significant impact against the stones and is directed approximately tangential to the slope. The uprush of the collapsing wave

TABLE 11

INFLUENCE OF BREAKER TYPE ON STABILITY NUMBER, N_s , FOR
DUMPED QUARRY STONE RIPRAP ON A SLOPE OF 1 ON 2.5

TEST	WAVE PERIOD	SURGING	COLLAPSING	PLUNGING	SPILLING
SPL-1	2.8 sec	----	----	2.66	----
2	5.7	2.25	----	----	----
3	4.2	----	1.87	----	----
4	8.5	2.64	----	----	----
5	11.3	2.75	----	----	----
6	8.5	2.34	----	----	----
7	5.7	2.25	----	----	----
8	4.2	----	1.87	----	----
9	2.8	----	----	2.66	----
10	4.2	----	1.87	----	----
11	5.7	----	1.88	----	----
12	8.5	2.47	----	----	----
13	2.8	----	----	2.47	----
14	4.2	----	1.94	----	----
15	11.3	2.56	----	----	----
16	5.7	----	1.89	----	----
Average		2.47	1.89	2.60	

$$\text{STABILITY NUMBER, } N_s = \frac{\gamma_s^{1/3} H_{D=0}}{W_{50}^{1/3} (S-1)}$$

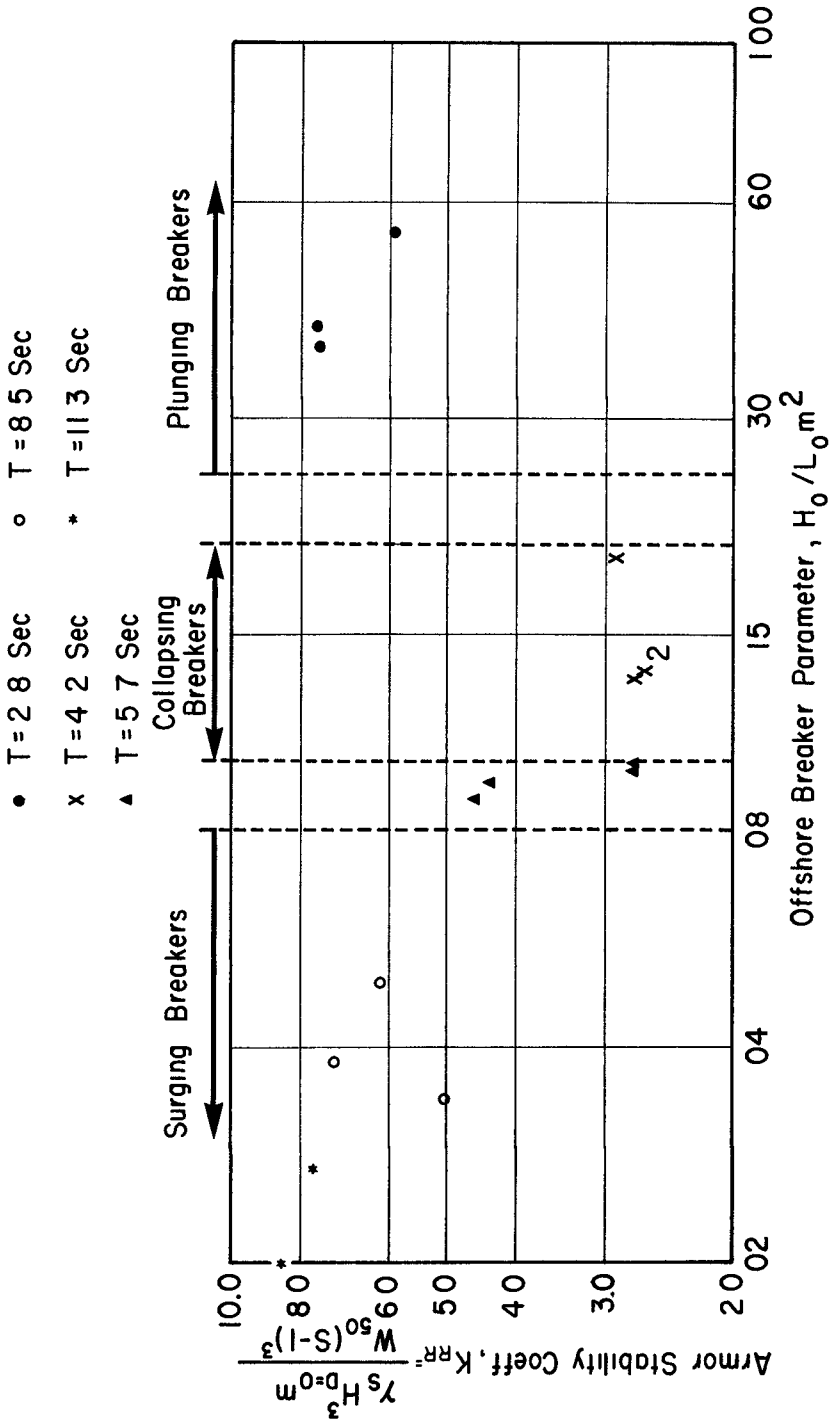


FIGURE I ARMOR STABILITY COEFF VS OFFSHORE BREAKER PARAMETER

also has dynamic properties which tend to lift the stones. The return flow of the runup can then dislodge or overturn stones which have been momentarily placed in a less stable position by the uprush. Since the return flow of the collapsing breaker seems to be significantly stronger than that of the plunging breaker it is possible that even stones which were not made unstable by the uprush could be dislodged by the downrush. It seems as if the physical characteristics of collapsing breakers have combined in an optimum way to yield low riprap stability.

ACKNOWLEDGEMENTS

The author is indebted to the numerous suggestions of Mr Thorndike Saville, Jr, Chief of the Research Division, CERC, and Mr George Simmons, Chief Technician, Research Division, CERC, which have materially improved this study. The study was supported jointly by the Office of Chief of Engineers and CERC of the U S Army Corps of Engineers, permission to publish this paper is gratefully acknowledged.

APPENDIX 1 - REFERENCES

- 1 Galvin, Cyril J, Jr, "Breaker Type Classification on Three Laboratory Beaches", Journal of Geophysical Research, Vol 73, No 12, June 15, 1968, p 3651-3659
- 2 Hudson, R Y, "Laboratory Investigations of Rubble-Mound Breakwaters", ASCE, Journal of the Waterways and Harbors Division, Vol 85, No WW3, Paper 2171, September, 1959

APPENDIX II - NOTATION

The following symbols are used in this paper

d = water depth

H = wave height

H_O = deep water wave height

$H_{D=0}$ = zero damage wave height

$H(\text{FAIL})$ = failure wave height

K_{RR} = stability coefficient for riprap

K_{Δ} = stability coefficient for rubble-mound breakwaters

L = wave length

L_O = deep water wave length

m = tangent of slope angle

N_S = stability number

\bar{F} = average riprap layer thickness

R = runup

S = specific gravity of riprap stone

T = wave period

W_{50} = median armor weight

γ_s = specific weight of riprap stone

CHAPTER 96

DAMAGE FUNCTIONS FOR A RUBBLE-MOUND BREAKWATER

UNDER THE EFFECT OF SWELLS

Juan B Font
Assistant Professor
College of Engineering, Central University
Caracas, Venezuela

ABSTRACT

In this paper experimental data are given to aid in the design of a rubble-mound breakwater. The use of armor damage functions is supported rather than the use of the wave height for the no damage condition. Damage curves defined experimentally are proposed, for both rocks and tetrapods, for different wave storm durations and for different placing techniques.

A determinant influence of storm duration is found for advanced damage of the armor layers.

The experiments with different placing techniques showed that stability coefficients based upon the no damage criteria, do not give a reliable picture of the ultimate strength of a rubble-mound breakwater.

INTRODUCTION

The experiments on which this paper is based have been made in a series of research works: Hernández, Pastor and Suárez (1968), Loreto (1969), Ibarra and Blumentals (1969), Neri and Santeliz (1970). These researches were accomplished in the Hydraulic Laboratory of the Central University of Venezuela, in partial fulfillment of their Civil Engineer Degree, under the writer's direction.

A preliminary paper on the influence of wave storm duration was submitted by the writer to the Eleventh Conference on Coastal Engineering (1968). In that paper were given damage functions for different storm durations with the number of waves as the only parameter. A strong dispersion of the

experimental data showed the importance of the ratio $H_{1\%} / H_{1/3}$, $H_{1\%}$ being the wave height that caused one percent damage and $H_{1/3}$ the so called significant wave height or mean of the larger one third. In this paper new data on wave storm duration is submitted, in which this ratio is also taken as a parameter, thus obtaining a better fitting of the experimental points

The Hudson's design wave height

Since the no damage criteria for rubble-mound breakwater design were defined (Hudson, 1959), most research work on this subject has focused its attention on the initial damage. However, it is generally accepted that rubble-mound breakwaters are expected to withstand the design storm with some damage, either reaching equilibrium or being repaired before next storm hits

The definition of the design condition for the one percent damage has the advantage of being equivalent to the no damage situation and thus numerically well defined. However, the stability of the one percent of the armor rocks that are first displaced, depends largely on random placing and geometrical factors, rather than on the armor capacity as a whole to resist waves. Rogan (1968) points out the fact, also observed by the writer, that the filter layers uncovering is simpler to observe and more significant than the number of displaced rocks, specially at the incipient stages of damage. In this sense, also the late Iribarren (1965) defined the design criteria based on the total failure of the breakwater. Iribarren proposed his most recent formula considering that the failure of the armour depended largely on the slope stability of about six rows of that could slide at the same time. Nevertheless, although this type of failure is often present at the final stages of failure, it has been largely induced by the continuous weakening of the armor in the manner considered by Hudson, it est rocks rolling or being lifted one by one

The design using the damage functions

The damage functions, rather than the no damage or total failure conditions alone, should be given to the design engineer, summarizing the afore discussion in the following reasons

- 1 Economic considerations in one hand and safety factor in the other, usually lead to a design damage different from either the no damage or total failure conditions
- 2 Neither the no damage or total failure conditions are solely determinant of the safety factor for a given design damage

Both Hudson and Iribarren, in the writings above mentioned, have presented experimental data in the form of damage functions in which the percentage of damage is related to parameters defined by themselves. The writer (1968) has proposed to relate the percentage of damage $\Delta\%$ to the ratio $H/H_{1/3}$, H being the wave height that causes the $\Delta\%$ damage, since technical literature is plenty of data for the $H_{1/3}$ selection. This representation also simplifies visual comparison of damage functions for different armor blocks and placing techniques.

The experimental data and curves given in this paper are believed to apply specially to the case of decayed swells, since the waves used in the laboratory are periodic waves of intermediate steepness. To the writer knowledge, the first reference given to the frequency spectrum shape influence appeared in a paper by Carstens et Al (1966). It could be said that the shape of the frequency spectrum is related to the tendency of higher waves to break in front of the breakwater, therefore it is suggested that in future experimentation, related with the non-uniform waves effect on breakwaters, the relation between the significant wave height and the breaker height for the mean wave period at the depth of the structure be considered as a significant parameter. In the present experiments this relation was

$$0.3 < \frac{H_{1/3}}{H_b} < 0.4$$

H_b being the breaker height corresponding to the wave period and water depth of the tests as computed after the experiments of Danel (1952).

The influence of duration of locally wind generated waves was studied in the laboratory by Rogan (1968). The main conclusion of the latter is that the effect of a local wave storm is similar to that of periodic waves with height equal to the storm significant wave height.

INFLUENCE OF SWELL DURATION

Fig 1 Shows the damage functions for rocks and tetrapods in which $\Delta\%$, the percentage of displaced elements, has been related to $H/H_{1/3}$, H being the height of the wave that causes the damage and $H_{1/3}$ the height of the wave for the 1% damage, usually defined as the limit of the no damage condition. The symbol n refers to the number of waves of the swell. The symbol $H_{1/3}$ refers to the significant wave height of swell.

Fig 2 Shows the total damage caused by swells of different durations with $H_{1/3} / H_{1/3}$ as parameter. H_{max} refers to the maximum wave height expected during the storm. For storms with more than 3 000 waves the $n = \infty$ curve could be used.

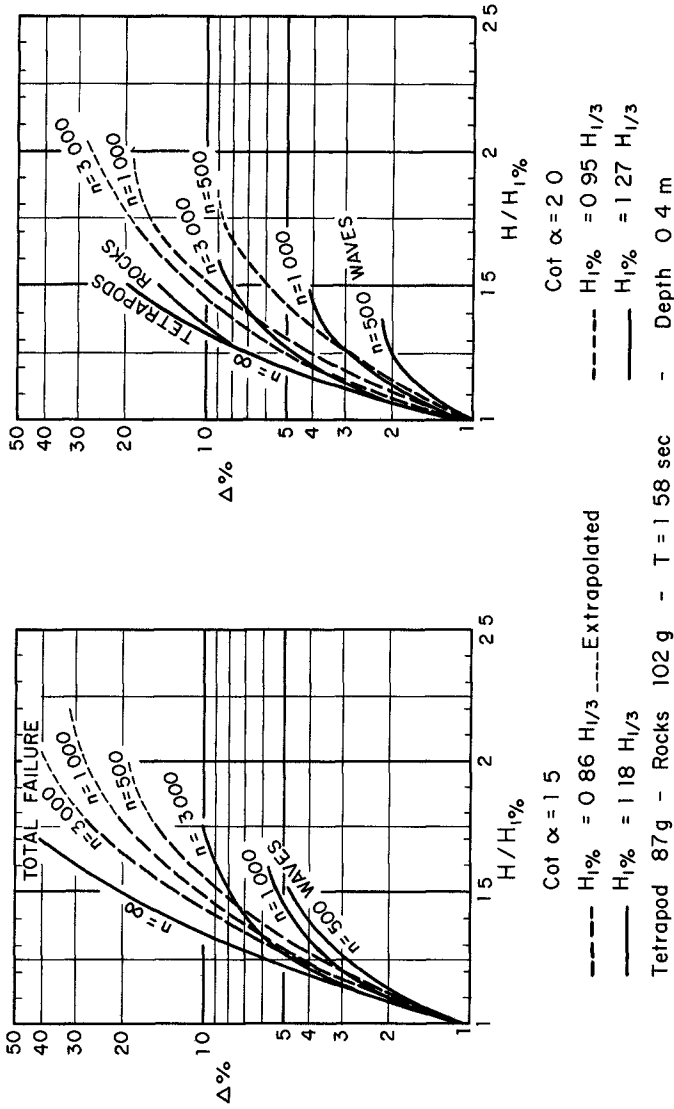


FIG 1 DAMAGE FUNCTIONS FOR ROCKS AND TETRAPODS
INFLUENCE OF SWELL DURATION

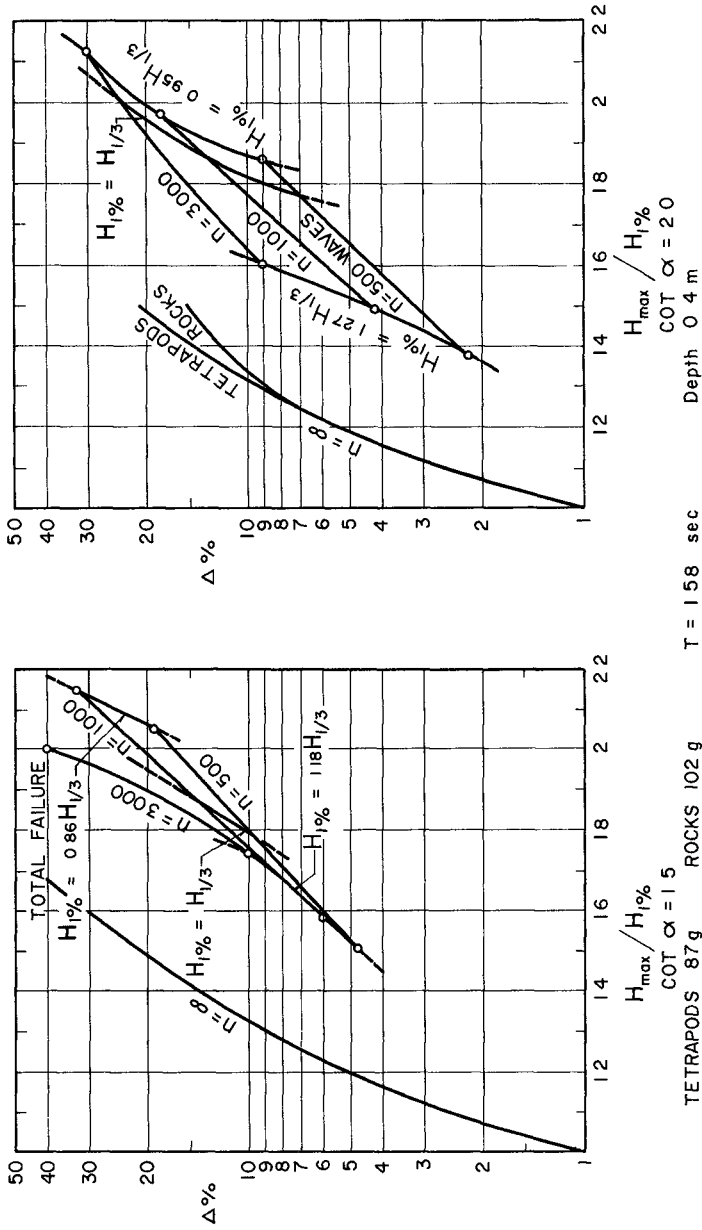


FIG 2 TOTAL DAMAGE FOR DIFFERENT DURATION SWELLS

Although a subject for future research, it is believed that design in shallow water, where the largest waves break far from the structure, could be carried using the curves in Fig 1 with H being the maximum active wave height Galvin (1969) has made experiments that may help in the selection of the maximum active wave height

INFLUENCE OF PLACING TECHNIQUES OF ARMOR ELEMENTS

Fig 3 shows the damage functions for rocks and tetrapods using different placing techniques Dashed curves correspond to careless random placing Full curves stand for careful placing, interlocking elements as much as possible

As it is shown by the experimental results, placing makes a big difference for the initial damage, but is less relevant for advanced damage, when the armor porosity and "dynamic" stability are essential

DAMAGE DISTRIBUTION ALONG BREAKWATER SLOPE

Fig 4 Shows the average damage distribution curve of four sets of experiments, with the 1 1 5 slope for both rocks and tetrapods It is seen that while at the beginning the the damage mostly occurs below the still surface level, for larger waves the portion immediately above that level is also strongly affected As a matter of fact it is in this region where uncovered filter first appears

THE ARMOR DENSITY COEFFICIENT

Usually the kind of armor block to be used in a breakwater (rock, tetrapod, tribar, tetrahedron, dolos, stabit, etc), as well as the constructive method (dumping, placed by crane, placed with special techniques, etc), are selected taking into account economic and functional considerations It is sometimes difficult, however, to make economic comparisons since authors do not give enough data, restricting it usually to the Hudson's Coefficient K_d , which is only indicative of the block weight and not of the volume required to cover a given breakwater slope area

In order to adopt a standard terminology and to simplify the economic design, the following coefficients and expressions are proposed

If we call A_t the area of the breakwater slope tributary to one block, then

$$A_t = \frac{\text{Area}}{\text{Number of blocks}}$$

In order to give this area in a dimensionless manner,

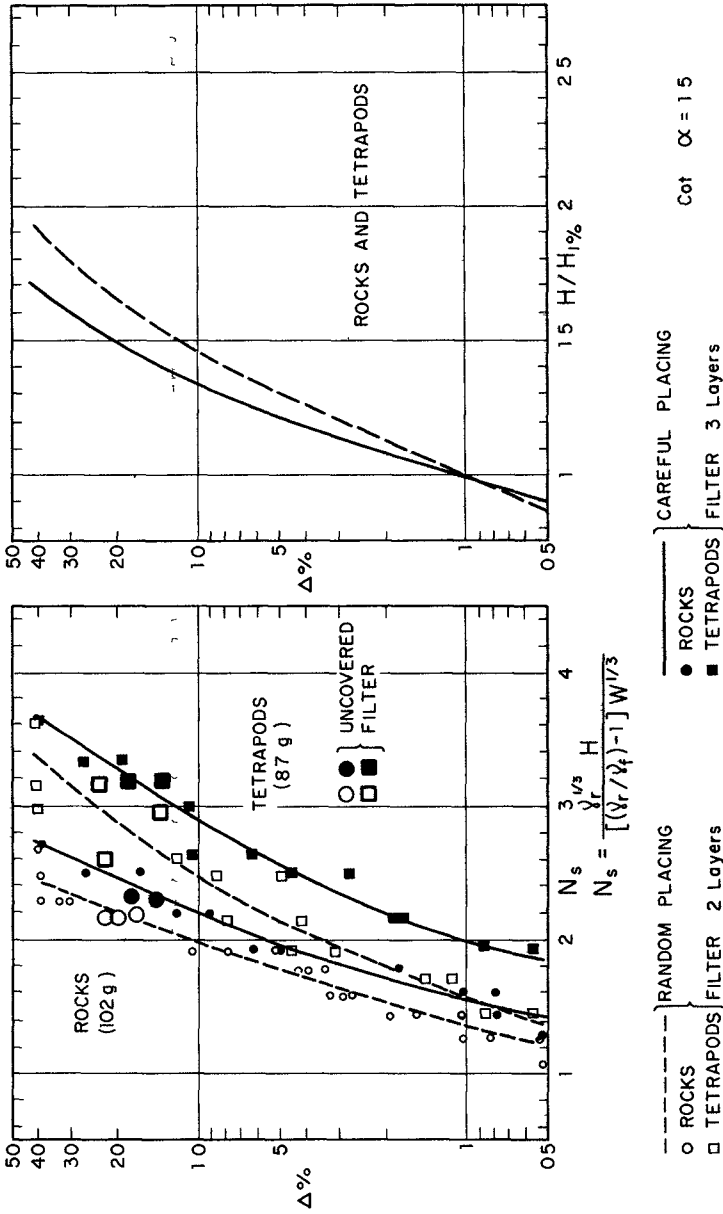


FIG 3 DAMAGE FUNCTIONS FOR DIFFERENT PLACING TECHNIQUES

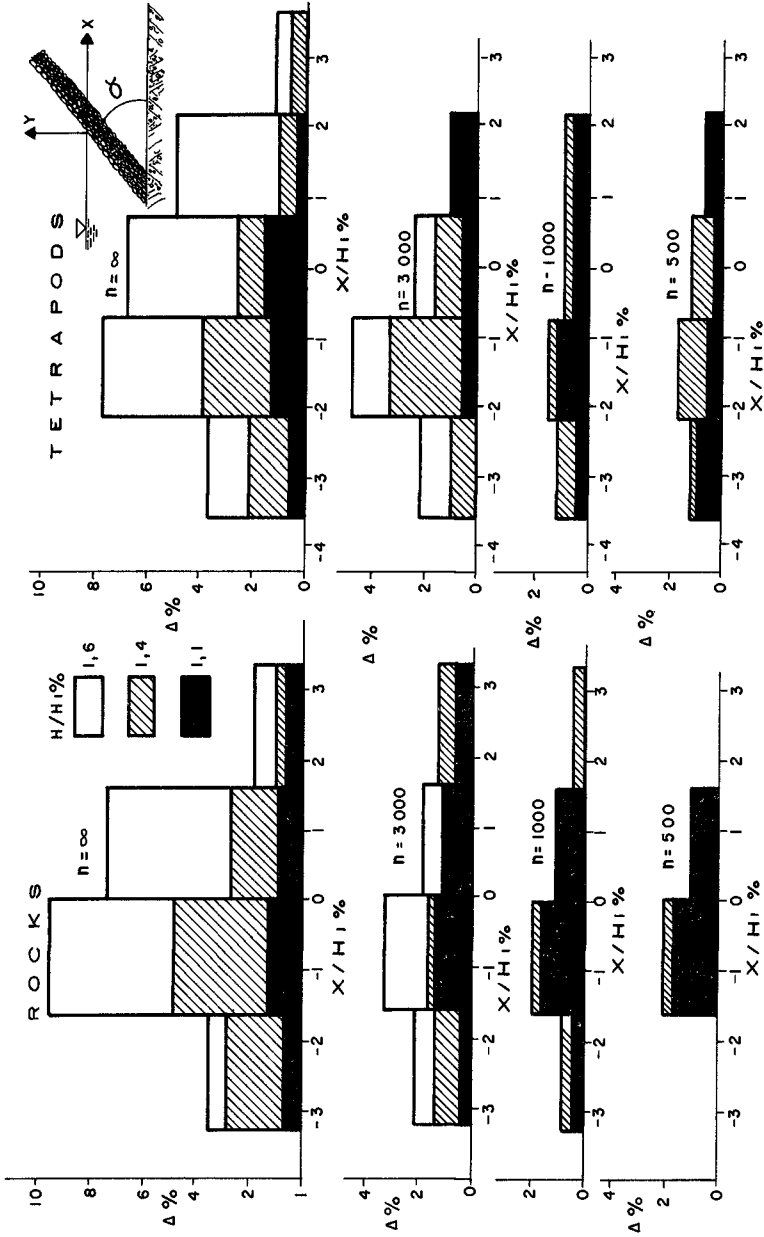


FIG 4 DAMAGE DISTRIBUTION ALONG BREAKWATER SLOPE
COT $\alpha = 1.5$ (MEAN OF TWO TESTS)

it may be defined the "revetment unit" U_r such that

$$U_r = \frac{A_t}{V^{2/3}} = \frac{A_t}{(W/\gamma_r)^{2/3}}$$

Where V is the solid volume of one block, W its weight and γ_r its specific weight

In the experiments reported in this paper, corresponding to the careful placing technique, the mean values for U_r were

Tetrapods 1,00 Rocks 0.95

Since the specific gravity of rocks is usually 2.7 and that of concrete 2.2, it may be defined a coefficient K_s such that

$$\frac{W}{A_t} = \frac{1}{K_s} \frac{\gamma_f H}{\cot \alpha}$$

Where γ_f is the water specific weight. In this manner the required weight per unit area would be inversely proportional to K_s for a given breakwater slope and wave height

If K_s is related with Hudson's formula

$$W = \frac{\gamma_r H^3}{K_D [(\gamma_r/\gamma_f) - 1]^3 \cot \alpha}$$

Then the following expressions result

$$K_s = \frac{\gamma_f H U_r}{\gamma_r^{2/3} W^{2/3} \cot \alpha} = \frac{K_D \gamma_f [(\gamma_r/\gamma_f) - 1]}{\gamma_r^{5/3}} \frac{U_r W^{2/3}}{H^2}$$

K_s could be named "armor density coefficient"

In Fig. 5 the "armor density coefficient" has been plotted against the damage percentage $\Delta\%$ for both rocks and Tetrapods. It is also shown a sample of economic comparison of both kinds of blocks for a 10% damage design. It is readily seen that a price per unit weight of tetrapods 1.26 times the price per unit weight of rocks will make both blocks economically equivalent for that condition.

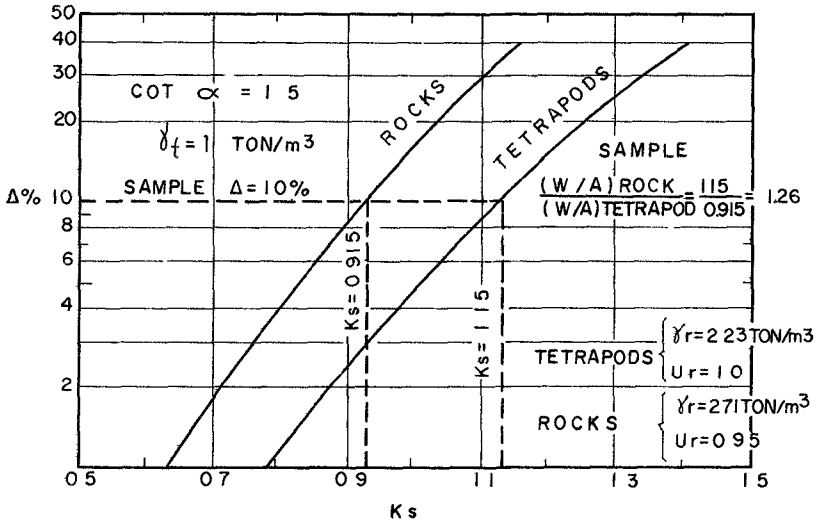


FIG 5 STABLE DENSITY COEFFICIENT (CAREFUL PLACING)

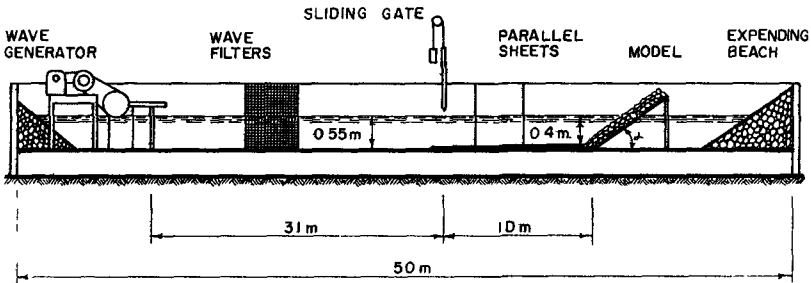


FIG 6 WAVE CHANNEL AND EXPERIMENTAL SET - UP

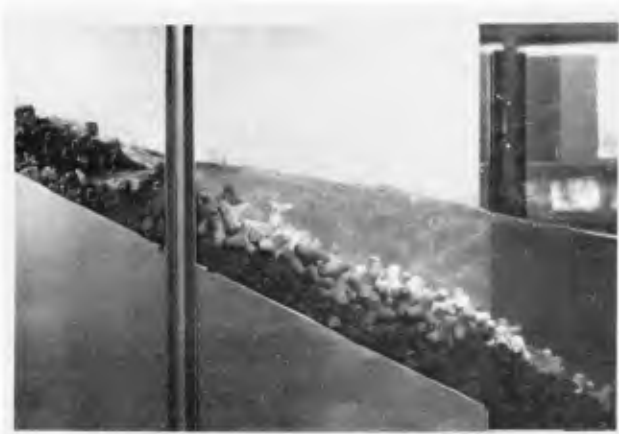


FIG. 7 WAVE ACTION ON THE MODEL BREAKWATER

DESCRIPTION OF THE EXPERIMENTAL WORK

The tests

For the limited duration storms the model breakwater was subjected to the attack of periodic waves of height and in number according with the known statistical distribution for actual swells (Putz, 1954) See in Fig 13 the wave height histogram actually used in the experiments In Fig 12 are shown records of a typical uniform wave train and a train of " three waves ", it est a train with three larger waves of mean height 2.7 times the mean wave height, as specified in the 1000 waves histogram

For the infinite duration swells, waves of a given height attacked the breakwater until equilibrium was reached Then the displaced blocks were counted and, without rebuilding the slope, the experiment followed increasing the wave height in steps of about one centimeter The test were conducted in bursts such that reflection from the breakwater would not interfere with wave generation; furthermore, a slide gate, close to the model, was used to interrupt the " last wave " of the train that is up to 20% larger than the preceeding waves In terms of Hudson's formula, a 10% difference in wave height means 33% difference in the stability coefficient K_d

The core of the breakwater was considered to be impervious and, as such, a board with stripes was used Completely different results are expected if a core with significant porosity were used

It was observed (See Fig 7) that all waves that caused some damage broke on the breakwater slope in the manner of a collapsing breaker as defined by Galvin (1969)

The Experimental Set - up

See fig 6 for a description of the experimental Set - up

CONCLUSIONS

1 For the initial movement of rocks and tetrapods it seems that the duration of the swell is not important The duration becomes relevant for advanced damage (See Figs N° 1 and 2)

2 Economic considerations in one hand and safety factor in the other, usually lead to a design damage different from either the no damage or total failure conditions Therefore the damage functions, rather than those criteria, should be given to the design engineer.

3 The experiments show that placing techniques of the armor blocks make a big difference for the initial damage, but are less relevant for advanced damage, when the armor porosity and "dynamic" stability are essential (See Fig 3.)

4 Uncovering of the filter layers in holes of diameter equal to two pieces ocured for armor damage percentages between 10% and 20% Usually, in the next wave height step, total failure would follow for damage between 30% and 40% (See Fig 3)

5 It was observed in the experiments that while at the beginning the damage mostly occurs below the still surface level, for larger waves the portion immediately above that level is also strongly affected (See Fig 4)

ACKNOWLEDGMENTS

Financial support for this research was provided by the "Consejo de Desarrollo Científico y Humanístico" of the Central University of Venezuela through the research project N° 273 The author is also grateful for the assistance given by the Ministry of Public Works, Ports and Airports Division, in the preparation of this report

REFERENCES

- Carstens, T , A Torum and A Traetteberg, "The stability of rubble mound breakwaters against irregular waves", Proc Tenth Conference on Coastal Engineering, A S C E , 1966, Volume 11, pp 958-971
- Danel, Pierre, "On the limiting clapotis", Gravity Waves, National Bureau of Standards Circular N° 521 (November, 1952), 35-38
- Pont, Juan B. "The effect of storm duration on rubble-mound break water stability", Proc 11 th Conference on Coastal Engineering, A S C E., 1968, pp 779-786
- Galvin, Cyril J "Breaker Travel and Choice of design wave height", proceedings, Journal of the Waterways and Harbors Division, ASCE, Vol 95, N° WW 2, May, 1969, pp 175-200
- Hernández, Pastor and Suárez " Estabilidad de rompeolas de roca," Graduation Research, Hydraulic Laboratory, Universidad Central de Venezuela, Aug, 1968
- Hudson, Robert Y , "Laboratory investigation of rubble-mound break waters", J Waterways Harbors Div ASCE, 85, WW 3, paper N° 2171 (September, 1959) 93-121

- Iribarren, R , "Formule pour le calcul des diques en enrochements Naturels ou elements artificiels" XXIst International Navigation Congress - Stokholm, 1965, P I A.N C,
- Ibarra E and T Blumentals, " Estabilidad de Rompeolas ", Graduation Research, Hyraulic Laboratory, Universidad Central de Venezuela, Dec , 1969.
- Loreto R., Alberto " Estabilidad del Talud de un Rompeolas de Roca,"Graduation Research, Hydraulic Laboratory, Universidad Central de Venezuela, May, 1969
- Neri, Lucila and Yandira Santeliz " Estabilidad de la Coraza de Rompeolas de Roca y Elementos de Concreto ", Graduation Research Hydraulic Laboratory, Universidad Central de Venezuela, July, 1970
- Putz, R R , "Statistical analysis of wave records" Proc Conference on Coastal Engineering, Berkeley, Calif , The Eng Foundation Council on wave Res, 1954 pp 13-24
- Rogan, Adels J " Destruction Criteria for rubble-mound breakwaters " Proc. 11th Conference on Coastal Engineering, ASCE, 1968, pp 761-778

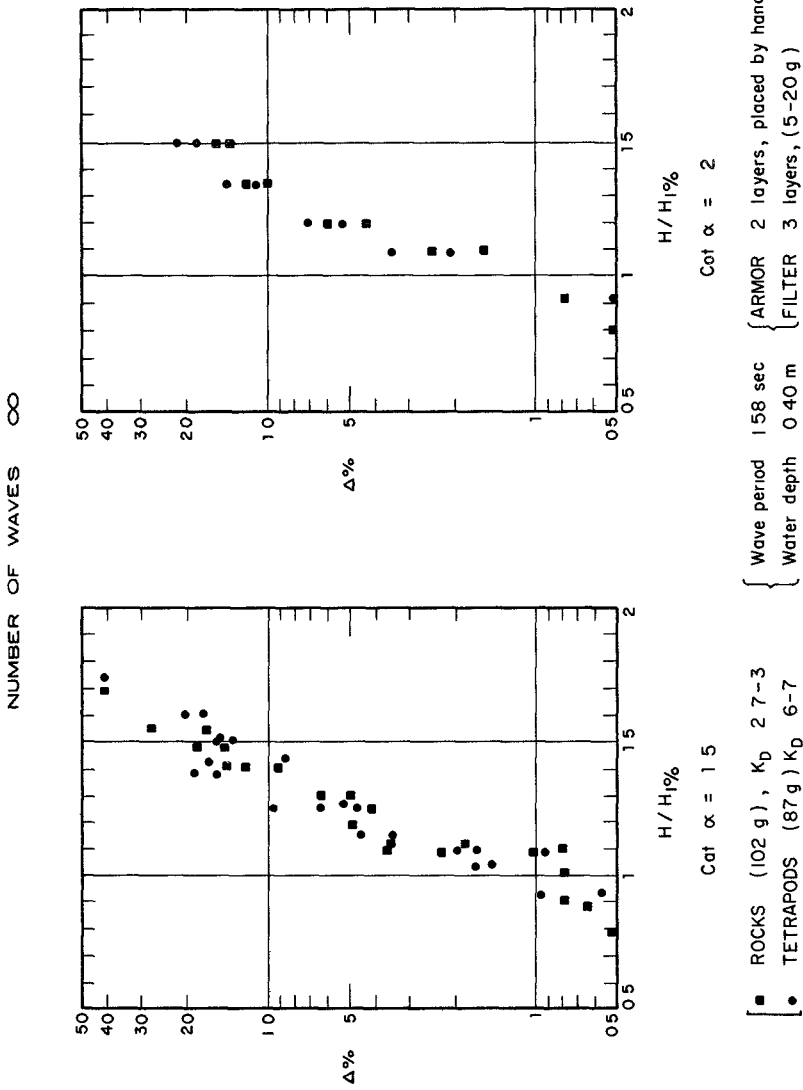
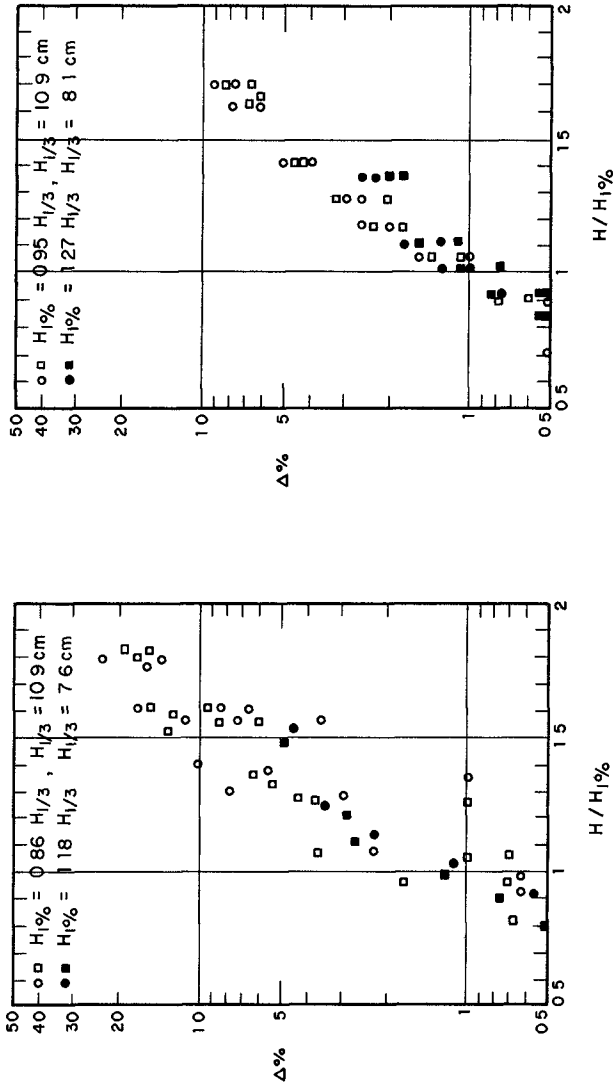


FIG 8 EXPERIMENTAL DATA

NUMBER OF WAVES 500



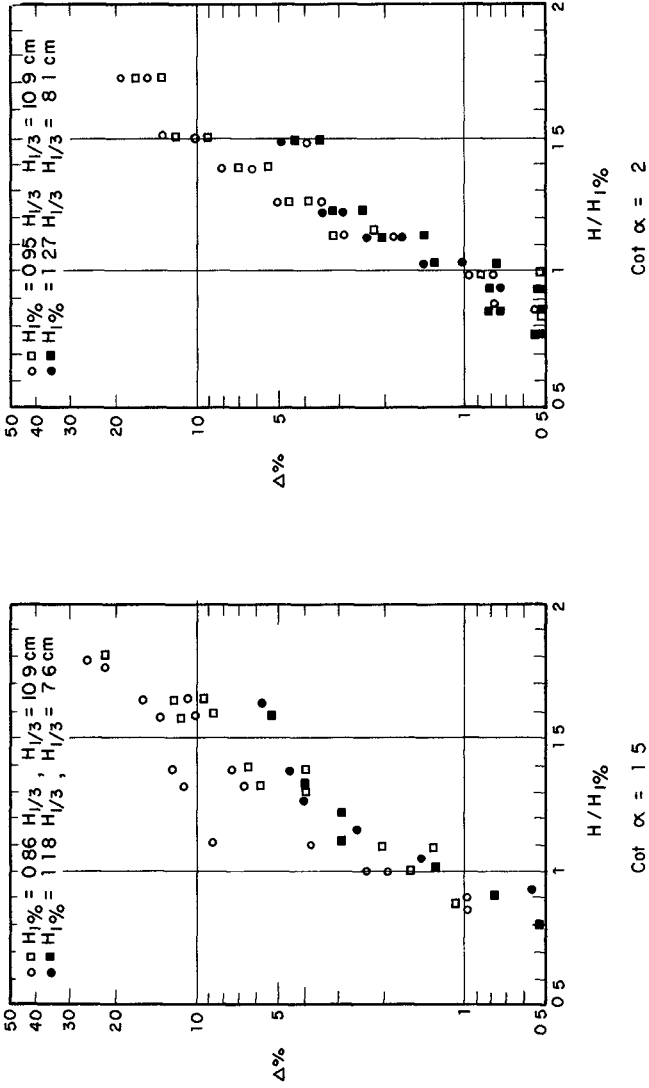
ROCKS (102 g), K_D 2.7-3
 TETRAPODS (87 g) K_D 6-7

ARMOR 2 layers, placed by hand
 FILTER 3 layers, (5-20 g)

Wave period 1.58 sec
 Water depth 0.40 m

FIG 9 EXPERIMENTAL DATA

NUMBER OF WAVES 1 000



■ ROCKS (102g)
 ○ TETRAPODS (87g)

FIG 10 EXPERIMENTAL DATA

NUMBER OF WAVES 3000

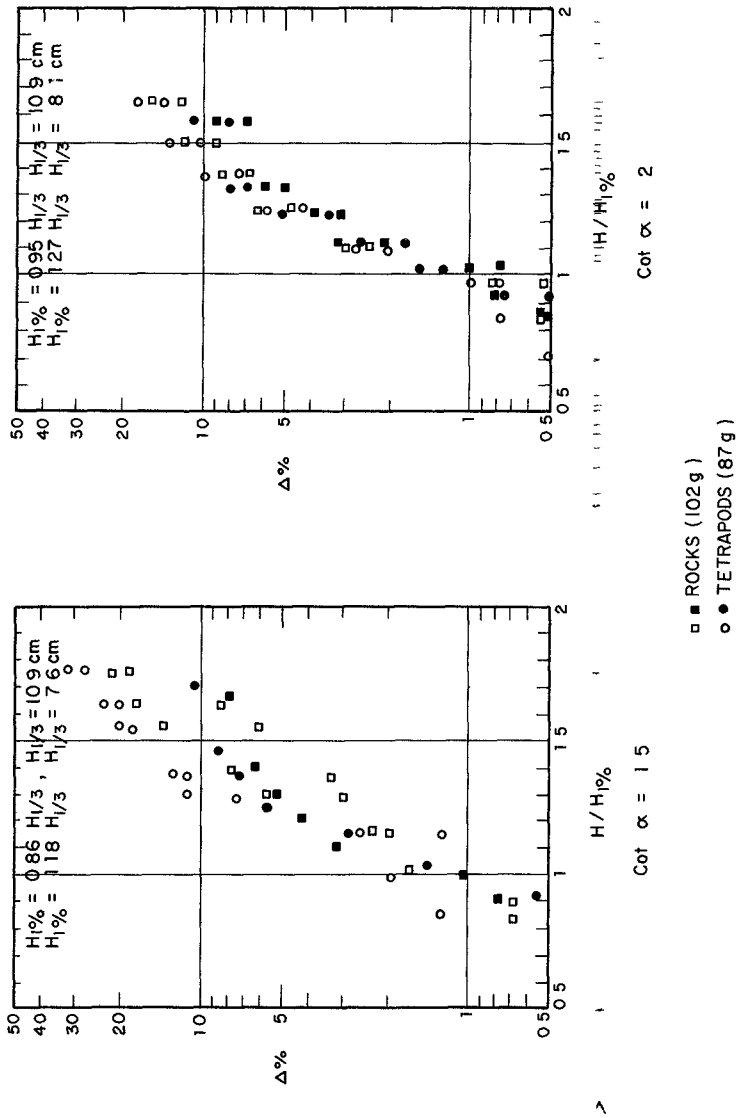


FIG 11 EXPERIMENTAL DATA

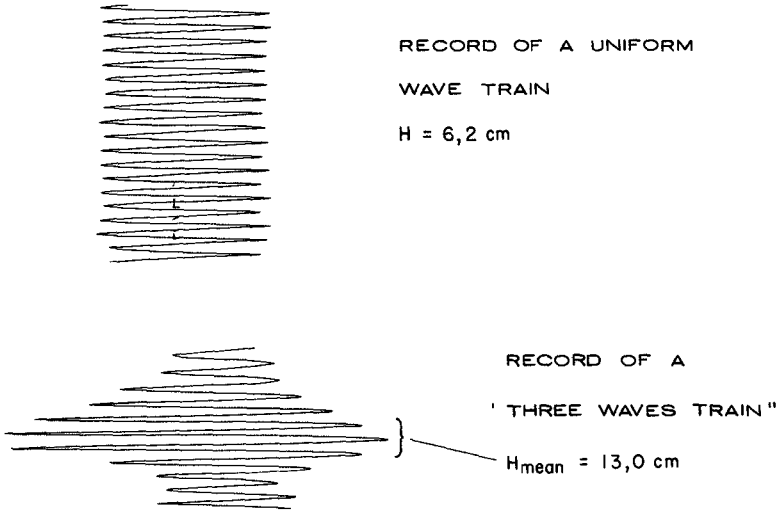


FIG 12 SAMPLE WAVE RECORDS

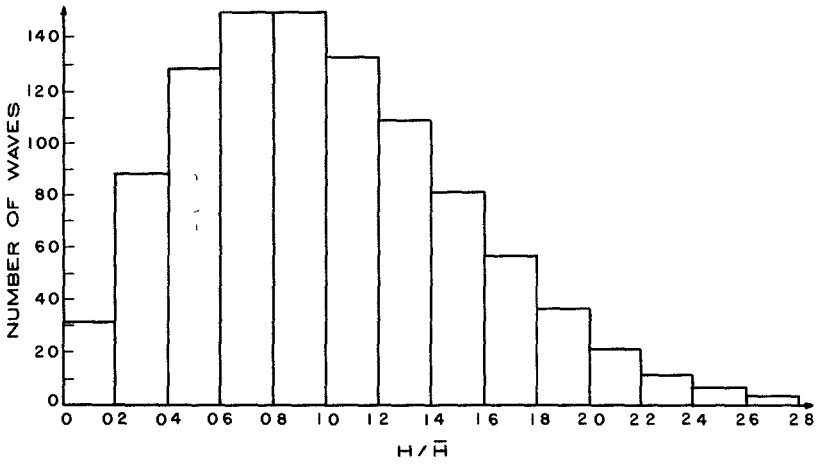


FIG 13 WAVE HEIGHT HISTOGRAM FOR 1000 WAVES

CHAPTER 97

HYDRAULIC RESISTANCE OF ARTIFICIAL CONCRETE BLOCKS

by

Nobuo Shuto

Associate Professor, Chuo University, Tokyo, Japan

and

Hiroshi Hashimoto

Senior Research Engineer,
Public Works Research Institute,
Ministry of Construction, Japan

Abstract

Theoretical analysis and experiments are made to clarify the mechanism of reducing the wave energy by the block structures. In order to express the hydraulic resistance of three different kinds of blocks, three different models are proposed. The hydraulic radius and the porosity of the block structures are essentially important factors in the expression of the hydraulic characteristics of the block structures.

It is recommended, from experimental results, to carry out the hydraulic experiments by using blocks heavier than at least 500 gr.

Resistance coefficients obtained in the steady and oscillatory flows show almost no difference.

1 Introduction

Several types of artificially made concrete blocks have been used in coastal and harbour areas. Main purposes of using block structures are

- (1) to reduce the wave forces acting on coastal structures,
- (2) to reduce the wave reflection from coastal structures,
- (3) to reduce the height of transmitted waves,
- (4) to reduce the wave run-up height,
- (5) to reduce the quantity of wave overtopping, and
- (6) to protect the toe of coastal structures against erosion.

Although the design of the block structures is usually based on hydraulic experiments, the similitude between model and prototype is not yet clearly understood.

In order to fulfill the above mentioned purposes, block structures must be able to effectively reduce wave energy. Thus, the knowledge of the mechanism of reducing the wave energy by the block structures is of essential importance. Naturally this mechanism should be considered by taking into account the effect of the scale of model.

The aim of the present study is to clarify the mechanism of energy reduction, and to express the hydraulic resistance law of the block structures in terms of their characteristic quantities. When this is once achieved, factors such as the reflection and transmission coefficients of block structures become computable and a part of the design may be satisfactorily done without conducting hydraulic experiments. In addition if the similitude is once established, the hydraulic experiment will give more reliable

design data

First, authors intend to explain the loss coefficient of block structures in terms of the characteristic quantities such as the porosity or the hydraulic radius by using the experimental results obtained in the steady flow

Secondly, authors try to determine whether the flow through the block structures is turbulent or laminar. Since a hydraulic model using small blocks does not produce a fully developed turbulent flow through its pores, the experimental results obtained from such a model are not likely to give any reliable design data. Therefore, the minimum allowable size of the blocks in the hydraulic experiment must be determined by taking into account the flow characteristics through the pores.

Thirdly, comparisons are made between the resistance law obtained by assuming the steady flow and that obtained by assuming the oscillatory flow. Naturally, the wave motion actually attacking the block structures in the field is not steady but unsteady. However, it is desired to determine the hydraulic resistance law of concrete blocks by the experiments in the steady flow which is simpler and more convenient than those in the oscillatory flow. Thus, it may be very useful to find a relationship between the resistance laws obtained in the steady and unsteady flow experiments.

2 Theoretical analysis

2-1 Steady flow

2-1-1 Resistance-pipe model

Figure 1 shows this model. The block structure is considered to have a number of fictitious pipes in it. The total volume of the fictitious pipes is set equal to the total volume of the pore in the block structure. The total area of the inner surface of the fictitious pipes is assumed equal to the total wetted area of the blocks.

Then, we have

$$nd^2L = \epsilon BLh \quad (1)$$

$$4nLd = S, \quad (2)$$

where n is the number of the pipes, d the diameter of the pipe, L the length of the block structure, B the width of the block structure, h the average water depth in the block structure, ϵ the porosity of the block structure, and S the surface area of the blocks.

From the above equations, we have

$$d = 4 \frac{\epsilon BLh}{S} = 4R \quad (3)$$

$$n = \frac{S}{16RL} \quad (4)$$

The hydraulic radius, R , is defined as $\epsilon BLh/S$ and is considered as a measure of the average size of the pore.

When the water flows down through these fictitious pipes, loss in energy occurs due to the friction along the inner surface of the pipe. By using the average velocity, v_p , in the pipe, the head loss, h_f , can be expressed as follows,

$$h_f = f \frac{L}{d} \frac{v_p^2}{2g} = f \frac{L}{4R} \frac{1}{2g} \frac{Q^2}{\epsilon^2 B^2 h^2}, \quad (5)$$

in which the average velocity is given as

$$v_p = \frac{Q}{nd} = \frac{Q}{\epsilon Bh} \quad (6)$$

and Q is the total discharge of water

In the experiment, the head loss is obtained as the difference between the energy heads in front of and behind the block structures

$$h_f = h_1 + \frac{v_1^2}{2g} - (h_2 + \frac{v_2^2}{2g}) \quad (7)$$

By using eqs (5) and (7), the loss coefficient f is determined

2-1-2 Fictitious pipe model with sudden expansion and contraction

In the model shown in Fig 2, the characteristic sizes of the pore and the block are considered equal to R_1 and D , respectively. The total number of pores in the block structure is m_p and that of blocks is m_b . The shapes of the pore and the block are assumed as cubes. Then, we have

$$m_p R_1^3 + m_b D^3 = V = BLh \quad (8)$$

$$m_p R_1^3 = \epsilon V \quad (9)$$

$$m_b D^3 = (1 - \epsilon) V \quad (10)$$

$$6m_b D^2 = S \quad (11)$$

$$R = \frac{V}{S} \quad (12)$$

Solving these equations, we can obtain a relation between a characteristic radius R_1 and the hydraulic radius R defined previously. The relation is, on neglecting the coefficient of proportionality,

$$R \propto \left(\frac{1 - \epsilon}{\epsilon} \right)^{\frac{2}{3}} R \quad (13)$$

Now, let us assume a homogeneous distribution of pores within the block structures, and let n_1 , n_2 , and n_3 be the numbers of the pores in the directions parallel to the length, width and height of the block structure, respectively. The assumption of the homogeneity gives the following relation

$$n_1 n_2 n_3 = L B h \quad (14)$$

The average total sectional area of the pore through which the water can flow down is

$$n_2 n_3 R_1' = \epsilon^{\frac{2}{3}} Bh, \quad (15)$$

where the equations (8) to (12) and $m_p = n_1 n_2 n_3$ are used

Average velocity, v_p , in the pore is, thus, given as

$$v_p = Q / \epsilon^{-\frac{2}{3}} Bh \quad (16)$$

Head loss which occurs when the water passes through a pore is expressed as

$$f \frac{1}{2g} v_p^2$$

Since the number of pores along the direction of flow is n , the total loss in energy is given as

$$n_1 f \frac{v_p^2}{2g}$$

The number n_1 is equal to $\epsilon^{\frac{2}{3}} L/R_1$, because

$$m_p R_1^3 = n_1 n_2 n_3 R_1^3 = n_1^3 \frac{Bh}{L^2} = \epsilon BhL \quad (17)$$

Finally, the total loss in energy is given as

$$n_1 f \frac{v_p^2}{2g} = f \frac{f}{R_1 \epsilon^{\frac{2}{3}}} \frac{1}{2g} \left(\frac{Q}{\epsilon^{\frac{2}{3}} Bh} \right)^2 \quad (18)$$

2-1-3 Resistance body model

If a body is placed in a flow, the force acting on the body changes the momentum of the flow. Total resistance, F , of the body in the flow is expressed as

$$F = \frac{w_0}{g} B \{ gh - v_1 v_2 \} \Delta h, \quad (19)$$

where v_1 and v_2 are the flow velocities in front of and behind the block structure, and Δh is the difference in heads. Other terms are as defined previously. We assume there are a number of rectangular piles in the block structure. The height of a pile is h , the sectional area of a pile is $d \times d$, and the number of piles in the block structure is m . This model is shown in Fig. 3.

The total volume and surface area of the fictitious piles are assumed equal to those of the actual blocks. Thus, we have

$$md^2h = (1 - \epsilon)LBh \quad (20)$$

$$4mdh = S \quad (21)$$

From these equations, the following expressions for d and m can be obtained

$$d = \frac{4LBh(1 - \epsilon)}{S} \quad (22)$$

$$m = \frac{S^2}{16BLh^2(1 - \epsilon)} \quad (23)$$

If a single fictitious pile is placed in the flow, the resistance F_{B1} may be expressed as follows by using the conventional expression C_D for a resistance coefficient,

$$F_{B1} = C_D \frac{v^2}{2g} dh \quad (24)$$

When all the piles are placed in the flow without mutual interaction, the total resistance of the piles is m -times larger than F_{B1} . The total resistance of the piles per unit width of the channel is then given as

$$m \frac{F_{B1}}{B} = C_D \frac{dh}{B} m \frac{v_1^2}{2g} = \frac{C_D}{4} \frac{S}{B} \frac{v_1^2}{2g} \frac{F}{B} \quad (25)$$

In an actual block structure, the adjacent piles interact each other because of the small spacings of the piles. The total drag coefficient may be a function of the number of the piles in the channel. The number of piles per unit width may be considered proportional to the surface area of the blocks per unit width of the channel. Thus, we have

$$\frac{F}{B} = f(S/B) \frac{v_1^2}{2g} \quad (26)$$

From this expression, it may be seen that the resistance coefficient is a function of the term S/B

2-2 Unsteady flow

The motion of the water column in a pipe without the block structure is given by the following equation,

$$\frac{d^2 z}{dt^2} + \frac{f}{2D} \frac{dz}{dt} \left| \frac{dz}{dt} \right| + \frac{2g}{L} z = 0, \quad (27)$$

where z is the water level, D and L are the diameter and the length of the water column, respectively, g is the gravitational acceleration, and f is the loss coefficient to be determined by the experiment

The motion of the water column with the block structure placed in it is expressed by the following equations,

$$\frac{1}{g} \frac{dV}{dt} + i_0 + \frac{f}{D} \frac{1}{2g} V|V| = 0, \quad (28)$$

$$\frac{1}{g} \frac{dv}{dt} + i_1 + \frac{f_1}{d} \frac{1}{2g} v|v| = 0, \quad (29)$$

$$i_1(L - l) + i_1 l = -2z, \quad (30)$$

$$V = \frac{a}{A} v = - \frac{dz}{dt}, \quad (31)$$

where V is the velocity of the water in the tank without the block structure, v the velocity of the water in the block structure, i_0 and i_1 the hydraulic gradients in the part of the tank without the block structure and in the block structure, respectively, L the total length of the water column, l the length of the block structure, A the sectional area of the tank, a the average sectional area of the pore in the block structure, f , the loss coefficient of the block structure, and other terms have the same meanings as defined previously

These four equations can be reduced to

$$\frac{d^2 z}{dt^2} + \frac{\left[\frac{f}{D} \left(1 - \frac{l}{L} \right) + \frac{1}{L} \left(\frac{A}{a} \right)^2 \frac{f_1}{d} \right] \frac{dz}{dt} \left| \frac{dz}{dt} \right| + \frac{2g}{L \left[1 + \frac{1}{L} \left(\frac{A}{a} - 1 \right) \right]} z = 0 \quad (32)$$

Comparing eq (27) with (32), we can determine the loss coefficient, f_1 , of the block structure in the unsteady flow

3 Experimental procedure

Three kinds of blocks were used in the experiment they are the tetrapod, the hollow tetrahedron and the hexaleg

Experiments in the steady flow were carried out by using an open channel, 12 m long, 0.7 m wide and 0.3 m deep. The water discharge was measured with a triangular weir placed at the end of the channel. The water depth in front of and behind the block structure were measured to give the change in the energy gradient. During the experiment, the bottom of the channel was kept horizontal.

Experiments in the unsteady flow were carried out by using an oscillatory tank shown in Fig 4. The length of the tank is variable to give different period of the free oscillation induced in the tank. The period of the unsteady flow used in the experiment varied from 3.4 sec to 4.9 sec. The tank was covered with a lid to form a chamber, which was vacuumized by a pump. A sudden removal of the lid induced the free oscillation of the water column. The amplitude of the free oscillation was damped partly due to the resistance of the block structure and partly due to the surface friction and loss at bends of the tank.

The tank has a square cross-section of 30 cm x 30 cm. In the middle part of the tank, the block structure was placed compactly to restrict their motion perpendicular to the motion of the water column.

Comparing the time history of the free oscillations with and without blocks, the effect of the blocks is determined. The rate of decay in the amplitude of the oscillation yields data for the determination of the resistance coefficient. Figure 5 illustrates this procedure.

4 Experimental result

Figure 6 shows the experimental results for the tetrapod. Among three models proposed by the authors, the resistance-pipe model was found the most adequate one for the tetrapod. Loss coefficients of the tetrapod structure are sufficiently well explained by this model. The weight of the tetrapods used in the experiment varied from 55 gr to 8 kg. The flow through the blocks heavier than 1 kg is estimated fully developed turbulent. This fact is more clearly shown in Fig 7, in which a relation between the loss coefficient and the Reynolds number is shown. The Reynolds number here is defined by using the hydraulic radius and the current velocity through the pore. When the Reynolds number becomes greater than about 1,000, the loss coefficient does not vary with the Reynolds number and is about 0.5. Judging from this result, an experiment should be carried out with the blocks heavier than at least 500 gr or under the condition of the Reynolds number higher than 1,000. Such an experiment will give us a satisfactory result.

The pipe model just mentioned was found only adequate for the tetrapod, but is not applicable to the other blocks. A hollow tetrahedron has six members which enclose and occupy one big space within itself. In the structure made with the hollow tetrahedron, the water flows down as if it flows down through the pipe which has the sudden expansions and contractions. A new hydraulic radius defined for this model is expressed by eq (18). Figure 8 shows the experimental results. The ordinate of the figure is the new hydraulic radius divided by the one-third power of the porosity. The weight of the blocks used in the experiment varied from 125 gr to 1,000 gr.

Figure 9 shows the variation of the loss coefficient with the Reynolds number. As the Reynolds number exceeds 1,000, the loss coefficient seems to tend to a constant which is equal to 0.6. Therefore, it seems desirable to carry out hydraulic experi-

ments, for the hollow tetrahedron, by using blocks heavier than 500 gr

In order to express the resistance of the hexaleg, assumption quite different from the other two, had to be made, because pipe models did not give any clear explanation. Figure 10 shows a relation between the drag coefficient and the surface area of the blocks per unit width of the channel. Except for the experimental results for 200 gr, a relation can be established. If the blocks heavier than 500 gr are used in the experiment, we will have the reliable design data.

In Figs 6 and 8, experimental results for the unsteady flow are also shown. The square marks correspond to the unsteady flow. The period of the unsteady flow used in the experiment varied from 3.4 sec to 4.9 sec. Within this range of the period, no remarkable differences are found between two loss coefficients for the tetrapod (Fig 6). The resistance coefficient in the unsteady flow is, however, a little smaller than that in the steady flow. This slight difference seems to be caused by the fact that blocks were not completely fixed in unsteady flow. The flow velocity relative to the motion of the blocks was a little lower than the velocity estimated from the motion of the water column. Thus, the resistance coefficient in the unsteady flow was a little smaller than that in the steady flow.

Figure 8 is for the hollow tetrahedron. Except for two points corresponding to the blocks with weight of 250 gr, the experimental results in the unsteady flow show the same tendency as in the results for the tetrapod.

5 Conclusions

On summarizing experimental results so far mentioned, the following conclusions were drawn.

- 1 In order to express the hydraulic resistance of blocks in terms of their characteristic quantities, different theoretical models should be used for different types of blocks.
- 2 For the tetrapod, the adequate model is the pipe model No. 1 in which loss in energy will be given as a result of the wall friction of the fictitious pipe.
- 3 For the hollow tetrahedron, the pipe model with sudden expansions and contractions is adequate.
- 4 For hexaleg, rectangular pile model is suitable.
- 5 For these three kinds of blocks, blocks heavier than at least 500 gr should be used in the hydraulic experiment.
- 6 Resistance coefficients obtained in the steady and oscillatory flows show almost no difference for the period of the oscillatory flow longer than 3.4 sec.

Acknowledgements

The work reported herein was partly supported by the Science Research Expense of Ministry of Education in Japan.

References

- 1) Lean, G. H. A simplified theory of permeable wave absorbers, J. Hydraulic Res., No. 1, 5, 1967.

- 2) Le Méhauté, B Perméabilité des digues en enrochements aux ondes de gravité périodiques, La Houille Blanche, No 6, 1957 et No 2, 1958
- 3) Murota, A and K Sato Basic study on the resistance law of the ground water flow, Memoir 21st Annual Conv , J S C E , 1966 (in Japanese)
- 4) Ozaki, A , H Sawamura, and Y Arai Basic study on the effect of pores in the rubble mound structures, Memoir 23rd Annual Conv , J S C E , 1968 (in Japanese)
- 5) Scheidegger, A E The physics of flow through porous media, Univ Toronto Press, 1957
- 6) Shuto, N Hydraulic resistance of concrete blocks, Proc 16th Conf on Coastal Eng in Japan, 1969 (in Japanese)
- 7) Tomimaga, M , N Shuto, and H Hashimoto Hydraulic characteristics of concrete blocks, Proc 14th Conf on Coastal Eng in Japan, 1967 (in Japanese)

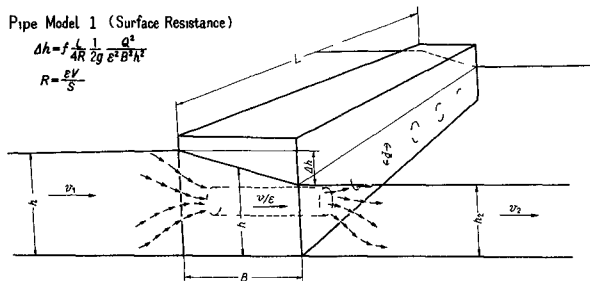


Fig 1 Resistance-pipe model

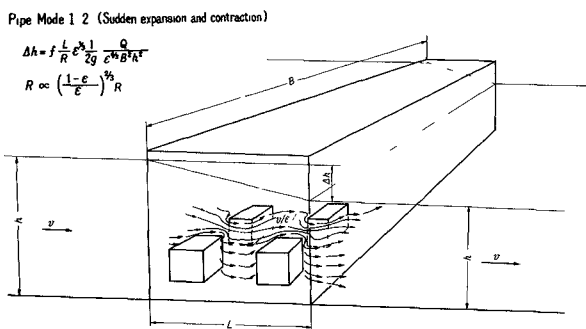


Fig 2 Pipe model with sudden expansions and contractions

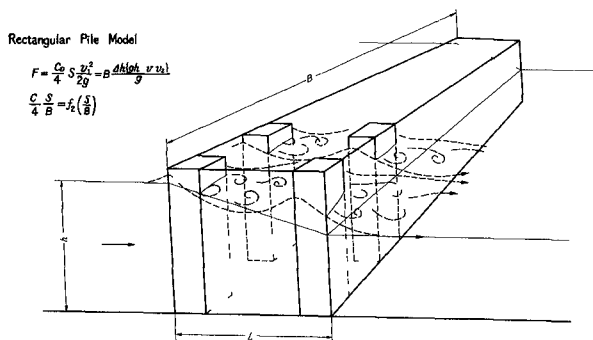


Fig 3 Resistance body model

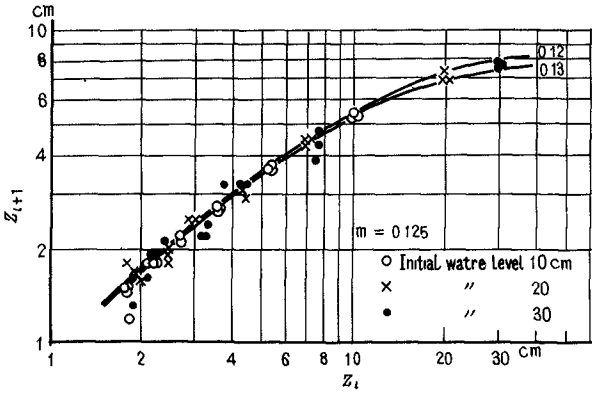


Fig 5 An example of the determination of the resistance coefficient

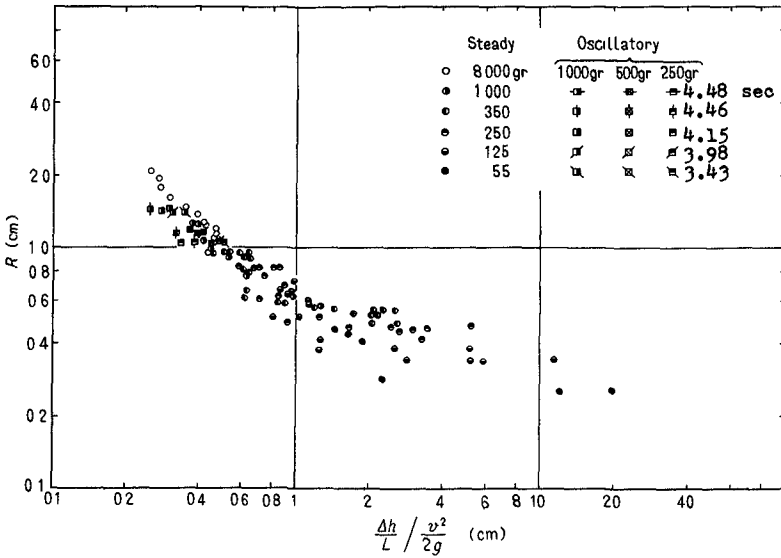


Fig 6 Loss coefficient vs hydraulic radius in case of the tetrapod

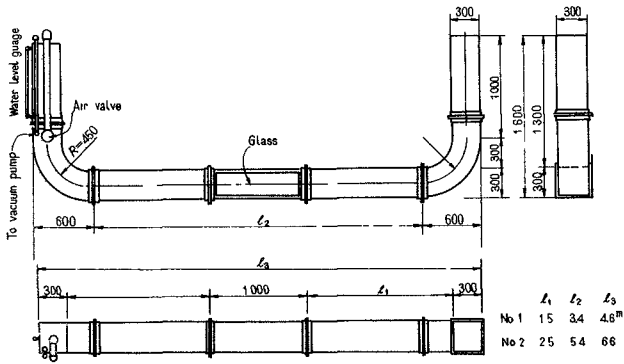


Fig 4 Oscillatory flow tank

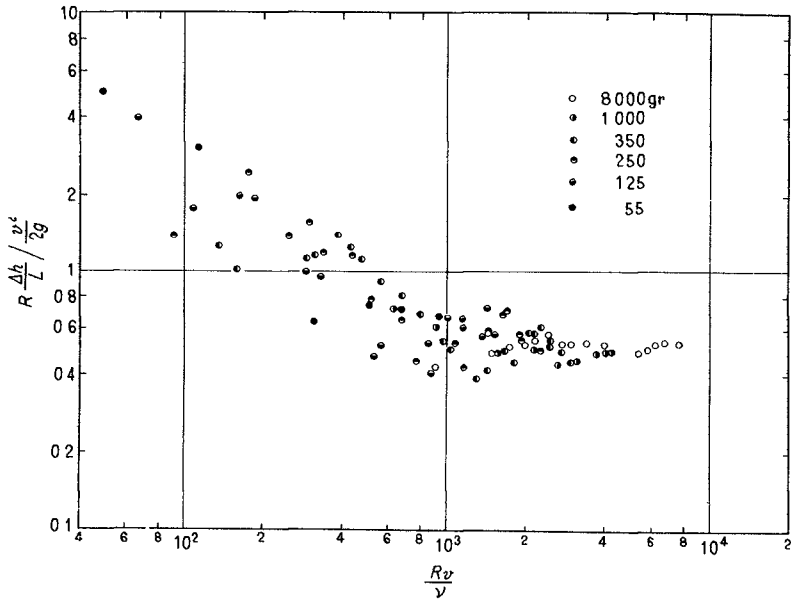


Fig 7 Loss coefficient vs Reynolds number in case of the tetrapod

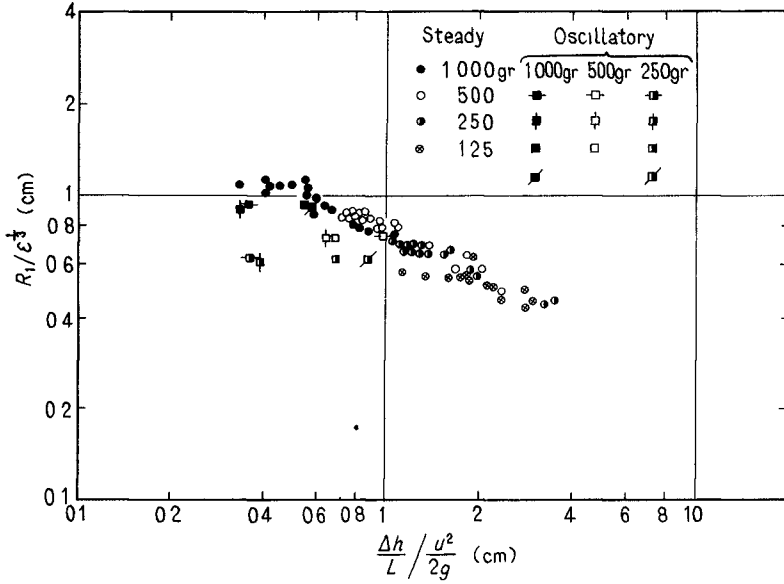


Fig 8 Loss coefficient vs hydraulic radius in case of the hollow tetrahedron

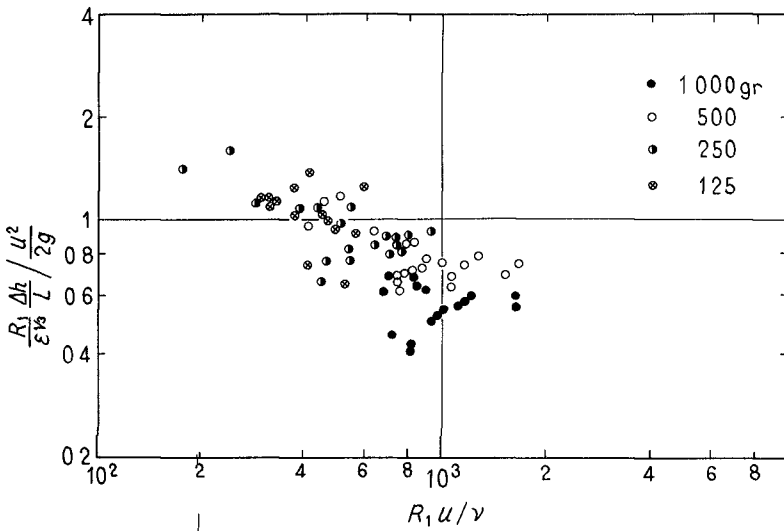


Fig 9 Loss coefficient vs Reynolds number in case of the hollow tetrahedron

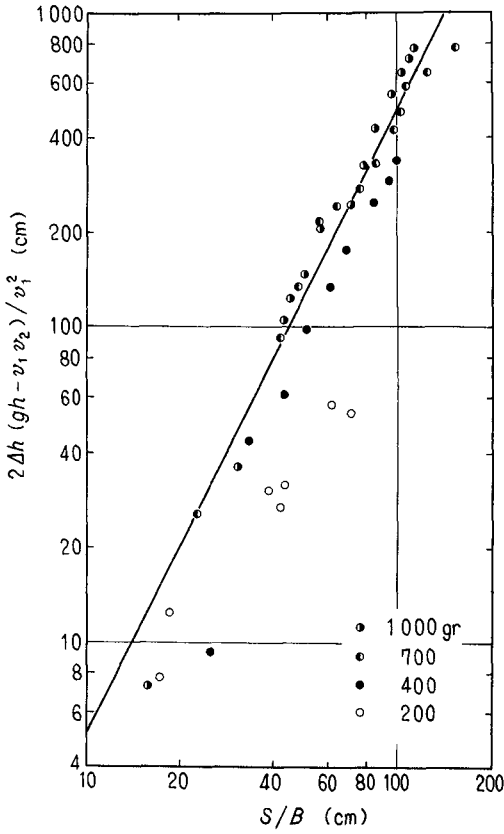


Fig 10 Drag coefficient vs surface area of blocks per unit width of the channel in case of the hexaleg

CHAPTER 98

USE OF ASPHALT IN BREAKWATER CONSTRUCTION

by

K. d'Angremond, Delft Hydraulics Laboratory
H. J. Th. Span, Royal Road Building Co.
J. van der Weide, Delft Hydraulics Laboratory
A. J. Waestenenk, Bitumarin

1 SUMMARY

Among the many types of breakwater constructions the so-called "rubble-mound" type is widely used. For the construction of exposed rubble-mound breakwaters relatively large units are necessary to create a stable structure. In many places in the world rock of the required size is not available at reasonable cost, which gave rise to the development of a great variety of armour units.

Lately also the use of asphalt in breakwater construction has proved feasible.

The experience gained during the construction of several projects in the Netherlands resulted in a special method of the use of stone-asphalt in breakwater construction. Several cross-sections based on this concept were subjected to model tests to compare their behaviour under wave-attack with that of conventional cross-sections. It appeared that the increase in stability can be expressed in terms of an "upgrading factor". Attention was also paid to wave run-up.

Finally, examples of other applications will be presented which incorporate both practical experience and basic research.

2 INTRODUCTION

The use of asphalt in road-building is well known, but in the past few decades the hydraulic uses of asphalt have also become common knowledge to civil engineers all over the world. Among the many publications in this field, van Asbeck's encyclopaedic work (Reference 1) should be mentioned.

An important contribution to the development of hydraulic applications of asphalt has been made by the Netherlands as a result of the interest shown in the subject by Rijkswaterstaat (State Traffic and Waterways Department) supported by investigations set up at the Delft Hydraulics Laboratory.

In 1960 two major Dutch road-building firms joined their efforts in the field by establishing BITUMARIN, an affiliate company specializing in the development and use of bitumen in hydraulic engineering. Close cooperation was established with the asphalt laboratory of the Royal Dutch/Shell Group, Kerckhove, one of their leading engineers, reported on the joint achievements reached together to the American Association of Asphalt Paving Technologists during its 1965 meeting at Philadelphia (2).

Now that the development of the various asphalt uses in hydraulic engineering has expanded it seems useful to outline specific developments like the use of asphalt in breakwater construction, which is the subject of this Paper.

In Chapter 3 a short historical review of asphalt techniques in breakwater construction is given, leading to a discussion of the pattern-grouting technique, which is believed to be most promising for the further development of asphalt uses in breakwater construction. As the average hydraulic engineer will not be familiar with the latest developments of asphalt technology, this Chapter ends with a summary of recently developed theories pertaining to the grouting of stones with asphalt mixes.

Chapter 4 is devoted to model investigations on the hydraulic properties of the constructions described in Chapter 3, introducing an "upgrading factor" for pattern-grouted slopes.

In Chapter 5 the recent construction of the Separating Jetty of the Hoek of Holland is discussed, illustrating the various techniques mentioned in this Paper.

3 DEVELOPMENT OF ASPHALT TECHNIQUES IN BREAKWATER CONSTRUCTION IN THE NETHERLANDS

3.1 Early marine uses

In the Netherlands the use of asphalt in sea defence works in the tidal zone started immediately after World War II. Examples are the grouting with mastic-asphalt of groyne at the North Sea Coast between the Hoek of Halland and The Hague, and at the breakwaters of the Hooft of Halland. The purpose of these repair works was to stabilize mounds and layers of discrete stones against heavy wave-attack by pouring hot mastic asphalt between the stones, thus keeping the stones in a fixed position.

Asphaltic grouting proved to be very effective for two reasons:

- (i) after having cooled down to ambient temperatures mastic-asphalt behaves like a solid mass with high elasticity modulus under short loading times such as wave-attack, and
- (ii) as a plastic material of very high viscosity under prolonged loading times, thus being able to follow subsoil settlements.

In due time it was recognized by the Authorities that the asphaltic grouting technique was suitable to replace the traditional pitching of stones, and thus, when the Delta Plan came into execution, the asphaltic grouting technique was adopted as a standard method of protecting the slopes of the dikes in the tidal zone. Examples of this use can be found in the cross-sections of the Veersegat Dam, the Grevelingen Dam, the Horingvliet Dam and the Brauwershavense Gat Dam (figure 1).

The first applications were "in the dry", even though in a tidal area. Before long, however, methods were developed for use under water. As a result of this development, the asphalt-ship "Jan Heijmans" was built, able to apply mastic-asphalt for grouting underwater sills or plainly for sea-bed protection in coastal inlets.

3.2 IJmuiden breakwaters

The first important use of asphalt in "full size" breakwater construction can be found in the IJmuiden breakwaters (1963 - 1967). The old southern and northern breakwater had to be extended into deeper water by 2,100 and 1,200 m respectively, as a result of which the southern breakwater would project 3 km (above 2 miles) into the open sea.

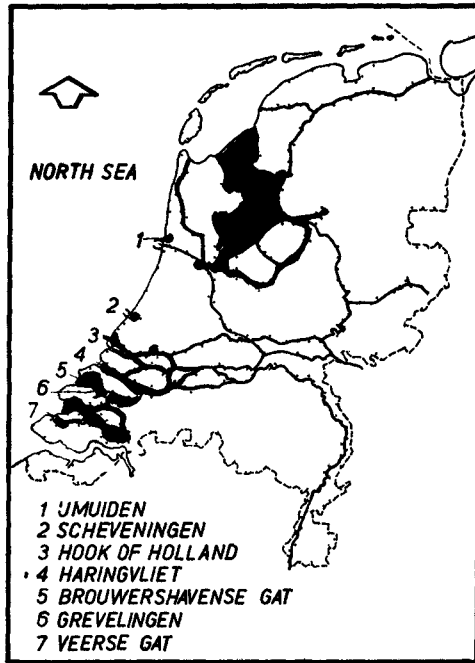


FIG 1

In principle the design of these breakwaters is of the "rubble-mound" type crowned with a prefab concrete crest-element. The core is made of 300 - 1,000 kg stone to obtain a reasonable degree of core-stability during construction. Nevertheless, frequent re-handling of the stone still appeared to be necessary because of the continuous bad weather conditions in the North Sea. In fact, the 300 - 1,000 kg stones showed considerable lack of stability during construction phases above a level of M S L - 4 m.

A substantial increase in core-stability was achieved by grouting the discrete stones with light stone-asphalt before receiving their final armour. The grouting material was designed in such a way that only the upper two layers of the core were penetrated, and that no further "cold" flow into the core took place. With mastic-asphalt, as was hitherto in use, such a controlled flow would have been impossible, but by the use in the mixture of stones up to 10 kg a kind of "clogging" effect was introduced, enabling control of flow of the grouting material.

Instead of the conventional armour layer of discrete though more or less interlocking elements, an impervious monolithic layer of stone-asphalt was adopted. The thickness of the layer was dictated by the internal water pressures caused by wave-action in the open rock-core against the impervious armour. The thickness of the armour was chosen to be 2.25 m (Figure 3).

The construction of asphaltic layers of such a thickness at the steepest slope possible constituted a problem in itself. By the time the breakwaters were designed the grouting techniques had not developed to the extent that controlled grouting of stone-layers of several thicknesses at water depths of 5 to 10 metres could be considered feasible.

Therefore a premixed product had to be used. Conventional asphaltic concrete with its aggregate-size limited to 6 - 8 centimeters lacked too much stability in the hot phase to enable the construction of thick layers as steep slopes. The solution to this problem was the development of a new mixture with aggregate-sizes up to 60 kg, called stone-asphalt, which has already been mentioned in this Paper. With this material slopes of 1 in 1.75 under water and 1 in 2 above water were found to be feasible.

The experience gained with the IJmuiden breakwaters after three years' service is satisfactory in general, but nevertheless continuous creep of the stone-asphalt layer is causing cracks, especially in summertime (temperatures of both water and air). However, the damage is decreasing every year as a result of the formation of an internal skeleton in the stone-asphalt aggregate.

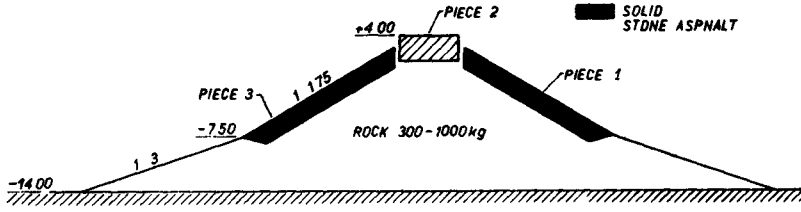


FIG 2

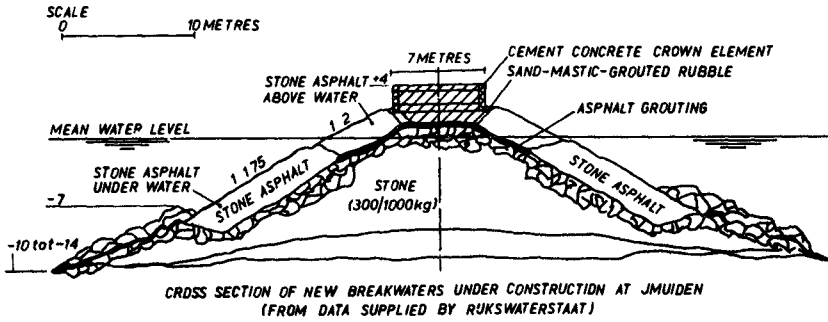


FIG 3

As has just been stated, the IJmuiden works gave new impulses to the development of grouting techniques. The grouting of the core-stone 300 - 1000 kg with light stone-aspalt has already been mentioned as standard procedure, but moreover a test-section was carried out successfully by grouting rock of 300 - 1000 kg with horizontal layers of 1.5 to 2 m thickness constructing a monolithic and stable cap of heavy stone grouted massively with light stone-aspalt.

In considering the first important use of aspalt in breakwater construction embodied by the IJmuiden breakwaters, it can be stated that its performance is satisfactory in general, but that for future works the following two drawbacks will have to be dealt with:

- a. The concept of an impervious layer covering a highly permeable rock-core should be abandoned to avoid the effect of internal water-pressures due to wave-action.
- b. Creep and extended setting-time of thick asphaltic layers should be avoided by replacing the use of premixed layers by the grouting of layers of discrete stones, which have already developed a skeleton of their own and are therefore no longer susceptible to setting.

The experience gained in the IJmuiden works made the solutions to these problems possible, as will be seen in the next paragraph.

3.3 Pattern grouting

To avoid the problem of internal water pressures originating from the impermeability of the stone-aspalt armour layer a new concept was introduced by the idea of increasing the stability of an already fairly stable rock slope by local grouting with stone-aspalt in a regular pattern, thus maintaining the permeable character of the slope. By using a grouting method the problem of creep and extended setting-time would also be coped with. This system of "internal armour" was made technically possible by the development of controlled grouting techniques during the IJmuiden works.

In working out the idea of pattern-grouting it was realized that in filling up more than about 70 % the interstices between the rocks no guarantee could be given for the overall permeability of the construction. Preliminary model tests executed in the Delft Hydraulics Laboratory showed an increase in stability as a function of an increasing degree of filling up the interstices, with a relatively slow increase beyond 50 %. So the filling up to 50 to 70 % of the interstices seemed to be optimal.

For the calculation of the required weights of armour-elements, layer thickness, etc. reference is made to Shore Protection, Planning and Design of the U.S. Corps of Engineers (Reference 7).

As to the size and spacing of the plots the following can be said
 An individual plot will penetrate to a depth of $2d$, d being one layer-thickness. The shape depends on the local conditions (shape and direction of interstices between the stones) but it can be idealized to the slope of a cube with contents $8d^3$, of which approximately 60% is solid rock and 40% grouting material. So the contents of one plot is $0,4 \cdot 8d^3 = 3,2 d^3$ and its weight

$$P = 3,2 \gamma_g d^3$$

The rock weight $W = \gamma_s d^3$

Thus

$$P = 3,2 \gamma_g / \gamma_s W$$

in which P = weight of plot in tons
 γ_g = spec weight of grout in tons/m³
 γ_s = spec weight of rock in tons/m³
 W = weight of rock in tons

The spacing of the plots should be such that 50 to 70% of the surface is covered

If placed in such a pattern the plots (each fixating 5 to 10 stones) will touch each other at the edges. This leaves stones uncovered at some places, which, however, are "keyed" between the others. For reasons of safety it is recommended to use three layers instead of two, only grouting the top two layers. A few loose stones will probably be washed away by the waves, which is not dangerous at all, but even if a whole plot were washed away for one reason or another, a third layer would still provide protection to the core, because it would be "keyed" to the surrounding plots.

As to the stability under wave-attack, a so-called "factor of upgrading" F could be attributed to the pattern-grouted system. This means that pattern-grouted rubble in the X -ton-class has the same stability as discrete rubble in the $F X$ -ton class.

From preliminary model tests a value of $F = 5$ seemed a conservative estimate, which has been confirmed by the more elaborate tests discussed in the next Chapter. This reduction of the required maximum stone-size has a favourable effect on the area of the cross-section of the breakwater because of the reduction in layer-thickness and the absence of secondary layers in most cases.

Ease of construction is obtained by the reduction of both crane-reach and crane-load, or by the possibility of working on more gentle slopes.

It seems that the time-proven asphalt grouting-technique has grown into a real competitor in rubble-mound breakwater design. With increasing demands on stability under wave-attack, quarries are proving steadily unable to produce heavy armour stone, and this has caused the development of a series of artificial armour-blocks. All these blocks have in common that increased stability can only be obtained by increased weight, which is necessarily accompanied by increased surface for wave-attack.

As distinct from these external armours, the internal armour presented in this paragraph has the advantage of diminishing the wave-attack on the discrete armour elements by partly filling up the interstices between them, while on the other hand their stability is increased as a result of the "keying" effect of the grouting material.

3.4 Asphalt mixtures for patch-grouting

The general principles for design and properties of asphaltic mixtures for hydraulic application, as developed in the Netherlands, are described by Kerkhoven (Reference 2).

For pattern grouting of the armour layer of large sized stones, some additional principles are necessary.

The mix-design of the patches must be related to the large size of the stones and the slope and weight of the patches. In this connection it is important whether the grouting is executed under water or not, as in the first case the hot stage of the mixture is rather short and, consequently, also the time for settlement.

Experiments have shown that for grouting with patches of limited size a relation exists as a blocking criterium between the small-sized stones in the armour layer, defined as d_{15}^1 , and the large-sized stones in the asphalt mixture, defined as d_{85}^1 . For underwater grouting the relation $d_{15}/d_{85} = \approx 10$ was found and for above-water-grouting $d_{15}/d_{85} = \approx 5$.

The mix design for small-sized stones, and sand inside the grouting material, depends on the working circumstances during execution and on the place of use in the total breakwater construction. It is common that for patch-grouting under water level, an asphaltic mixture in gap-grouting is adopted and for patch grouting above water level an asphaltic mixture in concrete-grouting.

The flow in the hot stage and the viscous creep in the cold stage, in relation to the size and slope of the armour large-sized stone layer, depend on the percentage and type of filler and bitumen in the grouting mixture.

1) d_{15} and d_{85} are the equivalent diameters d of stone size-distribution, passing in percentage of weight for 15 and 85 %

4 MODEL INVESTIGATIONS

4.1 Introduction

Since 1964 breakwaters with the use of asphalt have been the regular subject of model investigations in the Delft Hydraulics Laboratory. In the beginning the knowledge of the material was insufficient to reproduce the properties of the material on model scale. Therefore the "asphalt-design" for the IJmuiden breakwaters was originally not tested in a model. When, already during the execution of the works, again discussion arose on the required thickness of the stone-asphalt, it was decided to start simplified tests. In these tests the flexible structure was schematized applying rigid concrete mortar in the model, instead of stone-asphalt, which means that investigations into the mechanic and elastic behaviour of stone-asphalt were prevented. The cap of concrete and stone-asphalt was reproduced as 3 independent rigid and relatively strong pieces of concrete (compare Figures 2 and 3).

It was shown visually in these tests that the overall stability of the slope cap was insufficient due to water pressures under the cover layer. To solve this problem the toe of the slope was loaded with rubble and concrete blocks to a level of - 4 m for the exposed sections.

When, thereafter, Bitumarin proposed an application of stone-asphalt to prevent the uplift pressures by keeping the outer layer permeable, it was decided to carry out further model tests, by replacing asphalt by concrete grouting.

From a comparison between cross-sections with and without patch-grouting it appeared that the stability number k_D increased considerably. It must be noted, however, that the schematization of the tests was such that the elasticity and the strength of the patches were not to scale.

4.2 Reproduction of asphalt

Since pattern grouting proved to be a feasible method of stabilizing rubble-mound structures, a number of additional tests have been carried out to study the behaviour of grouted structures in more detail.

When pattern-grouting is used, the principle of the rubble-mound structure is maintained but the stability is increased considerably. Due to the effect of the grout, the surface of the structure is smoothed, resulting in a larger amount of uprush and overtopping.

Attention was paid, therefore, to the wave uprush and the stability of the armour layer, under various conditions using different cross-sections

Due regard was paid to the proper reproduction of asphalt to obtain both geometrical and dynamic similarity between model and prototype

Geometrical similarity was obtained by using the appropriate grading of the armour stone and a low viscosity of the grout to arrive at a depth and width of penetration comparable to those found on the site in question

Dynamic similarity was obtained by composing the grout in the model in such a way that the density of the mix, as well as its stiffness and strength, was reproduced correctly

Asphaltic bitumen is characterized in terms of the penetration and the ring and ball softening point (see Reference 1) Starting from these data, the stiffness modulus of the material, defined as the ratio between stress and strain

$$(S = \frac{\sigma}{\epsilon}),$$

can be determined for a given temperature and a given frequency of loading

When aggregates are added, the dynamic properties of the mix change, the stiffness of the mix being a function of the stiffness modulus of the asphalt and the concentration by volume (C_v) of the mineral aggregate

In the actual project a grouting mixture will be used which consists of (by weight) 94 % stone, sand and filler
6 % bitumen 80/100 pen

So the volume concentration of minerals in the mixture $C_v = 0.80$ to 0.82 and the density = 2300 kg/m^3 Two mixtures were tried out to give both the required density and stiffness

The compositions of the mixes used in the model were

Mixture No 1

(by weight) 40 % dune sand
40 % barium sulphate filler
20 % bitumen 80/100 pen

The volume concentration of minerals in the mix $C_v = 0.55$, the density = $2,300 \text{ kg/m}^3$

Mixture No 2

(by weight) 60 % barium sulphate filler
40 % bitumen 280/320 pen

The volume concentration of minerals in the mix is $C_v = 0.25$ and the density = $1,850 \text{ kg/m}^3$

The stiffness of the mixtures was calculated with the help of the monographs mentioned in References 3 and 4. The ambient temperature in nature is $T = 5 - 15^{\circ} \text{C}$, in the model it was 25°C . The results are plotted in Figure 4.

It is seen that mixture No. 1, which is on scale as the density is concerned, is too stiff, while mixture No. 11 is too light and also on the supple side as the stiffness-modulus is concerned. The strength of the material both in nature and in model is in the order of 1 to $5 \cdot 10^6 \text{ N/m}^2$ (Reference 4), meaning that the grout in the model is too strong.

From the above it follows that the density and the stiffness can be brought to scale (though not in one mix), while the tensile strength is always too high in the model. This means that in the event that the collapse of the armour layer would be caused by the cracking of the patches, the model would give too favourable results.

Therefore also some tests have been run in which the patches were already artificially broken beforehand, in order to eliminate any favourable effect of tensile strength of the grouting mixture, thus exaggerating the effect in the opposite direction.

For this purpose the pattern-grouted armour was frozen and then deliberately "demolished" by hitting with a bar, in such a way that the patches broke down internally, only leaving a three-dimensional "chinese puzzle". In the latter tests a situation is represented in which only the "keying" effect of the grout can be called upon, while the patches themselves have lost all internal bond.

To eliminate the adhesion between stone and asphalt, the stone in the model was covered with lime before grouting. This was done to represent the situation in nature, where due to the wet environment little or no adhesion of the grout to the stones can be expected.

4.3 Stability of grouted slopes

The results of stability tests for rubble-mound breakwaters are generally expressed in terms of the dimensionless stability number

$$K_D = \frac{H^3}{W \Delta \cdot 3 \cotg a}$$

Various authors have determined values for K_D in order to obtain a stable structure.

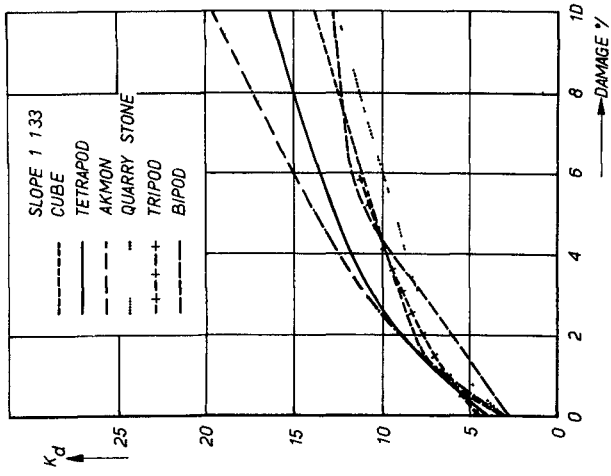


FIG 5

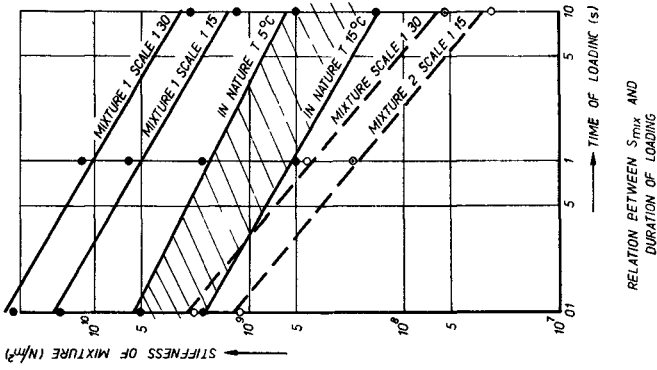


FIG 4

RELATION BETWEEN S_{mix} AND DURATION OF LOADING

A relation between the K_D value and the percentage of damage is given in Figure 5 (Reference 5)

Numerous references are present in literature describing artificial blocks which have a higher value of K_D for the no-damage criteria, due to the special interlocking effect. The results of the model tests indicate that the critical value of K_D can be increased by a factor 2 to 3 in this way. Pattern-grouting also increases the interlock between the various units, because of the three-dimensional effect, thus creating more or less irregular artificial units. Moreover, the wave-attack is reduced as a result of the filled voids. Obviously these aspects result in an increase in the stability of the structure which manifests itself in a higher K_D value.

The upgrading-factor F is defined as the ratio

$$F = \frac{K_D \text{ for pattern grouted armour layer}}{K_D \text{ for non-grouted armour layer}}$$

4.4 Test results

4.4.1 Cement grouting

The first series of stability tests on grouted slopes was performed on a cross-section as indicated in Figure 6. As already mentioned, the cement grouting was used in these early tests.

The patch-grouted test section was situated between - 8.5 and - 3 m. It has slopes of 1:2, 1:3 and consisted of rubble material from several weight classes during the various tests.

The dimensions of the patches and the pattern of grouting was also varied under the following conditions:

<u>Slope</u>	<u>Stone Weight</u> <u>armour layer</u>
1:3	1 - 6 ton
1:3	0.3 - 1 ton
1:3	0.5 - 3 ton
1:2	1 - 6 ton

The cross-section was subjected to regular waves with a period of 9.5 sec. The wave height was increased from 3 to 8 m in steps of 1 m. The duration of each step was 3 hours prototype. After each step the damage was determined by counting the displaced stones and expressing this number in a percentage of the

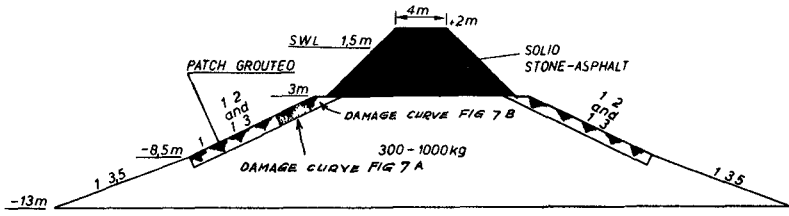


FIG 6

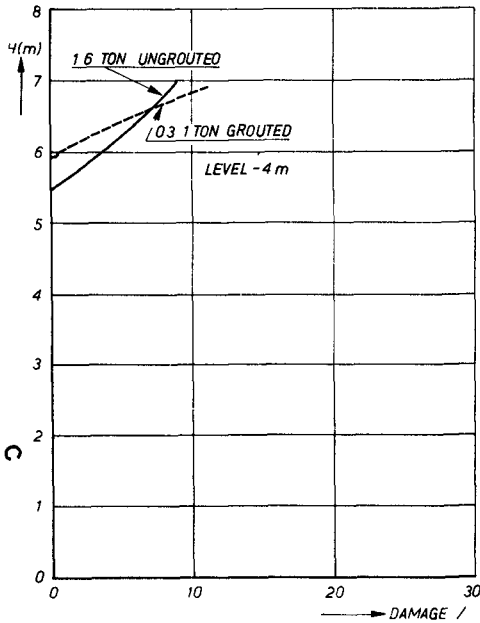


FIG 7A

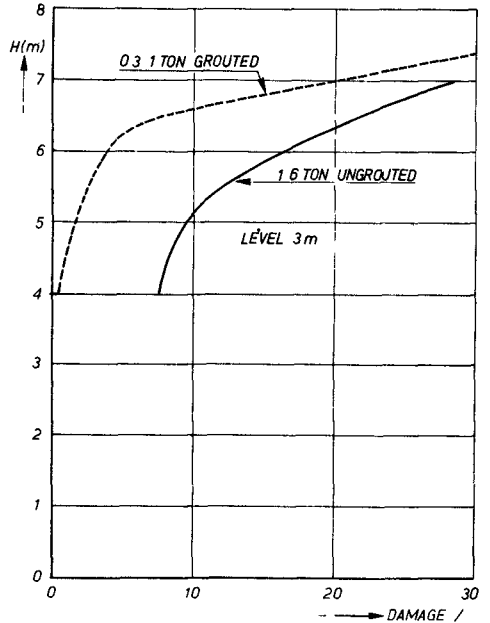


FIG 7B

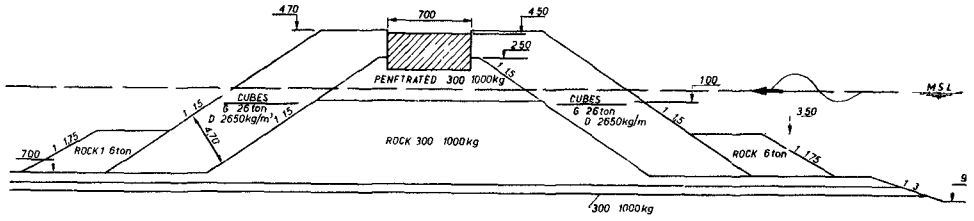


FIG 8 A

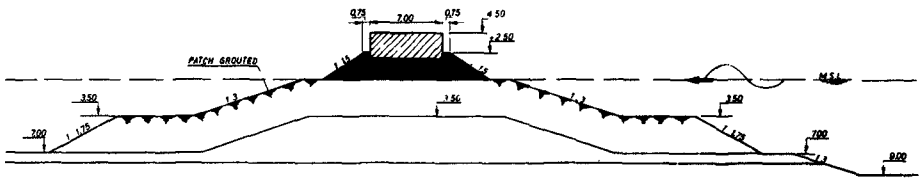


FIG 8 B

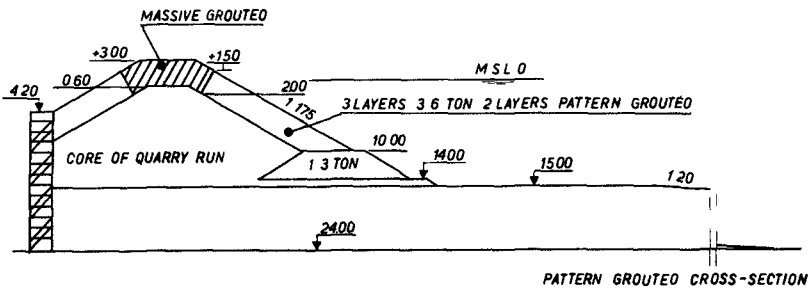
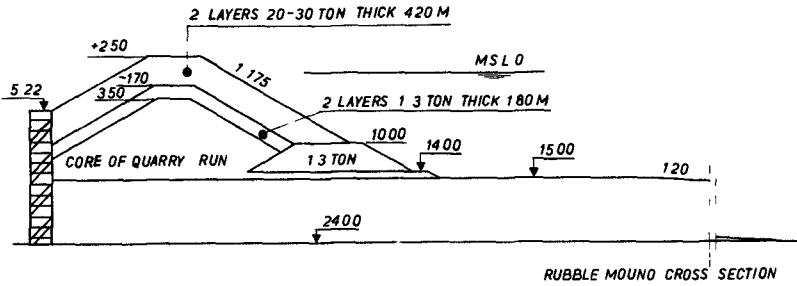


FIG 9

	Water-level - 0.5 H up to 5 m	Water-level + 0.5 H up to 5.5 m	Water-level + 2.5 H up to 6 m	Water-level + 3.5 H up to 7 m
Cross-section Fig 8A concrete blocks 26 ton berm 1 - 6 ton	no damage no damage	no damage no damage	no damage no damage	1 % no damage
Cross-section Fig 8B grouted slope berm 1 - 6 ton	no damage no damage	no damage no damage	no damage no damage	no damage moderate damage

Table 1 Results comparative tests with alternative design of Scheveningen breakwaters

total number of stones in the zone concerned. In this way it was possible to establish a relationship between damage percentage and wave height.

A comparison of the relation between damage and wave height for grouted slopes with stones of 0.3 - 1 ton and non-grouted slopes consisting of 1 - 6 ton quarry (Figures 7A and 7B) shows that these situations are comparable for damage less than 10 %. This leads to the conclusion that for a practical range of damage percentage the upgrading factor can be assumed to be about 5.

This conclusion has been verified for an alternative design of the Scheveningen breakwater, where a cross-section in stone asphalt was compared with a method using concrete blocks (Figures 8A and B). These tests were also performed in regular waves. Data on the damage are presented in Table 1.

In all conditions the grouted slope was equally as stable as the rubble-mound breakwater with cubes of 26 tons. Only in the most severe conditions did the smooth surface of the grouted slope increase the downrush in such a way that damage occurred to the non-grouted berms. This draw-back could be remedied by making the grouting slightly deeper. The stone-asphalt was also reproduced by a cement mortar in these tests.

4.4.2 Asphalt grouting

Since grouting proved to be a useful method for stabilizing rubble-mound structures, some additional tests were carried out to study the stability of grouted rubble-mounds in waves. For that purpose a number of grouted sections were compared with an equivalent number of traditional rubble-mound sections consisting of stones 5 times heavier than those used in the pattern-grouted section. Using the formula of Hudson, the rubble-mound section was so designed that no appreciable damage should occur under maximum wave attack.

As stated in Section 4.2 special care was taken to reproduce both the geometrical and dynamical properties of the asphalt grout. Since the strength of the material could not be reproduced correctly, the tests were repeated with broken patches.

Wave heights were increased step by step until maximum wave height were reached. A review of cross-sections tested in the model is given in Figures 9 to 11, whilst a summary of test conditions and the test results is given in Table 2.

Table 2 Test Conditions and Results for Various Grouted Sections

Profile	Fig	Scale of Test	Mixture	T (sec)	H _{max} (m)	Damage ₁ (%)
A	9	30	I	10	8.5	NONE
B	10	30		10	8.5	NONE
B	10	30		8	6-7	NONE
C	11	30		8	6-7	NONE
B	10	30	II ²⁾	10	7	NONE
B	10	30	II ²⁾	10	7	NONE

1) Damage expressed as % of stone removed

2) Patches broken

Test results indicated that both the traditional and the grouted sections showed little or no damage, even when the patches were broken. This proved the validity of an upgrading factor of 5.

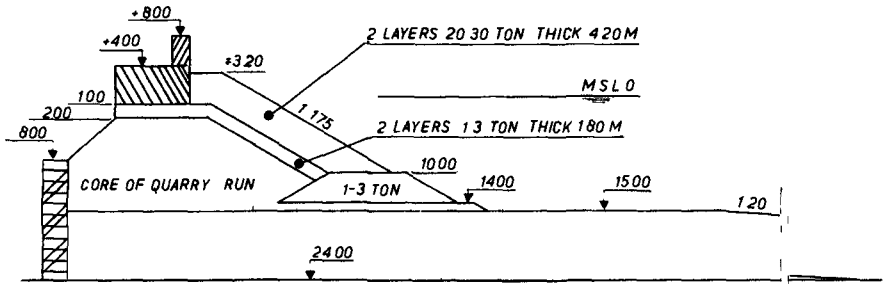
4.5 Run-up on grouted slopes

In many cases the crest level of a breakwater or a sea wall is determined on the basis of an acceptable amount of overtopping under extreme conditions, although sometimes the acceptable wave run-up is also used as a criterion.

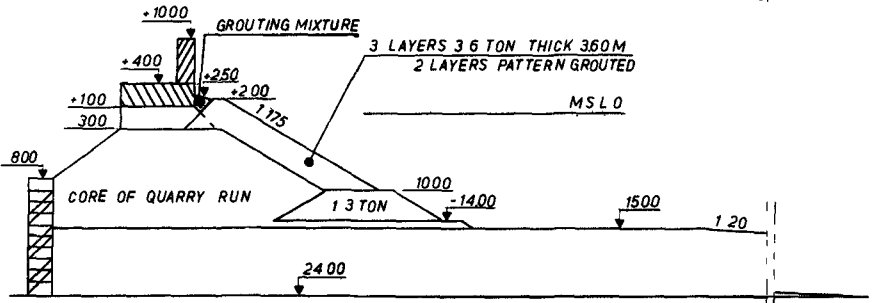
The level of wave run-up z above M.S.L. has been investigated extensively for smooth impermeable slopes by several authors (See also Reference 6, Reference 7 and Reference 8). An extract of these results is presented in Figures 12 and 13 for $d/H > 3$.

For slopes covered with rip-rap and for rubble-mounds the run-up is much less because of the roughness of the surface and the porosity of the outer layers. The reduction in run-up due to these effects is expressed by a reduction factor r , indicating the ratio between the run-up on the rough surface and the run-up on a smooth impermeable surface under the same conditions. Though the scatter of the measured figures is considerable, authors from different origin indicate for r a value of 0.5 to 0.6 (References 9, 10, 11).

With a patch-grouted slope, porosity and roughness are reduced in comparison with rubble slopes. Consequently the run-up must be expected to be greater. This may lead to a higher crest level of patch grouted breakwaters which involves a higher cost.

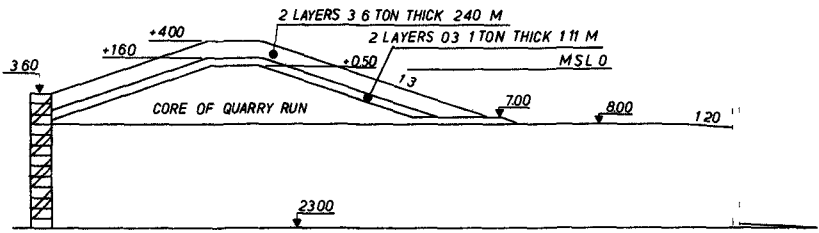


RUBBLE-MOUND CROSS-SECTION

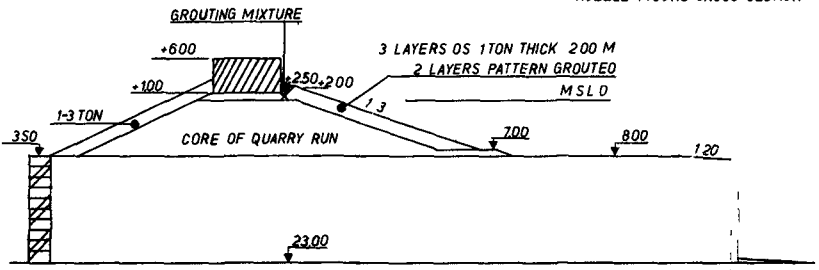


PATTERN GROUTED CROSS SECTION

FIG 10



RUBBLE-MOUND CROSS SECTION



PATTERN GROUTED CROSS-SECTION

FIG 11

Model tests have been carried out on fully grouted slopes, eliminating porosity completely. Any reduction in run-up was due to surface roughness.

The run-up z depends on the following factors

$$z = f(H, L, T, d, \nu, \rho, g, k, p \text{ and } \alpha)$$

in which H = wave height

L = wave length

T = wave period

d = water depth

ν = kinematic viscosity

ρ = density

g = gravity

k = roughness

p = porosity

$\cotg \alpha$ = slope

Because k and p were kept constant during the tests ($p = 0$) the relative run-up can be expressed as

$$z/H = f(H/gT^2, d/gT^2, \cotg \alpha)$$

H/gT^2 and d/gT^2 were varied from 0.0004 to 0.01 and from 0.009 to 0.095 respectively.

The slope $\cotg \alpha$ was 1.75 and 2.25. The grouted quarry stones weighed from 100 - 250 kg (prototype). As a check also tests have been made on a smooth impermeable slope and on a non-grouted slope covered with quarry stone.

As the plot of z/H versus H/gT^2 showed a scatter which could not be explained by the differences of d/gT^2 only, the maximum values of z/H have been plotted as a function of H/gT^2 , for both slopes separately (Figures 12 and 13).

To compare the actual model tests with the results of others, Figures 13 and 14 show also data obtained from References 7, 9 and 10.

From the Figures it can be concluded that reduction coefficients for the wave run-up can be used as indicated in Table 3.

Table 3 Reduction Coefficients

Slope	r	Source
smooth impermeable	1.0	-
rip-rap covered	0.5 to 0.6	model tests + literature
rubble-mounds	0.5 to 0.6	model tests + literature
100 % grouted	0.6 to 0.8	model tests
patch grouted	0.6 to 0.7	interpolation

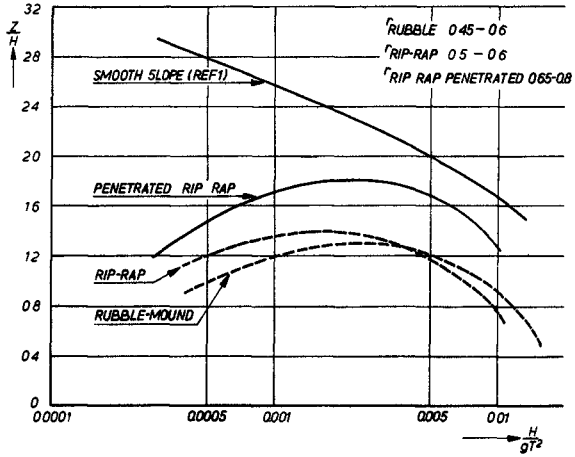


FIG 12

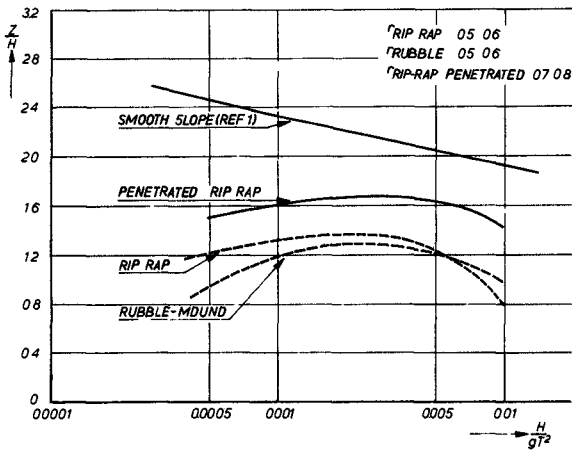


FIG 13

5 SEPARATING JETTY HOOK OF HOLLAND

5.1 Design conditions

A recent example of the use of asphalt in breakwater construction can be found in the so-called "Separating Jetty" at the Hook of Holland

This Separating Jetty (Figure 14) is situated in the new entrance being constructed for Rotterdam Harbour, separating both traffic and the tidal density currents of the Rotterdam Waterway leading to the inner harbours of Rotterdam, and the Caland Canal leading to the Eurapaart harbours for mammoth tankers. So its main objective is of a nautical nature, but by virtue of its exposed situation perpendicular wave-attack up to $H_{sign} = 6$ m can be expected at the head, and oblique attack along the trunk

From the inner and going seaward the seabed is descending from above water down to approx M S L - 5 m. Nevertheless it can hardly be regarded as a shallow water breakwater, due to the fact that the underwater banks will be dredged to 1 an 4 slopes going down beyond M S L - 20 m

5.2 Standard design

For the deeper part of the dam an embankment has been constructed consisting of fascine mattresses protecting the dam footing, and dumped stone and other waste materials from an ancient jetty to be cleared away, up to a level of M S L - 2 m

From an economical point of view two materials came into consideration for the dam core construction above water: mine-waste and lean sand asphalt. The latter was chosen because of its low permeability, which will be explained later.

In the standard design the armour was designed as an almost traditional fully graded stone-layer, which is to be regarded as impermeable. From investigations in an electric analogue, it appeared that in the lean sand asphalt dam core, being of the same permeability as the sand it is made of, pressure gradients develop during the tidal cycle which result in lower water pressures under the armour than the dam core were made of mine-waste.

This is why lean sand asphalt was chosen as the dam core material.

In view of the geometry of the dam and the moderate permeability of the dam core, the influence of wave action on the water pressures could be neglected.

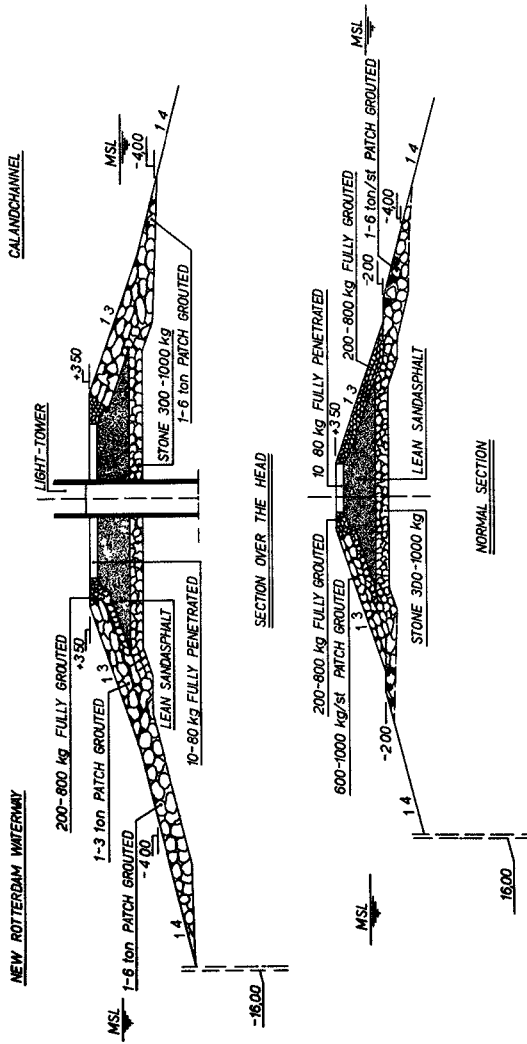


FIG 14

During the actual construction of the dam, which started in December 1969, the amplitude of lean sand asphalt for the dam core proved to be successful also as far as the stability under wave action during the execution of the works is concerned. Negligible losses of dam core material were suffered, in spite of several heavy storms encountered during construction time.

5.3 Test sections

As the Authorities (i.e., Rijkswaterstaat) are very much interested in the recently-developed pattern-grouting system as described in Paragraph 3.3, two test sections will be constructed in the near future to investigate the merits of this method actually. These sections are situated at the most exposed part of the dam, namely, the head and the adjacent part of the trunk.

Of these two wave attack on the head is assumed to be frontal with a significant wave height of $H_s = 6$ m, whereas the trunk is mainly attacked by oblique waves of the same height.

Using Hudson's formula with $K_D = 2.9$ for angular quarry stone as the head and an upgrading factor $F = 5$, 1 - 3 ton stones are used for the armour, to be pattern-grouted with 6 ton patches. Model investigations have confirmed the stability of this armour, and from these it could also be deduced that the pattern-grouting had to be used down to a level of M.S.L. - 4 m. Below this level stone 1 - 6 ton is sufficiently stable without pattern-grouting.

For economical reasons the recommended third layer is made of stone of a somewhat lighter class 200/800 kg. This layer is applied on a layer of light permeable stone-asphalt, which in its turn protects the lean sand asphalt core.

Wave attack on the trunk will be less than on the head, as it consists mainly of oblique waves. Therefore the trunk armour is designed assuming $K_D = 3.5$. Because trunk sections are also considered as test sections and upgrading factor $F = 10$ has been applied which possibly may lead to some damage within a few years. Together with the extensive wave measuring system of Rijkswaterstaat in the Europoort area it will be possible in this way to obtain insight in the behaviour of this type of structure under prototype conditions.

6 CONCLUSIONS

Considering the development of the use of asphalt in breakwater construction it appears that in view of its favourable properties and its peculiarities, the most profitable application in this part of hydraulic engineering is the use as a grouting-agent

As a matter of fact, asphalt grouting already constituted the beginning of the development of fixating unstable slopes. New techniques and working methods, however, grouting is developing into a system of internal armour protecting rubble-mound breakwaters and sea walls against the heaviest wave attack.

In the pattern-grouting technique described in this Paper a new tool is given to the designer of a rubble-mound breakwater. In practice it often happens that with the available rock-size from the quarry an armour-layer can be designed which is stable enough under wave attack of "normal" frequency, while just lacking stability in the exceptional design-storm. Pattern-grouting provides that extra "upgrading" which is needed for the exceptional design wave, at relatively reasonable costs. For design purposes an upgrading of 5 can be safely accepted.

REFERENCES

- 1 Boron W F von Asbeck, Bitumen in Hydraulic Engineering
Vol 1 and 2 Elsevier Publishing Company, 1964
- 2 R E Kerkhoven, Recent Developments in Asphalt Techniques
for Hydraulic Applications in the Netherlands
Paper to Annual Meeting, Association of Asphalt Paving
Technologists, Philadelphio, 1965
- 3 The testing of bituminous materials Kon -Shell Laboratorium,
Amsterdam, april 1969
- 4 W Heukelom, Observations on the rheology and fracture of
bitumens and asphalt mixes Shell-Bitumen Reprint no 19,
Febr 1966
- 5 A Poope and A W Wolther, Akmon Armour Unit for cover
layers of rubble-mound breakwaters
Proc VIIIth Conf on Coastal Engineering, Berkeley Calif ,
1963, Chapter 25, pp 430-443
- 6 Soville, Th , Wave run-up on shore structures,
Proc A S C E 82 W W 2, april 1956
- 7 Shore protection, Planning and Design,
C E R C , Techn Memorandum no 4, 1966
- 8 Fronzius, L , Wirkung und Wirtschaftlichkeit von Ronkdeckwerken
im Hinblick auf den Wellenouflouf
Mitt des Franzius Instituts 25, Honnover 1965
- 9 Hudson, R Y , Laboratory Investigations of rubble Mound
Breakwaters, Proc A S C E , 85 W W 3, sept 1959
- 10 Hydraulics Research Station, Wollingford, Hydraulics
Research, 1966
- 11 Savoge, R P , Wave run-up on rough and permeable slopes,
Proc A S C E 84 WW 3, may 1958

CHAPTER 99

HONOLULU REEF RUNWAY DIKE

Robert Q. Palmer, F. ASCE
Associate Researcher of Ocean Engineering
University of Hawaii
Honolulu, Hawaii

James R. Walker, M. S.
Assistant Researcher
University of Hawaii
Honolulu, Hawaii

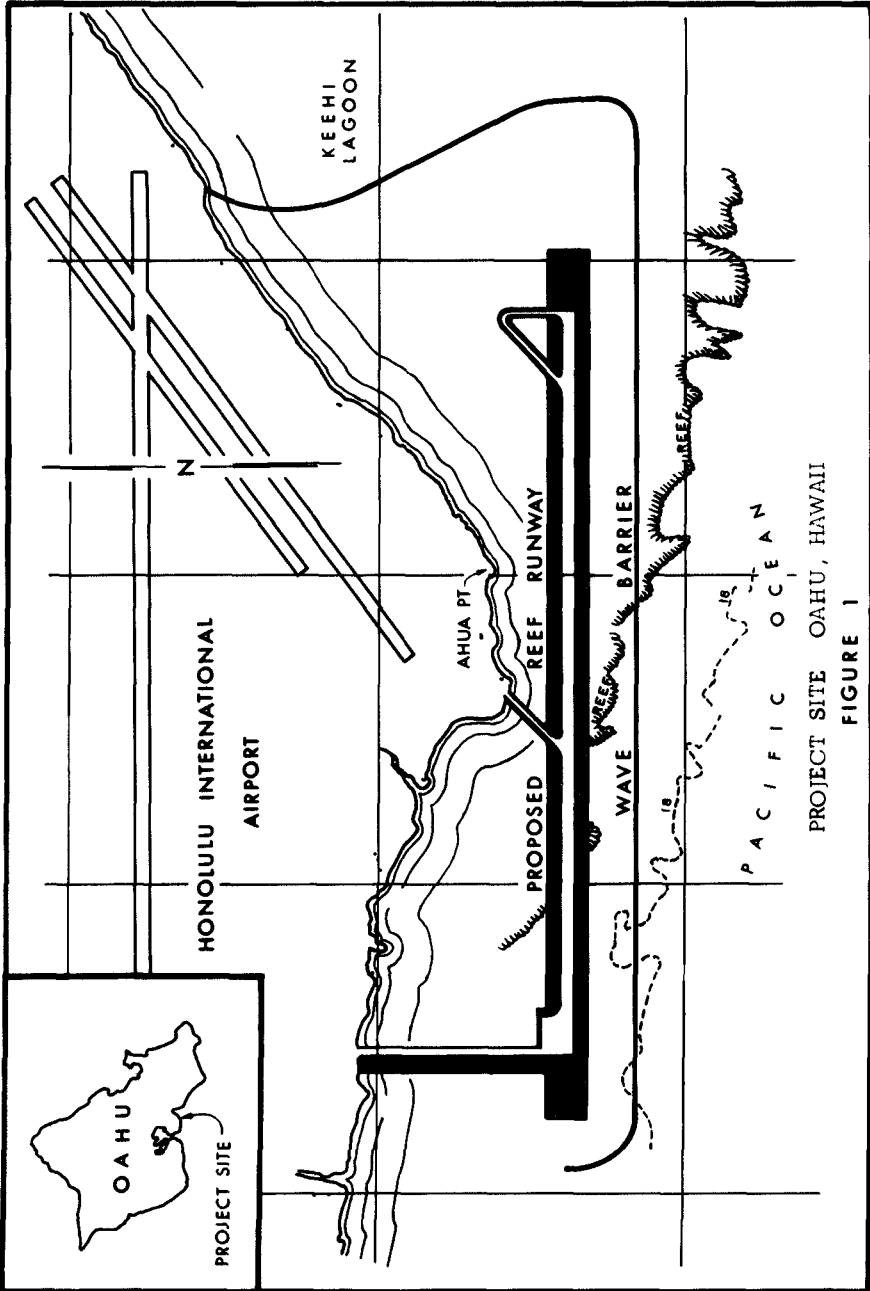
ABSTRACT

Criteria for design of a wave barrier to protect the proposed Honolulu International Airport Reef Runway from breaking waves were developed in wave flume model tests. Structures with tribar and quarry-stone armor units placed in single and multiple layers, on homogeneous and composite slopes, were subjected to both overtopping and non-overtopping breaking waves. Data on wave runup, armor unit stability, quantities of overtopping water, and transmitted wave heights were obtained using a 1:50 bottom slope, which modeled the irregular coral bathymetry seaward of the proposed structure. The model to prototype scale ratios ranged from 1:5 to 1:35.

Model Tests indicated that the weight of armor units placed below one-third the water depth may be three-fourths that of the units located near the water surface. It was noted that the maximum wave runup was 1.8 times the water depth fronting the structure. Data were obtained concerning quantities of overtopping water and transmitted wave heights over the low barriers. The study augments available criteria for economical design of structures subjected to breaking waves.

INTRODUCTION

The anticipated greater volume of future air traffic and larger aircraft imposes the need for an additional runway at the Honolulu International Airport, Oahu, Hawaii. The most practical site for the runway, shown in Figure 1, is on a coral reef, adjacent to the existing airport. The proposed runway location and alignment will not conflict with use of existing runways, but it will eliminate hazardous takeoffs and landings over the city, and will alleviate the present noise problem in urban areas.



The proposed wave protection for the reef runway would be situated in water ranging in depth from about one to twenty-five feet below mean low lower water (MLLW). Approximately one-third of the site would be located on a wide, flat coral reef, one to five feet deep and only 200 feet of the deeper portion would be in water greater than 25 feet deep. The bottom slope is approximately 1:50 to seaward. The design water surface of +3.5 feet MLLW allows for concurrence of a fairly high tide and storm surge. Southern hemisphere storms generate waves that approach the site with deep-water wave heights up to 15 feet, with 16-second periods. On rare occasions, local storms generate about 25-foot waves with shorter periods. A refraction analysis and a three-dimensional hydraulic model study⁷ indicated that waves are sufficiently high to break seaward of all reaches of the site at least ten hours per year.

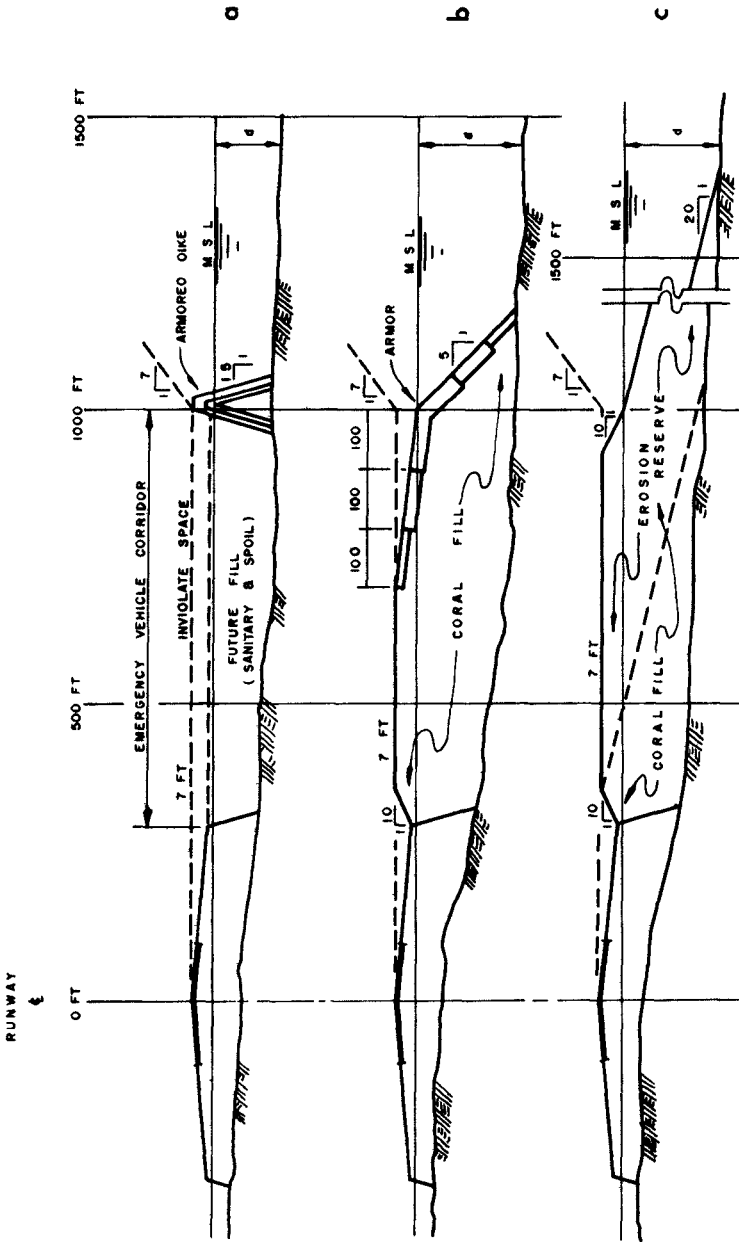
The purpose of this study was to develop the most economical system to protect the runway from storm waves. The runway, with 1,000-foot overruns, will be 14,000 feet long, 200 feet wide with 200-foot shoulders, and will have a centerline elevation of about seven feet above mean sea level (MSL). Air-space criteria require that there be no obstacles higher than the runway centerline for a distance of 1,000 feet from the centerline. Beyond 1,000 feet there is to be a side-clearance zone slope of one vertical to seven horizontal.

The apparent dearth of design data for structures subjected to breaking waves prompted the model investigation described herein. The testing objectives were divided into four categories, they were to determine wave runup, armor unit stability, quantities of overtopping water, and transmitted wave heights over low structures. In order to provide a basis for correlation of results with previous work, preliminary tests and procedures used by other investigators^{3, 8, 11} were made with non-breaking waves. Procedures were then modified as necessary to obtain the design breaking wave conditions.

The first three of six general concepts considered for the reef runway wave protection system are shown in Figure 2. These concepts are a) a seaward wave barrier which will contain future fill to provide access for emergency vehicles, b) a wide berm with flat armored slopes, and c) a wide berm with a flat beach slope similar to the Sand Dam of Europort in the Netherlands. Figure 3 shows the three other concepts which are d) a combination of a low seaward barrier and an artificial beach along the runway shoulder, e) a combination of a low seaward barrier and an armored levee along the runway, and f) a detached non-overtopped breakwater.

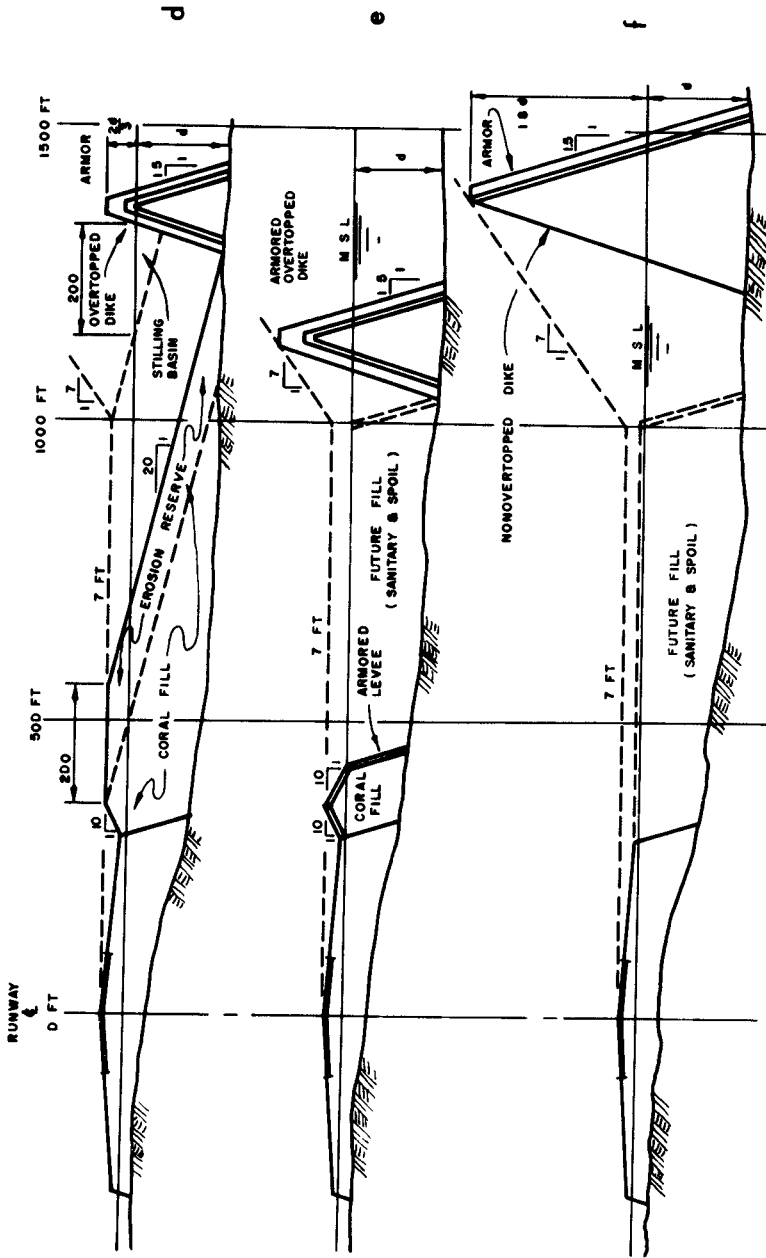
THE MODEL

The wave flume used for the two-dimensional tests was 180 feet long, four feet wide, and six feet deep. The walls were made of Transite and glass paneling. The glass panels were arranged to allow viewing



ALTERNATIVE WAVE PROTECTION CONCEPTS FOR HONOLULU REEF RUNWAY

FIGURE 2



ALTERNATIVE WAVE PROTECTION CONCEPTS FOR HONOLULU REEF RUNWAY
FIGURE 3

of the test section from one side of the flume. A plywood floor on a 1:50 slope simulated the offshore bathymetry. This slope extended approximately 65 feet seaward from the model test section.

The test sections were subjected to waves generated by a plunger-type wave generator. The wave generator was powered by a 20-HP electric motor coupled to a hydraulic pump. The hydraulic pump drove a high-torque, variable-speed hydraulic motor, which rotated an adjustable crank attached by a connecting rod to the plunger.

Wave heights were measured by resistance wave gauges, the signals were displayed on a light beam oscillograph recorder. Wave run-up elevations on structures were measured visually. Overtopping quantities were trapped in a one-foot wide box located in the center of the test section, at the core level, on the basin side of the structure. The trap door on top of the box opened and closed to capture the overtopping water of a selected series of waves.

The model breakwater sections had stone and tribar armor units. The armor stone was hand-shaped to simulate the type of stone that would be used in the prototype. The mean weight (saturated and surface-dried) of these units was 1.043 lb, with a standard deviation of 0.045 lb. The mean specific weight was 177.03 lb/cu ft, with a standard deviation of 2.83 lb/cu ft. However, the specific weight of the prototype stone may be as low as 165 lb/cu ft. The applicable model scales were determined by the WES (Hudson)¹ formula to range from 1.5 to 1.25 for these stones.

The model tribars were made of a mixture of concrete and barite sealed in a resin coating. The mean weight of these units was 2.10 lb, with a standard deviation of 0.023 lb. The specific weight of these units was 145.74 lb/cu ft, with a standard deviation of 1.05 lb/cu ft.

The armor stone and tribar underlayer stone mean weights were 0.055 lb and 0.189 lb, respectively, with specific gravities of 1.69 lb/cu ft. The impermeable core was made of a mixture of fines to gravel, 100 percent of the material passed a three-fourth inch sieve.

Test procedures were based upon the precedent set by related model studies^{3,8,9,11} and were modified as necessary to simulate prototype breaking waves. The incident wave heights were measured by a wave gauge located five feet seaward of the toe of the 1:50 bottom slope (70 feet from the test section). The incident wave heights were measured before reflections from the structure set up a standing wave. This wave height was used to estimate the deep water height, H_0 , by application of a shoaling coefficient. Another gauge was located one to five feet from the toe of the structure to measure the breaking-wave height. In order to generate a consistent wave of known height, the wave generator was stopped before wave reflections from the structure returned to the generator. The water was allowed to still before the generator was restarted.

Test sections were subjected to breaking waves to determine their stability under design conditions. The general procedure was to subject the structure to a series of small, non-breaking waves for a short period of time to allow the units to settle. Then the structure was subjected to the highest wave obtainable with the given depth to toe. The duration represented five to six hours of prototype wave attack. If the structure remained stable, the water depth was increased and a larger wave was allowed to attack the structure. This was done to determine if failure would occur with a slightly larger wave. Thus, a degree of safety was indicated.

Two types of armor stone placement were used in the models: in a single layer with the long axis perpendicular to the slope, and in multiple layers in a random fashion. Tribar armor units were either placed in a single layer arrangement or in multiple, random layers. Placement in the model was done to simulate, as closely as feasible, the placement in the prototype. For the majority of the tests, tribars were randomly placed in two layers below minus ten foot elevation. This placement was adopted in the model because of difficulties anticipated in prototype placement in murky water on an irregular bottom. Above minus ten feet, the units were placed upright with bars in contact with adjacent units.

The wave runup, R_u , as a function of deep-water wave height, H_o , wave period, T , and water depth d , was determined by visual observations. Runup, the elevation above the still-water surface to which a wave rises on a structure, was tested by increasing by increments wave height and period until the range of prototype conditions was covered. For a constant period, the wave height was increased from a small, non-breaking wave to a wave that broke sufficiently seaward of the structure to ensure that the maximum runup was observed. The wave attack was allowed to stabilize on the structure, and then the average runup of the next six to 15 waves was recorded. The number of waves used in the average runup was limited to the time it took for the first wave to reflect off the generator and return to the test section. When waves broke on or seaward of the structure, there was a large variation in the runup, therefore, the maximum runup value was recorded. In order to obtain a clear definition of the effect of location of the breaking wave, the generated wave height was increased by small increments when the wave started to break at the toe of the structure.

The quantity of water overtopping structures was trapped to determine the rate of over-swash. The procedure was to allow the wave attack to stabilize, then the over-swash of several waves was trapped and the quantity was measured. The procedures followed in obtaining the design wave in the overtopping tests were the same as described in the runup tests.

The water swashing over the top of the structure generated a transmitted wave height, H_T . This wave was measured by a gauge on the basin side, located five feet from the heel of the structure. The levees protecting the runway, as shown in Figures 3d and 3e, were modeled and also acted as wave absorbers for the transmitted waves.

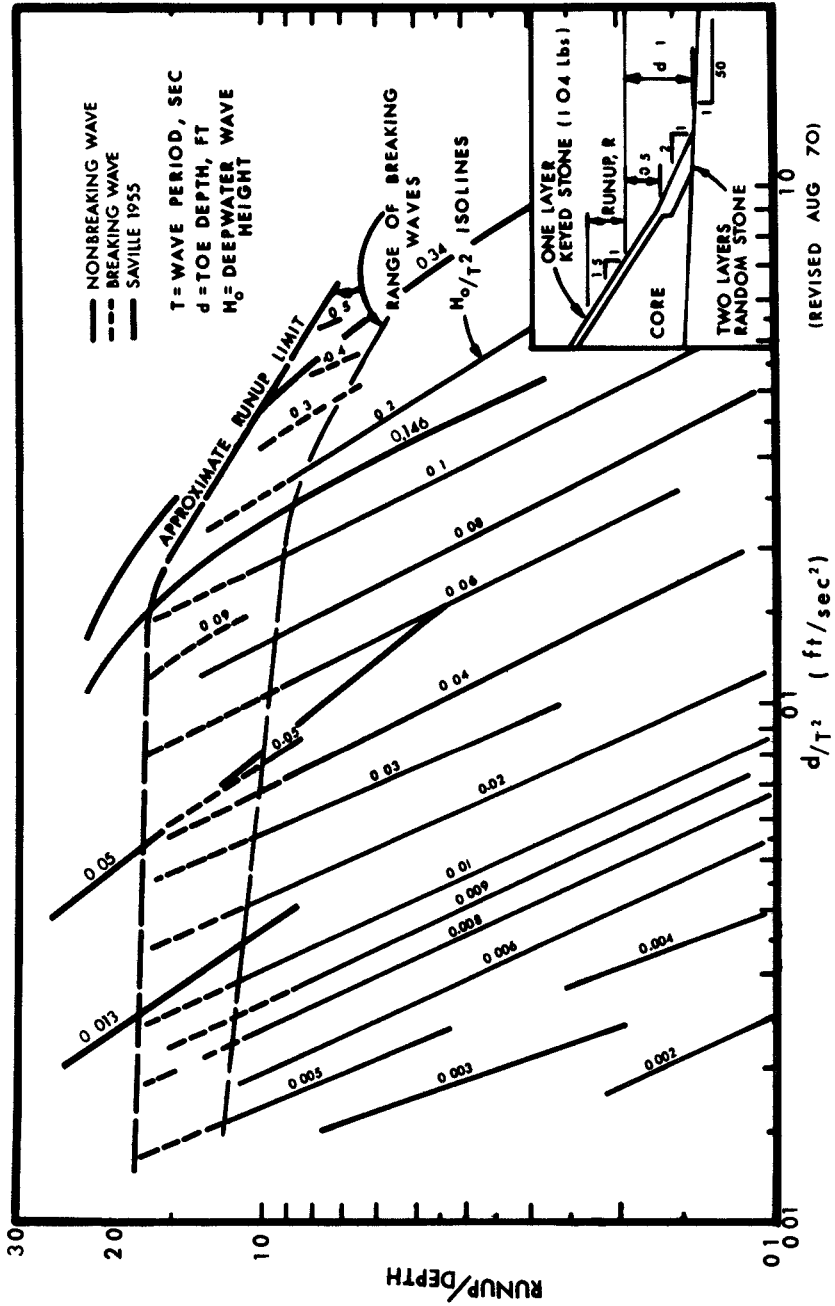
TESTS AND RESULTS

Runup on a structure subjected to breaking waves is a primary concern when considering a non-overtopping structure. For this reason, a typical dike section was designed and tested to determine the maximum runup. The inset in Figure 4 shows the test section. The core was impermeable and the material used has been described previously. Two layers of underlayer stone were randomly placed over the core, then a double layer of 1 04-lb stone was randomly placed on a 1 2 slope from the floor to -0 5 feet. From this point up to +3 5 feet, a single layer of fitted stone was placed on a 1 1 5 slope. The water depth was -1 0 foot at the toe of the structure.

One hundred and seventy-six tests were run on this structure to determine the maximum runup under prototype conditions. The results are shown in Figure 4 as a plot of the runup divided by depth, R_u/d vs d/T^2 for isolines of deep-water wave steepness, H_o/T^2 . These isolines are lines fitted through data points of non-breakers (solid line) and breakers (dashed line). The range of breaking waves is outlined by a line drawn approximately where the waves start to break at the toe of the structure. An increase in wave steepness approaches an upper limit of runup which is also drawn in Figure 4. This plot shows a rapid increase in runup as the wave period is increased until $d/T^2 = 0 15$ and $H_o/T^2 = 0 1$.

Saville⁸ previously conducted tests on a similar structure fronted by a 1 10 beach slope. Saville's results were plotted with the Reef Runway data for comparison. It was noted that the primary difference between the results of the two sets of data was that the runup Saville measured was about 45 percent greater than that of the Reef Runway data. Apparently, the steeper beach slope in Saville's experiment allowed a nearly 50 percent larger wave to break near the structure. This increase in breaker height, attributed to the difference in the bottom slope, was noted in the experimental work of Iversen² et al. The effect of the 1 2 slope at the toe of the Reef Runway test section does not account for such an increase in R/d when comparing the two structures using the composite slope method⁹. These runup data provide the designer of the Reef Runway project with an upper limit to which breaking waves will run up on a single-layer, stone-armor structure with a 1 1 5 slope.

Stability coefficients, K_D , were computed for each test section subjected to the breaking waves. When damage occurred to the armor, the degree was noted. The WES (Hudson)¹ formula was used in the analysis. The results indicate that a) published values of K_D for

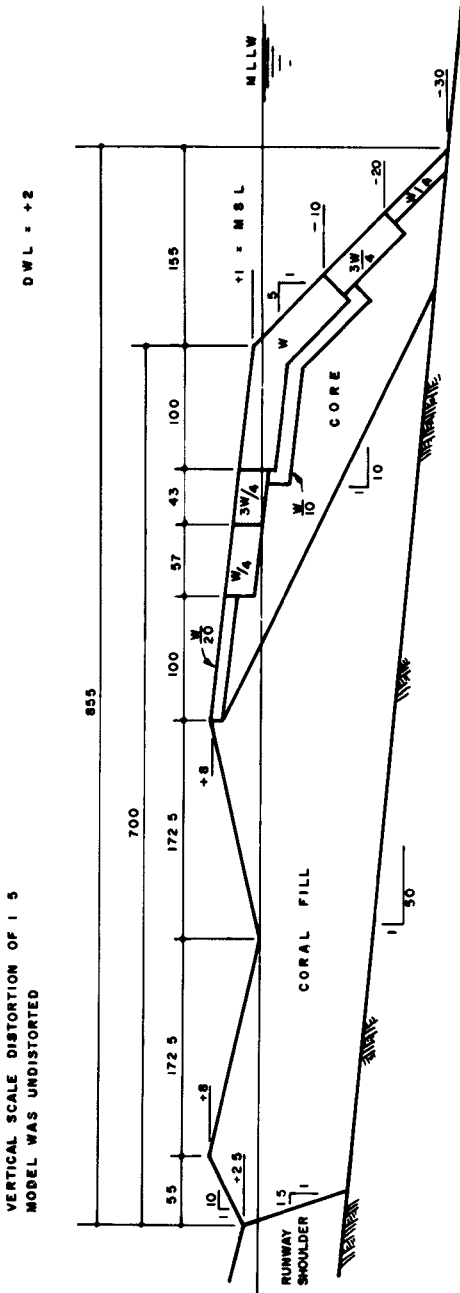


SHALLOW-WATER WAVE RUNUP ON A RUBBLE SLOPE
 FIGURE 4

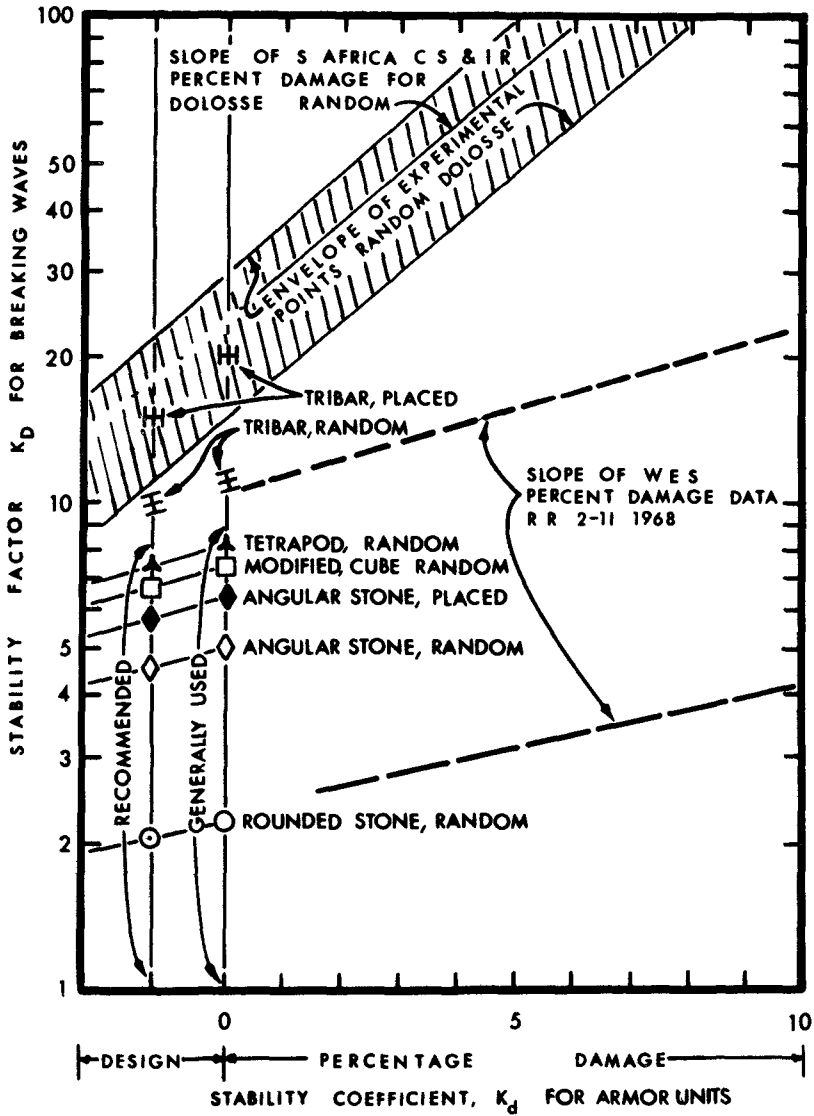
breaking waves are conservative, b) keyed and fitted armor is several times more stable than loosely-placed armor, c) displacement of one armor unit does not lead to sudden massive failure, in fact, the armor tends to heal unless it is grossly underweight, and d) the weight of armor may be reduced by one-fourth at depths below one-third of the toe depth and by three-fourths below the two-thirds depth as shown in Figure 5. A summation of stability coefficients for breaking waves is shown in Figure 6. The ordinate of the author's recommended design values are identified. However, it has been the general practice to design on the borderline of damage or even for a percentage of damage from infrequent waves.

Economically, the runway elevation should be kept as low as possible. A rise in water level behind the wave protection structure could affect the operation of the runway. In order to evaluate the effect of crest elevation upon the rate of overtopping water, series of tests were made on typical sections with various crest elevations. Results from two representative tests are given in Figures 7 and 8. The data is given in prototype dimensions and the test sections are shown in the insets. The linear model scale for these data was 1:15.2. The plots of these data are shown in Figure 7 for a crest elevation of 13.80 feet and in Figure 8 for a crest elevation of 9.35 feet. The rate of overtopping water per linear foot of crest, Q (cubic feet per second per foot of crest), is given as a function of deepwater wave height for isolines of wave periods. For a given wave period, the rate of overtopping rises rapidly with an increase in H_0 until the wave breaks at the toe of the structure. An increase in H_0 causes the wave to break seaward of the toe and the rate of overtopping approaches a maximum for a given wave period. The plots also indicate the effect of wave steepness. It was noted that it was inversely proportional to the amount of overtopping.

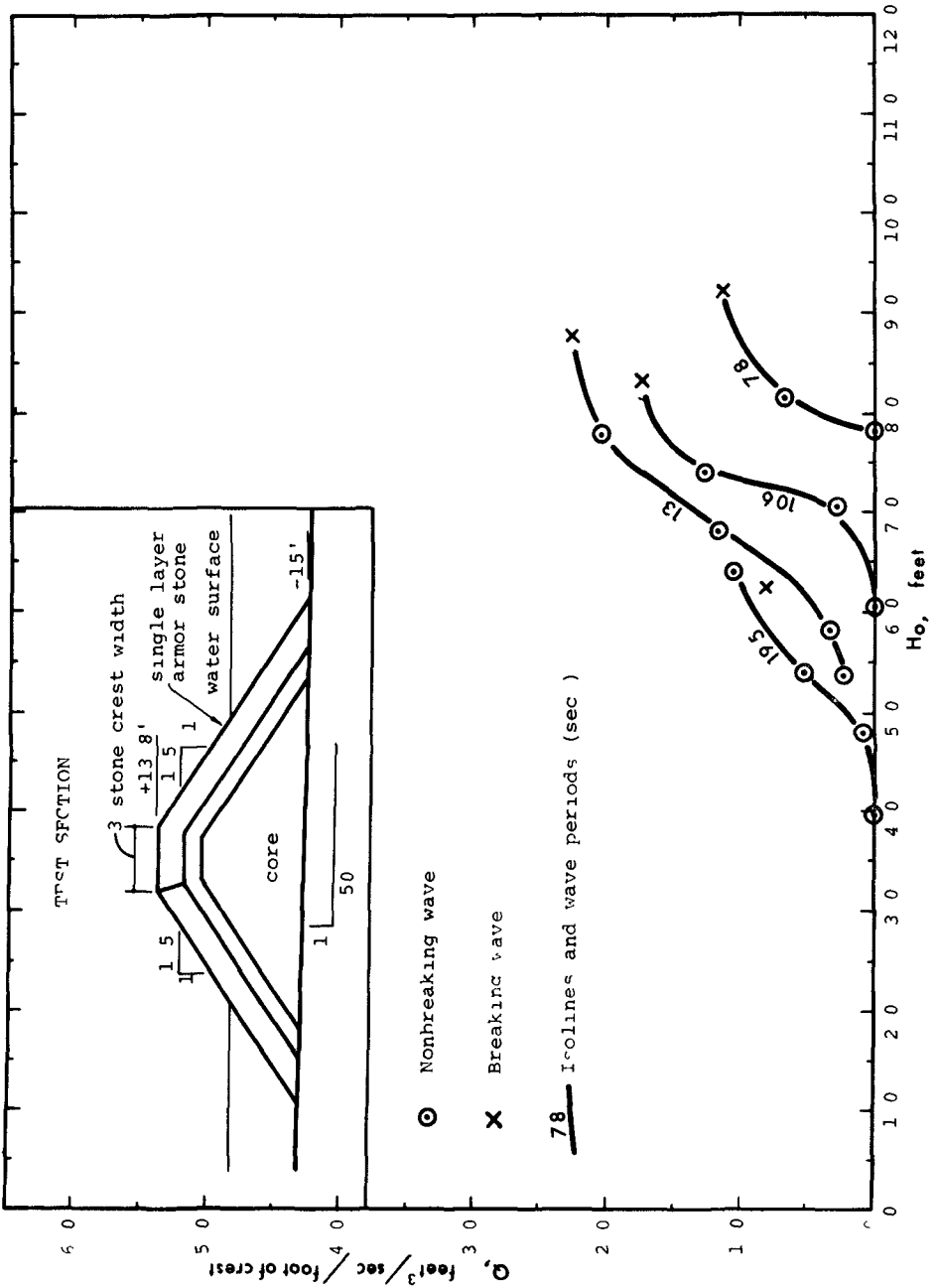
Wave swash over a structure generated waves in the basin behind the structure. When waves break just seaward of the structure, the maximum wave is generated in the basin. The relation of the effect of crest elevation is shown in Figure 9 as a plot of transmitted wave height, H_T , as a function of deep water wave height, H_0 , for two wave periods. The linear model scale was 1:15.2, and the test section in prototype dimensions is shown in Figure 9. The plots indicate that once the wave has broken, an increase in incident wave height does not produce an increase in transmitted wave height. An important observation noted during the testing program concerned the period of the transmitted wave, overswash of the incident wave generated a number of transmitted waves. This had a significant effect upon the runup on the runway levees. The size and depth of stilling basins also produced noticeable effects upon the transmitted wave. Due to these and other complicating factors, no general relations were developed for runup on the runway levees.



ARMOR WEIGHT RELATION & LOCATION ON STRUCTURE
FIGURE 5

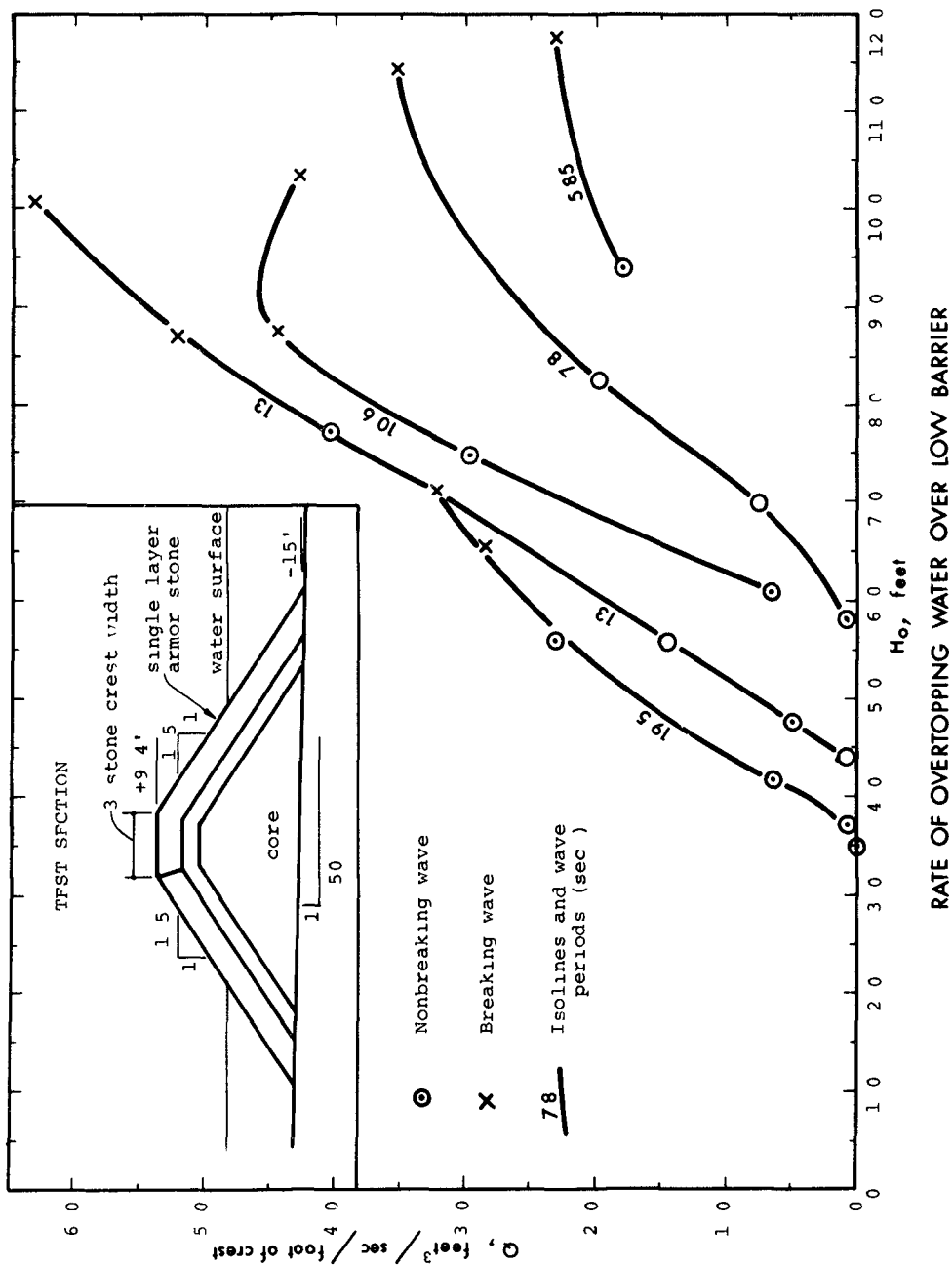


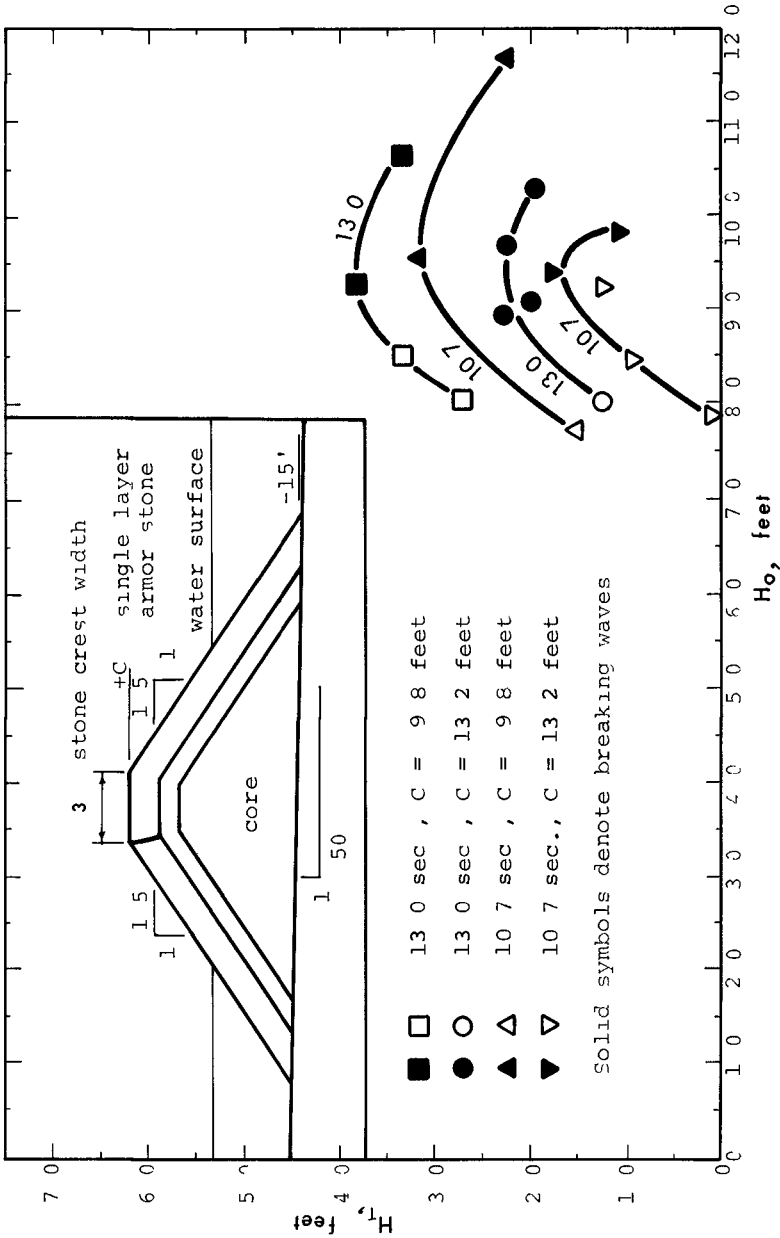
Note See references 4, 5, 9, 11



RATE OF OVERTOPPING WATER OVER LOW BARRIER

FIGURE 7





HEIGHT OF TRANSMITTED WAVE OVER LOW BARRIER

FIGURE 9

Forty-five sections were tested in this study. The results of these tests and comparative costs will be the subject of another paper. An example of one of the sections developed to attenuate runup is shown in Figure 10. Preliminary tests indicated that this high-void structure is stable and reduces runup.

CONCLUSIONS

A large scatter in the data was observed in the model testing of rubble structure with breaking waves. Even though a reasonably consistent wave train was generated, each wave broke in a different location, thus changing the effect of the wave upon the test. Since prototype waves are not consistent, the location of the breaking point varies even more. For this reason, maximum data points for the breaking waves were observed in the model tests.

Tests indicate that the maximum runup of a breaking wave for conditions shown on Figure 4 is 1.8 times the water depth fronting the structure. This was valid for the range of d/T^2 and H_o/T^2 tested.

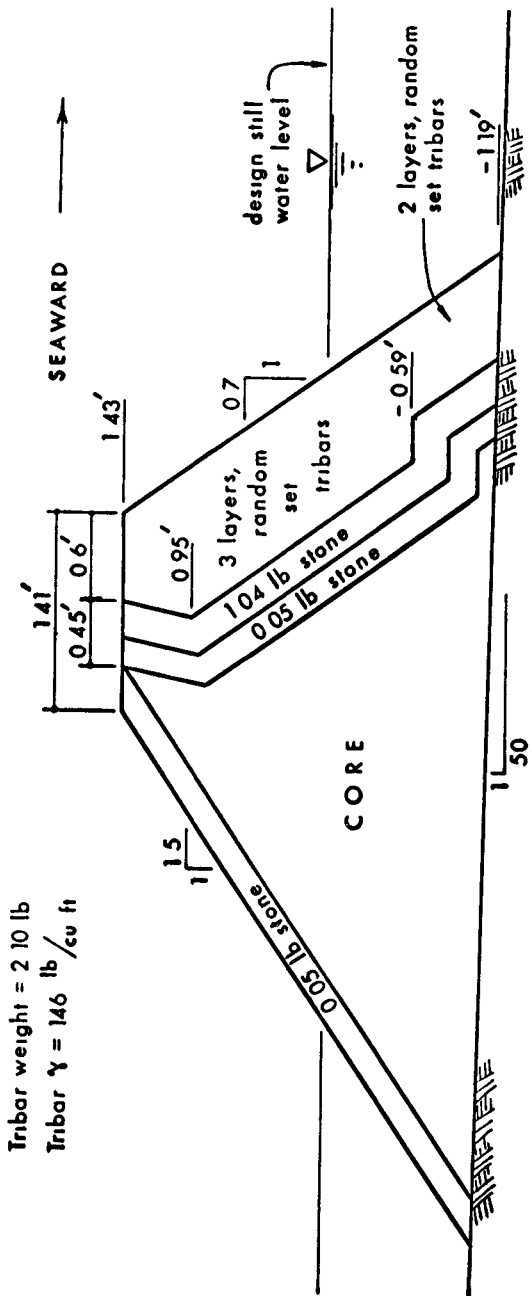
The tests confirmed the findings of previous investigations that the type of placement of armor is a major variable. Only skilled and experienced technicians can build rubble models which will yield fairly consistent results. Also, the designer and construction inspectors should be fully aware of the relationship between armor stability and placement. The tests confirmed that placement is as important a factor as the weight of the armor units. Specifically, the required weight of loosely placed stone may be twice that of a well-placed stone.

It is apparent that there is an overwhelming number of variables involved in analyzing breaking waves on complex rubble-mound structures. General design criteria can be developed for only a few unique conditions. It therefore appears that model tests should be made for all important rubble structures subject to breaking waves.

Scale effects¹⁰ should be considered when applying these data to prototype design.

ACKNOWLEDGEMENTS

The Honolulu International Airport Reef Runway model study was funded by the State of Hawaii. This work was performed by the University of Hawaii, Department of Ocean Engineering, Look Laboratory for Ralph M. Parsons Corporation representatives for the State of Hawaii Department of Transportation. The Department of Transportation's permission to publish this paper is appreciated.



NONOVERTOPPING DIKE WITH SMALL CROSS-SECTIONAL AREA

FIGURE 10

REFERENCES

- 1 Hudson, R Y , Laboratory Investigations of Rubble-Mound Breakwaters Proc , American Society of Civil Engineers , Waterways and Harbors Division, Vol 85, No WW3, Paper No 2171, September 1959
- 2 Iversen, H W "Discussion of Results from Studies of Wave Transformation in Shoaling Water " Institute of Engineering Research, Univ of California, Tech Report Series 3, No 331, March 1952
- 3 Jackson, R A , "Design of Cover Layers for Rubble-Mound Breakwaters Subjected to Nonbreaking Waves " U S Army Engineer Waterways Experiment Station, Research Report No 2-11, June 1968
- 4 Merrifield, Eric M , "DoLos Concrete Armor Protection," Civil Engineer, ASCE, December 1968
- 5 "Designs for Rubble-Mound Breakwater Repair, Morro Bay Harbor, Calif ," TR 2-567, WES, May 1961
- 6 Palmer, R Q , "Breakwaters in the Hawaiian Islands," Proc ASCE, WW1 and WW2, 1961
- 7 Palmer, R Q and J R Walker, "Three-Dimensional Storm Wave Study," Reef Runway Hydraulic Model Study, Honolulu International Airport, Honolulu, Hawaii, September 1969
- 8 Saville, T , Jr , "Laboratory Data on Wave Run-up and Overtopping on Shore Structures " U S Army Corps of Engineers, Beach Erosion Board, Tech Memo No 64, October 1955
- 9 Saville, T , Jr , "Wave Run-up on Composite Slopes," Proc of the 6th Conference on Coastal Engineering, Council on Wave Research, Univ of California, 1958
- 10 "Shore Protection Planning and Design," Beach Erosion Board, Technical Report No 4, Revised 1966
- 11 Tetra Tech, Inc , "Oceanographic Engineering For Reef Runway," Honolulu, International Airport (Final Report), Contract No TC-143, Pasadena, California, September 1968
- 12 Vanoni, Vito A and Fredric Raichlen, "Laboratory Design-Studies of the Effect of Waves on a Proposed Island Site for a Combined Nuclear Power and Desalting Plant," Report No KH-R-14, California Institute of Technology, July 1966

CHAPTER 100

FLOATING BREAKWATER FOR RESERVOIR MARINAS

by

Kenneth Chen, Research Assistant
University of California

and

R L Wiegel, Professor of Civil Engineering
University of California

ABSTRACT

The concept of multiple use of reservoirs is resulting in the construction of marinas for recreational boating requiring breakwaters that can function for a large range of water levels. A typical set of design criteria is an average water depth of 20 to 25 feet, wave lengths from 5 to 60 feet (wave periods of from 1 to 4 seconds) and wave heights from $\frac{1}{2}$ to 5 feet. Calculations based on Bulson's results showed a pneumatic breakwater to be too expensive. An extensive literature search revealed that floating structures based upon the concepts of large effective mass or moment of inertia resulting from "entrained" water, or structures which can dissipate energy might be more effective than one of the floating bag types of breakwaters. Several new-types of moored floating structures which combined two or more of the concepts mentioned above were tested in a wave tank, and several of the devices appear to have merit in that they were reasonably small compared with the longest design wave length and could reduce the highest design incident wave height to less than one foot, prototype, in the lee of the breakwater.

INTRODUCTION

Owing in part to the development of multiple purpose reservoir and inland lake recreation areas in recent years, the number of small craft used in these bodies of water has increased rapidly. In the design of small craft harbors for the protection of boats from storms, consideration must be given to the variation of the water level. This is of special importance for reservoirs because of draw-down during the summer and fall seasons. It appears that mobile breakwaters might be the best solution for such a condition.

Research on mobile breakwaters has been done in the past, but very few have been built. One purpose of this paper is to present the conclusions reached by the authors from a literature review. One can categorize mobile breakwaters into three main types: 1) pneumatic and hydraulic breakwaters, 2) flexible structures, and 3) rigid floating structures.

Based upon the conclusions derived from the literature review, three rigid floating breakwaters were designed, each making use of a different mechanism or combination of mechanisms of wave energy dissipation and reflection. The models were designated A, B and C. Later Mr J S Habel, Supervisor of Engineering of the Department of Harbors and Watercraft, State of California, and Professor J V Wehausen each suggested a concept of wave energy dissipation and reflection which resulted in the design and construction of Models

D and E

Almost no information was discovered on the maximum height and period of waves that are considered to be acceptable within a small craft marina. The Task Committee on Small Craft Harbors of the American Society of Civil Engineers (1969) state on page 57 that in general, wave heights should be reduced to approximately $\frac{1}{2}$ to 1 ft for small boat harbors. Some data on maximum wave heights in which different classes of working barges and vessels can operate have been given by Glenn (1950) and Santema (1955).

The problem of mooring so as to prevent damage to boat, mooring lines or dock is extremely complex, depending upon wave heights, periods and direction, and upon the weight, shape, natural periods of the boat and upon the characteristics of its moorings. A theoretical study was made by Raichlen (1968) for the simplified case of the surging motion of several classes of small boats (ranging from 2 to 8 tons - 20 to 40 ft in length) subjected to uniform periodic standing waves with crests normal to the longitudinal axis of the moored boats, with two bow lines and two stern lines. The restoring force versus displacement of the moorings were non-linear, as is apparently the normal case. A detailed analysis was made for one of the boats (Harbor Boat No 3), which had a length of 26 ft, beam of 9 ft -2 in, maximum draft of 2 ft -4 in and an approximate displacement (unloaded) of 5200 lbs. Details of the mooring configuration and mooring line characteristics were also presented. Measurements of the period of free oscillation of surge for three mooring line conditions (zero slack, 4 in and 8 in slack) for several different initial displacements were made and compared with theory. The comparisons, shown in Fig 1, are quite good.

Some of the complexities of the problem can be seen from Fig 2 which compares the maximum motion (in one direction only) of the boat as a function of wave period and the forcing function ζ for taut mooring lines and for 8 in slack. ζ is a rather complicated function, and Raichlen describes it as the maximum with respect to time of the water particle velocity averaged over the displaced volume of the moored body. All other things being equal, ζ is directly proportional to the standing wave amplitude. It is evident that a boat moored with slack lines at one tide stage may have taut lines at another stage of the tide, so that its response will vary with tide stage, all other conditions being equal.

Two other examples have been chosen from Raichlen's report, and are shown in Fig 3. The maximum positive displacement from rest is shown as a function of wave period and ζ for two boats, one of 3700 lbs with a length of 22 ft -5 in, and the other of 17,000 lbs and a length of 38 ft. First, it appears peculiar that the smaller boat should have larger "natural periods" than the larger boat. The reason for this was that the mooring lines of the larger boat were much stiffer compared with its weight than was the case for the smaller boat. This emphasizes again that the moorings are extremely important to the problem and there can be no simple wave height criteria for a harbor.

PREVIOUS WORK

Pneumatic and Hydraulic Breakwaters

An artificial surface current can be produced by air bubbles released from a comprised air manifold on the sea bed, or by means of horizontal water jets from a pipe floating on the water surface. If the surface current is of sufficient magnitude, and is directed towards the oncoming waves, the wave lengths are reduced and their heights increased until instability occurs, and the waves either break or are reflected.

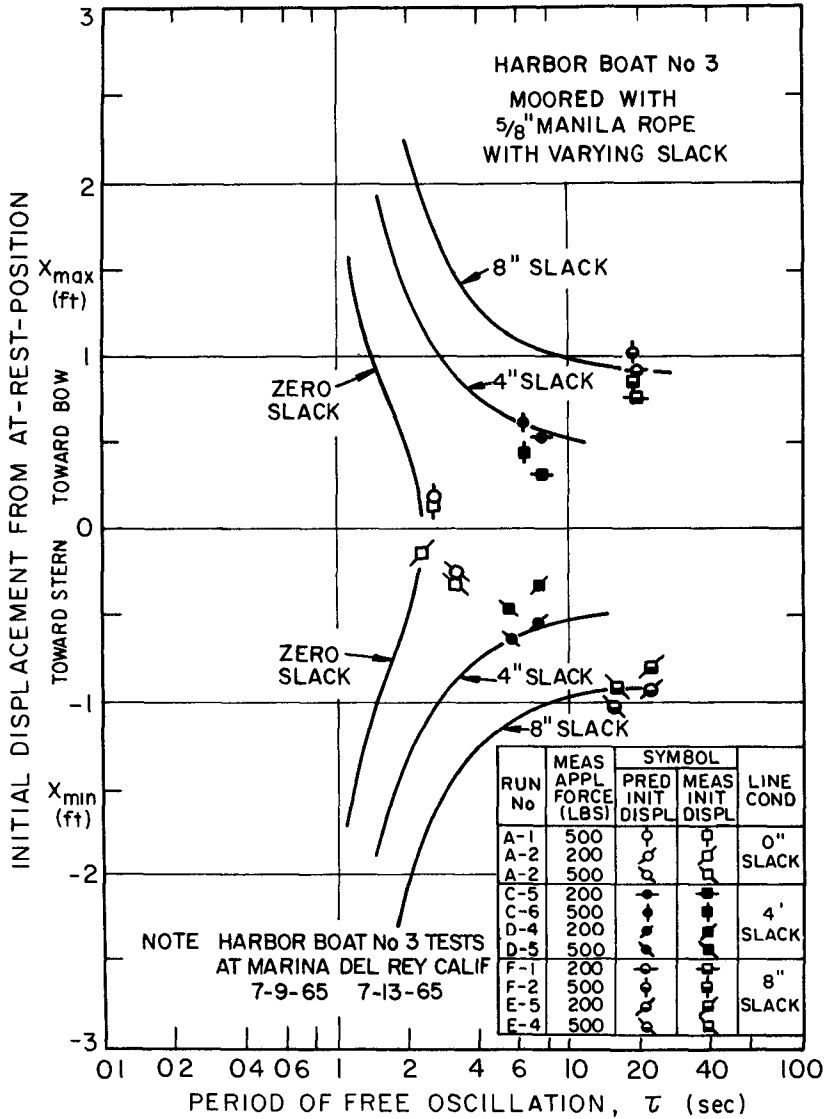


FIG 1 MEASURED AND PREDICTED PERIODS OF FREE OSCILLATION HARBOR BOAT No 3 (FROM RAICHLEN, 1968)

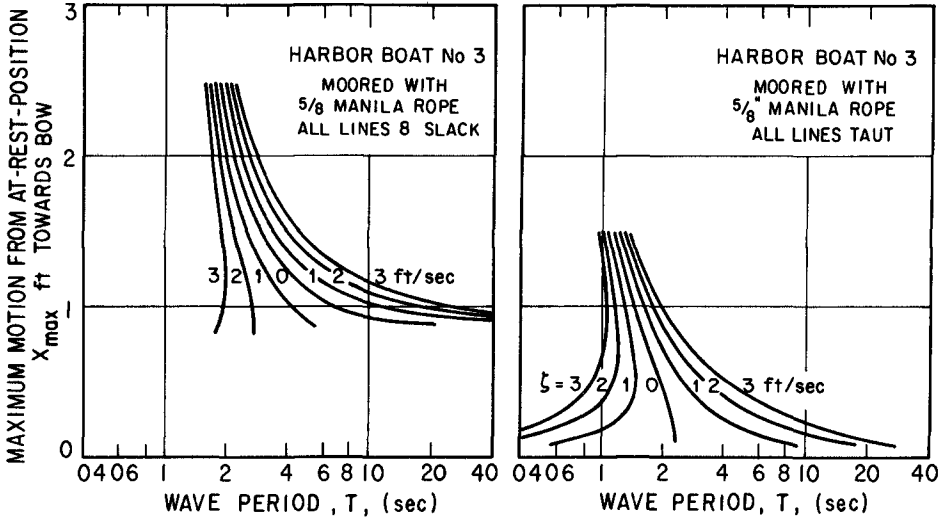


FIG 2 RESPONSE CURVES HARBOR BOAT No 3 (FROM RAICHLIN, 1968)

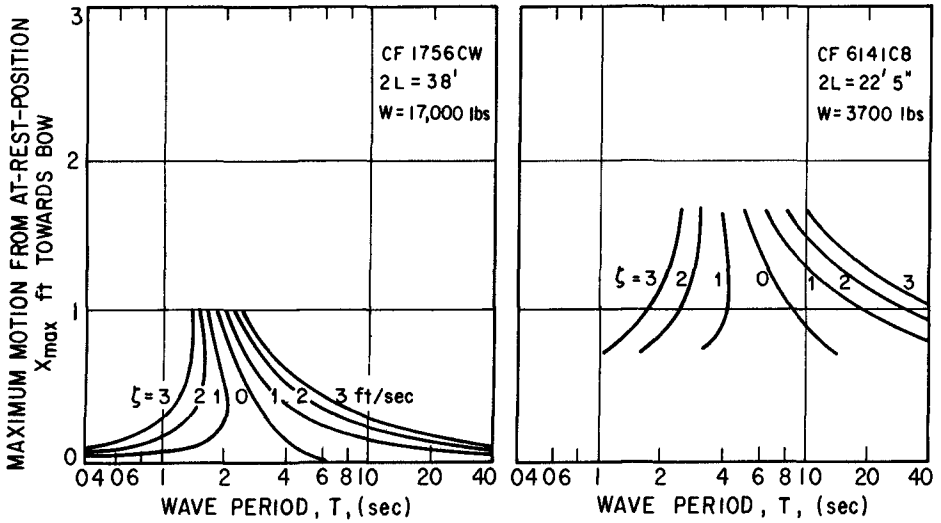


FIG 3 RESPONSE CURVES. 17,000 lb BOAT AND 3,700 lb BOAT (FROM RAICHLIN, 1968)

This concept was first employed by P Brasher (1915) in 1907 It was used by the Standard Oil Company in 1915 at El Segundo, California, apparently with little success In 1936 Professor Thyse of Delft University showed that the surface currents produced by the bubbles were the main mechanism The theoretical work was continued by White (1943) and Taylor (1955) in England during 1939-1945 As a result of their work, it became possible for the first time to predict the quantity of air required to produce a given surface current as well as the speed of current required to dissipate (and/or reflect) the energy of waves of known length After World War II, a large amount of research was done in connection with this subject

Williams and Wiegel (1963) generated waves in a tank by blowing air over the water surface and subjected them to a horizontal current of water created by horizontal water jets issuing from a manifold at the water surface (hydraulic breakwater) The energy spectra of the waves were computed for conditions before and after the hydraulic breakwater was turned on It was found that the shorter, steeper wave components were attenuated to a much greater extent than were the longer wave components They concluded that although a large portion of the wave energy could get past such a breakwater, the waves in the lee of the breakwater looked considerably lower to the observer, so that the claims made for the effectiveness of this type of breakwater were probably impressions rather than reality

Both experimental and analytical studies have been carried out by Bulson (1963, 1967, 1969), who concluded

"The experimental and theoretical studies during the past 25 years have made it possible for a reasonably accurate estimate to be made of the air quantity required to operate a bubble breakwater The quantity is astronomical and costly to supply The practical difficulties of operating a full scale system are immense It is doubtful whether any novel ideas of bubble formation and size can produce economies, and high cost is bound to be the basic feature of any apparatus of this type which is designed to combat the energy of the sea "

It was thought that perhaps a pneumatic breakwater might be a reasonable solution for the relatively short waves expected to be encountered in a reservoir Calculations were made for the following conditions water depth of 20 ft , wave lengths from 5 to 60 ft (wave periods from 1 to 4 seconds), and wave heights from $\frac{1}{2}$ to 5 ft Based on Bulson's results, one can calculate the quantity of air required to suppress waves of length L, height of H, in water depth, d

$$V_m = 1.46 \left[\frac{gQ_0P}{P+d} \right]^{1/3} \tag{1}$$

where V_m = the surface velocity of the current, feet per second

Q_0 = the quantity of free air delivered by compressors, cubic feet per second per foot

P = atmospheric pressure expressed as a head of water, feet of water

In this case the air supply manifold is placed on the bottom

The current velocity V diminishes approximately linearly with depth, until it equals zero at a depth D below the surface

$$D = 0.32 P \log_e \left[\frac{P+d}{P} \right] \text{ feet} \tag{2}$$

When the same quantity of air passes through a variety of orifice diameters and spacings, there is no significant difference in V_m , furthermore, results

for a single manifold at depth d are not noticeably different from those when two or more adjacent manifolds deliver the same total quantity of air. The critical current velocity at the surface to suppress completely deep water waves, \bar{V}_m , is given by

$$\bar{V}_m = \frac{1}{\alpha_m} \left[\frac{\lambda g}{2\pi} \right]^{-\frac{1}{2}} \quad (3)$$

$$\text{where } C^2 = gL/2\pi \quad \text{for deep water} \quad (4)$$

$$\text{and } \alpha_m^2/z = L/2\pi D \quad (5a)$$

$$z = Dg/\bar{V}_m^2 \quad (5b)$$

in which C is the wave speed in feet per second α_m can be obtained from Fig 5 of Bulson's 1969 paper. Combining Eqs (1) and (3)

$$Q_{cr} = \left[\frac{P+d}{P} \right] \left[\frac{gL}{2\pi} \right]^{-3/2} \left[\frac{1}{1-46\alpha_m} \right]^3 \quad (6)$$

According to Eq (6), Q_{cr} is independent of wave height, but experiments show that when waves are neither truly sinusoidal nor of infinitesimal height, the quantity of air necessary to produce complete damping can exceed Q_{cr} . It has been suggested by Bulson that Q_{max} can be represented by linear relationship between Q_{max}/Q_{cr} and the wave steepness, H/L

$$Q_{max}/Q_{cr} = 0.6 + (20 H/L)$$

Suppose one wishes to determine the quantity of air required to suppress waves 60 ft long, 5 ft high in a water depth of 20 ft. From Eq (2),

$$D = 0.32 \times 33 \times \text{Log}_e (63/33) = 6.83 \text{ ft} \quad \text{Also, } \frac{\alpha_m^2}{z} = 60 / (2\pi \times 6.83) = 1.4, \text{ and}$$

from Fig 5 of Bulson's paper, $\alpha_m = 3.05$. Substitution in Eq (6) gives $Q_{cr} = (33 + 20)/(33 \times 32) \times (g \times 60 / 2\pi)^{3/2} \times (1/1.46 \times 3.05)^3 = 3.59 \text{ cfs/ft}$. Finally, $Q_{max}/Q_{cr} = 0.6 + (20 H/L) = 2.27$, and $Q_{max} = 8.15 \text{ cfs/ft}$.

Therefore, the quantity of free air required is 8.15 cfs per ft. This represents an air power at the pipe of 26 horsepower per foot. Thus, a 300 yard long breakwater would require a total of 23,400 Hp. The operation alone is very costly, even if installation costs were not considered.

Flexible Breakwaters

In general a floating structure of relatively light weight will only be able to reflect a small amount of wave energy. If, however, the structure has sufficient length, a larger amount of wave damping and wave reflection will occur.

Model tests performed by Wiegell et al (1959), showed that floating sheets of plastic material will have a wave damping effect if the length of the plastic sheets, λ , is equal to many times the wave length, L . For a value of $\lambda/L = 5$, the wave height behind the structure appeared to be equal to $H_T = 0.8 H_I$, for $\lambda/L = 10$, $H_T = 0.4$ to $0.5 H_I$, and for $\lambda/L = 20$, $H_T = 0.2 H_I$. From a similar series of tests it appears that with a layer of plywood a wave reduction up to 50% could be obtained with $\lambda/L = 2$ to 3 . Other studies were made of the wave damping properties of waterfilled bags, ("hovering breakwater") floating in the water with their top at the water surface. The dimensions of the bags were $10' \times 10' \times 4'$. The results showed that within the

range of L/λ from 0.5 to 0.8, the ratio of the wave height in the lee of the "hovering breakwater" to that of the incident wave (H_1/H_I) was approximately equal to the ratio L/λ . This means that an effective damping requires a relatively wide structure.

Tests made with prototype waves in San Francisco Bay, with a hovering breakwater 20' x 24' x 4' deep in water 7' deep (below MLLW) by Wiegel, Shen and Cumming (1962) showed that H_T/H_I was one-half of the value obtained in the laboratory for the same value of L/λ , using the "significant wave length" computed from the measured "zero upcrossing period" of about 1.7 seconds. The reason why the "prototype" was more effective than the "model" was not determined.

Other extensive experiments were made by Ripken (1960). These experiments deal with the wave damping properties of cylindrical bags, filled with air or liquid, which are placed just below the water surface with their longitudinal axis parallel to the direction of wave propagation. It was found that a satisfactory attenuation requires a bag length of about 1.5 to 2 times the wave length. A diameter of 20% of the water depth was recommended for the cylindrical bags, although the influence of the relative depth appeared to be small. A filling of about 95% seems to be the most effective filling percentage for the bags. Use of fluids in the bag of a greater viscosity than water did not substantially increase the amount of wave attenuation. Ripken stated that the wave attenuation provided by water filled bags was associated with a progressive pressure wave in the bag. This pressure wave was found to be slightly out of phase with the wave motion. As a consequence of this, the material used for the bags must be strong.

Other studies were carried out by Ripken (1960) for two different types of wave absorbers: a blanket and a shallow moored floating structure. Ripken concluded:

The degree of attenuation achieved increases as the ratio of wave length to blanket length decreases and as the ratio of blanket thickness to water depth increases. The blanket thickness should be of the order of 15 percent or more of the water depth. For a thin blanket the length should be several times as long as the wave length. A multiple of about three or more is indicated depending on the attenuation desired.

A similar conclusion was reached in regard to the wave trap, a considerable length is needed to damp the oncoming waves.

An experimental study of fascine mattress composed of willow twigs and reeds has been made by Vinje (1966). It appeared that the wave attenuation was nearly 45-50% when the ratio of the length of mattress to the length of wave was larger than 1.

There are some other studies which have been made, and the general conclusion appears to be that the length of breakwater in the direction of wave propagation should be much larger than the wave length.

Floating Rigid Structures

Floating structures have three modes of oscillation due to the restoring force of gravity: rolling, pitching, and heaving. A moored floating structure has three additional modes of oscillation owing to the restoring force of the moorings. A floating structure which is to reflect wave energy must have the requisite long natural periods in each of these three modes of oscillation compared with the wave periods. To obtain a long natural period, it is necessary to combine a large mass with small "elasticity". In a floating structure the "elasticity" is represented by its change in buoyancy as it heaves, rolls, and pitches. A solution of this problem is the enclosure of a large

mass of water within a relatively light enclosing structure in such a way that the restoring force was reduced to a minimum. This was the principle of Bombardon floating breakwater designed for and used in the Normandy invasion of World War II (Lochner, Faber and Penney (1948)). In the official report on the operation of Bombardon floating breakwater the following statement was made

"A full scale breakwater, assembled off the Dorset coast in April 1944, successfully withstood an on-shore gale of force 7 (30 m p h) with gusts up to force 8 (39 m p h) "

"Both breakwaters were moored in 11-13 fathoms, giving sufficient depth inshore for Liberty ships to anchor. In this depth they reduced the height of the waves by the measured amount of 50%, which represents a 75% reduction in wave energy. These measurements were carefully made at the British harbour on the 16th June, 1944 with a wind blowing force 5-6. Unloading operations and small boat work were going on inside the breakwater at that time which would not have been possible outside the breakwater "

The requirement of large mass may be usefully replaced by large moment of inertia of mass in the development of floating breakwaters. This concept has been applied by Brebner and Ofuya (1969) in developing the "A" frame breakwater. The "A" Frame breakwater consists essentially of a central rigid curtain of wood, and two aluminum cylinders symmetrically located and rigidly connected to the curtain at intervals. The mass radius of gyration of the structure about a lateral axis through its center of gravity (axis parallel to wave crest) may be varied by altering the cylinder spacing. Laboratory experiments showed that an effective floating breakwater system can be developed in which a large moment of inertia of mass is the dominant factor rather than the mass. The reduction of wave heights is effected through the processes of wave reflection, dissipation, and wave interference. The best wave damping was obtained when the distance between the cylinders was nearly equal to the wave length.

The third concept is that of a perforated breakwater which was originally developed by Jarlan (1965). This study is concerned with the application of that breakwater as a mobile system and for possible operation in the floating-moored or fixed to the bottom. A recent study has been done by Marks (1967) who states

" The dynamic processes that result from the incidence of waves on the perforated breakwater can best be visualized by considering [Fig 3] * As the wave impinges on the porous front wall, part of its energy is reflected and the remainder passes through the perforations. The potential energy in the wave is converted to kinetic energy in the form of a jet, upon passage through the perforation, which then bends to be partially dissipated by viscosity in the channel and partially by turbulence in the fluid chamber behind the perforated wall. As the water in the fluid chamber flows back out of the holes, it encounters the next oncoming wave and partial energy destruction is accomplished even before that wave reaches the breakwater. If the walls were not perforated (e.g. a caisson), total reflection would occur on the face of the wall with resultant high impact forces and scouring on the base, if it is

fixed to the bottom. If the breakwater were floating and anchored, part of the incident wave force would be transmitted to the mooring cables and part would be directed to oscillating the breakwater thus inducing it to make waves on the shoreward side. In the case of the perforated breakwater, that part of the incident wave energy which is dissipated internally in the form of heat and eddies is not available for such deleterious activity. Hence, it is expected that less force would be felt in the mooring lines, and/or that smaller waves would be produced shoreward of the breakwater."

' It is clear that wave attenuation is most effective at low periods and least at high periods. The perforated unit is better up to about 9 seconds of wave period and worse beyond compared with caisson type."

"The breakwater geometry specifying 4-foot diameter holes, 4-foot wall thickness, and 40 feet between front and back wall was found to be most effective, as predicted by theory. The mooring lines in the perforated breakwater experienced less force by about a factor of 2 compared with caisson type. Wave reduction by the solid floating-breakwater varied from about 0.2 to 0.6. For the perforated floating breakwater, wave reduction varied from about 0.2 to 0.8. As expected, the perforated breakwater was far effective in reducing wave height for shorter waves (0.1 to 0.3) than for longer waves (0.6 to 0.7)."

NEW MODEL FLOATING BREAKWATERS

Introduction

It was decided to design three types of rigid structure breakwaters for laboratory testing, combining the principle of the use of a large entrained moment of inertia with the principle of partially absorbing the wave energy by a perforated wall or by a sloping board. The three types have been designated Type A, B, and C.

The experiments were performed in a 106 ft long by 1 ft wide by 3 ft deep wave channel. The water depth in the wave channel was set at 25 in, corresponding to a "prototype" depth of 25 ft. The floating breakwater model was placed about seventy feet from the wave generator. An energy absorbing beach was located at the other end of the channel. Wave measurements were obtained at a position about 15 ft 'seaward' of the floating breakwater model and at a location about 8 ft to the "lee" of the model, using parallel wire resistance wave gages (Wiegel, 1956).

Two wave heights were used for each wave length tested, one low and one high, to check approximately the effect of wave steepness (also, called the wave slope) on the phenomenon. The wave length, L, is related to the wave period, T, and water depth, d, by the equation

$$L = \frac{gT^2}{2\pi} \tanh \frac{2\pi d}{L} \tag{7}$$

in which g is the acceleration of gravity. For the water depth and wave periods tested, this equation could be approximated by

$$L \approx gT^2/2\pi \tag{8}$$

A portion of the wave energy was transmitted to the lee of each breakwater as a train of waves, a part of the energy was dissipated, and a part of the energy was reflected as a train of waves. Little wave energy was reflected by Model A breakwater, while Models B, C, D and E reflected a considerable amount of wave energy. No attempt was made to measure the amount of wave energy reflected.

The most important parameter of the study is the transmission coefficient, defined as

$$\text{Wave Transmission Coefficient} = \frac{\text{Transmitted Wave Height}}{\text{Incident Wave Height}} = \frac{H_T}{H_I}$$

A typical example of the record of both the incident and transmitted wave heights is shown in Fig. 4. It can be seen that the reflected waves interfered with the incident waves in a complex manner. Reported values of the wave transmission coefficient were based on the largest transmitted wave height and the average incident wave height.

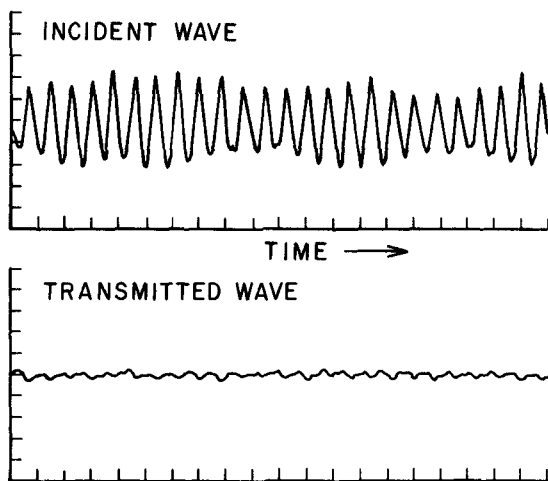


FIG 4 RECORD OF INCIDENT WAVE AND TRANSMITTED WAVE

One important factor that was not studied at this stage was the mooring line system and the mooring forces. The mooring line system forms an important feature of a floating breakwater since breakwater performance depends on the type of restraints imposed on its motion by the mooring lines. Three additional natural periods result from the mooring lines: yaw, sway and surge. Further studies must be made on the mooring system. Different types of floating breakwaters' moorings need to be studied to find out the best mooring system.

Model A

The basic concept of this design was the dissipation of wave energy by waves breaking on a sloping board "beach"

Model A, shown in Fig 5, consisted of a sloping board "beach," with the seaward end attached to a rectangular air chamber (pontoon) which provided buoyancy. The "lee side" of the sloping board was connected to a vertical wall (14" high) by steel frames. A "lee side" floating box (pontoon) was connected to the vertical wall by a steel frame. The total length, λ , of this model was 43.5 in (1 e, 43.5 ft, "prototype" as the ratio between the model and the contemplated breakwater for use in reservoirs is 1:12).

In order to check the effect of the height of the vertical wall on the wave transmission coefficient, the model was modified by increasing the height of the vertical wall to 22 in (22 ft, prototype), with about 19 in (19 ft, prototype) of it being submerged.

It was found that when the incident waves moved over the sloping board "beach," they started to break as if they were moving over a sand beach. The small amplitude waves broke completely on the board. The large amplitude waves did not break completely on the board "beach" owing to the limited length of the board. For waves which were about as long as the dimension λ of the breakwater, or shorter, a substantial amount of wave energy was dissipated in this breaking process. The top of the board "beach" was designed to have a saw tooth shape. The large amplitude waves partially broke on the board "beach," then ran over the top of the board, dropping through the space into the water on the lee side of the "beach." No water went over the top of the vertical wall. Considerable air entrainment and mixing occurred during the process. This periodic impact of the wave run-up dropping on the water surface eventually created a pressure fluctuation in the water under the board "beach," and in front of the vertical wall. The water moved up and down in this region. This resulted in a pressure fluctuation in the region between the bottom of the vertical wall and the bottom of the tank, which in turn caused a heaving motion of the water surface in the section between the vertical wall and the lee side pontoon. It appeared that the distance between the vertical wall and the lee side pontoon would be important, but lack of time prevented a study of various spacings.

A further observation was made by permitting the model drift (e.g., the mooring lines were removed from the model) in the waves. It was found that Model A drifted much more slowly than Model B. It was believed that the slow rate of drift indicated there would not be too great a problem in mooring the structure.

The results of the wave transmission coefficient vs the ratio of wave length to breakwater length (L/λ), and vs the wave length (given in "prototype" scale) are shown in Fig 6. The results show an irregular curve. In the range of wave lengths from 30 ft to 55 ft (prototype), the steep waves (wave slope = 0.055-0.075) had a higher transmission coefficient than did the waves of relatively small steepness (slope = 0.022-0.030). The term wave steepness refers to the ratio of the incident wave height to the wave length (H_i/L). The two curves crossed at a wave length of about 60 ft, and in the range of wave lengths from 65 ft to 90 ft, the relationship was opposite to that for the smaller wave lengths.

When the model was modified with the 22 in (22 ft, prototype) deep vertical wall, there was less difference in the transmission coefficients for the relatively flat waves than the steep wave. There was about a 10 percent improvement in the wave transmission coefficient for the range of wave lengths between 60 ft and 80 ft (prototype).

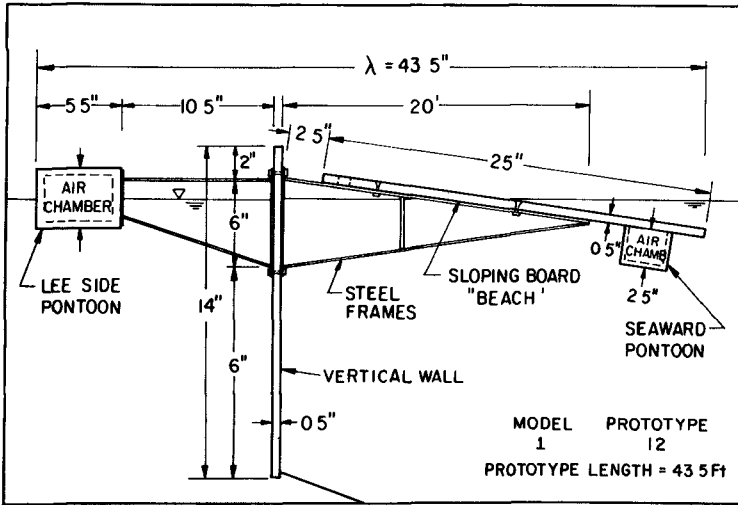


FIG 5 FLOATING BREAKWATER "TYPE A"

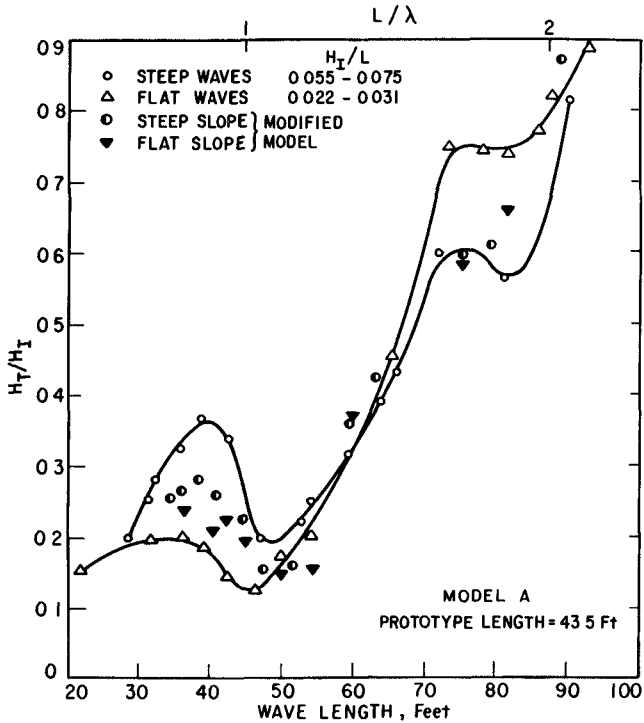


FIG 6 TRANSMISSION COEFFICIENT vs WAVE LENGTH (ALSO L/λ)

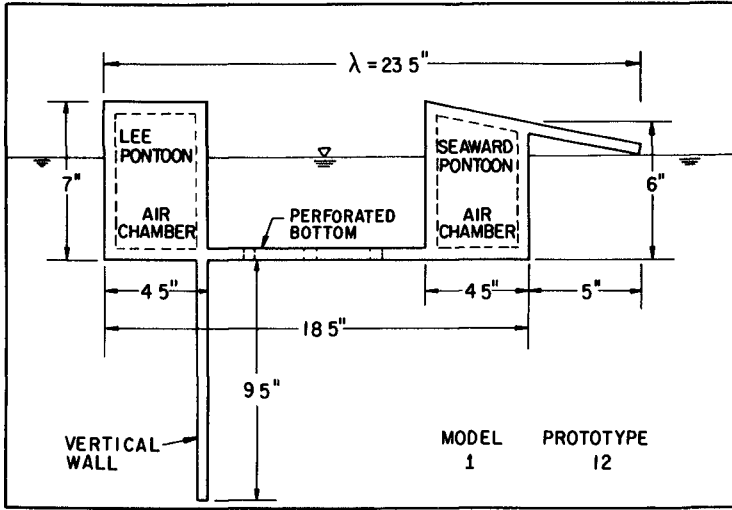


FIG 7 FLOATING BREAKWATER "TYPE B"

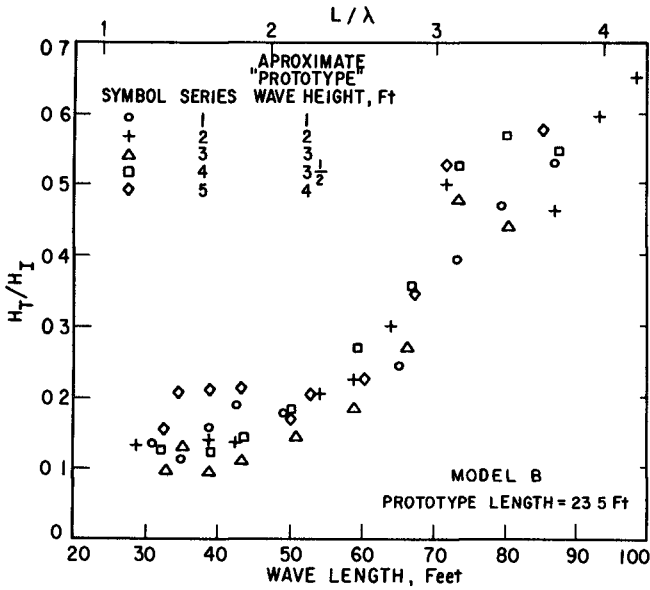


FIG 8 TRANSMISSION COEFFICIENT vs WAVE LENGTH (ALSO L/λ)

Model B

Floating breakwater Model B, shown in Fig 7, consisted of two pontoons separated by a perforated bottom. The length, λ , of the structure is 18.5 in (18.5 ft, prototype), with an additional 5 in (5 ft, prototype) of sloping "beach" extending seaward above the water surface for a total length of 23.5 in (23.5 ft, prototype). A vertical barrier was attached below the lee side of the perforated section. The pontoon on the lee side had a rectangular cross section. The pontoon on the weather side has unequal vertical sides, with a sloping top extending outwards a distance of 5 in (5 ft, prototype) towards the weather side.

The results of the wave transmission coefficient vs wave length and vs L/λ are shown in Fig 8 for five series of runs, each with a different wave height. For wave lengths less than 60 ft, prototype, (L/λ less than 2.7), the transmission coefficient is less than about 0.20. Considering the expected range of wave lengths in a reservoir, this is probably a satisfactory attenuation. For wave lengths between 65 ft and 80 ft (prototype), the transmission coefficient rises rapidly from about 0.3 to 0.5. For wave lengths of about 90 ft (L/λ of 3.8), the transmission coefficient rises to 0.60-0.65. Under the latter circumstances, a substantial portion of the wave energy is transmitted past the floating breakwater.

It appeared that more than half of the energy of the incident waves was reflected by the breakwater as a wave train, with an "apparent higher frequency" than the frequency of the incident waves. The breaking up of the oncoming waves into a series of smaller reflecting waves appeared to result in smaller forces acting on the mooring system. The action of the water and the structure is shown schematically in Fig 9. In Fig 9 the oncoming wave crest is shown striking surfaces A, B and C, it then reflects at different times in the form of a series of reflecting waves with a smaller amplitude compared with the incident waves, and with different phases.

Owing to the vertical barrier and the overall geometric arrangements, this floating breakwater had a rather large moment of inertia with respect to rolling motion. Also, the center "water channel" with the perforated bottom worked as a damping device, in some ways similar to an antirolling tank on a ship. For oncoming waves with large amplitude, the crest washed over the sloping top of the weather side pontoon, flowed into the center channel and then flowed through the perforated bottom. Part of the energy apparently was dissipated by water rolling over the top of the slope and by the eddies that formed in the water channel. Some air trapped under the surface of the extended portion of the sloping top of the seaward pontoon was compressed, and mixed with the water. This process was too complicated for analysis, but it appeared to be a good mechanism for dissipating some of the wave energy.

The tension in the mooring line consisted in general of two components, one caused by the rolling motion of the breakwater, and one caused by the wave crests striking the structure. However, the model was designed so that the two components would not cause maximum forces in the mooring line at the same time. Since the axis of rolling of the system is above the mooring point, when the incident waves strike on the system, the rolling motion of the body tended to release the tension in the mooring line. When the incident wave troughs reached the floating breakwater, the tension in the mooring line was caused only by the rolling motion.

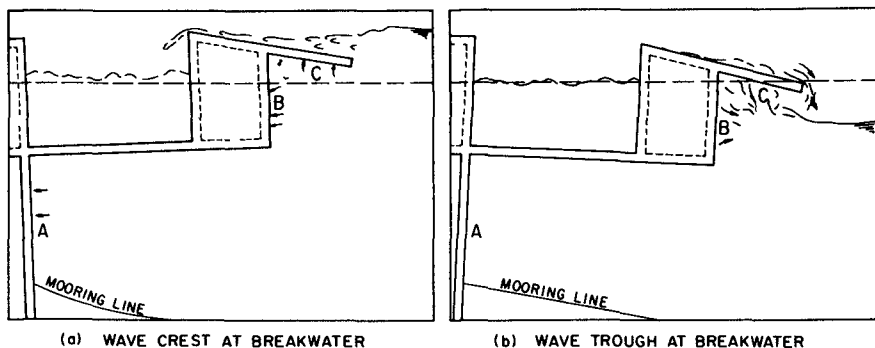


FIG 9 SKETCH SHOWING WAVE ACTION ON MODEL B

Model C

Model C (Fig 10) is a type of perforated breakwater the purpose of the perforated wall being to decrease the direct striking force by decreasing the reflecting area and to dissipate wave energy by the flow of water through the holes. The "water chamber" has two perforated walls. The back wall extends downward as a vertical barrier to provide sufficient moment of inertia of added mass. The air chamber (pontoon) serves as a walkway along the breakwater. During the model test, ballast was used to obtain proper balance of the structure. This model was the shortest of all five models, being only 14 in ($\lambda = 14$ ft, prototype) long.

Values of H_T/H_I vs wave length and vs L/λ are shown in Fig 11. For wave lengths up to about 40 ft, the result appears to be reasonably satisfactory. The curve of the wave transmission coefficient vs wave length (and vs L/λ) has a rather steep slope.

The expected amount of energy dissipation did not occur. The rest of the energy was either reflected or transmitted past the breakwater either through the motion of the breakwater which acted as a wave generator, or by wave energy passing under the structure.

Model D

The side and top views of Model D are shown in Fig 12. The platform, 32 in ($\lambda = 32$ ft prototype) in length, was ballasted sufficiently to cause it to be immersed with its bottom 6 in (6 ft prototype) beneath the water surface. A series of gates were suspended vertically upwards by their own buoyancy. Each gate was connected to the platform by a rubber sheet hinge. A string was used to restrain the motion of the gates to only one side from the vertical. The gates were designed so that the rolling motion of each row of gates could move in only one direction in an alternative manner. The model was carefully ballasted so that each gate emerged 0.5 in (0.5 ft, prototype) above the water surface. It was designed so that any water current could bypass the series of gates with a rather small striking force, and to dissipate the energy through turbulence. The restrained motion of the gates may interrupt the orbital motion of the waves and energy dissipation occurs. The motions of the water current and the gates are shown in Fig 13.

The experimental results are shown in Fig 14. The high wave transmission coefficients are due to the following two reasons. First, the joint between the gates and the platform was a one-inch wide (model dimension) rubber sheet instead of a simple hinge. Because of the inflexibility, the motion of the gates was not confined to a simple rolling motion, but also had a parallel displacement which regenerated the wave and transmitted the wave energy to the lee of the breakwater. In addition, the simple flat platform provided a smaller moment of inertia (largely due to added mass) than a structure with a vertical barrier.

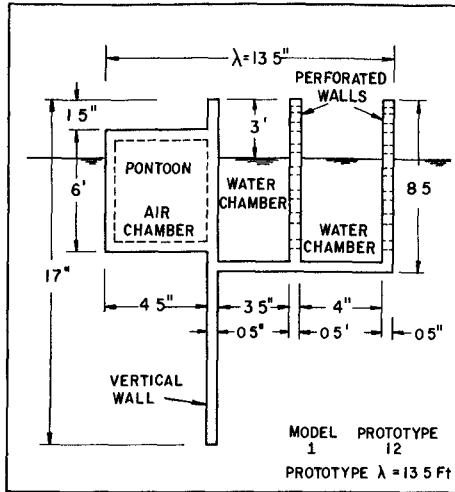


FIG 10 FLOATING BREAKWATER TYPE "C"

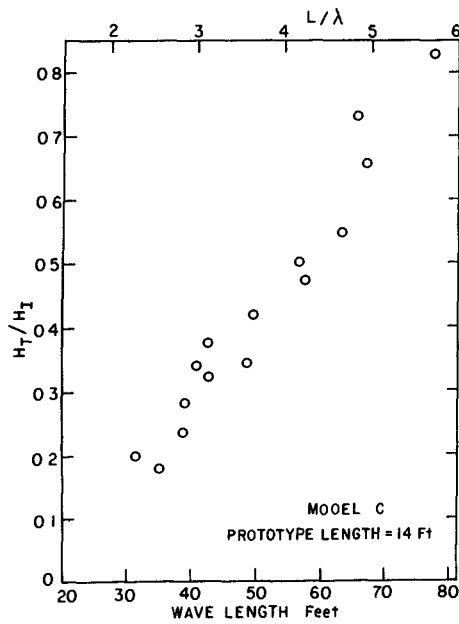


FIG 11 TRANSMISSION COEFFICIENT vs WAVE LENGTH (ALSO L/λ)

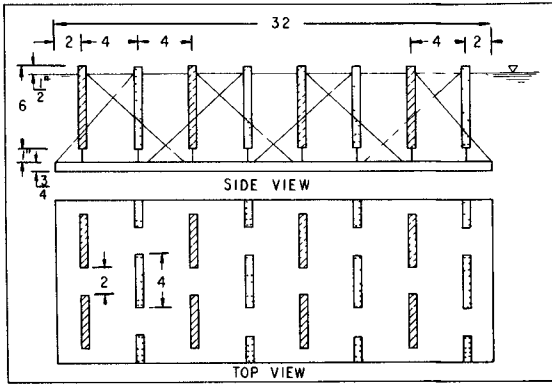


FIG 12 FLOATING BREAKWATER TYPE D

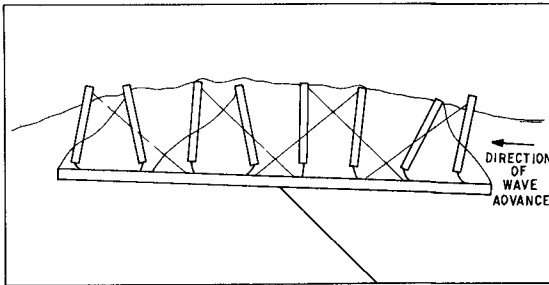


FIG 13 WAVE PASSING BREAKWATER TYPE D

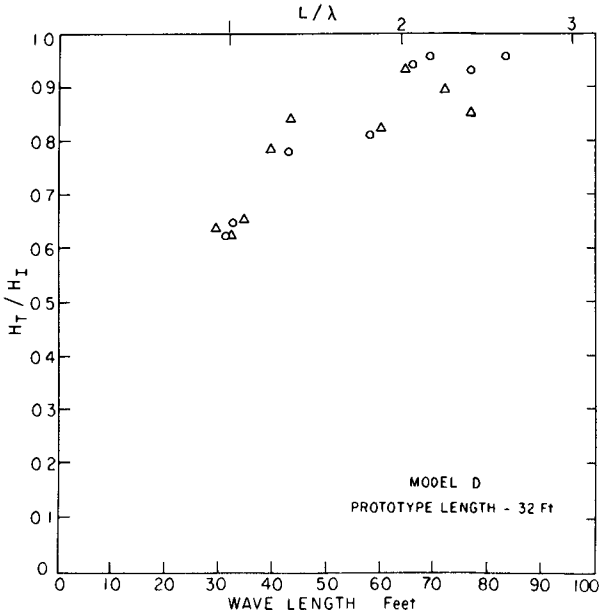


FIG 14 TRANSMISSION COEFFICIENT vs WAVE LENGTH (ALSO L / λ)

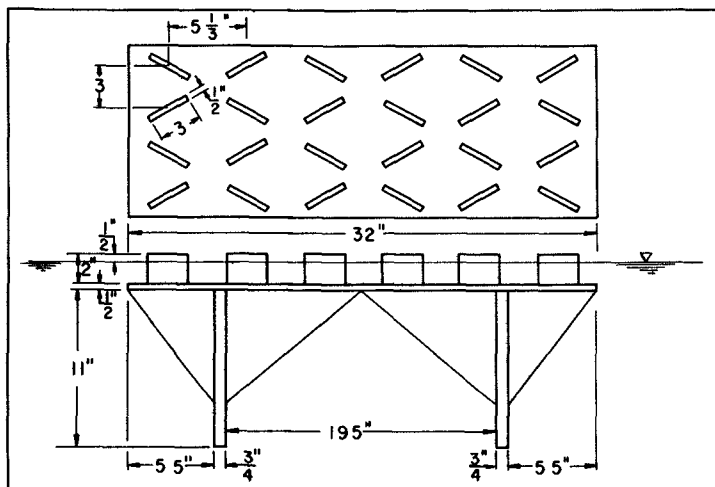


FIG 15 FLOATING BREAKWATER TYPE 'E'

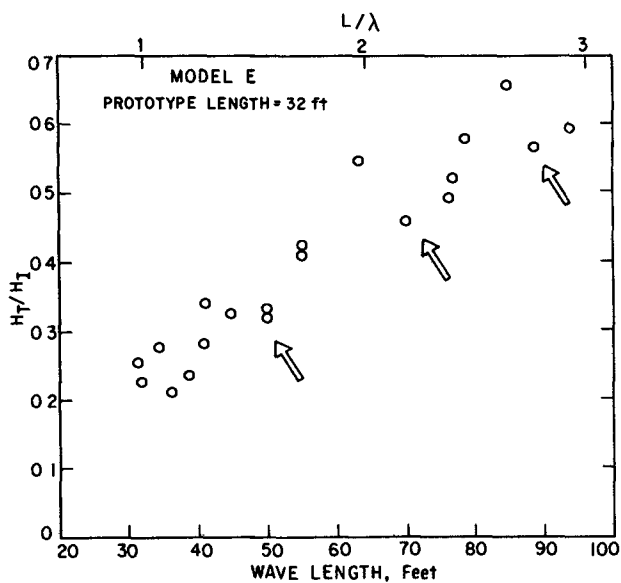


FIG 16 TRANSMISSION COEFFICIENT vs WAVE LENGTH (ALSO L/λ)

Model E

In order to avoid the transmission of energy through the gates, another model was adopted, based upon the concept of a fixed energy dissipator similar to those used at the foot of a spillway, rather than using the flapping gates. The vertical walls and the platform formed a π shape (Fig 15), which provided a large moment of inertia (largely due to added mass), and minimized the transmission of wave energy under the platform. The length, λ , of the structure was 32 ft, prototype. The vertical sections mounted on the top side of the horizontal submerged platform consisted of six rows of blocks. Each block was set at an angle of 30 degrees to the direction of wave propagation in an alternating pattern.

Energy dissipation occurred as the waves washed through the maze of vertical blocks, and formed eddies and turbulence. It was observed that the waves collided with the platform. This collision may have been caused by the combination of the motion of the platform and the wave motion. This occurred for wave lengths of about 50 ft, 70 ft, and 90 ft, prototype. The impact of this wave collision apparently resulted in the dissipation of some of the wave energy, this can be seen in the plot of wave transmission coefficient vs the wave length (and L/λ) for wave lengths of 50 ft, 70 ft, and 90 ft (see arrows in Fig 16).

As can be seen in Fig 16 the transmission coefficient was about 0.45 for a wave length of about 60 ft, prototype.

ACKNOWLEDGEMENTS

The work described herein was performed at the University of California, Berkeley, California, under contract to the Department of Harbors and Watercraft of the State of California. The authors wish to acknowledge the valuable advice of Mr. J. S. Habel of the Department and Professor J. V. Wehausen of the University during the course of this study.

REFERENCES

- 1 American Society of Civil Engineers, Task Committee on Small Craft Harbors, 'Report on Small Craft Harbors,' ASCE-Manuals and Reports on Engineering Practice-No 50, 1969, 139 pages.
- 2 Brasher, P., Compressed Air Magazine, Vol 20, 1915.
- 3 Brebner, A. and A. O. Ofuya, "Floating Breakwaters," Proceeding of Eleventh Conference on Coastal Engineering, London, 1968, Vol II, ASCE 1969, pp 1055-1094.
- 4 Bulson, P. S., 'Large Scale Bubble Breakwater Experiments,' The Dock and Harbour Authority, Vol XLIV, No 516, Oct 1963, pp 191-197.
- 5 Bulson, P. S., "Transportable Breakwater," The Dock and Harbour Authority, Vol XLVIII, No 560, June 1967, pp 41-46.
- 6 Bulson, P. S., "The Theory and Design of Bubble Breakwaters," Proceedings of the Eleventh Conference on Coastal Engineering, London, 1968, Vol II, American Society of Civil Engineers, 1969, pp 995-1015.

- 7 Glenn, A H , 'Progress Report on Solution of Wave, Tide, Current, and Hurricane Problems in Coastal Operations,' Oil and Gas Journal, Vol 49, No 7, 22 June 1950 pp 174-177
- 8 Jarlan, G E , "The Application of Acoustic Theory to the Reflective Properties of Coastal Engineering Structures," National Research Council of Canada, DML/NAE Quarterly Bulletin No 1965(1)
- 9 Lochner, R , Faber, O , & Penny, W G , "The Bombardon Floating Breakwater," The Civil Engineer in War, Vol 2, Docks and Harbors, The Institution of Civil Engineers, London, 1948, pp 256-290
- 10 Raichlen, Frederic, "Motions of Small Boats Moored in Standing Waves," California Institute of Technology, W M Keck Laboratory of Hydraulics and Water Resources, Report No KH-R-17, August 1968, 158 pages
- 11 Ripken J F , 'An Experimental Study of Flexible Floating Breakwaters,' University of Minnesota, St Anthony Falls Hydraulic Laboratory, Tech Paper No 31, Series B 1960, 72 pp
- 12 Ripken, J F , "Evaluation Studies of the United States Rubber Company Wave Blanket and Wave Trap," University of Minnesota, St Anthony Falls Hydraulic Laboratory, Project Report No 62, 1960, 77 pp
- 13 Santema, P 'About the Estimation of the Number of Days with Favorable Meteorological and Oceanographical Conditions for Engineering Operations on the Sea Coast and in Estuaries,' Proceedings of the Fifth Conference on Coastal Engineering, Council on Wave Research, The Engineering Foundation Berkeley, California, 1955, pp 405-410
- 14 Taylor, Sir Geoffrey "The Action of a Surface Current Used as a Breakwater," Proc Roy Soc (London), Ser A , Vol 231, No 1187, September 1955, pp 466-478
- 15 Vinje, J J , "Increase of Effective Working Time During Operations at Sea by Means of Movable Structures," Delft Hydraulics Laboratory, Publication No 42, 1966, 38 pp
- 16 Wiegel, R L , "Parallel Wire Resistance Wave Meter," Proceedings of the First Conference on Coastal Engineering Instruments, Council on Wave Research, The Engineering Foundation, Berkeley, California, 1956, pp 39-43
- 17 Wiegel, R L , Shen, H W and Cumming J D , "Final Report on Hovering Breakwater," University of California Berkeley Hydraulic Engineering Laboratory, Wave Research Projects Series 140, Issue 5, 1959
- 18 Wiegel, R L , Shen, H W and Cumming, J D , "Hovering Breakwater," Journal Waterways and Harbors Div , Proc ASCE, Vol 88, No WW 2, May 1962, pp 23-50
- 19 Williams John A and R L Wiegel, 'Attenuation of Wind Waves by a Hydraulic Breakwater, Proceedings of the Eighth Conference on Coastal Engineering, Council on Wave Research, The Engineering Foundation, Berkeley, California, 1963, pp 500-520

CHAPTER 101

FORCES ON A PONTOON IN THREE DIMENSIONAL WAVES

by

J. EIE, Research Engineer ^x

A TRÅTTEBERG, Senior Research Engineer ^x

A. TØRUM, Senior Research Engineer ^x

1. INTRODUCTION

Wave forces on a long pontoon (floating breakwater, floating bridges etc.) depend to a large extent on the three dimensional wave pattern. There is no deterministic method for calculating wave forces for such structures in a three dimensional sea and laboratory equipment for testing long structures in irregular three dimensional waves does hardly exist

Forces, bending moments etc on floating structures may in principle be calculated on basis of a transfer function $K(f, \theta)$ and the two dimensional wave power spectrum $E(f, \theta)$ giving the one dimensional force power spectrum $\phi(f)$ according to

$$\phi(f) = \int_{\theta} K^2(f, \theta) E(f, \theta) d\theta \quad (1)$$

where

f = frequency

θ = angle between mean wave direction and direction of the individual wave component

^xRiver and Harbour Laboratory

Technical University of Norway, Trondheim, Norway

This concept, which is being used to a certain extent in ship hydrodynamics, is based on a linear relationship between wave height and forces, bending moments etc.

The force distribution is calculated from the relationship derived by Longuet-Higgins (2) and is frequently used in wave statistics. This relationship is the following

$$F = k \sqrt{\int_f \phi(f) df} \quad (2)$$

where

F = force

k = coefficient, depending on which statistical force is wanted.

The force F is the zero-upcrossing force as defined in Fig. 7. (see chapter 3 1). For the significant force $F_{1/3}$, $k = 2,83$, (2), (3).

The whole concept is shown in Fig. 1.

The transfer function $K(f, \theta)$ can be found analytically or by model tests.

The purpose of the investigation described in this paper was to obtain some experimental data on the validity of the concept applied to a pontoon of rectangular cross-section. As the transfer function for such a pontoon, partly reflecting and partly transmitting the waves, is not so easily obtained by calculations, the force transfer function was found experimentally in regular waves. The wave forces in three dimensional waves were obtained in a wind wave flume. The scalar wave

power spectrum has been measured, but unfortunately we have not had the opportunity to measure the directional power spectrum of the waves. We have therefore in the calculations had to make assumption of the directional spread of the spectrum.

2. MODEL TEST ARRANGEMENT

The tested pontoon had a rectangular cross-section with width, draft and length of 0,44 m, 0,12 m and 3,00 meters respectively.

The two dimensional transfer function was obtained in tests using regular waves in a test arrangement as shown in Fig. 2 Fig. 3 shows details of the pontoon and its instrumentation. The total lateral forces were measured by use of strain gauges placed at both ends of the pontoon Except for the small motions necessary to obtain a response of the strain gauges the pontoon was fixed.

The tests in three dimensional waves were carried out in a wind/wave channel This channel is 78 meters long, and 3,8 meters wide. The water depth at the pontoon was 0,37 meters, while the depth in most parts of the channel was approximately 1,0 m. The test setup in the wave channel is shown in Fig. 4.

The waves were generated by wind with a velocity of approximately 10 m/sec. The ratio between wind velocity and wave celerity in such wind wave flumes is generally high, and the waves tend to have a steepness which is higher than normally found in fjords and in the ocean In order to reduce the wave steepness a wave filter was placed some distance in front of the pontoon as shown in Fig. 4.

3 TEST RESULTS

3.1. Transfer function

The transfer function was obtained by running tests with different wave periods, wave heights and wave directions.

The wave pattern in the test basin was as indicated in Fig 2. All measurements were made before the secondary reflected waves from the walls of the test basin reached the pontoon.

Fig 5 shows samples of the test results. The diagrams show wave force vs wave height. The angle between the direction of the wave propagation and the direction of force is indicated.

The relation between wave force and wave height is fairly linear and "best-fit" lines showing the linear relation is drawn by eye. This relation is given by

$$F^* = K^*(\theta, f)H \quad (3)$$

where

F^* = force

H = wave height

$K^*(\theta, f)$ = coefficient depending on wave frequency and wave direction

It is seen that the forces towards the "lee" direction of the waves are slightly larger than towards the "windward" side. This is also revealed in the force recordings, a sample of which is shown in Fig. 6.

The reason for the difference between the forces in the two directions is believed to be higher order effects

However, it is not possible within the simple linear concept we are dealing with to include these higher order effects. We have therefore combined the two directions by defining another coefficient $K(\theta, f)$ as

$$K(\theta, f) = K^*(\theta, f)_{lee} + K^*(\theta, f)_{windward} \quad (4)$$

The following relationship is then obtained

$$F = K(\theta, f) H \quad (5)$$

where F is the double amplitude force

F is comparable to H as indicated in Fig 7

The $K(\theta, f)$ values are shown in the diagram of Fig 8

Based on the diagram of Fig 8 we have made a contour "map" of the transfer function as shown in Fig 9

3.2 Directional spectrum

As mentioned in the introduction we have not had the opportunity to measure the directional spectrum of the waves in the wind wave flume. However, the scalar spectrum has been obtained. The waves were measured at the pontoon site in the flume when the pontoon was taken away. Fig 10 shows a sample of a paper record of the waves.

The waves were recorded on a magnetic tape. This record was then digitized with a time interval between samples of 0.128 sec and the power spectrum was calculated from a sample of 200 consecutive waves. The "raw" spectrum was smoothed by the method of Hanning (3). The calculated spectrum is shown in Fig 11.

It has been usual in theory on wave directional spectra to assume a spectrum directionality function

$$[a(f, \theta)]^2 = [a(f)]^2 y(\theta, \zeta_s) \quad (6)$$

where

$$y(\theta, \zeta_s) = \frac{(\cos \theta)^{\zeta_s}}{K(\zeta_s)} \quad (7)$$

and

$$K(\zeta_s) = \int_{-\pi/2}^{+\pi/2} (\cos \theta)^{\zeta_s} d\theta \quad (8)$$

Fig. 12 shows y vs θ for different values of ζ_s

We have estimated the directional power spectrum based on a $\cos^4 \theta$ -law. The estimate of the directional spectrum is shown as a contour map in Fig. 13. The implication of using a $\cos^4 \theta$ -law instead of, say, a $\cos^2 \theta$ -law will be discussed later.

3.3. Calculated force spectra and force distributions

Based on the transfer function and the estimated directional wave power spectrum, the force power spectrum was calculated according to equation (1). The numerical calculation was carried out by applying $\Delta f = 0,1$ sec and $\Delta \theta = \pi/96$. The result of the calculation is shown in Fig. 14.

The force distribution was calculated according to equation (2) and is shown in Fig. 15.

3.4. Measured forces and force distribution

The forces were recorded on both a paper and a magnetic tape. A sample of a force record is shown in Fig. 16.

The measured force power spectrum is shown in Fig 14 together with the calculated spectrum

The measured force distribution is shown in Fig 15
The measured force as well as the calculated force is the zero-upcrossing force as defined in Fig 7 d

4 COMMENTS

There is apparently a good agreement between the measured force distribution and the calculated force distribution as shown in Fig 15 however, the calculated force spectrum and the calculated force distribution is based on assumptions on the spectrum directionality function. The form of the transfer-function is such that a $\cos^2 \theta$ - directionality law will give lower calculated forces than a $\cos^4 \theta$ - law

It is therefore deemed necessary that the directional wave spectrum should be measured

5 CONCLUSIONS

The work described in this paper gives an indication that the concept of equation (1) is a useful tool for engineering purposes when dealing with forces on long floating pontoons like floating bridges, floating breakwaters etc

LITERATURE

1. TRITTEBERG, A The effect of wave crests on wave forces Proc of Eleventh Coastal Engineering Conference, London, England 1968
2. LONGUET-HIGGINS, M On the statistical distribution of the heights of sea waves Journal of Marine Research. Vol 11, 1952, no 3, pp, 246-266
- 3 KORVIN KROUKOVSKY, B V. Theory of seakeeping SHANE, New York, 1961

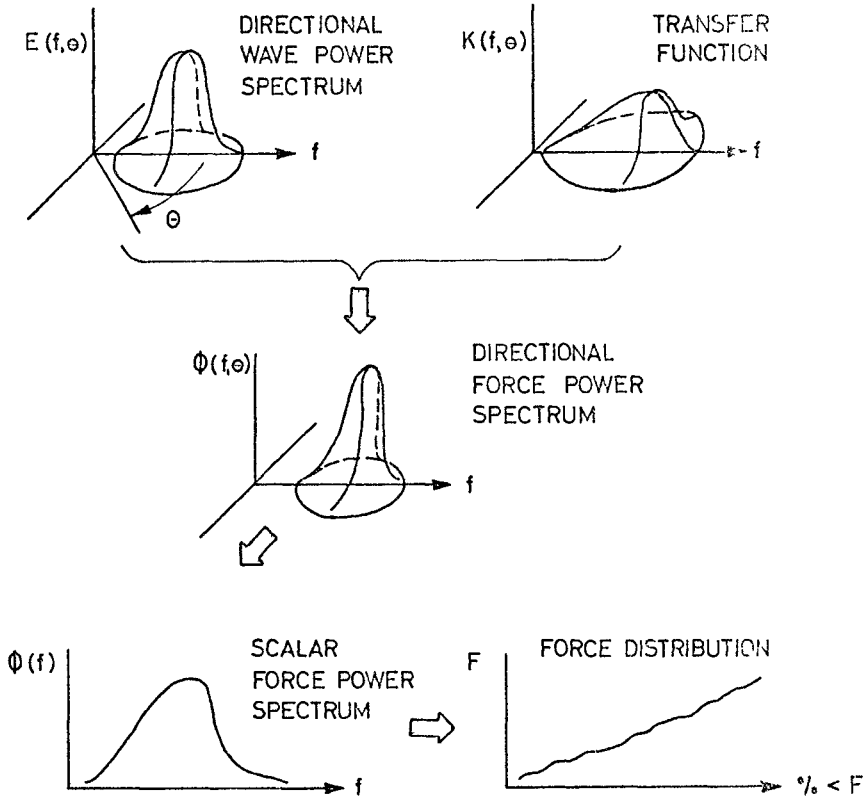


FIG 1

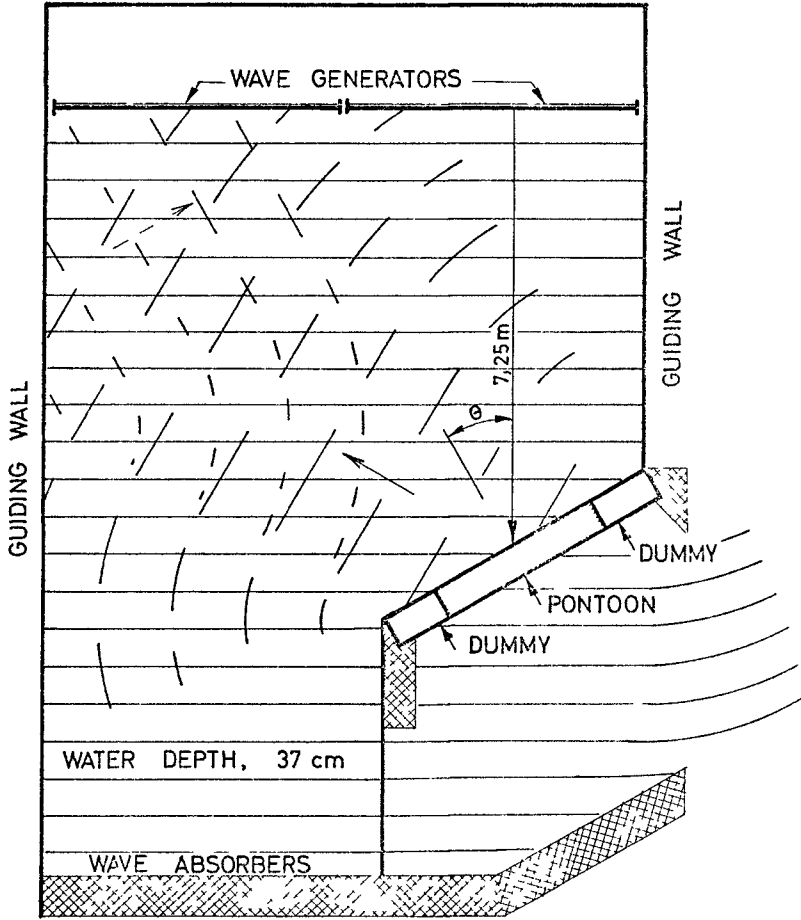
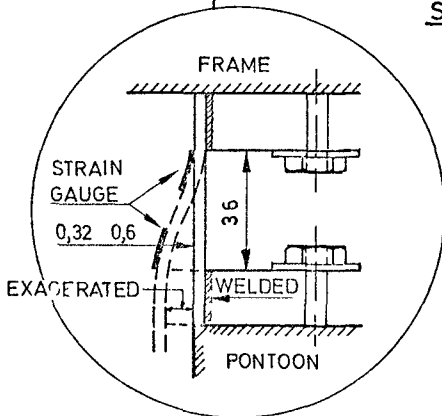
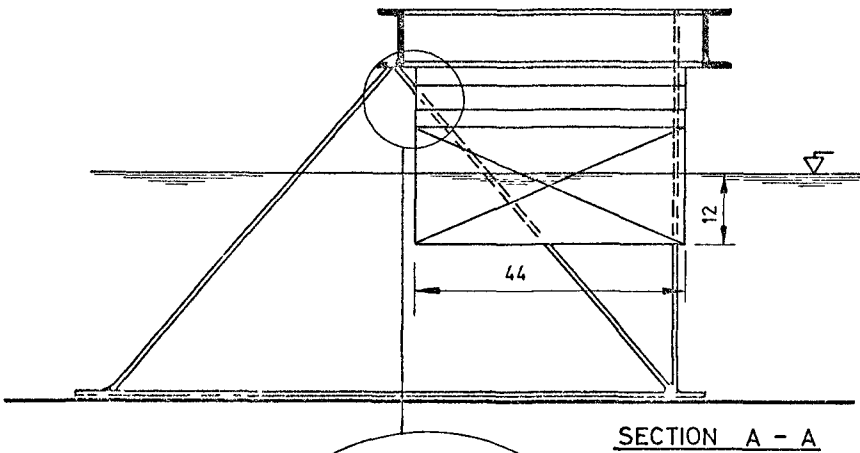
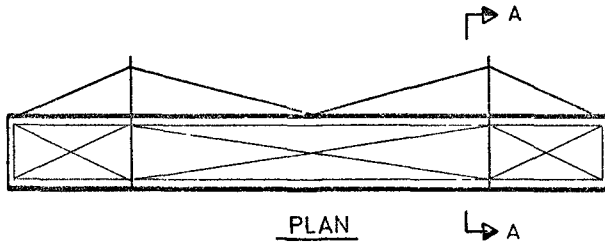
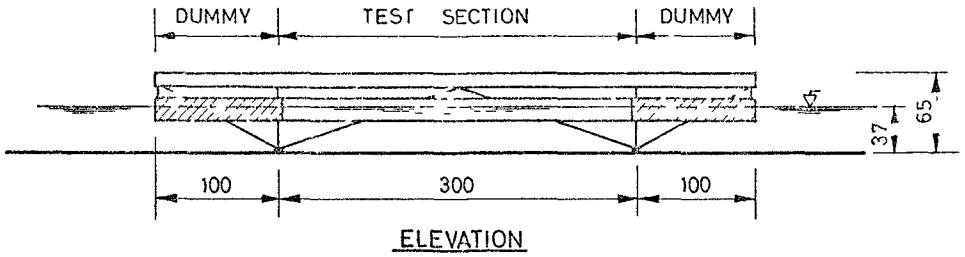


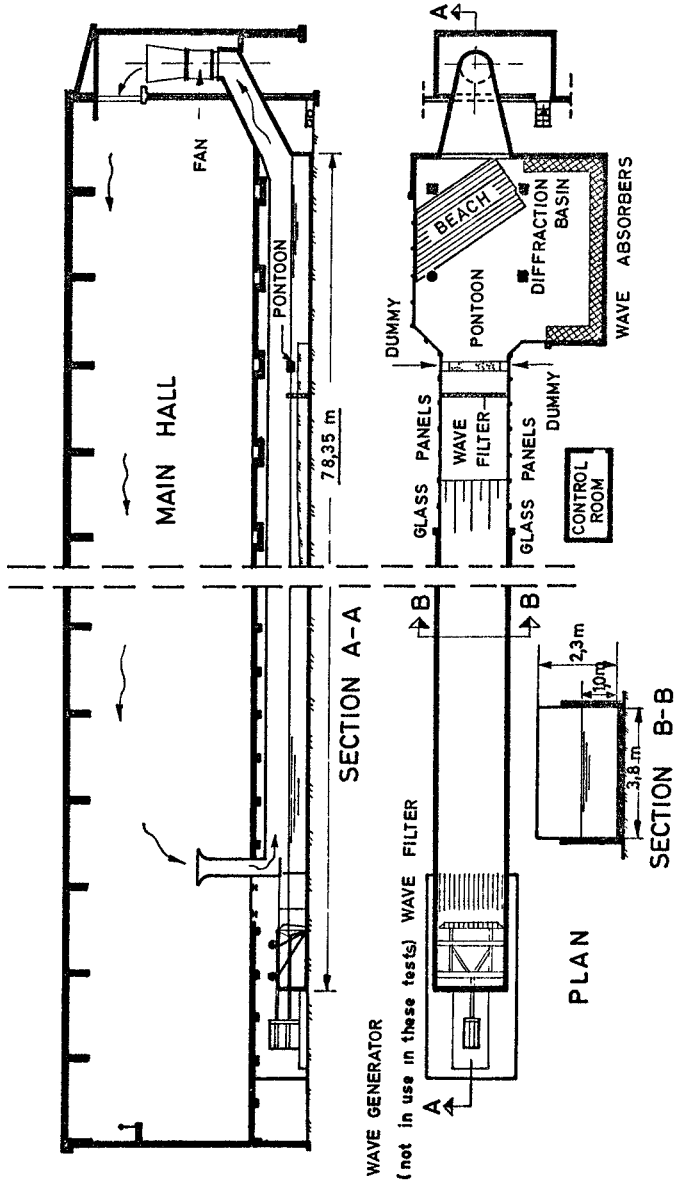
FIG 2 TEST ARRANGEMENT



DIMENSIONS IN CM

FIG 3

FIG. 4 WAVE CHANNEL



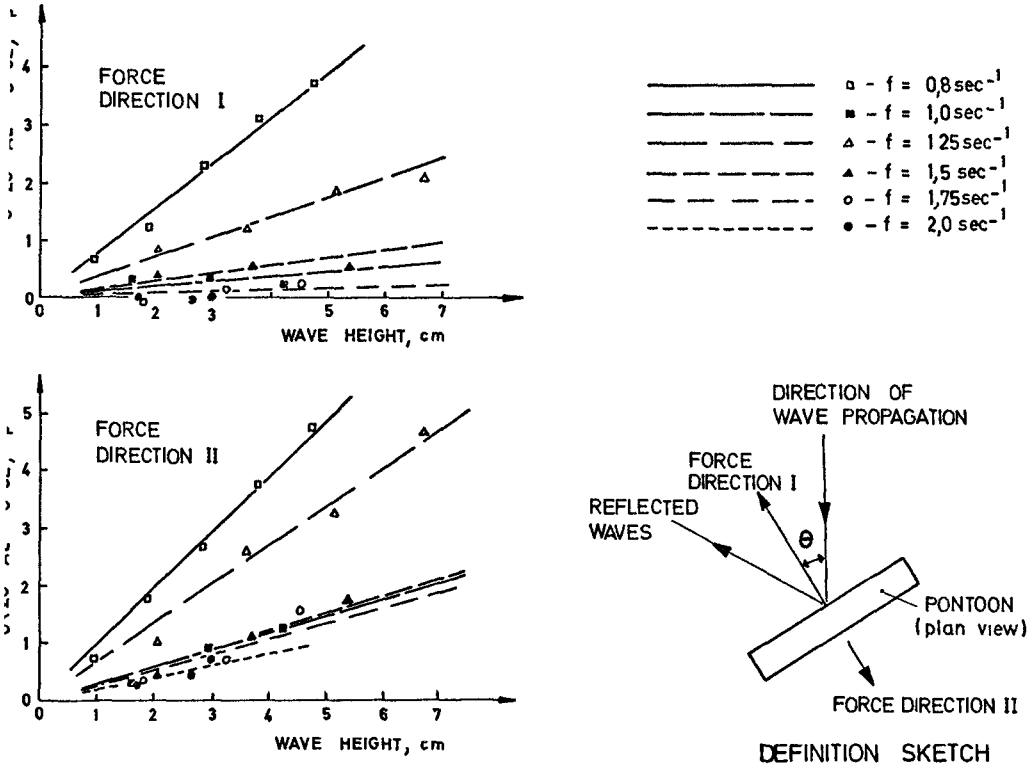


FIG 5 FORCE VS WAVEHEIGHT FOR $\theta = 30^\circ$

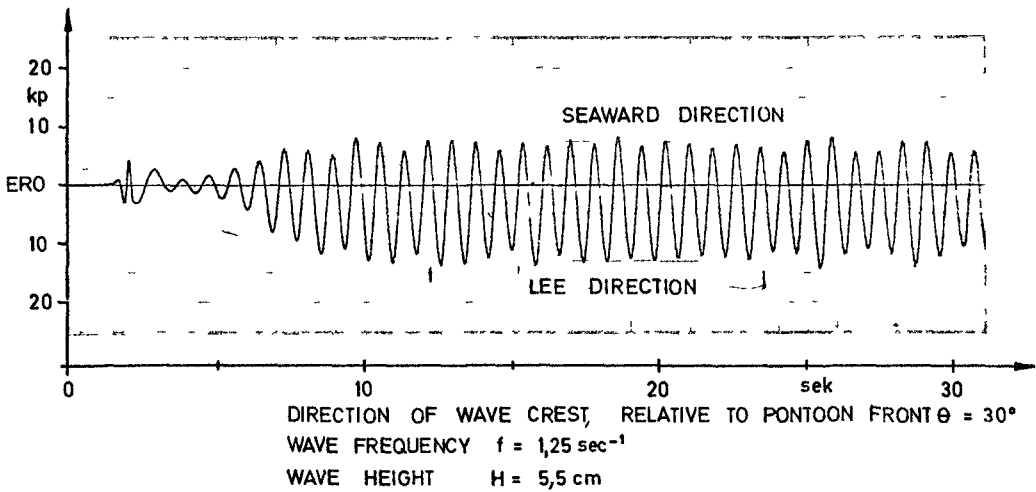


FIG 6 SAMPLE OF FORCE RECORD (regular waves)

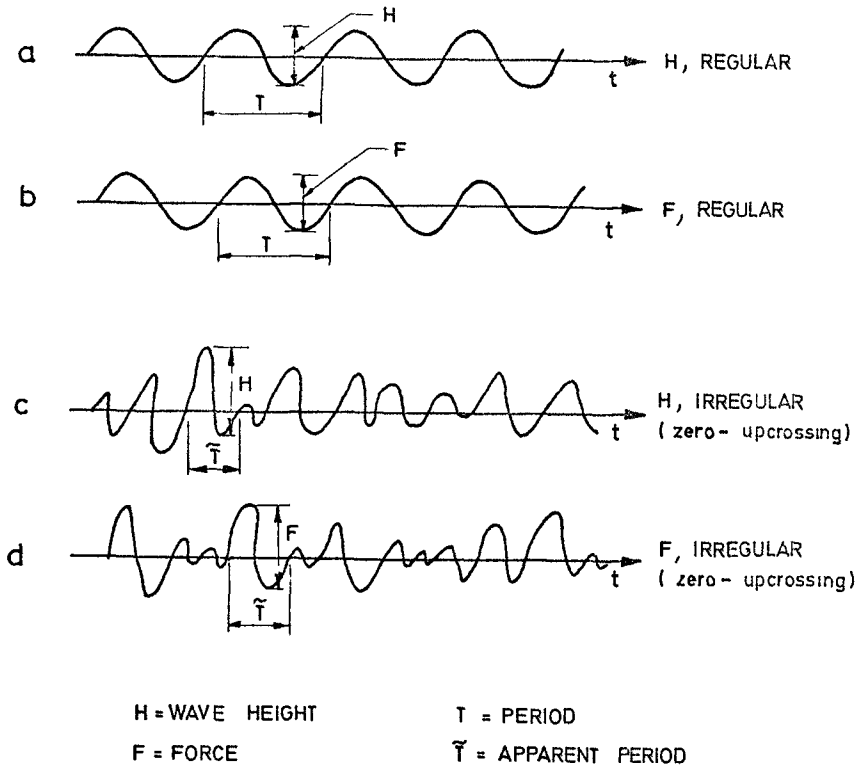


FIG 7 DEFINITION SKETCHES

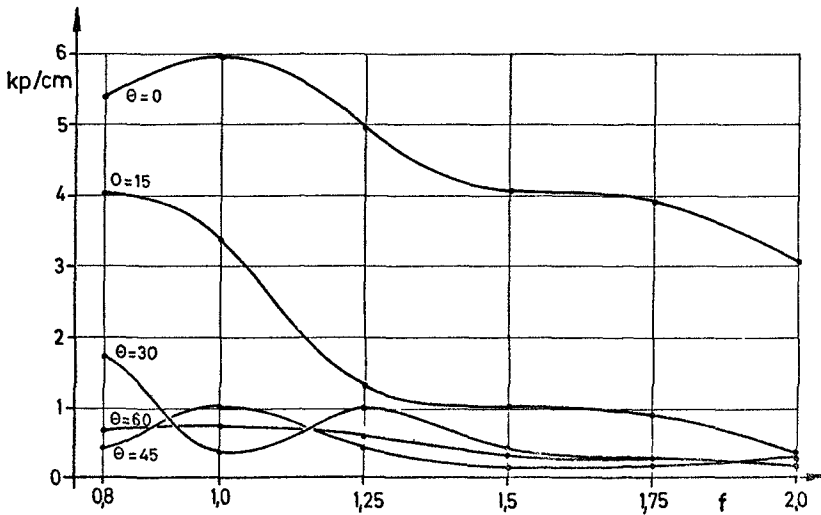


FIG 8 THE TRANSFER FUNCTION $K(\theta, f)$

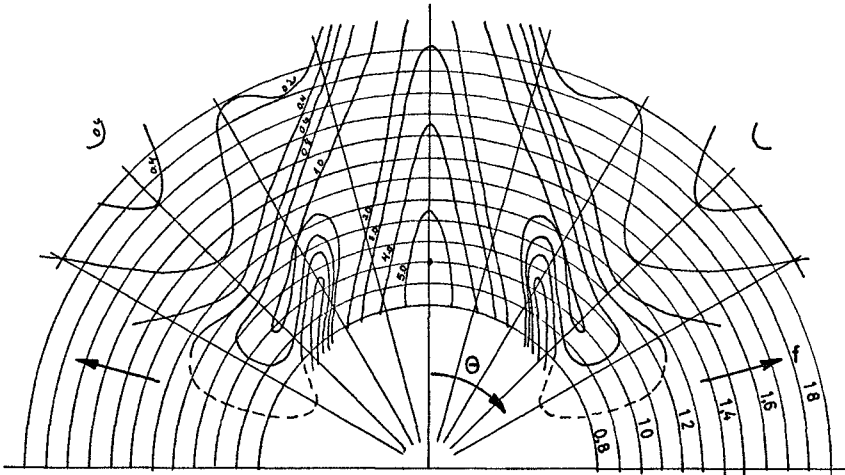


FIG 9 THE TRANSFER FUNCTION $K(\theta, f)$, kg/cm, AS A CONTOUR MAP

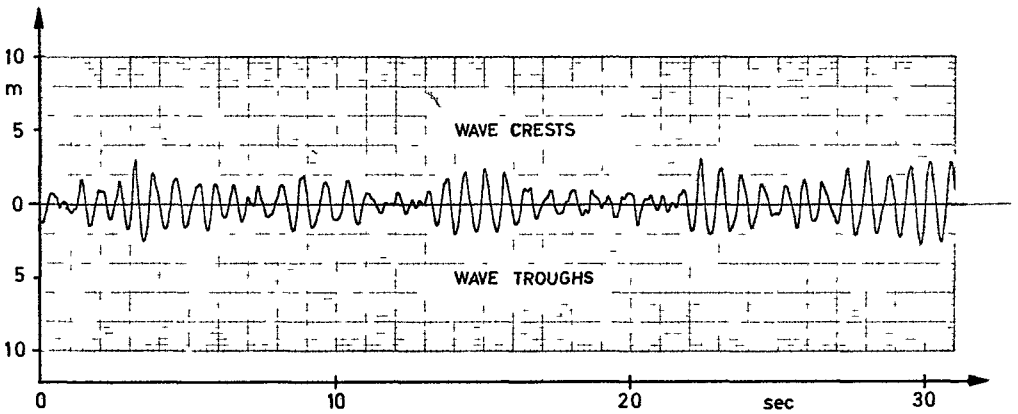


FIG 10 SAMPLE OF IRREGULAR WAVES

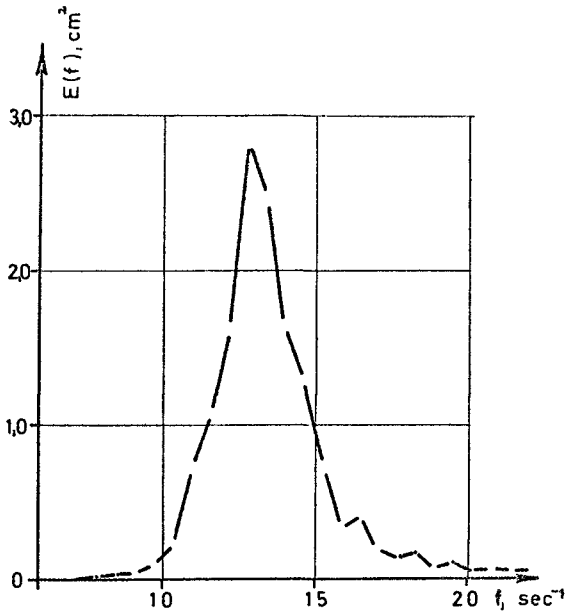


FIG 11 WAVE POWER SPECTRUM

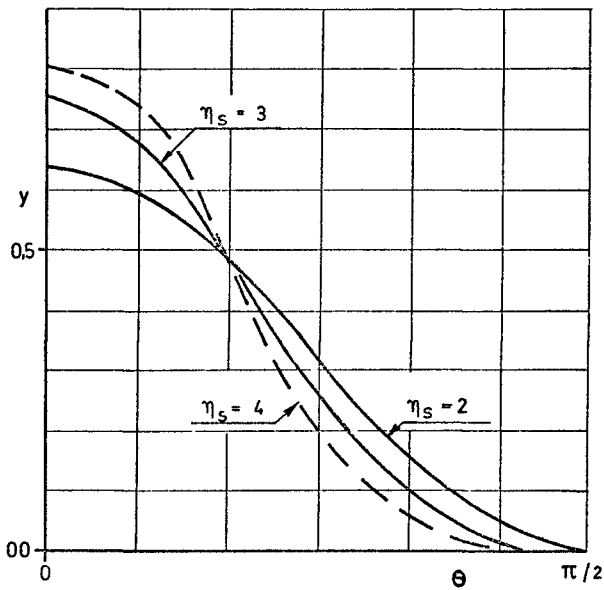


FIG 12 SPECTRUM DIRECTIONALITY FUNCTION

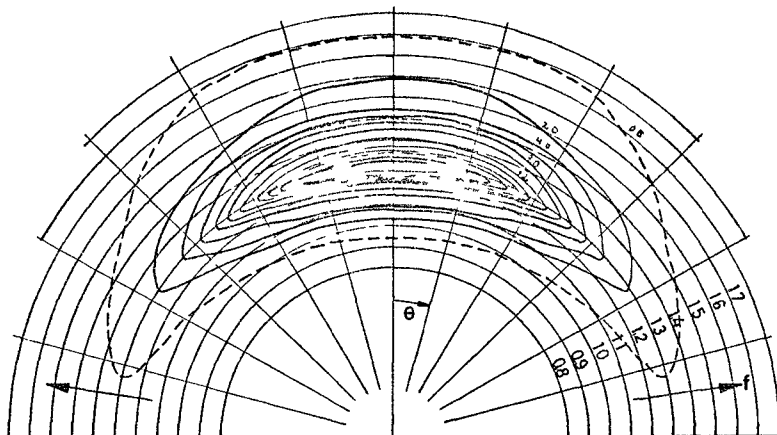


FIG 13 ESTIMATED DIRECTIONAL WAVE POWER SPECTRUM (COS⁴θ-LAW)

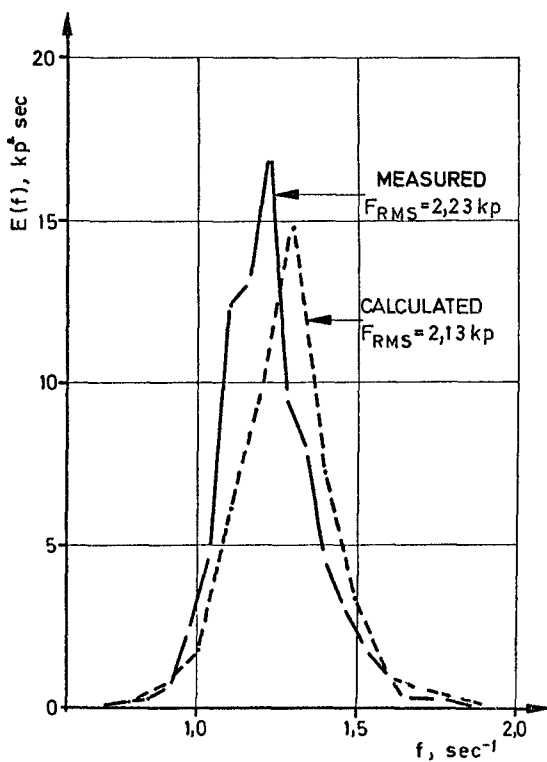


FIG 14 FORCE POWER SPECTRA

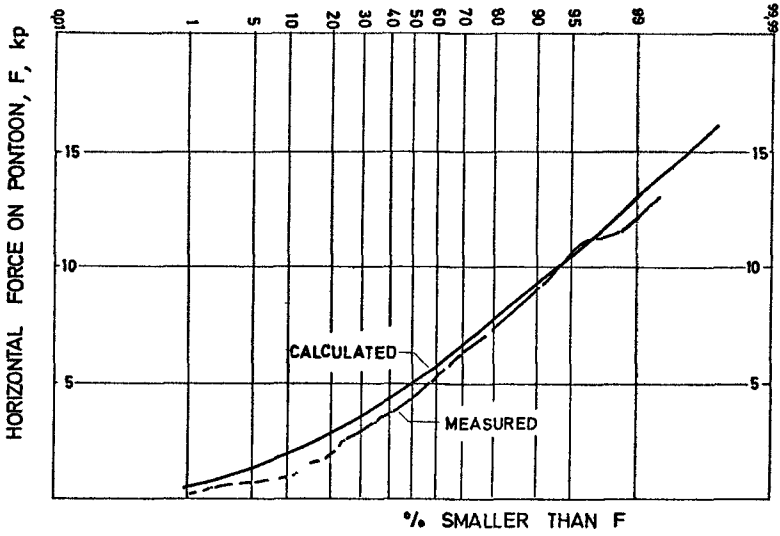


FIG 15 WAVE FORCE PROBABILITY DISTRIBUTIONS

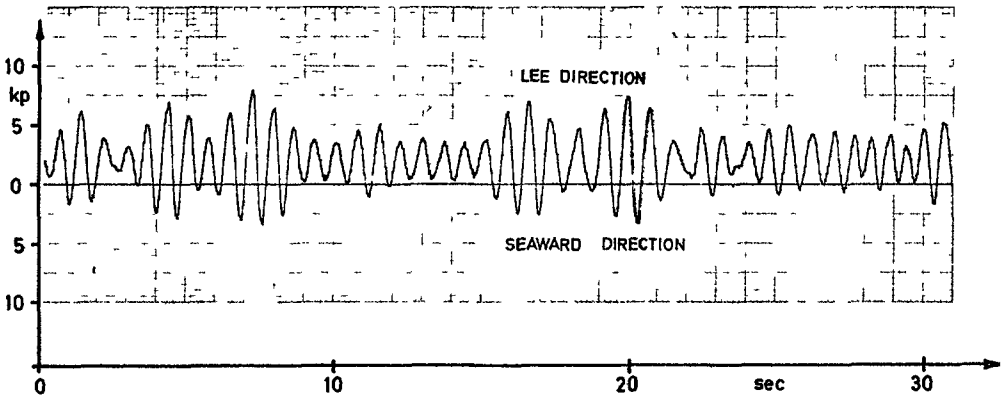


FIG 16 SAMPLE OF FORCE REGISTRATION IN IRREGULAR WAVES

CHAPTER 102

RESONANCE OF MOORED OBJECTS IN WAVE TRAINS

by

A.J. Hermans^x

G.F.M. Remery^{xx}

Abstract

In this paper the resonance of a moored object in wave trains is discussed and demonstrated with the help of some results obtained from model tests with a right angled barge. The measured results correspond well with a simple theory which calculates the slowly varying drifting force of regular wave trains.

^x Delft Technical University Working at the Courant Institute of Mathematical Sciences Adviser of the N S.M.B

^{xx} Head of the Wave and Current Laboratory of the N S.M.B.

1. Introduction

Due to the enormous increase of tanker size during the last years, a lot of harbours could not be adapted quick enough to receive these big ships.

That was, besides other reasons, why it became necessary to load and discharge large tankers in open sea near the coast. This caused a lot of problems, because now, the loading or unloading ship was fully exposed to wind, waves and current. In the course of time many different mooring systems have been developed and tested, such as.

- single buoy mooring
- spread mooring
- turret mooring
- ships moored to piers both rotating and fixed

Of these systems the single buoy mooring is probably the most used.

With this system the ship is moored by means of a bow hawser to a floating buoy.

The buoy itself is anchored to the sea bottom by means of one or more anchor legs.

At the Netherlands Ship Model Basin, extensive studies and model test programs have been executed concerning mooring of ships at sea.

A range of systems have been investigated and tested both as feasibility and as design studies.

Normally model tests with moored vessels are conducted in irregular waves.

From the results of this type of tests it was found that high peak forces can occur also in light weather conditions.

It appeared that these high forces often occurred after a group of higher waves had passed the ship.

These waves gave the moored vessel a horizontal excursion which induced a long periodical oscillating motion. The period of this oscillating excursion equalled the natural period of the horizontal motion of the moored vessel in still water.

Superimposed on the long periodical excursion, the moored object normally performed a high frequency oscillating sway, surge and yaw motion.

The periods of these motions corresponded to the period of the waves.

Especially when the relationship between the elongation and the tension of a mooring line is progressively non-linear, the resultant horizontal motion could induce rather high peak forces in the mooring lines.

A lot of literature is available concerning the vessel motions due to the higher frequency oscillating wave motion

However, only little information is available about the long periodical phenomena, which are important in studying mooring problems.

Therefore this paper is concerned with that problem

2. The wave drifting force

Considering the moored vessel as a mass spring system with a natural period T_n , it is known that big excursions will be induced by oscillating forces with a period near that natural period.

For the large ships under consideration the natural period of the horizontal motion will be 50 to 200 seconds or more

This indicates that the high frequency exciting forces due to the wave cannot induce important oscillating motions

So there has to be another source of forces

From the theory of Maruo [1] and the experiments of Ogawa [2] the phenomenon is known of the steady drifting force on bodies in regular waves

This steady drifting force per unit length equals:

$$\frac{1}{2} \rho g a^2$$

in which:

ρ = specific mass density of water

g = acceleration due to gravity

a = amplitude of the wave reflected and scattered by the body

For the case that the body is restrained, no waves can be generated by the motions of the body, which means that there is only wave reflection

When the direction of the reflected waves is just opposite to the direction of the incident waves the amplitude of the reflected wave can be written, according to Haskind [3], for deep water as:

$$a = \zeta_a R$$

in which:

ζ_a = amplitude of incident wave

R = reflection coefficient depending on $k T$ (see Figure 5)

k = wave number = $\frac{2\pi}{\lambda}$

λ = wave length

T = draft of body

This expression is exact for deep water and a vertical barrier of infinite length extending a distance T (= draft) below the still water surface

From this it will be clear that when the wave height is not constant but varies slowly with a certain period, also the drifting force will vary with that period.

In other words, when in an irregular sea wave groups are present which encounter a moored body with a frequency in the neighbourhood of the natural period of the mooring system, resonance phenomena may induce large slowly oscillating horizontal motions

In order to check this conception some model tests have been carried out with a simplified single point mooring system

3 Description of the tests

A vessel was moored by means of a single bow hawser to a fixed point

Generally the external conditions may be current, wind and waves, while the ship may have propulsion and steering capacity. However, from the point of simplicity only waves have been taken into consideration

The model represented a right angled barge of 107,000 metric tons displacement to a scale 1/80 (see Figure 1), in which also the main particulars are given for the full size barge

The bow hawser consisted of a linear spring with spring constant C . To avoid that the bow hawser became slack, a counter mass M was used as can be seen in Figure 1

The tests were executed in the Wave and Current Laboratory of the N.S.M.B. which has a length of 60 m and a breadth of 40 m

The water depth was 0.915 m, corresponding to 73.20 meters for the full scale

The barge was positioned with its centre line parallel to the direction of propagation of the waves

In Figure 2 an example is given of the wave trains generated. The period of the wave groups was kept constant during all tests and amounted to about 100 sec

By changing the spring constant of the bow hawser, the natural period of the surge motion of the moored barge could be varied

Tests have been executed with 5 different springs, inducing natural surge periods of 63, 88, 103, 113 and 134 seconds, in a number of wave trains different with regard to the mean period and the significant wave height

The wave train depicted in Figure 2 has a mean period of about 9 sec. and a significant wave height (double amplitude) of about 5 m.

The wave spectrum and the distribution of the wave elevation is given in Figure 4.

During the tests the force in the bow hawser was measured and recorded on magnetic tape and paper chart,

In Figure 2 an example is given of the measured force in the bow hawser for two different springs

From this it will be clear that the forces are much higher for the spring which gives the system a natural period T_n which almost equals the period of the wave groups

It is also easy to distinguish the slowly varying force component on which a high frequency component has been superimposed

The amplitude of the low frequency force has been plotted for each wave train as a function of the ratio

$$\Lambda = \frac{\text{natural period of vessel's surge motion}}{\text{period of wave groups} = 100 \text{ sec}}$$

An example is given in Figure 3 for two wave trains with a mean period of 9 seconds and a significant height of 5 and 8 meters. The same type of resonance curves were found for wave trains with mean periods of 7, 11, 13 and 15 seconds

4. Theoretical considerations

The generated wave trains can be considered to be built-up by two regular waves with different amplitudes and with only a small difference $\Delta\omega$ in frequency

Then the wave elevation ζ can be expressed as:

$$\zeta = b_1 \cos (kx - \omega t) + b_2 \cos (kx + \Delta kx - (\omega + \Delta\omega) t + \Delta\epsilon)$$

This can be written in a slowly varying form.

$$\zeta = a \cos (kx - \omega t)$$

with $a = b_1 + b_2 e^{i (\Delta kx - \Delta\omega t + \Delta\epsilon)}$

In which a is the envelope of the wave elevation or the slowly varying amplitude

It was already shown that the drifting force is a function of the square of the wave amplitude a

$$a^2 = b_1^2 + b_2^2 + 2 b_1 b_2 \cos (\Delta kx - \Delta\omega t + \Delta\epsilon)$$

Also notice that taking the square of the wave motion ζ , one finds

$$\zeta^2 = \frac{1}{2} (b_1^2 + b_2^2) + b_1 b_2 \cos (\Delta kx - \Delta\omega t + \Delta\epsilon) + \text{high frequency components}$$

Assuming that the heave and pitch motion of the barge can be neglected and that the waves will be reflected by the flat bow in a direction parallel to the direction of the incident waves, the drifting force F_d on the barge, according to Haskind [3], can be expressed as

$$F_d = \frac{1}{2} \rho g a^2 R^2 B$$

B = breadth of barge

in which:

$$a^2 = b_1^2 + b_2^2 + 2 b_1 b_2 \cos (\Delta kx - \Delta \omega t + \Delta \epsilon)$$

From this expression it follows that there is a slowly oscillating drift force component with frequency $\Delta \omega$ and amplitude F_{da} .

$$F_{da} = \rho g R^2 b_1 b_2 B$$

The equation of motion of the mass spring system representing the moored ship can be written as

$$M_x \ddot{x} + N_x \dot{x} + Cx = F_d$$

in which

$$\begin{aligned} M_x (\Delta \omega) &= \text{total mass of system} \\ &= M_{\text{ship}} + M_{\text{added}} + M_{\text{weight}} \end{aligned}$$

$$\begin{aligned} N_x (\Delta \omega) &= \text{damping coefficient} \\ C &= \text{spring constant} \\ F_d &= \text{drift force} \end{aligned}$$

M_x and N_x are functions of the frequency $\Delta \omega$ of the surge motion and have been determined from extinction tests

Because the force in the bow hawser F_b equals C x the amplitude F_{ba} of the bow hawser force due to the slowly oscillating drifting force component $F_{da} \cos (\Delta kx - \Delta \omega t + \Delta \epsilon)$ can be calculated from the solution of the equation of motion

$$F_{ba} = \frac{F_{da} C}{\sqrt{(C - M_x \Delta \omega^2)^2 + B_x^2 \Delta \omega^2}}$$

In Figure 3 the results of the calculations for two wave trains, with mean periods of about 9 seconds, have been plotted as a function of the non-dimensional frequency Λ .

$$\Lambda = \frac{2 \pi \sqrt{\frac{M_x}{C_x}}}{T_g}$$

$$T_g = \text{period of wave groups} = 100 \text{ sec}$$

The results of the calculations appear to be in a good agreement with the measured ones

For the wave trains with periods of 11 and 13 seconds the difference between measurement and calculation appeared to be larger

5 Discussion of the results

From the results of the tests it is clear that wave groups can induce resonance phenomena at moored ships

It has been illustrated by some simple calculations that the slowly varying drifting force can be determined from the square of the wave motion

Also for irregular waves the square of the wave motion gives information about the square of the irregular slowly varying wave envelop, which is a measure for the drifting force. Therefore, to obtain information about the occurrence of slowly varying drifting forces, one has to calculate the spectral density of the record representing the square of the wave motion.

From the distribution of this spectral density in the low frequency range it can be seen whether there will be important drifting force components near the natural period of the moored vessel.

This means that describing the sea state only by the spectral density distribution of the wave motion is not sufficient to predict what may happen with a moored vessel at a particular location.

What one really needs is the wave motion record itself or the spectral density distribution of the square of the wave motion.

What has been mentioned up to now are the results of a not yet finished study.

There are still a lot of items which have to be taken into consideration, like:

- vessel's pitch and heave motions
- influence of bow form
- influence of restricted water depth

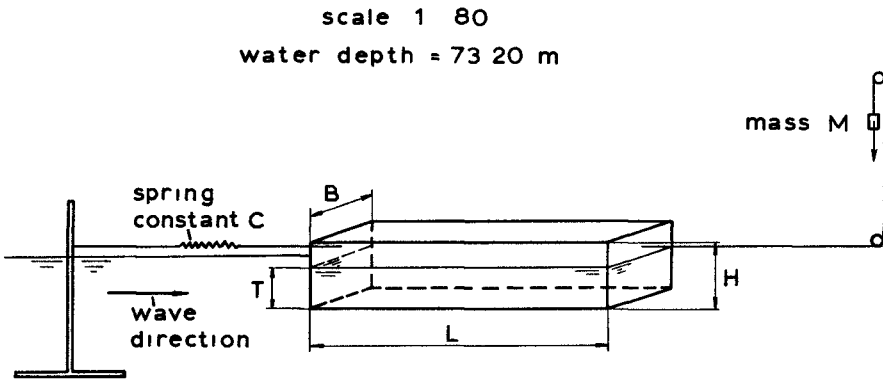
However, at this stage of the study two important conclusions have been obtained:

- Wave groups can induce resonance phenomena on moored ships
- The normal wave height spectrum does not provide sufficient information to predict the behaviour of the moored vessel.

Wageningen, October 1970

Literature

- [1] Maruo, H , "The drift of a body floating on waves"
Journal of Ship Research, Vol 4
Number 3, December 1960
- [2] Ogawa, A , "The drifting force and moment on a ship
in oblique regular waves"
Publication no 31 of the Delft Shipbuilding
Laboratory, Holland
- [3] Haskind, M D , "The pressure of waves on a barrier"
Inzhen S b. 4, no 2, 147-160 (1948)
see also "Encyclopedia of Physics"
Springer Verlag, Berlin 1960
"Surface waves" of Wehausen and Laitone
sect 17

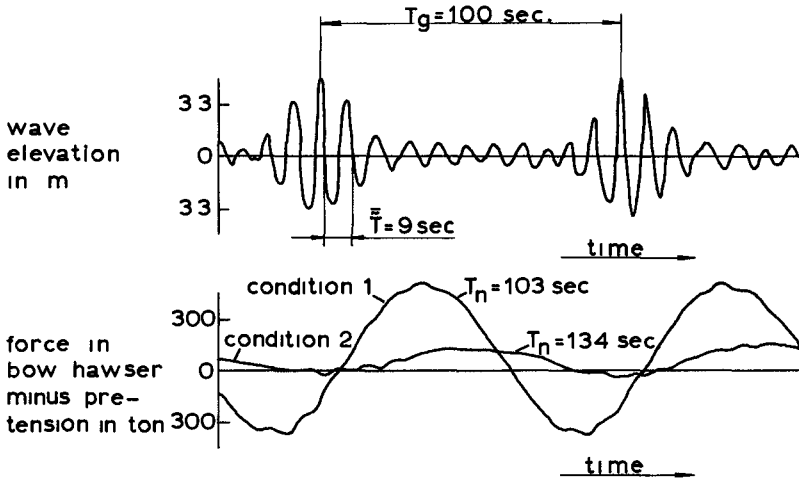
Test set-up and main particulars of barge

length	$L = 182\ 40$	m
breadth	$B = 48\ 96$	m
draft	$T = 12\ 00$	m
depth	$H = 19\ 20$	m
displacement	$\nabla = 107,163$	m^3
counter mass	$M = 819$	ton

natural period of heave motion	\approx	11 00 sec
natural period of pitch motion	\approx	13 00 sec
natural period of roll motion	\approx	11 35 sec

FIG 1

$\bar{H}_{1/3}$ = significant wave height = 5 m
 \bar{T} = mean wave period = 9 sec



T_n = natural period of vessel's surge motion

FIG 2

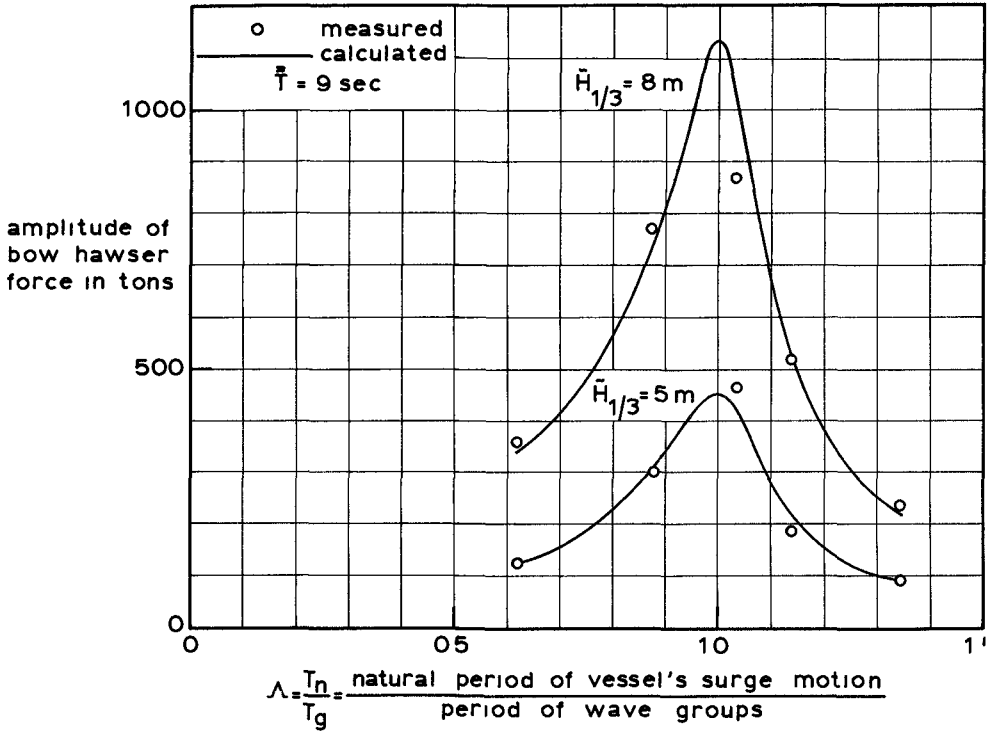


FIG 3

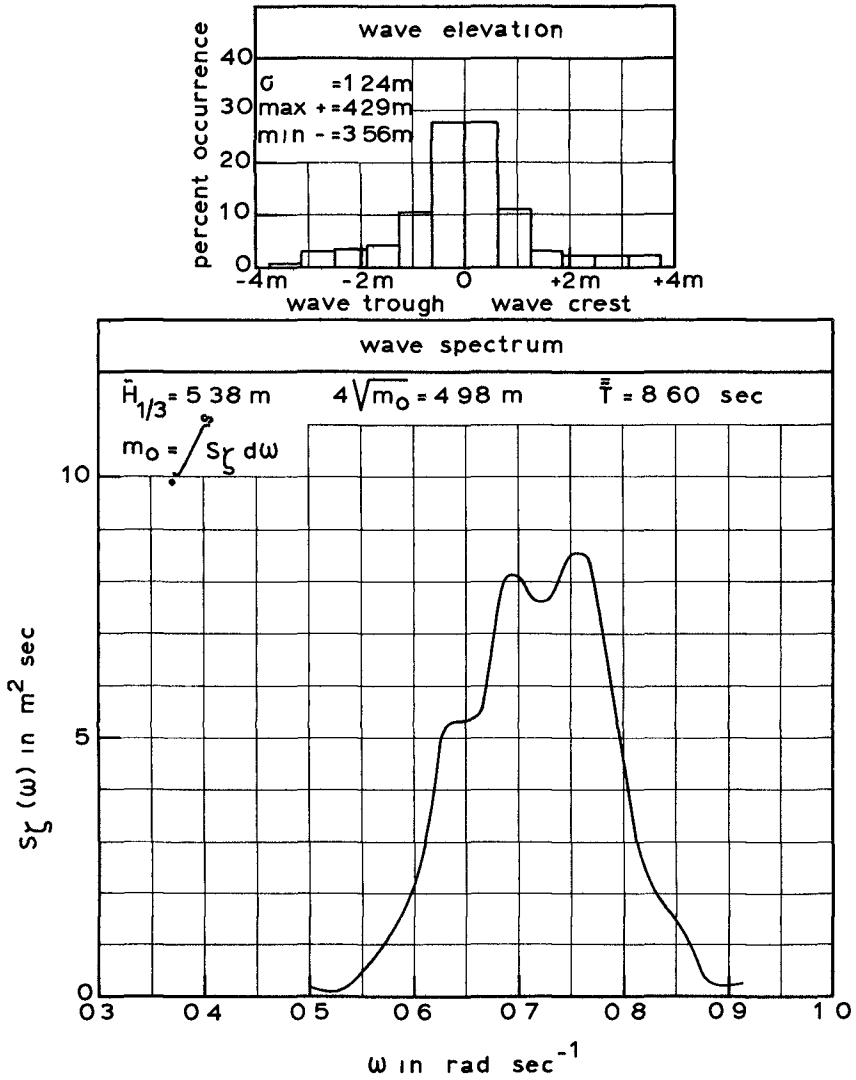


FIG 4

Reflection coefficient R as a function of kT

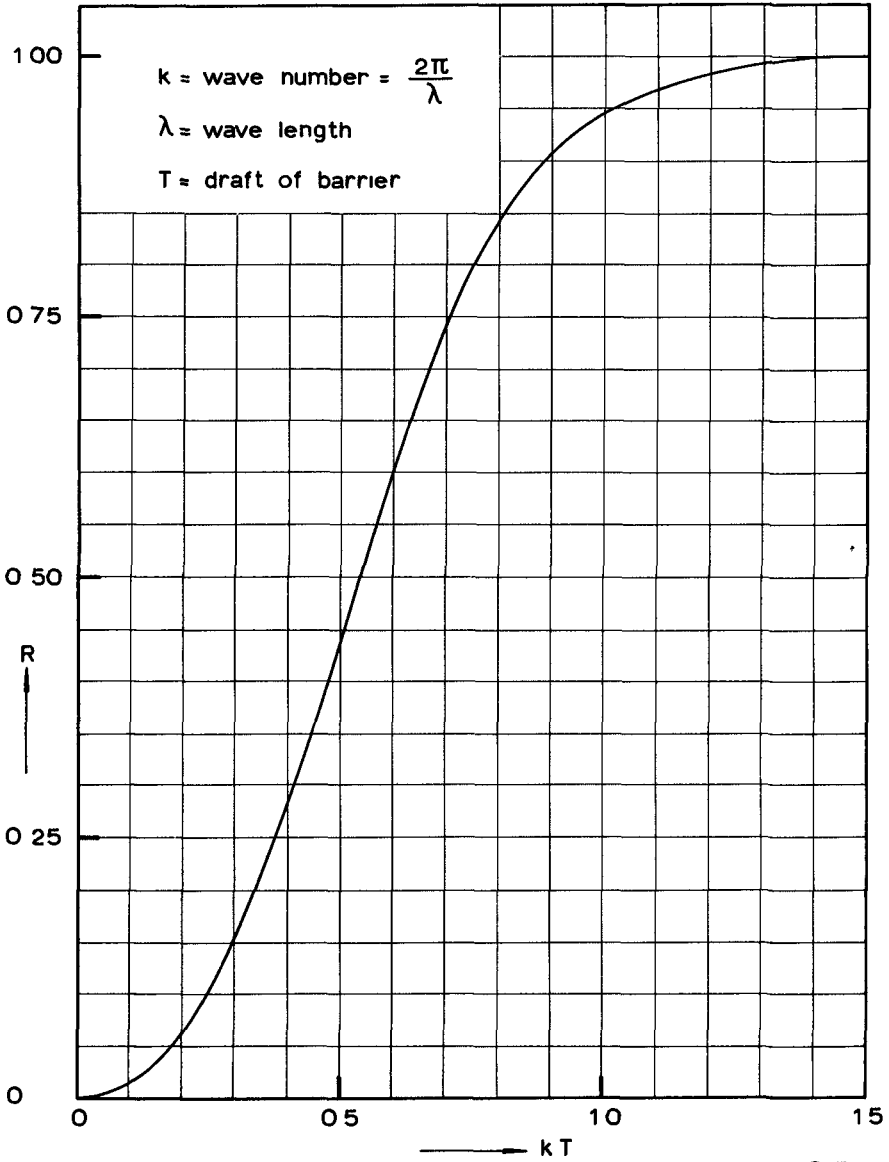


FIG 5

CHAPTER 103

ON THE HYDRODYNAMIC FORCES OF TWIN-HULL VESSELS

Shen Wang

Tetra Tech Inc
Pasadena, California

ABSTRACT

The added mass and damping coefficients for semi- and fully-submerged twin cylinders in vertical motion are determined as functions of the oscillation frequency, the cylinder spacing ratio, and the cylinder submergence ratio. It has been found that resonance may occur in particular combinations of cylinder spacing and oscillation frequency at which the hydrodynamic inertial and damping characteristics deviate from the trend curves for the case of a single cylinder. Justification of using the two-dimensional results to calculate motions of three-dimensional twin-hull vessels is discussed. It is suggested that, by means of strip theory approach, these results can be used to estimate the hydrodynamic forces for catamaran type vessels in pitch and heave motions.

1 INTRODUCTION

This paper presents a method to estimate the vertical hydrodynamic forces for twin-hull vessels, including the catamaran type surface ship which has two hulls floating on the free surface and a certain type of floating platforms which have two parallel and closely spaced hulls submerged under the free surface.

Analytical calculation of the mono-hull ship motions generally follows the method of strip theory approach. The validity of using the strip theory approach to calculate motions of twin-hull vessels has not been completely established. Objections certainly may raise, if one considers the overall width of the vessel as the beam, which is relatively too large for the strip theory to apply. However, one may feel different if he considers it as though there were only one hull plus a wall effect.

It is not the purpose of this paper to validate the strip theory for twin-hull vessels, but through the availability of the two-dimensional results for the twin-hull model, obtained from this and the previous analyses, investigations on motions of catamaran type vessels by means of strip theory approach may proceed

According to the strip theory, the hydrodynamic quantities, such as the added mass and damping coefficients, are estimated by making use of two-dimensional data of long cylinders. For the present purpose, we consider a body having two identical, rigidly connected, circular cylinders. As to the added mass and damping of the catamaran type surface vessels, the two cylinders are considered semi-submerged initially in the free surface. Theoretical and experimental investigation of this problem has been given by Wang and Wahab [1]. To complete the analysis, the present work considers the two cylinders being fully submerged. The problem is formulated as a linearized boundary value problem in the theory of small amplitude waves. Within this framework, a potential function is constructed by superimposing a series of various order singularities, and the solution is obtained through determining the singularity strength by means of satisfying the boundary conditions.

Numerical results of the added mass and damping coefficients are presented. For the convenience of discussion, the results of the semi-submerged case are also summarized and reviewed. Finally, applications of these results to calculating forces on catamaran type vessels are discussed.

2 SUBMERGED TWIN CYLINDERS

Formulation of the Problem

We consider two identical circular cylinders, each of radius a , rigidly connected with a spacing distance of $2b$ between their center-line axes. They are fully submerged and are forced to make small vertical harmonic oscillations about a mean level $f (> a)$ under the free surface. The problem reduces to the special case of semi-submerged cylinders oscillation if $f = 0$. The two cylinders are assumed to be infinitely long, and the resulting motion is two-dimensional.

Taking the undisturbed free surface as the x -axis, a Cartesian coordinate system is defined as shown in Figure 1. The center-line axes of the two cylinders are then (b, f) and $(-b, f)$. Two sets of polar coordinates are employed with their origins located at the two cylinder centers, they are related to the Cartesian coordinates as follows

$$\begin{aligned}
 x &= b + r \sin \theta = -b + r' \sin \theta' \\
 y &= f + r \cos \theta = f + r' \cos \theta' \\
 r &= [(x-b)^2 + (y-f)^2]^{1/2} \\
 r' &= [(x+b)^2 + (y-f)^2]^{1/2}
 \end{aligned} \tag{1}$$

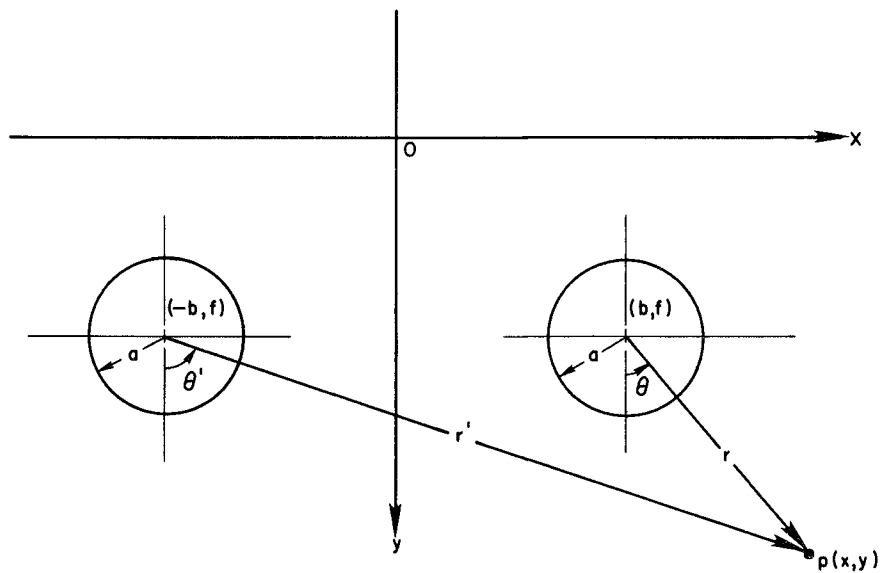


Figure 1 Coordinate systems

The fluid is assumed inviscid and incompressible, then the problem reduces to seeking a potential function for the described motion. Let the motion be simple harmonic of period $2\pi/\omega$. When the motion amplitude η_0 is sufficiently small, the velocity potential $\Phi(x, y, t)$ may be described by a series of singular function $\varphi_n(x, y)$, linearly superimposed in the following form

$$\Phi(x, y, t) = a\omega\eta_0 \operatorname{Re} \left[\sum_{n=0}^{\infty} A_n \varphi_n(x, y) e^{-i\omega t} \right] \quad (2)$$

The function $\varphi_n(x, y)$ satisfies

$$(A) \nabla^2 \varphi_n = 0 \text{ in the fluid} \quad (3)$$

$$(B) K\varphi_n + \frac{\partial \varphi_n}{\partial y} = 0 \text{ on the free surface } (K = \frac{\omega^2}{g}) \quad (4)$$

$$(C) \frac{\partial \varphi_n}{\partial x} = 0 \text{ at } x = 0 \quad (5)$$

$$(D) \operatorname{Lim} \left(\frac{\partial \varphi_n}{\partial x} \mp 1K\varphi_n \right) = 0 \text{ as } x \rightarrow \pm\infty \quad (6)$$

$$(E) \varphi_n = 0 \text{ as } y \rightarrow \infty \quad (7)$$

The coefficient A_n is a complex-valued number corresponding to the strength of the n^{th} order singularity. It is a function of the cylinder spacing b , submergence f and frequency ω . These coefficients are to be determined by satisfying the kinematic boundary conditions on the cylinder surface, which will be described later.

Method of Solution

The singular solution of the two dimensional Laplace equation (3) satisfying the boundary conditions (4), (6) and (7) may be written as a source function or its derivatives of any assigned order. For a singularity located at $(0, f)$ the solutions have been given by Thorne [2] as follows

$$G_0(x, y) = \log \frac{\rho}{\rho_1} + \int_0^{\infty} \frac{e^{-k(y+f)}}{K-k} \cos kx \, dk - i 2\pi e^{-K(y+f)} \cos Kx \quad (8)$$

$$G_{nc}(x, y) = \frac{\cos n\sigma}{\rho^n} + \frac{(-1)^{n-1}}{(n-1)!} \int_0^\infty \frac{K+k}{K-k} k^{n-1} e^{-k(y+f)} \cos kx \, dk$$

$$+ \frac{(-1)^n}{(n-1)!} 2\pi K^n e^{-K(y+f)} \cos Kx \tag{9}$$

$$G_{ns}(x, y) = \frac{\sin n\sigma}{\rho^n} + \frac{(-1)^n}{(n-1)!} \int_0^\infty \frac{K+k}{K-k} k^{n-1} e^{-k(y+f)} \sin kx \, dk$$

$$+ \frac{(-1)^{n-1}}{(n-1)!} 2\pi K^n e^{-K(y+f)} \sin Kx \tag{10}$$

Equations (8) and (9) are solutions for describing symmetrical motions, and Equation (10) for anti-symmetrical motion. In these equations, (ρ, σ) are the polar coordinates, measured from origin (o, f) and ρ_1 is the radial distance from the image of (o, f) , i.e., $(o, -f)$.

By expanding the integrals in Equations (9) and (10), one may show that any of the higher order potentials, G_{nc} and G_{ns} , can be constructed by the following functions

$$G_{1c}(x, y) = \frac{\cos \sigma}{\rho} + K \int_0^\infty \frac{e^{-k(y+f)}}{K-k} \cos kx \, dk$$

$$- 2\pi K e^{-K(y+f)} \cos Kx \tag{11}$$

$$G_{1s}(x, y) = \frac{\sin \sigma}{\rho} - K \int_0^\infty \frac{e^{-k(y+f)}}{K-k} \sin kx \, dk$$

$$+ 2\pi K e^{-K(y+f)} \sin Kx \tag{12}$$

$$G'_{nc}(x, y) = \frac{\cos n\sigma}{\rho^n} + \frac{K}{n-1} \frac{\cos (n-1)\sigma}{\rho^{n-1}} \tag{13}$$

} $n = 2, 3$

$$G'_{ns}(x, y) = \frac{\sin (n+1)\sigma}{\rho^{n+1}} + \frac{K}{n} \frac{\sin n\sigma}{\rho^n} \tag{14}$$

The functions G_{1c} and G_{1s} represent, respectively, the vertical and the horizontal dipoles, combining with appropriate wave function to satisfy the free surface condition (4) and the wave radiation condition (6). Each term in these equations satisfies the infinite depth condition (7). The functions G'_{nc} and G'_{ns} are wave-free potentials, they represent only local fluid motion which decays rapidly at a distance and yields no waves at infinity.

To derive the potential function $\varphi_n(x, y)$, one may construct it by using singular solutions corresponding to singularities located along the two cylinder axes, (b, f) and $(-b, f)$, so as to satisfy the symmetry condition, Equation (5) This may be obtained as follows

$$\varphi_o(x, y) = G_o(x-b, y) + G_o(x+b, y) \tag{15}$$

$$\varphi_{1c}(x, y) = G_{1c}(x-b, y) + G_{1c}(x+b, y) \tag{16}$$

$$\varphi_{1s}(x, y) = G_{1s}(x-b, y) - G_{1s}(x+b, y) \tag{17}$$

$$\varphi_{nc}(x, y) = G'_{nc}(x-b, y) + G'_{nc}(x+b, y) \tag{18}$$

$$\varphi_{ns}(x, y) = G'_{ns}(x-b, y) - G'_{ns}(x+b, y) \tag{19}$$

} n = 2, 3

Substituting Equations (8), (11), (12), (13) and (14) into (15) through (19) and invoking the following identities [3]

$$\frac{\cos n\theta}{r^n} = \frac{1}{(n-1)!} \int_0^\infty k^{n-1} e^{-k(y-f)} \cos(x-b) dk \tag{20}$$

$$\frac{\sin n\theta}{r^n} = \frac{1}{(n-1)!} \int_0^\infty k^{n-1} e^{-k(y-f)} \sin(x-b) dk \tag{21}$$

we obtain

$$\begin{aligned} \varphi_o(x, y) = & \log \frac{r}{r_1} \frac{r'}{r'_1} + 4 \int_0^\infty \frac{e^{-k(y+f)}}{K-k} \cos kb \cos kx dk \\ & - 1.4\pi e^{-K(y+f)} \cos Kb \cos Kx \end{aligned} \tag{22}$$

$$\begin{aligned} \varphi_{1c}(x, y) = & 4 \left\{ \int_0^\infty e^{-ky} \sinh kf \cos kb \cos kx dk \right. \\ & \left. + K \int_0^\infty \frac{e^{-k(y+f)}}{K-k} \cos kb \cos kx dk \right\} \\ & - 1.4\pi Ke^{-K(y+f)} \cos Kb \cos Kx \end{aligned} \tag{23}$$

$$\begin{aligned} \varphi_{1s}(x, y) = & -4 \left\{ \int_0^\infty e^{-ky} \cosh kf \sin kb \cos kx dk \right. \\ & \left. - K \int_0^\infty \frac{e^{-k(y+f)}}{K-k} \sin kb \cos kx dk \right\} \\ & - 1.4\pi Ke^{-K(y+f)} \sin Kb \sin Kx \end{aligned} \tag{24}$$

$$\varphi_{nc}(x, y) = \frac{4}{(n-1)!} \int_0^{\infty} (k+K)k^{n-2} e^{-ky} \frac{\cosh kf}{\sinh kf} \cos kb \cos kx \, dk, \quad n = \begin{array}{l} \text{even} \\ \text{odd} \end{array} \quad (25)$$

$$\varphi_{ns}(x, y) = -\frac{4}{(n-1)!} \int_0^{\infty} (k+K)k^{n-2} e^{-ky} \frac{\cosh kf}{\sinh kf} \sin kb \cos kx \, dk, \quad n = \begin{array}{l} \text{odd} \\ \text{even} \end{array} \quad (26)$$

If we put $A_n \varphi_n = A_{nc} \varphi_{nc} + A_{ns} \varphi_{ns}$, we may write Equation (2) in a different form as follows

$$\Phi(x, y, t) = a \omega \eta_0 \operatorname{Re} \left[A_0 \varphi_0 e^{-i\omega t} + \sum_{n=1}^{\infty} (A_{nc} \varphi_{nc} + A_{ns} \varphi_{ns}) e^{-i\omega t} \right] \quad (27)$$

To determine the expansion coefficients the velocity potential shall be forced to satisfy the normal velocity on the body surface

$$\frac{\partial \Phi}{\partial r} = \omega \eta_0 \cos \omega t \cos \theta \quad \text{on } r = a \quad (28a)$$

$$\frac{\partial \Phi}{\partial r'} = \omega \eta_0 \cos \omega t \cos \theta' \quad \text{on } r' = a \quad (28b)$$

assuming that the vertical velocity of the body is $\omega \eta_0 \cos \omega t$

Since the two cylinders are identical, the boundary condition (28b) is equivalent to (28a) and need not be considered. For the convenience of computation in this particular case, the potential functions (Equations (22) through (26)) are expanded into series about the cylinder axis (*b f*). The numerical computation then proceeds by formulating Equation (28a) into a set of simultaneous algebraic equations, and the expansion coefficients can be determined by a collocation technique

Added Mass and Damping Coefficients

The steady state vertical force on a unit length of the cylinders is

$$F_v = -2\rho a \int_0^{2\pi} \frac{\partial \Phi}{\partial t} \cos \theta \, d\theta \quad (29)$$

One may write F_v in terms of $\eta(t)$ ($= \eta_0 \sin \omega t$) as

$$F_v = -M_v \ddot{\eta}(t) - N_v \dot{\eta}(t) \quad (30)$$

then the added mass coefficient α and the nondimensional damping coefficient δ is defined as follows

$$\alpha \left(Ka, \frac{b}{a}, \frac{f}{a} \right) = \frac{M_v}{2\pi \rho a^2} \quad (31)$$

$$\delta \left(Ka, \frac{b}{a}, \frac{f}{a} \right) = \frac{N_v}{2\pi \rho \omega a^2} \quad (32)$$

These coefficients are directly related to the potential function ϕ , using the expression given in Equation (2), one obtains

$$\alpha = \frac{1}{\pi} \operatorname{Re} \left[\sum_{n=0}^{\infty} \int_0^{2\pi} A_n \left(Ka, \frac{b}{a}, \frac{f}{a} \right) \varphi_n \left(Ka, \frac{b}{a}, \frac{f}{a}, \theta \right) \cos \theta \, d\theta \right] \quad (33)$$

$$\delta = \frac{1}{\pi} \operatorname{Im} \left[\sum_{n=0}^{\infty} \int_0^{2\pi} A_n \left(Ka, \frac{b}{a}, \frac{f}{a} \right) \varphi_n \left(Ka, \frac{b}{a}, \frac{f}{a}, \theta \right) \cos \theta \, d\theta \right] \quad (34)$$

The Horizontal Force

Because of the unsymmetrical flow over the cylinder surface, there is a horizontal force component induced between the two cylinders, exciting sideway oscillations. For a unit length of the cylinder, this force is

$$F_h = -\rho a \int_0^{2\pi} \frac{\partial \phi}{\partial t} \sin \theta \, d\theta \quad (35)$$

or

$$F_h = \sqrt{M_h^2 + N_h^2} \sin(\omega t - \epsilon) \quad (36)$$

where

$$M_h = \rho \omega^2 \eta_0 a \operatorname{Re} \left[\sum_{n=0}^{\infty} \int_0^{2\pi} A_n \left(Ka, \frac{b}{a}, \frac{f}{a} \right) \varphi_n \left(Ka, \frac{b}{a}, \frac{f}{a}, \theta \right) \sin \theta \, d\theta \right] \quad (37)$$

$$N_h = \rho \omega^2 \eta_0 a \operatorname{Im} \left[\sum_{n=0}^{\infty} \int_0^{2\pi} A_n \left(Ka, \frac{b}{a}, \frac{f}{a} \right) \varphi_n \left(Ka, \frac{b}{a}, \frac{f}{a}, \theta \right) \sin \theta \, d\theta \right] \quad (38)$$

In terms of the maximum hydrostatic force variation during the oscillation a horizontal force coefficient is defined as

$$h = \frac{\sqrt{M_h^2 + N_h^2}}{2 \rho g a \eta_0} \quad (39)$$

and the phase angle by which the inward horizontal force falls behind the oscillating displacement is therefore

$$\epsilon = \tan^{-1} \frac{N_h}{M_h} \quad (40)$$

3 RESULTS AND DISCUSSION

Added Mass and Damping Coefficients

(1) Semi-submerged twin cylinders

Before entering into discussion of the results for the fully submerged case, we shall first review and summarize the results for the semi-submerged case, which has been obtained in [1]. The theoretical results of the added mass and damping coefficients for this case are shown in Figures 2 and 3. These results are presented as a function of nondimensional frequency Ka with the hull spacing ratio b/a as a parameter.

It is important to note that there exists a discrete set of characteristic frequencies at which the motion of the fluid between the two cylinders is strongly excited by the forcing oscillations. These characteristic frequencies can be obtained from the following equation

$$K(b-a) = n\pi \quad n = 1, 2, \quad (41)$$

They bear a correspondence to the natural modes of the motion of fluid between two vertical walls of $2(b-a)$ apart.

The first few characteristic numbers of Ka in accordance with the normal modes for four cylinder space ratios are listed below

$n \backslash b/a$	1	2	3	4
1 5	2π	4π	6π	8π
2 0	π	2π	3π	4π
3 0	$\pi/2$	π	$3\pi/2$	2π
4 0	$\pi/3$	$2\pi/3$	π	$4\pi/3$

Table I Characteristic frequencies as a function of hull spacing ratio

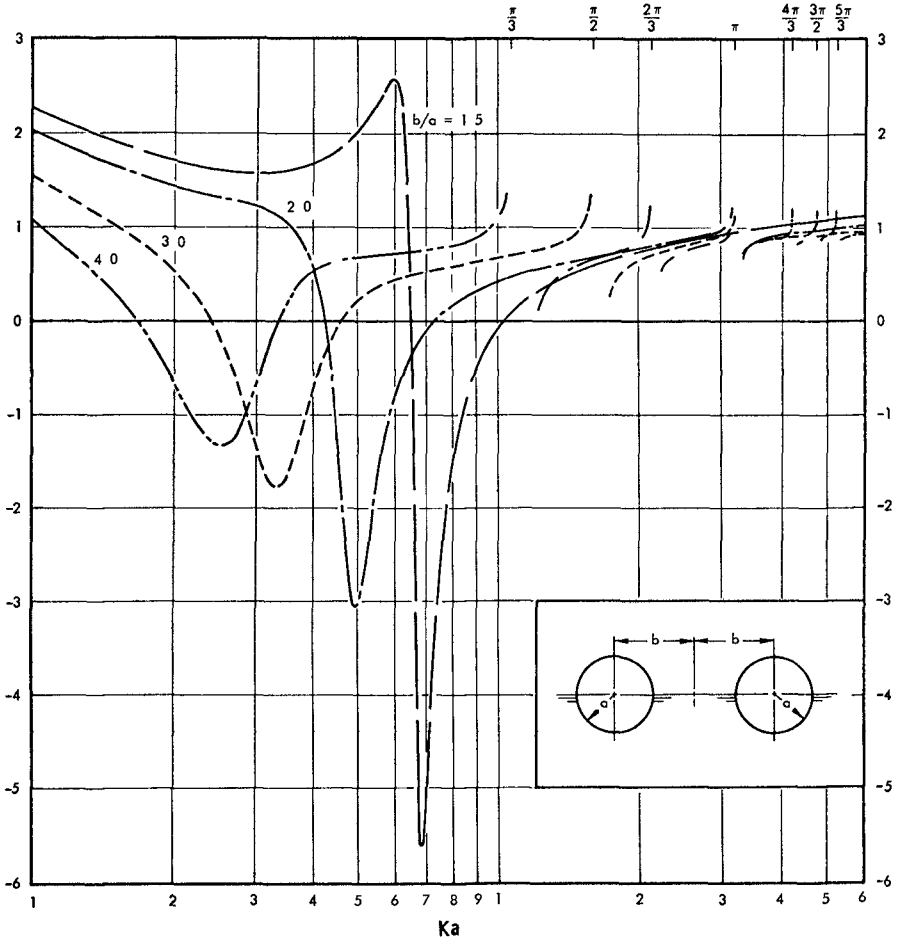


Figure 2 Added Mass Coefficient α as a Function of Ka
Semi-submerged Twin-cylinders, $f/a = 0$

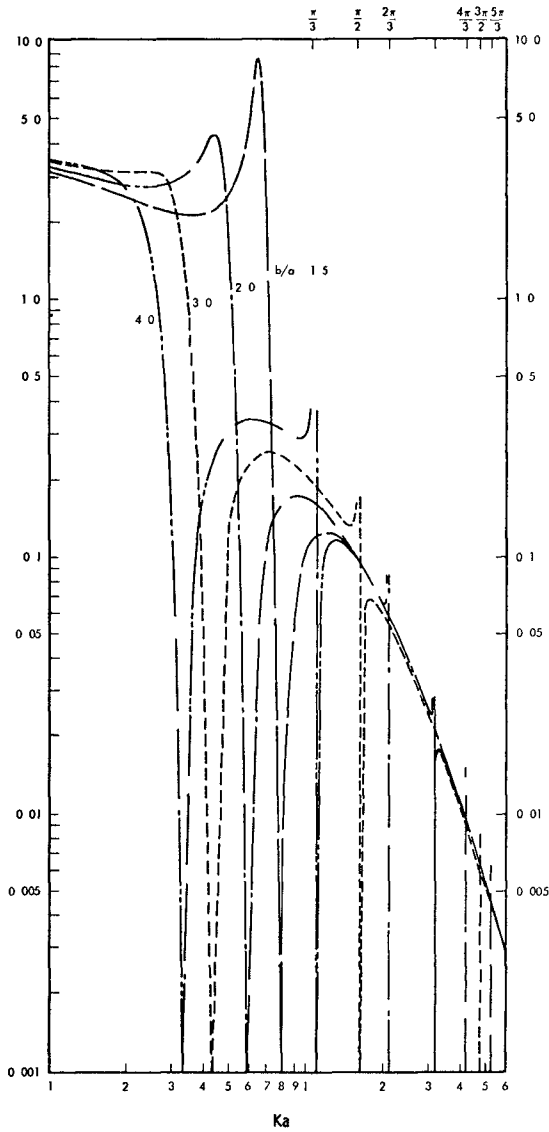


Figure 3 Nondimensional Damping Parameter δ as a Function of Ka Semi-submerged Twin-cylinders, $f/a = 0$

From the graphs, it can be seen that the added mass and damping coefficients are markedly peaked at values of Ka close to those specified above, and as the oscillation passes across the characteristic frequency (a phase change taking place in the surface waves), the added mass becomes negative in a very narrow band of frequencies and the damping coefficient falls down to zero at a certain frequency

Besides these normal modes of resonance, one may find, from Figures 2 and 3 that there is another peak occurring between $Ka = 0$ and the first characteristic frequency. This peak corresponds to the degenerate mode (or zero'th mode) at which the fluid displacement between the cylinders is approximately uniform and 180° out of phase with that immediately outside the cylinders. This peak occupies a rather wide range of frequencies, as compared to those which occur at higher modes

In regard to the resonance phenomena discussed above, it must be noted however that they are strictly two-dimensional characteristics. All the resonance peaks, except that of the zero'th mode, would disappear if the hull beams vary along the length (regular catamaran hull) or if the band width of the input oscillation is large. For a detailed discussion, one is referred to [1]

(2) Fully-submerged twin cylinders

The computation has been done for four cylinder spacing ratios, $b/a = 1.5, 2.0, 2.5$ and 3.0 and four submergence ratios, $f/a = 1.5, 2.0, 2.5$ and 3.0 . To demonstrate the spacing effect which arises from the interference between the two cylinders values of α and δ for different spacing ratios are superimposed and presented in Figures 4 through 11

Each plot is given for one given submergence ratio. As the frequency of interest for practical application is mostly in the neighborhood of $Ka = 1.0$, the presentation is limited to a frequency range up to $Ka = 2.0$

As discussed in the preceding case when the two cylinders are semi-submerged, there are certain characteristic frequencies, around which in a very narrow frequency band with the added mass deviates from its normal trend and the damping coefficient falls to zero while the radiated wave changes phase. When the two cylinders are fully submerged, although the spacing distance still has a tendency to amplify the surface waves between the two cylinders around those characteristic frequencies as given in Table I, there is no physical boundary on the free surface to characterize the wave length so that there is no equivalent resonant phenomenon as described for the semi-submerged case except that the radiated wave does change its phase around the neighborhood of those frequencies and that the damping falls to zero

Similar to the semi-submerged case, there is a peaked added mass and a zero damping occurring somewhere between $Ka = 0$ and the first characteristic frequency. It must be noted that, for both semi- and fully-submerged cases, these peaked added mass and deviated damping occupy a wide band of frequencies. This is very important to the twin-hull vessels, as these peaks and deviations will not be completely removed either by the effect of three-dimensional hull form or by random input oscillations

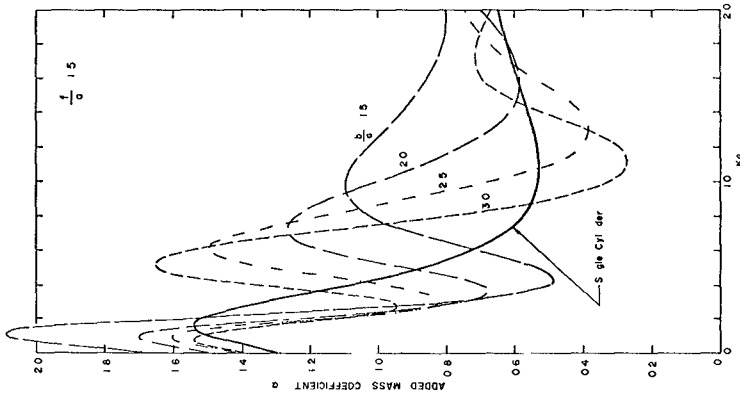


Fig 4 The Added Mass Coefficient for Fully-Submerged Cylinders, Submergence Ratio $f/a = 1.5$

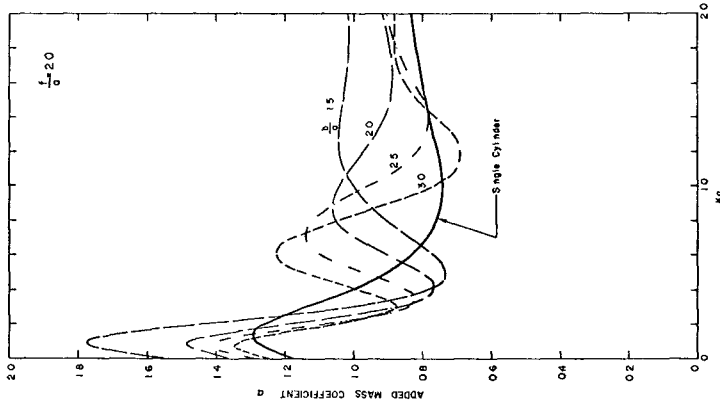


Fig 5 The Added Mass Coefficient for Fully-Submerged Cylinders, Submergence Ratio $f/a = 2.0$

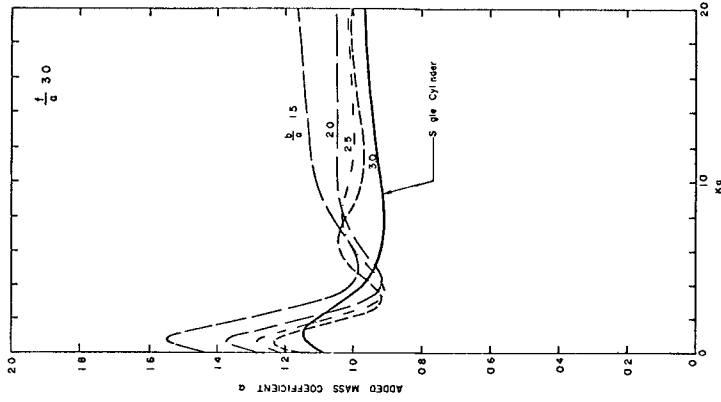


Fig 7 The Added Mass Coefficient for Fully-Submerged Cylinders, Submergence Ratio $f/a = 3.0$

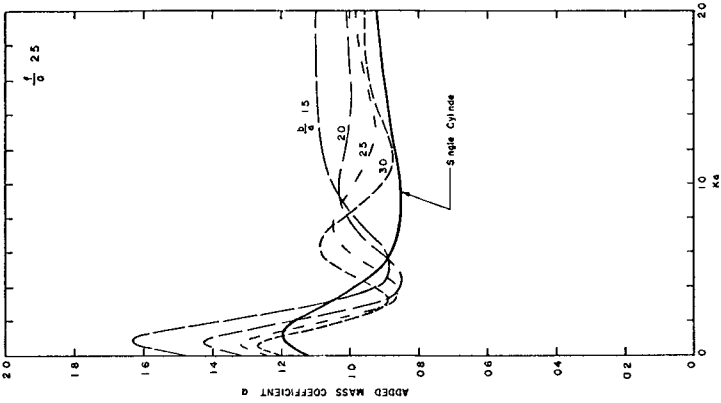


Fig 6 The Added Mass Coefficient for Fully-Submerged Cylinders, Submergence Ratio $f/a = 2.5$

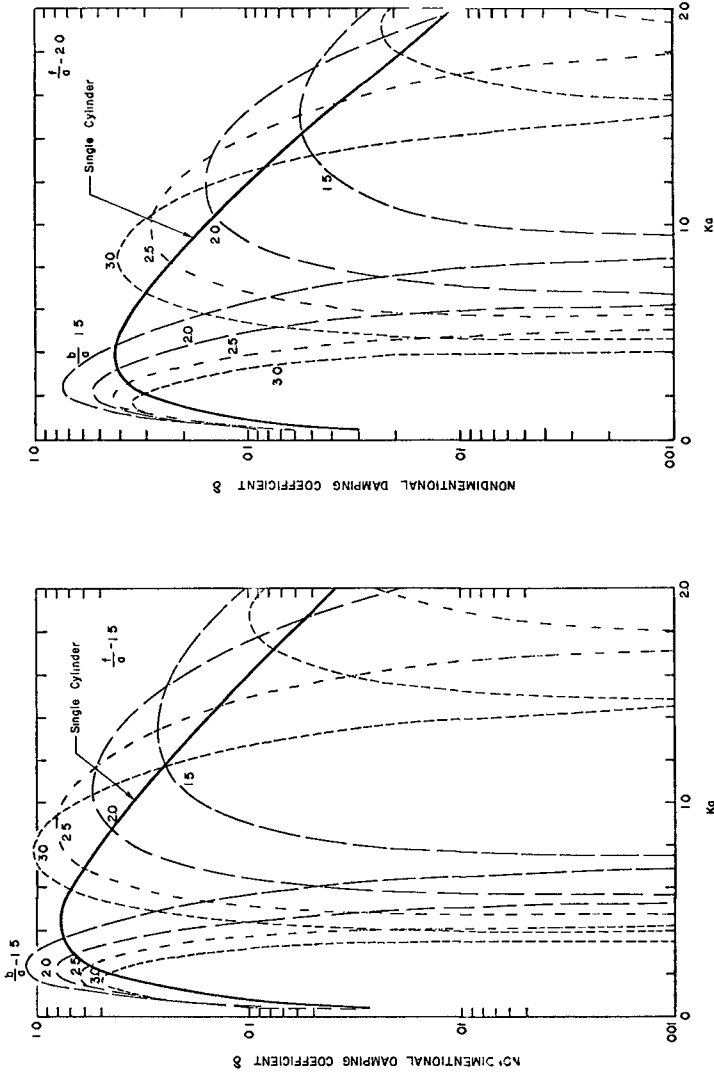


Figure 9 The Damping Coefficient for Fully-submerged Cylinders, Submergence Ratio $f/a = 2.0$

Figure 8 The Damping Coefficient for Fully-submerged Cylinders, Submergence Ratio $f/a = 1.5$

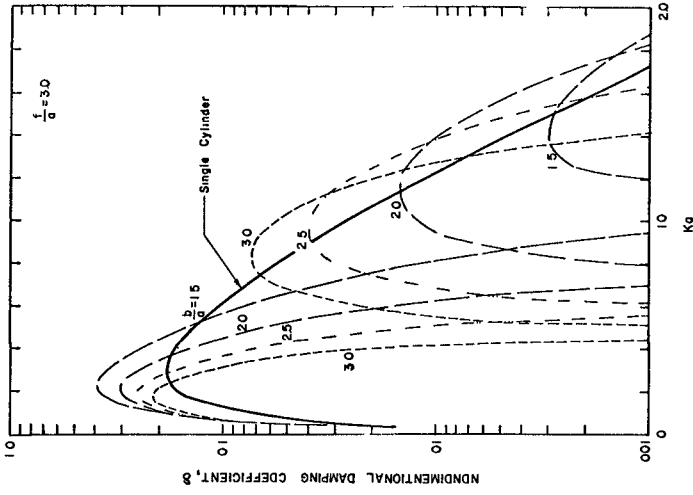


Figure 11 The Damping Coefficient for Fully-submerged Cylinders, Submergence Ratio $f/a = 3.0$

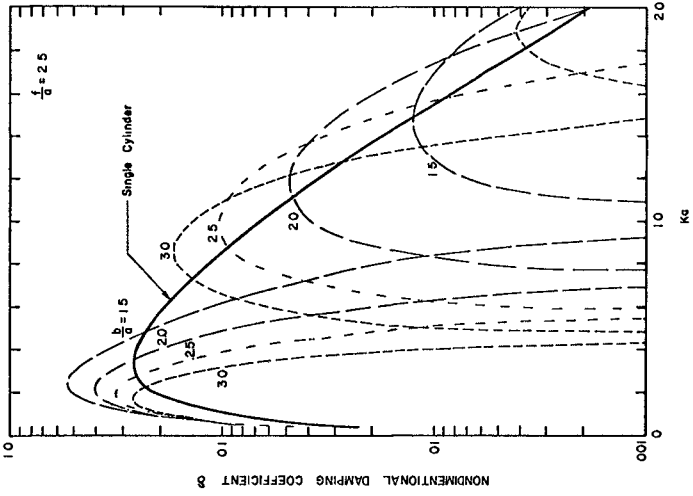


Figure 10 The Damping Coefficient for Fully-submerged Cylinders, Submergence Ratio $f/a = 2.5$

The Horizontal Force

The horizontal force, as well as the vertical component, added mass and damping oscillates in the neighborhood of the characteristic frequencies. It can be shown however, all the high frequency peaks are not larger than the first one. But this is not the case, when $f/a = 0$ (semi-submerged). The high frequency peaks for the semi-submerged case may be much larger because of the surface wave resonance. Nevertheless, this is strictly a two-dimensional phenomenon as discussed before and it occupies only a very narrow band of frequencies, the high frequency peaks, therefore, are of little importance to the practical applications.

In Figure 12, the dimensionless peak amplitude of the horizontal force are given as a function of cylinder spacing. All these values including those for the case $f/a = 0$, refer to the lowest frequency peaks. The hull spacing effect is clearly demonstrated in this figure for the semi-submerged case, the maximum side force can increase by ten times when the hull spacing ratio b/a is reduced from 3.0 to 1.5. For the fully submerged cases, the hull spacing effect is not as strong as that for the semi-submerged case, however, the submergence effect seems rather evident. The maximum side force may reduce approximately 70% when the submergence depth is increased by one cylinder radius. Based on the computed data, the maximum force coefficient h for the fully submerged case, can be interpolated in terms of the hull spacing ratio b/a and submergence ratio f/a as follows:

$$h = e^{2.0 - 2 \frac{b}{a} - 1.14 \frac{f}{a}} \quad \left(\begin{array}{l} 1.5 < \frac{b}{a} < 3.0 \\ 1.5 < \frac{f}{a} < 3.0 \end{array} \right) \quad (42)$$

4 APPLICATION

A group of floating platforms (such as the Mohole) and a certain type of the novel high speed vessels (such as the Trisec [4]) consist of two parallel cylindrical type hulls to facilitate good maneuverability, as well as to provide buoyancy. As to these kinds of vessels, the results of the present analysis on the fully submerged twin cylinders are to provide good hydrodynamic information and can be used directly for the vessel motion response estimation.

As to the catamaran type surface vessels, the results obtained from the semi-submerged twin cylinders analysis can be used to approximate the added mass and damping in both heaving and pitching by means of strip integration technique. As an example, the heave motion coefficients of an ASR (submarine rescue) catamaran are estimated. The procedure of this estimation begins with calculating the two-dimensional section added mass and damping of one hull of the catamaran by considering it independent from the interaction of the other hull. Then these values are corrected in considering the twin-hull interaction effect by multiplying the following ratio

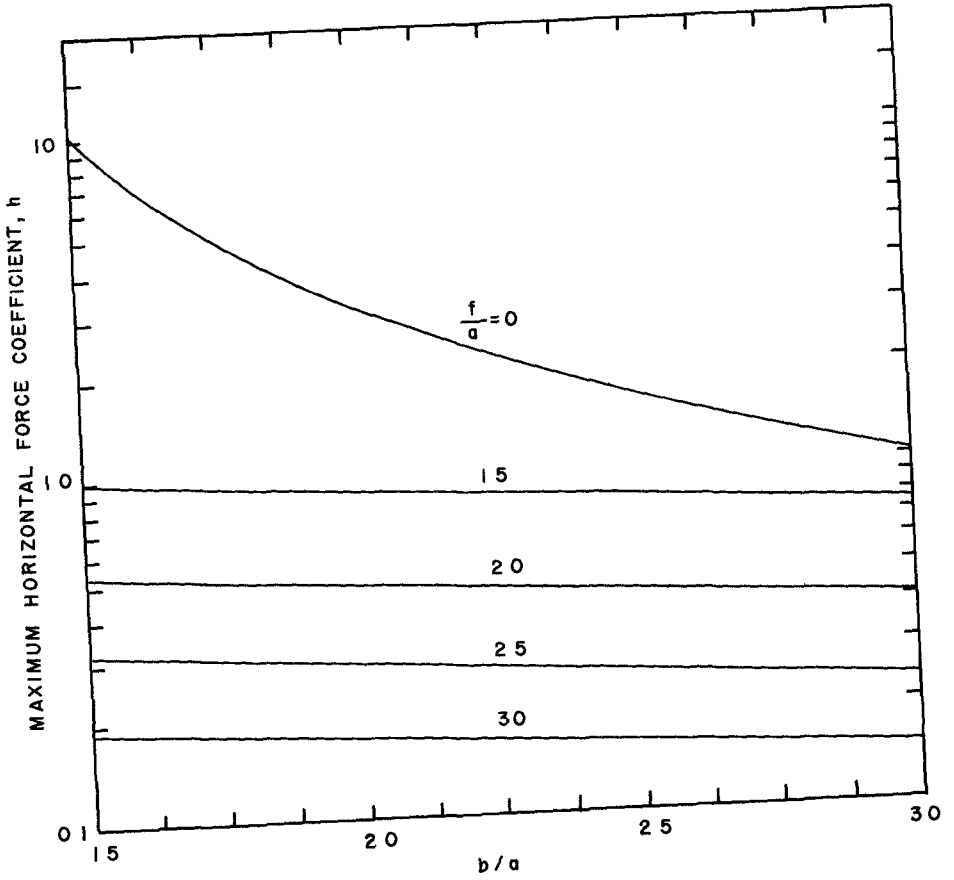


Figure 12 Effect of the Cylinder Spacing Ratio on the Maximum Horizontal Force Coefficient

$$R = \frac{a_s \left(\frac{b}{a}, Ka \right)}{a_o (Ka)} \quad (43)$$

where

a_s = added mass or damping coefficient (whichever applies)
for twin-cylinder oscillation

a_o = added mass or damping coefficient (whichever applies)
for single-cylinder oscillation

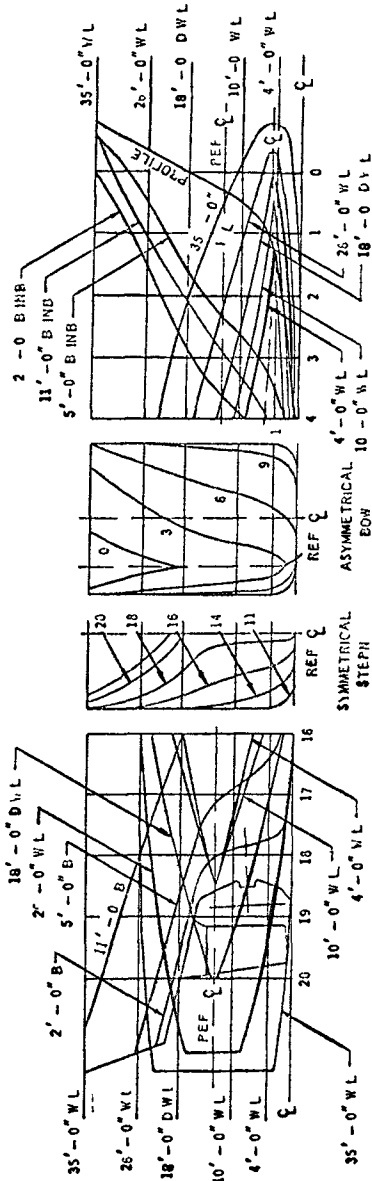
The ratio R is a function of the cylinder spacing ratio $\frac{b}{a}$ and the frequency parameter Ka , where the cylinder radius a here is assumed equivalent to and substituted by the local half-beam of one hull, and b is one-half of the spacing between center to center of the two hulls. This approximation implies that the effect of twin-hull interaction is not sensitive to the hull shape details.

The principal dimensions and the hull lines of this catamaran are shown in Figure 13. A 1/16 89 scale model of this catamaran was tested by NSRDC for the purpose of determining the added mass and damping coefficients in both pitching and heaving oscillations [5]. The model tests included investigations of the speed effects, covering a speed range up to Froude No = 0.316. The estimated results of the added mass and damping coefficients are compared with the experimental results for the catamaran at zero speed and shown in Figure 14. The agreement is fairly good in regard to the negative added mass in the neighborhood of $\mu = 2.5$, where μ is a non-dimensional frequency defined in Figure 14. The experimental results of damping are rather scattered. This is essentially due to the effect of resonance, which occurs in the neighborhood of $\mu = 2.5$.

5 REFERENCES

- [1] Wang, S & Wahab, R "Heaving Oscillations of Twin Cylinders in a Free Surface" Journal of Ship Research (in press)
- [2] Thorne, R C, "Multiple Expansions in the Theory of Surface Waves," Proc Comb Phil Soc 49, 1953
- [3] Whittaker, E T & Watson, G N, "A Course of Modern Analysis," Cambridge University Press, 1927
- [4] Leopold, R, "A New Hull Form for High-Speed Volume Limited Displacement-Type Ships," SNAME Spring Meeting, 1969
- [5] Jones, H D, "Experimental Determination of Coupled Catamaran Pitch and Heave Motion Coefficients" NSRDC T&E Report No 348-H-03, June, 1970

The author wishes to express his appreciation to Dr Li-San Hwang for his interest and support throughout this investigation.



Length (LBP)	210 ft
Beam (overall)	86 ft
Beam (one hull)	24 ft
Draft	18 ft
Displacement of each hull	1395 Tons

Figure 13 Lines plan of ASR catamaran

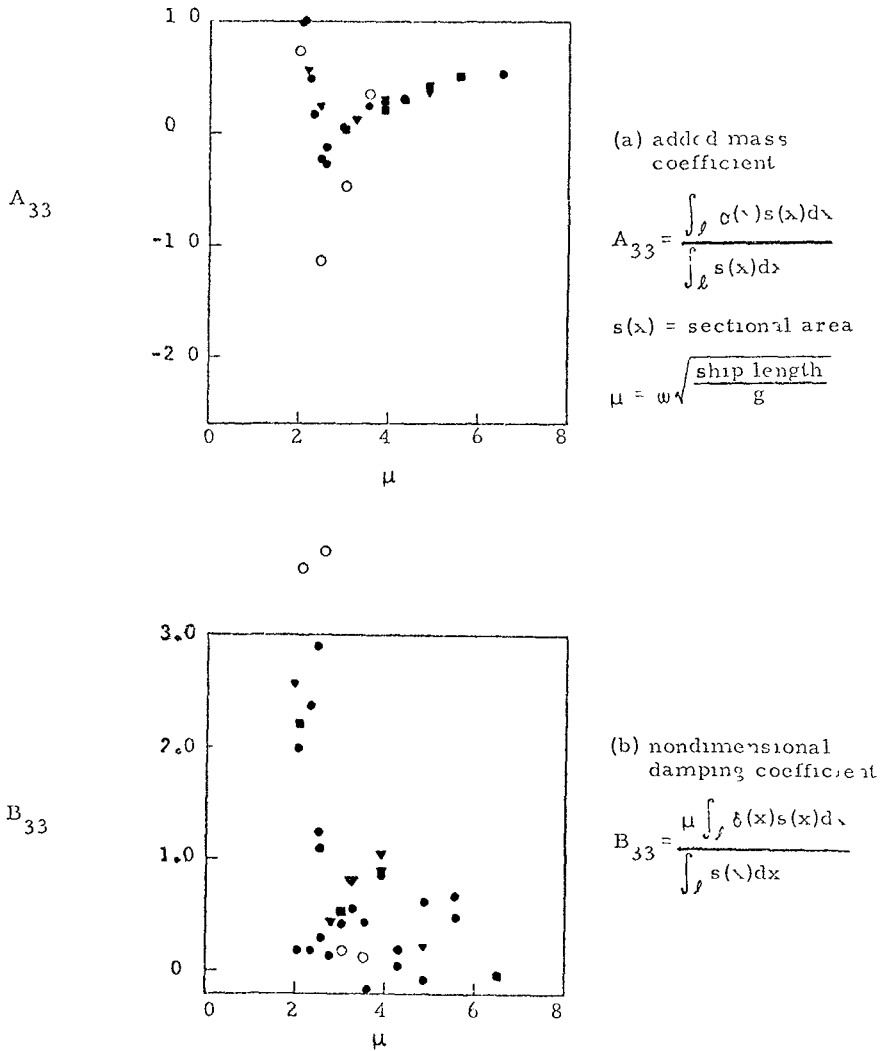


Figure 14 Hydrodynamic coefficients of ASR catamaran in heaving motion

Experimental	■	0.125''	motion amplitude
(Reference [5])	●	0.250''	motion amplitude
	▼	0.375''	motion amplitude
Computed	○		

CHAPTER 104

BEHAVIOR OF A SLENDER BODY IN SHALLOW-WATER WAVES

by

Hsiang Wang*

and

Li-San Hwang**

Abstract

The unsteady-state response of a slender body in nonlinear shallow-water wave environment was studied. Numerical scheme has been developed which permits rapid calculation of the following, which describe the motion of an arbitrarily shaped body in three degrees of freedom anywhere within such an environment

- a Unsteady-state response
- b Centroid locus
- c Forces and moments

Sample calculations are given for a typical submersible. Results are expressed in generalized parameters, defining the circumstances wherein various displacements, velocities, accelerations, etc., would occur.

Introduction

The primary objective of the present work was to study the unsteady state response of a slender body in nonlinear shallow-water wave environment. Consideration was restricted to the wave-induced motions of a rigid body confined to one plane, hence, involving only three degrees of freedom--either surge, pitch, and heave, or sway, heave, and roll. This would correspond to the case when the wave is long-crested and is incidental along the body in the former case and is incidental to the broad side in the latter case.

The hydrodynamic forces under consideration consist of four parts: pressure and inertial forces that can be derived from velocity potential, drag force that is proportional to the square of the relative velocity, restoring force due to the relative position and orientation of the body in the fluid, and thrust and uprighting moment due to the body.

* University of Delaware, Newark, Delaware 19711

** Tetra Tech, Inc., Pasadena, California 91107

The seaway which enters as the input to the system, is derived from the following wave theories

- a Cnoidal wave theory of Keulegan and Patterson for high, long, near-breaking and breaking waves
- b Airy linear theory for short period waves
- c McCowan solitary wave theory of matching period for very long waves

These theories are chosen on the basis that they provide the best approximation to internal wave characteristics as obtained experimentally

A numerical scheme has been developed which permits rapid calculation of the following, which describe the motion of an arbitrarily shaped body in three degrees of freedom anywhere within such an environment

- a Unsteady-state response
- b Centroid locus
- c Forces and moments

Results are expressed in generalized parameters, defining the circumstance wherein various displacements, velocities, accelerations, etc , would occur

The Equations of Motion of a Submerged Body

Consideration was restricted to the wave-induced motions of a rigid submerged body confined to one plane, hence involving only three degrees of freedom--either surge, pitch, and heave or sway, heave, and roll, as defined on Figure 1 This would correspond to the case when the wave is long-crested and is incident to along the body in the former case and incident to the broad side in the latter Although, in principle, these two cases are the same hydrodynamically, they differ somewhat in the method of obtaining an engineering solution

Two sets of coordinate systems were employed in analyzing the responses of a submerged body, they are

- a Fixed coordinate system used to describe the sea conditions and the position of the body, the origin is arbitrary and was chosen here at the sea bottom with the x-axis parallel to the longitudinal axis of the body, the y-axis pointing upward vertically, and the z-axis in the transverse direction
- b Body coordinate system used to describe the oscillations of the body The body had three principal axes, hence six degrees of freedom, corresponding to a translation and a rotation for each axis Symbol definitions are shown in Figure 1 The body axes have their origin at the center of gravity of the body and are coincident with the intersections of the principal planes of inertia

The problem of body response in a wave environment is treated in four steps

- a Derivation of flow environment
- b Derivation of hydrodynamic excitation
- c Derivation of body response and tracing of locus of body motion
- d Derivation of forces exerted on the body

Incident Wave Parallel to the Longitudinal Axis

For motions confined to the xy-plane, it is assumed that motion is described by three functions of time $X(t)$, $Y(t)$, and $\theta(t)$, which are such that the location of the center of gravity of the body is (X, Y) at time t , and the angle of inclination of the body is θ (Figure 1). Then the equations of motion of the body are

$$\left. \begin{aligned} M\ddot{X} &= F_x \\ MY &= F_y \\ I_\theta \ddot{\theta} &= F_\theta \end{aligned} \right\} (1)$$

where M is the natural mass, I_θ is the pitching moment of inertia, and F_x , F_y , and F_θ are the total hydrodynamic forces and moments on the body. The main problem is, of course, the estimation of these hydrodynamic forces.

It is convenient to separate the hydrodynamic forces into four parts: pressure and acceleration forces that can be derived from velocity potential, velocity force that has to be estimated using empirical drag coefficient, restoring force due to the relative position and orientation of the body in the fluid, and thrust or uprighting moment provided by the body.

For a body which is slender (i.e., has small cross-section relative to its length and to a typical wave length), the pressure forces, or Froude-Krylov forces (Korvin-Kroukovsky, 1961), are relatively easy to estimate. Suppose the given incident pressure field is $p(x, y, t)$ and the local horizontal and vertical pressure gradients at a station ξ of the body are calculated

$$P(\xi, t) = \frac{\partial p}{\partial x}(\lambda + \xi \cos \theta, Y + \xi \sin \theta, t) \quad (2)$$

$$Q(\xi, t) = \frac{\partial p}{\partial y}(X + \xi \cos \theta, Y + \xi \sin \theta, t) \quad (3)$$

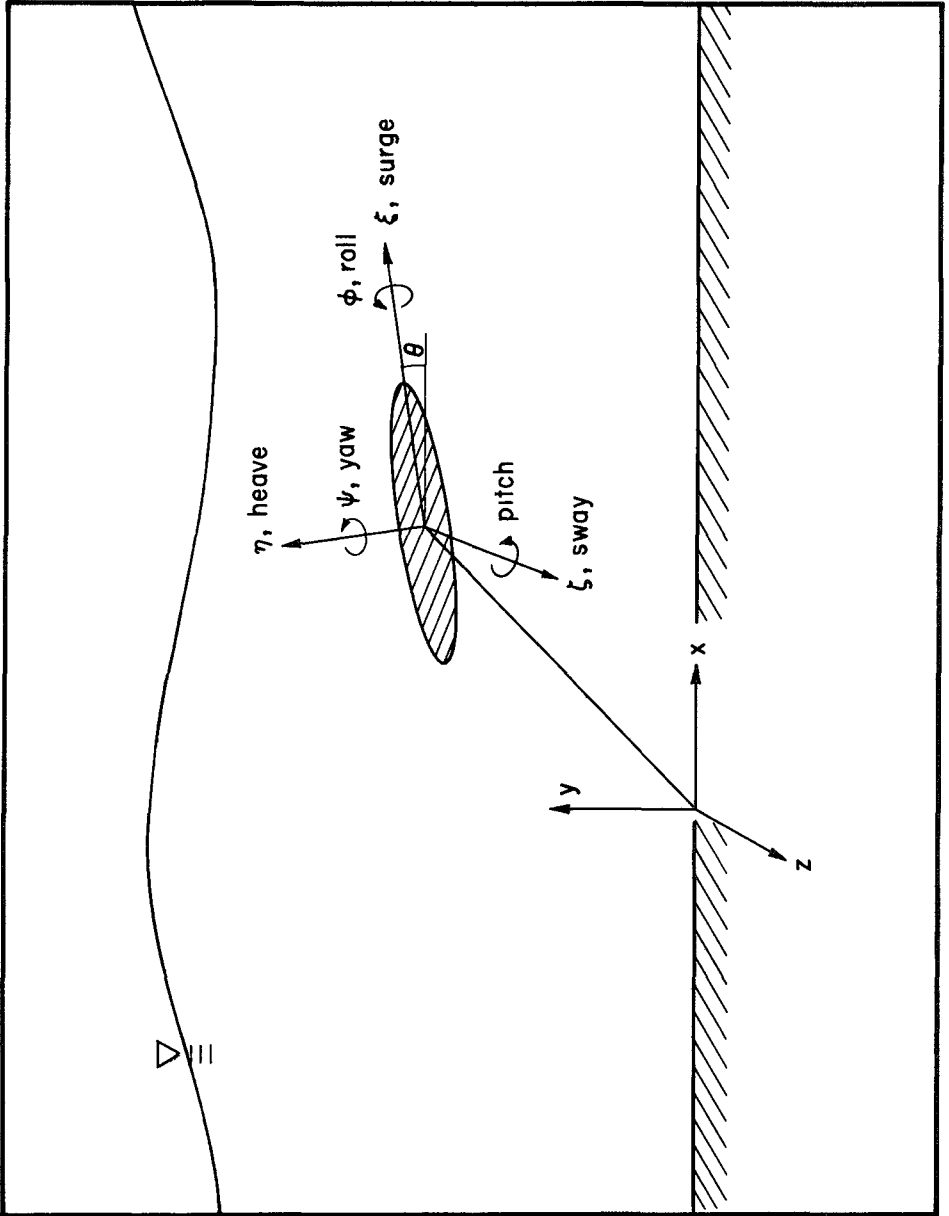


Figure 1 Coordinate system

then the pressure forces are easily seen to be

$$F_x^{FK} = - \int_{\ell} P(\xi, t) S(\xi) d\xi \quad (4)$$

$$F_y^{FK} = - \int_{\ell} Q(\zeta, t) S(\xi) d\xi \quad (5)$$

and the pitching moment is

$$F_{\theta}^{FK} = -\cos\theta \int_{\ell} \xi Q(\zeta, t) S(\xi) d\xi + \sin\theta \int_{\ell} \xi P(\xi, t) S(\xi) d\xi \quad (6)$$

Here $S(\xi)$ is the area of the cross-section of the body at station ξ , and the integrations extend over the length of the body. The acceleration forces include that due to the motion of the body and that due to the diffraction of the wave field by the body. If the body is slender, its effect on the fluid is sensible only when there is a relative motion across its axis. Thus, the longitudinal added mass of a spheroid with a thickness ratio 1 in 10 is only 2 percent of the displaced mass (Lamb, 1932), whereas the lateral added mass is nearly equal to the displaced mass. Hence, "strip" methods may be used to obtain the added inertia effects by considering only the cross flow at each station ξ . The fluid in the neighborhood of station ξ has an acceleration

$$\frac{1}{\rho} P(\xi, t) \sin\theta - \frac{1}{\rho} Q(\xi, t) \cos\theta$$

normal to the body axis, whereas the body itself has acceleration

$$-\ddot{X} \sin\theta + \ddot{Y} \cos\theta + \xi \ddot{\theta}$$

Hence, there is a relative acceleration of the section at ξ of

$$a(\xi) = -\left(\ddot{X} + \frac{1}{\rho} P\right) \sin\theta + \left(\ddot{Y} + \frac{1}{\rho} Q\right) \cos\theta + \xi \ddot{\theta} \quad (7)$$

The cross flow, or slender-body hypothesis, now asserts that the hydrodynamic effect of this relative motion is an opposing force $\mu(\xi)a(\xi)d\xi$ on a section of thickness $d\xi$, where $\mu(\xi)$ is the added mass of the section, calculated as if the flow were two dimensional, irrotational, and infinite in extent. Resolving horizontally and vertically and taking moments, we have inertia terms

$$F_x^A = - \int_l \mu(\xi)a(\xi)d\xi \sin\theta \quad (8)$$

$$F_y^A = \int_l \mu(\xi)a(\xi)d\xi \cos\theta \quad (9)$$

$$M_\theta^A = \int_l \xi \mu(\xi)a(\xi)d\xi \quad (10)$$

The force generated through the relative velocity between the body and the fluid flow is associated with the momentum defect of the fluid due to the body. This force is generally expressed in the form

$$F_D = \rho \frac{C_D}{2} A |V|V \quad (11)$$

where

C_D = drag coefficient

A = frontal area (normal to flow)

V = relative flow velocity

The drag coefficient is a function of Reynolds number and differs for different body geometry. The velocity force in the cross-flow direction and longitudinal-flow direction can be written separately as

$$\begin{aligned} F_{D\eta} &= \rho \frac{1}{2} \int_l C_D |V_{R\eta}| V_{R\eta} dA \\ &= \rho \frac{C_{DC}}{2} \int_l |V_{R\eta}| V_{R\eta} dA \end{aligned} \quad (12)$$

and

$$\begin{aligned}
 F_{D\xi} &= \rho \frac{1}{2} \int_B C_D |V_{R\xi}| V_{R\xi} dA \\
 &= \rho \frac{C_{DL}}{2} \int_B |V_{R\xi}| V_{R\xi} dA
 \end{aligned} \tag{13}$$

where

- $F_{D\eta}$ = drag force in the cross-flow direction
- $F_{D\xi}$ = drag force in the longitudinal-flow direction
- F_{DC} = average drag coefficient in the cross-flow direction
- F_{DL} = average drag coefficient in the longitudinal-flow direction

and the integral limits l and B denote that the integrations are performed along the longitudinal axis and along the vertical axis of the body

The relative velocities in the cross-flow direction $V_{R\eta}$ and in the longitudinal direction $V_{R\xi}$ are, respectively,

$$V_{R\eta} = -U_R \sin\theta + V_R \cos\theta + \xi \dot{\theta} \tag{14}$$

$$V_{R\xi} = U_R \cos\theta + V_R \sin\theta \tag{15}$$

with U_R and V_R defined as

$$U_R = X - u \tag{16}$$

$$V_R = Y - v \tag{17}$$

where X and Y are the velocity components of the body in the x - and y -directions and u and v are the velocity components of the fluid in the x - and y -directions

Again, like inertia terms, resolving horizontally and vertically and taking moments to obtain the drag forces

$$F_x^D = -F_{Dz} \cos \theta + \Gamma_{D\eta} \sin \theta \quad (18)$$

$$F_y^D = -F_{Dz} \sin \theta - \Gamma_{D\eta} \cos \theta \quad (19)$$

$$\Gamma_{\theta}^D = -\rho \frac{C_{DC}}{2} \int_{\ell} \xi |V_{R\eta}| V_{R\eta} dA \quad (20)$$

The restoring forces are simply

$$F_x^R = 0 \quad (21)$$

$$\begin{aligned} F_y^R &= -w_s && \text{for partial submergence} \\ &= 0 && \text{for full submergence} \end{aligned} \quad (22)$$

where w_s is the partial weight of the body that is surfaced

The restoring moments are

$$F_{\theta}^R = -\rho g \Psi_s \bar{ee} \sin \theta - \cos \theta \int_{\ell_1} \rho_s g \xi dV \quad (23)$$

for partial submergence and

$$F_{\theta}^R = -\rho g \Psi_s \bar{ee} \sin \theta$$

for full submergence

where

- Ψ_s = volume of displaced water
- ee = metacentric height of body
- ρ = density of sea water
- ρ_s = density of body
- ℓ_1 = body length above free surface

Finally, the thrust and righting moments produced by the body when resolved into x-, y-, and θ -directions, are

$$F_x^T = T_t \cos \theta \tag{21}$$

$$F_y^T = T_t \sin \theta \tag{25}$$

$$F_\theta^T = -M_r \theta \tag{26}$$

where T_t is the thrust, and $M_r \theta$ is the righting moment, which is assumed to be proportional to the pitch angle

Thus, we have completed the disposition of the total forces acting on the body, and the equations of motion become

$$\left. \begin{aligned} MX &= F_x^{FK} + F_x^A + F_x^D + F_x^T \\ MY &= F_y^{FK} + F_y^A + F_y^D + F_y^R + F_y^T \\ I_\theta \dot{\theta} &= F_\theta^{FK} + F_\theta^A + F_\theta^D + F_\theta^R + F_\theta^T \end{aligned} \right\} \tag{27}$$

When expressed explicitly, the equations of motion are

$$\left. \begin{aligned} M\ddot{X} &= - \int_l P(\xi, t) S(\xi) d\xi - \int_l u(\xi) a(\xi) d\xi \sin \theta - \rho \frac{C_{DL}}{2} \int_B |V_{R\xi}| |V_{R\xi}| dA \cos \theta \\ &\quad + \rho \frac{C_{DC}}{2} \int_l |V_{R\eta}| |V_{R\eta}| dA \sin \theta + T_t \cos \theta \\ MY &= - \int_l Q(\xi, t) S(\xi) d\xi + \int_l u(\xi) \eta(\xi) d\xi \cos \theta - \rho \frac{C_{DL}}{2} \int_B |V_{R\xi}| |V_{R\xi}| dA \cos \theta \\ &\quad - \rho \frac{C_{DC}}{2} \int_l |V_{R\eta}| |V_{R\eta}| dA \cos \theta + T_t \sin \theta + F_y^R \\ I_\theta \ddot{\theta} &= - \cos \theta \int_l \xi Q(\xi, t) S(\xi) d\xi + \sin \theta \int_l \xi P(\xi, t) S(\xi) d\xi + \int_l \xi u(\xi) a(\xi) d\xi \\ &\quad - \rho \frac{C_{DC}}{2} \int_l \xi |V_{R\eta}| |V_{R\eta}| dA - M_r \theta + F_\theta^R \end{aligned} \right\} \tag{28}$$

where F_y^R and F_θ^R are defined in Eqs 22 and 23, respectively. Once the flow field has been described, these three simultaneous equations can be solved using a high-speed computer.

The surging force, heaving force, and pitching moment are evaluated, respectively, according to the following equations

$$F_\xi = M(X\cos\theta + Y\sin\theta) - I_\theta(\dot{\theta})^2 \quad (29)$$

$$F_\eta = M(X\sin\theta + Y\cos\theta) - I_\theta\ddot{\theta} \quad (30)$$

$$M_T = I_\theta\dot{\theta} \quad (31)$$

where

F_ξ = surging force

F_η = heaving force

M_T = pitching moment

Incident Wave Perpendicular to the Longitudinal Axis

The equations of motion are similar to the previous case, except the evaluation of some forces were different. In the determination of the mass coefficients, the main body was treated as a cylindrical body of variable diameter. The drag term was calculated in a much similar way as the acceleration term, with due consideration in choosing drag coefficients for different parts.

The calculation of pressure force, and restoring force, remains the same as in the case of parallel waves. The complete calculations of motion for sway, heave, and roll, when expressed in force components, are, respectively,

$$\left. \begin{aligned} MZ &= \Gamma_z^K + \Gamma_z^A + \Gamma_z^D \\ M\dot{Y} &= \Gamma_y^K + \Gamma_y^A + \Gamma_y^D + F_y^T + \Gamma_y^R \\ I_\varphi\dot{\varphi} &= \Gamma_\varphi^K + \Gamma_\varphi^A + \Gamma_\varphi^D + \Gamma_\varphi^T + \Gamma_\varphi^R \end{aligned} \right\} (32)$$

Wave Environment and Flow Field

Three wave theories were used for evaluating excitation forces
They are

- a Cnoidal wave theory of Keulegan and Patterson for high, long, near-breaking, and breaking waves
- b Airy linear theory for short period waves
- c McCowan solitary wave theory for very long waves

The cnoidal wave has wave profile (Wiegel, 1964)

$$y_s = y_t + Hcn^2 \left[2K(k) \left(\frac{x}{L} - \frac{t}{T} \right) k \right] \tag{33}$$

with wave period to the first order

$$T = \frac{4d}{\sqrt{3gH}} \left\{ \frac{kK(k)}{\sqrt{1 + \frac{H}{d} \left[-1 + \frac{1}{k^2} \left(2 - 3 \frac{E(k)}{K(k)} \right) \right]}} \right\} \tag{34}$$

The corresponding wave length is

$$L = \sqrt{\frac{16d^3}{3H}} kK(k) \tag{35}$$

where

- y_s = water surface elevation measured from sea bottom
- H = wave height
- cn = one of the Jacobian elliptic functions
- k = a real number varied from 0 to 1
- $K(k)$ = elliptic integral of first kind
- $E(k)$ = elliptic integral of second kind
- $y_t = H \left(\frac{d}{H} - 1 + \frac{16d^3}{3L^2H} \right) \left\{ k(k) [K(k) \quad E(k)] \right\}$

In Eq 34, when T is plotted as a function of k for fixed d and H , it takes a form shown in Fig 2. Thus, if one starts at point A on the curve for increasing value of T , the corresponding k can increase or decrease depending upon which branch one follows. The left branch should be discarded because it corresponds to increasing values of T with decreasing values of L , which is physically meaningless. For waves of periods shorter than T_m , the Airy theory is to be applied. By differentiating Eq 34 with respect to k and equating the result to zero,

$$\frac{d}{dH} = 1 - \frac{1}{2k} \left[4 - 9 \frac{E(k)}{K(k)} + (1 - k^2) \frac{K(k)}{E(k)} \right] \quad (36)$$

for $T\sqrt{g/d} = \text{minimum}$

Thus, the value of $(T\sqrt{g/d})_{\min}$ versus d/H so obtained defines the matching line between the cnoidal wave and linear wave. It is also evident from Fig 5 that, when the elliptic parameter approaches unity, the period approaches infinity rapidly. For instance, when the k values are changed from 1 to 0.9999, the period $4K(k)$ is decreased from infinity to about 7π . In the numerical calculation, the wave period (or length) is specified, and the value of k is found by Eq 34 through iteration. For very long waves, the value of k is very nearly equal to 1, and it becomes impractical to obtain numerically the value of k through iteration. In this case, the solitary wave, which is the limiting case of the cnoidal wave, can be treated as having a finite period for many practical purposes. The upper limit of elliptic parameter has been chosen as equal to 0.9999 in the present study. Figure 3 shows the regions where the different wave theories apply.

Method of Computation

Numerical Analysis

The differential equations to be solved are a set of three simultaneous, nonlinear second-order equations. The fourth-order formula of Runge-Kutta (Hildebrand, 1956) is used to perform the numerical evaluation. This method, which extends forward the solution of differential equations from known conditions by an increment of the independent variable without using information outside this increment, has been applied extensively in solving initial value problems. In essence, the fourth-order formula evaluates the slope of the wave at the initial point, the 1/4 point, the 1/2 point, and the 3/4 point of the interval of increment. The numerical solution is then obtained in agreement with the Taylor series solution through terms of the fourth order of the interval h . The local truncated error is then of the order of h^5 , where h is the size of the increment. In the present case, the independent variable is the nondimensional time, which is equal to t/T , where t is real time, and T is the wave period.

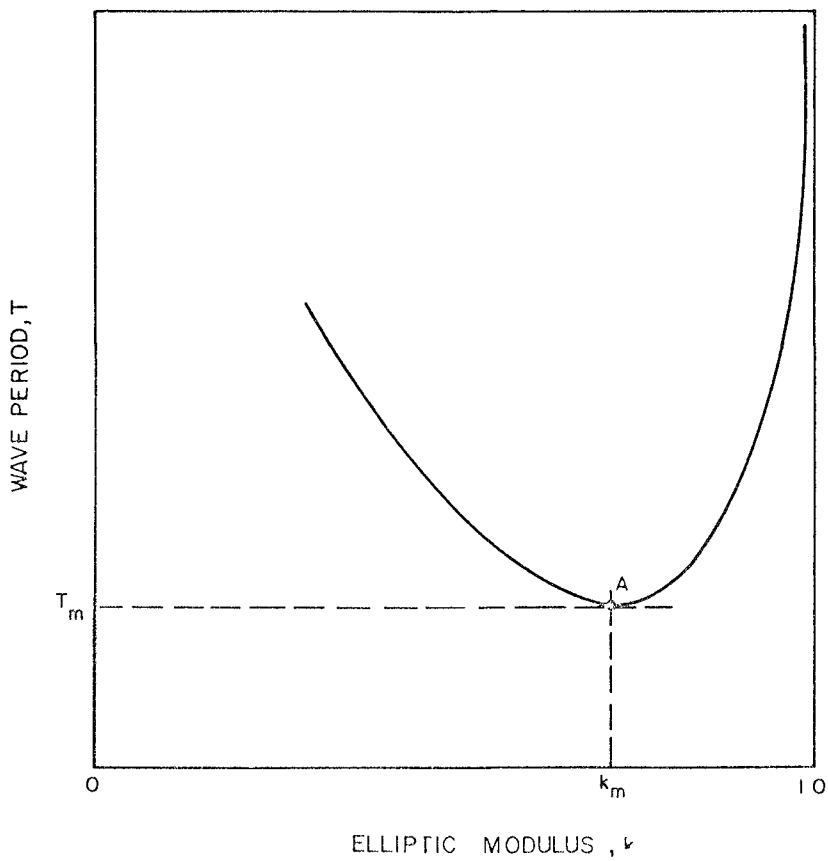


Figure 2 Wave period versus elliptic modulus for cnoidal wave

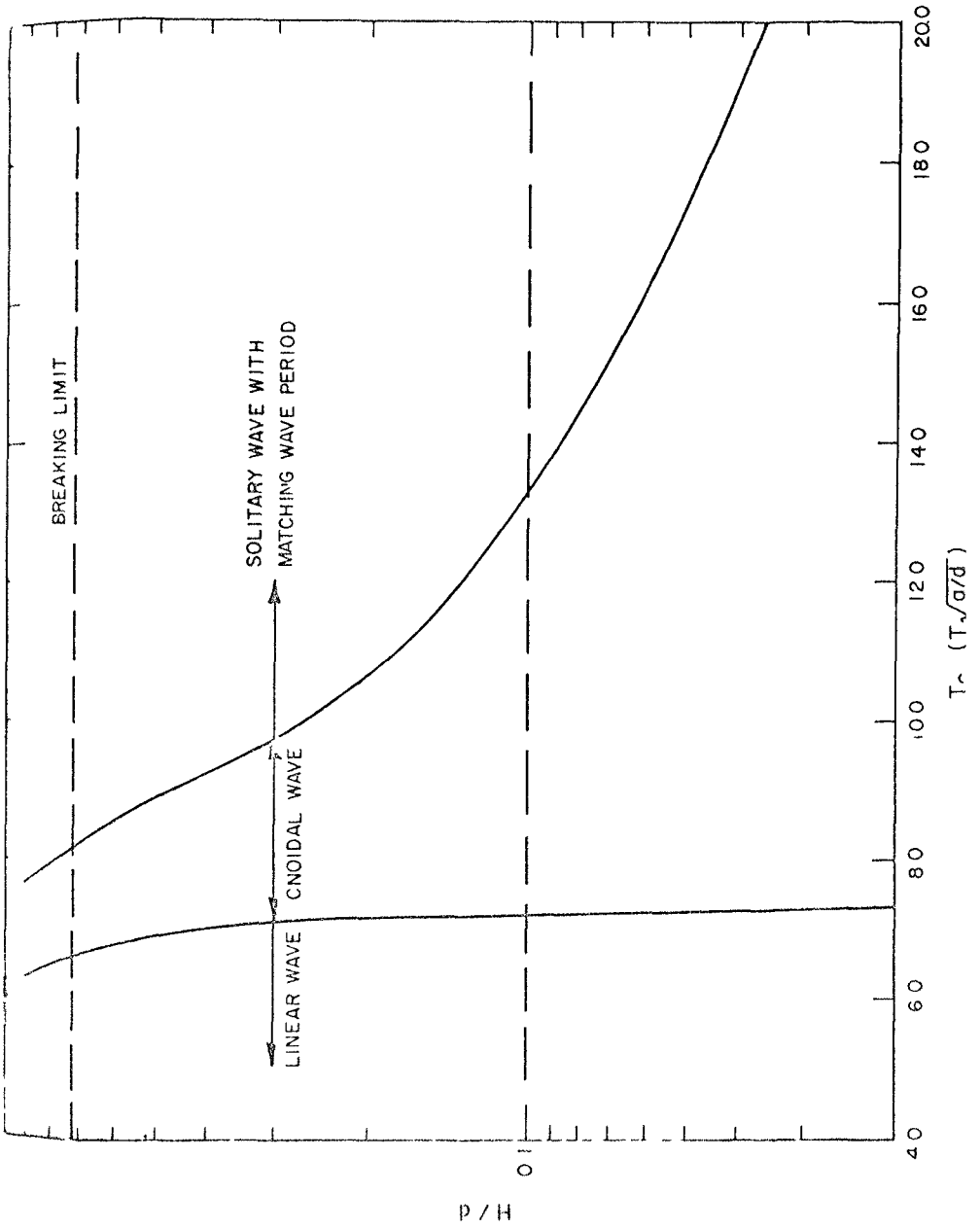


Figure 3 Region of wave theories

After several tests, the incremental interval $h = \Delta t/T$ was selected at $1/64$ throughout the computation

Input Conditions

The independent elements which affect the behavior of the body are

1 Environment

Wave height H
Wave period T
Water depth d
Gravity g

2 Fluid properties

Fluid density $\rho = 2.0$
Viscosity μ (Not explicitly involved, appears in terms of drag coefficients)

3 Submerged body

Length ℓ
Cross sectional areas along the longitudinal coordinate S_1
($i = 1$ to m number of station)
Longitudinal moment of inertia I_θ
Transverse moment of inertia I
Weight W
Metacentric height ee
Righting moment M_0
Added mass coefficients C_m 's

4 Initial conditions

Depth of submergence d_s
Velocity V_1
Angle of attack α_1
Form of first effective wave F
Orientating submerged body O

All of these factors are required inputs in the computer program

Numerical results

Figures 4 and 5 show, respectively, the vertical and horizontal displacements of the center of the body in a wave environment. In these figures, the free surface variation is drawn with respect to the gravity center of the submerged body. In the case of Figure 4, the body was initially placed at the middle water depth. The body has a tendency to surface. In the case of Figure 5, the body was placed right beneath the free surface, rose partially above the surface, and then dived down to hit the bottom, partially due to the additional downward force imposed on the body from the reduction of buoyancy force resulting from the surfacing.

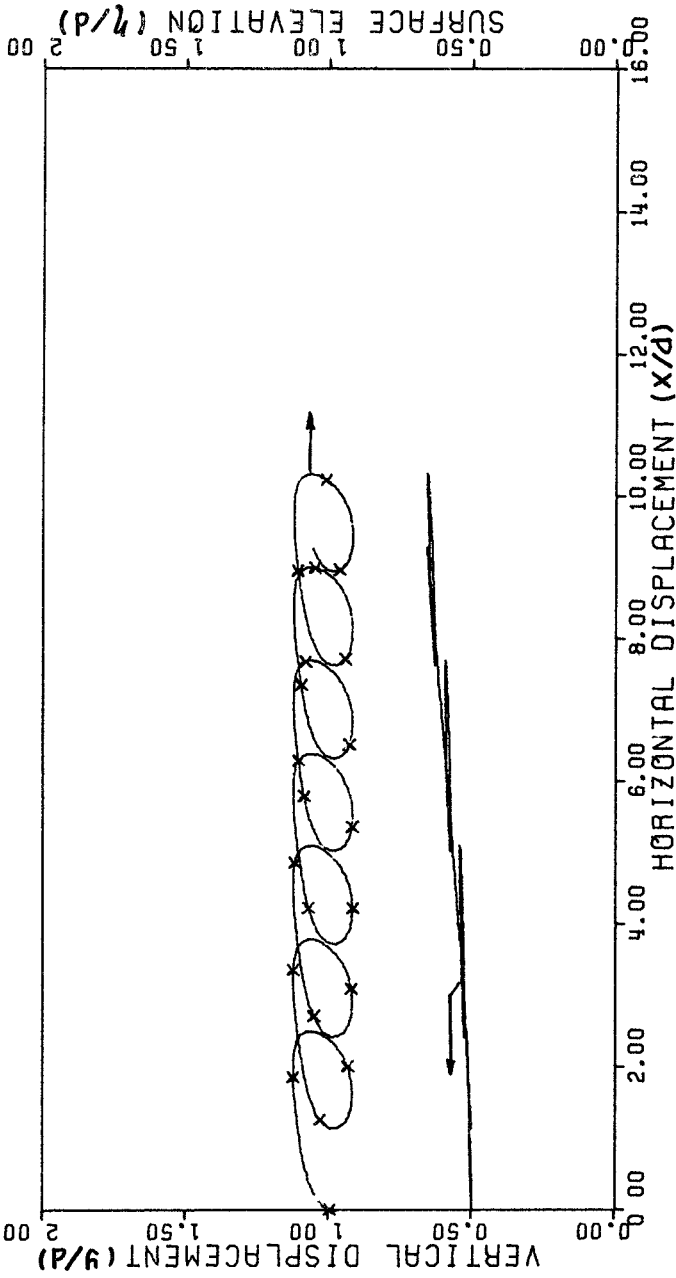


Figure 4 The locus of a submerged body which is initially placed at the middle depth

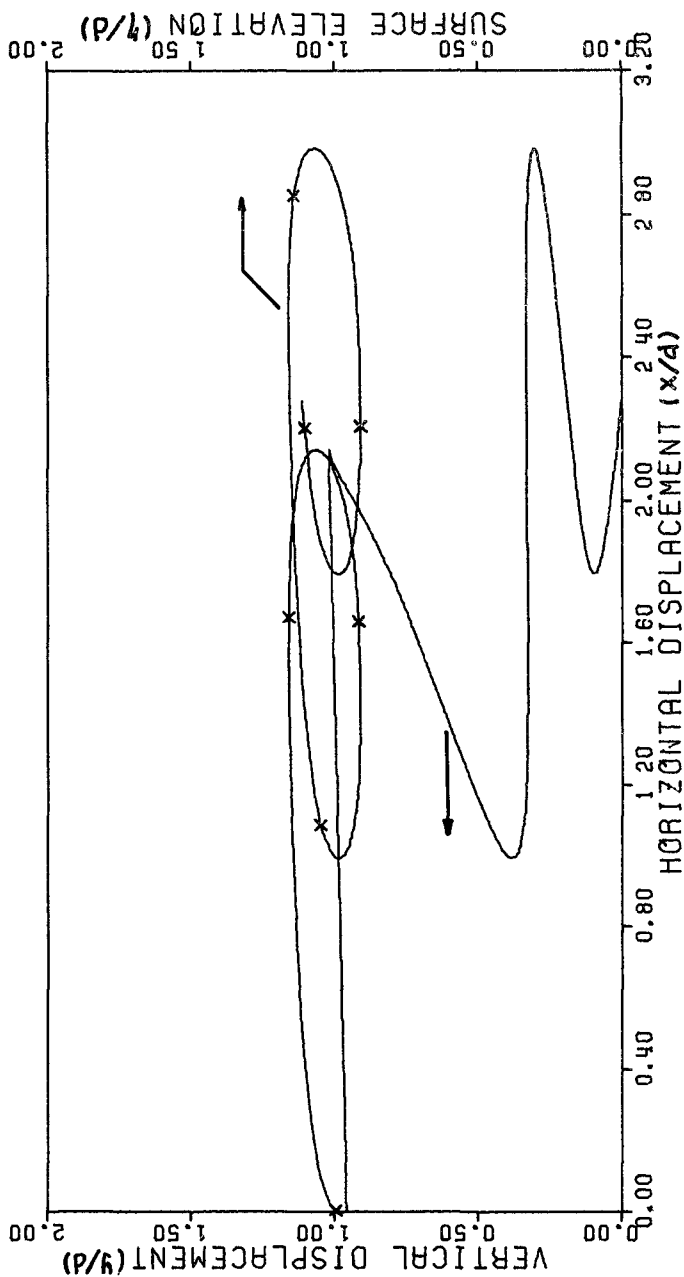


Figure 5 The locus of a submerged body which is initially placed right beneath surface

Figures 6 and 7 show the differences of the acceleration pattern of the body for different initial positions. The oscillation was more regular when the body was initially placed at mid-depth. The amplitude of the oscillation grew with time as the depth of the submergence decreased, as shown in Figure 4. Figure 7 shows the acceleration pattern for the case where the body was placed right beneath the free surface. The sudden increase of acceleration results from surfacing. Similar patterns were found for the heaving forces, which are closely related to these accelerations. A typical pitching motion is shown in Figure 8.

Discussion

The present work is to provide an analytical tool to examine the dynamic behavior of a submerged body when it is exposed in a shallow-water wave environment. A thorough investigation, considering every variable as listed in the previous section, though desirable, would be very cumbersome. Therefore, the consideration was restricted to specific hull configurations. Attempts were then made to examine the influence of environmental variables on the response of the structure. Even with such restriction, only qualitative evaluations can be made.

The wave height and the water depth were found to be the most influential variables. Dynamic stability, i.e., chance of capsize, depends significantly on them. Wave period is less important for the unsteady-state case considered. Original altitude of the body is also found to be of secondary importance, partially because the wave theories, even to the second order, yield hydrostatic pressure distribution in the vertical direction. This conclusion can not, however, be extended to the region where the body is close to the surface as illustrated in Figures 4 and 5.

The water inertia force, better known as the added mass effects, was found to vary with the altitude of the body. Correction was made by using experimentally determined added mass coefficients in the numerical computation. This coefficient, being approximately equal to 0.98 when the submergent depth is equal to or larger than six times the height of the body, decreases monotonically with the decreasing of submergence to a value of approximately 0.75 when the body is barely submerged. Further decrease in submergence will result in significant surface disturbance and was not considered. Because of the high waves used in the computation, it was found that the velocity-related force is no longer negligible. Entirely different results were obtained for the cases in which the velocity-related force was neglected, linearized and left to be proportional to the velocity square.

Also worth mentioning is the effect of the form of the first wave that encounters the body. Since waves are oscillatory in nature, the unsteady response of the body depends strongly on when the body is released in the wave cycle. In general, the body has a net translation in the wave direction when the first wave is in the form of a crest, whereas the net translation is opposite to the wave direction if the first wave is a trough. This phenomenon can easily be demonstrated experimentally.

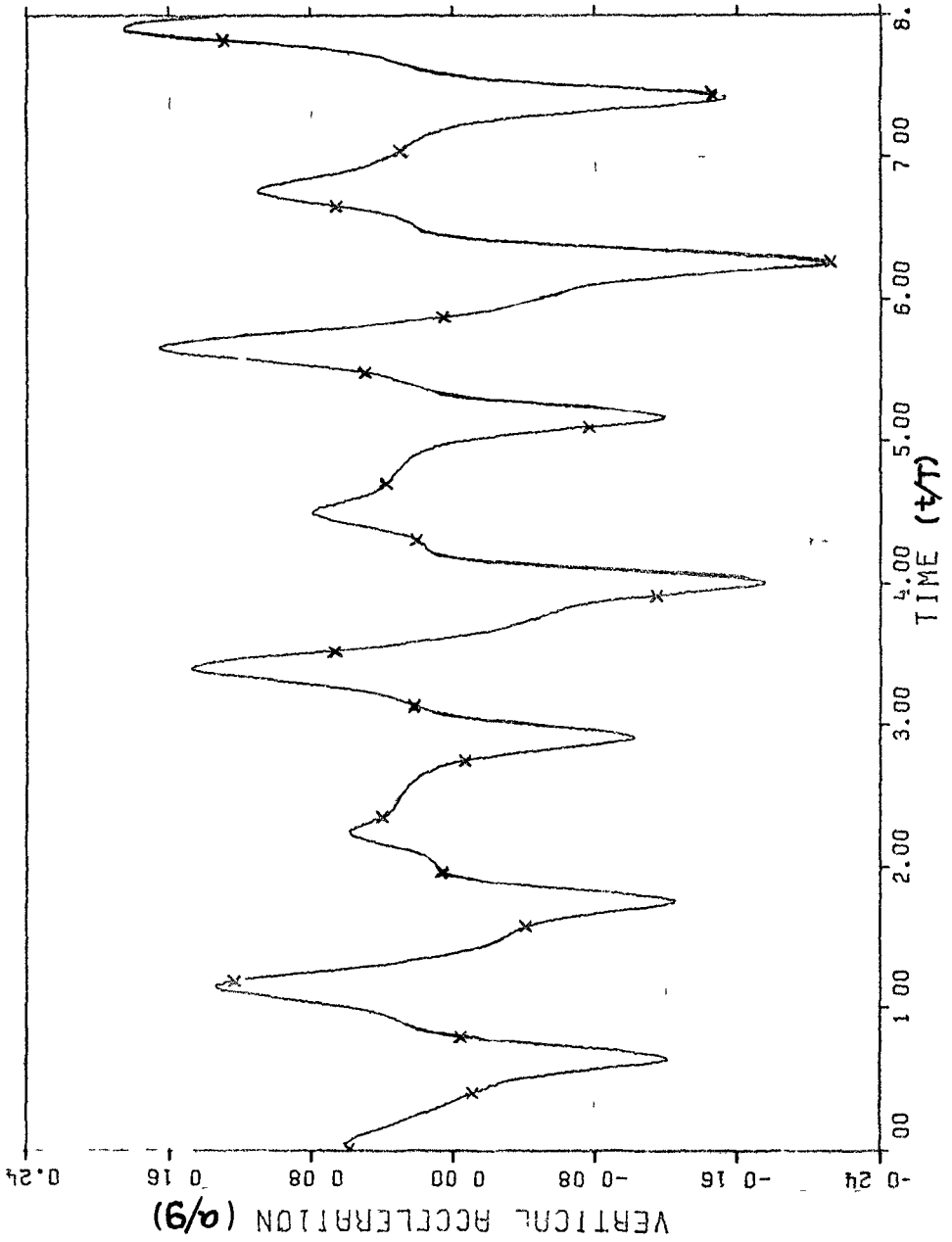


Figure 6 Vertical acceleration (mid-depth)

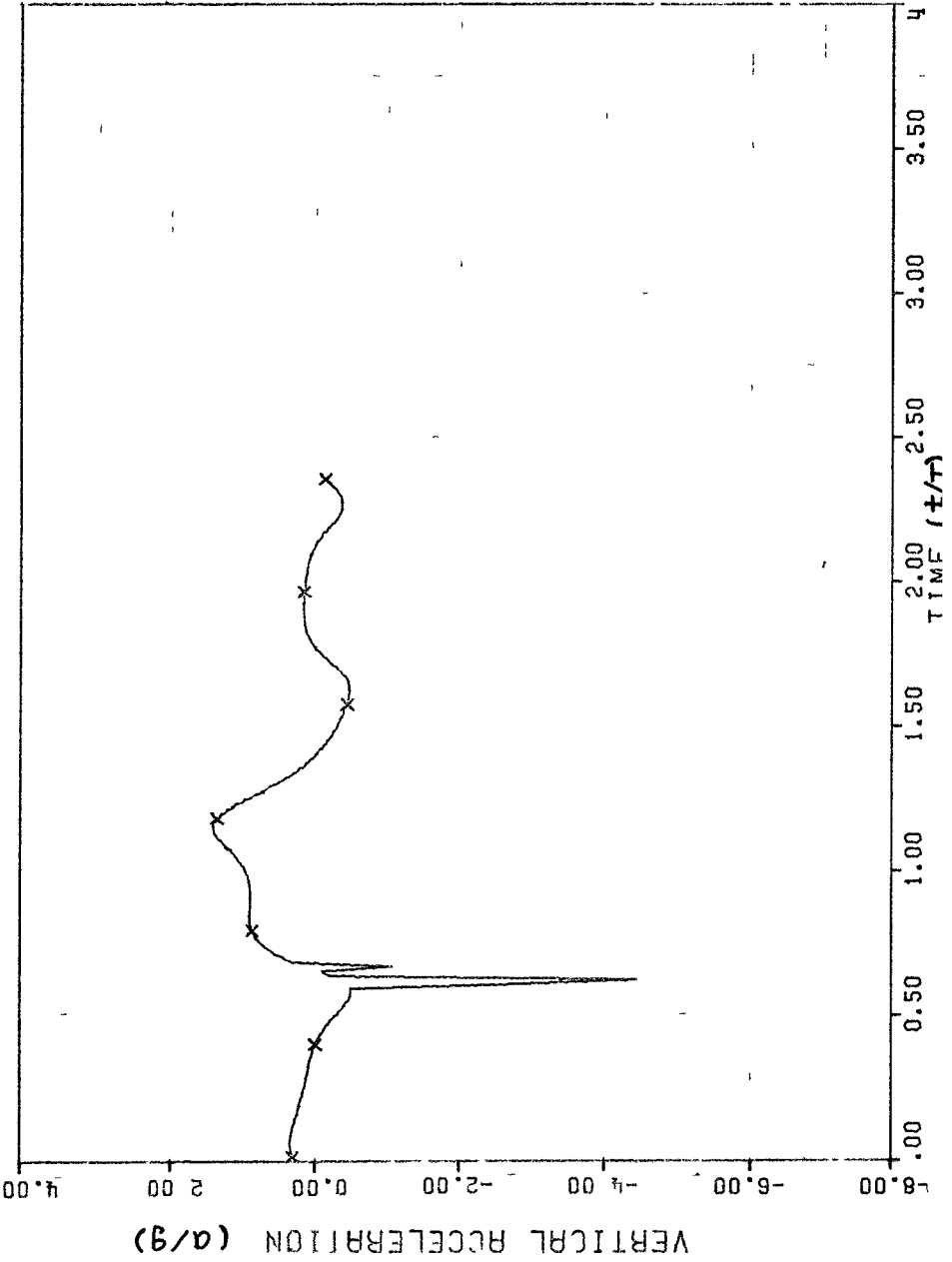


Figure 7 Vertical acceleration (beneath the free surface)

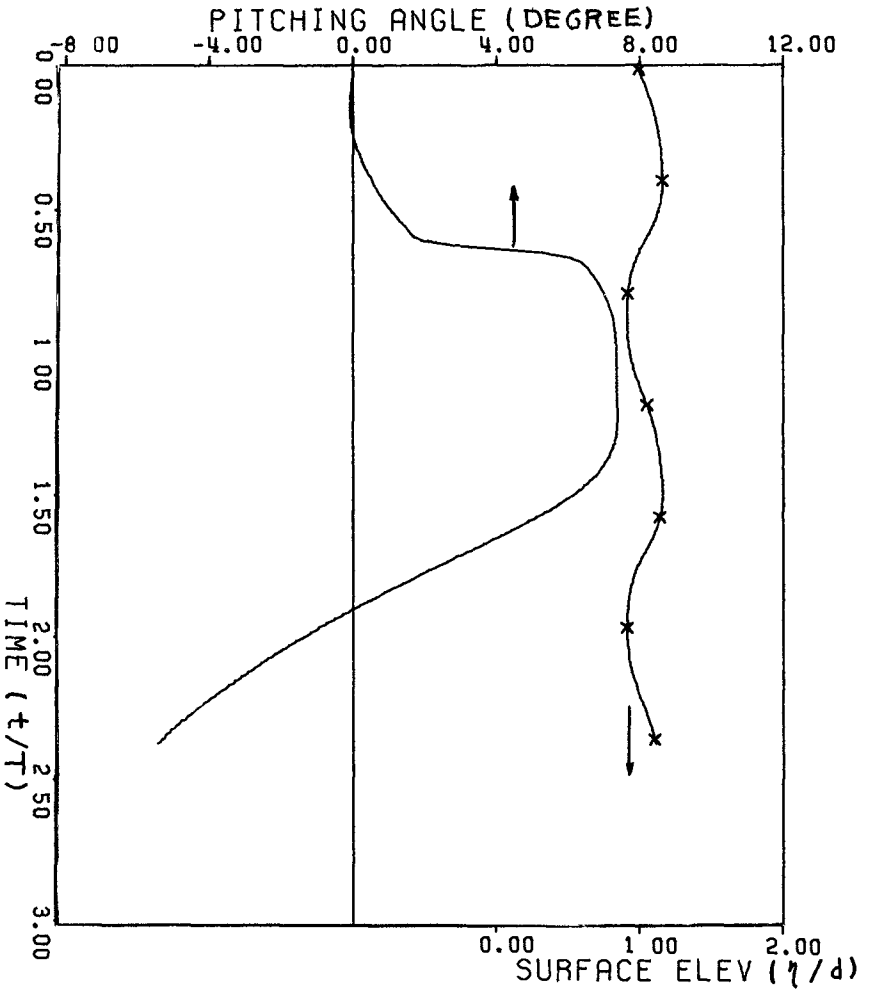


Figure 8 Pitching angle of a submerged body which is initially placed right beneath the free surface

Conclusion

Through analytical consideration, a numerical method was developed to suit the engineering purpose of quick assessment of the dynamic behavior of submerged slender body in high amplitude shallow water waves. To serve this purpose, as many variables as possible of engineering interest were included. In exchange, rigor in mathematics was compromised. Approximations such as strip theory, and empirical relations such as drag coefficient were used. Much desired are the future improvements of wave theory in shallow water region and a better understanding of velocity-related forces in oscillating fluid flows.

Acknowledgement

This work was performed under the sponsorship of ONR, and the authors would like to express their gratitude to Dr. B. LeMéhauté for his contribution.

References

- Hildebrand, F. B. (1956), Introduction to Numerical Analysis, McGraw-Hill Book Company, New York.
- Keulegan, C. H. and G. W. Patterson (1940), "Mathematical Theory of Irrotational Translation Waves," National Bureau of Standards Paper RP 1272.
- Korvin-Kroukovsky, B. V. (1961), Theory of Seakeeping, Society of Naval Architects and Marine Engineers, New York.
- Lamb, H. (1932), Hydrodynamics, 6th ed.

CHAPTER 105

OIL BOOMS IN TIDAL CURRENTS

by

Ralph H Cross¹ and David P Hoult²

INTRODUCTION

The classic, and most effective way to prevent the spread of oil spilled in harbors is by surrounding the spill with a floating barrier, or boom. In calm water, with no currents, early devices made from telephone poles and canvas were more or less effective. In the presence of currents, however, and particularly with larger spills, the problem rapidly becomes more complex, and the rational design of oil booms requires an understanding of the behavior of the oil and the boom in the current.

This paper presents the results of an investigation into the oil holding capacity of a boom in a steady current, and the forces and moments acting on such a boom.

I OIL CAPACITY

A floating oil boom anchored at each end in a current to form a U-shaped pocket, with the opening in the U facing upstream, can gather and hold significant volumes of oil under proper conditions. There are two main features which determine whether such a boom will hold oil, and how much oil can be held. The first is the existence of a critical Froude number, above which the boom holds no oil, and the second is the shape and behavior of the pool of oil held by the barrier.

A Critical Froude Number

A quick estimate of whether or not a boom will hold oil at all can be made by comparing the forces acting to draw a small column of oil under the barrier with the buoyancy of such a column of oil, for a section of barrier perpendicular to the current. For a column of oil of depth equal to the barrier depth, d , and unit cross-sectional area (in the horizontal plane), the force driving the oil downward is the difference between the stagnation pressure where the free surface of the water intersects the boom and the free-stream pressure near the bottom of the boom. Neglecting hydrostatic pressures (included in the buoyancy term), this difference is $U^2/2g$, where U is the current velocity and g is the acceleration due to gravity. The resulting downward force is, thus $1/2\rho_w U^2$. The net buoyancy is given by $\rho_w g \Delta d$, where ρ_w is the mass density of the water and Δ is the fractional density difference between the oil and the water, conveniently given by $\Delta = (1 - \text{specific gravity of oil})$. At incipient failure of the boom to hold any oil, these two expressions can be equated, yielding a densimetric Froude number

¹Assistant Professor, Department of Civil Engineering, M I T

²Associate Professor, Department of Mechanical Engineering, M I T

$$F' = \frac{U}{\sqrt{g\Delta d}} = 2^{1/2} \quad (1)$$

At Froude numbers above $\sqrt{2}$, the barrier will hold no oil, while below this figure, some quantity of oil will be held

Since the stagnation pressure depends on the component of the velocity normal to the barrier, this analysis also shows that failure will occur most readily in the apex of the boom (bottom of the U)

B Capacity of the Boom

Given conditions, then, under which a barrier will hold oil, the remaining question concerns the amount of oil held. This question can be approached by considering a two-dimensional pool of oil held up against a barrier by a current (Fig 1). If the oil is significantly more viscous than the water, motions in the oil itself are small, and the configuration of the pool, $h(x)$ vs x (see Fig 1), is determined by a balance between the shear stresses on the underside of the oil, τ , and the horizontal hydrostatic pressure gradient corresponding to an increase in thickness of the pool of oil

$$\rho_w g \Delta h \frac{dh}{dx} = \tau = \frac{1}{2} \rho_w C_f U^2, \quad (2)$$

where C_f is the friction coefficient. Rearranging and integrating,

$$h^2 = \frac{U^2}{g\Delta} \int_0^x C_f dx \quad (3)$$

which shows that the shape of the pool depends on the distribution of the shear stress coefficient along the underside of the slick

Near the leading edge of the pool ($x = 0$), the above analysis does not always apply. For velocities above 0.75 to 1.0 ft/sec, a "head wave" forms, as described in Wick (1969). While the details of this phenomena are not well understood, it has been noted that leakage of the barrier can occur by entrainment of oil droplets from the head wave into the floor, and, moreover, it is believed that the head wave does not scale according to the densimetric Froude number.

Near the barrier, the slick can become slightly thinner, due to stagnation pressures against the barrier. This, however, does not materially affect the volume of oil held.

C Experimental Results

A series of experiments were performed in the glass-walled sedimentation flume in the Ralph M. Parsons Laboratory for Water Resources and Hydrodynamics of the Department of Civil Engineering at M I T. This flume is

2.5 ft wide, 1.0 ft deep, and 40 ft long, and is equipped with a self-contained recirculating flow system capable of discharges up to 1.75 ft³/sec

The barrier used consisted of a masonite panel extending across the channel, and mounted from above so that its depth of immersion, or draft, d , could be adjusted. For given flow conditions, oil was added upstream, and allowed to collect against the barrier until leakage was imminent. Slight leakage at either end of the barrier, where it met the glass tank walls, was ignored. Measurements were then taken of the pool thickness, h , at various distances from the barrier, using a scale on the glass tank walls. Two types of oil were used in these experiments: soybean oil and No. 2 fuel oil, with the following properties:

<u>Oil</u>	<u>Δ</u>	<u>μ/μ_{water}</u>
No. 2 fuel	0.77	30
Soybean	1.38	2

The profiles so obtained are shown dimensionlessly as $g \Delta h/U^2$ vs $g \Delta x/U^2$ in Fig. 2, taken from work done by Robbins (1970). The scatter can be attributed to several sources:

1. As the water flow velocity was not constant across the tank, the position of the leading edge varied, the point chosen was an "eyeball average" of its position across the tank.
2. The presence of interfacial waves on the oil-water interface made an accurate measurement of thickness difficult. At higher flow rates, these waves were 1/8" - 1/4" high and an inch or two in length. Near the boom, especially, reflections from the boom acted to make the waves higher. Superposed on the interfacial waves were longer surface waves of similar height generated by the turbulence at the upstream end of the tank.

The data of Fig. 2 gives $h \propto x^{1/2}$, implying that C_f is independent of x , Eq. 3 then becomes

$$h^2 = \frac{U^2}{g\Delta} C_f x$$

or

$$\frac{g\Delta}{U^2} h = C_f^{1/2} \left(\frac{g\Delta}{U^2} x \right)^{1/2} \quad (4)$$

For the fuel oil, $C_f = 0.05$, while for the soybean oil, $C_f \approx 0.08$ for $g \Delta x/U^2 > 120$. (The deviation for low $g \Delta x/U^2$ for soybean oil is believed due to low Reynolds' numbers.)

The difference between the values of C_f observed is probably due in part to the scatter in the data, however, weak viscosity or surface tension effects cannot be ruled out

The argument for a constant C_f at sufficiently high Reynolds' number (based on x , the distance from the leading edge), has been made by Robbins and Hoult by analogy with a sand roughened flat plate. For low Reynolds numbers, the plate looks smooth, and C_f decreases with increasing x . For high Reynolds numbers, with the sand grain size, k_s , increasing with increasing x such that the ratio k_s/x is constant, C_f is constant (Schlichting 1960). In the oil slick, the sand roughness corresponds to the growing interfacial waves

Using a value of 0.08 for C_f Eq 4 can be written

$$\frac{g\Delta}{U^2} h = 0.09 \left(\frac{g\Delta}{U^2} x \right)^{1/2}$$

or

$$h = 0.09 \left(\frac{U^2}{g\Delta} \right)^{1/2} x^{1/2} \quad (5)$$

By inserting the effective boom draft, d , for h , and the slick length, ℓ , for x in Eq 5, a relation between slick length and boom draft is obtained

$$\ell = \frac{d^2}{(0.09)^2 (U^2/g\Delta)} \quad (6)$$

To obtain the volume stored per foot width, h can be integrated against x to give

$$V = \int_0^{\ell} h(x) dx = \frac{2}{3} \left[\frac{U^2}{g\Delta} C_f \right]^{1/2} \ell^{3/2}$$

or, in dimensionless form,

$$\frac{V}{d^2} = 82/F^{1/2} \quad (7)$$

The profile data was integrated numerically to find the volume stored, the results are shown in Fig 3. (Included in Fig 3 are data from preliminary runs using other oils. The scatter in this data is generally worse.) It can be seen from Fig 3 that Eq 7 gives good engineering prediction of oil retention capacity, and that the critical Froude number is approximately 1.3

II FORCES ON BARRIERS

This section treats the forces on a vertical flat plate oriented normal to the current, a geometry typical of most barriers. Two cases will be considered: the barrier alone, without oil, and the barrier full of oil to its depth, d .

A Two-Dimensional Forces

In the absence of oil, the barrier is simply a vertical flat plate, at high enough Reynolds numbers, the drag coefficient, C_D ($D = 1/2 \rho_w U^2 C_D d L$, where D is the drag force and L is the barrier length) is independent of Reynolds number. With a free surface present, however, one should anticipate a dependence on the Froude number, $F = U/\sqrt{gd}$, and a similar dependence for the location of the resultant force.

With the barrier full of oil, the densimetric Froude number must be less than 1.3. For a typical value of Δ of 0.10, the regular Froude number is thus less than 0.4. Since the Froude number squared represents the ratio of dynamic ($1/2 \rho U^2$) to hydrostatic ($\rho g d$) forces, and since this number is small, a balance of hydrostatic forces from the water on one side and the oil on the other can be made, recognizing that the free surface of the oil lies $d\Delta$ above the water surface.

$$D/L = \rho_o g \left(\frac{\rho_w d}{\rho_o} \right)^2 - \rho_w g \frac{d^2}{2} = g \rho_w \Delta \frac{d^2}{2} \quad (8)$$

Note that D is independent of the velocity, U . The location of the resultant force can be shown by a similar calculation to be approximately $2/3 d$ above the bottom of the barrier. For convenience, the force expressed by Eq. 8 can be converted to a drag coefficient, as

$$\frac{1}{2} \rho U^2 d L C_D = \frac{1}{2} L \rho g \Delta d^2$$

Thus,

$$C_D = 1/F'^2 \quad (9)$$

A series of experiments was performed in the tank described above, but with a barrier hung vertically from long wires, and constrained horizontally only by three LVDT-type force transducers, connected to an operational manifold and a digital voltmeter, arranged and adjusted to give direct readout of force and moment data. Dead-weight calibrations were used throughout.

Figs 4 and 5, from Robbins' paper, show values of C_D and the height, z , of the resultant force, both as functions of the Froude number. Without oil, the drag coefficient varies from about 1.6 at low Froude numbers to 1.2 at higher Froude numbers. With oil, the behavior predicted by Eq. 9 appears, verifying the hydrostatic assumptions.

The moment data, shown as z/d , the relative height of the resultant force, also support the assumptions, particularly for lower Froude numbers. With oil, z/d is approximately 0.55 to 0.65, and without oil, 0.45 to 0.55. It is important to note that a variation of approximately $0.2d$ will be encountered in the depth of the resultant force, so any barrier design has to have adequate roll stability to resist this varying moment.

III THE DEPLOYED BOOM

To find the total oil held by a boom anchored by its ends in a current (Fig. 6), the shape taken must be found. Since the momentum of the flow against the barrier depends on the velocity component normal to the barrier, as $\rho U^2 \cos^2 \theta$, one can assume for simplicity that the drag coefficient for a section of boom at an angle θ is

$$C_D(\theta) = C_D(\theta = 0) \cos^2 \theta \quad (10)$$

Assuming that tangential forces on the boom are negligible, and that the boom has zero bending stiffness, an analysis of a differential section of the boom shows that the tension is constant throughout, and that the normal force on the boom is balanced by the tension divided by the local radius of curvature of the boom. This can be expressed as

$$L \frac{d^2 x}{dy^2} = \frac{1}{\lambda} \left[1 + \left(\frac{dx}{dy} \right)^2 \right]^{1/2} \quad (11)$$

where L is the total length of the boom, λ is a tension factor which relates the tension in the boom, T , to the normal force on a "stretched-out" boom,

$$\lambda = \frac{T}{\frac{1}{2} \rho U^2 d L C_D(\theta = 0)} \quad (12)$$

Assuming d and $C_D(\theta = 0)$ to be constant, equation 11 can be integrated, using the boundary conditions

$$x(0) = x'(0) = 0$$

$$\frac{L}{2} = \int_0^{y_{\max}} \frac{dy}{\cos \theta}$$

The first boundary condition states that the slope of the barrier (dx/dy) is zero at the apex of the boom, and the second, that the boom has length L

The solution to Eq 11 gives the boom shape,

$$\frac{x}{L} = \lambda \left(\cosh \frac{y}{L\lambda} - 1 \right) \quad (13)$$

where λ is obtained as a function of y_{\max}/L (see Fig 6) from

$$\frac{1}{2} = \lambda \sinh \frac{y_{\max}}{L\lambda} \quad (14)$$

The table below gives values of λ for different values of y_{\max}/L

y_{\max}/L	λ	y_{\max}/L	λ
10	028	30	163
15	050	35	231
20	078	40	336
25	115	45	560

Note that the ratio of opening width to boom length is $2 y_{\max}/L$

The approximate spread of the mooring lines can be computed from the barrier angle at $y = y_{\max}$, from

$$\frac{dx}{dy} = \sin \frac{y_{\max}}{\lambda L} \quad (15)$$

For $y_{\max}/\lambda L < 1$, Eq 13 can be approximated by

$$\frac{x}{L} = \frac{1}{2\lambda} \left(\frac{y}{L} \right)^2 \quad (16)$$

In fact, $y_{\max}/\lambda L$ is less than 1 only for $y_{\max}/L > 0.42$, however, this parabolic approximation is useful over a much wider range of values

A final calculation of the total amount of oil held can now be made, using Eqs 5 and 16

$$\text{Volume} = 1.9 \times 10^3 L d^2 \left(\frac{\lambda d}{L} \right)^{1/2} \left(\frac{g \Delta h_o}{u^2} \right)^3 \quad (17)$$

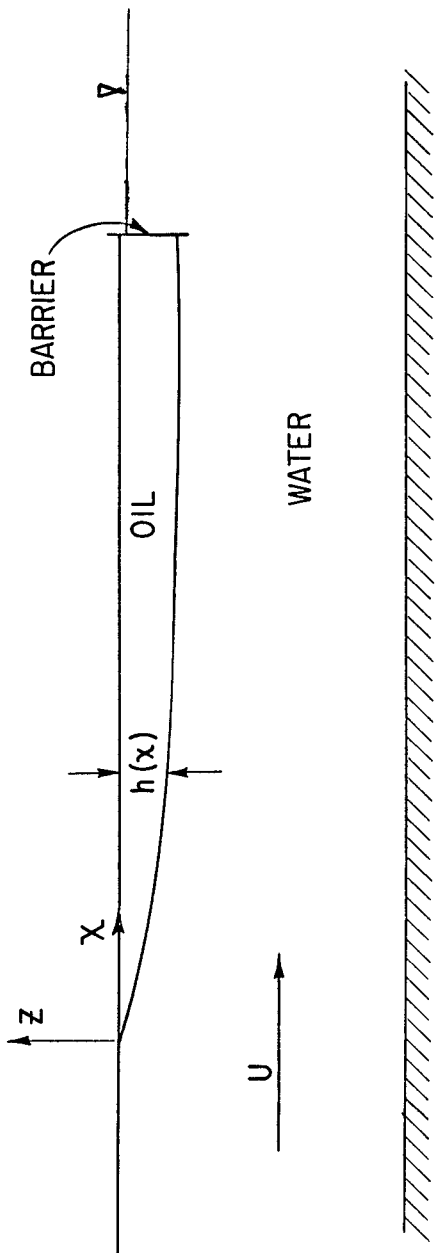
Here h_0 is the depth of the oil in the apex of the boom, this must be less than the draft, d . Moreover, $F = U/\sqrt{g\Delta h} < 1.2$, and $\ell < x_{\max}$

CONCLUSION

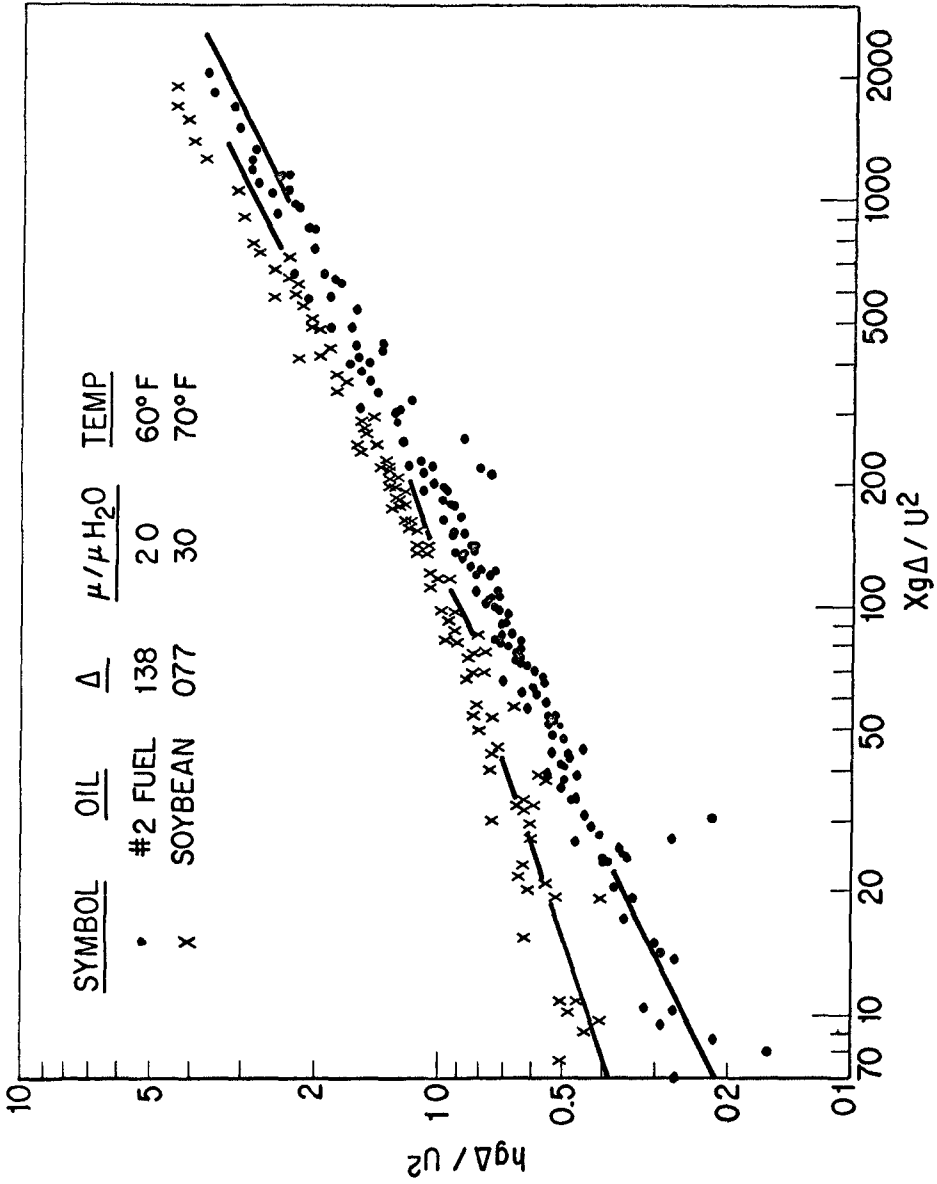
Using the above information on oil holding capacity, barrier shape, and forces on barriers, it is possible to design and operate floating barriers to capture oil spills in rivers and tidal currents, at least at modest velocities. At higher velocities, but sub-critical Froude numbers, some leakage from head wave entrainment can be expected. The concentration of oil in such a pool will greatly simplify the collection and removal of oil from the water surface.

REFERENCES

- Hoult, D. P., 1970, "Contained Oil Spills by Physical and Air Barriers", Joint Project sponsored by Department of Mechanical Engineering, Department of Civil Engineering and Department of Naval Architecture and Marine Engineering, Massachusetts Institute of Technology.
- Robbins, R. E., 1970, "The Oil Boom in a Current", M.S. Thesis, Department of Electrical Engineering, Massachusetts Institute of Technology.
- Schlichting, H., 1960, Boundary Layer Theory.
- Wicks, M., 1969, "Fluid Dynamics of Floating Oil Containment by Mechanical Barriers in the Presence of Water Currents", Shell Pipe Line Corporation Research and Development Laboratory, Houston, Texas.



PILE-UP OF A SLICK AGAINST A BARRIER
FIGURE 1



NON-DIMENSIONAL OIL THICKNESS, $hg\Delta/U^2$ VERSUS NON-DIMENSIONAL DISTANCE FROM THE LEADING EDGE OF THE SLICK $Xg\Delta/U^2$

FIGURE 2

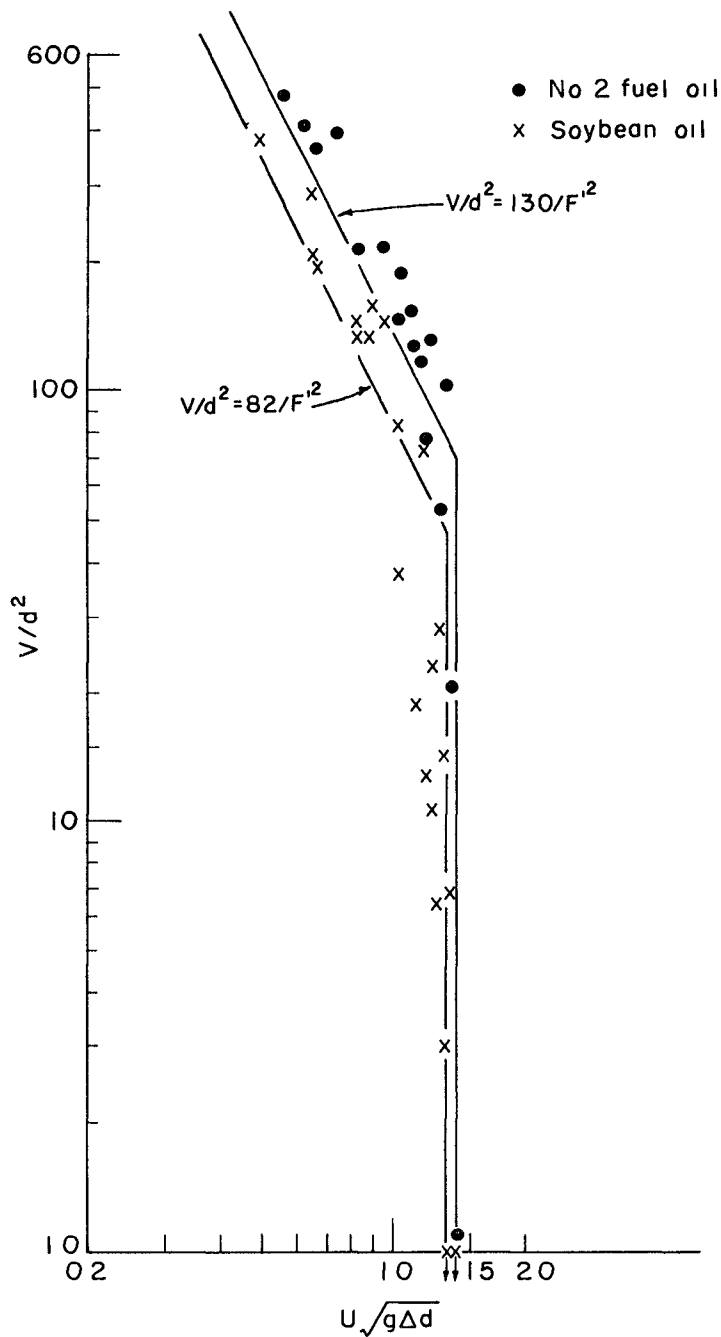


FIGURE 3 Non dimensional oil volume held, V/d^2 , versus densimetric Froude number, $U\sqrt{g\Delta d}$

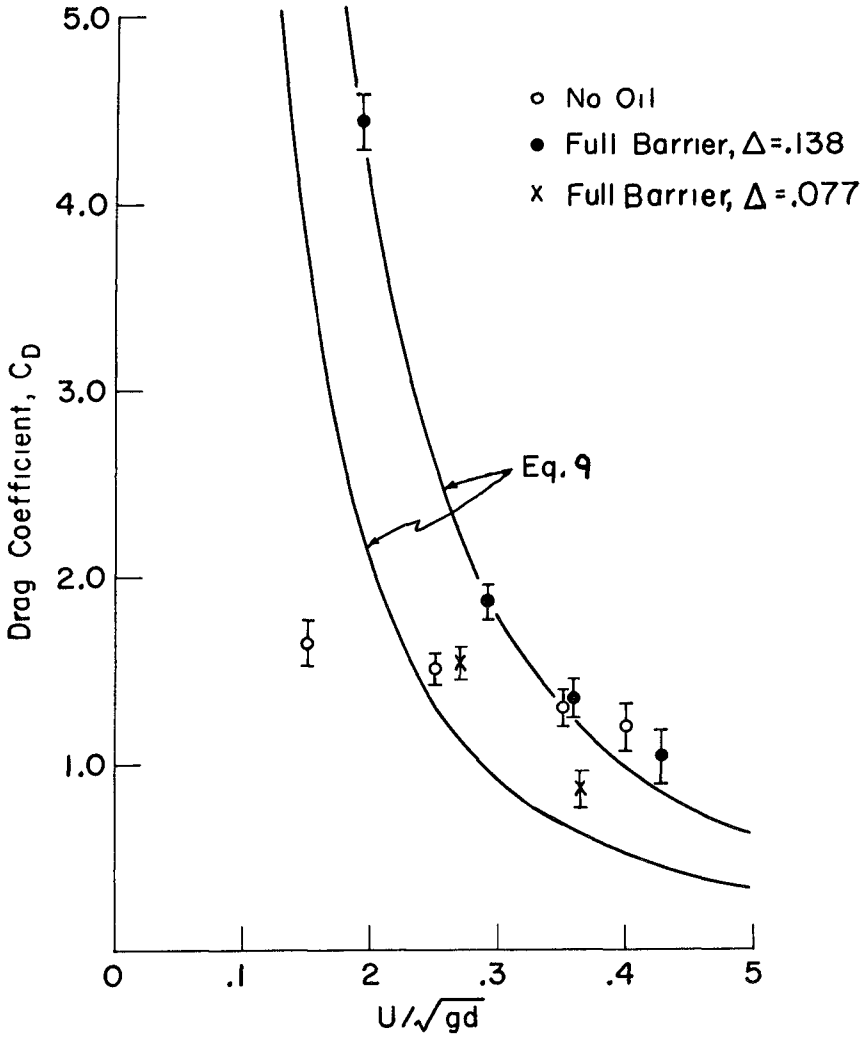


FIGURE 4 Drag coefficient, C_D , versus U/\sqrt{gd}

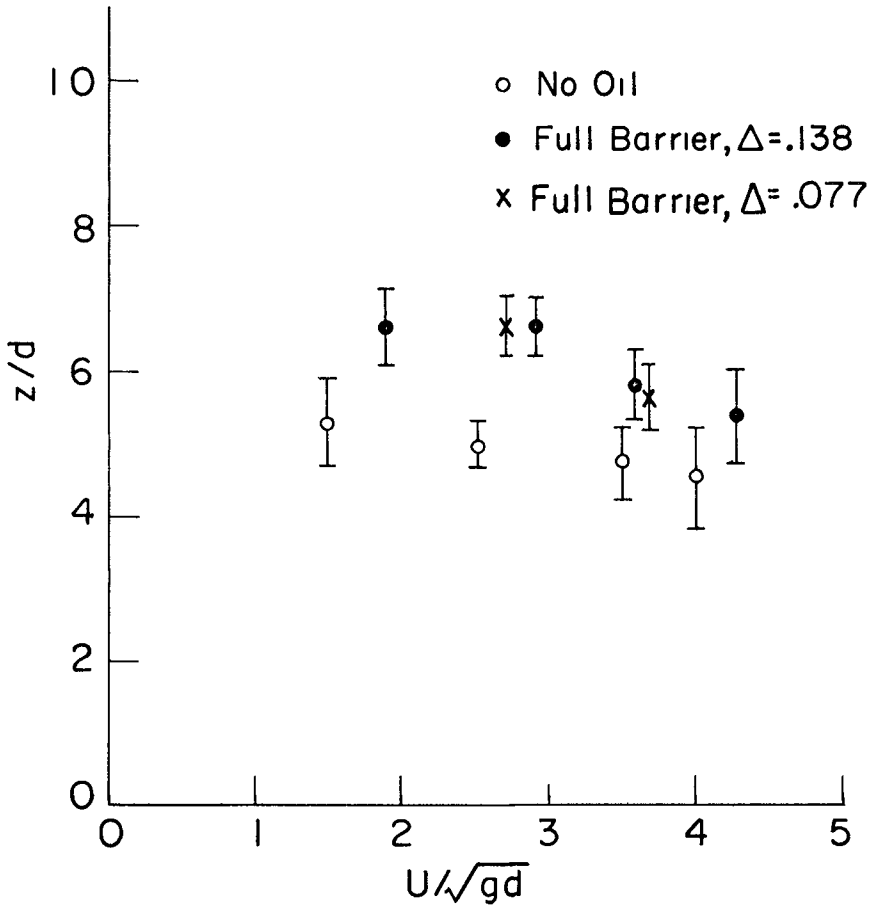


FIGURE 5 Location of drag force from lower edge of boom, z/d , versus U/\sqrt{gd}

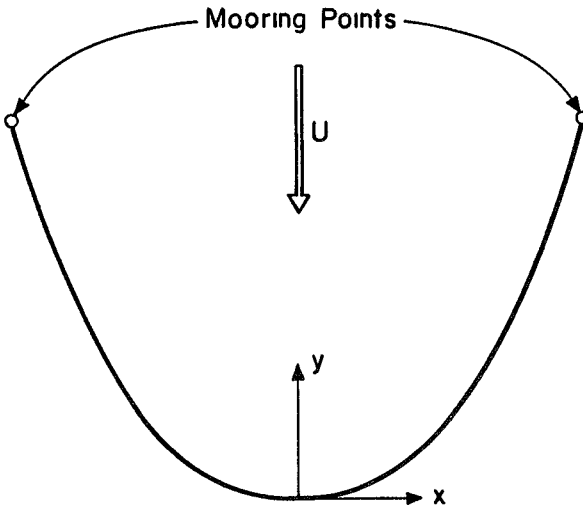


Figure 6 Sketch of planform of a boom in a current showing coordinates



Carolina Beach Inlet, North Carolina

PART 4. COASTAL, ESTUARINE, AND ENVIRONMENTAL PROBLEMS

Treasure Island, St. Petersburg, Florida



CHAPTER 106

ENVIRONMENTAL PLANNING OF A BAY AND COASTAL LAGOON SYSTEM

by

Norman T Gilroy
Architect and Environmental Planner
Norman T Gilroy and Associates
Mill Valley, California

The 1970s are, it seems, the beginning of an "age of environmental awareness " Never before has our nation been so conscious of the necessity for protection of the quality of its waters, its air, its aesthetic environment, and the productivity of its earth, and never has it been so aware of the potential, within man's actions for progress for the pollution of his environment or the creation of imbalance within the natural dynamic system. The realization is growing that the system of natural dynamics, the ecosystem and the natural aesthetic environment in which we live are, in fact, part of a complete interrelated, interdependent and synergistic "Environmental System " Man made modification of any part of the System carries with it the potential of effects extending throughout the rest of the system, often resulting in major, and at times catastrophic, modification of the natural balance of the physical environment as we know it today.

Though the principles of environmental sensitivity are only newly being adopted by our media, our community leaders and our elected officials, there are some who have been advocating and practicing the principles of environmental planning for some time. It has long seemed logical that major engineering or planning programs, capable of generating extensive modifications to the environment into which they are interposed, should be considered, throughout all their phases in terms of the entire spectrum of environmental factors which make up the site and its surroundings--yet rarely is this the case.

An area of particular environmental sensitivity lies in our ocean and along our coastline. Here nature's forces are at their most dynamic, while her ecological delicacy is often at its most vulnerable. The ocean's waters frequently act as a transfer medium, permitting the impact of man's modification at a specific location to be felt over great distances. We need only to remember any of numerous examples of the loss of beaches, radical modification of coastline characteristics, extensive changes or virtual annihilation of segments of our coastal ecosystem, and the effects of heated waste water emitted from power plant cooling systems upon adjacent ecosystems, to be aware of the potential effects of man's change upon downcoast areas within the ocean system.

Nature is not always capable of coping with her own problems, however. Frequently the natural sediment movement processes at work in our coastal waters or heavy growth of natural plant life can be as instrumental in smothering a portion of an ecosystem as any actions taken by man. Such is the case in many of the intertidal lagoons along the coastline, whose fate it is to disappear, transformed by sedimentation into a muddy meadow, if nature is allowed to run her course without man's intervention.

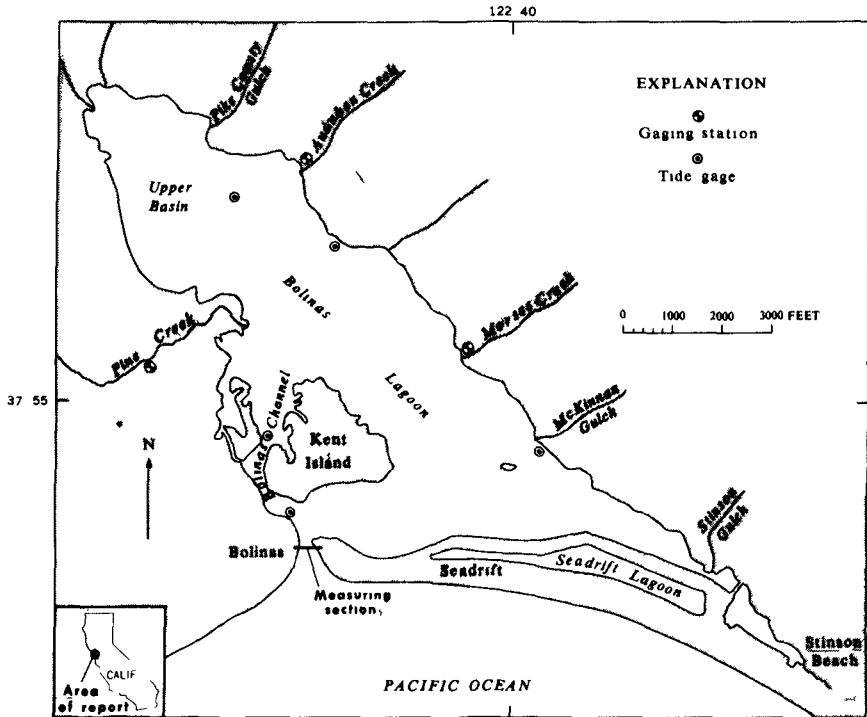


Figure 1 Bolinas Lagoon

Few more illustrative examples of such conditions, combined with the complete range of ocean environmental systems, exists than at Bolinas Lagoon on the west coast of California, twelve miles north of San Francisco (Figure 1). Bolinas Lagoon is a triangular, intertidal coastal lagoon three miles long and one and one-half miles wide, which lies in the rift valley of the San Andreas Earthquake fault which runs the length of the State of California. The Lagoon is separated from the Pacific Ocean by a curving sandspit, which, together with the high cliffs of the Bolinas Headland and Duxbury Reef to the west, form a typical hooked bay configuration. The main channel, the only link between the Lagoon and the ocean, lies between the sandspit and the beginning of the headland at the south-westerly corner of the Lagoon, adjacent to the historical town of Bolinas. Through a geological phenomenon, radically different geological formations flank the Lagoon on either side of the fault, contrasting the softly rolling, steep yet stable, Franciscan formation hills of the coastal range to the east, with the highly erodible miocene marine terraces of the Bolinas Mesa Headlands and the beginnings of the Point Reyes Peninsula to the west. Sedimentation has continued unchecked for centuries, with some encouragement by man's logging operations in the 1870s when the watershed lands were denuded to serve the need for timber for the building of San Francisco. Today the Lagoon's circulatory pattern is virtually

inoperative as a self-flushing, self-maintaining, dynamic system, and an offshore bar has grown across the channel mouth further minimizing the flow of oxygenated tidal water to the Lagoon. The extremely productive ecosystem of the Lagoon shows signs of faltering, with die-off occurring in areas no longer adequately supplied with tidal circulation. Clam populations, subsurface life systems, juvenile fish nurseries which serve the plentiful offshore fishery at the Farrallon Islands, bird feeding grounds, and harbor seal habitats all face the prospect of certain death if the process of nature continues unchecked, and with them will disappear many of man's recreational and sports opportunities, as well as a significant water resource of national and statewide importance.

Man has added to the complexity of the problem. The State of California has, for many years, designated Bolinas Lagoon as a priority site for a primary Harbor of Refuge to serve ocean sailors and fishermen from San Francisco Bay in times of fog, storm and emergency. The Lagoon is heavily polluted due to a continuous inflow of untreated effluent from an antiquated sewage collection system serving the town of Bolinas. The pressures for development of the watershed, as an extension of the growing metropolitan area of San Francisco, are mounting, and the growing flow of tourist visitors to the beaches of the area and to the newly-established Point Reyes National Seashore is placing new stress upon the small beach communities of the area, and upon the Lagoon itself, through a growing demand for use as a recreational resource.

There are still some who advocate inaction in the name of conservation, fearing, apparently, that man's modification of the natural processes may result in catastrophe rather than survival, apparently mindless of the fact that nature is on a suicide course of her own in Bolinas Lagoon, which can only be reversed by an act of God or by man's intervention. Fortunately there are others who recognize the potential for the survival and in the utilization of the Lagoon through a plan of action, created by man and based upon a deep understanding of the environmental systems which are Bolinas Lagoon.

In 1966 Norman T. Gilroy and Associates, Planners, Architects and Consultants in Environmental Design of Mill Valley, California, were engaged by local agencies to coordinate, implement and report on a multi-disciplinary program of study and research into the natural environmental systems of Bolinas Lagoon and its watershed, designed to act as the first step for planning the long-term conservation and use of the region and the Lagoon. From a virtually nonexistent economic base, thirty-six Federal, State, local, private and university research and funding programs were assembled into an integrated program of investigation valued at over \$208,000.

The natural environment of Bolinas Lagoon was analyzed in its three fundamental segments (1)*

a) The Watershed — Field investigations of the mineralogic and soil characteristics of sediment sources in the watershed lands, of the flow, velocity, and sediment transport characteristics of tributary water courses, and of local surface drainage systems and regional rainfall.

* See References

characteristics were undertaken by the U S Geological Survey (2) and the U S Soil Conservation Service over a 3-year period. An innovative graphic analysis system was utilized to define the sensitivity of the watershed to both erosion and change through development. Remedial measures to control and lessen natural sedimentation, and guidelines to guard against future acceleration of sedimentation through development in the watershed were defined for inclusion in local regulatory ordinances. Strong indications linked massive erosion of the Bolinas Headland, which has caused a 125-foot retreat in the 7,000 foot long, 120 foot high cliff-line over the past 56 years (and is caused by the combined action of groundwater-generated slides in the cliff face and the battering of heavy ocean storm waves), with the choking inundation of the Lagoon itself with light sediments. A combined buffer beach, intercept drainage gallery and surface drainage system are proposed to combat at source a problem which evidently pervades the entire dynamic system of Bolinas Lagoon.

b) The system of natural dynamics of Bolinas Lagoon and Bolinas Bay — A broad range of studies under the guidance of the U S Geological Survey was undertaken in the Lagoon itself. The Lagoon studies were supplemented by other studies in Bolinas Bay by the U S G S (2) and by the University of California under the guidance of J W Johnson. Following a detailed hydrographic and topographic survey of Bolinas Lagoon utilizing laser surveying techniques, periodic monitoring programs of flow velocities and sediment loads in the main channel to the ocean and in the circulatory network within the Lagoon were completed. The mineralogical characteristics of the bottom sediments of the Lagoon were analyzed and compared with the characteristics of sediment sources. Time lapse photography over a 15-month period monitored the changes in configuration of the sandspit and the main channel, and graphic comparisons were made between a series of quarterly bathymetric surveys of Bolinas Bay to plot the quantitative transport of sediments within the Bay itself. These studies were coupled with a mineralogical analysis of the bottom sediments of Bolinas Bay by P Wilde, a series of field observation studies and measurements of wave characteristics, a beach profile monitoring program, and mathematical analysis of the refraction of deep water storm waves as they impinge upon the shoreline of the sandspit. Much of this work is described in greater detail in companion papers by J W Johnson and P Wilde. (See Chapters 85 and 86)

The system of natural dynamics of Bolinas Lagoon and Bolinas Bay was thus defined. Contrary to previous assumptions, it was found that the littoral system of Bolinas Bay is largely self-contained, with sand moving onshore and offshore on a seasonal basis. This fact is confirmed by ecological studies of the bottom sediments of Bolinas Bay, which reveal a host ecosystem incapable of surviving in the everchanging conditions which would be consistent with an extensive downcoast littoral transport system. An arrowhead jetty channel stabilization system is recommended at a cost of \$2,500,000--a considerable reduction from the \$11,000,000 structures recommended previously using "worst case" design criteria without benefit of field research.

c) The Ecosystem — A series of 14 studies of the ecosystem of Bolinas Lagoon was completed by a team led by Joel Gustafson of Resources and Ecology Projects, Inc (3). Eighteen months of field studies mapped vegetation, fish nurseries, mollusk populations and defined key index species and the trophic food chain. A graphic "sensitivity analysis" of the Lagoon was completed, "grading" the Lagoon by degree of importance or sensitivity in the four major elements of the ecosystem, i.e., sub-surface life (clams, worms, shrimp, etc.), bird wading and feeding areas, fish and marine animal habitats, and marine aquatic and terrestrial plant life. A composite analysis of the four resulting charts indicates clearly the areas of greatest sensitivity in most need of preservation through establishment of a wildlife refuge, and those areas most able to cope with man's intrusion without damage to the ecosystem as a whole. Recommended restoration of the circulatory system of the Lagoon will renew the flow of oxygenated water to nourish the biota, while permitting flushing of pollutants and use of the Lagoon by man for recreation and harbor purposes. The study resulted in the moving of the primary harbor site location which had been deemed suitable for years, yet which, when scientifically examined, proved to be at the heart of the most delicate, ecologically important, area of the Lagoon system. A computer model of the circulatory system was built and tested, and is a medium for evaluation of all proposed physical change within the Lagoon for the future.

Having defined the natural systems of Bolinas Lagoon and evaluated their areas of sensitivity, decisions for the future of Bolinas Lagoon can be made in an atmosphere truly sensitive to the host environment. Examination of the future demands of man in the watershed have resulted in various recommendations which will permit nature and man's activities to co-exist, in some cases the improvements that will accompany man's uses will themselves be beneficial to the system as a whole. Not the least of these will be the maintenance of an open artery between the ocean and the Lagoon. Separation of the specific functions which the Harbor of Refuge must serve has prompted the innovative concept of a summer harbor located outside of the Lagoon behind the breakwater to cope with the maximum need for shelter in times of summer fog or emergency, and a small basin within the Lagoon to serve the lesser winter storm refuge need at a location protective of the overall ecological system. The quality of the natural biotic system has been recognized, and is utilized in a proposed marine biological research and education center and in various conservation-oriented recreation and park functions on the perimeter of the Lagoon. Large portions of the land necessary are already passing into the public domain through acquisition utilizing State and Federal funds. The Town of Bolinas is proposed for preservation and restoration as a historical landmark, with its beaches expanded through the cliff erosion solution recommended, and with its traffic problems largely solved as a part of the plan. Channel stabilization programs, cliff erosion solutions, harbor of refuge facilities, sewage treatment facilities and public use concepts have all been designed as multipurpose facilities, permitting funding through a number of State and Federal programs and enabling a relatively small community to implement solutions of considerable magnitude through proper structuring at the design concept stage.

REFERENCES

- 1 Gilroy, Norman T (1970) Bolinas Lagoon Its system of environmental dynamics and recommendations for its future preservation and utilization Prepared for the Advisory Commission on Navigation and Ocean Development, State of California, the Board of Harbor Commissioners of the Bolinas Harbor District and the County of Marin
- 2 Ritter, John R (1969) Preliminary studies of sedimentation and hydrology in Bolinas Lagoon, Marin County, California, May 1967-June 1968, U S G S Open-File Report, April 4, 1969
- 3 Gustafson, Joel F (1968-69) Ecological studies of Bolinas Lagoon, Parts 1, 2 and 3 (also see appendices of Reference 1)

CHAPTER 107

DETERIORATION AND RESTORATION OF COASTAL WETLANDS

By Sherwood M Gagliano
Hyuck J Kwon
Johannes L van Beek
Coastal Studies Institute
Louisiana State University
Baton Rouge, Louisiana 70803

ABSTRACT

Coastal Louisiana wetlands are a product of Mississippi River delta building that has occurred over a period of 5,000 years. The building process was a gradual one, for riverine and marine processes were very nearly balanced. In modern times man's use of the area (flood control, navigation improvement, exploitation of petroleum and other minerals, road building, etc) has seriously altered the natural balance. As a result, overbank flooding has been virtually eliminated and river flow is confined to channels discharging into the outer shelf area. Most transported sediment is now deposited in the deep Gulf of Mexico or along the continental shelf. Saltwater encroachment in the deltaic estuaries has been detrimental to fauna and flora. Even though considerable sediment deposition has resulted from the historic Atchafalaya River diversion and growth of subdeltas, comparative map studies indicate a net land loss rate of 16.5 miles²/year during the last 25 to 30 years. Land loss is only one symptom of general environmental deterioration.

A dynamic management plan is proposed for better utilization of combined freshwater discharge - dissolved solid and transported sediment input from the Mississippi River. Controlled flow into estuaries will reduce salinity encroachment and supply badly needed nutrients. Large areas of new marshland and estuarine habitat can be built by controlled subdelta diversion. Studies of natural subdeltas indicate that these systems are amenable to environmental management, salinities and sediment deposition may be manipulated to enhance desired conditions.

INTRODUCTION

Southern Louisiana is a 300-mile coastal lowland consisting of large tracts of marshes and swamps and innumerable lakes and bays. This extensive near-sea-level area, estimated at 4,000,000 acres (O'Neil, 1949), makes up the deltaic plain and marginal components of the Mississippi River delta system and is the result of deposition of river sediment during the past 5,000 years (Fig 1). Like all deltas, that of the Mississippi is a zone of interactions between fluvial and marine processes and constitutes one of the most dynamic situations in nature. The interaction of these processes through time results in a dynamically changing complex of environments within delta regions. Deposition of sediments vies with subsidence and erosion in a never-ending exchange of land and

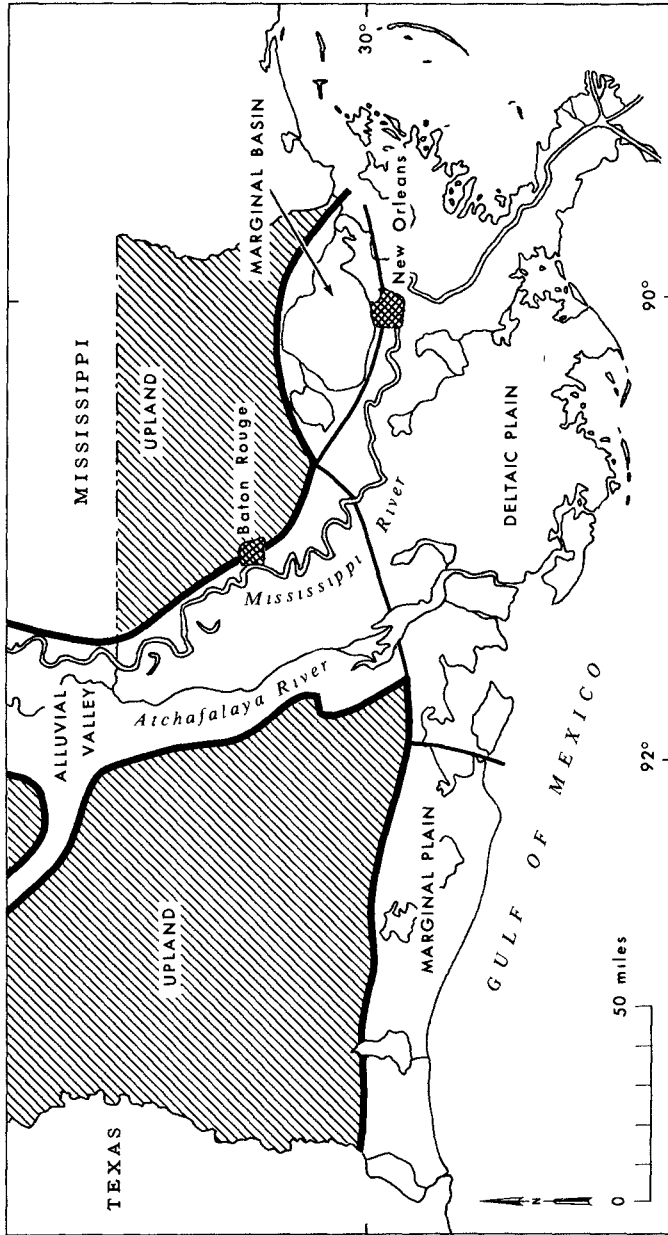


Fig 1 Major components of the Mississippi River delta system. Modern components of the delta system are bounded by geologically older Pleistocene terracelands (uplands). Marginal components lie updrift (marginal basin) and downdrift (marginal plain) of the area directly influenced by river distributary deposition (deltaic plain)

water areas. The balance between rates of deposition and the combined effects of subsidence and erosion by the sea causes shorelines of deltas alternately to advance seaward and to retreat. Seaward growth occurs at the mouths of active streams, whereas erosion results near the mouths of inactive streams which no longer transport sufficient sediment to sustain their seaward advance. This is the reason that delta building is so often depicted as a contest between the river and the sea. If the river deposits sediment faster than the sea is able to remove it, new land is added to the shore, and the delta is said to prograde. As the delta is extended, it gradually builds upward or aggrades by processes associated with lateral shifting of channels, by sediment deposition during overbank flooding, and by accumulation of plant and animal remains.

DETERIORATION OF THE DELTAIC COAST

Under Natural Conditions

Deterioration of the delta occurs if all or part of it is deprived of the necessary supply of river-borne sediment for its continued outward growth. This deprivation results in the reworking and/or removal of the seaward edge by wave attack, and the combined effects of compaction, consolidation, and subsidence lower the surface below sea level.

Under natural conditions progradation along any given segment of the deltaic shoreline is cyclic. During Recent geologic times southern Louisiana has witnessed development of numerous lobate extensions of the delta in areas of active discharge and sedimentation. After building one delta lobe, the Mississippi channel usually has shifted as a result of upstream diversion, and a new lobe has been built. Many repetitions of this process have produced a deltaic plain that is an aggregate of abandoned or inactive delta lobes, each of which has undergone a degree of deterioration dependent on its relative age.

Before the Mississippi occupied its present course, the river emptied its water and sediment discharge into shallow waters of the inner continental shelf, building lobes rapidly and efficiently. Under these circumstances the rate of new land building was always higher than that of land loss occurring concurrently in abandoned delta lobes.

From the preceding discussion it might be concluded that when viewed through geologic time a delta system is always in delicate balance--that is, on one side of the fulcrum there is an input of discharge and transported sediment and on the other side there are such factors as coastal erosion and subsidence, which cause shoreline retreat. The very existence of south Louisiana bears witness to the fact that there has been net progradation over the past 5,000 years.

Man's Effect on the System

Man's intervention in coastal Louisiana has seriously upset the natural balance in the delta system. In modern years it has been necessary to alter natural processes in order to prevent flooding and to improve navigation. As a result, virtually all overbank flow has been eliminated. Furthermore, the modern birdfoot delta is nearing the edge of the continental shelf,

and most transported sediments are now disappearing into the abyss. The river's attempt to divert to a new course that would allow development of a shallow-water delta lobe was aborted. The well-known attempted capture of the Mississippi by the Atchafalaya River has now been arrested by control structures, and the Atchafalaya is restricted to only 30 percent of the total Mississippi flow (U S Army Corps of Engineers, 1951, Fisk, 1952). As a result of these control measures the amount of land building has been sharply reduced, but the rate of land loss in abandoned portions of the deltaic plain continues.

These restrictions in themselves would have serious repercussions, but other developments have caused further imbalance in the delta system. Diking and drainage of marshland for agricultural purposes has been widespread and in many instances unsuccessful. After drainage organic marsh soils oxidize and shrink, reducing the drained land surface to below-sea-level elevations. Inundation by hurricane-generated storm surge has often resulted in abandonment, numerous rectangular lakes being left as mute testimony to land reclamation failure (Harrison, 1961). Equally serious has been the dredging of innumerable canals to provide access to oil well drilling sites and pipeline right-of-ways. These invariably alter circulation patterns in the estuaries, resulting in a general saltwater encroachment of the brackish swamps and marshes.

Map Studies of Land Loss

A fundamental question posed for this investigation, therefore, was, "Is the delta, and for that matter the coastal area on the whole, building or retreating?" The question has been approached by a number of workers (Morgan and Larimore, 1957, Treadwell, 1955, Kwon, 1969, Saucier, 1963, Russell, 1936, Peyronnin, 1962, Welder, 1959), who cited specific instances of shoreline advance or retreat. However, it has long been a common misconception that erosion occurring along some parts of the Louisiana coast is more than offset by the building of new land in other areas. We have attempted to reevaluate this problem by quantitative map studies, we used the ratio of land to water in a given sample area as an index of net loss or gain of land.

Fortunately, systematic planimetric mapping of coastal Louisiana was initiated in the 1890's by the U S Geological Survey. In the 1930's this area was remapped, and use was made of controlled aerial photomosaics. Mapping and remapping have continued since the 1940's, so that at present most of the 15-minute quadrangle areas have been covered at least twice. An example of changes that occurred in one small area between 1935 and 1953 is shown in Figure 2. This careful periodic remapping has made it possible to determine the ratio of land to water for a particular area and mapping interval, these values in turn can easily be converted into land loss or gain in acres per year.

The map shown in Figure 3 was constructed by contouring the land loss or gain rate obtained for each 7 1/2-minute quadrangle. From the map several things are immediately apparent. As indicated by the patterns, most of the deltaic plain is in a serious condition of deterioration. During the last 30 to 40 years land gain has been significant in only a few areas (notably in the lacustrine deltas of the Atchafalaya Basin). Areas of maximum loss generally occur inland from the Gulf shore, where brackish

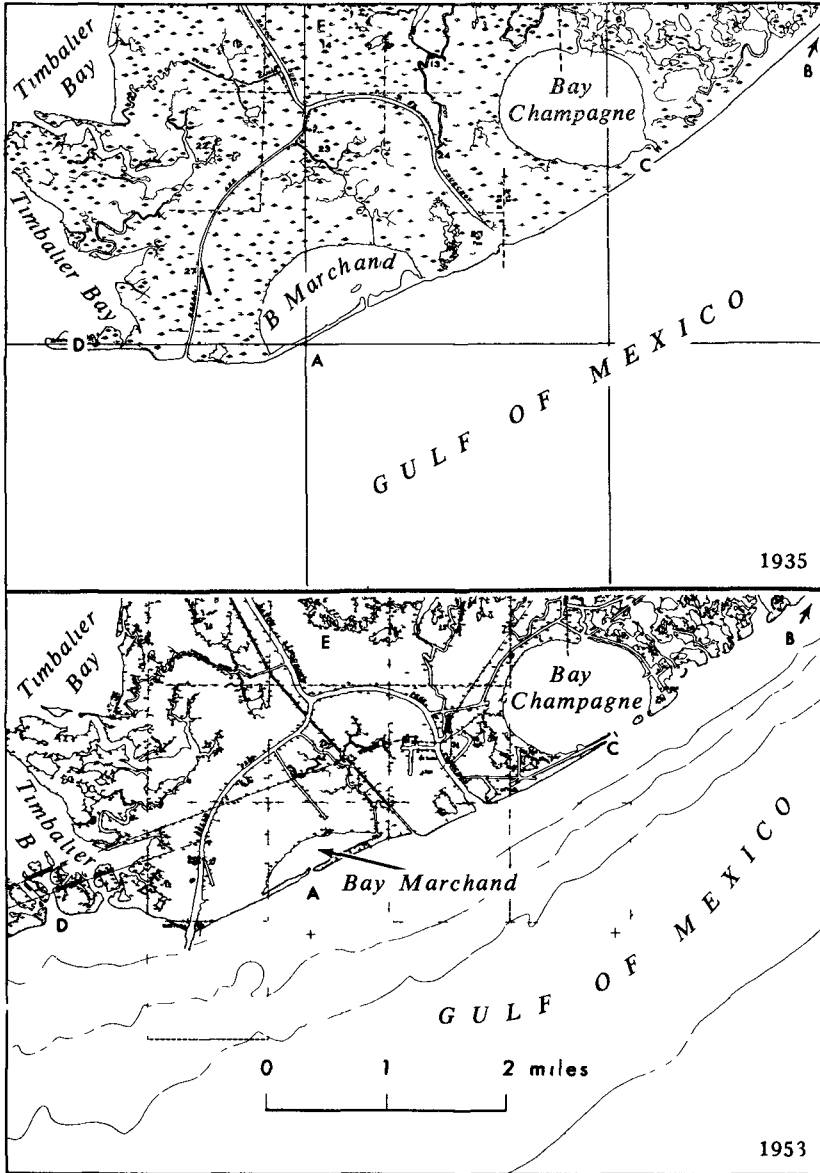


Fig 2 Land loss and shoreline change in the area covered by the Belle Pass quadrangle, south central Louisiana, 1935-1953 Several types of changes have occurred A, B, and C, Gulf shoreline retreat, D, washover fan development downdrift of retreating shoreline, E, marsh opening

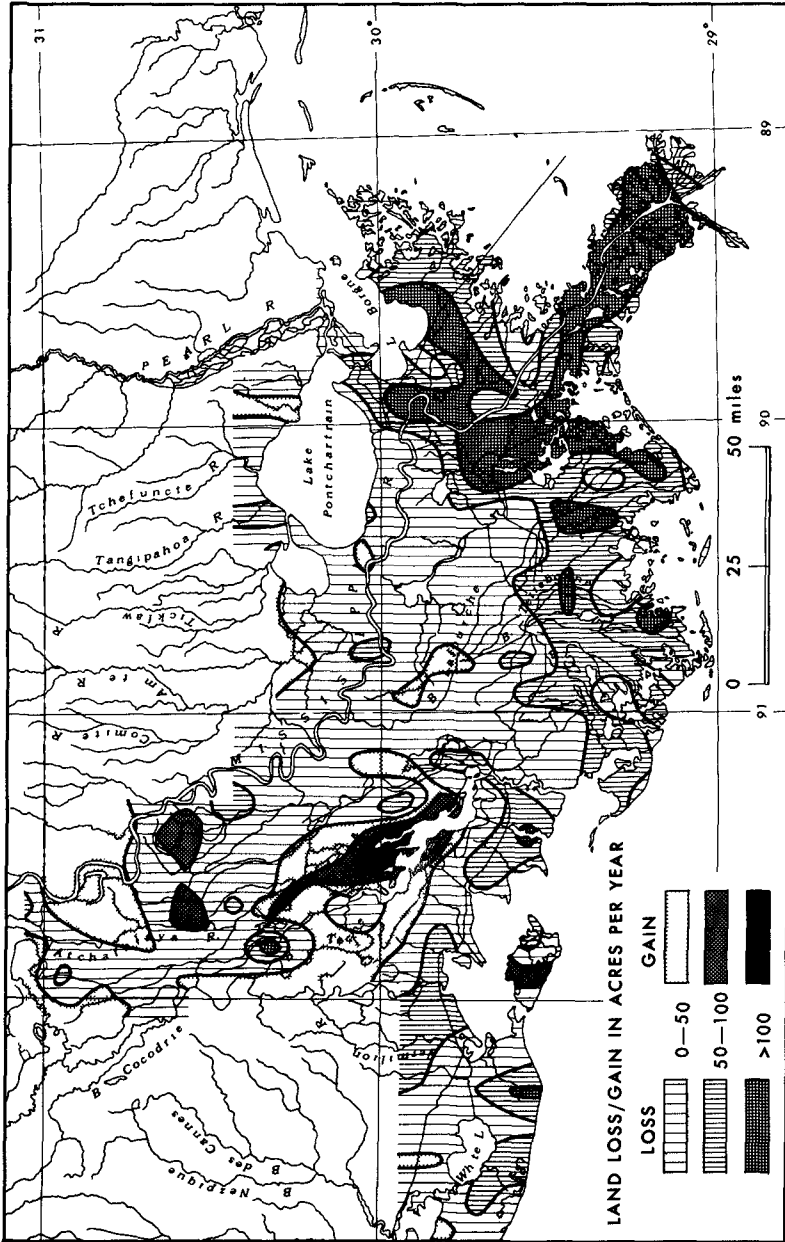


Fig 3 Rates of land loss and land gain in the Louisiana wetlands area Rates are calculated in acres per year per 7 1/2-minute quadrangle unit area An average 7 1/2-minute quadrangle covers 41,267 acres (After Gagliano and van Beek, 1970)

and fresh marshes are being subjected to saltwater intrusion (Chabreck, 1970, Palmisano, 1970) Subsidence is also undoubtedly a factor, as radiocarbon datings of buried marsh peats indicate that these are also areas of high subsidence rates (Coleman and Smith, 1964, Frazier and Osanik, 1969)

The net land loss figures are most impressive For the coastal Louisiana wetlands the land loss amounts to approximately 16 1/2 square miles per year (Gagliano and van Beek, 1970) This is an average for the last 25 to 30 years

The rates of change of land-to-water ratios established for each 7 1/2-minute quadrangle map can be analyzed in a number of ways One technique involves projection of the rates to establish land-water ratios for specific years within and beyond the period of map coverage Although such projections are based on the assumption that rates of change remain constant, the approach has some validity as a tool for prediction The map presented in Figure 4 depicts successive positions of the 50 percent land-water isopleth in the Mississippi deltaic plain for the years 1930, 1970, and 2000 The lines were constructed by determining land-water ratios for each 7 1/2-minute quadrangle for each year indicated Values were plotted at quadrangle center points, and contours were drawn on the basis of the points The 50 percent land-water line was selected as an index for analyzing the rate of land deterioration along the highly indented and irregular deltaic coast

The map indicates a progressive landward march of this line across the area The predicted position of the line in the year 2000 aids in identifying the most critical areas of deterioration Major estuaries are clearly undergoing rapid and drastic changes Within the estuaries the landward retreat of the line implies increases in both salinity and volume of the tidal prism

PROSPECTS FOR COASTAL RESTORATION

Areas of Active Sediment Deposition

The earlier discussion has attempted to define the symptoms of a disease, what are the prospects of a cure?

The key is obviously to be found in those areas where land gain is occurring For example, the Atchafalaya River--the Mississippi's only major distributary--is actively building a lacustrine delta (U S Army Corps of Engineers, 1951, Fisk, 1952) During the past 50 years Atchafalaya sediments have filled a series of large lakes, and the river is expected to construct a delta lobe into the Gulf within the next few decades

In the active delta, where one might anticipate the highest rates of land building, an anomalous situation exists As shown in Figure 5, approximately 75 percent of the total river flow and an equal proportion of transported sediment are discharged through four major outlets or passes As previously mentioned, and as shown in the figure, the mouths of these major passes lie in close proximity to deep water Consequently, most of the sediment transported by the Mississippi is simply dumped into the deep

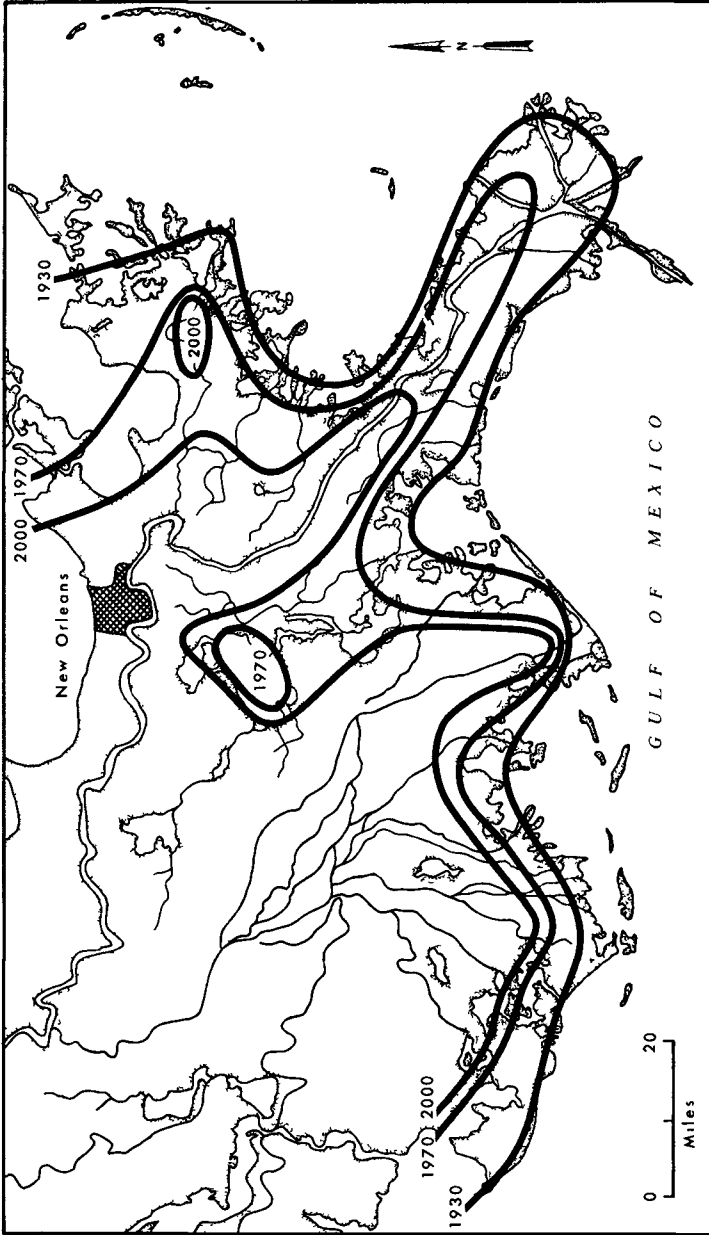


Fig. 4 Progressive position of the 50 percent land-water isopleth in the deltaic plain of the Mississippi River

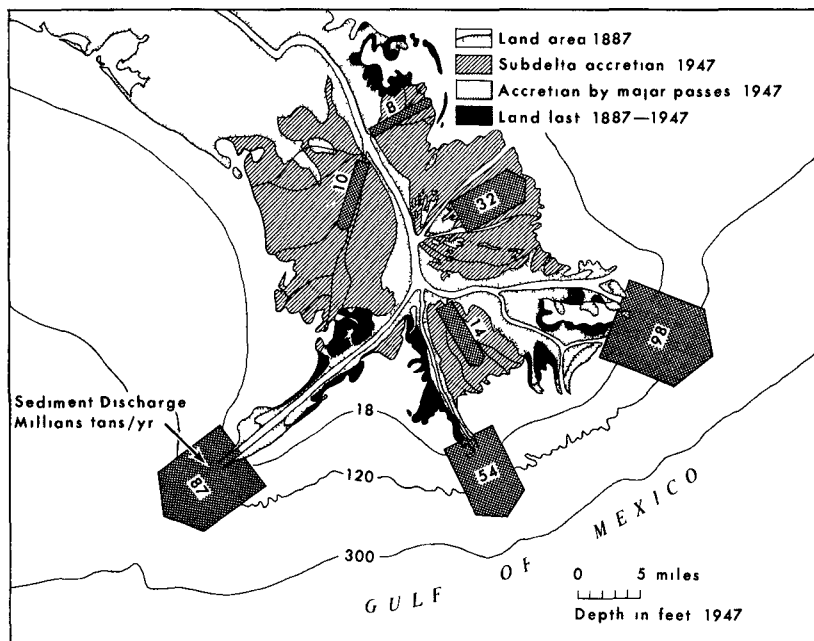


Fig 5 Relative sediment discharge and land accretion in the active birdfoot delta of the Mississippi River

Gulf, and there is little accretion of new land

In sharp contrast to the major passes, the 25 percent of river flow and transported sediment discharged through minor outlets has built a considerable landmass during historic times. This landmass is shown as subdelta accretion in Figure 5. From the standpoint of land building, then, these minor outlets, related to subdeltas, are of primary interest.

Subdeltas, which are appendages of major delta lobes, are usually active for periods of 50 to 100 years. As illustrated in Figures 5 and 6, much of the landmass of the lower delta has been constructed by such subdeltas during historic times. The dates shown in Figure 6 indicate the time of subdelta initiation. Prior to their development these areas were occupied by embayments. Comparative map studies reveal that the subdeltas account for over 80 percent of the new land built in the active delta during historic times.

One of the most interesting aspects of subdeltas is their cyclic nature—that is, during a period of 50 to 100 years they progress through a sequence of stages dictated by interaction of such factors as stream gradient, subsidence, and vegetation change (Welder, 1959, Coleman and Gagliano, 1964, Morgan, 1970). Figure 7 traces the life cycle of the

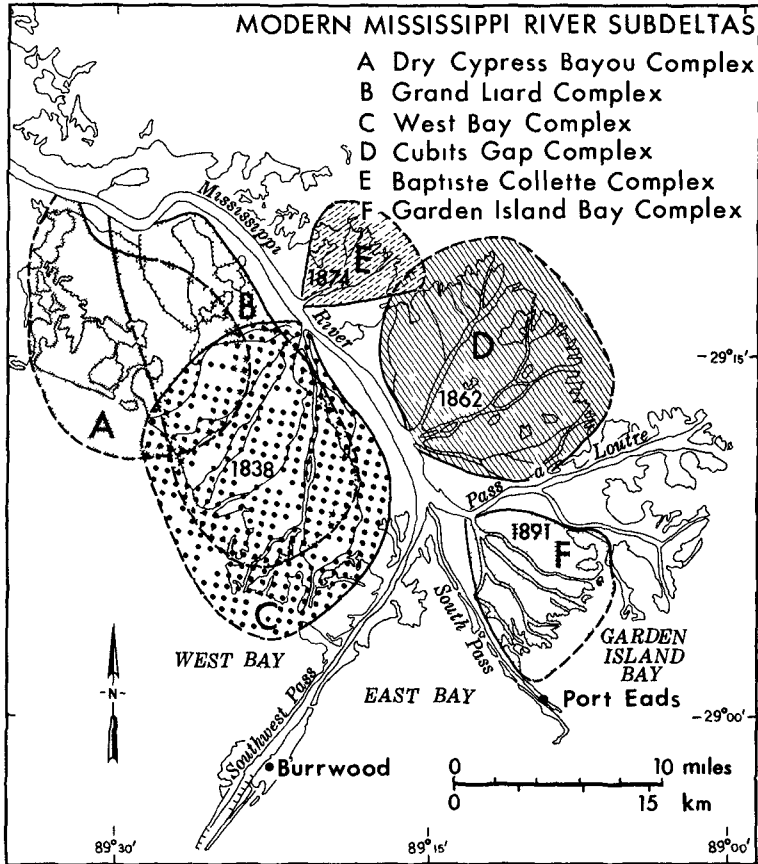


Fig 6 Subdeltas of the modern birdfoot delta Dates indicate year of crevasse breakthrough (After Coleman and Gagliano, 1964)

Garden Island Bay subdelta, as expressed by the gradual gain and loss of land area. Note that this subdelta was initiated by a crevasse or break in the natural levee of one of the major distributaries in 1891. It went through a short initial stage of subaqueous development until around 1900, when it started to increase in area rapidly. During this stage of fast subaerial growth land was added at an average rate of 0.75 miles²/year. Map measurements indicate that by 1940 the subdelta had built more than 30 square miles of land, utilizing less than 3 percent of the total flow of the river.

Since 1940 the Garden Island Bay subdelta has been in a stage of

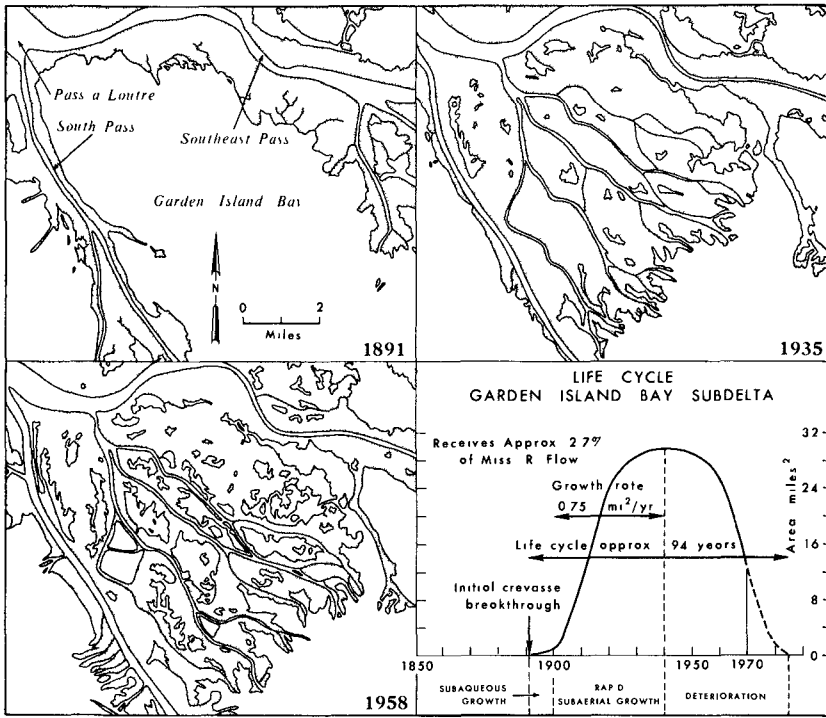


Fig 7 Progressive development of the Garden Island Bay subdelta after the crevasse breakthrough in 1891. Maps from U S C G S navigation charts

deterioration and has progressively decreased in land area as a consequence of subsidence and coastal erosion. This example clearly illustrates the relative rapidity of geological processes associated with subdelta building and deterioration and suggests that subdeltas are highly amenable to manipulation. Controlled diversions which will create new subdeltas are believed to be part of the solution to the environmental problem in coastal Louisiana.

A study correlating subdelta growth with sediment input has been conducted to provide a basis for estimating the likely effectiveness of controlled diversions of river flow in creating new land. This study centered on the four major historic subdeltas (indicated as C, D, E, and F in Fig 6). The average growth rate for the four subdeltas was found to be 0.7 square mile per year, using 5 percent of the total flow (Sporadic discharge measurements have been made in the major subdelta channels by the New Orleans District, U S Army Corps of Engineers). The efficiency of sediment retention ranged from about 50 to over 90

percent, and the average rate of retention was 70 percent

Controlled Diversions

Seven potential sites for the creation of new subdeltas have also been identified and evaluated three east of the Mississippi and four to the west (Fig 8) Assuming a configuration and size similar to one of the smaller modern subdeltas, average depth and volume for each of the proposed diversion sites have been determined

Long-term measurements indicate that the average sediment load of the Mississippi is 300 million tons per year If a 70 percent sediment retention efficiency figure for subdelta deposition is used, our data show that the river would be capable of building 12.3 square miles of new land per year if diversions were to be initiated along the lower reaches This is about 75 percent of the current net annual land loss of 16.5 square miles per year Thus it might be concluded that reestablishment of dynamic equilibrium in the Mississippi deltaic plain can only be approached However, other aspects of our studies indicate that relatively small volumes

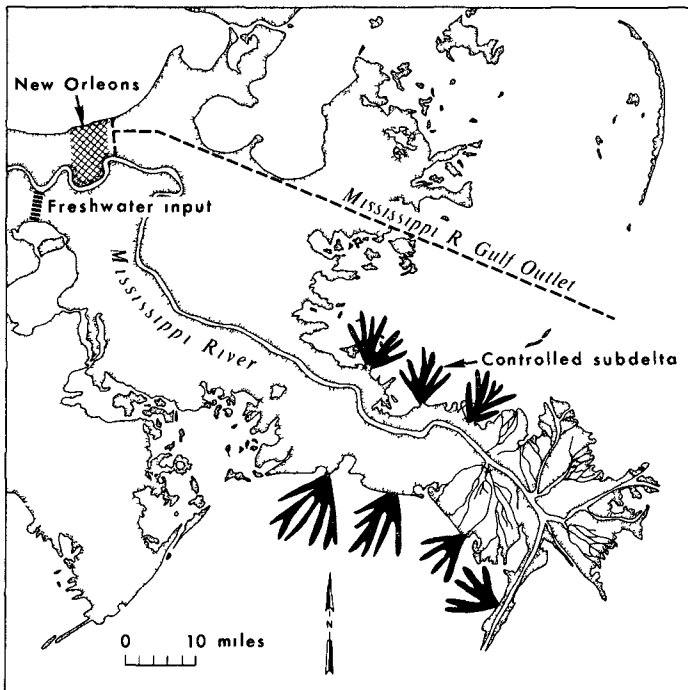


Fig 8 Suggested locations for controlled subdeltas and freshwater input canal in southeastern Louisiana

of fresh water introduced into the upper ends of interdistributary estuary systems could be used to offset salinity intrusion and introduce badly needed nutrients, both of which would offset conditions leading to rapid deterioration of brackish and fresh marshes (see Fig 8)

Such a dynamic management plan would have a number of benefits

- 1 The trend of land loss could be reversed,
- 2 Extension of the landmass would provide a valuable buffer zone for reducing hurricane-generated storm surges,
- 3 A highly irregular subdelta coast with maximum length of land-sea interface could be created, which would enhance productivity of fisheries and wild life,
- 4 Judicious spacing of controlled subdeltas could create new estuaries and increase the total areas of existing ones

During early settlement and initial utilization of the Mississippi valley and delta it was absolutely essential to prevent annual flooding and to improve navigation. Accomplishment of these tasks has made possible the unprecedented growth and development that south Louisiana is experiencing today. However, we have entered an era of total utilization of the Mississippi delta system. Because of the delicate natural balance associated with the delta, it is mandatory that a new long-term dynamic management plan be devised for orderly development and use of the area. It is the aim of our present studies to contribute to that goal.

ACKNOWLEDGMENTS

The Coastal Studies Institute, Louisiana State University, is supported by the Geography Programs, Office of Naval Research, under Contract N00014-69-A-0211-0003, NR 388 002. This study was funded by the Department of the Army, New Orleans District, Corps of Engineers, Contract No DACW 29-69-C-0092. The authors gratefully acknowledge the cooperation of personnel of the New Orleans District Office in providing data and guidance.

REFERENCES

- Chabreck, R H , 1970, Marsh zones and vegetative types in the Louisiana coastal marshes Ph D Dissertation, Dept Botany and Plant Pathology, La State Univ , Baton Rouge
- Coleman, J M , and S M Gagliano, 1964, Cyclic sedimentation in the Mississippi River deltaic plain Trans Gulf Coast Assoc Geol Soc , 14 67-80
- Coleman, J M , and W G Smith, 1964, Late Recent rise of sea level Bull Geol Soc Am , 75 833
- Fisk, H N , 1952, Geological investigation of the Atchafalaya basin and the problem of Mississippi River diversion U S Corps of Engineers Waterways Experiment Station, Vicksburg, Miss , 145 pp
- Frazier, D E , and A Osanik, 1969, Recent peat deposits--Louisiana coastal plain In (E C Dapples and M E Hopkins, eds) Environments of coal deposition, Geol Soc Am Spec Paper 114, pp 63-83
- Gagliano, S M , and J L van Beek, 1970, Geologic and geomorphic aspects of deltaic processes, Mississippi delta system In (S M Gagliano, R Muller, P Light, and M Al-Awady) Hydrologic and geologic studies of coastal Louisiana, La State Univ , Coastal Studies Institute and Dept of Marine Sciences, vol I, 140 pp
- Harrison, R W , 1961, Alluvial empire Arkansas (Pioneer Press)
- Kwon, H J , 1969, Barrier islands of the northern Gulf of Mexico coast sediment source and development La State Univ , Coastal Studies Series No 24, 51 pp
- Morgan, J P , 1970, Deltas--A résumé J Geologic Education, XVIII(3) 107-117
- _____, and P B Larimore, 1957, Changes in the Louisiana shoreline Trans Gulf Coast Assoc Geol Soc , 7 303-310
- O'Neil, Ted, 1949, The muskrat in the Louisiana coastal marshes La Dept Wildlife and Fisheries Commission Tech Report, 28 pp
- Palmisano, A W , 1970, Plant community-soil relationships in Louisiana coastal marshes Ph D dissertation, Dept Botany and Plant Pathology, La State Univ , Baton Rouge
- Peyronnin, C A , Jr , 1962, Erosion of Isles Dernieres and Timbalier Islands J Waterways and Harbors Div , Am Soc Civil Engrs , No WWL, pp 57-69

- Russell, R J , 1936, Physiography of the Lower Mississippi River Delta
La Dept Conservation Geol Bull 8, pp 3-199
- Saucier, R T , 1963, Recent geomorphic history of the Pontchartrain basin,
Louisiana La State Univ , Coastal Studies Series No 9, 114 pp
- Treadwell, R C , 1955, Sedimentology and ecology of southeast coastal
Louisiana La State Univ , Coastal Studies Institute Tech Report
No 6, 78 pp
- U S Army Corps of Engineers, 1951, The Atchafalaya River study Mississippi
River Commission, Vicksburg, Miss , vol 1, 47 pp
- Welder, F A , 1959, Processes of deltaic sedimentation in the Lower
Mississippi River La State Univ , Coastal Studies Institute
Tech Report No 12, 90 pp

CHAPTER 108

RESEARCH FOR THE COASTAL AREA OF THE DELTA REGION OF THE NETHERLANDS

by J J Dronkers

Hydraulics Division, Delta Works, The Hague, Netherlands

ABSTRACT

Tidal computations, wave studies, refraction computations, and morphological studies are discussed and practical results are mentioned. Theoretical investigations on refraction computations, in particular the accuracy, are dealt with in detail, because difficulties occurred in the practical applications. A former study of Morra, based on Kalinske's work on sand transport, has also been discussed in some detail in the section on morphological studies.

1 Introduction

The closing of the various sea-arms in the Deltaplan, the building of sluices, and the construction of Europort Harbour will cause great changes in the hydraulic and the morphologic situation along the south western part of the Netherlands. The practical purpose of these studies is the determination of the future conditions for the beaches and dunes, the discharge of the sluices, and the navigation. A big hydraulic model has been built at the Hydraulic Laboratory at Delft for the planning of the construction of Europort Harbour. The length scales are 1/640 in the horizontal plane, and 1/64 in the vertical.

The changes in the tidal motion can be computed in a satisfactory way, based on Leendertse's computational scheme. Difficulties do not occur with respect to the stability of this scheme. The accuracy of the method depends on the gridsize and the timestep.

In section 3, a discussion is given about wave research and practical determination of the energy wave spectrum. A relation of depth and breaking of waves is obtained from the wave observations.

Information is also obtained about the changes of the directions of the waves by means of refraction computations. These computations are based on the first order wave theory, which is an approximation of the irregular wave motion. Usually an iteration process has been applied for the determination of the celerity of the shallow water wave. In section 4 a direct formula for the celerity is derived by means of which the accuracy of the refraction computation is discussed.

The future depths must be determined in the coastal area. An iteration process must be carried out, because the changes in the currents and waves determine the morphological changes and reversely. The determination of the morphological changes is a difficult affair. The studies describe the physical factors in a general way. Simplifications must be accepted and the empirical coefficients in these formulae have to be determined from

observations in nature

The relation between the sediment transport and the currents is much better known than for the wave action. The methods of the determining of these relations will be discussed in section 5. The application of a physical scale model of the Haringvliet area for these studies has been considered, but rejected, because the sand in the Haringvliet mouths is very fine and the relation between sand transport along the bottom and that in suspension is unrepresentative in the scale model as compared to nature. For the future a great research program has been set up for getting observations from nature, during the period in which the great changes in the coastal area will take place. By means of the use of radio-active tracers, the direction and the relative significance of the sand transport can be determined. The most important tool is however the study of the changes in the shape of the bottom obtained from periodically repeated soundings after every three months.

The programs for the computations on the electronic computer of the Rijkswaterstaat (Elliott 503) are composed in Algol by the Mathematical Physical Division.

2 Tidal computations in the coastal areas of the Delta region

2.1 The effect of the Delta works on the tidal motion in the North Sea

The total quantity of water flowing to and from the sea-arms to be enclosed amounts about 2,000 million m^3 during normal tide, while the flood volume passing through the Strait of Dover is about 19,000 million m^3 and the ebb volume 17,000 million m^3 . The flood volume passing through a section crossing the North Sea from the isle of Walcheren to Harwich amounts about 50,000 million m^3 , so that the tide in the southern part of the North Sea comes mainly from the north and the effect of the tide passing through the Strait of Dover is limited. From these figures it is obvious that the closing of the sea-arms of the Delta-Works must have a small effect on the tidal motion in the North Sea and that the studies can be limited to the coastal area.

2.2 The tide along the Delta coast

The vertical tide changes considerably along the Dutch coast at Flushing (south of the Delta area) the mean tidal range is 3.8 m and at the Hook of Holland (north of the Delta area) 1.6 m, where the tide arrives 2.5 hours later.

The shoals along the coast of the Delta region are about 8 km wide. The transition from the 10 to 20 m contour line of depth can be considered as the boundary of the "underwater" delta. The greatest depth in the North Sea opposite the coast is 30 m. The bottom topography in the mouths of the sea-arms shows many gullies and shoals.

The pattern of the tidal currents in the mouths of the estuaries is complex because of the interference provided by currents flowing in the direction of the estuaries and tidal currents running parallel to the coastline caused by the prevailing tidal motion in the North Sea. The shape of the tidal current diagram changes from elongated in the direction of the coast to elliptical and then again to elongated, more or less perpendicular to those of the

North Sea currents

For the tidal studies in the coastal areas an extensive measuring programme has been set up in order to obtain a detailed insight into the vertical and horizontal tide in a strip 120 km along the Delta coast. The boundaries of the strip are shown in figure 1. Such programs were carried out on 27 and 28 June 1967 and on 22 May and 9 September 1969.

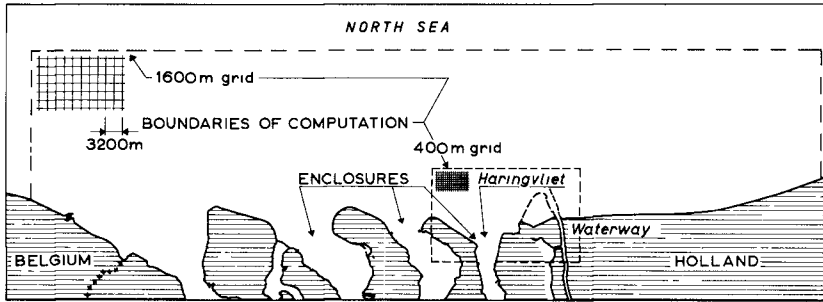


Fig 1 Coast Delta region and boundaries of the grid net

2.3 The tidal computations

The method, developed by Leendertse (1) has been used for the tidal computations. Some practical remarks are mentioned hereafter.

The vertical tides as measured at the seaward boundaries by pressure meters put on the bottom are used as a boundary condition for the tidal computations. The velocities in the sea, which depend more on local depth conditions than does the vertical tide, are not used as boundary conditions.

In the mouths of the sea-arms the vertical tides measured by means of tidal gauges or the velocities can be considered as boundary conditions. Obviously the components of the velocity perpendicular to the coastline of the islands are zero.

For computational reasons it is desirable to locate the boundaries so that the values of the second order terms in the tidal equations are small in the neighbourhood of the boundary. This is so at the boundary of the strip, but it must be expected that the results of the computation of the velocity vectors near the boundary will be less accurate than in the inner region.

There are however other factors which may cause more serious inaccuracies in the computation: the values of the resistance coefficient and the schematization of the depths. Tests for the accuracy of the computations are necessary.

Tidal computations are carried out for a square net of which the gridsize is 1600 m. This grid is too rough for adequately taking into account depth variations in the neighbourhood of the coast and in the sea-arms. In this region a 400 m square net is used.

(see fig 1) The boundary conditions (vertical tides) of the second net can be computed by means of the results of the coarser net, provided the tide is not influenced by the circumstances near the coast. Otherwise, a separate measuring programme is necessary for the determination of the boundary conditions.

The vertical tides at the various grid points along the seaward and land boundaries are determined by interpolation between the water levels at the locations where the vertical tide has been measured, as follows. The shapes of the measured vertical tides are represented by Fourier series with a basic period of 12h 50 m and the Fourier coefficients of the vertical tides in between are obtained by interpolation. These computations are performed by the computer. The velocities at a great number of locations were also measured in the program e.g. at locations in between the places where the vertical tides were measured. As the vertical and horizontal tides depend on each other a check can be performed by means of the equation of motion applied to the boundary line

$$\frac{\partial u}{\partial t} + u \frac{\partial u}{\partial x} + v \frac{\partial u}{\partial y} - \Omega v = -g \frac{\partial h}{\partial x} - g \frac{V u}{C^2 a}, \quad (1)$$

in which the x axis is directed along a part of the boundary, V is the magnitude of the velocity vector of which u and v are the components in x and y directions (counter clock wise) and h is the height of the water level with respect to a datum plane. By replacing the differentials by difference quotients, a relation is found for the differences in water levels between the vertical tides at both sides of the location where the velocity has been measured.

However, the term $v \frac{\partial u}{\partial y}$ could not be determined from the observations. The values of the Chézy coefficient, C, has been checked by means of these computations and from former research in the coastal area. The values of C depend also on the depths, e.g. according to the well-known logarithmic law. However such a relation could not be derived from the observations in the coastal area. The equation of continuity has also been applied to subregions of the coastal strip. Furthermore the importance of the various terms in equation (1) and the similar equation for the y-direction, has been determined, see Dronkers (2).

After preliminary computations detailed tidal computations were applied to the strip along the coast. The relative changes of the vertical and horizontal tide due to the enclosure of the sea-arms could then be determined.

Calculations were carried out after the Haringvliet was enclosed of which the flood volume was about 300 million m³. The future Europort Harbour was also included in the computations. Obviously the changes are maximal in the intermediate neighbourhood of this region. At a distance of 8 km from the coastline the changes are negligible. In fig 2 the results are shown for maximum flood and ebb. The directions of the velocities are denoted by arrows. A smaller gridsize, 400 m, has been used for these computations (see fig 1). Computations were also performed for discharges passing through the sluice during the low water period.

During this last case the timestep has been shortened in order to provide the necessary accuracy. For the 1600 m gridsize the time step was 10 minutes and the computed vertical tidal curves appeared

to have a smooth shape. Irregularities in the shape of these curves occurred in the case of a net with 400 m gridsize. Therefore in this case the time step has been taken $2\frac{1}{2}$ minutes. Obviously the propagation time in such a square is about 4 times shorter than in the case of 1600 m gridsize.

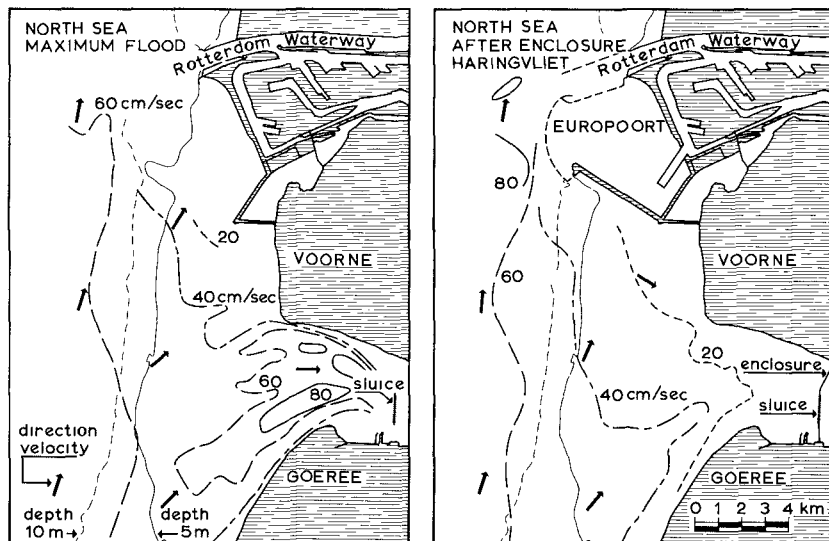


Fig. 2 Lines of equal velocities in the mouth of the Haringvliet

3 Practical wave investigations

For getting insight into the wave characteristics in the coastal area, a great number of wave observation piles are placed in the coastal area. The placing of heavy piles in the seabed is usually a costly affair and therefore the depth at these locations is limited to 10 m. Furthermore a wave instrument is put on a platform, which is at a location where the waterdepth is about 15 m. At some locations observations are taken for several years, maximal 5 years, usually they are observed for a shorter period, minimal one year, and then the piles are relocated. The instrument on the pile (which is an electrical step capacity gauge wave recorder with wireless transmission) does not measure wave heights smaller than 4 cm. The irregular waves and eventually the vertical tide observations are transmitted by radio to a coastal station where they can be observed on a pen recorder. By means of the so-called wave-rider, which is a wave buoy on which instruments are placed, the vertical accelerations of the movement of the buoy are measured. They can be used in the deeper parts of the coastal area. The directions of the waves cannot be measured by the instruments mentioned above. Radar

observations can be used for this purpose

Frequency and exceedance distributions of wave heights, distributions of periods, the wave period by zero crossing method and the energy spectral density function (energy spectrum) are determined for time intervals of about half an hour, during which the mean water level, due to the tide, does not change considerably in comparison to the depth. The significant wave height is one of the most important parameters for the practical applications. The largest and smallest value of the periods to be considered depend on the length of the measuring interval of the waves. Wave periods longer than 30 seconds or shorter than 1 second are eliminated by means of a filter procedure. For modern theories on waves, and in particular the energy spectrum, reference is made to Kindsman (3a) and Benda and Piersol (3b).

The mean wave period in the coastal areas of the Delta is about 5 seconds, although high waves generated by high winds, may have periods up to 10 seconds or more. A maximum wave height of 10 m has been measured at a water depth of 16 m. The significant wave height was about 7 m. Generally speaking the waves in the coastal area and even in a great part of the southern North Sea are of intermediate wave type between a long wave and a deep water wave (see section 4.1).

It has been found by Koele (4) that the distribution of the wave heights (trough to crest) over a sufficiently long measuring interval can approximately be represented by the well-known Rayleigh distribution even in rather shallow water, provided that small disturbances are omitted. In particular cases deviations from this distribution has been found.

From the wave observations in the coastal area of the Delta it has been found that the product of wind velocity and the frequency which occurs at maximum energy density is about 1.8. This is more than mentioned by Freudenthal (5). The definition of the wind velocity also effects the product mentioned above.

Waves may develop higher harmonics during their propagation in shallow water of which periods depend on the period of the original wave developed in deeper water. Consequently more waves of shorter period may be expected in such shallow regions than in deeper water under the same windfield.

It has also been found by Koele and de Bruyn (6) that in the breaker zone the significant wave height of irregular waves does not exceed about 0.5 of the local depth. The breaking of waves also depends on the steepness of the wave. In the example of fig 3, the bound is denoted by $H_S = 0.4a$, in which H_S is the significant wave height and a the depth. Particular circumstances may also have some influence on the coefficient, and therefore values between 0.4 and 0.5 occur.

Regular shaped wave profiles e.g. a trochoid and a cnoidal wave will break when the wave height is maximal about 0.8 of the local depth. During the propagation in a shallow region the regular wave deforms

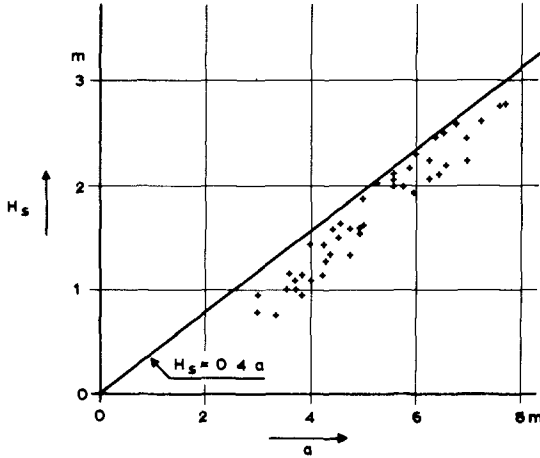


Fig 3 The relation between the significant wave height and the depth

For the statistical evaluation of wave conditions in reference to coastal engineering problems we may refer to Svasek (7) The relation between the significant wave height, H_s , and the area of the energy spectrum m_0 , is $H_s = 4 m_0^{1/2}$ This relation is based on the Rayleigh distribution and has also been verified by means of wave observations The deviation in the factor 4 is about 0.2

The calculation of the energy spectrum is based on the calculation of the well-known auto-covariance function $R(\tau)$, applied to the wave heights $h(t)$

$$R(\tau) = \frac{1}{P-\tau} \int_0^{P-\tau} h(t) h(t+\tau) dt = \int_{-\pi/30}^{\pi/30} S'(w) \cos(w\tau) dw,$$

where $S'(w)$ is the energy density and w is the frequency of a wave, while in practical applications the observational period P is usually 30 minutes (= 1800 seconds) The integral is replaced by a summation formula, in which $\Delta t = 0.2$ sec and $R(\tau)$ is calculated for successive values of τ at intervals of 0.2 seconds, from $\tau = 0$ up to $\tau_m = 30$ sec Thus if the mean wave period equals 5 seconds about 350 wave periods are considered for each observation period of 30 minutes The energy density $S'(w)$ is determined by

$$S'(w) = \frac{2}{\pi} \int_0^{\tau_m} R(\tau) \cos w\tau d\tau$$

(In practical applications $S(w) = \frac{1}{2} S'(w)$ has been considered)

4 Computation of the refraction diagrams4.1 Formula for the celerity of the wave

The purpose of the computation of wave refraction in the coastal areas of the Delta is to provide data on changes in the local wave characteristics that result from the morphological changes g for the determination of the attack on coastal structures.

Numerical refraction calculations on a computer for the case of a regular reference wave have been worked out by G M Griswold (8). The limitation for the accuracy of the wave ray computation is the accuracy of the depths which determine the celerity of the waves, c . A first approximation, based on linear wave theory, is applied

$$c = \frac{gT}{2\pi} \tanh \frac{2a\pi}{cT}, \quad (1)$$

in which T is the wave period and ' a ' the depth. This formula holds if $2\pi H/L \ll 1$ and $\pi H/L \ll (2\pi a)^3/L^3$, in which H is the wave height.

For the computation of c from (1) an iteration procedure may be applied (see e.g. Duthler (9)). Here a direct approximate formula for c as a function of depth and period is deduced. This formula is useful for the determination of the accuracy of the refraction computation (see 4.2). The derivation will be included here because the author has not found this method in the literature. Equation (1) may be written in the alternative form

$$u \tanh u = P, \text{ where } u = \frac{2\pi}{cT} a, \quad P = \frac{4\pi^2}{gT^2} a = \frac{4.0255}{T^2} a \quad (1a)$$

Let a_T be defined such that for $a < a_T$ the celerity c depends on the depth. For $a > a_T$ the wave propagates as a deep water wave. For deep water waves $\tanh u$ will be approximated by 1, e.g. if $u > 2.7$, $\tanh u$ does not depend on depth. Then for $a > a_T$,

$$c = \frac{gT}{2\pi} = 1.56 T \quad (2)$$

From equation (1a) an approximate solution for c can be determined for $a < a_T$ in the following way. After introducing the well-known series for $\tanh u$,

$$\tanh u = u - \frac{2u^3}{3!} + \frac{2^4 u^5}{5!} - \frac{2^4 17u^7}{7!} + \dots,$$

in (1a), which converges for $|u| < \frac{1}{2}\pi$, and after reversing the series of $u \tanh u$ in (1a) in a series of terms of P and by considering three terms of the reversed series, it is found that the approximation for c , c' , is obtained

$$(c')^2 \left(1 + \frac{1}{3} P + \frac{4}{45} P^2\right) = ag \quad (3)$$

This formula has an accuracy of 99% if $u < 1.5$. It appears that after the addition of a term, $0.007 P^3$, a better approximation is obtained, applicable now up to $u \approx 2.7$, with an accuracy of 98%

$$(c')^2 = \frac{ag}{1 + 0.333 P + 0.089 P^2 + 0.007 P^3} \quad (4)$$

Then it follows from (1a) and (4)

$$\frac{c^2}{(c')^2} = \frac{P}{u^2} \left(1 + 0.333 P + 0.089 P^2 + 0.007 P^3\right) \quad (5)$$

The transition depth, a_T , is defined by $a_T = \frac{c'T}{2\pi} u$ and $u = 2.7$ (see (1a)) Then $(c')^2 = 0.37 g a_T$ and $L' = c'T = 2.35 a_T$ (see (4)), and $P = 2.7 \tanh 2.7 \approx 2.7$ The line $(c')^2 = 0.37 g a$ is shown in fig 4

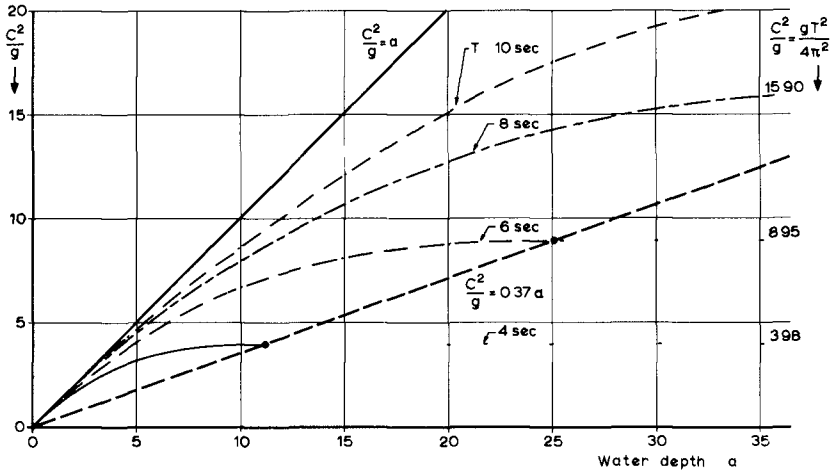


Fig 4 Relation between the celerity of the wave and the depth, according to first order wave theory

In fig 4 the relations (2) and (4) are represented for some periods T The wave propagates as a deep water wave on the right side of the line, $c^2 = 0.37 ag$ The derivation mentioned above is based on the required accuracy for the determination of c and a_T The criterion for the boundary between shallow and deep water waves, given in the literature, is $L = 2 a_T$ (see Kindsman (3a))

4.2 The formulae for the computation of the refraction and considerations on the accuracy

Difficulties concerning the accuracy of the computation are often met in the practical applications The computational method will be discussed in detail in connection with this During the propagation the wave front will change due to the change of the wave celerity, c

Let x and y be a perpendicular coordinate system and α the angle of the tangent to the ray at a point (x,y) with the x axis Furthermore let s be the distance from a fixed point (x_0, y_0) to (x,y) along the ray, and n the distance along the wave front at (x,y) perpendicular to the ray

The basic formulae for the computation of the wave refraction are

$$\frac{ds}{dt} = c, \quad \frac{\partial \alpha}{\partial t} = - \frac{\partial c}{\partial n}, \quad \text{and} \quad \frac{1}{\rho} = \frac{\partial \alpha}{\partial s} = - \frac{1}{c} \frac{\partial c}{\partial n} \quad (6)$$

in which ρ is the curvature radius

The transformation formulae between the coordinate systems (s, n) and (x, y) are

$$\frac{\delta}{\delta n} = -\sin \alpha \frac{\delta}{\delta x} + \cos \alpha \frac{\delta}{\delta y}, \quad \frac{\delta}{\delta s} = \cos \alpha \frac{\delta}{\delta x} + \sin \alpha \frac{\delta}{\delta y}$$

It follows that α satisfies the first order partial differential

$$\text{equation } \sin \alpha \frac{\delta c}{\delta x} - \cos \alpha \frac{\delta c}{\delta y} = c \cos \alpha \frac{\delta}{\delta x} + c \sin \alpha \frac{\delta}{\delta y} = \frac{c}{\rho}$$

Knowing the values of c , $\frac{\delta c}{\delta x}$, $\frac{\delta c}{\delta y}$ to obtain the path of the ray,

$\rho(x, y)$ must be solved in a numerical way

Assume that the path of the ray has been computed up to (x_1, y_1)

Then the point (x_{1+1}, y_{1+1}) of the wave ray can be computed, after

time $(\Delta t) = pT$, where $p = 1, \text{ or } 2, \text{ etc}$ is the number of wave lengths to be considered successively along the wave ray. The following numerical relations are considered

$$\Delta s_1 = c_{1,m} \Delta t, (a), \quad c_{1,m} = \frac{1}{2} (c_1 + c_{1+1}), (b), \quad \Delta \alpha_1 = \left(\frac{1}{\rho_1} + \frac{1}{\rho_{1+1}} \right) \frac{\Delta s_1}{2}, (c),$$

$$\frac{c_{1+1}}{\rho_{1+1}} = \sin (\alpha_1 + \Delta \alpha_1) \frac{\delta c_{1+1}}{\delta x} - \cos (\alpha_1 + \Delta \alpha_1) \frac{\delta c_{1+1}}{\delta y}, (d),$$

$$\Delta x = \Delta s_1 \cos (\alpha_1 + \frac{1}{2} \Delta \alpha_1), \quad \Delta y = \Delta s_1 \sin (\alpha_1 + \frac{1}{2} \Delta \alpha_1), (e), \quad (7)$$

$$c_{1+1} = c_1 + \frac{\delta c_1}{\delta x} \Delta x + \frac{\delta c_1}{\delta y} \Delta y + \frac{1}{2} \frac{\delta^2 c_1}{\delta x^2} (\Delta x)^2 + \frac{\delta^2 c_1}{\delta x \delta y} \Delta x \Delta y + \frac{1}{2} \frac{\delta^2 c_1}{\delta y^2} (\Delta y)^2, (f)$$

The functions $c_1, \frac{\delta c_1}{\delta x}$ etc occurring in (7, (f)) can be expressed in terms of $a, \frac{\delta a}{\delta x}$, and, $\frac{\delta a}{\delta y}$, by means of (3), if $a < a_T$ (see section 4 1)

For $a > a_T$, $\frac{\delta c_1}{\delta x} = 0$ etc

For $a < a_T$, it may be put

$$\frac{\delta c}{\delta x} = S(a, T) \frac{\delta a}{\delta x} \quad \text{and} \quad \frac{\delta c}{\delta y} = S(a, T) \frac{\delta a}{\delta y} \quad (8)$$

In fig 5 the function $S(a, T)$ is represented as a function of 'a' for $T = 4, 6$ and 8 seconds. The coefficient S is positive for shallow water. Then $c^2 < 0.37 ag$ (see fig 4). For $c^2 = 0.37 ag$, $\frac{\delta c}{\delta x} = 0$ and $S = 0$. In case $c^2 > 0.37 ag$ the value of S must be equal to zero. Then the wave is considered as a deep water wave.

The solution of the set of non-linear equations, (7), depends on the variations in the depths, so that the density of the sounding net is a very important factor for the accuracy of the solution. A second important factor is the accuracy of the numerical solution. In this respect great care is necessary. Assumptions must be made on the values of the derivatives of the celerity, c , and therefore on the depth.

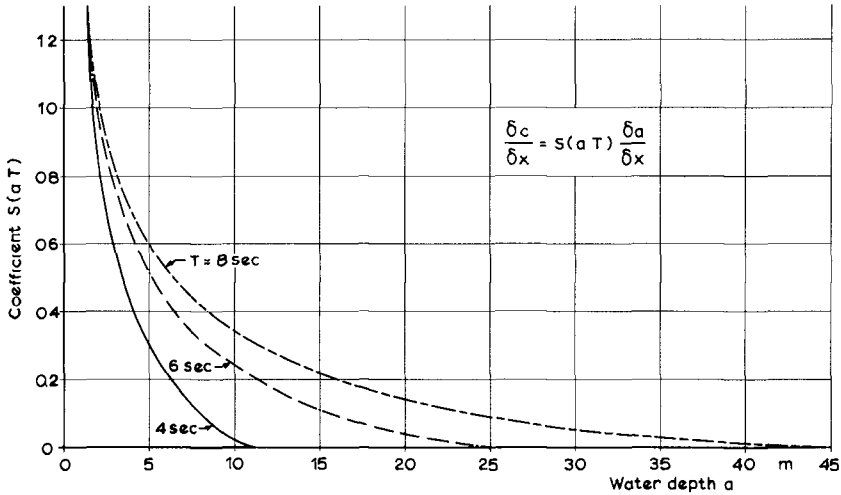


Fig 5 Graphical representation of the coefficient $S(a, T)$ as a function of depth. In the practical application is $S(a, T) > 0$ for $c^2 < 0.37$ ag and $S(a, T) = 0$ for $c^2 \geq 0.37$ ag

It is mentioned in the literature that $\frac{\delta a}{\delta x}$, or $\frac{\delta a}{\delta y}$, may not exceed the value, 0.1. A detailed research of the accuracy of the solution shows that this value is too great however for obtaining accurate results. The maximum value, 0.01, is recommended for the slopes $\frac{\delta a}{\delta x}$ and $\frac{\delta a}{\delta y}$.

The following example shows that in case $\frac{\delta a}{\delta x} = \frac{\delta a}{\delta y} = 0.1$, the computed value of $\Delta \alpha_1$ is much too large. Let be the value of $\sin(\alpha_1 + \Delta \alpha_1) = 1$. Then it follows from (7 d) and (8) that

$$\frac{c_{1+1}}{\rho_{1+1}} = \frac{\delta c_{1+1}}{\delta x} = S(a, T) \frac{\delta a_{1+1}}{\delta x},$$

and from (7a c), that $\Delta \alpha_1$ is of the order of $pT \frac{c}{\rho}$, and $\frac{\delta a}{\delta x} = 0.1$

If $p = 1$, $T = 5$ sec and the depth is about 2 m, then

$$\Delta \alpha_1 \approx 5 \frac{c}{\rho} \approx 5 \frac{\delta a}{\delta x} \approx 0.5$$

This value, 0.5, is much too large for an accurate numerical computation of $\Delta \alpha_1$. In the practical applications $\Delta \alpha_1$ may not exceed the value 0.05. Otherwise equation (7 c) and the relation $\sin \alpha_1 = \Delta \alpha_1$ etc are not accurate enough, unless $p < 1$. It is not desirable to consider parts of waves lengths from physical point of view. Therefore the value of p must be an integer.

Moreover restrictions must be made with respect to the values of the second derivatives $\frac{\delta^2 a}{\delta x^2}$ etc. The maximum values of these

second derivatives of 'a' have also to be limited to $0.005/\Delta s$ at the most. In that case the values of the terms which contain the second derivatives in the formula for $\Delta\alpha_1$, e.g. the terms $\frac{1}{2c_{1+i}}(\sin\alpha_1) \frac{\delta^2 c_1}{\delta x^2} \Delta x$ are smaller than 0.025.

The complete formula for $\Delta\alpha_1$, derived from (7 c) and (7 f), is

$$\begin{aligned} \frac{\Delta\alpha_1}{\Delta s} = & \frac{1}{\rho_1} + \frac{1}{2c_{1+1}} \left\{ \Delta\alpha \left[(\cos\alpha_1 \frac{\delta c_1}{\delta x} + \sin\alpha_1 \frac{\delta c_1}{\delta y}) + \right. \right. \\ & + (\Delta x \cos\alpha_1 \frac{\delta^2 c_1}{\delta x^2} - \Delta y \sin\alpha_1 \frac{\delta^2 c_1}{\delta y^2}) + (\Delta x \sin\alpha_1 + \Delta y \cos\alpha_1) \frac{\delta^2 c_1}{\delta x \delta y} \left. \right] \\ & + (\Delta x \sin\alpha_1 \frac{\delta^2 c_1}{\delta x^2} - \Delta y \cos\alpha_1 \frac{\delta^2 c_1}{\delta y^2}) + (-\Delta x \cos\alpha_1 + \\ & \left. + \Delta y \sin\alpha_1) \frac{\delta^2 c_1}{\delta x \delta y} \right\} \end{aligned} \quad (9)$$

It must be stressed that the accuracy of the refraction computation also depends on the wave length and thus on the period of the wave (see fig 5). The accuracy is greater for shorter waves, and in that case the maximum steepness of the slope of the bottom may be larger than in the case of longer waves.

Finally a remark follows on the practical determination of $\frac{\delta a}{\delta x}$ and $\frac{\delta a}{\delta y}$ etc. They are derived from the contour lines of the depth determined in intervals of 0.5 m. The location of the contour lines is usually irregular. Therefore it is often not possible to determine accurate values for the second derivatives. A grid net for the computation must be constructed on the map. The grid size depends on the accuracy of the contour lines. Various procedures can be followed for the numerical presentation of $\frac{\delta a}{\delta x}$, $\frac{\delta a}{\delta y}$ etc., e.g.

$$2\Delta x \frac{\delta a}{\delta x} = a_{p+1,q+1} + a_{q+1,q} - a_{p,q} - a_{p,q+1},$$

and a similar equation for $\frac{\delta a}{\delta y}$.

It is noted that the points (x_1, y_1) on the wave ray will usually not coincide with the grid points (p, q) of the grid net. The study of the accuracy of the refraction computation will be continued.

5 Considerations on studies of morphological changes

5 1 General remarks

This section deals with the methods to be applied for the determination of the morphological changes along the Delta coast. It was not possible to make satisfactory scientific forecast for these changes because of the uncertainty in the values of the various coefficients in the equations of the phenomena. It is intended that after the closing of the Haringvliet these coefficients will be determined based on extensive measurements in the new circumstances that will prevail along the coast. The sediment transport in the Delta estuaries and coastal regions occurs mainly in suspended form and bed load sediment is negligible. This is the reason that a hydraulic model has not been built for this research. In the preceding sections the basic factors influencing morphological studies have been mentioned. These factors are better defined from a physical and mathematical point of view than are the morphological changes. In this respect distinction must be made between the final shape of the seabed that will result when conditions have stabilized and the speed at which the change takes place. In particular this speed can be approached more theoretically. It is determined by the net sedimentation and erosion and is therefore related to the sand transport. However, simplifications must be accepted, and empirical quantities introduced which have to be evaluated by means of measurements in nature. Consequently only tendencies for the morphological changes can be given. Svasek has discussed these problems for the Delta area in his publications (10) and likewise Terwindt (11).

The concentration of the sand is determined by the currents in combination with the wave motion. The concentration can increase considerably by the wave action, because of the increased turbulence of the water, especially in the case of breaking waves. Tidal currents and wind waves vary with astronomical conditions and meteorological circumstances, especially during stormsurges. Reversely the tidal currents and the wave motion which is statistically distributed, are also affected by the bottom morphology.

The instruments for the measurement of sand in suspension that are currently in use are not accurate enough for all circumstances. Their application is very limited and is only possible during quiet weather. By means of radio-active tracers, the direction and the relative significance of the sand transport can be determined as a mean value over longer time periods. Quantitative evaluation of the sand transport directly related to the fluid motion, and of the net transport, still remains uncertain.

The most important tool for the determination of the net-sand transport is the study of the changes in the shape of the bottom, as obtained from periodically repeated soundings, combined with a knowledge about tidal currents and wave-action. The results of the soundings also give information for the estimation of the final situation of the bottom morphology. Along the Delta coast the soundings are repeated every three months, or at shorter intervals in regions where sand movement is considerable. The study of de Vries (12), on the applicability of tracer techniques for rivers must be mentioned. A discussion on sand transport processes is also given.

5.2 An empirical method for the determination of a cross-section area in the mouth of an enclosed estuary

An important problem is the estimation of the final cross-section area in the mouths of the enclosed estuaries, e.g. in the mouth of the Haringvliet, where the sluice is about 5 km inland and a gully must be maintained for the discharge of the sluices. It has been found that a relation exists between the quotient of the tidal volume (ebb + flood) and the total profile area of the inlet mouth for the various estuaries of the Delta region. This amount divided by the tidal period ($T = 44,700$ sec) determines a velocity \bar{v} over the tide, that appears to have a relation with the morphological conditions. Its value is 55 cm/sec for all the estuaries. The diameter of the sand is of the same order of magnitude for all the mouths, 0.15 mm to 0.2 mm.

It must be expected that in the future silt will be deposited in the mouth of Haringvliet and consequently the value of the scouring velocity will become somewhat higher. By means of laboratory tests it has been estimated as about 70 cm/sec in nature. The future discharges in the mouth can be determined from the discharges of the sluices and from tidal calculations. Then the future cross-section area can be computed. The time scale of the development must be determined from detailed knowledge about the sand transport and from comparative examples in nature, e.g. from the morphological changes after the closure of previous sea arms like Brielse Maas (1951) (see fig. 6) and Veerse Gat in the Delta region of which the mean grain-size at the bottom is the same. The mean value of the depth in the future gullies can also be estimated in an empirical way by comparison with these examples. Then the same relation between mean and maximum depth can be applied to the future gullies of the Haringvliet mouth, provided the widths of the gullies are fixed by banks. The preceding studies for the determination of the final cross-section have been applied by Terwindt in his morphological study of the Haringvliet mouth. Reference is also made to Bruun and Gerritsen (13).

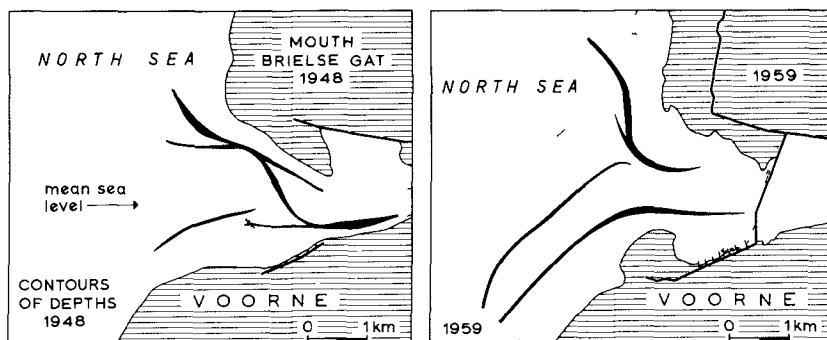


Fig. 6 Changes in the contours of depths due to the enclosing of the Brielse Maas

Extensive shoals have been formed with gullies at both sides after the enclosing of this sea-arm

5.3 A more theoretical method for the determination of the sand transport in a river

For the computation of the sediment transport due to the tidal currents in the Delta region, various sediment transport formulae can be used. They are however generally based on laboratory tests, trials in nature are limited. Various bed-load formulae are summarized in the book of A. J. Raudkivi (14). The formulae for the computation of suspended sediment movement, which is related to diffusion processes, are still more limited. The vertical distribution of the velocity in turbulent water is one of the determining factors, however the formulae for such distributions in nature are also more or less based on an empirical basis. The various quantities which are defined in the formulae under idealized circumstances must be redefined for the more irregular conditions in nature in an empirical way by adapting the formulae to the observations obtained from measurements in nature. After that the formula can be applied for different conditions and engineering purposes e.g. higher upland river discharges, or changes in the profiles of the river. Then the formula may give indications for changes in scour and sedimentation. The method has been applied by Morra (15) in the tidal region of the Delta, where the sand is fine, 0.15 mm to 0.2 mm. The calculation of the suspended sand transport is based on a formula for the distribution of the suspended sand concentration in the vertical, combined with the formula of Kalinske (16). The major feature of the method will be described. The exchange of sand over the vertical is determined by the equilibrium condition per unit of width,

$$cw = \epsilon \frac{dw}{dh}, \quad (1)$$

in which w is the local sediment concentration (the volume of sand per unit of volume water), h is the height above the bottom, c is the fall velocity of particles in the fluid at rest, and ϵ is an exchange coefficient. It is assumed to be equal to the momentum transfer coefficient in the relation for the shear stress τ ,

$\tau = \rho \epsilon \frac{dv}{dh}$, in which v is the velocity at height h , determined according to the parabolic formula

$$v = v_1 h^{1/q}, \quad (2)$$

and ρ is the density, q is of the order 5 to 7. Then

$$\frac{dv}{dh} = \frac{1}{q} v_1 h^{(1-q)/q} \quad (3)$$

It is well-known that the shear stress τ at the height h is defined by $\rho g a (1-z)$, in which $z = h/a$, a is the total depth, and i is the slope of the water surface in the case of steady flow. In the case of unsteady flow it is the difference in head, determined by the friction term, $i = v_m^2 / C^2 a$, (4), in which v_m is the mean velocity at time t in a cross-section, and C is the coefficient of Chezy. After integration and some calculation it is found from (1) and (3) that the vertical distribution of the sand concentration is

$$\frac{w_z}{w_{z_0}} = \left[\frac{(1-z)z^{1/q} e^{-(q+1)z^{1/q}}}{(1-z_0)z_0^{1/q} e^{-(q+1)z_0^{1/q}}} \right]^{p_c} \quad (5)$$

in which $z_0 = h_0/a$, and h_0 is a reference height above the bottom. For $h_0 = 0$, the formula is

$$\frac{w_z}{w_0} = \left[(1-z)z^{1/q} e^{-(q+1)z^{1/q}} \right]^{p_c} \quad (6)$$

in which $p_c = \frac{c}{g} \frac{C^2}{q v_m}$, v_m is the mean velocity over the vertical,

defined by $\frac{q}{q+1} v_1 a^{1/q}$ (see (4)), and w_0 is the suspended sand concentration near the bottom.

The formula of Kalinske determines the relation between w_0 and the bottom material. A brief explanation of this formula follows. Let v' be the velocity component in the vertical at the height h above the bottom and c the fall velocity in still water of a particle, and let the statistical distribution of v' be determined by the formula of Gauss. Then the formula

$$\Delta F(c) \int_c^\infty (v'-c) \frac{1}{2((v')^2)^{\frac{1}{2}}} \exp \frac{-v'^2}{2((v')^2)^{\frac{1}{2}}} dv' \quad (7)$$

in which $\Delta F(c)$ is an interval with equal diameters of bottom material with fall velocity c (expressed in percentages), determines the transport of sand from the bottom into suspension in course of time. The horizontal velocity component may not change considerably.

In the equilibrium situation the transport in vertical direction per unit of time equals the transport downwards, cw_0 .

It may be put for turbulent flow $((v')^2)^{\frac{1}{2}} = k(ga)^{\frac{1}{2}}$, (8)

in which k is an empirical constant. The transport of sand from the bottom, cw_0 , must be proportional to the expression (7). After the transformation, $v' = k(2ga)^{\frac{1}{2}}u$, it is found

$$cw_0 = \Lambda c \Delta F(c) \int_{u(c)}^\infty \left(\frac{u}{u(c)} - 1 \right) e^{-u^2} du \quad (9)$$

in which Λ is the proportional factor and $u(c) = c/k(2ga)^{\frac{1}{2}}$. The equation (9) may be rewritten in the form

$$\frac{w_0}{\Delta F(c)} = \frac{\Lambda}{(2\pi)^{\frac{1}{2}}} \left[\frac{1}{2u(c)} e^{-u^2(c)} - \frac{1}{2} \left(1 - \frac{2}{\pi^{\frac{1}{2}}} \int_0^{u(c)} e^{-u^2} du \right) \right] \quad (10)$$

Λ and k are empirical constants in (8) and (10). They depend on the local circumstances.

The following remark must be made for the application of the equation (10) in a tidal river. At a location in a tidal region the value of π , which is determined by the friction term, is usually different from the slope of the water surface caused by the tide at time t . This slope equals the algebraic sum of the friction term

and the inertia terms

It must be assumed in the practical applications that the changes of the tidal velocities are small enough, so that the equilibrium condition of the sand transport, defined above, is satisfied more or less

The bottom material can be considered as homogeneous in tidal regions with a standard grain diameter of d_{60} for this special purpose. In that case $\Delta F(c) = 100$. The practical determination of the empirical parameter, p_c , in formulae (5), and (6) is as follows. The relation between w_z and w_{z_0} is found from the measurements of the sand concentration w_z in the vertical, and the exponent q of the parabolic formula (2) is determined from velocity measurements. Then the exponent p_c in formula (5) can be computed. The value of p_c varies in the tidal regions of the Delta area between 0.25 and 2.5.

It is evident that due to the great variations of the sand transport in the course of time, a great number of measurements must be taken. Then the least square rule can be applied for the best fit of the sand concentration in the vertical.

After that w_0 can be calculated from (6) and introduced into the left member of equation (10). The values of A and k can be determined such that equation (10) is satisfied. A trial and error procedure is usually necessary. It is difficult to obtain reliable values for A and k .

It is also possible to determine A and k from the results of the measurements mentioned in Kalinske (10). However, Kalinske applies the logarithmic formula for the vertical velocity distribution, and ϵ_m , being the mean value for the exchange coefficient over the vertical. Kalinske found by this procedure $A \approx 39$ and $k \approx 0.75$.

5.4 Sand transport in the coastal area

The morphological conditions at the coast of the Delta region will change in the future as a consequence of the enclosing of the Haringvliet and the works which are in execution. The future situation depends on the new equilibrium of the sand transports, due to the combined effect of currents and waves. The new equilibrium in the channels, and seaward of the breaker zone is determined considerably by the changes in the tidal currents and in particular by the velocity components towards the coast line. A complicated sand transport process exists in the region of the sand banks, in front of the coast line between the existing gullies. Here the sand transport depends on the combined effect of currents and waves. Breaking waves produce very high sand concentrations in these regions. The combined effect has been studied by Bijker (17) on the basis of laboratory tests. He determines the combined shear stress at the bottom of currents and waves in the two dimensional case. Vertical velocity components and accelerations are not considered in his study. In the breaker zone where tidal currents are negligible a well-known procedure is to assume that the total long-shore transport rate is proportional to the loss of long-shore energy flux per unit of length. Reference is made to Bijker and Svašek (18). The basis of all the morphological studies are the tidal and refraction computations which determine the changes in the velocity.

components and the directions of the waves. These morphological studies are continued. An example of the changes in the coastal area is shown in fig 7. Some contours of depths in 1960 and 1969 are represented. It appears that the 2 and 5 m lines near the coast changed considerably, due to the wave action and the changes in the currents.

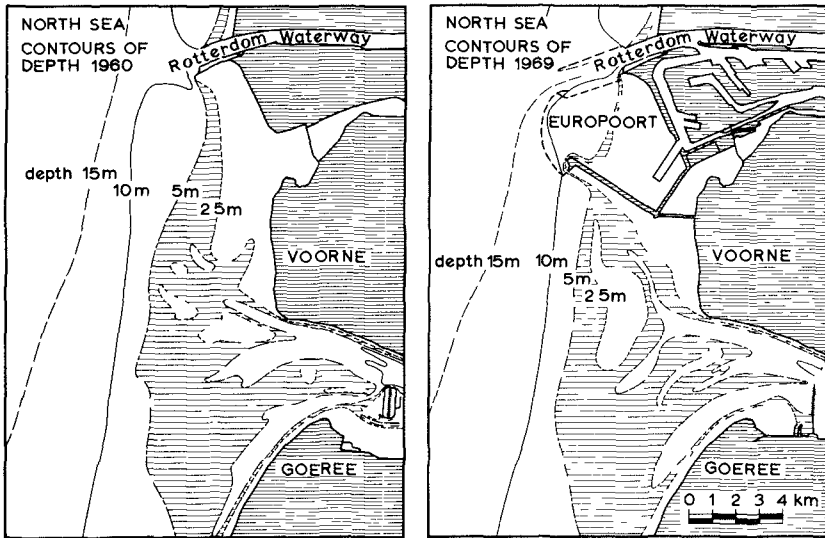


Fig 7 A comparison between the contours of depths in 1960 and 1969 in the mouth of Haringvliet and near Europort

REFERENCES

- 1, Leendertse, J , 1967, Aspects of a computational model for long-period water wave propagation, Thesis, The Rand Corporation, Santa Monica, California
- 2a, Dronkers, J J , 1969, Tidal computations for rivers, coastal areas and seas, J Hydraulics Div , Proc Am Soc Civ Eng, New York
- 2b, Dronkers, J J , 1969, Some practical aspects of tidal computations, Thirteenth Congr Int Ass Hydr Res , Proc vol 3, Tokyo
- 3a, Kindsman, B , 1965, Wind Waves, Prentice-Hall, Inc , Englewood Cliffs, New Jersey
- 3b, Benda, S J and Piersol, A G , 1966, Measurements and analysis of random data, John Wiley, New York

- 4, Koeló, L A , 1962, Statistical distribution of wave heights in shallow water, (Dutch text) Hydraulics Div., Delta works, The Hague
- 5, Freudenthal, A M , 1969, Determination sur base aleatoire des criteres pour le calcul des ouvrages maritimes, Ass Internat Perm des Congres de Navigation, Brussels
- 6, Koele, L A and de Bruyn, P A , 1964, Statistical distribution of wave heights in correlation with energy spectrum and water depth Ninth Confer on Coast Engin , Lisbon
- 7, Svašek, J N , 1969, Statistical evaluation of wave conditions in a deltaic area, Symposium on wave action, Delft, Hydraulics Lab
- 8, Griswold, G M , 1963, Numerical calculation of wave refraction, J of Geophys Res vol 68, no 6
- 9, Duthler, J W , 1968, Refraction computation by means of a digital computer, (Dutch text), Hydraulics Div , Delta works, The Hague
- 10, Svašek, J N , 1968, Influence of breaking waves on the stability of sandy coasts, (Dutch text), Hydraulics Div , Delta works, The Hague
- 11, Terwindt, J H J , 1970, Future depths in the gullies of the mouth of the enclosed Haringvliet, (Dutch text), Hydraulics Div , Delta works, The Hague
- 12, de Vries, M , 1966, Applications of luminophores in sand transport studies, Thesis 1966, Delft, Hydraulics Lab
- 13, Bruun, P and Gerritsen, F , 1953, Stability of coastal inlets, North-Holland Publ Comp, Amsterdam
- 14, Raudkivi, A J , 1967, Loose boundary hydraulics, Pergamon Press, Oxford
- 15, Morra, R H J , 1952, The sand movement in a tidal region, (Dutch text), Hydraulics Div , Delta works, The Hague
- 16, Kalinske, A A , 1939, Relations of suspended to bed materials, Nat Res Council, Transact Am Geoph Union
- 17, Bijker, E W , 1967, Some considerations about scales for coastal models with movable bed, Thesis, Delft, Hydraulics Lab
- 18, Bijker, E W and Svašek, J N , 1969, Two methods for determination of morphological changes included by coastal structures, XXII Internat Nav Congr , Paris

CHAPTER 109

SEDIMENT POLLUTION IN COASTAL WATERS

J van de Kreeke*

ABSTRACT

Sediment pollution can be defined as the increase in sediment concentration, due to artificial infusion of sediment, to a level harmful to fish and plant life

The coastal engineer may be called upon to evaluate the result of an artificial sediment influx in terms of characteristic parameters like concentration and turbidity and to determine eventual deposition areas of the sediment

This paper describes the field investigations carried out to evaluate a case of sediment infusion in one of the estuaries on the U S east coast. The sediment was discharged via a pipeline at a rate of approximately 10 lbs/sec. Nearly all the released sediment was in the silt range. In addition to the results of the field measurements a simple mathematical model is presented, describing the temporal and spatial distribution of the sediment in the resulting sediment plume.

DESCRIPTION OF THE STUDY AREA

The study area is located in a bend of the estuary, see Figure 1. The depth contours in this figure show a deep channel at the west side and a relative shallow plateau at the east side of the estuary. The hydraulic environment in the study area is governed by the tide and the freshwater inflow. The tide has a semidiurnal character with a mean tidal range of 2.1 ft and a mean spring tidal range of 2.4 ft. Maximum currents are on the order of 1 ft/sec, both for ebb and flood, but the ebb currents can be considerably higher during periods of high freshwater inflow. An order of magnitude of the freshwater discharge might be obtained from the following figures: During 50% of the time the average daily freshwater discharge is higher than 6,500 cfs and during 1% of the time exceeds 70,000 cfs. For comparison, the maximum tidal discharge in the study area is on the order of 100,000 cfs. Salinities in the shallow part, the area where the sediment is released, can be as high as 2‰ after long periods of low freshwater inflow and as low as 0.1‰ after periods of high freshwater inflow. The water is well mixed, at least for the shallow depths.

In order to gather additional information on the hydraulic environment in the study area, current measurements were carried out with a stationary and a movable current meter. Both instruments were equipped with a Savonius rotor. In addition, the stationary meter had a direction device. The readout of the movable current meter provided a record of instantaneous velocities.

*Research Associate, Dept of Coastal and Oceanographic Engineering,
University of Florida

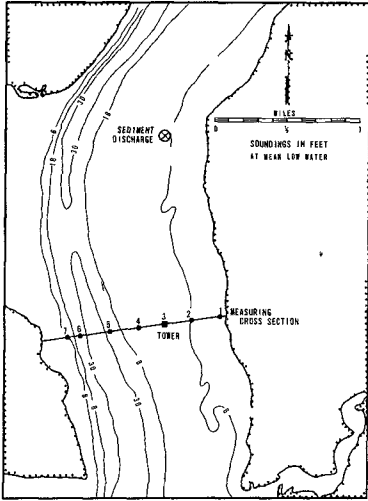


FIGURE 1 - STUDY AREA AND MEASURING STATIONS

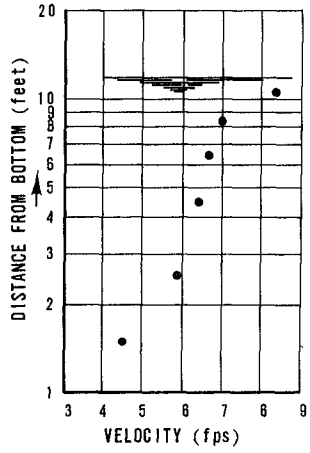


FIGURE 2 - MEASURED VELOCITY PROFILE IN STATION 3

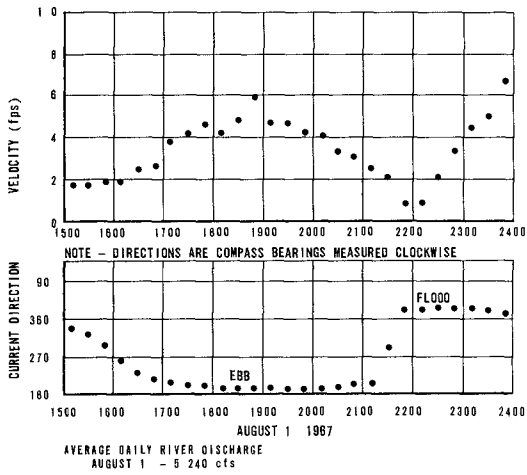


FIGURE 3 - CURRENT VELOCITY AND DIRECTION MEASURED IN STATION 3

The output of the stationary current meter consisted of velocities and directions averaged over time periods of 19 minutes. Calibration threshold for the rotor and direction device was approximately 0.1 ft/sec. The stationary meter was placed in a tower, for location see Figure 1, with the center of the rotor 1.5 ft and the center of the vane 3 ft above the bottom. The movable meter was used to determine the velocities at the stations 1-7, indicated in Figure 1. The measurements with the movable current meter were carried out during periods of definite ebb currents. It was hoped that by comparing measured and theoretical velocity profiles, an estimate could be made of the eddy diffusivity coefficient. This idea had to be abandoned, however, since the measured profiles did not comply with the theoretical logarithmic velocity distribution as may be seen from Figure 2.

Typical curves showing the variation in current velocity and direction during a tidal cycle are presented in Figure 3. Attention is drawn to the magnitudes and direction of the currents during slack tide. The transverse currents during these periods are one of the reasons why the sediment plume seems to disappear during periods of slack tide, as will be described later.

NATURAL SEDIMENT CONTENT IN THE ESTUARY

To determine the background sediment load in the study area, suspended load samples were taken when no sediment infusion took place. The samples were taken with a device consisting of two bottles connected by a short piece of pipe, see Figure 4. The lower bottle contains the sample while the displaced air is contained in the upper bottle. The whole system is buoyant even when the lower bottle is filled. A weight connected with the sampler by an anchor line is used to lower the sampler. When the weight reaches the bottom, the tension in the retrieval line is released, which automatically opens the intake. The positioning of the sampler above the bottom is controlled by the length of the anchor line.

The sediment samples were analyzed using the following procedure. The suspension was well mixed and 500 ml was poured into a cylinder. The suspended solids were then collected on filter paper. The filter paper was dried in an oven. When dry, the paper was burned and the ashes weighed.

The sediment samples were taken at three different depths at the stations used for the current measurements. The various sampling series were carried out for different freshwater discharges in order to study the influence of the freshwater inflow on the sediment content. All samples were taken during periods of definite ebb current. As an example, the results of one of the sampling series is plotted in Figure 5. It is noted that the data for the bottom samples are probably not very reliable, chances are that the sampler was in the mud layer covering the bottom instead of just above this layer.

In Figure 6, the average sediment concentration for each sampling series, that is the average of all 7 sampling stations, is plotted versus the average daily freshwater inflow. In the averaging procedure, bottom samples were neglected for the reason mentioned in the previous paragraph. Although only five data points are available, it may be safely concluded that a definite relation exists between sediment content and freshwater inflow. Because of the

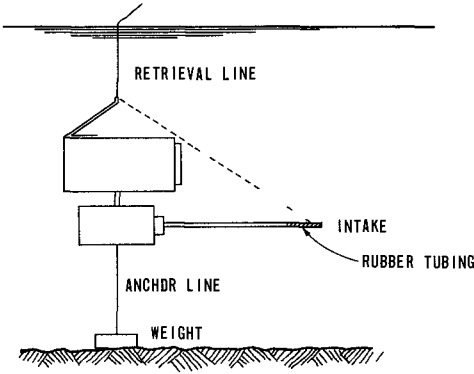


FIGURE 4 - SUSPENDEAD LOAD SAMPLER

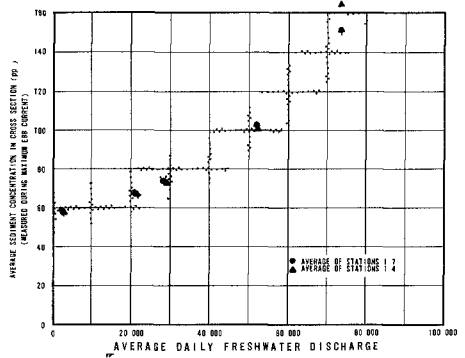


FIGURE 6 - NATURAL SEDIMENT CONTENT AS A FUNCTION OF FRESHWATER INFLW

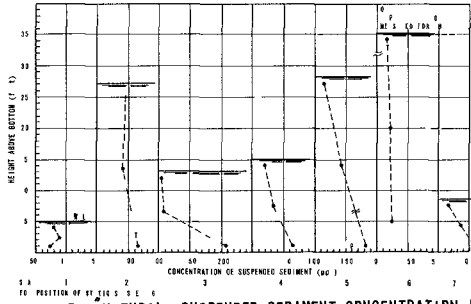


FIGURE 5 - NATURAL SUSPENDEAD SEDIMENT CONCENTRATION IN DIFFERENT MEASURING STATIONS

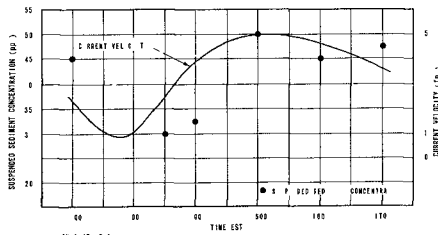


FIGURE 7 - VARIATION IN SUSPENDEAD SEDIMENT CONCENTRATION DURING A TIDAL CYCLE

special importance of the natural sediment in the area of sediment infusion, the average sediment concentration for stations 1 through 4 only, neglecting again the bottom samples, were also plotted versus the freshwater inflow in the same figure. No significant differences exist between the average sediment concentration in the shallow area (stations 1-4) and the average sediment concentration when regarding the total estuary cross-section (stations 1-7).

To study the variation in sediment concentration during a tidal cycle, a series of samples was taken at station No. 3 (tower) at a depth of 6 ft each hour for a period of six hours. The results are shown in Figure 7. A definite variation in suspended sediment content with the tidal currents seems to exist. This agrees with observations by other investigators, see Nichols and Poor [3]. At the time of the measurements, it was observed that during periods of high velocity the water looked cloudy while during slack tide the water had a less turbid appearance.

CHANGES IN THE SEDIMENT FIELD DUE TO THE SEDIMENT INFLUX

The sediment was discharged via a pipeline on the shallow plateau, see Figure 1. The discharge point was approximately 10 ft below the water surface. The total discharge was on the order of 10 lbs of solids/sec. Most of the discharged material appeared to be in the silt range, 90% of the particles are smaller than 85 μ , the median particle diameter is 45 μ and 10% of the particles are smaller than 10 μ . The sediment influx resulted in a plume visible during periods of relative low turbidity of the receiving waters. Visual observations, which are of course restricted to what happens at the surface, indicated that the end of the plume moved approximately with the speed of the current. The maximum length of the plume, just before slack tide, was approximately 3 miles. The width of the plume remained practically constant. At slack tide, the discoloring disappeared indicating that the sediment had settled or was dispersed by the reversing tide.

Sediment samples were taken to determine more accurately the effect of the sediment influx. The samples were taken in the measuring stations 1-7 and along the center line of the sediment plume. As an example, the distribution of suspended sediment across the estuary is presented in Figure 8. This figure clearly shows an increase in suspended load at the stations 2A and 3. The influence of the sediment infusion still is restricted to a narrow band at this distance.

Sediment concentrations in the axis of the plume are indicated in Figure 9, the concentrations decrease rapidly with downstream distance. The concentration near the discharge point varied between 1000 ppm and 1500 ppm and is already decreased to 200-500 ppm at a distance of 400 ft downstream of the discharge point.

It is clear from Figure 9 that large amounts of sediment settle close to the point of release. Fluorescent tracer was used to gain insight into the deposition areas of the remainder of the sediment. The range of particle sizes of the tracer material covered approximately that of the released sediment.

COASTAL ENGINEERING

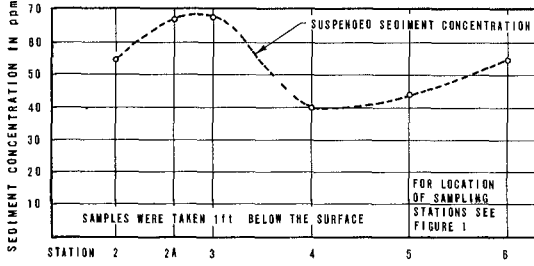


FIGURE 8 - HORIZONTAL DISTRIBUTION OF SUSPENDED SEDIMENT

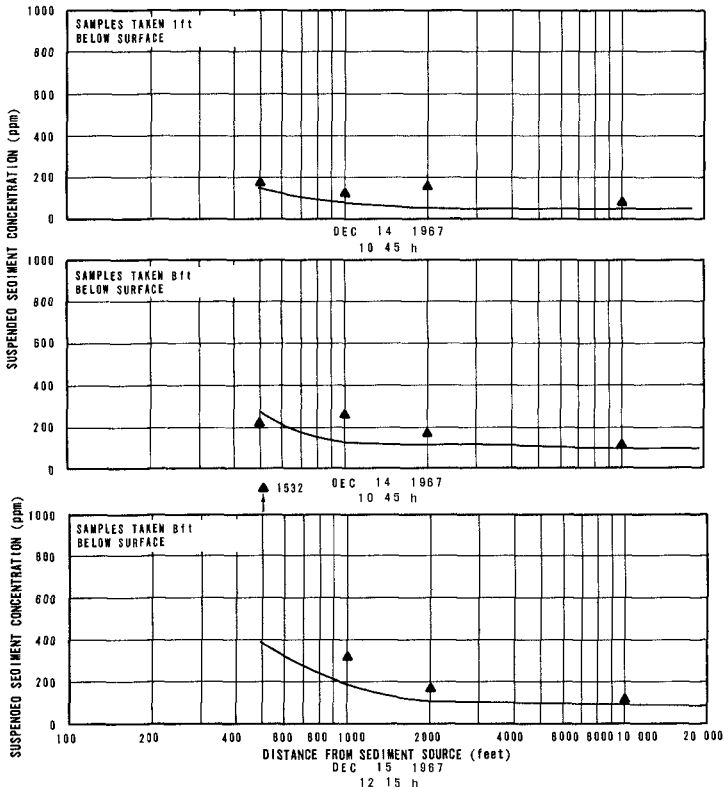


FIGURE 9 - SEDIMENT CONCENTRATION IN THE CENTER OF THE SEDIMENT PLUME

The tracer was released at the location of the sediment discharge point, at a rate of approximately 0.8 lbs/min for a period of two hours, leading to a total amount of released tracer of 100 lbs. The same day and the next day, suspended load samples were taken at different depths in the study area. The results were somewhat meager, probably because of the relative small quantity of tracer material, but some tracer grains were found as far away as stations 1 and 5 of the measuring cross-section.

MATHEMATICAL DESCRIPTION

Assuming that lateral and longitudinal diffusion are negligible (as suggested by the results of the measurements), and furthermore assuming a gradient type diffusion, the conservation of matter equation may be written as

$$\frac{\partial \phi}{\partial t} = \frac{\partial (\epsilon \frac{\partial \phi}{\partial y})}{\partial y} - u \frac{\partial \phi}{\partial x} + w \frac{\partial \phi}{\partial y} \quad (1)$$

in which ϕ = sediment concentration

ϵ = diffusion coefficient

u = current velocity

w = fall velocity of a sediment particle

The coordinate system has its origin at the bottom, the horizontal x-axis is positive in the current direction, the vertical y-axis is positive upward. Attempts to arrive at a computer solution for Equation (1) indicated that, with conventional numerical methods and for the dimensions of the computational field encountered in this study (water depth 10 ft, length of the sediment plume 20,000 ft), it is questionable whether even the larger computers can handle this problem. Therefore, a simplified and admittedly more crude model is presented here to describe the sediment concentration in the plume.

It is assumed that a block of polluted water travels at the average current velocity $u(t)$, and thus the position x , of the block at time t is $x = u t$. Only vertical diffusion is considered. It is also assumed that all particles reaching the bottom stick to it, while a steady sediment source at the bottom of the moving block of polluted water simulates the stir-up capacity of the flow. Only periods of definite ebb and flood current are considered. It is assumed that during periods of slack tide, the sediment particles in the plume settle and/or are distributed over the width of the estuary.

In deriving the equations, it is assumed that

- The convective velocity $u(t)$ is constant over the depth
- The eddy diffusivity coefficient ϵ is constant

- The fluid properties are not altered by the suspended sediment
- The diffusion is proportional to the gradient of the concentration
- The sediment concentration in the vertical at the dredging site is constant
- No flocculation occurs

The coordinate system is the same as the one described in the previous paragraph. Time (t) is zero at the moment the block of polluted water leaves the dredge. For the above assumptions the equations relating the sediment concentration $\phi(y,t)$ and the independent variables y and t are

Field equation

$$\frac{\delta \phi}{\delta t} = \epsilon \frac{\delta^2 \phi}{\delta y^2} + W \frac{\delta \phi}{\delta y} \quad (2)$$

Boundary conditions

$$y = 0 \quad \epsilon \frac{\delta \phi}{\delta y} = -\lambda$$

in which λ = rate of erosion

$$y = h \quad \epsilon \frac{\delta \phi}{\delta y} = -W\phi$$

in which h = average depth

For a more detailed discussion of the boundary condition, see Partheniades [2]

Initial condition

$$t = 0 \quad \phi = \phi_0$$

The solution of the above system of equations is

$$\phi = \frac{\lambda}{W} e^{-2ay} + \sum_{n=1}^{\infty} B(n) e^{-\alpha_n y} \left[\cos \alpha_n y + \frac{a}{\alpha_n} \sin \alpha_n y \right] e^{-(\alpha_n^2 + a^2) \epsilon t}$$

in which

$$\alpha_n \text{'s are the solution of } \operatorname{tg} \alpha_n h = \frac{2\alpha_n a}{\alpha_n^2 - a^2} \quad \alpha_n > 0$$

$$B(n) = \frac{\phi_0 e^{ah} \frac{\sin \alpha_n h}{\alpha_n} - \frac{\lambda}{2a} e^{-ah} \frac{\left[\frac{\alpha_n^2 - a^2}{\alpha_n} \sin \alpha_n h + 2a - 2a \cos \alpha_n h \right]}{a^2 + \alpha_n^2}}{(\alpha_n^2 + a^2)h + 2a} \frac{1}{2\alpha_n^2}$$

$$a = \frac{W}{2\epsilon}$$

Note that the second term in the solution goes to zero for large values of t , the first term represents the natural sediment concentration

To check the validity of the model a comparison is made between measured and computed concentrations. In the computations, $\phi_0 = 1250$ ppm. The value of λ was obtained by assuming a natural sediment concentration $\phi = 100$ ppm at $y = 4$ ft. The average depth $h = 10$ ft. An estimate of the diffusion coefficient was made by using Elders [1] expression

$$\epsilon = 0.068 hu_*$$

in which u_* = shear velocity

In the computations, $\epsilon = 0.05$ ft²/sec is used. The value $W = 0.008$ ft/sec was taken as a representative value of the fall velocity of the particle distribution. Computed and measured concentrations are plotted in Figure 9. The results agree reasonably well in spite of the many assumptions made in deriving the mathematical description and the limited accuracy of the measurements.

CONCLUSIONS

The artificial sediment infusion results in a sediment plume visible during periods of low turbidity of the receiving waters. The end of the plume moves approximately with the speed of the current. The width of the plume remains practically constant. The sediment concentration in the plume decreases rapidly with increasing distance from the point of sediment influx. During periods of slack tide, the plume disappears, the sediment settles and at the same time is dispersed by secondary currents.

A crude mathematical model is presented describing the sediment concentration in the plume. In its present form, it should be mainly regarded as a first step to a rational and universal solution.

Finally, it is noted that the title of the paper is somewhat of a misnomer as the case of sediment infusion discussed here has never been proven to be harmful.

ACKNOWLEDGEMENT

The study described here was carried out by the author while employed with Science Engineering Associates, San Marino, California. The guidance of Dr. Per Bruun during the initial stages of the project is gratefully acknowledged.

REFERENCES

1. Elder, J., "The Dispersion of Marked Fluid in Turbulent Shear Flow", J. Fluid Mech., Vol. 5, Part 5, 1959.

- 2 Partheniades, E , "A Summary of the Present Knowledge of the Behavior of Fine Sediments in Estuaries", Technical Note No 8, M I T , Hydrodynamics Laboratory, June, 1964
- 3 Nichols, M M and Poor, G , "Sediment Transport in a Coastal Plain Estuary," Journal of the Waterways and Harbors Division, ASCE, Vol 93, No WW4, November, 1967

CHAPTER 110

RECIRCULATION IN SHALLOW BAYS AND RIVERS

by

R K Price, Visiting Assistant Professor
R A Dalrymple, Assistant in Engineering
R G Dean, Professor, and Chairman

Department of Coastal and Oceanographic Engineering
University of Florida, Gainesville, Florida

ABSTRACT

A theoretical model is presented to provide an approximation of the water and temperature recirculation in a shallow bay, lake or river, between the outlet and inlet canals of the cooling system for a power plant. In particular, a temperature recirculation factor relating the outlet and inlet temperatures is derived.

INTRODUCTION

Since the efficiency of a power plant depends critically on a low intake water temperature, an injudicious siting of the discharge canal terminus may cause recirculation of the discharge water, with a consequent increase in the temperature of the intake water. Thus a prior knowledge of the effect of particular locations for the terminus of the discharge canal is important.

The quantitative evaluation of the siting of the outlet and inlet canals, taking into account tides, meteorological conditions, the diffusion and convection of momentum and temperature, and the stratification due to temperature and salinity, is a difficult problem. The complexity of the boundary conditions and governing equations for the system requires the use of numerical modeling. The recent work of Wada (1966, 1967, 1968) has clarified many of the problems involved and given some solutions to particular models.

The following work presupposes that steady conditions prevail and that, to the first order, temperature variations have no effect on the flow. This rather crude assumption can be partially strengthened by considering the receiving water system to be shallow and by assuming that the turbulence in the flow is sufficient to ensure that the mixing of the water is complete throughout the water column. These assumptions and conditions thus avoid the more difficult problems of variations in time, and vertical stratification of temperature.

To simplify the analysis, the equations governing the flow in the bay are linearized. This procedure is reasonable except near the outlet for the plant cooling system where the non-linear convection of momentum terms may well be important. We assume that the flow in the neighborhood of the outlet can be treated as a source rather than as a jet, whence the convection terms can be neglected.

For steady flow, the equations of momentum and continuity can be written as

$$-fv = -g \frac{\partial \eta}{\partial x} + \frac{\tau^{sx}}{\rho h} - \frac{\kappa \bar{U}}{h} u \quad (1)$$

$$fu = -g \frac{\partial \eta}{\partial y} + \frac{\tau^{sy}}{\rho h} - \frac{\kappa \bar{U}}{h} v \quad (2)$$

and

$$\frac{\partial}{\partial x} (hu) + \frac{\partial}{\partial y} (hv) = 0 \quad (3)$$

Here u and v are the water particle velocities in the x and y directions respectively, η is the displacement of the free surface from its mean level, τ^{sx} and τ^{sy} are the stresses exerted by the wind on the flow, h is the mean depth, f is the Coriolis parameter, κ is related to the Chezy bottom stress coefficient, C , by $\kappa = g/C^2$, \bar{U} is a scale velocity and g is the acceleration due to gravity

The linearization of equations (1) and (2) involved firstly the neglect of the non-linear inertia terms, as commented above, and also the adoption of a linear form for the bottom stress terms. The linearization of these latter terms has been shown to be reasonable for oscillating flows such as tides in estuaries. However, the use of the linear form for steady flows has not been so readily confirmed. It is used here because the basic equations can be written in a particularly useful form and also, the resulting flows appear to give a good representation of the physical situation. Equations (1), (2) and (3) also require $\eta \ll h$.

From equation (3), a stream function ψ can be defined such that

$$u = -\frac{1}{h} \frac{\partial \psi}{\partial y} \quad \text{and} \quad v = \frac{1}{h} \frac{\partial \psi}{\partial x} \quad (4)$$

By eliminating η between (1) and (2),

$$\frac{\partial^2 \psi}{\partial x^2} + \frac{\partial^2 \psi}{\partial y^2} = \frac{2}{h} \left(\frac{\partial \psi}{\partial x} \frac{\partial h}{\partial x} + \frac{\partial \psi}{\partial y} \frac{\partial h}{\partial y} \right) + \frac{f}{\kappa \bar{U}} \left(\frac{\partial \psi}{\partial x} \frac{\partial h}{\partial y} - \frac{\partial \psi}{\partial y} \frac{\partial h}{\partial x} \right) - \frac{h^2}{\rho \kappa \bar{U}} \left\{ \frac{\partial}{\partial y} \left(\frac{\tau^{sx}}{h} \right) - \frac{\partial}{\partial x} \left(\frac{\tau^{sy}}{h} \right) \right\} \quad (5)$$

Equation (5) takes on a particularly simple form if h is uniform and $\tau^{sx} = \tau^{sy} = 0$

$$\frac{\partial^2 \psi}{\partial x^2} + \frac{\partial^2 \psi}{\partial y^2} = 0 \quad (6)$$

In this case the streamlines are given by potential flow theory, whence sources and sinks can readily be modeled. This method is used as the basis for the study of recirculation of the water between the outlet and inlet canals. The extension of this type of model in the case of a variable depth and a non-zero wind stress requires the use of numerical solutions of (5).

WATER RECIRCULATION

Consider inlet and outlet canals embedded in a straight coastline bordering a receiving water system which covers the half-plane and has a uniform depth. If the distance between the outlet and inlet canals is $2a$, then the complex velocity potential for the flow in the receiving system is

$$w \equiv \phi + i\psi = -\mu \log \frac{z-a}{z+a} - \bar{U}z \quad (7)$$

where μ is the strength of the source-sink flow, $z \equiv x + iy$, the source is at $z = a$ and the sink at $z = -a$, and \bar{U} is the speed of a uniform steady current along the coast, cf. Figures 1 and 2. This current can be regarded as a steady river flow, or a "steady state" tidal current. In either case, \bar{U} may be a function of time t , subject to the condition that the time scale T for changes in \bar{U} are large compared with $h/\kappa\bar{U}$ and $2a/\bar{U}$. If $\bar{U} = 1.0$ ft/sec, the (varying) tidal amplitude is 1.5 ft and $\kappa = 0.02$, then for $T \approx 12$ hrs, it can be shown that h must be less than approximately 14 ft. Further, a must be less than 33,000 ft. These are fairly strict conditions on h and a . The conditions may be realistic only for a few situations.

From equation (7), the non-dimensional form for the streamlines is

$$x'^2 = 1 - y'^2 - 2y' \cot(\bar{U}'y' + \psi') \quad (8)$$

where $\bar{U}' \equiv \bar{U}a/\mu$, $\psi' \equiv \psi/\mu$ is the dimensionless value for the streamline, and $x' = x/a$, $y' = y/a$. It can be shown from equation (8) that the percentage recirculation of water is 100% for a zero current ($\bar{U}' = 0$) or for a current aided recirculation ($\bar{U}' < 0$). However, for an opposing current ($\bar{U}' > 0$), the percentage circulation is reduced. Figure 3 shows the percentage recirculation of water for aiding and opposing non-dimensionalized currents. It can be seen that for an opposing current \bar{U}' greater than 2.0, there will be no recirculating water.

Other elementary shaped coastlines can be treated by the technique of conformal mapping. In the general situation, equation (5) can readily be solved numerically. Further details on this technique will be discussed by Price (1971). Figure 4 gives the streamlines in an idealized model of a bay connected to the ocean. This model includes variations in the depth and coastline configuration and permits an inflow of water across two of the boundaries.

It is of interest to point out that uniform depth flows can be modeled experimentally using a Hele-Shaw apparatus. A Hele-Shaw model has been used at the University of Florida to determine the streamline patterns for flow into a bay.

THERMAL RECIRCULATION

The temperature difference between the outlet and inlet canal of a cooling system depends, in part, on the decay of temperature in the recirculating fluid with distance from the outlet. It should be noted that mixing effects are not

included in this treatment. Under the assumption that there is no heat flow through the bottom or the fixed side boundaries, heat can only be lost or gained by the recirculating water in exchange with the surrounding receiving water or with the atmosphere. We assume that the diffusion of temperature in the receiving system is negligible compared with the convection of temperature. Thus the primary mechanism for extracting heat from the water is assumed to be via the atmosphere.

The components of heat loss (or gain) from the surface of a body of water include

- Q_s solar radiation by the sun
- Q_b back radiation from the water to the atmosphere
- Q_c heat loss due to convection
- Q_e heat loss due to evaporation
- Q_r heat advection by rain or other inflows

The "s" refer to differentiation with respect to time t . Consider the anomalous heat flux due to the heated water, that is

$$Q_{net} = Q_E + Q'$$

$$T_w = T_{wE} + T_w'$$

where the primes denote incremental heat fluxes due to the increased water temperature T_w' . The quantities Q_E and T_{wE} are defined such that the water body is in equilibrium (in the average sense) for $T_w = T_{wE}$. This implies that $Q_E = 0$.

The heat flux budget can be written as

$$Q' = Q_s - Q_b - Q_c - Q_e + Q_r \quad (9)$$

where the various components of heat flux are defined in the following equations

$$\begin{aligned} Q_s &= (1 - r) Q_m \\ \dot{Q}_b &= 0.97 \sigma (\theta_w^4 - \beta \theta_a^4) \\ Q_c &= 0.00407 PW (T_w - T_a) \\ Q_e &= 12 W(e_w - e_a) \end{aligned} \quad (10)$$

$$Q_r = M_r C_{w_r} (T_r - T_w)$$

here

Q_m = the solar radiation on a horizontal surface,

r = the reflectivity, assumed to be 0.05,

σ = the Stefan-Boltzmann radiation constant = 1.714×10^{-9}
BTU/hr/ft²/°R⁴,

θ_w = absolute water temperature in °R ($T(^{\circ}\text{F}) + 459.69$),

θ_a = absolute air temperature,

β = radiation factor, depending on cloud cover, vapor pressure,
etc. An average value of β is 0.85,

W = wind speed in knots,

P = atmospheric pressure in inches of mercury,

e_w = vapor pressure of water in saturated air at the temperature
of water, in inches of mercury (For temperature ranges of
interest, $e_w \approx 0.045T_w - 2.6$),

e_a = vapor pressure of water in air, in inches of mercury
($e_a \approx e_w \times$ relative humidity),

M_r = mass rate of rainfall,

c_r = specific heat of rainwater,

T_r = temperature of the rainwater,

and

T_a = temperature of the air

We assume for the purposes of this paper, that $Q_r = 0$. By utilizing the various definitions for the Q 's from (10) and substituting in equation (9), then the incremental heat flux Q' , due to the water temperature increased an amount T_w' above the equilibrium temperature, is approximately

$$Q' \text{ (BTU/ft}^2\text{/hr)} = \{1.04 + 0.66 W\} T_w' \quad (11)$$

Thus if Q is the amount of heat above ambient in a volume of water with unit surface area

$$\begin{aligned} \frac{dQ}{dt} &= Q' \\ &= -KT_w' \end{aligned} \quad (12)$$

where $K = 1.04 + 0.66W$. K can be called the heat transfer coefficient, and as such includes the effects of radiation, convection and evaporation as outlined above

$$Q = \gamma h c_p \overline{T'_w} \quad (13)$$

where γ is the specific weight of water with heat capacity c_p . Thus from equation (13)

$$\frac{dQ}{dt} = \gamma h c_p \frac{dT'_w}{dt} = -K T'_w \quad (14)$$

To examine the relation between the flow and temperature fields, consider Figure 5. If the flow is divided into N streamtubes of equal flow Δq , then it can be seen that for the flow between two particular streamlines is

$$\Delta q = h \ell \, ds/dt \quad (15)$$

where ℓ is the spacing normal to the streamlines, and ds/dt is the local water particle velocity parallel to the local streamline. Using equations (14) and (15)

$$\frac{dT'_w}{ds} = - \frac{K \ell T'_w}{\gamma c_p \Delta q} \quad (16)$$

The integration of equation (16) gives

$$\ln T_{w_i} = - \frac{K A_j}{\gamma c_p \Delta q} + \ln T_{w_o}$$

where T_{w_i} and T_{w_o} are the inlet and outlet temperatures respectively for the flow between the $(j-1)$ th and the j th streamlines, and A_j is the surface area between the two streamlines. By summing over the N streamlines and averaging the thermal recirculation is expressed by

$$C_R = \frac{\overline{T_{w_i}}}{T_{w_o}} = \frac{1}{N} \sum_{j=1}^N e^{-\beta A_j} \quad (17)$$

where

$$\beta = \frac{K a^2}{\gamma c_p q} \quad (18)$$

The A_j 's are the non-dimensional areas between the streamlines (i.e. $A_j = A_j/a^2$), where $2a$ is the distance between the outlet and inlet), and q is the total volume recirculating ($q = \pi \mu h$). C_R can be termed the temperature recirculation factor. It can be seen that C_R depends on the sum of exponential terms, and of course must be less than unity.

A numerical evaluation of C_R in the case when the equations of the streamlines are known can be carried out on a computer. In the case of the source and sink embedded in the boundary of the half plane, with $\beta = 0.78$ and $\bar{U}' = -0.75$, (an aiding current and 100% water recirculation), $C_R = 43\%$, with only 50% recirculation of the outlet water ($\bar{U}' = 0.326$) and $\beta = 0.78$, $C_R = 127$. In this example $N = 10$, cf. Figure 6.

The extension of the technique to more complicated flows as considered briefly in Figure 4 is straightforward. For example, one can divide the flow from the outlet using 9 interior streamlines, whence $N = 10$. The areas A_j can readily be found from graph paper when the streamlines have been plotted. For a representative value of K and the proper dimensions and discharge, β can be calculated (equation 18), and the temperature recirculation determined from equation (17).

CONCLUSION

The analysis presented here can readily be used to obtain an estimate of the temperature circulation for particular locations of the inlet and outlet canals for a power plant located by a shallow bay, lake or river which is being used in the cooling system. A numerical solution of equation (5) can be used for particular cases, including the effects of prevailing wind stresses as well as an arbitrary bottom topography.

The limitations of the above technique are obvious due to neglecting temperature gradients, diffusion, and any unsteady feature of the flow. Also there may be some doubt about the validity of the linear form for the bottom stress in the case of large variations in the velocity of the water in the receiving system. However, despite these limitations, the authors have found that the technique provides a realistic approximation of the temperature recirculation.

REFERENCES

1. Wada, A, "A Study on Phenomena of Flow and Thermal Diffusion Caused by Outfall of Cooling Water", Proc 10th Conf on Coastal Engr, Tokyo, 1966
2. Wada, A, "Studies of Recirculation of Cooling Water in a Bay", Proc 11th Conf on Coastal Engr, London, 1968
3. Wada, A, "Numerical Analysis of Distribution of Flow and Thermal Diffusion Caused by Outfall of Cooling Water", 13th Congress I A H R, Tokyo, 1969
4. Price, R. K., "Wind Generated Coastal Currents" - in preparation

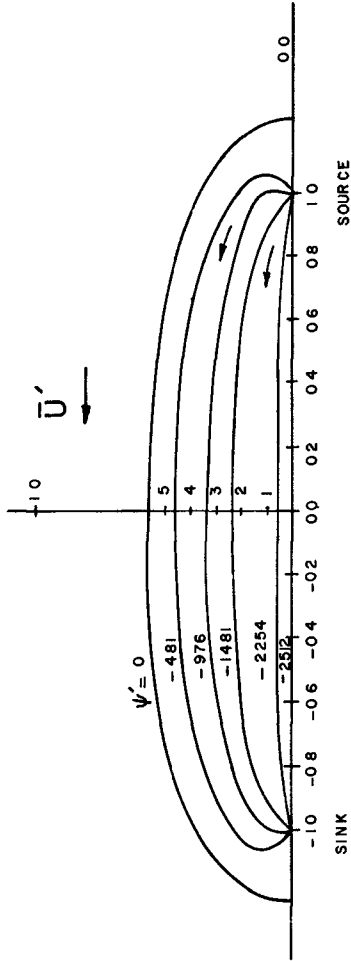


FIGURE 1' 100% RECIRCULATION WITH $\bar{U}' = -3.75$

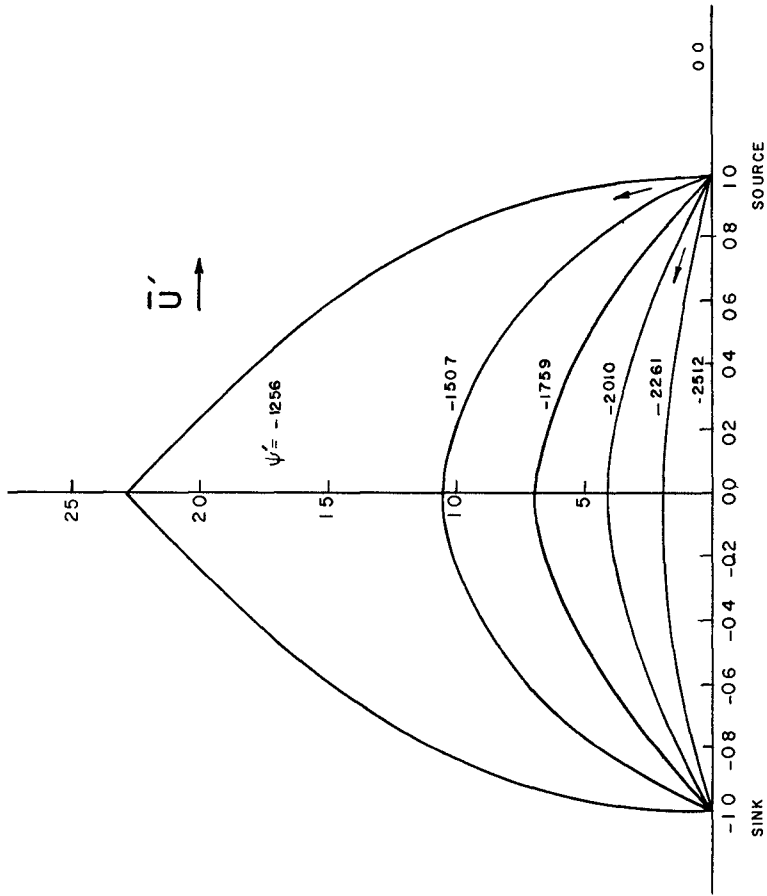


FIGURE 2 50% RECIRCULATION WITH $\bar{U} = 0.325$

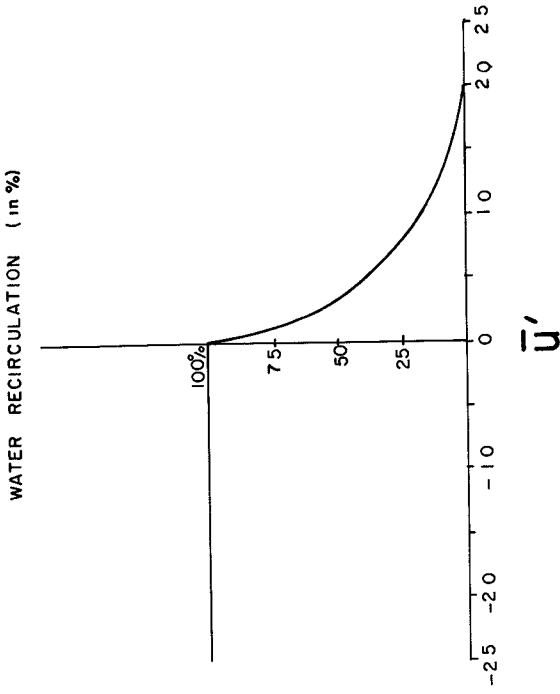


FIGURE 3 PERCENTAGE OF RECIRCULATED WATER FOR AIDING AND OPPOSING
NONDIMENSIONAL UNIFORM CURRENTS

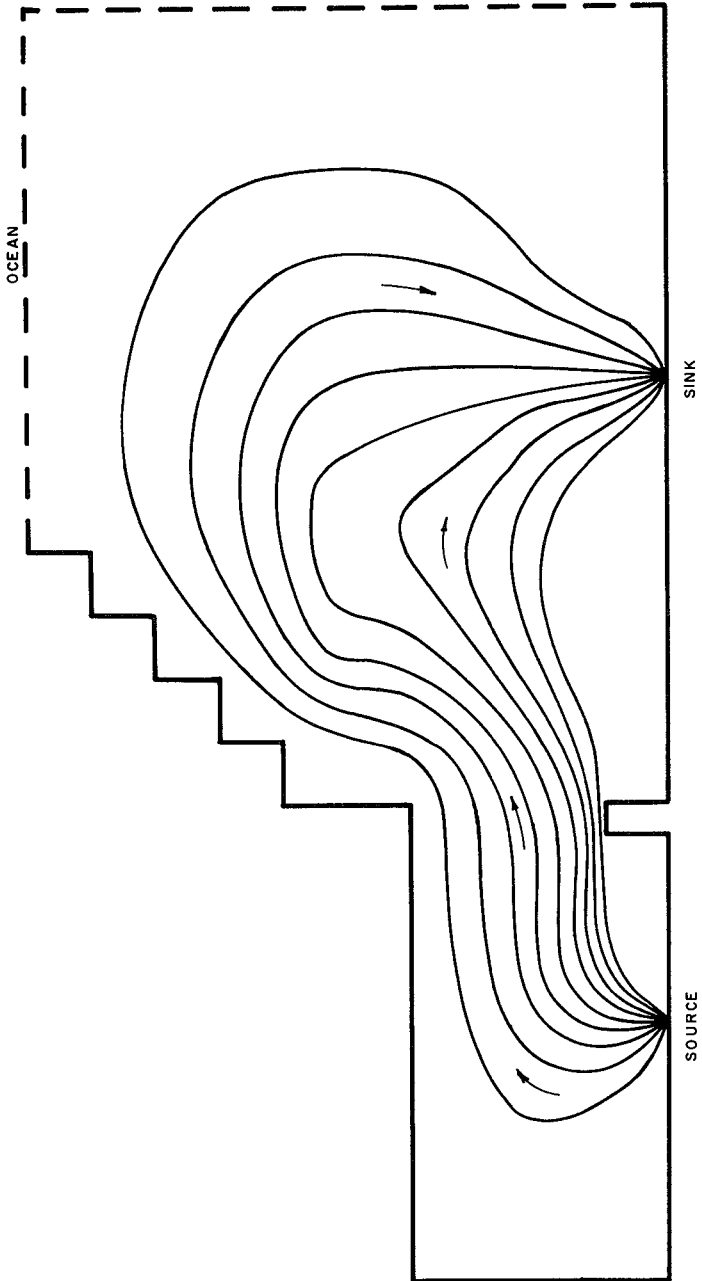


FIGURE 4 STREAMLINES IN AN IDEALIZED BAY

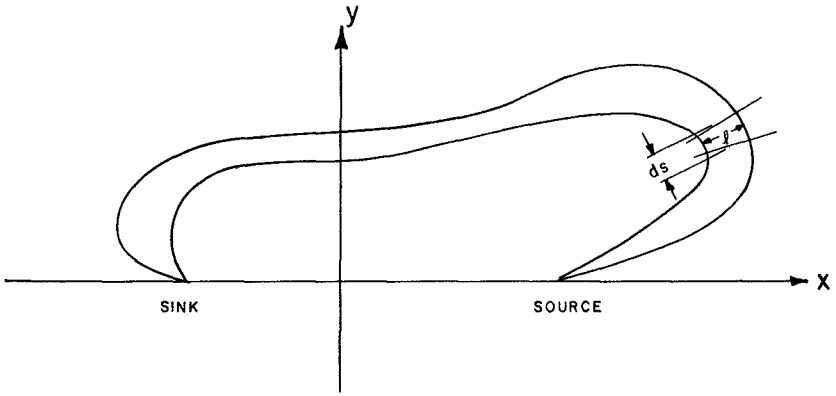


FIGURE 5 DEFINITION SKETCH

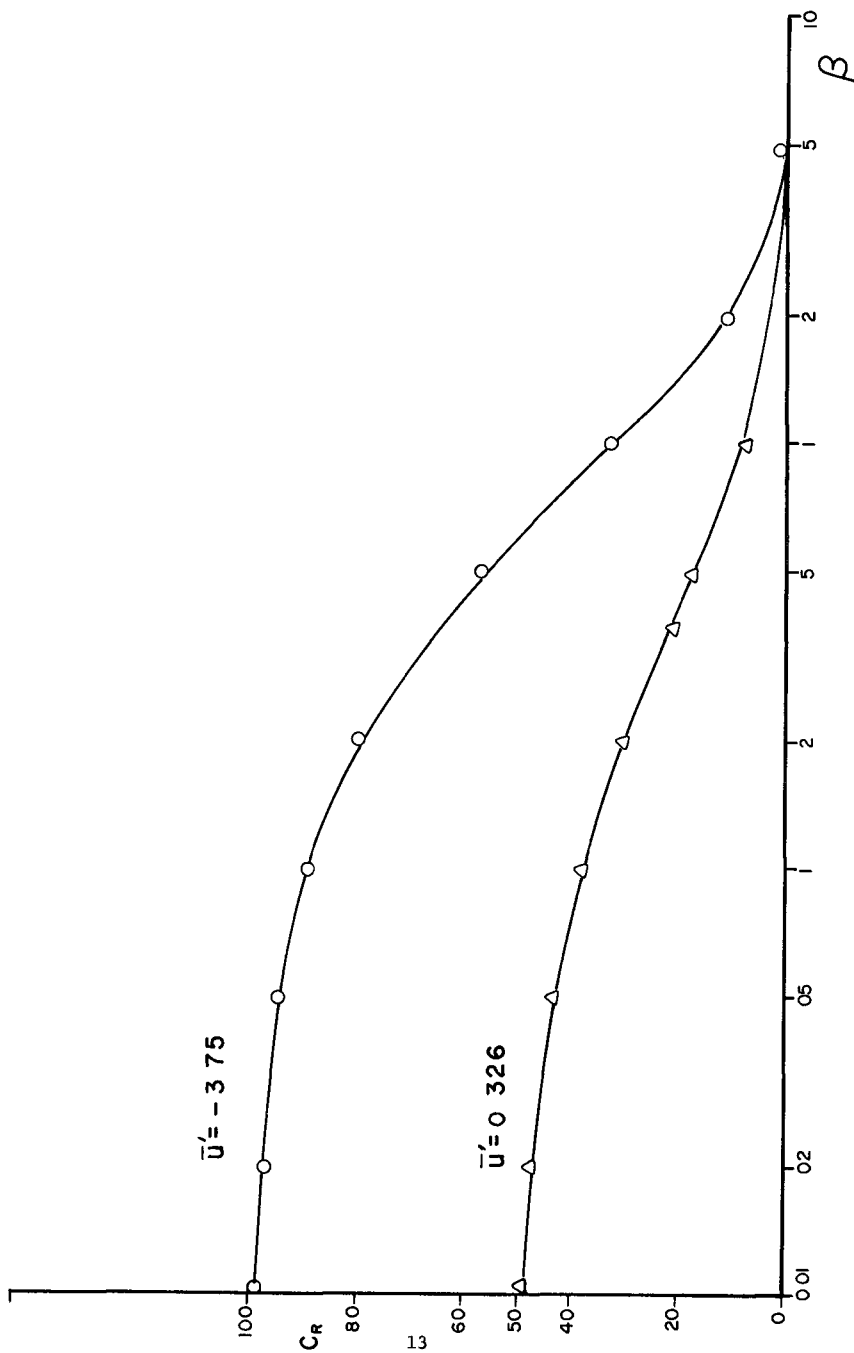


FIGURE 6 C_R VS β FOR TWO CASES OF FIGS 1 & 2

CHAPTER III

NATURAL FRESHING ABILITY IN TIDAL INLETS

L. S. Mota Oliveira*

1 - ABSTRACT

The main object of this work is to study the relationship between the freshening ability of tidal inlets with the degree of shoaling, assuming that the water level fluctuations in the lagoon are uniform over

It was assumed that natural freshening ability is proportional to the bed-load capacity of tidal currents and that this capacity can be characterized both by the hydraulic power consumed in the connecting channel and by the 3rd or 6th power of the mean velocity. Influence of the slope of the inlet banks and of the inner head losses was also analysed.

2 - INTRODUCTION

In 1951 E. H. Keulegan [1] undertook the analytical study of the hydrodynamic behaviour of the inlet-lagoon system, but some restricting hypotheses were assumed which diminish the practical interest of the results obtained. For instance, he assumed the relationship between the depth of the inlet channel and the tidal range to be very great (and therefore he considered the flow section constant during a tidal cycle). Also the banks of the lagoon were considered vertical, and the level variation law the same for all points of the lagoon.

The hydrodynamic behaviour of the system could thus be characterized by the equations

$$\frac{dh_1}{d\theta} = K \sqrt{h_2 - h_1} \quad \text{when } h_2 > h_1 \quad (\text{flood}) \quad \text{and}$$

$$\frac{dh_1}{d\theta} = K \sqrt{h_1 - h_2} \quad \text{when } h_1 > h_2 \quad (\text{ebb})$$

where (see Fig. 1),

$h_1 = \frac{H_1}{H}$, $h_2 = \frac{H_2}{H}$, H being the ocean tide amplitude, H_1 and H_2 sea and lagoon levels respectively referred to the mean sea level, $\theta = \frac{2\pi}{T}t$,

* - Trainee Research Officer - Laboratorio Nacional de Engenharia Civil, Lisbon, Portugal

T the tidal period, t the time variable, K a dimensionless parameter which the author has called repletion coefficient, and which condenses the influence of several parameters, namely, lagoon and channel dimensions, channel roughness, and sea tide amplitude and period

Owing to the simplifying hypotheses made, the coefficient K is constant all along the tidal cycle and, consequently, the mean level of the lagoon is equal to the mean sea level, the behaviour of the level law in the lagoon is symmetrical with respect to that level, and the flood velocities and rates of flow are symmetrical to those at the ebb. In the study of natural flushing ability of a tidal inlet we cannot make use of the results of such a simplified scheme, since the most interesting cases to be analysed are obviously those which are characterized by faulty inlets needing correction, which present small values for the channel depth/tidal range ratio

In the first studies it was sought to analyse the influence of the channel flow section variation and that of the lagoon area during a tidal cycle, subsequently, the influences of head losses in the lagoon were also analysed for a very schematic case

3 - INFLUENCE OF FLOW SECTION VARIATION OF INLET CHANNEL AND OF BANK SLOPE

3 1 - Characteristic equation of the system

Assuming the inlet channel to be well shaped, to have constant width and depth over its entire length, and the level variation in the lagoon to be uniform, we obtain similarly to Keulegan

$$\frac{dH_1}{dt} = \frac{a}{A} \sqrt{\frac{C^2 r}{L + \frac{C^2 r}{2g}}} \sqrt{H_2 - H_1} \quad (1)$$

where

- A - lagoon area
- a - flow section area of the inlet
- L - length of inlet channel
- r - hydraulic radius of inlet channel

C - Chezy coefficient ($C^2 = \frac{r^{1/3}}{n^2}$)

n - Strickler coefficient

Assuming further that the hydraulic radius (r) is equal to the depth of the channel, that this depth corresponds to the arithmetic mean of sea and lagoon levels, and that the lagoon area varies linearly with its level, we get

$$r = d + \frac{H_1 + H_2}{2}, \text{ where } d \text{ is the depth referred to the mean sea level} \\ \text{(Fig 1)}$$

a = br, b being the width of the channel,

$A = A_o (1 + N \frac{H_1}{H})$, A_o being the area of the basin corresponding to the mean sea level (Fig 2)

Parameters H_2 , H_1 , r and d were reduced to a dimensionless form by relating them to the sea tidal amplitude

$$h_2 = \frac{H_2}{H} = \sin \theta, h_1 = \frac{H_1}{H}, r_o = \frac{r}{H} = d_o + \frac{h_1 + \sin \theta}{2}$$

Besides, $\theta = \frac{2\pi}{T} t$, so that equation (1) will be

$$\frac{dh_1}{d\theta} = \frac{Tb}{\pi A_o} \sqrt{\frac{gH}{2}} \frac{1}{1 + N h_1} \frac{r_o^{3/2}}{(\frac{2gn^2L}{H^{4/3}r_o^{1/3}} + r_o)^{1/2}} (|h_2 - h_1|)^{1/2} \quad (2)$$

Making $D = \frac{Tb}{\pi A_o} \sqrt{\frac{gH}{2}}$ (3)

$E = \frac{2gn^2L}{H^{4/3}}$ (4)

we get $\frac{dh_1}{d\theta} = J \frac{D}{1 + N h_1} \frac{r_o^{3/2}}{(\frac{E}{r_o^{1/3}} + r_o)^{1/2}} (|\sin \theta - h_1|)^{1/2}$ (5)

J = 1 for $\sin \theta > h_1$ (flood)

J = -1 for $\sin \theta \leq h_1$ (ebb)

Since $r_o = d_o + \frac{h_1 + \sin \theta}{2}$, it follows that the inlet-lagoon system is well characterized by the dimensionless parameters D, E, d_o and N. On the other hand, it is easy to see that Keulegan repletion coefficient is related to these parameters by the expression

$$K = \frac{D d_o^{3/2}}{\left(\frac{E}{d_o^{1/3}} + d_o\right)^{1/2}}, N=0 \quad (6)$$

The numerical integration of equation (5) was made in the NCR-Elliott 4100 computer of the Laboratório Nacional de Engenharia Civil, using one of its library programs. An integration step $\Delta\theta = 0.1$ radians was adopted, to which corresponds, in the case of a semi-diurnal lunar type tide ($T=12$ h 25 min), $\Delta t \approx 11$ min 52 s. The numerical integration of equation (5) was effected starting from a situation in which the level inside and outside the basin were equal to the mean sea level. After some attempts it was concluded that the second tidal cycle no longer depended on initial conditions, so that integration was made to comprehend two tidal cycles, of which the first was discarded. While integrating equation (5) the computer also calculated the other parameters necessary for the study of the natural flushing capacity of the inlet, namely, rate of flow, velocity, 3rd and 6th power of the velocity and consumed power.

3.2 - Rate of flow

From the continuity equation

$$Q = A \frac{dh}{dt} = \frac{2\pi H A_o}{T} (1+Nh) \frac{dh}{d\theta}$$

we get

$$Q_a = \frac{Q}{\frac{2\pi H A_o}{T}} = (1+Nh) \frac{dh}{d\theta} \quad (7)$$

where Q_a is the dimensionless rate of flow, whose term of comparison

$$\frac{2\pi H A_o}{T} = \frac{2H A_o}{T/2} \frac{\pi}{2}$$

represents the peak discharge corresponding to the sinusoidal flow of the lagoon's maximum admissible prism ($2H A_o$).

3.3 - Mean velocity

From $Q = aV = A \frac{dh}{dt}$ there results

$$V_a = \frac{V}{\frac{2\pi H A_o}{T}} = \frac{1+Nh}{r_o} \frac{dh}{d\theta} \quad (8)$$

where V_a is the dimensionless velocity whose comparison term

$$\frac{2 \pi A_o}{T b} = \frac{2 H A_o}{T/2} \frac{\pi}{2} \frac{1}{b H}$$

represents the mean velocity of flow, through section bH , of the peak sinusoidal discharge corresponding to the lagoon's maximum admissible prism ($2H A_o$)

Another dimensionless velocity (V'_a) was further considered, in which the comparison term adopted was $\sqrt{2gH}$. It is easy to prove that

$$V'_a = \frac{V}{\sqrt{2gH}} = \frac{1+N h_1}{D r_o} \frac{dh_1}{d\theta} = \frac{V_a}{D} \tag{9}$$

In Keulegan's study a coefficient C was determined, which relates the maximum flow with the one that would occur if the effective prism Pr (and not the maximum possible one $2H A_o$) would flow out sinusoidally. As this author considers the flow section (bd) invariable, constant C also gives the relationship between the maximum velocity and the peak velocity corresponding to the sinusoidal flow of the effective prism Pr . In our case, as we take into account the variation of the flow section, there are reasons for the determination of a value C_1 for the rates of flow and of a value C_2 for the velocities, adopting as term of comparison for them the maximum velocity corresponding to the sinusoidal flow of the effective prism Pr through the mean sea level section.

We will then have

$$C_1 = \frac{Q_{max}}{\frac{Pr}{T/2} \frac{\pi}{2}} = \frac{Q_{max}}{\frac{\pi}{T} A_o (H_{1max} - H_{1min})} = \frac{Q_{max}}{2 \pi H A_o} \frac{1}{\frac{H_{1max} - H_{1min}}{2H}}$$

From expression (7) we will thus get, for $N=0$ (vertical banks)

$$C_1 = \frac{2}{\Delta h_1} Q_{a max} \tag{10}$$

where Δh_1 represents the lagoon tidal range in the dimensionless form

In the same way

$$C_2 = \frac{V_{max}}{\frac{Pr}{T/2} \frac{\pi}{2} \frac{1}{bd}} = \frac{V_{max}}{\frac{2 \pi A_o}{Tb} \frac{1}{d_o} \frac{H_{1max} - H_{1min}}{2H}}$$

Thus, from expression (8) there results for $N=0$ (vertical banks)

$$C_2 = \frac{2}{\Delta h_1} d_o V_{max} \tag{11}$$

We must say that the comparison of C_1 with the value of C obtained by Keulegan seems to be more logical than the comparison of C_2 . In fact C_2 relates the maximum effective velocity which, as a rule, will occur for a level other than the mean one, with the peak velocity corresponding to the sinusoidal flow through the section fixed arbitrarily for the mean level. On the other hand, in the calculation of C_1 , and since we are relating rates of flow, it is not necessary to take into account the value of the flow section. This comes close to the Keulegan scheme, in which this section was considered invariable.

3.4 - 3rd and 6th powers of the mean velocity

According to Colby [3], "the relationship of bed-material discharge to mean velocity is the most convenient to apply. The computations are simple, and the energy gradient is not required. The relationship may be as accurate as any of the other three [which relate bed load capacity, respectively, with shear velocity $\sqrt{\frac{\tau}{\rho}}$, shear velocity relative to the particles $\sqrt{\frac{\tau'}{\rho}}$ and stream power] unless antidunes extend across much of the flow."

From the curves presented by this author it can be concluded that bed-load capacity of an unidirectional current varies almost linearly with a very high power of the mean velocity. In the present work it was assumed that for the velocity range occurring in a given inlet, this variation was in fact linear with the 3rd or 6th power of the mean velocity and that natural flushing ability of the inlet was proportional to the integral value, during the ebb and flood periods, of that bed load capacity. Again, it was logically assumed that for a given natural flushing ability the more the integral ebb bed load capacity exceeds that of the flood, the better would be conditions offered by the inlet.

While integrating equation (5) the computer therefore calculated the values of function $V_a^3(\theta)$ and $V_a^6(\theta)$ (see expression (8)) and then obtained the integral value of these parameter by the trapezoidal rule.

3.5 - Hydraulic power consumed in the inlet channel

It was sought to relate natural flushing ability of the inlet with the hydraulic energy consumed in it during a tidal cycle.

To achieve this, and in accordance with the hypothesis made when deducing the expression (5), it was assumed that the kinetic energy of flow $\frac{V^2}{2g}$ is totally dissipated in the sea or lagoon, in a turbulent expansion process, and

that, therefore, the hydraulic power consumed in the channel can be calculated through the expression

$$W = \gamma Q (|H_2 - H_1| - \frac{V_a^2}{2g})$$

It was deemed unnecessary to present here the deduction of the consumed power in its dimensionless form, which is as follows

$$W_a = \frac{\gamma Q (|H_2 - H_1| - \frac{V_a^2}{2g})}{\frac{2 \pi \gamma A_o H^2}{T}} = Q_a \left[|\sin \theta - h_1| - (V'_a)^2 \right] \quad (12)$$

where the comparison term, which may be written,

$$\frac{2 \pi \gamma A_o H^2}{T} = \frac{\gamma 2 H A_o}{T/2} \frac{\pi}{2} H$$

represents the power developed, under a difference of levels equal to the sea tide amplitude, by the peak discharge corresponding to the sinusoidal flow of the maximum prism admissible in the lagoon

The expression of W_a may also be given as

$$W_a = \frac{E}{D^2} \frac{V_a^3}{r_o^{1/3}} \quad (13)$$

from which it is concluded that the behaviour of the $W_a(\theta)$ function should be analogous to that of the 3rd power of the dimensionless velocity (V_a). This similarity will increase with the mean depth of the channel, considering the smaller relative fluctuation of the dimensionless hydraulic radius (r_o) during the tidal cycle

3.6 - Results obtained by the computer

Through its plotter output and for each of the cases studied, the computer gave in graphic form all the functions just mentioned $\sin(\theta)$, $h_1(\theta)$, $Q_a(\theta)$, $V_a(\theta)$, $V_a^3(\theta)$, $V_a^6(\theta)$ and $W_a(\theta)$. Fig 4 shows the results concerning a lagoon-inlet system characterized by $D=0.2$, $E=10.0$, $d_o=6.0$, $N=0.0$ as given by the plotter, the curves $V_a^3(\theta)$ and $V_a^6(\theta)$ regarding the system characterized by

$$D = 0.2 \quad E = 10.0 \quad d_o = 6.0 \quad N = 0.2$$

being added only to illustrate the effect of the lagoon bank slope, which only differs from the previous system in so far as parameter N is concerned, which charac

terizes the slope referred to (Fig. 2)

4 - INFLUENCE OF HEAD LOSSES IN THE LAGOON

4.1 - Equilibrium in the study

It can be concluded, by mere energetic considerations that head losses through friction in a lagoon will bring about a decrease in actual flushing ability of its inlet. In fact, the tidal wave energy dissipated in the inner basin will cease to be available to remove the littoral drift material which tends to obstruct it.

As, however, flushing ability of an inlet depends not only on the integral bed load capacity of the tidal currents but also on the difference between the flood and ebb capacity, and considering that the friction damping effect of the tidal wave inside the lagoon causes the displacement of the discharge curve

with respect to that of the levels in the inlet, so that for the same discharge the ebb flow section will be smaller than that for the flood, one cannot a priori and in a general way state that head losses in the lagoon impair the natural flushing ability of its inlet.

A very simple mathematical model was therefore prepared, mainly to evaluate the change in the relation between the ebb bed load capacity and that of the flood, as a result of interior head losses.

Let us imagine a lagoon constituted by two basins, in both of which levels vary uniformly over their entire area, and which are connected to one another by a channel with well defined morphological characteristics (section, length and roughness). These basins are connected to the sea by a single inlet in which the bed load capacities of tidal currents will be studied. The channel connecting the two basins is the energy dissipating factor (Fig. 3). In this study the lagoon banks are considered to be vertical.

Index 2 will denote the sea, index 1 the basin directly connected to the sea and the inlet, and index 3 the inner basin and the channel connecting the two basins.

The equations characteristic of the system were derived from the equations relative to flow in the inlet and inner channel, and from the continuity equations relative to the inner basin and the entire lagoon, that is

$$V_1 = \sqrt{\frac{2g r_1}{C_1^2 L_1 r_1}} \sqrt{H_2 - H_1} \quad Q_1 = r_1 V_1 = A_1 \frac{dH_1}{dt} + r_3 \frac{dH_3}{dt}$$

$$V_3 = \sqrt{\frac{2g r_3}{C_3^2 L_3 r_3}} \sqrt{H_1 - H_3} \quad Q_3 = a_3 V_3 = A_3 \frac{dH_3}{dt}$$

After some manipulation whose presentation can be dispensed with, a system of two differential equations of the 1st order, identical in form to equation (5), is obtained, which characterizes the hydrodynamic behaviour of the inlet-lagoon system, namely

$$\frac{dh_1}{dt} + e \frac{dh_3}{dt} = i \frac{D_1 r_{10}^{3/2}}{\left(\frac{E_1}{r_{10}^{1/3}} + r_{10}\right)^{1/2}} (|\sin \theta - h_1|)^{1/2}, \text{ with } r_{10} = d_{10} + \frac{h_1 + \sin \theta}{2} \quad (14)$$

$$\frac{dh_3}{dt} = j \frac{D_3 r_{30}^{3/2}}{\left(\frac{E_3}{r_{30}^{1/2}} + r_{30}\right)^{1/2}} (|h_1 - h_3|)^{1/2}, \text{ with } r_{20} = d_{30} + \frac{h_1 + h_3}{2}$$

where

$$i = 1 \text{ for } \sin \theta > h_1 \quad j = 1 \text{ for } h_1 > h_3 \quad e = \frac{A_3}{A_1}$$

$$i = -1 \text{ for } \sin \theta \leq h_1 \quad j = -1 \text{ for } h_1 \leq h_3 \quad A = A_1 + A_3 = \text{Total area of the lagoon}$$

and

$$h_1 = \frac{H_1}{H}, \quad h_3 = \frac{H_3}{H}, \quad r_{10} = \frac{r_1}{H}, \quad \text{where } H \text{ is the sea tide amplitude}$$

The numerical integration of system (14) was made in the NCR Elliot 4100 computer of the Laboratorio Nacional de Engenharia Civil, using one of its library programs [2]

The integration step was $\Delta \theta = 0.1$ radians, the initial situation was cha-

racterized by equal levels in the sea and inner basins, so that to obtain results independent of initial conditions, the 1st calculation cycle, corresponding to a tidal period, had to be discarded

Together with the numerical integration of system (14) the computer also calculated other quantities with interest for the study of the natural flushing capacity of the inlet

As in item 3.2 and following, these quantities, in their dimensionless form, were calculated by means of the following expressions which, for the sake of brevity, will not be deduced here

$$\text{- Flow} \quad Q_{1a} = \frac{Q_1}{\frac{2\pi r_1 A}{T}} = \frac{1}{1+e} \frac{dh_1}{d\theta} + \frac{e}{1+e} \frac{dh_3}{d\theta} \quad (15)$$

- Velocity

$$V_{1a} = \frac{V_1}{\frac{2\pi r_1 A}{T b_1}} = \frac{1}{r_{10}} \left(\frac{1}{1+e} \frac{dh_1}{d\theta} + \frac{e}{1+e} \frac{dh_3}{d\theta} \right) \quad (16)$$

- 3rd and 6th power of the velocity

$$V_{1a}^3 = V_{1a}^3(\theta) \quad , \quad V_{1a}^6 = V_{1a}^6(\theta)$$

- Power consumed in inlet channel

$$W_{1a} = \frac{\gamma Q_1 \left(|H_2 - H_1| - \frac{V_1}{2g} \right)}{\frac{2\pi \gamma A H^2}{T}} = Q_{1a} \left[|\sin \theta - h_1| - \left(\frac{1+e}{D} \right)^2 V_{1a}^2 \right] \quad (17)$$

which may be written

$$W_{1a} = \frac{E_1}{D^2} \frac{V_{1a}^3}{r_{10}^{1/3}}$$

where D is the dimensionless parameter relative to the total lagoon basin with area A ($A=A_1+A_3$) and its inlet width b_1

4.2 - Results obtained in the computer

Fig 5 shows, as an example, the different curves studied for a system characterized by

$$D_1 = 0.4 \quad E_1 = 10.0 \quad d_{10} = 6.0$$

$$D_3 = 0.4 \quad E_3 = 10.0 \quad d_{30} = 3.0$$

which can be compared with the system shown in Fig 4

In view of expressions (3) and (4) defining parameters D and E, and moreover assuming that one considers the same outside tide (equal values of T and H) and an inlet channel with the same width and roughness (equal values of b and n), one may in fact conclude that the systems to which Figs 4 and 5 refer have lagoons with the same total area. Nevertheless these lagoons differ in that the lagoon of the latter system is formed by two basins with the same area (e=1.0) connected by a channel half as deep as the channel of the outer inlet, with reference to the mean sea level.

5 - ANALYSIS OF THE RESULTS

The studied cases were characterized by the set of the following parameters (in order to make clearer the prototype cases referred to, it is convenient to enclose in parentheses the lagoon area A_o , the length L and the depth d of the inlet channel referred to the mean sea level, that are compatible with these parameters and with the following conditions: semi-diurnal lunar tide with an external amplitude H=1.0 m, inlet b=200 m wide and n=0.0226 rough)

$N=0.0$

I - $D=0.5$ ($A_o=12.6 \text{ km}^2$), $E=19$ (L=1900 m), $d_o=2,3,4,5,6,8,10$
 (d=2,3,4,5,6,8,10 m)

II - $D=0.2$ ($A_o=31.6 \text{ km}^2$), $E=10$ (L=1000 m), $d_o = \text{idem}$

III - $D=0.2$ ($A_o=31.6 \text{ km}^2$), $E=19$ (L=1900 m), $d_o = \text{idem}$

$N=0,1,0.2$ for $D=0.5$, $E=19$, $d_o=4.0$
 $D=0.2$, $E=10$, $d_o=6.0$
 $D=0.2$, $E=19$, $d_o=6.0$

Although this work was mainly directed to the study of the bed load capacity of tidal currents in the inlet channel other results were obtained that should be compared with those obtained by Keulegan.

It has been shown that an inlet-lagoon system can be well defined only by the set of parameters D, E, d_o and N (expression (5)). Hence, the great variety of possible cases. As an attempt to reduce such a variety of cases, it was tried to make use of the Keulegan's coefficient of repletion which, in

some way, condenses the influence of the first three parameters. This parameter has proved satisfactory for the interpretation of some of the studied quantities.

Thus Fig. 6 gives the variation of the tidal prism against the parameter K in a vertical bank lagoon.

$$Pr = A_o (H_{1 \max} - H_{1 \min}) = A_o H (h_{1 \max} - h_{1 \min}) = A_o H \Delta h_1$$

the following function is represented in that figure

$$\Delta h_1 = \Delta h_1(K)$$

and compared with Keulegan's results (upper continuous curve). The effective prism is found to be well defined by the parameter K , although it is slightly superior to the one obtained by that author. The same figure also shows the functions $h_{1 \max} = f_1(K)$ and $|h_{1 \min}| = f_2(K)$ which are similarly compared with Keulegan's results (lower continuous curve), it being concluded that both the parameter K and Keulegan's scheme are less satisfactory in this case. In fact since the connecting channel is not "many times deeper than the tidal range" (Keulegan's hypothesis) a rise of the lagoon mean level results, which is better explained in Fig. 7.

Fig. 8 illustrates the variation of the flood and ebb times against the coefficient K . It may be concluded that ebb is always longer than flood and the difference between them increases as the entrance conditions of the tidal inlet grow worse (lower K values).

Fig. 9 illustrates the variation of C_1 and C_2 with the coefficient K . This variation is compared with the results obtained by Keulegan. As was shown in 3.3, C_1 and C_2 respectively relate rates of flow and maximum velocity values with those of the sinusoidal flow of the effective prism. From the figure it may be derived that in any case the function $C_2(K)$ satisfactorily agrees with the function $C(K)$ obtained by Keulegan, that is not the case with the function $C_1(K)$, concerning the rates of flow, which is clearly different from $C(K)$. In the zone of small K values, the behaviour of the curves obtained seems rather anomalous and, thus, it is intended to carry out laboratory experiments in order to verify them.

Fig. 10 presents, for the case of a lagoon having vertical banks ($N=0.0$),

the variation of the integral bed load capacities of the flood and ebb currents against the coefficient K , which are assumed to be proportional to V^3 and V^6 . It should be noticed firstly, that the general conclusions to be derived from this figure are practically independent from the power that affects mean velocity in its relation with bed load capacity

The most evident indication given by the figure is that the bed load capacity of tidal currents (which we assimilate to natural flushing ability in the tidal inlet) reaches a maximum for values of the coefficient of repletion K within the range

$$0.6 < K < 0.8$$

Then it may be stated that a tidal inlet characterized by a K value greater than 0.8 has an extra natural flushing ability that will allow it to overcome an occasional increase of the littoral drift. In fact, as the entrance conditions of the tidal inlet worsen as a consequence of that increase, the coefficient of repletion K decreases and then the natural flushing ability of the tidal inlet improves. In other words, it can be said that a tidal inlet characterized by a coefficient of repletion $K > 0.8$ is in a condition of steady alluvial equilibrium. On the other hand, following a similar reasoning, we can state that a tidal inlet characterized by a coefficient $K < 0.6$ is in a condition of non-steady alluvial equilibrium, which means that shoaling may be in progress there.

The same Fig. 10 supplies further information that may be useful to the interpretation of the evolution of such tidal inlets. In fact, for K values greater than 0.8 bed load capacity is found to be higher in the flood than in the ebb which may contribute to introducing littoral drift into the lagoon and to the corresponding formation of shoals and inner bars. Both facts would bring about a continuous reduction of the coefficient of repletion. Conversely, in a tidal inlet where $K < 0.6$, though the inlet is located in a zone of non-steady alluvial equilibrium, ebb currents overcome the flood ones as regards bed load capacity, which may represent the last resort of the tidal inlet in order to fight against its increasing obstruction.

It should be emphasized that the above remarks concern lagoons with vertical banks and in which the fluctuation of levels is uniform over their entire area. Nevertheless actual lagoons always deviate more or less from this theoretical condition. In fact banks are never truly vertical, sometimes the water

successively overflows and withdraws from the surrounding land in accordance with the tidal cycle, the extent of the lagoon and the head losses inside it do not allow the hypothesis of a uniform law of levels to be valid

In Figs 11 and 12 it is tried to evaluate the influence of bank slopes and of the internal head losses over the bed load capacity of tidal currents

Fig 11 shows that the slope of banks, given by the parameter N (see Fig 2), and thus the existence of large zones that the tide overflows or uncovers, improves the ebb bed load capacity in detriment of that of the flood

In Fig 12 the most significant results of the study relative to lagoons with internal head losses are condensed In 4.1 it has been shown that these head losses are artificially introduced by considering an inner channel that connects the two basins in which the lagoon is divided This inner channel is characterized as an energy dissipating factor by means of the parameter

$$F = \frac{E_3}{d_{30}} = \frac{2g L_3}{d_3 C_3^2}$$

If there are no head losses in the lagoon ($L_3 = 0$, d_3 or $C_3 = \infty$), F equals 0 The variation of F was obtained only by varying d_{30} , that is, a study was made of four different cases characterized by an inner channel with progressively lower depth

$$d_{30} = 6, 5, 4, 3$$

Fig 12 shows the general decrease of the bed load capacity of the tidal currents in the outer inlet as the internal head losses increase, which is the result logically expected Nevertheless the same figure also shows the increase of the relative importance of the ebb bed load capacity as compared with that of the flood This figure also shows the percentage with which a capacity overcomes the other for each case considered Such a percentage is found to reach very significant values in some cases which will favourably influence the natural flushing ability of the inlet

Summing up the main conclusions drawn from this work, we have

- The natural flushing ability of the inlet of a vertical bank lagoon where the law of levels can be assumed uniform, reaches a maximum for values of the coefficient of repletion of about 0.6 to 0.8,

- The slope of the lagoon banks or the existence of areas overflowed and uncovered during tidal cycle, increase the bed load capacity of the ebb currents as compared to the flood ones, and thus improve the natural flushing ability of the inlet,
- The existence of head losses in the lagoon or the effect of propagation of the tidal wave decrease the tidal prism and the integral bed load capacity of the tidal currents, but improve the ebb capacity as compared to that of the flood which has a favourable influence on the natural flushing conditions of the inlet

REFERENCES

- [1] - Keulegan, G H , "Water level fluctuations of basins in communication with seas", Third progress report on tidal flow in intrances, Beach Erosion Board, 1951
- [2]- Sieck, A N , "Numerical integration of ordinary differential equations", Mathematics of Computation, Jan 1962
- [3] - Colby, B R , "Practical computations of bed-material discharge" Proc ASCE, 90 (Hy2), March 1964

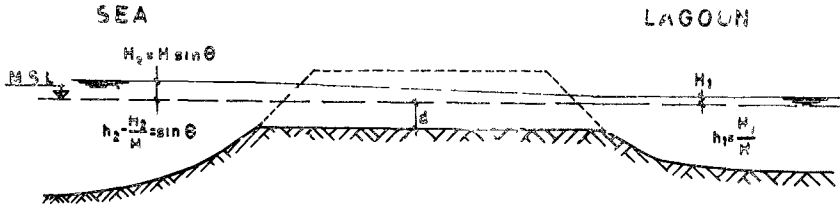


Fig 1 - SCHEMATIC LONGITUDINAL SECTION OF INLET CHANNEL

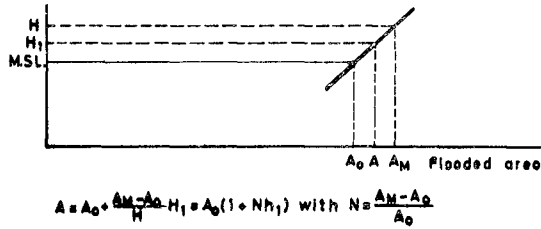


Fig 2 - LINEAR VARIATION OF FLOODED AREA IN LAGOON BASIN

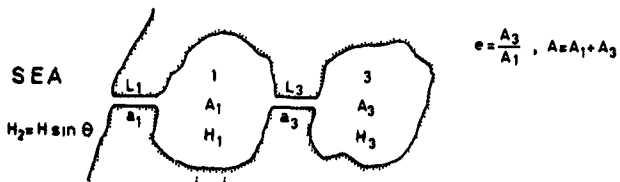


Fig 3 - TWO CHANNEL-LINKED BASINS FORMING A LAGOON

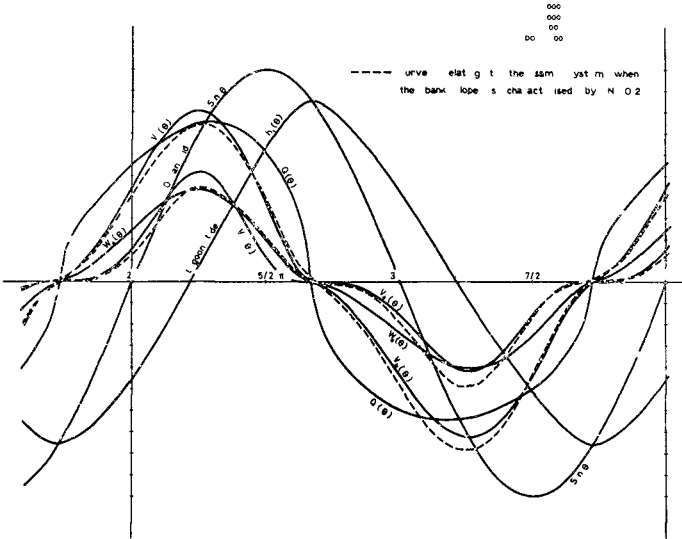


Fig 4 - CHARACTERISTIC CURVES OF AN INLET-LAGOON SYSTEM WITH VERTICAL BANKS, AS OBTAINED FROM THE COMPUTER

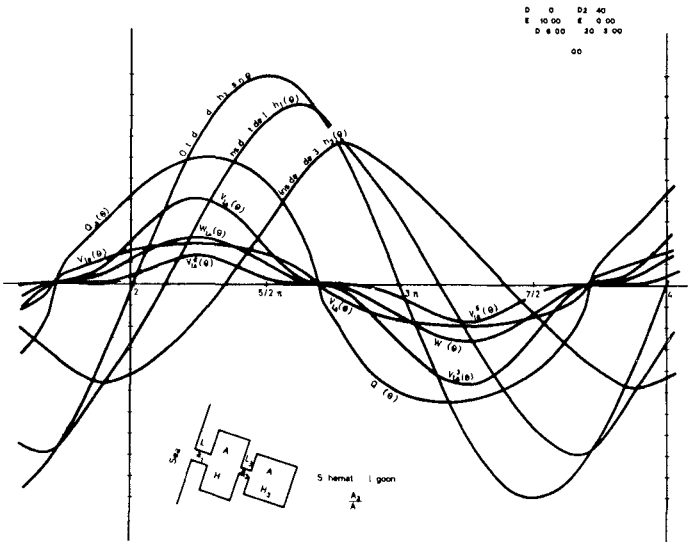


Fig 5 - CHARACTERISTI CURVES OF A TWO-BASIN LAGOON INLET

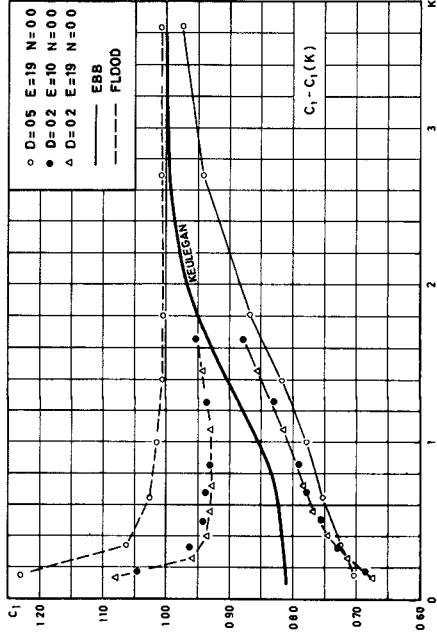
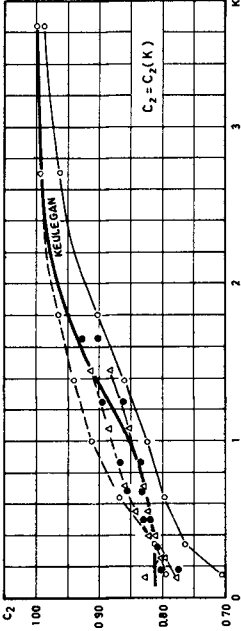


Fig 9 - C_1 AND C_2 VARIATION (VD ITEM 3 3) AS A FUNCTION OF THE COEFFICIENT OF REPLETION K

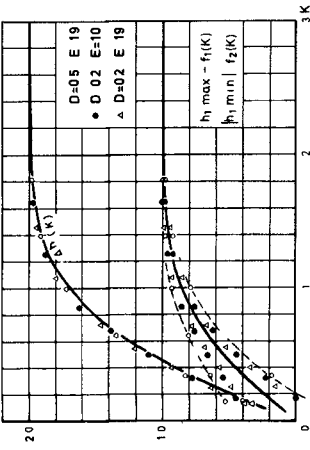


Fig 6 - TIDAL PRISM VARIATION AS A FUNCTION OF THE COEFFICIENT OF REPLETION K

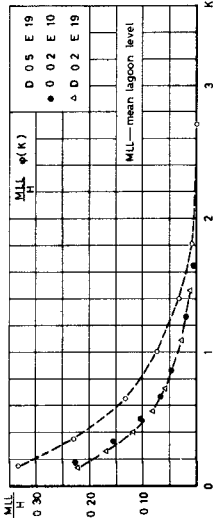


Fig 7 - MEAN LAGOON LEVEL VARIATION AS A FUNCTION OF THE COEFFICIENT OF REPLETION K

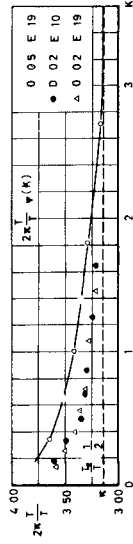


Fig 8 - EBB PERIOD VARIATION AS A FUNCTION OF THE COEFFICIENT OF REPLETION K

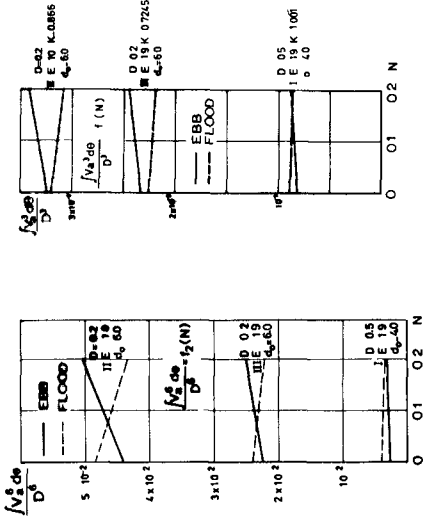


Fig 11 - INFLUENCE OF LAGOON BANK SLOPE

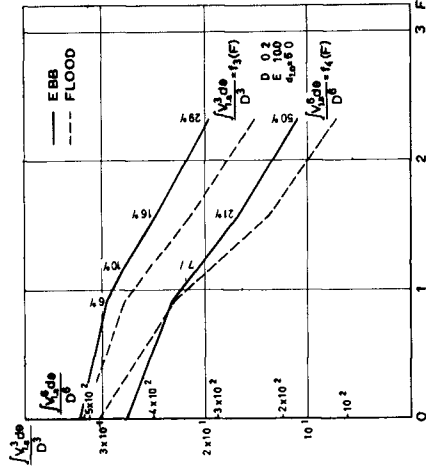


Fig 12 - INFLUENCE OF HEAD LOSSES IN THE LAGOON

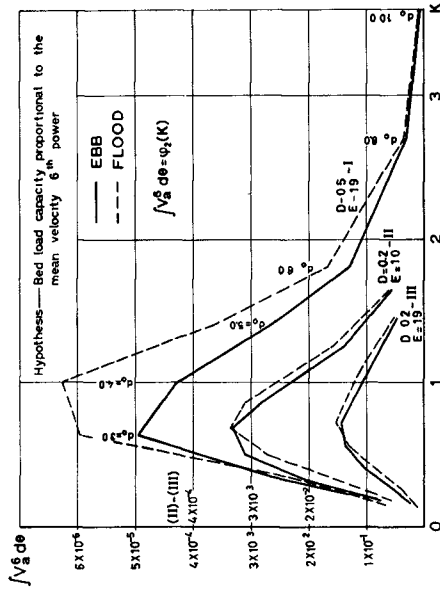
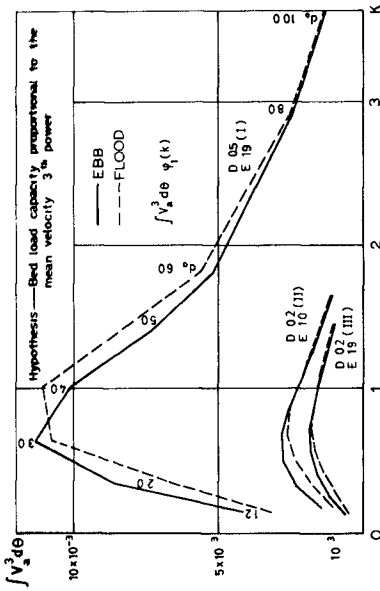


Fig 10 - VARIATION OF TIDAL CURRENT BED LOAD CAPACITY WITH THE COEFFICIENT OF REFLECTION

CHAPTER 112

MATHEMATICAL MODEL OF MIXING IN NEW HAVEN HARBOR

by

Michael D. Disko¹
Robert A. Norris²
Francis C. Lutz¹

ABSTRACT

A mathematical model of New Haven Harbor, a shallow embayment with approximately 8 square nautical miles of water surface within boundaries established by Long Island Sound and the mouths of the Quinnipiac, West and Mill Rivers, has been developed. The Harbor has extensive tidal flats and dredged channels which help to produce large lateral variations of velocity and mixing over a tidal cycle.

In order to adequately consider these lateral variations, a two-dimensional model of mixing, dispersion, pollutant reactions, and reaeration is made by linking together 28 segments of the Harbor, using a series of mass-balance equations. Mixing, or dispersion, is a complex function of reversing tidal currents, salinity-induced circulation patterns, fresh-water inflow, and the physical boundaries of the Harbor. Field measurements of salinity, dissolved oxygen, BOD, and tidal and hydraulic factors are used, in conjunction with laboratory studies, to evaluate coefficients and rate constants for the model. The linked system of equations is solved by matrix inversion procedures on a large computer.

After verification, the model was used to predict the effect of treatment levels, outfall locations, and hydrologic parameters on oxygen levels and water quality in the Harbor. An important aspect of the work is that it presents a rational evaluation of estuarine water quality as a function of tidal mixing, outfall location, and the degree of BOD removal by proposed treatment plants, rather than the acceptance of arbitrary treatment standards.

1. INTRODUCTION

A critical problem confronting engineers and scientists working in the field of water-quality control is the evaluation of the required degree of treatment necessary for waste effluent discharges into river or estuarine waters. Some typical sources of

¹ Consulting Engineers, M. Disko Associates, West Orange, N. J.

² Associate, Quirk, Lawler & Matusky Engineers, NYC

waste effluents are industrial and domestic discharges, periodic purgings of accumulated solids from combined storm and sanitary sewerage systems, surface runoff containing quantities of nutrients and pesticides, and seepage from sanitary landfill operations in marshlands.

Each receiving water body has the capacity to assimilate a certain quantity of introduced waste materials as a direct result of naturally occurring physical, chemical, and biological interactions and conversion processes. Evaluation of the assimilation capacity for a particular river or estuary is a complex and difficult task.

Typical methods used to determine the required degree of waste treatment necessary to maintain oxygen levels and other water quality parameters, within the framework of the natural assimilation capacity, include field measurements and testing in the receiving water body, experimentation in verified hydraulic models, and formulation of a rational mathematical model. Each of these methods is only approximate. A number of basic research questions still remain to be answered before any engineer or scientist can predict, with complete certainty, the response of a receiving water body to a waste effluent discharge.

The object of this paper is to describe the formulation and use of a mathematical model to determine the relationships between the degree of waste treatment prior to effluent discharge and the resulting level of dissolved oxygen in the receiving water body which is New Haven Harbor. The mathematical model described, herein, is a two-dimensional system which considers pollutant variations in the lateral and longitudinal direction of the Harbor.

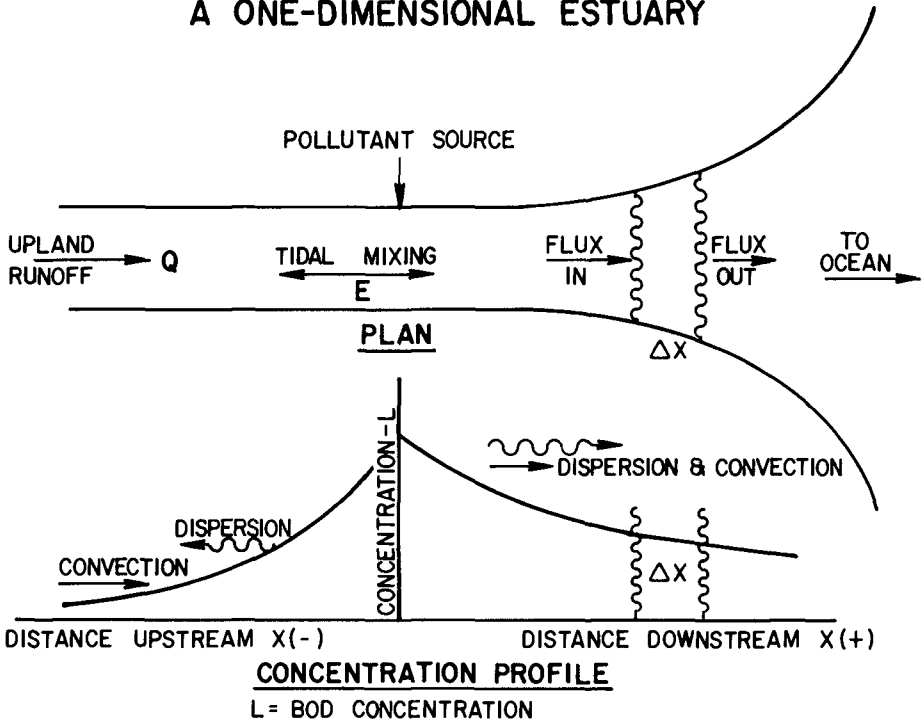
Municipal sewage wastes are discharged into the Harbor from three existing primary sewage treatment plants, i.e. the Boulevard Sewage Treatment Plant, the East Street Sewage Treatment Plant, and the East Shore Sewage Treatment Plant, and from a secondary plant located in West Haven. It was desired to evaluate the degree of BOD treatment required to insure water quality standards, for a number of alternate design schemes under consideration in a sewage treatment plant modification program.

2. MATHEMATICAL FUNDAMENTALS FOR TWO-DIMENSIONAL MODELLING

Transport of any substance in an estuary is governed by the Law of Conservation of Mass. Figure 1 illustrates the application of this law in a one-dimensional estuary. Waste particles discharged to an estuary are transported from the discharge point by convection and by dispersion. The rate of convective mass transport across any river section is equal to the product of fresh-water runoff, and the contaminant concentration.

Mixing, or dispersion, is a complex function of reversing tidal currents, salinity-induced circulation patterns, fresh-water inflow, and the physical boundaries of the Harbor. Dispersive

MASS TRANSPORT RELATIONSHIPS IN A ONE-DIMENSIONAL ESTUARY



MASS BALANCE OVER VOLUME ELEMENT, $A \Delta x$

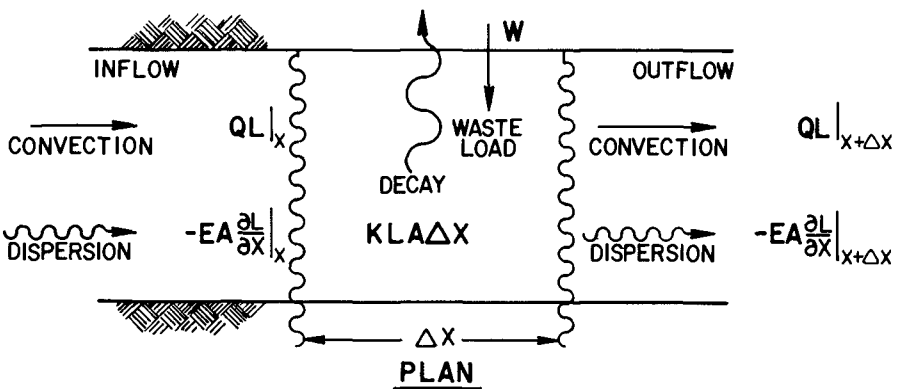


FIGURE 1

transport occurs only in the presence of a concentration gradient of the material being transported. The rate of dispersive transport is equal to the product of a dispersion coefficient, E , and the negative of the longitudinal concentration gradient, dL/dx . The dispersion coefficient, E , is a measure of the estuary's ability to transport material in the direction of a concentration gradient, regardless of the direction of net water movement.

The biochemical oxygen demand, BOD, is a measure of the oxygen required to reduce waste products by biochemical oxidation. The rate of BOD decay is equal to the product of the first order decay constant, the BOD, and the volume within which the reactions are occurring.

For the case of an estuary with both longitudinal and lateral mixing and dispersion, linked volume segments in a mathematical model can be used to represent the physical system. In such a model, system parameters such as BOD are assumed to be approximately constant with depth. Each volume segment can be considered a regular polyhedron. The top and bottom of each polyhedron represent the water surface and harbor bottom, respectively. Figure 2 shows how each volume segment is directly linked to a number of other segments.

A mass balance over any volume segment shown in Figure 2 is written

$$\text{INFLOW} - \text{OUTFLOW} + \text{PRODUCTION} - \text{LOSSES} = \text{ACCUMULATION} \dots (1)$$

For a steady-state case, the ACCUMULATION of BOD within any particular volume segment is zero, and EQUATION (1) gives

$$\text{INFLOW} - \text{OUTFLOW} + \text{PRODUCTION} - \text{LOSSES} = 0 \dots \dots \dots (2)$$

Each of the terms are described in detail below.

The INFLOW and OUTFLOW terms are the sums of convective and dispersive transport across the faces of the volume segments. A direction is assigned for convective and dispersive transport, and, using this sign convention, a consistent material balance is developed for each linked segment. The convective components are the product of each flowrate, Q , and each respective BOD concentration, L . The dispersive component is the term, $EA(dL/dS)$, where E is the average dispersion coefficient at the interface of each segment linkage, A is the interfacial area, and S is a distance in the direction normal to the area, A .

The PRODUCTION of BOD in a volume segment represents the sum of the inputs of waste effluents, surface runoff, and additions of BOD from the scour, by currents, of bottom deposits in the benthic layer of partly decomposed organic products. The net PRODUCTION is, therefore, estimated as a BOD load of W pounds per day.

TWO-DIMENSIONAL MASS TRANSPORT RELATIONSHIPS

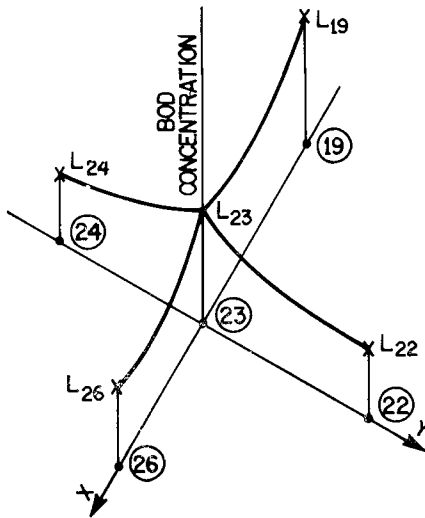
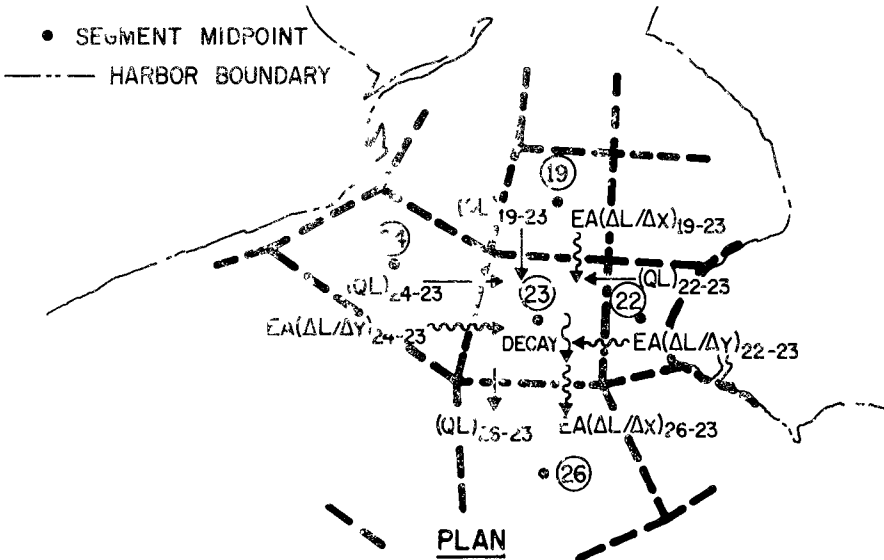


FIGURE 2

The LOSSES of BOD in a segment would include the removal of BOD by sedimentation or absorption, and decay. The BOD reduction, by sedimentation or absorption, may be assumed proportional to the amount of insoluble BOD in the water. The decay of BOD is assumed to be a first-order reaction, proportional to the concentration of BOD. The net decay of BOD in any segment is given by K_rLV , where K_r is the composite BOD decay coefficient (to the base e) due to decay and sedimentation, L is the average BOD concentration in the segment, and V represents the segment volume.

In New Haven Harbor, losses of BOD due to sedimentation and absorption were small because of the high tidal flushing rate. If, however, these effects were substantial in any particular volume segment representing a portion of the Harbor, allowance could be made to reflect these parameters in the coefficients of that segment's mass balance equation.

An algebraic substitution of the individual contributions into Equation 2, for each volume segment, gives

$$\Sigma OL - \Sigma EA(dL/dS) + W - K_rLV = 0 \dots\dots\dots (3)$$

Equations for each segment are developed and linked, noting the relative interconnection, the advective and dispersive transport conventions assumed, and appropriate coefficients such as K_r , E , and A .

Dissolved oxygen concentration is used as a principal index of organic waste pollution in a waterway. As the level of DO concentration is decreased, the capacity of a waterway to assimilate waste discharges is reduced, requiring upgrading of treatment facilities for waste flows. The important source of replenishment of DO is atmospheric oxygen transferred to the waterway in proportion to the currents and other estuarine parameters.

Application of Equation 2 to oxygen transport follows the approach outlined above for BOD and yields an equation analogous to Equation 3. The INFLOW and OUTFLOW terms are similar to the BOD terms. The convective term is the product of O and D , the dissolved oxygen deficit or the difference between oxygen saturation and actual oxygen concentration in the water. The dispersive term is the product, $EA(dD/dS)$.

The PRODUCTION of DO in a volume segment is the external input of oxygen reaeration from the atmosphere through the water surface, and the addition of oxygen by photosynthesis. The mechanism of reaeration is represented by $K_A DV$, where K_A is the coefficient of oxygen transfer from the atmosphere into the segment. K_A is, of course, a parameter that varies as a function of water depth and current velocity in various sections of the Harbor.

The LOSSES of DO in a volume segment would include the removal of oxygen from the water by diffusion into the benthic layer to

satisfy the oxygen demand in the aerobic zone, by the purging action of gases rising from the benthal deposits, and by the respiration of plankton, diatoms, and other life. The rate of removal of oxygen, or deoxygenation, is represented as KLV , where K is the coefficient of deoxygenation or rate of loss of oxygen associated with satisfying the BOD.

The production of oxygen by photosynthesis, the removal of oxygen by respiration and benthic effects were all judged to be minor effects that tended to balance one another in New Haven Harbor over long-term periods.

An algebraic substitution of the individual contributions into Equation 2, for each volume segment, gives

$$\sum QD - \sum EA(dD/dS) - K_A DV + KLV = 0 \dots\dots\dots (4)$$

The mass balance technique employed to develop Equations 3 and 4 is used to formulate a series of equations for BOD and dissolved oxygen deficit, D , in each segment. After solution of these equations, the corresponding DO in each segment is then obtained by subtraction of the dissolved oxygen deficit, D , from the saturation oxygen concentration.

3. GENERAL DESCRIPTION OF NEW HAVEN HARBOR

New Haven Harbor is a shallow embayment with approximately 8 square nautical miles of water surface within boundaries established by the Long Island Sound breakwaters and the mouths of the Quinnipiac, West, and Mill Rivers. The Harbor width varies from less than a thousand feet just downstream of the juncture of the Mill and Quinnipiac Rivers to approximately two miles at its mouth. Extensive tidal flats exist on the west shoreline of the Harbor, while the east shore is generally irregular.

The existence of extensive areas of tidal flats, variable harbor width, shore irregularities, deep navigational channels, breakwaters, and localized fresh-water inflows in a tidal waterway, all require that the mathematical modelling consider both lateral and longitudinal directions. The generally accepted one-dimensional estuarine model leaves lateral mixing effects unaccountable. Such a scheme would be forced to employ a cross-sectional average velocity in its development, and would result in potentially substantial errors in contaminant concentration predictions.

The mean depth of the Harbor below mean low water is about 11.5 ft. The mean tidal range for the Harbor is about 6.2 ft. The tidal prism, which is the mean volume of water that is exchanged from the Harbor between mean high and mean low water, is approximately 1.87×10^9 ft.³. The volume of the Harbor is about 4.4×10^9 ft.³ at mean water level. The ratio of the tidal prism to the mean volume of the Harbor is a measure of the flushing that occurs. It should be noted that this exchange occurs twice a day, since the period of the tide is about 12.4 hours. The

total tidal flushing is equivalent to the replacement of 84% of the Harbor volume each day.

The large variation in Harbor width controls the relative magnitudes of fresh-water and ocean-water velocities. The shore irregularities, breakwaters, and the deep navigational channels produce localized currents. Current data was obtained from "A Hydrographic Survey of New Haven Harbor, 1962-1963", by Alyn Crandall Duxbury of the Bingham Oceanographic Laboratory of Yale University. The survey is published as Connecticut Water Resources Bulletin No. 3A.

Shellfish breeding areas are maintained within the breakwaters, and extensive shellfish harvesting grounds are maintained beyond the breakwaters. In addition, portions of the Harbor are also reserved for recreational purposes. Bathing beaches line both the east and west shores at the Harbor entrance.

4. APPLICATION OF MODELLING TECHNIQUES TO NEW HAVEN HARBOR

In order to apply the material balance approach described in the previous section of this report, the Harbor was divided into 28 volume segments as shown in Figure 3. Segments 1 through 5 are associated with the Quinnipiac River, segment 6 with the Mill River and segments 13 and 14 with the West River.

Segmentation was made on the basis of current and depth patterns. Current patterns were determined from composite Bingham Oceanographic Laboratory hydrographic measurements of ebb and flood tide conditions. Depth patterns were obtained by constructing over 60 profile sections of the Harbor.

Each segment was linked to the adjoining segments by applying the material balance, defined by Equations 3 and 4, for BOD and DO conditions. Many of the segments are linked to four other segments. Evaluation of Equations 3 and 4 often required consideration of ten or more separate coefficients for each segment.

The model could have been divided into a larger number of segments if comprehensive field surveys and measurements were available to justify the additional complexity involved. The amount of total complexity increases as an exponential function when the number of segments increases. Division of the Harbor into 28 segments was judged to be the optimum segmentation for the available field data on DO, currents, BOD, etc.

Evaluation of the many parameters required for Equations 3 and 4 was a time-consuming process. The following parameters had to be computed for each segment: the BOD load per unit of time; cross-sectional areas at each boundary; fresh-water flow into and out of each segment; volume of waste effluent into each segment; the decay rate of BOD; the oxygen saturation concentration; the oxygen transfer from the atmosphere to water, the prevailing currents, and the mean water volumes.

NEW HAVEN HARBOR
SEGMENTATION
FOR
MATHEMATICAL MODEL
OF
BOD AND DO
DISTRIBUTION

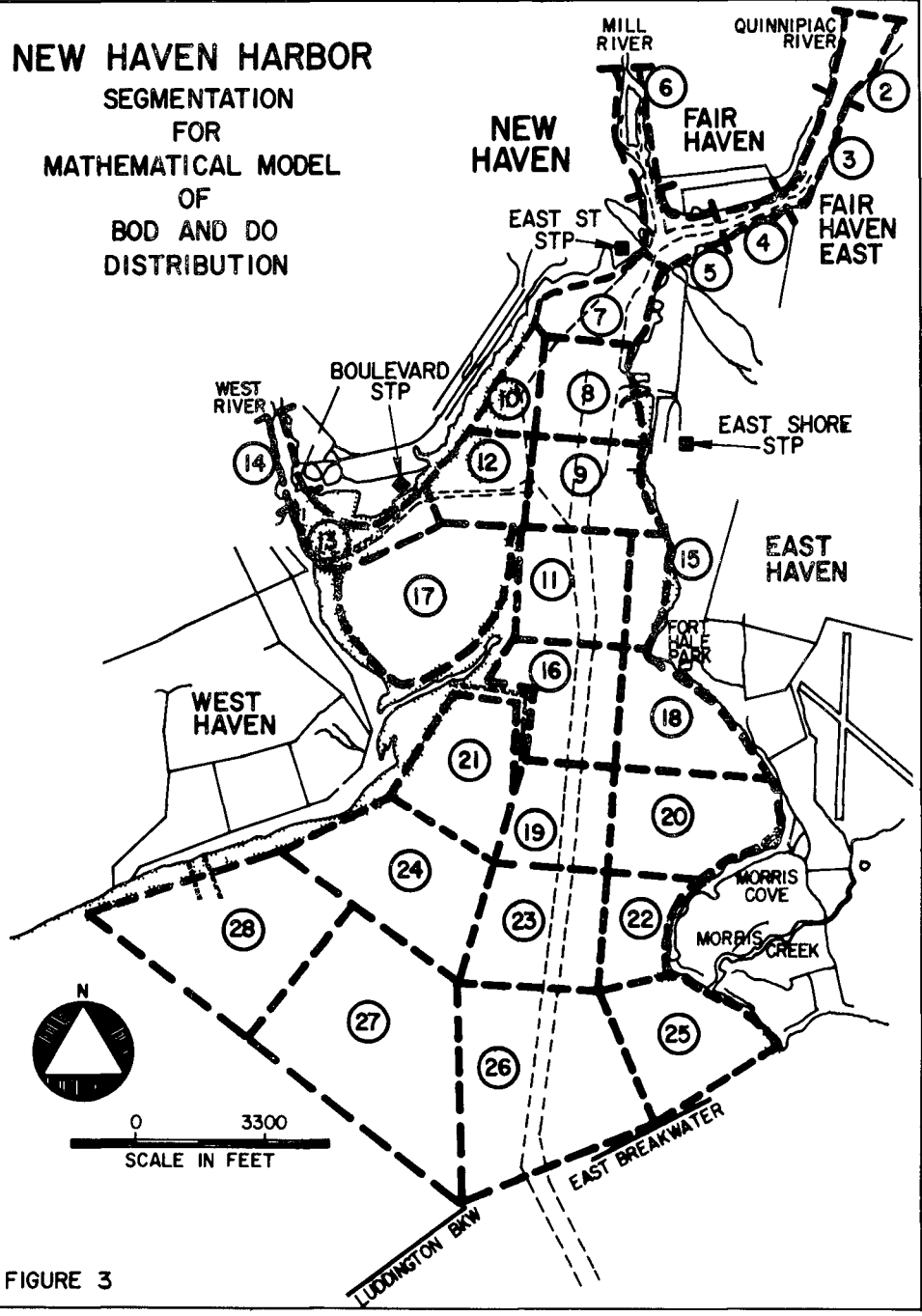


FIGURE 3

Information required for cross-sectional areas, segment volumes, depths, and tidal range were obtained from U. S. Geological Survey maps, U. S. Coast and Geodetic Survey maps, and other published Harbor data.

Fresh-water flowrates for the Quinnipiac River Basin at Wallingford, Connecticut were obtained from Geological Survey records. Flowrates for the Mill River and the West River were estimated from a study of watershed areas, and watershed characteristics. Critical flowrates from all three rivers into the Harbor were computed.

Tidal currents were obtained from composite Bingham survey measurements for ebb and flood conditions. Average current values were computed, based on tidal cycle relationships and the ebb and flood value .

The longitudinal dispersion coefficient at each segment boundary was computed from a knowledge of tidal currents, fresh-water flow, and salinity measurements obtained by the Bingham hydrographic survey. Longitudinal dispersion can be directly computed from the mean salinity concentration, the salinity gradients, and the average current at the segment boundary. In several non-critical areas of the Harbor, Bingham velocity data was not available. In these cases, the longitudinal dispersion coefficients were estimated from a study of the overall patterns of the computed longitudinal dispersion coefficients and the measured currents in the Harbor.

The first-order, BOD decay rates, or coefficients, were determined from a laboratory analysis of Harbor water samples. Seven representative water samples were obtained from predetermined Harbor locations on April 9, 1969. Long-term BOD evaluations were performed to determine the present K_r decay coefficient of Harbor waters. The K_r rate was determined to be about 0.31/day. This measured value is normal for primary effluent and was used for model verification and to estimate the future decay rates of secondary effluent. All seven samples showed K_r rates that were similar. An estimated decay rate of 0.20/day was used for the 1990 secondary effluent.

The coefficient of atmospheric reaeration, K_A , was computed, using the well-known O'Connor-Dobbins formula, and another equation developed by U. S. Geological Survey personnel. Atmospheric reaeration in streams is a function of velocity and depth. The expressions developed for streams are commonly adopted for estuarine reaeration.

Application of the mass balance approach to each segment, including all the above computed parameters, results in 28 equations for BOD and another 28 equations for the dissolved oxygen deficit, D . A system of equations, based on Equations 3 and 4, can be written in terms of the midpoint concentrations, in the following form

$$a_{1-1}L_1 + a_{1-2}L_2 + \dots + a_{1-28}L_{28} = W_1$$

⋮

$$a_{28-1}L_1 + a_{28-2}L_2 + \dots + a_{28-28}L_{28} = W_{28} \dots \dots \dots (5)$$

and

$$b_{1-1}D_1 + b_{1-2}D_2 + \dots + b_{1-28}D_{28} = C_1L_1$$

⋮

$$b_{28-1}D_1 + b_{28-2}D_2 + \dots + b_{28-28}D_{28} = C_{28}L_{28} \dots \dots \dots (6)$$

In the above system of equations, the a and b coefficients are obtained by summation of all the terms pertaining to a respective subscripted L or D parameter. The C coefficients are equivalent to the respective segment values of KV. Many of the a and b coefficients have zero values.

Equations 5 and 6 are sets of simultaneous linear algebraic equations with unique solutions, which are readily solved by any number of standard numerical techniques. Of those available, matrix inversion was chosen because of its ease of application, and directness for the system studied.

Using matrix algebra, the BOD waste loads into each segment become a column matrix. This column matrix is equated to a coefficient matrix which has 28 rows and 28 columns, and a column matrix which consists of the unknown BOD concentrations in each model segment. Each element of the 28 by 28 coefficient matrix is computed from the various parameters described above.

The coefficient matrix is inverted using standard numerical techniques on a computer. After matrix multiplication of the inverted coefficient matrix and the waste load column matrix, the unknown BOD concentration column matrix can be computed. A similar procedure is performed on the 28 equations for D. However, the computed BOD concentrations are required in order to solve the D equations.

The solution of the BOD and oxygen deficit system, Equations 5 and 6, was programmed in FORTRAN V for processing by a UNIVAC 1108 computer. One main program was constructed with a subroutine for matrix inversion. The program can be converted to most FORTRAN IV systems with few changes. An overall flowchart of the program is shown in Figure 4.

FLOW CHART FOR COMPUTER PROGRAMMING

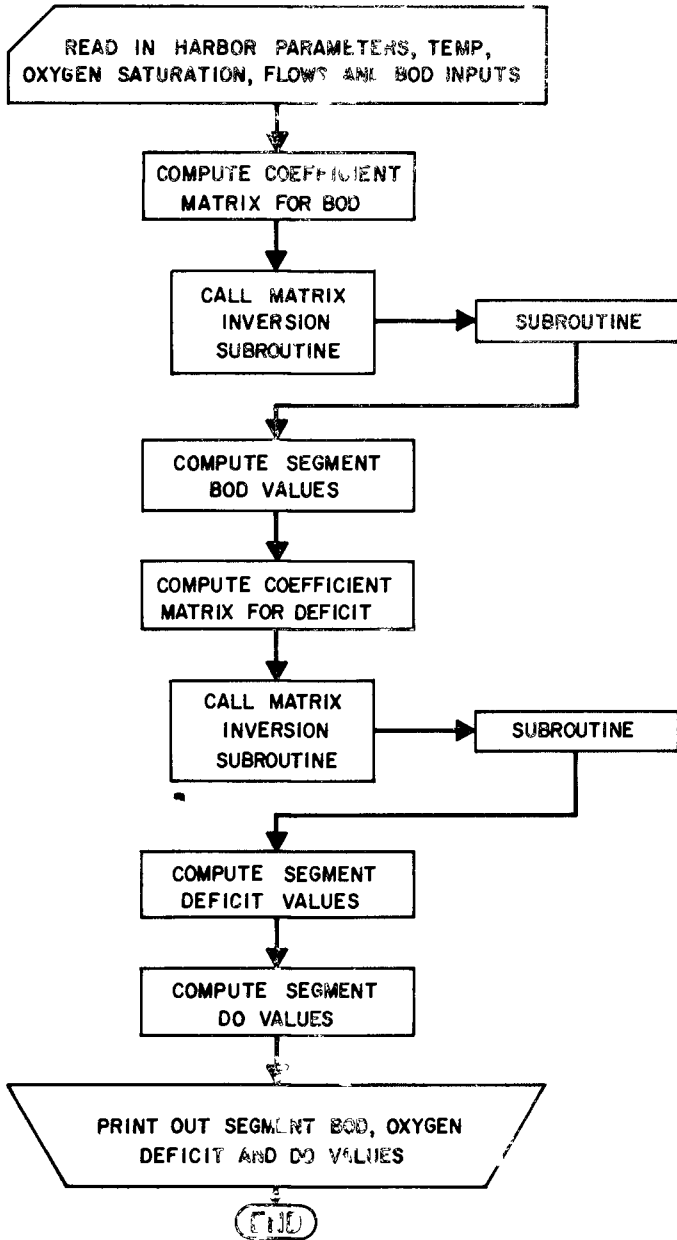


FIGURE 4

The computer program and mathematical model can be adopted and modified to compute coliform patterns, radioactivity distributions, temperature distributions, and contaminant patterns resulting from various input loadings. Program and model modifications would require additional field measurements for the particular type of parameter simulated.

5. MODEL VERIFICATION IN NEW HAVEN HARBOR

Model verification is accomplished by comparing predicted DO concentrations to measured DO concentrations. Measurements of DO in the Harbor are limited. The only survey giving a reasonable representation of the DO patterns of the Harbor was performed by the Bingham Oceanographic Laboratory from October 1962 through September 1963. In this survey, DO measurements were made approximately once a week, at nine stations in the Harbor and at three depths at each station.

The DO measurements showed significant variation, depending on the tidal phase of the survey and the cumulative rainfall for the period immediately prior to the survey date. The mathematical model, which was developed for steady-state conditions, is not applicable to measurements of a duration less than a full tidal cycle. Thus, for valid comparisons of model values to field data, predicted DO concentrations must be compared to measured DO concentrations that represent the average DO for a complete tidal cycle. Since numerous measurements within a tidal cycle are not available, the exact tidal cycle average DO must be estimated.

Absolute verification of the mathematical model requires complete and up-to-date field surveys to measure prescribed parameters. These types of field surveys must be designed with the mathematical model in mind so that the data obtained may be optimally employed. To accomplish this goal, the data must be collected at specific times and locations as prescribed by the model.

Model analysis indicated that the model DO predictions were relatively insensitive to local variations in E , K_r , and Q when compared to its sensitivity to variations in waste loads. Changes in waste loads are directly related to changes in DO. Consequently, model verification depends upon accurate determination of the waste loads that constituted an input to the Harbor coincident with the survey selected for verification purposes. All surveys that followed periods of excessive rainfall would be unsuitable for verification purposes because the actual waste loads during these periods are unknown. During the Bingham hydrographic surveys, the waste loads from the existing sewage treatment plants were determined from flow and BOD measurements made on the effluents.

Industrial waste loads were computed based on discharge flow estimates as reported to the Water Resources Commission by each industry. BOD measurements of the discharge flows were available for the largest flows. Where measurements were not available, reasonable estimates were used.

The following waste loads were estimated for dry weather conditions during the Bingham hydrographic surveys of 1962-1963:

<u>Source</u>	<u>Load. Lb. BOD₅/Day</u>
Boulevard STP	13,900
East Street STP	14,500
East Shore STP	3,940
West Haven STP	9,900
Central Business District (temporary during this period)	6,550
Industries	<u>3,800</u>
Total	52,590

The Bingham survey of April 17, 1963 can be selected to illustrate the problems involved in verification of the model. For a six-day period prior to April 17, 1963, the cumulative rainfall was 0.07 inches.

Measurements of oxygen were made on a rising tide. The hydrographic survey started at the breakwaters in the outer Harbor and proceeded inward to the Quinnipiac River. Bingham station OH2 is recorded as sampled within 2 hours after low water slack. Bingham stations MC3, MC1, FH2, OP3, OP2, and OP1 were sampled within one hour of mean tidal stage. Stations H1 and Q1 were sampled within one hour after mean tidal stage. In general, surveys will show a lower value of DO at low water conditions, and a higher DO at high water.

Measurements from several of the nine stations are not suitable for direct comparison to the model output. Analysis of measured data at a station showed considerable variations in oxygen concentrations, temperatures, and salinities for the three grab samples taken at the surface, 10-foot and 20-foot depths. The following listing shows a comparison between April 17, 1963 survey estimates of oxygen concentrations and model predictions at several stations:

<u>Bingham Survey Station</u>	<u>Range of Oxygen Deficit from Survey Data (ppm)</u>	<u>Oxygen Deficit from Model (ppm)</u>
OP1	1.1-0.8	0.9
OP2	0.8	0.9
OP3	1.1-0.8	0.9
FH2	0.4-0.1	0.8
MC1	1.1-0.6	0.6
OH2	0.7-0.6	0.5

In general, the model output closely matches the oxygen deficits measured in the hydrographic survey. Stations OP1, OP3, and OH2 are within 0.2 ppm. Other stations are within the survey range or relatively close to it.

6. USE OF THE VERIFIED MATHEMATICAL MODEL FOR WATER QUALITY PREDICTION

The mathematical model of New Haven Harbor was used to predict the effect of the degree of BOD removal during effluent treatment on the dissolved oxygen concentration in the waters, and also to evaluate the water quality resulting from the use of long outfalls to discharge waste effluent into deeper sections of the Harbor with higher mixing characteristics. The estimates of future waste loads, during the maximum month in 1990, were used for model predictions.

The major waste contributions to the Harbor are discharged from the Boulevard, East Street, East Shore, and West Haven Sewage Treatment Plants. Additional waste sources are direct industrial discharges and overflows from the municipal sewage system.

At present, more than two-thirds of the tributary drainage areas of the Boulevard, East Street, East Shore, and West Haven Sewage Treatment Plants are served by a combined sewer system. Consequently, sewage that settles and forms deposits in sewers during dry periods is flushed from the system during significant rainfalls, resulting in an instantaneous load several times larger than the normal BOD discharge. These irregular, instantaneous loads are a direct cause of the low DO conditions that sometimes occur. Future plans for New Haven include modifying the present combined system into a completely separate system.

The following is a list of the 5-day BOD loads for the maximum month in 1990

<u>Sewage Treatment Plant</u>	<u>Load, Lb. BOD₅/Day</u>
Boulevard	52,500
East Street	63,500
East Shore	64,000
West Haven	37,500
	<u>217,500</u>

The Boulevard, East Street, and East Shore operations are older, primary treatment plants. The West Haven operation is a secondary treatment plant.

Since the primary treatment plants were under consideration for renovation, the model was used to evaluate whether any substantial water quality benefit could result from combining the flow in one or more larger, rebuilt operations. Five alternate treat-

ment schemes were proposed as follows

<u>Scheme</u>	<u>BOD₅ lb/Day into Boulevard Site</u>	<u>BOD₅ lb/Day into East St Site</u>	<u>BOD₅ lb/Day into East Shore Site</u>
1	52,500	63,500	64,000
2	52,500 63,500 <u>116,000</u>	--	64,000
3	52,500	--	63,500 64,000 <u>127,500</u>
4	--	52,500 63,500 <u>116,000</u>	64,000
5	--	--	64,000 63,500 52,500 <u>180,000</u>

The estimated average monthly BOD loads for 1990 are about eighty percent of the maximum monthly loads above. The West Haven secondary treatment plant will, under all schemes, discharge 37,500 lbs. of 5-day BOD per day

One positive result that the computer model showed was that no particular alternate scheme offered significant advantages over the others in terms of average BOD and DO levels resulting in the Harbor. The basic reason for the essentially similar water quality patterns produced by the 5 schemes was that the Boulevard, East Street and East Shore Plants are all located in the inner section of the Harbor within a distance of 8,000 feet from each other. Hence, the high degree of tidal flushing that occurs effectively spreads and mixes the BOD waste loads throughout the inner Harbor, with similar dissolved oxygen concentration patterns resulting.

The conclusion drawn from these computer model results is that selection of an alternate scheme, at a given BOD removal rate, should be governed by the economics of construction and operation of the rebuilt plant or plants. In terms of the resulting water quality, and protection of the beach areas, outputs from all the schemes are essentially equal. This conclusion is predicted on the condition that discharge at or near the shoreline will be into tidal waters and will not be allowed to spill onto tidal mud flats where BOD concentrations can build up.

In order to evaluate the relationship between the degree of effluent treatment and resulting dissolved oxygen in the Harbor,

a series of computer runs was made for each of the 5 alternate schemes at BOD removal rates of 25%, 50%, 75%, 85%, and 90%. Printout 1 shows typical BOD output. Table 1 lists a typical result for the minimum dissolved oxygen in the Harbor, versus the percent of BOD removal.

The type of output displayed in the above Printout and Table 1 is an example of the type of rational engineering analysis that can be obtained from a predictive mathematical model. Instead of designing a waste treatment operation to an arbitrary set of BOD removal standards or effluent concentration levels, a verified mathematical model can be constructed to determine the relationship between the degree of BOD removal and the approximate distribution of dissolved oxygen, longitudinally and laterally, in the receiving waterbody. For example, if a minimum tidal average of 6 ppm of dissolved oxygen was desired in the Harbor, approximately 85% BOD removal would be required for the projected effluent discharges.

TABLE 1
EFFECT OF DEGREE OF BOD REMOVAL
ON MINIMUM DISSOLVED OXYGEN IN
NEW HAVEN HARBOR

% BOD Removal During Treatment	TIDAL AVERAGED NEW HAVEN HARBOR MINIMUM DO, PPM	
	Scheme 1 Separate Effluent Discharges at Boulevard, East St., and East Shore STP	Scheme 5 All Effluent Directed to East Shore STP
25	3.8	4.1
50	4.7	4.9
75	5.6	5.7
85	6.0	6.0
90	6.1	6.2

Another important predictive feature of the verified mathematical model is the ability to evaluate the effect of the use of outfalls to dilute the discharged effluent and, hence, to effectively reduce the level of BOD removal required. Table 2 shows a typical summary of computer runs at various percentages of BOD removal. Inspection of the table shows that extension of the outfall into deeper water of the Harbor allows reduction of the degree of sewage treatment, but maintains the desired minimum dissolved oxygen concentration. The economic feasibility of using outfall extensions must be evaluated after detailed construction cost estimates.

BOD VALUES IN (SEGMENTS) OF NEW HAVEN HARBOR
CONCENTRATIONS IN PPM

RUN NUMBER 6

Run No.	Location	DO	BOD
(1)	GUTWINNIPAC RIVER	1.35	
(2)		1.68	
(3)		1.04	
(4)		1.34	
(5)		1.56	
(7)		2.13	
(8)		2.07	
(9)		2.10	
(11)		1.75	1.70
(16)		1.18	1.11
(19)		.85	.90
(23)		.71	.73
(26)		.56	.64
(28)	LONG ISLAND SOUND	.36	
(13)	WEST RIVER	1.93	
(10)		2.14	
(12)		2.33	
(17)		2.03	
(21)		.68	
(24)		.52	
(27)		.40	
(6)	MILL RIVER	1.17	
(14)	71		
(15)			1.70
(18)			1.11
(20)			.90
(22)			.73
(25)			.64
(29)			
(30)			
(31)			
(32)			
(33)			
(34)			
(35)			
(36)			
(37)			
(38)			
(39)			
(40)			
(41)			
(42)			
(43)			
(44)			
(45)			
(46)			
(47)			
(48)			
(49)			
(50)			
(51)			
(52)			
(53)			
(54)			
(55)			
(56)			
(57)			
(58)			
(59)			
(60)			
(61)			
(62)			
(63)			
(64)			
(65)			
(66)			
(67)			
(68)			
(69)			
(70)			
(71)			
(72)			
(73)			
(74)			
(75)			
(76)			
(77)			
(78)			
(79)			
(80)			
(81)			
(82)			
(83)			
(84)			
(85)			
(86)			
(87)			
(88)			
(89)			
(90)			
(91)			
(92)			
(93)			
(94)			
(95)			
(96)			
(97)			
(98)			
(99)			
(100)			

PRINTOUT 1

LISTING OF COMPUTER PROGRAM RESULTS OF BOD AND

DO DISTRIBUTIONS IN NEW HAVEN HARBOR FOR

DRY WEATHER SUMMER CONDITIONS FOR SCHEME 1

OPERATION AT 50% BOD REMOVAL

TABLE 2
COMPARISON OF THE EFFECT OF LONG OUTFALLS
ON NEW HAVEN HARBOR WATER QUALITY
FOR SCHEME 5

% BOD REMOVAL	OUTFALL @ SEGMENT 16		OUTFALL @ SEGMENT 19		OUTFALL @ SEGMENT 23		OUTFALL @ SEGMENT 26	
	Maximum BOD ppm	Minimum DO ppm	Maximum BOD ppm	Minimum DO ppm	Maximum BOD ppm	Minimum DO ppm	Maximum BOD ppm	Minimum DO ppm
50%	2.0	5.1	1.6	5.3	1.5	5.4	1.4	5.6
75%	1.0	5.8	0.8	5.9	0.7	6.0	0.7	6.0
85%	0.6	6.1	0.5	6.2	0.4	6.2	0.4	6.2

Note: 1. Effluent from Boulevard, East St., and East Shore drainage areas treated and discharged from East Shore STP.
2. Effluent from West Haven is treated and discharged at West Haven STP.
3. Outfall runs from plant to midpoint of above model segments.

7. ACKNOWLEDGEMENTS

This work was performed under the sponsorship of the Water Resources Commission of the State of Connecticut, and was performed by Quirk, Lawler and Matusky Engineers, NYC.

CHAPTER 113

FLUSHING PATTERN OF NON-REACTIVE EFFLUENTS

by

Adel M. Kamel, AM.ASCE
Associate Professor of Civil Engineering
Louisiana State University, Baton Rouge, La. USA.

ABSTRACT

In south central Louisiana non-reactive liquid effluents are introduced into man-made relatively straight prismatic canals which are comparatively narrow and have brackish water. To study the flushing pattern of liquid effluents introduced into those canals (or estuaries), a one-dimensional numerical model is considered for a simplified system consisting of a long straight gently sloping reach with a sinusoidal tidal variation at the mouth of the estuary, sinusoidal tidal variation with a phase lag and an attenuated amplitude at the upstream end, a variable inflow hydrograph, and a variable inflow or outflow. For this system, the continuity and momentum equations are solved numerically by an explicit finite difference scheme. The output of the model describes the spatial and temporal variations in flow velocity (also in water depth and discharge) from which the flushing pattern is obtained for a liquid effluent introduced at any time during the tidal cycle at any section along the estuary. The numerical model is applied to Charenton drainage canal in south central Louisiana and good agreement is obtained between the velocities and stage elevations predicted from the model and recorded in the field. An IBM 360/65 computer is utilized.

INTRODUCTION

In south central Louisiana non-reactive liquid effluents mainly from sugar mills are introduced into man-made relatively straight prismatic canals which are comparatively narrow and have brackish water. Effluents introduced oscillate up and down the canals with tidal movement and are carried slowly to the Gulf of Mexico with the net flow.

The study of the flushing pattern of effluents introduced into those estuaries is of interest in the selection of the location of new outfalls and the time of release of effluents. The flushing pattern would depend on the flow velocity and the density of the effluent. The presence of tidal movement in the estuaries under consideration (for a 1.5 ft tide at the mouth of estuary, Gulf of Mexico, tidal variation of more than 1.0 ft is obtained about 6 miles upstream) result in unsteady flow which makes the evaluation of flow velocity based on steady state conditions no longer feasible. Resort to the evaluation of the flow by either empirical methods or continuous field measurements are also not feasible because of the lack of generality in the first and the incredible amount of work and expense in the latter.

Hydraulic and analog studies could be employed for predicting the flushing pattern in estuaries. However, such models provide results that are unique to the particular tidal reach for which they are applied. Application of those models to another tidal reach would require the construction of new hydraulic or analog model. On the other hand a general purpose numerical model would be applicable to any tidal reach in the area as long as the characteristics of the reach under consideration (such as length, roughness coefficient, shape of cross section of flow, tidal amplitude and phase angle, .. etc.) are provided as input to the numerical model.

Techniques for one-dimensional numerical modeling of both natural and artificially induced transient flows in rivers and estuaries have been developed by investigators such as (1,2,4,5,8,10,11,12, and 18)*. Recently work has begun on two-dimensional numerical modeling of tidal flows such as the work of (3,6,7,13, and 17). Those techniques involve the solution of the shallow water equations for the appropriate initial and boundary conditions.

This paper constitutes the results of a pilot study on the numerical simulation of the flushing pattern of a non-reactive liquid effluent (no decay or absorption of effluent across flow boundaries) which has a density similar to that of the estuarine water. The estuaries considered are

*Numerals in brackets refer to similarly numbered items in Appendix I-References.

comparatively narrow and straight with brackish waters. The numerical model is applied to Charenton drainage canal (figure 1) in south central Louisiana and good agreement is obtained between predicted and measured water stage elevations and velocities in the canal.

ANALYSIS

Simulation of Spatial and Temporal Velocity Changes.- The estuaries considered are sectionally homogeneous making a one-dimensional presentation adequate for the study of the flushing pattern and concentration distribution of liquid effluents having density similar to that of the receiving waters. The hydromechanics of the estuaries considered could be studied by developing a one-dimensional numerical model for a simplified system consisting of a long straight gently sloping reach with a sinusoidal tidal variation at mouth of estuary, a sinusoidal tidal variation with phase lag and amplitude attenuation at the upstream end, an inflow hydrograph, and lateral inflow or outflow.

The equations of continuity and of motion for one-dimensional unsteady flow of homogeneous density in a straight gently sloping prismatic tidal reach are expressed as:

$$\frac{\partial H}{\partial t} + H \frac{\partial u}{\partial x} + u \frac{\partial H}{\partial x} + u s_0 - \frac{q}{B} = 0 \quad -1-$$

$$\frac{\partial u}{\partial t} + u \frac{\partial u}{\partial x} + \sigma \frac{\partial H}{\partial x} + \alpha s_e - \frac{q u}{A} = 0 \quad -2-$$

Equations 1 and 2 are the familiar forms of the shallow water equations and are valid under the following assumptions 1. the effect of the coriolis force and the wind stress term are negligible, 2. in the direction normal to the axis of the channel the surface particles lie transversely on a horizontal line. Since the reach section is prismatic in form, it follows that the width B would be a function of depth only, 3. hydrostatic pressure prevails at any point and a uniform velocity distribution exists over any cross section.

*Symbols used are defined in Appendix II-Notation.

Further assuming that the coefficient of roughness for unsteady flow is the same as that for steady flow and can be expressed by the Manning's equation, the friction slope term in equation 2 could be expressed as

$$g S_e = \frac{g k}{(R)^{4/3}} u |u| \quad -3-$$

Substituting equation 3 into 2, the later becomes,

$$\frac{\partial u}{\partial t} + u \frac{\partial u}{\partial x} + g \frac{\partial E}{\partial x} + \frac{g k}{(R)^{4/3}} u |u| + \frac{c u}{A} = 0 \quad -4-$$

Equations 1 and 4 are two simultaneous quasi-linear partial differential equations with two dependent variables u and E and two independent variables x and t . To solve equations 1 and 4 numerically three methods were considered namely, characteristics, explicit, and implicit. Results obtained from the explicit method only are reported herein.

The computational scheme employed in this study is based on operating with finite differences by using a fixed rectangular net in the x - t plane. In this case it is not necessary to calculate the values of the coordinates x, t of the net points themselves. The reach of length L is divided into N equal sections of length Δx . The time interval Δt is selected to satisfy the Courant condition for empirical stability,

$$\Delta t = \frac{\Delta x}{V (|u| + c)} \quad -5-$$

The boundary conditions of water surface elevation were selected since in canals considered gaging stations are usually operated by the Corps of Engineers and supply continuous record of E . The computational procedure starts by assuming the initial condition (values of u and E at $t = t_0$) along the reach length and advancing the solution one step to time $t_1 = \Delta t$. Now that all values of u and E are known at each point in the grid at time $t_1 = \Delta t$, the same procedure is used to advance the solution from $t_1 = \Delta t$ to $t_2 = 2 \Delta t$. In this case the values of u and E

obtained at $t_1 = \Delta t$ are considered as initial conditions.

Simulation of Flushing Pattern of Index Particles.- The differential equations describing the movement of index particles released at any time at any location along the reach is expressed as

$$\frac{dx}{dt} = u(X,t) \quad -6-$$

A particle released at X_0 at t_0 would be located at X_{j+1} at time $t = t_0 + n \cdot \Delta t$. where:

$$X_{j+1} = X_j + u_{x_j} \cdot n \cdot \Delta t, \quad (n, j = 0, 1, 2, 3, \dots) \quad -7-$$

To obtain the flushing pattern of an effluent introduced at any time t_0 at any section X_0 along the reach, the value of u at that section at that time is read and multiplied by the time increment Δt to give the increment $\Delta x'$ which the effluent has advanced. $\Delta x'$ is added algebraically to X_0 to yield the new location X_j of the effluent at time $t_0 + \Delta t$. At this new location X_j , the value of u is obtained by linear interpolation from the corresponding values of u in the mesh of length Δx to the right and to the left of point X_j . The same procedure is repeated to obtain the flushing pattern for any length of time.

APPLICATION

Simulation of Spatial and Temporal Velocity Changes.- To establish the range of conditions under which the computational scheme would yield satisfactory results, the following factors are considered

1. effect of assumed initial conditions, 2. effect of Manning's coefficient of roughness, 3. stability of the scheme.

Effect of Initial Condition.- The initial conditions employed are the water level elevation E and the flow velocity u at $t = 0$. Since the water level is known at the two ends of the reach from gaging stations, an elevation of the water level at different sections along the reach by linear interpolation would be satisfactory for obtaining the initial values of E . The corresponding values of u could be computed

from Manning's formula, in this case a value of $u_0 = 1.45$ ft/sec is obtained and is assumed to be the same along the entire reach at $t = 0$. To establish the effect of u_0 on the convergence of the solution, computations were carried out with $u_0 = 1.45, 0.725, \text{ and } 0.00$ ft/sec. It was noted that all values computed converged to a unique value in less than 5 hours (figure 2). Five hours would seem as a short duration in the study of the velocity variation during a whole tidal cycle. However, in the study of the flushing pattern during periods of large velocities, the variation in the velocity obtained from the computational scheme during the first hours could result in an appreciable error in evaluating the flushing pattern. This suggests that a careful estimate of the initial velocity u_0 would be necessary if accurate flushing patterns are to be obtained.

Effect of Manning's Coefficient of Roughness - The effect of the value of n selected for the calculations on the spatial and temporal variation of the velocity was investigated for n values of 0.0, 0.02, 0.03, and 0.10. Other parameters are held constant. The results are shown in figure 3 and indicate that convergence does not occur and a variation in the magnitude of the velocity of as much as 80% occurs by changing the value of n from 0.02 to 0.03. Although the computational scheme is sensitive to variations in the value of n employed in the calculations, this should not be of great concern since the value of n can be estimated with a reasonable degree of accuracy for either an existing canal or for one which is in the planning stage.

Stability.- Questions regarding the stability of the explicit scheme has been raised. For instance (14) showed that the method is unstable when $\Delta x \rightarrow 0$ even though $\Delta t \rightarrow 0$ in such a manner as to satisfy equation 5. It was reported by (19) that satisfying equation 5 does not guarantee that the equation of continuity would be satisfied. According to the same author, over a long period of time the inflow might be greater or less than the outflow plus the accumulated storage. In his study of overland flow (15) noticed a tendency of the hydrograph to overshoot at equilibrium flow. In the present study instability was observed when the rate of change of discharge with respect to time is large. This was corrected for by selecting a value of Y variable in equation 5 to ensure stability in convenient means since a rigorous stability criteria for nonlinear equations cannot be established (16).

After exploring the effect of the initial conditions, the coefficient of roughness, and the stability of the method on results obtained by the computational scheme, it would be necessary to examine the effect of the different hydraulic parameters (such as tidal amplitude and inflow hydrograph) on the spatial and temporal variations of the flow velocity. This is summarized in the following paragraphs.

Effect of Tidal Amplitude.- The effect of tidal amplitude on the velocity, discharge, and water level for two semi-amplitudes of $a = 4.00$ ft, $a_1 = 3.5$ ft, and $a = 1.50$ ft, $a_1 = 1.25$ ft indicated minor spatial variation in the values of u, Q , and E obtained for the same tidal amplitude. This is believed to be due to the small coefficient of roughness ($n=0.002$) employed in the numerical model.

Effect of Inflow Hydrograph.- The four inflow hydrographs tested have a sinusoidal form with a peak amplitude (h) of 7.5 ft above existing water level at upstream end of reach. The duration of the inflow hydrograph (τ) varied from $T/16$ to $T/4$. The results are shown in figure 4 and indicate an equal peak velocity for different values of τ and a longer duration of high flows for larger values of τ .

Simulation of Flushing Pattern of Index Particles.- After examining the effect of the different hydraulic parameters on the spatial and temporal variation of the flow velocity, two typical examples are selected for the study of the flushing pattern. The first situation is representative of conditions during unusual weather activities. The following hydraulic parameters are selected: $a=4.0$ ft, $a_1=3.5$ ft, $q=0.10$ ft²/sec, $u_0=1.45$ ft/sec, $h=4.0$ ft, $\tau=T/2$, $T=24.83$ hrs., and $n=0.02$. The flushing pattern of an effluent introduced at time $t_0=T/2$ at section 1 through 12 of the reach under study is shown in figure 5. The second situation is representative of conditions that prevail during the dry season with normal tidal activity in the Gulf of Mexico. The following hydraulic parameters are selected: $a=0.75$ ft, $a_1=0.50$ ft, $q=0.0$, $u_0=0.0$, $h=0.0$, $\tau=0.0$, $T=24.834$ hrs., and $n=0.02$. The flushing pattern for an effluent introduced at time $t_0=T/2$ at sections 1 through 12 of the reach under study is shown in figure 6.

VERIFICATION OF NUMERICAL MODEL

For verifying the stages and velocities predicted from the numerical model the stage elevations recorded on three Stevens tide recorders were utilized. Tide charts were obtained for stations No.1 (at Southern Pacific Railroad bridge), No.2 (1 mile downstream from station No.1) and No.13 (0.25 miles below junction with IWW 6 miles downstream from station No.1), figure 1. The tide stages from stations No.1 and 13 were digitized and provided boundary condition input to the model. A comparison between the predicted and measured stage elevations for station No.2 is shown in figure 7 for $n=0.045$. The agreement between the predicted and measured stage elevations is good and could be improved by optimizing for the value of n . The predicted and measured temporal changes of the average velocity for station No.1 is shown in figure 8 and indicates good agreement. The velocity measurements were made from the Railroad bridge utilizing a cub current meter. Again it is believed that better agreement between predicted and measured velocities could be obtained by optimizing for the value of n .

CONCLUSIONS

1. The numerical model is sensitive to input values assumed for starting the computations such as the initial velocity, and the Manning's coefficient of roughness. This would call for a careful selection of these values but does not pose a great concern as to the validity of the model.
2. The computational scheme has a tendency to become unstable when the rate of change of discharge with respect to time is large. This difficulty is overcome by taking smaller time increments Δt , in equation 5.
3. The flushing pattern depends on the prevailing hydraulic conditions and on the time and location of release of effluent. For instance during normal conditions where a tide amplitude at mouth of estuary is about 1.5 ft and about 1.0 ft at a distance 6 miles upstream of the mouth, with no lateral inflow or outflow and no inflow hydrograph, the flushing pattern shown in figure 5 is predicted for effluents released at low water slack ($t_0 = 0.0$). It can be seen from figure 5 that an effluent released at the Southern Pacific Railroad bridge 6 miles upstream of the IWW will be flushed in a downstream direction to a distance of about 14,700 ft after 5 hours. Figure 6 shows typical flushing pattern during unusual weather activities which may prevail during the hurricane season where the variation in water level at the mouth of the estuary may reach as high as 8.0 ft with an inflow hydrograph at the

upstream end of the reach and lateral inflow caused by rainstorms. It can be seen from figure 6 that effluents released at the upstream end of the reach at $t=t_0 + 15.30$ hours (i.e. 15.30 hrs after high water slack) would be flushed in only 1.39 hrs into the mouth of the estuary. The same figure indicates that effluents released during high water slack ($t_0 = T/2$) as far downstream as 0.5 miles from mouth of estuary would reach the upstream end of reach in 3.89 hrs.

4. Computer time is an important factor in the appraisal of simulation techniques. In the scheme represented herein, for a time interval $\Delta t = 1.0$ minute and a section length $\Delta x = 0.5$ miles, a complete run required 2.67 minutes on a IBM 360/65 computer. A complete run involved predicting the spatial and temporal variations in water level elevation, flow velocity, discharge, and flushing pattern for a tidal reach 6 miles long during a tidal period of 24.834 hrs. Time required for plotting or printing out of the results is not included in the 2.67 minutes.

5. Agreement between predicted and measured temporal variations of water stage elevations and velocities is good and could be improved by optimizing for the value of n .

6. Development of two-dimensional stochastic models for predicting the flushing pattern and concentration distribution for non-reactive liquid effluents discharged into large water bodies such as rivers and lakes would seem to be the logical extension of this work.

ACKNOWLEDGMENT

The study was sponsored by the Louisiana Water Resources Research Institute. The continued financial support of the National Science Foundation for the operation of the Computer Facility at LSU is acknowledged.

APPENDIX I- REFERENCES

- 1- Abbott, M.B., and Ionesca, F., "On the Numerical Computation of Nearly Horizontal Flows," Journal of Hydraulic Research, IAHR, Vol.5, No.2, 1967.
- 2- Amien, M., "Streamflow Routing on Computer by Characteristics," Water Resources Research, Vol. 2, No.1, 1966.
- 3- Argelo, S.M., "Tidal Computation in Two-Dimensions", Report Rijkwaterstaat, 1965.
- 4- Ballofet, A., and Kupferman, A., "Hydraulic Studies in Jamaica Bay", Journal of the Hydraulics Division, ASCE, Vol.90, No.HY6, Nov. 1964.

- 5- Collins, J.I., "Mixed Techniques for Computing Surges in Channels", Journal of the Hydraulics Division, ASCE, Vol.94, No. HY2, March 1968.
- 6- Daubert, A., and Graffe, O., "Mathematical Model of Tidal Propagation in a Coastal Area," Proceedings 12 Congress, IAHR, Vol.4, Part II, Colorado State University, Fort Collins, Col., 1967.
- 7- Dronkers, J.J., "Tidal Computations for Rivers, Coastal Areas and Seas", Journal of Hydraulics Division, ASCE, Vol.95, No. HYL, Jan. 1969.
- 8- Einstein, H.A., and Harder, J.A , "Analytical and Numerical Methods for Prediction of Tidal Elevations and Tidal Flows in Canals and Estuaries", Report to the Committee on Tidal Hydraulics, Corps of Engineers, U.S Army, 1960.
- 9- Harris, D.L., and Yelismarski, C.P., "Some Problems Involved in the Numerical Solution of Tidal Hydraulics Equations", Monthly Weather Review, Vol.92, 1964.
- 10- Isaacson, E., Stoker, J.J, and Troash, A., "Numerical Solution of Flood Prediction and River Regulation Problems", Report No. IMM-235, Institute of Mathematical Science, New York University, New York, 1956.
- 11- Kamphius, J.W., "Mathematical Tidal Study of St. Lawrence River," Journal of the Hydraulics Division, ASCE, Vol.96, No. HY3, March 1970.
- 12- Lai, Chintu, "Computation of Transient Flows in Rivers and Estuaries by Multiple-Reach Method of Characteristics", U.S. Geological Survey Prof. Paper 575-D, pp. D273-D280, 1967.
- 13- Leendertsee, J J , "Aspects of the Computational Model for Long-Period Water Wave Propagation," Rand Memorandum R.M.-5294-P.R., Delft, 1967.
- 14- Liggett, J.J., and Woolhiser, D.A., "Difference Solutions of the Shallow-Water Equations", Journal of Engineering Mechanics, ASCE., Vol. 93, No.EM2, April 1967.
- 15- Morgali, J.R , "Laminar and Turbulent Overland Flow Hydrographs", Journal of the Hydraulics Division, ASCE, Vol.96, No.HY2, February 1970.
- 16- Richtmeyer, R.D., "Difference Methods for Initial Value Problems", Interscience Publishers, New York, 1957.
- 17- Schonfeld, J.C., "The Boundary Value Problem for Two-Dimensional Long Waves", Report Rijkswaterstaat, 1965.
- 18- Stoker, J.J., "Numerical Solution of Flood Predictions and River Regulations Problems, Report I: Derivation of Basic Theory and Formulation of Numerical Method of Attack," Report No. IMM-200, Institute of Mathematical Science, New York University, New York, 1953.
- 19- Strelkoff, T., and Amarocho, J., "Gradually Varied Unsteady Flow in a Controlled Canal System", Proceedings 11th Congress, IAHR, Leningrad, USSR, Paper 3-16, 1965.

APPENDIX II - NOTATION

The following symbols are used in this paper

- A = flow cross sectional area, (L^2),
 a = semi-amplitude of tide at downstream end of estuary, (L),
 a_1 = semi-amplitude of tide at upstream end of estuary, (L),
 B = surface width, (L),
 c = celerity of gravity wave, (L/T);
 E = elevation of water surface, (L);
 g = gravity acceleration, (L/T^2);
 H = average depth of flow in cross section, (L),
 h = height of inflow hydrograph above pre-existing water level at upstream end of reach, (L),
 k = a function of Manning's coefficient of resistance, ($T^2/L^{2/3}$);
 L = length of reach, (L);
 m = number of time intervals of duration Δt ,
 n = Manning's coefficient of resistance, ($T/L^{1/3}$),
 N = number of reach sections having a length Δx ,
 q = lateral inflow per unit length of reach, (L^2/T),
 Q = discharge, (L^3/T),
 R = hydraulic radius, (L);
 S_e = friction slope,
 S_o = bottom slope,
 T = tidal period, (T);
 t = time, (T);
 τ = duration of inflow hydrograph, (T),
 Δt = time interval, (T),
 u = flow velocity in longitudinal direction, (L/T),
 u_o = initial velocity in longitudinal direction, (L/T),
 x = distance measured in longitudinal direction, (L),
 Y = variable ≥ 1 ,
 Δx = length of equal section of reach, (L), and
 ϵ = phase angle between tides at downstream and upstream ends of reach.

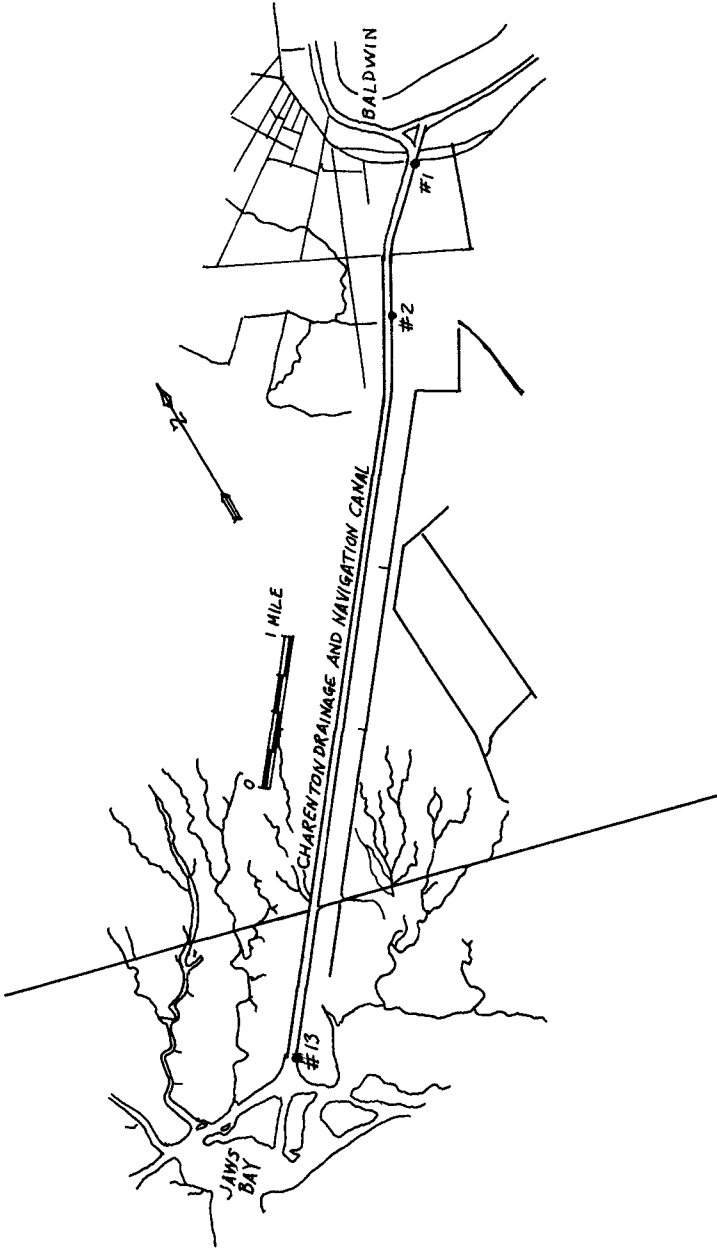


FIGURE 1. LOCATION MAP

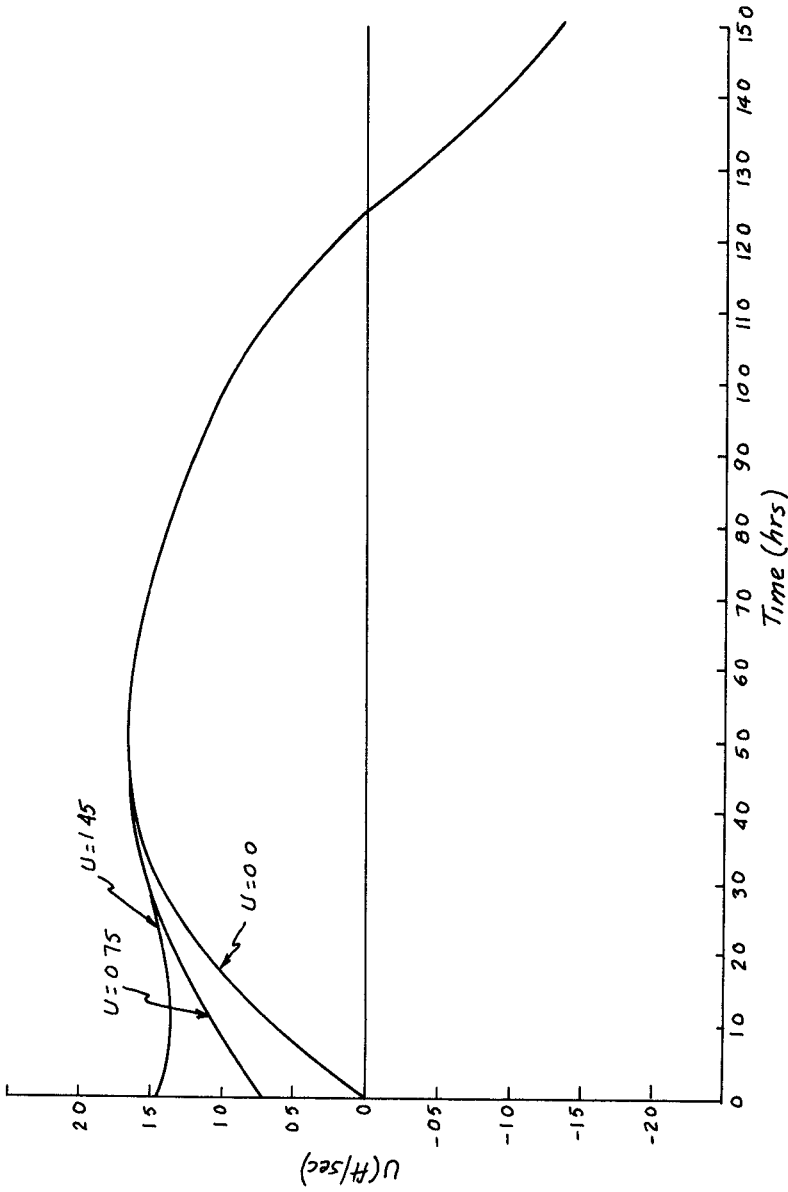


FIGURE 2. EFFECT OF INITIAL VELOCITY ON CONVERGENCE OF SOLUTION

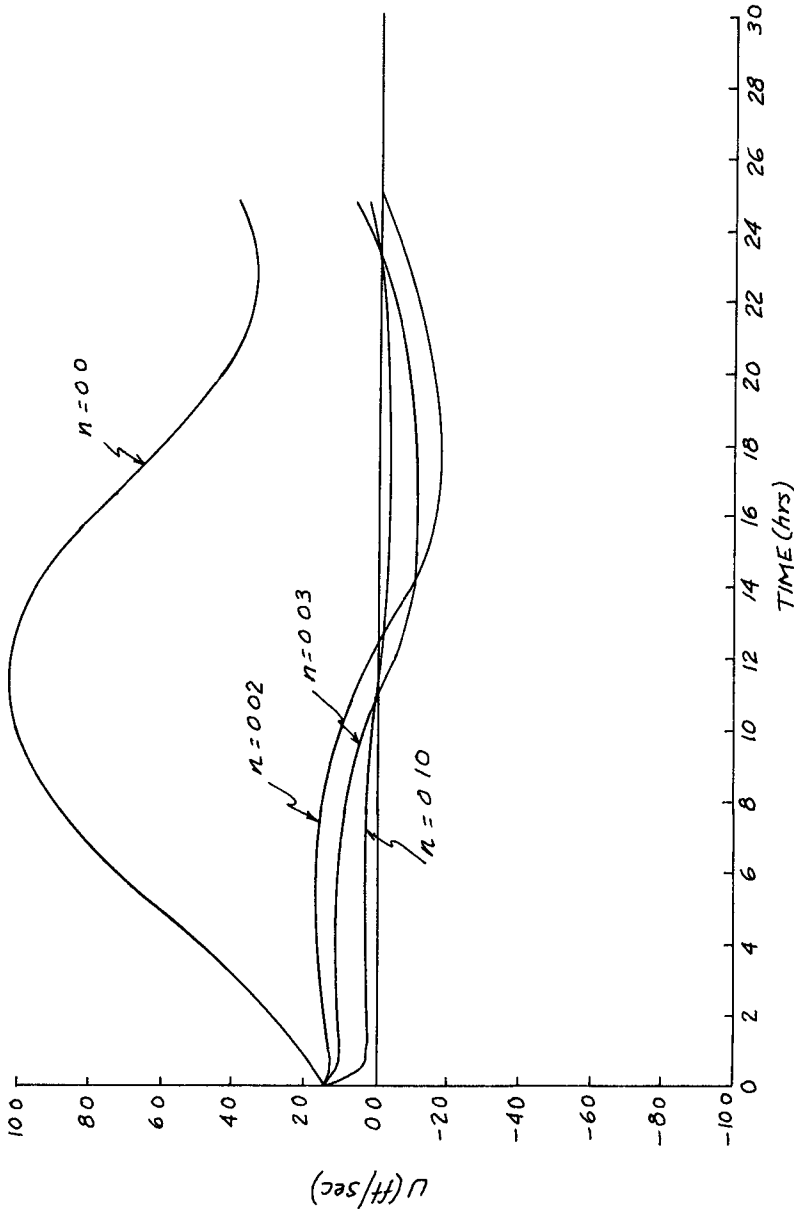


FIGURE 3 EFFECT OF MANNING'S COEFFICIENT OF ROUGHNESS ON CONVERGENCE OF SOLUTION

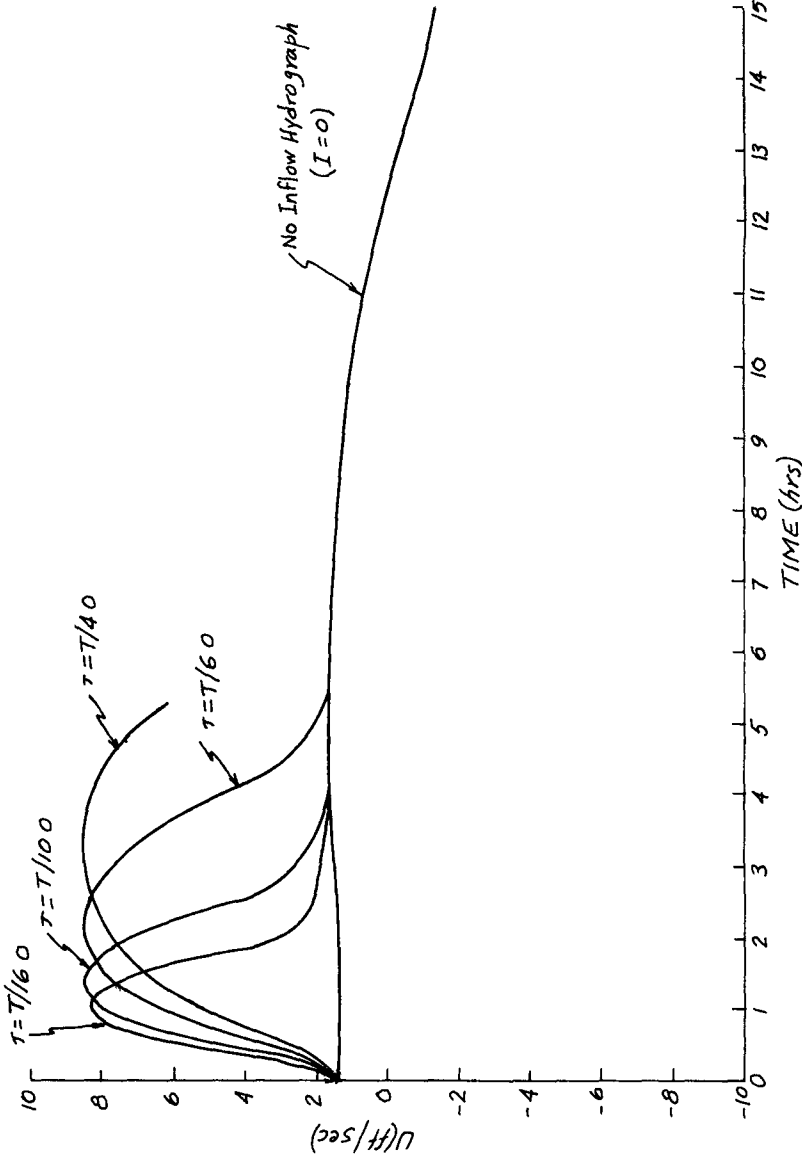


FIGURE 4 EFFECT OF DURATION OF INFLOW HYDROGRAPH ON TEMPORAL VELOCITY CHANGES AT STATION 7

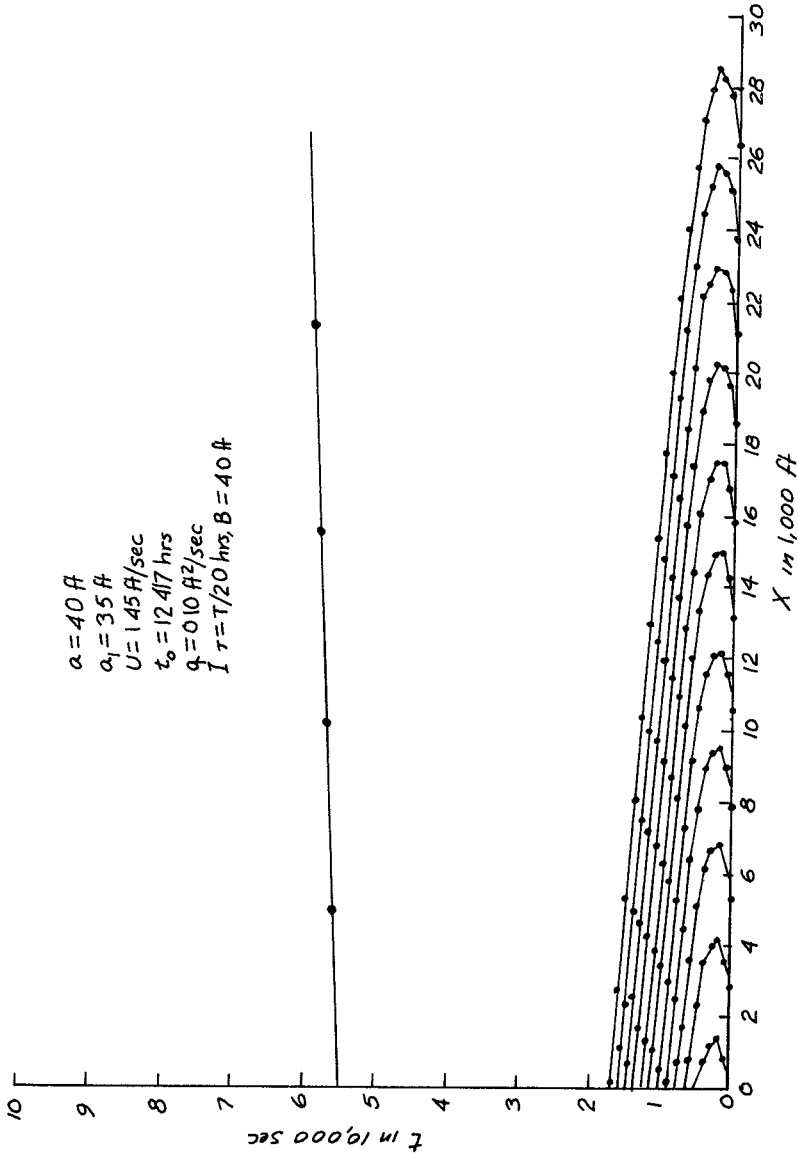


FIGURE 5. FLUSHING PATTERN OF INDEX PARTICLES

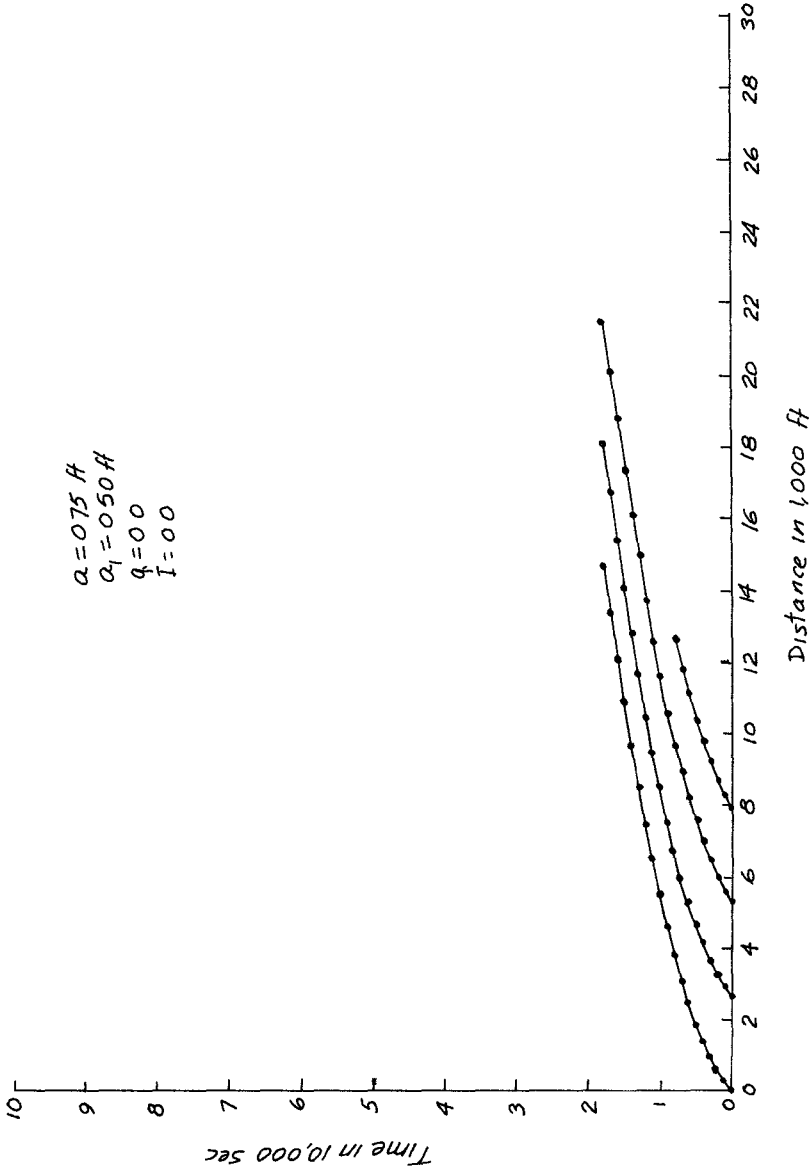


FIGURE 6. FLUSHING PATTERN OF INDEX PARTICLES

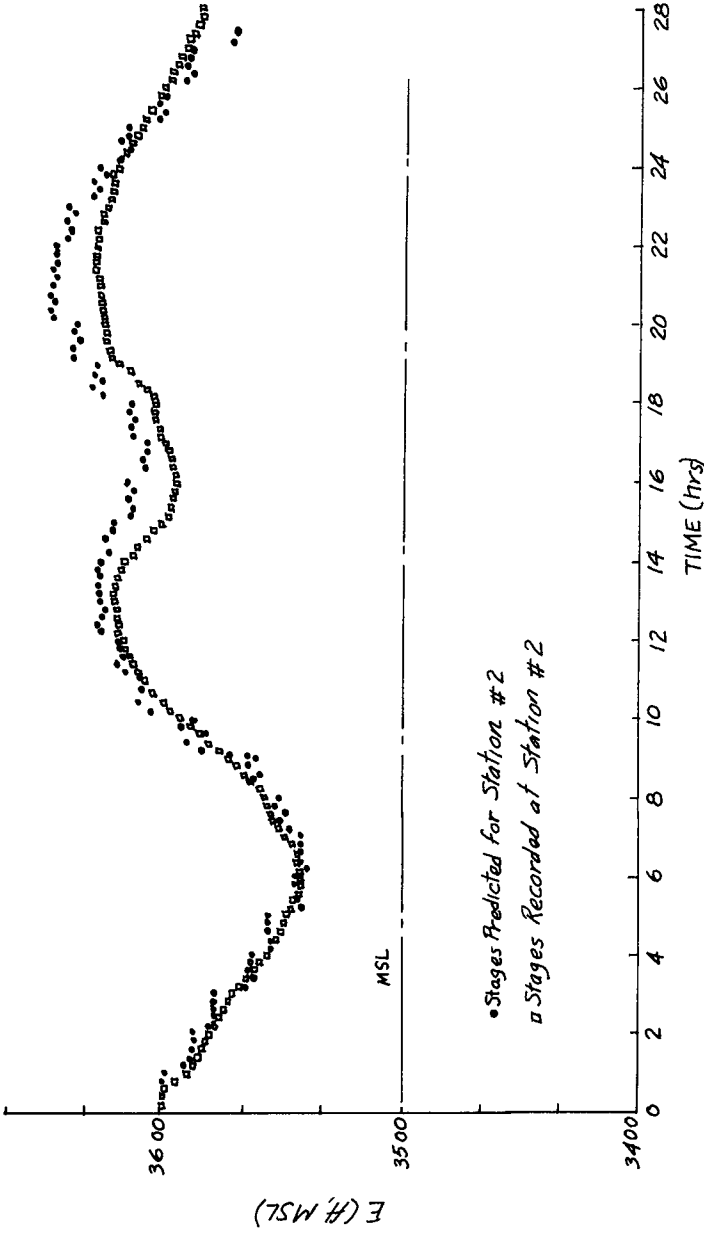


FIGURE 7 PREDICTED AND RECORDED STAGE ELEVATIONS FOR STATION 2

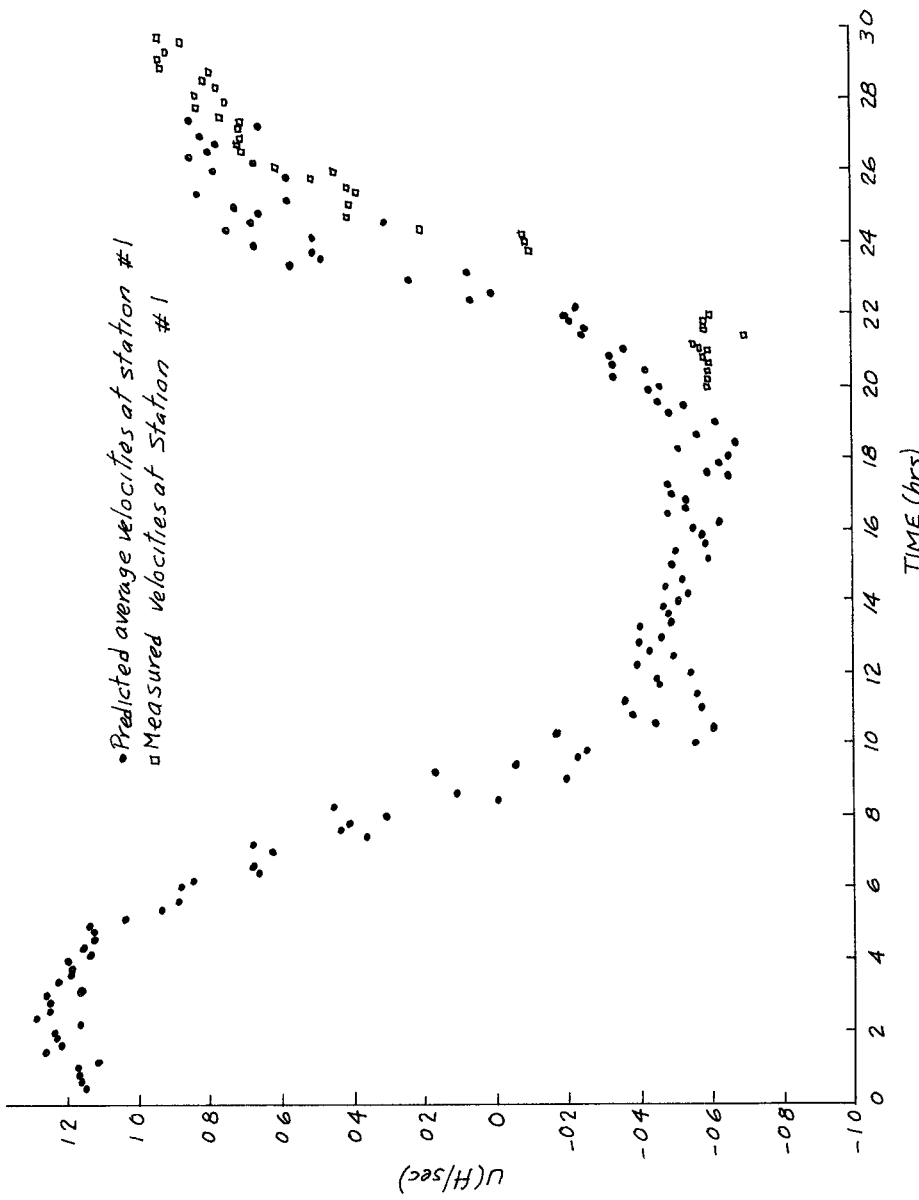


FIGURE 8 PREDICTED TEMPORAL CHANGES IN AVERAGE VELOCITY AT STATION 1

CHAPTER 114

THE MEASUREMENT OF TIDAL WATER TRANSPORT IN CHANNELS

R.E. Klein*

Summary

For the electromagnetic flow measurement in straits, channels etc use is made of the electric potential difference between two points in the bottom, near the moving water. The potential difference can be put down to natural causes the water is an electric conductor and moves in the magnetic field of the earth There are a number of quantities and variables that are of importance for the measured signal Beside this, the measurement is above all a matter of eliminating some disturbances

Information about the two measuring systems as applied in The Netherlands is given in this article

Introduction

The principle of the electromagnetic flow measurement in rivers, straits etc. has been known now for about 140 years ever since Faraday conceived the idea in 1832. But it is only in the last 30 years that it has more or less successfully been used at several places in the world [2, 3, 4, 5, 6]

In The Netherlands it has now been adapted to far smaller flows (the measurements in Washington excepted [4])

In 1964 Schumm started the investigations [7, 8]

Several difficulties had to be overcome, some of them may be of importance to those who want to apply the method themselves At present there are two measuring systems in use

This research work has been commissioned by the Rijkswaterstaat

*Technisch Fysische Dienst TNO-TH (Institute of Applied Physics)
Delft, The Netherlands.

The physical background

The method makes use of a natural phenomenon. Throughout the world, water moves in the magnetic field of the earth. Because water is an electric conductor, an electric potential field occurs in the water and, as a result, also in the surrounding ground, fig 1. The potential difference measured between the electrodes in P and Q or P and R is a function of all velocities in the channel, and depends also on other quantities and variables such as "the" conductivity of the water and the bottom, the shape and size of the channel, relative changes of the depth by changes of the waterlevel, the vertical component of the magnetic field B etc.

The theoretical basis was laid by M.S. Longuett-Higgins in 1949 [1] and in 1964 extended by Schumm [7], but the problem is very complicated, so that our knowledge remains relatively limited. The proposition is now, that this potential difference depends only little on the velocity distribution (except in very shallow, wide straits), so that in many cases it is allowed to calibrate against mean velocity, discharge etc.

The influence of the vertical component of the magnetic induction B on the calibration is obvious. Fortunately in most cases it is constant enough when taken over a few years to neglect its variations. The magnetic disturbances are very small relatively and they are only an additional effect that can be compensated. The effect of the other quantities and variables is very complicated. Therefore the systems are calibrated with a number of simultaneous velocity measurements, for instance once a year. The measured potential difference is highly dependent on the conductive properties of the bottom. The higher it is, the lower the potential difference measured will be and the higher the influence of changes of the conductivity of the water and the waterlevel (tidal range). In The Netherlands the conductivity of the bottom is very high up to a depth of 1 km it is about one tenth of that of seawater. It causes a loss of 80 percent and it is necessary to take into account the influence of the temperature on the conductivity of the water (knowledge within 3° C is adequate).

In the two cases with which we are concerned it was found that the influence of the waterlevel is such that the system does not give the mean velocity but the discharge
It may be expected that the accuracy will range from 5 to 10%

The problem of the disturbances

The elimination of all kinds of disturbances is an important problem, especially in The Netherlands where the level of the signals is very low.

Four kinds are mentioned here

1. Magnetic disturbances

Along the surface of the earth potential gradients are generated by the fluctuating magnetic field (especially the horizontal component) of the earth

As already stated they give additional signals

They are eliminated by compensation by means of two signals, measured far away from any flow, in two directions perpendicular to each other, between electrodes in the ground in the same way as the measurement of the flow signal fig. 2

Thus

$$V_{\text{flow}} = V_{PQ} - \alpha V_{AB} - \beta V_{BC},$$

is formed,

where α and β are suitable constants

In our cases, where the distance between P and B is for example 15 km, the elimination is very satisfactory

2. Earth currents caused by the electric DC railway traffic

They may cause heavy disturbances, depending on the distance to the railway system, the intensity of the traffic, the conductivity of the top layers of the bottom etc

In most cases the only thing to do is to avoid them, for instance by choosing great distances (10, 20 km) to the disturbing railway. In one case the influence could be reduced by compensation with a signal measured between two points in the neighbourhood of the railway and also by choosing an adequate direction of the line between the measuring points.

3 Electro-chemical disturbances in the bottom and in the electrodes

There are always fairly constant potential differences between two points in the earth. They are caused by local and extended differences in the composition of the ground water and the bottom. The variations in the compositions result in a drift of the zero level. It can be a long-term drift, but drift with the tidal frequency is also possible for example if the electrode is placed in the neighbourhood of the boundary between the fresh and the salt water in the shore. This boundary may move under the influence of the tidal changes of the water pressure, giving a slight mixing each time.

The electrodes are now placed in 5 to 10 m deep pipes, as far as possible from moving or fluctuating ground water. This also has the advantage of a sufficiently constant temperature.

We developed special purpose Ag-AgCl-electrodes. They are constant within $\pm 0,5$ mV for a period of one year (in the laboratory). We found that many kinds of electrodes (and also ours) are extremely sensitive to electric currents, giving a long-term drift. Therefore it was necessary to place a voltage follower between the electrode and the long line that connects the measuring point with the mV-meter. In one place we found a drift of the zero level as low as 0,5 mV in a week, but at other places it is greater.

4. Noise

The noise that is picked up by the wires used in the telephone cables to connect the measuring points with the apparatus mainly consists of pulses and hum

Sometimes the peak value is 1000 times the signal to be measured

It is eliminated by normal filtering after the compensation of the magnetic and other disturbances has taken place, this to avoid differences between the compensating and the compensated signals

The measuring systems in The Netherlands

At present there are two measuring systems in use in the north of The Netherlands, fig. 3, for measuring the tidal flow in the Borndiep and the Marsdiep. A third, in the Eyerlandse Gat, is being prepared

The Borndiep system

The Borndiep system, fig. 4, has three measurements for the flow (between wD and WM, OD and WM and ZD and ZM). The measurement for the magnetic compensation is between WM and OM and WM and ZM. There is a level gauge for additional data on the "Vrijheidsplaat". An example of the measurement between ZD and ZM, the two magnetic signals and the result is given in fig. 5. The amplitude of the flow signal is 3 mV, it is the lowest signal we can measure (low electro-chemical disturbances).

Fig. 6 gives an example of the flow according to "ZD - ZM" and the water level measured on the "Vrijheidsplaat".

In the middle the effect of a storm in the far distance the region between the Atlantic Ocean and the North Sea

The Marsdiep system, fig 7

The potential difference according to the flow has been measured between ZD and ND, between the electrodes in ZM, NM and OM the two magnetic signals are measured

The electric DC railway traffic causes heavy disturbances

Fortunately it is an uncomplicated case In this case compensation is possible We use the (large) signal measured between ZD and T

Due to the extensive clay layers deep in the bottom pronounced induced polarisation influence occurs It causes differences in the shape of the disturbances measured between the several points and these differences grow with the distance to the railway The ZD-T-signal must therefore be filtered so that it gets the right forms before it is used for compensation

Fig 8 is an example the disturbed flow signal, the three compensation signals and finally the result

The compensation of the railway disturbances is satisfactory, but not of the same quality as that of the magnetic disturbances If necessary, it is possible to make improvements by digital filtering or the extension of the compensation system.

The only calibration available at the moment is that of a former experimental system at the Marsdiep, fig 9

It did not work with ZD and ND but it did at two other points, one of them with more than normal electro-chemical disturbances, as will be seen on the right

We are now building a third system for measuring the flow in the Eyerlandse Gat It measures the flow signal between ZD' and N and uses the magnetic compensation signals of the Marsdiep system A fourth system may be built next year in the straits east of Ameland

Other applications

The method is also suitable to obtain information on the flow along a coast The most simple set-up makes use of one electrode near the coast and one far inland

The signal gives a weighted average of all velocities, the weighting factor depending on the distances to the two electrodes. Unfortunately we know only little about these factors. Theoretical research is necessary.

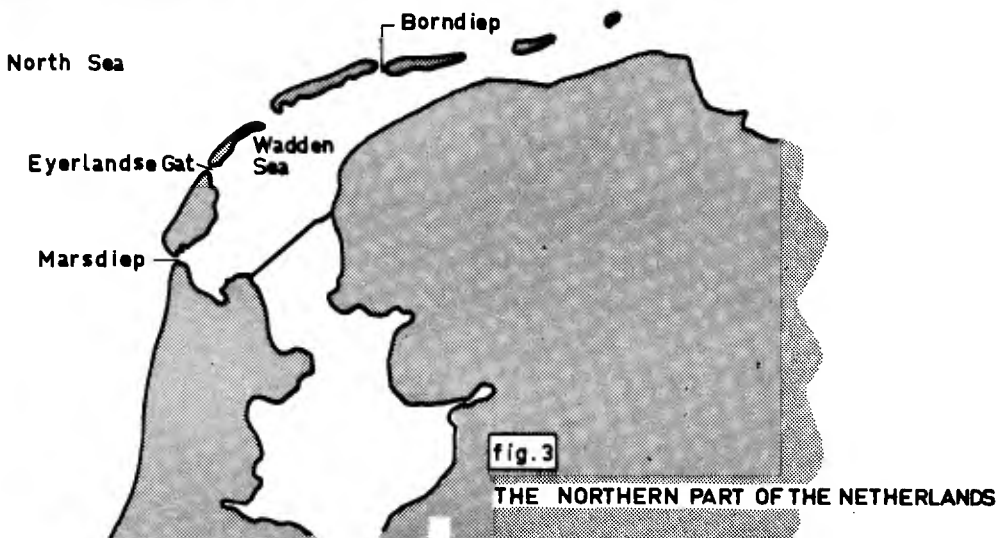
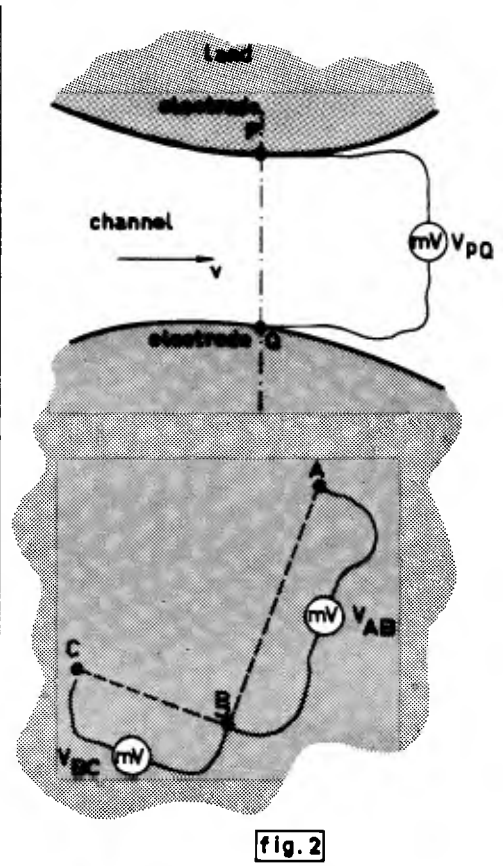
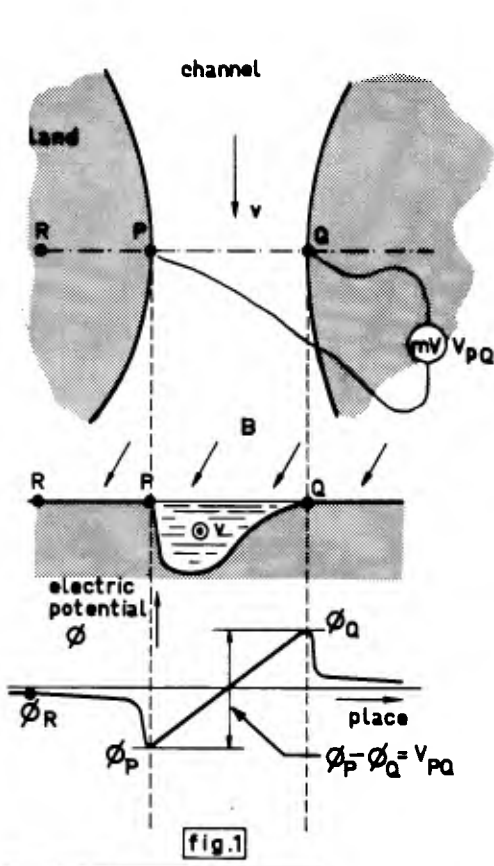
The flow signals of rivers are usually too small to be measured by applying the present method, due to the relatively small discharges.

We are now working on a modified method for fairly big rivers. This method makes use of an artificial alternating magnetic field in order to separate the signal from the noise.

References

- 1 M S Longuett-Higgins The electrical and magnetic effects of tidal streams
Monthly Not Roy Astr Soc , Geoph Suppl 1949, 5, 8, 285-307
- 2 G L Bloom Water transport and temperature measurement in the eastern Bering Strait, 1953-1958
J Geoph Res, Aug 1964, 69, 16, 3335-3354
3. K F. Bowden The flow of water through the Straits of Dover related to wind and differences in sea level
Phil Trans. Roy Soc. of London, series A, no 953.
Feb 1956, 248, 517-551.
- 4 R M Morse, M Rattray Jr , R G Paguette, C A Barnes
The measurement of transports and currents in small tidal streams by an electromagnetic method
Univ of Washington, Dep of Oceanography, Techn Rep 57, 1958
- 5 B H Olsson The electrical effects of tidal streams in Cook Strait, New Zealand
Deep-Sea Res 1955, 2, 204-212
- 6 G K Wertheim Studies of the electric potential between Key West, Florida and Havana, Cuba Woods Hole Oceanogr Inst Ref 53-95, 1954.

- 7 C Schumm Elektromagnetische debietmetingen in het Marsdiep
(Electromagnetic flow measurements in the Marsdiep)
Delft Techn. Univ , Lab for Techn Phys , 1964.
- 8 C Schumm. Potentiaalmetingen in het Marsdiep.
TNO-nieuws 1966, 21, 110-121.



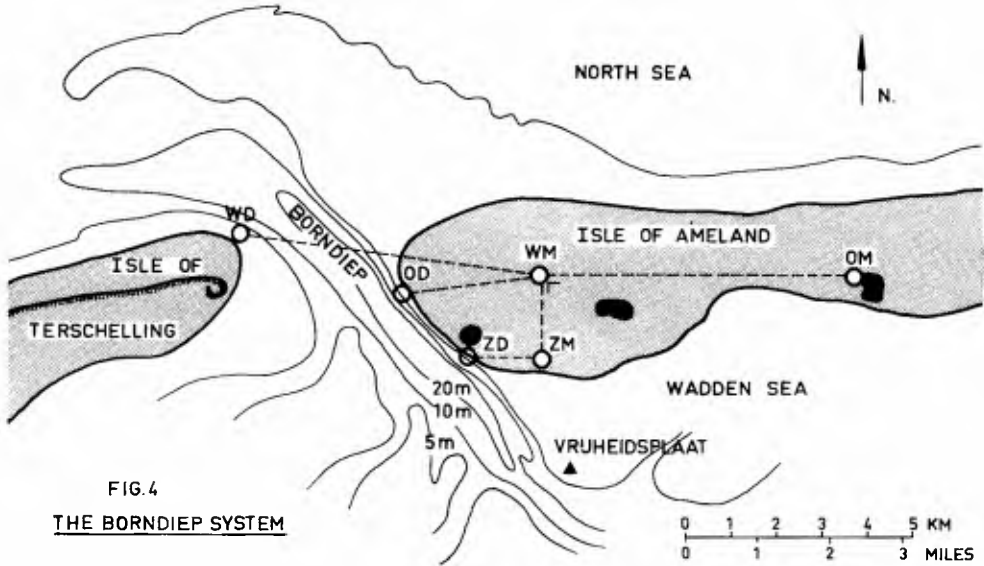


FIG. 4
THE BORNDIEP SYSTEM

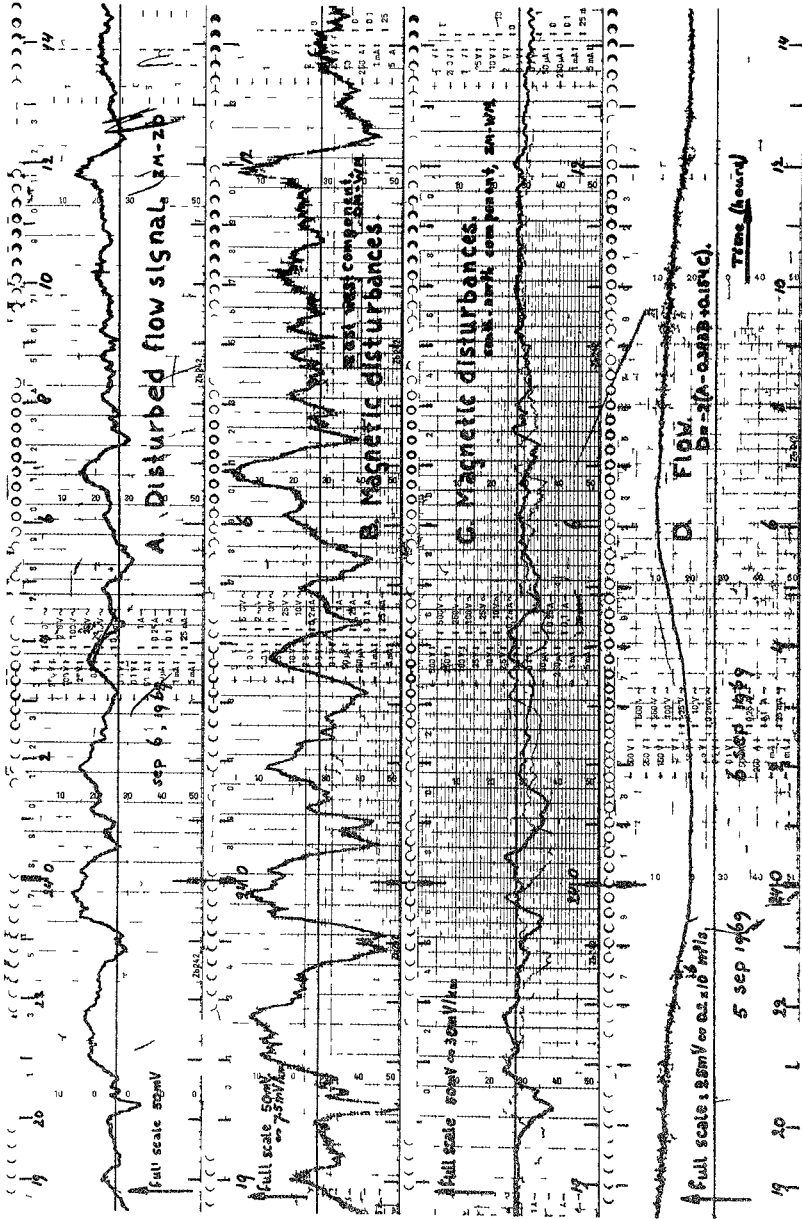


FIG 5

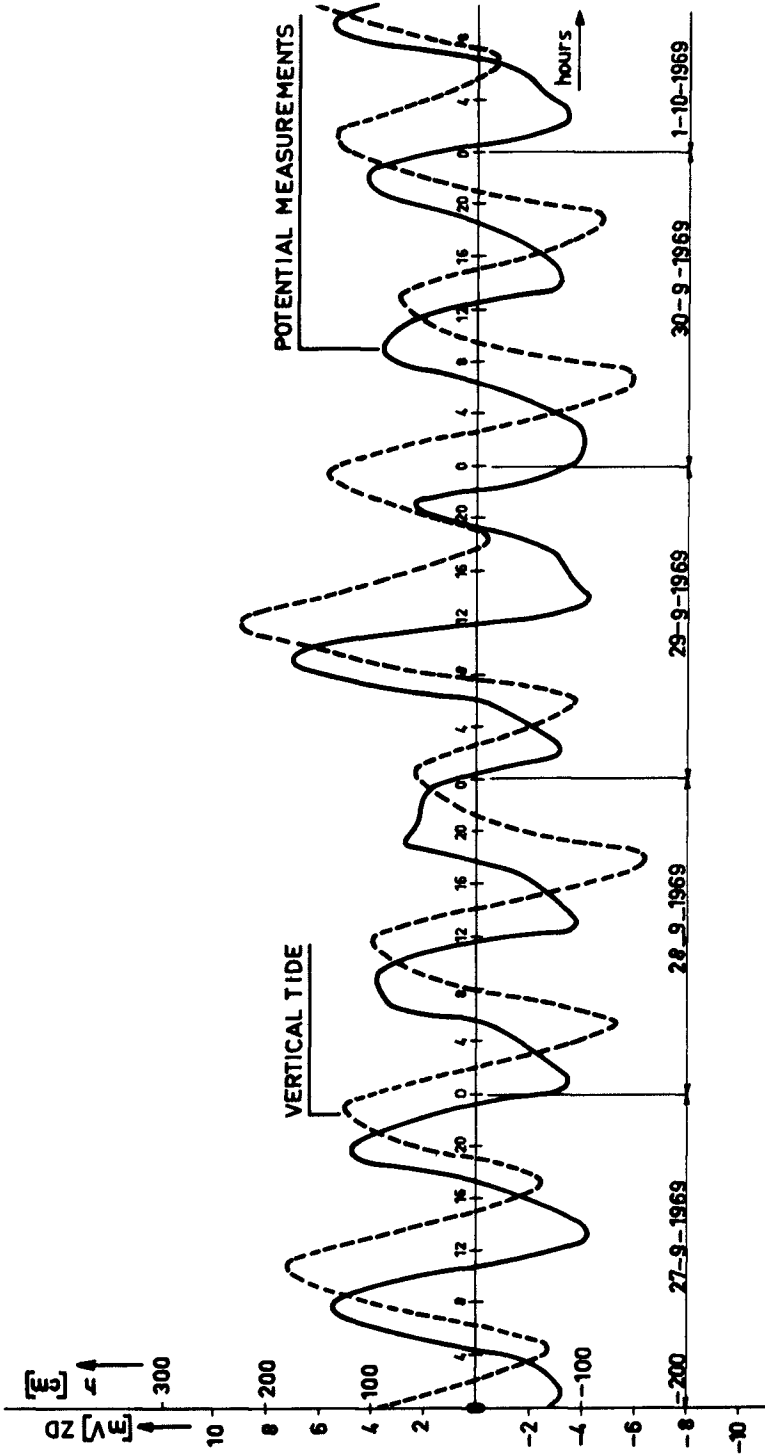


FIG 6 BORNDIEP SYSTEM
Flow and tide from 27 sep to 1 oct 1969

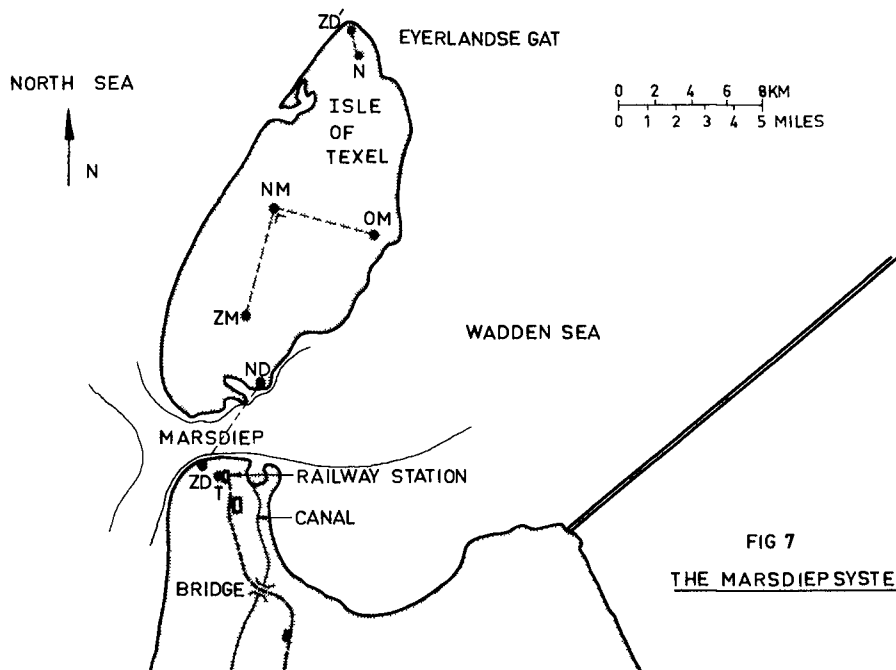


FIG 7
THE MARS DIEP SYSTEM

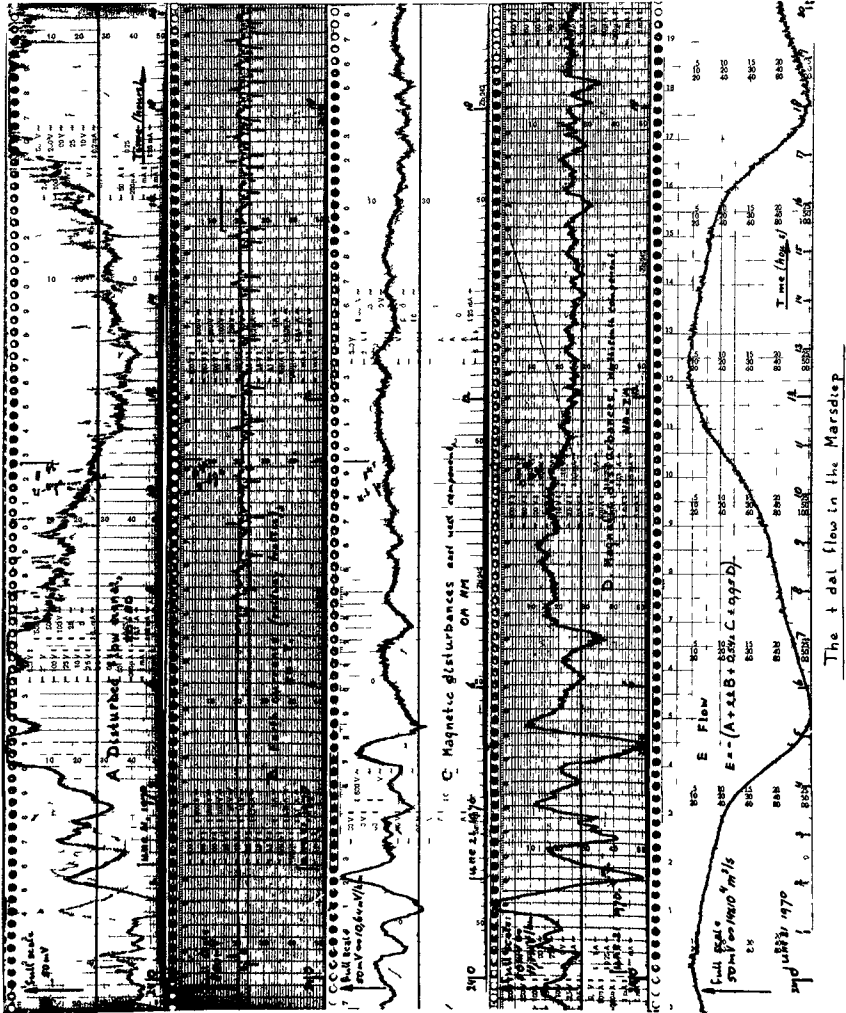
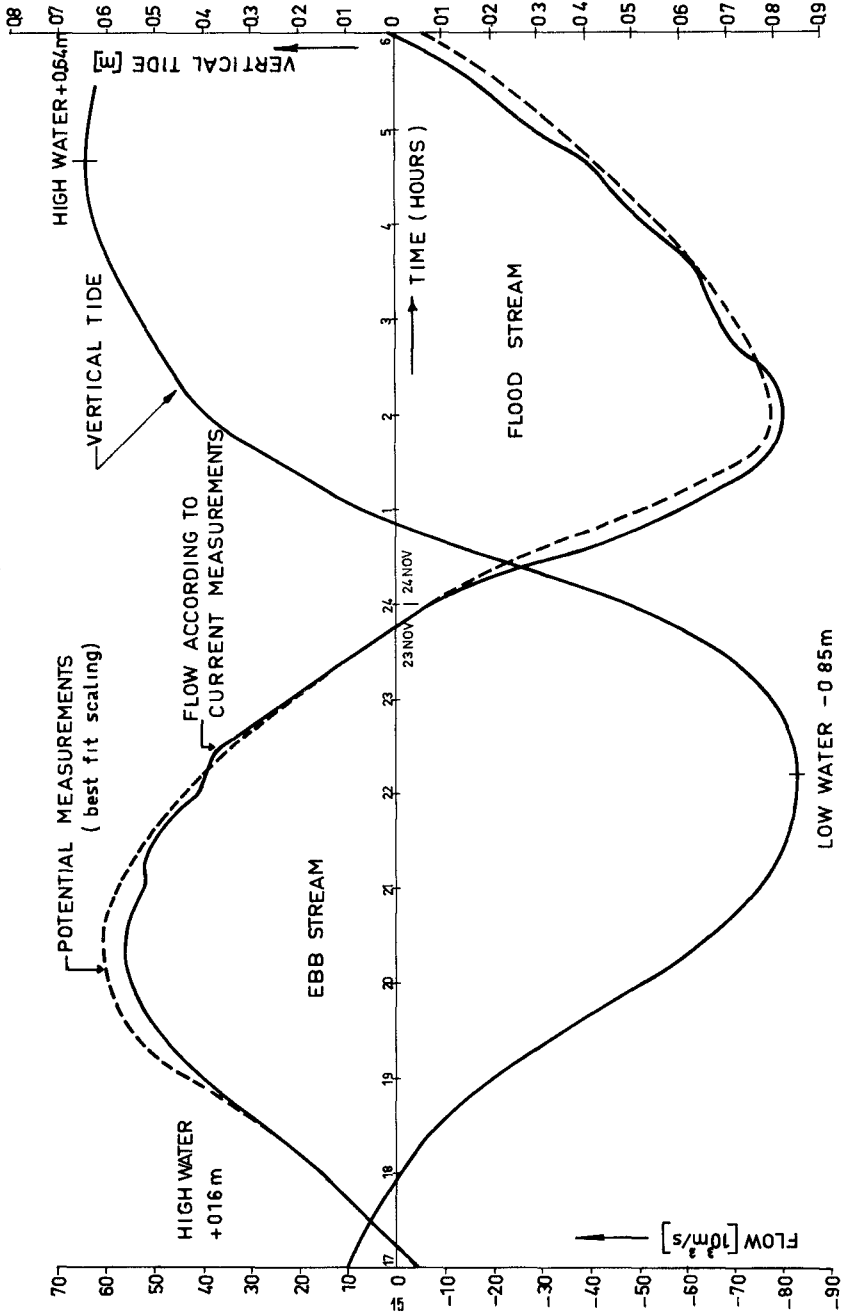


FIG 8

FIG 9 MARSDIEP NOV 23th-24th-1966
Calibration of a former, experimental system



CHAPTER 115

WATER CURRENT METER FOR MEAN FLOW MEASUREMENTS¹

DAVID SMITH

Instrument Research Division
NASA, Langley Research Center, Hampton, Va 23365

W HARRISON

Division of Physical, Chemical, and Geological Oceanography
Virginia Institute of Marine Science, Gloucester Point, Va 23062

ABSTRACT

A drag-sphere water current meter with a 0 to 6 ft/sec range has been developed for velocity measurements of relatively steady flows. A two-component strain-gage type force transducer is mounted within a 3.7-inch-diameter perforated drag sphere. Drag force measurements are related to the flow velocity around the meter. Several drag sphere configurations were tested in selecting the 336-hole pattern.

Frequency response data have been recorded and evaluation tests were made with current meters deployed in an estuary. Use of these current meters in studies of steady-state fluid processes and sediment responses is feasible. They are simple, relatively inexpensive, and well suited to applications where several simultaneous measurements are needed to determine velocity profiles or map flow distributions.

Contribution 358 of the Virginia Institute of Marine Science

INTRODUCTION

This water current meter was developed to satisfy the need for a relatively simple, inexpensive device to measure generally steady flows characterize certain nearshore waters. The design is compatible with automatic data acquisition and reduction equipment in order that several meters can be deployed and monitored simultaneously. This capability makes it feasible to determine and map the velocity distribution and/or profiles in the nearshore areas under study. The meter (fig 1) employs strain-gage techniques to measure the force exerted on a submerged drag sphere over a flow velocity range of 0 to 6 ft/sec. This drag force is then related to the flow velocity around the meter.

Inman and Nasu [1] were perhaps the first to develop a drag force meter for measuring fluid flow in the nearshore environment. Their device consisted of "a small flexible beryllium-copper rod with a sphere mounted on one end and the other mounted rigidly to support". Other efforts toward developing this type current meter are noted [2, 3, 4] in which the drag sphere or cylinders used were found to be subject to both an acceleration-dependent force and a fluid drag force. Consequently, this type of current meter is suitable for use only if fluid accelerations such as those in oscillatory flow are of low magnitude relative to the mean flow velocity.

DESCRIPTION OF THE CURRENT METER

The current meter (fig 1) consists of a two-component strain-gage force balance designed to fit within a 3.7-inch-diameter polyethylene drag sphere, similar to the anemometer developed by Reed and Lynch [5]. The force balance is constructed of Armco 17-4 PH Steel, with a 1/2-inch-diameter mounting "sting" extending approximately 14.5 inches from the sphere. A machined flat is located on the "sting" for alignment purposes.

Each of two perpendicular force components is sensed by 4 active foil-type strain gages. The meter is designed to be insensitive to moments or couples and detects only the forces exerted on the drag sphere. The output signal is approximately 2.4 mv per volt for a one pound force. The 0 to ± 6 ft/sec velocity range of interest corresponds to an electrical signal of about 0 to ± 18 mv for each component. Support equipment for each meter consists of a regulated power supply for the 4.0 to 6.0 v input to each strain-gage bridge, and a recorder with two channels. Strain-gage bridges used in this application are compensated for temperature variations over a suitable 100°F range. A 3M product designated EC870 is used to waterproof the strain gages and wiring on these devices.

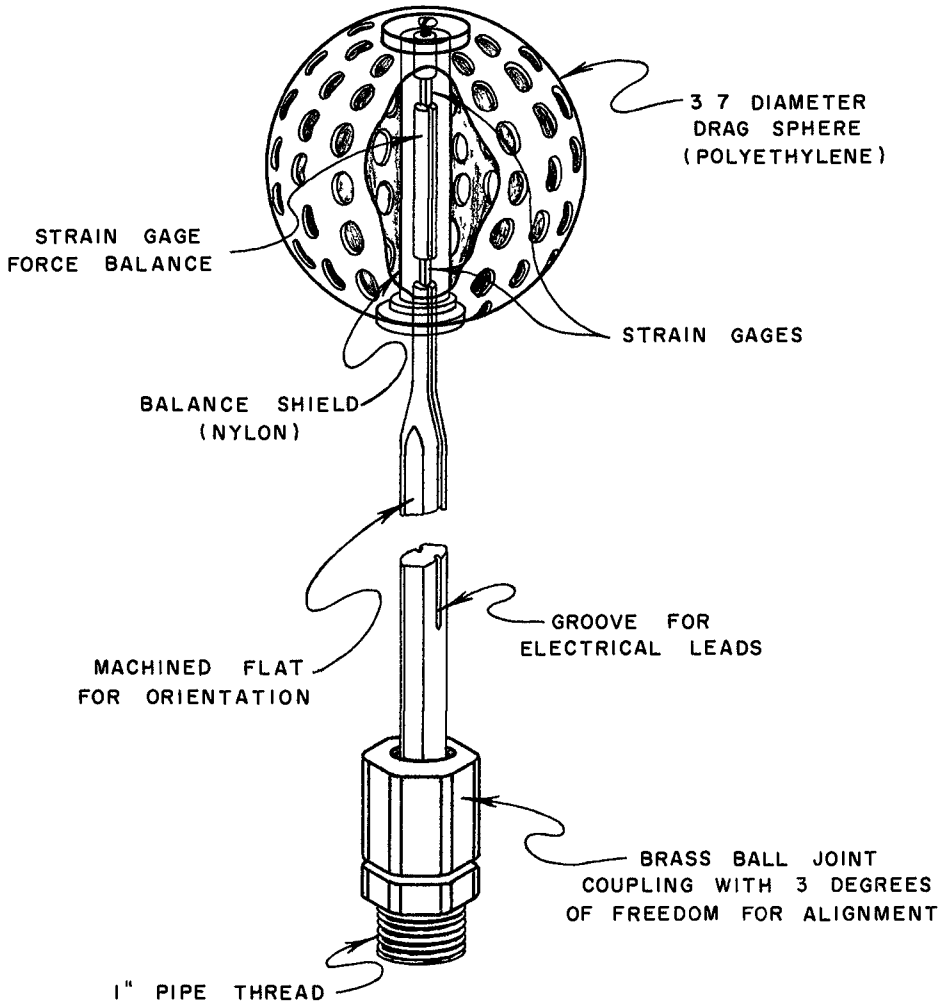


FIG 1 SCHEMATIC OF DRAG-SPHERE CURRENT METER

SELECTION OF THE DRAG SPHERE

Initial tow tank experiments with drag spheres were made in the Virginia Polytechnical Institute's towing basin at Blacksburg, Virginia. Smooth spheres were found to be very unstable in the flow velocity range of interest (0 to 6 ft/sec). The smooth spheres oscillated very erratically in the lateral direction of perpendicular to the flow past the sphere, as observed in other studies [6, 7]. Several methods of stabilizing sphere response were investigated, including various hole patterns, dimples, and bumps on the surface of the sphere, as shown in figure 2.

Several significant observations were made in the tow-tank tests. Figure 3 shows the variation of force with velocity for three spheres: the dimpled sphere, the smooth sphere, and the 336-hole-pattern sphere. All of the data points lie on or very near the theoretical lines for the appropriate drag coefficients C_D , showing that the force exerted on the sphere is a function of the velocity squared. Differences in the drag coefficients of the three sphere configurations are quite significant. Roughening sphere surfaces by dimples or bumps tends to reduce drag, as also noted by early golfers. Smooth golf balls do not go as far and as straight as old balls that are battered or have a roughened surface. On the other hand, placing holes in the surface of the sphere increases the drag coefficient in the 0 to ± 6 ft/sec velocity range. Larger holes or more holes of the same size increased the drag coefficients.

Based on these experimental results, the 3 7-inch-diameter sphere with the 336-hole pattern was selected for use on this water current meter. The drag coefficient of this sphere configuration was determined experimentally to be 0.69, with a standard deviation of 0.017 over the Reynolds Number range considered (35,000 to 211,000). All the surface alterations discussed increased the stability of the spheres, but the 336-hole pattern had the most stabilizing effect, as shown in current meter outputs in figure 4 ("component perpendicular to flow").

RELATION OF FORCE TO FLOW VELOCITY

Steady Flow

In steady flow conditions, the drag force exerted on a submerged object is related to the flow velocity by the following equation:

$$F = C_D Q A \quad (1)$$

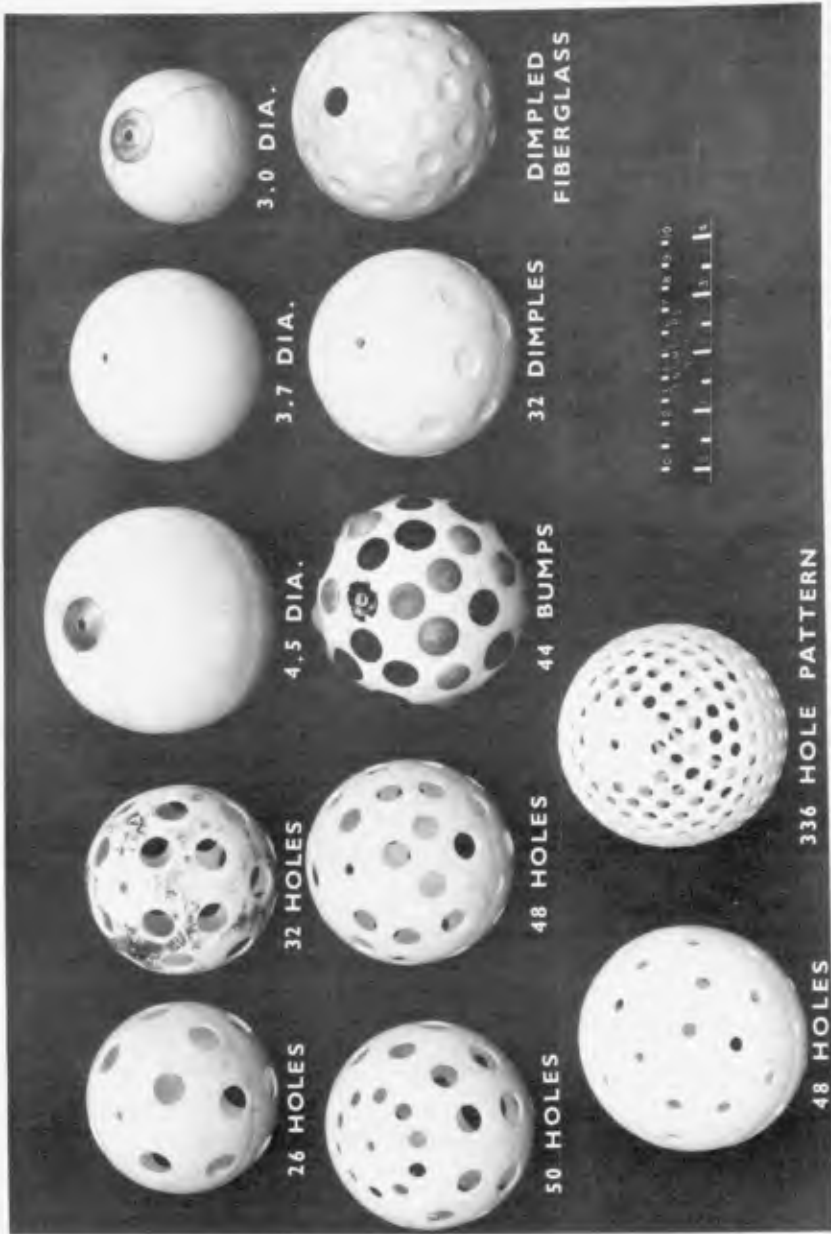


FIG. 2 DRAG SPHERE CONFIGURATIONS EVALUATED IN V.P.I. TOWING BASIN TESTS

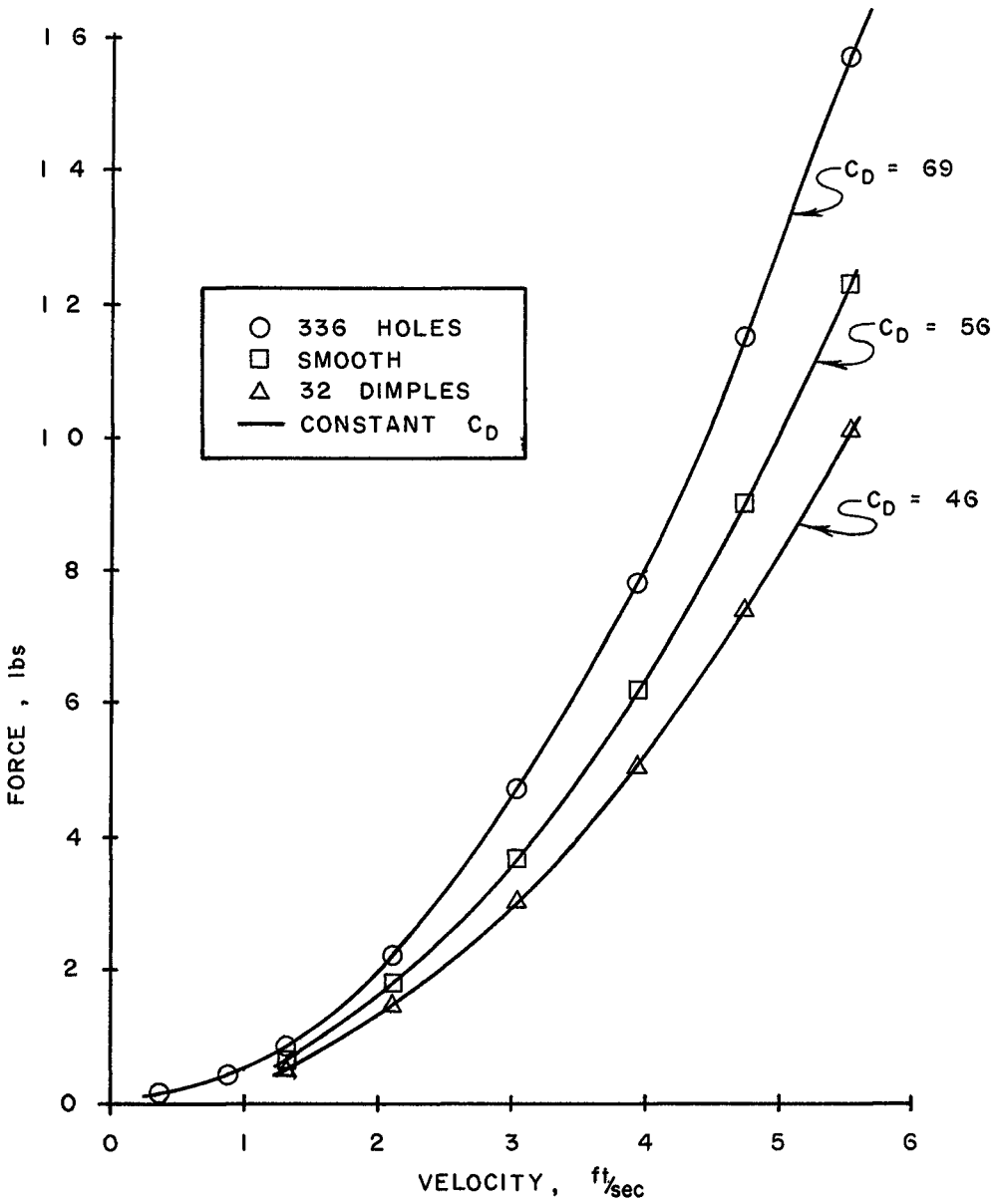
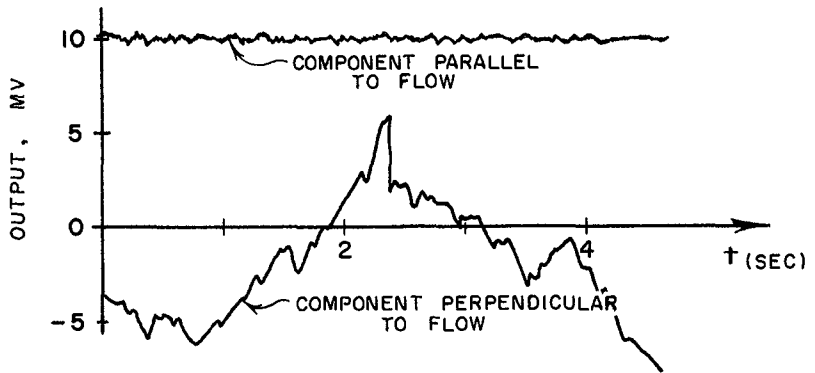


FIG 3

FORCE VS VELOCITY FOR THREE SPHERE-ROUGHNESS CONFIGURATIONS:

SMOOTH BALL , V = 5 6 FT/SEC



336-HOLE-PATTERN CONFIGURATION ,

V = 5 6 FT/SEC

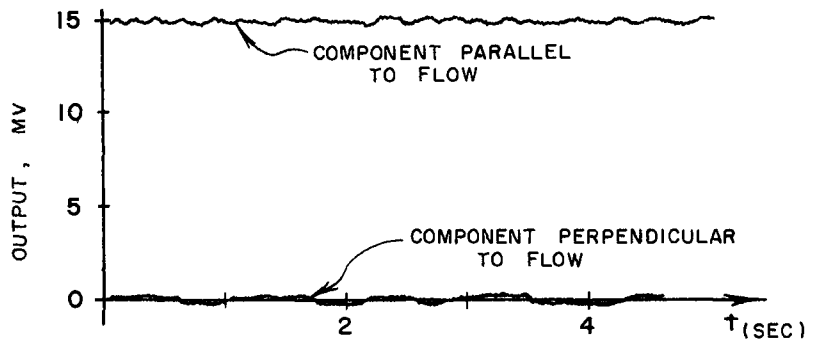


FIG 4 STABILIZING EFFECT OF 336 HOLE PATTERN COMPARED TO SMOOTH SPHERE'S OSCILLATION

Substituting $Q = \frac{1}{2}\rho U^2$, and solving for U yields

$$U = \left(\frac{2F}{\rho A C_D} \right)^{1/2} \quad (2)$$

where U = flow velocity, ft/sec

F = drag force, lb

C_D = drag coefficient

ρ = mass density, slugs/ft³

A = frontal area of drag sphere, ft²

The velocity vector has the same direction as the force vector

By having a well defined, constant C_D in the velocity range of interest, and knowing the density of the water as well as the projected area of the drag sphere, measuring the drag force vector enables the determination of the flow vector. A significant point is that the total force vector must be used in calculating the velocity, $\underline{i} \underline{e}$, velocity components cannot be correctly computed from the individual force components using equation (2)

The velocity range of 0 to 60 ft/sec corresponds to drag forces on the order of 0 to 1.7 lb for the 336-hole-pattern drag sphere used

Accelerating flow

In unsteady or accelerating flow conditions, the forces exerted on the drag sphere are a function of both the flow velocity and the acceleration of the water [3, 8]. The general expression for the force exerted on a submerged object in an accelerating flow is given as

$$\vec{F} = C_m \left(U, \frac{dU}{dt} \right) \rho V \frac{d\vec{U}}{dt} + \frac{1}{2} C_D \rho A |U| \vec{U} \quad (3)$$

where V = drag sphere volume, ft³,

and $C_m = C_m \left(U, \frac{dU}{dt} \right)$ = coefficient of mass

Since C_m is a function of both the flow velocity and any fluid acceleration in the flow region near the drag sphere [9, 10], solving equation (3) for the velocity becomes very impractical, if not impossible. Also, experimental results show that C_m is the same order of magnitude as C_D (3). Consequently, force-sensitive current meters must be used where the fluid acceleration is of very low magnitude and the $\frac{dU}{dt}$ term of equation (3) can be neglected.

ERROR ANALYSIS

Error in velocity measurements can be obtained from a Taylor's expansion of equation [2], which yields

$$\frac{\Delta U}{U} = \frac{1}{2} \left(\frac{\Delta F}{F} + \frac{\Delta \rho}{\rho} + \frac{\Delta A}{A} + \frac{\Delta C_D}{C_D} \right) \quad (4)$$

The following maximum percent errors were determined

$$\frac{\Delta F}{F} = 0.5\%$$

$$\frac{\Delta \rho}{\rho} = 0.5\%$$

$$\frac{\Delta A}{A} = 1.0\%$$

$$\frac{\Delta C_D}{C_D} = 4.0\%$$

Substituting these values into equation [4] shows that the maximum overall error of the velocity magnitude is 3 percent of full scale. A similar analysis of the vector direction shows that it is determined within 0.3° of the true value. A significant point here is that only the $\frac{\Delta F}{F}$ term changes at lower range velocities, e.g., at half scale, the inaccuracy of $\frac{\Delta F}{F}$ the current meter would be 3.25 percent of the reading, instead of 6 percent as would normally be expected.

FIELD TESTS

Four drag-sphere current meters were deployed simultaneously in the York River estuary in an investigation of the tidal current regime near Gloucester Point, Virginia. The meters were deployed by mounting them to rigid frames as shown in figure 5. Orientations of the current sensors were established by relating the location and position of the mounting frames to fixed landmarks. The sensors were oriented to detect two horizontal drag force components, from which the flow vector in the horizontal plane was determined at each meter. Because four meters were used simultaneously, the drag-force data were acquired by a portable digital data acquisition system and recorded on computer-compatible magnetic tape. Initial zeroing and force calibrations of each meter in the X and Y directions were made just prior to placing the current meters in the water.

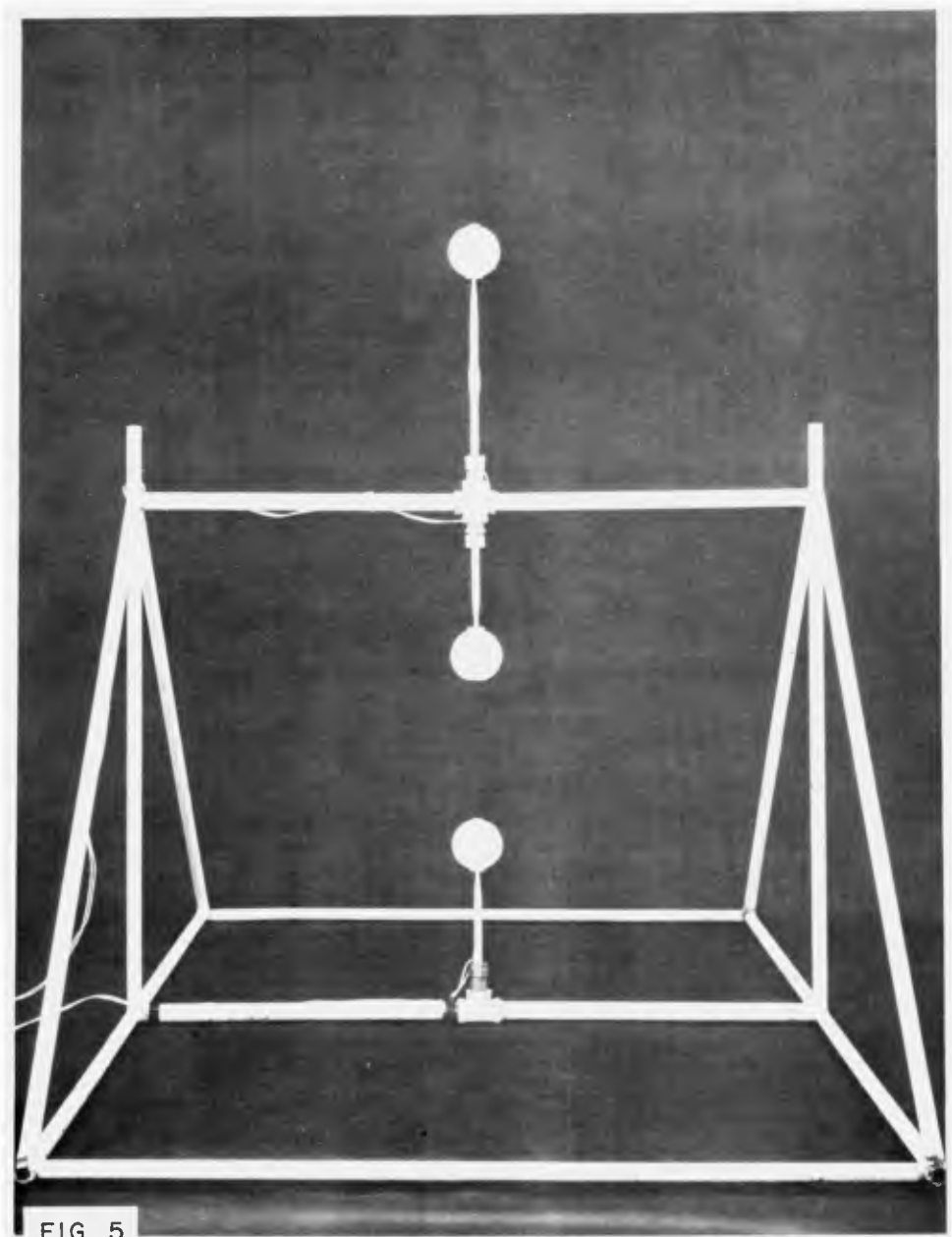


FIG. 5

RIGID FRAME FOR DEPLOYING DRAG-SPHERE CURRENT METERS

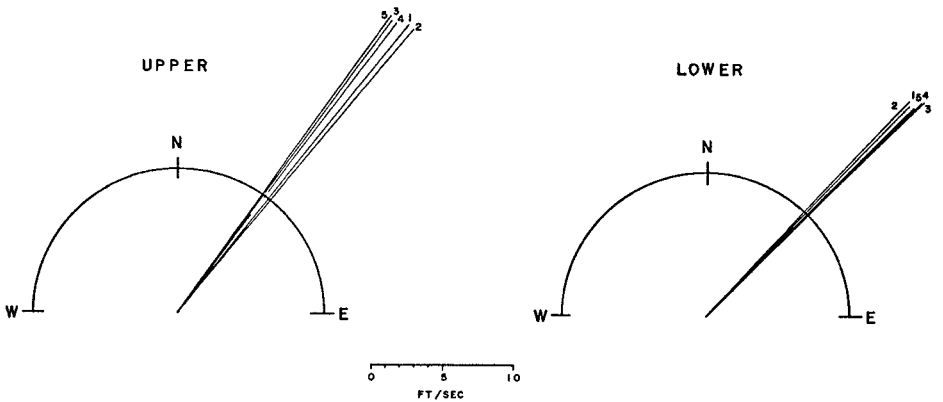
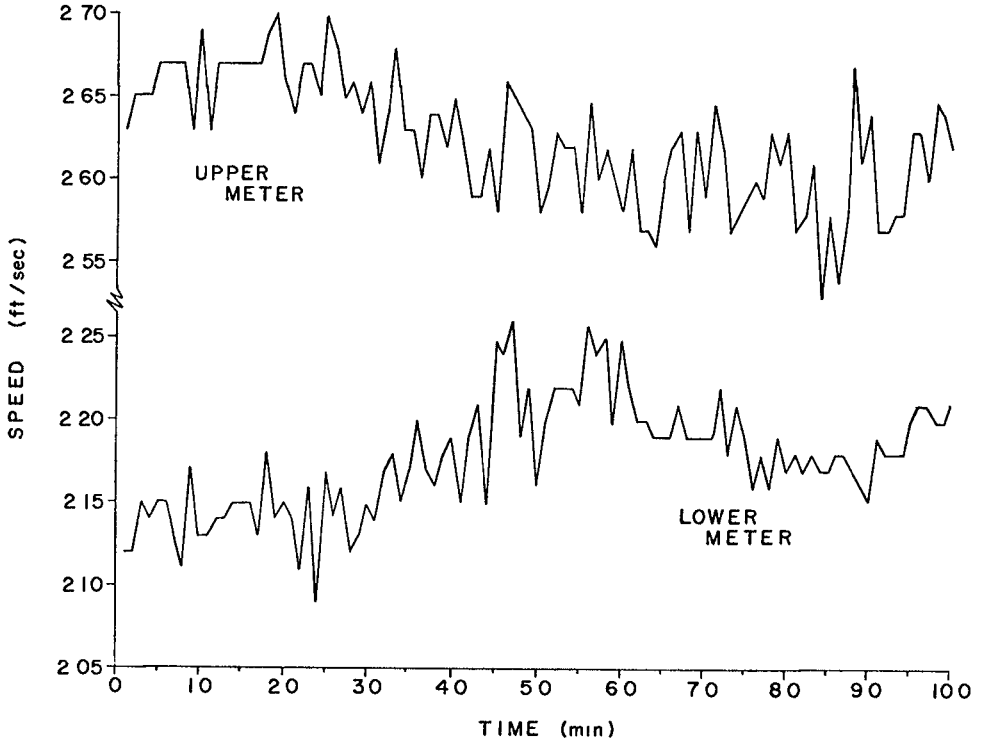


FIG 6 TYPICAL DATA FROM DRAG SPHERE CURRENT METERS VECTORS REPRESENT TWO-MINUTE AVERAGES OF SPEED AND DIRECTIONAL DATA EQUATOR OF UPPER DRAG SPHERE 46 IN ABOVE BOTTOM, LOWER SPHERE 16 IN ABOVE BOTTOM

At the end of one week, the meters were removed from the water, and the force calibrations were checked. Only small discrepancies were noted for three of the meters. The fourth meter had developed an electrical short-circuit within a few hours after deployment and was disconnected for the duration of the test. This short-circuit appeared to result from a breakdown of the bond between the water-proofing compound and the force transducer.

X and Y force-component data were then resolved to flow velocity vectors via a computer program. Analyzed data (fig 6) revealed vertical differences in the flow consistent with expectable velocity profiles, and directions compatible with those of the known tidal-current field. The net drift for various time intervals of interest was easily calculated.

CONCLUDING REMARKS

These evaluations have shown that use of the drag-force water current meters in fluid-process and sediment-response studies is feasible in the 0 to 6 ft/sec range. The net velocity vector at several points in a plane parallel to the sea floor may be obtained with these current meters over periods of a few minutes to several weeks.

Rigid frames are convenient for deploying the current meters, or they can be mounted to a pile or permanent structure.

The meter can be oriented to sense either the horizontal or the vertical flow vector.

If the meters are deployed unattended for extended periods during seasons of significant marine fouling, it will be necessary to impregnate the polyethylene drag spheres with an antifouling compound.

Since drag-force type current meters sense both acceleration-dependent forces and velocity-dependent forces, application of this meter is restricted to basically steady flows.

The drag-sphere velocity meters are simple, relatively inexpensive, and when combined with an appropriate data acquisition system, they are well suited to applications where a large number of simultaneous measurements are needed.

ACKNOWLEDGMENTS

We are indebted to Carl Roberts, IRD, NASA, for assistance in meter development. Thanks are due to the Civil Engineering Department, VPI, for assistance in tow tank tests and to Dr. R. L. Miller, University of Chicago, for use of his calibration gear and wave channel.

REFERENCES

- 1 Inman, D L and Nasu, N 1956 Orbital velocity associated with wave action near the breaker zone Corps of Eng , Beach Erosion Board, Tech Memo No 79 1-43
- 2 Beardsley, G F , Jr , Knollman, G C , Hamamoto, A S and Eisler, J D 1963 A device for measuring orbital velocities in an underwater wave field Rev Sci Insts 34 516-519
- 3 Olson, J R 1967 Flowmeters in shallow-water oceanography Naval Undersea Warfare Center, U S Navy, San Diego, Calif , NUWC TP 5 1-44
- 4 Earl, M D and Beardsley, G F 1969 A three component drag probe for use in wave fields and tidal channels Abstract Vol , Amer Geophy Union, Washington, D C , meeting, p 631
- 5 Reed, Wilmer H , III, and Lynch, J W 1963 A simple fast response anemometer Jour Appl Meteorol 2 412-416
- 6 Hirsch, P 1924 Motion of spheres in still fluids NACA Technical Memo No 257
- 7 Shapiro, Ascher H 1961 Shape and Flow, the Fluid Dynamics of Drag Doubleday and Company, Inc , Fig 13
- 8 O'Brien, M P and Morison, J R 1952 The forces exerted by waves on objects Amer Geophy Union Trans 33 32-38
- 9 Boussinesq, J 1885 Sur la resistance d'une sphere solide Compt rend 100 935
- 10 Basset, A B 1888 On the motion of a sphere in a viscous liquid Phil Trans Roy Soc , London 179 1-43

CHAPTER 116

TRAPPING OF OUTFALL CONSTITUENTS BEHIND SILLS

by T CARSTENS, River and harbour Laboratory,
Technical University of Norway,
Trondheim

and A SJØBERG, Hydraulic Division, Chalmers Institute
of Technology, Gothenburg

ABSTRACT

Communication between such coastal recipients of waste water as bays and fjords and the ocean is often through an outlet of small cross section

The combined effects of a topography with transverse ridges and a brackish surface layer creates a rather stagnant body of water. The ridge or sill deflects the tidal currents away from the bottom so that only the upper part of the water column is continually flushed. The stability of the pycnocline prevents surface-generated turbulence from penetrating downwards, so the turbulence in the deep pool is weak.

A scheme has been proposed to store the nutrients of sewage outfalls behind the sill at Drøbak in the Oslo-fjord. The storage capability of that fjord was estimated for a conservative outfall constituent by means of a one dimensional dispersion equation. From the analysis the gains of deep outfalls through diffusers compared with surface outfalls can be estimated for various periods between deep water inflows, which are observed to occur.

INTRODUCTION

Topographic traps

The effect of a given waste water release on the coastal

environment depends to a large extent on the coastal morphology. Indentations as well as promontories tend to create sheltered water bodies with long residence times in large scale circulations. This tendency is often enhanced by the constricted outlet of many bays and fjords.

A very efficient kind of constriction is the transverse bottom ridges or sills which are characteristic of the coastal inlets carved by glaciers and known as fjords. A longitudinal section of a fjord (Oslofjord) is shown in Fig. 1. Several sills divide the deep fjord into smaller sub-basins of varying size. It is obvious that this type of topography prevents large bodies of water from participating in the normal movements of coastal waters. In fact, only two significant transport processes seem to exist in the deep basins. One, the vertical diffusion, is continuous, while the other is a discrete process of flood-like inflows.

Inflows. Occasional renewal of the water occurs whenever the water density at the sill level exceeds the density of the bottom water inside the sill. The water mass occupying the basin is then forced upward by densimetric displacement, and a complete or partial renewal of the basin water takes place within a relatively short period of time. The inflowing volume depends on the density surplus and its duration and is governed primarily by meteorological variables such as wind and atmospheric pressure (upwelling).

Vertical diffusion. The density surplus responsible for the initial inflow is caused by a salinity surplus and a temperature defect, compared with the overlying layers. Thus a salinity gradient is established for a slow diffusive transport of salt upward, and a temperature gradient for a similar transport of heat.

downwards. with time this diffusion depletes the density surplus of the basin water, and the stage is set for a repeat performance, beginning with a new inflow.

Fig 2 shows observed salinities in the two innermost basins of the Oslofjora during 1962-65, demonstrating the two processes described above, and first by GADE (5).

The pycnocline lid

Even on open coasts pycnoclines develop near river mouths, but the fjoras are particularly prone to stratification, for topographic and climatic reasons. A regular feature of any fjord is therefore a pycnocline which is usually very stable in the summer half of the year.

The pycnocline acts as a lid on the deep pool. Vertical circulation that would go right to the bottom in water of constant density, is replaced by a layered flow. The shear motion in the pycnocline filters out most of the horizontal momentum, so that only very weak flows are set up below the pycnocline.

The effect of the density gradient on the surface-generated turbulence is equally strong. When entraining or eroding water of higher density, some of the turbulent energy is converted into potential energy. In this way the pycnocline acts as a sink of turbulence.

The combined effects of topography and layering thus create bodies of water with a rather special flow regime, characterized by long residence times and a low exchange with the surface layer.

Sewage disposal behind sills

The sheltered deep basins inside the sill at Drøbak (Fig 1) have been proposed for disposal of sewage from Oslo (6,7). The reasoning is that nutrients can be stored in these basins without causing algal blooms, in contrast to the disposal through shallow outfalls presently in use. A high production of algae is undesirable for two reasons, first because it decreases the esthetic and recreational value of the fjord, and secondly because the organic debris exhausts the oxygen supply at the lower depths.

The usefulness of this scheme hinges on the inflows discussed above. A renewal of the deep water must take place before the steady state of maximum storage has been reached, for which the supply through the sewers equals the vertical diffusion of a nutrient

A MODEL FOR CIRCULATION AND DIFFUSION OF DISCHARGED SEWAGEEarlier work

A model for the mixing and the convection in a confined region induced by a source of buoyancy has been advanced by BAINES and TURNER (1) neglecting the effect of turbulence in the environment on the rising plume, they obtained asymptotic solutions of the density distribution valid at large times. The model proposed by CEDERWALL (2) for mixing and convection induced by discharged sewage follows closely that of BAINES and TURNER, but is mostly concerned with the distribution of disposed pollutants

The simplifying assumptions made by CEDERWALL agree well with those first introduced by the authors of this paper (3), however, he neglects the diffusion of constituents through the pycnocline into the surface layer

The present model

A cross section of the fjord is shown in Fig 3. The source of the constituent is the effluent outfall at level $z = 0$, and its strength is $Q_0 c_0$, where Q_0 is the volume flux and c_0 the concentration. Because of its buoyancy, the effluent jet will rise to the level h in the pycnocline where the density of the surrounding fluid equals that of the jet, and the diluted effluent is trapped in a submerged field referred to as the cloud.

Assumptions In order to simplify the analysis we introduce the following assumptions

1. There is no exchange in the deep waters after the complete renewal that we choose as initial condition
2. The density profile is not significantly affected by the induced circulation of sewage
3. The vertical constituent flux is given by

$$-D_z \frac{dc}{dz} A_z \quad (1)$$

where D_z is the diffusion coefficient, dc/dz the concentration gradient and A_z the horizontal area

4. The effluent is trapped just below the halocline and instantaneously spread into a thin layer which will be successively convected and diffused downwards as new sewage reaches the trapping level
5. Any two scalar components are transported by the same mechanism. Thus the concentration distribution of the constituent across the halocline in steady-state condition is just a scaling of the salinity distribution, or

$$\frac{\Delta c}{\Delta z}_{h^+} = \frac{\Delta c}{\Delta s} \left[\frac{ds}{dz} \right]_{h^+} \quad (2)$$

where Δc and Δs are the difference in concentration of the constituent. $z=n$ is the trapping level and h^+ refers to "just above" and accordingly n^- to "just below". The time lag to reach steady-state from initial conditions is of the order of one week and may be neglected (3). The vertical constituent flux upwards to the surface layer is then given by

$$-\left[D_z \frac{1}{\Delta s} \cdot \frac{\delta s}{\delta z} \cdot A_z \right]_h + c(h,t) = Q_v c(h,t) \quad (3)$$

For simplicity the concentration of the constituent in the surface is assumed to be zero

6. The amount of sewage discharged to the fjord during a year is small compared with the fjord water available for dilution.
7. The freshwater runoff is sufficient to maintain a density stratification, but does not induce appreciable upward entrainment (CARSTENS (4))

The dispersion equation

The convection and mixing within the trapped cloud outside the plume is now described by the one dimensional dispersion model

$$\frac{\delta c}{\delta t} - U \frac{\delta c}{\delta z} = \frac{\delta}{\delta z} (D_z \frac{\delta c}{\delta z}) \quad (4)$$

where $U = Q(z)/A(z)$ is the induced convective velocity and $Q(z)$ the plume flow rate at level z . Eq. (4) can be solved numerically together with the continuity equation for the constituent within the cloud

$$\begin{aligned} Q_0 c_0 + \int_0^z c dQ - Q_v c(h,t) + U(z) A_z(z) c(z,t) \\ - D_z \frac{\delta c}{\delta z} A_z = \int_z^h \frac{\delta c}{\delta t} A_z dz \end{aligned} \quad (5)$$

which for $z=h$ has the following form

$$\begin{aligned} Q_0 c_0 + \int_0^z c dQ - Q_v c(h,t) + U(z) A_z(z) c(z,t) \\ - \left[D_z \frac{\delta c(h,t)}{\delta z} A_z \right]_h = 0 \end{aligned} \quad (6)$$

The first term is the source, the second term accounts for the recirculation of the constituent, and the third term is the constituent flux into the surface layer. The fourth and the fifth terms, respectively, represent the convective and the diffusive downward flux.

A straight forward numerical treatment of Eqs. (4) and (6) is not feasible at present. We have not completely solved the problem of supporting convenient mathematical

models with sound physical arguments. We shall, however, use Eqs. (5) and (6) to estimate the time history $c(h,t)$ of the cloud concentration at the trapping level. We feel our solutions for small and for large values of t are acceptable, but we do not yet have a solution for intermediate values of t .

Solution for small t For small t the thickness of the cloud is small compared with the height h . Hence, the recirculation of the constituent may be neglected

$$\int_0^h \alpha c Q \approx 0, \text{ and } U(h) \cdot A_z(h) \approx Q_0 S_0 \quad (7)$$

where S_0 is the dilution at the trapping level. For small t we may also assume the vertical distribution of the constituent concentration above the trapping level to be a mirror image of that below. Thus, the upward diffusive flux equals the downward flux and

$$-\left[D_z \frac{\delta c(z,t)}{\delta z} A_z \right]_{z=h} \cdot c(h,t) = Q_v c(h,t) \quad (8)$$

With these assumptions Eq (6) has the solution

$$\frac{c(n,t)}{c_0} = \frac{Q_0}{(1+\alpha)Q_v + Q_0 S_0} \quad (9)$$

where $\alpha \approx 2$ for small t . As the concentration in the surface layer is assumed to be constant $=0$, α decreases with growing t . Fig. 4 shows Eq. (9) for a particular case in the Oslofjora.

Solution for large t . The effluent cloud is successively convected and diffused downwards. In order to get a rough estimate of the transport velocity we consider only the convection and neglect the diffusion. We then have to find the rate of advance of the first

front. If we take U_0 as the front velocity and z_0 as the front level, it follows from continuity that

$$U_0 = \frac{Q(z_0)}{A_z(z_0)} \quad (10)$$

and the travel time T is given by

$$T = \int_{z_0}^h \frac{dz}{U_0} = \int_{z_0}^h \frac{A_z}{Q} dz \quad (11)$$

For a particular diffusor arrangement ($S_0=50$) in the Oslofjord with $Q_0=10 \text{ m}^3/\text{s}$ and $h=60$, T required for $z_0=0.1 \text{ h}$ may be calculated to about 14 months

For $t > 14$ months most of the deep water has recycled once and the effluent may be assumed to be approximately uniformly mixed into the deep water. In this case of ideal mixing we have

$$c(h,t) = c(z,t) = c(t) \\ \int_0^h \frac{\delta c}{\delta t} A_z dz = \frac{\delta c}{\delta t} \int_0^h A_z dz = \frac{\delta c}{\delta t} V \quad (12)$$

where V is the deep water volume between the levels $z=0$ and $z=h$. We also have $U(0)=0$. With $z=0$ Eq. (5) then takes the form

$$Q_0 c_0 - Q_V c(t) = \frac{\delta c}{\delta t} V \quad (13)$$

which has the solution

$$\frac{c}{c_0} = \frac{Q_0}{Q_V} \left(1 - e^{-\frac{Q_V t}{V}} \right)$$

Fig. 4 shows Eq. (14) for a particular case in the Oslofjord

$$Q_0=10 \text{ m}^3/\text{s}, S_0=50, D_z=3 \cdot 10^{-5} \text{ m}^2/\text{s}$$

$$\frac{1}{\Delta s} \frac{ds}{dz_h} = 0,15/m, A_z(h) = 1,1 \cdot 10^8 m^2,$$

$$V = 4,2 \cdot 10^9 m^3$$

CONCLUSIONS

A transverse ridge or sill on the bottom shelters the water mass below the sill depth from tidal flushing. A pycnocline provides additional sheltering from surface-generated turbulence, and so the body of water behind a sill and below a pycnocline is characterized by long residence times.

The buildup of the concentration of an outfall constituent released in such a stagnant body of water was investigated for the special case of the Oslofjord, based on a set of assumptions leading to a general one-dimensional dispersion equation.

Solutions were obtained for small and large periods of constituent release, respectively. The solution for small t assumes a rapid horizontal spread compared with the vertical transport. The solution for large t assumes ideal mixing. A tentative "probable curve" has been inserted for intermediate times.

From the analysis the gains of deep outfalls through diffusers compared with surface outfalls can be estimated for various periods between deepwater inflows.

REFERENCES

1. BAINES, W.D. and TURNER, J.S. Turbulent buoyant Convection from a Source in a Confined Region. - J. Fluid Mech. Vol. 37 Part 1, 1969
2. CEDERWALL, K. The Oslo Fjord - A Model for Circulation and Diffusion of Discharged Sewage. - Technical Memorandum 70-1. W.M. Keck Laboratory of Hydraulics and Water Resources, Cal. Inst. of Techn. 1970.
3. CARSTENS, T. and SJØBERG, A. Oslofjorden II An evaluation of sewage outfalls inside Drøbak. - NIVA, Oslo 1969. (In Norwegian).
4. CARSTENS, T. Turbulent diffusion and entrainment in two-layer flow - ASCE VW1, 77-104, Feb 1970.
5. GADE, H. Oslofjordens hydrografi. Delrapport nr. 2. - NIVA, Oslo 1967. (In Norwegian).
6. The Oslofjord and its pollution problems Samle-rapport I. NIVA, Oslo, 1968. (In Norwegian).
7. The Oslofjord and its pollution problems Samle-rapport II. NIVA, Oslo, 1970. (In Norwegian).

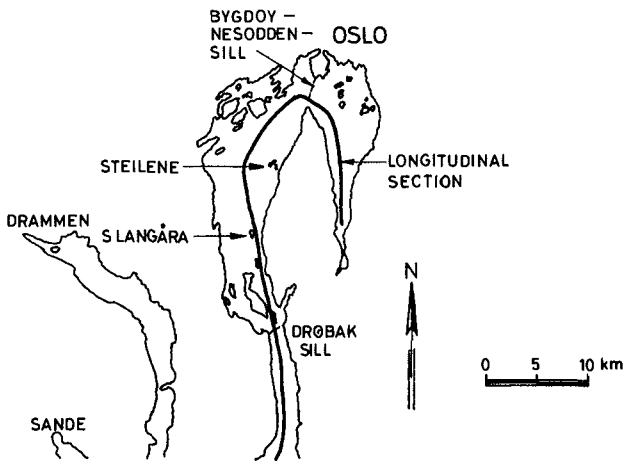
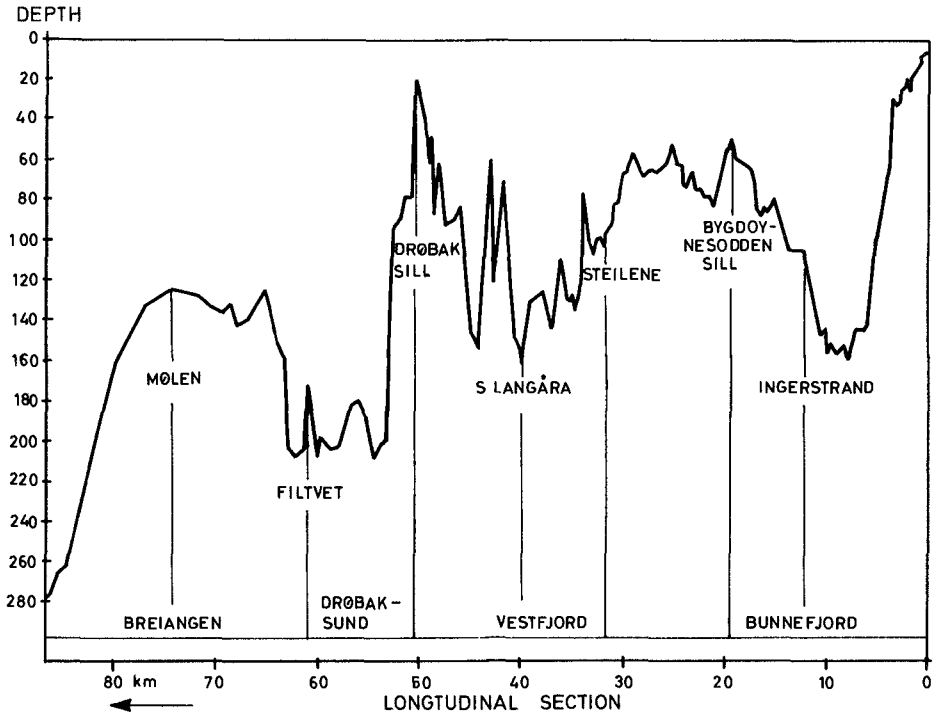


FIG 1 THE OSLOFJORD, PLAN AND SECTION

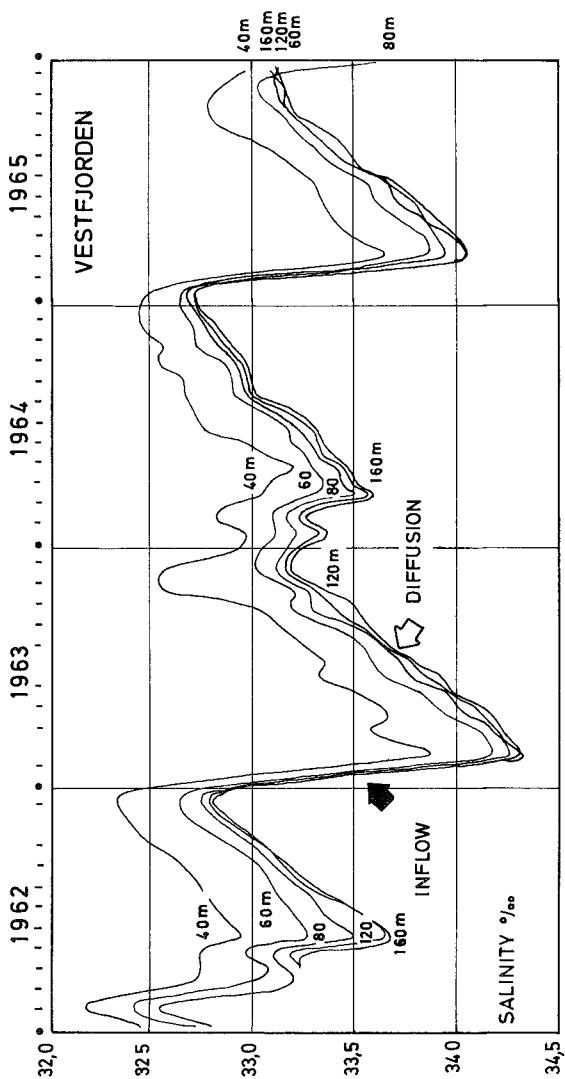


FIG 2 OBSERVED ISOHALINES , OSLOFJORD

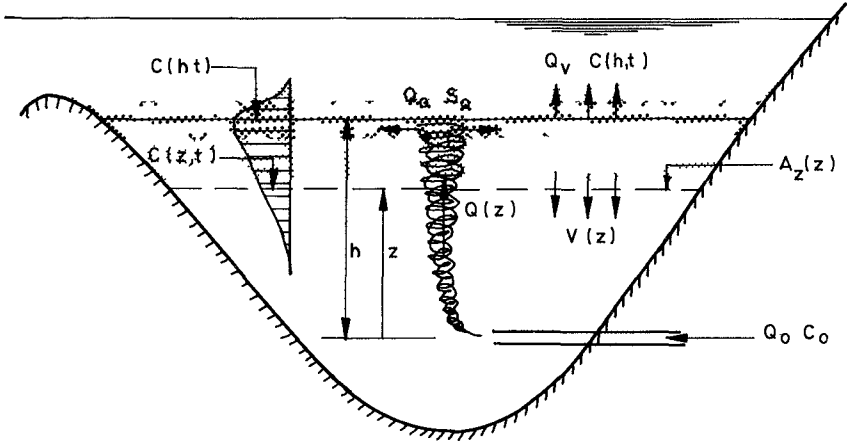


FIG 3 SCHEMATIC OF A SECTION THROUGH THE FJORD

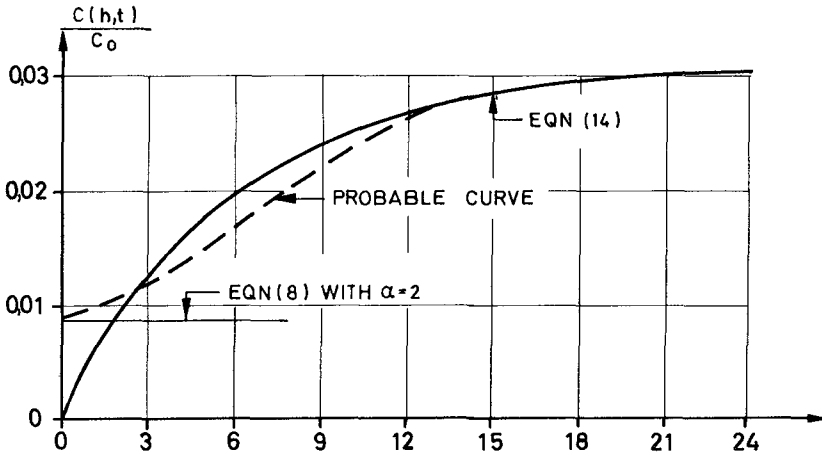


FIG 4 TIME HISTORY OF CLOUD CONCENTRATION AT TRAPPING LEVEL (OSLOFJORD)

CHAPTER 117

SUSPENDED LOAD CALCULATIONS IN A TIDAL ESTUARY

By BRIAN A O'CONNOR

Lecturer, Department of Civil Engineering,
University of Manchester, Manchester, England

ABSTRACT

The present work describes the derivation of equations which can represent the vertical distribution of sediment in a well mixed tidal estuary. The starting point for the analysis is the two dimensional longitudinal equation of motion, including the longitudinal salinity gradient term. Equations are given which represent a steady state sediment profile and it is shown that these are similar to the expression used in uni-directional flow e.g. Rouse's equation.

It is argued that the derived equations could be applied to a real estuary, subject to certain restrictions on sediment size and estuary type.

An application of the theoretical equations to the Mersey Estuary indicates reasonable agreement between observed and predicted sediment quantities for medium and coarse sand particles. Agreement is shown to be worst for fine grained sediments and it is concluded that much better results can be obtained by using the non-steady one dimensional sediment distribution equation in discrete steps throughout the tidal cycle.

INTRODUCTION

The calculation of the distribution of sediment in a real estuary is an exceedingly difficult task. All the problems of uni-directional flow are present together with the added complications of unsteady flow, varying bed resistance and salt/freshwater density currents.

The present paper endeavours to show how the distribution of certain sediment may be estimated in a particular type of well mixed estuary. It is not

intended to be the panacea for tidal sediment problems, but represents a comparatively simple engineering solution to certain tidal sediment distributions

METHOD

In uni-directional flow problems, the distribution of sediment is specified by assuming that a steady state is reached between sediment eroded from the river bed and sediment depositing on the river bed. Clearly, if no sediment is present in the water and erosion is started then a finite time is required for a steady state to be reached. The time will be dependent upon particle size, water depth, turbulence level and initial sediment distribution and will thus be expected to be small for large sized particles, whose equilibrium profile is close to the river bed and large for fine sediment, whose equilibrium is more uniformly distributed throughout the water depth. A first look at the sediment distribution in a tidal environment would thus be to assume that the sediment particles reached the steady state distribution in a short time, during which the tidal flow characteristics were unaltered i.e. the tide is considered to be a succession of uni-directional flows. The sediment distribution for the large sized particles would thus be given by the steady state profile appropriate for each elemental uni-directional flow.

The effects of the salt/freshwater density profile and the inertia of the flow system must also be incorporated into the problem. This can be done by assuming the tidal flow is frozen at each instant of time and then using the resultant shear stress distribution to predict the distribution of sediment.

ANALYSIS

The flow of water in a tidal estuary is governed in two-dimensions by the equation¹

$$A + F + 2D(1-n) - \frac{1}{\rho g H} \frac{\partial \tau}{\partial n} = I \quad (1)$$

where $A = \frac{1}{g} \frac{\partial U}{\partial t}$, U = horizontal water velocity in the horizontal direction (x),

t = time, g = acceleration due to gravity, $F = \frac{\partial}{\partial x} \left(\frac{U^2}{2g} \right)$, $D = \frac{H}{2\rho} \frac{\partial \rho}{\partial x}$, ρ = water density, $\eta = \frac{y}{H}$, y = elevation above the bed, H = water depth, τ = horizontal shear stress, I = water surface slope (positive in the ebb direction)

Equation (1) also assumes that the term $\frac{U^2}{gH}$ is small and the vertical velocity term is small

The shear stress distribution with depth is obtained from equation (1) by integration w r t η , after first specifying the distributions of A and F with depth It has been shown¹ that simple linear distributors for A and F are not vastly different than logarithmic or parabolic distributions Thus the variation of A and F are taken as

$$A = A_b + (A_s - A_b) \tag{2}$$

$$F = F_b + (F_s - F_b) \tag{3}$$

where b and s refer to bed and surface values respectively Equation (2) and (3) uses known or estimated values of A and F at small distances above the estuary bed and below the estuary surface

Inserting equations (2) and (3) in equation (1) and integrating w r t η gives the expression for the shear stress distribution with depth as

$$\frac{\tau}{\rho g H} = I' (1-\eta) - B(1-\eta)^2 - D(1-\eta)^2 \tag{4}$$

$$\frac{\tau}{\rho g H} = S' - 2P' \eta - D' \eta^2 \tag{5}$$

where $I' = I - A_b - F_b$, $B = \frac{1}{2}(\Delta A + \Delta F)$, $\Delta A = A_s - A_b$, $\Delta F = F_s - F_b$, $S' = I' - B - D$, $P' = \frac{1}{2}(S' - D')$, $D' = D - B$

The solution of equation (4) requires the knowledge of six prototype quantities at each instant of time However, equation (5) is a function of only the two quantities S' and D' These quantities can be determined by considering the velocity distribution with depth, as follows

The shear stress (τ) is first related to the velocity gradient by Prandtl's mixing length concept i e

$$\tau = \rho \mathcal{L}^2 \left| \frac{du}{dy} \right| \left| \frac{du}{dy} \right| \quad (6)$$

where \mathcal{L} = a mixing length, $||$ = absolute value

A suitable mixing length distribution to use in equation (6) is that found by Agnew² in the Haringvliet (Holland) i e

$$\mathcal{L} = Ky \left[\frac{1-\eta}{1-\delta} \right]^2 \quad \text{for the region } 1 > \eta > \delta \quad (7)$$

$$\text{and } \mathcal{L} = Ky \quad \text{for the region } \delta > \eta > 0 \quad (8)$$

where K = Von Karmans Constant, $\delta = \frac{h}{H}$, h = height of position of zero nett motion of the residual salinity circulation

Equation (5), (6), (7), and (8) thus lead to the following expressions for the variation of velocity (U) with depth (η)

$$\frac{K(U-U_g)}{\sqrt{gH}} = \sqrt{1-\delta} \int_{\delta}^{\eta} \frac{(1S' + D' \eta I)^{\frac{1}{2}}}{\eta} d\eta \quad \text{for } 1 > \eta > \delta \quad (9)$$

$$\frac{KU}{\sqrt{gH}} = \int_{\eta_0}^{\eta} \frac{(1S' - 2P' \eta - D' \eta^2 J)}{\eta} d\eta \quad \text{for } \delta > \eta > \eta_0 \quad (10)$$

where $\eta_0 = y_0/H$, y_0 = height at which $U = 0$

The solutions to equations (9) and (10) depend on the magnitude and sign of the terms S' and D' . If the sign convention, ebb slopes are positive is used¹, then S' is a maximum (+ve) about mid-ebb and mid-flood (-ve)¹ while D' is negative near high water, and greater than S' , and positive at low water and greater than S' . The latter is to be expected as the flow reverses at the bed first at low water due to the density circulation. Values of S' and D' can be found by fitting the prototype velocity observations to equations (9) and (10) viz table 3

The sediment distribution may now be found from the general sediment

diffusion equation in two dimensions

$$\frac{\partial C}{\partial t} = \frac{\partial}{\partial x} (\epsilon_x \frac{\partial C}{\partial x} - UC) + \frac{\partial}{\partial y} (\epsilon_y \frac{\partial C}{\partial y} + \omega C) \quad (11)$$

where ϵ_x, ϵ_y are diffusion equations in the x, y directions $\omega =$ particle fall velocity

If attention is confined to a particular type of estuary in which the variation of U with distance (x) is small and the sediment is equally distributed along the estuary then $\partial C/\partial x = 0$ and equations (11) will reduce to

$$\frac{\partial C}{\partial t} = \frac{\partial}{\partial y} (\epsilon_y \frac{\partial C}{\partial y} + \omega C) \quad (12)$$

An analytical solution of equation (12) is unknown for $\epsilon_y = f(y,t)$ Finite Difference methods can be used and are being studied at present. However, if only large particles are considered then a steady state profile will be quickly reached and a mathematical expression for the distribution of the sediment can be obtained from equation (12) with $\partial C/\partial t = 0$ i.e.

$$\ln\left(\frac{C}{C_a}\right) = -\omega \int_a^y \frac{dy}{\epsilon_y} \quad (13)$$

where $C_a =$ a reference concentration at level "a" above the bed. The distribution curve specified by equation (13), could also be used to describe the distribution of medium to fine sand particles by replacing C_a with an observed prototype concentration value (C_t). Clearly, $C_t < C_a$ and the concentration given by the modified equation (13) will be greater than in prototype, the error being greatest for the finest sized sediments.

The steady state solution is obtained from equation (13) by integration on specifying the variation of ϵ_y with depth. This is done by relating ϵ_y to the momentum transfer coefficient ϵ_m i.e.

$$\epsilon_y = \beta \epsilon_m \quad (14)$$

and ϵ_m is obtained from the equation

$$\tau = \rho \epsilon_m \frac{\partial u}{\partial y} \quad (15)$$

$$\text{i.e. } \epsilon_m = \tau^2 \left| \frac{\partial u}{\partial y} \right| \quad (16)$$

$$\text{Thus } \epsilon_y = \beta l \sqrt{\frac{\tau}{\rho}} \quad (17)$$

$$\text{i.e. } \epsilon_y = \beta K y \left[gH \left| S' - 2P'_{\eta} - D'_{\eta} \right|^2 \right]^{\frac{1}{2}} \text{ for } 0 < \eta < \delta \quad (18)$$

$$\epsilon_y = \beta K y \frac{(1-\eta)}{(1-\delta)^{\frac{1}{2}}} \left[gH \left| S' + D'_{\eta} \right|^2 \right]^{\frac{1}{2}} \text{ for } \delta < \eta < 1 \quad (19)$$

The variation of ϵ_y with depth as given by equations (18) and (19) is shown in Figure 1 for mean tide level ($S' \gg D'$) and near low water ($S' = D'$ and $S' = 0$) conditions, together with field data (average tidal cycle values) taken by Bowden³ and Sharaf⁴ in the Narrows Area of the Mersey Estuary, England

Bowden's data is seen from Figure 1 to indicate smaller values in the upper half of the vertical profile and indeed it was found that the velocity equations (9) and (10) gave better answers over the low water period if the following expressions were used for ϵ_y i.e.

$$\epsilon_y = 2\beta Kh(1-\eta)^{3/2} \left[gH \left| S' + D'_{\eta} \right| \right]^{\frac{1}{2}} \quad (20)$$

$$\epsilon_y = 2\sqrt{2}\beta Kh(1-\eta)^2 \left[gH \left| S' + D'_{\eta} \right| \right]^{\frac{1}{2}} \quad (21)$$

for the region $\delta < \eta < 1$

Equations (20) and (21) are also shown in Figure 1 and give a better fit to Bowden's data

The solution of equation (13) is thus dependent upon the sign and magnitude of S' and D' , as were equations (9) and (10). The various solutions to equation (13) have been presented elsewhere⁵. The solutions for the case $|S'| > |D'| > 0$, which apply for the majority of the tidal cycle are given below i.e.

$$\frac{C}{C_a} = \left[\frac{(1/n - \alpha_0) + \left[(1/n - \alpha_0)^2 - (1 - \alpha_0)^2 \right]^{\frac{1}{2}}}{(1/n_a - \alpha_0) + \left[(1/n_a - \alpha_0)^2 - (1 - \alpha_0)^2 \right]^{\frac{1}{2}}} \right]^Z \text{ for } n_a < n < \delta \quad \dots (22)$$

where $Z = \frac{\omega}{\beta K U_*}$ and $U_*^Z = \tau_b / \rho$ where $\tau_b = \rho g H S^i$

$$\frac{C}{C_\delta} = \left[\frac{(1 + \sqrt{1+n(1-2\alpha_0)}) \times (1 - \sqrt{1+\delta(1-2\alpha_0)})}{(1 - \sqrt{1+n(1-2\alpha_0)}) \times (1 + \sqrt{1+\delta(1-2\alpha_0)})} \right]^{Z(1-\delta)^{\frac{1}{2}}} \times \left[\frac{(\sqrt{2(1-\alpha_0)} - \sqrt{1+n(1-2\alpha_0)}) \times (\sqrt{2(1-\alpha_0)} + \sqrt{1+\delta(1-2\alpha_0)})}{(\sqrt{2(1-\alpha_0)} + \sqrt{1+n(1-2\alpha_0)}) \times (\sqrt{2(1-\alpha_0)} - \sqrt{1+\delta(1-2\alpha_0)})} \right]^{\frac{Z(1-\delta)^{\frac{1}{2}}}{\sqrt{2(1-\alpha_0)}^i}} \text{ for } \delta < n < 1 \quad (23)$$

where $\alpha_0 = \frac{P^i}{S} = \frac{1}{2}(1 - D^i/S^i)$, C_δ = concentration at height δ

Equation (23) is seen to be indeterminate for the case $\alpha_0 = \frac{1}{2}$ i.e. $D^i = 0$. If this condition is substituted in equation (18), (19) and (13), the expression for the variation of concentration with depth is

$$\frac{C}{C_a} = \left[\frac{(1 + \sqrt{1-n}) \times (1 - \sqrt{1-n_a})}{(1 - \sqrt{1-n}) \times (1 + \sqrt{1-n_a})} \right]^Z \text{ for } n_a < n < \delta \quad (24)$$

and

$$\frac{C}{C_\delta} = \left[\frac{1-n}{n} \times \frac{\delta}{1-\delta} \right]^{Z(1-\delta)^{\frac{1}{2}}} \text{ for } \delta < n < 1 \quad (25)$$

Equation (24) is the same as that derived by Tanaka and Sugimoto⁶ for uni-directional flow i.e. $D = 0$, $A = F = 0$ and $S^i = I$. Thus equations (22) and (23) are also similar to the expressions for uni-directional flow, except that the density circulation and inertia and kinetic terms are included. It should be noted that equation (22) reduces to Rouse's equation⁷ for uni-directional flow for $\alpha_0 = 1/2$. However, equations (21-23) predict a greater quantity of sediment in suspension than found by Rouse's equation. This is shown in Fig. 2. It will be noticed that both Rouse's equation and that of Tanaka and Sugimoto give values

almost identical to that of equation (22) below $\alpha_0 = 0.50$. However, the different mixing length distribution contained in equation (19) leads to smaller sediment values in the upper half of the water flow at $\alpha_0 = 1.0$ and 0.50 respectively.

Application of theory to field data

The theory was applied to the Mersey Estuary in order to predict the quantity of sediment in suspension at position H (Figure 3). The latter satisfies the requirements, on the flood tide, of complete sediment cover and little velocity variation with distance. Prototype sediment data was also available at position H in sufficient detail to be usable. The sediment data available is shown in Figure 4.

In order to apply the theory, values of C_a or C_t , α_0 , S' or $U_* \omega$, β and K must be available or capable of being calculated from the field data. The determination of these quantities is now considered in detail below.

(1) Determination of U_* values

This could be calculated from equation (5), with $n=0$, provided sufficient velocity and tide gauge data was available. A lack of data prohibits the use of this method. An alternative method is to use semi-log plots of the horizontal water velocity and equate the slope of the graph to U_*/K , where $K = 0.40$. This is likely to over-estimate U_* on the ebb tide and under-estimate it on the flood tide. A further method is to take $U_* = K\bar{U}^1$ where \bar{U} is the depth mean velocity and K has the value 5.2×10^{-2} . The method used eventually was to make semi-log plots of velocity and adjust the answer if necessary by the third method. The results are shown in Table 2.

Table 2 Calculated U_* values from Prototype Velocity Data - 25th Nov 1965

	Mersey Estuary Position H					
Time (GMT)	0801	0845	0924	1003	1044	1115
U_* (fps)	0.099	0.288	0.344	0.342	0.261	0.209

(2) Choice of β

Flume tests by Vanoni⁸, Laursen⁹ and River observations by Anderson¹⁰ indicate values of β between 0.63 - 4.10. Einstein¹¹ uses a value of $\beta = 1.0$ if the momentum (ϵ_m) and sediment (ϵ_s) transfer coefficients are equal. In a tidal estuary, it is to be expected that $\beta < 1.0$ due to the salinity circulation. It is also probable that the value of U_* to be used in the suspension exponent (Z) will also be reduced (to U_*') due to the presence of sand waves on the estuary bed. The product $\beta U_*'$ will thus be expected to be less than U_* .

In view of the lack of theory from which to estimate U_*' , the quantity ($\beta U_*'/U_*$) was determined from two simultaneous sand samples taken at a station in the Irish Sea. The samples were taken at maximum velocities from mid-depth and approximately 1ft above the bottom. The value of ($\beta U_*'/U_*$) for sand sizes between 63μ - 355μ was found to be 0.62. This implies a value of $\beta = 0.62$ for no reduction in U_* . In the present work a value of ($\beta U_*'/U_*$) of 0.658 has been used.

It is interesting to note that Tofaletti's work¹⁵ indicates a value of U_*' of 0.21 fps, which implies a β value of 1.065 for a U_* value of 0.34. Englund's work¹⁶, however, would suggest that in deep water (68ft) the reduction in shear due to sand waves is small (<2%), this implies a value of β closer to 0.658.

The value of $Z = \omega/\beta KU_*'$ is thus known at all points during the tidal cycle, ω was taken from standard tables¹² while a value of $K = 0.40$ was used since the concentration values are relatively low.

(3) Determination of α_0 values

The circulation of α_0 requires a knowledge of both S' and D' . These could be determined if all the terms in equation (5) are known. There are, however, no adequate tide gauge readings to the North of position H. α_0 values are thus computed for position C (Figure 4) and used for the calculation at position H. Velocity observations from positions H, C and N were used, together with the tide gauge information from Princes Pier and Gladstone Lock¹ to determine approximate

values of S' and D' . The velocity expressions (9) and (10) were then used to give a better estimate of S' and D' . The values found at C are shown in Table 3 in terms of the density term (D) $D = 3.86 \times 10^{-6}$

Table 3

S' and D' values calculated for Position C Mersey Estuary
for a Spring Tide (28ft H W above Liverpool Datum)

TIME Rel to H W Princes Pier	0	-½	-1	-2	-2½	-3½	-4	-5	-5.3
S'	-3.39	-7.58	-13.51	-18.88	-17.86	-10.0	-5.0	-0.885	-0.22
D'	-2.4	-1.78	1.4	0.5	0.38	6.15	5.27	1.77	1.73
α_0	0.146	0.383	0.552	0.513	0.511	0.808	1.027	1.50	4.43

The α_0 values for position H were found by super-imposing the time scale for the prototype observations (25th November 1965) on the values shown in Table 3 and simplifying the results - viz table 5

(4) Determination of sediment concentrations

The control concentration (C_t) was determined from the prototype data. Sediment samples were taken over successive half hourly periods from a fixed distance of 18 inches above the estuary bed using a pump sampler. The half hourly sampling trial was necessary in order to obtain sufficient sand for analysis.

The samples were washed, dried and weighed in the laboratory and the concentration determined. A grain size analysis was performed for each sample using a sedimentation tube¹³, where sufficient sediment existed, and sieves where the sample size was small. The results are shown in Table 4.

Table 4

Mean concentration (ppm) of sand at 18" above the estuary bed
at Position H Mersey Estuary 25th November 1965

Sample	Mean Sample Time (GMT)	Mean Grain Size (μ)							Water Depth (ft)
		76	106	138	165	195	227	298	
-	0810	0	0	0	0	0	0	0	
A	0825	1 76	3 29	2 17	1 13	1 03	0 04	0 05	60
B	0856	6 20	16 3	9 4	8 36	5 4	4 08	0 71	65
O	0925	9 9	24 6	30 1	33 8	20 6	15 1	2 46	68
E	0955	3 98	16 4	21 5	17 3	36 3	18 8	1 88	72
G	1022	7 87	12 57	20 19	26 04	40 39	17 15	0 38	73
I	1050	2 55	9 5	9 5	10 25	14 3	4 44	0 26	75
J	1120	2 2	7 7	9 3	10 4	13 9	14 5	0	76
K	1148	1 26	2 06	2 4	1 75	0 89	0 34	0	77
-	1200	0	0	0	0	0	0	0	

The usefulness of the preceding theory is checked by computing the quantity of sand that should have been caught in a suspended Oelft Bottle. This was kept at approximately 10ft below the water surface during the period 0830-0930 (Sample C) and 0934 - 1030 (Sample F) HRS GMT.

In order to use the theoretical distribution curves, the C_t values should be instantaneous values. A correction procedure was thus adopted to allow for the finite sampling time.

The method consisted of first calculating the quantity of sediment that would be collected over each sampling period, assuming that the variation of C_t with time was proportional to $(U_*^2/U_{*c}^2 - 1)$, where U_{*c} is the value of U_* at threshold conditions. The calculated quantity was then compared with the quantity that would be collected if conditions operating at the mean sampling time had prevailed over the full sampling period. Clearly, the ratio of these two terms

should be unity for small time intervals or for little variation of C_t with time. Only those samples collected near maximum velocities showed ratios of about unity, all others indicated greater values.

The correction procedure thus made the above ratio equal to unity by finding an equivalent mean time, which was a function of grain size, during the sampling interval. The observed concentrations were then accredited to this equivalent mean time. The concentration at the actual sample mean time was then obtained by interpolation between the equivalent mean times of all the samples.

The position of the Oelft Bottle varied between 5-25% of the depth during the two sampling periods (C and F). The concentration at 25% and 5% was determined using the appropriate formula (equations 22-25). The correction procedure was then used and the concentration at the Oelft Bottle level found by interpolation. The corrected concentration values are shown in Table 5.

The quantity of sediment collected in the Oelft Bottle was then determined by summing up the product of the theoretical concentration values and the observed water velocity at the Oelft Bottle level. The latter quantity was found by mounting an Ott Mark V Arkansas current meter on the Oelft Bottle framework.

Table 5
Estimated Theoretical Concentration at Oelft Bottle Level

<u>Time (GMT)</u>		<u>Mean Grain Size (μ)</u>						<u>% Level</u>	
HRS		76	106	138	165	195	227	298	
$\alpha_o=0.70$	0825	0.293	0.27	0.017	0	0	0	0	25
		0	0	0	0	0	0	0	5
		0.173	0.117	0.01	0	0	0	0	16.7*
$\alpha_o=0.60$	0856	2.05	3.2	0.64	0.20	0.025	0.015	0	25
		1.24	1.45	0.20	0.036	0.004	0	0	5
		1.66	2.36	0.43	0.1215	0.015	0.0078	0	15.4*
$\alpha_o=0.50$	0925	3.96	6.22	3.5	1.9	0.589	0.216	0	25
		2.89	3.93	1.69	0.712	0.175	0.051	0	5
		3.29	4.79	2.37	1.157	0.33	0.113	0	12.5*
$\alpha_o=0.50$	0955	1.61	4.21	2.56	0.99	1.04	0.28	0	25
		1.14	2.67	1.25	0.38	0.33	0.07	0	5
		1.184	2.81	1.37	0.436	0.396	0.0894	0	6.95*
$\alpha_o=0.50$	1022	2.79	2.617	1.716	0.97	0.684	0.133	0	25
		1.985	1.559	0.7664	0.3264	0.1757	0.027	0	5
		2.06	1.657	0.8544	0.3859	0.2221	0.037	0	6.85*
$\alpha_o=0.50$	1050	0.70	1.344	0.447	0.1755	0.092	0.0121	0	25
		0.46	0.7024	0.1635	0.0464	0.0175	0	0	5
		0.526	0.9044	0.2525	0.087	0.0411	0.0038	0	11.3*

*Oelft Bottle Level

The results of the calculation for sampling periods C and F are shown in Table 6. This also includes an estimated quantity which is the measured prototype values, corrected¹⁴ for sediment loss due to high water velocities within the Delft Bottle.

Table 6
Comparison of Theoretical and Observed Sediment Quantities

Sample	Grain size (μ)	75	106	138	165	195	227	298
C	Theory (gms)	4.06	5.89	2.11	0.925	0.261	0.094	0
	Measured (gms)	1.61	3.74	2.18	2.18	1.30	0.40	0.09
	Estimated (gms)	2.48	5.20	2.84	2.70	1.56	0.465	0.095
	Theory (gms)	4.03	6.0	2.96	1.15	0.72	0.164	0
F	Measured (gms)	0.72	1.26	0.86	0.63	0.40	0.116	0.012
	Estimated (gms)	2.04	2.56	1.44	0.97	0.59	0.16	0.015

Comments

It would appear, from Table 6, that the theory predicts the sediment quantities reasonably well for grain sizes in excess of 138μ , but less well for sizes below this value. It is particularly noticeable that the 75μ sand is predicted to be approximately double the observed value in both cases. The lack of agreement of the theory for small sized sediment is undoubtedly due to the longer time required for the fine sediments to reach an equilibrium profile as compared with the larger sized sediments, e.g. the majority of the steady state profile for 195μ particles is much closer to the estuary than that of the 75μ particles.

A better method of prediction, particularly for the fine sand size would be to solve equation (12) and use this solution in discrete time steps to determine the concentrations throughout the tidal cycle. Preliminary work on this method indicates that the difference between the non-steady state distribution and the steady state distribution is the order of 10% for 165μ particles at a level of 10% above the estuary bed. This increases to approximately 35% at the same level.

for 75μ particles. If the method is applied to the 75μ particles and adjusted for the observed sediment concentrations, then values of 1.9 gms and 3.4 gms are obtained for samples C and F respectively. These quantities are much closer to the observed values than the steady state solution.

A further improvement, which is being developed at present, is to allow for variations in sediment concentration with distance and for diffusion in the longitudinal direction.

All three methods mentioned above are still dependent upon the values of β and U_* which were used in the present theory to determine the suspension exponent Z . Clearly, the shape of the distribution curve assumes less significance in view of the uncertainty of β , U_* and to a lesser extent ω and K . The present results do, however, suggest that in the Mersey Estuary reasonable quantitative results can be obtained by using standard values of ω and K , together with U_* values calculated from the velocity data¹ and a β value of 0.66.

Conclusions

The present work leads to expressions for the vertical distribution of sediment which are similar to those of uni-directional flow. The derived equations indicate the vertical distribution of sediment in a real estuary subject to restrictions on grain size and estuary type. Preliminary work also indicates that the prediction of fine sediment concentrations is better represented by using the non-steady state equation in discrete steps throughout the tidal cycle.

NOTATION

a	a distance above the estuary bed
A	inertia term
B	$= \frac{1}{2} (\Delta A + \Delta F)$, a composite slope term
C	concentration
D	density slope
D'	effective density slope = D - B
F	kinetic energy term
H	water depth
h	height of zero nett motion
I	water surface slope (positive when sloping downwards from land to sea)
I'	the slope term $I - A'_b - F'_b$
K	Von Karmans Constant (=0.40)
λ	a mixing length
P'	the slope term $\frac{1}{2}(S' - D')$
S'	an effective energy slope = $I' - B - D$
t	time
u	velocity in the x direction
u_*	$(\tau_b/\rho)^{\frac{1}{2}}$ = shear velocity
x	distance measured along the estuary, seawards
y	distance vertically above the bed
Z	suspension exponent = $\omega/\beta KU_*$
α_0	ratio P'/S'
β	Ratio of eddy diffusivities for sediment and momentum (ϵ_s/ϵ_m)
δ	$\frac{1}{2} h/H$
ΔA	$= A_s - A_b$
ΔF	$= F_s - F_b$
ϵ	an eddy diffusivity coefficient
η	$= y/H$

- ρ = density
 τ = shear stress
 ω = sediment fall velocity

Subscripts

- a referring to level a and $t = \infty$
b bed and near bed
S near surface
t referring to time t
y level y
o level at which $U = 0$

REFERENCES

- 1 A R Halliwell and B A O'Connor "Shear Velocity in a Tidal Estuary" Proc 11th Conference on Coastal Engineering Chapter 88 pp 1377 - 1396 September 1968
- 2 R Agnew "Estuarine Currents and Tidal Streams" Proc 8th Conf on Coastal Engineering September 1960 Chapter 28 pp 510-535
- 3 K F Bowden "The Mixing Processes in a Tidal Estuary" Int J Air and Water Pollution Vol 7 p 343-356, 1963
- 4 K F Bowden and S H Sharaf El Din "Circulation, Salinity and River Discharge in the Mersey Estuary" Geophysics J 1965 Vol 10
- 5 B A O'Connor "Sediment Movement in a Tidal Estuary" Ph D Thesis Liverpool University April 1969
- 6 S Tanaka and S Sugimoto On the Distribution of Suspended Sediment in Experimental Flume Flow No 5 Memoirs of Faculty of Engineering Kyoto Japan 1958
- 7 H Rouse Experiments on the Mechanics of Sediment Suspension Proc 5th International Cong for App Mechanics Vol 55 N Y 1938
- 8 V A Vanoni "Transportation of Suspended Sediment by Water" Trans ASCE Vol 111 1946 pp 67-133
- 9 E M Laursen "The Total Sediment Load of Streams" Journal Hyd Div Proc ASCE Vol 84 No HY1 Feb 1958
- 10 A G Anderson "Distribution of Sediment in a Natural Stream" Trans A G U pt II 1942 pp 678-683
- 11 H A Einstein "The Bed Load Function for Sediment Transportation in Open Channel Flows" United States Department of Agriculture Tech Bull No 1026 September 1950
- 12 W W Rubey "Settling Velocities of Gravel, Sand and Silt Amer J Soc No 25 1933 p 325-338
- 13 P Sly Marine Geological Studies in the Eastern Irish Sea and Adjacent Estuaries with Special Reference to Sedimentation in Liverpool Bay and River Mersey Ph D thesis Liverpool University 1966
- 14 Delft Bottle- Directions for use - Delft Hydraulics Laboratory Pub No 8 November 1963
- 15 F B Toffaletti Computation of Sand Loads and its Vertical Distribution Nat Meeting on Wat Res Eng New York 1967
- 16 F Engelund - Hydraulic Resistance of Alluvial Streams Journal Hyd Div Proc ASCE Vol 92 No NY2 March 1966 pp 315-328

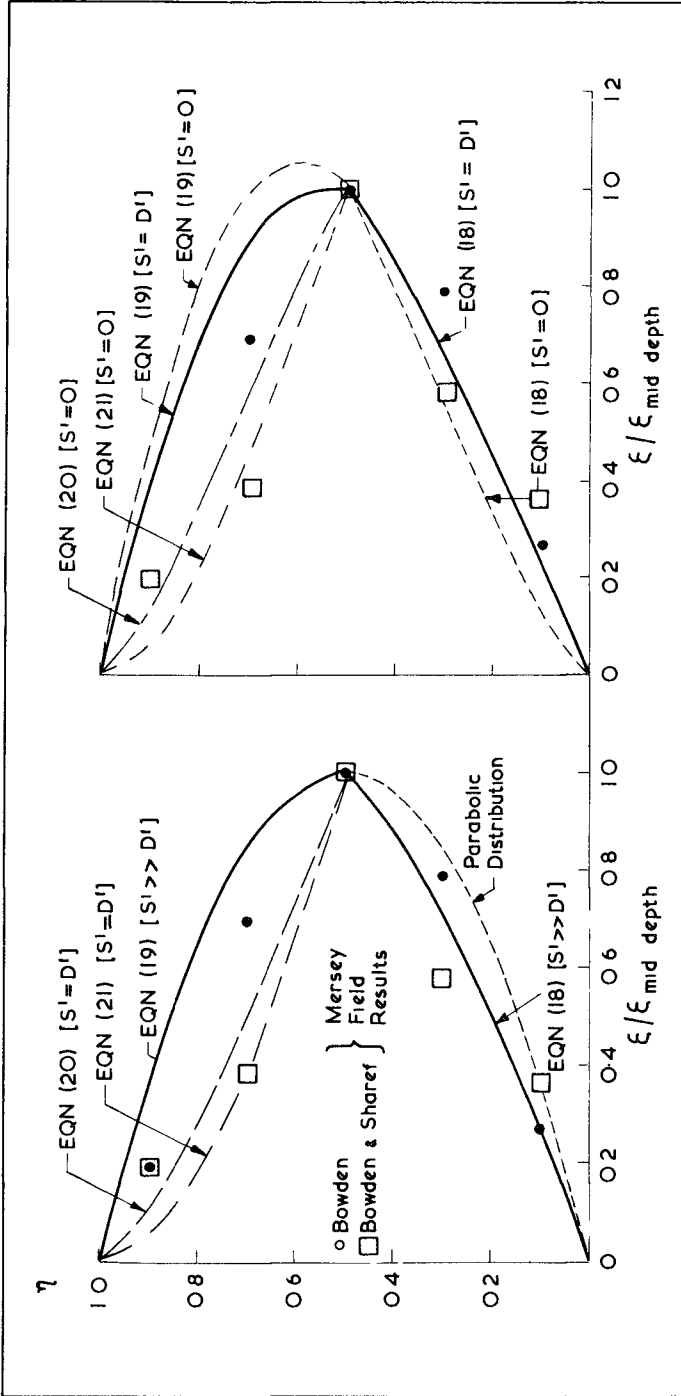


FIG 1 COMPARISON OF WITH FIELD DATA

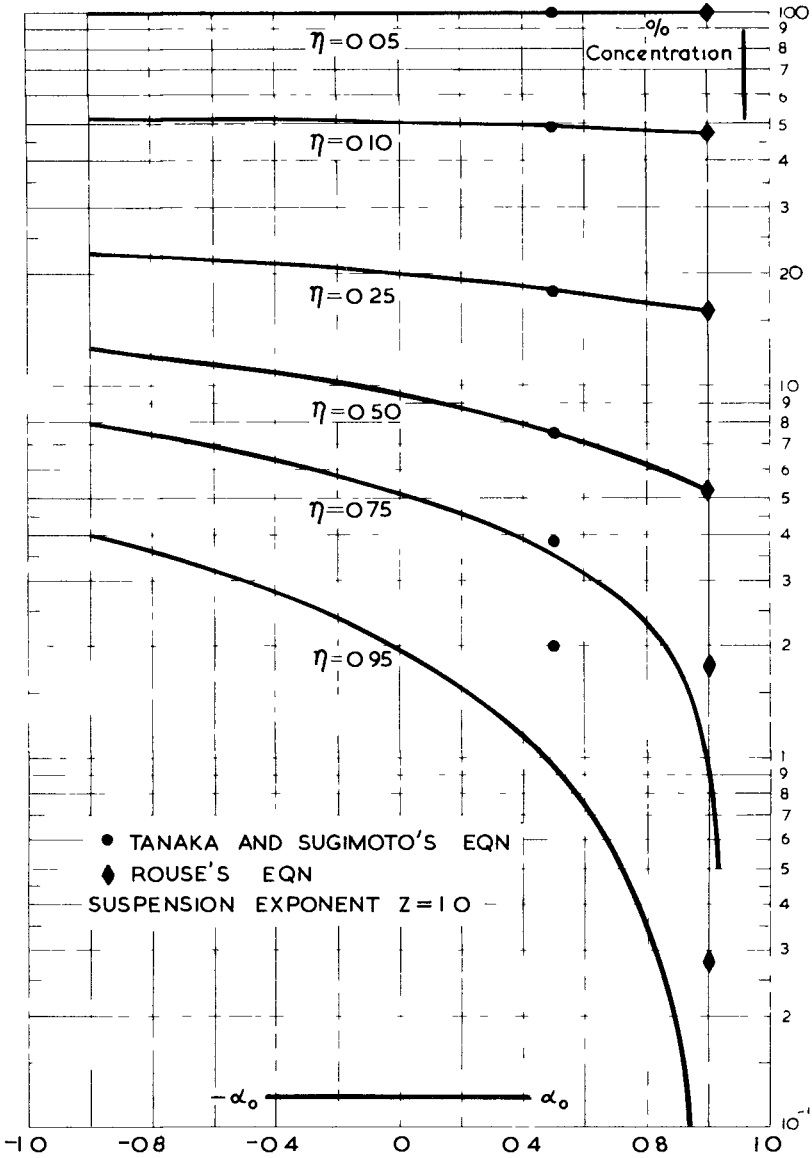


FIG 2 VARIATION OF CONCENTRATION WITH THE PARAMETER

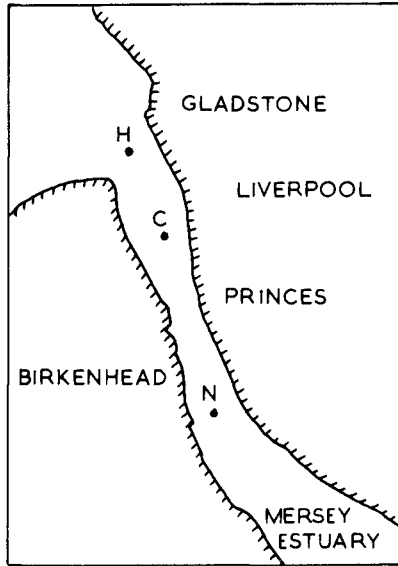


FIG 3 SELECTED OBSERVATION STATIONS - MERSEY ESTUARY

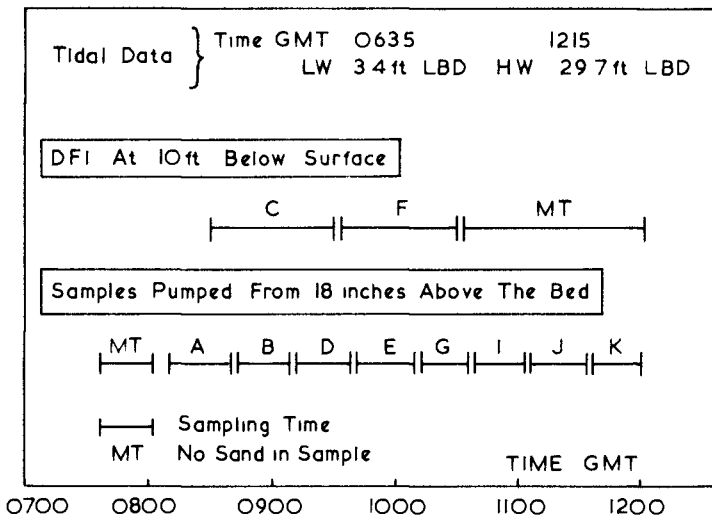


FIG 4 SEDIMENT SAMPLES AT POSITION H - MERSEY ESTUARY (25.11.65)

CHAPTER 118

PARTICLE VELOCITY MEASUREMENTS WITH A LASER DEVICE.

by

C.A. Greated¹ and N.B. Webber² M.A.S.C.E.

ABSTRACT

A laser velocimeter has been used to measure particle velocities in a turbulent suspension in open channel flow.

Both mean and fluctuating velocity components can be determined and the system may also be used to give records of instantaneous fluid velocities.

INTRODUCTION

Fundamental to the study of those coastal engineering problems which involve diffusion processes or transport of sedimentary material by tidal currents and wave action, is the measurement of particle velocities in turbulent flow. Particles of neutral buoyancy which are small compared with the largest wave number eddies will follow the flow pattern precisely and can therefore be thought of as fluid markers. In diffusion and sedimentation problems, however, the particles of interest are generally of non-neutral buoyancy and the gravity effect causes them to migrate vertically carrying them across streamlines of the mean flow. In addition to this, the fact that the inertial response of the particles will be different from that of an equal volume of fluid, will cause the particles to move relative to the fluid in accelerating turbulent eddies. Thus detailed studies must involve the statistical properties of both the fluid motion and the particle velocities.

Experimental research on these complex motions has hitherto been handicapped by lack of satisfactory instrumentation. Photographic methods have been used to measure particle movements in a Lagrangian manner but necessarily entail the laborious analysis of exhaustive data and tend to be very inaccurate. Hot film probes and other conventional turbulence measuring systems, on the other hand, are extremely difficult to use in water and further do not give any indication of particle velocities.

In the optical system described here, particles moving within a prescribed measuring volume cause a signal to be produced which has a frequency directly proportional to their velocity and thus the Eulerian

1. Lecturer, Mathematics Dept., Southampton University, England.

2. Lecturer, Civil Engineering Dept, Southampton University, England

statistics of their motion can be determined Fluid velocities can be measured by using extremely fine grain neutral buoyancy tracer particles, assumed to have a negligible influence on the flow.

OPTICAL MEASURING SYSTEM

Optical Configuration Light from a small laser (here 1mW helium-neon) is spread and collimated by two cylindrical lenses L_1 and L_2 and the parallel beam is then split by a mask M containing two small square apertures of size a and spacing b (figure 1)

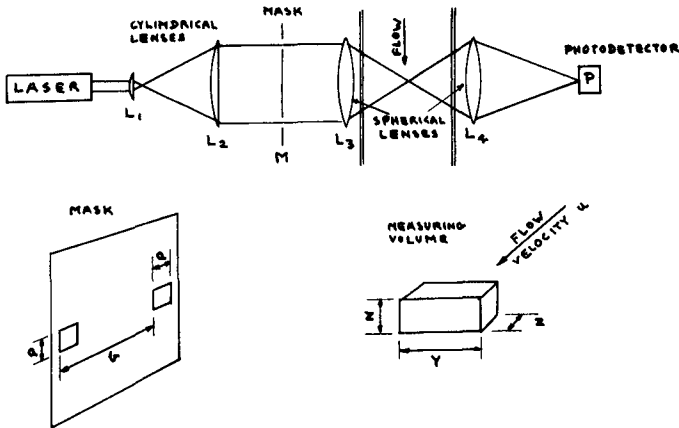


Figure 1. Optical layout.

A spherical lens L_3 is then used to bring the two beams to a focus at the required measuring point in the flow, a further spherical lens L_4 being used to image to focus on to a photodetector P .

Interference of the two beams causes a fringe pattern to be formed within a small volume at the focus and as particles move through this volume with velocity u , small patches will move across the image observed by the photodetector causing a signal of frequency

$$f_1 = \frac{b}{\lambda L} u \quad \text{where } \begin{cases} \lambda = \text{wavelength of laser light} \\ L = \text{focal length of lens } L_3 \end{cases}$$

i.e. proportional to velocity.

Measuring Volume Although the fringes die away gradually to infinity, the measuring volume at the focus from which significant signals are produced can be taken as being approximately of size $Z \times Z \times Y$ where

$$Z = \frac{\lambda L}{a} \quad \text{and} \quad Y = \frac{\lambda L^2}{ab}$$

This should be chosen so that Z is greater than the diameter of the largest particles.

SIGNAL ANALYSIS

Frequency Domain The simplest method of analysis, illustrated in figure 2, is to feed the photodetector output directly into an analogue spectrum analyser and integrate the output with an R-C circuit. The spectrum, which can be recorded on an X-Y plotter, then represents the probability distribution of velocity for particles in the measuring volume.

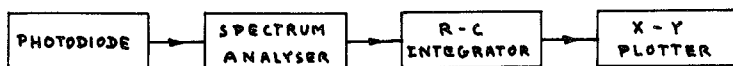


Figure 2. Frequency domain system

Ambiguity in the frequency measurement will occur here due to the finite number of fringes, but the magnitude of this can be predicted by taking the Fourier transform of the input signal giving

$$\text{r m s. ambiguity} = \frac{a f_1}{\sqrt{6} b} .$$

This should normally be of order 1% of f_1 for negligible error in velocity measurement i.e. $\frac{b}{a} = 40$

The details of this analysis have already been published (ref 2) but it is assumed here that the spectrum analyser used gives the modulus of

the Fourier components of the signal i.e. the frequency spectrum, rather than the power spectrum. This is the case with nearly all commercial spectrum analysers. It is also worth noting that the band width of the spectrum analyser should be small and the sweep rate long.

Figure 3 shows a typical spectrum obtained in a small flume.

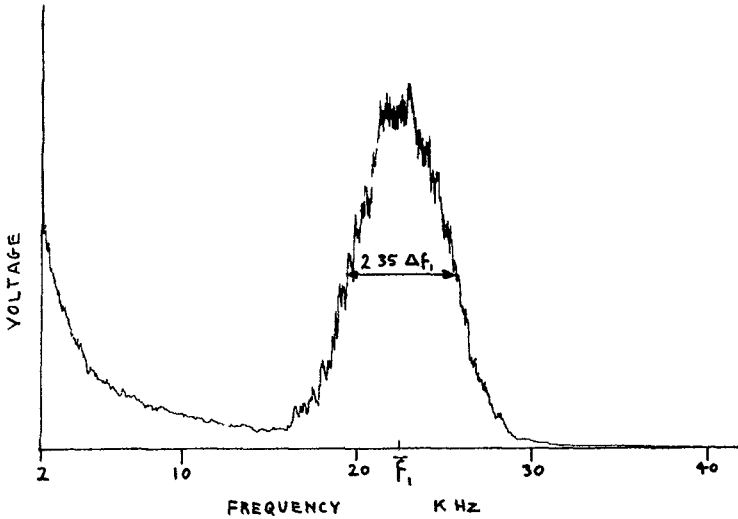


Figure 3. Spectrum of signal from photodetector.

Velocity Cross-Correlations The technique of rotating a hot-wire probe relative to the mean flow direction, or alternatively using an 'X' probe, has been used extensively for the measurement of Reynolds stresses in wind tunnels. In the same way the fringe pattern in the laser flowmeter can be rotated relative to the optical axis to give cross-correlations of particle velocities. Referring to figure 4, let us consider a mean velocity \bar{u} with fluctuating component u' in that direction, the fluctuating component perpendicular to \bar{u} being v' .

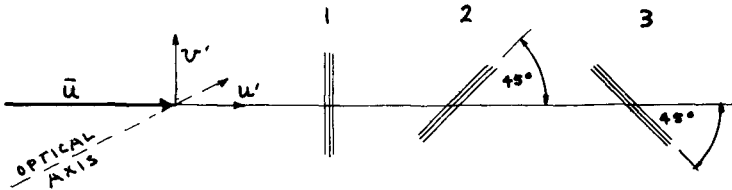


Figure 4. Alignment positions of the fringes.

Take the constant of proportionality for conversion from frequency to velocity as K i e with the fringes in position 1 the mean frequency (see figure 3) will be

$$\bar{f}_1 = K \bar{u}$$

If the r.m.s. width of the spectrum is Δf_1 then the r m s velocity fluctuation is

$$\sqrt{\overline{u'^2}} = \frac{1}{K} \Delta f_1$$

It can then be shown (Ref 2) that by measuring the r m s spectral widths Δf_2 and Δf_3 from recordings taken in positions 2 and 3 i e at $+45^\circ$ and -45° to the mean flow direction, the transverse velocity fluctuation $\sqrt{\overline{v'^2}}$ and the cross-correlation $\sqrt{\overline{u'v'}}$ can be found from

$$\sqrt{\overline{v'^2}} = \frac{1}{K} \sqrt{(\Delta f_2^2 + \Delta f_3^2 - \Delta f_1^2)}$$

and
$$\sqrt{\overline{u'v'}} = \frac{1}{K} \sqrt{(\Delta f_3^2 - \Delta f_2^2)}$$

For most practical purposes it will be satisfactory to assume that the velocity probability distributions are Gaussian whence the width at half the height is equal to $2.35 \Delta f$, as indicated in figure 3

Time Domain Analysis If the system is to be used to record velocities of tracer particles in the fluid then it is possible to construct the electronics in such a way that a continuous signal, proportional to the instantaneous velocity is obtained This will be called the 'time domain' method and the essential elements of the circuitry are shown in figure 5 More details are given in reference 1

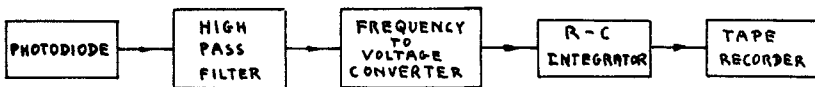


Figure 5. Time domain system

Firstly, the signal produced by the photodiode contains unwanted low frequencies produced by the total amount of light cut off as particles move across the observation volume, together with the noise caused by the passage of particles across points in the beam outside the observation volume. These frequencies are eliminated with a high-pass filter and a frequency-voltage converter is used to give an output signal proportional to the rate of zero crossings

Even if the fluid velocity were absolutely constant, the signal from the frequency-voltage converter would contain small fluctuations due to the finite number of fringes, the r.m.s. value of this fluctuation being equal to $a/(\sqrt{6} b)$ times the mean value. These can be damped before recording by using an R-C integrator, thus improving the resolution, but the integrating time should not be so long as to damp fluctuations due to velocity changes

PRELIMINARY RESULTS

Some preliminary results using the 'frequency domain' method are illustrated in figure 6 for the motion of glass spheres of diameter about 0.075mm in steady free surface flow. The velocities in the direction of mean flow were recorded in a channel 5cm wide with a measuring volume of size $z = 0.4\text{mm}$, $Y = 1\text{cm}$. These show the characteristic fall off in mean velocity and increase in r.m.s. velocity fluctuation towards the bed

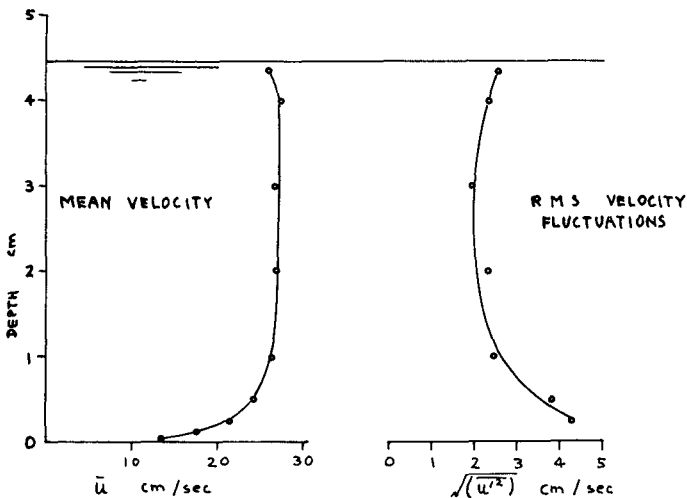


Figure 6 Particle velocities in open channel flow

At present the system is being adapted for measurements in a flume of 1m width and it is hoped that it will be possible to make simultaneous measurements of velocities and particle concentrations

POTENTIALITIES OF MEASURING SYSTEM

The system described would seem to fulfill the main requirements of a coastal engineering laboratory. Both fluid velocities and velocities of larger suspended particles can be measured with precision and to within a fraction of a millimeter of a wall. The instrument is directionally sensitive and rotation of the fringe pattern will give transverse velocity components and cross-correlations.

REFERENCES

- 1 Greated C, 1970 Journal of Physics E Sci. Instrum
Vol 3, pp 158-160
- 2 Greated C, 1970 Journal of Physics E Sci Instrum
Vol 3, pp 753-756

CHAPTER 119

DENSITY CURRENTS AND TURBULENT DIFFUSION IN LOCKS

by

A Roy Halliwell* and Martin O'Dell[†]

ABSTRACT

The paper describes a study of density-currents in locks where there is a net inflow of water into the dock. The velocity profiles occurring are different than might be expected by simply superimposing the net flow onto a normal density-current profile. The differences are shown to be due to the non-uniform salinity profiles occurring in the docks and a semi-theoretical study is presented which illustrates the importance of this salinity profile.

The accretion in the docks is explained by the transport of material into the docks during the levelling period. The quantitative agreement between estimates based on measurements during the levelling period and the dredged quantities from the dock are good. The locking operation is also shown to be an important factor in certain cases.

An attempt to describe the flow of silt into the dock using the one-dimensional diffusion equation has shown that allowance must be made for the pick up of silt off the bed of the lock and the settling of silt (as the velocities drop) if quantitative agreement is to be obtained.

* Senior Lecturer, Department of Civil Engineering, Liverpool University, Liverpool, England

[†] Research Student, Department of Civil Engineering, Liverpool University, Liverpool, England

INTRODUCTION

It is common practice in some docks on the Mersey Estuary (and elsewhere) to have a "levelling" period of about one hour (before high water). This is achieved, of course, by opening the gates at both ends of the lock communicating with the estuary, the water level in the dock having been run down (if necessary) in order to meet the rising tide level in the estuary. Thus, water can be impounded in the dock by inward flow, vessels can enter or leave without delay, and those longer than the lock itself can come and go at this time.

In the last few years, the problem of siltation in some of the Mersey docks has been investigated. Velocities, silt-concentrations and salinities have all been measured during the levelling periods. During this period, there is an influx of water into the dock, as the tide rises, but there is also a density-current between the estuary and the less-dense dock water.

The observations in two particular docks are discussed - Gladstone and Bromborough. In the case of Gladstone the water is impounded into the dock system by means of the levelling process and also by pumping. At Bromborough dock there is a fresh water discharge into the dock from a small river, which along with the levelling process provides the impounded water. Another important difference between the two docks is that the lock at Gladstone is long enough to cope with all the ships using the dock and therefore the levelling process is not essential (although of course it may be desirable) whereas the Bromborough lock is relatively small and the levelling period provides the only means for some ships to use the dock.

MEASUREMENTS

The measurements made in each of the locks have been similar in type, but partly because the sizes of the locks are very different the detail

execution of these measurements has been different at Bromborough than at Gladstone. In each case vertical traverses have been made of velocity, silt, salinity and temperature using in-situ measurement with direct-reading instruments. These traverses have been made throughout the levelling period and also for different tides (i.e. spring/neap) and different season (i.e. summer/winter). In addition to these, measurements of the silt in suspension near to the river entrance of the lock were made. These were made using the same type of silt-meter as for the traverses, based on the light-extinction method, along with a recorder. These allowed a continuous record of silt in suspension near the lock entrance to be made.

Bromborough dock is relatively small, the lock is some 70ft wide, 160ft long and 30ft deep. The vertical traverses in this case were made using a cantilever truss fixed to a dock transport bogie, the observation-bogie was driven up to the edge of the lock, the truss being of sufficient length to reach the centre of the lock. Two sets of instruments were suspended from the truss so that traverses could be made at above 25ft and 10ft from the lock wall. Each unit consisted of silt and salinity/temperature probes attached to a current meter and the unit was lowered and raised by hand. Readings were made at approximately six or seven levels and each traverse took about twelve minutes to complete. In addition to these, measurements were sometimes taken at fixed levels above the bed so that an almost continuous record of velocity etc. was obtained throughout the levelling period at these positions. This particular rig had the advantage of cheapness and more important still, it allowed the instruments to be removed from the lock when necessary, for example the passage of ships in and out of the lock.

Gladstone lock is some 130ft wide, 600ft long and 50ft deep and this meant that measurements were somewhat more difficult in this situation.

than at Bromborough. In general, traverses were made by lowering the instruments from a vessel in the lock. However, some traverses were made at about the middle of the lock and on the centre line of the lock by raising and lowering the instruments from a swinging foot-bridge across the lock.

DENSITY-CURRENT PROFILES

Although there is a considerable amount of literature published on density exchange flow the authors are not aware of any which deal with the situation where there is a net influx of water across the section. In the case of the Gladstone lock the influx of velocity at the start of the level (when the tide is still rising at approximately 5ft per hour) is considerably greater than the density current. At high water, of course, there is no net influx of water and the velocities are entirely due to the differences in density. In Bromborough lock the density differences are greater than at Gladstone, while the influx velocities are about the same as those at Gladstone.

When the lock gates are opened to the estuary, at say $1\frac{1}{2}$ hours before high water, water enters the dock through the lock due to the rising tide - this velocity is termed continuity velocity and is defined as

$$\bar{v} = \frac{\text{plan area of dock} \times \text{rate of rise of tide}}{\text{cross-sectional area of lock}} \quad (1)$$

Superimposed upon this continuity velocity there is a density-current between the estuary and the less-dense lock water which produces an outward flow at the surface and an inward flow near the bed. Figure 1 shows some examples of the vertical velocity profile occurring at the centre of the Bromborough lock during the levelling period on a spring tide. The importance of the continuity velocity at the start of the level can be seen by comparing figure 1(a) with 1(c).

The average influx velocity is defined as

$$\frac{1}{H} \int_0^H u \, dy \quad (2)$$

where u is velocity into dock at depth y ,

H is the depth of water

The velocity profile due to density differences alone is seen around the high water period in figure 1(c) when the average influx velocity is almost zero (and the continuity velocity is zero). The zero velocity point occurs at a level above the mid-depth position (approximately 40% depth) and the velocities out of the dock (in the upper surface layers) are considerably greater than those entering the dock (in the lower layers). It is immediately apparent therefore that the velocity profile due to the density-current alone is not that occurring in the situation illustrated in case (A), Figure 2, where the zero velocity point occurs at 50% depth and the overflow velocity is approximately 1.25 x the underflow velocity (see refs 1 and 2).

Measurements of salinity within the Bromborough dock on a number of occasions have shown that the salinity profile within the dock is in fact far from uniform. Two examples are given in Figure (3), and it is clear that the starting conditions are more likely to be similar to the situation illustrated in case (B) of Figure (2) than those of case (A). Some model tests have been made of both cases A and B and these have indicated the velocity profiles for the two cases are indeed different as illustrated in Figure (2). The model tests are still continuing and the results cannot therefore be discussed in detail in this paper but the profile indicated for case (B) in Figure (2) is clearly very close to that measured in the docks on a number of occasions and in particular to that given in Figure 1 (c).

The underflow velocity occurring in the situation illustrated in case A (fig 2) is given theoretically by

$$V_u = 0.5 V_\Delta \tag{3}$$

and has been assessed experimentally by a number of researchers (e.g. ref. 1) as

$$V_u = 0.465 V_\Delta \tag{4}$$

where

$$V_\Delta = \left(\frac{\Delta\rho}{\rho_m} gH \right)^{\frac{1}{2}}$$

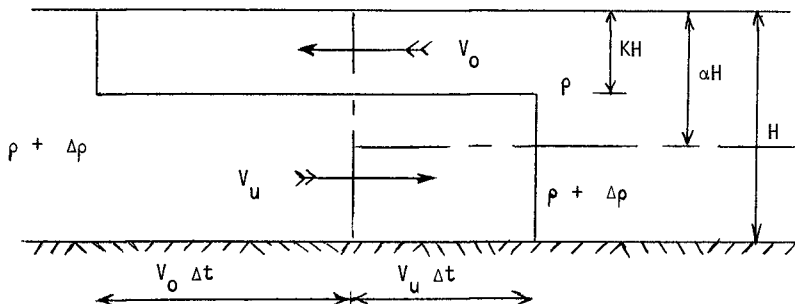
g = the acceleration due to gravity

ρ_m = the average density of the two liquids

$\Delta\rho$ = the density difference between the two liquids

H = the depth of the lock

Consider the general case for the situation illustrated in case B (fig 2), let the freshwater occupy the depth αH before the exchange flow starts. Assume that the exchange flow is rectangular block flow as illustrated in the sketch below and that the crossover point (or zero velocity) is at depth KH . Let the underflow and overflow velocities be denoted by V_u and V_o respectively. Then at time Δt after the barrier is removed the fronts will be in the positions illustrated in the sketch



The continuity equation gives

$$V_o = \left(\frac{1-K}{K}\right) V_u \quad (5)$$

The gain in kinetic energy is

$$\frac{1}{2} \rho \{KH(V_o + V_u) \Delta t\} V_o^2 + \frac{1}{2} (\rho + \Delta\rho) \left\{ (1-K)H (V_o + V_u) \Delta t \right\} V_u^2 \quad (6)$$

so substituting equation (5) into equation (6) and assuming $\Delta\rho$ is small compared to ρ

$$\text{gain in kinetic energy} = \frac{1}{2} \rho_m V_u^3 \Delta t H \left(\frac{1-K}{K^2}\right) \quad (7)$$

The loss of potential energy is

$$\begin{aligned} \Delta\rho(V_o \Delta t) g KH (\alpha - 0.5K)H \\ - \Delta\rho(V_u \Delta t)g (\alpha - K)H \left\{ 0.5(\alpha - K)H \right\} \end{aligned} \quad (8)$$

or

$$\Delta\rho g \Delta t H^2 V_u \left[\alpha - 0.5\alpha^2 - 0.5K \right] \quad (9)$$

Equating the gain in kinetic energy to the loss in potential energy gives

$$V_u^2 = \left\{ \frac{2K^2 (\alpha - 0.5\alpha^2 - 0.5K)}{(1-K)} \right\} V_\Delta^2 \quad (10)$$

Case 1 $\alpha = 1.0$ and $K = 0.5$ equation (10) and (5) yields

$$V_u = 0.5 V_\Delta \text{ and } V_o = V_u \quad (11)$$

which is the theoretical result for Case A and confirms equation (3)

Case 2 $\alpha = 0.5$ and $K = 0.4$ equations (10) and (5) yield

$$V_u = 0.33 V_\Delta \text{ and } V_o = 1.5 V_u \quad (12)$$

and this represents the model test results of Case B (fig 2)

Case 3 $\alpha = 0.2$ and $K = 0.15$ equations (10) and (5) yield

$$V_u = 0.075 V_\Delta \text{ and } V_o = 5.67 V \quad (13)$$

Equation (10) shows the importance of the salinity profiles occurring within the docks. The overflow velocity may not alter very much with changes in salinity profile within the dock, but the underflow velocity is greatly reduced compared with that given by equations (3) or (4)

If the density difference is expressed in terms of a difference of salinity then for the situations in Bromborough lock (H=32ft approximately) and Gladstone lock (H=50ft approximately), the underflow velocity according to equation (4) can be expressed as

$$\begin{aligned} V_u &= 0.403 (\Delta S)^{\frac{1}{2}} \text{ at Bromborough} \\ V_u &= 0.507 (\Delta S)^{\frac{1}{2}} \text{ at Gladstone} \end{aligned} \quad (14)$$

Using equation (12) the corresponding relationships are

$$\begin{aligned} V_u &= 0.27 (\Delta S)^{\frac{1}{2}} \\ V_u &= 0.34 (\Delta S)^{\frac{1}{2}} \end{aligned} \quad (15)$$

(allowing for the theoretical value to be reduced by 0.93 in a similar way to equation (3))

The velocities measured at Bromborough and Gladstone compare very well with those obtained using equation (15) whereas the values obtained using equation (14) which is based on equation (4) are considerably in error. The profile is also more closely described by the modified block flow illustrated in the sketch and the surface velocity is close to the value given in equation (12)

Fig (4) shows the velocities measured at a fixed level above the bed. These confirm that the resulting velocity during the levelling process is the simple addition of the average inflow velocity (or continuity velocity) and the density-current. The density-current is almost constant throughout the level period and equal in this case to 0.75 ft/sec. The maximum underflow velocity due to the density difference is about 1.0 ft/sec (occurring at a depth of about 65%) and compares very closely with the value obtained using equation (15) - the value of ΔS being approximately 12%

ACCRETION IN THE DOCKS

The main practical interest of the work was centred on the dredging requirements for the docks and the possible means of reducing them. The transport of silt through the lock into the dock was determined from the measurements of velocity and silt. For example the variation of silt concentration with depth for the traverse corresponding to Fig 1(a) is given in Fig 6(a) and the resultant transport of silt is proportional to (velocity x silt concentration). This figure immediately shows the silt burdened estuary water entering the dock in the lower layers and the relatively clear dock water leaving in the upper surfaces. By integrating traverses such as these the variation throughout the level period of silt transport into the docks has been determined (see for example Fig 6(a)) and thence the total amount of material entering during the level period

In the case of Bromborough, measurements on the 10th December 1969 - a spring tide - showed that a total amount of 350 tons dry weight of silt entered the dock during the levelling period. The amount of solids in the material dredged from the docks depends on the type of material and the consolidation occurring. The density of the material in the hoppers of the dredgers has been measured on a number of occasions and has indicated that the percentage of solids is usually less than 40% and that a reasonable figure is 36% so that

$$\text{dredged tonnage} = 2.8 \times (\text{tons of dry silt transported into the dock})$$

This figure also implies that one cubic yard of dredged material weighs approximately one ton, assuming that the specific gravity of the solids is 2.7. Using this value the amount of material entering the dock in the level period during a spring tide in winter conditions is approximately 1000 dredged tons.

Before any attempt can be made to calculate the total amount of silt

entering the docks throughout the year the variation with tide and season of the silt in suspension in the estuary near the entrance is required. The silt concentration varies with tide range and with season and the silt pattern at any position can be very different from that occurring relatively short distances away (see ref 3). Continuous silt measurements were therefore made near the entrance to the locks and the results from these instruments were used to allow for the variations throughout the year.

When this was done for Bromborough Dock the amount entering the dock during the levelling processes was estimated as 270,000 dredged tons (or cubic yards) per annum. The average amount of material dredged during the period 1964-68 was 300,000 dredged tons per annum. The estimated figure therefore compares very well with the actual amount, however there is another mechanism by which a significant amount of material can enter the dock - the locking procedure or operation.

During a locking operation the water in the lock is almost always of different density than that in the estuary. At Bromborough the water is usually less saline in the lock (due to the freshwater inflow into the dock) and the estuary water is also carrying a high suspended load which further increases the density difference. When the outer gates are opened therefore a density exchange flow starts with the heavier estuary water intruding into the lock near the bed and eventually, if the gates are open long enough, replacing almost all the lock water (ref 2). If the water in the lock is more dense than that in the estuary, for example near the period of low water, then the heavier lock water leaves the lock in the lower layers bringing the estuary water into the lock in the upper layers. Whichever mechanism occurs silt is brought into the lock from the estuary during the locking operation. When the inner gates (into the dock) are next opened, then a similar mechanism carries the water and

silt from the lock into the dock so that all the silt carried into the lock during the locking procedure is eventually deposited on the bed of the dock

The relatively small size of Bromborough lock and the large density differences mean that the time needed for say 80% of the lock water to be replaced by estuary water is not very great (of the order of 10 minutes) At Gladstone the lock is relatively large and the density differences are small so that the time needed for 80% of the lock water to be replaced by estuary water may be quite large (of the order of an hour) Obviously, therefore, the locking procedure may be a significant factor for Bromborough, but is unlikely to be so in the case of Gladstone Estimates for Bromborough, allowing for half the volume of water in the lock to be exchanged during each locking operation, indicate that approximately 75,000 dredged tons per annum enter the dock through this mechanism The estimated total quantity of material entering the Bromborough dock is therefore approximately 350,000 dredged tons per annum and this, considering the various assumptions made, compares very well with the actual figure of 300,000 dredged tons per annum (averaged)

A number of estimates have been made for the Gladstone lock and these have all shown that the average annual dredging figure of 265,000 hopper tons (1966-68) is accounted for to within a few percent by the levelling process (ref 4) and that the locking procedure does not contribute significantly in this situation

As a result of this work the levelling process at Gladstone dock has been stopped - the water now being impounded entirely by pumping - and at Bromborough (where the levelling period provides the only means of some ships using the dock) the levelling period has been reduced to a minimum There has been immediate reductions in the quantities dredged at both docks

ONE-DIMENSIONAL TURBULENT DIFFUSION EQUATION

The one-dimensional convective diffusion equation for a soluble substance in turbulent flow is (see ref 5)

$$\frac{\partial c}{\partial t} + U \frac{\partial c}{\partial x} = \frac{\partial}{\partial x} (D_{tx} \frac{\partial c}{\partial x})$$

where U is the average flow velocity across the section

D_{tx} is the turbulent diffusion coefficient

c is the concentration of the soluble substance

If a point injection of material is made into the flow at position $x=0$ and time $t=0$ then the concentration at time t and position x is given by Taylor as

$$c = \frac{M}{A\rho (4\pi D_t t)^{\frac{1}{2}}} e^{-\frac{(x - Ut)^2}{4D_t t}}$$

where M is the mass of material introduced

A is the cross-sectional area of flow

ρ is the density of the fluid

The solution for a series of point injections can obviously be obtained by superimposing the solutions for each separate injection. This type of solution is well suited to the digital computer and a computer program has been written (ref 4) incorporating the Taylor solution for finite source injections. The program allows for the possibility of injections at various points along the x -axis (i.e. at points other than $x=0$) and this allows various initial boundary conditions to be imposed upon the system, i.e. at $t=0$, $c=c(x)$ is simulated by a series of injections of different strengths at various points along the x -axis.

Silt measurements in the estuary at the entrance to the Gladstone lock presented the attractive possibility of comparing the measured dis-

tributions of silt at stations along the lock with computed values using the computer program. The vertical distribution of silt was simulated by dividing the lock into five layers with injections being made into each layer, the magnitude of each injection being arranged to produce the measured vertical distribution of silt occurring at the time near the river entrance to the lock. The technique for determining a suitable dispersion coefficient for each layer was empirical and to some extent arbitrary (ref 4). Eventually after consulting the various literature a value of approximately $100 \text{ ft}^2/\text{sec}$ was used.

Comparison of the field measurements taken with the results obtained from the computer solution showed that there were large differences in magnitude between the two sets of curves. However, the basic patterns exhibited by corresponding curves were similar. The computed concentration results showed that the times of the peaks occurring in the 90% and 70% layers agreed reasonably with the observed results. The average difference in concentration over the levelling period between the computed and observed results were determined for each layer and these suggested that material was being picked up from the bed and being diffused upwards into each layer, the quantity becoming successively smaller towards the surface layer. This process is almost certain to be occurring since on the day in question a layer of fluid mud was present on the lock sill at most times during the levelling period.

Close to high water the observed concentration in the lock decreased especially in the 70% and 90% layers, whereas the computed concentrations were still slowly increasing. This is thought to be due to the occurrence of flocculation which in turn causes rapid settling of the suspended silt. If quantitative agreement is to be obtained therefore it would seem that allowance must be made for both pick-up and settling of silt.

CONCLUSIONS

- (1) When there is a net influx of water superimposed upon a density-current situation the resulting velocity distribution is given (to a first approximation) by superimposing a uniform velocity throughout the depth (equal to the influx flow) upon the density-current profile
- (2) The density-current profile is considerably influenced by the salinity profiles occurring within the docks
- (3) The practice of levelling is responsible for most of the accretion occurring in the docks examined in the Mersey Estuary. The locking operations account for some material and of course if water is impounded by pumping this may also be an important contribution
- (4) Comparison of field measurements of suspended solids in the lock, with results obtained using a computer solution incorporating the Taylor solution for a finite source injection (and dividing the depth of flow in the lock into layers), show that the general pattern of silt transport into the dock can be qualitatively described by the semi-theoretical results. However, quantitative agreement is poor and this is considered to be due to
 - (a) the pick-up of silt off the bed of the lock
 - (b) the settling of silt (when flocculation occurs)neither of these processes being allowed for in the computer solution

ACKNOWLEDGEMENTS

The field measurements described were sponsored by the Mersey Docks and Harbour Board and Unilever Merseyside Ltd, and the helpful co-operation of both these organisations is acknowledged. The authors are particularly grateful to Mr J D Littler of the University Civil Engineering Department, for his considerable help with many of the measurements taken

REFERENCES

- (1) D I H Barr Aspects of density surge phenomena
Educational Fluid Mechanics No 3 1968 Arnfield Engineering Ltd
- (2) G H Keulegan An experimental study of the motion of saline
water from locks into fresh water channels
U S Dept of Commerce, Nat Bureau of Standards, Report
No 5168, 1957
- (3) A R Halliwell and M O Dell Differences in silt patterns
across an estuary
The Dock and Harbour Authority Vol L, No 585, July 1969
- (4) M O Dell Silt distributions and siltation processes (with
particular reference to the Mersey Estuary and Dock systems)
Ph D Thesis Liverpool University Dec 1969
- (5) A T Ippen Estuary and coastline hydrodynamics published by
McGraw Hill

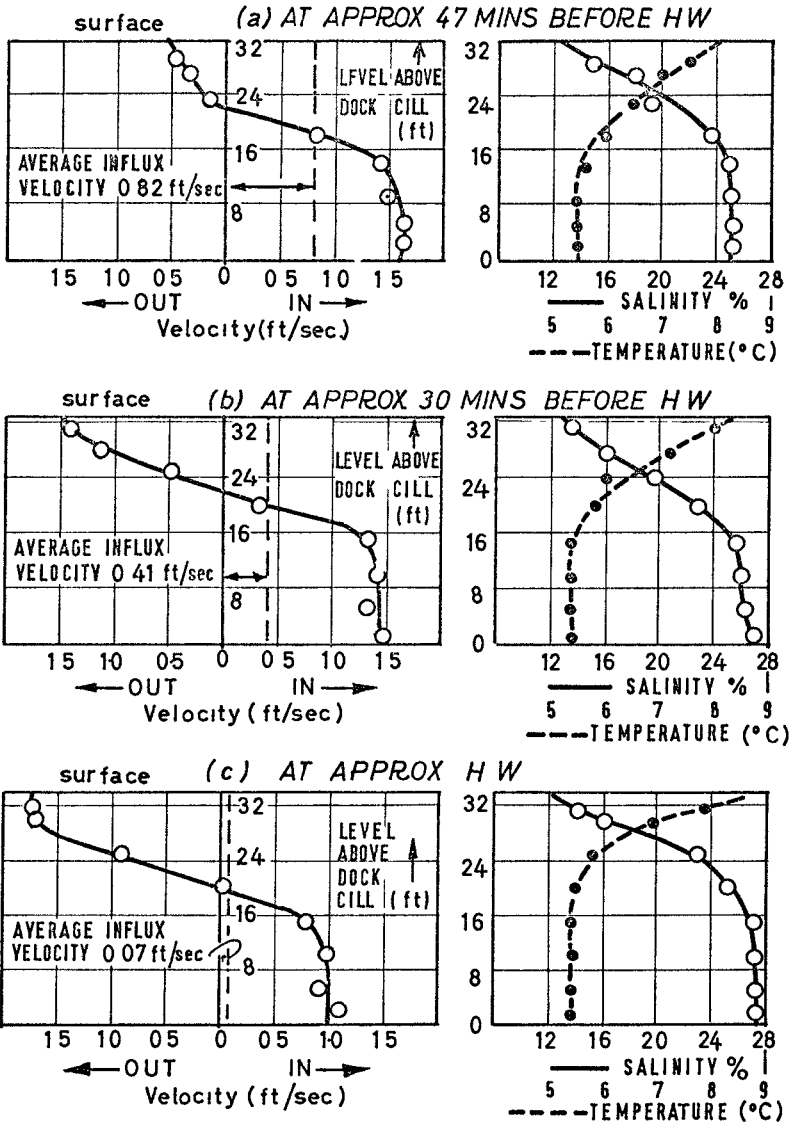


FIG 1 DENSITY-CURRENT PROFILES WITH NET INFLUX-VELOCITIES (Bromborough Lock 10-12-69)

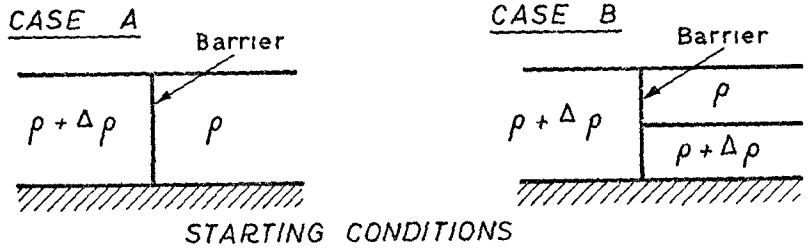
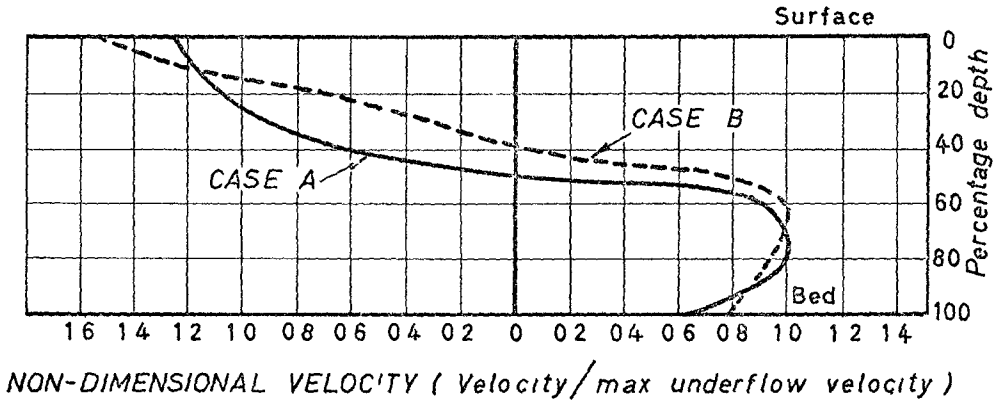


FIG 2 COMPARISON OF VELOCITY PROFILES DURING EXCHANGE FLOW FOR DIFFERENT STARTING CONDITIONS (MODEL TESTS)

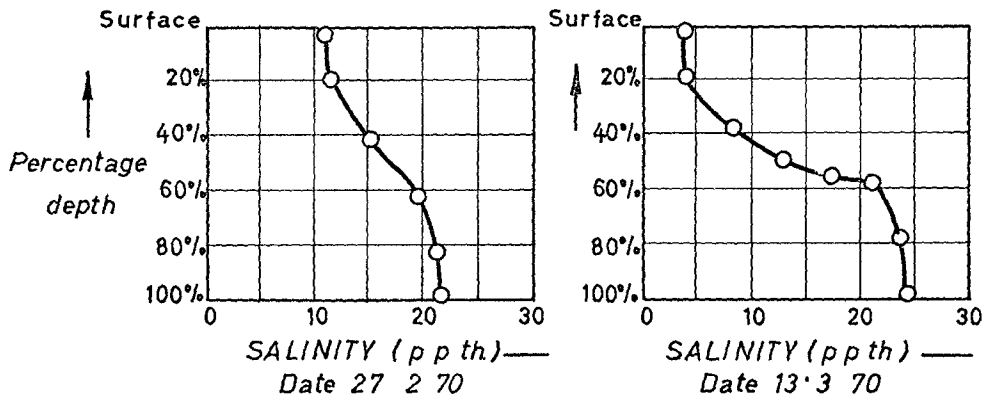


FIG 3 EXAMPLES OF SALINITY PROFILES IN BROMBOROUGH DOCK (MERSEY ESTUARY)

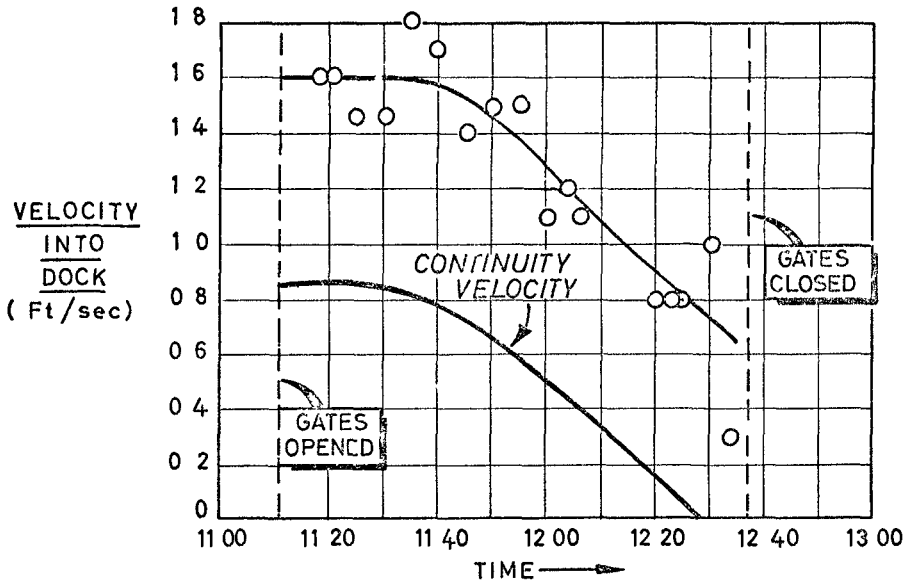


FIG 4 VELOCITY INTO DOCK MEASURED AT A POSITION 1 1/2 FT ABOVE DOCK CILL (ie at approx 56% depth)
BROMBOROUGH LOCK 10-12-69

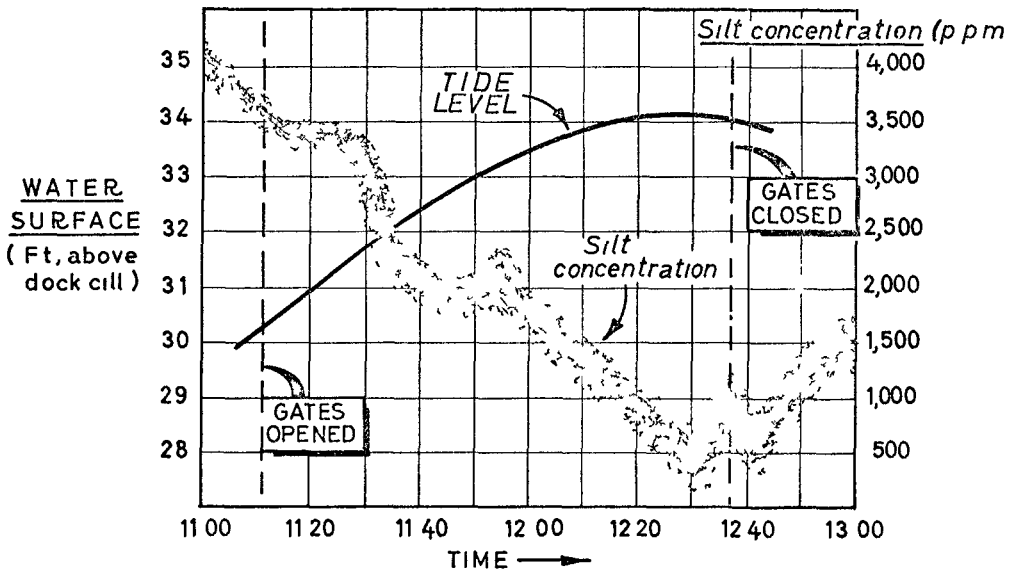


FIG 5 VARIATION OF SILT CONCENTRATION AT JETTY (NEAR BED) AND TIDE LEVEL
BROMBOROUGH LOCK 10~12~69

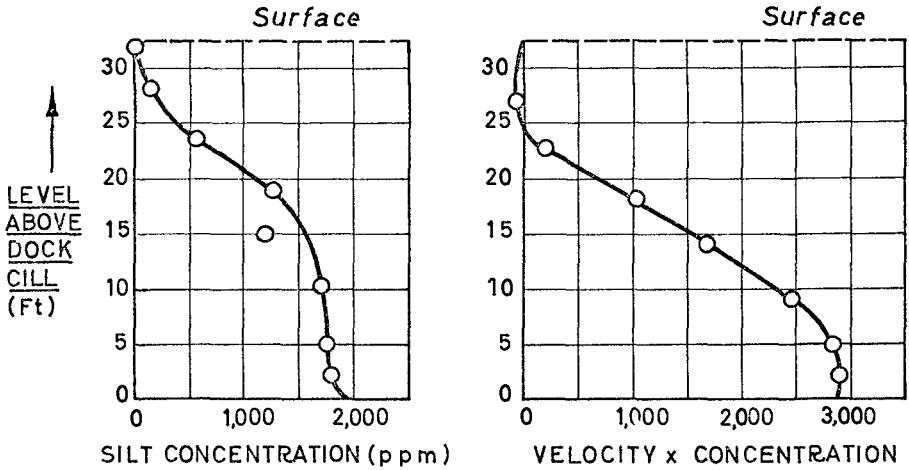


FIG 6(a) VARIATION WITH DEPTH OF SILT CONCENTRATION AND INFLUX OF SILT INTO THE DOCK AT APPROX 47 MINS BEFORE HIGH WATER
 (Corresponding velocity distribution is given in Fig 1 (a))

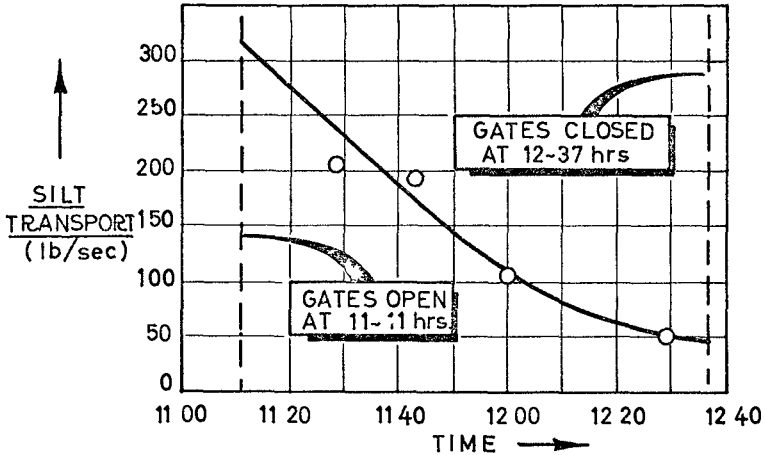


FIG 6(b) TRANSPORT OF SILT INTO DOCK
 (BROMBOROUGH DOCK 10-12-69)

CHAPTER 120

MEASUREMENT OF DENSITY CURRENTS IN AN IDEALIZED MODEL

By T1mm STUCKRATH 1)

1 INTRODUCTION

The mixing of salt and fresh water in estuaries of tidal rivers is related to two major phenomenons turbulent diffusion and density currents

The turbulent diffusion can be read off from the horizontal and vertical salinity distribution, the density current can be determined from the velocity distribution on the vertical axes

The physical description of tidal mixing in a mathematically closed system is not possible, because turbulent diffusion and gravitational convection are varied by such different influences as tidal action, fresh water flow, river bed form and roughnes, and gravitational and CORIOLIS forces

Most research in this field has been done on turbulent diffusion, especially to predict the mean horizontal (longitudinal) salinity distribution IPPEN, HARLEMAN (ref 11, 12), and others have found out by various model tests that FICK's law of diffusion used in one-dimensional form is a good physical description for the longitudinal salinity distribution and that the tidal energy dissipation, the cross section, and the fresh water flow are a good means of classifying tidal estuaries from the viewpoint of stratification

1) Diplom-Engineer, Scientific Assistant of the FRANZIUS-INSTITUT, Technical University of Hannover, Germany

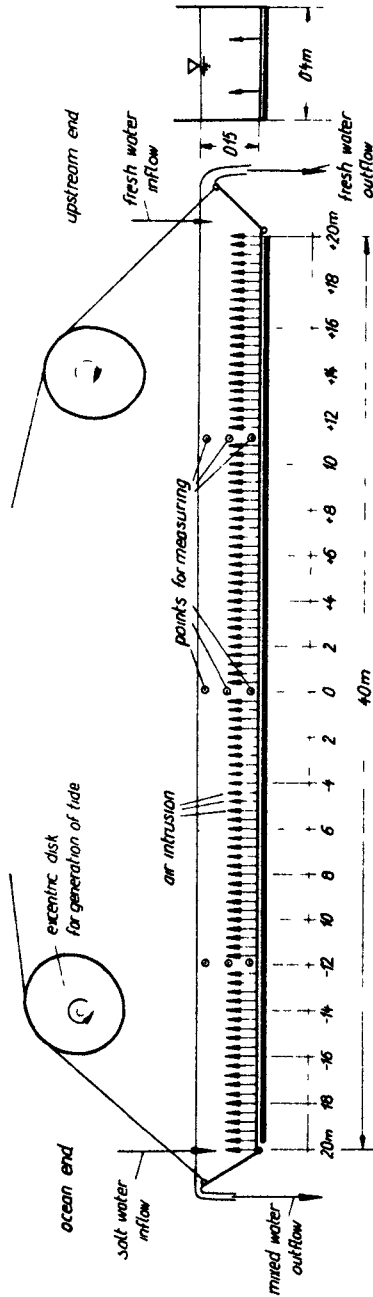


FIG 1 TIDAL FLUME OF THE FRANZIUSUS-INSTITUT

Much research is still needed to predict the density currents in tidal estuaries. Most theoretical and practical research on density currents is still limited to rivers or model tests without tide and with high stratification. In these channels salt and fresh water are separated into layers. The model tests which were carried out with sponsorship of the DEUTSCHE FORSCHUNGSGEMEINSCHAFT in the FRANZSIUS-INSTITUT in Hannover, were assigned to obtain informations about density currents in mixed estuaries.

2 EXPERIMENTAL EQUIPMENT

The flume that was used, is shown in fig 1. It was 40 m long, 0.4 m wide and 0.3 m deep. The flume was supplied with fresh water from the upstream end and with salt water from the ocean end. The tide was generated on both sides with tidal weirs which were moved by excentric disks. The flume should represent the zone of brackish water in an estuary. Due to the water supply the upstream end of the brackish zone during the whole tidal circle was within the flume, while the ocean end of the brackish zone could move downstream past the ocean end of the flume (fig 2).

As the intensity of turbulence in the model was nearly zero, artificial turbulence was generated by an air supply from the bottom of the flume (fig 1). Constant supply with air gives constant energy dissipation per unit of mass, even if there are great differences in water depth due to the tidal amplitude or changes in bed level. An artificial air supply is therefore a good means of achieving a definite turbulent energy dissipation in tidal models.

About 70 model tests were carried out with variation of

fresh water velocity from 0.20 to 1.35 cm/sec (4 series),
ocean salinity from 0 to 35 ‰,
air supply from 4 to 85 cm³/sec m²

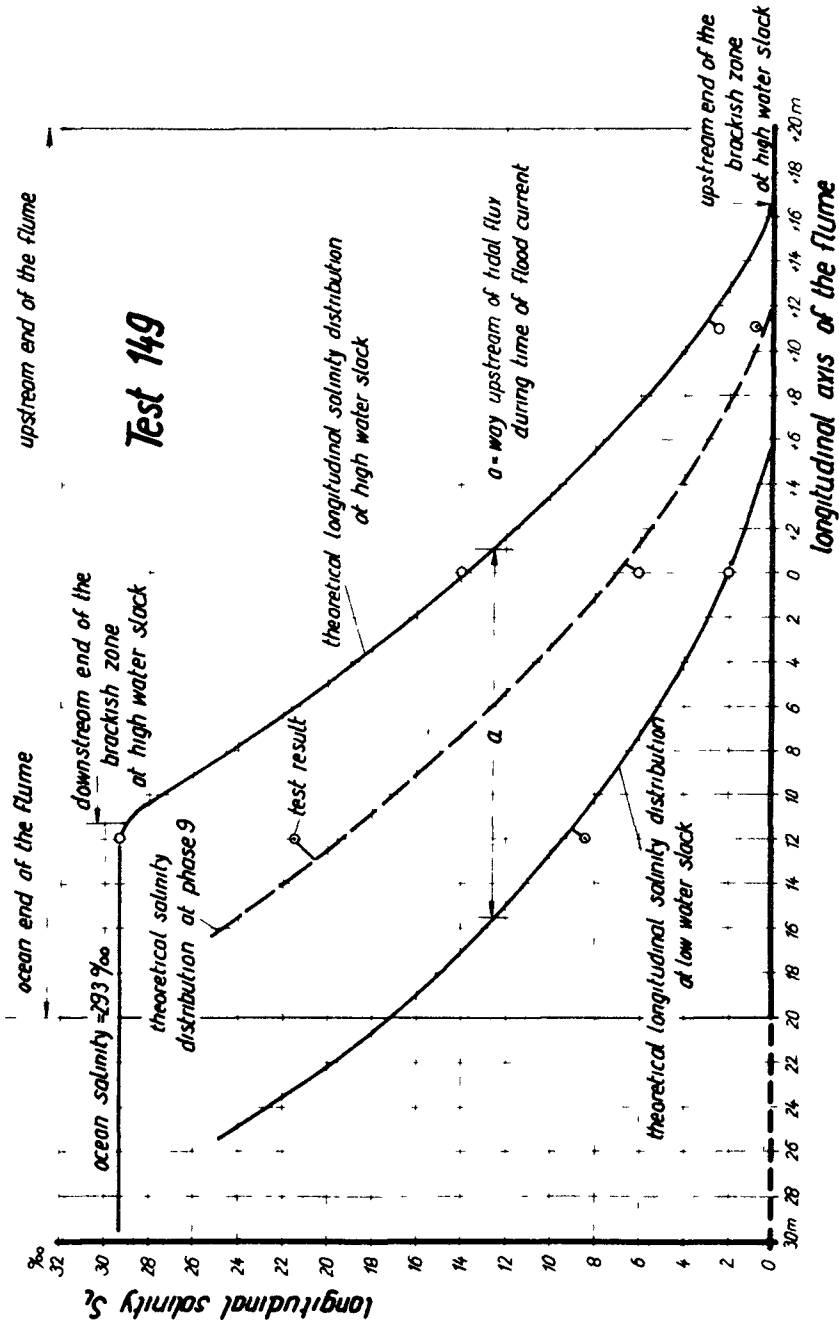


FIG. 2 LONGITUDINAL SALINITY DISTRIBUTION IN THE FLUME

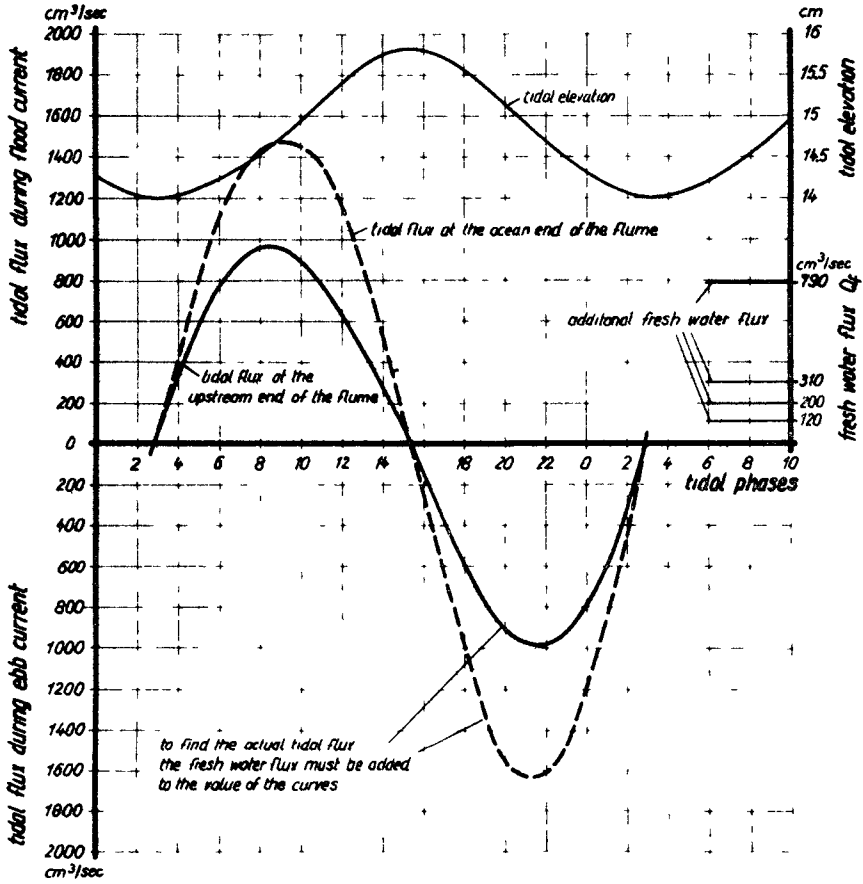


FIG 3 TIDAL AND FRESH WATER FLUX

Since the tide in the model had nearly no influence on turbulence, the experiments were carried out with a single tide which changed the depth from 14 cm (low water) to 15.8 cm (high water). The time for one tidal circle was 30 minutes. The tidal flux on both ends of the flume during one tidal circle (24 tidal phases) and the fresh water flux of the 4 series conducted, can be read from fig. 3.

The salinity was measured by the electrical conductivity of salt water at 9 fixed points (3 vertical axes with 3 levels) (fig. 1). The low speed currents were measured in the vicinity of these points with elastic pendulums as shown on fig. 4.

The elastic flexion of the pendulum is restricted to a short spring plate and recorded by strain gauges which were attached to both sides of the spring. Currents of 0.2 cm/sec up to 10 cm/sec could be measured with this technique with good accuracy.

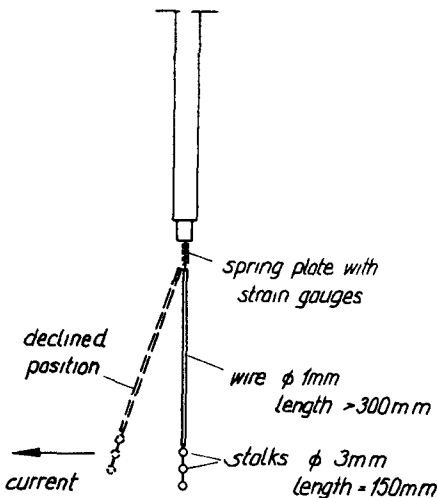


FIG 4 INSTRUMENT FOR MEASURING LOW SPEED CURRENTS

3 SALINITY DISTRIBUTION

Tidal research has shown that FICK's law of diffusion can be applied to rivers of various conditions of mixing (ref 5, 8, 9, 14, 15). It was therefore also important to verify the model tests of the FRANZIUS-INSTITUT with this theory. Since the applied theoretical developments and their agreements with the test results cannot be shortened

appreciably without harming their understanding, they shall not be explained here. It was worthwhile to know that all test results could be approximated with this theory closely (fig. 2) and that the longitudinal and vertical salinity distribution in the model could be expressed by physical parameters.

Instead of the tidal energy dissipation - which is the major cause for mixing in prototype estuaries - the energy dissipation of the air introduced was used, similar to the experiments which were carried out at the MASSACHUSETTS INSTITUTE OF TECHNOLOGY with oscillating grids (ref 6, 7, 10).

For the analysis of density currents it is not necessary to have a theoretical prediction of the salinity distribution. It is however presumed that the salinity at any point and at any time is known, because its distribution and changing is the cause for density currents.

4 DENSITY CURRENTS

One classical problem of density current was to determine the initial velocity v_1 which occurs, when a vertical separation between two liquids of different density (ρ_1 and ρ_2) is suddenly removed (fig 5).

The equation which describes this velocity is

$$v_1 = K \sqrt{\frac{\rho_1 - \rho_2}{\rho} g h}$$

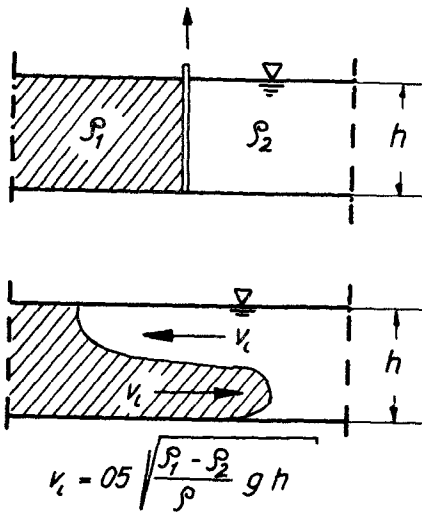
K = constant

ρ_1 = density of the water with greater density

ρ_2 = density of the water with lesser density

$$\rho = \frac{\rho_1 + \rho_2}{2}$$

g = acceleration of gravity



$h =$ water depth

Many model experiments have been carried out to determine the initial velocity. O'BRIEN and CHERNO (ref. 13), KEULEGAN (ref 4), YIH (ref. 3), BARR (ref 4), and others have proved that the constant before the root, which can also be computed by theoretical considerations as ABRAHAM and v d. BURGH (ref. 2) have shown, has nearly the value of

$$K = 0,5.$$

FIG 5 THE INITIAL VELOCITY v_1

ALLEN and PRICE (ref. 3) ascertained this value at ship locks.

After the vertical separation is removed (fig 5) the density current is

$$\Delta v = 2v_1.$$

So the equation of the initial velocity can be rewritten

$$\Delta v = 2K \sqrt{\frac{\rho_1 - \rho_2}{\rho} \cdot g \cdot h}$$

$$F_d = 2K = \frac{\Delta v}{\sqrt{\frac{\rho_1 - \rho_2}{\rho} \cdot g \cdot h}}$$

F_d is called the densimetric FROUDE number For the initial velocity (fig 5) is $F_d = 1$.

In a river mouth the density current can be determined as in fig 6 as the difference between the measured velocity and the tidal velocity without density.

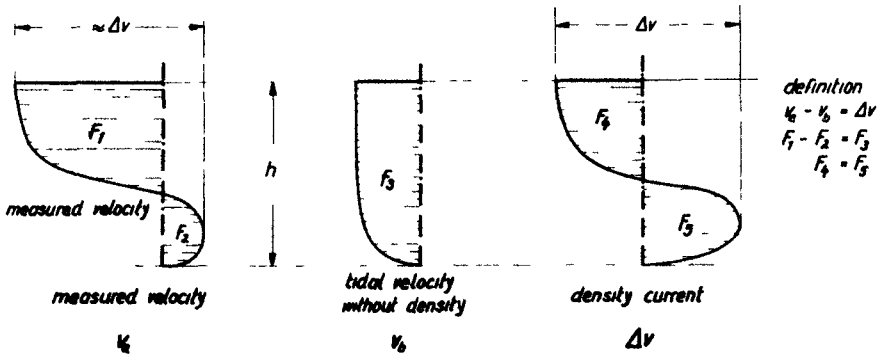


FIG. 6 DEFINITION OF DENSITY CURRENT

The experiments in the flume of the FRANZIUS-INSTITUT have shown that the densimetric FROUDE number is a good parameter for approximating the density currents in mixed channels also. In one vertical axis ρ_1 is the density on the bottom and ρ_2 is the density on the surface of the flume

Fig 7 compares the average density differences (which are linear to the salinity differences) over the whole tidal circle in the three vertical axes of fig 1 with the average density current Fig 7 shows that all experiments give an average densimetric FROUDE number smaller than $F_d = 1$

The compensating straight line gives

$$F_d = 0.6$$

The computed densimetric FROUDE numbers for every test result of fig. 7 are shown on fig. 8 with the average hori-

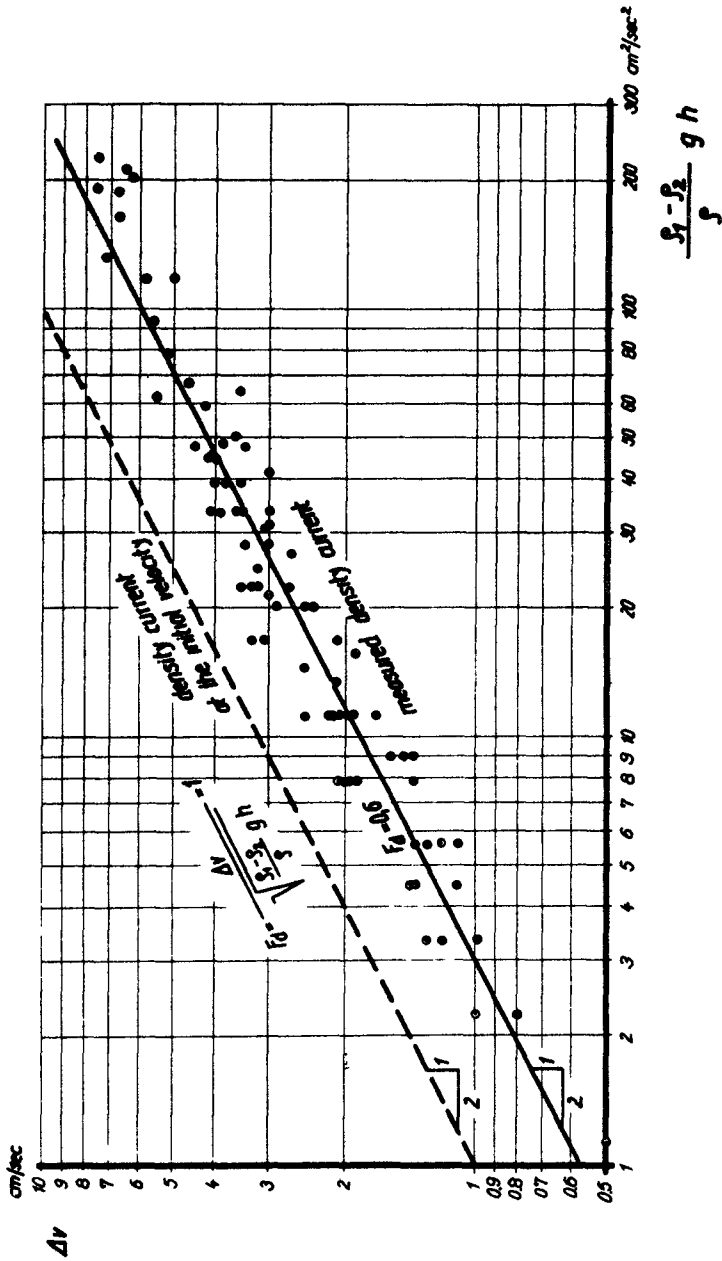


FIG. 7 DENSITY CURRENT VERSUS VERTICAL DENSITY DIFFERENCE

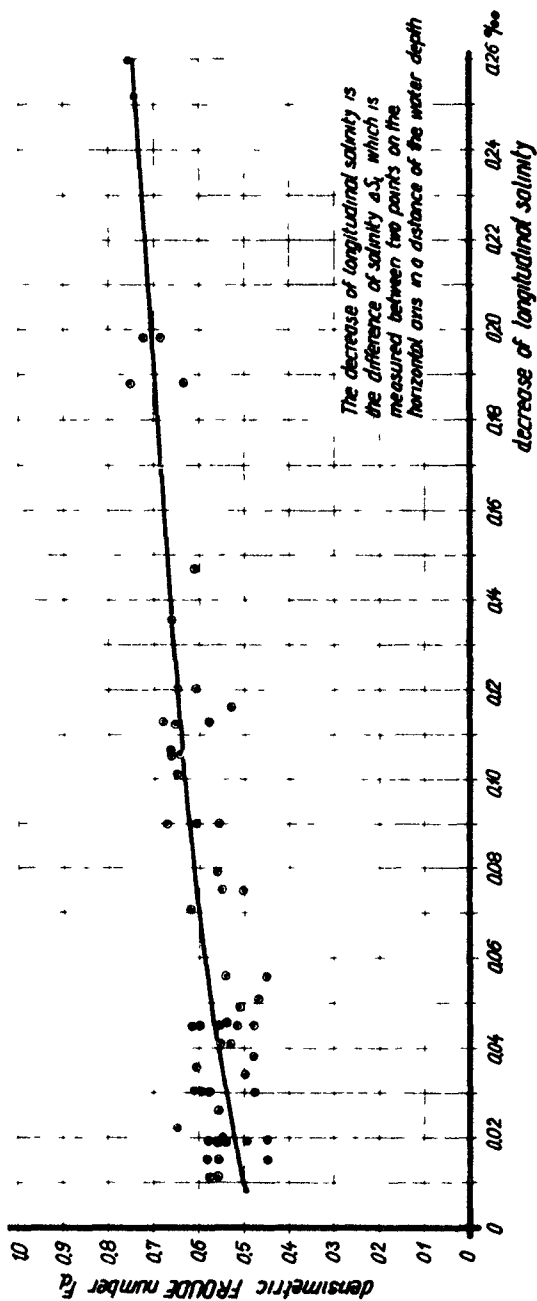


FIG. 8 DENSIMETRIC FROUDE NUMBER AND AVERAGE DECREASE OF LONGITUDINAL SALINITY

zontal salinity gradient of the same experiment. The average horizontal salinity gradient here is explained as the decrease of longitudinal salinity in a horizontal distance of the same length as the water depth.

From fig 8 can be derived what ABBOTT (ref 1) has proposed in a different form from prototype observation. If two estuaries have the same vertical salinity distribution and the same depth but unequal lengths of the salinity intrusion, the estuary with the shorter intrusion length has higher density currents than the longer one.

Fig 8 cannot show the dependence of density currents on the change of the salinity distribution, because it is derived from time-averaged measurements. This dependence can be read from fig 9 which shows the maximum density currents. In the flume the maximum density currents occurred shortly before the highest density on the bottom was reached. On fig 9 the densimetric FROUDE number is compared with the change of density difference during the time of two tidal phases (2/24 of one tidal circle).

$\Delta\rho_n$ denotes the vertical density difference at the tidal phase of maximum density current, $\Delta\rho_{n-2}$ denotes the vertical density difference measured 2 tidal phases before. If the change of density difference is zero, the value on the abscissa is

$$\frac{\Delta\rho_n}{\Delta\rho_{n-2}} = \frac{\Delta S_n}{\Delta S_{n-2}} = 1$$

At this point fig 9 gives $F_d =$ about 0,5. So the maximum density current in an estuary where the salinity differences do not change quickly, can be computed as the average density current in fig 8.

If

$$\frac{\Delta\rho_n}{\Delta\rho_{n-2}} = \frac{\Delta S_n}{\Delta S_{n-2}} \quad \text{tends to } \infty, \quad F_d \text{ tends to } 1$$

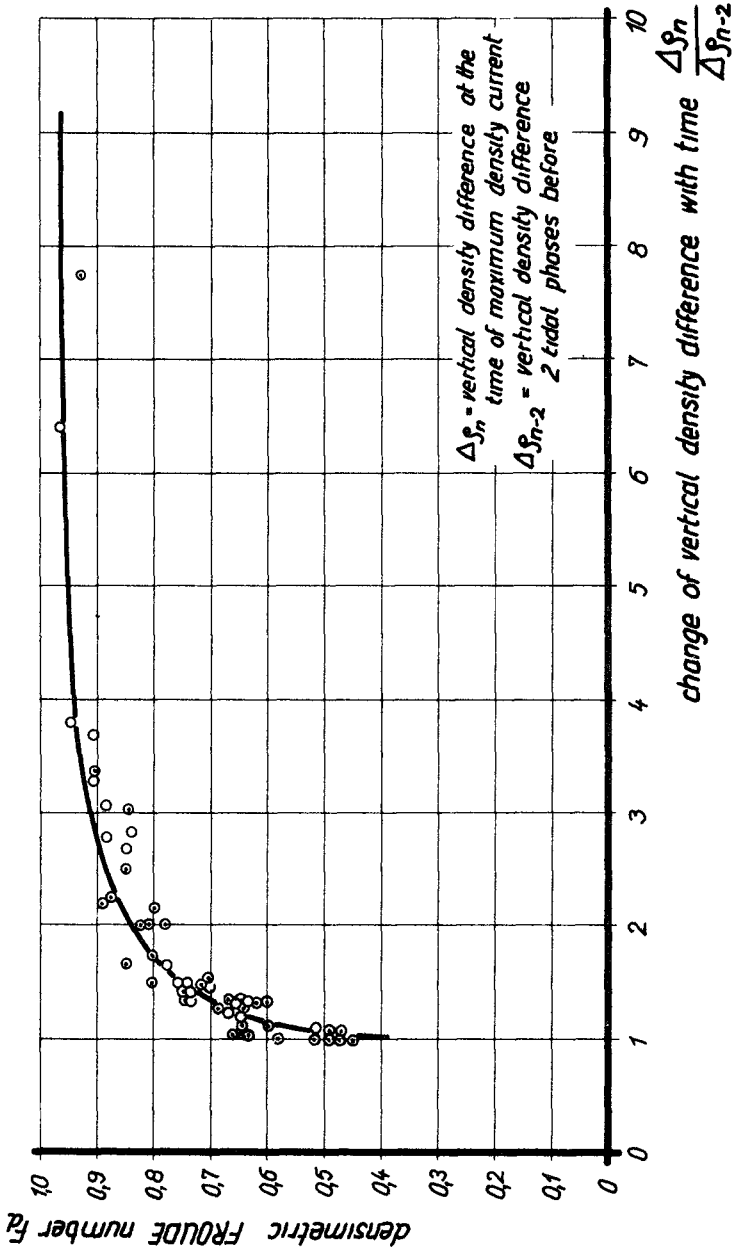


FIG 9 DENSIMETRIC FROUDE NUMBER AND CHANGE OF DENSITY DIFFERENCE WITH TIME

This is evident, because estuaries in which density differences change abruptly, approach the state of the initial velocity as in the experiment of fig 5

5 CONCLUSIONS

The model experiments of the FRANZIUS-INSTITUT represented the salinity distribution in an idealized estuary of various mixing stages. The density currents show a dependence on the vertical salinity distribution (densimetric FROUDE number), on the longitudinal salinity distribution, and on the change of salinity with time

6. REFERENCES

- 1 ABBOTT, M B Salinity effects in estuaries. Sears Foundation, Journal of Marine Research, Vol 18, No. 2, October 1960
- 2 ABRAHAM, G and Pneumatic reduction of salt intrusion
v d BURGH, P. through locks. Proceedings ASCE, Journal of the Hydraulics Division, January 1964
- 3 ALLEN, F H and Density currents and siltation in
PRICE, W.A docks and tidal basins. The Dock and Harbour Authority, July 1959
- 4 BARR, D.I H Densimetric exchange flow in rectangular channels. La Houille Blanche, November 1963
- 5 GOLE, C V and Progressive salinity intrusion during
THAKER, V S dry season in the Hooghly estuary. Proceedings, 13th Congress IAHR, Vol 3, Subj C, Kyoto 1969
- 6 HARLEMAN, D.R F , The diffusion of two fluids of different
JORDAN, J.M , and density in a homogenous turbulent
LIN, J D field. Massachusetts Institute of Technology, Hydrodynamics Laboratory, Techn Report No 31, 1959

- 7 HARLEMAN, D R.F.,
McDOUGALL, D W ,
GALVIN, C J , and
HOOPES, J.A. An analysis on one-dimensional con-
vective diffusion phenomena in an
idealized estuary Massachusetts
Institute of Technology, Hydrodynam-
ics Laboratory, Techn Report No 42,
1961
- 8 HARLEMAN, D.R.F
and HOOPES, J.A The prediction of salinity intru-
sion changes in partially mixed
estuaries. 10th Congress IAHR,
Vol 1, 1 15, London 1963
- 9 HARLEMAN, D.R F
and ABRAHAM, G One dimensional analysis of sali-
nity intrusion in the Rotterdam
Waterway. Delft Hydraulics Laborato-
ry, Publ No 44, 1966
- 10 IPPEN, A T ,
HARLEMAN, D.R.F
and LIN, J D. Turbulent diffusion and gravitatio-
nal convection in an idealized
estuary Massachusetts Institute of
Technology, Hydrodynamics Laborato-
ry, Techn Report No 38, 1960
- 11 IPPEN, A T and
HARLEMAN, D R F One dimensional analysis of salini-
ty intrusion in estuaries Corps of
Engineers, U.S Army, Committee on
Tidal Hydraulics, Techn Bull No 5,
January 1961
- 12 IPPEN, A T. ed Estuary and coastline hydrodynamics
McGraw-Hill, 1966
- 13 O'BRIEN, M P and
CHERNO, J Model law for motion of salt water
through fresh Transactions ASCE,
No 99, 1934
- 14 PARTENSCKY, H W
and LOUCHARD, L Etude sur le vartion cyclique de la
salinité moyenne dans l'estuaire du
Saint-Laurent Université de
Montréal, École Polytechnique, Di-
vision d'Hydraulique, Sep. 1967
- 15 PARTHENIADES, E Field investigations to determine
sediment sources and salinity in-
trusion in the Maracaibo estuary,
Venezuela Massachusetts Institute
of Technology, Hydrodynamics Labo-
ratory, Report No 94, June 1966

CHAPTER 121

Computation of Storm Surge

RICHARD SILVESTER

Professor of Coastal Engineering
Asian Institute of Technology, Bangkok, Thailand

ABSTRACT

From knowledge of wind resistance coefficients measured over the sea, it is possible to compute the shear stress of a wind field on its surface. Where a body of water is relatively shallow, such a shear stress will transport water to the downwind end and so create a high water level or surge. Graphs are presented for ready application of the relevant formulae to cases of lakes and Continental Shelves. The wind fields of either uniform or triangular horizontal distribution in velocity are included, as well as conditions of stationary or moving fetches. Surges from seven typhoons travelling towards Hong Kong are computed and compared to actual records.

INTRODUCTION

Wind stress on a water surface is a function of its roughness, particularly in respect to the shorter period waves in the spectrum. Hence an enclosed body of water can be hydrodynamically rougher than the open sea where the shorter waves are dissipated with the assistance of the longer ones. Formulae available can be put in graphical form for the computation of surge heights. These apply to lakes or Continental Shelves. With the latter the ratio of fetch length to Shelf width assumes importance, as well as velocity of approach of the fetch and the horizontal distribution of the wind velocity. Application of the graphs to a number of typhoons approaching Hong Kong indicates the accuracy of the procedure.

WIND STRESS

The shear stress applied by the wind to a water surface depends upon its smaller roughnesses and hence the wave conditions. Wu⁽¹⁾ has shown that waves in the order of 0.7 seconds period and 0.1 metre height are the main roughness element. The stress thus varies with the wind velocity and the fetch available. For this reason it is understandable that optimum values can be reached which are different for enclosed bodies of water of limited size and the open sea. The former contain a larger proportion of short waves that are reaching, or are at, their limiting steepness. The latter, however, when they approach the fully arisen state, contain less of the short period components and more of the longer period waves⁽²⁾. For this reason the

sea is slightly smoother as far as wind stress is concerned. It can be presumed therefore that the stress of a given steady wind can also vary with duration.

The shear stress is given by

$$\tau = \rho_a U^2 \text{-----(1)}$$

where ρ_a = density of air
 U^a = shear velocity near the water surface
 this can be expressed as

$$\tau = \rho_a C_y U_y^2 \text{-----(2)}$$

where C_y = resistance coefficient varying with U_y
 U_y = wind velocity at y metres above water surface

Many workers (3)(4)(5) have evolved relationships for C_y and U_y from measurements over lakes and the sea. Wu (6) has summarised these data and discussed their significance, from which Figure 1 has been prepared. This shows C_{10} for a range of U_{10} , as most wind measurements have been made at the 10 metre height. Within the boundary of the experimental values the relationships presented by various workers is also shown, including the stepped curve of Wu. It is now generally accepted that a limiting value of $C_{10} = 2.6 \times 10^{-3}$ can be applied to limited water bodies when the 10 metre high wind exceeds 10 metres/sec or 30 knots. The optimum for the ocean is $C_{10} = 2.4 \times 10^{-3}$. For winds less than this a relationship of

$$C_{10} = 0.65 \cdot 10^{-3} U_{10}^{-\frac{1}{2}} \text{-----(3)}$$

would follow Sheppard's curve reasonably well to the aforesaid limits. To convert wind velocities from other levels to the 10 metre height, graphs have been provided elsewhere (7).

In storm surge calculations it is more appropriate to use the relationship

$$\tau = k \rho U_{10}^2 \text{-----(4)}$$

where ρ = density of the water

so that $k = \frac{\rho_a}{\rho} C_y$, which for seawater = $\frac{1}{800} C_{10}$

the limiting values of $k = 3.3 \times 10^{-6}$ and 3.0×10^{-6} apply to lakes and ocean areas respectively.

A scale for k is included in Figure 1, together with scales for U_{10} in knots and designations of Beaufort Number and Sea State.

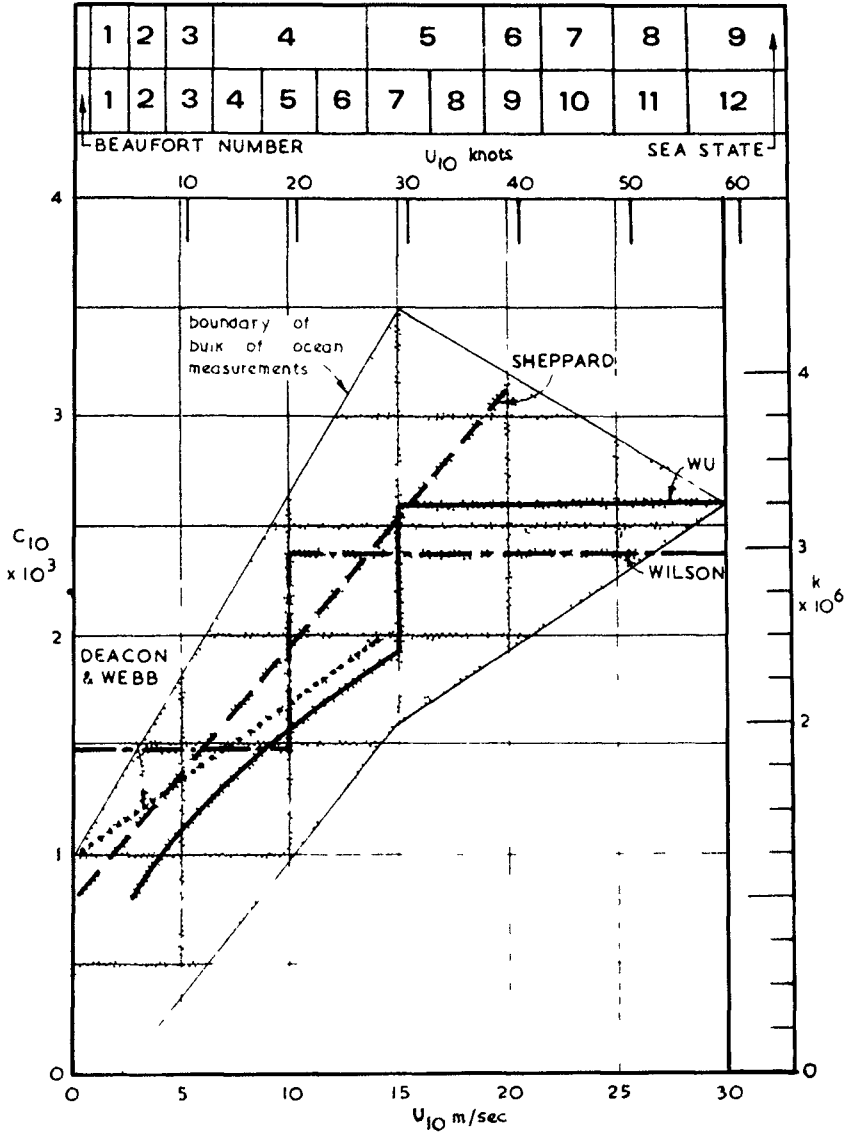


Fig 1 Variation of wind resistance coefficient with wind velocity

ENCLOSED BODIES OF WATER

Considering a lake of rectangular proportions in plan, its longitudinal cross-section can be equated to a rectangular one of equal area, giving an equivalent depth d and length or fetch L . The equation for the water surface profile⁽⁸⁾⁽⁹⁾⁽¹⁰⁾ when a steady wind velocity U_{10} is applied to it is

$$\frac{S}{d} = \frac{k_{10} U_{10}^2 L}{2 g d(d+S)} = \frac{k_{10} U_{10}^2 L}{2 g d^2} \text{ -----(5)}$$

where S = surge height at the down wind end. The last form of the equation assumes S to be small in respect to d . Equation (5) also approximates the nodal point at the centre of the length L .

The variables in this dimensionless equation must be chosen consistently. The values of the fall and rise of the water surface at the upwind and downwind ends of the lake are presented in graphical form in Figures 2 and 3, for the two conditions of bottom exposure at the upwind end. The surface passes through the mean depth plane around the centre of the water body⁽⁸⁾ even when part of the bed is exposed. Lakes of irregular depth can be treated similarly by determining an equivalent rectangular section.

In the case of narrow bodies of water such as canals the same value of $k_{10} = 3.3 \times 10^{-6}$ is applicable since the optimum roughness is due to waves of about 1 second period⁽¹¹⁾ reaching their maximum steepness of 1/7.

For the case of non-rectangular planar shapes, of uniform depth or sloping bottoms, Keulegan⁽¹¹⁾ has derived some form factors N by which the values of S/d in equation (5) should be multiplied. These are illustrated in Figure 4, where the exponential form analysed by Langhaar for constant depth d , and trapezoidal shapes with uniform depth or uniformly sloping bottom are presented. The high values of N resulting from the downwind depth decreasing should be noted. The same order of magnification will be observed for similar shoaling on the Continental Shelf.

CONTINENTAL SHELF - STATIC WIND FIELD

Where a wind is applied to the Continental Shelf blowing towards the shore, the Shelf width can be taken as half the length of the lake considered previously. The water feeding the surge comes from the deep ocean. The major difference from the previous situation is the decreasing depth towards the shore. For the purposes of surge calculation it is reasonable to assume a uniform variation from a depth d_1 at the Shelf edge to d_2 near the coast (see inset of Figure 5).

Surge problems assume importance on reasonably wide Continental Shelves. The majority of these have been constructed by sediment deposition for which waves are the predominant distributing factor.

It is not surprising, therefore, that most of these Shelf edges occur at around 65 fathoms⁽¹²⁾, or the reach of the 12-14 second waves, which are the most persistent swell waves of the oceans⁽¹³⁾. Thus, unless more specific information is available the depth d_1 may be taken as 400 feet (120 metres). On sandy shorelines the beach profile is parabolic from the breaker line, which produces depths of 5 fathoms very close to shore. It is such depths, rather than zero values at the beach, that are more effective in the surge phenomenon. Where a large tidal range occurs, or sediment of silt character exists, large tidal flats will necessitate the use of much smaller values of d_2 .

The width of the Shelf will be designated as L , which can be different from the fetch length F of the wind zone. As seen in Figure 5 the depth ratio d_1/d_2 can be equally expressed by L/x where x is distance inland where the plane of the bed meets the mean water level.

Where a storm zone has a fetch length (F) in excess of the Shelf width (L), only that portion across the relatively shallow zone is effective in producing surge, thus $F = L$. This is likely to be the case in extra-tropical cyclones, where wide expanses of ocean can suffer winds of uniform speed and direction. In tropical cyclones the fetch lengths are smaller and are more likely to be less than the Shelf width. This case is discussed later, together with the problem of velocity of advance (V) of the wind field.

(a) Uniform Wind Velocity ($V=0$)

For a wind of steady and uniform speed applied to a Continental Shelf the following formula has been derived⁽¹⁴⁾

$$S = \frac{k U^2 L}{g(d_1 - d_2 - S)} \ln \left(\frac{d_1}{d_2 + S} \right) \quad \text{-----(6)}$$

Since S is small compared to d_2 equation (6) can be rewritten

$$\frac{S}{d_1} = \frac{k U^2}{g d_1} \left(\frac{L}{d_1 - d_2} \right) \ln \frac{d_1}{d_2} \quad \text{-----(7)}$$

so that
$$\frac{S}{d_1} = \frac{k U^2 L}{g d_1^2 (1 - d_2/d_1)} \ln \frac{d_1}{d_2} \quad \text{-----(8)}$$

Values of S/d_1 versus $k U^2 L / g d_1^2$ have been graphed in Figure 5 for the range of $L/x = F/x = 0.01$ to 1000 or $d_1/d_2 = 1.01$ to 1001 (the latter approximating $d_2 = 0$)

(b) Triangular Wind Velocity ($V=0$)

The wind in a tropical cyclone is circular in character, but is deflected towards the centre such that it is around 45° to the radii

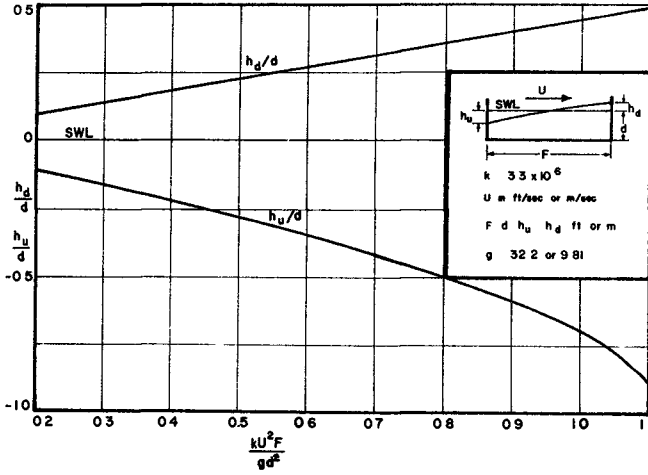


Fig 2 Upwind and downwind surge levels in a lake of uniform depth

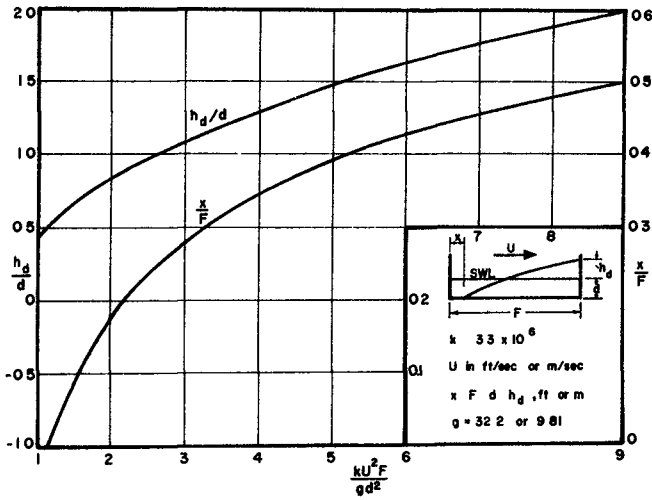


Fig 3 Surge levels in a lake when the upwind bed is exposed

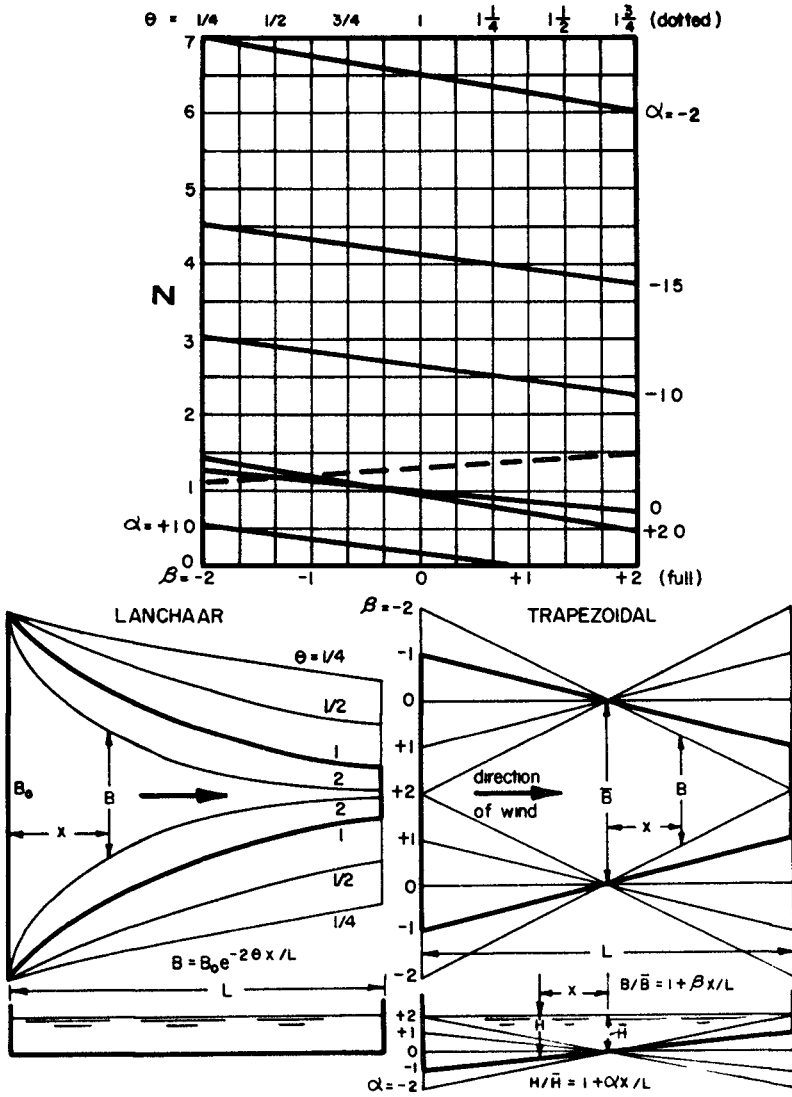


Fig 4 Amplification factor N for Langhaaar shaped and trapezoidal lakes

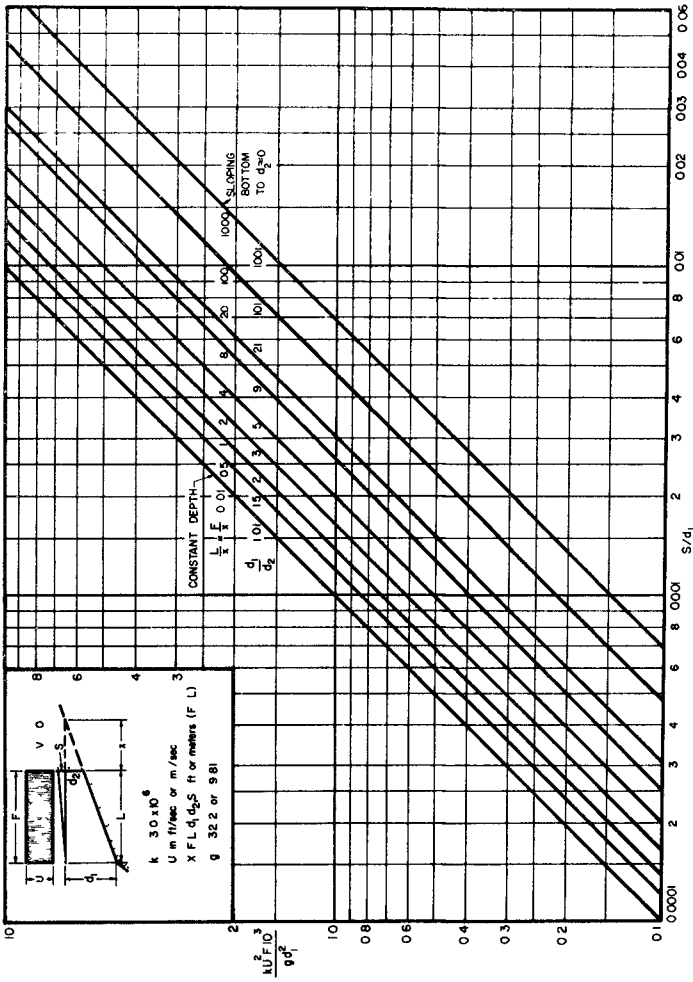


Fig 5 Surge produced by a static uniform wind field extending across the Continental Shelf

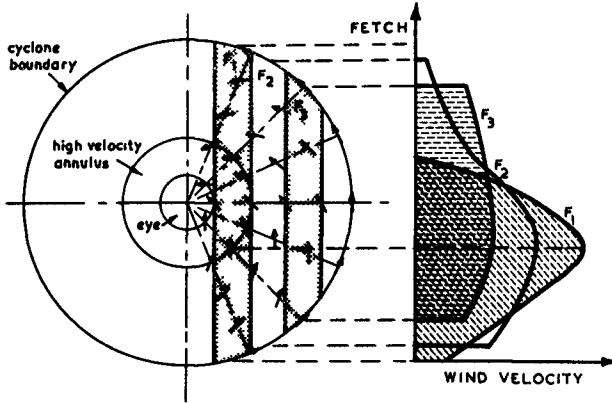


Fig 6 Typical surface wind structure inside a tropical cyclone

(See Figure 6) As the cyclonic centre moves forward the critical conditions as far as surge as well as wave generation is concerned are contained in the quadrant for which the centre and wind vectors are in same direction. The cyclone depicted in Figure 6 represents air circulation for the northern hemisphere in which the right rear quadrant contains the critical conditions for surge generation. The worst affected coastal zone will be that in line with fetch F_1 passing through the high velocity annulus. The assessment of wind components along this alignment will result in a triangular distribution of velocity (See Figure 6), the shape of which depends greatly on the radial distribution of the wind around the centre.

For a triangular wind distribution of more-or-less isosceles shape Reid⁽¹⁵⁾ has derived the following surge formula

$$s = \frac{k U^2 T}{C_1} \left(\frac{d_1}{d_2}\right)^{\frac{1}{2}} z \quad \text{-----(9)}$$

where T = mean time for surge wave to traverse the Shelf
 C_1 = celerity of the surge wave at the Shelf edge ($= \sqrt{gd_1}$)
 z = factor, ($= 0.56$ for $F = L$ and $V = 0$)

Substituting $T = \frac{L}{\frac{1}{2}(\sqrt{gd_1} + \sqrt{gd_2})}$ into equation (9) gives

$$\frac{s}{d_1} = \frac{k U_{\max}^2 L}{gd_1^2} \left[\frac{1.12}{1 + \sqrt{d_2/d_1}} \left(\frac{d_1}{d_2}\right)^{\frac{1}{2}} \right] \quad \text{-----(10)}$$

Equation (1) has been graphed in Figure 7 in a similar manner to Figure 5 for a similar range of $\frac{d_1}{d_2}$ or $\frac{L}{x} + 1$.

CONTINENTAL SHELF - MOVING WIND FIELD

In the case of the storm centre travelling towards the coast the initial surge wave is being reflected as later portions are still approaching. The interaction of these establishes a new surge system which Reid⁽¹⁵⁾ has analysed for various ratios of F/L and V/C

where $\bar{C} = L/T = \frac{1}{2}(\sqrt{gd_1} + \sqrt{gd_2})$ -----(11)

From the graphs so presented the ratio R of maximum surge (S_{max}) to that for static storm conditions (S) (i.e. F = L and V = 0) has been plotted as in Figure 8, for both uniform and triangular wind distributions. To find S_{max} it is necessary first to compute S for a hypothetical shelf whose width L equals the fetch length F (not the reverse). With this noted, then R is obtained from the combination of F/L and V/C. It is seen that the influence of the storm-centre speed differs in the two wind distributions. Reid's analysis⁽¹⁵⁾ also provides information on the timing of the maximum surge in respect to the location of the fetch, but this has not been included.

The absolute resultant is determined also by the depression of atmospheric pressure, which may precede or be concurrent with S_{max} from the wind alone. The surge due to air pressure is given by

$S_a = (\frac{1013-p_c}{34}) \frac{13.59}{121.003} = (1013-p_c) 0.033$ -----(12)

where S_a = storm surge in feet of seawater
and h_c^a = pressure at the storm centre in millibars (34 millibars = 1" mercury)

This value should be added to that obtained in the previous equations

EXAMPLES OF HONG KONG TYPHOONS

Since 1962 the Department of Public Works in Hong Kong has collated some valuable data on typhoons approaching the vicinity of the island. These have been summarised in a data sheet for each event, in which rainfall, wind speed, wind direction, atmospheric pressure, and sea-level are plotted against time in hours. On the sea-level graph is traced the normal tide curve as predicted in tide tables, from which the surge level can be obtained. The chronological relationship between the variables listed provides sufficient information to draw a plan of the cyclone and to determine its diameter. A geographic plan of the ocean area with the typhoon path traced on it with time markings, permits the speed of travel to be assessed. The distance across the Continental Shelf that the typhoon has traversed can also be measured. The wind speed trace indicates whether a triangular or rectangular distribution has produced the surge. A modified reproduction of one PWD data sheet is illustrated in Figure 9.

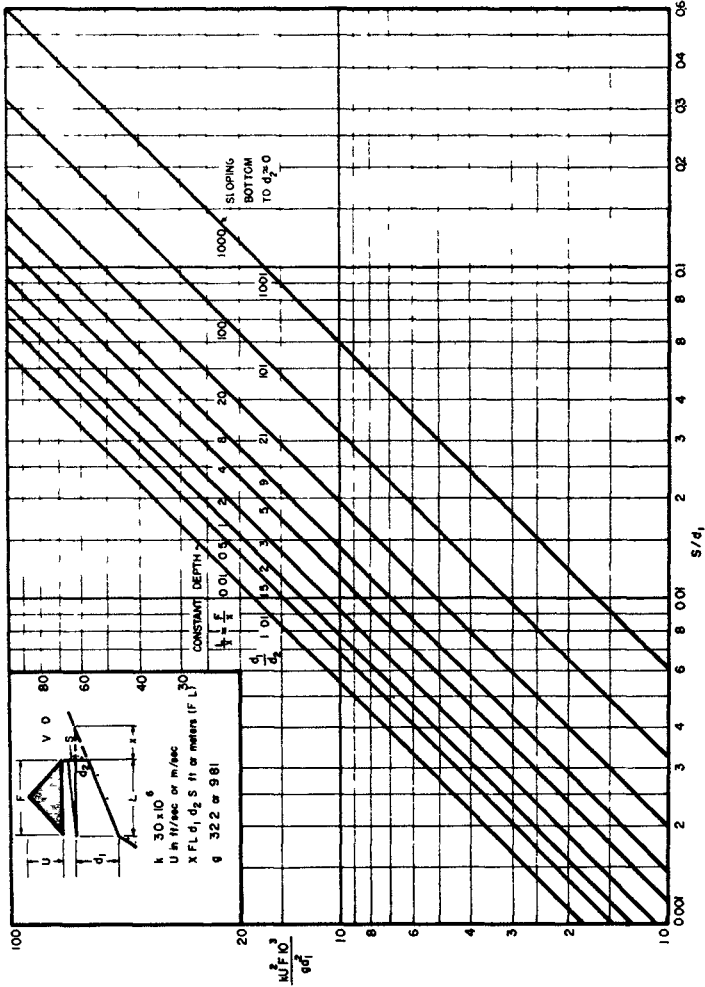


Fig 7 Surge produced by a static triangular wind field extending across the Continental Shelf

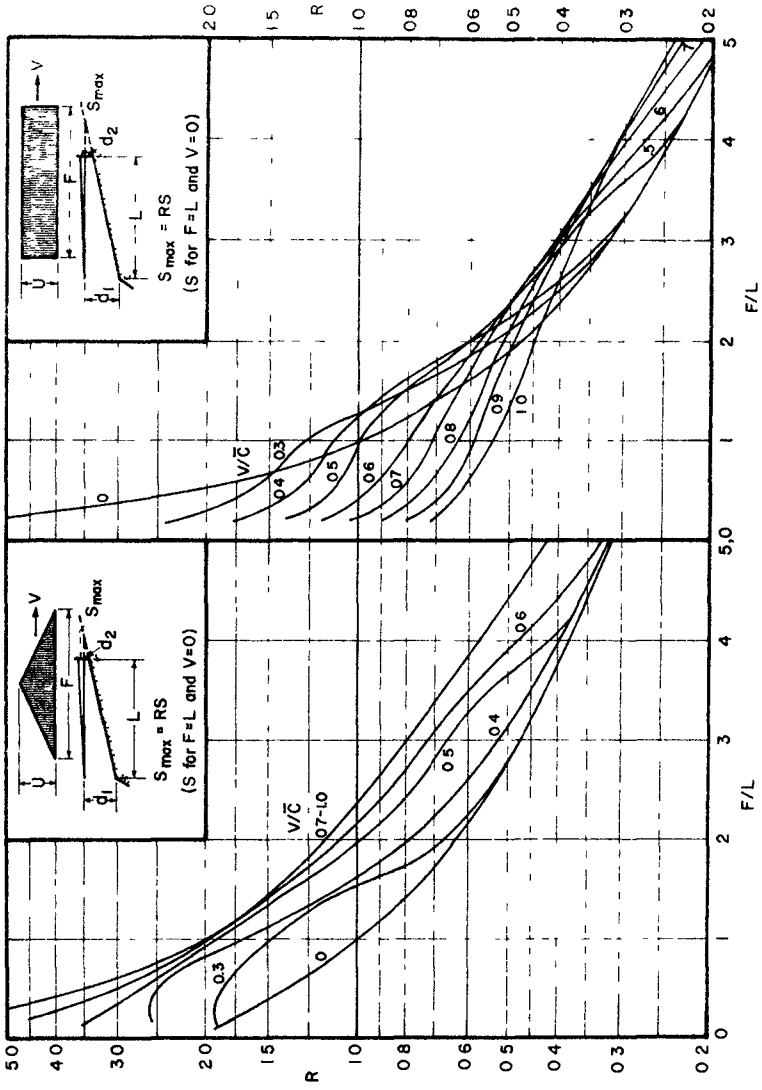


Fig 8 Optimum surge resulting from various fetch lengths and velocities of advance

**DATA SHEET FOR TYPHOON RUBY
PREPARED BY PORT WORKS OFFICE
(PWD) HONG KONG**

INFORMATION OMITTED FROM ORIGINAL

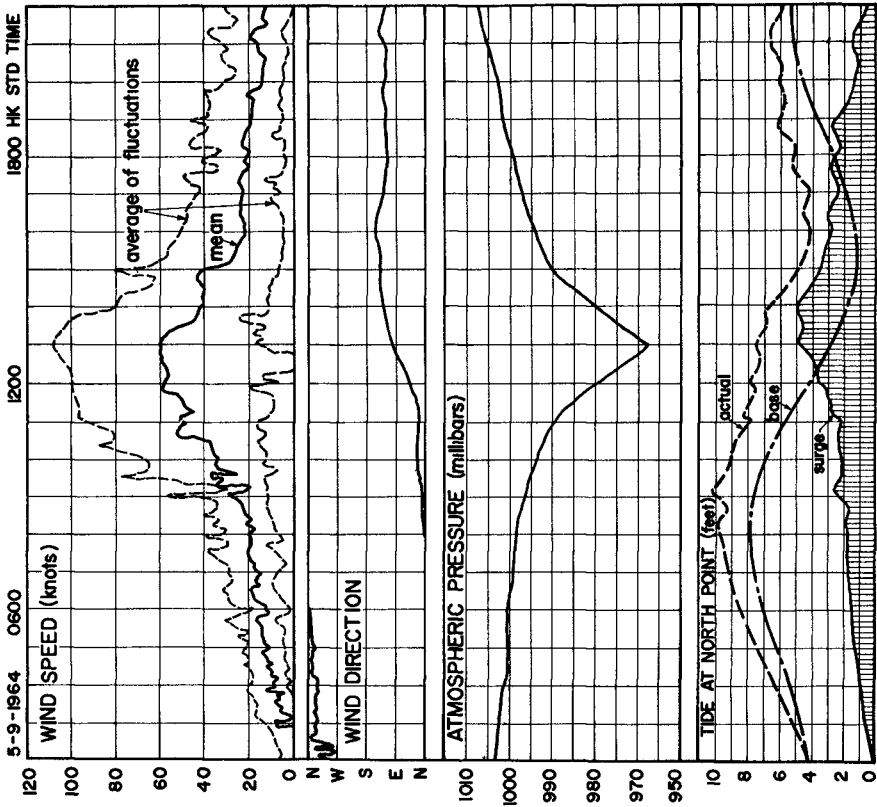
RAINFALL

TIDES AT OTHER LOCATIONS

PLAN OF HONGKONG & VICINITY

DATA PRIOR TO & SUBSEQUENT TO

5TH SEPTEMBER



TRACK OF TYPHOON

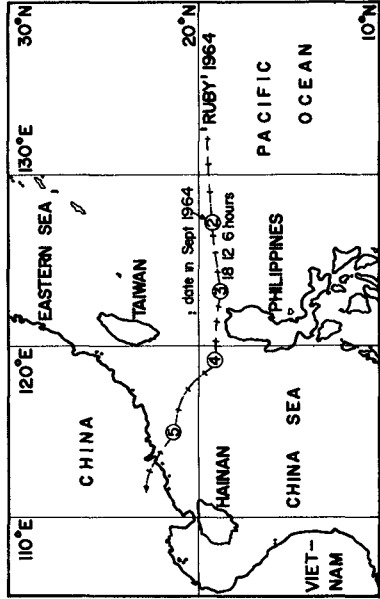


Fig 9 Limited reproduction of a typhoon data sheet produced by the Department of Public Works, Hong Kong

Data as above are available for seven typhoons, as listed in Table I, where relevant parameters leading to the final surge (S_f) are included. Comparison of the computed and measured values indicates the accuracy of the procedure presented.

To determine a surge prior to its arrival, the possible path in respect to the site must be assessed. The maximum wind speed at the boundary of the eye is a function of the atmospheric depression at the centre. Kraft⁽¹⁶⁾ provides an equation for Atlantic hurricanes as follows

$$U_{\max} = 14 \sqrt{1013 - p_c} \quad \text{-----(13)}$$

where U_{\max} is expressed in knots for p_c in millibars

Equation (13) may not be applicable to typhoons or more modest tropical cyclones

From table I the only typhoon which was centered on Hong Kong, and for which values could be used for verification, is that of Wanda when $U_{\max} = 80$ knots for $1013 - 952 = 61$ millibars. This would indicate a relationship of

$$U_{\max} = 10.3 \sqrt{1013 - p_c} \quad \text{-----(14)}$$

The overall diameter of typhoons in the Western Pacific is around half of those normally recorded for Atlantic hurricanes. It is not unreasonable, therefore, to expect lower wind velocities for any given atmospheric depression. Such data should be compiled for a region under study, when optimum storm surges are required to be calculated.

The optimum water level to be expected can be computed from a knowledge of the most severe tropical cyclones known to exist in the area. The fetch for this should then be traversed across the Continental Shelf at the critical speed, to hit the coast just to the left (northern hemisphere) or right (southern hemisphere) of the port under study. This maximum surge should then be added to MHW level which can occur during the cyclone period of the year. Should the harbour be located near the head of a funnel shaped inlet, or one that has a shoaling approach channel, an amplification factor⁽¹⁷⁾ may have to be determined for the surge level computed for the mouth.

ACKNOWLEDGEMENTS

Appreciation is expressed to the Department of Public Works, Hong Kong, who supplied copies of their typhoon data sheets and gave permission for publication of this material.

Table I Comparison of computed and measured surges at North Point, Hong Kong harbour

Name Date	Wanda Sept 62	Faye Sept 63	Viola May 64	Ida Aug 64	Ruby Sept 64	Sally Sept 64	Shirley Aug 68
Δp (mb)	61	17	21	38	45	24	44
S_a (feet)	2 02	0 57	0 70	1 27	1 50	0 80	1 47
U_{max} (knots)	80	25	30	45	60	35	42
Distribution	Δ	\square	\square	Δ	Δ	Δ	Δ
F (NM's)	55	220	110	210	166	107	90
d_1 (feet)	400	400	400	400	270 ⁽¹⁾	400	400
$k U^2 F 10^3 / g d_1^2$	3 55	1 4	1 0	4 3	13 7	1 32	1 6
$S/d_1 \times 10^3$ (Figs 5 & 7) ⁽²⁾	5 5	3 8	2 7	6 5	20 0	2 0	2 5
S (feet)	2 2	1 52	1 08	2 6	5 4	0 8	1 0
L (NM's)	180 ⁽³⁾	240 ⁽⁴⁾	120	120	80 ⁽¹⁾	120	120
F/L	0 3	0 92	0 92	1.75	2 08	0 89	0 75
V (knots)	12	10	8	15	12 8	13 3	9 1
V/\bar{C}	0 280	0 234	0 187	0 350	0 348	0 312	0 213
R (Fig 8)	1 9	1 3	1 4	0 9	0 7	1 6	1 5
S_{max} (= RS)	4 18	1 98	1 51	2 34	3 78	1 28	1 5
S_t (= $S_a + S_{max}$)	6 20	2 55	2 21	3 61	5 28	2 08	2 97
S (measured)	4 6 ⁽⁵⁾	2 8	3 0	4 0	5 0	1 8	3 0

- (1) Typhoon changed direction part way across Shelf where $d_1 = 270$ feet and $L = 80$ NM's
- (2) Assuming $d_2 = 30$ feet
- (3) Approach was from ESE, equivalent $L = 180$ NM's
- (4) Approach was from east, equivalent $L = 240$ NM's
- (5) Tide gauge out, water mark observations only

REFERENCES

- (1) Wu J "A criterion for determining air-flow separation from wind waves", *Tellus* 21, 1969, 707-714
- (2) Barnett T P and A J Sutherland "A note on an overshoot effect in wind generated waves" *J Geoph Res* , 1968, 6879-6885
- (3) Sheppard P A "Transfer across the earth's surface and through the air above", *Quart J Roy Met Soc* , 84, 1958, 205-224
- (4) Deacon E L and E K Webb "Small scale interaction" *The Sea* (Ed M N Hill) Interscience N Y 1962
- (5) Wilson B W "Note on surface wind stress over water at low and high wind speeds", *J Geoph Res* 65, 1960, 3377-3382
- (6) Wu J "Wind stress and surface roughness at sea interface" *J Geoph Res* 74, 1969, 444-455
- (7) Silvester R and S Vongvisessomjai "Energy distribution curves of developing and fully arisen seas" *J Hyd Res* (In Press)
- (8) Hellstrom B "Wind effect on lakes and rivers" *Roy Inst of Tech Stockholm, Bull* 41, 1941
- (9) Langhaar H L "Wind tides in inland waters" *Proc Mid Western Conf on Fluid Mechs* , 1951, p 278
- (10) Keulegan G H "Wind tides in small closed channels" *J Res of Nat Bur Stds* , 46, 1951
- (11) Keulegan G H "The form factor in wind-tide formulas", *Nat Bur Stds Rep No* 1835, 1952
- (12) Shepard F D Submarine Geology (2nd Ed) Harper & Row N Y , 1963
- (13) Silvester R and S Vongvisessomjai "Computation of Storm Waves and Swell" *Proc I,C E* (In Press)
- (14) Bretschneider C L "Engineering aspects of hurricane surge" *Estuary and Coastline Hydrodynamics* (Ed A T Ippen), McGraw-Hill, 1966, 231-256
- (15) Reid R O "Approximate response of water level on a sloping shelf to a wind fetch which moves towards shore" *Beach Erosion Board, Tech Mem No* 83, 1956
- (16) Kraft R H "The hurricane's central pressure and highest winds" *Mariners Weather Log* 5(5), 1961
- (17) Silvester R "Tides and long period waves on continental margins" *Proc 13th Congress I A H R* , 3, 1969, 113-121

CHAPTER 122

STATISTICAL PREDICTION OF HURRICANE STORM SURGE

by

C Y Yang, A M Parisi, and W S Gaither*

Abstract

High water associated with a hurricane is an important design parameter in coastal engineering. Long range rational predictions can be made on the basis of Gumbel's theory of extremes and Wemelsfelder's theory respectively. Fundamentals and underlying assumptions of the two theories are investigated and predictions are made for Breakwater Harbor, Lewes, Delaware, and Atlantic City, New Jersey. Gumbel's theory is found satisfactory according to a criterion. A crucial point, the ground rule of counting exceedances, is found to be vague in Wemelsfelder's method. The ground rule must be made definite in a meaningful prediction.

Introduction

In coastal protection projects, marine operations in harbors, and marine structural design, a reliable prediction of the extreme sea state associated with a hurricane is of utmost importance because of damages to lives and property.¹ The engineer would want to know the answers to the following simple questions: How high will the sea level rise? How often do the high water levels occur in the future? How long does each high water level last when it occurs? How high will the highest wave crest be? How often does the high waves occur and how long do they last? What are the oscillatory characteristics of the extremely strong waves? In answering these questions a large amount of research work has been conducted generally in two categories -- deterministic and probabilistic approaches. In 1966 Harris investigated the characteristics of observed hurricane surges in the States.² Bretschneider in 1959 studied local surges for the Delaware Bay.³ He made predictions of water level and waves in the bay for a given hurricane storm nearshore by a deterministic approach.⁴ Such a study and similar ones as by LaSeur⁵ and Moore⁶ in 1966, provide useful information for short-time (days) forecast and warning systems.

¹All superscript numbers refer to those in the Bibliography

* Associate Professor of Civil Engineering, Research Fellow of Civil Engineering and Dean of the College of Marine Studies, respectively, University of Delaware, Newark, Delaware 19711

For long-time (50 years) predictions, a deterministic approach based on laws of mechanics is too complicated and consequently the only rational approach is one based on laws of probability and statistics of past records. Indeed this was recognized for quite sometime and important research work was published by Wemelsfelder in 1961, on high water levels, by Pierson and Marks in 1952 on wave spectrum analysis, and by Cartwright and Lonquet-Higgins in 1956 on high wave crests. More recently Frendenthal in 1969 outlined the many important aspects of probabilistic design of marine structures. He and Gaither further investigated the economic aspects in design.¹⁰ In a series of papers Borgman investigated wave force on piles¹¹ and spectral density for ocean wave forces.¹²

In this paper we are concerned with the prediction of extreme mean sea levels generally associated with hurricanes near the Delaware coast by a statistical approach. The term hurricane surge is used as by Weigel¹³ to indicate a general association between extreme high water and a hurricane storm, though the analysis is not restricted to those caused by hurricanes. This study is aimed at answering the question of how high the extreme water level will be and how often each extreme water level will occur near the Delaware coast in the future years and decades. It is based on a rational analysis by Gumbel and Wemelsfelder, respectively.

Gumbel's Theory

The well known statistical theory of extremes now associated with Gumbel's name was originated in the early twentieth century. In the 1930's in a series of papers Gumbel presented important developments of the theory and its applications in a variety of problems -- breaking strength of materials, floods and gust winds and stock market trends.¹⁴ The fundamentals may be introduced by its application to our title problem.

At Breakwater Harbor, Lewes, Delaware mean sea-level records have been obtained giving monthly maximum levels for the period 1953-1969. Our problem is to predict the occurrence of high water levels in the future based on these available records and Gumbel's theory. First we concentrate our attention on the maximum height in each year of 365 days. Clearly the annual maximum level is a random variable which we can not predict definitely rather only with probability statements. Let the random annual maximum be denoted by X . The probability that X be less or equal to a certain quantity x is the same as the probability that all 365 daily water levels are less or equal to x . Furthermore, if we assume that random daily levels are independent to one another and have a common probability distribution, then

$$F_X(x) = [F_{X_0}(x)]^n$$

where X_n denotes the random daily level and $n = 365$. Therefore, if the probability distribution $F_{X_n}(x)$ of the random daily level X_n is known, the above simple relation gives the desired probability distribution of the annual maxima. Since $F_{X_n}(x)$ is derived from $F_X(x)$, the latter is known as the parent distribution. Now clearly the parent distribution is not known. Fortunately, it has been shown that if we can assume that the number of random daily levels can be very high, then the distribution

$$F_{X_n}(x) = e^{-\alpha(x-\mu)}$$

for large n , in which α and μ are parameters. This is known as the first asymptote of the extreme distribution. The problem is reduced to one of determination of the parameters α and μ suitable to our particular case. This may be accomplished by plotting all available data points on an extreme probability paper and then fitting the points by a straight line. The two independent parameters of the line then correspond to the desired parameters α and μ respectively. So if all goes well we now find what we are looking for, namely, the probability distribution of the annual maximum water levels, $F_{X_n}(x)$. Whether all things go well or not must be pointed out so that reliable predictions can be made and the direction of future improvement can be understood. These are the basic assumptions of independence among daily random levels, common parent distribution, the ground rule of plotting data points on the probability paper and the quality of fitting a straight line to these points. In addition, the assumption of time invariant of the parent distribution must also be valid.

Wemelsfelder's Theory

The essential difference between Gumbel's and Wemelsfelder's theory lies in the initial manipulation of available data and in the final presentation of results. Instead of picking annual maximum out of 365 daily records in a year, Wemelsfelder proposed to count the number of exceedances of high water levels in the entire period of observations. Thus in any one year the number of exceedance of a level may range from 0 up to 5 or 10, and all high water occurrences are to be counted in a year. This is a clear distinction from the data collection method under Gumbel's theory in which one and only one high water level, the annual maximum, is considered in one year. Having counted the number of exceedances of high water levels, Wemelsfelder proposed to plot the yearly rate or the number per year v versus the corresponding level H and called such a plot a frequency curve. Assuming that the high water levels are rare and independent events, he then applied the Poisson probability law.¹⁹ According to this law we can state that the probability p of no exceedance of a level in a specified period of T years is

$$p = e^{-vT}$$

where the parameter ν is the mean rate of exceedance This parameter can be estimated from the frequency curve Finally the probability of exceeding that level is

$$q = 1 - e^{-\nu T}$$

This probability implies a chance of failure and is therefore, defined as the risk In summary, an analytic relation is thus established among three variables, namely, the risk q , the design period T and the design water height H Recall that the mean rate ν is a function of the height H as established by the frequency curve Wemelsfelder presented the theory in a two dimensional plot, with ordinates H , abscissa T for various risks q This presentation is very appealing and different from that by Gumbel as will be shown later in applications

Applications and Results

All data used in this paper was recorded by the Coast and Geodetic Survey, Environmental Science Services Administration, U S Department of Commerce through tide gauges located at Breakwater Harbor, Lewes, Delaware, and at Atlantic City, New Jersey Highest tides above the 1929 Mean Sea-Level Datum in each month were tabulated by the Coast and Geodetic Survey for Lewes from 1953-1969, and for Atlantic City from 1923-69 These are reproduced here as Tables 1 and 2 respectively The number in parenthesis indicate estimations and the blanks indicate missing data Based on some of this data, the Corp of Engineers in 1964 made studies on hurricanes along the Atlantic Coast Delaware-Maryland line to Virginia,^{16,17} and presented frequency curves* with extrapolations In our study the same frequency curves were used but were extrapolated by means of linear regression computer program where a polynomial was fitted to the curve¹⁸ The output of the program yields a straight line for Breakwater Harbor, Lewes, Delaware, and a curve for Atlantic City These extrapolated frequency curves are shown as Figures 1 and 2

Figures 3 and 4 show the predictions of high water levels for Breakwater Harbor, Lewes, Delaware and Atlantic City, New Jersey, respectively by Gumbel's theory and with the data obtained from Tables 1 and 2 The ordinate is water height in feet; the abscissa on the bottom is probability distribution of the asymptote of the annual extremes and on the top is the return period in years A fourth scale is a linear transformation

* The references used there is Mean Low Water which is 2 5' and 4 53' above the datum of 1929, Mean Sea-Level for Lewes, Delaware, and Atlantic City, New Jersey, respectively

variable which is not important in physical interpretations. The plotted points are data points. The theoretical prediction is represented by the central straight line. A point on the line in Figure 3 for example, indicates that the height of 11 feet has a chance of 9 of not being exceeded in any one future year, and on the average it will be exceeded once in every ten years. Looking at the upper portion of the line for Breakwater Harbor, Lewes, Delaware, in Figure 3, we find that a height of 12 2' has a chance of 98 of not being exceeded in one year and on an average of once in 50 years. The remaining feature in Figure 3 is the two curves forming a band along the theoretical line. These curves are called control curves, indicating an allowable deviation of data points from the line. When all data points fall within this band, the theory is considered valid according to Gumbel. Fortunately, this is the case for both Breakwater and Atlantic City. Furthermore, the control curves supplement the straight line predictions. For example, in Figure 3, in addition to the statement made for the point 12 2' height, we can make two more statements. First, the height 12 2' will be exceeded within the interval of 18 to 160 years on the average with probability of 68. Secondly, in 50 years on the average the height will exceed 11 4' and not exceed 13 1', with a probability of 68. This fixed probability corresponds to a one standard deviation from the straight line. Consequently, different control curves can be plotted for different probabilities, and standard deviations. Figure 5 shows a comparative prediction for Atlantic City, New Jersey. Important computations are presented in Tables 3 and 4.

Now consider applying Wemelsfelder's theory to available data, monthly extremes in Tables 1 and 2, and frequency curves in Figures 1 and 2. By the method previously outlined risk curves of Breakwater Harbor, Lewes, Delaware, are constructed and shown in Figure 5 and for Atlantic City, New Jersey in Figure 6. In Figure 5 the ordinate is height of the water level and abscissa design period in years. The curves indicate, for example, in 50 years a height of 13 5' will be exceeded with probability or risk of 10%, 15 3' with a risk of 1% and 17 2' with a risk of 0.1% at Breakwater Harbor, Lewes, Delaware.

Conclusions and Discussions

Through the course of study, we feel that both Gumbel's and Wemelsfelder's theories are founded on rational basis and are useful in practical predictions. However, it is very important to be cautious about the validity of assumptions when applied to a particular location. Unfortunately, no rational method is known to the authors in case any assumption is violated. Consequently, an educated guess must be made to modify the theoretical prediction in those cases. As for the questions of which of these two theories is more reliable, our investigation at this point does not permit us

to answer it satisfactorily. However, we did find out one crucial point which must be resolved before any meaningful comparison can be made. That is in the Wemelsfelder's theory, we could not find a clear ground rule for making the count of exceedances. Suppose that a severe hurricane storm hits a coastal area for three days with highest water levels on the first and third day. Such an event may be counted as two if the unit of time intervals is a day, counted 1 if it is a month, or counted as 1 if the entire hurricane event is considered a unit. This ambiguity must be removed by a clearly defined ground rule. Since we have not been able to find out the precise ground rule in Wemelsfelder's paper nor that used by the Corp of Engineers in their frequency curves, we can only assume that the count was made in a more or less arbitrary manner depending on the engineers. As a result it is proposed here that a universal ground rule be established, say a daily unit so that the ambiguity can be removed and precise communication among engineers can be established.

Finally, we wish to point out that neither of the two theories take into account the important parameter of the time-span of an occurrence of high water. Since this parameter is obviously significant in the characterization of the damaging effect of a storm, even a crude modification of the two theories for this effect is extremely useful. Also, we wish to mention that during the conference presentation of the paper Lee Harris raised an important question. He argued that the astronomical tides should be subtracted from the total water heights to get that part of the height due to hurricane surge alone. This question was responded by both J. B. Schijf and C. L. Bretschneider. The general agreement is that in a location where the water heights are governed by a non-linear law and sufficiently large quantity of records are available, then the separation of the astronomical tide and hurricane surge is neither possible nor useful. However, if a linear law prevails then the separation is justifiable.

Acknowledgement

This work is supported in part by the Office of Naval Research under the contract, 2-97-815, N00014-69-A-0407, with the University of Delaware. Data used in this study was obtained through Lee Harris of the Coastal Engineering Research Center, Corp of Engineers, Washington, D. C., Martha Winn of the Coast and Geodetic Survey, Environmental Science Service Administration, Rockville, Maryland, and Vance Myers of the Weather Bureau, Environmental Science Service Administration, Silver Springs, Maryland.

TABLE 1

Monthly Extreme Tides for Breakwater Harbor*

Year	Jan.	Feb.	Mar.	Apr.	May	June	July	Aug	Sep.	Oct	Nov.	Dec
1953	8.3	8.9	7.9	8.5	8.6	8.3	7.8	8.5	8.2	10.1	9.5	7.8
1954	8.2	8.2	7.4	7.9	8.9	8.4	7.7	(8.0)	8.2	8.7	8.2	8.5
1955	9.8	7.8	8.1	9.0	7.9	9.2	8.2	9.0	8.7	9.2	8.8	8.0
1956	8.4	8.8	8.3	8.8	8.3	8.7	8.5	8.6	9.7	8.7	8.2	8.2
1957	8.0	8.6	8.6	7.6	7.8	8.3	8.1	8.2	7.9	9.1	8.4	8.7
1958	8.3	8.6	9.0	9.2	8.7	8.1	7.9	8.2	8.2	8.5	8.2	8.9
1959	8.3	8.4	8.9	8.3	8.3	8.3	8.0	8.3	8.2	9.2	8.3	8.9
1960	9.7	8.4	8.9	8.0	8.4	9.0	8.1	8.4	9.8	10.5	8.8	9.7
1961	8.0	8.1	12.0	7.5	8.1	8.2	8.5	7.9	8.4	8.8	10.2	8.6
1962	8.4	7.7	7.9	8.6	8.2	8.2	8.3	8.1	8.4	8.2	8.8	8.6
1963	10.0	9.1	8.4	8.6	8.5	8.6	8.6	7.6	9.0	8.2	8.6	8.0
1964	9.4	8.2	8.4	7.9	7.8	8.5	8.4	8.5	8.7	8.1	8.3	8.5
1965	9.4	8.0	8.5	7.9	9.7	8.5	8.4	8.1	8.1	8.2	8.7	8.5
1966	8.6	9.6	8.5	8.4	8.7	9.0	8.0	8.0	9.6	7.7	8.7	8.7
1967	8.8	8.5	8.4	8.4	8.4	8.6	8.2	8.0	8.3	8.6	8.4	8.7
1968	8.8	8.7	9.2	8.4	8.4	9.1	8.7	8.9	8.7	8.8	9.9	8.8
1969	8.9	8.7	9.2	8.4	8.4	8.6	8.7	8.9	8.8	8.5	9.9	8.8

* The height above the 1929 Mean Sea-level Datum is listed according to U S. Coast and Geodetic Survey tables

TABLE 2

Monthly Extreme Tides for Atlantic City*

Year	Jan.	Feb.	Mar.	Apr.	May	June	July	Aug.	Sep.	Oct.	Nov.	Dec.
1923	10.2	9.9	10.6	10.3	9.8	10.2	9.7	9.3	9.5	10.9	10.5	11.0
1924	9.6	10.6	11.1	9.9	9.9	10.1	9.8	9.9	9.6	10.6	9.8	9.4
1925	10.5	9.6	9.1	9.5	10.1	10.1	9.7	10.2	9.9	9.9	9.8	10.6
1926	9.9	10.5	9.6	9.1	9.6	9.6	10.0	10.2	10.1	10.1	9.6	9.5
1927	9.8	11.2	10.6	10.7	10.2	9.9	10.1	10.5	9.8	10.3	9.9	10.7
1928	9.5	9.8	10.6	10.6	10.4	10.6	9.7	10.5	9.9	10.4	10.5	10.4
1929	9.9	9.7	9.3	10.6	9.9	9.8	9.8	11.2	9.6	10.0	10.4	10.3
1930	10.6	9.6	10.2	9.6	9.9	9.9	10.0	10.6	10.1	10.0	10.8	9.7
1931	11.0	9.4	11.5	10.5	9.4	9.9	9.7	9.6	11.0	9.5	(11.8)	10.2
1932	10.5	9.9	10.9	10.2	10.2	10.2	11.0	11.2	11.4	10.4	9.9	10.4
1933	11.8	9.4	10.1	10.2	10.0	(9.8)	9.8	9.8	9.9	10.7	9.9	10.4
1934	9.8	10.0	9.9	10.2	9.6	10.5	9.8	9.8	11.8	9.8	11.5	10.3
1935	9.9	9.9	10.3	9.6	9.4	9.9	9.9	9.9	10.9	10.6	10.6	10.7
1936	9.9	10.8	10.5	11.1	10.2	10.2	10.0	9.8	10.2	11.0	10.6	10.7
1937	9.7	10.3	10.0	9.6	10.7	10.6	10.0	9.8	10.2	(10.5)	10.0	10.3
1938	10.6	10.2	10.2	9.9	11.6	10.2	10.2	10.2	9.9	10.5	10.5	10.2
1939	10.2	10.5	(10.3)	10.6	10.9	10.0	9.6	10.3	10.5	11.4	10.7	10.7
1940	11.3	10.2	10.2	9.9	10.2	10.3	10.3	10.2	10.2	10.8	9.9	9.8
1941	10.7	10.2	10.2	9.7	10.2	10.2	10.4	10.3	11.1	11.7	10.4	10.2
1942	10.2	10.3	11.4	9.9	10.8	10.4	10.4	10.3	(13.8)	11.1	12.0	10.1
1943	9.9	10.8	10.0	10.5	10.4	10.5	10.6	10.8	10.7	11.1	10.6	11.4
1944	11.1	10.2	10.0	9.9	10.2	(10.5)	10.1	10.6	10.5	11.1	12.0	10.1
1945	10.9	9.8	9.9	10.5	10.9	10.9	10.2	10.2	10.7	11.1	10.8	10.3
1946	10.5	9.8	9.9	10.5	10.9	10.9	10.2	10.2	10.3	11.1	12.1	9.9
1947	10.4	10.5	10.0	10.8	10.0	10.6	10.2	10.6	10.3	11.1	12.1	10.8
1948	10.4	10.6	10.5	9.9	10.2	10.3	10.7	10.5	10.1	11.5	11.0	10.8

TABLE 2 (Continued)

Year	Jan.	Feb.	Mar.	Apr.	May	June	July	Aug.	Sep.	Oct.	Nov.	Dec.
1949	10.2	10.2	10.1	10.5	10.9	10.1	10.0	10.1	10.4	11.0	9.9	9.6
1950	9.3	10.5	9.7	10.0	10.2	10.2	9.8	9.7	11.2	10.2	13.2	11.1
1951	10.3	10.0	10.7	9.8	10.8	10.5	10.5	10.3	11.2	10.7	11.4	10.4
1952	10.6	10.5	10.0	10.1	10.6	10.1	10.2	10.0	10.3	10.1	11.8	11.0
1953	10.6	10.6	9.8	10.1	10.3	10.1	9.8	10.1	10.1	12.3	11.2	9.8
1954	10.4	10.1	9.2	9.8	11.0	10.5	9.7	10.6	10.8	10.8	10.1	10.3
1955	10.3	9.5	10.3	11.1	9.9	11.1	10.2	10.2	9.7	11.2	11.0	10.0
1956	11.4	9.8	10.4	10.6	10.2	10.7	10.5	11.2	11.1	10.5	10.6	10.1
1957	10.5	10.9	10.6	9.9	9.7	10.3	10.0	10.7	10.2	10.8	10.3	10.1
1958	10.4	10.7	11.1	11.3	10.6	10.0	9.9	10.0	10.5	10.5	10.2	(10.8)
1959	10.4	10.7	10.7	10.4	10.6	10.0	10.1	(10.3)	10.0	10.5	10.1	11.5
1960	10.4	10.8	10.2	9.9	10.6	11.1	10.0	10.5	12.2	10.8	10.6	10.4
1961	11.6	(11.2)	11.2	10.8	9.9	(10.3)	10.8	10.6	11.0	12.2	10.1	10.3
1962	10.0	10.3	13.4	10.6	10.3	10.2	10.4	10.2	10.3	10.4	10.1	10.7
1963	10.6	9.9	9.9	10.4	10.3	10.4	10.8	9.8	11.1	10.4	11.1	10.2
1964	11.0	11.0	10.5	10.6	10.3	10.4	10.4	10.3	10.5	10.2	10.3	10.6
1965	11.1	11.0	10.3	9.8	9.9	10.8	10.4	10.4	10.2	10.2	(10.5)	10.4
1966	12.1	(10.3)	10.4	9.9	9.8	10.0	10.3	10.4	10.6	9.9	10.5	10.9
1967	10.7	11.3	10.4	11.3	11.3	11.0	9.8	9.9	10.9	10.8	11.0	11.1
1968	10.7	10.7	10.3	10.5	10.8	11.2	10.4	10.3	10.3	11.0	11.9	11.0
1969	10.3	10.9	11.0	10.1	10.5	10.7	10.8	11.0	10.7	10.5	11.7	11.0

* The height above the 1929 Mean Sea-level Datum is listed according to U.S. Coast and Geodetic Survey Tables

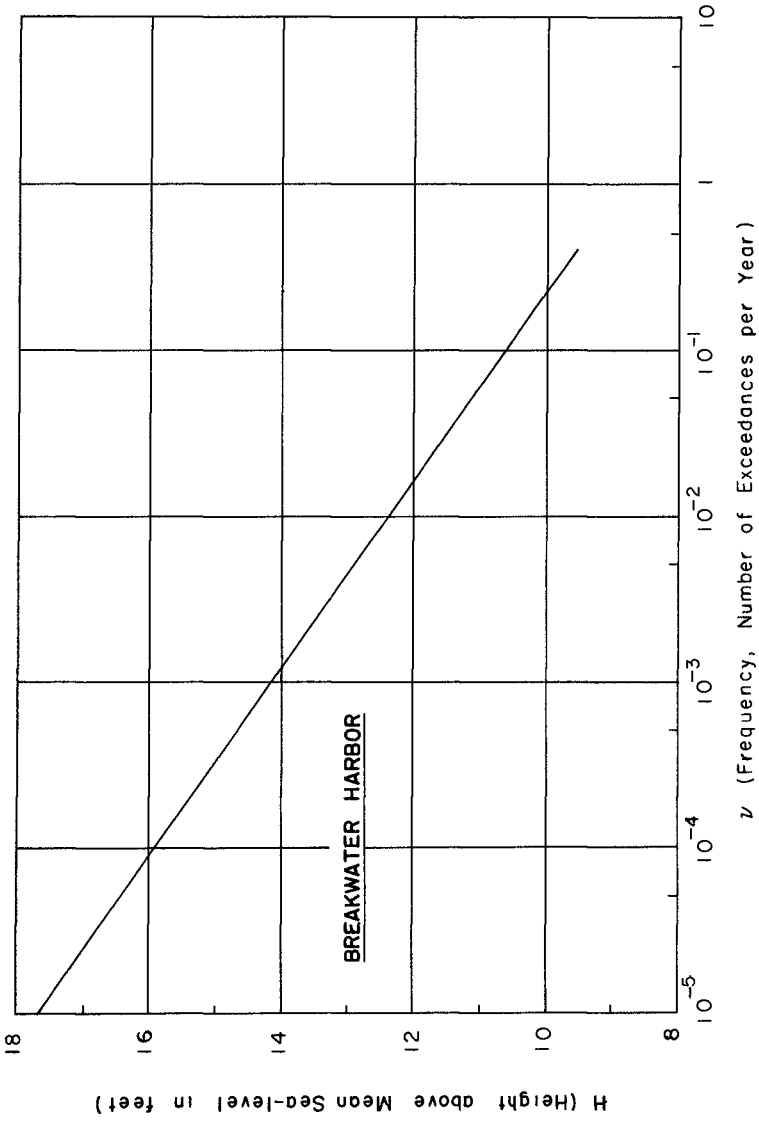


FIGURE 1 Frequency Curve for Breakwater Harbor

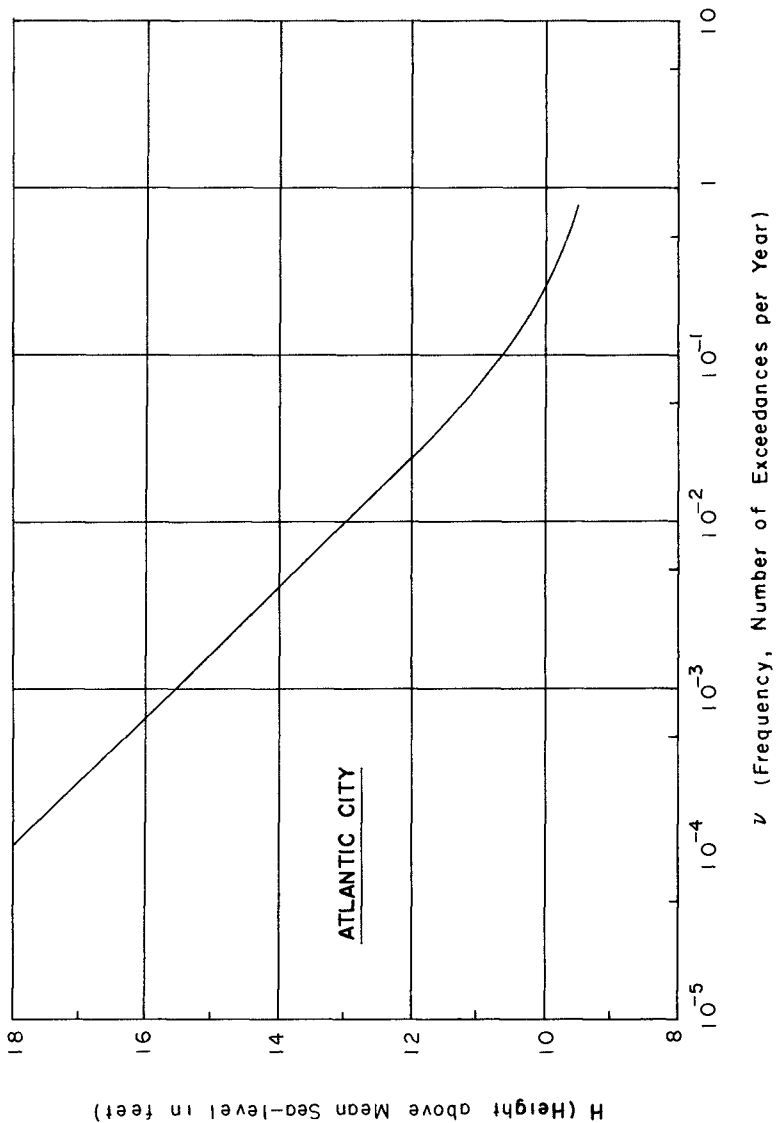


FIGURE 2 Frequency Curve for Atlantic City

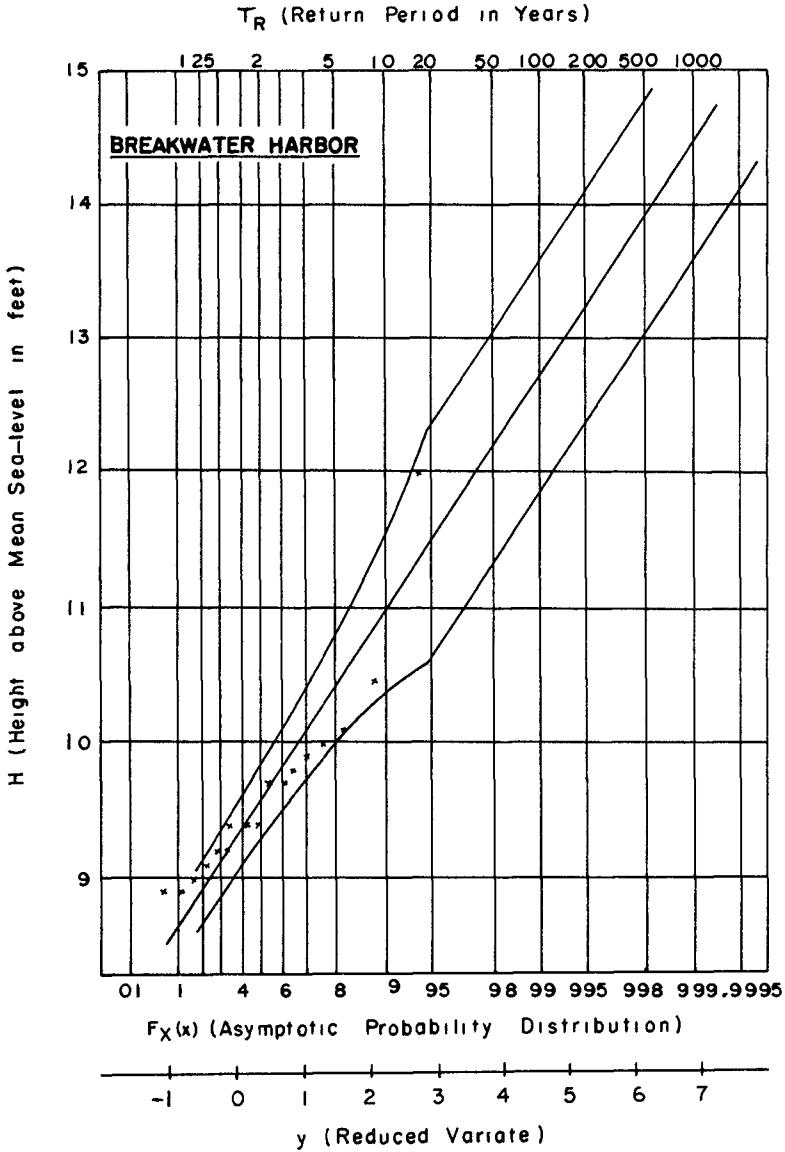


FIGURE 7 Gumbel Analysis for Breakwater Harbor

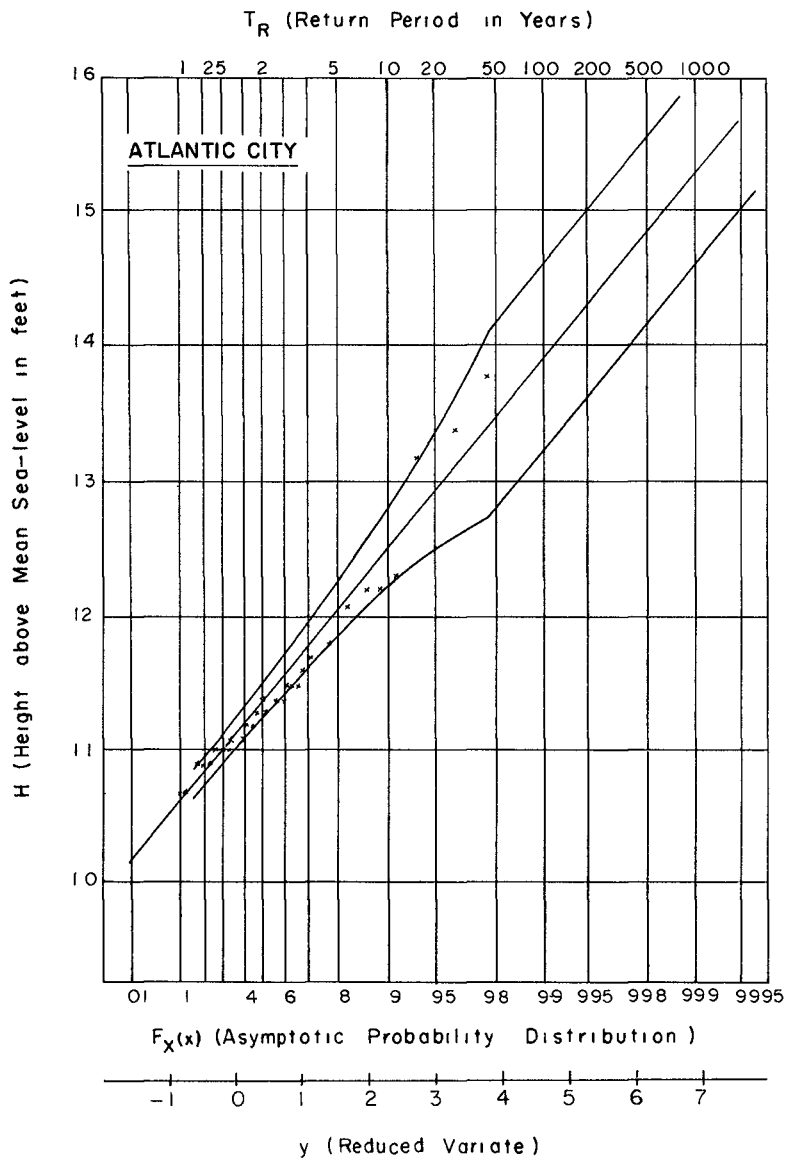


FIGURE 8 Gumbel Analysis for Atlantic City

TABLE 7

Gumbel Analysis of Breakwater Harbor Data

i	H*	H ²	$\frac{i}{N+1}$	y
1	8.9	79.21	0.056	-1.059
2	8.9	79.21	0.111	-0.788
3	9.0	81.00	0.167	-0.582
4	9.1	82.81	0.222	-0.409
5	9.2	84.64	0.278	-0.247
6	9.2	84.64	0.333	-0.095
7	9.4	88.36	0.389	-0.057
8	9.4	88.36	0.444	+0.208
9	9.4	88.36	0.500	0.366
10	9.7	94.09	0.556	0.533
11	9.7	94.09	0.611	0.708
12	9.8	96.04	0.667	0.904
13	9.9	98.01	0.722	1.122
14	10.0	100.00	0.778	1.382
15	10.1	102.01	0.833	1.700
16	10.5	110.25	0.889	2.140
17	12.0	144.00	0.944	2.854

$\Sigma H=164.2 \quad \Sigma H^2=1595.08$

$\bar{y}_N = 0.5181$

$\bar{H} = 9.65$

$\bar{H}^2 = 93.828$

$\sigma_N = 1.0411$

$\bar{H}^2 = 93.292$

$s_H^2 = 0.535 \quad s_H = 0.731$

$1/\alpha_N = 0.761$

$u_N = \bar{H} - (1/\alpha_N)\bar{y}_N = 9.264$

Φ	0.150	0.200	0.300	0.400	0.500	0.600	0.700	0.800	0.850
$\sigma(y)/N$	1.255	1.243	1.268	1.337	1.443	1.598	1.835	2.241	2.585
$\sigma(H)$	0.232	0.230	0.234	0.247	0.267	0.295	0.339	0.414	0.478

$\Delta_{H,N} = 0.869$

$\Delta_{H,N-1} = 0.578$

* Yearly Extremes from Table 1

TABLE 8

Gumbel Analysis of Atlantic City Data

i	H*	H ²	$\frac{i}{N+1}$	y
1	10.5	110.25	0.021	-1.35
2	10.6	112.36	0.043	-1.14
3	10.7	114.49	0.064	-1.01
4	10.7	114.49	0.085	-0.90
5	10.7	114.49	0.106	-0.80
6	10.9	118.81	0.128	-0.72
7	10.9	118.81	0.149	-0.64
8	10.9	118.81	0.170	-0.57
9	10.9	118.81	0.191	-0.50
10	10.9	118.81	0.213	-0.44
11	11.0	121.00	0.234	-0.37
12	11.0	121.00	0.255	-0.31
13	11.0	121.00	0.277	-0.25
14	11.0	121.00	0.298	-0.19
15	11.0	121.00	0.319	-0.13
16	11.1	123.21	0.340	-0.08
17	11.1	123.21	0.362	-0.02
18	11.1	123.21	0.383	+0.04
19	11.1	123.21	0.404	0.10
20	11.2	125.44	0.426	0.16
21	11.2	125.44	0.447	0.22
22	11.2	125.44	0.468	0.28
23	11.3	127.69	0.489	0.33
24	11.3	127.69	0.512	0.40
25	11.4	129.96	0.532	0.46
26	11.4	129.96	0.553	0.52
27	11.4	129.96	0.574	0.59
28	11.4	129.96	0.596	0.66
29	11.4	129.96	0.617	0.73
30	11.5	132.25	0.638	0.80
31	11.5	132.25	0.660	0.88
32	11.5	132.25	0.681	0.96
33	11.6	134.56	0.702	1.04
34	11.7	136.89	0.723	1.13
35	11.8	139.24	0.745	1.22
36	11.8	139.24	0.766	1.32
37	11.8	139.24	0.787	1.43
38	11.9	141.61	0.809	1.55

TABLE 8 (Continued)

1	H*	H ²	$\frac{1}{N+1}$	y
39	12.1	146.41	0.830	1.68
40	12.1	146.41	0.851	1.82
41	12.2	148.84	0.872	1.99
42	12.2	148.84	0.894	2.19
43	12.3	151.29	0.915	2.42
44	13.2	174.24	0.936	2.72
45	13.4	179.56	0.957	3.12
46	13.8	190.44	0.979	3.85

$\Sigma H = 526.7 \quad \Sigma H^2 = 6053.03$

$\bar{y}_N = 0.5468 \quad \bar{H} = 11.45 \quad \bar{H}^2 = 131.103$

$\sigma_N = 1.1538 \quad \overline{H^2} = 131.588$

$s_H^2 = 0.485 \quad s_H = 0.697$

$1/\alpha_N = 0.604 \quad u_N = \bar{H} - (1/\alpha_N)\bar{y}_N = 11.120$

Φ	0.150	0.200	0.300	0.400	0.500	0.600	0.700	0.800	0.850
$\sigma(y)/\bar{N}$	1.255	1.243	1.268	1.337	1.443	1.598	1.835	2.241	2.585
$\sigma(H)$	0.112	0.111	0.113	0.119	0.128	0.142	0.163	0.199	0.230

$\Delta_{H,N} = 0.689 \quad \Delta_{H,N-1} = 0.458$

* Yearly Extremes from Table 2

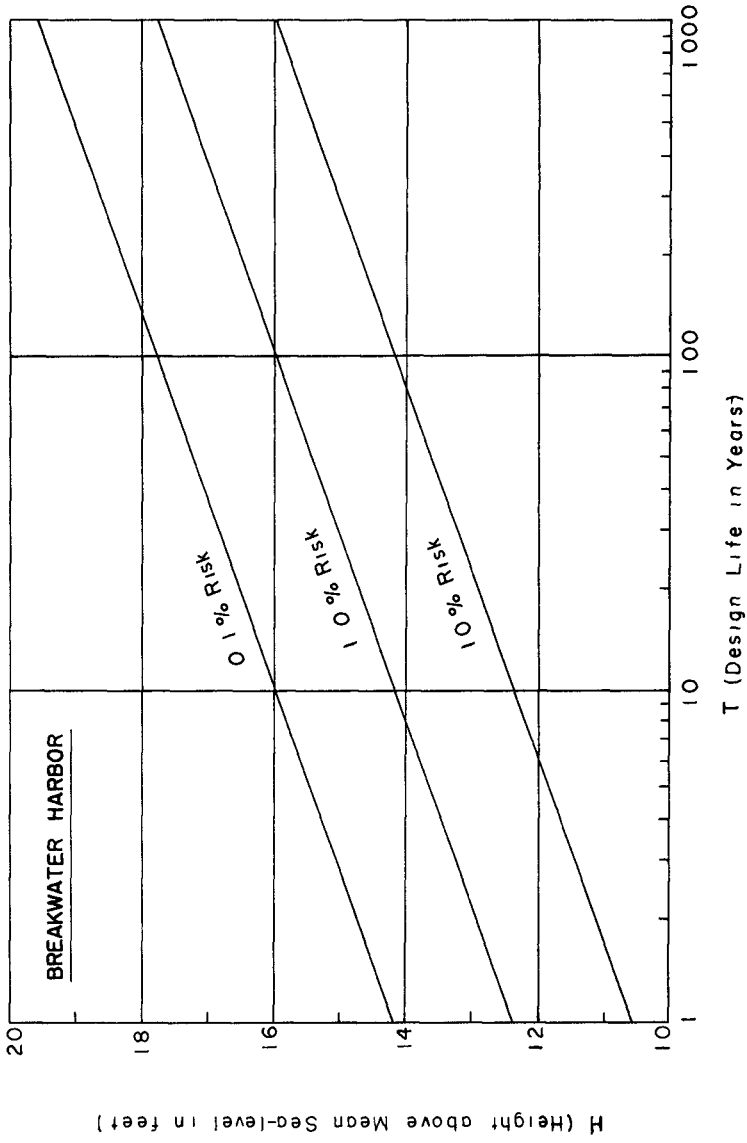


FIGURE 5 Wemelsfelder Risk Curves

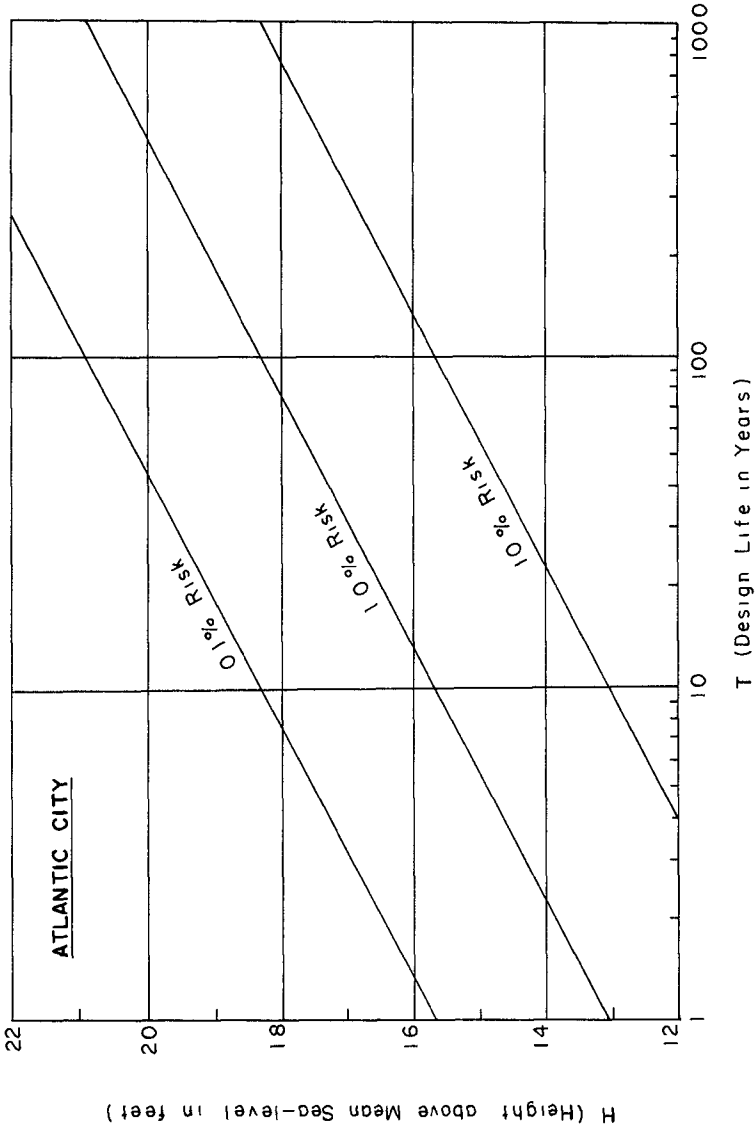


FIGURE 6 Wemelsfelder Risk Curves

BIBLIOGRAPHY

- 1 Mather, J R et al "Storm Damage Hazard Along the East Coast of the United States," Journal Applied Meteorology, Vol 6, No 1, February 1967, pp 20-30
- 2 Harris, D L "The Hurricane Surge," Hurricane Symposium, Am So Oceanography, No 1, October 1966, Houston, Texas, pp 200-228
- 3 Bretschneider, C "Hurricane Surge Predictions for Delaware Bay and River," Misc Paper 4-59, November 1959, Beach Erosion Board, Corp of Engineers, Department Army
- 4 LaSeur, N E "On the Description and Understanding of Hurricane Structure," Hurricane Symposium, Am So Oceanography, No 1, October 1966, Houston, Texas, pp 71-81
- 5 Moore, P L "Forecasting and Warning Systems," Hurricane Symposium, Am So Oceanography, No 1, October 1966, Houston, Texas, pp 102-113
- 6 Wemelsfelder, P J "On the Use of Frequency Curves of Storm Floods," Proc Seventh Conference Coastal Engineers, Berkeley, California, The Engineering Foundation Council on Wave Research, 1961, pp 617-632
- 7 Pierson, W J and Marks, W "The Power Spectrum Analysis of Ocean Wave Records," Transactions, American Geophysical Union, V 33, No 6, December 1952, 835-844
- 8 Cartwright, D E and Longuet-Higgins, M S "The Statistical Distribution of Maxima of a Random Function," Proc Roy Soc, A237, 1956, 212-232
- 9 Freudenthal, A M "Probabilistic Evaluation of Design Criteria for Marine Structures," Bulletin of the Permanent International Association of Navigation Congresses, Vol III, 1968-1969, No 2 17-33
- 10 Freudenthal, A M and W S Gaither, "Probabilistic Approach to Economic Design of Maritime Structures," Sec 2, Subject 5, XXII and Permanent International Association of Navigation Congress, Paris, France, 1969
- 11 Borgman, L E "The Statistical Distribution of Ocean Waves Forces on Vertical Piling," Institute of Engineering Res Tech Rep HEL-9-3, University of California, Berkeley, 1964

- 12 Borgman, L E "The Spectral Density for Ocean Waves Forces," Coastal Engineering ASCE Special Conference, Santa, Barbara, 1965, Am Soc of Civil Engineers, 1966, 147-182
- 13 Weigel, R L Oceanographical Engineering, Prentice Hall, 1964, pp 105-113
- 14 Gumbel, E J Statistics of Extremes, Columbia Press, 1958
- 15 Parzen, E Modern Probability Theory and Its Applications, John Wiley, 1960, p 251
- 16 Corps of Engineers, U S Army, "Atlantic City, New Jersey," Letter from Chief of Engineers Submitting Report of Interim Hurricane Survey," April 14, 1964 Item 334-A, D103, 22 AT6
- 17 Corps of Engineers, U S Army, "Delaware River and Delaware Bay, Letter from Chief Engineers Submitting Report on Interim Hurricane Survey and Review of Reports," August 17, 1964 Item 334-A, D103 22 D3716
- 18 Parisi, A M "Statistical Prediction of Design Still Water Level in Delaware Bay, M S Thesis, Civil Engineering Department, University of Delaware, July, 1970

CHAPTER 123

ANALYSIS OF HURRICANE TIDES AT PADRE ISLAND, TEXAS

Frank D Masch¹, Robert J Brandes²,
Floyd R Hill³ and William A White⁴

ABSTRACT

To establish design data, a study was undertaken to determine expected hurricane tide elevations, durations and frequencies of occurrence for events of various magnitudes in the vicinity of a proposed development at Padre Island, Texas. A set of synthetic hurricanes with selected sizes, translation speeds, wind fields, and pressure patterns were generated corresponding to various frequencies of occurrence of the CPI. Two numerical computer models were developed to determine the offshore surge hydrograph and to route the surge through the bay waters for each synthetic hurricane moving directly over the site.

Results included storm tide hydrographs at selected locations near the development. Synthetic storms were also routed across the coast at locations north and south of the site and storm hydrographs again computed.

INTRODUCTION

This study was undertaken to investigate hurricane tides on the Laguna Madre and Corpus Christi Bay sides of Padre Island. The location shown in Fig. 1 represents an extensive property development on the northernmost end of Padre Island and is connected to the mainland near Corpus Christi, Texas, by the John F. Kennedy Causeway. Of particular concern at the site were hurricane tide elevations, durations, and frequencies of occurrence of storm events of various magnitudes.

The specific objectives of this study are summarized as follows: (1) Determine the offshore storm tide hydrographs near the site which result from hurricane events of various frequencies of occurrence, (2) Route these same hurricanes over the shallow waters of Corpus Christi Bay and the Laguna Madre and calculate the storm tide hydrographs generated on the bay side of the development site on both the Corpus Christi Bay and Laguna Madre sides.

¹ Special Consultant on Fiscalin, Austin, Texas and Zurich, Switzerland, on leave from The University of Texas at Austin.

² Special Consultant on Fiscalin, Austin, Texas and Zurich, Switzerland.

³ Engineer, Frank D. Masch and Associates, Austin, Texas.

⁴ Engineer, Texas Water Development Board, Austin, Texas.

of the causeway, and (3) Determine the effects of hurricanes moving across the coastline at distances north and south of the development site and calculate the storm tides generated on both sides of the causeway and at the development site

Because there are insufficient data to develop a reliable statistical representation of hurricane tides in Corpus Christi Bay and the Laguna Madre, two computer models based on the fundamental equations of motion were developed for computing offshore storm surge and for routing this surge through the shallow bay waters. These models were first verified for measured astronomical and hurricane tides. They then were used to develop synthetic offshore hydrographs for storms of various frequencies of occurrence and to compute the storm tides at selected points in Corpus Christi Bay and the Laguna Madre resulting from these hurricanes.

For calculating hurricane tides, many of the hydrographic and physiographic features characteristic of the region needed to be described. These features include shallow water depths in Corpus Christi Bay and Laguna Madre, small islands, spoil dumps and limited exchange of waters between the Gulf of Mexico and the bay and lagoon. In the immediate vicinity of the development, other conditions exist that could affect the magnitudes of hurricane tides. A step type seawall, Ref [1], is now in existence over a portion of the Gulf side of the development site and is proposed to be extended to eliminate the possibility of Packery Channel cutting open to the Gulf of Mexico during hurricanes.

The John F. Kennedy Causeway which connects Padre Island with the mainland is an earth-fill dike with openings for the Intracoastal Canal and the Humble Channel. For hurricanes crossing the coast north of the development site, the causeway serves as a barrier and restricts the flow of water into the Laguna Madre until tides reach an elevation that produces overtopping of the causeway. Similarly, the causeway restricts flow into Corpus Christi Bay for hurricanes moving up the coast from the south. Islands formed by placement of dredge spoil from the construction of the Intracoastal Canal on the Laguna Madre side of the site also act as partial barriers to restrict somewhat the flow of water and consequently lower peak hurricane tide elevations slightly.

PROBLEM ANALYSIS

To obtain answers to the stated objectives, the problem analysis was divided into the following three parts: (1) Establishment of storm

characteristics for synthetic hurricanes with various frequencies of occurrence, (2) Determination of synthetic hurricane surges offshore of the site, and (3) Determination of storm hydrographs at the development site utilizing the hydrographic and physiographic features of Corpus Christi Bay and Laguna Madre, the synthetic hurricane characteristics and the corresponding offshore surges

Frequency Analysis After an extensive literature review, it was decided that within the scope and time frame available for this study, the most meaningful frequency analysis could be accomplished through the generation of a set of synthetic hurricanes. The U S Weather Bureau, Ref [2], has divided hurricanes affecting the Gulf Coast into three zones of approximately 80,000 square nautical miles each, one of which covers the Texas Coast and a small portion of the coasts of Louisiana and Mexico. Hurricanes within each zone have been analyzed for frequency of occurrence of the Central Pressure Index (CPI) and for size, translation speed, wind magnitudes, and other characteristics. From these analyses, the frequency of occurrence of the CPI is determined for selected locations along the Gulf Coast, including Corpus Christi. The CPI is the minimum estimated pressure in a storm and is a good indicator of storm intensity.

Once the CPI has been determined for a specified frequency, Ref [2] presents a series of steps by which synthetic hurricanes or "standard project storms" can be constructed. Utilizing the CPI as basic information, it is possible to determine the radius to maximum winds for various radius storms, the variations of this radius with longitude and latitude, the translation speed of the storm, probable azimuth, maximum cyclostrophic wind, maximum gradient wind and maximum wind speed 30 feet over water. Table I is a summary of the principal characteristics of synthetic hurricanes developed at Corpus Christi with frequencies from 3.3 years to 100 years. These characteristics were determined in part by the methods of Ref [2] and by adjustments based on judgment to more nearly reflect conditions near the Corpus Christi area.

In reviewing the relation between CPI and the radius to maximum winds, it was noted that data for the Texas coastal zone and in particular that for the Corpus Christi area indicate that the local mean radius storm is smaller than the average mean radius storm for all events. Similarly, the longitudinal correction to the radius to maximum winds shows a negative departure from the mean of about five nautical miles for a longitude near 96° W. Hence, the values of radius to maximum wind were adjusted to reflect these Corpus Christi characteristics. Also in selecting the translation speed for the hurricane center, a modal value based on the cumulative percent of occurrences of all events was chosen. From Ref [2], eleven knots is considered as a representative moderate speed and was taken as constant for all frequency hurricanes.

TABLE 1 SUMMARY OF SYNTHETIC HURRICANE CHARACTERISTICS

S_o (ft)	T_r (yrs)	CPI (in)	R (n mi)	V_{cx} (mph)	V_{gx} (mph)	V_x (mph)
2 0	100	27 44	12	110	108 2	99 9
2 0	75	27 50	12 5	108	106 2	98 3
2 0	50	27 60	13	107	105 1	97 3
2 0	30	27 73	13 5	103	101 1	93 8
1 5	20	27 88	14	99	97 0	90 4
1 5	15	27 94	14 5	97	95 0	88.3
1 5	10	28 16	15	92	90 0	84 2
1 0	5	28 56	15 5	82	79 9	75 3
1 0	3 3	28 84	16	68	65 9	63 3

LIST OF SYMBOLS

- S_o = Initial hurricane surge
 T_r = Return period of storm
 CPI = Central Pressure Index or the estimated minimum pressure for a particular hurricane
 R = Distance from center of storm to region of maximum winds
 V_{cx} = Maximum cyclostrophic wind
 V_{gx} = Maximum gradient wind
 V_x = Estimated maximum 30 foot over-water speed

Synthetic Storm Development Before the storm tide hydrographs could be determined at selected points in Corpus Christi Bay and Laguna Madre, it was necessary to know the hurricane surge hydrograph offshore in the vicinity of the development. It is this storm surge that acts at the tidal inlets and, depending on magnitude, may overtop Padre Island. As such, offshore tide represents one of the boundary conditions necessary to calculate tides within the bay and lagoon.

In hydrograph form the offshore surge gives a complete picture of the effects of the hurricane. Information required for the solution of this tide includes definition of the bottom profile offshore from the site to the edge of the continental shelf and knowledge of the wind's magnitude and direction across the entire width of the hurricane. U S C G S Hydrographic Charts provided the required data for the bottom profile. Wind patterns for the design storms could be taken either from actual historical hurricanes which have been documented or from synthetic storms such as illustrated in Ref [2].

Total storm surge offshore associated with a given hurricane is normally broken into several components for calculation. The total hurricane surge above mean sea level consists of an initial surge, an astronomical tide, a pressure tide and the components of wind tide due to winds blowing perpendicular and parallel to the coast. The initial surge is that associated with Gulf hurricanes and usually varies from one to two feet. To be conservative, the astronomical high tide above mean sea level was selected to coincide with the peak of the storm tide. The pressure tide was taken as 1/4 times the pressure differential expressed in inches of mercury. Wind tides were computed from wind magnitude, wind direction, duration and from a consideration of bottom and water surface shear stress coefficients.

In determining hurricane tide hydrographs there is the problem of appropriate values for the bottom friction and surface wind stress parameters used in the calculations. The most direct way to evaluate such parameters is to compare actual measured hurricane tide hydrographs with computed hydrographs, determined as above but with actual data on the wind patterns, wind magnitudes, storm directions, CPI, etc. It then becomes a matter of adjusting the bottom friction and wind stress coefficients until the computed hydrograph can be made to agree reasonably well with that actually measured.

The final hydrographs at the coast for a series of synthetic storms were obtained by placing the hurricane wind patterns with their leading edge at the coast, calculating the wind tides shoreward from the edge of the continental shelf, and then moving the wind patterns shoreward a prescribed distance and again performing the wind tide calculations. This process was repeated until the end of the hurricane passed over the coastline. Synthetic surge hydrographs were computed for hurricanes with return periods of 3, 3, 5, 10, 20, 30, 50, 75 and 100 years, and those for 10, 30 and 100 year return periods are included in Fig. 6. The isovel pattern used in the calculations is that of a mean radius moderate speed of translation standard project hurricane. To reflect the lower winds in the more frequent hurricanes, the wind magnitudes at specified radii were scaled proportionally by the ratio of the maximum wind speeds of the lesser storms to that of the standard project storm.

Storm Hydrographs at the Development Site The calculation of the storm tide hydrographs in Corpus Christi Bay and the Laguna Madre involved a numerical solution to the two-dimensional vertically integrated equations of motion and continuity. These equations were solved for the boundary configurations of the bay and lagoon and included such significant features as spoil banks, causeway, barrier islands, tidal inlets, flow controls, and the Intracoastal Canal. The boundary conditions for the equations included the storm surge hydrographs off-coast at Port Aransas, other tidal inlets and locations where Padre

Island was likely to be overtopped. Wind was another external surface force applied to the water surface within Corpus Christi Bay and the Laguna Madre.

The method utilized in the bay tide computations is based on work described in Ref. [3]. The first step was construction of an Eulerian type grid, one nautical mile square, which approximated the general physiographic and hydrographic features of the development area. Figure 2 is a small scale map of Corpus Christi Bay, Laguna Madre and Baffin Bay with the computational grid superimposed. Figure 3 illustrates the control features included within the computational model. The dash lines correspond to reefs, spoil banks or other flow control situations. The solid lines correspond to impermeable barriers such as islands and the causeway.

In a manner similar to that used for the offshore hurricane surge hydrographs, it was also necessary to calibrate this computational model. In a complicated configuration such as that represented by the combination of Corpus Christi Bay, Laguna Madre and Baffin Bay, this calibration was done in two steps. The first involved calibrating the bay for normal astronomical tides without the influence of wind, or with wind effects minimized. When the model was verified for astronomical tides, it was then operated using the offshore hurricane surge at tidal inlets and with varying wind on the water surface to compute the hurricane tide within the bay.

Verification of the computational model for astronomical tide was obtained by comparing the computed tide with the actual tide measurements at the Naval Air Station in response to a known tide imposed at Aransas Pass. The Naval Air Station is a location near the development site, Fig. 2, where normal astronomical tides were recorded by the Corps of Engineers. Figure 4 illustrates an astronomical tide measured at Corpus Christi Naval Air Station compared with the computed tide from the numerical model. The maximum departure of the computed curve from the measured tide is on the order of 0.1 feet. For the purpose of this study, this agreement is considered adequate verification of the astronomical tides and bottom friction conditions in Corpus Christi Bay.

Further hurricane tide verification was accomplished by introducing into the model, conditions associated with Hurricane Beulah. The storm tide recorded at Port Aransas was introduced at the jetties, and utilizing the winds associated with Beulah, the hurricane storm tide was computed at the Corpus Christi Naval Air Station. This hydrograph is illustrated in Fig. 5 where it can be seen that the model reproduced the actual measured tide quite satisfactorily. Tides were also computed at several other locations but are not included in this paper. The major difficulty in this calibration process was the inclusion

of the high runoff resulting from the large rainfall which accompanied Beulah and the rainfall on the bay itself. These conditions were approximated for this model from available data in Ref [4]. Winds recorded at the Corpus Christi Airport during the passage of Hurricane Beulah were applied in the time-dependent fashion measured at the airport to duplicate the tides recorded at different stations within Corpus Christi Bay.

To predict the tides on the Corpus Christi Bay and Laguna Madre side of the development and to simulate those conditions during which the Kennedy Causeway would be overtopped, the model had to be extended to include the Laguna Madre to a point south of Baffin Bay. Another extensive data search was undertaken to acquire quantitative information on the hydrodynamic characteristics of the Laguna Madre-Baffin Bay area. No tide data were available for this location and it was necessary to synthesize the behavior of tides south of the causeway. Although it was not possible to verify the computed tides in the Laguna Madre or Baffin Bay area, it was possible to compare qualitatively the computed results with those obtained during Hurricanes Beulah and Carla, and to note that the same general trends and characteristics existed. It was found that after allowing the Kennedy Causeway to be overtopped, very good verification of the Beulah hurricane tide at the Corpus Christi Naval Air Station was achieved. For this reason, it is believed that the total model including Corpus Christi Bay, Laguna Madre and Baffin Bay was sufficiently verified for the analysis used in this study.

ASSUMPTIONS AND MODEL LIMITATIONS

It is not difficult to envision a great number of combinations of hurricane events each of which may contribute to the storm hydrographs developed offshore and in the bays and lagoons. Such factors as storm path, storm size, CPI, translation speed, winds, and storm azimuth are some of the variable hurricane characteristics. Similarly, unpredictable factors such as the time during which the storm remains offshore and any unusual changes in storm course also control the formation of hurricane surge. Once within a bay, such variables as the amount, intensity, distribution and duration of rainfall on the bay itself and the runoff from contiguous land areas are also factors which affect the height, shape, and duration of the storm tide hydrograph. Obviously with so many variables very few of which are statistically predictable, caution must be used in attempts at generalizations of hurricane events at a given site.

Although it was necessary to make assumptions on the distribution of rainfall during Hurricane Beulah for proper verification of storm tides at the Naval Air Station, the synthetic storms on which the results of this study are based do not include rainfall. Since the storms themselves are synthetic and rainfall frequencies are not established relative to the hurricane frequencies,

attempts at introducing rainfall and rainfall distributions within the time frame available for this study would not be meaningful. It also was noted in the offshore storm hydrographs that the surges rise and fall rapidly, even though a decay factor was included in the model. Part of these rapid changes is due to the synthetic nature of the storms, but part is also due to the absence of rainfall which normally accompanies such storm events.

The computational model used in this study does not allow for inundation of adjacent land mass. The 10 and 15-foot contours lie very near the water line throughout most of the area in the vicinity of the development with the exception of the Laguna Madre side of Padre Island. Actually the volume of water involved in land inundation in the area covered by the model is very small in relation to the volume of water in Corpus Christi Bay and the Laguna Madre, and omission of land inundation should not have a noticeable effect on the computed tides in this area. Furthermore, this assumption is conservative, for if there is any effect at all, it would be to produce lower tides than those calculated.

Although the results in the following section are based totally on synthetic storms, they provide an indication of the magnitude and duration of hurricane tides due to storms of specified frequencies. The results are also conservative in that the lesser magnitude storms are based on the isovel patterns for a 100-year storm with a linear adjustment applied to the wind velocities for the less severe events. Hence, the duration of the smaller events may be somewhat greater than would occur in an actual small storm. On the other hand, these storms do not include rainfall and runoff and the computed tides could be of lower amplitude than those of a true storm with heavy precipitation.

DISCUSSION OF RESULTS

The operation of the simulation model of Corpus Christi Bay, Laguna Madre, and Baffin Bay with synthetically generated offshore inputs at Port Aransas, Corpus Christi Pass, and Yarborough Pass has permitted the computation of tide hydrographs at selected points at the development site. Synthetic hurricanes were routed across the shoreline with the eye crossing approximately 15 miles south of Port Aransas. This produced maximum storm tides at the Port Aransas jetties, the major tidal inlet to the Corpus Christi Bay area. Since the actual development site is protected on the Gulf side by a seawall and by proposed stabilization measures for Packery Channel and vicinity, it would appear that even though the maximum storm tides were allowed to exist immediately at the site, it would be unlikely that serious overtopping of Padre Island would occur at that point. However, in the computational model, allowances have been made for flow and tide at Corpus Christi Pass, which presumably will be opened and maintained in the future. Port Aransas also was

selected as the point for application of maximum storm tide since it was a location for which some surge data were available and was the input location for verification tides at the Naval Air Station during Hurricane Beulah. Also, since frequencies are based on average conditions for the Texas Coast, the probabilities of an event crossing at a specific point are undoubtedly less. Thus, the slight shift of the storm to permit tide computations at a point where some data were available is not considered significant.

Development Site Tides Corresponding to the offshore hydrographs from the synthetic storms, tide hydrographs in the bay were computed near the development site at the points defined in Fig. 1. The location of the two points considered most representative of the site were defined as Packery Channel and Padre Island Site West. Three of the computed hydrographs for these two locations are shown in Fig. 6 and are based on a causeway elevation of 4.5 feet which is near the present average elevation. These hydrographs account for overtopping of the causeway when storm tides increase beyond an elevation of 4.5 feet. For convenience, the input tides used in the calculations have also been included on these figures.

The maximum storm tide elevations at Aransas Pass, Padre Island Site West, and at Packery Channel are summarized in Fig. 10 where the maximum computed storm tide has been plotted against the probability of occurrence in any one year. The input tide at Aransas Pass varies from 6.2 feet for a storm with 3.3-year return period to 11.7 feet for the 100-year storm. The 30-year computed storm tide elevation is 11.2 feet although the curve indicates an elevation of about 10.8 feet. Figure 10 also shows that the storm tides at Packery Channel, i.e., on the Corpus Christi Bay side of the causeway, are always higher than tides on the Laguna Madre side of the development site. The maximum storm tide at Packery Channel computed from the 100-year storm is 7.9 feet whereas at Padre Island Site West it is 7 feet. The 30-year storm for the same sites produces tides of 7.4 and 6.7 feet respectively.

It is also significant to note that for the less frequent storms there is less change in the magnitude of storm tide at all locations including Aransas Pass. For example, it can be seen from Fig. 10 that for the existing causeway elevation of 4.5 feet, the tides expected from a 30-year storm differ from a 100-year storm by less than 0.6 feet. This small change in maximum tide is due to the small difference in maximum average wind speed between the less frequent storms. This can be noted in Table I.

As also illustrated in Fig. 6, the Padre Island Site West tide always lags the Packery Channel tide indicating the delaying influence of the causeway. Actually the storm tides on the Laguna Madre side of the development do not begin to increase appreciably until the tides on the Corpus Christi Bay side are of sufficient magnitude to overtop the causeway at elevation of 4.5

feet The Intracoastal Canal alone is not large enough to enable the exchange necessary for the tide to build up on the Laguna Madre side as rapidly as it does on the bay side This delay varies from about six to eight hours depending on storm magnitude It can also be noted that the Packery Channel tide reaches a peak shortly before the eye crosses the coastline and then falls rapidly as the eye crosses the coast and winds reverse direction This wind reversal also contributes to the rapid rise in the Padre Island Site West tide immediately after the storm passes the coast and winds begin to blow up Laguna Madre When the Padre Island Site West tide reaches its peak the eye has already crossed the coast and the Packery Channel tide has begun to fall Water from the Laguna Madre then flows back over the causeway into Corpus Christi Bay This, coupled with the fact that no sudden changes in wind direction occur after the eye has passed the site, produces a flatter peak on the Laguna Madre side The oscillation noted in the storm hydrographs after the passage of the peaks actually represents the astronomical component of the total tide

Further insight into the tide behavior on both sides of the causeway for different storm events can be obtained from Fig 7 These curves are computed for various frequency storms at points identified as Intracoastal Canal South, Intracoastal Canal North, Humble Channel South and Humble Channel North The locations of these points also are illustrated in Fig 1 These hydrographs give comparisons of the storm tide elevations for the three storm events of 10, 30 and 100 years at two points on each side of the causeway It is not possible to construct a duration of overtopping-frequency relationship because by the nature of the synthetic hurricanes the more severe events tend to be somewhat tighter storms in order to produce the lower CPI's This leads to the apparently anomalous condition in which the less frequent events produce shorter periods of overtopping once overtopping is significant The study of the isovel patterns for less severe storms requires analysis considerably in excess of that available to this study

It can also be noted from Fig 7 that the tides on the south side of the causeway are characterized initially by very low tides followed by a rapid rise in the water surface In fact, the tide at Humble Channel South becomes less than mean sea level meaning that water is blown out of the computational cell at that point No verification data of this condition are available, however, qualitative data obtained during Carla, Ref [5], indicates very low tides in this area Also an astronomical tide study south of the causeway, Ref [6], shows that tides change very rapidly with relatively small changes in wind velocity or direction In the case of the synthetic hurricanes, the winds are northerly to northeasterly until the eye crosses the coast As already noted, overtopping of the causeway occurs at about this same time This overtopping together with the sudden reversal to winds from the south and southwest lead to this very rapid rise in water surface elevation

Storms at Other Locations In order to obtain some insight into the tides generated from hurricanes crossing the coast at locations other than at the development site, two conditions were considered. These included the 30-year storm crossing the coast at points 50 miles south and 50 miles north of the site. The storm hydrographs computed for these conditions at Packery Channel and Padre Island Site West are shown in Fig. 8. Also the corresponding tides on each side of the causeway are given in Fig. 9. These computations have been carried out for a causeway elevation of 4.5 feet.

Rather than re-route the 30-year storm with its attendant adjustments into the coast over different offshore profiles, a linear adjustment based on observations made during Hurricane Carla, Ref. [5] was applied to the input tide used in the previous computations. It is well established that hurricane tides to the right of the eye when viewed in the direction of travel are larger than tides to the left of the eye. This is because of the large component of tide resulting from onshore winds. Thus, a hurricane crossing the Texas Coast south of the development site will produce a larger tide at the site than if the same storm moved inland north of the site. Corresponding to the Carla results, the input tide at Aransas Pass was reduced to 90% for the storm south of the site and by 75% for the storm north of the site. No adjustment was made to the storm duration.

All the tides thus computed are lower than those produced by the 30-year storm at the site. This can most easily be seen in Fig. 11 which summarizes the maximum tides at Aransas Pass, Packery Channel and Padre Island Site West for the various storm locations. One point of note is that for the storm south of the site, the Padre Island Site West tide is slightly higher than the Packery Channel tide. Although the difference in actual magnitude may not be of numerical significance, the behavior of the tide in Laguna Madre relative to the Packery Channel tide is different than for a storm crossing at the site or to the north of the site. It is possible that a slightly more severe storm or possibly one at some other location south of the site could produce a higher tide in the Laguna Madre than in Corpus Christi Bay. This, of course, assumes that sufficient overtopping of Padre Island occurs so that a large enough volume of water is available for the tide buildup. Although different storm paths were involved, a similar effect can be noted by comparing the computed tides with the spot tide elevations reported for Hurricane Carla and Beulah. Carla which crossed the coast at Port O'Conner caused high tides at the Naval Air Station near the site and very low tides in the Laguna Madre. Beulah, which affected the southern part of the coast, produced high tides in the Laguna Madre as well as Corpus Christi Bay.

REFERENCES

- [1] Masch, F D et al, (1968), "Design Considerations for the Padre Island Seawall," Austin, Texas
- [2] Graham, H E and Nunn, D E , (1959), National Hurricane Project Report 33, "Meteorological Considerations Pertinent to Standard Project Hurricane, Atlantic and Gulf Coasts of the United States "
- [3] Masch, F D et al, (1969), "A Numerical Model for the Simulation of Tidal Hydrodynamics in Shallow Irregular Estuaries," Technical Report HYD 12-6901, The University of Texas at Austin
- [4] U S Army Engineers District, Galveston, (1967), Report on Hurricane Beulah, U S Corps of Engineers, Galveston, Texas
- [5] U S Army Engineers District, Galveston, (1962), Report on Hurricane Carla, U S Corps of Engineers, Galveston, Texas
- [6] Copeland, B J and Thompson, Jr , J H , (1968), Effects of Wind on Water Levels in the Texas Laguna Madre, The Texas Journal of Science, Vol VV, No 2, December, 1968

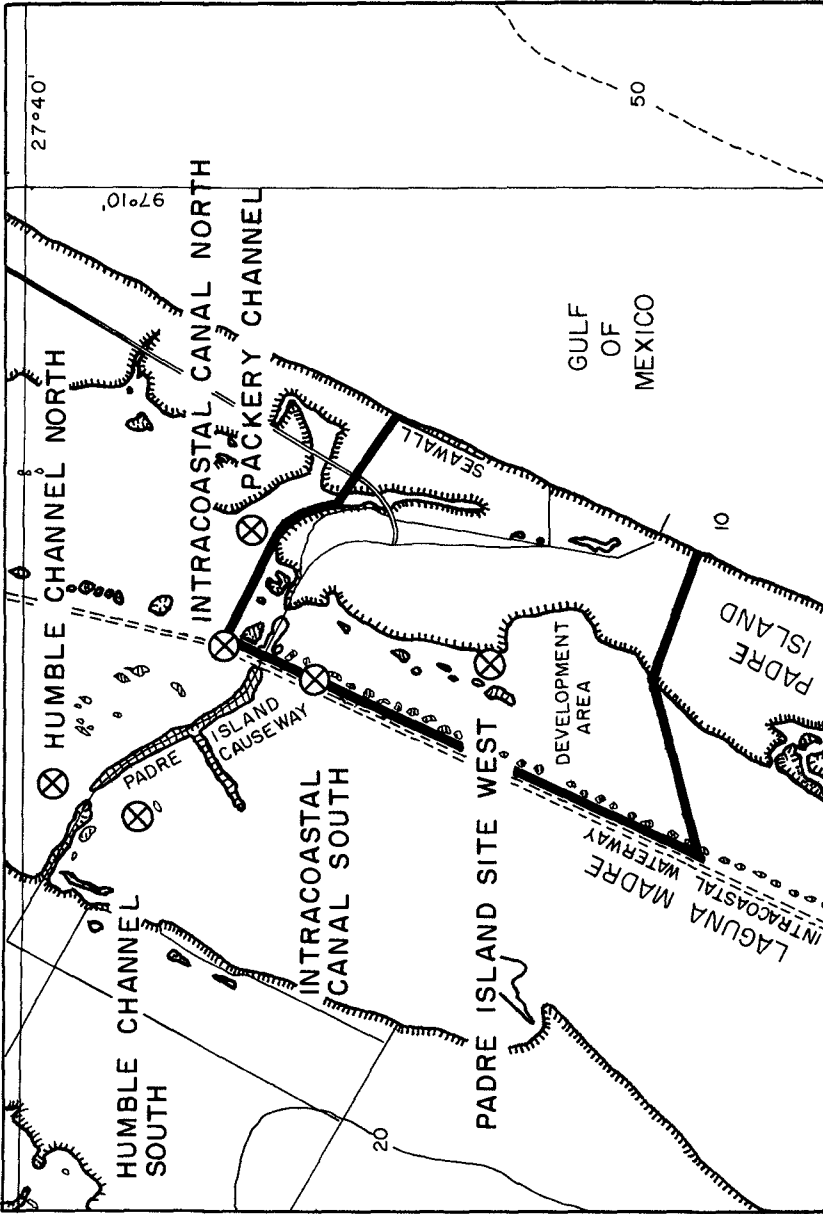


FIGURE 1 TIDE STATION LOCATIONS

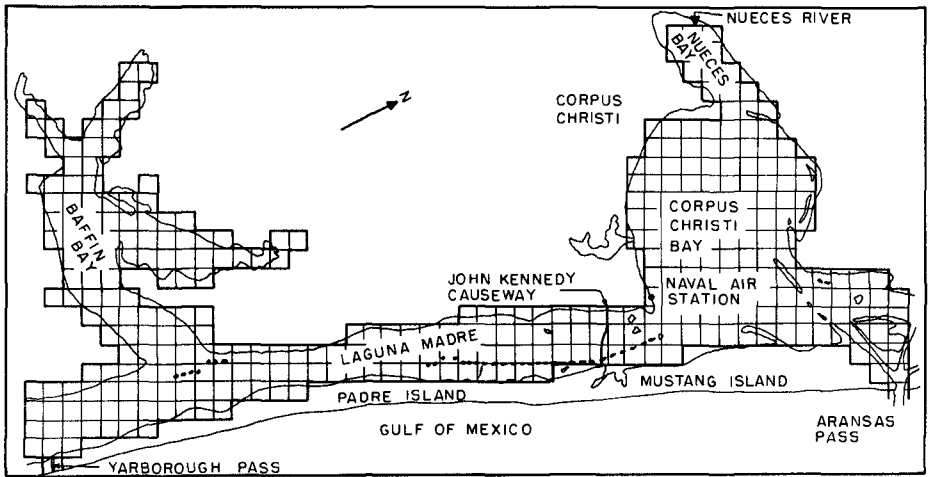


FIGURE 2 CORPUS CHRISTI AND BAFFIN BAY GRID LAYOUT

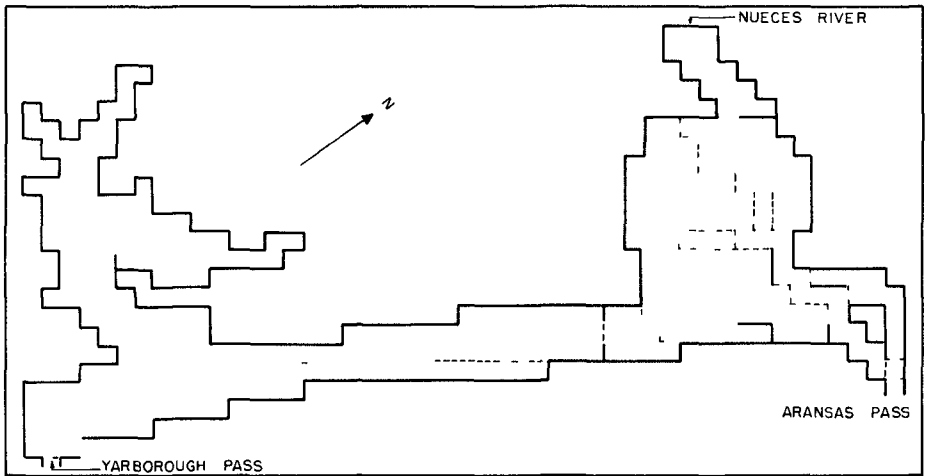


FIGURE 3 COMPUTATIONAL GRID SHOWING FLOW CONTROLS AND BARRIERS

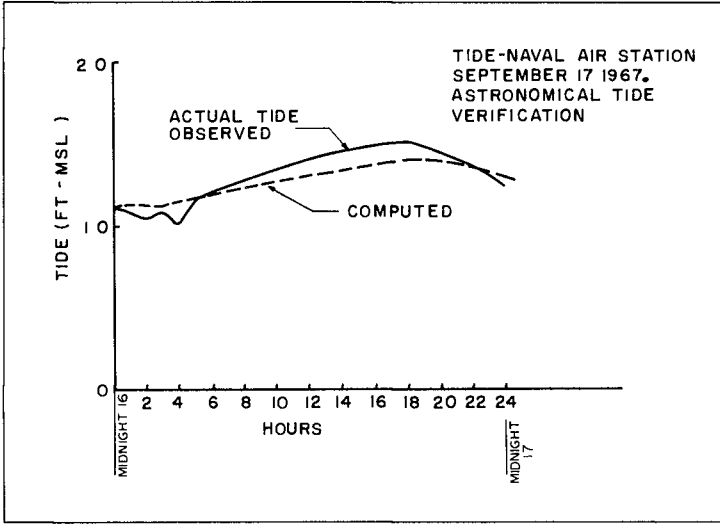


FIGURE 4 VERIFICATION OF ASTRONOMICAL TIDE - NAVAL AIR STATION

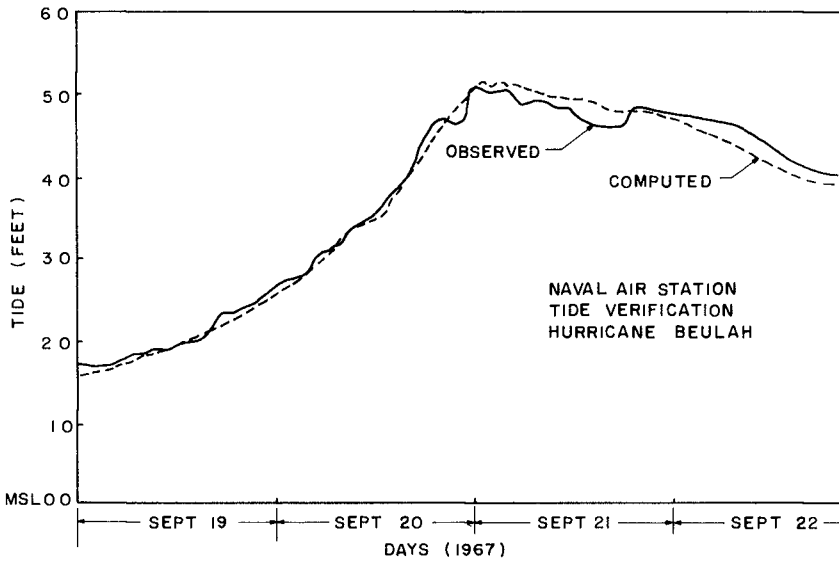


FIGURE 5 VERIFICATION OF HURRICANE TIDE-NAVAL AIR STATION

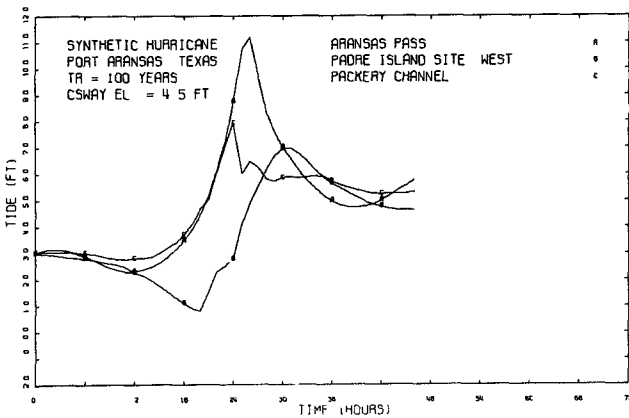
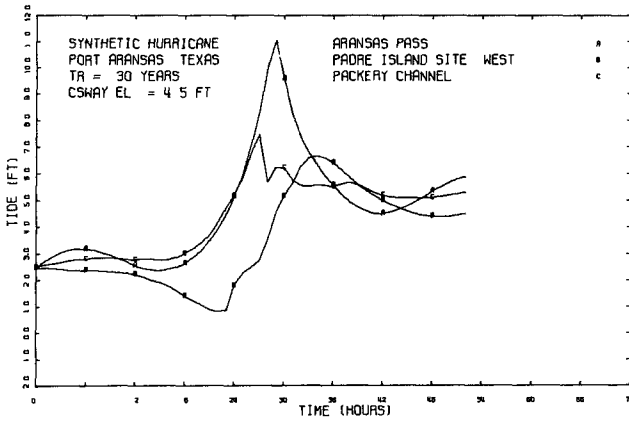
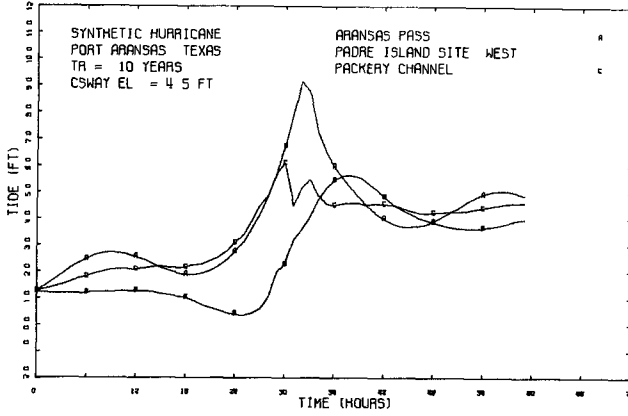


FIGURE 6

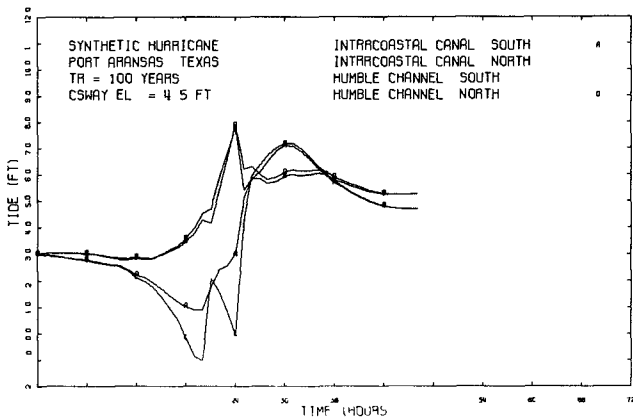
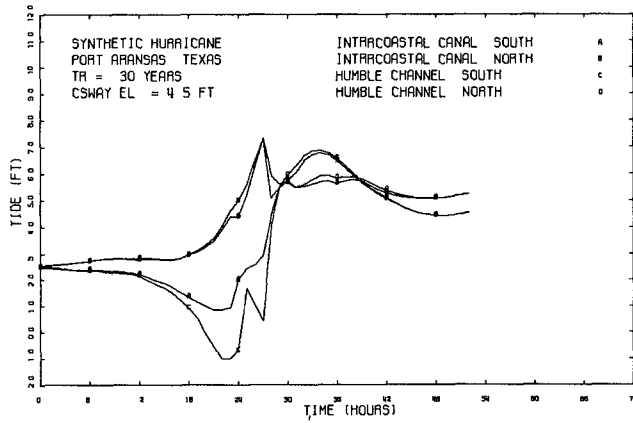
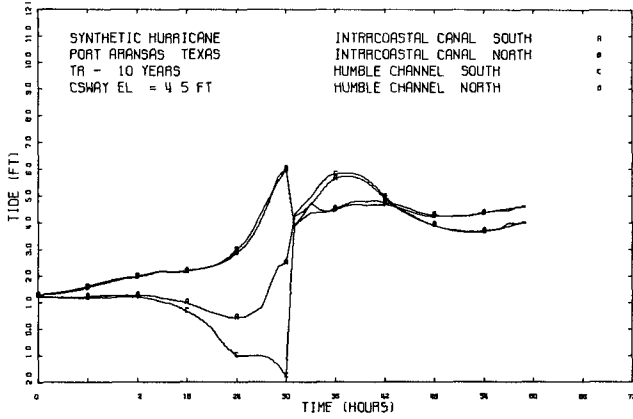


FIGURE 7

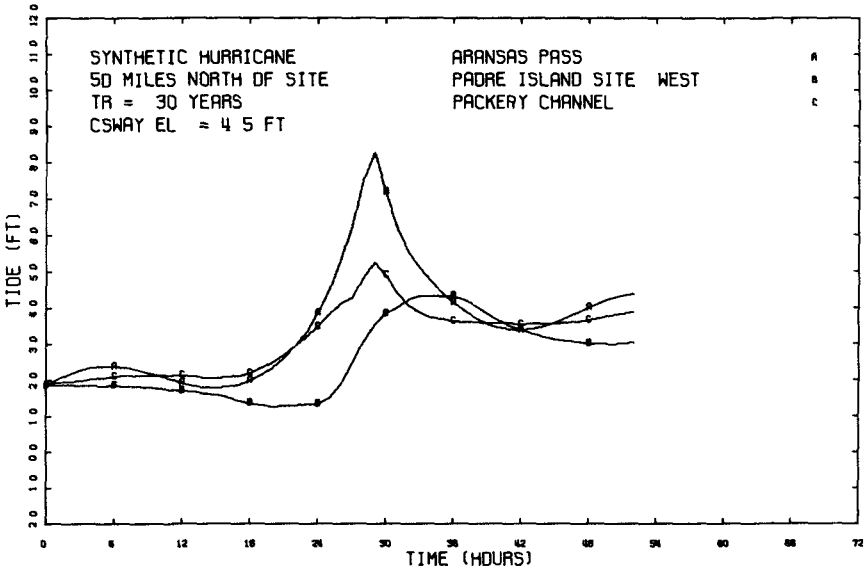
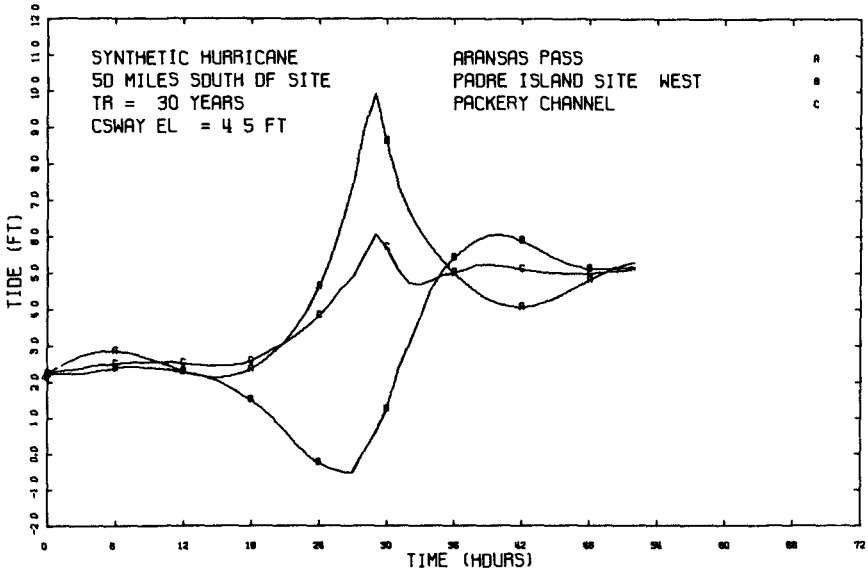


FIGURE 8

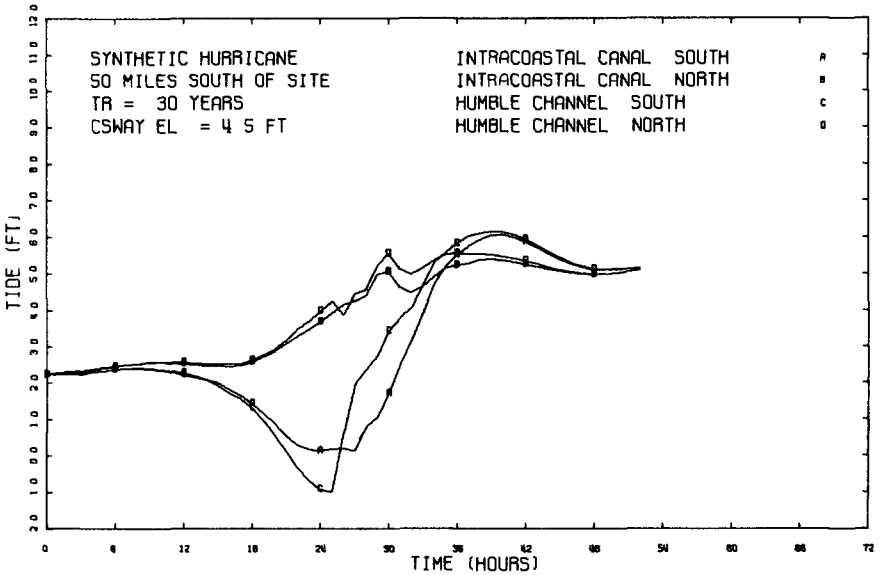
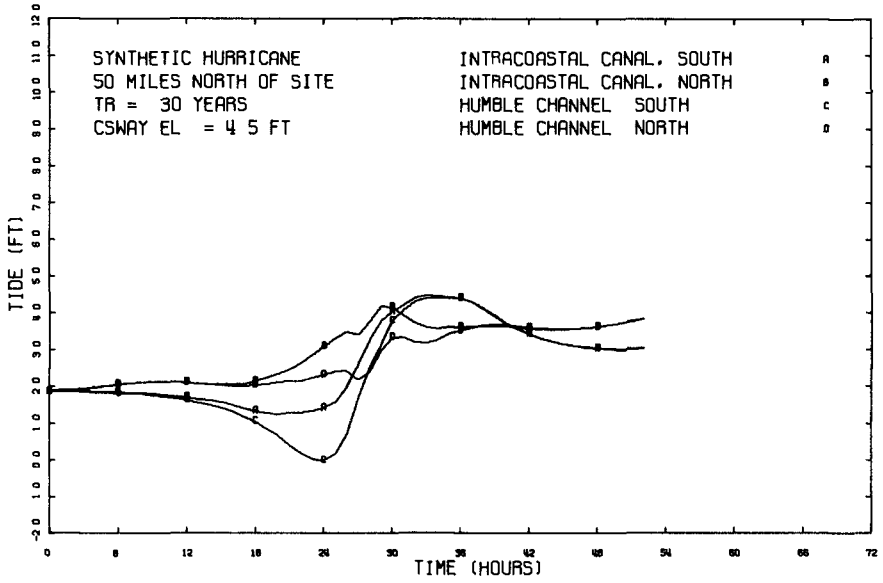


FIGURE 9

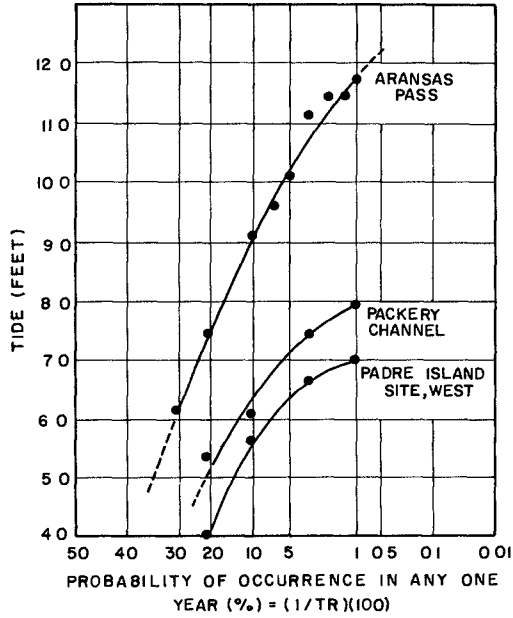


FIGURE 10 OFFSHORE AND DEVELOPMENT SITE TIDES AS COMPUTED FROM VARIOUS FREQUENCY SYNTHETIC STORMS

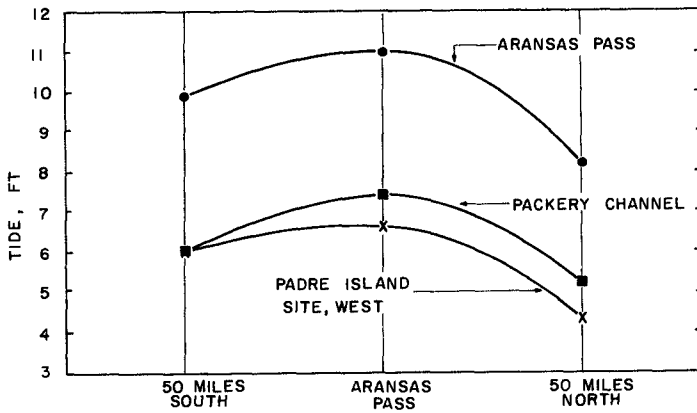


FIGURE 11 VARIATION OF MAXIMUM TIDE FOR STORMS CROSSING COASTLINE AT DIFFERENT LOCATIONS

CHAPTER 124

TURBULENCE IN HURRICANE-GENERATED COASTAL CURRENTS

By Stephen P Murray
Coastal Studies Institute
Louisiana State University
Baton Rouge, Louisiana 70803

ABSTRACT

Wind and current meter records taken during the passage of a hurricane were subjected to time series analysis. Filtering techniques isolated the speed fluctuations in the 10-60 CPH frequency band. These turbulent fluctuations proved to follow the Gaussian distribution for both wind and current. With the passage of the storm front the turbulence intensity of the wind actually decreased, while, on the other hand, the turbulence intensity of the current rose to extremely large values, even exceeding 27 percent of the mean flow speed.

Three phases of the storm were examined separately, and the energy density of the wind varied with the -1 power of the frequency in all phases. With respect to the energy density of the current, a -1 power dependency on the frequency was approximated by the first two phases, whereas in the third phase, which was the most intense, the energy density varied approximately as the -0.5 power of the frequency. The characteristics of the spectra indicate that there is little direct transfer of energy from the wind to the current in the frequency range studied. Energy is passing into the 10-60 CPH band of the current from still lower frequencies.

INTRODUCTION

Hurricane-generated coastal currents can attain enormous magnitude and are instrumental in inflicting material damage and producing changes in coastal topographies which result in great monetary losses. The undermining of piers and jetties and the destruction of sea buoys and other navigation aids illustrate this point clearly. However, owing to scarcity of data, the characteristics of currents produced by hurricane winds remain essentially unknown.

Hurricane Camille traversed the Gulf of Mexico on a northwesterly track during the period August 15-17, 1969, and made its landfall at Gulfport, Mississippi (Fig. 1). During this time the Coastal Studies Institute was conducting a shallow-water oceanographic measuring program at its field facility on the Eglin Air Force Base Santa Rosa Island Testing Grounds. This locality, 160 km to the east of the hurricane landfall, was subjected to severe winds, high waves, and storm surge. Of several current meters installed on the nearshore bottom prior to the storm, one placed at the depth of 6.3 meters beyond the outer bar provided an excellent time series record of the current during the storm.

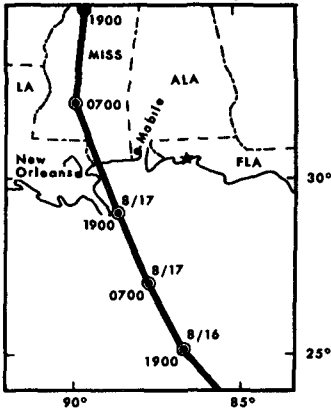


Fig 1 Track of the eye of Hurricane Camille, August 16 and 17, 1969

with a threshold speed rated at 0.08 knots. The duct is fitted with a vane that is long relative to the wave's orbital diameter, thus the vane holds the meter with its axis aligned with the steady current. A magnetic compass assembly within the instrument determines magnetic north, the orientation of the vane then determines the current direction.

The current speed sensor contains two reed switches that are activated by magnets on the blades of the impeller. The reed switches are mounted so that they open and close at slightly different times, which allows the electronic circuitry to determine the direction of rotation of the impeller. If the impeller is turning in the direction of the net current, a differential amplifier integrator integrates the pulses in the positive direction, if the impeller turns in the opposite direction, the amplifier integrates in the negative direction. There is then produced at the output of the amplifier a DC voltage proportional to the net current through the speed sensor. This voltage represents a time average over a time interval determined by the fixed time constant τ of the proper RC circuit. Given a step function increase in the current speed up to a value V_0 , the output speed V lags the true speed V_0 according to

$$V = V_0 (1 - e^{-t/\tau})$$

Thus one time constant is the time required for the output speed to reach $(1 - e^{-1}) \sim 63$ percent of the true speed. In the present case, the time constant was fixed at 6.2 seconds.

Instruments with time constants function as filters which smooth, lag, and damp cycles in the output as a function of the frequency f . The frequency response $R(f)$ (the ratio of output amplitude to true amplitude)

An anemometer mounted 12 meters above the water level on the adjacent beach operated concurrently.

The correlative aspects, especially in respect to the coastal circulation, of mean speeds and directions of both the current record and the wind record were discussed in Murray (1970). The purpose of the present paper is to discuss the properties of the turbulence associated with the hurricane winds and currents, with special reference to the turbulence, the energy density spectra, and cross spectra and coherence between these two signals.

INSTRUMENTATION

The current sensor was a Marine Advisers bottom-mounted Q-16 bidirectional integrating meter which utilizes a ducted impeller assembly of small mass

of a "time constant" filter is (Holloway, 1958)

$$R(f) = (1 + 4 \pi^2 \tau^2 f^2)^{-1/2}, \quad (1)$$

and the phase lag is

$$\phi = \tan^{-1} (-2\pi\tau f) \quad (2)$$

The frequency response function with $\tau = 6.2$ seconds, together with the phase lag, is shown in Figure 2. It is seen from the figure that there is at least 88 percent response for frequencies below 50 CPH. Since the frequency range of surface waves during the hurricane was between 450 and 720 CPH (5-8 second periods), the sensor response to waves was held to only 12-20 percent (frequency response at the output).

The Q-16 current meter assembly was situated on the bottom 360 meters seaward of the shoreline in 6.3 meters of water. The speed sensor duct was 1.5 meters above the sandy bottom.

The anemometer was a Science Associates No. 162 General Purpose Wind Recording System. The response characteristics of this particular instrument are not precisely known, but the sensitivity of this standard type three-cup anemometer has been well studied in the past. Fergusson (1935) measured 2.30, 0.60, and 0.33 seconds for a standard three-cup anemometer to accelerate from zero speed up to 5, 20, and 35 m/sec respectively. It is conservative to say that our anemometer of this type has a full response for cycles with a period of 10 seconds or 360 CPH.

ANALYSIS TECHNIQUES

Strip chart recorders were used which had response times of 0.8 seconds for the current recorder and 0.5 seconds for the wind recorder. The factors exerting ultimate control over the frequency response, however, were the recorder chart speeds--4 inches per hour for the current recorder and 3 inches per hour for the wind recorder. The trace width allowed only frequencies less than 50 CPH to be absolutely discriminated on both strip charts at these chart speeds.

The strip chart records were digitized on a Calma Model 303 Digitizer, which transfers graphical analog data to digital magnetic tapes by visually tracing the graphic data. Visual tracing in this case represents a smoothing filter which insures that no frequencies higher than about 60 CPH are transferred to the magnetic tape. The digitizer was set to record incrementally the coordinates of 100 points per inch of strip chart data. Owing to the two different chart speeds, this procedure produces a data density discrepancy which is eliminated by an interpolation option in the Calma software programs. The selected interpolation procedure yielded 100 data points per hour of record.

Thirteen hours of data between 0400 and 1700 hours August 17 (2600 data points) were placed on the magnetic tape for analysis. This interpolated version of the original observations was plotted by computer and

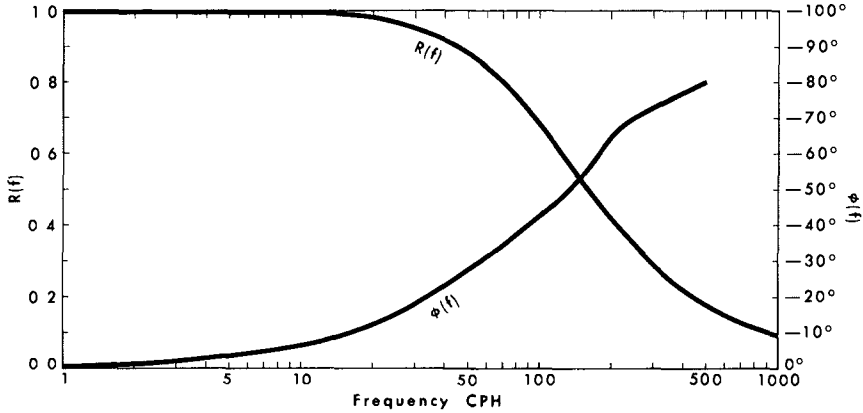


Fig 2 Frequency response and phase lag for a "time constant" filter with $\tau = 6.2$ seconds

is shown as Figure 3. Inspection of the figure shows that (a) the initial one third of this record (phase I) represents a pre-storm front phase, (b) the middle one third (II) represents an accelerative phase during which both the wind and current speeds increased rapidly after the storm front passage, and (c) the final third is a relatively steady phase (III) for both mean wind and mean current speeds.

The data length and time increment selects the highest and lowest frequencies which are present in the data. For N observations taken at ΔT seconds apart this spectral band is approximately

$$\frac{1}{2N\Delta T} < f < \frac{1}{2\Delta T}$$

In this study $N = 2600$, $\Delta T = 0.005$ hours, and the observable frequency band is $0.04 < f < 100$ CPH. The frequency $1/2\Delta T = 100$ CPH is known as the Nyquist frequency f_c . In spectral analysis all power contained in frequencies higher than f_c is folded back into the spectra below f_c , resulting in aliasing. One method of avoiding this problem (Bendat and Piersol, 1966) is to select a Nyquist frequency sufficiently higher than the maximum frequency of interest to insure that there is little power in the frequencies $f > f_c$. From the discussion of the digitizing of the relatively slow chart speeds and the frequency response curve in Figure 2, it is clear that there is little power above $f_c = 100$ CPH for aliasing.

Before spectral analysis of time series data is performed, any trends or very low frequency oscillations must be eliminated from the data, or the resulting spectra may be considerably distorted (Bendat and Piersol, 1966). A smoothing function which is essentially a low

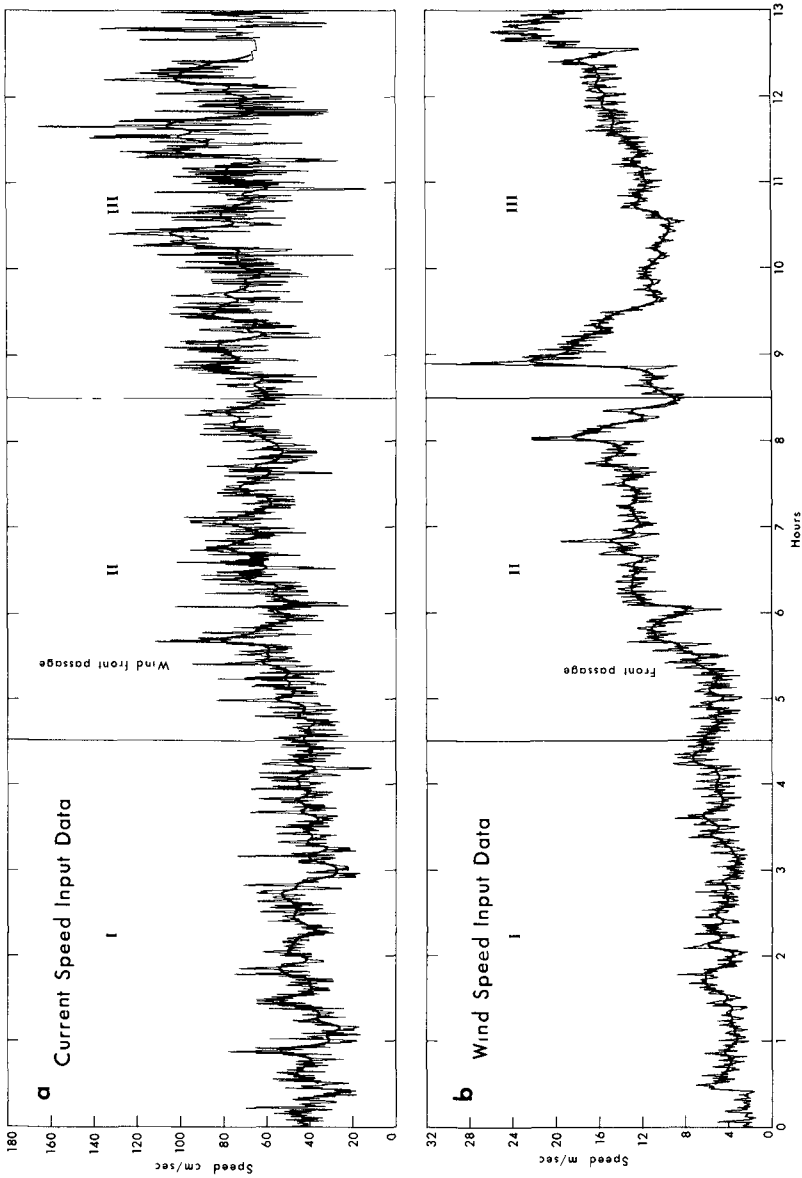


Fig 3 The time series observations of (a) the current and (b) the wind speeds together with the smoothed speeds determined by a 201-point binomial filter. The three phases subjected to separate analyses are shown in Roman numerals

pass filter can be used to isolate the trends and low frequency components. In Figure 3 the smoothed curve running through the observed data was derived from a 201-point binomial filter whose frequency response $R(f)_{BF201}$ is plotted in Figure 4 using the relation $R(f) = \cos^n(\pi f \Delta T)$ where n is the number of terms in the filter less one. This smoothing function passes only 8 percent of the amplitude of frequencies above 10 CPH and completely cuts out those amplitudes with $f \geq 15$ CPH.

The next step is the subtraction of the smoothed time series from the original time series, which is a high pass filtering technique (Holloway, 1958, Panofsky and Brier, 1963) with a frequency response $R'(f)$ in this case

$$R'(f) = 1 - R(f)_{BF201},$$

also plotted in Figure 4. All frequencies with $f \geq 10$ CPH have at least 90 percent of their amplitudes transmitted through the filter, and, again considering the filtering performed in digitizing, the final form of the data is a band pass $10 \lesssim f \lesssim 60$ CPH.

Also plotted in Figure 4 for comparison is the response of a high pass filter produced by subtracting a 30-point equally weighted running mean from an original time series. This type filter provides a sharper cut with minimal data loss but has distinct disadvantages in that it amplifies and damps certain frequencies, the troughs in the response curve turn maxima into minima and may produce a falsely rippled power spectrum (Holloway, 1958). A preliminary analysis of the present data with a 30-point equally weighted running mean high pass filter did in fact produce pronounced peaks at 30 and 50 CPH which could have been erroneously interpreted as surf beat effects.

TURBULENCE

Let us denote the original time series observations of speed by u_o and the smoothed record using the 201 binomial smoothing "function" by U_{BF} . The turbulent speed u' may be defined following the conventional theory by

$$u' \equiv u_o - U_{BF}$$

The random nature of u' is indicated by the histograms of u' (both wind and current), which show a good agreement with the corresponding best-fit Gaussian curves (Figure 5)--typical of most turbulence measurements.

In Figure 6 the turbulence intensity $(\overline{u'^2})^{1/2}$ and the relative turbulence intensity $(u'^2)^{1/2} / \bar{U}_{BF}$ are plotted as a function of time. The term $(u'^2)^{1/2}$ was calculated each half hour as the root-mean-square value of the 100 observations in that time interval, whereas the term \bar{U}_{BF} is the average of the corresponding 100 values of U_{BF} in that same time interval. The turbulence intensity of the current increased fairly

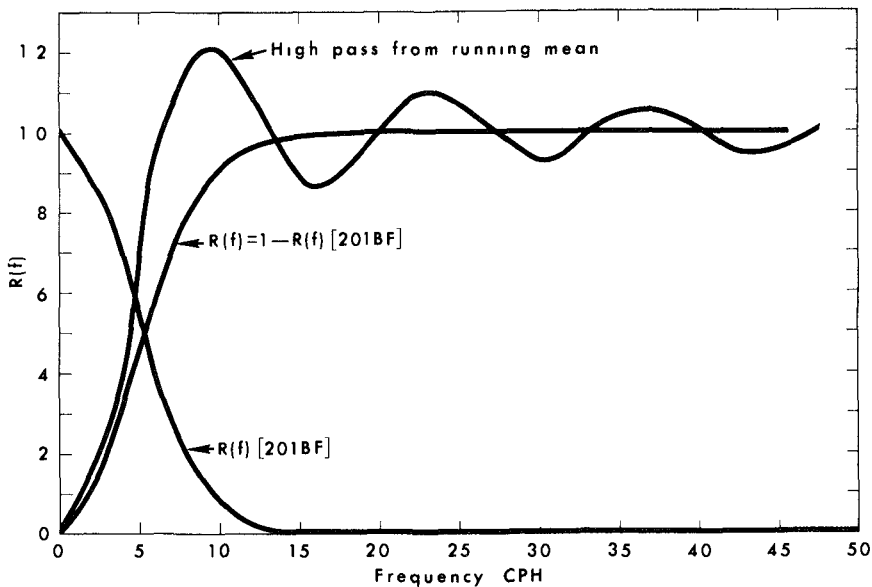


Fig 4 Frequency response curves for the high and low pass filters discussed in the text

regularly as the storm progressed from 8 cm/sec up to 22 cm/sec, while relative to the mean speed it oscillated around a value of about 0.18 cm/sec, even reaching as high as 0.27 cm/sec near the end of the record. Many previous studies in both field and laboratory have shown that the turbulence intensity under more normal conditions varies between 0.05 and 0.15 cm/sec of the mean flow speed. The turbulence intensity of the wind increased from an initial value of 75 cm/sec up to 150 cm/sec in the seventh hour. The relative value stayed at about 0.20 cm/sec until it dropped precipitously with the arrival of the storm front and its high mean speeds at hour 5.3 (see Fig. 3b).

It is notable that the turbulence intensity of the wind was decidedly damped after the front passed (excepting the effect of the large gust at 8.9 hours). The current turbulence intensity, on the other hand, increased after the front passed. It is significant that the current direction abruptly shifted (see Murray, 1970) after the wind front passed from westerly to southwesterly and south, reflecting, it is believed, a seaward return flow caused by setup against the coast. The increase in current turbulence intensity was probably caused by (a) the large vertical shear inherent within a reversing velocity profile and (b) the effects of large groups of wind-driven waves associated with the suddenly increased mean wind.

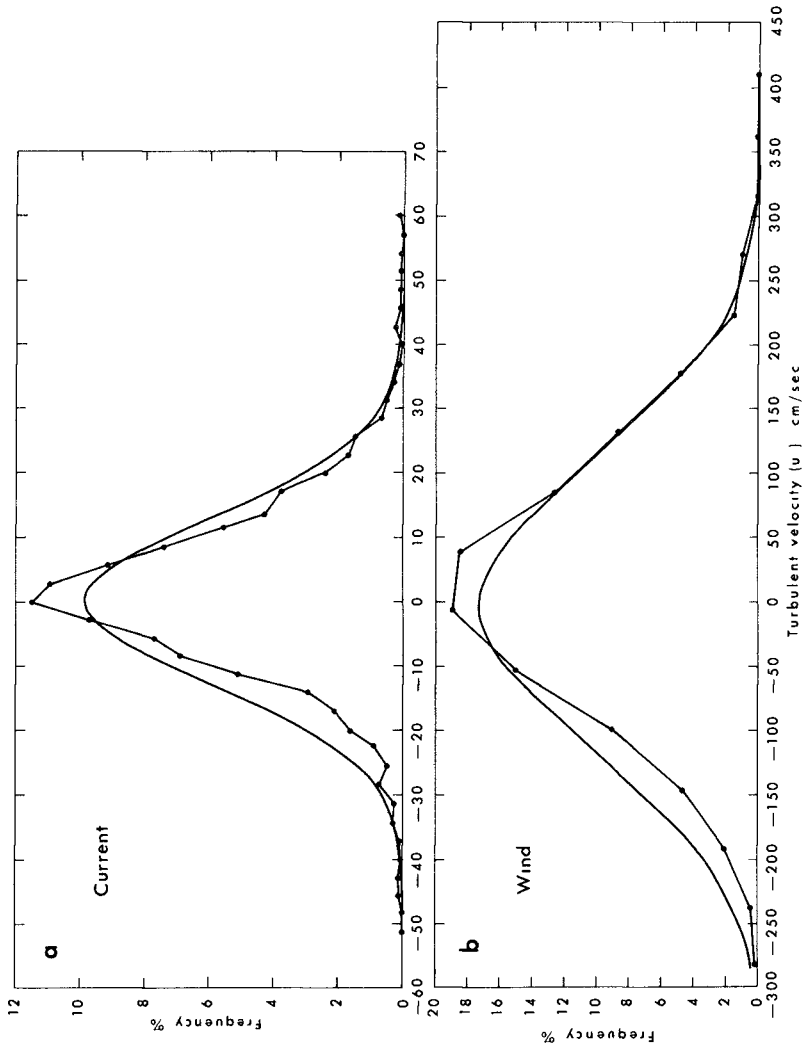


Fig 5 Frequency distributions of (a) the turbulent current speeds and (b) the turbulent wind speed together with the best-fit Gaussian curves

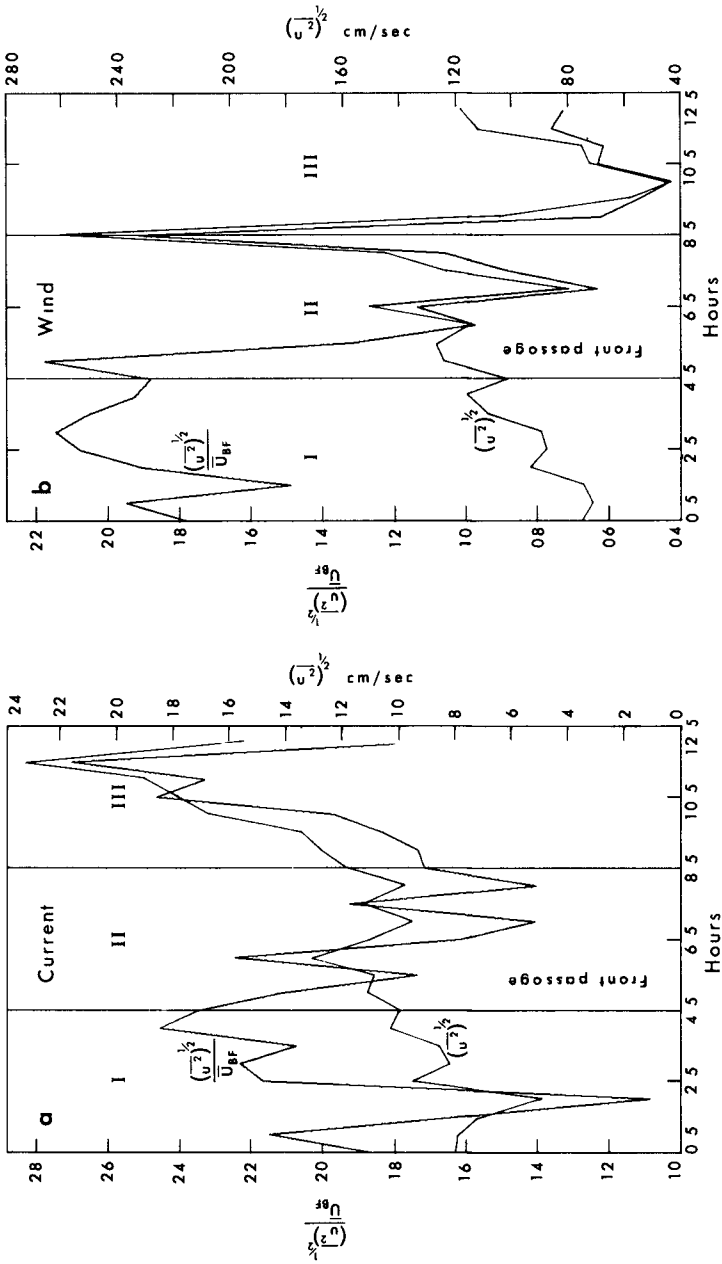


Fig 6 Turbulence intensity and relative turbulence intensity for (a) the current speed and (b) the wind speed

TURBULENCE SPECTRA

Energy density spectra $F(f)$ of the two u' time series were calculated from the procedure outlined in Bendat and Piersol (1966, p 291) and modified by the use of a Fast Fourier Transform. The 2400 data points were first divided into three segments (I, II, and III), as discussed earlier, each containing 800 points, so that the change of the energy density with the progress of the storm could be investigated. The resulting current speed spectra are shown in Figure 7. In the frequency range $15 < f < 60$ CPH there are no significant gaps or peaks apparent in any of the intervals, the energy density decreases smoothly with increasing frequency. The apparent peak in spectrum II is not significant at the 0.05 level at $f \approx 50$ CPH. The peaks at about 12 CPH, of course, are a result of the low frequency cutoff by the filter. As shown in Table 1, the total relative energy (the area under the spectral curve) more than quadruples from intervals I to III. There is considerably more energy at all frequencies in successively higher intervals, but the greatest increase is clearly at the lowest frequencies. Also listed in Table 1 is the absolute energy E associated with the turbulence in the mean flow direction, which is given by Taylor (1935) as

$$E = \frac{\rho}{2} \overline{(u'^2)}$$

The spectra in Figure 7 have also been corrected for the instrument frequency response $R(f)$ plotted in Figure 2. The corrected spectral density $F'(f)$, shown as a dashed line in Figure 7 and calculated from

$$F'(f) = \frac{F(f)}{R(f)^2},$$

has little effect other than to increase the energy at the high frequencies.

The wind speed spectra in Figure 8 display the same lack of peaks or gaps as the current spectra. Most notable is the fact that the energy content (see Table 1) does not increase at all from intervals II to III, in sharp contrast to the twofold increase observed in the content of the current spectra between these intervals. This suggests again a lack of direct energy transfer between wind and current in the frequency band $10 < f < 60$ CPH under study here. This inference is

Table 1 Total Energy Associated with Energy Density Spectra

Interval	RELATIVE $\int F(f) df$ (cm/sec) ²		ABSOLUTE E (ergs/cm ³)	
	Current	Wind	Current	Wind
I	69	8281	34	4.1
II	119	15006	59	7.5
III	279	15126	139	7.6

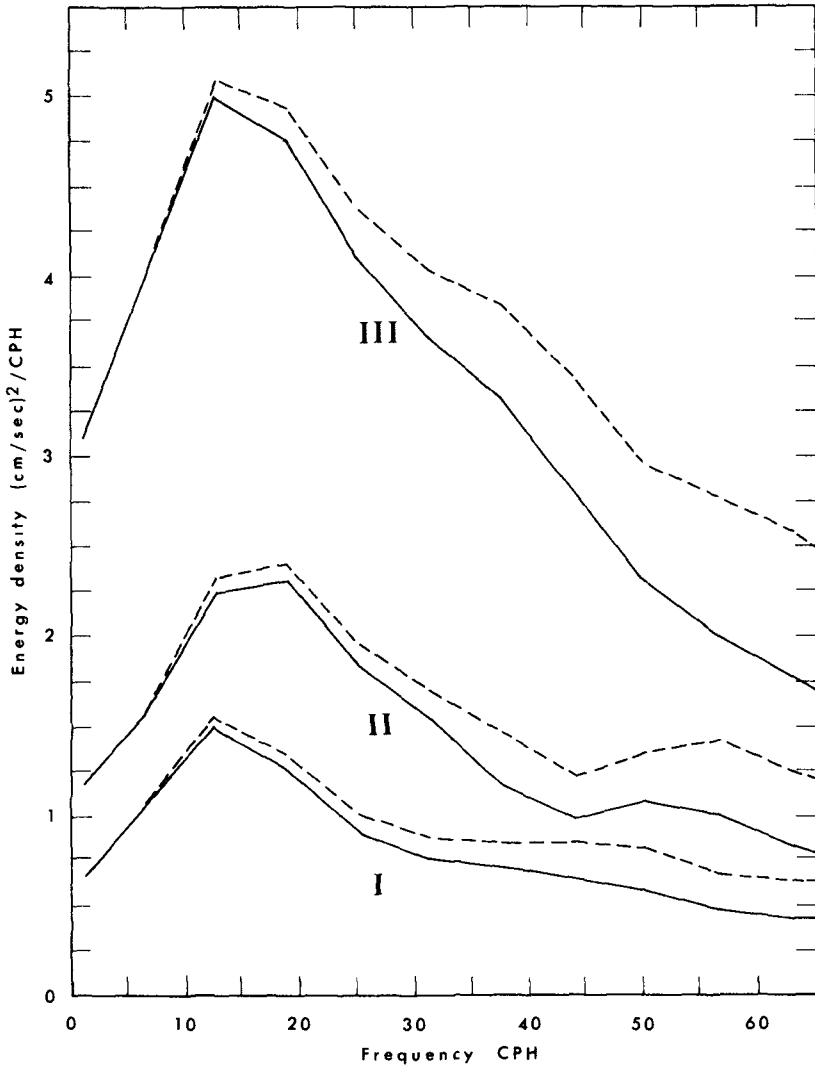


Fig 7 Energy density spectra of the current for the three phases of the storm. The dashed line is a correction for the instrument frequency response.

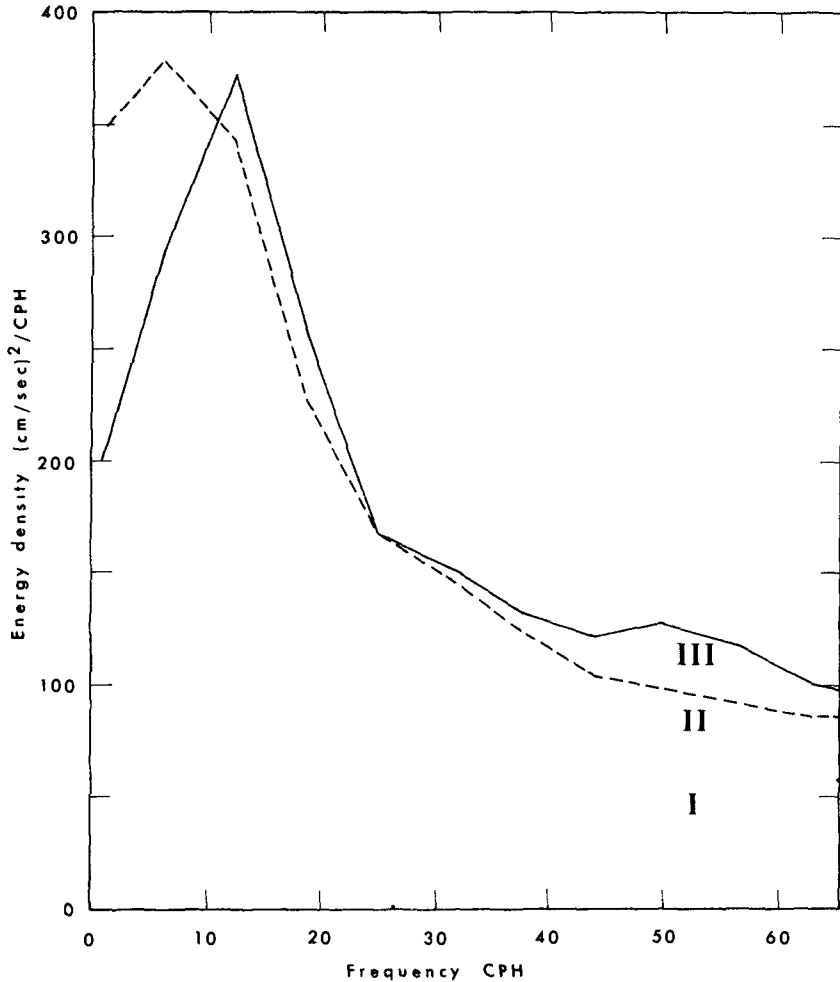


Fig 8 Energy density spectra of the wind speed for the three phases of the storm

supported by the data in Table 1, which shows that there are more ergs of energy per unit volume associated with the turbulence in the water than with that in the air at these frequencies

The data seem to indicate that the energy is entering the 10-60 CPH frequency band of the current from the lower frequency oscillations of the current itself, which are presumably generated by the low frequencies of the wind. A good correlation does clearly exist between

the DC levels (mean values) of the wind and the current (see Fig 3 and Murray, 1970)

In Figure 9 the $F(f)$ spectra of the wind are replotted on a log-log scale. In studies of air turbulence over water Pond *et al.* (1966) found that in the low frequency ranges of their data the energy density dropped off with the -1 power of the frequency $F(f) \propto f^{-1}$. Their -1 power range extended between $10^{-5} < k < 3 \times 10^{-3}$ where k is the wave number. Using Taylor's hypothesis $f = Uk/2\pi$ (Taylor, 1938) and the limits of the mean values for this study $500 < U_{BF} < 1300$ cm/sec, the corresponding frequency band for their -1 power range is $3 < f < 2300$ CPH. The present data which fall in the low frequency end of the range are also represented very well by the -1 power slope. Tchen (1953) has suggested that the -1 power law would hold below the inertial sub-range

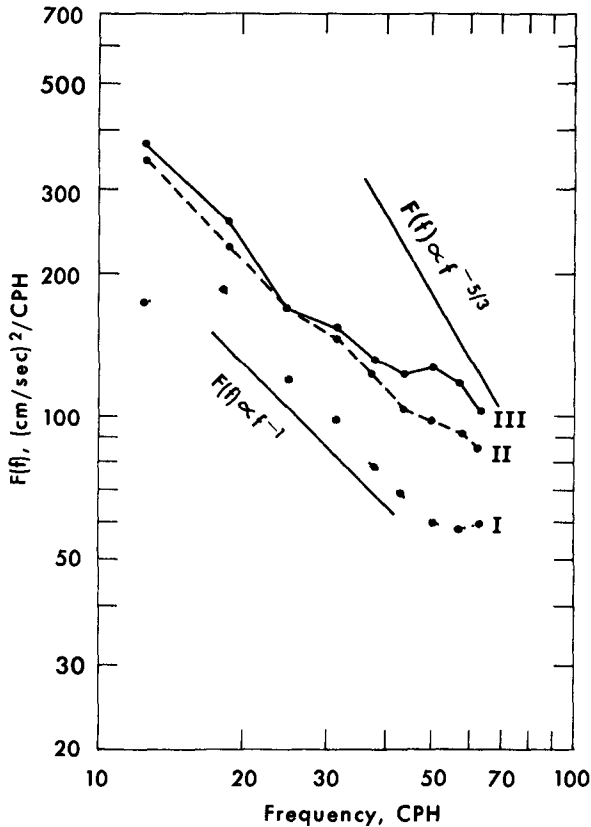


Fig 9 Energy density spectra of the wind on a log-log plot. The straight lines show a -1 and a $-5/3$ power dependency on the frequency.

in the presence of strong vertical shear--a situation which certainly existed in the lower 10 meters of the atmosphere during this storm as a result of surface drag

So that the energy drop-off with frequency of the $F(f)$ spectra of the current speed may be similarly investigated, the spectra of Figure 7 are replotted on a log-log scale in Figure 10 Cannon (1969) has presented excellent and comprehensive data which clearly established the presence of a $-5/3$ law governing the drop-off of energy with frequency in an estuarine tidal flow in the frequency band $1 < f < 72$ CPH Cannon also reported, however, several experiments in which strong vertical shear was suspected and the log-log plots showed that $F(f) \propto f^{-1}$ During a large part of the 13-hour record used in this study the Q-16 meter was bounded by two shear zones (a) the bottom boundary layer and (b) the transition zone (probably near mid-depth) between upper-layer wind-driven

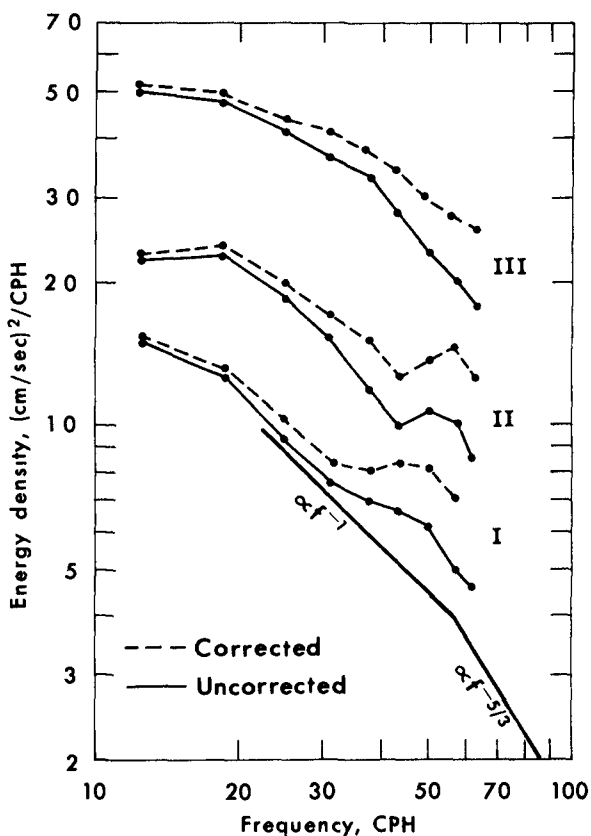


Fig 10 Energy density spectra of the current on a log-log plot The straight lines show a -1 and a $-5/3$ power dependency on the frequency

currents and lower-layer return flows caused by the setup against the coast (Murray, 1970) Figure 10 may reflect that this phenomenon as the -1 power is a reasonable fit for the spectra (both corrected and uncorrected) in intervals I and II. However, in interval III of the current record, when the energy content was highest (Table 1), the slope of the spectra (on a log-log plot) was considerably flatter than the -1 value--having a value close to -0.5 . These observations suggest that with increasing energy content (or perhaps increasing vertical shear) the $F(f)$ dependency on the frequency may shift from $f^{-5/3}$ to f^{-1} to $\sim f^{-0.5}$ in this intermediate frequency range.

CROSS CORRELATION

All attempts to relate the turbulent energy distribution in the wind to that of the current yielded negative results. Figure 11 shows a typical wind-current coherence function (interval II), the coherence level is insignificant at all frequencies. Similarly, the phase lags (Fig 12) from the same data set oscillate with no apparent pattern. Such results are not unexpected since Cannon (1969), in carefully controlled experiments, found no significant coherence between the records of adjacent current meters in frequencies above 10 CPH.

CONCLUDING REMARKS

The principal conclusions from this study of wind and water turbulence in the frequency band $10 < f < 60$ CPH are as follows:

- 1 As the storm progresses there is no systematic change in the energy spectra common to both wind and current.
- 2 As the storm progresses the energy content of the current spectra increases markedly, the maximum increase in energy is in the lowest frequencies.
- 3 The coherence between wind and current is insignificant (< 1) in this band.
- 4 For reasons 1, 2, and 3 above it is concluded that energy is fed into the 10-60 CPH frequency band of the current from the lower frequencies of the current itself.
- 5 The energy density of the wind decreases proportionally to the -1 power of the frequency in all three storm intervals.
- 6 The energy density of the current decreases proportionally to the -1 power of frequency in the first two intervals of the storm but proportionally to ~ 0.5 power of the frequency during the third storm interval, which was the most intense.

ACKNOWLEDGMENTS

Myron Young and Choule Sonu of Louisiana State University developed the programs which permitted this time series analysis to be carried out. The project was sponsored by the Geography Programs, Office of Naval Research, under Contract N00014-69-A-0211-0003, NR 388 002.

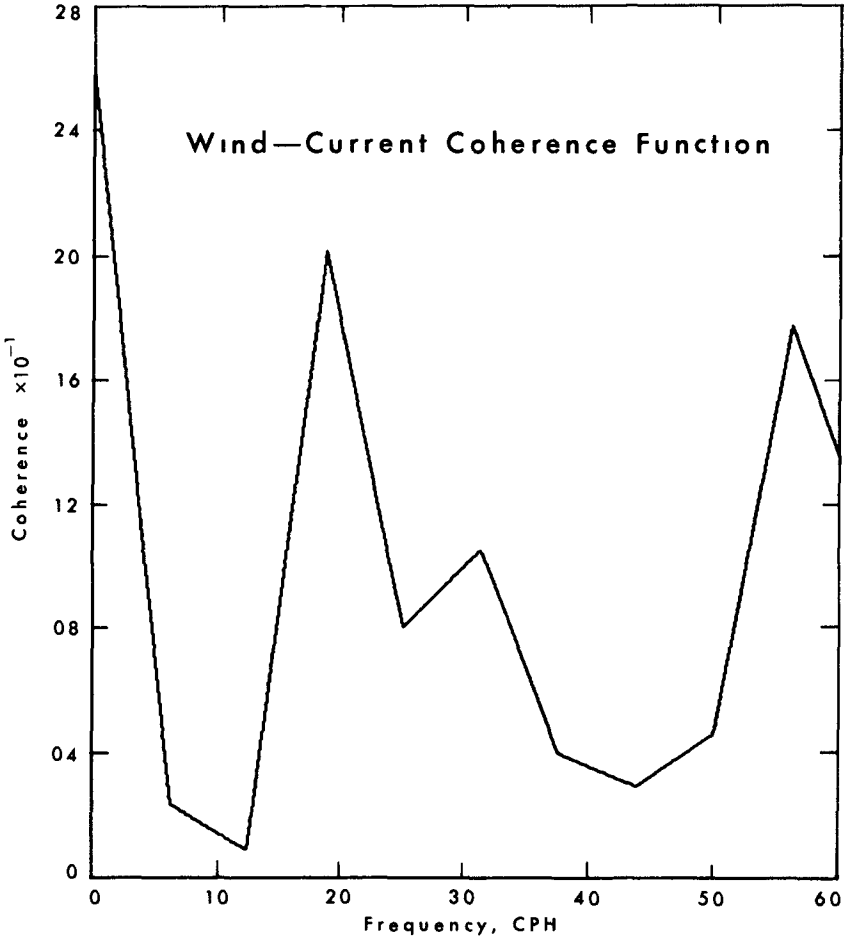


Fig 11 The coherence function between the wind and the current from interval II

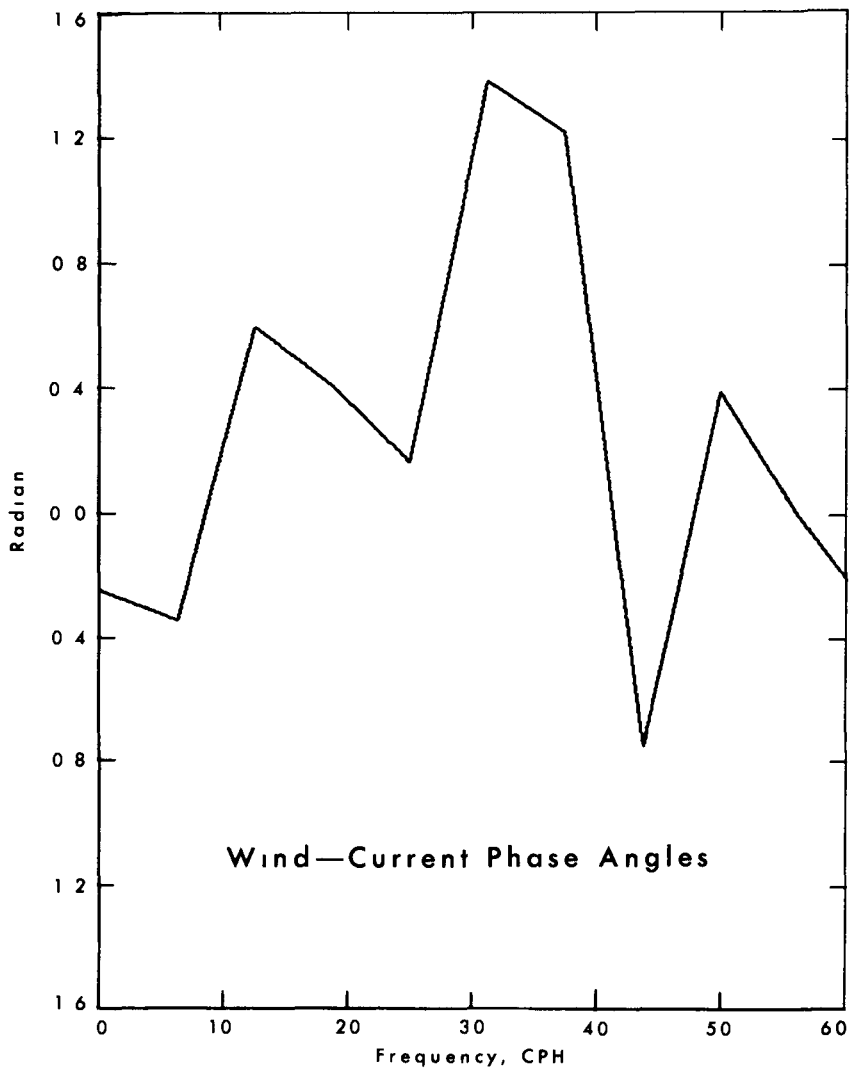


Fig 12 The phase lags of the wind and the current from interval II

REFERENCES

- Bendat, J S , and A G Piersol, 1966, Measurement and analysis of random noise data New York (John Wiley), 390 pp
- Cannon, G A , 1969, Observations of motion at intermediate and large scales in a coastal plain estuary Technical Report No 52, Ref 69-5, Chesapeake Bay Institute, The Johns Hopkins Univ , 113 pp
- Fergusson, S P , 1935, The sensitiveness of anemometers Bull Am Meteorol Soc , 15 95-99
- Holloway, J L , Jr , 1958, Smoothing and filtering of time series and space fields In (H E Landsberg, ed) Advances in geophysics, 4 351-388
- Murray, S P , 1970, Bottom currents near the coast during Hurricane Camille J Geophys Res , 75(24) 4579-4582
- Panofsky, H A , and G W Brier, 1963, Some applications of statistics to meteorology The Pennsylvania State Univ , University Park, Pennsylvania, 224 pp
- Pond, S , S D Smith, P F Hamblin, and R W Burling, 1966, Spectra of velocity and temperature fluctuations in the atmospheric boundary layer over the sea J Atmospheric Sci, 23(4) 376-386
- Taylor, G I , 1935, Statistical theory of turbulence Parts I-IV Proc Roy Soc London, A151, pp 421-478
- _____, 1938, The spectrum of turbulence Proc Roy Soc London, A164, pp 476-479
- Tchen, C M , 1953, On the spectrum of energy in turbulent shear flow J Res NBS, 50(51)

CHAPTER 125

Jamaica Bay Hurricane Barrier

by

Frank L Panuzio ^{1/}

Fellow American Society of Civil Engineers

ABSTRACT

A 12.4 mile beach erosion control and hurricane flood protection project includes Jamaica Bay and the Rockaway Inlet in the southwest corner of Long Island, New York. The project would provide 6.1 miles of beach fill and floodwalls along the Atlantic Ocean shore and 6.3 miles of inland structures to tie back to high ground, including a 0.9 mile barrier across the inlet. The barrier, with a 300 foot gated opening and a 300 foot ungated opening, would permit suppression of the design hurricane surge so as to eliminate the need of flood protection works within the bay. Linear mathematical models were used to determine these openings. Because of the limitation of these models to produce adequate data in the bay pertinent to environmental and ecological considerations, three hydraulic models were utilized. General conclusions drawn from the hydraulic model test data are that the results of the mathematical models were upheld, a design storm with high peak is critical for determining the height of protection, a design storm with high volume rather than high peak plus rainfall runoff is critical in determining ungated openings and suppression of bay levels, and there is a combination of gated and ungated openings that would meet the flood protection, navigation, environmental and ecological objectives.

GENERAL

Project The Jamaica Bay hurricane barrier is a part of a 12.4 mile, Federal beach erosion control and hurricane flood protection project, authorized by the Congress of the United States in June 1965 at more than 50 million dollars ^{1,2}

Location The project extends along the Atlantic Ocean side of the Rockaway peninsula from high ground in the vicinity of East Rockaway Inlet to high ground in the vicinity of Rockaway Inlet and includes Jamaica Bay (Figure 1). Jamaica Bay is a coastal body of water in the southwest corner of Long Island and connects to the lower bay of New York Harbor and the Atlantic Ocean through the Rockaway Inlet. The bay is bounded by the boroughs of Brooklyn and Queens and Rockaway peninsula in New York City and by Nassau County, all in the southeast corner of New York State. Long Island is a long, narrow island in the north Atlantic Ocean at a significant indentation of the northeastern coast line of the United States. The Rockaway peninsula is a barrier beach which extends westward from the mainland of Long Island and separates Jamaica Bay from the Atlantic Ocean.

Objectives The project objective is to provide protection against storm water flooding due to hurricanes along the developed shore line of the Rockaway peninsula and of Jamaica Bay and to restore and to stabilize the beach along the ocean shore line of the Rockaway peninsula.

The barrier objective is to provide a practicable solution of a tieback to high ground for the coastal works and to suppress the design hurricane surge to a non-damaging level in the bay so as to eliminate the need of protective works along the shores of the bay without any detrimental change in the existing bay environment and ecology during the no-storm period.

Problem In the preauthorization studies, the size of the barrier openings during normal and storm periods was determined by the use of a simplified linear mathematical model. While this model is adequate to predict water surface elevations and the discharges and average velocities in the openings, it did not produce adequate values of local hydraulic changes in the bay such as local

^{1/} Senior Engineer Consultant for Civil Works
U S Army, Corps of Engineers, New York District



OBLIQUE LOOKING GENERALLY EASTWARD



ROCKAWAY INLET TO EAST ROCKAWAY INLET

FIGURE 1 JAMAICA BAY, LONG ISLAND, NEW YORK, U.S.A.

velocities and currents, salinities, tidal levels and circulation which are essential to pollution, fish and wildlife, and other environmental and ecological considerations^{1,5,6} Therefore, environmental and ecological interests, recognizing this deficiency, requested that additional field studies and hydraulic model investigations be conducted during the final design of the project to determine the specific effects of the hurricane barrier on water quality, fish and wildlife, and currents in Jamaica Bay The authorization by Congress was subject to this consideration

AUTHORIZED PROJECT

Description The authorized project from east to west, with all elevations referred to mean sea level, would consist of (Figure 1) a 0.3 mile concrete closure wall at East Rockaway Inlet with a top elevation from 18 to 15 feet at closure and with a 6 foot high and 40 foot wide stoplog structure, a beach fill of more than 4 million cubic yards with a 100 to 200 foot wide berm at an elevation of 10 feet and with a 1 on 20 oceanward slope, backed up by a concrete-clad, steel sheet pile floodwall with a top elevation of 18 feet along 6.1 miles of the ocean side of the Rockaway peninsula, a 0.9 mile flood dike with a top elevation of 18 to 15 feet across the Rockaway peninsula to Rockaway Inlet, a 0.6 mile concrete floodwall and levee along the inlet with a top elevation of 15 to 18 feet, a 0.9 mile gated barrier across the inlet with a top elevation of 18 feet, a 1.2 mile levee and dike, and a 2.4 mile natural ground closure with a top elevation of 18 feet at the barrier to 15 feet at the closure

The Barrier The solid portion of the barrier would consist of (Figure 2) two sections with lengths of 1,860 and 1,670 feet, with a top width of 12 feet at an elevation of 18 feet, with side slopes of 1 on 1.5 and with fishing platforms on both sides at an elevation of 8.0 feet The middle 1,000 feet of the barrier with a bottom elevation of minus 42.5 feet would consist of a 600 foot navigation opening and two side rolling gates, each 150 feet wide with gate recesses, to permit closure of this opening to 300 feet during the storm periods

Still Water Level The design still water level for the authorized project is the peak of the Standard Project Hurricane surge occurring at the mean astronomical tide (Figure 3) For the prediction of surges at the mouth of the New York Harbor for a design storm, a research investigation was conducted at The A and M College of Texas⁴ From this research, a correlation-prediction formula was developed empirically, with some degree of theoretical guidance, from observed tides and corresponding meteorological parameters of storms inducing them On this basis, using the meteorological parameters of the September 1944 hurricane transposed to a path critical to the New York Harbor area, the Standard Project Hurricane surge was determined to be 12.3 feet^{3,4} The meteorological parameters were a maximum wind of 116 miles per hour, a central pressure range of 27.55 to 27.95 inches of mercury with a normal pressure of 30.12 inches of mercury, a radius to maximum winds of 30 nautical miles and a forward speed of 40 knots

Protection Height The design height of the protection works is the design still water level plus the wave runup Based on the solitary wave theory, the maximum breaking wave at the beach fill was found to be 20.5 feet with a 12 second period Using the composite slope method and experimental data,⁷ the runup for this wave would be 5.7 feet Thus, the top of protection was placed at an elevation of 18 feet At the barrier, based on a generalized relationship between winds and wave observations,⁸ an effective fetch of 3.9 miles, a wind speed of 80 miles per hour and an effective depth of 32 feet at the design still water level would result in a wave of 6.7 feet with a period of 5 seconds This wave, based on experimental data on riprap structures,^{7,8} would produce a wind setup and runup of 5.7 feet Thus, the top of protection was also placed at elevation 18

Mathematical Model The propagation of tides inside a bay may be expressed by dynamic and continuity equations^{1,5,6} These equations, due to boundary conditions

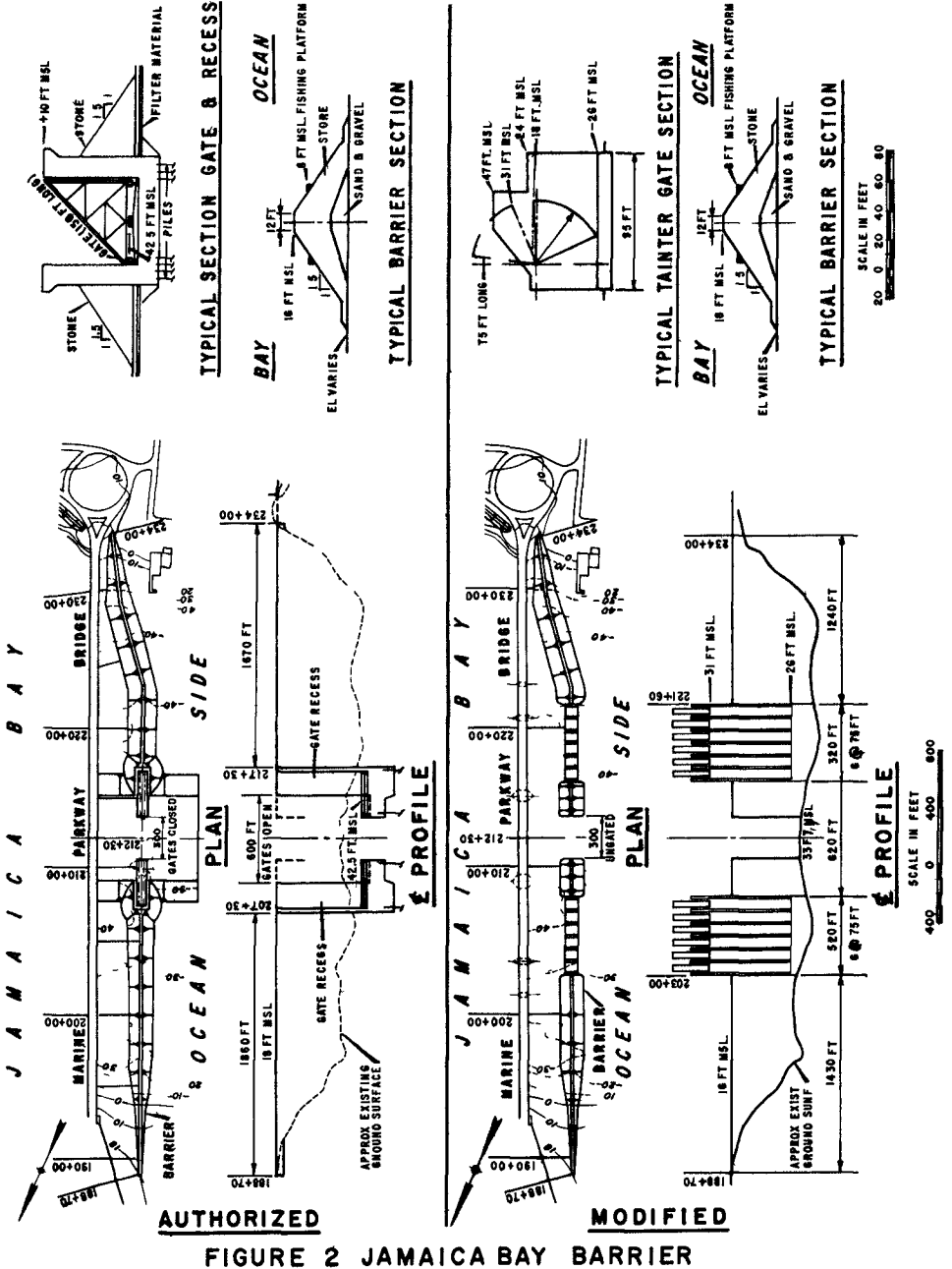


FIGURE 2 JAMAICA BAY BARRIER

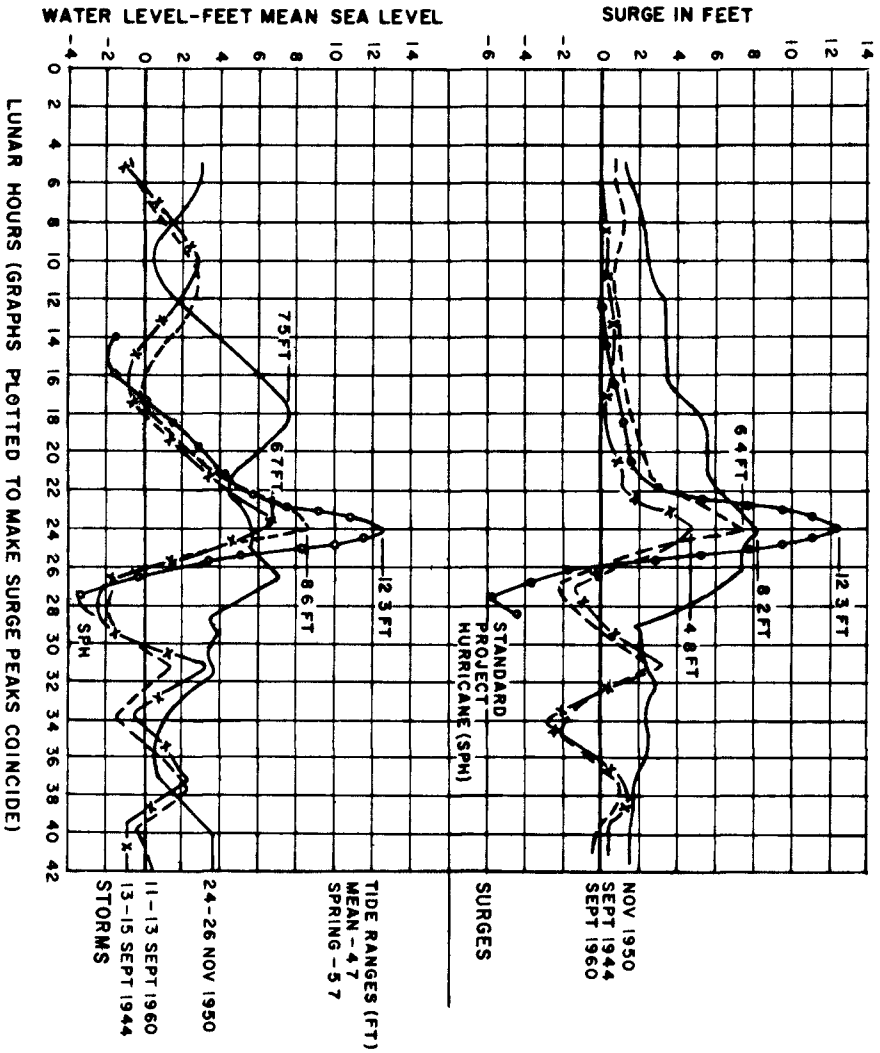


FIGURE 3 CRITICAL DESIGN HURRICANES-FORT HAMILTON,NY

and many complex terms involved, could not be solved analytically within the scope and time frame of the study. In order to obtain a practical solution, assumptions were made to simplify the equations by neglecting and simplifying the terms of the equations without substantial loss in accuracy. The bay is, basically, a basin connected to the ocean by a relatively long and narrow channel of the Rockaway Inlet. So, a simple, one-dimensional model for current natural conditions of the bay was developed on the assumption that the flow through the channel is governed only by the functional resistance in the channel with negligible inertia forces and that the level inside of the bay is variable only with time with an adjustment for wind setup and rainfall. The adequacy and adjustment of this model were developed by routing the hurricane of September 1960 to produce recorded bay levels. When the barrier is placed across the natural Rockaway Inlet, the mathematical model must be adjusted for the increased resistance to flow at the barrier. Thus, the one-dimensional model was based on two principal assumptions. The resistance to flow through the barrier opening and the inlet channel is the only significant force acting on the dynamic system. The water surface throughout the bay is assumed horizontal and related to the ocean surface elevation only by the law of continuity and the loss through the barrier and inlet channel. With these basic assumptions, the dynamic relationships were expressed by the following equations

$$Q = C A_b \sqrt{2g} \sqrt{Z_a - Z_j}$$

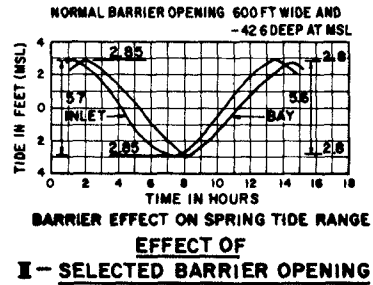
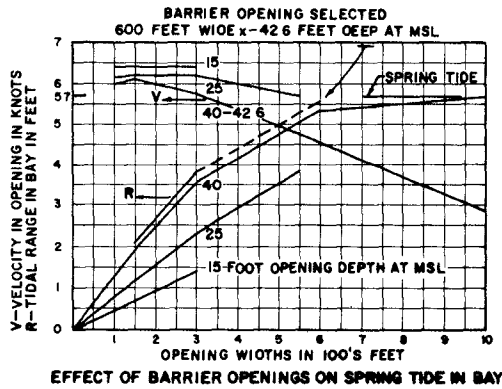
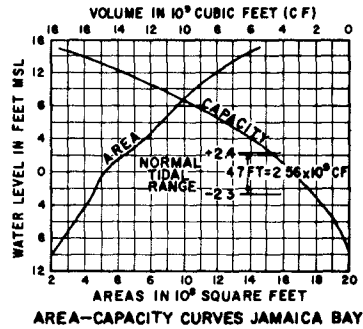
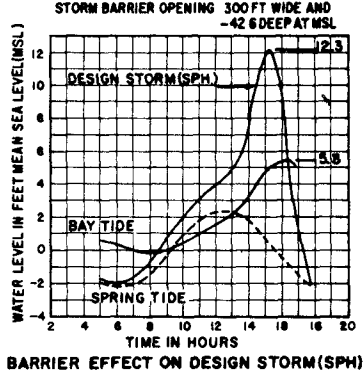
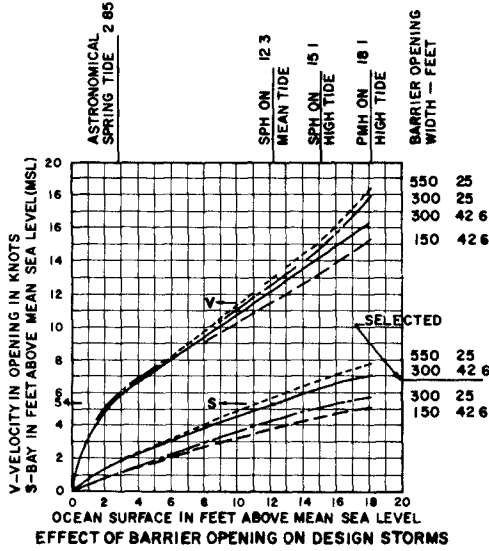
in which Q = discharge through barrier opening, C = discharge coefficient, A_b = area of opening, Z_a = water surface elevation on ocean side, and Z_j = water surface elevation on bay side

$$Q = S_j \frac{dZ_j}{dt} - I_r$$

in which S_j = surface area of bay, and dZ_j = change in bay water surface elevation for time interval of dt and I_r = rainfall-runoff inflow rate

Barrier Opening The initial barrier opening was sized to be large enough to minimize any change in the natural bay environment and ecology during no-storm periods, to satisfy the projected navigation vessel and traffic, and to suppress the design hurricane level to about zero damage stage in the bay. To accomplish the first two objectives, 14 routings were made for the spring astronomical tidal range of 5.7 feet, utilizing the mathematical model, the area capacity curve, navigation depths of 15 to 42.6 feet mean sea level and openings from 100 to 1,000 feet with results as shown on Figure 4. On the basis of these results, the minimum opening that would have minimal effect on the astronomical spring tidal range and would satisfy the navigation depths and velocities was the 600 foot opening with a depth of 42.5 feet at mean sea level, a 4.5 knot maximum velocity in the opening, and a reduction in range of 0.10 feet. The 1,000 foot opening showed no significant change in tidal range, and a 3.0 knot maximum velocity. The average velocity in the Rockaway Inlet for the existing conditions is in the order of 2.7 knots. However, average velocities up to 5 knots are considered tolerable for navigation.

Based on a gross appreciation of the hydraulic system of Jamaica Bay and Rockaway Inlet, a quasi theoretical mathematical model of BOD vs Tidal Prism relationship for Jamaica Bay was developed.⁹ This relationship assumed that change in total waste load as measured by the BOD is directly related to the volume of the tidal prism. This model was used with waste loads measured during the summer of 1959-1962 and anticipated future waste loads obtained from city sources to predict accumulation of waste in Jamaica Bay and Rockaway Inlet for the tidal prism change estimated from the effect of each barrier opening. The results from the model for the 600 and 1,000 foot openings were that the change in waste load accumulation



I - SECTION OF BARRIER OPENING

II - SELECTED BARRIER OPENING

FIGURE 4 BASIS OF AUTHORIZED BARRIER OPENING DESIGN

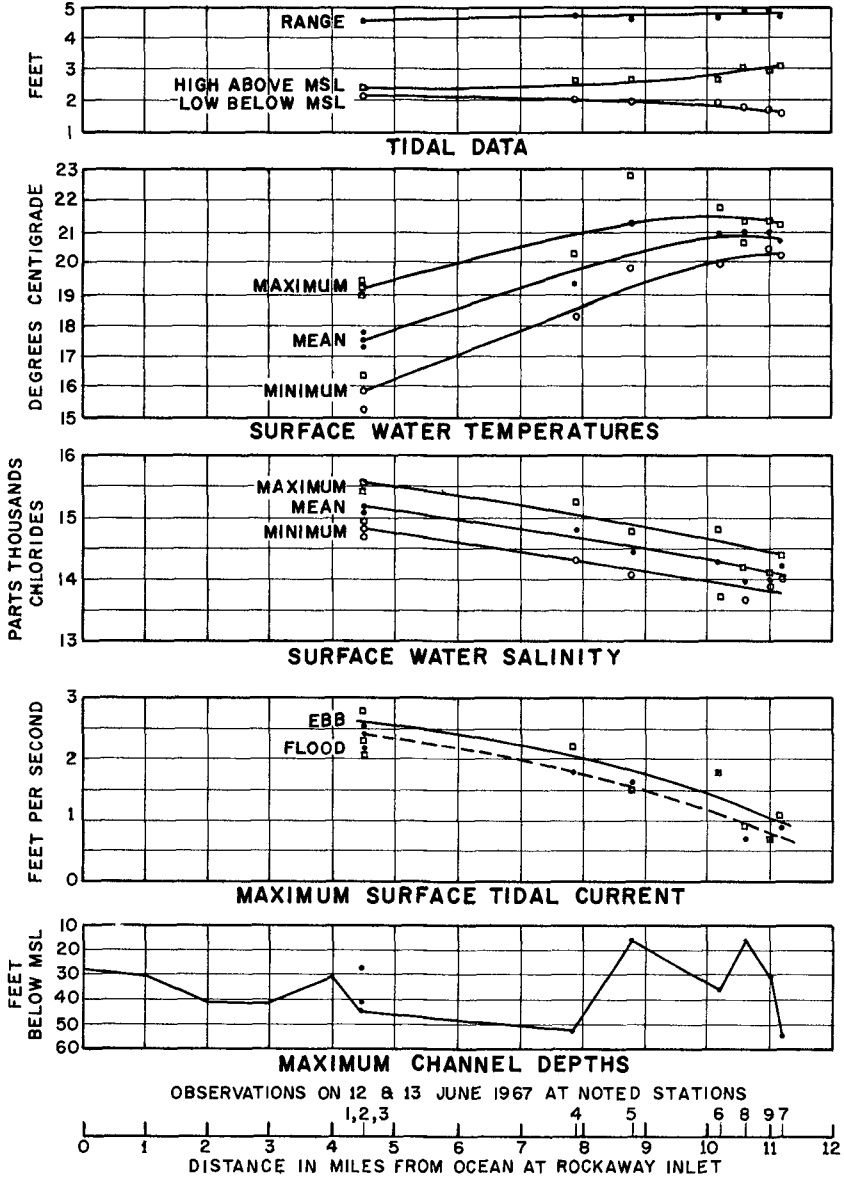
would be virtually zero and that there would be no significant damage to water quality. In the interest of minimum first cost, since the selected opening would have to be gated to obtain suppression of the design hurricane, the 600 foot opening was selected for the normal operating conditions.

To obtain the third objective, to suppress the design hurricane level to about zero damage stage in the bay, 13 routings were performed utilizing the mathematical model, the area capacity curve, navigation depths of 25 and 42.6 feet below mean sea level and openings of 150, 300, and 550 feet with results as shown in Figure 4. On this basis, the storm opening of 300 feet with a depth of 42.6 feet at mean sea level was selected to produce a bay level for the Standard Project surge on mean tide of 5.3 feet at mean sea level, about zero damage stage.

Limitations While these models are adequate to predict water surface elevations, discharges and average velocities in the opening, and gross evaluation of the water quality, they cannot produce adequate values of local hydraulic changes in various parts of the bay such as velocities and currents, salinities, tidal levels and circulation which are essential to pollution, fish and wildlife, and other environmental and ecological considerations. Therefore, recognizing this deficiency, the Congressional authorization was subject to the condition that additional field studies and hydraulic model investigations would be conducted in the final stage of design to evaluate and to minimize the specific effects of the hurricane barrier on water quality, fish and wildlife, and currents in Jamaica Bay.

FIELD INVESTIGATIONS

Measurements Field measurements were started in January 1967 with a view to developing data to construct and verify a hydraulic model of Jamaica Bay. To develop the physical characteristics of the bay, a photographic and topographic survey of the area was made to a horizontal scale of 1 inch = 1,000 feet and to a vertical relief of two foot contours up to elevation 20 feet mean sea level. The underwater contours were developed by a sounding survey at sufficient sections to delineate the underwater topography. For hydraulic verification, measurements were made on 12 and 13 June 1967. Current velocities were recorded at nine stations in Jamaica Bay at locations shown on Figure 1 and identified by letter V. Current velocities were taken every one half hour over a complete tidal cycle at surface, mid-depth, and bottom. Tidal current observations were timed generally to cover a period between successive low tides, during daylight hours, for a period in excess of 13 hours when the diurnal inequality was a minimum. Simultaneous measurements were taken at stations 1V, 2V, and 3V, at stations 2V, 4V, 5V, and 6V, and at stations 2V, 7V, 8V, and 9V in order to obtain the distribution of flow in the channel system of the bay. Each group of stations was tied into the other two groups through continuous reading at station 2V. Three Ott meters with F4 counter and two Gurley Price meters with 611 counter were used. Each meter was connected to an electric revolution counter and watch. Reduction of field data was by use of laboratory calibration curves for each meter. At each station, current meter measurements were made for a total period of one minute at just below the surface, at 2 feet above the bottom and at mid-depth where depths exceed 6 feet at mean low water. At each velocity station depth, water samples were taken with one or two liter Kemmerer samplers after water was permitted to flow freely out of the sampler. The temperature of each sample was taken immediately with armored thermometers with a range of -1° to 50° Centigrade in 0.1° divisions. The salinity of each sample was determined in the laboratory and recorded in parts per thousands of chlorides. The hydrography at each of these stations was also obtained with depths referred to mean sea level. Data were also developed as to sanitary and storm water inflow at four sewage treatment plant overflows and five storm water outfalls and on weather conditions as to rain, wind, and temperature.



FIGURES 5 FIELD OBSERVATIONS-JAMAICA BAY CHARACTERISTICS

Results The Jamaica Bay characteristics measured as to tidal currents, tidal range, temperatures, salinities and hydrography are shown in Figure 5¹⁰. The water depth varies from 15 to 55 feet at mean sea level. For the measured tidal cycle, the tidal range varies from 4.6 to 4.9 feet with the higher values in the interior of the bay and with time of high and low water almost identical at the five interior stations. The surface tidal currents vary from 2.5 to 0.7 feet per second on flood and from 2.8 to 0.7 feet per second on ebb with the lower values at the interior. The currents were found to be greatest at the surface and minimum at the bottom. Slack water was found to be coincident with or within one half hour of the times of high and low tides. The surface water salinity varied between 15.2 and 14.0 parts per thousand of chloride with the higher values at the entrance. The salinities increased with depth and were maximum near the end of flood and minimum near end of ebb. The surface water temperature varied from 17.3° to 21.0° Centigrade with the higher temperatures in the interior. The temperature decreased with depth and was greatest near end of ebb and least near end of flood.

HYDRAULIC MODEL INVESTIGATIONS

Purpose The model studies of Jamaica Bay were to determine the effects of the hurricane surge protection barrier in the Rockaway Inlet on (a) water quality in the bay as to public health, recreation, and fish and wildlife, (b) recreational and commercial navigation, and (c) suppression of the design storm surge to such a level as to provide protection to the area surrounding the bay from storm flooding.

Facilities The hydraulic model studies were carried out in three research facilities at the U.S. Army, Corps of Engineers, Waterways Experiment Station, Vicksburg, Mississippi, Figure 6. Jamaica Bay is a small section of the basic comprehensive model of the New York Harbor complex. This model, constructed to linear scale ratio (model to prototype) of 1/100 vertically and 1/1,000 horizontally, produces velocities at the ratio of 1/10, time at 1/100, discharge at 1/1,000,000 and salinity at 1/1. The Jamaica Bay area was reconstructed to reproduce prototype hydrographic and topographic conditions below +20 feet mean sea level as of June 1967. Tides and their associated flood and ebb tidal currents are controlled in the model by the interaction of a primary programmable tide generator located in the Atlantic Ocean at Sandy Hook and two secondary tide generators, one located in Long Island Sound and another located in the Hudson River at Hyde Park at the upstream limit of the model. Weirs are used to control the upland freshwater inflow from tributaries. A surge generator is used to produce the time-elevation history of the design storms. This model is used to develop data on the tidal regime, currents, salinities, dispersion characteristics, surge suppression and the barrier composition.

A second model reproduced a short reach of the Rockaway Inlet to an undistorted linear scale of 1/100. The velocity or time ratio is 1/10 and the discharge ratio is 1/100,000. Various designs of gated and ungated barrier openings were tested to determine their hydraulic efficiency under conditions of normal tides and storm surges and to determine in detail the flow patterns and velocities in and adjacent to the openings that might be significant to the design of the structure or to navigation through the structure.

The third model, to the scale of the basic model, was used to develop the distorted scale structures that have the hydraulic efficiencies as developed in the undistorted model for use in the distorted comprehensive model. This procedure ensured that when the distorted scale structures are placed in the comprehensive model they would pass the proper flows into and out of Jamaica Bay under any combination of head differentials imposed by the tides and storm surges.

Bay Model Verification The Jamaica Bay portion of the comprehensive model was first corrected to reproduce the latest topographic and hydrographic conditions. Then, the bay area was adjusted to reproduce prototype data for tides, tidal currents, and salinities, as observed on 12 and 13 June 1967 (Figure 5)¹⁰. The high



JAMAICA BAY AREA

MODEL SCALES
1:100 VERTICAL | 1:100
1:1000 HORIZONTAL | 1:1000
COMPREHENSIVE MODEL

ENTIRE MODEL



UNDISTORTED

DISTORTED

MODEL SCALES
1:100 VERTICAL | 1:100
1:100 HORIZONTAL | 1:1000
BARRIER MODELS

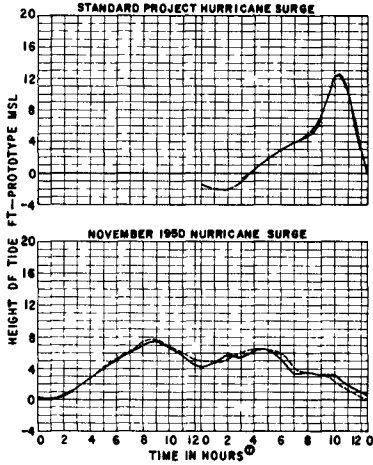
FIGURE 6 JAMAICA BAY MODELS

degree of accuracy attained in the model verification as to tides, current velocities, salinities, and design storms is illustrated by the comparative model and prototype curves shown on Figure 7¹¹. While there are some differences between model and prototype data, these differences were probably attributable to local winds and other disturbances that occurred when the prototype measurements were taken and that could neither be identified nor simulated to scale in the model verification tests.

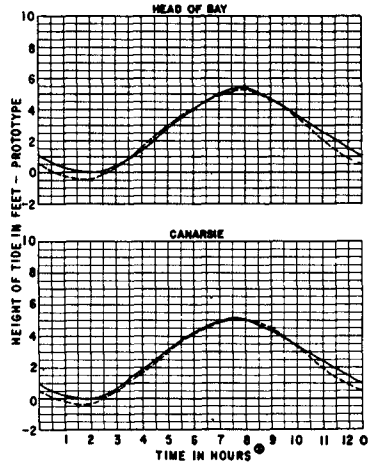
Barrier Model Verification The barrier gated and ungated openings were constructed to the undistorted scale of the second model (Figure 6). For steady flood flow conditions, and various combinations of the ungated opening with open gates, the ocean level was varied and the bay levels were determined. The procedure was reversed for the ebb conditions, the bay levels were varied and the ocean levels were determined. The results of this procedure for a 150 foot opening are shown on Figure 8. A distorted model was designed and adjusted until its calibration by the same procedure would match the undistorted model calibration. The results of this procedure for a 150 foot opening are shown on Figure 8. These tests were made to develop undistorted models for ungated openings of 300, 150, and 110 foot openings with combinations of 12 or 16 gate openings and sill levels in the ungated openings at natural ground, -23 feet and -26 feet at mean sea level. The hydraulic efficiency of the openings expressed as a discharge coefficient for various degrees of submergence and differential head for various steady flow discharges were developed as shown for the 150 foot ungated opening on Figure 8. It is noticeable that with decrease of submergence and increase in differential head and discharge, the efficiency of the opening becomes constant as the discharge coefficient becomes constant, a value slightly greater than 0.90. The conditions of surface currents are developed by vertical photographs of three-second time lapse exposure of floating confetti in the undistorted model (Figure 8). The length of confetti streak is converted to surface velocity. The barrier openings so developed in the distorted scales were inserted in the comprehensive model for water quality, navigation, and environmental tests.

Base Tests Once the model verification was accepted as being sufficiently accurate, model base tests or tests of existing conditions under carefully controlled conditions of tides, freshwater inflow, pollution input and hurricane surges were conducted. The results of these base tests (Figure 9), rather than the verification tests (Figure 7), were used to evaluate the effects of the barrier plans investigated in subsequent model tests. Thus, the model tests with and without barriers were made under identical and carefully controlled conditions. In this manner, any differences noted in tides, tidal currents, salinities, dispersion of pollutants or surge elevations with various barrier plans installed are attributable to the barrier plan under study and are not affected in any way by minor differences between model and prototype phenomena noted during verification.

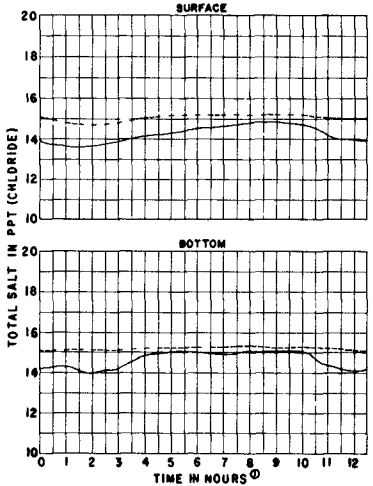
The base tests were conducted with a mean repetitive tide, a constant source of salinity, freshwater inflows and pollution sources and rates. All necessary phenomena were measured at predetermined sampling stations that would reflect conditions throughout the bay area. The repetitive mean tide had a duration of 12.45 hours and a range of 4.7 feet measured at Sandy Hook. The sump salinity was maintained at 30 parts per thousand (ppt). The primary freshwater inflow was 12,000 cfs from the Hudson River at Hyde Park and 1,770 cfs from the Raritan River at head of tide. Additional freshwater inflow sources were from treatment plant outfalls and storm water overflows in the amount of 130.69 cfs from two sources into the inlet downstream of any barrier and of 236.93 cfs from seven sources into the bay upstream of any barrier. Under these conditions, the model was operated for 25 cycles, equivalent to 12.5 days in nature to assure that salinity stability had been obtained before data collection was begun. Tides were measured with point gauges graduated to the nearest 0.01 foot (0.1 foot prototype).



DESIGN STORMS-FORT HAMILTON

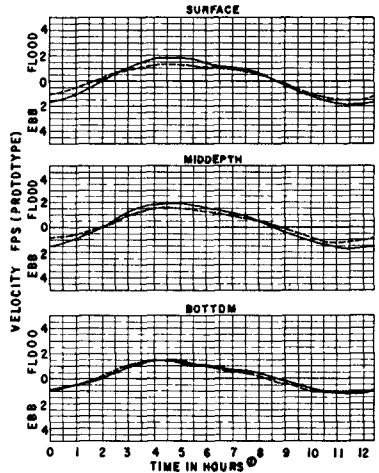


BAY TIDAL HEIGHTS



BAY SALINITIES-STATION 6V

⊙-AFTER MOON'S TRANSIT OF 74TH MERIDIAN



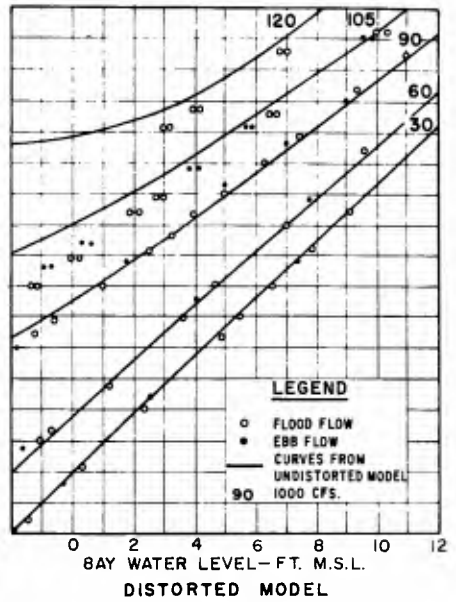
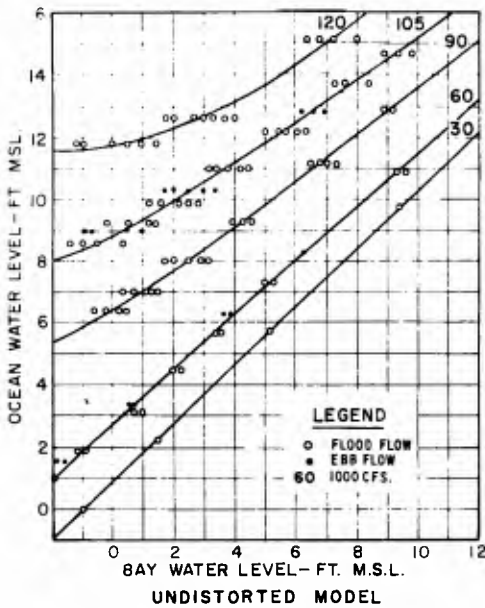
BAY CURRENT VELOCITIES-STATION 6V

LEGEND
 — PROTOTYPE
 - - - - - BASE TEST

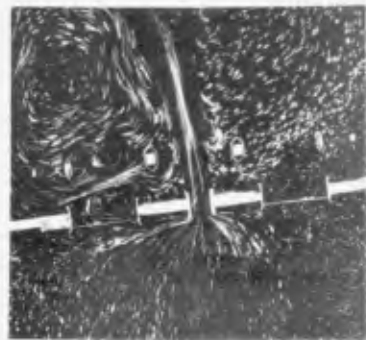
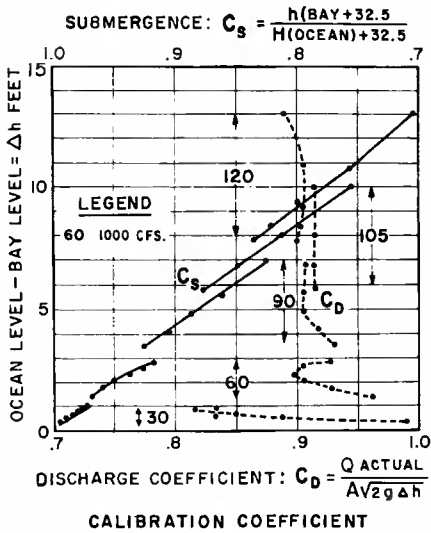
MODEL TEST DATA
 TIDE MEAN RANGE = 47 FEET
 FRESH WATER DISCHARGES
 HUDSON R - 12 000 CFS
 RARITAN R - 1 770 CFS
 OCEAN SALINITY 30 PPT

MODEL SCALE
 HORIZONTAL - 1 : 100
 VERTICAL - 1 : 100

FIGURE 7 BASIC MODEL VERIFICATION



DEVELOPMENT AND CALIBRATION OF DISTORTED MODEL OPENING



5 0 5 10
VELOCITY SCALE, FPS.
90,000 CFS. - FLOOD TIDE - $\Delta h = 6.7$ FEET
CURRENT STUDY - UNDISTORTED MODEL

FIGURE 8 CALIBRATION OF 150 FOOT UNGATED OPENING (ONLY) NO SILL

Current velocities were measured for each lunar half hour at 23 locations throughout Rockaway Inlet and Jamaica Bay (Figure 1). At each location where depths were 15 feet or more, velocities were measured at surface and bottom depths. Where depths were less than 15 feet, only mid-depth measurements were made. Current velocity measurements were made in the model by using miniature Price-type current meters. The meter cups are 0.02 foot in diameter, and the diameter of the cup wheels is about 0.08 foot. Wheel revolutions per 10 seconds were visually counted and subsequently converted to current velocities in feet per second prototype by referring to calibration curves which were checked frequently. The meters are capable of measuring actual velocities of 0.05 foot per second (0.5 fps in prototype).

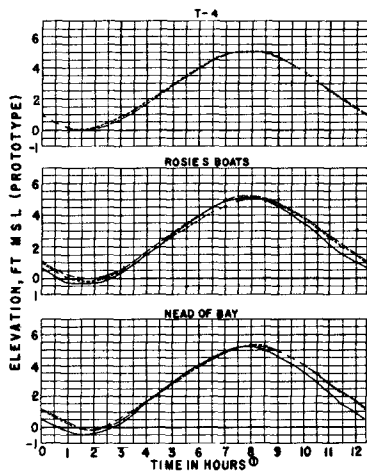
Salinities were measured for each lunar hour at surface and bottom depths at 18 stations located throughout Rockaway Inlet and Jamaica Bay. At each station, 5 milliliter samples were taken, labeled as to depth and time, and stored under a constant temperature until salinities were determined. Meters, operating on an electrical conductivity principle, were used to measure the sampled salinities. The electrical output of the conductivity meter, attached to a dip cell, is calibrated in terms of total salts within the concentration range of 0 to 40 parts per thousand.

Water samples for determination of dye concentration were taken at 34 stations at surface and bottom depths during high and low water slack periods. The model was operated until salinity stability had been obtained. Then, either uranine or pontacyl, brilliant pink dye, was injected at the nine pollution sources (Figure 9). Freshwater with pontacyl dye adjusted to an initial concentration of 10,000 ppb was released continuously at the two sources in the Rockaway Inlet, located oceanward of Jamaica Bay. Freshwater with uranine dye adjusted to an initial concentration of 10,000 ppb was released continuously at the seven pollution sources inside Jamaica Bay. The introduction of the dyed inflows was continued for 100 tidal cycles, which is equivalent to about 50 lunar days. During this time, water samples were taken and stored for later analysis. Dye concentrations were measured by utilizing G. K. Turner Fluorometers capable of accurately measuring concentrations ranging from 0 to 10,000 ppb, (parts per billion).

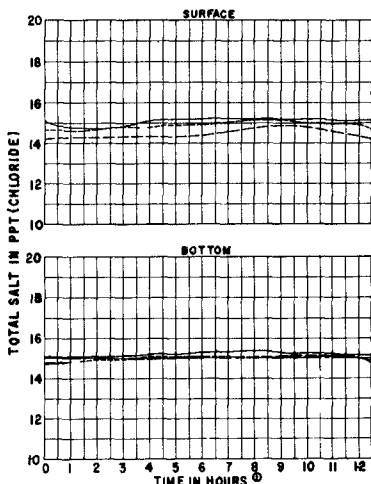
The hurricane surge generator used to simulate hurricane surges in the model was a vertically displacing steel constructed box with variable speed automatic drive mechanism which could be programmed to cause the water surface elevation to rise and fall as required with respect to time to reproduce the desired hurricane surges. Elevations were recorded throughout the problem area by means of automatic float-type recording gauges and by utilizing manual observations with the permanent point gauges described previously.

Barrier Plan 3 The first plan subjected to model testing, Barrier Plan 3, consisted of a 300 foot wide, ungated opening at natural bottom at about 32.5 feet below mean sea level, flanked by two gated sections (Figures 2 and 6). Each gate section consisted of six 75 foot wide tainter gates with sills at 26 feet below mean sea level (Figure 2). The tidal ranges with the gates fully open were not affected significantly (Figure 7). The time phasing of the tides in the interior of the bay was somewhat delayed, a matter of minutes. The mean low water was raised slightly, a matter of tenths of a foot (Figure 7). The current velocities on the whole throughout the bay were not changed significantly (Figure 7).

The results of the dye dispersion test of plan 3 are summarized in Figure 9. For the purpose of this summary, the region seaward from the barrier was divided into three areas (the approach channel, Coney Island Beach, and the basins), and Jamaica Bay was divided into four areas (Beach Channel, Island Channel, the tidal flats, and the basins). For the last 10 tidal cycles of the base and plan tests, the results of all sampling performed in the above seven areas were averaged, and the average concentrations are shown on Figure 9 for both dye sources seaward and



TIDAL HEIGHTS



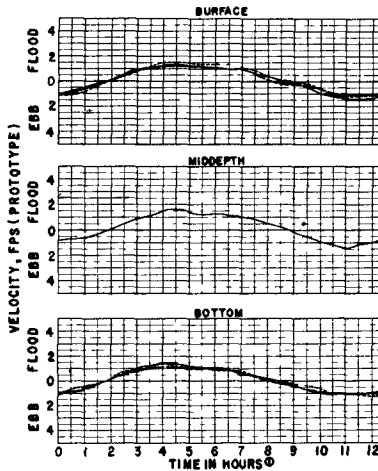
SALINITIES—STATION 6V

MODEL DATA

TIDE MEAN
 FRESH WATER HUDSON R - 12 000 CFS
 RARITAN R - 1 TTO CFS
 OCEAN SALINITY 30 PPT

LEGEND

— BASE TEST
 - - - PLAN 3 (300 FT UNGATE OPENING)
 ⊙ AFTER MOON'S TRANSIT OF T4 TH MERIDIAN



VELOCITIES—STATION 6V

SIMULATED CONTINUOUS PROTOTYPE IN FLOWS

STATION	NAME OF PLANT	CFS
INLET		
A	BNEEPSHEAD BAY OVERFLOW	1 86
B	CONEY ISLAND PLANT & OVERFLOW	128 83
BAY		
C	PAERDEGAT BASIN OVERFLOW	21 97
O	FRESH CREEK OVERFLOW	10 68
E	28TH WARD PLANT & OVERFLOW	77 38
F	BERGEN BASIN OVERFLOW	7 74
G	JAMAICA PLANT OUTFALL	77 68
H	THURSTON BASIN OVERFLOW	14 24
I	ROCKAWAY PLANT B OVERFLOW	27 24
TOTAL		367 82

FOR STATION LOCATION SEE FIGURE 1

MEASURED DYE CONCENTRATIONS*

LOCATION (SEE FIGURE 1)	DYE SOURCES OUTSIDE BARRIER		DYE SOURCES INSIDE BARRIER	
	BASE	PLAN	BASE	PLAN
AREAS OUTSIDE BARRIER				
APPROACH CHANNEL	35	32	196	136
CONEY ISLAND BEACH BASIN	24	11	39	26
	183	231	115	34
AREAS INSIDE BARRIER				
BEACH CHANNEL	70	47	708	327
ISLAND CHANNEL	82	53	887	579
TIGAL FLATS BASINS	75	33	815	696
	90	58	1948	1807

*PARTS PER BILLION (PPB)
 INITIAL DYE CONCENTRATIONS AT RELEASE POINT 100 000 PPB
 100 CYCLES 50 LUNAR DAYS

DYE DISPERSION TESTS

FIGURE 9 BASE TEST RESULTS

landward from the barrier For dye sources seaward from the barrier, average dye concentrations for the plan test were reduced slightly in six of the seven areas from those observed in the base test For dye sources inside Jamaica Bay, the plan test showed slightly reduced concentrations in all seven areas as compared to the base test The results of these tests do not prove conclusively that pollutants will be flushed from Jamaica Bay as rapidly or more rapidly under plan 3 conditions than under existing conditions, since the sampling performed was not sufficiently comprehensive to account for all dye released in the model for the tests However, the fact that the average plan dye concentrations for plan 3 were less than those of the base test in essentially all areas used for this evaluation suggests strongly that the flushing characteristics of the bay will be as good or better under plan 3 conditions than for existing conditions

The two storm surges were used for the hurricane surge tests in the model as shown on Figures 2 and 7 One is an actual hurricane surge that occurred in November 1950 and the other is the Standard Project Hurricane (SPH) surge that would be produced by a hurricane of maximum recorded intensity moving over the problem area on a critical path It is important to note that the November 1950 surge with a peak of 8.2 feet is considerably less in amplitude but is of much longer duration than the SPH surge with a peak of 12.3 feet The duration of rise of the surge or the volume of the surge is critical in considering total flow through an ungated opening, and the resulting bay level due to available bay storage

These surges were reproduced with the model water surface pooled at mean sea level For these tests, the gated openings were closed so that the passage of the surge into the bay was only through the ungated opening A comparison of levels with and without Barrier Plan 3 is shown on Table 1 The maximum elevation recorded in Jamaica Bay for the Standard Project Hurricane base test was 11.3 feet above mean sea level for a natural bay suppression of about 1 foot Under the Barrier Plan 3, the bay elevation was reduced to 4.8 feet above mean sea level for an additional bay suppression of 6.5 feet For the November 1950 hurricane surge, the maximum elevation recorded in the bay was 8.4 feet above mean sea level for no natural bay suppression Under Barrier Plan 3, the bay elevation was reduced to 6.6 feet above mean sea level for a bay suppression of 1.8 feet These suppressions would have to be reduced because of the increase in bay level that would occur due to runoff from a coincidental rainfall No correction was made for wind setup

Bay Rise Due to Rainfall The drainage area that reaches Jamaica Bay through drainage systems or overland was determined from U S G S quadrangles as being 102 square miles of which 18 square miles would represent bay water area at mean sea level A study of rainfall associated with hurricane storms and extra-tropical storms for the last 30 years showed that rainfall accompanying the hurricane of September 1944 would yield the greatest rainfall excess The study also revealed that the bulk of the rainfall would precede the hurricane surge so as reasonably to assume that the rainfall excess would totally contribute to the bay rise The total rainfall for this storm would be 3.62 inches of which 1.15 inches would be rainfall excess On this basis, the runoff into the bay would result in a rise of 3.74 inches which, added to rainfall onto the bay of 3.62 inches, would equal 7.36 inches or about 0.6 foot rise in the bay surface

Discussion of Barrier Plan 3 The plan could meet the environment and navigation objectives Further, the plan could meet the flood damage level objective of 5.3 feet mean sea level if the Standard Project Hurricane were the critical storm However, it is apparent from the surge tests that although the Standard Project Hurricane Surge with the higher peak is the basis for establishment of the height of the protective works, the November 1950 surge with the greater volume is critical for determining the size of the ungated opening that will obtain the no-damage level for the bay Therefore, the Barrier Plan 3 opening does not meet the zero flood damage bay level objective

TABLE I - EFFECTS OF BARRIERS ON HURRICANE TIDES
A - DIMENSIONS OF BARRIER OPENINGS FOR SURGE TESTS

Plan No	Ungated Opening ^a			Gated Openings ^{a,b}			Total Opening
	Width (FT)	Depth	Area Below	No of Gates	Depth	Area Below	Area ^a of Openings Below MSL (SQ FT)
		at MSL (FT)	MSL (SQ FT)		at MSL (FT)	MSL (SQ FT)	
Base	3,700	--	117,750	--	--	--	117,750
6	110	33	3,630	16	26	31,200	34,830
8	150	23	3,450	16	26	31,200	34,650
7	150	26	3,900	16	26	31,200	35,100
9	200	23	4,600	16	26	31,200	35,800
3	300	33	9,900	12	26	23,400	33,300

a - MSL = mean sea level

b - all gates 75 feet wide

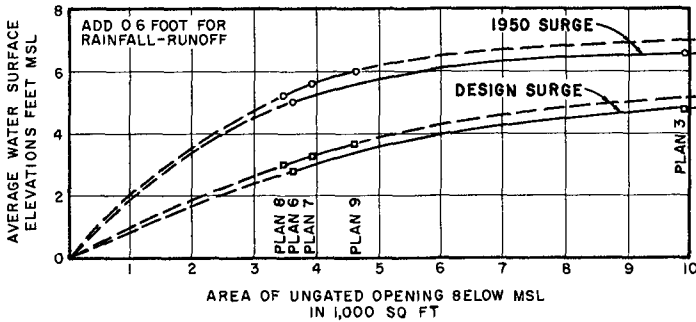
B - MAXIMUM BAY LEVELS FOR PLANS 3 AND 6 (FT MSL)

Location	1950 Surge		Standard Project Hurricane(SPH)	
	Without Barrier	With Barrier	Without Barrier	With Barrier
		Plan 3	Plan 6	Plan 3
OUTSIDE BARRIER				
Fort Hamilton	8 2	8 1	8 2	12 3
Parkway West	8 2	8 0	8 3	11 7
INSIDE BARRIER				
Parkway East	8 3	6 6	4 8	11 0
Canarsie	8 3	6 7	5 0	11 3
Grassy Bay	8 4	6 7	5 0	11 3
Rosie's Boats	8 3	6 6	5 0	11 3

C - SUMMARY OF MAXIMUM BAY LEVELS FOR ALL PLANS (FT MSL)

Plan No	1950 Surge	Rain Runoff*	Total	Design Surge	Rain Runoff*	Total
Base	8 4	0 6	9 0	11 3	0 5	11 8
6	5 0	0 6	5 6	2 8	0 7	3 5
8	5 3	0 6	5 9	2 9	0 7	3 6
7	5 6	0 6	6 2	3 3	0 6	3 9
9	6 0	0 6	6 6	3 7	0 6	4 3
3	6 6	0 6	7 2	4 8	0 6	5 4

* - computed based on 3 65 inch rainfall and 1 15 inch rainfall excess



Other Barrier Plans Alternative plans were developed to meet the multiobjectives. The overall open area through the barrier was generally maintained to meet the environmental objective as to tides, currents, velocities, salinities, and diffusion and flushing of pollutants by compensating any loss in ungated area by an increase in the gated area (Table 1). The reduction in ungated area to meet the zero damage flood level was effected by reduction in width and depth of the ungated opening. The principal elements of four alternative plans are shown in Table 1. The Barrier Plan 6 with 110 foot ungated opening and with all gates open had only minor effects on tides, current velocities, salinities, and dye dispersion, generally less than measured for Barrier Plan 3. The results of the suppression tests for both the November 1950 and Standard Project Hurricane surges, as shown in Table 1, most closely meet the flood surge suppression objective. However, the needs of commercial navigation require that the ungated opening be not less than 150 feet wide with a sill at a depth not less than 28.5 feet below mean sea level. From the test results for the plans tested, it is noted that either a 110 foot wide opening at natural depth, or a 150 foot wide opening with a sill at 23 feet below mean sea level, would hold the maximum water surface elevation in Jamaica Bay essentially at or below the critical zero damage level. Wider openings, or those with lower sill elevations, would have to be partially gated to insure necessary surge suppression during a recurrence of the November 1950 hurricane surge to about zero damage level in the bay.

CONCLUSIONS

General Findings Hydraulic model techniques, utilizing distorted and undistorted scale models, can be used to resolve the multiobjectives with a moderate amount of field investigations to assure acceptable degrees of verification of the model required to obtain reliability and acceptability of results. The results of the mathematical models were upheld. The discharge coefficient of the ungated opening is fairly constant except for low discharges and submergence above 97 percent. The suppression is more sensitive to width changes than depth changes. The design storm for determination of height of protection must be based on a high-peak storm such as Standard Project Hurricane. The design of ungated barrier openings to suppress bay levels must be based on the hurricane of critical volume, in this instance, the November 1950 hurricane. Any future change in bay storage would effect the degree of suppression. A bay barrier having the necessary combination of ungated and gated openings can be constructed that will simultaneously meet the requirements of hurricane surge suppression, recreational boating and commercial navigation, and environmental and ecological objectives as water quality, recreation, and fish and wildlife considerations.

ACKNOWLEDGEMENTS

The material presented herein is the result of studies conducted by the U S Army, Corps of Engineers, New York District, and model studies conducted at the Corps of Engineers Waterways Experiment Station at Vicksburg, Mississippi. The permission of the Chief of Engineers to use this information is appreciated. Corps of Engineers personnel to whom acknowledgement is due for their assistance are Colonel James W Barnett, District Engineer, Messrs Jesse Rosen, Herman Simensky, Joseph Tennen, Joseph Palminteri, Laszlo Makai, and Mrs Arlene Posner of the New York District, Messrs Henry Simmons, William H Bobb, Thomas C Hill, and Richard A Sager of Waterways Experiment Station. Any conclusions drawn are those of the author and do not necessarily reflect the policy or views of the Corps of Engineers or the Chief of Engineers.

REFERENCES

- 1 New York District, Corps of Engineers - Cooperative Beach Erosion Control and Hurricane Study of the Atlantic Coast of New York City from East Rockaway Inlet to Rockaway Inlet and Jamaica Bay (Interim Survey Report, 1964), printed as House Document No 215, 89th Congress, 1st Session, 1965
- 2 Panuzio, Frank L - The Atlantic Coast of Long Island Proceedings of Eleventh Conference on Coastal Engineering, Volume II, 1968, published by American Society of Civil Engineers
- 3 Gofseyeff, Samuel and Panuzio, Frank L - Hurricane Studies of New York Harbor Journal of the Waterways and Harbors Division, Proceedings of American Society of Civil Engineers, February 1962
- 4 Wilson, Basil W - The Prediction of Hurricane Storm Tides in New York Bay Final Technical Report No 165-3, October 1959, Department of Oceanography and Meteorology, The A and M College of Texas
- 5 Tippetts-Abbett-McCarthy-Stratton, Engineers and Architects, New York - Study of Hurricane Barriers Across Jamaica Bay for Corps of Engineers, U S Army Engineer District, New York (unpublished), February 1963
- 6 Balloffet, Armando and Kupferman, Arnold - Hydraulic Studies of Jamaica Bay Journal of the Hydraulics Division, Proceedings of American Society of Civil Engineers, November 1964
- 7 Coastal Engineering Research Center, Corps of Engineers, U S Army, Technical Report No 4 Shore Protection Planning and Design, 1966
- 8 Saville, J T , McClendon, E W , and Cochran, A L - Freeboard Allowances for Waves in Inland Reservoirs Journal of the Waterways and Harbors Division, Proceedings of American Society of Civil Engineers, May 1962
- 9 Taft, Robert - Investigation of the Effects of Hurricane Surge Control Structures on the Water Quality of Jamaica Bay Division of Water Supply and Pollution Control, Public Health Service, U S Department of Health, Education, and Welfare, Appendix N of Reference No 1
- 10 Norman Porter Associates, Engineers - Current Velocity Measurements in Jamaica Bay on 12-13 June 1967, for U S Army, Corps of Engineers, New York District, (unpublished)
- 11 U S Army, Corps of Engineers, Waterways Experiment Station - Test Data, Model Studies of Jamaica Bay Hurricane Barrier, 1970, (unpublished)

CHAPTER 126

MODEL STUDY OF TRANSFORMATION OF TSUNAMIS IN URADO BAY

Shigehisa NAKAMURA
Research Assistant,
Disaster Prevention Research Institute,

Yuichi IWAGAKI
Professor,
Department of Civil Engineering
and

Yoshito TSUCHIYA
Professor,
Disaster Prevention Research Institute,
Kyoto University, Kyoto, Japan

ABSTRACT

For the city and harbour of Kochi, including Urado Bay, facing the Pacific Ocean, an experimental study has been carried out on the problem of protection from tsunami disasters, and future harbour planning; that is, dredging, reclamation and construction of breakwaters against tsunamis. A hydraulic model of horizontal scale 1/250 and vertical 1/100 was used according to Froude's similitude. The transformation of the design tsunami in the bay was studied to find the effect of the tsunami breakwaters, dredging and reclamations by use of the model which was able to reproduce the Chilean Tsunami.

INTRODUCTION

The city and harbour of Kochi, including Urado Bay, located in Shikoku Island facing the Pacific Ocean as shown in Fig.1, have in the past 30 years been severely damaged by several tsunamis, for instance, the one due to the Nankai Earthquake in 1946 and the Chilean Tsunami in 1960. Tsunamis are mainly caused by Japan's position in a seismic active zone so that a historical review will show plenty of damage by the tsunamis and their causative earthquakes.

The characteristics of tsunamis have been studied theoretically, experimentally, and through field observations; but they should be studied too from the view point of coastal disaster prevention. A countermeasure has been the construction of seawalls. Recently the development of industries and of the harbour in Urado Bay have been planned, so it is necessary to study the effects of the construction of breakwaters and of the dredging and land reclamation in the bay on the behaviour of tsunamis. It

was decided that the best approach would be conducting hydraulic model studies.

This paper deals to study the transformations of tsunamis in the bay before and after completion of this project.

TSUNAMI GENERATOR

For this study, a tsunami generator of the plunger type was constructed, driven by an oil-hydraulic servo system. The plunger was made of steel, 7 m x 3 m x 0.5 m, located as shown in Fig.2. Power is supplied by an oil-hydraulic controller, shown in Fig.3. Transmission of an input signal is performed by a servo system, schematically given in the block diagram of Fig.1, to drive the plunger. The input signal is given by the cam of acrylicite. In order to produce not only sinusoidal regular waves but arbitrary waves, cams of various forms were used. According to the radius of the cam, the servo system controls the displacement and phase of the plunger through which the amplitude of the model tsunami wave is produced. By controlling the angular velocity of the cam, the period of the generated wave will be given. The stroke of the plunger is continuously variable and its maximum is ± 100 mm, and the period of the cam for a cycle is variable continuously in the range of 3 to 30 min.

SIMILITUDE AND THE MODEL

First of all, the area of the model should be determined with consideration of tsunamis around the bay mouth.

The tsunamis which attacked this bay were from off Nankaido, Hyuganada, the Aleutian Islands, the Chilean coast, and so on. These tsunamis propagated and attacked the bay after refraction, deflection and rectifying the wave rays to the contours. The propagation maps of the tsunamis show that the fronts of the tsunamis were almost parallel to the contours in the coastal area of 15 to 20 m deep, which was taken as a criterion to limit the model area. The tsunamis which entered the bay should run up the rivers so that the phenomena caused by the tsunamis should be found in the estuaries. The other criterion to limit the model is to find the limit of the tidal and the tsunami influences referring to the field data.

Second, the distortion of the model should be checked in relation to the characteristics of the tsunamis. When the model experiment is carried out by use of a distorted model which has different vertical and horizontal scales, the slope of the bottom is distorted so that the reflection and refraction of the tsunamis might be generally different compared to those in the non-distorted and distorted models. And graphical analysis to give a refraction diagram of the tsunami in the bay shows a little

difference up to the distortion of 2.5 (1/50 of horizontal and 1/100 of vertical) with consideration of recording and processing errors of the data. It was reported that the Hilo harbour tsunami model gave a distortion 3.0 (1/600 of horizontal and 1/200 of vertical) without effect of distortion to refraction and reflection of the tsunamis (Palmer et al., 1965).

In the estuary, saline water contacts fresh river water to mix vertically or to stratify into a stable double layer by the effect of the density difference of the waters. The river discharges flowing into the bay were so small compared to the tidal flushing that there should be prevailed vertical mixing which suggests that the consideration of the density difference might give little errors in the model experiment.

The similitude for the model was derived by the equation of motion and continuity. Froude's similitude was applied to the model experiment; the scale ratios of the prototype to the model are 250 for horizontal length, 100 for vertical length, 10 for current velocity, 25 for time, 2.5×10^5 for river discharge, and 100 for kinetic energy, respectively.

Generally, the flow regime of the prototype are turbulent so that the friction coefficient may be taken as a certain constant value. And for the model the coefficient is a function of a Reynolds number, therefore it is difficult to hold the similitude mentioned above for a whole period of experiment. Simulation was given for an average of current velocity in the model area.

Roughness of the bottom was simulated by use of Manning's formula for the current velocity as an average. The similitude gives the scale ratio 1.365 of Manning's roughness parameter. An artificial roughness was given in the model for simulation fulfilling the above condition. With the consideration of size distributions of sediments, the roughness parameter is 0.03 in the harbour part which is simulated as 0.022 in the model to give the roughness of 0.2 to 0.3 cm by brushing up the mortar surface. For the river part in the model, the roughness was given by fixing sands of 0.3 to 0.5 cm in size on the river bed mortar. Judging from the result of the experiment, the effect of the roughness was not distinctive compared to topographical influences.

The water level was recorded on the photographic chart continuously and simultaneously. For dynamical understanding, current velocity was obtained from movies tracking floats of 1 cm in diameter in several areas in the model.

The model of Urado Bay is schematically shown in Fig.1 for present topography and is shown in Fig.4 as a bird's eye view.

REPRODUCTION OF CHILEAN TSUNAMI

There are many records of damage caused by tsunami inundation, there is a few records of tsunamis for Urado Bay. One of the representative tsunamis in Urado Bay was the Chilean tsunami of 1960, which was recorded at three stations in the bay: Katsurahama(St.1), Urado(St.3), and Wakamatsu-cho(St.21). The locations are shown in Fig.1. Trials were carried out to reproduce this tsunami in the model basin. Tsunami records for the first four hours were reproduced using a cam as input under the dynamical consideration and repeating correction of the cam until the tsunami records of the prototype coincide with the wave records in the model experiments. One of the records is shown in Fig.5, in which the scales of elevation and time are in prototype according to the similitude. From Fig.5 it is found that the wave forms in the model coincide well with each other in amplitude and phase as a whole. Especially, the wave form at St.1 is well reproduced. The details do not perfectly coincide at St.3 and St.21. At St.3, the experimental result shifts about 20 cm high compared to the prototype records. The distorted model might give the shift of the water level. At St.21, the wave height in the experiment is up to twice as large as the tsunami records in the mareograms, which might be caused by the local topography around St.21. The river elevation increases from the end of the navigation course to the Kagami river so that the water passing St.21 is affected by local topographical effects and shoaling effect. These detailed discrepancies between the prototype and the experiment should be studied for more accurate reproduction of the tsunami in the model experiment.

DESIGN TSUNAMI AND ITS TRANSFORMATION

Inundation from tsunamis in Kochi Harbour was studied by numerical computation (Hamada et al., 1961). Scouring problems near the tsunami breakwaters at the entrance of Kochi Harbour were studied experimentally by Shibayama et al.(1964). The behaviour of tsunamis at the junctions of rivers were studied numerically by Horiguchi (1965). These computations and experiments were carried out by use of a design tsunami determined by the records of the tsunami of the Nankaido Earthquake and of the Chilean tsunami. Hamada (1961) gave the design tsunami at St.1 such as the crest height is 2.4 m above and the trough 1.5 m below the mean high water level with the period of 30 min for the numerical computation.

Spectral analysis of the Chilean tsunami gave the significant period of 30 to 35 min. For the Hyuganada Earthquake tsunami in 1968, the significant period was about 25 min.

These results suggest that the suitable period of the design tsunami is probably to be 30 min (Iwagaki et al., 1970). In this experiment the same conditions were given for the design tsunami. The initial water level before the tsunami inundation was taken to be the mean high water level (D.L. + 1.89 m).

The design tsunami that entered the bay propagates through the bay mouth; that is, the waves are transformed and their phases are delayed with the progress including the effects of the boundary and topography of the bay. There should be many factors affecting the transformation of the design tsunami, such as: phase velocity as a function of water depth, refraction caused by the bottom slope, deflection around a sharp edge, reflection at the coast and shoaling in the river mouth. The resultant effect of these factors gives the wave transformation. When the design tsunami at the entrance of the bay is given, the transformation of the wave in the model is obtained through the experiment as shown in Fig.6 in model scale. In Fig.6, wave height and time are shown in the model scale. The wave profiles are arranged ordinally for the stations, the locations of which are illustrated by numbers in circles in this figure.

The wave profile at St.1 is a sinusoidal which is found the lowest part of Fig.6. The wave is transformed and decreases its height at the narrow, the fact of which is found by comparison of the wave form at St.1, St.2 and St.5. There should be energy dissipation of the wave at the narrow caused by the confused configuration of the coast lines and to the curved water way. At the inlets, resonance occurred by produce higher harmonics of the incidental tsunami. For example, the wave form at St.10 suggests that the third harmonics of the tsunami is amplified in the small rectangular resonator in which the location of St.10 is included.

In the river part, the wave height increases with inundation of the tsunami as found the wave forms of St.22, 23 and 25 in Fig.6. In the Kuma river, the wave height increases from St.23 to St.25. The wave form is transformed to be assymetry; that is, the steep profile before the crest and the gentle slope after the crest of the wave. These transformed wave profiles differ from the incidental sinusoidal wave at the entrance of the bay.

CREST HEIGHT CHANGE AND TSUNAMI BREAKWATERS

The crest height distributions of the design tsunami were considered for the model of the present topography, the model without the tsunami breakwater for after dredging and reclamations, and the model with the tsunami breakwaters for after dredging and reclamations. The distributions were obtained as

two dimensional or areal distributions which will give understanding about the complexity of the wave characteristics in the bay. In this paper, the distributions are shown only along the navigation course from the entrance to the head of the bay and along the Kagami River and Kokubu River or Kuma River, as shown in Fig.7. In Fig.7, the distances of the stations from the bay mouth are shown in reduced prototype scale in Km and the crest height of the tsunami in meter with reference to the elevation of the mean high water level. The locations of the stations in Fig.7 are shown by the numbers in circles. The dots, the circles and the semi-circles show respectively the case for the present topography, the case for after dredging and reclamations, and the case with the tsunami breakwaters for after dredging and reclamations. The model for the conditions after dredging and reclamations is shown in Fig.8. Tsunami breakwaters are under planning for construction at the narrow point of the entrance of the bay, as shown in Fig.8.

The crest height distributions are shown in Fig.8 along the navigation course and the Kagami River. Comparing to the distribution for the present topography, the distribution for after dredging and reclamations suggests that the tsunami propagates with a little decrease of wave height because of water depth increase. But it is not clear why the crest height at St,2 became anomalously high after dredging. The effect of the reclamations is not so remarkable for the crest height distribution. When the tsunami breakwaters are constructed for the harbour after dredging and reclamations, it is found a remarkable effect of the tsunami-breakwaters to diminish the wave height in the bay and to protect the harbour from tsunami inundations around the bay mouth and in the bay. For the crest height distributions, the effect of the tsunami breakwaters is not remarkable at the end of the navigation course. In the Kagami River, there should be found a topographical effect for the tsunami inundations.

About the Kuma River or Kokubu River, the crest height distributions are shown in the up-right part of Fig.7 to compare those to the main profiles of the crest height in the same scale. There are found a little effect of the tsunami breakwater, dredging and reclamations in the profiles of the crest height distributions of the design tsunami.

CONCLUSION

From the results of the model experiment on tsunamis in Urado Bay, the authors obtained the following conclusions.

- 1) By use of the tsunami generator with consideration of Froude's similitude, the Chilean tsunami was reproduced in the model experiment. This result shows the possibility of studying future problems in the bay.

2) Transformation of the design tsunami and crest height distribution of the tsunami were studied to find the negative effect of dredging of the navigation course and to find the active effect of tsunami breakwaters for protection of the harbour from tsunami inundation. Reclamations gave a little influence on the crest height distribution and on the wave height of the tsunami.

Kochi was attacked directly by the typhoon 7010 on 21, August, 1970 so that they suffered from heavy damages by the storm surge accompanied with the typhoon. This fact suggests that it should be promoted not only to study on tsunami but to investigate on storm surges in Urado Bay. Future plan of the harbour should be referred on the studies mentioned above to protect from coastal disasters.

ACKNOWLEDGEMENT

The authors wish to express their thanks for the help given by the Ministry of Transport and Kochi Prefecture.

REFERENCES

- Hamada, T., Horiguchi, T., Kato, H. and Kaneko, M. (1961). Calculation of tsunami inundation in a channel --- a case of Kochi Harbour ---, Proc. 8th Conf. Coastal Eng. in Japan, pp.30 - 35 (in Japanese).
- Horiguchi, T. and Ko, R. (1965). Calculation of tsunami inundation in bay and river junctions, Proc. 12th Conf. Coastal Eng. in Japan, pp.14 - 18 (in Japanese).
- Iwagaki, Y., Tsuchiya, Y. and Nakamura, S. (1969). On a tsunami generator, Proc. 16th Conf. Coastal Eng. in Japan, pp.321 - 326 (in Japanese).
- Iwagaki, Y., Tsuchiya, Y. and Nakamura, S. (1970). Tsunami model experiment of Kochi Harbour, Ann. Dis. Prev. Res. Inst., Kyoto University, No. 13 B, pp.471 - 488 (in Japanese).
- Palmer, R.Q., Mulvihill, M.E. and Funasaki, G.T. (1965). Hilo Harbour tsunami model --- reflected waves superimposed, Coastal Eng., Santa Barbara, Sp. Conf., ASCE, pp.21 - 31.
- Shibayama, H., Kimura, H. and Takemura, K. (1964). Model experiment on tsunami breakwater of Kochi Harbour, Rep. Port and Harbour Res. Inst., Ministry of Transport, Vol.3, No.2, pp.14 - 18 (in Japanese).

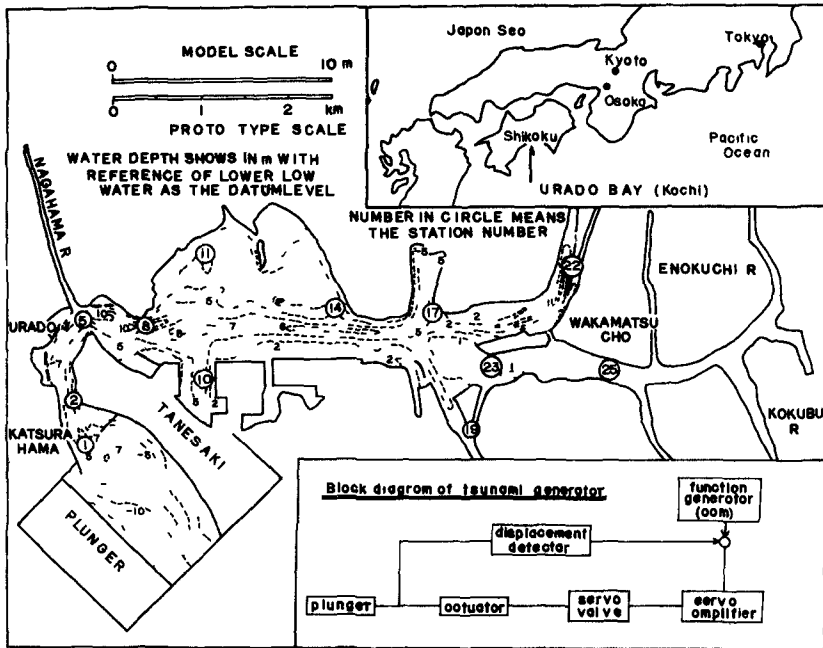


Fig.1 SCHEMATIC PLANE OF THE TSUNAMI MODEL OF URADO BAY (including locations of stations where water levels were recorded in the tsunami model, and tide gauges are located at St.2, St.3, St.7, St.17 and St.21 in the prototype of the harbour)
 UP-RIGHT: LOCATION OF URADO BAY
 DOWN-RIGHT: BLOCK DIAGRAM OF THE SERVO SYSTEM



Fig.2 PLUNGER OF THE TSUNAMI GENERATOR



Fig.3 OIL-HYDRAULIC CONTROLLER OF THE
TSUNAMI GENERATOR



Fig.4 BIRD'S EYE VIEW OF THE TSUNAMI MODEL
(The plunger shown in Fig.2 is at
the end of the model. The controller
is in the white cottage. The head
tank at the center of this photograph
supplies river discharges in the model.)

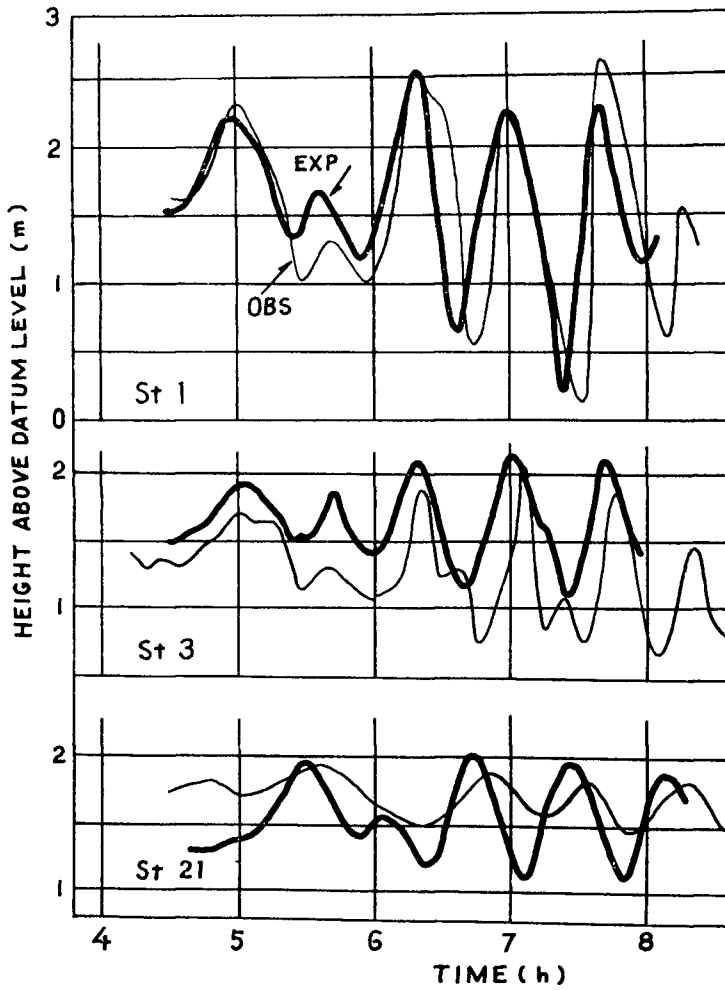


Fig.5 REPRODUCTION OF THE CHILEAN TSUNAMI IN URADO BAY

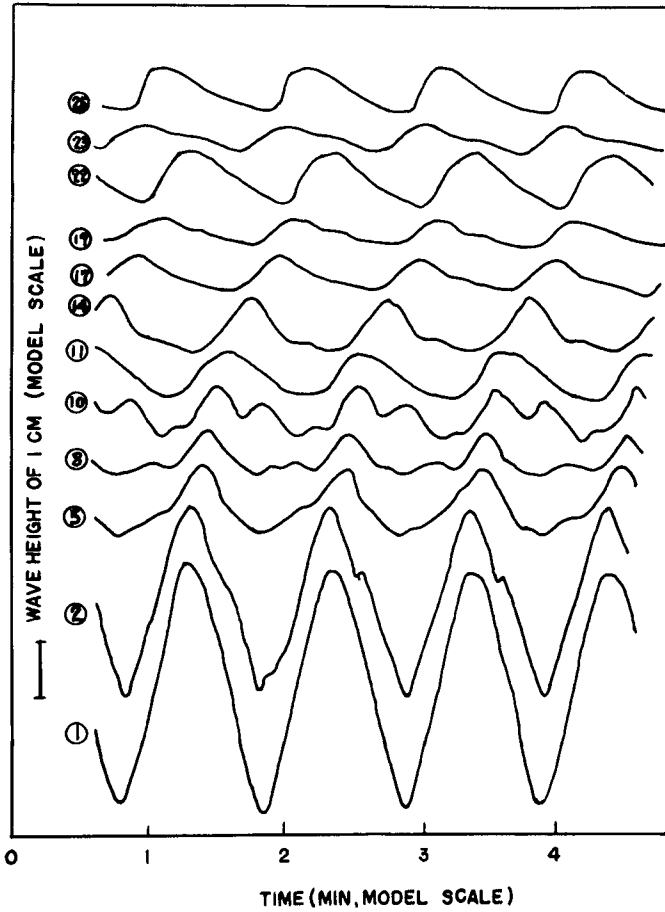
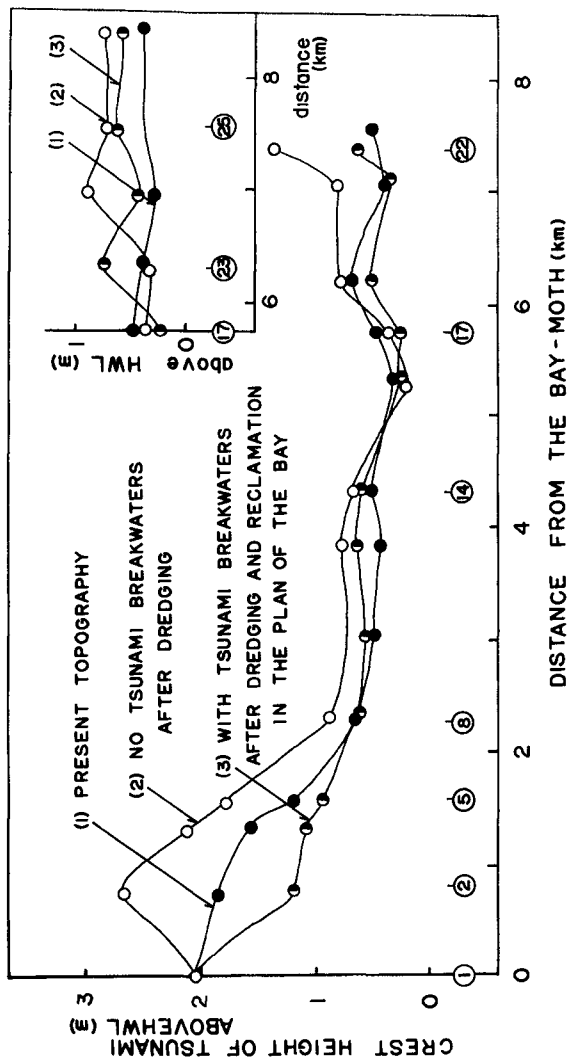


Fig. 6 TRANSFORMATION OF A DESIGN TSUNAMI



F-g.7 CREST HEIGHT PROFILES OF A DESIGN TSUNAMI

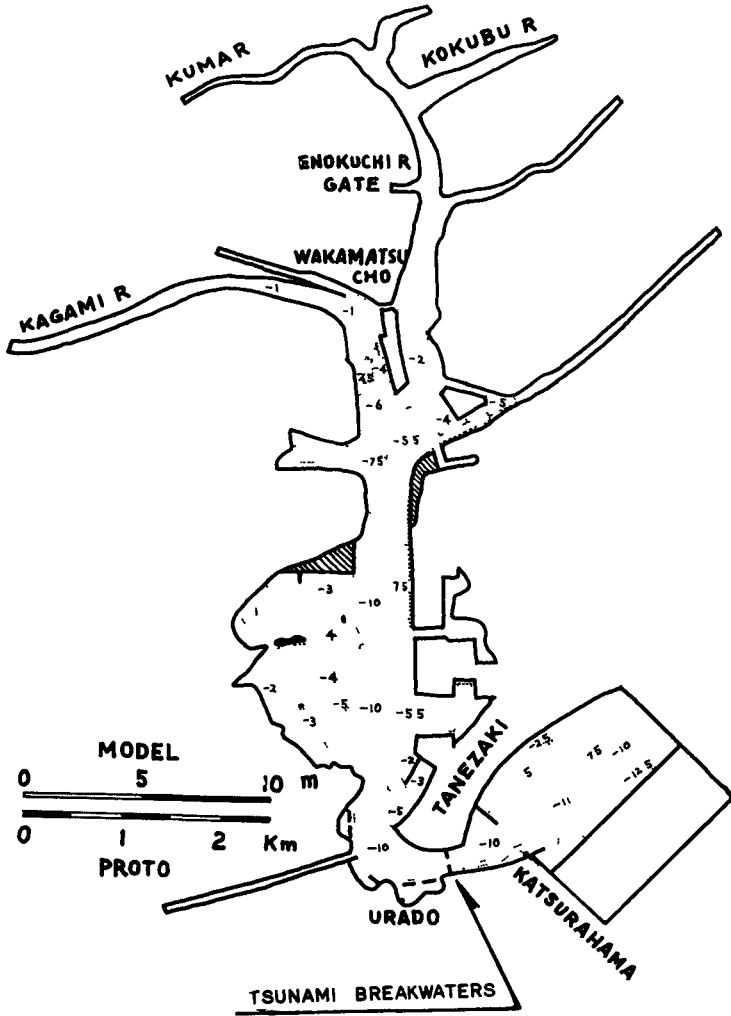


Fig.8 TSUNAMI MODEL AFTER DREDGING AND RECLAMATIONS
(The location of the tsunami breakwaters is indicated by an arrow.)

CHAPTER 127

TSUNAMIS SOME LABORATORY AND FIELD OBSERVATIONS

by Fredric Raichlen Assoc Prof of Civil Engineering
W M Keck Laboratory of Hydraulics and Water Resources,
California Institute of Technology, Pasadena, California, U S A

ABSTRACT

A unique laboratory facility to generate waves by impulsive movements of the bottom of a wave tank is described and examples of the wave forms which result are shown. An analytical model is presented for the case of rapid bottom movements which describes, in a qualitative way, certain features of the experiments.

Marigrams from various field stations for the tsunamis from the Chilean earthquake of 1960 and the Alaskan earthquake of 1964 have been analyzed using spectral analysis techniques to determine the harmonic components of these records. Comparisons are made between the spectra of the two tsunamis at each of several locations.

INTRODUCTION

The problems associated with earthquake generated sea waves, known as tsunamis, are serious in many parts of the world particularly around the rim of the Pacific Ocean which is such a seismically active region. Perhaps one of the worst tsunamis of historical times was generated off the coast of Japan on June 15, 1896. The maximum wave which was generated ran up on the near-by land to an elevation of 75 ft to 100 ft above the normal tide level resulting in the death of more than 27,000 persons and the destruction of over 10,000 homes. A much more recent example of the widespread property damage that such a wave system can cause is the tsunami associated with the Alaskan earthquake of March 27, 1964. This tsunami which originated in the Gulf of Alaska caused loss of life and extensive damage as far away as Crescent City California (\$11 million damage). In addition to this distant damage, an estimated \$350 million damage to a number of coastal towns in Alaska could be attributed to the combined effect of the tsunami, soil failure and vibrations.

To learn more about the generation, propagation, and coastal effects of the tsunamis a laboratory study has been initiated which deals with the generation of waves by impulsive bottom movements and the propagation of these waves in the near field. (The near field region is of particular importance to Southern California which appears to be reasonably protected from distant tsunamis, but may be vulnerable to sea waves generated by earthquakes near the coastline.) This investigation is directed toward understanding the phenomenon of bottom generation and the effect of linear and nonlinear dispersion on the resultant wave system. Some preliminary results of the laboratory study are presented herein, thereby demonstrating some of the characteristics and capabilities of the wave generating system which has been developed.

In addition to this laboratory program, field data have been analyzed to gain a better understanding of the interaction of tsunamis with the coastline.

Using spectral analysis techniques certain conclusions can be drawn regarding the effect of the tsunami which resulted from the Alaskan earthquake of 1964 and that resulting from the Chilean earthquake of 1960 on the harbors and embayments where tidal records are available. Hence, this paper is divided into two parts: the first dealing with the laboratory simulation of earthquake generated sea waves and the second dealing with the analysis of field data.

LABORATORY OBSERVATIONS

Experimental Equipment - The experimental program is being conducted in a wave tank which is 31.6 m long, 39 cm wide, and 61 cm deep with glass side-walls throughout. The impulsive wave generator is located at one end of the wave tank and consists, in the initial phases of this study, of a moveable section of the bottom of the wave tank 61 cm long and nearly the same width as the wave tank (39 cm). The section of the bottom can be moved in a pre-determined fashion either upwards or downwards, hence, this system can be thought of as modeling a tectonic movement in nature which is either a simple block upthrust or downthrow. In the laboratory the maximum movement of the bottom in a vertical direction is ± 15 cm with one of the design criterion being that the bottom should be capable of moving ± 3 cm in 0.05 sec. With some modifications the surface area of the generator can be changed.

A schematic drawing of the tsunami generator and the wave tank is presented in Fig. 1. It should be noted that the wave system under investigation is two-dimensional and the rigid wall which exists at $x=0$ represents a plane of symmetry in the true problem. Therefore, with reference to Fig. 1, the total length of the moveable section of the bottom, l , is one-half of the length of the block in nature which is being modeled.

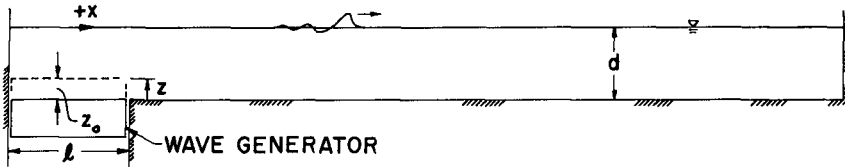


Fig. 1 Schematic Drawing of Impulsive Wave Generator

The wave generator is driven by a hydraulic-servo-system which accepts an input voltage which is proportional to the desired displacement of the bottom, and in this way a variety of bottom motions can be obtained. Basically the system can be divided into three parts: the hydraulic supply unit, the servo-system, and the moveable bed unit assembly.

The hydraulic supply system consisting of oil reservoir, pump, filter, and heat exchange unit supplies the main hydraulic cylinder which actuates the bed with hydraulic fluid at a pressure of 3200 psi. An accumulator is installed in the system primarily to provide a sufficient supply of hydraulic fluid at high pressure to drive the bed for programs which initially demand large flow rates.

The servo-system consists of a servo-valve and its associated electronics used in conjunction with a linear variable differential transformer (LVDT) which senses the motion of the bed. The LVDT with its core mounted to the moving bed and the coil fixed in position provides the electrical feed-back signal which is compared to the input signal supplied by the function generator, by comparing these two signals minor adjustments of the movement of the spool of the servo-valve are made automatically to achieve the desired program of bed movement.

A photograph is presented in Fig. 2 showing in detail the moveable bed unit assembly consisting of the hydraulic cylinder, its supporting structure, two flexures, the load cell, the guide cylinder, the bearing support box, and the bed unit. The hydraulic cylinder which drives the bed is a double-throw type mounted vertically and attached by means of flexures to the laboratory floor and to the bed unit. The flexures provide a means of correcting for any small vertical mis-alignment of the hydraulic cylinder upon installation. The upper flexure is connected to a load cell, for measuring the total applied force, which in turn is connected to the moveable bed unit. The guide cylinder, seen in Fig. 2 moves against two fixed bronze bearings and insures that the bed unit moves in a vertical direction. The bed unit is firmly fixed to the upper surface of the guide cylinder.

Fig. 3 shows the tsunami generator attached to the upstream section of the wave tank with the bed unit in its maximum upward position. A problem in the design of the generator which had to be overcome for successful operation was the sealing of the bed unit around its four sides, two of which are in proximity to glass walls and the other two near machined aluminum surfaces. The seal which was designed and fabricated was a one-piece unit molded of a relatively flexible material and mounted directly to the moveable portion of the bed. Details of this seal can be seen in both Figs. 2 and 3, this type of design (with water on only one side of the generator) minimizes the forces which arise in wave generation.

Some Experimental Results - The time-displacement of the bed which is being used initially is an exponential motion described by the following expression

$$\frac{z}{z_0} = 1 - e^{-\alpha t} \quad (1)$$

where z is the motion of the bed measured positive upwards from the fixed elevation of the bottom of the wave tank, z_0 is the maximum motion of the bed, varying time is represented by t , and α is a coefficient which is equal to the bed velocity divided by the maximum bed displacement, z_0 at $t=0$.

Figs. 4 and 5 are examples of the water surface motions which are generated by such exponential motions of the generator for a water depth of 10 cm and for positive and negative motions respectively. The ratio of the maximum displacement to the depth, z_0/d , for all cases shown was 0.1, and for positive and for negative motions examples are presented for two different non-dimensional times, $t_R(g/d)^{1/2}$, the time t_R is defined as the time that it takes the bed to rise to one-half its maximum value. The two values of the non-dimensional time for which results are shown in Fig. 4 and 5 are $t_R(g/d)^{1/2} = 0.4$ and 3.5 which, for these experiments, correspond to $\alpha = 17.2 \text{ sec}^{-1}$ and 1.96 sec^{-1} respectively. The motion of the bottom is shown as the upper record in each of these figures and is labelled as z .

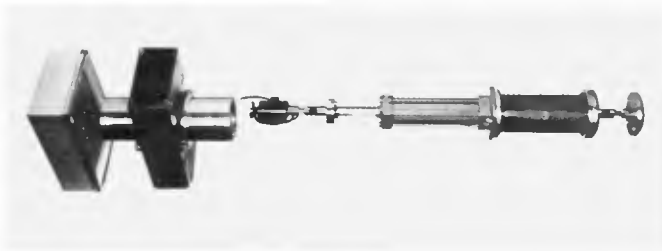


Fig. 2 Exploded View of Moveable
Bed Unit Assembly



Fig. 3 Assembled Impulsive Wave
Generator Attached to Wave Tank

POSITIVE DISPLACEMENT

$$z_0/d = +0.1$$

$$t_R \sqrt{g/d} = 0.4$$

$$t_R \sqrt{g/d} = 3.5$$

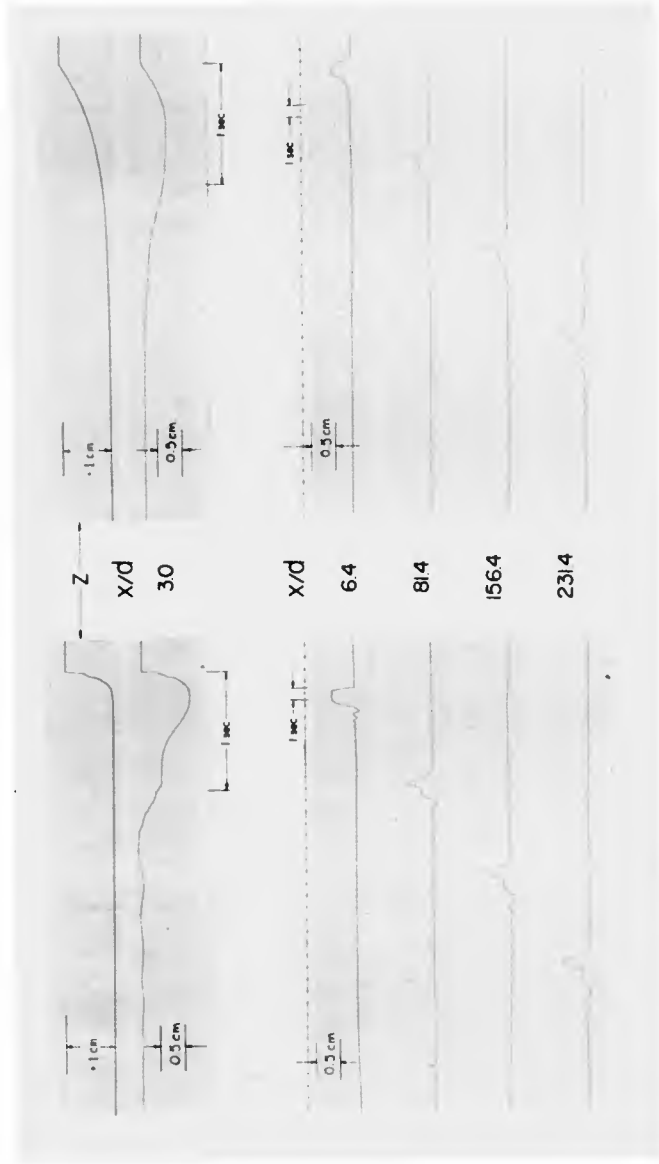


Fig. 4 Oscillograph Records of Bottom Motion and Waves Which Result from a Positive Bottom Displacement, z

Negative DISPLACEMENT

$$Z_0/d = -0.1$$

$$t_R \sqrt{g/d} = 0.4$$

$$t_R \sqrt{g/d} = 3.5$$

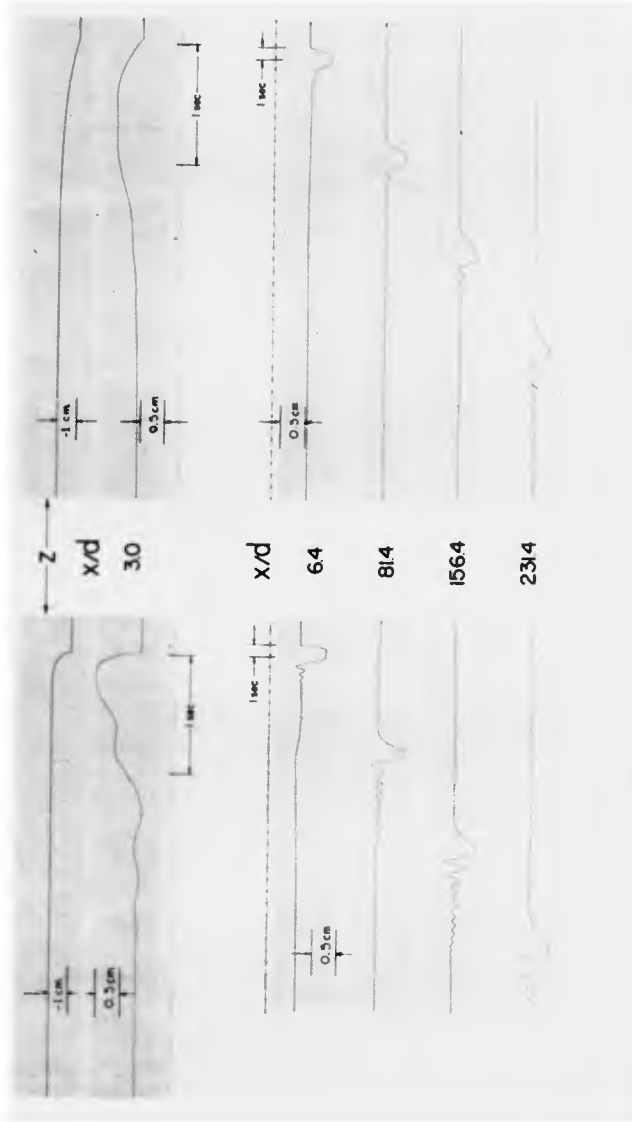


Fig. 5 Oscillograph Records of Bottom Motion and Waves Which Result from a Negative Bottom Displacement, z

In Figs 4 and 5 the variation of the water surface with time measured using resistance wave gages is shown at five different locations along the wave tank. The first location is $x/d = 3.0$ which is approximately midway over the moveable bottom. (Since the wall at $x/d = 0$ also can be thought of as a plane of symmetry for the case of a moving block of length $2l$ centered at $x/d = 0$ for this depth the location $x/d = 3.0$ represents the quarter-point of that moving block, i.e. $x/2l \approx 0.25$.) It should be noted in the oscillograph records which are shown, for the motion of the bottom (z) and for the variation of the water surface at the first location ($x/d = 3.0$) positive movements and water surface displacements are downward at all other locations the positive water surface displacements which are shown on the oscillograph records are upwards. In all of the records time increases to the left, the length of the record which corresponds to one second is indicated in the figure. Four of the wave gages are equally spaced ($x/d = 6.4, 8.1, 15.6, 23.1$) with the first gage located quite close to the "leading edge" of the moving bottom. Since the electronic amplification of the various wave gages has been adjusted to be approximately the same and the gages are equally spaced, a characteristic diagram could be constructed from these four records.

In Fig 4 for the two different non-dimensional times, the upper records show the exponential motion of the bottom. At the location $x/d = 3.0$ for the condition of rapid bottom movement the water surface rises in nearly the same way as does the bottom and begins to fall near the time of maximum bottom displacement. For the experiment with a slower bottom motion the water surface at the same location reaches a maximum before the bottom has fully risen and then begins to fall. For the former case the ratio of the maximum amplitude to the maximum bottom displacement is approximately unity whereas for the latter this ratio is about one-half. Thus, one effect of the magnitude of the non-dimensional time, $t_R(g/d)^{1/2}$, can be seen.

For a non-dimensional time of 0.4, near the edge of the generator ($x/d = 6.4$) the water surface rises quickly to a maximum and remains there for a short period of time before falling. In falling, the water surface elevation first becomes less than the still water level, then rises above the still water level and then oscillates in a damped periodic manner about the quiescent level. As the lead wave progresses downstream it tends to change radically as additional waves are generated from it. In addition to this, groups of waves are evident in the lee of the main wave system and these waves appear to be left further behind in time as the distance from the generation area increases probably due to frequency dispersion.

Similar effects can be seen for the example at a larger non-dimensional time (3.5) except that the dispersive effects are not nearly as pronounced as for the case of the faster bottom movement. Comparing the amplitude of the lead wave for locations $x/d \geq 6.4$ to that at $x/d = 3.0$ it is seen that the waves are approximately 0.8 of the amplitude of the wave over the generator. For the case of a more rapid bottom movement this same ratio was about 0.5 demonstrating another effect of the velocity of the generator on the waves generated.

The comparable case for negative waves is presented in Fig 5. The conditions for the two cases shown are identical to those presented in Fig 4 except a negative motion of $z_0/d = -0.1$ is used. In this case, for the

displacement of the bottom and of the water surface at $x/d = 3.0$ negative displacements are upwards on the oscillograph paper, at all other locations negative displacements are downwards. Comparing the water surface displacements in Figs. 4 and 5 at $x/d = 3.0$ and 6.4 for both non-dimensional times it is seen that the negative displacements are nearly mirror images of the positive displacements. However, for a normalized distance of 81.4 major differences are seen between the positive and negative cases. Perhaps the most obvious is the significant growth of a train of waves in the lee of the negative system compared to the positive case which supports the arguments proposed by Keulegan and Patterson (1940) in their paper dealing with non-linear long waves. The effect of dispersion on the lead wave can be seen readily in Fig. 5 for the example with the rapid bottom motion from the decrease of the slope of the leading edge of the main wave as the distance from the region of generation increases.

Similar features are evident for the case of a slower bottom movement, i.e., a larger non-dimensional time (3.5). Again the features in the lee of the main wave have grown much more rapidly than their positive counterpart. If a comparison is made of the amplitude of the lead wave over the generator to those for $x/d \geq 6.4$, for the case of rapid motion it is found that away from the generator the amplitude is approximately 0.6 of that over the generator. For the slower generator motion this ratio varies from about 0.85 to 0.90. The ratio of the amplitude of the lead wave to the maximum displacement of the generator for the two examples of negative displacements are comparable in magnitude to the corresponding positive cases. Thus, with respect to wave amplitudes there is little difference between the lead wave amplitude resulting from the negative and positive bottom motions for comparable initial conditions.

Some Analytical Considerations - To investigate, in a qualitative sense, some of the features of the wave systems observed in Figs. 4 and 5 an analytical method developed by Peregrine (1966) for the treatment of non-linear long waves has been applied. The equations of continuity and momentum can be written in non-dimensional form as

$$\frac{\partial \eta}{\partial t} + \frac{\partial}{\partial x} [(1 + \eta)u] = 0 \quad (2)$$

$$\frac{\partial u}{\partial t} + u \frac{\partial u}{\partial x} + \frac{\partial \eta}{\partial x} = \frac{1}{3} \frac{\partial^3 u}{\partial x^3 \partial t} + O(\epsilon^2 \sigma^3) \quad (3)$$

All length quantities in Eqs. 2 and 3 have been normalized with respect to the depth d , the velocities with respect to the shallow water wave velocity, $(gd)^{1/2}$, and time by multiplying by $(g/d)^{1/2}$. (In the following discussion the same notation as used in Eqs. 2 and 3 will be used to denote dimensional and dimensionless quantities; the meaning will be clear from the context of the discussion.) In Eqs. 2 and 3 the distance η to the water surface is measured from the still water level, the velocity u is the horizontal velocity averaged over the depth, σ is the ratio of water depth to wavelength, ϵ is the ratio of wave amplitude to water depth, and the notation $O(\)$ indicates terms of the order of the quantity in parentheses and smaller. The solution of these two equations allows for waves traveling in the positive and the negative x -directions; Peregrine's finite difference scheme was used for the numerical solution.

The problem of waves which are formed by an impulsive movement of the bottom was then treated as an initial value problem where the fluid in a long tank is initially at rest everywhere and a mass of fluid is added to (or subtracted

from) the still water surface over a portion of the tank at $t=0$. This theoretical model is crude in the sense that the movement of the bottom is not included instead an assumed form of the water surface is chosen at a time near the end of the wave-maker stroke and before the wave has left the generation area (defined for this analysis as $t=0$). The assumption that the horizontal velocity is initially zero everywhere just when this surface disturbance is formed is probably reasonably close to the experimental conditions for rapid bottom movements. In addition to these features of the analysis, similar to the laboratory conditions, the two ends of the tank in the theory are considered to be solid walls with zero water particle velocity at these walls for all time. This type of initial value problem is similar to that treated by Long (1964) using basically the same expressions as Eqs 2 and 3 but manipulated in such a way that solutions could be obtained by integrating along the characteristics in the (x, t) plane.

The initial amplitude distribution of the water surface which was used was

$$\frac{\eta}{d} = \pm 0.05 \left[1 - \tanh \left(\frac{x}{d} - 6 \right) \right] \quad (4)$$

From Eq 4 it is seen that for $x/d < 3$ the amplitude of the water surface is essentially constant and approximately equal to 0.1 and for $x/d > 9$ the amplitude is essentially zero. Such an expression allows for a smooth transition from one water surface elevation to another for the conditions chosen the length of the moveable bed corresponds to $x/d = 6$. With reference to Figs 4 and 5 it is evident that Eq 4 compares more favorably with the example which corresponds to the rapid bottom movement. Consider first the amplitude at $x/d = 3$, Eq 4 gives this amplitude as essentially 0.1 times the depth. In Figs 4 and 5 the amplitude at this location for the case of rapid motions is approximately the same as the maximum bed motion which is, in relative terms, $z_0/d = \pm 0.1$. From Eq 4 the relative amplitude at $x/d = 6$ is ± 0.05 which corresponds reasonably well to the observed values of +0.046 and -0.057 at about this location in the experiments for $t_R (g/d)^{1/2} = 0.4$. Thus, although this representation of the water surface is perhaps crude, it does retain some of the important features of the observed distributions.

The analytical results for the case of the positive disturbance are presented in Fig 6 where the variation in the water surface displacement, η/d is plotted as a function of non-dimensional time $\tau = t(g/d)^{1/2}$, for various values of normalized distance, i.e. $x/d = 0, 3, 10, 20, 30, 40$. A number of interesting features of the problem emerge from this analytical treatment and these will be discussed separately before comparing them to the experimental results. At $x/d = 0$ the wave amplitude decreases with time from the initial value of $\eta/d = 0.1$ to a magnitude less than zero and then oscillates with time about the still water level with the amplitude of oscillation decreasing with time and approaching zero. At $x/d = 10$ the water surface increases gradually with time from zero reaches a maximum, decreases and then increases slightly before decreasing and approaching zero. Hence, a second wave appears to be forming from the lead wave. An additional interesting feature of Fig 6 is that another group of waves appears in the lee of the main wave for $\tau > 30$. Both of these occurrences is a strong indication of the dispersive nature of such a wave system. For larger values of x/d the main wave appears to begin to move out in front, leaving behind the secondary wave system. If the computer storage had been sufficient to enable the computations to be made for a larger tank and thus to proceed to large values of x/d and τ it might have been possible to see the lead wave approach a solitary wave in form. As it is, because of this limitation the reflection of the wave from the far tank wall can be seen at $x/d = 40$ for $\tau > 80$.

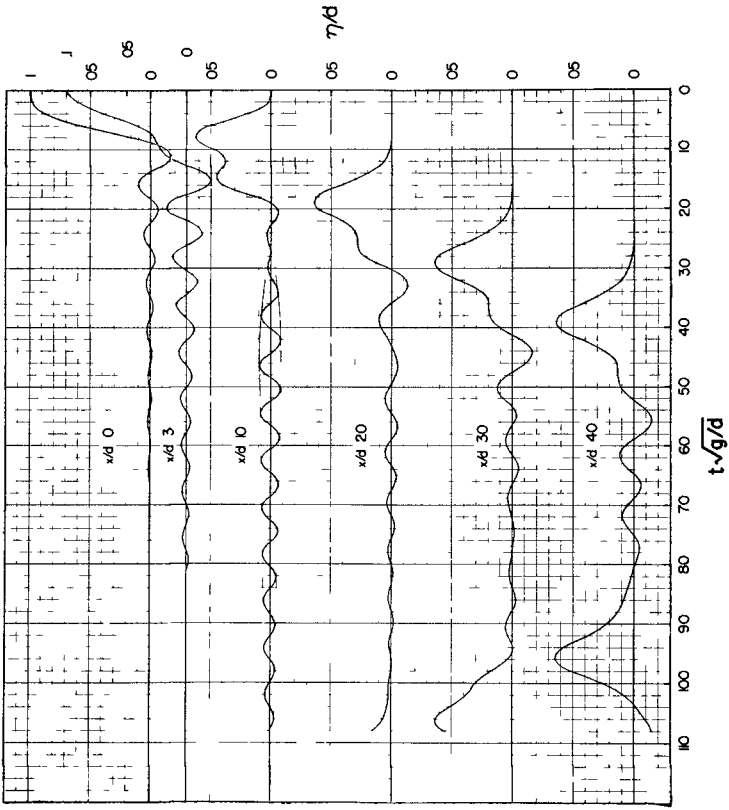


Fig 6 Analytical Results of Waves from a Positive Disturbance

It is interesting to compare Figs 4 and 6 in a qualitative sense. In Fig 4, for either $x/d = 3.0$ or 6.4 the same trailing-edge wave system is observed as at $x/d = 0$ in the analytical solution (Fig 6). The wave systems in both cases decrease to zero with increasing time. Unfortunately, as mentioned previously the analytical solution could not be extended further than $x/d = 40$ so that a station comparable to the next experimental station $x/d = 81.4$ could not be reached. However, in the analytical results similar changes in wave form are observed as in the experiments although perhaps the dispersion occurs more rapidly in the analytical solution than it does in the experiments.

In Fig 7 analytical results are presented for the comparable case of a negative disturbance which propagates from the initial conditions given by Eq 4. At $x/d = 0$ the shape of the disturbance is nearly the mirror image of the positive disturbance shown at the same location in Fig 6, and again trailing waves are seen in the lee of the lead wave. Fig 7 shows that the slope of the leading edge of the main wave decreases with distance as the wave propagates downstream. The same effect is observed when the results are plotted as a function of distance for constant times. If Fig 6 and 7 are compared it is seen that the lead negative disturbance is well formed for a given location compared to the positive wave, and also the trailing waves appear to have grown more rapidly in the case of the negative disturbance compared to the positive one. In addition it has been found that for the last station shown in Fig 7 the variation of the normalized velocity with time is nearly identical to the water surface variation even though at $x/d = 0$ these distributions are different.

If, as before, Fig 7 is compared to its experimental counterpart, Fig 5, the same general trends can be seen: the decreasing slope of the lead wave with distance, the rapid development of the form of the lead wave, and the rapid growth of the waves in the lee of the main disturbance.

In summary, it is felt that this analytical method describes the changes in a wave system due to both linear and nonlinear dispersion. Even though the initial conditions assumed appear crude, the resultant wave forms agree qualitatively with the experiments.

ANALYSIS OF FIELD OBSERVATIONS

In addition to the experimental and analytical studies of which this paper presents only some preliminary results, tide gage records of various tsunamis obtained at certain locations around the Pacific Ocean have been studied to investigate the interaction of these waves with the coastline. An obvious feature of such records is that, even though the particular earthquake has a relatively short duration (of the order of minutes or less), the tide gage records generally exhibit oscillations which last longer than 24 hrs. In addition, the major waves at many of these locations occur within the first few hours of the arrival of the lead wave. An example of such records is presented in Fig 8 for three locations in Southern California for the tsunami which resulted from the Alaskan earthquake of March 27, 1964; these and subsequent records were taken from Spaeth & Berkman (1965) and Berkman & Symons (1964). Such water surface fluctuations at the coastline raise the question whether the wave train which is measured at the coast bears any resemblance to the wave which existed in the open-sea. It is possible that the waves where are recorded are the result of a short impulsive wave train triggering the oscillation of the water masses in local embayments and coastal waters which then oscillate with small damping for long periods of time.

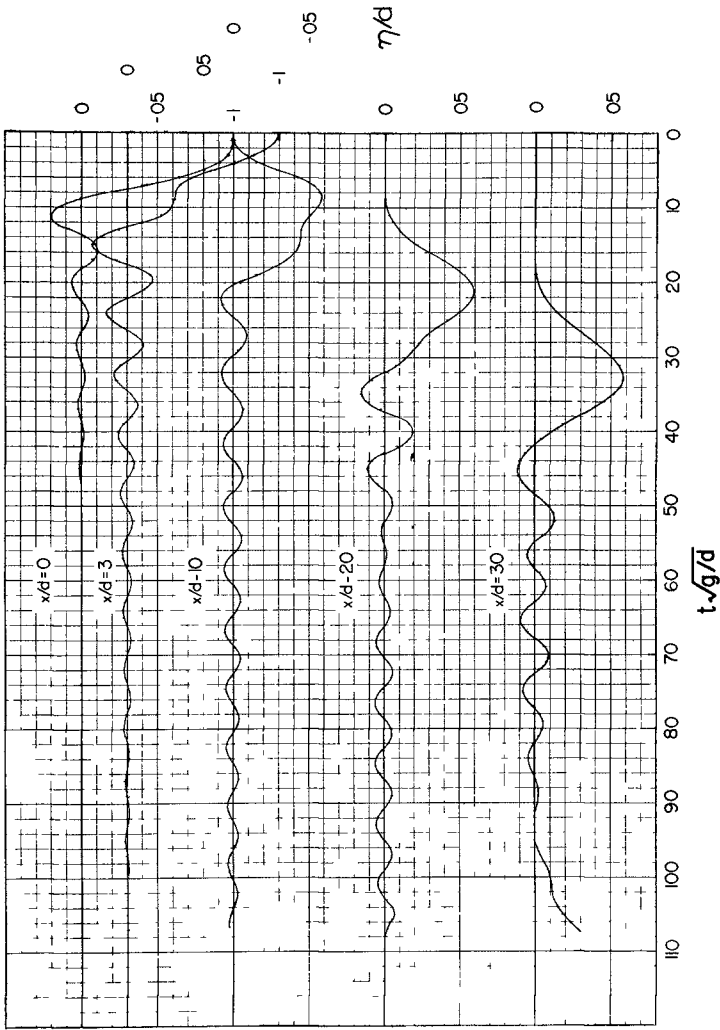


Fig 7 Analytical Results of Waves from a Negative Disturbance

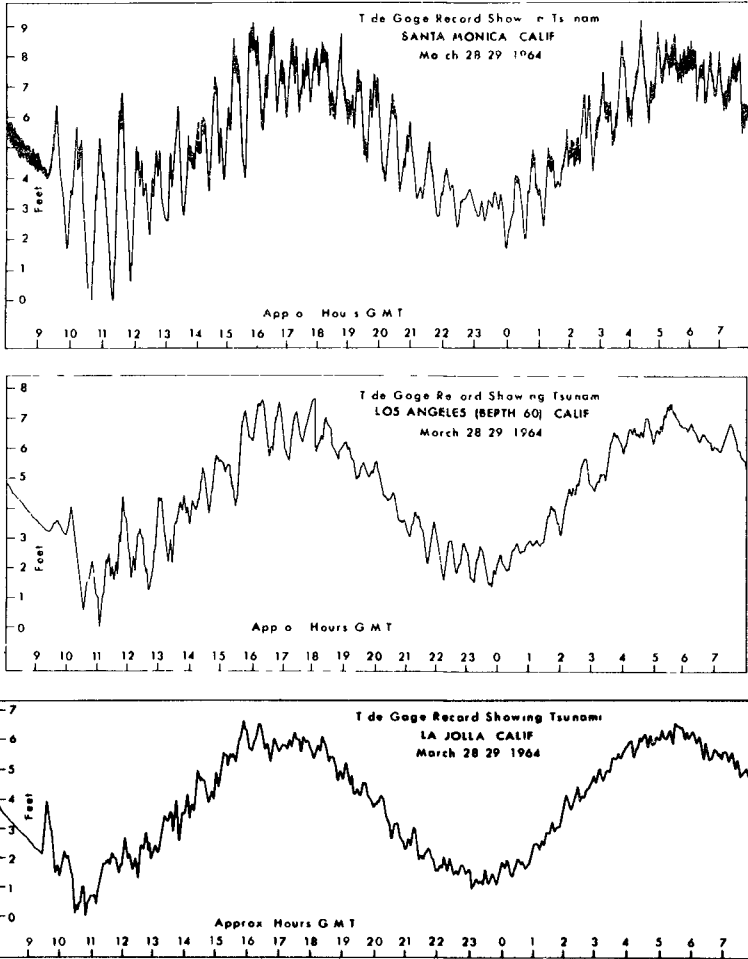


Fig 8 Tide Gage Records from the Tsunami of the Alaskan Earthquake of March 27 1964 (After Spaeth & Berkman (1965))

To investigate this type of question by obtaining information regarding the distribution of wave energy in these records as a function of frequency (or wave period) the wave records were analyzed using spectral analysis procedures similar to those used for analyzing ocean wave records. In essence these methods treat the record as if it were a stationary process. This is not considered too serious a limitation since the primary objective is to compare spectra from various harbors for the same event and from the same harbor for various events, and if approximately the same length of record is treated in the same way for all cases a reasonable comparison can be made. (Of course the same questions regarding stationarity also can be raised about other analytical methods such as harmonic analysis.)

The spectra of the tsunami associated with the Alaskan earthquake of March 27, 1964 for three Southern California locations are presented in Fig. 9. The ordinate in Fig. 9 is the normalized energy density, normalized with respect to the mean square of the deviation of the water surface from the tide level in units of hours and the abscissa is the frequency in cycles per hour (cph). Therefore, the area under each spectrum is unity. The spectra were obtained after subtracting from the marigram the effect of the tide so that this low frequency component would not completely distort the energy content of the spectrum. This was accomplished by first subtracting the predicted or fitted tide from the record and then passing the resultant digitized record through a numerical high-pass filter such as that described by Kinsman (1965). This, as well as the spectral analysis computation was accomplished on a digital computer using the procedure for spectral analysis described by Blackman and Tukey (1958) and by Rachlen (1967). In all cases the confidence limits of the spectra were obtained by applying the method described by Kinsman (1965). For the spectra which are presented it is expected that, for a given frequency-band, if the process were stationary, there is a probability that 90% of all spectral estimates will exceed 0.69 times the ordinate and 10% of all values will exceed 1.30 times the ordinate with 50% of all values exceeding 0.98 times the ordinate value. The frequency resolution which was used was chosen based on the available record lengths, the confidence limits, the sampling interval, and the fact that spectra from different events were to be compared.

Returning now to Fig. 9, spectra are presented for Santa Monica, Los Angeles Harbor (Berth 60) and La Jolla, all in Southern California with the first and last of these locations approximately 125 mi (200 km) apart in a North-South direction. Values of the root-mean-square of the water surface fluctuations about the tide (r_{ms}) are shown in Fig. 9 for these locations. The r_{ms} tends to decrease in a Southerly direction with distance from the tsunami source, in fact, the r_{ms} decreases by a factor of nearly 2.5 comparing the two furthest stations. Considering the problems usually associated with spectral analysis, the spectra for these locations are remarkably similar indicating a major concentration of energy between frequencies of 1.6 cph and 1.8 cph (wave periods between 33.4 min and 37.5 min). In addition, there is a secondary concentration of energy between frequencies of 0.4 cph and 0.6 cph (wave periods between 1.67 hrs and 2.5 hrs). Before discussing in detail some conclusions which may be drawn from these spectra it is useful to view others that have been obtained.

Spectra for four locations are presented in Figs. 10 and 11 for both the tsunami which resulted from the earthquake in Alaska of March 27, 1964 and the earthquake in Chile of May 22, 1960. In all cases the spectra were obtained

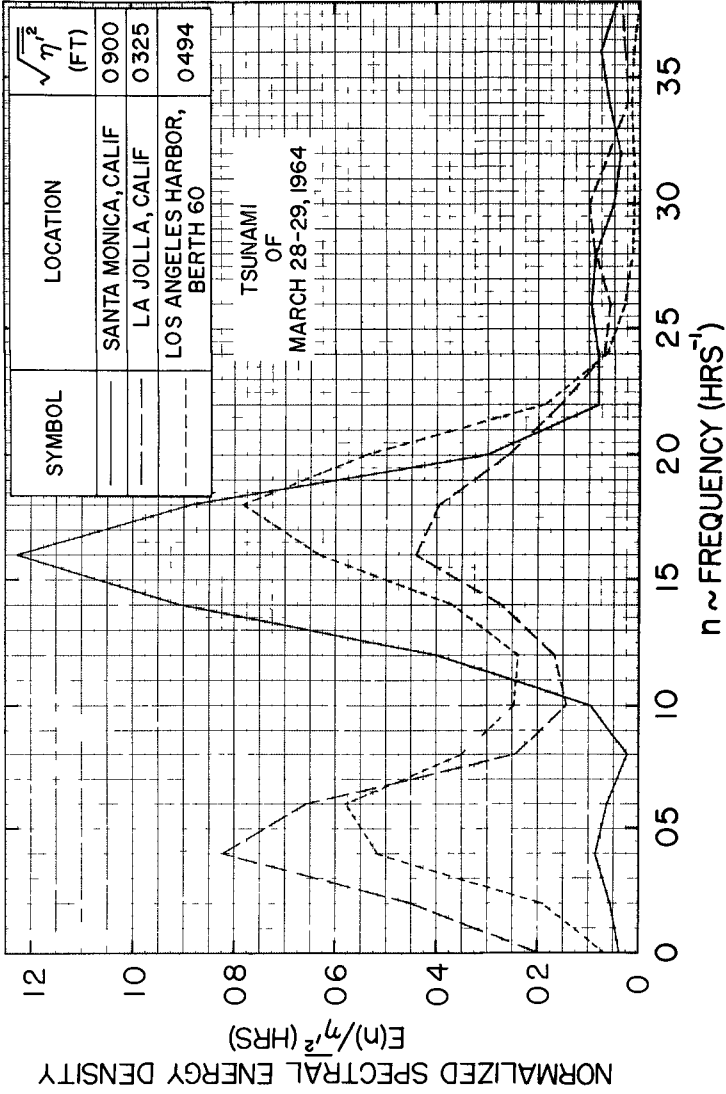


Fig 9 Normalized Energy Spectra for Tsunamis at Three Southern California Locations for the Alaskan Earthquake of March 27 1964

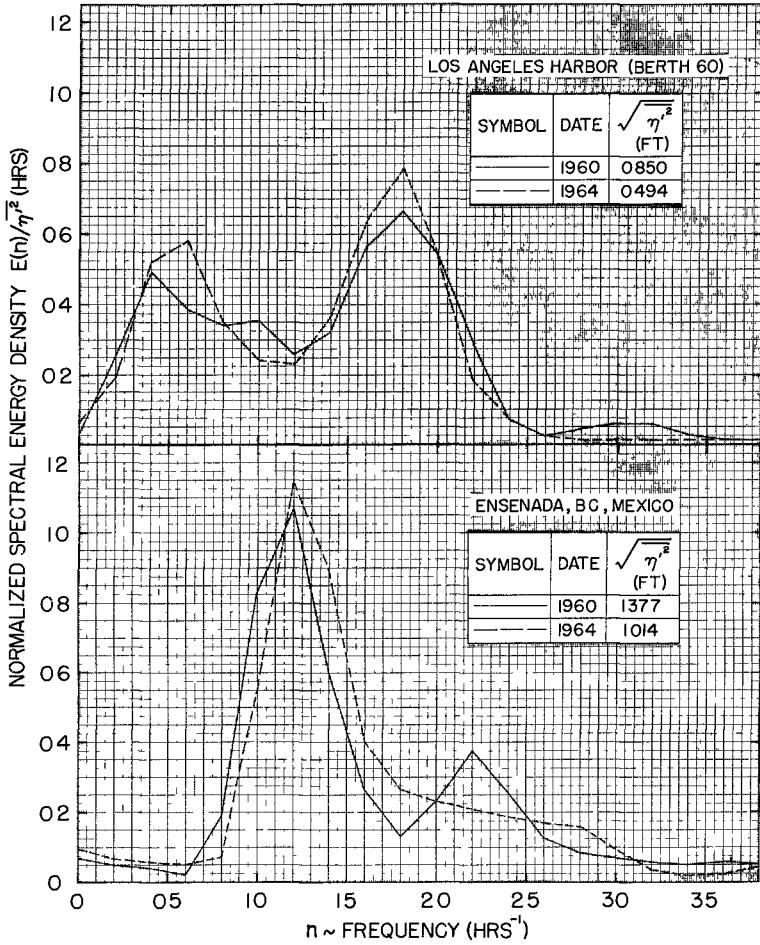


Fig 10 Normalized Energy Spectra for Tsunamis at Los Angeles Harbor (Berth 60) and Ensenada B C , Mexico Caused by Chilean (1960) and Alaskan (1964) Earthquakes

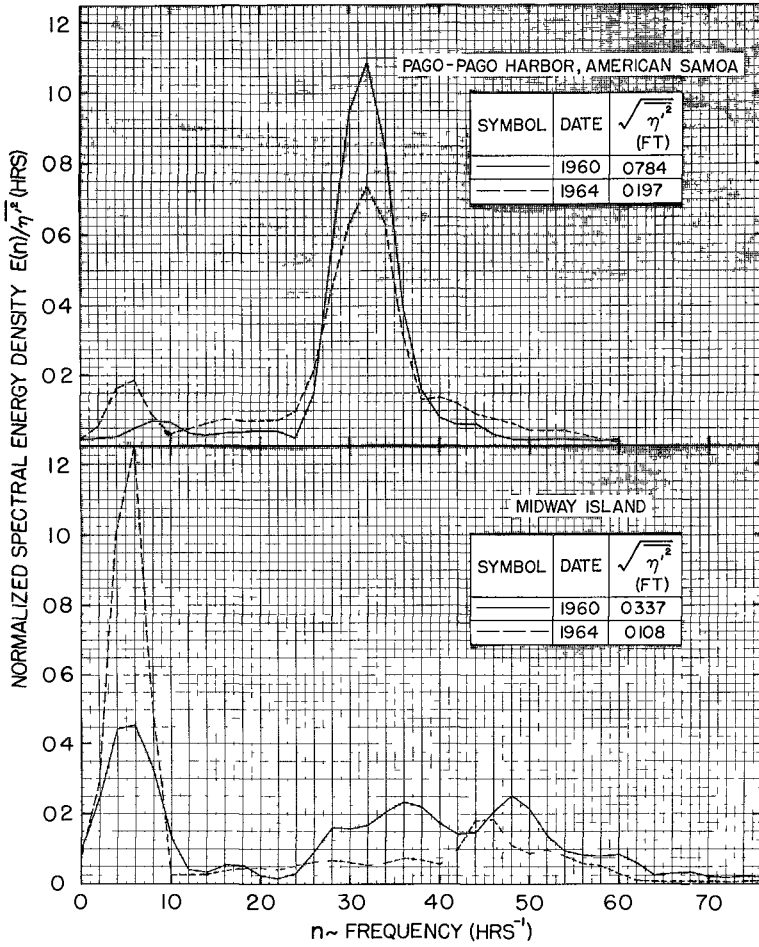


Fig 11 Normalized Energy Spectra for Tsunamis at Pago-Pago Harbor, American Samoa and Midway Island Caused by Chilean (1960) and Alaskan (1964) Earthquakes

and plotted in the same way as those shown in Fig 9 and the values of the $r m s$ are indicated in the figures. There are two obvious features of Figs 10 and 11 (1) the spectra at each location for the two different tsunamis are quite similar, and (2) in all cases the $r m s$ value for the Chilean tsunami is greater than that for the Alaskan tsunami (the ratio varying from nearly 1.4 to 4)

Wilson (1969) in a general investigation of earthquake movements and tsunamis concludes that the tectonic movement associated with both the Chilean earthquake of 1960 and the Alaskan earthquake of 1964 were probably similar and that evidence indicates that a molar upthrust combined with a down-throw played an important role in the earth movement. This similarity may be the reason for the relatively good agreement between spectra at each of the locations shown in Figs 10 and 11. It is also quite possible, as suggested earlier, that each location is very strongly responsive to particular frequencies which are in the tsunami wave train. Therefore, even if the tsunamis were quite different in the open-sea as long as a small amount of energy existed at the preferred frequencies for that particular location, due to the resonant nature of harbors and coastal waters, frequencies to which the harbor is not strongly responsive would be masked. In this way it is possible that spectra at a particular location could be similar even though the spectra of the events in the open-sea were quite different. For the records analyzed it is probable that both of these explanations are true in part, however, from these limited data a more definite conclusion cannot be made.

Wilson (1969) and Munk et al (1959) also have discussed the possibility of the excitation of harbors by these transient wave systems. Munk and Cepeda (1962) have attempted to analyse in some detail the marigram at Acapulco, Mexico due to the tsunami associated with the Mexican earthquake of 1957 to determine whether the response of Acapulco Harbor could be the cause of a sharp peak observed in the spectrum at a frequency of 1.98 cph (a period of about 0.5 hrs). They treated the harbor as if it were a rectangular harbor of constant depth and applied the method of Miles and Munk (1961) to determine the frequencies of various modes of oscillation of this harbor. Their conclusion was that the observed wave period of 0.5 hrs was probably not due to the harbor alone but it was probably caused by the oscillation of a much larger body of water offshore. Their method of determining the response was admittedly crude, and without determining the response by a more exact method such as that developed by Lee (1969) it is difficult to draw a definite conclusion as to the cause of the observed periodicity except to say that the peak which was observed in their spectrum was probably due to local excitations.

Comparing Figs 9, 10, and 11 it is seen that for both tsunamis at three of the four locations investigated there is a peak in all spectra in the period range between 1.67 and 2.5 hrs. (For the Alaskan tsunami alone this periodicity is common to five of the six sites studied.) Ensenada, Mexico is the only location which does not exhibit such a peak, and this may be due to the method of analysis. If the tide is not completely subtracted in the procedure, and if small amounts of energy exist at frequencies near that of the tide, it is possible that the remaining tidal energy can completely mask periodicities with small energy content at low frequencies.

The peaks which are observed in the spectra of Figs 10 and 11 at higher frequencies appear to be common for a particular location, however, these frequencies are not common among locations. Therefore, the energy concentrations which appear at wave periods between 20 min and 50 min are probably due to the bathymetric and coastal configuration of the particular location.

Wilson (1969) and Wilson and Tørum (1968) have concluded that the period of the primary tsunami wave for both the Alaskan tsunami of 1964 and the Chilean tsunami of 1960 was of the order of 1.7 hrs. Since the peaks at the lower frequencies in the spectra presented herein are approximately at the same frequency independent of location, the same conclusion may be made. If one agrees with this conclusion then, considering the periodicity between 33 min and 38 min, Fig 9 indicates that the Alaskan tsunami of 1964 must also have excited a large mass of water off the coast of Southern California extending at least from Santa Monica, California to La Jolla, California. Therefore, in order to learn more about local tsunami effects such as run-up and forces on structures, which are important from engineering considerations, then more must be understood about the response of off-shore water masses to impulsive wave systems.

CONCLUSIONS

The unique laboratory wave generating facility described herein is capable of producing an impulsively generated wave system which shows the same dispersive effects as predicted by a simple theory. The analysis which is used considers the wave system to originate from an initial condition of a disturbed water surface in a still tank of water. It shows, in addition to dispersive effects, the same distinct differences between positive and negative initial disturbances as are observed in the laboratory.

Spectra determined from the tide gage records at four locations around the Pacific Ocean for the tsunamis from the Alaskan earthquake of 1964 and the Chilean earthquake of 1960 had similar shapes at each location. The results indicate that there is a periodicity of approximately 2 hrs which is common to nearly all of the locations investigated. Other concentrations of energy at higher frequencies which for a given location are similar in period for both tsunamis are not similar for different locations. This shows that local embayments and bathymetry tend to influence significantly the wave amplitudes due to tsunamis measured near the shore.

ACKNOWLEDGEMENTS

This research is sponsored by the National Science Foundation under Grant No. GK-2370. The work which deals with the analytical simulation of surface waves was conducted at the Technical University of Denmark while the author was on leave of absence there, the assistance of the Northern Europe University Computing Center in making those computations is appreciated.

REFERENCES

- Berkman S C and Symons, J M "The Tsunami of May 22, 1960 as Recorded at Tide Stations" U S Dept of Commerce, U S Coast and Geodetic Survey, Feb 1964
- Blackman, R B , and Tukey J W , The Measurement of Power Spectra Dover Publications New York N Y , 1958
- Keulegan, G H , and Patterson, G W , "Mathematical Theory of Irrotational Translation Waves", Journal of Research of the National Bureau of Standards Vol 24, Jan 1940, pp 47-101
- Kinsman, B Wind Waves Prentice-Hall, Inc , Englewood Cliffs, New Jersey, 1965, pp 448-455
- Lee, J -J "Wave Induced Oscillations in Harbors of Arbitrary Shape", Report KH-R-20, W M Keck Lab of Hydr & Wat Res , California Institute of Technology Pasadena Calif , Dec 1969
- Long R R "The Initial-Value Problem for Long Waves of Finite Amplitude" Journal of Fluid Mechanics, Vol 20, Part 1, Sept 1964, pp 161-170
- Miles J , and Munk W H , "The Harbor Paradox" Journal of Waterways and Harbors Division, ASCE, Vol 87, No WW3, 1961, pp 111-130
- Munk, W and Cepeda H , "Concerning a Remarkably Sharp Peak in the Sea Level Spectra at Acapulco", Contributions University of California, San Diego, Scripps Institution of Oceanography, Vol 32, 1962 pp 1031-1040
- Munk W H Snodgrass, F E and Tucker, M J , "Spectra of Low Frequency Ocean Waves", Bulln Scripps Instit of Oceanography Vol 7(4), 1959, pp 283-362
- Peregrine, D H , "Calculations of the Development of an Undular Bore", Journal of Fluid Mechanics Vol 25 Part 2 June 1966, pp 321-330
- Rachlen, F , "Some Turbulence Measurements in Water", Journal of the Engineering Mechanics Division, ASCE EM2, Paper 5195, April 1967, pp 78-80
- Spaeth, M B and Berkman, S C , "The Tsunami of March 28, 1964 as Recorded at Tide Stations", U S Dept of Commerce, U S Coast and Geodetic Survey, April 1965
- Wilson, B W "Earthquake Occurrence and Effects in Ocean Areas", Technical Report CR 69 027, prepared for U S N C E L , Port Hueneme, Calif Feb 1969
- Wilson, B W and Tørum, A , "The Alaskan Tsunami of March 1964 Engineering Evaluation", Tech Memo No 25 Coastal Engr Res Cent , Corps Engrs , U S Army, Washington, D C , 1968

CHAPTER 128

HEAD LOSS AT TSUNAMI-BREAKWATER OPENING

by Yoshiyuki ITO*

Abstract

The head loss at breakwater opening is an important factor for evaluating the effect of breakwaters against tsunami. This paper examines the coefficient of the head loss term in the equation of motion by comparing the results of numerical calculations with the actual record observed in the Port of Ofunato at the time of 1968 tsunami. Numerical calculations are repeated changing the head loss coefficient from zero to 3.0 with the interval of 0.5. The calculated water level variation is quite different from the record if no head loss is taken into consideration. Although the most suitable value of the coefficient is not definitely determined, the value of 1.5, which has been adopted in our previous calculations, seems to be reasonable for practical purpose.

Introduction

The construction of tsunami-breakwaters in the Port of Ofunato and several other harbours was started after the disaster due to Chilean Earthquake Tsunami in 1960. Concerning this project the author studied the effect of breakwaters against tsunami mainly by numerical calculations. The method of calculation and some results obtained were reported to 10th Coastal Engineering Conference held in Tokyo in 1966 (Reference 1).

In May 1968, the tsunami-breakwater in the Port of Ofunato experienced the first remarkable tsunami since its completion in 1967. The water level variation was recorded by two tide gauges located outside and inside the breakwater. The author immediately applied the method of calculation and obtained a good agreement between calculation and observation. The effect of the tsunami-breakwater was also confirmed by this analysis. The details were already reported to 13th IAHR Congress in Kyoto, 1969 (Reference 2).

The term of head loss included in the equation of motion at the breakwater opening plays an important role in numerical calculation. If no head loss is taken into account, the effect of breakwaters against tsunami is not appropriately evaluated due to the appearance of so-called harbor-paradox. The author has so far adopted the head loss coefficient of 1.5 in previous calculations. The influence of this coefficient on the calculated results is examined in this paper by comparing the calculations with the actual observation of 1968 tsunami in the Port of Ofunato.

* Hydraulics Division, Port and Harbour Research Institute, Ministry of Transport 3-1-1, Nagase, Yokosuka, Japan

Basic Equations

The principle of calculation is to solve numerically the equations of motion and of continuity for two-dimensional long wave under certain initial and boundary conditions. Fundamental equations are as follows,

$$\begin{aligned}\frac{\partial u}{\partial t} &= -g \frac{\partial \zeta}{\partial x} \\ \frac{\partial v}{\partial t} &= -g \frac{\partial \zeta}{\partial y} \\ \frac{\partial \zeta}{\partial t} &= -\frac{\partial}{\partial x} (hu) - \frac{\partial}{\partial y} (hv)\end{aligned}\quad (1)$$

where, u, v = velocity component in x - and y -direction, respectively
 ζ = water level elevation with respect to mean water level
 h = water depth below mean water level

These differential equations are transformed into difference equations. Figure 1 shows the grid system around the breakwater in the Port of Ofunato. The grid interval in this case is 280 metres and the time interval is 10 seconds.

The outer sea is replaced by a channel of constant depth and width, where the computation is only aimed at supplying the incoming tsunami without being affected by reflected waves from the breakwater and shorelines. As a boundary condition, velocity components normal to the breakwater and shorelines are given to be zero. The calculation is started from the time when the front of tsunami arrives at the bay-mouth. Initial water level and velocity inside the bay are accordingly zero, while those in the outer sea correspond to the incident tsunami profile.

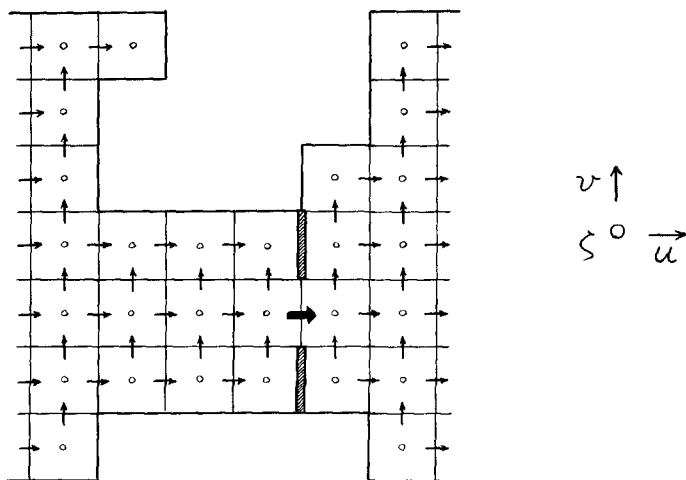


Figure 1 Grid System for Numerical Calculation

Although higher order terms for inertia or bottom friction are neglected in Equation (1), a term representing the head loss is added to the equation of motion at the breakwater opening as shown in the following difference equation,

$$\frac{\Delta_t u}{\Delta t} = -g \frac{\Delta_x \zeta}{\Delta x} - \frac{f}{2\Delta x} - u|u| \quad (2)$$

The head loss coefficient f in this equation has been assumed to be 1.5 in previous calculations. In this paper numerical calculations are carried out with f of 0, 0.5, 1.0, .., 3.0.

1968 tsunami in the Port of Ofunato

Figure 2 shows the plan of Ofunato Bay situated in the north-eastern part of Japan along the Pacific Coast. The tsunami-breakwater near the bay-mouth, where the maximum water depth reaches almost 40 metres, was constructed after Chilean Earthquake Tsunami in 1960 and was completed in 1967.

On May 16, 1968, an earthquake of magnitude 7.8 occurred off this district. A tsunami accompanied by this earthquake attacked the coast and caused certain damages to several ports. The tsunami-breakwater in the Port of Ofunato effectively protected the harbour and the city by reducing the water level elevation in the inner basin.

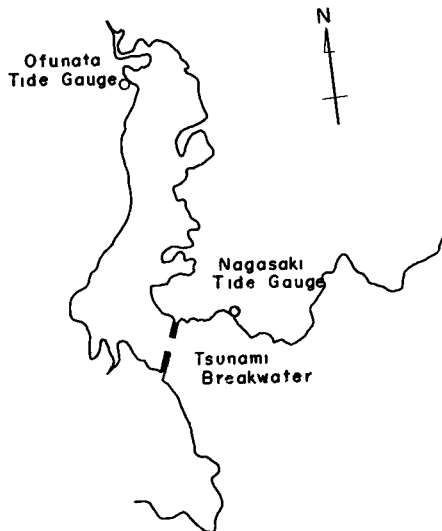


Figure 2 Tsunami-breakwater and Tide Gauges in the Port of Ofunato

Actual records of water level variation were obtained at two tide gauges, the one is located between the bay-mouth and the breakwater (Nagasaki) and the other is at the innermost part of the bay (Ofunato). The position of these tide gauges is indicated in Figure 2.

Figure 3 shows the water level variations during the first two hours, the astronomical tide being subtracted.

In the analysis of this tsunami by applying the author's method, the incident tsunami profile for calculation was determined so that the calculated water level variation at the outside tide gauge might be as close as possible to the observation. The outline of the procedure for this determination is as the following,

1) The water level variation at the outside tide gauge during the first 124 minutes, in which most of the major fluctuations are included, is analyzed into Fourier sine series.

2) Calculations are repeated for component regular sinusoidal waves in order to obtain the amplifying factor at the outside tide gauge. The amplifying factor obtained varies from 1.7 to 2.9.

3) The amplitude of each component obtained in the item 1) is divided by the corresponding amplifying factor in the item 2). The Fourier sine series consisting of thus determined amplitudes gives the approximate profile of the incident tsunami.

With this incident tsunami profile, a good agreement was confirmed between the calculation and the observation at the inside tide gauge. A calculation with the same incident tsunami was also carried out for the harbour before the construction of the tsunami-breakwater. The highest water level elevation in the harbour after the breakwater construction is 1.1-1.2 metres, while without the breakwater it reaches more than 2 metres. The effect of the tsunami-breakwater is definitely evaluated by these numerical calculations

Influence of the head loss coefficient on calculated results

The incident tsunami profile determined by the above-mentioned procedure will be affected to a certain extent by the head loss coefficient at the breakwater opening. However, the profile for $f=1.5$ is commonly used in this paper to all the cases from $f=0$ to 3.0. The influence of the value of f on the water level at the outside tide gauge is comparatively small, as shown in Figure 4.

Figure 5 is the comparison between calculation and observation at the inside tide gauge. This figure indicates that the curve for $f=0$ is quite different from the actual record, not only in the value at each peak or trough but also in the form of the curve itself.

Table 1 shows the computed and observed water level elevations at several peaks and troughs. The value of f fitted to the observation differs at each position, as indicated by the mark (*) in the column of calculation.

Figure 6 shows the goodness of fit of computed water level. The goodness is measured by the root mean square (σ) of the residuals at every two minutes during two hours ($N=60$).

$$\sigma = \sqrt{\sum (\xi_{\text{cal}} - \xi_{\text{obs}})^2 / N} \quad (3)$$

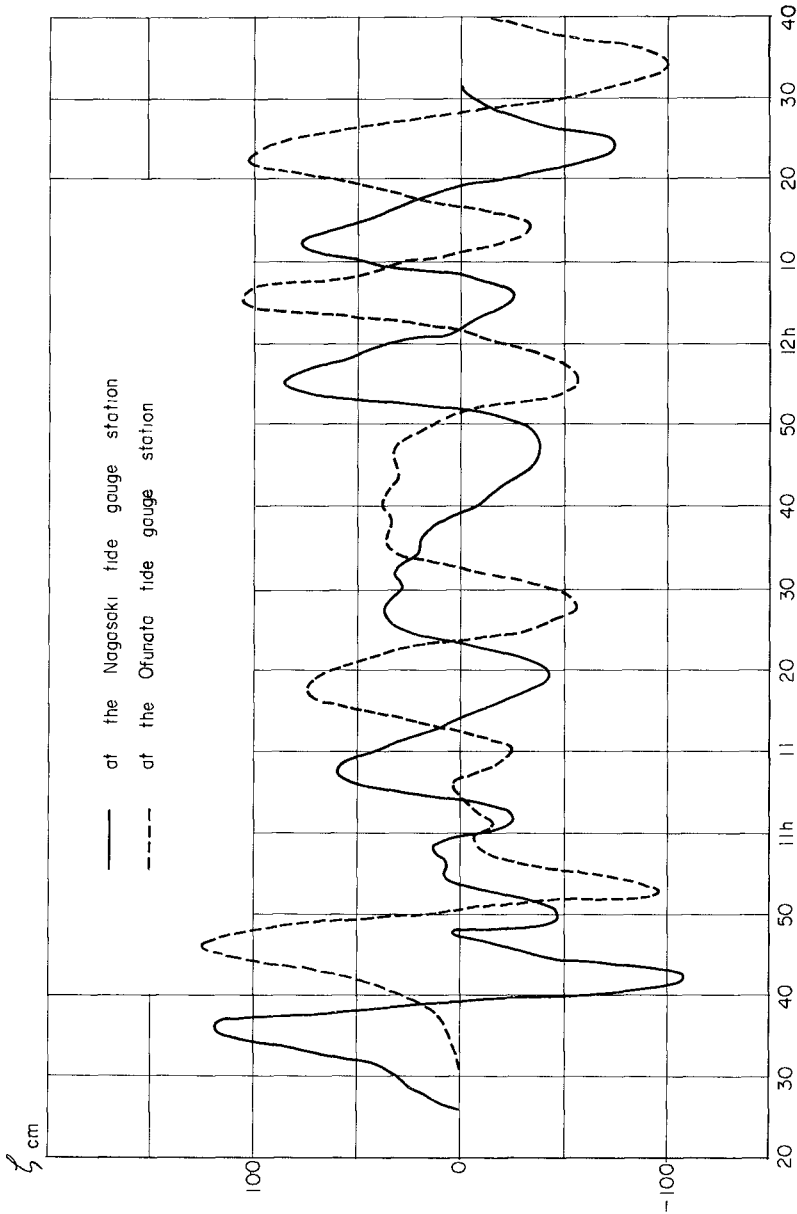


Figure 3 Water Level Variation due to 1968 Tsunami in the Port of Ofunata

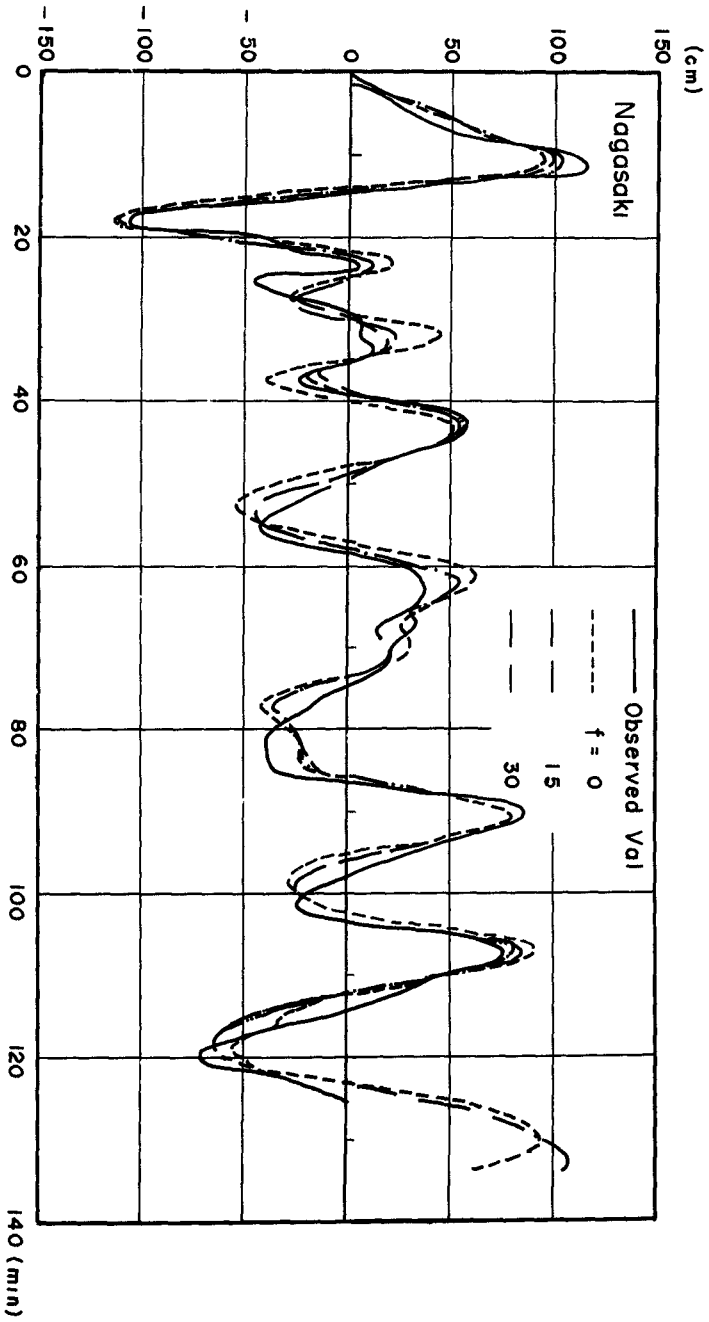


Figure 4 Comparison of Calculation and Observation at the Outside Tide Gauge

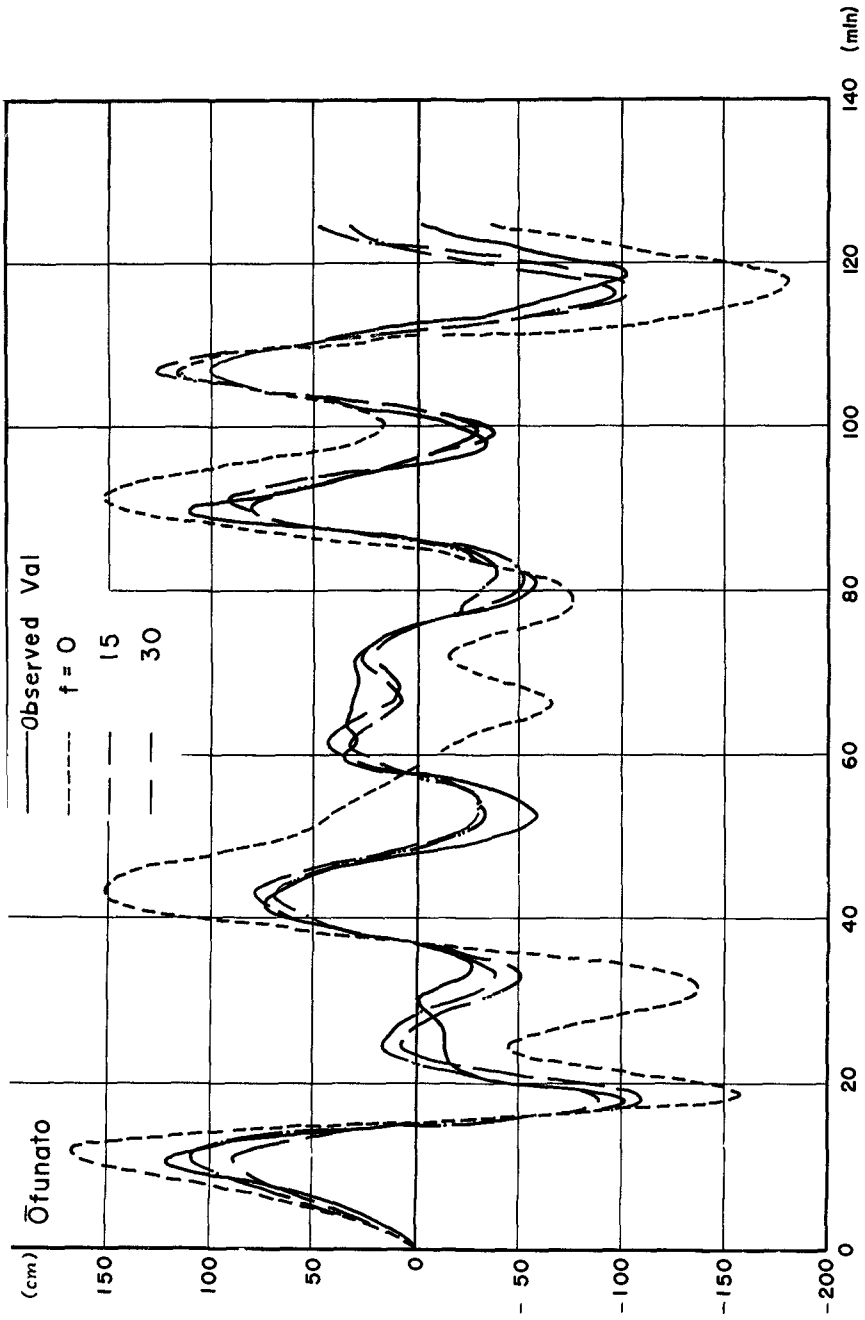


Figure 5 Comparison of Calculation and Observation at the Inside Tide Gauge

Table 1 Comparison of Calculation and Observation
at Peaks and Troughs (unit cm)

Position	Observation	Calculation						
		f=0	0.5	1.0	1.5	2.0	2.5	3.0
1st peak	124	169	140	123*	111	103	96	91
1st trough	-102	-159	-137	-120	-108	-101*	-95	-90
3rd peak	74	153	104	88	80	75*	72	69
4th peak	112	153	108*	100	94	90	85	81
6th peak	102	119	138	134	129	123	119	115*
6th trough	-101	-180	-121	-111	-105	-102*	-99	-97

Although the incident tsunami profile has been determined so that the computed water level at the outside tide gauge might coincide with the observed record, there still remain some differences between calculation and observation. The deviation of calculation for the inside tide gauge will depend on both the accuracy of the incident tsunami profile and the value of the head loss coefficient f .

At the inside tide gauge, the root mean square of the residuals is very big at $f=0$. It decreases rapidly with the increase of f and becomes almost constant for f of bigger than 1.0.

It is not easy to find out definitely the most suitable value of f from these results. However, the analysis in this paper suggests the practical validity of the adoption of 1.5 or so as the head loss coefficient at the tsunami-breakwater opening, as far as the form of the equation of motion in our method of calculation is concerned.

References

- 1) H. Fukuuchi, Y. Ito On the Effect of Breakwaters against Tsunami, Proc. 10th Conference on Coastal Engineering (Tokyo, 1966), pp.821-839
- 2) Y. Ito On the Effect of Ofunato Tsunami-Breakwater against 1968 Tsunami, Proc. 13th Congress of IAHR (Kyoto, 1969), Vol.3, pp.85-93

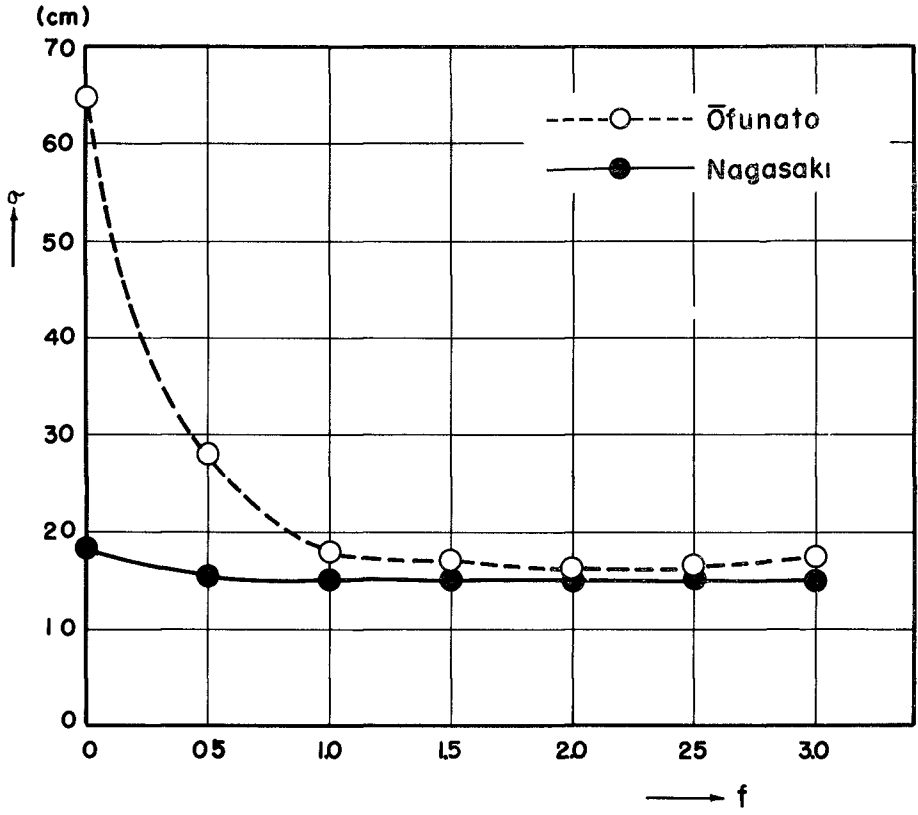


Figure 6 Goodness of Fit

CHAPTER 129

TIDAL WAVES IN SCHEMATIC ESTUARIES

Hans Vollmers

Bundesanstalt für Wasserbau Hamburg

and

Jürgen Sundermann

Institut für Meereskunde der Universität Hamburg

ABSTRACT

An investigation of tidal waves in schematic estuaries has been carried out simultaneously for hydraulic and hydrodynamic-numerical (HN) models. Thereby a far-reaching agreement of results is obtained for geometrically simple shapes. In these cases hydraulic investigations can be replaced equivalently by HN-computations.

INTRODUCTION AND GENERAL VIEW

The knowledge of the tidal caused motion processes in the near shore area, especially in the estuaries, is of great importance for coastal engineering and navigation. The quantitative determination of these processes, e.g. finding out of water levels and current velocities depending on space and time, can be done by direct measurements in the natural area. In recent years for this purpose also hydraulic and hydrodynamic-numerical (HN) models are used which simulate the natural conditions. The application of such models requires e.g. much less effort and costs and gives, further on, the possibility to study the effect of prospected coastal engineering structures. On these grounds model techniques succeeded in the last years on a large scale. Especially, the HN-methods belong to the most effective tools of dynamical oceanography.

The following results on the propagation of tidal waves in estuaries are obtained by means of hydraulic and HN-models. It was a main intention thereby to find out by a systematic investigation of geometrical simple estuarine shapes the degree of agreement and the possibilities and restrictions of the two principally different methods. It appears, that in this way a senseful mutual completion of both methods could be reached. Now, the more expensive hydraulic model experiments will be carried out only in those

complicated cases, for which theoretical solutions are not yet available. On the other hand, HN-investigations can relieve the hydraulic model testing plants of time-consuming routine experiments and be very useful if the constructional equipment of the laboratory do not allow the study of certain questions e.g. the influence of the Coriolis force. The investigations which result from a co-operation of the Bundesanstalt für Wasserbau Hamburg and the Institut für Meereskunde der Universität Hamburg, are sponsored by the Deutsche Forschungsgemeinschaft (Vo 153/1/2). The whole study will be reported later on. We are very thankful to W. Wulzinger for his assistance in the hydraulic model investigations.

The hydraulic processes in a tidal estuary without a steady inflow are mainly influenced by two aspects

- (a) Geometry of the estuary
- (b) Shape of the incoming tidal wave

In the following only the effect (a) is discussed. Fig. 1 shows the considered schematic estuaries. The types B and E are developed from tidal rivers at the German coast. By this time the comparison between the two models was realized for the types A and D.

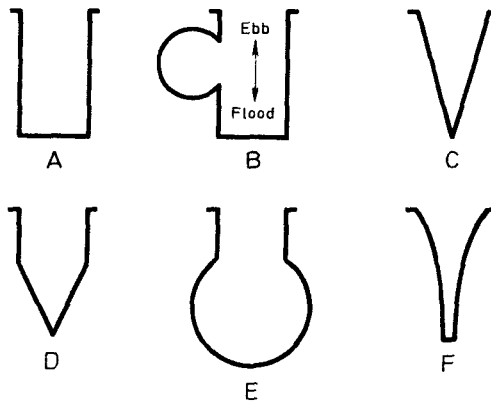


Fig. 1 Types of Estuaries

In all cases a uniform M_2 -tide with a mean amplitude of 1,5 m has been used.

Actually, the HN-models produce vertically integrated horizontal velocities. It is intended, furtherly, to consider the vertical dimension too.

THE NUMERICAL MODEL

The foundation of the mathematical model is, that flow movements (especially instationary tidal waves which are of interest here) take place according to the well-known fundamental equations of hydrodynamics. Therefore, the mathematical treatment of these equations gives the possibility, in principal, to determine the motion processes in a certain area. The mathematical model has to be adapted extensively to natural conditions.

In general, due to the nonlinearity of the hydrodynamic differential equations, an analytic solution is not available. Therefore the application of numerical methods is necessary, e. g. the HN-difference method (HANSEN [1]). This requires the application of electronic computers. In the last years, the HN-method was proved for many natural sea areas (Technical Report [4], SUNDERMANN [2]). The following differential equations have been used:

$$(11) \quad \frac{\partial u}{\partial t} + \frac{r}{h+\xi} u \sqrt{u^2+v^2} - A_H \Delta u - fv + g \frac{\partial \xi}{\partial x} = 0$$

$$(12) \quad \frac{\partial v}{\partial t} + \frac{r}{h+\xi} v \sqrt{u^2+v^2} - A_H \Delta v + fu + g \frac{\partial \xi}{\partial y} = 0$$

$$(13) \quad \frac{\partial \xi}{\partial t} + \frac{\partial}{\partial x} ((h+\xi)u) + \frac{\partial}{\partial y} ((h+\xi)v) = 0$$

The first two equations are motion equations and 13 is the continuity equation. The system is two-dimensional. For this a cartesian system of coordinates has been used. The x-axis is directed to East, the y-axis to North, the z-axis indicates the vertical direction (see Fig. 2).

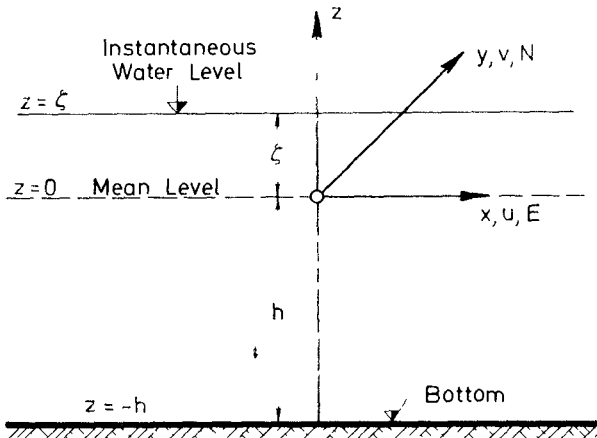


Fig. 2 System of Coordinates

Herein denotes

u, v components of the vertical averaged current velocity
 w in the x - or y -direction, respectively

ξ water level = distance from the mean level

h mean water depth = distance between the mean
 water level and bottom

t time

A_H horizontal turbulence coefficient

f Coriolis parameter

g gravitational acceleration

r friction factor

$$(2) \quad (2.1) \quad w_n = 0 \quad \text{along the coastline}$$

$$(2.2) \quad \xi(t) = A \cos(\sigma t - \alpha) \quad \text{at the entrance of the estuary}$$

The boundary conditions are given in the equations (2)
 2.1 signifies that no normal component of the velocity appears at the coast. In 2.2 A denotes the amplitude, σ the frequency and α the phase of the incoming tidal wave. Geometry, A and α must be given

The initial conditions are

$$(3) \quad u = v = 0, \quad \xi = 0$$

The water level ξ is included in the total depth $H = h + \xi$ and the bottom friction is given by a quadratical law. Therefore, the system (1) becomes nonlinear

As shown by computation with and without horizontal turbulence term, this effect can be neglected for the model types A, C, D and F ($A_H = 0$). The Coriolis parameter has been taken as $f = 0$, because the hydraulic model installations did not allow to realize this effect. A numerical experiment has shown however the influence of the earth's rotation on the distribution of current velocities, while the water level nearly did not change

With these assumptions it is sufficient to use instead of (1) the one-dimensional equations for the types A, C, D, F

$$(4.1) \quad \frac{\partial u}{\partial t} + \frac{r}{h + \xi} u |u| + g \frac{\partial \xi}{\partial x} = 0$$

$$(4.2) \quad \frac{\partial \xi}{\partial t} + \frac{\partial}{\partial x} ((h + \xi)u) = 0$$

Because the used calculation method was utilized mainly for natural areas, the hydraulic model was fitted with a corresponding scale.

For the difference method the use of a horizontal grid system is indispensable. Fig 3 illustrates the two-dimensional grid system of a rectangular estuary.

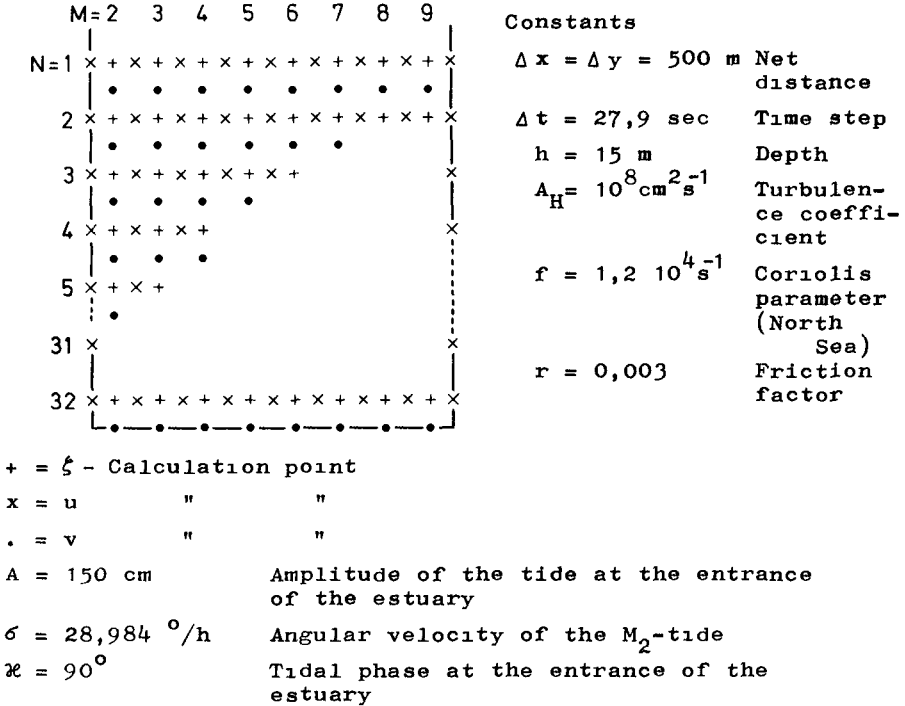
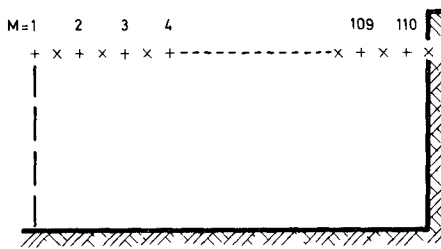


Fig 3 Grid System for 16 km Estuary (Type A)

Steady flow conditions occur in the two-dimensional consideration after about 12 periods

The one-dimensional treatment is based on a 55 km canal (Type A) The grid system and the constants are given in Fig 4



Constants

$\Delta x = 500$ m Net distance
 $\Delta t = 30$ sec Time step
 $h = 15$ m Depth
 $r = 0,003$ Friction factor

+ = ξ - Calculation point

x = u - " "

A = 162,5 resp 164 cm Amplitude of the tide at the entrance of the estuary

$\sigma = 28,984$ °/h Angular velocity of the M_2 -tide

$\alpha = 90^\circ$ Tidal phase at the entrance of the estuary

Fig 4 Grid System for 55 km Estuary (Type A)

In the HN-model, the amplitude of the incoming tidal wave was adapted to the value measured in the hydraulic model. The steady state was reached after about 5 periods.

All programs are written in FORTRAN IV.

As an example, in Fig. 5 the tidal and the velocity curves are given for 3 selected points. The tidal wave increases to the end of the estuary. The velocity curves show the typical steep gradient in the flood branch and the smoother distribution of the ebb.

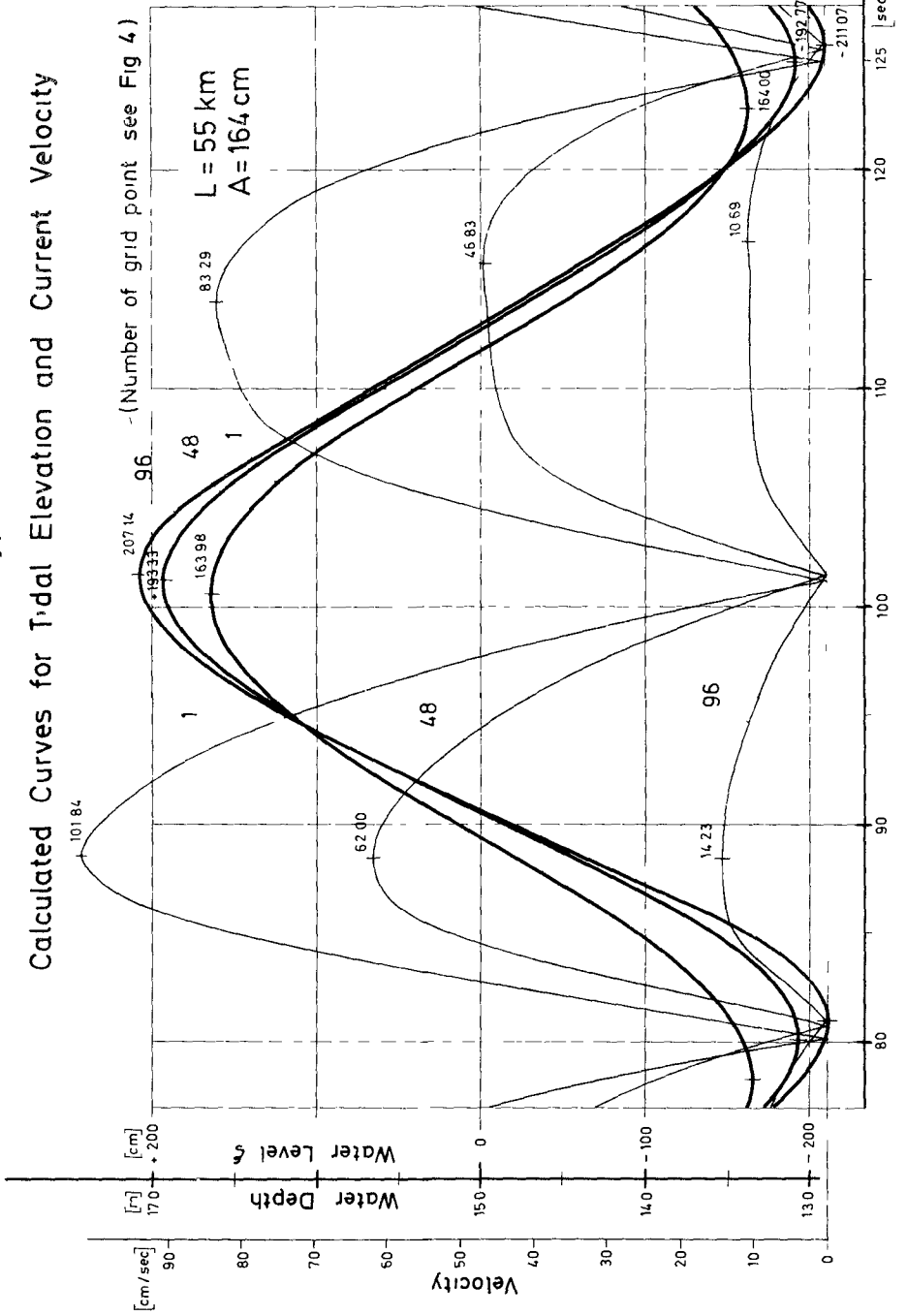
THE HYDRAULIC MODEL

The hydraulic model of type A is 55 m long, 4 m wide, the mean water depth amounts 0.15 m. Fig. 6 shows the model installation. The entrance of the model has a fixed bed with artificial roughness. The estuary itself was filled by sand which was not moved by the current. In this part of the model the roughness was simulated by artificial 1-cm-ripples. This kind of roughness corresponded with the assumed friction factor $r = 0.003$ in the HN-model.

According to natural conditions, the following scales were appointed: the extensions of length and width 1:1000, depths 1:100, e.g. the distortion is tenfold. The whole hydraulic data were reduced by Froude. The tidal period is 74.5 minutes in the model. The water levels were measured with mechanical and electrical water gages and the current velocities with micro-current meters (VOLLMERS [3]).

Meerwijk Estuary 55 km
(Type A)

Calculated Curves for Tidal Elevation and Current Velocity



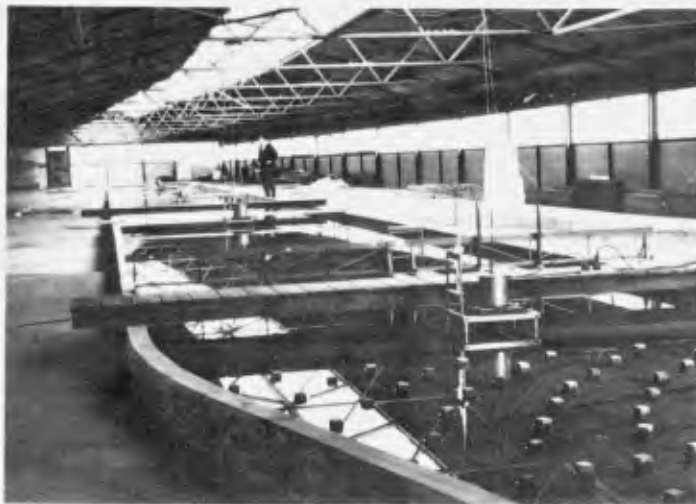


Fig. 6 Model Installation

The first tests were carried out in a 16 m long rectangular basin (e.g. 16 km in nature), but it was not possible to get clear results because the model was too short and therefore the differences for the speed are too small for measuring.

The measurement of the hydraulic data yields good results in the long canal (55 km in nature) of the Type A. Fig. 7 demonstrates side by side the measured and calculated water levels for different points during one tide. It was necessary to draw the curves side by side, because the good agreement shows nearly no differences between measurement and calculation. The tidal curve increases, as it is well-known, at the end of the canal and the time ratio between flood and ebb will be displaced. The tidal range increases from 3.28 to 4.18 m, the time ratio, tide low water to tide high water and tide high water to tide low water decreases from 1 at the entrance to about 0.80 at the end of the canal.

The current velocities were measured at different water depths.

Due to the restriction of the HN-model to vertically averaged velocities, the comparison between the two models was possible only for mean conditions. Fig. 8 shows this comparison for a mean calculated and measured curve. The agreement is good as well in shape as in order of magnitude.

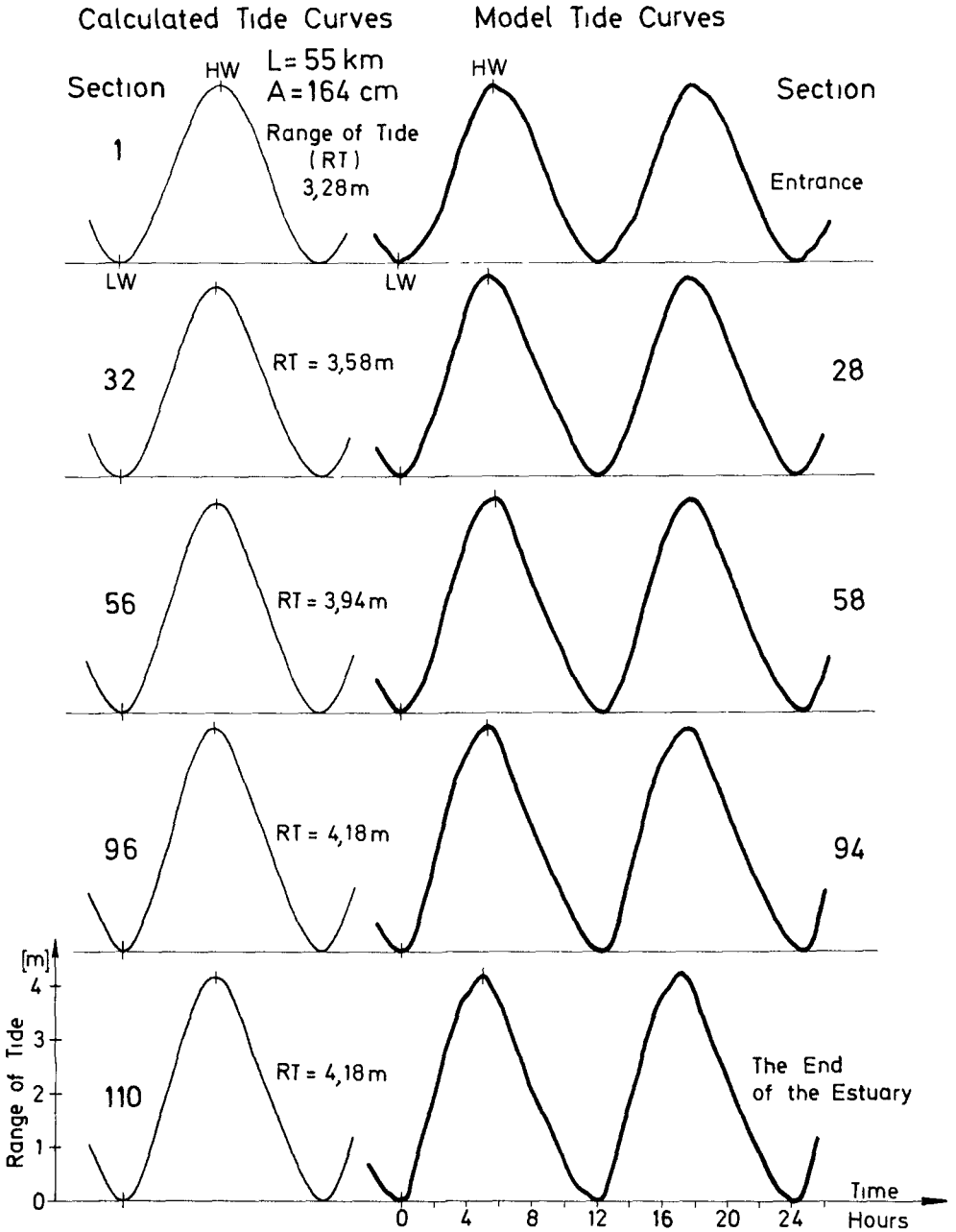


Fig 7 Rectangular Estuary 55 km (Type A)

The characteristic shows, that acceleration and deceleration are considerable and oscillations are small during the flood. The distribution curve is more filled and the oscillations are greater during ebb stream.

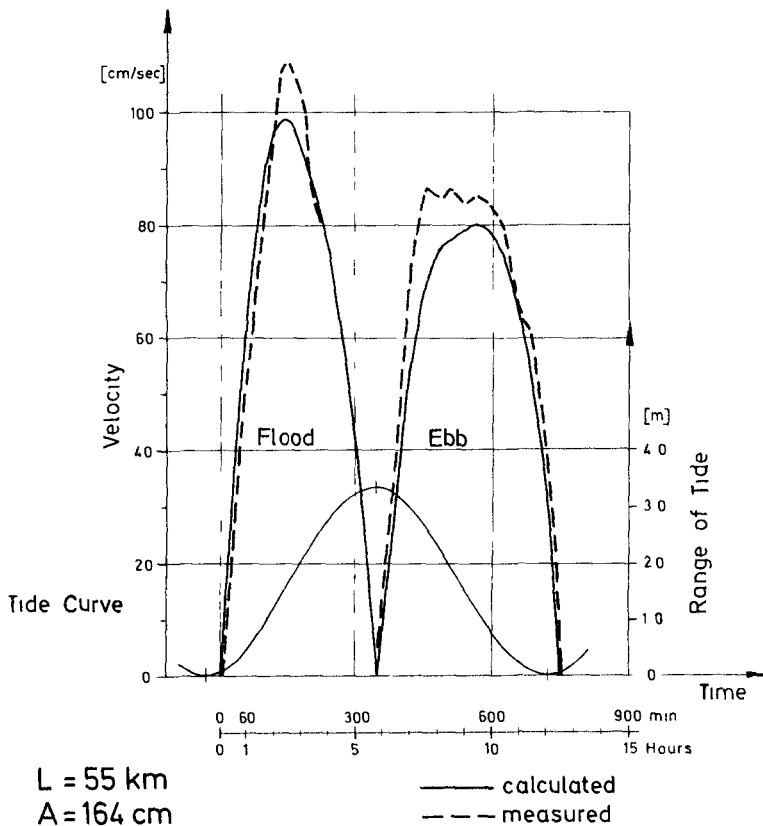


Fig 8 Typical velocity curve

The mean current velocities, averaged over cross section 5 (see Fig 4) for different water depths, are drawn in Fig. 9. The agreement with the corresponding calculated curve is satisfactory.

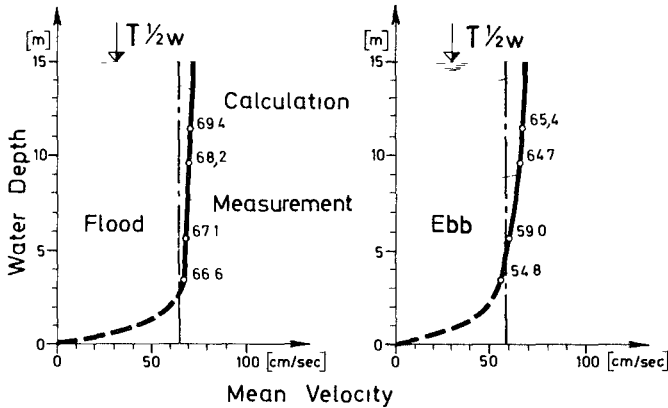


Fig. 9 Typical vertical distribution of velocity

Fig 10 shows the tidal ranges along the canal. In order to make also a comparison between other canal sizes (16 km and 50 kilometer), the calculated curves are listed with another amplitude. The differences between calculation and measurement for the 55-km canal are small. With regard to the model scale, only differences of 0.3 to 0.6 mm are present. 50 % of these data are already inside of the accuracy of measurement.

SUMMARY

It was shown by a systematic comparison between the hydraulic and the mathematical model, that the water levels and the mean current velocities for the investigated estuarine forms are in a fair agreement. In these cases the one-dimensional method was sufficient.

For the types B and E, however, the cross extension plays an important role. Therefore the corresponding HN-model must be considered two-dimensionally.

Finally, further investigations will include the vertical dimension, in order to study the shear stress distribution at the bottom.

REFERENCES

- [1] Hansen Hydrodynamical methods applied to oceanographic problems
Mitt. Inst. f. Meereskunde,
Universität Hamburg, Nr 1, 1962
- [2] Sundermann Ein Vergleich zwischen der analytischen und der numerischen Rechnung winderzeugter Stromungen und Wasserstände in einem Modellmeer mit Anwendungen auf die Nordsee
Mitt Inst. f Meereskunde,
Universität Hamburg, Nr 4, 1966
- [3] Vollmers Großflächige Tidemodelle
Das Gas-und Wasserfach,Heft 42, 1969
- [4] --- Die Reproduktion der Bewegungsvorgänge im Meer mit Hilfe hydrodynamisch-numerischer Methoden
Mitt. Inst f. Meereskunde,
Universität Hamburg, Nr. 5, 1966

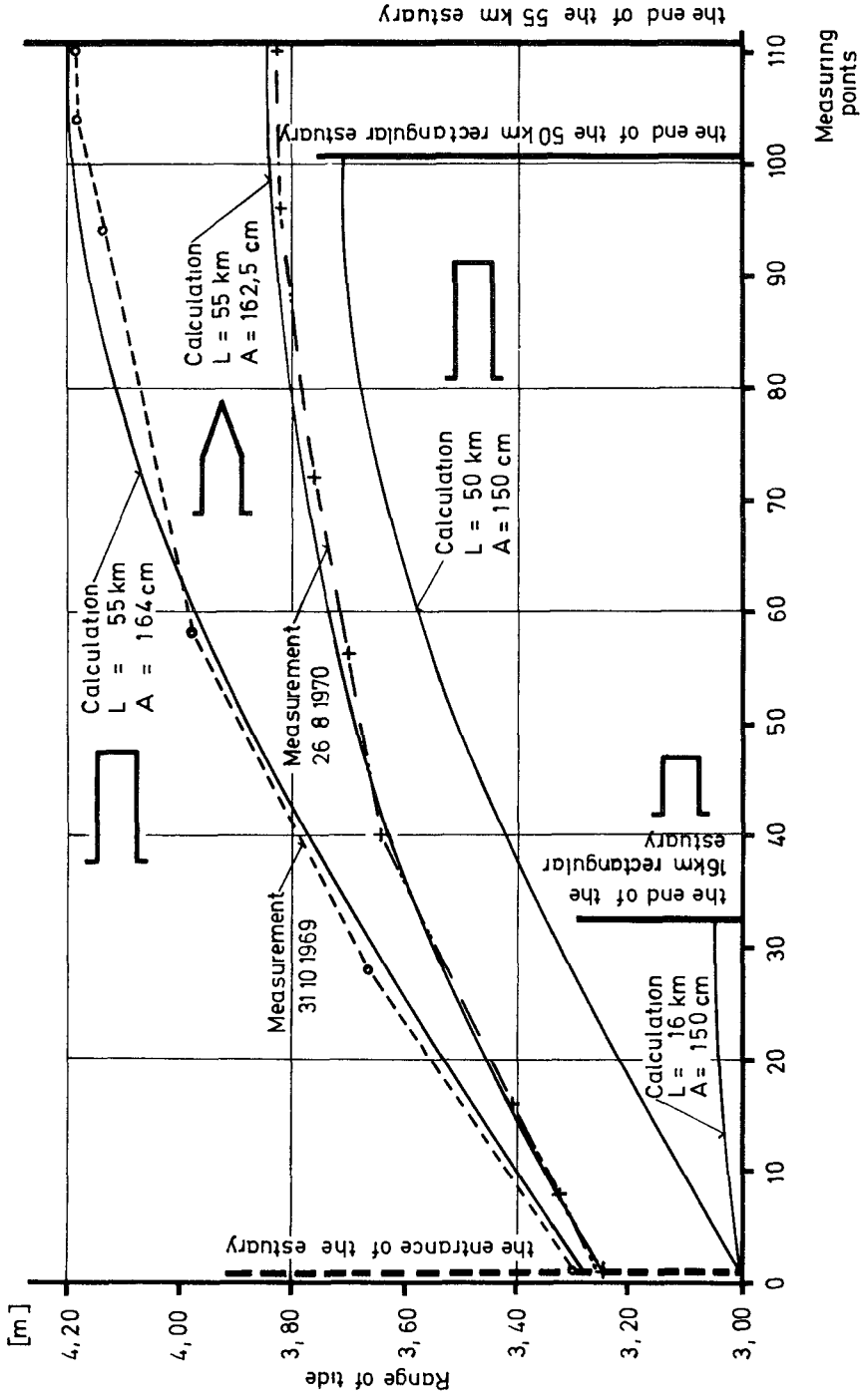


Fig 10 The Range of Tides in Relation to Different Types of Estuaries
 Model (Measurement) and Calculation

CHAPTER 130

DEFORMATION OF ROTATIONAL TIDAL CURRENTS IN SHALLOW COASTAL WATER

Dr -Ing Harald Gohren

Strom- und Hafenbau Hamburg
Forschungsgruppe Neuwerk

Abstract =====

Along gently sloping coasts of seas having rotary tidal currents, the symmetry of the rotary current is interrupted where the water is shallow. As a result, residual counter currents are formed. The dynamics of such a current system are described based on current measurements in the Elbe Estuary (southeastern North Sea). The residual currents of this area result in the movement of bottom sediment and are most likely responsible for a series of similar appearing morphologic features.

1 Rotary Tidal Waves

A typical effect of tidal motion in oceans as well as in bays is the formation of rotary tidal waves. They are characterized by cotidal lines radiating out from a nodal or amphidromic point, where the tide vanishes to zero. Amphidromic regions can be developed through the superposition of longitudinal and transverse oscillations. Normally, however, they form as a result of the Coriolis

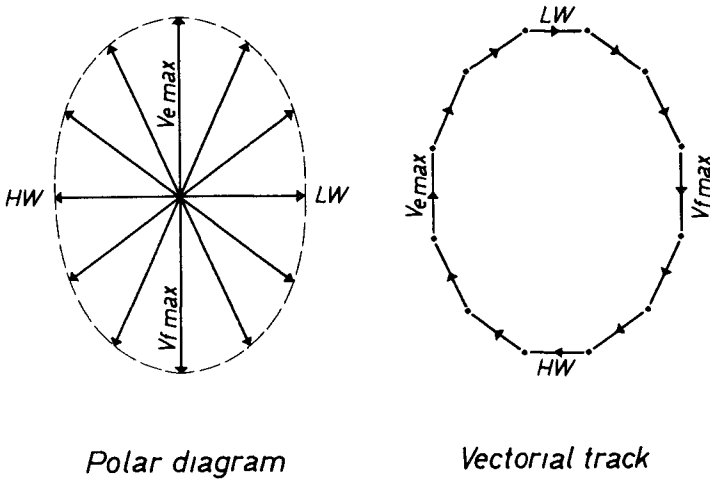


Fig 1
 Pattern of a rotational tidal current
 (schematic)

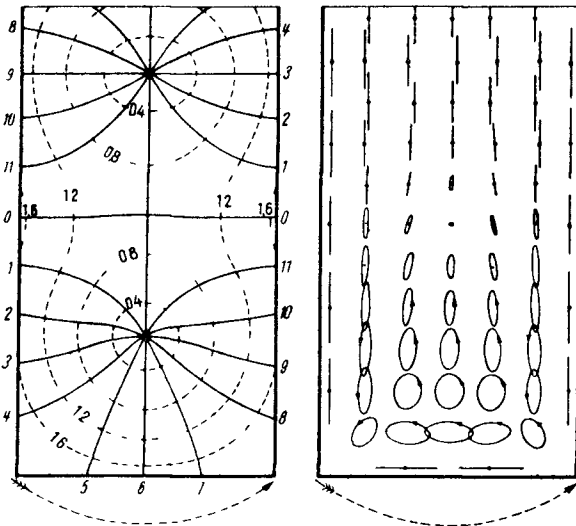


Fig 2
 Reflection of a Kelvin Wave in a basin
 open at one end (from Dietrich, 1957)
 Left cotidal lines and tide range
 Right currents

force acting on progressive or on standing long-period waves This effect was described by W Thomson (Lord Kelvin) in 1879 (Kelvin Waves)

Observations of tidal currents within an amphidromic system show characteristic circular or elliptical current patterns when the measurements from a complete tidal phase are plotted in vector form (Fig 1) Figure 2 shows Taylor's (1920) mathematical description of a Kelvin Wave in a basin open at one end The dimensions of his theoretical basin are comparable to the North Sea Two counterclockwise-rotating amphidromic systems are developed, the southernmost of which has rotating currents The general pattern of this example corresponds to the actual tidal motion found in the North Sea

2 Deformation of Rotational Current in Shallow Coastal Water

In the theoretical model of Fig 2, simplified marginal conditions result in the formation of reversing currents along the coastline On natural coasts the relationships are much more complex The deformation of the rotary current flow along the shallow coasts of the southern North Sea results in an interesting effect which can be of consequence for sand transport Large parts of this coast are composed of tidal flats ("Wattenmeere") (Fig 3), which are covered with water at high tide and fall dry at low tide Even further away from the coast the southern North Sea remains quite shallow, seldom reaching depths of over 30 or 40 m

If symmetrical rotary currents with elliptical current patterns exist in deep water off such a shallow coast, then this symmetry will be altered in the shallower water zones This is illustrated in schematic form in Figure 4 The left drawing shows the symmetrical rotary current in deep water. The pattern is based on a counterclockwise current flow whose maximum velocity (reached during flood and ebb) is

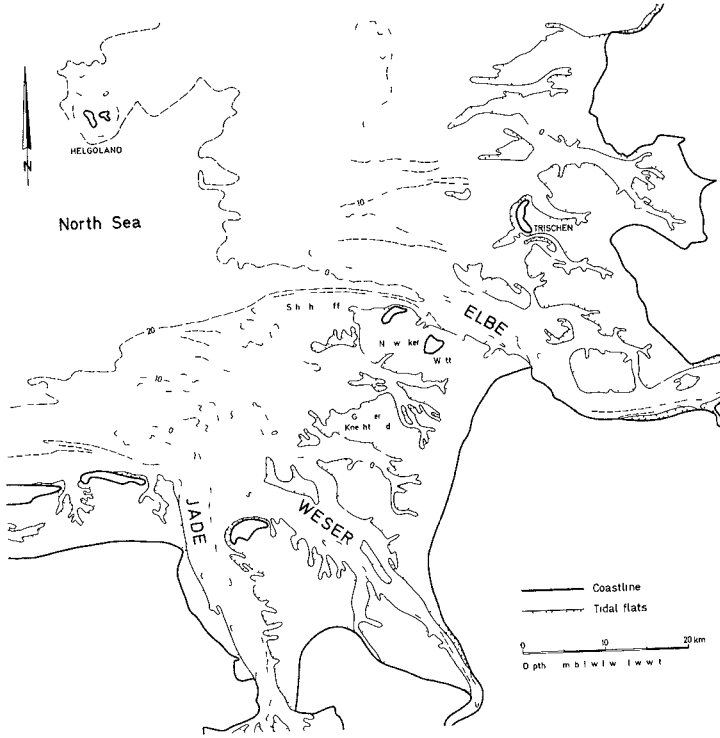


Fig 3
Map of the coastal area in the
southeastern North Sea

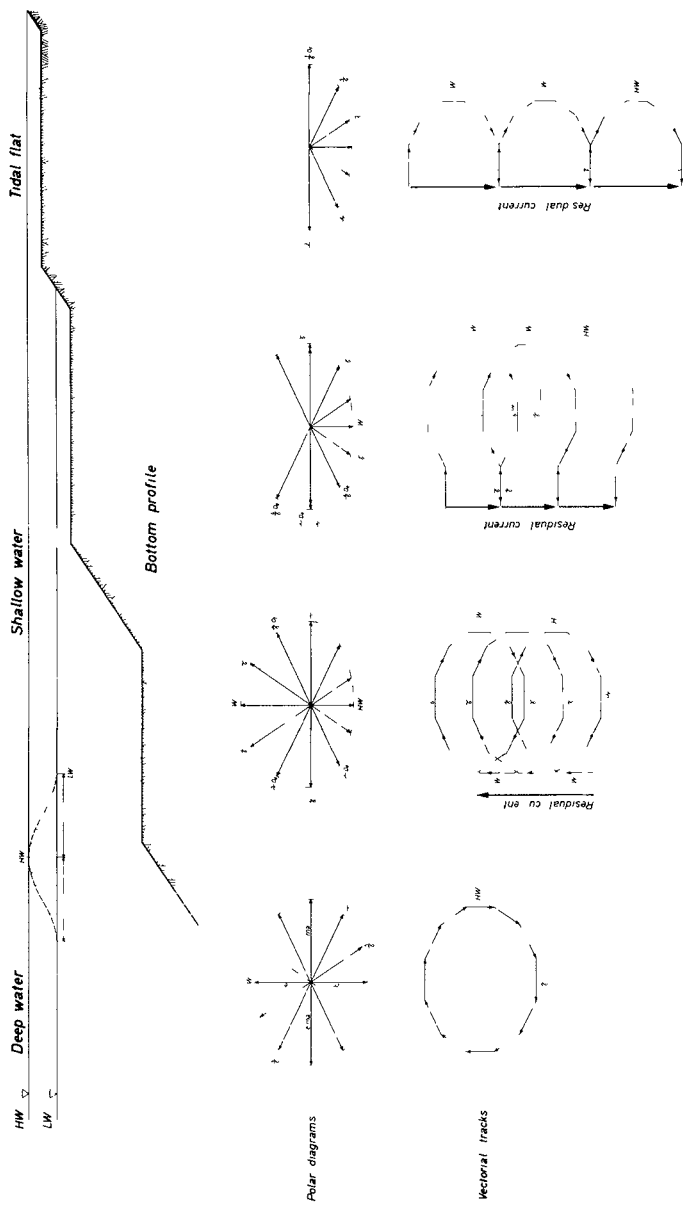


Fig 4
Deformation of rotational currents in shallow coastal water
(schematic)

developed normal to the coast, and whose minimum velocity (at high and low water) runs parallel to the coast. In general this compares to the relationships in the southern Elbe Estuary.

On the tidal flat (right in Fig. 4) only the high water phase of the tidal current ellipse can be effective. The current vectors yield a garland pattern with a strong residual current developed in the current direction which prevails at high tide.

Two factors lead to the conclusion that opposing residual currents, like those on the tidal flat, must also develop in the shallow water zone between tidal flat and deep water (middle, Fig. 4). Even without a net transport of water, the current velocities reached during low water are greater because of the decreased water depth in comparison to the tidal range. Consequently, the vectorial plot takes the form of a series of elongated loops showing a shift in the direction of flow at low water. This shift is intensified through an actual transport of water in the same direction; the total movement counterbalances the residual flow in the tidal flat.

The combination of these two factors changes the tidal ellipse into a spiraling current pattern which has a residual flow corresponding to the current direction found at low tide. In this way a system of opposing residual currents is developed which can influence both bottom morphology and sediment movement.

3. Data from the Elbe Estuary (southeastern North Sea)

The Elbe Estuary is presently the site of a wide-ranging scientific program concerned with harbor planning (Laucht, 1968). Figure 5 shows the "Scharhornriff" portion of the investigation area (cf. Fig. 3), a broad shallow-

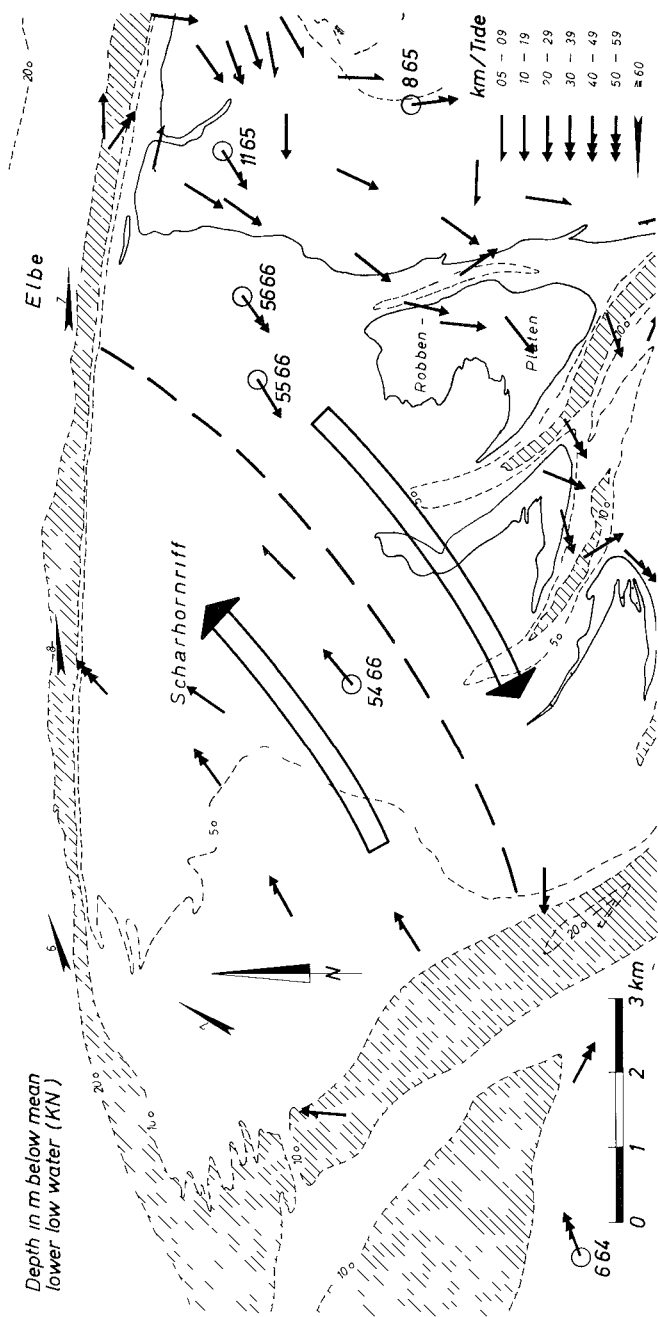


Fig 5
Residual counter currents on the "Scharhornriff"
(Elbe Estuary, southern North Sea, cf Fig 3)

water zone bordering the Neuwerk tidal flat. Using the continuous recording current meters pictured in Figs. 10 and 11, current measurements have been made at numerous points throughout the zone (Gohren, 1969). Each recording lasted approximately two weeks. Calculations based on these records show a uniform residual current toward the northeast in the outer portion of the zone and an opposing southwest residual current in the inner portion and on the tidal flat. A sharp boundary line can be drawn between these two residual current systems.

Plots of current velocity and direction for several stations are given in Fig. 6. The rotary nature of the current can be clearly seen, especially at the outermost stations (6.64 and 54.66).

At stations 55.66 and 56.66 the decreased water depth is reflected in a disturbance of the rotary current pattern. On the tidal flat itself (stations 11.65 and 8.65) the motion is interrupted during the low tide period, however, during the time when the flat is covered with water, the rotary nature of the current is clearly present, especially at station 11.65.

Figure 7 presents further substantiation that the residual counter currents illustrated in Fig. 5 are actually caused by the distortion of the rotary current in shallow water. Here, the measurements from several stations are presented as vector tracks. The closely spaced measurement intervals (5 min) result in nearly continuous curves. The loop-shaped current paths correspond exactly to the theoretical picture presented in Fig. 4. This seems to be confirmation that the residual current system in Fig. 5 is not an isolated occurrence but rather a hydrodynamic process, which may be expected on any shallow coast where rotary tidal waves are developed. Similar measurements are not yet available for other coastal sections in the

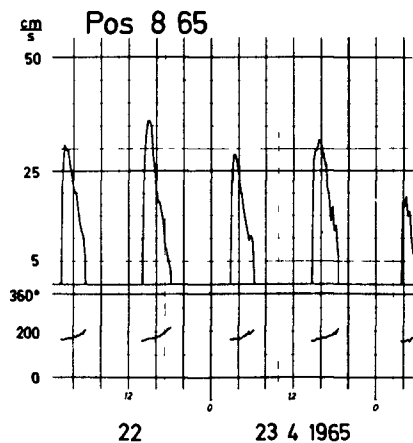
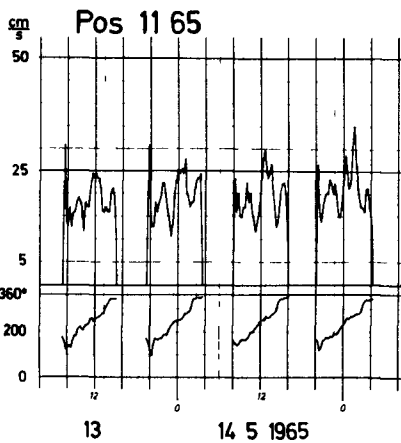
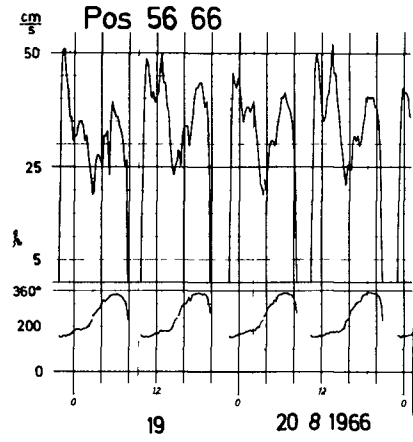
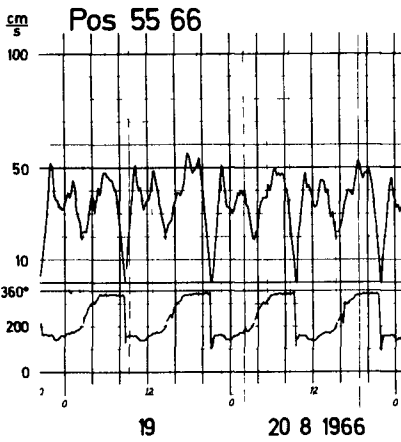
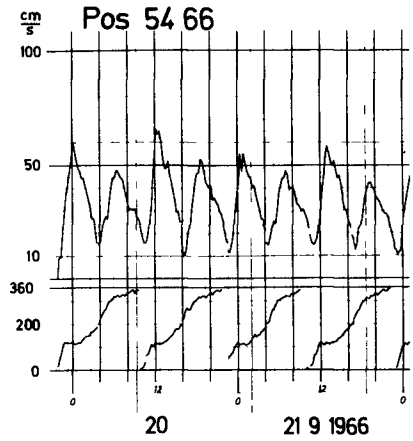
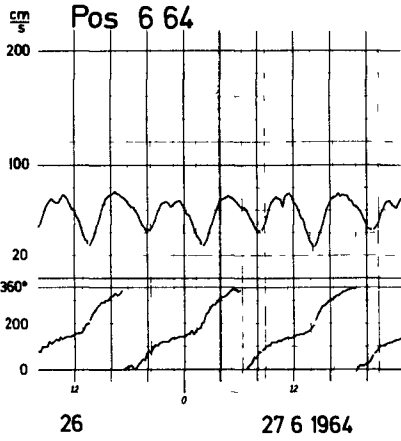


Fig 6

Results of current measurements from several stations on the "Scharhornriff" (cf Fig 5)

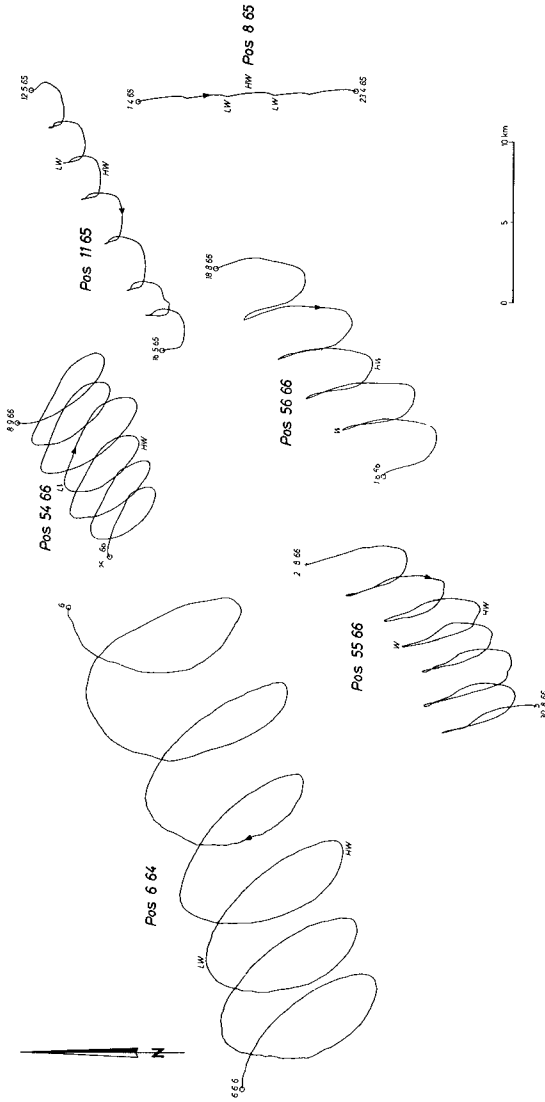


Fig 7
Results of current measurements from the "Scharhornriff",
plotted as vectorial tracks (cf Fig 5 and 6)

southeastern North Sea This is due to the fact that current measurements in exposed shallow water areas are extremely difficult to obtain and were possible in the Elbe Estuary only after the development of the equipment pictured in Figs 10 and 11

4 Influence of Residual Counter Currents on Sand Movement and Morphology

The direction of sand movement cannot be categorically equated with the residual current direction Figure 6 shows how difficult it is, when rotary tidal currents are present, to single out a dominant sand transport direction However, the maximum velocities developed in the "Scharhornriff" area are sufficient to move sand grains, particularly when one considers the added action of wind generated waves and surf

In order to establish the principal directions of sediment movement within this area of complex currents, a large number of tracer sand experiments were carried out (Gohren, 1969) Figure 8 shows the dispersion of the tracer grains at the conclusion of 5 of these experiments A comparison with Figure 5 shows good agreement between tracer movement and residual current direction The sediment movement on the outer portion of the "Scharhornriff" is toward the northeast or east, on the tidal flat near the island of Scharhorn it is clearly toward the south A circulation of bed material is present which almost certainly exerts an influence on the bottom morphology

Southwest of the "Scharhornriff", the V-form sand banks of the "Robbenplatten" form conspicuous morphologic features bordering the tidal flat Figure 9 shows this area together with the outlying parts of the Trischen and Knechtsand tidal flats, which lie north and south of the Elbe Estuary (cf Fig 3) Isolated measurements

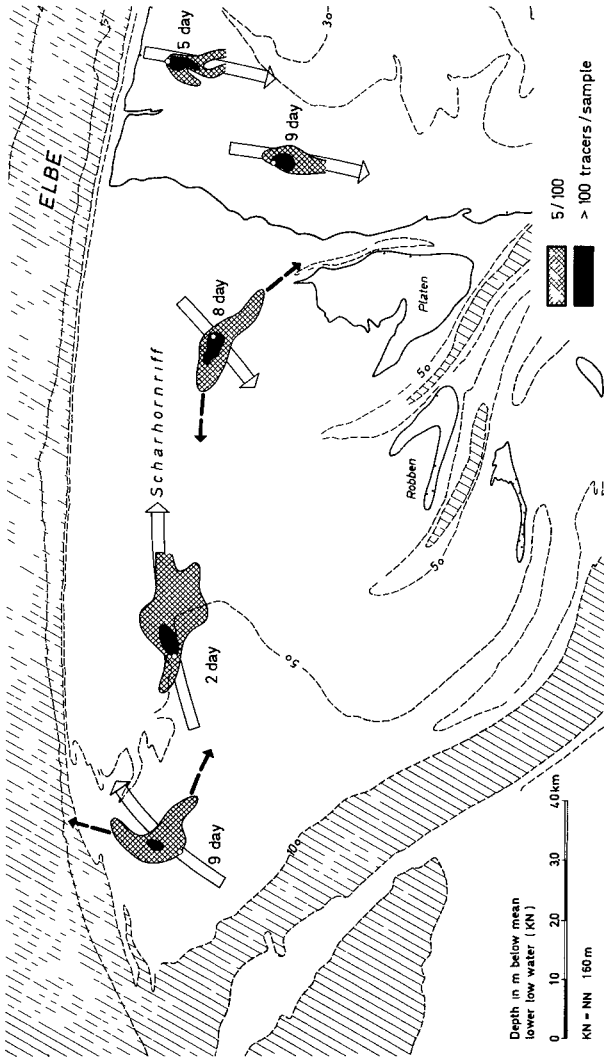


Fig 8

Direction of sand transport on the "Scharhornriff" found by tracer experiments (Scale of tracer countours = 2,5 x scale of the map)

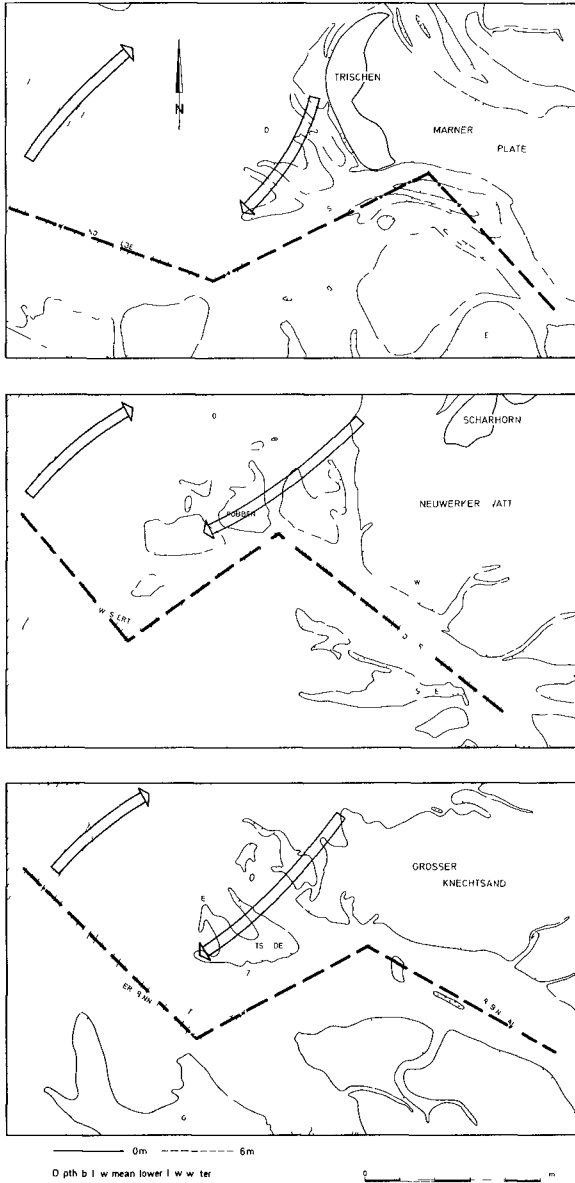


Fig 9

Influence of residual counter currents on the morphology of the outlying parts of the Trischen, Neuwerk and Knechtsand tidal flats (cf Fig 3)



Fig. 10
Recording current meter
for use in tidal flats



Fig. 11
Recording current meter for
use in shallow coastal water

have revealed opposing residual currents similar to those of the "Scharhornriff" in these areas, and it is apparent that the morphologic development in all three areas exhibits great similarity. The sand banks seem to be areas of accumulation for the south or south-westward moving sediment. This is also apparent from the configuration of the larger tidal channels south of the three flat areas (Neufahrwasser, Till and Robinsbalje). All three exhibit a decided S-form in their channels; the bends opposite the sandbanks reflect the southwestward directed forces. Further seaward the channels revert to a northwesterly course. Here, as previously indicated, the sediment transport is directed toward the northeast and most likely exerts a force against the channels in this direction.

The morphologic character and general similarity of the three areas mentioned above indicate an analogous mode of development which probably has its basis in comparable hydrodynamic conditions, i.e., the generation of residual counter currents caused by the interruption of the rotary tidal current in shallow water.

REFERENCES

- Dietrich, G. and Kalle, H. (1957) Allgemeine Meereskunde
- Gohren, H. (1969) Die Stromungsverhältnisse im Elbmündungsgebiet. Hamburger Küstenforschung, Heft 6
- Gohren, H. (1969) Untersuchungen mit fluoreszierenden Leitstoffen im südlichen Außenelbegebiet. Hamburger Küstenforschung, Heft 10
- Hansen, W. (1952) Gezeiten und Gezeitenströme der halbtägigen Hauptmondflut M_2 in der Nordsee. Deutsche Hydrographische Zeitschrift, Erg. Heft 1

Laucht, H. (1968). Ursachen und Ziele der Hamburger Küstenforschung. Hamburger Küstenforschung, Heft 1

Taylor, G.J (1920) Tidal oscillations in gulfs and rectangular basins. Proc. London Math. Soc., 70

Thomson, W. (1879). On gravitational oscillations of rotating Water. Proc. Roy Soc Edinburgh 10

CHAPTER 131

RESONANCE IN HARBORS OF ARBITRARY SHAPE

by Jun-Jen Lee,* Visiting Assistant Professor of Civil Engineering,
University of Southern California Los Angeles, California, U S A
and

Fredric Raichlen Associate Professor of Civil Engineering,
W M Keck Laboratory of Hydraulics & Water Resources
California Institute of Technology Pasadena California U S A

ABSTRACT

A theory is presented for analyzing the wave induced oscillations in an arbitrary shape harbor with constant depth which is connected to the open-sea. The solution is formulated as an integral equation which is then approximated by a matrix equation. The final solution is obtained by equating, at the harbor entrance, the wave amplitude and its normal derivative obtained from the solutions for the regions outside and inside the harbor.

The results of experiments conducted using a harbor model of the East and West Basins of Long Beach Harbor (Long Beach, California) are presented and compared to the theory. Good agreement has been found between the theory and experiments.

INTRODUCTION

Experience has shown that a natural or an artificial harbor can be excited by incident waves from the open-sea in such a way that large water surface oscillations can result for certain wave periods. This phenomena of resonance is similar to the dynamic response of mechanical or acoustical systems when exposed to time-varying forces, pressures, or displacements.

Resonant oscillations in harbors (also termed seiche and harbor surging) can cause significant damage to moored ships and marine structures especially if the resonant period is close to that of the ship-mooring system. In addition the currents induced by these oscillations can create navigation hazards. Such resonant oscillations have occurred at many locations around the world and have damaged moored ships and dockside facilities, e.g. Table Bay Harbor Cape Town, South Africa. In order to correct an existing resonance problem or design a harbor which is free of such problems one must be able to predict the resonant frequencies and the expected wave amplitude at various locations within the harbor as a function of the wave period.

Many previous investigators have studied various aspect of the harbor resonance problem. McNown (1952) studied seiches in circular harbors with small entrances by assuming an antinode occurred at the harbor entrance when the harbor was in resonance. A similar method was applied to rectangular harbors by Kravtchenko and McNown (1955). Thus, due to this assumption the resonant periods were identical to those of the eigenvalues for the free oscillations of a completely closed circular (or rectangular) basin. The problem of a rectangular harbor connected directly to the open-sea was investigated by Miles and Munk (1961). They included the effect of the wave radiation from the harbor.

* Formerly Research Fellow in Civil Engineering W M Keck Labr of Hydr & Water Res , California Institute of Technology, Pasadena, Calif , U S A

mouth to the open-sea thereby limiting the maximum wave amplitude within the harbor for the inviscid case to a finite value even at resonance. Ippen and Goda (1963) also studied the problem of a rectangular harbor connected to the open-sea by using the Fourier transformation method to evaluate the wave radiation from the entrance to the open-sea. Good agreement was found by them between the theory and experiments.

In recent years studies on more complicated harbor geometries have been conducted. Wilson, Hendrickson and Kilmer (1965) studied the oscillations induced by long waves in a basin with a complicated shape and variable depth incorporating an assumption of a nodal line (a line of zero amplitude) at the harbor entrance. Leendertse (1967) developed a finite-difference numerical scheme for the propagation of long-period waves in an arbitrary shape basin of variable depth given the water surface elevations at the open boundary. Recently, Hwang and Tuck (1970) in a study independent of the authors' study investigated the wave induced oscillations in an arbitrary shape basin with constant depth connected to the open-sea. Their approach was to superimpose scattered waves which were computed using a distribution of sources on the standing wave system. In their analysis the calculation of the source strengths along the entire reflecting boundary must be terminated at some distance from the entrance; the location of such a termination is not obvious unless trial solutions are made.

The present theoretical analysis is developed by applying Weber's solution of the Helmholtz equation in both the regions inside and outside the harbor with the final solution obtained by matching the wave amplitudes and their normal derivatives at the harbor entrance. In this way some of the problems of application which other investigators have experienced are eliminated since only the wave characteristics at infinity in the open-sea need be specified to obtain a complete solution. Experiments were performed in the laboratory to verify the theoretical solutions.

THEORETICAL ANALYSIS

For the theoretical analysis the flow is assumed irrotational and the fluid incompressible; thus one can define a velocity potential ϕ such that the fluid particle velocity can be expressed as a vector as $\vec{u} = \nabla\phi$, where ∇ is the gradient

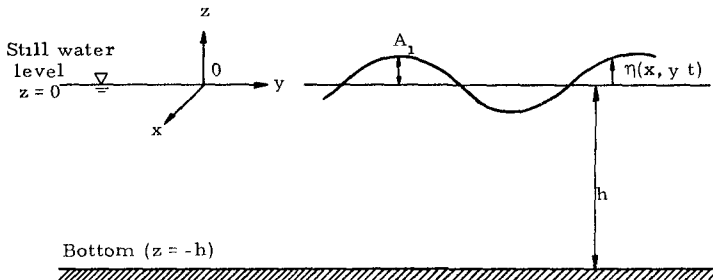


Fig. 1 Definition sketch of the coordinate system

operator (The coordinate system is defined in Fig 1) The velocity potential ϕ must satisfy Laplace's equation

$$\frac{\partial^2 \phi}{\partial x^2} + \frac{\partial^2 \phi}{\partial y^2} + \frac{\partial^2 \phi}{\partial z^2} = 0 \tag{1}$$

and a number of prescribed boundary conditions one of these is that the fluid does not penetrate the solid boundaries which define the limits of the domain of interest i.e. $\partial\phi/\partial n = 0$ on solid boundaries (where n is normal to the boundary and directed outward)

If the water depth is considered constant the method of separation of variables can be used to obtain the function which represents the depthwise variation of the velocity potential ϕ Thus, within the limitation of small amplitude water wave theory the following form of the velocity potential ϕ is found

$$\phi(x, y, z, t) = \frac{1}{i\sigma} \frac{A_1 g \cosh k(h+z)}{\cosh kh} f(x, y) e^{-\lambda\sigma t} \tag{2}$$

where σ is the angular frequency defined as $2\pi/T$ (T is the wave period) $\lambda = \sqrt{-1}$, A_1 is the wave amplitude at the crest of the incident wave h is the water depth (assumed constant), g is the acceleration of gravity k is the wave number defined as $2\pi/L$ (L is the wave length), and the function $f(x, y)$ termed the wave function describes the variation of ϕ in the x-y directions The function $f(x, y)$ must satisfy the Helmholtz equation

$$\frac{\partial^2 f}{\partial x^2} + \frac{\partial^2 f}{\partial y^2} + k^2 f = 0 \tag{3}$$

To complete the expression for the velocity potential ϕ the remaining problem is to determine the function $f(x, y)$ which satisfies Eq 3 (known as the Helmholtz equation) and the following boundary conditions

- (i) $\partial f/\partial n = 0$ along all fixed boundaries such as the coastline and the boundary of the harbor
- (ii) as $\sqrt{x^2 + y^2} \rightarrow \infty$ there is no effect of the harbor on the wave system this is termed the radiation condition Mathematically the radiation condition is necessary to ensure a unique solution of the function $f(x, y)$ in the unbounded domain

A method for solving the Helmholtz equation Eq 3 for an arbitrary shape harbor is presented in the following The domain of interest is divided at the harbor entrance into two regions as shown in Fig 2 the infinite ocean (Region I) and the region bounded by the limits of the harbor (Region II) For convenience the function f of Eq 3 in Region II is denoted as f_2 and in Region I it is denoted as f_1

In Region II the function f_2 that satisfies the Helmholtz equation at any position \vec{x} inside the harbor can be expressed as the following line integral

$$f_2(\vec{x}) = -\frac{\lambda}{4} \int_s \left\{ f_2(\vec{x}_0) \frac{\partial}{\partial n} [H_0^{(1)}(kr)] - H_0^{(1)}(kr) \frac{\partial}{\partial n} f_2(\vec{x}_0) \right\} ds(\vec{x}_0) \tag{4}$$

where \vec{x}_0 is the position vector of the boundary point r is the distance $|\vec{x} - \vec{x}_0|$ and n is normal to the boundary and is directed outward The function

$H_0^{(1)}(kr) = J_0(kr) + iY_0(kr)$ and is termed the Hankel function of the first kind and zeroth order. The integration in Eq. 4 is to be performed along the boundary of the harbor traveling in a counter-clockwise direction.

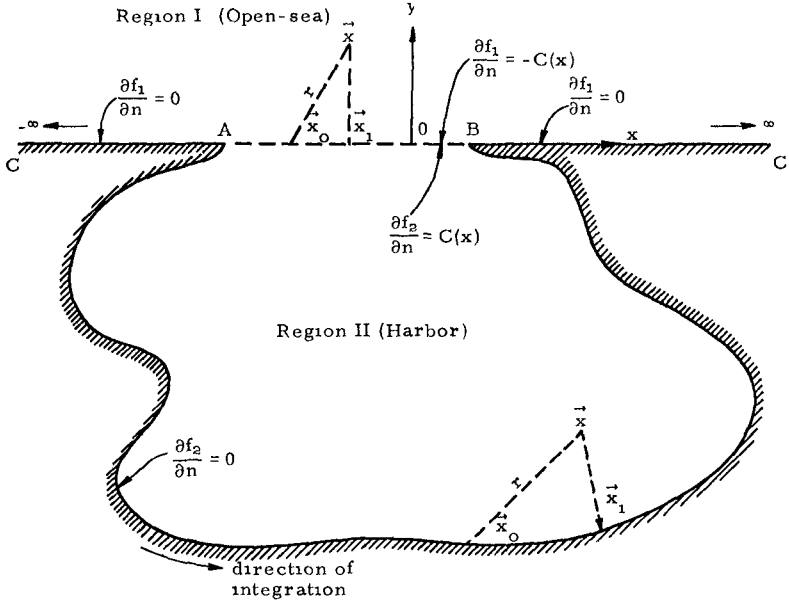


Fig. 2 Definition sketch of an arbitrary shape harbor

Eq. 4 indicates that if one knows the value of f_2 and $\partial f_2 / \partial n$ at the harbor boundary the function f_2 at any position \vec{x} inside the harbor can be obtained readily. However, the value of f_2 at the boundary (including the harbor entrance) is not known at this stage of the development; the value of $\partial f_2 / \partial n$ at the harbor entrance is also not known although it is known that $\partial f_2 / \partial n$ is zero on all solid boundaries within the harbor. In order to evaluate $f_2(\vec{x}_0)$ at the boundary as a function of the value of $\partial f_2 / \partial n$ at the harbor entrance, the field point \vec{x} is allowed to approach a boundary point \vec{x}_1 . If the boundary is sectionally smooth an integral equation is obtained as follows:

$$f_2(\vec{x}_1) = -\frac{i}{2} \int_{\Gamma} [f_2(\vec{x}_0) \frac{\partial}{\partial n} H_0^{(1)}(kr) - H_0^{(1)}(kr) \frac{\partial f_2}{\partial n}(\vec{x}_0)] ds(\vec{x}_0) \quad (5)$$

where $r = |\vec{x}_0 - \vec{x}_1|$. Although the exact solution of the integral equation (Eq. 5)

is difficult to obtain it is possible to obtain an approximate solution of Eq 5 by converting this integral equation into a matrix equation This is accomplished by dividing the boundary into a sufficiently large number of segments (N) and the value of f_2 (or $\partial f_2 / \partial n$) at each boundary segment is considered constant and equal to the value at the mid-point of each segment Thus Eq 5 can be approximated by the following matrix equation

$$(F)_i = -\frac{\lambda}{2} \left[\sum_{j=1}^N (G_n)_{ij} (F)_j - \sum_{j=1}^N (G)_{ij} (F_n)_j \right], \tag{6}$$

for $i = 1, 2, \dots, N$

using the notation

$$(F)_i = f_2(\vec{x}_i), \quad i = 1, 2, \dots, N \tag{7a}$$

$$(G_n)_{ij} = -kH_1^{(1)}(kr_{ij}) \frac{\partial r_{ij}}{\partial n} \Delta s_j$$

$$= -k [J_1(kr_{ij}) + \lambda Y_1(kr_{ij})] \left[-\frac{x_i - x_j}{r_{ij}} \left(\frac{\partial y}{\partial s} \right)_j + \frac{y_i - y_j}{r_{ij}} \left(\frac{\partial x}{\partial s} \right)_j \right] \Delta s_j, \quad i, j = 1, 2, \dots, N \quad i \neq j \tag{7b}$$

$$(G_n)_{i1} = 2 \int_0^{\frac{1}{2} \Delta s_1} (-kH_1^{(1)}(kr) \frac{\partial r}{\partial n}) dr$$

$$\approx \frac{\lambda}{\pi} \left(\frac{\partial x}{\partial s} \frac{\partial^2 y}{\partial s^2} - \frac{\partial^2 x}{\partial s^2} \frac{\partial y}{\partial s} \right) \Delta s_1, \quad i = 1, 2, \dots, N \tag{7c}$$

$$(G)_{ij} = H_0^{(1)}(kr_{ij}) \Delta s_j, \quad i, j = 1, 2, \dots, N \quad i \neq j \tag{7d}$$

$$(F_n)_i = \partial f_2 / \partial n(\vec{x}_i), \quad i = 1, 2, \dots, N \tag{7e}$$

$$(G)_{i1} = 2 \int_0^{\frac{1}{2} \Delta s_1} H_0^{(1)}(kr) dr$$

$$\approx \left[1 + \lambda \frac{2}{\pi} \left[\log \frac{k \Delta s_1}{4} - 0.42278 \right] \right] \Delta s_1, \quad i = 1, 2, \dots, N \tag{7f}$$

The vector F_n in Eq 6 involves the unknown value of $\partial f_2 / \partial n$ at the harbor entrance as well as the value of $\partial f_2 / \partial n$ at the solid boundaries (these latter values are zero) Thus the vector F_n can be represented as

$$F_n = \sum_{j=1}^p \delta_{ij} C_j = UC \tag{8}$$

where p is the total number of segments into which the harbor entrance is divided the vector C represents the p unknown values of $\partial f_2 / \partial n$ at the mid-point of each entrance segment, and the matrix

$$U = \delta_{ij} = \begin{cases} 0 & \text{for } i \neq j \\ 1 & \text{for } i = j \end{cases} \text{ (with the index } i=1, 2, \dots, N \text{ and the index } j=1, 2, \dots, p)$$

Substituting Eq 8 into Eq 6 and rearranging one obtains

$$f_2(\vec{x}_1) - \sum_{j=1}^p M_{1j} C_j = M \underline{C} \quad (\text{for } i=1, 2, \dots, N), \tag{9}$$

in which the matrix $M = (\lambda/2G_n + I)^{-1} (\lambda/2GU)$ is a $N \times p$ matrix and can be computed directly (I is an identity matrix). Eq 9 shows that the function $f_2(\vec{x}_1)$ on the harbor boundary can be expressed as a function of the unknown value of $\partial f_2 / \partial n$ at the entrance. Eq 19 can also be interpreted as the contribution to the value of f_2 on the harbor boundary from the superposition of the effect of p small harbor openings.

In order to evaluate the unknown vector \underline{C} defined in Eq 9, i.e. the value of $\partial f_2 / \partial n$ at the entrance, the function f_1 in Region I at the harbor entrance must be expressed as a function of $\partial f_1 / \partial n$. Thus using the "matching condition" at the entrance $f_1 = f_2$, $\partial f_1 / \partial n = -\partial f_2 / \partial n$, one is able to solve for the vector \underline{C} and the complete solution to the response problem can be obtained.

For the region outside the harbor (Region I) the function f_1 may be expressed as follows

$$f_1(x, y) = f_i(x, y) + f_r(x, y) + f_3(x, y) \tag{10}$$

where f_i represents an incident wave function, f_r represents a reflected wave function considered to occur as if the harbor entrance were closed, and f_3 (termed the radiated wave function) represents a correction to f_r due to the presence of the harbor. For the case of a periodic incident wave with the wave ray perpendicular to the coastline, the function $f_1(x, y)$ can be represented by $\frac{1}{2} e^{-\lambda ky}$ (the factor $\frac{1}{2}$ is taken for convenience). Thus the reflected wave function f_r can be represented by $f_r(x, y) = f_1(x, y) = \frac{1}{2} e^{-\lambda ky}$.

The function $f_3(x, y)$ can be obtained by the same procedure as used in Eq 4 for determining the function f_2 ; the reader is referred to Lee (1969) for its development as well as other details of the analysis.

For the condition of a periodic incident wave propagating in a direction perpendicular to the coastline (x -axis) the function f_1 at the harbor entrance can be expressed as

$$f_1(x, 0) = 1 + \left(-\frac{\lambda}{2}\right) \int_{\overline{AB}} H_0^{(1)}(k|x-x_0|) \left[\frac{\partial}{\partial n} f_2(x_0, 0) \right] dx_0 \tag{11}$$

The first term on the right-hand side of Eq 11 represents the incident wave plus the reflected wave; if the harbor entrance is closed, the second term represents the contribution from the radiated wave function f_3 . It is noted that in deriving Eq 11 the relation $\partial f_1 / \partial n = \partial f_3 / \partial n = -\partial f_2 / \partial n$ has been used at the harbor entrance.

Eq 11 can be approximated by a matrix equation as

$$f_1(\vec{x}_1) = 1 + \left(-\frac{\lambda}{2}\right) \sum_{j=1}^p H_{1j} C_j, \quad (\text{for } i=1 \ 2 \ \dots \ p) \quad (12)$$

where

$$H_{ij} = H_0^{(1)}(kr_{ij}) \Delta s_j \quad \text{for } i, j=1 \ 2 \ \dots \ p \ i \neq j$$

$$H_{11} = \left[1 + \lambda \frac{2}{\pi} \left(\log \left(\frac{k \Delta s_1}{4} \right) - 0.42278 \right) \right] \Delta s_1 \quad \text{for } i=1 \ 2 \ \dots \ p,$$

and the vector \underline{C} is the derivative $\partial f_2 / \partial n$ at the harbor entrance as defined in Eq 8

Eqs 9 and 12 can now be equated to solve for the unknown value of $\partial f_2 / \partial n$ at the harbor entrance i.e. the vector \underline{C} . This is done by first taking the first p equations from Eq 9

$$f_2(x_i) = \sum_{j=1}^p M_{ij} C_j = M_p \cdot \underline{C} \quad (13)$$

in which the index $i=1 \ 2, \dots \ p$ and the matrix M_p is a $p \times p$ matrix obtained from the first p rows of the matrix M. Then by equating Eq 13 to Eq 12 and solving for the unknown vector \underline{C} one obtains

$$\underline{C} = \left(M_p + \frac{\lambda}{2} H \right)^{-1} \underline{1} \quad (14)$$

where $\left(M_p + \frac{\lambda}{2} H \right)^{-1}$ is the inverse of the matrix $\left(M_p + \frac{\lambda}{2} H \right)$, and $\underline{1}$ is the vector with each p element equal to unity

With the value of $\partial f_2 / \partial n$ at the entrance i.e. the vector \underline{C} determined from Eq 14 the value of $f_2(\vec{x}_1)$ at the harbor boundary can be evaluated from Eq 9 and the value of $f_2(\vec{x})$ at any position inside the harbor can be obtained from the following discrete form of Eq 4

$$f_2(\vec{x}) = -\frac{\lambda}{4} \left\{ \sum_{j=1}^N f_2(\vec{x}_j) \left[-k H_1^{(1)}(kr) \frac{\partial r}{\partial n} \right] \Delta s_j - \sum_{j=1}^p H_0^{(1)}(kr) C_j \Delta s_j \right\} \quad (15)$$

where \vec{x}_j is at the midpoint of the j^{th} boundary segment and $r = |\vec{x} - \vec{x}_j|$

The response of a harbor to incident waves is described by a parameter called the "amplification factor" which is defined as the ratio of the wave amplitude at any position (x, y) inside the harbor to the sum of the incident and the reflected wave amplitude at the coastline (with the harbor entrance closed)

$$R = \frac{|\eta_B(x, y, t)|}{|A_1(f_I + f_R) e^{-\lambda \sigma t}|} = \frac{|A_1 f_2(x, y) e^{-\lambda \sigma t}|}{|A_1 \cdot 1 \cdot e^{-\lambda \sigma t}|} = |f_2(x, y)| \quad (16)$$

EXPERIMENTAL EQUIPMENT

Experiments were conducted in the laboratory in a wave basin 11 ft 9 in deep, 15 ft 5 in wide, and 31 ft 5 in long. An overall view of the wave basin is presented in Fig. 3. The wave generator was a pendulum type 11 ft 8 in long, 2 ft high located at one end of the basin and it was designed to operate either as a paddle- or piston-type wave generator with a maximum stroke of ± 6 in. (For detailed description and design considerations the reader is referred to Raichlen (1965).) Wave periods ranging from 0.34 sec to 3.8 sec can be obtained.

The wave period was determined by a pulse counting technique. The pulses are generated by interrupting a light beam which was directed at a photo cell by a disc with 360 evenly spaced holes arranged in a circle around its outer edge. The voltage pulses which are produced in this manner are counted by an industrial counter over an interval of 10 sec. Thus the wave period measured was an average over 10 sec and throughout an experiment this period varied at most by $\pm 0.05\%$.

Wave amplitudes were measured electronically using resistance wave gages and an oscillograph recorder. The wave gage was calibrated before and after an experiment (approximately one hour apart). Even though these calibrations showed very little difference, a calibration curve representing an average over the duration of an experiment was used in reducing the experimental data (see Lee (1969)).

In order to simulate the open-sea in the laboratory wave basin, two types of wave energy dissipators were employed: a wave filter placed in front of the wave generator and wave absorbers located along the side-walls of the wave basin. These can be seen in Fig. 3. The wave filter was 11 ft 9 in long, 1 ft 4 in high and 5 ft thick in the direction of wave propagation and was constructed of 70 sheets of galvanized iron wire screen with each sheet spaced 0.8 in apart. The wire diameter of the screens was 0.011 in with 18 wires per inch in one direction and 14 wires per inch in the other. The wave absorbers placed along the sidewalls of the basin were each 1 ft 6 in high, 1 ft 10 in thick normal to the sidewall, and 30 ft long and consisted of 50 equally spaced layers of the same galvanized iron screen as used in the wave filter. The majority of waves used in the experiments were reduced in amplitude by at least 80% as the result of passing through the wave filter (or absorber) reflecting from the wave machine (or wall) and passing through the wave filter (or absorber) again. Such wave energy dissipating materials were necessary in order to simulate the open-sea condition satisfactorily. Without this wave filter and these absorbers, waves radiated from the harbor entrance would be reflected from the wave paddle and the sidewalls of the basin creating a wave system which is quite different from the open-sea. This problem was described by Raichlen and Ippen (1965) in which it was shown that, due to coupling between the harbor and the wave basin, the response of a rectangular harbor in a highly reflective basin was radically different from that of a similar harbor connected to the open sea.

In order to fully test the theory developed, it was decided to use a model of Long Beach Harbor which in the past experienced problems from long period waves. This model shown in Fig. 4 was constructed from $\frac{1}{4}$ in thick lucite



Fig. 3 Over-all view of the wave basin and wave generator with wave filter and absorbers in place



Fig. 4 Model of the East and West Basins of Long Beach Harbor (Long Beach, California, U. S. A.)

plate with a plattform which was simplified from the prototype East and West Basins of Long Beach Harbor. The harbor model built to a horizontal scale equal to 1/4700 was designed so that it would fit into an opening at the center of a false wall simulating a perfectly reflecting coastline which was installed 27 ft 6 in from and parallel to the wave paddle.

PRESENTATION AND DISCUSSION OF RESULTS

Prior to applying this theory to a complicated harbor the theory was applied to harbors of simpler shapes—circular and rectangular. The circular harbor represents an extreme where the harbor boundary is curved and the tangent to the boundary is continuously changing direction. The rectangular shape harbor represents the other extreme since the harbor boundary is composed of straight lines, along each line the direction of the tangent to the boundary remains the same. It has been found (see Lee 1969, 1970) that the results of this theory applied to circular and rectangular harbors agree well with corresponding experiments.

As mentioned previously in order to verify the theory for a harbor of complicated shape Long Beach Harbor was studied theoretically and experimentally in the laboratory. A sketch of the harbor model which was used is presented in Fig. 5 which shows the width of the entrance as 0.2 ft and the characteristic dimension of the harbor a equal to 1.44 ft. The water depth was constant in both the harbor and the "open-sea" and equal to 1 ft.

Response curves at four different locations inside the harbor are presented in Figs. 6 to 9. The four points are designated as A, B, C, D and their relative positions in the model are shown in Fig. 5 as A (0.30 ft, -0.525 ft), B (0.30 ft, -0.96 ft), C (1.32 ft, -0.96 ft), and D (-0.45 ft, -1.245 ft), where the first number inside the parenthesis is the x-coordinate and the second number is the y-coordinate. For all the response curves the abscissa is the wave number parameter ka (where k is the wave number, and "a" is shown in Fig. 5) the ordinate is the amplification factor R , defined as the wave amplitude at point A (or B, C, D) divided by the average standing wave amplitude at the harbor entrance when the entrance is closed (see Eq. 16).

The theoretical results obtained are shown as solid lines in the response curves while the experimental results are shown as circles. In applying the theory the boundary of the harbor is divided into 75 unequal straight-line segments including two segments for the harbor entrance. The segments are numbered counter-clockwise starting from the right-hand limit of the harbor entrance and this numbering system is also shown in Fig. 5. For accurate results the length of these boundary segments should be less than approximately one-tenth of the smallest wave length investigated (see Lee 1969).

From Figs. 6, 7, 8, and 9 it is seen that the theoretical results agree well with the experimental data at all four locations which were investigated. The complicated shape of the response curves are due to the irregular shape of the harbor and the fact that this harbor really consists of two coupled basins. One common feature of the four response curves is that while the theory has predicted the frequency of every resonant mode of oscillation correctly the theoretical amplification factor at resonance is slightly larger than the experimental data especially for the resonant modes at larger values of ka . There are two possible reasons for this. First in applying

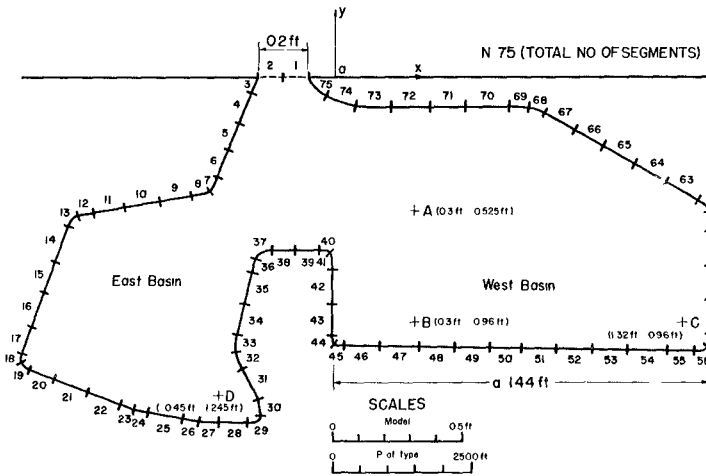


Fig 5 Dimensions sketch of the Long Beach Harbor model

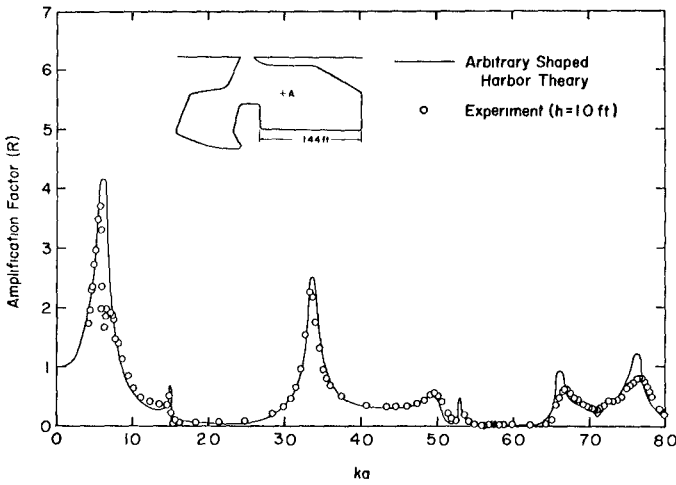


Fig 6 Response curve at point A of the Long Beach Harbor model

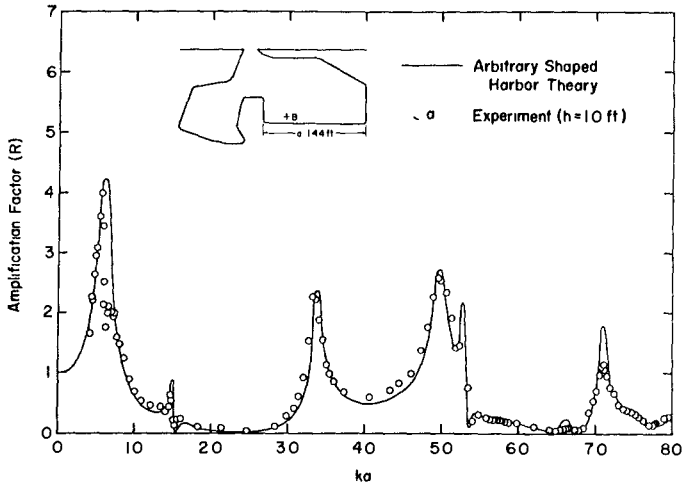


Fig 7 Response curve at point B of the Long Beach Harbor model

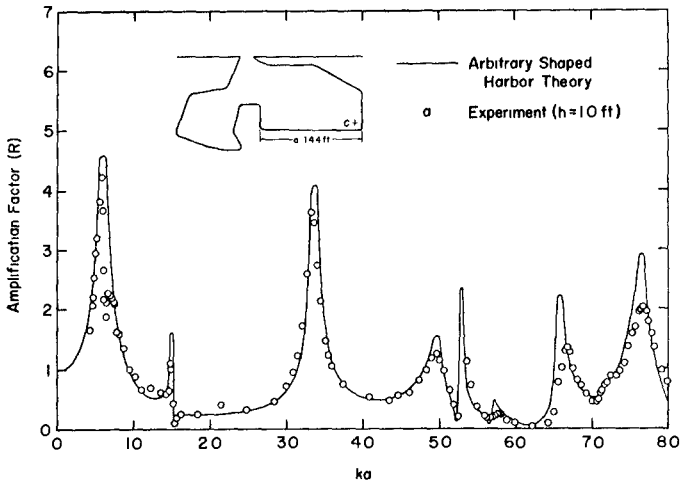


Fig 8 Response curve at point C of the Long Beach Harbor model

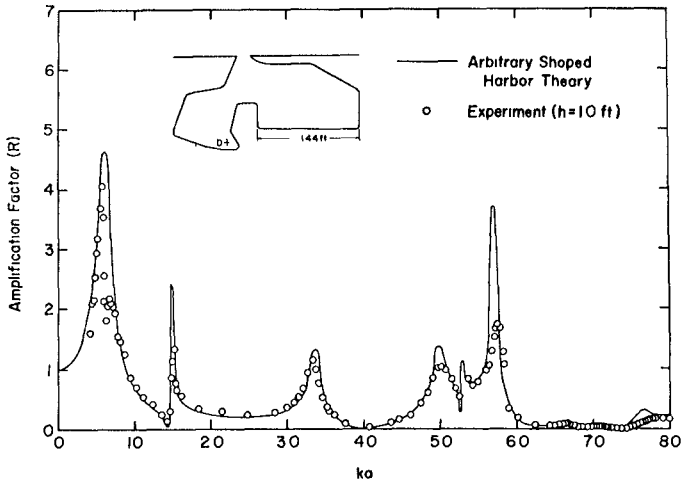


Fig 9 Response curve at point D of the Long Beach Harbor model

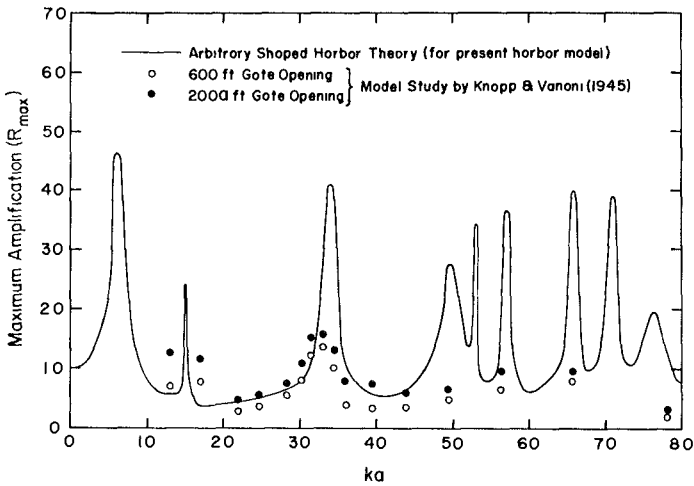


Fig 10 Response curve of the maximum amplification for the model of Long Beach Harbor compared with the data of the model study by Knapp and Vanoni (1945)

the theory the harbor boundary was divided into the same number of segments for all wave numbers thus the ratio of the segment length Δs to wave length L is smaller for the smaller values of ka than for larger values of ka . Therefore the theoretical results for small ka are more accurate than the results which correspond to large ka and thus better agreement between the theory and experiments is to be expected. Second energy dissipation is larger near resonance for large values of ka which also tends to decrease the experimental amplification factors compared to those determined theoretically.

It can also be seen from the response curves that the agreement between the theoretical solution and the experimental data is uniformly good at each of the locations. This suggests that the theory has also accurately predicted the wave amplitude distribution inside the harbor for each mode of resonant oscillation.

It is interesting to note that for larger values of ka , the shape of the mode of oscillation inside the harbor becomes more complex. For example for the first resonant mode ($ka = 0.61$) the amplification factors at the four positions (A, B, C and D) are approximately the same. In fact for this mode of oscillation the wave amplitude is fairly uniform throughout the harbor and either positive or negative water surface displacements occur simultaneously throughout the harbor. Thus the first resonant mode ($ka = 0.61$) is usually termed the "pumping mode". However for the mode corresponding to $ka = 7.62$ the amplification factors at the four locations differ considerably indicating that this is a much more complicated mode of oscillation than the "pumping mode."

The variation of the maximum amplification within the entire basin plotted as a function of ka is presented in the response curve of Fig. 10. The ordinate is the ratio of the maximum wave amplitude within the harbor regardless of location to the standing wave amplitude with the entrance closed. This curve shows every possible mode of resonant oscillation for the range of ka that has been investigated, as well as the maximum amplification for each mode. Experimental data from a model study conducted by Knapp and Vanoni (1945) are included in Fig. 10 for comparison. (The gate or entrance width used in the present model corresponds to a prototype width of 940 ft.) The original data of Knapp and Vanoni were presented by them as the maximum amplification factor as a function of prototype wave period. In order to convert their wave period to the wave number parameter (ka) used herein an average prototype water depth of 40 ft was used throughout the harbor along with a characteristic dimension of the harbor $a = 6768$ ft. These hydraulic model data and the present theoretical curve show qualitative agreement of the wave periods of resonant oscillations especially the mode of oscillation at $ka = 3.38$. However there is a considerable difference between the predicted maximum amplification and the measured. There are two factors that may contribute to such differences. First the maximum amplification factor used by Knapp and Vanoni was defined as the ratio of the maximum wave amplitude inside the harbor model to the maximum wave amplitude measured outside the harbor thus it differs from the definition used in the present theory. Second, the water depth in the model used by Knapp and Vanoni was small increasing the importance of viscous effects in their model compared either to the inviscid theory or the experiments of this study.

Fig 11 shows the distribution of wave amplitude inside the harbor for the resonant mode at $ka = 3.38$ determined from the present theory. The wave amplitude has been normalized with respect to the wave amplitude at point C (the coordinates of this position are shown in Fig 8). Two nodal lines (lines with zero amplitude) occur: one in the East Basin and one in the West Basin with maxima at the ends of each basin and a minimum near the confluence of the two. Data are presented in Fig 12 from Knapp and Vanoni (1945) on the wave amplitude distribution for a prototype wave period of 6 minutes ($ka = 3.30$). By comparing Figs 11 and 12 it is seen that the general shape of wave amplitude are similar for the two models (e.g., the location of the two nodds and the maximum) even though the boundary of the model used for present study is simplified compared to the hydraulic model.

Fig 13 shows the average maximum total velocity at the harbor entrance (maximum in time averaged across the harbor entrance) as a function of the wave number parameter ka . The ordinate has been normalized with respect to the maximum horizontal water particle velocity for a small amplitude shallow water wave $\sqrt{gh} A_1/h$. From this figure it is seen that there are nine maxima in the range of ka presented which correspond to the nine resonant modes shown in Fig 10 demonstrating that each maximum of the total entrance velocity is associated with a mode of resonant oscillation inside the harbor. Fig 13 also shows that the velocity at the entrance for the pumping mode ($ka = 0.61$) is significantly larger than that of any other mode of oscillation. Using the prototype dimensions mentioned previously the wave period of this mode is about 33 minutes and could possibly be excited by tsunamis. If $A_1 = 0.5$ ft and $h = 40$ ft, Fig 12 indicates that the maximum entrance velocity for the pumping mode would be 10 fps and for other modes it would be of the order of 2 fps. Such velocities may cause damage to structures located near the entrance as well as creating navigation problems.

CONCLUSIONS

The following major conclusions may be drawn from this study:

1. The present linear-inviscid-theory predicts the response to periodic incident waves of an arbitrary shape harbor with constant depth connected to the open-sea quite well even near resonance.
2. The theoretical prediction of the resonant wave numbers (or resonant frequencies) agree well with the experimental data. The theoretical amplification factor at resonance is generally somewhat larger than the experimental data especially for the resonance modes at larger values of ka .
3. The average total velocity across the harbor entrance reaches a maximum when a resonant oscillation develops inside the harbor. The magnitude of such entrance velocities may be much larger than the corresponding water particle velocity of the incident wave.
4. The present theoretical results also agree qualitatively with the experimental data obtained from a model study conducted by Knapp and Vanoni (1945) although the planform of the model investigated by them was more complicated and their study included depthwise variations.

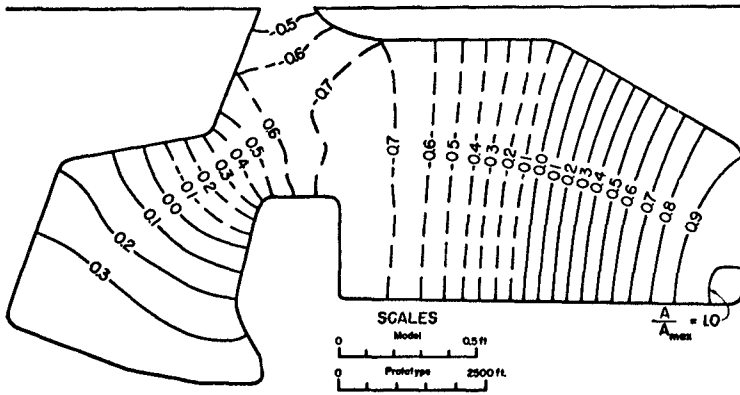


Fig 11 The theoretical wave amplitude distribution in the Long Beach Harbor model ($ka = 3.38$)

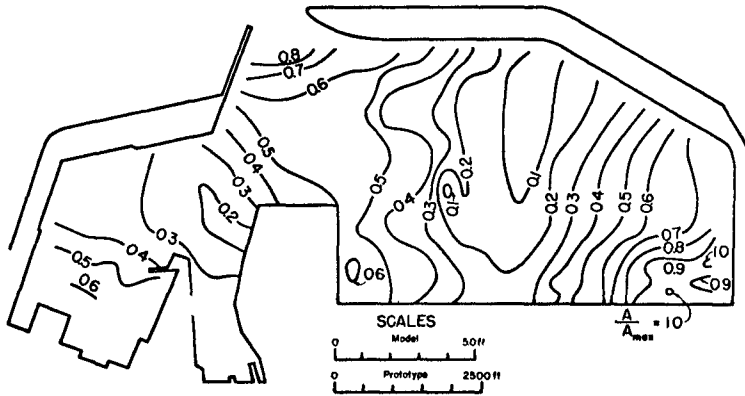


Fig 12 Wave amplitude distribution inside the harbor model of Knapp and Vanoni (1945) for six minute waves ($ka = 3.30$) (see Knapp and Vanoni (1945) p 133)

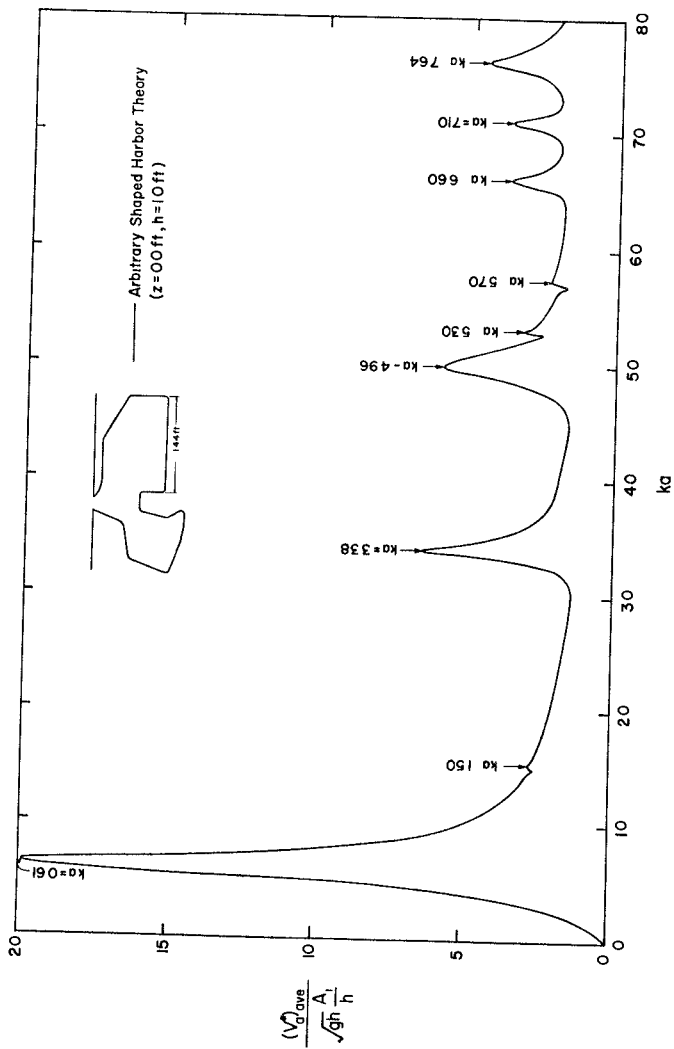


Fig 13 Average maximum total velocity on the water surface at the harbor entrance as a function of ka for the Long Beach Harbor model

ACKNOWLEDGEMENT

This study was supported by the U S Army Corps of Engineers under Contract No DA-22-079-CIVENG-64-11 and was conducted at the W M Keck Laboratory of Hydraulics and Water Resources California Institute of Technology

LIST OF REFERENCES

- Hwang L S and Tuck, E O "On the Oscillations of Harbors of Arbitrary Shape", Journal of Fluid Mechanics Vol 42, 1970, pp 447-464
- Ippen, A T and Goda Y, "Wave Induced Oscillations in Harbors The Solution for a Rectangular Harbor Connected to the Open-Sea", MIT Hydrodynamics Laboratory Report No 59, 1963
- Knapp R T and Vanoni, V A "Wave and Surge Study for the Naval Operating Base Terminal Island California", Hydraulic Structure Lab Calif Inst of Tech Pasadena, Calif, 1945
- Kravtchenko, J and McNown J S, "Seiche in Rectangular Ports", Quarterly of Applied Math, Vol 13 1955, pp 19-26
- Lee, J -J, "Wave Induced Oscillations in Harbors of Arbitrary Shape", Report KH-R-20, W M Keck Lab of Hydraulics and Water Resources, Calif Inst of Tech, Pasadena Calif 1969
- Lee J -J, "Wave-Induced Oscillations in Harbours of Arbitrary Geometry", Journal of Fluid Mechanics, 1970 (in press)
- Leendertse, J J "Aspects of a Computational Model for Long-Period Water Wave Propagation", RM-5294-PR The Rand Corporation Santa Monica, Calif 1967
- McNown J S "Waves and Seiche in Idealized Ports" Gravity Waves Symposium N B S Circular 521, 1952
- Miles, J, and Munk W, "Harbor Paradox" Journal of Waterways and Harbors Div, ASCE Vol 87 No WW3, 1961 pp 111-130
- Rachlen F "Wave-Induced Oscillations of Small Moored Vessels", Report KH-R-10 W M Keck Lab of Hydraulics and Water Resources, Calif Inst of Tech Pasadena Calif, 1965
- Rachlen, F, and Ippen A T "Wave Induced Oscillations in Harbors", Journal of Hydraulics Div, ASCE, Vol 91, No HY2 1965, pp 1-26
- Wilson, B W, Hendrickson, J A, and Kilmer, R C "Feasibility Study for a Surge-Action Model of Monterey Harbor, California", Report 2-136, Science Engineering Associates, San Marino, Calif, 1965

CHAPTER 132

SPECTRAL RESPONSE OF HARBOR RESONATOR CONFIGURATIONS

William James*

ABSTRACT

An outline is given of methods devised recently by the author to predict the spectral response of rectangular resonators, and to improve the response of resonators generally. A simple small scale acoustic model of the ocean-resonator-harbor configuration was developed and is described. The acoustic "ocean" is effectively decoupled from the rest of the system by means of sound absorbent material placed along the "infinite" boundaries, and standard audio-frequency equipment is used. The results demonstrate that the open end contraction for rectangular resonators may not differ significantly from the contraction for resonators of similar geometry placed in a semi-infinite (or effectively decoupled) wave channel, at least if the wavelengths are not smaller than the width of the harbor entrance channel.

INTRODUCTION

It is desirable to design harbor entrances to eliminate (as far as possible) those bandwidths in the incident wave spectra that cause difficulties such as range action, high mooring forces, unreasonable wave impact, wave overtopping and drift of littoral sediments into the harbor. In many problems these difficulties are functionally related to approximately the second (or higher) power of the wave height, and hence any reduction in the incident wave height will produce real benefits.

Resonators placed at the harbor entrance can be tuned to radiate back into the ocean those frequency bandwidths considered to be harmful without hindering navigation¹. Readers are cautioned against using the blanket quarter-wavelength recommendation^{2,3,4}, the initial design should accord with the fact that the tuning of individual resonators is considerably dependent on the width of the harbor entrance channel^{5,6}. Readers should also note that resonators are not effective

**Senior Lecturer, University of Natal, Durban, South Africa, presently visiting at Queen's University, Canada*

for wavelengths smaller than the width of the harbor entrance channel. Hence this paper relates to incident wavelengths that exceed the horizontal distance between the leading edges of symmetrically opposed rectangular resonators.

The transmitted and reflected spectra can be predicted for given geometry and incident spectra, assuming a linear system⁷, and this procedure is outlined below. Certain innovations⁸ that both broaden the tuning of the resonators and decrease the cost of construction are also briefly described in this paper. An acoustic model has been devised⁶ and this is used to check the ocean-resonator-harbor coupling. The results of the latter tests constitute the major contribution of this paper.

SPECTRAL RESPONSE

The method devised for computing the spectral response of individual rectangular resonators is based on experimental results. It is usual to plot frequency response curves in the frequency domain⁹ but in this study observed transmissivity and reflectivity were plotted against the tuning parameter d/L (i.e., in the ka domain). For details of the wave measurement and wave analysis procedure, readers are referred to earlier publications^{10,11}. The geometrical conditions for distinct resonance are summarized in fig. 1.

Approximate rectilinear apexes were fitted into the ka domain resonance curves, and the resulting maxima and minima are summarized in fig. 2. The tuning parameter bandwidths at the half resonant values were measured and found to be reasonably constant for various values of W/L . The information is summarized in fig. 3. Sufficient data are available in these three figures to allow the computation of the spectral response of any rectangular resonator to given incident spectra, *but only for the first resonant mode*.

Briefly, the procedure is to transform the incident spectrum into an amplitude/wavelength relationship for the particular harbor entrance. The dimensions of the resonator are chosen such that distinct resonance obtains for the dominant wavelength, using fig. 1. For discrete wavelengths the ratios W/L , w/L and d/L are calculated. The resonant tuning parameter is obtained from fig. 1, and the resonance curves "reconstructed" graphically or digitally using figs. 2 and 3. Values of transmissivity and reflectivity are then interpolated for various tuning parameters.

Finally, the incident spectra are transformed using these values. Two examples are presented elsewhere⁷, and it is shown that a standard quarter-wavelength resonator may reflect *only one quarter of the peak energy*, nearly all of which is reflected by a resonator designed according to fig. 1.

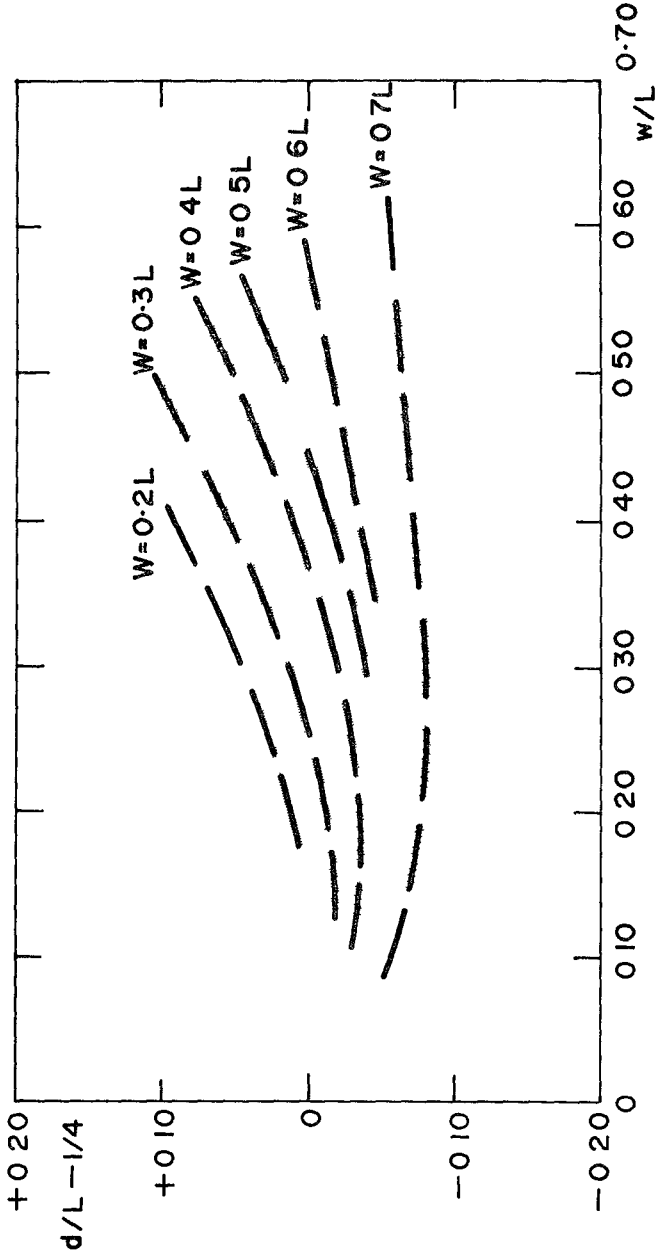


FIG 1 GEOMETRY FOR FIRST RESONANT MODE

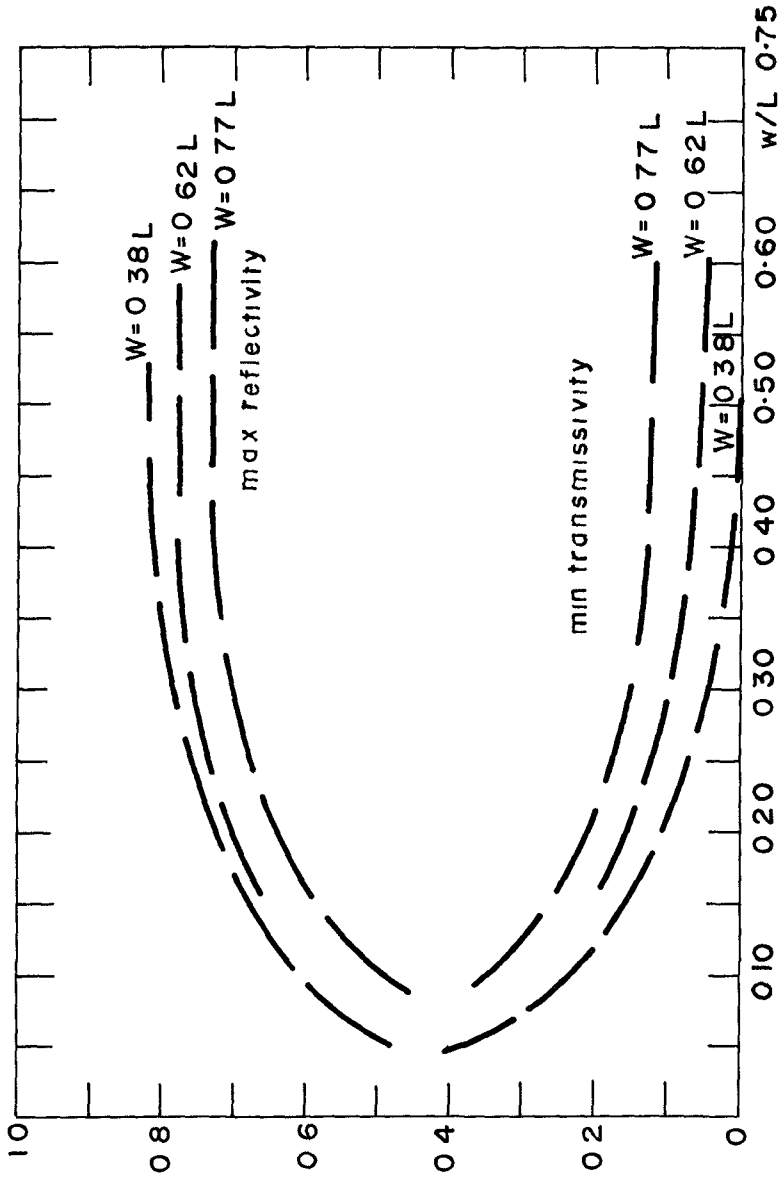


FIG. 2 RESONANT MAXIMA AND MINIMA

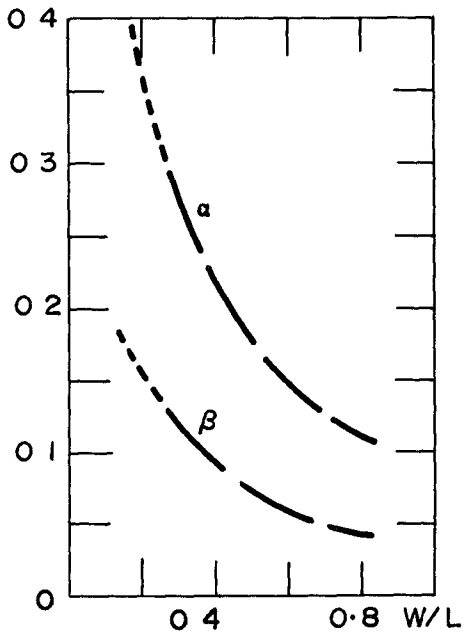


FIG. 3 TUNING PARAMETER BANDWIDTH
AT HALF RESONANT VALUE

TWO INNOVATIONS

Experiments were performed on

- (a) variable distances between three resonators in a battery configuration, and
- (b) non-uniform depths in a resonator/harbor entrance area

Triple Resonator Batteries

Rayleigh¹² recommended that the ratio of the fundamental periods of the individual resonators in a battery configuration should be $1/\sqrt{2}$. In this study resonators were constructed from 3/4 inch thick "perspex", geometries are shown in fig 4

Reflectivity and transmissivity were measured at points approximately one wavelength upstream and downstream of the battery respectively. In these tests the water depth was held constant, and wavelengths were systematically varied.

The results showed resonant peaks at those individual resonator frequencies obtained in earlier tests on single resonators, as is to be expected. Hence fig 1 can be used to predict the response of battery configurations. Superimpose the equation (a straight line) for each battery geometry (e.g. $w/L = 1.61 d/L$) on fig 1 and scan the line for the location such that the harbor entrance and resonator geometry satisfy the geometrical conditions for resonance. This identifies the tuning parameter for resonance, and performance can be estimated using the same computational procedure for spectral response described above.

By increasing the distances between the resonators, the water mass in the entrance channel contiguous with the leading edges of two adjacent resonators is brought into the system response. This effectively broadens the overall tuning of the battery configuration and hence improves the spectral performance of the battery. Because of the end-contractions, the distance should be significant, e.g. commensurate with resonator dimensions, and chosen by careful *ad hoc* model tests (acoustic models preferably).

Non-Uniform Depths

In the experiments on non-uniform depths an artificial invert was inserted into a single resonator, as depicted in fig 5. The still water depth and wavelength were held constant and the resonator planform was varied systematically (by gradually retracting the rear wall outwards). Reflectivity and transmissivity were measured as in early tests.

The results indicated a reduced efficiency for resonators of comparatively small still water depth, but less upstream agitation.

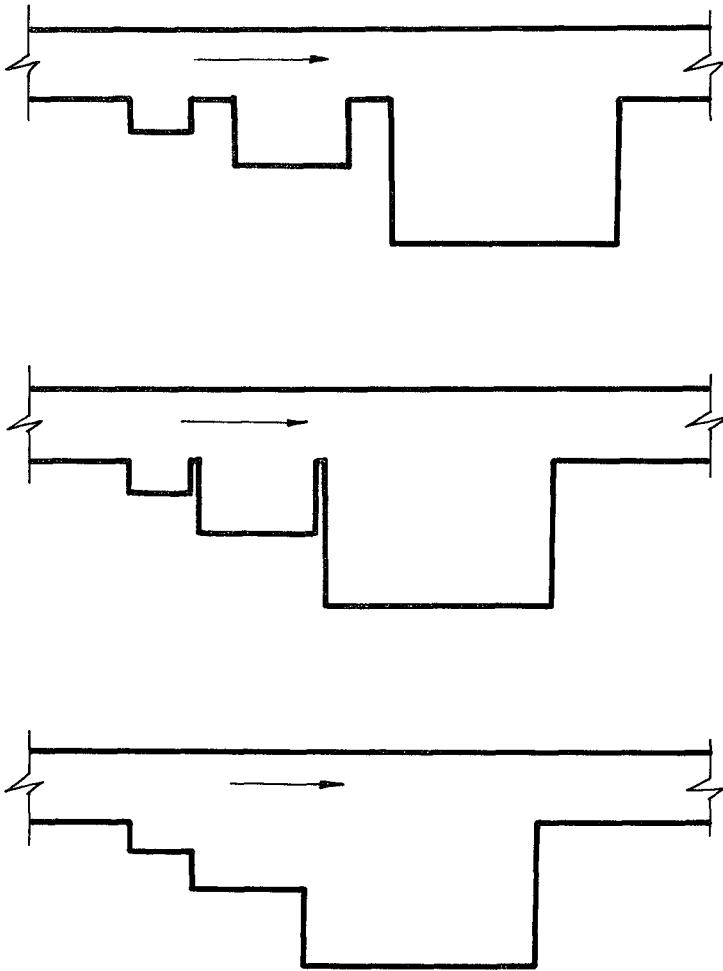


FIG 4 BATTERY GEOMETRIES EXAMINED

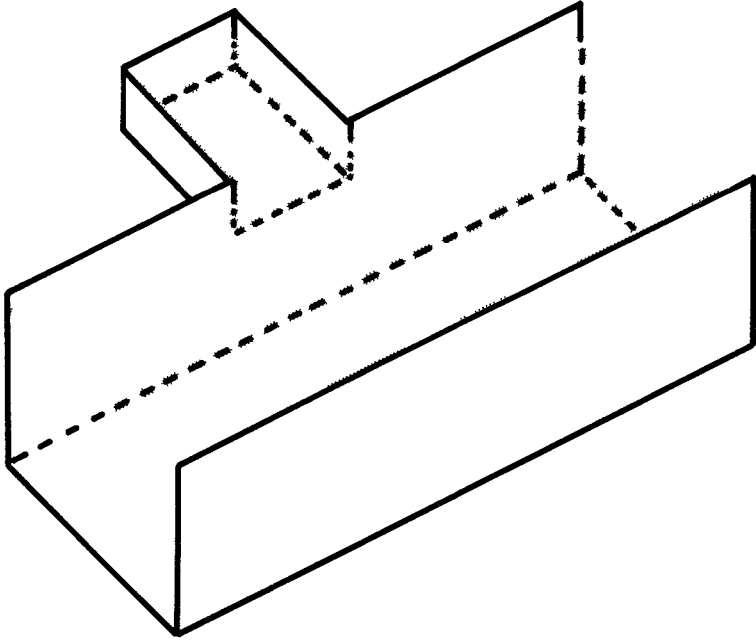


FIG. 5 NON-UNIFORM DEPTHS

(reflectivity) was associated with given transmissivity

It was found that the length of the resonator could easily be halved, if the still water depth in the resonator is reduced to a fraction of the harbor entrance channel depth, a point of considerable practical significance. However, tidal ranges will detune the resonator, the effect being related to the proportional reduction in depth and to the actual tidal range.

THE ACOUSTIC MODEL

An acoustic model evidently has certain advantages over a hydraulic model. Wave generation and absorption are easier, the fluid does not have to be isolated, wavelengths are generally shorter, and measuring equipment, speed and accuracy are generally better.

To test the model, earlier experiments on resonators in a water wave channel were reproduced. The variable geometry was built up from 3 inch movable timber walls and placed on a glass plate on top of a desk. A second glass plate was placed on top of the walls, and a loudspeaker was connected to an oscillator and placed against sponge rubber at the entry to the main duct. A microphone was placed against the sponge rubber absorber at the harbor end of the main duct, and was connected through a small pre-amplifier to an oscilloscope. By setting the widths of the main entrance duct and of the resonator, and by holding the oscillator frequency constant, the length of the resonator was adjusted until resonance occurred. This was monitored by a minimum signal on the oscilloscope.

The effect of imperfect sound absorption was checked and found to be unimportant. Tests on scale effects were also negative, although these were not exhaustive. In addition the effects of sound waves entering the duct along its length were also found to be insignificant. The signal-to-noise ratio was easily improved by means of the amplifier on the oscilloscope.

The results showed slight differences from those of the water wave experiments. Reasonably accurate predictions of harbor resonance modes for frequencies can be obtained in this way, but further development of the method will be necessary if absolute values of harbor amplification are required.

OCEAN-RESONATOR-HARBOR COUPLING

Fig 6 shows the experimental apparatus used to examine the coupling problem. In this case the model was set up on a reasonably clean office floor, again using 3 inch high timber walls. The cover to the ocean domain was supported on 3 inch iron nails. Cotton batting (reflectivity about 5%) was arranged along the "infinite"

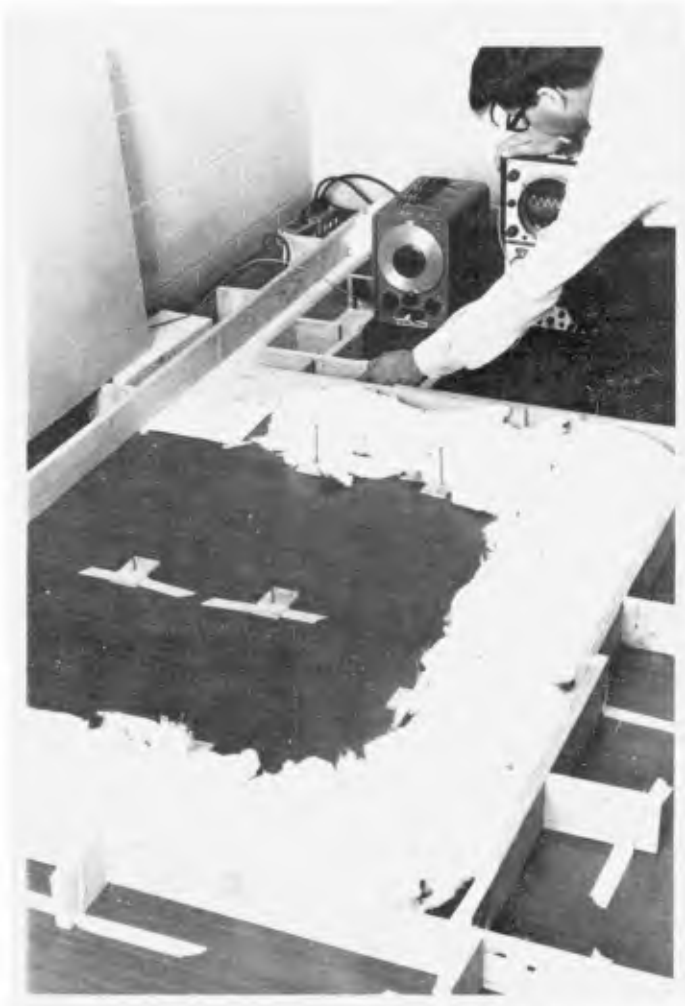


FIG. 6 ACOUSTIC MODEL: OCEAN-RESONATOR-HARBOR

boundaries, and this effectively decoupled the ocean domain. Total cost of the model excluding audio equipment was \$8 50.

Acoustic waves were generated from a virtual point source, and so the ocean domain had to be long enough for the radiating incident waves to achieve an approximately parallel wave front at the harbor entrance. It follows that re-reflections from the harbor off the loudspeaker were negligible.

The experimental procedure adopted was similar to that above resonance monitored by a minimum acoustic pressure signal in the harbor, and achieved by systematic variation of resonator geometry. This method was better than incident wave frequency variation, since system attenuation, transmissivity and reflectivity, parasitic vibrations, and also wave generation and recording were frequency dependent.

Geometrical conditions obtained for distinct resonance are presented in fig 7. Results for semi-infinite ocean coupling and semi-infinite wave channel coupling almost coincided, consequently both results could not be plotted on the figure. However the ocean coupling curves were slightly flatter, as indicated by the dashed curve.

Evidently, then, harbor resonance studies may be carried out at the end of water wave channels (provided that the incident wavelength exceeds the width of the harbor entrance channel) without material loss of accuracy.

Further tests on the acoustic model confirmed that resonators should be located at the ocean end of the entrance channel, and at an amplitude antinode in the wave envelope, if the harbor is reflective at the resonator tuning frequency. Since partial re-reflections occur off the ocean end of the entrance channel, the downstream harbor and channel oscillations are generally not amplified by resonators. For *transparent* frequencies there is no effect and for *opaque* frequencies there is no penetration.

CONCLUSIONS

Three figures are presented for estimating the spectral response of individual rectangular resonators, *but only for the first resonant mode*. No account is taken of the second resonant mode even though this is important when considering the response of a battery of resonators.

Individual resonators in a battery respond in an additive manner, and hence this response can also be predicted. The mass of water contiguous with adjacent resonators in the harbor entrance channel can

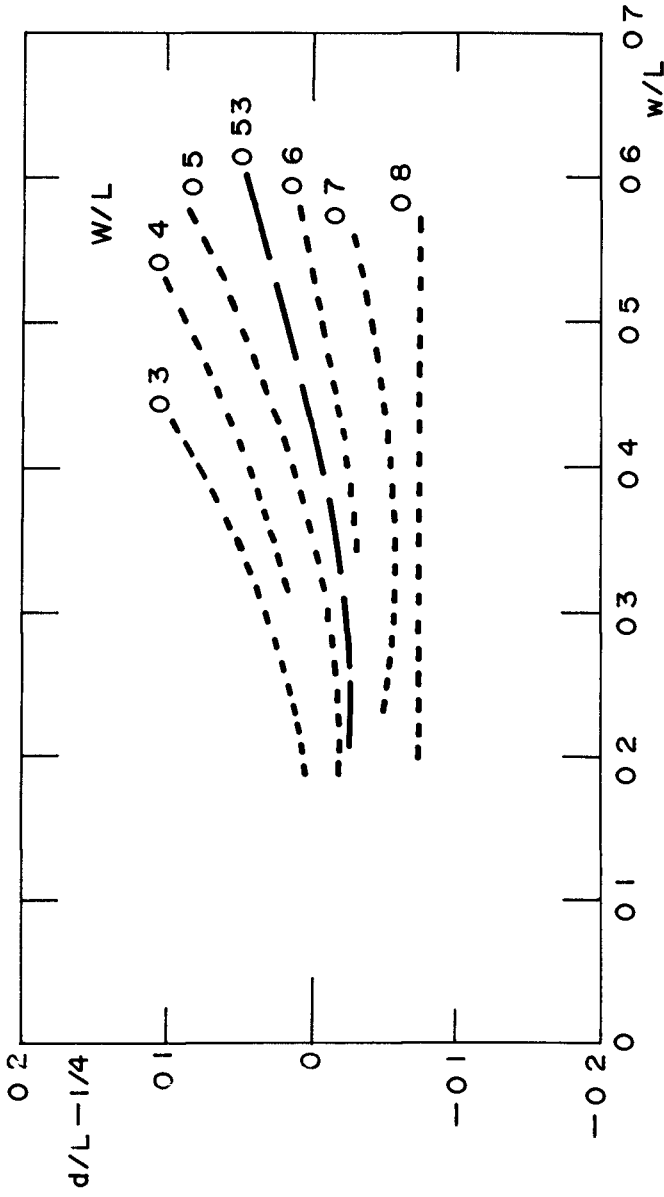


FIG 7 OCEAN-RESONATOR-HARBOR COUPLING

also be incorporated in the system response. For this reason the resonators should not be contiguous, if at all possible.

Comparatively shallow still water depths in individual resonators detunes the resonator downwards, i.e. towards smaller frequencies. Hence, for a particular tuning, non-uniform depths, with smaller depths in the resonator, result in smaller geometry, and concomitant savings in construction and excavation costs. Large tidal amplitudes would effectively detune such systems, however.

The acoustic analogy is an extremely fast and cheap method for evaluating eigen frequencies for any harbor planform. The method could probably be elaborated for estimation of orbital velocities and even of mooring forces, for uniform water depths in the harbor and harbor entrance. No scale effects were detected in the tests reported.

An acoustic model was constructed to check the ocean-resonator-harbor coupling. *The results indicated that the end-effect does not differ significantly from the contraction for resonators of similar geometry placed in a semi-infinite wave channel, at least for wavelengths greater than the harbor entrance width.*

This result validates the experimental results obtained in the wave channel, the method for predicting the spectral response of resonators for a real situation (i.e. on the edge of a semi-infinite ocean) is evidently reliable to the first order.

REFERENCES

- 1 James, W , "Rectangular Resonators for Harbour Entrances", Chapter 98, Coastal Engineering, A S C E , August 1969, pp 1512 - 1530
- 2 Valembais, J , "Etude de l'Action d'Ouvrages Resonants sur la Propagation de la Houle" Proc Minnesota Int Hydraulics Conf , Minneapolis 1953, pp 193-200
- 3 Wiegel, R L , Oceanographical Engineering, Pub Prentice Hall, 1964, p 144
- 4 Ippen, A T (Ed) Estuary and Coastline Hydrodynamics, pub McGraw Hill, 1966, p 397
- 5 James, W , "An Experimental Study on End-Effects for Rectangular Resonators", Journal of Fluid Mechanics, in press
- 6 James, W , "A Desk-top Model of Harbour Resonators", Journal of the Acoustical Society of America, in press

- 7 James, W , "The Spectral Response of Harbour Resonators", The Institution of Civil Engineers (London), in press
- 8 James, W , "Two Innovations for Harbour Resonators", A S C E , in press
- 9 Miles, J , and Munk, W , "Harbor Paradox", Proc A S C E , Vol 87 No WW3, Aug 1961, pp 111-130
- 10 James, W , "Accurate Wave Measurements in the Presence of Reflections", Jour Instn Water Engrs (London), Vol 23, No 8, Nov 1969
- 11 James, W , "Resolution of Partial Clapotis", Proc A S C E Vol 96, No WW1, Feb 1970
- 12 Strutt, J W (Lord Rayleigh), The Theory of Sound, Dover, 2nd Ed 1945, Chap XVI

NOTATION

a = lineal dimension
 d = length of resonator
 k = wave number
 L = incident wavelength
 w = width of resonator
 W = width of harbor entrance channel
 α = reflectivity
 β = transmissivity

ACKNOWLEDGEMENTS

The work reported was developed and the paper written while the author was visiting at Queen's University. Thanks are due to that Institution for the opportunity to visit Canada and to the University of Natal for leave of absence. The work was based on experimental results obtained mostly at Aberdeen University, Scotland, where guidance was readily given by Professor Jack Allen and Dr G D Matthew. Professor H Stewart, former Head of the Dept of Electrical Engineering at Queen's kindly loaned the audio equipment. The idea of the acoustic analogy crystallised out of discussion in Honolulu and Washington with Dr Dick Shaw of Buffalo University.

CHAPTER 133

HARBOR STUDY FOR SAN NICOLAS BAY, PERU

By James M Keith¹ and Emmett J Murphy²

ABSTRACT

A pair of ducted impeller current meters, one mounted vertically and the other horizontally, were used to measure wave action at San Nicolas Harbor, Peru. The horizontal water velocity records are superior to conventional wave records because they measure directly the wave property which induces adverse horizontal ship motion, and provide directional wave data. Spectral analysis methods proved well-suited to detailed interpretation of the particle velocity records, while considerable insight into the wave phenomena was gained by simple, rational inspections and interpretations of the records. Time-lapse movies of a moored ship, when correlated with simultaneous water particle velocity records, provided an exceptionally clear picture of ship response to wave action, and led to the rather surprising observation that long-period ship motion is not necessarily caused by long-period waves. The foregoing ship response was duplicated in hydraulic model tests.

INTRODUCTION

The results of a study program were used to determine the source of difficulties in mooring ore carriers at Marcona Mining Company's iron ore loading facility at San Nicolas Harbor, Peru. Observations of wave action were primarily obtained by time-lapse movies of a moored ship and by an orbital velocity meter consisting of two ducted impeller current meters, one mounted vertically and the other horizontally. The horizontal water velocity records are superior to conventional wave height records in two important respects: (1) They provide direct data regarding the wave property most directly affecting horizontal ship movement, and (2) they provide directional wave data.

Analyses were performed in two distinct stages. A direct, rational application of the records as a time-history of the horizontal water velocity was used to derive the time-history of horizontal water displacement. Using this approach, a mechanism was established whereby a relatively short-period swell of 16 sec induced long-period (50 sec to 150 sec) ship motion transverse to the pier. Spectral analyses by digital computer were then employed to derive a clear insight into the various wave trains existing at particular times, and to quantitatively evaluate the relative energy contents of selected wave frequencies. Simple hydraulic model tests were utilized to verify that swell generated periodic transverse ship motions having a period many times longer than the period of the swell. This occurred when a quartering stern swell acted on a ship moored with slack elastic mooring lines to a pier with elastic fenders.

¹ Vice President, John A. Blume & Associates, Engineers, San Francisco, California

² Project Manager, Marcona Corporation, San Francisco, California

BACKGROUND

The port at San Nicolas Bay is utilized by Marcona for the annual shipment of approximately 9 million tons of iron ore concentrates and pellets. The bay is a typical hooked embayment not fully protected from the ocean. At times, serious mooring problems have been experienced at the pier due to adverse water motion which has resulted in the breaking of many mooring lines and damage to the pier by the ship's impact (see Fig 1). Individual ships have broken more than twenty mooring lines and some of the impacts against the pier have been estimated to exceed the pier's design load by a substantial margin.

In general, rough water conditions in the bay occur during the winter months when storms in the lower southern latitudes frequently cause heavy swells along the coast. During these periods, which vary from a few hours to three or four days, ships are forced to anchor well out from the pier awaiting calmer water, and many ships have been delayed in this manner.

The pier deck (see Fig 2) is constructed of prestressed concrete sections supported on prestressed concrete piling. The fender system consists of hollow, end-loaded rubber cylinder buffers 18 in OD, 9 in ID, by 21 in long for energy absorption. Timber piles bear on the outer ends of rubber cylinders and support 12-in x 12-in rubbing timbers.

Fig 3 is a map of San Nicolas Bay showing the pier projecting into the bay from the south shore line. The harbor is relatively deep, water depth at the pier when the latter was completed in 1962 was 45 ft at the south end and 59 ft at the north end.

The mooring problem at San Nicolas Bay is further complicated by the large vessels currently using the pier facilities. Marcona Corporation owns and operates a fleet of the largest dry bulk, ore, and combination ore-oil carriers available. These carriers are used to transport Peruvian iron ore mined and concentrated by Marcona to Japan. To date, ships of over 100,000 OWT have been loaded at San Nicolas pier, by early 1970, ships of 130,000 OWT will be in service. Use of carriers exceeding 150,000 OWT is foreseen in the future, and the west side of the pier, where ships are moored for loading, has been dredged to 57 ft to meet the draft requirements for vessels of this size. Table 1 shows typical dimensions of bulk and ore carriers.

The economic advantage of larger ships is easily demonstrated by comparison of crew requirements and tonnage capacities. A crew of 45 was required to man a 10,000-ton Liberty ship, the highly automated 100,000-ton ships of today require 35-man crews. The 10-knot Liberty ship could make about four Peru-Japan voyages per year for a total annual ore lift of about 39,000 tons, or about 850 tons for each crew member, the 16-knot 100,000 OWT ore carrier can average about 6-1/4 voyages per year, lifting about 635,000 tons annually or over 18,000 tons per year for each crew member, 21 times the rate of the Liberty ship.



FIG. 1. - FENDER DAMAGED FROM IMPACT OF MOORED SHIP

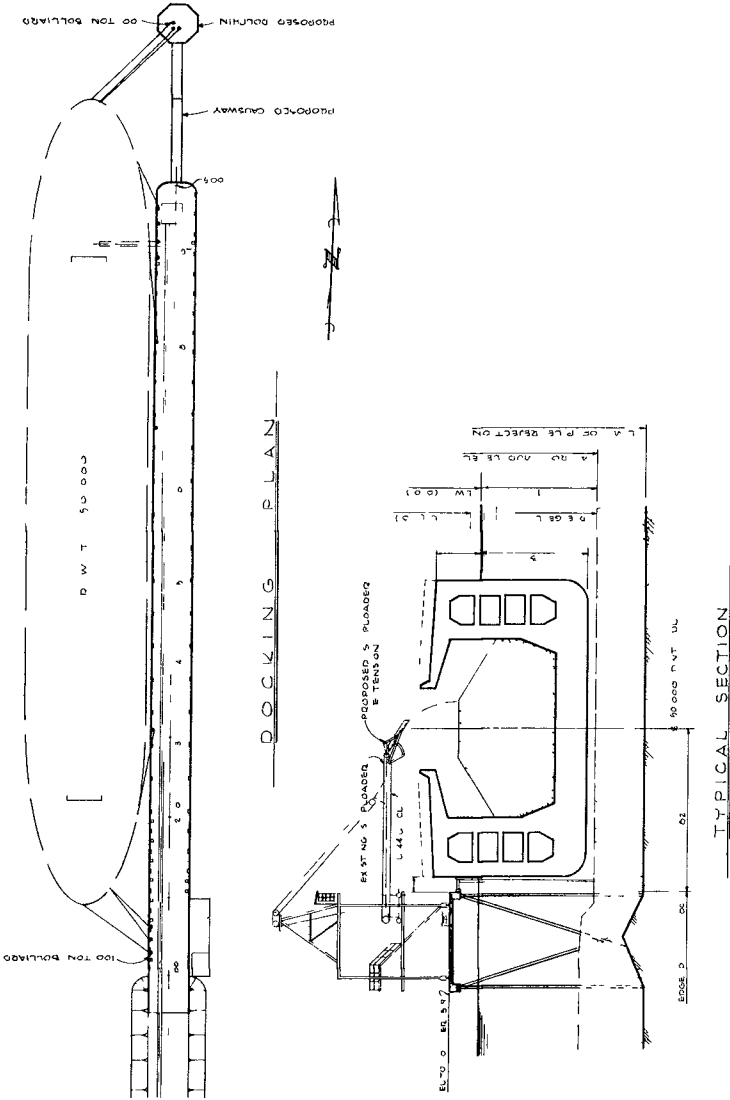


FIG 2 - SAN NICOLAS PIER

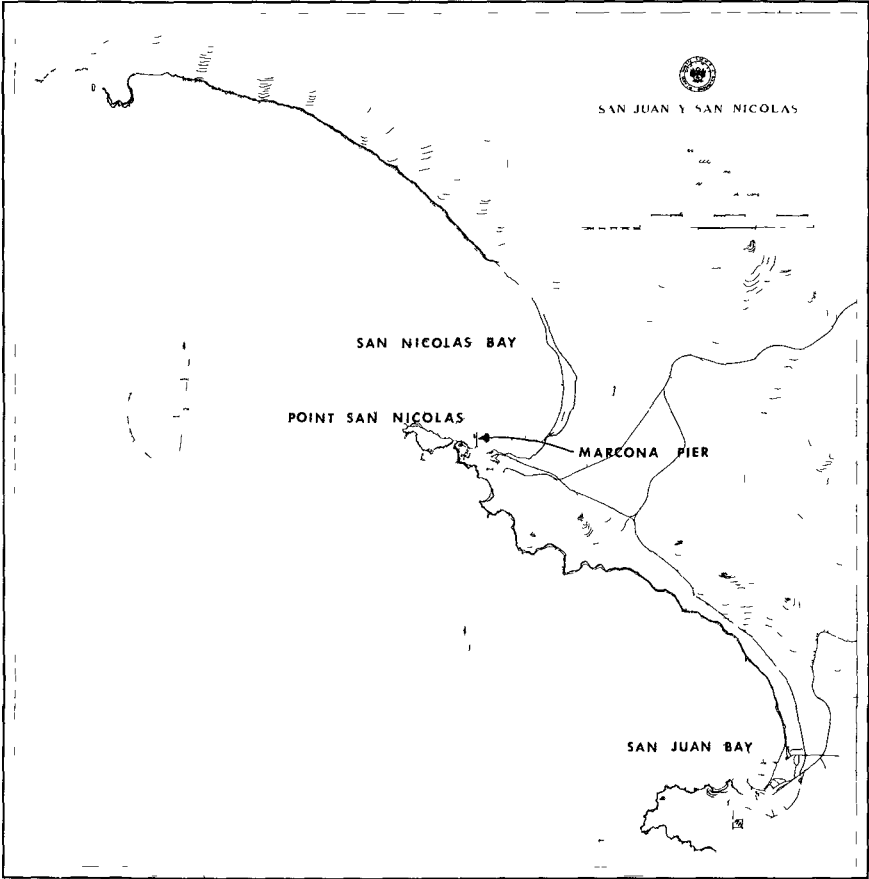


FIG 3 - SAN NICOLAS BAY, PERU

TABLE 1 - TYPICAL DIMENSIONS, BULK AND ORE CARRIERS

Vessel type	Vessel size, DWT	Displacement	Length overall, in feet and inches	Beam, in feet and inches	Depth, in feet and inches	Draft summer, in feet and inches
(1)	(2)	(3)	(4)	(5)	(6)	(7)
Liberty	10,800	14,100	441-6	56-11	37-4	27-8
Oread	31,662	41,641	655-0	87-0	46-6	34-2
San Juan Pathfinder	71,205	89,122	835-0	106-0	65-0	44-9
San Juan Exporter	106,000	123,852	865-3	124-8	68-11	50-10
-	130,000 ^a	154,400	948-2	138-10	74-2	51-9
-	150,000 ^b	180,000	1,014-0	150-0	75-0	53-0

^a Under construction

^b Possible design

Considering the trend toward larger ships and the problems encountered in mooring ships currently in service, Marcona Corporation retained John A. Blume & Associates, Engineers, to conduct a study to define wave action in the harbor. This information was considered essential to an evaluation of various proposals for improvement of the harbor.

Initial observations suggested that the ship motion to and from the pier was caused by harbor surge, since the period of motion ranged from 1 min to 3 min, and since the pier tide gage indicated occurrence of long-period waves ranging up to 20 min. Some ships at anchor appeared to swing on their anchors at periods approximately 20 min, an additional indication of surge. Discussion of the problem with local pilots indicated that swell might be a dominant factor in disturbances to moored vessels. The pilots relied upon the height of breakers on the north side of Point San Nicolas and the height of the surf along the beach southeast of the pier to estimate mooring conditions. It was therefore evident that if surge was the problem, it occurred only during periods of adverse weather as evidenced by the heavy swell.

The offshore swell approaching San Nicolas Bay from the south and southwest is refracted around Point San Nicolas and directed toward the pier from a northwesterly direction. It was noted that placement of a breakwater west of the pier would provide an excellent means of shielding the pier from the swell. Additional information, however, was needed to determine the effects of the breakwater on ship motion caused by surge, since a breakwater might well have little effect on reducing a long-period surge. An observation program was initiated to determine whether swell, surge, or a combination of these forces was causing the adverse motion.

OBSERVATION PROGRAM

Most conventional wave instruments record only wave height, and additional observations must be made to determine wave direction. Since wave direction at San Nicolas Bay is difficult to observe because of relatively low heights of swell and surge, a method of measurement was required which would eliminate the need to determine horizontal water motion from wave height data and observations of wave direction. Horizontal water motion from the swell or surge or both of these was the dominant factor causing ship motion, the most promising approach to the problem, therefore, was to measure this motion directly at the pier location.

Several marine instrument manufacturers were contacted for proposals to supply instrumentation which would record horizontal water particle direction and velocity. Two ducted impeller current meters arranged orthogonally on vertical and horizontal axes (see Fig. 4) were purchased from Marine Advisors, Inc. These meters were suspended approximately 10 ft below the low tide water surface and readings from each were simultaneously recorded on strip charts. A direction-sensing vane was installed in addition to the meters, and data from the vane was also recorded on a strip chart. Fig. 5 shows the instruments being placed off the north end of the pier.



FIG. 4. - PROTOTYPE: ORTHOGONALLY MOUNTED DUCTED IMPELLER CURRENT METERS



FIG. 5. - INSTALLING METER AT SAN NICOLAS PIER

Marine Advisors, Inc indicated that threshold current velocity for operation of the meters would be less than 3 cm per sec (0.06 knots), and that the meters would have a response time of 40 msec to 70 msec and a directional response approaching a cosine function of the angle between the meters' axes and the direction of water motion. Development data for these meters is available in another publication (3).

Since conditions causing mooring problems occurred relatively infrequently, readings were only taken during the rough sea periods. Recordings were made at 30° increments for six successive headings from 270° to 60°, with a 4-hr recording period for each heading. On April 8, April 15, and April 19, 1968, recordings of moderately rough conditions considered typical of problem-type storms were obtained. On July 26-27, 1968, recordings of the most severe wave disturbances since construction of the pier were obtained. These disturbances were considerably worse than any conditions previously experienced at the pier. The storm generating these waves caused damage to many marine installations along the Chilean and Peruvian coasts. In addition to the instrument records, a time-lapse motion picture study was filmed on April 19, 1968, of an ore carrier of 74,730 tons displacement moored at the pier. The camera mounted on the mole at the south end of the pier and focused on the bow of the ship recorded one frame every two seconds. Data from the wave instruments and the camera records were used to analyze water motion conditions within the harbor.

INITIAL ANALYSIS

The initial data analysis was a noncomputerized, rational comparison of the time-lapse movie and the horizontal water velocity record as shown in Fig. 6. The movement of the ship's bow was obtained by plotting sequential positions of a point on the ship's bow as the film was projected one frame at a time. The horizontal movement of a water particle was obtained by integrating the horizontal velocity record. Integration was done by measuring the area between the velocity curve and the zero line with a planimeter. The ship's bow movement consisted of a clockwise circular motion which showed excellent correlation with the swell period, but which was distorted by a long-period motion toward and away from the pier. Although the horizontal water motion also has a long-period component, the correlation between the long-period motions of the ship and the water was very poor.

In seeking an explanation of the long-period ship movements, the following hypothesis was proposed: the ship, fender system, and mooring lines comprised a vibrating system wherein the fender and the mooring lines were springs having slack or free travel space and the ship represented a mass having circular motion excited by the swell. Figs. 7 and 8 depict the idealized system. A model test was run in a University of California wave tank to confirm this hypothesis. The model simulated the conditions depicted by Fig. 8 at a linear scale of 1 to 159. Movies of the bow of the model ship indicated that a motion very similar to that shown in the lower portion of Fig. 8 could be generated in the

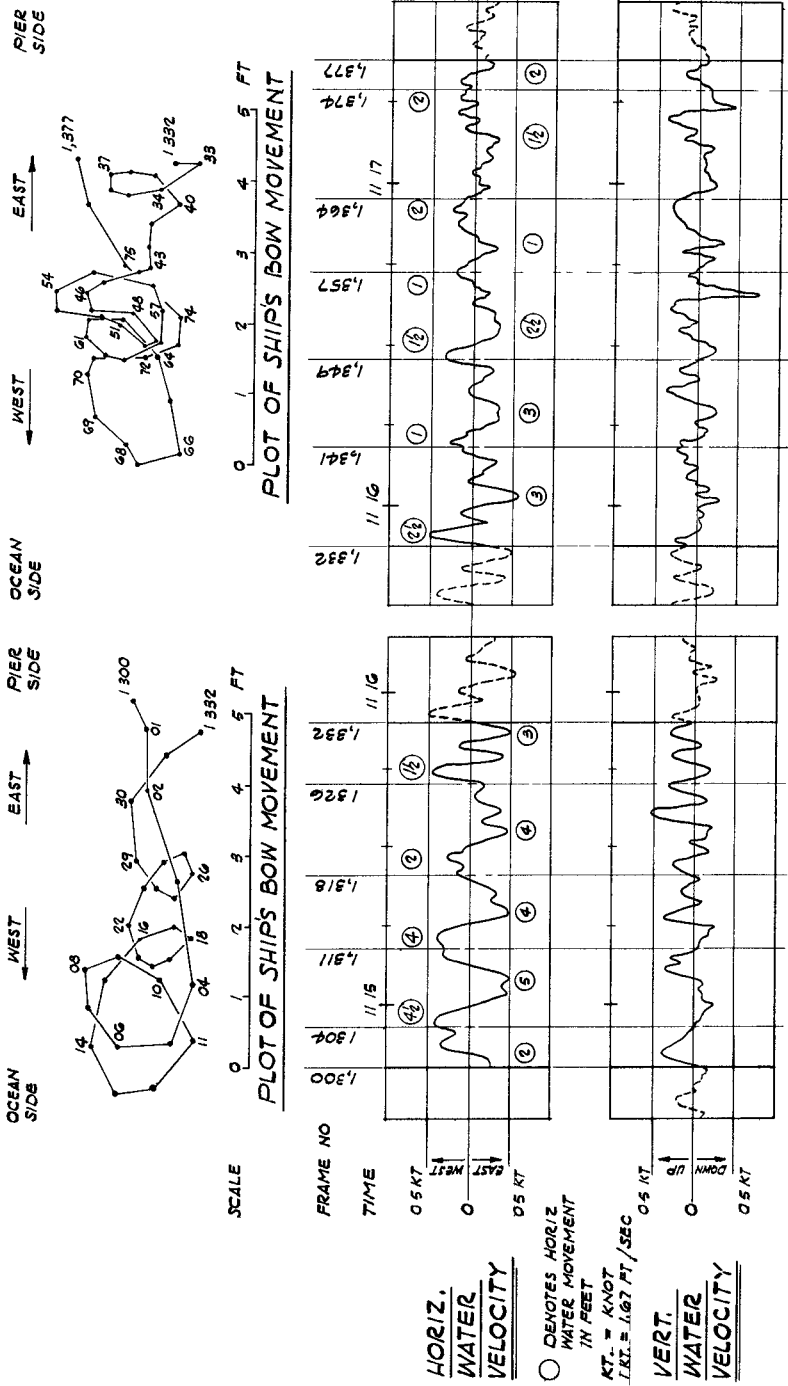


FIG 6 - PLOTS OF SIMULTANEOUS BOW MOVEMENT AND WATER VELOCITIES AT SAN NICOLAS BAY

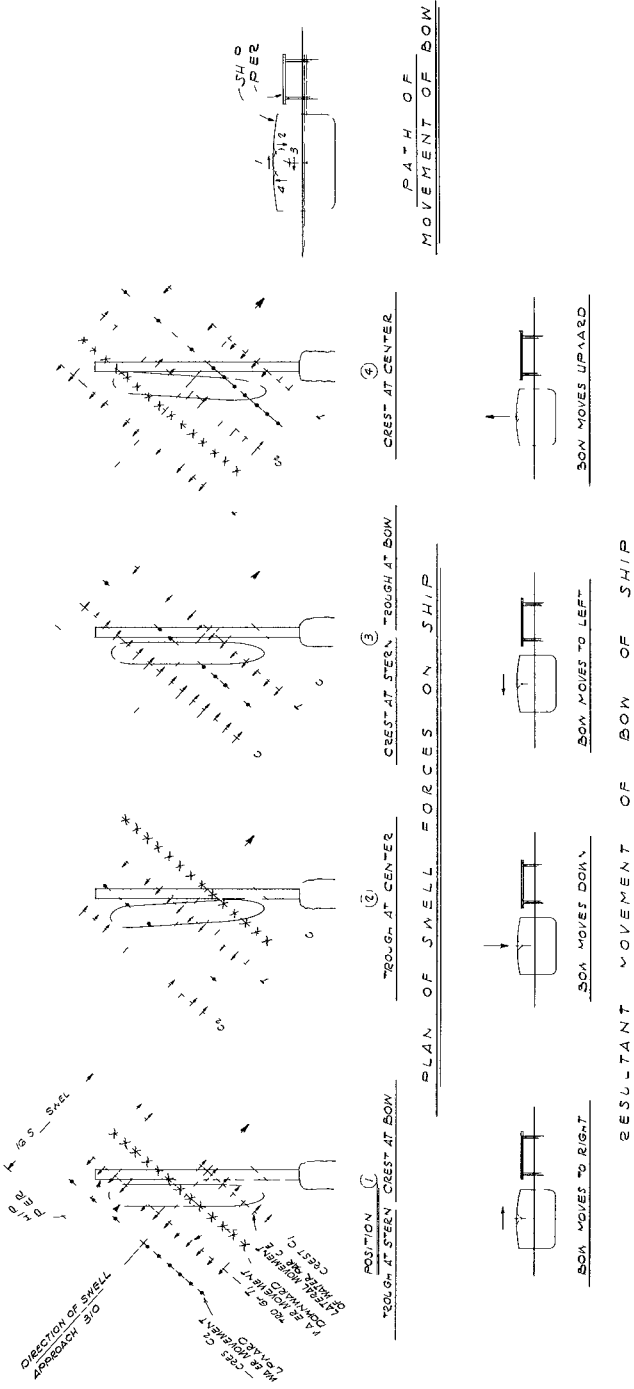


FIG 7 - SHIP MOVEMENT DIAGRAM, SWELL FORCES ONLY

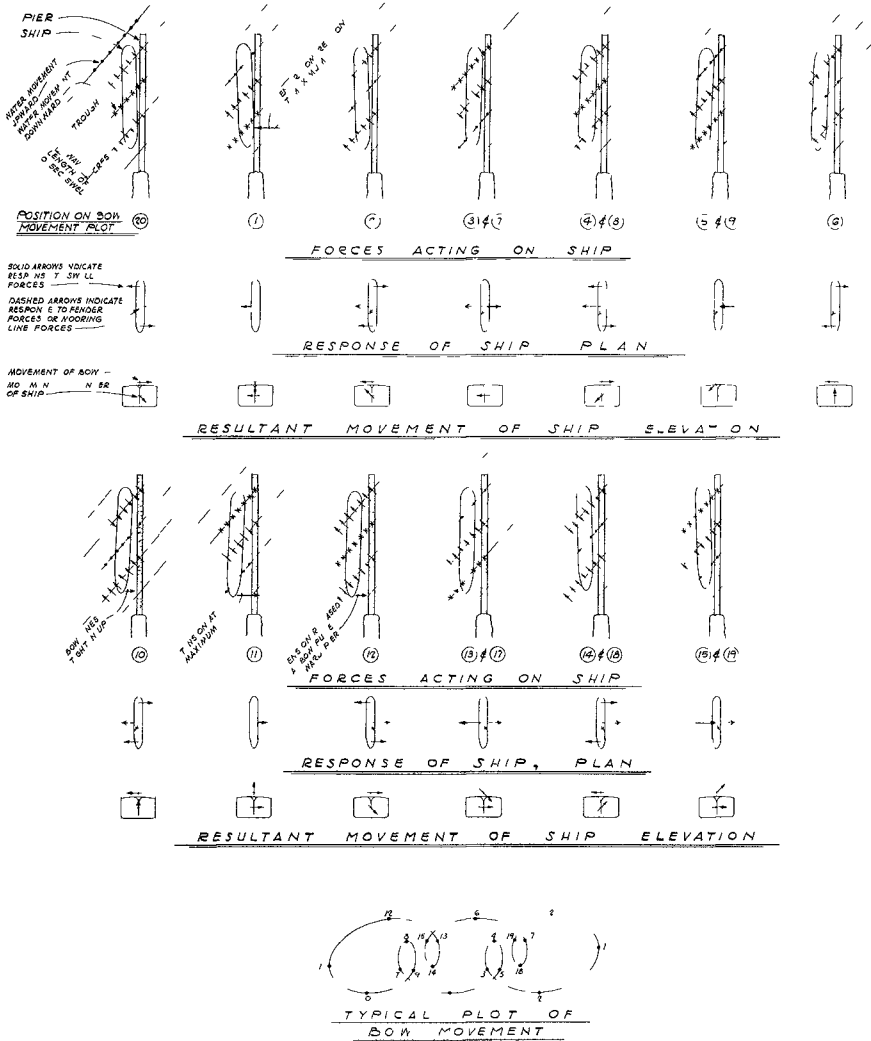


FIG 8 - SHIP MOVEMENT DIAGRAM, COMBINED SWELL AND MOORING FORCES

model It was also noted that the amount of slack in the mooring lines directly controlled the period of the transverse excursions of the model ship Another interesting observation was that a nonelastic or energy dissipating fender system attenuated the long-period excursions irrespective of the amount of slack in the mooring lines

The directional response of the ducted impellers of the current meters was essentially flat for a 60° sector centered parallel to the duct's axis, with the duct's axis at right angles to the water movement, however, a good null was obtained Direction was thus shown more clearly by a null position than by a centered position An inspection of the April, 1968, recordings confirmed the assumed swell approach azimuth of $\pm 300^\circ$

Upon completion of the water motion analysis and the model test observations, it was concluded that the major cause of the adverse ship motion was swell and not surge While the possibility of a surge problem could not be completely discounted, it was simply evident that swell was the greatest contributor to the ship motion problem The model tests confirmed also that the direction of swell approach to the pier caused the ship to oscillate with a yawing motion, and elastic fenders and mooring lines accentuated the problem

Additionally, it was established by calculation and model testing that this swell could be effectively attenuated by the construction of a break-water

SPECTRAL ANALYSIS

In comparing the April storms and the July storm, it was noted that the July storm contained significant long-period wave action of high energy content This surge was not evident during the April storms Because the July storm was of such exceptional intensity, a rather complete analysis of the water motion records was warranted

To precisely interpret this July record, a more sophisticated approach based on computer analysis was used The first objective was to obtain a power spectral density analysis for each direction of the horizontal velocity sensor by use of a digital computer Essentially, the computer program splits the total energy in the record into a number of frequency bands, and determines the uniform sinusoidal motion in every frequency band which would have the same power as the original record had in each band When performed on an analog computer, the analysis is more readily understood Here the input signal is an electrical current wherein voltage represents the quantity being measured, and the computer consists of a series of narrow band pass filters which ideally have square cut-offs The signal passing each filter is squared and averaged for the duration of the record to give a measure of the power in the original record which was contained in each frequency band Spectral analyses were computed by FORTRAN program ACAPS (Auto Correlation and Power Spectrum)(1) on a CDC 6600 computer

For the program used, the equivalent uniform sinusoidal motion could be calculated from

$$V_{\max} = 2\sqrt{SB_e} = \text{maximum velocity} \quad (1)$$

$$D = \gamma \frac{V_{\max}}{\omega} = \text{displacement} \quad (2)$$

and $T = \frac{2\pi}{\omega} = \text{period in seconds} \quad (3)$

in which S = spectral density, B_e = bandwidth in radians per second, and ω = mid-frequency of the band in radians per second. The equivalence can be applied to each bandwidth, individual peaks, or a group of peaks.

Record input for the spectral density calculation consists of discrete values of the velocity determined at a constant time interval, Δt , the sampling interval. The number of "lags" used in the calculation, m , is predetermined. The selection of total record length to be analyzed (which must be continuous), the sampling interval, and the number of lags are influenced by the following factors:

- 1 The maximum period for which the spectral density can be calculated with reasonable accuracy is approximately 1/10 of the total record time.
- 2 The minimum period for which the spectral density can be calculated is 2 times the sampling interval.
- 3 The number of frequency bands is equal to the number of lags.
- 4 The bandwidth is $\pi/(m\Delta t)$ or 1/ m times the frequency of the minimum calculated period.
- 5 The maximum calculated period (irrespective of accuracy of computation) is $2m\Delta t$.
- 6 The sampling interval, Δt , should be not more than approximately 1/4 of the minimum period in the record that contains a significant proportion of the total energy in the record.

If criterion 6 is not observed, the energy in these shorter periods will show up at spurious frequencies of longer period. For the instrument location at San Nicolas Harbor, the prevailing wind is offshore. This limits the fetch for local wind waves and gives assurance that the energy content in waves of less than 10-sec period is nominal. On this basis, a sampling interval of 3 sec was considered ideal.

For all wave records taken to date at San Nicolas Harbor, an attempt was made to obtain 4 hr of continuous record for each orientation of the horizontal velocity sensor. This method was based on the assumption that periods up to 24 min would be of interest. Subsequent studies have shown

that only tsunamis such as from the Alaskan earthquake in 1964 have significant velocities in this period range, and that an upper period limit of 6 min is reasonable for all wave action except tsunamis. On this basis, one hour of record was considered ideal for each spectral analysis.

Analyses were run with 720 lags and 360 lags for comparison. The 720-lag solution gave better definition of the component peaks, showed essentially the same total energy content, and was used for most of the data analysis.

Fig. 9 is a typical spectral density plot for the horizontal water motion of the seven successive headings for the July 26-27 wave conditions.

CROSS SPECTRAL ANALYSIS

A further development of spectral analysis is the cross-spectral analysis, in which two separate records are analyzed. Output of this analysis includes the spectral densities of each record, the cross-spectra consisting of two parts, real and imaginary, the coherence, and the phase coherence.

The cross-spectral analyses were computed for the study by FORTRAN program CROSPEC on a CDC 6600 computer. CROSPEC computes cross-correlation and cross-power spectral density functions for two or more time-series, and was developed from subroutines published by Robinson (2).

Cross-spectral analyses were run on the simultaneous vertical and horizontal velocity records for the 270° heading of July 26, and for the simultaneous ship's horizontal bow velocity and the horizontal water velocity of April 19. For the latter analysis, the displacement plots from the time-lapse movie sequence were converted to horizontal velocity rates by determining the horizontal distance moved every 2 sec.

The results of this analysis are shown in Figs. 10, 11, and 12. Fig. 10 shows the power spectrum of each motion plotted on the same graph. The excellent correlation in the range of periods for swell is readily apparent, while in the long-period range, especially from 90 sec to 110 sec, the ship motion has considerably more energy than the water motion. These results are also shown in Fig. 11, which presents a tabulation of the equivalent uniform sinusoidal motions corresponding to the energy peaks of the two spectra.

Fig. 12 shows the coherence and phase coherence from this analysis. For the coherence between the two records, a value of 1.0 shows excellent correlation and a value of 0.0 represents a completely random relationship. Here again, good coherence is shown in the swell range, some coherence in the 90-sec to 110-sec range, and an essentially random relationship in all other frequencies.

The phase coherence shows consistent values only in the swell range where the phase-angle values are clustered close to 0° . There is actually a 90° phase lag in the ship's response to the swell, but this phase difference was compensated by a time shift in the input data for the ship's

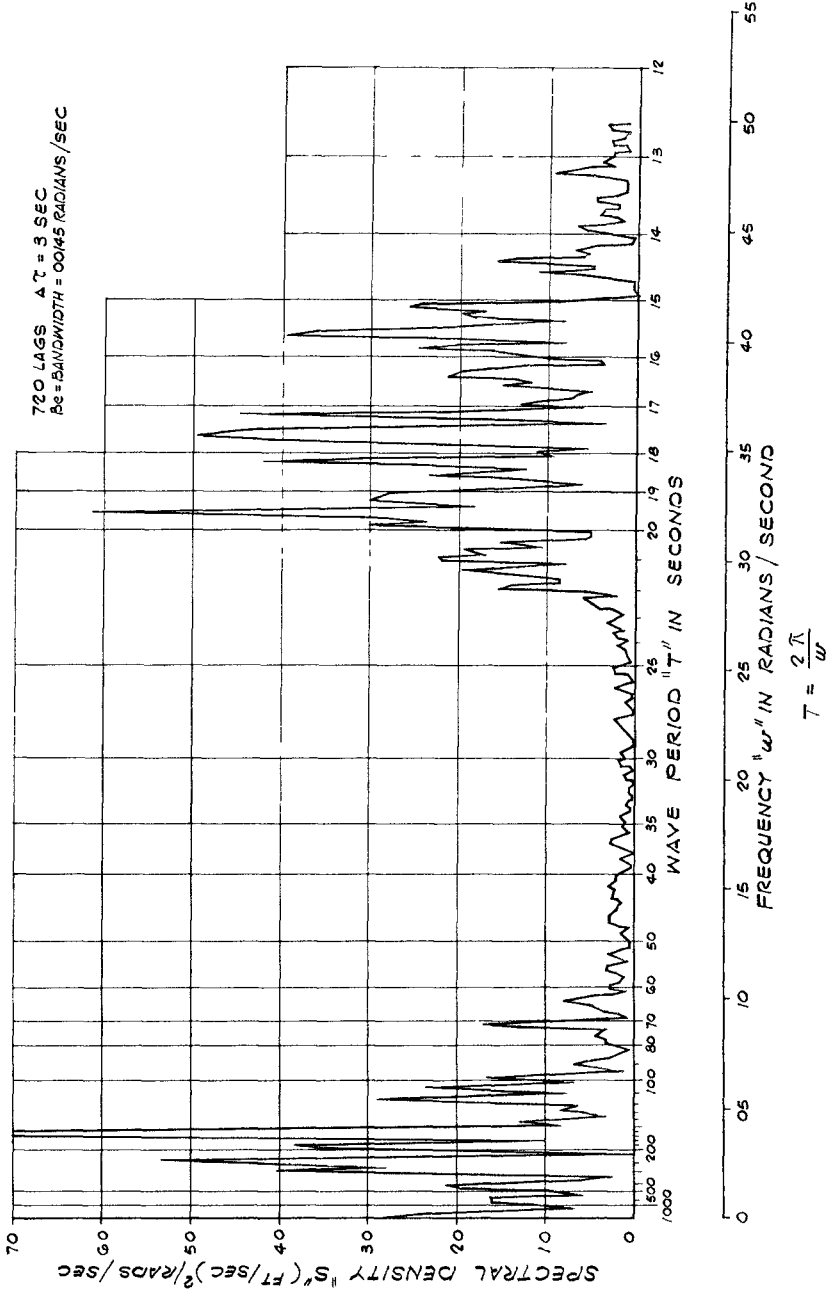


FIG 9 - HORIZONTAL WATER VELOCITY SPECTRUM 270° AZIMUTH,
 10 30-11 30, JULY 26, 1968

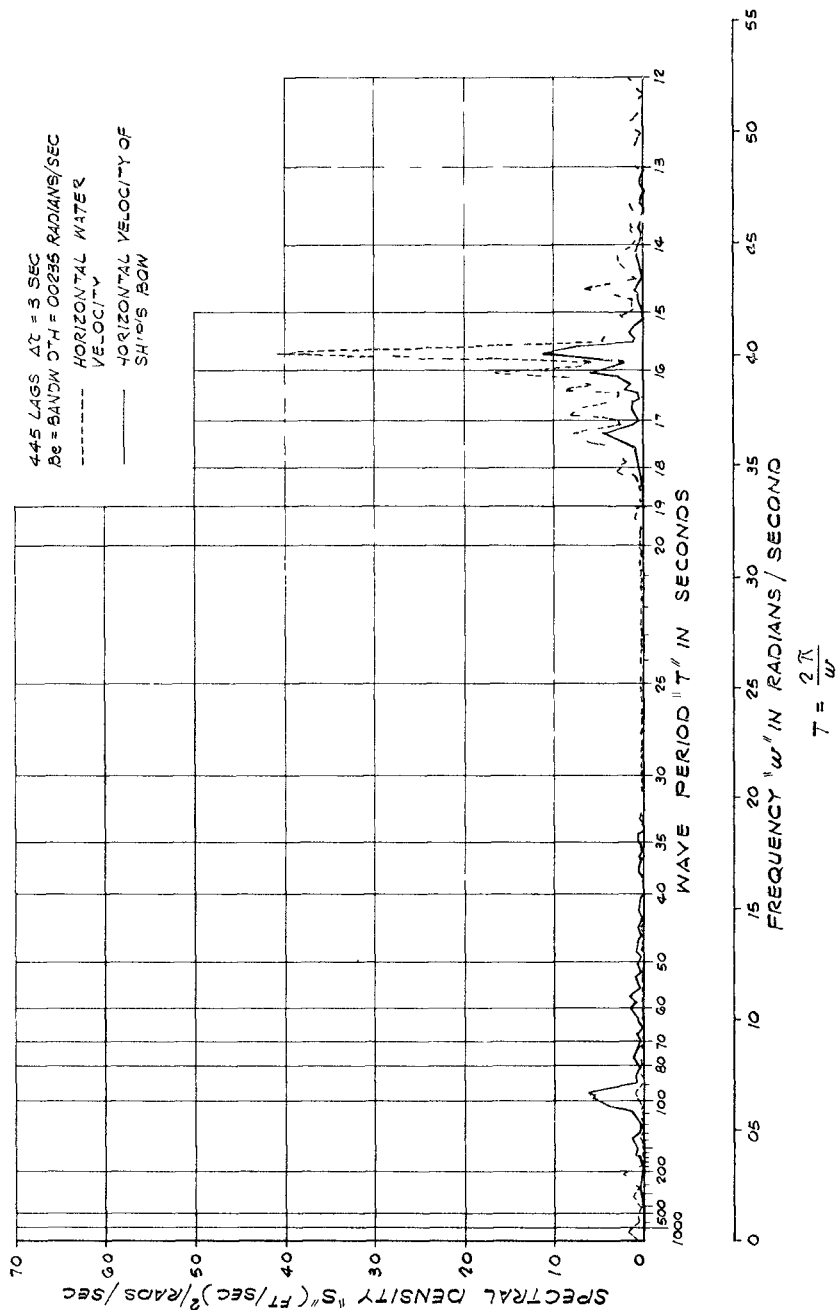


FIG 10 - SPECTRA OF HORIZONTAL WATER VELOCITY AND HORIZONTAL VELOCITY OF SHIP'S BOW 270° AZIMUTH, 11 12-11 53, APRIL 19, 1963

T = PERIOD IN SECONDS
 V = MAXIMUM HORIZONTAL VELOCITY
 D = HORIZONTAL DISPLACEMENT - FT

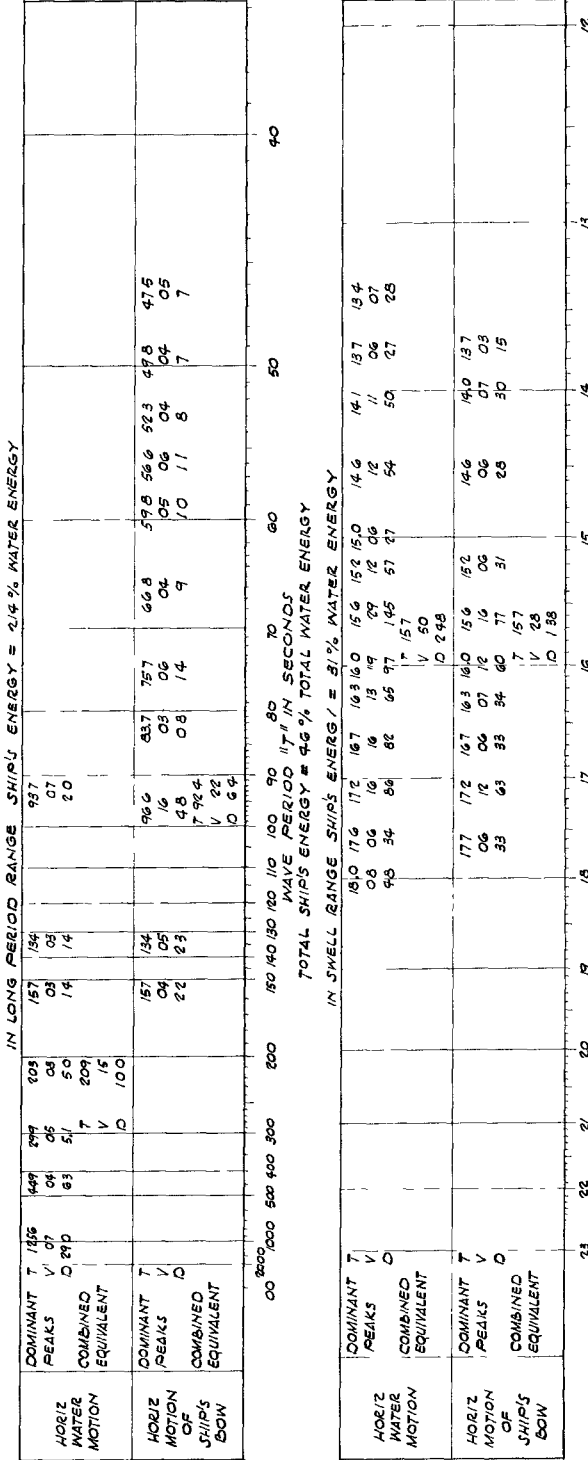


FIG 11 - TABULATION OF EQUIVALENT SINUSOIDAL MOTION EAST-WEST HORIZONTAL WATER MOTION AND MOTION OF SHIP'S BOW, 11 15-11 53, APRIL 19, 1968

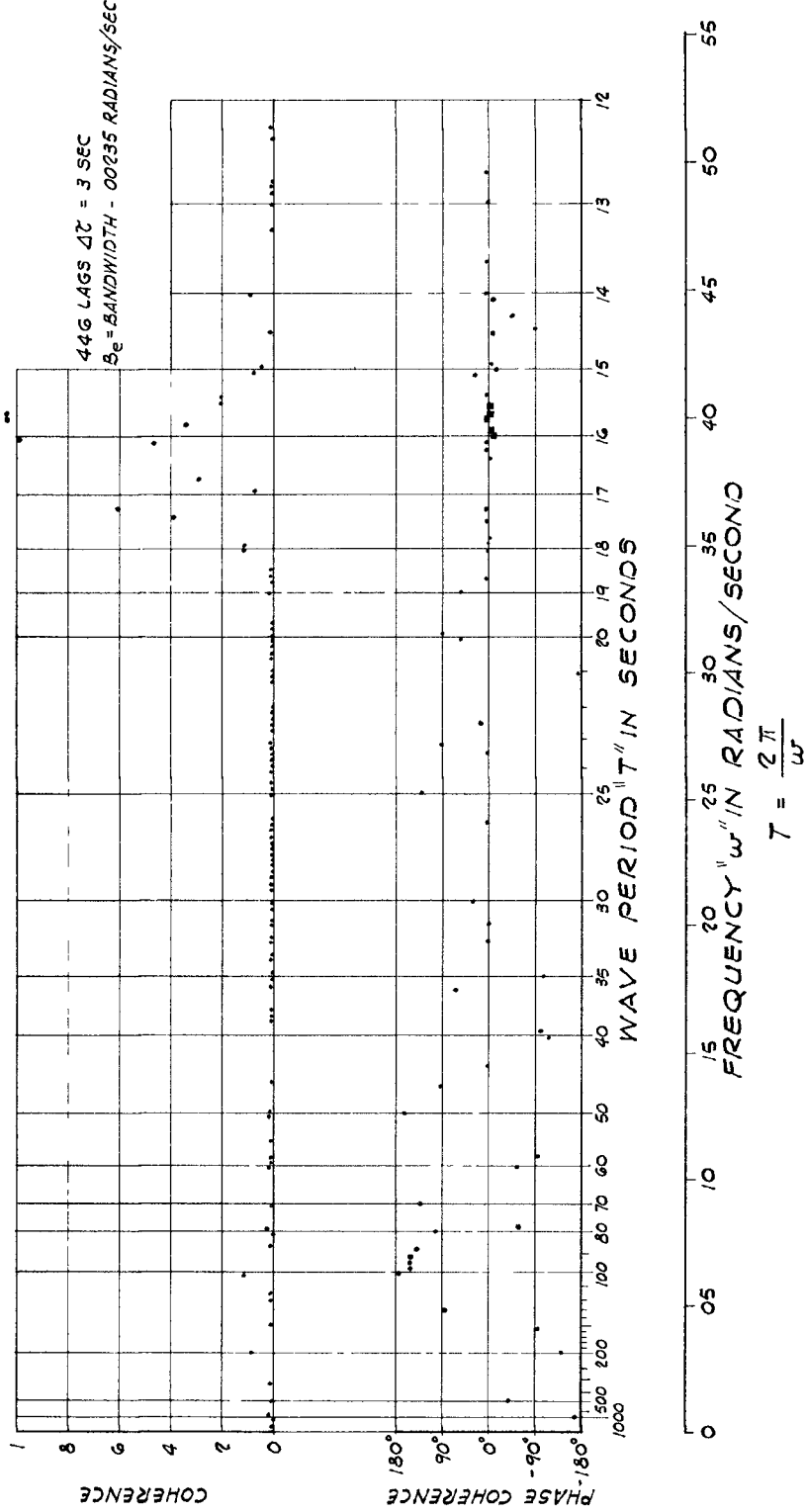


FIG 12 - CROSS-SPECTRA ANALYSIS OF EAST-WEST HORIZONTAL VELOCITY OF WATER AND MOTION OF SHIP'S BOW, 11 15-11 53, APRIL 19, 1968

motion. Elsewhere, the phase-angle relationship is essentially random except for a tendency of values to cluster around 180° at 90 sec to 110 sec. No firm explanation is offered for this last trend, but it might be that the time shift from 90° to 0° in the input data for the periods for swell may have shifted the long-period coherence in a direction opposite to the anticipated value of 90° . No clear physical significance of the real and imaginary cross-spectral functions could be determined, hence, plots of these values are not shown.

The results for the vertical and horizontal water velocity cross-spectral analyses were not as consistent as analysis results for the ship motion and horizontal water motion. Fig. 13 shows a dual plot of the spectral densities for both the horizontal and the vertical water velocities, and Fig. 14 shows a plot of the equivalent sinusoidal wave components corresponding to the peaks in each power spectrum. In Fig. 13, the spectral density scale for the vertical velocity is expanded to better illustrate the correlation between the two. It can be noted that the period range for swell again has good correlation, but the long-period correlation is rather inconsistent. Especially significant are a few frequencies, such as those near 36 sec, where the vertical spectral density function value is proportionally higher than elsewhere. This relationship could be interpreted in three possible ways:

1. The instrument was near an anti-node of a standing wave. For such a wave the water particle motion would be vertical only and a corresponding horizontal peak would not exist.
2. An incident wave of that period passed at right angles to the horizontal sensor. In this null direction, the horizontal velocity component would not register.
3. The relatively high horizontal velocities, combined with floating seaweed caught on the instrument supporting pipe, deflected the vertical duct out of plumb and thereby caused the vertical sensor to register some of the horizontal velocity as a false downward component. For a heavy swell, the false velocity component would not reverse since the false downward component would not be affected by the direction in which the instrument was out of plumb. Such behavior would show up as an unduly high peak in the power spectrum of the vertical velocity, indicating a false downward displacement.

This last interpretation was believed to be correct, since the displacement plot derived from the vertical velocity record also showed a false downward movement of the water surface considerably greater than that normally expected. Fig. 15 shows the displacement plot and the horizontal velocity record to the same time scale. Correlation between the rate of downward displacement and the magnitude of horizontal velocity is insufficient for this condition to be interpreted as the sole cause of the anomalous peaks in the power spectrum of the vertical velocity record. The availability of velocity readings, however, were deemed unreliable due to the downward reading and no further analysis was done using the vertical velocity records. In further applications, this problem could probably be eliminated by modification of the instrument mounting arrangement.

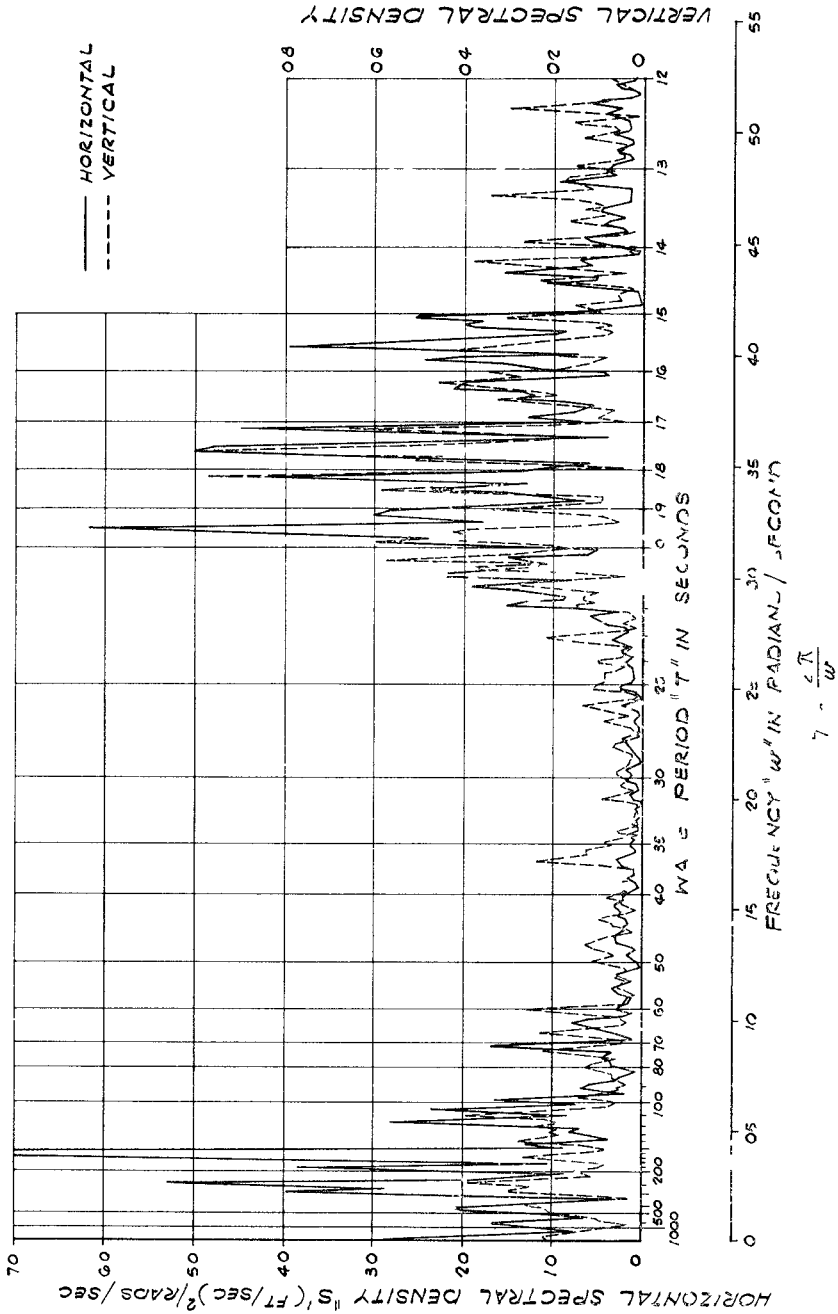


FIG 13 - SPECTRA OF HORIZONTAL AND VERTICAL WATER VELOCITIES, 270° AZIMUTH, 10 30-11 30 JULY 26, 1968

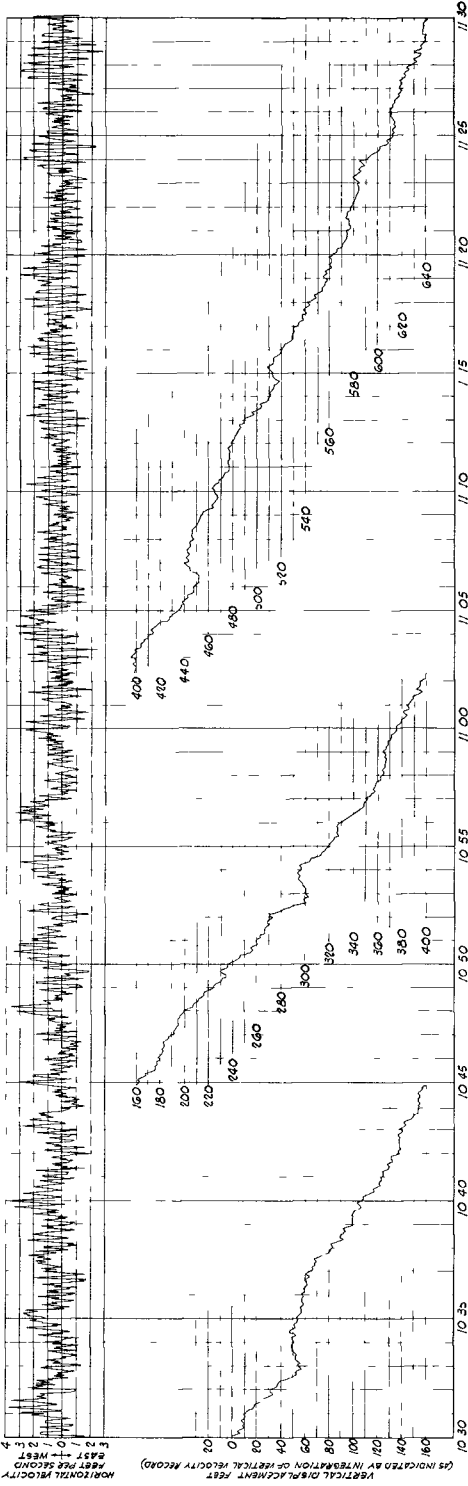


FIG 15 - HORIZONTAL WATER VELOCITY, 270° AZIMUTH DISPLACEMENT DERIVED FROM VERTICAL VELOCITY RECORD, 10 30-11 30, JULY 26, 1968

A primary purpose of the analysis of the July 26-27 data was to determine the magnitude and type of long-period waves. The magnitude as shown by the power spectra of the horizontal velocity records left no doubt as to the importance of the long-period waves. Energy content was nearly as high as that of the swell, and the energy content recorded for both long-period waves and swell depicted conditions much too rough for mooring a large ship alongside the pier. The cross-spectral analysis of the vertical and horizontal velocity records was expected to provide a major contribution in determining whether long-period waves were incident waves similar to the swell, resonant or standing waves, or a combination of incident and reflected waves. Since the questionable validity of the vertical velocity readings eliminated this possibility, the power spectra of the horizontal velocities were used instead.

Fig. 16 shows a tabulation of the equivalent uniform sinusoidal wave components corresponding to each energy peak of the horizontal spectra in the swell range, Fig. 17 shows a similar tabulation for the energy peaks of the horizontal spectra in the long-period range. For each heading a combined equivalent wave for each period range is also included.

If the long-period waves were a resonance phenomenon, nearly identical peaks would be expected, especially for waves approaching from azimuths of 295° and 300° , and long-period waves caused by a beat generated by the swell periods would be expected to change in period in accordance with shifts in the swell periods.

A study of Fig. 16 indicates that during the recorded interval

- 1 The periods of swell shifted towards the shorter range
- 2 The total swell energy decreased in magnitude by a little more than 40%
- 3 Most of the swell approached the north end of the pier from an azimuth of approximately 300°
- 4 Several of the peak periods were present throughout the entire recording period

A similar study of Fig. 17 indicates that during this interval

- 1 The energy content of the long-period waves decreased in magnitude by approximately 80%
- 2 The null direction of the long-period waves was not as clearly defined as for the swell, the dominant direction, however, was similar to the direction of swell
- 3 Shifts in period were apparently rather random and did not correspond to the shift to shorter periods of the swell
- 4 Very few of the peaks were apparent throughout the recording period

V - MAXIMUM HORIZONTAL VELOCITY - FT SEC
 D - HORIZONTAL DISPLACEMENT - FT
 T - PERIOD SECONDS

270 D 30, 11 30 26 JUL 68	DOMINANT	T	21.8	21.2	20.5	20.3	19.6	19.0	18.5	18.2	17.6	17.1	17.2	16.5	16.1	15.2	14.8	14.3	14.2	13.9	13.5	13.1	13.0	
	PEAKS	V	165	210	250	150	400	239	222	260	384	270	150	236	230	300	254	125	152	076	118	076	118	100
	COMBINED EQUIVALENT	D	115	148	165	97	250	145	131	150	215	147	80	122	116	143	123	58	70	43	52	41	49	41
300 D 30, 15 30 26 JUL 68	DOMINANT	T	22.3	21.7	20.9	20.3	19.7	19.2	18.9	18.3	17.7	17.2	17.2	16.5	16.1	15.2	14.4	14.1	14.1	13.7	13.7	13.7	13.0	
	PEAKS	V	112	117	183	287	239	327	255	163	401	274	274	383	163	290	194	251	156	190	156	190	153	
	COMBINED EQUIVALENT	D	79	81	122	147	150	120	153	95	212	152	171	204	84	145	94	115	51	81	81	81	65	
330 D 00, 19 00 26 JUL 68	DOMINANT	T	21.7	21.1	20.8	20.3	19.4	19.0	18.6	18.0	17.7	17.3	17.0	16.4	16.2	15.8	14.8	14.5	14.3	13.8	13.5	13.3	12.9	
	PEAKS	V	163	248	326	177	372	214	233	282	187	310	316	306	294	282	265	165	144	120	182	138	152	
	COMBINED EQUIVALENT	D	71	63	50	114	230	189	138	164	105	171	171	160	152	142	129	78	67	55	80	60	64	
360 D 30, 23 30 26 JUL 68	DOMINANT	T	19.4	19.0	18.3	17.9	17.3	17.0	16.4	15.9	15.5	15.5	15.5	14.9	14.6	14.3	13.5	13.7	13.5	13.7	13.5	13.7	12.9	
	PEAKS	V	119	086	125	187	153	239	107	229	131	142	107	142	107	100	184	119	100	121	111	100	121	
	COMBINED EQUIVALENT	D	74	59	73	107	84	189	56	116	65	167	50	159	50	46	55	82	40	47	46	40	47	
30 D 30, 02 30 27 JUL 68	DOMINANT	T	18.3	18.0	17.5	17.1	16.7	16.3	15.9	15.5	15.2	15.2	15.2	14.8	14.5	14.3	13.6	13.8	13.6	13.8	13.6	13.8	12.9	
	PEAKS	V	071	074	099	079	067	079	067	079	067	079	067	079	067	079	067	079	067	079	067	079	067	
	COMBINED EQUIVALENT	D	57	43	55	43	36	41	37	43	36	41	37	43	36	41	37	43	36	41	37	43	36	
60 D 30, 06 30 27 JUL 68	DOMINANT	T	19.2	18.6	17.9	17.3	16.9	16.5	16.4	15.8	15.5	15.2	15.2	14.8	14.5	14.3	13.6	13.8	13.6	13.8	13.6	13.8	12.9	
	PEAKS	V	094	073	117	110	098	102	074	110	066	091	083	091	083	38	26	38	26	38	26	38	26	
	COMBINED EQUIVALENT	D	45	43	78	61	59	50	53	37	67	32	43	38	24	24	38	26	24	24	38	26	24	
99 D 30, 10 30 27 JUL 68	DOMINANT	T	19.0	18.3	17.6	17.0	16.6	16.1	15.8	15.4	15.4	15.4	15.4	14.8	14.5	14.2	13.5	13.7	13.5	13.7	13.5	13.7	12.9	
	PEAKS	V	120	079	119	319	223	271	232	118	334	192	113	140	154	068	102	154	068	102	154	068	102	
	COMBINED EQUIVALENT	D	78	46	74	147	148	141	137	114	56	62	87	63	27	40	59	63	27	40	59	63	27	

FIG 16 - TABULATION OF EQUIVALENT SINUSOIDAL WAVE COMPONENTS FOR SWELL

These observations implied that the long-period waves are progressive waves originating from the same storm center as the swell, and that resonance of the bay is probably not an important factor. Unlike the energy of the swell, very little of the long-period wave energy is dissipated in breakers on the shore and most of the waves are reflected back to the ocean.

Some of the long-period waves are probably reflected more than once before returning to the ocean, which would explain their lack of a clear null direction.

APPLICATION TO HARBOR PROGRAM

Based on the preceding analysis, it was concluded that ocean swells refracted around Point San Nicolas and approaching the pier from the $\pm 30^\circ$ azimuth were the primary source of adverse mooring conditions at the pier. A breakwater similar to that shown in Fig. 18 is currently under construction at San Nicolas. The breakwater is expected to attenuate ocean swell so that wave action in the swell range will no longer cause interpretations to ore loading operations. Attenuation of long-period waves of high energy content will be nominal, but for these unusual occurrences, the breakwater will have some beneficial effect by reorienting these long-period waves so that their horizontal water motion will be primarily north-south or parallel to moored ships rather than east-west as at present.

CONCLUSIONS

The age-old problems of harbor design are becoming increasingly complex due to phenomenal increases in the sizes of modern ships. Fortunately, our burgeoning technology is developing many new and powerful tools which can be applied in solving these problems. The harbor study at San Nicolas adequately defined wave movement so that an economical solution could be obtained. The full potential of the techniques used was not applied, but experience gained during the study indicates the capability for improved results in similar applications.

Ducted impeller meters provided an extremely valuable means for studying harbor wave action. These instruments were especially useful in measuring long-period swells and surges which were difficult to identify by sight.

Spectral analysis methods proved well-suited to detailed interpretation of the particle velocity records, considerable insight into the wave phenomena was gained by simple, rational inspections and interpretations of the records.

Time-lapse movies of a moored ship in motion, when correlated with simultaneous water particle velocity records, provided an exceptionally clear picture of ship response to wave action, and led to the rather surprising observation that long-period ship motion is not necessarily caused by long-period waves.

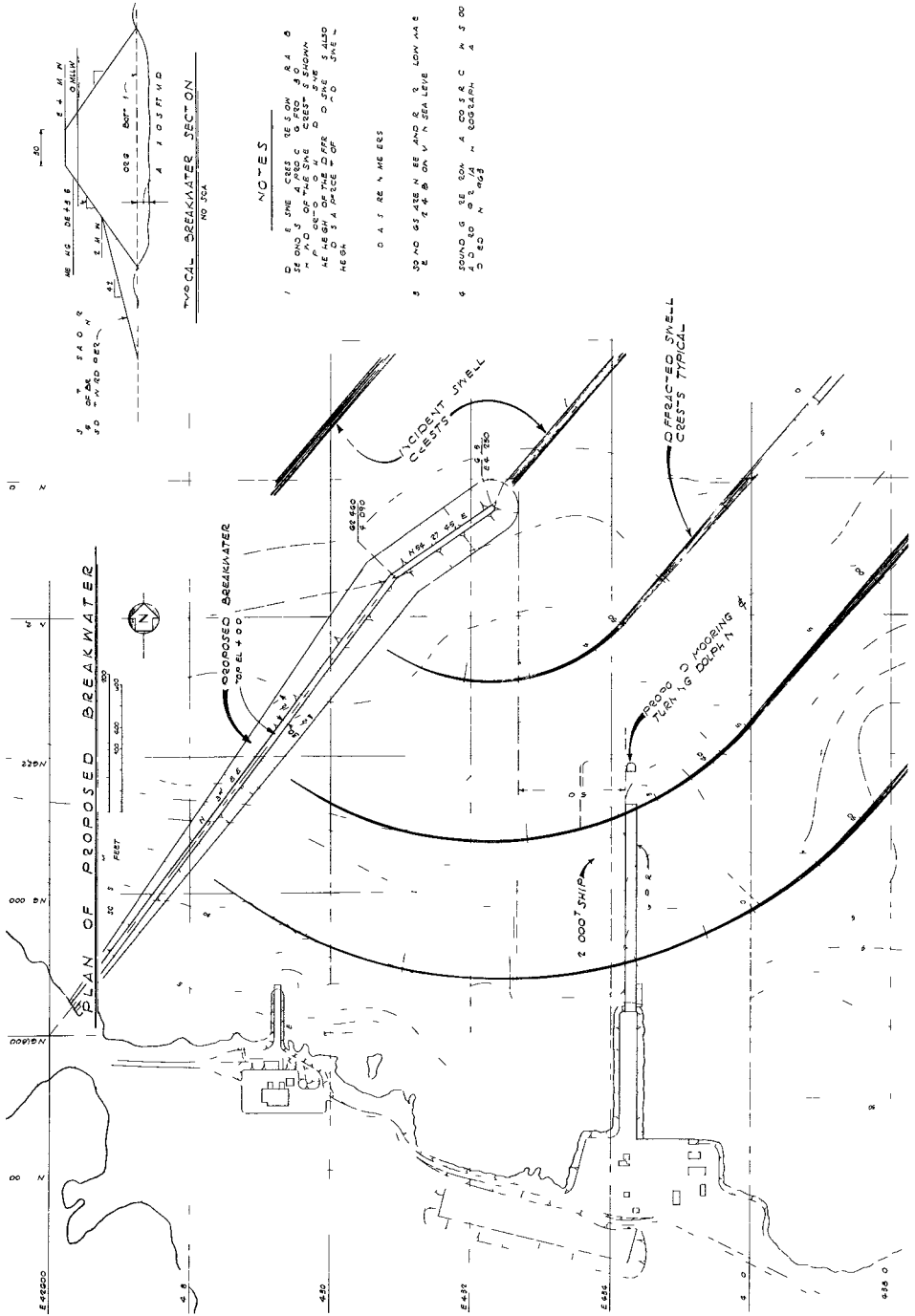


FIG 18 - PRELIMINARY STUDY OF BREAKWATER FOR SAN NICOLAS BAY, PERU

The usefulness of hydraulic model tests was again demonstrated, and it should be noted that very useful results can be obtained from model tests at modest expense if the test goals are clearly defined and the test work performed simply and judiciously

ACKNOWLEDGMENTS

The writers especially wish to express their appreciation to Marcona Corporation for permission to publish this paper. The writers also wish to thank the many individuals within Marcona Corporation and John A. Blume & Associates who participated in the harbor study. Dilip Jhaveri, who selected and modified the computer programs used for the spectral analyses, and J. W. Johnson, who was an engineering consultant for the harbor study, deserve special mention for their contributions to the study program.

APPENDIX-REFERENCES

- 1 Liu, S. C., and Jhaveri, D. P., "Spectral and Correlation Analysis of Ground-Motion Accelerograms," *Bulletin, Seismological Society of America*, Vol. 59, No. 4, August, 1969, pp. 1517-1534.
- 2 Robinson, E. A., *Multichannel Time Series Analysis with Digital Computer Programs*. Holden-Day, Inc., San Francisco, 1967.
- 3 Shanting, D. H., "Observations of Particle Motions in Ocean Waves," AD 658876, Clearinghouse for Federal Scientific and Technical Information, Springfield, Virginia, July, 1967.

CHAPTER 134

TIDAL MOTION IN BAYS

by

O H Shemdin, Associate Professor
R M Forney, Research Assistant

Department of Coastal and Oceanographic Engineering
University of Florida, Gainesville, Florida

ABSTRACT

A method is proposed to investigate periodic tidal motion in single or multiple basins connected to the ocean by an inlet. Non-sinusoidal tidal motion in the ocean and square friction law in the inlet are both considered. The method is applied to Boca Raton inlet, Florida. The calculated tidal elevation and velocity in the inlet are found to be in reasonable agreement with measured values. The bottom shear friction coefficient is defined

$$\tau_{to} = \rho r u|u|$$

where ρ is the water density, τ_{to} is the shear stress, and u is the average velocity in the inlet. The results of the study yield $r = 0.0039$, and predict net transport of sediment into the bay.

INTRODUCTION

The dynamics of tidal motion in a bay connected to the ocean by an inlet was investigated by Brown (1928) who considered only sinusoidal tidal motion in the ocean and linear bottom friction in the inlet. Later, Keulegan (1951) treated the same problem but included the square friction law in the inlet and predicted a non-sinusoidal oscillation in the bay elevation. Van de Kreeke (1968) developed a scheme which predicted tidal oscillations in bays in the presence of freshwater inflow by rainfall or streams. The above investigations were all limited to a sinusoidal tidal oscillation in the ocean and all neglected flow acceleration in the inlet.

An extensive treatise on tides and tidal propagation is given by Dronkers (1964). It is known that tidal motion is not simple but has many harmonic constituents. The principal components are shown in Table I.

Table 1 Principal Tidal Components

<u>Symbol</u>	<u>Component</u>	<u>Periods (hrs)</u>
M2	Principal lunar semidiurnal	12 421
S2	Principal solar semidiurnal	12 000
N2	Lunar elliptic semidiurnal	12 658
K1	Lunisolar declinational diurnal	23 936
O1	Lunar declinational diurnal	25 819

The relative importance of the different constituents depends on geographical location and depth of water. The principal lunar semidiurnal component (M-2) has usually the highest amplitude.

This study proposes a general method for analyzing tidal oscillation in bays connected to the ocean by inlets. It includes acceleration of flow in the inlet, square friction law, and a non-sinusoidal tidal oscillation in the ocean. The method utilizes the general equations of motion and approximates the periodic tidal oscillation by a series in circular functions. Use is made of complex variables to simplify computations. The method can be applied to multiple basins connected to each other and to the ocean. The present study is restricted to relatively deep bays in which negligible spacial variation in water elevation exist. The inlet area is assumed constant and equal to the mean area during one tidal cycle. The method can be applied, however, to shallow bays. The method has a resemblance to Dronker's (1964) harmonic method of tidal propagation although he did not specifically apply the method to inlets. A method proposed by Sidjabat (1970) for describing the nonlinear friction is employed in this study.

THEORETICAL APPROACH

The theoretical development to follow describes the dynamics of flow in an inlet with a constant cross sectional area connected on one side to a basin with uniform water level and on the other side to an ocean which has harmonic but non-sinusoidal tidal oscillation. The flow in the inlet is assumed one-dimensional. Resonance and bottom friction in the bay are neglected. Quantitatively bays satisfying these conditions must be at least 20 feet deep when the longest dimension equals 5 miles.

A Single Bay Coupled to Ocean

A definition sketch is shown in Figure 1. The equation of motion in the x-direction (direction of inlet flow) is used to describe the inlet flow

$$\frac{\partial u}{\partial t} + u \frac{\partial u}{\partial x} + w \frac{\partial u}{\partial z} = - \frac{1}{\rho} \frac{\partial p}{\partial x} + \frac{1}{\rho} \frac{\partial T_v}{\partial z}, \quad (1)$$

where u is the inlet velocity, p is the pressure, ρ is the water density, and T_v is the viscous shear stress. Denoting

$$u(x,y,z,t) = U_m(x,z,t) + u'(x,y,z,t)$$

$$w(x,y,z,t) = w'(x,y,z,t) \quad ,$$

where U_m denotes the mean flow over a length of time, T , which is small compared to tidal period by long compared to time scale turbulence. The overbar is taken to denote averaging over period T .

$$\bar{u} = \frac{1}{T} \int_0^T u dt = U_m$$

Equation (1) becomes

$$\frac{\partial U_m}{\partial t} + \frac{\partial}{\partial x} (U_m^2 + \overline{u'^2}) = -\frac{1}{\rho} \frac{\partial p}{\partial x} + \frac{1}{\rho} \frac{\partial}{\partial z} (\tau_v + \tau_t) \quad , \quad (2)$$

where τ_v is the turbulent Reynolds stress defined by

$$\tau_t = -\rho \overline{u'w'} = -\rho \int_0^T u' w' dt$$

Next, a vertical average over the depth h is specified. We define

$$U(x,t) = \frac{1}{h} \int_0^h U_m(x,z,t) dz \quad (3)$$

Integrating Equation (2) over depth and assuming hydrostatic pressure distribution

$$\frac{\partial U}{\partial t} + \alpha \frac{\partial}{\partial x} U^2 = -g \frac{\partial h}{\partial x} - \frac{1}{\rho h} (\tau_v + \tau_t)_0 \quad , \quad (4)$$

where

$$\alpha U^2 = \frac{1}{h} \int_0^h (U_m^2 + \overline{u'^2}) dz \quad ,$$

and the subscript 0 denotes bottom values ($z = 0$). From open channel considerations α is the momentum factor and is of the order of 1.05. The value of 1.0 will be assumed sufficiently accurate. In inlets, the flow is mostly turbulent except when it approaches zero during a tidal reversal. The bottom shear stress will be assumed to be primarily due to turbulence rather than viscosity ($\tau_v \ll \tau_t$) and to have the empirical square-law form

$$\tau_{t0} = \rho r U|U| \quad , \quad (5)$$

where r is the friction coefficient Equation (4) now becomes

$$\frac{\partial U}{\partial t} + \frac{\partial}{\partial x} U^2 = -g \frac{\partial h}{\partial x} - \frac{r}{h} U|U| \quad (6)$$

Equation (6) is applied to the inlet shown in Figure 1 Integration of Equation (6) along the x -direction yields an equation which relates the ocean level to that in the basin Assuming the inlet is finite in length and the velocity accelerates towards the inlet but achieves a constant velocity, U_1 , in the inlet, Equation (6) is integrated to yield

$$h_s = h_{b_1} + \frac{\partial U_1}{\partial t} \frac{L_1}{g} + \left(1 + \frac{r}{h_1} L_1\right) \frac{U_1 |U_1|}{g} \quad , \quad (7)$$

where h_s , h_{b_1} , L_1 and h_1 are defined in Figure 1 The equation of mass conservation consistent with the above assumptions becomes

$$U_1 A_1 = A_{b_1} \frac{dh_{b_1}}{dt} \quad , \quad (8)$$

where \hat{A}_1 and A_{b_1} are as defined in Figure 1 Equation (8) further assumes that the changes in A_{b_1} and A_1 due to depth changes are small over a tidal cycle Eliminating U_1 in Equation (7) yields

$$h_s = h_{b_1} + \left(\frac{A_{b_1}}{A_1}\right) \frac{L_1}{g} \frac{d^2 h_{b_1}}{dt^2} + \left(1 + \frac{r L_1}{h_1}\right) \frac{1}{g} \left(\frac{A_{b_1}}{A_1}\right)^2 \frac{dh_{b_1}}{dt} \left| \frac{dh_{b_1}}{dt} \right| \quad (9)$$

1 The Linearized Solution for Simple Motion

The tidal motion in the ocean is described by complex variables to simplify computations

$$h_s(t) = \hat{h}_s e^{i\sigma t} \quad , \quad (10)$$

where \hat{h}_s is a complex number and σ is the tidal frequency Let

$$h_{b_1} = -i \hat{h}_{b_1} e^{i\sigma t} \quad ,$$

where \hat{h}_{b1} is a real number representing the bay tidal amplitude. Linearization of the last term in Equation (9) implies

$$\frac{dh_{b1}}{dt} \left| \frac{dh_{b1}}{dt} \right| \approx \frac{8}{3\pi} \sigma^2 h_{b1} e^{i\sigma t} + \dots$$

which yields the solution

$$\hat{h}_s = \hat{h}_{b1} [\zeta \hat{h}_{b1} - i\eta] \quad (11)$$

where

$$\zeta = \frac{8}{3\pi} \left(1 + \frac{r_1}{h_1} L_1 \right) \frac{1}{g} \left(\frac{A_{b1}}{A_1} \right)^2 \sigma^2$$

and

$$\eta = \left[1 - \left(\frac{A_{b1}}{A_1} \right) \frac{L_1}{g} \sigma^2 \right]$$

The term $\left(\frac{A_{b1}}{A_1} \right) \frac{L_1}{g} \sigma^2$ represents the flow acceleration and has been traditionally neglected. It need not be always negligible compared to 1.0, it was found to be equal to 0.25 for Macquarie Harbor which was studied by Van de Kreeke (1968). The amplitude and phase shift of the ocean fluctuation are given respectively,

$$|\hat{h}_s| = \hat{h}_{b1} \sqrt{(\zeta \hat{h}_{b1})^2 + \eta^2} \quad (12)$$

and

$$\tan \theta = - \frac{\eta}{\zeta \hat{h}_{b1}} \quad (13)$$

O'Brien (1969) proposed an empirical relationship between the tidal prism, P, and inlet area A_1

$$A_1 = CP \quad (14)$$

where C is a constant. The present analysis yields an analytical representation for C which can be used to test the empirical constant of O'Brien

$$C = \frac{\left(\frac{8}{3\pi} \right) \left(1 + \frac{r_1}{h_1} L_1 \right) \frac{\sigma^2}{g} \left(\frac{A_{b1}}{A_1} \right)^2 \tan \theta}{2 \left[\left(\frac{A_{b1}}{A_1} \right) \frac{L_1}{g} \sigma^2 - 1 \right]} \quad (15)$$

2 Solution for Non-sinusoidal Motion

The tidal motion in the ocean is not simple as indicated previously so that sinusoidal simplifications introduce errors. Since the bay motion is affected by nonlinear friction, motion is not simple even when the ocean motion is. The latter case was investigated in detail by Keulegan (1951). When the tidal motion in the ocean is periodic but not simple, the bay motion is even more complex since each ocean harmonic constituent generates its own harmonic as well as multiple harmonics due to nonlinear friction. Thus a linearized procedure becomes invalid, in fact it is unrealistic and suggests negative friction at the higher harmonics.

In the following a method is proposed to describe the harmonic motion in both bay and ocean. The complex representation is employed

$$h_s = \sum_n \frac{1}{2} (r_n - i s_n) e^{i n \sigma t} \quad , \quad (16)$$

and

$$h_{b_1} = \sum_n \frac{1}{2} (c_n - i d_n) e^{i n \sigma t} \quad , \quad (17)$$

where the summation ranges over both positive and negative values of the index n which specifies the principal tidal frequencies, linear combinations thereof, and higher harmonics. The terms corresponding to $n = 0$ reflect mean levels in ocean and bay. Since h_s and h_{b_1} are real functions, the following relationships must be satisfied (Lee b_1 (1967))

$$\begin{aligned} r_n &= r_{-n} & , & & s_n &= -s_{-n} \\ c_n &= c_{-n} & , & & d_n &= -d_{-n} \end{aligned} \quad (18)$$

The average velocity is specified by

$$U(t) = \sum_n \frac{1}{2} (a_n - i b_n) e^{i n \sigma t} \quad (19)$$

where

$$a_n = a_{-n} \quad , \quad b_n = -b_{-n}$$

The representation of τ_{to} in series form was considered by Sidjabat (1970) in conjunction with tidal propagation in wide shallow bays. His description of the nonlinear term is conveniently adopted. Equation (15) may be expressed

$$\tau_{to} = \rho r \left[\sum_{\ell} \sum_m \frac{1}{4} (a_{\ell} - i b_{\ell}) (a_m - i b_m) e^{i(\ell+m)t} \right]^{1/2} \sum_n (a_n - i b_n) e^{i n \sigma t}$$

which is equivalent to

$$\tau_{to} = \rho r \left[\sum_{\rho} \frac{1}{4} (a_{\rho}^2 + b_{\rho}^2) + \sum_{\rho} \sum_{\ell \neq m} \sum_{m} \frac{1}{4} (a_{\rho} - 1b_{\rho}) (a_m - 1b_m) e^{1(\ell+m)t} \right]^{1/2} \sum_n (a_n - 1b_n) e^{1n\sigma t} \quad (20)$$

Denote

$$\lambda^2 = \sum_{\rho=-\infty}^{\infty} \frac{1}{4} (a_{\rho}^2 + b_{\rho}^2) = \frac{1}{2} \sum_{\rho=0}^{\infty} (a_{\rho}^2 + b_{\rho}^2) \quad (21)$$

Then

$$\tau_{to} = \rho r \lambda (1+\epsilon)^{1/2} \sum_n (a_n - 1b_n) e^{1n\sigma t} \quad , \quad (22)$$

where

$$\epsilon = \frac{1}{\lambda^2} \sum_{\rho} \sum_{\ell \neq m} \sum_{m} \frac{1}{4} (a_{\rho} - 1b_{\rho}) (a_m - 1b_m) e^{1(\ell+m)\sigma t}$$

It was found by Sidjabat (1970) that in areas where M2 is the dominant tide λ is determined primarily by the M-2 component and ϵ does not exceed the value 0.25. Equation (22) is approximated by

$$\tau_{to} \approx \rho r \lambda \sum_n \frac{1}{2} (a_n - 1b_n) e^{1n\sigma t} \quad (23)$$

The error in the friction term is less than 12.5% and corresponds to smaller errors in computing tidal elevation. In studies where such an error is significant, it is possible to calculate ϵ and to include its effect in Equation (22). The above method will be applied to Boca Raton inlet, the terms comprising ϵ will be neglected subject to comparison with measured tidal elevations.

The non-linear term in Equation (9) becomes according to the above analysis (See Equation (17))

$$\left| \frac{dh_{b1}}{dt} \right| \left| \frac{dh_{b1}}{dt} \right| = \lambda_1 \sum_n \frac{1}{2} (1n\sigma c_n + n\sigma d_n) e^{1n\sigma t} \quad , \quad (24)$$

where

$$\lambda_1 = \frac{1}{\sqrt{2}} \left[\sum_{k=0}^{\infty} \sigma^2 k^2 (c_n + d_n) \right]^{\frac{1}{2}} \quad (25)$$

Substituting for h_s , h_{b_1} , and $|dh_{b_1}/dt|$ (dh_{b_1}/dt) and equating the real and imaginary coefficients, the following algebraic equations for the coefficients of different harmonic constituents are deduced

$$\begin{aligned} r_n &= \left[1 - n^2 \sigma^2 \left(\frac{A_{b_1}}{A_1} \right) \frac{L_1}{g} \right] c_n + \frac{\lambda_1}{g} \left(1 + \frac{r}{h_1} L_1 \right) \left(\frac{A_{b_1}}{A_1} \right)^2 n \sigma d_n, \\ s_n &= \left[1 - n^2 \sigma^2 \left(\frac{A_{b_1}}{A_1} \right) \frac{L_1}{g} \right] d_n - \frac{\lambda_1}{g} \left(1 + \frac{r}{h_1} L_1 \right) \left(\frac{A_{b_1}}{A_1} \right)^2 n \sigma c_n \end{aligned} \quad (26)$$

Equations (26) relate the bay motion to the ocean tidal oscillation. The non-linear friction is specified by the term λ_1 which also couples the different harmonic constituents of the ocean elevation.

The procedure for solution depends on the available information. If the tidal elevations in both ocean and bay are measured, it is possible to evaluate the friction coefficient r . When only the motion in the bay is known, it is possible to predict the tidal motion in the ocean for any given r . However, when the tidal motion in the ocean is given the motion in the bay can only be computed by an iterative procedure for any given r .

B* Two Bays Coupled to Ocean

A definition sketch for two bays coupled together and to the ocean is shown in Figure 2. The second bay is not connected to the ocean. The tidal elevations in the ocean and first bay are specified by Equations (16) and (17), respectively. The tidal motion in the second bay is specified by

$$h_{b_2} = \sum_n \frac{1}{2} (p_n - i q_n) e^{i n \sigma t} \quad (27)$$

Subject to all assumptions stated previously, the equation which relates the motions in the two bays becomes

$$h_{b_1} = h_{b_2} + \left(\frac{A_{b_2}}{A_2} \right) \frac{L_2}{g} \frac{d^2 h_{b_2}}{dt^2} + \left(1 + \frac{r}{h_2} L_2 \right) \frac{1}{g} \left(\frac{A_{b_2}}{A_2} \right) \frac{dh_{b_2}}{dt} \left| \frac{dh_{b_2}}{dt} \right|, \quad (28)$$

where the equation of continuity in the second inlet

$$U_2 A_2 = A_{b_2} \frac{dh_{b_2}}{dt}, \quad (29)$$

was used. The resulting algebraic coefficient equations relating the two bays become

$$\begin{aligned}
 c_n &= [1 - n^2\sigma^2 \left(\frac{A_{b2}}{A_2}\right) \frac{L_2}{g}] p_n + \frac{\lambda_2}{g} \left(1 + \frac{r}{h_2} L_2\right) \left(\frac{A_{b2}}{A_2}\right)^2 n\sigma q_n, \\
 d_n &= [1 - n^2\sigma^2 \left(\frac{A_{b2}}{A_2}\right) \frac{L_2}{g}] q_n - \frac{\lambda_2}{g} \left(1 + \frac{r}{h_2} L_2\right) \left(\frac{A_{b2}}{A_2}\right)^2 n\sigma p_n,
 \end{aligned}
 \tag{30}$$

where

$$\lambda_2 = \frac{1}{\sqrt{2}} \left[\sum_{\ell=0}^{\infty} \sigma^2 \ell^2 (p_n^2 + q_n^2) \right]^{\frac{1}{2}}
 \tag{31}$$

The motion of the first bay may now be related to the motions of both ocean and second bay. Equation (7) remains valid for the first inlet, but the continuity equation now takes the form

$$U_1 A_1 = A_{b1} \frac{dh_{b1}}{dt} + U_2 A_2$$

Using Equation (29)

$$U_1 = \frac{A_{b1}}{A_1} \frac{dh_{b1}}{dt} + \frac{A_{b2}}{A_1} \frac{dh_{b2}}{dt},
 \tag{32}$$

and substituting for U_1 in Equation (7) the equation which relates the first bay to the ocean is obtained

$$\begin{aligned}
 h_s &= h_b + \frac{L_1}{g} \left(\frac{A_{b1}}{A_1}\right) \frac{d^2 h_{b1}}{dt^2} + \frac{L_1}{g} \left(\frac{A_{b2}}{A_2}\right) \frac{d^2 h_{b2}}{dt^2} \\
 &+ \left(1 + \frac{r}{h_1} L_1\right) \frac{1}{g} \left(\frac{A_{b1}}{A_1} \frac{dh_{b1}}{dt} + \frac{A_{b2}}{A_1} \frac{dh_{b2}}{dt}\right) \left[\frac{A_{b1}}{A_1} \frac{dh_{b1}}{dt} + \frac{A_{b2}}{A_1} \frac{dh_{b2}}{dt} \right]
 \end{aligned}
 \tag{33}$$

Using the representation for h_s , h_{b1} , and h_{b2} , given by Equation (16), (17) and (27), respectively, the following algebraic coefficient equations are deduced

$$\begin{aligned}
 r_n &= c_n [1 - n^2\sigma^2 \frac{L_1}{g} \left(\frac{A_{b1}}{A_1}\right)] - p_n [n^2\sigma^2 \frac{L_1}{g} \left(\frac{A_{b2}}{A_1}\right)] \\
 &+ \frac{\lambda_3}{g} \left(1 + \frac{r}{h_1} L_1\right) \left[\left(\frac{A_{b1}}{A_1}\right) n\sigma d_n + \left(\frac{A_{b2}}{A_1}\right) n\sigma q_n \right] \\
 s_n &= d_n [1 - n^2\sigma^2 \frac{L_1}{g} \left(\frac{A_{b1}}{A_1}\right)] - q_n [n^2\sigma^2 \frac{L_1}{g} \left(\frac{A_{b2}}{A_1}\right)] \\
 &- \frac{\lambda_3}{g} \left(1 + \frac{r}{h_1} L_1\right) \left[\left(\frac{A_{b1}}{A_1}\right) n\sigma c_n + \left(\frac{A_{b2}}{A_1}\right) n\sigma p_n \right],
 \end{aligned}
 \tag{34}$$

where

$$\lambda_3 = \frac{1}{\sqrt{2}} \left[\sum_{k=0}^{\infty} \left\{ \left(\frac{A_{b1}}{A_1} \right) n \sigma d_n + \left(\frac{A_{b2}}{A_1} \right) n \sigma q_n \right\}^2 + \left\{ \left(\frac{A_{b1}}{A_1} \right) n \sigma c_n + \left(\frac{A_{b2}}{A_1} \right) n \sigma p_n \right\}^2 \right]^{1/2} \quad (35)$$

The procedure for solution again depends on the available information. The friction factor can be determined when the motion in the ocean and both bays are known. The elevations in the first bay and ocean can be obtained deterministically for any given r when the motion in the second bay is known. The motion in the bays can be determined by an iterative scheme for any given r when the motion in the ocean is known.

APPLICATION - BOCA RATON INLET

The theoretical method outlined above was applied to Boca Raton Inlet, Florida. The inlet connects the Atlantic Ocean to Boca Raton Lake which is also connected to Lake Wyman. A plan view of these lakes is shown in Figure 3. The intercoastal waterway which connects Lake Wyman and Boca Raton Lake extends to South Lake Worth Inlet north and Hillsboro Inlet south. Comparisons of tide records obtained at Boca Raton Lake and at a station on the Intercoastal Waterway south of Boca Raton indicated no possible flow to or from the Intercoastal Waterway south of Boca Raton Lake. Boca Raton Inlet primarily influences Boca Raton Lake, Lake Wyman, and areas occupied by boating marinas north of Lake Wyman.

Boca Raton Inlet was chosen for this study because tide records were available at the Inlet North Jetty (denoted by Station 1 in Figure 3), at Boca Raton Lake (denoted by Station 2), and at Lake Wyman (denoted by Station 3). Actually tide records at three stations around Boca Raton Lake were also available. These records indicated no special variation of tide elevation in Boca Raton Lake and verifies the representation of conservation of mass given by Equation (8). The tide elevations recorded at Stations 1, 2 and 3 are shown in Figure 4. They indicate the magnitude and phase shift of tidal motion in the two bays relative to the ocean. Other available data included velocity measurements over a tidal cycle at Station 1 to be shown later in comparison with computed velocities.

Since tidal records were available in both bays and at the inlet, the multiple bay analysis was used to determine the friction factor r for the system. The tidal record in Lake Wyman was used to predict the tidal elevation in Boca Raton Lake using Equation (30). The computed elevation was then compared with the measured one. With the tidal elevation in Boca Raton Lake known, the ocean elevation in the ocean (Station 1) was computed using Equations (34) and the results compared with the measured values. The variances between the computed and measured elevations were computed at Stations 1 and 2 for different friction coefficients. The quantities which describe the bay system (see Figure 2) $A_1, L_1, A_{b1}, h_1, A_2, L_2, h_2$ were all known. The area A_{b2} was not known. The computed motion which gave the best fit to measured tidal elevations at Stations 1 and 2 corresponded to $r = 0.0039$ and $A_{b2} = 23 \times 10^6$ ft². The latter area is much larger than Lake Wyman's area and suggests that the tidal motion extends to areas occupied by marinas north of Lake Wyman. Table 2 summarizes the physical properties of the above two-bay system.

TABLE 2 Properties of the Two-Bay System

	<u>Boca Raton Lake</u>	<u>Lake Lyman</u>
Inlet area (ft ²)	1 40 x 10 ³	1 68 x 10 ³
Bay Area (ft ²)	3 74 x 10 ⁶	23 00 x 10 ⁶
Inlet depth (ft)	7 0	8 0
Inlet length (ft)	2 67 x 10 ³	7 33 x 10 ³
M-2 measured amplitude (ft)	1 57	1 40

The variances between computed and measured tidal elevations at Boca Raton Lake (station 2) and at the Ocean (station 1) were 1.9×10^{-2} and 2.0×10^{-2} , respectively for $r = 0.0039$. The difference in computed and measured phase shifts of the M-2 component were 2 degrees for Boca Raton Lake and 4 degrees for the ocean.

SIGNIFICANCE OF NON-SINUSOIDAL TIDAL COMPUTATION

A comparison between the measured tide record at station 1 and the M-2 constituent is shown in Figure 5. The agreement is reasonable only over part of the tide cycle. A comparison between the measured tide elevation at station 1 and the computed elevation using six harmonics is shown in Figure 6. Better agreement is recognized over most of the tidal cycle. The importance of considering the different harmonics in tidal computations appears more dramatically in velocity computations, however. In Figure 7, the measured velocity at station 1 is compared to the computed velocity using the M-2 constituent only. Near the maximum three velocity peaks appear in the measured record but are absent in the sinusoidal computation. These peaks appear in computations which include different harmonics as shown in Figure 8. Since the contribution of each harmonic to velocity depends on frequency and amplitude of that harmonic the higher harmonic contributes significantly to velocity even when the amplitude is small.

The velocity cycle has an important influence on sediment transport in the inlet. The sand trapping capability of an inlet may play an important role in shoreline stability in the vicinity of the inlet. The trapping capability of Boca Raton Inlet is investigated in what follows.

The theoretical basis for describing movable beds is empirical. Many relationships exist that relate volume of sediment transport to bottom shear stress. While there is no one relationship which is far superior to others, the empirical result arrived at by Einstein (1942) is used.

$$q_s' = 40 \rho F \frac{U_*^3}{[g(s_s - 1)]^{2/3}}, \quad (36)$$

where q_s' = the weight rate (in water) of sediment transport per unit width, ρ = water density, U_* = shear velocity ($= \tau_{0}/\rho$), g = gravitational acceleration,

s_s = specific gravity of sand, and F is given by

$$F = \left[\frac{2}{3} + \frac{36 \nu^2}{gd^3 (s_s - 1)} \right]^{1/2} - \left[\frac{36 \nu^2}{gd^3 (s_s - 1)} \right]^{1/2}, \quad (37)$$

where ν = kinematic viscosity of water Equation (36) was used successfully by Shemdin (1970) in modeling of sediment flow in the coastal zone Equation (5) relates the average velocity to the shear velocity

$$U_* = r^{1/2} U$$

For a wide channel with width B the weight rate of sediment transport, q_s , becomes

$$q_s = q_s' B = 40 \rho F B \frac{r^3 U^6}{[g (s_s - 1) d]^{3/2}} \quad (38)$$

The net sediment transport into Boca Raton Inlet was computed from results similar to those shown in Figure 8 Tide records were found to fluctuate in amplitude and typical records were used for two different days The net transport into the inlet for the two days was calculated to be 15 and 47 (yd^3/day) which correspond to 5,400 and 17,000 yd^3/yr , respectively A recent dredging operation in Boca Raton inlet have been removing 30,000 - 40,000 cubic yards of sand per year from the inlet The computed transport in the inlet is of the same order of magnitude Figure research on inlets may fruitfully include field measurements of sand transport

CONCLUSIONS

A non-linear coupled procedure is proposed to analyze tidal motion in inlets and bays The importance of the different tidal constituents is shown to be more important in velocity computation compared to surface elevation The exchange of sediment between bays and the ocean is dependent on the velocity variation over the tidal cycle and can only be computed accurately by considering different harmonic constituents in a tidal record The procedure is applied to Boca Raton Inlet and the result indicate that more sand transport occurs during the flood period compared to the ebb period The inlet consequently behaves like a sand trap

REFERENCES

- 1 Brown, E I (1928), Inlets on Sandy Coasts, Proc ASCE, Vol IIV
- 2 Dronkers, J J (1964), Tidal Computations in Rivers and Coastal Waters, North - Holland Publishing Co., Amsterdam
- 3 Einstein, H A (1942), Formulas for the Transportation of Bed Load, Trans ASCE, Vol 107, pp 561-577
- 4 Keulegan, G H (1951), Water-level Fluctuations of Basins in Communication with Seas, Report No 1146, National Bureau of Standards, Washington, D C

- 5 Lee, Y W (1967), Statistical Theory of Communication, John Wiley & Sons, Inc , New York
- 6 O'Brien, M P (1969), Equilibrium Flow Areas of Inlets on Sandy Coasts, J Waterways and Harbors Div , Vol 95, No WW1, pp 43-52
- 7 Shemdin, O H (1970), River-Coast Interaction Laboratory Simulation, J Waterways and Harbors Div , Vol 96, WW4
- 8 Sidjabat, M M (1970), The Numerical Modeling of Tides in a Shallow Semi-enclosed Basin by a Modified Elliptic Method, Ph D Dissertation Submitted to the University of Miami, Coral Gables, Florida
- 9 Van de Kreeke, J (1968), Water Level Fluctuations and Flow in Tidal Inlets, J Waterways and Harbors Div , Vol 93, No WW4, pp 97 - 106

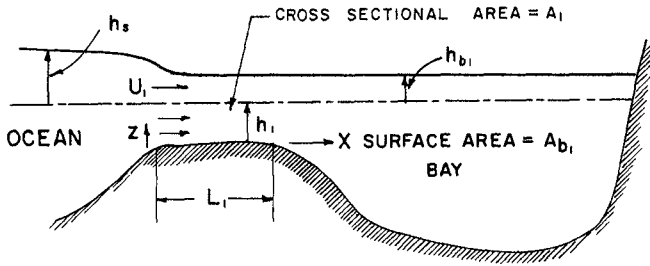


Figure 1 Definition sketch for a single bay coupled to ocean

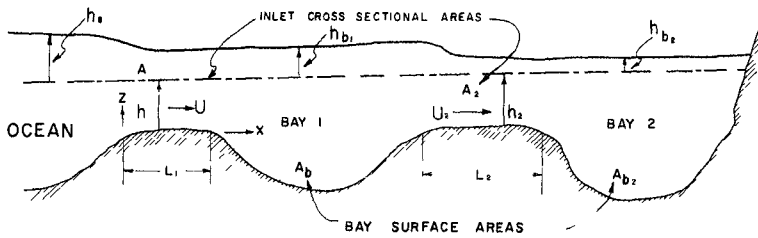


Figure 2 Definition sketch for two bays coupled to ocean

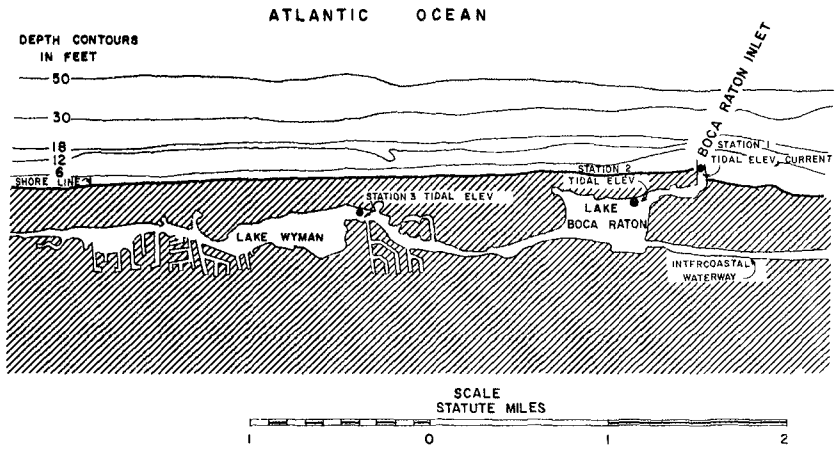


Figure 3 Plan view of Boca Raton Inlet and lake, and Lake Wyman

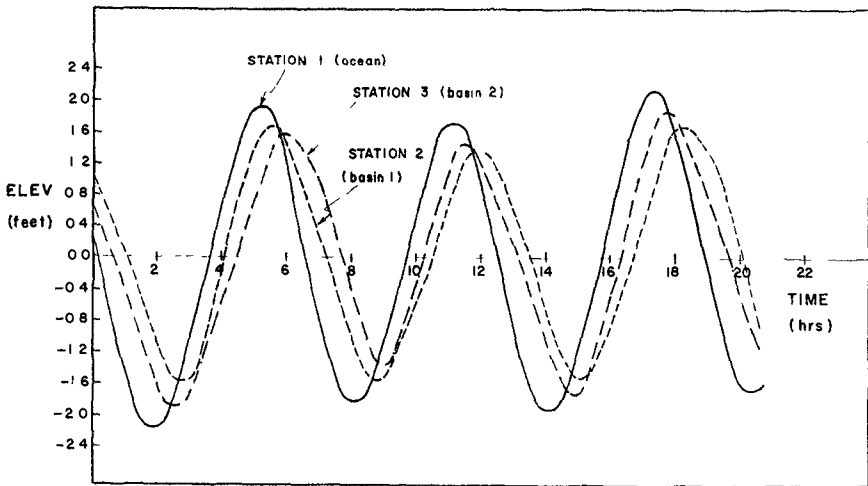


Figure 4 Tide elevations at Boca Raton Inlet, Boca Raton Lake, and Lake Wyman

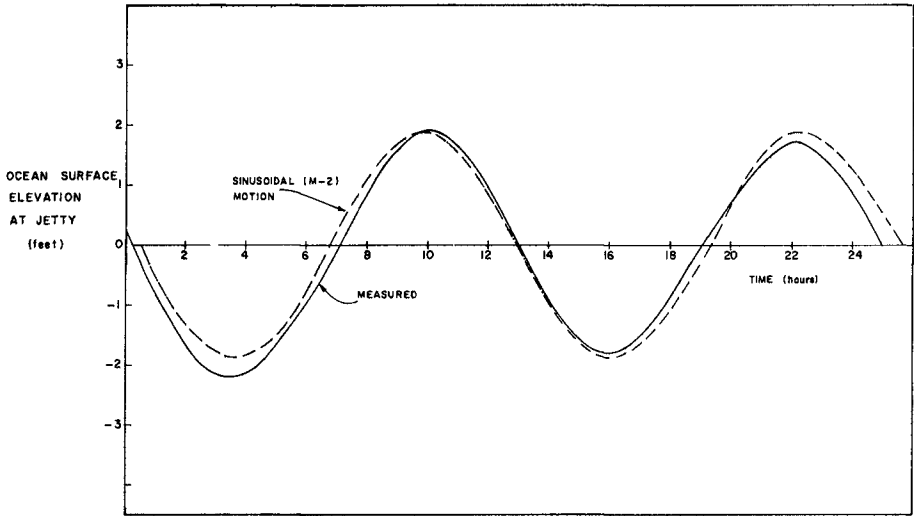


Figure 5 Comparison between measured and computed (M-2) component of tidal motion at Boca Raton Inlet

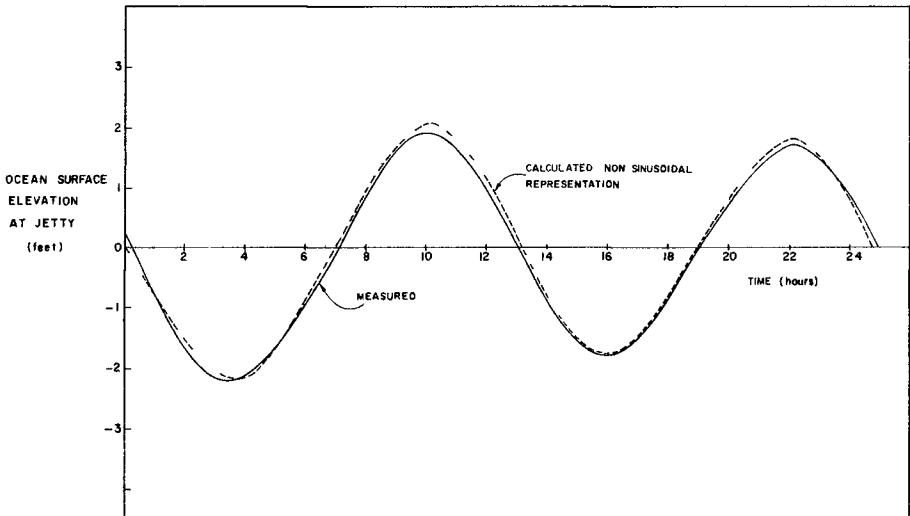


Figure 6 Comparison between measured and computed tidal motion using six harmonics at Boca Raton Inlet

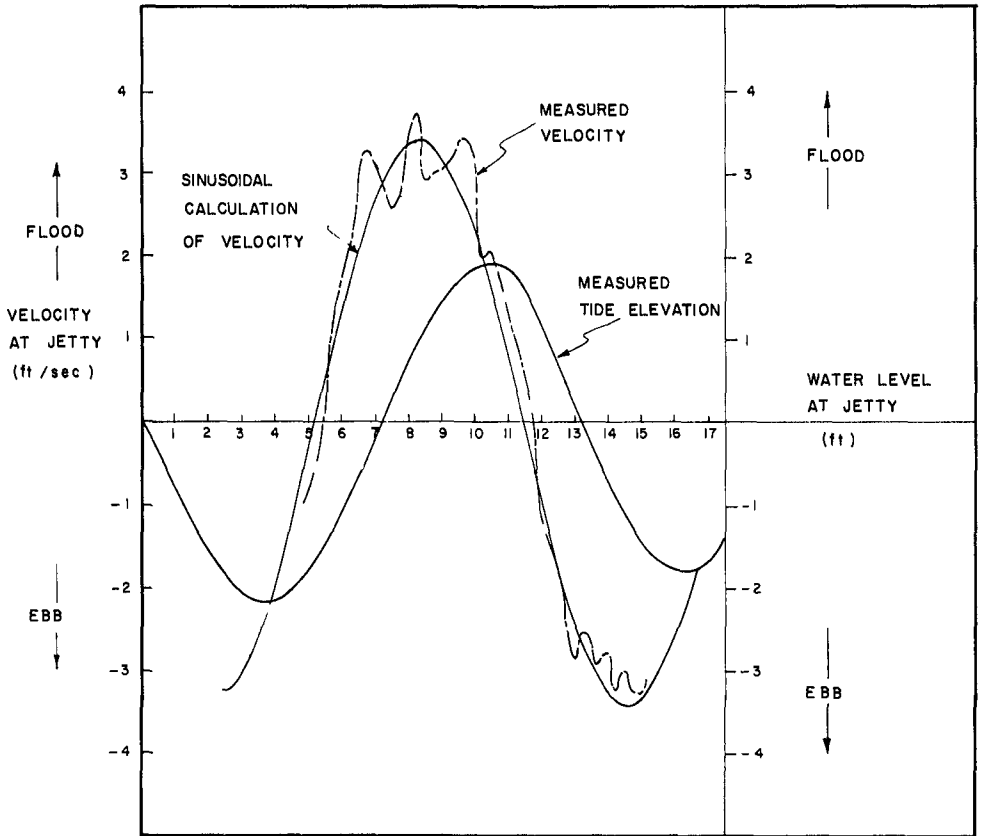


Figure 7 Comparison between measured and computed velocity using (M-2) component only at Boca Raton Inlet

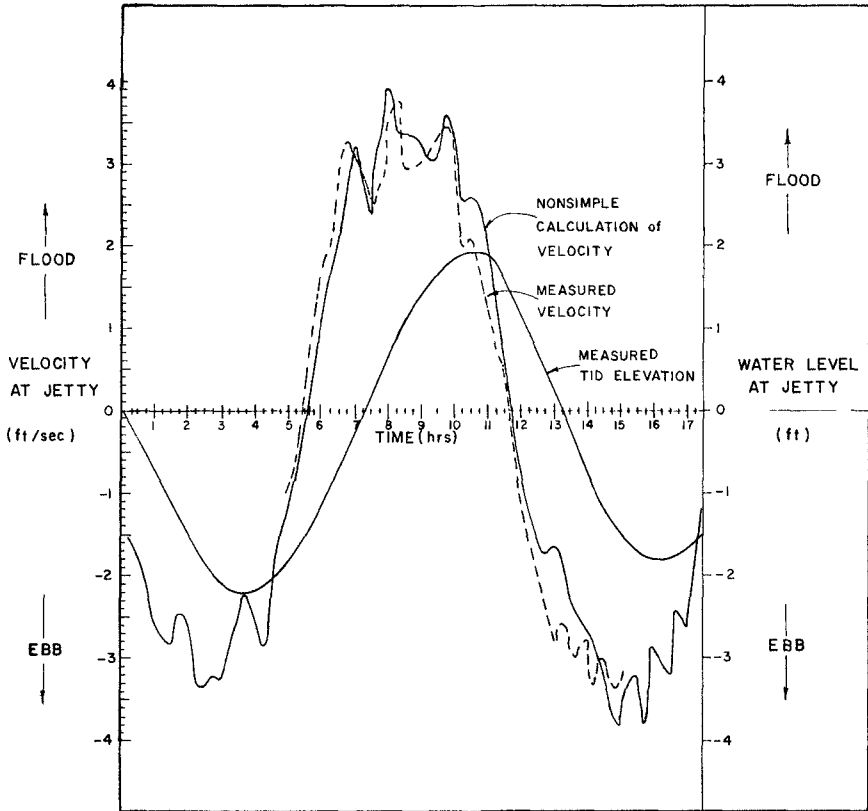


Figure 8 Comparison between measured and computed velocity using six harmonics at Boca Raton Inlet

CHAPTER 135

SURFACE OSCILLATIONS IN A WATER TANK CAUSED BY A SUBMERGED JET

By

Juan B Font ¹

Orar Azpurua ²

Flora Aranguren ³

ABSTRACT

In this paper are studied the surface oscillations that form in a water tank when a jet emerges from the bottom

The experimental system consisted of a circular water tank with the water intake at the bottom close to its circumference. Surface oscillations were recorded for different situations

The experimental results are presented in both dimensional and dimensionless plottings where the oscillations amplitude is related with water depth and jet diameter and velocity

The dimensionless graphs show that the oscillation amplification is, within the variables ranges studied, mostly independent of tank diameter

INTRODUCTION

When water flows into a shallow tank, in the form of a jet emerging from the bottom, small surface oscillations appear as a result of jet diffusion and supply pipe turbulence. These oscillations are reflected in the tank walls increasing the water surface movement which interferes with the jet flow, starting a horizontal oscillation of the latter. A complex surface oscillation results, which under determined conditions is continuously amplified until wave breaking puts a limit on wave height.

The oscillation pattern, no matter the degree of amplification,

¹ Asst. Prof. College of Engrg, Universidad Central - Venezuela

² Civil Engineer - CONPASA - Caracas - Venezuela

³ Civil Engineer - INOS - Caracas - Venezuela

is a complex and unsteady one, with standing wave type movement being dominant, with nodes and antinodes continuously changing their location

VARIABLES INVOLVED AND THEIR RELATIVE IMPORTANCE

According to the physical description of the phenomenon, the amplification is a function of the magnitudes that describe the boundary geometry and surface movement, i.e. tank and supply pipe geometry and Froude Number. In the amplification processes inertia and gravity forces are obviously much more important than viscous forces. The wave breaking is determined by oscillation characteristics. Thus the amplification and its upper limit will not be a function of Reynolds Number.

The amplification must result from a resonant combination of jet movement, surface movement and tank geometry. However, and due to the surface oscillation variability, the tank geometry plays a secondary role as shown in Fig. 1.

To back this experimental conclusion we may consider several reasons. First, the boundary conditions imposed by the circular vertical walls of the tank, determinant of the oscillation pattern in the steady case, are now almost irrelevant since a great number of instantaneous patterns will exist, some of them being close to the maximum amplification situation for the existing set of depth and jet variables. This is specially true when tank diameter is several times the mean wave length. As a matter of fact, it was observed in the experiments that the jet always followed a random sequence of quiet and oscillation periods. Second, specially at resonance situations, when breaking takes place, waves are non-linear and, therefore, continuously changing wave heights will cause that a range of frequencies be allowed with the circular boundary for every oscillation mode. As it can be seen in the sample record shown in Fig. 5, energy is mainly related to a wave frequency, but nevertheless, the oscillation is not monochromatic.

Dimensionless parameters

The variables thus involved are wave height H , jet diameter d , water depth h , jet velocity V and gravity force per unit mass g . With these five secondary magnitudes, the theorem shows that, since only length and time are involved, there will exist a function ϕ such that

$$\phi(\pi_1, \pi_2, \pi_3) = 0$$

where π_1 , π_2 , and π_3 are independent dimensionless combinations of the above listed variables. For graphical representation a convenient set of expressions is

$$\pi_1 = \frac{H}{d}, \quad \pi_2 = \frac{V}{\sqrt{gd}}, \quad \pi_3 = \frac{V}{\sqrt{gh}}$$

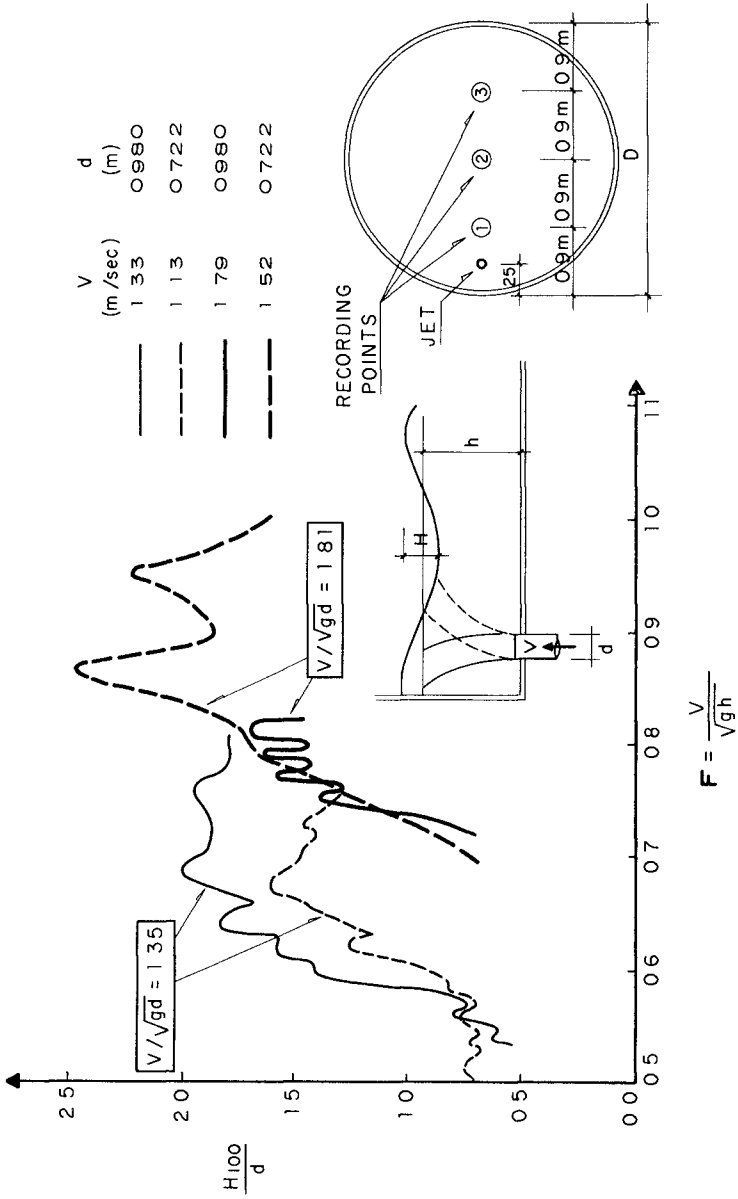


FIG 1 DIMENSIONLESS GRAPH OF SURFACE OSCILLATION

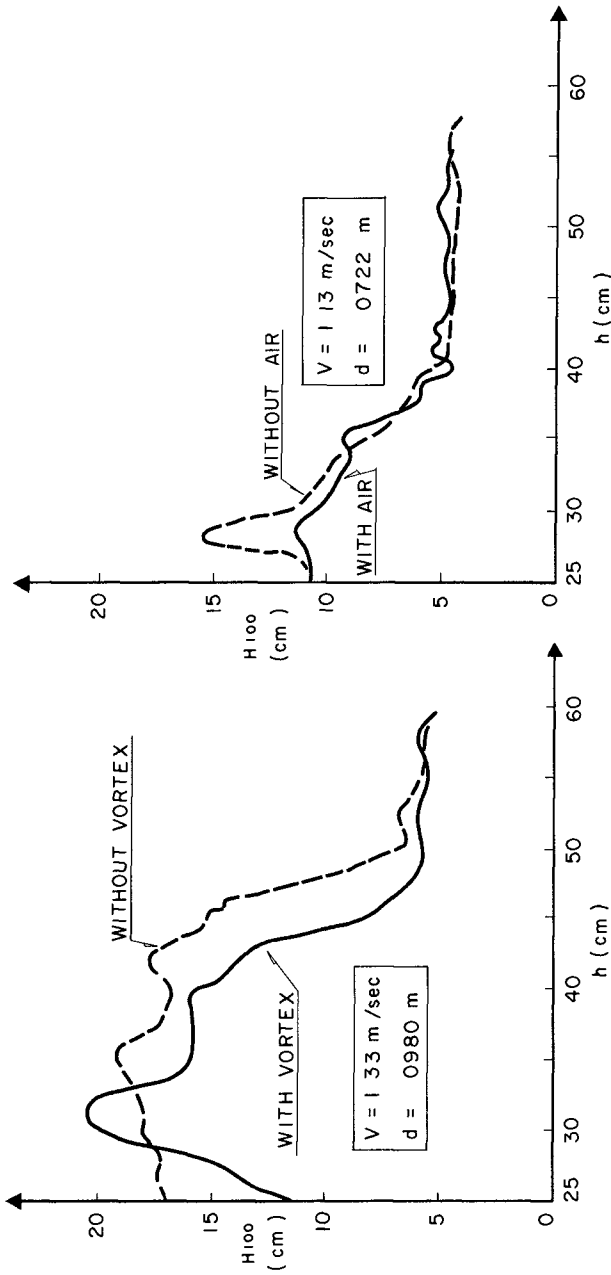


FIG 2 EFFECT OF A VORTEX AT THE SUPPLY PIPE ENTRANCE
 FIG 3 EFFECT OF AIR INTRUSION IN THE SUPPLY PIPE

EXPERIMENTAL CONDITIONS

For a description of the experimental set-up see figures 1, 5, and 6

Tests were run starting with the tank full of water, and allowing the outflow to be a little larger than the inflow such that water depth would slow and continuously decrease, until the possible minimum was attained, the water discharge was held constant through the experiment by means of a weir controlled elevated supply tank. Two supply pipe diameters were used with two different velocities for each one. Velocity was measured indirectly in terms of discharge by weir and elbow meters, previously calibrated in the experimental system with a weir meter.

The water surface elevation was recorded continuously at the three points shown in Fig 1.

As an indication of surface oscillation H_{100} has been defined as the average of the one percent largest wave of the two recordings taken at electrodes N° 2 and N° 3.

Influence of supply pipe disturbances

To investigate the influence of water flow disturbances in the supply pipe, one test was run allowing the formation of a vortex in the supply tank. In another test air was allowed to enter in the supply pipe. Figures N° 2 and 3 show the results with these conditions.

Oscillation damping

In one of the tests, after maximum amplification was reached, water outflow and inflow were stopped and the water surface was continuously recorded until oscillation nearly disappeared. At the beginning, a rather fast damping took place as a result of wave breaking, thereafter having a very weak damping. Calling $H_{100}(t=0)$ the one percent highest wave at an arbitrary time when wave breaking is over, the damping factor, in terms of the highest one percent height, has been plotted in fig 3. This graph shows that laminar type damping takes place. As a matter of fact Reynolds numbers computed for both bottom and tank walls, in the manner shown in fig 3, fall below the critical Reynolds numbers given by several authors (Li, Ref 2, Jonsson, Ref 1) for transition from laminar to turbulent regime on a smooth boundary. Comparison of the Reynolds numbers for the bottom and the tank wall, and the respective areas of these boundaries, leads to the conclusion that wall friction is much more important than bottom friction in this specific case, and therefore that the tank diameter plays an important role in the free oscillation damping.

CONCLUSIONS

- 1 The oscillation in the water surface that takes place in a water tank when a jet emerges from the bottom is a very complex one, with many frequencies superimposed and nonlinear-

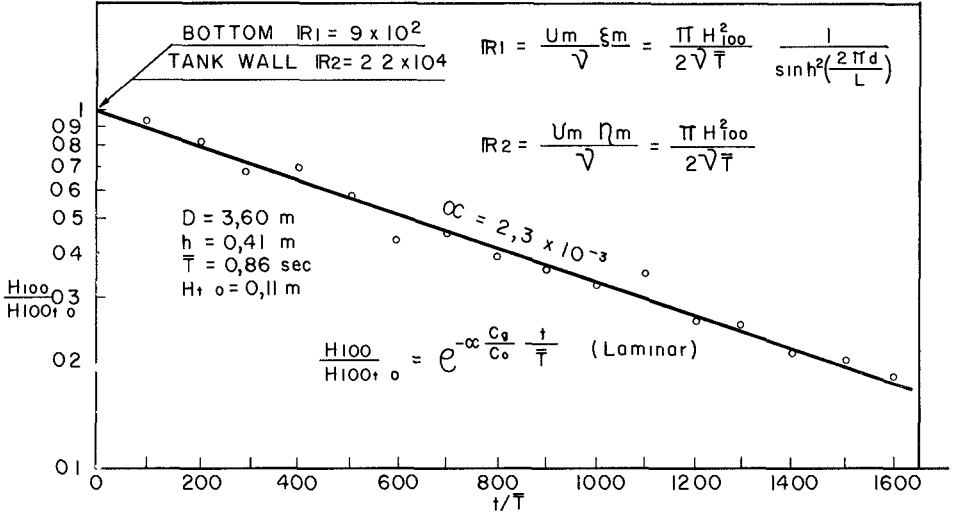


FIG 3 FREE OSCILLATION DAMPING

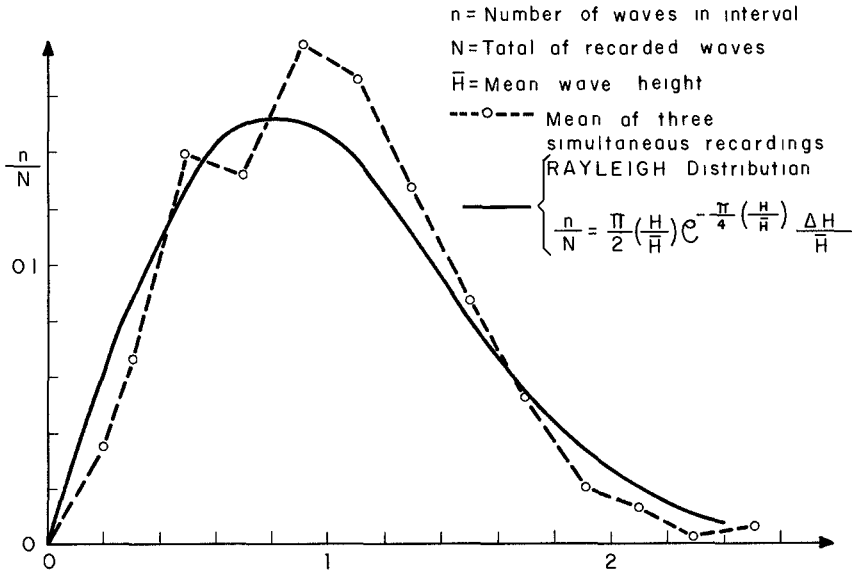


FIG 4 WAVE HEIGHTS HISTOGRAPH

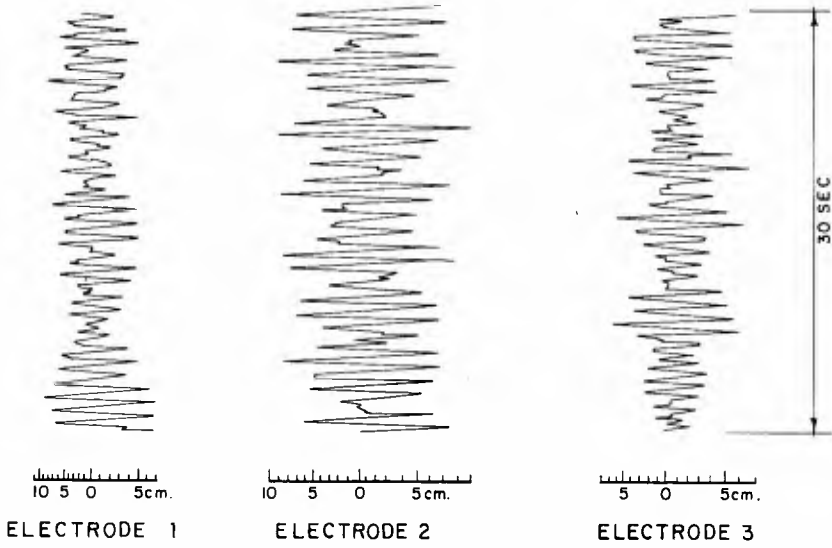


FIG. 5 SAMPLE SURFACE RECORDS



FIG. 6 VIEW OF LABORATORY SET-UP

ties characteristic of impulsive wave generation and breaking wave breaking puts a limit to wave height in resonant situations

- 2 The maximum amplification that reaches the oscillation is mainly due to a resonance among the emerging jet and the free surface movement
- 3 The experimental results summarized in Fig 1 show that the resonance depends mostly on jet characteristics and water depth, rather than on tank diameter
- 4 Flow disturbances in the supply pipe, such as longitudinal vorticity and air intrusion, are of second order importance in the amplification phenomena
- 5 Once the jet flow has been stopped, the wave breaking disappear shortly and after that, the oscillation damping is very slow

ACKNOWLEDGMENTS

It is appreciated the cooperation and assistance provided by the Laboratory "Ernesto León D , INOS" in the experiments reported in this paper

The authors are also grateful for the assistance given by the Ministry of Public Works, Ports and Airports Division, in the preparation of this report

REFERENCES

- 1 - Jonsson, Ivar G "Wave boundary layers and friction factors" Coastal Engineering 1966, Chapter 10, pp 127- 48, Pub American Society of Civil Engineers, New York, 1967
- 2 - Li, H "Stability of Oscillatory Laminar Flow Along a Wall" Beach Erosion Board Tech Memo N° 47, Washington, 1954

CHAPTER 136

EFFECT OF LONG PERIOD WAVES ON HYDROGRAPHIC SURVEYS

by

Orville T Magoon
Coastal Engineering Branch, U S Army Engineer Division,
South Pacific, 630 Sansome Street, San Francisco, California 94111

and

William O Sarlin
Chief, Technical Service Branch, U S Army Engineer District,
San Francisco, 100 McAllister Street, San Francisco, California 94102

ABSTRACT

In conjunction with routine hydrographic surveys at Santa Cruz Harbor, California, bottom elevation discrepancies were observed which were not associated with positional errors. It was suspected that these errors were associated with long period wave activity, common at this particular location on the Pacific Coast.

The existing practice for obtaining hydrographic soundings is by use of floating craft using either echo sounding techniques or a "lead line". Both of the above techniques utilize the instantaneous water surface at the survey boat as a datum reference. Normally the water surface elevation is determined by use of a water level recorder.

Based on the analysis of 50 repetitions of a well monumented cross section in Santa Cruz Harbor, it was concluded that long period waves affect the results of hydrographic surveys by slowly varying the datum plane. In the case of Santa Cruz Harbor, the maximum error due to this effect would be about ± 1.5 feet.

INTRODUCTION

Santa Cruz Harbor is located at the northerly end of Monterey Bay, California, about 65 nautical miles south of the entrance to San Francisco Bay, as shown in Figure 1 and Photo 1. The hydrography of the general coastal area and of Monterey Bay are shown on charts published by the United States Coast and Geodetic Survey, Nos 5402 and 5403 respectively. In connection with studies of Monterey Harbor, located at the southerly end of Monterey Bay, and at Santa Cruz Harbor

It has been shown that Monterey Bay and Santa Cruz Harbor are subject to pronounced seicheing. Individual maximum trough to crest heights of over three feet have been observed. Nominal periods associated with these seiches vary from 80 seconds to over 10 minutes with oscillations of about 3 minutes in period being most evident.

During the analyses of surveys made in the vicinity of Santa Cruz Harbor, an unexplained ambiguity in the sounding depths became apparent. Although the cause of these ambiguities was unknown, it was hypothesized that they were caused by shifts in the sounding datum by long period waves. Water level changes caused by these long period waves had previously been observed at Santa Cruz Harbor on numerous occasions by the authors. These long wave oscillations of Monterey Bay and Santa Cruz Harbor are discussed by Wilson⁽¹⁾, Grauzinis⁽²⁾, and Lynch⁽³⁾. The existing practice for obtaining hydrographic survey information is by use of floating craft and either echo sounding techniques or by lead line. The above techniques both utilize the instantaneous water surface at the survey boat as a datum reference. Generally a recording tide gage mounted on a 4" pipe well with a suitable orifice, a float, and recorder, are used in determining the instantaneous water surface. Attenuated long period fluctuations in the water surface may be observed in the resulting marigram trace. Discussion of tide gage attenuation is discussed by Cross⁽⁴⁾. These long period undulations vary spacially both in period and height, however, it appears that their presence, but not their relative magnitude, may be determined by conventional portable tide gages. Only the relatively flat bottom areas of the channel were used for purposes of this study and, therefore, the side slope areas are not involved.

SURVEY TECHNIQUE

In order to measure the effects of long period waves on hydrographic surveys, a test project was started at Santa Cruz Harbor by establishing a "repetitive line" and this line is indicated on Figure 2. Cross-section surveys were taken along this line using an aluminum hydrographic boat with a length of 14 feet, a beam of 62 inches, a draft of approximately 12 inches. The boat was equipped with a conventional tag-line reel with a cable marked at one foot intervals and a "Raytheon" fathometer, Model DE 119D, operating at a frequency of 200 kilo Hertz. Leadline soundings were then taken with an eight pound lead to verify fathometer soundings. A typical method used for hydrographic surveys is shown in Figure 3.

Fifty (50) measurements of the repetitive lines were taken on 21-22 March 1968. Initially, ten (10) cross-sections were taken of the repetitive line on 20 March 1968, however, these lines were discarded from this

Numbers in parentheses indicate listed references at end of text

study because they were considered practice lines for the crew to become accustomed to the survey techniques. The tide was recorded continuously during the survey period with an automatic tide recorder mounted on a 4-inch pipe attached to a dock. Tide corrections were applied to the fathometer soundings in order to correct the water depths. The boat was controlled in the forward motion by a tag line calibrated at one (1) foot intervals with the zero end attached to a baseline on shore. The side motion of the boat was controlled by an instrumentman with a transit on shore, giving signals to the boat operator for keeping the boat precisely on line. The marigrams shown on Figures 4 and 5 are taken from a previous project and are included for typical data. Figure 4 shows a typical record with an open end well, Figure 5 shows a typical record with a damped well.

Then the plotted lines of soundings were superimposed on a chart to compare the results. A sampling of these lines is shown on Figures 6, 7 and 8. These plottings indicate a data envelope of the echo sounding measurements of about one foot. As the survey boat was traversing the reference line with closely controlled position, the sounding variations are then due to the datum changes as produced by the long period waves.

These soundings are believed to be accurate since the location of the boat was controlled very carefully with an instrumentman on shore for the left and right directions or side motion of the boat. The distances of the boat from the shore baseline were read on the tag line which was calibrated in feet. Soundings were read to the closest tenth of a foot on the fathograms.

DISCUSSION

The effect of long period waves on hydrographic surveys has been demonstrated at Santa Cruz Harbor, and the effect of these waves at other locations along the Northern California Coast is believed to be of similar magnitude. An effective monitor appears to be a recording tide gage located at an anti-nodal position in the survey area with a suitable orifice that would filter out short period waves. A direct correction for the long wave effect could be obtained by use of a datum other than the water surface. However, consideration of these techniques is beyond the scope of this study.

In adjusting the soundings to account for the effect of tides, care must be taken to filter out the long wave excursions on the applicable marigrams. In Santa Cruz Harbor, water elevations at locations away from the tide gage may be experiencing different water level elevations than at the tide gage. In the extreme case, the water level at the tide gage could represent a maximum or peak on a wave and at the survey boat location in the harbor could represent a minimum or trough. If the instantaneous water elevation is used at both the tide gage and at the survey boat, the sounding error will equal plus or minus the long period wave height.

In the reduction of hydrographic sounding data, the water surface at the survey boat location is taken as a temporary datum. This datum, is, of course, influenced by any water level fluctuations. In the case presented in this paper, the actual fluctuation is considered to be due to long waves alone. This is shown diagrammatically in Figure 9A, where the total long wave height is taken as " H " and it is further assumed that a recording gage and also the survey boat are located at anti-nodal positions in a standing wave situation. Under these conditions, and with the recording tide gage operating correctly, a mean line may be drawn through the tide gage record (obviously the tide gage record may be damped mechanically or electrically). In this example, the maximum error due to the long wave effect will be equal to $\pm H/2$. When the survey boat is at position A, the water level at the gage is A' , but the average gage reading will be A'' . Similarly, when the survey boat is at position B, the water level at the gage is B' , and the average gage reading will be B'' . If the actual water surfaces at both the survey boat and the gage are used, then the situation shown in Figure 9B results. In this case, when the survey boat is at position C, the water level and the tide gage datum are at position C' . Similarly, when the survey boat is at position D, the water surface and tide gage datum are at position D' . In this instance, the maximum error will be $\pm H$ or twice the error as resulting in Case A, above.

In a real harbor, the situation becomes much more complex due to the inability to describe the instantaneous water surface elevation at the gage and survey boat. In instances where long waves are known to have occurred during surveys, it is suggested that a note be added to the survey information and resulting charts to indicate the situation.

CONCLUSIONS

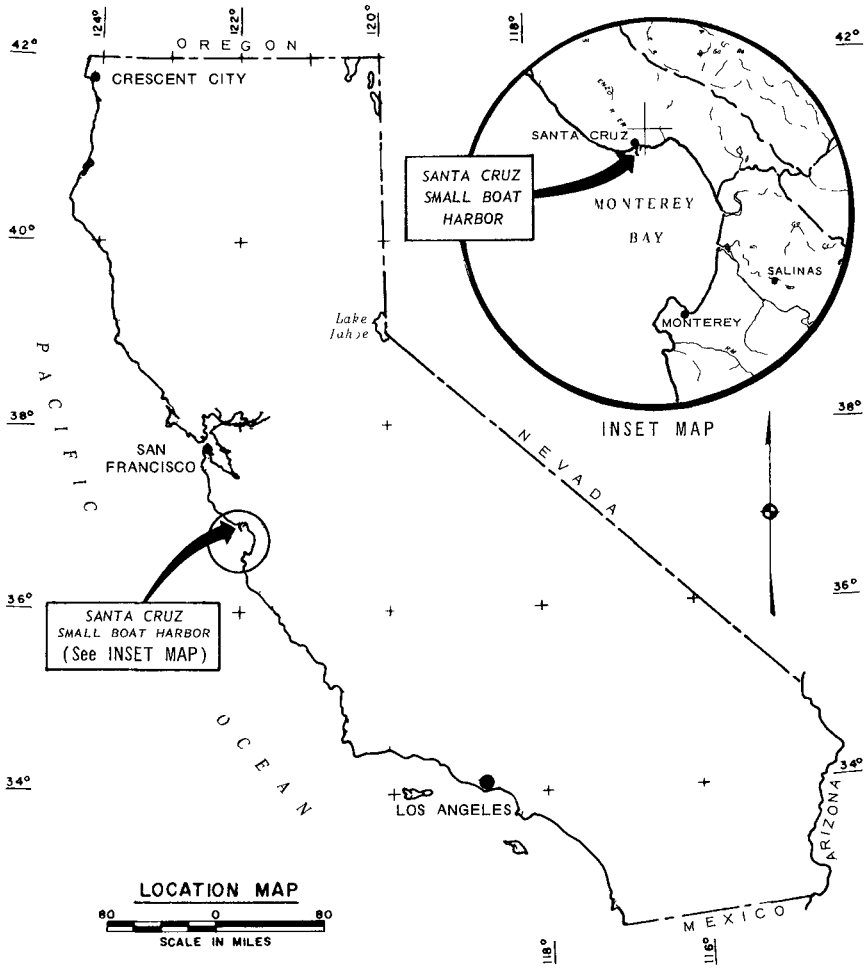
Based on the results of this study, it is concluded that long period waves affect the results of hydrographic surveys by slowly varying the datum plane in a manner that cannot be corrected by existing techniques. Experience at Santa Cruz Harbor indicates that long period waves reach heights slightly in excess of 3 feet and thus during times of occurrence of such waves, the maximum expected error in hydrographic surveys would be approximately equal to $1/2$ this value or about $\pm 1-1/2$ feet due to this effect if the tide gage record has been properly reduced. Incorrect reduction of the tide gage record may result in the sounding error equal to plus or minus the long wave height, or in this example ± 3 feet.

ACKNOWLEDGEMENT

Acknowledgement is gratefully made to the Corps of Engineers for access and permission to use this study material, available from the U S Army Engineer District, San Francisco, California.

REFERENCES

- 1 Wilson, Basil W , Hendrickson, James A , and Kilmer, Robert E , "Feasibility Study for a Surge Action Model of Monterey Harbor, California," prepared for U S Army Engineer Waterways Experiment Station, Corps of Engineers, Vicksburg, Mississippi, under Contract No DA 22-079-CIVENG-65-10, October 1965 Science Engineering Associates, a Division of Kaman Aircraft Corporation, San Marino, California
- 2 Grauzinis, V J , "An Analysis of Seiche Conditions in Santa Cruz Harbor, California, and Some Implications for the Proposed Harbor Extension," for U S Army Engineer District, San Francisco, Corps of Engineers, Contract No DACW07-68-C-0034, March 1968
- 3 Lynch, Thomas John, "Long Wave Study of Monterey Bay," Thesis at United States Naval Postgraduate School, September 1970
- 4 Cross, Ralph H , "Non-Linear Wave Effects on Tide Gages," Hydraulic Engineering Laboratory, College of Engineering, University of California, Berkeley, May 1967



SANTA CRUZ HARBOR

FIGURE 1

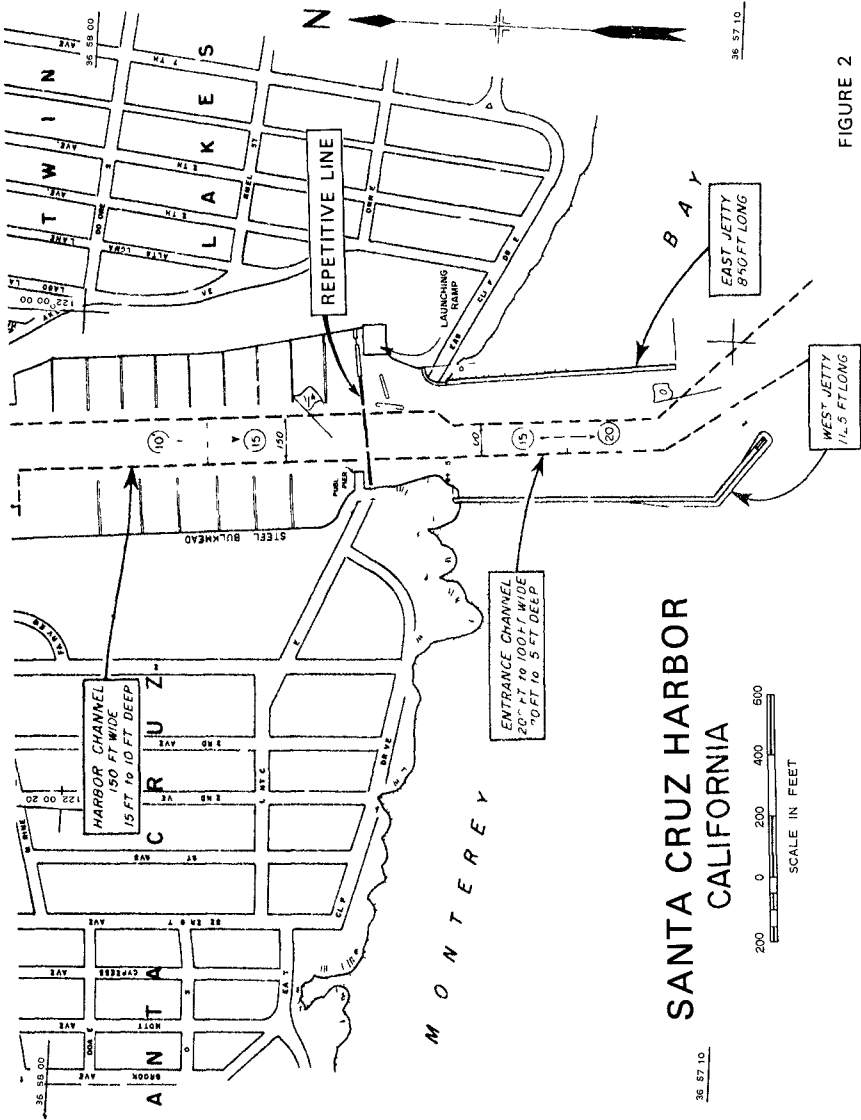


FIGURE 2

SANTA CRUZ HARBOR
CALIFORNIA

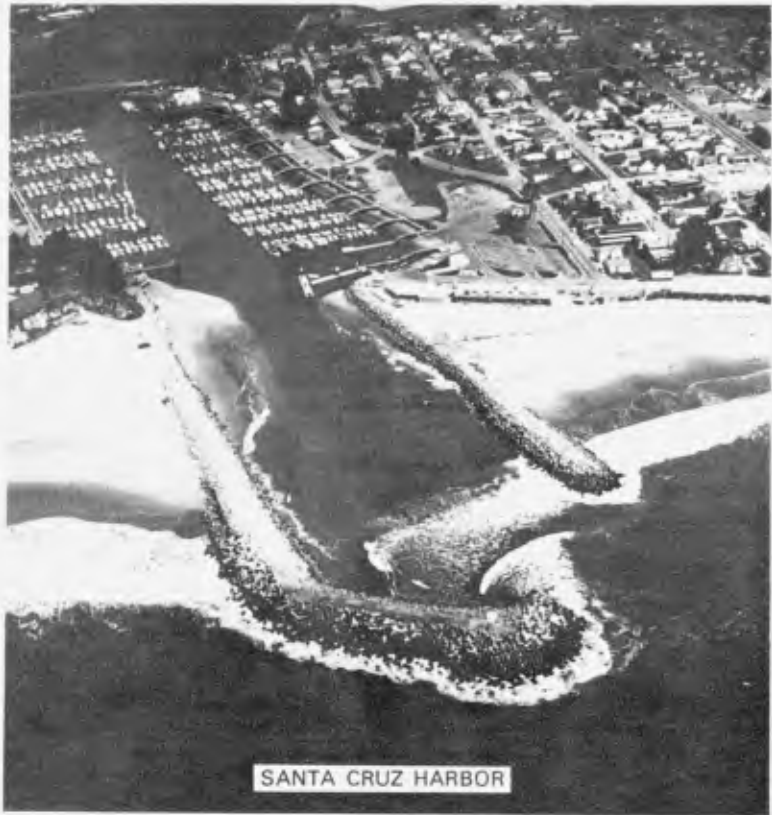
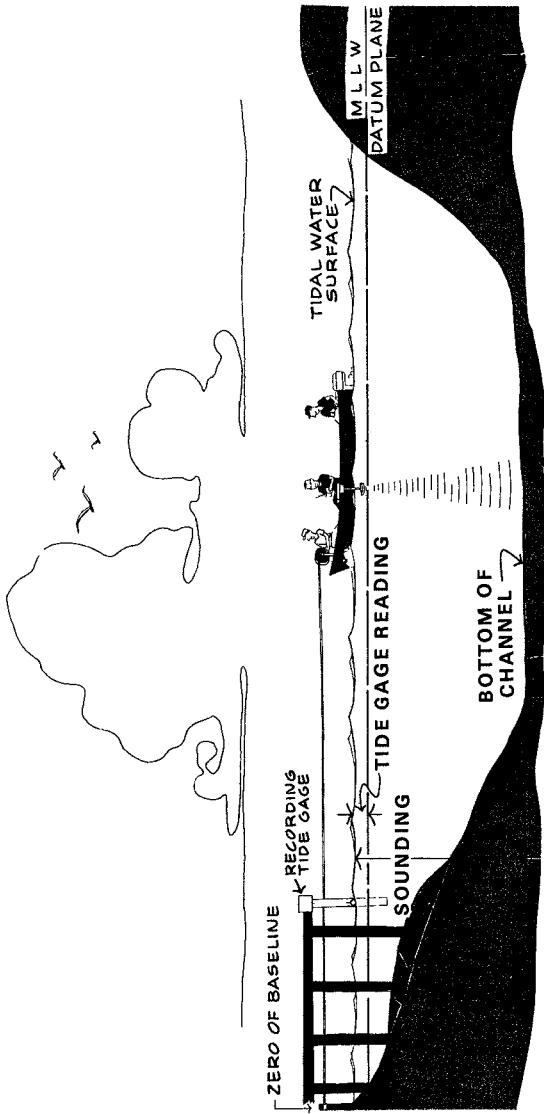


PHOTO 1



SANTA CRUZ HARBOR
SCHEMATIC DRAWING
OF HYDROGRAPHIC SURVEY
1970

FIGURE 3

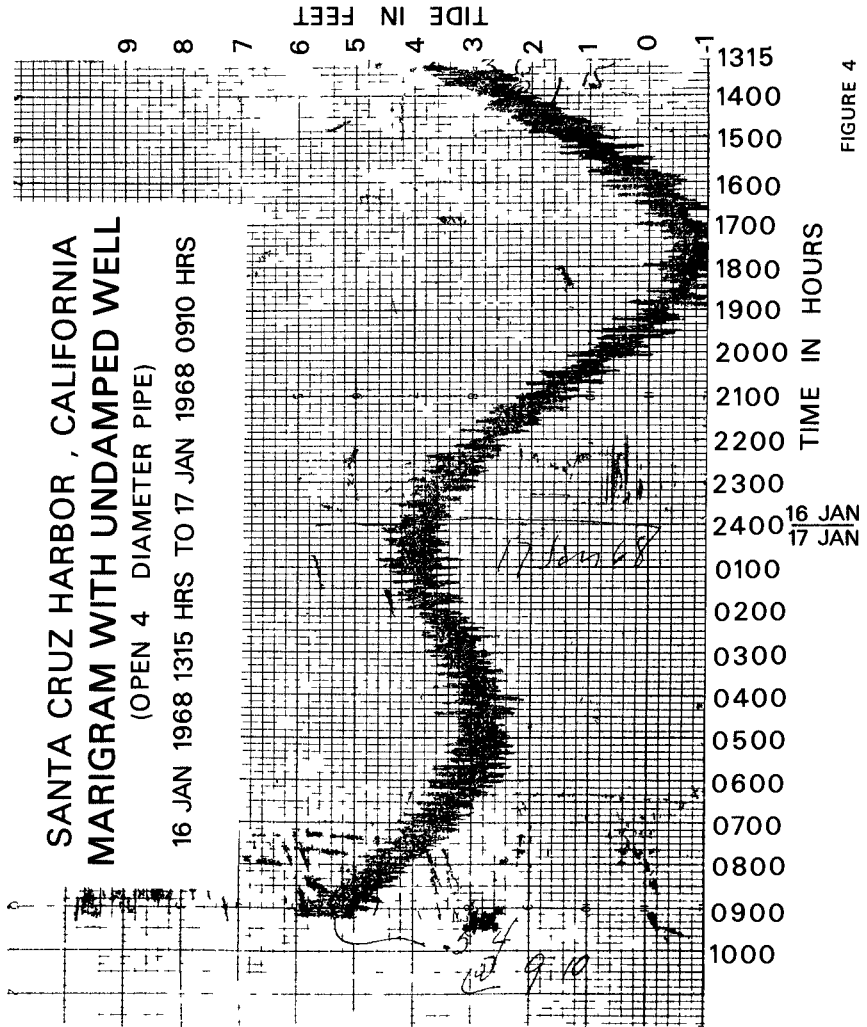


FIGURE 4

SANTA CRUZ HARBOR, CALIFORNIA
MARIGRAM WITH DAMPED WELL

(4 DIAMETER PIPE WITH 1/4 INLET)

17 JAN 1968 0920 TO 1440 HRS PST

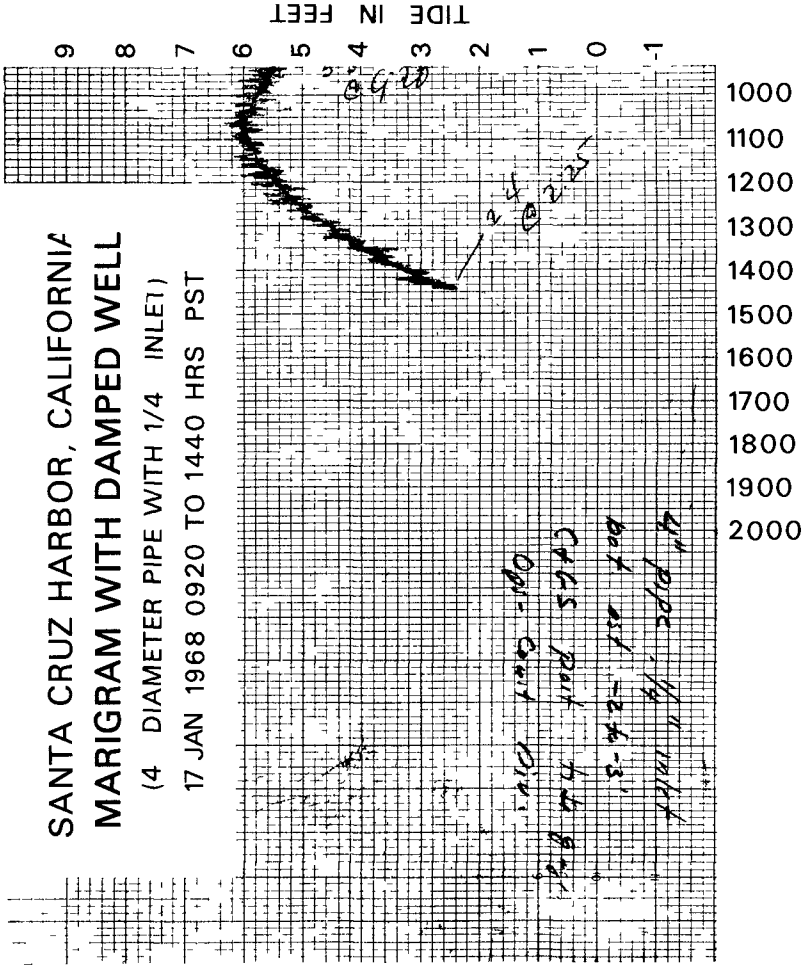


FIGURE 5

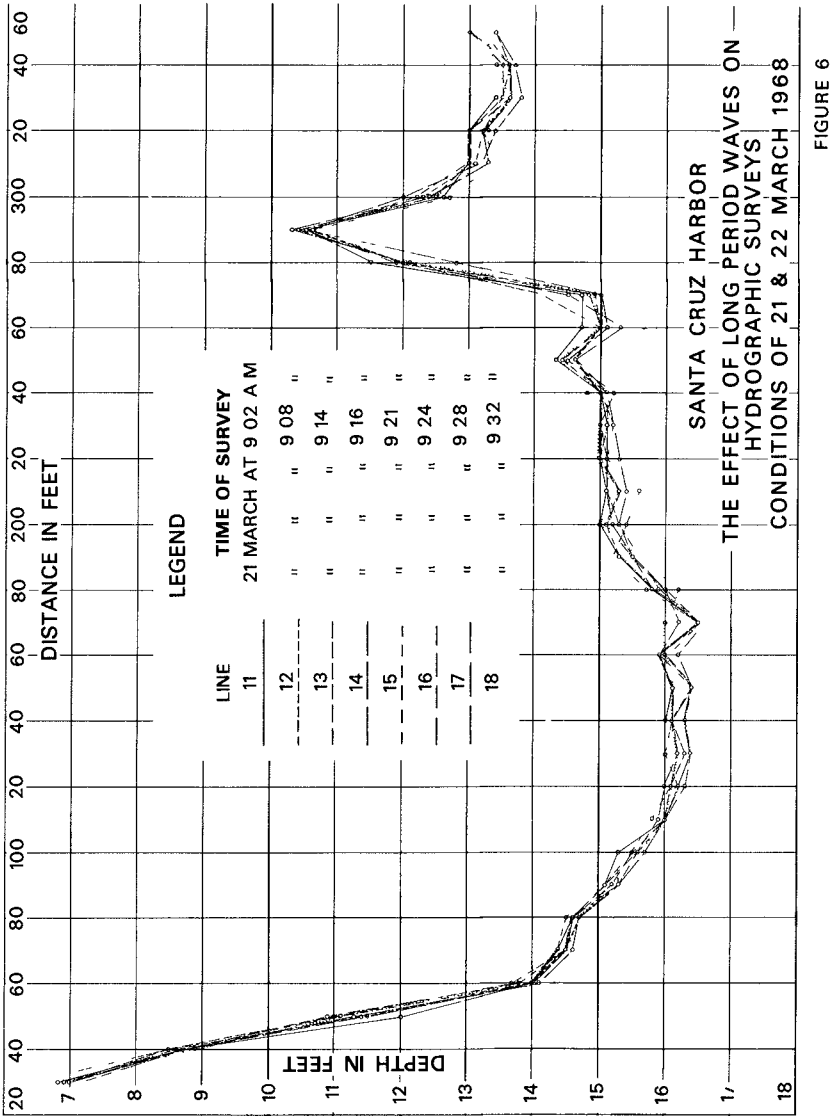
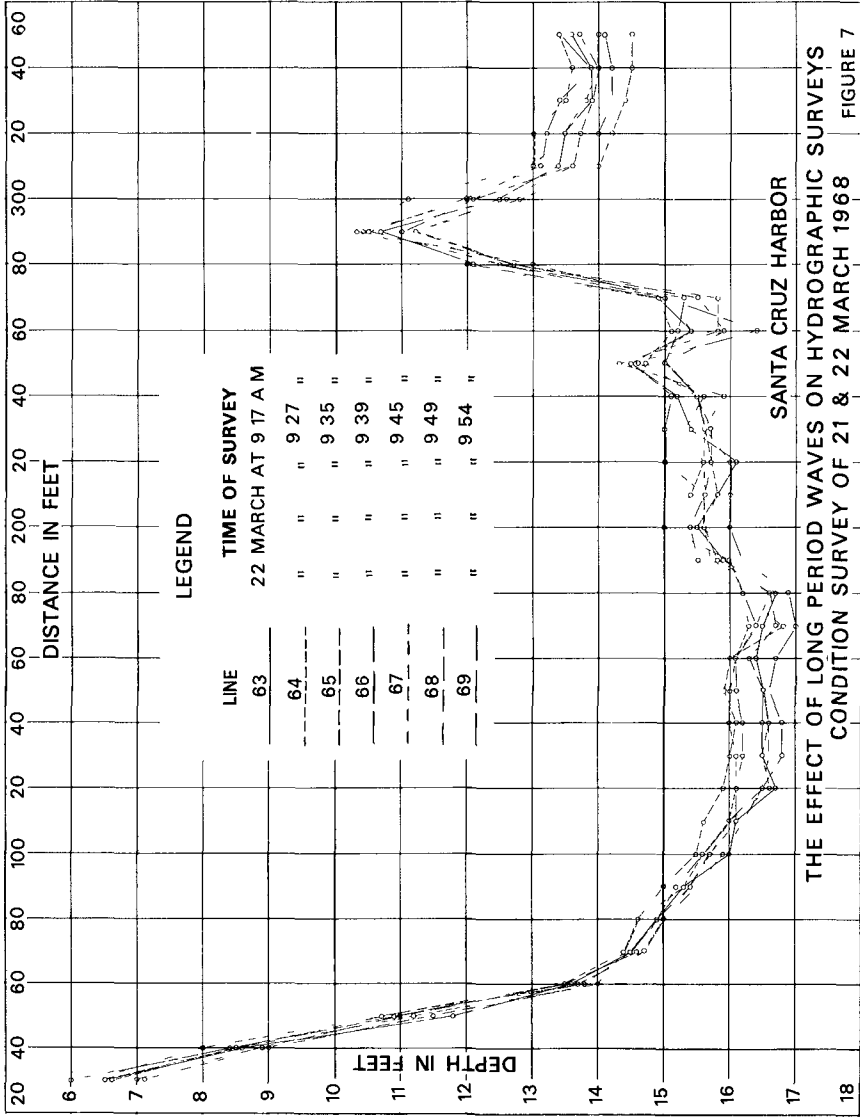


FIGURE 6



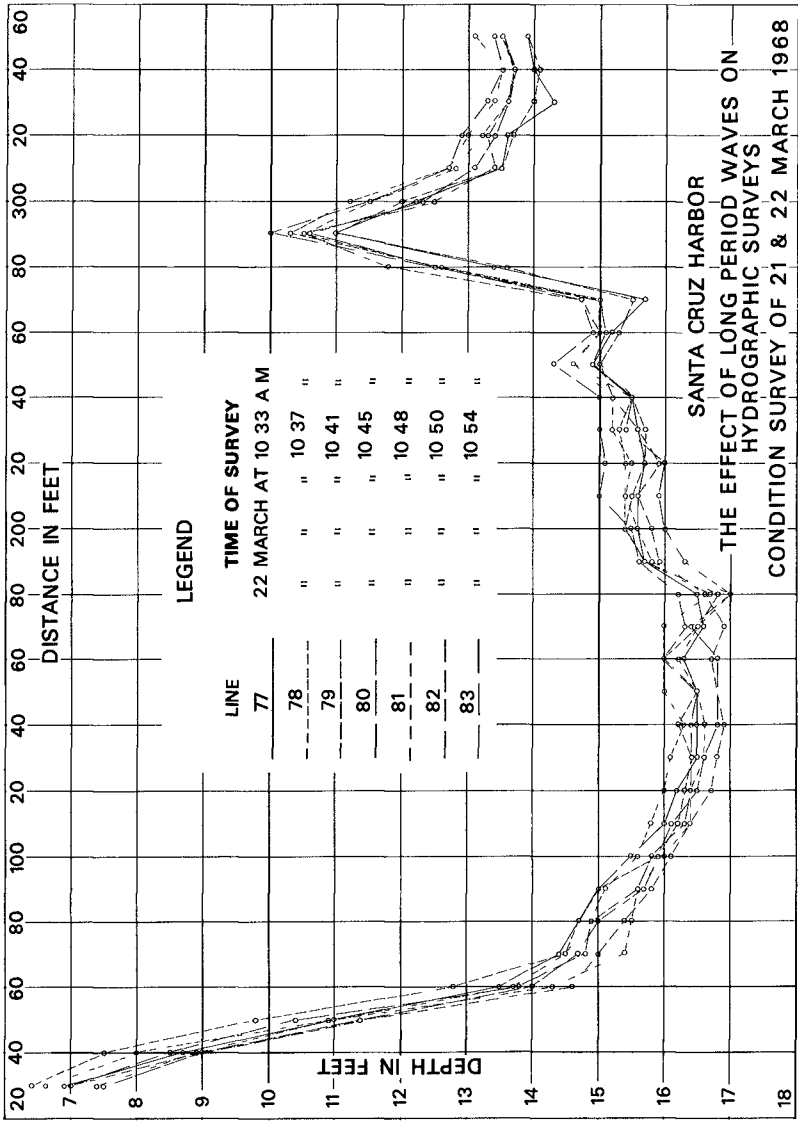
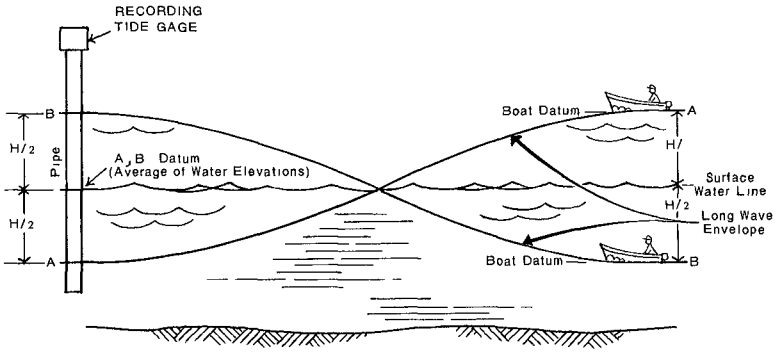


FIGURE 8

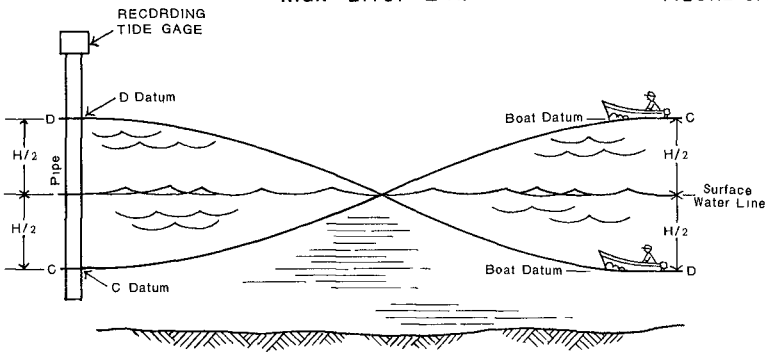
SANTA CRUZ HARBOR



(A) NORMAL METHOD OF SOUNDING REDUCTION FOR TIDES

Max Error = $\pm H/2$

FIGURE 9A



(B) INCORRECT METHOD OF SOUNDING REDUCTION FOR TIDES

Max Error = $\pm H$

H = Long Period Wave Height

FIGURE 9B

CHAPTER 137

SELECTION OF DISPOSAL AREAS FOR SPOIL FROM BALTIMORE HARBOR

By John F Hoffman¹, M ASCE

ABSTRACT

Selection of sites for the diked disposal of 100 million cubic yards of spoil dredged from Baltimore Harbor presented a formidable problem. Fifty percent of this spoil will be derived from harbor improvement in the next ten years. The remainder will result from maintenance dredging and some private dredging over a 20 to 25 year period.

The number of sites available for diked disposal areas, the various methods used for dredging and the fact that the dike material required transportation to site gave rise to a number of variables. The decision making process was facilitated by an econometric model.

Concentrations of metals such as chromium, cadmium, zinc, lead, and copper have been found in the sediments of Chesapeake Bay. An investigation as to the mode of their occurrence in the material to be dredged was made to appraise any possibility of toxic concentrations occurring in filter feeders such as oysters for shellfish constitute a sizeable industry in the Chesapeake Bay.

Stabilization of the deposited dredged spoil was investigated in order to determine whether the unstable loosely-deposited fine grain material extending over a three to five square mile area could be economically converted to a firm foundation material suitable for industrial parks, harbor terminals or water-oriented parks.

INTRODUCTION

Deepening the 25 miles of channel extending from Baltimore Harbor to a depth of 50 feet from its present depth of 42 feet and maintaining continuously that depth of channel will result in 100 million cubic yards of spoil in about twenty to twenty-five years.

¹Associate Professor of Oceanography, U S Naval Academy, Annapolis, Maryland and Senior Associate, Trident Engineering Associates, Inc

Senate Bill No 623 approved by the Congress of the State of Maryland on May 2, 1969 provides for the funding of " the design and construction of one or more diked disposal areas and other and appurtenant facilities to receive dredging spoil from the harbor and the approach channels in the water and adjacent areas known generally as the Harbor of Baltimore City "

This paper deals with the method of the selection of candidate sites rather than the specific sites themselves Site selection involved the following overall considerations

- 1 Economy as it is related to the transportation of spoil and the material for the construction of the dike
- 2 Economy of dike construction from a standpoint of partitioning the overall diked area as well as consolidation of the underlying sediments
- 3 Ecology of the Bay as it pertains to oyster beds, sports and commercial fishing, and fish spawning areas
- 4 The various Federal and State regulations concerning the construction of diked areas
- 5 Possible utilization of the three to five square miles of land created

Disposal of dredged spoil in previous years was by open dumping in designated submarine disposal points within Chesapeake Bay, for the open ocean is more than 150 miles downbay However, the economic value of the fishing grounds and the lack of control of the deposition of the fine-grained sediments in the free fall through deep water has outmoded this method of disposal

Owing to the essentially free storage volume between the level of the Chesapeake Bay and its bottom, diked disposal areas within the Bay itself were the ones evaluated primarily At first view this may appear to be against the best interests of the bay, however, valuable real estate is created by filling the diked area Spoil dumped in a depth of water of 18 feet to an elevation of 9 feet above the bay level would produce about $3\frac{1}{2}$ square miles of land

FUTURE DREDGING REQUIREMENTS IN BALTIMORE HARBOR

It is estimated that approximately ten years would be needed to dredge the channel from 42 feet to 50 feet without widening it Removal of some 50 million cubic yards of spoil would be involved From 1975 to 1983 there should be a steady increase in the total amount of spoil due to greater maintenance dredging and private dredging A slight decline should be realized after 1983, and should level off at

about 1985 to approximately 3 million cubic yards annually. As maintenance is a continuing operation, more than one diked disposal area will be required in the long range picture.

CURRENT DREDGING PRACTICES AND COSTS

Dredging in the vicinity of Baltimore Harbor and its approach channels is accomplished by means of bucket and scow, hopper dredge, and pipeline dredge. The first is used for new dredging work, the second for maintenance dredging by the Corps of Engineers, and the third for special work.

The cost projected in every dredging contract will be peculiar to the specific job to be performed and will be based on the following factors:

- 1 Dredging Site Distance from disposal area and depth of water in disposal area
- 2 Type of material Sand, silt, and clay are dredged at different rates and have different effects on the equipment
- 3 Depth of water in the area to be dredged
- 4 Whether dredging is classified "maintenance" or "new work "
- 5 Volume of material to be dredged
- 6 Financial posture of the bidding firm
- 7 Mobilization and demobilization costs involved
- 8 Time of the year in which dredging is to be performed

Contact was made with a number of dredging firms and various districts of the Corps of Engineers and approximate cost ranges were determined for the three types of dredging. These were used in the Econometric Model discussed later in this paper. The total costs involved in bucket and scow and hopper dredging included mobilizing and demobilizing equipment and cutting, loading, transporting, and off-loading spoil. Pipeline dredging costs, except for mobilization and demobilization, cannot easily be separated into component costs. Accordingly, the figures used in the study represent the best estimates available from firms contacted.

SITE SELECTION

Federal and State Regulations Important to Spoil Disposal

Any dredging project in navigable waters is affected by certain Federal and State regulations as well as by local interests and concerns. Following is a resume of the basic Federal and State statutes and authority important to a spoil disposal project.

1 Federal Jurisdiction

The Federal agency most critically involved in any dredging project is the U S Army Corps of Engineers. Authority for this body's jurisdiction goes back to, and is still primarily based on, the Rivers and Harbors Act of 1899. Chief among the areas of jurisdiction are the following:

- a Dams and dikes across navigable waterways
- b Piers, dredging, etc , in waterways. Plans for wharves, piers, dolphins, booms, weirs, breakwaters, bulkheads, jetties, or other structures, and excavation or fill in navigable waters must be recommended by the Chief of Engineers and approved by the Secretary of the Army. Section 10 of the River and Harbor Act of March 3, 1899 and Section 4(f) of the Outer Continental Shelf Lands Act of August 7, 1953, extend the authority of the Secretary of the Army to prevent obstructions to navigation by artificial islands and structures on the Outer Continental Shelf. (Bridges and Causeways are now (1970) under Coast Guard jurisdiction.)
- c Use of government works
- d Harbor Lines
- e Improvement of any navigable river
- f Pollution. Section 13 of the River and Harbor Act of 1899 states that, " it shall not be lawful to throw, discharge or deposit any refuse matter of any kind or description whatever other than that flowing from streets and sewers into any navigable water of the United States, or into any tributary of any navigable water. " The River and Harbor Act of 1888 defines pollutants as "refuse, mud, sand, dredgings, sludge, acid or any other matter of any kind. " Furthermore, Executive Order #11288 specifies the responsibilities of all Federal agencies to improve water quality through prevention, control, and abatement of water pollution.

from Federal government activities in the United States. The provisions of this Order are applicable to the pollutional aspects of all dredging operations including the disposal of dredged materials.

2 State Jurisdiction

In any dredging project, the Maryland state agency most intimately involved at present is the Board of Public Works. This body issues permits when state money is involved and also is the coordinating voice of all state groups involved. While the Corps of Engineers' has the ultimate power in granting or refusing a permit, it will probably never override serious objections raised by the State's Board of Public Works. In addition to the Board as a major voice of the State, the Submerged Lands Commission acts in an advisory capacity particularly in very large or controversial projects.

As a coordinating body, the Board of Public Works gathers opinions from various state agencies in the process of considering an application for a permit. Some of these agencies are

- a Department of Water Resources
- b Maryland Geological Survey
- c Department of Chesapeake Bay Affairs
- d Department of Health
- e Department of Game and Inland Fish
- f Department of Forests and Parks
- g Department of Natural Resources

Selection of Potential Sites

In order to evaluate all possible spoil disposal sites available a comprehensive study was made of navigational charts covering the Chesapeake Bay area from the mouth of the Susquehanna River south to Tangier Island.

Potential sites that were considered feasible for spoil disposal purposes were categorized as follows:

- ° Island and shoreline sites which could border a diked area and serve as a base for eventual fast land recovery.

- ° Marsh and swamp areas which could receive dredged harbor spoil providing eventual land recovery or possible nutritive enrichment of wetlands for wildlife use
- ° Relatively shallow open water areas suitable for diking for use as contained spoil disposal areas
- ° Deep bay areas such as trenches or holes where spoil disposal would not be subject to the spreading of spoil

Seventy sites were selected on this basis. These were then critically examined on the basis of economic, ecological, and environmental factors. These factors included site's proximity to oyster beds and other valuable seafood areas, the size and distance from the area to be dredged, the impact of the containment on water flow and navigation, the potential utilization as a reclaimed land area including accessibility to populated areas, and the present value as wetlands or wildlife refuge areas.

Following this, a review of each site was made with personnel of various state, commercial, civic, and private interests to insure the fact that all groups were represented.

Concurrently, the potential sites were examined from an economic standpoint by means of a mathematical model, hereafter termed Econometric Model. Details concerning this model are discussed below.

The Econometric Model

Input data to the Econometric Model were based on current dredging practices and costs. Assumed constant in the model were (1) the cost of excavating the dike material, (2) the cost of off-loading the spoil, and (3) the cost of purchasing the dike material at \$ 10 per cubic yard.

Variables in the model included (1) transportation distance of the spoil to the disposal site, (2) cost of cutting channels to some sites, (3) transportation of dike material, (4) construction of the dike, (5) partitioning, and (6) compressibility of the bottom sediments. Costs were computed for purposes of the comparison of sites on the basis of unit cost of cubic yard of dredged spoil.

For convenience, the shipping channel to be dredged was divided into five zones. As the bottom contour of the bottom varies, the centroid of the volume to be cut for each zone was located after the channel had been divided. Navigable distances to the sites were computed from these centroids.

One of the most important factors in choosing the site was the dike itself. For comparisons and to enable certain conclusions to be drawn, a structural model had to be formulated early in the study. The dike used for the model had a 1.4 slope on each face with elevation of +9 above mean low water (MLW). It was trapezoidal in shape with 4 yards across the top. The water depth at each of the sites was 15 feet or 18 feet MLW. In order for the unit cost of constructing the dike to be incorporated in the model, the following equation was used:

$$\text{Unit cost/yd}^3 = \frac{\text{Volume of Dike}}{\text{Vol. of Spoil in Site}} \quad (\$2.77/\text{yd}^3)$$

The figure \$2.77/yd³ was the unit cost assumed for constructing the dike. In keeping with the design of the model, the cost was divided by the amount of spoil in the site. This gives a unit cost per cubic yard of spoil.

The four most common horizontal configurations for the finished dike are the circle, square, rectangle, and equilateral triangle. The following table gives the amount of dike material in cubic yards required to contain 100 million cubic yards of spoil at 18 feet MLW. Calculations for the volume of the dike material are based on dimensions measured to the top inner edge of slope. Furthermore, it was assumed for the sake of simplicity that the volume of dike material underlying the face of the inner slope had a negligible effect on the storage capability of this enclosure.

Circle	Square	Rectangle (3000 x 3740 yards)	Triangle
4,254 million yd ³	4,800 million yd ³	4,826 million yd ³	5,471 million yd ³

From the above table it is clear that the circle would be the best, since the dike required the least material. This conclusion requires modification when partitioning is considered. Details concerning this matter are discussed below.

In the disposal of spoil in diked areas the question arises whether to build one continuous dike for the entire volume to be contained, awaiting a long period for filling and stabilization, or to partition the site into sections and thereby create stabilized acreage at a much faster rate. In partitioning, however, extra dike material is required and the most economical dike shape may change. Since the triangle was by far the most costly of the configurations, the effect of partitioning was examined only on the circle, square, and rectangle. A table of unit costs for the three shapes with varying numbers of partitions is given below, assuming 100 million cubic yards to be placed in the site and the bay bottom to be 18 feet below mean low water.

<u>Number of Partitions</u>	<u>Circle</u>	<u>Square</u>	<u>Rectangle</u>
4	\$ 194/yd ³	\$ 199/yd ³	\$ 221/yd ³
5	\$ 210/yd ³	\$ 210/yd ³	\$ 253/yd ³
6	\$ 229/yd ³	\$ 233/yd ³	\$ 283/yd ³
7	\$ 248/yd ³	\$ 243/yd ³	\$ 314/yd ³
8	\$ 266/yd ³	\$ 255/yd ³	\$ 344/yd ³
9	\$ 285/yd ³	\$ 266/yd ³	\$ 375/yd ³
10	\$ 303/yd ³	\$ 277/yd ³	\$ 406/yd ³

Although the circle does at times seem the best economically, the unit cost for a square is never more than one-half cent higher than that of a circle per cubic yard. As the number of partitions increases, the square becomes the more desirable shape.

Initially, the compressibility of the sub-bottom was assumed zero. An analysis was pursued for the purpose of determining a multiplier to be applied to the unit cost for zero compressibility to adjust for the estimated compressibility of the bottom sediments. When settlement takes place more dike material is required if a predetermined elevation of top of dike is to be maintained. Thus, initially the dike must be built to a higher elevation. Once the amount and rate of settling is estimated from tests on bottom core samples, compensation for settling can be achieved by considering a pad of trapezoidal cross-section with the same 1 4 side slope as existing beneath the dike. The height of the cross-section would be equal to the estimated settlement. As a result both studies may proceed simultaneously.

Economic Projection

Selecting an area for a diked enclosure involves a decision whether to build for long range use at the present time or to build smaller enclosures filling them in shorter intervals. All are aware of the diminishing value of the construction dollar with time, however, the more rapidly land is created the more rapidly its worth can be realized from both a sale and tax income standpoint.

The Engineering News-Record Construction Cost Index, which is an aggregate combination of common labor cost and material cost, was examined to determine the effects of inflation on construction. The Construction Cost Index in December, 1949, for Baltimore was 424. In December 1969, it was 1015. This is an increase of about 240 percent. A construction project in 1949 costing \$10 million would cost \$24 million today.

Projections of the ENR Construction Cost Index were made to the year 2000. Three straight line projections were made: maximum, median, and minimum rates of growth based on past recorded growth rates. Median rates have been extrapolated from the average trend line between 1950 and 1970. Maximum rates are based upon the trend line between 1963 and 1970 and minimum growth rates upon the trend between 1949 and 1963. Projection of the costs for any project to some future date were obtained by multiplying today's estimated construction costs by a ratio of the estimated future cost index to the present cost index. Space prevents further elaboration here of the studies made.

SUB-BOTTOM INVESTIGATION

A program of sub-bottom investigation was undertaken for four purposes:

1. To determine the types of sediment to be dredged
2. To determine the compressibility of the material underlying the dikes for dike design purposes
3. To obtain exact information as to the bathymetry in the candidate spoil areas
4. To obtain samples from the channel to be dredged for the chemical analysis of selected metal ions

The investigation was divided into two parts--a seismic survey and a test boring program.

The seismic survey technique chosen for sub-bottom profiling employed a 3.5 KH output frequency sub-bottom profiling device provided and operated by personnel from the Oceans International Company, Mystic, Connecticut.

The profiling equipment used on this project emitted an acoustic signal strong enough to penetrate to approximately 30-50 feet of the sub-bottom. About equivalent to the noise of a small sledge-hammer blow on a hard surface, the signal energy which is transmitted through the water and then absorbed and/or reflected by the sub-bottom in no way disturbed the bottom of the bay.

The position of the vessel at any time during the seismic survey was automatically recorded by the Motorola Range Positioning System (RPS). RPS operates at line-of-sight ranges up to 50 nautical miles and the usual system range measurement accuracy is considerably better

than 50 feet. The RPS was chosen for this project because of its 50-mile range, its all-weather capability, and its unique coding for non-interference with shipping or other communications in the congested harbor area.

To eliminate the necessity for shifting the transponders to new line-of-site visible fixed reference stations, two high elevation sites were selected which could be "seen" electronically at all times from any planned position of the survey boat. One of these, an outside observation-type terrace area of the Maryland National Bank Building in downtown Baltimore, which the Chesapeake and Potomac Telephone Company made available, is approximately 475 feet above sea level. The other was atop one of the high towers on the suspension bridge of the Chesapeake Bay Bridge at an elevation of about 400 feet above sea level. Each transponder and its antennas weighed approximately four pounds.

The seismic data which were acquired in less than one week, when correlated with test boring data acquired at a slightly later date, and over a period of six weeks, gave an extended picture as to the composition and compressibility of the sub-stratum in the areas concerned.

The test boring program consisted of basically taking continuous samples with a four-foot long 3" diameter piston corer according to ASTM Specification D1587-63T. Twenty borings in 4" cased holes spaced 6600 feet apart to a depth of 15 feet in the various channels to be deepened formed the backbone of this phase of the program. These were supplemented by 20 additional single four-foot piston cores (uncased) taken midway between the cased holes.

Immediately upon removal from the drilling rig the sample tubes were placed in dry ice and frozen in preparation for chemical analysis and to preserve intact any samples with a high water content. At the laboratory the long cores were cut laterally into 6-inch long cylinders and then longitudinally into hemi-cylinders. One of the hemi-cylinders was used for grain size analysis of the sediments, the other was utilized for chemical analysis.

The second part of the test boring program consisted of making piston core borings at each of the candidate sites to depths ranging from 36 to 50 feet below the bay bottom. Samples from this phase were used to obtain a quantitative estimate of dike settlement.

FUTURE USES OF THE FILLED CONTAINMENT AREA

Once filled to capacity and stabilized, the filled containment area will present the state with the pleasant dilemma of deciding upon one or even several of the many possible uses of this newly created piece of real estate. If land were a goal, the State could expect to spend upwards of \$25,000,000 for sandfill alone. Where the area is located offshore some means of access must be provided in order to accomplish any of the uses. Accordingly, sites adjacent to existing land where connections with the existing transit facilities are possible are particularly attractive.

One often-proposed utilization for newly created waterfront land is the construction of an airport. The location of an airport on or near water has a number of distinct advantages. However, the problems and disadvantages of offshore airports must also be considered. The proximity to water presents a weather problem in that fog is always more prevalent near the water. This fog or haze enhances the risk commercial carriers must face in take-offs or landings.

There will also be air traffic problems resulting from the proximity of Washington National, Dulles, Friendship, and Andrews Air Force Base to this offshore airport. Even without a fifth major airport, air traffic controllers have claimed that the air space in this region is too crowded.

Industries of various types might be attracted to new land on a waterfront site. The end result is more employment opportunities for Marylanders and a general increase in the tempo of economic activity in the Baltimore area. A shipping terminal would be another possibility. The present Dundalk Marine Terminal in Baltimore, old and new sections, totals about 540 acres.

Prices for industrially-zoned land in metropolitan areas start at about \$6,500 per acre while industrial sites with all utilities and rail frontage range upward from about \$15,000 per acre. A conservative estimate of the worth of waterfront land in the large cities places its value in a range between \$15,000 and \$25,000 with the shoreline lots being the most valuable. Assuming the most conservative price (\$15,000) as an average sale price per acre, the state could consider the stabilized filled disposal area as an asset worth in excess of \$30,000,000.

Turning from industrial development, it can be advantageous to consider the new land in terms of a recreation area. The State Department of Forests and Parks presently prefers at least 500 acres for a state park. Each of the prime sites meets this requirement. Along with a park, an 18-hole championship golf course (approximately 150

acres) could be scenically positioned on the Chesapeake Bay. With golf and aquatic sports readily available, it would be logical to also construct marinas, hotels, and motels. Athletic stadiums and wildlife preserves are other possibilities.

The Federal Government, through the Bureau of Outdoor Recreation of the Department of the Interior, provides matching grants to states to help defray the costs experienced in the construction of recreation areas. Funds for this type of outlay are authorized under the Land and Water Conservation Fund Act of 1965. As a result, this recreation benefit could be realized for only half of the actual cost.

SPECIAL SITUATIONS STUDIED

Heavy Metal Content

In recent years brief investigations indicated that heavy metals exist in the bottom sediments of Chesapeake Bay. Knowledge of the solubility and concentration of these metals is necessary for the proper evaluation of the possible disposal sites. Concurrently, with the present investigation, a study is being made of the effect of these metals on shellfish. This is being undertaken in a cooperative effort by the Chesapeake Biological Laboratory, the Chesapeake Bay Institute, the Department of Chesapeake Bay Affairs, and the Department of Water Resources.

Chemical analysis of the sediments by Atomic Absorption Method for the Chromium, Copper, Cadmium, Zinc, Lead, Nickel, Cobalt, Mercury, Manganese, and Molybdenum was made. Although other methods are available, Atomic Absorption Spectrometry was chosen as the method for making the desired analyses. This method is generally accepted as the most desirable because it is rapid and inexpensive and requires the least interpretation to obtain actual concentrations. In addition, standards used can be prepared to take into account amounts of interfering metals which may be included in the samples.

Initially, several digestion procedures for the sediments were utilized. One was acetic acid-sodium acetate buffer system. Another was 1.0 Molar concentration of hydrochloric acid (HCL) at 70° C for 48 hours. A third procedure used was digestion with aqua regia.

There was little difference in the results obtained using HCL and aqua regia digestions. The latter method was therefore discontinued. A considerable difference between the other two digestion procedures was observed, however, and, therefore, a dual set of analyses was made.

Digestion with the acetate buffer method would be expected to extract all of the soluble portions or lightly-bound particles while the HCL method would extract the more tightly-bound particles. These two methods, then, probably enable distinction between the readily available or soluble metal ions and the more tightly-bound metal ions.

Spoil Stabilization

During the initial period of spoil disposal the spoil, which is largely silt, will be covered by the water contained in the diked area. A large lake within the Bay will be delineated by the dike. Subsequent spoil disposal will cause the level of the spoil to rise above the water level within the dike. Slow movement of water entrapped in the interstitial spaces of the fine-grained material, however, will preclude the soil from bearing safely superimposed loads, such as buildings, for a number of years. In hopes of converting the created land into valuable real estate more rapidly, a search was made of the technical literature pertaining to soil stabilization by vibro-flotation, by electro-osmosis, and by chemicals. Agencies concerned with this type of problem such as the Corps of Engineers in Buffalo and Detroit and those concerned with the dry land phase, such as the Highway Research Board, were contacted.

The results of both parts of this investigation indicates that few inroads, if any, have been made into the problem and no satisfactory method of rapidly stabilizing the water-deposited dredged spoil is available.

ACKNOWLEDGMENTS

This work was carried out for the State of Maryland under the general supervision of Mr. George Lewis, Secretary of the Department of General Services. Site selection and associated studies were performed by Trident Engineering Associates, Annapolis, Maryland. The author was project manager of this phase. Preliminary design of the diked disposal areas was performed by Green Associates, Inc., Baltimore, Maryland.

CHAPTER 138

WAVES GENERATED BY LARGE SHIPS AND SMALL BOATS

M M Das and J W Johnson
University of California
Berkeley

The peak wave energy in a system of waves resulting from the passage of a ship is of importance in such problems as bank erosion, the motion of moored vessels, forces on fixed and floating docks, etc. With respect to the bank erosion problem, the question often asked is whether the single passage of a large ship during a day, for example, is more damaging than numerous passages of small pleasure craft during the day. With this in mind this study was conducted to determine the relative importance of the peak energy resulting from the passage of a Mariner class cargo ship and a pleasure cruiser. The characteristics of these vessels are as follows.

TABLE 1 MODEL CHARACTERISTICS

Scale	Overall length (inches)	Beam (inches)	Draft (inches)	Total Displace- ment (lbs)	
Mariner class cargo ship	1 96	70 75	9 25	3	37 32
Cruiser	1 16	48 75	-	2	24 91

The characteristics of the waves generated by these vessels moving at various speeds in deep and shallow water were determined from towing tests in a model basin (Ref 1)

The energy density or total energy per unit surface area is equivalent to the mean-square-height of the waves. The value of this term in a finite wave train varies with distance outward from the sailing line. From the point of view of the design of the banks of navigable channels and forces on docks or moored vessels, the peak wave energy associated with the maximum wave height in a wave train is of importance. For example, Figure 1 shows the peak energy density, H_m^2 , at various distances from the sailing line resulting from the cruiser model moving through shallow water (prototype depth = 5.5 ft) at various speeds (Froude Numbers). It is obvious from Figure 1 how important the ship speed is in generating high waves,

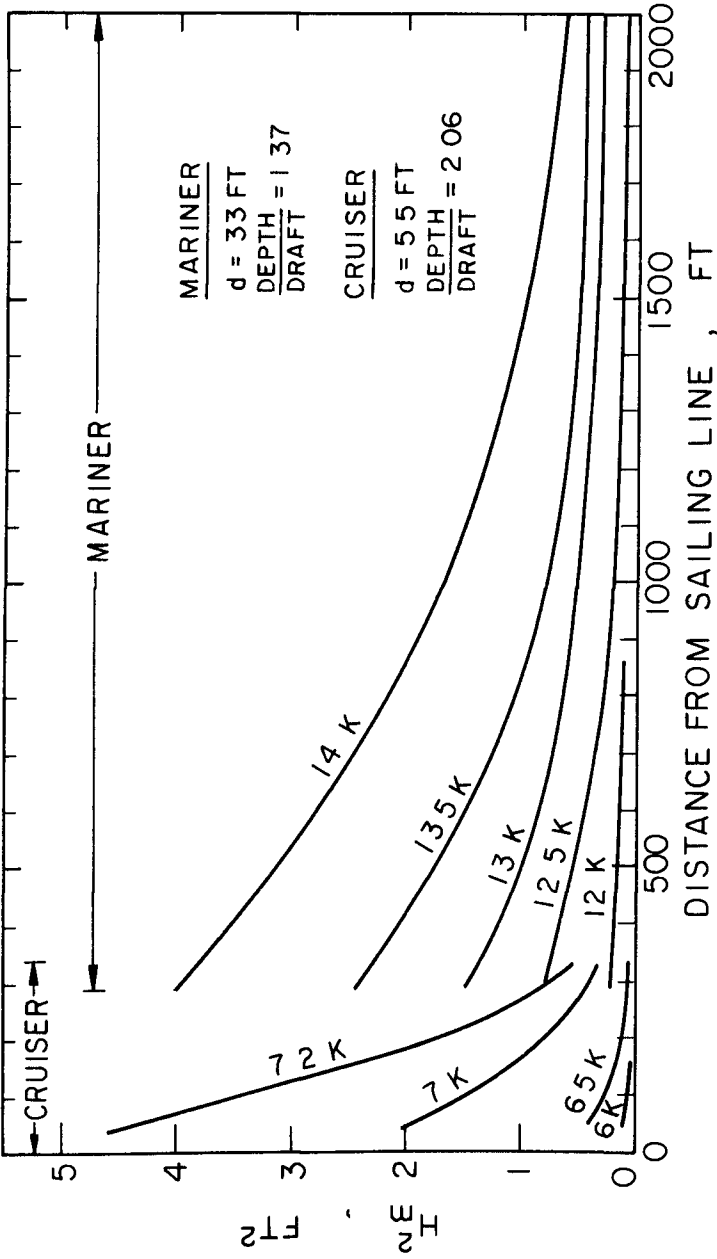


FIG 3 PROTOTYPE VALUES OF H_m^2 AS A FUNCTION OF DISTANCE FROM THE SAILING LINE WITH SHIP SPEED IN KNOTS AS A PARAMETER FOR A CARGO SHIP AND A CRUISER OPERATING IN SHALLOW WATER

particularly near the sailing line. Figure 1 also shows that the peak energy density is reduced by about 90 percent at a distance of five ship lengths from the sailing line for high ship speeds.

A plot similar to Figure 1, shown in Figure 2, is for the cargo ship model also moving in shallow water (prototype depth = 33 ft). It is obvious from Figures 1 and 2 that the wave-making resistance of the cruiser is much greater than the cargo ship, especially at high speeds and near the sailing line. A cross-plot of data from the tests on the two models in prototype values is shown in Figure 3 where H_m^2 , a measure of peak energy density, is given as a function of distance from the sailing line for various ship speeds in knots. In both instances the models operated under shallow-water conditions, that is, a low value of the ratio of water depth to ship draft. Comparisons of peak energy density for the two vessels can be made from Figure 3. For example, the cruiser travelling at 7 knots creates the same peak energy density at 150 ft from the sailing line as does the cargo ship travelling at 13 knots at 500 ft from the sailing line. Another comparison is that at 300 ft from the sailing line the cruiser travelling at 7 knots creates the same peak density as the cargo ship does when travelling slightly more than 12 knots. It therefore appears from these comparisons that for vessels of the sizes used in this study that small boats can induce more serious wave conditions than can a large ship.

ACKNOWLEDGEMENTS

The work reported both in this paper and in the references below was completed on a project supported by the U S Army Coastal Engineering Research Center, Washington, D C

REFERENCES

- 1 Das, M M (1969) Relative effect of waves generated by large ships and small boats in restricted waterways Univ of Calif Hyd Engin Lab Rept No HEL-12-9, Nov 1969
- 2 Hay, D (1969) Ship waves in navigable waterways Proc Eleventh Conf of Coastal Engin , pp 1472-1487
- 3 Johnson, J W , (1969) Ship waves at recreational beaches Shore and Beach, Vol 37, No 1, pp 11-15
- 4 Johnson, J W , (1969) Ship waves in shoaling water Proc Eleventh Conf on Coastal Engin , pp 1488-1498
- 5 Sorensen, R M (1967) Investigation of ship-generated waves Jour , Waterways and Harbors Div , A S C E , Vol 93, Feb 1967, pp 85-99
- 6 Sorensen, R M (1968) Stereo photogrammetric analysis of wave surfaces Jour , Hydraulics Div , A S C E , Vol 94 Jan 1968 pp 181-194
- 7 Sorensen, R M (1969) Waves generated by model ship hull Jour , Waterways and Harbors Div , A S C E , Nov 1969, pp 513-538